



INCLUDES
CD-ROM

HEAT TRANSFER HANDBOOK

ADRIAN BEJAN
ALLAN D. KRAUS
EDITORS

HEAT TRANSFER HANDBOOK

Adrian Bejan

J. A. Jones Professor of Mechanical Engineering
Department of Mechanical Engineering
Duke University
Durham, North Carolina

Allan D. Kraus

Department of Mechanical Engineering
University of Akron
Akron, Ohio



WILEY

JOHN WILEY & SONS, INC.

Designations used by companies to distinguish their products are often claimed as trademarks. In all instances where John Wiley & Sons, Inc. is aware of a claim, the product names appear in initial capital or all capital letters. Readers, however, should contact the appropriate companies for more complete information regarding trademarks and registration.

This book is printed on acid-free paper. (∞)

Copyright © 2003 by John Wiley & Sons, Inc. All rights reserved.

Published by John Wiley & Sons, Inc., Hoboken, New Jersey
Published simultaneously in Canada

No part of this publication may be reproduced, stored in a retrieval system, or transmitted in any form or by any means, electronic, mechanical, photocopying, recording, scanning or otherwise, except as permitted under Sections 107 or 108 of the 1976 United States Copyright Act, without either the prior written permission of the Publisher, or authorization through payment of the appropriate per-copy fee to the Copyright Clearance Center, Inc., 222 Rosewood Drive, Danvers, MA 01923, (978) 750-8400, fax (978) 750-4470, or on the web at www.copyright.com. Requests to the Publisher for permission should be addressed to the Permissions Department, John Wiley & Sons, Inc., 111 River Street, Hoboken, NJ 07030, (201) 748-6011, fax (201) 748-6008, e-mail: permcoordinator@wiley.com.

Limit of Liability/Disclaimer of Warranty: While the publisher and author have used their best efforts in preparing this book, they make no representations or warranties with respect to the accuracy or completeness of the contents of this book and specifically disclaim any implied warranties of merchantability or fitness for a particular purpose. No warranty may be created or extended by sales representatives or written sales materials. The advice and strategies contained herein may not be suitable for your situation. You should consult with a professional where appropriate. Neither the publisher nor author shall be liable for any loss of profit or any other commercial damages, including but not limited to special, incidental, consequential, or other damages.

For general information on our other products and services or for technical support, please contact our Customer Care Department within the United States at (800) 762-2974, outside the United States at (317) 572-3993 or fax (317) 572-4002.

Wiley also publishes its books in a variety of electronic formats. Some content that appears in print may not be available in electronic books. For more information about Wiley products, visit our web site at www.wiley.com.

Library of Congress Cataloging-in-Publication Data:

Bejan, Adrian, 1948–

Heat transfer handbook / Adrian Bejan, Allan D. Kraus.

p. cm.

ISBN 0-471-39015-1 (cloth : alk. paper)

1. Heat—Transmission—Handbooks, manuals, etc. I. Kraus, Allan D. II. Title.

TJ250 .B35 2003

621.402'2—dc21

2002028857

Printed in the United States of America

10 9 8 7 6 5 4 3 2 1

To Warren Rohsenow and James Hartnett

Heat transfer has emerged as a central discipline in contemporary engineering science. The research activity of a few decades ago—the material reviewed in the first handbooks—has distilled itself into textbook concepts and results. Heat transfer has become not only a self-standing discipline in the current literature and engineering curricula, but also an indispensable discipline at the interface with other pivotal and older disciplines. For example, fluid mechanics today is capable of describing the transport of heat and other contaminants because of the great progress made in modern convective heat transfer. Thermodynamics today is able to teach modeling, simulation, and optimization of “realistic” energy systems because of the great progress made in heat transfer. Ducts, extended surfaces, heat exchangers, and other features that may be contemplated by the practitioner are now documented in the heat transfer literature.

To bring this body of results to the fingertips of the reader is one of the objectives of this new handbook. The more important objective, however, is to inform the reader on what has been happening in the field more recently. In brief, heat transfer marches forward through new ideas, applications, and emerging technologies. The vigor of heat transfer has always come from its usefulness. For example, the challenges of energy self-sufficiency and aerospace travel, which moved the field in the 1970s, are still with us; in fact, they are making a strong comeback. Another example is the miniaturization revolution, which continues unabated. The small-scale channels of the 1980s do not look so small anymore. Even before “small scale” became the fashion, we in heat transfer had “compact” heat exchangers. The direction for the future is clear.

The importance of optimizing the architecture of a flow system to make it fit into a finite volume with purpose has always been recognized in heat transfer. It has been and continues to be the driving force. Space comes at a premium. Better and better shapes of extended surfaces are evolving into networks, bushes, and trees of fins. The many surfaces designed for heat transfer augmentation are accomplishing the same thing: They are increasing the heat transfer rate *density*, the size of the heat transfer enterprise that is packed into a given volume.

The smallest features are becoming smaller, but this is only half of the story. The other is the march toward greater complexity. More and more small-scale features must be connected and assembled into a device whose specified size is always macroscopic. Small-scale technologies demand the optimization of increasingly complex heat-flow architectures.

A highly distinguished group of colleagues who are world authorities on the frontiers of heat transfer today have contributed to this new handbook. Their chapters provide a bird's-eye view of the state of the field, highlighting both the foundations

and, especially, the edifices that rest on them. Because space comes at a premium, we have allocated more pages to those chapters dedicated to current applications. The latest important references are acknowledged; the classical topics are presented more briefly.

One feature of the handbook is that the main results and correlations are summarized at the ends of chapters. This feature was chosen to provide quick access and to help the flow of heat transfer knowledge from research to computer-aided design. It is our hope that researchers and practitioners of heat transfer will find this new handbook inspiring and useful.

Adrian Bejan acknowledges with gratitude the support received from Professor Kristina Johnson, Dean of the Pratt School of Engineering, and Professor Kenneth Hall, Chairman of the Department of Mechanical Engineering and Materials Science, Duke University. Allan Kraus acknowledges the assistance of his wife, who has helped in the proofreading stage of production.

Both authors acknowledge the assistance of our editor at John Wiley, Bob Argentieri, our production editor, Milagros Torres, and our fantastic copy editor, known only to us as Barbara from Pennsylvania.

ADRIAN BEJAN
ALLAN D. KRAUS

Cristina Amon
Department of Mechanical
Engineering
Carnegie Mellon University
Pittsburgh, PA 15213-3980

Benjamin T. F. Chung
F. Theodore Harrington Emeritus
Professor
Department of Mechanical
Engineering
302 East Buchtel Mall
University of Akron
Akron, OH 44325-3903

Avram Bar-Cohen
Professor and Chair
Department of Mechanical
Engineering
2181B Martin Hall
University of Maryland
College Park, MD 20742-3035

Sadik Kakac
Department of Mechanical
Engineering
University of Miami
Coral Gables, FL 33124-0624

G. P. Peterson
Provost
Rensselaer Polytechnic Institute
110 Eighth Street
Troy, NY 12180-3590

James Welty
Department of Mechanical
Engineering
Rogers Hall
Oregon State University
Corvallis, OR 97330

Michael M. Yovanovich
Department of Mechanical
Engineering
University of Waterloo
Waterloo, Ontario N2L 3G1
Canada

A. Aziz, Department of Mechanical Engineering, Gonzaga University, Spokane, WA 99258-0026

Avram Bar-Cohen, Department of Mechanical Engineering, University of Minnesota, Minneapolis, MN 55455-0213

Current address: Glenn L. Martin Institute of Technology, A. James Clark School of Engineering, Department of Mechanical Engineering, 2181 Glenn L. Martin Hall, College Park, MD 20742-3035

Adrian Bejan, J. A. Jones Professor of Mechanical Engineering, Department of Mechanical Engineering and Materials Science, Duke University, Durham, NC 27708-0300

Robert F. Boehm, University of Nevada–Las Vegas, Las Vegas, NV 89154-4027

J. C. Chato, Department of Mechanical and Industrial Engineering, University of Illinois–Urbana-Champaign, Urbana, IL 61801

C. Haris Doumanidis, Department of Mechanical Engineering, Tufts University, Medford, MA 02150

R. T. Jacobsen, Idaho National Engineering and Environmental Laboratory, Idaho Falls, ID 83415-3790

Yogesh Jaluria, Mechanical and Aerospace Engineering Department, Rutgers University, New Brunswick, NJ 08901-1281

Yogendra Joshi, George W. Woodruff School of Mechanical Engineering, Georgia Institute of Technology, Atlanta, GA 30332-0405

M. A. Kedzierski, Building and Fire Research Laboratory, National Institute of Standards and Technology, Gaithersburg, MD 20899

Allan D. Kraus, University of Akron, Akron, OH 44325-3901

José L. Lage, Laboratory of Porous Materials Applications, Mechanical Engineering Department, Southern Methodist University, Dallas, TX 75275-0337

E. W. Lemmon, Physical and Chemical Properties Division, National Institute of Standards and Technology, Boulder, CO 80395-3328

R. M. Manglik, Thermal-Fluids and Thermal Processing Laboratory, Department of Mechanical, Industrial and Nuclear Engineering, University of Cincinnati, 598 Rhodes Hall, P.O. Box 210072, Cincinnati, OH 45221-0072

E. E. Marotta, Senior Engineer/Scientist, Thermal Technologies Group, IBM Corporation, Poughkeepsie, NY 12801

Michael F. Modest, Professor of Mechanical and Nuclear Engineering, College of Engineering, Pennsylvania State University, University Park, PA 16802-1412

Wataru Nakayama, Therm Tech International, Kanagawa, Japan 255-0004

Pamela M. Norris, Associate Professor, Department of Mechanical and Aerospace Engineering, University of Virginia, Charlottesville, VA 22903

Jay M. Ochterbeck, College of Engineering and Science, Department of Mechanical Engineering, Clemson University, Clemson, SC 29634-0921

S. G. Penoncello, Center for Applied Thermodynamic Studies, College of Engineering, University of Idaho, Moscow, ID 83844-1011

Ranga Pitchumani, Department of Mechanical Engineering, University of Connecticut, Storrs, CT 06269-3139

Ravi S. Prasher, Intel Corporation, Chandler, AZ 85225

T. J. Rabas, Consultant, Downers Grove, IL 60516

Z. Shan, Center for Applied Thermodynamic Studies, College of Engineering, University of Idaho, Moscow, ID 83844-1011

Andrew N. Smith, Department of Mechanical Engineering, United States Naval Academy, Annapolis, MD 21402-5000

Richard N. Smith, Department of Mechanical Engineering, Aeronautical Engineering and Mechanics, Rensselaer Polytechnic Institute, Troy, NY 12180-3590

John R. Thome, Laboratory of Heat and Mass Transfer, Faculty of Engineering Science, Swiss Federal Institute of Technology Lausanne, CH-1015 Lausanne, Switzerland

Abhay A. Watwe, Intel Corporation, Chandler, AZ 85225

N. T. Wright, Department of Mechanical Engineering, University of Maryland, Baltimore, MD 21250

M. M. Yovanovich, Distinguished Professor Emeritus, Department of Mechanical Engineering, University of Waterloo, Waterloo, Ontario, N2L 3G1, Canada

Preface	ix
Contributors	xi
1. Basic Concepts	1
<i>Allan D. Kraus</i>	
2. Thermophysical Properties of Fluids and Materials	43
<i>R. T. Jacobsen, E. W. Lemmon, S. G. Penoncello, Z. Shan, and N. T. Wright</i>	
3. Conduction Heat Transfer	161
<i>A. Aziz</i>	
4. Thermal Spreading and Contact Resistances	261
<i>M. M. Yovanovich and E. E. Marotta</i>	
5. Forced Convection: Internal Flows	395
<i>Adrian Bejan</i>	
6. Forced Convection: External Flows	439
<i>Yogendra Joshi and Wataru Nakayama</i>	
7. Natural Convection	525
<i>Yogesh Jaluria</i>	
8. Thermal Radiation	573
<i>Michael F. Modest</i>	
9. Boiling	635
<i>John R. Thome</i>	
10. Condensation	719
<i>M. A. Kedzierski, J. C. Chato, and T. J. Rabas</i>	
11. Heat Exchangers	797
<i>Allan D. Kraus</i>	
12. Experimental Methods	913
<i>José L. Lage</i>	
13. Heat Transfer in Electronic Equipment	947
<i>Avram Bar-Cohen, Abhay A. Watwe, and Ravi S. Prasher</i>	
14. Heat Transfer Enhancement	1029
<i>R. M. Manglik</i>	

15. Porous Media	1131
<i>Adrian Bejan</i>	
16. Heat Pipes	1181
<i>Jay M. Ochterbeck</i>	
17. Heat Transfer in Manufacturing and Materials Processing	1231
<i>Richard N. Smith, C. Haris Doumanidis, and Ranga Pitchumani</i>	
18. Microscale Heat Transfer	1309
<i>Andrew N. Smith and Pamela M. Norris</i>	
19. Direct Contact Heat Transfer	1359
<i>Robert F. Boehm</i>	
Author Index	1401
Subject Index	1427

Basic Concepts

ALLAN D. KRAUS

University of Akron
Akron, Ohio

- 1.1 Heat transfer fundamentals
 - 1.1.1 Introduction
 - 1.1.2 Conduction heat transfer
 - One-dimensional conduction
 - One-dimensional conduction with internal heat generation
 - 1.1.3 Spreading resistance
 - 1.1.4 Interface–contact resistance
 - 1.1.5 Lumped-capacity heating and cooling
 - 1.1.6 Convective heat transfer
 - Heat transfer coefficient
 - Dimensionless parameters
 - Natural convection
 - Forced convection
 - 1.1.7 Phase-change heat transfer
 - 1.1.8 Finned surfaces
 - 1.1.9 Flow resistance
 - 1.1.10 Radiative heat transfer
- 1.2 Coordinate systems
 - 1.2.1 Rectangular (Cartesian) coordinate system
 - 1.2.2 Cylindrical coordinate system
 - 1.2.3 Spherical coordinate system
 - 1.2.4 General curvilinear coordinates
- 1.3 Continuity equation
- 1.4 Momentum and the momentum theorem
- 1.5 Conservation of energy
- 1.6 Dimensional analysis
 - 1.6.1 Friction loss in pipe flow
 - 1.6.2 Summary of dimensionless groups
- 1.7 Units
 - 1.7.1 SI system (Système International d’Unités)
 - 1.7.2 English engineering system (U.S. customary system)
 - 1.7.3 Conversion factors

Nomenclature

References

1.1 HEAT TRANSFER FUNDAMENTALS

1.1.1 Introduction

Practitioners of the thermal arts and sciences generally deal with four basic thermal transport modes: conduction, convection, phase change, and radiation. The process by which heat diffuses through a solid or a stationary fluid is termed *heat conduction*. Situations in which heat transfer from a wetted surface is assisted by the motion of the fluid give rise to *heat convection*, and when the fluid undergoes a liquid–solid or liquid–vapor state transformation at or very near the wetted surface, attention is focused on this *phase-change heat transfer*. The exchange of heat between surfaces, or between a surface and a surrounding fluid, by long-wavelength electromagnetic radiation is termed *thermal heat radiation*.

It is our intent in this section to describe briefly these modes of heat transfer, with emphasis on an important parameter known as the *thermal resistance* to heat transfer. Simple examples are given for illustration; detailed descriptions of the same topics are presented in specialized chapters.

1.1.2 Conduction Heat Transfer

One-Dimensional Conduction Thermal diffusion through solids is governed by *Fourier's law*, which in one-dimensional form is expressible as

$$q = -kA \frac{dT}{dx} \quad (\text{W}) \quad (1.1)$$

where q is the heat current, k the thermal conductivity of the medium, A the cross-sectional area for heat flow, and dT/dx the temperature gradient, which, because it is negative, requires insertion of the minus sign in eq. (1.1) to assure a positive heat flow q . The temperature difference resulting from the steady-state diffusion of heat is thus related to the thermal conductivity of the material, the cross-sectional area A , and the path length L (Fig. 1.1), according to

$$(T_1 - T_2)_{cd} = q \frac{L}{kA} \quad (\text{K}) \quad (1.2)$$

The form of eq. (1.2), where k and A are presumed constant, suggests that in a way that is analogous to Ohm's law governing electrical current flow through a resistance, it is possible to define a conduction thermal resistance as

$$R_{cd} \equiv \frac{T_1 - T_2}{q} = \frac{L}{kA} \quad (\text{K/W}) \quad (1.3)$$

One-Dimensional Conduction with Internal Heat Generation Situations in which a solid experiences internal heat generation, such as that produced by the flow of an electric current, give rise to more complex governing equations and require

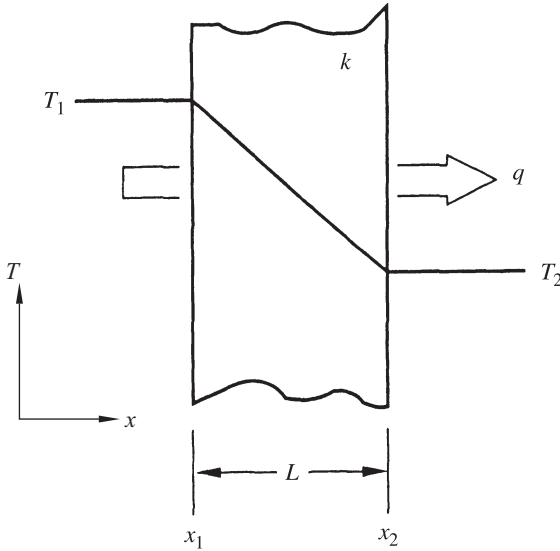


Figure 1.1 Heat transfer by conduction through a slab.

greater care in obtaining the appropriate temperature differences. The axial temperature variation in the slim, internally heated conductor shown in Fig. 1.2 is found to equal

$$T = T_o + q_g \frac{L^2}{2k} \left[\frac{x}{L} - \left(\frac{x}{L} \right)^2 \right]$$

where T_o is the edge temperature. When the two ends are cooled to an identical temperature, and when the volumetric heat generation rate q_g (W/m^3) is uniform throughout, the peak temperature is developed at the center of the solid and is given by

$$T_{\max} = T_o + q_g \frac{L^2}{8k} \quad (\text{K}) \quad (1.4)$$

Alternatively, because q_g is the volumetric heat generation $q_g = q/LW\delta$, the center-edge temperature difference can be expressed as

$$T_{\max} - T_o = q \frac{L^2}{8kLW\delta} = q \frac{L}{8kA} \quad (1.5)$$

where the cross-sectional area A is the product of the width W and the thickness δ . An examination of eq. (1.5) reveals that the thermal resistance of a conductor with a distributed heat input is only one-fourth that of a structure in which all of the heat is generated at the center.

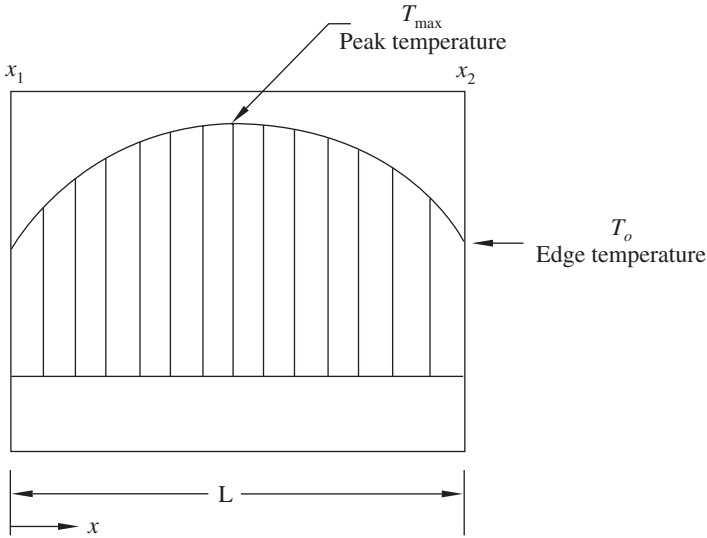


Figure 1.2 Temperature variation in an internally heated conductor.

1.1.3 Spreading Resistance

In configurations where there is a discrete heat source on the surface of a conducting medium, provision must be made for the lateral spreading of the heat generated in successive “layers” in the conducting medium below the source. The additional resistance associated with this lateral flow of heat is called the *spreading resistance*. According to Yovanovich and Antonetti (1988), the spreading resistance for a small heat source on a thick conductor or heat spreader (required to be three to five times thicker than the square root of the heat source area) can be expressed as

$$R_{\text{sp}} = \frac{1 - 1.410\epsilon + 0.344\epsilon^3 + 0.043\epsilon^5 + 0.034\epsilon^7}{4ka} \quad (\text{K/W}) \quad (1.6)$$

where ϵ is the ratio of the heat source area to the substrate area, k the thermal conductivity of the conductor, and a the square root of the area of the heat source.

For relatively thin conducting layers on thicker substrates, such as encountered in the cooling of microcircuits, eq. (1.6) cannot provide an acceptable prediction of R_{sp} . Instead, use can be made of the numerical results plotted in Fig. 1.3 to obtain the requisite value of the spreading resistance.

1.1.4 Interface–Contact Resistance

Heat transfer across the interface between two solids is generally accompanied by a measurable temperature difference, which can be ascribed to a contact or interface thermal resistance. For perfectly adhering solids, geometrical differences in the crystal structure (lattice mismatch) can impede the flow of phonons and electrons

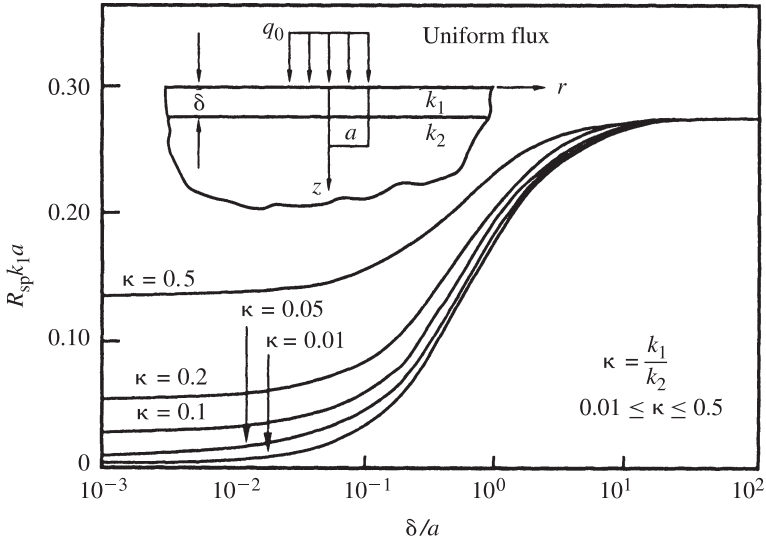


Figure 1.3 Thermal resistance for a circular discrete heat source on a two-layer conducting medium. (From Yovanovich and Antonetti, 1988.)

across the interface, but this resistance is generally negligible in engineering design. However, when dealing with real interfaces, the asperities present on each of the surfaces (Fig. 1.4) limit actual contact between the two solids to a very small fraction of the apparent interface area. The flow of heat across the gap between two solids in nominal contact is by solid conduction in areas of actual contact and fluid conduction across the “open” spaces. Radiation across the gap can be important in a vacuum environment or when surface temperatures are high. The heat transferred across an interface can be found by adding the effects of solid-to-solid conduction and conduction through the fluid and recognizing that solid-to-solid conduction in the contact zones involves heat flowing sequentially through the two solids. With the total contact conductance h_{co} , taken as the sum of solid-to-solid conductance h_c and the gap conductance h_g ,

$$h_{co} = h_c + h_g \quad (\text{W/m}^2 \cdot \text{K}) \quad (1.7a)$$

the contact resistance based on the apparent contact area A_a may be defined as

$$R_{co} = \frac{1}{h_{co} A_a} \quad (\text{K/W}) \quad (1.7b)$$

In eq. (1.7a), h_c is given by (Yovanovich and Antonetti, 1988)

$$h_c = 1.25 k_s \frac{m}{\sigma} \left(\frac{P}{H} \right)^{0.95} \quad (1.8a)$$

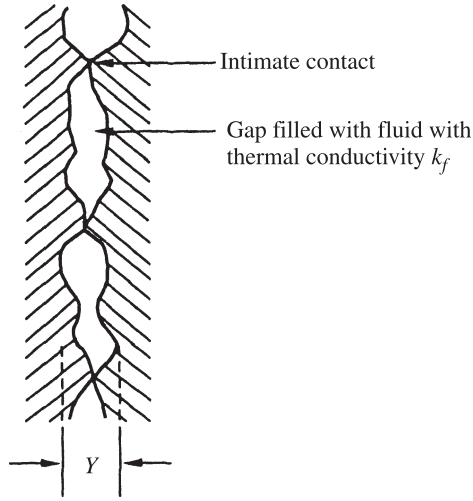


Figure 1.4 Physical contact between two nonideal surfaces.

where k_s is the harmonic mean thermal conductivity for solid 1 and solid 2,

$$k_s = \frac{2k_1k_2}{k_1 + k_2} \quad (\text{W/m} \cdot \text{K})$$

σ is the effective root mean square (rms) surface roughness,

$$\sigma = (\sigma_1^2 + \sigma_2^2)^{1/2} \quad (\mu\text{m})$$

m is the effective absolute surface slope,

$$m = (m_1^2 + m_2^2)^{1/2}$$

P is the contact pressure, and H is the microhardness of the softer material, both in N/m^2 . In the absence of detailed information, the σ/m ratio can be taken as 5 to 9 μm for relatively smooth surfaces.

In eq. (1.7a), h_g is given by

$$h_g = \frac{k_g}{Y + M} \quad (1.8b)$$

where k_g is the thermal conductivity of the gap fluid, Y is the distance between the mean planes (Fig. 1.4), given by

$$\frac{Y}{\sigma} = 1.185 \left[-\ln \left(3.132 \frac{P}{H} \right) \right]^{0.547}$$

and M is a gas parameter used to account for rarified gas effects,

$$M = \alpha\beta\Lambda$$

where α is an accommodation parameter (approximately equal to 1.7 for air and clean metals), Λ is the mean free path of the molecules (equal to approximately $0.06 \mu\text{m}$ for air at atmospheric pressure and 15°C), and β is a fluid property parameter (equal to approximately 1.7 for air and other diatomic gases). Equations (1.8a) and (1.8b) can be added and, in accordance with eq. (1.7a), the contact resistance becomes

$$R_{co} = \left\{ \left[1.25k_s \frac{m}{\sigma} \left(\frac{P}{H} \right)^{0.95} + \frac{k_g}{Y + M} \right] A_a \right\}^{-1} \quad (1.9)$$

1.1.5 Lumped-Capacity Heating and Cooling

An internally heated solid of relatively high thermal conductivity that is experiencing no external cooling will undergo a constant rise in temperature according to

$$\frac{dT}{dt} = \frac{q}{mc} \quad (\text{K/s}) \quad (1.10)$$

where q is the rate of internal heat generation, m the mass of the solid, and c the specific heat of the solid. Equation (1.10) assumes that all the mass can be represented by a single temperature. This approach is commonly called the *lumped-capacity model for transient heating*.

Expanding on the analogy between thermal and electrical resistances suggested previously, the product of mass and specific heat can be viewed as analogous to electrical capacitance and thus to constitute the *thermal capacitance*.

When this same solid is externally cooled, the temperature rises asymptotically toward the steady-state temperature, which is itself determined by the external resistance to heat flow, R . Consequently, the time variation of the temperature of the solid is expressible as

$$T(t) = T(t=0) + qR(1 - e^{-t/Rmc}) \quad (\text{K}) \quad (1.11)$$

where the product of the external resistance R and the thermal capacitance mc is seen to constitute the *thermal time constant* of the system.

1.1.6 Convective Heat Transfer

Heat Transfer Coefficient Convective thermal transport from a surface to a fluid in motion can be related to the heat transfer coefficient h , the surface-to-fluid temperature difference, and the “wetted” surface area S in the form

$$q = hS(T_s - T_f) \quad (\text{W}) \quad (1.12)$$

The differences between convection to a rapidly moving fluid, a slowly flowing fluid, or a stagnant fluid, as well as variations in the convective heat transfer rate among various fluids, are reflected in the values of h . For a particular geometry and flow regime, h may be found from available empirical correlations and/or theoretical relations. Use of eq. (1.12) makes it possible to define the convective thermal resistance as

$$R_{cv} \equiv \frac{1}{hS} \quad (\text{K/W}) \quad (1.13)$$

Dimensionless Parameters Common dimensionless quantities that are used in the correlation of heat transfer data are the *Nusselt number* Nu , which relates the convective heat transfer coefficient to the conduction in the fluid:

$$Nu \equiv \frac{h}{k/L} = \frac{hL}{k}$$

The *Prandtl number* Pr , which is a fluid property parameter:

$$Pr \equiv \frac{c_p \mu}{k} = \frac{\nu}{\alpha}$$

the *Grashof number* Gr , which accounts for the buoyancy effect:

$$Gr \equiv \frac{\rho^2 \beta g L^3 \Delta T}{\mu^2}$$

and the *Reynolds number* Re , which relates the momentum in the flow to the viscous dissipation:

$$Re \equiv \frac{\rho \hat{V} L}{\mu}$$

All thermal properties in the foregoing dimensionless groups apply to the fluid at its bulk temperature.

Natural Convection In natural convection, fluid motion is induced by density differences resulting from temperature gradients in the fluid. The heat transfer coefficient for this regime can be related to the buoyancy and the thermal properties of the fluid through the *Rayleigh number* Ra , which is the product of the Grashof and Prandtl numbers:

$$Ra \equiv \frac{\rho^2 \beta g c_p}{\mu k} L^3 \Delta T = \frac{g \beta}{\alpha \nu} L^3 \Delta T$$

where the fluid properties ρ , β , c_p , μ , and k are evaluated at the fluid bulk temperature. Empirical correlations for the heat transfer coefficient in natural convection boundary layer flow have taken the form

$$h = C \frac{k}{L} (\text{Ra})^n \quad (\text{W/m}^2 \cdot \text{K}) \quad (1.14)$$

where n is found to be approximately 0.25 for $10^3 < \text{Ra} < 10^9$, representing laminar flow; 0.33 for $10^9 < \text{Ra} < 10^{12}$, the region associated with the transition to turbulent flow; and 0.4 for $\text{Ra} > 10^{12}$, when strong turbulent flow prevails. The precise value of the correlating coefficient C depends on fluid, the geometry of the surface, and the Rayleigh number range. Nevertheless, for common plate, cylinder, and sphere configurations, it is found to vary in the relatively narrow range of 0.45 to 0.65 for laminar flow and 0.11 to 0.15 for turbulent flow past the heated surface.

Natural convection in vertical channels such as those formed by arrays of longitudinal fins is of major significance. Elenbaas (1942) was the first to document a detailed study of this configuration, and his experimental results for isothermal plates were later confirmed numerically by Bodoia and Osterle (1964). A uniform picture of the thermal transport in such a vertical channel has emerged from these and complementary studies.

It has been shown that the value of the Nusselt number lies between two extremes that are based on the size of the space between the plates or width of channel. For wide spacing, the plates appear to have little influence on one another, and the Nusselt number in this case achieves its *isolated plate limit*. On the other hand, for closely spaced plates or for relatively long channels, the fluid attains its *fully developed value* and the Nusselt number reaches its *fully developed limit*. Intermediate values of the Nusselt number can be obtained from a correlating method suggested by Churchill and Usagi (1972) for smoothly varying processes, and these values have been verified by a plethora of detailed experimental and numerical studies.

Thus, the correlation for the average value of h along isothermal vertical channels spaced z units apart is

$$h = \frac{k}{z} \left(\frac{576}{\text{El}} + \frac{2.873}{\text{El}^{1/2}} \right)^{1/2} \quad (1.15)$$

where El is the *channel Elenbaas number*:

$$\text{El} \equiv \frac{\rho^2 \beta g c_p z^4 \Delta T}{\mu k L}$$

and ΔT is the surface temperature minus the bulk fluid temperature, $\Delta T = T_s - T_f$. Natural convection fundamentals and results are covered in more detail in Chapter 7.

Forced Convection For forced flow in long or very narrow parallel-plate channels, the heat transfer coefficient attains an asymptotic value (the fully developed limit), which for symmetrically heated channel surfaces is equal approximately to

$$h = \frac{4k}{d_e} \quad (\text{W/m}^2 \cdot \text{K}) \quad (1.16)$$

where d_e is the *hydraulic diameter* defined in terms of the flow area A and the wetted perimeter of the surfaces p :

$$d_e \equiv \frac{4A}{p}$$

In the inlet zones of such parallel-plate channels and along isolated plates, the heat transfer coefficient varies with the distance from the leading edge. The low-velocity, or laminar flow, average convective heat transfer coefficient along a surface of length L for $\text{Re} \leq 3 \times 10^5$ is found to be

$$h = 0.664 \frac{k}{L} \text{Re}^{1/2} \cdot \text{Pr}^{1/3} \quad (\text{W/m}^2 \cdot \text{K}) \quad (1.17)$$

where k is the fluid thermal conductivity, L the characteristic dimension of the surface, and Re the *Reynolds number* based on L : namely, $\hat{V}L/\nu$.

A similar relation applies to a flow in tubes, pipes, annuli or channels, with the equivalent diameter d_e serving as the characteristic dimension in both the Nusselt and Reynolds numbers. For laminar flow, $\text{Re} \leq 2100$,

$$\frac{hd_e}{k} = 1.86 \left(\text{Re} \cdot \text{Pr} \frac{d_e}{L} \right)^{1/3} \left(\frac{\mu}{\mu_w} \right)^{0.14} \quad (1.18)$$

which is attributed to Sieder and Tate (1936) and where μ_w is the viscosity of the convective medium at the channel wall temperature. Observe that this relationship shows that the heat transfer coefficient attains its maximum value at the inlet to the channel and decreases as d_e/L decreases.

In higher-velocity turbulent flow along plates, the dependence of the convective heat transfer coefficient on the Reynolds number increases, and in the range $\text{Re} \geq 3 \times 10^5$,

$$h = 0.036 \frac{k}{L} \text{Re}^{0.8} \cdot \text{Pr}^{1/3} \quad (\text{W/m}^2 \cdot \text{K}) \quad (1.19)$$

In pipes, tubes, annuli, and channels, turbulent flow occurs at an equivalent diameter-based Reynolds number of 10,000, with the regime bracketed by $2100 \leq \text{Re} \leq 10,000$ usually referred to as the *transition region*. For the transition region, Hausen (1943) has provided the correlating equation

$$\frac{hd_e}{k} = 0.116(\text{Re} - 125)\text{Pr}^{1/3} \left[1 + \left(\frac{d_e}{L} \right)^{2/3} \right] \left(\frac{\mu}{\mu_w} \right)^{0.14} \quad (1.20)$$

and Sieder and Tate (1936) give for turbulent flow

$$\frac{hd_e}{k} = 0.023 \text{Re}^{0.8} \cdot \text{Pr}^{1/3} \left(\frac{\mu}{\mu_w} \right)^{0.14} \quad (1.21)$$

Forced convection in internal and external flows is treated in greater detail in Chapters 5 and 6.

1.1.7 Phase-Change Heat Transfer

Boiling heat transfer displays a complex dependence on the temperature difference between the heated surface and the saturation temperature (boiling point) of the liquid. Following Rohsenow (1952), the heat transfer rate in nucleate boiling, the primary region of interest, can be approximated by a relation of the form

$$q_\phi = C_{sf} A (T_s - T_{\text{sat}})^3 \quad (\text{W}) \quad (1.22)$$

where C_{sf} is a function of the surface–fluid combination. For comparison purposes, it is possible to define a boiling heat transfer coefficient h_ϕ :

$$h_\phi = C_{sf} (T_s - T_{\text{sat}})^2 \quad (\text{W/m}^2 \cdot \text{K})$$

which, however, will vary strongly with surface temperature. Boiling and condensation are treated in greater detail in Chapters 9 and 10, respectively.

1.1.8 Finned Surfaces

Frequent use is made of finned or extended surfaces, and while such finning can substantially increase the surface area in contact with the coolant, conduction in the fin reduces the average temperature of the exposed surface relative to the fin base. In the analysis of such finned surfaces, it is common to define a fin efficiency η as being equal to the ratio of the actual heat dissipated by the fin to the heat that would be dissipated if the fin possessed an infinite thermal conductivity. Using this approach, heat transferred from a fin or a fin structure can be expressed in the form

$$q_f = h S_f \eta (T_b - T_s) \quad (\text{W}) \quad (1.23)$$

where S_f is the surface area of the fin, T_b the temperature at the base of the fin, T_s the surrounding temperature, and q_b the heat entering the base of the fin, which in the steady state is equal to the heat dissipated by the fin. The thermal resistance of a finned surface is given by

$$R_f \equiv \frac{1}{h S_f \eta} \quad (1.24)$$

and η is approximately 0.63 for a thermally optimum rectangular-cross-section fin.

1.1.9 Flow Resistance

The transfer of heat to a flowing gas or liquid that is not undergoing a phase change results in an increase in the coolant temperature from an inlet temperature of T_{in} to an outlet temperature of T_{out} , according to

$$q = \dot{m} c_p (T_{\text{out}} - T_{\text{in}}) \quad (\text{W}) \quad (1.25)$$

Based on this relation, it is possible to define an effective flow resistance, R_{fl} , as

$$R_{fl} \equiv \frac{1}{\dot{m}c_p} \quad (\text{K/W}) \quad (1.26)$$

1.1.10 Radiative Heat Transfer

Unlike conduction and convection, radiative heat transfer between two surfaces or between a surface and its surroundings is not linearly dependent on the temperature difference and is expressed instead as

$$q = \sigma A \mathcal{F} (T_1^4 - T_2^4) \quad (\text{W}) \quad (1.27)$$

where \mathcal{F} includes the effects of surface properties and geometry and σ is the Stefan–Boltzmann constant, $\sigma = 5.669 \times 10^{-8} \text{ W/m}^2 \cdot \text{K}^4$. For modest temperature differences, this equation can be linearized to the form

$$q_r = h_r S (T_1 - T_2) \quad (\text{W}) \quad (1.28)$$

where h_r is the effective “radiation” heat transfer coefficient,

$$h_r = \sigma \mathcal{F} (T_1^2 + T_2^2) (T_1 + T_2) \quad (\text{W/m}^2 \cdot \text{K}) \quad (1.29a)$$

and for small $\Delta T = T_1 - T_2$ is approximately equal to

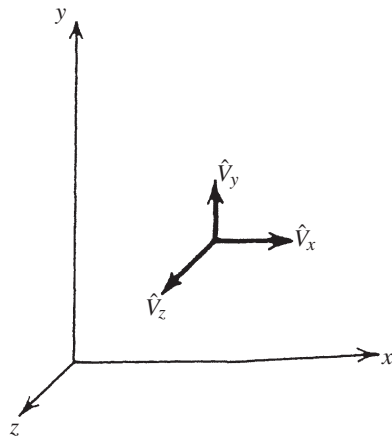
$$h_r = 4\sigma \mathcal{F} (T_1 T_2)^{3/2} \quad (\text{W/m}^2 \cdot \text{K}) \quad (1.29b)$$

It is of interest to note that for temperature differences on the order of 10 K, the radiative heat transfer coefficient h_r for an ideal (or “black”) surface in an absorbing environment is approximately equal to the heat transfer coefficient in natural convection of air. Noting the form of eq. (1.27), the radiation thermal resistance, analogous to the convective resistance, is seen to equal

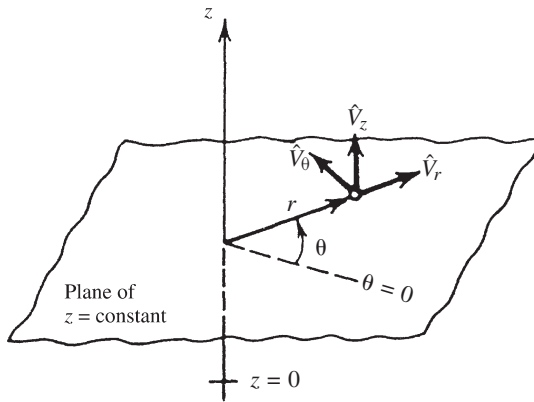
$$R_r \equiv \frac{1}{h_r S} \quad (\text{K/W}) \quad (1.30)$$

1.2 COORDINATE SYSTEMS

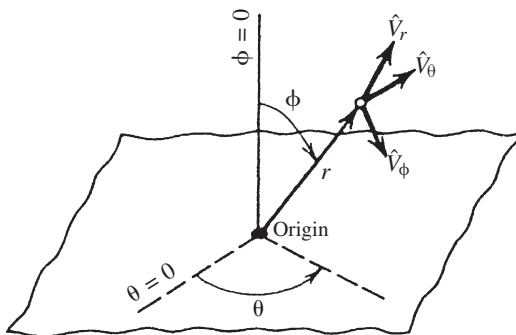
Heat transfer and fluid flow analyses of objects of various sizes and shapes and their corresponding flow fields are facilitated by working in a coordinate system that provides a good fit to the flow geometry. Figure 1.5 presents diagrams for the rectangular (Cartesian), cylindrical, and spherical coordinate systems. Equations for the gradient of a scalar, divergence and curl of a vector, and the Laplacian are given below for the three coordinate systems.



Cartesian coordinates



Cylindrical coordinates



Spherical coordinates

Figure 1.5 Rectangular (Cartesian), cylindrical, and spherical coordinate systems.

1.2.1 Rectangular (Cartesian) Coordinate System

For a rectangular coordinate system with coordinates x , y , and z and unit vectors \mathbf{e}_x , \mathbf{e}_y , and \mathbf{e}_z , the gradient of the scalar T is

$$\text{grad } T = \nabla T = \mathbf{e}_x \frac{\partial T}{\partial x} + \mathbf{e}_y \frac{\partial T}{\partial y} + \mathbf{e}_z \frac{\partial T}{\partial z} \quad (1.31)$$

The divergence of a vector \mathbf{V} having components V_x , V_y , and V_z is

$$\text{div } \mathbf{V} = \nabla \cdot \mathbf{V} = \frac{\partial V_x}{\partial x} + \frac{\partial V_y}{\partial y} + \frac{\partial V_z}{\partial z} \quad (1.32)$$

The curl of the vector \mathbf{V} is

$$\begin{aligned} \text{curl } \mathbf{V} = \nabla \times \mathbf{V} &= \mathbf{e}_x \left(\frac{\partial V_z}{\partial y} - \frac{\partial V_y}{\partial z} \right) \\ &+ \mathbf{e}_y \left(\frac{\partial V_x}{\partial z} - \frac{\partial V_z}{\partial x} \right) + \mathbf{e}_z \left(\frac{\partial V_y}{\partial x} - \frac{\partial V_x}{\partial y} \right) \end{aligned} \quad (1.33)$$

Alternatively, curl \mathbf{V} may be written as the determinant

$$\begin{vmatrix} \mathbf{e}_x & \mathbf{e}_y & \mathbf{e}_z \\ \frac{\partial}{\partial x} & \frac{\partial}{\partial y} & \frac{\partial}{\partial z} \\ V_x & V_y & V_z \end{vmatrix} \quad (1.34)$$

The Laplacian of the scalar T is

$$\nabla^2 T = \frac{\partial^2 T}{\partial x^2} + \frac{\partial^2 T}{\partial y^2} + \frac{\partial^2 T}{\partial z^2} \quad (1.35)$$

1.2.2 Cylindrical Coordinate System

For a cylindrical coordinate system with coordinates r , θ , and z and unit vectors \mathbf{e}_r , \mathbf{e}_θ , and \mathbf{e}_z , the gradient of the scalar T is

$$\text{grad } T = \nabla T = \mathbf{e}_r \frac{\partial T}{\partial r} + \mathbf{e}_\theta \frac{1}{r} \frac{\partial T}{\partial \theta} + \mathbf{e}_z \frac{\partial T}{\partial z} \quad (1.36)$$

The divergence of a vector \mathbf{V} having components, V_r , V_θ , and V_z is

$$\text{div } \mathbf{V} = \nabla \cdot \mathbf{V} = \frac{1}{r} \frac{\partial(r V_r)}{\partial r} + \frac{1}{r} \frac{\partial V_\theta}{\partial \theta} + \frac{\partial V_z}{\partial z} \quad (1.37)$$

The curl of the vector \mathbf{V} is

$$\begin{aligned}\text{curl } \mathbf{V} = \nabla \times \mathbf{V} &= \mathbf{e}_r \left(\frac{1}{r} \frac{\partial V_z}{\partial \theta} - \frac{\partial V_\theta}{\partial z} \right) \\ &+ \mathbf{e}_\theta \left(\frac{\partial V_r}{\partial z} - \frac{\partial V_z}{\partial r} \right) + \mathbf{e}_z \frac{1}{r} \left[\frac{\partial(r V_\theta)}{\partial r} - \frac{\partial V_r}{\partial \theta} \right]\end{aligned}\quad (1.38)$$

Alternatively, curl \mathbf{V} may be written as the determinant

$$\begin{vmatrix} \mathbf{e}_r \frac{1}{r} & \mathbf{e}_\theta & \mathbf{e}_z \frac{1}{r} \\ \frac{\partial}{\partial r} & \frac{\partial}{\partial \theta} & \frac{\partial}{\partial z} \\ V_r & r V_\theta & V_z \end{vmatrix}\quad (1.39)$$

The Laplacian of the scalar T is

$$\nabla^2 T = \frac{1}{r} \frac{\partial}{\partial r} \left(r \frac{\partial T}{\partial r} \right) + \frac{1}{r^2} \frac{\partial^2 T}{\partial \theta^2} + \frac{\partial^2 T}{\partial z^2}\quad (1.40)$$

1.2.3 Spherical Coordinate System

For a spherical coordinate system with coordinates r , θ , and ϕ and unit vectors \mathbf{e}_r , \mathbf{e}_θ , and \mathbf{e}_ϕ , the gradient of the scalar T is

$$\text{grad } T = \nabla T = \mathbf{e}_r \frac{\partial T}{\partial r} + \mathbf{e}_\phi \frac{1}{r} \frac{\partial T}{\partial \phi} + \mathbf{e}_\theta \frac{1}{r \sin \phi} \frac{\partial T}{\partial \theta}\quad (1.41)$$

The divergence of a vector \mathbf{V} having components, V_r , V_θ , and V_ϕ is

$$\text{div } \mathbf{V} = \nabla \cdot \mathbf{V} = \frac{1}{r^2} \frac{\partial(r^2 V_r)}{\partial r} + \frac{1}{r \sin \phi} \frac{\partial(V_\phi \sin \phi)}{\partial \phi} + \frac{1}{r \sin \phi} \frac{\partial V_\theta}{\partial \theta}\quad (1.42)$$

The curl of the vector \mathbf{V} is

$$\begin{aligned}\text{curl } \mathbf{V} = \nabla \times \mathbf{V} &= \mathbf{e}_r \frac{1}{r \sin \phi} \left[\frac{\partial(V_\theta \sin \phi)}{\partial \phi} - \frac{\partial V_\phi}{\partial \theta} \right] \\ &+ \mathbf{e}_\phi \frac{1}{r} \left[\frac{1}{\sin \phi} \frac{\partial V_r}{\partial \theta} - \frac{\partial(r V_\theta)}{\partial r} \right] + \mathbf{e}_\theta \frac{1}{r} \left[\frac{\partial(r V_\phi)}{\partial r} - \frac{\partial V_r}{\partial \phi} \right]\end{aligned}\quad (1.43)$$

The Laplacian of the scalar T is

$$\nabla^2 T = \frac{1}{r^2} \frac{\partial}{\partial r} \left(r^2 \frac{\partial T}{\partial r} \right) + \frac{1}{r^2 \sin \phi} \frac{\partial}{\partial \phi} \left(\sin \phi \frac{\partial T}{\partial \phi} \right) + \frac{1}{r^2 \sin^2 \phi} \frac{\partial^2 T}{\partial \theta^2}\quad (1.44)$$

1.2.4 General Curvilinear Coordinates

In general, a curvilinear coordinate system can be proposed where a vector \mathbf{V} has components V_1 , V_2 , and V_3 in the x_1 , x_2 , and x_3 coordinate directions. The unit vectors are \mathbf{e}_1 , \mathbf{e}_2 , and \mathbf{e}_3 in the coordinate directions x_1 , x_2 , and x_3 and there are scale factors, s_1 , s_2 , and s_3 that relate the general curvilinear coordinate system to the rectangular, cylindrical, and spherical coordinate systems.

In the general curvilinear coordinate system, the gradient of a scalar T is

$$\text{grad } T = \nabla T = \mathbf{e}_1 \frac{1}{s_1} \frac{\partial T}{\partial x_1} + \mathbf{e}_2 \frac{1}{s_2} \frac{\partial T}{\partial x_2} + \mathbf{e}_3 \frac{1}{s_3} \frac{\partial T}{\partial x_3} \quad (1.45)$$

The divergence of a vector \mathbf{V} having components, V_1 , V_2 , and V_3 is

$$\text{div } \mathbf{V} = \nabla \cdot \mathbf{V} = \frac{1}{s_1 s_2 s_3} \left[\frac{\partial (s_2 s_3 V_1)}{\partial x_1} + \frac{\partial (s_3 s_1 V_2)}{\partial x_2} + \frac{\partial (s_1 s_2 V_3)}{\partial x_3} \right] \quad (1.46)$$

The curl of the vector \mathbf{V} is

$$\begin{aligned} \text{curl } \mathbf{V} = \nabla \times \mathbf{V} = & \mathbf{e}_1 \frac{1}{s_2 s_3} \left[\frac{\partial (s_3 V_3)}{\partial x_2} - \frac{\partial (s_2 V_2)}{\partial x_3} \right] \\ & + \mathbf{e}_2 \frac{1}{s_1 s_3} \left[\frac{\partial (s_1 V_1)}{\partial x_3} - \frac{\partial (s_3 V_3)}{\partial x_1} \right] + \mathbf{e}_3 \frac{1}{s_1 s_2} \left[\frac{\partial (s_2 V_2)}{\partial x_1} - \frac{\partial (s_1 V_1)}{\partial x_2} \right] \end{aligned} \quad (1.47)$$

The Laplacian of the scalar T is

$$\begin{aligned} \nabla^2 T = \frac{1}{s_1 s_2 s_3} \left[\frac{\partial}{\partial x_1} \left(\frac{s_2 s_3}{s_1} \frac{\partial T}{\partial x_1} \right) \right. \\ \left. + \frac{\partial}{\partial x_2} \left(\frac{s_1 s_3}{s_2} \frac{\partial T}{\partial x_2} \right) + \frac{\partial}{\partial x_3} \left(\frac{s_1 s_2}{s_3} \frac{\partial T}{\partial x_3} \right) \right] \end{aligned} \quad (1.48)$$

In eqs. (1.45) through (1.48), the conversion from the general curvilinear coordinate system to the rectangular, cylindrical, and spherical coordinate systems depends on the assignment of values to the coordinates x_1 , x_2 , and x_3 and the scale factors s_1 , s_2 , and s_3 .

	x_1	x_2	x_3	s_1	s_2	s_3
Rectangular:	x	y	z	1	1	1
Cylindrical:	r	θ	z	1	r	1
Spherical:	r	ϕ	θ	1	r	$r \sin \phi$

1.3 CONTINUITY EQUATION

A control volume is a region in space selected for analysis. An incremental control volume carrying a mass flux is shown in Fig. 1.6. The conservation of mass principle

can be applied to the control volume by noting that the net rate of mass flux out of the control volume plus the rate of accumulation of mass within the control volume must equal zero:

$$\iint_A \rho (\hat{\mathbf{V}} \cdot \mathbf{n}) dA = \frac{\partial}{\partial t} \iiint_V \rho dV \quad (1.49)$$

Observe that the mass within the control volume is

$$m = \rho \Delta x \Delta y \Delta z$$

and that the mass flux at each of the faces of Fig. 1.6 will be $\rho(\hat{\mathbf{V}} \cdot \mathbf{n})$, where \mathbf{n} is the normal to the area dA .

Noting that the density can vary from point to point and with time, $\rho = f(x, y, z, t)$, the net mass flux out of the control volumes in each of the coordinate directions will be

$$\begin{aligned} & (\rho \hat{V}_{x|x+\Delta x} - \rho \hat{V}_{x|x}) \Delta y \Delta z \\ & (\rho \hat{V}_{y|y+\Delta y} - \rho \hat{V}_{y|y}) \Delta x \Delta z \\ & (\rho \hat{V}_{z|z+\Delta z} - \rho \hat{V}_{z|z}) \Delta x \Delta y \end{aligned}$$

With all of the foregoing substituted into eq. (1.49),

$$\begin{aligned} & (\rho \hat{V}_{x|x+\Delta x} - \rho \hat{V}_{x|x}) \Delta y \Delta z + (\rho \hat{V}_{y|y+\Delta y} - \rho \hat{V}_{y|y}) \Delta x \Delta z \\ & + (\rho \hat{V}_{z|z+\Delta z} - \rho \hat{V}_{z|z}) \Delta x \Delta y + \frac{\partial \rho}{\partial t} \Delta x \Delta y \Delta z = 0 \end{aligned}$$

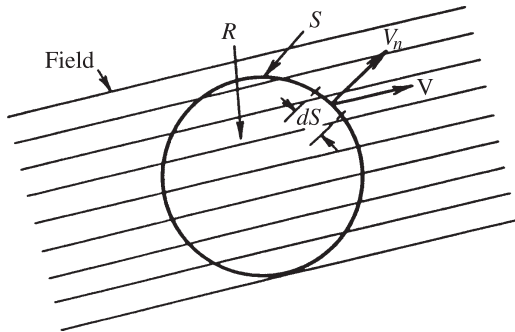


Figure 1.6 Mass flux through an incremental flow volume.

and after division by $\Delta x \Delta y \Delta z$, the result is

$$\frac{\rho \hat{V}_{x|x+\Delta x} - \rho \hat{V}_{x|x}}{\Delta x} + \frac{\rho \hat{V}_{y|y+\Delta y} - \rho \hat{V}_{y|y}}{\Delta y} + \frac{\rho \hat{V}_{z|z+\Delta z} - \rho \hat{V}_{z|z}}{\Delta z} + \frac{\partial \rho}{\partial t} = 0$$

In the limit as Δx , Δy , and Δz all tend to zero, the result is

$$\frac{\partial}{\partial x}(\rho \hat{V}_x) + \frac{\partial}{\partial y}(\rho \hat{V}_y) + \frac{\partial}{\partial z}(\rho \hat{V}_z) + \frac{\partial \rho}{\partial t} = 0 \quad (1.50)$$

This may be written as

$$\nabla \cdot \rho \hat{\mathbf{V}} + \frac{\partial \rho}{\partial t} = 0 \quad (1.51)$$

where $\nabla \cdot \rho \hat{\mathbf{V}} = \text{div } \rho \hat{\mathbf{V}}$ is the divergence of the vector $\hat{\mathbf{V}}$. This equation is general: It applies to unsteady three-dimensional flow with variable ρ .

Equation (1.51) is a vector equation that represents the *equation of continuity* in rectangular, cylindrical, and spherical coordinates. If the flow is incompressible, so that ρ is independent of time, eq. (1.51) reduces to

$$\nabla \cdot \rho \hat{\mathbf{V}} = 0 \quad (1.52)$$

which applies to both steady and unsteady flow. This equation is also a vector equation that applies to rectangular, cylindrical, and spherical coordinates.

Equation (1.50) can be written as

$$\frac{\partial \rho}{\partial t} + \hat{V}_x \frac{\partial \rho}{\partial x} + \hat{V}_y \frac{\partial \rho}{\partial y} + \hat{V}_z \frac{\partial \rho}{\partial z} + \rho \left(\frac{\partial \hat{V}_x}{\partial x} + \frac{\partial \hat{V}_y}{\partial y} + \frac{\partial \hat{V}_z}{\partial z} \right) = 0$$

or

$$\frac{D\rho}{Dt} + \rho \nabla \cdot \hat{\mathbf{V}} = 0 \quad (1.53)$$

where

$$\frac{D\rho}{Dt} = \frac{\partial \rho}{\partial t} + \hat{V}_x \frac{\partial \rho}{\partial x} + \hat{V}_y \frac{\partial \rho}{\partial y} + \hat{V}_z \frac{\partial \rho}{\partial z} \quad (1.54)$$

is called the *substantial derivative* of the density ρ . Thus, in rectangular coordinates,

$$\frac{D}{Dt} = \frac{\partial}{\partial t} + \hat{V}_x \frac{\partial}{\partial x} + \hat{V}_y \frac{\partial}{\partial y} + \hat{V}_z \frac{\partial}{\partial z} \quad (1.55)$$

The substantial derivative in cylindrical coordinates is

$$\frac{D}{Dt} = \frac{\partial}{\partial t} + \hat{V}_r \frac{\partial}{\partial r} + \frac{\hat{V}_\theta}{r} \frac{\partial}{\partial \theta} + \hat{V}_z \frac{\partial}{\partial z} \quad (1.56)$$

and in spherical coordinates, it is

$$\frac{D}{Dt} = \frac{\partial}{\partial t} + \hat{V}_r \frac{\partial}{\partial r} + \frac{\hat{V}_\phi}{r} \frac{\partial}{\partial \phi} + \frac{\hat{V}_\theta}{r \sin \phi} \frac{\partial}{\partial \theta} \quad (1.57)$$

The equation of continuity representing the conservation of mass can be summarized for the three coordinate systems. For the rectangular coordinate system,

$$\frac{\partial \rho}{\partial t} + \frac{\partial(\rho \hat{V}_x)}{\partial x} + \frac{\partial(\rho \hat{V}_y)}{\partial y} + \frac{\partial(\rho \hat{V}_z)}{\partial z} = 0 \quad (1.58)$$

for the cylindrical coordinate system,

$$\frac{\partial \rho}{\partial t} + \frac{1}{r} \frac{\partial(\rho r \hat{V}_r)}{\partial r} + \frac{1}{r} \frac{\partial(\rho \hat{V}_\theta)}{\partial \theta} + \frac{\partial(\rho \hat{V}_z)}{\partial z} = 0 \quad (1.59)$$

and for the spherical coordinate system,

$$\frac{\partial \rho}{\partial t} + \frac{1}{r^2} \frac{\partial(\rho r^2 \hat{V}_r)}{\partial r} + \frac{1}{r \sin \phi} \frac{\partial(\rho \hat{V}_\phi \sin \phi)}{\partial \phi} + \frac{1}{r \sin \phi} \frac{\partial(\rho \hat{V}_\theta)}{\partial \theta} = 0 \quad (1.60)$$

In the event that the flow may be modeled as incompressible,

$$\frac{\partial \hat{V}_x}{\partial x} + \frac{\partial \hat{V}_y}{\partial y} + \frac{\partial \hat{V}_z}{\partial z} = 0 \quad (1.61)$$

for the cylindrical coordinate system,

$$\frac{1}{r} \frac{\partial(r \hat{V}_r)}{\partial r} + \frac{1}{r} \frac{\partial \hat{V}_\theta}{\partial \theta} + \frac{\partial \hat{V}_z}{\partial z} = 0 \quad (1.62)$$

and for the spherical coordinate system,

$$\frac{1}{r^2} \frac{\partial(r^2 \hat{V}_r)}{\partial r} + \frac{1}{r \sin \phi} \frac{\partial(\hat{V}_\phi \sin \phi)}{\partial \phi} + \frac{1}{r \sin \phi} \frac{\partial \hat{V}_\theta}{\partial \theta} = 0 \quad (1.63)$$

1.4 MOMENTUM AND THE MOMENTUM THEOREM

The momentum theorem of fluid mechanics provides a relation between a group of field points. It is especially useful when the details of the flow field are more than moderately complicated and it is based on Newton's law, which can be written as

$$\mathbf{F} = m \frac{d\hat{\mathbf{V}}}{dt} = \frac{d(m\hat{\mathbf{V}})}{dt} \quad (1.64)$$

where $m\mathbf{V}$ is the *momentum*. Equation (1.64) is the statement of the *conservation of momentum principle*.

Note that the conservation of momentum principle is stated in terms of the properties of particles and not in terms of the properties of a field. To derive the momentum theorem, a region in a fluid confined by the control surface S_1 , shown in Fig. 1.7, is employed. The surface S_1 contains a definite and fixed number of particles at time t_1 . At time t_2 , these particles will have moved to a region bounded by the control surface S_2 , which is shown as a dashed curve to distinguish it from S_1 .

The control surfaces S_1 and S_2 enclose three separate and distinct regions, designated by a , b , and c . Let the momentum in the three regions be \mathbf{P}_a , \mathbf{P}_b , and \mathbf{P}_c , respectively. At time t_1 the particles within surface S_1 will possess momentum $\mathbf{P}_a + \mathbf{P}_{b1}$. At time t_2 these particles will have momentum, $\mathbf{P}_{b2} + \mathbf{P}_c$ because they have moved into the region enclosed by surface S_2 . Hence the momentum change during the time interval $t_2 - t_1$ may be described by

$$(\mathbf{P}_{b2} + \mathbf{P}_c) - (\mathbf{P}_{b1} + \mathbf{P}_a) = (\mathbf{P}_{b2} - \mathbf{P}_{b1}) + (\mathbf{P}_c - \mathbf{P}_a)$$

and the time rate of change of momentum will be

$$\lim_{t_2 \rightarrow t_1} \left(\frac{\mathbf{P}_{b2} - \mathbf{P}_{b1}}{t_2 - t_1} + \frac{\mathbf{P}_c - \mathbf{P}_a}{t_2 - t_1} \right) \quad (1.65)$$

As t_2 approaches t_1 as a limit, the control surface S_2 will coincide with S_1 . The first term in eq. (1.65) is therefore the time rate of change of momentum of the fluid contained within region 1, R_1 , contained within S_1 . This may be written as the integral over R_1 . Because the mass of fluid contained in R_1 is

$$\iiint_{R_1} \rho \, dR_1$$

the time rate of change of momentum of the fluid contained within region 1 will be

$$\frac{\partial}{\partial t} \iiint_{R_1} \rho \hat{\mathbf{V}} \, dR_1$$

The second term in eq. (1.65) is the momentum efflux through the control surface S_1 . If the flux in the outward direction is taken as positive, this efflux can be expressed by the integral

$$\iint_{S_1} \rho \hat{\mathbf{V}} \hat{V}_n \, dS_1$$

where V_n is the component of velocity normal to S_1 .

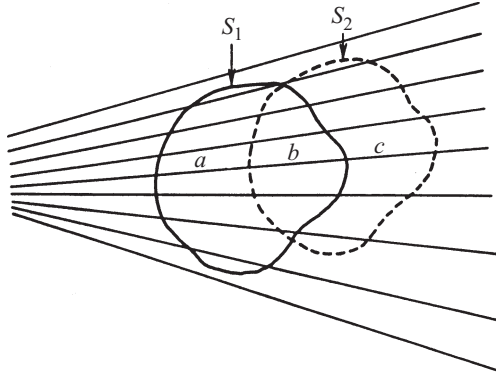


Figure 1.7 Regions bounded by control surfaces used for the development of the momentum theorem.

The conservation of momentum principle then becomes

$$F = m \frac{d\hat{\mathbf{V}}}{dt} = \frac{\partial}{\partial t} \iiint_{R_1} \rho \hat{\mathbf{V}} dR_1 + \iint_{S_1} \rho \hat{\mathbf{V}} \hat{V}_n dS_1 \quad (1.66)$$

or, by rearrangement of terms,

$$\frac{\partial}{\partial t} \iiint_{R_1} \rho \hat{V}_x dR_1 = F_x - \iint_{S_1} \rho \hat{V}_x \hat{V}_n dS_1 \quad (1.67a)$$

$$\frac{\partial}{\partial t} \iiint_{R_1} \rho \hat{V}_y dR_1 = F_y - \iint_{S_1} \rho \hat{V}_y \hat{V}_n dS_1 \quad (1.67b)$$

$$\frac{\partial}{\partial t} \iiint_{R_1} \rho \hat{V}_z dR_1 = F_z - \iint_{S_1} \rho \hat{V}_z \hat{V}_n dS_1 \quad (1.67c)$$

in the three rectangular coordinate directions.

The foregoing development leads to the statement of the *momentum theorem*: The time rate of increase of momentum of a fluid within a fixed control volume R will be equal to the rate at which momentum flows into R through its confining surface S , plus the net force acting on the fluid within R . When the flow is incompressible, the viscosity is constant, and the flow is laminar, the *Navier–Stokes equations* result. In Cartesian coordinates, with F_x , F_y , and F_z taken as the components of the body force per unit volume, the Navier–Stokes equations are

$$\rho \left(\frac{\partial \hat{V}_x}{\partial t} + \hat{V}_x \frac{\partial \hat{V}_x}{\partial x} + \hat{V}_y \frac{\partial \hat{V}_x}{\partial y} + \hat{V}_z \frac{\partial \hat{V}_x}{\partial z} \right)$$

$$= -\frac{\partial P}{\partial x} + \mu \left(\frac{\partial^2 \hat{V}_x}{\partial x^2} + \frac{\partial^2 \hat{V}_x}{\partial y^2} + \frac{\partial^2 \hat{V}_x}{\partial z^2} \right) + F_x \quad (1.68a)$$

$$\begin{aligned} & \rho \left(\frac{\partial \hat{V}_y}{\partial t} + \hat{V}_x \frac{\partial \hat{V}_y}{\partial x} + \hat{V}_y \frac{\partial \hat{V}_y}{\partial y} + \hat{V}_z \frac{\partial \hat{V}_y}{\partial z} \right) \\ &= -\frac{\partial P}{\partial y} + \mu \left(\frac{\partial^2 \hat{V}_y}{\partial x^2} + \frac{\partial^2 \hat{V}_y}{\partial y^2} + \frac{\partial^2 \hat{V}_y}{\partial z^2} \right) + F_y \end{aligned} \quad (1.68b)$$

$$\begin{aligned} & \rho \left(\frac{\partial \hat{V}_z}{\partial t} + \hat{V}_x \frac{\partial \hat{V}_z}{\partial x} + \hat{V}_y \frac{\partial \hat{V}_z}{\partial y} + \hat{V}_z \frac{\partial \hat{V}_z}{\partial z} \right) \\ &= -\frac{\partial P}{\partial z} + \mu \left(\frac{\partial^2 \hat{V}_z}{\partial x^2} + \frac{\partial^2 \hat{V}_z}{\partial y^2} + \frac{\partial^2 \hat{V}_z}{\partial z^2} \right) + F_z \end{aligned} \quad (1.68c)$$

In cylindrical coordinates with F_r , F_θ , and F_z taken as the components of the body force per unit volume, the Navier–Stokes equations are

$$\begin{aligned} & \rho \left(\frac{\partial \hat{V}_r}{\partial t} + \hat{V}_r \frac{\partial \hat{V}_r}{\partial r} + \frac{\hat{V}_\theta}{r} \frac{\partial \hat{V}_r}{\partial \theta} - \frac{\hat{V}_\theta^2}{r} + \hat{V}_z \frac{\partial \hat{V}_r}{\partial z} \right) = -\frac{\partial P}{\partial r} \\ & + \mu \left(\frac{\partial^2 \hat{V}_r}{\partial r^2} + \frac{1}{r} \frac{\partial \hat{V}_r}{\partial r} - \frac{\hat{V}_r}{r^2} + \frac{1}{r^2} \frac{\partial^2 \hat{V}_r}{\partial \theta^2} - \frac{2}{r^2} \frac{\hat{V}_\theta}{\partial \theta} + \frac{\partial^2 \hat{V}_r}{\partial z^2} \right) + F_r \end{aligned} \quad (1.69a)$$

$$\begin{aligned} & \rho \left(\frac{\partial \hat{V}_\theta}{\partial t} + \hat{V}_r \frac{\partial \hat{V}_\theta}{\partial r} + \frac{\hat{V}_\theta}{r} \frac{\partial \hat{V}_\theta}{\partial \theta} - \frac{\hat{V}_r \hat{V}_\theta}{r} + \hat{V}_z \frac{\partial \hat{V}_\theta}{\partial z} \right) = -\frac{1}{r} \frac{\partial P}{\partial \theta} \\ & + \mu \left(\frac{\partial^2 \hat{V}_\theta}{\partial r^2} + \frac{1}{r} \frac{\partial \hat{V}_\theta}{\partial r} - \frac{\hat{V}_\theta}{r^2} + \frac{1}{r^2} \frac{\partial^2 \hat{V}_\theta}{\partial \theta^2} + \frac{2}{r^2} \frac{\partial \hat{V}_r}{\partial \theta} + \frac{\partial^2 \hat{V}_\theta}{\partial z^2} \right) + F_\theta \end{aligned} \quad (1.69b)$$

$$\begin{aligned} & \rho \left(\frac{\partial \hat{V}_z}{\partial t} + \hat{V}_r \frac{\partial \hat{V}_z}{\partial r} + \frac{\hat{V}_\theta}{r} \frac{\partial \hat{V}_z}{\partial \theta} + \hat{V}_z \frac{\partial \hat{V}_z}{\partial z} \right) = -\frac{\partial P}{\partial z} \\ & + \mu \left(\frac{\partial^2 \hat{V}_z}{\partial r^2} + \frac{1}{r} \frac{\partial \hat{V}_z}{\partial r} + \frac{1}{r^2} \frac{\partial^2 \hat{V}_z}{\partial \theta^2} + \frac{\partial^2 \hat{V}_z}{\partial z^2} \right) + F_z \end{aligned} \quad (1.69c)$$

Finally, in spherical coordinates with F_r , F_θ , and F_ϕ taken as the components of the body force per unit volume and with

$$\begin{aligned} \frac{D}{DT} &= \frac{\partial}{\partial t} + \hat{V}_r \frac{\partial}{\partial r} + \frac{\hat{V}_\phi}{r} \frac{\partial}{\partial \phi} + \frac{\hat{V}_\theta}{r \sin \phi} \frac{\partial}{\partial \theta} \\ \nabla^2 &= \frac{1}{r^2} \frac{\partial}{\partial r} \left(r^2 \frac{\partial}{\partial r} \right) + \frac{1}{r^2 \sin \phi} \frac{\partial}{\partial \phi} \left(\sin \phi \frac{\partial}{\partial \phi} \right) + \frac{1}{r^2 \sin^2 \phi} \frac{\partial^2}{\partial \theta^2} \end{aligned}$$

the Navier–Stokes equations are

$$\rho \left(\frac{D\hat{V}_r}{Dt} - \frac{\hat{V}_\phi^2 + \hat{V}_\theta^2}{r} \right) = -\frac{\partial P}{\partial r} + \mu \left(\nabla^2 \hat{V}_r - \frac{2\hat{V}_r}{r^2} - \frac{2}{r^2} \frac{\partial \hat{V}_\phi}{\partial \phi} - \frac{2\hat{V}_\theta \cot \phi}{r^2} - \frac{2}{r^2 \sin \phi} \frac{\partial \hat{V}_\theta}{\partial \theta} \right) + F_r \quad (1.70a)$$

$$\rho \left(\frac{D\hat{V}_\phi}{Dt} - \frac{\hat{V}_r \hat{V}_\phi}{r} - \frac{\hat{V}_\theta^2 \cot \phi}{r} \right) = -\frac{1}{r} \frac{\partial P}{\partial \phi} + \mu \left(\nabla^2 \hat{V}_\phi + \frac{2}{r^2} \frac{\partial \hat{V}_r}{\partial \phi} - \frac{\hat{V}_\phi}{r^2 \sin \phi} - \frac{2 \cos \phi}{r^2 \sin^2 \phi} \frac{\partial \hat{V}_\theta}{\partial \theta} \right) + F_\phi \quad (1.70b)$$

$$\rho \left(\frac{D\hat{V}_\theta}{Dt} + \frac{\hat{V}_\theta \hat{V}_r}{r} + \frac{\hat{V}_\phi \hat{V}_\theta \cot \phi}{r} \right) = -\frac{\hat{V}_\theta}{r \sin \phi} \frac{\partial P}{\partial \theta} + \mu \left(\nabla^2 \hat{V}_\theta - \frac{\hat{V}_\theta}{r^2 \sin^2 \phi} + \frac{2}{r^2 \sin \phi} \frac{\partial \hat{V}_r}{\partial \theta} + \frac{2 \cos \phi}{r^2 \sin^2 \phi} \frac{\partial \hat{V}_\phi}{\partial \theta} \right) + F_\theta \quad (1.70c)$$

1.5 CONSERVATION OF ENERGY

In Fig. 1.8, an imaginary two-dimensional control volume of finite size $\Delta x \Delta y$ with flow velocity $\hat{\mathbf{V}} = \mathbf{e}_x \hat{V}_x + \mathbf{e}_y \hat{V}_y$, heat flux $\mathbf{q}'' = \mathbf{e}_x q_x'' + \mathbf{e}_y q_y''$, specific internal energy u , and rate of internal heat generation q''' , the *first law of thermodynamics* requires that

$$\begin{aligned} & \left(\begin{array}{c} \text{rate of energy} \\ \text{accumulation within} \\ \text{the control volume} \end{array} \right) \\ &= \left(\begin{array}{c} \text{net transfer} \\ \text{of energy by} \\ \text{fluid flow} \end{array} \right) + \left(\begin{array}{c} \text{net heat} \\ \text{transfer by} \\ \text{conduction} \end{array} \right) \\ &\quad \times \left(\begin{array}{c} \text{rate of} \\ \text{internal heat} \\ \text{generation} \end{array} \right) - \left(\begin{array}{c} \text{net work} \\ \text{transfer from the} \\ \text{control volume to} \\ \text{the environment} \end{array} \right) \end{aligned} \quad (1.71)$$

Four of the five terms indicated do not involve work transfer from the control volume to the environment.

- The rate of energy accumulated in the control volume is

$$\Delta x \Delta y \frac{\partial}{\partial t} (\rho u) \quad (1.72a)$$

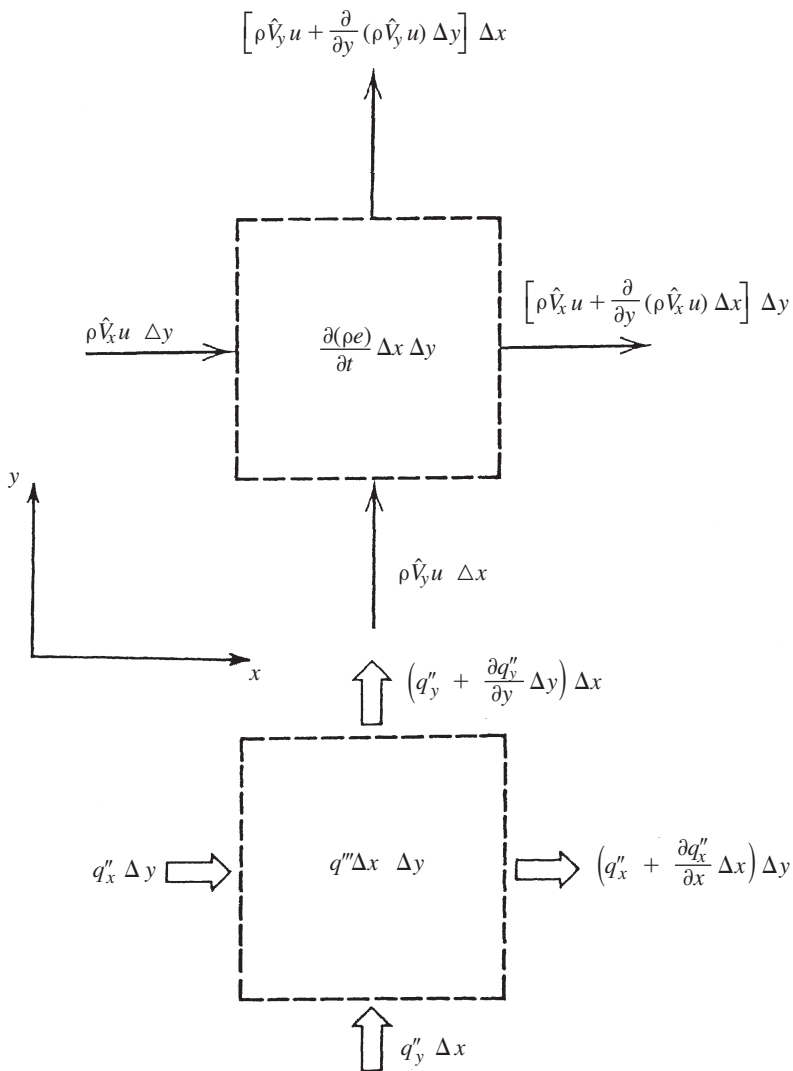


Figure 1.8 First law of thermodynamics applied to an imaginary control volume in two-dimensional flow.

- The net transfer of energy by fluid flow is

$$- (\Delta x \Delta y) \left[\frac{\partial}{\partial x} (\rho \hat{V}_x u) + \frac{\partial}{\partial y} (\rho \hat{V}_y u) \right] \quad (1.72b)$$

- The net heat transfer by conduction is

$$- (\Delta x \Delta y) \left(\frac{\partial q''_x}{\partial x} + \frac{\partial q''_y}{\partial y} \right) \quad (1.72c)$$

- The rate of internal heat generation is

$$(\Delta x \Delta y) q''' \quad (1.72d)$$

The origin of the term involving the net work transferred from the control volume to the environment is shown in Fig. 1.9, where the normal and tangential stresses are sketched. For example, the work done per unit time by the normal stress σ_x on the left

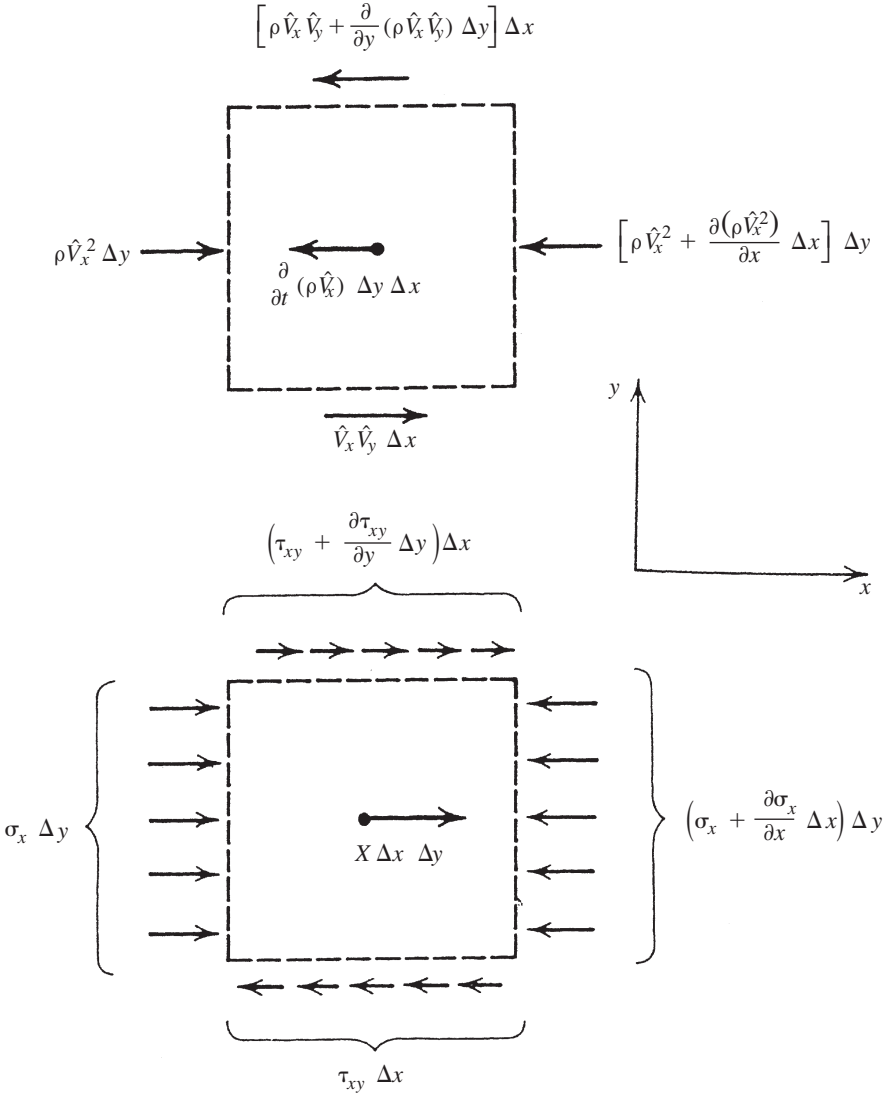


Figure 1.9 Force balance in the x direction of an imaginary control volume in two-dimensional flow.

side of the $\Delta x \Delta y$ element is negative and equal to the force acting on the boundary σ_y , multiplied by the boundary displacement per unit time \hat{V}_x . This yields $-\hat{V}_x \sigma_x \Delta y$. Similarly, the work transfer associated with normal stresses acting on the right side of the element is positive and equal to

$$\left(\sigma_x + \frac{\partial \sigma_x}{\partial x} \Delta x \right) \left(\hat{V}_x + \frac{\partial \hat{V}_x}{\partial x} \Delta x \right) \Delta y$$

The net work transfer rate due to these two contributions is

$$\left(\sigma_x \frac{\partial \hat{V}_x}{\partial x} + \hat{V}_x \frac{\partial \sigma_x}{\partial x} \right) (\Delta x \Delta y)$$

Three more work transfer rates can be calculated in the same way by examining the effect of the remaining three stresses, τ_{xy} in the x direction and σ_y and τ_{yx} in the y direction. This gives

$$\begin{aligned} (\Delta x \Delta y) & \left(\sigma_x \frac{\partial \hat{V}_x}{\partial x} - \tau_{xy} \frac{\partial \hat{V}_x}{\partial y} + \sigma_y \frac{\partial \hat{V}_y}{\partial y} - \tau_{yx} \frac{\partial \hat{V}_y}{\partial x} \right) \\ & + (\Delta x \Delta y) \left(\hat{V}_x \frac{\partial \sigma_x}{\partial x} - \hat{V}_x \frac{\partial \tau_{xy}}{\partial y} + \hat{V}_y \frac{\partial \sigma_y}{\partial y} - \hat{V}_x \frac{\partial \tau_{yx}}{\partial x} \right) \end{aligned}$$

where the eight terms have been separated into two groups. It can be shown that the second group reduces to

$$- \rho \frac{D}{Dt} \frac{\hat{V}_x^2 + \hat{V}_y^2}{2}$$

which represents the change of kinetic energy of the fluid in the control volume. This change may be considered negligible relative to the internal energy change, $\partial(\rho u)/\partial t$, so that the work transfer becomes

$$(\Delta x \Delta y) \left(\sigma_x \frac{\partial \hat{V}_x}{\partial x} - \tau_{xy} \frac{\partial \hat{V}_x}{\partial y} + \sigma_y \frac{\partial \hat{V}_y}{\partial y} - \tau_{yx} \frac{\partial \hat{V}_y}{\partial x} \right) \quad (1.72e)$$

The stresses σ_x and τ_{xy} can be related to the flow field via the constitutive relations given by Rohsenow and Choi (1961):

$$\sigma_x = P - 2\mu \frac{\partial \hat{V}_x}{\partial x} + \frac{2}{3}\mu \left(\frac{\partial \hat{V}_x}{\partial x} + \frac{\partial \hat{V}_y}{\partial y} \right) \quad (1.73a)$$

and

$$\tau_{xy} = \mu \left(\frac{\partial \hat{V}_x}{\partial y} + \frac{\partial \hat{V}_y}{\partial x} \right) \quad (1.73b)$$

The bookkeeping required by eq. (1.71) dictates the assembly of eqs. (1.72), using eqs. (1.73), into

$$\rho \frac{Du}{Dt} + u \left(\frac{Dp}{Dt} + \rho \nabla \cdot \hat{\mathbf{V}} \right) = -\nabla \cdot \mathbf{q}'' + q''' - P \nabla \cdot \hat{\mathbf{V}} + \mu \Phi \quad (1.74)$$

where μ is the dynamic viscosity of the fluid and Φ is the *viscous dissipation function*, which is detailed subsequently in rectangular, cylindrical, and spherical coordinates. However, eq. (1.53) shows that the term in parentheses on the left-hand side of eq. (1.74) is equal to zero, so that eq. (1.74) reduces to

$$\rho \frac{Du}{Dt} = -\nabla \cdot \mathbf{q}'' + q''' - P \nabla \cdot \hat{\mathbf{V}} + \mu \Phi \quad (1.75)$$

In the special case where the flow can be modeled as incompressible and two-dimensional, the viscous dissipation function reduces to

$$\Phi = 2 \left[\left(\frac{\partial \hat{V}_x}{\partial x} \right)^2 + \left(\frac{\partial \hat{V}_y}{\partial y} \right)^2 \right] + \left(\frac{\partial \hat{V}_x}{\partial y} + \frac{\partial \hat{V}_y}{\partial x} \right)^2 \quad (1.76)$$

To express eq. (1.74) in terms of enthalpy, the definition

$$h = u + Pv = u + \frac{P}{\rho}$$

is invoked. Hence,

$$\frac{Dh}{Dt} = \frac{Du}{Dt} + \frac{1}{\rho} \frac{DP}{Dt} - \frac{P}{\rho^2} \frac{D\rho}{Dt} \quad (1.77)$$

Moreover, the heat fluxes q_x'' and q_y'' can be expressed in terms of local temperature gradients through use of Fourier's law:

$$\mathbf{q}'' = -k \nabla T \quad (1.78)$$

Thus, the combination of eqs. (1.74), (1.77), and (1.78) results in

$$\rho \frac{Dh}{Dt} = \nabla \cdot (k \nabla T) + q''' + \frac{DP}{Dt} + \mu \Phi - \frac{P}{\rho} \left(\frac{D\rho}{Dt} + \rho \nabla \cdot \hat{\mathbf{V}} \right) \quad (1.79)$$

Here, too, eq. (1.53) points out that the terms in parentheses in eq. (1.79) are equal to zero, so that eq. (1.75) reduces to

$$\rho \frac{Dh}{Dt} = \nabla \cdot (k \nabla T) + q''' + \frac{DP}{Dt} + \mu \Phi \quad (1.80)$$

Bejan (1995) points out that the change in specific enthalpy for a single-phase fluid is given by

$$dh = T ds + v dP = T ds + \frac{dP}{\rho} \quad (1.81)$$

where T is the absolute temperature and ds is the specific entropy change:

$$ds = \left(\frac{ds}{dT} \right)_P dT + \left(\frac{ds}{dP} \right)_T dP \quad (1.82)$$

The last of the Maxwell relations given by Bejan (1997)

$$\left(\frac{\partial s}{\partial P} \right)_T = - \left[\frac{\partial(1/\rho)}{\partial T} \right]_P = \frac{1}{\rho^2} \left(\frac{\partial \rho}{\partial T} \right)_P = - \frac{\beta}{\rho} \quad (1.83)$$

where β is the *volumetric coefficient of thermal expansion*,

$$\beta = - \frac{1}{\rho} \left(\frac{\partial \rho}{\partial T} \right)_P \quad (1.84)$$

With c_p taken as the *specific heat at constant pressures*, it can be shown that

$$\left(\frac{ds}{dT} \right)_P = \frac{c_p}{T} \quad (1.85)$$

and eqs. (1.81) through (1.85) can be combined,

$$dh = c_p dT + \frac{1}{\rho} (1 - \beta T) dP \quad (1.86)$$

so that the left-hand side of eq. (1.80) can be written as

$$\rho \frac{Dh}{Dt} = \rho c_p \frac{DT}{Dt} + (1 - \beta T) \frac{DP}{Dt} \quad (1.87)$$

Thus, the temperature formulation of the first law of thermodynamics is

$$\rho c_p \frac{DT}{Dt} = \nabla \cdot (k \nabla T) + q''' + \beta T \frac{DT}{Dt} + \mu \Phi \quad (1.88)$$

with the special forms for the ideal gas where $\beta = 1/T$,

$$\rho c_p \frac{DT}{Dt} = \nabla \cdot (k \nabla T) + q''' + \frac{DP}{Dt} + \mu \Phi \quad (1.89a)$$

and for an incompressible fluid where $\beta = 0$,

$$\rho c_p \frac{DT}{Dt} = \nabla \cdot (k \nabla T) + q''' + \mu \Phi \quad (1.89b)$$

Most convection problems concern an even simpler model where the fluid has constant thermal conductivity k , negligible viscous dissipation Φ , zero internal heat

generation ($q''' = 0$), and a negligible compressibility effect, $\beta T(DP/Dt) \approx 0$. The energy equation for this model is simply

$$\rho c_p \frac{DT}{Dt} = k \nabla^2 T \quad (1.90)$$

or, in the rectangular coordinate system,

$$\rho c_p \left(\frac{\partial T}{\partial t} + \hat{V}_x \frac{\partial T}{\partial x} + \hat{V}_y \frac{\partial T}{\partial y} + \hat{V}_z \frac{\partial T}{\partial z} \right) = k \left(\frac{\partial^2 T}{\partial x^2} + \frac{\partial^2 T}{\partial y^2} + \frac{\partial^2 T}{\partial z^2} \right) \quad (1.91)$$

in the cylindrical coordinate system,

$$\begin{aligned} \rho c_p \left(\frac{\partial T}{\partial t} + \hat{V}_r \frac{\partial T}{\partial r} + \frac{\hat{V}_\theta}{r} \frac{\partial T}{\partial \theta} + \hat{V}_z \frac{\partial T}{\partial z} \right) \\ = k \left[\frac{1}{r} \frac{\partial}{\partial r} \left(r \frac{\partial T}{\partial r} \right) + \frac{1}{r^2} \frac{\partial^2 T}{\partial \theta^2} + \frac{\partial^2 T}{\partial z^2} \right] \end{aligned} \quad (1.92)$$

and in the spherical coordinate system,

$$\begin{aligned} \rho c_p \left(\frac{\partial T}{\partial t} + \hat{V}_r \frac{\partial T}{\partial r} + \frac{\hat{V}_\phi}{r} \frac{\partial T}{\partial \phi} + \frac{\hat{V}_\theta}{r \sin \phi} \frac{\partial T}{\partial \theta} \right) \\ = k \left[\frac{1}{r^2} \frac{\partial}{\partial r} \left(r^2 \frac{\partial T}{\partial r} \right) + \frac{1}{r^2 \sin \phi} \frac{\partial}{\partial \phi} \left(\sin \phi \frac{\partial T}{\partial \phi} \right) + \frac{1}{\sin^2 \phi} \frac{\partial^2 T}{\partial \theta^2} \right] \end{aligned} \quad (1.93)$$

If the fluid can be modeled as incompressible then, as in eq. (1.89b), the specific heat at constant pressure c_p is replaced by c . And when dealing with extremely viscous flows, the model is improved by taking into account the internal heating due to viscous dissipation,

$$\rho c_p \frac{DT}{Dt} = k \nabla^2 T + \mu \Phi \quad (1.94)$$

In the rectangular coordinate system, the viscous dissipation can be expressed as

$$\begin{aligned} \Phi = 2 \left[\left(\frac{\partial \hat{V}_x}{\partial x} \right)^2 + \left(\frac{\partial \hat{V}_y}{\partial y} \right)^2 + \left(\frac{\partial \hat{V}_z}{\partial z} \right)^2 \right] \\ + \left(\frac{\partial \hat{V}_x}{\partial y} + \frac{\partial \hat{V}_y}{\partial x} \right)^2 + \left(\frac{\partial \hat{V}_y}{\partial z} + \frac{\partial \hat{V}_z}{\partial y} \right)^2 + \left(\frac{\partial \hat{V}_z}{\partial x} + \frac{\partial \hat{V}_x}{\partial z} \right)^2 \\ - \frac{2}{3} \left(\frac{\partial \hat{V}_x}{\partial x} + \frac{\partial \hat{V}_y}{\partial y} + \frac{\partial \hat{V}_z}{\partial z} \right)^2 \end{aligned} \quad (1.95)$$

in the cylindrical coordinate system as

$$\begin{aligned}\Phi = 2 \left[\left(\frac{\partial \hat{V}_r}{\partial r} \right)^2 + \left(\frac{1}{r} \frac{\partial \hat{V}_\theta}{\partial \theta} + \frac{\hat{V}_r}{r} \right)^2 + \left(\frac{\partial \hat{V}_z}{\partial z} \right)^2 \right. \\ \left. + \frac{1}{2} \left(\frac{\partial \hat{V}_\theta}{\partial r} - \frac{\hat{V}_\theta}{r} + \frac{1}{r} \frac{\partial \hat{V}_r}{\partial \theta} \right)^2 + \frac{1}{2} \left(\frac{1}{r} \frac{\partial \hat{V}_z}{\partial \theta} + \frac{\partial \hat{V}_\theta}{\partial z} \right)^2 \right. \\ \left. + \frac{1}{2} \left(\frac{\partial \hat{V}_r}{\partial z} + \frac{\partial \hat{V}_z}{\partial r} \right)^2 - \frac{1}{3} (\nabla \cdot \hat{\mathbf{V}})^2 \right] \quad (1.96)\end{aligned}$$

and in the spherical coordinate system as

$$\begin{aligned}\Phi = 2 \left\{ \left[\left(\frac{\partial \hat{V}_r}{\partial r} \right)^2 + \left(\frac{1}{r} \frac{\partial \hat{V}_\theta}{\partial \phi} + \frac{\hat{V}_r}{r} \right)^2 + \left(\frac{1}{r \sin \phi} \frac{\partial \hat{V}_\theta}{\partial \theta} + \frac{\hat{V}_r}{r} + \frac{\hat{V}_\phi \cot \phi}{r} \right)^2 \right] \right. \\ \left. + \frac{1}{2} \left[r \frac{\partial}{\partial r} \left(\frac{\hat{V}_\phi}{r} \right) + \frac{1}{r} \frac{\partial \hat{V}_r}{\partial \phi} \right]^2 + \frac{1}{2} \left[\frac{\sin \phi}{r} \frac{\partial}{\partial \phi} \left(\frac{\hat{V}_\theta}{r \sin \phi} \right) + \frac{1}{r \sin \phi} \frac{\partial \hat{V}_\theta}{\partial \theta} \right]^2 \right. \\ \left. + \frac{1}{2} \left[\frac{1}{r \sin \phi} \frac{\partial \hat{V}_r}{\partial \theta} + r \frac{\partial}{\partial r} \left(\frac{\hat{V}_\theta}{r} \right) \right]^2 \right\} - \frac{2}{3} (\nabla \cdot \hat{\mathbf{V}})^2 \quad (1.97)\end{aligned}$$

1.6 DIMENSIONAL ANALYSIS

Bejan (1995) provides a discussion of the rules and promise of *scale analysis*. *Dimensional analysis* provides an accounting of the dimensions of the variables involved in a physical process. The relationship between the variables having a bearing on friction loss may be obtained by resorting to such a dimensional analysis whose foundation lies in the fact that all equations that describe the behavior of a physical system must be dimensionally consistent. When a mathematical relationship cannot be found, or when such a relationship is too complex for ready solution, dimensional analysis may be used to indicate, in a semiempirical manner, the form of solution. Indeed, in considering the friction loss for a fluid flowing within a pipe or tube, dimensional analysis may be employed to reduce the number of variables that require investigation, suggest logical groupings for the presentation of results, and pave the way for a proper experimental program.

One method for conducting a dimensional analysis is by way of the *Buckingham- π theorem* (Buckingham, 1914): If r physical quantities having s fundamental dimensions are considered, there exists a maximum number q of the r quantities which, in themselves, cannot form a dimensionless group. This maximum number of quantities q may never exceed the number of s fundamental dimensions (i.e., $q \leq s$). By combining each of the remaining quantities, one at a time, with the q quantities, n

dimensionless groups can be formed, where $n = r - q$. The dimensionless groups are called π terms and are represented by $\pi_1, \pi_2, \pi_3, \dots$.

The foregoing statement of the Buckingham- π theorem may be illustrated quite simply. Suppose there are eight variables that are known or assumed to have a bearing on a certain problem. Then $r = 8$ and if it is desired to express these variables in terms of four physical dimensions, such as length L , mass M , temperature θ , and time T , then $s = 4$. It is then possible to have $q = r - s = 8 - 4 = 4$ physical quantities, which, by themselves, cannot form a dimensionless group.

The usual practice is to make $q = s$ in order to minimize labor. Moreover, the q quantities should be selected, if possible, so that each contains each of the physical quantities at least once. Thus, if $q = 4$, there will be $n = r - q = 8 - 4 = 4$ different π terms, and the functional relationship in the equation that relates the eight variables will be

$$f(\pi_1, \pi_2, \pi_3, \pi_4)$$

1.6.1 Friction Loss in Pipe Flow

It is expected that the pressure loss per unit length of pipe or tube will be a function of the mean fluid velocity \hat{V} , the pipe diameter d , the pipe roughness e , and the fluid properties of density ρ and dynamic viscosity μ . These variables are assumed to be the only ones having a bearing on $\Delta P/L$ and may be related symbolically by

$$\frac{\Delta P}{L} = f(\hat{V}, d, e, \rho, \mu)$$

Noting that $r = 6$, the fundamental dimensions of mass M , length L , and time T are selected so that $s = 3$. This means that the maximum number of variables that cannot, by themselves, form a dimensionless group will be $q = r - s = 6 - 3 = 3$.

The variables themselves, together with their dimensions, are displayed in Table 1.1. Observe that because mass in kilograms is a fundamental dimension, pressure must be represented by N/m^2 , not kg/m^2 . Pressure is therefore represented by $F/A = mg/A$ and dimensionally by $MLT^{-2}/L^2 = M/LT^2$.

Suppose that v , ρ , and d are selected as the three primary quantities ($q = 3$). These clearly contain all three of the fundamental dimensions and there will be $n = r - q = 6 - 3 = 3$ dimensionless π groups:

$$\pi_1 = \frac{\Delta P}{L} \hat{V}^a \rho^b d^c$$

$$\pi_2 = e \hat{V}^a \rho^b d^c$$

$$\pi_3 = \mu \hat{V}^a \rho^b d^c$$

In each of the π groups, the exponents are collected and equated to zero. The equations are then solved simultaneously for the exponents. For π_1 ,

TABLE 1.1 Variables and Dimensions for the Example of Section 1.6.1, SI System

Variable	Dimension
Pressure loss ΔP	M/LT^2
Length L	L
Velocity V	L/T
Diameter d	L
Roughness e	L
Density ρ	M/L^3
Viscosity μ	M/LT
Pressure loss per unit length $\Delta P/L$	M/L^2T^2

$$\pi_1 = \frac{\Delta P}{L} \hat{V}^a \rho^b d^c = \frac{M}{L^2 T^2} \left(\frac{L}{T} \right)^a \left(\frac{M}{L^3} \right)^b L^c$$

Then

$$\begin{aligned} M: \quad 0 &= 1 + b \\ L: \quad 0 &= -2 + a - 3b + c \\ T: \quad 0 &= -2 - a \end{aligned}$$

A simultaneous solution quickly yields $a = -2$, $b = -1$, and $c = +1$, so that

$$\pi_1 = \frac{\Delta P}{L} \hat{V}^{-2} \rho^{-1} d = \frac{\Delta P d}{\rho L \hat{V}^2} = \frac{\Delta P}{(L/d) \rho \hat{V}^2}$$

For π_2 ,

$$\pi_2 = e \hat{V}^a \rho^b d^c = L \left(\frac{L}{T} \right)^a \left(\frac{M}{L^3} \right)^b L^c$$

Then

$$\begin{aligned} M: \quad 0 &= b \\ L: \quad 0 &= 1 + a - 3b + c \\ T: \quad 0 &= -a \end{aligned}$$

This time, the simultaneous solution provides $a = b = 0$ and $c = -1$, so that

$$\pi_2 = e d^{-1} = \frac{e}{d}$$

For π_3 ,

$$\pi_3 = \mu \hat{V}^a \rho^b d^c = \frac{M}{LT} \left(\frac{L}{T} \right)^a \left(\frac{M}{L^3} \right)^b L^c$$

Then

$$\begin{aligned} M: \quad 0 &= 1 + b \\ L: \quad 0 &= -1 + a - 3b + c \\ T: \quad 0 &= -1 - a \end{aligned}$$

from which $a = b = c = -1$, so that

$$\pi_3 = \mu \hat{V}^{-1} \rho^{-1} d^{-1} = \frac{\mu}{\rho \hat{V} d}$$

the reciprocal of the Reynolds number.

Let a friction factor f be defined as

$$f = \frac{2(\Delta P/L)d}{\rho \hat{V}^2} \quad (1.98)$$

such that the pressure loss per unit length will be given by

$$\frac{\Delta P}{L} = \frac{\rho f \hat{V}^2}{2d} \quad (1.99)$$

Equation (1.99) is a modification of the *Darcy–Fanning* head-loss relationship, and the friction factor defined by eq. (1.95), as directed by the dimensional analysis, is a function of the Reynolds number and the *relative roughness* of the containing pipe or tube. Hence,

$$f = \frac{2g(\Delta P/L)}{\rho \hat{V}^2 d} = \phi \left(\frac{\rho \hat{V} d}{\mu}, \frac{e}{L} \right) \quad (1.100)$$

A representation of eq. (1.100) was determined by Moody (1944) (see Fig. 5.13).

1.6.2 Summary of Dimensionless Groups

A summary of the dimensionless groups used in heat transfer is provided in Table 1.2. A summary of the dimensionless groups used in mass transfer is provided in Table 1.3. Note that when there can be no confusion regarding the use of the Stanton and Stefan numbers, the Stefan number, listed in Table 1.2, is sometimes designated as St.

TABLE 1.2 Summary of Dimensionless Groups Used in Heat Transfer

Group	Symbol	Definition
Bejan number	Be	$\Delta P L^2 / \mu \alpha$
Biot number	Bi	$h L / k$
Colburn j -factor	j_h	$St \cdot Pr^{2/3}$
Eckert number	Ec	$\hat{V}_\infty^2 / c_p (T_w - T_\infty)$
Elenbass number	El	$\rho^2 \beta g c_p z^4 \Delta T / \mu k L$
Euler number	Eu	$\Delta P / \rho \hat{V}^2$
Fourier number	Fo	$\alpha t / L^2$
Froude number	Fr	$\hat{V}^2 / g L$
Graetz number	Gz	$\rho c_p \hat{V} d^2 / k L$
Grashof number	Gr	$g \beta \Delta T L^3 / \nu^2$
Jakob number	Ja	$\rho_l c_{pl} (T_w - T_{sat}) / \rho g g h_{fg}$
Knudsen number	Kn	λ / L
Mach number	Ma	\hat{V} / a
Nusselt number	Nu	$h L / k$
Péclet number	Pe	$Re \cdot Pr = \rho c_p \hat{V} L / k$
Prandtl number	Pr	$c_p \mu / k = \nu / \alpha$
Rayleigh number	Ra	$Gr \cdot Pr = \rho g \beta \Delta T L^3 / \mu \alpha$
Reynolds number	Re	$\rho \hat{V} L / \mu$
Stanton number	St	$Nu / Re \cdot Pr = h / \rho c_p \hat{V}$
Stefan number	Ste	$c_p (T_w - T_m) / h_{sf}$
Strouhal number	Sr	$L f / \hat{V}$
Weber number	We	$\rho \hat{V}^2 L / \sigma$

TABLE 1.3 Summary of Dimensionless Groups Used in Mass Transfer

Group	Symbol	Definition
Biot number	Bi	$h_D L / D$
Colburn j -factor	j_D	$ST_D \cdot Sc^2/3$
Lewis number	Le	$Sc / Pr = \alpha / D$
Péclet number	Pe_D	$Re \cdot Sc = \hat{V} L / D$
Schmidt number	Sc	ν / D
Sherwood number	Sh	$h_D L / D$
Stanton number	St_D	$Sh / Re \cdot Sc = h_D / \hat{V}$

1.7 UNITS

As shown in Table 1.4, there are seven primary dimensions in the SI system of units and eight in the English engineering system. Luminous intensity and electric current are not used in a study of heat transfer and are not considered further.

TABLE 1.4 Primary Dimensions and Units for the SI and English Engineering Systems

Dimension (Quantity)	Unit and Symbol	
	SI System	English System
Mass	kilogram (kg)	pound-mass (lb _m)
Length	meter (m)	foot (ft)
Time	second (s)	second (s)
Temperature	kelvin (K)	rankine (°R)
Amount of substance	mole (mol)	mole (mol)
Luminous intensity	candela (Cd)	candle
Electric current	ampere (A)	ampere (A)
Force	newton (N)	pound-force (lb _f)

1.7.1 SI System (Système International d'Unités)

The SI system of units is an extension of the metric system and has been adopted in many countries as the only system accepted legally. The primary dimensions used in a study of the thermal sciences embrace the first five entries in the center column of Table 1.1. There are standards for all these units. For example, the standard for the second is the duration of 9,192,631,770 periods, corresponding to the transition states between two levels of the ground state of the cesium-133 atom.

The mole is defined as the molecular weight of a substance expressed in the appropriate mass unit. For example, a gram-mole (g-mol) of nitrogen contains 28.01 grams (g) and 1 kg-mol of nitrogen contains 28.01 kilograms (kg). The number of moles of a substance, N , is related to its mass m and molecular weight by the simple expression

$$N = \frac{m}{M} \quad (1.101)$$

In the SI system, force is a secondary dimension. The unit of force is therefore a secondary or derived unit and is the *newton* (N), which can be obtained from Newton's second law, $F = ma$, as

$$1 \text{ N} = 1 \text{ kg}(\text{m}/\text{s}^2) = 1 \text{ kg} \cdot \text{m}/\text{s}^2$$

and the constant of proportionality is unity, or

$$\frac{1 \text{ N} \cdot \text{s}^2}{\text{kg} \cdot \text{m}} = 1 \quad (1.102)$$

Because pressure is force per unit area, $P = F/A$, the unit of pressure, the *pascal* (Pa), can be expressed as

$$1 \text{ Pa} = 1 \text{ N}/\text{m}^2 = (1 \text{ kg} \cdot \text{m}/\text{s}^2)(1/\text{m}^2) = \frac{1 \text{ kg}}{\text{m} \cdot \text{s}^2} \quad (1.103)$$

A work interaction, or work, is represented by

$$\delta W = Fx$$

The unit of work or *energy* is the *joule* (J), defined as

$$W = 1 \text{ J} = 1 \text{ N} \cdot \text{m} \quad (1.104)$$

and because *power* P is the rate of doing work, the unit of power is the *watt*:

$$P = \frac{dW}{dt} = \dot{W} = 1 \text{ J/s} = 1 \text{ N} \cdot \text{m/s} \quad (1.105)$$

Note that quantities that pertain to a rate can be designated by a dotted quantity.

Observe that the *weight* of a body is equal to the force of gravity on the body. Hence, weight always refers to a force, and in the SI system this force is always in newtons. The mass of the body can always be related to its weight via

$$W = mg \quad (1.106)$$

where g , the local gravitational acceleration, has a mean value at sea level of

$$g = 9.807 \text{ m/s}^2$$

and is a function of location. This shows that the weight of a body may vary, whereas the mass of the body is always the same.

1.7.2 English Engineering System (U.S. Customary System)

The *English engineering system* (sometimes referred to as the *U.S. customary system* of units) is often used in the United States. This system takes the first five entries and the last entry in the right-hand column of Table 1.4. Here both mass and force are taken as primary dimensions and the pound is used as the unit of mass (the lb_m) and the unit of force (the lb_f). This leads to more than a little confusion when this system is used.

Because there are now six primary dimensions to be used with Newton's second law, it must be written as

$$F \propto ma$$

When the proportionality constant g_c is inserted, the result is

$$F = \frac{ma}{g_c} \quad (1.107)$$

with $g_c = 32.174 \text{ ft/s}^2$ taken as the *standard acceleration of gravity*. This means that a force of 1 lb_f will accelerate a mass of 1 lb_m at a rate of 32.174 ft/s^2 . Thus,

$$1 \text{ lb}_f = \frac{(32.174 \text{ ft/s}^2)(1 \text{ lb}_m)}{g_c}$$

or

$$g_c = \frac{32.174 \text{ lb}_m\text{-ft}}{\text{lb}_f\text{-s}^2} \quad (1.108)$$

Thus Newton's second law must be written as

$$F = \frac{ma}{32.174} \quad (1.109)$$

It is important to remember that the SI system of units does not require this conversion factor.

1.7.3 Conversion Factors

Conversion factors from English engineering units to SI units are given in Table 1.5. Conversion factors for commonly used heat transfer parameters are given in Table 1.6.

TABLE 1.5 Conversion Factors from English Engineering Units to SI Units

To Convert from:	To:	Multiply by:
Acceleration		
ft/sec ²	m/s ²	3.048×10^{-1}
Area		
ft ²	m ²	9.2903×10^{-2}
in ²	m ²	6.4516×10^{-4}
Density		
lb _m /in ³	kg/m ³	2.7680×10^4
lb _m /ft ³	kg/m ³	16.018
Energy, heat, and work		
Btu	J	1.0544×10^3
ft-lb _f	J	1.3558
kW-hr	J	3.60×10^6
Force		
lb _f	N	4.4482
Length		
ft	m	3.048×10^{-1}
in.	m	2.54×10^{-2}
mi	km	1.6093
Mass		
lb _m	kg	4.5359×10^{-1}
ton	kg	9.0718×10^2
Power		
ft-lb _f /min	W	2.2597×10^{-2}
horsepower (hp)	W	7.457×10^2
Pressure		
atm	Pa	1.0133×10^5
lb _f /ft ²	Pa	47.880
lb _f /in ²	Pa	6.8948×10^3
Velocity		
ft/sec	m/s	3.048×10^{-1}
mi/hr	m/s	4.4704×10^{-1}

TABLE 1.6 Conversion Factors for Heat Transfer Parameters from English Engineering Units to SI Units

To Convert from:	To:	Multiply by:
Heat flux		
btu/hr-ft ²	W/m ²	3.1525
kcal/h · m ²	W/m ²	1.163
Heat transfer coefficient		
Btu/hr-ft ² -°F	W/m ² · K	5.678
kcal/h · m ² · °C	W/m ² · K	1.163
Heat transfer rate		
Btu/hr	W	0.2931
Mass flow rate		
lb _m /hr	kg/s	1.26 × 10 ⁻⁴
lb _m /sec	kg/s	4.536 × 10 ⁻¹
Specific heat		
Btu/lb _m -°F	J/kg · K	4.187 × 10 ³
Surface tension		
lb _m /ft	N/m	1.4594 × 10 ¹
Temperature		
1°R	K	0.5555
Thermal conductivity		
Btu/hr-ft-°F	W/m · K	1.731
kcal/h · m · °F	W/m · K	1.163
Thermal diffusivity		
ft ² /sec	m ² /s	9.29 × 10 ⁻²
ft ² /h	m ² /s	2.581 × 10 ⁻⁵
Thermal resistance		
°F-hr/Btu	K/W	1.8958
Viscosity (dynamic)		
lb _m /ft-sec	N · s/m ²	1.4881
centipoise	N · s/m ²	1 × 10 ³
Viscosity (kinematic)		
ft ² /hr	m ² /s	9.29 × 10 ⁻²
ft ² /hr	stoke	929

NOMENCLATURE

Roman Letter Symbols

- A* cross-sectional area, m²
- a* square root of heat source area, m²
speed of sound, m/s
- C* constant, dimensionless
- c* specific heat, W/m · K
- D* substantial differential, dimensionless
mass diffusivity, m²/s

d	differential, dimensionless diameter, m
\mathbf{e}	unit vector, dimensionless
e	roughness, m specific energy, J/kg · K
\mathbf{F}	force vector, N
F	force, N
\mathcal{F}	radiation factor, dimensionless
f	frequency, m ⁻¹
G	mass velocity, kg/m ² · s
g	acceleration of gravity, m/s ²
H	microhardness, N/m ²
h	heat transfer coefficient, W/m ² · K specific enthalpy, J/kg
k	thermal conductivity, W/m · K
L	path length, m physical dimension, dimensionless
M	gas parameter, m physical dimension, kg
m	surface slope, dimensionless mass, kg
\dot{m}	mass flow rate, kg/s
n	number of moles, dimensionless number of dimensionless groups, dimensionless
\mathbf{n}	normal direction, dimensions vary
P	pressure, N/m ²
p	wetted perimeter, m
q	heat flow, W maximum number of quantities, dimensionless
q_g	heat generation, W/m ³
q''	heat flux, W/m ²
q'''	heat generation, W/m ³
\mathbf{q}'	heat flux vector, W/m ²
R	thermal resistance, K/W region, dimensionless
r	radial direction, m radius, m number of physical quantities, dimensionless
S	surface area, m ²
s	specific entropy, J/kg · K scale factor, dimensions vary number of fundamental dimensions, dimensionless
T	temperature, K
t	time, s physical dimension, s

u	specific internal energy, J/kg
V	volume, m^3
\mathbf{V}	velocity vector, m/s
\hat{V}	velocity, m/s
W	width, m
x	length coordinate, m generalized coordinate, dimensions vary
Y	mean plane distance, m
y	length coordinate, m
z	length coordinate, m fin spacing, m

Greek Letter Symbols

α	accommodation parameter, dimensionless thermal diffusivity, m^2/s
β	coefficient of volumetric expansion, m^{-1}
Δ	change, dimensionless
δ	thickness, m
ϵ	area ratio, dimensionless
η	fin efficiency, dimensionless
θ	angle in cylindrical coordinate system, rad angle in spherical coordinate system, rad
Λ	mean free path of molecules, m
μ	dynamic viscosity, $\text{N}/\text{m} \cdot \text{s}$
ν	kinematic viscosity, m^2/s
π	group, dimensionless
ρ	density, kg/m^3
σ	surface roughness, m surface tension, N/m Stefan–Boltzmann constant, $\text{W}/\text{m}^2 \cdot \text{K}^4$ normal stress, N/m^2
τ	shear stress, N/m^2
Φ	viscous dissipation factor, s^{-1}
ϕ	angle in spherical coordinate system, rad
∇	vector operator, s^{-1}
∇^2	Laplacian operator, s^{-2}

Roman Letter Subscripts

c	contact
cd	conduction
co	contact
cv	convection
D	diffusion
e	equivalent
f	fin fluid

fl	flow
g	generated gap
	standard acceleration of gravity
in	inlet condition
ℓ	liquid
m	melting
max	maximum condition
min	minimum condition
n	normal direction
o	nominal value
out	outlet condition
p	constant pressure
r	radiation radial direction
s	harmonic mean surface condition
sat	saturated condition
sp	spreading
sf	surface parameter in boiling
w	wall condition
x	x -coordinate direction
y	y -coordinate direction
z	z -coordinate direction
∞	free stream condition

Greek Letter Subscripts

θ	θ -coordinate direction
ϕ	phase change ϕ -coordinate direction

Superscripts

a	exponent in dimensional analysis
b	exponent in dimensional analysis
c	exponent in dimensional analysis
n	exponent in natural convection correlation

REFERENCES

- Bejan, A. (1995). *Convection Heat Transfer*, 2nd Ed, Wiley, New York.
- Bejan, A. (1997). *Advanced Engineering Thermodynamics*, 2nd Ed, Wiley, New York.
- Bodoia, J. R., and Osterle, J. F. (1964). The development of free convection between heated vertical plates, *Trans. ASME, J. Heat Transfer*, 84, 40–44.

- Buckingham, E. (1914). On Physically Similar Systems: Illustrations of the Use of Dimensional Equations, *Phys. Rev.*, 4(4), 345–376.
- Churchill, S. W., and Usagi, R. (1972). A General Expression for the Correlation of Rates of Heat Transfer and Other Phenomena, *AIChE J.*, 18(6), 1121–1138.
- Elenbaas, W. (1942). Heat Dissipation of Parallel Plates by Free Convection, *Physica*, 9(1), 2–28.
- Hausen, H. (1943). Darstellung des Wärmeüberganges in Rohren durch verallgemeinerte Potenzbeziehungen, *Z. VDI*, 4, 91–98.
- Moody, L. F. (1944). Friction Factors for Pipe Flow, *Trans. ASME*, 66, 671–684.
- Rohsenow, W. M. (1952). A Method for Correlation Heat Transfer Data for Surface Boiling in Liquids, *Trans. ASME*, 74, 969–975.
- Rohsenow, W. M., and Choi, H. Y. (1961). *Heat Mass and Momentum Transfer*, Prentice-Hall, Englewood Cliffs, NJ.
- Sieder, E. N., and Tate, G. E. (1936). Heat Transfer and Pressure Drop of Liquids in Tubes, *Ind. Eng. Chem.*, 28, 1429–1436.
- Yovanovich, M. M., and Antonetti, V. W. (1988). Application of Thermal Contact Resistance Theory to Electronic Packages, in *Advances in Thermal Modeling of Electronic Components and Systems*, A. Bar-Cohen and A. D. Kraus, eds.), Hemisphere Publishing, New York.

Thermophysical Properties of Fluids and Materials*

R. T. JACOBSEN

Idaho National Engineering and Environmental Laboratory
Idaho Falls, Idaho

E. W. LEMMON

Physical and Chemical Properties Division
National Institute of Standards and Technology
Boulder, Colorado

S. G. PENONCELLO and Z. SHAN

Center for Applied Thermodynamic Studies
College of Engineering
University of Idaho
Moscow, Idaho

N. T. WRIGHT

Department of Mechanical Engineering
University of Maryland
Baltimore, Maryland

2.1 Introduction

2.2 Thermophysical properties of fluids

2.2.1 Thermodynamic properties

Equation of state

Calculation of properties

Thermodynamic properties of mixtures

2.2.2 Transport properties

Extended corresponding states

Dilute-gas contributions

Density-dependent contributions

Transport properties of mixtures

2.3 Thermophysical properties of solids

2.3.1 Conservation of energy

2.3.2 Behavior of thermophysical properties of solids

*The material in this chapter is a contribution in part of the National Institute of Standards and Technology, not subject to copyright in the United States. We gratefully thank Mark McLinden for permission to use portions of his work for the section on extended corresponding states, as well as the help and suggestions of Daniel Friend and Joan Sauerwein, all of the National Institute of Standards and Technology.

- 2.3.3 Property values of solid materials
- 2.3.4 Measuring thermophysical properties of solids
 - Thermal conductivity
 - Specific heat
 - Thermal diffusivity
 - Thermal expansion
- Nomenclature
- References
- Graphs of thermophysical properties

2.1 INTRODUCTION

The need for accurate thermophysical properties in the design and analysis of engineered systems is well established. The industrial applications of various working fluids and solids require a variety of property values with accuracies that range from crude estimates to precisions of 1 part in 10,000 for some sensitive applications. It is particularly true that small errors in properties for custody transfer of fluids can result in significant costs or benefits to those involved in commercial transactions. It is the responsibility of the engineer to decide what level of accuracy is needed for a particular application and to establish the uncertainty of the related design or analysis in light of the accuracy of the properties used.

In addition to the individual properties for system design and analysis, there is a need for combined heat transfer parameters and dimensionless groups that occur in equations for conduction, convection, and radiation. These include:

Biot number	Boussinesq number	Eckert number
Fourier number	Graetz number	Grashof number
Lewis number	Nusselt number	Péclet number
Prandtl number	Rayleigh number	Reynolds number
Schmidt number	Sherwood number	

Only the Prandtl number is a fluid property; the others incorporate system characteristics such as velocity, length, or diameter. These groups are defined elsewhere in this book and are not discussed in this chapter.

The term *thermophysical properties* is used here to refer to both thermodynamic (equilibrium) properties and transport properties. The thermodynamic properties define equilibrium states of the system and include such properties as temperature, pressure, density, internal energy, heat capacity, speed of sound, enthalpy, and entropy. The transport properties are those such as thermal conductivity, viscosity, and thermal diffusivity which pertain to the transfer of momentum or energy within the system. In a practical sense, design and analysis of heat transfer systems require information about both transport and thermodynamic properties. The thermodynamic properties are generally well defined by measurement for most common fluids and

mixtures and are usually of higher accuracy than the transport properties available for the same fluids and mixtures. This is, in part, because the experimental methods for measuring transport properties are generally less accurate than those for the thermodynamic properties, although the state of the art is improving for such measurements (see Wakeham et al., 1991).

Current practice in the design and analysis of fluid systems requires the use of computer programs in various forms for thermophysical properties. Based on the experience of the authors in the development and evaluation of computer programs for engineered systems, we recommend the use of the most accurate computer databases available to the engineer. Such sources of highly accurate properties are often referred to as *standard reference quality* sources, and many are the result of international agreements among qualified experts on the current best values of properties. A typical accurate equation of state is a polynomial with 15 to 35 terms, as described later. If special applications require equations with fewer terms for rapidly estimating properties or for calculating abbreviated tables, these can be developed based on properties calculated by means of the best available models, and estimates of uncertainties in the properties used in design can be determined by comparisons to values from the source, the accuracies of which are generally well specified.

We have assumed that the user of this book has access to a reasonably current personal computer and to the World Wide Web. Because the National Institute of Standards and Technology (NIST) databases generally incorporate the best available fluid properties algorithms and equations, we rely heavily on those sources in the recommended values given in this chapter. We provide summary tables of properties of common fluids and materials for estimating purposes and, at the end of the chapter, graphical comparisons of various properties of different fluids to assist in the selection of materials for design. We have not, in general, attempted to repeat tabular values for fluid properties that are readily available in other sources, including common engineering textbooks and other handbooks, although some general tables of property values at common conditions are given for completeness.

The values of the thermodynamic and transport properties for a large number of fluids may be calculated using several comprehensive computer programs from NIST, including NIST Standard Reference Databases 10, 12, 14, and 23. A limited computer program is included in this book for use in calculating properties for design and analysis of heat transfer systems using the most common fluids. Some properties are also available on the NIST Chemistry Webbook at <http://webbook.nist.gov/chemistry>.

Although the NIST programs provide the most accurate values currently available, additional research, experimentation, and correlation activities worldwide will increase the accuracy, the number of fluids, and the ranges of available states for the covered fluids. The full programs with source code and mixture capabilities are available from NIST at a nominal cost and are updated periodically. Details concerning the current databases available from the Standard Reference Data Office of NIST are located at the Web address <http://www.nist.gov/srd> by searching for the key words NIST10, NIST12, NIST14, or NIST23.

There are fewer sources of properties of solids for design than there are for fluids, and the data available have not yet been incorporated into evaluated wide-range computer models. The uncertainties associated with published values for many properties

of solids are generally larger than those for properties of fluids, in part because of impurities or compositional variations in experimental samples. In this chapter we have included selected properties of solids from reliable published sources.

This chapter contains a minimum of theory and no details on the correlation and analysis of thermophysical property data for determining the recommended values for both fluids and solids. Literature references are given for the best available sources known for the various properties. The references should be useful to the reader who is interested in greater detail about the correlation methods and about the data on which the correlations and recommended values are based.

2.2 THERMOPHYSICAL PROPERTIES OF FLUIDS

The thermodynamic and transport properties of fluids are discussed separately in this section. Sources of calculated values and brief descriptions of the methods used to determine values in the tables and graphs in this book are given. References to original works that contain details of both correlation and measurement techniques are also included.

2.2.1 Thermodynamic Properties

A *property formulation* is the set of equations used to calculate properties of a fluid at specified thermodynamic states defined by the appropriate independent variables. A typical thermodynamic property formulation is based on an equation of state that allows the correlation and computation of all thermodynamic properties of the fluid, including properties such as entropy that cannot be measured directly.

The general term *equation of state* in this chapter refers to an empirical model developed for calculating thermodynamic properties of fluids. The term *fundamental equation* is often used in the literature to refer to empirical descriptions of one of four fundamental relations: internal energy as a function of volume and entropy, enthalpy as a function of pressure and entropy, Gibbs energy as a function of pressure and temperature, and Helmholtz energy as a function of density and temperature. Modern equations of state for the thermodynamic properties of pure fluids are usually fundamental equations explicit in the Helmholtz energy as a function of density and temperature.

The equation of state for a pure fluid using the Helmholtz energy as the fundamental property is given by

$$a(\rho, T) = a^0(\rho, T) + a^r(\rho, T) \quad (2.1)$$

where a is the molar Helmholtz energy, $a^0(\rho, T)$ is the ideal gas contribution to the Helmholtz energy, and $a^r(\rho, T)$ is the residual Helmholtz energy that corresponds to the influence of intermolecular forces. All thermodynamic properties can be calculated as derivatives of the Helmholtz energy. For example, the pressure derived from this expression is

$$p = \rho^2 \left(\frac{\partial a}{\partial \rho} \right)_T \quad (2.2)$$

Also, the thermodynamic properties at saturation conditions can be calculated without additional ancillary equations through the use of the Maxwell criterion (equal pressures and Gibbs energies at constant temperature during phase changes).

The quality of a thermodynamic property formulation is determined by its ability to model the physical behavior of the fluid as represented by the available data as well as by its conformance to theory (to assure reasonable extrapolation behavior). Published correlations should include estimates of the accuracy of calculated properties as well as a careful definition of the range of validity. A modern thermodynamic property formulation is generally capable of representing all data values within the estimated experimental uncertainty of the measurements (see Table 2.1). The practical models of today are empirical or semiempirical in nature, although virtually all are based on sound theoretical principles. The limitations of the model selected must be understood by the user for effective system optimization and related work.

Correct behavior of the equation of state in the critical region (bounded by $\pm 0.25\rho_c$ and $\pm 0.05T_c$) is sometimes a concern of users of property formulations. Classical equations (those that do not use an additional scaling theory) cannot represent the theoretically expected behavior at the critical point. However, state-of-the-art multi-parameter equations of state are sufficiently accurate in the critical region to satisfy

TABLE 2.1 General Standard Uncertainty Estimates for Various Fluid Properties

Calculated Property	Region	State-of-the-Art Experimental Uncertainty (%)	Uncertainty to Be Expected from a Modern Equation of State (%)
Pressure	—	0.02	
Temperature	—	0.001 K	
Density	—	0.02	0.1
Isochoric heat capacity	$\rho > \rho_c$	0.5	0.5
	$\rho < \rho_c$	1	1
Isobaric heat capacity	$\rho > \rho_c$	0.5	1
	$\rho < \rho_c$	2	1
Speed of sound	$\rho > \rho_c$	0.1	0.5
	$\rho < \rho_c$	0.01	0.1
Vapor pressure	$p < 0.1$ MPa	0.05	0.5
	$p > 0.1$ MPa	0.01	0.2
Thermal conductivity	$\rho > \rho_c$	0.5	0.5
	$\rho < \rho_c$	2	2
Viscosity	$\rho > \rho_c$	2	2
	$\rho < \rho_c$	0.5	0.5

most data needs (although they should not be used as the basis for theoretical calculations regarding the limiting behavior at the critical point). Older or less accurate equations of state may show significant shortcomings with regard to the representation of properties in the critical region.

Most modern reference equations of state yield reasonable extrapolation behavior up to the limits of chemical stability of the corresponding substance. However, in general, multiparameter equations of state should not be extrapolated beyond the given range of validity, especially when using older equations or equations where the functional form was not optimized to the experimental data. When extrapolation is necessary, the reliability of the results must be checked carefully, unless reasonable extrapolation behavior is stated explicitly by the authors of the equation. The extrapolation behavior of empirical multiparameter equations of state has been discussed by Span and Wagner (1997) and Span (2000).

Table 2.2 lists sources of recommended multiparameter equations of state that are suitable for use in system design and analysis and in scientific applications. We believe that these are the most accurate published equations available for these fluids. To assess whether an equation is suitable for a certain application, details given in the original publications should be considered. The fluids listed in bold type in Table 2.2 can be considered primary standards with typical uncertainties of 0.02% in density, 0.5% in heat capacities and the liquid speed of sound, and 0.02% in the vapor speed of sound. Properties of italicized fluids are also represented by equations of high accuracy with typical uncertainties in density of 0.1%, 0.5% in heat capacities and the liquid speed of sound, and 0.1% in the vapor speed of sound. The uncertainties of the correlations for the other fluids are generally greater depending on the quality of data used in the fit and the ability of the correlator to develop a thermodynamically consistent equation with proper extrapolation behavior. Uncertainties in viscosities and thermal conductivities are generally within 2% for fluids with published equations. The uncertainty rises for fluids using extended corresponding states (ECS) techniques that were fitted to data, and can exceed 10% for those fluids that use the ECS model in a purely predictive mode (see Section 2.2.2).

Table 2.3 displays the molecular weight, critical temperature, critical pressure, critical density, triple-point temperature, normal boiling point temperature (at 0.101325 MPa), acentric factor (defined as $[-\log(p_{\text{sat}}/p_c) - 1]$ at $T/T_c = 0.7$), and dipole moment for the fluids listed in Table 2.2. These values were taken from the references listed in Table 2.2. Tables 2.4, 2.5, and 2.6 give the ideal gas isobaric heat capacity, dilute gas thermal conductivity, and dilute gas viscosity. The thermodynamic and transport properties along the saturated liquid and vapor lines are given in Table 2.7. Values of the thermodynamic properties, transport properties, and surface tension given in these tables were calculated using NIST databases. Additional details of the fitted equations are given in the databases.

Equation of State The functional form for the equation of state used for the fluid properties given here is explicit in the dimensionless Helmholtz energy α , using independent variables of dimensionless density and temperature. The form of this equation is

TABLE 2.2 Equations of State and Transport Equations for Pure Fluids^a

Fluid	Equation of State	Thermal Conductivity Equation	Viscosity Equation	Temp. Range (K) (EOS)	Max. Pressure (MPa)
Methane	Setzmann and Wagner (1991)	Friend et al. (1989)	Younglove and Ely (1987)	90.6941–625	1000
<i>Ethane</i>	<i>Friend et al. (1991)</i>	Friend et al. (1991)	Friend et al. (1991)	90.352–625	70
<i>Propane</i>	<i>Miyamoto and Watanabe (2000)</i>	Marsh et al. (2002)	Vogel et al. (1998)	85.48–623	103
Butane	Miyamoto and Watanabe (2001a)	Perkins et al. (2002)	Vogel et al. (1999)	134.87–589	69
Isobutane	Miyamoto and Watanabe (2001b)	Perkins (2002)	Vogel et al. (2000)	113.56–573	35
Pentane	Span (2000)	NIST14, Version 9.08	NIST14, Version 9.08	143.47–600	100
Isopentane	Polt et al. (1992)	NIST14, Version 9.08	NIST14, Version 9.08	200–553	7.5
Neopentane	Polt et al. (1992)	Not currently available	Not currently available	273–498	20
Hexane	Span (2000)	NIST14, Version 9.08	NIST14, Version 9.08	177.83–600	100
Heptane	Span (2000)	NIST14, Version 9.08	NIST14, Version 9.08	182.55–600	100
Octane	Span (2000)	Not currently available	Not currently available	216.37–600	100
<i>Ammonia</i>	<i>Tillner-Roth et al. (1993)</i>	Tufeu et al. (1984)	Fenghour et al. (1995)	195.495–700	1000
Argon	Tegeler et al. (1999)	Lemmon and Jacobsen (2001)	Lemmon and Jacobsen (2001)	83.806–700	1000
Benzene	Polt et al. (1992)	Not currently available	Not currently available	283–635	78
Carbon dioxide	Span and Wagner (1996)	Vesovic et al. (1990)	Fenghour et al. (1998)	216.592–1100	800
Carbon monoxide	Lemmon and Span (2001)	NIST14, Version 9.08	NIST14, Version 9.08	68.127–1000	100
Cyclohexane	Penoncello et al. (1995)	Not currently available	Not currently available	279.47–700	80
Cyclopropane	Polt et al. (1992)	Not currently available	Not currently available	273–473	28
Deuterium	McCarty (1989)	Not currently available	Not currently available	18.71–423	320
Ethylene	Smukala et al. (2000)	Holland et al. (1983)	Holland et al. (1983)	103.986–450	260
<i>Fluorine</i>	<i>de Reuck (1990)</i>	Not currently available	Not currently available	53.4811–300	20
<i>Heavy water</i>	<i>Hill et al. (1982)</i>	IAPWS (1994)	IAPWS (1994)	276.97–800	100
<i>Helium</i>	<i>McCarty and Arp (1990)</i>	Hands and Arp (1981)	Arp et al. (1998)	2.1768–1500	100
Hydrogen (normal)	Younglove (1982)	McCarty and Weber (1972)	McCarty and Weber (1972)	13.957–400	121

continued

TABLE 2.2 Equations of State and Transport Equations for Pure Fluids^a (Continued)

Fluid	Equation of State	Thermal Conductivity Equation	Viscosity Equation	Temp. Range (K) (EOS)	Max. Pressure (MPa)
Hydrogen sulfide	Lemmon and Span (2001)	NIST14, Version 9.08	NIST14, Version 9.08	187.7–760	170
Krypton	Lemmon and Span (2001)	ECS (fitted)	ECS (fitted)	115.77–800	300
Methanol	de Reuck and Craven (1993)	Not currently available	Not currently available	175.61–620	800
Neon	Katti et al. (1986)	ECS (fitted)	ECS (fitted)	24.562–700	700
Nitrogen	Span et al. (2000)	Lemmon and Jacobsen (2001)	Lemmon and Jacobsen (2001)	63.151–2000	2200
Nitrogen trifluoride	Younglove (1982)	Not currently available	Not currently available	85–500	50
Oxygen	Schmidt and Wagner (1985)	Lemmon and Jacobsen (2001)	Lemmon and Jacobsen (2001)	54.361–1000	82
Parahydrogen	Younglove (1982)	McCarty and Weber (1972)	McCarty and Weber (1972)	13.8–400	121
Perfluorobutane	ECS (fitted)	Not currently available	Not currently available	189–500	30
Perfluoropentane	ECS (fitted)	Not currently available	Not currently available	200–500	30
Perfluoropropane	Lemmon and Span (2001)	Not currently available	Not currently available	113–500	30
Propylene	Angus et al. (1980)	Not currently available	Not currently available	100–600	200
Propyne	Polt et al. (1992)	Not currently available	Not currently available	273–474	32
Sulfur dioxide	Polt (1987)	Not currently available	Not currently available	273–523	32
Sulfur hexafluoride	de Reuck et al. (1991)	Not currently available	Not currently available	222.38–525	55
Toluene	Lemmon and Span (2001)	Not currently available	Not currently available	179–750	100
Water	Wagner and Pruss (2002)	IAPWS (1998)	IAPWS (1997)	273.16–1275	1000
Xenon	Lemmon and Span (2001)	McCarty (1989)	McCarty (1989)	161.36–800	300
R-11	Jacobsen et al. (1992)	ECS (fitted)	ECS (fitted)	162.68–625	30
R-113	Marx et al. (1992)	ECS (fitted)	ECS (fitted)	236.93–525	200
R-114	Platzter et al. (1990)	ECS (fitted)	ECS (fitted)	273.15–507	21
R-115	ECS (fitted)	ECS (fitted)	ECS (fitted)	173.76–500	60
R-116	Kozlov (1996)	ECS (predictive)	ECS (predictive)	176–423	50
R-12	Marx et al. (1992)	ECS (fitted)	ECS (fitted)	116.099–525	200

<i>R-123</i>	<i>Younglove and McLinden (1994)</i>	Laesecke et al. (1996)	Tanaka and Sotani (1995)	166–600	40
<i>R-124</i>	<i>de Vries et al. (1995)</i>	ECS (predictive)	ECS (predictive)	120–470	40
<i>R-125</i>	<i>Sunaga et al. (1998)</i>	ECS (fitted)	ECS (fitted)	172.52–500	60
<i>R-13</i>	Magee et al. (2000)	ECS (fitted)	ECS (fitted)	92–403	35
<i>R-134a</i>	<i>Tillner-Roth and Baehr (1994)</i>	Perkins et al. (2000)	Laesecke (2000)	169.85–455	70
<i>R-14</i>	Platzter et al. (1990)	ECS (predictive)	ECS (predictive)	98.94–623	51
<i>R-141b</i>	Lemmon and Span (2001)	ECS (predictive)	ECS (predictive)	169.85–500	100
<i>R-142b</i>	Lemmon and Span (2001)	ECS (fitted)	ECS (fitted)	142.72–500	60
<i>R-143a</i>	<i>Lemmon and Jacobsen (2000)</i>	ECS (fitted)	ECS (fitted)	161.34–650	100
<i>R-152a</i>	<i>Outcalt and McLinden (1996)</i>	Krauss et al. (1996)	Krauss et al. (1996)	154.56–500	60
<i>R-22</i>	<i>Kamei et al. (1995)</i>	ECS (fitted)	ECS (fitted)	115.73–550	60
<i>R-227ea</i>	ECS (fitted)	ECS (fitted)	ECS (fitted)	200–500	60
<i>R-23</i>	<i>Penoncello et al. (2003)</i>	Shan et al. (2000)	Shan et al. (2000)	118.20–475	120
<i>R-236ea</i>	ECS (fitted)	ECS (predictive)	ECS (predictive)	242–500	60
<i>R-236fa</i>	Outcalt and McLinden (1995)	ECS (predictive)	ECS (predictive)	179.52–500	40
<i>R-245ca</i>	ECS (fitted)	ECS (fitted)	ECS (fitted)	200–500	60
<i>R-245fa</i>	ECS (fitted)	ECS (fitted)	ECS (fitted)	200–500	60
<i>R-32</i>	<i>Tillner-Roth and Yokozeki (1997)</i>	ECS (fitted)	ECS (fitted)	136.340–435	70
<i>R-41</i>	Outcalt (1996)	ECS (predictive)	ESC (predictive)	175–500	60
<i>RC318</i>	Platzter et al. (1990)	ECS (predictive)	ECS (predictive)	233.35–623	60

^aThe equations of state for the fluids in bold type can be considered primary standards, and those for the italicized fluids are high-accuracy equations. See the text for additional details.

TABLE 2.3 Physical Constants and Fixed Points

	Molecular Weight (g/mol)	Critical Temperature (K)	Critical Pressure (MPa)	Critical Density (kg/m ³)	Triple Point (K)	Normal Boiling Point (K)	Acentric Factor	Dipole Moment (D)
Methane	16.043	190.56	4.5992	162.66	90.694	111.67	0.0114	0
Ethane	30.070	305.33	4.8718	206.58	90.352	184.55	0.0993	0
Propane	44.096	369.82	4.2471	218.50	85.480	231.06	0.1524	0.083
Butane	58.122	425.13	3.7960	227.84	134.87	272.59	0.2000	0.02
Isobutane	58.122	407.82	3.6400	224.36	113.56	261.48	0.1850	0.132
Pentane	72.149	469.70	3.3700	232.00	143.47	309.21	0.2510	0.37
Isopentane	72.149	460.35	3.3957	236.00	112.65	300.97	0.2296	0.10
Neopentane	72.151	433.75	3.1963	232.00	256.60	282.63	0.1960	0
Hexane	86.175	507.82	3.0340	233.18	177.83	341.86	0.2970	0.05
Heptane	100.20	540.13	2.7360	232.00	182.55	371.53	0.3480	
Octane	114.23	569.32	2.4970	234.90	216.37	398.77	0.3930	
Ammonia	17.030	405.40	11.333	225.00	195.50	239.82	0.2560	1.47
Argon	39.948	150.69	4.8630	535.60	83.806	87.302	−0.0022	0
Benzene	78.108	562.05	4.8940	309.00	278.70	353.23	0.2092	
Carbon dioxide	44.010	304.13	7.3773	467.60	216.59	—	0.2239	0
Carbon monoxide	28.011	132.80	3.4935	303.92	67.127	81.648	0.0510	0.10
Cyclohexane	84.161	553.64	4.0750	273.00	279.47	353.89	0.2093	0.30
Cyclopropane	42.081	398.30	5.5797	258.50	145.70	241.67	0.1305	
Deuterium	4.0282	38.340	1.6653	69.797	18.710	23.309	−0.1750	0
Ethylene	28.054	282.35	5.0418	214.24	103.99	169.38	0.0866	0
Fluorine	37.997	144.41	5.1724	592.86	53.481	85.037	0.0449	0
Heavy water	20.027	643.89	21.671	358.00	276.97	374.56	0.3640	1.90
Helium	4.0026	5.1953	0.2275	69.641	2.1768	4.2304	−0.3820	0
Hydrogen	2.0159	33.190	1.3150	30.118	13.957	20.277	−0.2140	0
Hydrogen sulfide	34.082	373.60	9.1100	337.41	187.70	212.86	0.0960	0.90

Krypton	83.804	209.48	5.5100	908.44	115.77	119.78	−0.0017	0
Methanol	32.042	513.38	8.2158	281.50	175.61	337.63	0.5625	1.70
Neon	20.179	44.492	2.6786	481.91	24.562	27.104	−0.0387	0
Nitrogen	28.013	126.19	3.3958	313.30	63.151	77.355	0.0372	0
Nitrogen trifluoride	71.019	234.00	4.4607	562.47	66.360	144.14	0.1260	0.20
Oxygen	31.999	154.58	5.0430	436.14	54.361	90.188	0.0222	0
Parahydrogen	2.0159	32.938	1.2838	31.360	13.800	20.277	−0.2180	0
Perfluorobutane	238.03	386.33	2.3234	599.84	145.00	271.06	0.3740	
Perfluoropentane	288.03	420.56	2.0450	609.47	200.00	302.90	0.4230	0.14
Perfluoropropane	188.02	345.10	2.6710	628.00	113.00	236.32	0.3210	0.14
Propylene	42.080	365.57	4.6646	223.39	87.950	225.46	0.1408	0.40
Propyne	40.060	402.38	5.6260	244.90	170.50	191.00	0.2040	0.70
Sulfur dioxide	64.066	430.65	7.8800	525.00	197.70	256.61	0.2300	1.60
Sulfur hexafluoride	146.06	318.73	3.7546	743.81	222.38	—	0.2100	0
Toluene	92.138	593.88	4.2380	290.24	179.00	383.70	0.2610	0.40
Water	18.015	647.10	22.064	322.00	273.16	373.12	0.3440	1.855
Xenon	131.30	289.73	5.8400	1099.0	161.36	165.03	0.0036	0
R-11	137.37	471.11	4.4076	554.00	162.68	296.86	0.1888	0.45
R-113	187.38	487.21	3.3922	560.00	236.93	320.74	0.2525	0.803
R-114	170.93	418.83	3.2570	580.00	179.00	276.74	0.2523	0.658
R-115	154.47	353.10	3.1200	613.10	173.76	234.21	0.2520	0.52
R-116	138.01	293.03	3.0420	622.00	176.00	194.98	0.2540	0
R-12	120.91	385.12	4.1361	565.00	116.10	243.40	0.1795	0.51
R-123	152.93	456.83	3.6618	550.00	166.00	300.97	0.2819	1.356
R-124	136.47	395.43	3.6243	560.00	74.000	261.19	0.2881	1.469
R-125	120.02	339.17	3.6290	568.00	172.52	225.02	0.3061	1.563
R-13	104.46	302.00	3.8790	582.88	92.000	191.67	0.1723	0.51
R-134a	102.03	374.21	4.0593	511.90	169.85	247.08	0.3268	2.058
R-14	88.010	227.51	3.7500	625.70	98.940	145.10	0.1785	0
R-141b	116.95	479.96	4.4600	460.00	169.85	305.21	0.2235	2.014

continued

TABLE 2.3 Physical Constants and Fixed Points *(Continued)*

	Molecular Weight (g/mol)	Critical Temperature (K)	Critical Pressure (MPa)	Critical Density (kg/m ³)	Triple Point (K)	Normal Boiling Point (K)	Acentric Factor	Dipole Moment (D)
R-142b	100.50	410.26	4.0700	446.00	142.72	264.04	0.2337	2.14
R-143a	84.041	345.86	3.7610	431.00	161.34	225.91	0.2615	2.34
R-152a	66.051	386.41	4.5168	368.00	154.56	249.13	0.2752	2.262
R-22	86.468	369.30	4.9900	523.84	115.73	232.34	0.2208	1.458
R-227ea	170.03	374.88	2.9290	584.00	146.35	256.71	0.3632	1.456
R-23	70.014	299.29	4.8280	526.50	118.02	191.13	0.2646	1.649
R-236ea	152.04	412.44	3.5020	563.00	—	279.35	0.3794	1.129
R-236fa	152.04	398.07	3.2000	551.29	179.52	271.71	0.3772	1.982
R-245ca	134.05	447.57	3.9250	523.59	—	298.28	0.3536	1.74
R-245fa	134.05	427.20	3.6400	517.00	—	288.05	0.3724	1.549
R-32	52.024	351.25	5.7820	424.00	136.34	221.50	0.2769	1.978
R-41	34.033	317.28	5.8970	316.51	129.82	195.02	0.2012	1.851
RC318	200.04	388.38	2.7775	620.00	233.35	267.18	0.3553	

TABLE 2.4 Ideal Gas Isobaric Heat Capacity (kJ/kg · K)

	100 K	150 K	200 K	250 K	300 K	350 K	400 K	450 K	500 K	550 K	600 K
Methane	2.0742	2.0759	2.0890	2.1360	2.2301	2.3663	2.5312	2.7118	2.8989	3.0868	3.2720
Ethane	1.1871	1.2846	1.4048	1.5617	1.7523	1.9626	2.1785	1.3904	2.5935	2.7858	2.9671
Propane	0.9365	1.1064	1.2714	1.4616	1.6771	1.9050	2.1321	2.3496	2.5537	2.7434	2.9194
Butane	—	1.1579	1.3157	1.4944	1.7024	1.9251	2.1472	2.3595	2.5581	2.7422	2.9126
Isobutane	—	1.0373	1.2359	1.4442	1.6713	1.9078	2.1411	2.3624	2.5681	2.7574	2.9313
Pentane	—	1.1214	1.2966	1.4703	1.6716	1.8915	2.1143	2.3292	2.5313	2.7194	2.8939
Isopentane	—	0.9488	1.1782	1.4163	1.6563	1.8927	2.1210	2.3380	2.5416	2.7308	2.9058
Neopentane	—	—	—	—	1.6849	1.9344	2.1664	2.3840	2.5894	2.7846	2.9704
Hexane	—	—	1.2832	1.4607	1.6625	1.8829	2.1062	2.3212	2.5222	2.7078	2.8786
Heptane	—	—	1.2739	1.4518	1.6565	1.8787	2.1023	2.3164	2.5159	2.6997	2.8684
Octane	—	—	—	1.4453	1.6519	1.8753	2.0988	2.3121	2.5107	2.6934	2.8608
Ammonia	—	—	2.0084	2.0364	2.0953	2.1743	2.2666	2.3681	2.4759	2.5879	2.7024
Argon	0.5203	0.5203	0.5203	0.5203	0.5203	0.5203	0.5203	0.5203	0.5203	0.5203	0.5203
Benzene	—	—	—	—	1.0547	1.2518	1.4337	1.6010	1.7543	1.8941	2.0211
Carbon dioxide	—	—	—	0.7916	0.8458	0.8951	0.9392	0.9786	1.0141	1.0463	1.0755
Carbon monoxide	1.0388	1.0390	1.0390	1.0388	1.0385	1.0384	1.0384	1.0386	1.0390	1.0396	1.0405
Cyclohexane	—	—	—	—	1.2730	1.5342	1.7852	2.0280	2.2591	2.4756	2.6759
Cyclopropane	—	—	—	—	1.3371	1.5814	1.8225	2.0480	2.2519	2.4339	2.5999
Deuterium	7.4682	7.3039	7.2477	7.2459	7.2499	7.2526	7.2570	7.2667	7.2842	7.3108	7.3468
Ethylene	—	1.1999	1.2602	1.3768	1.5338	1.7098	1.8889	2.0169	2.2248	2.3762	2.5166
Fluorine	0.7662	0.7693	0.7812	0.8013	0.8247	0.8475	0.8681	0.8859	0.9012	0.9142	0.9253
Heavy water	—	—	—	—	1.7122	1.7439	1.7788	1.8164	1.8560	1.8971	1.9393
Helium	5.1931	5.1931	5.1931	5.1931	5.1931	5.1931	5.1931	5.1931	5.1931	5.1931	5.1931
Hydrogen	11.195	12.591	13.530	14.045	14.309	14.429	14.473	14.492	14.511	14.529	14.535
Hydrogen sulfide	—	—	0.9809	0.9913	1.0059	1.0241	1.0451	1.0683	1.0931	1.1189	1.1454
Krypton	—	0.2480	0.2480	0.2480	0.2480	0.2480	0.2480	0.2480	0.2480	0.2480	0.2480

continued

TABLE 2.4 Ideal Gas Isobaric Heat Capacity (kJ/kg · K) (Continued)

	100 K	150 K	200 K	250 K	300 K	350 K	400 K	450 K	500 K	550 K	600 K
Methanol	—	—	1.2384	1.2923	1.3775	1.4873	1.6101	1.7368	1.8616	1.9814	2.0952
Neon	1.0301	1.0301	1.0301	1.0301	1.0301	1.0301	1.0301	1.0301	1.0301	1.0301	1.0301
Nitrogen	1.0389	1.0390	1.0391	1.0392	1.0397	1.0412	1.0441	1.0490	1.0559	1.0646	1.0748
Nitrogen trifluoride	0.4793	0.5287	0.6024	0.6809	0.7541	0.8178	0.8711	0.9150	0.9514	0.9830	1.0127
Oxygen	0.9098	0.9098	0.9102	0.9126	0.9183	0.9280	0.9409	0.9558	0.9717	0.9876	1.0030
Parahydrogen	13.408	16.188	16.071	15.329	14.836	14.624	14.573	14.587	14.615	14.633	14.638
Perfluorobutane	—	—	0.6181	0.7188	0.8069	0.8835	0.9495	1.0059	1.0537	1.0938	1.1273
Perfluoropentane	—	—	—	0.7283	0.8176	0.8952	0.9621	1.0192	1.0676	1.1083	1.1422
Perfluoropropane	—	0.5023	0.6100	0.7054	0.7894	0.8627	0.9263	0.9809	1.0274	1.0667	1.0996
Propylene	—	1.0550	1.1898	1.3545	1.5375	1.7259	1.9116	2.0901	2.2592	2.4178	2.5658
Propyne	—	—	—	—	1.5199	1.6703	1.8100	1.9398	2.0602	2.1722	2.2763
Sulfur dioxide	—	—	—	—	0.6229	0.6518	0.6785	0.7029	0.7252	0.7454	0.7635
Sulfur hexafluoride	—	—	—	0.5779	0.6674	0.7397	0.7971	0.8427	0.8790	0.9082	0.9318
Toluene	—	—	0.7409	0.9347	1.1347	1.3316	1.5206	1.6978	1.8608	2.0093	2.1439
Water	—	—	—	—	1.8648	1.8806	1.9018	1.9272	1.9554	1.9852	2.0163
Xenon	—	—	0.1583	0.1583	0.1583	0.1583	0.1583	0.1583	0.1583	0.1583	0.1583
R-11	—	—	0.4719	0.5283	0.5738	0.6106	0.6402	0.6641	0.6836	0.6996	0.7128
R-113	—	—	—	0.5896	0.6501	0.6998	0.7413	0.7761	0.8055	0.8303	0.8513
R-114	—	—	—	—	0.6925	0.7454	0.7912	0.8308	0.8648	0.8933	0.9156
R-115	—	—	0.5458	0.6380	0.7156	0.7801	0.8330	0.8757	0.9098	0.9368	0.9582
R-116	—	—	0.5985	0.6890	0.7722	0.8445	0.9060	0.9580	1.0020	1.0391	1.0707
R-12	—	0.4113	0.4873	0.5511	0.6045	0.6490	0.6860	0.7166	0.7421	0.7633	0.7810
R-123	—	—	0.5312	0.6069	0.6731	0.7310	0.7819	0.8267	0.8667	0.9031	0.9369
R-124	—	0.4935	0.5777	0.6557	0.7284	0.7968	0.8619	0.9247	0.9862	1.0474	1.1092
R-125	—	—	0.6187	0.7079	0.7901	0.8658	0.9345	0.9957	1.0492	1.0957	1.1358
R-13	0.3445	0.4304	0.5081	0.5776	0.6389	0.6921	0.7371	0.7738	0.8024	0.8228	0.8350
R-134a	—	—	0.6457	0.7448	0.8367	0.9230	1.0047	1.0828	1.1577	1.2299	1.2998

R-14	0.3944	0.4576	0.5361	0.6187	0.6972	0.7664	0.8238	0.8698	0.9080	0.9445	0.9887
R-141b	—	—	0.5943	0.6789	0.7562	0.8263	0.8891	0.9445	0.9927	1.0336	1.0673
R-142b	—	0.5331	0.6406	0.7402	0.8319	0.9157	0.9916	1.0596	1.1196	1.1718	1.2160
R-143a	—	—	0.7119	0.8260	0.9329	1.0318	1.1221	1.2038	1.2771	1.3427	1.4015
R-152a	—	—	0.7968	0.9101	1.0259	1.1417	1.2548	1.3626	1.4625	1.5518	1.6278
R-22	—	0.4660	0.5292	0.5915	0.6518	0.7088	0.7613	0.8086	0.8506	0.8877	0.9204
R-227ea	—	—	—	0.7126	0.8018	0.8818	0.9524	1.0138	1.0660	1.1088	1.1424
R-23	—	0.5261	0.5887	0.6590	0.7318	0.8035	0.8712	0.9333	0.9894	1.0393	1.0836
R-236ea	—	—	—	0.7699	0.8505	0.9261	0.9966	1.0621	1.1224	1.1777	1.2278
R-236fa	—	—	0.6610	0.7412	0.8226	0.9052	0.9889	1.0738	1.1598	1.2470	1.3354
R-245ca	—	—	—	0.7738	0.8923	0.9968	1.0874	1.1640	1.2265	1.2751	1.3097
R-245fa	—	—	—	0.7684	0.8640	0.9541	1.0389	1.1183	1.1924	1.2610	1.3243
R-32	—	0.6667	0.7058	0.7597	0.8282	0.9060	0.9871	1.0666	1.1421	1.2124	1.2773
R-41	—	—	0.9882	1.0368	1.1077	1.1955	1.2951	1.4012	1.5085	1.6119	1.7062
RC318	—	—	—	0.7005	0.7848	0.8599	0.9264	0.9848	1.0358	1.0799	1.1178

TABLE 2.5 Dilute Gas Thermal Conductivity (mW/m · K)

	100 K	150 K	200 K	250 K	300 K	350 K	400 K	450 K	500 K	550 K	600 K
Methane	9.9026	15.868	21.802	27.874	34.479	41.870	50.076	59.003	68.524	78.519	88.889
Ethane	3.4561	6.6236	10.488	15.264	21.126	28.070	35.953	44.583	53.783	63.407	73.350
Propane	2.4171	5.3426	8.9969	13.380	18.492	24.333	30.902	38.200	46.277	54.983	64.467
Butane	—	5.5793	8.5006	12.224	16.749	22.075	28.204	35.134	42.867	51.401	60.737
Isobutane	—	4.4607	8.0380	12.264	17.139	22.662	28.834	35.655	43.125	51.243	60.010
Pentane	—	4.3338	6.9608	10.186	14.217	19.058	24.571	30.583	36.944	43.542	50.300
Isopentane	—	5.1984	6.7668	10.433	14.946	20.218	26.125	32.531	39.301	46.321	53.501
Hexane	—	—	6.4043	9.4223	13.207	17.797	23.080	28.891	35.078	41.521	48.133
Heptane	—	—	5.6156	8.3151	11.723	15.857	20.608	25.826	31.375	37.151	43.074
Ammonia	—	—	19.670	21.331	24.988	30.369	37.130	44.854	53.052	61.163	68.551
Argon	6.3522	9.5054	12.427	15.143	17.683	20.073	22.332	24.479	26.527	28.488	30.372
Carbon dioxide	—	—	—	12.897	16.747	20.887	25.110	29.317	33.465	37.358	41.533
Carbon monoxide	10.021	14.905	19.199	23.039	26.545	29.794	32.833	35.702	38.431	41.044	43.562
Ethylene	—	8.3718	11.061	14.860	20.458	27.290	34.643	42.151	49.908	58.435	68.602
Heavy water	—	—	—	—	18.236	22.218	26.556	31.260	36.330	41.766	47.558
Helium	73.632	96.857	117.90	137.46	155.90	173.45	190.29	206.52	222.23	237.48	252.33
Hydrogen (normal)	68.059	100.76	132.27	160.44	185.63	210.20	233.94	256.84	280.40	304.11	327.99
Hydrogen sulfide	—	—	11.372	14.611	17.981	21.445	24.977	28.563	32.194	35.864	39.571
Krypton	—	4.7716	6.3942	7.9417	9.3899	10.743	12.014	13.216	14.360	15.454	16.504
Neon	22.510	30.298	36.923	42.828	48.261	53.356	58.191	62.814	67.259	71.549	75.704
Nitrogen	9.9841	14.527	18.623	22.365	25.828	29.079	32.181	35.183	38.123	41.025	43.901
Oxygen	9.2232	13.938	18.367	22.568	26.635	30.654	34.673	38.705	42.738	46.753	50.729
Parahydrogen	80.159	127.56	155.47	174.04	192.13	212.10	232.94	253.84	274.90	296.11	317.49
Water	—	—	—	—	18.571	22.066	26.148	30.672	35.559	40.758	46.230
Xenon	—	—	3.7573	4.6490	5.5177	6.3636	7.1858	7.9837	8.7574	9.5073	10.234
R-11	—	—	—	6.4835	8.4849	10.564	12.667	14.753	16.796	18.784	20.710
R-113	—	—	—	6.4431	8.5520	10.770	13.050	15.348	17.629	19.871	22.062

R-114	—	—	—	—	10.265	12.898	15.602	18.326	21.026	23.655	26.160
R-115	—	—	6.2130	9.0983	12.240	15.493	18.748	21.928	24.986	27.903	30.679
R-116	—	—	7.7455	11.135	14.872	18.749	22.639	26.471	30.209		
R-12	—	—	5.3594	7.5944	10.008	12.510	15.027	17.511	19.933	22.280	24.547
R-123	—	—	3.6100	6.4575	9.3050	12.154	15.004	17.852	20.699	23.546	26.393
R-124	—	—	6.1013	8.6795	11.567	14.694	18.014	21.497	25.138	28.945	32.938
R-125	—	—	7.2748	10.483	14.099	18.026	22.157	26.397	30.673	34.937	39.159
R-13	—	4.2020	6.6108	9.3773	12.361	15.440	18.515	21.504	24.342	26.970	
R-134a	—	—	5.4948	9.4998	13.505	17.510	21.514	25.519	29.524	33.529	37.534
R-14	—	5.6385	8.7606	12.450	16.482	20.629	24.713				
R-141b	—	—	—	7.1637	9.5957	12.253	15.064	17.957	20.870	23.745	26.530
R-142b	—	—	5.9144	8.5481	11.542	14.803	18.240	21.771	25.325	28.839	32.262
R-143a	—	—	7.1323	10.703	15.005	19.968	25.509	31.549	38.021	44.873	52.069
R-152a	—	—	4.5237	9.3901	14.256	19.123	23.989	28.856	33.722	38.589	43.455
R-22	—	—	5.5304	7.8754	10.655	13.835	17.362	21.180	25.243	29.516	33.973
R-227ea	—	—	—	9.3315	12.617	16.146	19.807	23.502	27.147	30.670	34.009
R-23	—	5.5120	8.1950	10.878	13.583	16.244	18.927	21.610	24.293	26.976	29.659
R-236ea	—	—	—	9.5352	12.680	16.110	19.747	23.525	27.384	31.278	35.165
R-236fa	—	—	6.5632	9.2338	12.327	15.809	19.646	23.814	28.294	33.075	38.149
R-245ca	—	—	—	8.9551	12.420	16.204	20.171	24.191	28.144	31.924	35.434
R-245fa	—	—	—	9.0415	12.231	15.764	19.563	23.559	27.689	31.901	36.150
R-32	—	—	7.2338	9.6396	12.434	15.602	19.081	22.791	26.665	30.653	24.722
R-41	—	—	10.345	13.591	17.327	21.564	26.279	31.411	36.861	42.495	
RC318	—	—	—	9.0906	12.250	15.640	19.163	22.737	26.301	29.811	33.234

TABLE 2.6 Dilute Gas Viscosity ($\mu\text{Pa} \cdot \text{s}$)

	100 K	150 K	200 K	250 K	300 K	350 K	400 K	450 K	500 K	550 K	600 K
Methane	3.9829	5.9087	7.7900	9.5673	11.233	12.795	14.264	15.652	16.969	18.225	19.426
Ethane	3.3157	4.8014	6.3522	7.8926	9.3864	10.820	12.192	13.504	14.759	15.963	17.118
Propane	2.9792	4.2268	5.5379	6.8715	8.2038	9.5190	10.807	12.060	13.273	14.443	15.568
Butane	—	3.7091	4.9832	6.2381	7.4730	8.6883	9.8849	11.064	12.226	13.371	14.502
Isobutane	—	3.7994	5.0857	6.3403	7.5639	8.7583	9.9253	11.067	12.184	13.279	14.353
Pentane	—	3.4241	4.5472	5.7121	6.8932	8.0678	9.2197	10.339	11.421	12.465	13.472
Isopentane	—	3.9857	4.8092	6.0426	7.2928	8.5359	9.7548	10.939	12.084	13.189	14.254
Hexane	—	—	4.3039	5.4420	6.5526	7.6788	8.8014	9.9075	10.989	12.041	13.063
Heptane	—	—	3.5540	4.9393	5.9304	6.9437	7.9569	8.9564	9.9342	10.886	11.810
Ammonia	—	—	6.9639	8.4513	10.188	12.052	13.977	15.922	17.862	19.783	21.678
Argon	8.1386	12.179	15.922	19.402	22.656	25.718	28.612	31.363	33.987	36.499	38.913
Carbon dioxide	—	—	—	12.556	15.014	17.395	19.690	21.896	24.013	26.044	27.995
Carbon monoxide	6.8135	10.031	12.857	15.385	17.696	19.836	21.836	23.720	25.507	27.212	28.847
Ethylene	—	5.3064	7.0041	8.6638	10.361	12.008	13.575	15.061	16.478	17.838	19.149
Heavy water	—	—	—	—	10.235	11.879	13.740	15.724	17.780	19.876	21.991
Helium	9.7650	12.491	15.135	17.597	19.926	22.151	24.290	26.356	28.361	30.311	32.213
Hydrogen (normal)	4.1824	5.5558	6.7762	7.8996	8.9507	9.9440	10.890	11.797	12.670	13.516	14.337
Hydrogen sulfide	—	—	8.4917	10.686	12.882	15.035	17.121	19.129	21.056	22.905	24.685
Krypton	—	12.825	17.186	21.346	25.238	28.875	32.291	35.532	38.598	41.538	44.361
Neon	14.568	19.609	23.897	27.718	31.235	34.532	37.662	40.654	43.530	46.307	48.996
Nitrogen	6.9167	10.063	12.900	15.490	17.882	20.111	22.205	24.185	26.069	27.868	29.594
Oxygen	7.6302	11.275	14.609	17.682	20.539	23.214	25.735	28.124	30.399	32.575	34.663
Parahydrogen	4.1824	5.5558	6.7762	7.8996	8.9507	9.9440	10.890	11.797	12.670	13.516	14.337
Water	—	—	—	—	9.9262	11.531	13.347	15.285	17.294	19.345	21.416
Xenon	—	—	15.942	19.472	23.021	26.536	29.984	33.346	36.615	39.787	42.864
R-11	—	—	—	8.5895	10.366	12.144	13.899	15.613	17.277	18.887	20.444
R-113	—	—	—	8.0710	9.7388	11.413	13.070	14.694	16.275	17.807	19.290

R-114	—	—	—	—	10.967	12.823	14.633	16.384	18.072	19.696	21.259
R-115	—	—	8.3439	10.501	12.633	14.700	16.684	18.581	20.394	22.131	23.800
R-116	—	—	9.4781	11.889	14.212	16.420	18.510	20.493	22.382	24.188	
R-12	—	—	7.8613	9.8945	11.925	13.914	15.838	17.688	19.463	21.166	22.803
R-123	—	—	6.9649	8.9742	10.863	12.632	14.281	15.810	17.219	18.507	19.675
R-124	—	—	7.7230	9.7203	11.697	13.617	15.461	17.225	18.912	20.529	22.082
R-125	—	—	8.6666	10.903	13.102	15.223	17.252	19.188	21.035	22.805	24.504
R-13	—	6.9581	9.3573	11.747	14.059	16.264	18.355	20.340	22.231	24.040	25.777
R-134a	—	—	7.7659	9.8718	11.893	13.830	15.686	17.468	19.181	20.831	22.423
R-14	—	8.7213	11.679	14.491	17.118	19.570	21.873	24.051			
R-141b	—	—	—	7.7183	9.3140	10.914	12.495	14.042	15.547	17.004	18.414
R-142b	—	—	6.6993	8.4275	10.166	11.881	13.550	15.163	16.714	18.206	19.643
R-143a	—	—	7.3820	9.2892	11.169	12.987	14.729	16.392	17.982	19.504	20.965
R-152a	—	—	6.7055	8.4826	10.367	12.174	13.909	15.577	17.182	18.731	20.288
R-22	—	—	8.4013	10.575	12.735	14.840	16.868	18.813	20.674	22.459	24.174
R-227ea	—	—	—	9.6938	11.678	13.615	15.484	17.277	18.996	20.644	22.228
R-23	—	7.1874	9.9500	12.554	15.012	17.329	19.533	21.634	23.645	25.576	27.436
R-236ea	—	—	—	9.1613	11.052	12.918	14.735	16.491	18.181	19.807	21.372
R-236fa	—	—	7.3159	9.2059	11.101	12.964	14.772	16.515	18.189	19.797	21.345
R-245ca	—	—	—	8.5345	10.301	12.059	13.785	15.464	17.089	18.657	20.170
R-245fa	—	—	—	8.6749	10.468	12.245	13.981	15.663	17.286	18.849	20.355
R-32	—	—	8.3720	10.538	12.695	14.801	16.834	18.784	20.653	22.446	24.169
R-41	—	—	7.3138	9.1921	11.022	12.775	14.443	16.030	17.543	18.991	20.381
RC318	—	—	—	9.6361	11.616	13.556	15.435	17.242	18.977	20.641	22.243

TABLE 2.7 Thermophysical Properties of Fluids along the Saturation Line^a

<i>Methane (R-50)</i>											
T	100.00	110.00	120.00	130.00	140.00	150.00	160.00	170.00	180.00	185.00	190.00
p	0.0344	0.0881	0.1914	0.3673	0.6412	1.0400	1.5921	2.3283	3.2852	3.8617	4.5186
ρ (liq.)	438.89	424.78	409.90	394.04	376.87	357.90	336.31	310.50	276.23	251.36	200.78
ρ (vap.)	0.6746	1.5982	3.2619	5.9804	10.152	16.328	25.382	38.974	61.375	80.435	125.18
h (liq.)	-40.269	-5.8134	29.405	65.628	103.20	142.64	184.80	231.24	285.94	320.51	378.27
h (vap.)	490.21	508.02	524.02	537.66	548.34	555.23	557.07	551.54	532.83	512.49	459.03
s (liq.)	-0.3793	-0.0522	0.2521	0.5385	0.8116	1.0761	1.3378	1.6054	1.8991	2.0765	2.3687
s (vap.)	4.9255	4.6191	4.3738	4.1695	3.9912	3.8267	3.6645	3.4895	3.2707	3.1142	2.7937
c_v (liq.)	2.1136	2.0642	2.0196	1.9795	1.9452	1.9186	1.9037	1.9095	1.9669	2.0623	2.6022
c_v (vap.)	1.5887	1.6108	1.6390	1.6739	1.7172	1.7727	1.8473	1.9556	2.1404	2.3118	2.8546
c_p (liq.)	3.4084	3.4692	3.5493	3.6580	3.8129	4.0474	4.4354	5.1872	7.2923	11.109	94.012
c_p (vap.)	2.1458	2.2053	2.2930	2.4208	2.6108	2.9083	3.4189	4.4585	7.5740	13.527	140.81
w (liq.)	1452.0	1354.7	1253.5	1148.1	1037.7	920.85	795.43	657.52	497.01	398.59	250.31
w (vap.)	260.09	270.01	277.76	283.13	285.93	285.97	283.01	276.66	266.04	258.03	238.55
η (liq.)	155.78	121.34	97.432	79.868	66.333	55.437	46.266	38.115	30.193	25.773	18.982
η (vap.)	3.9976	4.3964	4.1823	5.2517	5.7254	6.2526	6.8688	7.6515	8.8251	9.8238	12.455
λ (liq.)	199.67	186.18	172.15	157.91	143.65	129.43	115.19	100.73	85.799	78.733	96.970
λ (vap.)	10.015	11.350	12.811	14.449	16.334	18.581	21.423	25.477	33.392	43.706	119.40
σ	0.0163	0.0137	0.0113	0.0091	0.0071	0.0052	0.0035	0.0021	0.0009	0.0004	0.0000
<i>Ethane (R-170)</i>											
T	100.00	120.00	140.00	160.00	180.00	200.00	220.00	240.00	260.00	280.00	300.00
p	0.000011	0.00035	0.0038	0.0215	0.0787	0.2174	0.4923	0.9673	1.7125	2.8076	4.3565
ρ (liq.)	641.24	619.31	596.90	573.82	549.66	523.96	496.10	465.08	429.02	383.15	303.22
ρ (vap.)	0.0004	0.0107	0.0991	0.4893	1.6257	4.1746	9.0367	17.492	31.703	56.583	114.50
h (liq.)	-199.04	-152.04	-105.35	-58.612	-11.027	38.151	89.685	144.53	204.23	272.18	363.80
h (vap.)	386.60	410.88	435.96	460.84	484.38	505.82	524.45	539.23	548.17	546.52	512.98

s (liq.)	-1.4399	-1.0115	-0.6516	-0.3398	-0.0603	0.1974	0.4403	0.6745	0.9066	1.1481	1.4478
s (vap.)	4.4165	3.6795	3.2149	2.9067	2.6920	2.5357	2.4165	2.3190	2.2294	2.1279	1.9451
c_v (liq.)	1.6012	1.5345	1.4647	1.4282	1.4184	1.4281	1.4536	1.4941	1.5513	1.6356	1.8781
c_v (vap.)	0.9080	0.9168	0.8995	0.9217	1.0065	1.1280	1.2633	1.4047	1.5560	1.7365	2.0507
c_p (liq.)	2.3318	2.3453	2.3284	2.3497	2.4082	2.5019	2.6377	2.8398	3.1805	3.9711	9.9832
c_p (vap.)	1.1840	1.1875	1.1618	1.1888	1.3017	1.4791	1.7090	2.0151	2.4986	3.6068	12.744
w (liq.)	1938.3	1795.5	1647.8	1498.5	1347.7	1194.8	1039.0	878.23	708.85	520.93	276.76
w (vap.)	189.89	207.39	223.45	236.89	246.81	252.96	254.94	252.03	243.27	227.16	200.47
η (liq.)	877.99	488.15	320.91	231.74	176.39	138.23	109.90	87.650	69.273	52.962	34.918
η (vap.)	3.3157	3.8961	4.4956	5.1100	5.7388	6.3908	7.0891	7.8826	8.8799	10.381	14.023
λ (liq.)	248.15	230.30	210.90	191.08	171.51	152.56	134.47	117.37	101.18	85.534	71.371
λ (vap.)	3.4562	4.6535	5.9584	7.4110	9.0663	10.997	13.305	16.179	20.060	26.418	46.929
σ	0.0300	0.0267	0.0233	0.0200	0.0168	0.0136	0.0105	0.0076	0.0048	0.0023	0.0003

Propane (R-290)

T	100.00	125.00	150.00	175.00	200.00	225.00	250.00	275.00	300.00	325.00	350.00
p	2.5×10^{-8}	7.5×10^{-6}	0.00028	0.0034	0.0201	0.0769	0.2179	0.5020	0.9980	1.7832	2.9510
ρ (liq.)	718.54	693.01	667.73	642.23	615.98	588.40	558.78	526.17	489.14	444.89	384.02
ρ (vap.)	0.0000	0.0003	0.0100	0.1026	0.5404	1.8711	4.9424	10.941	21.658	40.480	77.052
h (liq.)	-168.39	-119.73	-70.291	-19.808	32.227	86.460	143.65	204.67	270.61	343.27	427.71
h (vap.)	379.56	404.10	430.71	459.04	488.58	518.59	548.27	576.71	602.56	623.16	630.91
s (liq.)	-1.0920	-0.6577	-0.2973	0.0138	0.2915	0.5465	0.7863	1.0168	1.2428	1.4699	1.7116
s (vap.)	4.3876	3.5329	3.0427	2.7501	2.5733	2.4670	2.4048	2.3697	2.3493	2.3311	2.2921
c_v (liq.)	1.3436	1.3339	1.3391	1.3582	1.3926	1.4423	1.5065	1.5839	1.6738	1.7794	1.9248
c_v (vap.)	0.7480	0.8366	0.9184	1.0016	1.0946	1.2040	1.3313	1.4736	1.6281	1.7975	2.0004
c_p (liq.)	1.9310	1.9613	1.9956	2.0461	2.1194	2.2196	2.3515	2.5233	2.7572	3.1371	4.2091
c_p (vap.)	0.9365	1.0252	1.1075	1.1933	1.2950	1.4244	1.5908	1.8048	2.0984	2.5937	4.0530
w (liq.)	2026.4	1857.6	1684.4	1515.0	1349.7	1187.5	1027.5	868.89	710.10	544.17	350.19
w (vap.)	153.65	169.94	184.59	197.65	208.68	216.87	221.28	220.90	214.52	200.36	175.23

continued

TABLE 2.7 Thermophysical Properties of Fluids along the Saturation Line^a (Continued)

<i>Propane (R-290) (Continued)</i>											
η (liq.)	3821.5	1269.7	655.97	415.28	289.68	212.58	160.60	123.31	95.085	72.351	51.632
η (vap.)	2.9792	3.5913	4.2258	4.8708	5.5148	6.1540	6.8026	7.5026	8.3405	9.5083	11.634
λ (liq.)	203.49	192.17	178.46	163.55	148.25	133.13	118.62	105.08	92.755	81.720	71.502
λ (vap.)	2.4171	3.7887	5.3418	7.0722	8.9711	11.040	13.323	15.957	19.248	23.915	32.636
σ	0.0354	0.0315	0.0277	0.0239	0.0203	0.0167	0.0132	0.0099	0.0068	0.0039	0.0014
<i>Butane (R-600)</i>											
T	150.00	200.00	225.00	250.00	275.00	300.00	325.00	350.00	375.00	400.00	425.00
p	8.8×10^{-6}	0.0020	0.0106	0.0393	0.1109	0.2580	0.5206	0.9447	1.5821	2.4950	3.7828
ρ (liq.)	720.91	673.73	649.75	624.93	598.78	570.67	539.76	504.77	463.27	408.14	256.91
ρ (vap.)	0.0004	0.0687	0.3336	1.1234	2.9507	6.5301	12.847	23.402	40.982	72.839	201.07
h (liq.)	-58.828	41.883	93.960	147.89	204.27	263.73	326.94	394.69	468.29	551.10	680.26
h (vap.)	422.68	484.26	517.46	551.89	587.15	622.77	685.13	692.20	722.98	745.40	709.19
s (liq.)	-0.2501	0.3289	0.5741	0.8011	1.1055	1.2215	1.4223	1.6206	1.8200	2.0282	2.3307
s (vap.)	2.9600	2.5407	2.4563	2.4171	2.4078	2.4183	2.4414	2.4707	2.4992	2.5140	2.3988
c_v (liq.)	1.4290	1.4718	1.5135	1.5709	1.6422	1.7248	1.8161	1.9147	2.0215	2.1482	2.4543
c_v (vap.)	1.0149	1.1748	1.2650	1.3681	1.4849	1.6133	1.7508	1.8955	2.0485	2.2178	2.4822
c_p (liq.)	1.9824	2.0537	2.1155	2.2004	2.3092	2.4435	2.6082	2.8194	3.1351	3.8592	211.56
c_p (vap.)	1.1580	1.3198	1.4147	1.5282	1.6644	1.8266	2.0227	2.2764	2.6684	3.6114	242.27
w (liq.)	1719.0	1430.6	1290.7	1153.3	1018.2	884.92	752.87	620.83	483.83	328.58	119.17
w (vap.)	156.47	178.85	188.13	195.52	200.40	202.11	199.83	192.54	178.61	154.97	113.84
η (liq.)	1370.6	494.94	349.26	259.20	198.78	155.62	123.09	97.300	75.697	55.863	27.110
η (vap.)	3.7090	4.9792	5.5998	6.2086	6.8131	7.4364	8.1245	8.9613	10.110	12.016	21.260
λ (liq.)	171.21	149.19	137.42	125.77	114.53	103.94	94.180	85.386	77.581	70.526	118.63
λ (vap.)	5.5793	8.4973	10.250	12.197	14.357	16.785	19.604	23.061	27.664	34.993	123.39
σ	0.0313	0.0243	0.0210	0.0177	0.0146	0.0116	0.0088	0.0061	0.0037	0.0015	0.0000

Isobutane (2-Methylpropane, R-600a)

T	150.00	175.00	200.00	225.00	250.00	275.00	300.00	325.00	350.00	375.00	400.00
p	0.000023	0.00045	0.0038	0.0185	0.0631	0.1672	0.3698	0.7162	1.2577	2.0551	3.1920
ρ (liq.)	706.14	682.48	658.25	633.09	606.61	578.29	547.48	513.31	474.24	425.57	340.74
ρ (vap.)	0.0011	0.0179	0.1318	0.5807	1.8175	4.5187	9.6081	18.417	33.238	59.391	119.80
h (liq.)	-49.648	-3.4665	44.680	95.083	148.13	204.27	264.00	327.86	396.67	472.64	566.69
h (vap.)	404.10	431.22	460.56	491.72	524.22	557.51	591.00	623.83	654.41	679.12	683.39
s (liq.)	-0.1998	0.0848	0.3419	0.5791	0.8023	1.0155	1.2220	1.4243	1.6250	1.8296	2.0643
s (vap.)	2.8252	2.5688	2.4212	2.3419	2.3066	2.3000	2.3121	2.3350	2.3614	2.3802	2.3561
c_v (liq.)	1.3103	1.3524	1.4019	1.4620	1.5336	1.6160	1.7077	1.8073	1.9144	2.0356	2.2388
c_v (vap.)	0.8943	0.9947	1.0959	1.2040	1.3230	1.4541	1.5954	1.7446	1.9021	2.0749	2.3041
c_p (liq.)	1.8104	1.8850	1.9684	2.0652	2.1781	2.3095	2.4623	2.6446	2.8911	3.3822	6.5400
c_p (vap.)	1.0374	1.1383	1.2419	1.3564	1.4894	1.6466	1.8340	2.0676	2.4005	3.0674	7.3172
w (liq.)	1612.0	1470.8	1332.1	1195.1	1059.3	924.64	791.59	660.70	528.31	378.18	183.42
w (vap.)	157.76	169.14	179.38	188.05	194.51	198.00	197.70	192.61	181.32	161.42	128.34
η (liq.)	1751.4	903.05	551.15	369.87	262.91	194.15	147.22	113.53	87.888	66.264	42.436
η (vap.)	3.7993	4.4453	5.0797	5.6991	6.3047	6.9095	7.5457	8.2773	9.2413	10.815	14.857
λ (liq.)	148.49	139.48	129.36	118.75	108.11	97.862	88.323	79.776	72.402	66.126	62.048
λ (vap.)	4.4606	6.1666	8.0276	10.032	12.174	14.477	17.026	20.030	23.954	30.110	46.264
σ	0.0285	0.0253	0.0221	0.0189	0.0158	0.0128	0.0099	0.0071	0.0045	0.0022	0.0003

Pentane

T	150.00	200.00	250.00	275.00	300.00	325.00	350.00	375.00	400.00	425.00	450.00
p	2.7×10^{-7}	0.0002	0.0076	0.0266	0.0732	0.1685	0.3396	0.6177	1.0384	1.6429	2.4836
ρ (liq.)	756.28	711.19	666.32	643.13	618.95	593.35	565.69	535.02	499.73	456.47	395.85
ρ (vap.)	0.0000	0.0086	0.2651	0.8533	2.1937	4.8038	9.3842	16.939	29.117	49.281	87.430
h (liq.)	-334.92	-235.81	-132.70	-78.400	-21.633	38.051	101.10	168.03	239.58	317.05	404.03
h (vap.)	139.41	199.97	268.35	305.08	343.22	382.47	422.37	462.26	500.99	536.24	561.62

continued

TABLE 2.7 Thermophysical Properties of Fluids along the Saturation Line^a (Continued)

<i>Pentane (Continued)</i>											
s (liq.)	-1.5046	-0.9346	-0.4749	-0.2681	-0.0709	0.1197	0.3056	0.4889	0.6714	0.8561	1.0503
s (vap.)	1.6576	1.2443	1.1292	1.1264	1.1453	1.1794	1.2235	1.2735	1.3249	1.3719	1.4005
c_v (liq.)	1.4426	1.4869	1.5862	1.6572	1.7397	1.8310	1.9284	2.0303	2.1363	2.2488	2.3821
c_v (vap.)	1.0061	1.1817	1.3597	1.4629	1.5763	1.6983	1.8272	1.9619	2.1029	2.2543	2.4328
c_p (liq.)	1.9682	2.0091	2.1283	2.2171	2.3239	2.4480	2.5916	2.7620	2.9808	3.3177	4.1782
c_p (vap.)	1.1214	1.2972	1.4793	1.5889	1.7141	1.8562	2.0189	2.2132	2.4707	2.9032	4.2191
w (liq.)	1788.3	1500.5	1244.1	1122.1	1002.5	884.21	765.87	645.89	522.16	391.45	246.17
w (vap.)	138.80	159.00	175.83	182.32	186.93	189.09	188.17	183.35	173.48	156.77	130.14
η (liq.)	2750.8	689.40	344.14	267.51	214.42	174.84	143.56	117.61	95.070	74.436	53.842
η (vap.)	3.4236	4.5515	5.7318	6.3409	6.9672	7.6198	8.3158	9.0883	10.004	11.222	13.312
λ (liq.)	172.92	152.50	130.68	120.37	110.64	101.54	93.033	85.073	77.560	70.311	62.809
λ (vap.)	4.3338	6.9615	10.207	12.164	14.393	16.928	19.811	23.099	26.897	31.431	37.367
σ	0.0323	0.0265	0.0208	0.0180	0.0153	0.0126	0.0100	0.0075	0.0051	0.0030	0.0011
<i>Isopentane (2-Methylbutane)</i>											
T	260.00	280.00	300.00	320.00	340.00	360.00	380.00	400.00	420.00	440.00	460.00
p	0.0189	0.0461	0.0980	0.1872	0.3284	0.5382	0.8347	1.2377	1.7700	2.4600	3.3570
ρ (liq.)	652.36	633.24	613.33	592.35	569.95	545.63	518.63	487.67	450.35	400.63	287.45
ρ (vap.)	0.6394	1.4647	2.9606	5.4417	9.3072	15.089	23.563	36.004	54.920	86.923	190.32
h (liq.)	-89.675	-46.927	-2.2196	44.614	93.760	145.45	199.99	257.89	320.05	388.70	482.73
h (vap.)	283.21	312.03	341.94	372.68	403.97	435.42	466.50	496.36	523.38	543.59	525.56
s (liq.)	-0.3195	-0.1613	-0.0074	0.1432	0.2914	0.4380	0.5840	0.7304	0.8792	1.0350	1.2378
s (vap.)	1.1147	1.1207	1.1398	1.1685	1.2038	1.2435	1.2853	1.3265	1.3633	1.3870	1.3309
c_v (liq.)	1.5651	1.6409	1.7196	1.8006	1.8832	1.9673	2.0530	2.1412	2.2348	2.3440	2.5665
c_v (vap.)	1.3572	1.4595	1.5639	1.6702	1.7785	1.8887	2.0017	2.1188	2.2439	2.3883	2.6252
c_p (liq.)	2.0902	2.1834	2.2843	2.3939	2.5142	2.6495	2.8094	3.0149	3.3265	4.0252	42.070
c_p (vap.)	1.4807	1.5904	1.7064	1.8305	1.9659	2.1186	2.3018	2.5477	2.9552	4.0178	69.567

w (liq.)	1138.6	1041.7	946.48	852.31	758.32	663.63	567.22	467.82	363.47	249.42	102.20
w (vap.)	178.39	182.73	185.71	187.00	186.27	183.10	176.93	167.00	152.15	130.49	96.500
η (liq.)	410.30	310.40	241.39	192.27	156.15	128.61	106.74	88.534	72.481	57.021	28.956
η (vap.)	6.2933	6.7963	7.3046	7.8224	8.3586	8.9291	9.5620	10.310	11.286	12.827	18.849
λ (liq.)	106.77	100.93	95.472	90.390	85.637	81.154	76.898	72.801	68.750	64.508	54.273
λ (vap.)	11.321	13.160	15.181	17.403	19.849	22.552	25.565	28.972	32.944	37.914	47.550
σ	0.0187	0.0164	0.0143	0.0121	0.0101	0.0081	0.0062	0.0044	0.0027	0.0012	0.0000

Neopentane (2,2-Dimethylpropane)

T	280.00	300.00	320.00	340.00	360.00	370.00	380.00	390.00	400.00	410.00	420.00
p	0.0921	0.1819	0.3267	0.5443	0.8539	1.0497	1.2766	1.5378	1.8370	2.1782	2.5670
ρ (liq.)	606.22	583.28	559.16	533.36	505.00	489.41	472.49	453.76	432.43	407.01	374.05
ρ (vap.)	2.9706	5.6289	9.8434	16.232	25.712	32.056	39.849	49.555	61.938	78.430	102.36
h (liq.)	−5.8227	39.477	87.305	137.73	190.96	218.75	247.47	277.28	308.47	341.55	377.75
h (vap.)	312.19	341.69	371.77	401.99	431.75	446.19	460.11	473.26	485.20	495.16	501.37
s (liq.)	−0.0206	0.1351	0.2885	0.4401	0.5905	0.6656	0.7409	0.8169	0.8941	0.9738	1.0586
s (vap.)	1.1151	1.1424	1.1775	1.2174	1.2594	1.2803	1.3005	1.3194	1.3359	1.3484	1.3529
c_v (liq.)	1.5236	1.6487	1.7722	1.8881	1.9973	2.0507	2.1043	2.1592	2.2171	2.2810	2.3577
c_v (vap.)	1.4748	1.5909	1.7088	1.8300	1.9560	2.0217	2.0897	2.1610	2.2369	2.3197	2.4140
c_p (liq.)	2.2006	2.3239	2.4512	2.5860	2.7422	2.8372	2.9526	3.1027	3.3181	3.6796	4.5015
c_p (vap.)	1.6124	1.7470	1.8952	2.0660	2.2777	2.4110	2.5762	2.7952	3.1163	3.6677	4.9415
w (liq.)	1004.3	877.57	757.88	644.46	535.00	480.86	426.56	371.55	315.16	256.39	193.67
w (vap.)	180.13	181.48	180.61	177.10	170.36	165.54	159.57	152.24	143.28	132.30	118.65

Hexane

T	200.00	250.00	300.00	325.00	350.00	375.00	400.00	425.00	450.00	475.00	500.00
p	0.000021	0.0015	0.0219	0.0578	0.1299	0.2582	0.4661	0.7803	1.2313	1.8567	2.7139

continued

TABLE 2.7 Thermophysical Properties of Fluids along the Saturation Line^a (Continued)

<i>Hexane (Continued)</i>											
ρ (liq.)	741.90	697.89	652.98	629.48	604.84	578.59	550.08	518.24	481.07	433.62	350.12
ρ (vap.)	0.0011	0.0639	0.7683	1.9057	4.0858	7.8720	14.046	23.808	39.364	66.089	129.04
h (liq.)	-306.56	-206.69	-98.600	-40.702	20.138	84.182	151.72	223.16	299.18	381.51	478.78
h (vap.)	121.00	189.30	265.66	306.52	348.84	392.27	436.28	480.06	522.13	559.07	577.03
s (liq.)	-1.1456	-0.7005	-0.3070	-0.1219	0.0581	0.2342	0.4075	0.5793	0.7510	0.9260	1.1209
s (vap.)	0.9922	0.8835	0.9072	0.9465	0.9972	1.0557	1.1189	1.1838	1.2464	1.2998	1.3174
c_v (liq.)	1.4405	1.5804	1.7503	1.8457	1.9453	2.0475	2.1508	2.2547	2.3600	2.4716	2.6218
c_v (vap.)	1.1868	1.3657	1.5758	1.6930	1.8161	1.9433	2.0731	2.2053	2.3409	2.4847	2.6579
c_p (liq.)	1.9301	2.0713	2.2598	2.3714	2.4933	2.6263	2.7743	2.9479	3.1796	3.6056	6.5887
c_p (vap.)	1.2833	1.4636	1.6817	1.8086	1.9478	2.1011	2.2746	2.4853	2.7854	3.4001	7.5559
w (liq.)	1515.7	1269.4	1047.6	942.17	838.85	736.47	633.63	528.43	417.67	294.59	138.19
w (vap.)	144.44	160.40	172.79	176.83	178.87	178.39	174.77	167.09	153.94	132.74	98.609
η (liq.)	1306.4	529.19	290.31	227.83	183.11	149.58	123.38	101.98	83.551	66.222	45.006
η (vap.)	4.2946	5.4709	6.6161	7.2117	7.8304	8.4853	9.2018	10.031	11.090	12.712	16.804
λ (liq.)	154.97	142.43	125.48	117.26	109.61	102.62	96.301	90.550	85.124	79.386	70.105
λ (vap.)	6.4043	9.4265	13.258	15.531	18.065	20.879	24.003	27.502	31.520	36.488	44.807
σ	0.0293	0.0234	0.0177	0.0151	0.0125	0.0100	0.0077	0.0055	0.0035	0.0017	0.0003
<i>Heptane</i>											
T	200.00	250.00	300.00	325.00	350.00	375.00	400.00	425.00	450.00	475.00	500.00
p	2.1×10^{-6}	0.00031	0.0067	0.0204	0.0514	0.1121	0.2182	0.3887	0.6451	1.0120	1.5191
ρ (liq.)	761.24	719.62	677.94	656.47	634.23	610.90	586.03	558.97	528.70	493.27	448.22
ρ (vap.)	0.0001	0.0150	0.2702	0.7680	1.8293	3.8189	7.2279	12.736	21.379	34.995	57.736
h (liq.)	-380.96	-279.59	-171.54	-114.10	-54.026	8.9028	74.888	144.16	217.04	294.13	376.79
h (vap.)	47.527	115.51	192.43	234.17	277.88	323.27	369.98	417.53	465.21	511.77	554.66
s (liq.)	-1.3567	-0.9047	-0.5112	-0.3274	-0.1495	0.0238	0.1936	0.3609	0.5264	0.6915	0.8588
s (vap.)	0.7857	0.6757	0.7020	0.7442	0.7987	0.8621	0.9314	1.0041	1.0779	1.1497	1.2146

c_v (liq.)	1.5143	1.6246	1.7815	1.8727	1.9689	2.0678	2.1676	2.2674	2.3669	2.4667	2.5700
c_v (vap.)	1.1910	1.3692	1.5776	1.6923	1.8118	1.9344	2.0586	2.1837	2.3095	2.4372	2.5703
c_p (liq.)	1.9825	2.0836	2.2477	2.3479	2.4574	2.5748	2.7007	2.8386	2.9977	3.2033	2.5488
c_p (vap.)	1.2739	1.4526	1.6644	1.7838	1.9115	2.0475	2.1934	2.3540	2.5425	2.7963	3.2569
w (liq.)	1576.5	1336.1	1120.1	1018.0	918.29	819.96	721.82	622.51	520.31	412.79	295.82
w (vap.)	133.23	148.24	160.82	165.69	169.16	170.85	170.28	166.88	159.83	147.86	128.88
η (liq.)	2171.4	741.16	380.04	293.16	233.07	189.27	155.88	129.39	107.48	88.425	70.558
η (vap.)	3.5470	4.9751	6.0076	6.5434	7.0975	7.6775	8.2967	8.9798	9.7730	10.775	12.243
λ (liq.)	153.82	143.43	130.74	124.39	118.19	112.17	106.32	100.56	94.763	88.670	81.714
λ (vap.)	5.6156	8.3161	11.741	13.757	15.983	18.427	21.103	24.041	27.294	30.978	35.390
σ	0.0310	0.0253	0.0198	0.0172	0.0148	0.0123	0.0100	0.0078	0.0058	0.0038	0.0021

Octane

T	250.00	300.00	350.00	375.00	400.00	425.00	450.00	475.00	500.00	525.00	550.00
p	0.000063	0.0021	0.0207	0.0497	0.1048	0.1993	0.3489	0.5717	0.8882	1.3229	1.9082
ρ (liq.)	736.69	696.69	655.47	633.81	611.07	586.81	560.43	530.96	496.64	453.63	389.70
ρ (vap.)	0.0035	0.0946	0.8269	1.8851	3.8175	7.0696	12.255	20.289	32.752	53.043	92.190
h (liq.)	-347.92	-240.35	-123.85	-61.705	3.2520	71.155	142.17	216.57	294.82	378.01	469.56
h (vap.)	46.050	123.10	209.74	256.28	304.60	354.35	405.08	456.14	506.48	554.02	592.73
s (liq.)	-1.0811	-0.6893	-0.3306	-0.1593	0.0081	0.1724	0.3341	0.4941	0.6533	0.8139	0.9816
s (vap.)	0.4947	0.5222	0.6225	0.6887	0.7615	0.8387	0.9183	0.9984	1.0767	1.1491	1.2055
c_v (liq.)	1.6551	1.8107	1.9962	2.0936	2.1916	2.2891	2.3854	2.4806	2.5754	2.6724	2.7811
c_v (vap.)	1.3726	1.5808	1.8108	1.9299	2.0498	2.1699	2.2896	2.4092	2.5299	2.6547	2.7926
c_p (liq.)	2.0786	2.2333	2.4311	2.5400	2.6544	2.7750	2.9049	3.0521	3.2372	3.5293	4.3831
c_p (vap.)	1.4455	1.6551	1.8916	2.0180	2.1498	2.2887	2.4391	2.6120	2.8367	3.2176	4.4619
w (liq.)	1344.5	1138.6	948.81	857.47	767.20	676.95	585.56	491.62	393.17	287.24	168.34
w (vap.)	138.40	150.71	160.16	163.15	164.51	163.85	160.64	154.15	143.24	125.94	98.584
σ	0.0259	0.0210	0.0163	0.0141	0.0119	0.0098	0.0078	0.0058	0.0040	0.0023	0.0008

continued

TABLE 2.7 Thermophysical Properties of Fluids along the Saturation Line^a (Continued)

<i>Ammonia (R-717)</i>											
<i>T</i>	200.00	220.00	240.00	260.00	280.00	300.00	320.00	340.00	360.00	380.00	400.00
<i>p</i>	0.0087	0.0338	0.1022	0.2553	0.5509	1.0617	1.8728	3.0802	4.7929	7.1402	10.305
ρ (liq.)	728.12	705.76	681.75	656.22	629.08	599.97	568.19	532.44	490.26	436.07	344.56
ρ (vap.)	0.0891	0.3188	0.8969	2.1154	4.3817	8.2507	14.510	24.395	40.187	67.368	131.09
<i>h</i> (liq.)	18.997	104.71	192.70	282.79	374.99	469.71	567.90	671.27	783.03	910.32	1085.0
<i>h</i> (vap.)	1492.9	1528.9	1561.7	1589.9	1612.3	1627.7	1634.2	1629.2	1607.8	1558.3	1431.9
<i>s</i> (liq.)	0.0960	0.5042	0.8866	1.2461	1.5860	1.9098	2.2221	2.5287	2.8384	3.1686	3.5949
<i>s</i> (vap.)	7.4653	6.9780	6.5907	6.2735	6.0051	5.7697	5.5542	5.3462	5.1294	4.8739	4.4622
<i>c_v</i> (liq.)	2.9264	2.8894	2.8545	2.8213	2.7898	2.7624	2.7430	2.7388	2.7636	2.8531	3.1772
<i>c_v</i> (vap.)	1.5649	1.6196	1.7054	1.8232	1.9719	2.1482	2.3490	2.5745	2.8322	3.1467	3.5984
<i>c_p</i> (liq.)	4.2270	4.3423	4.4488	4.5477	4.6562	4.8001	5.0184	5.3846	6.0817	7.8177	22.728
<i>c_p</i> (vap.)	2.0755	2.1599	2.2984	2.5028	2.7878	3.1767	3.7181	4.5302	5.9545	9.3949	34.924
<i>w</i> (liq.)	2080.2	1913.7	1766.9	1624.5	1481.0	1333.2	1177.9	1011.8	830.62	628.75	384.58
<i>w</i> (vap.)	357.91	373.38	386.30	396.20	402.59	404.95	402.70	395.05	380.83	357.96	318.22
η (liq.)	507.28	346.68	254.85	197.34	158.12	129.33	106.91	88.555	72.796	58.315	41.802
η (vap.)	6.9515	7.4846	8.0587	8.6558	9.2664	9.8938	10.561	11.330	12.346	14.025	18.529
λ (liq.)	803.14	733.17	665.09	600.07	538.50	480.25	424.83	371.51	319.25	266.57	216.00
λ (vap.)	19.684	20.132	20.978	22.258	24.034	26.408	29.568	33.945	40.752	54.556	113.54
σ	0.0604	0.0523	0.0447	0.0374	0.0306	0.0242	0.0183	0.0129	0.0080	0.0038	0.0005
<i>Argon (R-740)</i>											
<i>T</i>	90.000	100.00	110.00	115.00	120.00	125.00	130.00	135.00	140.00	145.00	150.00
<i>p</i>	0.1335	0.3238	0.6653	0.9098	1.2130	1.5823	2.0255	2.5509	3.1682	3.8896	4.7346
ρ (liq.)	1378.6	1313.7	1242.8	1204.2	1162.8	1117.9	1068.1	1011.5	943.71	854.28	680.43
ρ (vap.)	7.4362	16.859	33.287	45.126	60.144	79.194	103.56	135.39	178.86	244.44	394.50
<i>h</i> (liq.)	−114.49	−103.06	−91.129	−84.874	−78.353	−71.488	−64.161	−56.177	−47.162	−36.192	−17.880
<i>h</i> (vap.)	44.572	47.401	48.840	48.899	48.413	47.268	45.295	42.211	37.472	29.757	11.522

s (liq.)	1.4090	1.5278	1.6390	1.6928	1.7461	1.7995	1.8538	1.9102	1.9712	2.0425	2.1589
s (vap.)	3.1763	3.0324	2.9114	2.8560	2.8025	2.7495	2.6957	2.6390	2.5757	2.4973	2.3550
c_v (liq.)	0.5268	0.4976	0.4747	0.4653	0.4576	0.4520	0.4492	0.4509	0.4598	0.4893	0.7060
c_v (vap.)	0.3309	0.3445	0.3633	0.3752	0.3893	0.4064	0.4275	0.4544	0.4940	0.5662	0.8218
c_p (liq.)	1.1212	1.1537	1.2176	1.2663	1.3324	1.4253	1.5638	1.7903	2.2247	3.3994	23.582
c_p (vap.)	0.5757	0.6269	0.7122	0.7760	0.8627	0.9857	1.1717	1.4822	2.1036	3.8959	35.468
w (liq.)	819.45	746.91	669.20	627.79	584.19	537.83	487.88	433.10	371.63	297.06	174.74
w (vap.)	172.83	178.91	183.03	184.33	185.09	185.28	184.85	183.74	181.50	176.57	157.01
η (liq.)	247.64	183.99	140.92	123.88	108.89	95.502	83.326	72.024	61.193	50.126	35.321
η (vap.)	7.3861	8.3516	9.4080	9.9908	10.628	11.341	12.166	13.165	14.466	16.416	21.305
λ (liq.)	122.07	108.87	95.888	89.504	83.208	77.005	70.891	64.854	58.883	53.102	50.932
λ (vap.)	5.7436	6.6691	7.8579	8.6048	9.5027	10.612	12.031	13.935	16.706	21.516	40.853
σ	0.0119	0.0094	0.0071	0.0060	0.0050	0.0040	0.0030	0.0021	0.0013	0.0006	0.0000

Benzene

T	300.00	325.00	350.00	375.00	400.00	425.00	450.00	475.00	500.00	525.00	550.00
p	0.0138	0.0388	0.0916	0.1894	0.3528	0.6053	0.9724	1.4820	2.1651	3.0585	4.2145
ρ (liq.)	871.65	844.82	817.14	788.52	758.60	726.83	692.37	653.91	609.15	553.06	466.88
ρ (vap.)	0.4357	1.1393	2.5361	5.0014	9.0028	15.138	24.226	37.522	57.259	88.461	150.30
h (liq.)	−95.464	−51.903	−6.0993	42.075	92.593	145.52	201.07	259.71	322.22	390.29	469.81
h (vap.)	336.21	362.75	390.92	420.32	450.58	481.27	511.90	541.72	569.48	592.42	600.44
s (liq.)	−0.2922	−0.1529	−0.0173	0.1153	0.2451	0.3726	0.4984	0.6235	0.7495	0.8793	1.0230
s (vap.)	1.1467	1.1230	1.1170	1.1239	1.1401	1.1626	1.1891	1.2172	1.2441	1.2643	1.2605
c_v (liq.)	1.1906	1.2529	1.3416	1.4289	1.5092	1.5840	1.6568	1.7314	1.8130	1.9106	2.0533
c_v (vap.)	0.9505	1.0545	1.1573	1.2597	1.3626	1.4666	1.5728	1.6828	1.7999	1.9316	2.1038
c_p (liq.)	1.7055	1.7839	1.8779	1.9710	2.0643	2.1640	2.2794	2.4258	2.6373	3.0331	4.7654
c_p (vap.)	1.0608	1.1696	1.2807	1.3967	1.5206	1.6573	1.8161	2.0169	2.3136	2.9126	5.8688
w (liq.)	1295.7	1180.0	1060.9	947.23	839.45	735.77	633.92	531.41	425.31	311.24	179.15
w (vap.)	187.37	192.67	196.74	199.21	199.73	197.89	193.24	185.11	172.54	153.85	125.56
σ	0.0280	0.0247	0.0215	0.0185	0.0155	0.0126	0.0099	0.0072	0.0048	0.0025	0.0006

continued

TABLE 2.7 Thermophysical Properties of Fluids along the Saturation Line^a (Continued)

<i>Carbon Dioxide (R-744)</i>											
<i>T</i>	220.00	230.00	240.00	250.00	260.00	270.00	280.00	285.00	290.00	295.00	300.00
<i>p</i>	0.5991	0.8929	1.2825	1.7850	2.4188	3.2033	4.1607	4.7123	5.3177	5.9822	6.7131
ρ (liq.)	1166.1	1128.7	1088.9	1046.0	998.89	945.83	883.58	847.05	804.67	752.56	679.24
ρ (vap.)	15.817	23.271	33.295	46.644	64.417	88.374	121.74	143.92	171.96	209.72	268.58
<i>h</i> (liq.)	86.728	106.57	126.84	147.71	169.44	192.41	217.30	230.86	245.63	262.38	283.38
<i>h</i> (vap.)	431.64	434.60	436.49	437.04	435.92	432.56	425.94	420.80	413.75	403.64	387.08
<i>s</i> (liq.)	0.5517	0.6387	0.7235	0.8068	0.8895	0.9732	1.0598	1.1056	1.1544	1.2087	1.2759
<i>s</i> (vap.)	2.1194	2.0649	2.0137	1.9641	1.9144	1.8626	1.8050	1.7720	1.7341	1.6876	1.6215
<i>c_v</i> (liq.)	0.9698	0.9567	0.9454	0.9364	0.9323	0.9396	0.9605	0.9748	0.9937	1.0265	1.1199
<i>c_v</i> (vap.)	0.6389	0.6700	0.7053	0.7459	0.7943	0.8517	0.9232	0.9686	1.0260	1.1060	1.2476
<i>c_p</i> (liq.)	1.9618	1.9970	2.0510	2.1320	2.2554	2.4534	2.8141	3.1333	3.6756	4.7939	8.6979
<i>c_p</i> (vap.)	0.9303	1.0053	1.1033	1.2366	1.4295	1.7307	2.2769	2.7668	3.6142	5.4316	11.921
<i>w</i> (liq.)	951.21	879.09	806.38	731.78	652.58	565.46	471.54	422.75	371.95	315.91	245.67
<i>w</i> (vap.)	223.15	223.57	222.96	221.22	218.19	213.75	207.72	203.94	199.45	193.84	185.33
η (liq.)	242.01	204.23	172.96	146.74	124.40	105.02	87.731	79.548	71.409	62.936	53.107
η (vap.)	11.135	11.689	12.272	12.902	13.614	14.469	15.601	16.361	17.357	18.792	21.306
λ (liq.)	176.15	163.28	150.75	138.47	126.35	114.25	102.03	95.810	89.546	83.558	80.593
λ (vap.)	11.301	12.221	13.297	14.610	16.306	18.687	22.468	25.424	29.821	37.215	53.689
σ	0.0163	0.0139	0.0115	0.0093	0.0071	0.0051	0.0033	0.0024	0.0017	0.0010	0.0003
<i>Carbon Monoxide</i>											
<i>T</i>	70.000	80.000	90.000	95.000	100.00	105.00	110.00	115.00	120.00	125.00	130.00
<i>p</i>	0.0210	0.0836	0.2384	0.3685	0.5443	0.7741	1.0663	1.4299	1.8745	2.4112	3.0556
ρ (liq.)	840.21	798.97	754.42	730.36	704.70	677.01	646.65	612.68	573.40	525.22	455.45
ρ (vap.)	1.0232	3.6494	9.6370	14.530	21.137	29.920	41.533	56.990	78.080	108.67	161.99
<i>h</i> (liq.)	−25.074	−3.5476	18.162	29.279	40.692	52.515	64.903	78.078	92.410	108.66	129.41
<i>h</i> (vap.)	205.08	213.81	220.88	223.56	225.53	226.64	226.69	225.37	222.13	215.82	202.48

s (liq.)	−0.3301	−0.0436	0.2097	0.3280	0.4426	0.5547	0.6658	0.7778	0.8933	1.0180	1.1730
s (vap.)	2.9578	1.6734	2.4621	2.3731	2.2909	2.2130	2.1366	2.0586	1.9744	1.8752	1.7323
c_v (liq.)	1.2779	1.1803	1.1075	1.0780	1.0525	1.0312	1.0147	1.0049	1.0063	1.0305	1.1232
c_v (vap.)	0.7540	0.7727	0.8056	0.8280	0.8546	0.8857	0.9225	0.9673	1.0249	1.1072	1.2555
c_p (liq.)	2.1606	2.1448	2.1877	2.2355	2.3068	2.4110	2.5651	2.8045	3.2168	4.1075	7.9566
c_p (vap.)	1.0669	1.1157	1.2115	1.2858	1.3860	1.5243	1.7245	2.0383	2.5995	3.8853	9.7719
w (liq.)	967.52	872.05	773.63	722.64	670.00	615.20	557.54	495.94	428.49	351.29	253.47
w (vap.)	169.27	178.52	184.85	186.78	187.83	187.97	187.16	185.34	182.45	178.27	171.80
η (liq.)	255.08	178.90	139.80	125.97	114.09	103.40	93.380	83.643	73.841	63.508	51.253
η (vap.)	4.7766	5.6070	6.6165	7.2220	7.9187	8.7333	9.7056	10.903	12.453	14.661	18.685
λ (liq.)	162.95	145.12	126.19	116.48	106.76	97.193	87.895	78.967	70.419	61.995	52.280
λ (vap.)	6.8841	7.9811	9.1267	9.7277	10.359	11.039	11.803	12.730	13.986	15.999	20.331
σ	0.0119	0.0098	0.0078	0.0067	0.0057	0.0047	0.0037	0.0027	0.0018	0.0010	0.0003

Cyclohexane

T	300.00	325.00	350.00	375.00	400.00	425.00	450.00	475.00	500.00	525.00	550.00
p	0.0141	0.0388	0.0900	0.1833	0.3373	0.5729	0.9133	1.3839	2.0124	2.8316	3.8928
ρ (liq.)	772.06	748.08	723.43	697.80	670.77	641.79	609.94	573.73	530.62	475.08	349.73
ρ (vap.)	0.4810	1.2313	2.6979	5.2621	9.4161	15.830	25.495	40.045	62.573	100.85	198.59
h (liq.)	−107.66	−59.864	−8.3171	46.568	104.68	166.10	231.07	300.04	373.80	454.16	559.79
h (vap.)	283.43	315.78	350.42	386.93	424.83	463.47	502.44	540.44	576.11	606.53	617.68
s (liq.)	−0.3290	−0.1761	−0.0236	0.1275	0.2769	0.4249	0.5722	0.7196	0.8685	1.0221	1.2136
s (vap.)	0.9747	0.9797	1.0014	1.0351	1.0772	1.1248	1.1752	1.2257	1.2731	1.3123	1.3188
c_v (liq.)	1.3176	1.4866	1.6165	1.7279	1.8312	1.9316	2.0139	2.1344	2.2419	2.3598	2.5605
c_v (vap.)	1.1713	1.3075	1.4443	1.5846	1.7297	1.8806	2.0381	2.2032	2.3752	2.5444	2.6403
c_p (liq.)	1.8265	1.9899	2.1282	2.2570	2.3858	2.5224	2.6760	2.8629	3.1201	3.6393	11.570
c_p (vap.)	1.2732	1.4148	1.5618	1.7199	1.8951	2.0972	2.3452	2.6798	3.1989	4.2107	11.408
w (liq.)	1245.3	1108.1	996.64	895.44	797.11	697.60	594.66	487.67	378.12	263.49	108.39
w (vap.)	177.99	182.88	186.30	187.76	186.80	182.91	175.58	164.25	148.10	124.78	87.229
σ	0.0244	0.0214	0.0185	0.0157	0.0130	0.0104	0.0079	0.0056	0.0034	0.0016	0.0001

continued

74 **TABLE 2.7 Thermophysical Properties of Fluids along the Saturation Line^a (Continued)**

<i>Cyclopropane</i>											
<i>T</i>	290.00	300.00	310.00	320.00	330.00	340.00	350.00	360.00	370.00	380.00	390.00
<i>p</i>	0.5777	0.7615	0.9849	1.2529	1.5709	1.9441	2.3784	2.8796	3.4546	4.1114	4.8609
ρ (liq.)	631.52	616.18	600.11	583.17	565.14	545.75	524.57	500.93	473.63	440.16	393.04
ρ (vap.)	11.361	14.851	19.140	24.390	30.814	38.698	48.459	60.747	76.696	98.678	133.76
<i>h</i> (liq.)	240.80	263.98	287.23	311.06	335.82	361.86	389.49	419.11	451.33	487.35	530.72
<i>h</i> (vap.)	655.85	663.68	671.20	678.30	684.84	690.64	695.42	698.72	699.73	696.75	684.85
<i>s</i> (liq.)	1.1437	1.2213	1.2964	1.3705	1.4450	1.5208	1.5985	1.6791	1.7642	1.8564	1.9643
<i>s</i> (vap.)	2.5749	2.5537	2.5350	2.5182	2.5027	2.4878	2.4726	2.4558	2.4355	2.4074	2.3595
<i>c_v</i> (liq.)	1.4862	1.4188	1.4010	1.4173	1.4571	1.5130	1.5800	1.6556	1.7388	1.8322	1.9471
<i>c_v</i> (vap.)	1.1838	1.2513	1.3221	1.3961	1.4735	1.5546	1.6400	1.7305	1.8276	1.9341	2.0566
<i>c_p</i> (liq.)	2.3257	2.3054	2.3424	2.4242	2.5449	2.7051	2.9144	3.1994	3.6306	4.4382	6.9802
<i>c_p</i> (vap.)	1.5298	1.6387	1.7615	1.9024	2.0682	2.2705	2.5304	2.8917	3.4598	4.5706	8.1541
<i>w</i> (liq.)	875.75	836.04	789.18	736.55	679.48	618.85	554.99	487.71	416.20	338.70	251.34
<i>w</i> (vap.)	239.65	238.29	236.10	232.99	228.84	223.51	216.83	208.55	198.34	185.70	169.73
<i>Deuterium</i>											
<i>T</i>	20.000	22.000	24.000	26.000	28.000	30.000	32.000	34.000	36.000	37.000	38.000
<i>p</i>	0.0333	0.0678	0.1232	0.2055	0.3209	0.4767	0.6814	0.9432	1.2621	1.4389	1.6903
ρ (liq.)	171.96	167.25	161.96	156.41	150.64	144.33	136.77	126.83	113.42	103.75	83.193
ρ (vap.)	0.7929	1.4776	2.5031	3.9668	6.0163	8.9050	13.070	19.017	26.539	30.756	83.193
<i>h</i> (liq.)	−22.077	−9.5250	5.3945	22.156	40.366	60.234	82.614	109.06	140.62	160.36	195.52
<i>h</i> (vap.)	303.50	315.14	325.69	334.40	340.44	342.68	339.65	330.70	319.19	313.41	195.52
<i>s</i> (liq.)	−0.9991	−0.4114	0.2224	0.8721	1.5187	2.1673	2.8420	3.5829	4.4081	4.9041	5.7696
<i>s</i> (vap.)	15.280	14.346	13.568	12.882	12.236	11.582	10.874	10.102	9.3686	9.0408	5.7696
<i>c_v</i> (liq.)	3.5194	4.1411	4.6767	4.9486	4.9985	4.9028	4.7342	4.5971	4.7493	5.1300	6.4594
<i>c_v</i> (vap.)	2.4782	2.2988	2.1682	2.1164	2.1737	2.3814	2.8067	3.5034	4.3132	4.6790	6.4594

c_p (liq.)	5.6785	6.7969	7.8537	8.5907	9.2946	10.320	12.182	15.584	21.483	40.467	75.419
c_p (vap.)	4.1521	3.9417	3.8780	4.0466	4.5882	5.7989	8.3068	12.743	18.581	23.229	75.419
w (liq.)	1023.8	919.13	858.60	830.29	801.77	755.58	683.32	578.05	437.40	337.51	243.33
w (vap.)	266.64	280.24	292.49	302.87	310.72	315.32	316.51	315.63	313.14	309.68	243.33
σ	0.0038	0.0034	0.0030	0.0026	0.0021	0.0017	0.0013	0.0009	0.0005	0.0003	0.0000

Ethylene (Ethene, R-1150)

T	120.00	140.00	160.00	180.00	200.00	220.00	240.00	250.00	260.00	270.00	280.00
p	0.0014	0.0118	0.0562	0.1818	0.4555	0.9566	1.7730	2.3295	3.0035	3.8125	4.7835
ρ (liq.)	634.17	608.02	580.87	552.20	521.22	486.67	446.11	422.02	393.47	356.39	290.70
ρ (vap.)	0.0385	0.2876	1.2123	3.5889	8.4936	17.452	33.066	44.970	61.542	86.795	140.70
h (liq.)	-119.17	-70.809	-22.661	25.871	75.686	128.03	184.88	216.09	250.40	290.30	347.75
h (vap.)	428.29	451.32	473.00	492.31	508.13	519.07	522.74	520.39	513.45	498.32	457.49
s (liq.)	-0.8307	-0.4581	-0.1372	0.1473	0.4070	0.6516	0.8911	1.0132	1.1413	1.2836	1.4814
s (vap.)	3.7314	3.2714	2.9607	2.7386	2.5692	2.4290	2.2989	2.2304	2.1530	2.0541	1.8733
c_v (liq.)	1.5530	1.4655	1.3948	1.3464	1.3214	1.3196	1.3435	1.3679	1.4068	1.4839	1.7784
c_v (vap.)	0.8937	0.9064	0.9335	0.9783	1.0431	1.1320	1.2540	1.3344	1.4387	1.5918	1.9809
c_p (liq.)	2.4271	2.4081	2.4067	2.4413	2.5286	2.7002	3.0430	3.3629	3.9457	5.4086	19.562
c_p (vap.)	1.1920	1.2125	1.2598	1.3467	1.4920	1.7382	2.2112	2.6608	3.5116	5.7658	29.260
w (liq.)	1660.4	1520.9	1376.7	1227.0	1069.9	903.49	724.39	628.10	524.13	404.99	246.68
w (vap.)	217.51	233.95	247.39	256.98	261.94	261.54	254.88	248.80	240.47	229.17	208.88
η (liq.)	427.51	277.58	200.13	153.02	120.52	95.681	74.961	65.398	55.950	46.028	33.085
η (vap.)	3.3390	4.8414	5.6998	6.4011	7.1332	8.0066	9.1616	9.9344	10.957	12.506	16.176
λ (liq.)	248.79	222.34	197.46	174.60	153.73	134.45	116.07	106.84	97.241	86.860	83.422
λ (vap.)	6.7795	7.8923	9.1146	10.360	11.862	13.943	17.142	19.563	23.219	30.451	71.723
σ	0.0250	0.0212	0.0175	0.0140	0.0106	0.0075	0.0046	0.0033	0.0021	0.0010	0.0001

Fluorine

T	60.000	70.000	80.000	90.000	100.00	110.00	120.00	125.00	130.00	135.00	140.00
p	0.0015	0.0120	0.0547	0.1730	0.4275	0.8891	1.6342	2.1389	2.7475	3.4739	4.3357

continued

TABLE 2.7 Thermophysical Properties of Fluids along the Saturation Line^a (Continued)

<i>Fluorine (Continued)</i>											
ρ (liq.)	1665.4	1602.3	1536.5	1466.3	1390.0	1305.2	1207.4	1150.6	1084.8	1003.7	890.17
ρ (vap.)	0.1134	0.7882	3.1953	9.2442	21.494	43.338	80.165	107.32	143.72	195.17	278.28
h (liq.)	-37.242	-22.484	-7.5901	7.5700	23.208	39.593	57.183	66.712	77.048	88.724	103.17
h (vap.)	157.21	164.56	171.31	177.09	181.58	184.41	184.90	183.83	181.40	176.84	168.02
s (liq.)	-0.5175	-0.2901	-0.0916	0.0860	0.2488	0.4016	0.5494	0.6237	0.7005	0.7834	0.8817
s (vap.)	2.7233	2.3819	2.1446	1.9696	1.8325	1.7182	1.6138	1.5607	1.5032	1.4361	1.3449
c_v (liq.)	0.9015	0.8618	0.8352	0.8062	0.7772	0.7517	0.7329	0.7285	0.7314	0.7504	0.8149
c_v (vap.)	0.5482	0.5522	0.5622	0.5793	0.6027	0.6303	0.6641	0.6868	0.7186	0.7697	0.8707
c_p (liq.)	1.4654	1.4810	1.4964	1.5295	1.5855	1.6788	1.8572	2.0212	2.3048	2.8936	4.7992
c_p (vap.)	0.7686	0.7787	0.8043	0.8519	0.9269	1.0440	1.2591	1.4604	1.8232	2.6291	5.5472
w (liq.)	1043.5	973.15	871.16	779.02	692.27	603.67	506.54	452.05	391.41	321.84	238.35
w (vap.)	135.46	145.85	154.65	161.52	166.12	168.12	167.26	165.81	163.76	161.03	156.46
σ	0.0208	0.0177	0.0148	0.0120	0.0093	0.0067	0.0044	0.0033	0.0022	0.0013	0.0005
<i>Heavy Water (Deuterium oxide)</i>											
T	300.00	350.00	400.00	425.00	450.00	475.00	500.00	525.00	550.00	575.00	600.00
p	0.0031	0.0388	0.2374	0.4893	0.9205	1.6075	2.6406	4.1228	6.1713	8.9205	12.530
ρ (liq.)	1104.0	1080.3	1040.2	1015.3	987.24	955.76	920.48	880.63	834.82	780.47	712.24
ρ (vap.)	0.0246	0.2690	1.4704	2.9030	5.2871	9.0422	14.735	23.177	35.632	54.331	83.999
h (liq.)	-313.36	-102.51	105.78	209.99	315.22	422.31	532.19	646.06	765.72	894.20	1037.4
h (vap.)	1951.3	2032.9	2106.1	2136.7	2161.4	2178.8	2187.4	2185.2	2169.4	2134.8	2071.1
s (liq.)	-0.9330	-0.2829	0.2729	0.5250	0.7646	0.9946	1.2178	1.4368	1.6550	1.8773	2.1127
s (vap.)	6.6158	5.8181	5.2737	5.0585	4.8673	4.6926	4.5282	4.3685	4.2071	4.0349	3.8356
c_v (liq.)	4.2158	3.9214	3.5946	3.4528	3.3293	3.2237	3.1347	3.0614	3.0045	2.9694	2.9721
c_v (vap.)	1.3169	1.3891	1.4982	1.5800	1.6917	1.8413	2.0334	2.2679	2.5414	2.8503	3.1963
c_p (liq.)	4.2420	4.1850	4.1541	4.1763	4.2306	4.3211	4.4572	4.6615	4.9842	5.5435	6.7062
c_p (vap.)	1.7387	1.8326	2.0042	2.1482	2.3575	2.6583	3.0848	3.6902	4.5816	6.0279	8.8990

w (liq.)	1394.9	1457.7	1413.3	1366.2	1306.7	1235.6	1152.3	1056.2	946.14	820.49	674.99
w (vap.)	404.89	434.21	457.95	466.94	473.39	476.73	476.36	471.63	461.90	446.35	423.35
η (liq.)	1046.6	433.25	253.36	207.17	174.50	150.33	131.71	116.77	104.18	92.820	81.477
η (vap.)	10.228	11.828	13.544	14.395	15.229	16.050	16.871	17.722	18.655	19.769	21.290
λ (liq.)	596.96	631.93	633.11	624.05	609.65	590.46	566.82	538.88	506.76	470.46	430.22
λ (vap.)	18.277	22.532	27.812	31.041	34.820	39.366	45.081	52.701	63.267	76.284	98.667
σ	0.0716	0.0632	0.0536	0.0484	0.0429	0.0372	0.0313	0.0254	0.0194	0.0136	0.0079

Helium (R-704)

T	2.5000	2.7500	3.0000	3.2500	3.5000	3.7500	4.0000	4.2500	4.5000	4.7500	5.0000
p	0.0100	0.0159	0.0237	0.0339	0.0466	0.0622	0.0810	0.1032	0.1292	0.1594	0.1945
ρ (liq.)	144.96	143.37	141.35	138.91	136.06	132.75	128.90	124.35	118.81	111.65	100.83
ρ (vap.)	2.1163	3.1344	4.4284	6.0404	8.0221	10.443	13.406	17.077	21.756	28.103	38.213
h (liq.)	-6.1796	-5.5295	-4.8686	-4.1185	-3.2577	-2.2773	-1.1643	0.1065	1.5856	3.3849	5.8545
h (vap.)	16.972	17.858	18.659	19.361	19.947	20.396	20.679	20.749	20.525	19.838	18.183
s (liq.)	-1.6199	-1.3874	-1.1767	-0.9599	-0.7324	-0.4941	-0.2439	0.0216	0.3106	0.6427	1.0809
s (vap.)	7.6406	7.1170	6.6658	6.2645	5.8975	5.5522	5.2169	4.8785	4.5193	4.1065	3.5467
c_v (liq.)	2.5212	2.0330	2.0609	2.1996	2.3317	2.4323	2.5045	2.5575	2.6013	2.6462	2.7093
c_v (vap.)	3.4863	3.4759	3.4520	3.4184	3.3779	3.3325	3.2839	3.2328	3.1794	3.1221	3.0526
c_p (liq.)	2.7003	2.3729	2.5978	2.9782	3.4138	3.9093	4.5230	5.3796	6.7756	9.6775	20.240
c_p (vap.)	6.2582	6.4127	6.5921	6.8185	7.1215	7.5475	8.1786	9.1817	10.964	14.856	29.094
w (liq.)	216.03	216.77	214.33	209.15	202.40	194.56	185.70	175.63	164.00	150.22	132.96
w (vap.)	87.618	90.530	93.038	95.167	96.937	98.367	99.469	100.26	100.75	101.05	101.63
η (liq.)	3.7456	3.7462	3.6940	3.6113	3.5106	3.3987	3.2785	3.1500	3.0100	2.8488	2.6342
η (vap.)	0.6382	0.7164	0.7961	0.8783	0.9640	1.0544	1.1509	1.2554	1.3718	1.5075	1.6874
λ (liq.)	14.894	15.783	16.553	17.209	17.751	18.173	18.476	18.668	18.785	18.915	19.301
λ (vap.)	4.7651	5.3301	5.8927	6.4659	7.0604	7.6838	8.3555	9.1128	10.036	11.314	13.587
σ	0.0003	0.0002	0.0002	0.0002	0.0002	0.0001	0.0001	0.0001	0.0001	0.0000	0.0000

continued

TABLE 2.7 Thermophysical Properties of Fluids along the Saturation Line^a (Continued)

<i>Hydrogen (R-702)</i>											
<i>T</i>	14.000	16.000	18.000	20.000	22.000	24.000	26.000	28.000	30.000	31.000	32.000
<i>p</i>	0.0079	0.0215	0.0481	0.0932	0.1631	0.2641	0.4025	0.5852	0.8199	0.9596	1.1168
ρ (liq.)	76.867	75.116	73.220	71.110	68.727	65.997	62.801	58.916	53.838	50.432	45.636
ρ (vap.)	0.1391	0.3380	0.6880	1.2429	2.0666	3.2435	4.9001	7.2581	10.814	13.459	17.503
<i>h</i> (liq.)	−51.323	−36.642	−20.891	−2.7322	18.221	42.350	70.318	103.40	144.51	170.44	204.55
<i>h</i> (vap.)	397.84	415.41	430.92	443.88	453.66	459.49	460.25	454.04	436.68	420.39	392.55
<i>s</i> (liq.)	−2.9267	−1.9580	−1.0526	−0.1300	0.8199	1.8035	2.8358	3.9492	5.2217	5.9839	6.9620
<i>s</i> (vap.)	29.156	26.296	24.048	22.201	20.613	19.184	17.833	16.472	14.961	14.047	12.837
<i>c_v</i> (liq.)	5.4352	4.7859	5.1897	5.6168	5.9417	6.1793	6.3692	6.5599	6.8276	7.0430	7.4038
<i>c_v</i> (vap.)	6.5127	6.4022	6.4898	6.5876	6.7038	6.8464	7.0274	7.2696	7.6185	7.8644	8.2019
<i>c_p</i> (liq.)	7.7121	7.2964	8.2552	9.4843	10.881	12.575	14.893	18.656	26.883	37.140	70.365
<i>c_p</i> (vap.)	10.885	11.012	11.469	12.128	13.096	14.572	16.982	21.456	32.270	46.373	92.295
<i>w</i> (liq.)	1359.6	1271.6	1185.5	1110.7	1038.2	960.99	874.29	773.58	652.73	581.16	497.24
<i>w</i> (vap.)	305.17	325.05	340.22	352.59	362.25	369.34	373.96	376.19	375.97	374.91	373.31
η (liq.)	25.310	19.784	16.182	13.607	11.641	10.057	8.7151	7.5160	6.3620	5.7518	5.0391
η (vap.)	0.6670	0.8106	0.9355	1.0569	1.1819	1.3151	1.4619	1.6331	1.8628	2.0375	2.3378
λ (liq.)	76.650	90.079	98.405	103.01	104.87	104.60	102.53	98.654	92.547	88.221	82.176
λ (vap.)	10.431	12.681	14.669	16.716	18.956	21.493	24.477	28.202	33.407	37.226	43.200
σ	0.0030	0.0027	0.0023	0.0020	0.0017	0.0014	0.0011	0.0007	0.0004	0.0003	0.0002
<i>Hydrogen Sulfide</i>											
<i>T</i>	200.00	220.00	240.00	260.00	280.00	300.00	320.00	330.00	340.00	350.00	360.00
<i>p</i>	0.0504	0.1436	0.3374	0.6870	1.2555	2.1116	3.3296	4.1000	4.9939	6.0257	7.2129
ρ (liq.)	971.76	936.62	899.77	860.53	817.99	770.74	716.26	684.82	648.98	606.07	549.45
ρ (vap.)	1.0479	2.7604	6.1003	11.898	21.243	35.712	57.989	73.601	93.816	121.19	161.67
<i>h</i> (liq.)	−25.538	14.221	54.188	94.816	136.65	180.44	227.37	252.68	279.89	310.11	346.08
<i>h</i> (vap.)	534.46	551.02	565.59	577.58	586.27	590.63	588.92	584.82	577.57	565.71	545.98

s (liq.)	-0.1235	0.0655	0.2385	0.3994	0.5519	0.6992	0.8453	0.9198	0.9970	1.0798	1.1753
s (vap.)	2.6765	2.5055	2.3693	2.2562	2.1577	2.0665	1.9752	1.9263	1.8725	1.8101	1.7306
c_v (liq.)	1.2344	1.1873	1.1483	1.1162	1.0900	1.0697	1.0561	1.0529	1.0534	1.0604	1.0806
c_v (vap.)	0.7538	0.7721	0.7962	0.8254	0.8595	0.8990	0.9453	0.9720	1.0021	1.0369	1.0794
c_p (liq.)	1.9878	1.9854	2.0037	2.0468	2.1242	2.2577	2.5040	2.7174	3.0656	3.7338	5.5180
c_p (vap.)	1.0162	1.0547	1.1118	1.1936	1.3123	1.4961	1.8187	2.0937	2.5378	3.3708	5.4584
w (liq.)	1386.6	1280.4	1173.3	1064.3	951.91	834.38	708.55	640.77	568.10	488.44	398.78
w (vap.)	252.66	262.30	269.67	274.46	276.40	275.21	270.62	267.00	262.49	257.21	251.56
η (liq.)	386.41	311.85	252.16	204.45	165.98	134.42	107.82	95.796	84.274	72.846	60.710
η (vap.)	8.5566	9.4845	10.455	11.485	12.606	13.873	15.397	16.328	17.454	18.919	21.089
λ (liq.)	241.07	219.71	199.10	179.34	160.41	142.13	124.18	115.11	105.74	95.684	84.012
λ (vap.)	11.438	12.822	14.334	16.022	17.954	20.231	23.039	24.759	26.822	29.451	33.217

Krypton

T	120.00	130.00	140.00	150.00	160.00	170.00	180.00	185.00	190.00	195.00	200.00
p	0.1031	0.2108	0.3873	0.6547	1.0363	1.5562	2.2396	2.6512	3.1145	3.6339	4.2148
ρ (liq.)	2411.5	2334.5	2253.2	2166.2	2071.6	1966.5	1846.2	1777.8	1701.2	1613.0	1505.6
ρ (vap.)	8.9533	17.276	30.370	49.827	77.728	117.09	172.91	209.69	255.02	312.65	390.21
h (liq.)	0.1163	5.4315	10.873	16.509	22.422	28.727	35.606	39.354	43.396	47.852	52.975
h (vap.)	107.33	108.90	110.09	110.79	110.91	110.28	108.66	107.33	105.53	103.08	99.598
s (liq.)	0.0010	0.0431	0.0829	0.1209	0.1579	0.1946	0.2318	0.2511	0.2712	0.2928	0.3168
s (vap.)	0.8944	0.8391	0.7915	0.7495	0.7110	0.6743	0.6377	0.6185	0.5983	0.5760	0.5499
c_v (liq.)	0.2555	0.2454	0.2369	0.2299	0.2242	0.2202	0.2187	0.2194	0.2218	0.2271	0.2375
c_v (vap.)	0.1607	0.1673	0.1755	0.1853	0.1965	0.2095	0.2252	0.2347	0.2459	0.2598	0.2783
c_p (liq.)	0.5251	0.5335	0.5481	0.5706	0.6044	0.6566	0.7439	0.8130	0.9158	1.0866	1.4338
c_p (vap.)	0.2753	0.2928	0.3172	0.3510	0.3988	0.4707	0.5913	0.6890	0.8377	1.0909	1.6167
w (liq.)	685.71	643.02	598.86	552.79	504.18	452.07	394.88	363.54	329.61	292.16	249.52
w (vap.)	138.00	141.81	144.75	146.78	147.90	148.07	147.23	146.39	145.21	143.62	141.42

continued

88 TABLE 2.7 Thermophysical Properties of Fluids along the Saturation Line^a (Continued)

<i>Krypton (Continued)</i>											
η (liq.)	405.25	319.90	258.92	213.53	178.25	149.55	125.00	113.68	102.69	91.727	80.323
η (vap.)	10.282	11.243	12.261	13.353	14.550	15.900	17.506	18.466	19.599	21.008	22.922
λ (liq.)	110.26	101.11	92.317	83.757	75.416	67.252	59.207	55.204	51.199	47.196	43.284
λ (vap.)	3.6296	3.9992	4.4367	4.9695	5.6654	6.6462	8.1320	9.2053	10.663	12.775	16.186
σ	0.0155	0.0135	0.0115	0.0095	0.0076	0.0058	0.0041	0.0033	0.0025	0.0017	0.0011
<i>Methanol</i>											
T	200.00	250.00	300.00	325.00	350.00	375.00	400.00	425.00	450.00	475.00	500.00
p	6.1×10^{-6}	0.00081	0.0187	0.0603	0.1617	0.3748	0.7737	1.4561	2.5433	4.1688	6.5250
ρ (liq.)	880.28	831.52	784.51	760.74	735.84	708.86	678.59	643.38	600.49	544.35	451.53
ρ (vap.)	0.0001	0.0126	0.2462	0.7463	1.9053	4.2757	8.7343	16.754	30.831	54.371	109.88
h (liq.)	-334.31	-221.69	-100.87	-35.064	35.664	112.27	195.83	287.71	390.11	507.42	656.91
h (vap.)	955.68	1013.1	1065.3	1089.5	1111.6	1129.6	1140.4	1140.3	1129.3	1117.9	1048.0
s (liq.)	-1.2581	-0.7559	-0.3161	-0.1057	0.1035	0.3140	0.5281	0.7483	0.9783	1.2257	1.5223
s (vap.)	5.1918	4.1834	3.5711	3.3546	3.1777	3.0268	2.8894	2.7543	2.6209	2.5109	2.3044
c_v (liq.)	1.7695	1.8828	2.1179	2.2679	2.4278	2.5914	2.7555	2.9204	3.0907	3.2830	3.6076
c_v (vap.)	1.1423	1.9688	2.9830	3.3331	3.5800	3.7842	4.0140	4.2985	4.4435	4.0231	3.9538
c_p (liq.)	2.2141	2.3121	2.5461	2.7223	2.9362	3.1891	3.4912	3.8713	4.4067	5.3805	9.9683
c_p (vap.)	1.4194	2.3704	3.6638	4.1950	4.6631	5.1821	5.9366	7.1409	8.2711	8.1500	19.040
w (liq.)	1471.1	1266.7	1093.5	1015.5	938.89	859.31	772.84	676.21	567.09	441.11	269.59
w (vap.)	253.63	276.25	297.15	305.94	312.61	316.20	315.37	308.41	295.26	275.02	236.75
σ	0.0313	0.0264	0.0221	0.0200	0.0179	0.0155	0.0130	0.0103	0.0073	0.0042	0.0012
<i>Neon (R-720)</i>											
T	26.000	28.000	30.000	32.000	34.000	36.000	38.000	40.000	42.000	43.000	44.000
p	0.0716	0.1316	0.2231	0.3545	0.5344	0.7720	1.0770	1.4603	1.9355	2.2121	2.5168

ρ (liq.)	1226.1	1191.2	1154.0	1113.1	1068.3	1018.9	963.27	897.21	807.59	739.37	632.15
ρ (vap.)	6.9815	12.168	19.828	30.680	45.664	66.143	94.361	134.66	197.94	248.26	333.79
h (liq.)	-2.0721	1.6942	5.6339	9.8416	14.330	19.129	24.344	30.236	37.552	42.540	49.772
h (vap.)	84.820	86.375	87.428	88.045	88.180	87.726	86.492	84.107	79.688	75.959	69.666
s (liq.)	-0.0771	0.0606	0.1937	0.3257	0.4568	0.5874	0.7200	0.8604	1.0251	1.1340	1.2900
s (vap.)	3.2649	3.0849	2.9202	2.7696	2.6288	2.4928	2.3554	2.2072	2.0283	1.9112	1.7421
c_v (liq.)	0.9016	0.8822	0.8608	0.8401	0.8233	0.8140	0.8146	0.8283	0.8683	0.9153	1.0016
c_v (vap.)	1.0924	0.7929	0.7237	0.7218	0.7434	0.7774	0.8233	0.8852	0.9730	1.0319	1.1005
c_p (liq.)	1.8756	1.8931	2.0117	2.1481	2.2966	2.4903	2.8047	3.4429	5.3776	8.7614	22.206
c_p (vap.)	1.6402	1.3352	1.3141	1.3990	1.5570	1.8104	2.2403	3.0926	5.4496	9.1322	27.296
w (liq.)	617.51	579.65	548.99	514.19	474.28	429.96	381.08	325.39	256.54	213.78	170.57
w (vap.)	121.12	130.23	135.55	138.54	140.26	141.11	141.18	140.49	138.95	137.87	136.83
η (liq.)	130.15	106.36	88.574	74.741	63.597	54.286	46.180	38.726	31.144	26.666	20.958
η (vap.)	4.3247	4.7040	5.1031	5.5284	5.9702	6.4766	7.0646	7.8037	8.9012	9.8049	11.526
λ (liq.)	161.88	149.59	137.57	125.73	114.09	102.69	91.512	80.499	69.885	66.995	129.48
λ (vap.)	6.3618	6.9727	7.7049	8.6200	9.9203	11.433	13.666	17.259	24.333	31.873	54.986
σ	0.0050	0.0041	0.0034	0.0026	0.0020	0.0014	0.0010	0.0006	0.0003	0.0001	0.0000

Nitrogen (R-728)

T	70.000	80.000	85.000	90.000	95.000	100.00	105.00	110.00	115.00	120.00	125.00
p	0.0385	0.1369	0.2289	0.3605	0.5405	0.7783	1.0833	1.4658	1.9370	2.5106	3.2069
ρ (liq.)	838.51	793.94	770.13	745.02	718.26	689.35	657.52	621.45	578.70	523.36	426.08
ρ (vap.)	1.8960	6.0894	9.8241	15.079	22.272	31.961	44.959	62.579	87.294	125.09	205.18
h (liq.)	-136.97	-116.58	-106.16	-95.517	-84.571	-73.209	-61.268	-48.486	-34.389	-17.870	6.4029
h (vap.)	71.098	79.099	82.352	84.970	86.828	87.766	87.557	85.835	81.911	74.173	55.034
s (liq.)	2.6321	2.9028	3.0277	3.1473	3.2630	3.3761	3.4882	3.6015	3.7198	3.8514	4.0373
s (vap.)	5.6045	5.3487	5.2454	5.1527	5.0672	4.9858	4.9055	4.8226	4.7311	4.6185	4.4263
c_v (liq.)	1.1297	1.0691	1.0429	1.0196	0.9996	0.9832	0.9715	0.9667	0.9742	1.0106	1.2380
c_v (vap.)	0.7580	0.7773	0.7909	0.8078	0.8288	0.8548	0.8874	0.9284	0.9896	1.0985	1.4021

continued

TABLE 2.7 Thermophysical Properties of Fluids along the Saturation Line^a (Continued)

<i>Nitrogen (Continued)</i>											
c_p (liq.)	2.0145	2.0555	2.0906	2.1407	2.2126	2.3180	2.4789	2.7433	3.2403	4.5076	16.717
c_p (vap.)	1.0816	1.1449	1.1957	1.2655	1.3628	1.5026	1.7139	2.0618	2.7490	4.6309	23.743
w (liq.)	925.74	824.36	772.44	719.01	663.50	605.23	543.30	476.44	402.67	317.33	195.48
w (vap.)	168.42	176.72	179.68	181.78	182.99	183.25	182.51	180.76	177.75	172.61	160.26
η (liq.)	219.88	145.05	121.11	102.53	87.656	75.375	64.882	55.566	46.895	38.206	27.250
η (vap.)	4.8792	5.6413	6.0405	6.4592	6.9056	7.3920	7.9386	8.5822	9.4010	10.611	13.460
λ (liq.)	161.84	140.20	129.93	119.89	110.09	100.50	91.091	81.788	72.515	63.318	59.228
λ (vap.)	6.7968	7.7802	8.3518	9.0210	9.8408	10.893	12.314	14.350	17.541	23.495	45.040
σ	0.0106	0.0083	0.0072	0.0061	0.0050	0.0041	0.0031	0.0022	0.0014	0.0007	0.0001
<i>Nitrogen Trifluoride</i>											
T	100.00	120.00	140.00	160.00	170.00	180.00	190.00	200.00	210.00	220.00	230.00
p	0.00095	0.0128	0.0752	0.2719	0.4576	0.7246	1.0918	1.5791	2.2073	3.0003	3.9918
ρ (liq.)	1734.8	1648.8	1557.5	1459.6	1406.8	1350.1	1288.0	1217.8	1135.4	1030.8	862.72
ρ (vap.)	0.0809	0.9158	4.7318	15.700	25.765	40.315	60.917	89.943	131.52	194.82	317.54
h (liq.)	-44.273	-24.275	-4.2035	16.448	27.219	38.442	50.264	62.889	76.645	92.252	112.76
h (vap.)	142.74	152.12	161.00	168.69	171.85	174.41	176.21	177.00	176.36	173.29	163.59
s (liq.)	-0.3661	-0.1838	-0.0295	0.1075	0.1720	0.2350	0.2974	0.3601	0.4246	0.4938	0.5802
s (vap.)	1.5040	1.2861	1.1505	1.0590	1.0228	0.9904	0.9603	0.9307	0.8995	0.8621	0.8012
c_v (liq.)	0.6268	0.5889	0.5693	0.5659	0.5689	0.5750	0.5844	0.5983	0.6189	0.6508	0.7112
c_v (vap.)	0.3627	0.3806	0.4100	0.4513	0.4764	0.5044	0.5357	0.5705	0.6099	0.6568	0.7232
c_p (liq.)	1.0016	0.9983	1.0106	1.0543	1.0923	1.1451	1.2190	1.3278	1.5091	1.9114	4.3165
c_p (vap.)	0.4804	0.5022	0.5441	0.6151	0.6662	0.7329	0.8236	0.9566	1.1806	1.6856	4.6205
w (liq.)	1018.1	894.02	779.79	671.28	614.73	554.78	490.50	421.22	346.33	264.69	171.03
w (vap.)	124.38	135.01	142.91	147.30	147.95	147.44	145.68	142.53	137.79	131.07	121.80

Oxygen (R-732)

<i>T</i>	60.000	70.000	80.000	90.000	100.00	110.00	120.00	130.00	140.00	145.00	150.00
<i>p</i>	0.00073	0.0063	0.0301	0.0994	0.2540	0.5434	1.0223	1.7491	2.7878	3.4477	4.2186
ρ (liq.)	1282.0	1237.0	1190.5	1142.1	1090.9	1035.5	973.85	902.48	813.24	755.13	675.48
ρ (vap.)	0.0466	0.3457	1.4684	4.3871	10.425	21.281	39.308	68.369	116.76	154.91	214.94
<i>h</i> (liq.)	−184.19	−167.42	−150.61	−133.69	−116.45	−98.641	−79.904	−59.662	−36.695	−23.219	−6.6708
<i>h</i> (vap.)	54.188	63.092	71.695	79.551	86.155	91.054	93.754	93.466	88.474	82.830	72.562
<i>s</i> (liq.)	2.2571	2.5155	2.7397	2.9383	3.1184	3.2855	3.4444	3.6001	3.7612	3.8498	3.9546
<i>s</i> (vap.)	6.2300	5.8086	5.5185	5.3076	5.1445	5.0100	4.8915	4.7780	4.6552	4.5812	4.4828
<i>c_v</i> (liq.)	1.0886	1.0167	0.9697	0.9296	0.8949	0.8658	0.8430	0.8293	0.8323	0.8497	0.9057
<i>c_v</i> (vap.)	0.6818	0.7052	0.6950	0.6758	0.6752	0.6988	0.7415	0.8002	0.8834	0.9461	1.0492
<i>c_p</i> (liq.)	1.6734	1.6781	1.6816	1.6989	1.7375	1.8068	1.9271	2.1534	2.6907	3.3684	5.4639
<i>c_p</i> (vap.)	0.9475	0.9780	0.9743	0.9705	1.0064	1.1014	1.2763	1.6002	2.3696	3.3693	6.6254
<i>w</i> (liq.)	1127.4	1066.3	987.43	905.90	822.19	734.77	641.52	539.50	423.10	355.20	273.80
<i>w</i> (vap.)	147.03	158.07	168.36	177.30	184.06	188.14	189.41	187.75	182.82	178.78	172.82
η (liq.)	648.81	395.81	268.59	196.85	152.43	122.72	101.36	84.640	69.800	62.062	52.886
η (vap.)	4.4773	5.2944	6.1260	6.9976	7.9429	9.0060	10.253	11.812	14.010	15.663	18.361
λ (liq.)	194.02	180.49	166.32	151.89	137.31	122.49	107.41	92.121	77.064	70.180	64.843
λ (vap.)	5.2712	6.2754	7.2936	8.3487	9.4862	10.795	12.450	14.807	18.760	22.190	28.695
σ	0.0211	0.0184	0.0158	0.0132	0.0108	0.0084	0.0061	0.0040	0.0021	0.0013	0.0005

Parahydrogen (R-702p)

<i>T</i>	14.000	16.000	18.000	20.000	22.000	24.000	26.000	28.000	30.000	31.000	32.000
<i>p</i>	0.0079	0.0215	0.0481	0.0932	0.1631	0.2641	0.4025	0.5852	0.8199	0.9596	1.1168
ρ (liq.)	76.867	75.116	73.220	71.110	68.727	65.997	62.801	58.916	53.838	50.432	45.636
ρ (vap.)	0.1391	0.3380	0.6880	1.2429	2.0666	3.2435	4.9001	7.2581	10.814	13.459	17.503
<i>h</i> (liq.)	−51.158	−36.595	−20.869	−2.7300	18.209	42.329	70.294	103.39	144.50	170.45	204.57
<i>h</i> (vap.)	398.00	415.46	430.94	443.88	453.65	459.47	460.22	454.02	436.67	420.40	392.57
<i>s</i> (liq.)	−2.9159	−1.9553	−1.0514	−0.1299	0.8193	1.8025	2.8347	3.9483	5.2213	5.9839	6.9625

continued

TABLE 2.7 Thermophysical Properties of Fluids along the Saturation Line^a (Continued)

<i>Parahydrogen (R-702p) (Continued)</i>											
s (vap.)	29.167	26.298	24.049	22.201	20.612	19.183	17.832	16.471	14.960	14.047	12.838
c_v (liq.)	5.2321	4.7725	5.1779	5.6085	5.9359	6.1759	6.3695	6.5651	6.8381	7.0562	7.4195
c_v (vap.)	6.3096	6.3887	6.4780	6.5793	6.6980	6.8430	7.0278	7.2748	7.6290	7.8776	8.2177
c_p (liq.)	7.5091	7.2829	8.2434	9.4761	10.875	12.572	14.894	18.661	26.893	37.153	70.380
c_p (vap.)	10.682	10.998	11.457	12.120	13.090	14.569	16.982	21.461	32.280	46.387	92.311
w (liq.)	1367.4	1272.2	1186.0	1111.1	1038.4	961.13	874.28	773.39	652.36	580.72	496.76
w (vap.)	307.13	325.20	340.35	352.69	362.33	369.39	373.96	376.10	375.77	374.65	372.98
η (liq.)	25.310	19.784	16.182	13.607	11.641	10.057	8.7151	7.5160	6.3620	5.7518	5.0391
η (vap.)	0.6670	0.8106	0.9355	1.0569	1.1819	1.3151	1.4619	1.6331	1.8628	2.0375	2.3378
λ (liq.)	76.869	90.003	98.339	103.00	104.89	104.64	102.56	98.669	92.543	88.209	82.155
λ (vap.)	10.649	12.604	14.603	16.705	18.981	21.529	24.507	28.217	33.404	37.214	43.179
σ	0.0030	0.0026	0.0023	0.0020	0.0016	0.0013	0.0010	0.0007	0.0004	0.0003	0.0001
<i>Perfluorobutane (Decafluorobutane)</i>											
T	200.00	220.00	240.00	260.00	280.00	300.00	320.00	340.00	360.00	370.00	380.00
p	0.0016	0.0071	0.0238	0.0635	0.1432	0.2846	0.5131	0.8582	1.3548	1.6737	2.0512
ρ (liq.)	1790.9	1739.5	1684.9	1626.1	1561.8	1490.0	1407.5	1308.1	1176.4	1084.1	943.56
ρ (vap.)	0.2240	0.9323	2.8907	7.2680	15.730	30.613	55.438	96.371	167.48	226.83	331.05
h (liq.)	-69.244	-50.453	-31.173	-11.288	9.2884	30.651	52.937	76.393	101.61	115.40	131.16
h (vap.)	49.696	62.322	75.566	89.260	103.22	117.22	130.99	144.10	155.65	160.06	161.84
s (liq.)	-0.2952	-0.2057	-0.1219	-0.0424	0.0336	0.1070	0.1784	0.2487	0.3196	0.3566	0.3976
s (vap.)	0.2995	0.3069	0.3228	0.3443	0.3691	0.3955	0.4223	0.4478	0.4697	0.4773	0.4783
c_v (liq.)	0.7851	0.7959	0.8142	0.8353	0.8571	0.8794	0.9022	0.9269	0.9572	0.9784	1.0086
c_v (vap.)	0.5841	0.6273	0.6696	0.7112	0.7528	0.7946	0.8372	0.8820	0.9327	0.9638	1.0069
c_p (liq.)	0.9301	0.9504	0.9779	1.0099	1.0463	1.0885	1.1414	1.2184	1.3753	1.5773	2.3729
c_p (vap.)	0.6196	0.6639	0.7084	0.7545	0.8038	0.8595	0.9279	1.0271	1.2313	1.4992	2.6364
w (liq.)	665.06	602.10	538.46	476.02	414.72	353.81	292.10	227.66	156.85	117.66	76.452

w (vap.)	85.873	89.483	92.376	94.250	94.770	93.564	90.163	83.851	73.248	65.430	54.827
σ	0.0178	0.0155	0.0133	0.0111	0.0090	0.0070	0.0051	0.0033	0.0017	0.0009	0.0003

Perfluoropentane (Dodecafluoropentane)

T	220.00	240.00	260.00	280.00	300.00	320.00	340.00	360.00	380.00	400.00	420.00
p	0.0010	0.0044	0.0147	0.0397	0.0909	0.1832	0.3348	0.5664	0.9016	1.3696	2.0154
ρ (liq.)	1866.0	1804.0	1740.9	1675.7	1607.4	1534.5	1454.6	1364.2	1256.0	1110.4	790.04
ρ (vap.)	0.1538	0.6356	1.9857	5.0554	11.073	21.731	39.427	67.915	114.18	195.87	446.07
h (liq.)	-85.533	-65.657	-45.368	-24.559	-3.1602	18.896	41.695	65.373	90.197	116.87	150.50
h (vap.)	31.600	45.274	59.599	74.444	89.660	105.08	120.51	135.67	150.13	162.82	166.32
s (liq.)	-0.3288	-0.2424	-0.1612	-0.0842	-0.0105	0.0605	0.1293	0.1965	0.2629	0.3303	0.4105
s (vap.)	0.2036	0.2199	0.2425	0.2694	0.2989	0.3298	0.3611	0.3918	0.4206	0.4451	0.4482
c_v (liq.)	0.7650	0.7831	0.8089	0.8368	0.8647	0.8921	0.9191	0.9463	0.9756	1.0122	1.0786
c_v (vap.)	0.6404	0.6816	0.7215	0.7605	0.7988	0.8368	0.8749	0.9136	0.9546	1.0021	1.0877
c_p (liq.)	0.9862	1.0029	1.0265	1.0542	1.0850	1.1198	1.1606	1.2131	1.2944	1.4863	7.2710
c_p (vap.)	0.6696	0.7115	0.7528	0.7944	0.8375	0.8838	0.9363	1.0023	1.1034	1.3447	9.1686
w (liq.)	690.92	625.87	560.34	496.98	435.94	376.54	317.78	258.33	196.07	127.37	47.747
w (vap.)	81.346	84.569	87.264	89.195	90.088	89.644	87.507	83.193	75.897	63.940	42.446
σ	0.0175	0.0154	0.0134	0.0114	0.0095	0.0076	0.0059	0.0042	0.0026	0.0011	0.0000

Perfluoropropane (Octafluoropropane, R-218)

T	140.00	160.00	180.00	200.00	220.00	240.00	260.00	280.00	300.00	320.00	340.00
p	0.000028	0.00041	0.0030	0.0138	0.0455	0.1193	0.2637	0.5142	0.9123	1.5087	2.3722
ρ (liq.)	1944.6	1876.2	1808.5	1740.1	1669.4	1594.6	1513.5	1422.4	1314.7	1174.7	918.89
ρ (vap.)	0.0045	0.0583	0.3796	1.5753	4.8108	11.891	25.406	49.244	90.244	164.29	339.94
h (liq.)	77.035	93.906	111.07	128.75	147.08	166.20	186.24	207.38	229.92	254.58	284.94
h (vap.)	213.34	223.37	234.24	245.79	257.81	270.09	282.37	294.32	305.43	314.56	317.26
s (liq.)	0.3920	0.5046	0.6057	0.6987	0.7860	0.8690	0.9488	1.0264	1.1032	1.1811	1.2705

continued

TABLE 2.7 Thermophysical Properties of Fluids along the Saturation Line^a (Continued)

<i>Perfluoropropane (Octafluoropropane, R-218) (Continued)</i>											
<i>s</i> (vap.)	1.3656	1.3138	1.2899	1.2839	1.2893	1.3018	1.3185	1.3369	1.3549	1.3686	1.3656
<i>c_v</i> (liq.)	0.5459	0.5699	0.5994	0.6314	0.6643	0.6977	0.7312	0.7653	0.8009	0.8411	0.9086
<i>c_v</i> (vap.)	0.4350	0.4807	0.5247	0.5682	0.6121	0.6571	0.7028	0.7494	0.7978	0.8517	0.9276
<i>c_p</i> (liq.)	0.8413	0.8487	0.8696	0.8989	0.9346	0.9764	1.0259	1.0885	1.1796	1.3643	2.9357
<i>c_p</i> (vap.)	0.4792	0.5250	0.5696	0.6150	0.6633	0.7165	0.7772	0.8517	0.9598	1.1880	2.8405
<i>w</i> (liq.)	1011.3	892.00	787.19	692.48	604.62	521.14	440.07	359.64	277.92	191.43	87.125
<i>w</i> (vap.)	82.581	87.853	92.650	96.748	99.796	101.38	101.04	98.200	92.062	81.308	63.602
σ	0.0228	0.0201	0.0175	0.0150	0.0125	0.0101	0.0078	0.0056	0.0036	0.0018	0.0003
<i>Propylene (Propene, R-1270)</i>											
<i>T</i>	160.00	180.00	200.00	220.00	240.00	260.00	280.00	300.00	320.00	340.00	360.00
<i>p</i>	0.0012	0.0070	0.0269	0.0785	0.1877	0.3874	0.7150	1.2118	1.9231	2.9015	4.2202
ρ (liq.)	685.79	663.00	639.79	615.80	590.59	563.65	534.23	501.22	462.62	413.59	329.22
ρ (vap.)	0.0386	0.1968	0.6889	1.8601	4.1883	8.2949	15.017	25.615	42.352	70.506	133.82
<i>h</i> (liq.)	−46.027	−5.6479	35.723	78.278	122.36	168.41	216.94	268.70	324.84	388.00	471.23
<i>h</i> (vap.)	457.53	479.22	501.31	523.35	544.87	565.30	583.97	599.91	611.43	614.68	593.11
<i>s</i> (liq.)	−0.1487	0.0889	0.3067	0.5090	0.7000	0.8828	1.0604	1.2356	1.4119	1.5964	1.8237
<i>s</i> (vap.)	2.9985	2.7827	2.6346	2.5321	2.4604	2.4093	2.3712	2.3396	2.3075	2.2631	2.1622
<i>c_v</i> (liq.)	1.2910	1.3130	1.3325	1.3589	1.3949	1.4404	1.4950	1.5584	1.6321	1.7217	1.8578
<i>c_v</i> (vap.)	0.8826	0.9368	0.9987	1.0695	1.1496	1.2393	1.3389	1.4493	1.5731	1.7160	1.8962
<i>c_p</i> (liq.)	1.9939	2.0426	2.0941	2.1592	2.2433	2.3518	2.4940	2.6918	3.0073	3.7071	9.4092
<i>c_p</i> (vap.)	1.0812	1.1385	1.2081	1.2941	1.4014	1.5369	1.7144	1.9649	2.3754	3.2987	10.060
<i>w</i> (liq.)	1573.5	1450.8	1328.3	1203.5	1075.9	946.08	814.70	681.71	545.64	401.15	229.03
<i>w</i> (vap.)	196.55	206.90	215.70	222.51	226.88	228.30	226.21	219.92	208.55	190.85	164.25
σ	0.0272	0.0239	0.0207	0.0176	0.0146	0.0118	0.0090	0.0064	0.0041	0.0020	0.0003

Propyne (Methyl Acetylene)

<i>T</i>	280.00	300.00	320.00	330.00	340.00	350.00	360.00	370.00	380.00	390.00	400.00
<i>p</i>	0.3335	0.6142	1.0494	1.3399	1.6878	2.0999	2.5834	3.1460	3.7958	4.5427	5.4015
ρ (liq.)	640.72	608.37	574.86	557.05	538.14	517.73	495.22	469.69	439.34	399.70	328.84
ρ (vap.)	6.2075	11.137	18.918	24.310	31.044	39.505	50.262	64.241	83.182	111.33	170.13
<i>h</i> (liq.)	214.96	259.99	308.98	335.53	363.70	393.70	425.83	460.54	498.76	542.80	604.67
<i>h</i> (vap.)	702.61	723.17	741.02	748.48	754.64	759.16	761.59	761.21	756.71	744.86	709.59
<i>s</i> (liq.)	1.0537	1.2074	1.3631	1.4432	1.5254	1.6101	1.6979	1.7898	1.8878	1.9976	2.1481
<i>s</i> (vap.)	2.7953	2.7514	2.7132	2.6945	2.6752	2.6542	2.6305	2.6024	2.5666	2.5157	2.4104
<i>c_v</i> (liq.)	0.7129	0.9966	1.2488	1.3648	1.4750	1.5802	1.6812	1.7799	1.8800	1.9922	2.1785
<i>c_v</i> (vap.)	1.3614	1.4656	1.5825	1.6484	1.7212	1.8028	1.8957	2.0031	2.1290	2.2788	2.4494
<i>c_p</i> (liq.)	2.1869	2.3279	2.5802	2.7406	2.9274	3.1507	3.4333	3.8296	4.4951	6.1004	20.603
<i>c_p</i> (vap.)	1.6777	1.8543	2.0974	2.2624	2.4748	2.7607	3.1683	3.8008	4.9329	7.6836	30.312
<i>w</i> (liq.)	1574.9	1180.1	937.04	839.03	748.75	662.69	578.26	493.25	405.36	311.27	202.30
<i>w</i> (vap.)	246.19	245.98	242.39	239.13	234.76	229.17	222.15	213.39	202.31	187.67	166.14
σ	0.0137	0.0109	0.0083	0.0071	0.0059	0.0047	0.0036	0.0026	0.0016	0.0008	0.0001

Sulfur Dioxide (R-764)

<i>T</i>	280.00	300.00	320.00	340.00	360.00	370.00	380.00	390.00	400.00	410.00	420.00
<i>p</i>	0.2337	0.4440	0.7897	1.3224	2.1006	2.6020	3.1898	3.8734	4.6632	5.5711	6.6128
ρ (liq.)	1441.8	1373.2	1307.1	1239.8	1167.2	1127.2	1083.4	1034.5	978.02	909.56	817.46
ρ (vap.)	6.8047	12.411	21.500	35.666	57.320	72.134	90.627	114.07	144.64	186.69	251.94
<i>h</i> (liq.)	200.59	208.65	223.87	244.45	269.61	283.90	299.45	316.45	335.26	356.62	382.49
<i>h</i> (vap.)	524.14	532.10	538.57	543.11	545.00	544.62	543.07	539.99	534.77	526.21	511.17
<i>s</i> (liq.)	1.0020	1.0291	1.0773	1.1384	1.2083	1.2463	1.2863	1.3288	1.3744	1.4248	1.4842
<i>s</i> (vap.)	2.1576	2.1073	2.0608	2.0167	1.9733	1.9509	1.9274	1.9020	1.8732	1.8384	1.7906
<i>c_v</i> (liq.)						0.5977	0.6615	0.7193	0.7753	0.8350	0.9090
<i>c_v</i> (vap.)	0.5446	0.5786	0.6167	0.6598	0.7100	0.7389	0.7715	0.8089	0.8533	0.9085	0.9825
<i>c_p</i> (liq.)						1.5129	1.6701	1.8742	2.1738	2.7111	4.1931

continued

88 **TABLE 2.7 Thermophysical Properties of Fluids along the Saturation Line^a (Continued)**

<i>Sulfur Dioxide (R-764) (Continued)</i>											
c_p (vap.)	0.7273	0.7888	0.8690	0.9790	1.1435	1.2631	1.4278	1.6715	2.0740	2.8740	5.2428
w (liq.)						623.50	545.29	473.03	402.63	330.91	254.54
w (vap.)	207.80	210.92	212.27	211.55	208.35	205.67	202.14	197.66	192.05	185.08	176.18
σ	0.0252	0.0214	0.0176	0.0138	0.0102	0.0085	0.0068	0.0052	0.0037	0.0023	0.0010
<i>Sulfur Hexafluoride</i>											
T	230.00	240.00	250.00	260.00	270.00	280.00	290.00	295.00	300.00	305.00	310.00
p	0.3056	0.4445	0.6264	0.8590	1.1502	1.5088	1.9447	2.1952	2.4696	2.7698	3.0984
ρ (liq.)	1814.6	1762.4	1706.3	1646.1	1580.7	1508.0	1424.1	1375.7	1320.8	1256.3	1176.3
ρ (vap.)	25.484	36.561	51.245	70.523	95.801	129.25	174.58	203.77	239.35	284.28	344.86
h (liq.)	160.42	168.75	177.65	187.01	196.81	207.12	218.08	223.91	230.05	236.63	243.90
h (vap.)	266.93	271.10	275.12	278.93	282.42	285.46	287.79	288.56	288.94	288.75	287.60
s (liq.)	0.8450	0.8801	0.9161	0.9522	0.9885	1.0251	1.0626	1.0819	1.1018	1.1228	1.1456
s (vap.)	1.3081	1.3066	1.3059	1.3057	1.3056	1.3049	1.3029	1.3010	1.2981	1.2937	1.2865
c_v (liq.)	0.4792	0.5205	0.5523	0.5787	0.6023	0.6250	0.6485	0.6611	0.6749	0.6908	0.7120
c_v (vap.)	0.4943	0.5206	0.5476	0.5756	0.6050	0.6362	0.6704	0.6893	0.7102	0.7341	0.7637
c_p (liq.)	0.7963	0.8624	0.9126	0.9581	1.0085	1.0751	1.1778	1.2566	1.3718	1.5592	1.9345
c_p (vap.)	0.5784	0.6167	0.6609	0.7138	0.7808	0.8727	1.0161	1.1278	1.2952	1.5798	2.1856
w (liq.)	539.86	489.70	440.25	391.49	343.00	294.10	243.92	218.04	191.41	163.77	134.40
w (vap.)	112.77	112.19	110.92	108.86	105.91	101.93	96.707	93.543	89.944	85.845	81.148
σ	0.0104	0.0089	0.0075	0.0061	0.0048	0.0036	0.0024	0.0019	0.0014	0.0009	0.0005
<i>Toluene (Methylbenzene)</i>											
T	200.00	250.00	300.00	350.00	400.00	425.00	450.00	475.00	500.00	525.00	550.00
p	1.1×10^{-6}	0.00018	0.0042	0.0348	0.1576	0.2878	0.4875	0.7775	1.1804	1.7220	2.4326
ρ (liq.)	951.41	905.53	859.98	813.06	762.88	735.78	706.70	674.88	639.11	597.24	544.89

ρ (vap.)	0.0001	0.0078	0.1546	1.1231	4.6109	8.1655	13.600	21.661	33.501	51.153	78.960
h (liq.)	-312.30	-236.54	-154.93	-65.411	33.182	86.171	141.80	200.27	261.90	327.27	397.62
h (vap.)	164.08	205.88	257.25	317.25	383.99	419.15	454.98	491.00	526.46	560.19	589.90
s (liq.)	-1.0886	-0.7508	-0.4537	-0.1781	0.0845	0.2125	0.3391	0.4646	0.5897	0.7156	0.8441
s (vap.)	1.2933	1.0188	0.9203	0.9152	0.9615	0.9960	1.0350	1.0766	1.1189	1.1592	1.1937
c_v (liq.)	1.0597	1.1466	1.2799	1.4315	1.5884	1.6664	1.7432	1.8189	1.8938	1.9690	2.0480
c_v (vap.)	0.6507	0.8447	1.0465	1.2501	1.4528	1.5530	1.6523	1.7508	1.8496	1.9504	2.0581
c_p (liq.)	1.4803	1.5643	1.7064	1.8771	2.0664	2.1682	2.2774	2.3987	2.5429	2.7358	3.0588
c_p (vap.)	0.7409	0.9351	1.1387	1.3493	1.5705	1.6877	1.8130	1.9532	2.1236	2.3641	2.8127
w (liq.)	1746.0	1505.2	1287.9	1088.3	898.66	805.26	711.52	616.36	518.61	416.90	309.53
w (vap.)	143.36	157.98	170.97	181.24	186.72	186.88	184.82	180.07	171.98	159.69	141.94
σ	0.0406	0.0340	0.0278	0.0219	0.0163	0.0136	0.0111	0.0087	0.0064	0.0043	0.0024

Water (R-718)

T	300.00	350.00	400.00	425.00	450.00	475.00	500.00	525.00	550.00	575.00	600.00
p	0.0035	0.0417	0.2458	0.5003	0.9322	1.6160	2.6392	4.1019	6.1172	8.8140	12.345
ρ (liq.)	996.51	973.70	937.49	915.27	890.34	862.49	831.31	796.13	755.81	708.30	649.41
ρ (vap.)	0.0256	0.2603	1.3694	2.6693	4.8120	8.1598	13.199	20.617	31.474	47.607	72.842
h (liq.)	112.56	321.79	532.95	640.17	749.16	860.62	975.43	1094.8	1220.5	1355.4	1505.4
h (vap.)	2549.9	2637.7	2715.7	2748.1	2774.4	2793.1	2802.5	2800.3	2783.3	2746.0	2677.8
s (liq.)	0.3931	1.0380	1.6013	1.8606	2.1087	2.3480	2.5810	2.8104	3.0394	3.2727	3.5190
s (vap.)	8.5174	7.6549	7.0581	6.8205	6.6092	6.4164	6.2351	6.0591	5.8809	5.6912	5.4731
c_v (liq.)	4.1305	3.8895	3.6324	3.5149	3.4077	3.3112	3.2255	3.1515	3.0913	3.0510	3.0475
c_v (vap.)	1.4422	1.5053	1.6435	1.7594	1.9074	2.0800	2.2714	2.4818	2.7181	2.9928	3.3271
c_p (liq.)	4.1809	4.1946	4.2555	4.3120	4.3927	4.5055	4.6635	4.8901	5.2331	5.8055	6.9532
c_p (vap.)	1.9141	2.0033	2.2183	2.4105	2.6742	3.0181	3.4631	4.0622	4.9332	6.3560	9.1809
w (liq.)	1501.4	1554.8	1509.5	1461.8	1400.4	1326.1	1239.6	1140.5	1027.9	899.25	749.57
w (vap.)	427.89	459.58	484.67	493.86	500.41	504.09	504.55	501.23	493.31	479.46	457.33
η (liq.)	853.84	368.77	218.60	180.07	152.98	133.02	117.66	105.27	94.746	85.206	75.773

continued

TABLE 2.7 Thermophysical Properties of Fluids along the Saturation Line^a (Continued)

<i>Water (R-718) (Continued)</i>											
η (vap.)	9.9195	11.487	13.192	14.056	14.917	15.779	16.653	17.564	18.563	19.749	21.350
λ (liq.)	610.28	668.00	683.64	681.72	674.59	662.21	644.05	619.08	585.95	544.05	495.46
λ (vap.)	18.673	22.707	28.347	31.873	35.904	40.471	45.666	51.756	59.456	70.685	91.052
σ	0.0717	0.0632	0.0536	0.0483	0.0429	0.0373	0.0315	0.0256	0.0197	0.0139	0.0084
<i>Xenon</i>											
T	180.00	190.00	200.00	210.00	220.00	230.00	240.00	250.00	260.00	270.00	280.00
p	0.2216	0.3477	0.5207	0.7499	1.0446	1.4146	1.8700	2.4215	3.0807	3.8611	4.7805
ρ (liq.)	2837.0	2766.5	2692.6	2614.8	2532.0	2443.0	2346.0	2238.0	2114.4	1965.5	1764.6
ρ (vap.)	20.542	31.174	45.483	64.297	88.648	119.90	159.97	211.82	280.44	375.85	525.13
h (liq.)	5.1356	8.6275	12.193	15.858	19.653	23.614	27.795	32.271	37.165	42.717	49.568
h (vap.)	97.052	97.849	98.437	98.785	98.853	98.589	97.919	96.734	94.846	91.891	86.911
s (liq.)	0.0295	0.0482	0.0661	0.0836	0.1007	0.1177	0.1346	0.1519	0.1699	0.1894	0.2125
s (vap.)	0.5402	0.5178	0.4974	0.4785	0.4607	0.4436	0.4268	0.4098	0.3918	0.3716	0.3459
c_v (liq.)	0.1613	0.1567	0.1528	0.1493	0.1463	0.1438	0.1420	0.1411	0.1418	0.1454	0.1565
c_v (vap.)	0.1066	0.1102	0.1143	0.1189	0.1241	0.1297	0.1361	0.1436	0.1527	0.1649	0.1838
c_p (liq.)	0.3442	0.3498	0.3579	0.3691	0.3842	0.4049	0.4342	0.4780	0.5496	0.6897	1.1092
c_p (vap.)	0.1865	0.1970	0.2104	0.2274	0.2493	0.2785	0.3193	0.3806	0.4834	0.6918	1.3341
w (liq.)	599.04	570.00	540.11	509.18	476.96	443.11	407.13	368.28	325.30	275.99	215.47
w (vap.)	133.38	135.47	137.12	138.33	139.09	139.38	139.19	138.48	137.18	135.11	131.75
η (liq.)	398.17	349.91	308.34	272.06	240.00	211.31	185.32	161.41	138.96	117.20	94.450
η (vap.)	14.780	15.592	16.460	17.398	18.428	19.577	20.889	22.432	24.333	26.859	30.802
λ (liq.)	64.909	61.180	57.451	53.748	50.081	46.442	42.812	39.160	35.494	32.045	29.622
λ (vap.)	3.5348	3.7825	4.0521	4.3506	4.6887	5.0845	5.5731	6.2321	7.2516	9.1505	13.683
σ	0.0157	0.0138	0.0121	0.0104	0.0087	0.0072	0.0057	0.0042	0.0029	0.0017	0.0007

R-11 (Trichlorofluoromethane, CFC-11)

<i>T</i>	200.00	225.00	250.00	275.00	300.00	325.00	350.00	375.00	400.00	425.00	450.00
<i>p</i>	0.00043	0.0030	0.0134	0.0435	0.1131	0.2492	0.4847	0.8570	1.4074	2.1811	3.2329
ρ (liq.)	1691.9	1639.2	1585.4	1529.9	1471.9	1410.2	1343.5	1269.9	1185.7	1084.1	943.21
ρ (vap.)	0.0358	0.2212	0.8909	2.6678	6.4840	13.590	25.648	45.010	75.450	124.37	212.96
<i>h</i> (liq.)	138.94	159.42	180.30	201.59	223.40	245.84	269.08	293.34	318.92	346.46	377.77
<i>h</i> (vap.)	353.48	365.46	377.93	390.72	403.59	416.24	428.30	439.34	448.79	455.64	457.26
<i>s</i> (liq.)	0.7403	0.8368	0.9247	1.0058	1.0815	1.1530	1.2214	1.2876	1.3524	1.4175	1.4867
<i>s</i> (vap.)	1.8130	1.7525	1.7153	1.6936	1.6822	1.6774	1.6763	1.6769	1.6771	1.6744	1.6633
<i>c_v</i> (liq.)	0.5569	0.5687	0.5790	0.5886	0.5984	0.6085	0.6191	0.6307	0.6439	0.6611	0.6891
<i>c_v</i> (vap.)	0.4135	0.4469	0.4790	0.5090	0.5367	0.5624	0.5871	0.6119	0.6383	0.6685	0.7082
<i>c_p</i> (liq.)	0.8101	0.8273	0.8427	0.8605	0.8826	0.9105	0.9461	0.9935	1.0636	1.1918	1.5893
<i>c_p</i> (vap.)	0.4748	0.5096	0.5441	0.5781	0.6123	0.6489	0.6919	0.7488	0.8358	1.0024	1.5284
<i>w</i> (liq.)	1099.1	996.42	900.09	810.44	725.77	644.16	563.73	482.57	398.34	307.60	203.77
<i>w</i> (vap.)	117.77	124.15	129.86	134.61	138.07	139.87	139.68	137.09	131.61	122.37	107.74
η (liq.)	1752.4	1028.3	702.05	516.70	396.78	312.19	248.58	198.16	156.21	119.39	83.759
η (vap.)		7.6997	8.5563	9.4064	10.244	11.077	11.931	12.857	13.960	15.481	18.227
λ (liq.)	118.01	109.32	101.20	93.558	86.285	79.291	72.483	65.765	59.050	52.286	46.661
λ (vap.)		5.5342	6.4895	7.4898	8.5279	9.6226	10.801	12.138	13.754	16.074	20.850
σ	0.0311	0.0275	0.0241	0.0207	0.0175	0.0143	0.0113	0.0085	0.0058	0.0034	0.0013

R-113 (1,1,2-Trichloro-1,2,2-trifluoroethane, CFC-113)

<i>T</i>	260.00	280.00	300.00	320.00	340.00	360.00	380.00	400.00	420.00	440.00	460.00
<i>p</i>	0.0076	0.0208	0.0482	0.0989	0.1840	0.3166	0.5113	0.7840	1.1522	1.6354	2.2568
ρ (liq.)	1652.1	1605.8	1558.6	1510.0	1459.3	1405.9	1348.5	1285.7	1215.0	1131.6	1023.5
ρ (vap.)	0.6670	1.6931	3.7087	7.2565	13.018	21.851	34.881	53.693	80.766	120.59	183.51
<i>h</i> (liq.)	188.29	206.16	224.37	242.98	262.01	281.52	301.58	322.27	343.77	366.38	390.82
<i>h</i> (vap.)	350.90	362.90	375.16	387.54	399.91	412.16	424.11	435.57	446.26	455.69	462.82

continued

TABLE 2.7 Thermophysical Properties of Fluids along the Saturation Line^a (Continued)

<i>R-113 (1,1,2-Trichloro-1,2,2-trifluoroethane, CFC-113) (Continued)</i>											
<i>s</i> (liq.)	0.9561	1.0223	1.0850	1.1449	1.2025	1.2580	1.3118	1.3643	1.4160	1.4676	1.5207
<i>s</i> (vap.)	1.5815	1.5821	1.5876	1.5967	1.6081	1.6208	1.6342	1.6475	1.6600	1.6706	1.6772
<i>c_v</i> (liq.)	0.6368	0.6535	0.6712	0.6885	0.7053	0.7214	0.7372	0.7531	0.7700	0.7895	0.8159
<i>c_v</i> (vap.)	0.5605	0.5867	0.6118	0.6360	0.6598	0.6833	0.7069	0.7309	0.7560	0.7834	0.8165
<i>c_p</i> (liq.)	0.8855	0.9014	0.9196	0.9396	0.9617	0.9868	1.0165	1.0540	1.1063	1.1925	1.3875
<i>c_p</i> (vap.)	0.6063	0.6342	0.6619	0.6904	0.7206	0.7541	0.7929	0.8413	0.9087	1.0201	1.2754
<i>w</i> (liq.)	828.94	759.92	692.84	628.04	565.13	503.50	442.41	380.97	317.99	251.65	179.46
<i>w</i> (vap.)	111.03	114.38	117.08	118.97	119.89	119.66	118.07	114.87	109.72	102.05	90.902
η (liq.)	1217.5	859.37	645.95	504.29	403.15	326.93	266.92	217.88	176.32	139.65	105.13
η (vap.)	8.3780	9.0218	9.6611	10.288	10.918	11.561	12.237	12.986	13.879	15.069	16.948
λ (liq.)	76.719	72.151	67.853	63.782	59.900	56.168	52.545	48.991	45.465	41.934	38.567
λ (vap.)	6.8569	7.7005	8.5700	9.4607	10.385	11.348	12.370	13.485	14.754	16.351	18.804
σ	0.0216	0.0193	0.0170	0.0148	0.0126	0.0105	0.0085	0.0066	0.0048	0.0031	0.0016
<i>R-114 (1,2-Dichloro-1,1,2,2-tetrafluoroethane, CFC-114)</i>											
<i>T</i>	280.00	300.00	320.00	330.00	340.00	350.00	360.00	370.00	380.00	390.00	400.00
<i>p</i>	0.1145	0.2275	0.4102	0.5350	0.6862	0.8670	1.0811	1.3323	1.6246	1.9630	2.3530
ρ (liq.)	1508.8	1449.0	1384.6	1350.1	1313.5	1274.5	1232.4	1186.1	1134.0	1073.5	998.95
ρ (vap.)	8.7845	16.788	29.651	38.550	49.568	63.201	80.128	101.34	128.36	163.86	213.09
<i>h</i> (liq.)	206.60	226.22	246.49	256.91	267.54	278.42	289.59	301.10	313.05	325.60	339.09
<i>h</i> (vap.)	341.38	353.56	365.44	371.18	376.73	382.04	387.03	391.61	395.62	398.84	400.80
<i>s</i> (liq.)	1.0238	1.0912	1.1562	1.1880	1.2194	1.2505	1.2815	1.3125	1.3436	1.3754	1.4086
<i>s</i> (vap.)	1.5052	1.5157	1.5279	1.5343	1.5405	1.5466	1.5522	1.5571	1.5609	1.5632	1.5629
<i>c_v</i> (liq.)	0.6839	0.7019	0.7215	0.7317	0.7421	0.7527	0.7637	0.7753	0.7878	0.8018	0.8189
<i>c_v</i> (vap.)	0.6250	0.6523	0.6804	0.6950	0.7102	0.7262	0.7431	0.7615	0.7818	0.8047	0.8317
<i>c_p</i> (liq.)	0.9661	0.9945	1.0300	1.0511	1.0754	1.1043	1.1400	1.1867	1.2530	1.3589	1.5650

c_p (vap.)	0.6833	0.7193	0.7624	0.7883	0.8189	0.8562	0.9035	0.9673	1.0600	1.2106	1.5052
w (liq.)	617.82	545.01	472.58	436.26	399.72	362.81	325.38	287.21	248.03	207.45	164.86
w (vap.)	116.64	117.29	116.25	115.00	113.19	110.75	107.63	103.71	98.885	92.999	85.834
η (liq.)	343.29	272.64	218.66	195.98	175.46	156.71	139.36	123.11	107.63	92.535	77.218
η (vap.)	10.092	10.793	11.506	11.878	12.268	12.689	13.158	13.704	14.376	15.264	16.560
λ (liq.)	64.871	60.564	56.352	54.262	52.173	50.077	47.963	48.825	43.667	41.544	39.809
λ (vap.)	9.2879	10.359	11.507	12.125	12.780	13.475	14.238	15.108	16.157	17.541	19.640
σ	0.0129	0.0107	0.0085	0.0074	0.0064	0.0054	0.0045	0.0035	0.0027	0.0018	0.0011

R-115 (Chloropentafluoroethane, CFC-115)

T	180.00	200.00	220.00	240.00	260.00	280.00	300.00	310.00	320.00	330.00	340.00
p	0.0038	0.0162	0.0512	0.1303	0.2820	0.5412	0.9480	1.2209	1.5489	1.9398	2.4037
ρ (liq.)	1744.4	1677.4	1608.8	1537.2	1460.6	1376.4	1279.5	1223.5	1159.4	1082.0	978.74
ρ (vap.)	0.3895	1.5196	4.4456	10.647	22.183	42.028	75.066	99.259	131.38	175.92	244.04
h (liq.)	115.98	132.53	149.80	167.90	186.92	207.02	228.47	239.86	251.85	264.73	279.15
h (vap.)	259.35	269.56	280.23	291.10	301.89	312.24	321.65	325.74	329.18	331.56	331.93
s (liq.)	0.6278	0.7150	0.7972	0.8756	0.9513	1.0251	1.0980	1.1346	1.1718	1.2104	1.2521
s (vap.)	1.4244	1.4002	1.3900	1.3890	1.3935	1.4009	1.4086	1.4117	1.4135	1.4129	1.4073
c_v (liq.)	0.5034	0.5368	0.5739	0.6103	0.6454	0.6797	0.7151	0.7343	0.7558	0.7820	0.8174
c_v (vap.)	0.4522	0.4958	0.5384	0.5806	0.6230	0.6660	0.7111	0.7352	0.7613	0.7912	0.8290
c_p (liq.)	0.8125	0.8442	0.8824	0.9253	0.9746	1.0351	1.1198	1.1821	1.2746	1.4387	1.8463
c_p (vap.)	0.5072	0.5529	0.6000	0.6506	0.7081	0.7789	0.8799	0.9559	1.0710	1.2797	1.8218
w (liq.)	871.69	771.03	674.85	584.54	498.43	414.26	329.28	285.28	239.30	190.47	138.88
w (vap.)	103.84	108.30	111.73	113.72	113.87	111.69	106.57	102.61	97.474	90.861	82.340
η (liq.)	883.93	580.60	414.58	309.63	236.71	182.31	139.13	120.23	102.44	85.077	66.950
η (vap.)	7.4741	8.3095	9.1393	9.9536	10.782	11.658	12.674	13.297	14.067	15.112	16.776
λ (liq.)	91.430	83.457	76.095	69.224	62.726	56.481	50.364	47.312	44.256	41.293	39.563
λ (vap.)	5.1681	6.2202	7.3494	8.5499	9.8470	11.289	12.986	14.022	15.315	17.123	20.245
σ	0.0193	0.0166	0.0140	0.0115	0.0090	0.0067	0.0046	0.0035	0.0026	0.0017	0.0008

continued

TABLE 2.7 Thermophysical Properties of Fluids along the Saturation Line^a (Continued)

<i>R-116 (Hexafluoroethane, FC-116)</i>											
<i>T</i>	180.00	200.00	210.00	220.00	230.00	240.00	250.00	260.00	270.00	280.00	290.00
<i>p</i>	0.0419	0.1317	0.2128	0.3271	0.4824	0.6866	0.9483	1.2771	1.6854	2.1908	2.8203
ρ (liq.)	1669.5	1582.0	1537.3	1490.1	1439.1	1382.8	1319.4	1247.0	1163.4	1060.3	881.57
ρ (vap.)	3.9752	11.637	18.328	27.699	40.517	57.843	81.290	113.61	160.16	233.17	380.08
<i>h</i> (liq.)	100.42	118.94	128.53	138.45	148.77	159.58	170.94	182.96	195.76	209.77	227.86
<i>h</i> (vap.)	222.95	232.88	237.76	242.54	247.17	251.58	255.64	259.13	261.65	262.42	258.44
<i>s</i> (liq.)	0.5658	0.6630	0.7096	0.7554	0.8008	0.8461	0.8917	0.9378	0.9849	1.0341	1.0953
<i>s</i> (vap.)	1.2465	1.2328	1.2297	1.2285	1.2286	1.2295	1.2305	1.2308	1.2289	1.2222	1.2007
<i>c_v</i> (liq.)	0.6433	0.6589	0.6701	0.6828	0.6965	0.7107	0.7247	0.7377	0.7496	0.7642	0.7935
<i>c_v</i> (vap.)	0.5151	0.5648	0.5917	0.6194	0.6474	0.6754	0.7029	0.7297	0.7553	0.7782	0.7928
<i>c_p</i> (liq.)	0.9172	0.9427	0.9720	1.0088	1.0535	1.1083	1.1760	1.2613	1.3855	1.6746	4.1002
<i>c_p</i> (vap.)	0.5872	0.6513	0.6890	0.7309	0.7779	0.8328	0.9010	0.9954	1.1497	1.4589	3.6372
<i>w</i> (liq.)	542.56	509.57	479.05	442.11	400.49	356.12	311.45	268.70	226.45	176.28	107.44
<i>w</i> (vap.)	107.94	110.51	110.91	110.58	109.36	107.03	103.37	98.137	91.227	82.842	72.721
η (liq.)	412.30	288.78	245.42	209.55	179.11	152.66	129.14	107.81	88.060	68.961	46.463
η (vap.)	8.4436	9.4174	9.8763	10.330	10.784	11.251	11.759	12.372	13.256	14.894	19.069
λ (liq.)	75.336	67.094	63.241	59.495	55.816	52.169	48.525	44.893	41.403	38.798	53.980
λ (vap.)	6.5676	7.8096	8.4927	9.2285	10.038	10.939	11.938	13.109	14.691	17.614	27.103
σ	0.0130	0.0103	0.0090	0.0077	0.0064	0.0052	0.0040	0.0029	0.0018	0.0009	0.0001
<i>R-12 (Dichlorodifluoromethane, CFC-12)</i>											
<i>T</i>	125.00	150.00	175.00	200.00	225.00	250.00	275.00	300.00	325.00	350.00	375.00
<i>p</i>	1.6×10^{-6}	0.000092	0.0014	0.0100	0.0430	0.1331	0.3273	0.6839	1.2694	2.1593	3.4527
ρ (liq.)	1805.2	1739.6	1674.3	1608.0	1539.6	1467.5	1390.1	1304.3	1205.0	1080.3	883.06
ρ (vap.)	0.0002	0.0089	0.1174	0.7307	2.8376	8.1095	18.930	38.700	73.003	133.91	269.11
<i>h</i> (liq.)	73.862	94.438	114.83	135.52	156.77	178.78	201.74	225.90	251.69	280.08	314.63

<i>h</i> (vap.)	286.44	296.19	306.91	318.39	330.28	342.18	353.63	364.09	372.80	378.21	374.56
<i>s</i> (liq.)	0.3405	0.4907	0.6164	0.7269	0.8269	0.9193	1.0063	1.0894	1.1705	1.2522	1.3438
<i>s</i> (vap.)	2.0411	1.8357	1.7140	1.6412	1.5980	1.5729	1.5586	1.5501	1.5431	1.5326	1.5036
<i>c_v</i> (liq.)	0.5533	0.5288	0.5275	0.5370	0.5515	0.5683	0.5862	0.6050	0.6258	0.6544	0.7208
<i>c_v</i> (vap.)	0.3009	0.3426	0.3827	0.4208	0.4578	0.4944	0.5317	0.5706	0.6126	0.6620	0.7423
<i>c_p</i> (liq.)	0.8371	0.8152	0.8194	0.8371	0.8631	0.8961	0.9376	0.9934	1.0802	1.2618	2.1896
<i>c_p</i> (vap.)	0.3696	0.4115	0.4250	0.4920	0.5334	0.5794	0.6344	0.7072	0.8204	1.0658	2.5120
<i>w</i> (liq.)	1265.2	1143.1	1026.5	915.19	808.46	705.34	604.49	504.07	400.97	289.31	158.26
<i>w</i> (vap.)	102.76	111.28	119.04	125.92	131.52	135.31	136.70	135.10	129.75	119.47	102.14
η (liq.)	—	—	965.60	612.98	431.42	320.10	243.90	187.31	142.19	103.30	63.988
η (vap.)	—	—	6.8573	7.8481	8.8378	9.8222	10.816	11.866	13.091	14.819	18.726
λ (liq.)	—	—	115.83	104.39	93.947	84.277	75.197	66.250	58.063	49.727	46.867
λ (vap.)	—	—	4.3416	5.3635	6.4653	7.6492	8.9383	10.411	12.293	15.258	23.499
σ	0.0343	0.0302	0.0262	0.0223	0.0185	0.0149	0.0115	0.0083	0.0053	0.0027	0.0006

R-123 (2,2-Dichloro-1,1,1-trifluoroethane, HCFC-123)

<i>T</i>	200.00	225.00	250.00	275.00	300.00	325.00	350.00	375.00	400.00	425.00	450.00
<i>p</i>	0.00025	0.0020	0.0101	0.0355	0.0978	0.2248	0.4515	0.8185	1.3722	2.1672	3.2806
ρ (liq.)	1694.4	1638.4	1581.1	1521.6	1459.1	1392.7	1320.8	1240.6	1146.8	1026.4	819.52
ρ (vap.)	0.0230	0.1660	0.7469	2.4243	6.2595	13.752	26.977	49.027	85.321	148.41	296.39
<i>h</i> (liq.)	130.25	153.55	177.37	201.83	227.03	253.01	279.89	307.88	337.44	369.62	409.08
<i>h</i> (vap.)	339.57	353.25	367.66	382.55	397.63	412.60	427.11	440.74	452.74	461.52	460.11
<i>s</i> (liq.)	0.7034	0.8132	0.9135	1.0067	1.0942	1.1771	1.2563	1.3327	1.4078	1.4840	1.5713
<i>s</i> (vap.)	1.7500	1.7007	1.6747	1.6638	1.6629	1.6681	1.6769	1.6870	1.6960	1.7002	1.6847
<i>c_v</i> (liq.)	0.6361	0.6473	0.6649	0.6855	0.7070	0.7289	0.7514	0.7749	0.8011	0.8335	0.8881
<i>c_v</i> (vap.)	0.4770	0.5168	0.5553	0.5932	0.6309	0.6687	0.7068	0.7458	0.7872	0.8348	0.9048
<i>c_p</i> (liq.)	0.9253	0.9408	0.9648	0.9923	1.0219	1.0545	1.0939	1.1481	1.2375	1.4385	2.9067
<i>c_p</i> (vap.)	0.5315	0.5720	0.6123	0.6540	0.6988	0.7488	0.8078	0.8846	1.0044	1.2728	3.3587
<i>w</i> (liq.)	1104.3	998.61	894.26	793.34	696.37	602.81	511.47	420.73	328.57	231.85	119.97

continued

TABLE 2.7 Thermophysical Properties of Fluids along the Saturation Line^a (Continued)

<i>R-123 (2,2-Dichloro-1,1,1-trifluoroethane, HCFC-123) (Continued)</i>											
<i>w</i> (vap.)	110.02	116.07	121.40	125.72	128.63	129.74	128.62	124.74	117.30	104.85	84.236
η (liq.)	1795.0	1124.7	768.49	551.59	408.74	309.64	238.12	184.60	142.78	107.74	71.220
η (vap.)	6.9646	7.9822	8.9646	9.9065	10.804	11.664	12.515	13.445	14.683	16.913	23.904
λ (liq.)	105.59	98.545	90.832	83.129	75.902	69.320	63.340	57.789	52.407	46.810	40.476
λ (vap.)	3.6080	5.0248	6.4350	7.8477	9.2909	10.815	12.497	14.451	16.867	20.168	26.721
σ	0.0275	0.0242	0.0211	0.0180	0.0150	0.0121	0.0093	0.0067	0.0043	0.0021	0.0003
<i>R-124 (1-Chloro-1,2,2,2-tetrafluoroethane, HCFC-124)</i>											
<i>T</i>	125.00	150.00	175.00	200.00	225.00	250.00	275.00	300.00	325.00	350.00	375.00
<i>p</i>	9.2×10^{-8}	0.000011	0.00029	0.0030	0.0166	0.0619	0.1747	0.4050	0.8136	1.4717	2.4663
ρ (liq.)	1839.6	1774.6	1709.8	1644.3	1576.9	1506.4	1431.2	1349.0	1255.7	1143.4	987.37
ρ (vap.)	0.0000	0.0012	0.0273	0.2443	1.2235	4.1891	11.131	24.975	50.266	95.626	185.30
<i>h</i> (liq.)	53.743	77.013	100.64	124.81	149.68	175.36	202.01	229.85	259.21	290.76	326.38
<i>h</i> (vap.)	278.64	290.42	303.28	317.07	331.55	346.36	361.10	375.32	388.44	399.39	405.30
<i>s</i> (liq.)	0.2365	0.4062	0.5518	0.6809	0.7979	0.9060	1.0073	1.1036	1.1965	1.2884	1.3840
<i>s</i> (vap.)	2.0357	1.8289	1.7097	1.6422	1.6063	1.5900	1.5858	1.5885	1.5942	1.5988	1.5945
<i>c_v</i> (liq.)	0.6433	0.6426	0.6534	0.6706	0.6915	0.7147	0.7396	0.7660	0.7948	0.8293	0.8796
<i>c_v</i> (vap.)	0.3878	0.4326	0.4759	0.5185	0.5620	0.6082	0.6582	0.7120	0.7693	0.8326	0.9134
<i>c_p</i> (liq.)	0.9276	0.9363	0.9550	0.9798	1.0096	1.0445	1.0863	1.1391	1.2133	1.3428	1.7183
<i>c_p</i> (vap.)	0.4488	0.4936	0.5371	0.5807	0.6273	0.6807	0.7452	0.8258	0.9360	1.1240	1.6905
<i>w</i> (liq.)	1271.2	1157.4	1043.8	932.36	824.09	719.17	617.30	517.54	417.74	313.56	198.17
<i>w</i> (vap.)	93.870	102.10	109.63	116.42	122.21	126.48	128.63	128.00	123.82	114.94	99.240
η (liq.)	—	—	—	1045.8	634.47	432.13	311.61	230.86	171.82	125.13	84.022
η (vap.)	—	—	6.7326	7.7137	8.6921	9.6539	10.604	11.575	12.648	14.035	16.477
λ (liq.)	—	—	—	102.64	92.804	83.792	75.439	67.582	60.047	52.635	45.323
λ (vap.)	—	—	4.9531	6.1026	7.3533	8.7039	10.165	11.778	13.665	16.178	21.002
σ	0.0330	0.0294	0.0258	0.0224	0.0190	0.0157	0.0125	0.0094	0.0065	0.0039	0.0015

R-125 (Pentafluoroethane, HFC-125)

T	180.00	200.00	220.00	240.00	260.00	270.00	280.00	290.00	300.00	310.00	320.00
p	0.0057	0.0247	0.0787	0.2003	0.4327	0.6064	0.8279	1.1049	1.4459	1.8604	2.3597
ρ (liq.)	1666.4	1600.2	1531.5	1458.3	1378.2	1334.4	1287.4	1236.0	1178.6	1112.4	1031.7
ρ (vap.)	0.4576	1.8130	5.3578	12.946	27.244	38.100	52.361	71.093	95.933	129.69	178.02
h (liq.)	95.143	116.24	137.89	160.34	183.84	196.07	208.69	221.77	235.43	249.87	265.50
h (vap.)	281.44	292.86	304.36	315.62	326.28	331.25	335.86	339.99	343.45	345.90	346.72
s (liq.)	0.5353	0.6464	0.7494	0.8467	0.9400	0.9857	1.0310	1.0761	1.1214	1.1676	1.2157
s (vap.)	1.5703	1.5295	1.5061	1.4937	1.4879	1.4864	1.4852	1.4838	1.4815	1.4774	1.4696
c_v (liq.)	0.6746	0.6963	0.7199	0.7447	0.7710	0.7850	0.7998	0.8160	0.8343	0.8564	0.8858
c_v (vap.)	0.5142	0.5594	0.6103	0.6660	0.7236	0.7528	0.7824	0.8131	0.8457	0.8820	0.9255
c_p (liq.)	1.0459	1.0658	1.0994	1.1445	1.2034	1.2405	1.2855	1.3433	1.4234	1.5481	1.7857
c_p (vap.)	0.5857	0.6358	0.6974	0.7725	0.8635	0.9183	0.9839	1.0676	1.1845	1.3706	1.7372
w (liq.)	909.89	800.94	701.53	606.80	513.52	466.60	419.00	370.32	320.00	267.33	211.15
w (vap.)	118.55	123.47	126.98	128.59	127.77	126.27	123.91	120.57	116.10	110.29	102.86
η (liq.)	1003.1	635.17	442.77	324.15	242.88	210.77	182.60	157.44	134.54	113.17	92.452
η (vap.)	7.7601	8.6274	9.4598	10.303	11.180	11.652	12.167	12.753	13.458	14.372	15.691
λ (liq.)	116.42	105.35	95.117	85.528	76.421	71.996	67.625	63.281	58.935	54.566	50.240
λ (vap.)	6.1300	7.2865	8.5383	9.9061	11.438	12.302	13.252	14.341	15.665	17.427	20.135
σ	0.0206	0.0174	0.0144	0.0114	0.0087	0.0073	0.0060	0.0048	0.0036	0.0025	0.0015

R-13 (Chlorotrifluoromethane, CFC-13)

T	100.00	120.00	140.00	160.00	180.00	200.00	220.00	240.00	260.00	280.00	300.00
p	2.7×10^{-6}	0.00013	0.0019	0.0125	0.0518	0.1550	0.3714	0.7602	1.3878	2.3316	3.7065
ρ (liq.)	1838.1	1773.3	1706.8	1637.8	1565.5	1488.9	1406.1	1313.8	1205.2	1063.8	777.60
ρ (vap.)	0.0003	0.0139	0.1691	0.9949	3.7116	10.304	23.541	47.397	88.789	164.64	388.24
h (liq.)	39.457	55.920	72.678	89.538	106.70	124.44	143.02	162.81	184.36	208.88	244.14
h (vap.)	229.98	237.21	245.04	253.25	261.55	269.66	277.27	283.96	288.96	290.35	276.51

continued

TABLE 2.7 Thermophysical Properties of Fluids along the Saturation Line^a (Continued)

<i>R-13 (Chlorotrifluoromethane, CFC-13) (Continued)</i>											
s (liq.)	0.1008	0.2508	0.3799	0.4924	0.5934	0.6864	0.7742	0.8590	0.9432	1.0309	1.1470
s (vap.)	2.0060	1.7615	1.6111	1.5156	1.4536	1.4125	1.3844	1.3638	1.3455	1.3218	1.2549
c_v (liq.)	0.5665	0.5346	0.5103	0.5056	0.5167	0.5376	0.5637	0.5919	0.6210	0.6525	0.7094
c_v (vap.)	0.2649	0.3004	0.3359	0.3731	0.4133	0.4561	0.5005	0.5458	0.5923	0.6439	0.7231
c_p (liq.)	0.7968	0.8358	0.8393	0.8481	0.8691	0.9031	0.9526	1.0262	1.1497	1.4407	7.1130
c_p (vap.)	0.3445	0.3802	0.4169	0.4577	0.5058	0.5629	0.6319	0.7219	0.8650	1.2201	8.7804
w (liq.)	1032.1	1072.1	992.15	879.99	763.71	653.03	549.57	451.26	354.31	252.29	122.38
w (vap.)	101.74	109.91	117.29	123.73	128.85	132.18	133.16	131.16	125.37	114.75	98.019
η (liq.)	—	—	1074.8	619.60	413.61	295.83	218.78	163.36	120.15	83.240	42.014
η (vap.)	—	5.5560	6.4782	7.4051	8.3561	9.2869	10.222	11.203	12.357	14.113	20.216
λ (liq.)	—	—	108.32	99.067	90.580	82.644	75.047	67.555	59.925	52.204	33.975
λ (vap.)	—	2.9848	3.7768	4.6577	5.6304	6.7144	7.9588	9.5027	11.666	15.535	36.022
σ	0.0302	0.0265	0.0228	0.0193	0.0159	0.0126	0.0095	0.0067	0.0041	0.0018	0.0001
<i>R-134a (1,1,1,2-Tetrafluoroethane, HFC-134a)</i>											
T	180.00	200.00	220.00	240.00	260.00	280.00	300.00	320.00	340.00	360.00	370.00
p	0.0011	0.0063	0.0244	0.0725	0.1768	0.3727	0.7028	1.2166	1.9715	3.0405	3.7278
ρ (liq.)	1564.2	1510.5	1455.2	1397.7	1337.1	1271.8	1199.7	1116.8	1015.0	870.11	740.32
ρ (vap.)	0.0770	0.3898	1.3850	3.8367	8.9052	18.228	34.193	60.715	105.73	193.58	293.90
h (liq.)	83.483	107.39	131.78	156.79	182.56	209.27	237.19	266.77	298.88	336.06	360.64
h (vap.)	340.88	353.06	365.65	378.34	390.76	402.55	413.27	422.25	428.17	427.08	417.68
s (liq.)	0.4814	0.6073	0.7235	0.8321	0.9349	1.0333	1.1287	1.2226	1.3178	1.4207	1.4857
s (vap.)	1.9114	1.8356	1.7865	1.7552	1.7357	1.7236	1.7156	1.7085	1.6981	1.6735	1.6398
c_v (liq.)	0.7912	0.8016	0.8193	0.8403	0.8631	0.8877	0.9144	0.9443	0.9802	1.0390	1.1146
c_v (vap.)	0.5267	0.5732	0.6204	0.6700	0.7234	0.7810	0.8426	0.9093	0.9852	1.0854	1.1690
c_p (liq.)	1.1871	1.2058	1.2332	1.2669	1.3082	1.3606	1.4324	1.5426	1.7507	2.4368	5.1048

c_p (vap.)	0.6097	0.6586	0.7109	0.7705	0.8418	0.9296	1.0438	1.2109	1.5238	2.6064	6.8622
w (liq.)	1068.3	967.61	869.85	775.00	682.14	590.17	497.89	404.00	306.37	196.05	127.23
w (vap.)	130.05	135.98	141.01	144.73	146.75	146.63	143.88	137.86	127.57	111.25	99.370
η (liq.)	1478.6	866.56	585.96	425.63	321.76	248.50	193.32	149.30	111.95	76.801	55.825
η (vap.)	6.8981	7.7531	8.5863	9.3983	10.199	11.014	11.892	12.927	14.353	17.043	20.660
λ (liq.)	139.12	127.74	117.17	107.27	97.920	88.990	80.335	71.774	63.074	54.117	52.102
λ (vap.)	3.8934	5.4978	7.1080	8.7325	10.389	12.118	14.009	16.294	19.687	27.401	40.656
σ	0.0263	0.0230	0.0197	0.0165	0.0135	0.0106	0.0078	0.0053	0.0030	0.0010	0.0002

R-14 (Tetrafluoromethane, FC-14)

T	120.00	130.00	140.00	150.00	160.00	170.00	180.00	190.00	200.00	210.00	220.00
p	0.0113	0.0304	0.0697	0.1412	0.2593	0.4405	0.7030	1.0663	1.5523	2.1864	3.0022
ρ (liq.)	1731.1	1681.6	1630.3	1576.9	1520.9	1461.3	1396.8	1325.4	1243.2	1142.5	998.53
ρ (vap.)	1.0025	2.5092	5.4125	10.433	18.464	30.643	48.512	74.366	112.10	169.77	272.45
h (liq.)	188.05	196.60	205.35	214.43	223.87	233.71	244.03	254.95	266.70	279.76	295.60
h (vap.)	334.63	338.60	342.46	346.14	349.52	352.48	354.86	356.44	356.86	355.39	349.79
s (liq.)	0.2722	0.3406	0.4052	0.4675	0.5279	0.5868	0.6448	0.7023	0.7607	0.8217	0.8918
s (vap.)	1.4937	1.4328	1.3846	1.3456	1.3132	1.2855	1.2605	1.2365	1.2115	1.1819	1.1381
c_v (liq.)	0.4752	0.4596	0.4713	0.4890	0.5060	0.5212	0.5352	0.5494	0.5656	0.5870	0.6217
c_v (vap.)	0.3228	0.3363	0.3514	0.3685	0.3878	0.4098	0.4349	0.4641	0.4989	0.5428	0.6059
c_p (liq.)	0.8547	0.8604	0.8883	0.9224	0.9598	1.0028	1.0572	1.1335	1.2558	1.5008	2.3618
c_p (vap.)	0.4193	0.4354	0.4554	0.4807	0.5132	0.5561	0.6155	0.7034	0.8505	1.1593	2.3090
w (liq.)	849.39	800.48	736.34	669.70	604.18	539.97	476.19	411.57	344.50	272.56	190.63
w (vap.)	120.58	124.35	127.42	129.66	130.96	131.18	130.22	127.94	124.21	118.82	111.42
η (liq.)	580.41	438.50	343.99	276.40	225.43	185.34	152.62	124.97	100.76	78.511	55.883
η (vap.)	6.9030	7.4762	8.0467	8.6194	9.2032	9.7925	10.420	11.125	11.987	13.178	15.320
λ (liq.)	118.21	109.59	101.36	93.465	85.871	78.518	71.345	64.302	57.364	50.825	50.943
λ (vap.)	4.1155	4.6071	5.1432	5.7360	6.3544	7.0923	7.9818	9.1167	10.713	13.357	19.379
σ	0.0170	0.0150	0.0131	0.0113	0.0095	0.0077	0.0061	0.0045	0.0031	0.0017	0.0006

continued

TABLE 2.7 Thermophysical Properties of Fluids along the Saturation Line^a (Continued)

<i>R-141b (1,1-Dichloro-1-fluoroethane, HCFC-141b)</i>											
<i>T</i>	260.00	280.00	300.00	320.00	340.00	360.00	380.00	400.00	420.00	440.00	460.00
<i>p</i>	0.0149	0.0381	0.0841	0.1657	0.2982	0.4990	0.7872	1.1835	1.7104	2.3943	3.2695
ρ (liq.)	1305.2	1268.4	1230.4	1190.8	1149.0	1104.5	1056.0	1002.3	940.91	866.87	766.81
ρ (vap.)	0.8134	1.9487	4.0769	7.6901	13.399	21.977	34.459	52.370	78.256	117.23	183.52
<i>h</i> (liq.)	185.26	207.74	230.64	254.08	278.17	303.04	328.85	355.79	384.22	414.78	449.24
<i>h</i> (vap.)	428.86	442.35	456.02	469.74	483.35	496.67	509.47	521.42	531.99	540.17	543.32
<i>s</i> (liq.)	0.9447	1.0280	1.1068	1.1822	1.2549	1.3255	1.3945	1.4626	1.5306	1.5999	1.6741
<i>s</i> (vap.)	1.8816	1.8658	1.8581	1.8562	1.8584	1.8633	1.8698	1.8767	1.8824	1.8849	1.8786
<i>c_v</i> (liq.)	0.7839	0.7953	0.8096	0.8258	0.8432	0.8615	0.8805	0.9003	0.9210	0.9439	0.9729
<i>c_v</i> (vap.)	0.6309	0.6672	0.7037	0.7403	0.7766	0.8124	0.8477	0.8829	0.9184	0.9559	0.9991
<i>c_p</i> (liq.)	1.1154	1.1327	1.1562	1.1853	1.2205	1.2629	1.3157	1.3854	1.4873	1.6681	2.1653
<i>c_p</i> (vap.)	0.7065	0.7468	0.7895	0.8350	0.8843	0.9390	1.0028	1.0836	1.2005	1.4126	2.0258
<i>w</i> (liq.)	965.48	888.40	813.58	740.44	668.42	596.95	525.39	453.00	378.62	300.17	212.70
<i>w</i> (vap.)	142.44	146.37	149.41	151.38	152.08	151.30	148.75	144.11	136.84	126.18	110.96
η (liq.)	660.72	505.40	400.16	323.93	265.87	219.82	182.01	149.94	121.83	96.148	70.787
η (vap.)	8.0066	8.6210	9.2309	9.8432	10.463	11.103	11.785	12.546	13.465	14.722	16.914
λ (liq.)	106.81	100.03	93.619	87.517	81.666	76.008	70.484	65.042	59.635	54.319	50.633
λ (vap.)	7.6353	8.6087	9.6283	10.704	11.841	13.060	14.402	15.941	17.844	20.568	25.867
σ	0.0232	0.0206	0.0181	0.0157	0.0133	0.0110	0.0088	0.0067	0.0047	0.0028	0.0012
<i>R-142b (1-Chloro-1,1-difluoroethane, HCFC-142b)</i>											
<i>T</i>	150.00	175.00	200.00	225.00	250.00	275.00	300.00	325.00	350.00	375.00	400.00
<i>p</i>	0.000012	0.00028	0.0028	0.0150	0.0553	0.1548	0.3575	0.7169	1.2941	2.1600	3.4073
ρ (liq.)	1425.6	1375.0	1324.8	1273.8	1221.0	1165.0	1104.4	1036.8	958.28	860.13	708.10
ρ (vap.)	0.0009	0.0196	0.1681	0.8190	2.7584	7.2444	16.064	31.807	58.788	106.36	210.67
<i>h</i> (liq.)	55.776	85.033	113.63	142.39	171.82	202.30	234.18	267.87	303.98	343.71	391.51

<i>h</i> (vap.)	340.74	354.67	369.69	385.48	401.70	418.00	433.99	449.10	462.40	471.95	470.74
<i>s</i> (liq.)	0.3000	0.4805	0.6332	0.7687	0.8925	1.0084	1.1187	1.2254	1.3307	1.4376	1.5567
<i>s</i> (vap.)	2.1997	2.0212	1.9135	1.8490	1.8120	1.7927	1.7847	1.7830	1.7833	1.7796	1.7548
<i>c_v</i> (liq.)	0.8464	0.8029	0.7937	0.8026	0.8214	0.8461	0.8745	0.9056	0.9396	0.9789	1.0407
<i>c_v</i> (vap.)	0.4506	0.5073	0.5663	0.6294	0.6960	0.7643	0.8320	0.8983	0.9643	1.0342	1.1227
<i>c_p</i> (liq.)	1.1998	1.1502	1.1430	1.1605	1.1946	1.2426	1.3055	1.3898	1.5154	1.7576	2.9075
<i>c_p</i> (vap.)	0.5335	0.5910	0.6527	0.7221	0.8002	0.8874	0.9857	1.1047	1.2740	1.6106	3.3426
<i>w</i> (liq.)	1272.4	1155.1	1041.8	933.10	828.22	726.06	625.29	524.42	421.36	311.75	179.80
<i>w</i> (vap.)	121.20	129.73	137.45	144.09	149.20	152.24	152.62	149.69	142.54	129.67	107.82
η (liq.)	—	—	1005.4	615.63	423.84	309.47	232.80	176.91	133.20	96.421	60.679
η (vap.)	—	—	6.6910	7.5308	8.3658	9.1971	10.046	10.965	12.073	13.676	17.213
λ (liq.)	—	—	122.50	110.57	99.635	89.593	80.345	71.782	63.794	56.323	51.519
λ (vap.)	—	—	5.9167	7.1925	8.5903	10.127	11.852	13.893	16.566	20.899	32.411
σ	0.0317	0.0281	0.0245	0.0210	0.0176	0.0143	0.0112	0.0082	0.0054	0.0028	0.0006

R-143a (1,1,1-Trifluoroethane, HFC-143a)

<i>T</i>	180.00	200.00	220.00	240.00	260.00	280.00	300.00	310.00	320.00	330.00	340.00
<i>p</i>	0.0059	0.0246	0.0759	0.1890	0.4025	0.7628	1.3234	1.6983	2.1483	2.6850	3.3250
ρ (liq.)	1285.0	1234.8	1182.4	1127.0	1067.2	1000.4	922.32	876.21	822.31	754.94	654.79
ρ (vap.)	0.3359	1.2699	3.6364	8.5946	17.796	33.738	60.818	81.198	109.18	150.42	224.36
<i>h</i> (liq.)	75.254	100.17	125.91	152.68	180.72	210.37	242.26	259.41	277.77	298.05	322.63
<i>h</i> (vap.)	331.08	343.78	356.59	369.08	380.80	391.15	399.14	401.68	402.62	400.80	392.40
<i>s</i> (liq.)	0.4475	0.5786	0.7010	0.8170	0.9284	1.0370	1.1449	1.1998	1.2564	1.3167	1.3873
<i>s</i> (vap.)	1.8687	1.7967	1.7496	1.7187	1.6980	1.6826	1.6679	1.6587	1.6465	1.6280	1.5925
<i>c_v</i> (liq.)	0.8139	0.8308	0.8564	0.8862	0.9184	0.9528	0.9911	1.0135	1.0406	1.0785	1.1501
<i>c_v</i> (vap.)	0.5794	0.6357	0.6948	0.7587	0.8277	0.9014	0.9815	1.0259	1.0757	1.1362	1.2253
<i>c_p</i> (liq.)	1.2286	1.2638	1.3095	1.3653	1.4357	1.5325	1.6872	1.8139	2.0205	2.4501	4.2484
<i>c_p</i> (vap.)	0.6848	0.7483	0.8205	0.9077	1.0175	1.1653	1.3973	1.5895	1.9129	2.6199	5.7113
<i>w</i> (liq.)	969.14	874.04	778.88	683.65	587.94	490.70	389.93	337.04	281.21	220.39	149.32

continued

TABLE 2.7 Thermophysical Properties of Fluids along the Saturation Line^a (Continued)

<i>R-143a (1,1,1-Trifluoroethane, HFC-143a) (Continued)</i>											
<i>w</i> (vap.)	143.91	149.60	153.71	155.74	155.15	151.36	143.59	137.85	130.56	121.34	109.29
η (liq.)	598.25	418.61	310.60	238.18	185.70	145.21	112.04	97.149	82.830	68.425	52.084
η (vap.)	6.6109	7.3509	8.0868	8.8271	9.5960	10.444	11.716	12.423	13.342	14.693	17.360
λ (liq.)	125.83	114.66	104.42	94.972	86.152	77.777	69.619	65.523	61.342	57.032	53.120
λ (vap.)	5.9266	7.1478	8.5171	10.059	11.830	13.974	17.067	19.371	22.801	28.686	43.217
σ	0.0138	0.0132	0.0122	0.0107	0.0089	0.0067	0.0044	0.0033	0.0022	0.0012	0.0003
<i>R-152a (1,1-Difluoroethane, HFC-152a)</i>											
<i>T</i>	180.00	200.00	220.00	240.00	260.00	280.00	300.00	320.00	340.00	360.00	380.00
<i>p</i>	0.0011	0.0061	0.0228	0.0665	0.1602	0.3354	0.6298	1.0873	1.7577	2.7000	3.9966
ρ (liq.)	1146.0	1108.4	1069.9	1030.0	988.11	943.43	894.75	840.12	775.99	694.20	559.36
ρ (vap.)	0.0504	0.2432	0.8374	2.2727	5.1996	10.519	19.497	34.064	57.642	98.069	189.74
<i>h</i> (liq.)	52.162	82.726	113.69	145.33	177.92	211.73	247.07	284.40	324.50	369.16	425.84
<i>h</i> (vap.)	437.63	452.68	467.99	483.19	497.90	511.72	524.16	534.55	541.68	542.84	526.44
<i>s</i> (liq.)	0.3416	0.5026	0.6501	0.7875	0.9176	1.0422	1.1629	1.2816	1.4006	1.5245	1.6719
<i>s</i> (vap.)	2.4831	2.3524	2.2605	2.1953	2.1482	2.1135	2.0866	2.0634	2.0394	2.0069	1.9366
<i>c_v</i> (liq.)	1.0305	1.0310	1.0399	1.0578	1.0817	1.1097	1.1410	1.1763	1.2177	1.2713	1.3632
<i>c_v</i> (vap.)	0.6286	0.6764	0.7291	0.7877	0.8522	0.9224	0.9978	1.0785	1.1660	1.2655	1.3998
<i>c_p</i> (liq.)	1.5220	1.5356	1.5620	1.6022	1.6550	1.7220	1.8094	1.9327	2.1336	2.5736	5.4456
<i>c_p</i> (vap.)	0.7558	0.8069	0.8669	0.9389	1.0260	1.1326	1.2677	1.4523	1.7462	2.3930	6.6870
<i>w</i> (liq.)	1236.1	1131.3	1031.8	933.98	836.44	738.29	638.61	536.30	429.89	316.40	183.93
<i>w</i> (vap.)	164.78	172.27	178.66	183.57	186.60	187.33	185.34	180.10	170.91	156.55	134.10
η (liq.)	1346.4	799.04	546.26	366.72	253.77	198.37	159.59	128.39	101.41	76.671	50.477
η (vap.)	6.0336	6.6946	7.3581	8.0896	8.8523	9.6064	10.371	11.199	12.226	13.850	18.080
λ (liq.)	158.94	146.60	135.25	124.73	115.02	105.93	97.294	88.992	80.876	72.836	67.267
λ (vap.)	2.5785	4.5306	6.4952	8.4883	10.540	12.704	15.087	17.914	21.728	28.123	45.999
σ	0.0275	0.0243	0.0211	0.0181	0.0151	0.0122	0.0095	0.0069	0.0044	0.0022	0.0004

R-22 (Chlorodifluoromethane, HCFC-22)

<i>T</i>	160.00	180.00	200.00	220.00	240.00	260.00	280.00	300.00	320.00	340.00	360.00
<i>p</i>	0.00052	0.0037	0.0167	0.0547	0.1432	0.3169	0.6186	1.0970	1.8061	2.8081	4.1837
ρ (liq.)	1605.8	1553.2	1499.7	1444.5	1386.6	1324.9	1257.9	1183.4	1097.4	990.07	823.43
ρ (vap.)	0.0341	0.2145	0.8752	2.6485	6.5009	13.759	26.226	46.539	79.186	133.94	246.68
<i>h</i> (liq.)	76.746	97.975	119.22	140.63	162.40	184.80	208.10	232.62	258.89	288.07	324.43
<i>h</i> (vap.)	352.65	362.31	372.15	381.91	391.27	399.92	407.49	413.50	417.16	416.77	406.25
<i>s</i> (liq.)	0.4212	0.5462	0.6581	0.7599	0.8544	0.9435	1.0289	1.1122	1.1949	1.2804	1.3798
<i>s</i> (vap.)	2.1456	2.0147	1.9227	1.8567	1.8080	1.7709	1.7411	1.7151	1.6895	1.6589	1.6071
<i>c_v</i> (liq.)	0.6776	0.6671	0.6585	0.6545	0.6562	0.6635	0.6759	0.6926	0.7137	0.7413	0.7921
<i>c_v</i> (vap.)	0.3827	0.4093	0.4378	0.4692	0.5044	0.5439	0.5879	0.6368	0.6919	0.7580	0.8579
<i>c_p</i> (liq.)	1.0617	1.0611	1.0643	1.0763	1.1001	1.1368	1.1893	1.2653	1.3907	1.6650	3.0011
<i>c_p</i> (vap.)	0.4792	0.5071	0.5391	0.5778	0.6262	0.6880	0.7698	0.8851	1.0710	1.4696	3.4689
<i>w</i> (liq.)	1190.6	1095.0	1001.1	908.04	814.96	721.58	627.58	532.11	433.11	326.68	201.90
<i>w</i> (vap.)	138.70	145.98	152.37	157.61	161.35	163.24	162.92	159.98	153.86	143.71	127.92
η (liq.)	1140.0	740.55	531.77	403.35	315.93	252.00	202.53	162.37	128.17	97.172	64.683
η (vap.)	—	7.5310	8.3851	9.2315	10.075	10.926	11.810	12.780	13.957	15.654	19.259
λ (liq.)	150.39	139.46	129.14	119.33	109.91	100.76	91.777	82.820	73.742	64.397	57.477
λ (vap.)	—	4.7194	5.5390	6.4424	7.4444	8.5755	9.9012	11.573	13.956	18.143	29.834
σ	0.0305	0.0269	0.0235	0.0201	0.0168	0.0137	0.0107	0.0078	0.0051	0.0027	0.0007

R-227ea (1,1,1,2,3,3,3-Heptafluoropropane, HFC-227ea)

<i>T</i>	220.00	240.00	260.00	280.00	300.00	310.00	320.00	330.00	340.00	350.00	360.00
<i>p</i>	0.0151	0.0464	0.1165	0.2510	0.4814	0.6439	0.8446	1.0891	1.3834	1.7347	2.1517
ρ (liq.)	1662.6	1599.4	1532.3	1459.7	1379.4	1335.2	1287.3	1234.6	1175.2	1105.5	1018.0
ρ (vap.)	1.4175	4.0605	9.6473	20.061	38.012	51.061	67.842	89.545	118.06	156.81	213.24
<i>h</i> (liq.)	144.21	164.54	185.65	207.64	230.69	242.69	255.05	267.86	281.22	295.33	310.62
<i>h</i> (vap.)	290.25	303.10	316.19	329.29	342.06	348.20	354.08	359.58	364.52	368.59	371.14

continued

TABLE 2.7 Thermophysical Properties of Fluids along the Saturation Line^a (Continued)

<i>R-227ea (1,1,1,2,3,3,3-Heptafluoropropane, HFC-227ea) (Continued)</i>											
<i>s</i> (liq.)	0.7738	0.8621	0.9463	1.0275	1.1064	1.1454	1.1841	1.2229	1.2621	1.3021	1.3441
<i>s</i> (vap.)	1.4375	1.4394	1.4485	1.4619	1.4777	1.4857	1.4936	1.5009	1.5071	1.5114	1.5122
<i>c_v</i> (liq.)	0.7251	0.7494	0.7753	0.8022	0.8300	0.8444	0.8594	0.8753	0.8932	0.9149	0.9448
<i>c_v</i> (vap.)	0.6088	0.6512	0.6941	0.7381	0.7838	0.8075	0.8322	0.8581	0.8859	0.9171	0.9552
<i>c_p</i> (liq.)	0.9988	1.0341	1.0751	1.1230	1.1821	1.2185	1.2627	1.3194	1.3988	1.5258	1.7832
<i>c_p</i> (vap.)	0.6607	0.7071	0.7574	0.8145	0.8841	0.9272	0.9799	1.0485	1.1472	1.3120	1.6716
<i>w</i> (liq.)	704.83	628.41	553.77	480.06	406.17	368.65	330.34	290.81	249.41	205.28	157.36
<i>w</i> (vap.)	106.83	109.94	111.73	111.79	109.68	107.62	104.77	100.98	96.058	89.744	81.651
<i>η</i> (liq.)	847.91	578.41	419.33	313.80	237.79	206.86	179.27	154.26	131.15	109.22	87.430
<i>η</i> (vap.)	8.4734	9.2457	10.012	10.787	11.609	12.062	12.566	13.153	13.878	14.852	16.345
<i>λ</i> (liq.)	74.567	68.652	63.124	57.901	52.897	50.448	48.016	45.588	43.159	40.758	38.679
<i>λ</i> (vap.)	7.5338	8.7314	10.008	11.376	12.873	13.693	14.587	15.591	16.776	18.296	20.564
<i>σ</i>	0.0164	0.0139	0.0115	0.0091	0.0068	0.0057	0.0046	0.0036	0.0026	0.0017	0.0009
<i>R-23 (Trifluoromethane, HCFC-23)</i>											
<i>T</i>	120.00	140.00	160.00	180.00	200.00	220.00	240.00	250.00	260.00	270.00	280.00
<i>p</i>	0.000082	0.0014	0.0111	0.0508	0.1649	0.4204	0.9041	1.2631	1.7194	2.2893	2.9920
<i>ρ</i> (liq.)	1695.5	1628.6	1559.3	1487.4	1411.4	1329.1	1236.5	1184.2	1125.9	1058.8	977.25
<i>ρ</i> (vap.)	0.0057	0.0861	0.5881	2.4451	7.3704	18.002	38.444	54.440	76.250	106.63	151.12
<i>h</i> (liq.)	−1.2359	22.757	46.716	70.930	95.679	121.36	148.55	162.98	178.20	194.54	212.60
<i>h</i> (vap.)	290.22	300.04	309.78	319.10	327.57	334.58	339.33	340.46	340.39	338.64	334.23
<i>s</i> (liq.)	−0.0502	0.1348	0.2947	0.4371	0.5671	0.6885	0.8051	0.8628	0.9210	0.9806	1.0438
<i>s</i> (vap.)	2.3786	2.1154	1.9388	1.8159	1.7265	1.6577	1.6000	1.5727	1.5448	1.5143	1.4781
<i>c_v</i> (liq.)	0.7912	0.7298	0.7180	0.7138	0.7155	0.7232	0.7373	0.7474	0.7604	0.7776	0.8024
<i>c_v</i> (vap.)	0.3822	0.4117	0.4527	0.5023	0.5589	0.6218	0.6912	0.7290	0.7701	0.8160	0.8700
<i>c_p</i> (liq.)	1.2133	1.1953	1.2020	1.2201	1.2542	1.3123	1.4106	1.4868	1.5970	1.7732	2.1125

c_p (vap.)	0.5020	0.5350	0.5841	0.6493	0.7341	0.8476	1.0131	1.1344	1.3075	1.5860	2.1324
w (liq.)	1217.4	1113.6	995.20	883.92	775.28	665.63	552.13	492.95	431.40	366.62	297.21
w (vap.)	136.73	146.52	154.86	161.50	165.88	167.34	165.16	162.43	158.45	153.03	145.89
η (liq.)	1888.0	927.24	551.43	369.10	265.41	198.77	151.35	131.88	114.19	97.630	81.441
η (vap.)	5.4612	6.6166	7.7511	8.8611	9.9521	11.048	12.216	12.874	13.633	14.580	15.907
λ (liq.)	261.13	204.73	169.63	145.56	127.55	112.93	100.02	93.782	87.452	80.781	73.342
λ (vap.)	3.9025	4.9794	6.0746	7.2269	8.5073	10.028	11.971	13.198	14.689	16.580	19.152
σ	0.0339	0.0291	0.0245	0.0200	0.0158	0.0118	0.0081	0.0064	0.0048	0.0033	0.0019

R-236ea (1,1,1,2,3,3-Hexafluoropropane, HFC-236ea)

T	260.00	280.00	300.00	320.00	340.00	350.00	360.00	370.00	380.00	390.00	400.00
p	0.0429	0.1040	0.2196	0.4157	0.7231	0.9290	1.1760	1.4692	1.8141	2.2172	2.6856
ρ (liq.)	1539.6	1480.7	1418.5	1351.4	1277.3	1236.5	1192.4	1143.9	1089.5	1026.5	949.53
ρ (vap.)	3.0942	7.1277	14.508	26.974	47.043	61.109	78.831	101.35	130.44	169.14	223.41
h (liq.)	184.21	208.33	233.15	258.82	285.52	299.34	313.54	328.19	343.42	359.44	376.70
h (vap.)	358.49	373.18	387.77	402.04	415.72	422.20	428.34	434.02	439.04	443.11	445.66
s (liq.)	0.9408	1.0301	1.1154	1.1977	1.2780	1.3175	1.3570	1.3964	1.4362	1.4768	1.5193
s (vap.)	1.6112	1.6188	1.6308	1.6453	1.6609	1.6686	1.6759	1.6824	1.6878	1.6914	1.6917
c_v (liq.)	0.8695	0.8913	0.9152	0.9399	0.9648	0.9776	0.9907	1.0045	1.0192	1.0355	1.0547
c_v (vap.)	0.7413	0.7812	0.8228	0.8663	0.9118	0.9354	0.9598	0.9852	1.0121	1.0411	1.0729
c_p (liq.)	1.1914	1.2209	1.2591	1.3062	1.3664	1.4046	1.4522	1.5148	1.6040	1.7478	2.0323
c_p (vap.)	0.8048	0.8527	0.9075	0.9722	1.0537	1.1052	1.1692	1.2536	1.3749	1.5716	1.9597
w (liq.)	692.02	620.13	548.27	475.96	402.79	365.76	328.35	290.46	251.87	212.17	170.38
w (vap.)	121.07	123.12	123.69	122.45	119.00	116.28	112.80	108.44	103.11	96.688	88.985
η (liq.)	487.80	371.39	289.51	228.30	180.18	159.53	140.55	122.90	106.22	90.109	73.980
η (vap.)	9.4904	10.254	11.008	11.793	12.657	13.146	13.697	14.346	15.152	16.222	17.787
λ (liq.)	81.617	75.536	69.810	64.355	59.085	56.493	53.916	51.347	48.795	46.333	44.346
λ (vap.)	10.154	11.425	12.776	14.233	15.861	16.784	17.824	19.046	20.569	22.627	25.712
σ	0.0166	0.0142	0.0117	0.0092	0.0068	0.0056	0.0045	0.0034	0.0024	0.0015	0.0007

continued

TABLE 2.7 Thermophysical Properties of Fluids along the Saturation Line^a (Continued)

<i>R-236fa (1,1,1,3,3,3-Hexafluoropropane, HFC-236fa)</i>											
<i>T</i>	200.00	220.00	240.00	260.00	280.00	300.00	320.00	340.00	360.00	380.00	390.00
<i>p</i>	0.0013	0.0061	0.0216	0.0604	0.1415	0.2897	0.5346	0.9107	1.4595	2.2351	2.7324
ρ (liq.)	1656.8	1598.7	1540.2	1480.5	1418.8	1353.5	1282.3	1200.8	1100.1	955.88	838.36
ρ (vap.)	0.1164	0.5132	1.6746	4.3901	9.8077	19.515	35.820	62.567	107.75	195.16	284.95
<i>h</i> (liq.)	116.72	138.54	161.04	184.28	208.33	233.27	259.23	286.49	315.64	348.26	367.66
<i>h</i> (vap.)	309.52	322.84	336.52	350.41	364.34	378.10	391.36	403.62	413.82	419.02	416.49
<i>s</i> (liq.)	0.6465	0.7504	0.8483	0.9412	1.0300	1.1157	1.1988	1.2805	1.3624	1.4485	1.4975
<i>s</i> (vap.)	1.6105	1.5881	1.5794	1.5801	1.5872	1.5984	1.6118	1.6250	1.6351	1.6347	1.6227
<i>c_v</i> (liq.)	0.7932	0.7981	0.8139	0.8389	0.8686	0.8997	0.9311	0.9630	0.9985	1.0474	1.0879
<i>c_v</i> (vap.)	0.6073	0.6413	0.6774	0.7159	0.7568	0.8000	0.8457	0.8950	0.9518	1.0281	1.0863
<i>c_p</i> (liq.)	1.0731	1.1078	1.1427	1.1808	1.2223	1.2691	1.3271	1.4097	1.5568	1.9736	2.9554
<i>c_p</i> (vap.)	0.6627	0.6982	0.7374	0.7815	0.8318	0.8909	0.9647	1.0702	1.2673	1.9382	3.7265
<i>w</i> (liq.)	785.19	767.34	723.90	664.16	594.57	518.80	438.37	353.27	262.22	162.46	107.86
<i>w</i> (vap.)	109.04	113.74	117.69	120.57	122.02	121.60	118.77	112.82	102.72	87.507	78.176
η (liq.)	1333.2	822.85	569.41	418.88	319.33	248.35	194.64	151.71	115.24	80.986	61.838
η (vap.)	7.3120	8.0565	8.7977	9.5318	10.261	10.998	11.778	12.684	13.951	16.457	19.508
λ (liq.)	97.208	89.557	82.508	75.997	69.951	64.290	58.917	53.708	48.488	43.104	41.351
λ (vap.)	6.5637	7.5810	8.6731	9.8431	11.100	12.464	13.988	15.782	18.227	23.348	31.175
σ	0.0207	0.0188	0.0167	0.0145	0.0122	0.0099	0.0075	0.0052	0.0030	0.0012	0.0004
<i>R-245ca (1,1,2,2,3-Pentafluoropropane, HFC-245ca)</i>											
<i>T</i>	240.00	260.00	280.00	300.00	320.00	340.00	360.00	380.00	400.00	420.00	440.00
<i>p</i>	0.0055	0.0179	0.0476	0.1082	0.2179	0.3991	0.6778	1.0834	1.6493	2.4161	3.4432
ρ (liq.)	1522.4	1477.5	1430.8	1381.6	1329.4	1273.0	1210.7	1139.9	1055.5	945.62	750.95
ρ (vap.)	0.3739	1.1282	2.8168	6.1026	11.886	21.382	36.317	59.394	95.583	156.83	301.50
<i>h</i> (liq.)	158.71	183.36	208.81	235.12	262.34	290.58	319.97	350.77	383.44	419.08	463.03

h (vap.)	388.91	403.85	419.34	435.15	451.03	466.73	481.95	496.23	508.80	517.83	515.08
s (liq.)	0.8390	0.9376	1.0318	1.1224	1.2100	1.2951	1.3785	1.4608	1.5432	1.6283	1.7276
s (vap.)	1.7982	1.7857	1.7837	1.7892	1.7996	1.8132	1.8284	1.8436	1.8566	1.8634	1.8459
c_v (liq.)	0.9241	0.9528	0.9828	1.0130	1.0430	1.0727	1.1024	1.1324	1.1639	1.2021	1.2882
c_v (vap.)	0.6934	0.7478	0.8021	0.8570	0.9127	0.9693	1.0267	1.0855	1.1477	1.2191	1.3280
c_p (liq.)	1.2131	1.2516	1.2926	1.3363	1.3837	1.4375	1.5024	1.5890	1.7250	2.0237	4.5489
c_p (vap.)	0.7584	0.8160	0.8759	0.9402	1.0110	1.0913	1.1872	1.3136	1.5136	1.9727	5.9950
w (liq.)	868.33	793.28	720.25	648.66	577.85	507.13	435.77	362.99	287.61	205.82	104.18
w (vap.)	126.83	130.82	133.92	135.88	136.40	135.20	131.92	126.07	116.91	103.10	81.608
η (liq.)	1680.5	1033.2	716.21	528.66	404.54	315.87	248.68	195.14	150.27	110.05	66.093
η (vap.)	8.1691	8.8554	9.5368	10.217	10.906	11.628	12.424	13.371	14.638	16.709	22.618
λ (liq.)	106.65	99.625	93.059	86.882	81.025	75.413	69.965	64.578	59.133	53.525	51.435
λ (vap.)	8.3146	9.6231	11.007	12.465	14.002	15.637	17.419	19.472	22.143	26.633	43.415
σ	0.0241	0.0215	0.0189	0.0163	0.0137	0.0112	0.0087	0.0063	0.0040	0.0020	0.0004

R-245fa (1,1,1,3,3-Pentafluoropropane, HFC-245fa)

T	220.00	240.00	260.00	280.00	300.00	320.00	340.00	360.00	380.00	400.00	420.00
p	0.0022	0.0091	0.0283	0.0726	0.1599	0.3135	0.5605	0.9322	1.4639	2.1977	3.1929
ρ (liq.)	1530.7	1484.5	1436.7	1386.6	1333.7	1277.1	1215.1	1145.3	1063.2	958.96	790.91
ρ (vap.)	0.1653	0.6151	1.7875	4.3238	9.1230	17.393	30.801	51.868	85.032	140.30	258.30
h (liq.)	133.87	158.13	183.17	208.89	235.36	262.71	291.13	320.86	352.33	386.52	427.27
h (vap.)	366.14	380.40	395.10	410.08	425.13	440.06	454.61	468.41	480.79	490.21	490.65
s (liq.)	0.7313	0.8368	0.9369	1.0321	1.1232	1.2110	1.2966	1.3806	1.4644	1.5501	1.6467
s (vap.)	1.7871	1.7629	1.7521	1.7506	1.7557	1.7652	1.7774	1.7905	1.8024	1.8094	1.7976
c_v (liq.)	0.8035	0.8602	0.8911	0.9180	0.9459	0.9755	1.0067	1.0397	1.0758	1.1187	1.1835
c_v (vap.)	0.6480	0.6906	0.7344	0.7798	0.8271	0.8763	0.9277	0.9820	1.0409	1.1088	1.2000
c_p (liq.)	1.1852	1.2347	1.2681	1.3027	1.3428	1.3906	1.4502	1.5299	1.6525	1.9037	3.2693
c_p (vap.)	0.7111	0.7557	0.8034	0.8554	0.9134	0.9794	1.0583	1.1607	1.3172	1.6510	3.5853
w (liq.)	1078.1	946.32	843.61	752.12	665.21	580.24	496.00	411.62	325.85	235.78	132.14

continued

TABLE 2.7 Thermophysical Properties of Fluids along the Saturation Line^a (Continued)

<i>R-245fa (1,1,1,3,3-Pentafluoropropane, HFC-245fa) (Continued)</i>											
<i>w</i> (vap.)	122.04	126.65	130.49	133.30	134.77	134.58	132.35	127.57	119.55	107.08	87.604
η (liq.)	1949.4	1096.6	727.44	522.67	392.66	302.53	235.84	183.76	140.96	103.52	65.435
η (vap.)	7.5986	8.2993	9.0067	9.7051	10.404	11.118	11.878	12.749	13.862	15.549	19.436
λ (liq.)	108.44	100.64	93.361	86.554	80.146	74.064	68.227	62.541	56.903	51.242	47.573
λ (vap.)	7.3261	8.4555	9.6593	10.938	12.298	13.754	15.346	17.166	19.453	22.967	31.829
σ	0.0239	0.0214	0.0189	0.0164	0.0138	0.0113	0.0087	0.0063	0.0040	0.0020	0.0004
<i>R-32 (Difluoromethane, HFC-32)</i>											
<i>T</i>	140.00	160.00	180.00	200.00	220.00	240.00	260.00	280.00	300.00	320.00	340.00
<i>p</i>	0.000084	0.0010	0.0069	0.0295	0.0938	0.2396	0.5216	1.0069	1.7749	2.9194	4.5614
ρ (liq.)	1420.4	1371.6	1321.9	1270.6	1217.1	1160.3	1098.9	1031.1	953.22	857.19	714.82
ρ (vap.)	0.0037	0.0408	0.2408	0.9422	2.7796	6.7367	14.239	27.430	49.971	89.651	172.78
<i>h</i> (liq.)	−13.253	18.272	49.508	80.723	112.21	144.31	177.42	212.09	249.17	290.38	341.38
<i>h</i> (vap.)	446.71	459.81	472.65	484.76	495.69	504.99	512.14	516.34	516.27	509.21	486.63
<i>s</i> (liq.)	−0.0628	0.1477	0.3316	0.4959	0.6457	0.7848	0.9163	1.0430	1.1682	1.2970	1.4451
<i>s</i> (vap.)	3.2226	2.9073	2.6824	2.5161	2.3888	2.2877	2.2037	2.1297	2.0586	1.9809	1.8723
<i>c_v</i> (liq.)	1.0568	1.0138	0.9807	0.9569	0.9417	0.9343	0.9344	0.9422	0.9598	0.9952	1.0878
<i>c_v</i> (vap.)	0.5019	0.5193	0.5479	0.5929	0.6539	0.7248	0.8000	0.8783	0.9634	1.0647	1.2130
<i>c_p</i> (liq.)	1.5875	1.5668	1.5586	1.5641	1.5847	1.6231	1.6853	1.7848	1.9578	2.3336	3.9321
<i>c_p</i> (vap.)	0.6622	0.6819	0.7177	0.7782	0.8670	0.9828	1.1291	1.3275	1.6420	2.2966	5.0360
<i>w</i> (liq.)	1395.1	1289.9	1185.7	1082.1	978.59	874.35	768.33	658.88	543.11	415.41	263.77
<i>w</i> (vap.)	171.76	182.88	192.69	200.85	206.99	210.73	211.65	209.26	202.95	191.66	172.68
η (liq.)	—	724.13	500.13	370.61	286.05	226.15	181.04	145.28	115.50	89.141	62.690
η (vap.)	—	6.6699	7.5068	8.3476	9.1881	10.033	10.898	11.821	13.170	14.796	17.853
λ (liq.)	—	231.95	218.25	204.67	191.12	177.46	163.51	149.01	133.54	116.30	94.871
λ (vap.)	—	5.5629	6.3769	7.2546	8.2175	9.3075	10.610	12.322	15.620	22.973	51.021
σ	0.0382	0.0337	0.0294	0.0251	0.0210	0.0171	0.0133	0.0098	0.0065	0.0035	0.0010

R-41 (Fluoromethane, HFC-41)

<i>T</i>	180.00	200.00	220.00	230.00	240.00	250.00	260.00	270.00	280.00	290.00	300.00
<i>p</i>	0.0408	0.1325	0.3398	0.5090	0.7357	1.0310	1.4070	1.8766	2.4542	3.1558	4.0010
ρ (liq.)	912.22	870.42	825.48	801.43	776.07	749.13	720.24	688.82	653.89	613.62	564.05
ρ (vap.)	0.9532	2.8703	7.0096	10.354	14.866	20.868	28.796	39.280	53.307	72.619	100.95
<i>h</i> (liq.)	-7.3311	34.553	77.148	98.902	121.10	143.88	167.42	191.99	217.99	246.13	277.89
<i>h</i> (vap.)	502.72	515.86	525.59	528.99	531.30	532.37	531.96	529.75	525.15	517.15	503.56
<i>s</i> (liq.)	0.0886	0.3087	0.5105	0.6063	0.6995	0.7909	0.8812	0.9714	1.0628	1.1577	1.2604
<i>s</i> (vap.)	2.9222	2.7153	2.5489	2.4762	2.4087	2.3449	2.2833	2.2224	2.1598	2.0922	2.0127
<i>c_v</i> (liq.)	1.2475	1.2202	1.1962	1.1880	1.1834	1.1826	1.1860	1.1940	1.2075	1.2288	1.2642
<i>c_v</i> (vap.)	0.7982	0.8752	0.9754	1.0314	1.0900	1.1502	1.2114	1.2736	1.3369	1.4027	1.4743
<i>c_p</i> (liq.)	2.0820	2.1038	2.1506	2.1887	2.2405	2.3110	2.4089	2.5503	2.7686	3.1447	3.9440
<i>c_p</i> (vap.)	1.0916	1.2251	1.4178	1.5395	1.6822	1.8526	2.0633	2.3383	2.7290	3.3634	4.6729
<i>w</i> (liq.)	1247.6	1107.9	971.29	903.70	836.30	768.77	700.58	630.89	558.39	481.04	395.35
<i>w</i> (vap.)	238.64	246.68	250.94	251.49	250.88	249.06	245.91	241.33	235.16	227.13	216.80
η (liq.)	455.12	324.11	241.69	210.69	184.25	161.29	141.01	122.78	106.06	90.314	74.809
η (vap.)	6.5276	7.2516	7.9823	8.3587	8.7503	9.1664	10.007	10.630	11.381	12.347	13.743
λ (liq.)	269.60	241.95	215.71	202.99	190.45	178.05	165.72	153.35	140.82	127.87	114.06
λ (vap.)	9.2053	10.449	11.887	12.725	13.689	14.842	16.714	19.220	23.312	30.715	46.326
σ	0.0220	0.0181	0.0143	0.0124	0.0107	0.0090	0.0073	0.0058	0.0043	0.0029	0.0016

RC318 (Octafluorocyclobutane, FC-C318)

<i>T</i>	240.00	260.00	280.00	300.00	320.00	330.00	340.00	350.00	360.00	370.00	380.00
<i>p</i>	0.0281	0.0745	0.1674	0.3314	0.5954	0.7749	0.9921	1.2519	1.5601	1.9239	2.3532
ρ (liq.)	1707.8	1640.4	1568.6	1490.8	1404.3	1356.3	1303.7	1244.9	1176.5	1091.9	970.93
ρ (vap.)	2.8694	7.1467	15.360	29.698	53.394	70.324	92.014	120.21	158.00	211.83	301.19
<i>h</i> (liq.)	166.25	186.32	207.28	229.18	252.10	264.00	276.26	288.95	302.22	316.40	332.43
<i>h</i> (vap.)	292.33	305.65	319.15	332.58	345.64	351.90	357.86	363.38	368.24	371.93	373.07

continued

TABLE 2.7 Thermophysical Properties of Fluids along the Saturation Line^a (Continued)

<i>RC318 (Octafluorocyclobutane, FC-C318) (Continued)</i>											
<i>s</i> (liq.)	0.8686	0.9488	1.0262	1.1014	1.1748	1.2110	1.2471	1.2833	1.3199	1.3579	1.3995
<i>s</i> (vap.)	1.3940	1.4078	1.4258	1.4461	1.4671	1.4773	1.4871	1.4959	1.5033	1.5080	1.5065
<i>c_v</i> (liq.)	0.7084	0.7397	0.7739	0.8070	0.8385	0.8541	0.8699	0.8862	0.9040	0.9246	0.9524
<i>c_v</i> (vap.)	0.6425	0.6803	0.7183	0.7571	0.7976	0.8189	0.8413	0.8652	0.8914	0.9215	0.9597
<i>c_p</i> (liq.)	0.9819	1.0244	1.0699	1.1182	1.1752	1.2109	1.2557	1.3173	1.4133	1.6004	2.2182
<i>c_p</i> (vap.)	0.6873	0.7291	0.7746	0.8270	0.8931	0.9360	0.9910	1.0680	1.1911	1.4390	2.2820
<i>w</i> (liq.)	654.66	579.81	504.72	430.19	355.56	317.77	279.32	239.80	198.61	154.70	105.83
<i>w</i> (vap.)	101.56	103.78	104.61	103.64	100.37	97.668	94.081	89.431	83.456	75.752	65.658
<i>η</i> (liq.)	506.03	375.90	287.28	222.61	172.66	151.41	131.94	113.78	96.438	79.162	60.232
<i>η</i> (vap.)	9.1935	9.9598	10.697	11.458	12.270	12.721	13.232	13.844	14.638	15.803	17.976
<i>λ</i> (liq.)	63.039	58.334	53.929	49.767	45.779	43.825	41.886	39.956	38.064	36.443	37.590
<i>λ</i> (vap.)	8.5065	9.7277	11.014	12.394	13.905	14.731	15.633	16.657	17.908	19.659	22.983
<i>σ</i>	0.0153	0.0128	0.0103	0.0080	0.0058	0.0047	0.0037	0.0028	0.0019	0.0011	0.0004

^a*T*, temperature (K); *p*, pressure (MPa); *ρ*, density (kg/m³); *h*, enthalpy (kJ/kg); *s*, entropy (kJ/kg · K); *c_v*, isochoric heat capacity (kJ/kg · K); *c_p*, isobaric heat capacity (kJ/kg · K); *w*, speed of sound (m/s); *η*, viscosity (μPa · s); *λ*, thermal conductivity (mW/m · K); *σ*, surface tension (N/m).

$$\frac{\alpha(\rho, T)}{RT} = \alpha(\delta, \tau) = \alpha^0(\delta, \tau) + \alpha'(\delta, \tau) \quad (2.3)$$

where $\delta = \rho/\rho_c$, $\tau = T_c/T$, and the ideal gas constant R is $8.314472 \text{ J/mol} \cdot \text{K}$ (Mohr and Taylor, 1999). The Helmholtz energy of the ideal gas (the fluid in the limit of noninteracting particles realized at zero density, where $p = \rho RT$) is given by

$$a^0 = h^0 - RT - Ts^0 \quad (2.4)$$

The ideal gas enthalpy is given by

$$h^0 = h_0^0 + \int_{T_0}^T c_p^0 dT \quad (2.5)$$

where h_0^0 is the enthalpy reference point at T_0 and c_p^0 is the ideal gas heat capacity given by eq. (2.9). The ideal gas entropy is given by

$$s^0 = s_0^0 + \int_{T_0}^T \frac{c_p^0}{T} dT - R \ln \frac{\rho T}{\rho_0 T_0} \quad (2.6)$$

where s_0^0 is the entropy reference point at T_0 and p_0 , and ρ_0 is the ideal gas density at T_0 and p_0 . The values for h_0^0 and s_0^0 are chosen arbitrarily for each fluid. Combining these equations results in the following equation for the Helmholtz energy of the ideal gas:

$$a^0 = h_0^0 + \int_{T_0}^T c_p^0 dT - RT - T \left(s_0^0 + \int_{T_0}^T \frac{c_p^0}{T} dT - R \ln \frac{\rho T}{\rho_0 T_0} \right) \quad (2.7)$$

This ideal gas Helmholtz energy can be expressed in dimensionless form by

$$\alpha^0 = \frac{h_0^0 \tau}{RT_c} - \frac{s_0^0}{R} - 1 + \ln \frac{\delta \tau_0}{\delta_0 \tau} - \frac{\tau}{R} \int_{\tau_0}^{\tau} \frac{c_p^0}{\tau^2} d\tau + \frac{1}{R} \int_{\tau_0}^{\tau} \frac{c_p^0}{\tau} d\tau \quad (2.8)$$

where $\delta_0 = \rho_0/\rho_c$ and $\tau_0 = T_c/T_0$.

In the calculation of the thermodynamic properties using an equation of state explicit in the Helmholtz energy, an equation for the ideal gas heat capacity, c_p^0 , is needed to calculate the Helmholtz energy for the ideal gas, α^0 . Equations for the ideal gas heat capacity are generally given in the form

$$\frac{c_p^0}{R} = \sum_k N_k T^{i_k} + \sum_k N_k \frac{u_k^2 \exp(u_k)}{[\exp(u_k) - 1]^2} \quad (2.9)$$

where u_k is M_k/T . N_k and M_k are constants determined from spectroscopic or other experimental data. Table 2.4 gives values of the ideal gas isobaric heat capacity for

selected fluids. The values were calculated from the ideal gas heat capacity equations given in the references in Table 2.2.

Unlike the equations for the ideal gas, dense fluid or residual behavior is often described using empirical models that are only loosely tied with theory. The dimensionless residual Helmholtz energy is generally given as

$$\alpha^r(\delta, \tau) = \sum_k N_k \delta^{i_k} \tau^{j_k} + \sum_k N_k \delta^{i_k} \tau^{j_k} \exp(-\delta^{l_k}) \\ + \sum_k N_k \delta^{i_k} \tau^{j_k} \exp[-\varphi_k(\delta - 1)^2 - \beta_k(\tau - \gamma_k)^2] \quad (2.10)$$

Although the values of i_k , j_k , and l_k are empirical fitting constants, j_k is generally expected to be greater than zero, and i_k and l_k are integers greater than zero. The terms in the third sum correspond to *modified Gaussian bell-shaped terms*, introduced by Setzmann and Wagner (1991) to improve the description of properties in the critical region.

Calculation of Properties The functions used for calculating pressure, compressibility factor, internal energy, enthalpy, entropy, Gibbs energy, isochoric heat capacity, isobaric heat capacity, and the speed of sound from eq. (2.3) are given as eqs. (2.11 to 2.19). These equations were used in calculating values of thermodynamic properties given in the tables.

$$p = \rho RT \left[1 + \delta \left(\frac{\partial \alpha^r}{\partial \delta} \right)_\tau \right] \quad (2.11)$$

$$Z = \frac{P}{\rho RT} = 1 + \delta \left(\frac{\partial \alpha^r}{\partial \delta} \right)_\tau \quad (2.12)$$

$$\frac{u}{RT} = \tau \left[\left(\frac{\partial \alpha^0}{\partial \tau} \right)_\delta + \left(\frac{\partial \alpha^r}{\partial \tau} \right)_\delta \right] \quad (2.13)$$

$$\frac{h}{RT} = \tau \left[\left(\frac{\partial \alpha^0}{\partial \tau} \right)_\delta + \left(\frac{\partial \alpha^r}{\partial \tau} \right)_\delta \right] + \delta \left(\frac{\partial \alpha^r}{\partial \delta} \right)_\tau + 1 \quad (2.14)$$

$$\frac{s}{R} = \tau \left[\left(\frac{\partial \alpha^0}{\partial \tau} \right)_\delta + \left(\frac{\partial \alpha^r}{\partial \tau} \right)_\delta \right] - \alpha^0 - \alpha^r \quad (2.15)$$

$$\frac{g}{RT} = 1 + \alpha^0 + \alpha^r + \delta \left(\frac{\partial \alpha^r}{\partial \delta} \right)_\tau \quad (2.16)$$

$$\frac{c_v}{R} = -\tau^2 \left[\left(\frac{\partial^2 \alpha^0}{\partial \tau^2} \right)_\delta + \left(\frac{\partial^2 \alpha^r}{\partial \tau^2} \right)_\delta \right] \quad (2.17)$$

$$\frac{c_p}{R} = \frac{c_v}{R} + \frac{[1 + \delta(\partial \alpha^r / \partial \delta)_\tau - \delta \tau (\partial^2 \alpha^r / \partial \delta \partial \tau)]^2}{[1 + 2\delta(\partial \alpha^r / \partial \delta)_\tau + \delta^2 (\partial^2 \alpha^r / \partial \delta^2)_\tau]} \quad (2.18)$$

$$\frac{w^2 M}{RT} = 1 + 2\delta \left(\frac{\partial \alpha^r}{\partial \delta} \right)_\tau + \delta^2 \left(\frac{\partial^2 \alpha^r}{\partial \delta^2} \right)_\tau - \frac{[1 + \delta(\partial \alpha^r / \partial \delta)_\tau - \delta \tau (\partial^2 \alpha^r / \partial \delta \partial \tau)]^2}{\tau^2 [(\partial^2 \alpha^0 / \partial \tau^2)_\delta + (\partial^2 \alpha^r / \partial \tau^2)_\delta]} \quad (2.19)$$

Equations for additional thermodynamic properties are given in Lemmon et al. (2000). Table 2.3 displays the molecular weight, critical temperature, and critical density used in these equations for various fluids. The thermodynamic properties of various fluids along the saturated liquid and vapor lines are given in Table 2.7.

Thermodynamic Properties of Mixtures The Helmholtz energy for mixtures of fluids can be calculated from a generalized mixture model using the equations of state for the pure fluids in the mixture and an excess function to account for the interactions between different species, as given by Lemmon and Jacobsen (1999). This model is used in the REFPROP program available from the Standard Reference Data Program of NIST for mixture calculations. (See the introduction for additional details on the NIST databases.)

The Helmholtz energy of a mixture is

$$a = a^{\text{idmix}} + a^E \quad (2.20)$$

where the Helmholtz energy for an ideal mixture defined at constant reduced temperature and density (similar to simple corresponding states) is

$$a^{\text{idmix}} = \sum_{i=1}^n x_i [a_i^0(\rho, T) + a_i^r(\delta, \tau) + RT \ln x_i] \quad (2.21)$$

where n is the number of components in the mixture, a_i^0 is the ideal gas Helmholtz energy for component i , and a_i^r is the pure fluid residual Helmholtz energy of component i evaluated at a reduced density and temperature defined below.

The excess contribution to the Helmholtz energy from mixing is

$$\frac{a^E}{RT} = \alpha^E(\delta, \tau, \mathbf{x}) = \sum_{i=1}^{n-1} \sum_{j=i+1}^n x_i x_j F_{ij} \sum_{k=1}^{10} N_k \delta^{d_k} \tau^{t_k} \quad (2.22)$$

where the coefficients and exponents are obtained from nonlinear regression of experimental mixture data. The same set of mixture coefficients (N_k , d_k , and t_k) is used for all mixtures in the model, and the parameter F_{ij} is a scaling factor that relates the excess properties of one binary mixture to those of another. Multicomponent mixtures can then be calculated without any additional ternary or higher interaction parameters.

All single-phase thermodynamic properties [such as those given in eqs. (2.11 to 2.19)] can be calculated from the Helmholtz energy using the relations

$$\alpha^0 = \sum_{i=1}^n x_i \left[\frac{a_i^0(\rho, T)}{RT} + \ln x_i \right] \quad (2.23)$$

$$\alpha^r = \sum_{i=1}^n x_i \alpha_i^r(\delta, \tau) + \alpha^E(\delta, \tau, \mathbf{x}) \quad (2.24)$$

where the derivatives are taken at constant composition. The reduced values of density and temperature for the mixture are

$$\delta = \frac{\rho}{\rho_{\text{red}}} \quad (2.25)$$

$$\tau = \frac{T_{\text{red}}}{T} \quad (2.26)$$

where ρ and T are the mixture density and temperature, respectively, and ρ_{red} and T_{red} are the reducing values,

$$\rho_{\text{red}} = \left[\sum_{i=1}^n \frac{x_i}{\rho_{c_i}} + \sum_{i=1}^{n-1} \sum_{j=i+1}^n x_i x_j \xi_{ij} \right]^{-1} \quad (2.27)$$

$$T_{\text{red}} = \sum_{i=1}^n x_i T_{c_i} + \sum_{i=1}^{n-1} \sum_{j=i+1}^n x_i x_j \zeta_{ij} \quad (2.28)$$

The parameters ζ_{ij} and ξ_{ij} are used to define the shapes of the reducing temperature line and reducing density line. These reducing parameters are not the same as the critical parameters of the mixture and are determined simultaneously with the other parameters of the mixture model for each binary pair in the nonlinear fit of experimental data.

2.2.2 Transport Properties

The equations used for calculating the transport properties of fluids are given in the references cited in Table 2.2. For many substances, equations for transport properties have not been developed or published, and alternative techniques must be used. A widely used method for calculating the transport properties of fluids is based on predictions using the extended corresponding states (ECS) concept. In Table 2.2, those fluids for which the ECS method is used to determine the best current values are identified. Values for some of the fluids have been improved by fitting experimental data, while others are used in a purely predictive mode.

Extended Corresponding States The principle of corresponding states stems from the observation that the properties of many fluids are similar when scaled by their respective critical temperatures and densities. Extended corresponding states models modify this scaling by using additional shape factors to improve the representation of data. ECS methods may be used to predict both the thermodynamic and transport properties, especially for fluids with limited data. The method starts with

the ECS model of Huber et al. (1992) and Ely and Hanley (1983) and combines this predictive model with the best available thermodynamic equations of state (see Klein et al., 1997; McLinden et al., 2000).

The viscosity of a fluid can be represented as the sum of the dilute gas and the real fluid contributions,

$$\eta(T, \rho) = \eta^*(T) + \eta^r(T, \rho) \quad (2.29)$$

where η^* is the Chapman–Enskog dilute gas contribution described later. The thermal conductivity of a fluid can be represented as the sum of energy transfer due to translational and internal contributions.

$$\lambda(T, \rho) = \lambda^{\text{int}}(T) + \lambda^{\text{trans}}(T, \rho) \quad (2.30)$$

where the superscript “trans” designates the translational term (i.e., contributions arising from collisions between molecules) and the superscript “int” designates the contribution from internal motions of the molecule). The internal term is assumed to be independent of density. The translational term is divided into a dilute-gas contribution λ^* and a density-dependent term, which is further divided into a residual part (superscript r) and a critical enhancement (superscript “crit”). The thermal conductivity is thus the sum of four terms:

$$\lambda(T, \rho) = \lambda^{\text{int}}(T) + \lambda^*(T) + \lambda^r(T, \rho) + \lambda^{\text{crit}}(T, \rho) \quad (2.31)$$

Dilute-Gas Contributions The standard formulas for the dilute-gas contributions that arise from kinetic theory and which have been used by Ely and Hanley (1983), Huber et al. (1992), and others, but with an empirical modification, are used here. The transfer of energy associated with internal degrees of freedom of the molecule is assumed to be independent of density and can be calculated from the Eucken correlation for polyatomic gases given in Hirschfelder et al. (1967),

$$\lambda_j^{\text{int}}(T) = \frac{f_{\text{int}} \eta_j^*(T)}{M_j} \left(c_{p,j}^0 - \frac{5}{2} R \right) \quad (2.32)$$

where c_p^0 is the ideal gas heat capacity, R the gas constant, and M the molar mass. The subscript j emphasizes that all quantities are to be evaluated for fluid j . The factor f_{int} accounts for the energy conversion between internal and translational modes.

The dilute-gas part of the translational term is given by

$$\lambda_j^*(T) = \frac{15 R \eta_j^*(T)}{4 M_j} \quad (2.33)$$

The Chapman–Enskog dilute-gas viscosity is given by standard kinetic gas theory from Hirschfelder et al. (1967):

$$\eta_j^*(T) = \frac{(M_j T)^{1/2}}{\sigma_j^2 \Omega^{(2,2)}(kT/\epsilon_j)} \quad (2.34)$$

where σ_j and ε/k are the molecular size and energy parameters associated with an intermolecular potential function such as the Lennard-Jones 12-6 potential, and $\Omega^{(2,2)}$ is the collision integral (again for the Lennard-Jones fluid), which is a function of the reduced temperature, kT/ε_j . The empirical function of Neufeld et al. (1972) is often used for $\Omega^{(2,2)}$. While the dilute-gas viscosity equation is derived from theory, the molecular size and energy parameters are most often evaluated from low-density viscosity data. This function can thus be treated as a theoretically based correlating function.

Where experimentally based Lennard-Jones parameters are not available, they may be estimated by the relations suggested by Huber and Ely (1992):

$$\varepsilon_j/k = \frac{\varepsilon_0}{k} \frac{T_j^{\text{crit}}}{T_0^{\text{crit}}} \quad (2.35)$$

$$\sigma_j = \sigma_0 \left(\frac{\rho_0^{\text{crit}}}{\rho_j^{\text{crit}}} \right)^{1/3} \quad (2.36)$$

where the zero subscript refers to the reference fluid used in the ECS described below. Tables 2.5 and 2.6 give values for the dilute-gas thermal conductivity and viscosity.

Density-Dependent Contributions The principle of corresponding states can be used to model the residual part of the thermal conductivity and viscosity. Such models have been applied to a wide variety of fluids by many authors, including Leland and Chapplear (1968), Hanley (1976), Ely and Hanley (1983), and Huber et al. (1992). This approach is especially useful for fluids for which limited experimental data exist.

The simple corresponding states model is based on the assumption that different fluids are conformal; that is, they obey, in reduced coordinates, the same intermolecular force laws. A reduced property may be obtained by dividing the individual state values by the value of the property at the critical point. This assumption leads to the conclusion that with appropriate scaling of temperature and density, the reduced residual Helmholtz energies and compressibilities of the unknown fluid j and a reference fluid 0 (for which an accurate, wide-ranging equation of state is available) are equal:

$$\alpha_j^r(T, \rho) = \alpha_0^r(T_0, \rho_0) \quad (2.37)$$

$$Z_j(T, \rho) = Z_0(T_0, \rho_0) \quad (2.38)$$

The reference fluid is usually chosen as one that has a molecular structure similar to the fluid of interest. The conformal temperature T_0 and density ρ_0 are related to the actual T and ρ of the fluid of interest by

$$T_0 = \frac{T}{f} = T \frac{T_0^{\text{crit}}}{T_j^{\text{crit}} \theta(T, \rho)} \quad (2.39)$$

$$\rho_0 = \rho h = \rho \frac{\rho_0^{\text{crit}}}{\rho_j^{\text{crit}}} \phi(T, \rho) \quad (2.40)$$

where the multipliers $1/f$ and h are termed *equivalent substance reducing ratios*, or simply *reducing ratios*.

Initially, the corresponding states approach was developed for spherically symmetric molecules for which the reducing ratios are simple ratios of the critical parameters (θ and ϕ both equal to 1). The ECS model extends the method to other types of molecules by the introduction of the shape factors θ and ϕ . These shape factors are functions of temperature and density, although the density dependence is often neglected.

The ECS method has been applied to both the thermodynamic and transport properties. In this model, the thermal conductivity is

$$\lambda_j^r(T, \rho) = F_\lambda \lambda_0^r(T_0, \rho_0) \quad (2.41)$$

and the viscosity is

$$\eta_j^r(T, \rho) = F_\eta \eta_0^r(T_0, \rho_0) \quad (2.42)$$

where

$$F_\lambda = f^{1/2} h^{-2/3} \left(\frac{M_0}{M_j} \right)^{1/2} \quad (2.43)$$

$$F_\eta = f^{1/2} h^{-2/3} \left(\frac{M_j}{M_0} \right)^{1/2} \quad (2.44)$$

Following the methods of Klein et al. (1997) and McLinden et al. (2000), the reducing ratios $1/f$ and h are further modified by empirical viscosity shape factors and thermal conductivity shape factors fitted to experimental data. The thermal conductivity approaches infinity at the critical point, and even well removed from the critical point the critical enhancement can be a significant portion of the total thermal conductivity. The transport properties of various fluids along the saturated liquid and vapor lines are given in Table 2.7.

Transport Properties of Mixtures For mixtures, the calculation of thermal conductivity and viscosity from extended corresponding states principles uses the same terms as those given in equations for pure fluids. For the thermal conductivity, the internal and translational contributions are calculated using

$$\lambda_{\text{mix}}^{\text{int}}(T, x) + \lambda_{\text{mix}}^*(T, x) = \sum_{j=1}^n \frac{x_j [\lambda_j^{\text{int}}(T) + \lambda_j^*(T)]}{\sum_{i=1}^n x_i \phi_{ji}} \quad (2.45)$$

where

$$\varphi_{ji} = \left[1 + \left(\frac{\eta_j^*}{\eta_i^*} \right)^{1/2} \left(\frac{M_j}{M_i} \right)^{1/4} \right]^2 \left[8 \left(1 + \frac{M_j}{M_i} \right) \right]^{-1/2} \quad (2.46)$$

All quantities in the dilute-gas terms are evaluated at the temperature of the mixture rather than at some conformal temperature. The residual viscosity includes an additional term,

$$\eta_{\text{mix}}^r = \Delta\eta_0 \left(\frac{T}{f_x, \rho h_x} \right) F_\eta + \Delta\eta^*(\rho, x) \quad (2.47)$$

where $\Delta\eta_0$ is the residual viscosity of the reference fluid and the additional term $\Delta\eta^*$ is an Enskog hard-sphere correction for effects of differences in size and mass in a mixture.

The F_λ term in the residual part of the transport equations is

$$F_\lambda = f_x^{1/2} h_x^{-2/3} g_x^{1/2} \quad (2.48)$$

where the subscript x indicates a mixture quantity, and

$$g_x^{1/2} = \frac{M_0^{1/2}}{f_x^{1/2} h_x^{4/3}} \sum_{i=1}^n \sum_{j=1}^n x_i x_j (f_i f_j)^{1/4} \left(\frac{2}{1/g_i + 1/g_j} \right)^{-1/2} \left[\frac{1}{8} (h_i^{1/3} + h_j^{1/3})^3 \right]^{4/3} \quad (2.49)$$

The g_i are

$$g_i = M_0 \left[\frac{\lambda_0^r(T_0, \rho_0)}{\lambda_j^r(T_j, \rho_j)} \right]^2 f_j h_j^{-4/3} \quad (2.50)$$

The reducing ratios are defined as $f_x = T/T_0$, $h_x = \rho_0/\rho$, $f_j = T_j f_x/T$, and $h_j = \rho h_x/\rho_j$. The conformal conditions for component j and the mixture are found by solving the equations

$$\alpha_j^r(T_j, \rho_j) = \alpha_{\text{mix}}^r(T, \rho, x) \quad (2.51)$$

$$Z_j(T_j, \rho_j) = Z_{\text{mix}}(T, \rho, x) \quad (2.52)$$

$$\alpha_j^r(T_0, \rho_0) = \alpha_{\text{mix}}^r(T, \rho, x) \quad (2.53)$$

$$Z_j(T_0, \rho_0) = Z_{\text{mix}}(T, \rho, x) \quad (2.54)$$

where the mixture properties are calculated using the Helmholtz energy mixture model described earlier.

2.3 THERMOPHYSICAL PROPERTIES OF SOLIDS

In this section we discuss the transport properties associated with heat transfer in solid materials. Starting with the equation for the conservation of energy, we demonstrate the need for constitutive models for the internal energy and heat flux. A brief

discussion of the physical mechanisms that contribute to heat transfer in solids follows. Next, several common measurement techniques are discussed to assist the reader in assessing their applicability should property measurements be needed. In practice, such measurements might be desired because the tabulated property values of a listed material may differ from those of the material obtained for use because of differences in alloying, level of impurities, or crystalline structure, for example.

Introduction to the molecular modeling of thermal conductivity may be found in Klemens (1969) and Parrott and Stuckes (1975). Brief discussions of thermal conductivity, specific heat, and thermal expansion may be found in introductory texts in solid-state physics (e.g., Reif, 1965; Brown, 1967; Kittel, 1996). The general behavior of material properties with respect to temperature may also be found in Jakob (1955) and in introductory texts (e.g., Incropera and DeWitt, 1996).

2.3.1 Conservation of Energy

The equation for the conservation of energy in the absence of stress power may be written as

$$\frac{di}{dt} = -\nabla \cdot \dot{\mathbf{q}} + q''' \quad (2.55)$$

where i the enthalpy per unit volume, t the time, $\dot{\mathbf{q}}$ the heat flux vector, and q''' the volumetric rate of heat generation due, for example, to chemical reaction or to absorption of electromagnetic radiation. The stress power is the rate of work done by the stress field during deformation. It is identically zero for rigid-body motion. In general, i may be a function of deformation and temperature and $\dot{\mathbf{q}}$ may be a function of the temperature gradient as well. Two constitutive equations are needed for eq. (2.55), one for i and another for $\dot{\mathbf{q}}$. Changes in the specific internal energy may be written as

$$\frac{di}{dt} = \rho_m c_p \frac{dT}{dt} \quad (2.56)$$

where c_p is the specific heat per unit mass at constant pressure, ρ_m the mass density, and T the temperature. For solids, it may easily be shown that the specific heat is nearly independent of pressure (i.e., $c_p \approx c_v$, where c_v is the specific heat at constant volume) (see, e.g., Reif, 1965). Similarly, it is usually assumed that c_p is independent of internal stresses (Parrott and Stuckes, 1975). Fourier's equation is most often assumed to relate $\dot{\mathbf{q}}$ to temperature. It agrees well with most measurements and may be written as

$$\dot{\mathbf{q}} = -\lambda \cdot \nabla T \quad (2.57)$$

where λ is the thermal conductivity tensor. In most common circumstances, the thermal conductivity is isotropic and eq. (2.57) may be rewritten as $\dot{\mathbf{q}} = -\lambda \nabla T$.

In the absence of internal heat generation and assuming isotropic thermal conductivity, substituting eqs. (2.56) and (2.57) into eq. (2.55) yields

$$\rho_m c_p \frac{dT}{dt} = \lambda \nabla^2 T \quad (2.58)$$

Grouping the material properties, the thermal diffusivity is defined as $\alpha_D = \lambda / \rho_m c_p$. Thus, the important thermophysical properties are α_D , λ , ρ_m , and c_p . In general, these properties can be functions of direction, deformation, and temperature. Some crystalline elements, such as carbon, bismuth, and tin, have anisotropic thermal conductivities. Some polymers develop anisotropy after finite deformation (Choy et al., 1978; Broerman et al., 1999; Ortt et al., 2000). The temperature dependence of α is sometimes less strong than that of λ , which can simplify analytical solutions of conduction problems (Ozisik, 1980). For analyses of transient heat transfer, α_D is the important parameter, while for analyses of steady heat transfer and boundary conditions of transient analyses, λ is required.

Equation (2.58) is nonphysical because it predicts an infinite speed of propagation of temperature change, that is, a temperature change in one part of the body causes an immediate change in temperature throughout the body. Substituting the Maxwell–Cattaneo equation for Fourier’s equation yields

$$\frac{1}{\alpha_D} \frac{dT}{dt} + \frac{1}{c^2} \frac{d^2 T}{dt^2} = \nabla^2 T \quad (2.59)$$

where c has dimensions of velocity. If c is approximated as the speed of sound in the body, then for good conductors the ratio of the coefficients is $\alpha_D/c = 10^{-11}$ s (Parrott and Stuckes, 1975). Thus, except in rare circumstances, finite propagation speeds are important only for very short times. Joseph and Preziosi (1989, 1990) provide an extensive review of studies examining Maxwell–Cattaneo conduction.

In general, analyses of thermal conduction assume that materials are rigid and incompressible. This is not strictly so. Relaxing this assumption requires the addition of the simultaneous solution of the balance of linear momentum and the addition of the stress work term (see, e.g., Day, 1985). The linear coefficient of thermal expansion may be defined as $\mu = (L - L_0) / [L_0(T - T_0)]$, where L is the length of the solid at its new temperature T , and L_0 is its length at the reference temperature T_0 . At room temperature, μ typically ranges from $0.6 \times 10^{-6} \text{ } ^\circ\text{C}^{-1}$ for silicon carbide to $500 \times 10^{-6} \text{ } ^\circ\text{C}^{-1}$ for rubber (Brown, 1967). The volumetric coefficient of thermal expansion $\mu_v = (1 + \mu)^3 \approx (1 + 3\mu)$ relates the specific volume at T to the specific volume at T_0 .

2.3.2 Behavior of Thermophysical Properties of Solids

The thermal conductivity and specific heat are defined above as continuum properties. Some indication of their behavior may be found by considering the molecular nature of materials. In solids, thermal transport properties result from molecular vibrations, and in electrical conductors, from electron transport. The vibrations of the molecules in a crystal lattice may be analyzed as harmonic oscillators and quantized (see, e.g., Reif, 1965 or Brown, 1967). These quanta are called *phonons*, and heat conduction

can be pictured as the diffusion of phonons from a hotter region to a colder one. Transport of electrons dominates that of phonons in metals at moderate temperatures, which explains why their thermal conductivities are typically larger than those of dielectrics. Typical values of thermal conductivity for metallic elements at 300 K range from 23 W/m · K for zirconium to 427 W/m · K for silver, whereas typical values for dielectrics run from 0.12 W/m · K for paper to almost 3.0 W/m · K for granite and marble (Baehr and Stephan, 1998). Diamond is anomalous in that it has a thermal conductivity as high as 2310 W/m · K at 300 K (Ho et al., 1974).

As the temperature approaches absolute zero, both the thermal conductivity and the specific heat tend toward zero, in accordance with the third law of thermodynamics. In dielectrics, the change in conductivity decreases as $1/T^3$, while in metals it decreases as $1/T$, owing to the transport of electrons. As the material warms, the conductivity usually reaches a maximum and then decreases with increasing temperature. The trend at higher temperatures is not universal, however, and the thermal conductivity may still increase with temperature for some materials that melt or decompose before the maximum is reached. The molar specific heat of many simple materials reaches approximately $3R$ at moderate temperatures, in accordance with the observations of Dulong and Petit (see, e.g., Brown, 1967; Reif, 1965). Modeling of materials such as glasses and amorphous polymers is less complete (Kittel, 1996). Dashora (1994) examined the temperature dependence of the thermal diffusivity of elastomers, and Eiermann (1966) discussed a resistive network model of heat conduction in amorphous polymers.

Some material systems, such as heterogeneous polymers (Bigg, 1995), biological tissues (Chato, 1985), and composite materials (Dowding et al., 1996) have been modeled using apparent thermal properties. In fact, these material systems are composed of materials with different densities, thermal conductivities, and specific heats. Prediction of the performance of material systems that include continuous fibers of dispersed particles or voids within a matrix material is difficult. Measurement of apparent properties may then be more expedient and accurate for a given system. Cooper and Trezek (1971), for example, proposed correlations for the apparent conductivity of biological soft tissue as functions of the mass fractions of water, protein, and fat. Even so, tabulated and correlated values of the thermophysical properties of biological materials must be used with caution because of potential anisotropy, specimen-to-specimen variation, and changes due to denaturation of protein during heating.

2.3.3 Property Values of Solid Materials

Unlike gases and liquids, there is no standard, reference-quality computer package for the calculation of thermophysical properties of solids. Perhaps the most extensive compilation of solid properties comes from the Center for Information and Numerical Data Synthesis and Analysis (CINDAS) at Purdue University, which was established by Yeram S. Touloukian (1981) as the Thermophysical Properties Research Center (TPRC). The reference materials produced by this group have been used extensively as a resource for this part of the chapter. Tables of typical values for metallic alloys and nonmetallic solids have been taken from the introductory text by Bejan (1993).

Tables 2.8, 2.9, and 2.10 list the properties of solids that have been grouped into categories of solid elements, solid metallic alloys, and miscellaneous nonmetallic solids. Unlike those of fluids, the properties of solids vary little with changes in pressure, and thus the tables in this section neglect the effects of pressure on solid property values.

The thermal conductivities of elements are sensitive to even minute levels of impurity, especially at low temperatures, although the purity of the samples measured is often omitted in reports of measurements. Even near room temperature, values quoted by different sources may vary by 15% or more. The values of thermal conductivity for all elements recommended by Ho et al. (1974), listed in Table 2.8, were derived from critical and comprehensive evaluations by CINDAS of the data available in the literature up to the early 1970s. Accuracy for the thermal conductivity values may vary from 2 to 20%, depending on the purity and temperature levels. The reader should refer to the original work for detailed information if requirements for accuracy are high.

2.3.4 Measuring Thermophysical Properties of Solids

Measuring thermal conductivity and thermal diffusivity requires the development of experimental approximations of boundary value problems. Carslaw and Jaeger (1959) provide analytical solutions to many classical boundary value problems that have been useful in the measurement of thermal transport properties. Reviews of methods for measuring thermal transport properties may be found in Maglic et al. (1984, 1992), Shirliffe and Tye (1985), Parrott and Stuckes (1975), and Jakob (1955). The American Society for Testing and Materials (ASTM) has established several standards for measuring transport properties, and the National Institute of Standards and Technology (NIST) can provide some standard reference materials (SRMs). As noted above, sources of error include impurities in the sample and variables omitted from the analysis, such as deformation of polymers (Choy et al., 1978; Greig and Sahota, 1978; Doss and Wright, 2000). New methods of measurement are constantly being developed to overcome such sources of error, and the results are published as appropriate.

Thermal Conductivity Direct measurement of thermal conductivity has traditionally used steady-state methods. For materials of moderate to high thermal conductivity (~ 10 to $500 \text{ W/m} \cdot \text{K}$), axial heat flow, radial heat flow, and direct electrical heating methods are often used (Maglic et al., 1984). Materials of lower thermal conductivity are most commonly tested in using the guarded hot plate (thermal insulation materials) or hot wire methods; the latter is a transient method. These methods can provide high accuracy and simple data reduction but require a relatively long time to reach steady state. This reduces their suitability for measuring properties of a material that may change during measurement, such as biological tissues. Thermal conductivity is sometimes determined via indirect methods by measuring the diffusivity and using the density and specific heat to calculate the conductivity. The 3ω technique

(text continues on page 140)

TABLE 2.8 Thermophysical Properties of Solid Elements^a

<i>Aluminum (Al)</i>												
T	50	100	150	200	273	298	400	500	600	700	800	900
ρ	2736	2732	2726	2719	2706	2701	2681	2661	2639	2616	2591	2564
c_p	—	481	—	797	881	893	944	994	1044	1094	1144	1194
λ	1350	302	248	237	236	237	240	236	231	225	218	210
α_D	—	230	—	109	99.0	98.3	94.8	89.2	83.8	78.6	73.6	68.6
<i>Antimony (Sb)</i>												
T	50	100	150	200	273	298	400	400	600	700	800	900
ρ	—	6724	6714	6704	6688	6683	6660	6636	6613	6590	6568	
c_p	—	—	—	—	206	208	214	220	226	232	238	244
λ	88.3	46.4	35.6	30.2	25.5	24.4	21.3	19.5	18.3	17.4	16.8	16.7
α_D	—	—	—	—	18.5	17.6	15.0	13.4	12.2	11.4	10.7	
<i>Beryllium (Be)</i>												
T	—	100	200	273	298	400	500	600	800	1000	1200	1400
ρ	—	—	—	—	1850	1843	1835	1826	1807	1785	1763	1739
c_p	—	195	1109	1624	1764	2119	2317	2458	2671	2847		
λ	—	990	301	218	201	161	139	126	106	90.8	78.7	69.4
α_D	—	—	—	—	61.6	41.2	32.7	28.1	22.0	17.9		
<i>Bismuth (Bi)</i>												
T	50	100	200	273	298	350	400	500				
ρ	9872	9855	9817	9788	9778	9758	9738	9700				
c_p	—	109	120	122	123	126	129	134				

(continued)

TABLE 2.8 Thermophysical Properties of Solid Elements^a (Continued)

<i>Bismuth (Bi) (Continued)</i>												
λ	32.6	16.5	9.69	8.20	7.89	7.39	7.04	6.63				
α_D	—	15.4	8.2	6.9	6.5	6.0	5.6	5.1				
<i>Boron (B)</i>												
T	50	100	150	200	273	298	400	600	800	1000	1100	1300
ρ	—	—	—	—	—	2500	2496	2488	2479	2470	2465	2455
c_p	—	—	—	—	1061	1104	1277	1618	1958	2299	2469	
λ	404	190	93.5	55.1	31.8	27.4	16.8	10.6	9.60	9.85	10.1	
α_D	—	—	—	—	—	9.9	5.3	2.6	2.0	1.7	1.7	
<i>Cadmium (Cd)</i>												
T	50	100	200	273	298	373	400	473	500	573		
ρ	—	8799	8724	8666	8646	8585	8562	8499	8475	8405		
c_p	—	—	—	228	231	237	240	247	249	256		
λ	120	103	99.3	97.5	96.9	95.3	94.7	92.8	92.0	89.1		
α_D	—	—	—	49.3	48.6	46.7	46.1	44.3	43.6	41.4		
<i>Calcium (Ca)</i>												
T	—	100	200	273	298	350	400	500	573	600	800	1000
ρ	—	1568	1559	1552	1549	1544	1539	1528	1520	1517		
c_p	—	—	—	649	658	676	693	728	754	763	774	
λ	—	—	222	206	201	193	188	181	179	178	153	128
α_D	—	—	—	204	197	185	176	163	156	154		

Carbon (C)

T	50	100	150	200	273	298	400	600	800	1000	1500	2500
ρ (amorphous)	—	—	—	—	—	1950	1948	1944	1940	1936	1924	1892
c_p (graphite)	—	—	—	—	633	744	1040	1364	1595	1800		
λ (amorphous)	0.377	0.668	0.938	1.18	1.50	1.59	1.89	2.19	2.37	2.53	3.48	

Cerium (Ce)

T	50	100	150	200	273	298	400	500	600	700	800	1000
ρ	—	—	—	—	—	6899	6888	6875	6861	6846	6831	6795
c_p	—	—	—	—	186	187	190	194	198	201	205	
λ	3.79	6.00	7.66	9.00	10.8	11.3	13.3	15.0	16.5	18.0	19.3	21.8
α_D	—	—	—	—	—	8.8	10.1	11.3	12.2	13.1	13.8	

Cesium (Cs)

T	50	100	150	200	273	298						
ρ	1962	1944	1926	1907	1880	1871						
c_p	—	—	—	—	218	232						
λ	44.7	39.7	37.8	36.8	36.1	35.9						
α_D	—	—	—	—	88.0	82.5						

Chromium (Cr)

T	50	100	200	273	298	400	600	800	1000	1200	1500	1800
ρ	—	—	—	—	7139	7124	7086	7042	6995	6944	6860	6761
c_p	—	190	382	454	460	484	532	579	627	674	746	817
λ	317	159	111	96.5	93.9	90.9	80.7	71.3	65.4	61.9	57.2	52.6
α_D	—	—	—	—	28.6	26.3	21.4	17.5	14.9	13.2	11.2	9.5

(continued)

TABLE 2.8 Thermophysical Properties of Solid Elements^a (Continued)

<i>Cobalt (Co)</i>												
T	50	100	200	273	298	400	600	800	1000	1200	1400	1700
ρ	—	8919	8892	8869	8860	8823	8744	8642	8561	8475		
c_p	—	234	376	428	434	458	505	553	600	647	694	765
λ	299	167	122	105	100	85.4	67.4	58.2	52.1	49.3	41.7	43.0
α_D	—	80.0	36.5	27.7	26.0	21.1	15.3	12.2	10.1	8.99		
<i>Copper (Cu)</i>												
T	50	100	200	273	298	400	600	800	1000	1100	1200	1300
ρ	—	9009	8973	8942	8931	8884	8788	8686	8576	8519	8458	8396
c_p	—	254	357	384	387	397	416	435	454	464	474	483
λ	1250	482	413	403	401	393	379	366	352	346	339	332
α_D	—	210.6	128.9	117.2	116.1	111.5	103.7	96.8	90.3	87.5	84.6	81.8
<i>Gold (Au)</i>												
T	50	100	200	273	298	400	600	800	1000	1100	1200	1300
ρ	—	19,030	18,950	18,900	18,880	18,790	18,620	18,440	18,250	18,140	18,030	17,920
c_p	—	109	124	128	128	131	138	144	150	153	156	159
λ	421	327	323	319	318	311	298	284	270	262	255	247
α_D	—	157.7	137.4	132.4	131.3	125.9	116.4	107.2	98.8	94.5	90.7	86.7
<i>Iron (Fe)</i>												
T	50	100	200	273	298	400	600	800	1000	1200	1400	1600
ρ	7918	7913	7895	7876	7869	7838	7772	7699	7624	7632	7527	7424
c_p	—	216	384	440	452	501	596	692	787	629	629	629
λ	405	134	94.0	83.5	80.4	69.5	54.7	43.3	32.8	28.3	31.2	33.0
α_D	—	78.4	31.0	24.1	22.6	17.7	11.8	8.1	5.5	5.9	6.6	7.1

Lead (Pb)

T	50	100	200	273	298	400	500	600
ρ	—	11,520	11,430	11,360	11,340	11,230	11,130	11,010
c_p	—	118	125	128	129	133	137	141
λ	43.6	39.7	36.7	35.6	35.3	34.0	32.8	31.4
α_D	—	29.2	25.7	24.5	24.2	22.8	21.5	20.2

Lithium (Li)

T	50	100	200	273	298	300	350	400	450
ρ	547	546	541	535	534	533	530	526	521
c_p	—	—	—	3373	3644	3666	4208	4751	5293
λ	235	104	90.1	85.9	84.8	84.7	82.8	80.4	
α_D	—	—	—	47.6	43.6	43.3	37.1	32.2	

Magnesium (Mg)

T	50	100	200	273	298	400	500	600	700	800	900
ρ	—	1761	1751	1742	1739	1726	1711	1696	1680	1663	1645
c_p	—	648	929	973	1004	1086	1135	1172	1204	1232	1259
λ	465	169	159	157	156	153	151	149	147	146	145
α_D	—	148.1	97.7	92.6	89.3	81.6	77.7	74.9	72.7	71.2	70.0

Manganese (Mn)

T	50	100	200	273	298	400	600	800	900	1000
ρ	—	—	7474	7440	7428	7376	7257	7109	7020	
c_p	—	—	—	442	456	514	628	741	198	855
λ	4.06	5.79	7.17	7.68	7.81					
α_D	—	—	—	2.3	2.3					

(continued)

TABLE 2.8 Thermophysical Properties of Solid Elements^a (Continued)

<i>Nickel (Ni)</i>												
T	50	100	200	273	298	400	600	800	1000	1200	1500	1700
ρ	—	—	—	—	8898	8860	8779	8694	8606	8516	8372	
c_p	—	232	383	428	440	486	577	550	563	576	595	608
λ	400	164	107	94.1	90.0	80.2	65.6	67.6	71.8	76.2	82.6	
α_D	—	—	—	—	23.2	18.6	12.9	14.1	14.8	15.5	16.6	
<i>Platinum (Pt)</i>												
T	50	100	200	273	298	400	600	800	1000	1400	1800	1900
ρ	—	21,500	21,500	21,460	21,450	21,390	21,270	21,140	21,010	20,720	20,400	20,310
c_p	—	101	127	134	134	137	142	147	152	162	172	
λ	109	77.5	72.6	71.7	71.6	71.8	73.2	75.6	78.7	87.1	96.1	97.8
α_D	—	35.6	26.6	25.0	24.8	24.5	24.3	24.4	24.7	26.0	27.4	
<i>Potassium (K)</i>												
T	50	100	200	273	298	300	323	336				
ρ	911	904	888	874	869	869	864	861				
c_p	—	—	—	723	738	739	753	760				
λ	112	107	104	104	103	102	100	99				
α_D	—	—	—	165	160	160	154	150				
<i>Silicon (Si)</i>												
T	50	100	200	273	298	400	600	800	1000	1200	1400	1600
ρ	2422	2422	2421	2420	2420	2418	2413	2407	2401	2394	2388	2381
c_p	—	—	—	678	713	798	868	905	932			
λ	2680	884	264	168	149	98.9	61.9	42.2	31.2	25.7	23.5	22.1
α_D	—	—	—	102.3	86.4	51.3	29.5	19.4	13.9			

Silver (Ag)

T	50	100	200	273	298	400	500	600	700	800	1000	1200
ρ	—	—	10,550	10,500	10,490	10,430	10,360	10,300	10,230	10,160	10,010	9855
c_p	—	187	225	233	235	240	246	252	258	264	275	287
λ	700	444	430	429	429	425	419	412	404	396	379	361
α_D	—	—	181	175	174	169	164	159	153	148	137	128

Sodium (Na)

T	50	100	200	273	298	300	371
ρ	—	1007	990	975	970	970	955
c_p	—	—	—	1178	1202	1204	1274
λ	158	136	142	142	142	141	132
α_D	—	—	—	124	122	121	109

Tantalum (Ta)

T	50	100	200	273	298	400	600	800	1000	1500	2000	3000
ρ	—	—	—	—	16,600	16,570	16,500	16,430	16,360	16,180	15,970	15,340
c_p	—	—	—	143	143	146	150	155	160			
λ	72.0	59.2	57.5	57.4	57.5	57.8	58.6	59.4	60.2	62.2	64.1	66.6
α_D	—	—	—	—	24.1	23.9	23.6	23.3	23.1			

Tin (Sn)

T	50	100	200	273	298	400	500
ρ	—	5815	5783	5757	7307	7255	7199
c_p	—	189	214	224	228	246	263
λ	115	85.3	73.3	68.2	66.8	62.2	59.6
α_D	—	77.6	59.2	52.8	40.0	34.9	31.5

(continued)

TABLE 2.8 Thermophysical Properties of Solid Elements^a (Continued)

<i>Titanium (Ti)</i>												
T	50	100	200	273	298	400	600	800	1000	1200	1400	1600
ρ	—	—	4510	4502	4499	4487	4461	4432	4402	4379	4348	4315
c_p	—	—	—	298	382	582	733					
λ	37.4	30.5	24.5	22.4	21.9	20.4	19.4	19.7	20.7	22.0	23.6	25.3
α_D	—	—	—	16.7	12.7	7.8	5.9					
<i>Tungsten (W)</i>												
T	50	100	200	273	298	400	500	1000	1500	2000	3000	3600
ρ	—	—	—	—	19,300	19,270	19,250	19,110	18,950	18,790	18,380	18,050
c_p	—	—	—	182	187	207	227	326	424	523		
λ	428	208	186	177	174	159	146	118	107	100	91.4	89.5
α_D	—	—	—	—	48.1	39.8	33.4	19.0	13.3	10.2		
<i>Uranium (U)</i>												
T	50	100	200	273	298							
ρ	—	—	—	—	19,070							
c_p	—	—	—	117	117							
λ	18.9	21.7	25.1	27.0	27.5							
α_D	—	—	—	—	12.4							
<i>Vanadium (V)</i>												
T	50	100	200	273	298	400	600	800	1000	1400	1800	2000
ρ	—	—	—	—	6198	6214	6244	6272	6298	6339	6364	6369
c_p	—	—	—	479	481	489	505	521	537	569	601	
λ	40.5	35.8	31.3	30.7	30.7	31.3	33.3	35.7	38.2	43.4	48.4	50.9
α_D	—	—	—	—	10.3	10.3	10.6	10.9	11.3	12.0	12.7	

Zinc (Zn)

T	50	100	200	273	298	400	500	600
ρ	—	7258	7199	7153	7137	7070	7002	6933
c_p	—	295	366	383	387	405	422	440
λ	205	117	118	117	116	111	107	103
α_D	—	54.6	44.8	42.7	41.9	38.8	36.2	33.8

^a T , temperature (K); ρ , density (kg/m³); c_p , heat capacity (J/kg · K); λ , thermal conductivity (W/m · K); α_D , thermal diffusivity (10^{−6} m²/s). The heat capacities are from Liley et al. (1997). The densities are calculated from the formulations of thermal linear expansion by Touloukian et al. (1975, 1977). Those at temperatures higher than 273 K are calculated from the formulations compiled by Liley et al. (1997). The uncertainties of these formulations are about 2% for most elements listed.

TABLE 2.9 Thermophysical Properties of Metallic Alloys

	Properties at 20°C (293 K)				Thermal Conductivity λ (W/m · K)					
	ρ (kg/m ³)	c_p (kJ/kg · K)	λ (W/m · K)	α_D (cm ² /s)	−100°C 173 K	0°C 273 K	100°C 373 K	200°C 473 K	400°C 673 K	600°C 873 K
Aluminum										
Duralumin (94–96% Al, 3–5% Cu, trace Mg)	2787	0.883	164	0.667	126	159	182	194		
Silumin (87% Al, 13% Si)	2659	0.871	164	0.710	149	163	175	185		
Copper										
Commercial	8300	0.419	372	1.07						
Aluminum bronze (95% Cu, 5% Al)	8666	0.410	83	0.233						
Brass (70% Cu, 30% Zn)	8522	0.385	111	0.341	88	—	128	144	147	
Brass (60% Cu, 40% Zn)	8400	0.376	113	0.358						
Bronze (75% Cu, 25% Sn)	8666	0.343	26	0.086						
Bronze (85% Cu, 6% Sn, 9% Zn, 1% Pb)	8800	0.377	61.7	0.186						
Constantan (60% Cu, 40% Ni)	8922	0.410	22.7	0.161	21	—	22.2	26		
German silver (62% Cu, 15% Ni, 22% Zn)	8618	0.394	24.9	0.073	19.2	—	31	40	48	
Iron										
Cast (5% C)	7272	0.420	52	0.170						
Carbon steel, 0.5% C	7833	0.465	54	0.148	—	55	52	48	42	35
Carbon steel, 1.0% C	7801	0.473	43	0.117	—	43	43	42	36	33
Carbon steel, 1.5% C	7753	0.486	36	0.097	—	36	36	36	33	31
Chrome steel, 1% Cr	7865	0.460	61	0.167	—	62	55	52	42	36
Chrome steel, 5% Cr	7833	0.460	40	0.111	—	40	38	36	33	29
Chrome steel, 20% Cr	7689	0.460	22	0.064	—	22	22	22	24	24
Chrome-nickel steel										
15% Cr, 10% Ni	7865	0.460	19	0.053						
20% Cr, 15% Ni	7833	0.460	15.0	0.042						
Invar (36% Ni)	8137	0.460	10.7	0.029						

Manganese steel 1% Mn	7865	0.460	50	0.139						
Manganese steel 5% Mn	7849	0.460	22	0.064						
Nickel-chrome steel										
80% Ni, 15% Cr	8522	0.460	17	0.045						
20% Ni, 15% Cr	7865	0.460	14	0.039	—	14	15.1	15.1	17	19
Silicon steel, 1% Si	7769	0.460	42	0.116						
Silicon steel, 5% Si	7417	0.460	19	0.056						
Stainless steel, type 304	7817	0.460	13.8	0.040	—	—	15	17	21	25
Stainless steel, type 347	7817	0.420	15	0.044	13	—	16	18	20	23
Tungsten steel, 2% W	7961	0.444	62	0.176	—	62	59	54	48	45
Tungsten steel, 10% W	8314	0.419	48	0.139						
Wrought (0.5% CH)	7849	0.460	59	0.163	—	59	57	52	45	36
Magnesium										
6–8% Al, 1–2% Zn electrolytic	1810	1.000	66	0.360	—	52	62	74		
2% Mn	1778	1.000	114	0.640	93	111	125	130		
Manganese										
Manganin (84% Cu, 4% Ni, 12% Mn)	8400	0.406	21.9	0.064						
Monel 505 (at 60°C)	8360	0.544	19.7	0.043						
Nickel										
Nichrome (24% Fe, 16% Cr)	8250	0.448	12.6	0.034						
90% Ni, 10% Cr	8666	0.444	17	0.044	—	17.1	18.9	20.9	24.6	

Source: Bejan (1993), with permission.

TABLE 2.10 Thermophysical Properties of Nonmetallic Solids

	T (°C)	ρ (kg/m ³)	c_p (kJ/kg · K)	λ (W/m · K)	α_D (cm ² /s)
Asbestos					
Cement board	20			0.6	
Felt (16 laminations per centimeter)	40			0.057	
Fiber	50	470	0.82	0.11	0.0029
Sheet	20			0.74	
	50			0.17	
Asphalt	20	2120	0.92	0.70	0.0036
Bakelite	20	1270	1.59	0.230	0.0011
Bark	25	340	1.26	0.074	0.0017
Brick					
Carborundum	1400			11.1	
Cement	10	720		0.34	
Common	20	1800	0.84	0.38–0.52	0.0028–0.0034
Chrome	100			1.9	
Facing	20			1.3	
Firebrick	300	2000	0.96	0.1	0.00054
Magnesite (50% MgO)	20	2000		2.68	
Masonry	20	1700	0.84	0.66	0.0046
Silica (95% SiO ₂)	20	1900		1.07	
Zircon (62% ZrO ₂)	20	3600		2.44	
Brickwork, dried in air	20	1400–1800	0.84	0.58–0.81	0.0049–0.0054
Carbon					
Diamond (type IIb)	20	3250	0.51	1350	8.1
Graphite (firm, natural)	20	2000–2500	0.61	155	1.02–1.27
Carborundum (SiC)	100	1500	0.62	58	0.62
Cardboard	0–20	~790		~0.14	

Celluloid	20	1380	1.67	0.23	0.001
Cement (portland, fresh, dry)	20	3100	0.75	0.3	0.0013
Chalk (CaCO ₃)	20	2000–3000	0.74	2.2	0.01–0.015
Clay	20	1450	0.88	1.28	0.01
Fireclay	100	1700–2000	0.84	0.5–1.2	0.35–0.71
Sandy Clay	20	1780		0.9	
Coal	20	1200–1500	1.26	0.26	0.0014–0.0017
Anthracite	900	1500		0.2	
Brown coal	900			0.1	
Bituminous in situ		1300		0.5–0.7	0.003–0.004
Dust	30	730	1.3	0.12	0.0013
Concrete, made with gravel, dry	20	2200	0.88	1.28	0.0066
Cinder	24			0.76	
Cork					
Board	20	150	1.88	0.042	0.0015
Expanded	20	120		0.036	
Cotton	30	81	1.15	0.059	0.0063
Earth					
Clayey (28% moisture)	20	1500		1.51	
Coarse-grained	20	2040	1.84	0.59	0.0016
Diatomaceous	20	466	0.88	0.126	0.0031
Sandy (8% moisture)	20	1500		1.05	
Fat	20	910	1.93	0.17	0.001
Felt, hair	–7	130–200		0.032–0.04	
	94	130–200		0.054–0.051	
Fiber insulating board	20	240		0.048	
Glass					
Borosilicate	30	2230		1.09	
Fiber	20	220		0.035	

(continued)

TABLE 2.10 Thermophysical Properties of Nonmetallic Solids (Continued)

	T (°C)	ρ (kg/m ³)	c_p (kJ/kg · K)	λ (W/m · K)	α_D (cm ² /s)
Glass (<i>Continued</i>)					
Lead	20	2890	0.68	0.7–0.93	0.0036–0.0047
Mirror	20	2700	0.80	0.76	0.0035
Pyrex	60–100	2210	0.75	1.3	0.0078
Quartz	20	2210	0.73	1.4	0.0087
Window	20	2800	0.80	0.81	0.0034
Wool	0	200	0.66	0.037	0.0028
Granite	20	2750	0.89	2.9	0.012
Gypsum	20	1000	1.09	0.51	0.0047
Ice	0	917	2.04	2.25	0.012
Ivory	80			0.5	
Kapok	30			0.035	
Leather, dry	20	860	1.5	0.12–0.15	~0.001
Limestone (Indiana)	100	2300	0.9	1.1	~0.005
Linoleum	20	535		0.081	
Lunar surface dust, in high vacuum	250	1500±300	~0.6	~0.0006	
Magnezia (85%)	38–204			0.067–0.08	
Marble	20	2600	0.81	2.8	0.013
Meat					
Beef	25				~0.0014
Chuck	43–66	1060			0.0012
Liver	27			0.5	
Eye of loin, parallel to fiber	2–7			0.3	
Ground	6			0.35	
Lean	2–47			0.45	
Chicken					

Muscle, perpendicular to fiber	5–27		0.41	
Skin	5–27		0.03	
Egg, white	33–38		0.55	
Egg, whole	–8		0.46	
Egg, albumen gel, freez-dried	41		0.04	
Egg, yolk	24–38		0.42	
Fish				
Cod fillets	–19		1.17	
Halibut	43–66	1080		0.0014
Herring	–19		0.8	
Salmon, perpendicular to fiber	–23		1.3	
Salmon, freeze-dried, parallel to fiber	–29		0.04	
Horse	25		0.41	
Lamb, lean	7–57		0.45	
Pork				
Ham, smoked	43–66	1090		0.0014
Fat	25		0.15	
Lean, perpendicular to fiber	27–57		0.52	
Lean, parallel to fiber	7–57		0.45	
Pig skin	25		0.37	
Sausage				
23% fat	25		0.38	
15% fat	25		0.43	
Seal, blubber	(–13)–(–2)		0.21	
Turkey				
Breast, perpendicular to fiber	–3		1.05	
	2		0.7	
Breast, parallel to fiber	–8		1.4	
Leg, perpendicular to fiber	2		0.7	

(continued)

TABLE 2.10 Thermophysical Properties of Nonmetallic Solids (Continued)

	T (°C)	ρ (kg/m ³)	c_p (kJ/kg · K)	λ (W/m · K)	α_D (cm ² /s)
Mica	20	2900		0.52	
Mortar	20	1900	0.8	0.93	0.0061
Paper	20	700	1.2	0.12	0.0014
Paraffin	30	870–925	2.9	0.24–0.27	~0.001
Plaster	20	1690	0.8	0.79	0.0058
Plexiglas (acrylic)	20	1180	1.44	0.184	0.0011
Plums	–16			0.3	
Polyethylene	20	920	2.30	0.35	0.0017
Polystyrene	20	1050		0.157	
Polyurethane	20	1200	2.09	0.32	0.0013
Polyvinyl chloride (PVC)	20	1380	0.96	0.15	0.0011
Porcelain	95	2400	1.08	1.03	0.004
Quartz	20	2100–2500	0.78	1.40	~0.008
Rubber					
Foam	20	500	1.67	0.09	0.0011
Hard (ebonite)	20	1150	2.01	0.16	0.0006
Soft	20	1100	1.67	~0.2	~0.001
Synthetic	20	1150	1.97	0.23	0.001
Salt (rock salt)	0	2150–2500	0.92	7	0.003–0.036
Sand					
Dry	20			0.58	
Moist	20	1640		1.13	
Sandstone	20	2150–2300	0.71	1.6–2.1	0.01–0.013
Sawdust, dry	20	215		0.07	
Silica stone (85% SiC)	700	2720	1.05	1.56	0.055
Silica aerogel	0	140		0.024	

Silicon	20	2330	0.703	153	0.94
Silk (artificial)	35	100	1.33	0.049	0.0037
Slag	20	2500–3000	0.84	0.57	0.0023–0.0027
Slate					
Parallel to lamination	20	2700	0.75	2.9	0.014
Perpendicular to lamination	20	2700	0.75	1.83	0.009
Snow, firm	0	560	2.1	0.46	0.0039
Soil (<i>see also</i> Earth)					
Dry	15	1500	1.84	1	0.004
Wet	15	1930		2	
Strawberries, dry	–18			0.59	
Sugar (fine)	0	1600	1.25	0.58	0.0029
Sulfur	20	2070	0.72	0.27	0.0018
Teflon (polytetrafluoroethylene)	20	2200	1.04	0.23	0.001
Wood, perpendicular to grain					
Ash	15	740		0.14–0.3	
Balsa	15	100		0.05	
Cedar	15	480		0.11	
Mahogany	20	700		0.16	
Oak	20	600–800	2.4	0.17–0.25	~0.0012
Pine, fir, spruce	20	416–421	2.72	0.15	0.0012
Plywood	20	590		0.11	
Wool					
Sheep	20	100	1.72	0.036	0.0021
Mineral	50	200	0.92	0.042	0.0025
Slag	25	200	0.8	0.05	0.0031

Source: Bejan (1993), with permission.

(Cahill, 1990) is being applied widely to measure the thermal conductivity of thin films, especially for microelectronic applications. A single metal strip is fabricated on the film to be tested, which is in turn mounted on a substrate of another material (e.g., silicon). The metal film acts as both heater and temperature sensor. Analysis of the oscillation of electrical resistance at a frequency of 3ω , in response to oscillations of power and temperature of 2ω , provides the in-plane thermal conductivity.

Specific Heat Differential scanning calorimetry (DSC) has become widely used because modern commercial instrumentation allows simple use, although the construction and control system of the device may be complex (Richardson, 1992). In DSC, a small test sample and a reference sample of similar size are placed in adjacent separate holders. The samples are heated simultaneously at a specified rate, often 1 to $10^\circ\text{C}/\text{min}$. Thermocouples are typically used to monitor the temperature of each sample. The change in enthalpy of the sample is then determined by measurement of how much energy must be added to the test sample to make its temperature track that of the reference. By keeping the sample and the reference the same size and temperature and making the two holders of the same material, the effects of parasitic convective and radiative losses are automatically canceled in the comparison of the two samples. Modulating the temperature rise of a DSC (e.g., by adding an ac component to the steady rise in temperature) provides additional insight into phase transitions in polymers.

Thermal Diffusivity Measurements of thermal diffusivity are popular because they typically require only measurement of a temperature history due to a thermal perturbation of the sample, which is easier than measuring heat flux as required in many steady-state methods. Formerly hampered by complex error analysis, microprocessors have made commercial devices relatively easy to use. The flash method (Parker et al., 1961) is a standard method for measuring the out-of-plane component of diffusivity in a variety of materials (ASTM, 1992). Extensions of the flash method have been made to allow measuring components of α (Donaldson and Taylor, 1975; Mallet et al., 1990; Fujii et al., 1997; Doss and Wright, 2000). Other methods have been employed to measure multiple components of α in anisotropic thin films (Ju et al., 1999), carbon-carbon composite specimens (Dowding et al., 1996), and in elongated polymers (Broerman et al., 1999).

Thermal Expansion The linear coefficient of expansion is easier to measure than the volumetric coefficient of expansion. Usually, a cylindrical specimen is heated and its change in length measured either mechanically or with optical methods, such as interferometry.

Heat conduction in solids is a mature field. Even so, new materials, applications, and methods of analysis require new measurement of, and increased accuracy in, the values of thermal transport properties. New challenges exist for properties in biological systems, micro- and nanoscale devices, and composites.

NOMENCLATURE

Roman Letter Symbols

a	molar Helmholtz energy, J/mol
c_p	isobaric (constant pressure) heat capacity, J/mol · K
c_v	isochoric (constant volume) heat capacity, J/mol · K
f	equivalent substance reducing ratio for temperature, dimensionless
f_{int}	factor in Eucken correlation for dilute-gas thermal conductivity, dimensionless
F_λ, F_η	multiplier for thermal conductivity and viscosity, dimensionless
F_{ij}	mixture parameter, dimensionless
g	molar Gibbs energy, J/mol
h	molar enthalpy, J/mol
i	enthalpy per unit volume, J/m ³
k	Boltzmann constant, J/K
L	length, m
M	molar mass, g/mol
N	coefficient, dimensionless
p	pressure, MPa
Pr	Prandtl number, dimensionless [= $\eta c_p / \lambda$]
$\dot{\mathbf{q}}$	heat flux vector, W/m ²
R	molar gas constant, J/(mol · K)
s	molar entropy, J/mol · K
T	temperature, K
u	molar internal energy, J/mol
	coefficient, dimensionless
v	molar volume, dm ³ /mol
w	speed of sound, m/s
x	composition (mole fraction), dimensionless
Z	compressibility factor, dimensionless [= $p/\rho RT$]

Greek Letter Symbols

α	reduced Helmholtz energy, dimensionless [= a/RT]
α_D	thermal diffusivity, m ² /s [= $\lambda/\rho c_p$]
α	thermal diffusivity tensor, m ² /s
β	coefficient in critical region terms, dimensionless
γ	coefficient in critical region terms, dimensionless
δ	reduced density, dimensionless [= ρ/ρ_c]
ε/k	molecular energy parameter, K
ζ	mixture parameter, dimensionless
η	viscosity, dimensionless $\mu\text{Pa} \cdot \text{s}$
θ	shape factor for temperature, dimensionless

λ	thermal conductivity, W/m · K
	thermal conductivity tensor, W/m · K
μ	coefficient of linear thermal expansion, K ⁻¹
μ_v	coefficient of volumetric thermal expansion, K ⁻¹
ν	kinematic viscosity, m ² /s
ξ	mixture parameter, dimensionless
ρ	molar density, mol/dm ³
ρ_m	mass density, kg/m ³
σ	molecular size parameter, nm
	surface tension, N/m
τ	inverse reduced temperature, [= T_c/T], dimensionless
ϕ	shape factor for density, dimensionless
φ	coefficient in critical region terms, dimensionless
ω	fundamental frequency in the 3 ω method, dimensionless
$\Omega^{(2,2)}$	collision integral, dimensionless

Superscripts

0	ideal gas property
crit	critical point
E	excess-like property
idmix	ideal mixture
int	thermal conductivity arising from internal motions
r	residual or real gas property
trans	translational part of thermal conductivity
*	dilute-gas (ideal gas) state

Subscripts

0	reference state property
c	critical point property
i, j	pure fluid properties
mix	mixture quantity
red	reducing property

REFERENCES

- Angus, S., Armstrong, B., and de Reuck, K. M. (1980). *International Thermodynamic Tables of the Fluid State: 7. Propylene*, IUPAC, Pergamon Press, Oxford.
- Arp, V. D., McCarty, R. D., and Friend, D. G. (1998). Thermophysical Properties of Helium-4 from 0.8 to 1500 K with Pressures to 2000 MPa, *Technical Note 1334*, NIST, Boulder, CO.
- ASTM (1992). Standard Test Method for Thermal Diffusivity of Solids by the Flash Method, *E 1461-92*, ASTM, Philadelphia.
- Baehr, H. D., and Stephan, K. (1998). *Heat and Mass Transfer*, Springer-Verlag, Berlin.
- Bejan, A. (1993). *Heat Transfer*, Wiley, New York.

- Bigg, D. M. (1995). Thermal Conductivity of Heterophase Polymer Compositions, in *Thermal and Electrical Conductivity of Polymer Materials*, Y. K. Godovsky and V. P. Privalko, eds., Advances in Polymer Science, Vol. 119, Springer-Verlag, Berlin, pp. 1–30.
- Broerman, A. W., Venerus, D. C., and Schieber, J. D. (1999). Evidence for the Stress-Thermal Rule in an Elastomer Subjected to Simple Elongation, *J. Chem. Phys.*, 111(15), 6965–6969.
- Brown, F. C. (1967). *The Physics of Solids*, W. A. Benjamin, New York.
- Cahill, D. G. (1990). Thermal Conductivity Measurement from 30 to 750 K: The 3ω Method, *Rev. Sci. Instrum.*, 61, 802–808.
- Carslaw, H. S., and Jaeger, J. C. (1959). *Conduction of Heat in Solids*, Oxford University Press, London.
- Chato, J. C. (1985). In *Heat Transfer in Biology and Medicine*, A. Shitzer and R. C. Eberhart, eds., Plenum Press, New York.
- Choy, C. L., Luk, W. H., and Chen, F. C. (1978). Thermal Conductivity of Highly Oriented Polyethylene, *Polymer*, 19, 155–162.
- Cooper, T. E., and Trezek, G. J. (1971). Correlation of Thermal Properties of Some Human Tissues with Water Content, *Aerosp. Med.*, 42, 24–27.
- Dashora, P. (1994). A Study of Variation of Thermal Conductivity of Elastomers with Temperature, *Phys. Scr.*, 49, 611–614.
- Day, W. A. (1985). *Heat Conduction within Linear Thermoelasticity*, Springer-Verlag, New York.
- de Reuck, K. M. (1990). *International Thermodynamic Tables of the Fluid State: 11. Fluorine*, IUPAC, Pergamon Press, Oxford.
- de Reuck, K. M., and Craven, R. J. B. (1993). *International Thermodynamic Tables of the Fluid State: 12. Methanol*. IUPAC, Blackwell Scientific Publications, London.
- de Reuck, K. M., Craven, R. J. B., and Cole, W. A. (1991). *Report on the Development of an Equation of State for Sulphur Hexafluoride*, IUPAC Thermodynamic Tables Project Centre, London.
- de Vries, B., Tillner-Roth, R., and Baehr, H. D. (1995). Thermodynamics Properties of HCFC 124, *Proc. 19th International Congress of Refrigeration*, The Hague, The Netherlands, International Institute of Refrigeration, Vol. IVa, pp. 582–589.
- Donaldson, A. B., and Taylor, R. E. (1975). Thermal Diffusivity Measurement by a Radial Heat Flow Method, *J. Appl. Phys.*, 46(10), 4584–4589.
- Doss, D. J., and Wright, N. T. (2000). Simultaneous Measurement of the Orthogonal Components of Thermal Diffusivity in PVC Sheet, *J. Heat Transfer*, 122, 27–32.
- Dowding, K. J., Beck, J. V., and Blackwell, B. F. (1996). Estimation of Directional-Dependent Thermal Properties in a Carbon–Carbon Composite, *Int. J. Heat Mass Transfer*, 39(15), 3157–3164.
- Eiermann, K. (1966). Model Interpretation of Thermal Conductivity in High Polymers, I: Amorphous High Polymers, *Rubber Chem. Technol.*, 39, 841–857.
- Ely, J. F., and Hanley, H. J. M. (1983). Prediction of Transport Properties, 2: Thermal Conductivity of Pure Fluids and Mixtures, *Ind. Eng. Chem. Fundam.*, 22, 90–97.
- Fenghour, A., Wakeham, W. A., Vesovic, V., Watson, J. T. R., Millat, J., and Vogel, E. (1995). The Viscosity of Ammonia, *J. Phys. Chem. Ref. Data*, 24, 1649–1667.
- Fenghour, A., Wakeham, W. A., Vesovic, V. (1998). The Viscosity of Carbon Dioxide, *J. Phys. Chem. Ref. Data*, 27, 31–44.

- Friend, D. G., Ely, J. F., and Ingham, H. (1989). Tables for the Thermophysical Properties of Methane, *Technical Note 1325*, NIST, Boulder, CO.
- Friend, D. G., Ingham, H., and Ely, J. F. (1991). Thermophysical Properties of Ethane, *J. Phys. Chem. Ref. Data*, 20(2), 275–347.
- Fujii, M., Park, S. C., Tomimura, T., and Zhang, X. (1997). A Non-contact Method for Measuring Thermal Conductivity and Thermal Diffusivity of Anisotropic Materials, *Int. J. Thermophys.*, 18(1), 251–267.
- Greig, D., and Sahota, M. (1978). Thermal Conductivity of Extruded Polyethylene, *Polymer*, 19, 503–506.
- Hands, B. A., and Arp, V. D. (1981). A Correlation of Thermal Conductivity Data for Helium, *Cryogenics*, 21(12), 697–703.
- Hanley, H. J. M. (1976). Prediction of the Viscosity and Thermal Conductivity Coefficients of Mixtures, *Cryogenics*, 16(11), 643–651.
- Hill, P. G., MacMillan, R. D. C., and Lee, V. (1982). A Fundamental Equation of State for Heavy Water, *J. Phys. Chem. Ref. Data*, 11(1), 1–14.
- Hirschfelder, J. O., Curtiss, C. F., and Bird, R. B. (1967). *Molecular Theory of Gases and Liquids*, Wiley, New York/Chapman & Hall, London.
- Ho, C. Y., Powell, R. W., and Liley, P. E. (1974). Thermal Conductivity of the Elements: A Comprehensive Review, *J. Phys. Chem. Ref. Data*, 3 Suppl. 1.
- Holland, P. M., Eaton, B. E., and Hanley, H. J. M. (1983). A Correlation of the Viscosity and Thermal Conductivity Data of Gaseous and Liquid Ethylene, *J. Phys. Chem. Ref. Data*, 12(4), 917–932.
- Huber, M. L., and Ely, J. F. (1992). Prediction of Viscosity of Refrigerants and Refrigerant Mixtures, *Fluid Phase Equilib.*, 80, 239–248.
- Huber, M. L., Friend, D. G., and Ely, J. F. (1992). Prediction of the Thermal Conductivity of Refrigerants and Refrigerant Mixtures, *Fluid Phase Equilib.*, 80, 249–261.
- Incropera, F. P., and DeWitt, D. P. (1996). *Introduction to Heat and Mass Transfer*, Wiley, New York.
- International Association for the Properties of Water and Steam (IAPWS) (1994). Viscosity and Thermal Conductivity of Heavy Water Substance, in *Physical Chemistry of Aqueous Systems (Proc. 12th International Conference on the Properties of Water and Steam)*, Orlando, FL, pp. A107–A138.
- International Association for the Properties of Water and Steam (IAPWS) (1997). *Revised Release on the IAPS Formulation 1985 for the Viscosity of Ordinary Water Substance*.
- International Association for the Properties of Water and Steam (IAPWS) (1998). *Revised Release on the IAPS Formulation 1985 for the Thermal Conductivity of Ordinary Water Substance*.
- Jacobsen, R. T., Penoncello, S. G., and Lemmon, E. W. (1992). A Fundamental Equation for Trichlorofluoromethane (R-11), *Fluid Phase Equilibria*, 80, 45–56.
- Jakob, M. (1955). *Heat Transfer*, Vol. 1, Wiley, New York.
- Joseph, D. D., and Preziosi, L. (1989). Heat Waves, *Rev. Modern Phys.*, 61(1), 41–73.
- Joseph, D. D., and Preziosi, L. (1990). Addendum to the paper “Heat Waves,” *Rev. Modern Phys.*, 62(2), 375–391.
- Ju, Y. S., Kurabayashi, K., and Goodson, K. E. (1999). Thermal Characterization of Anisotropic Thin Dielectric Films Using Harmonic Joule Heating, *Thin Solid Films*, 339, 160–164.

- Kamei, A., Beyerlein, S. W., and Jacobsen, R. T (1995). Application of Nonlinear Regression in the Development of a Wide Range Formulation for HCFC-22, *Int. J. Thermophys.* 16, 1155–1164.
- Katti, R. S., Jacobsen, R. T, Stewart, R. B., and Jahangiri, M. (1986). Thermodynamic Properties for Neon for Temperatures from the Triple Point to 700 K at Pressures to 700 MPa, *Adv. Cryog. Eng.*, 31, 1189–1197.
- Kittel, C. (1996). *Introduction to Solid State Physics*, 7th ed., Wiley, New York.
- Klein, S. A., McLinden, M. O., and Laesecke, A. (1997). An Improved Extended Corresponding States Method for Estimation of Viscosity of Pure Refrigerants and Mixtures, *Int. J. Refrig.*, 20, 208–217.
- Klemens, P. G. (1969). Theory of the Thermal Conductivity of Solids, in *Thermal Conductivity*, Vol. 1, R. P. Tye, ed., Academic Press, London.
- Kozlov, A. D. (1996). Personal communication, Moscow.
- Krauss, R., Weiss, V. C., Edison, T. A., Sengers, J. V., and Stephan, K. (1996). Transport Properties of 1,1-Difluoroethane (R152a), *Int. J. Thermophys.*, 17, 731–757.
- Laesecke, A. (2000). Data Reassessment and Full Surface Correlation of the Viscosity of HFC-134a (1,1,1,2-tetrafluoroethane), *J. Phys. Chem. Ref. Data*.
- Laesecke, A., Perkins, R. A., and Howley, J. B. (1996). An Improved Correlation for the Thermal Conductivity of HCFC123 (2,2-Dichloro-1,1,1-trifluoroethane), *Int. J. Refrig.*, 19, 231–238.
- Leland, T. W., and Chappelaar, P. S. (1968). The Corresponding States Principle, *AIChE J.*, 14, 568–576.
- Lemmon, E. W., and Jacobsen, R. T (1999). A Generalized Model for the Thermodynamic Properties of Mixtures, *Int. J. Thermophys.*, 20(3), 825–835.
- Lemmon, E. W., and Jacobsen, R. T (2000). An International Standard Formulation for the Thermodynamic Properties of 1,1,1-Trifluoroethane (HFC-143a) for Temperatures from 161 to 450 K and Pressures to 50 MPa, *J. Phys. Chem. Ref. Data*, 29(4), 521–552.
- Lemmon, E. W., and Jacobsen, R. T (2001). Preliminary equation.
- Lemmon, E. W., and Span, R. (2001). Preliminary equation.
- Lemmon, E. W., Jacobsen, R. T, Penoncello, S. G., and Friend, D. G. (2000). Thermodynamic Properties of Air and Mixtures of Nitrogen, Argon, and Oxygen from 60 to 2000 K at Pressures to 2000 MPa, *J. Phys. Chem. Ref. Data*, 29(3), 331–385.
- Liley, P. E., Thomson, G. H., Friend, D. G., Daubert, T. E., and Buck, E. (1997). Physical and Chemical Data, in R. H. Perry, D. W. Green, and J. O. Maloney, eds., *Perry's Chemical Engineers' Handbook*, 7th ed., McGraw-Hill, New York.
- Magee, J. W., Outcalt, S. L., and Ely, J. F. (2000). Molar Heat Capacity C_v , Vapor Pressure, and (p , ρ , T) Measurements from 92 to 350 K at Pressures to 35 MPa and a New Equation of State for Chlorotrifluoromethane (R13), *Int. J. Thermophys.*, 21(5), 1097–1121.
- Maglic, K. D., Cezailliyan, A., and Peletsky, V. E., eds. (1984). *Compendium of Thermophysical Property Measurement Methods: Survey of Measurement Techniques*, Plenum Press, New York.
- Maglic, K. D., Cezailliyan, A., and Peletsky, V. E., eds. (1992). *Compendium of Thermophysical Property Measurement Methods: Recommended Measurement Techniques and Practices*, Plenum Press, New York.
- Mallet, D., Lachi, M., and Degiovanni, A. (1990). Simultaneous Measurements of Axial and

- Radial Thermal Diffusivities of an Anisotropic Solid in Thin Plate: Application to Multi-layered Materials, in *Thermal Conductivity*, vol. 21, C. J. Cremers and H. A. Fine, eds., Plenum Press, New York, pp. 91–107.
- Marsh, K., Perkins, R., and Ramires, M. L. V. (2002). Measurement and Correlation of the Thermal Conductivity of Propane from 86 to 600 K at Pressures to 700 MPa, *J. Chem. Eng. Data*, 47(4), 932–940.
- Marx, V., Pruss, A., and Wagner, W. (1992). Neue Zustandsgleichungen fuer R 12, R 22, R 11 und R 113: Beschreibung des thermodynamischen Zustandsverhaltens bei Temperaturen bis 525 K und Druecken bis 200 MPa, *Waermetechnik/Kaeltechnik*, Ser. 19, No. 57, VDI Verlag, Duesseldorf, Germany.
- McCarty, R. D. (1989). *Correlations for the Thermophysical Properties of Deuterium*, NIST, Boulder, CO.
- McCarty, R. D., and Arp, V. D. (1990). A New Wide Range Equation of State for Helium, *Adv. Cryog. Eng.*, 35, 1465–1475.
- McCarty, R. D., and Weber, L. A. (1972). Thermophysical Properties of Parahydrogen from the Freezing Liquid Line to 5000 R for Pressures to 10,000 psia, *Tech. Note 617*, National Bureau of Standards, Washington, DC.
- McLinden, M. O., Klein, S. A., and Perkins, R. A. (2000). An Extended Corresponding States Model for the Thermal Conductivity of Refrigerants and Refrigerants Mixtures, *Int. J. Refrig.*, 23, 43–63.
- Miyamoto, H., and Watanabe, K. (2000). A Thermodynamic Property Model for Fluid-Phase Propane, *Int. J. Thermophys.*, 21(5), 1045–1072.
- Miyamoto, H., and Watanabe, K. (2001a). A Thermodynamic Property Model for Fluid-Phase *n*-Butane, *Int. J. Thermophys.*, 22(2), 459–475.
- Miyamoto, H., and Watanabe, K. (2001b). A Thermodynamic Property Model for Fluid-Phase Isobutane, *Int. J. Thermophys.*, 23(2), 477–499.
- Mohr, P. J., and Taylor, B. N. (1999). CODATA Recommended Values of the Fundamental Physical Constants: 1998, *J. Phys. Chem. Ref. Data*, 28(6), 1713–1852.
- Neufeld, P. D., Janzen, A. R., and Aziz, R. A. (1972). Empirical Equations to Calculate 16 of the Transport Collision Integrals for the Lennard-Jones (12-6) Potential, (2000). *J. Chem. Phys.*, 57(3), 1100–1102.
- Ortt, E., Doss, D. J., LeGall, E., Wright, N. T., and Humphrey, J. D. (2000). A Device to Measure the Thermophysical and Thermoelastic Behavior of Elastomers, *J. Appl. Mech.*, 67, 465–471.
- Ozisik, M. N. (1980). *Heat Conduction*, Wiley, New York.
- Outcalt, S. L. (1996). MBWR equation of state as reported in W. M. Haynes, *Thermophysical Properties of HCFC Alternatives*, NIST, Boulder, CO, Final Report for ARTI MCLR Project 660-50800.
- Outcalt, S. L., and McLinden, M. O. (1995). An Equation of State for the Thermodynamic Properties of R236fa, NIST report to sponsor (U.S. Navy, David Taylor Model Basin) under contract N61533-94-F-0152.
- Outcalt, S. L., and McLinden, M. O. (1996). A Modified Benedict–Webb–Rubin Equation of State for the Thermodynamic Properties of R152a (1,1-difluoroethane), *J. Phys. Chem. Ref. Data*, 25(2), 605–636.
- Parker, W. J., Jenkins, R. J., Butler, C. P., and Abbott, G. L. (1961). Flash Method of Determining Thermal Diffusivity, Heat Capacity and Thermal Conductivity, *J. Appl. Phys.*, 32(9), 1679–1684.

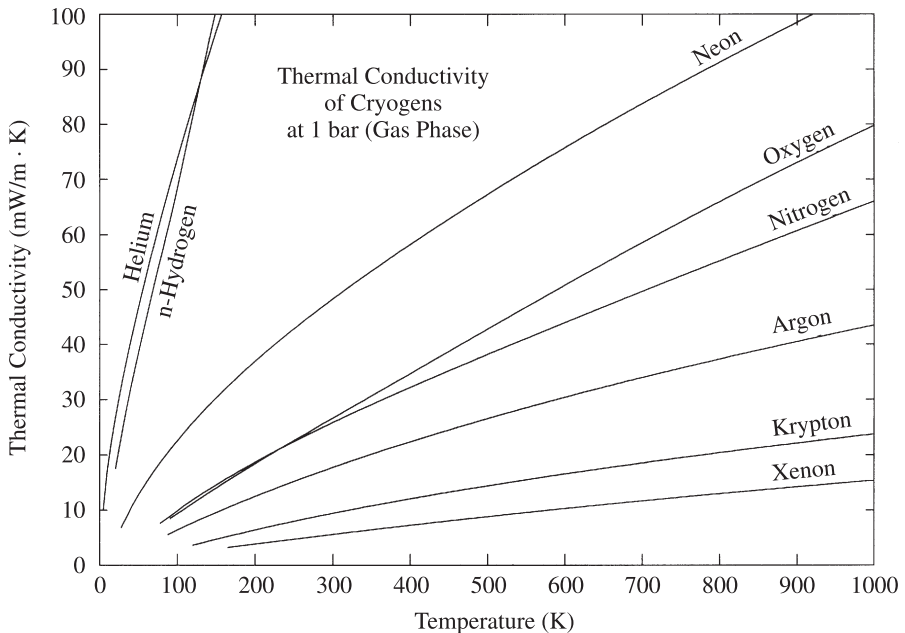
- Parrott, J. E., and Stuckes, A. D. (1975). *Thermal Conductivity of Solids*, Pion, London.
- Penoncello, S. G., Goodwin, A. R. H., and Jacobsen, R. T. (1995). A Preliminary Thermodynamic Property Formulation for Cyclohexane, *Int. J. Thermophys.*, 16(2), 519–531.
- Penoncello, S. G., Lemmon, E. W., Shan, Z., and Jacobsen, R. T. (2001). A Fundamental Equation for the Calculation of the Thermodynamic Properties of Trifluoromethane (R-23), *J. Phys. Chem. Ref. Data*.
- Perkins, R. A. (2001). Measurement and Correlation of the Thermal Conductivity of Isobutane from 114 K to 600 K at Pressures to 70 MPa, *J. Chem. Eng. Data*.
- Perkins, R. A., Laesecke, A., Howley, J., Ramires, M. L. V., Gurova, A. N., and Cusco, L. (2000). Experimental Thermal Conductivity Values for the IUPAC Round-Robin Sample of 1,1,1,2-Tetrafluoroethane (R134a), NISTIR, Boulder, CO.
- Perkins, R. A., Ramires, M. L. V., Nieto de Castro, C. A., and Cusco, L. (2002). Measurement and Correlation of the Thermal Conductivity of Butane from 135 K to 600 K at Pressures to 70 MPa, *J. Chem. Eng. Data*, 47(5), 1263–1271.
- Platzer, B., Polt, A., and Maurer, G. (1990). *Thermophysical Properties of Refrigerants*, Springer-Verlag, Berlin.
- Polt, A. (1987). Zur Beschreibung der thermodynamischen Eigenschaften reiner Fluide mit “Erweiterten BWR-Gleichungen,” Ph.D. dissertation, Universitaet Kaiserslautern, Germany.
- Polt, A., Platzer, B., and Maurer, G. (1992). Parameter der Thermischen Zustandsgleichung von Bender fuer 14 Mehratomige reine Stoffe, *Chem. Technol. (Leipzig)*, 44(6), 216–224.
- Reif, F. (1965). *Fundamentals of Statistical and Thermal Physics*, McGraw-Hill, New York.
- Richardson, M. J. (1992). The Application of Differential Scanning Calorimetry to the Measurement of Specific Heat, in *Compendium of Thermophysical Property Measurement Methods: Recommended Measurement Techniques and Practices*, K. D. Maglic, A. Cezaillian, and V. E. Peletsky, eds., Plenum Press, New York.
- Schmidt, R., and Wagner, W. (1985). A New Form of the Equation of State for Pure Substances and Its Application to Oxygen, *Fluid Phase Equilibria*, 19, 175–200.
- Setzmann, U., and Wagner, W. (1991). A New Equation of State and Tables of Thermodynamic Properties for Methane Covering the Range from the Melting Line to 625 K at Pressures up to 1000 MPa, *J. Phys. Chem. Ref. Data*, 20(6), 1061–1155.
- Shan, Z., Penoncello, S. G., and Jacobsen, R. T. (2000). A Generalized Model for Viscosity and Thermal Conductivity of Trifluoromethane (R-23), *ASHRAE Trans.*, 106, 1–11.
- Shircliffe, C. J., and Tye, R. P. (1985). *Guarded Hot Plate and Heat Flow Meter Methodology*, ASTM, Philadelphia.
- Smukala, J., Span, R., and Wagner, W. (2000). A New Equation of State for Ethylene Covering the Fluid Region for Temperatures from the Melting Line to 450 K at Pressures up to 300 MPa, *J. Phys. Chem. Ref. Data*, 29(5), 1053–1122.
- Span, R. (2000). *Multiparameter Equations of State: An Accurate Source of Thermodynamic Property Data*, Springer-Verlag, New York.
- Span, R., and Wagner, W. (1996). A New Equation of State for Carbon Dioxide Covering the Fluid Region from the Triple-Point Temperature to 1100 K at Pressures up to 800 MPa, *J. Phys. Chem. Ref. Data*, 25(6), 1509–1596.
- Span, R., and Wagner, W. (1997). On the Extrapolation Behavior of Empirical Equations of State, *Int. J. Thermophys.*, 18(6), 1415–1443.
- Span, R., Lemmon, E. W., Jacobsen, R. T., and Wagner, W. (2000). A Reference Quality

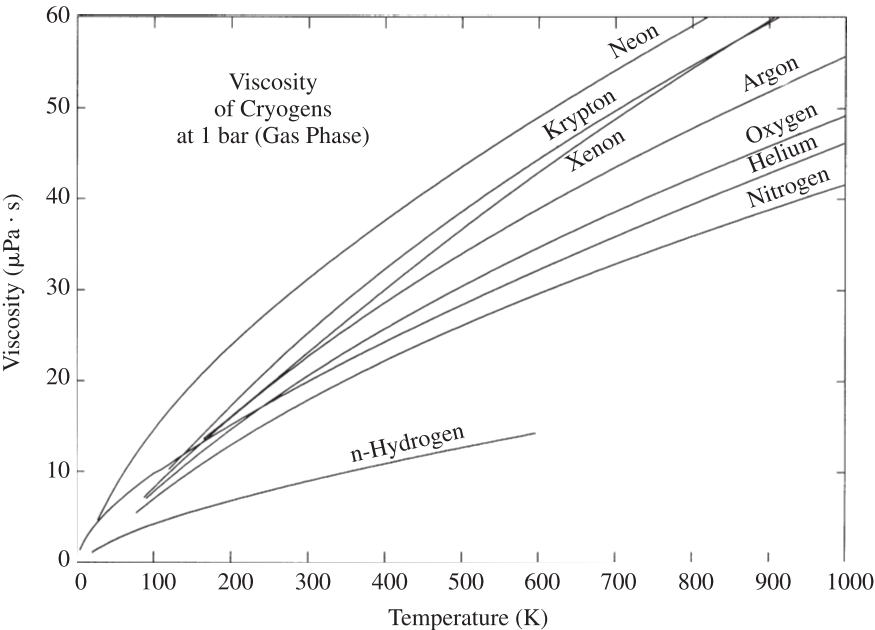
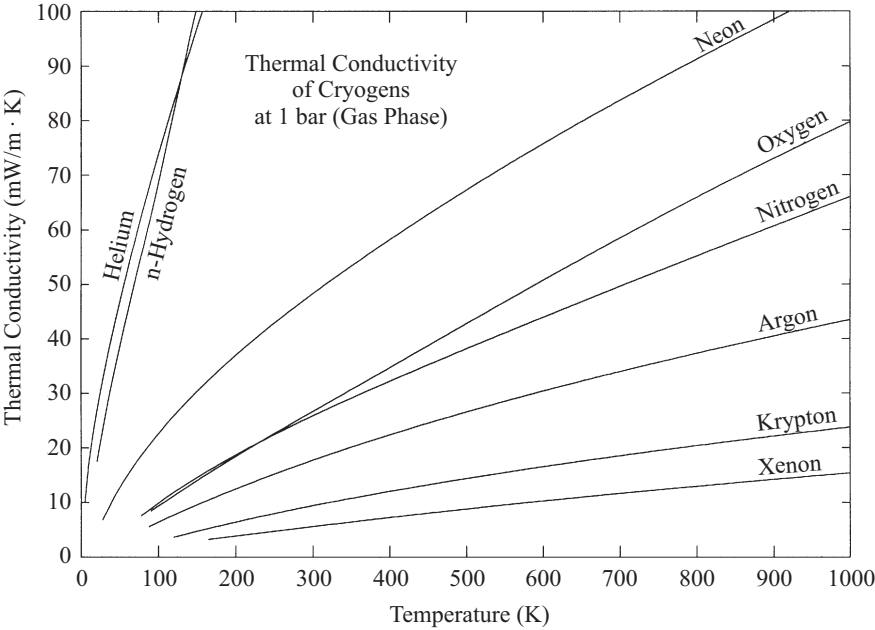
- Thermodynamic Property Formulation for Nitrogen, *J. Phys. Chem. Ref. Data*, 29(6), 1361–1433. See also *Int. J. Thermophys.*, 14(4), 1121–1132, 1998.
- Sunaga, H., Tillner-Roth, R., Sato, H., and Watanabe, K. (1998). A Thermodynamic Equation of State for Pentafluoroethane (R-125), *Int. J. Thermophys.*, 19(6), 1623–1635.
- Tanaka, Y., and Sotani, T. (1995). Transport Properties (Thermal Conductivity and Viscosity), in *R-123: Thermodynamic and Physical Properties*, M. O. McLinden, ed. International Institute of Refrigeration, Paris. See also *Int. J. Thermophys.*, 17(2), 293–328, 1996.
- Tegeler, Ch., Span, R., and Wagner, W. (1999). A New Equation of State for Argon Covering the Fluid Region for Temperatures from the Melting Line to 700 K at Pressures up to 1000 MPa, *J. Phys. Chem. Ref. Data*, 28(3), 779–850.
- Tillner-Roth, R., and Baehr, H. D. (1994). An International Standard Formulation of the Thermodynamic Properties of 1,1,1,2-Tetrafluoroethane (HFC-134a) Covering Temperatures from 170 K to 455 K at Pressures up to 70 MPa, *J. Phys. Chem. Ref. Data*, 23, 657–729.
- Tillner-Roth, R., and Yokozeki, A. (1997). An International Standard Equation of State for Difluoromethane (R-32) for Temperatures from the Triple Point at 136.34 K to 435 K and Pressures up to 70 MPa, *J. Phys. Chem. Ref. Data*, 25(6), 1273–1328.
- Tillner-Roth, R., Harms-Watzenberg, F., and Baehr, H. D. (1993). Eine neue Fundamentalgleichung fuer Ammoniak, *DKV-Tagungsbericht*, 20, 167–181.
- Touloukian, Y. S. (1981). Twenty-five Years of Pioneering Accomplishments by CINDAS: A Retrospective Review, *Int. J. Thermophys.*, 2(3), 205–222.
- Touloukian, Y. S., Kirby, R. K., Taylor, R. E., and Desai, P. D. (1975). Thermal Expansion Metallic Elements and Alloys, in *Thermophysical Properties of Matter*, Vol. 12, IFI/Plenum Press, New York.
- Touloukian, Y. S., Kirby, R. K., Taylor, R. E., and Lee, T. Y. R. (1977). Thermal Expansion Nonmetallic Solids, *Thermophysical Properties of Matter*, Vol. 13, IFI/Plenum Press, New York.
- Tufeu, R., Ivanov, D. Y., Garrabos, Y., and Le Neindre, B. (1984). Thermal Conductivity of Ammonia in a Large Temperature and Pressure Range including the Critical Region, *Ber. Bunsenges. Phys. Chem.*, 88, 422–427.
- Vesovic, V., Wakeham, W. A., Olchoway, G. A., Sengers, J. V., Watson, J. T. R., and Millat, J. (1990). The Transport Properties of Carbon Dioxide, *J. Phys. Chem. Ref. Data*, 19, 763–808.
- Vogel, E., Kuechenmeister, C., Bich, E., and Laesecke, A. (1998). Reference Correlation of the Viscosity of Propane, *J. Phys. Chem. Ref. Data*, 27(5), 947–970.
- Vogel, E., Kuechenmeister, C., and Bich, E. (1999). Viscosity for *n*-Butane in the Fluid Region, *High Temp. High Pressures*, 31(2), 173–186.
- Vogel, E., Kuechenmeister, C., and Bich, E. (2000). Viscosity Correlation for Isobutane over Wide Ranges of the Fluid Region, *Int. J. Thermophys.*, 21(2), 343–356.
- Wagner, W., and Pruss, A. (2002). New International Formulation for the Thermodynamic Properties of Ordinary Water Substance for General and Scientific Use, *J. Phys. Chem. Ref. Data*, 31(2), 387–535.
- Wakeham, W. A., Nagashima, A., and Sengers, J. V. (1991). Measurement of the Transport Properties of Fluids, in *Experimental Thermodynamics*, Vol. 3, Blackwell Science, Malden, MA.
- Younglove, B. A. (1982). Thermophysical Properties of Fluids: I. Argon, Ethylene, Parahydrogen, Nitrogen, Nitrogen Trifluoride, and Oxygen, *J. Phys. Chem. Ref. Data*, 11, Suppl. 1, 1–11.

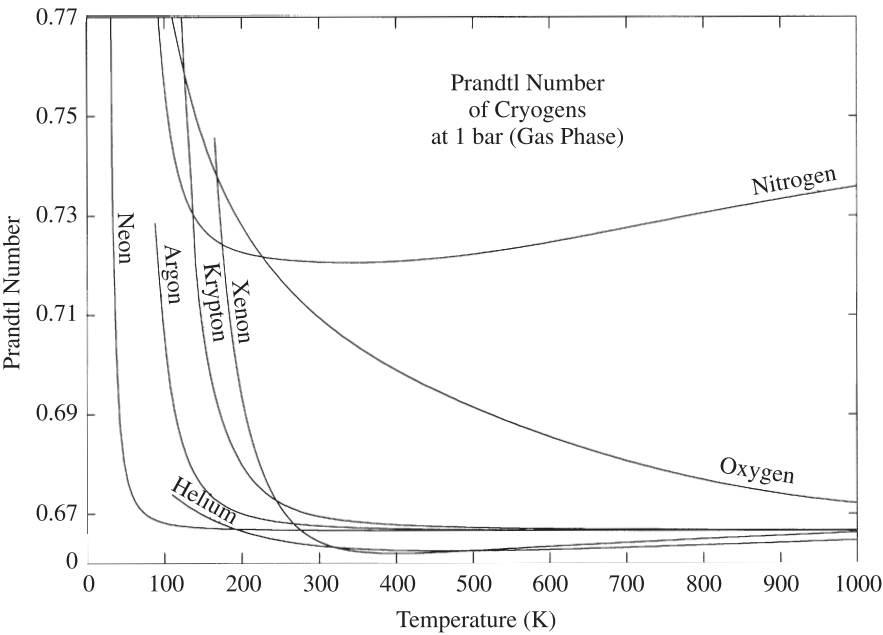
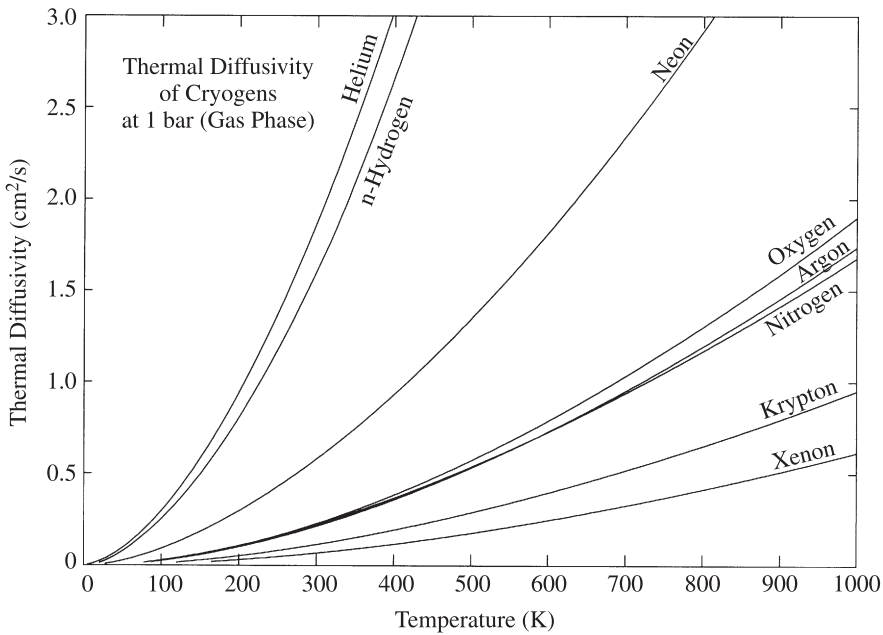
- Younglove, B. A., and Ely, J. F. (1987). Thermophysical Properties of Fluids: II. Methane, Ethane, Propane, Isobutane and Normal Butane, *J. Phys. Chem. Ref. Data*, 16, 577–798.
- Younglove, B. A., and McLinden, M. O. (1994). An International Standard Equation-of-State Formulation of the Thermodynamic Properties of Refrigerant 123 (2,2-dichloro-1,1,1-trifluoroethane), *J. Phys. Chem. Ref. Data*, 23, 731–779.

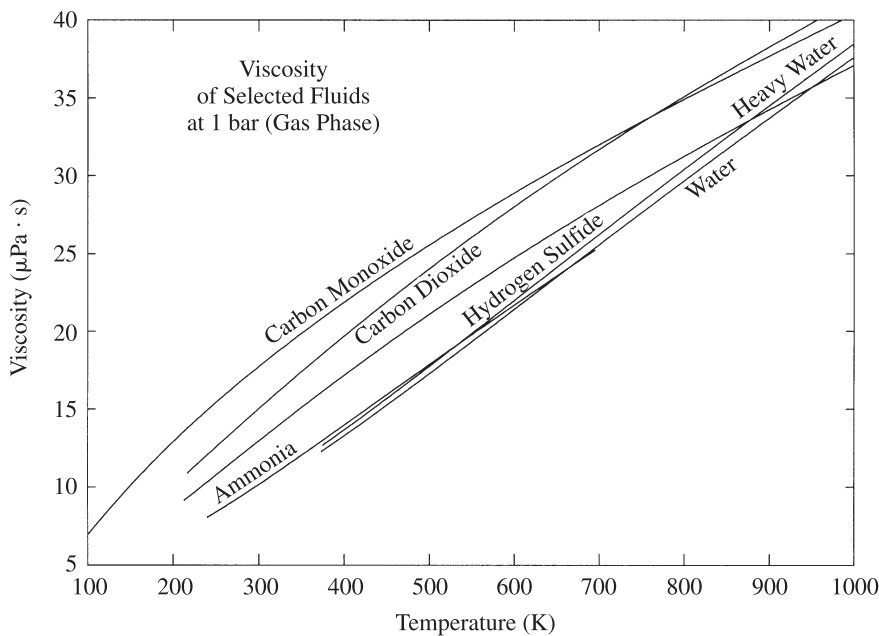
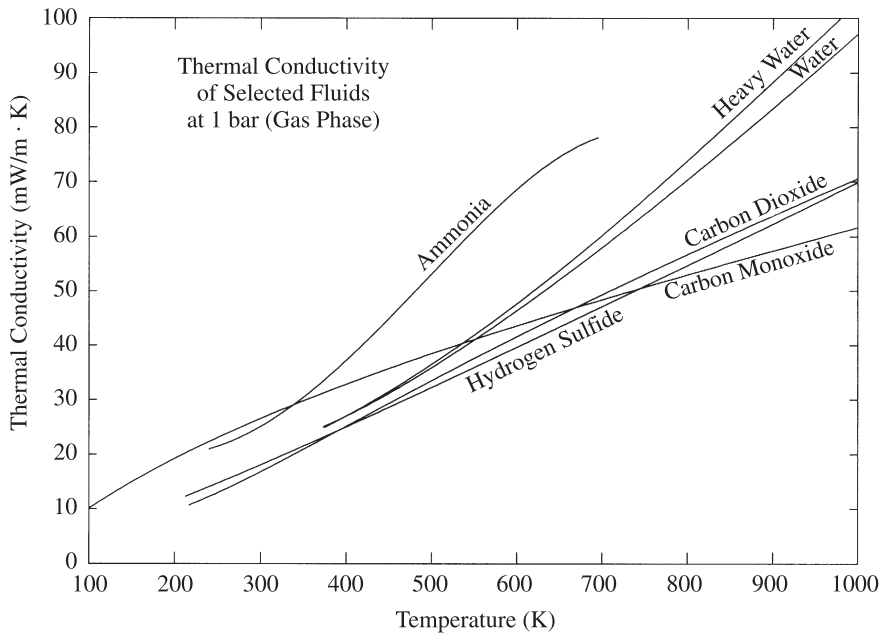
GRAPHS OF THERMOPHYSICAL PROPERTIES

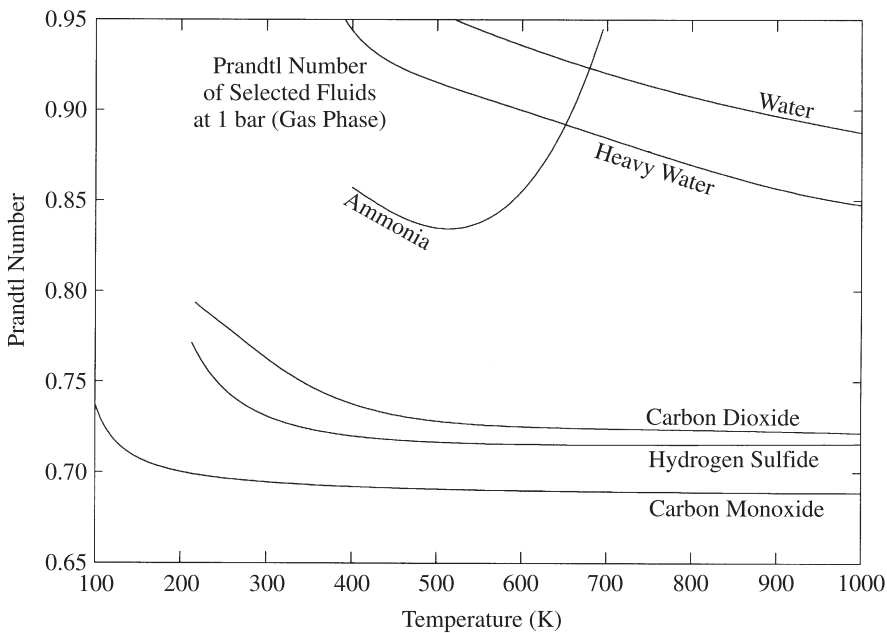
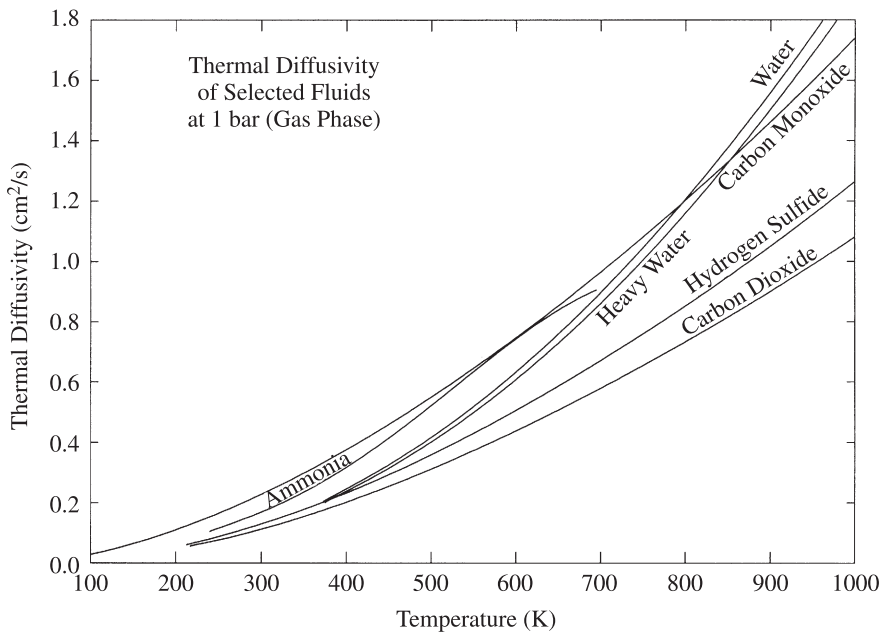
The following figures show property behavior for several groups of similar fluids in the gas phase. The fluid groups include atmospheric gases, hydrocarbons, refrigerants, and other inorganic gases. The plots are given to allow qualitative comparisons of properties of the various fluids. Properties displayed include those important to heat transfer calculations, including thermal conductivity, viscosity, thermal diffusivity and Prandtl number. These plots provide assistance in the selection of working fluids in thermal system design. The plots were constructed using values calculated from the NIST databases.

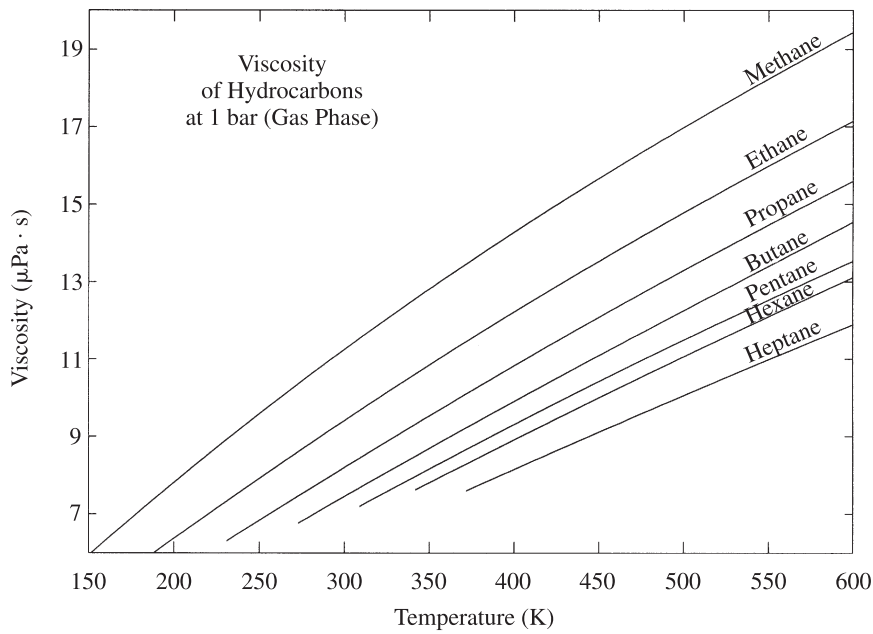
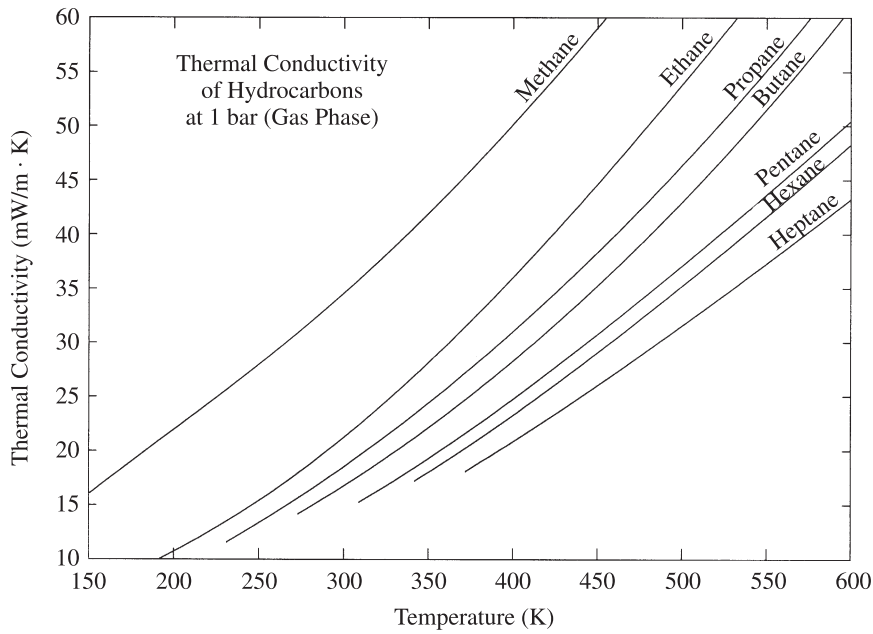


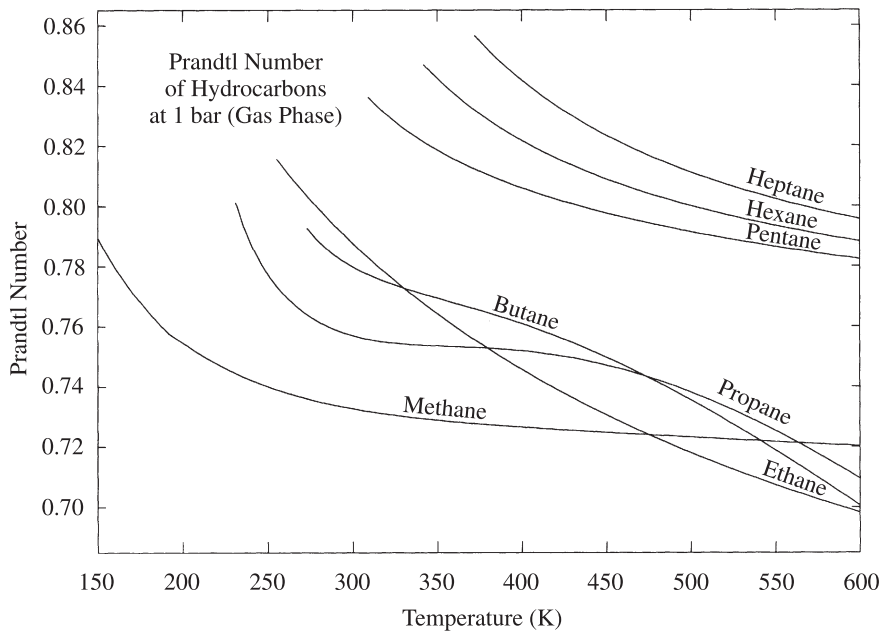
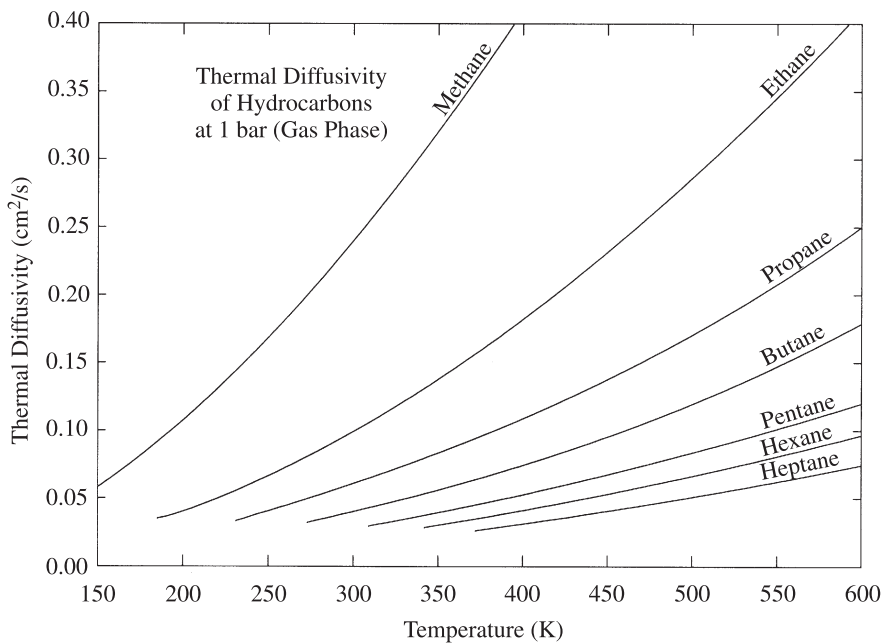


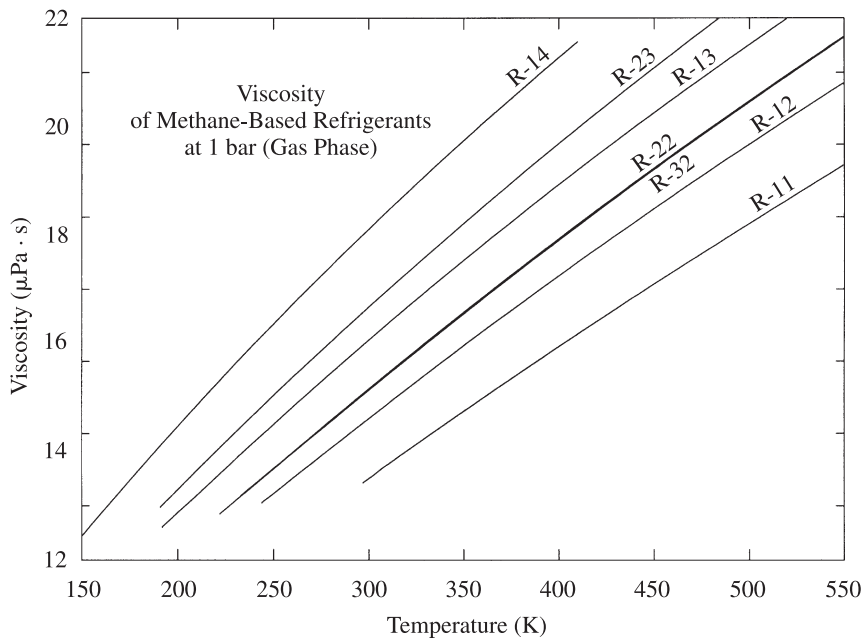
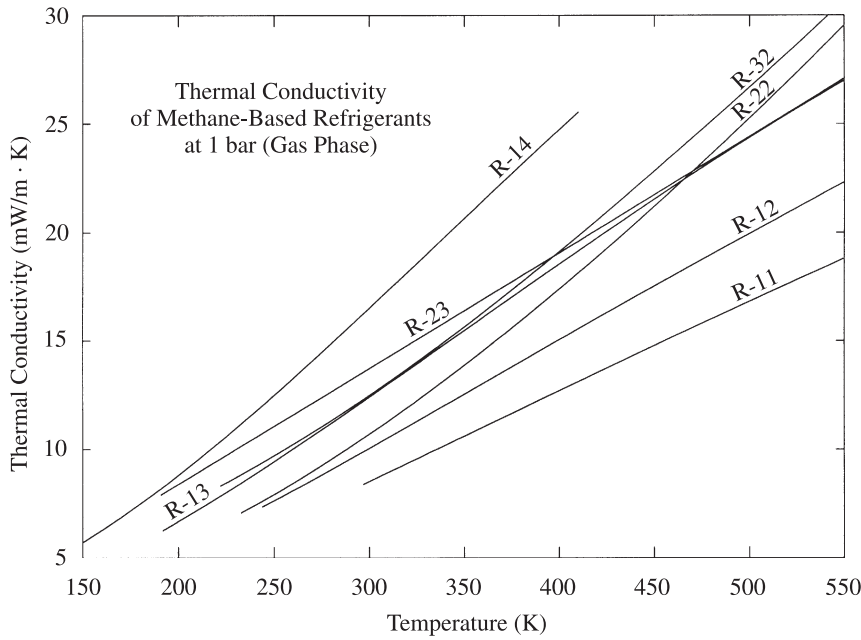


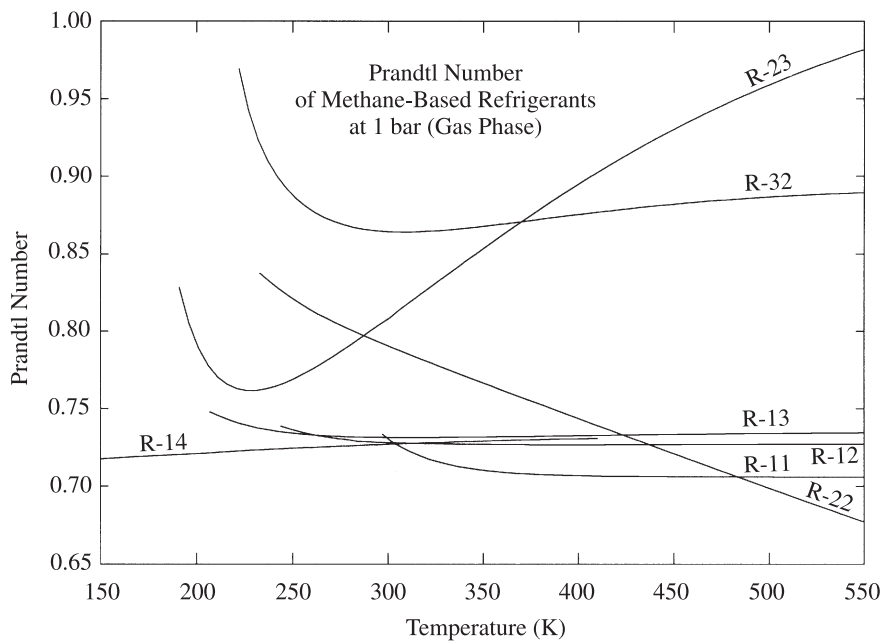
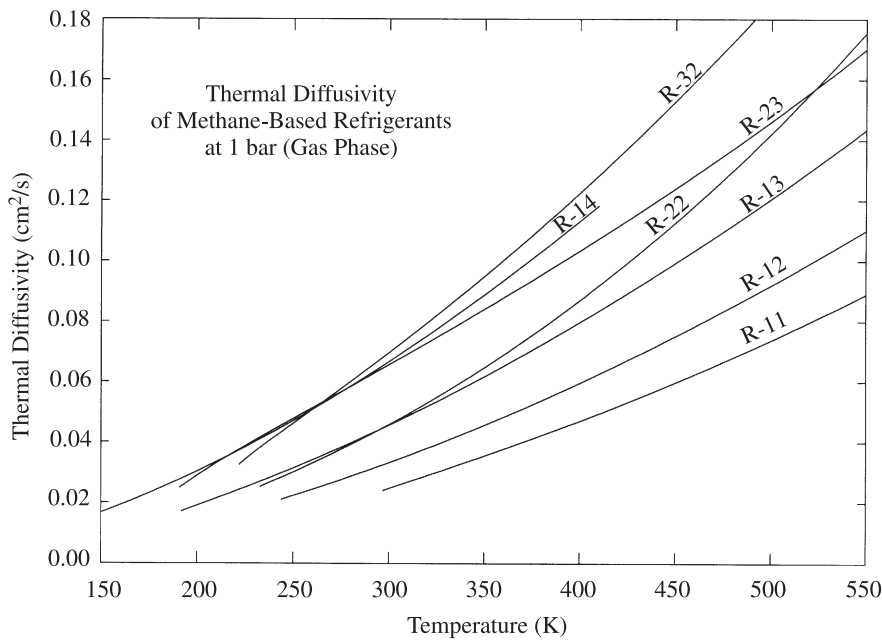


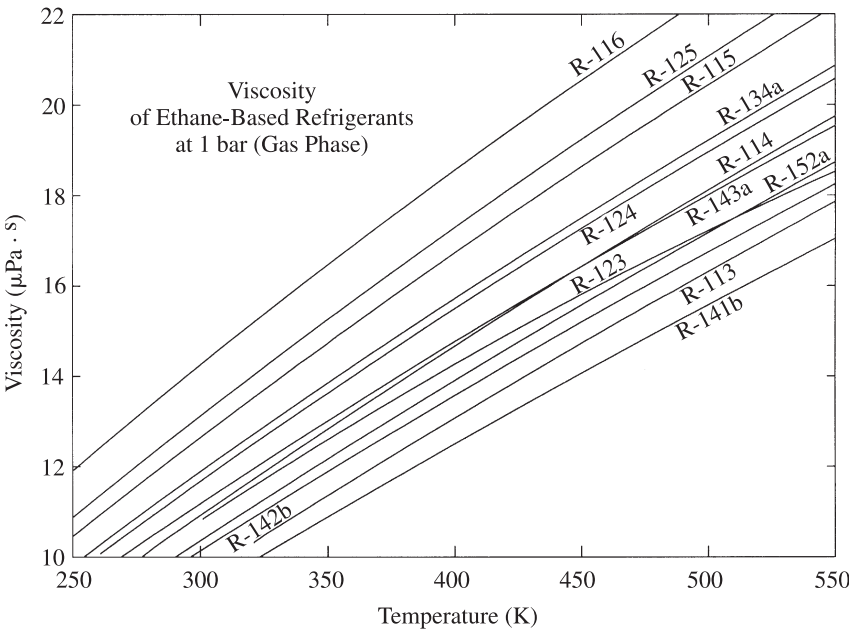
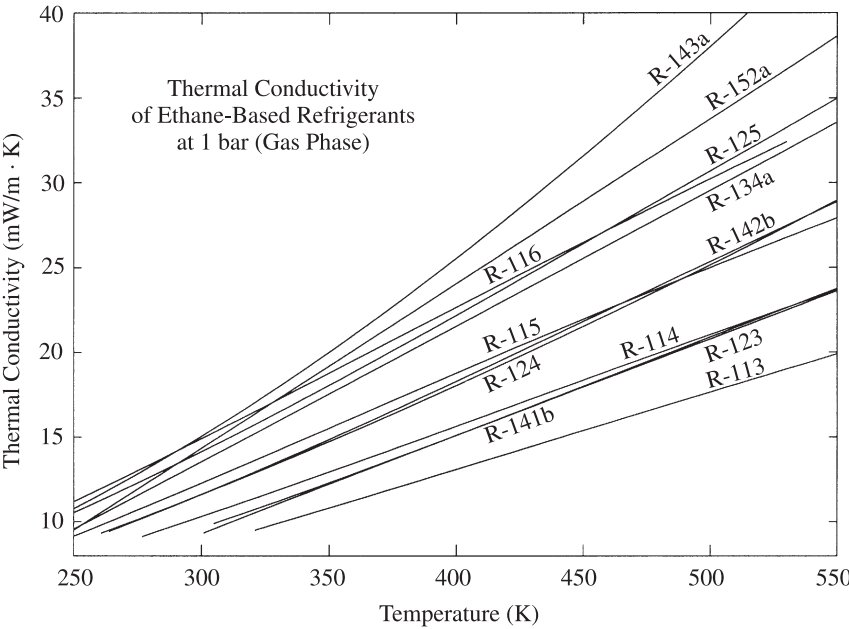


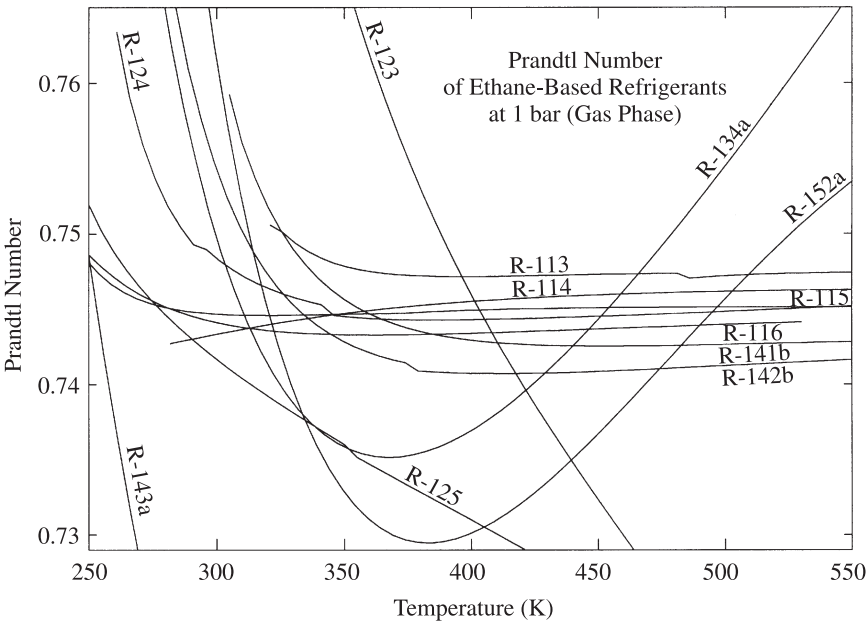
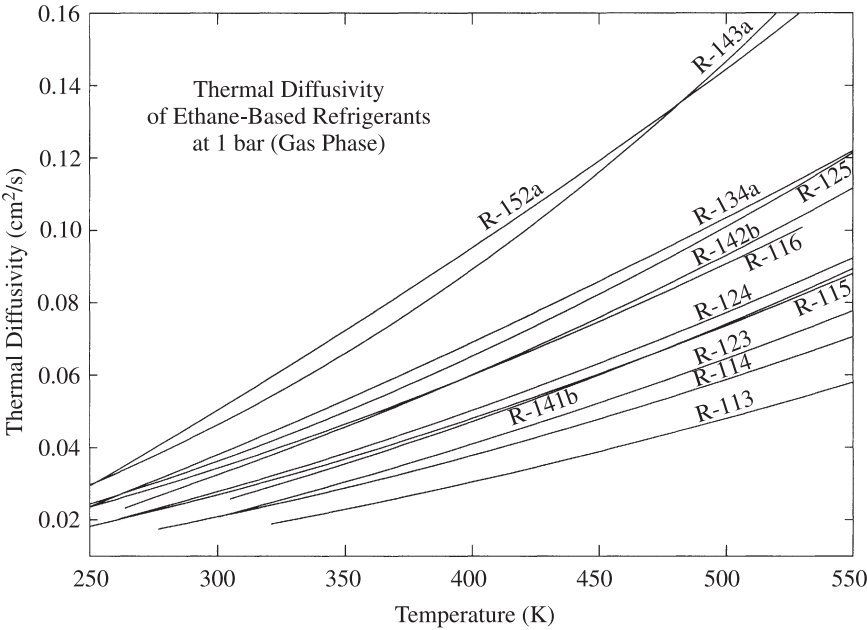












Conduction Heat Transfer*

A. AZIZ

Department of Mechanical Engineering
Gonzaga University
Spokane, Washington

- 3.1 Introduction
- 3.2 Basic equations
 - 3.2.1 Fourier's law
 - 3.2.2 General heat conduction equations
 - 3.2.3 Boundary and initial conditions
- 3.3 Special functions
 - 3.3.1 Error functions
 - 3.3.2 Gamma function
 - 3.3.3 Beta functions
 - 3.3.4 Exponential integral function
 - 3.3.5 Bessel functions
 - 3.3.6 Legendre functions
- 3.4 Steady one-dimensional conduction
 - 3.4.1 Plane wall
 - 3.4.2 Hollow cylinder
 - 3.4.3 Hollow sphere
 - 3.4.4 Thermal resistance
 - 3.4.5 Composite systems
 - Composite plane wall
 - Composite hollow cylinder
 - Composite hollow sphere
 - 3.4.6 Contact conductance
 - 3.4.7 Critical thickness of insulation
 - 3.4.8 Effect of uniform internal energy generation
 - Plane wall
 - Hollow cylinder
 - Solid cylinder
 - Hollow sphere
 - Solid sphere
- 3.5 More advanced steady one-dimensional conduction
 - 3.5.1 Location-dependent thermal conductivity

*The author dedicates this chapter to little Senaan Asil Aziz whose sparkling smile “makes my day.”

- Plane wall
- Hollow cylinder
- 3.5.2 Temperature-dependent thermal conductivity
 - Plane wall
 - Hollow cylinder
 - Hollow sphere
- 3.5.3 Location-dependent energy generation
 - Plane wall
 - Solid cylinder
- 3.5.4 Temperature-dependent energy generation
 - Plane wall
 - Solid cylinder
 - Solid sphere
- 3.5.5 Radiative–convective cooling of solids with uniform energy generation
- 3.6 Extended surfaces
 - 3.6.1 Longitudinal convecting fins
 - Rectangular fin
 - Trapezoidal fin
 - Triangular fin
 - Concave parabolic fin
 - Convex parabolic fin
 - 3.6.2 Radial convecting fins
 - Rectangular fin
 - Triangular fin
 - Hyperbolic fin
 - 3.6.3 Convecting spines
 - Cylindrical spine
 - Conical spine
 - Concave parabolic spine
 - Convex parabolic spine
 - 3.6.4 Longitudinal radiating fins
 - 3.6.5 Longitudinal convecting–radiating fins
 - 3.6.6 Optimum dimensions of convecting fins and spines
 - Rectangular fin
 - Triangular fin
 - Concave parabolic fin
 - Cylindrical spine
 - Conical spine
 - Concave parabolic spine
 - Convex parabolic spine
- 3.7 Two-dimensional steady conduction
 - 3.7.1 Rectangular plate with specified boundary temperatures
 - 3.7.2 Solid cylinder with surface convection
 - 3.7.3 Solid hemisphere with specified base and surface temperatures
 - 3.7.4 Method of superposition
 - 3.7.5 Conduction of shape factor method
 - 3.7.6 Finite-difference method

- Cartesian coordinates
- Cylindrical coordinates

3.8 Transient conduction

- 3.8.1 Lumped thermal capacity model
 - Internal energy generation
 - Temperature-dependent specific heat
 - Pure radiation cooling
 - Simultaneous convective–radiative cooling
 - Temperature-dependent heat transfer coefficient
 - Heat capacity of the coolant pool
- 3.8.2 Semi-infinite solid model
 - Specified surface temperature
 - Specified surface heat flux
 - Surface convection
 - Constant surface heat flux and nonuniform initial temperature
 - Constant surface heat flux and exponentially decaying energy generation
- 3.8.3 Finite-sized solid model
- 3.8.4 Multidimensional transient conduction
- 3.8.5 Finite-difference method
 - Explicit method
 - Implicit method
 - Other methods

3.9 Periodic conduction

- 3.9.1 Cooling of a lumped system in an oscillating temperature environment
- 3.9.2 Semi-infinite solid with periodic surface temperature
- 3.9.3 Semi-infinite solid with periodic surface heat flux
- 3.9.4 Semi-infinite solid with periodic ambient temperature
- 3.9.5 Finite plane wall with periodic surface temperature
- 3.9.6 Infinitely long semi-infinite hollow cylinder with periodic surface temperature

3.10 Conduction-controlled freezing and melting

- 3.10.1 One-region Neumann problem
- 3.10.2 Two-region Neumann problem
- 3.10.3 Other exact solutions for planar freezing
- 3.10.4 Exact solutions in cylindrical freezing
- 3.10.5 Approximate analytical solutions
 - One-region Neumann problem
 - One-region Neumann problem with surface convection
 - Outward cylindrical freezing
 - Inward cylindrical freezing
 - Outward spherical freezing
 - Other approximate solutions
- 3.10.6 Multidimensional freezing (melting)

3.11 Contemporary topics

Nomenclature

References

3.1 INTRODUCTION

This chapter is concerned with the characterization of conduction heat transfer, which is a mode that pervades a wide range of systems and devices. Unlike convection, which pertains to energy transport due to fluid motion and radiation, which can propagate in a perfect vacuum, conduction requires the presence of an intervening medium. At microscopic levels, conduction in stationary fluids is a consequence of higher-temperature molecules interacting and exchanging energy with molecules at lower temperatures. In a nonconducting solid, the transport of energy is exclusively via lattice waves (phonons) induced by atomic motion. If the solid is a conductor, the transfer of energy is also associated with the translational motion of free electrons.

The microscopic approach is of considerable contemporary interest because of its applicability to miniaturized systems such as superconducting thin films, microsensors, and micromechanical devices (Duncan and Peterson, 1994; Tien and Chen, 1994; Tzou, 1997; Tien et al., 1998). However, for the vast majority of engineering applications, the macroscopic approach based on Fourier's law is adequate. This chapter is therefore devoted exclusively to macroscopic heat conduction theory, and the material contained herein is a unique synopsis of a wealth of information that is available in numerous works, such as those of Schneider (1955), Carslaw and Jaeger (1959), Gebhart (1993), Ozisik (1993), Poulikakos (1994), and Jiji (2000).

3.2 BASIC EQUATIONS

3.2.1 Fourier's Law

The basic equation for the analysis of heat conduction is *Fourier's law*, which is based on experimental observations and is

$$q_n'' = -k_n \frac{\partial T}{\partial n} \quad (3.1)$$

where the *heat flux* q_n'' (W/m²) is the heat transfer rate in the n direction per unit area perpendicular to the direction of heat flow, k_n (W/m · K) is the thermal conductivity in the direction n , and $\partial T/\partial n$ (K/m) is the *temperature gradient* in the direction n . The thermal conductivity is a thermophysical property of the material, which is, in general, a function of both temperature and location; that is, $k = k(T, n)$. For *isotropic materials*, k is the same in all directions, but for *anisotropic materials* such as wood and laminated materials, k is significantly higher along the grain or lamination than perpendicular to it. Thus for anisotropic materials, k can have a strong directional dependence. Although heat conduction in anisotropic materials is of current research interest, its further discussion falls outside the scope of this chapter and the interested reader can find a fairly detailed exposition of this topic in Ozisik (1993).

Because the thermal conductivity depends on the atomic and molecular structure of the material, its value can vary from one material to another by several orders of

magnitude. The highest values are associated with metals and the lowest values with gases and thermal insulators. Tabulations of thermal conductivity data are given in Chapter 2.

For three-dimensional conduction in a Cartesian coordinate system, the Fourier law of eq. (3.1) can be extended to

$$\mathbf{q}'' = \mathbf{i}q_x'' + \mathbf{j}q_y'' + \mathbf{k}q_z'' \quad (3.2)$$

where

$$q_x'' = -k \frac{\partial T}{\partial x} \quad q_y'' = -k \frac{\partial T}{\partial y} \quad q_z'' = -k \frac{\partial T}{\partial z} \quad (3.3)$$

and \mathbf{i} , \mathbf{j} , and \mathbf{k} are unit vectors in the x , y , and z coordinate directions, respectively.

3.2.2 General Heat Conduction Equations

The general equations of heat conduction in the rectangular, cylindrical, and spherical coordinate systems shown in Fig. 3.1 can be derived by performing an energy balance.

Cartesian coordinate system:

$$\frac{\partial}{\partial x} \left(k \frac{\partial T}{\partial x} \right) + \frac{\partial}{\partial y} \left(k \frac{\partial T}{\partial y} \right) + \frac{\partial}{\partial z} \left(k \frac{\partial T}{\partial z} \right) + \dot{q} = \rho c \frac{\partial T}{\partial t} \quad (3.4)$$

Cylindrical coordinate system:

$$\frac{1}{r} \frac{\partial}{\partial r} \left(kr \frac{\partial T}{\partial r} \right) + \frac{1}{r^2} \frac{\partial}{\partial \phi} \left(k \frac{\partial T}{\partial \phi} \right) + \frac{\partial}{\partial z} \left(k \frac{\partial T}{\partial z} \right) + \dot{q} = \rho c \frac{\partial T}{\partial t} \quad (3.5)$$

Spherical coordinate system:

$$\begin{aligned} \frac{1}{r^2} \frac{\partial}{\partial r} \left(kr^2 \frac{\partial T}{\partial r} \right) + \frac{1}{r^2 \sin^2 \theta} \frac{\partial}{\partial \phi} \left(k \frac{\partial T}{\partial \phi} \right) \\ + \frac{1}{r^2 \sin \theta} \frac{\partial}{\partial \theta} \left(k \sin \theta \frac{\partial T}{\partial \theta} \right) + \dot{q} = \rho c \frac{\partial T}{\partial t} \end{aligned} \quad (3.6)$$

In eqs. (3.4)–(3.6), \dot{q} is the volumetric energy addition (W/m^3), ρ the density of the material (kg/m^3), and c the specific heat ($\text{J/kg} \cdot \text{K}$) of the material. The general heat conduction equation can also be expressed in a general curvilinear coordinate system (Section 1.2.4). Ozisik (1993) gives the heat conduction equations in prolate spheroidal and oblate spheroidal coordinate systems.

3.2.3 Boundary and Initial Conditions

Each of the general heat conduction equations (3.4)–(3.6) is second order in the spatial coordinates and first order in time. Hence, the solutions require a total of six

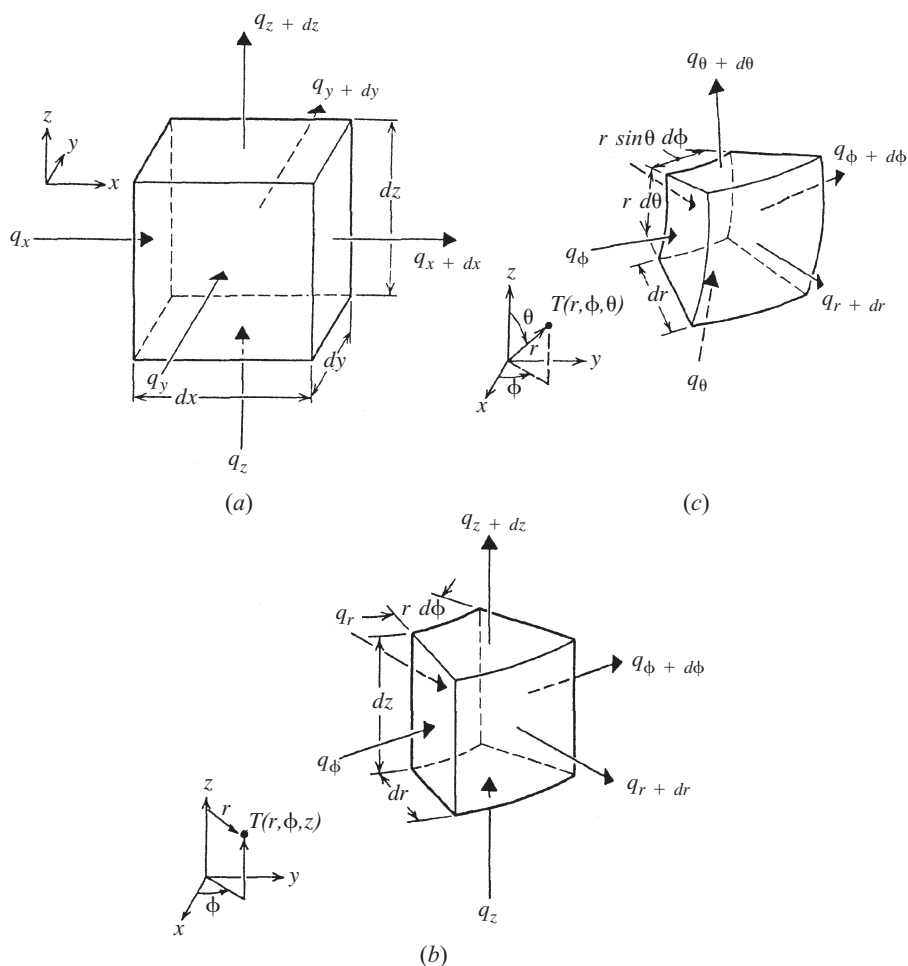


Figure 3.1 Differential control volumes in (a) Cartesian, (b) cylindrical, and (c) spherical coordinates.

boundary conditions (two for each spatial coordinate) and one initial condition. The initial condition prescribes the temperature in the body at time $t = 0$. The three types of boundary conditions commonly encountered are that of constant surface temperature (the boundary condition of the first kind), constant surface heat flux (the boundary condition of the second kind), and a prescribed relationship between the surface heat flux and the surface temperature (the convective or boundary condition of the third kind). The precise mathematical form of the boundary conditions depends on the specific problem.

For example, consider one-dimensional transient condition in a semi-infinite solid that is subject to heating at $x = 0$. Depending on the characterization of the heating, the boundary condition at $x = 0$ may take one of three forms. For constant surface temperature,

$$T(0, t) = T_s \quad (3.7)$$

For constant surface heat flux,

$$-k \frac{\partial T(0, t)}{\partial x} = q_s'' \quad (3.8)$$

and for convection at $x = 0$,

$$-k \frac{\partial T(0, t)}{\partial x} = h [T_\infty - T(0, t)] \quad (3.9)$$

where in eq. (3.9), $h(\text{W/m}^2 \cdot \text{K})$ is the convective heat transfer coefficient and T_∞ is the temperature of the hot fluid in contact with the surface at $x = 0$.

Besides the foregoing boundary conditions of eqs. (3.7)–(3.9), other types of boundary conditions may arise in heat conduction analysis. These include boundary conditions at the interface of two different materials in perfect thermal contact, boundary conditions at the interface between solid and liquid phases in a freezing or melting process, and boundary conditions at a surface losing (or gaining) heat simultaneously by convection and radiation. Additional details pertaining to these boundary conditions are provided elsewhere in the chapter.

3.3 SPECIAL FUNCTIONS

A number of special mathematical functions frequently arise in heat conduction analysis. These cannot be computed readily using a scientific calculator. In this section we provide a modest introduction to these functions and their properties. The functions include error functions, gamma functions, beta functions, exponential integral functions, Bessel functions, and Legendre polynomials.

3.3.1 Error Functions

The error function with argument (x) is defined as

$$\text{erf}(x) = \frac{2}{\sqrt{\pi}} \int_0^x e^{-t^2} dt \quad (3.10)$$

where t is a dummy variable. The error function is an odd function, so that

$$\text{erf}(-x) = -\text{erf}(x) \quad (3.11)$$

In addition,

$$\text{erf}(0) = 0 \quad \text{and} \quad \text{erf}(\infty) = 1 \quad (3.12)$$

The complementary error function with argument (x) is defined as

$$\text{erfc}(x) = 1 - \text{erf}(x) = \frac{2}{\sqrt{\pi}} \int_x^\infty e^{-t^2} dt \quad (3.13)$$

The derivatives of the error function can be obtained by repeated differentiations of eq. (3.10):

$$\frac{d}{dx} \operatorname{erf}(x) = \frac{2}{\sqrt{\pi}} e^{-x^2} \quad \text{and} \quad \frac{d^2}{dx^2} \operatorname{erf}(x) = -\frac{4}{\sqrt{\pi}} x e^{-x^2} \quad (3.14)$$

The repeated integrals of the complementary error function are defined by

$$i^n \operatorname{erfc}(x) = \int_x^\infty i^{n-1} \operatorname{erfc}(t) dt \quad (n = 1, 2, 3, \dots) \quad (3.15)$$

with

$$i^0 \operatorname{erfc}(x) = \operatorname{erfc}(x) \quad \text{and} \quad i^{-1} \operatorname{erfc}(x) = \frac{2}{\sqrt{\pi}} e^{-x^2} \quad (3.16)$$

The first two repeated integrals are

$$i \operatorname{erfc}(x) = \frac{1}{\sqrt{\pi}} e^{-x^2} - x \operatorname{erfc}(x) \quad (3.17)$$

$$i^2 \operatorname{erfc}(x) = \frac{1}{4} \left[(1 + 2x^2) \operatorname{erfc}(x) - \frac{2}{\sqrt{\pi}} x e^{-x^2} \right] \quad (3.18)$$

Table 3.1 lists the values of $\operatorname{erf}(x)$, $d \operatorname{erf}(x)/dx$, $d^2 \operatorname{erf}(x)/dx^2$, and $d^3 \operatorname{erf}(x)/dx^3$ for values of x from 0 to 3 in increments of 0.10. Table 3.2 lists the values of $\operatorname{erfc}(x)$, $i \operatorname{erfc}(x)$, $i^2 \operatorname{erfc}(x)$, and $i^3 \operatorname{erfc}(x)$ for the same values of x . Both tables were generated using Maple V (Release 6.0).

3.3.2 Gamma Function

The *gamma function*, denoted by $\Gamma(x)$, provides a generalization of the factorial $n!$ to the case where n is not an integer. It is defined by the *Euler integral* (Andrews, 1992):

$$\Gamma(x) = \int_0^\infty t^{x-1} e^{-t} dt \quad (x > 0) \quad (3.19)$$

and has the property

$$\Gamma(x + 1) = x \Gamma(x) \quad (3.20)$$

which for integral values of x (denoted by n) becomes

$$\Gamma(n + 1) = n! \quad (3.21)$$

Table 3.3 gives values of $\Gamma(x)$ for values of x from 1.0 through 2.0. These values were generated using Maple V, Release 6.0.

TABLE 3.1 Values of $\operatorname{erf}(x)$, $d \operatorname{erf}(x)/dx$, $d^2 \operatorname{erf}(x)/dx^2$, and $d^3 \operatorname{erf}(x)/dx^3$

x	$\operatorname{erf}(x)$	$d \operatorname{erf}(x)/dx$	$d^2 \operatorname{erf}(x)/dx^2$	$d^3 \operatorname{erf}(x)/dx^3$
0.00	0.00000	1.12838	0.00000	-2.25676
0.10	0.11246	1.11715	-0.22343	-2.18962
0.20	0.22270	1.08413	-0.43365	-1.99481
0.30	0.32863	1.03126	-0.61876	-1.69127
0.40	0.42839	0.96154	-0.76923	-1.30770
0.50	0.52050	0.87878	-0.87878	-0.87878
0.60	0.60386	0.78724	-0.94469	-0.44086
0.70	0.67780	0.69127	-0.96778	-0.02765
0.80	0.74210	0.59499	-0.95198	0.33319
0.90	0.79691	0.50197	-0.90354	0.62244
1.00	0.84270	0.41511	-0.83201	0.83021
1.10	0.88021	0.33648	-0.74026	0.95560
1.20	0.91031	0.26734	-0.64163	1.00521
1.30	0.93401	0.20821	-0.54134	0.99107
1.40	0.95229	0.15894	-0.44504	0.92822
1.50	0.96611	0.11893	-0.35679	0.83251
1.60	0.97635	0.08723	-0.27913	0.71877
1.70	0.98379	0.06271	-0.21322	0.59952
1.80	0.98909	0.04419	-0.15909	0.48434
1.90	0.99279	0.03052	-0.11599	0.37973
2.00	0.99532	0.02067	-0.08267	0.28934
2.10	0.99702	0.01372	-0.05761	0.21451
2.20	0.99814	0.00892	-0.03926	0.15489
2.30	0.99886	0.00569	-0.02617	0.10900
2.40	0.99931	0.00356	-0.01707	0.07481
2.50	0.99959	0.00218	-0.01089	0.05010
2.60	0.99976	0.00131	-0.00680	0.03275
2.70	0.99987	0.76992×10^{-3}	-0.00416	0.02091
2.80	0.99992	0.44421×10^{-3}	-0.00249	0.01305
2.90	0.99996	0.25121×10^{-3}	-0.00146	0.00795
3.00	0.99997	0.13925×10^{-3}	-0.83552×10^{-3}	0.00473

The *incomplete gamma function* is defined by the integral (Andrews, 1992)

$$\Gamma(a, x) = \int_x^\infty t^{a-1} e^{-t} dt \quad (3.22)$$

Values of $\Gamma(1.2, x)$ for $0 \leq x \leq 1$ generated using Maple V, Release 6.0 are given in Table 3.4.

3.3.3 Beta Functions

The *beta function*, denoted by $B(x, y)$, is defined by

$$B(x, y) = \int_0^1 (1-t)^{x-1} t^{y-1} dt \quad (3.23)$$

TABLE 3.2 Values of $\operatorname{erfc}(x)$, $i \operatorname{erfc}(x)$, $i^2 \operatorname{erfc}(x)$, and $i^3 \operatorname{erfc}(x)$

x	$\operatorname{erfc}(x)$	$i \operatorname{erfc}(x)$	$i^2 \operatorname{erfc}(x)$	$i^3 \operatorname{erfc}(x)$
0.00	1.00000	0.56419	0.25000	0.09403
0.10	0.88754	0.46982	0.19839	0.07169
0.20	0.77730	0.38661	0.15566	0.05406
0.30	0.67137	0.31422	0.12071	0.04030
0.40	0.57161	0.25213	0.09248	0.02969
0.50	0.47950	0.19964	0.06996	0.02161
0.60	0.39614	0.15594	0.05226	0.01554
0.70	0.32220	0.12010	0.03852	0.01103
0.80	0.25790	0.09117	0.02801	0.00773
0.90	0.20309	0.06820	0.02008	0.00534
1.00	0.15730	0.05025	0.01420	0.00364
1.10	0.11979	0.03647	0.00989	0.00245
1.20	0.08969	0.02605	0.00679	0.00162
1.30	0.06599	0.01831	0.00459	0.00106
1.40	0.04771	0.01267	0.00306	0.68381×10^{-3}
1.50	0.03389	0.00862	0.00201	0.43386×10^{-3}
1.60	0.02365	0.00577	0.00130	0.27114×10^{-3}
1.70	0.01621	0.00380	0.82298×10^{-3}	0.16686×10^{-3}
1.80	0.01091	0.00246	0.51449×10^{-3}	0.10110×10^{-3}
1.90	0.00721	0.00156	0.31642×10^{-3}	0.60301×10^{-4}
2.00	0.00468	0.97802×10^{-3}	0.19141×10^{-3}	0.35396×10^{-4}
2.10	0.00298	0.60095×10^{-3}	0.11387×10^{-3}	0.20445×10^{-4}
2.20	0.00186	0.36282×10^{-3}	0.66614×10^{-4}	0.11619×10^{-4}
2.30	0.00114	0.21520×10^{-3}	0.38311×10^{-4}	0.64951×10^{-5}
2.40	0.68851×10^{-3}	0.12539×10^{-3}	0.21659×10^{-4}	0.35711×10^{-5}
2.50	0.40695×10^{-3}	0.71762×10^{-4}	0.12035×10^{-4}	0.19308×10^{-5}
2.60	0.23603×10^{-3}	0.40336×10^{-4}	0.65724×10^{-5}	0.10265×10^{-5}
2.70	0.13433×10^{-3}	0.22264×10^{-4}	0.35268×10^{-5}	0.53654×10^{-6}
2.80	0.75013×10^{-4}	0.12067×10^{-4}	0.18595×10^{-5}	0.27567×10^{-6}
2.90	0.41098×10^{-4}	0.64216×10^{-5}	0.96315×10^{-6}	0.13922×10^{-6}
3.00	0.22090×10^{-4}	0.33503×10^{-5}	0.49007×10^{-6}	0.69101×10^{-7}

The beta function is related to the gamma function:

$$B(x, y) = \frac{\Gamma(x)\Gamma(y)}{\Gamma(x + y)} \quad (x > 0, y > 0) \quad (3.24)$$

has the symmetry property

$$B(x, y) = B(y, x) \quad (3.25)$$

and for nonnegative integers,

$$B(m, n) = \frac{(m - 1)!(n - 1)!}{(m + n - 1)!} \quad m, n \text{ nonnegative integers} \quad (3.26)$$

TABLE 3.3 Gamma Function

x	$\Gamma(x)$	x	$\Gamma(x)$	x	$\Gamma(x)$	x	$\Gamma(x)$
1.00	1.00000	1.25	0.90640	1.50	0.88623	1.75	0.91906
1.01	0.99433	1.26	0.90440	1.51	0.88659	1.76	0.92137
1.02	0.98884	1.27	0.90250	1.52	0.88704	1.77	0.92376
1.03	0.98355	1.28	0.90072	1.53	0.88757	1.78	0.92623
1.04	0.97844	1.29	0.89904	1.54	0.88818	1.79	0.92877
1.05	0.97350	1.30	0.89747	1.55	0.88887	1.80	0.93138
1.06	0.96874	1.31	0.89600	1.56	0.88964	1.81	0.93408
1.07	0.96415	1.32	0.89464	1.57	0.89049	1.82	0.93685
1.08	0.95973	1.33	0.89338	1.58	0.89142	1.83	0.93969
1.09	0.95546	1.34	0.89222	1.59	0.89243	1.84	0.94261
1.10	0.95135	1.35	0.89115	1.60	0.89352	1.85	0.94561
1.11	0.94740	1.36	0.89018	1.61	0.89468	1.86	0.94869
1.12	0.94359	1.37	0.88931	1.62	0.89592	1.87	0.95184
1.13	0.93993	1.38	0.88854	1.63	0.89724	1.88	0.95507
1.14	0.93642	1.39	0.88785	1.64	0.89864	1.89	0.95838
1.15	0.93304	1.40	0.88726	1.65	0.90012	1.90	0.96177
1.16	0.92980	1.41	0.88676	1.66	0.90167	1.91	0.96523
1.17	0.92670	1.42	0.88636	1.67	0.90330	1.92	0.96877
1.18	0.92373	1.43	0.88604	1.68	0.90500	1.93	0.97240
1.19	0.92089	1.44	0.88581	1.69	0.90678	1.94	0.97610
1.20	0.91817	1.45	0.88566	1.70	0.90864	1.95	0.97988
1.21	0.91558	1.46	0.88560	1.71	0.91057	1.96	0.98374
1.22	0.91311	1.47	0.88563	1.72	0.91258	1.97	0.98768
1.23	0.91075	1.48	0.88575	1.73	0.91467	1.98	0.99171
1.24	0.90852	1.49	0.88595	1.74	0.91683	1.99	0.99581
						2.00	1.00000

TABLE 3.4 Incomplete Gamma Function, $\Gamma(a, x)$, $a = 1.2$

x	$\Gamma(a, x)$
0.00	0.91817
0.10	0.86836
0.20	0.80969
0.30	0.75074
0.40	0.69366
0.50	0.63932
0.60	0.58813
0.70	0.54024
0.80	0.49564
0.90	0.45426
1.00	0.41597

TABLE 3.5 Incomplete Beta Function, $B_t(0.3, 0.5)$

x	$B_t(0.3, 0.5)$
0.00	0.00000
0.10	0.64802
0.20	0.94107
0.30	1.18676
0.40	1.41584
0.50	1.64284
0.60	1.87920
0.70	2.13875
0.80	2.44563
0.90	2.86367
1.00	4.55444

The *incomplete beta function*, $B_t(x, y)$, is defined by

$$B_t(x, y) = \int_0^t (1 - t)^{x-1} t^{y-1} dt \tag{3.27}$$

Values of $B_t(0.3, 0.5)$ for the range $0 \leq t \leq 1$ generated using Maple V, Release 6.0 are given in Table 3.5.

3.3.4 Exponential Integral Function

The *exponential integral function* $E_1(x)$ or $-E_i(-x)$ for a real argument x is defined by

$$E_1(x) \quad \text{or} \quad -E_i(-x) = \int_x^\infty \frac{e^{-t}}{t} dt \tag{3.28}$$

and has the following properties:

$$E_1(0) = \infty \quad E_1(\infty) = 0 \quad \frac{dE_1(x)}{dx} = -\frac{e^{-x}}{x} \tag{3.29}$$

As indicated by the entries in Table 3.6, the function decreases monotonically from the value $E_1(0) = \infty$ to $E_1(\infty) = 0$ as x is varied from 0 to ∞ .

3.3.5 Bessel Functions

Bessel functions of the first kind of order n and argument x , denoted by $J_n(x)$, and *Bessel functions of the second kind* of order n and argument x , denoted by $Y_n(x)$, are defined, respectively, by the infinite series

TABLE 3.6 Exponential Integral Function

x	$E_1(x)$	x	$E_1(x)$
0.00	∞	0.80	0.31060
0.01	4.03793	0.90	0.26018
0.02	3.35471	1.00	0.21938
0.03	2.95912	1.10	0.18599
0.04	2.68126	1.20	0.15841
0.05	2.46790	1.30	0.13545
0.06	2.29531	1.40	0.11622
0.07	2.15084	1.50	0.10002
0.08	2.02694	1.60	0.08631
0.09	1.91874	1.70	0.07465
0.10	1.82292	1.80	0.06471
0.15	1.46446	1.90	0.05620
0.20	1.22265	2.00	0.04890
0.30	0.90568	2.20	0.03719
0.40	0.70238	2.40	0.02844
0.50	0.55977	2.60	0.02185
0.60	0.45438	2.80	0.01686
0.70	0.37377	3.00	0.01305

$$J_n(x) = \sum_{m=0}^{\infty} \frac{(-1)^m (x/2)^{2m+n}}{m! \Gamma(m+n+1)} \quad (3.30)$$

and

$$Y_n(x) = \frac{J_n(x) \cos n\pi - J_{-n}(x)}{\sin n\pi} \quad (n \neq 0, 1, 2, \dots) \quad (3.31a)$$

or

$$Y_n(x) = \lim_{m \rightarrow n} \frac{J_m(x) \cos m\pi - J_{-m}(x)}{\sin m\pi} \quad (n = 0, 1, 2, \dots) \quad (3.31b)$$

Numerous recurrence relationships involving the Bessel functions are available (Andrews, 1992). Some that are relevant in this chapter are

$$J_{-n}(x) = (-1)^n J_n(x) \quad (3.32)$$

$$\frac{dJ_n(x)}{dx} = J_{n-1}(x) - \frac{n}{x} J_n(x) = \frac{n}{x} J_n(x) - J_{n+1}(x) \quad (3.33)$$

$$\frac{d}{dx} [x^n J_n(x)] = x^n J_{n-1}(x) \quad (3.34)$$

$$\frac{d}{dx} [x^{-n} J_n(x)] = -x^{-n} J_{n+1}(x) \quad (3.35)$$

The relations given by eqs. (3.32)–(3.35) apply to the Bessel functions of the second kind when the J 's are replaced by Y 's.

Modified Bessel functions of the first kind of order n and argument x , denoted by $I_n(x)$, and *modified Bessel functions of the second kind* of order n and argument x , denoted by $K_n(x)$, are defined, respectively, by the infinite series

$$I_n(x) = \sum_{m=0}^{\infty} \frac{(x/2)^{2m+n}}{m! \Gamma(m+n+1)} \quad (3.36)$$

and

$$K_n(x) = \frac{\pi}{2 \sin n\pi} [I_{-n}(x) - I_n(x)] \quad (n \neq 0, 1, 2, \dots) \quad (3.37a)$$

or

$$K_n(x) = \lim_{m \rightarrow n} \frac{\pi}{2 \sin n\pi} [I_{-m}(x) - I_m(x)] \quad (n = 0, 1, 2, \dots) \quad (3.37b)$$

$I_n(x)$ and $K_n(x)$ are real and positive when $n > -1$ and $x > 0$.

A selected few of the numerous recurrence relationships involving the modified Bessel functions are

$$I_n(x) = (\iota)^{-n} J_n(\iota x) \quad (3.38)$$

$$I_{-n}(x) = (\iota)^n J_{-n}(\iota x) \quad (3.39)$$

$$\frac{dI_n(x)}{dx} = I_{n-1}(x) - \frac{n}{x} I_n(x) = \frac{n}{x} I_n(x) + I_{n+1}(x) \quad (3.40)$$

$$\frac{d}{dx} [x^n I_n(x)] = x^n I_{n-1}(x) \quad (3.41)$$

$$\frac{d}{dx} [x^{-n} I_n(x)] = x^{-n} I_{n+1}(x) \quad (3.42)$$

$$K_{-n}(x) = K_n(x) \quad (n = 0, 1, 2, 3, \dots) \quad (3.43)$$

$$\frac{dK_n(x)}{dx} = \frac{n}{x} K_n(x) - K_{n+1}(x) = -K_{n-1}(x) - \frac{n}{x} K_n(x) \quad (3.44)$$

$$\frac{d}{dx} [x^n K_n(x)] = -x^n K_{n-1}(x) \quad (3.45)$$

$$\frac{d}{dx} [x^{-n} K_n(x)] = -x^{-n} K_{n+1}(x) \quad (3.46)$$

Fairly extensive tables for the Bessel functions and modified Bessel functions of orders 1 and 2 and those of fractional order $I_{-1/3}(x)$, $I_{-2/3}(x)$, $I_{1/3}(x)$, and $I_{2/3}(x)$ in the range $0 \leq x \leq 5$ with a refined interval are given in Kern and Kraus (1972), and polynomial approximations are given by Kraus et al. (2001), culled from the work of Abramowitz and Stegun (1955). Maple V, Release 6.0 can also be used to

generate these tables. Figure 3.2 displays graphs of $J_0(x)$, $J_1(x)$, $Y_0(x)$, and $Y_1(x)$. These functions exhibit oscillatory behavior with amplitude decaying as x increases. Figure 3.3 provides plots of $I_0(x)$, $I_1(x)$, $K_0(x)$, and $K_1(x)$ as a function of x and these functions exhibit monotonic behavior.

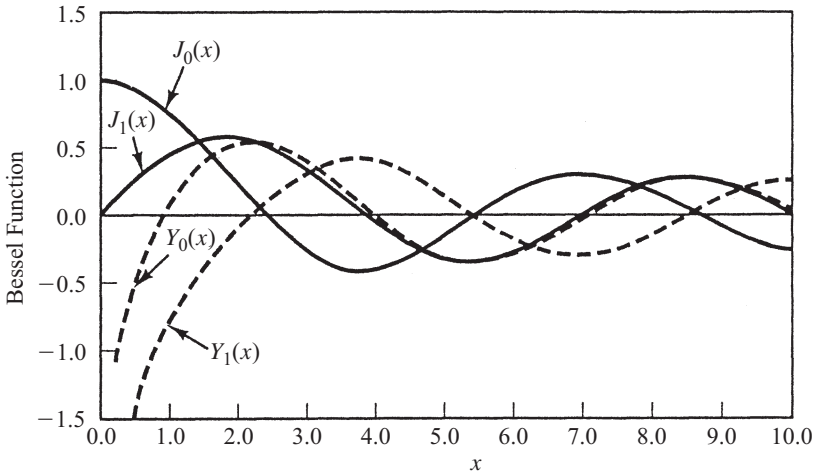


Figure 3.2 Graphs of $J_0(x)$, $J_1(x)$, $Y_0(x)$, and $Y_1(x)$.

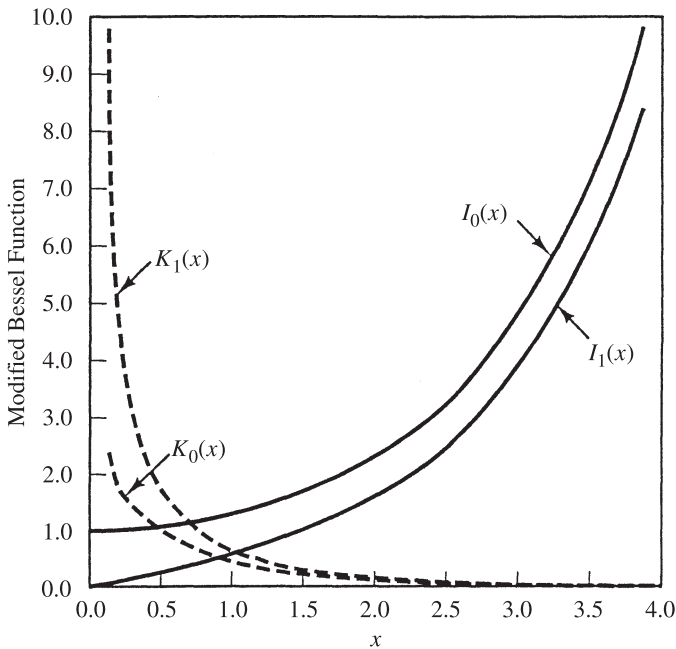


Figure 3.3 Graphs of $I_0(x)$, $I_1(x)$, $K_0(x)$, and $K_1(x)$.

Thomson functions $\text{ber}_i(x)$, $\text{bei}_i(x)$, $\text{ker}_i(x)$, and $\text{kei}_i(x)$ arise in obtaining the real and imaginary parts of the modified Bessel functions of imaginary argument. The subscripts i denote the order of the Thomson functions. Note that it is customary to omit the subscript when dealing with Thomson functions of zero order. Hence $\text{ber}_0(x)$, $\text{bei}_0(x)$, $\text{ker}_0(x)$, and $\text{kei}_0(x)$ are written as $\text{ber}(x)$, $\text{bei}(x)$, $\text{ker}(x)$, and $\text{kei}(x)$. The Thomson functions are defined by

$$I_0(x\sqrt{\imath}) = \text{ber}(x) + \imath \text{bei}(x) \tag{3.47}$$

$$K_0(x\sqrt{\imath}) = \text{ker}(x) + \imath \text{kei}(x) \tag{3.48}$$

with

$$\text{ber}(0) = 1 \qquad \text{bei}(0) = 0 \qquad \text{ker}(0) = \infty \qquad \text{kei}(0) = -\infty \tag{3.49}$$

Expressions for the derivatives of the Thomson functions are

$$\frac{d}{dx} [\text{ber}(x)] = \frac{1}{\sqrt{2}} [\text{ber}_1(x) + \text{bei}_1(x)] \tag{3.50}$$

$$\frac{d}{dx} [\text{bei}(x)] = \frac{1}{\sqrt{2}} [\text{bei}_1(x) - \text{ber}_1(x)] \tag{3.51}$$

$$\frac{d}{dx} [\text{ker}(x)] = \frac{1}{\sqrt{2}} [\text{ker}_1(x) + \text{kei}_1(x)] \tag{3.52}$$

$$\frac{d}{dx} [\text{kei}(x)] = \frac{1}{\sqrt{2}} [\text{kei}_1(x) - \text{ker}_1(x)] \tag{3.53}$$

Table 3.7 gives the values of $\text{ber}(x)$, $\text{bei}(x)$, $\text{ker}(x)$, and $\text{kei}(x)$ for $1 \leq x \leq 5$, and the values of $d\text{ber}(x)/dx$, $d\text{bei}(x)/dx$, $d\text{ker}(x)/dx$, and $d\text{kei}(x)/dx$ are provided for the same range of x values in Table 3.8. Figure 3.4 displays graphs of $\text{ber}(x)$, $\text{bei}(x)$, $\text{ker}(x)$, and $\text{kei}(x)$.

TABLE 3.7 Functions $\text{ber}(x)$, $\text{bei}(x)$, $\text{ker}(x)$, and $\text{kei}(x)$

x	$\text{ber}(x)$	$\text{bei}(x)$	$\text{ker}(x)$	$\text{kei}(x)$
1.00	0.98438	0.24957	0.28671	−0.49499
1.50	0.92107	0.55756	0.05293	−0.33140
2.00	0.75173	0.97229	−0.04166	−0.20240
2.50	0.39997	1.45718	−0.06969	−0.11070
3.00	−0.22138	1.93759	−0.06703	−0.05112
3.50	−1.19360	2.28325	−0.05264	−0.01600
4.00	−2.56342	2.29269	−0.03618	0.00220
4.50	−4.29909	1.68602	−0.02200	0.00972
5.00	−6.23008	0.11603	−0.01151	0.01119

TABLE 3.8 Functions $d \operatorname{ber}(x)/dx$, $d \operatorname{bei}(x)/dx$, $d \operatorname{ker}(x)$, dx , and $d \operatorname{kei}(x)/dx$

x	$d \operatorname{ber}(x)/dx$	$d \operatorname{bei}(x)/dx$	$d \operatorname{ker}(x)/dx$	$d \operatorname{kei}(x)/dx$
1.00	-0.06245	0.49740	-0.69460	0.35237
1.50	-0.21001	0.73025	-0.29418	0.29561
2.00	-0.49307	0.91701	-0.10660	0.21981
2.50	-0.94358	0.99827	-0.01693	0.14890
3.00	-1.56985	0.88048	0.02148	0.09204
3.50	-2.33606	0.43530	0.03299	0.05098
4.00	-3.13465	-0.49114	0.03148	0.02391
4.50	-3.75368	-2.05263	0.02481	0.00772
5.00	-3.84534	-4.35414	0.01719	-0.00082

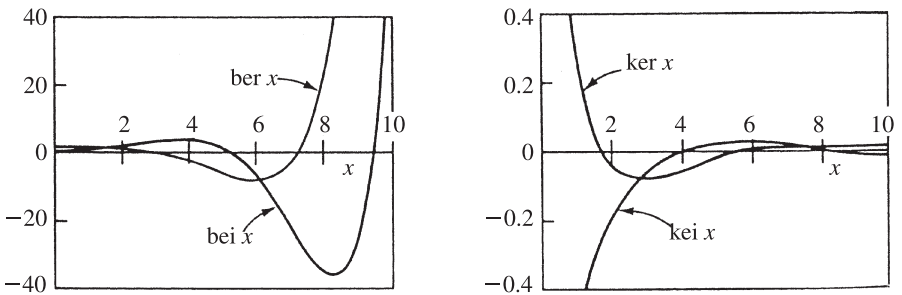


Figure 3.4 Thomson functions.

3.3.6 Legendre Functions

The *Legendre function*, also known as the *Legendre polynomial* $P_n(x)$, and the associated Legendre function of the first kind $P_n^m(x)$, are defined by

$$P_n(x) = \frac{1}{2^n n!} \frac{d^n}{dx^n} (x^2 - 1)^n \quad (3.54)$$

$$P_n^m(x) = (1 - x^2)^{m/2} \frac{d^m}{dx^m} [P_n(x)] \quad (3.55)$$

The *Legendre function* $Q_n(x)$ and the associated Legendre function of the second kind, $Q_n^m(x)$, are defined by

$$Q_n(x) = \frac{(-1)^{n/2} \cdot 2^n [(n/2)!]^2}{n!} \times \left[x - \frac{(n-1)(n+2)}{3!} x^3 + \frac{(n-1)(n-3)(n+2)(n+4)}{5!} x^5 - \dots \right] \quad (n = \text{even}, |x| < 1) \quad (3.56)$$

$$Q_n(x) = \frac{(-1)^{(n+1)/2} \cdot 2^{n-1} \{[(n-1)/2]!\}^2}{1 \cdot 3 \cdot 5 \cdots n} \\ \times \left[1 - \frac{n(n+1)}{2!}x^2 - \frac{n(n-2)(n+1)(n+3)}{4!}x^4 - \cdots \right] \\ (n = \text{odd}, |x| < 1) \quad (3.57)$$

$$Q_n^m(x) = (1-x^2)^{m/2} \frac{d^m}{dx^m} [Q_n(x)] \quad (3.58)$$

Several relationships involving $P_n(x)$, $Q_n(x)$, $P_n^m(x)$, and $Q_n^m(x)$ are useful in heat conduction analysis. They are

$$P_n(-x) = (-1)^n P_n(x) \quad (3.59)$$

$$P_{n+1}(x) = \frac{2n+1}{n+1}x P_n(x) - \frac{n}{n+1}P_{n-1}(x) \quad (3.60)$$

$$\frac{d}{dx} [P_{n+1}(x)] - \frac{d}{dx} [P_{n-1}(x)] = 2(n+1)P_n(x) \quad (3.61)$$

$$Q_n(x = \pm 1) = \infty \quad (3.62)$$

$$P_n^m(x) = 0 \quad (m > n) \quad (3.63)$$

$$Q_n^m(x = \pm 1) = \infty \quad (3.64)$$

The numerical values of the Legendre functions and their graphs can be generated with Maple V, Release 6.0. Table 3.9 lists the values of $P_0(x)$ through $P_4(x)$ for the range $-1 \leq x \leq 1$, and a plot of these functions appears in Fig. 3.5.

3.4 STEADY ONE-DIMENSIONAL CONDUCTION

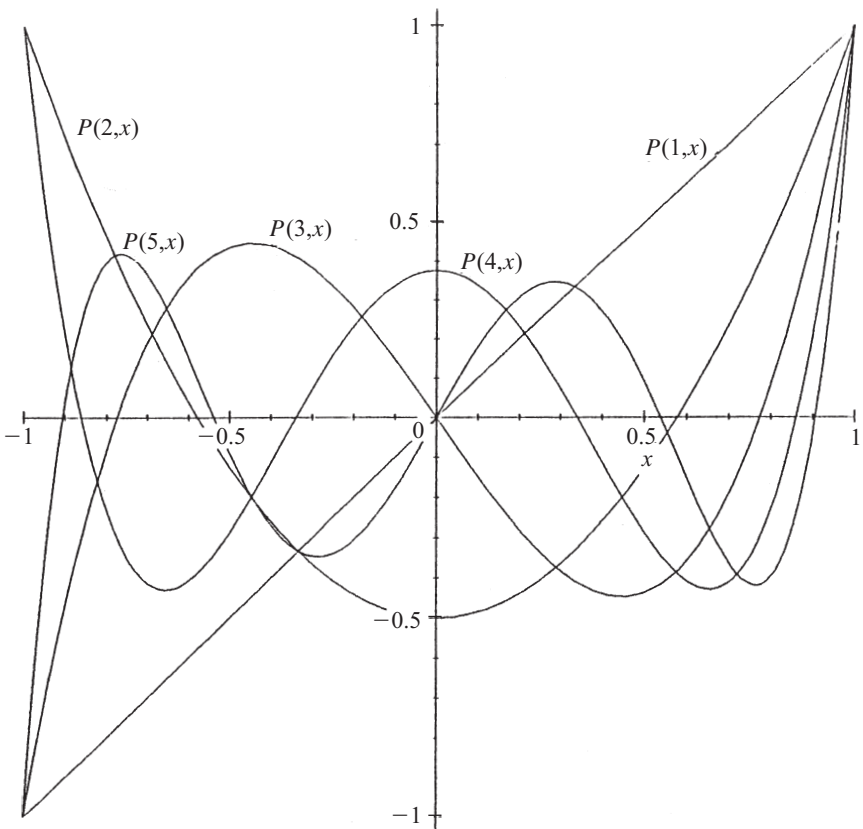
In this section we consider one-dimensional steady conduction in a plane wall, a hollow cylinder, and a hollow sphere. The objective is to develop expressions for the temperature distribution and the rate of heat transfer. The concept of thermal resistance is utilized to extend the analysis to composite systems with convection occurring at the boundaries. Topics such as contact conductance, critical thickness of insulation, and the effect of uniform internal heat generation are also discussed.

3.4.1 Plane Wall

Consider a plane wall of thickness L made of material with a thermal conductivity k , as illustrated in Fig. 3.6. The temperatures at the two faces of the wall are fixed at $T_{s,1}$ and $T_{s,2}$ with $T_{s,1} > T_{s,2}$. For steady conditions with no internal heat generation and constant thermal conductivity, the appropriate form of the general heat conduction equation, eq. (3.4), is

TABLE 3.9 Numerical Values of $P_n(x)$

x	$P_0(x)$	$P_1(x)$	$P_2(x)$	$P_3(x)$	$P_4(x)$
-1.00	1.00000	-1.00000	1.00000	-1.00000	1.00000
-0.80	1.00000	-0.80000	0.46000	-0.08000	-0.23300
-0.60	1.00000	-0.60000	0.04000	0.36000	-0.40800
-0.40	1.00000	-0.40000	-0.26000	0.44000	-0.11300
-0.20	1.00000	-0.20000	-0.44000	0.28000	0.23200
0.00	1.00000	0.00000	-0.50000	0.00000	0.37500
0.20	1.00000	0.20000	-0.44000	-0.28000	0.23200
0.40	1.00000	0.40000	-0.26000	-0.44000	-0.11300
0.60	1.00000	0.60000	0.04000	-0.36000	-0.40800
0.80	1.00000	0.80000	0.46000	0.08000	-0.23300
1.00	1.00000	1.00000	1.00000	1.00000	1.00000

**Figure 3.5** Legendre polynomials.

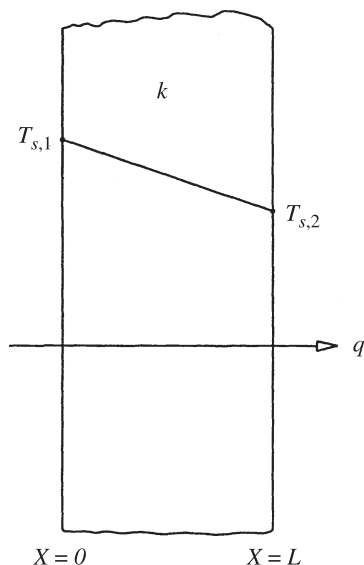


Figure 3.6 One-dimensional conduction through a plane wall.

$$\frac{d^2 T}{dx^2} = 0 \quad (3.65)$$

with the boundary conditions expressed as

$$T(x = 0) = T_{s,1} \quad \text{and} \quad T(x = L) = T_{s,2} \quad (3.66)$$

Integration of eq. (3.65) with subsequent application of the boundary conditions of eq. (3.66) gives the linear temperature distribution

$$T = T_{s,1} + (T_{s,2} - T_{s,1}) \frac{x}{L} \quad (3.67)$$

and application of Fourier's law gives

$$q = \frac{kA(T_{s,1} - T_{s,2})}{L} \quad (3.68)$$

where A is the wall area normal to the direction of heat transfer.

3.4.2 Hollow Cylinder

Figure 3.7 shows a hollow cylinder of inside radius r_1 , outside radius r_2 , length L , and thermal conductivity k . The inside and outside surfaces are maintained at constant temperatures $T_{s,1}$ and $T_{s,2}$, respectively with $T_{s,1} > T_{s,2}$. For steady-state conduction

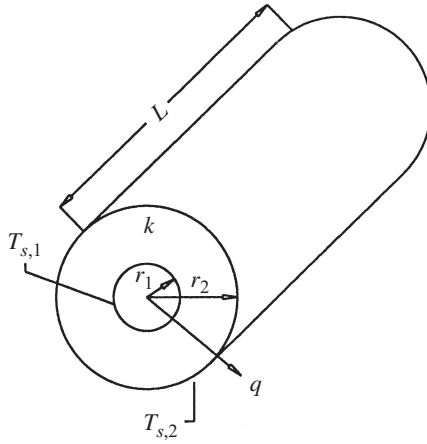


Figure 3.7 Radial conduction through a hollow cylinder.

in the radial direction with no internal heat generation and constant thermal conductivity, the appropriate form of the general heat conduction equation, eq. (3.5), is

$$\frac{d}{dr} \left(r \frac{dT}{dr} \right) = 0 \quad (3.69)$$

with the boundary conditions expressed as

$$T(r = r_1) = T_{s,1} \quad \text{and} \quad T(r = r_2) = T_{s,2} \quad (3.70)$$

Following the same procedure as that used for the plane wall will give the temperature distribution

$$T = T_{s,1} + \frac{T_{s,1} - T_{s,2}}{\ln(r_1/r_2)} \ln \frac{r}{r_1} \quad (3.71)$$

and the heat flow

$$q = \frac{2\pi k L (T_{s,1} - T_{s,2})}{\ln(r_2/r_1)} \quad (3.72)$$

3.4.3 Hollow Sphere

The description pertaining to the hollow cylinder also applies to the hollow sphere of Fig. 3.8 except that the length L is no longer relevant. The applicable form of eq. (3.6) is

$$\frac{d}{dr} \left(r^2 \frac{dT}{dr} \right) = 0 \quad (3.73)$$

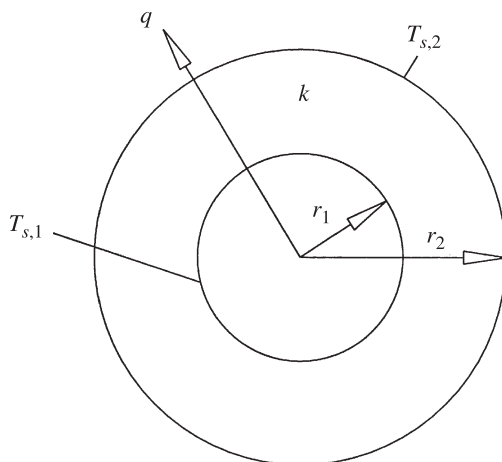


Figure 3.8 Radial conduction through a hollow sphere.

with the boundary conditions expressed as

$$T(r = r_1) = T_{s,1} \quad \text{and} \quad T(r = r_2) = T_{s,2} \quad (3.74)$$

The expressions for the temperature distribution and heat flow are

$$T = T_{s,1} + \frac{T_{s,1} - T_{s,2}}{1/r_2 - 1/r_1} \left(\frac{1}{r_1} - \frac{1}{r} \right) \quad (3.75)$$

$$q = \frac{4\pi k(T_{s,1} - T_{s,2})}{1/r_1 - 1/r_2} \quad (3.76)$$

3.4.4 Thermal Resistance

Thermal resistance is defined as the ratio of the temperature difference to the associated rate of heat transfer. This is completely analogous to electrical resistance, which, according to Ohm's law, is defined as the ratio of the voltage difference to the current flow. With this definition, the thermal resistance of the plane wall, the hollow cylinder, and the hollow sphere are, respectively,

$$R_{\text{cond}} = \frac{L}{kA} \quad (3.77)$$

$$R_{\text{cond}} = \frac{\ln(r_2/r_1)}{2\pi kL} \quad (3.78)$$

$$R_{\text{cond}} = \frac{1/r_1 - 1/r_2}{4\pi k} \quad (3.79)$$

When convection occurs at the boundaries of a solid, it is convenient to define the convection resistance from Newton's law of cooling:

$$q = hA(T_s - T_\infty) \quad (3.80)$$

where h is the convection heat transfer coefficient and T_∞ is the convecting fluid temperature. It follows from eq. (3.80) that

$$R_{\text{conv}} = \frac{T_s - T_\infty}{q} = \frac{1}{hA} \quad (3.81)$$

3.4.5 Composite Systems

The idea of thermal resistance is a useful tool for analyzing conduction through composite members.

Composite Plane Wall For the series composite plane wall and the associated thermal network shown in Fig. 3.9, the rate of heat transfer q is given by

$$q = \frac{T_{\infty,1} - T_{\infty,2}}{1/h_1A + L_1/k_1A + L_2/k_2A + 1/h_2A} \quad (3.82)$$

Once q has been determined, the surface and interface temperatures can be found:

$$T_{s,1} = T_{\infty,1} - q \frac{1}{h_1A} \quad (3.83)$$

$$T_2 = T_{\infty,1} - q \left(\frac{1}{h_1A} + \frac{L_1}{k_1A} \right) \quad (3.84)$$

$$T_{s,2} = T_{\infty,1} - q \left(\frac{1}{h_1A} + \frac{L_1}{k_1A} + \frac{L_2}{k_2A} \right) \quad (3.85)$$

Figure 3.10 illustrates a series-parallel composite wall. If materials 2 and 3 have comparable thermal conductivities, the heat flow may be assumed to be one-dimensional. The network shown in Fig. 3.10 assumes that surfaces normal to the direction of heat flow are isothermal. For a wall of unit depth, the heat transfer rate is

$$q = \frac{T_{s,1} - T_{s,2}}{L_1/k_1H_1 + L_2L_3/(k_2H_2L_3 + k_3H_3L_2) + L_4/k_4H_4} \quad (3.86)$$

where $H_1 = H_2 + H_3 = H_4$ and the rule for combining resistances in parallel has been employed. Once q has been determined, the interface temperatures may be computed:

$$T_1 = T_{s,1} - q \frac{L_1}{k_1H_1} \quad (3.87)$$

$$T_2 = T_{s,2} + q \frac{L_4}{k_4H_4} \quad (3.88)$$

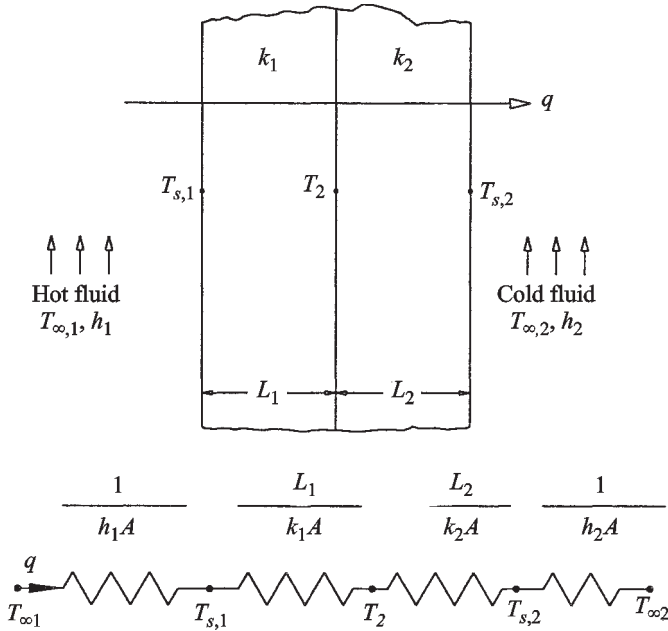


Figure 3.9 Series composite wall and its thermal network.

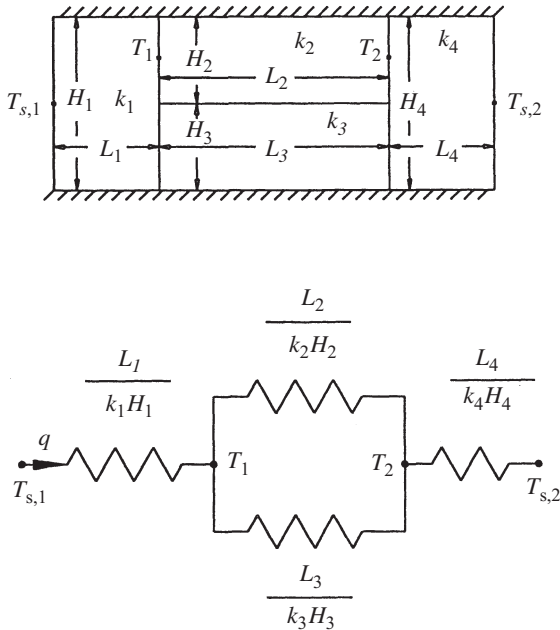


Figure 3.10 Series-parallel composite wall and its thermal network.

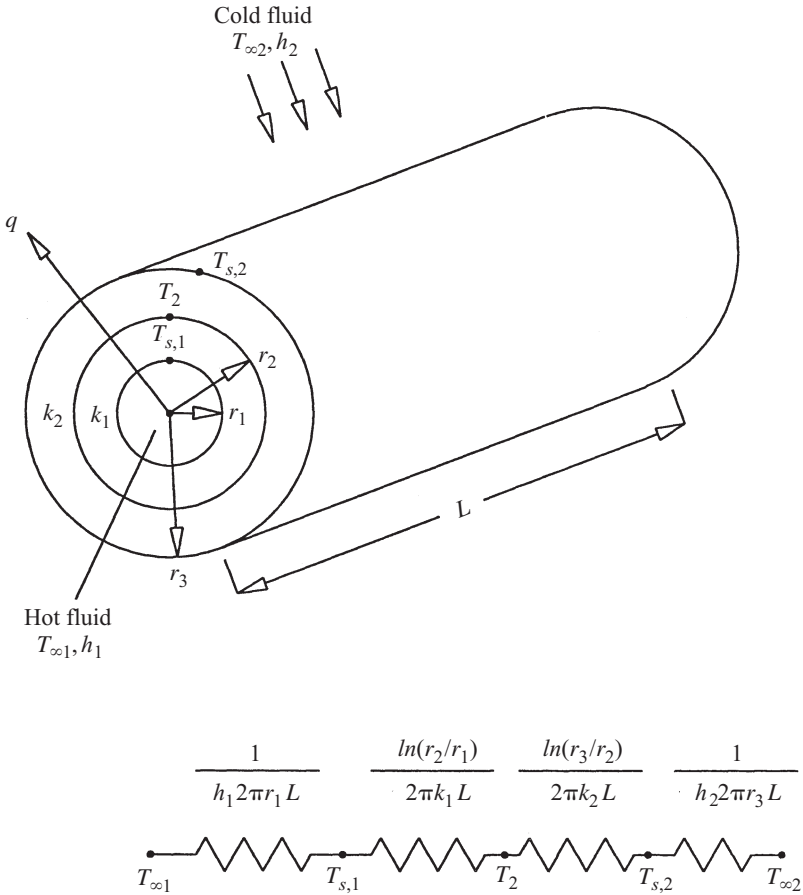


Figure 3.11 Series composite hollow cylinder and its thermal network.

Composite Hollow Cylinder A typical composite hollow cylinder with both inside and outside experiencing convection is shown in Fig. 3.11. The figure includes the thermal network that represents the system. The rate of heat transfer q is given by

$$q = \frac{T_{\infty,1} - T_{\infty,2}}{1/2\pi h_1 r_1 L + \ln(r_2/r_1)/2\pi k_1 L + \ln(r_3/r_2)/2\pi k_2 L + 1/2\pi h_2 r_3 L} \quad (3.89)$$

Once q has been determined, the inside surface $T_{s,1}$, the interface temperature T_2 , and the outside surface temperature $T_{s,2}$ can be found:

$$T_{s,1} = T_{\infty,1} - q \frac{1}{2\pi h_1 r_1 L} \quad (3.90)$$

$$T_2 = T_{\infty,1} - q \left[\frac{1}{2\pi h_1 r_1 L} + \frac{\ln(r_2/r_1)}{2\pi k_1 L} \right] \quad (3.91)$$

$$T_{s,2} = T_{\infty,2} + q \frac{1}{2\pi h_2 r_3 L} \quad (3.92)$$

Composite Hollow Sphere Figure 3.12 depicts a composite hollow sphere made of two layers and experiencing convective heating on the inside surface and convective cooling on the outside surface. From the thermal network, also shown in Fig. 3.12, the rate of heat transfer q can be determined as

$$q = \frac{T_{\infty,1} - T_{\infty,2}}{1/4\pi h_1 r_1^2 + (r_2 - r_1)/4\pi k_1 r_1 r_2 + (r_3 - r_2)/4\pi k_2 r_3 r_2 + 1/4\pi h_2 r_3^2} \quad (3.93)$$

Once q has been determined, temperatures $T_{s,1}$, T_2 , and $T_{s,2}$ can be found:

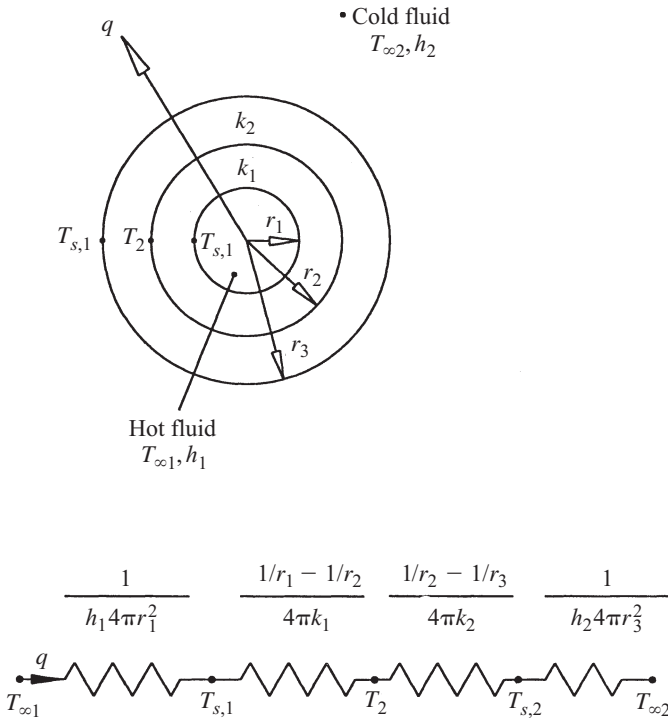


Figure 3.12 Series composite hollow sphere and its thermal network.

$$T_{s,1} = T_{\infty,1} - q \frac{1}{4\pi h_1 r_1^2} \quad (3.94)$$

$$T_2 = T_{\infty,1} - q \left[\frac{1}{4\pi h_1 r_1^2} + \frac{1}{4\pi k_1} \left(\frac{1}{r_1} - \frac{1}{r_2} \right) \right] \quad (3.95)$$

$$T_{s,2} = T_{\infty,2} + q \frac{1}{4\pi h_2 r_2^2} \quad (3.96)$$

3.4.6 Contact Conductance

The heat transfer analyses for the composite systems described in Section 3.4.5 assumed perfect contact at the interface between the two materials. In reality, however, the mating surfaces are rough and the actual contact occurs at discrete points (*asperities* or *peaks*), as indicated in Fig. 3.13. The gaps or voids are usually filled with air, and the heat transfer at the interface is the sum of solid conduction across the contact points and fluid conduction through the gaps. Because of the imperfect contact, there is a temperature drop across the gap or interface, ΔT_c . The contact conductance h_c ($\text{W/m}^2 \cdot \text{K}$) is defined as the ratio of the heat flux q/A through the interface to the interface temperature drop:

$$h_c = \frac{q/A}{\Delta T_c} = \frac{1}{R_c''} \quad (3.97)$$

where q/A is the heat flux through the interface and R_c'' ($\text{m}^2 \cdot \text{K/W}$), the inverse of h_c , is the contact resistance.

The topic of contact conductance is of considerable contemporary interest, as reflected by a review paper of Fletcher (1988), a book by Madhusudana (1996),

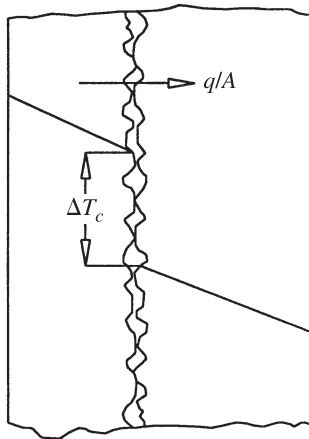


Figure 3.13 Contact interface for actual surfaces.

and numerous contributions from several research groups. Chapter 4 of this book is devoted exclusively to this subject.

3.4.7 Critical Thickness of Insulation

When a plane surface is covered with insulation, the rate of heat transfer always decreases. However, the addition of insulation to a cylindrical or spherical surface increases the conduction resistance but reduces the convection resistance because of the increased surface area. The *critical thickness of insulation* corresponds to the condition when the sum of conduction and convection resistances is a minimum. For a given temperature difference, this results in a maximum heat transfer rate, and the critical radius r_c is given by

$$r_c = \begin{cases} \frac{k}{h} & \text{(cylinder)} \\ \frac{2k}{h} & \text{(sphere)} \end{cases} \quad (3.98)$$

$$(3.99)$$

where k is the thermal conductivity of the insulation and h is the convective heat transfer coefficient for the outside surface.

The basic analysis for obtaining the critical radius expression has been modified to allow for:

- The variation of h with outside radius
- The variation of h with outside radius, including the effect of temperature-dependent fluid properties
- Circumferential variation of h
- Pure radiation cooling
- Combined natural convection and radiation cooling

The analysis for a circular pipe has also been extended to include insulation boundaries that form equilateral polygons, rectangles, and concentric circles. Such configurations require a two-dimensional conduction analysis and have led to the conclusion that the concept of critical perimeter of insulation, $P_c = 2\pi(k/h)$, is more general than that of critical radius. The comprehensive review article by Aziz (1997) should be consulted for further details.

3.4.8 Effect of Uniform Internal Energy Generation

In some engineering systems, it becomes necessary to analyze one-dimensional steady conduction with internal energy generation. Common sources of energy generation are the passage of an electric current through a wire or busbar or a rear window defroster in an automobile. In the fuel element of a nuclear reactor, the energy is generated due to neutron absorption. A vessel containing nuclear waste experiences energy generation as the waste undergoes a slow process of disintegration.

Plane Wall Consider first a plane wall of thickness $2L$, made of a material having a thermal conductivity k , as shown in Fig. 3.14. The volumetric rate of energy generation in the wall is \dot{q} (W/m^3). Let $T_{s,1}$ and $T_{s,2}$ be the two surface temperatures, and assuming the thermal conductivity of the wall to be constant, the appropriate form of eq. (3.4) is

$$\frac{d^2T}{dx^2} + \frac{\dot{q}}{k} = 0 \quad (3.100)$$

and the boundary conditions are

$$T(x = -L) = T_{s,1} \quad \text{and} \quad T(x = L) = T_{s,2} \quad (3.101)$$

The solution for the temperature distribution is

$$T = \frac{\dot{q}}{2k} (L^2 - x^2) + \frac{T_{s,2} - T_{s,1}}{2L}x + \frac{T_{s,2} + T_{s,1}}{2} \quad (3.102)$$

The maximum temperature occurs at $x = k(T_{s,2} - T_{s,1})/2L\dot{q}$ and is given by

$$T_{\max} = \frac{\dot{q}L^2}{2k} + \frac{k(T_{s,2} - T_{s,1})^2}{8\dot{q}L^2} + \frac{T_{s,2} + T_{s,1}}{2} \quad (3.103)$$

If the face at $x = -L$ is cooled by convection with a heat transfer coefficient h_1 and coolant temperature $T_{\infty,1}$, and the face at $x = +L$ is cooled by convection with a heat transfer coefficient h_2 and coolant temperature $T_{\infty,2}$, the overall energy balance gives

$$2\dot{q}L = h_1(T_{s,1} - T_{\infty,1}) + h_2(T_{s,2} - T_{\infty,2}) \quad (3.104)$$

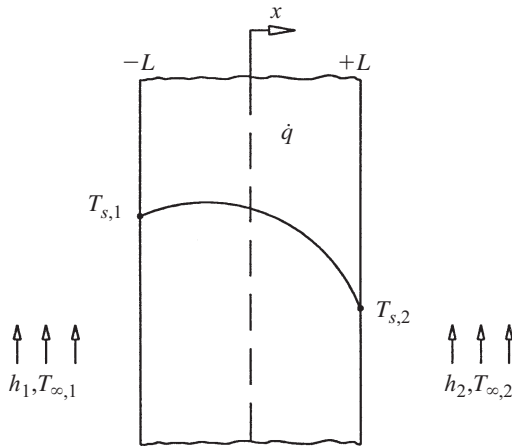


Figure 3.14 Conduction in a plane wall with uniform internal energy generation.

When $T_{s,1} = T_{s,2}$, the temperature distribution is symmetrical about $x = 0$ and is given by

$$T = \frac{\dot{q}}{2k} (L^2 - x^2) + T_s \quad (3.105)$$

and the maximum temperature occurs at the midplane ($x = 0$), which can be expressed as

$$T_{\max} = \frac{\dot{q}L^2}{2k} + T_s \quad (3.106)$$

When $T_{\infty,1} = T_{\infty,2} = T_{\infty}$ and $h_1 = h_2 = h$, eq. (3.104) reduces to

$$T_s - T_{\infty} = \frac{\dot{q}L}{h} \quad (3.107)$$

Hollow Cylinder For the hollow cylinder shown in Fig. 3.15, the appropriate form of eq. (3.5) for constant k is

$$\frac{1}{r} \frac{d}{dr} \left(r \frac{dT}{dr} \right) + \frac{\dot{q}}{k} = 0 \quad (3.108)$$

and the boundary conditions are

$$T(r = r_1) = T_{s,1} \quad \text{and} \quad T(r = r_2) = T_{s,2} \quad (3.109)$$

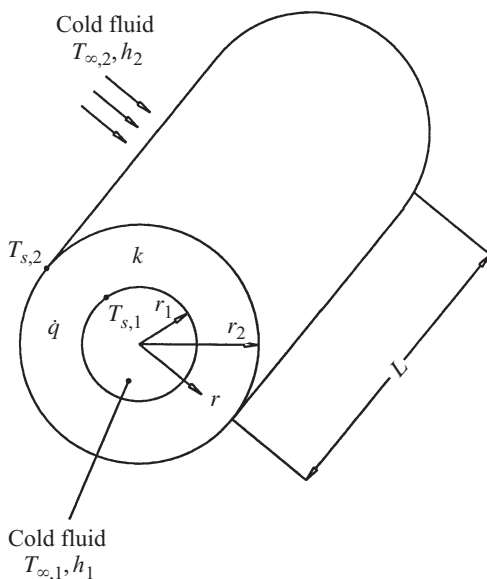


Figure 3.15 Conduction in a hollow cylinder with uniform internal energy generation.

The solution of eq. (3.108) that satisfies eqs. (3.109) is

$$T = T_{s,2} + \frac{\dot{q}r_2^2}{4k} \left[1 - \left(\frac{r}{r_2} \right)^2 \right] - \left\{ \frac{\dot{q}r_2^2}{4k} \left[1 - \left(\frac{r_1}{r_2} \right)^2 \right] + (T_{s,2} - T_{s,1}) \right\} \frac{\ln(r_2/r)}{\ln(r_2/r_1)} \quad (3.110)$$

If the inside and outside surfaces are cooled by convection, the inside with fluid at $T_{\infty,1}$ with heat transfer coefficient h_2 , the overall energy balance gives

$$\dot{q}(r_2^2 - r_1^2) = 2h_1r_1(T_{s,1} - T_{\infty,1}) + 2h_2r_2(T_{s,2} - T_{\infty,2}) \quad (3.111)$$

and for the case of $T_{s,1} = T_{s,2}$, eq. (3.110) is reduced to

$$T = T_s + \frac{\dot{q}r_2^2}{4k} \left[1 - \left(\frac{r}{r_2} \right)^2 \right] - \frac{\dot{q}r_2^2}{4k} \left[1 - \left(\frac{r_1}{r_2} \right)^2 \right] \frac{\ln(r_2/r)}{\ln(r_2/r_1)} \quad (3.112)$$

Similarly, when $T_{\infty,1} = T_{\infty,2} = T_{\infty}$ and $h_1 = h_2 = h$, eq. (3.111) is reduced to

$$T_s - T_{\infty} = \frac{\dot{q}(r_2 - r_1)}{2h} \quad (3.113)$$

Solid Cylinder Equation (3.108) also applies to the solid cylinder of Fig. 3.16, but the boundary conditions change to

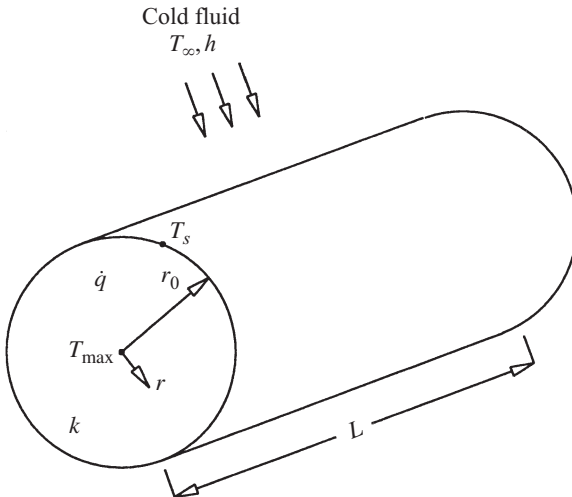


Figure 3.16 Conduction in a solid cylinder with uniform internal energy generation.

$$\left. \frac{dT}{dr} \right|_{r=0} = 0 \quad \text{and} \quad T(r = r_0) = T_s \quad (3.114)$$

The temperature distribution is given by

$$T = T_s + \frac{\dot{q}}{4k} (r_0^2 - r^2) \quad (3.115)$$

and the maximum temperature occurs along the centerline at $r = 0$:

$$T_{\max} = T_s + \frac{\dot{q}r_0^2}{4k} \quad (3.116)$$

If the outside surface of the cylinder is cooled by convection to a fluid at T_∞ through a heat transfer coefficient h , the overall energy balance gives

$$T_s - T_\infty = \frac{\dot{q}r_0}{2h} \quad (3.117)$$

Hollow Sphere For the hollow sphere shown in Fig. 3.17, the appropriate form of eq. (3.6) with constant thermal conductivity k is

$$\frac{1}{r^2} \frac{d}{dr} \left(r^2 \frac{dT}{dr} \right) + \frac{\dot{q}}{k} = 0 \quad (3.118)$$

and eq. (3.109) provides the boundary conditions

$$T(r = r_1) = T_{s,1} \quad \text{and} \quad T(r = r_2) = T_{s,2} \quad (3.109)$$

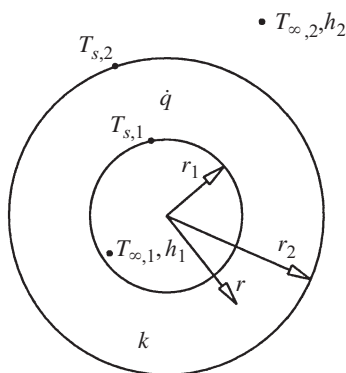


Figure 3.17 Conduction in a hollow sphere with uniform internal energy generation.

The temperature distribution is found to be

$$T = T_{s,2} + \frac{\dot{q}r_2^2}{6k} \left[1 - \left(\frac{r}{r_2} \right)^2 \right] - \left\{ \frac{\dot{q}r_2^2}{6k} \left[1 - \left(\frac{r_1}{r_2} \right)^2 \right] + (T_{s,2} - T_{s,1}) \right\} \frac{1/r - 1/r_2}{1/r_1 - 1/r_2} \quad (3.119)$$

If the inside and outside surfaces are cooled by convection, the inside with fluid at $T_{\infty,1}$ with heat transfer coefficient h_1 and the outside with fluid at $T_{\infty,2}$ with heat transfer coefficient h_2 , the overall energy balance gives

$$\frac{\dot{q} (r_2^3 - r_1^3)}{3} = h_1 r_1^2 (T_{s,1} - T_{\infty,1}) + h_2 r_2^2 (T_{s,2} - T_{\infty,2}) \quad (3.120)$$

and when $T_{s,1} = T_{s,2} = T_s$, eq. (3.119) reduces to

$$T = T_s + \frac{\dot{q}r_2^2}{6k} \left[1 - \left(\frac{r}{r_2} \right)^2 \right] - \frac{\dot{q}r_2^2}{6k} \left[1 - \left(\frac{r_1}{r_2} \right)^2 \right] \frac{1/r - 1/r_2}{1/r_1 - 1/r_2} \quad (3.121)$$

When $T_{\infty,1} = T_{\infty,2} = T_{\infty}$, and $h_1 = h_2 = h$, eq. (3.120) is reduced to

$$T_s - T_{\infty} = \frac{\dot{q} (r_2^3 - r_1^3)}{3h (r_1^2 + r_2^2)} \quad (3.122)$$

Solid Sphere For the solid sphere, eq. (3.118),

$$\frac{1}{r^2} \frac{d}{dr} \left(r^2 \frac{dT}{dr} \right) + \frac{\dot{q}}{k} = 0 \quad (3.118)$$

must be solved subject to the boundary conditions of eqs. (3.114):

$$\left. \frac{dT}{dr} \right|_{r=0} = 0 \quad \text{and} \quad T(r = r_0) = T_s \quad (3.114)$$

The solution is

$$T = T_s + \frac{\dot{q}}{6k} (r_0^2 - r^2) \quad (3.123)$$

The maximum temperature that occurs at the center of the sphere where $r = 0$ is

$$T_{\max} = T_s + \frac{\dot{q}r_0^2}{6k} \quad (3.124)$$

and if the cooling at the outside surface is to a fluid at T_∞ via a heat transfer coefficient of h , the overall energy balance gives

$$T_s - T_\infty = \frac{\dot{q}r_0}{3h} \quad (3.125)$$

For additional analytical results for one-dimensional steady conduction with uniform internal heat generation, the reader should consult Incropera and DeWitt (1996, App. C).

3.5 MORE ADVANCED STEADY ONE-DIMENSIONAL CONDUCTION

The results presented in Section 3.4 have been based on assumptions such as constant thermal conductivity, uniform heat generation, and pure convective cooling or heating at the boundary. In some applications, these assumptions may introduce significant errors in predicting the thermal behavior of the system.

The conducting medium may be nonhomogeneous, causing thermal conductivity to vary with location. Similarly, the temperature dependence of thermal conductivity cannot be ignored if the temperature difference driving the conduction process is large and the assumption of uniform heat generation may prove too restrictive. For example, when the shield of a nuclear reactor is irradiated with gamma rays, the resulting release of energy decays exponentially with distance from the irradiated surface, making the heat generation location dependent. A more realistic modeling of heat generation due to the passage of electric current or a chemical reaction requires that \dot{q} be treated as temperature dependent. Finally, if the heat transfer process at a boundary is driven by natural convection, radiation becomes equally important and must be taken into account. This section is devoted to a discussion of such situations.

3.5.1 Location-Dependent Thermal Conductivity

Plane Wall Consider the plane wall of Fig. 3.6 and let the thermal conductivity k increase linearly with x in accordance with

$$k = k_0(1 + ax) \quad (3.126)$$

where k_0 is the thermal conductivity at $x = 0$ and a is a measure of the variation of k with x . The equation governing the temperature distribution is

$$\frac{d}{dx} \left(k \frac{dT}{dx} \right) = 0 \quad (3.127)$$

Solving eq. (3.127) subject to the boundary conditions of eq. (3.66),

$$T(x = 0) = T_{s,1} \quad \text{and} \quad T(x = L) = T_{s,2} \quad (3.66)$$

gives

$$T = T_{s,1} + (T_{s,2} - T_{s,1}) \frac{\ln(1 + ax)}{\ln(1 + aL)} \quad (3.128)$$

and the rate of heat transfer will be

$$q = \frac{k_0 A a (T_{s,1} - T_{s,2})}{\ln(1 + aL)} \quad (3.129)$$

In the limit, as $a \rightarrow 0$, eqs. (3.128) and (3.129) reduce to eqs. (3.67) and (3.68), respectively.

Now consider the case where k is of the form

$$k = k_0(1 + ax^2) \quad (3.130)$$

The solutions for T and q are given by

$$T = T_{s,1} + (T_{s,2} - T_{s,1}) \frac{\arctan(\sqrt{ax})}{\arctan(\sqrt{aL})} \quad (3.131)$$

and the rate of heat transfer will be

$$q = \frac{k_0 A \sqrt{a} (T_{s,1} - T_{s,2})}{\arctan(\sqrt{aL})} \quad (3.132)$$

Hollow Cylinder When modified to allow for the location-dependent thermal conductivity of the form

$$k = a(1 + br) \quad (3.133)$$

analysis of Section 3.4.2 for a hollow cylinder (Fig. 3.7) gives the following results for the temperature distribution and the rate of heat transfer:

$$T = \frac{T_{s,1} \ln \left(\frac{r_2}{1 + br_2} \frac{1 + br}{r} \right) + T_{s,2} \ln \left(\frac{1 + br_1}{r_1} \frac{r}{1 + br} \right)}{\ln \left(\frac{1 + br_1}{1 + br_2} \frac{r_2}{r_1} \right)} \quad (3.134)$$

$$q = \frac{2\pi a L (T_{s,1} - T_{s,2})}{\ln \left(\frac{1 + br_1}{1 + br_2} \frac{r_2}{r_1} \right)} \quad (3.135)$$

When $b = 0$, $k = a$ and the thermal conductivity is constant. In this case, eqs. (3.134) and (3.135) are reduced to eqs. (3.71) and (3.72), respectively.

3.5.2 Temperature-Dependent Thermal Conductivity

Plane Wall Let the thermal conductivity k of the plane wall of Fig. 3.6 be a linear function of the temperature T , expressed as

$$k = k_0(1 + aT) \quad (3.136)$$

Equation (3.127) will then take the form

$$\frac{d}{dx} \left[k_0(1 + aT) \frac{dT}{dx} \right] = 0 \quad (3.137)$$

which must be integrated using the boundary conditions of eqs. (3.66):

$$T(x = 0) = T_{s,1} \quad \text{and} \quad T(x = L) = T_{s,2} \quad (3.66)$$

The solution is facilitated by the introduction of a new variable, T^* , defined by the Kirchhoff transformation:

$$T^* = \int_0^T (1 + aT) dT = T + \frac{1}{2}aT^2 \quad (3.138)$$

Differentiation of eq. (3.138) with respect to x gives

$$\frac{dT^*}{dx} = (1 + aT) \frac{dT}{dx} \quad (3.139)$$

which allows eq. (3.137) to be written as

$$\frac{d^2T^*}{dx^2} = 0 \quad (3.140)$$

The boundary conditions of eq. (3.66) in terms of T^* become

$$T_{s,1}^*(x = 0) = T_{s,1} + \frac{1}{2}aT_{s,1}^2 \quad \text{and} \quad T_{s,2}^*(x = L) = T_{s,2} + \frac{1}{2}aT_{s,2}^2 \quad (3.141)$$

The solution for T^* is

$$T^* = T_{s,1}^* + (T_{s,2}^* - T_{s,1}^*) \frac{x}{L} \quad (3.142)$$

Once T^* has been found, T can be reclaimed by solving the quadratic of eq. (3.138), which gives

$$T = \frac{1}{a} \left(-1 + \sqrt{1 + 2aT^*} \right) \quad (3.143)$$

and the rate of heat transfer can be shown to be

$$q = \frac{k_m A (T_{s,1} - T_{s,2})}{L} \quad (3.144)$$

where $k_m = k_0(1 + aT_{s,m})$ is the thermal conductivity at the mean temperature,

$$T_{s,m} = \frac{T_{s,1} + T_{s,2}}{2}$$

For a variation of the thermal conductivity with temperature represented by

$$k = k_0(1 + aT^2) \quad (3.145)$$

the temperature distribution in the plane wall (Fig. 3.6) is given by the cubic equation

$$T + \frac{1}{3}aT^3 = T_{s,1} + \frac{1}{3}aT_{s,1}^3 + \left[\frac{1}{3}a(T_{s,2}^3 - T_{s,1}^3) + (T_{s,2} - T_{s,1}) \right] \frac{x}{L} \quad (3.146)$$

and the corresponding rate of heat transfer is

$$q = \frac{Ak_0(T_{s,1} - T_{s,2}) \left[1 + (a/3)(T_{s,1}^2 + T_{s,1}T_{s,2} + T_{s,2}^2) \right]}{L} \quad (3.147)$$

Hollow Cylinder For the thermal conductivity–temperature relation of eq. (3.136), the Kirchhoff transformation of eq. (3.138) can also be used for the hollow cylinder of Fig. 3.7. The final result for T^* is

$$T^* = T_{s,1}^* + \frac{T_{s,1}^* - T_{s,2}^*}{\ln(r_1/r_2)} \ln \frac{r}{r_1} \quad (3.148)$$

where $T_{s,1}^*$ and $T_{s,2}^*$ are as given in eq. (3.141). Once T^* for any radius r is found from eq. (3.148), eq. (3.143) can be used to find the corresponding value of T . The rate of heat transfer then follows as

$$q = \frac{2\pi k_m L (T_{s,1} - T_{s,2})}{\ln(r_2/r_1)} \quad (3.149)$$

where k_m is the thermal conductivity at the mean temperature,

$$T_{s,m} = \frac{T_{s,1} + T_{s,2}}{2}$$

Hollow Sphere The results for a hollow sphere (Fig. 3.8) whose thermal conductivity–temperature variation follows eq. (3.136) are

$$T^* = T_{s,1}^* + \frac{T_{s,1}^* - T_{s,2}^*}{1/r_2 - 1/r_1} \left(\frac{1}{r_1} - \frac{1}{r} \right) \quad (3.150)$$

$$T = \frac{1}{a} \left(-1 + \sqrt{1 + 2aT^*} \right) \quad (3.151)$$

$$q = \frac{4\pi k_m (T_{s,1} - T_{s,2})}{1/r_1 - 1/r_2} \quad (3.152)$$

Gebhart (1993) provides one-dimensional steady conduction analyses for single and composite solids when the thermal conductivity varies simultaneously with location and temperature. He also gives expressions for the conduction resistances of a plane wall, a hollow cylinder, and a hollow sphere for three cases of variable thermal conductivity: $k = k(T)$, $k = k(x)$ or $k(r)$, and $k = k(x, T) = k(T)f(x)$. Note that the last case assumes that $k(x, T)$ can be expressed as a product of two functions, $k(T)$ and $f(x)$, each a function of a single variable.

3.5.3 Location-Dependent Energy Generation

Plane Wall Figure 3.18 presents a plane wall that experiences location-dependent energy generation of the form

$$\dot{q} = \dot{q}_0 \left(1 - \frac{x}{L} \right) \quad (3.153)$$

The temperature distribution in the wall is given by

$$T = T_{s,1} + \frac{\dot{q}_0 L x}{2k} - \frac{\dot{q}_0}{2k} \left(x^2 - \frac{x^3}{3L} \right) \quad (3.154)$$

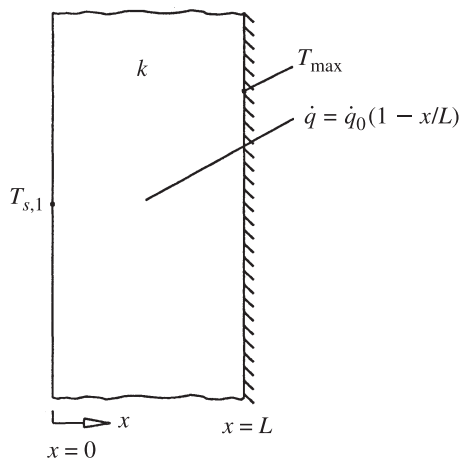


Figure 3.18 Plane wall with linearly decaying, location-dependent internal energy generation.

and the maximum temperature occurs at $x = L$ for an insulated face:

$$T = T_{s,1} + \frac{\dot{q}_0 L^2}{6k} \quad (3.155)$$

Next, assume that the plane wall of Fig. 3.6 represents the shield of a nuclear reactor. The absorption of gamma radiation at the left surface ($x = 0$) triggers energy release into the shield which decays exponentially with the penetration distance x and can be represented by the relation

$$\dot{q} = q_0'' a e^{-ax} \quad (3.156)$$

where q_0'' (W/m^2) is the incident radiation heat flux and a (m^{-1}) is the absorption coefficient of the shield.

The temperature distribution in the shield is

$$T = T_{s,1} + \frac{q_0''}{ak} (1 - e^{-ax}) + \left[(T_{s,2} - T_{s,1}) + \frac{q_0''}{ak} (e^{-aL} - 1) \right] \frac{x}{L} \quad (3.157)$$

and the maximum temperature occurs at

$$x = \frac{1}{a} \ln \frac{q_0'' a L}{ak(T_{s,1} - T_{s,2}) + q_0''(1 - e^{-aL})} \quad (3.158)$$

Solid Cylinder Reconsidering the solid cylinder of Fig. 3.16, \dot{q} will now be assumed to vary linearly with the radial distance r , that is,

$$\dot{q} = ar \quad (3.159)$$

where a (W/m^4) is a constant. The temperature distribution in this case is

$$T = T_\infty + \frac{ar_0^2}{3h} + \frac{a}{9k} (r_0^3 - r^3) \quad (3.160)$$

from which the centerline ($r = 0$) temperature T_c and the surface ($r = r_0$) temperature T_s follow as

$$T_c = T_\infty + \frac{ar_0^2}{3h} + \frac{ar_0^3}{9k} \quad (3.161)$$

$$T_s = T_\infty + \frac{ar_0^2}{3h} \quad (3.162)$$

3.5.4 Temperature-Dependent Energy Generation

In this section we present a collection of results for one-dimensional steady conduction in a plane wall, a solid cylinder, and a solid sphere when each experiences energy generation that increases linearly with local temperature in accordance with

$$\dot{q} = \dot{q}_s [1 + a(T - T_s)] \quad (3.163)$$

where \dot{q}_s is the energy generation at the surface temperature T_s and a is a constant.

Plane Wall For a plane wall of thickness $2L$ having identical surface temperatures T_s on both faces, the temperature distribution is

$$T = T_s + \frac{1}{a} \left(\frac{\cos nx}{\cos nL} - 1 \right) \quad (3.164)$$

where $n = \sqrt{a\dot{q}_s/k}$ and $nL < \pi/2$ to ensure that the temperatures remain finite.

If the convection cooling, characterized by the temperature T_∞ and heat transfer coefficient h , is identical on both faces of the wall, the relationship between T_s and T_∞ is given by

$$T_s = T_\infty + \frac{m}{h} \tan nL \quad (3.165)$$

where $m = \sqrt{\dot{q}_s k/a}$.

Solid Cylinder For a solid cylinder of radius r_0 , the temperature distribution is

$$T = T_s + \frac{1}{a} \left[\frac{J_0(nr)}{J_0(nr_0)} - 1 \right] \quad (3.166)$$

where $n = \sqrt{a\dot{q}_s/k}$ and J_0 is the Bessel function of the first kind of zero order (see Section 3.3.5). The parallel counterpart of eq. (3.165) is

$$T_s = T_\infty + \frac{m}{h} \frac{J_1(nr_0)}{J_0(nr_0)} \quad (3.167)$$

where $m = \sqrt{\dot{q}_s k/a}$, $n = \sqrt{a\dot{q}_s/k}$, and J_1 is the Bessel function of the first kind of order 1. In eqs. (3.166) and (3.167), $nr_0 < 2.4048$ to assure finite temperatures in the cylinder.

Solid Sphere For a solid sphere of radius r_0 , the temperature distribution is

$$T = T_s + \frac{1}{a} \left(\frac{r_0}{r} \frac{\sin nr}{\sin nr_0} - 1 \right) \quad (3.168)$$

where $nr_0 < \pi$ to assure finite temperatures in the sphere and the relationship between T_s and the coolant temperature T_∞ is

$$T = T_s + \frac{k}{hr_0 a} [1 - (nr_0) \cot nr_0] \quad (3.169)$$

where, here too, $nr_0 < \pi$ to assure finite temperatures in the sphere.

3.5.5 Radiative–Convective Cooling of Solids with Uniform Energy Generation

The solutions obtained in Section 3.4.8 for a plane wall (the thermal symmetry case), a solid cylinder, and a solid sphere are now extended to accommodate surface cooling by simultaneous convection and radiation. The surface energy balance for each geometry gives

$$h(T_s - T_\infty) + \epsilon\sigma(T_s^4 - T_\infty^4) + k \left. \frac{dT}{dx} \right|_{x=L} = 0 \quad (\text{plane wall}) \quad (3.170)$$

$$h(T_s - T_\infty) + \epsilon\sigma(T_s^4 - T_\infty^4) + k \left. \frac{dT}{dr} \right|_{r=r_0} = 0 \quad (\text{solid cylinder and sphere}) \quad (3.171)$$

where ϵ is the surface emissivity, σ the Stefan–Boltzmann constant, and T_∞ represents the surrounding or ambient temperature for both convection and radiation. In eqs. (3.170) and (3.171), the last terms can be evaluated using eqs. (3.105), (3.115), and (3.123), respectively.

Because eqs. (3.170) and (3.171) require a numerical approach for their solutions, it is convenient to recast them in dimensionless form as

$$N_1(\theta_s - 1) + N_2(\theta_s^4 - 1) + \left. \frac{d\theta}{dX} \right|_{X=1} = 0 \quad (\text{plane wall}) \quad (3.173)$$

$$N_1(\theta_s - 1) + N_2(\theta_s^4 - 1) + \left. \frac{d\theta}{dR} \right|_{R=1} = 0 \quad (\text{cylinder and sphere}) \quad (3.173)$$

where $\theta = T_s/T_\infty$, $N_1 = hL/k$ for the plane wall, $N_1 = hr_0/k$ for the cylinder and sphere, $N_2 = \epsilon\sigma T_\infty^3 L/k$ for the plane wall, and $N_2 = \epsilon\sigma T_\infty^3 r_0/k$ for the cylinder and sphere, $X = x/L$, $R = r/r_0$, and $\theta = T/T_\infty$. The numerical values for θ_s are given in Table 3.10 for a range of values of N_1 and N_2 and $\dot{q}L^2/kT_\infty = 1$ for the plane wall and $\dot{q}r_0^2/kT_\infty = 1$ for the cylinder and sphere.

3.6 EXTENDED SURFACES

The term *extended surface* is used to describe a system in which the area of a surface is increased by the attachment of *fins*. A fin accommodates energy transfer by conduction within its boundaries, while its exposed surfaces transfer energy to the surroundings by convection or radiation or both. Fins are commonly used to augment heat transfer from electronic components, automobile radiators, engine and compressor cylinders, control devices, and a host of other applications. A comprehensive treatment of extended surface technology is provided by Kraus et al. (2001).

In this section we provide the performance characteristics (temperature distribution, rate of heat transfer, and fin efficiency) for convecting, radiating, and convecting–radiating fins. Configurations considered include longitudinal fins, radial fins, and spines. The section concludes with a discussion of optimum fin designs.

TABLE 3.10 Dimensionless Surface Temperature in Solids with Uniform Energy Generation and Radiative–Convective Surface Cooling

N_1	N_2	θ_s		
		Plane Wall	Solid Cylinder	Solid Sphere
0.25	0.25	1.4597	1.2838	1.2075
0.50	0.25	1.4270	1.2559	1.1840
0.75	0.25	1.3970	1.2320	1.1646
1.00	0.25	1.3698	1.2115	1.1484
0.25	0.50	1.2993	1.1759	1.1254
0.50	0.50	1.2838	1.1640	1.1159
0.75	0.50	1.2693	1.1534	1.1076
1.00	0.50	1.2559	1.1439	1.1004
0.25	0.75	1.2258	1.1288	1.0905
0.50	0.75	1.2164	1.1221	1.0853
0.75	0.75	1.2075	1.1159	1.0807
1.00	0.75	1.1991	1.1103	1.0764
0.25	1.00	1.1824	1.1020	1.0710
0.50	1.00	1.1759	1.0976	1.0677
0.75	1.00	1.1698	1.0935	1.0647
1.00	1.00	1.1640	1.0897	1.0619

3.6.1 Longitudinal Convecting Fins

The five common profiles of longitudinal fins shown in Fig. 3.19 are rectangular, trapezoidal, triangular, concave parabolic, and convex parabolic. The analytical expressions obtained are based on several assumptions.

1. The heat conduction in the fin is steady and one-dimensional.
2. The fin material is homogeneous and isotropic.
3. There is no energy generation in the fin.
4. The convective environment is characterized by a uniform and constant heat transfer coefficient and temperature.
5. The fin has a constant thermal conductivity.
6. The contact between the base of the fin and the primary surface is perfect.
7. The fin has a constant base temperature.

Rectangular Fin For the rectangular fin (Fig. 3.19a), the temperature distribution, rate of heat transfer, and fin efficiency are given for five cases of thermal boundary conditions.

1. *Constant base temperature and convecting tip:*

$$\frac{\theta}{\theta_b} = \frac{\cosh m(b-x) + H \sinh m(b-x)}{\cosh mb + H \sinh mb} \tag{3.174}$$

$$q_f = kmA\theta_b \frac{\sinh mb + H \cosh mb}{\cosh mb + H \sinh mb} \quad (3.175)$$

$$q_{id} = (hPb + h_t A)_{\theta_b} \quad (3.176)$$

$$\eta = \frac{q_f}{q_{id}} \quad (3.177)$$

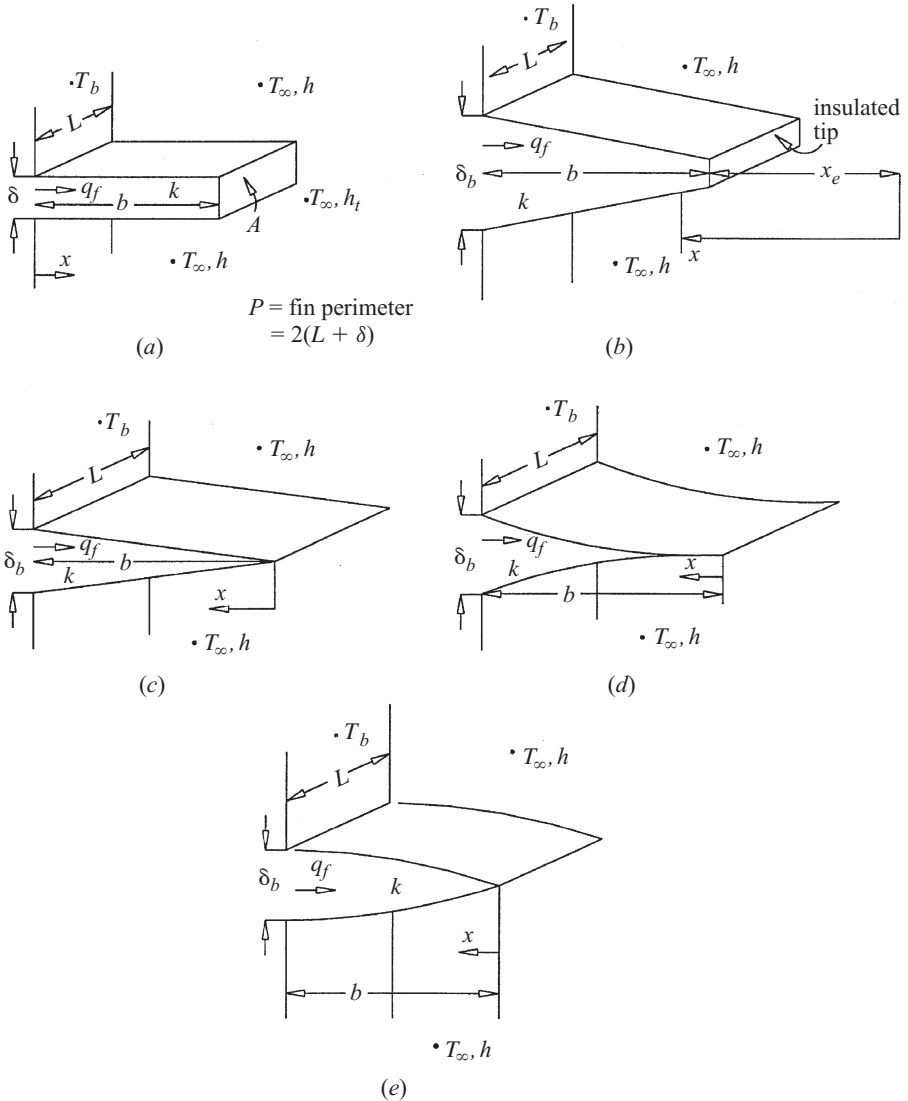


Figure 3.19 Longitudinal fins of (a) rectangular, (b) trapezoidal, (c) triangular, (d) concave parabolic, and (e) convex parabolic profiles.

where $\theta = T - T_\infty$, $\theta_b = T_b - T_\infty$, $m^2 = hP/kA = 2h/k\delta$, $H = h_t/km$, and T_b is the fin base temperature, T the fin temperature at location x , T_∞ the convective environmental temperature, b the fin height, A the fin cross-sectional area, P the fin perimeter, k the fin thermal conductivity, h the convective heat transfer coefficient for surfaces other than the fin tip, h_t the tip convective heat transfer coefficient, q_f the fin heat dissipation, and q_{id} the ideal fin heat dissipation.

2. *Constant base temperature and insulated tip ($H = 0$):*

$$\frac{\theta}{\theta_b} = \frac{\cosh m(b-x)}{\cosh mb} \quad (3.178)$$

$$q_f = kmA\theta_b \tanh mb \quad (3.179)$$

$$\eta = \frac{\tanh mb}{mb} \quad (3.180)$$

3. *Constant base and tip temperatures:*

$$\frac{\theta}{\theta_b} = \frac{(\theta_t/\theta_b) \sinh mx + \sinh m(b-x)}{\sinh mb} \quad (3.181)$$

$$q_f = kmA\theta_b \frac{\cosh mb - (\theta_t/\theta_b)}{\sinh mb} \quad (3.182)$$

with q_{id} and η given by eqs. (3.176) and (3.177), respectively, T_t taken as the prescribed tip temperature, and $\theta_t = T_t - T_\infty$.

4. *Convective heating at the base and insulated tip:*

$$\frac{\theta}{\theta_f} = \frac{\text{Bi} \cosh(mb-x)}{\text{Bi} \cosh mb + mb \sinh mb} \quad (3.183)$$

$$q_f = kmA\theta_f \frac{\text{Bi} \sinh mb}{\text{Bi} \cosh mb + mb \sinh mb} \quad (3.184)$$

where $\text{Bi} = h_f b/k$, $\theta_f = T_f - T_\infty$, and h_f and T_f characterize the convection process at the fin base. Equations (3.176) and (3.177) can be used to find q_{id} and η , but θ_b must be found first from eq. (3.183).

5. *Infinitely high fin with constant base temperature:*

$$\frac{\theta}{\theta_b} = e^{-mx} \quad (3.185)$$

$$q_f = kmA\theta_b \quad (3.186)$$

Because the fin is infinitely high, q_{id} and η cannot be calculated. Instead, one may calculate the *fin effectiveness* ϵ as the ratio of q_f to the rate of heat transfer from the *base surface* without the fin, $hA\theta_b$. Thus

$$\epsilon = \frac{q_f}{hA\theta_b} = \left(\frac{kP}{hA} \right)^{1/2} \quad (3.187)$$

Several important conclusions can be drawn from eq. (3.187). First, the fin effectiveness is enhanced by choosing a material with high thermal conductivity. Copper has a high value ($k = 401 \text{ W/m} \cdot \text{K}$ at 300K), but it is heavy and expensive. Aluminum alloys have lower k ($k = 168$ to $237 \text{ W/m} \cdot \text{K}$ at 300 K) but are lighter, offer lower cost, and in most instances are preferable to copper. Second, the fins are more effective when the convecting fluid is a gas (low h) rather than a liquid (higher h). Moreover, there is a greater incentive to use the fin under natural convection (lower h) than under forced convection (higher h). Third, the greater the perimeter/area (P/A) ratio, the higher the effectiveness. This, in turn, suggests the use of thin, closely spaced fins. However, the gap between adjacent fins must be sufficient to prevent interference of the boundary layers on adjacent surfaces.

Trapezoidal Fin For a constant base temperature and insulated tip, the temperature distribution, rate of heat transfer, ideal rate of heat transfer, and fin efficiency for a trapezoidal fin (Fig. 3.19b) are

$$\frac{\theta}{\theta_b} = \frac{I_0(2m\sqrt{bx})K_1(2m\sqrt{bx_e}) + K_0(2m\sqrt{bx})I_1(2m\sqrt{bx_e})}{I_0(2mb)K_1(2m\sqrt{bx_e}) + K_0(2mb)I_1(2m\sqrt{bx_e})} \quad (3.188)$$

$$q_f = km\delta_b L\theta_b \frac{I_1(2mb)K_1(2m\sqrt{bx_e}) - K_1(2mb)I_1(2m\sqrt{bx_e})}{I_0(2mb)K_1(2m\sqrt{bx_e}) + K_0(2mb)I_1(2m\sqrt{bx_e})} \quad (3.189)$$

$$q_{id} = 2Lbh\theta_b \quad (3.190)$$

and eq. (3.177) gives the fin efficiency. In eqs. (3.188) and (3.189), $m = \sqrt{2h/k\delta_b}$ and x_e is the distance to the fin tip. The modified Bessel functions appearing here and in subsequent sections are discussed in Section 3.3.5.

Triangular Fin The rectangular fin (Fig. 3.19c) is a special case of the trapezoidal fin with $x_e = 0$ and

$$\frac{\theta}{\theta_b} = \frac{I_0(2m\sqrt{bx})}{I_0(2mb)} \quad (3.191)$$

$$q_f = km\delta_b L\theta_b \frac{I_1(2mb)}{I_0(2mb)} \quad (3.192)$$

$$\eta = \frac{I_1(2mb)}{mbI_0(2mb)} \quad (3.193)$$

Concave Parabolic Fin For the concave parabolic fin shown in Fig. 2.19d, the temperature distribution, rate of heat transfer, and fin efficiency are

$$\frac{\theta}{\theta_b} = \left(\frac{x}{b}\right)^{-1/2+1/2(1+4m^2b^2)^{1/2}} \quad (3.194)$$

$$q_f = \frac{k\delta_b L\theta_b}{2b} \left[-1 + (1 + 4m^2b^2)^{1/2} \right] \quad (3.195)$$

$$\eta = \frac{2}{1 + (1 + 4m^2b^2)^{1/2}} \quad (3.196)$$

Convex Parabolic Fin For the convex parabolic fin shown in Fig. 3.19e, the temperature distribution, rate of heat transfer, and fin efficiency are

$$\frac{\theta}{\theta_b} = \left(\frac{x}{b}\right)^{1/4} \left[\frac{I_{-1/3} \left(\frac{4}{3}mb^{1/4}x^{3/4} \right)}{I_{-1/3} \left(\frac{4}{3}mb \right)} \right] \quad (3.197)$$

$$q_f = km\delta_b L\theta_b \frac{I_{2/3} \left(\frac{4}{3}mb \right)}{I_{-1/3} \left(\frac{4}{3}mb \right)} \quad (3.198)$$

$$\eta = \frac{1}{mb} \frac{I_{2/3} \left(\frac{4}{3}mb \right)}{I_{-1/3} \left(\frac{4}{3}mb \right)} \quad (3.199)$$

The efficiency of longitudinal fins of rectangular, triangular, concave parabolic, and convex parabolic fins are plotted as a function of mb in Fig. 3.20.

3.6.2 Radial Convecting Fins

The radial fin is also referred to as an *annular fin* or *circumferential fin*, and the performance of three radial fin profiles is considered. These are the rectangular, triangular, and hyperbolic profiles. Analytical results are presented for the rectangular profile, and graphical results are provided for all three profiles.

Rectangular Fin For the radial fin of rectangular profile shown in the inset of Fig. 3.21, the expressions for the temperature distribution, rate of heat transfer, and fin efficiency are

$$\frac{\theta}{\theta_b} = \frac{K_1(mr_a)I_0(mr) + I_1(mr_a)K_0(mr)}{I_0(mr_b)K_1(mr_a) + I_1(mr_a)K_0(mr_b)} \quad (3.200)$$

$$q_f = 2\pi r_b km\delta_b \frac{I_1(mr_a)K_1(mr_b) - K_1(mr_a)I_1(mr_b)}{I_0(mr_b)K_1(mr_a) + I_1(mr_a)K_0(mr_b)} \quad (3.201)$$

$$\eta = \frac{2r_b}{m(r_a^2 - r_b^2)} \frac{I_1(mr_a)K_1(mr_b) - K_1(mr_a)I_1(mr_b)}{I_0(mr_b)K_1(mr_a) + I_1(mr_a)K_0(mr_b)} \quad (3.202)$$

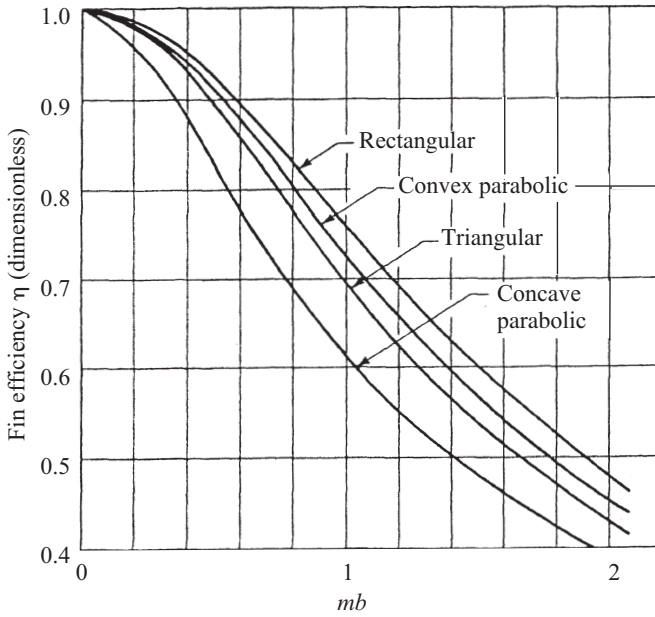


Figure 3.20 Efficiencies of longitudinal convecting fins.

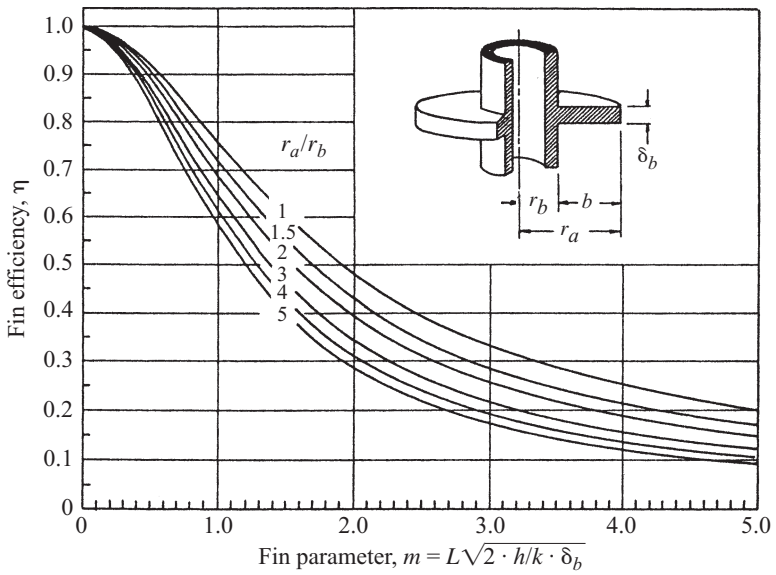


Figure 3.21 Efficiency of radial (annular) fins of rectangular profile. (Adapted from Ullman and Kalman, 1989.)

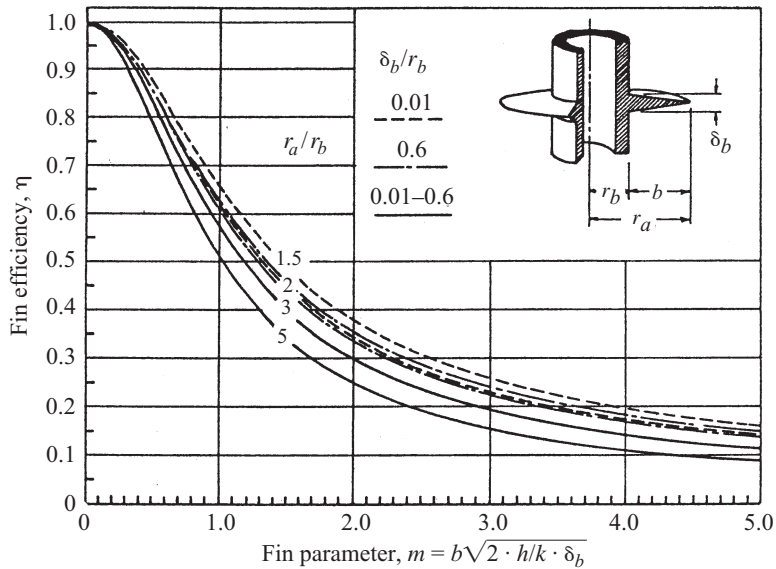


Figure 3.22 Efficiency of radial (annular) fins of triangular profile. (Adapted from Ullman and Kalman, 1989.)

The efficiency of a radial fin of rectangular profile given by eq. (3.202) is plotted as a function of mb in the main body of Fig. 3.21 for $r_a/r_b = 1$ (longitudinal fin), 1.5, 2.0, 3.0, 4.0, and 5.0.

Triangular Fin The inset in Fig. 3.22 shows a radial fin of triangular profile. The analysis for this profile is given in Kraus et al. (2001) and involves an infinite series that is omitted in favor of numerical results for the fin efficiency, which are graphed in Fig. 3.22. Note that η is a function of m , r_a/r_b , and δ_b/r_b . Once η is known, $q_f = 2\pi(r_a^2 - r_b^2)h\theta_b\eta$.

Hyperbolic Fin A radial fin of hyperbolic profile appears as an inset in Fig. 3.23. The lengthy analytical results are presented in Kraus et al. (2001) and a graph of the fin efficiency is presented in Fig. 3.23. Note that η is a function of m , r_a/r_b , and δ_b/r_b , and once η is known, $q_f = 2\pi(r_a^2 - r_b^2)h\theta_b\eta$.

3.6.3 Convecting Spines

Four commonly used shapes of spines, shown in Fig. 3.24, are the cylindrical, conical, concave parabolic, and convex parabolic. Analytical results for the temperature distribution, rate of heat transfer, and fin efficiency are furnished.

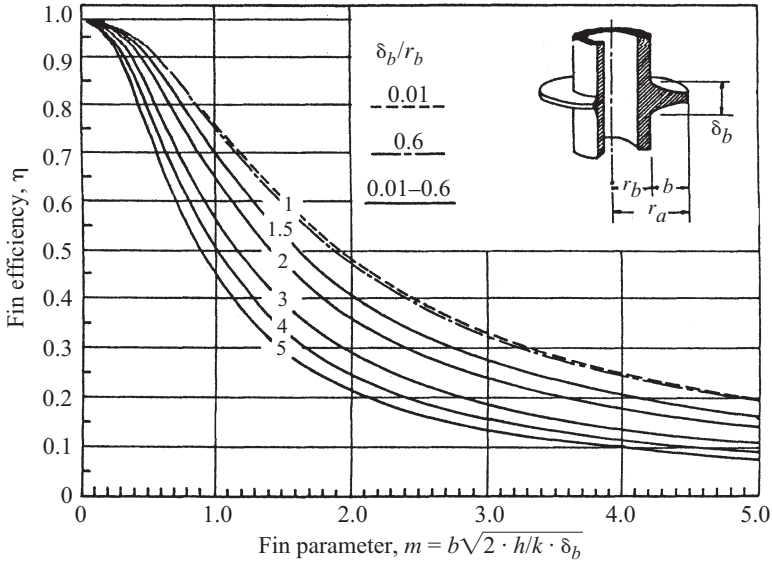


Figure 3.23 Efficiency of radial (annular) fins of hyperbolic profile. (Adapted from Ullman and Kalman, 1989.)

Cylindrical Spine For the cylindrical spine, the results for the rectangular fins are applicable if $m = (4h/kd)^{1/2}$ is used instead of $m = (2h/kδ)^{1/2}$. If the spine tip is insulated, eqs. (3.178)–(3.180) can be used.

Conical Spine

$$\frac{\theta}{\theta_b} = \left(\frac{b}{x}\right)^{1/2} \frac{I_1(2M\sqrt{x})}{I_1(2M\sqrt{b})} \quad (3.203)$$

$$q_f = \frac{\pi k d_b^2 M \theta_b}{4\sqrt{b}} \frac{I_2(2M\sqrt{b})}{I_1(2M\sqrt{b})} \quad (3.204)$$

$$\eta = \frac{2}{M\sqrt{b}} \frac{I_2(2M\sqrt{b})}{I_1(2M\sqrt{b})} \quad (3.205)$$

where $M = (4hb/kd_b)^{1/2}$.

Concave Parabolic Spine

$$\frac{\theta}{\theta_b} = \left(\frac{x}{b}\right)^{-3/2+1/2(9+4M^2)^{1/2}} \quad (3.206)$$

$$q_f = \frac{\pi k d_b^2 \theta_b [-3 + (9 + 4M^2)^{1/2}]}{8b} \quad (3.207)$$

$$\eta = \frac{2}{1 + (1 + \frac{8}{9}m^2b^2)^{1/2}} \quad (3.208)$$

where $M = (4hb/kd_b)^{1/2}$ and $m = (2h/kd_b)^{1/2}$.

Convex Parabolic Spine

$$\frac{\theta}{\theta_b} = \frac{I_0(\frac{4}{3}Mx^{3/4})}{I_0(\frac{4}{3}Mb^{3/4})} \quad (3.209)$$

$$q_f = \frac{\pi k d_b^2 M \theta_b}{2b^{1/4}} \frac{I_1(\frac{4}{3}Mb^{3/4})}{I_0(\frac{4}{3}Mb^{3/4})} \quad (3.210)$$

$$\eta = \frac{3}{2\sqrt{2}} \frac{I_1(\frac{4}{3}\sqrt{2}mb)}{mb I_0(\frac{4}{3}\sqrt{2}mb)} \quad (3.211)$$

where $M = (4hb^{1/2}/kd_b)^{1/2}$ and $m = (2h/kd_b)^{1/2}$.

Figure 3.25 is a plot of η as a function of mb for the four spines discussed.

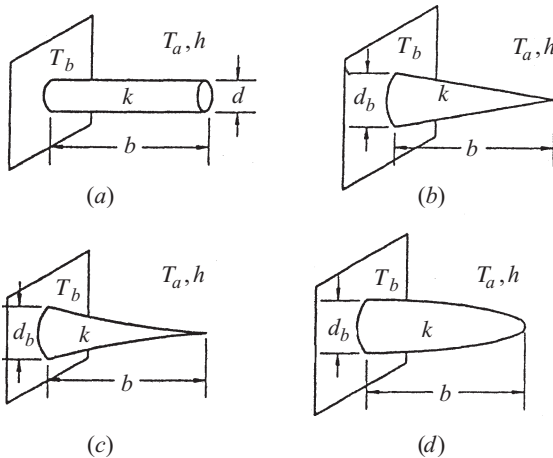


Figure 3.24 Spines: (a) cylindrical; (b) conical; (c) concave parabolic; (d) convex parabolic.

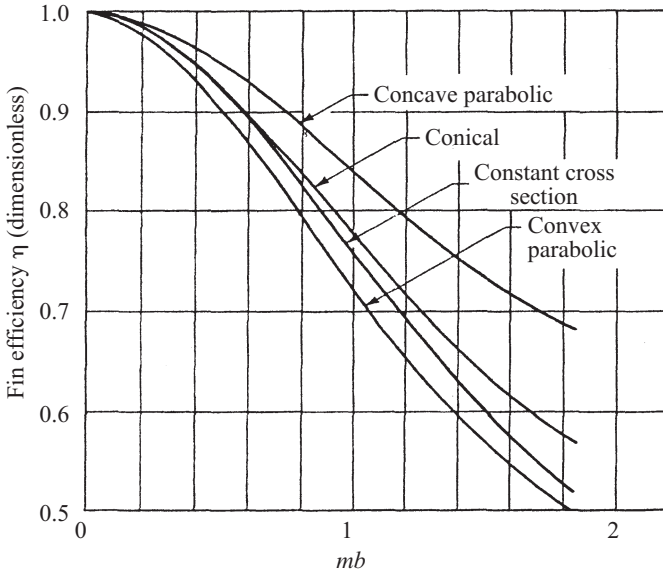


Figure 3.25 Efficiencies of convecting spines.

3.6.4 Longitudinal Radiating Fins

Unlike convecting fins, for which exact analytical solutions abound, few such solutions are available for radiating fins. Consider the longitudinal fin of rectangular profile shown in Fig. 3.19a and let the fin radiate to free space at 0 K. The differential equation governing the temperature in the fin is

$$\frac{d^2 T}{dx^2} = \frac{2\sigma\epsilon}{k\delta} T^4 \quad (3.212)$$

with the boundary conditions

$$T(x=0) = T_b \quad \text{and} \quad \left. \frac{dT}{dx} \right|_{x=b} = 0 \quad (3.213)$$

where ϵ is the emissivity of the fin surface and σ is the Stefan–Boltzmann constant ($\sigma = 5.667 \times 10^{-8} \text{ W/m}^2 \cdot \text{K}^4$).

The solution for the temperature distribution, rate of heat transfer, and fin efficiency are

$$B(0.3, 0.5) - B_u(0.3, 0.5) = b \left(\frac{20\sigma\epsilon T_i^3}{k\delta} \right)^{1/2} \quad (3.214)$$

$$q_f = 2k\delta L \left(\frac{\sigma\epsilon}{5k\delta} \right)^{1/2} (T_b^5 - T_i^5)^{1/2} \quad (3.215)$$

$$\eta = \frac{2k\delta L(\sigma\epsilon/5k\delta)^{1/2} \left(T_b^5 - T_i^5\right)^{1/2}}{2\sigma\epsilon bLT_b^4} \tag{3.216}$$

where B and B_u are complete and incomplete beta functions discussed in Section 3.3.3, $u = (T_i/T)^5$ and T_i is the unknown tip temperature. Because T_i is not known, the solution involves a trial-and-error procedure.

Sen and Trinh (1986) reported the solution of eqs. (3.212) and (3.213) when the surface heat dissipation is proportional to T^m rather than T^4 . Their solution appears in terms of hypergeometric functions which bear a relationship to the incomplete beta function. Kraus et al. (2001) provide an extensive collection of graphs to evaluate the performance of radiating fins of different profiles.

3.6.5 Longitudinal Convecting–Radiating Fins

A finite-difference approach was taken by Nguyen and Aziz (1992) to evaluate the performance of longitudinal fins (Fig. 3.19) of rectangular, trapezoidal, triangular, and concave parabolic profiles when the fin surface loses heat by simultaneous convection and radiation. For each profile, the performance depends on five parameters, $2b/\delta_b$, $h\delta_b/2k$, T_∞/T_b , T_s/T_b , and $2b^2\sigma\epsilon T_b^3/k\delta_b$, where T_s is the effective sink temperature for radiation. A sample result for the fin efficiency is provided in Table 3.11. These results reveal a more general trend—that a convecting–radiating fin has a lower efficiency than that of a purely convecting fin ($2b^2\sigma\epsilon T_b^3/k\delta_b = 0$).

3.6.6 Optimum Dimensions of Convecting Fins and Spines

The classical fin or spine optimization involves finding the profile so that for a prescribed volume, the fin or spine rate of heat transfer is maximized. Such optimizations result in profiles with curved boundaries that are difficult and expensive to fabricate. From a practical point of view, a better approach is to select the profile first and then find the optimum dimensions so that for a given profile area or volume, the fin or spine rate of heat transfer is maximized. The results of the latter approach are provided here. For each shape, two sets of expressions for optimum dimensions are given, one set for

TABLE 3.11 Efficiency of Longitudinal Convecting–Radiating Fins, $T_\infty/T_b = T_s/T_b = 0.8$, $2hb^2/k\delta_b = 1$

$2b^2\sigma\epsilon T_b^3/k\delta$	Rectangular	Trapezoidal $\delta t/\delta_b = 0.25$	Triangular	Concave Parabolic
0.00	0.6968	0.6931	0.6845	0.6240
0.20	0.4679	0.4677	0.4631	0.4244
0.40	0.3631	0.3644	0.3616	0.3324
0.60	0.3030	0.3051	0.3033	0.2811
0.80	0.2638	0.2666	0.2655	0.2471
1.00	0.2365	0.2396	0.2390	0.2233

when the profile area or volume is specified and another set for when the fin or spine rate of heat transfer is specified. Note that q_f for fins in the expressions to follow is the fin rate of heat transfer per unit length L of fin.

Rectangular Fin When the weight or profile area A_p is specified,

$$\delta_{\text{opt}} = 0.9977 \left(\frac{A_p^2 h}{k} \right)^{1/3} \quad (3.217)$$

$$b_{\text{opt}} = 1.0023 \left(\frac{A_p k}{h} \right)^{1/3} \quad (3.218)$$

and when the fin rate of heat transfer (per unit length) q_f is specified,

$$\delta_{\text{opt}} = \frac{0.6321 [q_f / (T_b - T_\infty)]^2}{hk} \quad (3.219)$$

$$b_{\text{opt}} = \frac{0.7978 q_f}{h(T_b - T_\infty)} \quad (3.220)$$

Triangular Fin When the weight or profile area A_p is specified,

$$\delta_{b,\text{opt}} = 1.6710 \left(\frac{A_p^2 h}{k} \right)^{1/3} \quad (3.221)$$

$$b_{\text{opt}} = 1.1969 \left(\frac{A_p k}{h} \right)^{1/3} \quad (3.222)$$

and when the fin rate of heat transfer (per unit length) q_f is specified,

$$\delta_{b,\text{opt}} = \frac{0.8273 [q_f / (T_b - T_\infty)]^2}{hk} \quad (3.223)$$

$$b_{\text{opt}} = \frac{0.8422 q_f}{h(T_b - T_\infty)} \quad (3.224)$$

Concave Parabolic Fin When the weight or profile area A_p is specified,

$$\delta_{\text{opt}} = 2.0801 \left(\frac{A_p^2 h}{k} \right)^{1/3} \quad (3.225)$$

$$b_{\text{opt}} = 1.4422 \left(\frac{A_p k}{h} \right)^{1/3} \quad (3.226)$$

and when the fin rate of heat transfer (per unit length) q_f is specified,

$$\delta_{b,\text{opt}} = \left(\frac{1}{hk} \right) \left[\frac{q_f}{(T_b - T_\infty)} \right]^2 \quad (3.227)$$

$$b_{\text{opt}} = \frac{q_f}{h(T_b - T_\infty)} \quad (3.228)$$

Cylindrical Spine When the weight or volume V is specified,

$$d_{\text{opt}} = 1.5031 \left(\frac{hV^2}{k} \right)^{1/5} \quad (3.229)$$

$$b_{\text{opt}} = 0.5636 \left(\frac{Vk^2}{h^2} \right)^{1/5} \quad (3.230)$$

and when the spine rate of heat transfer q_f is specified,

$$d_{\text{opt}} = 0.9165 \left[\frac{q_f^2}{hk(T_b - T_\infty)^2} \right]^{1/3} \quad (3.231)$$

$$b_{\text{opt}} = 0.4400 \left[\frac{q_f k}{h^2(T_b - T_\infty)} \right]^{1/3} \quad (3.232)$$

Conical Spine When the weight or volume V is specified,

$$d_{b,\text{opt}} = 1.9536 \left(\frac{hV^2}{k} \right)^{1/5} \quad (3.233)$$

$$b_{\text{opt}} = 1.0008 \left(\frac{Vk^2}{h^2} \right)^{1/5} \quad (3.234)$$

and when the spine rate of heat transfer q_f is specified,

$$d_{b,\text{opt}} = 1.0988 \left[\frac{q_f^2}{hk(T_b - T_\infty)^2} \right]^{1/3} \quad (3.235)$$

$$b_{\text{opt}} = 0.7505 \left[\frac{q_f k}{h^2(T_b - T_\infty)^2} \right]^{1/3} \quad (3.236)$$

Concave Parabolic Spine When the weight or volume V is specified,

$$d_{b,\text{opt}} = 2.0968 \left(\frac{hV^2}{k} \right)^{1/5} \quad (3.237)$$

$$b_{\text{opt}} = 1.4481 \left(\frac{Vk^2}{h^2} \right)^{1/5} \quad (3.238)$$

and when the spine rate of heat transfer q_f is specified,

$$d_{b,\text{opt}} = 1.1746 \left[\frac{q_f^2}{hk(T_b - T_\infty)^2} \right]^{1/3} \quad (3.239)$$

$$b_{\text{opt}} = 1.0838 \left[\frac{q_f k}{h^2(T_b - T_\infty)^2} \right]^{1/3} \quad (3.240)$$

Convex Parabolic Spine When the weight or volume V is specified,

$$d_{b,\text{opt}} = 1.7980 \left(\frac{hV^2}{k} \right)^{1/5} \quad (3.241)$$

$$b_{\text{opt}} = 0.7877 \left(\frac{Vk^2}{h^2} \right)^{1/5} \quad (3.242)$$

and when the spine rate of heat transfer q_f is specified,

$$d_{b,\text{opt}} = 1.0262 \left[\frac{q_f^2}{hk(T_b - T_\infty)^2} \right]^{1/3} \quad (3.243)$$

$$b_{\text{opt}} = 0.5951 \left[\frac{q_f k}{h^2(T_b - T_\infty)^2} \right]^{1/3} \quad (3.244)$$

The material presented here is but a small fraction of the large body of literature on the subject of optimum shapes of extended surfaces. The reader should consult Aziz (1992) for a comprehensive compilation of results for the optimum dimensions of convecting extended surfaces. Another article by Aziz and Kraus (1996) provides similar coverage for radiating and convecting–radiating extended surfaces. Both articles contain a number of examples illustrating the design calculations, and both are summarized in Kraus et al. (2001).

3.7 TWO-DIMENSIONAL STEADY CONDUCTION

The temperature field in a two-dimensional steady-state configuration is controlled by a second-order partial differential equation whose solution must satisfy four boundary conditions. The analysis is quite complex, and consequently, exact analytical solutions are limited to simple geometries such as a rectangular plate, a cylinder, and a sphere under highly restrictive boundary conditions. Problems that involve complex geometries and more realistic boundary conditions can only be solved by using an

approximate technique or a numerical method. Approximate techniques that are employed include the integral method, the method of scale analysis, and the method of conduction shape factors. The two most popular numerical techniques are the finite-difference and finite-element methods. There are numerous sources for information on approximate and numerical techniques, some of which are Bejan (1993), Ozisik (1993, 1994), Comini et al. (1994), and Jaluria and Torrance (1986). In the following section we provide an example of an exact solution, a table of conduction shape factors, and a brief discussion of the finite-difference method and its application to two-dimensional conduction in a square plate and a solid cylinder.

3.7.1 Rectangular Plate with Specified Boundary Temperatures

Figure 3.26 shows a rectangular plate with three sides maintained at a constant temperature T_1 , while the fourth side is maintained at another constant temperature, T_2 ($T_2 \neq T_1$). Defining

$$\theta = \frac{T - T_1}{T_2 - T_1} \quad (3.245)$$

the governing two-dimensional temperature distribution becomes

$$\frac{\partial^2 \theta}{\partial x^2} + \frac{\partial^2 \theta}{\partial y^2} = 0 \quad (3.246)$$

with the boundary conditions

$$\theta(0, y) = 1 \quad (3.247a)$$

$$\theta(x, 0) = 0 \quad (3.247b)$$

$$\theta(L, y) = 0 \quad (3.247c)$$

$$\theta(x, H) = 0 \quad (3.247d)$$

Use of the separation of variables method gives the solution for θ as

$$\theta = \frac{4}{\pi} \sum_{n=0}^{\infty} \frac{\sinh [(2n+1)\pi(L-x)/H]}{\sinh [(2n+1)\pi L/H]} \frac{\sin [(2n+1)\pi y/H]}{2n+1} \quad (3.248)$$

Using eq. (3.248), Bejan (1993) developed a network of isotherms and heat flux lines, which is shown in Fig. 3.27 for $H/L = 2$ (a rectangular plate) and for $H/L = 1$ (a square plate).

The heat flow into the plate from a hot left face is given by

$$\frac{q}{W} = \frac{8}{\pi} k(T_2 - T_1) \sum_{n=0}^{\infty} \frac{1}{(2n+1) \tanh [(2n+1)\pi L/H]} \quad (3.249)$$

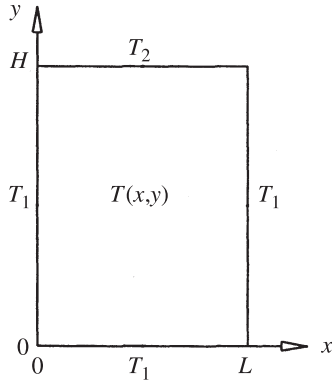


Figure 3.26 Two-dimensional steady conduction in a rectangular plate.

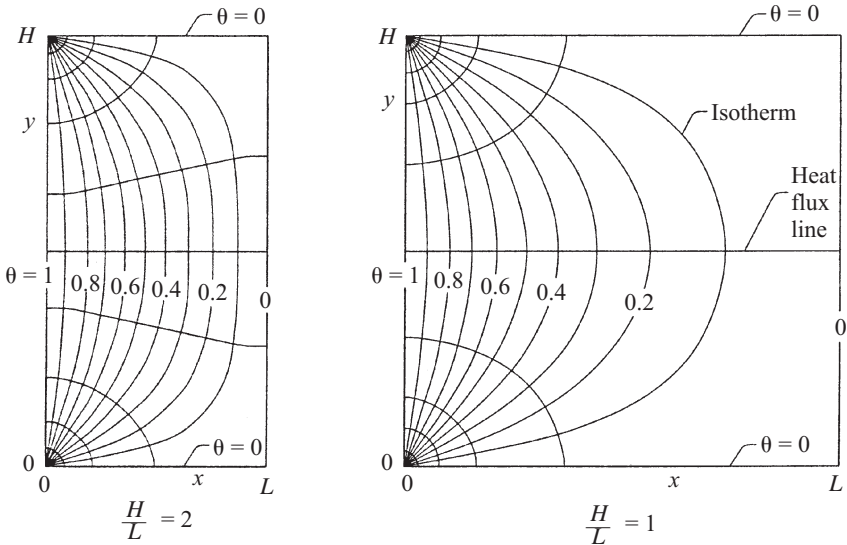


Figure 3.27 Isotherms and heat flux lines in a rectangular plate and a square plate. (From Bejan, 1993.)

where W is the plate dimension in the z direction. Solutions for the heat flux and convective boundary conditions are given in Ozisik (1993) and Poulidakos (1994).

3.7.2 Solid Cylinder with Surface Convection

Figure 3.28 illustrates a solid cylinder of radius r_0 and length L in which conduction occurs in both radial and axial directions. The face at $z = 0$ is maintained at a constant

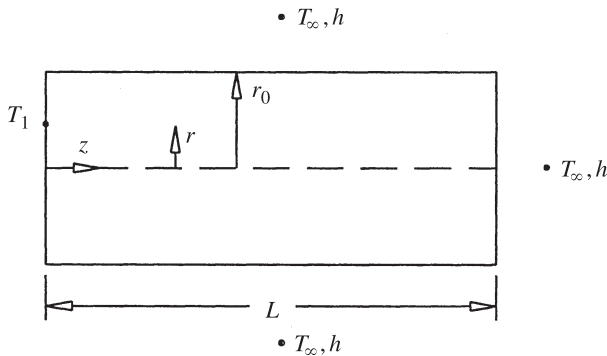


Figure 3.28 Radial and axial conduction in a hollow cylinder.

temperature T_1 , while both the lateral surface and the face at $z = L$ lose heat by convection to the environment at T_∞ via the heat transfer coefficient h . The system described represents a two-dimensional (r, z) convecting spine discussed by Aziz and Lunardini (1995). The equation governing the two-dimensional heat conduction in the cylinder is

$$\frac{\partial^2 \theta}{\partial R^2} + \frac{1}{R} \frac{\partial \theta}{\partial R} + \frac{\partial^2 \theta}{\partial Z^2} = 0 \quad (3.250)$$

where

$$\theta = \frac{T - T_\infty}{T_1 - T_\infty} \quad R = \frac{r}{r_0} \quad Z = \frac{z}{L} \quad \gamma = \frac{L}{r_0}$$

and Bi is the *Biot number*, $\text{Bi} = hr_0/k$. The boundary conditions are

$$\theta(R, 0) = 1 \quad (3.251a)$$

$$\frac{\partial \theta}{\partial R}(0, Z) = 0 \quad (3.251b)$$

$$\frac{\partial \theta}{\partial R}(1, Z) = -\text{Bi} \cdot \theta(1, Z) \quad (3.251c)$$

$$\frac{\partial \theta}{\partial R}(R, 1) = -\text{Bi} \cdot \gamma \theta(R, 1) \quad (3.251d)$$

The solution obtained via the separation of the variables is

$$\theta = \sum_{n=1}^{\infty} \frac{2\lambda_n J_1(\lambda_n) J_0(\lambda_n R)}{(\lambda_n^2 + \text{Bi}^2) [J_0(\lambda_n)]^2} (\cosh \lambda_n \gamma Z - \gamma \sinh \lambda_n \gamma Z) \quad (3.252)$$

where

$$\Upsilon = \frac{\lambda_n \sinh \lambda_n \gamma + \text{Bi} \cosh \lambda_n \gamma}{\lambda_n \cosh \lambda_n \gamma + \text{Bi} \sinh \lambda_n \gamma}$$

and where J_0 and J_1 are the Bessel functions of the first kind (Section 3.3.5) and the eigenvalues λ_n are given by

$$\lambda_n J_1(\lambda_n) = \text{Bi} \cdot J_0(\lambda_n) \quad (3.253)$$

The heat flow into the cylinder from the hot left face is

$$q = 4\pi k r_0 (T_1 - T_\infty) \sum_{n=1}^{\infty} \frac{\lambda_n [J_1(\lambda_n)]^2}{(\lambda_n^2 + \text{Bi}^2) [J_0(\lambda_n)]^2} \Upsilon \quad (3.254)$$

A three-dimensional plot of θ as a function of r and z is shown in Fig. 3.29 for $r_0 = 1$, $L = 1$, and $h/k = 1$. This plot was generated using Maple V, Release 5.0. As expected, the temperature decreases along both the radial and axial directions. Ozisik (1993) has devoted a complete chapter to the method of separation of variables in cylindrical coordinates and provides solutions for several other configurations.

3.7.3 Solid Hemisphere with Specified Base and Surface Temperatures

Poulikakos (1994) considers a hemispherical droplet condensing on a cold horizontal surface as shown in Fig. 3.30. The heat conduction equation for the two-dimensional (r, θ) steady-state temperature distribution in the droplet is given by

$$\frac{\partial}{\partial r} \left(r^2 \frac{\partial \phi}{\partial r} \right) + \frac{1}{\sin \theta} \frac{\partial}{\partial \theta} \left(\sin \theta \frac{\partial \phi}{\partial \theta} \right) = 0 \quad (3.255)$$

where $\phi = T - T_c$. Two of the boundary conditions are

$$\theta(r_0, \theta) = T_s - T_c = \phi_s \quad (3.256a)$$

$$\phi \left(r, \frac{\pi}{2} \right) = 0 \quad (3.256b)$$

Because the boundary condition at $r = 0$ falls on the $\theta = \pi/2$ plane, which is the base of the hemispherical droplet, it must meet the boundary condition of eq. (3.256b), that is,

$$\phi \left(r, \frac{\pi}{2} \right) = 0 \quad (3.256c)$$

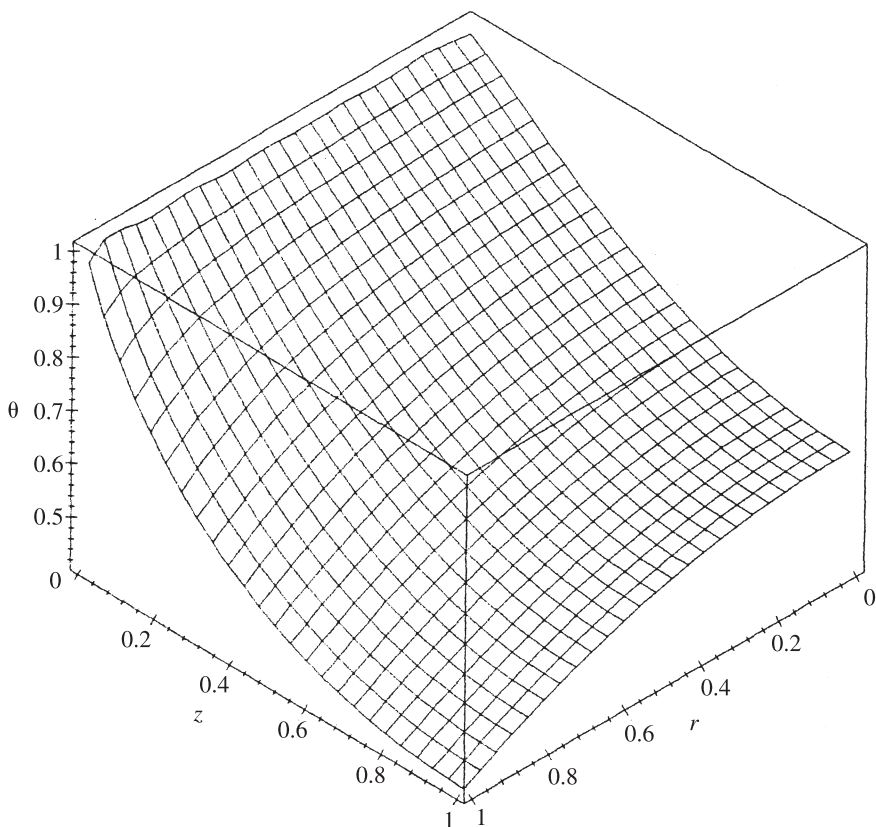


Figure 3.29 Three-dimensional plot of the temperature distribution in a solid cylinder. (From Aziz, 2001.)

The fourth boundary condition at $\theta = 0$ is obtained by invoking the condition of thermal symmetry about $\theta = 0$, giving

$$\frac{\partial \phi}{\partial \theta}(r, 0) = 0 \quad (3.256d)$$

Use of the method of separation of the variables provides the solution for ϕ as

$$\phi = \phi_s \sum_{n=1}^{\infty} \left[P_{n+1}(1) - P_{n-1}(1) - P_{n+1}(0) + P_{n-1}(0) \right] \left(\frac{r}{r_0} \right)^n P_n(\cos \theta) \quad (3.257)$$

where the P 's are the Legendre functions of the first kind, discussed in Section 3.3.6.

Ozisik (1993) may be consulted for a comprehensive discussion of the method of separation of the variables in spherical coordinates.

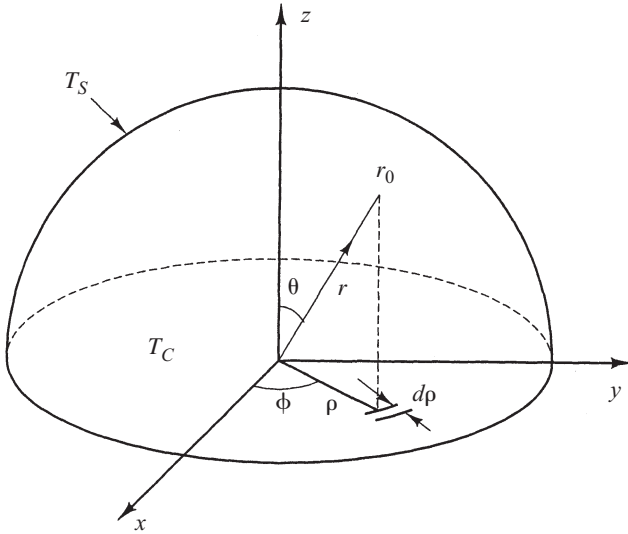


Figure 3.30 Hemispherical droplet condensing on an isothermal surface. (Adapted from Poulikakos, 1994.)

3.7.4 Method of Superposition

The configuration considered in the preceding section involved one nonhomogeneous boundary condition [either eq. (3.247a), (3.251a), or (3.256a)]. When two or more nonhomogeneous boundary conditions occur, the analysis can be split into two subanalyses each containing one nonhomogeneous boundary condition. Each subanalysis can then be solved using the method of separation of the variables, and the sum of the solutions to the two subanalyses will provide the solution to the overall problem. This approach is illustrated in Fig. 3.31 for a rectangular plate with two homogeneous boundary conditions.

The mathematical description of the problem is

$$\frac{\partial^2 \theta}{\partial x^2} + \frac{\partial^2 \theta}{\partial y^2} = 0 \quad (3.258)$$

where $\theta = T - T_3$. The boundary conditions are

$$\theta(0, y) = \theta_1 = T_1 - T_3 \quad (3.259a)$$

$$\theta(x, 0) = \theta_2 = T_2 - T_3 \quad (3.259b)$$

$$\theta(L, y) = 0 \quad (3.259c)$$

$$\theta(x, H) = 0 \quad (3.259d)$$

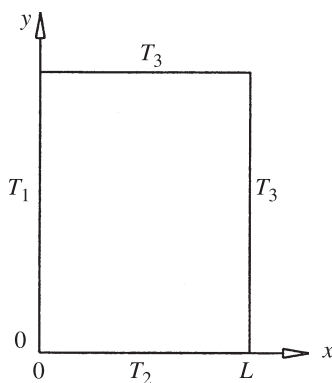


Figure 3.31 Rectangular plate with two nonhomogeneous boundary conditions.

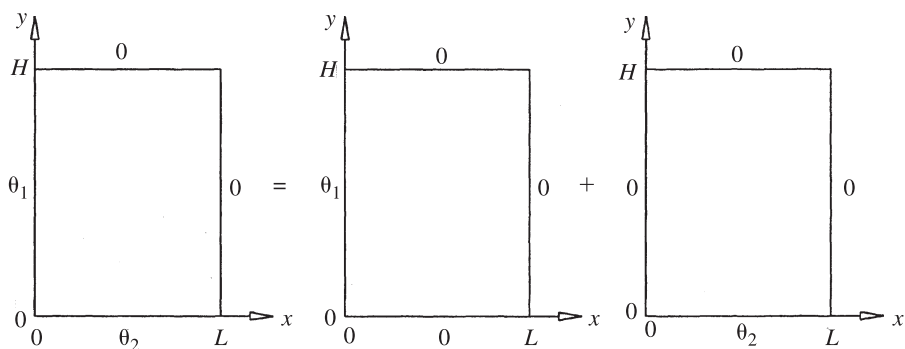


Figure 3.32 Splitting the problem of Fig. 3.31 into two subproblems with known solutions.

The problem is split into two subproblems, as indicated in Fig. 3.32, and the two solutions can be obtained from eq. (3.248) with appropriate adjustment to account for the definition of θ and the coordinates, x and y . The sum of the two solutions is

$$\begin{aligned} \theta = & \frac{4\theta_1}{\pi} \sum_{n=0}^{\infty} \frac{\sinh [(2n+1)\pi(L-x)/H]}{\sinh [(2n+1)\pi L/H]} \frac{\sin [(2n+1)(\pi y/H)]}{2n+1} \\ & + \frac{4\theta_2}{\pi} \sum_{n=0}^{\infty} \frac{\sinh [(2n+1)\pi(H-y)/L]}{\sinh [(2n+1)(\pi H/L)]} \frac{\sin [(2n+1)(\pi x/L)]}{2n+1} \end{aligned} \quad (3.260)$$

3.7.5 Conduction Shape Factor Method

Although the conduction shape factor method does not give the temperature distribution, it provides a simple equation for the rate of heat transfer:

$$q = kS \Delta T \quad (3.261)$$

where k is the thermal conductivity of the conducting medium, ΔT the temperature difference driving the heat flow, and S the conduction shape factor. Table 3.12 provides expressions for the conduction shape factor for various two-dimensional configurations.

The conduction resistance for a two-dimensional system follows from eq. (3.261) as

$$R_{\text{cond}} = \frac{1}{Sk} \quad (3.262)$$

3.7.6 Finite-Difference Method

Cartesian Coordinates In the finite-difference approach, the conducting region is covered with a grid consisting of intersecting lines. The points of intersection are called *nodes*. For a rectangular region, the grid lines are drawn parallel to the boundaries. For simplicity, the spacings Δx and Δy are chosen so that $\Delta x = \Delta y$. Nodes are identified by double-subscript notation, ij , where i and j count the grid lines along the x - and y -coordinate directions, respectively. The node i, j , which represents a particular subvolume, is presumed to be isothermal at the temperature, $T_{i,j}$. In Fig. 3.33, five different types of nodes are identified together with their control volumes, which are shown as dashed enclosures. The finite-difference approximation for each type of node is given here with the control volume assumed to have no energy generation.

1. *Internal node:*

$$-T_{i,j} + \frac{1}{4}(T_{i+1,j} + T_{i,j+1} + T_{i-1,j} + T_{i,j-1}) = 0 \quad (3.263)$$

2. *Node on plane convecting surface:*

$$2T_{i-1,j} + T_{i,j-1} + T_{i,j+1} + \frac{2h \Delta x}{k} T_{\infty} - 2 \left(\frac{h \Delta x}{k} + 2 \right) T_{i,j} = 0 \quad (3.264)$$

3. *External corner node with convection:*

$$T_{i,j-1} + T_{i-1,j} + \frac{2h \Delta x}{k} T_{\infty} - 2 \left(1 + \frac{h \Delta x}{k} \right) T_{i,j} = 0 \quad (3.265)$$

4. *Internal corner node with convection:*

$$\begin{aligned} 2(T_{i,j-1} + T_{i,j+1}) + T_{i+1,j} + T_{i,j-1} + \frac{2h \Delta x}{k} T_{\infty} \\ - 2 \left(3 + \frac{h \Delta x}{k} \right) T_{i,j} = 0 \end{aligned} \quad (3.266)$$

TABLE 3.12 Conduction Shape Factors for Selected Two-Dimensional Systems
[$q = Sk(T_1 - T_2)$]

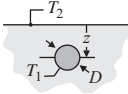
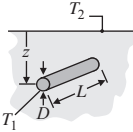
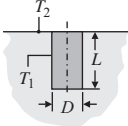
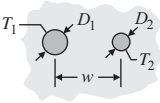
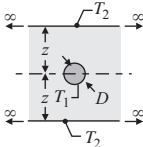
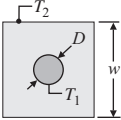
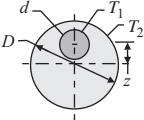
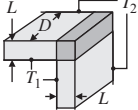
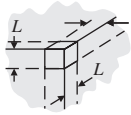
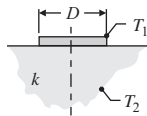
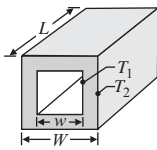
System	Schematic	Restrictions	Shape Factor
Case 1: Isothermal sphere buried in a semi-infinite medium		$z > D/2$	$\frac{2\pi D}{1 - D/4z}$
Case 2: Horizontal isothermal cylinder of length L buried in a semi-infinite medium		$L \gg D$ $L \gg D$ $z > 3D/2$	$\frac{2\pi L}{\cosh^{-1}(2z/D)}$ $\frac{2\pi L}{\ln(4z/D)}$
Case 3: Vertical cylinder in a semi-infinite medium		$L \gg D$	$\frac{2\pi L}{\ln(4L/D)}$
Case 4: Conduction between two cylinders of length L in infinite medium		$L \gg D_1, D_2$ $L \gg w$	$\frac{2\pi L}{\cosh^{-1}\left(\frac{4w^2 - D_1^2 - D_2^2}{2D_1 D_1}\right)}$
Case 5: Horizontal circular cylinder of length L midway between parallel planes of equal length and infinite width		$z \gg D/2$ $L \gg z$	$\frac{2\pi L}{\ln(8z/\pi D)}$
Case 6: Circular cylinder of length L centered in a square solid of equal length		$w > D$ $L \gg w$	$\frac{2\pi L}{\ln(1.08w/D)}$
Case 7: Eccentric circular cylinder of length L in a cylinder of equal length		$D > d$ $L \gg D$	$\frac{2\pi L}{\cosh^{-1}\left(\frac{D^2 + d^2 - 4z^2}{2Dd}\right)}$
Case 8: Conduction through the edge of adjoining walls		$D > L/5$	$0.54D$

TABLE 3.12 Conduction Shape Factors for Selected Two-Dimensional Systems
[$q = Sk(T_1 - T_2)$] (Continued)

System	Schematic	Restrictions	Shape Factor
Case 9: Conduction through corner of three walls with a temperature difference ΔT_{1-2} across the wall		$L \ll \text{length and width of wall}$	$0.15L$
Case 10: Disk of diameter D and T_1 on a semi-infinite medium of thermal conductivity k and T_2		None	$2D$
Case 11: Square channel of length L		$\frac{W}{w} < 1.4$ $\frac{W}{w} > 1.4$	$\frac{2\pi L}{0.785 \ln(W/w)}$ $\frac{2\pi L}{0.930(W/w) - 0.050}$

5. Node on a plane surface with a uniform heat flux:

$$(2T_{i+1,j} + T_{i,j+1} + T_{i,j-1}) + \frac{2q'' \Delta x}{k} - 4T_{i,j} = 0 \quad (3.267)$$

In eqs. (3.264)–(3.266), $h = 0$ applies to a node on an adiabatic boundary and $h = \infty$ applies to a node on an isothermal boundary.

By writing an appropriate finite-difference approximation for each node in the grid, a set of n -linear algebraic equations (one for each of the n nodes) in the unknown node temperatures can be produced. A standard numerical procedure or a computer code can be used to solve the system of equations giving the temperatures at all the nodes.

Consider the square plate shown in Fig. 3.34. For $\Delta x = \Delta y = 0.1/16 = 0.00625$ m, the finite-difference solution generated by Aziz (2001) gives the temperatures on the convecting surface. For $j = 1, 3, 5, 7, \dots, 17$,

$T_{17,j} = 67.85, 68.24, 70.19, 73.24, 77.13, 81.67, 86.81, 92.66$, and 100.00 all in $^{\circ}\text{C}$.

Cylindrical Coordinates Consider the solid cylinder of radius r_0 and length L (Fig. 3.35) in which steady conduction occurs along the r and z directions. The conduction equation is

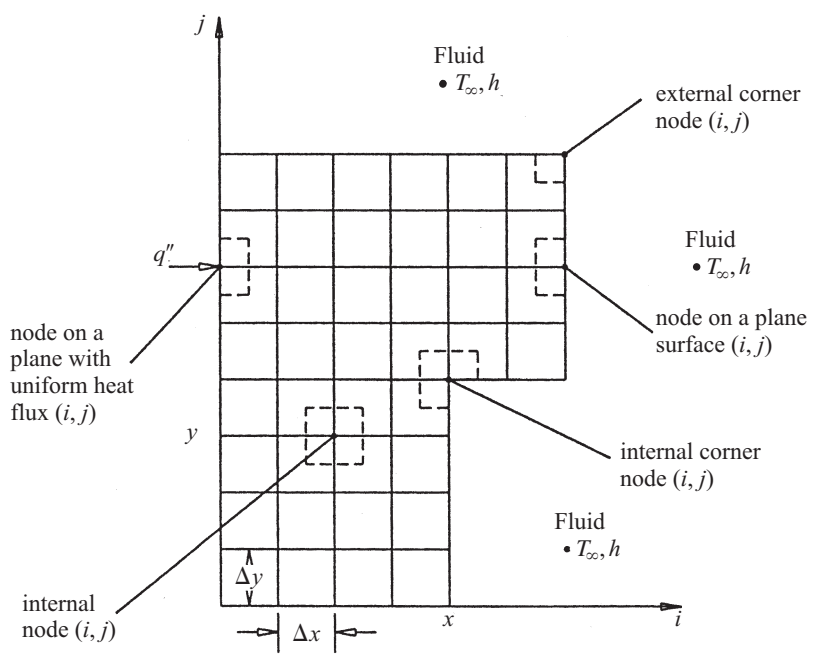


Figure 3.33 Types of nodes and the corresponding control volumes.

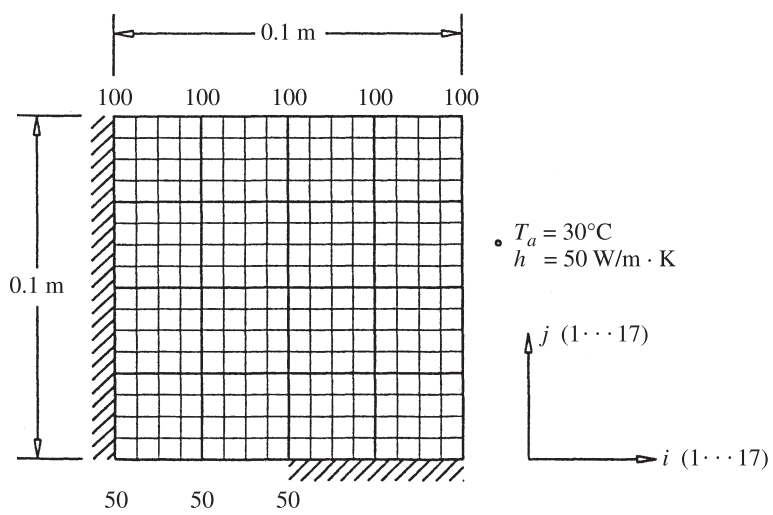


Figure 3.34 Grid for two-dimensional conduction in a square plate.

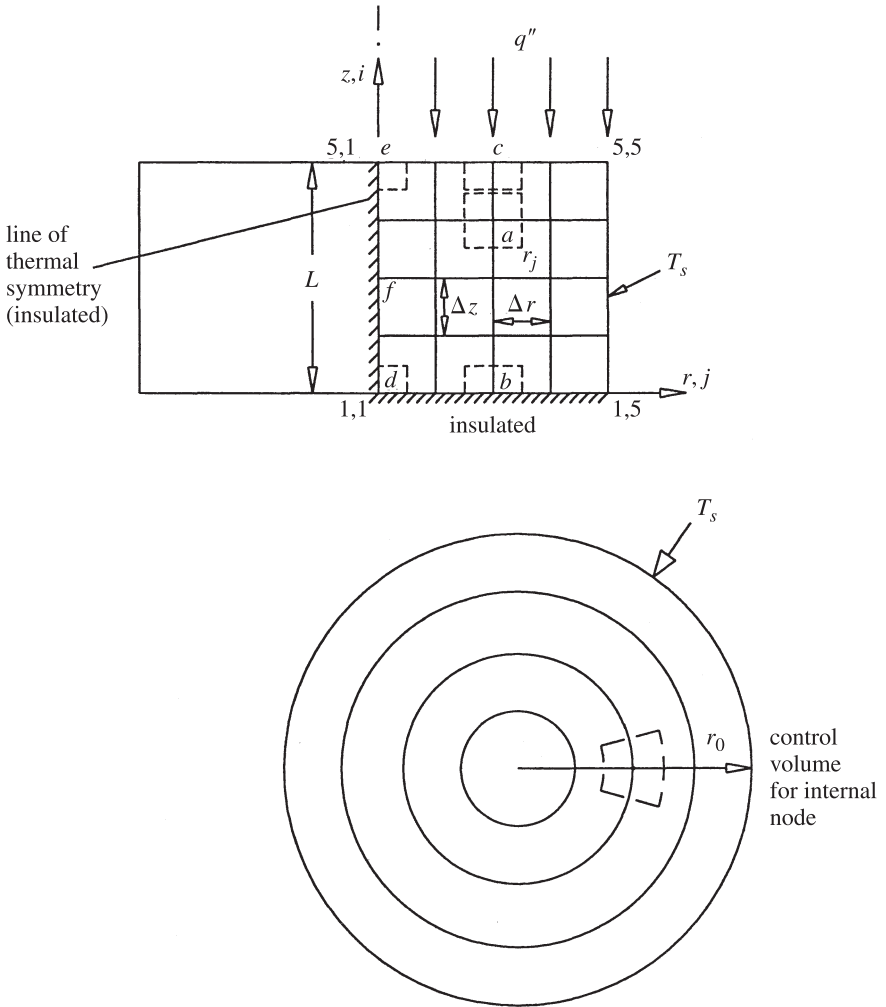


Figure 3.35 Finite-difference grid for radial and axial conduction in a solid cylinder with six different types of nodes.

$$\frac{\partial^2 T}{\partial r^2} + \frac{1}{r} \frac{\partial T}{\partial r} + \frac{\partial^2 T}{\partial z^2} = 0 \quad (3.268)$$

Let the outer surface temperature of the cylinder be T_s . The face at $z = 0$ is insulated while the face at $z = L$ experiences a constant heat flux q'' . This description gives the boundary conditions

$$\frac{\partial T(0,z)}{\partial r} = 0 \quad (\text{thermal symmetry}) \quad (3.269a)$$

$$T(r_0, z) = T_s \quad (3.269b)$$

$$\frac{\partial T(r, 0)}{\partial z} = 0 \quad (3.269c)$$

$$\frac{\partial T(r, L)}{\partial z} = q'' \quad (3.269d)$$

Six different nodes (*a*, *b*, *c*, *d*, *e*, and *f*) have been identified in Fig. 3.35. The finite-difference approximations for these nodes are as follows:

1. *Node a (internal node):*

$$-T_{i,j} + \frac{1}{4} \left[\left(1 - \frac{\Delta r}{2r_j}\right) T_{i,j-1} + \left(1 + \frac{\Delta r}{2r_j}\right) T_{i,j+1} + T_{i+1,j} + T_{i-1,j} \right] = 0 \quad (3.270)$$

2. *Node b (node on an insulated surface, $z = 0$):*

$$-T_{i,j} + \frac{1}{4} \left[2T_{i+1,j} + \left(1 - \frac{\Delta r}{2r_j}\right) T_{i,j-1} + \left(1 + \frac{\Delta r}{2r_j}\right) T_{i,j+1} \right] = 0 \quad (3.271)$$

3. *Node c (node on a constant heat flux surface, $z = L$):*

$$\begin{aligned} -T_{i,j} + \frac{1}{4} \left[\left(1 - \frac{\Delta r}{2r_j}\right) T_{i,j-1} + \left(1 + \frac{\Delta r}{2r_j}\right) T_{i,j+1} + 2T_{i-1,j} \right] \\ + \frac{q'' \Delta r}{2k} = 0 \end{aligned} \quad (3.272)$$

4. *Node d (node at the corner of two insulated surfaces):*

$$-T_{i,j} + \frac{1}{3} (T_{i+1,j} + 2T_{i,j+1}) = 0 \quad (i = 1, j = 1) \quad (3.273)$$

5. *Node e (node at the corner of an insulated surface and a constant heat flux surface):*

$$-T_{i,j} + \frac{1}{3} \left(T_{i-1,j} + 2T_{i,j+1} + \frac{q'' \Delta r}{k} \right) = 0 \quad (3.274)$$

6. *Node f (node on the longitudinal axis):*

$$-T_{i,j} + \frac{1}{6} (T_{i-1,j} + T_{i+1,j} + 4T_{i,j+1}) = 0 \quad (3.275)$$

Taking $r_0 = 1\text{m}$, $L = 1\text{m}$, $T_s = 25^\circ\text{C}$, $k = 20\text{W/m} \cdot \text{K}$, and $q'' = 1000\text{W/m}^2$, Aziz (2001) produced the following temperatures at the 20 nodes shown in Fig. 3.35:

$T_{1,1} = 31.03^\circ\text{C}$	$T_{3,3} = 32.33^\circ\text{C}$
$T_{1,2} = 30.54^\circ\text{C}$	$T_{3,4} = 28.95^\circ\text{C}$
$T_{1,3} = 29.14^\circ\text{C}$	$T_{4,1} = 41.42^\circ\text{C}$
$T_{1,4} = 27.13^\circ\text{C}$	$T_{4,2} = 40.43^\circ\text{C}$
$T_{2,1} = 32.02^\circ\text{C}$	$T_{4,3} = 37.38^\circ\text{C}$
$T_{2,2} = 31.46^\circ\text{C}$	$T_{4,4} = 32.15^\circ\text{C}$
$T_{2,3} = 29.87^\circ\text{C}$	$T_{5,1} = 51.59^\circ\text{C}$
$T_{2,4} = 27.53^\circ\text{C}$	$T_{5,2} = 50.42^\circ\text{C}$
$T_{3,1} = 35.24^\circ\text{C}$	$T_{5,3} = 46.69^\circ\text{C}$
$T_{3,2} = 34.50^\circ\text{C}$	$T_{5,4} = 39.35^\circ\text{C}$

A thorough discussion of the finite-difference method appears in Ozisik (1994). The book also features a large number of examples.

3.8 TRANSIENT CONDUCTION

The term *transient conduction* is used when the temperature in a heat conduction process depends on both time and the spatial coordinates. Three models that are commonly used to study transient conduction are the lumped thermal capacity model, the semi-infinite solid model and the finite-sized model. The finite-difference method provides one of many numerical methods that are used to analyze complicated configurations.

3.8.1 Lumped Thermal Capacity Model

The lumped thermal capacity model assumes that spatial temperature variations within the body are negligible and the temperature variation is solely a function of time. Consider a body of arbitrary shape of volume V , surface area A_s , density ρ , and specific heat c , initially at a temperature T_i , as indicated in Fig. 3.36. At time $t \geq 0$, the body is immersed in a convective environment (T_∞, h) , where $T_\infty < T_i$, and allowed to cool. The differential equation describing the cooling process is

$$\rho V c \frac{dT}{dt} = -h A_s (T - T_\infty) \quad (3.276)$$

with the initial condition

$$T(t = 0) = T_i \quad (3.277)$$

The solution is

$$\frac{T - T_\infty}{T_i - T_\infty} = e^{-h A_s t / \rho V c} \quad (3.278)$$

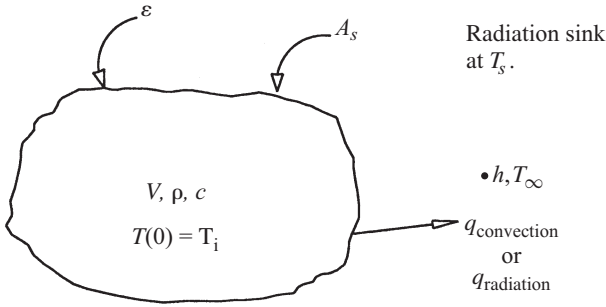


Figure 3.36 Cooling of a lumped thermal capacity body.

and the cumulative energy transfer to the coolant Q over a period of time t is

$$Q = \rho V c (T_i - T_\infty) (1 - e^{-h A_s t / \rho V c}) \quad (3.279)$$

The lumped thermal capacity model is valid for $Bi = hV/kA_s < 0.10$, a condition that is met in many engineering applications, such as the annealing of metals.

Attention now turns to some refinements of the basic lumped thermal capacity model.

Internal Energy Generation If the body experiences uniform thermal energy generation \dot{E}_g (W) at time $t = 0$, the temperature variation in the body is given by

$$\frac{\dot{E}_g - h A_s (T - T_\infty)}{\dot{E}_g - h A_s (T_i - T_\infty)} = e^{-h A_s t / \rho V c} \quad (3.280)$$

This situation occurs when an electronic component is suddenly energized.

Temperature-Dependent Specific Heat If the specific heat varies linearly with temperature, that is,

$$c = c_\infty [1 \pm \beta (T - T_\infty)] \quad (3.281)$$

the temperature variation given by Aziz and Hamad (1977) is

$$\ln \frac{T - T_\infty}{T_i - T_\infty} \pm \beta (T_i - T_\infty) \frac{T - T_i}{T_i - T_a} = -\frac{h A_s t}{\rho V c_\infty} \quad (3.282)$$

Pure Radiation Cooling If the body is cooled solely by radiation, the term $h A_s (T - T_\infty)$ is replaced in eq. (3.276) by $\epsilon \sigma A_s (T^4 - T_s^4)$, where ϵ is the surface emissivity and T_s is the effective sink temperature for radiation. The solution for T in this case is given by Aziz and Hamad (1977):

$$\ln \left(\frac{T_s + T}{T_s - T} \frac{T_s - T_i}{T_s + T_i} \right) + 2 \left(\arctan \frac{T}{T_s} - \arctan \frac{T_i}{T_s} \right) = \frac{4\epsilon\sigma A_s T_s^3 t}{\rho V c} \quad (3.283)$$

Equation (3.283) is useful, for example, in designing liquid droplet radiation systems for heat rejection on a permanent space station.

Simultaneous Convective–Radiative Cooling In this case, the radiative term, $-\sigma A_s(T^4 - T_s^4)$ appears on the right-hand side of eq. (3.276) in addition to $-hA_s(T - T_\infty)$. An exact solution for this case does not exist except when $T_\infty = T_s = 0$. For this special case the exact solution is

$$\frac{1}{3} \ln \left[\frac{1 + (\epsilon\sigma T_i^3)/h(T/T_i)^3}{(1 + \epsilon\sigma T_i^3/h)(T/T_i)^3} \right] = \frac{hA_s t}{\rho V c} \quad (3.284)$$

Temperature-Dependent Heat Transfer Coefficient For natural convection cooling, the heat transfer coefficient is a function of the temperature difference, and the functional relationship is

$$h = C(T - T_\infty)^n \quad (3.285)$$

where C and n are constants. Using eq. (3.285) in (3.276) and solving the resulting differential equation gives

$$\frac{T - T_\infty}{T_i - T_\infty} = \left(1 + \frac{nh_i A_s t}{\rho V c} \right)^{-1/n} \quad (3.286)$$

where $n \neq 0$ and $h_i = C(T_i - T_\infty)^n$.

Heat Capacity of the Coolant Pool If the coolant pool has a finite heat capacity, the heat transfer to the coolant causes T_∞ to increase. Denoting the properties of the hot body by subscript 1 and the properties of the coolant pool by subscript 2, the temperature–time histories as given by Bejan (1993) are

$$T_1(t) = T_1(0) - \frac{T_1(0) - T_2(0)}{1 + \rho_1 V_1 c_1 / \rho_2 V_2 c_2} (1 - e^{-nt}) \quad (3.287)$$

$$T_2(t) = T_2(0) + \frac{T_1(0) + T_2(0)}{1 + (\rho_2 V_2 c_2 / \rho_1 V_1 c_1)} (1 - e^{-nt}) \quad (3.288)$$

where $T_1(0)$ and $T_2(0)$ are the initial temperatures and

$$n = hA_s \frac{\rho_1 V_1 c_1 + \rho_2 V_2 c_2}{(\rho_1 V_1 c_1)(\rho_2 V_2 c_2)} \quad (3.289)$$

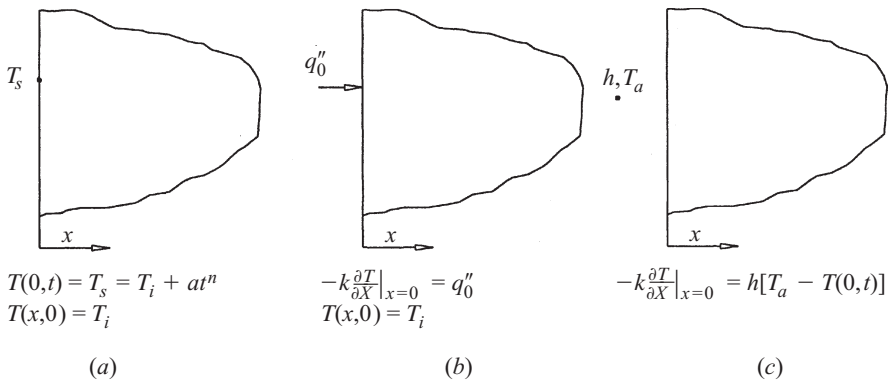


Figure 3.37 Semi-infinite solid with (a) specified surface temperature, (b) specified surface heat flux, and (c) surface convection.

3.8.2 Semi-infinite Solid Model

As indicated in Fig. 3.37, the semi-infinite solid model envisions a solid with one identifiable surface and extending to infinity in all other directions. The parabolic partial differential equation describing the one-dimensional transient conduction is

$$\frac{\partial^2 T}{\partial x^2} = \frac{1}{\alpha} \frac{\partial T}{\partial t} \quad (3.290)$$

Specified Surface Temperature If the solid is initially at a temperature T_i , and if for time $t > 0$ the surface at $x = 0$ is suddenly subjected to a specified temperature–time variation $f(t)$, the initial and boundary conditions can be written as

$$T(x, 0) = T_i \quad (x \geq 0) \quad (3.291a)$$

$$T(0, t) = f(t) = T_i + at^{n/2} \quad (3.291b)$$

$$T(\infty, t) = T_i \quad (t \geq 0) \quad (3.291c)$$

where a is a constant and n is a positive integer.

Using the Laplace transformation, the solution for T is obtained as

$$T = T_i + a\Gamma\left(1 + \frac{n}{2}\right)(4t)^{n/2}i^n \operatorname{erfc}\left(\frac{x}{2\sqrt{\alpha t}}\right) \quad (3.292)$$

where Γ is the gamma function (Section 3.3.2) and $i^n \operatorname{erfc}$ is the n th repeated integral of the complementary error function (Section 3.3.1). The surface heat flux q_0'' is

$$q_0'' = \frac{2^{n-1}}{\sqrt{\alpha}} t^{(n-1)/2} ka\Gamma\left(1 + \frac{n}{2}\right)\left[i^{n-1} \operatorname{erfc}\left(\frac{x}{2\sqrt{\alpha t}}\right)\right]_{x=0} \quad (3.293)$$

Several special cases can be deduced from eqs. (3.292) and (3.293).

Case 1: $f(t) = T_0$ This is the case of constant surface temperature which occurs when $n = 0$ and $a = T_0 - T_i$:

$$\frac{T(x, t) - T_i}{T_0 - T_i} = \operatorname{erfc}\left(\frac{x}{2\sqrt{\alpha t}}\right) \quad (3.294)$$

$$q_0'' = \frac{k(T_0 - T_i)}{(\pi\alpha t)^{1/2}} \quad (3.295)$$

Case 2: $f(t) = T_i + at$ This is the case of a linear variation of surface temperature with time which occurs when $n = 2$:

$$T(x, t) = T_i + 4ati^2 \operatorname{erfc}\left(\frac{x}{2\sqrt{\alpha t}}\right) \quad (3.296)$$

$$q_0'' = \frac{2kat}{(\pi\alpha t)^{1/2}} \quad (3.297)$$

Case 3: $f(t) = T_i + at^{1/2}$ This is the case of a parabolic surface temperature variation with time with $n = 1$.

$$T(x, t) = T_i + a\sqrt{\pi t} i \operatorname{erfc}\left(\frac{x}{2\sqrt{\alpha t}}\right) \quad (3.298)$$

$$q_0'' = \frac{ka}{2} \sqrt{\frac{\pi}{\alpha}} \quad (3.299)$$

Specified Surface Heat Flux For a constant surface heat flux q_0'' , the boundary conditions of eq. (3.291b) is replaced by

$$-k \frac{\partial T(0, t)}{\partial x} = q_0'' \quad (3.300)$$

and the solution is

$$T(x, t) = T_i + \frac{2q_0''\sqrt{\alpha t}}{k} i \operatorname{erfc}\left(\frac{x}{2\sqrt{\alpha t}}\right) \quad (3.301)$$

Surface Convection The surface convection boundary condition

$$-k \frac{\partial T(0, t)}{\partial x} = h [T_\infty - T(0, t)] \quad (3.302)$$

replaces eq. (3.291b) and the solution is

$$\frac{T(x, t) - T_i}{T_\infty - T_i} = \operatorname{erfc}\left(\frac{x}{2\sqrt{\alpha t}}\right) - e^{(hx/k) + (h^2\alpha t/k^2)} \operatorname{erfc}\left(\frac{h}{k}\sqrt{\alpha t} + \frac{x}{2\sqrt{\alpha t}}\right) \quad (3.303)$$

Constant Surface Heat Flux and Nonuniform Initial Temperature Zhuang et al. (1995) considered a nonuniform initial temperature of the form

$$T(x, 0) = a + bx \quad (3.304)$$

where a and b are constants to find a modified version of eq. (3.301) as

$$T(x, t) = a + bx + 2\sqrt{\alpha t} \left(\frac{q_0''}{k} + b \right) i \operatorname{erfc} \left(\frac{x}{2\sqrt{\alpha t}} \right) \quad (3.305)$$

The surface temperature is obtained by putting $x = 0$ in eq. (3.305), which gives

$$T(0, t) = a + 2\sqrt{\frac{\alpha t}{\pi}} \left(\frac{q_0''}{k} + b \right) \quad (3.306)$$

Zhuang et al. (1995) found that the predictions from eqs. (3.305) and (3.306) matched the experimental data obtained when a layer of asphalt is heated by a radiant burner, producing a heat flux of 41.785 kW/m². They also provided a solution when the initial temperature distribution decays exponentially with x .

Constant Surface Heat Flux and Exponentially Decaying Energy Generation When the surface of a solid receives energy from a laser source, the effect of this penetration of energy into the solid can be modeled by adding an exponentially decaying heat generation term, $\dot{q}_0 e^{-ax}/k$ (where a is the surface absorption coefficient), to the left side of eq. (3.290). The solution for this case has been reported by Sahin (1992) and Blackwell (1990):

$$\begin{aligned} T = T_i + (T_0 + T_i) \operatorname{erfc} \left(\frac{x}{2\sqrt{\alpha t}} \right) \\ + \frac{\dot{q}_0}{ka^2} \left[\operatorname{erfc} \left(\frac{x}{2\sqrt{\alpha t}} \right) - \frac{1}{2} e^{a^2 \alpha t + ax} \operatorname{erfc} \left(\frac{x}{2\sqrt{\alpha t}} + a\sqrt{\alpha t} \right) \right. \\ \left. - \frac{1}{2} e^{a^2 \alpha t - ax} \operatorname{erfc} \left(\frac{x}{2a\sqrt{\alpha t}} - a\sqrt{\alpha t} \right) + e^{-ax} e^{(a^2 \alpha t - 1)} \right] \quad (3.307) \end{aligned}$$

Both Sahin (1992) and Blackwell (1990) have also solved this case for a convective boundary condition (h, T_∞) at $x = 0$. Blackwell's results show that for a given absorption coefficient a , thermal properties of α and k , initial temperature T_i , and surface heat generation \dot{q}_0 , the location of the maximum temperature moves deeper into the solid as time progresses. If h is allowed to vary, for a given time the greater value of h provides the greater depth at where the maximum temperature occurs. The fact that the maximum temperature occurs inside the solid provides a possible explanation for the "explosive removal of material" that has been observed to occur when the surface of a solid is given an intense dose of laser energy.

3.8.3 Finite-Sized Solid Model

Consider one-dimensional transient conduction in a plane wall of thickness $2L$, a long solid cylinder of radius r_0 , and a solid sphere of radius r_0 , each initially at a uniform temperature T_i . At time $t = 0$, the exposed surface in each geometry is exposed to a hot convective environment (h, T_∞). The single parabolic partial differential equation describing the one-dimensional transient heating of all three configurations can be written as

$$\frac{1}{s^n} \frac{\partial}{\partial s} \left(s^n \frac{\partial T}{\partial s} \right) = \frac{1}{\alpha} \frac{\partial T}{\partial t} \quad (3.308)$$

where $s = x, n = 0$ for a plane wall, $s = r, n = 1$ for a cylinder, and $s = r, n = 2$ for a sphere. In the case of a plane wall, x is measured from the center plane. The initial and boundary conditions for eq. (3.308) are

$$T(s, 0) = T_i \quad (3.309a)$$

$$\frac{\partial T(0, t)}{\partial s} = 0 \quad (\text{thermal symmetry}) \quad (3.309b)$$

$$k \frac{\partial T(L \text{ or } r_0, t)}{\partial s} = h [T_\infty - T(L \text{ or } r_0, t)] \quad (3.309c)$$

According to Adebisi (1995), the separation of variables method gives the solution for θ as

$$\theta = \sum_{n=1}^{\infty} \frac{2 \text{Bi}}{\lambda_n^2 + \text{Bi}^2 + 2\nu \cdot \text{Bi}} \frac{R^\nu J_{-\nu}(\lambda_n R)}{J_{-\nu}(\lambda_n)} e^{-\lambda_n^2 \tau} \quad (3.310)$$

where $\theta = (T_\infty - T)/(T_\infty - T_i)$, $R = x/L$ for a plane wall, $R = r/r_0$ for both cylinder and sphere, $\text{Bi} = hL/k$ or hr_0/k , $\tau = \alpha t/L^2$ or $\tau = \alpha t/r_0^2$, $\nu = (1 - n)/2$, and the λ_n are the eigenvalues given by

$$\lambda_n J_{-(\nu-1)}(\lambda_n) = \text{Bi} \cdot J_{-\nu}(\lambda_n) \quad (3.311)$$

The cumulative energy received over the time t is

$$Q = \rho c V (T_\infty - T_i) \sum_{n=1}^{\infty} \frac{2(1+n) \text{Bi}^2 (1 - e^{-\lambda_n^2 \tau})}{\lambda_n^2 (\lambda_n^2 + \text{Bi}^2 + 2\nu \cdot \text{Bi})} \quad (3.312)$$

Solutions for a plane wall, a long cylinder, and a sphere can be obtained from eqs. (3.310) and (3.312) by putting $n = 0$, ($\nu = \frac{1}{2}$), $n = 1$ ($\nu = 0$), and $n = 2$ ($\nu = -\frac{1}{2}$), respectively. It may be noted that

$$J_{-1/2}(z) = \left(\frac{2}{\pi z} \right)^{1/2} \cos z$$

$$J_{1/2}(z) = \left(\frac{2}{\pi z}\right)^{1/2} \sin z$$
$$J_{3/2}(z) = \left(\frac{2}{\pi z}\right)^{1/2} \left(\frac{\sin z}{z} - \cos z\right)$$

With these representations, eqs. (3.310) and (3.312) reduce to the standard forms appearing in textbooks. Graphical representations of eqs. (3.310) and (3.312) are called *Heisler charts*.

3.8.4 Multidimensional Transient Conduction

For some configurations it is possible to construct multidimensional transient conduction solutions as the product of one-dimensional results given in Sections 3.8.2 and 3.8.3. Figure 3.38 is an example of a two-dimensional transient conduction situation in which the two-dimensional transient temperature distribution in a semi-infinite plane wall is the product of the one-dimensional transient temperature distribution in an infinitely long plane wall and the one-dimensional transient temperature distribution in a semi-infinite solid. Several other examples of product solutions are given by Bejan (1993).

3.8.5 Finite-Difference Method

Explicit Method For two-dimensional transient conduction in Cartesian coordinates, the governing partial differential equation is

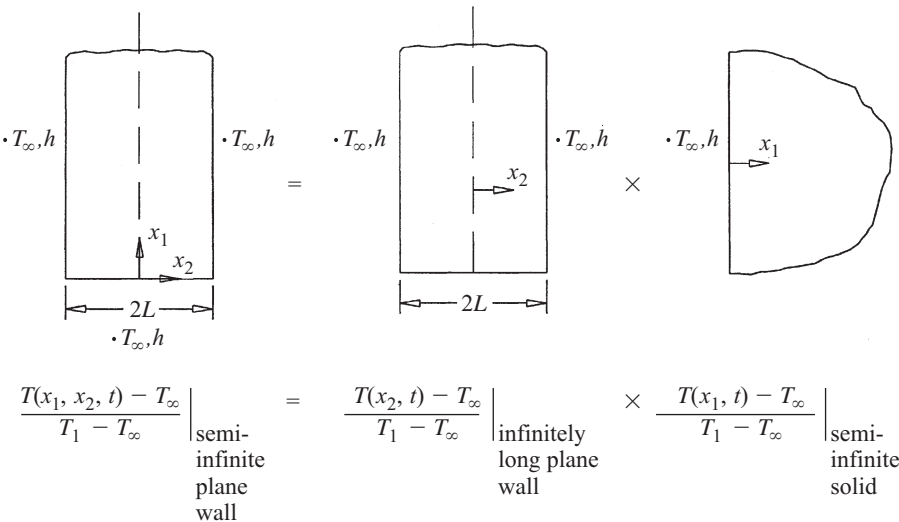


Figure 3.38 Product solution for a two-dimensional transient conduction problem.

$$\frac{\partial^2 T}{\partial x^2} + \frac{\partial^2 T}{\partial y^2} = \frac{1}{\alpha} \frac{\partial T}{\partial t} \quad (3.313)$$

which assumes no internal heat generation and constant thermal properties. Approximating the second-order derivatives in x and y and the first-order derivative in t by *forward differences*, the explicit finite-difference approximations (using $\Delta x = \Delta y$) for various nodes (see Fig. 3.33) can be expressed using the Fourier modulus, $Fo = \alpha \Delta t / (\Delta x)^2$, $Bi = h \Delta x / k$, and $t = p \Delta t$.

- *Internal node:* With $Fo \leq \frac{1}{4}$,

$$T_{i,j}^{p+1} = Fo \left(T_{i+1,j}^p + T_{i-1,j}^p + T_{i,j+1}^p + T_{i,j-1}^p \right) + (1 - 4Fo) T_{i,j}^p \quad (3.314)$$

- *Node at interior corner with convection:* With $Fo(3 + Bi) \leq \frac{3}{4}$,

$$T_{i,j}^{p+1} = \frac{2}{3} Fo \left(T_{i+1,j}^p + 2T_{i-1,j}^p + 2T_{i,j+1}^p + T_{i,j-1}^p + 2Bi T_{\infty} \right) + \left(1 - 4Fo - \frac{4}{3} Bi \cdot Fo \right) T_{i,j}^p \quad (3.315)$$

- *Node on a plane surface with convection:* With $Fo(2 + Bi) \leq \frac{1}{2}$,

$$T_{i,j}^{p+1} = Fo \left(2T_{i-1,j}^p + T_{i,j+1}^p + T_{i,j-1}^p + 2Bi \cdot T_{\infty} \right) + (1 - 4Fo - 2Bi \cdot Fo) T_{i,j}^p \quad (3.316)$$

- *Node at exterior corner with convection:* With $Fo(1 + Bi) \leq \frac{1}{4}$,

$$T_{i,j}^{p+1} = 2Fo \left(T_{i-1,j}^p + T_{i,j-1}^p + 2Bi \cdot T_{\infty} \right) + (1 - 4Fo - 4Bi \cdot Fo) T_{i,j}^p = 0 \quad (3.317)$$

- *Node on a plane surface with uniform heat flux:* With $Fo \leq \frac{1}{4}$,

$$T_{i,j}^{p+1} = (1 - 4Fo) T_{i,j}^p + Fo \left(2T_{i-1,j}^p + T_{i,j+1}^p + T_{i,j-1}^p \right) + 2Fo \cdot q'' \frac{\Delta x}{k} \quad (3.318)$$

The choice of Δx and Δt must satisfy the stability constraints, introducing each of the approximations given by eqs. (3.314)–(3.318) to ensure a solution free of numerically induced oscillations. Once the approximations have been written for each node on the grid, the numerical computation is begun with $t = 0$ ($p = 0$), for which the node temperatures are known from the initial conditions prescribed. Because eqs. (3.313)–(3.318) are explicit, node temperatures at $t = \Delta t$ ($p = 1$) can be determined from a knowledge of the node temperatures the preceding time, $t = 0$ ($p = 0$). This

“marching out” in time type of computation permits the transient response of the solid to be determined in a straightforward manner. However, the computational time necessary to cover the entire transient response is excessive because extremely small values of Δt are needed to meet the stability constraints.

Implicit Method In the implicit method, the second derivatives in x and y are approximated by *central differences* but with the use of temperatures at a subsequent time, $p + 1$, rather than the current time, p , while the derivative in t is replaced by a *backward difference* instead of a forward difference. Such approximations lead to the following equations:

- *Internal node:*

$$(1 + 4\text{Fo})T_{i,j}^{p+1} - \text{Fo} \left(T_{i+1,j}^{p+1} + T_{i-1,j}^{p+1} + T_{i,j+1}^{p+1} + T_{i,j-1}^{p+1} \right) = T_{i,j}^p \quad (3.319)$$

- *Node at interior corner with convection:*

$$\begin{aligned} \left[(1 + 4\text{Fo}) \left(1 + \frac{1}{3}\text{Bi} \right) \right] T_{i,j}^{p+1} - \frac{2}{3}\text{Fo} \left(T_{i+1,j}^{p+1} + 2T_{i-1,j}^{p+1} \right. \\ \left. + 2T_{i,j+1}^{p+1} + T_{i,j-1}^{p+1} \right) = T_{i,j}^p + \frac{4}{3}\text{Fo} \cdot \text{Bi} \cdot T_{\infty} \end{aligned} \quad (3.320)$$

- *Node on a plane surface with convection:*

$$\begin{aligned} [1 + 2\text{Fo}(2 + \text{Bi})] T_{i,j}^{p+1} - \text{Fo} \left(2T_{i-1,j}^{p+1} + T_{i,j+1}^{p+1} + T_{i,j-1}^{p+1} \right) \\ = T_{i,j}^p + 2\text{Bi} \cdot \text{Fo} \cdot T_{\infty} \end{aligned} \quad (3.321)$$

- *Node at exterior corner with convection:*

$$1 + 4\text{Fo}(1 + \text{Bi})T_{i,j}^{p+1} - 2\text{Fo} \left(T_{i-1,j}^{p+1} + T_{i,j-1}^{p+1} \right) = T_{i,j}^p + 4\text{Bi} \cdot \text{Fo} \cdot T_{\infty} \quad (3.322)$$

- *Node on a plane surface with uniform heat flux:*

$$(1 + 4\text{Fo})T_{i,j}^{p+1} + \text{Fo} \left(2T_{i-1,j}^{p+1} + T_{i,j+1}^{p+1} + T_{i,j-1}^{p+1} \right) = T_{i,j}^p + \frac{2\text{Fo} \cdot q'' \Delta x}{k} \quad (3.323)$$

The implicit method is unconditionally stable and therefore permits the use of higher values of Δt , thereby reducing the computational time. However, at each time t , the implicit method requires that the node equations be solved *simultaneously* rather than *sequentially*.

Other Methods Several improvements of the explicit and implicit methods have been advocated in the numerical heat transfer literature. These include the three-time-level scheme of Dufort and Fankel, the Crank–Nicholson method, and alternating

direction explicit methods. For a discussion of these methods as well as stability analysis, the reader should consult Pletcher et al. (1988).

3.9 PERIODIC CONDUCTION

Examples of periodic conduction are the penetration of atmospheric temperature cycles into the ground, heat transfer through the walls of internal combustion engines, and electronic components under cyclic operation. The periodicity may appear in the differential equation or in a boundary condition or both. The complete solution to a periodic heat conduction problem consists of a transient component that decays to zero with time and a steady oscillatory component that persists. It is the steady oscillatory component that is of prime interest in most engineering applications. In this section we present several important solutions.

3.9.1 Cooling of a Lumped System in an Oscillating Temperature Environment

Revisit the lumped thermal capacity model described in Section 3.8.1 and consider a scenario in which the convective environmental temperature T_∞ oscillates sinusoidally, that is,

$$T_\infty = T_{\infty,m} + a \sin \omega t \quad (3.324)$$

where a is the amplitude of oscillation, $\omega = 2\pi f$ the angular frequency, f the frequency in hertz, and $T_{\infty,m}$ the mean temperature of the environment.

The method of complex combination described by Arpaci (1966), Myers (1998), Poulikakos (1994), and Aziz and Lunardini (1994) gives the steady periodic solution as

$$\theta = \frac{1}{\sqrt{1+B^2}} \sin(B\tau - \beta) \quad (3.325)$$

where

$$\theta = \frac{T - T_{\infty,m}}{a} \quad B = \frac{\rho V c}{h A} \omega \quad \tau = \frac{h A t}{\rho V c} \quad \beta = \arctan B \quad (3.326)$$

A comparison of eq. (3.325) with the dimensionless environmental temperature variation ($\sin B\tau$) shows that the temperature of the body oscillates with the same frequency as that of the environment but with a phase lag of β . As the frequency of oscillation increases, the phase angle $\beta = \arctan B$ increases, but the amplitude of oscillation $1/(1+B^2)^{1/2}$ decreases.

3.9.2 Semi-infinite Solid with Periodic Surface Temperature

Consider the semi-infinite solid described in Section 3.8.2 and let the surface temperature be of the form

$$T(0, t) = T_s = T_i + a \cos \omega t \quad (3.327)$$

In this case, eqs. (3.291) are still applicable, although the initial condition of eq. (3.291a) becomes irrelevant for the steady periodic solution, which is

$$T(x, t) = T_i + ae^{-[(\omega/2\alpha)^{1/2}x]} \cos \left[\omega t - \left(\frac{\omega}{2\alpha} \right)^{1/2} x \right] \quad (3.328)$$

Three conclusions can be drawn from this result. First, the temperatures at all locations oscillate with the same frequency as the thermal disturbance at the surface. Second, the amplitude of oscillation decays exponentially with x . This makes the solution applicable to the finite thickness plane wall. Third, the amplitude of oscillation decays exponentially with the square root of the frequency ω . Thus, higher-frequency disturbances damp out more rapidly than those at lower frequencies. This explains why daily oscillations of ambient temperature do not penetrate as deeply into the ground as annual and millennial oscillations. The surface heat flux variation follows directly from eq. (3.328):

$$q''(0, t) = -k \frac{\partial T(0, t)}{\partial x} = ka \left(\frac{\omega}{\alpha} \right)^{1/2} \cos \left(\omega t - \frac{\pi}{4} \right) \quad (3.329)$$

and this shows that $q''(0, t)$ leads $T(0, t)$ by $\pi/4$ radians.

3.9.3 Semi-infinite Solid with Periodic Surface Heat Flux

In this case, the boundary condition of eq. (3.327) is replaced with

$$q''(0, t) = -k \frac{\partial T}{\partial x}(0, t) = q_0'' \cos \omega t \quad (3.330)$$

and the solution takes the form

$$T(x, t) = T_i + \frac{q_0''}{k} \left(\frac{\alpha}{\omega} \right)^{1/2} e^{-[(\omega/2\alpha)^{1/2}x]} \cos \left[\omega t - \left(\frac{\omega}{2\alpha} \right)^{1/2} x - \frac{\pi}{4} \right] \quad (3.331)$$

It is interesting to note that the phase angle increases as the depth x increases with the minimum phase angle of $\pi/4$ occurring at the surface ($x = 0$). A practical situation in which eq. (3.331) becomes useful is in predicting the steady temperature variations induced by frictional heating between two reciprocating parts in contact in a machine. This application has been described by Poulikakos (1994).

3.9.4 Semi-infinite Solid with Periodic Ambient Temperature

The surface boundary condition in this case is

$$T_\infty = T_{\infty, m} + a \cos \omega t \quad (3.332)$$

and the steady periodic temperature distribution is given by

$$\theta = \frac{\text{Bi}}{(\text{Bi}^2 + 2\text{Bi} + 2)^{1/2}} e^{-\sqrt{\pi} X} \cos(2\pi\tau - \sqrt{\pi} X - \beta) \quad (3.333)$$

where

$$\theta = \frac{T - T_{\infty, m}}{a} \quad (3.334a)$$

$$X = \left(\frac{\omega}{2\pi\alpha} \right)^{1/2} x \quad (3.334b)$$

$$\tau = \frac{\omega t}{2\pi} \quad (3.334c)$$

$$\text{Bi} = \frac{h}{k} \left(\frac{2}{\alpha} \right)^{1/2} \omega \quad (3.334d)$$

$$\beta = \arctan \frac{1}{1 + \text{Bi}} \quad (3.334e)$$

Note that as $h \rightarrow \infty$, $\text{Bi} \rightarrow \infty$, and $\beta \rightarrow 0$, eqs. (3.333) reduce to eq. (3.328) with $T_{\infty, m} = T_i$. The presence of the factor $\text{Bi}/(\text{Bi} + 2\text{Bi} + 2)^{1/2}$ in eq. (3.333) shows that convection enhances the damping effect and that it also increases the phase angle by an amount $\beta = \arctan 1/(1 + \text{Bi})$.

3.9.5 Finite Plane Wall with Periodic Surface Temperature

Consider a plane wall of thickness L with the face at $x = 0$ insulated and the face at $x = L$ subjected to a periodic temperature change of the form

$$T(L, t) = T_i + a \cos \omega t \quad (3.335)$$

where T_i is the initial temperature of the wall and the insulated boundary condition at $x = 0$ gives

$$\frac{\partial T(0, t)}{\partial x} = 0 \quad (3.336)$$

The steady periodic solution is

$$T(x, t) = T_i + a\phi_1 \left[\frac{x}{L}, \left(\frac{\omega}{2\alpha} \right)^{1/2} L \right] \cos \left\{ \omega t + \phi_2 \left[\frac{x}{L}, \left(\frac{\omega}{2\alpha} \right)^{1/2} L \right] \right\} \quad (3.337)$$

where the numerical values of ϕ_1 as a function of x/L and $(w/2\alpha)^{1/2}L$ are supplied in Table 3.13, and ϕ_2 , which is also a function of x/L and $(w/2\alpha)^{1/2}L$, is given by

$$\phi_2 = \arctan \frac{\phi_a \phi_d - \phi_b \phi_c}{\phi_a \phi_b - \phi_c \phi_d} \quad (3.338)$$

TABLE 3.13 Values of the Amplitude Decay Function, ϕ as a Function of x/L and $\sigma = (\omega/2\alpha)^{1/2}L$

σ	$x/L = 0$	0.125	0.250	0.375	0.500	0.625	0.750	0.875	1.000
0.0	1.00	1.00	1.00	1.00	1.00	1.00	1.00	1.00	1.00
0.5	0.98	0.98	0.98	0.98	0.98	0.98	0.98	0.99	1.00
1.0	0.77	0.77	0.77	0.78	0.79	0.81	0.85	0.91	1.00
1.5	0.47	0.47	0.47	0.48	0.52	0.58	0.68	0.83	1.00
2.0	0.27	0.27	0.28	0.30	0.36	0.45	0.58	0.77	1.00
4.0	0.04	0.04	0.05	0.08	0.13	0.22	0.37	0.64	1.00
8.0	0.00	0.00	0.01	0.01	0.02	0.05	0.14	0.36	1.00
∞	0.00	0.00	0.00	0.00	0.00	0.00	0.00	0.00	

where

$$\phi_a = \cos \left[\left(\frac{\omega}{2\alpha} \right)^{1/2} L \right] \cosh \left[\left(\frac{\omega}{2\alpha} \right)^{1/2} L \right] \quad (3.339a)$$

$$\phi_b = \cos \left[\left(\frac{\omega}{2\alpha} \right)^{1/2} x \right] \cosh \left[\left(\frac{\omega}{2\alpha} \right)^{1/2} x \right] \quad (3.339b)$$

$$\phi_c = \sin \left[\left(\frac{\omega}{2\alpha} \right)^{1/2} L \right] \sinh \left[\left(\frac{\omega}{2\alpha} \right)^{1/2} L \right] \quad (3.339c)$$

$$\phi_d = \sin \left[\left(\frac{\omega}{2\alpha} \right)^{1/2} x \right] \sinh \left[\left(\frac{\omega}{2\alpha} \right)^{1/2} x \right] \quad (3.339d)$$

3.9.6 Infinitely Long Semi-infinite Hollow Cylinder with Periodic Surface Temperature

Consider an infinitely long cylinder of inside radius, r_i , extending to infinity in the radial direction. The inner surface is subjected to a periodic temperature variation of the form

$$T(r_i, t) = T_i + a \cos \omega t \quad (3.340)$$

where T_i is the initial temperature of the cylinder. The equation governing the temperature distribution is

$$\frac{\partial^2 T}{\partial r^2} + \frac{1}{r} \frac{\partial T}{\partial r} = \frac{1}{\alpha} \frac{\partial T}{\partial t} \quad (3.341)$$

The other boundary condition is

$$T(\infty, t) = T_i, \quad \frac{\partial T(\infty, t)}{\partial r} = 0 \quad (3.342)$$

and the initial condition is

$$T(r, 0) = T_i \quad (3.343)$$

An application of the method of complex combination gives the steady-state periodic solution as

$$\theta = \frac{T - T_i}{a} = \Lambda_1 \cos \omega t - \Lambda_2 \sin \omega t \quad (3.344)$$

where

$$\Lambda_1 = \frac{\ker(\sqrt{\omega/\alpha} r_i) \ker(\sqrt{\omega/\alpha} r) + \operatorname{kei}(\sqrt{\omega/\alpha} r_i) \operatorname{kei}(\sqrt{\omega/\alpha} r)}{\ker^2(\sqrt{\omega/\alpha} r_i) + \operatorname{kei}^2(\sqrt{\omega/\alpha} r_i)} \quad (3.345a)$$

$$\Lambda_2 = \frac{\ker(\sqrt{\omega/\alpha} r_i) \operatorname{kei}(\sqrt{\omega/\alpha} r) - \operatorname{kei}(\sqrt{\omega/\alpha} r_i) \ker(\sqrt{\omega/\alpha} r)}{\ker^2(\sqrt{\omega/\alpha} r_i) + \operatorname{kei}^2(\sqrt{\omega/\alpha} r_i)} \quad (3.345b)$$

and \ker and kei are the Thomson functions discussed in Section 3.3.5.

As indicated in Section 3.9.1, the method of complex combination is described by Arpaci (1966), Myers (1998), Poulikakos (1994), and Aziz and Lunardini (1994). The method may be extended to numerous other periodic heat problems of engineering interest.

3.10 CONDUCTION-CONTROLLED FREEZING AND MELTING

Heat conduction with freezing (melting) occurs in a number of applications, such as ice formation, permafrost melting, metal casting, food preservation, storage of latent energy, and organ preservation and cryosurgery. Books and review articles on the subject include those of Lunardini (1991), Cheng and Seki (1991), Rubinsky and Eto (1990), Aziz and Lunardini (1993), Viskanta (1983, 1988), and Alexiades and Solomon (1993). Because of the vastness of the literature, only selected results that are judged to be of fundamental importance are discussed in this section.

3.10.1 One-Region Neumann Problem

The one-region Neumann problem deals with a semi-infinite region of liquid initially at its freezing temperature, T_f . At time $t > 0$, the face at $x = 0$ is suddenly reduced and kept at T_0 such that $T_0 < T_f$, as shown in Fig. 3.39. This initiates the extraction of heat by conduction from the saturated liquid to the surface and the liquid begins to freeze. As the cooling continues, the interface (assumed sharp) between the solid and liquid phases penetrates deeper into the liquid region. The prediction of the location of the interface calls for determination of the one-dimensional transient temperature distribution in the solid assuming that the liquid continues to remain at T_f at all times. The governing partial differential equation is

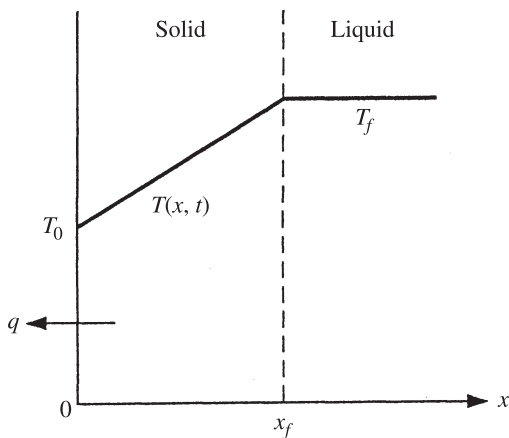


Figure 3.39 One-region Neumann problem (freezing).

$$\frac{\partial^2 T}{\partial x^2} = \frac{1}{\alpha} \frac{\partial T}{\partial t} \quad (3.346)$$

with the boundary conditions

$$T(0, t) = T_0 \quad (3.347a)$$

$$T(x_f, t) = T_f \quad (3.347b)$$

where x_f denotes the location of the interface, which is not known a priori and must be determined as part of the solution. An energy balance at the interface gives

$$k \left. \frac{\partial T}{\partial x} \right|_{x=x_f} = \rho L \frac{\partial x_f}{\partial t} \quad (3.348)$$

where k and ρ are the thermal conductivity and density of the solid phase, respectively, and L is the latent heat.

The temperature distribution in the solid is given as

$$\frac{T_f - T}{T_f - T_0} = 1 - \frac{\operatorname{erf}(x/2\sqrt{\alpha t})}{\operatorname{erf}(x_f/2\sqrt{\alpha t})} \quad (3.349)$$

where $x_f/2\sqrt{\alpha t}$, denoted by λ , is a root of the transcendental equation

$$\sqrt{\pi} \lambda \operatorname{erf}(\lambda e^{\lambda^2}) = \operatorname{St} \quad (3.350)$$

TABLE 3.14 Interface Location Parameter λ

λ	St
0.0	0.0000
0.2	0.0822
0.4	0.3564
0.6	0.9205
0.8	1.9956
1.0	4.0601
1.2	8.1720

and

$$\text{St} = \frac{c(T_f - T_0)}{L} \quad (3.351)$$

is the *Stefan number*, the ratio of the sensible heat to the latent heat. For water, St is about 0.10, for paraffin wax about 0.90, for copper about 2.64, and for silicon dioxide about 436. Table 3.14 gives selected values of λ and St that satisfy eq. (3.350). Viskanta (1983) reports that the Neumann model accurately predicts the solidification of *n*-octadecane on a horizontal plate.

The solution presented here applies to the one-region melting problem if T_f is replaced by the melting temperature T_m . With $T_0 > T_m$, eq. (3.349) gives the temperature in the liquid region.

3.10.2 Two-Region Neumann Problem

The two-region Neumann problem allows for heat conduction in both the solid and liquid phases. For the configuration in Fig. 3.40, the mathematical description of the problem is

$$\frac{\partial^2 T_s}{\partial x^2} = \frac{1}{\alpha_s} \frac{\partial T_s}{\partial t} \quad (0 < x < x_f \text{ and } t > 0) \quad (3.352)$$

$$\frac{\partial^2 T_l}{\partial x^2} = \frac{1}{\alpha_l} \frac{\partial T_l}{\partial t} \quad (x_f < x < \infty \text{ and } t > 0) \quad (3.353)$$

with initial and boundary conditions

$$T_l(x, 0) = T_i \quad (3.354a)$$

$$T_s(0, t) = T_0 \quad (3.354b)$$

$$T_s(x_f, t) = T_l(x_f, t) = T_f \quad (3.354c)$$

$$\left(k_s \frac{\partial T_s}{\partial x} - k_l \frac{\partial T_l}{\partial x} \right)_{x=x_f} = \rho L \frac{dx_f}{dt} \quad (3.354d)$$

where the subscripts s and l refer to the solid and liquid phases, respectively.

The solutions for T_s and T_l are

$$\frac{T_s - T_0}{T_f - T_0} = \frac{\operatorname{erf}(x/2\sqrt{\alpha_s t})}{\operatorname{erf}(x_f/2\sqrt{\alpha_s t})} \quad (3.355)$$

$$\frac{T_i - T_l}{T_i - T_f} = \frac{\operatorname{erfc}(x/2\sqrt{\alpha_l t})}{\operatorname{erfc}(x_f/2\sqrt{\alpha_l t})} \quad (3.356)$$

With $x_f/2\sqrt{\alpha_s t}$ denoted by λ , the interface energy balance given by eq. (3.354d) leads to the transcendental equation for λ :

$$\frac{e^{-\lambda^2}}{\lambda \operatorname{erf}(\lambda)} - \frac{T_i - T_f}{T_f - T_0} \left[\frac{(k\rho c)_l}{(k\rho c)_s} \right]^{1/2} \frac{e^{-\lambda^2(\alpha_s/\alpha_l)}}{\lambda \operatorname{erfc}[\lambda(\alpha_s/\alpha_l)^{1/2}]} = \frac{\sqrt{\pi} L}{c(T_f - T_0)} \quad (3.357)$$

Churchill and Evans (1971) noted that λ is a function of three parameters:

$$\theta^* = \frac{T_i - T_f}{T_f - T_0} \left[\frac{(k\rho c)_l}{(k\rho c)_s} \right]^{1/2} \quad \alpha^* = \frac{\alpha_s}{\alpha_l} \quad \text{St} = \frac{c(T_f - T_0)}{L}$$

and solved eq. (3.357) for a range of values of these parameters. Table 3.15 summarizes these results for λ .

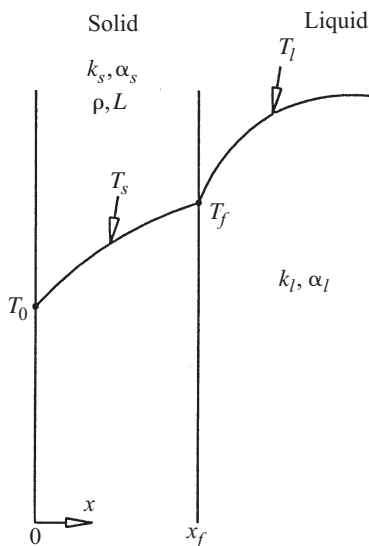


Figure 3.40 Two-region Neumann problem (freezing).

TABLE 3.15 Values of λ

St	α^*	θ^*						
		0.50	1.0	1.5	2.0	3.0	5.0	10.0
0.1	2.0	0.202	0.187	0.173	0.161	0.141	0.111	0.071
0.1	1.5	0.203	0.188	0.175	0.163	0.142	0.113	0.072
0.1	1.0	0.204	0.189	0.176	0.164	0.144	0.114	0.073
0.2	2.0	0.270	0.241	0.216	0.195	0.165	0.123	0.074
0.2	1.5	0.271	0.243	0.219	0.199	0.167	0.125	0.075
0.2	1.0	0.273	0.245	0.222	0.202	0.170	0.128	0.076
0.5	2.0	0.374	0.313	0.268	0.234	0.186	0.133	0.077
0.5	1.5	0.378	0.320	0.273	0.240	0.192	0.135	0.078
0.5	1.0	0.383	0.325	0.280	0.246	0.197	0.139	0.079
1.0	2.0	0.452	0.358	0.298	0.254	0.198	0.137	0.077
1.0	1.5	0.460	0.367	0.305	0.261	0.203	0.140	0.079
1.0	1.0	0.470	0.378	0.315	0.270	0.209	0.144	0.080
2.0	2.0	0.517	0.391	0.317	0.267	0.204	0.139	0.078
2.0	1.5	0.530	0.403	0.327	0.275	0.210	0.142	0.079
2.0	1.0	0.546	0.418	0.339	0.286	0.217	0.146	0.080

3.10.3 Other Exact Solutions for Planar Freezing

Besides the one- and two-region Neumann solutions, several other exact solutions for planar freezing problems are available. These include:

1. The two-region problem with different solid- and liquid-phase densities (Lunardini, 1991)
2. The two-region problem with phase change occurring over a temperature range (Cho and Sunderland, 1969)
3. The one-region problem with a mushy zone separating the pure solid and pure liquid phases (Solomon et al., 1982)
4. The two-region problem with temperature-dependent thermal conductivities k_s and k_l (Cho and Sunderland, 1974)
5. The two-region problem with arbitrary surface temperature and initial conditions (Tao, 1978)

3.10.4 Exact Solutions in Cylindrical Freezing

Carslaw and Jaeger (1959) give an exact solution for the freezing of a subcooled liquid while the solid phase remains at the freezing temperature. The latent heat released is used to bring the subcooled liquid to its freezing temperature. The process is described by the differential equation

$$\frac{1}{r} \frac{\partial}{\partial r} \left(r \frac{\partial T}{\partial r} \right) = \frac{1}{\alpha} \frac{\partial T}{\partial t} \quad (r < r_f) \quad (3.358)$$

and the initial boundary conditions

$$T(r_f, t) = T_f \quad (3.359a)$$

$$\lim_{r \rightarrow \infty} T(r, t) = T_0 \quad (3.359b)$$

$$T(r, 0) = T_0 \quad (3.359c)$$

where r_f represents the radial growth of the solid phase and $T_0 < T_f$ is the subcooled liquid temperature.

The solution of eq. (3.358) satisfying the conditions of eqs. (3.359) is

$$T = T_0 + (T_f - T_0) \frac{\text{Ei}(-r^2/4\alpha t)}{\text{Ei}(-r_f^2/4\alpha t)} \quad (3.360)$$

where $\lambda = r_f^2/4\alpha t$ is given by

$$\lambda^2 \cdot \text{Ei}(-\lambda^2) e^{\lambda^2} + \text{St} = 0 \quad (3.361)$$

In eqs. (3.360) and (3.361), Ei is the exponential integral function discussed in Section 3.3.4, and in eq. (3.361), St is the Stefan number. Table 3.16 provides the solution of eq. (3.361).

Another situation for which an exact solution is available is shown in Fig. 3.41. A line heat sink of strength Q_s (W/m) located at $r = 0$ and activated at time $t = 0$ causes the infinite extent of liquid at a uniform temperature T_i ($T_i > T_f$) to freeze. The interface grows radially outward. The mathematical formulation for the solid and liquid phases leads to

$$\frac{1}{r} \frac{\partial}{\partial r} \left(r \frac{\partial T_s}{\partial r} \right) = \frac{1}{\alpha_s} \frac{\partial T_s}{\partial t} \quad (0 < r < r_f) \quad (3.362)$$

$$\frac{1}{r} \frac{\partial}{\partial r} \left(r \frac{\partial T_l}{\partial r} \right) = \frac{1}{\alpha_l} \frac{\partial T_l}{\partial t} \quad (r_f < r < \infty) \quad (3.363)$$

with initial and boundary conditions

$$T_l(\infty, t) = T_i \quad (3.364a)$$

$$T_l(r, 0) = T_i \quad (3.364b)$$

$$T_s(r_f, t) = T_l(r_f, t) = T_f \quad (3.364c)$$

$$\left(k_s \frac{\partial T_s}{\partial r} - k_l \frac{\partial T_l}{\partial r} \right)_{r=r_f} = \rho L \frac{dr_f}{dt} \quad (3.364d)$$

TABLE 3.16 Stefan Number and Interface Location Parameter

St	λ
0.1	0.1846
0.2	0.3143
0.3	0.4491
0.4	0.6006
0.5	0.7811
0.6	1.0095
0.7	1.3237
0.8	1.8180

Ozisik (1993) gives the solution as

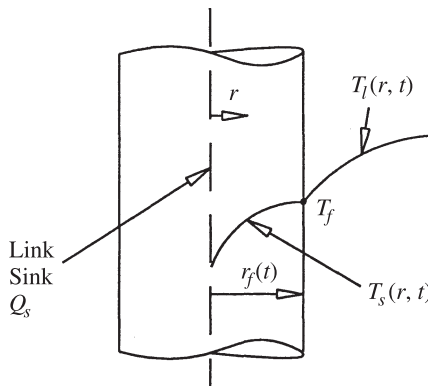
$$T_s = T_f + \frac{Q_s}{4\pi k_s} \left[\text{Ei} \left(-\frac{r^2}{4\alpha_s t} \right) - \text{Ei} \left(-\frac{r_f^2}{4\alpha_s t} \right) \right] \quad (0 < r < r_f) \quad (3.365)$$

$$T_l = T_i - \frac{T_i - T_f}{\text{Ei} \left(-\frac{r_f^2}{4\alpha_l t} \right)} \text{Ei} \left(-\frac{r^2}{4\alpha_l t} \right) \quad (r_f < r < \infty) \quad (3.366)$$

where $\lambda = r_f/2\sqrt{\alpha_s t}$ is obtained from the transcendental equation

$$\frac{Q_s}{4\pi} e^{-\lambda^2} + \frac{k_l(T_i - T_f)}{\text{Ei}(-\lambda^2\alpha_s/\alpha_l)} e^{-\lambda^2\alpha_s/\alpha_l} = \lambda^2\alpha_s\rho L \quad (3.367)$$

The solution presented by eqs. (3.365) through (3.367) has been extended by Ozisik and Uzzell (1979) for a liquid with an extended freezing temperature.

**Figure 3.41** Cylindrical freezing due to a line strength of fixed strength.

3.10.5 Approximate Analytical Solutions

Because of the mathematical complexity and the restrictive nature of exact analytical solutions, several approaches have been employed to generate approximate analytical solutions that provide rapid results in a number of practical situations. The methods used are the quasi-steady solution, the heat balance integral approach of Goodman (1958) and Lunardini (1991), and the perturbation method of Aziz and Na (1984), Aziz and Lunardini (1993), and others. A collection of such solutions is provided next.

One-Region Neumann Problem The quasi-steady-state solution where $St = 0$ for this problem is

$$T = T_0 + (T_f - T_0) \frac{x}{x_f} \quad (3.368)$$

$$x_f^2 = \frac{2k(T_0 - T_f)}{\rho L} t \quad (3.369)$$

One-Region Neumann Problem with Surface Convection With convective cooling, the boundary condition of eq. (3.347a) is replaced by

$$k \frac{\partial T}{\partial x} \bigg|_{x=0} = h [T(0, t) - T_\infty] \quad (3.370)$$

where T_∞ is now the coolant temperature. The quasi-steady-state approach with $St = 0$ yields

$$T = T_f + \frac{h(T_f - T_\infty)(x - x_f)}{k + hx_f} \quad (3.371)$$

$$t = \frac{\rho L x_f}{h(T_f - T_\infty)} \left(1 + \frac{hx_f}{2k} \right) \quad (3.372)$$

as the results.

Outward Cylindrical Freezing Consider a saturated liquid at the freezing temperature T_f , surrounding a cylinder of radius r_0 whose outer surface is kept at a sub-freezing temperature, $T_0 < T_f$. If a quasi-steady-state assumption ($St = 0$) is used, the solution is

$$T = T_0 + \frac{T_f - T_0}{\ln(r_f/r_0)} \ln \frac{r}{r_0} \quad (3.373)$$

$$t = \frac{\rho L}{k(T_f - T_0)} \left[\frac{1}{2} r_f^2 \ln \frac{r_f}{r_0} - \frac{1}{4} (r_f^2 - r_0^2) \right] \quad (3.374)$$

An improvement on the quasi-steady-state solution can be achieved with the regular perturbation analysis provided by Aziz and Na (1984). The improved version of eq. (3.374) is

$$t = \frac{\rho L}{k(T_f - T_0)} \left[\frac{1}{2} r_f^2 \ln \frac{r_f}{r_0} - \frac{1}{4} (r_f^2 - r_0^2) - \frac{1}{4} \text{St} (r_f^2 - r_0^2) \left(1 + \frac{1}{\ln(r_f/r_0)} \right) \right] \quad (3.375)$$

If the surface of the cylinder is convectively cooled, the boundary condition is

$$k \frac{\partial T}{\partial r} \bigg|_{r=r_0} = h [T(r_0, t) - T_\infty] \quad (3.376)$$

and the quasi-steady-state solutions for $\text{St} = 0$ in this case is

$$T = \frac{T_f - T_\infty}{(k/hr_0) + \ln(r_f/r_0)} \ln \frac{r}{r_f} + T_f \quad (3.377)$$

$$t = \frac{\rho L}{k(T_f - T_\infty)} \left[\frac{1}{2} r_f^2 \ln \frac{r_f}{r_0} - \frac{1}{4} (r_f^2 - r_0^2) \left(1 - \frac{2k}{hr_0} \right) \right] \quad (3.378)$$

Noting that the quasi-steady-state solutions such as eqs. (3.377) and (3.378) strictly apply only when $\text{St} = 0$, Huang and Shih (1975) used them as zero-order solutions in a regular perturbation series in St and generated two additional terms. The three-term perturbation solution provides an improvement on eqs. (3.377) and (3.378).

Inward Cylindrical Freezing Consider a saturated liquid at the freezing temperature contained in a cylinder of inside radius r_i . If the surface temperature is suddenly reduced to and kept at T_0 such that $T_0 < T_f$, the liquid freezes inward. The governing equation is

$$\frac{1}{r} \frac{\partial}{\partial r} \left(r \frac{\partial T}{\partial r} \right) = \frac{1}{\alpha} \frac{\partial T}{\partial t} \quad (3.379)$$

with initial and boundary conditions

$$T(r_i, t) = T_0 \quad (3.380a)$$

$$T(r_f, 0) = T_f \quad (3.380b)$$

$$k \frac{\partial T}{\partial r} \bigg|_{r=r_f} = \rho L \frac{dr_f}{dt} \quad (3.380c)$$

Equations (3.373) and (3.374) also give the quasi-steady-state solutions in this case except that r_0 now becomes r_i .

If the surface cooling is due to convection from a fluid at temperature T_∞ , with heat transfer coefficient h , the quasi-steady-state solutions for T and t are

$$T = T_\infty + \left[\frac{T_f - T_\infty}{\ln(r_f/r_i) - (k/hr_i)} \right] \left(\ln \frac{r}{r_i} - \frac{k}{hr_i} \right) \quad (3.381)$$

$$t = \frac{\rho L}{k(T_f - T_\infty)} \left[\frac{1}{2} r_f^2 \ln \frac{r_f}{r_i} + \frac{1}{4} (r_i^2 - r_f^2) \left(1 + \frac{2k}{hr_i} \right) \right] \quad (3.382)$$

Outward Spherical Freezing Consider a situation where saturated liquid at the freezing temperature T_f is in contact with a sphere of radius r_0 whose surface temperature T_0 is less than T_f . The differential equation for the solid phase is

$$\frac{1}{r} \frac{\partial^2 (Tr)}{\partial r^2} = \frac{1}{\alpha} \frac{\partial T}{\partial t} \quad (3.383)$$

which is to be solved subject to the conditions of eqs. (3.380) (r_i replaced by r_0).

In this case, the quasi-steady-state solution with $St = 0$ is

$$T = T_0 + \frac{T_f - T_0}{1/r_f - 1/r_0} \left(\frac{1}{r} - \frac{1}{r_0} \right) \quad (3.384)$$

$$t = \frac{\rho L r_0^2}{k(T_f - T_0)} \left[\frac{1}{3} \left(\frac{r_f}{r_0} \right)^3 - \frac{1}{2} \left(\frac{r_f}{r_0} \right)^2 + \frac{1}{6} \right] \quad (3.385)$$

A regular perturbation analysis allows an improved version of eqs. (3.384) and (3.385) to be written as

$$\frac{T - T_0}{T_f - T_0} = \frac{1 - 1/R}{1 - 1/R_f} + St \left[\frac{R_f^2 - 3R_f + 2}{6(R_f - 1)^4} \left(1 - \frac{1}{R} \right) - \frac{R^2 - 3R + 2}{6R_f(R_f - 1)^3} \right] \quad (3.386)$$

and

$$\tau = \frac{1}{6} \left[(1 + 2R_f^3 - 3R_f^2) + St (1 + R_f^2 - 2R_f) \right] \quad (3.387)$$

where

$$R = \frac{r}{r_0} \quad R_f = \frac{r_f}{r_0} \quad St = \frac{c(T_f - T_0)}{L} \quad \tau = \frac{k(T_f - T_0)t}{\rho L r_0^2}$$

If the surface boundary condition is changed to eq. (3.376), the quasi-steady-state solutions ($St = 0$) for T and t are

$$T = T_f + \frac{(T_f - T_0)r_0}{1 - r_0/r_f + k/hr_0} \left(\frac{1}{r_f} - \frac{1}{r} \right) \quad (3.388)$$

$$t = \frac{\rho L r_0^2}{k(T_f - T_\infty)} \left\{ \frac{1}{3} \left[\left(\frac{r_f}{r_0} \right)^3 - 1 \right] \left(1 + \frac{k}{h r_0} \right) - \frac{1}{2} \left(\frac{r_f}{r_0} \right)^2 + \frac{1}{2} \right\} \quad (3.389)$$

A three-term solution to the perturbation solution which provides an improvement over eqs. (3.388) and (3.389) is provided by Huang and Shih (1975).

Other Approximate Solutions Yan and Huang (1979) have developed perturbation solutions for planar freezing (melting) when the surface cooling or heating is by simultaneous convection and radiation. A similar analysis has been reported by Seniraj and Bose (1982). Lock (1971) developed a perturbation solution for planar freezing with a sinusoidal temperature variation at the surface. Variable property planar freezing problems have been treated by Pedroso and Domato (1973) and Aziz (1978). Parang et al. (1990) provide perturbation solutions for the inward cylindrical and spherical solidification when the surface cooling involves both convection and radiation.

Alexiades and Solomon (1993) give several approximate equations for estimating the time needed to melt a simple solid body initially at its melting temperature T_m . For the situation when the surface temperature T_0 is greater than T_m , the melt time t_m can be estimated by

$$t_m = \frac{l^2}{2\alpha_l(1 + \omega)\text{St}} \left[1 + (0.25 + 0.17\omega^{0.70})\text{St} \right] \quad (0 \leq \text{St} \leq 4) \quad (3.390)$$

where

$$\omega = \frac{lA}{V} - 1 \quad \text{and} \quad \text{St} = \frac{c_l(T_l - T_m)}{L} \quad (3.391)$$

and l is the characteristic dimension of the body, A the surface area across which heat is transferred to the body, and V the volume of the body. For a plane solid heated at one end and insulated at the other, $\omega = 0$ and l is equal to the thickness. For a solid cylinder and a solid sphere, l becomes the radius and $\omega = 1$ for the cylinder and $\omega = 2$ for the sphere.

If a hot fluid at temperature T_∞ convects heat to the body with heat transfer coefficient h , the approximate melt time for $0 \leq \text{St} \leq 4$ and $\text{Bi} \geq 0.10$ is

$$t_m = \frac{l^2}{2\alpha_l(1 + \omega)\text{St}} \left[1 + \frac{2}{\text{Bi}} + (0.25 + 0.17\omega^{0.70})\text{St} \right] \quad (3.392)$$

where $\text{Bi} = hl/k$.

In this case, the surface temperature $T(0, t)$ is given by the implicit relationship

$$t = \frac{\rho c_l k_l}{2h^2 \cdot \text{St}} \left\{ 1.18\text{St} \left[\frac{T(0, t) - T_m}{T_\infty - T(0, t)} \right]^{1.83} + \left[\frac{T_\infty - T_m}{T_\infty - T(0, t)} \right]^2 - 1 \right\} \quad (3.393)$$

Equations (3.390), (3.392), and (3.393) are accurate to within 10%.

3.10.6 Multidimensional Freezing (Melting)

In Sections 3.10.1 through 3.10.5 we have discussed one-dimensional freezing and melting processes where natural convection effects were assumed to be absent and the process was controlled entirely by conduction. The conduction-controlled models described have been found to mimic experimental data for freezing and melting of water, *n*-octadecane, and some other phase-change materials used in latent heat energy storage devices.

Multidimensional freezing (melting) problems are far less amenable to exact solutions, and even approximate analytical solutions are sparse. Examples of approximate analytical solutions are those of Budhia and Kreith (1973) for freezing (melting) in a wedge, Riley and Duck (1997) for the freezing of a cuboid, and Shamshundar (1982) for freezing in square, elliptic, and polygonal containers. For the vast majority of multidimensional phase-change problems, only a numerical approach is feasible. The available numerical methods include explicit finite-difference methods, implicit finite-difference methods, moving boundary immobilization methods, the isotherm migration method, enthalpy-based methods, and finite elements. Ozisik (1994) and Alexiades and Solomon (1993) are good sources for obtaining information on the implementation of finite-difference schemes to solve phase-change problems. Papers by Comini et al. (1974) and Lynch and O'Neill (1981) discuss finite elements with reference to phase-change problems.

3.11 CONTEMPORARY TOPICS

A major topic of contemporary interest is microscale heat conduction, mentioned briefly in Section 3.1, where we cited some important references on the topic. Another area of active research is inverse conduction, which deals with estimation of the surface heat flux history at the boundary of a heat-conducting solid from a knowledge of transient temperature measurements inside the body. A pioneering book on inverse heat conduction is that of Beck et al. (1985), and the book of Ozisik and Orlande (2000) is the most recent, covering not only inverse heat conduction but inverse convection and inverse radiation as well.

Biothermal engineering, in which heat conduction appears prominently in many applications, such as cryosurgery, continues to grow steadily. In view of the increasingly important role played by thermal contact resistance in the performance of electronic components, the topic is pursued actively by a number of research groups. The development of constructal theory and its application to heat and fluid flow discussed in Bejan (2000) offers a fresh avenue for research in heat conduction. Although Green's functions have been employed in heat conduction theory for many decades, the codification by Beck et al. (1992) is likely to promote their use further. Similarly, hybrid analytic–numeric methodology incorporating the classical integral transform approach has provided an alternative route to fully numerical methods. Numerous heat conduction applications of this numerical approach are given by Cotta and Mikhailov (1997). Finally, symbolic algebra packages such as *Maple V* and

Mathematica are influencing both teaching and research in heat conduction, as shown by Aziz (2001), Cotta and Mikhailov (1997), and Beltzer (1995).

NOMENCLATURE

Roman Letter Symbols

A	cross-sectional area, m^2 area normal to heat flow path, m^2
A_p	fin profile area, m^2
A_s	surface area, m^2
a	constant, dimensions vary absorption coefficient, m^{-1}
B	frequency, dimensionless
b	constant, dimensions vary fin or spine height, m^{-1}
Bi	Biot number, dimensionless
C	constant, dimensions vary
c	specific heat, $\text{kJ/kg} \cdot \text{K}$
d	spine diameter, m
\dot{E}_g	rate of energy generation, W
$ Fo$	Fourier number, dimensionless
f	frequency, s^{-1}
H	height, m fin tip heat loss parameter, dimensionless
h	heat transfer coefficient, $\text{W/m}^2 \cdot \text{K}$
h_c	contact conductance, $\text{W/m}^2 \cdot \text{K}$
\mathbf{i}	unit vector along the x coordinate, dimensionless
\mathbf{j}	unit vector along the y coordinate, dimensionless
k	thermal conductivity, $\text{W/m} \cdot \text{K}$
\mathbf{k}	unit vector along the z coordinate, dimensionless
L	thickness, length, or width, m
l	thickness, m characteristic dimension, m
M	fin parameter, $\text{m}^{-1/2}$
m	fin parameter, m^{-1}
N_1	convection–conduction parameter, dimensionless
N_2	radiation–conduction parameter, dimensionless
n	exponent, dimensionless integer, dimensionless heat generation parameter, m^{-1} normal direction, m parameter, s^{-1}
P	fin perimeter, m
p	integer, dimensionless

Q	cumulative heat loss, J
Q_s	strength of line sink, W/m
q	rate of heat transfer, W
\dot{q}	volumetric rate of energy generation, W/m ³
q''	heat flux, W/m ²
R	radius, dimensionless
	thermal resistance, K/W
R_c''	contact resistance, m ² ·K/W
R_f	freezing interface location, dimensionless
r	cylindrical or spherical coordinate, m
S	shape factor for two-dimensional conduction, m
St	Stefan number, dimensionless
s	general coordinate, m
T	temperature, K
T^*	Kirchhoff transformed temperature, K
t	time, s
V	volume, m ³
W	depth, m
X	distance, dimensionless
x	Cartesian length coordinate, m
y	Cartesian length coordinate, m
Z	axial distance, dimensionless
z	Cartesian or cylindrical length coordinate, m

Greek Letter Symbols

α	thermal diffusivity, m ² /s
α^*	ratio of thermal diffusivities, dimensionless
β	constant, K ⁻¹
	phase angle, rad
γ	length-to-radius ratio, dimensionless
δ	fin thickness, m
ϵ	fin effectiveness, dimensionless
	surface emissivity or emittance, dimensionless
η	fin efficiency, dimensionless
θ	temperature difference, K
	temperature parameter, dimensionless
	coordinate in cylindrical or spherical coordinate system, dimensionless
θ^*	temperature, dimensionless
λ_n	n th eigenvalue, dimensionless
ν	order of Bessel function, dimensionless
ρ	density, kg/m ³
σ	Stefan–Boltzmann constant, W/m ² ·K ⁴
τ	time, dimensionless
ϕ	temperature difference, K

	indicates a function, dimensionless
	spherical coordinate, dimensionless
ω	angular frequency, rad/s
	shape parameter, dimensionless

Roman Letter Subscripts

a	fin tip
b	fin base
cond	conduction
conv	convection
f	fin
	freezing interface
	fluid
i	integer
	initial
	ideal
j	integer
l	liquid
m	mean
	melting
max	maximum
n	normal direction
opt	optimum
s	surface condition
	solid
t	fin tip
0	condition at $x = 0$ or $r = 0$

Additional Subscript and Superscript

∞	free stream condition
p	integer

REFERENCES

- Abramowitz, M., and Stegun, I. A. (1955). *Handbook of Mathematical Functions*, Dover Publications, New York.
- Adebiyi, G. A. (1995). A Single Expression for the Solution of the One-Dimensional Transient Conduction Equation for the Simple Regular Shaped Solids, *J. Heat Transfer*, 117, 158–160.
- Alexaides, V., and Solomon, A. D. (1993). *Mathematical Modeling of Melting and Freezing Processes*, Hemisphere Publishing, Washington, DC.
- Andrews, L. C. (1992). *Special Functions of Mathematics for Engineers*, McGraw-Hill, New York.
- Arpaci, V. S. (1966). *Conduction Heat Transfer*, Addison-Wesley, Reading, MA.

- Aziz, A. (1978). New Asymptotic Solutions for the Variable Property Stefan Problem, *Chem. Eng. J.*, 16, 65–68.
- Aziz, A. (1992). Optimum Dimensions of Extended Surfaces Operating in a Convecting Environment, *Appl. Mech. Rev.*, 45, 155–173.
- Aziz, A. (1997). The Critical Thickness of Insulation, *Heat Transfer Eng.*, 18, 61–91.
- Aziz, A. (2001). *Heat Conduction with Maple™*. To be published.
- Aziz, A., and Hamad, G. (1977). Regular Perturbation Expansions in Heat Transfer, *Int. J. Mech. Eng.*, 5, 167–182.
- Aziz, A., and Kraus, A. D. (1996). Optimum Design of Convecting and Convecting–Radiating Fins, *Heat Transfer Eng.*, 17, 44–78.
- Aziz, A., and Lunardini, V. J. (1993). Perturbation Techniques in Phase Change Heat Transfer, *Appl. Mech. Rev.*, 46, 29–68.
- Aziz, A., and Lunardini, V. J. (1994). Analytical and Numerical Modeling of Steady, Periodic, Heat Transfer in Extended Surfaces, *Comput. Mech.*, 14, 387–410.
- Aziz, A., and Lunardini, V. J. (1995). Multi-dimensional Steady Conduction in Convecting, Radiating and Convecting–Radiating Fins and Fin Assemblies, *Heat Transfer Eng.*, 16, 32–64.
- Aziz, A., and Na, T. Y. (1984). *Perturbation Methods in Heat Transfer*, Hemisphere Publishing, Washington, DC.
- Beck, J. V., Blackwell, B. F., and St. Clair, C. A., Jr. (1985). *Inverse Heat Conduction*, Wiley, New York.
- Beck, J. V., Cole, K. D., Haji-Sheikh, A., and Litkouhi, B. (1992). *Heat Conduction Using Green's Functions*, Hemisphere Publishing, Washington, DC.
- Bejan, A. (1993). *Heat Transfer*, Wiley, New York.
- Bejan, A. (2000). *Shape and Structure from Engineering to Nature*, Cambridge University Press, Cambridge.
- Beltzer, A. I. (1995). *Engineering Analysis with Maple™/Mathematica™*, Academic Press, San Diego, CA.
- Blackwell, B. F. (1990). Temperature Profile in Semi-infinite Body with Exponential Source and Convective Boundary Condition, *J. Heat Transfer*, 112, 567–571.
- Budhia, H., and Kreith, F. (1973). Heat Transfer with Melting or Freezing in a Corner, *Int. J. Heat Mass Transfer*, 16, 195–211.
- Carslaw, H. S., and Jaeger, J. C. (1959). *Conduction of Heat in Solids*, Oxford University Press, Oxford.
- Cheng, K. C., and Seki, N., eds. (1991). *Freezing and Melting Heat Transfer in Engineering*, Hemisphere Publishing, Washington, DC.
- Cho, S. H., and Sunderland, J. E. (1969). Heat Conduction Problems with Freezing or Melting, *J. Heat Transfer*, 91, 421–428.
- Cho, S. H., and Sunderland, J. E. (1974). Phase Change Problems with Temperature Dependent Thermal Conductivity, *J. Heat Transfer*, 96, 214–217.
- Churchill, S. W., and Evans, L. B. (1971). Calculation of Freezing in a Semi-infinite Region, *J. Heat Transfer*, 93, 234–236.
- Comini, G., Del Guidice, S., Lewis, R. W., and Zienkiewicz, O. G. (1974). Finite Element Solution of Nonlinear Heat Conduction Problems with Special Reference to Phase Change, *Int. J. Numer. Methods Eng.*, 8, 613–623.

- Comini, G., Del Guidice, S., and Nonino, C. (1994). *Finite Element Analysis in Heat Transfer*, Taylor & Francis, Washington, DC.
- Cotta, R. M., and Mikhailov, M. D. (1997). *Heat Conduction: Lumped Analysis, Integral Transforms and Symbolic Computation*, Wiley, New York.
- Duncan, A. B., and Peterson, G. P. (1994). Review of Microscale Heat Transfer, *Appl. Mech. Rev.*, 47, 397–428.
- Fletcher, L. S. (1988). Recent Developments in Contact Conductance Heat Transfer, *J. Heat Transfer*, 110, 1059–1070.
- Gebhart, B. (1993). *Heat Conduction and Mass Diffusion*, McGraw-Hill, New York.
- Goodman, T. R. (1958). The Heat Balance Integral and Its Application to Problems Involving a Change of Phase, *Trans. ASME*, 80, 335–342.
- Huang, C. L., and Shih, Y. P. (1975). A Perturbation Method for Spherical and Cylindrical Solidification, *Chem. Eng. Sci.*, 30, 897–906.
- Incropera, F., and DeWitt, D. P. (1996). *Introduction to Heat Transfer*, Wiley, New York.
- Jaluria, Y., and Torrance, K. E. (1986). *Computational Heat Transfer*, Hemisphere Publishing, Washington, DC.
- Jiji, L. M. (2000). *Heat Conduction*, Begell House, New York.
- Kern, D. Q., and Kraus, A. D. (1972). *Extended Surface Heat Transfer*, McGraw-Hill, New York.
- Kraus, A. D., Aziz, A., and Welty, J. R. (2001). *Extended Surface Heat Transfer*, Wiley, New York.
- Lock, G. H. S. (1971). On the Perturbation Solution of the Ice-Layer Problem, *Int. J. Heat Mass Transfer*, 14, 642–644.
- Lunardini, V. J. (1991). *Heat Transfer with Freezing and Thawing*, Elsevier Science, Amsterdam.
- Lynch, D. R., and O'Neill, K. (1981). Continuously Deforming Finite Elements for the Solution of Parabolic Problems with and without Phase Change, *Int. J. Numer. Methods Eng.*, 17, 81–93.
- Madhusadana, C. V. (1996). *Thermal Contact Conductance*, Springer-Verlag, New York.
- Myers, G. E. (1998). *Analytical Methods in Conduction Heat Transfer*, AMCHT Publications, Madison, WI.
- Nguyen, H., and Aziz, A. (1992). Heat Transfer from Conducting–Radiating Fins of Different Profile Shapes, *Waerme-Stoffuebertrag.*, 27, 67–72.
- Ozisk, M. N. (1993). *Heat Conduction*, Wiley, New York.
- Ozisk, M. N. (1994). *Finite Difference Methods in Heat Transfer*, CRC Press, Boca Raton, FL.
- Ozisk, M. N., and Orlande, H. R. B. (2000). *Inverse Heat Transfer*, Taylor & Francis, New York.
- Ozisk, M. N., and Uzzell, J. C., Jr. (1979). Exact Solution for Freezing in Cylindrical Symmetry with Extended Freezing Temperature Range, *J. Heat Transfer*, 101, 331–334.
- Parang, M., Crocker, D. S., and Haynes, B. D. (1990). Perturbation Solution for Spherical and Cylindrical Solidification by Combined Convective and Radiative Cooling, *Int. J. Heat Fluid Flow*, 11, 142–148.
- Pedroso, R. I., and Domato, G. A. (1973). Technical Note on Planar Solidification with Fixed Wall Temperature and Variable Thermal Properties, *J. Heat Transfer*, 93, 553–555.

- Pletcher, R. H., Minkowycz, W. J., Sparrow, E. M., and Schneider, G. E. (1988). Overview of Basic Numerical Methods, in *Handbook of Numerical Heat Transfer*, W. J. Minkowycz, E. M. Sparrow, G. E. Schneider, and R. H. Pletcher, eds., Wiley, New York, Chap. 1.
- Poulikakos, D. (1994). *Conduction Heat Transfer*, Prentice Hall, Englewood Cliffs, NJ.
- Riley, D. S., and Duck, P. W. (1977). Application of the Heat Balance Integral Method to the Freezing of a Cuboid, *Int. J. Heat Mass Transfer*, 20, 294–296.
- Rubinsky, B., and Eto, T. K. (1990). Heat Transfer during Freezing of Biological Materials, in *Annual Review of Heat Transfer*, C. L. Tien, ed., Hemisphere Publishing, Washington, DC, Chap. 1.
- Sahin, A. Z. (1992). Transient Heat Conduction in Semi-infinite Solid with Spatially Decaying Exponential Heat Generation, *Int. Commun. Heat Mass Transfer*, 19, 349–358.
- Schneider, P. J. (1955). *Conduction Heat Transfer*, Addison-Wesley, Reading, MA.
- Sen, A. K., and Trinh, S. (1986). An Exact Solution for the Rate of Heat Transfer from a Rectangular Fin Governed by Power Law Type Temperature Difference, *J. Heat Transfer*, 108, 457–459.
- Seniraj, R. V., and Bose, T. K. (1982). One-Dimensional Phase Change Problems with Radiation–Convection, *J. Heat Transfer*, 104, 811–813.
- Shamsundar, N. (1982). Approximate Calculation of Multidimensional Solidification Using Conduction Shape Factors, *J. Heat Transfer*, 104, 8–12.
- Solomon, A. D., Wilson, D. G., and Alexiades, V. (1982). A Mushy Zone Model with an Exact Solution, *Lett. Heat Mass Transfer*, 9, 319–324.
- Tao, L. N. (1978). The Stefan Problem with Arbitrary Initial and Boundary Conditions, *Q. Appl. Math.*, 36, 223–233.
- Tien, C. L., and Chen, G. (1994). Challenges in Microscale Conduction and Radiative Heat Transfer, *J. Heat Transfer*, 116, 799–807.
- Tien, C. L., Majumdar, A., and Gerner, F. M. (1998). *Microscale Energy Transport*, Taylor & Francis, Washington, DC.
- Tzou, D. Y. (1997). *Macro- to Microscale Heat Transfer*, Taylor & Francis, Washington, DC.
- Ullman, A., and Kalman, H. (1989). Efficiency and Optimized Dimensions of Annular Fins of Different Cross Sections, *Int. J. Heat Mass Transfer*, 32, 1105–1111.
- Viskanta, R. (1983). *Phase Change Heat Transfer*, in *Solar Heat Storage: Latent Heat Materials*, G. A. Lane, ed., CRC Press, Boca Raton, FL, pp. 153–222.
- Viskanta, R. (1988). Heat Transfer during Melting and Solidification of Metals, *J. Heat Transfer*, 110, 1205–1219.
- Yan, M. M., and Huang, P. N. S. (1979). Perturbation Solutions to Phase Change Problem Subject to Convection and Radiation, *J. Heat Transfer*, 101, 96–100.
- Zhuang, J. R., Werner, K., and Schlünder, E. U. (1995). Study of Analytical Solution to the Heat Transfer Problem and Surface Temperature in a Semi-infinite Body with a Constant Heat Flux at the Surface and an Initial Temperature Distribution, *Heat Mass Transfer*, 30, 183–186.

Thermal Spreading and Contact Resistances

M. M. YOVANOVICH

Department of Mechanical Engineering
University of Waterloo
Waterloo, Ontario, Canada

E. E. MAROTTA

Thermal Technologies Group
IBM Corporation
Poughkeepsie, New York

4.1 Introduction

- 4.1.1 Types of joints or interfaces
- 4.1.2 Conforming rough solids
- 4.1.3 Nonconforming smooth solids
- 4.1.4 Nonconforming rough solids
- 4.1.5 Single layer between two conforming rough solids
- 4.1.6 Parameters influencing contact resistance or conductance
- 4.1.7 Assumptions for resistance and conductance model development

4.2 Definitions of spreading and constriction resistances

- 4.2.1 Spreading and constriction resistances in a half-space
- 4.2.2 Spreading and constriction resistances in flux tubes and channels

4.3 Spreading and constriction resistances in an isotropic half-space

- 4.3.1 Introduction
- 4.3.2 Circular area on a half-space
 - Isothermal circular source
 - Isoflux circular source
- 4.3.3 Spreading resistance of an isothermal elliptical source area on a half-space
- 4.3.4 Dimensionless spreading resistance of an isothermal elliptical area
- 4.3.5 Approximations for dimensionless spreading resistance
- 4.3.6 Flux distribution over an isothermal elliptical area

4.4 Spreading resistance of rectangular source areas

- 4.4.1 Isoflux rectangular area
- 4.4.2 Isothermal rectangular area
- 4.4.3 Isoflux regular polygonal area
- 4.4.4 Arbitrary singly connected area
- 4.4.5 Circular annular area
 - Isoflux circular annulus
 - Isothermal circular annulus

- 4.4.6 Other doubly connected areas on a half-space
Effect of contact conductance on spreading resistance
- 4.5 Transient spreading resistance in an isotropic half-space
 - 4.5.1 Isoflux circular area
 - 4.5.2 Isoflux hyperellipse
 - 4.5.3 Isoflux regular polygons
- 4.6 Spreading resistance within a compound disk with conductance
 - 4.6.1 Special cases of the compound disk solution
 - 4.6.2 Half-space problems
 - 4.6.3 Semi-infinite flux tube problems
 - 4.6.4 Isotropic finite disk with conductance
- 4.7 Spreading resistance of isotropic finite disks with conductance
 - 4.7.1 Correlation equations
 - 4.7.2 Circular area on a single layer (coating) on a half-space
Equivalent isothermal circular contact
 - 4.7.3 Isoflux circular contact
 - 4.7.4 Isoflux, equivalent isothermal, and isothermal solutions
Isoflux contact area
Equivalent isothermal contact area
Isothermal contact area
- 4.8 Circular area on a semi-infinite flux tube
 - 4.8.1 General expression for a circular contact area with arbitrary flux on a circular flux tube
Flux distributions of the form $(1 - u^2)^\mu$
Equivalent isothermal circular source
Isoflux circular source
Parabolic flux distribution
Asymptotic values for dimensionless spreading resistances
Correlation equations for spreading resistance
Simple correlation equations
 - 4.8.2 Accurate correlation equations for various combinations of source areas, flux tubes, and boundary conditions
- 4.9 Multiple layers on a circular flux tube
- 4.10 Spreading resistance in compound rectangular channels
 - 4.10.1 Square area on a semi-infinite square flux tube
 - 4.10.2 Spreading resistance of a rectangle on a layer on a half-space
 - 4.10.3 Spreading resistance of a rectangle on an isotropic half-space
- 4.11 Strip on a finite channel with cooling
- 4.12 Strip on an infinite flux channel
 - 4.12.1 True isothermal strip on an infinite flux channel
 - 4.12.2 Spreading resistance for an abrupt change in the cross section
- 4.13 Transient spreading resistance within isotropic semi-infinite flux tubes and channels
 - 4.13.1 Isotropic flux tube
 - 4.13.2 Isotropic semi-infinite two-dimensional channel
- 4.14 Spreading resistance of an eccentric rectangular area on a rectangular plate with cooling
 - 4.14.1 Single eccentric area on a compound rectangular plate
 - 4.14.2 Multiple rectangular heat sources on an isotropic plate
- 4.15 Joint resistances of nonconforming smooth solids

- 4.15.1 Point contact model
 - Semiaxes of an elliptical contact area
- 4.15.2 Local gap thickness
- 4.15.3 Contact resistance of isothermal elliptical contact areas
- 4.15.4 Elastogap resistance model
- 4.15.5 Joint radiative resistance
- 4.15.6 Joint resistance of sphere–flat contact
 - Contacts in a vacuum
 - Effect of gas pressure on joint resistance
- 4.15.7 Joint resistance of a sphere and a layered substrate
- 4.15.8 Joint resistance of elastic–plastic contacts of hemispheres and flat surfaces in a vacuum
 - Alternative constriction parameter for a hemisphere
- 4.15.9 Ball-bearing resistance
- 4.15.10 Line contact models
 - Contact strip and local gap thicknesses
 - Contact resistance at a line contact
 - Gap resistance at a line contact
 - Joint resistance at a line contact
 - Joint resistance of nonconforming rough surfaces
- 4.16 Conforming rough surface models
 - 4.16.1 Plastic contact model
 - Plastic contact geometric parameters
 - Correlation of geometric parameters
 - Relative contact pressure
 - Vickers microhardness correlation coefficients
 - Dimensionless contact conductance: plastic deformation
 - 4.16.2 Radiation resistance and conductance for conforming rough surfaces
 - 4.16.3 Elastic contact model
 - Elastic contact geometric parameters
 - Dimensionless contact conductance
 - Correlation equations for surface parameters
 - 4.16.4 Conforming rough surface model: elastic–plastic deformation
 - Correlation equations for dimensionless contact conductance: elastic–plastic model
 - 4.16.5 Gap conductance for large parallel isothermal plates
 - 4.16.6 Gap conductance for joints between conforming rough surfaces
 - 4.16.7 Joint conductance for conforming rough surfaces
- 4.17 Joint conductance enhancement methods
 - 4.17.1 Metallic coatings and foils
 - Mechanical model
 - Thermal model
 - 4.17.2 Ranking metallic coating performance
 - 4.17.3 Elastomeric inserts
 - 4.17.4 Thermal greases and pastes
 - 4.17.5 Phase change materials
- 4.18 Thermal resistance at bolted joints

Nomenclature

References

4.1 INTRODUCTION

When two solids are joined, imperfect joints (interfaces) are formed. The imperfect joints occur because “real” surfaces are not perfectly smooth and flat. A mechanical joint consists of numerous discrete microcontacts that may be distributed in a random pattern over the apparent contact area if the contacting solids are nominally flat (conforming) and rough, or they may be distributed over a certain portion of the apparent contact area, called the *contour area*, if the contacting solids are nonconforming and rough. The contact spot size and density depend on surface roughness parameters, physical properties of the contacting asperities, and the apparent contact pressure. The distribution of the contact spots over the apparent contact area depends on the local out-of-flatness of the two solids, their elastic or plastic or elastic–plastic properties, and the mechanical load. Microgaps and macrogaps appear whenever there is absence of solid-to-solid contact. The microgaps and macrogaps are frequently occupied by a third substance, such as gas (e.g., air), liquid (e.g., oil, water), or grease, whose thermal conductivities are frequently much smaller than those of the contacting solids.

The joint formed by explosive bonding may appear to be perfect because there is metal-to-metal contact at all points in the interface that are not perfectly flat and perpendicular to the local heat flux vector. When two metals are brazed, soldered, or welded, a joint is formed that has a small but finite thickness and it consists of a complex alloy whose thermal conductivity is lower than that of the joined metals. A complex joint is formed when the solids are bonded or epoxied.

As a result of the “imperfect” joint, whenever heat is transferred across the joint, there is a measurable temperature drop across the joint that is related directly to the joint resistance and the heat transfer rate.

There are several review articles by Fletcher (1972, 1988, 1990), Kraus and Bar-Cohen (1983), Madhusudana and Fletcher (1986), Yovanovich (1986, 1991), Madhusudana (1996), Lambert and Fletcher (1996), and Yovanovich and Antonetti (1988), that should be consulted for details of thermal joint resistance and conductance of different types of joints.

4.1.1 Types of Joints or Interfaces

Several definitions are required to define heat transfer across joints (interfaces) formed by two solids that are brought together under a static mechanical load. The heat transfer across the joint is frequently related to *contact* resistances or *contact* conductances and the effective temperature drop across the joint (interface). The definitions are based on the type of joint (interface), which depends on the macro- and microgeometry of the contacting solids, the physical properties of the substrate and the contacting asperities, and the applied load or apparent contact pressure.

Figure 4.1 illustrates six types of joints that are characterized by whether the contacting surfaces are smooth and nonconforming (Fig. 4.1*a*), rough and conforming (nominally flat) (Fig. 4.1*c*), or rough and nonconforming (Fig. 4.1*b*). One or more layers may also be present in the joint, as shown in Fig. 4.1*d–f*.

If the contacting solids are nonconforming (e.g., convex solids) and their surfaces are smooth (Fig. 4.1*a* and *d*), the joint will consist of a single macrocontact and a

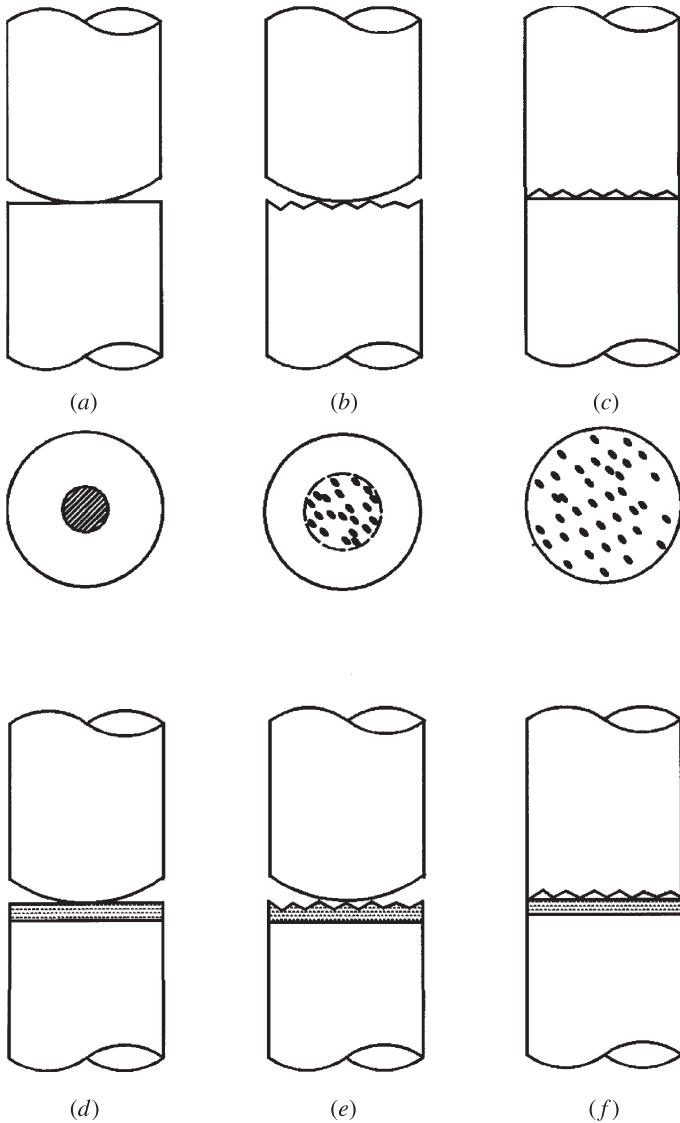


Figure 4.1 Six types of joints.

macrogap. The macrocontact may be formed by elastic, plastic, or elastic–plastic deformation of the substrate (bulk). The presence of a single “layer” will alter the nature of the joint according to its physical and thermal properties relative to those of the contacting solids. Thermomechanical models are available for finding the joint resistance of these types of joints.

The surfaces of the solids may be conforming (nominally flat) and rough (Fig. 4.1c and f). Under a static load, elastic, plastic, or elastic–plastic deformation of the contacting surface asperities occurs. The joint (interface) is characterized by many

discrete microcontacts with associated microgaps that are more or less *uniformly* distributed in the apparent (nominal) contact area. The sum of the microcontact areas, called the *real area of contact*, is a small fraction of the apparent contact area. Thermomechanical models are available for obtaining the contact, gap, and joint conductances (or resistances) of these types of joints.

A third type of joint is formed when nonconforming solids with surface roughness on one or both solids (Fig. 4.1*b* and *e*) are brought together under load. In this more complex case the microcontacts with associated microgaps are formed in a region called the *contour area*, which is some fraction of the apparent contact area. The substrate may undergo elastic, plastic, or elastic–plastic deformation, while the microcontacts may experience elastic, plastic, or elastic–plastic deformation. A few thermomechanical models have been developed for this type of joint.

The substance in the microgaps and macrogaps may be a gas (air, helium, etc.), a liquid (water, oil, etc.), grease, or some compound that consists of grease filled with many micrometer-sized solid particles (zinc oxide, etc.) that increase its effective thermal conductivity and alter its rheology. The interstitial substance is assumed to wet the surfaces of the bounding solids completely, and its effective thermal conductivity is assumed to be isotropic.

If one (or more) layers are present in the joint, the contact problem is much more complex and the associated mechanical and thermal problems are more difficult to model because the layer thickness, and its physical and thermal properties and surface characteristics, must be taken into account.

The total (joint) heat transfer rate across the interface may take place by conduction through the microcontacts, conduction through the interstitial substance, and radiation across the microgaps and macrogaps if the interstitial substance is transparent to radiation. Definitions of thermal *contact*, *gap*, and *joint* resistances and *contact*, *gap*, and *joint* conductances for several types of joints are given below.

4.1.2 Conforming Rough Solids

If the solids are conforming and their surfaces are rough (Fig. 4.1*c* and *f*), heat transfer across the joint (interface) occurs by conduction through the contacting microcontacts and through the microgap substance and by radiation across the microgap if the substance is transparent (e.g., dry air). The total or joint heat transfer rate Q_j , in general, is the sum of three separate heat transfer rates:

$$Q_j = Q_c + Q_g + Q_r \quad (\text{W}) \quad (4.1)$$

where Q_j , Q_c , Q_g , and Q_r represent the joint, contact, gap, and radiative heat transfer rates, respectively. The heat transfer rates are generally coupled in some complex manner; however, in many important problems, the coupling is relatively weak. The joint heat transfer rate is related to the effective temperature drop across the joint ΔT_j , nominal contact area A_a , joint resistance R_j , and joint conductance h_j by the definitions

$$Q_j = h_j A_a \Delta T_j \quad \text{and} \quad Q_j = \frac{\Delta T_j}{R_j} \quad (\text{W}) \quad (4.2)$$

These definitions result in the following relationships between joint conductance and joint resistance:

$$h_j = \frac{1}{A_a R_j} \quad (\text{W/m}^2 \cdot \text{K}) \quad \text{and} \quad R_j = \frac{1}{A_a h_j} \quad (\text{K/W}) \quad (4.3)$$

The component heat transfer rates are defined by the relationships

$$Q_c = h_c A_a \Delta T_j \quad Q_g = h_g A_g \Delta T_j, \quad Q_r = h_r A_g \Delta T_j \quad (4.4)$$

which are all based on the effective joint temperature drop ΔT_j and their respective heat transfer areas: A_a and A_g , the apparent and gap areas, respectively. It is the convention to use the apparent contact area in the definition of the contact conductance. Since $A_g = A_a - A_c$ and $A_c/A_a \ll 1$, then $A_g \approx A_a$. Finally, using the relationships given above, one can write the following relationships between the resistances and the conductances:

$$\frac{1}{R_j} = \frac{1}{R_c} + \frac{1}{R_g} + \frac{1}{R_r} \quad (\text{W/K}) \quad (4.5)$$

$$h_j = h_c + h_g + h_r \quad (\text{W/m}^2 \cdot \text{K}) \quad (4.6)$$

If the gap substance is opaque, then $R_r \rightarrow \infty$ and $h_r \rightarrow 0$, and the relationships reduce to

$$\frac{1}{R_j} = \frac{1}{R_c} + \frac{1}{R_g} \quad (\text{W/K}) \quad (4.7)$$

$$h_j = h_c + h_g \quad (\text{W/m}^2 \cdot \text{K}) \quad (4.8)$$

For joints (interfaces) placed in a vacuum where there is no substance in the microgaps, $R_g \rightarrow \infty$ and $h_g \rightarrow 0$ and the relationships become

$$\frac{1}{R_j} = \frac{1}{R_c} + \frac{1}{R_r} \quad (\text{W/K}) \quad (4.9)$$

$$h_j = h_c + h_r \quad (\text{W/m}^2 \cdot \text{K}) \quad (4.10)$$

In all cases there is heat transfer through the contacting asperities and h_c and R_c are present in the relationships. This heat transfer path is therefore very important. For most applications where the joint (interface) temperature level is below 600°C, radiation heat transfer becomes negligible, and therefore it is frequently ignored.

4.1.3 Nonconforming Smooth Solids

If two smooth, nonconforming solids are in contact (Fig. 4.1a and d), heat transfer across the joint can be described by the relationships given in earlier sections. The

radiative path becomes more complex because the enclosure and its radiative properties must be considered. If the apparent contact area is difficult to define, the use of conductances should be avoided and resistances should be used. The joint resistance, neglecting radiation, is

$$\frac{1}{R_j} = \frac{1}{R_c} + \frac{1}{R_g} \quad (\text{W/K}) \quad (4.11)$$

4.1.4 Nonconforming Rough Solids

If two rough, nonconforming solids make contact (Fig. 4.1*b* and *e*), heat transfer across the joint is much more complex when a substance “fills” the microgaps associated with the microcontacts and the macrogap associated with the contour area. The joint resistance, neglecting radiative heat transfer, is defined by the relationship

$$\frac{1}{R_j} = \frac{1}{R_{ma,c} + (1/R_{mi,c} + 1/R_{mi,g})^{-1}} + \frac{1}{R_{ma,g}} \quad (\text{W/K}) \quad (4.12)$$

where the component resistances are $R_{mi,c}$ and $R_{mi,g}$, the microcontact and microgap resistances, respectively, and $R_{ma,c}$ and $R_{ma,g}$, the macrocontact and macrogap resistances, respectively. If there is no interstitial substance in the microgaps and macrogap, and the contact is in a vacuum, the joint resistance (neglecting radiation) consists of the macro and micro resistances in series:

$$R_j = R_{ma,c} + R_{mi,c} \quad (\text{K/W}) \quad (4.13)$$

4.1.5 Single Layer between Two Conforming Rough Solids

If a single thin metallic or nonmetallic layer of uniform thickness is placed between the contacting rough solids, the mechanical and thermal problems become more complex. The layer thickness, thermal conductivity, and physical properties must also be included in the development of joint resistance (conductance) models. There are now two interfaces formed, which are generally different.

The presence of the layer can increase or decrease the joint resistance, depending on several geometric, physical, and thermal parameters. A thin isotropic silver layer bonded to one of the solids can decrease the joint resistance because the layer is relatively soft and has a high thermal conductivity. On the other hand, a relatively thick oxide coating, which is hard and has low thermal conductivity, can increase the joint resistance. The joint resistance, neglecting radiation, is given by the general relationship

$$R_j = \left(\frac{1}{R_{mi,c1}} + \frac{1}{R_{mi,g1}} \right)^{-1} + R_{\text{layer}} + \left(\frac{1}{R_{mi,c2}} + \frac{1}{R_{mi,g2}} \right)^{-1} \quad (\text{K/W}) \quad (4.14)$$

where $R_{mi,c1}$, $R_{mi,g1}$ and $R_{mi,c2}$, $R_{mi,g2}$ are the microcontact and microgap resistances at the two interfaces formed by the two solids, which are separated by the layer. The thermal resistance of the layer is modeled as

$$R_{\text{layer}} = \frac{t}{k_{\text{layer}} A_a} \quad (\text{K/W}) \quad (4.15)$$

where t is the layer thickness under loading conditions. Except for very soft metals (e.g., indium, lead, tin) at or above room temperature, the layer thickness under load conditions is close to the thickness before loading. If the layers are nonmetallic, such as elastomers, the thickness under load may be smaller than the preload thickness and elastic compression should be included in the mechanical model.

To develop thermal models for the component resistances, it is necessary to consider single contacts on a half-space and on semi-infinite flux tubes and to find relations for the spreading–constriction resistances.

4.1.6 Parameters Influencing Contact Resistance or Conductance

Real surfaces are not perfectly smooth (specially prepared surfaces such as those found in ball and roller bearings can be considered to be almost ideal surfaces) but consist of microscopic peaks and valleys. Whenever two real surfaces are placed in contact, intimate solid-to-solid contact occurs only at discrete parts of the joint (interface) and the real contact area will represent a very small fraction ($< 2\%$) of the nominal contact area. The real joint (interface) is characterized by several important factors:

- Intimate contact occurs at numerous discrete parts of the nominal contact area.
- The ratio of the real contact area to the nominal contact area is usually much less than 2%.
- The pressure at the real contact area is much greater than the apparent contact pressure. The real contact pressure is related to the flow pressure of the contacting asperities.
- A very thin gap exists in the regions in which there is no solid–solid contact, and it is usually occupied by a third substance.
- The third substance can be air, other gases, liquid, grease, grease filled with very small solid particles, and another metallic or nonmetallic substance.
- The joint (interface) is idealized as a line; however, the actual “thickness” of the joint (interface) ranges from $0.5 \mu\text{m}$ for very smooth surfaces to about 60 to $80 \mu\text{m}$ for very rough surfaces.
- Heat transfer across the interface can take place by conduction through the real contact area, by conduction through the substance in the gap, or by radiation across the gap if the substance in the gap is transparent to radiation or if the gap is under a vacuum. All three modes of heat transfer may occur simultaneously; but usually, they occur in pairs, with solid–solid conduction always present.

The process of heat transfer across a joint (interface) is complex because the joint resistance may depend on many geometrical, thermal, and mechanical parameters, of which the following are very important:

- Geometry of the contacting solids (surface roughness, asperity slope, and out-of-flatness or waviness)
- Thickness of the gap (noncontact region)
- Type of interstitial fluid (gas, liquid, grease, or vacuum)
- Interstitial gas pressure
- Thermal conductivities of the contacting solids and the interstitial substance
- Microhardness or flow pressure of the contacting asperities (plastic deformation of the highest peaks of the softer solid)
- Modulus of elasticity and Poisson's ratio of the contacting solids (elastic deformation of the wavy parts of the joint)
- Average temperature of the joint influences radiation heat transfer as well as the thermophysical properties
- Load or apparent contact pressure

4.1.7 Assumptions for Resistance and Conductance Model Development

Because thermal contact resistance is such a complex problem, it is necessary to develop simple thermophysical models that can be analyzed and verified experimentally. To achieve these goals the following assumptions have been made in the development of the several contact resistance models, which will be discussed later:

- Contacting solids are isotropic: thermal conductivity and physical parameters are constant.
- Contacting solids are thick relative to the roughness or waviness.
- Surfaces are clean: no oxide effect.
- Contact is static: no vibration effects.
- First loading cycle only: no hysteresis effect.
- Relative apparent contact pressure (P/H_p for plastic deformation and P/H_e for elastic deformation) is neither too small ($> 10^{-6}$) nor too large ($< 10^{-1}$).
- Radiation is small or negligible.
- Heat flux at microcontacts is steady and not too large ($< 10^7 \text{ W/m}^2$).
- Contact is in a vacuum or the interstitial fluid can be considered to be a continuum if it is not a gas.
- Interstitial fluid perfectly wets both contacting solids.

4.2 DEFINITIONS OF SPREADING AND CONSTRICTION RESISTANCES

4.2.1 Spreading and Constriction Resistances in a Half-Space

Heat may enter or leave an isotropic *half-space* (a region whose dimensions are much larger than the characteristic length of the heat source area) through planar singly or

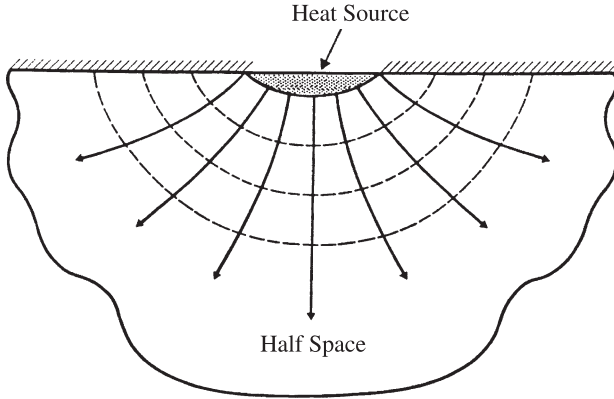


Figure 4.2 Heat flow lines and isotherms for steady conduction from a finite heat source into a half-space. (From Yovanovich and Antonetti, 1988.)

doubly connected areas (e.g., circular or annular area). The free surface of the half-space is adiabatic except for the source area. If heat enters the half-space, the flux lines spread apart as the heat is conducted away from the small source area (Fig. 4.2); then the thermal resistance is called *spreading resistance*.

If the heat leaves the half-space through a small area, the flux lines are constricted and the thermal resistance is called *constriction resistance*. The heat transfer may be steady or transient. The temperature field T in the half-space is, in general, three-dimensional, and steady or transient. The temperature in the source area may be two-dimensional, and steady or transient.

If heat transfer is into the half-space, the spreading resistance is defined as (Carslaw and Jaeger, 1959; Yovanovich, 1976c; Madhusudana, 1996; Yovanovich and Antonetti, 1988)

$$R_s = \frac{\bar{T}_{\text{source}} - \bar{T}_{\text{sink}}}{Q} \quad (\text{K/W}) \quad (4.16)$$

where T_{source} is the source temperature and T_{sink} is a convenient thermal sink temperature; and where Q is the steady or transient heat transfer rate:

$$Q = \iint_A q_n dA = \iint_A -k \frac{\partial T}{\partial n} dA \quad (\text{W}) \quad (4.17)$$

where q_n is the heat flux component normal to the area and $\partial T / \partial n$ is the temperature gradient normal to the area. If the heat flux distribution is uniform over the area, $Q = qA$. For singly and doubly connected source areas, three source temperatures have been used in the definition: maximum temperature, centroid temperature, and area-averaged temperature, which is defined according to Yovanovich (1976c) as

$$\bar{T}_{\text{source}} = \frac{1}{A} \iint_A T_{\text{source}} dA \quad (\text{K}) \quad (4.18)$$

where A is the source area. Because the sink area is much larger than the source area, it is, by convention, assumed to be isothermal (i.e., $T_{\text{sink}} = T_{\infty}$). The maximum and centroid temperatures are identical for singly connected axisymmetric source areas; otherwise, they are different (Yovanovich, 1976c; Yovanovich and Burde, 1977; Yovanovich et al., 1977). For doubly connected source areas (e.g., circular annulus), the area-averaged source temperature is used (Yovanovich and Schneider, 1977). If the source area is assumed to be isothermal, $\bar{T}_{\text{source}} = T_0$.

The general definition of spreading (or constriction) resistance leads to the following relationship for the dimensionless spreading resistance:

$$k\mathcal{L}R_s = \frac{\mathcal{L}}{A} \frac{\iint_A \theta \, dA}{\iint_A (\partial\theta/\partial z)_{z=0} \, dA} \quad (4.19)$$

where $\theta = T(x,y) - T_{\infty}$, the rise of the source temperature above the sink temperature. The arbitrary characteristic length scale of the source area is denoted as \mathcal{L} . For convenience the dimensionless spreading resistance, denoted as $\psi = k\mathcal{L}R_s$ (Yovanovich, 1976c; Yovanovich and Antonetti, 1988), is called the *spreading resistance parameter*. This parameter depends on the heat flux distribution over the source area and the shape and aspect ratio of the singly or doubly connected source area. The spreading resistance definition holds for transient conduction into or out of the half-space. If the heat flux is uniform over the source area, the temperature is nonuniform; and if the temperature of the source area is uniform, the heat flux is nonuniform (Carslaw and Jaeger, 1959; Yovanovich, 1976c). The relation for the dimensionless spreading resistance is mathematically identical to the dimensionless constriction resistance for identical boundary conditions on the source area. For a nonisothermal singly connected area the spreading resistance can also be defined with respect to its maximum temperature or the temperature at its centroid (Carslaw and Jaeger, 1959; Yovanovich, 1976c; Yovanovich and Burde, 1977). These temperatures, in general, are not identical and they are greater than the area-averaged temperature (Yovanovich and Burde, 1977).

The definition of spreading resistance for the isotropic half-space is applicable for single and multiply isotropic layers which are placed in perfect thermal contact with the half-space, and the heat that leaves the source area is conducted through the layer or layers before entering into the half-space. The conductance h cannot be defined for the half-space problem because the corresponding area is not defined.

4.2.2 Spreading and Constriction Resistances in Flux Tubes and Channels

If a circular heat source of area A_s is in contact with a very long circular flux tube of cross-sectional area A_t (Fig. 4.3), the flux lines are constrained by the adiabatic sides to “bend” and then become parallel to the axis of the flux tube at some distance $z = \ell$ from the contact plane at $z = 0$. The isotherms, shown as dashed lines, are everywhere orthogonal to the flux lines. The temperature in planes $z = \ell \gg \sqrt{A_t}$

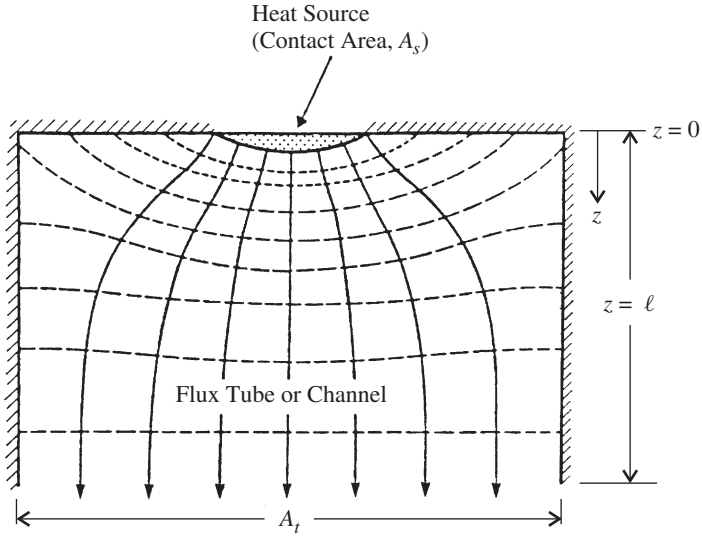


Figure 4.3 Heat flow lines and isotherms for steady conduction from a finite heat source into a flux tube or channel. (From Yovanovich and Antonetti, 1988.)

“far” from the contact plane $z = 0$ becomes isothermal, while the temperature in planes near $z = 0$ are two- or three-dimensional. The thermal conductivity of the flux tube is assumed to be constant.

The total thermal resistance R_{total} for steady conduction from the heat source area in $z = 0$ to the arbitrary plane $z = \ell$ is given by the relationship

$$QR_{\text{total}} = \bar{T}_s - \bar{T}_{z=\ell} \quad (\text{K}) \quad (4.20)$$

where \bar{T}_s is the mean source temperature and $\bar{T}_{z=\ell}$ is the mean temperature of the arbitrary plane. The one-dimensional resistance of the region bounded by $z = 0$ and $z = \ell$ is given by the relation

$$QR_{\text{1D}} = \bar{T}_{z=0} - \bar{T}_{z=\ell} \quad (\text{K}) \quad (4.21)$$

The total resistance is equal to the sum of the one-dimensional resistance and the spreading resistance:

$$R_{\text{total}} = R_{\text{1D}} + R_s \quad \text{or} \quad R_{\text{total}} - R_{\text{1D}} = R_s \quad (\text{K}) \quad (4.22)$$

By subtraction, the relationship for the spreading resistance, proposed by Mikic and Rohsenow (1966), is

$$R_s = \frac{\bar{T}_s - \bar{T}_{z=0}}{Q} \quad (\text{K/W}) \quad (4.23)$$

where Q is the total heat transfer rate from the source area into the flux tube. It is given by

$$Q = \iint_{A_s} -k \frac{\partial T}{\partial z} \bigg|_{z=0} dA_s \quad (\text{W}) \quad (4.24)$$

The dimensionless spreading resistance parameter $\psi = k\mathcal{L}R_s$ is introduced for convenience. The arbitrary length scale \mathcal{L} is related to some dimension of the source area. In general, ψ depends on the shape and aspect ratio of the source area, the shape and aspect ratio of the flux tube cross section, the relative size of the source area, the orientation of the source area relative to the cross section of the flux tube, the boundary condition on the source area, and the temperature basis for definition of the spreading resistance.

The definitions given above are applicable to singly and doubly connected source areas; however, $A_s/A_t < 1$ in all cases. The source area and flux tube cross-sectional area may be circular, square, elliptical, rectangular, or any other shape. The heat flux and temperature on the source area may be uniform and constant. In general, both heat flux and temperature on the source area are nonuniform. Numerous examples are presented in subsequent sections.

4.3 SPREADING AND CONSTRICTION RESISTANCES IN AN ISOTROPIC HALF-SPACE

4.3.1 Introduction

Steady or transient heat transfer occurs in a half-space $z > 0$ which may be isotropic or may consist of one or more thin isotropic layers bonded to the isotropic half-space. The heat source is some planar singly or doubly connected area such as a circular annulus located in the “free” surface $z = 0$ of the half-space. The dimensions of the half-space are much larger than the largest dimension of the source area. The “free” surface $z = 0$ of the half-space outside the source area is adiabatic. If the source area is isothermal, the heat flux over the source area is nonuniform. If the source is subjected to a uniform heat flux, the source area is nonisothermal.

4.3.2 Circular Area on a Half-Space

There are two classical steady-state solutions available for the circular source area of radius a on the surface of a half-space of thermal conductivity k . The solutions are for the isothermal and isoflux source areas. In both problems the temperature field is two-dimensional in circular-cylinder coordinates [i.e., $\theta(r, z)$]. The important results are presented here.

Isothermal Circular Source In this problem the mixed-boundary conditions (Sneddon, 1966) in the free surface are

$$z = \begin{cases} 0 & 0 \leq r < a & \theta = \theta_0 \\ 0 & r > a & \frac{\partial \theta}{\partial z} = 0 \end{cases} \quad (4.25)$$

and the condition at remote points is: As $\sqrt{r^2 + z^2} \rightarrow \infty$, then $\theta \rightarrow 0$. The temperature distribution throughout the half-space $z \geq 0$ is given by the infinite integral (Carslaw and Jaeger, 1959)

$$\theta = \frac{2}{\pi} \theta_0 \int_0^\infty e^{-\lambda z} J_0(\lambda r) \sin \lambda a \frac{d\lambda}{\lambda} \quad (K) \quad (4.26)$$

where $J_0(x)$ is the Bessel function of the first kind of order zero (Abramowitz and Stegun, 1965) and λ is a dummy variable. The solution can be written in the following alternative form according to Carslaw and Jaeger (1959):

$$\theta = \frac{2}{\pi} \theta_0 \sin^{-1} \frac{2a}{\sqrt{(r-a)^2 + z^2} + \sqrt{(r+a)^2 + z^2}} \quad (K) \quad (4.27)$$

The heat flow rate from the isothermal circular source into the half-space is found from

$$\begin{aligned} Q &= \int_0^a -k \left(\frac{\partial \theta}{\partial z} \right)_{z=0} 2\pi r \, dr \\ &= 4ka\theta_0 \int_0^\infty J_1(\lambda a) \sin \lambda a \frac{d\lambda}{\lambda} \\ &= 4ka\theta_0 \quad (W) \end{aligned} \quad (4.28)$$

From the definition of spreading resistance one finds the relationship for the spreading resistance (Carslaw and Jaeger, 1959):

$$R_s = \frac{\theta_0}{Q} = \frac{1}{4ka} \quad (K/W) \quad (4.29)$$

The heat flux distribution over the isothermal heat source area is axisymmetric (Carslaw and Jaeger, 1959):

$$q(r) = \frac{Q}{2\pi a^2} \frac{1}{\sqrt{1 - (r/a)^2}} \quad 0 \leq r < a \quad (W/m^2) \quad (4.30)$$

This flux distribution is minimum at the centroid $r = 0$ and becomes unbounded at the edge $r = a$.

Isoflux Circular Source In this problem the boundary conditions in the free surface are

$$\theta = \begin{cases} 0 & 0 \leq r < a & \frac{\partial \theta}{\partial z} = -\frac{q_0}{k} \\ 0 & r > a & \frac{\partial \theta}{\partial z} = 0 \end{cases} \tag{4.31}$$

where $q_0 = Q/\pi a^2$ is the uniform heat flux. The condition at remote points is identical. The temperature distribution throughout the half-space $z \geq 0$ is given by the infinite integral (Carslaw and Jaeger, 1959)

$$\theta = \frac{q_0 a}{k} \int_0^\infty e^{-\lambda z} J_0(\lambda r) J_1(\lambda a) \frac{d\lambda}{\lambda} \tag{K} \tag{4.32}$$

where $J_1(x)$ is the Bessel function of the first kind of order 1 (Abramowitz and Stegun, 1965), and λ is a dummy variable. The temperature rise in the source area $0 \leq r \leq a$ is axisymmetric and is given by (Carslaw and Jaeger, 1959):

$$\theta(r) = \frac{q_0 a}{k} \int_0^\infty J_0(\lambda r) J_1(\lambda a) \frac{d\lambda}{\lambda} \tag{K} \tag{4.33}$$

The alternative form of the solution according to Yovanovich (1976c) is

$$\theta(r) = \frac{2}{\pi} \frac{q_0 a}{k} E\left(\frac{r}{a}\right) \quad 0 \leq r \leq a \tag{K} \tag{4.34}$$

where $E(r/a)$ is the complete elliptic integral of the second kind of modulus r/a (Byrd and Friedman, 1971) which is tabulated, and it can be calculated by means of computer algebra systems. The temperatures at the centroid $r = 0$ and the edge $r = a$ of the source area are, respectively,

$$\theta(0) = \frac{q_0 a}{k} \quad \text{and} \quad \theta(a) = \frac{2}{\pi} \frac{q_0 a}{k} \tag{K} \tag{4.35}$$

The centroid temperature rise relative to the temperature rise at the edge is greater by approximately 57%. The values of the dimensionless temperature rise defined as $k\theta(r/a)/(q_0 a)$ are presented in Table 4.1.

TABLE 4.1 Dimensionless Source Temperature

r/a	$k\theta(r/a)/q_0 a$	r/a	$k\theta(r/a)/q_0 a$
0.0	1.000	0.6	0.9028
0.1	0.9975	0.7	0.8630
0.2	0.9899	0.8	0.8126
0.3	0.9771	0.9	0.7459
0.4	0.9587	1.0	0.6366
0.5	0.9342		

The area-averaged source temperature is

$$\bar{\theta} = \frac{1}{\pi a^2} \frac{q_0 a}{k} \int_0^a \left[\int_0^\infty J_0(\lambda r) J_1(\lambda a) \frac{d\lambda}{\lambda} \right] 2\pi r dr \quad (\text{K}) \quad (4.36)$$

The integrals can be interchanged, giving the result (Carslaw and Jaeger, 1959):

$$\bar{\theta} = \frac{2q_0}{k} \int_0^\infty J_1^2(\lambda a) \frac{d\lambda}{\lambda^2} = \frac{8}{3\pi} \left(\frac{q_0 a}{k} \right) \quad (\text{K}) \quad (4.37)$$

According to the definition of spreading resistance, one obtains for the isoflux circular source the relation (Carslaw and Jaeger, 1959)

$$R_s = \frac{\bar{\theta}}{Q} = \frac{8}{3\pi^2} \left(\frac{1}{ka} \right) \quad (\text{K/W}) \quad (4.38)$$

The spreading resistance for the isoflux source area based on the area-averaged temperature rise is greater than the value for the isothermal source by the factor

$$\frac{(R_s)_{\text{isoflux}}}{(R_s)_{\text{isothermal}}} = \frac{32}{3\pi^2} = 1.08076$$

4.3.3 Spreading Resistance of an Isothermal Elliptical Source Area on a Half-Space

The spreading resistance for an isothermal elliptical source area with semiaxes $a \geq b$ is available in closed form. The results are obtained from a solution that follows the classical solution presented for finding the capacitance of a charged elliptical disk placed in free space as given by Jeans (1963), Smythe (1968), and Stratton (1941). Holm (1967) gave the solution for the electrical resistance for current flow from an isopotential elliptical disk. The thermal solution presented next will follow the analysis of Yovanovich (1971).

The elliptical contact area $x^2/a^2 + y^2/b^2 = 1$ produces a three-dimensional temperature field where the isotherms are ellipsoids described by the relationship

$$\frac{x^2}{a^2 + \zeta} + \frac{y^2}{b^2 + \zeta} + \frac{z^2}{\zeta} = 1 \quad (4.39)$$

The three-dimensional Laplace equation in Cartesian coordinates can be transformed into the one-dimensional Laplace equation in ellipsoidal coordinates:

$$\nabla^2 \theta = \frac{\partial}{\partial \zeta} \left[\sqrt{f(\zeta)} \frac{\partial \theta}{\partial \zeta} \right] = 0 \quad (4.40)$$

where ζ is the ellipsoidal coordinate for the ellipsoidal temperature rise $\theta(\zeta)$ and where

$$\sqrt{f(\zeta)} = \sqrt{(a^2 + \zeta)(b^2 + \zeta)\zeta} \quad (4.41)$$

The solution of the differential equation according to Yovanovich (1971) is

$$\theta = C_2 - C_1 \int_{\zeta}^{\infty} \frac{d\zeta}{\sqrt{f(\zeta)}} \quad (\text{K}) \quad (4.42)$$

The boundary conditions are specified in the contact plane ($z = 0$) where

$$\begin{aligned} \theta &= \theta_0 \quad \text{within} \quad \frac{x^2}{a^2} + \frac{y^2}{b^2} = 1 \\ \frac{\partial \theta}{\partial z} &= 0 \quad \text{outside} \quad \frac{x^2}{a^2} + \frac{y^2}{b^2} = 1 \end{aligned} \quad (4.43)$$

The regular condition at points remote to the elliptical area is $\theta \rightarrow 0$ as $\zeta \rightarrow \infty$. This condition is satisfied by $C_2 = 0$, and the condition in the contact plane is satisfied by $C_1 = -Q/4\pi k$, where Q is the total heat flow rate from the isothermal elliptical area. The solution is, therefore, according to Yovanovich (1971),

$$\theta = \frac{Q}{4\pi k} \int_{\zeta}^{\infty} \frac{d\zeta}{\sqrt{(a^2 + \zeta)(b^2 + \zeta)\zeta}} \quad (\text{K}) \quad (4.44)$$

When $\zeta = 0$, $\theta = \theta_0$, constant for all points within the elliptical area, and when $\zeta \rightarrow \infty$, $\theta \rightarrow 0$ for all points far from the elliptical area. According to the definition of spreading resistance for an isothermal contact area, we find that

$$R_s = \frac{\theta_0}{Q} = \frac{1}{4\pi k} \int_0^{\infty} \frac{d\zeta}{\sqrt{(a^2 + \zeta)(b^2 + \zeta)\zeta}} \quad (\text{K/W}) \quad (4.45)$$

The last equation can be transformed into a standard form by setting $\sin t = a/\sqrt{a^2 + \zeta}$. The alternative form for the spreading resistance is

$$R_s = \frac{1}{2\pi k a} \int_0^{\pi/2} \frac{dt}{\{1 - [(a^2 - b^2)/a^2] \sin^2 t\}^{1/2}} \quad (\text{K/W}) \quad (4.46)$$

The spreading resistance depends on the thermal conductivity of the half-space, the semimajor axis a , and the aspect ratio of the elliptical area $b/a \leq 1$. It is clear that when the axes are equal (i.e., $b = a$), the elliptical area becomes a circular area and the spreading resistance is $R_s = 1/(4ka)$. The integral is the complete elliptic integral of the first kind $K(\kappa)$ of modulus $\kappa = \sqrt{(a^2 - b^2)/a^2}$ (Byrd and Friedman, 1971; Gradshteyn and Ryzhik, 1965). The spreading resistance for the isothermal elliptical source area can be written as

$$R_s = \frac{1}{2\pi k a} K(\kappa) \quad (\text{K/W}) \quad (4.47)$$

The complete elliptic integral is tabulated (Abramowitz and Stegun, 1965; Magnus et al. (1966); Byrd and Friedman, 1971). It can also be computed efficiently and very accurately by computer algebra systems.

TABLE 4.2 Dimensionless Spreading Resistance of an Isothermal Ellipse

a/b	$k\sqrt{A} R_s$	a/b	$k\sqrt{A} R_s$
1	0.4431	6	0.3678
2	0.4302	7	0.3566
3	0.4118	8	0.3466
4	0.3951	9	0.3377
5	0.3805	10	0.3297

4.3.4 Dimensionless Spreading Resistance of an Isothermal Elliptical Area

To compare the spreading resistances of the elliptical area and the circular area, it is necessary to nondimensionalize the two results. For the circle, the radius appears as the length scale, and for the ellipse, the semimajor axis appears as the length scale. For proper comparison of the two geometries it is important to select a length scale that best characterizes the two geometries. The proposed length scale is based on the square root of the active area of each geometry (i.e., $\mathcal{L} = \sqrt{A}$) (Yovanovich, 1976c; Yovanovich and Burde, 1977; Yovanovich et al., 1977). Therefore, the dimensionless spreading resistances for the circle and ellipse are

$$(k\sqrt{A} R_s)_{\text{circle}} = \frac{\sqrt{\pi}}{4}$$

$$(k\sqrt{A} R_s)_{\text{ellipse}} = \frac{1}{2\sqrt{\pi}} \sqrt{\frac{a}{b}} K(\kappa)$$

where $\kappa = \sqrt{1 - (b/a)^2}$. The dimensionless spreading resistance values for an isothermal elliptical area are presented in Table 4.2 for a range of the semiaxes ratio a/b .

The tabulated values of the dimensionless spreading resistance reveal an interesting trend beginning with the first entry, which corresponds to the circle. The dimensionless resistance values decrease with increasing values of a/b . Ellipses with larger values of a/b have smaller spreading resistances than the circle; however, the decrease has a relatively weak dependence on a/b . For the same area the spreading resistance of the ellipse with $a/b = 10$ is approximately 74% of the spreading resistance for the circle.

4.3.5 Approximations for Dimensionless Spreading Resistance

Two approximations are presented for quick calculator estimations of the dimensionless spreading resistance for isothermal elliptical areas:

$$k\sqrt{A} R_s = \begin{cases} \frac{\sqrt{\pi\alpha}}{(\sqrt{\alpha} + 1)^2} & \text{for } 1 \leq \alpha \leq 5 \\ \frac{1}{2\sqrt{\pi\alpha}} \ln 4\alpha & \text{for } 5 \leq \alpha < \infty \end{cases} \quad (4.48)$$

where $\alpha = a/b \geq 1$. Although both approximations can be used at $\alpha = 5$, the second approximation is slightly more accurate, and therefore it is recommended.

4.3.6 Flux Distribution over an Isothermal Elliptical Area

The heat flux distribution over the elliptical area is given by (Yovanovich, 1971)

$$q(x,y) = \frac{Q}{2\pi ab} \left[1 - \left(\frac{x}{a}\right)^2 - \left(\frac{y}{b}\right)^2 \right]^{-1/2} \quad (\text{W/m}^2) \quad (4.49)$$

The heat flux is minimum at the centroid, where its magnitude is $q_0 = Q/2\pi ab$, and it is “unbounded” on the perimeter of the ellipse.

4.4 SPREADING RESISTANCE OF RECTANGULAR SOURCE AREAS

4.4.1 Isoflux Rectangular Area

The dimensionless spreading resistances of the rectangular source area $-a \leq x \leq a$, $-b \leq y \leq b$ with aspect ratio $a/b \geq 1$ are found by means of the integral method (Yovanovich, 1971). Employing the definition of the spreading resistance based on the area-averaged temperature rise with $Q = 4qab$ gives the following dimensionless relationship (Yovanovich, 1976c; Carslaw and Jaeger, 1959):

$$k\sqrt{A} R_s = \frac{\sqrt{\epsilon}}{\pi} \left\{ \sinh^{-1} \frac{1}{\epsilon} + \frac{1}{\epsilon} \sinh^{-1} \epsilon + \frac{\epsilon}{3} \left[1 + \frac{1}{\epsilon^3} - \left(1 + \frac{1}{\epsilon^2} \right)^{3/2} \right] \right\} \quad (4.50)$$

where $\epsilon = a/b \geq 1$. Employing the definition based on the centroid temperature rise, the dimensionless spreading resistance is obtained from the relationship (Carslaw and Jaeger, 1959)

$$k\sqrt{A} R_s = \frac{\sqrt{\epsilon}}{\pi} \left(\frac{1}{\epsilon} \sinh^{-1} \epsilon + \sinh^{-1} \frac{1}{\epsilon} \right) \quad (4.51)$$

Typical values of the dimensionless spreading resistance for the isoflux rectangle based on the area-average temperature rise for $1 \leq a/b \leq 10$ are given in Table 4.3.

Table 4.3 Dimensionless Spreading Resistance of an Isoflux Rectangular Area

a/b	$k\sqrt{A} R_s$	a/b	$k\sqrt{A} R_s$
1	0.4732	6	0.3950
2	0.4598	7	0.3833
3	0.4407	8	0.3729
4	0.4234	9	0.3636
5	0.4082	10	0.3552

TABLE 4.4 Dimensionless Spreading Resistance of an Isothermal Rectangular Area

a/b	$k\sqrt{A} R_s$
1	0.4412
2	0.4282
3	0.4114
4	0.3980

4.4.2 Isothermal Rectangular Area

Schneider (1978) presented numerical values and a correlation of those values for the dimensionless spreading resistance of an isothermal rectangle for the aspect ratio range: $1 \leq a/b \leq 4$. The correlation equation is

$$k\sqrt{A} R_s = \sqrt{\frac{a}{b}} \left[0.06588 - 0.00232 \left(\frac{a}{b} \right) + \frac{0.6786}{a/b + 0.8145} \right] \quad (4.52)$$

The numerical values are given in Table 4.4.

A comparison of the values for the isothermal rectangular area and the isothermal elliptical area reveals a very close relationship. The maximum difference of approximately -0.7% is found at $a/b = 4$. It is expected that the close agreement observed for the four aspect ratios will hold for higher aspect ratios because the dimensionless spreading resistance is a weak function of the shape if the areas are geometrically similar. In fact, the correlation values for the rectangle and the analytical values for the ellipse are within $\pm 1.5\%$ over the wider range, $1 \leq a/b \leq 13$.

4.4.3 Isoflux Regular Polygonal Area

The spreading resistances of isoflux regular polygonal areas has been examined extensively. The regular polygonal areas are characterized by the number of sides $N \geq 3$, the side dimension s , and the radius of the inscribed circle denoted as r_i . The perimeter is $P = Ns$; the relationship between the inscribed radius and the side dimension is $s/r_i = 2 \tan(\pi/N)$. The area of the regular polygon is $A = Nr_i^2 \tan(\pi/N)$. The temperature rises from the minimum values located on the edges to a maximum value at the centroid. It can be found easily by means of integral methods based on the superposition of point sources. The general relationship for the spreading resistance based on the *centroid* temperature rise is found to be

$$k\sqrt{A} R_s = \frac{1}{\pi} \sqrt{\frac{N}{\tan(\pi/N)}} \ln \frac{1 + \sin(\pi/N)}{\cos(\pi/N)} \quad N \geq 3 \quad (4.53)$$

The expression above gives $k\sqrt{A} R_s = 0.5516$ for the equilateral triangle $N = 3$, which is approximately 2.3% smaller than the value for the circle where $N \rightarrow \infty$.

Numerical methods are required to find the dimensionless spreading resistance for regular polygons subjected to a uniform heat flux. The corresponding value for the area-averaged basis was reported by Yovanovich and Burde (1977) to be $k\sqrt{A} R_s = 0.4600$ for the equilateral triangle, which is approximately 4% smaller than the value for the circle.

4.4.4 Arbitrary Singly Connected Area

The spreading resistances for isoflux, singly connected source areas were obtained by means of numerical methods applied to the integral formulation of the spreading resistance. The source areas examined were isosceles triangles having a range of aspect ratios, the semicircle, L-shaped source areas (squares with corners removed), and the hyperellipse area defined by

$$\left(\frac{x}{a}\right)^n + \left(\frac{y}{b}\right)^n = 1 \tag{4.54}$$

where a and b are the semiaxes along the x and y axes, respectively. The shape parameter n lies in the range $0 < n < \infty$. Many interesting geometries can be generated by the parameters a , b , and n . The area of the hyperellipse is given by the relationship

$$A = \frac{4ab}{n} \frac{\Gamma(1 + 1/n)\Gamma(1/n)}{\Gamma(1 + 2/n)} \quad (\text{m}^2) \tag{4.55}$$

where $\Gamma(x)$ is the gamma function which is tabulated (Abramowitz and Stegun, 1965), and it can be computed accurately by means of computer algebra systems. The dimensionless spreading resistance was found to be a weak function of the shape of the source area for a wide range of values of n . Typical values are given in Table 4.5.

The dimensionless spreading resistances were based on the centroid temperature rise denoted as R_0 and the area-averaged temperature rise, denoted \bar{R} . The dimensionless spreading resistance was based on the length scale $\mathcal{L} = \sqrt{A}$. All numerical results were found to lie in narrow ranges: $0.4424 \leq k\sqrt{A} \bar{R} \leq 0.4733$ and $0.5197 \leq k\sqrt{A} R_0 \leq 0.5614$. The corresponding values for the equilateral triangle are $k\sqrt{A} \bar{R} = 0.4600$ and $k\sqrt{A} R_0 = 0.5616$, and for the semicircle they are $k\sqrt{A} \bar{R} = 0.4610$ and $k\sqrt{A} R_0 = 0.5456$.

TABLE 4.5 Effect of n on Dimensionless Spreading Resistances

n	$k\sqrt{A} \bar{R}$	$k\sqrt{A} R_0$
0.5	0.4440	0.5468
1	0.4728	0.5611
2	0.4787	0.5642
4	0.4770	0.5631
∞	0.4732	0.5611

The following approximations were recommended by Yovanovich and Burde (1977) for quick approximate calculations: $k\sqrt{A} R_0 = \frac{5}{9}$ and $k\sqrt{A} \bar{R} = 0.84 k\sqrt{A} R_0$.

The ratios of the area-averaged and centroid temperature rises for all geometries examined were found to be closely related such that $\bar{\theta}/\theta_0 = 0.84 \pm 1.7\%$.

4.4.5 Circular Annular Area

Analytical methods have been used to obtain the spreading resistance for the isoflux and isothermal circular annulus of radii a and b in the surface of an isotropic half-space having thermal conductivity k .

Isoflux Circular Annulus The temperature rise of points in the annular area $a \leq r \leq b$ was reported by Yovanovich and Schneider (1977) to have the distribution

$$\theta(r) = \frac{2}{\pi} \frac{qb}{k} \left\{ E\left(\frac{r}{b}\right) - \frac{r}{b} E\left(\frac{a}{r}\right) + \frac{r}{b} \left[1 - \left(\frac{a}{r}\right)^2 \right] K\left(\frac{a}{r}\right) \right\} \quad (\text{K}) \quad (4.56)$$

where the special functions $K(x)$ and $E(x)$ are the complete elliptic integrals of the first and second kinds, respectively, of arbitrary modulus x (Abramowitz and Stegun, 1965; Byrd and Friedman, 1971). The dimensionless spreading resistance, based on the area-averaged temperature rise, of the isoflux circular annulus was reported by Yovanovich and Schneider (1977) to have the form

$$kbR_s = \frac{8}{3\pi^2} \frac{1}{(1 - \epsilon^2)^2} [1 + \epsilon^3 - (1 + \epsilon^2)E(\epsilon) + (1 - \epsilon^2)K(\epsilon)] \quad (4.57)$$

where the modulus is $\epsilon = a/b < 1$. When $\epsilon = 0$, the annulus becomes a circle of radius b , and the relationship above gives $kbR = 8/(3\pi^3)$, which is in agreement with the result obtained for the isoflux circular area.

Isothermal Circular Annulus The spreading resistance for the isothermal circular annulus cannot be obtained directly by the integral method. Mathematically, this is a mixed boundary value problem that requires special solution methods, which are discussed by Sneddon (1966). Smythe (1951) reported the solution for the capacitance of a charged annulus. Yovanovich and Schneider (1977) used the two results of Smythe to determine the spreading resistance. Yovanovich and Schneider (1977) reported the following relationships for the spreading resistance of an isothermal circular annular contact area:

$$kbR_s = \frac{1}{\pi^2} \frac{\ln 16 + \ln[(1 + \epsilon)/(1 - \epsilon)]}{1 + \epsilon} \quad (4.58)$$

for $1.000 < 1/\epsilon < 1.10$, and

$$kbR_s = \frac{\pi/8}{(\cos^{-1} \epsilon + \sqrt{1 - \epsilon^2} \tanh^{-1} \epsilon)[1 + 0.0143\epsilon^{-1} \tan^3(1.28\epsilon)]} \quad (4.59)$$

for $1.1 < 1/\epsilon < \infty$. When $\epsilon = 0$, the annulus becomes a circle, and the spreading resistance gives $R_s = 1/(4kb)$, in agreement with the result obtained for the isothermal circular area.

4.4.6 Other Doubly Connected Areas on a Half-Space

The numerical data of spreading resistance from Martin et al. (1984) for three doubly connected regular polygons: equilateral triangle, square, and circle were nondimensionalized as $k\sqrt{A_c} R_s$. The dimensionless spreading resistance is a function of $\epsilon = \sqrt{A_i/A_o}$, where A_i and A_o are the inner and outer projected areas of the polygons. The active area is $A_c = A_o - A_i$.

Accurate correlation equations with a maximum relative error of 0.6% were given. For the range $0 \leq \epsilon \leq 0.995$,

$$k\sqrt{A_c} R_s = a_0 \left[1 - \left(\frac{\epsilon}{a_1} \right)^{a_2} \right]^{a_3} \tag{4.60}$$

and for the range $0.995 \leq \epsilon \leq 0.9999$,

$$k P_o R_s = a_5 \ln \frac{a_4}{(1/\epsilon) - 1} \tag{4.61}$$

where P_o is the outer perimeter of the polygons and the correlation coefficients: a_0 through a_5 are given in Table 4.6.

The correlation coefficient a_0 represents the dimensionless spreading resistance of the full contact area, in agreement with results presented above. Since the results for the square and the circle are very close for all values of the parameter ϵ , the correlation equations for the square or the circle may be used for other doubly connected regular polygons, such as pentagons, hexagons, and so on.

Effect of Contact Conductance on Spreading Resistance Martin et al. (1984) used a novel numerical technique to determine the effect of a uniform contact conductance h on the spreading resistance of square and circular contact areas. The dimensionless spreading resistance values were correlated with an accuracy of 0.1% by the relationship

TABLE 4.6 Correlation Coefficients for Doubly Connected Polygons

	Circle	Square	Triangle
a_0	0.4789	0.4732	0.4602
a_1	0.99957	0.99980	1.00010
a_2	1.5056	1.5150	1.5101
a_3	0.35931	0.37302	0.38637
a_4	39.66	68.59	115.91
a_5	0.31604	0.31538	0.31529

TABLE 4.7 Correlation Coefficients for Squares and Circles

	Circle	Square
c_1	0.46159	0.45733
c_2	0.017499	0.016463
c_3	0.43900	0.47035
c_4	1.1624	1.1311

$$k\sqrt{A} R_s = c_1 - c_2 \tanh(c_3 \ln \text{Bi} - c_4) \quad 0 \leq \text{Bi} < \infty \quad (4.62)$$

with $\text{Bi} = h\sqrt{A}/k$. The correlation coefficients c_1 through c_4 are given in Table 4.7.

When $\text{Bi} \leq 0.1$, the predicted values approach the values corresponding to the isoflux boundary condition, and when $\text{Bi} \geq 100$, the predicted values are within 0.1% of the values obtained for the isothermal boundary condition. The transition from the isoflux values to the isothermal values occurs in the range $0.1 \leq \text{Bi} \leq 100$.

4.5 TRANSIENT SPREADING RESISTANCE IN AN ISOTROPIC HALF-SPACE

Transient spreading resistance occurs during startup and is important in certain micro-electronic systems. The spreading resistance may be defined with respect to the area-averaged temperature or with respect to a single point temperature such as the centroid temperature. Analytical solutions have been reported for a circular area on an isotropic half-space with isothermal, isoflux, and other heat flux distributions (Beck, 1979; Blackwell, 1972; Dryden et al., 1985; Keltner, 1973; Normington and Blackwell, 1964, 1972; Schneider et al., 1976; Turyk and Yovanovich, 1984; Negus and Yovanovich (1989); Yovanovich et al. (1984). Various analytical and numerical methods were employed to obtain short- and long-time solutions.

4.5.1 Isoflux Circular Area

Beck (1979) reported the following integral solution for a circular area of radius a which is subjected to a uniform and constant flux q for $t > 0$:

$$4kaR_s = \frac{8}{\pi} \int_0^\infty \text{erf}(\zeta\sqrt{\text{Fo}}) J_1^2(\zeta) \frac{d\zeta}{\zeta^2} \quad (4.63)$$

where erf is the error function, $J_1(x)$ is a Bessel function of the first kind of order 1 (Abramowitz and Stegun, 1965), and ζ is a dummy variable. The dimensionless time is defined as $\text{Fo} = at/a^2$, where α is the thermal diffusivity of the half-space. The spreading resistance is based on the area-averaged temperature. Steady state is obtained when $\text{Fo} \rightarrow \infty$, and the solution goes to $4kaR_s = 32/(3\pi^2)$.

Beck (1979) gave approximate solutions for short and long times. For short times where $\text{Fo} < 0.6$,

$$4kaR_s = \frac{8}{\pi} \left(\sqrt{\frac{Fo}{\pi}} - \frac{Fo}{\pi} + \frac{Fo^2}{8\pi} + \frac{Fo^3}{32\pi} + \frac{15Fo^4}{512\pi} \right) \quad (4.64)$$

and for long times where $Fo \geq 0.6$,

$$4kaR_s = \frac{32}{3\pi^2} - \frac{2}{\pi^{3/2}\sqrt{Fo}} \left[1 - \frac{1}{3(4Fo)} + \frac{1}{6(4Fo)^2} - \frac{1}{12(4Fo)^3} \right] \quad (4.65)$$

The maximum errors of about 0.18% and 0.07% occur at $Fo = 0.6$ for the short- and long-time expressions, respectively.

4.5.2 Isoflux Hyperellipse

The hyperellipse is defined by $(x/a)^n + (y/b)^n = 1$ with $b \leq a$, where n is the shape parameter and a and b are the axes along the x and y axes, respectively. The hyperellipse reduces to many special cases by setting the values of n and the aspect ratio parameter $\gamma = b/a$, which lies in the range $0 \leq \gamma \leq 1$. Therefore, the solution developed for the hyperellipse can be used to obtain solutions for many other geometries, such as ellipse and circle, rectangle and square, diamondlike geometries, and so on. The transient dimensionless centroid constriction resistance $k\sqrt{A} R_0$, where $R_0 = T_0/Q$, is given by the double-integral solution (Yovanovich, 1997)

$$k\sqrt{A} R_0 = \frac{2}{\pi\sqrt{A}} \int_0^{\pi/2} \int_0^{r_0} \operatorname{erfc} \left(\frac{r}{2\sqrt{A}\sqrt{Fo}} \right) dr d\omega \quad (4.66)$$

with $Fo = \alpha t/A$, and the area of the hyperellipse is given by $A = (4\gamma/n)B(1 + 1/n, 1/n)$ and $B(x, y)$ is the beta function (Abramowitz and Stegun, 1965). The upper limit of the radius is given by $r_0 = \gamma/[(\sin \omega)^n + \gamma^n(\cos \omega)^n]^{1/n}$ and the aspect ratio parameter $\gamma = b/a$. The solution above has the following characteristics: (1) for small dimensionless times, $Fo \leq 4 \times 10^{-2}$, $k\sqrt{A} R_0 = (2/\sqrt{\pi})\sqrt{Fo}$ for all values of n and γ ; (2) for long dimensionless times, $Fo \geq 10^3$, the results are within 1% of the steady-state values, which are given by the single integral

$$k\sqrt{A} R_0 = \frac{2\gamma}{\pi\sqrt{A}} \int_0^{\pi/2} \frac{d\omega}{[(\sin \omega)^n + \gamma^n(\cos \omega)^n]^{1/n}} \quad (4.67)$$

which depends on the aspect ratio γ and the shape parameter n . The dimensionless spreading resistance depends on the three parameters Fo , γ , and n in the transition region $4 \times 10^{-2} \leq Fo \leq 10^3$ in some complicated manner that can be deduced from the solution for the circular area. For this axisymmetric shape we put $\gamma = 1$, $n = 2$ into the hyperellipse double integral, which yields the following closed-form result valid for all dimensionless time (Yovanovich, 1997):

$$k\sqrt{A} R_0 = \sqrt{Fo} \left[\frac{1}{\sqrt{\pi}} - \frac{1}{\sqrt{\pi}} \exp \left(-\frac{1}{4\pi Fo} \right) \right]$$

$$+ \frac{1}{2\sqrt{\pi}\sqrt{Fo}} \operatorname{erfc}\left(\frac{1}{2\sqrt{\pi}\sqrt{Fo}}\right) \Bigg] \quad (4.68)$$

where the dimensionless time for the circle of radius a is $Fo = \alpha t / \pi a^2$.

4.5.3 Isoflux Regular Polygons

For regular polygons having sides $N \geq 3$, the area is $A = Nr_i^2 \tan(\pi/N)$, where r_i is the radius of the inscribed circle. The dimensionless spreading resistance based on the centroid temperature rise $k\sqrt{A} R_0$ is given by the following double integral (Yovanovich, 1997):

$$k\sqrt{A} R_0 = 2\sqrt{\frac{N}{\tan(\pi/N)}} \int_0^{\pi/N} \int_0^{1/\cos\omega} \operatorname{erfc}\left[\frac{r}{2\sqrt{N \tan(\pi/N)}\sqrt{Fo}}\right] dr d\omega \quad (4.69)$$

where the polygonal area is expressed in terms of the number of sides N , and for convenience the inscribed radius has been set to unity. This double-integral solution has characteristics identical to those of the double-integral solution given above for the hyperellipse; that is, for small dimensionless time, $Fo \leq 4 \times 10^{-2}$, $k\sqrt{A} R_0 = (2/\sqrt{\pi})\sqrt{Fo}$ for all polygons $N \geq 3$; and for long dimensionless times, $Fo \geq 10^3$, the results are within 1% of the steady-state values, which are given by the following closed-form expression (Yovanovich, 1997):

$$k\sqrt{A} R_0 = \frac{1}{\pi} \sqrt{\frac{N}{\tan(\pi/N)}} \ln \frac{1 + \sin(\pi/N)}{\cos(\pi/N)} \quad (4.70)$$

The dimensionless spreading resistance $k\sqrt{A} R_0$ depends on the parameters: Fo and N in the transition region: $4 \times 10^{-2} \leq Fo \leq 10^3$ in some complex manner which, as described above, may be deduced from the solution for the circular area. The steady-state solution gives the values $k\sqrt{A} R_o = 0.5617, 0.5611$, and 0.5642 for the equilateral triangle, $N = 3$, the square, $N = 4$, and the circle, $N \rightarrow \infty$. The difference between the values for the triangle and the circle is approximately 2.2%, whereas the difference between the values for the square and the circle is less than 0.6%. The following procedure is proposed for computation of the centroid-based transient spreading resistance for the range $4 \times 10^{-2} \leq Fo \leq 10^6$. The closed-form solution for the circle is the basis of the proposed method. For any planar singly connected contact area subjected to a uniform heat flux, take

$$\begin{aligned} \frac{\psi_0}{\psi_0(Fo \rightarrow \infty)} &= 2\sqrt{Fo} \left[1 - \exp\left(-\frac{1}{4\pi \cdot Fo}\right) \right. \\ &\quad \left. + \frac{1}{2\sqrt{Fo}} \operatorname{erfc}\left(\frac{1}{2\sqrt{\pi}\sqrt{Fo}}\right) \right] \end{aligned} \quad (4.71)$$

where $\psi_0 = k\sqrt{A} R_0$. The right-hand side of eq. (4.71) can be considered to be a *universal* dimensionless time function that accounts for the transition from small times to near steady state. The procedure proposed should provide quite accurate results for any planar, singly connected area. A simpler expression that is based on the Greene (1989) approximation of the complementary error function is proposed (Yovanovich, 1997):

$$\frac{\psi_0}{\psi_0(\text{Fo} \rightarrow \infty)} = \frac{1}{z\sqrt{\pi}} \left[1 - e^{-z^2} + a_1\sqrt{\pi} z e^{-a_2(z+a_3)^2} \right] \tag{4.72}$$

where $z = 1/(2\sqrt{\pi}\sqrt{\text{Fo}})$ and the three correlation coefficients are $a_1 = 1.5577$, $a_2 = 0.7182$, and $a_3 = 0.7856$. This approximation will provide values of ψ_0 with maximum errors of less than 0.5% for $\text{Fo} \geq 4 \times 10^{-2}$.

4.6 SPREADING RESISTANCE WITHIN A COMPOUND DISK WITH CONDUCTANCE

The spreading, one-dimensional flow and total resistances for steady conduction within compound disks is important in many microelectronic applications. The heat enters a compound disk of radius b through a circular area of radius a located in the top surface of the first layer of thickness t_1 and thermal conductivity k_1 , which is in perfect thermal contact with the second layer (called the *substrate*) of thickness t_2 and thermal conductivity k_2 .

The lateral boundary $r = b$ is adiabatic, the face at $z = t = t_1 + t_2$ is either cooled by a fluid through the film conductance h or it is in contact with a heat sink through a contact conductance h . In either case, h is assumed to be uniform. A compound disk with uniform heat flux and uniform conductance along the lower surface is shown in Fig. 4.4.

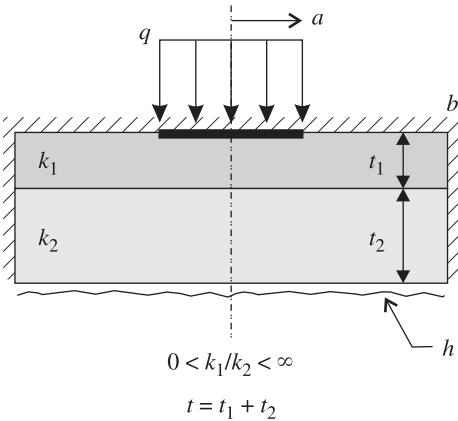


Figure 4.4 Compound disk with uniform heat flux and conductance. (From Yovanovich et al., 1980.)

The boundary condition over the source area may be modeled as either uniform heat flux or isothermal. The complete solution for these two boundary conditions has been reported by Yovanovich et al. (1980). The spreading resistance R_s and one-dimensional system resistance R_{1D} are related to the total system resistance R_{total} in the following manner:

$$R_{\text{total}} = R_s + R_{1D} = R_s + \frac{t_1}{k_1 A} + \frac{t_2}{k_2 A} + \frac{1}{hA} \quad (\text{K/W}) \quad (4.73)$$

where $A = \pi b^2$. The general solution for the dimensionless spreading resistance parameter $\psi = 4k_1 a R_s$ depends on several dimensionless geometric and thermophysical parameters: $\epsilon = a/b$, $\tau = t/b$, $\tau_1 = t_1/b$, $\tau_2 = t_2/b$, $\kappa = k_1/k_2$, $\text{Bi} = hb/k_2$, and μ , a parameter that describes the heat flux distribution over the source area. The general relationship between the total heat flow rate Q and the axisymmetric heat flux distribution $q(u)$ is

$$q(u) = \frac{Q}{\pi a^2} (1 + \mu)(1 - u^2)^\mu \quad 0 \leq u \leq 1 \quad (4.74)$$

The heat flux distributions corresponding to three values of the parameter μ are presented in Table 4.8, where $Q/\pi a^2$ is the average flux on the area. When $\mu = 0$, the heat flux is uniform, and when $\mu = -\frac{1}{2}$, the heat flux distribution is called the *equivalent isothermal distribution* because it produces an *almost* isothermal area provided that $a/b < 0.6$.

The independent system parameters have the ranges given in Table 4.9. If the first layer conductivity is lower than the substrate conductivity (i.e., $0 < \kappa < 1$), the layer (coating) is said to be *thermally resistive*, and if the conductivity ratio parameter lies in the range $1 < \kappa < \infty$, the layer is said to be *thermally conductive*.

The general dimensionless spreading resistance relationship was given as (Yovanovich et al., 1980):

$$4k_1 a R_s = \frac{8(\mu + 1)}{\pi \epsilon} \sum_{n=1}^{\infty} A_n(\epsilon) B_n(\tau, \tau_1, \kappa, \text{Bi}) \frac{J_1(\delta_n \epsilon)}{\delta_n} \quad (4.75)$$

The first layer thermal conductivity and the radius of the heat source were used to nondimensionalize the spreading resistance. If the substrate thermal conductivity

TABLE 4.8 Three Heat Flux Distributions

μ	$q(u)$
$-\frac{1}{2}$	$\frac{Q}{2\pi a^2 \sqrt{1-u^2}}$
0	$\frac{Q}{\pi a^2}$
$\frac{1}{2}$	$\frac{3Q}{2\pi a^2} \sqrt{1-u^2}$

TABLE 4.9 System Parameter Ranges

$0 < \epsilon < 1$
$0 < \tau_1 < \infty$
$0 < \tau_2 < \infty$
$0 < \kappa < \infty$
$0 < \text{Bi} < \infty$

is used, the right-hand side of the relationship must be multiplied by the thermal parameter κ .

The coefficients A_n are functions of the heat flux parameter μ . They are

$$A_n = \begin{cases} \frac{-2 \sin \delta_n \epsilon}{\delta_n^2 J_0^2(\delta_n)} & \text{for } \mu = -\frac{1}{2} \\ \frac{-2 J_1(\delta_n \epsilon)}{\delta_n^2 J_0^2(\delta_n)} & \text{for } \mu = 0 \\ \frac{-2 \sin \delta_n \epsilon}{\delta_n^2 J_0^2(\delta_n)} \left[\frac{1}{(\delta_n \epsilon)^2} - \frac{1}{(\delta_n \epsilon) \tan \delta_n \epsilon} \right] & \text{for } \mu = \frac{1}{2} \end{cases} \quad (4.76)$$

The function B_n , which depends on the system parameters (τ_1 , τ_2 , κ , Bi), was defined as

$$B_n = \frac{\phi_n \tanh(\delta_n \tau_1) - \varphi_n}{1 - \phi_n} \quad (4.77)$$

and the two functions that appear in the relationship above are defined as

$$\phi_n = \frac{\kappa - 1}{\kappa} (\cosh \delta_n \tau_1 - \varphi_n \sinh \delta_n \tau_1) \cosh \delta_n \tau_1 \quad (4.78)$$

$$\varphi_n = \frac{\delta_n + \text{Bi} \tanh \delta_n \tau}{\delta_n \tanh(\delta_n \tau) + \text{Bi}} \quad (4.79)$$

The eigenvalues δ_n are the positive roots of $J_1(\cdot) = 0$ (Abramowitz and Stegun, 1965). For the special case of an isotropic disk where $\kappa = 1$, $B_n = -\varphi_n$, which depends on τ and Bi only. Since the general solution depends on several independent parameters, it is not possible to present the results in tabular or graphical form. The full solution can, however, be programmed easily into computer algebra systems.

Characteristics of φ_n This function accounts for the effects of the parameters: δ_n , τ , and Bi . For extreme values of the parameter Bi , it reduces to

$$\varphi_n \rightarrow \begin{cases} \tanh \delta_n \tau & \text{as } \text{Bi} \rightarrow \infty \\ \coth \delta_n \tau & \text{as } \text{Bi} \rightarrow 0 \end{cases} \quad (4.80)$$

For all values in the range $0 < Bi < \infty$ and for all values $\tau > 0.72$, $\tanh \delta_n \tau \approx 1$ for all $n \geq 1$. Therefore, $\phi_n \approx 1$ for values $n \geq 1$.

Characteristics of B_n When $\tau_1 > 0.72$, $\tanh \delta_n \tau = 1$, $\phi_n = 1$ for all $0 < Bi < \infty$; therefore, $B_n = 1$ for $n \geq 1$.

4.6.1 Special Cases of the Compound Disk Solution

The general solution for the compound disk may be used to obtain spreading resistances for several special cases examined previously by many researchers. These special cases arise when some of the system parameters go to certain limits. The special cases fall into the following two categories: isotropic half-space, semi-infinite flux tube, and finite disk problems; and layered half-space and semi-infinite flux tube problems. Figures 4.5 and 4.6 show the several special cases that arise from the general case presented above. Results for several special cases are discussed in more detail in subsequent sections.

4.6.2 Half-Space Problems

If the dimensions of the compound disk (b, t) become very large relative to the radius a and the first layer thickness t_1 , the general solution approaches the solution for the case of a single layer in perfect thermal contact with an isotropic half-space. In this case $\epsilon \rightarrow 0$, $\tau_1 \rightarrow 0$ and the spreading resistance depends on the four system parameters (a, t_1, k_1, k_2) and the heat flux parameter μ . If we set $t_1 = 0$ or $k_1 = k_2$, the general solution goes to the special case of a circular heat source in perfect contact with an isotropic half-space. In this case the spreading resistance depends on two system parameters (a, k_2) and the heat flux parameter μ . The dimensionless spreading resistance is now defined as $\psi = 4k_2 a R_s$, and it is a constant depending on the heat flux parameter. The total resistance is equal to the spreading resistance in both cases because the one-dimensional resistance is negligible. The half-space problems are shown in Figs. 4.5d and 4.6d.

4.6.3 Semi-infinite Flux Tube Problems

The general solution goes to the semi-infinite flux tube solutions when the system parameter $\tau_2 \rightarrow \infty$. In this case the spreading resistance will depend on the system parameters (a, b, t_1, k_1, k_2) and the heat flux parameter μ . The dimensionless spreading resistance will be a function of the parameters (ϵ, τ_1, κ) and μ . If one sets $t_1 = 0$ or $k_1 = k_2 = k$, the dimensionless spreading resistance $\psi = 4ka R_s$ depends on the system parameters (a, b, k) and μ or $\epsilon = a/b$ and μ only. The semi-infinite flux tube problems are shown in Figs. 4.5c and 4.6c.

4.6.4 Isotropic Finite Disk with Conductance

In this case, one puts $k_1 = k_2 = k$ or $\kappa = 1$. The dimensionless spreading resistance $\psi = 4ka R_s$ depends on the system parameters (a, b, t, k, h) and μ or the

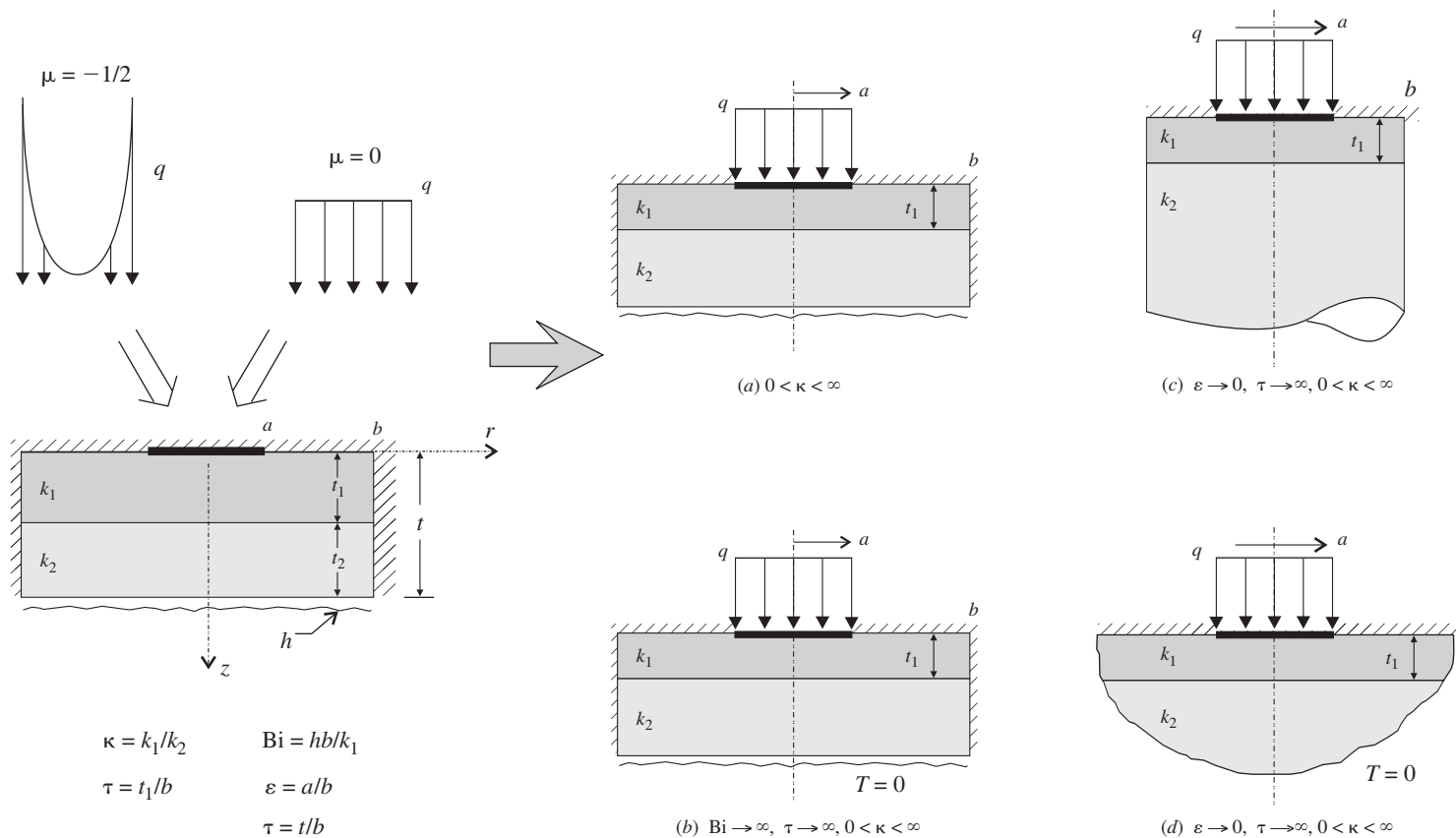
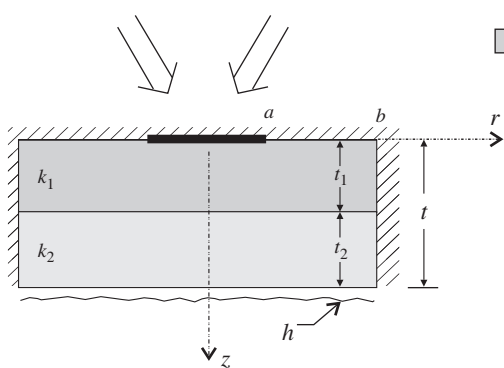
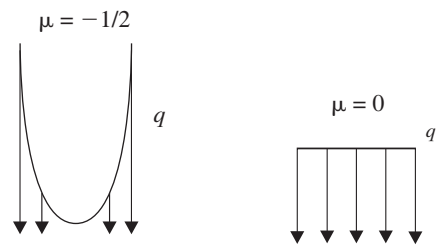


Figure 4.5 Four problems with a single layer on a substrate. (From Yovanovich et al., 1998.)



$$\kappa = k_1/k_2 \quad \text{Bi} = hb/k_1$$

$$\tau_1 = t_1/b \quad \varepsilon = a/b$$

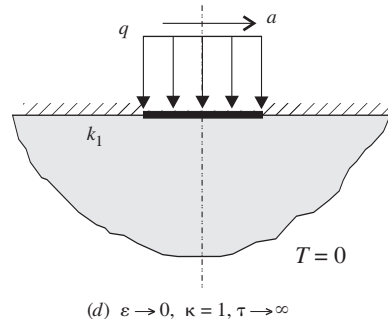
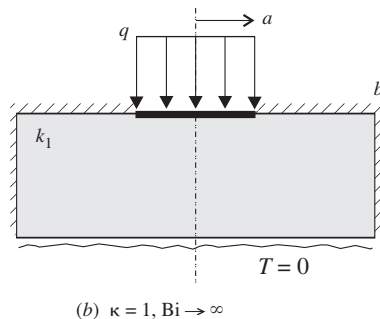
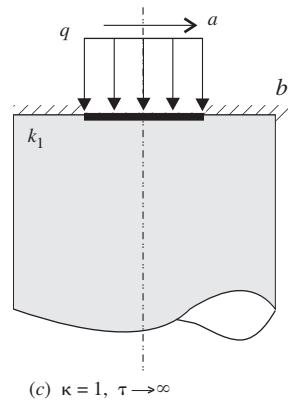
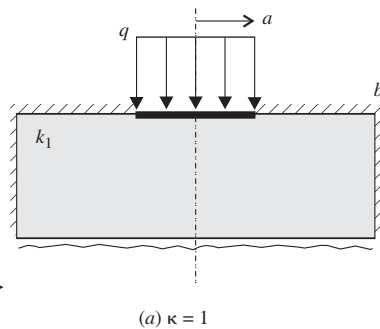
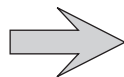


Figure 4.6 Four problems for isotropic systems. (From Yovanovich et al., 1998.)

dimensionless system parameters ($\epsilon = a/b$, $\tau = t/b$, $Bi = hb/k$) and μ . This problem is shown in Fig. 4.6b. These special cases are presented in the following sections.

4.7 SPREADING RESISTANCE OF ISOTROPIC FINITE DISKS WITH CONDUCTANCE

The dimensionless spreading resistance for isotropic ($\kappa = 1$) finite disks ($\tau_1 < 0.72$) with negligible thermal resistance at the heat sink interface ($Bi = \infty$) is given by the following solutions (Kennedy, 1960; Mikic and Rohsenow, 1966; Yovanovich et al., 1998): For $\mu = -\frac{1}{2}$:

$$4kaR_s = \frac{8}{\pi\epsilon} \sum_{n=1}^{\infty} \frac{J_1(\delta_n\epsilon) \sin \delta_n\epsilon}{\delta_n^3 J_0^2(\delta_n)} \tanh \delta_n\tau \quad (4.81)$$

For $\mu = 0$:

$$4kaR_s = \frac{16}{\pi\epsilon} \sum_{n=1}^{\infty} \frac{J_1^2(\delta_n\epsilon)}{\delta_n^3 J_0^2(\delta_n)} \tanh \delta_n\tau \quad (4.82)$$

If the external resistance is negligible $Bi \rightarrow \infty$, the temperature at the lower face of the disk is isothermal. The solutions for isoflux $\mu = 0$ heat source and isothermal base temperature were given by Kennedy (1960) for the centroid temperature and the area-averaged contact area temperature.

4.7.1 Correlation Equations

A circular heat source of radius a is attached to one end of a circular disk of thickness t , radius b , and thermal conductivity k . The opposite boundary is cooled by a fluid at temperature T_f through a uniform heat transfer coefficient h . The sides of the disk are adiabatic and the region outside the source area is also adiabatic. The flux over the source area is uniform. The heat transfer through the disk is steady. The external resistance is defined as $R_{ext} = 1/hA$, where $A = \pi b^2$.

The solution for the isoflux boundary condition and with external thermal resistance was recently reexamined by Song et al. (1994) and Lee et al. (1995). They nondimensionalized the constriction resistance based on the centroid and area-averaged temperatures using the square root of the source area (as recommended by Yovanovich, 1976b, 1991, 1997; Yovanovich and Burde, 1977; Yovanovich and Schneider, 1977; Chow and Yovanovich, 1982; Yovanovich et al., 1984; Yovanovich and Antonetti, 1988) and compared the analytical results against the numerical results reported by Nelson and Sayers (1992) over the full range of independent parameters: $Bi = hb/k$, $\epsilon = a/b$, $\tau = t/b$. Nelson and Sayers (1992) also chose the square root of the source area to report their numerical results. The agreement between the analytical and numerical results were reported to be in excellent agreement.

Lee et al. (1995) recommended a simple closed-form expression for the dimensionless constriction resistance based on the area-averaged and centroid temperatures. They defined the dimensionless spreading resistance parameter as $\psi = \sqrt{\pi} ka R_c$, where R_c is the constriction resistance, and they recommended the following approximations: For the area-averaged temperature

$$\psi_{\text{ave}} = \frac{1}{2}(1 - \epsilon)^{3/2}\phi_c \quad (4.83)$$

and for the centroid temperature:

$$\psi_{\text{max}} = \frac{1}{\sqrt{\pi}}(1 - \epsilon)\varphi_c \quad (4.84)$$

with

$$\varphi_c = \frac{\text{Bi} \tanh(\delta_c \tau) + \delta_c}{\text{Bi} + \delta_c \tanh \delta_c \tau} \quad (4.85)$$

$$\delta_c = \pi + \frac{1}{\sqrt{\pi} \epsilon} \quad (4.86)$$

The approximations above are within $\pm 10\%$ of the analytical results (Song et al., 1994; Lee et al., 1995) and the numerical results of Nelson and Sayers (1992). The locations of the maximum errors were not given.

4.7.2 Circular Area on a Single Layer (Coating) on a Half-Space

Integral solutions are available for the spreading resistance for a circular source of radius a in contact with an isotropic layer of thickness t_1 and thermal conductivity k_1 which is in perfect thermal contact with an isotropic half-space of thermal conductivity k_2 . The solutions were obtained for two heat flux distributions corresponding to the flux parameter values $\mu = -\frac{1}{2}$ and $\mu = 0$.

Equivalent Isothermal Circular Contact Dryden (1983) obtained the solution for the equivalent isothermal circular contact flux distribution:

$$q(r) = \frac{Q}{2\pi a^2 \sqrt{1 - u^2}} \quad 0 \leq u \leq 1 \quad (\text{W/m}^2) \quad (4.87)$$

The problem is depicted in Fig. 4.7.

The dimensionless spreading resistance, based on the area-averaged temperature, is obtained from the integral (Dryden, 1983):

$$\psi = 4k_2 a R_s = \frac{4}{\pi} \frac{k_2}{k_1} \int_0^\infty \frac{\lambda_2 \exp(\zeta t_1/a) + \lambda_1 \exp(-\zeta t_1/a)}{\lambda_2 \exp(\zeta t_1/a) - \lambda_1 \exp(-\zeta t_1/a)} \frac{J_1(\zeta) \sin \zeta}{\zeta^2} d\zeta \quad (4.88)$$

with $\lambda_1 = (1 - k_2/k_1)/2$ and $\lambda_2 = (1 + k_2/k_1)/2$. The parameter ζ is a dummy variable of integration. The constriction resistance depends on the thermal conductivity

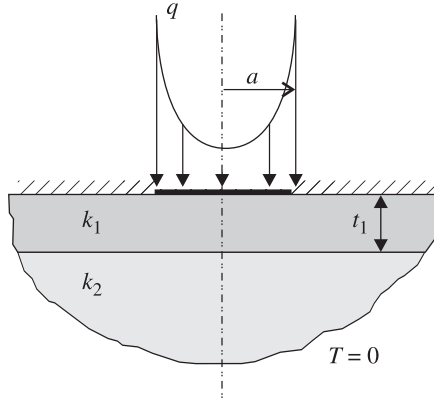


Figure 4.7 Layered half-space with an equivalent isothermal flux. (From Yovanovich et al., 1998.)

ratio k_1/k_2 and the relative layer thickness t_1/a . Dryden (1983) presented simple asymptotes for thermal spreading in thin layers, $t_1/a \leq 0.1$, and in thick layers, $t_1/a \geq 10$. These asymptotes were also presented as dimensionless spreading resistances defined as $4k_2aR_s$. They are:

Thin-layer asymptote:

$$(4k_2aR_s)_{\text{thin}} = 1 + \frac{4}{\pi} \frac{t_1}{a} \left(\frac{k_2}{k_1} - \frac{k_1}{k_2} \right) \quad (4.89)$$

Thick-layer asymptote:

$$(4k_2aR_s)_{\text{thick}} = \frac{k_2}{k_1} - \frac{2}{\pi} \frac{a}{t_1} \frac{k_2}{k_1} \ln \frac{2}{1 + k_1/k_2} \quad (4.90)$$

These asymptotes provide results that are within 1% of the full solution for relative layer thickness: $t_1/a < 0.5$ and $t_1/a > 2$.

The dimensionless spreading resistance is based on the substrate thermal conductivity k_2 . The general solution above is valid for conductive layers where $k_1/k_2 > 1$ as well as for resistive layers where $k_1/k_2 < 1$. The infinite integral can be evaluated numerically by means of computer algebra systems, which provide accurate results.

4.7.3 Isoflux Circular Contact

Hui and Tan (1994) presented an integral solution for the isoflux circular source. The dimensionless spreading resistance is

$$4k_2aR_s = \frac{32}{3\pi^2} \left(\frac{k_2}{k_1} \right)^2 + \frac{8}{\pi} \left[1 - \left(\frac{k_2}{k_1} \right)^2 \right] \int_0^\infty \frac{J_1^2(\zeta) d\zeta}{[1 + (k_1/k_2) \tanh(\zeta t_1/a)] \zeta^2} \quad (4.91)$$

which depends on the thermal conductivity ratio k_1/k_2 and the relative layer thickness t_1/a . The dimensionless spreading resistance is based on the substrate thermal conductivity k_2 . The general solution above is valid for conductive layers, where $k_1/k_2 > 1$, as well as resistive layers, where $k_1/k_2 < 1$.

4.7.4 Isoflux, Equivalent Isothermal, and Isothermal Solutions

Negus et al. (1985) obtained solutions by application of the Hankel transform method for flux-specified boundary conditions and with a novel technique of linear superposition for the mixed boundary condition (isothermal contact area and zero flux outside the contact area). They reported results for three flux distributions: isoflux, equivalent isothermal flux, and true isothermal source. Their results were presented below.

Isoflux Contact Area For the isoflux boundary condition, they reported the result for $\psi^q = 4k_1aR_s$:

$$\psi^q = \frac{32}{3\pi^2} + \frac{8}{\pi^2} \sum_{n=1}^{\infty} (-1)^n \alpha^n I_q \quad (4.92)$$

The first term is the dimensionless isoflux spreading resistance of an isotropic half-space of thermal conductivity k_1 , and the second term accounts for the effect of the layer relative thickness and relative thermal conductivity. The thermal conductivity parameter α is defined as

$$\alpha = \frac{1 - \kappa}{1 + \kappa}$$

with $\kappa = k_1/k_2$. The layer thickness–conductivity parameter I_q is defined as

$$I_q = \frac{1}{2\pi} \left\{ 2\sqrt{2(\gamma+1)} E \left[\sqrt{2/(\gamma+1)} \right] - \frac{\pi}{2\sqrt{2\gamma}} I_\gamma - 2\pi n \tau_1 \right\}$$

with

$$I_\gamma = 1 + \frac{0.09375}{\gamma^2} + \frac{0.0341797}{\gamma^4} + \frac{0.00320435}{\gamma^6}$$

The relative layer thickness is $\tau_1 = t/a$ and the relative thickness parameter is

$$\gamma = 2n^2\tau_1^2 + 1$$

The special function $E(\cdot)$ is the complete elliptic integral of the second kind (Abramowitz and Stegun, 1965).

Equivalent Isothermal Contact Area For the equivalent isothermal flux boundary condition, they reported the result for $\psi_{ei} = 4k_1aR_s$:

$$\psi_{ei} = 1 + \frac{8}{\pi} \sum_{n=1}^{\infty} (-1)^n \alpha^n I_{ei} \quad (4.93)$$

where as discussed above, the first term represents the dimensionless spreading resistance of an isothermal contact area on an isotropic half-space of thermal conductivity k_1 and the second term accounts for the effect of the layer relative thickness and the relative thermal conductivity. The thermal conductivity parameter α is defined above. The relative layer thickness parameter I_{ei} is defined as

$$I_{ei} = \left[\sqrt{1 - \beta^{-2}} (\beta - \beta^{-1}) + \frac{1}{2} \sin^{-1} (\beta^{-1}) - 2n\tau_1 \right]$$

with $\tau_1 = t/a$ and

$$\beta = n\tau_1 + \sqrt{n^2\tau_1^2 + 1}$$

Isothermal Contact Area For the isothermal contact area, Negus et al. (1985) reported a correlation equation for their numerical results. They reported that $\psi^T = 4k_1aR_s$ in the form

$$\psi^T = F_1 \tanh F_2 + F_3 \quad (4.94)$$

where

$$F_1 = 0.49472 - 0.49236\kappa - 0.0034\kappa^2$$

$$F_2 = 2.8479 + 1.3337\tau + 0.06864\tau^2 \quad \text{with } \tau = \log_{10}\tau_1$$

$$F_3 = 0.49300 + 0.57312\kappa - 0.06628\kappa^2$$

where $\kappa = k_1/k_2$. The correlation equation was developed for resistive layers: $0.01 \leq \kappa \leq 1$ over a wide range of relative thickness $0.01 \leq \tau_1 \leq 100$. The maximum relative error associated with the correlation equation is approximately 2.6% at $\tau_1 = 0.01$ and $\kappa = 0.2$. Numerical results for ψ^q , ψ_{ei} , and ψ^T for a range of values of τ_1 and κ were presented in tabular form for easy comparison. They found that the values for ψ^q were greater than those for ψ_{ei} and that $\psi_{ei} \leq \psi^T$. The maximum difference between ψ^q and ψ^T was approximately 8%. The values for $\psi_T > \psi_{ei}$ for very thin layers, $\tau_1 \leq 0.1$ and for $\kappa \leq 0.1$; however, the differences were less than approximately 8%. For most applications the equivalent isothermal flux solution and the true isothermal solution are similar.

4.8 CIRCULAR AREA ON A SEMI-INFINITE FLUX TUBE

The problem of finding the spreading resistance in an semi-infinite isotropic circular flux tube has been investigated by many researchers (Roess, 1950; Mikic and

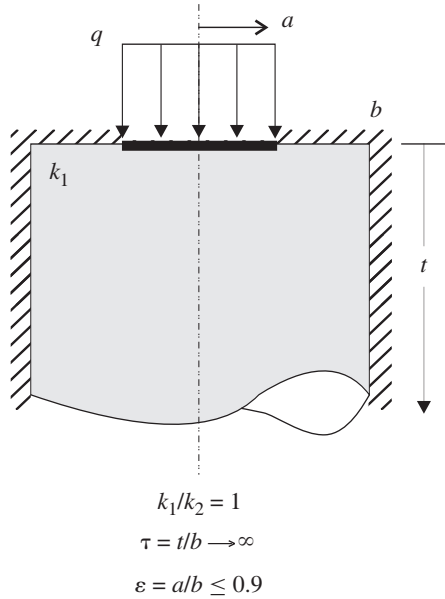


Figure 4.8 Isotropic flux tube with an isoflux area. (From Yovanovich et al., 1998.)

Rohsenow, 1966; Gibson, 1976; Yovanovich, 1976a,b; Negus and Yovanovich, 1984a,b; Negus et al., 1989). The system with uniform heat flux on the circular area is shown in Fig. 4.8.

This problem corresponds to the case where $\kappa = 1$ and $\tau \rightarrow \infty$, and therefore the spreading resistance depends on the system parameters (a, b, k) and the flux distribution parameter μ . The dimensionless spreading resistance defined as $\psi = 4kaR_s$, where R_s is the spreading resistance, depends on ϵ and μ . The results of several studies are given below.

4.8.1 General Expression for a Circular Contact Area with Arbitrary Flux on a Circular Flux Tube

The general expression for the dimensionless spreading (constriction) resistance $4kaR_s$ for a circular contact subjected to an arbitrary axisymmetric flux distribution $f(u)$ (Yovanovich, 1976b) is obtained from the series

$$4kaR_s = \frac{8/\pi}{\int_0^1 u f(u) du} \sum_{n=1}^{\infty} \frac{J_1(\delta_n \epsilon)}{\delta_n^2 J_0^2(\delta_n)} \int_0^1 u f(u) J_0(\delta_n \epsilon u) du \quad (4.95)$$

where δ_n are the positive roots of $J_1(\cdot) = 0$ and $\epsilon = a/b$ is the relative size of the source area.

Flux Distributions of the Form $(1 - u^2)^\mu$ Yovanovich (1976b) reported the following general solution for axisymmetric flux distributions of the form $f(u) = (1 - u^2)^\mu$, where the parameter μ accounts for the shape of the flux distribution. The general expression above reduces to the following general expression:

$$4kaR_s = \frac{16}{\pi}(\mu + 1)2^\mu \Gamma(\mu + 1) \frac{1}{\epsilon} \sum_{n=1}^{\infty} \frac{J_1(\delta_n \epsilon) J_{\mu+1}(\delta_n \epsilon)}{\delta_n^3 J_0(\delta_n)(\delta_n \epsilon)^\mu} \quad (4.96)$$

where $\Gamma(\cdot)$ is the gamma function (Abramowitz and Stegun, 1965) and $J_\nu(\cdot)$ is the Bessel function of arbitrary order ν (Abramowitz and Stegun, 1965).

The general expression above can be used to obtain specific solutions for various values of the flux distribution parameter μ . Three particular solutions are considered next.

Equivalent Isothermal Circular Source The isothermal contact area requires solution of a difficult mathematical problem that has received much attention by numerous researchers (Roess, 1950; Kennedy, 1960; Mikic and Rohsenow, 1966; Gibson, 1976; Yovanovich, 1976b; Negus and Yovanovich, 1984a,b).

Mikic and Rohsenow (1966) proposed use of the flux distribution corresponding to $\mu = -\frac{1}{2}$ to approximate an isothermal contact area for small relative contact areas $0 < \epsilon < 0.5$. The general expression becomes

$$4kaR_s = \frac{8}{\pi} \frac{1}{\epsilon} \sum_{n=1}^{\infty} \frac{J_1(\delta_n \epsilon) \sin \delta_n \epsilon}{\delta_n^3 J_0^2(\delta_n)} \quad (4.97)$$

An accurate correlation equation of this series solution is given below.

Isoflux Circular Source The general solution above with $\mu = 0$ yields the isoflux solution reported by Mikic and Rohsenow (1966):

$$4kaR_s = \frac{16}{\pi} \frac{1}{\epsilon} \sum_{n=1}^{\infty} \frac{J_1^2(\delta_n \epsilon)}{\delta_n^3 J_0^2(\delta_n)} \quad (4.98)$$

An accurate correlation equation of this series solution is given below.

Parabolic Flux Distribution Yovanovich (1976b) reported the solution for the parabolic flux distribution corresponding to $\mu = \frac{1}{2}$.

$$4kaR_s = \frac{24}{\pi} \frac{1}{\epsilon} \sum_{n=1}^{\infty} \frac{J_1(\delta_n \epsilon) \sin \delta_n \epsilon}{\delta_n^3 J_0^2(\delta_n)} \left[\frac{1}{(\delta_n \epsilon)^2} - \frac{1}{\delta_n \epsilon \tan \delta_n \epsilon} \right] \quad (4.99)$$

An accurate correlation equation of this series solution is given below.

Asymptotic Values for Dimensionless Spreading Resistances The three series solutions given above converge very slowly as $\epsilon \rightarrow 0$, which corresponds to the

TABLE 4.10 Correlation Coefficients for Three Flux Distributions

C_n	$\mu = -\frac{1}{2}$	$\mu = 0$	$\mu = \frac{1}{2}$
C_0	1.00000	1.08085	1.12517
C_1	-1.40981	-1.41002	-1.41038
C_3	0.303641	0.259714	0.235387
C_5	0.0218272	0.0188631	0.0117527
C_7	0.0644683	0.0420278	0.0343458

case of a circular contact area on a half-space. The corresponding half-space results were reported by Strong et al. (1974):

$$4kaR_s = \begin{cases} 1 & \text{for } \mu = -\frac{1}{2} \\ \frac{32}{3\pi^2} & \text{for } \mu = 0 \\ 1.1252 & \text{for } \mu = \frac{1}{2} \end{cases} \quad (4.100)$$

Correlation Equations for Spreading Resistance Since the three series solutions presented above for the three heat flux distributions $\mu = -\frac{1}{2}, 0, \frac{1}{2}$ converge slowly as $\epsilon \rightarrow 0$, correlation equations for the dimensionless spreading resistance $\psi = 4kaR_s$ for the three flux distributions were developed having the general form

$$\psi = C_0 + C_1\epsilon + C_3\epsilon^3 + C_5\epsilon^5 + C_7\epsilon^7 \quad (4.101)$$

with the correlation coefficients given in Table 4.10. The correlation equations, applicable for the parameter range $0 \leq \epsilon \leq 0.8$, provide four-decimal-place accuracy.

Simple Correlation Equations Yovanovich (1976b) recommended the following simple correlations for the three flux distributions:

$$4kaR_s = a_1(1 - a_2\epsilon) \quad (4.102)$$

in the range $0 < \epsilon \leq 0.1$ with a maximum error of 0.1%, and

$$4kaR_s = a_1(1 - \epsilon)^{a_3} \quad (4.103)$$

in the range $0 < \epsilon \leq 0.3$ with a maximum error of 1%. The correlation coefficients for the three flux distributions are given in Table 4.11.

TABLE 4.11 Correlation Coefficients for $\mu = -\frac{1}{2}, 0, \frac{1}{2}$

	$-\frac{1}{2}$	0	$\frac{1}{2}$
a_1	1	1.0808	1.1252
a_2	1.4197	1.4111	1.4098
a_3	1.50	1.35	1.30

TABLE 4.12 Coefficients for Correlations of Dimensionless Spreading Resistance $4kaR_s$

Flux Tube Geometry and Contact Boundary Condition	C_0	C_1	C_3	C_5	C_7
Circle/circle					
Uniform flux	1.08076	−1.41042	0.26604	−0.00016	0.058266
True isothermal flux	1.00000	−1.40978	0.34406	0.04305	0.02271
Circle/square					
Uniform flux	1.08076	−1.24110	0.18210	0.00825	0.038916
Equivalent isothermal flux	1.00000	−1.24142	0.20988	0.02715	0.02768

4.8.2 Accurate Correlation Equations for Various Combinations of Source Areas, Flux Tubes, and Boundary Conditions

Solutions are also available for various combinations of source areas and flux tube cross-sectional areas, such as circle/circle and circle/square for the uniform flux, true isothermal, and equivalent isothermal boundary conditions (Negus and Yovanovich, 1984a,b).

Numerical results were correlated with the polynomial

$$4kaR_s = C_0 + C_1\epsilon + C_3\epsilon^3 + C_5\epsilon^5 + C_7\epsilon^7 \tag{4.104}$$

The dimensionless spreading (constriction) resistance coefficient C_0 is the half-space value, and the correlation coefficients C_1 through C_7 are given in Table 4.12.

4.9 MULTIPLE LAYERS ON A CIRCULAR FLUX TUBE

The effect of single and multiple isotropic layers or coatings on the end of a circular flux tube has been determined by Antonetti (1983) and Muzychka et al. (1999). The heat enters the end of the circular flux tube of radius b and thermal conductivity k_3 through a coaxial, circular area that is in perfect thermal contact with an isotropic layer of thermal conductivity k_1 and thickness t_1 . This layer is in perfect contact with a second layer of thermal conductivity k_2 and thickness t_2 , which is in perfect contact with the flux tube having thermal conductivity k_3 (Fig. 4.9).

The lateral boundary of the flux tube is adiabatic and the contact plane outside the contact area is also adiabatic. The boundary condition over the contact area may be isoflux or isothermal. The system is depicted in Fig. 4.9. The dimensionless constriction resistance $\psi_{2 \text{ layers}} = 4k_3aR_c$ is defined with respect to the thermal conductivity of the flux tube, which is often referred to as the substrate. This constriction resistance depends on several dimensionless parameters: relative contact size $\epsilon = a/b$ where $0 < \epsilon < 1$; two conductivity ratios: $\kappa_{21} = k_2/k_1$, $\kappa_{32} = k_3/k_2$; two relative layer thicknesses: $\tau_1 = t_1/a$, $\tau_2 = t_2/a$; and the boundary condition over the contact area. The solution for two layers is given as

$$\psi_{2 \text{ layers}} = \frac{16}{\pi \epsilon} \sum_{n=1}^{\infty} \phi_{n,\epsilon} \kappa_{21} \kappa_{32} \frac{\vartheta^+}{\vartheta^-} \quad (4.105)$$

where

$$\phi_{n,\epsilon} = \frac{J_1^2(\delta_n \epsilon)}{\delta_n^3 J_0^2(\delta_n)} \rho_{n,\epsilon} \quad (4.106)$$

and the boundary condition parameter is according to Muzychka et al. (1999):

$$\rho_{n,\epsilon} = \begin{cases} \frac{\sin \delta_n \epsilon}{2 J_1(\delta_n \epsilon)} & \text{isothermal area} \\ 1 & \text{isoflux area} \end{cases}$$

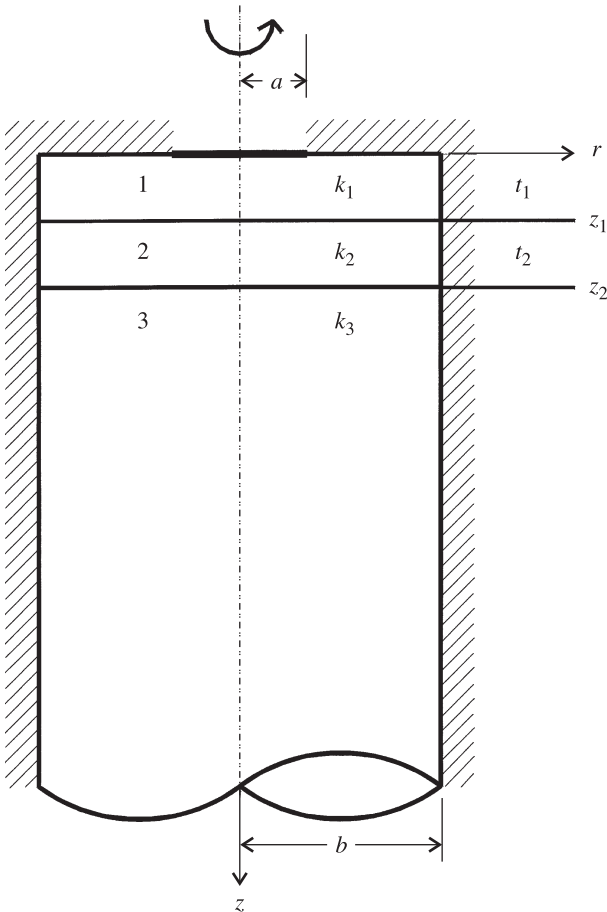


Figure 4.9 Two layers in a flux tube. (From Muzycha et al., 1999.)

The thermal conductivity ratios are defined above. The layer parameters ϑ^+ and ϑ^- come from the following general relationship:

$$\begin{aligned}\vartheta^\pm &= (1 + \kappa_{21})(1 + \kappa_{32}) \pm (1 - \kappa_{21})(1 + \kappa_{32}) \exp(-2\delta_n \epsilon \tau_1) \\ &\quad + (1 - \kappa_{21})(1 - \kappa_{32}) \exp(-2\delta_n \epsilon \tau_2) \\ &\quad \pm (1 + \kappa_{21})(1 - \kappa_{32}) \exp[-2\delta_n \epsilon (\tau_1 + \tau_2)]\end{aligned}$$

The eigenvalues δ_n that appear in the solution are the positive roots of $J_1(\cdot) = 0$.

The two-layer solution may be used to obtain the relationship for a single layer of thermal conductivity k_1 and thickness t_1 in perfect contact with a flux tube of thermal conductivity k_2 . In this case the dimensionless spreading resistance $\psi_{1 \text{ layer}}$ depends on the relative contact size ϵ , the conductivity ratio κ_{21} , and the relative layer thickness τ_1 :

$$\psi_{1 \text{ layer}} = \frac{16}{\pi \epsilon} \sum_{n=1}^{\infty} \phi_{n, \epsilon} \kappa_{21} \frac{\vartheta^+}{\vartheta^-} \quad (4.107)$$

and the general layer relationship becomes

$$\vartheta^\pm = 2[(1 + \kappa_{21}) \pm (1 - \kappa_{21}) \exp(-2\delta_n \epsilon \tau_1)]$$

4.10 SPREADING RESISTANCE IN COMPOUND RECTANGULAR CHANNELS

Consider the spreading resistance R_s and total one-dimensional resistance R_{1D} for the system shown in Fig. 4.10. The system is a rectangular flux channel $-c \leq x \leq c$, $-d \leq y \leq d$, consisting of two isotropic layers having thermal conductivities k_1, k_2 and thicknesses t_1, t_2 , respectively. The interface between the layers is assumed to be thermally perfect. All four sides of the flux channel are adiabatic. The planar rectangular heat source area $-a \leq x \leq a$, $-b \leq y \leq b$ is subjected to a uniform heat flux q , and the region outside the planar source area is adiabatic. The steady heat transfer rate $\dot{Q} = qA = 4qcd$ occurs in the system and the heat leaves the system through the lower face $z = t_1 + t_2$. The heat is removed by a fluid through a uniform heat transfer coefficient h or by a heat sink characterized by an effective heat transfer coefficient h .

The total thermal resistance of the system is given by the relation

$$R_{\text{total}} = R_s + R_{1D} \quad (\text{K/W}) \quad (4.108)$$

where R_s is the thermal spreading resistance of the system and R_{1D} is the one-dimensional thermal resistance, defined as

$$R_{1D} = \frac{1}{A} \left(\frac{t_1}{k_1} + \frac{t_2}{k_2} + \frac{1}{h} \right) \quad \text{where } A = 4cd \quad (\text{K/W}) \quad (4.109)$$

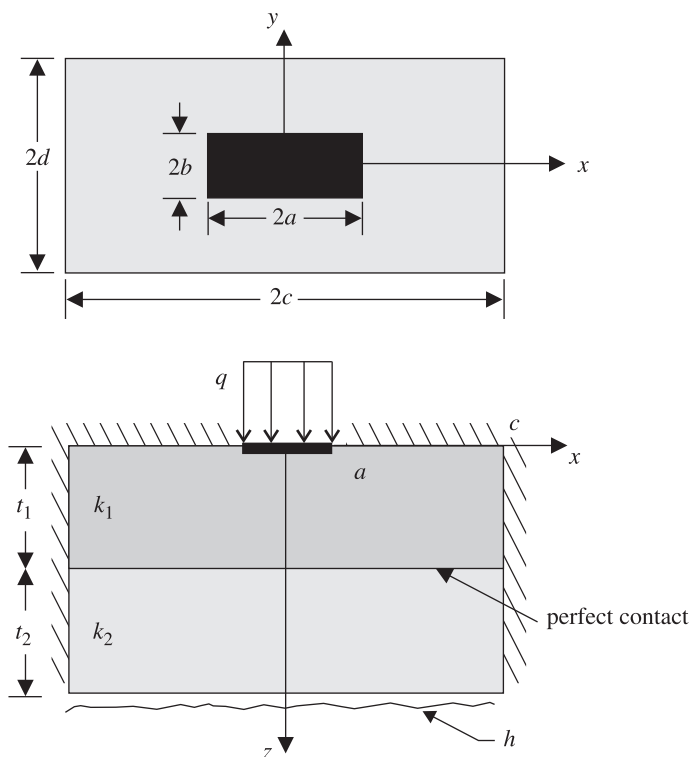


Figure 4.10 Rectangular isoflux area on a compound rectangular channel. (From Yovanovich et al., 1999.)

The spreading resistance is given by the general relationship (Yovanovich et al., 1999)

$$\begin{aligned}
 R_s = & \frac{1}{2a^2cdk_1} \sum_{m=1}^{\infty} \frac{\sin^2(a\delta)}{\delta^3} \phi_m(\delta) \\
 & + \frac{1}{2b^2cdk_1} \sum_{n=1}^{\infty} \frac{\sin^2(b\lambda)}{\lambda^3} \phi_n(\lambda) \\
 & + \frac{1}{a^2b^2cdk_1} \sum_{m=1}^{\infty} \sum_{n=1}^{\infty} \frac{\sin^2(a\delta) \sin^2(b\lambda)}{\delta^2 \lambda^2 \beta} \phi_{m,n}(\beta) \quad (\text{K/W}) \quad (4.110)
 \end{aligned}$$

The general relationship for the spreading resistance consists of three terms. The two single summations account for two-dimensional spreading in the x and y directions, respectively, and the double summation accounts for three-dimensional spreading from the rectangular heat source.

The eigenvalues δ_m and λ_n , corresponding to the two strip solutions, depend on the flux channel dimensions and the indices m and n , respectively. The eigenvalues $\beta_{m,n}$ for the rectangular solution are functions of the other two eigenvalues and both indices:

$$\lambda_n = \frac{n\pi}{d} \quad \delta_m = \frac{m\pi}{c} \quad \beta_{m,n} = \sqrt{\delta_m^2 + \lambda_n^2} \quad (4.111)$$

The contributions of the layer thicknesses t_1, t_2 , the layer conductivities k_1, k_2 , and the uniform conductance h to the spreading resistance are determined by means of the general expression

$$\phi(\zeta) = \frac{\alpha(\kappa\zeta\mathcal{L} - \text{Bi})e^{4\zeta t_1} + (\kappa\zeta\mathcal{L} - \text{Bi})e^{2\zeta t_1} + \alpha(\kappa\zeta\mathcal{L} - \text{Bi})e^{4\zeta t_1} - (\kappa\zeta\mathcal{L} - \text{Bi})e^{2\zeta t_1} + (\kappa\zeta\mathcal{L} + \text{Bi})e^{2\zeta(2t_1+t_2)} + \alpha(\kappa\zeta\mathcal{L} + \text{Bi})e^{2\zeta(t_1+t_2)}}{(\kappa\zeta\mathcal{L} + \text{Bi})e^{2\zeta(2t_1+t_2)} - \alpha(\kappa\zeta\mathcal{L} + \text{Bi})e^{2\zeta(t_1+t_2)}}$$

where the thermal conductivity ratio parameter is

$$\alpha = \frac{1 - \kappa}{1 + \kappa}$$

with $\kappa = k_2/k_1$, $\text{Bi} = h\mathcal{L}/k_1$, and \mathcal{L} an arbitrary length scale employed to define the dimensionless spreading resistance:

$$\psi = \mathcal{L}k_1 R_s \quad (4.112)$$

which is based on the thermal conductivity of the layer adjacent to the heat source. Various system lengths may be used and the appropriate choice depends on the system of interest.

In all summations $\phi(\zeta)$ is evaluated in each series using $\zeta = \delta_m, \lambda_n$, and $\beta_{m,n}$ as defined above. The general relationship for $\phi(\zeta)$ reduces to simpler relationships for two important special cases: the semi-infinite flux channel where $t_2 \rightarrow \infty$, shown in Fig. 4.11, and the finite isotropic rectangular flux channel where $\kappa = 1$, shown in Fig. 4.12. The respective relationships are

$$\phi(\zeta) = \frac{(e^{2\zeta t_1} - 1)\kappa + (e^{2\zeta t_1} + 1)}{(e^{2\zeta t_1} + 1)\kappa + (e^{2\zeta t_1} - 1)} \quad (4.113)$$

where the influence of the contact conductance has vanished, and

$$\phi(\zeta) = \frac{(e^{2\zeta t} + 1)\zeta\mathcal{L} - (1 - e^{2\zeta t})\text{Bi}}{(e^{2\zeta t} - 1)\zeta\mathcal{L} + (1 + e^{2\zeta t})\text{Bi}} \quad (4.114)$$

where the influence of κ has vanished.

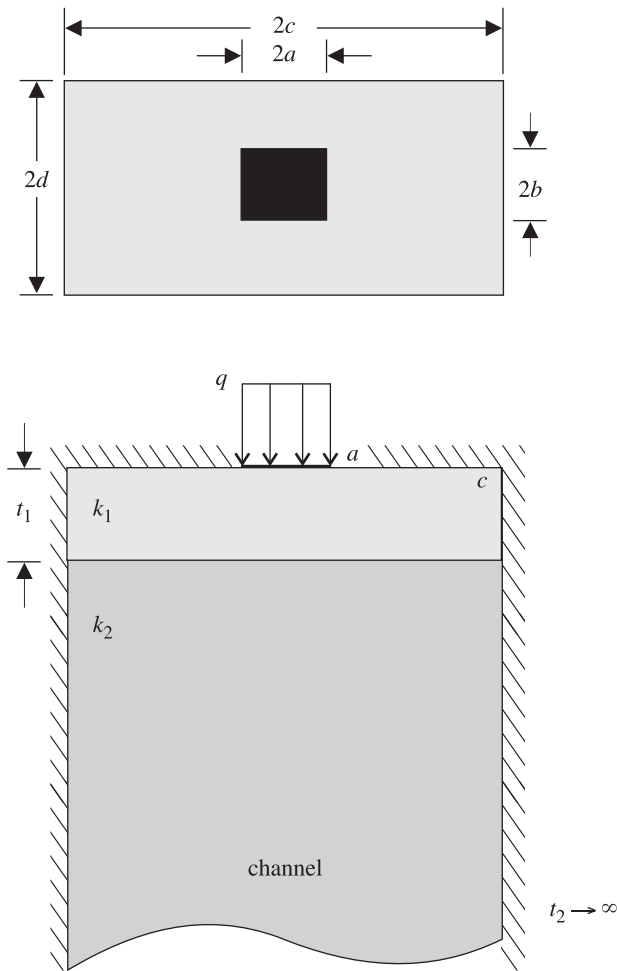


Figure 4.11 Rectangular isoflux area on a layer bonded to a rectangular flux channel. (From Yovanovich et al., 1999.)

The dimensionless spreading resistance ψ depends on six independent dimensionless parameters, such as the relative size of the rectangular source area $\epsilon_1 = a/c$, $\epsilon_2 = b/d$, the layer conductivity ratio $\kappa = k_2/k_1$, the relative layer thicknesses $\tau_1 = t_1/L$, $\tau_2 = t_2/L$, and the Biot number $Bi = hL/k_1$.

The general relationship reduces to several special cases, such as those described in Table 4.13. The general solution may also be used to obtain the relationship for an isoflux square area on the end of a square semi-infinite flux tube.

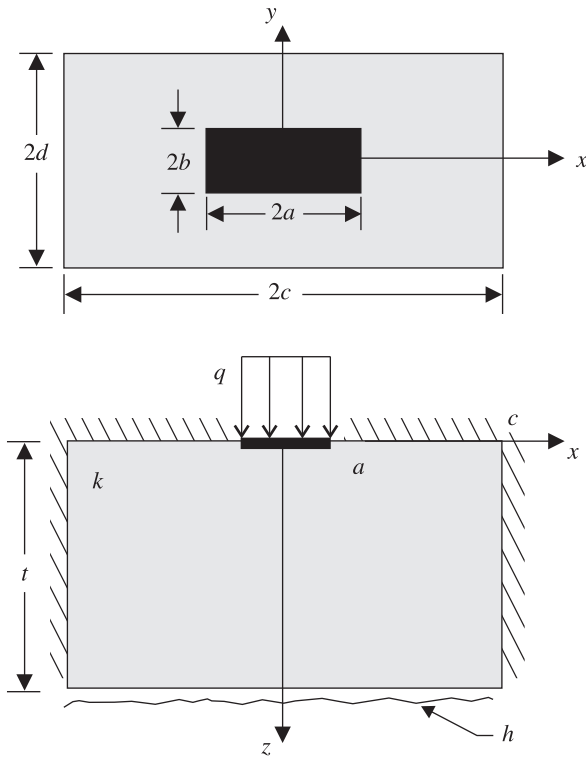


Figure 4.12 Rectangular isoflux area on an isotropic rectangular channel. (From Yovanovich et al., 1999.)

TABLE 4.13 Summary of Relationships for Isoflux Area

Configuration	Limiting Values
Rectangular heat source	
Finite compound rectangular flux channel	$a, b, c, d, t_1, t_2, k_1, k_2, h$
Semi-infinite compound rectangular flux channel	$t_2 \rightarrow \infty$
Finite isotropic rectangular flux channel	$k_1 = k_2$
Semi-infinite isotropic rectangular flux channel	$t_1 \rightarrow \infty$
Strip heat source	
Finite compound rectangular flux channel	$a, c, b = d, t_1, t_2, k_1, k_2, h$
Semi-infinite compound rectangular flux channel	$t_2 \rightarrow \infty$
Finite isotropic rectangular flux channel	$k_1 = k_2$
Semi-infinite isotropic rectangular flux channel	$t_1 \rightarrow \infty$
Rectangular source on a half-space	
Isotropic half-space	$c \rightarrow \infty, d \rightarrow \infty, t_1 \rightarrow \infty$
Compound half-space	$c \rightarrow \infty, d \rightarrow \infty, t_2 \rightarrow \infty$

4.10.1 Square Area on a Semi-infinite Square Flux Tube

For the special case of a square heat source on a semi-infinite square isotropic flux tube, the general solution reduces to a simpler expression which depends on one parameter only. The dimensionless spreading resistance relationship (Mikic and Rohsenow, 1966; Yovanovich et al., 1999) was recast in the form

$$k\sqrt{A_s} R_s = \frac{2}{\pi^3\epsilon} \left[\sum_{m=1}^{\infty} \frac{\sin^2 m\pi\epsilon}{m^3} + \frac{1}{\pi^2\epsilon^2} \sum_{m=1}^{\infty} \sum_{n=1}^{\infty} \frac{\sin^2 m\pi\epsilon \sin^2 n\pi\epsilon}{m^2 n^2 \sqrt{m^2 + n^2}} \right] \quad (4.115)$$

where the characteristic length was selected as $\mathcal{L} = \sqrt{A_s}$. The relative size of the heat source was defined as $\epsilon = \sqrt{A_s/A_t}$, where A_s and A_t are the source and flux tube areas, respectively. A correlation equation was reported for eq. (4.115) (Negus et al., 1989):

$$k\sqrt{A_s} R_s = 0.47320 - 0.62075\epsilon + 0.1198\epsilon^3 \quad (4.116)$$

in the range $0 \leq \epsilon \leq 0.5$, with a maximum relative error of approximately 0.3%. The constant on the right-hand side of the correlation equation is the value of the dimensionless spreading resistance of an isoflux square source on an isotropic half-space when the square root of the source area is chosen as the characteristic length.

4.10.2 Spreading Resistance of a Rectangle on a Layer on a Half-Space

The solution for the rectangular heat source on a compound half-space is obtained from the general relationship for the finite compound flux channel, provided that $t_2 \rightarrow \infty$, $c \rightarrow \infty$, $d \rightarrow \infty$. No closed-form solution exists for this problem.

4.10.3 Spreading Resistance of a Rectangle on an Isotropic Half-Space

The spreading resistance for an isoflux rectangular source of dimensions $2a \times 2b$ on an isotropic half-space whose thermal conductivity is k has the closed-form relationship (Carslaw and Jaeger, 1959)

$$k\sqrt{A_s} R_s = \frac{\sqrt{\varrho}}{\pi} \left\{ \sinh^{-1} \frac{1}{\varrho} + \frac{1}{\varrho} \sinh^{-1} \varrho + \frac{\varrho}{3} \left[1 + \frac{1}{\varrho^3} - \left(1 + \frac{1}{\varrho^2} \right)^{3/2} \right] \right\} \quad (4.117)$$

where $\varrho = a/b \geq 1$ is the aspect ratio of the rectangle. If the scale length is $\mathcal{L} = \sqrt{A_s}$, the dimensionless spreading resistance becomes a weak function of ϱ . For a square heat source, the numerical value of the dimensionless spreading resistance is $k\sqrt{A_s} R_s = 0.4732$, which is very close to the numerical value for the isoflux circular source on an isotropic half-space and other singly connected heat source geometries such as an equilateral triangle and a semicircular heat source.

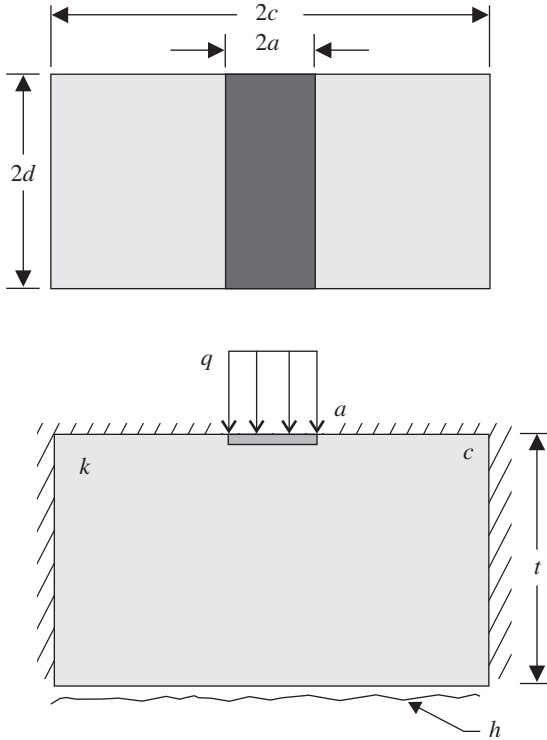


Figure 4.13 Strip on a finite rectangular channel with cooling. (From Yovanovich et al., 1999.)

4.11 STRIP ON A FINITE CHANNEL WITH COOLING

Spreading resistance due to steady conduction from a strip of width $2a$ and length $L = 2d$ through a finite rectangular flux channel of width $2c$ and thickness t and thermal conductivity k is considered here. A uniform conductance h is specified on the bottom surface to account for cooling by a fluid or to represent the cooling by a heat sink. The system is shown in Fig. 4.13.

This is a special case of the general relationships presented above for a rectangular area on a compound rectangular channel. A general flux distribution on the strip is given by

$$q(x) = \frac{Q}{L} \frac{\Gamma(\mu + 3/2)}{\sqrt{\pi} a^{1+2\mu} \Gamma(\mu + 1)} (a^2 - x^2)^\mu \quad 0 \leq x \leq a \quad (\text{W/m}^2) \quad (4.118)$$

where Q is the total heat transfer rate from the strip and $\Gamma(\cdot)$ is the gamma function (Abramowitz and Stegun, 1965). The parameter μ defines the heat flux distribution

on the strip, which may have the following values: (1) $\mu = -\frac{1}{2}$ to approximate an isothermal strip provided that $a/c \ll 1$, (2) $\mu = 0$ for an isoflux distribution, and (3) $\mu = \frac{1}{2}$, which gives a parabolic flux distribution. The three flux distributions are

$$q(x) = \begin{cases} \frac{Q}{L\pi} \frac{1}{\sqrt{a^2 - x^2}} & \text{for } \mu = -\frac{1}{2} \\ \frac{Q}{2La} & \text{for } \mu = 0 \\ \frac{2Q}{L\pi a^2} \sqrt{a^2 - x^2} & \text{for } \mu = \frac{1}{2} \end{cases} \quad (4.119)$$

The dimensionless spreading resistance relationship based on the mean source temperature is

$$kLR_s = \frac{\Gamma(\mu + 3/2)}{\pi^2 \epsilon} \sum_{n=1}^{\infty} \left(\frac{2}{n\pi\epsilon} \right)^{\mu+1/2} \frac{\sin n\pi\epsilon}{n^2} J_{\mu+1/2}(n\pi\epsilon) \varphi_n \quad (4.120)$$

where

$$\varphi_n = \frac{n\pi + \text{Bi} \tanh n\pi\tau}{n\pi \tanh n\pi\tau + \text{Bi}} \quad n = 1, 2, 3, \dots$$

and the three dimensionless system parameters and their ranges are

$$0 < \epsilon = \frac{a}{c} < 1 \quad 0 < \text{Bi} = \frac{hc}{k} < \infty \quad 0 < \tau = \frac{t}{c} < \infty$$

The general relationship gives the following three relationships for the three flux distributions:

$$kLR_s = \begin{cases} \frac{1}{\epsilon\pi^2} \sum_{n=1}^{\infty} \frac{\sin n\pi\epsilon}{n^2} J_0(n\pi\epsilon) \varphi_n & \text{for } \mu = -\frac{1}{2} \\ \frac{1}{\epsilon^2\pi^3} \sum_{n=1}^{\infty} \frac{\sin^2 n\pi\epsilon}{n^3} \varphi_n & \text{for } \mu = 0 \\ \frac{2}{\epsilon^2\pi^3} \sum_{n=1}^{\infty} \frac{\sin n\pi\epsilon}{n^3} J_1(n\pi\epsilon) \varphi_n & \text{for } \mu = \frac{1}{2} \end{cases} \quad (4.121)$$

The influence of the cooling along the bottom surface on the spreading resistance is given by the function φ_n , which depends on two parameters, Bi and τ . If the channel is relatively thick (i.e., $\tau \geq 0.85$), $\varphi_n \rightarrow 1$ for all values $n = 1 \dots \infty$, and the influence of the parameter Bi becomes negligible. When $\tau \geq 0.85$, the finite channel may be modeled as though it were infinitely thick. This special case is presented next.

4.12 STRIP ON AN INFINITE FLUX CHANNEL

If the relative thickness of the rectangular channel becomes very large (i.e., $\tau \rightarrow \infty$), the relationships given above approach the relationships appropriate for the infinitely thick flux channel. The dimensionless spreading resistance for this problem depends on two parameters: the relative size of the strip ϵ and the heat flux distribution parameter μ . The three relationships for the dimensionless spreading resistance are obtained from the relationships given above with $\varphi_n = 1$.

Numerical values for LkR_s for three values of μ are given in Table 4.14. From the tabulated values it can be seen that the spreading resistance values for the isothermal strip are smaller than the values for the isoflux distribution, which are smaller than the values for the parabolic distribution for all values of ϵ . The differences are large as $\epsilon \rightarrow 1$; however, the differences become negligibly small as $\epsilon \rightarrow 0$.

4.12.1 True Isothermal Strip on an Infinite Flux Channel

There is a closed-form relationship for the true isothermal area on an infinitely thick flux channel. According to Sexl and Burkhard (1969), Veziroglu and Chandra (1969), and Yovanovich et al. (1999), the relationship is

$$kLR_s = \frac{1}{\pi} \ln \frac{1}{\sin(\pi\epsilon/2)} \tag{4.122}$$

Numerical values are given in Table 4.14. A comparison of the values corresponding to $\mu = -\frac{1}{2}$ and those for the true isothermal strip shows close agreement provided that $\epsilon < 0.5$. For very narrow strips where $\epsilon < 0.1$, the differences are less than 1%.

4.12.2 Spreading Resistance for an Abrupt Change in the Cross Section

If steady conduction occurs in a two-dimensional channel whose width decreases from $2a$ to $2b$, there is spreading resistance as heat flows through the common

TABLE 4.14 Dimensionless Spreading Resistance kLR_s in Flux Channels

ϵ	μ			Isothermal Strip	Change
	$-\frac{1}{2}$	0	$\frac{1}{2}$		
0.01	1.321	1.358	1.375	1.322	1.343
0.1	0.5902	0.6263	0.6430	0.5905	0.6110
0.2	0.3729	0.4083	0.4247	0.3738	0.3936
0.3	0.2494	0.2836	0.2995	0.2514	0.2699
0.4	0.1658	0.1984	0.2134	0.1691	0.1860
0.5	0.1053	0.1357	0.1496	0.1103	0.1249
0.6	0.0607	0.0882	0.1007	0.0675	0.0794
0.7	0.0283	0.0521	0.0628	0.0367	0.0456
0.8	0.0066	0.0255	0.0338	0.0160	0.0214

interface. The true boundary condition at the common interface is unknown. The temperature and the heat flux are both nonuniform. Conformal mapping leads to a closed-form solution for the spreading resistance.

The relationship for the spreading resistance is, according to Smythe (1968),

$$kLR_s = \frac{1}{2\pi} \left[\left(\epsilon + \frac{1}{\epsilon} \right) \ln \frac{1+\epsilon}{1-\epsilon} + 2 \ln \frac{1-\epsilon^2}{4\epsilon} \right] \quad (4.123)$$

where $\epsilon = a/b < 1$. Numerical values are given in Table 4.14. An examination of the values reveals that they lie between the values for $\mu = -\frac{1}{2}$ and $\mu = 0$. The average value of the first two columns corresponding to $\mu = -\frac{1}{2}$ and $\mu = 0$ are in very close agreement with the values in the last column. The differences are less than 1% for $\epsilon \leq 0.20$, and they become negligible as $\epsilon \rightarrow 0$.

4.13 TRANSIENT SPREADING RESISTANCE WITHIN ISOTROPIC SEMI-INFINITE FLUX TUBES AND CHANNELS

Turyk and Yovanovich (1984) reported the analytical solutions for transient spreading resistance within semi-infinite circular flux tubes and two-dimensional channels. The circular contact and the rectangular strip are subjected to uniform and constant heat flux.

4.13.1 Isotropic Flux Tube

The dimensionless transient spreading resistance for an isoflux circular source of radius a supplying heat to a semi-infinite isotropic flux tube of radius b , constant thermal conductivity k , and thermal diffusivity α is given by the series solution

$$4kaR_s = \frac{16}{\pi\epsilon} \sum_{n=1}^{\infty} \frac{J_1^2(\delta_n\epsilon) \operatorname{erf}(\delta_n\epsilon\sqrt{\text{Fo}})}{\delta_n^3 J_0^2(\delta_n)} \quad (4.124)$$

where $\epsilon = a/b < 1$, $\text{Fo} = \alpha t/a^2 > 0$, and δ_n are the positive roots of $J_1(\cdot) = 0$. The average source temperature rise was used to define the spreading resistance. The series solution approaches the steady-state solution presented in an earlier section when the dimensionless time satisfies the criterion $\text{Fo} \geq 1/\epsilon^2$ or when the real time satisfies the criterion $t \geq a^2/\alpha\epsilon^2$.

4.13.2 Isotropic Semi-infinite Two-Dimensional Channel

The dimensionless transient spreading resistance for an isoflux strip of width $2a$ within a two-dimensional channel of width $2b$, length L , constant thermal conductivity k , and thermal diffusivity α was reported as (Turyk and Yovanovich, 1984)

$$LkR_s = \frac{1}{\pi^3\epsilon} \sum_{m=1}^{\infty} \frac{\sin^2 m\pi\epsilon \operatorname{erf}(m\pi\epsilon\sqrt{\text{Fo}})}{m^3} \quad (4.125)$$

where $\epsilon = a/b < 1$ is the relative size of the contact strip and the dimensionless time is defined as $Fo = \alpha t/a^2$. There is no half-space solution for the two-dimensional channel. The transient solution is within 1% of the steady-state solution when the dimensionless time satisfies the criterion $Fo \geq 1.46/\epsilon^2$.

4.14 SPREADING RESISTANCE OF AN ECCENTRIC RECTANGULAR AREA ON A RECTANGULAR PLATE WITH COOLING

A rectangular isoflux area with side lengths c and d lies in the surface $z = 0$ of a rectangular plate with side dimensions a and b . The plate thickness is t_1 and its thermal conductivity is k_1 . The top surface outside the source area is adiabatic, and all sides are adiabatic. The bottom surface at $z = t_1$ is cooled by a fluid or a heat sink that is in contact with the entire surface. In either case the heat transfer coefficient is denoted as h and is assumed to be uniform. The origin of the Cartesian coordinate system (x,y,z) is located in the lower left corner. The system is shown in Fig. 4.14.

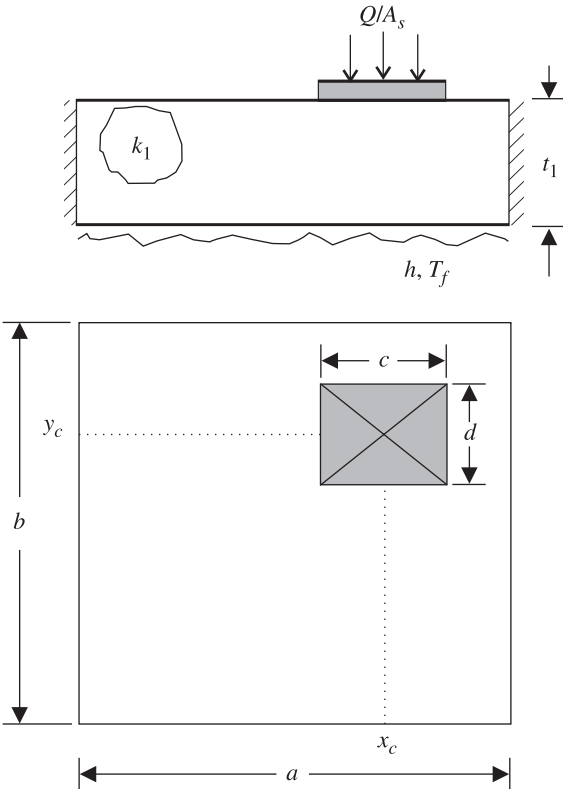


Figure 4.14 Isotropic plate with an eccentric rectangular heat source. (From Muzychka et al., 2000.)

The temperature rise of points in the plate surface $z = 0$ is given by the relationship

$$\begin{aligned}\theta(x, y, z) = & A_0 + B_0 z \\ & + \sum_{m=1}^{\infty} \cos \lambda_m x (A_1 \cosh \lambda_m z + B_1 \sinh \lambda_m z) \\ & + \sum_{n=1}^{\infty} \cos \delta_n y (A_2 \cosh \delta_n z + B_2 \sinh \delta_n z) \\ & + \sum_{m=1}^{\infty} \sum_{n=1}^{\infty} \cos \lambda_m x \cos \delta_n y (A_3 \cosh \beta_{m,n} z + B_3 \sinh \beta_{m,n} z) \quad (4.126)\end{aligned}$$

The Fourier coefficients are obtained by means of the following relationships:

$$A_0 = \frac{Q}{ab} \left(\frac{t_1}{k_1} + \frac{1}{h} \right) \quad \text{and} \quad B_0 = -\frac{Q}{k_1 ab} \quad (4.127)$$

$$A_1 = \frac{2Q \left[\sin \left(\frac{2X_c + c}{2} \lambda_m \right) - \sin \left(\frac{2X_c - c}{2} \lambda_m \right) \right]}{abck_1 \lambda_m^2 \phi(\lambda_m)} \quad (4.128)$$

$$A_2 = \frac{2Q \left[\sin \left(\frac{2Y_c + d}{2} \delta_n \right) - \sin \left(\frac{2Y_c - d}{2} \delta_n \right) \right]}{abck_1 \delta_n^2 \phi(\delta_n)} \quad (4.129)$$

$$A_3 = \frac{16Q \cos(\lambda_m X_c) \sin \left(\frac{1}{2} \lambda_m c \right) \cos(\delta_n Y_c) \sin \left(\frac{1}{2} \delta_n d \right)}{abcdk_1 \beta_{m,n} \lambda_m \delta_n \phi(\beta_{m,n})} \quad (4.130)$$

The other Fourier coefficients are obtained by the relationship

$$B_i = -\phi(\zeta) A_i \quad i = 1, 2, 3 \quad (4.131)$$

where ζ is replaced by λ_m , δ_n , or $\beta_{m,n}$ as required. The eigenvalues are

$$\lambda_m = \frac{m\pi}{a} \quad \delta_n = \frac{n\pi}{b} \quad \beta_{m,n} = \sqrt{\lambda_m^2 + \delta_n^2}$$

The mean temperature rise of the source area is given by the relationship

$$\begin{aligned}\bar{\theta} = & \bar{\theta}_{1D} + 2 \sum_{m=1}^{\infty} A_m \frac{\cos(\lambda_m X_c) \sin \left(\frac{1}{2} \lambda_m c \right)}{\lambda_m c} + 2 \sum_{n=1}^{\infty} A_n \frac{\cos(\delta_n Y_c) \sin \left(\frac{1}{2} \delta_n d \right)}{\delta_n d} \\ & + 4 \sum_{m=1}^{\infty} \sum_{n=1}^{\infty} A_{mn} \frac{\cos(\delta_n Y_c) \sin \left(\frac{1}{2} \delta_n d \right) \cos(\lambda_m X_c) \sin \left(\frac{1}{2} \lambda_m c \right)}{\lambda_m c \delta_n d} \quad (4.132)\end{aligned}$$

where the one-dimensional temperature rise is

$$\bar{\theta}_{1D} = \frac{Q}{ab} \left(\frac{t_1}{k_1} + \frac{1}{h} \right) \quad (\text{K}) \quad (4.133)$$

for an isotropic plate. The total resistance is related to the spreading resistance and the one-dimensional resistance:

$$R_{\text{total}} = \frac{\bar{\theta}}{Q} = R_{1D} + R_s \quad (\text{K/W}) \quad (4.134)$$

where

$$R_{1D} = \frac{1}{ab} \left(\frac{t_1}{k_1} + \frac{1}{h} \right) \quad (\text{K/W}) \quad (4.135)$$

4.14.1 Single Eccentric Area on a Compound Rectangular Plate

If a single source is on the top surface of a compound rectangular plate that consists of two layers having thicknesses t_1 and t_2 and thermal conductivities k_1 and k_2 , as shown in Fig. 4.15, the results are identical except for the system parameter ϕ , which now is given by the relationship

$$\phi(\zeta) = \frac{(\alpha e^{4\zeta t_1} - e^{2\zeta t_1}) + \varrho(e^{2\zeta(2t_1+t_2)} - \alpha e^{2\zeta(t_1+t_2)})}{(\alpha e^{4\zeta t_1} + e^{2\zeta t_1}) + \varrho(e^{2\zeta(2t_1+t_2)} + \alpha e^{2\zeta(t_1+t_2)})} \quad (4.136)$$

where

$$\varrho = \frac{\zeta + h/k_2}{\zeta - h/k_2} \quad \text{and} \quad \alpha = \frac{1 - \kappa}{1 + \kappa} \quad (4.137)$$

with $\kappa = k_2/k_1$ and ζ is replaced by λ_m , δ_n , or $\beta_{m,n}$, accordingly. The one-dimensional temperature rise in this case is

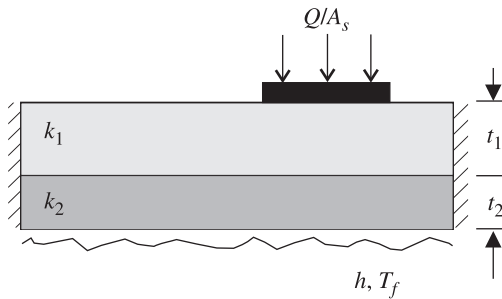


Figure 4.15 Compound plate with an eccentric rectangular heat source. (From Muzychka et al., 2000.)

$$\bar{\theta}_{1D} = \frac{Q}{ab} \left(\frac{t_1}{k_1} + \frac{t_2}{k_2} + \frac{1}{h} \right) \quad (\text{K}) \quad (4.138)$$

4.14.2 Multiple Rectangular Heat Sources on an Isotropic Plate

The multiple rectangular sources on an isotropic plate are shown in Fig. 4.16. The surface temperature by superposition is given by the following relationship (Muzychka et al., 2000):

$$T(x, y, 0) - T_f = \sum_{i=1}^N \theta_i(x, y, 0) \quad (\text{K}) \quad (4.139)$$

where θ_i is the temperature excess for each heat source by itself and $N \geq 2$ is the number of discrete heat sources. The temperature rise is given by

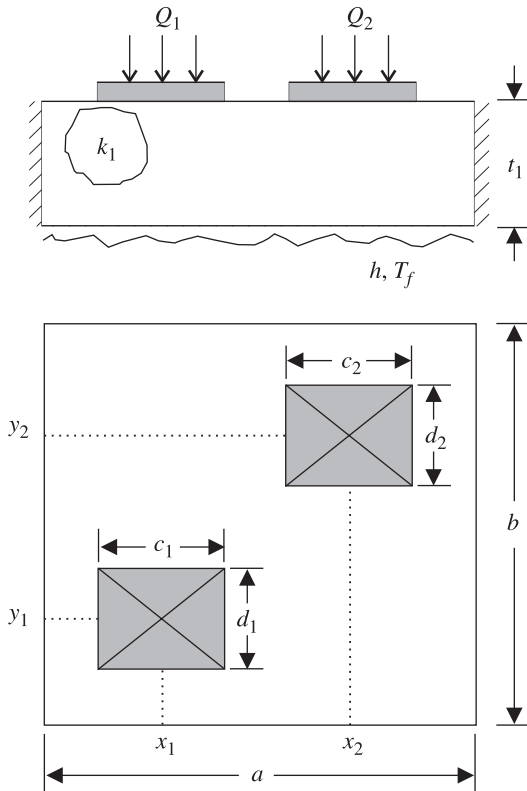


Figure 4.16 Isotropic plate with two eccentric rectangular heat sources. (From Muzychka et al., 2000.)

$$\begin{aligned}\theta_i(x, y, 0) = & A_0^i + \sum_{m=1}^{\infty} A_m^i \cos \lambda_m x + \sum_{n=1}^{\infty} A_n^i \cos \delta_n y \\ & + \sum_{m=1}^{\infty} \sum_{n=1}^{\infty} A_{mn}^i \cos \lambda_m x \cos \delta_n y\end{aligned}\quad (4.140)$$

where ϕ and $A_0^i = \bar{\theta}_{ID}$ are defined above for the isotropic and compound plates.

The mean temperature of an arbitrary rectangular area of dimensions c_j and d_j , located at $X_{c,j}$ and $Y_{c,j}$, may be obtained by integrating over the region $A_j = c_j d_j$:

$$\bar{\theta}_j = \frac{1}{A_j} \iint_{A_j} \theta_i dA_j = \frac{1}{A_j} \iint_{A_j} \sum_{i=1}^N \theta_i(x, y, 0) dA_j \quad (4.141)$$

which may be written as

$$\bar{\theta}_j = \sum_{i=1}^N \frac{1}{A_j} \iint_{A_j} \theta_i(x, y, 0) dA_j = \sum_{i=1}^N \bar{\theta}_i \quad (4.142)$$

The mean temperature of the j th heat source is given by

$$\bar{T}_j - T_f = \sum_{i=1}^N \bar{\theta}_i \quad (4.143)$$

where

$$\begin{aligned}\bar{\theta}_i = & A_0^i + 2 \sum_{m=1}^{\infty} A_m^i \frac{\cos(\lambda_m X_{c,j}) \sin\left(\frac{1}{2} \lambda_m c_j\right)}{\lambda_m c_j} + 2 \sum_{n=1}^{\infty} A_n^i \frac{\cos(\delta_n Y_{c,j}) \sin\left(\frac{1}{2} \delta_n d_j\right)}{\delta_n d_j} \\ & + 4 \sum_{m=1}^{\infty} \sum_{n=1}^{\infty} A_{mn}^i \frac{\cos(\delta_n Y_{c,j}) \sin\left(\frac{1}{2} \delta_n d_j\right) \cos(\lambda_m X_{c,j}) \sin\left(\frac{1}{2} \lambda_m c_j\right)}{\lambda_m c_j \delta_n d_j}\end{aligned}\quad (4.144)$$

Equation (4.143) represents the sum of the effects of all sources over an arbitrary location. Equation (4.143) is evaluated over the region of interest c_j, d_j located at $X_{c,j}, Y_{c,j}$, with the coefficients A_0^i, A_m^i, A_n^i , and A_{mn}^i evaluated at each of the i th source parameters.

4.15 JOINT RESISTANCES OF NONCONFORMING SMOOTH SOLIDS

The elastoconstriction and elastogap resistance models (Yovanovich, 1986) are based on the Boussinesq point load model (Timoshenko and Goodier, 1970) and the Hertz

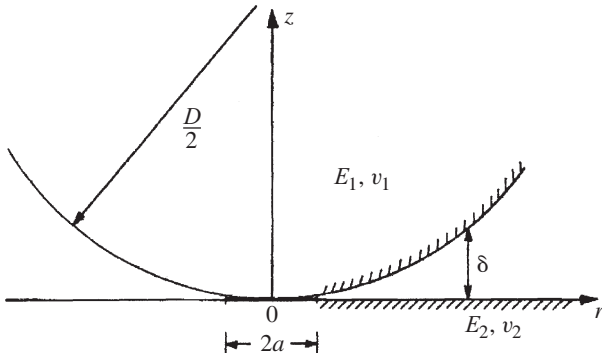


Figure 4.17 Joint formed by elastic contact of a sphere or a cylinder with a smooth flat surface. (From Kitscha, 1982.)

distributed-load model (Hertz, 1896; Timoshenko and Goodier, 1970; Walowit and Anno, 1975; Johnson, 1985). Both models assume that bodies have “smooth” surfaces, are perfectly elastic, and that the applied load is static and normal to the plane of the contact area. In the general case the contact area will be elliptical, having semimajor and semiminor axes a and b , respectively. These dimensions are much smaller than the dimensions of the contacting bodies. The circular contact area produced when two spheres or a sphere and a flat are in contact are two special cases of the elliptical contact. Also, the rectangular contact area, produced when two ideal circular cylinders are in line contact or an ideal cylinder and a flat are in contact, are special cases of the elliptical contact area.

Figure 4.17 shows the contact between two elastic bodies having physical properties (Young’s modulus and Poisson’s ratio): E_1, ν_1 and E_2, ν_2 , respectively. One body is a smooth flat and the other body may be a sphere or a circular cylinder having radius $D/2$. The contact $2a$ is the diameter of a circular contact area for the sphere/flat contact and the width of the contact strip for the cylinder/flat contact. A gap is formed adjacent to the contact area, and its local thickness is characterized by δ .

Heat transfer across the joint can take place by conduction by means of the contact area, conduction through the substance in the gap, and by radiation across the gap if the substance is “transparent,” or by radiation if the contact is formed in a vacuum. The thermal joint resistance model presented below was given by Yovanovich (1971, 1986). It was developed for the elastic contact of paraboloids (i.e., the elastic contact formed by a ball and the inner and outer races of an instrument bearing).

4.15.1 Point Contact Model

Semiaxes of an Elliptical Contact Area The general shape of the contact area is an ellipse with semiaxes a and b and area $A = \pi ab$. The semiaxes are given by the relationships (Timoshenko and Goodier, 1970)

$$a = m \left[\frac{3F\Delta}{2(A+B)} \right]^{1/3} \quad \text{and} \quad b = n \left[\frac{3F\Delta}{2(A+B)} \right]^{1/3} \quad (4.145)$$

where F is the total normal load acting on the contact area, and Δ is a physical parameter defined by

$$\Delta = \frac{1}{2} \left(\frac{1 - \nu_1^2}{E_1} + \frac{1 - \nu_2^2}{E_2} \right) \quad (\text{m}^2/\text{N}) \quad (4.146)$$

when dissimilar materials form the contact. The physical parameters are Young's modulus E_1 and E_2 and Poisson's ratio ν_1 and ν_2 . The geometric parameters A and B are related to the radii of curvature of the two contacting solids (Timoshenko and Goodier, 1970):

$$\begin{aligned} 2(A+B) &= \frac{1}{\rho_1} + \frac{1}{\rho'_1} + \frac{1}{\rho_2} + \frac{1}{\rho'_2} \\ &= \frac{1}{\rho^*} \end{aligned} \quad (4.147)$$

where the local radii of curvature of the contacting solids are denoted as ρ_1 , ρ'_1 , ρ_2 , and ρ'_2 . The second relationship between A and B is

$$\begin{aligned} 2(B-A) &= \left[\left(\frac{1}{\rho_1} - \frac{1}{\rho'_1} \right)^2 + \left(\frac{1}{\rho_2} - \frac{1}{\rho'_2} \right)^2 \right. \\ &\quad \left. + 2 \left(\frac{1}{\rho_1} - \frac{1}{\rho'_1} \right) \left(\frac{1}{\rho_2} - \frac{1}{\rho'_2} \right) \cos 2\phi \right]^{1/2} \end{aligned} \quad (4.148)$$

The parameter ϕ is the angle between the principal planes that pass through the contacting solids.

The dimensionless parameters m and n that appear in the equations for the semi-axes are called the *Hertz elastic parameters*. They are determined by means of the following Hertz relationships (Timoshenko and Goodier, 1970):

$$m = \left[\frac{2}{\pi} \frac{E(k')}{k^2} \right]^{1/3} \quad \text{and} \quad n = \left[\frac{2}{\pi} k E(k') \right]^{1/3} \quad (4.149)$$

where $E(k')$ is the complete elliptic integral of the second kind of modulus k' (Abramowitz and Stegun, 1965; Byrd and Friedman, 1971), and

$$k' = \sqrt{1 - k^2} \quad \text{with} \quad k = \frac{n}{m} = \frac{b}{a} \leq 1 \quad (4.150)$$

The additional parameters k and k' are solutions of the transcendental equation (Timoshenko and Goodier, 1970):

$$\frac{B}{A} = \frac{(1/k^2)E(k') - K(k')}{K(k') - E(k')} \quad (4.151)$$

where $K(k')$ and $E(k')$ are complete elliptic integrals of the first and second kind of modulus k' .

The Hertz solution requires the calculation of k , the ellipticity, $K(k')$, and $E(k')$. This requires a numerical solution of the transcendental equation that relates k , $K(k')$, and $E(k')$ to the local geometry of the contacting solids through the geometric parameters A and B . This is usually accomplished by an iterative numerical procedure.

To this end, additional geometric parameters have been defined (Timoshenko and Goodier, 1970):

$$\cos \tau = \frac{B - A}{B + A} \quad \text{and} \quad \omega = \frac{A}{B} \leq 1 \quad (4.152)$$

Computed values of m and n , or m/n and n , are presented with τ or ω as the independent parameter. Table 4.15 shows how k , m , and n depend on the parameter ω over a range of values that should cover most practical contact problems. The parameter k' may be computed accurately and efficiently by means of the Newton–Raphson iteration method applied to the following relationships (Yovanovich, 1986):

$$k'_{\text{new}} = k' + \frac{N(k')}{D(k')} \quad (4.153)$$

TABLE 4.15 Hertz Contact Parameters and Elastoconstriction Parameter

ω	k	m	n	ψ^*
0.001	0.0147	14.316	0.2109	0.2492
0.002	0.0218	11.036	0.2403	0.3008
0.004	0.0323	8.483	0.2743	0.3616
0.006	0.0408	7.262	0.2966	0.4020
0.008	0.0483	6.499	0.3137	0.4329
0.010	0.0550	5.961	0.3277	0.4581
0.020	0.0828	4.544	0.3765	0.5438
0.040	0.1259	3.452	0.4345	0.6397
0.060	0.1615	2.935	0.4740	0.6994
0.080	0.1932	2.615	0.5051	0.7426
0.100	0.2223	2.391	0.5313	0.7761
0.200	0.3460	1.813	0.6273	0.8757
0.300	0.4504	1.547	0.6969	0.9261
0.400	0.5441	1.386	0.7544	0.9557
0.500	0.6306	1.276	0.8045	0.9741
0.600	0.7117	1.1939	0.8497	0.9857
0.700	0.7885	1.1301	0.8911	0.9930
0.800	0.8618	1.0787	0.9296	0.9972
0.900	0.9322	1.0361	0.9658	0.9994
1.000	1.0000	1.0000	1.0000	1.0000

where

$$N(k') = k^2 \frac{E(k')}{K(k')} \left(k^2 + \frac{A}{B} \right) - k^4 \left(1 + \frac{A}{B} \right) \quad (4.154)$$

$$D(k') = \frac{E(k')}{K(k')} \left(k'k^2 - 2k' \frac{A}{B} \right) + \frac{A}{B} k^2 k' \quad (4.155)$$

If the initial guess for k' is based on the following correlation of the results given in Table 4.15, the convergence will occur within two to three iterations:

$$k' = \left\{ 1 - \left[0.9446 \left(\frac{A}{B} \right)^{0.6135} \right]^2 \right\}^{1/2} \quad (4.156)$$

Polynomial approximations of the complete elliptic integrals (Abramowitz and Stegun, 1965) may be used to evaluate them with an absolute error less than 10^{-7} over the full range of k' .

4.15.2 Local Gap Thickness

The local gap thickness is required for the elastogap resistance model developed by Yovanovich (1986). The general relationship for the gap thickness can be determined by means of the following surface displacements (Johnson, 1985; Timoshenko and Goodier, 1970):

$$\delta(x, y) = \delta_0 + w(x, y) - w_0 \quad (\text{m}) \quad (4.157)$$

where $\delta_0(x, y)$ is the local gap thickness under zero load conditions, $w(x, y)$ is the total local displacement of the surfaces of the bodies outside the loaded area, and w_0 is the approach of the contact bodies due to loading.

The total local displacement of the two bodies is given by

$$\frac{3F\Delta}{2\pi} \int_{\mu}^{\infty} \left(1 - \frac{x^2}{a^2 + t} - \frac{y^2}{b^2 + t} \right) \frac{dt}{[(a^2 + t)(b^2 + t)t]^{1/2}} \quad (4.158)$$

where μ is the positive root of the equation

$$\frac{x^2}{a^2 + \mu} + \frac{y^2}{b^2 + \mu} = 1 \quad (4.159)$$

When $\mu > 0$, the point of interest lies outside the elliptical contact area:

$$\frac{x^2}{a^2} + \frac{y^2}{b^2} = 1 \quad (4.160)$$

When $\mu = 0$, the point of interest lies inside the contact area, and when $x = y = 0$, $w(0, 0) = w_0$, the total approach of the contacting bodies is

$$\begin{aligned}
 w_0 &= \frac{3F\Delta}{2\pi} \int_0^\infty \frac{dt}{[(a^2 + t)(b^2 + t)t]^{1/2}} \\
 &= \frac{3F\Delta}{\pi a} K(k') \quad (\text{m})
 \end{aligned} \tag{4.161}$$

The relationships for the semiaxes and the local gap thickness are used in the following subsections to develop the general relationships for the contact and gap resistances.

4.15.3 Contact Resistance of Isothermal Elliptical Contact Areas

The general spreading–constriction resistance model, as proposed by Yovanovich (1971, 1986), is based on the assumption that both bodies forming an elliptical contact area can be taken to be a conducting half-space. This approximation of actual bodies is reasonable because the dimensions of the contact area are very small relative to the characteristic dimensions of the contacting bodies.

If the free (noncontacting) surfaces of the contacting bodies are adiabatic, the total ellipsoidal spreading–constriction resistance of an isothermal elliptical contact area with $a \geq b$ is (Yovanovich, 1971, 1986)

$$R_c = \frac{\psi}{2k_s a} \quad (\text{K/W}) \tag{4.162}$$

where a is the semimajor axis, k_s is the harmonic mean thermal conductivity of the joint,

$$k_s = \frac{2k_1 k_2}{k_1 + k_2} \quad (\text{W/m} \cdot \text{K}) \tag{4.163}$$

and ψ is the spreading/constriction parameter of the isothermal elliptical contact area developed in the section for spreading resistance of an isothermal elliptical area on an isotropic half-space:

$$\psi = \frac{2}{\pi} K(k') \tag{4.164}$$

in which $K(k')$ is the complete elliptic integral of the first kind of modulus k' and is related to the semiaxes

$$k' = \left[1 - \left(\frac{b}{a} \right)^2 \right]^{1/2}$$

The complete elliptic integral can be computed accurately by means of accurate polynomial approximations and by computer algebra systems. This important special function can also be approximated by means of the following simple relationships:

$$K(k') = \begin{cases} \ln \frac{4a}{b} & 0 \leq k < 0.1736 \\ \frac{2\pi}{(1 + \sqrt{b/a})^2} & 0.1736 < k \leq 1 \end{cases} \quad (4.165)$$

These approximations have a maximum error less than 0.8%, which occurs at $k = 0.1736$. The ellipsoidal spreading-constriction parameter approaches the value of 1 when $a = b$, the circular contact area.

When the results of the Hertz elastic deformation analysis are substituted into the results of the ellipsoidal constriction analysis, one obtains the elastoconstriction resistance relationship developed by Yovanovich (1971, 1986):

$$k_s(24F \Delta \rho^*)^{1/3} R_c = \frac{2}{\pi} \frac{K(k')}{m} \equiv \psi^* \quad (4.166)$$

where the effective radius of the ellipsoidal contact is defined as $\rho^* = [2(A + B)]^{-1}$. The left-hand side is a dimensionless group consisting of the known total mechanical load F , the effective thermal conductivity k_s of the joint, the physical parameter Δ , and the isothermal elliptical spreading/constriction resistance R_c . The right-hand side is defined to be ψ^* , which is called the *thermal elastoconstriction parameter* (Yovanovich, 1971, 1986). Typical values of ψ^* for a range of values of ω are given in Table 4.15. The elastoconstriction parameter $\psi^* \rightarrow 1$ when $k = b/a = 1$, the case of the circular contact area.

4.15.4 Elastogap Resistance Model

The thermal resistance of the gas-filled gap depends on three local quantities: the local gap thickness, thermal conductivity of the gas, and temperature difference between the bounding solid surfaces. The gap model is based on the subdivision of the gap into elemental heat flow channels (flux tubes) having isothermal upper and lower boundaries and adiabatic sides (Yovanovich and Kitscha, 1974). The heat flow lines in each channel (tube) are assumed to be straight and perpendicular to the plane of contact.

If the local effective gas conductivity $k_g(x, y)$ in each elemental channel is assumed to be uniform across the local gap thickness $\delta(x, y)$, the differential gap heat flow rate is

$$dQ_g = \frac{k_g(x, y) \Delta T_g(x, y)}{\delta(x, y)} dx dy \quad (\text{W}) \quad (4.167)$$

The total gap heat flow rate is given by the double integral $Q_g = \iint_{A_g} dQ_g$, where the integration is performed over the entire effective gap area A_g .

The thermal resistance of the gap, R_g , is defined in terms of the overall joint temperature drop ΔT_j (Yovanovich and Kitscha, 1974):

$$\frac{1}{R_g} = \frac{Q_g}{\Delta T_j} = \iint_{A_g} \frac{k_g(x, y) \Delta T_g(x, y)}{\delta(x, y) \Delta T_j} dA_g \quad (\text{W/K}) \quad (4.168)$$

The local gap thickness in the general case of two bodies in elastic contact forming an elliptical contact area is given above.

The local effective gas conductivity is based on a model for the effective thermal conductivity of a gaseous layer bounded by two infinite isothermal parallel plates. Therefore, for each heat flow channel (tube) the effective thermal conductivity is approximated by the relation (Yovanovich and Kitscha, 1974)

$$k_g(x, y) = \frac{k_{g,\infty}}{1 + \alpha\beta\Lambda/\delta(x, y)} \quad (\text{W/m} \cdot \text{K}) \quad (4.169)$$

where $k_{g,\infty}$ is the gas conductivity under continuum conditions at STP. The accommodation parameter α is defined as

$$\alpha = \frac{2 - \alpha_1}{\alpha_1} + \frac{2 - \alpha_2}{\alpha_2} \quad (4.170)$$

where α_1 and α_2 are the accommodation coefficients at the solid–gas interfaces (Wiedemann and Trumpler, 1946; Hartnett, 1961; Wachman, 1962; Thomas, 1967; Kitscha and Yovanovich, 1975; Madhusudana, 1975, 1996; Semyonov et al., 1984; Wesley and Yovanovich, 1986; Song and Yovanovich, 1987; Song, 1988; Song et al., 1992a, 1993b). The fluid property parameter β is defined by

$$\beta = \frac{2\gamma}{(\gamma + 1)/\text{Pr}} \quad (4.171)$$

where γ is the ratio of the specific heats and Pr is the Prandtl number. The mean free path Λ of the gas molecules is given in terms of $\Lambda_{g,\infty}$, the mean free path at STP, as follows:

$$\Lambda = \Lambda_{g,\infty} \frac{T_g}{T_{g,\infty}} \frac{P_{g,\infty}}{P_g} \quad (\text{m}) \quad (4.172)$$

Two models for determining the local temperature difference, $\Delta T_g(x, y)$, are proposed (Yovanovich and Kitscha, 1974). In the first model it is assumed that the bounding solid surfaces are isothermal at their respective contact temperatures; hence

$$\Delta T_g(x, y) = \Delta T_j \quad (\text{K}) \quad (4.173)$$

This is called the *thermally decoupled model* (Yovanovich and Kitscha, 1974), since it assumes that the surface temperature at the solid–gas interface is independent of the temperature field within each solid.

In the second model (Yovanovich and Kitscha, 1974), it is assumed that the temperature distribution of the solid–gas interface is induced by conduction through the solid–solid contact, under vacuum conditions. This temperature distribution is approximated by the temperature distribution immediately below the surface of an insulated half-space that receives heat from an isothermal elliptical contact. Solving for this temperature distribution, using ellipsoidal coordinates it was found that

$$\frac{\Delta T_g(x, y)}{\Delta T_j} = 1 - \frac{F(k', \psi)}{K(k')} \quad (4.174)$$

where $F(k', \psi)$ is the incomplete elliptic integral of the first kind of modulus k' and amplitude angle ψ (Abramowitz and Stegun, 1965; Byrd and Friedman, 1971). The modulus k' is given above and the amplitude angle is

$$\psi = \sin^{-1} \left(\frac{a^2}{a^2 + \mu} \right)^{1/2} \quad (4.175)$$

where the parameter μ is defined above. It ranges between $\mu = 0$, the edge of the elliptical contact area, to $\mu = \infty$, the distant points within the half-space. Since the solid–gas interface temperature is coupled to the interior temperature distribution, it is called the coupled half-space model temperature drop.

The general elastogap model has not been solved. Two special cases of the general model have been examined. They are the sphere–flat contact, studied by Yovanovich and Kitscha (1974) and Kitscha and Yovanovich (1975), and the cylinder–flat contact, studied by McGee et al. (1985). The two special cases are discussed below.

4.15.5 Joint Radiative Resistance

If the joint is in a vacuum, or the gap is filled with a transparent substance such as dry air, there is heat transfer across the gap by radiation. It is difficult to develop a general relationship that would be applicable for all point contact problems because radiation heat transfer occurs in a complex enclosure that consists of at least three nonisothermal convex surfaces. The two contacting surfaces are usually metallic, and the third surface forming the enclosure is frequently a reradiating surface such as insulation.

Yovanovich and Kitscha (1974) and Kitscha and Yovanovich (1975) examined an enclosure that was formed by the contact of a metallic hemisphere and a metallic circular disk of diameter D . The third boundary of the enclosure was a nonmetallic circular cylinder of diameter D and height $D/2$. The metallic surfaces were assumed to be isothermal at temperatures T_1 and T_2 with $T_1 > T_2$. These temperatures correspond to the extrapolated temperatures from temperatures measured on both sides of the joint. The joint temperature was defined as $T_j = (T_1 + T_2)/2$. The dimensionless radiation resistance was found to have the relationship

$$Dk_s R_r = \frac{k_s}{\pi \sigma D T_j^3} \left(\frac{1 - \epsilon_2}{\epsilon_2} + \frac{1 - \epsilon_1}{2\epsilon_1} + 1.103 \right) \quad (4.176)$$

where $\sigma = 5.67 \times 10^{-8} \text{ W/m}^2 \cdot \text{K}^4$ is the Stefan–Boltzmann constant, ϵ_1 and ϵ_2 are the emissivities of the hemisphere and disk, respectively, and k_s is the effective thermal conductivity of the joint.

4.15.6 Joint Resistance of Sphere–Flat Contact

The contact, gap, radiative, and joint resistances of the sphere–flat contact shown in Fig. 4.17 are presented here. The contact radius a is much smaller than the sphere diameter D . Assuming an isothermal contact area, the general elastoconstriction resistance model (Yovanovich, 1971, 1986; Yovanovich and Kitscha, 1974), becomes

$$R_c = \frac{1}{2k_s a} \quad (\text{K/W}) \quad (4.177)$$

where $k_s = 2k_1 k_2 / (k_1 + k_2)$ is the harmonic mean thermal conductivity of the contact, and the contact radius is obtained from the Hertz elastic model (Timoshenko and Goodier, 1970):

$$\frac{2a}{D} = \left(\frac{3F\Delta}{D^2} \right)^{1/3} \quad (4.178)$$

where F is the mechanical load at the contact and Δ is the joint physical parameter defined above.

The general-coupled elastogap resistance model for point contacts reduces, for the sphere–flat contact, to (Yovanovich and Kitscha, 1974; Kitscha and Yovanovich 1975; Yovanovich, 1986):

$$\frac{1}{R_g} = \frac{D}{L} k_{g,0} I_{g,p} \quad (\text{W/K}) \quad (4.179)$$

where $L = D/2a$ is the relative contact size. The gap integral for point contacts proposed by Yovanovich and Kitscha (1974) and Yovanovich (1975) is defined as

$$I_{g,p} = \int_1^L \frac{2x \tan^{-1} \sqrt{x^2 - 1}}{2\delta/D + 2M/D} dx \quad (4.180)$$

The local gap thickness δ is obtained from the relationship

$$\begin{aligned} \frac{2\delta}{D} = 1 - \left[1 - \left(\frac{x}{L} \right)^2 \right]^{1/2} \\ + \frac{1}{\pi L^2} \left[(2 - x^2) \sin^{-1} \frac{1}{x} + \sqrt{x^2 - 1} \right] - \frac{1}{L^2} \end{aligned} \quad (4.181)$$

where $x = r/a$ and $1 \leq x \leq L$. The gap gas rarefaction parameter is defined as

$$M = \alpha \beta \Lambda \quad (\text{m}) \quad (4.182)$$

where the gas parameters α , β , and Γ are as defined above.

Contacts in a Vacuum The joint resistance for a sphere–flat contact in a vacuum is (Yovanovich and Kitscha, 1974; Kitscha and Yovanovich, 1975)

$$\frac{1}{R_j} = \frac{1}{R_c} + \frac{1}{R_r} \quad (\text{W/K}) \tag{4.183}$$

The models proposed were verified by experiments conducted by Kitscha (1982). The test conditions were: sphere diameter $D = 25.4$ mm; vacuum pressure $P_g = 10^{-6}$ torr; mean interface temperature range $316 \leq T_m \leq 321$ K; harmonic mean thermal conductivity of sphere–flat contact $k_s = 51.5$ W/(m · K); emissivities of very smooth sphere and lapped flat (rms roughness is $\sigma = 0.13$ μm) $\epsilon_1 = 0.2$ and $\epsilon_2 = 0.8$, respectively; elastic properties of sphere and flat $E_1 = E_2 = 206$ GPa and $\nu_1 = \nu_2 = 0.3$.

The dimensionless joint resistance is given by the relationship

$$\frac{1}{R_j^*} = \frac{1}{R_c^*} + \frac{1}{R_r^*} \tag{4.184}$$

where

$$R_j^* = Dk_s R_j \qquad R_c^* = Dk_s R_c = L \qquad R_r^* = 1415 \left(\frac{300}{T_m} \right)^3 \tag{4.185}$$

The model and vacuum data are compared for a load range in Table 4.16. The agreement between the joint resistance model and the data is excellent over the full range of tests.

Effect of Gas Pressure on Joint Resistance According to the Model of Yovanovich and Kitscha (1974), the dimensionless joint resistance with a gas in the gap is given by

$$\frac{1}{R_j^*} = \frac{1}{R_c^*} + \frac{1}{R_r^*} + \frac{1}{R_g^*} \tag{4.186}$$

TABLE 4.16 Dimensionless Load, Constriction, Radiative, and Joint Resistances

F (N)	L $D/2a$	T_m (K)	R_r^* Model	R_j^* Model	R_j^* Test
16.0	115.1	321	1155	104.7	107.0
22.2	103.2	321	1155	94.7	99.4
55.6	76.0	321	1155	71.3	70.9
87.2	65.4	320	1164	61.9	61.9
195.7	50.0	319	1177	48.0	48.8
266.9	45.1	318	1188	43.4	42.6
467.0	37.4	316	1211	36.4	35.4

Source: Kitscha (1982).

where

$$R_g^* = Dk_s R_g = \frac{k_s L^2}{k_{g,\infty} I_{g,p}} \quad (4.187)$$

The joint model for the sphere–flat contact is compared against data obtained for the following test conditions: sphere diameter $D = 25.4$ mm; load is 16 N; dimensionless load $L = 115.1$; mean interface temperature range $309 \leq T_m \leq 321$ K; harmonic mean thermal conductivity of sphere–flat contact $k_s = 51.5$ W/m · K; emissivities of smooth sphere and lapped flat are $\epsilon_1 = 0.2$ and $\epsilon_2 = 0.8$, respectively.

The load was fixed such that $L = 115.1$ for all tests, while the air pressure was varied from 400 mmHg down to a vacuum. The dimensionless resistances are given in Table 4.17. It can be seen that the dimensionless radiative resistance was relatively large with respect to the dimensionless gap and contact resistances. The dimensionless gap resistance values varied greatly with the gas pressure. The agreement between the joint resistance model and the data is very good for all test points.

4.15.7 Joint Resistance of a Sphere and a Layered Substrate

Figure 4.18 shows three joints: contact between a hemisphere and a substrate, contact between a hemisphere and a layer of finite thickness bounded to a substrate, and contact between a hemisphere and a very thick layer where $t/a \gg 1$.

In the general case, contact is between an elastic hemisphere of radius ρ and elastic properties: E_3, ν_3 and an elastic layer of thickness t and elastic properties: E_1, ν_1 , which is bonded to an elastic substrate of elastic properties: E_2, ν_2 . The axial load is F . It is assumed that $E_1 < E_2$ for layers that are less rigid than the substrate.

The contact radius a is much smaller than the dimensions of the hemisphere and the substrate. The solution for arbitrary layer thickness is complex because the contact radius depends on several parameters [i.e., $a = f(F, \rho, t, E_i, \nu_i), i = 1, 2, 3$]. The contact radius lies in the range $a_S \leq a \leq a_L$, where a_S corresponds to the very thin

TABLE 4.17 Effect of Gas Pressure on Gap and Joint Resistances for Air

T_m (K)	P_g (mmHg)	R_g^* Model	R_r^* Model	R_j^* Model	R_j^* Test
309	400.0	77.0	1295	44.5	46.8
310	100.0	87.6	1282	47.9	49.6
311	40.0	97.4	1270	50.7	52.3
316	4.4	138.3	1211	59.7	59.0
318	1.8	168.9	1188	64.7	65.7
321	0.6	231.3	1155	72.1	73.1
322	0.5	245.9	1144	73.4	74.3
325	0.2	352.8	1113	80.5	80.3
321	vacuum	∞	1155	104.7	107.0

Source: Kitscha (1982).

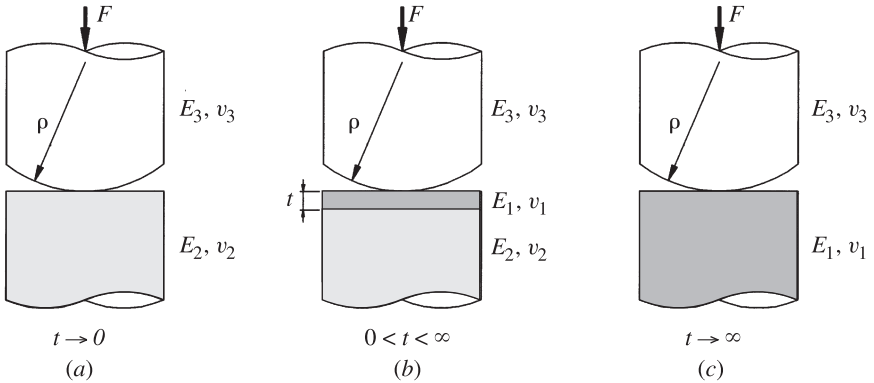


Figure 4.18 Contact between a hemisphere and a layer on a substrate: (a) hemisphere and substrate; (b) hemisphere and layer of finite thickness; (c) hemisphere and very thick layer. (From Stevanović et al., 2001.)

layer limit, $t/a \rightarrow 0$ (Fig. 4.18a) and a_L corresponds to the very thick layer limit, $t/a \rightarrow \infty$ (Fig. 4.18c).

For the general case, a contact in a vacuum, and if there is negligible radiation heat transfer across the gap, the joint resistance is equal to the contact resistance, which is equal to the sum of the spreading–constriction resistances in the hemisphere and layer–substrate, respectively.

The joint resistance is given by Fisher (1985), Fisher and Yovanovich (1989), and Stevanović et al. (2001, 2002)

$$R_j = R_c = \frac{1}{4k_3a} + \frac{\psi_{12}}{4k_2a} \quad (\text{K/W}) \quad (4.188)$$

where a is the contact radius. The first term on the right-hand side represents the constriction resistance in the hemisphere, and ψ_{12} is the spreading resistance parameter in the layer–substrate. The thermal conductivities of the hemisphere and the substrate appear in the first and second terms, respectively. The layer–substrate spreading resistance parameter depends on two dimensionless parameters: $\tau = t/a$ and $\kappa = k_1/k_2$. This parameter was presented above under spreading resistance in a layer on a half-space. To calculate the joint resistance the contact radius must be found.

A special case arises when the rigidity of the layer is much smaller than the rigidity of the hemisphere and the layer. This corresponds to “soft” metallic layers such as indium, lead, and tin; or nonmetallic layers such as rubber or elastomers. In this case, since $E_1 \ll E_2$ and $E_1 \ll E_3$, the hemisphere and substrate may be modeled as perfectly rigid while the layer deforms elastically.

The dimensionless numerical values for a/a_L obtained from the elastic contact model of Chen and Engel (1972) according to Stevanović et al. (2001) are plotted in Fig. 4.19 for a wide range of relative layer thickness $\tau = t/a$ and for a range of values of the layer Young’s modulus E_1 . The contact model, which is represented by the correlation equation of the numerical values, is (Stevanović et al., 2002)

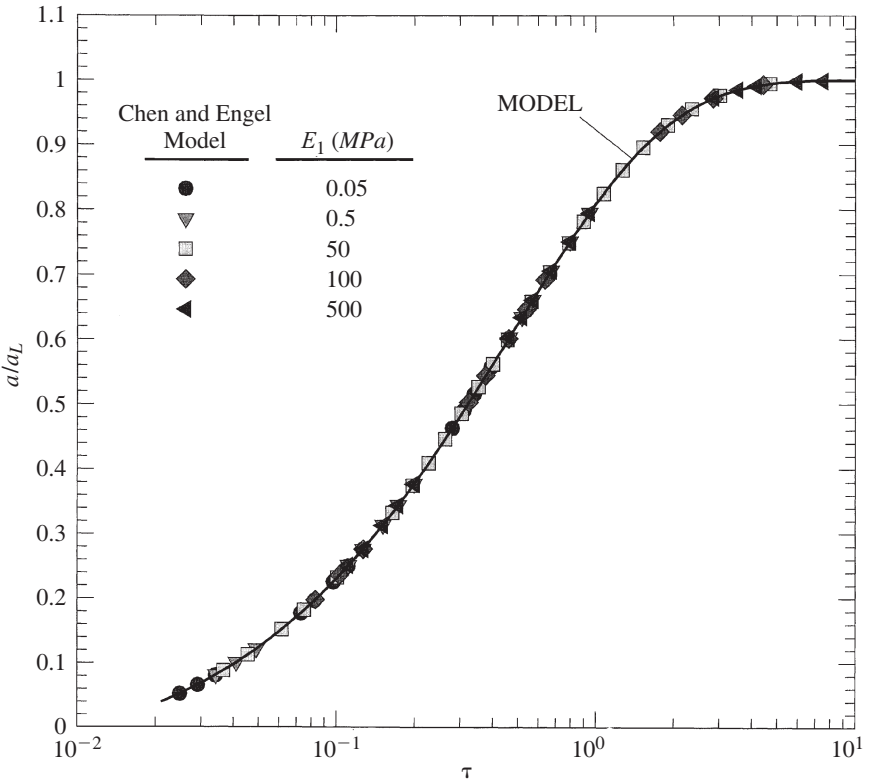


Figure 4.19 Comparison of data and model for contact between a rigid hemisphere and an elastic layer on a rigid substrate. (From Stevanović et al., 2001.)

$$\frac{a}{a_L} = 1 - c_3 \exp(c_1 \tau^{c_2}) \quad (4.189)$$

with correlation coefficients: $c_1 = -1.73$, $c_2 = 0.734$, and $c_3 = 1.04$. The reference contact radius is a_L , which corresponds to the very thick layer limit given by

$$a_L = \left(\frac{3}{4} \frac{F \rho}{E_{13}} \right)^{1/3} \quad \text{for } \frac{t}{a} \rightarrow \infty \quad (4.190)$$

The maximum difference between the correlation equation and the numerical values obtained from the model of Chen and Engel (1972) is approximately 1.9% for $\tau = 0.02$. The following relationship, based on the Newton–Raphson method, is recommended for calculation of the contact radius (Stevanović et al., 2001):

$$a_{n+1} = \frac{a_n - a_L \{1 - 1.04 \exp[-1.73(t/a_n)^{0.734}]\}}{1 + 1.321(a_L/a_S)(t/a_n)^{0.734} \exp[-1.73(t/a_n)^{0.734}]} \quad (4.191)$$

If the first guess is $a_0 = a_L$, fewer than six iterations are required to give eight-digit accuracy.

In the general case where the hemisphere, layer, and substrate are elastic, the contact radius lies in the range $a_S \leq a \leq a_L$ for $E_2 < E_1$. The two limiting values of a are, according to Stevanović et al. (2002),

$$a = \begin{cases} a_S = \left(\frac{3}{4} \frac{F \rho}{E_{23}} \right)^{1/3} & \text{for } \frac{t}{a} \rightarrow 0 \\ a_L = \left(\frac{3}{4} \frac{F \rho}{E_{13}} \right)^{1/3} & \text{for } \frac{t}{a} \rightarrow \infty \end{cases} \quad (4.192)$$

where the effective Young's modulus for the two limits are defined as

$$E_{13} = \left(\frac{1 - \nu_1^2}{E_1} + \frac{1 - \nu_3^2}{E_3} \right)^{-1} \quad E_{23} = \left(\frac{1 - \nu_2^2}{E_2} + \frac{1 - \nu_3^2}{E_3} \right)^{-1} \quad (4.193)$$

The dimensionless contact radius and dimensionless layer thickness were defined as (Stevanović et al., 2002)

$$a^* = \frac{a - a_S}{a_L - a_S} \quad \text{where } 0 < a^* < 1 \quad (4.194)$$

$$\tau^* = \left(\frac{t}{a} \sqrt{\alpha} \right)^{1/3} \quad \text{where } \alpha = \frac{a_L}{a_S} = \left(\frac{E_{23}}{E_{13}} \right)^{1/3} \quad (4.195)$$

The dimensionless numerical values obtained from the full model of Chen and Engel (1972) for values of α in the range $1.136 \leq \alpha \leq 2.037$ are shown in Fig. 4.20. The correlation equation is (Stevanović et al., 2002)

$$\frac{a - a_S}{a_L - a_S} = 1 - \exp \left[-\pi^{1/4} \left(\frac{t \sqrt{\alpha}}{a} \right)^{\pi/4} \right] \quad (4.196)$$

Since the unknown contact radius a appears on both sides, the numerical solution of the correlation equation requires an iterative method (Newton–Raphson method) to find its root. For all metal combinations, the following solution is recommended (Stevanović et al., 2002):

$$a = a_S + (a_L - a_S) \left\{ 1 - \exp \left[-\pi^{1/4} \left(\frac{t \sqrt{\alpha}}{a_0} \right)^{\pi/4} \right] \right\} \quad (4.197)$$

where

$$a_0 = a_S + (a_L - a_S) \left\{ 1 - \exp \left[-\pi^{1/4} \left(\frac{2t \sqrt{\alpha}}{a_S + a_L} \right)^{\pi/4} \right] \right\} \quad (4.198)$$

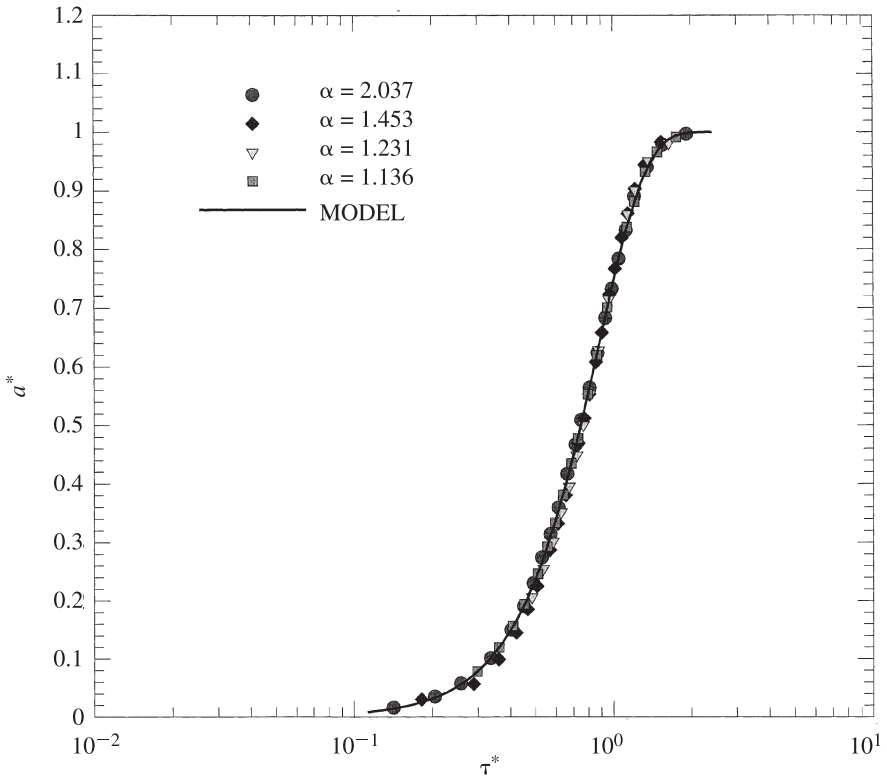


Figure 4.20 Comparison of the data and model for elastic contact between a hemisphere and a layer on a substrate. (From Stevanović et al., 2002.)

4.15.8 Joint Resistance of Elastic–Plastic Contacts of Hemispheres and Flat Surfaces in a Vacuum

A model is available for calculating the joint resistance of an elastic–plastic contact of a portion of a hemisphere whose radius of curvature is ρ attached to a cylinder whose radius is b_1 and a cylindrical flat whose radius is b_2 . The elastic properties of the hemisphere are E_1 , ν_1 , and the elastic properties of the flat are E_2 , ν_2 . The thermal conductivities are k_1 and k_2 , respectively.

If the contact strain is very small, the contact is elastic and the Hertz model can be used to predict the elastic contact radius denoted as a_e . On the other hand, if the contact strain is very large, plastic deformation may occur in the flat, which is assumed to be fully *work hardened*, and the plastic contact radius is denoted as a_p . Between the fully elastic and fully plastic contact regions there is a transition called the *elastic–plastic contact region*, which is very difficult to model. In the region the contact radius is denoted as a_{ep} , the elastic–plastic contact radius. The relationship between a_e , a_p , and a_{ep} is $a_e \leq a_{ep} \leq a_p$.

The elastic–plastic radius is related to the elastic and plastic contact radii by means of the composite model based on the method of Churchill and Usagi (1972) for combining asymptotes (Sridhar and Yovanovich, 1994):

$$a_{ep} = (a_e^n + a_p^n)^{1/n} \quad (m) \quad (4.199)$$

where n is the combination parameter, which is found empirically to have the value $n = 5$. The elastic and plastic contact radii may be obtained from the relationships (Sridhar and Yovanovich, 1994)

$$a_e = \left(\frac{3}{4} \frac{F\rho}{E'} \right)^{1/3} \quad \text{and} \quad a_p = \left(\frac{F}{\pi H_B} \right)^{1/2} \quad (m) \quad (4.200)$$

with the effective modulus

$$\frac{1}{E'} = \frac{1 - \nu_1^2}{E_1} + \frac{1 - \nu_2^2}{E_2} \quad (m^2/N) \quad (4.201)$$

The plastic parameter is the Brinell hardness H_B of the flat. The elastic–plastic deformation model assumes that the hemispherical solid is harder than the flat. The static axial load is F .

The joint resistance for a smooth hemispherical solid in elastic–plastic contact with smooth flat is given by (Sridhar and Yovanovich, 1994)

$$R_j = \frac{\psi_1}{4k_1 a_{ep}} + \frac{\psi_2}{4k_2 a_{ep}} \quad (K/W) \quad (4.202)$$

The spreading–constriction resistance parameters for the hemisphere and flat are

$$\psi_1 = \left(1 - \frac{a_{ep}}{b_1} \right)^{1.5} \quad \text{and} \quad \psi_2 = \left(1 - \frac{a_{ep}}{b_2} \right)^{1.5} \quad (4.203)$$

Alternative Constriction Parameter for a Hemisphere The following spreading–constriction parameter can be derived from the hemisphere solution:

$$\psi_1 = 1.0014 - 0.0438\epsilon - 4.0264\epsilon^2 + 4.968\epsilon^3 \quad (4.204)$$

where $\epsilon = a/b_1$.

If the contact is in a vacuum and the radiation heat transfer across the gap is negligible, $R_j = R_c$. Also, if $b_1 = b_2 = b$,

$$\psi_1 = \psi_2 = \left(1 - \frac{a}{b} \right)^{1.5} \quad (4.205)$$

The joint and dimensionless joint resistances for this case become

$$R_j = \frac{\psi}{2k_s a} \quad \text{and} \quad R_j^* = 2bk_s R_j = \frac{(1 - a/b)^{1.5}}{a/b} \quad (4.206)$$

where $k_s = 2k_1 k_2 / (k_1 + k_2)$.

Sridhar and Yovanovich (1994) compared the dimensionless joint resistance against data obtained for contacts between a carbon steel ball and several flats of Ni 200, carbon steel, and tool steel. The nondimensional data and the dimensionless joint resistance model are compared in Fig. 4.21 for a range of values of the reciprocal contact strain b/a . The agreement between the model and the data over the entire range $20 < b/a < 120$ is very good. The points near $b/a \approx 100$ are in the elastic contact region, and the points near $b/a \approx 20$ are close to the plastic contact region. In between the points are in the transition region, called the *elastic-plastic contact region*.

If the material of the flat work-hardens as the deformation takes place, the model for predicting the contact radius is much more complex, as described by Sridhar and Yovanovich (1994) and Johnson (1985). This case is not given here.

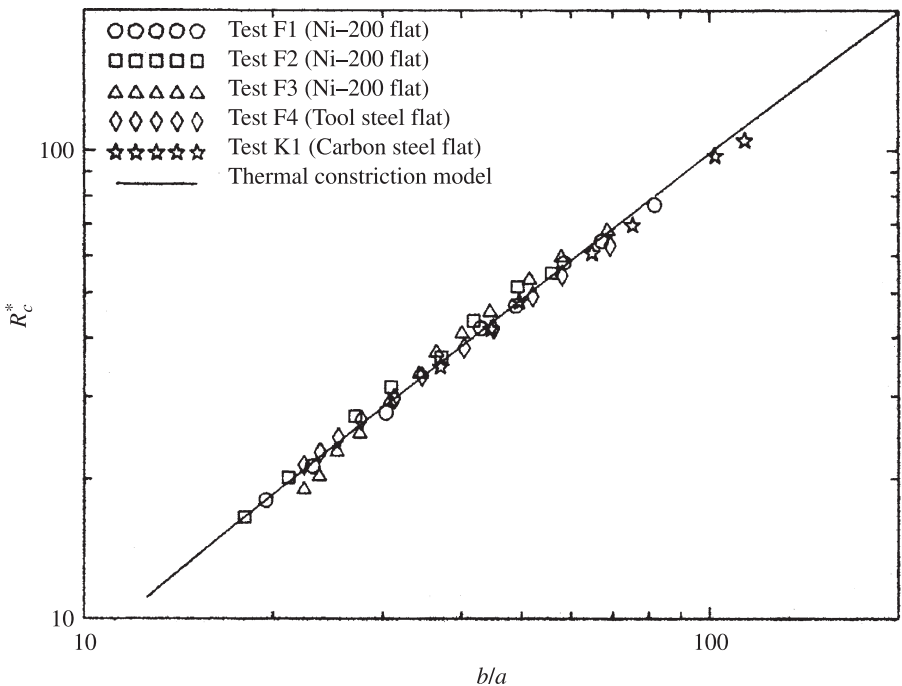


Figure 4.21 Comparison of the data and model for an elastic-plastic contact between a hemisphere and a flat. (From Sridhar and Yovanovich, 1994.)

4.15.9 Ball-Bearing Resistance

Models have been presented (Yovanovich, 1967, 1971, 1978) for calculating the overall thermal resistance of slowly rotating instrument bearings, which consist of many very smooth balls contained by very smooth inner and outer races. The thermal resistance models for bearings are based on elastic contact of the balls with the inner and outer races and spreading and constriction resistances in the balls and in the inner and outer races. For each ball there are two elliptical contact areas, one at the inner race and one at the outer race. The local thickness of the adjoining gap is very complex to model. There are four spreading–constriction zones associated with each ball. The full elastoconstriction resistance model must be used to obtain the overall thermal resistance of the bearing. Since these are complex systems, the contact resistance models are also complex; therefore, they are not presented here. The references above should be consulted for the development of the contact resistance models and other pertinent references.

4.15.10 Line Contact Models

If a long smooth circular cylinder with radius of curvature $\rho_1 = D_1/2$, length L_1 , and elastic properties: E_1, ν_1 makes contact with another long smooth circular cylinder with radius of curvature $\rho_2 = D_2/2$, length L_1 , and elastic properties: E_2, ν_2 , then in general, if the axes of the cylinders are not aligned (i.e., they are crossed), an elliptical contact area is formed with semiaxes a and b , where it is assumed that $a < b$. If the cylinder axes are aligned, the contact area becomes a strip of width $2a$, and the larger axes are equal to the length of the cylinder. The general Hertz model presented may be used to find the semiaxes and the local gap thickness if the axes are not aligned. For aligned axes, the general equations reduce to simple relationships, which are given below.

Contact Strip and Local Gap Thickness If the two cylinder axes are aligned, the contact area is a strip of width $2a$ and length L_1 , where (Timoshenko and Goodier, 1970; Walowit and Anno, 1975)

$$a = 2 \left(\frac{2F\rho\Delta}{\pi L_1} \right)^{1/2} \quad (\text{m}) \quad (4.207)$$

where the effective curvature is

$$\frac{1}{\rho} = \frac{1}{\rho_1} + \frac{1}{\rho_2} \quad (1/\text{m}) \quad (4.208)$$

and the contact parameter is

$$\Delta = \frac{1}{2} \left(\frac{1 - \nu_1^2}{E_1} + \frac{1 - \nu_2^2}{E_2} \right) \quad (\text{m}^2/\text{N}) \quad (4.209)$$

The contact pressure is maximum along the axis of the contact strip, and it is given by the relationship

$$P_0 = \frac{2}{\pi} \frac{F}{aL_1} = \left(\frac{F}{2\pi L_1 \rho \Delta} \right)^{1/2} \quad (\text{N/m}^2) \quad (4.210)$$

and the pressure distribution has the form (Timoshenko and Goodier, 1970; Walowit and Anno, 1975)

$$P(x) = P_0 \sqrt{1 - \left(\frac{x}{a} \right)^2} \quad \text{for } 0 \leq x \leq a \quad (\text{N/m}^2) \quad (4.211)$$

The mean contact area pressure is

$$P_m = \frac{F}{2aL_1} = \frac{4P_0}{\pi} \quad (\text{N/m}^2) \quad (4.212)$$

The normal approach of the two aligned cylinders is (Timoshenko and Goodier, 1970; Walowit and Anno, 1975)

$$\alpha = \frac{2F'}{\pi} \left[\frac{1 - \nu_1^2}{E_1} \left(\ln \frac{4\rho_1}{a} - \frac{1}{2} \right) + \frac{1 - \nu_2^2}{E_2} \left(\ln \frac{4\rho_2}{a} - \frac{1}{2} \right) \right] \quad (\text{m}) \quad (4.213)$$

where $F' = F/L_1$ is the load per unit cylinder length. The general local gap thickness relationship is (Timoshenko and Goodier, 1970; Walowit and Anno, 1975)

$$\begin{aligned} \frac{2\delta}{\rho} &= \left(1 - \frac{1}{L^2} \right)^{1/2} - \left(1 - \frac{\xi^2}{L^2} \right)^{1/2} \\ &+ [\xi(\xi^2 - 1)^{1/2} - \cosh^{-1}\xi - \xi^2 + 1] 2L \end{aligned} \quad (4.214)$$

where

$$L = \frac{\rho}{2a} \quad \xi = \frac{x}{L} \quad 1 \leq \xi \leq L \quad (4.215)$$

If a single circular cylinder of diameter D or ($\rho_1 = D_1/2 = D/2$) is in elastic contact with a flat ($\rho_2 = \infty$), put $\rho = D/2$ in the relationships above.

Contact Resistance at a Line Contact The thermal contact resistance for the very narrow contact strip of width $2a$ formed by the elastic contact of a long smooth circular cylinder of diameter D and a smooth flat whose width is $2b$ and whose length L_1 is identical to the cylinder length is given by the approximate relationship (McGee et al., 1985)

$$R_c = \frac{1}{\pi L_1 k_1} \left(\ln \frac{4}{\epsilon_1} - \frac{\pi}{2} \right) + \frac{1}{\pi L_1 k_2} \ln \frac{2}{\pi \epsilon_2} \quad (\text{K/W}) \quad (4.216)$$

where the thermal conductivities of the cylinder and flat are k_1 and k_2 , respectively. The contact parameters are $\epsilon_1 = 2a/D$ for the cylinder and $\epsilon_2 = a/b$ for the flat. For elastic contacts, $2a/D \ll 1$ and $2a/b \ll 1$ for most engineering applications. The approximate relationship for R_c becomes more accurate for very narrow strips.

The width of the flat relative to the cylinder diameter may be $2b > D$, $2b = D$, or $2b < D$. McGee et al. (1985) proposed the use of the dimensionless form of the contact resistance:

$$R_c^* = L_1 k_s R_c = \frac{1}{2\pi} \frac{k_s}{k_1} \ln \frac{\pi}{F^*} - \frac{k_s}{2k_1} + \frac{1}{2\pi} \frac{k_s}{k_2} \ln \frac{1}{4\pi F^*} \quad (4.217)$$

where

$$F^* = \frac{F\Delta}{L_1 D} \quad \text{and} \quad k_s = \frac{2k_1 k_2}{k_1 + k_2} \quad (4.218)$$

Gap Resistance at a Line Contact The general elastogap resistance model for line contacts proposed by Yovanovich (1986) reduces for the circular cylinder–flat contact to

$$\frac{1}{R_g} = \frac{4aL_1}{D} k_{g,\infty} I_{g,l} \quad (\text{W/K}) \quad (4.219)$$

where $k_{g,\infty}$ is the gas thermal conductivity and the line contact elastogap integral is defined as (Yovanovich, 1986)

$$I_{g,l} = \frac{2}{\pi} \int_1^L \frac{\cosh^{-1}(\xi) d\xi}{2\delta/D + M/D} \quad (4.220)$$

where

$$L = \frac{D}{2a} \quad \xi = \frac{x}{L} \quad 1 \leq \xi \leq L \quad (4.221)$$

This is the coupled elastogap model. Numerical integration is required to calculate values of $I_{g,l}$.

The gas rarefaction parameter that appears in the gap integral is

$$M = \alpha\beta\Lambda \quad (\text{m}) \quad (4.222)$$

where the accommodation parameter and other gas parameters are defined as

$$\alpha = \frac{2 - \alpha_1}{\alpha_1} + \frac{2 - \alpha_2}{\alpha_2} \quad \beta = \frac{2\gamma}{(\gamma + 1)\text{Pr}} \quad \gamma = \frac{C_p}{C_v} \quad (4.223)$$

and the molecular mean free path is

$$\Lambda = \Lambda_{g,\infty} \frac{T_g}{T_{g,\infty}} \frac{P_{g,\infty}}{P_g} \quad (\text{m}) \quad (4.224)$$

where $\Lambda_{g,\infty}$ is the value of the molecular mean free path at the reference temperature $T_{g,\infty}$ and gas pressure $P_{g,\infty}$.

Joint Resistance at a Line Contact The joint resistance at a line contact, neglecting radiation heat transfer across the gap, is

$$\frac{1}{R_j} = \frac{1}{R_c} + \frac{1}{R_g} \quad (\text{W/K}) \quad (4.225)$$

McGee et al. (1985) examined the accuracy of the contact, gap, and joint resistance relationships for helium and argon for gas pressures between 10^{-6} torr and 1 atm. The effect of contact load was investigated for mechanical loads between 80 and 8000 N on specimens fabricated from Keewatin tool steel, type 304 stainless steel, and Zircaloy 4. The experimental data were compared with the model predictions, and good agreement was obtained over a limited range of experimental parameters. Discrepancies were observed at the very light mechanical loads due to slight amounts of form error (crowning) along the contacting surfaces.

Joint Resistance of Nonconforming Rough Surfaces There is ample empirical evidence that surfaces may not be conforming and rough, as shown in Fig. 4.1c and f. The surfaces may be both nonconforming and rough, as shown in Fig. 4.1b and e, where a smooth hemispherical surface is in contact with a flat, rough surface.

If surfaces are nonconforming and rough, the joint that is formed is more complex from the standpoint of defining the micro- and macrogeometry before load is applied, and the definition of the micro- and macrocontacts that are formed after load is applied. The deformation of the contacting asperities may be elastic, plastic, or elastic-plastic. The deformation of the bulk may also be elastic, plastic, or elastic-plastic. The mode of deformation of the micro- and macrogeometry are closely connected under conditions that are not understood today.

The thermal joint resistance of such a contact is complex because heat can cross the joint by conduction through the microcontacts and the associated microgaps and by conduction across the macrogap. If the temperature level of the joint is sufficiently high, there may be significant radiation across the microgaps and macrogap. Clearly, this type of joint represents complex thermal and mechanical problems that are coupled.

Many vacuum data have been reported (Clausing and Chao, 1965; Burde, 1977; Kitscha, 1982) that show that the presence of roughness can alter the joint resistance of a nonconforming surface under light mechanical loads and have negligible effects at higher loads. Also, the presence of out-of-flatness can have significant effects on the joint resistance of a rough surface under vacuum conditions.

It is generally accepted that the joint resistance under vacuum conditions may be modeled as the superposition of microscopic and macroscopic resistance (Clausing and Chao, 1965; Greenwood and Tripp, 1967; Holm, 1967; Yovanovich, 1969; Burde and Yovanovich, 1978; Lambert, 1995; Lambert and Fletcher, 1997). The joint resistance can be modeled as

$$R_j = R_{\text{mic}} + R_{\text{mac}} \quad (\text{K/W}) \quad (4.226)$$

The microscopic resistance is given by the relationship

$$R_{\text{mic}} = \frac{\psi_{\text{mic}}}{2k_s N a_s} \quad (\text{K/W}) \quad (4.227)$$

where ψ_{mic} is the average spreading–constriction resistance parameter, N is the number of microcontacts that are distribution in some complex manner over the contour area of radius a_L and a_s represents some average microcontact spot radius, and the harmonic mean thermal conductivity of the joint is $k_s = 2k_1 k_2 / (k_1 + k_2)$.

The macroscopic resistance is given by the relationship

$$R_{\text{mac}} = \frac{\psi_{\text{mac}}}{2k_s a_L} \quad (\text{K/W}) \quad (4.228)$$

where ψ_{mac} is the spreading–constriction resistance parameter for the contour area of radius a_L .

The mechanical model should be capable of predicting the contact parameters: a_s , a_L , and N . These parameters are also required for the determination of the thermal spreading–constriction parameters ψ_{mic} and ψ_{mac} .

At this time there is no simple mechanical model available for prediction of the geometric parameters required in microscopic and macroscopic resistance relationships. There are publications (e.g., Greenwood and Tripp, 1967; Holm, 1967; Burde and Yovanovich, 1978; Johnson, 1985; Lambert and Fletcher, 1997; Marotta and Fletcher, 2001) that deal with various aspects of this very complex problem.

4.16 CONFORMING ROUGH SURFACE MODELS

There are models for predicting contact, gap, and joint conductances between conforming (nominally flat) rough surfaces developed by Greenwood and Williamson (1966), Greenwood (1967), Greenwood and Tripp (1970), Cooper et al. (1969), Mikic (1974), Sayles and Thomas (1976), Yovanovich (1982), and DeVaal (1988).

The three mechanical models—elastic, plastic, or elastic–plastic deformation of the contacting asperities—are based on the assumptions that the surface asperities have Gaussian height distributions about some mean plane passing through each surface and that the surface asperities are distributed randomly over the apparent contact area A_a . Figure 4.22 shows a very small portion of a typical joint formed between two nominally flat rough surfaces under a mechanical load.

Each surface has a mean plane, and the distance between them, denoted as Y , is related to the effective surface roughness, the apparent contact pressure, and the plastic or elastic physical properties of the contacting asperities.

A very important surface roughness parameter is the surface roughness: either the rms (root-mean-square) roughness or the CLA (centerline-average) roughness, which are defined as (Whitehouse and Archard, 1970; Onions and Archard, 1973; Thomas, 1982)

$$\text{CLA roughness} = \frac{1}{L} \int_0^L |y(x)| dx \quad (\text{m}) \quad (4.229)$$

$$\text{rms roughness} = \sqrt{\frac{1}{L} \int_0^L y^2(x) dx} \quad (\text{m}) \quad (4.230)$$

where $y(x)$ is the distance of points in the surface from the mean plane (Fig. 4.22) and L is the length of a trace that contains a sufficient number of asperities. For Gaussian asperity heights with respect to the mean plane, these two measures of surface roughness are related (Mikic and Rohsenow, 1966):

$$\sigma = \sqrt{\frac{\pi}{2}} \cdot \text{CLA}$$

A second very important surface roughness parameter is the absolute mean asperity slope, which is defined as (Cooper et al., 1969; Mikic and Rohsenow, 1966; and DeVaal et al. 1987).

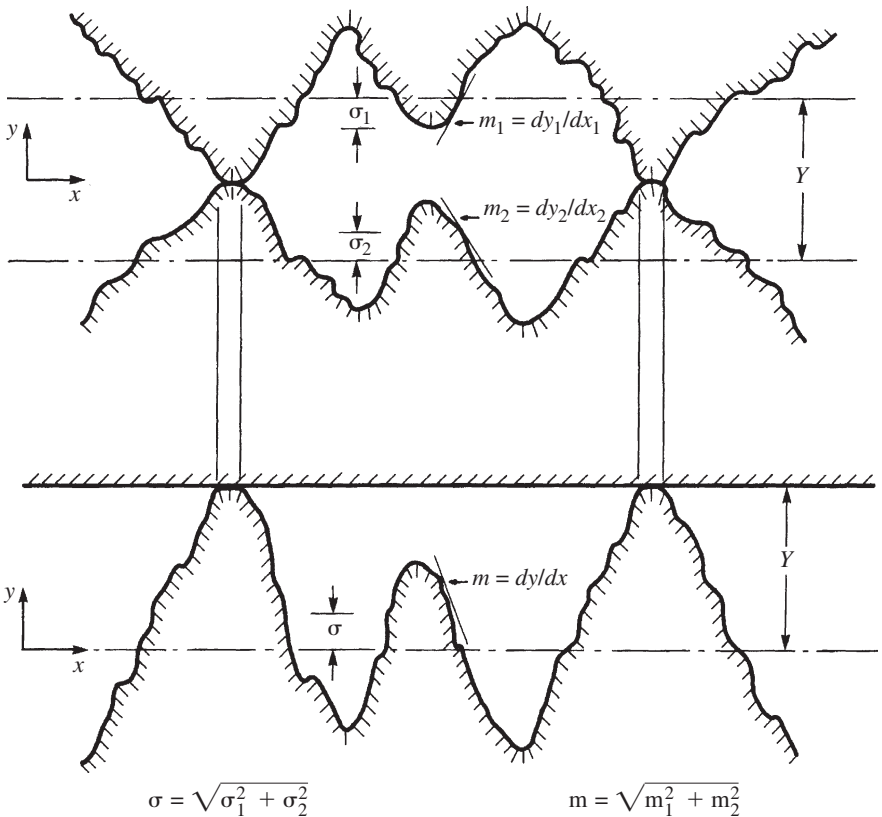


Figure 4.22 Typical joint between conforming rough surfaces. (From Hegazy, 1985.)

$$m = \frac{1}{L} \int_0^L \left| \frac{dy(x)}{dx} \right| dx \quad (\text{rad}) \quad (4.231)$$

The effective rms surface roughness and the effective absolute mean asperity slope for a typical joint formed by two conforming rough surfaces are defined as (Cooper et al., 1969; Mikic, 1974; Yovanovich, 1982)

$$\sigma = \sqrt{\sigma_1^2 + \sigma_2^2} \quad \text{and} \quad m = \sqrt{m_1^2 + m_2^2} \quad (4.232)$$

Antonetti et al. (1991) reported approximate relationships for m as a function of σ for several metal surfaces that were bead-blasted.

The three deformation models (elastic, plastic, or elastic-plastic) give relationships for three important geometric parameters of the joint: the relative real contact area A_r/A_a , the contact spot density n , and the mean contact spot radius a in terms of the relative mean plane separation defined as $\lambda = Y/\sigma$. The mean plane separation Y and the effective surface roughness are illustrated in Fig. 4.22 for the joint formed by the mechanical contact of two nominally flat rough surfaces.

The models differ in the mode of deformation of the contacting asperities. The three modes of deformation are plastic deformation of the softer contacting asperities, elastic deformation of all contacting asperities, and elastic-plastic deformation of the softer contacting asperities. For the three deformation models there is one thermal contact conductance model, given as (Cooper et al., 1969; Yovanovich, 1982)

$$h_c = \frac{2nak_s}{\psi(\epsilon)} \quad (\text{W/m}^2 \cdot \text{K}) \quad (4.233)$$

where n is the contact spot density, a is the mean contact spot radius, and the effective thermal conductivity of the joint is

$$k_s = \frac{2k_1k_2}{k_1 + k_2} \quad (\text{W/m} \cdot \text{K}) \quad (4.234)$$

and the spreading/constriction parameter ψ , based on isothermal contact spots, is approximated by

$$\psi(\epsilon) = (1 - \epsilon)^{1.5} \quad \text{for} \quad 0 < \epsilon < 0.3 \quad (4.235)$$

where the relative contact spot size is $\epsilon = \sqrt{A_r/A_a}$. The geometric parameters n , a and A_r/A_a are related to the relative mean plane separation $\lambda = Y/\sigma$.

4.16.1 Plastic Contact Model

The original plastic deformation model of Cooper et al. (1969) has undergone significant modifications during the past 30 years. First, a new, more accurate correlation equation was developed by Yovanovich (1982). Then Yovanovich et al. (1982a) and

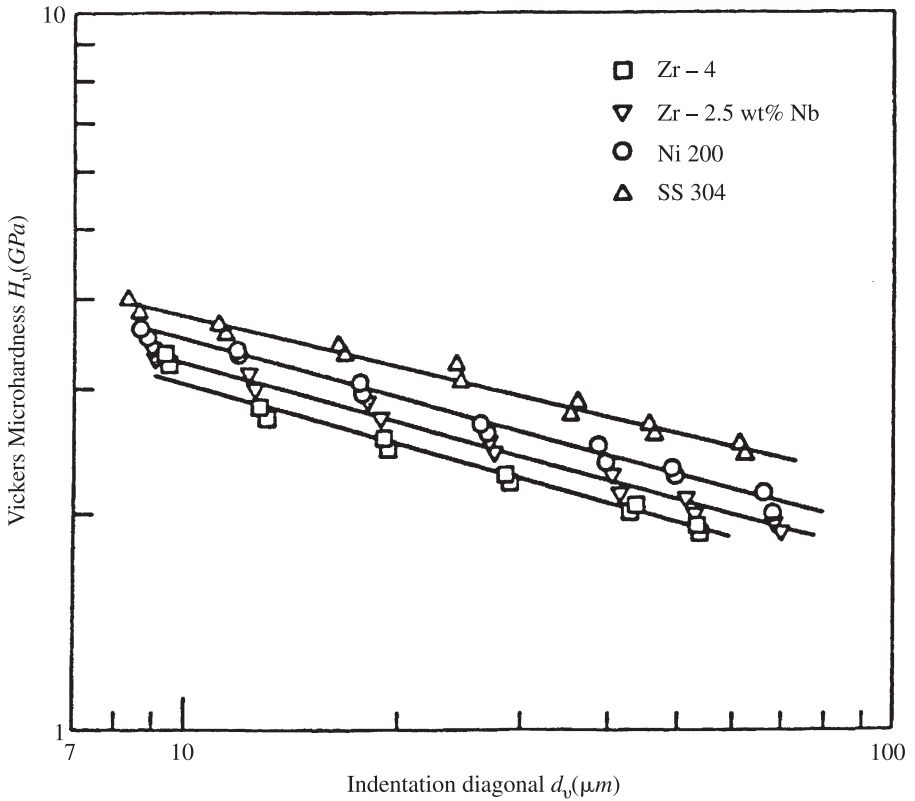


Figure 4.23 Vickers microhardness versus indentation diagonal for four metal types. (From Hegazy, 1985.)

Hegazy (1985) introduced the microhardness layer which appears in most *worked* metals. Figures 4.23 and 4.24 show plots of measured microhardness and macrohardness versus the penetration depth t or the Vickers diagonal d_v . These two measures of indenter penetration are related: $d_v/t = 7$. Figure 4.23 shows the measured Vickers microhardness versus indentation diagonal for four metal types (Ni 200, stainless steel 304, Zr-4 and Zr-2.5 wt % Nb). The four sets of data show the same trends: that as the load on the indenter increases, the indentation diagonal increases and the Vickers microhardness decreases with increasing diagonal (load). The indentation diagonal was between 8 and 70 μm .

Figure 4.24 shows the Vickers microhardness measurements and the Brinell and Rockwell macrohardness measurements versus indentation depth. The Brinell and Rockwell macrohardness values are very close because they correspond to large indentations, and therefore, they are a measure of the bulk hardness, which does not change with load. According to Fig. 4.24, the penetration depths for the Vickers microhardness measurements are between 1 and 10 μm , whereas the larger penetration

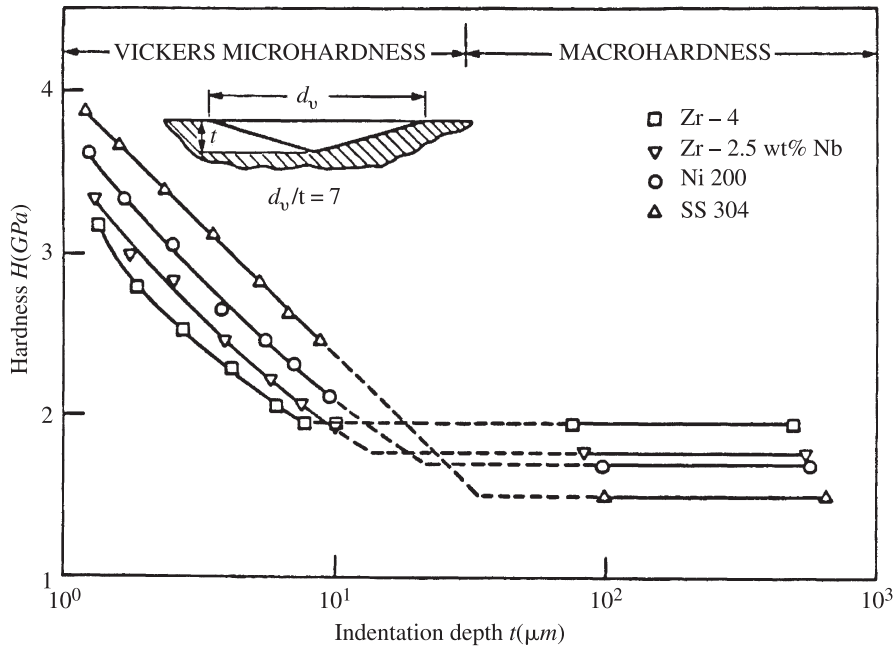


Figure 4.24 Vickers, Brinell, and Rockwell hardness versus indentation depth for four metal types. (From Hegazy, 1985.)

depths for the Brinell and Rockwell macrohardness measurements lie between approximately 100 and 1000 μm .

The microhardness layer may be defined by means of the Vickers microhardness measurements, which relate the Vickers microhardness H_V to the Vickers average indentation diagonal d_V (Yovanovich et al., 1982a; Hegazy, 1985):

$$H_V = c_1 \left(\frac{d_V}{d_0} \right)^{c_2} \quad (\text{GPa}) \quad (4.236)$$

where d_0 represents some convenient reference value for the average diagonal, and c_1 and c_2 are the correlation coefficients. It is conventional to set $d_0 = 1 \mu\text{m}$. Hegazy (1985) found that c_1 is closely related to the metal bulk hardness, such as the Brinell hardness, denoted as H_B .

The original mechanical contact model (Yovanovich et al., 1982a; Hegazy, 1985) required an iterative procedure to calculate the appropriate microhardness for a given surface roughness σ and m , given the apparent contact pressure P and the coefficients c_1 and c_2 .

Song and Yovanovich (1988) developed an explicit relationship for the microhardness H_p , which is presented below. Recently, Sridhar and Yovanovich (1996b) developed correlation equations between the Vickers correlation coefficients c_1 and

c_2 and Brinell hardness H_B over a wide range of metal types. These relationships are also presented below.

Plastic Contact Geometric Parameters For plastic deformation of the contacting asperities, the contact geometric parameters are obtained from the following relationships (Cooper et al., 1969; Yovanovich, 1982):

$$\frac{A_r}{A_a} = \frac{1}{2} \operatorname{erfc} \left(\frac{\lambda}{\sqrt{2}} \right) \quad (4.237)$$

$$n = \frac{1}{16} \left(\frac{m}{\sigma} \right)^2 \frac{\exp(-\lambda^2)}{\operatorname{erfc}(\lambda/\sqrt{2})} \quad (4.238)$$

$$a = \sqrt{\frac{8}{\pi}} \frac{\sigma}{m} \exp \left(\frac{\lambda^2}{2} \right) \operatorname{erfc} \left(\frac{\lambda}{\sqrt{2}} \right) \quad (4.239)$$

$$na = \frac{1}{4\sqrt{2\pi}} \frac{m}{\sigma} \exp \left(-\frac{\lambda^2}{2} \right) \quad (4.240)$$

Correlation of Geometric Parameters

$$\begin{aligned} \frac{A_r}{A_a} &= \exp(-0.8141 - 0.61778\lambda - 0.42476\lambda^2 - 0.004353\lambda^3) \\ n &= \left(\frac{m}{\sigma} \right)^2 \exp(-2.6516 + 0.6178\lambda - 0.5752\lambda^2 + 0.004353\lambda^3) \\ a &= \frac{\sigma}{m} (1.156 - 0.4526\lambda + 0.08269\lambda^2 - 0.005736\lambda^3) \end{aligned}$$

and for the relative mean plane separation

$$\lambda = 0.2591 - 0.5446 \left(\ln \frac{P}{H_p} \right) - 0.02320 \left(\ln \frac{P}{H_p} \right)^2 - 0.0005308 \left(\ln \frac{P}{H_p} \right)^3 \quad (4.241)$$

The relative mean plane separation for plastic deformation is given by

$$\lambda = \sqrt{2} \operatorname{erfc}^{-1} \left(\frac{2P}{H_p} \right) \quad (4.242)$$

where H_p is the microhardness of the softer contacting asperities.

Relative Contact Pressure The appropriate microhardness may be obtained from the relative contact pressure P/H_p . For plastic deformation of the contacting asperities, the explicit relationship is (Song and Yovanovich, 1988)

$$\frac{P}{H_p} = \left[\frac{P}{c_1(1.62\sigma/m)^{c_2}} \right]^{1/(1+0.071c_2)} \quad (4.243)$$

where the coefficients c_1 and c_2 are obtained from Vickers microhardness tests. The Vickers microhardness coefficients are related to the Brinell hardness for a wide range of metal types.

Vickers Microhardness Correlation Coefficients The correlation coefficients c_1 and c_2 are obtained from Vickers microhardness measurements. Sridhar and Yovanovich (1996b) developed correlation equations for the Vickers coefficients:

$$\frac{c_1}{3178} = 4.0 - 5.77 H_B^* + 4.0 (H_B^*)^2 - 0.61 (H_B^*)^3 \quad (4.244)$$

$$c_2 = -0.370 + 0.442 \left(\frac{H_B}{c_1} \right) \quad (4.245)$$

where H_B is the Brinell hardness (Johnson, 1985; Tabor, 1951) and $H_B^* = H_B/3178$. The correlation equations are valid for the Brinell hardness range 1300 to 7600 MPa. The correlation equations above were developed for a range of metal types (e.g., Ni200, SS304, Zr alloys, Ti alloys, and tool steel). Sridhar and Yovanovich (1996b) also reported a correlation equation that relates the Brinell hardness number to the Rockwell C hardness number:

$$\text{BHN} = 43.7 + 10.92 \text{ HRC} - \frac{\text{HRC}^2}{5.18} + \frac{\text{HRC}^3}{340.26} \quad (4.246)$$

for the range $20 \leq \text{HRC} \leq 65$.

Dimensionless Contact Conductance: Plastic Deformation The dimensionless contact conductance C_c is

$$C_c \equiv \frac{h_c \sigma}{k_s m} = \frac{1}{2\sqrt{2}\pi} \frac{\exp(-\lambda^2/2)}{\left[1 - \sqrt{\frac{1}{2}} \text{erfc}(\lambda/\sqrt{2}) \right]^{1.5}} \quad (4.247)$$

The correlation equation of the dimensionless contact conductance obtained from theoretical values for a wide range of λ and P/H_p is (Yovanovich, 1982)

$$C_c \equiv \frac{h_c \sigma}{k_s m} = 1.25 \left(\frac{P}{H_p} \right)^{0.95} \quad (4.248)$$

which agrees with the theoretical values to within $\pm 1.5\%$ in the range $2 \leq \lambda \leq 4.75$.

It has been demonstrated that the plastic contact conductance model of eq. (4.248) predicts accurate values of h_c for a range of surface roughness σ/m , a range of metal types (e.g., Ni 200, SS 304, Zr alloys, etc.), and a range of the relative contact pressure P/H_p (Antonetti, 1983; Hegazy, 1985; Sridhar, 1994; Sridhar and Yovanovich, 1994, 1996a). The very good agreement between the contact conductance models and experiments is shown in Fig. 4.25.

In Fig. 4.25 the dimensionless contact conductance model and the vacuum data for different metal types and a range of surface roughnesses are compared over two

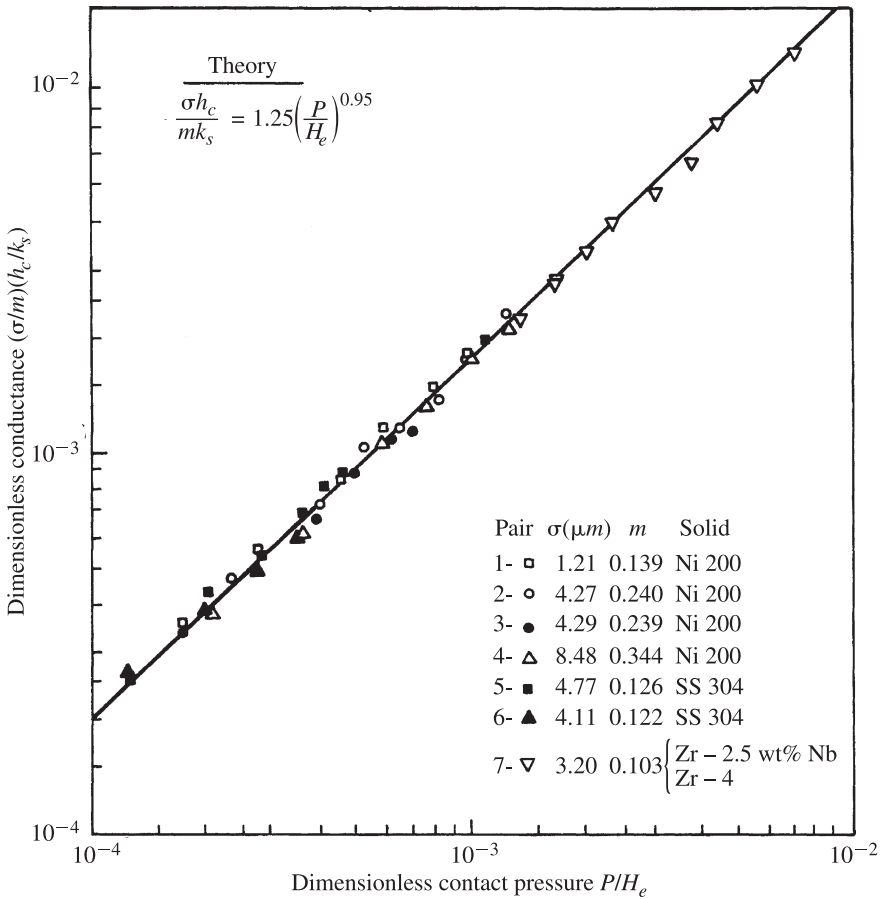


Figure 4.25 Comparison of a plastic contact conductance model and vacuum data. (From Antonetti, 1983; Hegazy, 1985.)

decades of the relative contact pressure defined as P/H_e , where H_e was called the *effective microhardness* of the joint. The agreement between the theoretical model developed for conforming rough surfaces that undergo plastic deformation of the contacting asperities is very good over the entire range of dimensionless contact pressure. Because of the relatively high contact pressures and high thermal conductivity of the metals, the effect of radiation heat transfer across the gaps was found to be negligible for all tests.

4.16.2 Radiation Resistance and Conductance for Conforming Rough Surfaces

The radiation heat transfer across gaps formed by conforming rough solids and filled with a transparent substance (or its in a vacuum) is complex because the geometry of

TABLE 4.18 Radiative Conductances for Black Surfaces

ΔT_j	T_j	h_r	ΔT_j	T_j	h_r
100	350	9.92	600	600	61.24
200	400	15.42	700	650	80.34
300	450	22.96	800	700	103.2
400	500	32.89	900	750	130.1
500	550	45.53	1000	800	161.5

the microgaps is very difficult to characterize and the temperatures of the bounding solids vary in some complex manner because they are coupled to heat transfer by conduction through the microcontacts.

The radiative resistance and the conductance can be estimated by modeling the heat transfer across the microgaps as equivalent to radiative heat transfer between two gray infinite isothermal smooth plates. The radiative heat transfer is given by

$$Q_r = \sigma A_a \mathcal{F}_{12} (T_{j1}^4 - T_{j2}^4) \quad (\text{W}) \quad (4.249)$$

where $\sigma = 5.67 \times 10^{-8} \text{ W}/(\text{m}^2 \cdot \text{K}^4)$ is the Stefan–Boltzmann constant and T_{j1} and T_{j2} are the absolute joint temperatures of the bounding solid surfaces. These temperatures are obtained by extrapolation of the temperature distributions within the bounding solids. The radiative parameter is given by

$$\frac{1}{\mathcal{F}_{12}} = \frac{1}{\epsilon_1} + \frac{1}{\epsilon_2} - 1 \quad (4.250)$$

where ϵ_1 and ϵ_2 are the emissivities of the bounding surfaces. The radiative resistance is given by

$$R_r = \frac{T_{j1} - T_{j2}}{Q_r} = \frac{T_{j1} - T_{j2}}{\sigma A_a \mathcal{F}_{12} (T_{j1}^4 - T_{j2}^4)} \quad (\text{K/W}) \quad (4.251)$$

and the radiative conductance by

$$h_r = \frac{Q_r}{A_a (T_{j1} - T_{j2})} = \frac{\sigma \mathcal{F}_{12} (T_{j1}^4 - T_{j2}^4)}{T_{j1} - T_{j2}} \quad (\text{W}/\text{m}^2 \cdot \text{K}) \quad (4.252)$$

The radiative conductance is seen to be a complex parameter which depends on the emissivities ϵ_1 and ϵ_2 and the joint temperatures T_{j1} and T_{j2} . For many interface problems the following approximation can be used to calculate the radiative conductance:

$$\frac{T_{j1}^4 - T_{j2}^4}{T_{j1} - T_{j2}} \approx 4(\bar{T}_j)^3$$

where the mean joint temperature is defined as

$$\bar{T}_j = \frac{1}{2}(T_{j1} + T_{j2}) \quad (\text{K})$$

If we assume blackbody radiation across the gap, $\epsilon_1 = 1, \epsilon_2 = 1$ gives $\mathcal{F}_{12} = 1$. This assumption gives the upper bound on the radiation conductance across gaps formed by conforming rough surfaces. If one further assumes that $T_{j2} = 300$ K and $T_{j1} = T_{j2} + \Delta T_j$, one can calculate the radiation conductance for a range of values of ΔT_j and T_j . The values of h_r for black surfaces represent the maximum radiative heat transfer across the microgaps. For microgaps formed by real surfaces, the radiative heat transfer rates may be smaller. Table 4.18 shows that when the joint temperature is $T_j = 800$ K and $\Delta T_j = 1000$ K, the maximum radiation conductance is approximately $161.5 \text{ W/m}^2 \cdot \text{K}$. This value is much smaller than the contact and gap conductances for most applications where $T_j < 600$ K and $\Delta T_j < 200$ K. The radiation conductance becomes relatively important when the interface is formed by two very rough, very hard low-conductivity solids under very light contact pressures. Therefore, for many practical applications, the radiative conductance can be neglected, but not forgotten.

4.16.3 Elastic Contact Model

The conforming rough surface model proposed by Mikic (1974) for elastic deformation of the contacting asperities is summarized below (Sridhar and Yovanovich, 1994, 1996a).

Elastic Contact Geometric Parameters The elastic contact geometric parameters are (Mikic, 1974)

$$\frac{A_r}{A_a} = \frac{1}{4} \text{erfc} \left(\frac{\lambda}{\sqrt{2}} \right) \quad (4.253)$$

$$n = \frac{1}{16} \left(\frac{m}{\sigma} \right)^2 \frac{\exp(-\lambda^2)}{\text{erfc}(\lambda/\sqrt{2})} \quad (4.254)$$

$$a = \frac{2}{\sqrt{\pi}} \frac{\sigma}{m} \exp \left(\frac{\lambda^2}{2} \right) \text{erfc} \left(\frac{\lambda}{\sqrt{2}} \right) \quad (4.255)$$

$$na = \frac{1}{8\sqrt{\pi}} \frac{m}{\sigma} \exp \left(-\frac{\lambda^2}{2} \right) \quad (4.256)$$

The relative mean plane separation is given by

$$\lambda = \sqrt{2} \text{erfc}^{-1} \left(\frac{4P}{H_e} \right) \quad (4.257)$$

The equivalent elastic microhardness according to Mikic (1974) is defined as

$$H_e = C m E' \quad \text{where} \quad C = \frac{1}{\sqrt{2}} = 0.7071 \quad (4.258)$$

where the effective Young's modulus of the contacting asperities is

$$\frac{1}{E'} = \frac{1 - \nu_1^2}{E_1} + \frac{1 - \nu_2^2}{E_2} \quad (\text{m}^2/\text{N}) \quad (4.259)$$

Greenwood and Williamson (1966), Greenwood (1967), and Greenwood and Tripp (1970) developed a more complex elastic contact model that gives a dimensionless elastic microhardness H_e/mE' that depends on the surface roughness bandwidth α and the separation between the mean planes of the asperity "summits," denoted as λ_s . For a typical range of values of α and λ_s (McWaid and Marschall, 1992a), the value of Mikic (1974) (i.e., $H_e/mE' = 0.7071$) lies in the range obtained with the Greenwood and Williamson (1966) model. There is, at present, no simple correlation for the model of Greenwood and Williamson (1966).

Dimensionless Contact Conductance The dimensionless contact conductance for conforming rough surfaces whose contacting asperities undergo elastic deformation is (Mikic, 1974; Sridhar and Yovanovich, 1994)

$$\frac{h_c \sigma}{k_s m} = \frac{1}{4\sqrt{\pi}} \frac{\exp(-\lambda^2/2)}{\left[1 - \sqrt{\frac{1}{4} \operatorname{erfc}(\lambda/\sqrt{2})}\right]^{1.5}} \quad (4.260)$$

The power law correlation equation based on calculated values obtained from the theoretical relationship is (Sridhar and Yovanovich, 1994)

$$\frac{h_c \sigma}{k_s m} = 1.54 \left(\frac{P}{H_e} \right)^{0.94} \quad (4.261)$$

has an uncertainty of about $\pm 2\%$ for the relative contact pressure range $10^{-5} \leq P/H_e \leq 0.2$.

Correlation Equations for Surface Parameters The correlation equations for A_r/A_a , n , and a for the relative contact pressure range $10^{-6} \leq P/H_e \leq 0.2$ are

$$\begin{aligned} \frac{A_r}{A_a} &= \frac{1}{2} \exp(-0.8141 - 0.61778\lambda - 0.42476\lambda^2 - 0.004353\lambda^3) \\ n &= \left(\frac{m}{\sigma}\right)^2 \exp(-2.6516 + 0.6178\lambda - 0.5752\lambda^2 + 0.004353\lambda^3) \\ a &= \frac{1}{\sqrt{2}} \frac{\sigma}{m} (1.156 - 0.4526\lambda + 0.08269\lambda^2 - 0.005736\lambda^3) \end{aligned}$$

and the relative mean planes separation

$$\lambda = -0.5444 - 0.6636 \left(\ln \frac{P}{H_e} \right) - 0.03204 \left(\ln \frac{P}{H_e} \right)^2 - 0.000771 \left(\ln \frac{P}{H_e} \right)^3 \quad (4.262)$$

Sridhar and Yovanovich (1994) reviewed the plastic and elastic deformation contact conductance correlation equations and compared them against vacuum data (Mikic and Rohsenow, 1966; Antonetti, 1983; Hegazy, 1985; Nho, 1989; McWaid and Marschall, 1992a, b) for several metal types, having a range of surface roughnesses, over a wide range of apparent contact pressure. Sridhar and Yovanovich (1996a) showed that the elastic deformation model was in better agreement with the vacuum data obtained for joints formed by conforming rough surfaces of tool steel, which is very hard.

The elastic asperity contact and thermal conductance models of Greenwood and Williamson (1966), Greenwood (1967), Greenwood and Tripp (1967, 1970), Bush et al. (1975), and Bush and Gibson (1979) are different from the Mikic (1974) elastic contact model presented in this chapter. However, they predict similar trends of contact conductance as a function apparent contact pressure.

4.16.4 Conforming Rough Surface Model: Elastic–Plastic Deformation

Sridhar and Yovanovich (1996c) developed an elastic–plastic contact conductance model which is based on the plastic contact model of Cooper et al. (1969) and the elastic contact model of Mikic (1974). The results are summarized below in terms of the geometric parameters A_r/A_a , the real-to-apparent area ratio; n , the contact spot density; a , the mean contact spot radius; and λ , the dimensionless mean plane separation:

$$\frac{A_r}{A_a} = \frac{f_{ep}}{2} \operatorname{erfc} \left(\frac{\lambda}{\sqrt{2}} \right) \quad (4.263)$$

$$n = \frac{1}{16} \left(\frac{m}{\sigma} \right)^2 \frac{\exp(-\lambda^2)}{\operatorname{erfc}(\lambda/\sqrt{2})} \quad (4.264)$$

$$a = \sqrt{\frac{8}{\pi}} \sqrt{f_{ep}} \frac{\sigma}{m} \exp \left(\frac{\lambda^2}{2} \right) \operatorname{erfc} \left(\frac{\lambda}{\sqrt{2}} \right) \quad (4.265)$$

$$na = \frac{1}{8} \sqrt{\frac{2}{\pi}} \sqrt{f_{ep}} \frac{m}{\sigma} \exp \left(-\frac{\lambda^2}{2} \right) \quad (4.266)$$

$$\frac{h_c \sigma}{k_s m} = \frac{1}{2\sqrt{2\pi}} \frac{\sqrt{f_{ep}} \exp(-\lambda^2/2)}{\left[1 - \sqrt{(f_{ep}/2) \operatorname{erfc}(\lambda/\sqrt{2})} \right]^{1.5}} \quad (4.267)$$

$$\lambda = \sqrt{2} \operatorname{erfc}^{-1} \left(\frac{1}{f_{ep}} \frac{2P}{H_{ep}} \right) \quad (4.268)$$

The important elastic–plastic parameter f_{ep} is a function of the dimensionless contact strain ϵ_c^* , which depends on the amount of work hardening. This physical parameter lies in the range $0.5 \leq f_{ep} \leq 1.0$. The smallest and largest values correspond to zero and infinitely large contact strain, respectively. The elastic–plastic parameter is related to the contact strain:

$$f_{ep} = \frac{[1 + (6.5/\epsilon_c^*)^2]^{1/2}}{[1 + (13.0/\epsilon_c^*)^{1.2}]^{1/1.2}} \quad 0 < \epsilon_c^* < \infty \quad (4.269)$$

The dimensionless contact strain is defined as

$$\epsilon_c^* = 1.67 \left(\frac{mE'}{S_f} \right) \quad (4.270)$$

where S_f is the material yield or flow stress (Johnson, 1985), which is a complex physical parameter that must be determined by experiment for each metal.

The elastic–plastic microhardness H_{ep} can be determined by means of an iterative procedure which requires the following relationship:

$$H_{ep} = \frac{2.76S_f}{[1 + (6.5/\epsilon_c^*)^2]^{1/2}} \quad (4.271)$$

The elastoplastic contact conductance model moves smoothly between the elastic contact model of Mikic (1974) and the plastic contact conductance model of Cooper et al. (1969), which was modified by Yovanovich (1982), Yovanovich et al. (1982a), and Song and Yovanovich (1988) to include the effect of work-hardened layers on the deformation of the contacting asperities. The dimensionless contact pressure for elastic–plastic deformation of the contacting asperities is obtained from the following approximate explicit relationship:

$$\frac{P}{H_{ep}} = \left[\frac{0.9272P}{c_1(1.43 \sigma/m)^{c_2}} \right]^{1/(1+0.071c_2)} \quad (4.272)$$

where the coefficients c_1 and c_2 are obtained from Vickers microhardness tests. The Vickers microhardness coefficients are related to Brinell and Rockwell hardness for a wide range of metals.

Correlation Equations for Dimensionless Contact Conductance: Elastic–Plastic Model The complex elastic–plastic contact model proposed by Sridhar and Yovanovich (1996a, b, c, d) may be approximated by the following correlation equations for the dimensionless contact conductance:

$$C_c = \begin{cases} 1.54 \left(\frac{P}{H_{ep}} \right)^{0.94} & 0 < \epsilon_c^* < 5 \\ 1.245b_1 \left(\frac{P}{H_{ep}} \right)^{b_2} & 5 < \epsilon_c^* < 400 \\ 1.25 \left(\frac{P}{H_{ep}} \right)^{0.95} & 400 < \epsilon_c^* < \infty \end{cases} \quad (4.273)$$

$$C_c = \begin{cases} 1.245b_1 \left(\frac{P}{H_{ep}} \right)^{b_2} & 5 < \epsilon_c^* < 400 \end{cases} \quad (4.274)$$

$$C_c = \begin{cases} 1.25 \left(\frac{P}{H_{ep}} \right)^{0.95} & 400 < \epsilon_c^* < \infty \end{cases} \quad (4.275)$$

where the elastic-plastic correlation coefficients b_1 and b_2 depend on the dimensionless contact strain:

$$b_1 = \left[1 + \frac{46,690.2}{(\epsilon_c^*)^{2.49}} \right]^{1/30} \quad (4.276)$$

$$b_2 = \left[\frac{1}{1 + 2086.9/(\epsilon_c^*)^{1.842}} \right]^{1/600} \quad (4.277)$$

4.16.5 Gap Conductance for Large Parallel Isothermal Plates

Two infinite isothermal surfaces form a gap of uniform thickness d which is much greater than the roughness of both surfaces: $d \gg \sigma_1$ and σ_2 . The gap is filled with a stationary monatomic or diatomic gas. The boundary temperatures are T_1 and T_2 , where $T_1 > T_2$. The Knudsen number for the gap is defined as $\text{Kn} = \Lambda/d$, where Λ is the molecular mean free path of the gas, which depends on the gas temperature and its pressure. The gap can be separated into three zones: two boundary zones, which are associated with the two solid boundaries, and a central zone. The boundary zones have thicknesses that are related to the molecular mean free paths Λ_1 and Λ_2 , where

$$\Lambda_1 = \Lambda_0 \frac{T_1}{T_0} \frac{P_{g,0}}{P_g} \quad \text{and} \quad \Lambda_2 = \Lambda_0 \frac{T_2}{T_0} \frac{P_{g,0}}{P_g} \quad (4.278)$$

and Λ_0 , T_0 , and $P_{g,0}$ represent the molecular mean free path and the reference temperature and gas pressure. In the boundary zones the heat transfer is due to gas molecules that move back and forth between the solid surface and other gas molecules located at distances Λ_1 and Λ_2 from both solid boundaries. The energy exchange between the gas and solid molecules is *imperfect*. At the hot solid surface at temperature T_1 , the gas molecules that leave the surface after contact are at some temperature $T_{g,1} < T_1$, and at the cold solid surface at temperature T_2 , the gas molecules that leave the surface after contact are at a temperature $T_{g,2} > T_2$. The two boundary zones are called *slip regions*.

In the central zone whose thickness is modeled as $d - \Lambda_1 - \Lambda_2$, and whose temperature range is $T_{g,1} \geq T \geq T_{g,2}$, heat transfer occurs primarily by molecular

diffusion. Fourier's law of conduction can be used to determine heat transfer across the central zone.

There are two heat flux asymptotes, corresponding to very small and very large Knudsen numbers. They are: for a continuum,

$$\text{Kn} \rightarrow 0 \quad q \rightarrow q_0 = k_g \frac{T_1 - T_2}{d} \quad (4.279)$$

and for free molecules,

$$\text{Kn} \rightarrow \infty \quad q \rightarrow q_\infty = k_g \frac{T_1 - T_2}{M} \quad (4.280)$$

where

$$M = \alpha\beta\Lambda = \left(\frac{2 - \alpha_1}{\alpha_1} + \frac{2 - \alpha_2}{\alpha_2} \right) \frac{2\gamma}{(\gamma + 1)\text{Pr}} \Lambda \quad (4.281)$$

and k_g is the thermal conductivity, α_1 and α_2 the accommodation coefficients, γ the ratio of specific heats, and Pr the Prandtl number.

The gap conductance, defined as $h_g = q/(T_1 - T_2)$, has two asymptotes:

$$\text{for } \text{Kn} \rightarrow 0, \quad h_g \rightarrow \frac{k_g}{d} \quad \text{for } \text{Kn} \rightarrow \infty, \quad h_g \rightarrow \frac{k_g}{M}$$

For the entire range of the Knudsen number, the gap conductance is given by the relationship

$$h_g = \frac{k_g}{d + M} \quad \text{for } 0 < \text{Kn} < \infty \quad (\text{W/m}^2 \cdot \text{K}) \quad (4.282)$$

This relatively simple relationship covers the continuum, $0 < \text{Kn} < 0.1$, slip, $0.1 < \text{Kn} < 10$, and free molecule, $10 < \text{Kn} < \infty$, regimes. Song (1988) introduced the dimensionless parameters

$$G = \frac{k_g}{h_g d} \quad \text{and} \quad M^* = \frac{M}{d} \quad (4.283)$$

and recast the relationship above as

$$G = 1 + M^* \quad \text{for } 0 < M^* < \infty \quad (4.284)$$

The accuracy of the simple parallel-plate gap model was compared against the data (argon and nitrogen) of Teagan and Springer (1968), and the data (argon and helium) of Braun and Frohn (1976). The excellent agreement between the simple gap model and all data is shown in Fig. 4.26. The simple gap model forms the basis of the gap model for the joint formed by two conforming rough surfaces.

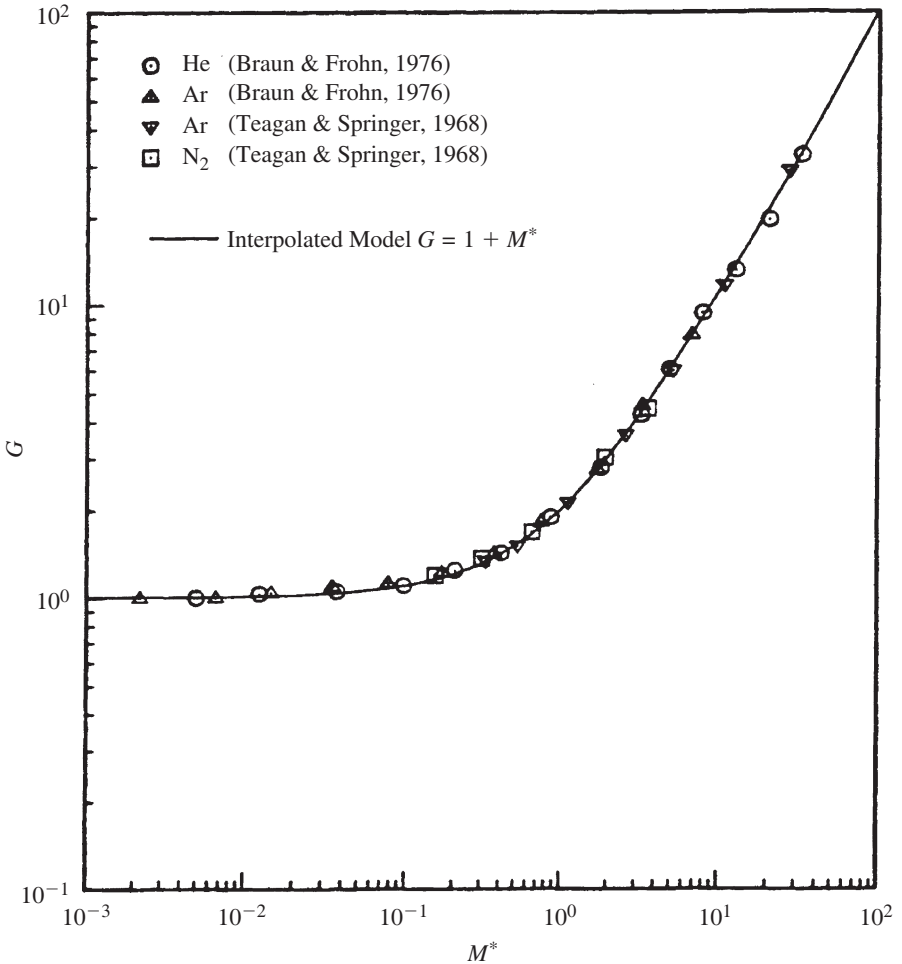


Figure 4.26 Gap conductance model and data for two large parallel isothermal plates. (From Song et al., 1992a.)

4.16.6 Gap Conductance for Joints between Conforming Rough Surfaces

If the gap between two conforming rough surfaces as shown in Fig. 4.22 is occupied by a gas, conduction heat transfer will occur across the gap. This heat transfer is characterized by the gap conductance, defined as

$$h_g = \frac{\Delta T_j}{Q_g} \quad (\text{W/m}^2 \cdot \text{K}) \quad (4.285)$$

with ΔT_j as the effective temperature drop across the gas gap and Q_g the heat transfer rate across the gap. Because the local gap thickness and local temperature drop vary in very complicated ways throughout the gap, it is difficult to develop a simple gap conductance model.

Several gap conductance models and correlation equations have been presented by a number of researchers (Cetinkale and Fishenden, 1951; Rapier et al., 1963; Shlykov, 1965; Veziroglu, 1967; Lloyd et al., 1973; Garnier and Begej, 1979; Loyalka, 1982; Yovanovich et al., 1982b); they are given in Table 4.19. The parameters that appear in Table 4.19 are $b_t = 2(\text{CLA}_1 + \text{CLA}_2)$, where CLA_i is the centerline-average surface

TABLE 4.19 Models and Correlation Equations for Gap Conductance for Conforming Rough Surfaces

Authors	Models and Correlations	
Cetinkale and Fishenden (1951)	$h_g = \frac{k_g}{0.305b_t + M}$	
Rapier et al. (1963)	$h_g = k_g \left[\frac{1.2}{2b_t + M} + \frac{0.8}{2b_t} \ln \left(1 + \frac{2b_t}{M} \right) \right]$	
Shlykov (1965)	$h_g = \frac{k_g}{b_t} \left\{ \frac{10}{3} + \frac{10}{X} + \frac{4}{X^2} - 4 \left[\frac{1}{X^3} + \frac{3}{X^2} + \frac{2}{X} \ln(1 + X) \right] \right\}$	
Veziroglu (1967)	$h_g = \begin{cases} \frac{k_g}{0.264 b_t + M} & \text{for } b_t > 15 \mu\text{m} \\ \frac{k_g}{1.78 b_t + M} & \text{for } b_t < 15 \mu\text{m} \end{cases}$	
Lloyd et al. (1973)	$h_g = \frac{k_g}{\delta + \beta\Lambda/(\alpha_1 + \alpha_2)}$	δ not given
Garnier and Begej (1979)	$h_g = k_g \left[\frac{\exp(-1/\text{Kn})}{M} + \frac{1 - \exp(-1/\text{Kn})}{\delta + M} \right]$	δ not given
Loyalka (1982)	$h_g = \frac{k_g}{\delta + M + 0.162(4 - \alpha_1 - \alpha_2)\beta\Lambda}$	δ not given
Yovanovich et al. (1982b)	$h_g = \frac{k_g/\sigma}{\sqrt{2\pi}} \int_0^\infty \frac{\exp[-(Y/\sigma - t/\sigma)^2/2]}{t/\sigma + M/\sigma} d\left(\frac{t}{\sigma}\right)$ $\frac{Y}{\sigma} = \sqrt{2} \operatorname{erfc}^{-1} \left(\frac{2P}{H_p} \right)$ $\frac{P}{H_p} = \left[\frac{P}{c_1(1.62\sigma/m)^{c_2}} \right]^{1/(1+0.071c_2)}$	

Source: Song (1988).

roughness of the two contacting surfaces, $M = \alpha\beta\Lambda$, $X = b_t/M$, $\sigma = \sqrt{\sigma_1^2 + \sigma_2^2}$, where the units of σ are μm . The Knudsen number Kn that appears in the Garnier and Begej (1979) correlation equation is not defined.

Song and Yovanovich (1987), Song (1988), and Song et al. (1993b) reviewed the models and correlation equations given in Table 4.19. They found that for some of the correlation equations the required gap thickness δ was not defined, and for other correlation equations an empirically based average gap thickness was specified that is constant, independent of variations of the apparent contact pressure. The gap conductance model developed by Yovanovich et al. (1982b) is the only one that accounts for the effect of mechanical load and physical properties of the contacting asperities on the gap conductance. This model is presented below.

The gap conductance model for conforming rough surfaces was developed, modified, and verified by Yovanovich and co-workers (Yovanovich et al., 1982b; Hegazy, 1985; Song and Yovanovich, 1987; Negus and Yovanovich, 1988; Song et al., 1992a, 1993b).

The gap contact model is based on surfaces having Gaussian height distributions and also accounts for mechanical deformation of the contacting surface asperities. Development of the gap conductance model is presented in Yovanovich (1982, 1986), Yovanovich et al. (1982b), and Yovanovich and Antonetti (1988).

The gap conductance model is expressed in terms of an integral:

$$h_g = \frac{k_g}{\sigma} \frac{1}{\sqrt{2\pi}} \int_0^\infty \frac{\exp[-(Y/\sigma - u)^2/2]}{u + M/\sigma} du = \frac{k_g}{\sigma} I_g \quad (\text{W/m}^2 \cdot \text{K}) \quad (4.286)$$

where k_g is the thermal conductivity of the gas trapped in the gap and σ is the effective surface roughness of the joint, and $u = t/\sigma$ is the dimensionless local gap thickness. The integral I_g depends on two independent dimensionless parameters: Y/σ , the mean plane separation; and M/σ , the relative gas rarefaction parameter.

The relative mean planes separation for plastic and elastic contact are given by the relationships

$$\begin{aligned} \left(\frac{Y}{\sigma}\right)_{\text{plastic}} &= \sqrt{2} \operatorname{erfc}^{-1} \left(\frac{2P}{H_p}\right) \\ \left(\frac{Y}{\sigma}\right)_{\text{elastic}} &= \sqrt{2} \operatorname{erfc}^{-1} \left(\frac{4P}{H_e}\right) \end{aligned} \quad (4.287)$$

The relative contact pressures P/H_p for plastic deformation and P/H_e for elastic deformation can be determined by means of appropriate relationships.

The gas rarefaction parameter is $M = \alpha\beta\Lambda$, where the gas parameters are defined as:

$$\alpha = \frac{2 - \alpha_1}{\alpha_1} + \frac{2 - \alpha_2}{\alpha_2} \quad (4.288)$$

$$\beta = \frac{2\gamma}{(\gamma + 1)\text{Pr}} \quad (4.289)$$

$$\Lambda = \Lambda_0 \frac{T_g}{T_{g,0}} \frac{P_g}{P_{g,0}} \quad (4.290)$$

where α is the accommodation coefficient, which accounts for the efficiency of gas-surface energy exchange. There is a large body of research dealing with experimental and theoretical aspects of α for various gases in contact with metallic surfaces under various surface conditions and temperatures (Wiedmann and Trumpler, 1946; Hartnett, 1961; Wachman, 1962; Thomas, 1967; Semyonov et al., 1984; Loyalka, 1982). Song and Yovanovich (1987) and Song et al. (1992a, 1993b) examined the several gap conductance models available in the literature and the experimental data and models for the accommodation coefficients.

Song and Yovanovich (1987) developed a correlation for the accommodation for engineering surfaces (i.e., surfaces with absorbed layers of gases and oxides). They proposed a correlation that is based on experimental results of numerous investigators for monatomic gases. The relationship was extended by the introduction of a monatomic equivalent molecular weight to diatomic and polyatomic gases. The final correlation is

$$\alpha = \exp(C_0 T) \left\{ \frac{M_g}{C_1 + M_g} + [1 - \exp(C_0 T)] \frac{2.4\mu}{(1 + \mu)^2} \right\} \quad (4.291)$$

with $C_0 = -0.57$, $T = (T_s - T_0)/T_0$, $M_g = M_g$ for monatomic gases ($= 1.4M_g$ for diatomic and polyatomic gases), $C_1 = 6.8$ in units of M_g (g/mol), and $\mu = M_g/M_s$, where T_s and $T_0 = 273$ K are the absolute temperatures of the surface and the gas, and M_g and M_s are the molecular weights of the gas and the solid, respectively. The agreement between the predictions according to the correlation above and the published data for diatomic and polyatomic gases was within $\pm 25\%$.

The gas parameter β depends on the specific heat ratio $\gamma = C_p/C_v$ and the Prandtl number Pr . The molecular mean free path of the gas molecules Λ depends on the type of gas, the gas temperature T_g and gas pressure P_g , and the reference values of the mean free path Λ_0 , the gas temperature $T_{g,0}$, and the gas pressure $P_{g,0}$, respectively.

Wesley and Yovanovich (1986) compared the predictions of the gap conductance model and experimental measurements of gaseous gap conductance between the fuel and clad of a nuclear fuel rod. The agreement was very good and the model was recommended for fuel pin analysis codes.

The gap integral can be computed accurately and easily by means of computer algebra systems. Negus and Yovanovich (1988) developed the following correlation equations for the gap integral:

$$I_g = \frac{f_g}{Y/\sigma + M/\sigma} \quad (4.292)$$

In the range $2 \leq Y/\sigma \leq 4$:

$$f_g = \begin{cases} 1.063 + 0.0471 \left(4 - \frac{Y}{\sigma}\right)^{1.68} \left(\ln \frac{\sigma}{M}\right)^{0.84} & \text{for } 0.01 \leq \frac{M}{\sigma} \leq 1 \\ 1 + 0.06 \left(\frac{\sigma}{M}\right)^{0.8} & \text{for } 1 \leq \frac{M}{\sigma} < \infty \end{cases}$$

The correlation equations have a maximum error of approximately 2%.

4.16.7 Joint Conductance for Conforming Rough Surfaces

The joint conductance for a joint between two conforming rough surfaces is

$$h_j = h_c + h_g \quad (\text{W/m}^2 \cdot \text{K}) \quad (4.293)$$

when radiation heat transfer across the gap is neglected. The relationship is applicable to joints that are formed by elastic, plastic, or elastic-plastic deformation of the contacting asperities. The mode of deformation will influence h_c and h_g through the relative mean plane separation parameter Y/σ .

The gap and joint conductances are compared against data (Song, 1988) obtained for three types of gases, argon, helium, and nitrogen, over a gas pressure range between 1 and 700 torr. The gases occupied gaps formed by conforming rough Ni 200 and stainless steel type 304 metals. In all tests the metals forming the joint were identical, and one surface was flat and lapped while the other surface was flat and glass bead blasted.

The gap and joint conductance models were compared against data obtained for relatively light contact pressures where the gap and contact conductances were comparable. Figure 4.27 shows plots of the joint conductance data and the model predictions for very rough stainless steel type 304 surfaces at $Y/\sigma = 1.6 \times 10^{-4}$. Agreement among the data for argon, helium, and nitrogen is very good for gas pressures between approximately 1 and 700 torr. At the low gas pressure of 1 torr, the measured and predicted joint conductance values for the three gases differ by a few percent because $h_g \ll h_c$ and $h_j \approx h_c$. As the gas pressure increases there is a large increase in the joint conductances because the gap conductances are increasing rapidly. The joint conductances for argon and nitrogen approach asymptotes for gas pressures approaching 1 atm. The joint conductances for helium are greater than for argon and nitrogen, and the values do not approach an asymptote in the same pressure range. The asymptote for helium is approached at gas pressures greater than 1 atm.

Figure 4.28 shows the experimental and theoretical gap conductances as points and curves for nitrogen and helium for gas pressures between approximately 10 and 700 torr. The relative contact pressure is 1.7×10^{-4} is based on the plastic deformation model. The joint was formed by Ni 200 surfaces (one flat and lapped and the second flat and glass bead blasted). The data were obtained by subtracting the theoretical value of h_c from the measured values of h_j to get the values of h_g that appear on the plots. The agreement between the data and the predicted curves is very good.

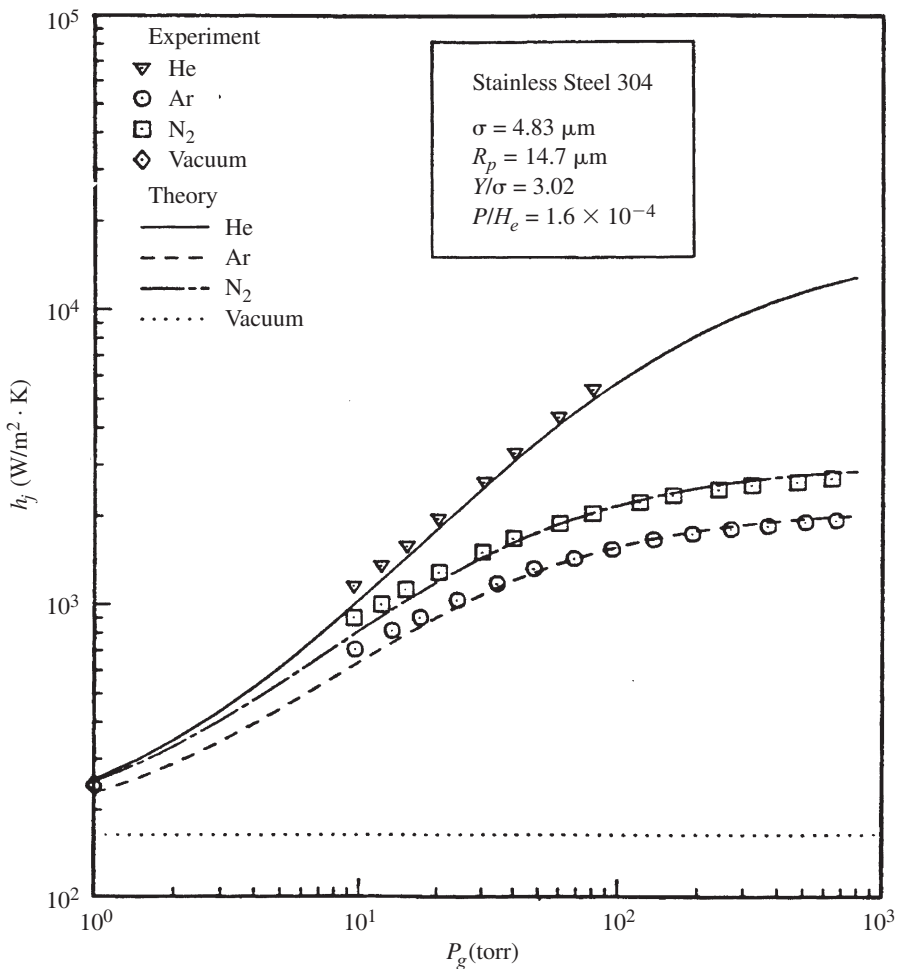


Figure 4.27 Joint conductance model and data for conforming rough stainless steel 304 surfaces. (From Song, 1988.)

Figure 4.29 shows the experimental data for argon, nitrogen, and helium and the dimensionless theoretical curve for the gap model recast as (Song et al., 1993b)

$$G = 1 + M^* \tag{4.294}$$

where

$$G = \frac{k_g}{h_g Y} \quad \text{and} \quad M^* = \frac{M}{Y} = \frac{\alpha \beta \Lambda}{Y} \tag{4.295}$$

There is excellent agreement between the model and the data over the entire range of the gas-gap parameter M^* . The joint was formed by very rough conforming Ni

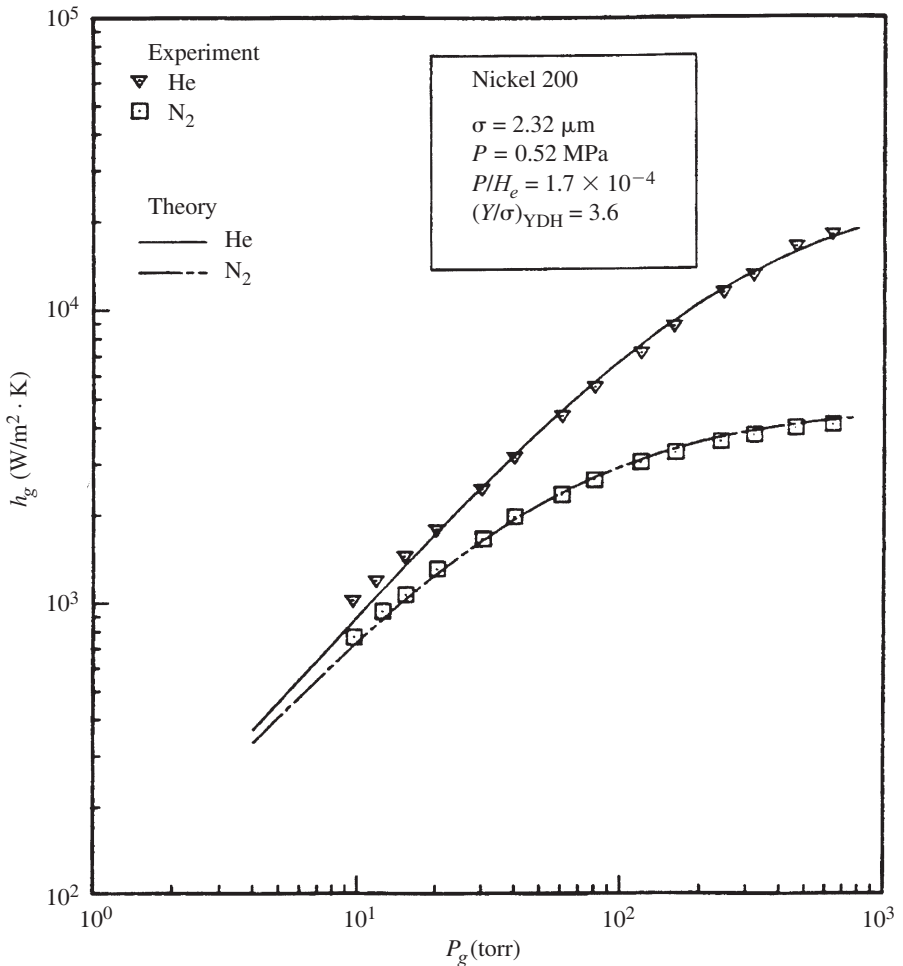


Figure 4.28 Gap conductance model and data for conforming rough Ni 200 surfaces. (From Song, 1988.)

200 surfaces. The plastic deformation model was used to calculate Y . The points for $M^* < 0.01$ correspond to the high-gas-pressure tests (near 1 atm), and the points for $M^* > 2$ correspond to the low-gas-pressure tests.

4.17 JOINT CONDUCTANCE ENHANCEMENT METHODS

In many electronics packages the thermal joint conductance across a particular joint must be improved for the thermal design to meet its performance objectives. If the joint cannot be made permanent because of servicing or other considerations, the joint

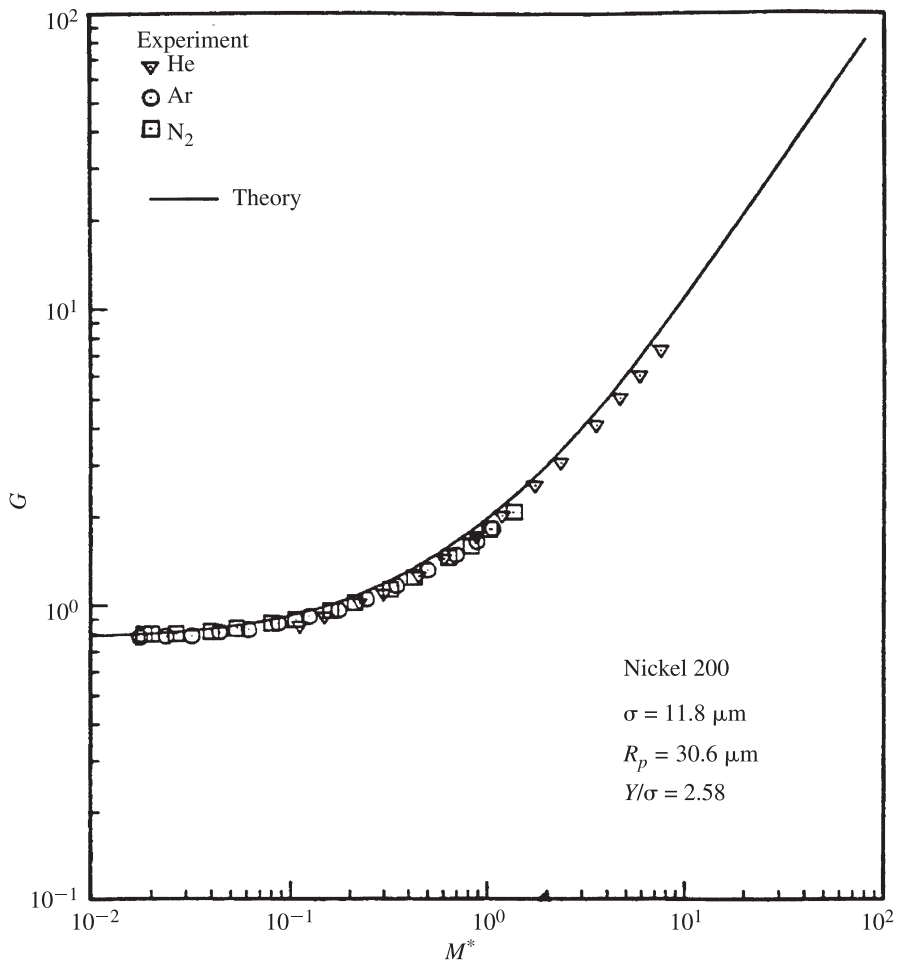


Figure 4.29 Dimensionless gap conductance model and data for conforming rough Ni 200 surfaces. (From Song, 1988.)

conductance must be “enhanced”; that is, it must be improved above the bare joint situation utilizing one of several known techniques, such as application of thermal interface materials (TIMs): for example, thermal grease, grease filled with particles (also called *paste*), oils, and phase-change materials (PCMs). Enhancement of the joint conductance has also been achieved by the insertion of soft metallic foils into the joint, or by the use of a relatively soft metallic coating on one or both surfaces. More recently, soft nonmetallic materials such as polymers and rubber have been used.

One may consult review articles by Fletcher (1972, 1990), Madhusudana and Fletcher (1986), Madhusudana (1996), Marotta and Fletcher (1996), Prasher (2001), Savija et al. (2002a, b), and other pertinent references may be found in these reviews. This section is limited to a few examples where models and data are available.

4.17.1 Metallic Coatings and Foils

An effective method for enhancement of joint conductance consists of vapor deposition of a very thin soft metallic layer on the surface of the substrate. The layer thickness is often less than 100 μm ; it is in “perfect” thermal and mechanical contact with the substrate, and its bulk resistance is negligibly small relative to the contact resistance. The thermal resistance at the layer–substrate interface is also negligible.

A comprehensive treatment of the theoretical development and experimental verification of the thermomechanical model can be found in Antonetti (1983) and Antonetti and Yovanovich (1983, 1985). In the following discussion, therefore, only those portions of the theory needed to apply the model to a thermal design problem are presented. The general expression for the contact conductance of the coated joint operating in a vacuum is

$$h'_c = h_c \left(\frac{H_S}{H'} \right)^{0.93} \frac{k_1 + k_2}{Ck_1 + k_2} \quad (\text{W/m}^2 \cdot \text{K}) \quad (4.296)$$

where h_c is the uncoated contact conductance, H_S the microhardness of the softer substrate, H' the effective microhardness of the layer–substrate combination, C a spreading–constriction parameter correction factor that accounts for the heat spreading in the coated substrate, and k_1 and k_2 the thermal conductivities of the two substrates, respectively.

The coated contact conductance relationship consists of the product of three quantities: the uncoated contact conductance h_c , the mechanical modification factor $(H_S/H')^{0.93}$, and the thermal modification factor. The uncoated (bare) contact conductance may be determined by means of the conforming, rough surface correlation equation based on plastic deformation:

$$h_c = 1.25 \left(\frac{m}{\sigma} \right) \frac{2k_1k_2}{k_1 + k_2} \left(\frac{P}{H_S} \right)^{0.95} \quad (\text{W/m}^2 \cdot \text{K}) \quad (4.297)$$

where H_S is the flow pressure (microhardness) of the softer substrate, m the combined average absolute asperity slope, and σ the combined rms surface roughness of the joint.

For a given joint, the only unknowns are the effective microhardness H' and the spreading–constriction parameter correction factor C . Thus, the key to solving coated contact problems is the determination of these two quantities.

Mechanical Model The substrate microhardness can be obtained from the following approximate relationship (Hegazy, 1985):

$$H_S = (12.2 - 3.54H_B) \left(\frac{\sigma}{m} \right)^{-0.26} \quad (\text{GPa}) \quad (4.298)$$

which requires the combined surface roughness parameters σ and m and the bulk hardness of the substrate H_B . In the correlation equation the units of the joint roughness parameter σ/m are micrometers. For Ni 200 substrates, $H_B = 1.67$ GPa.

The effective microhardness must be obtained empirically for the particular layer (coating)–substrate combination under consideration. This requires a series of Vickers microhardness measurements which will result in an effective microhardness plot similar to that shown in Fig. 4.30 (e.g., a silver layer on a Ni 200 substrate).

The effective Vickers microhardness measurements, denoted H' , are plotted against the relative indentation depth t/d , where t is the layer thickness and d is the indentation depth. The three microhardness regions were correlated as

$$H' = \begin{cases} H_S \left(1 - \frac{t}{d}\right) + 1.81 H_L \frac{t}{d} & \text{for } 0 \leq \frac{t}{d} < 1.0 \\ 1.81 H_L - 0.21 H_L \left(\frac{t}{d} - 1\right) & \text{for } 1.0 \leq \frac{t}{d} \leq 4.90 \\ H_L & \text{for } \frac{t}{d} > 4.90 \end{cases} \quad (4.299)$$

$$H' = \begin{cases} 1.81 H_L - 0.21 H_L \left(\frac{t}{d} - 1\right) & \text{for } 1.0 \leq \frac{t}{d} \leq 4.90 \end{cases} \quad (4.300)$$

$$H' = \begin{cases} H_L & \text{for } \frac{t}{d} > 4.90 \end{cases} \quad (4.301)$$

where H_S and H_L are the substrate and layer microhardness, respectively. The Ni 200 substrate microhardness is found to be $H_S = 2.97$ GPa for the joint roughness parameter values: $\sigma = 4.27$ μm and $m = 0.236$ rad. The Vickers microhardness of the silver layer is approximately $H_L = 40$ kg/mm² = 0.394 GPa.

The relative indentation depth is obtained from the following approximate correlation equation (Antonetti and Yovanovich, 1983, 1985)

$$\frac{t}{d} = 1.04 \left(\frac{t}{d}\right) \left(\frac{P}{H'}\right)^{-0.097} \quad (4.302)$$

To implement the procedure (Antonetti and Yovanovich, 1983, 1985) for finding H' from the three correlation equations requires an iterative method.

To initiate the iterative method, the first guess is based on the arithmetic average of the substrate and layer microhardness values:

$$H'_1 = \frac{H_S + H_L}{2} \quad (\text{GPa})$$

For a given value of t and P , the first value of t/d can be computed. From the three correlation equations, one can find a new value for H' : say, H'_2 . The new microhardness value, H'_2 , is used to find another value for t/d , which leads to another value, H'_3 . The procedure is continued until convergence occurs. This usually occurs within three or four iterations (Antonetti and Yovanovich, 1983, 1985).

Thermal Model The spreading–constriction resistance parameter correction factor C is defined as the ratio of the spreading–constriction resistance parameter for a substrate with a layer to a bare substrate, for the same value of the relative contact spot radius ϵ' :

$$C = \frac{\Psi(\epsilon', \phi_n)}{\Psi(\epsilon')} \quad (4.303)$$

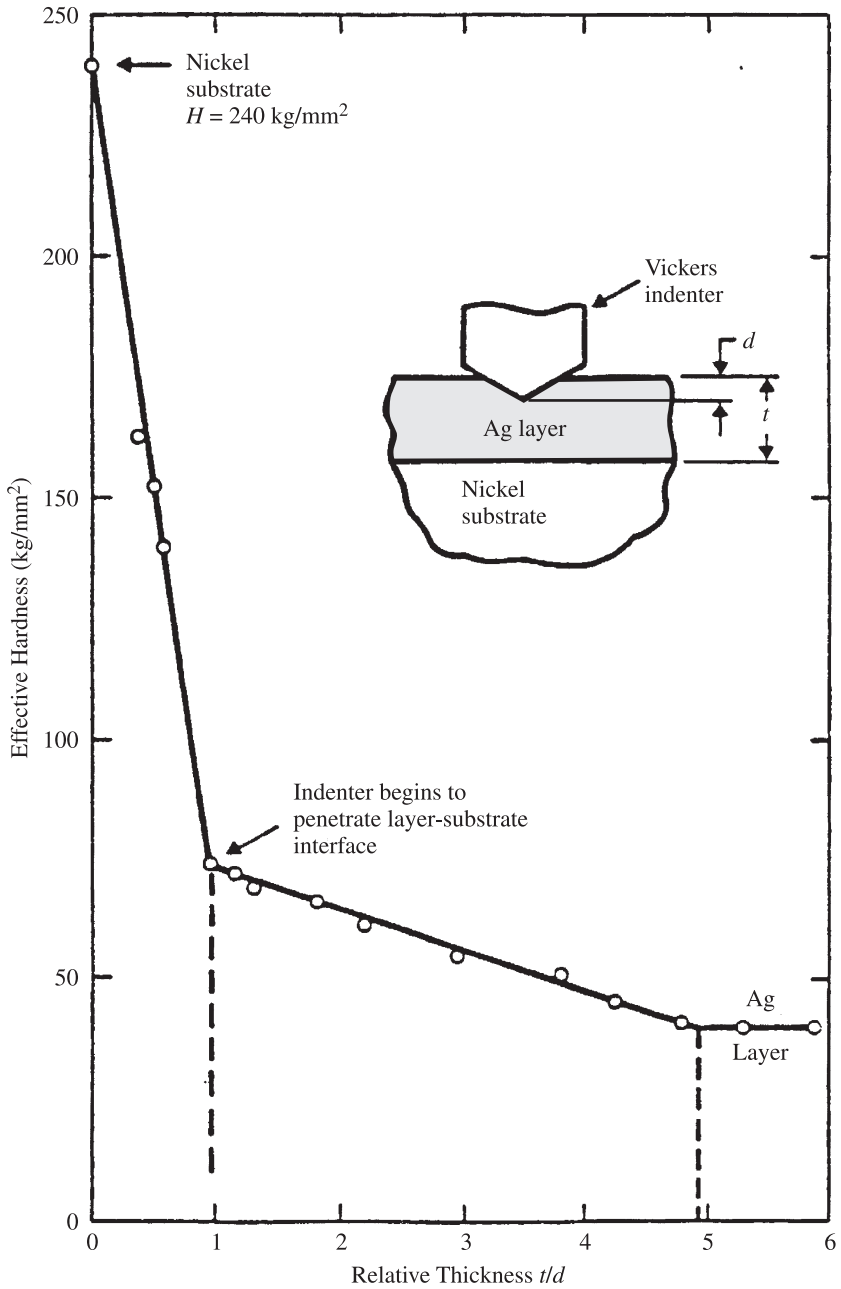


Figure 4.30 Vickers microhardness of a silver layer on a nickel substrate. (From Antonetti and Yovanovich, 1985.)

The dimensionless spreading–constriction resistance parameter is defined as

$$\Psi(\epsilon', \phi_n) = 4k_2 a' R'_c \quad (4.304)$$

where k_2 is the thermal conductivity of the substrate that is coated, a' is the contact spot radius for the layer on the substrate, and R'_c is the spreading–constriction resistance of the contact spot.

The spreading–constriction resistance parameter with a layer on the substrate is (Antonetti and Yovanovich, 1983, 1985)

$$\Psi(\epsilon', \phi_n) = \frac{16}{\pi \epsilon'} \sum_{n=1}^{\infty} \frac{J_1^2(\delta'_n \epsilon')}{(\delta'_n)^3 J_0^2(\delta'_n)} \phi_n \gamma_n \rho_n \quad (4.305)$$

The first of these, ϕ_n , accounts for the effect of the layer though its thickness and thermal conductivity; the second, γ_n , accounts for the contact temperature basis used to determine the spreading–constriction resistance; and the third, ρ_n , accounts for the contact spot heat flux distribution. For contacting surfaces it is usual to assume that the contact spots are isothermal. The modification factors in this case are $\gamma_n = 1.0$ and

$$\phi_n = K \frac{(1 + K) + (1 - K)e^{-2\delta'_n \epsilon' \tau'}}{(1 + K) - (1 - K)e^{-2\delta'_n \epsilon' \tau'}} \quad (4.306)$$

where K is the ratio of the substrate-to-layer thermal conductivity, $\tau' = t/a'$ is the layer thickness-to-contact spot radius ratio, and

$$\rho_n = \frac{\sin \delta'_n \epsilon'}{2J_1(\delta'_n \epsilon')} \quad (4.307)$$

The parameter δ'_n are the eigenvalues, which are roots of $J_1(\delta'_n) = 0$.

Tabulated values of C were reported by Antonetti (1983) for a wide range of the parameters K and τ' . Details of the thermomechanical model development are given in Antonetti (1983) and Antonetti and Yovanovich (1983, 1985).

The thermomechanical model of Antonetti and Yovanovich (1983, 1985) has been verified by extensive tests. First the bare joint was tested to validate that part of the model. Figure 4.31 shows the dimensionless joint conductance data and theory plotted versus the relative contact pressure for three joints having three levels of surface roughness. The two surfaces were flat; one was lapped and the other was glass bead blasted. All tests were conducted in a vacuum. The agreement between the model given by the correlation equation and all data is very good over the entire range of relative contact pressure.

The bare surface tests were followed by three sets of tests for joints having three levels of surface roughness. Figure 4.32 shows the effect of the vapor-deposited silver layer thickness on the measured joint conductance plotted against the contact pressure. For these tests the average values of the combined surface roughness parameters were $\sigma = 4.27 \mu\text{m}$ and $m = 0.236$ rad. For the contact pressure range the substrate

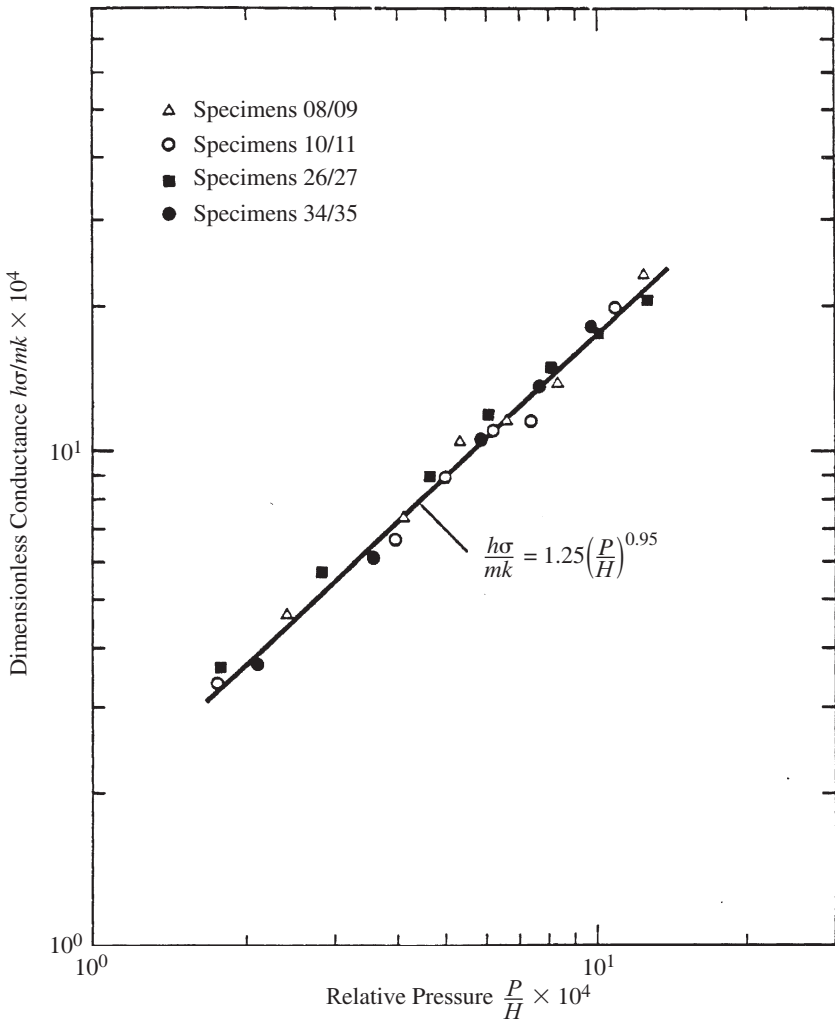


Figure 4.31 Dimensionless contact conductance versus relative contact pressure for bare Ni 200 surfaces in a vacuum. (From Antonetti and Yovanovich, 1985.)

microhardness was estimated to be $H_S = 2.97$ GPa. The layer thickness was between 0.81 and 39.5 μm . The lowest set of data and the theoretical curve correspond to the bare surface tests. Agreement between data and model is very good. The highest set of data for layer thickness of $t = 39.5$ μm corresponds to the infinitely thick layer where thermal spreading occurs in the layer only and the layer microhardness controls the formation of the microcontacts. Again, the agreement between experiment and theory is good.

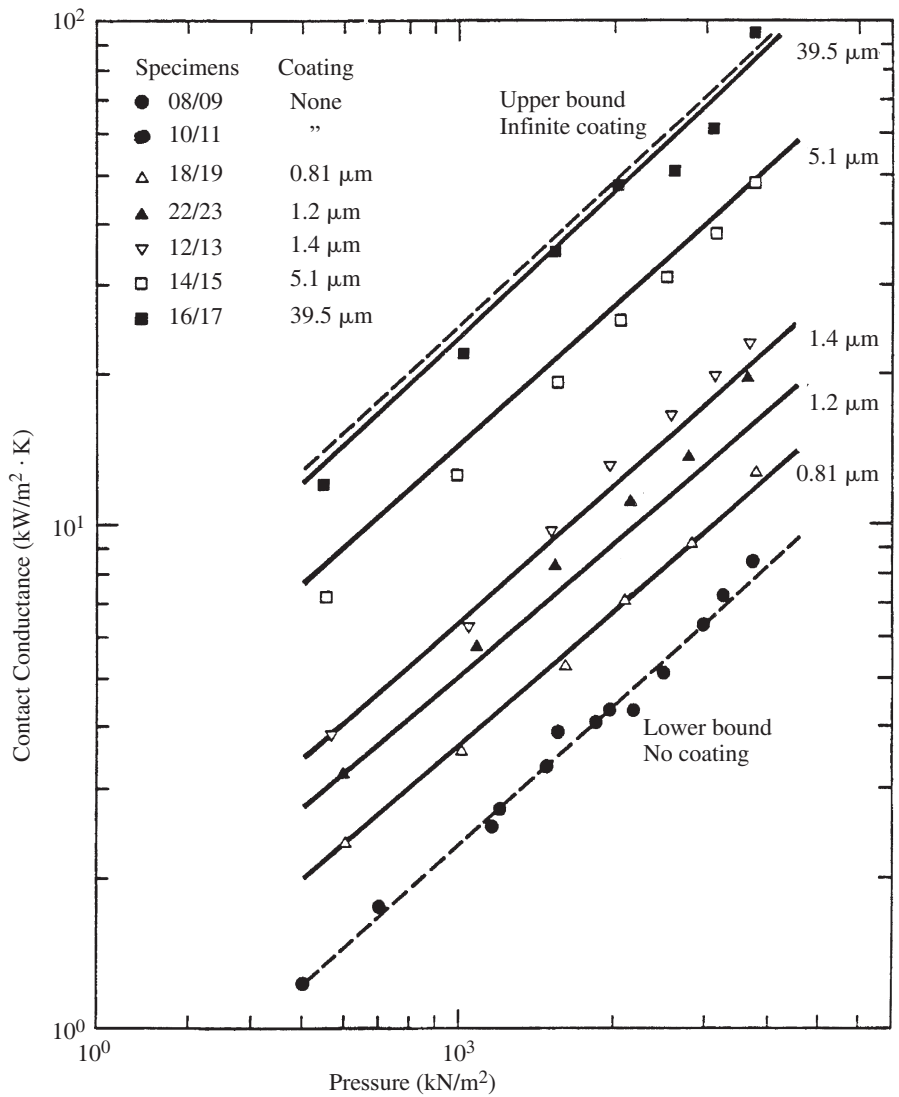


Figure 4.32 Effect of layer thickness and contact pressure on joint conductance: vacuum data and theory. (From Antonetti and Yovanovich, 1985.)

The difference between the highest and lowest joint conductance values is approximately a factor of 10. The enhancement is clearly significant. The agreement between the measured values of joint conductance and the theoretical curves for the layer thicknesses: $t = 0.81, 1.2, 1.4,$ and $5.1 \mu\text{m}$ is also very good, as shown in Fig. 4.32. All the test points for bare and coated surfaces are plotted in Fig. 4.33 as dimensionless joint conductance versus relative contact pressure. The agreement between experiment and theory is very good for all points.

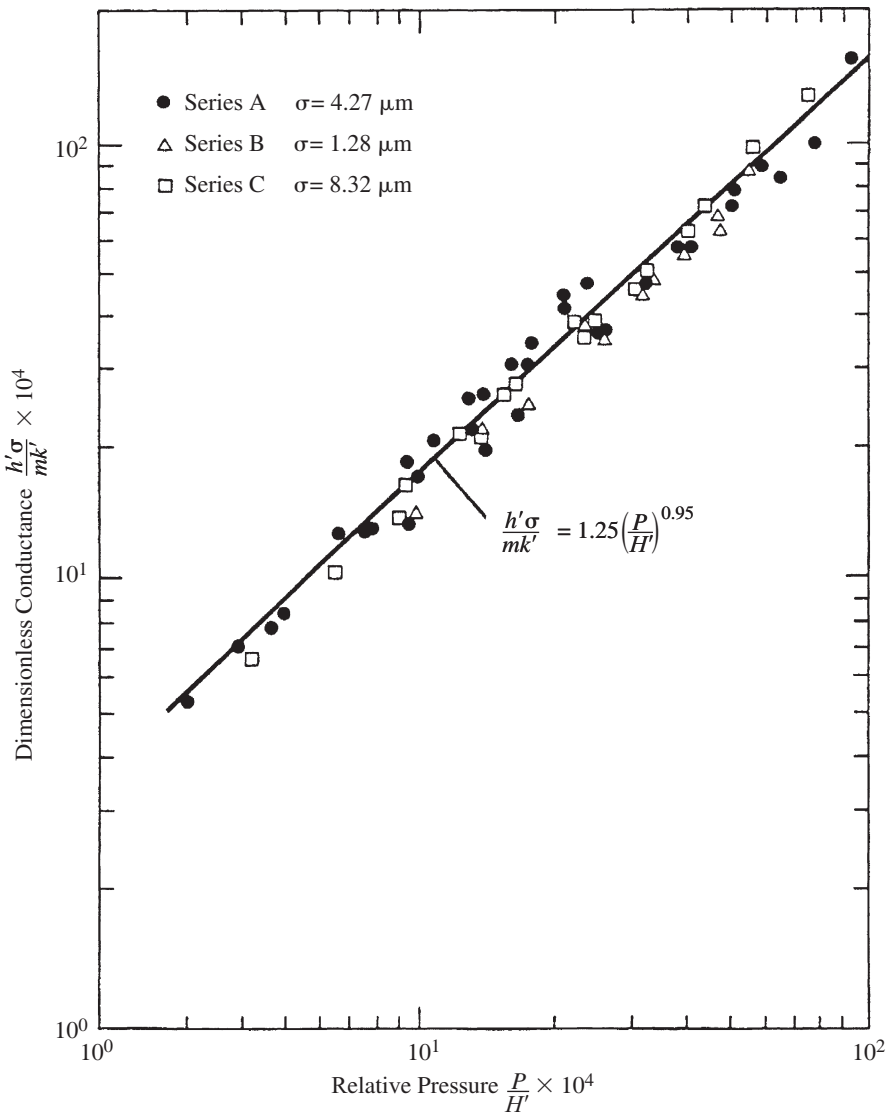


Figure 4.33 Dimensionless joint conductance for a bare and silver layer on Ni 200 substrates versus relative contact pressure. (From Antonetti and Yovanovich, 1985.)

A parametric study was conducted to calculate the enhancement that can be achieved when different metal types are used. The theory outlined earlier will now be applied to a common problem in electronics packaging: heat transfer across an aluminum joint. What is required is a parametric study showing the variation in joint conductance as a function of metallic coating type and thickness for fixed surface

TABLE 4.20 Assumed Nominal Property Values of Four Coatings

	k (W/m · K)	H (kg/mm ²)
Lead	32.4	3.0
Tin	58.4	8.5
Silver	406.0	40.0
Aluminum	190.0	85.0

roughness and contact pressure. The thermophysical properties of the coatings and the aluminum substrate material are presented in Table 4.20.

Figure 4.34 shows the effect of the metallic layers on joint conductance. As shown in this figure, except for a very thin layer (about 1 μm), the performance curves are arranged according to layer microhardness. Lead with the lowest microhardness has

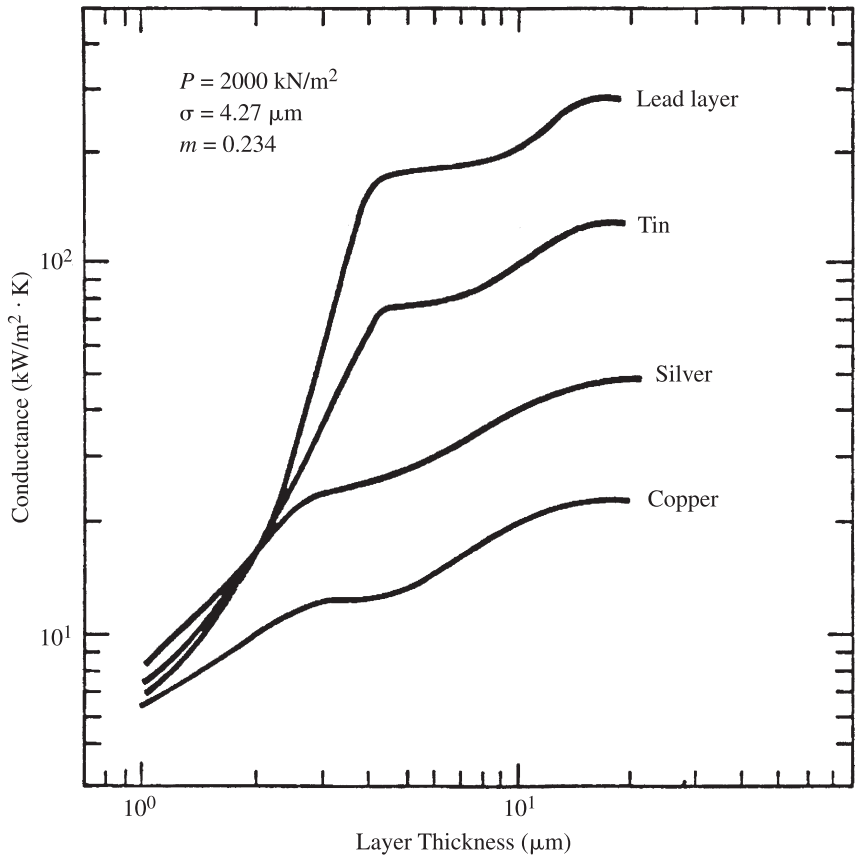


Figure 4.34 Effect of layer thickness for four metallic layers. (From Antonetti and Yovanovich, 1983.)

the highest contact conductance, and silver with the highest microhardness has the lowest contact conductance. The thermal conductivity of the coating appears to play a secondary role.

The unusual shape of the curves is attributable to the fact that the assumed effective hardness curve shown in Fig. 4.30 has three distinct zones. Moreover, because the microhardness of silver is much closer to aluminum than are the microhardness of lead and tin, respectively, the transition from one region to the next is not abrupt in the silver-on-aluminum effective microhardness curve, and this is reflected in the smoother contact conductance plot for the silver layer shown in Fig. 4.34. It should be noted that in the model that has been used, the load is assumed to be uniformly applied over the apparent contact area.

4.17.2 Ranking Metallic Coating Performance

In his research on the effects of soft metallic foils on joint conductance, Yovanovich (1972) proposed that the performance of various foil materials may be ranked according to the parameter k/H , using the properties of the foil material. He showed empirically that the higher the value of this parameter, the greater was the improvement in the joint conductance over a bare joint. Following this thought, Antonetti and Yovanovich (1983) proposed (but did not prove experimentally) that the performance of coated joints can be ranked by the parameter $k'/(H')^{0.93}$. Table 4.21 shows the variation in this parameter as the layer thickness is increased. Table 4.21 also suggests that even if the effective microhardness of the layer-substrate combinations being considered is not known, the relative performance of coating materials can be estimated by assuming an infinitely thick coating (where the effective microhardness is equal to the microhardness of the layer).

In this section we have shown how a thermomechanical model for coated substrates can be used to predict enhancement in thermal joint conductance. For the particular case considered, an aluminum-to-aluminum joint, it was demonstrated that up to an order of magnitude,

TABLE 4.21 Ranking the Effectiveness of Coatings [$k'/(H')^{0.93}$]

Coating Thickness (μm)	Lead	Tin	Silver
0	3.05	3.05	3.05
1	3.72	3.96	3.53
2	7.05	6.81	3.98
4	19.6	10.5	4.68
8	18.0	10.8	6.24
16	21.0	12.9	8.16
∞	19.9	12.2	8.38

$$P = 2000 \text{ kN/m}^2 \quad \sigma = 4.0 \text{ } \mu\text{m} \quad m = 0.20 \text{ rad}$$

improvement in the contact conductance is possible, depending on the choice of coating material and the thickness employed. It should also be noted that aluminum substrates are relatively soft and have a relatively high thermal conductivity, and if the joint in question had been, for example, steel against steel, improvement in the joint conductance would have been even more impressive.

4.17.3 Elastomeric Inserts

Thin polymers and organic materials are being used to a greater extent in power-generating systems. Frequently, these thin layers of relatively low thermal conductivity are inserted between two metallic rough surfaces assumed to be nominally flat. The joint that is formed consists of a single layer whose initial, unloaded thickness is denoted as t_0 and has thermal conductivity k_p . There are two mechanical interfaces that consist of numerous microcontacts with associated gaps that are generally occupied with air. If radiation heat transfer across the two gaps is negligible, the overall joint conductance is Yovanovich et al. (1997).

$$\frac{1}{h_j} = \frac{1}{h_{c,1} + h_{g,1}} + \frac{k_p}{t} + \frac{1}{h_{c,2} + h_{g,2}} \quad (\text{m}^2 \cdot \text{K/W}) \quad (4.308)$$

where t is the polymer thickness under mechanical loading. The contact and gap conductances at the mechanical interfaces are denoted as $h_{c,i}$ and $h_{g,i}$, respectively, and $i = 1, 2$.

Since this joint is too complex to study, Fuller (2000) and Fuller and Marotta (2002) choose to investigate the simpler joint, which consisted of thermal grease at interface 2, and the joint was placed in a vacuum. Under these conditions, they assumed that $h_{g,2} \rightarrow \infty$ and $h_{g,1} \rightarrow 0$. They assumed further that the compression of the polymer layer under load may be approximated by the relationship

$$t = t_0 \left(1 - \frac{P}{E_p} \right) \quad (\text{m}) \quad (4.309)$$

where E_p is Young's modulus of the polymer. Under these assumptions the joint conductance reduces to the simpler relationship

$$h_j = \left[\frac{1}{h_{c,1}} + \frac{t_0}{k_p} \left(1 - \frac{P}{E_p} \right) \right]^{-1} \quad (\text{W/m}^2 \cdot \text{K}) \quad (4.310)$$

On further examination of the physical properties of polymers, Fuller (2000) concluded that the polymers will undergo elastic deformation of the contacting asperities. Fuller examined use of the elastic contact model of Mikic (1974) and found that the disagreement between data and the predictions was large. To bring the model into agreement with the data, it was found that the elastic hardness of the polymers should be defined as

$$H_{ep} = \frac{E_p m}{2.3} \quad (\text{GPa}) \quad (4.311)$$

where m is the combined mean absolute asperity slope. The dimensionless contact conductance correlation equation was expressed as

$$\frac{h_c \sigma}{k_s m} = a_1 \left(\frac{2.3 P}{m E_p} \right)^{a_2} \quad (4.312)$$

where a_1 and a_2 are correlation coefficients. Fuller and Marotta (2000) chose the coefficient values $a_1 = 1.49$ and $a_2 = 0.935$, compared with the values that Mikic (1974) reported: $a_1 = 1.54$ and $a_2 = 0.94$. In the Mikic (1974) elastic contact model, the elastic hardness was defined as

$$H_e = \frac{m E'}{\sqrt{2}} \quad (\text{GPa}) \quad (4.313)$$

where E' is the effective Young's modulus of the joint. For most polymer-metal joints, $E' \approx E_p$ because $E_p \ll E_{\text{metal}}$.

Fuller (2000) conducted a series of vacuum tests for validation of the joint conductance model. The thickness, surface roughness and the thermophysical properties of the polymers and the aluminum alloy are given in Table 4.22. The polymer thickness in all cases is two to three orders of magnitude larger than the surface roughness (i.e., $t/\sigma > 100$).

The dimensionless joint conductance data for three polymers (delrin, polycarbonate, and PVC) are plotted in Fig. 4.35 against the dimensionless contact pressure over approximately three decades. Two sets of data are reported for delrin. The joint conductance model and the data show similar trends with respect to load. At the higher loads, the data and the model approach asymptotes corresponding to the bulk resistance of the polymers. The dimensionless joint conductance goes to different asymptotes because the bulk resistance is defined by the thickness of the polymer

TABLE 4.22 Thickness, Surface Roughness, and Thermophysical Properties of Test Specimens

Material	t_0 (10^3 m)	σ (10^6 m)	m (rad)	k (W/m · K)	E (GPa)	ν
Delrin B	1.88	1.02	0.492	0.38	3.59	0.38
Polycarbonate A	1.99	0.773	0.470	0.22	2.38	0.38
PVC A	1.83	0.650	0.436	0.17	4.14	0.38
Teflon A	1.89	0.622	0.305	0.25	0.135	0.38
Aluminum	—	0.511	0.267	183	72.0	0.32

Source: Fuller (2000).

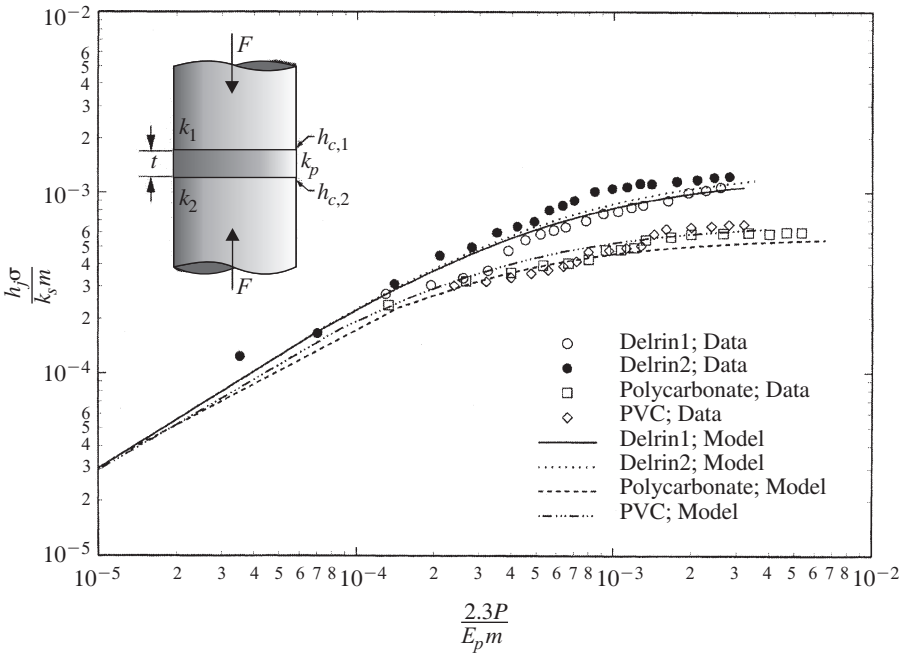


Figure 4.35 Dimensionless joint conductance versus dimensionless contact pressure for polymer layers. (From Fuller and Marotta, 2000.)

layers. In general, there is acceptable agreement between the vacuum data and the model predictions.

4.17.4 Thermal Greases and Pastes

There is much interest today in the use of thermal interface materials (TIMs) such as thermal greases and pastes to enhance joint conductance. Prasher (2001) and Savija et al. (2002a,b) have reviewed the use of TIMs and the models that are available to predict joint conductance. The thermal joint resistance or conductance of a joint formed by two nominally flat rough surfaces filled with grease (Fig. 4.22) depend on several geometric, physical, and thermal parameters. The resistance and conductance relations are obtained from a model that is based on the following simplifying assumptions:

- Surfaces are nominally flat and rough with Gaussian height distributions.
- The load is supported by the contacting asperities only.
- The load is light; nominal contact pressure is small; $P/H_c \approx 10^{-3}$ to 10^{-5} .
- There is plastic deformation of the contacting asperities of the softer solid.

- Grease is homogeneous, fills the interstitial gaps completely, and wets the bounding surfaces perfectly.

In general, the joint conductance h_j and joint resistance R_j depend on the contact and gap components. The joint conductance is modeled as

$$h_j = h_c + h_g \quad (\text{W/m}^2 \cdot \text{K}) \quad (4.314)$$

where h_c represents the contact conductance and h_g represents the gap conductance. The joint resistance is modeled as

$$\frac{1}{R_j} = \frac{1}{R_c} + \frac{1}{R_g} \quad (\text{W/K}) \quad (4.315)$$

where R_c is the contact resistance and R_g is the gap resistance. For very light contact pressures it is assumed that $h_c \ll h_g$ and $R_c \gg R_g$. The joint conductance and resistance depend on the gap only; therefore,

$$h_j = h_g \quad \text{and} \quad \frac{1}{R_j} = \frac{1}{R_g} \quad \text{where} \quad h_j = \frac{1}{A_a R_j} \quad (4.316)$$

Based on the assumptions given above, the gap conductance is modeled as an equivalent layer of thickness $t = Y$ filled with grease having thermal conductivity k_g . The joint conductance is given by

$$h_j = \frac{k_g}{Y} \quad (\text{W/m}^2 \cdot \text{K}) \quad (4.317)$$

The gap parameter Y is the distance between the mean planes passing through the two rough surfaces. This geometric parameter is related to the combined surface roughness $\sigma = \sqrt{\sigma_1^2 + \sigma_2^2}$, where σ_1 and σ_2 are the rms surface roughness of the two surfaces and the contact pressure P and effective microhardness of the softer solid, H_c . The mean plane separation Y , shown in Fig. 4.22, is given approximately by the simple power law relation (Antonetti, 1983)

$$\frac{Y}{\sigma} = 1.53 \left(\frac{P}{H_c} \right)^{-0.097} \quad (4.318)$$

The power law relation shows that Y/σ is a relatively weak function of the relative contact pressure. Using this relation, the joint conductance may be expressed as

$$h_j = \frac{k_g}{\sigma(Y/\sigma)} = \frac{k_g}{1.53\sigma(P/H_c)^{-0.097}} \quad (\text{W/m}^2 \cdot \text{K}) \quad (4.319)$$

which shows clearly how the geometric, physical, and thermal parameters influence the joint conductance. The relation for the specific joint resistance is

$$A_a R_j = \frac{1}{h_j} = 1.53 \left(\frac{\sigma}{k_g} \right) \left(\frac{P}{H_c} \right)^{-0.097} \quad (\text{m}^2 \cdot \text{K/W}) \quad (4.320)$$

In general, if the metals work-harden, the relative contact pressure P/H_c is obtained from the relationship

$$\frac{P}{H_c} = \left[\frac{P}{c_1 (1.62 \sigma / m)^{c_2}} \right]^{1/(1+0.071 c_2)} \quad (4.321)$$

where the coefficients c_1 and c_2 are obtained from Vickers microhardness tests. The Vickers microhardness coefficients are related to the Brinell hardness H_B for a wide range of metals. The units of σ in the relation above must be micrometers. The units of P and c_1 must be consistent.

The approximation of Hegazy (1985) for microhardness is recommended:

$$H_c = (12.2 - 3.54 H_B) \left(\frac{\sigma}{m} \right)^{-0.26} \quad (\text{GPa}) \quad (4.322)$$

where H_c , the effective contact microhardness, and H_B , the Brinell hardness, are in GPa and the effective surface parameter (σ/m) is in micrometers. If the softer metal does not work-harden, $H_c \approx H_B$. Since $H_B < H_c$, if we set $H_c = H_B$ in the specific joint resistance relationship, this will give a lower bound for the joint resistance or an upper bound for the joint conductance.

The simple grease model for joint conductance or specific joint resistance was compared against the specific joint resistance data reported by Prasher (2001). The surface roughness parameters of the bounding copper surfaces and the grease thermal conductivities are given in Table 4.23. All tests were conducted at an apparent contact pressure of 1 atm and in a vacuum. Prasher (2001) reported his data as specific joint resistance $r_j = A_a R_j$ versus the parameter σ/k_g , where k_g is the thermal conductivity of the grease.

TABLE 4.23 Surface Roughness and Grease Thermal Conductivity

Test	Roughness, $\sigma_1 = \sigma_2$ (μm)	Conductivity, k_g (W/m · K)
1	0.12	3.13
2	1	3.13
3	3.5	3.13
4	1	0.4
5	3.5	0.4
6	3.5	0.25
7	3.5	0.22

Source: Prasher (2001).

4.17.5 Phase-Change Materials

Phase-change materials (PCMs) are being used to reduce thermal joint resistance in microelectronic systems. PCMs may consist of a substrate such as an aluminum foil supporting a PCM such as paraffin. In some applications the paraffin may be filled with solid particles to increase the effective thermal conductivity of the paraffin.

At some temperature T_m above room temperature, the PCM melts, then flows through the microgaps, expels the air, and then fills the voids completely. After the temperature of the joint falls below T_m , the PCM solidifies. Depending on the level of surface roughness, out-of-flatness, and thickness of the PCM, a complex joint is formed. Thermal tests reveal that the specific joint resistance is very small relative to the bare joint resistance with air occupying the microgaps (Fig. 4.36). Because of the complex nature of a joint with a PCM, no simple models are available for the several types of joints that can be formed when a PCM is used.

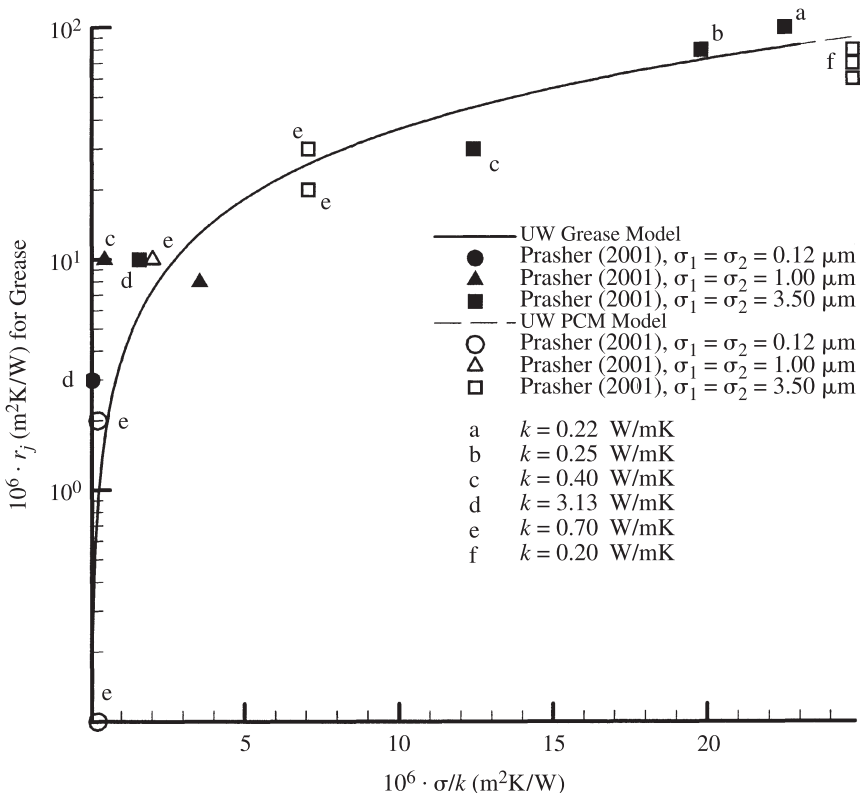


Figure 4.36 Specific joint resistance versus σ/k for grease. (From Prasher, 2001.)

4.18 THERMAL RESISTANCE AT BOLTED JOINTS

Bolted joints are frequently found in aerospace systems and less often in microelectronics systems. The bolted joints are complex because of their geometric configurations, the materials used, and the number of bolts and washers used. The pressure distributions near the location of the bolts are not uniform, and the region influenced by the bolts is difficult to predict. A number of papers are available to provide information on measured thermal resistances and to provide models to predict the thermal resistance under various conditions.

Madhusudana (1996) and Johnson (1985) present material on the thermal and mechanical aspects of bolted joints. For bolted joints used in satellite thermal design, the publications of Mantelli and Yovanovich (1996, 1998a, b) are recommended.

For bolted joints used in microelectronics cooling, the publications of Lee et al. (1993), Madhusudana et al. (1998) and Song et al. (1992b, 1993a) are recommended. Mikic (1970) describes variable contact pressure effects on joint conductance.

NOMENCLATURE

Roman Letter Symbols

A	area, m^2
	Fourier coefficient, dimensionless
	geometric parameter related to radii of curvature, dimensionless
A_a	apparent contact area, m^2
A_g	effective gap area, m^2
A_n	coefficient in summation, dimensionless
A_r	real contact area, m^2
a	radius of source area, m
	mean contact spot radius, m
	semimajor diameter of ellipse, m
	correlation coefficient, dimensionless
	radius of circle, m
	strip half-width, m
	side dimension of plate, m
	radius of flat contact, m
a_e	elastic contact radius, m
a_{ep}	composite elastic-plastic contact radius, m
a_L	thick-layer limit of contact radius, m
a_p	plastic contact radius, m
a_s	thin-layer limit of contact radius, m
a^*	combination of terms, dimensionless

B	Fourier coefficient, dimensionless geometric parameter related to radii of curvature, dimensionless
Bi	Biot modulus, dimensionless
$Bi(x, y)$	beta function of arguments x and y , dimensionless
B_n	coefficient in summation, dimensionless
b	semiminor diameter of ellipse, m side dimension of plate, m radius of compound disk, m correlation coefficient, dimensionless channel half-width, m
b_1	radius of cylinder, m
C	Fourier coefficient, dimensionless correction factor, dimensionless
C_c	contact conductance, dimensionless
c	correlation coefficient, dimensionless length dimension, m flux channel half-width, m side dimension of isoflux area, m
D	diameter of sphere, m diameter of circular cylinder, m
d	length dimension, m uniform gap thickness, m side dimension of isoflux area, m
d_o	reference value for average diagonal, m
d_v	Vickers diagonal, m
E	modulus of elasticity (Young's modulus), N/m^2 modulus of elasticity for polymer, N/m^2 complete elliptic integral of second kind, dimensionless
E'	effective modulus of elasticity, N/m^2
$\text{erf}(x)$	error function of argument x , dimensionless
$\text{erfc}(x)$	complementary error function of argument x , dimensionless
\mathcal{F}	emissivity factor, dimensionless
F_i	factor, dimensionless, $i = 1, 2, 3$ total normal load on a contact, N
$F(k', \psi)$	incomplete elliptic integral of the first kind of modulus k' and amplitude ψ , dimensionless
F^*	combination of terms, dimensionless
F'	load per unit cylinder length, N
Fo	Fourier modulus, dimensionless
f_{ep}	elastic-plastic parameter, dimensionless
f_g	combination of terms, dimensionless
$f(u)$	axisymmetric heat flux distribution, dimensionless
G	parameter, dimensionless

H'	effective microhardness, MPa
H_B	Brinnell hardness, MPa
	bulk microhardness of substrate, MPa
H_B^*	adjusted Brinnell hardness, MPa
H_e	effective microhardness, MPa
H_{ep}	elastic–plastic microhardness, MPa
H_p	microhardness of softer contacting asperities, MPa
	substrate microhardness, MPa
H_S	microhardness of softer material, MPa
H_V	Vickers microhardness, MPa
H_1	microhardness, layer 1, MPa
H_2	microhardness, layer 2, MPa
h	conductance or heat transfer coefficient, $\text{W/m}^2 \cdot \text{K}$
h'	coated joint conductance in vacuum, $\text{W/m}^2 \cdot \text{K}$
h_c	contact conductance, $\text{W/m}^2 \cdot \text{K}$
h_g	gap conductance, $\text{W/m}^2 \cdot \text{K}$
h_j	joint conductance, $\text{W/m}^2 \cdot \text{K}$
I_g	gap conductance integral, dimensionless
$I_{g,\ell}$	line contact elastogap integral, dimensionless
$I_{g,p}$	point contact elastogap integral, dimensionless
I_o	relative layer thickness, dimensionless
I_q	layer thickness conductivity parameter, dimensionless
I_γ	relative layer thickness conductivity parameter, dimensionless
K	thermal conductivity parameter, dimensionless
	complete elliptic integral of first kind, dimensionless
Kn	Knudsen number, dimensionless
k	modulus related to the ellipticity, dimensionless
	thermal conductivity, $\text{W/m} \cdot \text{K}$
k_g	effective gas thermal conductivity, $\text{W/m} \cdot \text{K}$
	grease thermal conductivity, $\text{W/m} \cdot \text{K}$
$k_{g,\infty}$	gas thermal conductivity under continuum conditions, $\text{W/m} \cdot \text{K}$
k_s	harmonic mean thermal conductivity of a joint, $\text{W/m} \cdot \text{K}$
k_1	layer 1 thermal conductivity, $\text{W/m} \cdot \text{K}$
k_2	layer 2 thermal conductivity, $\text{W/m} \cdot \text{K}$
L	strip length, m
L	relative contact size, dimensionless
ℓ	point in flux tube where flux lines are parallel, m
\mathcal{L}	length scale, m
M	gas rarefaction parameter, m
M_g	molecular weight of gas, g-mol
M_s	molecular weight of solid, g-mol
m	counter, dimensionless
	Hertz elastic parameter, dimensionless
	absolute asperity slope, dimensionless

N	number of sides in a polygon, dimensionless
	number of discrete sources, dimensionless
	number of microcontacts, dimensionless
$N(k')$	numerator function, dimensionless
n	counter, dimensionless
	Hertz elastic parameter, dimensionless
	combination parameter, dimensionless
	contact spot density, $1/\text{m}^2$
P	perimeter, m
	pressure, N/m^2 or Pa
$P_{g,\infty}$	reference gas pressure, N/m^2 or Pa
P_m	mean contact area pressure, N/m^2 or Pa
Pr	Prandtl number, dimensionless
Q	heat transfer rate, W
Q_g	gap heat transfer rate, W
q	heat flux, W/m^2
R	thermal resistance, K/W
R_g	thermal resistance of gap, K/W
R_{mac}	macroscopic thermal resistance of gap, K/W
R_{mic}	microscopic thermal resistance of gap, K/W
R_r	radiation resistance, K/W
R_c^*	combination of terms, dimensionless
R_g^*	combination of terms, dimensionless
R_j^*	combination of terms, dimensionless
R_r^*	combination of terms, dimensionless
r	radial coordinate, m
S_f	material yield or flow stress, N/m^2
s	side dimension, m
T	temperature, K
T_g	gas molecule temperature, K
$T_{g,\infty}$	reference temperature, K
ΔT	temperature drop or difference, K
ΔT_j	joint temperature drop, K
\bar{T}	area-averaged temperature, K
T_1	temperature, K
T_2	temperature, K
t	layer thickness, m
	thickness of elastic layer, m
	time, s
t_1	layer 1 thickness, m
	thickness of isotropic plate, m
t_2	layer 2 (substrate) thickness, m
u	local gap thickness, dimensionless
	position, dimensionless
$w(x, y)$	total local displacement, m

w_o	approach of contacting bodies due to loading, m
X_c	coordinate of center of eccentric rectangular area, m
x	length coordinate, m
Y	mean plane separation, m
Y_c	coordinate of center of eccentric rectangular area, m
y	distance, m
	length coordinate, m
z	length coordinate, m

Greek Letter Symbols

α	ratio of semimajor axes, dimensionless
	thermal diffusivity, m^2/s
	thermal conductivity ratio, dimensionless
	accommodation parameter or coefficient, dimensionless
α_1	accommodation coefficient, dimensionless
α_2	accommodation coefficient, dimensionless
β	combination of terms, dimensionless
	fluid property parameter, dimensionless
$\beta_{m,n}$	eigenvalue, dimensionless
$\Gamma(x)$	gamma function of argument x , dimensionless
γ	aspect ratio parameter, dimensionless
	ratio of specific heats, dimensionless
γ_T	combination of terms, dimensionless
Δ	change in, dimensionless
	physical parameter, m^2/N
δ	local gap thickness, m
δ_0	local gap thickness under zero-load conditions, m
δ_m	eigenvalue, dimensionless
δ_n	eigenvalues of $J_n(x)$, dimensionless
ϵ	radius ratio, dimensionless
	ellipse aspect ratio, dimensionless
	emissivity of hemisphere, dimensionless
	emissivity of disk, dimensionless
	relative contact spot size, dimensionless
ϵ_c	contact strain, dimensionless
ζ	ellipsoidal coordinate, m
	dummy variable, dimensionless
θ	temperature excess, K
$\bar{\theta}$	area averaged temperature rise, K
$\theta(r,z)$	temperature excess field, K
$\theta(\tau)$	ellipsoidal temperature rise, K
θ_o	centroid temperature rise, K
θ_s	temperature rise due to spreading, K
κ	parameter, dimensionless

	thermal conductivity ratio, dimensionless
Λ	mean free path length of gas molecules, m
Λ_g	molecular mean free path length at reference temperature, m
Λ_o	reference value of mean free path length, m
λ	dummy variable, dimensions vary
	relative mean free path length, dimensionless
λ_1	combination of terms, dimensionless
λ_2	combination of terms, dimensionless
λ_n	eigenvalue, dimensionless
μ	dynamic viscosity, $\text{N} \cdot \text{s}^2/\text{m}$
	positive root of an equation, dimensionless
	molecular weight ratio, dimensionless
ν	arbitrary order of Bessel function, dimensionless
	Poisson's ratio, dimensionless
ξ	length ratio, dimensionless
ρ	radius of curvature, m
	radius of elastic hemisphere, m
$\rho_{n,e}$	boundary condition parameter, dimensionless
ϱ	rectangular aspect ratio, dimensionless
	combination of terms, dimensionless
σ	Stefan-Boltzmann constant, $5.67 \times 10^{-8} \text{ W/m}^2 \cdot \text{K}^4$
	effective surface roughness, m or microns
τ	thickness, dimensionless
τ_1	thickness, dimensionless
τ_2	thickness, dimensionless
τ^*	combination of terms, dimensionless
ϕ	angle, rad
	combination of terms, dimensionless
ϕ_n	combination of terms, dimensionless
φ	combination of terms, dimensionless
φ^+	layer parameter, dimensionless
φ^-	layer parameter, dimensionless
ψ	combination of terms, dimensionless
	spreading resistance, dimensionless
	spreading-constriction parameter, dimensionless
	amplitude angle, rad
ψ_{mac}	macroscopic spreading-constriction parameter, dimensionless
ψ_{mic}	microscopic spreading-constriction parameter, dimensionless
ψ_o	combination of terms, dimensionless
ψ_n	combination of terms, dimensionless
$\psi_{e,i}$	combination of terms, dimensionless
ψ^*	thermal elasto constriction parameter, dimensionless
ψ_{12}	dimensional spreading resistance in layer-substrate
ω	angle, rad
∇^2	Laplacian operator, $1/\text{m}^2$

Subscripts

<i>a</i>	nominal value
ave	average
<i>B</i>	Brinnell
<i>c</i>	flux tube area
	active area
	contact
<i>c</i> , 1	contact 1
<i>c</i> , 2	contact 2
circle	circle
<i>e</i>	elastic contact radius
<i>ei</i>	layer thickness parameter
<i>ep</i>	elastic-plastic radius
ellipse	ellipse
<i>g</i>	gap
<i>g</i> , 1	gap 1
<i>g</i> , 2	gap 2
<i>g</i> , ∞	gas conductivity under continuum conditions
<i>j</i>	joint
layer	layer
1 layer	one layer
2 layer	two layers
<i>L</i>	thick layer
<i>m</i>	counter
	mean
<i>ma</i>	macrogap
<i>mi</i>	microcontact
mac	macroscopic
max	maximum
metal	metal
mic	microscopic
<i>n</i>	normal component
	counter
<i>n</i> , <i>e</i>	combination of terms
new	new value
<i>o</i>	outer
<i>p</i>	plastic contact radius
	polymer
<i>q</i>	layer thickness parameter
<i>r</i>	radiation or radiative
<i>s</i>	spreading
	thin layer
	source area
source	source
sink	sink

v	Vickers
t	tube
thick	thick
thin	thin
total	total
1D	one-dimensional
0	order 0
1	order 1
o	value at centroid of area
∞	sink temperature

Superscripts

i	identifies i th source parameter
n	shape parameter
q	isoflux boundary condition
T	isothermal boundary condition
*	composite value

REFERENCES

- Abramowitz, M., and Stegun, I. A. (1965). *Handbook of Mathematical Functions*, Dover, New York.
- Antonetti, V. W. (1983). On the Use of Metallic Coatings to Enhance Thermal Contact Conductance, Ph.D. dissertation, University of Waterloo, Waterloo, Ontario, Canada.
- Antonetti, V. W., and Yovanovich, M. M. (1983). Using Metallic Coatings to Enhance Thermal Contact Conductance of Electronic Packages, in *Heat Transfer in Electronic Equipment, 1983, ASME-HTD-28*, ASME, New York, pp. 71–77.
- Antonetti, V. W., and Yovanovich, M. M. (1985). Enhancement of Thermal Contact Conductance by Metallic Coatings: Theory and Experiments, *J. Heat Transfer*, 107, Aug., pp. 513–519.
- Antonetti, V. W., Whittle, T. D., and Simons, R. E. (1991). An Approximate Thermal Contact Conductance Correlation, in *Experimental/Numerical Heat Transfer in Combustion and Phase Change, ASME-HTD-170*, ASME, New York.
- Beck, J. V. (1979). Average Transient Temperature within a Body Heated by a Disk Heat Source, in *Heat Transfer, Thermal Control, and Heat Pipes*, Progress in Aeronautics and Astronautics, Vol. 70, AIAA, New York, pp. 3–24.
- Blackwell, J. H. (1972). Transient Heat Flow from a Thin Circular Disk Small-Time Solution, *J. Aust. Math. Soc.*, 14, 433–442.
- Braun, D., and Frohn, A. (1976). Heat Transfer in Simple Monatomic Gases and in Binary Mixtures of Monatomic Gases, *Int. J. Heat and Mass Transfer*, 19, 1329–1335.
- Burde, S. S. (1977). Thermal Contact Resistance between Smooth Spheres and Rough Flats, Ph.D. Dissertation, Department of Mechanical Engineering, University at Waterloo, Waterloo, Ontario, Canada.

- Burde, S. S., and Yovanovich, M. M. (1978). Thermal Resistance at Smooth Sphere/Rough Flat Contacts: Theoretical Analysis, AIAA, 78-871, 2nd AIAA/ASME Thermophysics and Heat Transfer Conference, Palo Alto, CA.
- Bush, A. W., and Gibson, R. D. (1979). A Theoretical Investigation of Thermal Contact Conductance, *J. Appl. Energy*, 5, 11-22.
- Bush, A. W., Gibson, R. D., and Thomas, T. R. (1975). The Elastic Contact of a Rough Surface, *Wear*, 35, 87-111.
- Byrd, P. F., and Friedman, M. D. (1971). *Handbook of Elliptic Integrals for Engineers and Scientists*, 2nd ed., Springer-Verlag, New York.
- Carslaw, H. S., and Jaeger, J. C. (1959). *Conduction of Heat in Solids*, 2nd ed., Oxford University Press, London.
- Cetinkale, T. N., and Fishenden, M. (1951). Thermal Conductance of Metal Surfaces in Contact, *Proc. General Discussion on Heat Transfer*, Institute of Mechanical Engineers, London, pp. 271-275.
- Chen, W. T., and Engel, P. A. (1972). Impact and Contact Stress Analysis in Multilayer Media, *Int. J. Solids Struct.*, 8, 1257-1281.
- Chow, Y. L., and Yovanovich, M. M. (1982). The Shape Factor of the Capacitance of a Conductor, *J. Appl. Physics*, 53(12), 8470-8475.
- Churchill, S. W., and Usagi, R. (1972). A General Expression for the Correlation of Rates of Transfer and Other Phenomena, *AIChE J.*, 18, 1121-1132.
- Clausing, A. M., and Chao, B. T. (1965). Thermal Contact Resistance in a Vacuum Environment," *J. Heat Transfer*, 87, 243-251.
- Cooper, M. G., Mikic, B. B., and Yovanovich, M. M. (1969). Thermal Contact Conductance, *Int. J. Heat Mass Transfer*, 12, 279-300.
- DeVaal, J. W. (1988). Thermal Joint Conductance of Surfaces Prepared by Grinding, Ph.D. dissertation, Department of Mechanical Engineering, University of Waterloo, Waterloo, Ontario, Canada.
- DeVaal, J. W., Yovanovich, M. M., and Negus, K. J. (1987). The Effects of Surface Slope Anisotropy on the Contact Conductance of Conforming Rough Surfaces, in *Fundamentals of Conduction and Recent Developments in Contact Resistance*, HTD-69, ASME, New York, pp. 123-134.
- Dryden, J. R. (1983). The Effect of a Surface Coating on the Constriction Resistance of a Spot on an Infinite Half-Plane, *J. Heat Transfer*, 105, May, 408-410.
- Dryden, J. R., Yovanovich, M. M., and Deakin, A. S. (1985). The Effect of Coatings on the Steady-State and Short Time Constriction Resistance for an Arbitrary Axisymmetric Flux, *J. Heat Transfer*, 107, Feb., 33-38.
- Fisher, N. J. (1985). Analytical and Experimental Studies of the Thermal Contact Resistance of Sphere Layered Contact, M.A.Sc. thesis, Department of Mechanical Engineering, University of Waterloo, Waterloo, Ontario, Canada.
- Fisher, N. J., and Yovanovich, M. M. (1989). Thermal Constriction Resistance of Sphere/Layered Flat Contacts: Theory and Experiments, *J. Heat Transfer*, 111, May, pp. 249-256.
- Fletcher, L. S. (1972). A Review of Thermal Control Materials for Metallic Junctions, *J. Spacecr. Rockets*, 9(12), 849-850.
- Fletcher, L. S. (1988). Recent Developments in Contact Conductance Heat Transfer, *J. Heat Transfer*, 110, 1059-1070.

- Fletcher, L. S. (1990). A Review of Thermal Enhancement Techniques for Electronic Systems, *IEEE Trans. Components Hybrids Manuf. Technol.*, 13(4), 1012–1021.
- Fuller, J. J. (2000). Thermal Contact Conductance of Metal/Polymer Joints: An Analytical and Experimental Investigation, M.S. thesis, Department of Mechanical Engineering, Clemson University, Clemson, SC.
- Fuller, J. J., and Marotta, E. E. (2000). Thermal Contact Conductance of Metal/Polymer Joints, *J. Thermophys. Heat Transfer*, 14(2), 283–286.
- Garnier, J. E., and Begej, S. (1979). Ex-reactor determination of Gap and Contact Conductance between Uranium Dioxide: Zircaloy-4 Interfaces, Report, Nuclear Regulatory Commission, Washington, DC.
- Gibson, R. D. (1976). The Contact Resistance for a Semi-infinite Cylinder in a Vacuum, *J. Appl. Energy*, 2, 57–65.
- Gradshteyn, I. S., and Ryzhik, I. M. (1965). *Table of Integrals, Series and Products*, Springer-Verlag, New York.
- Greene, P. R. (1989). A Useful Approximation to the Error Function: Applications to Mass, Momentum, and Energy Transport in Shear Layers, *J. Fluids Eng.*, 111, June, 224–226.
- Greenwood, J. A. (1967). The Area of Contact between Rough Surfaces and Flats, *J. Lubr. Technol.*, 81, 81–91.
- Greenwood, J. A., and Tripp, J. H. (1967). The Elastic Contact of Rough Spheres, *J. Appl. Mech.*, 89(1), 153–159.
- Greenwood, J. A., and Tripp, J. H. (1970). The Contact of Two Nominally Flat Rough Surfaces, *Proc. Inst. Mech. Eng.*, 185, 625–633.
- Greenwood, J. A., and Williamson, J. B. P. (1966). Contact of Nominally Flat Surfaces, *Proc. R. Soc. London*, A295, 300–319.
- Hartnett, J. P. (1961). A Survey of Thermal Accommodation Coefficients, in *Rarefied Gas Dynamics*, L. Talbot, ed., Academic Press, New York, pp. 1–28.
- Hegazy, A. A. (1985). Thermal Joint Conductance of Conforming Rough Surfaces: Effect of Surface Microhardness Variation, Ph.D. dissertation, University of Waterloo, Waterloo, Ontario, Canada.
- Hertz, H. R. (1896). *Miscellaneous Papers*, English Translation, Macmillan, London.
- Holm, R. (1967). *Electric Contacts: Theory and Applications*, Springer-Verlag, New York.
- Hui, P., and Tan, H. S. (1994). Temperature Distributions in a Heat Dissipation System Using a Cylindrical Diamond Heat Spreader on a Copper Sink, *J. Appl. Phys.*, 75(2), 748–757.
- Jeans, J. (1963). *The Mathematical Theory of Electricity and Magnetism*, Cambridge University Press, Cambridge, pp. 244–249.
- Johnson, K. L. (1985). *Contact Mechanics*, Cambridge University Press, Cambridge.
- Keltner, N. R. (1973). Transient Heat Flow in Half-Space Due to an Isothermal Disk on the Surface, *J. Heat Transfer*, 95, 412–414.
- Kennedy, D. P. (1960). Spreading Resistance in Cylindrical Semiconductor Devices, *J. Appl. Phys.*, 31(8), 1490–1497.
- Kitscha, W. W. (1982). Thermal Resistance of Sphere–Flat Contacts, M.A.Sc. thesis, Department of Mechanical Engineering, University of Waterloo, Waterloo, Ontario, Canada.
- Kitscha, W. W., and Yovanovich, M. M. (1975). Experimental Investigation on the Overall Thermal Resistance of Sphere–Flat Contacts, *Progress in Astronautics and Aeronautics*:

- Heat Transfer with Thermal Control Applications*, Vol. 39, MIT Press, Cambridge, MA, pp. 93–110.
- Kraus, A. D., and Bar-Cohen, A. (1983). *Thermal Analysis and Control of Electronic Equipment*, McGraw-Hill, New York, pp. 199–214.
- Lambert, M. A. (1995). Thermal Contact Conductance of Spherical Rough Surfaces, Ph.D. dissertation, Texas A&M University, College Station, TX.
- Lambert, M. A., and Fletcher, L. S. (1996). A Review of Models for Thermal Contact Conductance of Metals, *AIAA 96-0239*, 34th Aerospace Sciences Meeting and Exhibit, Jan. 15–18.
- Lambert, M. A., and Fletcher, L. S. (1997). Thermal Contact Conductance of Spherical Rough Surfaces, *J. Heat Transfer*, 119, 684–690.
- Lee, S., Yovanovich, M. M., Song, S., and Moran, K. P. (1993). Analysis of Thermal Constriction Resistance in Bolted Joint, *Int. J. Microcircuits Electron. Packag.*, 16(2), 125–136.
- Lee, S., Song, S., Au, V., and Moran, K. P. (1995). Constriction/Spreading Resistance Model for Electronics Packaging, *Proc. ASME/JSME Thermal Engineering Conference*, Vol. 4, pp. 199–206.
- Lloyd, W. R., Wilkins, D. R., and Hill, P. R. (1973). Heat Transfer in Multicomponent Monatomic Gases in the Low, Intermediate and High Pressure Regime, *Proc. Nuclear Thermionics Conference*.
- Loyalka, S. K. (1982). A Model for Gap Conductance in Nuclear Fuel Rods, *Nucl. Technol.*, 57, 220–227.
- Madhusudana, C. V. (1975). The Effect of Interface Fluid on Thermal Contact Conductance, *Int. J. Heat Mass Transfer*, 18, 989–991.
- Madhusudana, C. V. (1996). *Thermal Contact Conductance*, Springer-Verlag, New York.
- Madhusudana, C. V., and Fletcher, L. S. (1986). Contact Heat Transfer: The Last Decade, *AIAA J.*, 24(3), 510–523.
- Madhusudana, C. V., Peterson, G. P., and Fletcher, L. S. (1988). Effect of Non-uniform Pressures on the Thermal Conductance in Bolted and Riveted Joints, *Mech. Eng.*, 104, 57–67.
- Magnus, W., Oberhettinger, F., and Soni, R. P. (1966). *Formulas and Theorems for Special Functions of Mathematical Physics*, Springer-Verlag, New York.
- Mantelli, M. B. H., and Yovanovich, M. M. (1996). Experimental Determination of the Overall Thermal Resistance of Satellite Bolted Joints, *J. Thermophys. Heat Transfer*, 10(1), 177–179.
- Mantelli, M. B. H., and Yovanovich, M. M. (1998a). Parametric Heat Transfer Study of Bolted Joints, *J. Thermophys. Heat Transfer*, 12(3), 382–390.
- Mantelli, M. B. H., and Yovanovich, M. M. (1998b). Compact Analytical Model for Overall Thermal Resistance of Bolted Joints, *Int. J. Heat Mass Transfer*, 41(10), 1255–1266.
- Marotta, E. E., and Fletcher, L. S. (1996). Thermal Contact Resistance of Selected Polymeric Materials, *J. Thermophys. Heat Transfer*, 10(2), 334–342.
- Marotta, E. E., and Fletcher, L. S. (2001). Thermal Contact Resistance Modeling of Non-flat, Roughened Surfaces with Non-metallic Coatings, *J. Heat Transfer*, 123, 11–23.
- Martin, K. A., Yovanovich, M. M., and Chow, Y. L. (1984). Method of Moments Formulation of Thermal Constriction Resistance of Arbitrary Contacts, *AIAA-84-1745*, AIAA 19th Thermophysics Conference, Snowmass, CO, June 25–28.

- McGee, G. R., Schankula, M. H., and Yovanovich, M. M. (1985). Thermal Resistance of Cylinder-Flat Contacts: Theoretical Analysis and Experimental Verification of a Line-Contact Model, *Nucl. Eng. Des.*, 86, 369–381.
- McWaid, T. H., and Marschall, E. (1992a). Applications of the Modified Greenwood and Williamson Contact Model for Prediction of Thermal Contact Resistance, *Wear*, 152, 263–277.
- McWaid, T. H., and Marschall, E. (1992b). Thermal Contact Resistance across Pressed Metal Contacts in a Vacuum Environment, *Int. J. Heat Mass Transfer*, 35, 2911–2920.
- Mikic, B. B. (1970). Thermal Constriction Resistance Due to Nonuniform Surface Conditions: Contact Resistance at Nonuniform Interface Pressure, *Int. J. Heat Mass Transfer*, 13, 1497–1500.
- Mikic, B. B. (1974). Thermal Contact Conductance: Theoretical Considerations, *Int. J. Heat Mass Transfer*, 17, 205–214.
- Mikic, B. B., and Rohsenow, W. M. (1966). Thermal Contact Resistance, *Mech. Eng. Rep. DSR 74542-41*, MIT, Cambridge, MA.
- Muzychka, Y. S., Sridhar, M. R., Yovanovich, M. M., and Antonetti, V. W. (1999). Thermal Spreading Resistance in Multilayered Contacts: Applications in Thermal Contact Resistance, *J. Thermophys. Heat Transfer*, 13(4), 489–494.
- Muzychka, Y. S., Culham, J. R., and Yovanovich, M. M. (2000). Thermal Spreading Resistance of Eccentric Heat Sources on Rectangular Flux Channels, *ASME-HTD-366-4*, ASME, New York, pp. 347–355.
- Negus, K. J., and Yovanovich, M. M. (1984a). Constriction Resistance of Circular Flux Tubes with Mixed Boundary Conditions by Linear Superposition of Neumann Solutions, *ASME-84-HT-84*, ASME, New York.
- Negus, K. J., and Yovanovich, M. M. (1984b). Application of the Method of Optimized Images to Steady Three-Dimensional Conduction Problems, *ASME-84-WA/HT-110*, ASME, New York.
- Negus, K. J., and Yovanovich, M. M. (1988). Correlation of Gap Conductance Integral for Conforming Rough Surfaces, *J. Thermophys. Heat Transfer*, 12, 279–281.
- Negus, K. J., and Yovanovich, M. M. (1989). Transient Temperature Rise at Surfaces Due to Arbitrary Contacts on Half-Spaces, *CSME Trans.*, 13(1/2), 1–9.
- Negus, K. J., Yovanovich, M. M., and Thompson, J. C. (1985). Thermal Constriction Resistance of Circular Contacts on Coated Surfaces: Effect of Contact Boundary Condition, *AIAA-85-1014*, AIAA 20th Thermophysics Conference, Williamsburg, VA, June 19–21.
- Negus, K. J., Yovanovich, M. M., and Beck, J. V. (1989). On the Nondimensionalization of Constriction Resistance for Semi-infinite Heat Flux Tubes, *J. Heat Transfer*, 111, Aug., 804–807.
- Nelson, G. J., and Sayers, W. A. (1992). A Comparison of Two-Dimensional Planar, Axisymmetric and Three-Dimensional Spreading Resistance, *Proc. 8th Annual IEEE Semiconductor Thermal Measurement and Management Symposium*, 62–68.
- Nho, K. M. (1989). Experimental Investigation of Heat Flow Rate and Directional Effect on Contact Resistance of Anisotropic Gound/Lapped Interfaces, Ph.D. dissertation Department of Mechanical Engineering, University of Waterloo, Waterloo, Ontario, Canada.
- Normington, E. J., and Blackwell, J. H. (1964). Transient Heat Flow from Constant Temperature Spheroids and the Thin Circular Disk, *Q. J. Mech. Appl. Math.*, 17, 65–72.

- Normington, E. J., and Blackwell, J. H. (1972). Transient Heat Flow from a Thin Circular Disk: Small Time Solution, *J. Aust. Math. Soc.*, 14, 433–442.
- Onions, R. A., and Archard, J. F. (1973). The Contact of Surfaces Having a Random Structure, *J. Phys. D. Appl. Phys.*, 6, 289–304.
- Prasher, R. S. (2001). Surface Chemistry and Characteristics Based Model for the Thermal Contact Resistance of Fluidic Interstitial Thermal Interface Materials, *J. Heat Transfer*, 123, 969–975.
- Rapier, A. C., Jones, T. M., and McIntosh, J. E. (1963). The Thermal Conductance of Uranium Dioxide/Stainless Steel Interfaces, *Int. J. Heat Mass Transfer*, 6, 397–416.
- Roess, L. C. (1950). Theory of Spreading Conductance, Beacon Laboratories of Texas Company, Beacon, NY, App. A (unpublished report).
- Savija, I., Culham, J. R., Yovanovich, M. M., and Marotta, E. E. (2002a). Review of Thermal Conductance Models for Joints Incorporating Enhancement Materials, *AIAA-2002-0494*, 40th AIAA Aerospace Sciences Meeting and Exhibit, Jan. 14–17, Reno, NV.
- Savija, I., Yovanovich, M. M., Culham, J. R., and Marotta, E. E. (2002b). Thermal Joint Resistance Models for Conforming Rough Surfaces with Grease Filled Gaps, *AIAA-2002-0495*, 40th AIAA Aerospace Sciences Meeting and Exhibit, Jan. 14–17, Reno, NV.
- Sayles, R. S., and Thomas, T. R. (1976). Thermal Conductance of a Rough Elastic Contact, *J. Appl. Energy*, 2, 249–267.
- Schneider, G. E. (1978). Thermal Resistance Due to Arbitrary Dirichlet Contacts on a Half-Space, *Prog. Astronaut. Aeronaut. Thermophys. Therm. Control*, 65, 103–119.
- Schneider, G. E., Strong, A. B., and Yovanovich, M. M. (1976). Transient Heat Flow from a Thin Circular Disk, *AIAA Progress in Astronautics, Radiative Transfer and Thermal Control*, (Ed. A. M. Smith), MIT Press, 49, 419–432.
- Semyonov, Yu. G., Borisov, S. E., and Suetin, P. E. (1984). Investigation of Heat Transfer in Rarefied Gases over a Wide Range of Knudsen Numbers, *Int. J. Heat Mass Transfer*, 27, 1789–1799.
- Sexl, R. U., and Burkhard, D. G. (1969). An Exact Solution for Thermal Conduction through a Two-Dimensional Eccentric Constriction, *Prog. Astronaut. Aeronaut.*, 21, 617–620.
- Shlykov, Yu. P. (1965). Calculation of Thermal Contact Resistance of Machined Metal Surfaces, *Teploenergetika*, 12(10), 79–83.
- Smythe, W. R. (1951). The Capacitance of a Circular Annulus, *Am. J. Phys.*, 22(8), 1499–1501.
- Smythe, W. R. (1968). *Static and Dynamic Electricity*, 3rd ed., McGraw-Hill, New York.
- Sneddon, I. N. (1966). *Mixed Boundary Value Problems in Potential Theory*, North-Holland, Amsterdam.
- Song, S. (1988). Analytical and Experimental Study of Heat Transfer through Gas Layers of Contact Interfaces, Ph.D. dissertation, University of Waterloo, Waterloo, Ontario, Canada.
- Song, S., and Yovanovich, M. M. (1987). Correlation of Thermal Accommodation Coefficients for Engineering Surfaces, *ASME-HTD-69*, ASME, New York, 107–116.
- Song, S., and Yovanovich, M. M. (1988). Relative Contact Pressure: Dependence on Surface Roughness and Vickers Microhardness, *J. Thermophys. Heat Transfer*, 2(1), 43–47.
- Song, S., Yovanovich, M. M., and Nho, K. (1992a). Thermal Gap Conductance: Effects of Gas Pressure and Mechanical Load, *J. Thermophys. Heat Transfer*, 6(1), 62–68.
- Song, S., Park, C., Moran, K. P., and Lee, S. (1992b). Contact Area of Bolted Joint Interface: Analytical, Finite Element Modeling, and Experimental Study, *Comput. Aid. Des. Electron. Packag.*, 3, 73–81.

- Song, S., Moran, K. P., Augi, R., and Lee, S. (1993a). Experimental Study and Modeling of Thermal Contact Resistance across Bolted Joints, *AIAA-93-0844*, 31st Aerospace Sciences Meeting and Exhibit, Reno, NV, Jan. 11–14.
- Song, S., Yovanovich, M. M., and Goodman, F. O. (1993b). Thermal Gap Conductance of Conforming Rough Surfaces in Contact, *J. Heat Transfer*, 115, 533–540.
- Song, S., Lee, S., and Au, V. (1994). Closed-Form Equation for Thermal Constriction/Spreading Resistances with Variable Resistance Boundary Condition, *Proc. 1994 IEPS Conference*, Atlanta, GA, pp. 111–121.
- Sridhar, M. R. (1994). Elastoplastic Contact Models for Sphere-Flat and Conforming Rough Surface Applications, Ph.D. dissertation, University of Waterloo, Waterloo, Ontario, Canada.
- Sridhar, M. R., and Yovanovich, M. M. (1994). Review of Elastic and Plastic Contact Conductance Models: Comparison with Experiment, *J. Thermophys. Heat Transfer*, 8(4), 633–640.
- Sridhar, M. R., and Yovanovich, M. M. (1996a). Thermal Contact Conductance of Tool Steel and Comparison with Model, *Int. J. Heat Mass Transfer*, 39(4), 831–839.
- Sridhar, M. R., and Yovanovich, M. M. (1996b). Empirical Methods to Predict Vickers Microhardness, *Wear*, 193, pp. 91–98.
- Sridhar, M. R., and Yovanovich, M. M. (1996c). Elastoplastic Contact Model for Isotropic Conforming Rough Surfaces and Comparison with Experiments, *J. Heat Transfer*, 118(1), 3–9.
- Sridhar, M. R., and Yovanovich, M. M. (1996d). Elastoplastic Constriction Resistance Model for Sphere-Flat Contacts, *J. Heat Transfer*, 118(1), 202–205.
- Stevanović, M., Yovanovich, M. M., and Culham, J. R. (2002). Modeling Thermal Contact Resistance between Elastic Hemisphere and Elastic Layer on Bonded Elastic Substrate, *Proc. 8th Intersociety Conference on Thermal and Thermomechanical Phenomena in Electronic Systems*, San Diego, CA, May 29–June 1.
- Stratton, J. A. (1941). *Electromagnetic Theory*, McGraw-Hill, New York, pp. 207–211.
- Strong, A. B., Schneider, G. E., and Yovanovich, M. M. (1974). Thermal Constriction Resistance of a Disc with Arbitrary Heat Flux: Finite Difference Solutions in Oblate Spheroidal Coordinates, *AIAA-74-690*, AIAA/ASME 1974 Thermophysics and Heat Transfer Conference, Boston, July 15–17.
- Tabor, D. (1951). *The Hardness of Metals*, Oxford University Press, London.
- Teagan, W. P., and Springer, G. S. (1968). Heat-Transfer and Density Distribution Measurements between Parallel Plates in the Transition Regime, *Phys. of Fluids*, 11(3), 497–506.
- Thomas, L. B. (1967). *Rarefied Gas Dynamics*, Academic Press, New York.
- Thomas, T. R. (1982). *Rough Surfaces*, Longman Group, London.
- Timoshenko, S. P., and Goodier, J. N. (1970). *Theory of Elasticity*, 3rd ed., McGraw-Hill, New York.
- Turyk, P. J., and Yovanovich, M. M. (1984). Transient Constriction Resistance for Elemental Flux Channels Heated by Uniform Heat Sources, *ASME-84-HT-52*, ASME, New York.
- Veziroglu, T. N. (1967). Correlation of Thermal Contact Conductance Experimental Results, presented at AIAA Thermophysics Specialist Conference, New Orleans, LA.
- Veziroglu, T. N., and Chandra, S. (1969). Thermal Conductance of Two-Dimensional Constrictions, *Prog. Astronaut. Aeronaut.*, 21, 617–620.
- Wachman, H. Y. (1962). The Thermal Accommodation Coefficient: A Critical Survey, *ARS J.*, 32, 2–12.

- Walowit, J. A., and Anno, J. N. (1975). *Modern Developments in Lubrication Mechanics*, Applied Science Publishers, Barking, Essex, England.
- Wesley, D. A., and Yovanovich, M. M. (1986). A New Gaseous Gap Conductance Relationship, *Nucl. Technol.*, 72, Jan., 70–74.
- Whitehouse, D. J., and Archard, J. F. (1970). The Properties of Random Surfaces of Significance in Their Contact, *Proc. R. Soc. London*, A316, 97–121.
- Wiedmann, M. L., and Trumpler, P. R. (1946). Thermal Accommodation Coefficients, *Trans. ASME*, 68, 57–64.
- Yovanovich, M. M. (1967). Thermal Contact Resistance across Elastically Deformed Spheres, *J. Spacecr. Rockets*, 4, 119–122.
- Yovanovich, M. M. (1969). Overall Constriction Resistance between Contacting Rough, Wavy Surfaces, *Int. J. Heat Mass Transfer*, 12, 1517–1520.
- Yovanovich, M. M. (1971). Thermal Constriction Resistance between Contacting Metallic Paraboloids: Application to Instrument Bearings, in *Progress in Astronautics and Aeronautics: Heat Transfer and Spacecraft Control*, Vol. 24, J. W. Lucas, ed., AIAA, New York, pp. 337–358.
- Yovanovich, M. M. (1972). Effect of Foils on Joint Resistance: Evidence of Optimum Foil Thickness, *AIAA-72-283*. AIAA 7th Thermophysics Conference, San Antonio, TX, Apr.
- Yovanovich, M. M. (1976a). General Thermal Constriction Resistance Parameter for Annular Contacts on Circular Flux Tubes, *AIAA J.*, 14(6), 822–824.
- Yovanovich, M. M. (1976b). General Expressions for Constriction Resistances of Arbitrary Flux Distributions, in *Progress in Astronautics and Aeronautics: Radiative Transfer and Thermal Control*, Vol. 49, AIAA, New York, pp. 381–396.
- Yovanovich, M. M. (1976c). Thermal Constriction Resistance of Contacts on a Half-Space: Integral Formulation, in *Progress in Astronautics and Aeronautics: Radiative Transfer and Thermal Control*, Vol. 49, AIAA, New York, pp. 397–418.
- Yovanovich, M. M. (1978). Simplified Explicit Elastoconstriction Resistance for Ball/Race Contacts, *AIAA-78-84*. 16th Aerospace Sciences Meeting, Huntsville, AL, Jan. 16–18.
- Yovanovich, M. M. (1982). Thermal Contact Correlations, in *Progress in Astronautics and Aeronautics: Spacecraft Radiative Transfer and Temperature Control*, Vol. 83, T. E. Horton, ed., AIAA, New York, pp. 83–95.
- Yovanovich, M. M. (1986). Recent Developments in Thermal Contact, Gap and Joint Conductance Theories and Experiments, *Proc. 8th International Heat Transfer Conference*, San Francisco, Vol. 1, pp. 35–45.
- Yovanovich, M. M. (1991). Theory and Applications of Constriction and Spreading Resistance Concepts for Microelectronic Thermal Management, in *Cooling Techniques for Computers*, W. Aung, ed., Hemisphere Publishing, New York, pp. 277–332.
- Yovanovich, M. M. (1997). Transient Spreading Resistance of Arbitrary Isoflux Contact Areas: Development of a Universal Time Function, *AIAA-97-2458*, AIAA 32nd Thermophysics Conference, Atlanta, GA, June 23–25.
- Yovanovich, M. M., and Antonetti, V. W. (1988). Application of Thermal Contact Resistance Theory to Electronic Packages, in *Advances in Thermal Modeling of Electronic Components and Systems*, Vol. 1, A. Bar-Cohen and A. D. Kraus, eds., Hemisphere Publishing, New York, pp. 79–128.
- Yovanovich, M. M., and Burde, S. S. (1977). Centroidal and Area Average Resistances of Nonsymmetric, Singly Connected Contacts, *AIAA J.*, 15(10), 1523–1525.

- Yovanovich, M. M., and Kitscha, W. W. (1974). Modeling the Effect of Air and Oil upon the Thermal Resistance of a Sphere-Flat Contact, in *Progress in Astronautics and Aeronautics: Thermophysics and Spacecraft Control*, Vol. 35, R. G. Hering, ed., AIAA, New York, pp. 293–319.
- Yovanovich, M. M., and Schneider, G. E. (1977). Thermal Constriction Resistance Due to a Circular Annular Contact, in *Progress in Astronautics and Aeronautics*, Vol. 56, AIAA, New York, pp. 141–154.
- Yovanovich, M. M., Burde, S. S., and Thompson, J. C. (1977). Thermal Constriction Resistance of Arbitrary Planar Contacts with Constant Flux, in *Progress in Astronautics and Aeronautics: Thermophysics of Spacecraft and Outer Planet Entry Probes*, Vol. 56, AIAA, New York, pp. 127–139.
- Yovanovich, M. M., Tien, C. H., and Schneider, G. E. (1980). General Solution of Constriction Resistance within a Compound Disk, in *Progress in Astronautics and Aeronautics: Heat Transfer, Thermal Control, and Heat Pipes*, Vol. 70, AIAA, New York, pp. 47–62.
- Yovanovich, M. M., Hegazy, A. A., and DeVaal, J. (1982a). Surface Hardness Distribution Effects upon Contact, Gap and Joint Conductances, *AIAA-82-0887*, AIAA/ASME 3rd Joint Thermophysics, Fluids, Plasma and Heat Transfer Conference, St. Louis, MO, June 7–11.
- Yovanovich, M. M., DeVaal, J., and Hegazy, A. A. (1982b). A Statistical Model to Predict Thermal Gap Conductance between Conforming Rough Surfaces, *AIAA-82-0888*, AIAA/ASME 3rd Joint Thermophysics, Fluids, Plasma and Heat Transfer Conference, St. Louis, MO, June 7–11.
- Yovanovich, M. M., Negus, K. J., and Thompson, J. C. (1984). Transient Temperature Rise of Arbitrary Contacts with Uniform Flux by Surface Element Methods, *AIAA-84-0397*, AIAA 22nd Aerospace Sciences Meeting, Reno, NV, Jan. 9–12.
- Yovanovich, M. M., Culham, J. R., and Teerstra, P. (1997). Calculating Interface Resistance, *Electron. Cool.*, 3(2), 24–29.
- Yovanovich, M. M., Culham, J. R., and Teerstra, P. (1998). Analytical Modeling of Spreading Resistance in Flux Tubes, Half Spaces, and Compound Disks, *IEEE Trans. Components Packag. Manuf. Technol.*, A21(1), 168–176.
- Yovanovich, M. M., Muzychka, Y. S., and Culham, J. R. (1999). Spreading Resistance of Isoflux Rectangles and Strips on Compound Flux Channels, *J. Thermophys. Heat Transfer*, 13(4), 495–500.

Forced Convection: Internal Flows

ADRIAN BEJAN

Department of Mechanical Engineering and Materials Science
Duke University
Durham, North Carolina

- 5.1 Introduction
 - 5.2 Laminar flow and pressure drop
 - 5.2.1 Flow entrance region
 - 5.2.2 Fully developed flow region
 - 5.2.3 Hydraulic diameter and pressure drop
 - 5.3 Heat transfer in fully developed flow
 - 5.3.1 Mean temperature
 - 5.3.2 Thermally fully developed flow
 - 5.4 Heat transfer in developing flow
 - 5.4.1 Thermal entrance region
 - 5.4.2 Thermally developing Hagen–Poiseuille flow
 - 5.4.3 Thermally and hydraulically developing flow
 - 5.5 Optimal channel sizes for laminar flow
 - 5.6 Turbulent duct flow
 - 5.6.1 Time-averaged equations
 - 5.6.2 Fully developed flow
 - 5.6.3 Heat transfer in fully developed flow
 - 5.7 Total heat transfer rate
 - 5.7.1 Isothermal wall
 - 5.7.2 Wall heated uniformly
 - 5.8 Optimal channel sizes for turbulent flow
 - 5.9 Summary of forced convection relationships
- Nomenclature
- References

5.1 INTRODUCTION

An *internal flow* is a flow configuration where the flowing material is surrounded by solid walls. Streams that flow through ducts are primary examples of internal flows. Heat exchangers are conglomerates of internal flows. This class of fluid flow and

convection phenomena distinguishes itself from the class of an external flow, which is treated in Chapters 6 (forced-convection external) and 7 (natural convection). In an external flow configuration, a solid object is surrounded by the flow.

There are two basic questions for the engineer who contemplates using an internal flow configuration. One is the heat transfer rate, or the thermal resistance between the stream and the confining walls. The other is the friction between the stream and the walls. The fluid friction part of the problem is the same as calculation of the pressure drop experienced by the stream over a finite length in the flow direction. The fluid friction question is the more basic, because friction is present as soon as there is flow, that is, even in the absence of heat transfer. This is why we begin this chapter with the calculation of velocity and pressure drop in duct flow. The heat transfer question is supplementary, as the duct flow will convect energy if a temperature difference exists between its inlet and the wall.

To calculate the heat transfer rate and the temperature distribution through the flow, one must know the flow, or the velocity distribution. When the variation of temperature over the flow field is sufficiently weak so that the fluid density and viscosity are adequately represented by two constants, calculation of the velocity field and pressure drop is independent of that of the temperature field. This is the case in all the configurations and results reviewed in this chapter. When this approximation is valid, the velocity field is “not coupled” to the temperature field, although, as already noted, correct derivation of the temperature field requires the velocity field as a preliminary result, that is, as an input.

The following presentation is based on the method developed in Bejan (1995). Alternative reviews of internal flow convection are available in Shah and London (1978) and Shah and Bhatti (1978) and are recommended.

5.2 LAMINAR FLOW AND PRESSURE DROP

5.2.1 Flow Entrance Region

Consider the laminar flow through a two-dimensional duct formed between two parallel plates, as shown in Fig. 5.1. The spacing between the plates is D . The flow velocity in the inlet cross section ($x = 0$) is uniform (U). Mass conservation means that U is also the mean velocity at any position x downstream,

$$U = \frac{1}{A} \int_A u \, dA \quad (5.1)$$

where u is the longitudinal velocity component and A is the duct cross-sectional area in general. Boundary layers grow along the walls until they meet at the distance $x \approx X$ downstream from the entrance. The length X is called *entrance length* or *flow (hydrodynamic) entrance length*, to be distinguished from the thermal entrance length discussed in Section 5.4.1. In the entrance length region the boundary layers coexist with a core in which the velocity is uniform (U_c). Mass conservation and the fact that the fluid slows down in the boundary layers requires that $U_c > U$.

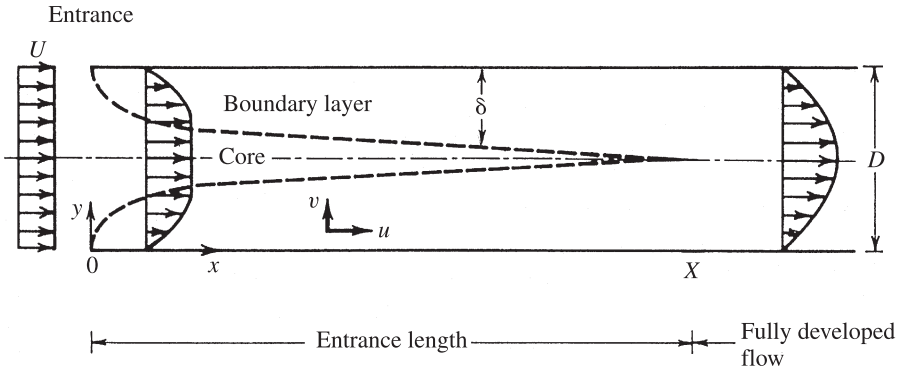


Figure 5.1 Developing flow in the entrance region of the duct formed between two parallel plates. (From Bejan, 1995.)

The length X divides the duct flow into an entrance region ($0 < x \leq X$) and a fully developed flow region ($x \geq X$). The flow friction and heat transfer characteristics of the entrance region are similar to those of boundary layer flows. The features of the fully developed region require special analysis, as shown in Section 5.2.2. The entrance length X is indicated approximately in Fig. 5.1. This is not a precise dimension, for the same reasons that the thickness of a boundary layer (δ) is known only as an order-of-magnitude length. The scale of X can be determined from the scale of δ , which according to the Blasius solution is

$$\delta \sim 5x \left(\frac{Ux}{\nu} \right)^{-1/2}$$

The transition from entrance flow to fully developed flow occurs at $x \sim X$ and $\delta \sim D/2$, and therefore it can be concluded that

$$\frac{X/D}{\text{Re}_D} \approx 10^{-2} \quad (5.2)$$

where $\text{Re}_D = UD/\nu$. The heat transfer literature also recommends the more precise value 0.04 in place of the 10^{-2} in eq. (5.2) (Schlichting, 1960), although as shown in Fig. 5.2 and 5.3, the transition from entrance flow to fully developed flow is smooth.

The friction between fluid and walls is measured as the local shear stress at the wall surface,

$$\tau_x(x) = \mu \left. \frac{\partial u}{\partial y} \right|_{y=0}$$

or the dimensionless local skin friction coefficient

$$C_{f,x} = \frac{\tau_w}{\frac{1}{2} \rho U^2} \quad (5.3)$$

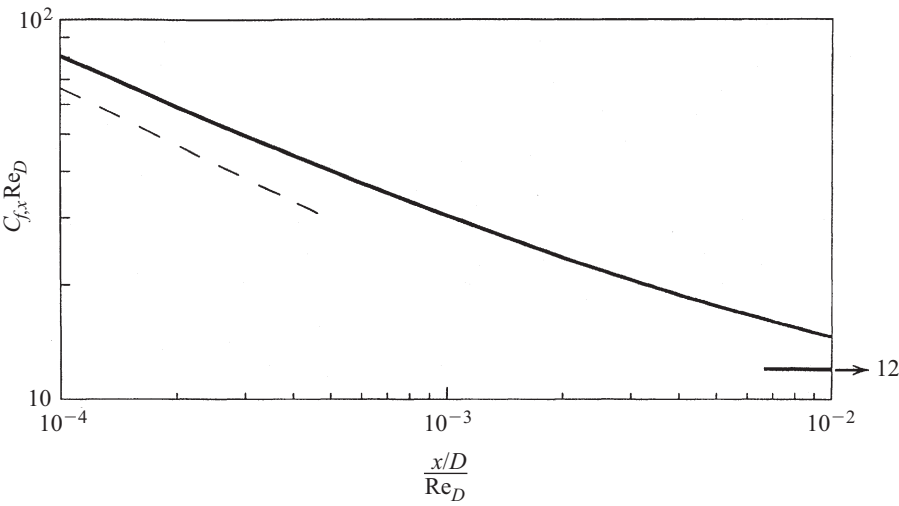


Figure 5.2 Local skin-friction coefficient in the entrance region of a parallel-plate duct. (From Bejan, 1995.)

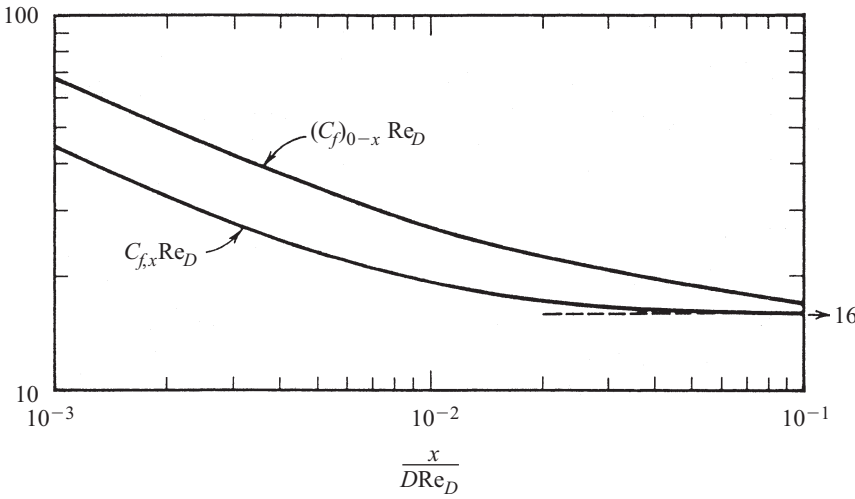


Figure 5.3 Local and average skin friction coefficients in the entrance region of a round tube. (From Bejan, 1995.)

Figure 5.2 shows a replotting (Bejan, 1995) of the integral solution (Sparrow, 1955) for $C_{f,x}$ in the entrance region of a parallel-plate duct. The dashed-line asymptote indicates the $C_{f,x}$ estimate based on the Blasius solution for the laminar boundary layer between a flat wall and a uniform free stream (U). If numerical factors of order 1 are neglected, the boundary layer asymptote is

$$C_{f,x} \approx \left(\frac{Ux}{\nu} \right)^{-1/2}$$

or

$$C_{f,x} \cdot \text{Re}_D \approx \left(\frac{x}{D \cdot \text{Re}_D} \right)^{-1/2}$$

The solid-line asymptote, $C_{f,x} \cdot \text{Re}_D = 12$, represents the skin friction solution for the fully developed flow region (Section 5.2.2).

The local skin friction coefficient in the entrance region of a round tube is indicated by the lower curve in Fig. 5.3. This is a replottting (Bejan, 1995) of the solution reported by Langhaar (1942). The upper curve is for the averaged skin friction coefficient,

$$C_f \Big|_{0-x} = \frac{1}{x} \int_0^x C_{f,\xi}(\xi) d\xi \quad (5.4a)$$

or

$$C_f \Big|_{0-x} = \frac{\bar{\tau}}{\frac{1}{2} \rho U^2} \quad (5.4b)$$

where

$$\bar{\tau} = \frac{1}{x} \int_0^x \tau_w(\xi) d\xi$$

The horizontal asymptote serves both curves,

$$C_{f,x} = 16 = C_f \Big|_{0-x}$$

and represents the solution for fully developed skin friction in a round tube as shown subsequently in eq. (5.18).

5.2.2 Fully Developed Flow Region

The key feature of the flow in the region downstream of $x \sim X$ is that the transverse velocity component ($v = 0$ in Fig. 5.1) is negligible. In view of the equation for mass conservation,

$$\frac{\partial u}{\partial x} + \frac{\partial v}{\partial y} = 0$$

the vanishing of v is equivalent to $\partial u / \partial x = 0$, that is, a velocity distribution that does not change or does not develop further from one x to the next. This is why this flow region is called fully developed. It is considered as defined by

$$v = 0 \quad \text{or} \quad \frac{\partial u}{\partial x} = 0 \quad (5.5)$$

This feature is a consequence of the geometric constraint that downstream of $x \sim X$, the boundary layer thickness δ cannot continue to grow. In this region, the length scale for changes in the transverse direction is the constant D , not the freely growing δ , and the mass conservation equation requires that $U/L \approx v/D$, where L is the flow dimension in the downstream direction. The v scale is then $v \approx UD/L$ and this scale vanishes as L increases, that is, as the flow reaches sufficiently far into the duct.

Another consequence of the full development of the flow is that the pressure is essentially uniform in each constant- x cross section ($\partial P/\partial y = 0$). This feature is derived by substituting $v = 0$ into the momentum (Navier–Stokes) equation for the y direction. With reference to Fig. 5.1, the pressure distribution is $P(x)$, and the momentum equation for the flow direction x becomes

$$\frac{dP}{dx} = \mu \frac{d^2 u}{dy^2} \quad (5.6)$$

Both sides of this equation must equal the same constant, because at most, the left side is a function of x and the right side a function of y . That constant is the pressure drop per unit length,

$$\frac{\Delta P}{L} = -\frac{dP}{dx}$$

The pressure drop and the flow distribution $u(y)$ are obtained by solving eq. (5.6) subject to $u = 0$ at the walls ($y \pm D/2$), where $y = 0$ represents the center plane of the parallel plate duct:

$$u(y) = \frac{3}{2}U \left[1 - \left(\frac{y}{D/2} \right)^2 \right] \quad (5.7)$$

with

$$U = \frac{D^2}{12\mu} \left(-\frac{dP}{dx} \right) \quad (5.8)$$

In general, for a duct of arbitrary cross section, eq. (5.6) is replaced by

$$\frac{dP}{dx} = \mu \nabla^2 u = \text{constant}$$

where the Laplacian operator ∇^2 accounts only for curvatures in the cross section,

$$\nabla^2 = \frac{\partial^2}{\partial y^2} + \frac{\partial^2}{\partial z^2}$$

that is, $\partial^2/\partial x^2 = 0$. The boundary conditions are $u = 0$ on the perimeter of the cross section. For example, the solution for fully developed laminar flow in a round tube of radius r_0 is

$$u = 2U \left[1 - \left(\frac{r}{r_0} \right)^2 \right] \quad (5.9)$$

with

$$U = \frac{r_0^2}{8\mu} \left(-\frac{dP}{dx} \right) \quad (5.10)$$

This solution was first reported by Hagen (1839) and Poiseuille (1840), which is why the fully developed laminar flow regime is also called *Hagen–Poiseuille flow* or *Poiseuille flow*.

5.2.3 Hydraulic Diameter and Pressure Drop

Equations (5.8) and (5.10) show that in fully developed laminar flow the mean velocity U (or the mass flow rate $\dot{m} = \rho AU$) is proportional to the longitudinal pressure gradient P/L . In general, and especially in turbulent flow, the relationship between \dot{m} and ΔP is nonlinear. Fluid friction results for fully developed flow in ducts are reported as friction factors:

$$f = \frac{\tau_w}{\frac{1}{2}\rho U^2} \quad (5.11)$$

where τ_w is the shear stress at the wall. Equation (5.11) is the same as eq. (5.3), with the observation that in fully developed flow, τ_w and f are x -independent.

The shear stress τ_w is proportional to $\Delta P/L$. This proportionality follows from the longitudinal force balance on a flow control volume of cross section A and length L ,

$$A \Delta P = \tau_w p L \quad (5.12)$$

where p is the perimeter of the cross section. Equation (5.12) is general and is independent of the flow regime. Combined with eq. (5.11), it yields the pressure drop relationship

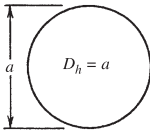
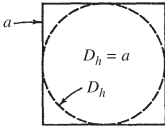
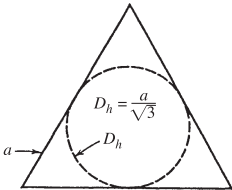
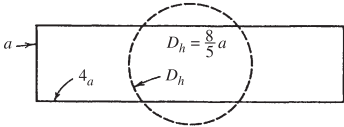
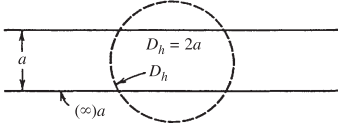
$$\Delta P = f \frac{pL}{A} \left(\frac{1}{2} \rho U^2 \right) \quad (5.13)$$

where A/p represents the transversal length scale of the duct:

$$r_h = \frac{A}{p} \quad \text{hydraulic radius} \quad (5.14)$$

$$D_h = \frac{4A}{p} \quad \text{hydraulic diameter} \quad (5.15)$$

TABLE 5.1 Scale Drawing of Five Different Ducts That Have the Same Hydraulic Diameter

Cross Section	Diagram
Circular	
Square	
Equilateral triangle	
Rectangular (4:1)	
Infinite parallel plates	

Source: Bejan (1995).

Table 5.1 shows five duct cross sections that have the same hydraulic diameter. The hydraulic diameter of the round tube coincides with the tube diameter. The hydraulic diameter of the channel formed between two parallel plates is twice the spacing between the plates. For cross sections shaped as regular polygons, D_h is the diameter of the circle inscribed inside the polygon. In the case of highly asymmetric cross sections, D_h scales with the smaller of the two dimensions of the cross section.

The general pressure drop relationship (5.2) is most often written in terms of hydraulic diameter,

$$\Delta P = f \frac{4L}{D_h} \left(\frac{1}{2} \rho U^2 \right) \quad (5.16)$$




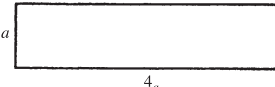


To calculate ΔP , the friction factor f must be known and it can be derived from the flow solution. The friction factors derived from the Hagen–Poiseuille flows described by eqs. (5.7) and (5.9) are

$$f = \begin{cases} \frac{24}{\text{Re}_{D_h}} & D_h = 2D \quad \text{parallel plates } (D = \text{spacing}) \\ \frac{16}{\text{Re}_{D_h}} & D_h = D \quad \text{round tube } (D = \text{diameter}) \end{cases} \quad (5.17)$$

$$(5.18)$$

Equations (5.17) and (5.18) hold for laminar flow ($\text{Re}_{D_h} \leq 2000$). Friction factors for other cross-sectional shapes are reported in Tables 5.2 and 5.3. Additional results can be found in Shah and London (1978). All Hagen–Poiseuille flows are characterized by

TABLE 5.2 Effect of Cross-Sectional Shape on f and Nu in Fully Developed Duct Flow

Cross Section	f/Re_{D_h}	$B = \frac{\pi D_h^2/4}{A}$	$\text{Nu} = h D_h / k$	
			Uniform q''	Uniform T_0
	13.3	0.605	3	2.35
	14.2	0.785	3.63	2.89
	16	1	4.364	3.66
	18.3	1.26	5.35	4.65
	24	1.57	8.235	7.54
 One side insulated	24	1.57	5.385	4.86

Source: Bejan (1995).

TABLE 5.3 Friction Factors and Nusselt Numbers for Heat Transfer to Laminar Flow through Ducts with Regular Polygonal Cross Sections

Cross Section	$f \cdot \text{Re}_{D_h}$ Fully Developed Flow	$\text{Nu} = hD_h/k$			
		Uniform Heat Flux		Isothermal Wall	
		Fully Developed Flow	Slug Flow	Fully Developed Flow	Slug Flow
Square	14.167	3.614	7.083	2.980	4.926
Hexagon	15.065	4.021	7.533	3.353	5.380
Octagon	15.381	4.207	7.690	3.467	5.526
Circle	16	4.364	7.962	3.66	5.769

Source: Data from Asako et al. (1988).

$$f = \frac{C}{\text{Re}_{D_h}} \tag{5.19}$$

where the constant C depends on the shape of the duct cross section. It was shown in Bejan (1995) that the duct shape is represented by the dimensionless group

$$B = \frac{\pi D_h/4}{A_{\text{duct}}} \tag{5.20}$$

and that $f \cdot \text{Re}_{D_h}$ (or C) increases almost proportionally with B . This correlation is illustrated in Fig. 5.4 for the duct shapes documented in Table 5.2.

5.3 HEAT TRANSFER IN FULLY DEVELOPED FLOW

5.3.1 Mean Temperature

Consider the stream shown in Fig. 5.5, and assume that the duct cross section A is not specified. According to the thermodynamics of open systems, the first law for the control volume of length dx is $q''p = \dot{m} dh/dx$, where h is the bulk enthalpy of the stream. When the fluid is an ideal gas ($dh = c_p dT_m$) or an incompressible liquid with negligible pressure changes ($dh = c dT_m$), the first law becomes

$$\frac{dT_m}{dx} = \frac{q''p}{\dot{m}c_p} \tag{5.21}$$

In heat transfer, the bulk temperature T_m is known as *mean temperature*. It is related to the bundle of ministreams of enthalpy ($\rho u c_p T dA$) that make up the bulk enthalpy stream (h) shown in the upper left corner of Fig. 5.5. From this observation it follows that the definition of T_m involves a u -weighted average of the temperature distribution over the cross section,

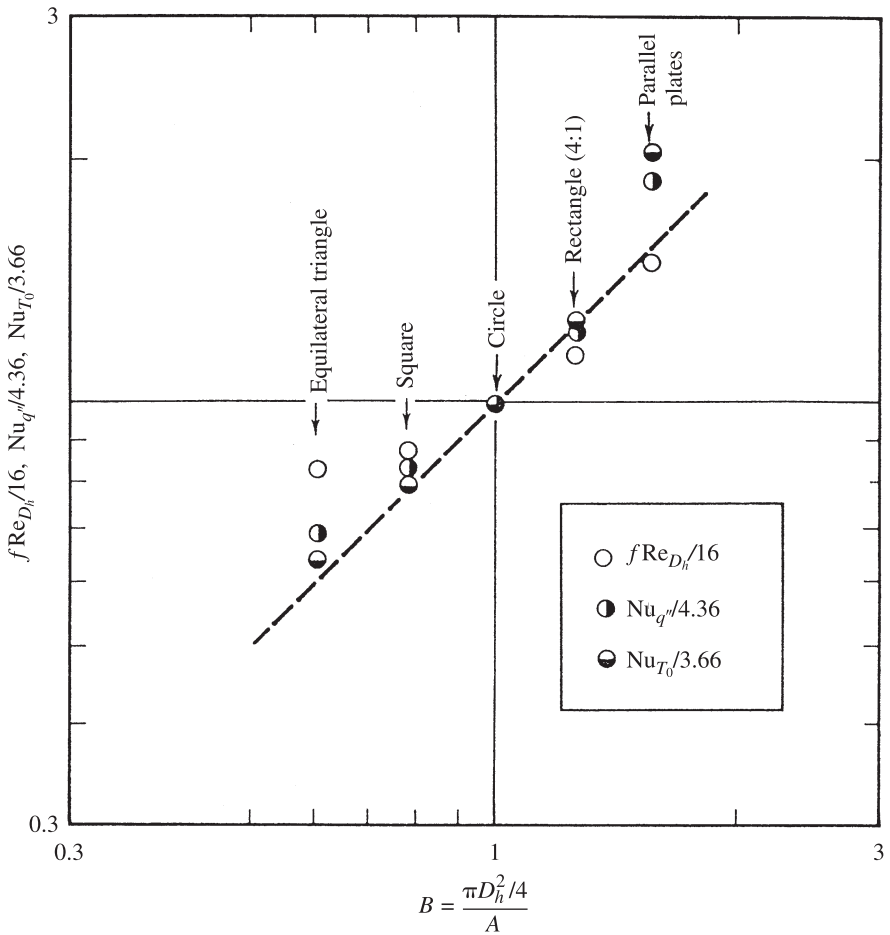


Figure 5.4 Effect of the cross-sectional shape (the number B) on fully developed friction and heat transfer in a straight duct. (From Bejan, 1995.)

$$T_m = \frac{1}{UA} \int_A uT \, dA \quad (5.22)$$

In internal convection, the heat transfer coefficient $h = q''/\Delta T$ is based on the difference between the wall temperature (T_0) and the mean temperature of the stream: namely, $h = q''/(T_0 - T_m)$.

5.3.2 Thermally Fully Developed Flow

By analogy with the developing velocity profile described in connection with Fig. 5.1, there is a thermal entrance region of length X_T . In this region the thermal boundary

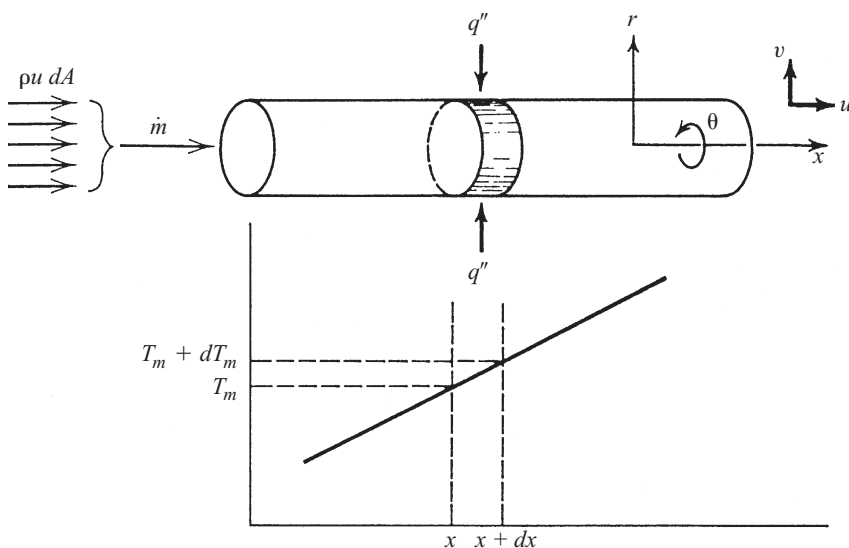


Figure 5.5 Nomenclature for energy conservation in a duct segment. (From Bejan, 1995.)

layers grow and effect changes in the distribution of temperature over the duct cross section. Estimates for X_T are given in Section 5.4.1. Downstream from $x \sim X_T$ the thermal boundary layers have merged and the shape of the temperature profile across the duct no longer varies. For a round tube of radius r_0 , this definition of a fully developed temperature profile is

$$\frac{T_0(x) - T(r, x)}{T_0(x) - T_m(x)} = \phi\left(\frac{r}{r_0}\right) \quad (5.23)$$

The function $\phi(r/r_0)$ represents the r -dependent shape (profile) that does not depend on the downstream position x .

The alternative to the definition in eq. (5.23) is the scale analysis of the same regime (Bejan, 1995), which shows that the heat transfer coefficient must be constant (x -independent) and of order k/D . The dimensionless version of this second definition is the statement that the Nusselt number is a constant of order 1:

$$\text{Nu} = \frac{hD}{k} = D \frac{\partial T / \partial r|_{r=r_0}}{T_0 - T_m} = O(1) \quad (5.24)$$

The second part of the definition refers to a tube of radius r_0 . The Nu values compiled in Tables 5.2 and 5.3 confirm the constancy and order of magnitude associated with thermally fully developed flow. The Nu values also exhibit the approximate proportionality with the B number that characterizes the shape of the cross section (Fig. 5.4). In Table 5.3, slug flow means that the velocity is distributed uniformly over the

cross section, $u = U$. Noteworthy are the Nu values for a round tube with uniform wall heat flux

$$\text{Nu} = \frac{48}{11} = 4.364 \quad \text{uniform wall heat flux}$$

and a round tube with isothermal wall

$$\text{Nu} = 3.66 \quad \text{isothermal wall}$$

5.4 HEAT TRANSFER IN DEVELOPING FLOW

5.4.1 Thermal Entrance Region

The heat transfer results listed in Tables 5.2 and 5.3 apply to laminar flow regions where the velocity and temperature profiles are fully developed. They are valid in the downstream section x , where $x > \max(X, X_T)$. The flow development length X is given by eq. (5.2). The thermal length X_T is determined from a similar scale analysis by estimating the distance where the thermal boundary layers merge, as shown in Fig. 5.6. When $\text{Pr} \ll 1$, the thermal boundary layers are thicker than the velocity boundary layers, and consequently, $X_T \ll X$. The Prandtl number Pr is the ratio of the molecular momentum and thermal diffusivities, ν/α . When $\text{Pr} \gg 1$, the thermal boundary layers are thinner, and X_T is considerably greater than X . The scale analysis of this problem shows that for both $\text{Pr} \ll 1$ and $\text{Pr} \gg 1$, the relationship between X_T and X is (Bejan, 1995)

$$\frac{X_T}{X} \approx \text{Pr} \quad (5.25)$$

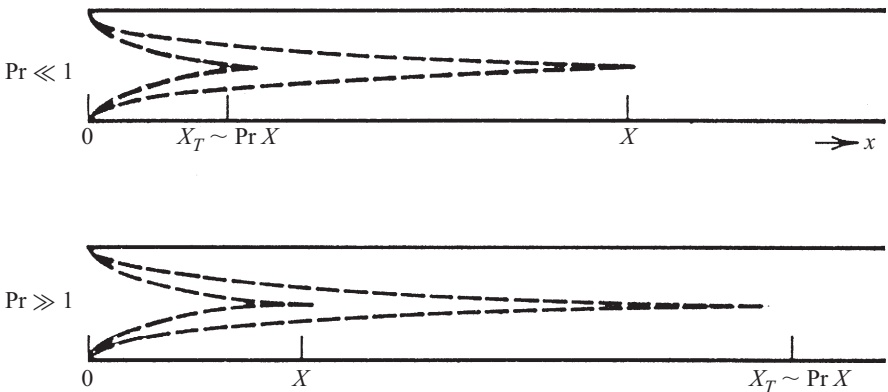


Figure 5.6 Prandtl number effect on the flow entrance length X and the thermal entrance length X_T . (From Bejan, 1995.)

Equations (5.25) and (5.2) yield the scale

$$X_T \approx 10^{-2} \text{Pr} \cdot D_h \cdot \text{Re}_{D_h} \tag{5.26}$$

which is valid over the entire Pr range.

5.4.2 Thermally Developing Hagen–Poiseuille Flow

When $\text{Pr} \gg 1$, there is a significant length of the duct ($X < x < X_T$) over which the velocity profile is fully developed, whereas the temperature profile is not. If the x -independent velocity profile of Hagen–Poiseuille flow is assumed, it is possible to solve the energy conservation equation and determine, as an infinite series, the temperature field (Graetz, 1883). The $\text{Pr} = \infty$ curve in Fig. 5.7 shows the main features of the Graetz solution for heat transfer in the entrance region of a round tube with an isothermal wall (T_0). The Reynolds number $\text{Re}_D = UD/\nu$ is based on the tube diameter D and the mean velocity U . The bulk dimensionless temperature of the stream (θ_m^*), the local Nusselt number (Nu_x), and the averaged Nusselt number (Nu_{0-x}) are defined by

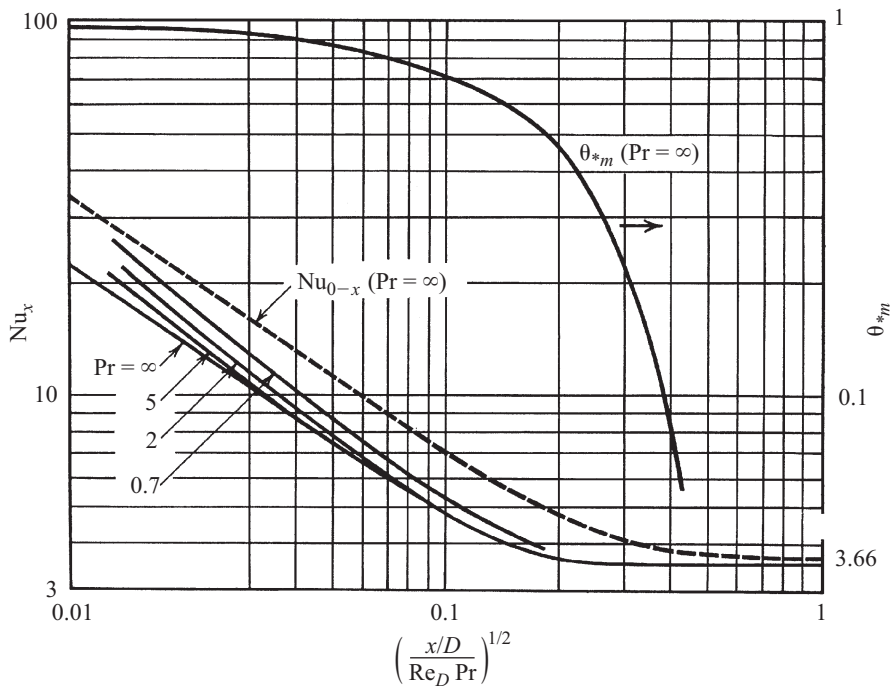


Figure 5.7 Heat transfer in the entrance region of a round tube with isothermal wall. (From Bejan, 1995; drawn based on data from Shah and London, 1978, and Hornbeck, 1965.)

$$\theta_m^* = \frac{T_m - T_0}{T_{in} - T_0} \quad (5.27)$$

$$\text{Nu}_x = \frac{q_x'' D}{k(T_0 - T_m)} \quad (5.28)$$

$$\text{Nu}_{0-x} = \frac{q_{0-x}'' D}{k \Delta T_m} \quad (5.29)$$

In these expressions, $T_m(x)$ is the local mean temperature, T_{in} the stream inlet temperature, q_x'' the local wall heat flux, and q_{0-x}'' the heat flux averaged from $x = 0$ to x , and ΔT_m the logarithmic mean temperature difference,

$$\Delta T_m = \frac{[T_0 - T_{in}(x)] - (T_0 - T_m)}{\ln [T_0 - T_m(x)/(T_0 - T_{in})]} \quad (5.30)$$

The dimensionless longitudinal position plotted on the abscissa is also known as x_* :

$$x_* = \frac{x/D}{\text{Re}_D \cdot \text{Pr}} \quad (5.31)$$

This group, and the fact that the knees of the Nu curves occur at $x_*^{1/2} \approx 10^{-1}$, support the X_T estimate anticipated by eq. (5.26).

The following analytical expressions are recommended by a simplified alternative to Graetz's series solution (L  v  que, 1928; Drew, 1931). The relationships for the $\text{Pr} = \infty$ curves shown in Fig. 5.7 are (Shah and London, 1978)

$$\text{Nu}_x = \begin{cases} 1.077x_*^{-1/3} - 0.70 & x_* \leq 0.01 \\ 3.657 + 6.874(10^3 x_*)^{-0.488} e^{-57.2x_*} & x_* > 0.01 \end{cases} \quad (5.32)$$

$$\text{Nu}_{0-x} = \begin{cases} 1.615x_*^{-1/3} - 0.70 & x_* \leq 0.005 \\ 1.615x_*^{-1/3} - 0.20 & 0.005 < x_* < 0.03 \\ 3.657 + 0.0499/x_* & x_* > 0.03 \end{cases} \quad (5.33)$$

The thermally developing Hagen–Poiseuille flow in a round tube with uniform heat flux q'' can be analyzed by applying Graetz's method (the $\text{Pr} = \infty$ curves in Fig. 5.8). The results for the local and overall Nusselt numbers are represented within 3% by the equations (see also Shah and London, 1978)

$$\text{Nu}_{x_*} = \begin{cases} 3.302x_*^{-1/3} - 1.00 & x_* \leq 0.00005 \\ 1.302x_*^{-1/3} - 0.50 & 0.00005 < x_* \leq 0.0015 \\ 4.364 + 8.68(10^3 x_*)^{-0.506} e^{-41x_*} & x_* > 0.001 \end{cases} \quad (5.34)$$

$$\text{Nu}_{0-x} = \begin{cases} 1.953x_*^{-1/3} & x_* \leq 0.03 \\ 4.364 + 0.0722/x_* & x_* > 0.03 \end{cases} \quad (5.35)$$

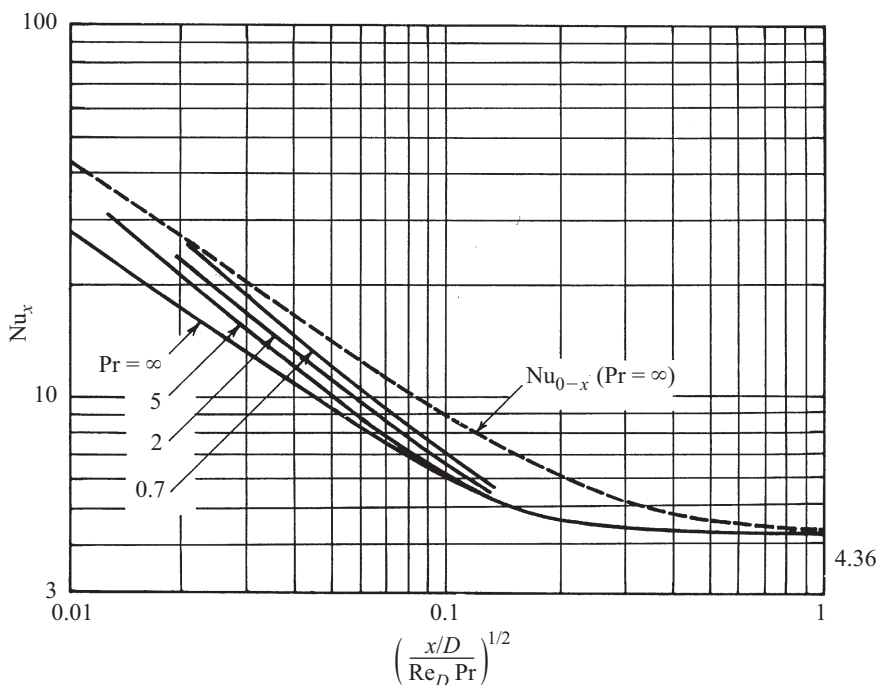


Figure 5.8 Heat transfer in the entrance region of a round tube with uniform heat flux. (From Bejan, 1995; drawn based on data from Shah and London, 1978, and Hornbeck, 1965.)

where

$$\text{Nu}_{x_*} = q'' \frac{D}{k [T_0(x) - T_m(x)]}$$

$$\text{Nu}_{0-x} = q'' \frac{D}{k \Delta T_{\text{avg}}}$$

with

$$\Delta T_{\text{avg}} = \left[\frac{1}{x} \int_0^x \frac{dx}{T_0(x) - T_m(x)} \right]^{-1} \quad (5.36)$$

Analogous results are available for the heat transfer to thermally developing Hagen–Poiseuille flow in ducts with other cross-sectional shapes. The Nusselt numbers for a parallel-plate channel are shown in Fig. 5.9. The curves for a channel with isothermal surfaces are approximated by (Shah and London, 1978)

$$\text{Nu}_{0-x} = \begin{cases} 1.233x_*^{-1/3} + 0.40 & x_* \leq 0.001 \\ 7.541 + 6.874(10^3 x_*)^{-0.488} e^{-245x_*} & x_* > 0.001 \end{cases} \quad (5.37)$$

$$\text{Nu}_{0-x} = \begin{cases} 1.849x_*^{-1/3} & x_* \leq 0.0005 \\ 1.849x_*^{-1/3} + 0.60 & 0.0005 < x_* \leq 0.006 \\ 7.541 + 0.0235/x_* & x_* > 0.006 \end{cases} \quad (5.38)$$

If the plate-to-plate spacing is D , the Nusselt numbers are defined as

$$\text{Nu}_x = \frac{q''(x)D_h}{k[T_0 - T_m(x)]}$$

$$\text{Nu}_{0-x} = \frac{q''_{0-x}D_h}{k\Delta T_{lm}}$$

where $D_h = 2D$ and ΔT_{lm} is given by eq. (5.30).

The thermal entrance region of the parallel-plate channel with uniform heat flux and Hagen–Poiseuille flow is characterized by (Shah and London, 1978)

$$\text{Nu}_x = \begin{cases} 1.490x_*^{-1/3} & x_* \leq 0.0002 \\ 1.490x_*^{-1/3} - 0.40 & 0.0002 < x_* \leq 0.001 \\ 8.235 + 8.68(10^3x_*)^{0.506}e^{-164x_*} & x_* > 0.001 \end{cases} \quad (5.39)$$

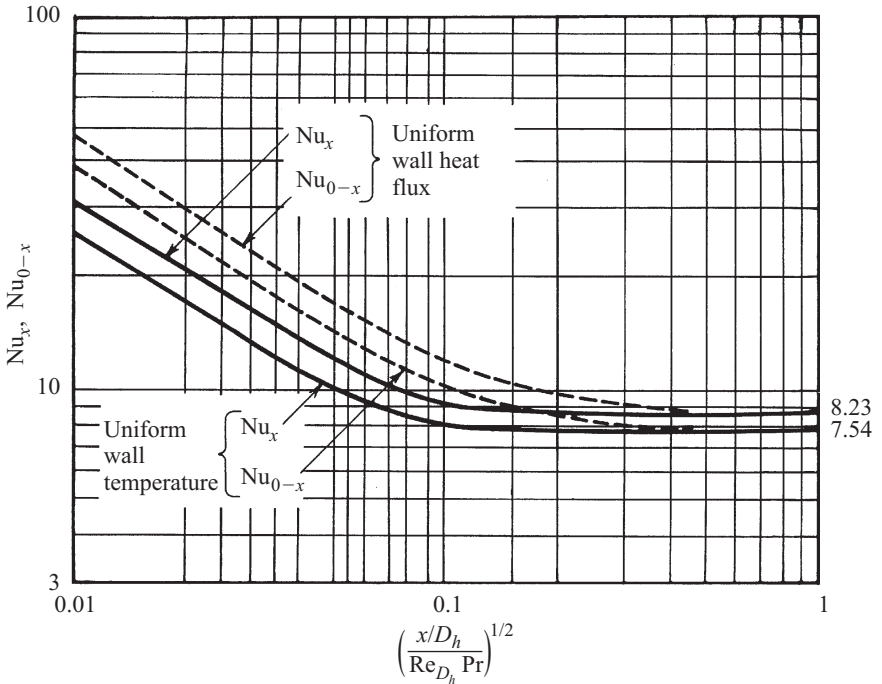


Figure 5.9 Heat transfer in the thermal entrance region of a parallel-plate channel with Hagen–Poiseuille flow. (From Bejan, 1995; drawn based on data from Shah and London, 1978.)

$$\text{Nu}_{0-x} = \begin{cases} 2.236x_*^{-1/3} & x_* \leq 0.001 \\ 2.236x_*^{-1/3} + 0.90 & 0.001 < x_* \leq 0.01 \\ 8.235 + 0.0364/x_* & x_* \geq 0.01 \end{cases} \quad (5.40)$$

The Nusselt number definitions are

$$\text{Nu}_x = \frac{q'' D_h}{k [T_0(x) - T_m(x)]}$$

$$\text{Nu}_{0-x} = \frac{q'' D_h}{k \Delta T_{\text{avg}}}$$

where ΔT_{avg} is furnished by eq. (5.36). It is worth repeating that x_* represents the dimensionless longitudinal coordinate in the thermal entrance region, eq. (5.31), which in the case of the parallel-plate channel becomes

$$x_* = \frac{x/D_h}{\text{Re}_{Dh} \cdot \text{Pr}}$$

All of the results compiled in this section hold in the limit $\text{Pr} \rightarrow \infty$.

5.4.3 Thermally and Hydraulically Developing Flow

When the Prandtl number is not much greater than 1, especially when X_T and X are comparable, the temperature and velocity profiles develop together, at the same longitudinal location x from the duct entrance. This is the most general case, and heat transfer results for many duct geometries have been developed numerically by a number of investigators. Their work is reviewed by Shah and London (1978). Here, a few leading examples of analytical correlations of the numerical data are shown.

Figure 5.7 shows a sample of the finite-Pr data available for a round tube with an isothermal wall. The recommended analytical expressions for the local (Shah and Bhatti, 1987) and overall (Stephan, 1959) Nusselt numbers in the range $0.1 \leq \text{Pr} \leq 1000$ in parallel-plate channels are

$$\text{Nu}_x = 7.55 + \frac{0.024x_*^{-1.14}(0.0179\text{Pr}^{0.17}x_*^{-0.64} - 0.14)}{(1 + 0.0358\text{Pr}^{0.17}x_*^{-0.64})^2} \quad (5.41)$$

$$\text{Nu}_{0-x} = 7.55 + \frac{0.024x_*^{-1.14}}{1 + 0.0358\text{Pr}^{0.17}x_*^{-0.64}} \quad (5.42)$$

The pressure drop over the hydrodynamically developing length x , or $\Delta P = P(0) - P(x)$, can be calculated using (Shah and London, 1978)

$$\frac{\Delta P}{\frac{1}{2}\rho U^2} = 13.74(x_+)^{1/2} + \frac{1.25 + 64x_+ - 13.74(x_+)^{1/2}}{1 + 0.00021(x_+)^{-2}} \quad (5.43)$$

On the right-hand side, x_+ is the dimensionless coordinate for the hydrodynamic entrance region,

$$x_+ = \frac{x/D}{\text{Re}_D} \quad (5.44)$$

which also appears on the abscissa of Fig. 5.3. Note the difference between X_+ and x_* . Equation (5.43) can be used instead of the $(C_f)_{0-x} \cdot \text{Re}_D$ curve shown in Fig. 5.3 by noting the force balance

$$\Delta P \frac{\pi D^2}{4} = \tau_{0-x} \pi D x$$

or

$$\frac{\Delta P}{\frac{1}{2} \rho U^2} = 4x_+ C_f \bigg|_{0-x} \cdot \text{Re}_D \quad (5.45)$$

Figures 5.8 and 5.9 show, respectively, several finite-Pr solutions for the local Nusselt number in the entrance region of a tube with uniform heat flux. A closed-form expression that covers both the entrance and fully developed regions was developed by Churchill and Ozoe (1973):

$$\begin{aligned} & \frac{\text{Nu}_x}{4.364 [1 + (\text{Gz}/29.6)^2]^{1/6}} \\ &= \left\{ 1 + \left[\frac{\text{Gz}/19.04}{[1 + (\text{Pr}/0.0207)^{2/3}]^{1/2} [1 + (\text{Gz}/29.6)^2]^{1/3}} \right]^{3/2} \right\}^{1/3} \end{aligned} \quad (5.46)$$

where

$$\text{Nu}_x = \frac{q'' D}{k [T_0(x) - T_m(x)]}$$

The Graetz number is defined as

$$\text{Gz} = \frac{\pi}{4x_*} = \frac{\pi \text{Re}_D \cdot \text{Pr}}{4 x/D}$$

Equation (5.46) agrees within 5% with numerical data for $\text{Pr} = 0.7$ and $\text{Pr} = 10$ and has the correct asymptotic behavior for large and small Gz and Pr .

5.5 OPTIMAL CHANNEL SIZES FOR LAMINAR FLOW

The geometry of the boundary layers in the entrance region of a duct (Fig. 5.6) brings with it a fundamental property of great importance in numerous and diverse heat

transfer applications. When the objective is to use many channels in parallel, for the purpose of cooling or heating a specified volume that is penetrated by these channels, there is an optimal channel geometry such that the heat transfer rate integrated over the volume is maximal. Alternatively, because the volume is fixed, use of a bundle of channels of optimal sizes means that the heat transfer density (the average heat transfer per unit volume) is maximal.

In brief, the optimal channel size (D , in Fig. 5.10 must be such that the thermal boundary layers merge just as the streams leave the channels. The streamwise length of the given volume (L) matches the scale of X_T . In this case most of the space occupied by fluid is busy transferring heat between the solid walls and the fluid spaces. This geometric optimization principle is widely applicable, as this brief review shows. The reason is that every duct begins with an entrance region, and from the *constructal* point of view of deducing flow architecture by maximizing global performance subject to global constraints (such as the volume) (Bejan, 2000), the most useful portion of the duct is its entrance length. This principle was first stated for bundles of vertical channels with natural convection (Bejan, 1984; Bar-Cohen and Rohsenow, 1984). It was extended to bundles of channels with forced convection by Bejan and Sciubba (1992). It continues to generate an expanding class of geometric results, which was

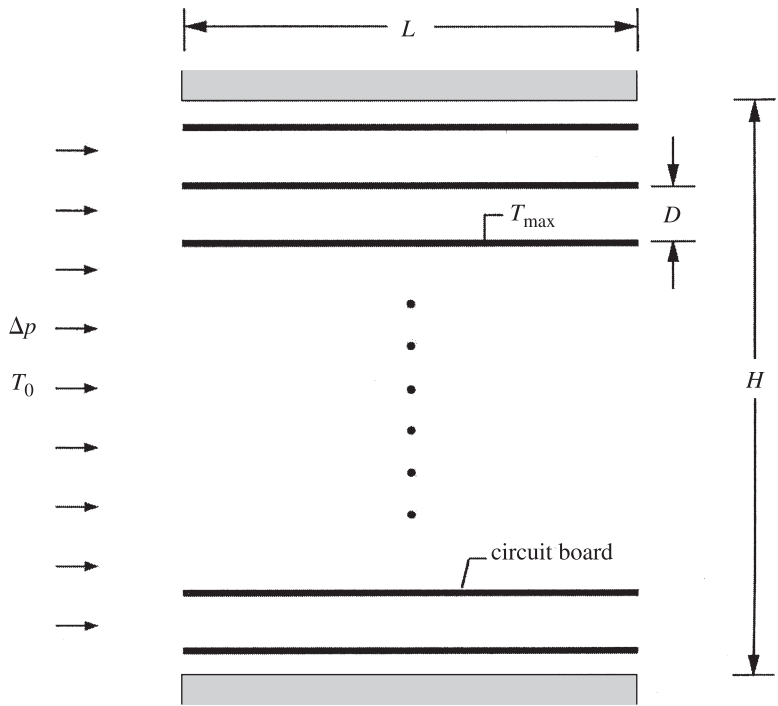


Figure 5.10 Two-dimensional volume that generates heat and is cooled by forced convection. (From Bejan, 2000.)

reviewed in Kim and Lee (1996) and Bejan (2000). In this section some of the forced convection results are reviewed.

The opportunity for optimizing internal channel geometry becomes evident if Fig. 5.10 is regarded as a single-stream heat exchanger intended for cooling electronics. The global thermal conductance of the electronics is the ratio between the total rate of heat generation in the package (q) and the maximum excess temperature registered in the hot spots ($T_{\max} - T_0$). The entrance temperature of the coolant is T_0 . Designs with more components and circuitry installed in a given volume are desirable as is a larger q . This can be accommodated by increasing the ceiling temperature T_{\max} (usually limited by the design of electronics) and by increasing the conductance ratio $q/(T_{\max} - T_{\min})$. The latter puts the design on a course of geometry optimization, because the conductance is dictated by the flow geometry. The degree of freedom in the design is the channel size D , on the number of channels, $n = H/D$.

The existence of an optimal geometry is discovered by designing the stack of Fig. 5.10 in its two extremes: a few large spacings, and many small spacings. When D is large, the total heat transfer surface is small, the global thermal resistance is high, and consequently, each heat-generating surface is overheated. When D is small, the coolant cannot flow through the package. The imposed heat generation rate can be removed only by allowing the entire volume to overheat. An optimal D exists in between and is located by intersecting the large D and small D asymptotes.

For the two-dimensional parallel-plate stack of Fig. 5.10, where $\text{Pr} \geq 1$ and the pressure difference ΔP is fixed, the optimal spacing is (Bejan and Sciubba, 1992)

$$\frac{D_{\text{opt}}}{L} \simeq 2.7\text{Be}^{-1/4} \quad (5.47)$$

where

$$\text{Be} = \Delta PL^2/\mu\alpha$$

is the specified pressure drop number, which Bhattacharjee and Grosshandler (1988) and Petrescu (1994) have termed the Bejan number. Equation (5.47) underestimates (by only 12%) the value obtained by optimizing the stack geometry numerically. Furthermore, eq. (5.47) is robust, because it holds for both uniform-flux and isothermal plates. Equation (5.47) holds even when the plate thickness is not negligible relative to the plate-to-plate spacing (Mereu et al., 1993). The maximized thermal conductance $q_{\max}/(T_{\max} - T_0)$, or maximized heat transfer rate per unit volume that corresponds to eq. (5.47), is

$$\frac{q_{\max}}{HLW} \simeq 0.60 \frac{k}{L^2} (T_{\max} - T_0) \text{Be}^{1/2} \quad (5.48)$$

where W is the volume dimension in the direction perpendicular to the plane of Fig. 5.10. Equation (5.48) overestimates (by 20%) the heat transfer density maximized numerically (Bejan and Sciubba, 1992).

The pressure drop number $\text{Be} = \Delta PL^2/\mu\alpha$ is important, because in the field of internal forced convection it plays the same role that the Rayleigh number plays

for internal natural convection (Petrescu, 1994). Specifically, the equivalent of eq. (5.47) for natural convection through a H -tall stack of vertical D -wide channels with a $\text{Pr} \geq 1$ fluid is

$$\frac{D_{\text{opt}}}{H} \simeq 2.3\text{Ra}^{-1/4} \quad (5.49)$$

where the Rayleigh number is specified (Bejan, 1984):

$$\text{Ra} = \frac{g\beta H^3 (T_{\text{max}} - T_0)}{\alpha \nu}$$

Equations (5.47) and (5.49) make the Be–Ra analogy evident. The Rayleigh number is the dimensionless group that indicates the slenderness of vertical thermal boundary layers in laminar natural convection,

$$\text{Ra} \approx \left(\frac{H}{\delta_T} \right)^4$$

where H is the wall height and δ_T is the thermal boundary layer thickness.

Campo and Li (1996) considered the related problem where the parallel-plate channels are heated asymmetrically: for example, with adiabatic or nearly adiabatic regions. Campo (1999) used the intersection of asymptotes method in the optimization of the stack of Fig. 5.10, where the plates are with uniform heat flux. His results confirmed the correctness and robustness of the initial result of eq. (5.47). The geometric optimization of round tubes with steady and periodic flows and $\text{Pr} \gg 1$ fluids was performed by Rocha and Bejan (2001). Related studies are reviewed in Kim and Lee (1996).

The optimal internal spacings belong to the specified volume as a whole, with its purpose and constraints, not to the individual channel. The robustness of this conclusion becomes clear when we look at other elemental shapes for which optimal spacings have been determined. A volume heated by an array of staggered plates in forced convection (Fig. 5.11a) is characterized by an internal spacing D that scales with the swept length of the volume (Fowler et al., 1997):

$$\frac{D_{\text{opt}}}{L} \simeq 5.4\text{Pr}^{-1/4} \left(\text{Re}_L \frac{L}{b} \right)^{-1/2} \quad (5.50)$$

In this relation the Reynolds number is $\text{Re}_L = U_\infty L/\nu$. The range in which this correlation was developed based on numerical simulations and laboratory experiments is $\text{Pr} = 0.72$, $10^2 \leq \text{Re}_L \leq 10^4$, and $0.5 \leq Nb/L \leq 1.3$, where N is the number of plate surfaces that face one elemental channel; that is, $N = 4$ in Fig. 5.11a.

Similarly, when the elements are cylinders in crossflow as in Fig. 5.11b, the optimal spacing S is influenced the most by the longitudinal dimension of the volume. The optimal spacing was determined based on the method of intersecting the asymptotes

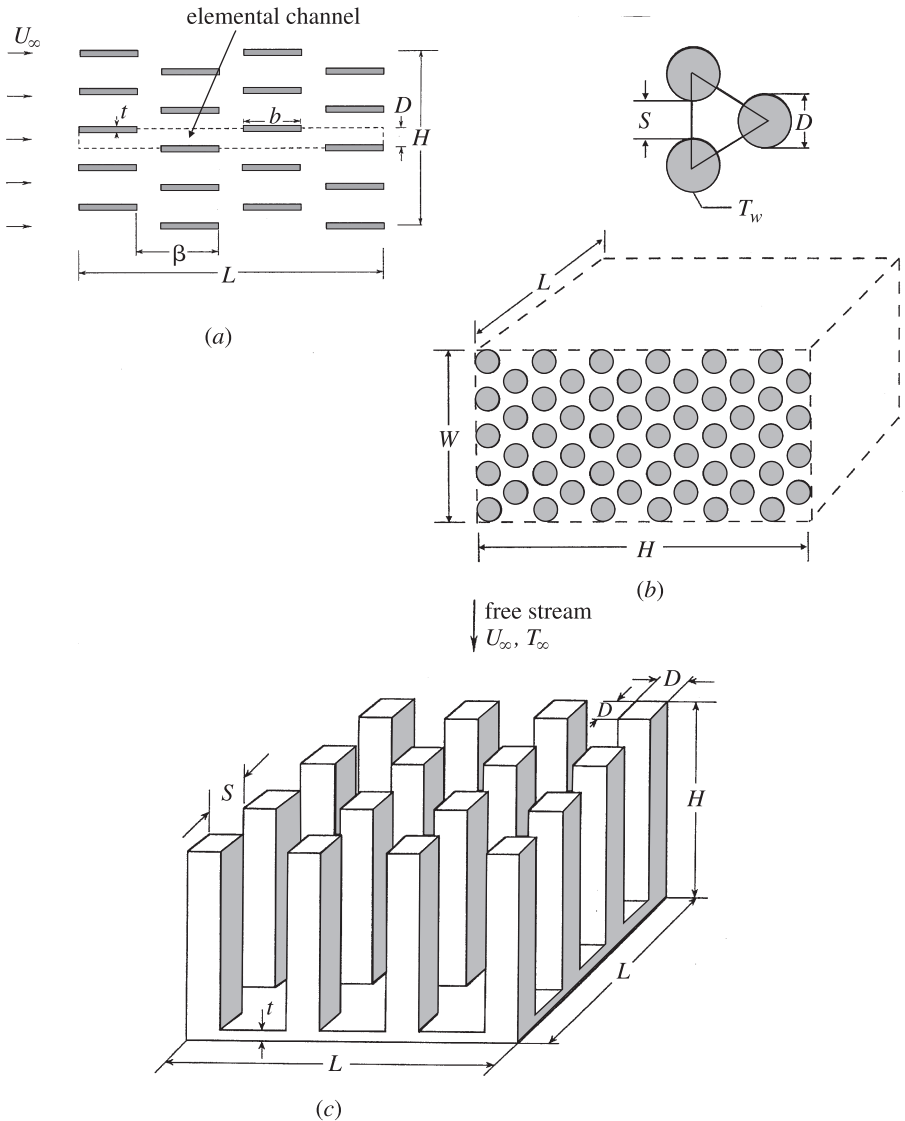


Figure 5.11 Forced-convection channels for cooling a heat-generating volume: (a) array of staggered plates; (b) array of horizontal cylinders; (c) square pins with impinging flow. (From Bejan, 2000.)

(Stanescu et al., 1996; Bejan, 2000). The asymptotes were derived from the large volume of empirical data accumulated in the literature for single cylinders in crossflow (the large- S limit) and for arrays with many rows of cylinders (the small- S limit). In the range $10^4 \leq \tilde{P} \leq 10^8$, $25 \leq H/D \leq 200$, and $0.72 \leq \text{Pr} \leq 50$, the optimal spacing is correlated to within 5.6% by

$$\frac{S_{\text{opt}}}{D} \simeq 1.59 \frac{(H/D)^{0.52}}{\tilde{P}^{0.13} \cdot \text{Pr}^{0.24}} \quad (5.51)$$

where \tilde{P} is an alternative dimensionless pressure drop number based on D : namely, $\tilde{P} = \Delta P D^2 / \mu v$. When the free stream velocity U is specified (instead of ΔP), eq. (5.51) may be transformed by noting that with ΔP approximately equal to $\Delta P \approx \rho U_\infty^2 / 2$:

$$\frac{S_{\text{opt}}}{D} \simeq 1.70 \frac{(H/D)^{0.52}}{\text{Re}_D^{0.26} \cdot \text{Pr}^{0.24}} \quad (5.52)$$

This correlation is valid in the range $140 \leq \text{Re}_D \leq 14,000$, where $\text{Re}_D = UD/v$. The minimized global thermal resistance that corresponds to this optimal spacing is

$$\frac{T_D - T_\infty}{qD/kLW} \simeq \frac{4.5}{\text{Re}_D^{0.90} \cdot \text{Pr}^{0.64}} \quad (5.53)$$

where T_D is the cylinder temperature and q is the total rate of heat transfer from the HLW volume to the coolant (T). If the cylinders are arranged such that their centers form equilateral triangles as in Fig. 5.11*b*, the total number of cylinders present in the bundle is $HW / [(S + D)^2 \cos 30^\circ]$. This number and the contact area based on it may be used to deduce from eq. (5.53) the volume-averaged heat transfer coefficient between the array and the stream.

Fundamentally, these results show that there always is an optimal spacing for cylinders (or tubes) in crossflow heat exchangers when compactness is an objective. This was demonstrated numerically by Matos et al. (2001), who optimized numerically assemblies of staggered round and elliptic tubes in crossflow. Matos et al. (2001) also found that the elliptic tubes perform better relative to round tubes: The heat transfer density is larger by 13%, and the overall flow resistance is smaller by 25%.

Optimal spacings emerge also when the flow is three-dimensional, as in an array of pin fins with impinging flow (Fig. 5.11*c*). The flow is initially aligned with the fins, and later makes a 90° turn to sweep along the base plate and across the fins. The optimal spacings are correlated to within 16% by Ledezma et al. (1996):

$$\frac{S_{\text{opt}}}{L} \simeq 0.81 \text{Pr}^{-0.25} \cdot \text{Re}_L^{-0.32} \quad (5.54)$$

which is valid in the range $0.06 < D/L \leq 0.14$, $0.28 \leq H/L \leq 0.56$, $0.72 \leq \text{Pr} \leq 7$, $10 \leq \text{Re}_D \leq 700$, and $90 \leq \text{Re}_L \leq 6000$. Note that the spacing S_{opt} is controlled by the linear dimension of the volume L . The corresponding minimum global thermal resistance between the array and the coolant is given within 20% by

$$\frac{T_D - T_\infty}{q/kH} \simeq \frac{(D/L)^{0.31}}{1.57 \text{Re}_L^{0.69} \cdot \text{Pr}^{0.45}} \quad (5.55)$$

The global resistance refers to the entire volume occupied by the array (HL^2) and is the ratio between the fin-coolant temperature difference ($T_D - T$) and the total heat

current q generated by the HL^2 volume. In the square arrangement of Fig. 5.11c the total number of fins is $L^2/(S+D)^2$. Application of the same geometric optimization method to ducts with turbulent flow is reviewed in Section 5.8.

5.6 TURBULENT DUCT FLOW

5.6.1 Time-Averaged Equations

The analysis of turbulent duct flow and heat transfer is traditionally presented in terms of time-averaged quantities, which are denoted by a bar superscript. For example, the longitudinal velocity is decomposed as $u(\mathbf{r}, t) = \bar{u}(\mathbf{r}) + u'(\mathbf{r}, t)$, where \bar{u} is the time-averaged velocity and u' is the fluctuation, or the time-dependent difference between u and \bar{u} . In the cylindrical coordinates (r, x) of the round tube shown in Fig. 5.12, the time-averaged equations for the conservation of mass, momentum, and energy are

$$\frac{\partial \bar{u}}{\partial x} + \frac{1}{r} \frac{\partial}{\partial r}(r\bar{v}) = 0 \quad (5.56)$$

$$\bar{u} \frac{\partial \bar{u}}{\partial x} + \bar{v} \frac{\partial \bar{u}}{\partial r} = -\frac{1}{\rho} \frac{d\bar{P}}{dx} + \frac{1}{r} \frac{\partial}{\partial r} \left[r(\nu + \epsilon_M) \frac{\partial \bar{T}}{\partial r} \right] \quad (5.57)$$

$$\bar{u} \frac{\partial \bar{T}}{\partial x} + \bar{v} \frac{\partial \bar{T}}{\partial r} = \frac{1}{r} \frac{\partial}{\partial r} \left[r(\alpha + \epsilon_H) \frac{\partial \bar{T}}{\partial r} \right] \quad (5.58)$$

These equations have been simplified based on the observation that the duct is a slender flow region; the absence of second derivatives in the longitudinal direction may be noted. Note also that $d\bar{P}/dx$, which means that $\bar{P}(r, x) \simeq \bar{P}(x)$. The momentum eddy diffusivity ϵ_M and the thermal eddy diffusivity ϵ_H are defined by

$$-\overline{\rho u'v'} = \rho \epsilon_M \frac{\partial \bar{u}}{\partial r} \quad \text{and} \quad -\rho c_p \overline{v'T'} = \rho c_p \epsilon_H \frac{\partial \bar{T}}{\partial r} \quad (5.59)$$

where u' , v' , and T' are the fluctuating parts of the longitudinal velocity, radial velocity, and local temperature. The eddy diffusivities augment significantly the transport

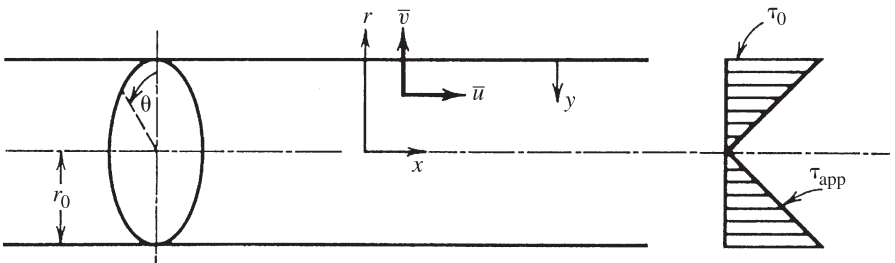


Figure 5.12 Distribution of apparent shear stress in fully developed turbulent flow.

effect that would occur in the presence of molecular diffusion alone, that is, based on ν for momentum and α for thermal diffusion.

5.6.2 Fully Developed Flow

The entrance region for the development of the longitudinal velocity profile and the temperature profile is about 10 times the tube diameter,

$$\frac{X}{D} \simeq 10 \simeq \frac{X_T}{D} \quad (5.60)$$

This criterion is particularly valid for fluids with Pr values of order 1 (air and water). For ducts with other cross sections, D is the smaller dimension of the cross section. The lengths X and X_T are considerably shorter than their laminar-flow counterparts when $\text{Re}_D \geq 2000$. Downstream of $x = (X, X_T)$ the flow is fully developed, and $\bar{v} = 0$ and $\partial \bar{u} / \partial x = 0$. The left side of eq. (5.57) is zero. For the quantity in brackets, the apparent (or total) shear stress notation is employed:

$$\tau_{\text{app}} = \rho(\nu + \epsilon_M) \frac{\partial \bar{u}}{\partial y} \quad (5.61)$$

where y is measured away from the wall, $y = r_0 - r$, as indicated in Fig. 5.12. The two contributions to τ_{app} , $\rho\nu\partial\bar{u}/\partial y$ and $\rho\epsilon_M\partial\bar{u}/\partial y$, are the molecular shear stress and the eddy shear stress, respectively. Note that $\tau_{\text{app}} = 0$ at $y = 0$. The momentum equation, eq. (5.57), reduces to

$$\frac{d\bar{P}}{dx} = \frac{1}{r} \frac{\partial}{\partial r} (r\tau_{\text{app}}) \quad (5.62)$$

where both sides of the equation equal a constant. By integrating eq. (5.62) from the wall to the distance y in the fluid, and by using the force balance of eq. (5.12), one can show that τ_{app} decreases linearly from τ_0 at the wall to zero on the centerline,

$$\tau_{\text{app}} = \tau_0 \left(1 - \frac{y}{r_0} \right)$$

Sufficiently close to the wall, where $y \ll r_0$, the apparent shear stress is nearly constant, $\tau_{\text{app}} \simeq \tau_0$. The mixing-length analysis that produced the law of the wall for the turbulent boundary layer applies near the tube wall. Measurements confirm that the time-averaged velocity profile fits the law of the wall,

$$u^+ = 2.5 \ln y^+ + 5.5 \quad (5.63)$$

where 2.5 and 5.5 are curve-fitting constants, and

$$u^+ = \frac{\bar{u}}{u_*} \quad y^+ = \frac{u_* y}{\nu} \quad u_* = \left(\frac{\tau_0}{\rho} \right)^{1/2} \quad (5.64)$$

The group u_* is known as the friction velocity. The major drawback of the τ_{app} approximation is that the velocity profile deduced from it, eq. (5.63), has a finite slope at the centerline. An empirical profile that has zero slope at the centerline and matches eq. (5.64) as $y^+ \rightarrow 0$ is that of Reichardt (1951):

$$u^+ = 2.5 \ln \left\{ \frac{3(1 + r/r_0)}{2[1 + 2(r/r_0)^2]} y^+ \right\} + 5.5 \quad (5.65)$$

The friction factor is defined by eq. (5.11) and is related to the friction velocity $(\tau_0/\rho)^{1/2}$:

$$\left(\frac{\tau_0}{\rho} \right)^{1/2} = U \left(\frac{f}{2} \right)^{1/2} \quad (5.66)$$

An analysis based on a velocity curve fit where, instead of eq. (5.63), u^+ is proportional to $(y^+)^{1/7}$ (Prandtl, 1969) leads to

$$f \simeq 0.078 \text{Re}_D^{-1/4} \quad (5.67)$$

where $\text{Re}_D = UD/\nu$ and $D = 2r_0$. Equation (5.67) agrees with measurements up to $\text{Re}_D = 8 \times 10^4$. An empirical relation that holds at higher Reynolds numbers in smooth tubes (Fig. 5.13) is

$$f \simeq 0.046 \text{Re}_D^{-1/5} \quad (2 \times 10^4 < \text{Re}_D < 10^6) \quad (5.68)$$

An alternative that has wider applicability is obtained by using the law of the wall, eq. (5.63), instead of Prandtl's $\frac{1}{7}$ power law, $u^+ \sim (y^+)^{1/7}$. The result is (Prandtl, 1969)

$$\frac{1}{f^{1/2}} = 1.737 \ln (\text{Re}_D f^{1/2}) - 0.396 \quad (5.69)$$

which agrees with measurements for Re_D values up to $O(10^6)$. The heat transfer literature refers to eq. (5.69) as the *Kármán–Nikuradse relation* (Kays and Perkins, 1973); this relation is displayed as the lowest curve in Fig. 5.13. This figure is known as the *Moody chart* (Moody, 1944). The laminar flow line in Fig. 5.13 is for a round tube. The figure shows that the friction factor in turbulent flow is considerably greater than that in laminar flow in the hypothetical case that the laminar regime can exist at such large Reynolds numbers.

For fully developed flow through ducts with cross sections other than round, the Kármán–Nikuradse relation of eq. (5.69) still holds if Re_D is replaced by the Reynolds number based on hydraulic diameter, Re_{D_h} . Note that for a duct of noncircular cross section, the time-averaged τ_0 is not uniform around the periphery of the cross section; hence, in the friction factor definition of eq. (5.11), τ_0 is the perimeter-averaged wall shear stress.

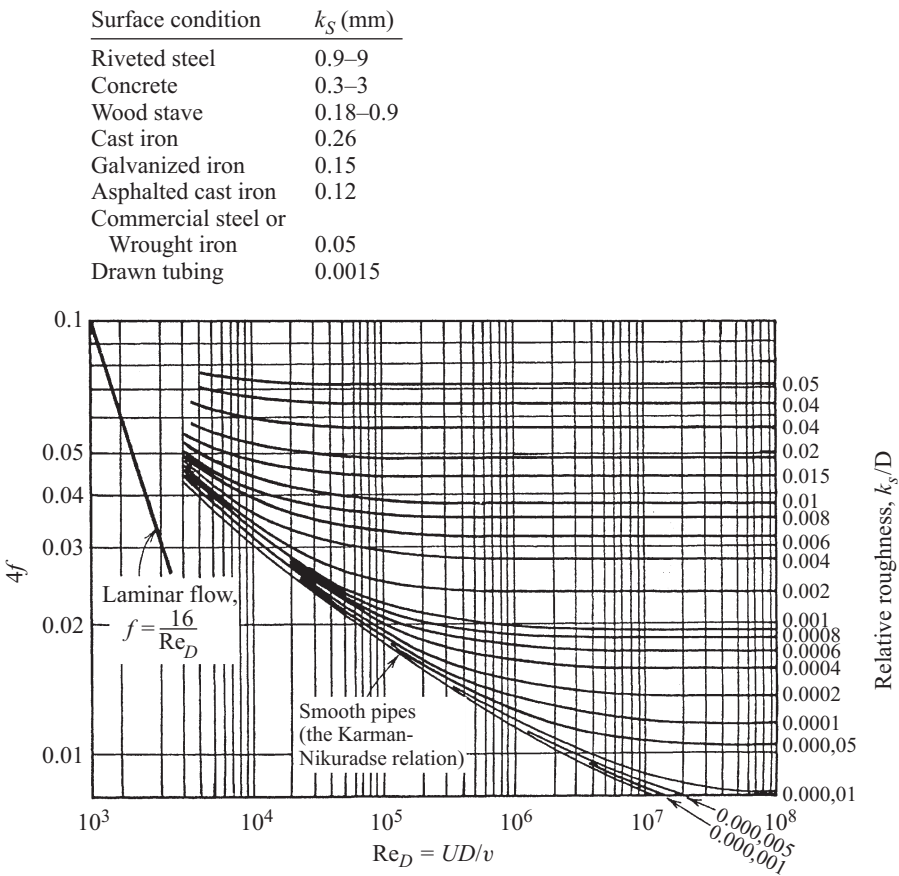


Figure 5.13 Friction factor for duct flow. (From Bejan, 1995; drawn after Moody, 1944.)

Figure 5.13 also documents the effect of wall roughness. It is found experimentally that the performance of commercial surfaces that do not feel rough to the touch departs from the performance of well-polished surfaces. This effect is due to the very small thickness acquired by the laminar sublayer in many applications [e.g., because $U_{y_{VSL}}/\nu$ is of order 10^2 (Bejan, 1995), where y_{VSL} is the thickness of the viscous sublayer]. In water flow through a pipe, with $U \approx 10\text{m/s}$ and $\nu \approx 0.01\text{cm}^2/\text{s}$, y_{VSL} is approximately 0.01 mm. Consequently, even slight imperfections of the surface may interfere with the natural formation of the laminar shear flow contact spots. If the surface irregularities are taller than y_{VSL} , they alone rule the friction process.

Nikuradse (1933) measured the effect of surface roughness on the friction factor by coating the inside surface of pipes with sand of a measured grain size glued as tightly as possible to the wall. If k_s is the grain size in Nikuradse’s sand roughness, the friction factor fully rough limit is the constant

$$f \simeq \left(1.74 \ln \frac{D}{k_s} + 2.28 \right)^{-2} \quad (5.70)$$

The fully rough limit is that regime where the roughness size exceeds the order of magnitude of what would have been the laminar sublayer in time-averaged turbulent flow over a smooth surface,

$$k_s^+ = \frac{k_s(\tau_0/\rho)^{1/2}}{\nu} \geq 10 \quad (5.71)$$

The roughness effect described by Nikuradse is illustrated by the upper curves in Fig. 5.13.

5.6.3 Heat Transfer in Fully Developed Flow

There are several empirical relationships for calculating the time-averaged coefficient for heat transfer between the duct surface and the fully developed flow, $h = q''/(T_0 - T_m)$. The analytical form of these relationships is based on exploiting the analogy between momentum and heat transfer by eddy rotation. One of the earliest examples is due to Prandtl in 1910 (Prandtl, 1969; Schlichting, 1960),

$$\text{St} = \frac{f/2}{\text{Pr}_t + (\bar{u}_1/U)(\text{Pr} - \text{Pr}_t)} \quad (5.72)$$

where St, Pr, and Pr_t are the Stanton number, Prandtl number, and turbulent Prandtl number,

$$\text{St} = \frac{h}{\rho c_p U} \quad \text{Pr} = \frac{\nu}{\alpha} \quad \text{Pr}_t = \frac{\epsilon_M}{\epsilon_H} \quad (5.73)$$

Equation (5.72) holds for $\text{Pr} \geq 0.5$, and if Pr_t is assumed to be 1, the factor \bar{u}_1/U is provided by the empirical correlation (Hoffmann, 1937)

$$\frac{\bar{u}_1}{U} \simeq 1.5 \text{Re}_{D_h}^{-1/8} \cdot \text{Pr}^{-1/6} \quad (5.74)$$

Better agreement with measurements is registered by Colburn's (1933) empirical correlation,

$$\text{St} \cdot \text{Pr}^{2/3} \simeq \frac{f}{2} \quad (5.75)$$

Equation (5.75) is analytically the same as the one derived purely theoretically for boundary layer flow (Bejan, 1995). Equation (5.75) holds for $\text{Pr} \geq 0.5$ and is to be used in conjunction with Fig. 5.13, which supplies the value of the friction factor f . It applies to ducts of various cross-sectional shapes, with wall surfaces having various degrees of roughness. In such cases D is replaced by D_h . In the special case of a pipe

with smooth internal surface, eqs. (5.75) and (5.68) can be combined to derive the Nusselt number relationship

$$\text{Nu}_D = \frac{hD}{k} = 0.023\text{Re}_D^{4/5} \cdot \text{Pr}^{1/3} \quad (5.76)$$

which holds in the range $2 \times 10^4 \leq \text{Re}_D \leq 10^6$. A popular version of this is a correlation due to Dittus and Boelter (1930),

$$\text{Nu}_D = 0.023\text{Re}_D^{4/5} \cdot \text{Pr}^n \quad (5.77)$$

which was developed for $0.7 \leq \text{Pr} \leq 120$, $2500 \leq \text{Re}_D \leq 1.24 \times 10^5$, and $L/D > 60$. The Prandtl number exponent is $n = 0.4$ when the fluid is being heated ($T_0 > T_m$), and $n = 0.3$ when the fluid is being cooled ($T_0 < T_m$). All of the physical properties needed for the calculation of Nu_D , Re_D , and Pr are to be evaluated at the bulk temperature T_m . The maximum deviation between experimental data and values predicted using eq. (5.77) is on the order of 40%.

For applications in which influence of temperature on properties is significant, the Sieder and Tate (1936) modification of eq. (5.76) is recommended:

$$\text{Nu}_D = 0.027\text{Re}_D^{4/5} \cdot \text{Pr}^{1/3} \left(\frac{\mu}{\mu_0} \right)^{0.14} \quad (5.78)$$

This correlation is valid for $0.7 \leq \text{Pr} \leq 16,700$ and $\text{Re}_D > 10^4$. The effect of temperature-dependent properties is taken into account by evaluating all the properties (except μ_0) at the mean temperature of the stream, T_m . The viscosity μ_0 is evaluated at the wall temperature $\mu_0 = \mu(T_0)$. Equations (5.76)–(5.78) can be used for ducts with constant temperature and constant heat flux.

More accurate correlations of this type were developed by Petukhov and Kirilov (1958) and Petukhov and Popov (1963); respectively:

$$\text{Nu}_D = \frac{(f/2)\text{Re}_D \cdot \text{Pr}}{1.07 + 900/\text{Re}_D - 0.63/(1 + 10\text{Pr}) + 12.7(f/2)^{1/2}(\text{Pr}^{2/3} - 1)} \quad (5.79a)$$

and

$$\text{Nu}_D = \frac{(f/2)\text{Re}_D \cdot \text{Pr}}{1.07 + 12.7(f/2)^{1/2}(\text{Pr}^{2/3} - 1)} \quad (5.79b)$$

for which f is supplied by Fig. 5.13. Additional information is provided by Petukhov (1970). Equation (5.79a) is accurate within 5% in the range $4000 \leq \text{Re}_D \leq 5 \times 10^6$ and $0.5 \leq \text{Pr} \leq 10^6$. Equation (5.79b) is an abbreviated version of eq. (5.79a) and was modified by Gnielinski (1976):

$$\text{Nu}_D = \frac{(f/2)(\text{Re}_D - 10^3)\text{Pr}}{1 + 12.7(f/2)^{1/2}(\text{Pr}^{2/3} - 1)} \quad (5.80)$$

which is accurate within $\pm 10\%$ in the range $0.5 \leq \text{Pr} \leq 10^6$ and $2300 \leq \text{Re}_D \leq 5 \times 10^6$. The Gnielinski correlation of eq. (5.80) can be used in both constant- q'' and constant- T_0 applications. Two simpler alternatives to eq. (5.80) are (Gnielinski, 1976)

$$\text{Nu}_D = 0.0214 (\text{Re}_D^{0.8} - 100) \text{Pr}^{0.4} \quad (5.81a)$$

valid in the range

$$0.5 \leq \text{Pr} \leq 1.5 \quad 10^4 \leq \text{Re}_D \leq 5 \times 10^6$$

and

$$\text{Nu}_D = 0.012 (\text{Re}_D^{0.87} - 280) \text{Pr}^{0.4} \quad (5.81b)$$

valid in the range

$$1.5 \leq \text{Pr} \leq 500 \quad 3 \times 10^3 \leq \text{Re}_D \leq 10^6$$

The preceding results refer to gases and liquids, that is, to the range $\text{Pr} \geq 0.5$. For liquid metals, the most accurate correlations are those of Notter and Sleicher (1972):

$$\text{Nu}_D = \begin{cases} 6.3 + 0.0167 \text{Re}_D^{0.85} \cdot \text{Pr}^{0.93} & q'' = \text{constant} \\ 4.8 + 0.0156 \text{Re}_D^{0.85} \cdot \text{Pr}^{0.93} & T_0 = \text{constant} \end{cases} \quad (5.82)$$

$$T_0 = \text{constant} \quad (5.83)$$

These are valid for $0.004 \leq \text{Pr} \leq 0.1$ and $10^4 \leq \text{Re}_D \leq 10^6$ and are based on both computational and experimental data. All the properties used in eqs. (5.82) and (5.83) are evaluated at the mean temperature T_m . The mean temperature varies with the position along the duct. This variation is linear in the case of constant q'' and exponential when the duct wall is isothermal (see Section 5.7). To simplify the recommended evaluation of the physical properties at the T_m temperature, it is convenient to choose as representative mean temperature the average value

$$T_m = \frac{1}{2}(T_{\text{in}} + T_{\text{out}}) \quad (5.84)$$

In this definition, T_{in} and T_{out} are the bulk temperatures of the stream at the duct inlet and outlet, respectively (Fig. 5.14).

5.7 TOTAL HEAT TRANSFER RATE

The summarizing conclusion is that in both laminar and turbulent fully developed duct flow the heat transfer coefficient h is independent of longitudinal position. This feature makes it easy to express analytically the total heat transfer rate q (watts) between a stream and duct of length L ,

$$q = hA_w \Delta T_{lm} \quad (5.85)$$

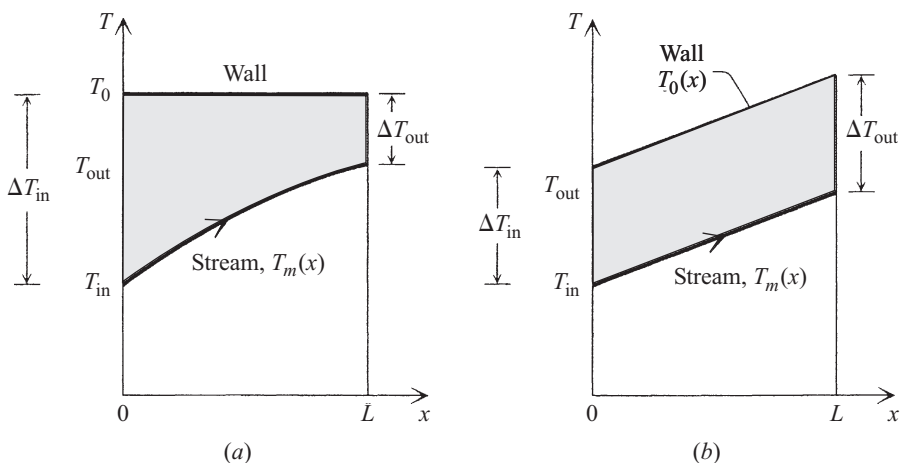


Figure 5.14 Variation of the mean temperature along the duct: (a) isothermal wall; (b) wall with uniform heat flux.

In this expression A_w is the total duct surface, $A_w = pL$. The effective temperature difference between the wall and the stream is the log-mean temperature difference T_{lm} .

5.7.1 Isothermal Wall

When the wall is isothermal (Fig. 5.14) the log-mean temperature difference is

$$\Delta T_{lm} = \frac{\Delta T_{in} - \Delta T_{out}}{\ln(\Delta T_{in}/\Delta T_{out})} \quad (5.86)$$

Equations (5.85) and (5.86) express the relationship among the total heat transfer rate q , the total duct surface conductance hA_w , and the outlet temperature of the stream. Alternatively, the same equations can be combined to express the total heat transfer rate in terms of the inlet temperatures, mass flow rate, and duct surface conductance,

$$q = \dot{m}c_p \Delta T_{in}(1 - e^{-hA_w/\dot{m}c_p}) \quad (5.87)$$

In cases where the heat transfer coefficient varies longitudinally, $h(x)$, the h factor on the right side of eq. (5.87) represents the L -averaged heat transfer coefficient: namely,

$$\bar{h} = \frac{1}{L} \int_0^L h(x) dx \quad (5.88)$$

5.7.2 Wall Heated Uniformly

In the analysis of heat exchangers (Bejan, 1993), it is found that the applicability of eqs. (5.85) and (5.86) is considerably more general than what is suggested by Fig. 5.14. For example, when the heat transfer rate q is distributed uniformly along the duct, the temperature difference ΔT does not vary with the longitudinal position. This case is illustrated in Fig. 5.14, where it was again assumed that A , p , h , and c_p are independent of x . Geometrically, it is evident that the effective value ΔT_{lm} is the same as the constant ΔT recorded all along the duct,

$$\Delta T_{lm} = \Delta T_{in} = \Delta T_{out} \quad (5.89)$$

Equation (5.89) is a special case of eq. (5.86): namely, the limit $\Delta T_{in}/\Delta T_{out} \rightarrow 1$.

5.8 OPTIMAL CHANNEL SIZES FOR TURBULENT FLOW

The optimization of packing of channels into a fixed volume, which in Section 5.5 was outlined for laminar duct flow, can also be pursued when the flow is turbulent (Bejan and Morega, 1994). With reference to the notation defined in Fig. 5.10, where the dimension perpendicular to the figure is W , the analysis consists of intersecting the two asymptotes of the design: a few wide spaces with turbulent boundary layers and many narrow spaces with fully developed turbulent flow. The plate thickness (t) is not negligible with respect to the spacing D . The optimal spacing and maximal global conductance of the *HWL* package are

$$\frac{D_{opt}/L}{(1 + t/D_{opt})^{4/11}} = 0.071 \text{Pr}^{-5/11} \cdot \text{Be}^{-1/11} \quad (5.90)$$

and

$$\frac{q_{max}}{HLW} \leq 0.57 \frac{k}{L^2} (T_{max} - T_0) \text{Pr}^{4/99} \left(1 + \frac{t}{D_{opt}}\right)^{-67/99} \cdot \text{Be}^{47/99} \quad (5.91)$$

where $\text{Be} = \Delta PL^2/\mu\alpha$. These results are valid in the range $10^4 \leq \text{Re}_{D_h} \leq 10^6$ and $10^6 \leq \text{Re}_L \leq 10^8$, which can be shown to correspond to the pressure drop number range $10^{11} \leq \text{Be} \leq 10^{16}$.

5.9 SUMMARY OF FORCED CONVECTION RELATIONSHIPS

- *Laminar flow entrance length:*

$$\frac{X/D}{\text{Re}_D} \approx 10^{-2} \quad (5.2)$$

- *Skin friction coefficient definition:*

$$C_{f,x} = \frac{\tau_w}{\frac{1}{2}\rho U^2} \quad (5.3)$$

- *Laminar fully developed (Hagen–Poiseuille) flow between parallel plates with spacing D :*

$$u(y) = \frac{3}{2}U \left[1 - \left(\frac{y}{D/2} \right)^2 \right] \quad (5.7)$$

with

$$U = \frac{D^2}{12\mu} \left(-\frac{dP}{dx} \right) \quad (5.8)$$

- *Laminar fully developed (Hagen–Poiseuille) flow in a tube with diameter D :*

$$u = 2U \left[1 - \left(\frac{r}{r_0} \right)^2 \right] \quad (5.9)$$

with

$$U = \frac{r_0^2}{8\mu} \left(-\frac{dP}{dx} \right) \quad (5.10)$$

- *Hydraulic radius and diameter:*

$$r_h = \frac{A}{p} \quad \text{hydraulic radius} \quad (5.14)$$

$$D_h = \frac{4A}{p} \quad \text{hydraulic diameter} \quad (5.15)$$

- *Friction factor:*

$$f = \begin{cases} \frac{\tau_w}{\frac{1}{2}\rho U^2} & \text{see Tables 5.1–5.3} \end{cases} \quad (5.11)$$

$$f = \begin{cases} \frac{24}{\text{Re}_{Dh}} & D_h = 2D \quad \text{parallel plates } (D = \text{spacing}) \end{cases} \quad (5.17)$$

$$f = \begin{cases} \frac{16}{\text{Re}_{Dh}} & D_h = D \quad \text{round tube } (D = \text{diameter}) \end{cases} \quad (5.18)$$

- *Pressure drop:*

$$\Delta P = f \frac{4L}{D_h} \left(\frac{1}{2} \rho U^2 \right) \quad (5.16)$$

- *Nusselt number* (see Tables 5.1 through 5.3):

$$\text{Nu} = \frac{hD}{k} = D \frac{\partial T / \partial r|_{r=r_0}}{T_0 - T_m} \quad (5.24)$$

- *Laminar thermal entrance length:*

$$X_T \approx 10^{-2} \text{Pr} \cdot D_h \cdot \text{Re}_{D_h} \quad (5.26)$$

- *Thermally developing Hagen–Poiseuille flow* ($\text{Pr} = \infty$):

- Round tube, isothermal wall:

$$\text{Nu}_x = \begin{cases} 1.077x_*^{-1/3} - 0.70 & x_* \leq 0.01 \\ 3.657 + 6.874(10^3 x_*)^{-0.488} e^{-57.2x_*} & x_* > 0.01 \end{cases} \quad (5.32)$$

$$\text{Nu}_{0-x} = \begin{cases} 1.615x_*^{-1/3} - 0.70 & x_* \leq 0.005 \\ 1.615x_*^{-1/3} - 0.20 & 0.005 < x_* < 0.03 \\ 3.657 + 0.0499/x_* & x_* > 0.03 \end{cases} \quad (5.33)$$

- Round tube, uniform heat flux:

$$\text{Nu}_x = \begin{cases} 3.302x_*^{-1/3} - 1.00 & x_* \leq 0.00005 \\ 1.302x_*^{-1/3} - 0.50 & 0.00005 < x_* \leq 0.0015 \\ 4.364 + 8.68(10^3 x_*)^{-0.506} e^{-41x_*} & x_* > 0.001 \end{cases} \quad (5.34)$$

$$\text{Nu}_{0-x} = \begin{cases} 1.953x_*^{-1/3} & x_* \leq 0.03 \\ 4.364 + 0.0722/x_* & x_* > 0.03 \end{cases} \quad (5.35)$$

- Parallel plates, isothermal surfaces:

$$\text{Nu}_{0-x} = \begin{cases} 1.233x_*^{-1/3} + 0.40 & x_* \leq 0.001 \\ 7.541 + 6.874(10^3 x_*)^{-0.488} e^{-245x_*} & x_* > 0.001 \end{cases} \quad (5.37)$$

$$\text{Nu}_{0-x} = \begin{cases} 1.849x_*^{-1/3} & x_* \leq 0.0005 \\ 1.849x_*^{-1/3} + 0.60 & 0.0005 < x_* \leq 0.006 \\ 7.541 + 0.0235/x_* & x_* > 0.006 \end{cases} \quad (5.38)$$

- Parallel plates, uniform heat flux:

$$\text{Nu}_x = \begin{cases} 1.490x_*^{-1/3} & x_* \leq 0.0002 \\ 1.490x_*^{-1/3} - 0.40 & 0.0002 < x_* \leq 0.001 \\ 8.235 + 8.68(10^3x_*)^{-0.506}e^{-164x_*} & x_* > 0.001 \end{cases} \quad (5.39)$$

$$\text{Nu}_{0-x} = \begin{cases} 2.236x_*^{-1/3} & x_* \leq 0.001 \\ 2.236x_*^{-1/3} + 0.90 & 0.001 < x_* \leq 0.01 \\ 8.235 + 0.0364/x_* & x_* \geq 0.01 \end{cases} \quad (5.40)$$

- *Thermally and hydraulically developing flow:*

- Round tube, isothermal wall:

$$\text{Nu}_x = 7.55 + \frac{0.024x_*^{-1.14} (0.0179\text{Pr}^{0.17}x_*^{-0.64} - 0.14)}{(1 + 0.0358\text{Pr}^{0.17}x_*^{-0.64})^2} \quad (5.41)$$

$$\text{Nu}_{0-x} = 7.55 + \frac{0.024x_*^{-1.14}}{1 + 0.0358\text{Pr}^{0.17}x_*^{-0.64}} \quad (5.42)$$

$$\frac{\Delta P}{\frac{1}{2}\rho U^2} = 13.74(x_+)^{1/2} + \frac{1.25 + 64x_+ - 13.74(x_+)^{1/2}}{1 + 0.00021(x_+)^{-2}} \quad (5.43)$$

$$x_+ = \frac{x/D}{\text{Re}_D} \quad (5.44)$$

- Round tube, uniform heat flux:

$$\frac{\text{Nu}_x}{4.364 [1 + (\text{Gz}/29.6)^2]^{1/6}} = \left\{ 1 + \left[\frac{\text{Gz}/19.04}{[1 + (\text{Pr}/0.0207)^{2/3}]^{1/2} [1 + (\text{Gz}/29.6)^2]^{1/3}} \right]^{3/2} \right\}^{1/3} \quad (5.46)$$

- *Optimal channel sizes:*

- Laminar flow, parallel plates:

$$\frac{D_{\text{opt}}}{L} \simeq 2.7\text{Be}^{-1/4} \quad \text{Be} = \frac{\Delta PL^2}{\mu\alpha} \quad (5.47)$$

$$\frac{q_{\text{max}}}{HLW} \simeq 0.60 \frac{k}{L^2} (T_{\text{max}} - T_0) \text{Be}^{1/2} \quad (5.48)$$

- Staggered plates:

$$\frac{D_{\text{opt}}}{L} \simeq 5.4 \text{Pr}^{-1/4} \left(\text{Re}_L \frac{L}{b} \right)^{-1/2} \quad (5.50)$$

for the range

$$\text{Pr} = 0.72 \quad 10^2 \leq \text{Re}_L \leq 10^4 \quad 0.5 \leq \frac{Nb}{L} \leq 1.3$$

- Bundle of cylinders in cross flow:

$$\frac{S_{\text{opt}}}{D} \simeq 1.59 \frac{(H/D)^{0.52}}{\tilde{P}^{0.13} \cdot \text{Pr}^{0.24}} \quad \tilde{P} = \frac{\Delta P D^2}{\mu v} \quad (5.51)$$

for the range

$$0.72 \leq \text{Pr} \leq 50 \quad 10^4 \leq \tilde{P} \leq 10^8 \quad 25 \leq \frac{H}{D} \leq 200$$

$$\frac{S_{\text{opt}}}{D} \simeq 1.70 \frac{(H/D)^{0.52}}{\text{Re}_D^{0.26} \cdot \text{Pr}^{0.24}} \quad (5.52)$$

$$\frac{T_D - T_\infty}{q D / k L W} \simeq \frac{4.5}{\text{Re}_D^{0.90} \cdot \text{Pr}^{0.64}} \quad (5.53)$$

with

$$\text{Re}_D = U_\infty \frac{D}{v} \quad 140 \leq \text{Re}_D \leq 14,000$$

- Array of pin fins with impinging flow:

$$\frac{S_{\text{opt}}}{L} \simeq 0.81 \text{Pr}^{-0.25} \cdot \text{Re}_L^{-0.32} \quad (5.54)$$

for the range

$$0.06 \leq \frac{D}{L} \leq 0.14 \quad 0.28 \leq \frac{H}{L} \leq 0.56 \quad 0.72 \leq \text{Pr} \leq 7$$

$$10 \leq \text{Re}_D \leq 700 \quad 90 \leq \text{Re}_L \leq 6000$$

- Turbulent duct flow:

$$\frac{D_{\text{opt}}/L}{(1 + t/D_{\text{opt}})^{4/11}} = 0.071 \text{Pr}^{-5/11} \cdot \text{Be}^{-1/11} \quad (5.90)$$

$$\frac{q_{\max}}{HLW} \leq 0.57 \frac{k}{L^2} (T_{\max} - T_0) \text{Pr}^{4/99} \left(1 + \frac{t}{D_{\text{opt}}}\right)^{-67/99} \cdot \text{Be}^{47/99} \quad (5.91)$$

with

$$\text{Be} = \frac{\Delta PL^2}{\mu \alpha}$$

for the range

$$10^4 \leq \text{Re}_{D_h} \leq 10^6 \quad 10^6 \leq \text{Re}_L \leq 10^8 \quad 10^{11} \leq \text{Be} \leq 10^{16}$$

- *Turbulent flow and entrance lengths:*

$$\frac{X}{D} \simeq 10 \simeq \frac{X_T}{D} \quad (5.60)$$

- *Turbulent flow friction factor:*

$$f \simeq 0.046 \text{Re}_D^{-1/5} \quad 2 \times 10^4 \leq \text{Re}_D \leq 10^5 \quad (\text{see Fig. 5.13}) \quad (5.68)$$

- *Turbulent flow heat transfer:*

$$\text{St} \cdot \text{Pr}^{2/3} \simeq \frac{f}{2} \quad (5.75)$$

for $\text{Pr} \geq 0.5$

$$\text{Nu}_D = \frac{hD}{k} = 0.023 \text{Re}_D^{4/5} \cdot \text{Pr}^{1/3} \quad (5.76)$$

for $\text{Pr} \geq 0.50$

$$2 \times 10^4 \leq \text{Re}_D \leq 10^6$$

$$\text{Nu}_D = 0.023 \text{Re}_D^{4/5} \cdot \text{Pr}^n \quad (5.77)$$

where $n = 0.4$ for heating the fluid and $n = 0.3$ for cooling the fluid in the range

$$\frac{L}{D} > 60 \quad 0.7 \leq \text{Pr} \leq 120 \quad 2500 \leq \text{Re}_D \leq 1.24 \times 10^5$$

$$\text{Nu}_D = 0.027 \text{Re}_D^{4/5} \cdot \text{Pr}^{1/3} \left(\frac{\mu}{\mu_0} \right)^{0.14} \quad (5.78)$$

in the range

$$0.70 \leq \text{Pr} \leq 16,700 \quad \text{Re}_D \geq 10^4$$

Here

$$\mu_0 = \mu(T_0) \quad (T_0 \text{ is the wall temperature})$$

$$\mu = \mu(T_m) \quad (T_m \text{ is the bulk temperature})$$

$$\text{Nu}_D = \frac{(f/2)\text{Re}_D \cdot \text{Pr}}{1.07 + 900/\text{Re}_D - 0.63/(1 + 10\text{Pr}) + 12.7(f/2)^{1/2}(\text{Pr}^{2/3} - 1)} \quad (5.79a)$$

$$\text{Nu}_D = \frac{(f/2)\text{Re}_D \cdot \text{Pr}}{1.07 + 12.7(f/2)^{1/2}(\text{Pr}^{2/3} - 1)} \quad (5.79b)$$

where

$$0.5 \leq \text{Pr} \leq 10^6 \quad 4000 \leq \text{Re}_D \leq 5 \times 10^6$$

and f from Fig. 5.13.

$$\text{Nu}_D = \frac{(f/2)(\text{Re}_D - 10^3)\text{Pr}}{1 + 12.7(f/2)^{1/2}(\text{Pr}^{2/3} - 1)} \quad (5.80)$$

where

$$0.5 \leq \text{Pr} \leq 10^6 \quad 2300 \leq \text{Re}_D \leq 5 \times 10^6$$

and f from Fig. 5.13.

$$\text{Nu}_D = 0.0214 (\text{Re}_D^{0.8} - 100) \text{Pr}^{0.4} \quad (5.81a)$$

where

$$0.5 \leq \text{Pr} \leq 1.5 \quad 10^4 \leq \text{Re}_D \leq 5 \times 10^6$$

$$\text{Nu}_D = 0.012 (\text{Re}_D^{0.87} - 280) \text{Pr}^{0.4} \quad (5.81b)$$

where

$$1.5 \leq \text{Pr} \leq 500 \quad 3 \times 10^3 \leq \text{Re}_D \leq 10^6$$

$$\text{Nu}_D = \begin{cases} 6.3 + 0.0167\text{Re}_D^{0.85} \cdot \text{Pr}^{0.93} & q_0'' = \text{constant} \\ 4.8 + 0.0156\text{Re}_D^{0.85} \cdot \text{Pr}^{0.93} & T_0 = \text{constant} \end{cases} \quad (5.82)$$

$$(5.83)$$

where for eqs. (5.82) and (5.83),

$$0.004 \leq \text{Pr} \leq 0.1 \quad 10^4 \leq \text{Re}_D \leq 10^6$$

- *Total heat transfer rate:*

$$q = h A_w \Delta T_{lm} \quad (5.85)$$

- *Isothermal wall:*

$$\Delta T_{lm} = \frac{\Delta T_{in} - \Delta T_{out}}{\ln(\Delta T_{in}/\Delta T_{out})} \quad (5.86)$$

$$q = \dot{m} c_p \Delta T_{in} (1 - e^{-h A_w / \dot{m} c_p}) \quad (5.87)$$

- *Uniform heat flux:*

$$\Delta T_{lm} = \Delta T_{in} = \Delta T_{out} \quad (5.89)$$

NOMENCLATURE

Roman Letter Symbols

A	cross-sectional area, m ²
A_w	wall area, m ²
(a)	pressure at point 1, Pa
B	cross-section shape number, dimensionless
Be	Bejan number, dimensionless
b	length, m
(b)	pressure at point 2, Pa
C	cross-section shape factor, dimensionless
$C_{f,x}$	local skin friction coefficient, dimensionless
c_p	specific heat at constant pressure, J/kg·K
D	spacing, diameter, m
D_h	hydraulic diameter, m
f	friction factor, dimensionless
G_z	Graetz number, dimensionless
H	height, m
h	heat transfer coefficient, W/m ² ·K
	specific bulk enthalpy, J/kg
k	thermal conductivity, W/m·K
k_s	size of sand grain, m
L	flow length, m
\dot{m}	mass flow rate, kg/s
N	number of plate surfaces in one elemental channel, dimensionless
Nu	Nusselt number, dimensionless
Nu_x	local Nusselt number, dimensionless

P	pressure, Pa
	pressure difference, dimensionless
ΔP	pressure difference, Pa
Pr	Prandtl number, dimensionless
Pr_t	turbulent Prandtl number, dimensionless
p	perimeter of cross section, m
q''	heat flux, W/m^2
r	radial position, m
r_h	hydraulic radius, m
r_0	tube radius, m
Ra	Rayleigh number, dimensionless
Re_D	Reynolds number based on D , dimensionless
Re_{D_h}	Reynolds numbers based on D_h , dimensionless
Re_L	Reynolds number based on L , dimensionless
S	spacing between cylinders, m
St	Stanton number, dimensionless
t	plate thickness, m
T	temperature, K
T_{in}	inlet temperature, K
T_{out}	outlet temperature, K
T_m	mean temperature, K
ΔT_{avg}	average temperature difference, K
ΔT_{lm}	log-mean temperature difference, K
u	longitudinal velocity, m/s
u_*	friction velocity, m/s
U	mean velocity, m/s
v	transversal velocity, m/s
W	width, m
x	longitudinal position, m
x_*	longitudinal position, dimensionless
x^+	longitudinal position, dimensionless
X	flow entrance length, m
X_T	thermal entrance length, m
y	transversal position, m
y_{VSL}	viscous sublayer thickness, m

Greek Letter Symbols

α	thermal diffusivity, m^2/s
ϵ_H	thermal eddy diffusivity, m^2/s
ϵ_M	momentum eddy diffusivity, m^2/s
θ_{*m}	bulk temperature, dimensionless
μ	viscosity, $kg/s\cdot m$
ν	kinematic viscosity, m^2/s
ρ	density, kg/m^3
τ_{app}	apparent shear stress, Pa

τ_{avg}	averaged wall shear stress, Pa
τ_w	wall shear stress, Pa
ϕ	fully developed temperature profile, dimensionless

Subscripts

in	inlet
max	maximum
opt	optimum
out	outlet
0	wall
0- x	averaged longitudinally
∞	free stream

Superscripts

—	time-averaged components
'	fluctuating components
+	wall coordinates

REFERENCES

- Asako, Y., Nakamura, H., and Faghri, M. (1988). Developing Laminar Flow and Heat Transfer in the Entrance Region of Regular Polygonal Ducts, *Int. J. Heat Mass Transfer*, 31, 2590–2593.
- Bar-Cohen, A., and Rohsenow, W. M. (1984). Thermally Optimum Spacing of Vertical, Natural Convection Cooled, Parallel Plates, *J. Heat Transfer*, 106, 116–123.
- Bejan, A. (1984). *Convection Heat Transfer*. Wiley, New York, p. 157, prob. 11.
- Bejan, A. (1993). *Heat Transfer*, Wiley, New York, Chap. 9.
- Bejan, A. (1995). *Convection Heat Transfer*, 2nd ed., Wiley, New York.
- Bejan, A. (2000). *Shape and Structure, from Engineering to Nature*, Cambridge University Press, Cambridge.
- Bejan, A., and Morega, A. M. (1994). The Optimal Spacing of a Stack of Plates Cooled by Turbulent Forced Convection, *Int. J. Heat Mass Transfer*, 37, 1045–1048.
- Bejan, A., and Sciubba, E. (1992). The Optimal Spacing of Parallel Plates Cooled by Forced Convection, *Int. J. Heat Mass Transfer*, 35, 3259–3264.
- Bhattacharjee, S., and Grosshandler, W. L. (1988). The Formation of a Wall Jet near a High Temperature Wall under Microgravity Environment, *ASME-HTD-96*, ASME, New York, pp. 711–716.
- Campo, A. (1999). Bounds for the Optimal Conditions of Forced Convective Flows Inside Multiple Channels Whose Plates Are Heated by Uniform Flux, *Int. Commun. Heat Mass Transfer*, 26, 105–114.
- Campo, A., and Li, G. (1996). Optimum Separation of Asymmetrically Heated Sub-channels Forming a Bundle: Influence of Simultaneous Flow and Temperature, *Heat Mass Transfer*, 32, 127–132.

- Churchill, S. W., and Ozoe, H. (1973). Correlations for Forced Convection with Uniform Heating in Flow over a Plate and in Developing and Fully Developed Flow in a Tube, *J. Heat Transfer*, 95, 78–84.
- Colburn, A. P. (1933). A Method of Correlating Forced Convection Heat Transfer Data and a Comparison with Fluid Friction, *Trans. Am. Inst. Chem. Eng.*, 29, 174–210.
- Dittus, F. W., and Boelter, L. M. K. (1930). Heat Transfer in Automobile Radiators of the Tubular Type, *Univ. Calif. Publ. Eng.*, 2(13), 443–461; *Int. Commun. Heat Mass Transfer*, 12(1985), 3–22.
- Drew, T. B. (1931). Mathematical Attacks on Forced Convection Problems: A Review, *Trans. Am. Inst. Chem. Eng.*, 26, 26–80.
- Fowler, A. J., Ledezma, G. A., and Bejan, A. (1997). Optimal Geometric Arrangement of Staggered Plates in Forced Convection, *Int. J. Heat Mass Transfer*, 40, 1795–1805.
- Gnielinski, V. (1976). New Equations for Heat and Mass Transfer in Turbulent Pipe and Channel Flow, *Int. Chem. Eng.*, 16, 359–368.
- Graetz, L. (1883). Über die Wärmeleitungsfähigkeit von Flüssigkeiten (On the Thermal Conductivity of Liquids), Part 1, *Ann. Phys. Chem.*, 18, 79–94; Part 2 (1885), *Ann. Phys. Chem.*, 25, 337–357.
- Hagen, G. (1839). Über die Bewegung des Wassers in engen zylindrischen Röhren, *Pogg. Ann.*, 46, 423.
- Hoffmann, E. (1937). Die Wärmeübertragung bei der Strömung im Rohr, *Z. Gesamte Kaelte-Ind.*, 44, 99–107.
- Hornbeck, R. W. (1965). An All-Numerical Method for Heat Transfer in the Inlet of a Tube, *ASME-65-WA/HT-36*, ASME, New York.
- Kays, W.M., and Perkins, H. C. (1973). Forced Convection, Internal Flow in Ducts, in *Handbook of Heat Transfer*, W. M. Rohsenow and J. P. Hartnett, eds., McGraw-Hill, New York, Sec. 7.
- Kim, S. J., and Lee, S. W., eds. (1996). *Air Cooling Technology for Electronic Equipment*, CRC Press, Boca Raton, FL, Chap. 1.
- Langhaar, H. L. (1942). Steady Flow in the Transition Length of a Straight Tube, *J. Appl. Mech.*, 9, A55–A58.
- Ledezma, G., Morega, A. M., and Bejan, A. (1996). Optimal Spacing between Pin Fins with Impinging Flow, *J. Heat Transfer*, 118, 570–577.
- Lévêque, M. A. (1928). Les lois de la transmission de chaleur par convection, *Ann. Mines Mem. Ser.*, 12, 13, 201–299, 305–362, 381–415.
- Matos, R. S., Vargas, J. V. C., Laursen, T. A., and Saboya, F. E. M. (2001). Optimization Study and Heat Transfer Comparison of Staggered Circular and Elliptic Tubes in Forced Convection, *Int. J. Heat Mass Transfer*, 44, 3953–3961.
- Mereu, S., Sciubba, E., and Bejan, A. (1993). The Optimal Cooling of a Stack of Heat Generating Boards with Fixed Pressure Drop, Flow Rate or Pumping Power, *Int. J. Heat Mass Transfer*, 36, 3677–3686.
- Moody, L. F. (1944). Friction Factors for Pipe Flow, *Trans. ASME*, 66, 671–684.
- Nikuradse, J. (1933). Strömungsgesetze in rauen Röhren, *VDI-Forschungsh.*, 361, 1–22.
- Notter, R. H., and Sleicher, C. A. (1972). A Solution to the Turbulent Graetz Problem, III: Fully Developed and Entry Region Heat Transfer Rates, *Chem. Eng. Sci.*, 27, 2073–2093.

- Petrescu, S. (1994). Comments on the Optimal Spacing of Parallel Plates Cooled by Forced Convection, *Int. J. Heat Mass Transfer*, 37, 1283.
- Petukhov, B. S. (1970). Heat Transfer and Friction in Turbulent Pipe Flow with Variable Physical Properties, *Adv. Heat Transfer*, 6, 503–564.
- Petukhov, B. S., and Kirilov, V. V. (1958). The Problem of Heat Exchange in the Turbulent Flow of Liquids in Tubes, *Teploenergetika*, 4(4), 63–68.
- Petukhov, B. S., and Popov, V. N. (1963). Theoretical Calculation of Heat Exchange in Turbulent Flow in Tubes of an Incompressible Fluid with Variable Physical Properties, *High Temp.*, 1(1), 69–83.
- Poiseuille, J. (1840). Recherches expérimentales sur le mouvement des liquides dans les tubes de très petit diamètres, *Comptes Rendus*, 11, 961, 1041.
- Prandtl, L. (1969). *Essentials of Fluid Dynamics*, Blackie and Son, London, p. 117.
- Reichardt, H. (1951). Die Grundlagen des turbulenten Wärmeüberganges, *Arch. Gesamte Waermetech.*, 2, 129–142.
- Rocha, L. A. O., and Bejan, A. (2001). Geometric Optimization of Periodic Flow and Heat Transfer in a Volume Cooled by Parallel Tubes, *J. Heat Transfer*, 123, 233–239.
- Schlichting, H. (1960). *Boundary Layer Theory*, 4th ed., McGraw-Hill, New York, pp. 169, 489.
- Shah, R. K., and Bhatti, M. S. (1987). Laminar Convective Heat Transfer in Ducts, in *Handbook of Single-Phase Convective Heat Transfer*, S. Kakaç, R. K. Shah, and W. Aung, Wiley, New York, Chap. 3.
- Shah, R. K., and London, A. L. (1978). *Laminar Flow Forced Convection in Ducts*, Suppl. 1 to *Advances in Heat Transfer*, Academic Press, New York.
- Sieder, E. N., and Tate, G. E. (1936). Heat Transfer and Pressure Drop of Liquids in Tubes, *Ind. Eng. Chem.*, 28, 1429–1436.
- Sparrow, E. M. (1955). Analysis of Laminar Forced Convection Heat Transfer in the Entrance Region of Flat Rectangular Ducts, *NACA-TN-3331*.
- Stanescu, G., Fowler, A. J., and Bejan, A. (1996). The Optimal Spacing of Cylinders in Free-Stream Cross-Flow Forced Convection, *Int. J. Heat Mass Transfer*, 39, 311–317.
- Stephan, K. (1959). Wärmeübertragung und Druckabfall beinichtausgebildeter Laminarströmung in Röhren und in ebenen Spalten, *Chem. Ing. Tech.*, 31, 773–778.

Forced Convection: External Flows

YOGENDRA JOSHI

George W. Woodruff School of Mechanical Engineering
Georgia Institute of Technology
Atlanta, Georgia

WATARU NAKAYAMA

Therm Tech International
Kanagawa, Japan

- 6.1 Introduction
- 6.2 Morphology of external flow heat transfer
- 6.3 Analysis of external flow heat transfer
- 6.4 Heat transfer from single objects in uniform flow
 - 6.4.1 High Reynolds number flow over a wedge
 - 6.4.2 Similarity transformation technique for laminar boundary layer flow
 - 6.4.3 Similarity solutions for the flat plate at uniform temperature
 - 6.4.4 Similarity solutions for a wedge
 - Wedge flow limits
 - 6.4.5 Prandtl number effect
 - 6.4.6 Incompressible flow past a flat plate with viscous dissipation
 - 6.4.7 Integral solutions for a flat plate boundary layer with unheated starting length
 - Arbitrarily varying surface temperature
 - 6.4.8 Two-dimensional nonsimilar flows
 - 6.4.9 Smith–Spalding integral method
 - 6.4.10 Axisymmetric nonsimilar flows
 - 6.4.11 Heat transfer in a turbulent boundary layer
 - Axisymmetric flows
 - Analogy solutions
 - 6.4.12 Algebraic turbulence models
 - 6.4.13 Near-wall region in turbulent flow
 - 6.4.14 Analogy solutions for boundary layer flow
 - Mixed boundary conditions
 - Three-layer model for a “physical situation”
 - Flat plate with an unheated starting length in turbulent flow
 - Arbitrarily varying heat flux
 - Turbulent Prandtl number
 - 6.4.15 Surface roughness effect
 - 6.4.16 Some empirical transport correlations
 - Cylinder in crossflow
 - Flow over an isothermal sphere

- 6.5 Heat transfer from arrays of objects
 - 6.5.1 Crossflow across tube banks
 - 6.5.2 Flat plates
 - Stack of parallel plates
 - Offset strips
- 6.6 Heat transfer from objects on a substrate
 - 6.6.1 Flush-mounted heat sources
 - 6.6.2 Two-dimensional block array
 - 6.6.3 Isolated blocks
 - 6.6.4 Block arrays
 - 6.6.5 Plate fin heat sinks
 - 6.6.6 Pin fin heat sinks
- 6.7 Turbulent jets
 - 6.7.1 Thermal transport in jet impingement
 - 6.7.2 Submerged jets
 - Average Nusselt number for single jets
 - Average Nusselt number for an array of jets
 - Free surface jets
- 6.8 Summary of heat transfer correlations
- Nomenclature
- References

6.1 INTRODUCTION

This chapter is concerned with the characterization of heat transfer and flow under forced convection, where the fluid movement past a heated object is induced by an external agent such as a fan, blower, or pump. The set of governing equations presented in Chapter 1 is nonlinear in general, due to the momentum advection terms, variable thermophysical properties (e.g., with temperature) and nonuniform volumetric heat generation. Solution methodologies for the governing equations are based on the nondimensional groups discussed in Section 6.3. Solutions can be obtained through analytical means only for a limited number of cases. Otherwise, experimental or numerical solution procedures must be employed.

6.2 MORPHOLOGY OF EXTERNAL FLOW HEAT TRANSFER

Various cases arise from the geometry of a heated object and the constraint imposed on the fluid flow. Figure 6.1 shows the general configuration in which it is assumed that the body is being cooled by the flow. The heated object is an arbitrary shape enclosed in a rectangular envelope. The dimensions of the envelope are L , the length in the streamwise direction, W , the length in the cross-stream direction (the width), and H , the height. Generally, the fluid flow is constrained by the presence of bounding

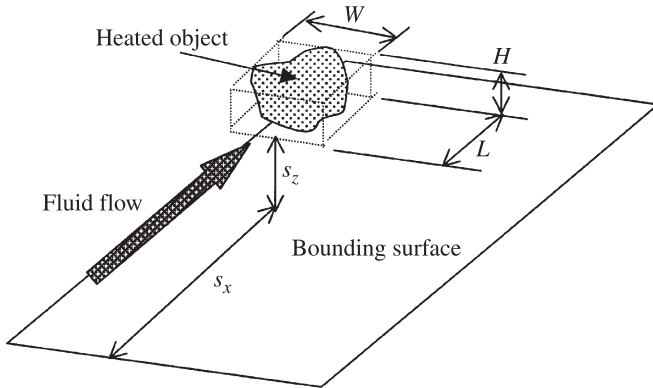


Figure 6.1 Heated object in a flow over a bounding surface.

surfaces. The bounding surface may be a solid wall or an interface with a fluid of a different kind, for instance, a liquid–vapor interface.

The distance s_x signifies the extent of the bounding surface in the streamwise direction, and s_z is the distance to the bounding surface. When $s_z \gg H$ or L and $s_z \gg s_x$, the flow around the object is uniform and free of the effect of the bounding surface. Otherwise, the object is within a boundary layer developing on a larger object. In laboratory experiments and many types of industrial equipment, one often finds a situation where the object is placed in a duct. When the duct cross section has dimensions comparable to the object size, the flow has a velocity distribution defined by the duct walls and the object. Hence, the foregoing relations between H , L , s_x , and s_z can be put into more precise forms involving the velocity and viscosity of the fluid as well. In an extreme case, the object is in contact with the bounding surface; that is, $s_z = 0$. In such cases the flow and temperature fields are generally defined by both the bounding surface and the object. Only in cases where the object dimensions are much smaller than those of the bounding surface is the external flow defined primarily by the bounding surface.

Several external flow configurations are illustrated in Fig. 6.2. The symbols used to define the dimensions are conventionally related to the flow direction. For the flat plate in Fig. 6.2a, ℓ is the plate length in the streamwise direction, w is the length (width) in the cross-stream direction, and t is the plate thickness. The cylinder in Fig. 6.2b has length ℓ and diameter d . For the rectangular block of Fig. 6.2c, ℓ is oriented in the streamwise direction, h is the height, and w is the width. Sometimes, these letters can be used as subscripts to a common symbol for the block. The sphere (Fig. 6.2d) is defined by only one dimension, that is, the diameter d . Although an infinite number of configurations can be conceived from the combination of external flow and object geometry, only a limited number of cases have been the subject of theoretical studies as well as practical applications. The most common are two-dimensional objects in uniform flow, which are used in basic research and teaching.

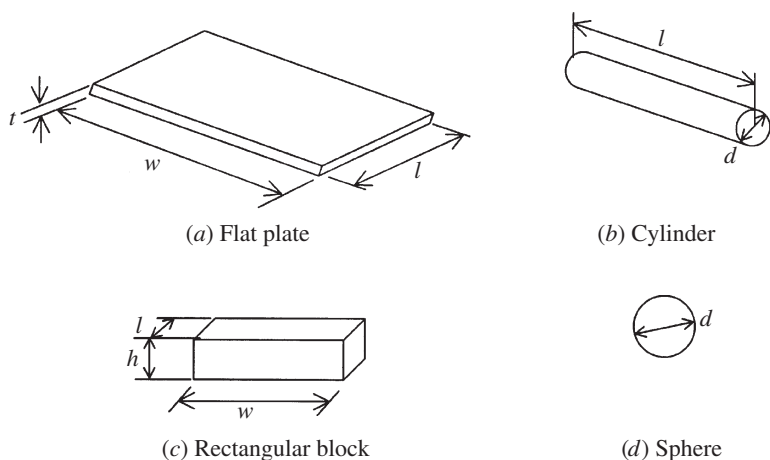


Figure 6.2 Basic configurations of objects.

A flat plate of large width ($w \gg \ell$) and small thickness ($t \ll \ell$) is often used to introduce the concept of boundary layer flow and heat transfer. An infinitely long cylinder ($\ell \gg d$) in cross flow is also a geometrically simple object, but the flow develops complexity at high velocities due to separation on the curved surface. Flow passing an infinitely long rectangular body ($w \gg h, w \gg \ell$) also involves complexities caused by flow separation at the sharp corners. A sphere in uniform flow is also one of the basic configurations, where axisymmetric flow prevails at low velocities.

The orientation of the heated object relative to the fluid flow has a significant influence on heat transfer. Well-studied configurations are parallel flow along a flat plate as in Fig. 6.3a, flows impinging on a plane (Fig. 6.3b), a wedge and a cone (Fig. 6.3c), and the side of a cylinder (Fig. 6.3d). In many studies the impinging flow is assumed to be parallel to the symmetry axis of the object as illustrated by the sketches in Fig. 6.3. The study of impinging heat transfer has as one objective the understanding of heat transfer near the symmetry axis. For the plane and the cylinder, the point on the symmetry axis is called the *stagnation point*.

Figure 6.4 illustrates flows through heated objects placed in regular geometric patterns. These arrays are commonly found in heat exchangers that transmit heat from the external surfaces of tubes or flat plates (strips) to the fluid. In heat exchanger applications, the array of cylinders (Fig. 6.4a and b) is called a *tube bank*. When the row of objects is deep, the fluid flow develops a repeating pattern after a few rows, that is, a *fully developed* pattern. The fluid temperature increases toward the end of the row as the fluid absorbs heat from the objects in the upstream rows and the thermal environment for an individual object bears the characteristics of internal flow. The case of a stack of parallel plates (Fig. 6.4c and d) involves an extra feature; that is, the fluid can bypass the plates in the stack. Such a situation is commonly found in the cooling of electronics.

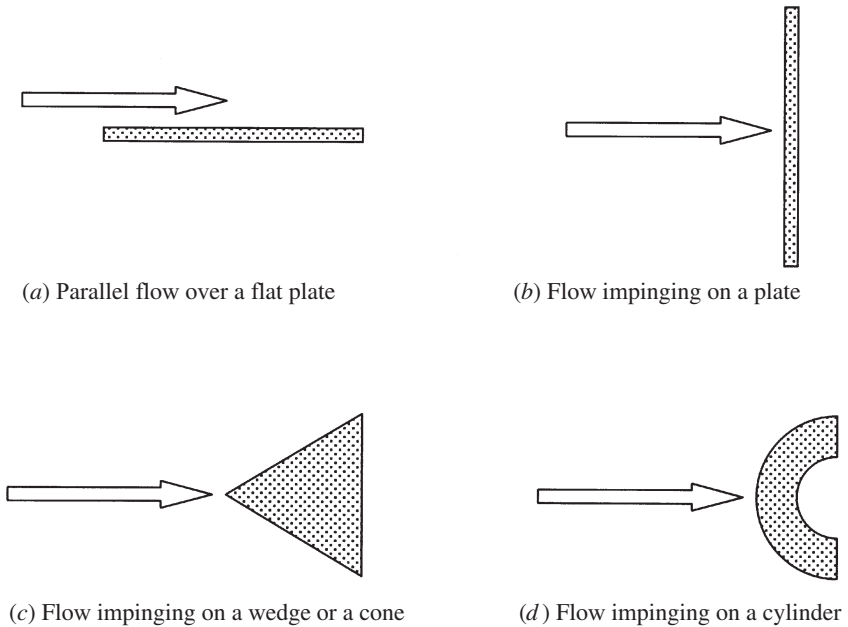


Figure 6.3 Flow configurations.

If the heated object is in contact with the bounding surface, the heat and fluid flow patterns become more complex. Figure 6.5 shows some configurations that are found in industrial equipment, particularly in electronic equipment. A rectangular block on a flat substrate simulates an integrated-circuit (IC) package on a printed wiring board (PWB) in Fig. 6.5*a*. If a certain number of rectangular packages are mounted on a PWB, with their longer sides extending laterally and leaving narrow edge-to-edge gaps between the packages on the same row, such a package array is modeled by an array of two-dimensional blocks (Fig. 6.5*b*). Two-dimensional blocks (frequently referred to as *ribs*) are also provided on a surface to enhance heat transfer. Longitudinal planar fins on a substrate are commonly used as a heat sink for the IC package (Fig. 6.5*c*). The pin fin array is a common heat sink device for electronic components (Fig. 6.5*d*).

In most of the examples illustrated in Fig. 6.5, the flow and the temperature field are three-dimensional. In addition, flow separation and vortex shedding from the objects are common features in the velocity range of practical interest. The contribution made by the substrate is another complicating factor because heat conduction in the substrate is coupled with surface heat transfer on the object as well as the substrate. This coupled process is called *conjugate heat transfer*. In the case of heat sinks, the substrate is usually made from the same (highly conductive) material as the fins and is in good thermal contact with the fins. The heat source is bonded to the lower side of the substrate, so that the heat flows from the substrate to the fins. These features

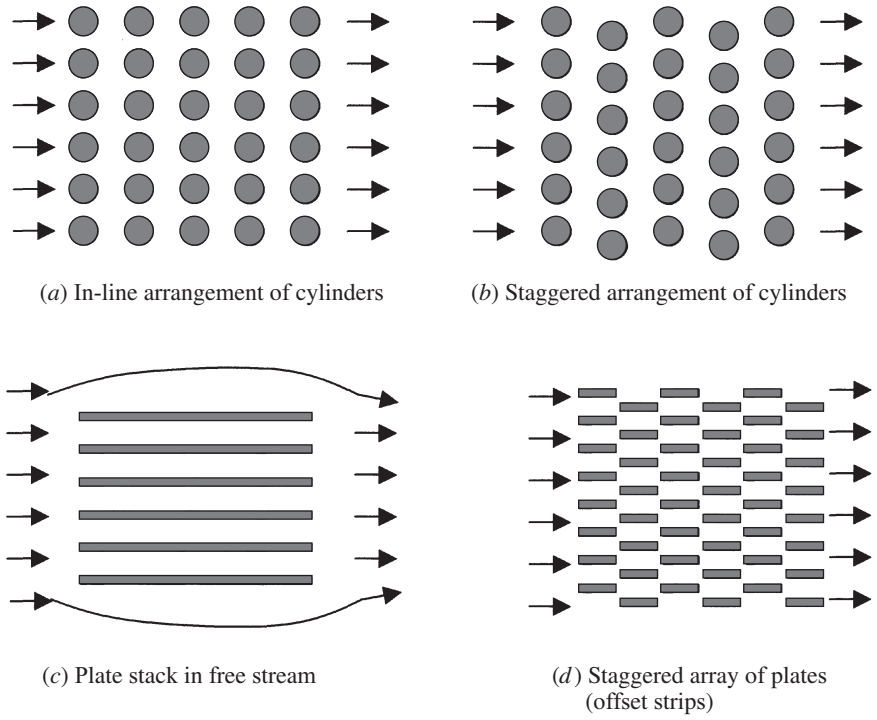


Figure 6.4 Arrays of objects.

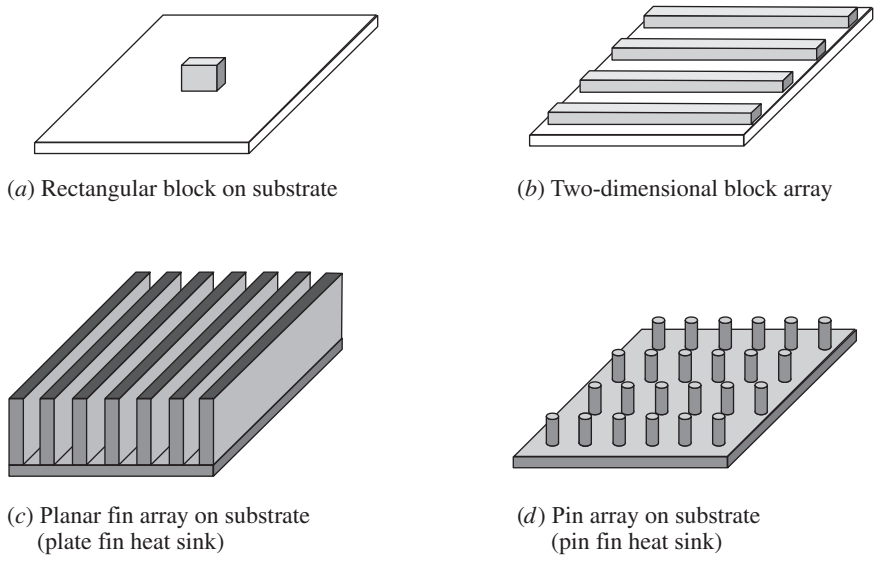


Figure 6.5 Objects on substrates.

often justify the assumption of an isothermal condition over the substrate, and as a result, conjugate heat transfer does not play a major role.

This section concludes with the following observations:

1. Classical analytical solutions are available for two-dimensional cases where the flow is laminar up to the point of transition to turbulent flow or flow separation. For turbulent flows in simple circumstances, approximate analytical solutions based on phenomenological laws of turbulence kinetics are also available. Results for both laminar and turbulent flows are discussed in Sections 6.4 and 6.6.

2. The advent of computational fluid dynamics (CFD) codes has expanded the possibility of finding detailed features of flow and heat transfer in many complex situations. Developments after flow separation (such as vortex shedding) can be studied in detail and three-dimensional situations can be considered, although the computational resource is finite and the scope of analysis in a narrower zone must be limited when the flow involves more complex features. For processes occurring outside the analysis zone, assumptions or approximations are frequently employed. These assumptions introduce inaccuracies in the solution, and experiments are required to justify solutions for a certain number of cases. Such experimental verification is called *benchmarking*, and only benchmarked CFD codes can be used as product design tools.

3. There are many circumstances where experiments are the only means for obtaining useful heat transfer data. In many instances empirical relationships still serve as invaluable tools to estimate heat transfer, particularly for the design of industrial equipment.

6.3 ANALYSIS OF EXTERNAL FLOW HEAT TRANSFER

For a general three-dimensional flow (Fig. 6.1), the six unknowns at any instant at a given location are the three velocity components and the pressure, temperature, and density. For constant fluid properties, the flow field is not coupled to the temperature field and can be obtained independently. With a known flow field, the energy equation subsequently provides the temperature variation. The determination of flow and temperature fields and gradients permits computation of the local heat transfer coefficient h :

$$h = \frac{-k_f(\partial T/\partial n)|_s}{T_s - T_{\text{ref}}} \quad (6.1a)$$

and its nondimensional representation, known as the Nusselt number:

$$\text{Nu} = \frac{hL}{k_f} \quad (6.1b)$$

The surface heat flux can be obtained from

$$q'' = h(T_s - T_{\text{ref}}) \quad (6.1c)$$

Here T_s is the local surface temperature and T_{ref} is the fluid reference temperature. For external flow, this is typically the local ambient environment temperature.

Experimental Determination of Convection Transport The experimental technique has been employed extensively. For a given geometrical configuration, it involves the simulation of thermal loads and flow conditions and the determination of resulting thermal fields. Experimental techniques are often used for validation of numerical simulations of laminar flows in complex geometries and for transport characterization for turbulent flow.

Analytical Solutions The key nondimensional flow parameter in convection analysis is the Reynolds number, Re , which is defined later. For $Re \ll 1$, the nonlinear advection terms in the momentum equations can be neglected, and the resulting linearized set of equations can then be solved analytically for a limited set of conditions.

Numerical Simulations of Transport With the advent of high-speed digital computers, it has become possible to carry out numerical simulations with great accuracy for virtually any geometrical configuration in laminar flow. The focus in these solutions is on the determination of generalized transport correlations and on the detailed descriptions of the thermal and flow fields. For turbulent and transitional flow, reliance must be placed on experimental data and correlations.

6.4 HEAT TRANSFER FROM SINGLE OBJECTS IN UNIFORM FLOW

6.4.1 High Reynolds Number Flow over a Wedge

In the absence of mass transfer, the governing equations in Cartesian coordinates (x, y, z) for constant property, incompressible three-dimensional flow with the velocity

$$\mathbf{V} = u\mathbf{i} + v\mathbf{j} + w\mathbf{k}$$

account for continuity (mass conservation), conservation of momentum, and conservation of energy. The mass conservation equation is

$$\nabla \cdot \mathbf{V} = 0 \quad (6.2)$$

For the conservation of momentum, the x , y , and z components are

$$\rho \frac{Du}{Dt} = \rho \left[\frac{\partial u}{\partial t} + \nabla \cdot (u\mathbf{V}) \right] = -\frac{\partial p}{\partial x} + \mu \nabla^2 u \quad (6.3a)$$

$$\rho \frac{Dv}{Dt} = \rho \left[\frac{\partial v}{\partial t} + \nabla \cdot (v\mathbf{V}) \right] = -\frac{\partial p}{\partial y} + \mu \nabla^2 v \quad (6.3b)$$

$$\rho \frac{Dw}{Dt} = \rho \left[\frac{\partial w}{\partial t} + \nabla \cdot (w\mathbf{V}) \right] = -\frac{\partial p}{\partial z} + \mu \nabla^2 w \quad (6.3c)$$

The conservation of energy requires

$$\rho c_p \frac{DT}{Dt} = \rho c_p \left[\frac{\partial T}{\partial t} + \nabla \cdot (T\mathbf{V}) \right] = k \nabla^2 T + \mu \Phi + \beta \frac{Dp}{Dt} \quad (6.4)$$

The last two terms on the right-hand side of the energy equation, eq. (6.4), account for viscous dissipation and pressure stress effects, where, as indicated in Chapters 1 and 5, Φ is given by

$$\begin{aligned} \Phi = 2 & \left[\left(\frac{\partial u}{\partial x} \right)^2 + \left(\frac{\partial v}{\partial y} \right)^2 + \left(\frac{\partial w}{\partial z} \right)^2 \right] \\ & \times \left(\frac{\partial v}{\partial x} + \frac{\partial u}{\partial y} \right)^2 + \left(\frac{\partial w}{\partial y} + \frac{\partial v}{\partial z} \right)^2 + \left(\frac{\partial u}{\partial z} + \frac{\partial w}{\partial x} \right)^2 \\ & - \frac{2}{3} (\nabla \cdot \mathbf{V})^2 \end{aligned}$$

Viscous dissipation effects are important in very viscous fluids or in the presence of large velocity gradients.

Two other orthogonal coordinate systems of frequent interest are the cylindrical and spherical coordinate systems. Governing equations for continuity, the force-momentum balance and the conservation of energy are provided in Chapter 1.

Equations (6.2)–(6.4) can be normalized using the variables

$$(x^*, y^*, z^*) = \frac{(x, y, z)}{L} \quad (6.5a)$$

$$(u^*, v^*, w^*) = \frac{(u, v, w)}{U} \quad (6.5b)$$

$$t^* = \frac{t}{L/U} \quad (6.5c)$$

$$p^* = \frac{p}{\rho U^2} \quad (6.5d)$$

where L and U are appropriate length and velocity scales, respectively. The normalized form of eq. (6.3a) is then

$$\begin{aligned} \frac{\partial u^*}{\partial t^*} + u^* \frac{\partial u^*}{\partial x^*} + v^* \frac{\partial u^*}{\partial y^*} + w^* \frac{\partial u^*}{\partial z^*} \\ = -\frac{\partial p^*}{\partial x^*} + \frac{\mu}{UL\rho} \left(\frac{\partial^2 u^*}{\partial x^{*2}} + \frac{\partial^2 u^*}{\partial y^{*2}} + \frac{\partial^2 u^*}{\partial z^{*2}} \right) \end{aligned} \quad (6.6)$$

The normalized forms of eqs. (6.3b) and (6.3c) are similar, and for brevity are not shown. Moreover, when all the variables in eq. (6.2) are replaced by their normalized versions, the Reynolds number emerges as the key nondimensional solution parameter, relating the inertia forces to the viscous forces:

$$\text{Re} = \frac{\rho U^2 L^2}{\mu(U/L)L^2} = \frac{\rho UL}{\mu} \quad (6.7)$$

To nondimensionalize the energy equation, a normalized temperature is defined as

$$T^* = \frac{T - T_\infty}{T_s - T_\infty} \quad (6.8)$$

where T_∞ and T_s are the local ambient and surface temperatures, respectively. Both temperatures could, in general, vary with location and/or time. The resulting normalized energy equation is

$$\frac{DT^*}{Dt^*} = \frac{1}{\text{Re} \cdot \text{Pr}} \left(\nabla^2 T^* + 2\text{Ec} \cdot \text{Pr} \cdot \Phi + 2\beta T \cdot \text{Re} \cdot \text{Pr} \cdot \text{Ec} \frac{Dp^*}{Dt^*} \right) \quad (6.9)$$

where β is the coefficient of volumetric thermal expansion and Pr is the Prandtl number:

$$\text{Pr} = \frac{\nu}{\alpha} = \frac{c_p \mu}{k} \quad (6.10a)$$

a measure of the ratio of diffusivity of momentum to diffusivity of heat. The Eckert number

$$\text{Ec} = \frac{V^2}{2c_p(T_s - T_\infty)} \quad (6.10b)$$

which expresses the magnitude of the kinetic energy of the flow relative to the enthalpy difference. In eq. (6.9), $\beta T = 1$ for ideal gases, and typically, $\beta T \ll 1$ for liquids. The pressure stress term is thus negligible in forced convection whenever the viscous dissipation is small.

The wall values of shear stress and heat flux are, respectively,

$$\tau_s = \mu \left. \frac{\partial u}{\partial y} \right|_s = \frac{\mu U}{L} \left. \frac{\partial u^*}{\partial y^*} \right|_{y^*=0} \quad (6.11a)$$

and

$$q_s'' = -k \left. \frac{\partial T}{\partial y} \right|_s = \frac{k(T_s - T_\infty)}{L} \left(- \left. \frac{\partial T^*}{\partial y^*} \right|_{y^*=0} \right) \quad (6.11b)$$

From a practical perspective, the friction drag and the heat transfer rate are the most important quantities. These are determined from the friction coefficient, C_f :

$$C_f = \frac{2\tau_s}{\rho U^2} = \frac{2}{\text{Re}} \left(\frac{\partial u^*}{\partial y^*} \right)_{y^*=0} \quad (6.12a)$$

and the Nusselt number Nu , defined as

$$\text{Nu} = \frac{q_s'' L}{k(T_s - T_\infty)} = - \frac{\partial T^*}{\partial y^*} \bigg|_{y^*=0} \quad (6.12b)$$

The boundary layer development for two-dimensional flow in the x - and y -coordinate directions over the wedge shown in Fig. 6.6 is based on the governing equations representing continuity, the x and y components of momentum, and the conservation of energy,

$$\frac{\partial u}{\partial x} + \frac{\partial v}{\partial y} = 0 \quad (6.13)$$

$$\frac{\partial u}{\partial t} + u \frac{\partial u}{\partial x} + v \frac{\partial u}{\partial y} = \frac{X}{\rho} - \frac{1}{\rho} \frac{\partial p}{\partial x} + \nu \left(\frac{\partial^2 u}{\partial x^2} + \frac{\partial^2 u}{\partial y^2} \right) \quad (6.14a)$$

$$\frac{\partial v}{\partial t} + u \frac{\partial v}{\partial x} + v \frac{\partial v}{\partial y} = \frac{Y}{\rho} - \frac{1}{\rho} \frac{\partial p}{\partial y} + \nu \left(\frac{\partial^2 v}{\partial x^2} + \frac{\partial^2 v}{\partial y^2} \right) \quad (6.14b)$$

$$\frac{\partial T}{\partial t} + u \frac{\partial T}{\partial x} + v \frac{\partial T}{\partial y} = \alpha \left(\frac{\partial^2 T}{\partial x^2} + \frac{\partial^2 T}{\partial y^2} \right) + \frac{\mu}{\rho c_p} \Phi + \frac{\beta T}{\rho c_p} \frac{Dp}{Dt} + \frac{q'''}{\rho c_p} \quad (6.15)$$

In eqs. (6.14), X and Y are the body forces in the x and y directions. The body force and the static pressure gradient terms on the right-hand sides of eqs. (6.14) can be combined to yield

$$- \frac{\partial p_m}{\partial x} = \frac{X}{\rho} - \frac{1}{\rho} \frac{\partial p}{\partial x} \quad \text{and} \quad - \frac{\partial p_m}{\partial y} = \frac{Y}{\rho} - \frac{1}{\rho} \frac{\partial p}{\partial y}$$

where the motion pressure p_m is the difference between the local static and local hydrostatic pressures.

On each face of the wedge shown in Fig. 6.6, the x direction is measured along the surface from the point of contact (the *leading edge*) and the y direction is measured normal to the surface. The free stream velocity, which is designated by $U(x)$ at a

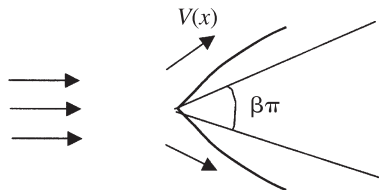


Figure 6.6 Boundary layer development for high-Reynolds-number flow over a wedge.

given x , remains unchanged for large values of y . The velocity varies from zero at the surface [$u(y = 0) = 0$] to the free stream velocity within a fluid layer, the thickness of which increases with x .

The region close to the surface where the velocity approaches a value close to the local free stream level defines the hydrodynamic boundary layer, which has the thickness $\delta(x)$. When heat transfer occurs, the temperature at the surface, $T(y = 0) = T_s$, is not equal to the free stream temperature T_∞ , and a thermal boundary layer also exists. In the thermal boundary, the temperature adjusts from the wall value to near the free stream level. The thermal boundary layer thickness $\delta_T(x)$ characterizes the thermal boundary layer.

When $R \gg 1$, thin hydrodynamic and thermal boundary layers of thickness $\delta(x)$ and $\delta_T(x)$, respectively, develop along an object in general and on the surfaces of the wedge in Fig. 6.6 in particular. Under this condition, $\delta/L \ll 1$ and $\delta_T/L \ll 1$ and the following scaled variables can be defined:

$$t^* = \frac{t}{t_0} \quad (6.16a)$$

$$x^* = \frac{x}{L} \quad (6.16b)$$

$$y^* = \frac{y}{\delta} \quad (6.16c)$$

$$u^* = \frac{u}{U(x)} \quad (6.16d)$$

$$v^* = \frac{v}{V_s} \quad (6.16e)$$

$$p_m^* = \frac{p_m - p_\infty}{\rho U^2} \quad (6.16f)$$

$$T^* = \frac{T - T_\infty}{T_s - T_\infty} \quad (6.16g)$$

$$y_T^* = \frac{y}{\delta_T} \quad (6.16h)$$

where V_s is the fluid velocity normal to the surface imposed by induced or forced fluid motion, $U(x)$ the velocity field in the potential flow region outside the boundary layers, t_0 a time reference, and T_∞ the temperature of the environment.

The corresponding continuity equation is

$$\frac{\partial u^*}{\partial x^*} + \frac{V_s L}{U \delta} \frac{\partial v^*}{\partial y^*} = 0 \quad (6.17)$$

and in order for the two terms to be of the same order of magnitude, V_s must be of the order of $\delta U/L$:

$$V_s = O\left(\frac{\delta U}{L}\right)$$

Then the normalized momentum equations become

$$\frac{L}{U t_0} \frac{\partial u^*}{\partial t^*} + u^* \frac{\partial u^*}{\partial x^*} + v^* \frac{\partial u^*}{\partial y^*} = -\frac{\partial p_m^*}{\partial x^*} + \frac{vL}{U \delta^2} \left[\left(\frac{\delta}{L}\right)^2 \frac{\partial^2 u^*}{\partial x^{*2}} + \frac{\partial^2 u^*}{\partial y^{*2}} \right] \quad (6.18)$$

and as $\text{Re} \gg 1$,

$$\frac{vL}{U \delta^2} = O(1) \quad \text{so that} \quad \frac{\delta}{L} = O\left(\frac{1}{\text{Re}_L^{1/2}}\right) \ll 1$$

and therefore,

$$\begin{aligned} \left(\frac{\delta}{L}\right)^2 \left(\frac{L}{U t_0} \frac{\partial v^*}{\partial t^*} + u^* \frac{\partial v^*}{\partial x^*} + v^* \frac{\partial v^*}{\partial y^*} \right) \\ = -\frac{\partial p_m^*}{\partial y^*} + \frac{1}{\text{Re}} \left[\left(\frac{\delta}{L}\right)^2 \frac{\partial^2 v^*}{\partial x^{*2}} + \frac{\partial^2 v^*}{\partial y^{*2}} \right] \end{aligned} \quad (6.19)$$

As $\text{Re} \rightarrow \infty$, eq. (6.19) becomes

$$0 = -\frac{\partial p_m^*}{\partial y^*} + 0$$

which implies that the pressure inside the boundary layer is a function of x and can be evaluated outside the boundary layer in the potential flow via the solution to the Euler equation

$$-\frac{1}{\rho} \frac{dp_m}{dx} = U \frac{dU}{dx}$$

The energy equation is

$$\begin{aligned} \frac{L}{U t_0} \frac{\partial T^*}{\partial t^*} + u^* \frac{\partial T^*}{\partial x^*} + \frac{\delta}{\delta_T} v^* \frac{\partial T^*}{\partial y_T^*} = \frac{k}{\rho c_p U L} \left[\frac{\partial^2 T^*}{\partial x^{*2}} + \left(\frac{L}{\delta_T}\right)^2 \frac{\partial^2 T^*}{\partial y_T^{*2}} \right] \\ + \frac{\mu U L}{\rho c_p \Delta T \delta^2} \Phi^* + \frac{\beta T U L}{c_p \Delta T t_0} \frac{Dp^*}{Dt^*} + \frac{q''' L}{\rho c_p U \Delta T} \end{aligned} \quad (6.20)$$

Here the transient term is important if $L/t_0 U = O(1)$ and steady conditions are approached for $L/t_0 U \ll 1$. In addition, the pressure stress term $v p_y \ll u p_x$ and the normalized equation resulting from letting $\text{Re} = O(L^2/\delta^2)$ is

$$\begin{aligned}
 u^* \frac{\partial T^*}{\partial x^*} + \frac{\delta}{\delta_T} v^* \frac{\partial T^*}{\partial y_T^*} &= \frac{1}{\text{Pr}} \left(\frac{\delta}{\delta_T} \right)^2 \frac{\partial^2 T^*}{\partial y_T^{*2}} \\
 &+ 2\text{Ec} \cdot \Phi^* + 2\beta T \cdot \text{Ec} \cdot u^* \frac{dp^*}{dx^*} + \frac{q''' L}{\rho c_p U \Delta T}
 \end{aligned} \quad (6.21)$$

The corresponding dimensional form of eq. (6.21) is

$$u \frac{\partial T}{\partial x} + v \frac{\partial T}{\partial y} = \alpha \frac{\partial^2 T}{\partial y^2} + \frac{\beta T}{\rho c_p} u \frac{dp}{dx} + \frac{\mu}{\rho c_p} \left(\frac{\partial u}{\partial y} \right)^2 + \frac{q'''}{\rho c_p} \quad (6.22)$$

Equation (6.20) can be used to demonstrate that when $\text{Pr} \ll 1$,

$$\frac{\delta_T}{\delta} = O\left(\frac{1}{\text{Pr}^{1/2}}\right)$$

and when $\text{Pr} \gg 1$,

$$\frac{\delta_T}{\delta} = O\left(\frac{1}{\text{Pr}^{1/3}}\right)$$

6.4.2 Similarity Transformation Technique for Laminar Boundary Layer Flow

Following the simplifications of eqs. (6.19)–(6.22), the two-dimensional steady-state boundary layer equations are:

$$u \frac{\partial u}{\partial x} + v \frac{\partial v}{\partial y} = 0 \quad (6.23)$$

$$u \frac{\partial u}{\partial x} + v \frac{\partial u}{\partial y} = -\frac{1}{\rho} \frac{\partial p}{\partial x} + \nu \frac{\partial^2 u}{\partial y^2} = U U_x + \nu \frac{\partial^2 u}{\partial y^2} \quad (6.24)$$

$$u \frac{\partial T}{\partial x} + v \frac{\partial T}{\partial y} = \alpha \frac{\partial^2 T}{\partial y^2} + \beta T u \frac{\partial p}{\partial x} + \frac{\mu}{\rho c_p} \left(\frac{\partial u}{\partial y} \right)^2 + \frac{q'''}{\rho c_p} \quad (6.25)$$

The boundary conditions for an impermeable surface are

$$u(x, 0) = v(x, 0) = 0 \quad (6.26a)$$

$$T(x, 0) = T_0(x) \quad (6.26b)$$

$$u(x, \infty) = U(x) \quad (6.26c)$$

$$T(x, \infty) = T_\infty(x) \quad (6.26d)$$

Equations (6.23)–(6.25) constitute a set of nonlinear partial differential equations. Under certain conditions similarity solutions can be found that allow conversion of this set into ordinary differential equations. The concept of similarity means that

certain features (e.g., velocity profiles) are geometrically similar. Analytically, this amounts to combining the x and y spatial dependence on a single independent variable η . The velocity components $u(x, y)$ and $v(x, y)$ are expressed by a single nondimensional stream function $f(\eta)$, and the temperature $T(x, y)$ into a nondimensional temperature $\phi(\eta)$.

Similarity for boundary layer flow follows from the observation that while the boundary layer thickness at each downstream location x is different, a scaled normal distance η can be employed as a universal length scale. Presence of natural length scales (such as a finite-length, plate, cylinder, or sphere) generally precludes the finding of similarity solutions. Using the scaled distance, the similarity procedure finds the appropriate normalized stream and temperature functions that are also valid at all locations. Following Gebhart (1980), the similarity variables are defined as

$$\eta(x, y) = yb(x) \quad (6.27)$$

$$f(\eta) = \frac{\Psi(x, y)}{vc(x)} \quad (6.28)$$

$$\phi(\eta) = \frac{T(x, y) - T_\infty(x)}{T_0(x) - T_\infty(x)} \quad (6.29)$$

where the allowable forms of $b(x)$ and $c(x)$ (defined later) and

$$d(x) = T_0(x) - T_\infty(x)$$

$$j(x) = T_\infty(x) - T_{\text{ref}}$$

need to be determined. The transformed governing equations in terms of the foregoing normalized variables are

$$f'''(\eta) + \frac{1}{b(x)} \frac{dc(x)}{dx} f(\eta) f''(\eta) - \frac{1}{b(x)} \left[\frac{dc(x)}{dx} + \frac{c(x)}{b(x)} \frac{db(x)}{dx} \right] [f'(\eta)]^2 - \frac{1}{\rho v^2 c(x) [(b(x))]^3} \frac{dp}{dx} = 0 \quad (6.30)$$

$$\begin{aligned} \frac{f''(\eta)}{\text{Pr}} + \frac{1}{b(x)} \frac{dc(x)}{dx} f(\eta) f''(\eta) - \frac{c(x)}{b(x)d(x)} \frac{dd(x)}{dx} f'(\eta) \phi(\eta) \\ - \frac{c(x)}{b(x)d(x)} \frac{dj(x)}{dx} f'(\eta) + \frac{\beta T}{\rho c_p} \frac{c(x)}{b(x)d(x)} \frac{dp}{dx} f'(\eta) \\ + \frac{v^2 [c(x)b(x)]^2}{c_p d(x)} [f''(\eta)]^2 + \frac{1}{d(x)[b(x)]^2} \frac{q'''}{k\text{Pr}} = 0 \end{aligned} \quad (6.31)$$

The boundary conditions are

$$f'(0) = f(0) = 1 - \phi(0) = \phi(\infty) = 0$$

and it is also noted that

$$\frac{dp}{dx} = -\rho U \frac{dU}{dx}$$

For the momentum equation to be entirely a function of the independent variable η ,

$$\begin{aligned} \frac{1}{b(x)} \frac{dc(x)}{dx} &= C_1 \\ \frac{c(x)}{[b(x)]^2} \frac{db(x)}{dx} &= C_2 \end{aligned}$$

This results in choices for the constants, C_1 and C_2 :

$$c(x) = \begin{cases} k' e^{kx} & (C_1 = C_2) \\ k'' x^q & (C_1 \neq C_2) \end{cases}$$

with C_1 and C_2 related by

$$C_2 = \frac{q-1}{q} C_1$$

For the pressure gradient term to be independent of x , the free stream velocity must be

$$U(x) \propto x^{2q-1}$$

Also known as *Falkner–Skan flow*, this form arises in the flow past a wedge with an included angle $\beta\pi$ as seen in Fig. 6.6. In this case,

$$U(x) = \bar{C} x^m$$

where

$$m = \frac{\beta}{2 - \beta}$$

as indicated in potential flow theory. From the similarity requirement, the exponent q becomes

$$q = \frac{m+1}{2} = \frac{1}{2-\beta}$$

Then the pressure gradient term in eq. (6.30) becomes

$$-\frac{1}{\rho v^2} \frac{1}{c(x)[b(x)]^3} \frac{dp}{dx} = \frac{(C_1 - C_2)^3 m \bar{C}^2}{v^2 k''^4} \frac{x^{2m-1}}{x^{4q-3}} = \beta$$

The arbitrary constants C_1 and C_2 may be chosen, without loss of generality, as

$$C_1 = 1 \quad \text{and} \quad C_2 = \beta - 1$$

This results in

$$\begin{aligned} c(x) &= \left(\frac{2}{m+1} \text{Re}_x \right)^{1/2} \\ b(x) &= \frac{1}{x} \left(\frac{m+1}{2} \text{Re}_x \right)^{1/2} \\ \eta &= \frac{y}{x} \left(\frac{m+1}{2} \text{Re}_x \right)^{1/2} \\ \psi(x, y) &= \nu f(\eta) \left(\frac{2}{m+1} \text{Re}_x \right)^{1/2} \end{aligned}$$

and for this choice of constants, the Falkner–Skan momentum equation and boundary conditions become

$$\begin{aligned} f'''(\eta) + f(\eta)f''(\eta) + [1 - f'(\eta)]^2 \beta &= 0 \\ f'(\eta = 0) = f(\eta = 0) &= 1 - f'(\eta = \infty) = 0 \end{aligned}$$

The often used (and much older) Blasius (1908) variables for flow past a flat plate ($\beta = 0$) are related to the Falkner–Skan variables η and $f(\eta)$ as

$$\eta_B = 2^{1/2} \eta \quad \text{and} \quad f(\eta_B) = 2^{1/2} f(\eta)$$

For similarity to hold, the energy equation must satisfy the conditions

$$\frac{c(x)}{b(x)d(x)} \frac{dd(x)}{dx} = C_5 \quad (6.32a)$$

$$\frac{\nu^2 [c(x)b(x)]^2}{c_p d(x)} = K_3 \frac{[c(x)b(x)]^2}{d(x)} = K_3 C_6 \quad (6.32b)$$

$$\frac{c(x)}{b(x)d(x)} \frac{dj(x)}{dx} = C_7 \quad (6.32c)$$

$$\frac{\beta T}{\rho c_p} \frac{c(x)}{b(x)d(x)} \frac{dp}{dx} = K_4 \frac{c(x)}{b(x)d(x)} \frac{dp}{dx} = K_4 C_{10} \quad (6.32d)$$

$$\frac{1}{d(x)[b(x)]^2} \frac{1}{\text{Pr}} \frac{q'''}{k} = F_1(\eta) \quad (6.32e)$$

6.4.3 Similarity Solutions for the Flat Plate at Uniform Temperature ($m = 0$)

For the case of the flat plate, the similarity equations and boundary conditions reduce to

$$f'''(\eta) + f(\eta)f''(\eta) = 0 \quad \phi''(\eta) + \text{Pr} \cdot f(\eta)\phi'(\eta) = 0 \quad (6.33)$$

and

$$1 - \phi(0) = \phi(\infty) = 0 \quad \text{and} \quad f(0) = f'(0) = 1 - f'(\infty) = 0 \quad (6.34)$$

Both the momentum and energy equations are ordinary differential equations in the form of two-point boundary value problems. The momentum equation is solved first because it is uncoupled from the energy equation. The velocity field is then substituted into the energy equation to obtain the temperature field and heat transfer characteristics.

The wall heat flux is obtained as

$$\begin{aligned} q''(x) &= h_x(T_0 - T_\infty) = -k \left. \frac{\partial T}{\partial y} \right|_{y=0} = -k(T_0 - T_\infty)\phi'(0) \frac{\partial \eta}{\partial y} \\ &= -k(T_0 - T_\infty)\phi'(0) \frac{1}{x} \cdot \text{Re}_x^{1/2} \end{aligned} \quad (6.35)$$

This results in the local Nusselt number

$$\text{Nu}_x = \frac{h_x x}{k} = \frac{-\phi'(0)}{\sqrt{2}} \text{Re}_x^{1/2} = \bar{F}(\text{Pr}) \text{Re}_x^{1/2}$$

where $\bar{F}(\text{Pr})$ is determined numerically and near $\text{Pr} \approx 1$ is well approximated by $0.332\text{Pr}^{1/3}$ so that,

$$\text{Nu}_x = 0.332 \text{Re}_x^{1/2} \cdot \text{Pr}^{1/3} \quad (6.36)$$

the surface-averaged heat transfer coefficient is determined as:

$$\bar{h} = \frac{1}{A_s} \int h \, dA_s = \frac{1}{L} \int_0^L h_x \, dx = 2h \Big|_{x=L} \quad (6.37)$$

6.4.4 Similarity Solutions for a Wedge ($m \neq 0$)

For a wedge at a uniform surface temperature, the expressions for the surface heat flux and the Nusselt number are

$$q''(x) = -k(T_0 - T_\infty)\phi'(0)\frac{1}{x}\left(\frac{m+1}{2}\text{Re}_x\right)^{1/2} \quad (6.38)$$

$$\text{Nu}_x = \frac{h_x x}{k} = \frac{-\phi'(0)}{\sqrt{2}}[(m+1)\text{Re}_x]^{1/2} = \bar{F}(m, \text{Pr})\text{Re}_x^{1/2} \quad (6.39)$$

For a wedge with a spatially varying surface temperature, eq. (6.32a)

$$C_5 = \frac{c(x)}{b(x)d(x)} \frac{dd(x)}{dx}$$

yields

$$\frac{1}{d(x)} \frac{dd(x)}{dx} = C_5 \frac{b(x)}{c(x)} = C_5 \frac{m+1}{2x} = \frac{n}{x}$$

where

$$n \equiv C_5 \frac{m+1}{2}$$

is a constant. This yields

$$d(x) = [T_0(x) - T_\infty] = Nx^n$$

where N is a constant arising from the integration for the surface temperature variation. The energy equation is transformed to

$$\phi''(\eta) + \text{Pr} \left[f(\eta)\phi'(\eta) - \frac{2n}{m+1} f'(\eta)\phi(\eta) \right] = 0$$

The resulting expressions for the heat flux and the local Nusselt number are

$$q''(x) = -k\phi'(0)N \left(\frac{(m+1)\bar{C}}{2v} \right)^{1/2} x^{(2n+m-1)/2} \quad (6.40)$$

$$\text{Nu}_x = -\phi'(0) \left(\frac{m+1}{2} \text{Re}_x \right)^{1/2} = \bar{F}(\text{Pr}, m, n)\text{Re}_x^{1/2} \quad (6.41)$$

In the range of $0.70 \leq \text{Pr} \leq 10$, Zhukauskas (1972, 1987) reports the correlation for the data computed by Eckert:

$$\frac{\text{Nu}}{\text{Re}_x^{1/2}} = \frac{0.56A}{(2 - \beta)^{1/2}} \quad (6.42)$$

where

$$\beta = \frac{2m}{m+1} \quad \text{and} \quad A = (\beta + 0.20)^{0.11} \cdot \text{Pr}^{0.333+0.067\beta-0.026\beta^2}$$

For the thermal boundary layer thickness to increase with x , two special cases of the foregoing solution corresponding to a flat plate ($m = 0$) are of interest (Fig. 6.7). These correspond respectively to a uniform heat flux surface and a line heat source at $x = 0$ (a line plume). The heat flux can be written as

$$q''(x) = -k\phi'(0)N \left(\frac{U}{\nu} \right)^{1/2} x^{(2n-1)/2}$$

For the first condition (Fig. 6.7a), $n = \frac{1}{2}$. For the second condition (Fig. 6.7b), the total energy convected by the flow per unit length of the source is written as

$$\begin{aligned} q'(x) &= \int_0^\infty \rho c_p u (T - T_\infty) dy \\ &= \nu \rho c_p c(x) d(x) \int_0^\infty f'(\eta) \phi(\eta) d\eta \propto x^{(2n+1)/2} \end{aligned} \quad (6.43)$$

For the convected energy to remain invariant with x , n must take on the value $n = -\frac{1}{2}$.

Wedge Flow Limits With regard to wedge flow limits, numerical solutions to the Falkner–Skan equations have been obtained for $-0.0904 \leq m \leq \infty$, where the lower limit is set by the onset of boundary layer separation. In addition, the hydrodynamic boundary layer thickness is

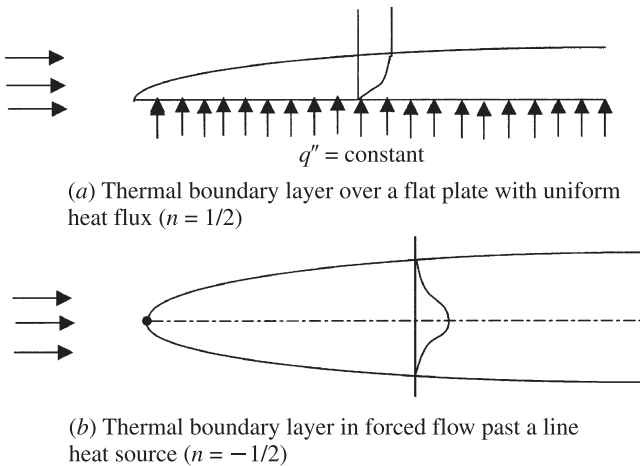


Figure 6.7 Two important cases for boundary layer flow at uniform free stream velocity.

$$\delta(x) = \eta_\delta \left[\frac{2\nu}{(m+1)\bar{C}} \right]^{1/2} x^{(1-m)/2}$$

where η_δ , the nondimensional thickness of the boundary layer, is bound at $x = 0$ only for $m \leq 1$. This requires that $1 \geq m \geq -0.0904$. Additionally, the total energy convected by the flow per unit width normal to the plane of flow is given by

$$q'(x) = \nu \rho c_p c(x) d(x) \int_0^\infty f'(\eta) \phi(\eta) d\eta \propto Nx^{(2n+m+1)/2}$$

This provides the condition

$$\frac{2n+m+1}{2} \geq 0 \quad \text{or} \quad n \geq -\frac{m+1}{2}$$

6.4.5 Prandtl Number Effect

Consider the case of $n = m = 0$ first. In the limiting cases of $\text{Pr} \ll 1$ and $\text{Pr} \gg 1$ (Fig. 6.8), the solution of the momentum equation can be approximated in closed form. Subsequently, the energy equation can be solved. For $\text{Pr} \ll 1$, the velocity components u and U are approximately equal throughout the thermal boundary layer. This results in $f'(\eta) \approx 1$ or $f(\eta) \approx \eta + K$. For an impermeable wall, $K = 0$ and the energy equation simplifies to

$$\phi''(\eta) + \text{Pr} \cdot \eta \phi'(\eta) = 0$$

This can be integrated to yield

$$\phi'(\eta) = e^{-\eta_1^2 + C}$$

where

$$\eta_1^2 = \frac{\eta^2 \cdot \text{Pr}}{2}$$

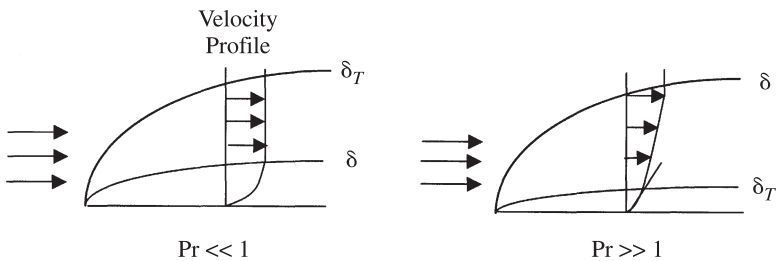


Figure 6.8 Laminar flat plate boundary layer flow at limiting Prandtl numbers.

and with the boundary conditions

$$1 = \phi(0) = \phi(\infty) = 0$$

another integration provides

$$\phi(\eta) = 1 - \operatorname{erf}(\eta_1)$$

where

$$\operatorname{erf}(\eta_1) = \frac{2}{\sqrt{\pi}} \int_0^{\eta_1} e^{-v^2} dv$$

From this the local Nusselt number is determined as

$$\operatorname{Nu}_x = -\frac{\phi'(0)}{\sqrt{2}} \operatorname{Re}_x^{1/2} = \frac{2}{\sqrt{\pi}} \left(\frac{\operatorname{Pr}}{2} \operatorname{Re}_x \right)^{1/2} = 0.565 \operatorname{Re}_x^{1/2} \cdot \operatorname{Pr}^{1/2} \quad (6.44)$$

and for $\operatorname{Pr} \gg 1$, the nondimensional stream function near the wall is expressed as

$$f(\eta) = \frac{f(0)}{0!} + \frac{f'(0)}{1!} \eta + \frac{f''(0)}{2!} \eta^2 + \frac{f'''(0)}{3!} \eta^3 + \dots \quad (6.45)$$

However, $f(0) = f'(0) = 0$ and the momentum equation shows that $f'''(0) = 0$. This results in

$$f(\eta) = \frac{f''(0)}{2!} \eta^2 = \frac{0.332}{\sqrt{2}} \eta^2 \quad (6.46)$$

upon using

$$f''(0) = \sqrt{2} f_B''(0) = 0.332\sqrt{2}$$

where the subscript B refers to the Blasius variables defined in Section 6.4.2. The energy equation then becomes

$$\phi''(\eta) + \frac{0.332\operatorname{Pr}}{\sqrt{2}} \eta^2 \phi'(\eta) = 0 \quad (6.47)$$

This can be integrated and evaluated at the surface to yield

$$-\frac{\phi'(0)}{\sqrt{2}} = 0.339\operatorname{Pr}^{1/3} \quad (6.48a)$$

$$\operatorname{Nu}_x = 0.339 \operatorname{Re}_x^{1/2} \cdot \operatorname{Pr}^{1/3} \quad (6.48b)$$

6.4.6 Incompressible Flow Past a Flat Plate with Viscous Dissipation

Using the Blasius normalized variables for the flow and then defining the normalized temperature as

$$\theta(\eta) = \frac{2c_p(T - T_\infty)}{U^2}$$

the energy equation and thermal boundary conditions become

$$\theta''(\eta) + \frac{1}{2}\text{Pr} \cdot f(\eta)\theta'(\eta) + 2\text{Pr} \cdot f''(\eta)^2 = 0 \quad (6.49)$$

and

$$\theta(\eta = \infty) = 0 \quad \text{and} \quad \theta(\eta = 0) = \frac{2c_p(T_0 - T_\infty)}{U^2} = \theta_o \quad (\text{constant}) \quad (6.50)$$

The solution to eq. (6.49), which is a nonhomogeneous equation, consists of the superposition of a homogeneous part:

$$\theta_H = C_1\phi(\eta) - C_2$$

and a particular solution

$$\theta_P = \theta_{AW}(\eta)$$

where the subscript AW refers to an adiabatic wall condition.

The governing equations and boundary conditions for these are

$$\theta''_{AW} + \frac{1}{2}\text{Pr} \cdot f\theta'_{AW} + 2\text{Pr}(f'')^2 = 0 \quad (6.51)$$

$$\phi'' + \frac{1}{2}\text{Pr} \cdot f\phi' = 0 \quad (6.52)$$

and

$$\theta'_{AW}(0) = \theta'_{AW}(\infty) = 0 \quad \text{and} \quad \phi(0) = 1 - \phi(\infty) \quad (6.53)$$

For the boundary conditions for the complete problem to be satisfied,

$$\theta(\infty) = 0 = \theta_{AW}(\infty) + C_1\phi(\infty) + C_2$$

which leads to $C_1 = -C_2$ and

$$\theta(0) = \frac{2c_p(T_0 - T_\infty)}{U^2} = \theta_{AW}(0) + C_1\phi(0) + C_2 = \frac{2c_p(T_{AW} - T_0)}{U^2} + C_2$$

or

$$C_2 = -C_1 = \frac{2c_p(T_0 - T_{AW})}{U^2}$$

The solution for $\theta_{AW}(\eta_B)$ is obtained numerically by solving eq. (6.51). From this

$$\theta_{AW}(0) \equiv r_c = b(\text{Pr}) \simeq \text{Pr}^{1/2} \quad (\text{for gases})$$

where r_c is called the *recovery factor*. Using this, the adiabatic wall temperature is calculated as

$$T_{AW} = T_\infty + r_c \frac{U^2}{2c_p}$$

For low velocities this can be approximated as

$$T_{AW} = T_\infty$$

The temperature profile for various choices of T_0 is shown in Fig. 6.9 from Gebhart (1971).

The heat flux can be written as

$$\begin{aligned} q_0'' &= -k \frac{\partial T}{\partial y} \Big|_{y=0} = -k \frac{U^2}{2c_p} \left(\frac{U}{\nu x} \right)^{1/2} [\theta'_{AW}(0) + C_1 \phi'(0)] \\ &= k(T_0 - T_{AW}) \left[0.332 \left(\frac{U}{\nu x} \right)^{1/2} \cdot \text{Pr}^{1/3} \right] \end{aligned} \quad (6.54)$$

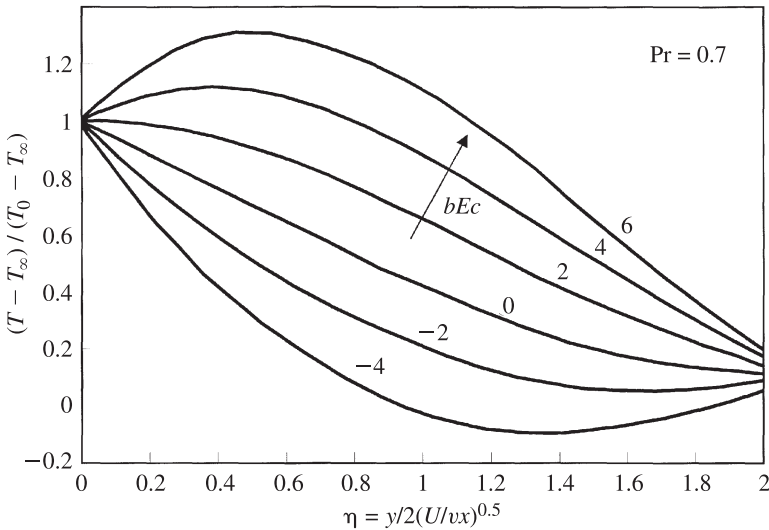


Figure 6.9 Boundary layer temperature profiles with viscous dissipation. (From Gebhart, 1971.)

and with the definition

$$q_0'' = h_x(T_0 - T_{AW})$$

the Nusselt number becomes the well-known Pohlhausen (1921) solution:

$$\text{Nu} = 0.332 \text{Re}_x^{1/2} \cdot \text{Pr}^{1/3}$$

where the properties can be evaluated at the reference temperature recommended by Eckert:

$$T^* = T_\infty + (T_W - T_\infty) + 0.22(T_{AW} - T_\infty)$$

6.4.7 Integral Solutions for a Flat Plate Boundary Layer with Unheated Starting Length

Consider the configuration illustrated in Fig. 6.10. The solution for this configuration can be used as a building block for an arbitrarily varying surface temperature where a similarity solution does not exist. Assuming steady flow at constant properties and no viscous dissipation, the boundary layer momentum and energy equations can be integrated across the respective boundary layers to yield

$$\frac{d}{dx} \int_0^\delta u(U - u) dy = \nu \left. \frac{\partial u}{\partial y} \right|_{y=0} \quad (6.55)$$

$$\frac{d}{dx} \int_0^{\delta_T} u(T_\infty - T) dy = \alpha \left. \frac{\partial T}{\partial y} \right|_{y=0} \quad (6.56)$$

To integrate eqs. (6.55) and (6.56), approximate profiles for tangential velocity and temperature across the boundary layer must be defined. For example, a cubic parabola profile of the type $T = a + by + cy^2 + dy^3$ can be employed, with the conditions

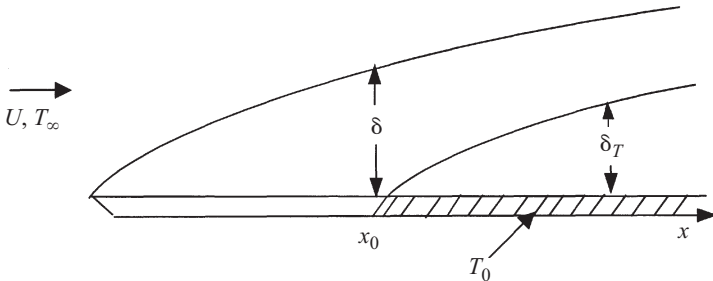


Figure 6.10 Hydrodynamic and thermal boundary layer development along a flat plate with an unheated starting length in a uniform stream.

$$y(T = T_0) = 0 \quad (6.57a)$$

$$y(T = T_\infty) = \delta_T \quad (6.57b)$$

$$\left. \frac{\partial T}{\partial y} \right|_{T=T_\infty} = 0 \quad (6.57c)$$

By evaluating the energy equation at the surface, an additional condition can be developed:

$$\left. \frac{\partial^2 T}{\partial y^2} \right|_{y=0} = 0$$

Using these boundary conditions, the temperature profile can be determined as

$$\frac{T - T_0}{T_\infty - T_0} = \frac{3}{2} \frac{y}{\delta_T} - \frac{1}{2} \left(\frac{y}{\delta_T} \right)^3 \quad (6.58)$$

Polynomials of higher order can be selected, with the additional conditions determined by prescribing additional higher-order derivatives set to zero at the edge of the boundary layer. In a similar manner, a cubic velocity profile can be determined by prescribing

$$u(y = 0) = v(y = 0) = 0$$

$$u(y = \delta) = u_\infty$$

$$\left. \frac{\partial u}{\partial y} \right|_{y=\delta} = 0$$

and determining

$$\left. \frac{\partial^2 u}{\partial y^2} \right|_{y=0} = 0$$

This results in

$$\frac{u}{U} = \frac{3}{2} \frac{y}{\delta} - \frac{1}{2} \left(\frac{y}{\delta} \right)^3 \quad (6.59)$$

These profiles are next substituted into the integral energy equation and the integration carried out. Assuming that $\text{Pr} > 1$, the upper limit needs only to be extended to $y = \delta_T$, because beyond this, $\theta = T_0 - T = T - T_\infty = \theta_\infty$ and the integrand is zero. In addition, defining, $r = \delta_T / \delta$, it noted that

$$\int_0^{\delta_T} (\theta_\infty - \theta) u \, dy = \theta_\infty U \delta \left(\frac{3}{20} r^2 - \frac{3}{280} r^4 \right) \quad (6.60)$$

Because $r < 1$, the second term may be neglected in comparison to the first. Now r is a function of x and the integral of eq. (6.60) may be put into the integral energy equation of eq. (6.56), yielding

$$2r^2\delta^2\frac{dr}{dx} + r^3\delta\frac{d\delta}{dx} = \frac{10\alpha}{U} \quad (6.61)$$

From the integral momentum equation, $\delta(x)$ can be determined as

$$\delta(x) = 4.64 \left(\frac{\nu x}{U} \right)^{1/2}$$

This yields

$$r^3 + 4r^2x\frac{dr}{dx} = \frac{13}{14\text{Pr}}$$

which can be solved to yield

$$r = \frac{1}{1.026\text{Pr}^{1/3}} \left[1 - \left(\frac{x_0}{x} \right)^{3/4} \right]^{1/3}$$

where x_0 is the unheated starting length. The heat transfer coefficient and the Nusselt number are then

$$h = \frac{-k(\partial T/\partial y)|_{y=0}}{T_0 - T_\infty} = \frac{k}{\theta_\infty} \frac{\partial \theta}{\partial y} \bigg|_{y=0} = \frac{3}{2} \frac{k}{\delta_T} = \frac{3}{2} \frac{k}{r\delta}$$

or

$$h = 0.332k \frac{\text{Pr}^{1/3}}{[1 - (x_0/x)^{3/4}]^{1/3}} \left(\frac{U}{\nu x} \right)^{1/2} \quad (6.62)$$

and

$$\text{Nu} = \frac{0.332\text{Pr}^{1/2} \cdot \text{Re}_x^{1/2}}{[1 - (x_0/x)^{3/4}]^{1/3}} \quad (6.63)$$

Arbitrarily Varying Surface Temperature The foregoing results can easily be generalized for any surface temperature variation of the type

$$T_0 = T_\infty + A + \sum_{n=1}^{\infty} B_n x^n \quad (6.64)$$

For a single step,

$$\frac{T_0 - T}{T_0 - T_\infty} = \theta(x_0, x, y)$$

and for an arbitrary variation,

$$T_0 - T_\infty = \int_0^x [1 - \theta(x_0, x, y)] \frac{\partial T}{\partial x_0} dx_0 + \sum_{i=1}^k [1 - \theta(x_{0i}, x, y)] \Delta T_{0,i} \quad (6.65)$$

$$q_0'' = k \int_0^x \frac{\partial \theta(x_0, x, 0)}{\partial y} \frac{dT_0}{dx_0} dx_0 + \sum_{i=1}^k \frac{\partial \theta(x_{0i}, x, 0)}{\partial y} \Delta T_{0,i} \quad (6.66)$$

This procedure using the integral momentum equation can also be generalized to a turbulent boundary layer with an arbitrary surface temperature variation.

6.4.8 Two-Dimensional Nonsimilar Flows

When similarity conditions do not apply, as in the case of an unheated starting length plate, two classes of approaches exist for solution of the governing equations. The integral method results in an ordinary differential equation with the downstream coordinate x as the independent variable and parameters associated with the body profile shape and the various boundary layer thicknesses as the dependent variable. Generally, such solutions result in correlation relationships that have a limited range of applicability. These are typically much faster to compute.

Differential methods solve the partial differential equations describing numerically the conservation of mass, force momentum balance, and conservation of energy. These equations are discretized over a number of control volumes, resulting in a set of algebraic equations that are solved simultaneously using numerical techniques. These solutions provide the detailed velocity, pressure, temperature, and density fields for compressible flows. The heat transfer rates from various surfaces can also be determined from these results. In the 1980s and 1990s, the computational hardware capabilities expanded dramatically and the differential methods have become the most commonly used methods for various complex and realistic geometries.

6.4.9 Smith–Spalding Integral Method

The heat transfer in a constant-property laminar boundary layer with variable velocity $U(x)$ but uniform surface temperature can be obtained via the Smith–Spalding integral method (1958), as described by Cebeci and Bradshaw (1984). A conduction thickness is defined as

$$\delta_c = \frac{k(T_0 - T_\infty)}{q_0''} = - \frac{T_0 - T_\infty}{(\partial T / \partial y)_{y=0}} \quad (6.67)$$

This is expressed in nondimensional form as

$$\frac{U(x)}{v} \frac{d\delta_c^2}{dx} = f \left(\frac{\delta_c^2}{v} \frac{dU}{dx}, \text{Pr} \right) = A - B \frac{\delta_c^2}{v} \frac{dU}{dx} \quad (6.68)$$

where A and B are Prandtl number–dependent constants. For similar laminar flows, the Nusselt number is given as

$$\text{Nu} = \frac{q''x}{k(T_0 - T_\infty)} = -\frac{x(\partial T/\partial y)_0}{T_0 - T_\infty} = f(\text{Pr}, m, 0)\text{Re}_x^{1/2} \quad (6.69)$$

and using the definition of the conduction thickness yields

$$\delta_c^2 = \frac{\nu x}{C^2 U} \quad (6.70)$$

where $C = f(\text{Pr}, m, 0)$. The parameters in eq. (6.68) can be expressed as

$$\frac{U(x)}{\nu} \frac{d\delta_c^2}{dx} = \frac{1-m}{C^2} \quad (6.71a)$$

$$\frac{\delta_c^2}{\nu} \frac{dU}{dx} = \frac{m}{C^2} \quad (6.71b)$$

Equation (6.69) is a first-order ordinary differential equation that can be integrated as

$$\delta_c^2 = -\frac{\nu A \int_0^x U^{B-1} dx}{U^B} + \delta_c^2 \frac{U_i^B}{U^B}$$

where the subscript i denotes initial conditions. The normalized heat transfer coefficient in the form of a local Stanton number ($\text{St} = \text{Nu}/\text{Re}_x \cdot \text{Pr}$) is

$$\text{St} = \frac{q''}{\rho c_p U (T_0 - T_\infty)} = \frac{k}{\rho c_p U \delta} = \frac{c_1 (U^*)^{c_2}}{\left[\int_0^{x^*} (U^*)^{c_3} dx^* \right]^{1/2}} \left(\frac{1}{\text{Re}_L} \right)^{1/2} \quad (6.72)$$

Here

$$c_1 = \text{Pr}^{-1} \cdot A^{-1/2}, \quad c_2 = \frac{B}{2}, \quad c_3 = B - 1$$

and provided in Table 6.1 and

$$U^* = \frac{U(x)}{U_\infty} \quad x^* = \frac{x}{L} \quad \text{Re}_L = \frac{U_\infty L}{\nu}$$

where U_∞ is a reference velocity, typically the uniform upstream velocity, and L is a length scale characteristic of the object.

As an example of the use of the Smith–Spalding approach, consider the heat transfer in cross flow past a cylinder of radius r_0 heated at a uniform temperature. The velocity distribution outside the boundary layer is given by

TABLE 6.1 Parameters c_1 , c_2 , and c_3 as Functions of the Prandtl Number

Pr	c_1	c_2	c_3
0.70	0.418	0.435	1.87
1.00	0.332	0.475	1.95
5.00	0.117	0.595	2.19
10.0	0.073	0.685	2.37

Source: Cebeci and Bradshaw (1984).

$$U(x) = 2U_\infty \sin \theta = 2U_\infty \sin \frac{x}{r_0} \tag{6.73}$$

where x is measured around the circumference, beginning with the front stagnation point. For small values of θ , $\sin \theta \approx \theta$, and the free stream velocity approaches that for a stagnation point where similarity exists. The computed results for $Nu_x/Re_x^{1/2}$ are shown in Fig. 6.11 for three values of Pr.

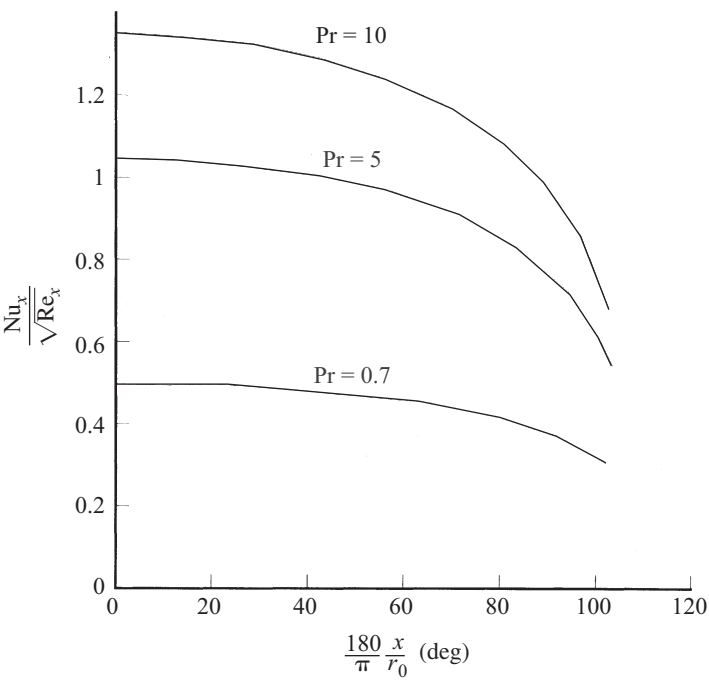


Figure 6.11 Local heat transfer results for crossflow past a heated circular cylinder at uniform temperature for various Pr values, using the integral method. (From Cebeci and Bradshaw, 1984.)

6.4.10 Axisymmetric Nonsimilar Flows

The Smith–Spalding method (1958) can be extended to axisymmetric flows by using the Mangler transformation. If the two-dimensional variables are denoted by the subscript 2 and the axisymmetric variables by the subscript 3 and neglecting transverse curvature, then

$$dx_2 = \left(\frac{r_0}{L}\right)^{2K} dx_3 \quad \theta_2 = \left(\frac{r_0}{L}\right)^K \theta_3 \quad (6.74)$$

where K is the flow index used in the Mangler transformation to relate the axisymmetric coordinates x and θ to two-dimensional coordinates and

$$r_0^2 (\delta_c)_3^2 = \frac{\nu A \int_0^{x_3} U^{B-1} dx_3}{U^B} \quad (6.75)$$

where r_0 is the distance from the axis to the surface (see Fig. 6.13).

The Stanton number is given in nondimensional form by

$$\text{St} = \frac{c_1 (r_0^*)^K (U^*)^{c_2}}{\left[\int_0^{x_3^*} (U^*)^{c_3} (r_0^*)^{2K} dx_3^* \right]^{1/2} \left(\frac{1}{\text{Re}_L} \right)^{1/2}} \quad (6.76)$$

where $U^* = U(x)/U_\infty$, $r_0^* = r_0/L$, and $x_3^* = x_3/L$. Here the constants c_1 , c_2 , and c_3 are given in Table 6.1.

As an example, heat transfer from a heated sphere of radius a at a uniform temperature placed in an undisturbed flow characterized by U_∞ can be calculated by this method. The velocity distribution in the inviscid flow is

$$U = \frac{3}{2} U_\infty \sin \phi = \frac{3}{2} U_\infty \sin \frac{x}{a} \quad (6.77)$$

The variation of $\text{Nu}_x (U_\infty a / \nu)^{-1/2}$ downstream from the front stagnation point is seen in Fig. 6.12. The result of the similarity solution for the case of axisymmetric stagnation flow is also shown. As described by Cebeci and Bradshaw (1984), this similarity solution requires the transformation of the axisymmetric equations into a nearly two-dimensional form through use of the Mangler transformation.

6.4.11 Heat Transfer in a Turbulent Boundary Layer

The two-dimensional boundary layer form of the time-averaged governing equations is

$$\frac{\partial \bar{u}}{\partial x} + \frac{\partial \bar{v}}{\partial y} = 0 \quad (6.78)$$

$$\begin{aligned}
 \rho \left(\bar{u} \frac{\partial \bar{u}}{\partial x} + \bar{v} \frac{\partial \bar{v}}{\partial y} \right) &= -\frac{d\bar{p}}{dx} + \mu \frac{\partial^2 \bar{u}}{\partial y^2} - \frac{\partial}{\partial y} (\rho \overline{u'v'}) \\
 &= -\frac{d\bar{p}}{dx} + \frac{\partial \tau_m}{\partial y} - \frac{\partial}{\partial y} (\rho \overline{u'v'})
 \end{aligned} \quad (6.79)$$

$$\rho c_p \left(\bar{u} \frac{\partial \bar{T}}{\partial x} + \bar{v} \frac{\partial \bar{T}}{\partial y} \right) = k \frac{\partial^2 \bar{T}}{\partial y^2} - \frac{\partial}{\partial y} (\rho c_p \overline{v'T'}) = -\frac{\partial q_m}{\partial y} - \frac{\partial}{\partial y} (\rho c_p \overline{v'T'}) \quad (6.80)$$

where $\tau_m = \mu(\partial \bar{u}/\partial y)$ and $q_m'' = -k(\partial \bar{T}/\partial y)$ are the mean shear stress and heat flux, respectively.

Axisymmetric Flows Equations (6.78) through (6.80) are derived for two-dimensional flow, with the velocity component as well as all derivatives of time-averaged quantities neglected in the z direction. For axisymmetric flow, such as in a circular jet or within the boundary layer on a body of circular cross section, also called a *body of revolution* (Fig. 6.13), Cebeci and Bradshaw (1984) show that the governing equations can be generalized:

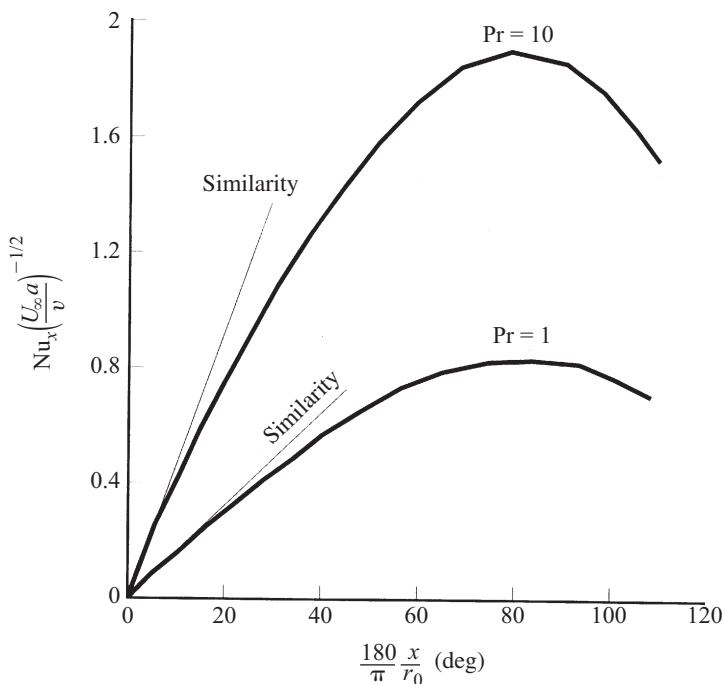


Figure 6.12 Local heat transfer behavior for flow past a heated sphere at uniform surface temperature for various Pr values, using the integral method. (From Cebeci and Bradshaw, 1984.)

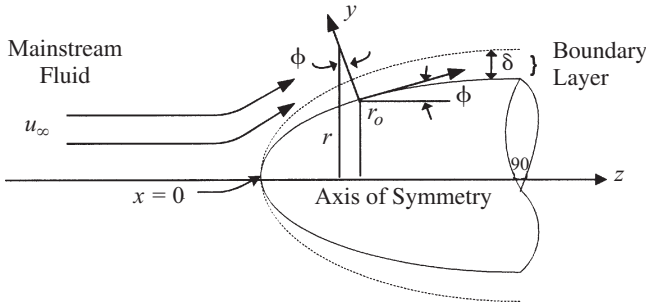


Figure 6.13 Boundary layer development on a body of revolution.

$$\frac{\partial r^N \bar{u}}{\partial x} + \frac{\partial r^N \bar{v}}{\partial y} = 0 \quad (6.81)$$

$$\rho \left(\bar{u} \frac{\partial \bar{u}}{\partial x} + \bar{v} \frac{\partial \bar{v}}{\partial y} \right) = -\frac{dp}{dx} + \frac{1}{r^N} \frac{\partial}{\partial y} \left[r^N \left(\mu \frac{\partial \bar{u}}{\partial y} - \rho \overline{u'v'} \right) \right] \quad (6.82)$$

$$\rho c_p \left(\bar{u} \frac{\partial \bar{T}}{\partial x} + \bar{v} \frac{\partial \bar{T}}{\partial y} \right) = \frac{1}{r^N} \frac{\partial}{\partial y} \left(k \frac{\partial \bar{T}}{\partial y} - \rho c_p \overline{v'T'} \right) \quad (6.83)$$

where $N = 1$ in axisymmetric flow and $N = 0$ in two-dimensional flow. The turbulent components of the shear stress and the heat flux are defined as

$$\tau_T = -\rho \overline{u'v'} = \rho \epsilon \frac{\partial \bar{u}}{\partial y} \quad \text{and} \quad q_T'' = -\rho c_p \overline{v'T'} = -\rho c_p \epsilon_H \frac{\partial \bar{T}}{\partial y}$$

where ϵ and ϵ_H are, respectively, the turbulent or eddy diffusivities of momentum and heat. The governing two-dimensional equations with these incorporated become

$$\bar{u} \frac{\partial \bar{u}}{\partial x} + \bar{v} \frac{\partial \bar{v}}{\partial y} = -\frac{1}{\rho} \frac{d\bar{p}}{dx} + \frac{\partial}{\partial y} \left[(v + \epsilon) \frac{\partial \bar{u}}{\partial y} \right] \quad (6.84)$$

and

$$\bar{u} \frac{\partial \bar{T}}{\partial x} + \bar{v} \frac{\partial \bar{T}}{\partial y} = \frac{\partial}{\partial y} \left[(\alpha + \epsilon_H) \frac{\partial \bar{T}}{\partial y} \right] = v \frac{\partial}{\partial y} \left(\frac{1}{\text{Pr}} + \frac{\epsilon}{v} \frac{1}{\text{Pr}_T} \frac{\partial \bar{T}}{\partial y} \right) \quad (6.85)$$

where $\text{Pr}_T = \epsilon/\epsilon_H$ is the turbulent Prandtl number. Solution of (6.84) and (6.85) requires modeling of the turbulent shear stress and heat flux.

Analogy Solutions The total shear stress and heat flux are written as a combination of the mean and turbulent components:

$$\tau = \tau_m + \tau_T = \rho(v + \epsilon) \frac{\partial \bar{u}}{\partial y} \quad (6.86)$$

$$q'' = q_m'' + q_T'' = -\rho c_p (\alpha + \epsilon_H) \frac{\partial \bar{T}}{\partial y} \quad (6.87)$$

These can be integrated to yield

$$\bar{u} = \int_0^y \frac{\tau}{\rho(v + \epsilon)} dy \quad (6.88)$$

$$T_0 - \bar{T} = \int_0^y \frac{q''}{\rho c_p (\alpha + \epsilon_H)} dy \quad (6.89)$$

6.4.12 Algebraic Turbulence Models

The simplest class of turbulence closure models is the *zero-equation model* or *first-order closure model*. Prandtl's mixing length model is an example of this class where the eddy diffusivities ϵ and ϵ_H are modeled in terms of the gradients of the mean flow:

$$\epsilon = \ell^2 \left| \frac{\partial \bar{u}}{\partial y} \right| \quad \text{and} \quad \epsilon_H = C \ell^2 \left| \frac{\partial \bar{u}}{\partial y} \right| \quad (6.90)$$

where ℓ is the mixing length. Here C is found from Pr_T :

$$C = \frac{\epsilon_H}{\epsilon} = \frac{1}{\text{Pr}_T}$$

where Pr_T is the turbulent Prandtl number.

6.4.13 Near-Wall Region in Turbulent Flow

The mean momentum equation can be written near the wall as

$$\rho \bar{u} \frac{\partial \bar{u}}{\partial x} + \rho \bar{v} \frac{\partial \bar{u}}{\partial y} - \frac{\partial \tau}{\partial y} + \frac{d\bar{p}}{dx} = 0 \quad (6.91)$$

In a region close to the wall, the approximations

$$\rho \bar{u} \frac{\partial \bar{u}}{\partial x} \approx 0 \quad (6.92a)$$

$$\bar{u} = \bar{u}(y) \quad (6.92b)$$

and the normal velocity at the wall,

$$\bar{v} = v_0 \quad (6.92c)$$

can be made. With these, the momentum equation becomes

$$\rho v_0 \frac{\partial \bar{u}}{\partial y} - \frac{\partial \tau}{\partial y} + \frac{d\bar{p}}{dx} = 0$$

which can be integrated using $\tau = \tau_0$ and $\bar{u} = 0$ at $y = 0$:

$$\frac{\tau}{\tau_0} = 1 + \frac{\rho v_0 \bar{u}}{\tau_0} + \frac{d\bar{p}}{dx} \frac{y}{\tau_0} \quad (6.93)$$

Near the wall, a friction velocity v^* can be defined as

$$\frac{\tau_0}{\rho} = C_f \frac{U^2}{2} = (v^*)^2$$

which yields

$$v^* = \left(\frac{\tau_0}{\rho} \right)^{1/2} \quad (6.94)$$

Moreover, normalized variables can be defined near the wall:

$$u^+ = \frac{\bar{u}}{v^*} = \frac{\bar{u}/U}{\sqrt{C_f/2}} \quad (6.95a)$$

$$v^+ = \frac{y v^*}{\nu} \quad (6.95b)$$

$$v_0^+ = \frac{v_0}{v^*} \quad (6.95c)$$

$$p^+ = \frac{\mu (d\bar{p}/dx)}{\rho^{1/2} \tau_0^{3/2}} \quad (6.95d)$$

and substitution of eqs. (6.95) into eq. (6.93) yields

$$\frac{\tau}{\tau_0} = 1 + v^+ u^+ + p^+ y^+ \quad (6.96)$$

In the absence of pressure gradient and transpiration ($p^+ = 0$, $v_0^+ = 0$),

$$\frac{\tau}{\tau_0} = 1 \quad \text{or} \quad \tau_0 = \rho(\nu + \epsilon) \frac{d\bar{u}}{dy} \quad (6.97)$$

In a region very close to the wall (called the *viscous sublayer*), $\nu \gg \epsilon$ and eq. (6.97) can be integrated from the wall to a nearby location (say, $0 \leq y^+ \leq 5$) in the flow

$$\int_0^{\bar{u}} d\bar{u} = \frac{\tau_0}{\mu} \int_0^{y^+} dy \quad \text{or} \quad u^+ = y^+ \quad (6.98)$$

In a region farther out from the wall, turbulence effects become important. However, the near-wall region still has effectively constant total shear stress and total heat flux:

$$\tau = \tau_0 + \rho(v + \epsilon) \frac{\partial \bar{u}}{\partial y} = \rho \left(v + l^2 \frac{\partial \bar{u}}{\partial y} \right) \frac{\partial \bar{u}}{\partial y} = \rho \left(v + \kappa^2 y^2 \frac{\partial \bar{u}}{\partial y} \right) \frac{\partial \bar{u}}{\partial y} \quad (6.99)$$

where the mixing length near the wall is taken as $\ell = \kappa y$, with $\kappa = 0.40$ being the *von Kármán constant*. In the fully turbulent *outer region*, $v \ll \epsilon$, resulting in

$$\tau_0 = \rho \kappa^2 y^2 \left(\frac{\partial \bar{u}}{\partial y} \right)^2 \quad \text{or} \quad \kappa y \frac{\partial \bar{u}}{\partial y} = \left(\frac{\tau_0}{\rho} \right)^{1/2} = v^* \quad (6.100)$$

This can be expressed as

$$\kappa y^+ \frac{\partial u^+}{\partial y^+} = 1$$

which can be integrated to yield the *law of the wall*:

$$u^+ = \frac{1}{\kappa} \ln y^+ + C \quad (6.101)$$

With $\kappa = 0.4$ and $C = 5.5$, this describes the data reasonably well for $y^+ > 30$, as seen in Fig. 6.14. Minor variations in the κ and C values are found in the literature, as indicated in Fig. 6.14. In the range $5 < y^+ < 30$, the *buffer region*, both v

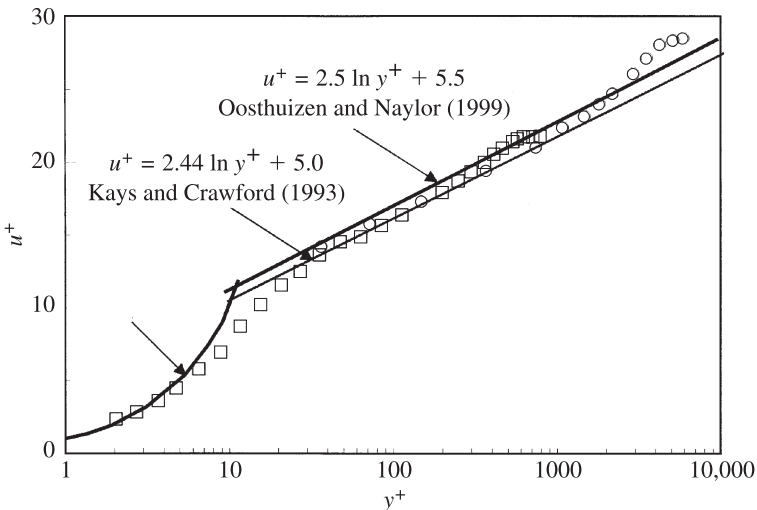


Figure 6.14 Velocity profiles in turbulent flow past a flat surface in the wall coordinates. (Data from the literature, as reported by Kays and Crawford, 1993.)

and ϵ are important and the experimental data from various investigators can be approximated by

$$u^+ = 5 \ln y^+ - 3.05$$

6.4.14 Analogy Solutions for Boundary Layer Flow

Consider the apparent shear stress and heat flux in turbulent flat plate boundary layer flow:

$$\tau = \rho(v + \epsilon) \frac{\partial \bar{u}}{\partial y} \quad \text{and} \quad \frac{\partial \bar{u}}{\partial y} = \frac{\tau}{\rho(v + \epsilon)} \quad (6.102)$$

$$q'' = -\rho c_p (\alpha + \epsilon_H) \frac{\partial \bar{T}}{\partial y} \quad \text{and} \quad \frac{\partial \bar{T}}{\partial y} = -\frac{q''}{\rho c_p (\alpha + \epsilon_H)} \quad (6.103)$$

These expressions can be integrated from the wall to a location ℓ in the free stream,

$$u_\ell = \int_0^\ell \frac{\tau}{\rho(v + \epsilon)} dy \quad (6.104)$$

$$T_0 - T_\ell = \int_0^\ell \frac{q''}{\rho c_p (\alpha + \epsilon_H)} dy \quad (6.105)$$

Under the assumptions that

$$\text{Pr} = \text{Pr}_T = 1 \quad \text{and} \quad \frac{q''}{q_0''} = \frac{\tau}{\tau_0}$$

then

$$T_0 - T_\ell = \int_0^\ell \frac{q''}{\rho c_p (v + \epsilon)} dy = \frac{q_0''}{\tau_0} \int_0^\ell \frac{\tau}{\rho c_p (v + \epsilon)} dy \quad (6.106)$$

Upon division by the velocity expression

$$\frac{T_0 - T_\ell}{u_\ell} = \frac{q_0''}{c_p \tau_0}$$

then

$$\frac{q_0''}{T_0 - T_\ell} \frac{x}{k} = \frac{\tau_0}{\rho u_\ell^2} \left(\frac{\rho u_1 x}{\mu} \right) \frac{\mu c_p}{k} \quad \text{or} \quad \text{Nu}_x = \frac{C_f}{2} \text{Re}_x \cdot \text{Pr} \quad (6.107)$$

For moderate Re_x

$$C_f = \frac{0.058}{\text{Re}_x^{0.2}}$$

and for $Pr = Pr_T = 1$ and no pressure gradient,

$$Nu_x = 0.0296 Re_x^{0.80} \quad (6.108)$$

Mixed Boundary Conditions Often, the boundary layer may start as laminar, undergo transition, and become turbulent along the plate length. The average heat transfer coefficient in such a case can be determined by assuming an abrupt transition at a location x_T :

$$\bar{h} = \frac{1}{L} \left(\int_0^{x_T} h_L dx + \int_{x_T}^L h_T dx \right) \quad (6.109)$$

where h_L and h_T are the local heat transfer coefficient variations for the laminar and turbulent boundary layers, respectively. A critical Reynolds number Re_T can be selected and eq. (6.109) can be normalized to obtain the average Nusselt number

$$\overline{Nu}_L = 0.664 Re_T^{0.50} + 0.036 (Re_L^{0.8} - Re_T^{0.8}) \quad (6.110)$$

Three-Layer Model for a “Physical Situation” Considering the total shear stress and heat flux in eqs. (6.102) and (6.103), division and introduction of the turbulent scales leads to

$$\frac{\tau}{\tau_0} = \left(1 + \frac{\epsilon}{\nu} \right) \frac{\partial u^+}{\partial y^+} \quad (6.111a)$$

$$\frac{q''}{q_0''} = \left(\frac{1}{Pr} + \frac{\epsilon/\nu}{Pr_T} \right) \frac{\partial T^+}{\partial y^+} \quad (6.111b)$$

The turbulent boundary layer may be considered to be divided into an inner region, a buffer region, and an outer region. For the inner region ($0 \leq y^+ < 5$), $\epsilon = 0$ and $q'' = q_0''$, which results in

$$1 = \frac{1}{Pr} \frac{\partial T^+}{\partial y^+} \quad \text{or} \quad T^+ = Pr \cdot y^+ \quad (6.112)$$

At the outer edge of the inner layer, $T_s^+ = 5Pr$.

For the buffer region ($5 \leq y^+ < 30$),

$$\tau = \tau_0 \quad q'' = q_0'' \quad u^+ = 5 + 5 \ln \frac{y^+}{5} \quad (6.113a)$$

or

$$\frac{\partial u^+}{\partial y^+} = \frac{5}{y^+} \quad (6.113b)$$

Substituting eq. (6.113a) into eqs. (6.111) provides

$$1 = \left(1 + \frac{\epsilon}{\nu}\right) \frac{5}{y^+} \quad (6.114a)$$

or

$$\frac{\epsilon}{\nu} = \frac{y^+}{5} - 1 \quad (6.114b)$$

With eq. (6.114b) put into eq. (6.112),

$$1 = \left(\frac{1}{\text{Pr}} + \frac{y^+ - 5}{5\text{Pr}_T} \right) \frac{\partial T^+}{\partial y^+} \quad (6.115)$$

Then integration across the buffer region gives

$$T^+ - T_s^+ = \int_5^{y^+} \frac{dy^+}{1/\text{Pr} + (y^+ - 5)/5\text{Pr}_T} \quad (6.116)$$

or

$$T^+ - T_s^+ = 5\text{Pr}_T \ln \left[1 + \frac{\text{Pr}}{\text{Pr}_T} \left(\frac{y^+}{5} - 1 \right) \right] \quad (6.117)$$

This may be applied across the entire buffer region:

$$T_b^+ - T_s^+ = 5\text{Pr}_T \ln \left[1 + \frac{\text{Pr}}{\text{Pr}_T} \left(\frac{30}{5} - 1 \right) \right] \quad (6.118)$$

For the outer region ($y^+ > 30$), where $\epsilon \gg \nu$ and $\epsilon_H \gg \nu$,

$$\frac{\tau}{\tau_0} = \frac{\epsilon}{\nu} \frac{\partial u^+}{\partial y^+} \quad (6.119)$$

$$\frac{q''}{q_0''} = \frac{\epsilon/\nu}{\text{Pr}} \frac{\partial T^+}{\partial y^+} \quad (6.120)$$

Similar distributions of shear stress and heat transfer rate in the outer region can be assumed so that

$$\frac{\tau}{\tau_b} = \frac{q''}{q_b''} \quad (6.121)$$

Because τ and q'' are constant across the inner two layers, $\tau_b = \tau_0$ and $q'' = q_0''$. Hence

$$\frac{\tau}{\tau_0} = \frac{q''}{q_0''} \quad (6.122)$$

With eqs. (6.121) and (6.122) in eq. (6.120),

$$\frac{\epsilon}{v} \frac{\partial u^+}{\partial y^+} = \frac{\epsilon}{v \text{Pr}_T} \frac{\partial T^+}{\partial y^+} \quad \text{and} \quad \frac{\partial T^+}{\partial y^+} = \text{Pr}_T \frac{\partial u^+}{\partial y^+} \quad (6.123)$$

Integrating across the outer layer yields

$$T_1^+ - T_b^+ = \text{Pr}_T (u_1^+ - u_b^+) \quad (6.124)$$

where T_1^+ and u_1^+ are in the free stream and

$$u_b^+ = 5 + 5 \ln 6$$

so that

$$T_1^+ - T_b^+ = \text{Pr}_T [u_1^+ - 5(1 + \ln 6)] \quad (6.125)$$

Addition of the temperature profiles across the three layers gives

$$T_1^+ = 5\text{Pr} + 5\text{Pr}_T \ln \frac{\text{Pr}_T + 5\text{Pr}}{6\text{Pr}_T} + \text{Pr}_T (u_1^+ - 5) \quad (6.126)$$

and because

$$T^+ = \frac{\rho c_p (T_0 - \bar{T})}{q_0''} v^* = \frac{\rho c_p (T_0 - \bar{T})}{q_0''} \left(\frac{\tau_0}{\rho} \right)^{1/2} = \frac{\text{Pr} \cdot \text{Re}_x}{\text{Nu}_x} \left(\frac{C_f}{2} \right)^{1/2} \quad (6.127)$$

the Nusselt number becomes

$$\text{Nu}_x = \frac{\text{Re}_x (C_f/2)^{1/2}}{5 + 5 \frac{\text{Pr}_T}{\text{Pr}} \ln \left(\frac{\text{Pr}_T + 5\text{Pr}}{6\text{Pr}_T} \right) + \frac{\text{Pr}_T}{\text{Pr}} (u_1^+ - 5)} \quad (6.128)$$

This yields the final expression with $\text{St} = \text{Nu}_x / \text{Re}_x \cdot \text{Pr}$:

$$\text{St}_x = \frac{(C_f/2)^{1/2}}{(C_f/2)^{1/2} \{5\text{Pr} + 5\text{Pr}_T \ln[(\text{Pr}_T + 5\text{Pr})/6\text{Pr}_T] - 5\text{Pr}_T\} + \text{Pr}_T} \quad (6.129)$$

For

$$C_f = \frac{0.058}{\text{Re}_x^{0.20}}$$

eq. (6.129) can be written as

$$\text{Nu}_x = 0.029 \text{Re}_x^{0.8} G \quad (6.130)$$

where the parameter G is

$$G = \frac{\text{Pr}}{(0.029/\text{Re}_x^{20})^{1/2}\{5\text{Pr} + 5 \ln[(1 + 5\text{Pr})/6] - 5\} + 1} \quad (6.131)$$

As pointed out by Oosthuizen and Naylor (1999), eq. (6.131) is based on $\text{Pr}_T = 1$ but does apply for various Pr .

Flat Plate with an Unheated Starting Length in Turbulent Flow The integral forms of the momentum and energy equations can also be developed for turbulent flow by integrating the mean flow equations across the boundary layer from the surface to a location H outside the boundary layer. The integral momentum equation can be written as

$$\frac{d}{dx} \int_0^H \bar{u}(\bar{u} - U) dy = -\frac{\tau_0}{\rho} = -U^2 \frac{d\delta_2}{dx} = -(v^*)^2 \quad (6.132)$$

where the momentum thickness δ_2 is

$$\delta_2 = \int_0^H \frac{\bar{u}}{U} \left(1 - \frac{\bar{u}}{U}\right) dy \quad (6.133)$$

Assume that both Pr and Pr_T are equal to unity and that the mean profiles for the mean velocity and temperature in the velocity (δ) and thermal (δ_T) boundary layers are given by

$$\frac{\bar{u}}{U} = \left(\frac{y}{\delta}\right)^{1/7} \quad \text{and} \quad \frac{T_0 - \bar{T}}{t_0 - T_\infty} = \left(\frac{y}{\delta_T}\right)^{1/7} \quad (6.134)$$

Then from the integral momentum equation

$$\frac{\tau}{\tau_0} = 1 - \left(\frac{y}{\delta}\right)^{1/7} \quad (6.135)$$

and because the total heat flux at any point in the flow is

$$v + \epsilon = \alpha + \epsilon_H = \frac{\tau/\rho}{\partial \bar{u}/\partial y} = 7\nu \frac{C_f}{2} \frac{\delta}{x} \text{Re}_x \left[1 - \left(\frac{y}{\delta}\right)^{9/7}\right] \left(\frac{y}{\delta}\right)^{6/7} \quad (6.136)$$

the total heat flux at any point in the flow is

$$q'' = -\rho c_p (\alpha + \epsilon_H) \frac{\partial \bar{T}}{\partial y} \quad (6.137)$$

For the assumed profiles this can be written as

$$\frac{q''}{\rho c_p U (T_0 - T_\infty)} = \frac{C_f}{2} \left[1 - \left(\frac{y}{\delta}\right)^{9/7}\right] \left(\frac{y}{\delta}\right)^{6/7} \quad (6.138)$$

The wall heat flux can be determined from eq. (6.138). This expression is substituted on the right-hand side of the integral energy equation. The \bar{u} and \bar{T} profiles and the δ as a function of x relations are substituted on the left side and δ_T is solved for as a function of x . The final result for the Stanton number St is

$$St = \frac{C_f}{2} \left[1 - \left(\frac{x_0}{x} \right)^{9/10} \right]^{-1/9} \quad (6.139)$$

With the same Prandtl number correction as in the case of the fully heated plate,

$$St \cdot Pr^{0.40} = 0.0287 Re_x^{-0.2} \left[1 - \left(\frac{x_0}{x} \right)^{9/10} \right]^{-1/9} \quad (6.140)$$

Just as for laminar flow, the result of eq. (6.140) can be generalized to an arbitrarily varying wall temperature through superposition (Kays and Crawford, 1980).

Arbitrarily Varying Heat Flux Based on eq. (6.134), which is Prandtl's $\frac{1}{7}$ power law for thermal boundary layers on smooth surfaces with uniform specified surface heat flux, a relationship that is nearly identical to eq. (6.140) for uniform surface temperature is recommended:

$$St \cdot Pr^{0.40} = 0.03 Re_x^{-0.2} \quad (6.141)$$

For a surface with an arbitrarily specified heat flux distribution and an unheated section, the temperature rise can be determined from

$$T_0(x) - T_\infty = \int_{x_0=0}^{x_0=x} \Gamma(x_0, x) q''(x_0) dx_0 \quad (6.142)$$

where

$$\Gamma(x_0, x) = \frac{\frac{9}{10} Pr^{-0.60} \cdot Re_x^{-0.80}}{\Gamma\left(\frac{1}{9}\right) \Gamma\left(\frac{8}{9}\right) (0.0287k)} \left[1 - \left(\frac{x_0}{x} \right)^{9/10} \right]^{-8/9} \quad (6.143)$$

Turbulent Prandtl Number An assumption of $Pr_T = 1$ has been made in the foregoing analyses. The turbulent Prandtl number is determined experimentally using

$$Pr_T = \frac{\overline{u'v'}(\partial \bar{T} / \partial y)}{\overline{v'T'}(\partial \bar{u} / \partial y)} \quad (6.144)$$

Kays and Crawford (1993) have pointed out that, in general, it is difficult to measure all four quantities accurately. With regard to the mean velocity data, mean temperature data in the logarithmic region show straight-line behavior when plotted in the wall coordinates. The slope of this line, relative to that of the velocity profile, provides Pr_T . Data for air and water reveal a Pr_T range from 0.7 to 0.9. No noticeable effect

due to surface roughness is noted, but at very low Pr , a Prandtl number effect on Pr_T is observed. This is believed to be due to the higher thermal conductivity based on existing analyses. At higher Pr , there is no effect on Pr_T . The Pr_T values are found to be constant in the “law of the wall” region but are higher in the sublayer, and the wall value of Pr_T approaches 1.09 regardless of Pr .

6.4.15 Surface Roughness Effect

If the size of the roughness elements is represented by a mean length scale k_s , a *roughness Reynolds number* may be defined as $Re_k = k_s(v^*/\nu)$. Three regimes of roughness may then be prescribed:

Smooth	$Re_k < 5$
Transitional rough	$5 < Re_k < 70$
Fully rough	$Re_k > 70$

Under the fully rough regime, the friction coefficient becomes independent of viscosity and Re_k . The role of the roughness is to destabilize the sublayer. For $Re_k > 70$, the sublayer disappears and the shear stress is transmitted to the wall by pressure drag on the roughness elements. The mixing length near a rough surface is given as $\ell = \kappa(y + \delta y_o)$, which yields a finite eddy diffusivity at $y = 0$. In the wall coordinates, based on experimental data,

$$\delta y_0^+ = \frac{\delta y_0 v^*}{\nu} = 0.031 Re_k \quad (6.145)$$

The law of the wall for a fully rough surface is

$$\frac{du^+}{dy^+} = \frac{1}{\kappa(y^+ + \delta y_0^+)} \quad (6.146)$$

Because no sublayer exists for fully rough surface, eq. (6.146) may be integrated from 0 to y^+ to provide

$$u^+ = \frac{1}{\kappa} \ln y^+ + \frac{1}{\kappa} \ln \frac{32.6}{Re_k} \quad (6.147)$$

The friction coefficient is calculated by evaluating u_∞^+ while including the additive effect of the outer wake. The latter results in a displacement by 2.3. The result is

$$u_\infty^+ = \frac{1}{(C_f/2)^{1/2}} = \frac{1}{\kappa} \ln \frac{848}{k_s} \quad (6.148)$$

The heat transfer down to the plane of the roughness elements is by eddy conductivity, but the final transfer to the surface is by molecular conduction through the almost stagnant fluid in the roughness cavities. The law of the wall is written as

$$T^+ - \delta T_0^+ = \int_0^{y^+} \frac{dy^+}{\epsilon_H/\nu} \quad (6.149)$$

where the second term on the left is the temperature difference across which heat is transferred by conduction. With

$$\frac{\epsilon_H}{\nu} = \frac{1}{\text{Pr}_T} \frac{\epsilon}{\nu} = \frac{\kappa}{\text{Pr}_T} (y^+ + \delta y_0^+) \quad (6.150a)$$

then

$$T^+ = \delta T_0^+ + \frac{\text{Pr}_T}{\kappa} \ln \frac{32.6 y^+}{\text{Re}_k} \quad (6.150b)$$

A local heat transfer coefficient can be defined based on δT_0 :

$$\delta T_0^+ = \frac{\rho c_p v^*}{h_k} = \frac{1}{\text{St}_k} \quad (6.151)$$

Based on experimental data for roughness from spheres,

$$\text{St}_k = C \cdot \text{Re}_k^{-0.20} \cdot \text{Pr}^{-0.40} \quad (6.152)$$

with $C \approx 0.8$ and $\text{Pr}_T \approx 0.9$, the law of the wall can be rewritten as

$$T^+ = \frac{1}{\text{St}_k} + \frac{\text{Pr}_T}{\kappa} \ln \frac{32.6 y^+}{\text{Re}_k} \quad (6.153)$$

and using a procedure similar to that used for a smooth surface,

$$\text{St} = \frac{C_f/2}{\text{Pr}_T + (C_f/2)^{1/2}/\text{St}_k} \quad (6.154)$$

6.4.16 Some Empirical Transport Correlations

Cylinder in Crossflow The analytical solutions described in Sections 6.4.9 and 6.4.10 provide local convection coefficients from the front stagnation point (using similarity theory) to the separation point of a cylinder using the Smith–Spalding method. At the front stagnation point, the free stream is brought to rest, with an accompanying rise in pressure. The initial development of the boundary layer along the cylinder following this point is under favorable pressure gradient conditions; that is, $dp/dx < 0$. However, the pressure reaches a minimum at some value of x , depending on the Reynolds number. Farther downstream, the pressure gradient is *adverse* (i.e., $dp/dx > 0$), until the point of boundary layer separation where the surface shear stress becomes zero. This results in the formation of a wake. For $\text{Re}_D \leq 2 \times 10^5$, the boundary layer remains laminar until the separation point, which

occurs at an arc of about 81° . For higher values of Re_D , the boundary layer undergoes transition to turbulence, which results in higher fluid momentum and the pushing back of the separation point to about 140° .

The foregoing changes result in large variations in the transport behavior with the angle θ . If the interest is on an average heat transfer coefficient, many empirical equations are available. One such correlation for an isothermal cylinder that is based on the data of many investigators for various Re_D and Pr , such that $Re_D \cdot Pr > 0.2$ was proposed by Churchill and Bernstein (1977):

$$\overline{Nu_D} \equiv \frac{\bar{h}D}{k} = 0.30 + \frac{0.62Re_D^{1/2} \cdot Pr^{1/3}}{[1 + (0.40/Pr)^{2/3}]^{1/4}} \left[1 + \left(\frac{Re_D}{282,000} \right)^{5/8} \right]^{4/5} \quad (6.155)$$

The fluid properties are evaluated at the film temperature, which is the average of the surface and ambient fluid values.

Flow Over an Isothermal Sphere Whitaker (1972) recommends the correlation

$$\overline{Nu_D} = 2 + \left(0.4Re_D^{1/2} + 0.06Re_D^{2/3} \right) Pr^{0.4} \left(\frac{\mu}{\mu_s} \right)^{1/4} \quad (6.156)$$

The uncertainty band around this correlation is $\pm 30\%$ in the range: $0.71 < Pr < 380$, $3.5 < Re_D < 7.6 \times 10^4$, and $1.0 < \mu/\mu_s < 3.2$. All properties except μ_s are evaluated at the ambient temperature.

6.5 HEAT TRANSFER FROM ARRAYS OF OBJECTS

6.5.1 Crossflow across Tube Banks

This configuration is encountered in many practical heat transfer applications, including shell-and-tube heat exchangers. Zhukauskas (1972, 1987) has provided comprehensive heat transfer and pressure drop correlations for tube banks in aligned and staggered configurations (Fig. 6.15). The heat transfer from a tube depends on its location within the bank. In the range of lower Reynolds numbers, typically the tubes in the first row show similar heat transfer to those in the inner rows. For higher Reynolds numbers, flow turbulence leads to higher heat transfer from inner tubes than from the first row. The heat transfer becomes invariant with tube location following the third or fourth row in the mixed-flow regime, occurring above $Re_{D,\max}$. The average Nusselt number from a tube is then of the form

$$\overline{Nu_D} = C \cdot Re_{D,\max}^m \cdot Pr^{0.36} \left(\frac{Pr}{Pr_s} \right)^{1/4} \quad (6.157)$$

for $0.7 \leq Pr < 5000$, $1 < Re_{D,\max} < 2 \times 10^4$, and $N_L \geq 20$ and where m is as given in Table 6.2. The Reynolds number $Re_{D,\max}$ in eq. (6.157) is based on the maximum

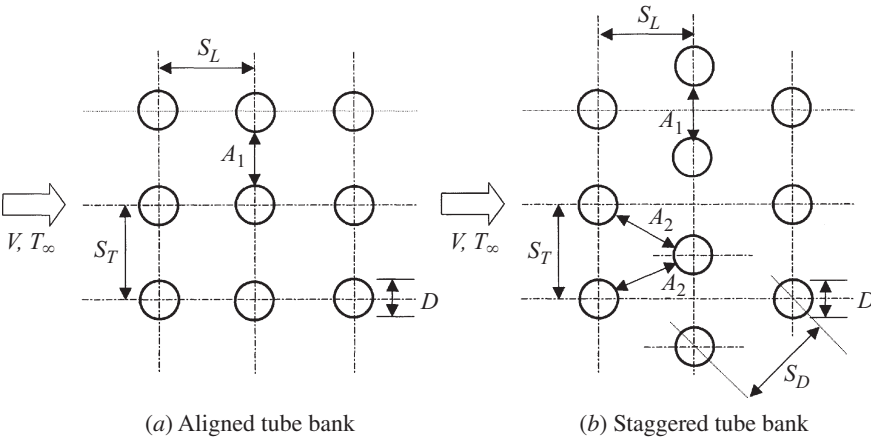


Figure 6.15 Tube bundle configurations studied by Zhukaukas (1987).

fluid velocity within the tube bank which occurs at the minimum-flow cross section. For the aligned arrangement, it occurs at A_1 in Fig. 6.15 and is given by

$$V_{\max} = \frac{S_T}{S_T - D} V \tag{6.158}$$

where V is the upstream fluid velocity.

For the staggered configuration, the maximum fluid velocity occurs at A_2 if $2(S_D - D) < (S_T - D)$, in which case

$$V_{\max} = \frac{S_T}{2(S_D - D)} V \tag{6.159}$$

Otherwise, the aligned tube expression of eq. (6.158) can be used.

TABLE 6.2 Parameters $Re_{D,\max}$, C , and m for Various Aligned and Staggered Tube Arrangements

Configuration	$Re_{D,\max}$	C	m
Aligned	16–100	0.90	0.40
Staggered	1.6–40	1.04	0.40
Aligned	100–1000	0.52	0.50
Staggered	40–1000	0.71	0.50
Aligned ($S_T/S_L > 0.7$)	$1000\text{--}2 \times 10^5$	0.27	0.63
Staggered ($S_T/S_L < 2$)	$1000\text{--}2 \times 10^5$	$0.35 (S_T/S_L)^{0.20}$	0.60
Staggered ($S_T/S_L > 2$)	$1000\text{--}2 \times 10^5$	0.40	0.60
Aligned	$2 \times 10^5\text{--}2 \times 10^6$	0.033	0.80
Staggered ($Pr > 0.70$)	$2 \times 10^5\text{--}2 \times 10^6$	$0.031 (S_T/S_L)^{0.20}$	0.80
Staggered ($Pr = 0.70$)	$2 \times 10^5\text{--}2 \times 10^6$	$0.027 (S_T/S_L)^{0.20}$	0.80

Source: Zhukauskas (1987).

TABLE 6.3 Parameter C_2 for Various Tube Rows and Configurations

N_L	1	2	3	4	5	7	10	13	16
Aligned ($Re_{D,\max} > 1000$)	0.70	0.80	0.86	0.90	0.92	0.95	0.97	0.98	0.99
Staggered ($Re_{D,\max}$ 100–1000)	0.83	0.87	0.91	0.94	0.95	0.97	0.98	0.98	0.99
Staggered ($Re_{D,\max} > 1000$)	0.64	0.76	0.84	0.89	0.92	0.95	0.97	0.98	0.99

Source: Zhukauskas (1987).

It is noted that all properties except Pr_s are evaluated at the arithmetic mean of the fluid inlet and outlet temperatures. The constants C and m are listed in Table 6.2, where it can be observed that for $S_T/S_L < 0.7$, heat transfer is poor and the aligned tube configuration should not be employed.

If $N_L < 20$, a corrected expression can be employed:

$$Nu_L \Big|_{N_L < 20} = C_2 \cdot Nu_L \Big|_{N_L \geq 20}$$

where $C_2 = 1.0$ for aligned tubes in the range $Re_{D,\max}$ and is provided for other conditions in Table 6.3.

6.5.2 Flat Plates

Stack of Parallel Plates Consider a stack of parallel plates placed in a free stream (Fig. 6.16). The envelope for the plate stack has a fixed volume, W (width) $\times L$ (length) $\times H$ (height). Morega et al. (1995) conducted numerical analyses on a two-dimensional model where $W \gg L$, t (the plate thickness), equal to $L/20$ and q'' (the heat flux) uniform over the plate surfaces, excluding the edges. The question addressed by Morega et al. is the number of plates needed to maximize the heat transfer performance from the entire plate stack. Fewer plates than the optimum

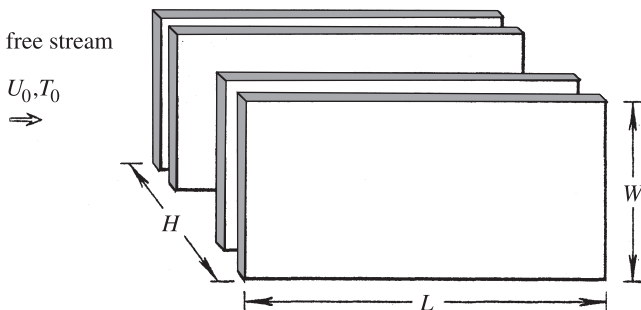


Figure 6.16 Plate stack. (From Morega et al., 1995.)

reduce the amount of heat transfer area in a given volume. A greater population of plates than the optimum increases the resistance to flow through the stack and hence diverts the flow to the free stream zone outside the stack. The heat transfer performance is represented by the nondimensional hot-spot temperature,

$$\theta_{\text{hot}} = \frac{k(T_{\text{max}} - T_0)}{q''(2nL)} \tag{6.160}$$

where T_{max} is the maximum surface temperature on the plate surface, T_0 is the free stream temperature, and k is the fluid thermal conductivity.

Figure 6.17 shows θ_{hot} versus the number of plates in the stack, n . The parameter is the Reynolds number $\text{Re}_L = U_0 L/\nu$, where U_0 is the free stream velocity and ν is the kinematic viscosity of the fluid. Figure 6.17 also shows the curves derived from Nakayama et al. (1988), where the experimental data were obtained with the finned heat sinks having nearly isothermal surfaces. Despite the difference in thermal boundary conditions, the two groups of curves imply a smooth transition of optimum n from low to high Reynolds number regimes. Morega et al. (1995) proposed a relationship for optimum n :

$$n_{\text{opt}} \simeq \frac{0.26(H/L)\text{Pr}^{1/4} \cdot \text{Re}_L^{1/2}}{1 + 0.26(t/L)\text{Pr}^{1/4} \cdot \text{Re}_L^{1/2}} \tag{6.161}$$

where Pr is the Prandtl number. Equation (6.161) is applicable to cases where $\text{Pr} \geq 0.7$ and $n \gg 1$.

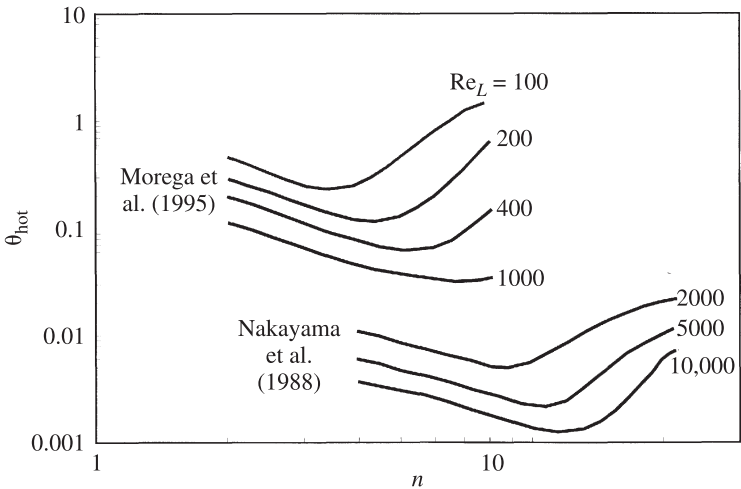
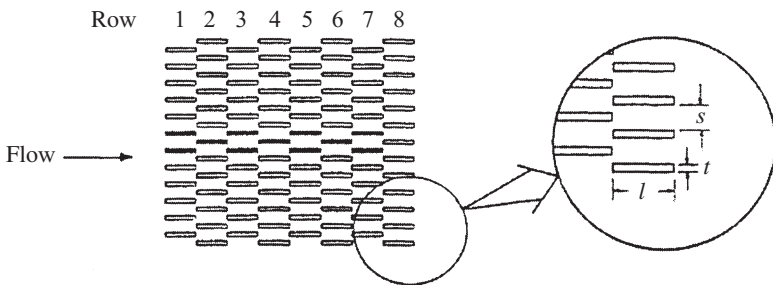


Figure 6.17 Nondimensional hot spot temperature (θ_{hot}) versus the number of plates (n). (From Morega et al., 1995.)

Offset Strips Offset arrangements of plates or strips (Fig. 6.1*d*) reproduced with the addition of the symbols in Fig. 6.18 offer the advantage of heat transfer enhancement. The boundary layer development is interrupted at the end of the strip and then resumes from the leading edge of the strip in the downstream row. This arrangement allows the boundary layer to be held thin everywhere in the strip array. A similar effect can be obtained with the in-line arrangement of strips, but offsetting the strips from row to row introduces additional favorable effects on heat transfer. The fluid in the offset strips has a longer distance to travel after leaving the trailing edge of a strip to the leading edge of the next strip than in the in-line counterpart. This elongated distance results in a longer elapsed time for the diffusion (or dispersion) of momentum and heat. When the fluid velocity is high enough, vortex shedding or turbulence attains a high level in the intervening space between the strips. Thus, the strips after the third row come to be exposed to highly dynamic flow; thermal wakes shed from the upstream strips tend to be diluted by increased level of turbulence so that the individual strip is washed by a cooler stream than in the in-line strip arrangement. Because of these advantages, the offset strip array has been studied by many researchers and used widely in compact heat exchangers.

Figure 6.18 includes a table showing the relative strip thicknesses (t/ℓ) and the relative strip spacings (s/ℓ) studied by DeJong et al. (1998). Those rectangles painted black in the sketch of the strip array are the strips covered with naphthalene to measure the mass transfer rate. The mass transfer data were converted to the heat transfer coefficient using the analogy between mass and heat transfer. The experimental data reveal row-by-row variations of heat transfer coefficient that depend on the Reynolds number. Figure 6.19 shows the friction factor f and Colburn j -factor j plotted as a function of the Reynolds number Re . They are defined as



Geometrical parameters for experimental and numerical arrays

geometrical parameter	experimental geometry	numerical geometry
t/l	0.125	0.117
s/l	0.375	0.507

Figure 6.18 Offset strips. Black strips were naphthalene coated to measure the mass transfer coefficient. The table shows the dimensions. (From DeJong et al., 1998.)

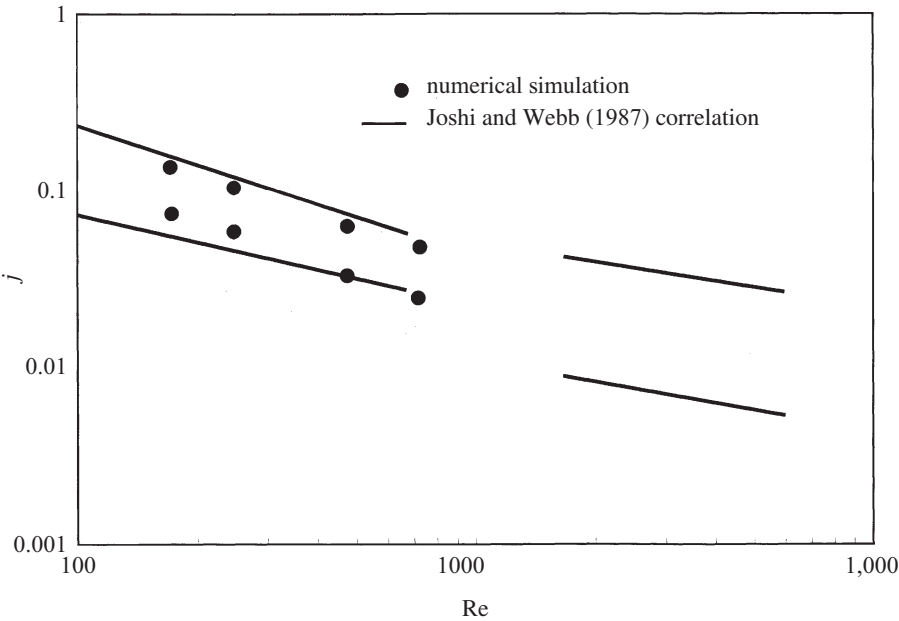


Figure 6.19 Colburn j -factors and friction factors versus Reynolds number. The curves were based on the Joshi and Webb correlations [eqs. (6.166)–(6.169)]. (From DeJong et al., 1998.)

$$Re = \frac{U_c d_h}{\nu} \tag{6.162}$$

where U_c is the flow velocity at the minimum free-flow area, d_h is the hydraulic diameter,

$$d_h = \frac{2(s - t)\ell}{l + t}$$

ν is the fluid kinematic viscosity, and

$$f = \frac{2\Delta p_{\text{core}}}{\rho U_c^2} \frac{d_h}{4L_{\text{core}}} \tag{6.163}$$

where Δp_{core} is the pressure drop across the entire eight-row test section, L_{core} is the total length of the strip array, ρ is the fluid density, and

$$j = \frac{Nu}{Re} Pr^m \tag{6.164}$$

where Nu is the Nusselt number, and $m = 0.40$ [DeJong et al. (1998)] or 0.30 [Joshi and Webb (1987)]. The original j -factor in DeJong et al. (1998) is defined using the

Sherwood and Schmidt numbers. For the sake of consistency throughout this section, they are replaced by heat transfer parameters in

$$\text{Nu} = \frac{d_h h_{av}}{k} \quad (6.165)$$

where h_{av} is the average heat transfer coefficient and k is the fluid thermal conductivity.

The curves in Fig. 6.19 show the correlations proposed by Joshi and Webb (1987). With the transition Reynolds number denoted as Re^* , in the laminar flow range where $\text{Re} \leq \text{Re}^*$,

$$f = 8.12\text{Re}^{-0.74} \left(\frac{\ell}{d_h} \right)^{-0.41} \alpha^{-0.02} \quad (6.166)$$

$$j = 0.53\text{Re}^{-0.50} \left(\frac{\ell}{d_h} \right)^{-0.15} \alpha^{-0.14} \quad (6.167)$$

where α is the aspect ratio; $\alpha = s/W$, with W taken as the strip width measured normal to the page in Fig. 6.18. In the turbulent flow range where $\text{Re} \geq \text{Re}^* + 1000$,

$$f = 1.12\text{Re}^{-0.36} \left(\frac{\ell}{d_h} \right)^{-0.65} \left(\frac{t}{d_h} \right)^{0.17} \quad (6.168)$$

$$j = 0.21\text{Re}^{-0.40} \left(\frac{\ell}{d_h} \right)^{-0.24} \left(\frac{t}{d_h} \right)^{0.02} \quad (6.169)$$

The transition Reynolds number Re^* is given by

$$\text{Re}^* = \text{Re}_b^* \frac{d_h}{b} \quad (6.170)$$

with

$$\text{Re}_b^* = 257 \left(\frac{\ell}{s} \right)^{1.23} \left(\frac{t}{\ell} \right)^{0.58} \quad (6.171)$$

$$b = t + \frac{1.328\ell}{(\text{Re}_\ell)^{1/2}} \quad (6.172)$$

and

$$\text{Re}_\ell = \frac{U_c \ell}{\nu} \quad (6.173)$$

The solid symbols in Fig. 6.19 are the results of numerical simulation on the same strip. Figure 6.19 shows the state-of-the-art accuracy in the predictions of f and j .

6.6 HEAT TRANSFER FROM OBJECTS ON A SUBSTRATE

Figure 6.20 shows a classification of the situations and models encountered in electronics cooling applications: (a) a heated strip that is flush bonded to the substrate surface, (b) a rectangular heat source which is also flush to the substrate surface, (c) an isolated two-dimensional block, (d) a two-dimensional block array, (e) a rectangular block and (f) an array of rectangular blocks. Ortega et al. (1994) suggest that in many practical situations the substrate is a heat conductor, so that a heat path from the heat source through the substrate to the fluid flow cannot be ignored in what is called *conductive/convective conjugate heat transfer*. The analytical solution of the

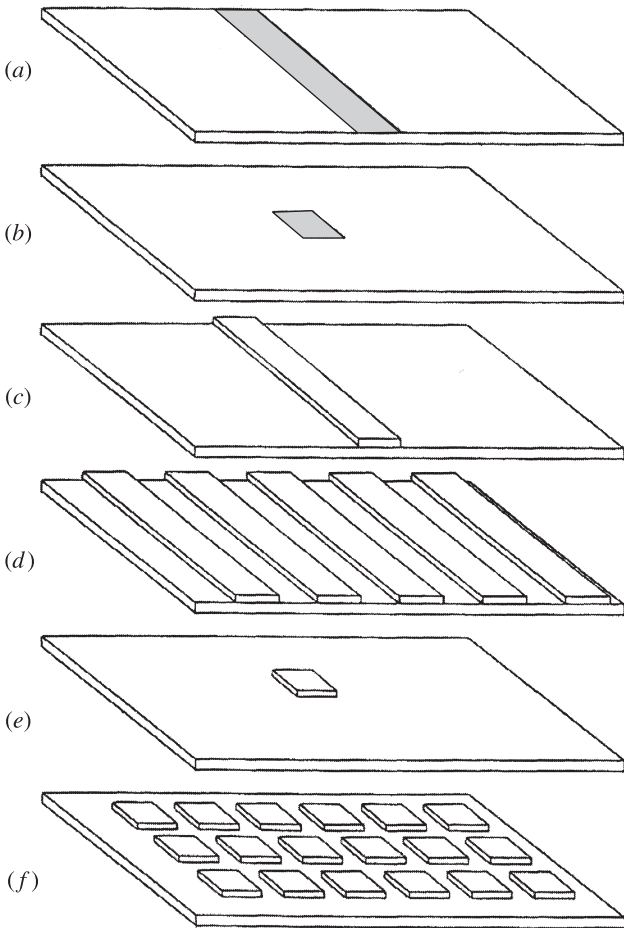


Figure 6.20 Configurations of heat sources on substrate. (From Ortega et al., 1994.)

conjugate heat transfer problem is difficult, and numerical solutions or experiments have been used in the studies reported in the literature.

6.6.1 Flush-Mounted Heat Sources

Heat transfer considerations in flush-mounted heat sources involve less complications than in those for fluid flow. The flow is described by the solution for boundary layer flow or duct flow, particularly where the flow is laminar and conjugate heat transfer is important in laminar flow cases. In turbulent flow, the heat transfer coefficient on the heat source surface is high enough to reduce the heat flow to the substrate to an insignificant level. Gorski and Plumb (1990, 1992) performed numerical analyses on the two-dimensional (Fig. 6.20a) and rectangular (Fig. 6.20b) patch problems. The cross section of the heat source and the substrate is shown in Fig. 6.21. The fluid flow is described by the analytical solution of Blasius for the laminar boundary layer, while the substrate is assumed to be infinitely thick and the numerical solutions are correlated for the two-dimensional strip by

$$\overline{\text{Nu}} = 0.486\text{Pe}^{0.53} \left(\frac{\ell_s}{x_s} \right)^{0.71} \left(\frac{k_{\text{sub}}}{k_f} \right)^{0.057} \quad (6.174)$$

where $\overline{\text{Nu}} = \bar{h}\ell_s/k_f$, \bar{h} is the average heat transfer coefficient based on the heat source area (per unit width normal to the page in Fig. 6.21), ℓ_s is the heat source length, x_s is the distance between the leading edge of the substrate and that of the heat source, k_{sub} is the substrate thermal conductivity, and k_f is the fluid thermal conductivity. Pe is the Péclet number, $\text{Pe} = U_0 x_s / \alpha$, where U_0 is the free stream velocity and α is the fluid thermal diffusivity. Equation (6.174) correlates the numerical solutions within 5% in the parameter ranges $10^3 \leq \text{Pe} \leq 10^5$, $0.10 \leq k_{\text{sub}}/k_f \leq 10$, and $5 \leq x_s/\ell_s \leq 100$.

For the rectangular patch:

$$\overline{\text{Nu}} = \begin{cases} 0.60\text{Pe}_c^{0.48} \left(\frac{2\ell_s}{2x_s + \ell_s} \right)^{0.63} \left(\frac{P\ell_s}{2A} \right)^{0.18} & \left(\frac{k_{\text{sub}}}{k_f} = 1 \right) \\ 0.43\text{Pe}_c^{0.52} \left(\frac{2\ell_s}{2x_s + \ell_s} \right)^{0.70} \left(\frac{P\ell_s}{2A} \right)^{0.07} & \left(\frac{k_{\text{sub}}}{k_f} = 10 \right) \end{cases} \quad (6.175)$$

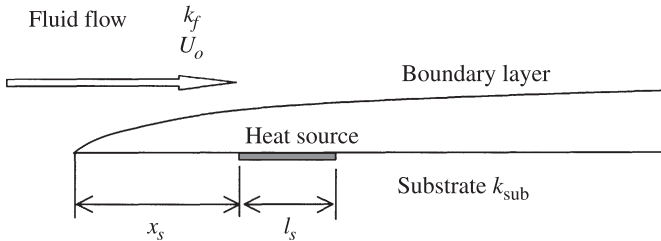


Figure 6.21 Two-dimensional flush-mounted heat source.

where Nu is as defined for the two-dimensional strip, $Pe_c = U_o(2x_s + \ell_s)/2\alpha$ and A/P is the source surface area/perimeter ratio. The correlations of eqs. (6.175) and (6.176) are valid for $10^3 \leq Pe_c \leq 10^5$, $5 \leq (2x_s + \ell_s) \leq 2\ell_s \leq 150$, and $0.2 \leq w_s/\ell_s \leq 5$, where w_s is the heat source width. Additional detailed treatments of the subject have been compiled by Ortega (1996).

6.6.2 Two-Dimensional Block Array

Figure 6.22 shows the pertinent dimensions, all nondimensionalized by the plate spacing for the two-dimensional block array. Arvizu and Moffat (1982) performed experiments for heat transfer from aluminum blocks in forced airflow in such channels. The parameter ranges covered are $P_h = 1/2, 1/4, 6$, and $1/7$, $s = 0.5, 1, 2, 3, 6$, and 8 , and $2200 < Re_{P_h} = UP'_h/\nu < 12,000$. P'_h = dimensional block height. For $s \geq 2$, the heat transfer coefficients for a fixed P_h almost collapse into a single curve. The effect of P_h on heat transfer is large for tightly placed blocks; for $s = 0.5$, when P_h is increased from $1/7$ to $1/2$, the Nusselt number almost doubles. However, Lehman and Wirtz (1985) found a near collapse of heat transfer data of various P_h ranging from $1/2$ to $1/6$ with $s = P_h$ and $P_\ell/P_h = 4$. The data of Lehman and Wirtz (1985) were obtained for $1000 < Re_{P_\ell} < 12,000$ and $\frac{2}{3} \leq P_\ell \leq 2$.

A visualization study was also conducted by Lehman and Wirtz and it revealed modes of convection that depend on the block spacing. For close block spacing, $s/P_\ell = 0.25$, cavity-type flow is formed in the interblock space, indicating that the forward and back surfaces of the block do not contribute much to the heat transfer. When the spacing is widened to $s/P_\ell = 1$, significant cavity-channel flow interactions were observed.

Davalath and Bayazitoglu (1987) performed numerical analysis on a three-row block array placed in a parallel-plate channel. Heat transfer correlations were derived for the cases where the following dimensions are fixed at, $P_\ell = s = 0.5$, $P_h = 0.25$, $\ell_1 = 3.0$, $\ell_2 = 9.5$, and $t = 0.1$. The Reynolds number is defined as $Re = U_0 H/\nu$, where U_0 is the average velocity in the channel (with an unobstructed cross section), H is the channel height, and ν is the fluid kinematic viscosity. The average Nusselt number is $\bar{Nu} = \bar{h}\ell/k$, where \bar{h} is the average heat transfer coefficient over the block surface, ℓ is the dimensional block length, and k_f is the fluid thermal conductivity. The correlation between \bar{Nu} , Re , and Pr is given in the form

$$\bar{Nu} = A \cdot Re^B \cdot Pr^C \quad (6.177)$$

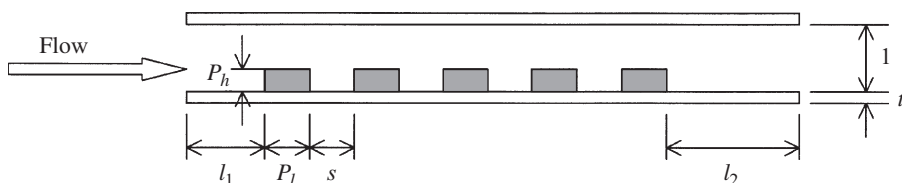


Figure 6.22 Three-row block array studied by Davalath and Bayazitoglu (1987).

TABLE 6.4 Correlating Constants A , B , and C for Use in Eq. (6.177) for the Case of Blocks on an Insulated Plate

Block Number	A	B	C
1	0.69085	0.43655	0.41081
2	0.57419	0.40087	0.37771
3	0.48004	0.39578	0.36405

TABLE 6.5 Correlating Constants A , B , and C for Use in Eq. (6.177) for the Case of Blocks on a Conducting Plate

Block Number	A	B	C
1	1.09064	0.37406	0.38605
2	0.89387	0.34568	0.33571
3	0.67149	0.36757	0.31054

TABLE 6.6 Ratio of Heat Dissipation from the Bottom Surface of a Plate to the Total Heat Dissipation by Block

k_{plate}^*	Percent of Total Heat Dissipation in Blocks
10	46.0
5	44.3
1	32.8

The correlation constants, A , B , and C are given in Table 6.4 for the blocks on an insulated plate and in Table 6.5 for the blocks on a conducting plate having the same thermal conductivity as the block. Table 6.6 shows the ratios, expressed as a percentage, of the heat transfer rate from the bottom surface of the plate to the total heat dissipation by the block. Here k_{plate}^* is the ratio of thermal conductivity of the plate to the fluid thermal conductivity.

6.6.3 Isolated Blocks

Roeller et al. (1991) and Roeller and Webb (1992) performed experiments with the protruded rectangular heat sources mounted on a nonconducting substrate. The pertinent dimensions are shown in Fig. 6.23, where it is observed that H and W are the height and the width, respectively, of the channel where the heat source/substrate composite is placed, P_h is the height, P_ℓ the length, and P_w the width of the heat

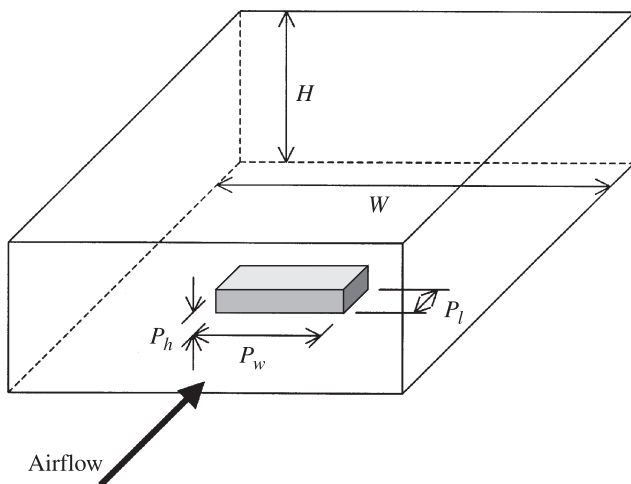


Figure 6.23 Rectangular block on a substrate surrounded by channel walls.

source. The channel width is fixed at $W = 12$ mm, and the height H was allowed to vary from 7 to 30 mm. The heat source dimensions covered by the experiments were $P_\ell = 12$ mm; $P_h = 4, 8$, and 12 mm, $H - P_h = 3, 8$, and 12 mm, and $P_w = W = 12$ mm. The heat transfer correlation is given by

$$\overline{\text{Nu}} = 0.150\text{Re}^{0.632}(A^*)^{-0.455}\left(\frac{H}{P_\ell}\right)^{-0.727} \quad (6.178)$$

where $\overline{\text{Nu}} = \bar{h}P_\ell/k$ and where in

$$\bar{h} = \frac{q}{A_s(\bar{T}_s - T_\infty)}$$

\bar{h} is the average heat transfer coefficient, q the heat transfer rate, A_s the heat transfer area,

$$A_s = 2P_hP_w + P_\ell P_w + 2P_hP_\ell$$

\bar{T}_s the average surface temperature, and T_∞ the free stream temperature. The Reynolds number is defined as $\text{Re} = UD_H/\nu$, where U is the average channel velocity upstream of the heat source, D_H the channel hydraulic diameter at a section unobstructed by the heat source, and ν the fluid (air) kinematic viscosity. A^* is the fraction of the channel cross section open to flow:

$$A^* = 1 - \frac{P_w}{W} \frac{P_h}{H}$$

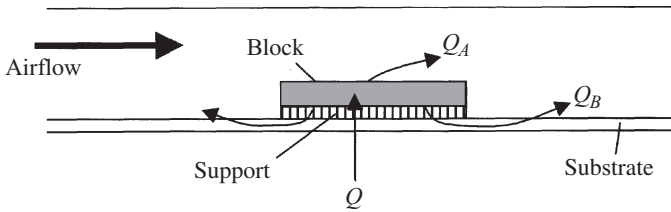


Figure 6.24 Heat transfer paths from a surface-mounted block to airflow. (From Nakayama and Park, 1996.)

Equation (6.178) is valid for $1500 \leq \text{Re} \leq 10,000$, $0.33 \leq P_h/P_\ell \leq 1.0$, $0.12 \leq P_w/W \leq 1.0$, and $0.583 \leq H/P_\ell \leq 2.5$. Here, a realistic error bound is 5%.

In actual situations of cooling electronic packages the heat flow generally follows two paths, one directly from the package surface to the coolant flow, and the other from the package through the lead pins or solder balls to the printed wiring board (PWB), then through the PWB, and finally, from the PWB surfaces to the coolant flow. Figure 6.24 depicts heat flows through such paths; Q is the total heat generation, Q_A the direct heat transfer component, and Q_B the conjugate heat transfer component through the substrate, hence

$$Q = Q_A + Q_B$$

which is due to Nakayama and Park (1996). Equation (6.178) can be used to estimate Q_A .

The ratio Q_B/Q_A depends on the thermal resistance between the heat source block and the substrate (the block support in Fig. 6.24 simulating the lead lines or the solder balls), the thermal conductivity and the thickness of the substrate, and the surface heat transfer coefficient. The estimation of Q_B is a complex process, particularly where the lower side of the substrate is not exposed to the coolant flow, which makes Q_B find its way through only the upper surface. This is the case often encountered in electronic equipment. Convective heat transfer from the upper surface is affected by flow development around the heat source block, which is three-dimensional, involving a horseshoe vortex and the thermal wake shed from the block, leading to a rise in the local fluid temperature above the free stream temperature. Nakayama and Park (1996) studied such cases using a heat source block typical to electronic package, 31 mm \times 31 mm \times 7 mm. A good thermal bond between the block and the substrate, of the order of $R = 0.01$ K/W, and a high thermal conductance of the substrate, such as that of a 1-mm-thick copper plate, maximizes the contribution of conjugate heat transfer Q_B to the total heat dissipation Q , raising the ratio Q_B/Q to a value greater than 0.50.

6.6.4 Block Arrays

Block arrays are common features of electronic equipment, particularly, large systems where a number of packages of the same size are mounted on a large printed wiring

board (PWB) and cooled by air in forced convection. Numerical analysis of three-dimensional airflow over a block array is possible only when a fully developed situation is assumed. For fully developed flow, a zone around a block is carved out, and a repeating boundary condition is assumed on the upstream and downstream faces of the zone. In general, the analysis of flow and heat transfer over an entire block array depends too much upon computational resources, and experiments are frequently the sole means of investigation. However, experiments can be costly, especially when it is desired to cover a wide range of cases where the heat dissipation varies from package to package. To reduce the demand for experimental (and computational as well) resources, a systematic methodology has been developed.

Consider the block array displayed in Fig. 6.25. Block A dissipates q_A and block B, q_B . Assume for the moment that the other blocks are inactive; that is, they do not dissipate. The temperature of air over block B can be written as

$$T_{\text{air},B} = T_0 + \theta_{B/A} q_A \quad (6.179)$$

where T_0 is the free stream temperature and $\theta_{B/A}$ in the second term represents the effect of heat dissipation from block A. Equation (6.179) is based on the *superposition* of solutions that is permissible because of the linearity of the energy equation. However, the factor $\theta_{B/A}$ results from nonlinear phenomena of dispersion of warm air from block A and is a function of the relative location of B to A and the flow velocity. To find $\theta_{B/A}$ by experiment, block A may be energized while block B remains inactive ($q_B = 0$). A measurement of the surface temperature of block B is then divided by q_A . Because $q_B = 0$, its measured surface temperature is called the *adiabatic temperature*.

The next step is to activate block B and inactivate block A ($q_A = 0$). The heat transfer coefficient measured in this situation is called the *adiabatic heat transfer coefficient* and is denoted as $h_{\text{ad},B}$. When both block A and block B are energized, the heat transfer from block B is driven by the temperature difference $T_{s,B} - T_{\text{air},B}$,

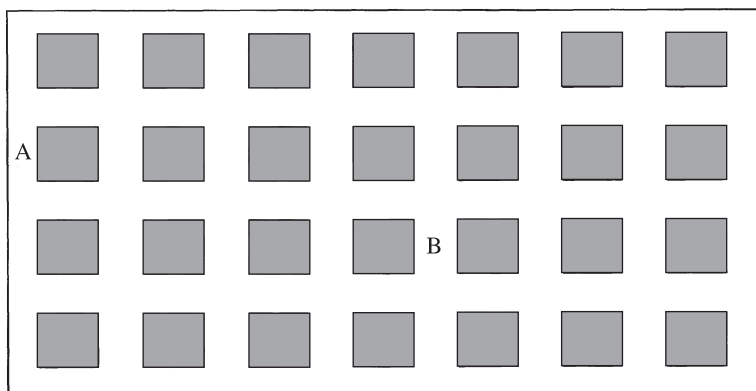


Figure 6.25 Block array on a substrate.

where $T_{s,B}$ is the surface temperature of block B and $T_{\text{air},B}$ is given by eq. (6.179). Again using the superposition principle, the heat flux at block B is

$$q_B = h_{\text{ad},B} (T_{s,B} - T_{\text{air},B}) \quad (6.180)$$

Once $\theta_{B/A}$ is determined, it is straightforward to estimate q_B (or $T_{s,B}$ when q_B is specified) for any value of q_A from eqs. (6.179) and (6.180).

Extension of this concept to a general case includes taking account of the contributions of all blocks upstream of block B in the equation for $T_{\text{air},B}$:

$$T_{\text{air},B} = T_0 + \sum_{i,j} \theta_{B/(i,j)} q_{(i,j)} \quad (6.181)$$

where (i,j) is the row and column index and the summation is performed for all the packages upstream of block B .

Although the foregoing concept looks convenient at first sight, it is a tedious and time-consuming task to determine $\theta_{B/(i,j)}$. Except for a limited number of cases, there have been few correlations that relate $\theta_{B/(i,j)}$ to the geometrical and flow parameters. Moffat and Ortega (1988) summarized the work on this subject, and Anderson (1994) extended the concept to the case of conjugate heat transfer.

The heat transfer data corresponding to the adiabatic heat transfer coefficient in downstream rows where the flow is fully developed were reported by Wirtz and Dykshoorn (1984). The data were correlated by the equation

$$\text{Nu}_{P_\ell} = 0.348 \text{Re}_{P_\ell}^{0.6} \quad (6.182)$$

where the characteristic length for Nu and Re is the streamwise length of the block, P_ℓ .

6.6.5 Plate Fin Heat Sinks

While the plate stack discussed in Section 4.2.1 allows bypass flow in two-dimensional domain, bypass flow around an actual heat sink is three-dimensional. Numerical analysis of such flow is possible but very resource demanding. Ashiwake et al. (1983) developed a method that allows approximate but rapid estimation of the heat sink performance. In their formulation the bypass flow rate is estimated using the balance between the dynamic pressure in front of the fin array and the flow resistance in the interfin passages. Although the validity of the modeling was well corroborated by the experimental data, the method requires computations of the several pressure balance and heat transfer correlations, and the task of developing a more concise formulation of heat sink performance estimation remains.

Presently, the performance estimation is largely in the realm of empirical art, although Ledezma et al. (1996) and Bejan and Sciubba (1992) clearly show optimum spacings which agree with the theory. The heat sink is placed in a wind tunnel and the thermal resistance is measured. The thermal resistance is defined as

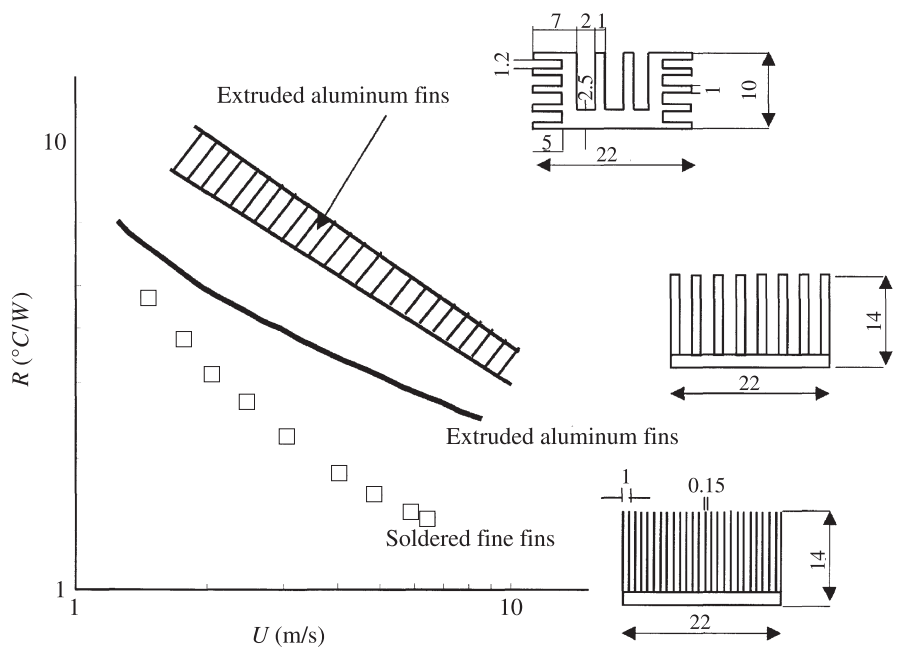


Figure 6.26 Thermal resistance of plate-fin heat sinks. (From Matsushima and Yanagida, 1993.)

$$R = \frac{Q}{T_b - T_0} \quad (\text{K/W}) \tag{6.183}$$

where Q is the power input to the heater bonded to the bottom of the heat sink, T_b the temperature at the bottom surface of the heat sink, and T_0 the airflow temperature in front of the heat sink. Figure 6.26 shows examples of thermal resistance data, where U is the free stream velocity. All the data were obtained with aluminum heat sinks having a 22 mm × 22 mm base area. Of course, there is trade-off between the heat transfer performance and the cost of heat sink. Conventional extruded heat sinks (see Fig. 6.26) are at the lowest in the cost ranking but also in the performance ranking. The heat sink having 19 thin fins (0.15 mm thick) on the 22-mm span provides low thermal resistance, particularly at high air velocities, but the manufacture of such a heat sink requires a costly process of bonding thin fins to the base.

6.6.6 Pin Fin Heat Sinks

As electronic systems become compact, the path for cooling airflow is constrained. This means increased uncertainty in the direction of airflow in front of the heat sink. The performance of plate fin heat sinks degrades rapidly as the direction of air flow deviates from the orientation of the fins. The pin fin heat sink has a distinct advantage

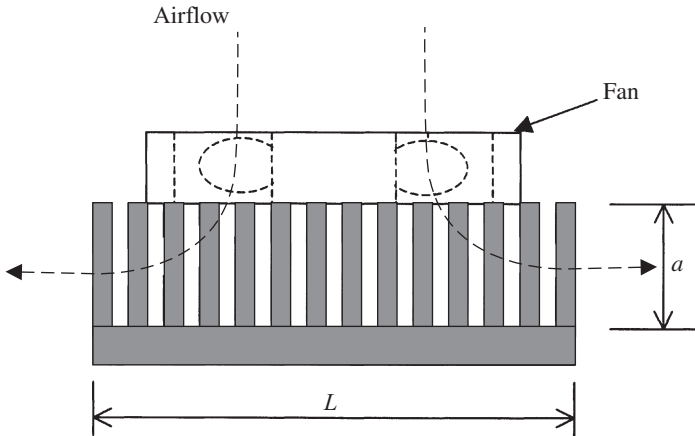


Figure 6.27 Pin-fin fan sink assembly.

over the plate fin heat sink in that its performance is relatively insensitive to the direction of the airflow.

Figure 6.27 shows a scheme that exploits the advantage of pin fin heat sink to the fullest extent. A small axial fan is mounted above the fin heat sink, and air is blown from above to the heat sink. The airflow is longitudinal to those pins in the central area, and the pins in the perimeter are exposed to cross flow. Recently, the scheme has become popular for cooling CPU chips in a constrained space.

The work of Wirtz et al. (1997) provides a guide for the estimation of the performance of a pin fin heat sink/fan assembly. The dimensions of the pin fin heat sinks tested by Wirtz et al. (1997) are as follows:

Foot print area:	63.5 mm × 63.5 mm
L in Fig. 6.26:	63.5 mm
Dimensionless pin diameter:	$d/L = 0.05$
Dimensionless pin height:	$a/L = 0.157 - 0.629$
Fin pitch-to-diameter ratio:	$p/d = 2.71 - 1.46$
Number of pins on a row or a column:	$n = 8, 10, \text{ and } 14$

The fan used in the experiment has overall dimensions of 52 mm × 52 mm × 10 mm, a 27-mm-diameter hub, and a 50-mm blade shroud diameter. The overall heat transfer coefficient U is defined as

$$U = \frac{Q}{A_T \Delta T} \quad (6.184)$$

where Q is the heat transfer rate, A_T the total surface area of the heat sink, and ΔT the temperature difference between the fin base and the incoming air. The Nusselt number is defined as $Nu = UL/k$, where k is the fluid thermal conductivity. Two

types of correlations are proposed, one for a given pressure rise maintained by the fan, Δp ,

$$\text{Nu} = 7.12 \times 10^{-4} C_{\Delta p}^{0.574} \left(\frac{a}{L}\right)^{0.223} \left(\frac{p}{d}\right)^{1.72} \quad (6.185)$$

where in

$$C_{\Delta p} = \frac{\rho L^2 \Delta p}{\mu^2} \quad (5 \times 10^6 < C_{\Delta p} < 1.5 \times 10^8)$$

μ is the dynamic viscosity of the air.

The other correlation is for a given fan power P_W :

$$\text{Nu} = 3.2 \times 10^{-6} C_{P_W}^{0.520} \left(\frac{a}{L}\right)^{-0.205} \left(\frac{p}{d}\right)^{0.89} \quad (6.186)$$

where

$$C_{P_W} = \frac{\rho L P_W}{\mu^3} \quad (10^{11} < C_{P_W} < 10^{13})$$

Wirtz et al. (1997) also reported on experimental results obtained with square and diamond-shaped pins.

6.7 TURBULENT JETS

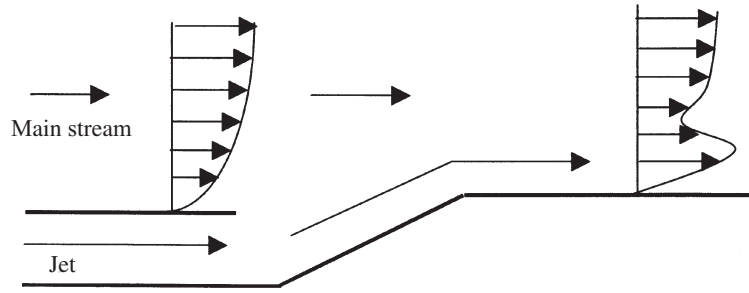
Jets are employed in a wide variety of engineering devices. In cases where the jets are located far from solid walls, they are classified as free shear flows. In most cases, however, solid walls are present and affect the flow and heat transfer significantly. These flows can take many configurations. Some of the practically important cases for heat transfer include wall jets and jets impinging on solid surfaces as indicated in Fig. 6.28.

Wall jets are frequently employed in turbomachinery applications and are not discussed here. Jet impingement on surfaces is of interest in materials packaging and electronics cooling.

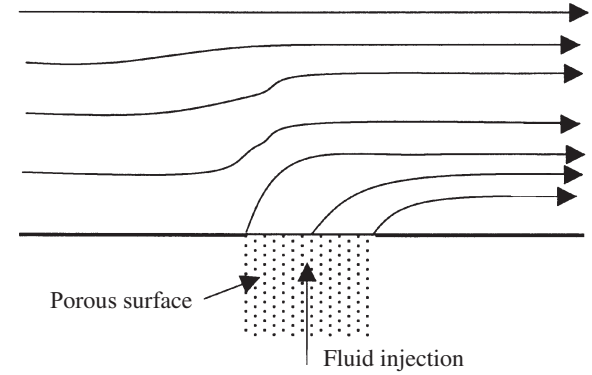
6.7.1 Thermal Transport in Jet Impingement

Due to the thin thermal and hydrodynamic boundary layers formed on the impingement surface, the heat transfer coefficients associated with jet impingement are large, making these flows suitable for large heat flux cooling applications. The relationship for impingement of a jet issuing from a nozzle at a uniform velocity and at ambient temperature T_e , with a surface at temperature T_s , can be written as

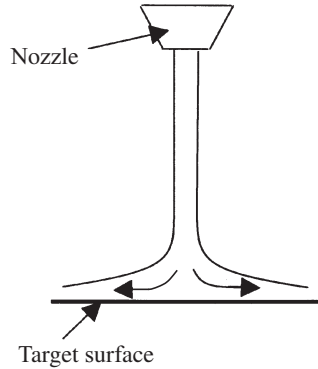
$$q'' = h(T_s - T_e) \quad (6.187)$$



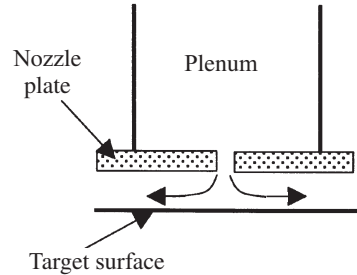
(a) Film cooling with tangential injection



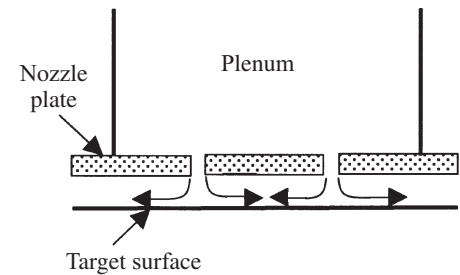
(b) Transpiration cooling



(c) Unconfined jet impingement



(d) Confined jet impingement



(e) Multiple confined jet impingement

Figure 6.28 Several configurations of jet cooling arising in applications.

The impinging jet may be circular (round) or planar (rectangular or slot), based on its cross section. It may be submerged (fluid discharged in the same ambient medium), or free surface (a liquid discharged into ambient gas). The flows in each of these cases may be *unconfined* or *partially confined*. Moreover, in the case of multiple jets, interaction effects arise.

6.7.2 Submerged Jets

A schematic of a single submerged circular or planar jet is seen in Fig. 6.29. Typically, the jet is turbulent at the nozzle exit and can be characterized by a nearly uniform axial velocity profile. With increasing distance from the nozzle exit, the potential core region within which the uniform velocity profile persists shrinks as the jet interacts with the ambient. Farther downstream, in the free jet region, the velocity profile is nonuniform across the entire jet cross section. The centerline velocity decreases with distance from the nozzle exit in this region. The effect of the impingement surface is not felt in this region. The impingement surface influences the flow in

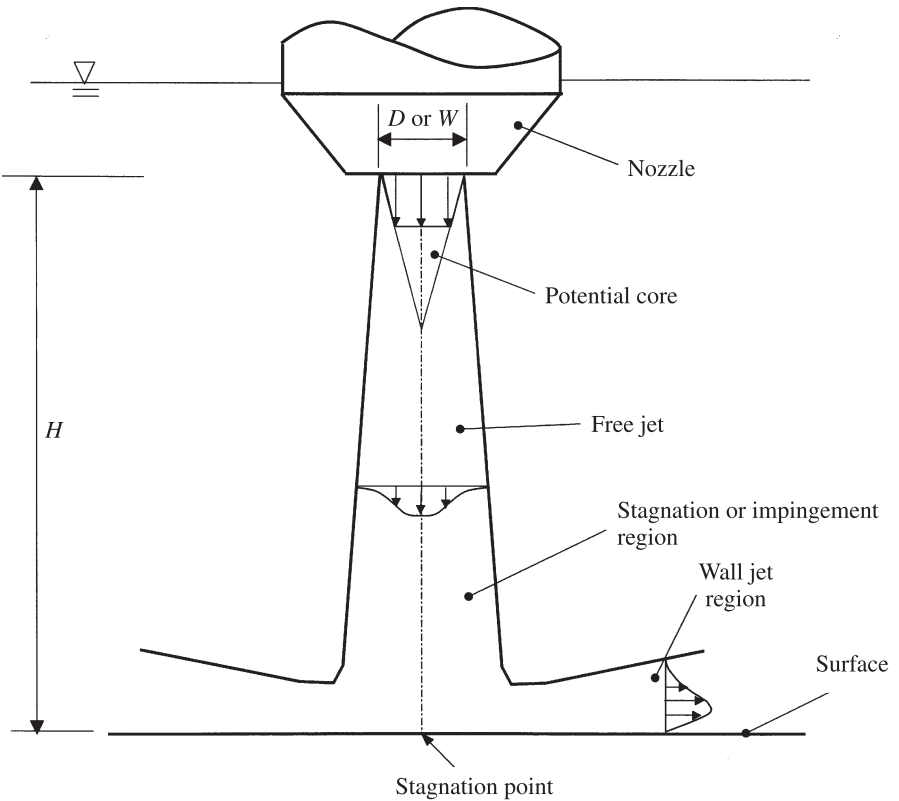


Figure 6.29 Transport regimes in a submerged circular unconfined jet impinging on a surface.

the *stagnation* or *impingement zone*. Within this region the flow accelerates in the transverse direction (r or x) and decelerates in the z direction. Farther away in the transverse direction (in the *wall jet region*), the flow starts to decelerate due to entrainment of the ambient fluid.

Average Nusselt Number for Single Jets Martin (1977) provides an extensive review of heat transfer data for impinging gas jets. For single nozzles, the average Nusselt number is of the form (Martin, 1977; Incropera and DeWitt, 1996)

$$\overline{\text{Nu}} = f\left(\text{Re}, \text{Pr}, \frac{r}{D_h}, \frac{H}{D_h}\right) \quad (6.188a)$$

or

$$\overline{\text{Nu}} = f\left(\text{Re}, \text{Pr}, \frac{x}{D_h}, \frac{H}{D_h}\right) \quad (6.188b)$$

where

$$\overline{\text{Nu}} = \frac{\bar{h}}{D_h} k \quad (6.189a)$$

and

$$\text{Re} = \frac{V_e D_h}{\nu} \quad (6.189b)$$

where V_e is the uniform exit velocity at the jet nozzle, $D_h = D$ for a round nozzle, and $D_h = 2W$ for a slot nozzle. Figure 6.29 defines the geometric parameters.

For a single round nozzle, Martin (1977) recommends

$$\frac{\overline{\text{Nu}}}{\text{Pr}^{0.42}} = G\left(\frac{D}{r}, \frac{H}{D}\right) f_1(\text{Re}) \quad (6.190)$$

where

$$f_1(\text{Re}) = 2\text{Re}^{1/2}(1 + 0.005\text{Re}^{0.55})^{1/2} \quad (6.191a)$$

and

$$G = \frac{D}{r} \frac{1 - 1.1(D/r)}{1 + 0.1[(H/D) - 6](D/r)} \quad (6.191b)$$

Replacing D/r by $2A_r^{1/2}$ yields

$$G = 2A_r^{1/2} \frac{1 - 2.20A_r^{1/2}}{1 + 0.20[(H/D) - 6]A_r^{1/2}} \quad (6.192)$$

The ranges of validity of eqs. (6.191) are

$$2000 \leq \text{Re} \leq 400,000 \quad 2 \leq \frac{H}{D} \leq 12$$

$$2.5 \leq \frac{r}{D} \leq 7.5 \quad \text{and} \quad 0.004 \leq A_r \leq 0.04$$

For $r < 2.5D$, the average heat transfer data are provided by Martin (1977) in graphical form.

For a single-slot nozzle, the recommended correlation is

$$\frac{\overline{\text{Nu}}}{\text{Pr}^{0.42}} = \frac{3.06\text{Re}^m}{(x/W) + (H/W) + 2.78} \quad (6.193)$$

where x is the distance from the stagnation point,

$$m = 0.695 - \left[\left(\frac{x}{2W} \right) + \left(\frac{H}{2W} \right)^{1.33} + 3.06 \right]^{-1} \quad (6.194)$$

and the corresponding ranges of validity are

$$3000 \leq \text{Re} \leq 90,000 \quad 4 \leq \frac{H}{W} \leq 20 \quad 4 \leq \frac{x}{W} \leq 50$$

For $x/W < 4$, these results can be used as a first approximation and are within 40% of measurements. More recent measurements by Womac et al. (1993) suggest that with the Prandtl number effect included in Martin (1977), these correlations are also applicable as a reasonable approximation for liquid jets.

Average Nusselt Number for an Array of Jets Martin (1977) also provides correlations for arrays of in-line and staggered nozzles, as well as for an array of slot jets. These configurations are illustrated in Fig. 6.30, and the following correlations are also provided by Incropera and DeWitt (1996).

For an array of round nozzles,

$$\frac{\overline{\text{Nu}}}{\text{Pr}^{0.42}} = K \left(A_r, \frac{H}{D} \right) G \left(A_r, \frac{H}{D} \right) f_2(\text{Re}) \quad (6.195)$$

where

$$f_2(\text{Re}) = 0.5\text{Re}^{2/3} \quad (6.196a)$$

$$K \left(A_r, \frac{H}{D} \right) = \left[1 + \left(\frac{H/D}{0.6/A_r^{1/2}} \right)^6 \right]^{-0.05} \quad (6.196b)$$

where G is the same as for the single nozzle, eq. (6.191b).

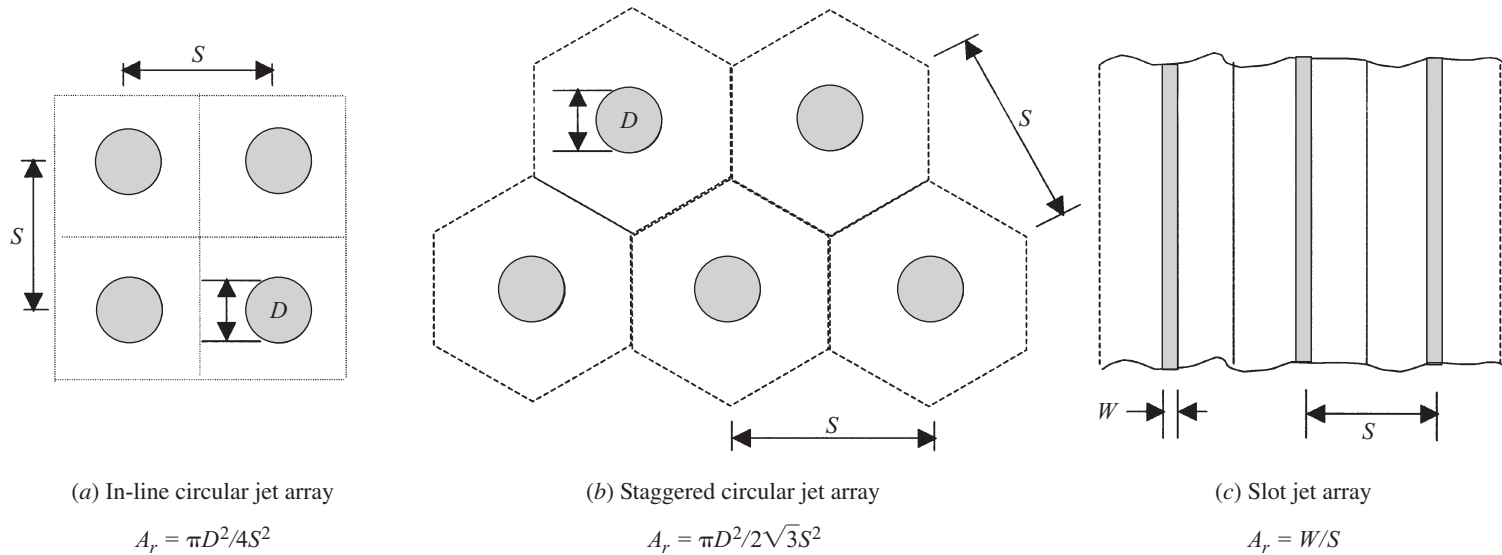


Figure 6.30 Commonly utilized jet array configurations. (From Incropera and DeWitt, 1996.)

The ranges of validity of eqs. (6.196) are

$$2000 \leq \text{Re} \leq 100,000 \quad 2 \leq \frac{H}{D} \leq 12 \quad 0.004 \leq A_r \leq 0.04$$

For an array of slot nozzles,

$$\frac{\overline{\text{Nu}}}{\text{Pr}^{0.42}} = \frac{2}{3} A_{r,0}^{3/4} \left(\frac{2\text{Re}}{A_r/A_{r,0} + A_{r,0}/A_r} \right)^{2/3} \quad (6.197)$$

where

$$A_{r,0} = \left[60 + 4 \left(\frac{H}{2W} - 2 \right)^2 \right]^{-1/2} \quad (6.198)$$

and

$$1500 \leq \text{Re} \leq 40,000 \quad 2 \leq \frac{H}{W} \leq 80 \quad 0.008 \leq A_r \leq 2.5 A_{r,0}$$

Free Surface Jets The flow regimes associated with a free surface jet are illustrated in Fig. 6.31. As the jet emerges from the nozzle, it tends to achieve a more uniform profile farther downstream, due to the elimination of wall friction. There is a corresponding reduction in jet centerline velocity (or midplane velocity for the slot jet). As for the submerged jet, a stagnation zone occurs. This zone is associated with the concurrent deceleration of the jet in a direction normal to surface and acceleration parallel to it and is also characterized by a strong favorable pressure gradient parallel to the surface.

Within the stagnation zone, hydrodynamic and thermal boundary layers are of uniform thickness. Beyond this region, the boundary layers begin to grow in the wall jet region, eventually reaching the free surface. The viscous effects extend throughout the film thickness $t(r)$, and the surface velocity V_s starts to decrease with increasing radius. The velocity profiles are similar to each other in a region that ends at $r = r_c$, where the transition to turbulence begins.

The flow development associated with the planar jet is less complicated. Following the bifurcation at the stagnation line, the two oppositely directed films are of a fixed film thickness and the free surface velocity is $V_s = V_i$. Boundary layers grow outside the stagnation zone. These reach the film thickness, before or after transition to turbulence, depending on the initial conditions.

Womac et al. (1993) considered free surface impinging jets of water and FC-77 on a square nearly isothermal heater of side 12.7 mm. Nozzle diameters D_n ranged from 0.978 to 6.55 mm, and nozzle-to-surface spacings varied from 3.5 to 10. They correlated their average heat transfer coefficient data using an area-weighted average of standard correlations for the impingement and wall jet regions. The correlation for the impingement region is of the form

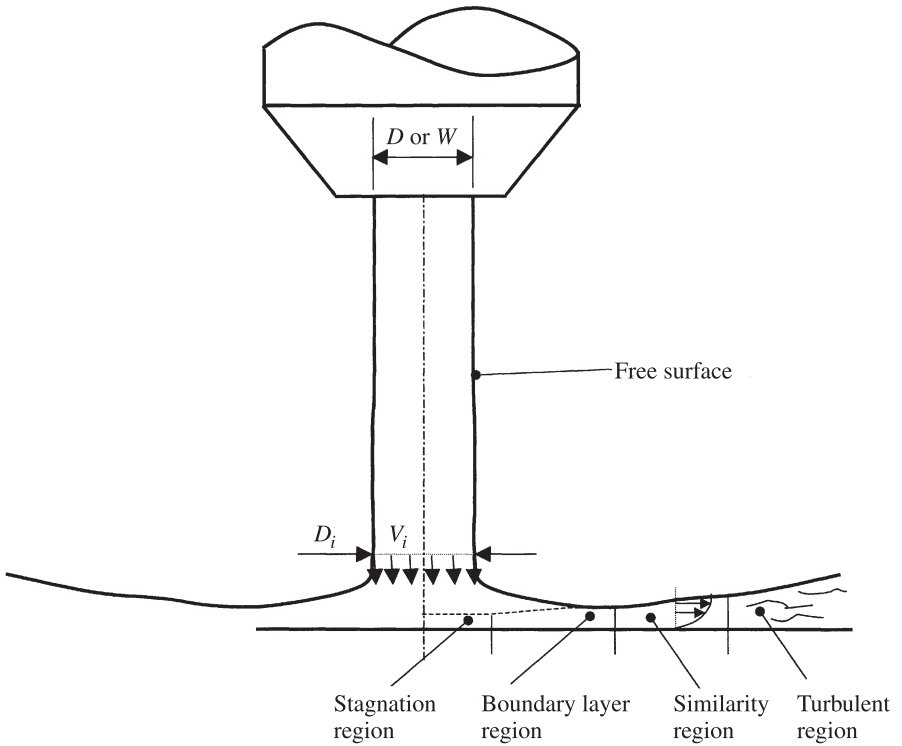


Figure 6.31 Transport regions in a circular, unconfined, free surface jet impinging on a surface.

$$\frac{\overline{Nu}}{Pr^{0.4}} = C_1 \cdot Re_{D_i}^m \quad (6.199)$$

where $m = 0.5$ and the Reynolds number is defined in terms of the impingement velocity V_i diameter $D_i = D_n(V_n/V_i)^{1/2}$. The wall jet correlation is of the form

$$\frac{\overline{Nu}}{Pr^{0.4}} = C_2 \cdot Re_{L^*}^n \quad (6.200)$$

where the Reynolds number is defined in terms of the impingement velocity v_i , and the average length L^* of the wall jet region for a square heater is

$$L^* = \frac{0.5(\sqrt{2} L_h - D_i) + 0.5(L_h - D_i)}{2} \quad (6.201)$$

Combining the correlations of eqs. (6.199) and (6.200) in an area-weighted fashion gives (Incropera, 1999)

$$\frac{\overline{\text{Nu}}}{\text{Pr}^{0.4}} = C_1 \cdot \text{Re}_{D_i}^m \frac{L_h}{D_i} A_r + C_2 \cdot \text{Re}_{L^*}^n \frac{L_h}{L^*} (1 - A_r) \quad (6.202)$$

where

$$A_r = \frac{\pi D_i^2}{4l_h^2}$$

The data were found to be best correlated in the range $1000 < \text{Re}_{D_h} < 51,000$ for $C_1 = 0.516$, $C_2 = 0.491$, and $n = 0.532$, where the fluid properties are evaluated at the mean of the surface and ambient fluid temperature.

6.8 SUMMARY OF HEAT TRANSFER CORRELATIONS

- Isothermal flat plate in uniform laminar flow (Sections 6.4.3 through 6.4.5): Near $\text{Pr} = 1$,

$$\text{Nu}_x = 0.332 \text{Re}_x^{1/2} \cdot \text{Pr}^{1/3} \quad (6.36)$$

For $\text{Pr} \ll 1$,

$$\text{Nu}_x = 0.565 \text{Re}_x^{1/2} \cdot \text{Pr}^{1/2} \quad (6.44)$$

For $\text{Pr} \gg 1$,

$$\text{Nu}_x = 0.339 \text{Re}_x^{1/2} \cdot \text{Pr}^{1/3} \quad (6.48b)$$

- Isothermal flat plate in uniform laminar flow with appreciable viscous dissipation (Section 6.4.6):

$$\text{Nu}_x = 0.332 \text{Re}_x^{1/2} \cdot \text{Pr}^{1/3} \quad (6.36)$$

The local heat flux is given by

$$q'' = h_x(T_o - T_{\text{AW}})$$

where

$$T_{\text{AW}} = T_\infty + r_c \frac{U^2}{2c_p}$$

and for gases

$$r_c = b(\text{Pr} \simeq \text{Pr})^{1/2}$$

and where the fluid properties are evaluated at

$$T^* = T_\infty + (T_W - T_\infty) + 0.22(T_{AW} - T_\infty)$$

The surface-averaged heat transfer coefficient in each of the foregoing cases for an isothermal flat plate is determined from its local value at $x = L$ (h_L) as

$$\bar{h} = 2h_L \quad (6.37)$$

- Flat plate in uniform laminar flow with an unheated starting length (x_0) and heated to a uniform temperature beyond Pr near 1 (Section 6.4.7):

$$Nu = \frac{0.332Pr^{1/2} \cdot Re_x^{1/2}}{[1 - (x_0/x)^{3/4}]^{1/3}} \quad (6.63)$$

- Wedge at uniform temperature with an included angle of $\beta\pi$ in a uniform laminar flow in the range $0.7 < Pr < 10$ (Section 6.4.4):

$$\frac{Nu_x}{Re_x^{1/2}} = \frac{0.56A}{(2 - \beta)^{1/2}} \quad (6.42)$$

where

$$\beta = \frac{2m}{m+1} \quad \text{and} \quad A = (\beta + 0.2)^{0.11} Pr^{0.333+0.067\beta-0.026\beta^2}$$

- Cylinder at uniform surface temperature in a laminar cross flow (Section 6.4.16):

$$\overline{Nu_D} \equiv \frac{\bar{h}D}{k} = 0.30 + \frac{0.62Re_D^{1/2} \cdot Pr^{1/3}}{[1 + (0.40/Pr)^{2/3}]^{1/4}} \left[1 + \left(\frac{Re_D}{282,000} \right)^{5/8} \right]^{4/5} \quad (6.155)$$

- General two-dimensional object at uniform surface temperature in a uniform laminar flow (Section 6.4.9):

$$St = \frac{q''}{\rho c_p U (T_0 - T_\infty)} = \frac{k}{\rho c_p U \delta} = \frac{c_1 (U^*)^{c_2}}{\left[\int_0^{x^*} (U^*)^{c_3} dx^* \right]^{1/2}} \left(\frac{1}{Re_L} \right)^{1/2} \quad (6.72)$$

where c_1 through c_3 are as given in Table 6.1.

- Laminar flow over a sphere at a uniform surface temperature (Section 6.4.16):

$$\overline{Nu_D} = 2 + \left(0.4Re_D^{1/2} + 6Re_D^{2/3} \right) Pr^{0.4} \left(\frac{\mu}{\mu_s} \right)^{1/4} \quad (6.156)$$

- General axisymmetric object at uniform surface temperature in a uniform laminar flow (Section 6.4.10):

$$\text{St} = \frac{c_1 (r_0^*)^K (U^*)^{c_2}}{\left[\int_0^{x_3^*} (U^*)^{c_3} (r_0^*)^{2K} dx_3^* \right]^{1/2}} \left(\frac{1}{\text{Re}_L} \right)^{1/2} \quad (6.76)$$

where c_1 through c_3 are as given in Table 6.1.

- Isothermal flat plate with a turbulent boundary layer from the leading edge for Pr and Pr_T near 1 (Section 6.4.14):

$$\text{Nu}_x = 0.0296 \text{Re}_x^{0.80} \quad (6.108)$$

- Isothermal flat plate with turbulent boundary layer transition from laminar to turbulent for Pr and Pr_T near 1 (Section 6.4.14):

$$\overline{\text{Nu}}_L = 0.664 \text{Re}_L^{0.5} + 0.36 (\text{Re}_L^{0.8} - \text{Re}_T^{0.8}) \quad (6.110)$$

- Isothermal flat plate with turbulent boundary Pr_T near 1 (Section 6.4.14):

$$\text{Nu}_x = 0.029 \text{Re}_x^{0.8} G \quad (6.130)$$

where

$$G = \frac{\text{Pr}}{(0.029/\text{Re}_x)^{1/2} \{5\text{Pr} + 5 \ln[(1 + 5\text{Pr})/6] - 5\} + 1} \quad (6.131)$$

- Flat plate with a turbulent boundary layer from the leading edge and with an unheated starting length followed by uniform surface temperature for Pr and Pr_T near 1 (Section 6.4.14):

$$\text{St} \cdot \text{Pr}^{0.8} = 0.287 \text{Re}_x^{-0.2} \left[1 - \left(\frac{x_0}{x} \right)^{9/10} \right]^{1/9} \quad (6.140)$$

- Uniform flux plate with a turbulent boundary layer from the leading edge for Pr and Pr_T near 1 (Section 6.4.14):

$$\text{St} \cdot \text{Pr}^{0.4} = 0.03 \text{Re}_x^{-0.2} \quad (6.141)$$

- Isothermal rough flat plate with a turbulent boundary layer from the leading for Pr and Pr_T near 1 (Section 6.4.15):

$$\text{St} = \frac{C_f/2}{\text{Pr}_T + (C_f/2)^{1/2}/\text{St}_k} \quad (6.154)$$

where

$$\text{St}_k \simeq 0.8 \text{Re}_k^{-0.2} \cdot \text{Pr}^{-0.4}$$

- Cross flow across a bank of cylinders at uniform surface temperature (Section 6.5.1):

$$\overline{\text{Nu}}_D = C \cdot \text{Re}_{D,\max}^m \cdot \text{Pr}^{0.36} \left(\frac{\text{Pr}}{\text{Pr}_s} \right)^{1/4} \quad (6.157)$$

for

$$N_L \geq 20 \quad 0.7 \leq \text{Pr} < 500 \quad 1 < \text{Re}_{D,\max} < 2 \times 10^6$$

where C and m are given in Table 6.2.

- Plate stack (Section 6.5.2): The optimum number of plates in a given cross-sectional area, $L \times H$,

$$n_{\text{opt}} \simeq \frac{0.26(H/L)\text{Pr}^{1/4} \cdot \text{Re}_L^{1/2}}{1 + 0.26(t/L)\text{Pr}^{1/4} \cdot \text{Re}_L^{1/2}} \quad (6.161)$$

for $\text{Pr} \geq 0.7$ and $n \gg 1$.

- Offset strips (Section 6.5.2): In the laminar range ($\text{Re} \leq \text{Re}^*$),

$$f = 8.12 \text{Re}^{-0.74} \left(\frac{\ell}{d_h} \right)^{-0.15} \alpha^{-0.02} \quad (6.166)$$

$$j = 0.53 \text{Re}^{-0.50} \left(\frac{\ell}{d_h} \right)^{-0.15} \alpha^{-0.14} \quad (6.167)$$

In the turbulent range ($\text{Re} \leq \text{Re}^* + 1000$),

$$f = 1.12 \text{Re}^{-0.36} \left(\frac{\ell}{d_h} \right)^{-0.65} \left(\frac{t}{d_h} \right)^{0.17} \quad (6.168)$$

$$j = 0.21 \text{Re}^{-0.40} \left(\frac{\ell}{d_h} \right)^{-0.24} \left(\frac{t}{d_h} \right)^{0.02} \quad (6.169)$$

The transition Reynolds number Re^* is obtained from the set of equations

$$\text{Re}^* = \text{Re}_b^* \frac{d_h}{b} \quad (6.170)$$

$$\text{Re}_b^* = 257 \left(\frac{\ell}{s} \right)^{1.23} \left(\frac{t}{\ell} \right)^{0.58} \quad (6.171)$$

$$b = t + \frac{1.328\ell}{(\text{Re}_\ell)^{1/2}} \quad (6.172)$$

$$\text{Re}_\ell = \frac{U_c \ell}{\nu} \quad (6.173)$$

The parameter α is the aspect ratio. $\alpha = s/W$, where W is the strip width.

- Flush-mounted heat sources (Section 6.6.1):

$$\overline{\text{Nu}} = 0.486\text{Pe}^{0.53} \left(\frac{\ell_{se}}{s_x} \right)^{0.71} \left(\frac{k_s}{k_f} \right)^{0.057} \quad (6.174)$$

For the rectangular patch,

$$\overline{\text{Nu}} = \begin{cases} 0.60\text{Pe}_c^{0.48} \left(\frac{2\ell_s}{2x_s + \ell_s} \right)^{0.63} \left(\frac{P\ell_s}{2A} \right)^{0.18} & \left(\frac{k_{\text{sub}}}{k_f} = 1 \right) \\ 0.43\text{Pe}_c^{0.52} \left(\frac{2\ell_s}{2x_s + \ell_s} \right)^{0.70} \left(\frac{P\ell_s}{2A} \right)^{0.07} & \left(\frac{k_{\text{sub}}}{k_f} = 10 \right) \end{cases} \quad (6.175)$$

Here $\overline{\text{Nu}}$ is as defined for the two-dimensional strip,

$$\text{Pe}_c = \frac{U_0 (s_x + \ell_{se})}{\alpha}$$

A/P is the source surface area/perimeter ratio. The foregoing correlations are valid for

$$10^3 \leq \text{Pe}_c \leq 10^5 \quad 5 \leq \frac{x_s + \ell_s/2}{\ell_s} \leq 150 \quad 0.2 \leq \frac{w_s}{\ell_s} \leq 5$$

In the foregoing, w_s is the heat source height, P_ℓ its length, and P_w its width. The channel width is $W = 12$ mm and the height H can vary from 7 to 30 mm. The heat source dimensions covered in the experiments are $P_\ell = 12$ mm, $P_h = 4, 8$, and 12 mm, $H - P_h = 3, 8$, and 12 mm, and $P_s = 12$ mm.

- Isolated blocks (Section 6.6.3):

$$\overline{\text{Nu}} = 0.150\text{Re}^{0.612} (A^*)^{-0.455} \left(\frac{H}{P_\ell} \right)^{0.727} \quad (6.178)$$

where $\overline{\text{Nu}} = \bar{h} P_\ell / k$, \bar{h} is the average heat transfer coefficient, and A_s is the heat transfer area,

$$A_s = 2P_h P_w + P_\ell P_w + 2P_h P_\ell$$

\bar{T}_s is the average surface temperature and T_∞ is the stream temperature. The Reynolds number is defined as $\text{Re} = UD_h/\nu$, where U is the average channel

velocity upstream of the heat source, D_H is the channel hydraulic diameter at a section unobstructed by the heat source, and ν is the fluid (air) kinematic viscosity. The fraction of the channel open to flow is

$$A^* = 1 - \frac{P_w/W}{P_h/H}$$

Equation (6.178) is valid for

$$\begin{aligned} 1500 \leq \text{Re} \leq 10^4 & \quad 0.33 \leq \frac{P_h}{P_\ell} \leq 1.00 \\ 0.12 \leq \frac{P_w}{W} \leq 1.00 & \quad 0.583 \leq \frac{H}{P_\ell} \leq 2.50 \end{aligned}$$

A realistic error bound is 5%.

- Block array (Section 6.6.4):

$$\text{Nu}_{P_\ell} = 0.348 \text{Re}_{P_\ell}^{0.6} \quad (6.182)$$

where the characteristic length for both Nu and Re is the streamwise length of the block, P_ℓ .

- Pin fin heat sinks (Section 6.6.6): Two correlations are given:

$$\text{Nu} = 7.12 \times 10^{-4} C_{\Delta p}^{0.574} \left(\frac{a}{L}\right)^{0.223} \left(\frac{p}{d}\right)^{1.72} \quad (6.185)$$

where in

$$C_{\Delta p} = \frac{\rho L^3 \Delta p}{\mu^2}$$

μ is the dynamic viscosity of the air. Equation (6.185) was derived from the data for $5 \times 10^6 < C_{\Delta p} < 1.5 \times 10^8$:

$$\text{Nu} = 3.2 \times 10^{-6} C_{P_w}^{0.520} \left(\frac{a}{L}\right)^{-0.205} \left(\frac{p}{d}\right)^{0.89} \quad (6.186)$$

where

$$C_{P_w} = \frac{\rho^2 L P_w}{\mu^3}$$

covers a range of 10^{11} to 10^{13} .

- Single round submerged jet impinging on an isothermal target surface (Section 6.7.2):

$$\frac{\overline{\text{Nu}}}{\text{Pr}^{0.42}} = G \left(\frac{D}{r}, \frac{H}{D} \right) f_1(\text{Re}) \quad (6.190)$$

where

$$f_1(\text{Re}) = 2\text{Re}^{1/2}(1 + 0.005\text{Re}^{0.55})^{1/2} \quad (6.191a)$$

$$G = \frac{D}{r} \frac{1 - 1.1(D/r)}{1 + 0.1[(H/D) - 6](D/r)} \quad (6.191b)$$

The range of applicability of the foregoing is

$$2000 \leq \text{Re} \leq 4 \times 10^5 \quad 2 \leq \frac{H}{D} \leq 12 \quad 2.5 \leq \frac{r}{D} \leq 7.5 \quad 0.004 \leq A_r \leq 0.04$$

- Single submerged slot jet impinging on an isothermal target surface (Section 6.7.2):

$$\frac{\overline{\text{Nu}}}{\text{Pr}^{0.42}} = \frac{3.06\text{Re}^m}{(x/W) + (H/W) + 2.78} \quad (6.193)$$

where

$$m = 0.695 - \left[\left(\frac{x}{2W} \right) + \left(\frac{H}{2W} \right)^{1.33} + 3.06 \right]^{-1} \quad (6.194)$$

The range of applicability is

$$3000 \leq \text{Re} \leq 9 \times 10^4 \quad 4 \leq \frac{H}{W} \leq 20 \quad 4 \leq \frac{x}{W} \leq 50$$

- Array of round submerged jets impinging on an isothermal target surface (Section 6.7.2):

$$\frac{\overline{\text{Nu}}}{\text{Pr}^{0.42}} = K \left(A_r, \frac{H}{D} \right), G \left(A_r, \frac{H}{D} \right) f_2(\text{Re}) \quad (6.195)$$

where

$$f_2(\text{Re}) = 0.5\text{Re}^{2/3} \quad (6.196a)$$

$$K = \left[1 + \left(\frac{H/D}{0.6/A_r^{1/2}} \right)^6 \right]^{-0.05} \quad (6.196b)$$

and G is given by eq. (1.191b). The range of validity of the foregoing is

$$2000 \leq \text{Re} \leq 10^5 \quad 2 \leq \frac{H}{D} \leq 12 \quad 2.5 \leq \frac{r}{D} \leq 7.5 \quad 0.004 \leq A_r \leq 0.04$$

- Array of submerged slot jets impinging on an isothermal target surface (Section 6.7.2):

$$\frac{\overline{\text{Nu}}}{\text{Pr}^{0.42}} = \frac{2}{3} A_{r,0}^{3/4} \left(\frac{2\text{Re}}{A_r/A_{r,0} + A_{r,0}/A_r} \right)^{2/3} \quad (6.197)$$

where

$$A_{r,0} = \left[60 + 4 \left(\frac{h}{2W} - 2 \right)^2 \right]^{-1/2} \quad (6.198)$$

with a range of validity of

$$1500 \leq \text{Re} \leq 4 \times 10^4 \quad 2 \leq \frac{H}{W} \leq 80 \quad 0.008 \leq A_r \leq 2.5 A_{r,0}$$

- Single round free surface jet impinging on a square isothermal target surface (Section 6.7.2):

$$\frac{\overline{\text{Nu}}}{\text{Pr}^{0.4}} = C_1 \cdot \text{Re}_{D_i}^m \frac{L_h}{D_i} A_r + C_2 \cdot \text{Re}_{L^*}^n \frac{L_h}{L^*} (1 - A_r) \quad (6.202)$$

where

$$A_r = \frac{\pi D_i^2}{4 L_h^2}$$

$$L^* = \frac{0.5(\sqrt{2} L_h - D_i) + 0.5(L_h - D_i)}{2} \quad (6.201)$$

These data have been found to be best correlated in the range $1000 \leq \text{Re}_{D_n} \leq 51,000$ for $C_1 = 0.516$, $C_2 = 0.491$, and $n = 0.532$, where the fluid properties are evaluated at the mean of the surface and ambient fluid temperature.

NOMENCLATURE

Roman Letter Symbols

A	constant or correlation constant, dimensionless
	Prandtl number-dependent constant, dimensionless
	source surface area, m^2
A_s	surface area, m^2
A_T	total heat sink surface area, m^2
A^*	fraction of channel cross section open to flow, m^2
A_1	flow area (aligned tube arrangement), m^2

A_2	flow area (staggered tube arrangement), m^2
a	sphere radius, m fin height, m
B	correlation constant, dimensionless
b	parameter defined by eq. (6.172), dimensionless
$b(x)$	similarity function, dimensionless
C	ratio of eddy to turbulent diffusivity, dimensionless constant or correlation constant, dimensionless
$C_{\Delta p}$	coefficient in eq. (6.185), dimensionless
C_{P_w}	coefficient in eq. (6.186), dimensionless
\bar{C}	coefficient in free stream velocity definition, dimensionless
C_f	friction coefficient, dimensionless
$c(x)$	similarity function, dimensionless
c_p	specific heat, $J/kg \cdot K$
D	substantial derivative, dimensionless cylinder or sphere diameter, m round jet diameter, m
D_h	hydraulic diameter, m
D_H	channel hydraulic diameter, m
d	pin diameter, m tube diameter, m
$d(x)$	similarity function, dimensionless
d_h	hydraulic diameter, m
Ec	Eckert number, dimensionless
F	function, dimensionless
\bar{F}	Prandtl number, dimensionless
f	friction factor, dimensionless
$f(\eta)$	stream function, dimensionless
G	parameter defined by eq. (6.131), dimensionless
H	envelope height, m location outside the boundary layer, m channel height (plate spacing), m
h	height, m heat transfer coefficient, $W/m^2 \cdot K$
\bar{h}	mean heat transfer coefficient, $W/m^2 \cdot K$
h_{ad}	adiabatic heat transfer coefficient, $W/m^2 \cdot K$
h_{av}	average heat transfer coefficient, $W/m^2 \cdot K$
h_L	heat transfer coefficient for laminar boundary layer, $W/m^2 \cdot K$
h_T	heat transfer coefficient for turbulent boundary layer, $W/m^2 \cdot K$
\mathbf{i}	unit vector in x -coordinate direction, dimensionless
i	step counter, dimensionless row counter, dimensionless
(i, j)	row and column index, dimensionless
j	column counter, dimensionless Colburn heat transfer factor, dimensionless

$j(x)$	similarity function, dimensionless
j	unit vector in y-coordinate direction, dimensionless
K	flow index, dimensionless
k	thermal conductivity, $\text{W/m} \cdot \text{K}$
k_{plate}^*	plate/fluid thermal conductivity ratio, $\text{W/m} \cdot \text{K}$
k_f	fluid thermal conductivity, $\text{W/m} \cdot \text{K}$
k_s	mean roughness length scale, dimensionless
k_{sub}	substrate thermal conductivity, $\text{W/m} \cdot \text{K}$
k	unit vector in z coordinate direction, dimensionless
L	envelope length, m
	length scale factor, m
	length of heat sink, m
	length in streamwise direction, m
L_{core}	core length, m
ℓ	plate length, m
	cylinder length, m
	mixing length, m
	spacing between plates, m
ℓ_1	leading edge to first block spacing, m
ℓ_2	last block to trailing edge spacing, m
ℓ_s	heat source length, m
m	exponent, dimensionless
N	constant, dimensionless
N_L	exponent, dimensionless
	number of tube rows, dimensionless
Nu	Nusselt number, dimensionless
$\bar{\text{Nu}}$	mean or average Nusselt number, dimensionless
Nu_D	Nusselt number based on diameter, dimensionless
$\bar{\text{Nu}}_D$	average Nusselt number based on diameter, dimensionless
Nu_L	Nusselt number based on length, dimensionless
Nu_x	Nusselt number based on diameter, dimensionless
n	exponent, dimensionless
	number of pins, dimensionless
	number of plates in stack, dimensionless
O	order, dimensionless
P	perimeter, m
P_h	height of block, m
	heat source height, m
P_ℓ	heat source length, m
	length of block, m
P_W	fan power, W
P_w	width of block, m
	heat source width
Pe	Péclet number, dimensionless
Pe_c	Péclet number used in eqs. (6.175) and (6.176), dimensionless

Pr	Prandtl number, dimensionless
Pr_T	turbulent Prandtl number, dimensionless
p	pressure, N/m^2
	fin pitch, m
p^+	normalized pressure, N/m^2
\bar{p}	mean or average pressure, N/m^2
p^*	normalized pressure, N/m^2
p_m	motion pressure, N/m^2
Q	total heat generated, W
	heat sink dissipation, W
	heater power input, W
Q_A	direct heat transfer component, W
Q_B	conjugate heat transfer component through substrate, W
q	exponent, dimensionless
q_A	heat dissipation, block A , W
q_B	heat dissipation, block B , W
q''	heat flux, W/m^2
q_m''	mean heat flux, W/m^2
q'''	volumetric heat generation, W/m^3
$q_{(i,j)}$	rate of heat dissipation by block (i,j) in the array, W
R	thermal resistance, K/W
Re	Reynolds number, dimensionless
Re_b^*	Reynolds number defined by eq. (6.171), dimensionless
Re_D	Reynolds number based on diameter, dimensionless
$Re_{D,\max}$	Reynolds number at maximum flow, dimensionless
Re_k	roughness Reynolds number, dimensionless
Re_L	Reynolds number based on length, dimensionless
Re_ℓ	Reynolds number defined by eq. (6.173), dimensionless
Re_{P_h}	Reynolds number based on P_h defined in Section 6.6.2, dimensionless
Re_{P_ℓ}	Reynolds number based on P_ℓ defined in Section 6.6.2, dimensionless
Re_T	critical Reynolds number, dimensionless
Re_x	Reynolds number based on x , dimensionless
Re^*	transition Reynolds number, dimensionless
r	boundary layer ratio, dimensionless
r_c	recovery factor, dimensionless
r_0	distance from axis to surface, m
S	jet spacing, m
S_D	diagonal tube spacing, m
S_L	longitudinal tube spacing, m
S_T	transverse tube spacing, m
St	Stanton number, dimensionless
St_k	roughness Stanton number, dimensionless

s	strip spacing, m clear space between blocks, m
s_x	x -coordinate distance, m
s_z	distance to bounding surface, m
T	temperature, K
\bar{T}	average or mean temperature, K
\bar{T}_s	average surface temperature, K
$T_{\text{air}, B}$	temperature of air at block B , K
T_b	temperature in buffer region, K temperature at bottom surface of heat sink, K
T_{max}	maximum surface temperature, K
T_{ref}	reference temperature, K
T_s	surface temperature, K
$T_{s, B}$	surface temperature of block B , K
T^*	normalized temperature in eq. (6.8), dimensionless
T_b^+	normalized buffer temperature, K
T_0	free stream temperature, K air temperature at front of heat sink, K
T_∞	ambient temperature, K
t	time, s plate thickness, m nondimensional substrate thickness, dimensionless
t^*	normalized time, s
t_0	time reference, s
U	overall heat transfer coefficient, $\text{W/m}^2 \cdot \text{K}$ velocity scale factor, m/s free stream velocity, m/s
U_∞	velocity in undisturbed flow, m/s
U_0	average velocity in unobstructed channel, m/s
U_c	core velocity, m/s
u	x -coordinate velocity, m/s
u^+	normalized x -coordinate velocity, m/s
u_∞^+	normalized free stream x -coordinate velocity, m/s
u_o	free stream x -coordinate velocity, m/s
\bar{u}	mean or average x -coordinate velocity, m/s
u^*	normalized x -coordinate velocity, m/s
V	velocity, m/s
V_{max}	maximum velocity, m/s
\mathbf{V}	velocity vector, m/s
v	y -coordinate velocity, m/s
v_0	free stream y -coordinate velocity, m/s
v^*	friction velocity in turbulent flow, m/s
v^+	normalized y -coordinate velocity, m/s
\bar{v}	mean or average y -coordinate velocity, m/s

W	envelope width, m channel width, m
w	width, m z -coordinate velocity, m/s slot jet width, m
w^*	normalized, z -coordinate velocity, m/s
X	body force, N
x_0	x coordinate, m
x	unheated starting length, m
x^*	normalized x -coordinate velocity, m/s
x_s	leading edge to heat source distance, m
Y	body force, N
y^*	normalized y -coordinate velocity, m/s
z^*	normalized z -coordinate velocity, m/s
Δp	pressure difference, N/m ²
Δp_{core}	core pressure difference, N/m ²
ΔT	temperature difference, K

Greek Letter Symbols

α	thermal diffusivity, m ² /s aspect ratio, dimensionless
β	volumetric expansion coefficient, K ⁻¹ wedge angle, rad constant, pressure difference, N/m ²
Γ	gamma function, dimensionless
Δ	change in, dimensionless
δ	hydrodynamic boundary layer, m
δ_2	momentum thickness, m
δ_c	conduction thickness, m
δ_T	thermal boundary layer, m
ϵ	eddy viscosity, m ² /s
ϵ_H	eddy diffusivity, m ² /s
η	similarity variable, dimensionless similarity function, dimensionless
η_B	Blasius similarity variable, dimensionless
η_δ	thickness of boundary layer, dimensionless
θ	normalized temperature, dimensionless angle, rad
$\theta_{B/A}$	effect of heat dissipation from block B on block A , K/W
$\theta_{B/(i,j)}$	contribution of all blocks upstream of block B , K/W
θ_{hot}	hot spot temperature, dimensionless
κ	von Kármán constant, dimensionless
μ	dynamic viscosity, kg/m · s
μ_s	dynamic viscosity at surface or wall temperature, kg/m · s
ν	kinematic viscosity, m ² /s

ξ	dummy variable, dimensionless
ρ	fluid density, kg/m^3
τ	shear stress, N/m^2
τ_b	mean shear stress, N/m^2
τ_o	free stream shear stress, N/m^2
τ_T	turbulent shear stress, N/m^2
Φ	viscous dissipation, s^{-2}
$\phi(x, y)$	stream function, dimensionless
$\phi(\eta)$	similarity function, dimensionless
$\psi(x, y)$	stream function, dimensionless

Roman Letter Subscripts

A	block designator
	direct heat transfer component
AW	adiabatic wall
ad, B	adiabatic heat transfer coefficient on block B
air, b	air temperature at block B
av	average
B	pertaining to Blasius
	conjugate heat transfer component
	block designator
B/A	effect on block B by dissipation from block A
$b/(i, j)$	contribution of upstream block
b	bottom of heat sink
c	conduction thickness
	recovery factor
core	core
D	diameter
f	fluid
	friction
H	homogeneous art of solution
h	height
hot	max
(i, j)	row and column index
L	length
ℓ	length
opt	optimum
P	particular part of solution
P_w	fan power
p	constant pressure
plate	plate
ref	reference
s	surface
se	heat source
sub	substrate

T	thermal turbulent
w	width
x	x -coordinate direction
y	y -coordinate direction
z	z -coordinate direction

Greek Letter Subscripts

∞	infinity
Δp	pressure loss
δ	thickness of boundary layer, dimensionless

Superscripts

m	exponent
N	exponent
q	exponent
$+$	normalized variable
$*$	normalized variable
$'$	first derivative
$''$	second derivative
$'''$	third derivative

Other

∂	partial derivative
∇	vector operator

REFERENCES

Anderson, A. M. (1994). Decoupling of Convective and Conductive Heat Transfer Using the Adiabatic Heat Transfer Coefficient, *ASME J. Electron. Packag.*, 116, 310–316.

Arvisu, D. E., and Moffat, R. J. (1982). The Use of Superposition in Calculating Cooling Requirements for Circuit Board Mounted Electronic Components, *Proc. 32nd Elect. Comp. Cont.*, San Diego, CA.

Ashiwake, N., Nakayama, W., and Daikoku, T. (1983). Convective Heat Transfer from LSI Packages in an Air-Cooled Wiring Card Array, *ASME-HTD-28*, ASME, New York, pp. 35–42.

Bejan, A., and Sciubba, E. (1992). The Optimal Spacing of Parallel Plates Cooled by Forced Convection, *Int. J. Heat Mass Transfer*, 35, 3259–3264.

Blasius, H. (1908). Grenzschichten in Flüssigkeiten mit kleiner Reibung, *Z. Math. Phys.*, 56, 1.

Cebeci, T., and Bradshaw, P. (1984). *Physical and Computational Aspects of Convective Heat Transfer*, Springer-Verlag, New York.

Churchill, S. W., and Bernstein, M. (1977). A Correlating Equation for Forced Convection from Gases and Liquids to a Circular Cylinder in Cross Flow, *J. Heat Transfer*, 99, 300–306.

- Davalath, J., and Bayazitoglu, Y. (1987). Forced Convection Cooling across Rectangular Blocks, *J. Heat Transfer*, 109, 321–328.
- DeJong, N. C., Zhang, L. W., Jacobi, A. M., Balachandar, A. M., and Tafti, D. K. (1998). A Complementary Experimental and Numerical Study of the Flow and Heat Transfer in Offset Strip-Fin Heat Exchangers, *J. Heat Transfer*, 120, 690–698.
- Gebhart, B. (1971). *Convective Heat Transfer*, McGraw-Hill, New York, Chap. 7.
- Gebhart, B. (1980). *Convective Heat Transfer*, Spring Course Notes, Department of Mechanical Engineering, State University of New York, Buffalo, NY.
- Gorski, M. A., and Plumb, O. A. (1990). Conjugate Heat Transfer from a Finite Strip Heat Source in a Plane Wall, *ASME-HTD-129*, AIAA-ASME Thermophysics and Heat Transfer Conference, Seattle, WA, ASME, New York, pp. 47–53.
- Gorski, M. A., and Plumb, O. A. (1992). Conjugate Heat Transfer from an Isolated Heat Source in a Plane Wall, in *Fundamentals of Forced Convection Heat Transfer*, *ASME-HTD-210*, M. A. Ebdian and P. H. Oosthuizen, eds., ASME, New York, pp. 99–105.
- Incropera, F. P. (1999). *Liquid Cooling of Electronic Devices by Single-Phase Convection*, Wiley, New York.
- Incropera, F. P., and DeWitt, D. P. (1996). *Fundamentals of Heat and Mass Transfer*, 4th ed., Wiley, New York.
- Joshi, H. M., and Webb, R. L. (1987). Heat Transfer and Friction in the Offset Strip-Fin Heat Exchanger, *Int. J. Heat Mass Transfer*, 30, 69–83.
- Kays, W. M., and Crawford, M. (1993). *Convective Heat and Mass Transfer*, McGraw Hill, New York.
- Ledezma, G., Morega, A. M., and Bejan, A. (1996). Optimal Spacing between Pin Fins with Impinging Flow, *J. Heat Transfer*, 118, 570–577.
- Lehman, G. L., and Wirtz, R. A. (1985). The Effect of Variations in Stream-wise Spacing and Length on Convection from Surface Mounted Rectangular Components, in *Heat Transfer in Electronic Equipment*, *ASME-HTD-48*, ASME, New York, pp. 39–47.
- Martin, H. (1977). Heat and Mass Transfer between Impinging Gas Jets and Solid Surfaces, in *Advances in Heat Transfer*, Vol. 13, J. P. Hartnett and T. F. Irvine, Jr., eds., Academic Press, New York.
- Matsushima, H., and Yanagida, T. (1993). Heat Transfer from LSI Packages with Longitudinal Fins in Free Air Stream, in *Advances in Electronic Packaging*, *ASME-EEP-4-2*, ASME, New York, pp. 793–800.
- Moffat, R. J., and Ortega, A. (1988). Direct Air Cooling of Electronic Components, in *Advances in Thermal Modeling of Electronic Components and Systems*, Vol. 1, A. Bar-Cohen and A. D. Kraus, eds., Hemisphere Publishing, New York.
- Morega, A. M., Bejan, A., and Lee, S. W. (1995). Free Stream Cooling of Parallel Plates, *Int. J. Heat Mass Transfer*, 38(3), 519–531.
- Nakayama, W., and Park, S.-H. (1996). Conjugate Heat Transfer from a Single Surface-Mounted Block to Forced Convective Air Flow in a Channel, *J. Heat Transfer*, 118, 301–309.
- Nakayama, W., Matsushima, H., and Goel, P. (1988). Forced Convective Heat Transfer from Arrays of Finned Packages, in *Cooling Technology for Electronic Equipment*, W. Aung, ed., Hemisphere Publishing, New York, pp. 195–210.

- Oosthuizen, P. H., and Naylor, D. (1999). *Convective Heat Transfer Analysis*, WCB/McGraw-Hill, New York, Chap. 6.
- Ortega, A. (1996). Conjugate Heat Transfer in Forced Air Cooling of Electronic Components, in *Air Cooling Technology for Electronic Equipment*, S. J. Kim and S. W. Lee, eds., CRC Press, Boca Raton, FL, pp. 103–171.
- Ortega, A., Wirth, U., and Kim, S. J. (1994). Conjugate Forced Convection from a Discrete Heat Source on a Plane Conducting Surface: A Benchmark Experiment, in *Heat Transfer in Electronic Systems, ASME-HTD-292*, ASME, New York, pp. 25–36.
- Pohlhausen, E. (1921). Der Wärmeaustausch zwischen festen Körpern und Flüssigkeiten mit kleiner Reibung und kleiner Wärmeleitung, *Z. Angew. Math. Mech.*, 1, 115–121.
- Roeller, P. T., and Webb, B. (1992). A Composite Correlation for Heat Transfer from Isolated Two- and Three Dimensional Protrusions in Channels, *Int. J. Heat Mass Transfer*, 35(4), 987–990.
- Roeller, P. T., Stevens, J., and Webb, B. (1991). Heat Transfer and Turbulent Flow Characteristics of Isolated Three-Dimensional Protrusions in Channels, *J. Heat Transfer*, 113, 597–603.
- Smith, A. G., and Spalding, D. B. (1958). Heat Transfer in a Laminar Boundary Layer with Constant Fluid Properties and Constant Wall Temperature, *J. R. Aeronaut. Soc.*, 62, 60–64.
- Whitaker, S. (1972). Forced Convection Heat Transfer Correlations for Flow in Pipes, Past Flat Plates, Single Cylinders, Single Spheres and for Flow in Packed Beds and Tube Bundles, *AIChE J.*, 18, 361–371.
- Wirtz, R. A., and Dykshoorn, P. (1984). Heat Transfer from Arrays of Flat Packs in Channel Flow, *Proc. 4th International Electronics Packaging Society Conferences*, New York, pp. 318–326.
- Wirtz, R. A., Sohal, R., and Wang, H. (1997). Thermal Performance of Pin-Fin Fan-Sink Assemblies, *J. Electron. Packag.*, 119, 26–31.
- Womac, D. J., Ramadhyani, S., and Incropera, F. P. (1993). Correlating Equations for Impingement Cooling of Small Heat Sources with Single Circular Liquid Jets, *J. Heat Transfer*, 115, 106–115.
- Zhukauskas, A. (1972). Heat Transfer from Tubes in Cross Flow, in *Advances in Heat Transfer*, J. P. Hartnett and T. F. Irvine, eds., Vol. 8, Academic Press, New York.
- Zhukauskas, A. (1987). Convective Heat Transfer in Cross Flow, in *Convective Heat Transfer*, S. Kakaç, R. K. Shah, and W. Aung, eds., Wiley, New York.

Natural Convection

YOGESH JALURIA

Mechanical and Aerospace Engineering Department
Rutgers University
New Brunswick, New Jersey

- 7.1 Introduction
 - 7.2 Basic mechanisms and governing equations
 - 7.2.1 Governing equations
 - 7.2.2 Common approximations
 - 7.2.3 Dimensionless parameters
 - 7.3 Laminar natural convection flow over flat surfaces
 - 7.3.1 Vertical surfaces
 - 7.3.2 Inclined and horizontal surfaces
 - 7.4 External laminar natural convection flow in other circumstances
 - 7.4.1 Horizontal cylinder and sphere
 - 7.4.2 Vertical cylinder
 - 7.4.3 Transients
 - 7.4.4 Plumes, wakes, and other free boundary flows
 - 7.5 Internal natural convection
 - 7.5.1 Rectangular enclosures
 - 7.5.2 Other configurations
 - 7.6 Turbulent flow
 - 7.6.1 Transition from laminar flow to turbulent flow
 - 7.6.2 Turbulence
 - 7.7 Empirical correlations
 - 7.7.1 Vertical flat surfaces
 - 7.7.2 Inclined and horizontal flat surfaces
 - 7.7.3 Cylinders and spheres
 - 7.7.4 Enclosures
 - 7.8 Summary
- Nomenclature
- References

7.1 INTRODUCTION

The convective mode of heat transfer involves fluid flow along with conduction, or diffusion, and is generally divided into two basic processes. If the motion of the

fluid arises from an external agent, for instance, a fan, a blower, the wind, or the motion of the heated object itself, which imparts the pressure to drive the flow, the process is termed *forced convection*. If, on the other hand, no such externally induced flow exists and the flow arises “naturally” from the effect of a density difference, resulting from a temperature or concentration difference in a body force field such as gravity, the process is termed *natural convection*. The density difference gives rise to buoyancy forces due to which the flow is generated. A heated body cooling in ambient air generates such a flow in the region surrounding it. The buoyant flow arising from heat or material rejection to the atmosphere, heating and cooling of rooms and buildings, recirculating flow driven by temperature and salinity differences in oceans, and flows generated by fires are other examples of natural convection. There has been growing interest in buoyancy-induced flows and the associated heat and mass transfer over the past three decades, because of the importance of these flows in many different areas, such as cooling of electronic equipment, pollution, materials processing, energy systems, and safety in thermal processes. Several books, reviews, and conference proceedings may be consulted for detailed presentations on this subject. See, for instance, the books by Turner (1973), Jaluria (1980), Kakaç et al. (1985), and Gebhart et al. (1988).

The main difference between natural and forced convection lies in the mechanism by which flow is generated. In forced convection, externally imposed flow is generally known, whereas in natural convection it results from an interaction of the density difference with the gravitational (or some other body force) field and is therefore inevitably linked with and dependent on the temperature and/or concentration fields. Thus, the motion that arises is not known at the onset and has to be determined from a consideration of the heat and mass transfer process which are coupled with fluid flow mechanisms. Also, velocities and the pressure differences in natural convection are usually much smaller than those in forced convection.

The preceding differences between natural and forced convection make the analytical and experimental study of processes involving natural convection much more complicated than those involving forced convection. Special techniques and methods have therefore been devised to study the former, with a view to providing information on the flow and on the heat and mass transfer rates.

To understand the physical nature of natural convection transport, let us consider the heat transfer from a heated vertical surface placed in an extensive quiescent medium at a uniform temperature, as shown in Fig. 7.1. If the plate surface temperature T_w is greater than the ambient temperature T_∞ , the fluid adjacent to the vertical surface gets heated, becomes lighter (assuming that it expands on heating), and rises. Fluid from the neighboring areas moves in, due to the generated pressure differences, to take the place of this rising fluid. Most fluids expand on heating, resulting in a decrease in density as the temperature increases, a notable exception being water between 0 and 4°C. If the vertical surface is initially at temperature T_∞ , and then, at a given instant, heat is turned on, say through an electric current, the flow undergoes a transient before the flow shown is achieved. It is the analysis and study of this time-dependent as well as steady flow that yields the desired information on the heat transfer rates, flow and temperature fields, and other relevant process variables.

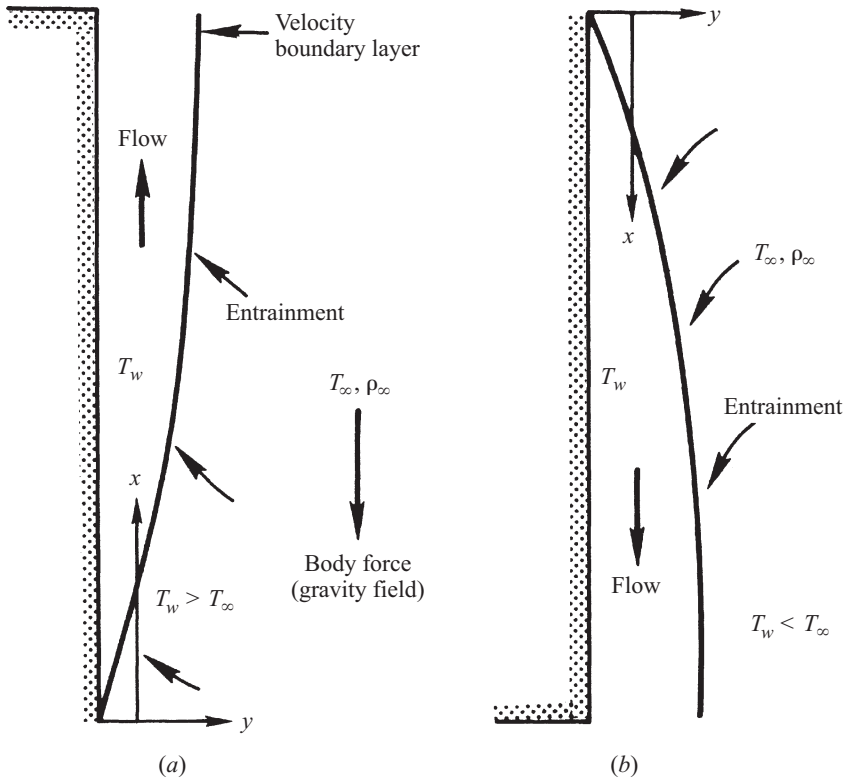


Figure 7.1 Natural convection flow over a vertical surface, together with the coordinate system.

The flow adjacent to a cooled surface is downward, as shown in Fig. 7.1*b*, provided that the fluid density decreases with an increase in temperature.

Heat transfer from the vertical surface may be expressed in terms of the commonly used Newton's law of cooling, which gives the relationship between the heat transfer rate q and the temperature difference between the surface and the ambient as

$$q = \bar{h}A(T_w - T_\infty) \quad (7.1)$$

where \bar{h} is the average convective heat transfer coefficient and A is the total area of the vertical surface. The coefficient \bar{h} depends on the flow configuration, fluid properties, dimensions of the heated surface, and generally also on the temperature difference, because of which the dependence of q on $T_w - T_\infty$ is not linear. Since the fluid motion becomes zero at the surface due to the no-slip condition, which is generally assumed to apply, the heat transfer from the heated surface to the fluid in its immediate vicinity is by conduction. It is therefore given by Fourier's law as

$$q = -kA \left(\frac{\partial T}{\partial y} \right)_0 \quad (7.2)$$

Here the temperature gradient is evaluated at the surface, $y = 0$, in the fluid and k is the thermal conductivity of the fluid. From this equation it is obvious that the natural convection flow largely affects the temperature gradient at the surface, since the remaining parameters remain essentially unaltered. The analysis is therefore directed at determining this gradient, which in turn depends on the nature and characteristics of the flow, temperature field, and fluid properties.

The heat transfer coefficient \bar{h} represents an integrated value for the heat transfer rate over the entire surface, since, in general, the local value h_x would vary with the vertical distance from the leading edge, $x = 0$, of the vertical surface. The local heat transfer coefficient h_x is defined by the equation

$$q' = h_x(T_w - T_\infty) \quad (7.3)$$

where q' is the rate of heat transfer per unit area per unit time at a location x , where the surface temperature difference is $T_w - T_\infty$, which may itself be a function of x . The average heat transfer coefficient \bar{h} is obtained from eq. (7.3) through integration over the entire surface area. Both \bar{h} and h_x are generally given in terms of a nondimensional parameter called the *Nusselt number* Nu . Again, an overall (or average) value \overline{Nu} , and a local value Nu_x , may be defined as

$$\overline{Nu} = \frac{\bar{h}L}{k} \quad Nu_x = \frac{h_x x}{k} \quad (7.4)$$

where L is the height of the vertical surface and thus represents a characteristic dimension.

The fluid far from the vertical surface is stationary, since an extensive medium is considered. The fluid next to the surface is also stationary, due to the no-slip condition. Therefore, flow exists in a layer adjacent to the surface, with zero vertical velocity on either side, as shown in Fig. 7.2. A small normal velocity component does exist at the edge of this layer, due to entrainment into the flow. The temperature varies from T_w to T_∞ . Therefore, the maximum vertical velocity occurs at some distance away from the surface. Its exact location and magnitude have to be determined through analysis or experimentation.

The flow near the bottom or leading edge of the surface is laminar, as indicated by a well-ordered and well-layered flow, with no significant disturbance. However, as the flow proceeds vertically upward or downstream, the flow gets more and more disorderly and disturbed, because of flow instability, eventually becoming chaotic and random, a condition termed *turbulent flow*. The region between the laminar and turbulent flow regimes is termed the *transition region*. Its location and extent depend on several variables, such as the temperature of the surface, the fluid, and the nature and magnitude of external disturbances in the vicinity of the flow. Most of the processes encountered in nature are generally turbulent. However, flows in many

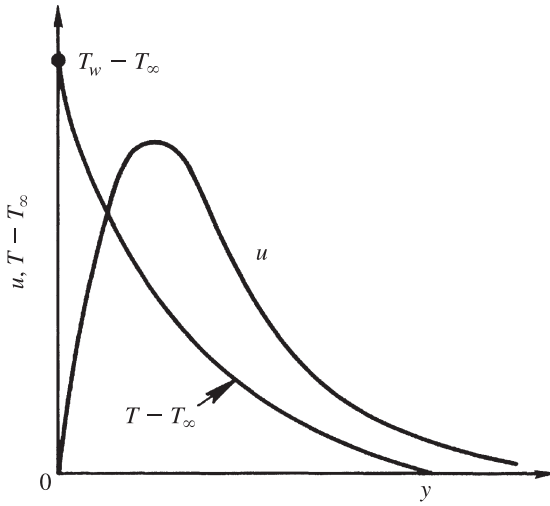


Figure 7.2 Velocity and temperature distributions in natural convection flow over a vertical surface.

industrial applications, such as those in electronic systems, are often in the laminar or transition regime. A determination of the regime of the flow and its effect on the flow parameters and heat transfer rates is therefore important.

Natural convection flow may also arise in enclosed regions. This flow, which is generally termed *internal natural convection*, is different in many ways from the *external natural convection* considered in the preceding discussion on a vertical heated surface immersed in an extensive, quiescent, isothermal medium. Buoyancy-induced flows in rooms, transport in complete or partial enclosures containing electronic equipment, flows in enclosed water bodies, and flows in the liquid melts of solidifying materials are examples of internal natural convection. In this chapter we discuss both external and internal natural convection for a variety of flow configurations and circumstances.

7.2 BASIC MECHANISMS AND GOVERNING EQUATIONS

7.2.1 Governing Equations

The governing equations for a convective heat transfer process are obtained by considerations of mass and energy conservation and of the balance between the rate of momentum change and applied forces. These equations may be written, for constant viscosity μ and zero bulk viscosity, as (Gebhart et al., 1988)

$$\frac{D\rho}{Dt} = \frac{\partial\rho}{\partial t} + \mathbf{V} \cdot \nabla\rho = -\rho\nabla \cdot \mathbf{V} \quad (7.5)$$

$$\rho \frac{D\mathbf{V}}{Dt} = \rho \left(\frac{\partial \mathbf{V}}{\partial t} + \mathbf{V} \cdot \nabla \mathbf{V} \right) = \mathbf{F} - \nabla p + \mu \nabla^2 \mathbf{V} + \frac{\mu}{3} \nabla (\nabla \cdot \mathbf{V}) \quad (7.6)$$

$$\rho c_p \frac{DT}{Dt} = \rho c_p \left(\frac{\partial T}{\partial t} + \mathbf{V} \cdot \nabla T \right) = \nabla \cdot (k \nabla T) + q''' + \beta T \frac{Dp}{Dt} + \mu \Phi_v \quad (7.7)$$

where \mathbf{V} is the velocity vector, T the local temperature, t the time, \mathbf{F} the body force per unit volume, c_p the specific heat at constant pressure, p the static pressure, ρ the fluid density, β the coefficient of thermal expansion of the fluid, Φ_v the viscous dissipation (which is the irreversible part of the energy transfer due to viscous forces), and q''' the energy generation per unit volume. The coefficient of thermal expansion $\beta = -(1/\rho)(\partial \rho / \partial T)_p$, where the subscript p denotes constant pressure. For a perfect gas, $\beta = 1/T$, where T is the absolute temperature. The total, or particle, derivative D/Dt may be expressed in terms of local derivative as $\partial/\partial t + \mathbf{V} \cdot \nabla$.

As mentioned earlier, in natural convection flows, the basic driving force arises from the temperature (or concentration) field. The temperature variation causes a difference in density, which then results in a buoyancy force due to the presence of the body force field. For a gravitational field, the body force $\mathbf{F} = \rho \mathbf{g}$, where \mathbf{g} is the gravitational acceleration. Therefore, it is the variation of ρ with temperature that gives rise to the flow. The temperature field is linked with the flow, and all the preceding conservation equations are coupled through variation in the density ρ . Therefore, these equations have to be solved simultaneously to determine the velocity, pressure, and temperature distributions in space and in time. Due to this complexity in the analysis of the flow, several simplifying assumptions and approximations are generally made to solve natural convection flows.

In the momentum equation, the local static pressure p may be broken down into two terms: one, p_a , due to the hydrostatic pressure, and other other, p_d , the dynamic pressure due to the motion of the fluid (i.e., $p = p_a + p_d$). The former pressure component, coupled with the body force acting on the fluid, constitutes the buoyancy force that is driving mechanism for the flow. If ρ_∞ is the density of the fluid in the ambient medium, we may write the buoyancy term as

$$\mathbf{F} - \nabla p = (\rho \mathbf{g} - \nabla p_a) - \nabla p_d = (\rho \mathbf{g} - \rho_\infty \mathbf{g}) - \nabla p_d = (\rho - \rho_\infty) \mathbf{g} - \nabla p_d \quad (7.8)$$

If \mathbf{g} is downward and the x direction is upward (i.e., $\mathbf{g} = -g\mathbf{i}$, where \mathbf{i} is the unit vector in the x direction and g is the magnitude of the gravitational acceleration, as is generally the case for vertical buoyant flows), then

$$\mathbf{F} - \nabla p = (\rho_\infty - \rho)g\mathbf{i} - \nabla p_d \quad (7.9)$$

and the buoyancy term appears only in the x -direction momentum equation. Therefore, the resulting governing equations for natural convection are the continuity equation, eq. (7.5), the energy equation, eq. (7.7), and the momentum equation, which becomes

$$\rho \frac{D\mathbf{V}}{Dt} = (\rho - \rho_\infty)g\mathbf{i} - \nabla p_d + \mu \nabla^2 \mathbf{V} + \frac{\mu}{3} \nabla (\nabla \cdot \mathbf{V}) \quad (7.10)$$

7.2.2 Common Approximations

The governing equations for natural convection flow are coupled, elliptic, partial differential equations and are therefore of considerable complexity. Another problem in obtaining a solution to these equations lies in the inevitable variation of the density ρ with temperature or concentration. Several approximations are generally made to simplify these equations. Two of the most important among these are the Boussinesq and the boundary layer approximations.

The Boussinesq approximations involve two aspects. First, the density variation in the continuity equation is neglected. Thus, the continuity equation, eq. (7.5), becomes $\nabla \cdot \mathbf{V} = 0$. Second, the density difference, which causes the flow, is approximated as a pure temperature or concentration effect (i.e., the effect of pressure on the density is neglected). In fact, the density difference is estimated for thermal buoyancy as

$$\rho_{\infty} - \rho = \rho\beta(T - T_{\infty}) \quad (7.11)$$

These approximations are employed very extensively for natural convection. An important condition for the validity of these approximations is that $\beta(T - T_{\infty}) \ll 1$ (Jaluria, 1980). Therefore, the approximations are valid for small temperature differences if β is essentially unchanged. However, they are not valid near the density maximum of water at 4°C, where β is zero and changes sign as the temperature varies across this value (Gebhart, 1979). Similarly, for large temperature differences encountered in fire and combustion systems, these approximations are generally not applicable.

Another approximation made in the governing equations is the extensively employed boundary layer assumption. The basic concepts involved in using the boundary layer approximation in natural convection flows are very similar to those in forced flow. The main difference lies in the fact that the pressure in the region outside the boundary layer is hydrostatic instead of being the externally imposed pressure, as is the case in forced convection. The velocity outside the layer is only the entrainment velocity due to the motion pressure and is not an imposed free stream velocity. However, the basic treatment and analysis are quite similar. It is assumed that the flow and the energy, or mass, transfer, from which it arises, are restricted predominantly to a thin region close to the surface. Several experimental studies have corroborated this assumption. As a consequence, the gradients along the surface are assumed to be much smaller than those normal to it.

The main consequences of the boundary layer approximations are that the downstream diffusion terms in the momentum and energy equations are neglected in comparison with the normal diffusion terms. The normal momentum balance is neglected since it is found to be of negligible importance compared to the downstream balance. Also, the velocity and thermal boundary layer thicknesses, δ and δ_T , respectively, are given by the order-of-magnitude expressions

$$\frac{\delta}{L} = O\left(\frac{1}{Gr^{1/4}}\right) \quad (7.12)$$

$$\frac{\delta_T}{\delta} = O\left(\frac{1}{\text{Pr}^{1/2}}\right) \quad (7.13)$$

where Gr is the Grashof number based on a characteristic length L and Pr is the Prandtl number. These are defined as

$$\text{Gr} = \frac{g\beta L^3 (T_w - T_\infty)}{\nu^2} \quad \text{Pr} = \frac{\mu c_p}{k} = \frac{\nu}{\alpha} \quad (7.14)$$

where ν is the kinematic viscosity and α the thermal diffusivity of the fluid. These dimensionless parameters are important in characterizing the flow, as discussed in the next section.

The resulting boundary layer equations for a two-dimensional vertical flow, with variable fluid properties except density, for which the Boussinesq approximations are used, are then written as (Jaluria, 1980; Gebhart et al., 1988)

$$\frac{\partial u}{\partial x} + \frac{\partial v}{\partial y} = 0 \quad (7.15)$$

$$u \frac{\partial u}{\partial x} + v \frac{\partial u}{\partial y} = g\beta(T - T_\infty) + \frac{1}{\rho} \frac{\partial}{\partial y} \left(\mu \frac{\partial u}{\partial y} \right) \quad (7.16)$$

$$\rho c_p \left[u \frac{\partial T}{\partial x} + v \frac{\partial T}{\partial y} \right] = \frac{\partial}{\partial y} \left(k \frac{\partial T}{\partial y} \right) + q''' + \beta T u \frac{\partial p_a}{\partial x} + \mu \left(\frac{\partial u}{\partial y} \right)^2 \quad (7.17)$$

where the last two terms in the energy equation are the dominant terms from pressure work and viscous dissipation effects. Here u and v are the velocity components in the x and y directions, respectively. Although these equations are written for a vertical, two-dimensional flow, similar approximations can be employed for many other flow circumstances, such as axisymmetric flow over a vertical cylinder and the wake above a concentrated heat source.

There are several other approximations that are commonly employed in the analysis of natural convection flows. The fluid properties, except density, for which the Boussinesq approximations are generally employed, are often taken as constant. The viscous dissipation and pressure work terms are generally small and can be neglected. However, the importance of various terms can be best considered by nondimensionalizing the governing equations and the boundary conditions, as outlined next.

7.2.3 Dimensionless Parameters

To generalize the natural convection transport processes, a study of the basic nondimensional parameters must be carried out. These parameters are important not only in simplifying the governing equations and the analysis, but also in guiding experiments that may be carried out to obtain desired information on the process and in the presentation of the data for use in simulation, modeling, and design.

In natural convection, there is no free stream velocity, and a convection velocity V_c is employed for the nondimensionalization of the velocity \mathbf{V} , where V_c is given by

$$V_c = [g\beta(T_w - T_\infty)]^{1/2} \quad (7.18)$$

The governing equations may be nondimensionalized by employing the following dimensionless variables (indicated by primes):

$$\begin{aligned} \mathbf{V}' &= \frac{\mathbf{V}}{V_c} & p' &= \frac{p}{\rho V_c^2} & \theta' &= \frac{T - T_\infty}{T_w - T_\infty} \\ \Phi'_v &= \Phi_v \frac{L^2}{V_c^2} & t' &= \frac{t}{t_c} & \nabla' &= L \nabla & (\nabla')^2 &= L^2 \nabla^2 \end{aligned} \quad (7.19)$$

where t_c is a characteristic time scale. The dimensionless equations are obtained as

$$\nabla' \cdot \mathbf{V}' = 0 \quad (7.20)$$

$$\text{Sr} \left(\frac{\partial v'}{\partial t'} + \mathbf{V}' \cdot \nabla' v' \right) = -\mathbf{e} \theta' - \nabla' p'_d + \frac{1}{\sqrt{\text{Gr}}} (\nabla')^2 \mathbf{V}' \quad (7.21)$$

$$\begin{aligned} \text{Sr} \left(\frac{\partial \theta'}{\partial t'} + \mathbf{V}' \cdot \nabla' \theta' \right) &= \frac{1}{\text{Pr} \sqrt{\text{Gr}}} (\nabla')^2 \theta' + (q''')' + \beta T \frac{g\beta L}{c_p} \left(\text{Sr} \frac{\partial p'}{\partial t'} + \mathbf{V}' \cdot \nabla' p' \right) \\ &+ \frac{g\beta L}{c_p} \frac{1}{\sqrt{\text{Gr}}} \Phi'_v \end{aligned} \quad (7.22)$$

where \mathbf{e} is the unit vector in the direction of the gravitational force.

Here $\text{Sr} = L/V_c t_c$ is the Strouhal number and q''' is nondimensionalized with $\rho c_p (T_w - T_\infty) V_c / L$ to yield the dimensionless value $(q''')'$. It is clear from the equations above that $\sqrt{\text{Gr}}$ replaces Re , which arises as the main dimensionless parameter in forced convection. Similarly, the Eckert number is replaced by $g\beta L / c_p$, which now determines the importance of the pressure and viscous dissipation terms. The Grashof number indicates the relative importance of the buoyancy term compared to the viscous term. A large value of Gr , therefore, indicates small viscous effects in the momentum equation, similar to the physical significance of Re in forced flow. The Prandtl number Pr represents a comparison between momentum and thermal diffusion. Thus, the Nusselt number may be expressed as a function of the Grashof and Prandtl numbers for steady flows if pressure work and viscous dissipation are neglected. The primes used for denoting dimensionless variables are dropped for convenience in the following sections.

7.3 LAMINAR NATURAL CONVECTION FLOW OVER FLAT SURFACES

7.3.1 Vertical Surfaces

The classical problem of natural-convection heat transfer from an isothermal heated vertical surface, shown in Fig. 7.1, with the flow assumed to be steady and laminar and the fluid properties (except density) taken as constant, has been of interest to investigators for a very long time. Viscous dissipation effects are neglected, and no

heat source is considered within the flow. Therefore, the problem is considerably simplified, although the complications due to the coupled partial differential equations remain. The governing differential equations may be obtained from eqs. (7.15)–(7.17) by using these simplifications.

An important method for solving the boundary layer flow over a heated vertical surface is the similarity variable method. A stream function $\psi(x, y)$ is first defined so that it satisfies the continuity equation. Thus, we define ψ by the equations

$$u = \frac{\partial \psi}{\partial y} \quad v = -\frac{\partial \psi}{\partial x} \quad (7.23)$$

Then the similarity variable η , the dimensionless stream function f , and the temperature θ are defined so as to convert the governing partial differential equations into ordinary differential equations. Gebhart et al. (1988) have presented a general approach to determine the conditions for similarity in a variety of flow circumstances. For flow over a vertical isothermal surface, the similarity variables which have been used in the literature and which may also be derived from this general approach may be written as

$$\eta = \frac{y}{x} \left(\frac{\text{Gr}_x}{4} \right)^{1/4} \quad \psi = 4\nu f(\eta) \left(\frac{\text{Gr}_x}{4} \right)^{1/4} \quad \theta = \frac{T - T_\infty}{T_w - T_\infty} \quad (7.24)$$

where

$$\text{Gr}_x = \frac{g\beta x^3 (T_w - T_\infty)}{\nu^2} \quad (7.25)$$

The boundary conditions are:

$$\text{at } y = 0: \quad u = v = 0, T = T_w; \quad \text{as } y \rightarrow \infty: \quad u \rightarrow 0, T \rightarrow T_\infty \quad (7.26)$$

These must also be written in terms of the similarity variables in order to obtain the solution. Note that the velocity component v for $y \rightarrow \infty$ is not specified as zero in order to account for the ambient fluid entrainment into the boundary layer.

The governing equations are obtained from the preceding similarity transformations as

$$f''' + 3ff'' - 2(f')^2 + \theta = 0 \quad (7.27)$$

$$\frac{\theta''}{\text{Pr}} + 3f\theta' = 0 \quad (7.28)$$

where the primes here indicate differentiation of $f(\eta)$ and $\theta(\eta)$ with respect to the similarity variable η , one prime representing the first derivative, two primes the second derivatives, and three primes the third derivative. The corresponding boundary conditions are

$$\text{at } \eta = 0: \quad f = f' = 1 - \theta = 0; \quad \text{as } \eta \rightarrow \infty: \quad f' \rightarrow 0, \theta \rightarrow 0$$

which may be written more concisely as

$$f(0) = f'(0) = 1 - \theta(0) = f'(\infty) = \theta(\infty) = 0 \quad (7.29)$$

where the quantity in parentheses indicates the location where the condition is applied.

The solution of these equations has been considered by several investigators. Schuh (1948) gave results for various values of the Prandtl number Pr , employing approximate methods. Ostrach (1953) numerically obtained the solution for the Pr range 0.01 to 1000. The velocity and temperature profiles thus obtained are shown in Figs. 7.3 and 7.4. An increase in Pr is found to cause a decrease in the thermal boundary layer thickness and an increase in the absolute value of the temperature gradient at the surface. This is expected from the physical nature of the Prandtl number, which represents the comparison between momentum and thermal diffusion. An increasing value of Pr indicates increasing viscous effects. The dimensionless maximum velocity is also found to decrease and the velocity gradient at the surface to decrease with increasing Pr , indicating the effect of greater viscous forces. The location of this maximum value is found to shift to higher η as Pr is decreased. The velocity boundary layer thickness is also found to increase as Pr is decreased to low values. These trends are expected from the physical mechanisms that govern this boundary layer flow, as discussed earlier. It is also worth noting that the results indicate the coupling between the velocity and temperature fields, as evidenced by the presence of flow wherever a temperature difference exists, such as the profiles at low Pr . Additional results and discussion on the flow are given in several books; see, for instance, the books by Kaviany (1994), Bejan (1995), and Oosthuizen and Naylor (1999).

The heat transfer from the heated surface may be obtained as

$$\begin{aligned} q'_x &= -k \left(\frac{\partial T}{\partial y} \right)_0 = -k(T_w - T_\infty) \frac{1}{x} \left(\frac{Gr_x}{4} \right)^{1/4} \left(\frac{\partial \theta}{\partial \eta} \right)_0 \\ &= [-\theta'(0)] \frac{k(T_w - T_\infty)}{x} \left(\frac{Gr_x}{4} \right)^{1/4} \end{aligned} \quad (7.30)$$

The local Nusselt number Nu_x is given by

$$Nu_x = \frac{h_x x}{k} = \frac{q'_x}{T_w - T_\infty} \frac{x}{k}$$

We have for an isothermal surface

$$Nu_x = [-\theta'(0)] \left(\frac{Gr_x}{4} \right)^{1/4} = \frac{-\theta'(0)}{\sqrt{2}} Gr_x^{1/4} = \phi(Pr) Gr_x^{1/4} \quad (7.31)$$

where $\phi(Pr) = [-\theta'(0)]/\sqrt{2}$. Therefore, the local surface heat transfer coefficient h_x varies as

$$h_x = Bx^{-1/4} \quad \text{where } B = \frac{k[-\theta'(0)]}{\sqrt{2}} \left[\frac{g\beta(T_w - T_\infty)}{\nu^2} \right]^{1/4}$$

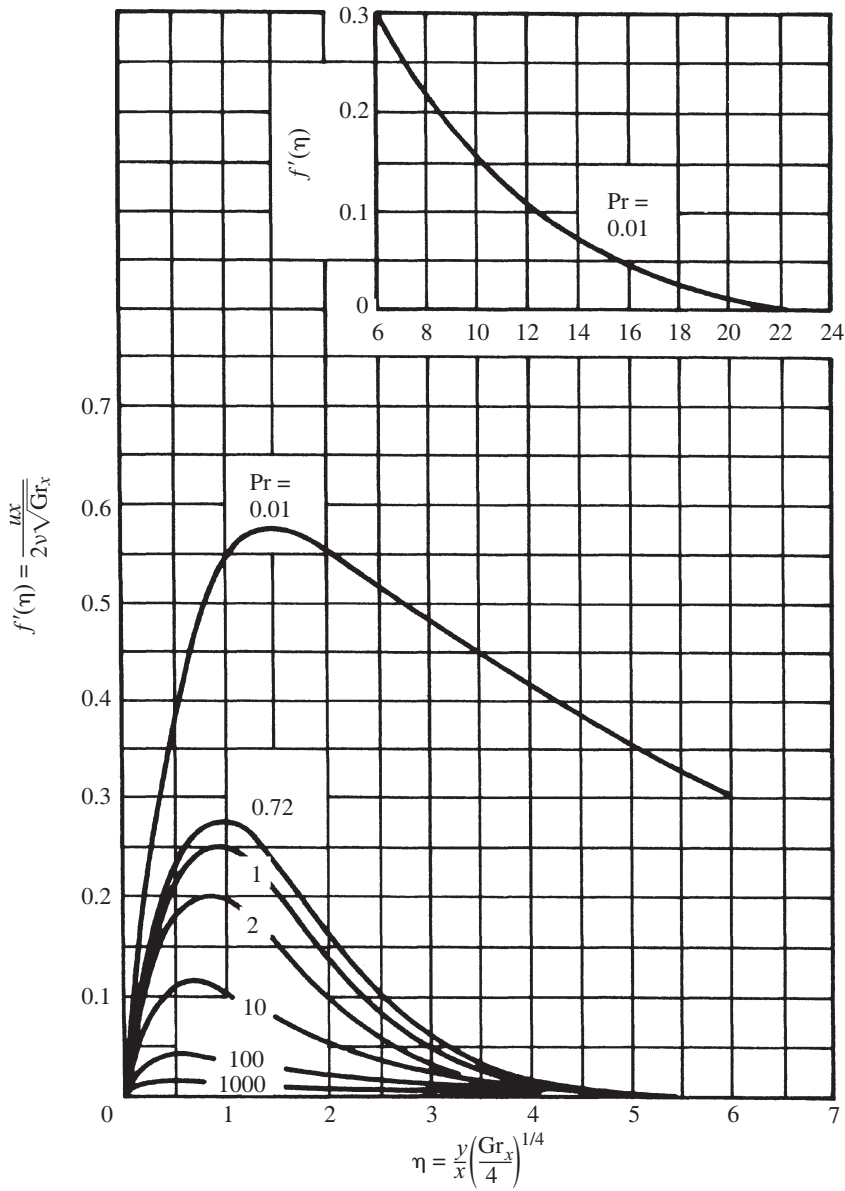


Figure 7.3 Calculated velocity distributions in the boundary layer for flow over an isothermal vertical surface. (From Ostrach, 1953.)

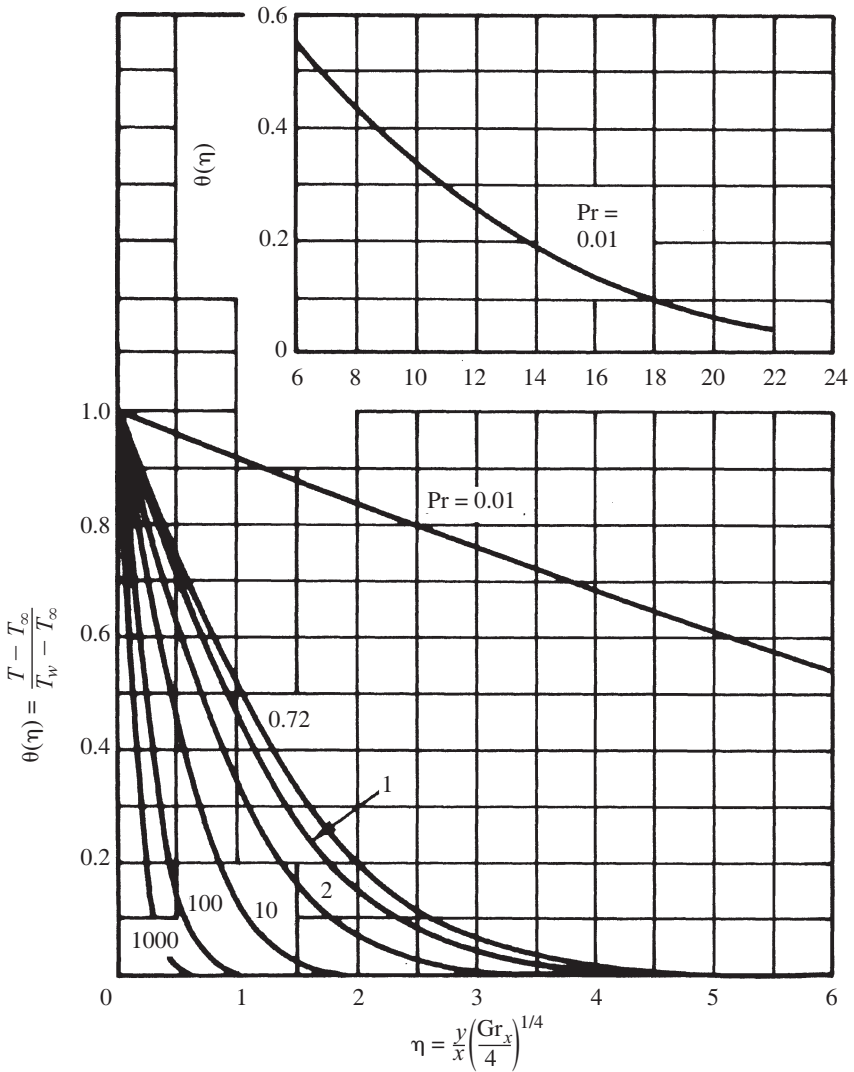


Figure 7.4 Calculated temperature distributions in the boundary layer for flow over an isothermal vertical surface. (From Ostrach, 1953.)

The average value of the heat transfer coefficient \bar{h} may be obtained by averaging the heat transfer over the entire length of the vertical surface, to yield

$$\bar{h} = \frac{1}{L} \int_0^L h_x dx = \frac{4}{3} \frac{B}{L} L^{3/4}$$

Therefore,

$$\overline{\text{Nu}} = \frac{4}{3} \frac{[-\theta'(0)]}{\sqrt{2}} \text{Gr}^{1/4} = \frac{4}{3} \phi(\text{Pr}) \text{Gr}^{1/4} = \frac{4}{3} \text{Nu}_L \tag{7.32}$$

The values of $\phi(\text{Pr})$ can be obtained from a numerical solution of the governing differential equations. Values obtained at various Pr are listed in Table 7.1. The significance of n and the uniform heat flux data in the table is discussed later. An approximate curve fit to the numerical results for $\phi(\text{Pr})$ has been given by Oosthuizen and Naylor (1999) as

$$\phi(\text{Pr}) = \left(\frac{0.316\text{Pr}^{5/4}}{2.44 + 4.88\text{Pr}^{1/2} + 4.95\text{Pr}} \right)^{1/4} \tag{7.33}$$

It must be mentioned that these results can be used for both heated and cooled surfaces (i.e., $T_w > \text{or} < T_\infty$), yielding respectively a positive q' value for heat transfer from the surface and a negative value for heat transfer to the surface.

In several problems of practical interest, the surface from which heat transfer occurs is nonisothermal. The two families of surface temperature variation that give rise to similarity in the governing laminar boundary layer equations have been shown by Sparrow and Gregg (1958) to be the power law and exponential distributions, given as

$$T_w - T_\infty = N x^n \quad \text{and} \quad T_w - T_\infty = M e^{m x} \tag{7.34}$$

TABLE 7.1 Computed Values of the Parameter $\phi(\text{Pr})$ for a Vertical Heated Surface

Pr	$\phi(\text{Pr})$ (Isothermal), $n = 0$	$\phi\left(\text{Pr}, \frac{1}{5}\right)$ (Uniform Heat Flux), $n = \frac{1}{5}$
0	$0.600\text{Pr}^{1/2}$	$0.711\text{Pr}^{1/2}$
0.01	0.0570	0.0669
0.72	0.357	—
0.733	—	0.410
1.0	0.401	—
2.0	0.507	—
2.5	—	0.616
5.0	0.675	—
6.7	—	0.829
7.0	0.754	—
10	0.826	0.931
10^2	1.55	1.74
10^3	2.80	—
10^4	5.01	—
∞	$0.503\text{Pr}^{1/4}$	$0.563\text{Pr}^{1/4}$

Source: Gebhart (1973).

where N , M , n , and m are constants. The power law distribution is of particular interest, since it represents many practical circumstances. The isothermal surface is obtained for $n = 0$. From the expression for q'_x , eq. (7.30), it can be shown that q'_x varies with x as $x^{(5n-1)/4}$. Therefore, a uniform heat flux condition, $q'_x = \text{constant}$, arises for $n = \frac{1}{5}$. It can also be shown that physically realistic solutions are obtained for $-\frac{3}{5} \leq n < 1$ (Sparrow and Gregg, 1958; Jaluria, 1980). The governing equations are obtained for the power law case as

$$f''' + (n+3)ff'' - 2(n+1)(f')^2 + \theta = 0 \quad (7.35)$$

$$\frac{\theta''}{\text{Pr}} + (n+3)f\theta' - 4nf'\theta = 0 \quad (7.36)$$

The local Nusselt number Nu_x is obtained as

$$\frac{\text{Nu}_x}{\text{Gr}_x^{1/4}} = \frac{-\theta'(0)}{\sqrt{2}} = \phi(\text{Pr}, n) \quad (7.37)$$

The function $\text{Nu}_x/\text{Gr}_x^{1/4}$ is plotted against n in Fig. 7.5. For $n < -\frac{3}{5}$, the function is found to be negative, indicating the physically unrealistic circumstance of heat transfer to the surface for $T_w > T_\infty$. The surface is adiabatic for $n = -\frac{3}{5}$, which thus represents the case of a line source at the leading edge of a vertical adiabatic surface, so that no energy transfer occurs at the surface for $x > 0$.

For the case of uniform heat flux, $n = \frac{1}{5}$ and $q'_x = q'$, a constant. Therefore, from eq. (7.30),

$$q' = k[-\theta'(0)]N \left(\frac{g\beta N}{4\nu^2} \right)^{1/4}$$

which gives

$$N = \left\{ \frac{q'}{k[-\theta'(0)]} \right\}^{4/5} \left(\frac{4\nu^2}{g\beta} \right)^{1/5} \quad (7.38)$$

Therefore, for a given heat flux q' , which may be known, for example, from the electrical input into the surface, the temperature of the surface varies as $x^{1/5}$ and its magnitude may be determined as a function of the heat flux and fluid properties from eq. (7.38). The parameter $-\theta'(0)$ is obtained from a numerical solution of the governing equations for $n = \frac{1}{5}$ at the given value of Pr . Some results obtained from Gebhart (1973) are shown in Table 7.1 as $\phi(\text{Pr}, \frac{1}{5})$.

7.3.2 Inclined and Horizontal Surfaces

In many natural convection flows, the thermal input occurs at a surface that is itself curved or inclined with respect to the direction of the gravity field. Consider, first, a flat surface at a small inclination γ from the vertical. Boundary layer approximations,

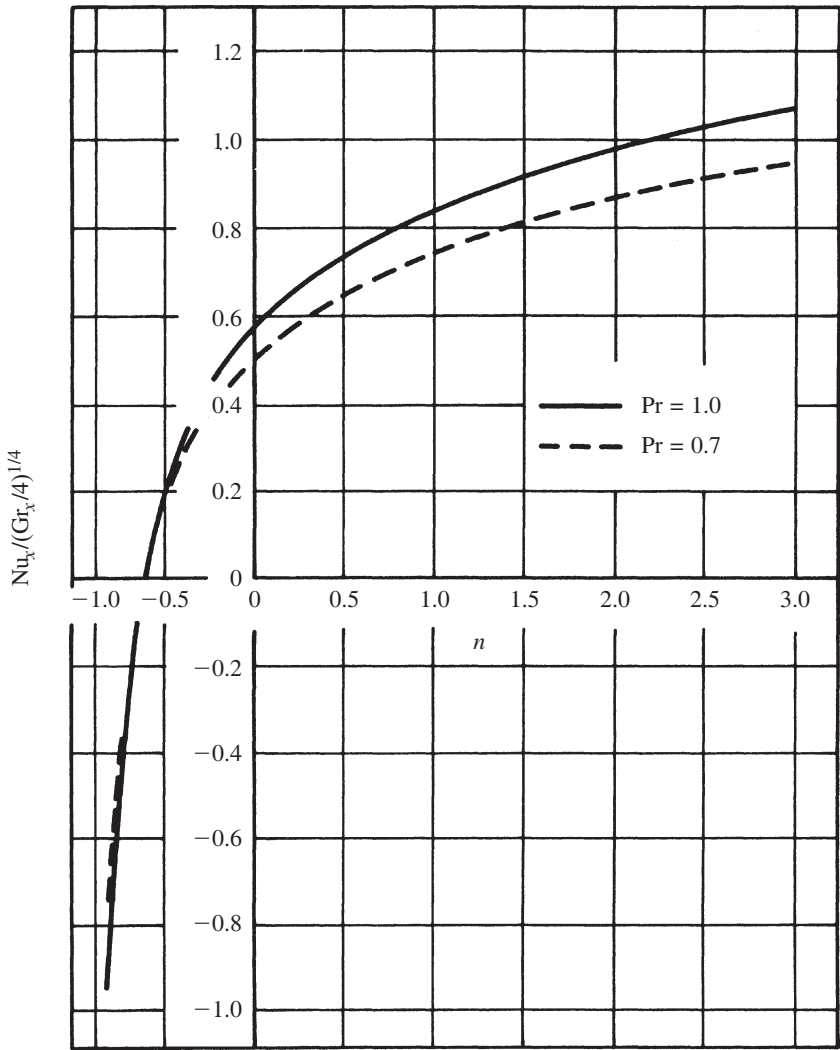


Figure 7.5 Dependence of the local Nusselt number on the value of n for a power law surface temperature distribution. (From Sparrow and Gregg, 1958.)

similar to those for a vertical surface, may be made for this flow. It can be shown that if x is taken along the surface and y normal to it, the continuity and energy equations, eqs. (7.15) and (7.17), respectively, remain unchanged and the x -direction momentum equation becomes

$$u \frac{\partial u}{\partial x} + v \frac{\partial u}{\partial y} = g\beta(T - T_\infty) \cos \gamma + \frac{1}{\rho} \frac{\partial}{\partial y} \left(\mu \frac{\partial u}{\partial y} \right) \tag{7.39}$$

Therefore, the problem is identical to that for flow over a vertical surface except that g is replaced by $g \cos \gamma$ in the buoyancy term. Therefore, a replacement of g by $g \cos \gamma$ in all the expressions derived earlier for a vertical surface would yield the corresponding results for an inclined surface. This implies using $Gr_x \cos \gamma$ for Gr_x and assuming equal rates of heat transfer on the two sides of the surface. This is strictly not the case since the buoyancy force is directed away from the surface at the top and toward the surface at the bottom, resulting in differences in boundary layer thicknesses and heat transfer rates. However, this difference is neglected in this approximation.

The preceding procedure for obtaining the heat transfer rate from an inclined surface was first suggested theoretically by Rich (1953), and his data are in good agreement with the values predicted. The data obtained by Vliet (1969) for a uniform-flux heated surface in air and in water indicate the validity of this procedure up to inclination angles as large as 60° . Additional experiments have confirmed that the replacement of g by $g \cos \gamma$ in the Grashof number is appropriate for inclination angles up to around 45° and, to a close approximation, up to a maximum angle of 60° . Detailed experimental results on this problem were obtained by Fujii and Imura (1972). They also discuss the separation of the boundary layer for the inclined surface facing upward.

The natural convection flow over horizontal surfaces is of considerable importance in a variety of applications, for instance, in the cooling of electronic systems and in flows over the ground and water surfaces. Rotem and Claassen (1969) obtained solutions to the boundary layer equations for flow over a semi-infinite isothermal horizontal surface. Various values of Pr , including the extreme cases of very large and small Pr , were treated. Experimental results indicated the existence of a boundary layer near the leading edge on the upper side of a heated horizontal surface. These boundary layer flows merge near the middle of the surface to generate a wake or plume that rises above the surface. Equations were presented for the power law case, $T_w - T_\infty = Nx^n$, and solved for the isothermal case, $n = 0$. Pera and Gebhart (1972) have considered flow over surfaces slightly inclined from the horizontal.

For a semi-infinite horizontal surface with a single leading edge, as shown in Fig. 7.6, the dynamic or motion pressure p_d drives the flow. Physically, the upper side of a heated surface heats up the fluid adjacent to it. This fluid becomes lighter than the ambient, if it expands on heating, and rises. This results in a pressure difference, which causes a boundary layer flow over the surface near the leading edge. Similar considerations apply for the lower side of a cooled surface. The governing equations are the continuity and energy equations (7.15) and (7.17) and the momentum equations

$$u \frac{\partial u}{\partial x} + v \frac{\partial u}{\partial y} = \frac{1}{\rho} \frac{\partial}{\partial y} \left(\mu \frac{\partial u}{\partial y} \right) - \frac{1}{\rho} \frac{\partial p_d}{\partial x} \quad (7.40)$$

$$g\beta(T - T_\infty) = \frac{1}{\rho} \frac{\partial p_d}{\partial y} \quad (7.41)$$

This problem may be solved by similarity analysis, as discussed earlier for vertical surfaces. The similarity variables, given by Pera and Gebhart (1972), are

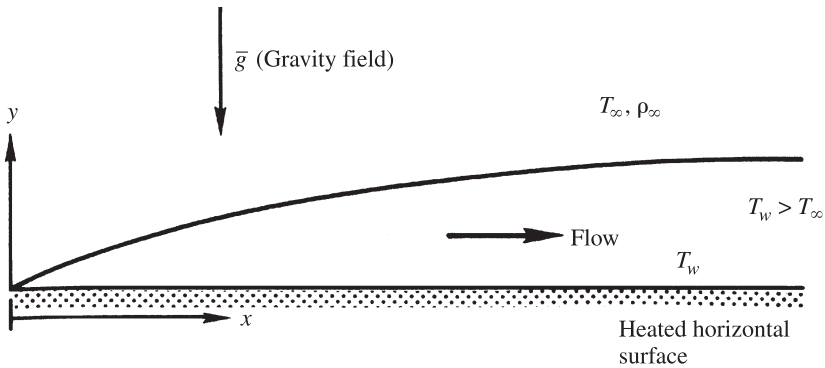


Figure 7.6 Natural convection boundary layer flow over a semi-infinite horizontal surface, with the heated surface facing upward.

$$\eta = \frac{y}{x} \left(\frac{\text{Gr}_x}{5} \right)^{1/5} \quad \psi = 5\nu f(\eta) \left(\frac{\text{Gr}_x}{5} \right)^{1/5} \quad (7.42)$$

Figure 7.7 shows the computed velocity and temperature profiles for flow over a heated horizontal surface facing upward or a cooled surface facing downward. For a heated surface facing downward or a cooled surface facing upward, a boundary layer type of flow is not obtained for a fluid that expands on heating. This is because the fluid does not flow away from the surface due to buoyancy. The local Nusselt number for horizontal surfaces is given by Pera and Gebhart (1972) for both the isothermal and the uniform-heat-flux surface conditions. The Nusselt number was found to be approximately proportional to $\text{Pr}^{1/4}$ over the Pr range 0.1 to 100. The expression given for an isothermal surface is

$$\text{Nu}_x = \frac{h_x x}{k} = 0.394 \text{Gr}_x^{1/5} \cdot \text{Pr}^{1/4} \quad (7.43)$$

and that for a uniform-flux surface, $\text{Nu}_{x,q}$, is

$$\text{Nu}_{x,q} = \frac{h_x x}{k} = 0.501 \text{Gr}_x^{1/5} \cdot \text{Pr}^{1/4} \quad (7.44)$$

It can be shown by integrating over the surface that for the isothermal surface, the average Nusselt number is $\frac{5}{3}$ times the value of the local Nusselt number at $x = L$.

Therefore, the natural convection heat transfer from inclined surfaces can be treated in terms of small inclinations from the vertical and horizontal positions, detailed results on which are available. For intermediate values of γ , an interpolation between these two regimes may be used to determine the resulting heat transfer rate. Numerical methods, such as the finite difference method, can also be used to solve the governing equations to obtain the flow and temperature distributions and the heat transfer rate. This regime has not received as much attention as the horizontal and

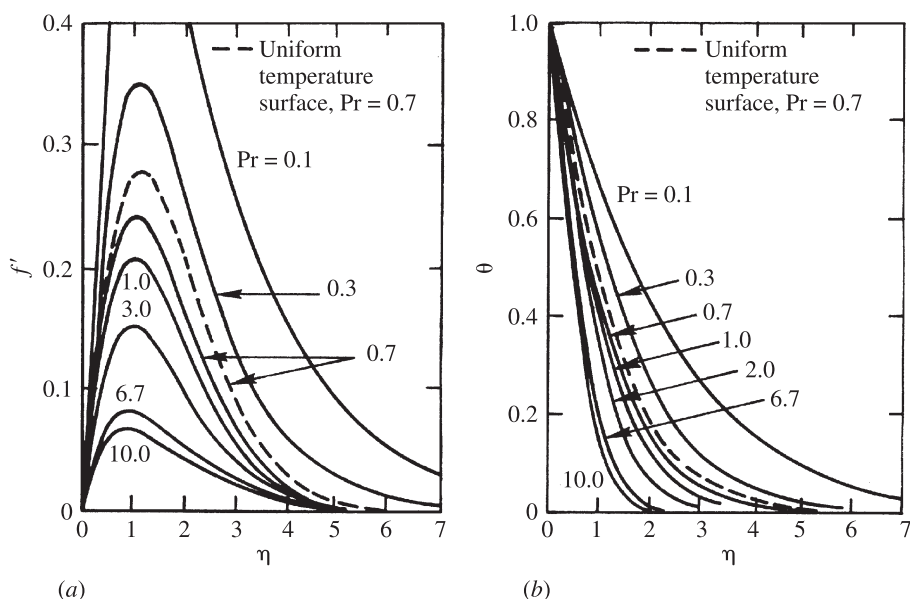


Figure 7.7 Calculated (a) velocity and (b) temperature distribution in natural convection boundary layer flow over a horizontal surface with a uniform heat flux. (From Pera and Gebhart, 1972.)

vertical surfaces, although some numerical and experimental results are available such as those of Fujii and Imura (1972).

7.4 EXTERNAL LAMINAR NATURAL CONVECTION FLOW IN OTHER CIRCUMSTANCES

7.4.1 Horizontal Cylinder and Sphere

Much of the information on laminar natural convection over heated surfaces, discussed in Section 7.3, has been obtained through similarity analysis. However, neither the horizontal cylindrical nor the spherical configuration gives rise to similarity, and therefore several other methods have been employed for obtaining a solution to the governing equations. Among the earliest detailed studies was that by Merk and Prins (1953–54), who employed integral methods with the velocity and thermal boundary layer thicknesses assumed to be equal. The variation of the local Nusselt number with ϕ , the angular position from the lower stagnation point $\phi = 0^\circ$, is shown in Fig. 7.8 for a horizontal cylinder and also for a sphere. The local Nusselt number Nu_ϕ decreases downstream due to the increase in the boundary layer thickness, which is predicted to be infinite at $\phi = 180^\circ$, resulting in a zero value for Nu_ϕ there. However, Merk and Prins (1953–54) indicated the inapplicability of the analysis for $\phi \geq 165^\circ$ due to boundary layer separation and realignment into a plume flow near the top.

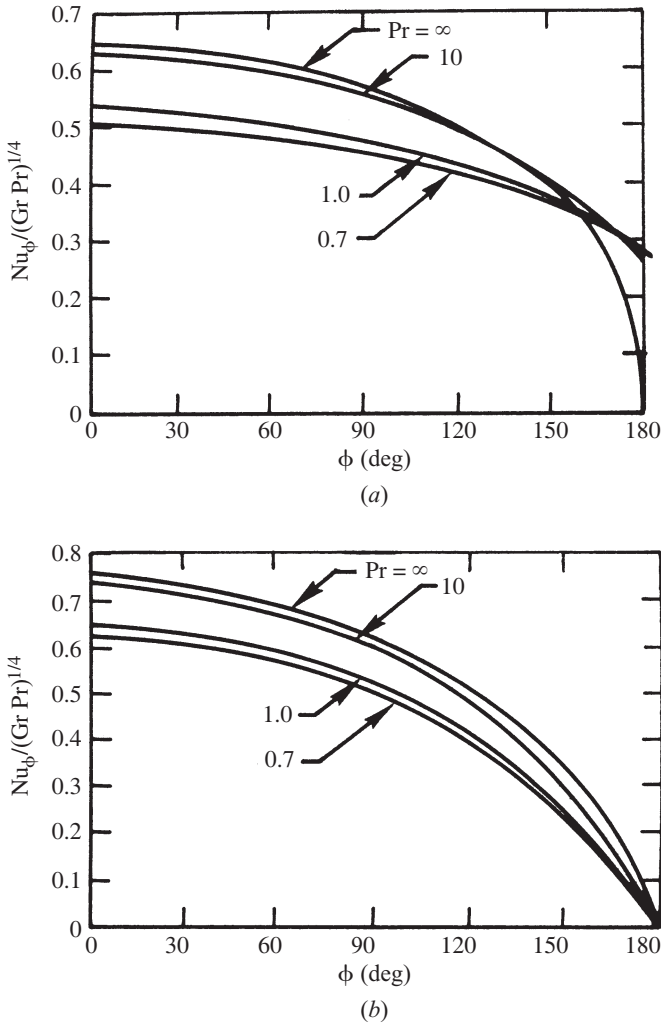


Figure 7.8 Variation of the local Nusselt number with downstream angular position ϕ for (a) a horizontal cylinder and (b) a sphere. (From Merk and Prins, 1953–54.)

The mean value of the Nusselt number \overline{Nu} is given by Merk and Prins (1953–54) for a horizontal isothermal cylinder as

$$\overline{Nu} = \frac{\bar{h}D}{k} = C(Pr)(Gr \cdot Pr)^{1/4} \tag{7.45}$$

where \overline{Nu} and Gr are based on the diameter D . The constant $C(Pr)$ was calculated as 0.436, 0.456, 0.520, 0.523, and 0.523 for Pr values of 0.7, 1.0, 10.0, 100.0, and ∞ , respectively.

The preceding expression is also suggested for spheres by Merk and Prins (1953–54), with $C(\text{Pr})$ given for the Pr values of 0.7, 1.0, 10.0, 100.0, and ∞ as 0.474, 0.497, 0.576, 0.592, and 0.595, respectively. There are many other analytical and experimental studies of the natural convection flow over spheres. Since this configuration is of particular interest in chemical processes, it has also been studied in detail for mass transfer. Chiang et al. (1964) solved the governing equations, using a series method, and presented heat transfer results. Trends similar to those discussed earlier were obtained. A considerable amount of experimental work has been done on the heat transfer from spheres. Amato and Tien (1972) have discussed such studies and have given the heat transfer correlation as

$$\overline{\text{Nu}} = 2 + 0.5(\text{Gr} \cdot \text{Pr})^{1/4} \quad (7.46)$$

where the constant 2 in the expression can be shown analytically to apply for pure conduction. Additional correlations for transport from horizontal cylinders and spheres are given later. Work has also been done on the separation of the flow to form a wake near the top of the body. This realignment of the flow can significantly affect the heat transfer rate in the vicinity of the top of a cylinder or a sphere (Jaluria and Gebhart, 1975).

7.4.2 Vertical Cylinder

Natural convection flow over vertical cylinders is another important problem, being relevant to many practical applications, such as flow over tubes and rods (as in nuclear reactors), over cylindrical heating elements, and over various closed bodies (including the human body) that can be approximated as a vertical cylinder. For large values of D/L , where D is the diameter of the cylinder and L its height, the flow can be approximated as that over a flat plate, since the boundary layer thickness is small compared to the diameter of the cylinder. As a result, the governing equations are the same as those for a flat plate. However, since this result is based on the boundary layer thickness, which in turn depends on the Grashof number, the deviation of the results obtained for a vertical cylinder from those for a flat plate must be given in terms of D/L and the Grashof number. Sparrow and Gregg (1956) obtained the following criterion for a difference in heat transfer from a vertical cylinder of less than 5% from the flat plate solution, for Pr values of 0.72 and 1.0:

$$\frac{D}{L} \geq \frac{35}{\text{Gr}^{1/4}} \quad (7.47)$$

where Gr is the Grashof number based on L .

When D/L is not large enough to ignore the effects of curvature, the relevant governing equations must be solved. Sparrow and Gregg (1956) employed similarity methods for obtaining a solution to these equations. Minkowycz and Sparrow (1974) obtained the solution using the local nonsimilarity method. Cebeci (1974) gave results on vertical slender cylinders. LeFevre and Ede (1956) employed an integral method to solve the governing equations and gave the following expression for the Nusselt number $\overline{\text{Nu}}$:

$$\overline{\text{Nu}} = \frac{\bar{h}L}{k} = \frac{4}{3} \left[\frac{7\text{Gr} \cdot \text{Pr}^2}{5(20 + 21\text{Pr})} \right]^{1/4} + \frac{4(272 + 315\text{Pr})L}{35(64 + 63\text{Pr})D} \quad (7.48)$$

where both $\overline{\text{Nu}}$ and Gr are based on the height L of the cylinder. Other studies on vertical axisymmetric bodies are reviewed by Gebhart et al. (1988).

7.4.3 Transients

We have so far considered steady natural convection flows in which the velocity and temperature fields do not vary with time. However, time dependence is important in many practical circumstances (Jaluria, 1998). For instance, the change in the thermal condition that generates the natural convection flow could be a sudden or a periodic one, leading to a time-dependent variation in the flow. The startup and shutdown of thermal systems, such as furnaces, ovens, and nuclear reactors, involves a consideration of time-dependent or unsteady natural convection if buoyancy effects are significant.

If the heat input at a surface is suddenly changed from zero to a specific value, the steady natural convection flow is eventually obtained following a transient process. As soon as the heat is turned on, the surface starts heating up, this change being essentially a step variation if the thermal capacity of the body is very small. In response to this sudden change, the fluid adjacent to the surface gets heated, becomes buoyant, and rises, if the fluid expands on heating. However, the flow at a given location is initially unaffected by flow at other portions of the surface. This implies that the fluid element behaves as isolated, and the heat transfer mechanisms are initially not influenced by the fluid motion. Consequently, the initial transport mechanism is predominantly conduction and can be approximated as a one-dimensional conduction problem up to the leading edge effect, which results from flow originating at the leading edge and which propagates downstream along the flow, is felt at a given location x . The heat transfer rates due to pure conduction being much smaller than those due to convection, it is to be expected that for a step change in the heat flux input, there may initially be an overshoot in the temperature above the steady-state value. Similarly, for a step change in temperature, a lower heat flux is expected initially, ultimately approaching the steady-state value, as the flow itself progresses through a transient regime to steady-state conditions.

The preceding discussion implies that at the initial stages of the transient, the solution for a step change in the surface temperature, or in the heat flux, is independent of the vertical location and is of the form obtained for semi-infinite conduction solutions. Employing Laplace transforms for a step change in the heat flux, the solution is obtained as (Ozisik, 1993)

$$\tilde{\theta} = \frac{2q'\sqrt{\alpha t}}{k} \left[\frac{\exp(-\eta^2)}{\sqrt{\pi}} - \eta \operatorname{erfc}(\eta) \right] \quad (7.49)$$

where $\eta = y/\sqrt{\alpha t}$, α being the thermal diffusivity of the fluid. Here, $\operatorname{erfc}(\eta)$ is the conjugate of the error function and q' is the constant heat flux input imposed at

time $t = 0$, starting from a no-flow, zero-heat-input condition. The temperature $\tilde{\theta}$ is simply the physical temperature excess over the initial temperature T_∞ . The heat transfer coefficient h is obtained from the preceding temperature expression, by using Fourier's law, as

$$h = \frac{q'}{[\tilde{\theta}]_0} = \frac{k}{2} \sqrt{\frac{\pi}{\alpha t}} \quad (7.50)$$

Similarly, for a step change in the surface temperature, the solution is (Ozisik, 1993)

$$\frac{T - T_\infty}{T_w - T_\infty} = \theta = \text{erf}(\eta) \quad (7.51)$$

The velocity profile is obtained by substituting the preceding temperature solution into the momentum equation and solving the resulting equation by Laplace transforms to obtain $u(y)$.

Numerical solutions to the governing time-dependent boundary layer equations have been obtained by Hellums and Churchill (1962) for a vertical surface subjected to a step change in the surface temperature. The results converge to the steady-state solution at large time and show a minimum in the local Nusselt number during the transient, as shown in Fig. 7.9. An integral method for analyzing unsteady natural convection has also been developed for time-dependent heat input and for finite thermal capacity of the surface element. This work has been summarized by Gebhart (1973, 1988) and is based on the analytical and experimental work of Gebhart and co-workers. This analysis is particularly suited to practical problems, since it considers the thermal capacity of the bounding material and determines the temperature variation with time over the entire transient regime.

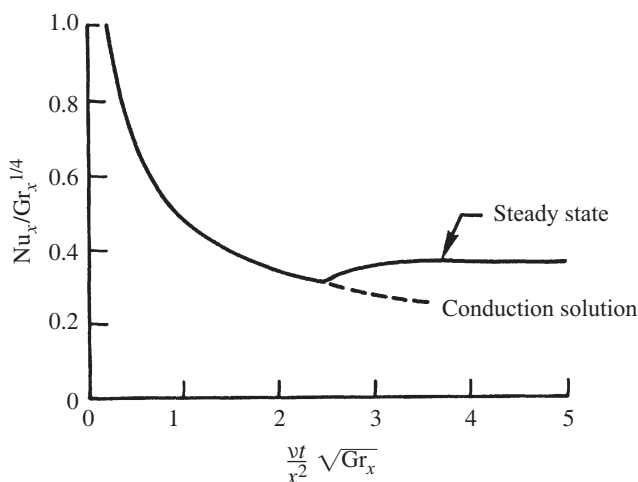


Figure 7.9 Variation of the heat transfer rate with time for a step change in the surface temperature of a vertical plate. (From Hellums and Churchill, 1962.)

Churchill (1975) has given a correlation for transient natural convection from a heated vertical plate, subjected to a step change in the heat flux. The thermal capacity of the plate is taken as negligible, and the local Nusselt number is given as

$$[\text{Nu}_{x,q}]^n = \left(\frac{\pi x^2}{4\alpha t} \right)^{n/2} + \left\{ \frac{\text{Ra}_x/10}{[1 + (0.437/\text{Pr})^{9/16}]^{16/9}} \right\}^{n/4} \quad (7.52)$$

where

$$\text{Ra}_x = \frac{g\beta(T_w - T_\infty)x^3}{\nu\alpha} \quad (7.53)$$

Employing the available experimental information, the appropriate value of n is given as 6. With this value of n , the preceding correlation was found to give Nusselt number values quite close to the experimental results. A temperature overshoot was not considered, since the experimental studies of Gebhart (1973) showed no significant overshoot. For a step change in surface temperature, Churchill and Usagi (1974) have obtained an empirical correlation approximating the entire transient domain.

7.4.4 Plumes, Wakes, and Other Free Boundary Flows

In the preceding sections we have considered external natural convection adjacent to heated or cooled surfaces. However, there are many important natural convection flows that, although generated by a heated or cooled surface, move beyond the buoyancy input so that they occur without the presence of a solid boundary. Figure 7.10 shows the sketches of a few common flows, which are often termed *free boundary flows*. Many of these flows are of interest in nature and in pollution and are usually turbulent (Gebhart et al., 1984).

Thermal plumes which are assumed to arise from heat input at point or horizontal line sources represent the wakes above heated bodies. The former circumstance is an axisymmetric flow and is generated by a heated body such as a sphere, whereas the latter case is a two-dimensional flow generated by a long, thin, heat source such as an electric heater. Figure 7.11 shows a sketch of the flow in a two-dimensional plume,

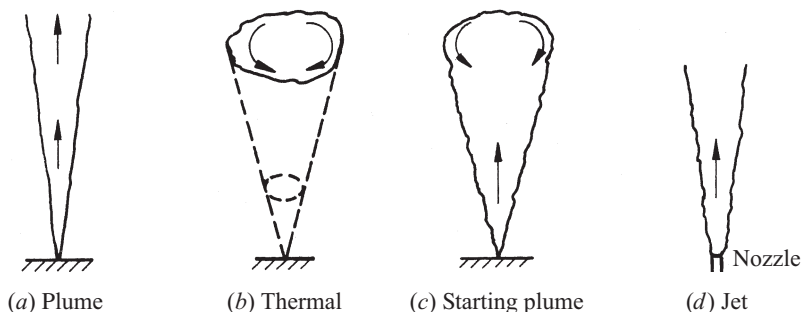


Figure 7.10 Common free boundary flows.

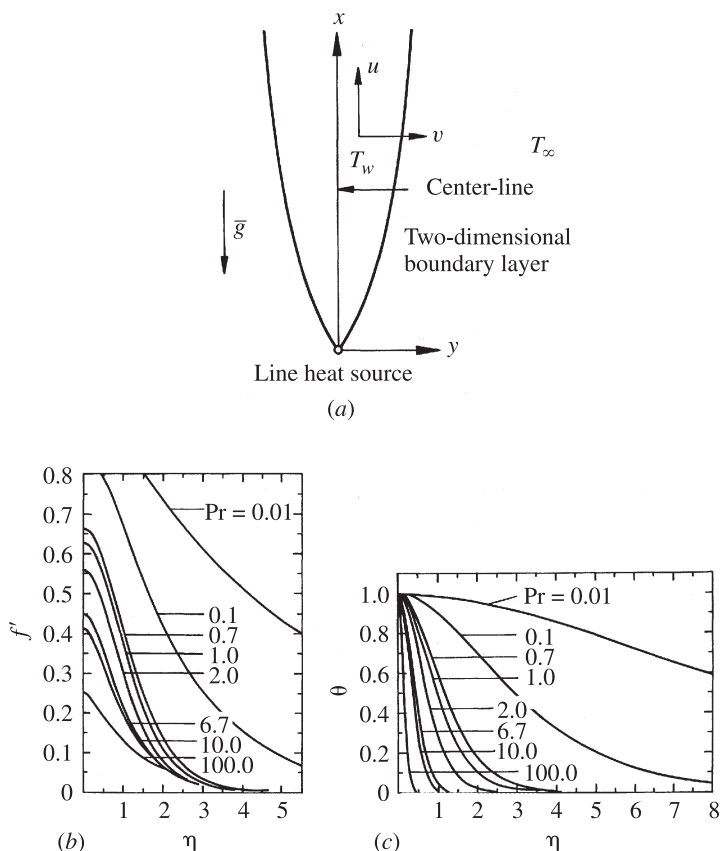


Figure 7.11 (a) Sketch and coordinate system for a two-dimensional thermal plume arising from a horizontal line source. Also shown are the calculated (b) velocity and (c) temperature distributions. (From Gebhart et al., 1970.)

along with a coordinate system which is similar to that for flow over a heated vertical surface. Using the nomenclature and analysis given earlier for a vertical surface, it can easily be seen that $n = \frac{3}{5}$ because the centerline, $y = 0$, is adiabatic due to symmetry. Also, the vertical velocity is not zero there but a maximum, since a no-shear condition applies there rather than the no-slip condition. Then the similarity variables given earlier in eq. (7.24) may be used with $T_w - T_\infty = Nx^{-3/5}$, where T_w is the centerline temperature. The governing equations are then obtained from eqs. (7.35) and (7.36) as

$$f''' + \frac{12}{5}ff'' - \frac{4}{5}(f')^2 + \theta = 0 \quad (7.54)$$

$$\frac{\theta''}{Pr} + \frac{12}{5}(f\theta' + f'\theta) = 0 \quad (7.55)$$

The boundary conditions for a two-dimensional plume are

$$\theta'(0) = f(0) = f''(0) = 1 - \theta(0) = f'(\infty) = 0 \quad (7.56)$$

The first and third conditions arise from symmetry at $y = 0$, or $\eta = 0$. The overall energy balance can also be written in terms of the total convected energy in the boundary layer q_c as

$$\begin{aligned} q_c &= \int_{-\infty}^{\infty} \rho c_p u (T - T_{\infty}) dy \\ &= 4\mu c_p N \left(\frac{g\beta N}{4\nu^2} \right)^{1/4} x^{(5n+3)/4} \int_{-\infty}^{\infty} f'(\eta)\theta(\eta) d\eta \end{aligned} \quad (7.57)$$

Therefore, the x dependence drops out for $n = -\frac{3}{5}$ and q_c represents the total energy input Q per unit length of the line source. Then the constant N in the centerline temperature distribution, $T_w - T_{\infty} = Nx^{-3/5}$, is obtained from eq. (7.57) as

$$N = \left(\frac{Q^4}{64g\beta\rho^2\mu^2c_p^4I^4} \right)^{1/5} \quad (7.58)$$

where I is the integral

$$I = \int_{-\infty}^{\infty} f'(\eta)\theta(\eta) d\eta \quad (7.59)$$

This integral I can be determined numerically by solving the governing similarity equations and then evaluating the integral. Values of I at several Prandtl numbers are given by Gebhart et al. (1970). For instance, the values of I calculated at $Pr = 0.7, 1.0, 6.7$, and 10.0 are given as $1.245, 1.053, 0.407$, and 0.328 , respectively.

Figure 7.11 also presents some calculated velocity and temperature profiles in a two-dimensional plume from Gebhart et al. (1970). These results can be used to calculate the velocity and thermal boundary layer thicknesses, which can be shown to vary as $x^{2/5}$, and the centerline velocity, which can be shown to increase with x as $x^{1/5}$. The centerline temperature, which decays with x as $x^{-3/5}$, can be calculated by obtaining the value of N from eq. (7.58) for a given Pr and heat input Q . Note that this analysis applies for a line source on a vertical adiabatic surface as well, since q_c is constant in this case, too, resulting in $n = -\frac{3}{5}$ (Jaluria and Gebhart, 1977). Therefore, the governing equations are eqs. (7.54) and (7.55). However, the boundary condition $f''(0) = 0$ is replaced by $f'(0) = 0$ because of the no-slip condition at the wall.

Similarly, a laminar axisymmetric plume can be analyzed to yield the temperature and velocity distributions (Jaluria, 1985a). The wake rising above a finite heated body is expected finally to approach the conditions of an axisymmetric plume far downstream of the heat input as the effect of the size of the source diminishes. However, as mentioned earlier, most of these flows are turbulent in nature and in most practical applications. Simple integral analyses have been carried out, along

with appropriate experimentation, to understand and characterize these flows (Turner, 1973). Detailed numerical studies have also been carried out on a variety of free boundary flows to provide results that are of particular interest in pollution, fires, and environmental processes.

7.5 INTERNAL NATURAL CONVECTION

In the preceding sections we have considered largely external natural convection in which the ambient medium away from the flow is extensive and stationary. However, there are many natural convection flows that occur within enclosed regions, such as flows in rooms and buildings, cooling towers, solar ponds, and furnaces. The flow domain may be completely enclosed by solid boundaries or may be a partial enclosure with openings through which exchange with the ambient occurs. There has been growing interest and research activity in buoyancy-induced flows arising in partial or complete enclosures. Much of this interest has arisen because of applications such as cooling of electronic circuitry (Jaluria, 1985b; Incropera, 1999), building fires (Emmons, 1978, 1980), materials processing (Jaluria, 2001), geothermal energy extraction (Torrance, 1979), and environmental processes. The basic mechanisms and heat transfer results in internal natural convection have been reviewed by several researchers, such as Yang (1987) and Ostrach (1988). Some of the important basic considerations are presented here.

7.5.1 Rectangular Enclosures

The two-dimensional natural convection flow in a rectangular enclosure, with the two vertical walls at different temperatures and the horizontal boundaries taken as adiabatic or at a temperature varying linearly between those of the vertical boundaries, has been thoroughly investigated over the past three decades. Figure 7.12a shows a typical vertical enclosure with the two vertical walls at temperatures T_h and T_c and the horizontal surfaces being taken as insulated. The dimensionless governing equations may be written as

$$\frac{1}{\text{Pr}} \mathbf{V} \cdot \nabla \omega = \nabla^2 \omega - \text{Ra} \frac{\partial \theta}{\partial Y} \quad (7.60)$$

$$\mathbf{V} \cdot \nabla \theta = \nabla^2 \theta \quad (7.61)$$

where the vorticity $\omega = -\nabla^2 \psi$, $\theta = (T - T_c)/(T_h - T_c)$, $Y = y/d$, and the Rayleigh number $\text{Ra} = \text{Gr} \cdot \text{Pr}$. The width d of the enclosure and the temperature difference $T_h - T_c$ are taken as characteristic quantities for nondimensionalization of the variables. The velocity is nondimensionalized by α/d here. This problem has been investigated numerically and experimentally for a wide range of Rayleigh and Prandtl numbers and of the aspect ratio $A = H/d$. Figure 7.12b shows the calculated isotherms at a moderate value of Pr . A recirculating flow arises and distorts the temperature field resulting from pure conduction.

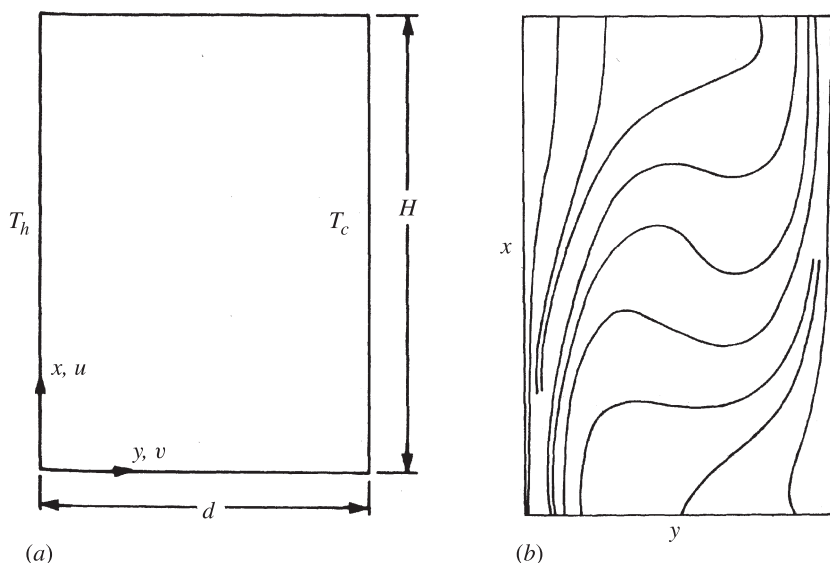


Figure 7.12 (a) Typical vertical rectangular enclosure; (b) calculated isotherms for $Pr = 1.0$ at $Ra = 2 \times 10^4$. (From Elder, 1966.)

At small values of Ra , $Ra \leq 1000$, there is little increase in the heat transfer over that due to conduction alone, for which the Nusselt number $Nu = hd/k = 1$. However, as Ra increases, several flow regimes have been found to occur, resulting in a significant increase in the Nusselt number. In laminar flow, these regimes include the conduction, transition, and boundary layer regimes. The conduction regime is characterized by a linear temperature variation in the central region of the enclosure. In the boundary layer regime, thin boundary layers appear along the vertical walls, with horizontal temperature uniformity between the two layers. In the transition regime, the two boundary regions are thicker and the isothermal interior region does not appear. The characteristics are seen clearly in Figs. 7.13 and 7.14. As Ra increases further, secondary flows appear, as characterized by additional cells in the flow, and transition to turbulence occurs at still higher Ra . Detailed studies of the different flow regimes and the corresponding heat transfer have been carried out, along with three-dimensional transport, for wide ranges of the governing parameters, as reviewed by Gebhart et al. (1988).

An interesting solution was obtained by Batchelor (1954) for large aspect ratios, $H/d \rightarrow \infty$. The flow can then be assumed to be fully developed, with the velocity and temperature as functions only of the horizontal coordinate y . This problem can be solved analytically to yield the velocity U and temperature θ distributions as

$$U = \frac{Ra}{12} Y(1 - Y)(1 - 2Y) \quad \text{and} \quad \theta = 1 - Y \quad (7.62)$$

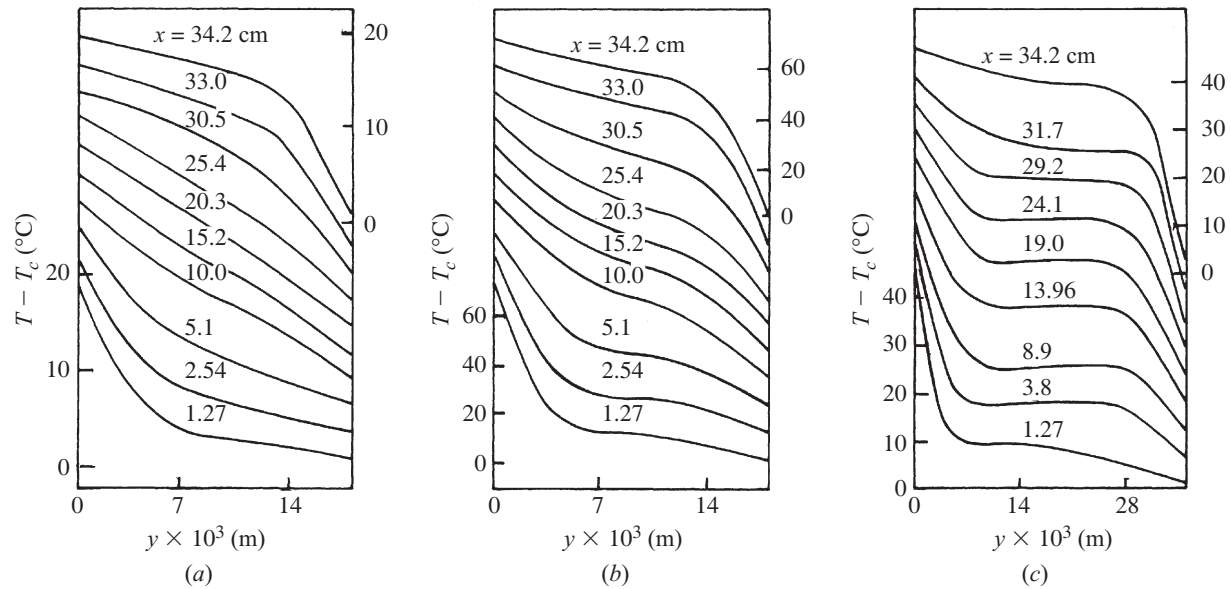


Figure 7.13 Measured temperature distributions in air in a vertical rectangular enclosure: (a) conduction regime; (b) transition regime; (c) boundary layer regime. (From Eckert and Carlson, 1961.)

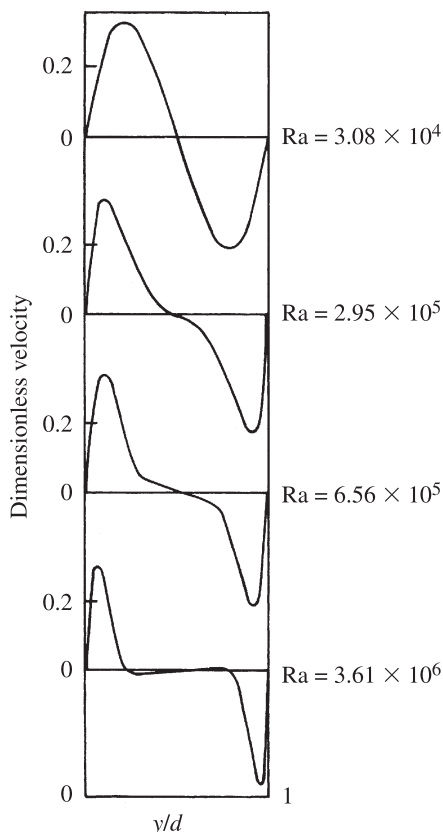


Figure 7.14 Measured velocity distributions at midheight in a rectangular enclosure at various values of Ra . (From Elder, 1965.)

where the nondimensionalization given earlier for eqs. (7.60) and (7.61) is used. Therefore, the temperature distribution is independent of the flow and the Nusselt number Nu is 1.0.

7.5.2 Other Configurations

Many other flow configurations in internal natural convection, besides the rectangular enclosure, have been studied because of both fundamental and applied interest. Inclined and horizontal enclosures have been of interest in solar energy utilization and have received a lot of attention. Horizontal layers, with heating from below, provide the classical Benard problem whose instability has been of interest to many researchers over many decades. Convective flow does not arise up to a Rayleigh number Ra , based on the layer thickness and temperature difference, of around 1700. The

exact value was obtained as 1708 by several researchers, using stability analysis, as reviewed by Gebhart et al. (1988). Therefore, the Nusselt number based on these characteristic quantities is 1.0 up to this value of Ra . As the Rayleigh number increases, convective flow arises and different flow regimes, including turbulent flow, and different instabilities have been studied in detail, as reviewed by Gebhart et al. (1988). Hollands et al. (1975) presented experimental results and correlated their own data and that from other studies for horizontal enclosures. Similarly, Hollands et al. (1976) presented correlations for inclined enclosures heated at the bottom.

Natural convection in cylindrical, spherical, and annular cavities has also been of interest. Ostrach (1972) reviewed much of the work done on the flow inside horizontal cylindrical cavities. Kuehn and Goldstein (1976) carried out a detailed experimental and numerical investigation of natural convection in concentric horizontal cylindrical annuli. A thermosyphon, which is a fully or partially enclosed circulating fluid system driven by buoyancy, has been of interest in the cooling of gas turbines, electrical machinery, nuclear reactors, and geothermal energy extraction. See, for instance, the review by Japikse (1973) and the detailed study by Mallinson et al. (1981). Partial enclosures are of importance in room ventilation, building fires, and cooling of electronic equipment. Several studies have been directed at the natural convection flow arising in enclosures with openings and the associated thermal or mass transport (Markatos et al., 1982; Abib and Jaluria, 1988). Figure 7.15 shows the schematic of the buoyancy-driven flow in an enclosure with an opening. Typical results for flow due to a thermal source on the left wall are shown in Fig. 7.16. The numbers in the figure indicate dimensionless stream function and temperature values. A strong stable stratification, with hot fluid overlying colder fluid, is observed. Many other such natural convection flows and the resulting transport processes have been investigated in the literature.

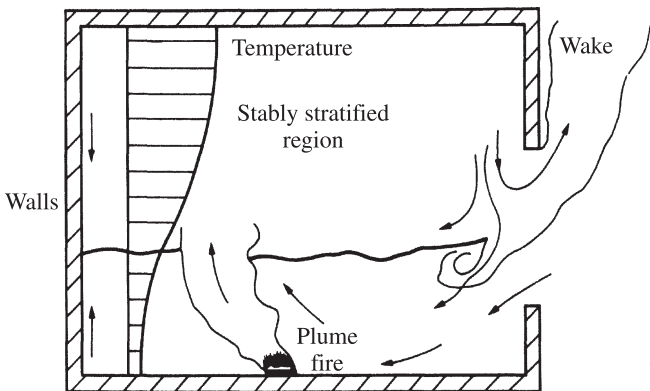


Figure 7.15 Buoyancy-driven flow due to a thermal energy source in an enclosure with an opening.

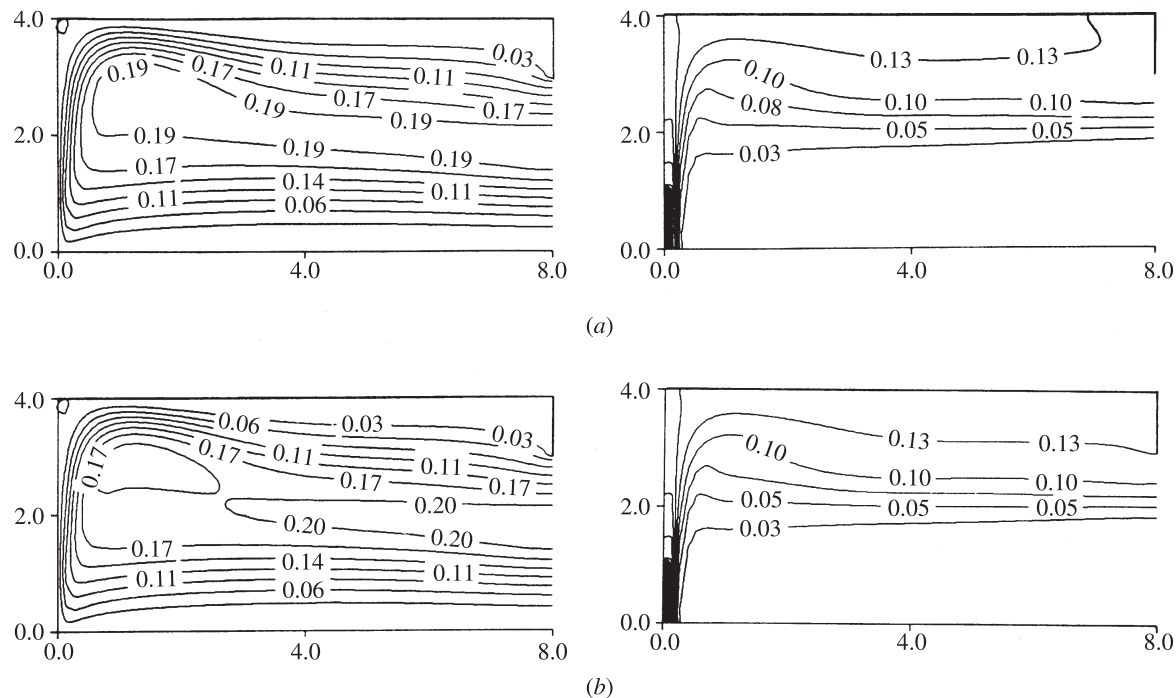


Figure 7.16 Calculated streamlines and isotherms for the buoyancy-driven flow in an enclosure with an opening at (a) $Ra = 10^5$ and (b) $Ra = 10^6$, where Ra is based on the thermal source height and temperature difference from the ambient. (From Abib and Jaluria, 1988.)

7.6 TURBULENT FLOW

7.6.1 Transition from Laminar Flow to Turbulent Flow

One of the most important questions to be answered in convection is whether the flow is laminar or turbulent, since the transport processes depend strongly on the flow regime. Near the leading edge of a surface, the flow is well ordered and well layered. The fluctuations and disturbances, if any, are small in magnitude compared to the mean flow. The processes can be defined in terms of the laminar governing equations, as discussed earlier. However, as the flow proceeds downstream from the leading edge, it undergoes transition to turbulent flow, which is characterized by disturbances of large magnitude. The flow may then be considered as a combination of a mean velocity and a fluctuating component. Statistical methods can generally be used to describe the flow field. In several natural convection flows of interest, particularly in industrial applications, the flow lies in the unstable regime or in the transition regime.

In a study of the transition of laminar flow to turbulence, it is necessary to determine the conditions under which a disturbance in the flow amplifies as it proceeds downstream. This involves a consideration of the stability of the flow, an unstable circumstance leading to disturbance growth. These disturbances enter the flow from various sources, such as building vibrations, fluctuations in heat input, and vibrations in equipment. Depending on the conditions in terms of frequency, location, and magnitude of the input disturbances, they may grow in amplitude due to a balance of buoyancy, pressure, and viscous forces. This form of instability, termed *hydrodynamic stability*, leads to disturbance growth.

The disturbances gradually amplify to large enough magnitudes to cause significant nonlinear effects and secondary mean flows which distort the mean velocity and temperature profiles. This leads to the formation of a shear layer, which fosters further amplification of the disturbances, and concentrated turbulent bursts arise. These bursts then increase in magnitude and in the fraction of time they occur, eventually crowding out the remaining laminar flow and giving rise to a completely turbulent flow. The general mechanisms underlying transition are shown in Fig. 7.17 from the work of Jaluria and Gebhart (1974). Several books on flow stability, such as those by Chandrasekhar (1961) and Drazin and Reid (1981), are available and may be consulted for further information on the underlying mechanisms.

7.6.2 Turbulence

Most natural convection flows of interest in nature and in technology are turbulent. The velocity, pressure, and temperature at a given point in these flows do not remain constant with time but vary irregularly at relatively high frequency. There is considerable amount of bulk mixing, with fluid packets moving around chaotically, giving rise to the fluctuations observed in the velocity and temperature fields rather than the well-ordered and well-layered flow characteristic of the laminar regime. Due to the importance of turbulent natural convection flows, a considerable amount of effort, both experimental and analytical, has been directed at understanding the basic

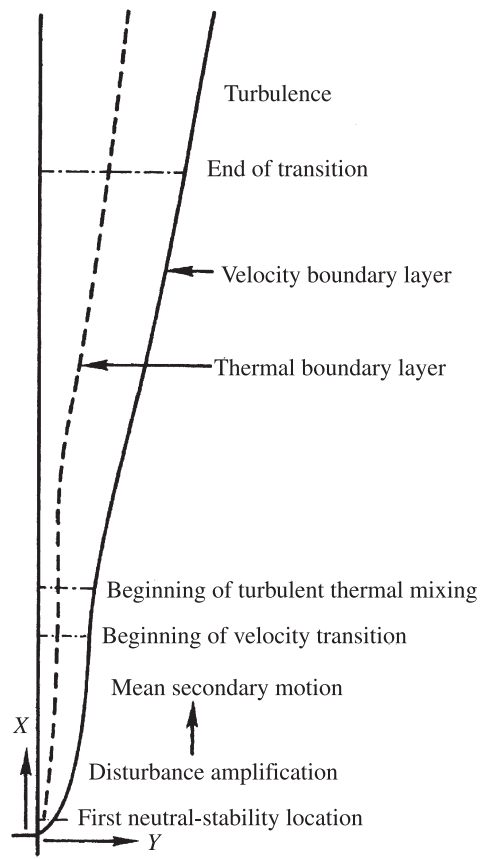


Figure 7.17 Growth of the boundary layer and the sequence of events during transition in natural convection flow over a vertical surface in water, $Pr = 6.7$. (From Jaluria and Gebhart, 1974.)

mechanisms and determining the transport rates. The work done in forced flows has been more extensive, and in fact, much of our understanding of turbulent flows in natural convection is based on this work. The transport mechanisms in turbulent flow are very different from those in laminar flow, and some of the basic considerations are given here. For further information, books on turbulent transport, such as those by Hinze (1975) and Tennekes and Lumley (1972), may be consulted.

In describing a turbulent flow, the fluctuating or eddy motion is superimposed on a mean motion. The flow may, therefore, be described in terms of the time-averaged values of the velocity components (denoted as \bar{u} , \bar{v} , and \bar{w}) and the disturbance or fluctuating quantities (u' , v' , and w'). The instantaneous value of each of the velocity components is then given as

$$u = \bar{u} + u' \quad v = \bar{v} + v' \quad w = \bar{w} + w' \quad (7.63)$$

Similarly, the pressure and temperature in the flow may be written as

$$p = \bar{p} + p' \quad T = \bar{T} + T' \quad (7.64)$$

The time averages are found by integrating the local instantaneous value of the particular quantity at a given point over a time interval that is long compared to the time period of the fluctuations. For steady turbulence, the time-averaged quantities do not vary with time. Then, from the definition of the averaging process, the time averages of the fluctuating quantities are zero. For unsteady turbulence, the time-averaged quantities are time dependent. Here we consider only the case of steady turbulence, so that the average quantities are independent of time and allow the flow and the transport processes to be represented in terms of time-independent variables.

If the instantaneous quantities defined by eqs. (63) and (64) are inserted into the governing continuity, momentum, and energy equations and a time average taken, additional transport terms, due to the turbulent eddies, arise. An important concept employed for treating these additional transport components is that of eddy viscosity ϵ_M and diffusivity ϵ_H . Momentum and heat transfer processes may then be expressed as a combination of a molecular component and an eddy component. This gives for $\bar{u}(y)$ and $\bar{T}(y)$

$$\frac{\tau}{\rho} = (\nu + \epsilon_M) \frac{d\bar{u}}{dy} \quad (7.65)$$

$$\frac{q'}{\rho c_p} = (\alpha + \epsilon_H) \frac{d\bar{T}}{dy} \quad (7.66)$$

where τ is the total shear stress and q' is the total heat flux. For isotropic turbulence, ϵ_M and ϵ_H are independent of direction and are of the form $-\bar{u}'v'/(\partial\bar{u}/\partial y)$ and $\bar{v}'T'/(\partial\bar{T}/\partial y)$, respectively.

If the preceding relationships for τ and q' are introduced into the governing equations for the mean flow, obtained by time averaging the equations written for the total instantaneous flow in boundary layer form, we obtain

$$\frac{\partial\bar{u}}{\partial x} + \frac{\partial\bar{v}}{\partial y} = 0 \quad (7.67)$$

$$\bar{u} \frac{\partial\bar{u}}{\partial x} + \bar{v} \frac{\partial\bar{u}}{\partial y} = g\beta(\bar{T} - T_\infty) + \frac{\partial}{\partial y} \left[(\nu + \epsilon_M) \frac{\partial\bar{u}}{\partial y} \right] \quad (7.68)$$

$$\bar{u} \frac{\partial\bar{T}}{\partial x} + \bar{v} \frac{\partial\bar{T}}{\partial y} = \frac{\partial}{\partial y} \left[(\alpha + \epsilon_H) \frac{\partial\bar{T}}{\partial y} \right] \quad (7.69)$$

where the viscous dissipation and energy source terms are neglected. A replacement of ν and α in the laminar flow equations by $\nu + \epsilon_M$ and $\alpha + \epsilon_H$, respectively, yields the governing equations for turbulent flow. However, ϵ_M and ϵ_H are not properties of the fluid but functions of the flow. As such, they are not known *a priori* and experimental results or various turbulence models are used for approximating them.

Several turbulence models have been developed in recent years and employed for solving various turbulent natural convection flows of practical interest. Among these, the κ - ϵ model, where κ is the turbulence kinetic energy and ϵ the rate of dissipation of turbulence energy, has been employed extensively. Both these quantities are calculated from differential equations which describe their transport in the flow and which are similar to the vorticity and energy transport equations. Launder and Spalding (1972) discuss this turbulence model, and similar models, in detail and also give the relevant constants and functions for these models.

Various researchers have employed different turbulence models to simulate complex turbulent natural convection flows. The algebraic eddy viscosity model has been a popular choice because of its simplicity and because the empirical constants in higher-order models may not be available for a given flow circumstance. A considerable amount of work has been done on recirculating turbulent flows in enclosures, such as those due to fire in a room (Abib and Jaluria, 1995). See, for instance, the review paper on such flows by Yang and Lloyd (1985).

Experimental work has also been done on turbulent natural convection flows and heat transfer. However, the data available for different flow configurations and circumstances are few. Cheesewright (1968) measured velocity and temperature profiles and provided heat transfer data from a heated surface in air. In turbulent flow, the generalized temperature profiles were found to remain largely unchanged downstream. This aspect was employed by Cheesewright to determine the end of the transition regime. The work of Vliet and Liu (1969) and of Vliet (1969) was directed at vertical and inclined uniform heat flux surfaces. The turbulence level, which was defined as u'/\bar{u} , was measured and found to be as high as 0.3. The velocity profile was found to widen with a decrease in the nondimensional velocity, as also observed by Jaluria and Gebhart (1974). Both water and air were employed. Vliet and Ross (1975) considered an inclined surface with a constant heat flux. In the Grashof number, g was replaced by $g \cos \gamma$, where γ is the angle at which the surface is inclined with the vertical. This is in line with the earlier discussion on inclined surfaces.

7.7 EMPIRICAL CORRELATIONS

In several problems of practical interest, the heat transfer and flow processes are so complicated that the analytical and numerical methods discussed earlier cannot be employed easily and one has to depend on experimental data. Over the years, a considerable amount of information on heat transfer rates for various flow configurations and thermal conditions has been gathered. Some of this information has already been presented earlier. The present section gives some of the commonly used results for a few important cases. The results included here are only a small fraction of what is available in the literature, and the attempt is only to present useful results in a few common circumstances and to indicate the general features of the empirical relationships. Unless mentioned otherwise, all fluid properties are to be evaluated at the film temperature $T_f = (T_w + T_\infty)/2$.

7.7.1 Vertical Flat Surfaces

To cover the range of Rayleigh number Ra from laminar to turbulent flow, the following correlations have been employed over many years for isothermal surfaces (McAdams, 1954; Warner and Arpaci, 1968):

$$\overline{Nu} = \begin{cases} 0.59Ra^{1/4} & \text{for } 10^4 < Ra < 10^9 \quad (\text{laminar}) \\ 0.10Ra^{1/3} & \text{for } 10^9 < Ra < 10^{13} \quad (\text{turbulent}) \end{cases} \quad (7.70)$$

These equations are applicable for Pr values that are not very far from 1.0. Churchill and Chu (1975a) have recommended the following correlation, which may be applied over the entire range of Ra :

$$\overline{Nu} = \left\{ 0.825 + \frac{0.387Ra^{1/6}}{[1 + (0.492/Pr)^{9/16}]^{8/27}} \right\}^2 \quad (7.72)$$

For laminar flow, greater accuracy is obtained with the correlation [Churchill and Chu (1975a)]

$$\overline{Nu} = 0.68 + \frac{0.67Ra^{1/4}}{[1 + (0.492/Pr)^{9/16}]^{4/9}} \quad \text{for } 0 < Ra \lesssim 10^9 \quad (7.73)$$

Here \overline{Nu} and Ra are both based on the plate height L . The preceding correlations are generally preferred to the others, since they have the best agreement with experimental data. The local Nusselt numbers Nu_x can be obtained from the results given in the preceding references.

For the uniform heat flux case, the heat transfer results given by Vliet and Liu (1969) in water yield the following relationships. For laminar flow,

$$Nu_{x,q} = 0.60(Gr_x^* \cdot Pr)^{1/5} \quad \text{for } 10^5 < Gr_x^* \cdot Pr < 10^{13} \quad (7.74)$$

$$\overline{Nu}_q = 1.25Nu_{L,q} \quad \text{for } 10^5 < Gr_x^* \cdot Pr < 10^{11} \quad (7.75)$$

For turbulent flow,

$$Nu_{x,q} = 0.568(Gr_x^* \cdot Pr)^{0.22} \quad \text{for } 10^{13} < Gr_x^* \cdot Pr < 10^{16} \quad (7.76)$$

$$\overline{Nu}_q = 1.136Nu_{L,q} \quad \text{for } 2 \times 10^{13} < Gr_x^* \cdot Pr < 10^{16} \quad (7.77)$$

where

$$Gr_x^* = \frac{g\beta q'x^4}{k\nu^2} \quad (7.78)$$

Here $Nu_{L,q}$ represents the Nusselt number at $x = L$ and $Gr^* = g\beta q' L^4 / kv^2$. In a later study, Vliet and Ross (1975) obtained a closer corroboration for data in air with the following relationships:

$$\overline{Nu}_{x,q} = \begin{cases} 0.55(Gr_x^* \cdot Pr)^{0.2} & \text{for laminar flow} \\ 0.17(Gr_x^* \cdot Pr)^{0.25} & \text{for turbulent flow} \end{cases} \quad (7.79)$$

\overline{Nu}_q can be obtained by computing the mean temperature difference and using the overall heat transfer rate provided by Vliet and Ross (1975).

7.7.2 Inclined and Horizontal Flat Surfaces

As discussed earlier, the results obtained for vertical surfaces may be employed for surfaces inclined at an angle γ up to about 45° with the vertical, by replacing g with $g \cos \gamma$ in the Grashof number. For inclined surfaces with constant heat flux, Vliet and Ross (1975) have suggested the use of eq. (7.74) for laminar flow, with the replacement of Gr_x^* by $Gr_x^* \cos \gamma$ for both upward- and downward-facing heated inclined surfaces. In the turbulent region also, eq. (7.76) is suggested, with Gr_x^* replaced by $Gr_x^* \cos \gamma$ for an upward-facing heated surface and with Gr_x^* replaced by $Gr_x^* \cos^2 \gamma$ for a downward-facing surface.

Several correlations for inclined surfaces, under various thermal conditions, were given by Fujii and Imura (1972). For an inclined plate with heated surface facing upward with approximately constant heat flux, the correlation obtained is of the form

$$\overline{Nu}_q = 0.14[(Gr \cdot Pr)^{1/3} - (Gr_{cr} \cdot Pr)^{1/3}] + 0.56(Gr_{cr} \cdot Pr \cos \gamma)^{1/4} \quad \text{for } 10^5 < Gr \cdot Pr \cos \gamma < 10^{11} \text{ and } 15^\circ < \gamma < 75^\circ \quad (7.81)$$

where Gr_{cr} is the critical Grashof number at which the Nusselt number starts deviating from the laminar relationship, which is the second expression on the right-hand side of eq. (7.81). This correlation applies for $Gr > Gr_{cr}$. The value of Gr_{cr} is also given for various inclination angles. For $\gamma = 15, 30, 60$, and 70° , Gr_{cr} is given as 5×10^9 , 2×10^9 , 10^8 , and 10^6 , respectively. For inclined heated surfaces facing downward, the expression given is

$$\overline{Nu}_q = 0.56(Gr \cdot Pr \cos \gamma)^{1/4} \quad \text{for } 10^5 < Gr \cdot Pr \cos \gamma < 10^{11}, \quad \gamma < 88^\circ \quad (7.82)$$

The fluid properties are evaluated at $T_w - 0.25(T_w - T_\infty)$, and β at $T_\infty + 0.25(T_w - T_\infty)$.

For horizontal surfaces, several classical expressions exist. For heated isothermal surfaces facing downward (lower surface of heated plate), or cooled ones facing upward (upper surface of cooled plate), the correlation given by McAdams (1954) which has been used extensively, is

$$\overline{Nu} = 0.27Ra^{1/4} \quad \text{for } 10^5 \lesssim Ra \lesssim 10^{10} \quad (7.83)$$

Fujii and Imura (1972) give the corresponding correlation as

$$\overline{Nu} = 0.58Ra^{1/5} \quad \text{for } 10^6 \leq Ra \leq 10^{11} \quad (7.84)$$

Over the overlapping range of the two studies by Fujii and Imura (1972) and Rotem and Claassen (1969), the agreement between the two Nusselt numbers is fairly good.

For the heated isothermal horizontal surface facing upward and cold surface facing downward, the correlations for heat transfer are given by McAdams (1954) as

$$\overline{Nu} = \begin{cases} 0.54Ra^{1/4} & \text{for } 10^4 \leq Ra \leq 10^7 \\ 0.15Ra^{1/3} & \text{for } 10^7 \leq Ra \leq 10^{11} \end{cases} \quad (7.85)$$

$$(7.86)$$

The corresponding correlation given by Fujii and Imura (1972) for an approximately uniform heat flux condition is

$$\overline{Nu}_q = 0.14Ra^{1/3} \quad \text{for } Ra > 2 \times 10^8 \quad (7.87)$$

7.7.3 Cylinders and Spheres

A considerable amount of information exists on natural convection heat transfer from cylinders. For vertical cylinders of large diameter, ascertained from eq. (7.47), the correlations for vertical flat surfaces may be employed. For cylinders of small diameter, correlations for Nu are suggested in terms of the Rayleigh number Ra , where Ra and Nu are based on the diameter D of the cylinder.

The horizontal cylinder has been of interest to several investigators. McAdams (1954) gave correlation for isothermal cylinders as

$$\overline{Nu} = \begin{cases} 0.53Ra^{1/4} & \text{for } 10^4 < Ra < 10^9 \\ 0.13Ra^{1/3} & \text{for } 10^9 < Ra < 10^{12} \end{cases} \quad (7.88)$$

$$(7.89)$$

For smaller values of Ra , graphs are presented by McAdams (1954). A general expression of the form $\overline{Nu} = C \cdot Ra^n$ is given by Morgan (1975), with C and n presented in tabular form. Churchill and Chu (1975b) have given a correlation covering a wide range of Ra , $Ra \leq 10^{12}$, for isothermal cylinders as

$$\overline{Nu} = \left(0.60 + 0.387 \left\{ \frac{Ra}{[1 + (0.559/Pr)^{9/16}]^{16/9}} \right\}^{1/6} \right)^2 \quad (7.90)$$

This correlation is recommended for horizontal cylinders since it is convenient to use and agrees closely with experimental results.

For natural convection from spheres, too, several experimental studies have provided heat transfer correlations. Amato and Tien (1972) have listed the correlations for \overline{Nu} obtained from various investigations of heat and mass transfer. In a review paper, Yuge (1960) suggested the following correlation for heat transfer from isothermal spheres in air and gases over a Grashof number range $1 < Gr < 10^5$, where Gr and \overline{Nu} are based on the diameter D :

TABLE 7.2 Summary of Natural Convection Correlations for External Flows over Isothermal Surfaces

Geometry	Recommended Correlation	Range	Reference
Vertical flat surfaces	$\overline{\text{Nu}} = \left\{ 0.825 + \frac{0.387\text{Ra}^{1/6}}{[1 + (0.492/\text{Pr})^{9/16}]^{8/27}} \right\}^2$	$10^{-1} < \text{Ra} < 10^{12}$	Churchill and Chu (1975a)
Inclined flat surfaces	Above equation with g replaced by $g \cos \gamma$	$\gamma \leq 60^\circ$	
Horizontal flat surfaces	$\overline{\text{Nu}} = 0.54\text{Ra}^{1/4}$	$10^5 \leq \text{Ra} \leq 10^7$	
Heated, facing upward	$\overline{\text{Nu}} = 0.15\text{Ra}^{1/3}$	$10^7 \leq \text{Ra} \leq 10^{10}$	McAdams (1954)
Heated, facing downward	$\overline{\text{Nu}} = 0.27\text{Ra}^{1/4}$	$3 \times 10^5 \leq \text{Ra} \leq 3 \times 10^{10}$	McAdams (1954)
Horizontal cylinders	$\overline{\text{Nu}} = \left(0.60 + 0.387 \left\{ \frac{\text{Ra}}{[1 + (0.559/\text{Pr})^{9/16}]^{16/9}} \right\}^{1/6} \right)^2$	$10^{-5} \leq \text{Ra} \leq 10^{12}$	Churchill and Chu (1975b)
Spheres	$\overline{\text{Nu}} = 2 + 0.43\text{Ra}^{1/4}$	$\text{Pr} = 1$ and $1 < \text{Ra} < 10^5$	Yuge (1960)

$$\overline{\text{Nu}} = 2 + 0.43\text{Ra}^{1/4} \quad \text{for } \text{Pr} = 1 \text{ and } 1 < \text{Ra} < 10^5 \quad (7.91)$$

For heat transfer in water, Amato and Tien (1972) obtained the correlation for isothermal spheres as

$$\overline{\text{Nu}} = 2 + C \cdot \text{Ra}^{1/4} \quad \text{for } 3 \times 10^5 \leq \text{Ra} \leq 8 \times 10^8 \quad (7.92)$$

with $C = 0.500 \pm 0.009$, which gave a mean deviation of less than 11%. A general correlation applicable for $\text{Pr} \geq 0.7$ and $\text{Ra} \lesssim 10^{11}$ is given by Churchill (1983) as

$$\overline{\text{Nu}} = 2 + \frac{0.589\text{Ra}^{1/4}}{[1 + (0.469/\text{Pr})^{9/16}]^{4/9}} \quad (7.93)$$

Several of the important correlations presented earlier are summarized in Table 7.2. Correlations for various other geometries are given by Churchill (1983) and Raithby and Hollands (1985). $\overline{\text{Nu}}$ and Ra are based on the height L for a vertical plate, length L for inclined and horizontal surfaces, and diameter D for horizontal cylinders and spheres. All fluid properties are evaluated at the film temperature $T_f = (T_w + T_\infty)/2$.

7.7.4 Enclosures

As mentioned earlier, the heat transfer across a vertical rectangular cavity is largely by conduction for $\text{Ra} \lesssim 10^3$, which implies a Nusselt number $\overline{\text{Nu}}$ of 1.0. For larger Ra , Catton (1978) has given the following correlation for the aspect ratio H/d in the range 2 to 10 and $\text{Pr} < 10^5$:

$$\overline{\text{Nu}} = 0.22 \left(\frac{\text{Pr}}{0.2 + \text{Pr}} \text{Ra} \right)^{0.28} \left(\frac{H}{d} \right)^{-1/4} \quad (7.94)$$

where the Nusselt and Rayleigh numbers are based on the distance d between the vertical walls and the temperature difference between them. For an aspect ratio between 1 and 2, the coefficient in this expression was changed from 0.22 to 0.18 and the exponent from 0.28 to 0.29, with the aspect ratio dependence dropped. Similarly, correlations are given for higher aspect ratios in the literature.

For horizontal cavities heated from below, the Nusselt number $\overline{\text{Nu}}$ is 1.0 for Rayleigh number $\text{Ra} \lesssim 1708$, as discussed earlier. Globe and Dropkin (1959) gave the following correlation for such cavities at larger Ra , $3 \times 10^5 < \text{Ra} < 7 \times 10^9$:

$$\overline{\text{Nu}} = 0.069\text{Ra}^{1/3} \cdot \text{Pr}^{0.074} \quad (7.95)$$

For inclined cavities, Hollands et al. (1976) gave the following correlation for air as the fluid with $H/d \gtrsim 12$ and $\gamma < \gamma^*$ on the basis of several experimental studies:

$$\overline{\text{Nu}} = 1 + 1.44 \left[1 - \frac{1708}{\text{Ra} \cos \gamma} \right] \left\{ 1 - \frac{1708(\sin 1.8\gamma)^{1.6}}{\text{Ra} \cos \gamma} \right\} + \left[\left(\frac{\text{Ra} \cos \gamma}{5830} \right)^{1/3} - 1 \right] \quad (7.96)$$

where γ is the inclination with the horizontal, γ^* is a critical angle tabulated by Hollands et al. (1976), and the term in the square brackets is set equal to zero if the quantity within these brackets is negative. This equation uses the stability limit of $Ra = 1708$ for a horizontal layer, given earlier. For a horizontal enclosure heated from below, with air as the fluid, Hollands et al. (1975) gave the correlation

$$\overline{Nu} = 1 + 1.44 \left[1 - \frac{1708}{Ra} \right] + \left[\left(\frac{Ra}{5830} \right)^{1/3} - 1 \right] \quad (7.97)$$

Similarly, correlations for other fluids, geometries, and thermal conditions are given in the literature.

7.8 SUMMARY

In this chapter we discuss the basic considerations relevant to natural convection flows. External and internal buoyancy-induced flows are considered, and the governing equations are obtained. The approximations generally employed in the analysis of these flows are outlined. The important dimensionless parameters are derived in order to discuss the importance of the basic processes that govern these flows. Laminar flows for various surfaces and thermal conditions are discussed, and the solutions obtained are presented, particularly those derived from similarity analysis. The heat transfer results and the characteristics of the resulting velocity and temperature fields are discussed. Also considered are transient and turbulent flows. The governing equations for turbulent flow are given, and experimental results for various flow configurations are presented. The frequently employed empirical correlations for heat transfer by natural convection from various surfaces and enclosures are also included. Thus, this chapter presents the basic aspects that underlie natural convection and the heat transfer correlations that may be employed for practical applications.

NOMENCLATURE

Roman Letter Symbols

c_p	specific heat at constant pressure, J/kg · K
D	diameter of cylinder or sphere, m
f	stream function, dimensionless
F	body force per unit volume, N/m ³
g	gravitational acceleration, m/s ²
Gr	Grashof number, dimensionless
Gr_x	local Grashof number, dimensionless
Gr^*	heat flux Grashof number, dimensionless
h_x	local heat transfer coefficient, W/m ² · K
\bar{h}	average heat transfer coefficient, W/m ² · K
h_ϕ	heat transfer coefficient at angular position ϕ , W/m ² · K

k	thermal conductivity, $\text{W/m} \cdot \text{K}$
L	characteristic length, height of vertical plate, m
m, n	exponents in exponential and power law distributions, dimensionless
M, N	constants employed for exponential and power law distributions of surface temperature, dimensionless
Nu_x	local Nusselt number, dimensionless $[= h_x x / k]$
$\overline{\text{Nu}}$	average Nusselt number for an isothermal surface, dimensionless
$\overline{\text{Nu}}_q$	average Nusselt number for a uniform heat flux surface, dimensionless
Nu_ϕ	local Nusselt number at angular position ϕ , dimensionless
p	pressure, Pa
Pr	Prandtl number, dimensionless
q	total heat transfer, W
q'_x	local heat flux, W/m^2
q'	constant surface heat flux, W/m^2
q'''	volumetric heat source, W/m^3
Ra	Rayleigh number, dimensionless $[= \text{Gr} \cdot \text{Pr}]$
Ra_x	local Rayleigh number, dimensionless $[= \text{Gr}_x \cdot \text{Pr}]$
Sr	Strouhal number, dimensionless
t	time, s
t_c	characteristic time, s
ΔT	temperature difference, K $[= T_w - T_\infty]$
T	local temperature, K
T_w	wall temperature, K
	plume centerline temperature, K
T_∞	ambient temperature, K
u, v, w	velocity components in x , y , and z directions, respectively, m/s
\mathbf{V}	velocity vector, m/s
V_c	convection velocity, m/s
x, y, z	coordinate distances, m

Greek Letter Symbols

α	thermal diffusivity, m^2/s
β	coefficient of thermal expansion, K^{-1}
γ	inclination with the vertical, degrees or radians
δ	velocity boundary layer thickness, m
δ_T	thermal boundary layer thickness, m
ε_H	eddy diffusivity, m^2/s
ε_M	eddy viscosity, m^2/s
η	similarity variable, dimensionless
θ	temperature, dimensionless $[= (T - T_\infty)/(T_w - T_\infty)]$
μ	dynamic viscosity, $\text{Pa} \cdot \text{s}$

ν	kinematic viscosity, m^2/s
Φ_v	viscous dissipation, s^{-2}
ψ	stream function, m^2/s

REFERENCES

- Abib, A., and Jaluria, Y. (1988). Numerical Simulation of the Buoyancy-Induced Flow in a Partially Open Enclosure, *Numer. Heat Transfer*, 14, 235–254.
- Abib, A., and Jaluria, Y. (1995). Turbulent Penetrative and Recirculating Flow in a Compartment Fire, *J. Heat Transfer*, 117, 927–935.
- Amato, W. S., and Tien, C. (1972). Free Convection Heat Transfer from Isothermal Spheres in Water, *Int. J. Heat Mass Transfer*, 15, 327–339.
- Batchelor, G. K. (1954). Heat Transfer by Free Convection across a Closed Cavity between Vertical Boundaries at Different Temperatures, *Q. Appl. Math.*, 12, 209–233.
- Bejan, A. (1995). *Convection Heat Transfer*, 2nd ed., Wiley, New York.
- Catton, I. (1978). Natural Convection in Enclosures, *Proc. 6th International Heat Transfer Conference*, Toronto, Ontario, Canada, pp. 6, 13–31.
- Cebeci, T. (1974). Laminar Free Convection Heat Transfer from the Outer Surface of a Vertical Slender Circular Cylinder, *Proc. 5th International Heat Transfer Conference*, Paper NC1.4, pp. 15–19.
- Chandrasekhar, S. (1961). *Hydrodynamic and Hydromagnetic Stability*, Clarendon Press, Oxford.
- Cheesewright, R. (1968). Turbulent Natural Convection from a Vertical Plane Surface, *J. Heat Transfer*, 90, 1–8.
- Chiang, T., Ossin, A., and Tien, C. L. (1964). Laminar Free Convection from a Sphere, *J. Heat Transfer*, 86, 537–542.
- Churchill, S. W. (1975). Transient Laminar Free Convection from a Uniformly Heated Vertical Plate, *Lett. Heat Mass Transfer*, 2, 311–317.
- Churchill, S. W. (1983). Free Convection around Immersed Bodies, in *Heat Exchanger Design Handbook*, E. U. Schlünder, ed., Hemisphere Publishing, New York, Sec. 2.5.7.
- Churchill, S. W., and Chu, H. H. S. (1975a). Correlating Equations for Laminar and Turbulent Free Convection from a Vertical Plate, *Int. J. Heat Mass Transfer*, 18, 1323–1329.
- Churchill, S. W., and Chu, H. H. S. (1975b). Correlating Equations for Laminar and Turbulent Free Convection from a Horizontal Cylinder, *Int. J. Heat Mass Transfer*, 18, 1049–1053.
- Churchill, S. W., and Usagi, R. (1974). A Standardized Procedure for the Production of Correlations in the Form of a Common Empirical Equation, *Ind. Eng. Chem. Fundam.*, 13, 39–46.
- Drazin, P. G., and Reid, W. H. (1981). *Hydrodynamic Stability*, Cambridge University Press, Cambridge.
- Eckert, E. R. G., and Carlson, W. O. (1961). Natural Convection in an Air Layer Enclosed between Two Vertical Plates at Different Temperatures, *Int. J. Heat Mass Transfer*, 2, 106–129.
- Elder, J. W. (1965). Laminar Free Convection in a Vertical Slot, *J. Fluid Mech.*, 23, 77–98.

- Elder, J. W. (1966). Numerical Experiments with Free Convection in a Vertical Slot, *J. Fluid Mech.*, 24, 823–843.
- Emmons, H. W. (1978). The Prediction of Fires in Buildings, *Proc. 17th Symposium (International) on Combustion*, Combustion Institute, Pittsburgh, PA, pp. 1101–1111.
- Emmons, H. (1980). Scientific Progress on Fire, *Annu. Rev. Fluid Mech.*, 12, 223–236.
- Fujii, T., and Imura, H. (1972). Natural Convection from a Plate with Arbitrary Inclination, *Int. J. Heat Mass Transfer*, 15, 755–767.
- Gebhart, B. (1973). Natural Convection Flows and Stability, *Adv. Heat Transfer*, 9, 273–348.
- Gebhart, B. (1979). Buoyancy Induced Fluid Motions Characteristic of Applications in Technology, *J. Fluids Eng.*, 101, 5–28.
- Gebhart, B. (1988). Transient Responses and Disturbance Growth in Buoyancy-Driven Flows, *J. Heat Transfer*, 110, 1166–1174.
- Gebhart, B., Pera, L., and Schorr, A. W. (1970). Steady Laminar Natural Convection Plumes above a Horizontal Line Heat Source, *Int. J. Heat Mass Transfer*, 13, 161–171.
- Gebhart, B., Hilder, D. S., and Kelleher, M. (1984). The Diffusion of Turbulent Buoyant Jets, *Adv. Heat Transfer*, 16, 1–57.
- Gebhart, B., Jaluria, Y., Mahajan, R. L., and Sammakia, B. (1988). *Buoyancy Induced Flows and Transport*, Hemisphere Publishing, New York.
- Globe, S., and Dropkin, D. (1959). Natural Convection Heat Transfer in Liquids Confined between Two Horizontal Plates, *J. Heat Transfer*, 81, 24.
- Hellums, J. D., and Churchill, S. W. (1962). Transient and Steady State, Free and Natural Convection, Numerical Solutions, I: The Isothermal, Vertical Plate, *AIChE J.*, 8, 690–692.
- Hinze, J. O. (1975). *Turbulence*, McGraw-Hill, New York.
- Hollands, K. G. T., Raithby, G. D., and Konicek, L. (1975). Correlating Equations for Free Convection Heat Transfer in Horizontal Layers of Air and Water, *Int. J. Heat Mass Transfer*, 18, 879–884.
- Hollands, K. G. T., Unny, T. E., Raithby, G. D., and Konicek, L. (1976). Free Convective Heat Transfer across Inclined Air Layers, *J. Heat Transfer*, 98, 189–193.
- Incropera, F. P. (1999). *Liquid Cooling of Electronic Devices by Single-Phase Convection*, Wiley-Interscience, New York.
- Jaluria, Y. (1980). *Natural Convection Heat and Mass Transfer*, Pergamon Press, Oxford.
- Jaluria, Y. (1985a). Thermal Plumes, in *Natural Convection: Fundamentals and Applications*, W. Aung, S. Kakaç and R. Viskanta, eds., Hemisphere Publishing, New York, pp. 51–74.
- Jaluria, Y. (1985b). Natural Convective Cooling of Electronic Equipment, in *Natural Convection: Fundamentals and Applications*, W. Aung, S. Kakaç, and R. Viskanta, eds., Hemisphere Publishing, New York, pp. 961–986.
- Jaluria, Y. (1998). *Design and Optimization of Thermal Systems*, McGraw-Hill, New York.
- Jaluria, Y. (2001). Fluid Flow Phenomena in Materials Processing: The 2000 Freeman Scholar Lecture, *J. Fluids Eng.*, 123, 173–210.
- Jaluria, Y., and Gebhart, B. (1974). On Transition Mechanisms in Vertical Natural Convection Flow, *J. Fluid Mech.*, 66, 309–337.
- Jaluria, Y., and Gebhart, B. (1975). On the Buoyancy-Induced Flow Arising from a Heated Hemisphere, *Int. J. Heat Mass Transfer*, 18, 415–431.
- Jaluria, Y., and Gebhart, B. (1977). Buoyancy-Induced Flow Arising from a Line Thermal Source on an Adiabatic Vertical Surface, *Int. J. Heat Mass Transfer*, 20, 153–157.

- Japikse, D. (1973). Heat Transfer in Open and Closed Thermosyphons, Ph.D. dissertation, Purdue University, West Lafayette, IN.
- Kakaç, S., Aung, W., and Viskanta, R., eds. (1985). *Natural Convection: Fundamentals and Applications*, Hemisphere Publishing, New York.
- Kaviany, M. (1994). *Principles of Convective Heat Transfer*, Springer-Verlag, New York.
- Kuehn, T. H., and Goldstein, R. J. (1976). An Experimental and Theoretical Study of Natural Convection in the Annulus between Horizontal Concentric Cylinders, *J. Fluid Mech.*, 74, 695–719.
- Launder, B. E., and Spalding, D. B. (1972). *Mathematical Models of Turbulence*, Academic Press, London.
- LeFevre, E. J., and Ede, A. J. (1956). Laminar Free Convection from the Outer Surface of a Vertical Circular Cylinder, *Proc. 9th International Congress on Applied Mechanics*, Brussels, Vol. 4, pp. 175–183.
- Mallinson, G. D., Graham, A. D., and De Vahl Davis, G. (1981). Three-Dimensional Flow in a Closed Thermosyphon, *J. Fluid Mech.*, 109, 259–275.
- Markatos, N. C., Malin, M. R., and Cox G. (1982). Mathematical Modeling of Buoyancy-Induced Smoke Flow in Enclosures, *Int. J. Heat Mass Transfer*, 25, 63–75.
- McAdams, W. H. (1954). *Heat Transmission*, 3rd ed., McGraw-Hill, New York.
- Merk, H. J., and Prins, J. A. (1953–54). Thermal Convection in Laminar Boundary Layers I, II, and III, *Appl. Sci. Res.*, A4, 11–24, 195–206, 207–221.
- Minkowycz, W. J., and Sparrow, E. M. (1974). Local Nonsimilar Solutions for Natural Convection on a Vertical Cylinder, *J. Heat Transfer*, 96, 178–183.
- Morgan, V. T. (1975). The Overall Convective Heat Transfer from Smooth Circular Cylinders, *Advances in Heat Transfer*, Vol. 11, Academic Press, New York, pp. 199–264.
- Oosthuizen, P. H., and Naylor, D. (1999). *Introduction to Convective Heat Transfer Analysis*, McGraw-Hill, New York.
- Ostrach, S. (1953). An Analysis of Laminar Free Convection Flow and Heat Transfer about a Flat Plate Parallel to the Direction of the Generating Body Force, *NACA Tech. Rep. 1111*.
- Ostrach, S. (1972). Natural Convection in Enclosures, *Adv. Heat Transfer*, 8, 161–227.
- Ostrach, S. (1988). Natural Convection in Enclosures, *J. Heat Transfer*, 110, 1175–1190.
- Ozisik, M. N. (1993). *Heat Conduction*, 2nd ed., Wiley-Interscience, New York.
- Pera, L., and Gebhart, B. (1972). Natural Convection Boundary Layer Flow over Horizontal and Slightly Inclined Surfaces, *Int. J. Heat Mass Transfer*, 16, 1131–1146.
- Raithby, G. D., and Hollands, K. G. T. (1985). In *Handbook of Heat Transfer Fundamentals*, W. M. Rohsenow, J. P. Hartnett, and E. N. Ganic, eds., McGraw-Hill, New York, Chap. 6.
- Rich, B. R. (1953). An Investigation of Heat Transfer from an Inclined Flat Plate in Free Convection, *Trans. ASME*, 75, 489–499.
- Rotem, Z., and Claassen, L. (1969). Natural Convection above Unconfined Horizontal Surfaces, *J. Fluid Mech.*, 39, 173–192.
- Schuh, H. (1948). Boundary Layers of Temperature, in *Boundary Layers*, W. Tollmien, ed., British Ministry of Supply, German Document Center, Ref. 3220T, Sec. B.6.
- Sparrow, E. M., and Gregg, J. L. (1956). Laminar Free Convection Heat Transfer from the Outer Surface of a Vertical Circular Cylinder, *Trans. ASME*, 78, 1823–1829.
- Sparrow, E. M., and Gregg, J. L. (1958). Similar Solutions for Free Convection from a Non-isothermal Vertical Plate, *J. Heat Transfer*, 80, 379–386.

- Tennekes, H., and Lumley, J. L. (1972). *Introduction to Turbulence*, MIT Press, Cambridge, MA.
- Torrance, K. E. (1979). Open-Loop Thermosyphons with Geological Applications, *J. Heat Transfer*, 101, 677–683.
- Turner, J. S. (1973). *Buoyancy Effects in Fluids*, Cambridge University Press, Cambridge.
- Vliet, G. C. (1969). Natural Convection Local Heat Transfer on Constant Heat Flux Inclined Surfaces, *J. Heat Transfer*, 9, 511–516.
- Vliet, G. C., and Liu, C. K. (1969). An Experimental Study of Turbulent Natural Convection Boundary Layers, *J. Heat Transfer*, 91, 517–531.
- Vliet, G. C., and Ross, D. C. (1975). Turbulent, Natural Convection on Upward and Downward Facing Inclined Heat Flux Surfaces, *J. Heat Transfer*, 97, 549–555.
- Warner, C. Y., and Arpaci, V. S. (1968). An Experimental Investigation of Turbulent Natural Convection in Air at Low Pressure along a Vertical Heated Flat Plate, *Int. J. Heat Mass Transfer*, 11, 397–406.
- Yang, K. T. (1987). Natural Convection in Enclosures, in *Handbook of Single-Phase Convective Heat Transfer*, S. Kakaç, R. K. Shah, and W. Aung, eds., Wiley-Interscience, New York, Chap. 13.
- Yang, K. T., and Lloyd, J. R. (1985). Turbulent Buoyant Flow in Vented Simple and Complex Enclosures, in *Natural Convection: Fundamentals and Applications*, S. Kakaç, W. Aung, and R. Viskanta, eds., Hemisphere Publishing, New York, pp. 303–329.
- Yuge, T. (1960). Experiments on Heat Transfer from Spheres Including Combined Natural and Forced Convection, *J. Heat Transfer*, 82, 214–220.

Thermal Radiation

MICHAEL F. MODEST

College of Engineering
Pennsylvania State University
University Park, Pennsylvania

- 8.1 Fundamentals
 - 8.1.1 Emissive power
 - 8.1.2 Solid angles
 - 8.1.3 Radiative intensity
 - 8.1.4 Radiative heat flux
- 8.2 Radiative properties of solids and liquids
 - 8.2.1 Radiative properties of metals
 - Wavelength dependence
 - Directional dependence
 - Hemispherical properties
 - Total properties
 - Surface temperature effects
 - 8.2.2 Radiative properties of nonconductors
 - Wavelength dependence
 - Directional dependence
 - Temperature dependence
 - 8.2.3 Effects of surface conditions
 - Surface roughness
 - Surface layers and oxide films
 - 8.2.4 Semitransparent sheets
 - 8.2.5 Summary
- 8.3 Radiative exchange between surfaces
 - 8.3.1 View factors
 - Direct integration
 - Special methods
 - View factor algebra
 - Crossed-strings method
 - 8.3.2 Radiative exchange between black surfaces
 - 8.3.3 Radiative exchange between diffuse gray surfaces
 - Convex surface exposed to large isothermal enclosure
 - 8.3.4 Radiation shields
 - 8.3.5 Radiative exchange between diffuse nongray surfaces
 - Semigray approximation method
 - Band approximation method

- 8.4 Radiative properties of participating media
 - 8.4.1 Molecular gases
 - 8.4.2 Particle clouds
 - Soot
 - Pulverized coal and fly ash dispersions
 - Mixtures of molecular gases and particulates
- 8.5 Radiative exchange within participating media
 - 8.5.1 Mean beam length method
 - 8.5.2 Diffusion approximation
 - 8.5.3 P-1 approximation
 - 8.5.4 Other RTE solution methods
 - 8.5.5 Weighted sum of gray gases
 - 8.5.6 Other spectral models

Nomenclature

References

8.1 FUNDAMENTALS

Radiative heat transfer or *thermal radiation* is the science of transferring energy in the form of electromagnetic waves. Unlike heat conduction, electromagnetic waves do not require a medium for their propagation. Therefore, because of their ability to travel across vacuum, thermal radiation becomes the dominant mode of heat transfer in low pressure (vacuum) and outer-space applications. Another distinguishing characteristic between conduction (and convection, if aided by flow) and thermal radiation is their temperature dependence. While conductive and convective fluxes are more or less linearly dependent on temperature differences, radiative heat fluxes tend to be proportional to differences in the fourth power of temperature (or even higher). For this reason, radiation tends to become the dominant mode of heat transfer in high-temperature applications, such as combustion (fires, furnaces, rocket nozzles), nuclear reactions (solar emission, nuclear weapons), and others.

All materials continuously emit and absorb electromagnetic waves, or photons, by changing their internal energy on a molecular level. Strength of emission and absorption of radiative energy depend on the temperature of the material, as well as on the wavelength λ , frequency ν , or wavenumber η , that characterizes the electromagnetic waves,

$$\lambda = \frac{c}{\nu} = \frac{1}{\eta} \quad (8.1)$$

where wavelength is usually measured in μm ($= 10^{-6} \text{ m}$), while frequency is measured in hertz = cycles/s), and wavenumbers are given in cm^{-1} . Electromagnetic waves or photons (which include what is perceived as “light”) travel at the *speed of light*, c . The speed of light depends on the medium through which the wave travels and is related to that in vacuum, c_0 , through the relation

$$c = \frac{c_0}{n} \quad c_0 = 2.998 \times 10^8 \text{ m/s} \quad (8.2)$$

where n is known as the *refractive index* of the medium. By definition, the refractive index of vacuum is $n \equiv 1$. For most gases the refractive index is very close to unity, and the c in eq. (8.1) can be replaced by c_0 . Each wave or photon carries with it an amount of energy ϵ determined from quantum mechanics as

$$\epsilon = h\nu \quad h = 6.626 \times 10^{-34} \text{ J} \cdot \text{s} \quad (8.3)$$

where h is known as *Planck's constant*. The frequency of light does not change when light penetrates from one medium to another because the energy of the photon must be conserved. On the other hand, the wavelength does change, depending on the values of the refractive index for the two media.

When an electromagnetic wave strikes an interface between two media, the wave is either reflected or transmitted. Most solid and liquid media absorb all incoming radiation over a very thin surface layer. Such materials are called *opaque* or *opaque surfaces* (even though absorption takes place over a thin layer). An opaque material that does not reflect any radiation at its surface is called a *perfect absorber*, *black surface*, or *blackbody*, because such a surface appears black to the human eye, which recognizes objects by visible radiation reflected off their surfaces.

8.1.1 Emissive Power

Every medium continuously emits electromagnetic radiation randomly into all directions at a rate depending on the local temperature and the properties of the material. The radiative heat flux emitted from a surface is called the *emissive power* E , and there is a distinction between *total* and *spectral emissive power* (heat flux emitted over the entire spectrum or at a given frequency per unit frequency interval), so that the spectral emissive power E_ν is the emitted energy/time/surface area/frequency, while the total emissive power E is emitted energy/time/surface area. Spectral and total emissive powers are related by

$$E(T) = \int_0^\infty E_\lambda(T, \lambda) d\lambda = \int_0^\infty E_\nu(T, \nu) d\nu \quad (8.4)$$

It is easy to show that a black surface is not only a perfect absorber, but it is also a perfect emitter, that is, the emission from such a surface exceeds that of any other surface at the same temperature (known as *Kirchhoff's law*). The emissive power leaving an opaque black surface, commonly called *blackbody emissive power*, can be determined from quantum statistics as

$$E_{b\lambda}(T, \lambda) = \frac{2\pi hc_0^2}{n^2 \lambda^5 (e^{hc_0/n\lambda kT} - 1)} \quad (n = \text{const}) \quad (8.5)$$

where it is assumed that the black surface is adjacent to a nonabsorbing medium of constant refractive index n . The constant $k = 1.3806 \times 10^{-23} \text{ J/K}$ is known as

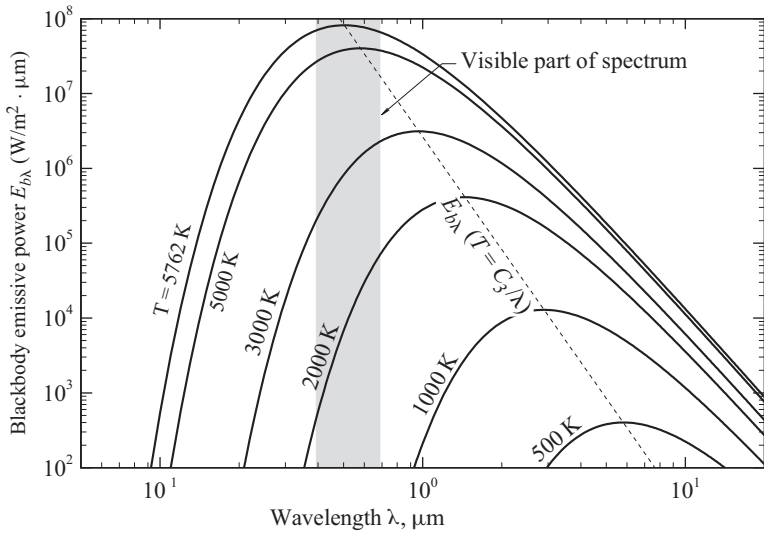


Figure 8.1 Blackbody emissive power spectrum.

Boltzmann's constant. The spectral dependence of the blackbody emissive power into vacuum ($n = 1$) is shown for a number of emitter temperatures in Fig. 8.1. It is seen that emission is zero at both extreme ends of the spectrum with a maximum at some intermediate wavelength. The general level of emission rises with temperature, and the important part of the spectrum (the part containing most of the emitted energy) shifts toward shorter wavelengths. Because emission from the sun ("solar spectrum") is well approximated by blackbody emission at an *effective solar temperature* of $T_{\text{sun}} = 5762$ K, this temperature level is also included in the figure. Heat transfer problems generally involve temperature levels between 300 and, say, 2000 K (plus, perhaps, solar radiation). Therefore, the spectral ranges of interest in heat transfer applications include the ultraviolet (0.1 to 0.4 μm), visible radiation (0.4 to 0.7 μm , as indicated in Figure 8.1 by shading), and the near- and mid-infrared (0.7 to 20 μm).

For quick evaluation, a scaled emissive power can be written as

$$\frac{E_{b\lambda}}{n^3 T^5} = \frac{C_1}{(n\lambda T)^5 (e^{C_2/n\lambda T} - 1)} \quad (n = \text{const}) \quad (8.6)$$

where

$$C_1 = 2\pi h c_0^2 = 3.7419 \times 10^{-16} \text{ W} \cdot \text{m}^2$$

$$C_2 = \frac{h c_0}{k} = 14,388 \mu\text{m} \cdot \text{K}$$

Equation (8.6) has its maximum at

$$(n\lambda T)_{\text{max}} = C_3 = 2898 \mu\text{m} \cdot \text{K} \quad (8.7)$$

which is known as *Wien's displacement law*. The constants C_1 , C_2 , and C_3 are known as the first, second, and third radiation constants, respectively.

The total blackbody emissive is found by integrating eq. (8.6) over the entire spectrum, resulting in

$$E_b(T) = n^2 \sigma T^4 \quad (8.8)$$

where $\sigma = 5.670 \times 10^{-8} \text{ W/m}^2 \cdot \text{K}^4$ is the *Stefan-Boltzmann constant*. It is often desirable to calculate fractional emissive powers, that is, the emissive power contained over a finite wavelength range, say between wavelengths λ_1 and λ_2 . It is not possible to integrate eq. (8.6) between these limits in closed form; instead, one resorts to tabulations of the fractional emissive power, contained between 0 and $n\lambda T$,

$$f(n\lambda T) = \frac{\int_0^\lambda \frac{E_{b\lambda}}{E_{b\lambda}} \frac{d\lambda}{b\lambda} = \int_0^{n\lambda T} \frac{E_{b\lambda}}{n^3 \sigma T^5} d(n\lambda T) \quad (8.9)$$

so that

$$\int_{\lambda_1}^{\lambda_2} E_{b\lambda} d\lambda = [f(n\lambda_2 T) - f(n\lambda_1 T)] n^2 \sigma T^4 \quad (8.10)$$

An extensive listing of $f(n\lambda T)$, as well as of the scaled emissive power, eq. (8.6), is given in Table 8.1. Both functions are also shown in Fig. 8.2, together with *Wien's distribution*, which is the short-wavelength limit of eq. (8.5),

$$E_{b\lambda} \simeq \frac{2\pi hc_0^2}{n^2 \lambda^5} e^{-hc_0/n\lambda kT} = \frac{C_1}{n^2 \lambda^5} e^{-C_2/n\lambda T} \quad \frac{hc_0}{n\lambda kT} \gg 1 \quad (8.11)$$

As seen from the figure, Wien's distribution is actually rather accurate over the entire spectrum, predicting a total emissive power approximately 8% lower than the one given by eq. (8.8). Because Wien's distribution can be integrated analytically over parts of the spectrum, it is sometimes used in heat transfer applications.

8.1.2 Solid Angles

Radiation is a directional phenomenon; that is, the radiative flux passing through a point generally varies with direction, such as the sun shining onto Earth from essentially a single direction. Consider an opaque surface element dA_i , as shown in Fig. 8.3. It is customary to describe the direction unit vector \hat{s} in terms of polar angle θ (measured from the surface normal \hat{n}) and azimuthal angle ψ (measured in the plane of the surface, between an arbitrary axis and the projection of \hat{s}); for a hemisphere $0 \leq \theta \leq \pi/2$ and $0 \leq \psi \leq 2\pi$.

The solid angle with which a surface A_j is seen from a certain point P (or dA_i in Fig. 8.3) is defined as the projection of the surface onto a plane normal to the direction vector, divided by the distance squared, as also shown in Fig. 8.3 for an infinitesimal

TABLE 8.1 Blackbody Emissive Power

$n\lambda T$ ($\mu\text{m} \cdot \text{K}$)	$E_{b\lambda}/n^3T^5$ ($\text{W}/\text{m}^2 \cdot \mu\text{m} \cdot \text{K}^5$) $\times 10^{-11}$	$f(n\lambda T)$	$n\lambda T$ ($\mu\text{m} \cdot \text{K}$)	$E_{b\lambda}/n^3T^5$ ($\text{W}/\text{m}^2 \cdot \mu\text{m} \cdot \text{K}^5$) $\times 10^{-11}$	$f(n\lambda T)$
1,000	0.02110	0.00032	5,600	0.56332	0.70101
1,100	0.04846	0.00091	5,700	0.54146	0.71076
1,200	0.09329	0.00213	5,800	0.52046	0.72012
1,300	0.15724	0.00432	5,900	0.50030	0.72913
1,400	0.23932	0.00779	6,000	0.48096	0.73778
1,500	0.33631	0.01285	6,100	0.46242	0.74610
1,600	0.44359	0.01972	6,200	0.44464	0.75410
1,700	0.55603	0.02853	6,300	0.42760	0.76180
1,800	0.66872	0.03934	6,400	0.41128	0.76920
1,900	0.77736	0.05210	6,500	0.39564	0.77631
2,000	0.87858	0.06672	6,600	0.38066	0.78316
2,100	0.96994	0.08305	6,700	0.36631	0.78975
2,200	1.04990	0.10088	6,800	0.35256	0.79609
2,300	1.11768	0.12002	6,900	0.33940	0.80219
2,400	1.17314	0.14025	7,000	0.32679	0.80807
2,500	1.21659	0.16135	7,100	0.31471	0.81373
2,600	1.24868	0.18311	7,200	0.30315	0.81918
2,700	1.27029	0.20535	7,300	0.29207	0.82443
2,800	1.28242	0.22788	7,400	0.28146	0.82949
2,900	1.28612	0.25055	7,500	0.27129	0.83436
3,000	1.28245	0.27322	7,600	0.26155	0.83906
3,100	1.27242	0.29576	7,700	0.25221	0.84359
3,200	1.25702	0.31809	7,800	0.24326	0.84796
3,300	1.23711	0.34009	7,900	0.23468	0.85218
3,400	1.21352	0.36172	8,000	0.22646	0.85625
3,500	1.18695	0.38290	8,200	0.21101	0.86396
3,600	1.15806	0.40359	8,400	0.19679	0.87115
3,700	1.12739	0.42375	8,600	0.18370	0.87786
3,800	1.09544	0.44336	8,800	0.17164	0.88413
3,900	1.06261	0.46240	9,000	0.16051	0.88999
4,000	1.02927	0.48085	9,200	0.15024	0.89547
4,100	0.99571	0.49872	9,400	0.14075	0.90060
4,200	0.96220	0.51599	9,600	0.13197	0.90541
4,300	0.92892	0.53267	9,800	0.12384	0.90992
4,400	0.89607	0.54877	10,000	0.11632	0.91415
4,500	0.86376	0.56429	10,200	0.10934	0.91813
4,600	0.83212	0.57925	10,400	0.10287	0.92188
4,700	0.80124	0.59366	10,600	0.09685	0.92540
4,800	0.77117	0.60753	10,800	0.09126	0.92872
4,900	0.74197	0.62088	11,000	0.08606	0.93184
5,000	0.71366	0.63372	11,200	0.08121	0.93479
5,100	0.68628	0.64606	11,400	0.07670	0.93758
5,200	0.65983	0.65794	11,600	0.07249	0.94021
5,300	0.63432	0.66935	11,800	0.06856	0.94270
5,400	0.60974	0.68033	12,000	0.06488	0.94505
5,500	0.58608	0.69087			(continued)

TABLE 8.1 Blackbody Emissive Power (*Continued*)

$n\lambda T$ ($\mu\text{m} \cdot \text{K}$)	$E_{b\lambda}/n^3T^5$ ($\text{W}/\text{m}^2 \cdot \mu\text{m} \cdot \text{K}^5$) $\times 10^{-11}$	$f(n\lambda T)$	$n\lambda T$ ($\mu\text{m} \cdot \text{K}$)	$E_{b\lambda}/n^3T^5$ ($\text{W}/\text{m}^2 \cdot \mu\text{m} \cdot \text{K}^5$) $\times 10^{-11}$	$f(n\lambda T)$
12,200	0.06145	0.94728	19,200	0.01285	0.98387
12,400	0.05823	0.94939	19,400	0.01238	0.98431
12,600	0.05522	0.95139	19,600	0.01193	0.98474
12,800	0.05240	0.95329	19,800	0.01151	0.98515
13,000	0.04976	0.95509	20,000	0.01110	0.98555
13,200	0.04728	0.95680	21,000	0.00931	0.98735
13,400	0.04494	0.95843	22,000	0.00786	0.98886
13,600	0.04275	0.95998	23,000	0.00669	0.99014
13,800	0.04069	0.96145	24,000	0.00572	0.99123
14,000	0.03875	0.96285	25,000	0.00492	0.99217
14,200	0.03693	0.96418	26,000	0.00426	0.99297
14,400	0.03520	0.96546	27,000	0.00370	0.99367
14,600	0.03358	0.96667	28,000	0.00324	0.99429
14,800	0.03205	0.96783	29,000	0.00284	0.99482
15,000	0.03060	0.96893	30,000	0.00250	0.99529
15,200	0.02923	0.96999	31,000	0.00221	0.99571
15,400	0.02794	0.97100	32,000	0.00196	0.99607
15,600	0.02672	0.97196	33,000	0.00175	0.99640
15,800	0.02556	0.97288	34,000	0.00156	0.99669
16,000	0.02447	0.97377	35,000	0.00140	0.99695
16,200	0.02343	0.97461	36,000	0.00126	0.99719
16,400	0.02245	0.97542	37,000	0.00113	0.99740
16,600	0.02152	0.97620	38,000	0.00103	0.99759
16,800	0.02063	0.97694	39,000	0.00093	0.99776
17,000	0.01979	0.97765	40,000	0.00084	0.99792
17,200	0.01899	0.97834	41,000	0.00077	0.99806
17,400	0.01823	0.97899	42,000	0.00070	0.99819
17,600	0.01751	0.97962	43,000	0.00064	0.99831
17,800	0.01682	0.98023	44,000	0.00059	0.99842
18,000	0.01617	0.98081	45,000	0.00054	0.99851
18,200	0.01555	0.98137	46,000	0.00049	0.99861
18,400	0.01496	0.98191	47,000	0.00046	0.99869
18,600	0.01439	0.98243	48,000	0.00042	0.99877
18,800	0.01385	0.98293	49,000	0.00039	0.99884
19,000	0.01334	0.98340	50,000	0.00036	0.99890

element dA_j . If the surface is projected onto a unit sphere above point P , the solid angle becomes equal to the projected area, or

$$\Omega = \int_{A_{jp}} \frac{dA_{jp}}{S^2} = \int_{A_j} \frac{\cos \theta_0 dA_j}{S^2} = A''_{jp} \quad (8.12)$$

where S is the distance between P and dA_j . Thus, an infinitesimal solid angle is simply an infinitesimal area on a unit sphere, or

$$d\Omega = dA''_{jp} = (1 \times \sin \theta \, d\psi)(1 \times d\theta) = \sin \theta \, d\theta \, d\psi \tag{8.13}$$

Integrating over all possible directions yields

$$\int_{\psi=0}^{2\pi} \int_{\theta=0}^{\pi/2} \sin \theta \, d\theta \, d\psi = 2\pi \tag{8.14}$$

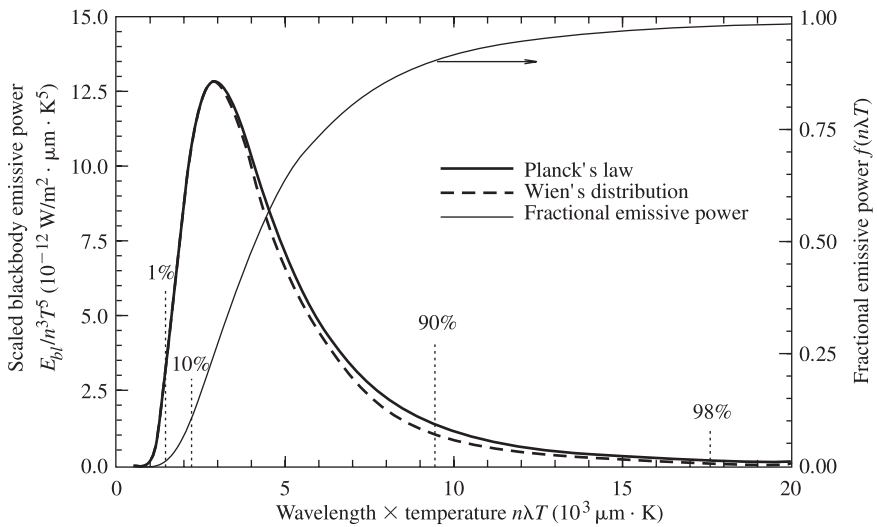


Figure 8.2 Normalized blackbody emissive power spectrum.

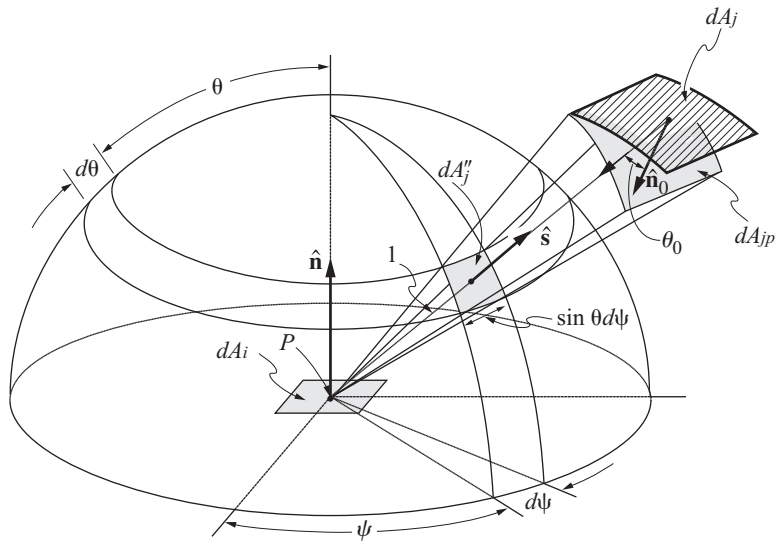


Figure 8.3 Definitions of direction vectors and solid angles.

for the total solid angle above the surface. If a point inside a medium removed from the surface is considered, radiation passing through that point can strike any point of an imaginary unit sphere surrounding it; that is, the total solid angle here is 4π , with $0 \leq \theta \leq \pi$, $0 \leq \psi \leq 2\pi$. Similarly, at a surface one can talk about an upper hemisphere (outgoing directions, $0 \leq \theta < \pi/2$), and a lower hemisphere (incoming directions, $\pi/2 < \theta \leq \pi$).

8.1.3 Radiative Intensity

The directional behavior of radiative energy traveling through a medium is characterized by the radiative intensity I , which is defined as

$I \equiv \text{radiative energy flow/time/area normal to the rays/solid angle}$

Like emissive power, intensity is defined on both spectral and total bases, related by

$$I(\hat{\mathbf{s}}) = \int_0^\infty I_\lambda(\hat{\mathbf{s}}, \lambda) d\lambda \quad (8.15)$$

However, unlike emissive power, which depends only on position (and wavelength), the radiative intensity depends, in addition, on the direction vector $\hat{\mathbf{s}}$. Emissive power can be related to emitted intensity by integrating this intensity over the 2π solid angles above a surface, and then realizing that the projection of dA normal to the rays is $dA \cos \theta$. Thus,

$$E(\mathbf{r}) = \int_0^{2\pi} \int_0^{\pi/2} I(\mathbf{r}, \theta, \psi) \cos \theta \sin \theta d\theta d\psi = \int_{2\pi} I(\mathbf{r}, \hat{\mathbf{s}}) \hat{\mathbf{n}} \cdot \hat{\mathbf{s}} d\Omega \quad (8.16)$$

which is, of course, also valid on a spectral basis. For a black surface it is readily shown, through a variation of Kirchhoff's law, that $I_{b\lambda}$ is independent of direction, or

$$I_{b\lambda} = I_{b\lambda}(T, \lambda) \quad (8.17)$$

Using this relation in eq. (8.16), it is observed that the intensity leaving a blackbody (or any surface whose outgoing intensity is independent of direction, or *diffuse*) may be evaluated from the blackbody emissive power (or outgoing heat flux) as

$$I_{b\lambda}(\mathbf{r}, \lambda) = \frac{E_{b\lambda}(\mathbf{r}, \lambda)}{\pi} \quad (8.18)$$

In the literature the spectral blackbody intensity is sometimes referred to as the *Planck function*.

8.1.4 Radiative Heat Flux

Emissive power is the total radiative energy streaming away from a surface due to emission. Therefore, it is a radiative flux, but not the net radiative flux at the surface,

because it only accounts for emission and not for incoming radiation and reflected radiation. Extending the definition of eq. (8.16) gives

$$(q_\lambda)_{\text{out}} = \int_{\cos \theta > 0} I_\lambda(\hat{\mathbf{s}}) \cos \theta \, d\Omega \geq 0 \quad (8.19)$$

where $I_\lambda(\theta)$ is now *outgoing* intensity (due to emission plus reflection). Similarly, for incoming directions ($\pi/2 < \theta \leq \pi$),

$$(q_\lambda)_{\text{in}} = \int_{\cos \theta < 0} I_\lambda(\hat{\mathbf{s}}) \cos \theta \, d\Omega < 0 \quad (8.20)$$

Combining the incoming and outgoing contributions, the net radiative flux at a surface is

$$(q_\lambda)_{\text{net}} = \mathbf{q}_\lambda \cdot \hat{\mathbf{n}} = (q_\lambda)_{\text{in}} + (q_\lambda)_{\text{out}} = \int_{4\pi} I_\lambda(\hat{\mathbf{s}}) \cos \theta \, d\Omega \quad (8.21)$$

The total radiative flux, finally, is obtained by integrating eq. (8.21) over the entire spectrum, or

$$\mathbf{q} \cdot \hat{\mathbf{n}} = \int_0^\infty \mathbf{q}_\lambda \cdot \hat{\mathbf{n}} \, d\lambda = \int_0^\infty \int_{4\pi} I_\lambda(\hat{\mathbf{s}}) \hat{\mathbf{n}} \cdot \hat{\mathbf{s}} \, d\Omega \, d\lambda \quad (8.22)$$

Of course, the surface described by the unit vector $\hat{\mathbf{n}}$ may be an imaginary one (located somewhere inside a radiating medium). Thus, removing the $\hat{\mathbf{n}}$ from eq. (8.22) gives the definition of the radiative heat flux vector inside a participating medium:

$$\mathbf{q} = \int_0^\infty \mathbf{q}_\lambda \, d\lambda = \int_0^\infty \int_{4\pi} I_\lambda(\hat{\mathbf{s}}) \hat{\mathbf{s}} \, d\Omega \, d\lambda \quad (8.23)$$

8.2 RADIATIVE PROPERTIES OF SOLIDS AND LIQUIDS

Because radiative energy arriving at a given point in space can originate from a point far away, without interacting with the medium in between, a *conservation of energy* balance must be performed on an *enclosure* bounded by *opaque walls* (i.e., a medium thick enough that no electromagnetic waves can penetrate through it). Strictly speaking, the surface of an enclosure wall can only reflect radiative energy or allow a part of it to penetrate into the substrate. A surface cannot absorb or emit photons: Attenuation takes place inside the solid, as does emission of radiative energy (and some of the emitted energy escapes through the surface into the enclosure). In practical systems the thickness of the surface layer over which absorption of irradiation from inside the enclosure occurs is very small compared with the overall dimensions of an enclosure—usually, a few angstroms for metals and a few micrometers for most non-metals. The same may be said about emission from within the walls that escapes into

the enclosure. Thus, in the case of opaque walls it is customary to speak of absorption by and emission from a “surface,” although a thin surface layer is implied.

If radiation impinging on a solid or liquid layer is considered, a fraction of the energy will be reflected (*reflectance* ρ , often also referred to as *reflectivity*), another fraction will be absorbed (*absorptance* α , often also referred to as *absorptivity*), and if the layer is thin enough, a fraction may be transmitted (*transmittance* τ , often also referred to as *transmissivity*). Because all radiation must be either reflected, absorbed, or transmitted,

$$\rho + \alpha + \tau = 1 \quad (8.24)$$

If the medium is sufficiently thick to be *opaque*, then $\tau = 0$ and

$$\rho + \alpha = 1 \quad (8.25)$$

All surfaces also emit thermal radiation (or, rather, radiative energy is emitted within the medium, some of which escapes from the surface). The *emittance* ϵ is defined as the ratio of energy emitted by a surface as compared to that of a black surface at the same temperature (the theoretical maximum).

All of these four properties may vary in magnitude between the values 0 and 1; for a black surface, which absorbs all incoming radiation and emits the maximum possible, $\alpha = \epsilon = 1$ and $\rho = \tau = 0$. They may also be functions of temperature as well as wavelength and direction (incoming and/or outgoing). One distinguishes between spectral and total properties (an average value over the spectrum) and also between directional and hemispherical properties (an average value over all directions).

It may be shown (through another variation of *Kirchhoff's law*) that, at least on a spectral, directional basis,

$$\alpha(T, \lambda, \hat{s}) = \epsilon(T, \lambda, \hat{s}) \quad (8.26)$$

This is also true for hemispherical values if either the directional emittance or the incoming radiation are *diffuse* (they do not depend on direction). It is also true for total values if either the spectral emittance does not depend on wavelength or if the spectral behavior of the incoming radiation is similar to blackbody radiation at the same temperature.

Typical directional behavior is shown in Fig. 8.4*a* (for nonmetals) and *b* (metals). In these figures the total, directional emittance, a value averaged over all wavelengths, is shown. For nonmetals the directional emittance varies little over a large range of polar angles but decreases rapidly at grazing angles until a value of zero is reached at $\theta = \pi/2$. Similar trends hold for metals, except that at grazing angles, the emittance first increases sharply before dropping back to zero (not shown). Note that emittance levels are considerably higher for nonmetals.

A surface whose emittance is the same for all directions is called a *diffuse* emitter, or a *Lambert surface*. No real surface can be a diffuse emitter because *electromagnetic wave theory* predicts a zero emittance at $\theta = \pi/2$ for all materials. However,

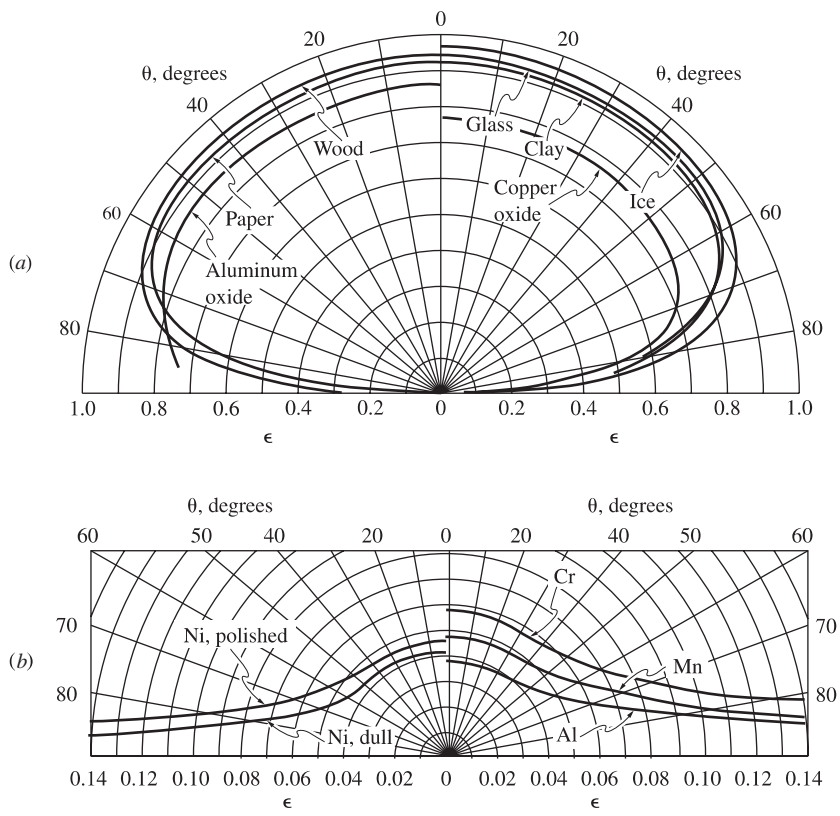


Figure 8.4 Directional variation of surface emittances: (a) for several nonmetals; (b) for several metals. (From Schmidt and Eckert, 1935.)

little energy is emitted into grazing directions, as seen from eq. (8.16), so that the assumption of diffuse emission is often a good one.

Typical spectral behavior of surface emittances is shown in Fig. 8.5 for a few materials, as collected by White (1984). Shown are values for directional emittances in the direction normal to the surface. However, the spectral behavior is the same for *hemispherical emittances*. In general, nonmetals have relatively high emittances, which may vary erratically across the spectrum, and metals behave similarly for short wavelengths but tend to have lower emittances with more regular spectral dependence in the infrared.

Mathematically, the *spectral, hemispherical emittance* is defined in terms of emissive power as

$$\epsilon_{\lambda}(T, \lambda) \equiv \frac{E_{\lambda}(T, \lambda)}{E_{b\lambda}(T, \lambda)} \quad (8.27)$$

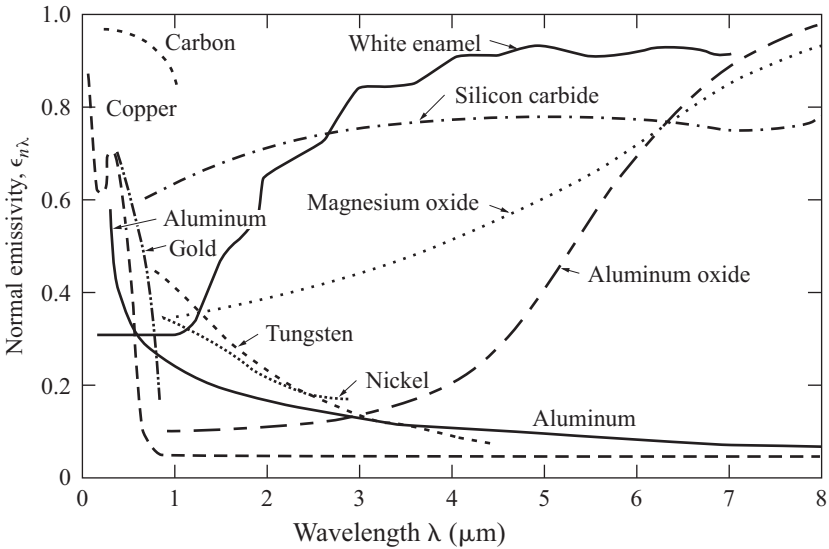


Figure 8.5 Normal, spectral emittances for selected materials. (From White, 1984.)

This property may be extracted from the *spectral, directional emittance* ϵ'_λ by integrating over all directions,

$$\begin{aligned}\epsilon_\lambda(T, \lambda) &= \frac{1}{\pi} \iint \epsilon'_\lambda(T, \lambda, \theta, \psi) \cos \theta \, d\Omega \\ &= \frac{1}{\pi} \int_0^{2\pi} \int_0^{\pi/2} \epsilon'_\lambda(T, \lambda, \theta, \psi) \cos \theta \sin \theta \, d\theta \, d\psi\end{aligned}\quad (8.28)$$

and finally, the *total, hemispherical emittance* may be related to the spectral hemispherical emittance through

$$\epsilon(T) = \frac{E(T)}{E_b(T)} = \frac{\int_0^\infty E_\lambda(T, \lambda) \, d\lambda}{E_b(T)} = \frac{1}{n^2 \sigma T^4} \int_0^\infty \epsilon_\lambda(T, \lambda) E_{b\lambda}(T, \lambda) \, d\lambda \quad (8.29)$$

Here a prime and subscript λ have been added temporarily to distinguish directional from hemispherical properties, and spectral from total (spectrally averaged) values. If the spectral emittance is the same for all wavelengths, eq. (8.29) reduces to

$$\epsilon(T) = \epsilon_\lambda(T) \quad (8.30)$$

Such surfaces are termed *gray*, and for the very special case of a *gray, diffuse surface*, this implies that

$$\epsilon(T) = \epsilon_\lambda = \epsilon' = \epsilon'_\lambda \quad (8.31)$$

Although no real surface is truly gray, it often happens that ϵ_λ is relatively constant over that part of the spectrum where $E_{b\lambda}$ is substantial, making the simplifying assumption of a gray surface warranted.

8.2.1 Radiative Properties of Metals

Wavelength Dependence Electromagnetic theory states that the radiative properties of interfaces are strong functions of the material's electrical conductivity. Metals are generally excellent electrical conductors because of an abundance of free electrons. For materials with large electrical conductivity, both the real and imaginary parts of the complex index of refraction, $m = n - ik$ ($t = \sqrt{-1}$), become large and approximately equal for long wavelengths, say $\lambda > 1 \mu\text{m}$, leading to an approximate relation for the normal, spectral emittance of the metal, known as the *Hagen–Rubens relation* (Modest, 2003),

$$\epsilon_{n\lambda} \simeq \frac{2}{n} \simeq \frac{2}{\sqrt{0.003\lambda\sigma_{\text{dc}}}} = 1 - \rho_{n\lambda} \quad \lambda \text{ in } \mu\text{m}, \quad \sigma_{\text{dc}} \text{ in } \Omega^{-1} \cdot \text{cm}^{-1} \quad (8.32)$$

where σ_{dc} is the dc conductivity of the material. Equation (8.32) indicates that for clean, polished metallic surfaces the normal emittance can be expected to be small, and the reflectance large (using typical values for conductivity, σ_{dc}), with a $1/\sqrt{\lambda}$ wavelength dependence. Comparison with experiment has shown that for sufficiently long wavelengths, the Hagen–Rubens relationship describes the radiative properties of polished (not entirely smooth) metals rather well, in contrast to the older, more sophisticated *Drude theory* (Modest, 2003). However, for optically smooth metallic surfaces (such as vapor-deposited layers on glass), radiative properties closely obey electromagnetic wave theory, and it is the Drude theory that gives excellent results.

Directional Dependence The spectral, directional reflectance for an optically smooth interface is given by *Fresnel's relations* (Modest, 2003). As noted before, in the infrared, n and k are generally fairly large for metals, and Fresnel's relations simplify to

$$\rho_{\parallel} = \frac{(n \cos \theta - 1)^2 + (k \cos \theta)^2}{(n \cos \theta + 1)^2 + (k \cos \theta)^2} \quad (8.33a)$$

$$\rho_{\perp} = \frac{(n - \cos \theta)^2 + k^2}{(n + \cos \theta)^2 + k^2} \quad (8.33b)$$

Here ρ_{\parallel} is the spectral reflectance for parallel-polarized radiation, which refers to electromagnetic waves whose oscillations take place in a plane formed by the surface normal and the direction of incidence. Similarly, ρ_{\perp} is the spectral reflectance for perpendicular-polarized radiation, which refers to waves oscillating in a plane normal to the direction of incidence. In all engineering applications (except lasers), radiation consists of many randomly oriented waves (randomly polarized or unpolarized), and the spectral, directional emittance and reflectance can be evaluated from

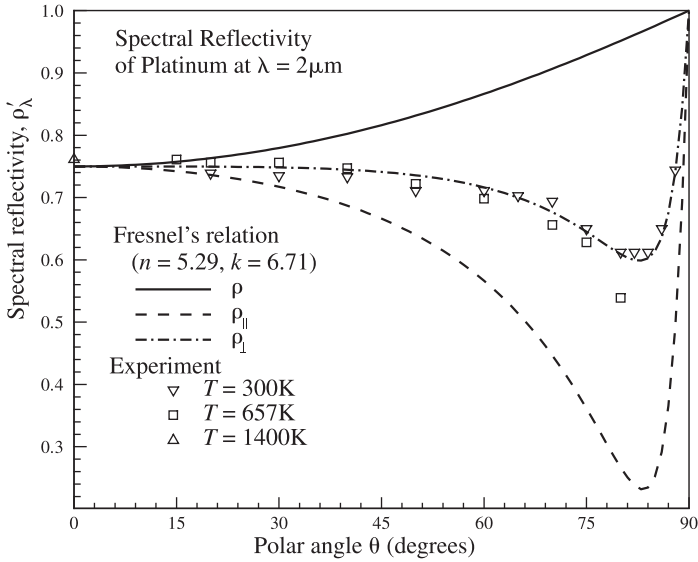


Figure 8.6 Spectral, directional reflectance of platinum at $\lambda = 2\mu\text{m}$.

$$\epsilon'_{\lambda} = 1 - \rho'_{\lambda} = 1 - \frac{1}{2} (\rho_{||} + \rho_{\perp}) \quad (8.34)$$

The directional behavior for the reflectance of polished platinum at $\lambda = 2\mu\text{m}$ is shown in Fig. 8.6 and is also compared with experiment (Brandenberg, 1963; Brandenberg and Clausen, 1965; Price, 1947). As already seen from Fig. 8.4, reflectance is large for near-normal incidence, and the unpolarized reflectance remains fairly constant with increasing θ . However, near grazing angles of $\theta \simeq 80\text{--}85^\circ$, the parallel-polarized component undergoes a sharp dip before going to $\rho_{||} = \rho_{\perp} = 1$ at $\theta = 90^\circ$. This behavior is responsible for the lobe of strong emittance near grazing angles commonly observed for metals. Fortunately, these near-grazing angles are fairly unimportant in the evaluation of radiative fluxes, due to the $\cos \theta$ in eq. (8.21); that is, even metals can usually be treated as “diffuse emitters” with good accuracy. It needs to be emphasized that the foregoing discussion is valid only for relatively long wavelengths (infrared). For shorter wavelengths, particularly the visible, the assumption of large values for n and k generally breaks down, and the directional behavior of metals resembles that of nonconductors (discussed in the next section).

Hemispherical Properties Equation (8.33) may be integrated analytically over all directions to obtain the spectral, hemispherical emittance. Figure 8.7 is a plot of the ratio of the hemispherical and normal emittances, $\epsilon_{\lambda}/\epsilon_{n\lambda}$. For the case of $k/n = 1$ the dashed line represents results from integrating equation (8.33), while the solid lines were obtained by numerically integrating the exact form of Fresnel's relations. For most metals $k > n > 3$, so that, as shown in Fig. 8.7, the hemispherical emittance is

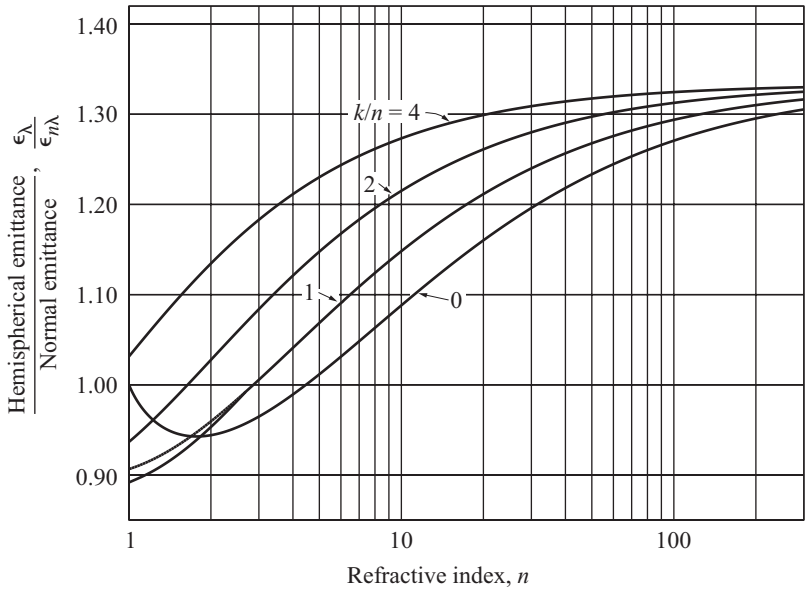


Figure 8.7 Ratio of hemispherical and normal spectral emittance for electrical conductors as a function of n and k . (From Dunkle, 1965.)

larger than the normal value, due to the strong emission lobe at near grazing angles. Again, this statement holds only for relatively long wavelengths.

Total Properties Equation (8.32) may be integrated over the spectrum, using eq. (8.29), and applying the correction given in Fig. 8.7 to convert normal emittance to hemispherical emittance. This leads to an approximate expression for the *total, hemispherical emittance* of a metal,

$$\epsilon(T) = 0.766 \left(\frac{T}{\sigma_{dc}} \right)^{1/2} - \left[0.309 - 0.0889 \ln \frac{T}{\sigma_{dc}} \right] \frac{T}{\sigma_{dc}} \quad (8.35)$$

where T is in K and σ_{dc} is in $\Omega^{-1} \cdot \text{cm}^{-1}$.

Because eq. (8.35) is based on the Hagen–Rubens relation, this expression is valid only for relatively low temperatures (where most of the blackbody emissive power lies in the long wavelengths; see Fig. 8.1). Figure 8.8 shows that eq. (8.35) does an excellent job predicting the total hemispherical emittances of polished metals as compared with experiment (Parker and Abbott, 1965), and that emittance is essentially linearly proportional to $(T/\sigma_{dc})^{1/2}$.

Surface Temperature Effects The Hagen–Rubens relation, eq. (8.32), predicts that the spectral, normal emittance of a metal should be proportional to $1/\sqrt{\sigma_{dc}}$. Because the electrical conductivity of metals is approximately inversely proportional

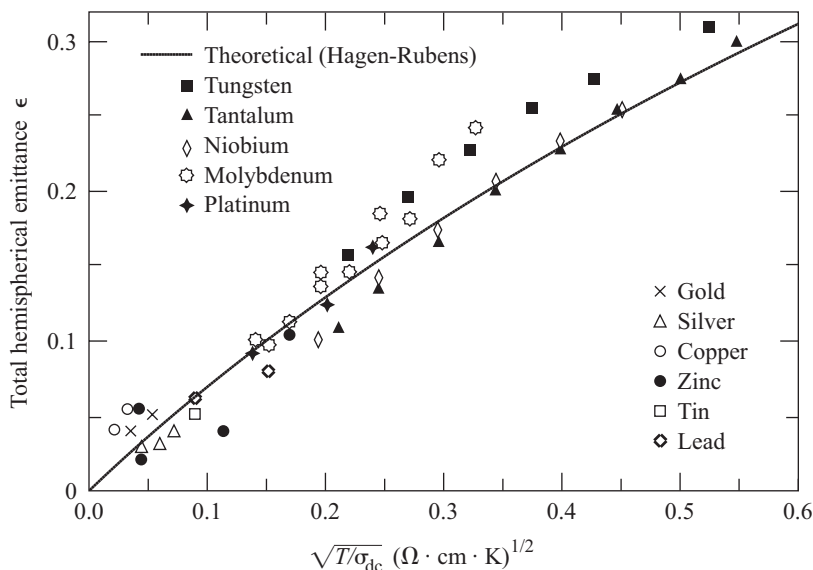


Figure 8.8 Total, hemispherical emittance of various polished metals as a function of temperature. (From Parker and Abbott, 1965.)

to temperature, the spectral emittance should therefore be proportional to the square root of absolute temperature for long enough wavelengths. This trend should also hold for the spectral, hemispherical emittance. Experiments have shown that this is indeed true for many metals. A typical example is given in Fig. 8.9, which shows the spectral dependence of the hemispherical emittance for tungsten for a number of temperatures. Note that the emittance for tungsten tends to increase with temperature beyond a *crossover wavelength* of approximately $1.3 \mu\text{m}$, while the temperature dependence is reversed for shorter wavelengths. Similar trends of a single crossover wavelength have been observed for many metals. Because the crossover wavelength is fairly short for many metals, the Hagen–Ruben temperature relation often holds for surprisingly high temperatures.

8.2.2 Radiative Properties of Nonconductors

Electrical nonconductors have few free electrons and thus do not display high reflectance/opacity behavior across the infrared as do metals.

Wavelength Dependence Reflection of light by insulators and semiconductors tends to be a strong, sometimes erratic function of wavelength. Crystalline solids generally have strong absorption–reflection bands (large k) in the infrared commonly known as *Reststrahlen bands*, which are due to transitions of intermolecular vibrations. These materials also have strong bands at short wavelengths (visible to ultraviolet), due to electronic energy transitions. In between these two spectral regions there

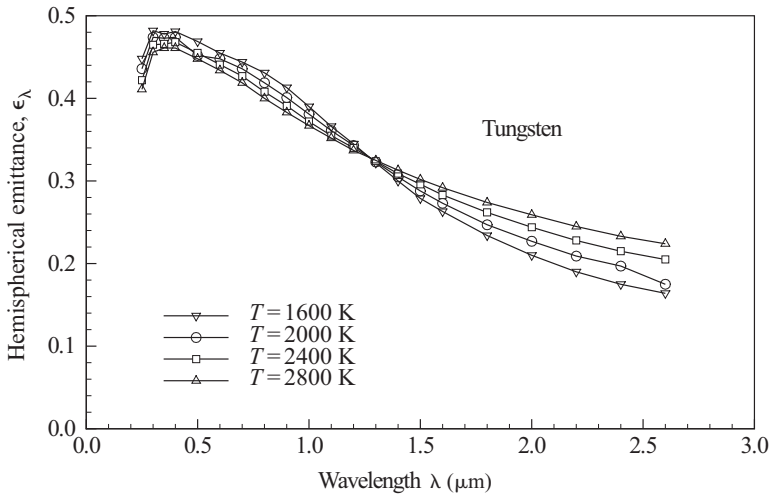


Figure 8.9 Temperature dependence of the spectral, hemispherical emittance of tungsten. (From Weast, 1988.)

generally is a region of fairly high transparency (and low reflectance), where absorption is dominated by impurities and imperfections in the crystal lattice. As such, these spectral regions often show irregular and erratic behavior. Defects and impurities may vary appreciably from specimen to specimen and even between different points on the same sample. As an example, the spectral, normal reflectance of silicon at room temperature is shown in Fig. 8.10. The strong influence of different types and levels of impurities is clearly evident. Therefore, looking up properties for a given material in published tables is problematical unless a detailed description of surface and material preparation is given.

In spectral regions outside Reststrahlen and electronic transition bands the absorptive index of a nonconductor is very small; typically, $k < 10^{-6}$ for a pure substance. While impurities and lattice defects can increase the value of k , one is very unlikely to find values of $k > 10^{-2}$ for a nonconductor outside the Reststrahlen bands. This implies that Fresnel's relations can be simplified significantly, and the spectral, normal reflectance may be evaluated as

$$\rho_{n\lambda} = \left(\frac{n - 1}{n + 1} \right)^2 \tag{8.36}$$

Therefore, for optically smooth nonconductors the radiative properties may be calculated from refractive index data. Refractive indices for a number of semitransparent materials at room temperature are displayed in Fig. 8.11 as a function of wavelength. All of these crystalline materials show similar spectral behavior: the refractive index drops rapidly in the visible region, then is nearly constant (declining very gradually) until the midinfrared, where n again starts to drop rapidly. This behavior is explained

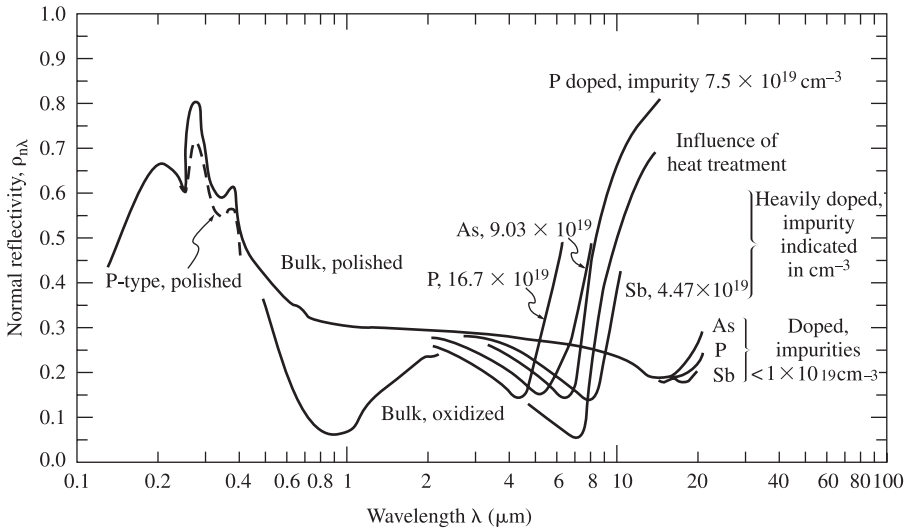


Figure 8.10 Spectral, normal reflectance of silicon at room temperature. (Redrawn from the data of Touloukian and DeWitt, 1972.)

by the fact that crystalline solids tend to have an absorption band due to electronic transitions near the visible and a Reststrahlen band in the infrared: The first drop in n is due to the tail end of the electronic band; the second drop in the midinfrared is due to the beginning of a Reststrahlen band.

Directional Dependence For optically smooth nonconductors, for the spectral region between absorption–reflection bands, experiment has been found to closely follow Fresnel’s equations of electromagnetic wave theory. Figure 8.12 shows a comparison between theory and experiment for the directional reflectance of glass (blackened on one side to avoid multiple reflections) for polarized, monochromatic irradiation. Because $k^2 \ll n^2$, the absorptive index may be eliminated from Fresnel’s relations, and the relations for a perfect dielectric become valid. For unpolarized light incident from vacuum (or a gas), this leads to

$$\epsilon'_\lambda = 1 - \frac{1}{2} (\rho_\parallel + \rho_\perp) = 1 - \frac{1}{2} \left[\left(\frac{n^2 \cos \theta - \sqrt{n^2 - \sin^2 \theta}}{n^2 \cos \theta + \sqrt{n^2 - \sin^2 \theta}} \right)^2 + \left(\frac{\cos \theta - \sqrt{n^2 - \sin^2 \theta}}{\cos \theta + \sqrt{n^2 - \sin^2 \theta}} \right)^2 \right] \quad (8.37)$$

Comparison with experiment agrees well with electromagnetic wave theory for a large number of nonconductors.

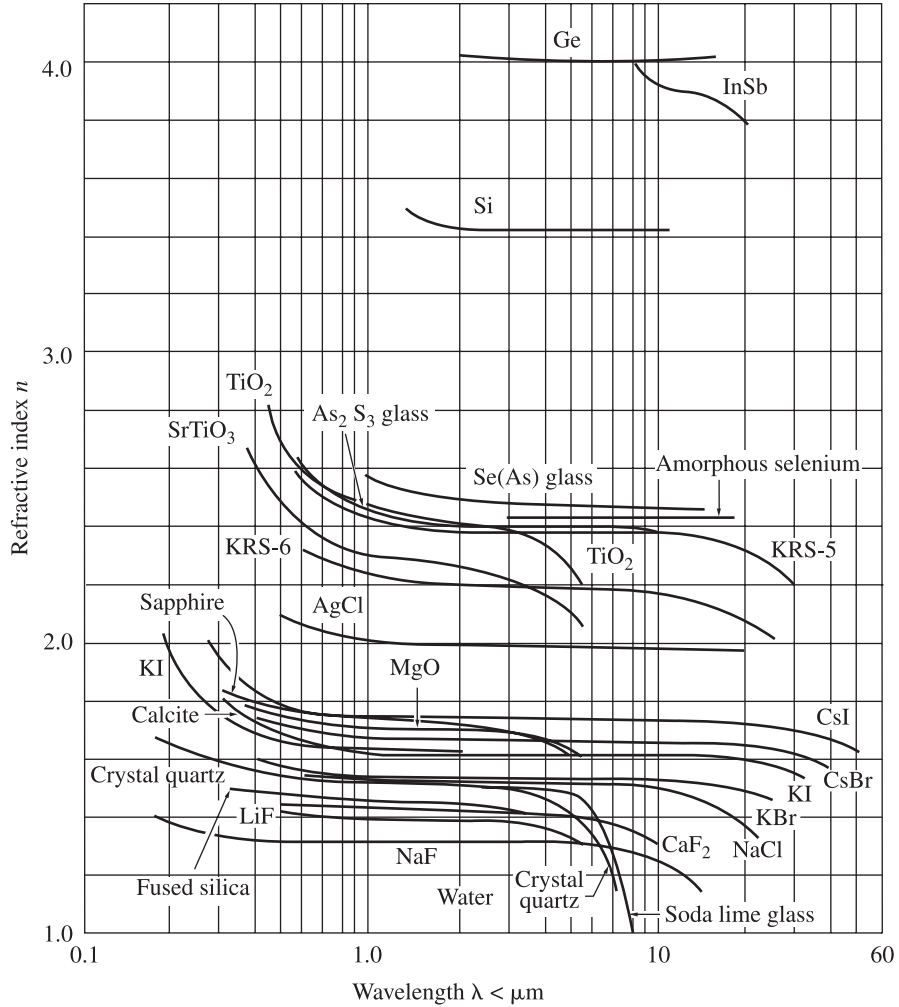


Figure 8.11 Refractive indices for various semitransparent materials. (From American Institute of Physics, 1972.)

Temperature Dependence The temperature dependence of the radiative properties of nonconductors is considerably more difficult to quantify than for metals. Infrared absorption bands in ionic solids due to excitation of lattice vibrations (Reststrahlen bands) generally increase in width and decrease in strength with temperature, and the wavelength of peak reflection-absorption shifts toward higher values. The reflectance for shorter wavelengths depends largely on the material's impurities. Often, the behavior is similar to that of metals, that is, the emittance increases with temperature for the near infrared while it decreases with shorter wavelengths. On the

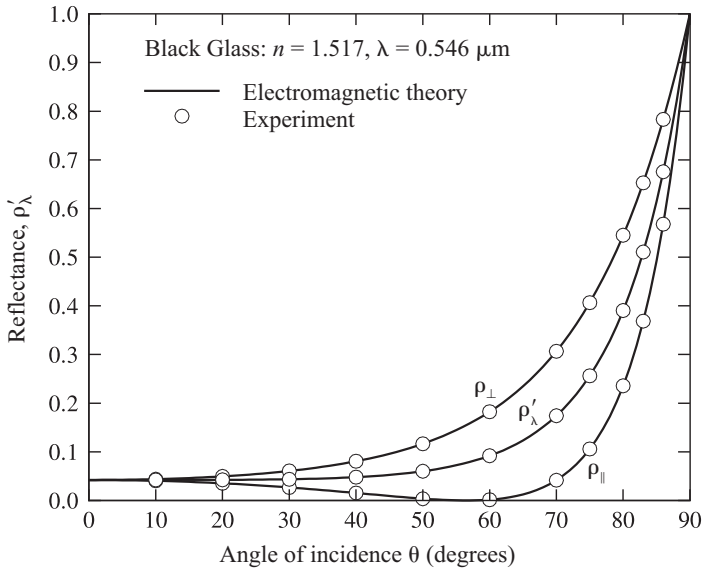


Figure 8.12 Spectral, directional reflectance of blackened glass at room temperature. (From Brandenburg, 1963.)

other hand, the emittance of amorphous solids (solids without a crystal lattice) tends to be independent of temperature.

8.2.3 Effects of Surface Conditions

Up to this point, the present discussion of radiative properties has assumed that the material is pure and homogeneous, and that its surface is isotropic and optically smooth. Very few real material surfaces come close to this idealization. In usually hostile industrial environments, even an initially ideal material will have its surface composition and quality altered: Heating of the material may be accompanied by strong oxidation or other chemical reaction, producing an opaque surface layer of a material quite different from the substrate. Similar statements can be made about materials exposed to corrosive atmospheres for extended periods of time. In addition, very few surfaces have an optically smooth finish when new; exposing them to heat and/or corrosive atmospheres is generally accompanied by further roughening of the surface finish.

Surface Roughness A surface is *optically smooth* if the average length scale of surface roughness is much less than the wavelength of the electromagnetic wave. Therefore, a surface that appears rough in visible light ($\lambda \simeq 0.5 \mu\text{m}$) may well be optically smooth in the intermediate infrared ($\lambda \simeq 50 \mu\text{m}$). This difference is the primary reason why results from electromagnetic wave theory cease to be valid for very short wavelengths.

The character of roughness may be very different from surface to surface, depending on the material, method of manufacture, and surface preparation, and classification of this character is difficult. A common measure of surface roughness is given by the root-mean-square (rms) roughness, σ_m . The rms roughness can be measured readily with a profilometer (a sharp stylus that traverses the surface, recording the height fluctuations). Unfortunately, σ_m alone is woefully inadequate to describe the roughness of a surface. Surfaces of identical σ_m may have vastly different frequencies of roughness peaks, as well as different peak-to-valley lengths; in addition, σ_m gives no information on second-order (or higher) roughness superimposed onto the fundamental roughness.

In general terms it may be stated that surfaces will become less reflective, and the behavior of reflection will become less specular and more diffuse as surface roughness increases. This behavior may be explained through geometric optics by realizing that, for a rough surface, incoming radiation hitting the surface may undergo two or more reflections off local peaks and valleys (resulting in increased absorption), after which it leaves the surface into an off-specular direction. Simple models predict sharp reflection peaks in the specular direction, and lesser reflection into other directions, with the strength of the peak depending on the surface roughness. This was also found to be true experimentally for most cases as long as the incidence angle was not too large. For large off-normal angles of incidence, experiment has shown that the reflectance has its peak at polar angles greater than the specular direction, and for larger incidence angles, rough surfaces tend to display off-specular peaks, apparently due to shadowing of parts of the surface by adjacent peaks.

Surface Layers and Oxide Films Even optically smooth surfaces have a surface structure that is different from the bulk material, due to either surface damage or the presence of thin layers of foreign materials. Surface damage is usually caused by the machining process, particularly for metals and semiconductors, which distorts or damages the crystal lattice near the surface. Thin foreign coats may be formed by chemical reaction (mostly oxidation), absorption (coats of grease or water), or electrostatics (dust particles). All of these effects may have a severe impact on the radiation properties of metals and may cause considerable changes in the properties of semiconductors. Because metals have large absorptive indices k and thus high reflectances, a thin, nonmetallic layer with small k can significantly decrease the composite's reflectance (and raise its absorptance). Dielectric materials, on the other hand, have small k 's, and their relatively strong emission and absorption take place over a very thick surface layer. The addition of a thin, different dielectric layer cannot significantly alter their radiative properties (Bennett et al., 1963; Dunkle and Gier, 1953).

Figure 8.13 shows the spectral, normal emittance (or absorptance) of aluminum for a surface prepared by the ultrahigh vacuum method and for several other aluminum surface finishes. While ultrahigh vacuum aluminum follows the Drude theory for $\lambda > 1 \mu\text{m}$, polished aluminum (clean and optically smooth for large wavelengths) has a much higher absorptance over the entire spectrum. Still, the overall level of absorptance remains very low, and the reflectance remains rather specular. As Fig. 8.13 shows, the absorptance is much larger still when off-the-shelf commercial aluminum

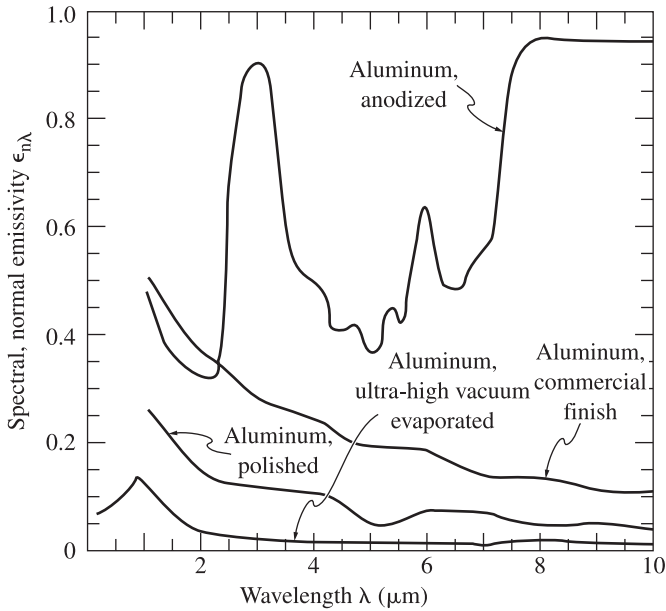


Figure 8.13 Spectral, normal emittance for aluminum with different surface finishes. (From Bennett et al., 1963; Dunkle and Gier, 1953.)

is tested, probably due to a combination of roughness, contamination, and slight atmospheric oxidation. Deposition of a thin oxide layer on aluminum (up to 100 \AA) appreciably increases the emittance only for wavelengths less than $1.5 \mu\text{m}$. This clearly is not true for thick oxide layers, as evidenced by Fig. 8.13: Anodized aluminum (electrolytically oxidized material with a thick layer of alumina, Al_2O_3) no longer displays the typical trends of a metal, but rather, shows the behavior of the dielectric alumina. The effects of thin and thick oxide layers have been measured for many metals, with similar results. As a rule of thumb, clean metal exposed to air at room temperature grows oxide films so thin that infrared emittances are not affected appreciably. On the other hand, metal surfaces exposed to high-temperature oxidizing environments (furnaces, laser heating) generally have radiative properties similar to those of their oxide layer.

Although most severe for metallic surfaces, the problem of surface modification is not unknown for nonmetals. For example, it is well known that when exposed to air at high temperature, silicon carbide (SiC) forms a layer of silica (SiO_2) on its surface, resulting in a reflection band around $9 \mu\text{m}$. Nonoxidizing chemical reactions can also significantly change the radiative properties of dielectrics. For example, the strong ultraviolet radiation in outer space (from the sun) as well as gamma rays (from inside Earth's van Allen belt) can damage the surface of spacecraft-protective coatings such as white acrylic paint or titanium dioxide epoxy coating, and similar results can be expected for ultraviolet laser irradiation.

8.2.4 Semitransparent Sheets

For an optically smooth semitransparent sheet of thickness L substantially larger than the laser wavelength, $L \gg \lambda$, radiative properties are readily determined through geometric optics and raytracing. Accounting for multiple reflections, the absorptance A_{slab} , reflectance R_{slab} , and transmittance T_{slab} of an absorbing layer with complex index of refraction $m = n - \iota k$ ($\iota = \sqrt{-1}$) are given by

$$R_{\text{slab}} = \rho \left[1 + \frac{(1 - \rho)^2 \tau^2}{1 - \rho^2 \tau^2} \right] \quad (8.38)$$

$$T_{\text{slab}} = \frac{(1 - \rho)^2 \tau}{1 - \rho^2 \tau^2} \quad (8.39)$$

$$A_{\text{slab}} = \frac{(1 - \rho)(1 - \tau)}{1 - \rho \tau} \quad (8.40)$$

and

$$A_{\text{slab}} + R_{\text{slab}} + T_{\text{slab}} = 1 \quad (8.41)$$

In these relations ρ is the reflectance of both sheet–air interfaces and τ is the transmittance of the sheet, as given for a nonscattering material (one without defects, inclusions, bubbles) by

$$\tau = e^{-\kappa L} \quad (8.42)$$

where $\kappa = 4\pi k/\lambda$ is the *absorption coefficient* of the material, which is related to the absorptive index k as shown.

If the thickness of the semitransparent sheet is on the order of the wavelength of the irradiation (thin film), interference effects need to be accounted for because phase differences between first- and second-surface reflected light make film reflectance a strongly oscillating function of wavelength, with near-zero reflectance at some wavelengths and very substantial reflectances in between. This phenomenon is commonly exploited by putting antireflection coatings onto optical components, optimized to minimize the reflectance of the optical elements at desired wavelengths.

8.2.5 Summary

Reflectance and absorptance for many materials have been compiled in a number of books and other publications, notably the handbooks by Touloukian et al. (Touloukian and DeWitt, 1970, 1972; Touloukian et al., 1973). These tabulations show large amounts of scatter, and radiative properties for opaque surfaces, when obtained from tabulations and figures in the literature, should be taken with a grain of salt. Unless detailed descriptions of surface purity, preparation, and treatment are available, the data may not give any more than an order-of-magnitude estimate. One should also keep in mind that the properties of a surface may change during a process or overnight

TABLE 8.2 Total Emittance and Solar Absorptance of Selected Surfaces

	Temperature (°C)	Total, Normal Emittance	Solar Absorptance
Alumina, flame-sprayed	−25	0.80	0.28
Aluminum foil			
As received	20	0.04	
Bright dipped	20	0.025	0.10
Aluminum, vacuum-deposited	20	0.025	0.10
Hard-anodized	−25	0.84	0.92
Highly polished plate, 98.3% pure	225–575	0.039–0.057	
Commercial sheet	100	0.09	
Rough polish	100	0.18	
Rough plate	40	0.055–0.07	
Oxidized at 600°C	200–600	0.11–0.19	
Heavily oxidized	95–500	0.20–0.31	
Antimony, polished	35–260	0.28–0.31	
Asbestos	35–370	0.93–0.94	
Beryllium	150	0.18	0.77
	370	0.21	
	600	0.30	
Beryllium, anodized	150	0.90	
	370	0.88	
	600	0.82	
Bismuth, bright	75	0.34	
Black paint			
Parson's optical black	−25	0.95	0.975
Black silicone	−25 to 750	0.93	0.94
Black epoxy paint	−25	0.89	0.95
Black enamel paint	95–425	0.81–0.80	
Brass, polished	40–315	0.10	
Rolled plate, natural surface	22	0.06	
Dull plate	50–350	0.22	
Oxidized by heating at 600°C	200–600	0.61–0.59	
Carbon, graphitized	100–320	0.76–0.75	
	320–500	0.75–0.71	
Candle soot	95–270	0.952	
Graphite, pressed, filed surface	250–510	0.98	
Chromium, polished	40–1100	0.08–0.36	
Copper, electroplated	20	0.03	0.47
Carefully polished electrolytic copper	80	0.018	
Polished	115	0.023	
Plate heated at 600°C	200–600	0.57	
Cuprous oxide	800–1100	0.66–0.54	
Molten copper	1075–1275	0.16–0.13	
Glass, pyrex, lead, and soda	260–540	0.95–0.85	
Gold, pure, highly polished	225–625	0.018–0.035	

(continued)

TABLE 8.2 Total Emittance and Solar Absorptance of Selected Surfaces (Continued)

	Temperature (°C)	Total, Normal Emittance	Solar Absorptance
Gypsum	20	0.903	
Inconel X, oxidized	−25	0.71	0.90
Lead, pure (99.96%), unoxidized	125–225	0.057–0.075	
Gray oxidized	25	0.28	
Oxidized at 150°C	200	0.63	
Magnesium, polished	35–260	0.07–0.13	
Magnesium oxide	275–825	0.55–0.20	
	900–1705	0.20	
Mercury	0–100	0.09–0.12	
Molybdenum, polished	35–260	0.05–0.08	
	540–1370	0.10–0.18	
	2750	0.29	
Nickel, electroplated	20	0.03	0.22
Polished	100	0.072	
Platinum, pure, polished	225–625	0.054–0.104	
Silica, sintered, powdered, fused silica	35	0.84	0.08
Silicon carbide	150–650	0.83–0.96	
Silver, polished, pure	40–625	0.020–0.032	
Stainless steel			
Type 312, heated 300 h at 260°C	95–425	0.27–0.32	
Type 301 with Armco black oxide	−25	0.75	0.89
Type 410, heated to 700°C in air	35	0.13	0.76
Type 303, sandblasted	95	0.42	0.68
Titanium, 75A	95–425	0.10–0.19	
75A, oxidized 300 h at 450°C	35–425	0.21–0.25	0.80
Anodized	−25	0.73	0.51
Tungsten, filament, aged	27–3300	0.032–0.35	
Zinc, pure, polished	225–325	0.045–0.053	
Galvanized sheet	100	0.21	

(by oxidation and/or contamination). A representative list of total normal emittances and total normal absorptances (= 1− reflectance) for solar irradiation is given in Table 8.2 for a number of metals and nonmetals, which may be enlisted for a gray analysis. All values are for stated temperature ranges and stated surface conditions: As explained earlier, these values may change significantly with temperature, surface roughness, and oxidation.

8.3 RADIATIVE EXCHANGE BETWEEN SURFACES

In many engineering applications the exchange of radiative energy between surfaces is virtually unaffected by the medium that separates them. Such (radiatively) *non-participating media* include vacuum as well as monatomic and most diatomic gases

(including air) at low to moderate temperature levels (i.e., in the absence of ionization and dissociation). Examples include spacecraft heat rejection systems, solar collector systems, radiative space heaters, illumination problems, and so on. This implies that photons will travel unimpeded from surface to surface, possibly over large distances. To account for all the radiative energy arriving at a point in space from all directions, the analysis has to be carried out over a complete enclosure of opaque surfaces. One or more of these surfaces may not be material, such as windows, in which case they are assigned equivalent properties and equivalent temperatures to account for the radiative energy entering or leaving the enclosure through them.

In the following sections the analysis of radiative heat transfer in the absence of a participating medium will be considered for different levels of complexity. To make the analysis tractable it is common practice to make the assumption of an *idealized enclosure* and/or *ideal surface properties*. An enclosure may be idealized in two ways, as indicated in Fig. 8.14: by replacing a complex geometrical shape with a few simple surfaces, and by assuming surfaces to be isothermal with constant (or average) heat flux values through them. Obviously, the idealized enclosure approaches the real enclosure for sufficiently small isothermal subsurfaces.

Surface properties may be idealized in a number of ways. The greatest simplification arises if all surfaces are assumed black: For such a situation no reflected radiation needs to be accounted for and all emitted radiation is diffuse. The next level of difficulty arises if surfaces are assumed to be diffuse gray emitters (and, thus, absorbers) as well as diffuse gray reflectors. This level of idealization tends to give results of acceptable accuracy for the vast majority of engineering problems. If the directional reflection behavior of a surface deviates strongly from a diffuse reflector (such a polished metal, which reflects almost like a mirror), one may often approximate the reflectance to consist of a purely diffuse and a purely specular component. However, this greatly complicates the analysis, in particular, if the enclosure includes curved surfaces. Luckily, the effects of specular (or, indeed, any type of nondiffuse) reflections tend to be very small in most engineering enclosures. Exceptions include light concentrators and collimators (in solar energy applications), long channels with specular sidewalls (optical fibers), and others. For the treatment of specular reflections the reader is referred to more detailed textbooks, such as the one by Modest (2003).

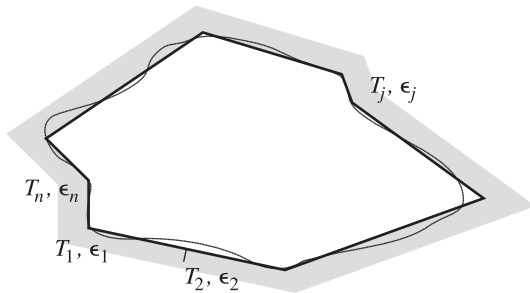


Figure 8.14 Real and ideal enclosures for radiative transfer calculations.

Of greater engineering importance is the case when the assumption of a gray surface is not acceptable. Simple methods to treat nongray behavior are outlined briefly at the end of this section.

8.3.1 View Factors

To make an energy balance on a surface, the incoming radiative flux, or *irradiation*, H must be evaluated. In a general enclosure the irradiation has contributions from all parts of the enclosure surface. Therefore, one needs to determine how much of the energy that leaves any surface of the enclosure travels toward the surface under consideration. The geometric relations governing this process for *diffuse surfaces* (which absorb and emit diffusely, and also reflect radiative energy diffusely) are known as *view factors*. Other names used in the literature are *configuration factor*, *angle factor*, and *shape factor*. The view factor between two surfaces A_i and A_j is defined as

$$F_{i-j} \equiv \frac{\text{diffuse energy leaving } A_i \text{ directly toward and intercepted by } A_j}{\text{total diffuse energy leaving } A_i} \quad (8.43)$$

where the word *directly* is meant to imply “on a straight path, without intervening reflections.” A list of relationships for some common view factors is given in Table 8.3, and Figs. 8.15 through 8.17 give convenient graphical representations of the three most important view factors.

Radiation view factors may be determined by a variety of methods, such as direct integration (analytical or numerical integration), statistical evaluation [through statistical sampling using a *Monte Carlo method* (Modest, 2003), or through a variety of special methods, some of which are described briefly in what follows.

Direct Integration Mathematically, view factors can be expressed in terms of a double surface integral, that is,

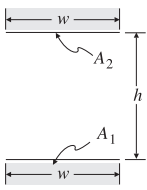
$$F_{i-j} = \frac{1}{A_i} \int_{A_i} \int_{A_j} \frac{\cos \theta_i \cos \theta_j}{\pi S_{ij}^2} dA_j dA_i \quad (8.44)$$

where S_{ij} is the distance between points on surfaces A_i and A_j , and θ_i and θ_j are the angles between S_{ij} and the local surface normals, as shown in Fig. 8.18. Using Stokes' theorem, eq. (8.44) can be converted into a double contour integral,

$$A_i F_{i-j} = \frac{1}{2\pi} \oint_{\Gamma_i} \oint_{\Gamma_j} \ln S_{ij} d\mathbf{s}_j \cdot d\mathbf{s}_i \quad (8.45)$$

where Γ_i is the contour of A_i (as also indicated in Fig. 8.18) and \mathbf{s}_i is a vector to a point on contour Γ_i .

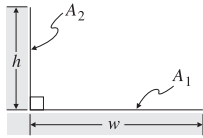
While the integration of eqs. (8.44) and (8.45) may be straightforward for some simple configurations, it is desirable to have a more generally applicable formula at

TABLE 8.3 Important View Factors


1. Two infinitely long, directly opposed parallel plates of the same finite width:

$$H = \frac{h}{w}$$

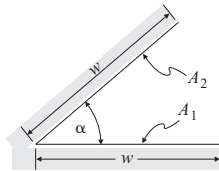
$$F_{1-2} = F_{2-1} = \sqrt{1 + H^2} - H$$



2. Two infinitely long plates of unequal widths h and w , having one common edge, and at an angle of 90° to each other:

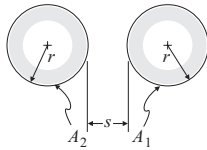
$$H = \frac{h}{w}$$

$$F_{1-2} = \frac{1}{2} \left(1 + H - \sqrt{1 + H^2} \right)$$



3. Two infinitely long plates of equal finite width w , having one common edge, forming a wedgelike groove with opening angle α :

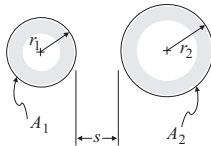
$$F_{1-2} = F_{2-1} = 1 - \sin \frac{\alpha}{2}$$



4. Infinitely long parallel cylinders of the same diameter:

$$X = 1 + \frac{s}{2r}$$

$$F_{1-2} = \frac{1}{\pi} \left(\sin^{-1} \frac{1}{X} + \sqrt{X^2 - 1} - X \right)$$

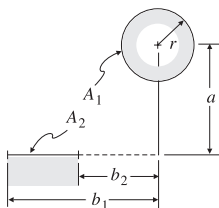


5. Two infinite parallel cylinders of different radius:

$$R = \frac{r_2}{r_1} \quad S = \frac{s}{r_1} \quad C = 1 + R + S$$

$$F_{1-2} = \frac{1}{2\pi} \left[\pi + \sqrt{C^2 - (R+1)^2} - \sqrt{C^2 - (R-1)^2} \right. \\ \left. + (R-1) \cos^{-1} \frac{R-1}{C} - (R+1) \cos^{-1} \frac{R+1}{C} \right]$$

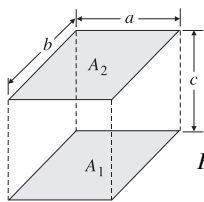
(continued)

TABLE 8.3 Important View Factors (Continued)

6. Exterior of infinitely long cylinder to unsymmetrically placed, infinitely long parallel rectangle; $r \leq a$:

$$B_1 = \frac{b_1}{a} \quad B_2 = \frac{b_2}{a}$$

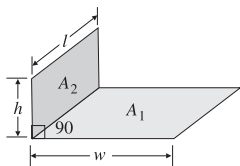
$$F_{1-2} = \frac{1}{2\pi} (\tan^{-1} B_1 - \tan^{-1} B_2)$$



7. Identical, parallel, directly opposed rectangles:

$$X = \frac{a}{c} \quad Y = \frac{b}{c}$$

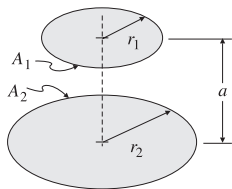
$$F_{1-2} = \frac{2}{\pi XY} \left\{ \ln \left[\frac{(1+X^2)(1+Y^2)}{1+X^2+Y^2} \right]^{1/2} + X\sqrt{1+Y^2} \tan^{-1} \frac{X}{\sqrt{1+Y^2}} \right. \\ \left. + Y\sqrt{1+X^2} \tan^{-1} \frac{Y}{\sqrt{1+X^2}} - X \tan^{-1} X - Y \tan^{-1} Y \right\}$$



8. Two finite rectangles of same length, having one common edge, and at an angle of 90° to each other:

$$H = \frac{h}{l} \quad W = \frac{w}{l}$$

$$F_{1-2} = \frac{1}{\pi W} \left(W \tan^{-1} \frac{1}{W} + H \tan^{-1} \frac{1}{H} - \sqrt{H^2 + W^2} \tan^{-1} \frac{1}{\sqrt{H^2 + W^2}} \right. \\ \left. + \frac{1}{4} \ln \left\{ \frac{(1+W^2)(1+H^2)}{1+W^2+H^2} \left[\frac{W^2(1+W^2+H^2)}{(1+W^2)(W^2+H^2)} \right]^{W^2} \left[\frac{H^2(1+H^2+W^2)}{(1+H^2)(H^2+W^2)} \right]^{H^2} \right\} \right)$$



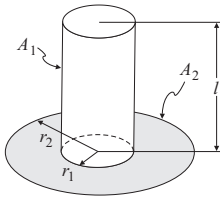
9. Disk to parallel coaxial disk of unequal radius:

$$R_1 = \frac{r_1}{a} \quad R_2 = \frac{r_2}{a}$$

$$X = 1 + \frac{1 + R_2^2}{R_1^2}$$

$$F_{1-2} = \frac{1}{2} \left[X - \sqrt{X^2 - 4 \left(\frac{R_2}{R_1} \right)^2} \right]$$

TABLE 8.3 Important View Factors (Continued)



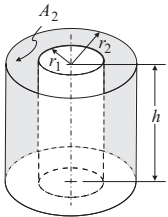
10. Outer surface of cylinder to annular disk at end of cylinder:

$$R = \frac{r_1}{r_2} \quad L = \frac{l}{r_2}$$

$$A = L^2 + R^2 - 1$$

$$B = L^2 - R^2 + 1$$

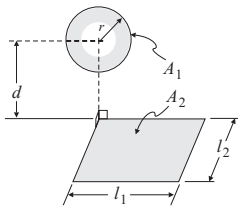
$$F_{1-2} = \frac{B}{8RL} + \frac{1}{2\pi} \left[\cos^{-1} \frac{A}{B} - \frac{1}{2L} \sqrt{\frac{(A+2)^2}{R^2} - 4} \cos^{-1} \frac{AR}{B} - \frac{A}{2RL} \sin^{-1} R \right]$$



11. Interior of finite-length, right-circular coaxial cylinder to itself:

$$R = \frac{r_2}{r_1} \quad H = \frac{h}{r_1}$$

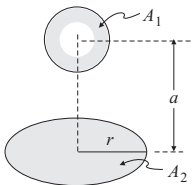
$$F_{2-2} = 1 - \frac{1}{R} - \frac{\sqrt{H^2 + 4R^2} - H}{4R} + \frac{1}{\pi} \left(\frac{2}{R} \tan^{-1} \frac{2\sqrt{R^2 - 1}}{H} - \frac{H}{2R} \left\{ \frac{\sqrt{4R^2 + H^2}}{H} \sin^{-1} \frac{H^2 + 4(R^2 - 1) - 2H^2/R^2}{H^2 + 4(R^2 - 1)} - \sin^{-1} \frac{R^2 - 2}{R^2} \right\} \right)$$



12. Sphere to rectangle,
- $r < d$
- :

$$D_1 = \frac{d}{l_1} \quad D_2 = \frac{d}{l_2}$$

$$F_{1-2} = \frac{1}{4\pi} \tan^{-1} \sqrt{\frac{1}{D_1^2 + D_2^2 + D_1^2 D_2^2}}$$



13. Sphere to coaxial disk:

$$R = \frac{r}{a}$$

$$F_{1-2} = \frac{1}{2} \left[1 - \frac{1}{\sqrt{1 + R^2}} \right]$$

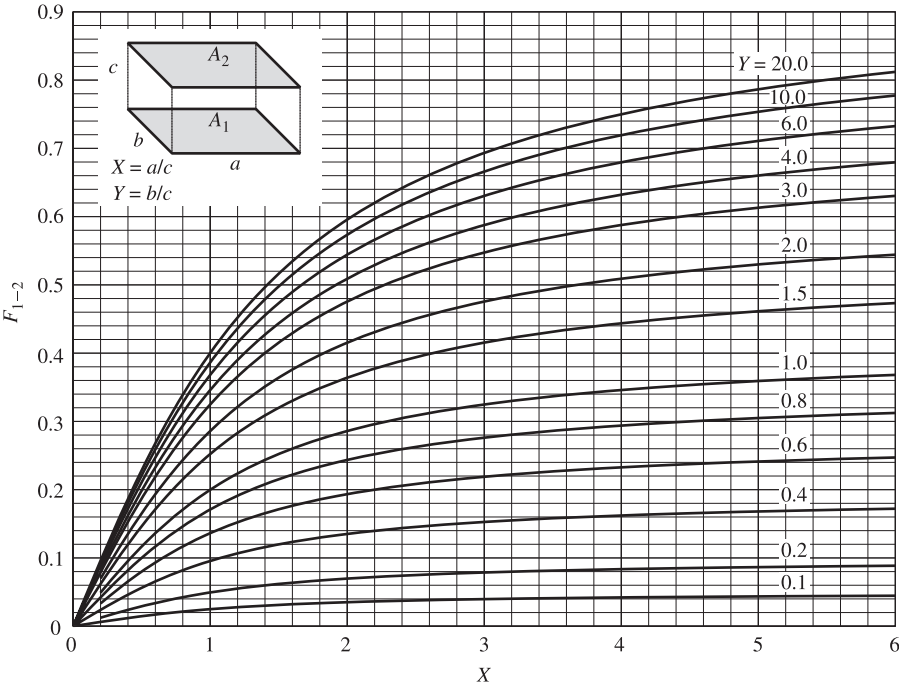


Figure 8.15 View factor between identical, parallel, directly opposed rectangles (configuration 7).

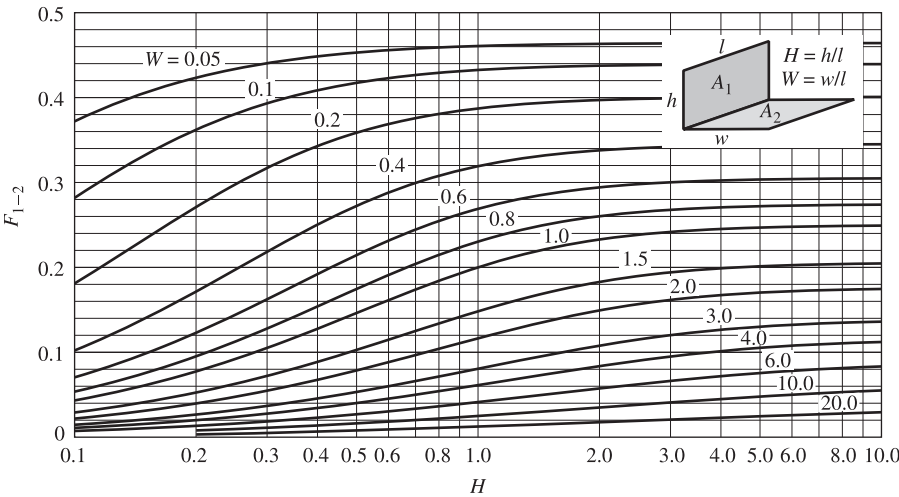


Figure 8.16 View factor between perpendicular rectangles with common edge (configuration 8).

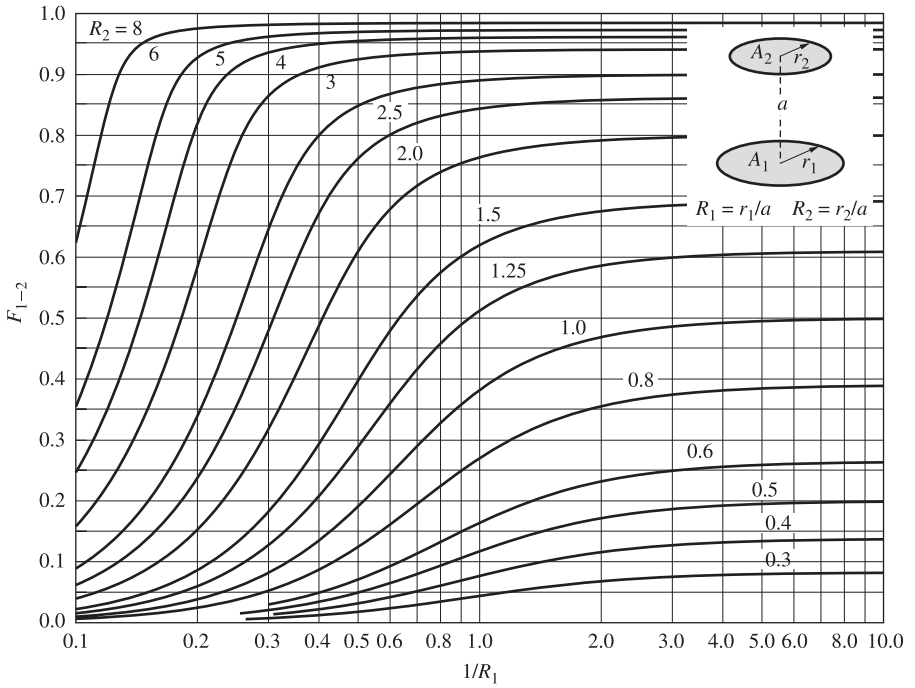


Figure 8.17 View factor between parallel coaxial disks of unequal radius (configuration 9).

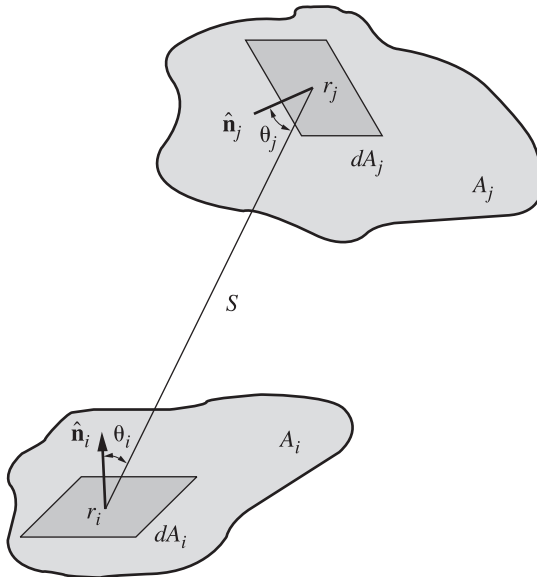


Figure 8.18 View factor evaluation between two surfaces.

one's disposal. Using an arbitrary coordinate origin, a vector pointing from the origin to a point on a surface may be written as

$$\mathbf{r} = x\hat{\mathbf{i}} + y\hat{\mathbf{j}} + z\hat{\mathbf{k}} \quad (8.46)$$

where $\hat{\mathbf{i}}$, $\hat{\mathbf{j}}$, and $\hat{\mathbf{k}}$ are *unit vectors* pointing into the x , y , and z directions, respectively. Thus the vector from dA_i going to dA_j is determined as

$$\mathbf{s}_{ij} = -\mathbf{s}_{ji} = \mathbf{r}_j - \mathbf{r}_i = (x_j - x_i)\hat{\mathbf{i}} + (y_j - y_i)\hat{\mathbf{j}} + (z_j - z_i)\hat{\mathbf{k}} \quad (8.47)$$

The length of this vector is determined as

$$|\mathbf{s}_{ji}|^2 = |\mathbf{s}_{ij}|^2 = S_{ij}^2 = (x_j - x_i)^2 + (y_j - y_i)^2 + (z_j - z_i)^2 \quad (8.48)$$

It will now be assumed that the local surface normals are known in terms of the unit vectors $\hat{\mathbf{i}}$, $\hat{\mathbf{j}}$, and $\hat{\mathbf{k}}$, or

$$\hat{\mathbf{n}} = l\hat{\mathbf{i}} + m\hat{\mathbf{j}} + n\hat{\mathbf{k}} \quad (8.49)$$

where l , m , and n are the *direction cosines* for the unit vector $\hat{\mathbf{n}}$. For example, $l = \hat{\mathbf{n}} \cdot \hat{\mathbf{i}}$ is the cosine of the angle between $\hat{\mathbf{n}}$ and the x axis, and m and n can be represented in a similar manner. Thus $\cos \theta_i$ and $\cos \theta_j$ may be evaluated as

$$\cos \theta_i = \frac{\hat{\mathbf{n}}_i \cdot \mathbf{s}_{ij}}{S_{ij}} = \frac{1}{S_{ij}} [(x_j - x_i)l_i + (y_j - y_i)m_i + (z_j - z_i)n_i] \quad (8.50)$$

$$\cos \theta_j = \frac{\hat{\mathbf{n}}_j \cdot \mathbf{s}_{ji}}{S_{ij}} = \frac{1}{S_{ij}} [(x_i - x_j)l_j + (y_i - y_j)m_j + (z_i - z_j)n_j] \quad (8.51)$$

For contour integration the tangential vectors $d\mathbf{s}$ are found from eq. (8.46), that is,

$$d\mathbf{s} = dx \hat{\mathbf{i}} + dy \hat{\mathbf{j}} + dz \hat{\mathbf{k}} \quad (8.52)$$

where dx is the change in the x coordinate along the contour Γ , and dy and dz follow in a similar fashion. Examples for the application of area and contour integration to view factor evaluation may be found in textbooks (Modest, 2003; Siegel and Howell, 2002).

Special Methods The mathematics of view factors follow certain rules, which may be exploited to simplify their evaluation. The two most important ones are the *summation rule* for a closed configuration consisting of N surfaces,

$$\sum_{j=1}^N F_{i-j} = 1 \quad (8.53)$$

stating that the sum of fractions must total unity, and the *reciprocity rule*,

$$A_i F_{i-j} = A_j F_{j-i} \quad (8.54)$$

which follows directly from eq. (8.44). The methods known as *view factor algebra* and the *crossed-strings method* are discussed briefly next.

View Factor Algebra Many view factors for fairly complex configurations may be calculated without any integration simply by using the rules of reciprocity and summation and perhaps the known view factor for a more basic geometry. For example, suppose that the view factor for a corner piece from configuration 8 in Table 8.3 is given. Using this knowledge, the view factor F_{3-4} between the two perpendicular strips shown in Fig. 8.19 can be evaluated.

From the definition of the view factor and because the energy traveling to A_4 is the energy going to A_2 and A_4 minus the energy going to A_2 , it follows that

$$F_{3-4} = F_{3-(2+4)} - F_{3-2}$$

and using reciprocity,

$$F_{3-4} = \frac{1}{A_3} [(A_2 + A_4) F_{(2+4)-3} - A_2 F_{2-3}]$$

Similarly,

$$F_{3-4} = \frac{A_2 + A_4}{A_3} [F_{(2+4)-(1+3)} - F_{(2+4)-1}] - \frac{A_2}{A_3} [F_{2-(1+3)} - F_{2-1}]$$

All view factors on the right-hand side are for corner pieces and may be found by evaluating view factor 8 with appropriate dimensions.

As a second example, the view factor from the inside surface of a finite-length cylinder to itself will be determined (as shown in the figure for view factor 11 for the

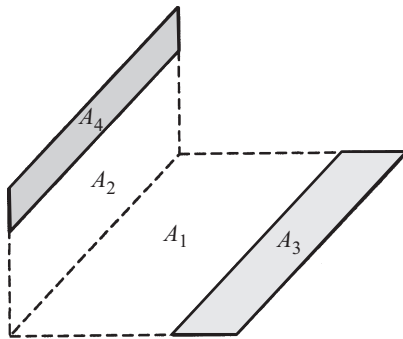


Figure 8.19 View factor between two strips on a corner.

limiting case of $r_1 \rightarrow 0$). Calling the cylinder A_1 , and top and bottom openings of the cylinder A_2 and A_3 , respectively, the summation rule gives

$$F_{1-1} + F_{1-2} + F_{1-3} = 1 \quad \text{or} \quad F_{1-1} = 1 - 2F_{1-2}$$

because $F_{1-2} = F_{1-3}$. Now, using reciprocity, or $A_1 F_{1-2} = A_2 F_{2-1}$, and summation once again,

$$F_{1-1} = 1 - 2 \frac{A_2}{A_1} F_{2-1} = 1 - 2 \frac{A_2}{A_1} (1 - F_{2-3})$$

because $F_{2-2} = 0$. Then F_{2-3} can be evaluated from configuration 9, with $R_1 = R_2 = r/h = R$, $X = 2 + 1/R^2$, or

$$F_{2-3} = \frac{1}{2} \left(2 + \frac{1}{R^2} - \sqrt{4 + \frac{4}{R^2} + \frac{1}{R^4} - 4} \right)$$

Finally, with $A_2/A_1 = \pi r^2/2\pi rh = r/2h = R/2$,

$$F_{1-1} = 1 - R \left(-\frac{1}{2R^2} + \frac{1}{R} \sqrt{1 + \frac{1}{4R^2}} \right) = 1 + \frac{1}{2R} - \sqrt{1 + \frac{1}{4R^2}}$$

Crossed-Strings Method View factor algebra may be used to determine all the view factors in long enclosures with constant cross section. The method is called the crossed-strings method because the view factors can be determined experimentally by a person armed with four pins, a roll of string, and a yardstick. Consider the configuration in Fig. 8.20, which shows the cross section of an infinitely long enclosure, continuing into and out of the plane of the figure: The determination of F_{1-2} is sought. Obviously, the surfaces shown are rather irregular (partly convex, partly concave), and the view between them may be obstructed. For such geometries, integration is out of the question; however, repeated application of the reciprocity and summation rules allows the evaluation of F_{1-2} as

$$F_{1-2} = \frac{(A_{bc} + A_{ad}) - (A_{ac} + A_{bd})}{2A_1} \quad (8.55)$$

where, in general, A_{ab} is the area (per unit depth) defined by the length of the string between points a and b . This relationship is easily memorized by looking at the configuration between any two surfaces as a generalized “rectangle,” consisting of A_1 , A_2 , and the two sides of A_{ac} and A_{bd} . Then

$$F_{1-2} = \frac{\text{diagonals} - \text{sides}}{2 \times \text{originating area}} \quad (8.56)$$

As an example, suppose that the calculation of F_{1-2} for configuration 1 in Table 8.3 via the crossed-strings method is desired. For that geometry, both “sides” would have

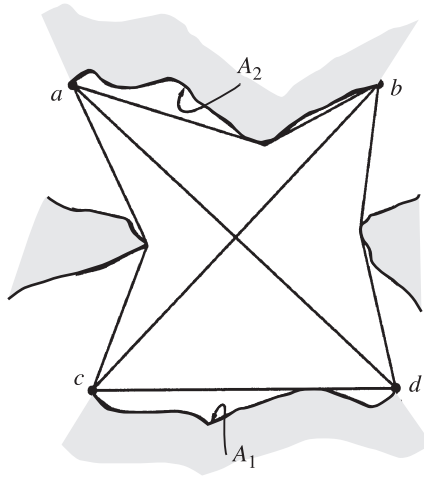


Figure 8.20 Crossed strings method for two-dimensional configurations.

length h , both diagonals would have length $\sqrt{h^2 + w^2}$, and the originating area would have width w . Thus,

$$F_{1-2} = \frac{2\sqrt{h^2 + w^2} - 2h}{2w} = \sqrt{1 + \left(\frac{h}{w}\right)^2} - \frac{h}{w} \quad (8.57)$$

as given in the table.

8.3.2 Radiative Exchange between Black Surfaces

Consider an enclosure consisting of N opaque, black, isothermal surfaces. One or more of these surfaces may not be actual material but a hole through which radiation escapes, and through which external radiation may enter the enclosure. A hole is usually best modeled as a cold black surface, because a hole does not reflect internal radiation (black) and because usually no diffuse energy is entering through the hole (no emission or $T = 0$ K). If external radiation is entering through an opening, this energy tends to be directional and is best accounted for in the energy balances for individual surfaces that receive it.

An energy balance for any isothermal surface A_i in the enclosure yields

$$\frac{Q_i}{A_i} = E_{bi} - H_i \quad H_i = \sum_{j=1}^N E_{bj} F_{i-j} + H_{oi} \quad i = 1, 2, \dots, N \quad (8.58)$$

where Q_i/A_i is the average radiative heat flux on A_i , $E_{bi} = \sigma T_i^4$ is the surface's emissive power, and H_i is the total irradiation onto A_i , consisting of the fractions of emitted radiation from all surfaces in the enclosure (including itself if A_i is concave)

that are intercepted by A_i , plus, possibly, external radiation H_{oi} that enters through a hole and hits A_i (per unit area of A_i). If the temperatures for all N surfaces making up the enclosure are known, eq. (8.58) constitutes a set of N explicit equations for the unknown radiative fluxes (Q_i/A_i).

Suppose that for surfaces $i = 1, 2, \dots, n$ the heat fluxes are prescribed (and temperatures are unknown), whereas for surfaces $i = n+1, \dots, N$ the temperatures are prescribed (heat fluxes unknown). Unlike for the heat fluxes, no explicit relations for the unknown temperatures exist. Placing all unknown temperatures on one side, eq. (8.58) may be written as

$$E_{bi} - \sum_{j=1}^n F_{i-j} E_{bj} = \frac{Q_i}{A_i} + H_{oi} + \sum_{j=n+1}^N F_{i-j} E_{bj} \quad i = 1, 2, \dots, n \quad (8.59)$$

where everything on the right-hand side of the equation is known. In matrix form this is written as

$$\mathbf{A} \cdot \mathbf{e}_b = \mathbf{b} \quad (8.60)$$

where

$$\mathbf{A} = \begin{bmatrix} 1 - F_{1-1} & -F_{1-2} & \cdots & -F_{1-n} \\ -F_{2-1} & 1 - F_{2-2} & \cdots & -F_{2-n} \\ \vdots & & \ddots & \vdots \\ -F_{n-1} & -F_{n-2} & \cdots & 1 - F_{n-n} \end{bmatrix} \quad (8.61)$$

$$\mathbf{e}_b = \begin{bmatrix} E_{b1} \\ E_{b2} \\ \vdots \\ E_{bn} \end{bmatrix} \quad \mathbf{b} = \begin{bmatrix} \frac{Q_1}{A_1} + H_{o1} + \sum_{j=n+1}^N F_{1-j} E_{bj} \\ \frac{Q_2}{A_2} + H_{o2} + \sum_{j=n+1}^N F_{2-j} E_{bj} \\ \vdots \\ \frac{Q_n}{A_n} + H_{on} + \sum_{j=n+1}^N F_{n-j} E_{bj} \end{bmatrix} \quad (8.62)$$

The $n \times n$ matrix \mathbf{A} is readily inverted on a computer (generally with the aid of a software library subroutine), and the unknown temperatures are calculated as

$$\mathbf{e}_b = \mathbf{A}^{-1} \cdot \mathbf{b} \quad (8.63)$$

8.3.3 Radiative Exchange between Diffuse Gray Surfaces

It will now be assumed that all surfaces are gray and that they are diffuse emitters, absorbers, and reflectors. Under these conditions, $\epsilon = \epsilon'_\lambda = \alpha'_\lambda = \alpha = 1 - \rho$. The

radiative heat flux leaving surface A_i now consists of emission plus the reflection of incoming radiation,

$$J_i = \epsilon_i E_{bi} + \rho_i H_i \quad (8.64)$$

which is called the *surface radiosity*. In the same way as eq. (8.58) was formulated, one can make an energy balance at surface A_i , but there are now two ways to make this balance,

$$\frac{Q_i}{A_i} = J_i - H_i = \epsilon_i E_{bi} - \alpha_i H_i \quad i = 1, 2, \dots, N \quad (8.65)$$

the first stating that the net flux is equal to outgoing minus incoming radiation, the other stating that net flux is equal to the emitted minus the absorbed radiation. Eliminating H_i between them gives an expression for radiosity in terms of local temperature and flux,

$$J_i = E_{bi} - \left(\frac{1}{\epsilon_i} - 1 \right) \frac{Q_i}{A_i} \quad (8.66)$$

Replacing emissive power by radiosities in eq. (8.58) and using eq. (8.65) leads to N simultaneous equations for the N unknown radiosities,

$$J_i = \epsilon_i E_{bi} + \rho_i \left(\sum_{j=1}^N F_{i-j} J_j + H_{oi} \right) \quad (8.67a)$$

or

$$J_i = \frac{Q_i}{A_i} + \sum_{j=1}^N F_{i-j} J_j + H_{oi} \quad (8.67b)$$

dependent on whether temperature (E_{bi}) or flux (Q_i/A_i) is known for surface i . While commonly solved for in the older literature, there is rarely ever any need to determine radiosities. Eliminating them through the use of eq. (8.66) yields a set of N simultaneous algebraic equations,

$$\frac{1}{\epsilon_i} \frac{Q_i}{A_i} - \sum_{j=1}^N \left(\frac{1}{\epsilon_j} - 1 \right) F_{i-j} \frac{Q_j}{A_j} + H_{oi} = E_{bi} - \sum_{j=1}^N F_{i-j} E_{bj} \quad i = 1, 2, \dots, N \quad (8.68)$$

Equation (8.68) contains N different E_{bi} and N different Q_i/A_i . Therefore, if the temperatures are specified for all N surfaces, all fluxes can be calculated. It is also possible to specify an arbitrary mix of N surface temperatures and heat fluxes, and eq. (8.68) allows determination of the remaining N unknowns (the one exception being

that it is not proper to specify all N heat fluxes: because from conservation of energy, $\sum_{i=1}^N Q_i = 0$, this amounts to only $N - 1$ specifications). As for black enclosures, holes are modeled as cold black surfaces; because for such surfaces $E_{bi} = J_i = 0$, they do not appear in eq. (8.68) (except for external irradiation, entering *through* holes, accounted for at the surfaces receiving this irradiation).

Convex Surface Exposed to Large Isothermal Enclosure In many important engineering applications a flat or convex surface (i.e., a surface that cannot “see itself”) is radiating into (and receiving radiation from) a large isothermal enclosure. In such a case, $N = 2$ (A_i being the convex surface and A_e the large enclosure), and, if $F_{i-e} = 1$, eq. (8.68) reduces to

$$\frac{Q_i}{A_i} = \frac{\sigma(T_i^4 - T_e^4)}{(1/\epsilon_i) + (A_i/A_e)[(1/\epsilon_e) - 1]} \simeq \epsilon_i \sigma (T_i^4 - T_e^4) \quad (8.69)$$

because for a large enclosure, $A_i \ll A_e$. Equation (8.69) provides a simple, yet accurate set of radiation boundary conditions for engineering problems, which are dominated by conduction and/or convection.

8.3.4 Radiation Shields

If it is desired to minimize radiative heat transfer between two surfaces, it is common practice to place one or more radiation shields between them (usually, thin metallic sheets of low emittance). In these situations any two shields A_i and A_j often enclose one another, or are very close together, such that $F_{i-j} \simeq 1$. The radiative heat transfer between two diffusely reflecting plates is then, from eq. (8.69),

$$Q = \frac{E_{bi} - E_{bj}}{R_{ij}} \quad R_{ij} = \frac{1}{\epsilon_i A_i} + \left(\frac{1}{\epsilon_j} - 1 \right) \frac{1}{A_j} \quad (8.70)$$

where R_{ij} is termed the *radiative resistance*. Equation (8.70) is seen to be analogous to an electrical circuit with current Q and voltage potential $E_{bi} - E_{bj}$. Therefore, expressing radiative fluxes in terms of radiative resistances is commonly known as the *network analogy* (Oppenheim, 1956). The network analogy is a very powerful method for solving one-dimensional problems (e.g., whenever only two isothermal surfaces see each other, such as infinite parallel plates, or when one surface totally encloses another). Consider, for example, two large parallel, or concentric, plates, A_1 and A_N , separated by $N - 2$ radiation shields, as shown in Fig. 8.21. Let each shield j have an emittance ϵ_j on both sides. Then by applying eq. (8.70) to any two consecutive surfaces and using the fact that Q remains constant throughout the gap,

$$Q = \frac{E_{b1} - E_{b2}}{R_{12}} = \dots = \frac{E_{bk-1} - E_{bk}}{R_{k-1,k}} = \dots = \frac{E_{bN-1} - E_{bN}}{R_{N-1,N}} = \frac{E_{b1} - E_{bN}}{\sum_{j=2}^N R_{j-1,j}} \quad (8.71)$$

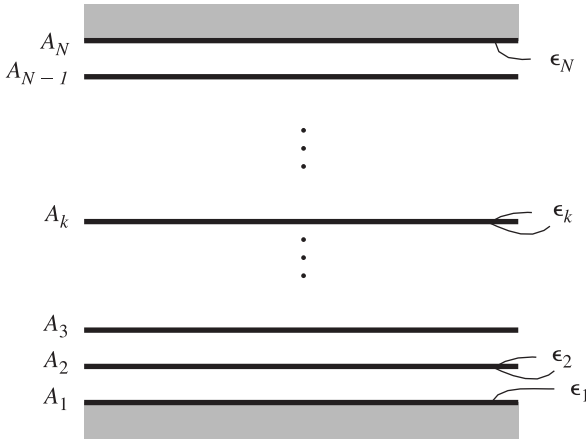


Figure 8.21 Arrangement of parallel or concentric radiation shields.

where

$$R_{j-1,j} = \frac{1}{\epsilon_{j-1}A_{j-1}} + \left(\frac{1}{\epsilon_j} - 1 \right) \frac{1}{A_j} \quad (8.72)$$

The analysis of radiation shields is one of the few applications where analysis of specularly reflecting surfaces is relatively simple and may lead to substantially different answers for concentric shields with strongly varying radii. For a specularly reflecting shield A_j (with A_{j-1} being specular *or* diffuse), the radiative resistance becomes

$$R_{j-1,j} = \left(\frac{1}{\epsilon_{j-1}} + \frac{1}{\epsilon_j} - 1 \right) \frac{1}{A_{j-1}} \quad (A_j \text{ specular}) \quad (8.73)$$

Note that it is desirable to make shields highly reflective (low ϵ), and this tends to make them specularly reflecting (also desirable, because it also increases the resistance).

Further simplifications arise if all shields are of identical material ($\epsilon_2 = \epsilon_3 = \dots = \epsilon_{N-1}$); on the other hand, eqs. (8.71) through (8.73) remain valid for shields with different emittances on both of its sides (different values for ϵ_j in $R_{j-1,j}$ and $R_{j,j+1}$).

While the network analogy can (and has been) applied to configurations with more than two surfaces seeing each other, this leads to very complicated circuits (because there is only one resistance between any two surfaces). For such problems the network analogy is not recommended, and the net radiation method, eq. (8.68), should be employed.

8.3.5 Radiative Exchange between Diffuse Nongray Surfaces

In a number of important engineering problems the assumption of gray surface properties may not provide adequate accuracy (when properties exhibit strong spectral variations across the important range of the spectrum). To deal with such effects, two simple models, known as the *semigray approximation* and the *band approximation*, will be described.

Semigray Approximation Method This method employs the principle of superposition: The radiative flux at any given point is the sum of the contributions from the various emitters in the enclosure, each one acting independently. In some applications there is a natural division of the radiative energy within an enclosure into two or more distinct spectral regions. For example, in a solar collector the incoming energy comes from a high-temperature source with most of its energy below $3\text{ }\mu\text{m}$, whereas radiation losses for typical collector temperatures are at wavelengths above $3\text{ }\mu\text{m}$. In the case of laser heating and processing, the incoming energy is monochromatic (at the laser wavelength); reradiation takes place over the entire near- to midinfrared (depending on the workpiece temperature). In such a situation, eq. (8.68) may be split into two sets of N equations each, one set for each spectral range, and with different radiative properties for each set. For example, consider an enclosure subject to external irradiation, which is confined to a certain spectral range (1). The surfaces in the enclosure, owing to their temperature, emit over spectral range (2).^{*} Then from eq. (8.68),

$$\frac{1}{\epsilon_i^{(1)}} \frac{Q_i^{(1)}}{A_j} - \sum_{j=1}^N \left(\frac{1}{\epsilon_j^{(1)}} - 1 \right) F_{i-j} \frac{Q_j^{(1)}}{A_j} + H_{oi} = 0 \quad (8.74a)$$

$$\frac{1}{\epsilon_i^{(2)}} \frac{Q_i^{(2)}}{A_j} - \sum_{j=1}^N \left(\frac{1}{\epsilon_j^{(2)}} - 1 \right) F_{i-j} \frac{Q_j^{(2)}}{A_j} = E_{bi} - \sum_{j=1}^N F_{i-j} E_{bj} \quad (8.74b)$$

$$\frac{Q_i}{A_i} = \frac{Q_i^{(1)}}{A_i} + \frac{Q_i^{(2)}}{A_i} \quad i = 1, 2, \dots, N \quad (8.74c)$$

where $\epsilon_j^{(1)}$ is the average emittance for surface j over spectral interval (1), and so on. The semigray approximation is not limited to two distinct spectral regions. Each surface of the enclosure may be given a set of absorptances and reflectances, one value for each different emission temperature (with its different emission spectra). However, while simple and straightforward, the method can never become exact no matter how many different values of absorptance and reflectance are chosen for each surface.

Band Approximation Method Another commonly used method to deal with nongray surfaces is the *band approximation method*. This method employs the fact

^{*}Note that spectral ranges (1) and (2) do not need to cover the entire spectrum, and indeed, they may overlap.

that even for nongray materials, eq. (8.68) remains valid on a spectral basis (replacing emissive power E_b by spectral emissive power $E_{b\lambda}$, related to the total emissive power by $E_b = \int_0^\infty E_{b\lambda} d\lambda$). In this method the spectrum is broken up into M bands, over which the radiative properties of *all* surfaces in the enclosure are constant. Therefore,

$$\frac{1}{\epsilon_i^{(m)}} \frac{Q_i^{(m)}}{A_i} - \sum_{j=1}^N \left(\frac{1}{\epsilon_i^{(m)}} - 1 \right) F_{i-j} \frac{Q_j^{(m)}}{A_j} + H_{oi}^{(m)} = E_{bi}^{(m)} - \sum_{j=1}^N F_{i-j} E_{bj}^{(m)}$$

$$i = 1, 2, \dots, N, \quad m = 1, 2, \dots, M \quad (8.75a)$$

$$E_{bj} = \sum_{m=1}^M E_{bj}^{(m)} \quad \frac{Q_j}{A_j} = \sum_{m=1}^M \frac{Q_j^{(m)}}{A_j} \quad H_{oi} = \sum_{m=1}^M H_{oi}^{(m)} \quad (8.75b)$$

Here, $E_b^{(m)}$ is the fractional emissive power contained in band m and so on. Equations (8.75) are, of course, nothing but a simple numerical integration of the spectral version of eq. (8.68), using the trapezoidal rule with varying steps. This method has the advantage that the widths of the bands can be tailored to the spectral variation of properties, resulting in good accuracy with relatively few bands. For very few bands the accuracy of this method is similar to that of the semigray approximation but is a little more cumbersome to apply. On the other hand, the *band approximation method* can achieve any desired accuracy by using many bands.

8.4 RADIATIVE PROPERTIES OF PARTICIPATING MEDIA

In many high-temperature applications, when radiative heat transfer is important, the medium between surfaces is not transparent but is “participating”; that is, it absorbs, emits, and (possibly) scatters radiation. In a typical combustion process this interaction results in (1) continuum radiation due to tiny, burning soot particles (of dimension $< 1 \mu\text{m}$) and also due to larger suspended particles, such as coal particles, oil droplets, and fly ash; (2) banded radiation in the infrared due to emission and absorption by molecular gaseous combustion products, mostly water vapor and carbon dioxide; and (3) chemiluminescence due to the combustion reaction itself. While chemiluminescence may normally be neglected, particulates as well as gas radiation generally must be accounted for.

8.4.1 Molecular Gases

When a photon (or an electromagnetic wave) interacts with a gas molecule, it may be absorbed, raising the energy level of the molecule. Conversely, a gas molecule may spontaneously lower its energy level by the emission of an appropriate photon. This leads to large numbers of narrow spectral lines, which partially overlap and together form vibration–rotation bands. As such, gases tend to be transparent over most of the spectrum but may be almost opaque over the spectral range of a band. The *absorption coefficient* κ_λ is defined as a measure of how strongly radiation is

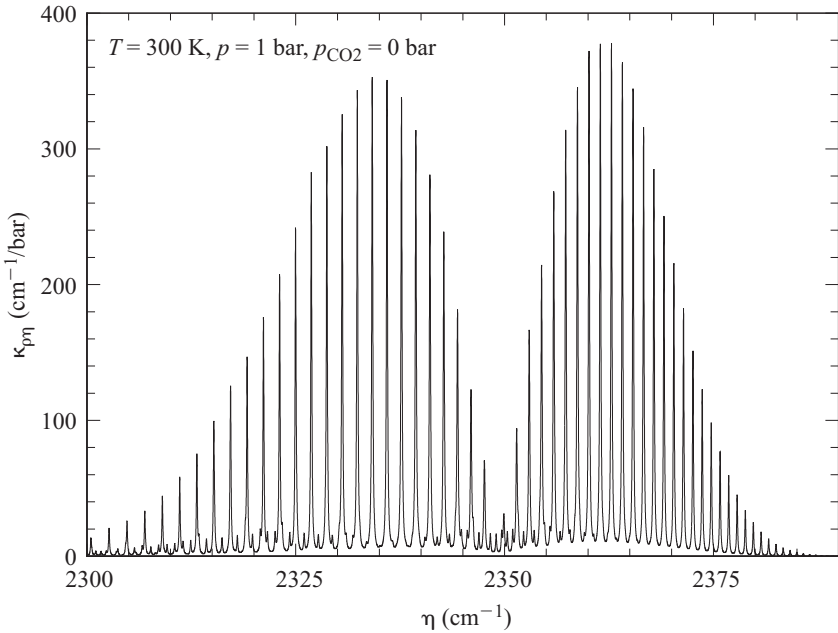


Figure 8.22 Absorption coefficient spectrum for the CO₂ 4.3-μm band.

absorbed or emitted along a path in a participating medium. Figure 8.22 shows the absorption coefficient of the important 4.3-μm vibration–rotation band of CO₂ (per partial pressure of CO₂), for small amounts of CO₂ contained in nitrogen, with a temperature of 300 K and a mixture pressure of 1 bar, generated from the HITRAN database (Rothman et al., 1998). The figure shows that the band consists of a large number of strong spectral lines, and a number of weak lines can also be observed. In reality, there are many more spectral lines than appear in the figure. However, at the relatively high total pressure of 1 bar, the lines strongly overlap, giving a relatively smooth appearance. Lowering the pressure would decrease line overlap, and more and more of the $\approx 12,500$ lines contained in the HITRAN database for this band would become distinguishable. Similarly, with increasing temperature, lines become narrower (less overlap), and many additional “hot lines” must be considered, which are negligible at room temperature. The new HITEMP database (Rothman et al., 2000), which is designed for temperatures up to 1000 K, includes $\approx 185,000$ lines for the 4.3-μm CO₂ band alone!

Fortunately, for many engineering problems, for simple heat transfer calculations, it is sufficient to determine the total emissivity for an isothermal, homogeneous path of length L ,

$$\epsilon = \frac{1}{E_b} \int_0^\infty (1 - e^{-\kappa_\lambda L}) E_{b\lambda}(T_g) d\lambda \quad (8.76)$$

For a mixture of gases the total emissivity is a function of path length L , gas temperature T_g , partial pressure(s) of the absorbing gas(es) p_a , and total pressure p .

Especially important in combustion application, the total emissivity in mixtures of nitrogen with water vapor and/or carbon dioxide may be calculated from Leckner (1972). First, the individual emissivities for water vapor and carbon dioxide, respectively, are calculated separately from

$$\epsilon(p_a L, p, T_g) = \epsilon_0(p_a L, T_g) \frac{\epsilon}{\epsilon_0}(p_a L, p, T_g) \quad (8.77a)$$

$$\frac{\epsilon}{\epsilon_0}(p_a L, p, T_g) = \left[1 - \frac{(a-1)(1-P_E)}{a+b-1+P_E} \exp \left\{ -c \left[\log_{10} \frac{(p_a L)_m}{p_a L} \right]^2 \right\} \right] \quad (8.77b)$$

$$\epsilon_0(p_a L, T_g) = \exp \left[\sum_{i=0}^M \sum_{j=0}^N c_{ji} \left(\frac{T_g}{T_0} \right)^j \left(\log_{10} \frac{p_a L}{(p_a L)_0} \right)^i \right] \quad (8.77c)$$

Here ϵ_0 is the total emissivity at a reference state, which is $p = 1$ bar total pressure and $p_a \rightarrow 0$ (but $p_a L > 0$). The correlation constants $a, b, c, c_{ji}, P_E, (p_a L)_0, (p_a L)_m$, and T_0 are given in Table 8.4 for water vapor and carbon dioxide (for convenience, plots of ϵ_0 are given in Fig. 8.23 for CO_2 and Fig. 8.24 for H_2O). The total emissivity of a mixture of nitrogen with both water vapor and carbon dioxide is calculated from

$$\epsilon_{\text{CO}_2+\text{H}_2\text{O}} = \epsilon_{\text{CO}_2} + \epsilon_{\text{H}_2\text{O}} - \Delta\epsilon \quad (8.78)$$

$$\Delta\epsilon = \left(\frac{\zeta}{10.7 + 101\zeta} - 0.0089\zeta^{10.4} \right) \left[\log_{10} \frac{(p_{\text{H}_2\text{O}} + p_{\text{CO}_2})L}{(p_a L)_0} \right]^{2.76} \quad (8.79)$$

TABLE 8.4 Correlation Constants for the Determination of the Total Emissivity for Water Vapor and Carbon Dioxide

	H_2O			CO_2			
M, N	2,2			2,3			
$c_{00} \cdots c_{N0}$	-2.2118	-1.1987	-0.035596	-3.9893	-2.7669	-2.1081	-0.39163
$\vdots \quad \ddots \quad \vdots$	-0.85667	-0.93048	-0.14391	-1.2710	-1.1090	-1.0195	-0.21897
$c_{0M} \cdots c_{NM}$	-0.10838	-0.17156	-0.045915	-0.23678	-0.19731	-0.19544	-0.044644
P_E	$(p + 2.56p_a/\sqrt{t})/p_0$			$(p + 0.28p_a)/p_0$			
$(p_a L)_m/(p_a L)_0$	$13.2t^2$			$0.054/t^2, t < 0.7$ $0.225t^2, t > 0.7$			
a	$2.144, \quad t < 0.75$ $1.888 - 2.053 \log_{10} t, t > 0.75$			$1 + 0.1/t^{1.45}$			
b	$1.10/t^{1.4}$			0.23			
c	0.5			1.47			

$$T_0 = 1000 \text{ K}, \quad p_0 = 1 \text{ bar}, \quad t = T/T_0, \quad (p_a L)_0 = 1 \text{ bar} \cdot \text{cm}$$

Source: Leckner (1972).

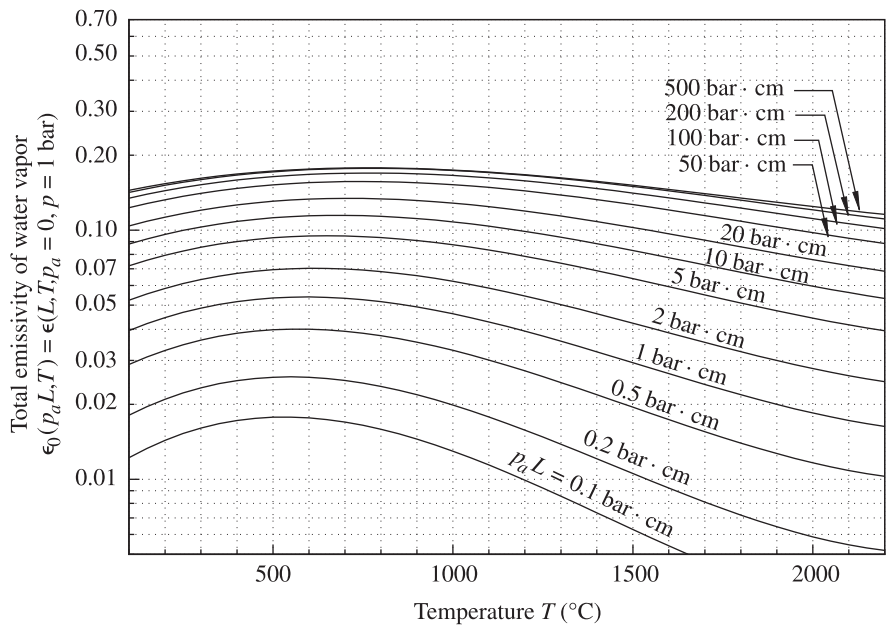


Figure 8.23 Total emissivity of carbon dioxide at a total pressure of 1 bar and zero partial pressure. (From Leckner, 1972.)

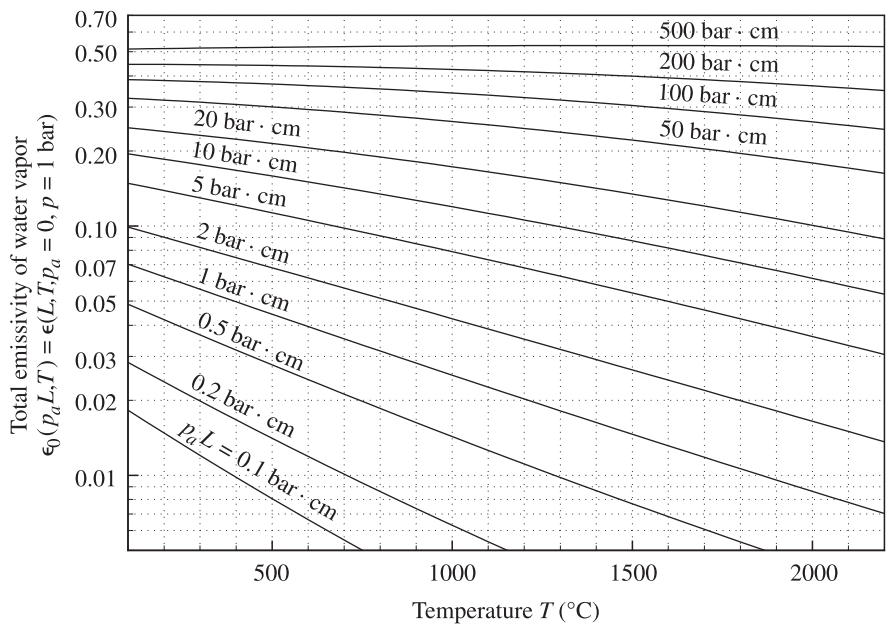


Figure 8.24 Total emissivity of water vapor at a total pressure of 1 bar and zero partial pressure. (From Leckner, 1972.)

where

$$\zeta = \frac{p_{\text{H}_2\text{O}}}{p_{\text{H}_2\text{O}} + p_{\text{CO}_2}}$$

and where the $\Delta\epsilon$ compensates for overlap effects between H_2O and CO_2 bands, and the ϵ_{CO_2} and $\epsilon_{\text{H}_2\text{O}}$ are calculated from eq. (8.77).

If radiation emitted externally to the gas (e.g., by emission from an adjacent wall at temperature T_w) travels through the gas, the total amount absorbed by the gas is of interest. This leads to the absorptivity of a gas path at T_g with a source at T_w :

$$\alpha(p_a L, p, T_g, T_w) = \frac{1}{E_b(T_w)} \int_0^\infty [1 - e^{-\kappa_\lambda(T_g)L}] E_{b\lambda}(T_w) d\lambda \quad (8.80)$$

which for water vapor or carbon dioxide may be estimated from

$$\alpha(p_a L, p, T_g, T_w) = \left(\frac{T_g}{T_w}\right)^{1/2} \epsilon\left(p_a L \frac{T_w}{T_g}, p, T_w\right) \quad (8.81)$$

where ϵ is the emissivity calculated from eq. (8.77) evaluated at the temperature of the surface, T_w , and using an adjusted pressure path length, $p_a L T_w / T_g$. For mixtures of water vapor and carbon dioxide, band overlap is again accounted for by taking

$$\alpha_{\text{CO}_2+\text{H}_2\text{O}} = \alpha_{\text{CO}_2} + \alpha_{\text{H}_2\text{O}} - \Delta\epsilon \quad (8.82)$$

with $\Delta\epsilon$ evaluated for a pressure path length of $p_a L T_w / T_g$.

8.4.2 Particle Clouds

Nearly all flames are visible to the human eye and are therefore called *luminous* (sending out light). Apparently, there is some radiative emission from within the flame at wavelengths where there are no vibration–rotation bands for any combustion gases. This luminous emission is today known to come from tiny *char* (almost pure carbon) particles, called *soot*, which are generated during the combustion process. The dirtier the flame, the higher the soot content and the more luminous the flame.

Soot Soot particles are produced in fuel-rich flames, or fuel-rich parts of flames, as a result of incomplete combustion of hydrocarbon fuels. As shown by electron microscopy, soot particles are generally small and spherical, ranging in size between approximately 5 and 80 nm and up to about 300 nm in extreme cases. Although mostly spherical in shape, soot particles may also appear in agglomerated chunks and even as long agglomerated filaments. It has been determined experimentally in typical diffusion flames of hydrocarbon fuels that the volume percentage of soot generally lies in the range 10^{-4} to $10^{-6}\%$.

Because soot particles are very small, they are generally at the same temperature as the flame and therefore strongly emit thermal radiation in a continuous spectrum over

the infrared region. Experiments have shown that soot emission often is considerably stronger than the emission from the combustion gases.

For a simplified heat transfer analysis it is desirable to use suitably defined mean absorption coefficients and emissivities. If the soot volume fraction f_v is known as well as an appropriate spectral average of the complex index of refraction of the soot, $m = n - \iota k$ ($\iota = \sqrt{-1}$), one may approximate the spectral absorption coefficient from Felske and Tien (1977) as

$$\kappa_\lambda = C_0 \frac{f_v}{\lambda} \quad C_0 = \frac{36\pi nk}{(n^2 - k^2 + 2)^2 + 4n^2k^2} \quad (8.83)$$

and a total or spectral-average value may be taken as

$$\kappa_m = \frac{3.72 f_v C_0 T}{C_2} \quad (8.84)$$

where $C_2 = 1.4388 \text{ cm} \cdot \text{K}$ is the second Planck function constant. Substituting eq. (8.84) into eq. (8.76) gives a total soot cloud emissivity of

$$\epsilon(f_v TL) = 1 - e^{-\kappa_m L} = 1 - e^{-3.72 C_0 f_v TL / C_2} \quad (8.85)$$

Pulverized Coal and Fly Ash Dispersions To calculate the radiative properties of arbitrary size distributions of coal and ash particles, one must have knowledge of their complex index of refraction as a function of wavelength and temperature. Data for carbon and different types of coal indicate that its real part, n , varies little over the infrared and is relatively insensitive to the type of coal (anthracite, lignite, bituminous), while the absorptive index, k , may vary strongly across the spectrum and from coal to coal. If the number and sizes of particles are known and if a suitable average value for the complex index of refraction can be found, the spectral absorption coefficient of the dispersion may be estimated by a correlation given by Buckius and Hwang (1980). They observed spectral behavior to be weak (similar to that of small soot particles) and that spectrally averaged properties do not depend appreciably on the optical properties of the coal. However, due to their larger size, coal particles tend to scatter radiation as well as absorb and emit radiation, leading to the definition of the *scattering coefficient* σ_s and *extinction coefficient* $\beta = \kappa + \sigma_s$. Interpolating the data of Buckius and Hwang, crude approximations for spectrally averaged absorption and extinction coefficients may be determined from

$$\frac{\kappa_m}{f_A} = \left[\left\{ 0.0032 \left[1 + \left(\frac{\phi}{425} \right)^{1.8} \right] \right\}^{-6/5} + \left(\frac{10.99}{\phi^{0.02}} \right)^{-6/5} \right]^{-5/6} \quad (8.86)$$

$$\frac{\beta_m}{f_A} = \left[\left\{ 0.0032 \left[1 + \left(\frac{\phi}{650} \right)^{2.0} \right] \right\}^{-5/4} + \left(\frac{13.75}{\phi^{0.13}} \right)^{-5/4} \right]^{-4/5} \quad (8.87)$$

where f_A is the total projected area of particles per unit volume (e.g., $f_A = \pi a^2 N$ for uniform spheres of radius a and a particle density of N particles/unit volume), and ϕ is a size parameter defined as

$$\phi = \bar{a}T \quad \bar{a} = \frac{3f_v}{4f_A} \quad a \text{ in } \mu\text{m}, \quad T \text{ in K} \quad (8.88)$$

where \bar{a} is an average particle size. This leads to total coal cloud emissivity and absorptivity:

$$\alpha(\phi) = \epsilon(\phi) = 1 - e^{-\kappa_m L} \quad (8.89)$$

On the other hand, if one is interested in transmitted radiation (i.e., radiation not absorbed or scattered away), the cloud transmissivity becomes

$$\tau(\phi) = e^{-\beta_m L} \quad (8.90)$$

If both soot as well as larger particles are present in the dispersion, the absorption coefficients of all constituents must be added before applying eqs. (8.89) and (8.90).

Mixtures of Molecular Gases and Particulates To determine the total emissivity of a mixture, it is generally necessary to find the spectral absorption coefficient κ_λ of the mixture (the sum of the absorption coefficient of all contributors), followed by numerical integration of eqs. (8.89) and (8.90). However, because molecular gases tend to absorb only over a small part of the spectrum, to some degree of accuracy

$$\epsilon_{\text{mix}} \simeq \epsilon_{\text{gas}} + \epsilon_{\text{particulates}} \quad (8.91)$$

Equation (8.91) gives an upper estimate because overlap effects result in lower emissivity [compare eq. (8.78) for gas mixtures].

8.5 RADIATIVE EXCHANGE WITHIN PARTICIPATING MEDIA

To calculate the radiative heat transfer rates within—and to the bounding wall of—a participating medium, it is necessary to solve the *radiative transfer equation* (RTE),

$$\frac{dI_\lambda}{ds} = \hat{s} \cdot \nabla I_\lambda = \kappa_\lambda I_{b\lambda} - \beta_\lambda I_\lambda + \frac{\sigma_{s\lambda}}{4\pi} \int_{4\pi} I_\lambda(\hat{s}_i) \Phi_\lambda(\hat{s}_i, \hat{s}) d\Omega_i \quad (8.92)$$

to some degree of accuracy, followed by integration over all directions and all wavelengths, to obtain the radiative heat flux desired. Here κ_λ is the medium's *absorption coefficient*, $\sigma_{s\lambda}$ its *scattering coefficient*, $\beta_\lambda = \kappa_\lambda + \sigma_{s\lambda}$ is known at the *extinction coefficient*, and Φ_λ is the *scattering phase function*.

As demonstrated in Fig. 8.25, this equation states that spectral radiative intensity I_λ along a path s in the direction of \hat{s} is augmented by emission along the path,

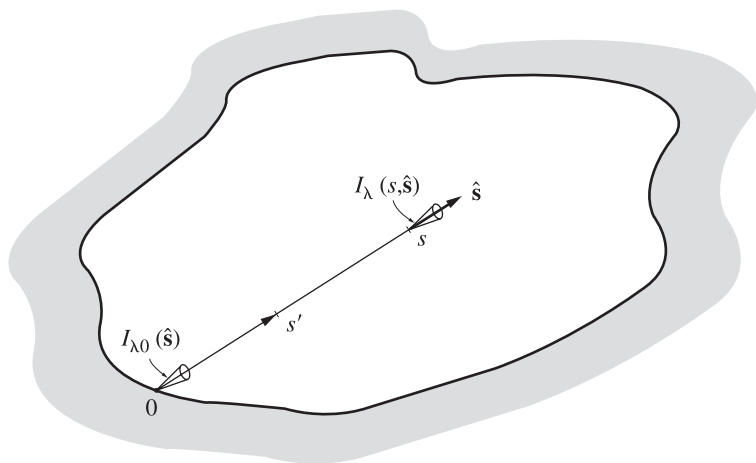


Figure 8.25 Coordinates for the formal solution to the radiative transfer equation.

diminished by extinction or absorption and outscattering (scattering of radiation away from \hat{s}), and augmented by in-scattering (scattering from all other directions \hat{s}_i into direction \hat{s}); κ_λ gives a measure of how much radiation is absorbed and/or emitted, $\sigma_{s\lambda}$ gives a measure of how much is scattered, and Φ_λ is the probability that radiation is scattered from direction \hat{s}_i into direction \hat{s} .

Finding a solution to eq. (8.92), which is an integrodifferential equation in five independent variables (three space coordinates and two direction coordinates), is a truly daunting task for all but the most trivial situations, even at the spectral level. Integration over all wavelengths, due to the complicated nature of radiative properties, tends to add another dimension to the level of difficulty. Consequently, the literature abounds with solutions to very simplistic scenarios as well as with approximate solution methods. A few of these simplified cases and methods are outlined in this section.

In most engineering applications scattering can be neglected, and eq. (8.92) can be formally integrated along a straight path from $s' = 0$ at a bounding wall to a point $s' = s$ inside the medium, to yield

$$I_\lambda(s) = I_\lambda(0)e^{-\kappa_\lambda s} + \int_0^s I_{b\lambda}(s')e^{-\kappa_\lambda(s-s')} \kappa_\lambda ds' \quad (8.93)$$

where it was also assumed that κ_λ is constant along the path. If the medium is isothermal along the path, eq. (8.93) can be reduced further to

$$I_\lambda(s) = I_\lambda(0)e^{-\kappa_\lambda s} + I_{b\lambda}(1 - e^{-\kappa_\lambda s}) \quad (8.94)$$

or

$$I_\lambda(s) = I_\lambda(0)\tau_\lambda(s) + I_{b\lambda}\epsilon_\lambda(s) \quad (8.95)$$

where $\epsilon_\lambda(s)$ is the *spectral emissivity* of a homogeneous column (isothermal, and with constant concentrations of absorbing/emitting material) and $\tau_\lambda(s)$ is its *spectral transmissivity*. For a homogeneous medium, on a spectral basis,

$$\epsilon_\lambda(s) = \alpha_\lambda(s) = 1 - \tau_\lambda(s) = 1 - e^{-\kappa_\lambda s} \quad (8.96)$$

where $\alpha_\lambda(s)$ is the *spectral absorptivity* of the medium.

8.5.1 Mean Beam Length Method

Relatively accurate yet simple heat transfer calculations can be carried out if an isothermal, absorbing–emitting, but not scattering medium is contained in an isothermal, black-walled enclosure. While these conditions are, of course, very restrictive, they are met to some degree by conditions inside furnaces. For such cases the local heat flux on a point of the surface may be calculated by putting eq. (8.94) into eq. (8.20), which leads to

$$q = [1 - \alpha(L_m)]E_{bw} - \epsilon(L_m)E_{bg} \quad (8.97)$$

where E_{bw} and E_{bg} are blackbody emissive powers for the walls and medium (gas and/or particulates), respectively, and $\alpha(L_m)$ and $\epsilon(L_m)$ are the total absorptivity and emissivity of the medium for a path length L_m through the medium. The length L_m , known as the *mean beam length*, is a directional average of the thickness of the medium as seen from the point on the surface. On a spectral basis, equation (8.97) is exact, provided that the foregoing conditions are met and that an accurate value of the (spectral) mean beam length is known. It has been shown that spectral dependence of the mean beam length is weak (generally less than $\pm 5\%$ from the mean). Consequently, total radiative heat flux at the surface may be calculated very accurately from eq. (8.97), provided that the emissivity and absorptivity of the medium are also known accurately. The mean beam lengths for many important geometries have been calculated and are collected in Table 8.5. In this table L_0 is known as the geometric mean beam length, which is the mean beam length for the optically thin limit ($\kappa_\lambda \rightarrow 0$), and L_m is a spectral average of the mean beam length. For geometries not listed in Table 8.5, the mean beam length may be estimated from

$$L_0 \simeq 4 \frac{V}{A} \quad L_m \simeq 0.9L_0 \simeq 3.6 \frac{V}{A} \quad (8.98)$$

where V is the volume of the participating medium and A is its entire bounding surface area.

8.5.2 Diffusion Approximation

A medium through which a photon can travel only a short distance without being absorbed is known as *optically thick*. Mathematically, this implies that $\kappa_\lambda L \gg 1$ for a

TABLE 8.5 Mean Beam Lengths for Radiation from a Gas Volume to a Surface on Its Boundary

Geometry of Gas Volume	Characterizing Dimension, L	Geometric Mean Beam Length, L_0/L	Average Mean Beam Length, L_m/L	L_m/L_0
Sphere radiating to its surface	Diameter, $L = D$	0.67	0.65	0.97
Infinite circular cylinder to bounding surface	Diameter, $L = D$	1.00	0.94	0.94
Semi-infinite circular cylinder to:	Diameter, $L = D$			
Element at center of base		1.00	0.90	0.90
Entire base		0.81	0.65	0.80
Circular cylinder (height/diameter = 1) to:	Diameter, $L = D$			
Element at center of base		0.76	0.71	0.92
Entire surface		0.67	0.60	0.90
Circular cylinder (height/diameter = 2) to:	Diameter, $L = D$			
Plane base		0.73	0.60	0.82
Concave surface		0.82	0.76	0.93
Entire surface		0.80	0.73	0.91
Circular cylinder (height/diameter = 0.5) to:	Diameter, $L = D$			
Plane base		0.48	0.43	0.90
Concave surface		0.53	0.46	0.88
Entire surface		0.50	0.45	0.90
Infinite semicircular cylinder to center of plane rectangular face	Radius, $L = R$		1.26	
Infinite slab to its surface	Slab thickness, L	2.00	1.76	0.88
Cube to a face	Edge, L	0.67	0.6	0.90
Rectangular $1 \times 1 \times 4$ parallelepipeds:	Shortest edge, L			
To 1×4 face		0.90	0.82	0.91
To 1×1 face		0.86	0.71	0.83
To all faces		0.89	0.81	0.91

characteristic dimension L , across which the temperature does not vary substantially. For such an optically thick, nonscattering medium, the spectral radiative flux may be calculated from

$$\mathbf{q}_\lambda = -\frac{4}{3\kappa_\lambda} \nabla E_{b\lambda} \quad (8.99)$$

similar to Fourier's diffusion law for heat conduction. Note that a medium may be optically thick at some wavelengths but thin ($\kappa_\lambda L \ll 1$) at others (such as in molecular gases). For a medium that is optically thick for all wavelengths, eq. (8.99) may be integrated over the spectrum, yielding the total radiative flux

$$\mathbf{q} = -\frac{4}{3\kappa_R} \nabla E_b = -\frac{4}{3\kappa_R} \nabla (\sigma T^4) = -\frac{16\sigma T^3}{3\kappa_R} \nabla T \quad (8.100)$$

where κ_R is a suitably averaged absorption coefficient, termed the *Rosseland mean absorption coefficient*. For a cloud of soot particles, $\kappa_R \simeq \kappa_m$ from eq. (8.76) is a reasonable approximation. Equation (8.100) may be rewritten by defining a radiative conductivity k_R ,

$$\mathbf{q} = -k_R \nabla T \quad k_R = \frac{16\sigma T^3}{3\kappa_R} \quad (8.101)$$

This form shows that the diffusion approximation is mathematically equivalent to conductive heat transfer with a (strongly) temperature-dependent conductivity.

The diffusion approximation can be expected to give accurate results for gas-particulate suspensions with substantial amounts of particulates (such as for very sooty flames and in fluidized beds), and for semitransparent solids and liquids (such as glass or ice/water at low to moderate temperatures, that is, where most of the emissive power lies in the infrared, $\lambda > 2.5 \mu\text{m}$, and where these materials exhibit large absorption coefficients). The method is not suitable for pure molecular gases (such as non- or mildly luminescent flames), because molecular gases are always optically thin across much of the spectrum.

Indeed, more accurate calculations show that in the absence of other modes of heat transfer (conduction, convection), there is generally a temperature discontinuity near the boundaries ($T_{\text{surface}} \neq T_{\text{adjacent medium}}$), and unless boundary conditions that allow such temperature discontinuities are chosen, the diffusion approximation will do very poorly in the vicinity of bounding surfaces.

8.5.3 P-1 Approximation

For the vast majority of engineering applications, very accurate (spectral) values for radiative fluxes \mathbf{q} (and internal radiative sources $\nabla \cdot \mathbf{q}$) can be obtained using the *P-1 approximation*, also known as the *spherical harmonics method* and *differential approximation*. The method assumes that radiative intensity at any point varies smoothly

with direction. Thus, it is particularly suited for optically thick situations (indeed, the diffusion approximation is simply an extreme limit of the P-1 approximation) and for situations in which radiation is emitted isotropically from a hot participating medium (as in combustion applications).

Under the smooth intensity assumption, the radiative transfer equation (8.92) (limited to isotropic scattering) can be integrated over all directions, leading to

$$\nabla \cdot \mathbf{q} = \kappa(4E_b - G), \quad (8.102)$$

$$\nabla G = -3\beta\mathbf{q} \quad (8.103)$$

where the *incident radiation* $G = \int_{4\pi} I d\Omega$ is intensity integrated over all solid angles. These equations are subject to *Marshak's boundary conditions* at the bounding walls:

$$2q_w = \frac{\epsilon_w}{2 - \epsilon_w}(4E_{bw} - G) \quad (8.104)$$

where ϵ_w is the emittance of the wall, q_w the net flux going into the medium, and E_{bw} is emissive power evaluated at the wall temperature (as opposed to the temperature of the medium next to the wall, which may be different in the absence of conduction and convection). Note that for optically thick situations (κ large), $G \rightarrow 4E_b$, and eq. (8.103) reduces to the diffusion approximation, eq. (8.100).

For multidimensional calculations it tends to be advantageous to eliminate the vector \mathbf{q} from eqs. (8.102)–(8.104), leading to an elliptic equation, which is readily incorporated into an overall heat transfer code:

$$\nabla \cdot \left(\frac{1}{\beta} \nabla G \right) - 3\kappa G = -12\kappa E_b \quad (8.105)$$

subject to the boundary condition

$$-\left(\frac{2}{\epsilon_w} - 1 \right) \frac{2}{3\beta} \frac{\partial G}{\partial n} + G = 4E_{bw} \quad (8.106)$$

where $\partial G / \partial n$ is the spatial derivative of G , taken along the surface normal pointing into the medium.

Equation (8.105) and its boundary condition, eq. (8.106), can be solved for suitable averaged values (across the spectrum) of the absorption and extinction coefficient, followed by the evaluation of wall fluxes from eq. (8.104) and/or the radiative source from eq. (8.102). Alternatively, these equations are evaluated on a spectral basis, followed by spectral integration,

$$\mathbf{q} = \int_0^\infty \mathbf{q}_\lambda d\lambda \quad \nabla \cdot \mathbf{q} = \int_0^\infty \kappa_\lambda(4E_{b\lambda} - G_\lambda) d\lambda \quad (8.107)$$

8.5.4 Other RTE Solution Methods

The diffusion approximation and P -1 approximation are powerful, yet simple methods that can give accurate solutions in many engineering applications (and are implemented in all important commercial heat transfer codes). However, they cannot be carried to levels of higher accuracy. This can be achieved by a number of finite volume methods, notably by the *discrete ordinates method* (Modest, 2003; Raithby and Chui, 1990; Chai et al., 1994; Fiveland and Jessee, 1994) and the zonal method (Modest, 1991; Hottel and Sarofim, 1967), and by statistical methods, called *Monte Carlo methods* (Modest, 2003). The discrete ordinate method is probably the most popular higher-order method today and is also implemented in most commercial heat transfer codes. In this method the RTE is solved for a set of discrete directions (ordinates) spanning the total solid angle of 4π . The resulting first-order differential equations are solved along the various directions by breaking up the physical domain into a number of finite volumes. In the presence of nonblack walls and/or scattering, because of the interdependence of different directions, the system of equations must be solved iteratively. Integrals over solid angle are approximated by numerical quadrature (to evaluate the radiative flux and the radiative source). In the zonal method the enclosure is also divided into a finite number of isothermal volume and surface area zones. An energy balance is then performed for the radiative exchange between any two zones, employing precalculated “exchange areas” and “exchange volumes.” This process leads to a set of simultaneous equations for the unknown temperatures or heat fluxes. Once used widely, the popularity of the zonal method has waned recently, and it does not appear to have been implemented in any commercial solver. Monte Carlo or statistical methods are powerful tools to solve even the most challenging problems. However, they demand enormous amounts of computer time, and because of their statistical nature, they are difficult to incorporate into finite volume/finite element heat transfer solvers and are best used for benchmarking (Modest, 2003).

8.5.5 Weighted Sum of Gray Gases

The weighted sum of gray gases (WSGG) is a simple, yet accurate method that has become very popular to address the nongrayness of participating media, in particular for molecular gas mixtures. In this method the nongray gas is replaced by a number of gray ones, for which the heat transfer rates are calculated separately, based on weighted emissive power. The total heat flux and/or radiation source are then found by adding the contributions of the gray gases. The gray gases are determined by a curve fit from the total emissivity and absorptivity of a gas column, such as given by eqs. (8.77) and (8.81),

$$\epsilon(T_g, p_a, s) \simeq \sum_{k=0}^K a_k(T_g, p_a)(1 - e^{-\kappa_k s}) \quad (8.108a)$$

$$\alpha(T_g, T_w, p_a, s) \simeq \sum_{k=0}^K a_k^*(T_g, T_w, p_a)(1 - e^{-\kappa_k s}) \quad (8.108b)$$

For mathematical simplicity the gray gas absorption coefficients κ_k are chosen to be constants, while the weight factors a_k may be functions of temperature. Neither a_k nor κ_k are allowed to depend on path length s . Depending on the material, the quality of the fit, and the accuracy desired, a K value of 2 or 3 usually gives results of satisfactory accuracy (Hottel and Sarofim, 1967). Because, for an infinitely thick medium, the absorptivity approaches unity,

$$\sum_{k=0}^K a_k(T) = 1 \quad (8.109)$$

Still, for a molecular gas with its spectral windows, it would take very large path lengths indeed for the absorptivity to be close to unity. For this reason, eq. (8.108) starts with $k = 0$ (with an implied $\kappa_0 = 0$), to allow for spectral windows.

Substituting this into eqs. (8.102) through (8.104) leads to

$$\nabla \cdot \mathbf{q}_k = \kappa_k(4a_k E_b - G_k) \quad (8.110)$$

$$\nabla G_k = -3\kappa_k \mathbf{q}_k \quad (8.111)$$

and for the bounding walls,

$$2q_{w,k} = \frac{\epsilon_w}{2 - \epsilon_w} (4a_k^* E_{bw} - G_k) \quad (8.112)$$

Total wall flux and internal source are then found from

$$q_w = \sum_{k=0}^K q_{w,k} \quad \nabla \cdot \mathbf{q} = \sum_{k=1}^K \nabla \cdot \mathbf{q}_k \quad (8.113)$$

Note that for $\kappa_0 = 0$ (spectral windows), the enclosure is without a participating medium, and q_w can (and should) be evaluated from eq. (8.68), while $\nabla \cdot \mathbf{q}_0 = 0$.

Mathematically, the weighted-sum-of-gray-gases method is equivalent to the “step-wise gray” assumption, that is, a system where the absorption coefficient is considered a step function in wavelength, with a gray value κ_k over the fraction a_k (based on emissive power) of the spectrum. Some weighted-sum-of-gray-gases absorptivity fits for important gases have been reported in the literature (Modest, 1991; Smith et al., 1982; Farag and Allam, 1981). Very recent work has shown that the weighted-sum-of-gray-gases method is a crude implementation of the also simple *full-spectrum correlated k distribution* method (FSCK) (Modest and Zhang, 2002), which produces almost exact results.

8.5.6 Other Spectral Models

More sophisticated spectral modeling than the weighted-sum-of-gray-gases method is rarely warranted, in particular, because accurate values for the spectral radiative properties are seldom known: in particle-laden media spectral behavior depends strongly on particle material, shape, and size distributions, which are rarely known to a high degree of accuracy; in gases the temperature and pressure behavior is still not perfectly understood, although the new HITEMP database (Rothman et al., 2000) is nearing that goal. For more detailed descriptions of particle models, the reader should consult textbooks (Modest, 2003; Bohren and Huffman, 1983), while the state of the art in gas modeling is described in Goody and Yung (1989) and Taine and Soufiani (1999).

NOMENCLATURE

Roman Letter Symbols

A	matrix of view factors, dimensionless
A	area, m ²
	absorptance of a slab, dimensionless
<i>a</i>	radius of sphere, m
\bar{a}	average particle size, m
a_k, a_k^*	gray gas weight factors, dimensionless
b	column vector of heat fluxes, W/m ²
C_0	constant for particulate absorption coefficient, dimensionless
C_1, C_2, C_3	radiation constants, dimensions vary
<i>c</i>	speed of light, m/s
c_0	speed of light in vacuum, 2.998×10^8 m/s
<i>E</i>	emissive power, W/m ²
e_b	column vector of emissive powers, W/m ²
F_{i-j}	view factor, dimensionless
<i>f</i>	fractional Planck function, dimensionless
f_A	projected area of particles per unit volume, m ⁻¹
f_v	soot volume fraction, dimensionless
<i>G</i>	incident radiation, W/m ²
<i>H</i>	irradiation, W/m ²
H_0	irradiation from external source, W/m ²
<i>h</i>	Planck's constant, 6.626×10^{-34} J · s
<i>I</i>	radiative intensity, W/m ² · sr
<i>i</i>	index or counter, dimensionless
$\hat{\mathbf{i}}$	unit vector, dimensionless
<i>J</i>	surface radiosity, W/m ²
$\hat{\mathbf{j}}$	unit vector, dimensionless
<i>j</i>	index or counter, dimensionless

$\hat{\mathbf{k}}$	unit vector, dimensionless
k	Boltzmann's constant, 1.3806×10^{-23} J/K
	imaginary part of complex index of refraction, dimensionless
k_R	radiative thermal conductivity, W/m · K
L	path length, m
	thickness of sheet, m
L_m	spectrally averaged mean beam length, m
L_0	geometric mean beam length, m
l	direction cosine in x -coordinate direction, dimensionless
m	complex index of refraction, dimensionless
	direction cosine in y -coordinate direction, dimensionless
N	number of surfaces in enclosure, dimensionless
$\hat{\mathbf{n}}$	normal unit vector, dimensionless
n	refractive index, dimensionless
	direction cosine in z -coordinate direction, dimensionless
P	point, dimensionless
p	pressure, Pa
Q	radiative heat flow, W
\mathbf{q}	radiative heat flux vector, W/m ²
q	radiative heat flux, W/m ²
R	radiation resistance, m ⁻²
	reflectance of a slab, dimensionless
	radius, m
\mathbf{r}	position vector, m
S	distance between points, m
\mathbf{s}	distance vector, m
$\hat{\mathbf{s}}$	direction unit vector, dimensionless
T	temperature, K
	transmittance of a slab, dimensionless
V	volume of participating medium, m ³
x	Cartesian length coordinate, m
y	Cartesian length coordinate, m
z	Cartesian length coordinate, m

Greek Letter Symbols

α	absorptance, dimensionless
β	extinction coefficient, m ⁻¹
Γ	contour, m
ϵ	surface emittance, dimensionless
	gas column emissivity, dimensionless
η	wavenumber, cm ⁻¹
θ	polar angle, rad
κ	absorption coefficient, m ⁻¹
κ_R	Rosseland mean absorption coefficient, m ⁻¹
λ	wavelength, μm

ν	frequency, Hz
ρ	reflectance, dimensionless
σ	Stefan–Boltzmann constant, $5.67 \times 10^{-8} \text{ W/m}^2 \cdot \text{K}^4$
σ_{dc}	electrical conductivity $\Omega^{-1} \cdot \text{m}^{-1}$
σ_m	rms roughness, m
σ_s	scattering coefficient, m^{-1}
τ	transmittance, dimensionless
	transmissivity of gas column, dimensionless
Φ	scattering phase function, dimensionless
ϕ	size parameter, dimensionless
ψ	azimuthal angle, rad
Ω	solid angle, sr

Roman Letter Subscripts

A	area
b	black
g	gas
i	incoming
n	normal direction
o	outgoing
p	associated with point P
s	slab (multiple reflections)
v	volume
w	wall
\parallel	parallel polarized component
\perp	perpendicular polarized component

Greek Letter Subscripts

λ	spectral (wavelength)
ν	spectral (frequency)

Superscripts

$'$	directional quantity
(m)	spectral range m , or band m

REFERENCES

- American Institute of Physics (1972). *American Institute of Physics Handbook*, 3rd ed., McGraw-Hill, New York, Chap. 6.
- Bennett, H. E., Silver, M., and Ashley, E. J. (1963). Infrared Reflectance of Aluminum Evaporated in Ultra-high Vacuum, *J. Opt. Soc. Am.*, Vol. 53(9), 1089–1095.
- Bohren, C. F., and Huffman, D. R. (1983). *Absorption and Scattering of Light by Small Particles*, Wiley, New York.

- Brandenberg, W. M. (1963). The Reflectivity of Solids at Grazing Angles, in *Measurement of Thermal Radiation Properties of Solids*, J. C. Richmond, NASA-SP-31, pp. 75–82.
- Brandenberg, W. M., and Clausen, O. W. (1965). The Directional Spectral Emittance of Surfaces between 200 and 600 C, in *Symposium on Thermal Radiation of Solids*, S. Katzoff, NASA-SP-55, pp. 313–319.
- Buckius, R. O., and Hwang, D. C. (1980). Radiation Properties for Polydispersions: Application to Coal, *Heat Transfer*, 102, 99–103.
- Chai, J. C., Lee, H. S., and Patankar, S. V. (1994). Finite Volume Method for Radiation Heat Transfer, *J. Thermophys. Heat Transfer*, 8(3), 419–425.
- Dunkle, R. V. (1965). Emissivity and Inter-reflection Relationships for Infinite Parallel Specular Surfaces, in *Symposium on Thermal Radiation of Solids*, S. Katzoff, ed., NASA-SP-55, pp. 39–44.
- Dunkle, R. V., and Gier, J. T. (1953). Snow Characteristics Project Progress Report, Technical report, University of California–Berkeley, June.
- Farag, I. H., and Allam, T. A. (1981). Gray-Gas Approximation of Carbon Dioxide Standard Emissivity, *J. Heat Transfer*, 103, 403–405.
- Felske, J. D., and Tien, C. L. (1977). The Use of the Milne–Eddington Absorption Coefficient for Radiative Heat Transfer in Combustion Systems, *J. Heat Transfer*, 99(3), 458–465.
- Fiveland, W. A., and Jessee, J. P. (1994). Finite Element Formulation of the Discrete-Ordinates Method for Multidimensional Geometries, *J. Thermophys. Heat Transfer*, 8(3), 426–433.
- Goody, R. M., and Yung, Y. L. (1989). *Atmospheric Radiation: Theoretical Basis*, 2nd ed., Oxford University Press, New York.
- Hottel, H. C., and Sarofim, A. F. (1967). *Radiative Transfer*, McGraw-Hill, New York.
- Leckner, B. (1972). Spectral and Total Emissivity of Water Vapor and Carbon Dioxide, *Combust. Flame*, 19, 33–48.
- Modest, M. F. (1991). The Weighted-Sum-of-Gray-Gases Model for Arbitrary Solution Methods in Radiative Transfer, *J. Heat Transfer*, 113(3), 650–656.
- Modest, M. F., and Zhang, H. (2002). The Full-Spectrum Correlated- k Distribution For Thermal Radiation from Molecular Gas–Particulate Mixtures, *J. Heat Transfer*, 124(1), 30–38.
- Modest, M. F. (2003). *Radiative Heat Transfer*, 2nd ed., Academic Press, New York, 118–131.
- Oppenheim, A. K. (1956). Radiation Analysis by the Network Method, *Trans. ASME, J. Heat Transfer*, 78, 725–735.
- Parker, W. J., and Abbott, G. L. (1965). Theoretical and Experimental Studies of the Total Emittance of Metals, in *Symposium on Thermal Radiation of Solids*, S. Katzoff, ed., NASA-SP-55, pp. 11–28.
- Price, D. J. (1947). The Emissivity of Hot Metals in the Infrared, *Proc. Phys. Soc.*, 59(311), 118–131.
- Raithby, G. D., and Chui, E. H. (1990). A Finite-Volume Method for Predicting Radiant Heat Transfer Enclosures with Participating Media, *J. Heat Transfer*, 112(2), 415–423.
- Rothman, L. S., Rinsland, C. P., Goldman, A., Massie, S. T., Edwards, D. P., Flaud, J. M., Perrin, A., Camy-Peyret, C., Dana, V., Mandin, J. Y., Schroeder, J., McCann, A., Gamache, R. R., Wattson, R. B., Yoshino, K., Chance, K. V., Jucks, K. W., Brown, L. R., Nemtchinov, V., and Varanasi, P. (1998). The HITRAN Molecular Spectroscopic Database and HAWKS (HITRAN Atmospheric Workstation): 1996 Edition, *J. Quant. Spectrosc. Radiat. Transfer*, 60, 665–710.

- Rothman, L. S., Camy-Peyret, C., Flaud, J.-M., Gamache, R. R., Goldman, A., Goorvitch, D., Hawkins, R. L., Schroeder, J., Selby, J. E. A., and Wattson, R. B. (2000). HITEMP, the High-Temperature Molecular Spectroscopic Database, *J. Quant. Spectrosc. Radiat. Transfer*, 62, 511–562.
- Schmidt, E., and Eckert, E. R. G. (1935). Über die Richtungsverteilung der Wärmestrahlung von Oberflächen, *Forsch. Geb. Ingenieurwes.*, 7, 175.
- Siegel, R., and Howell, J. R. (1992). *Thermal Radiation Heat Transfer*, 4th ed., Taylor and Francis, New York.
- Smith, T. F., Shen, Z. F., and Friedman, J. N. (1982). Evaluation of Coefficients for the Weighted Sum of Gray Gases Model, *J. Heat Transfer*, 104, 602–608.
- Taine, J., and Soufiani, A. (1999). *Gas IR Radiative Properties: From Spectroscopic Data to Approximate Models*, Vol. 33, Academic Press, New York, pp. 295–414.
- Touloukian, Y. S., and DeWitt, D. P., eds. (1970). *Thermal Radiative Properties: Metallic Elements and Alloys*, Vol. 7 of *Thermophysical Properties of Matter*, Plenum Press, New York.
- Touloukian, Y. S., and DeWitt, D. P., eds. (1972). *Thermal Radiative Properties: Nonmetallic Solids*, Vol. 8 of *Thermophysical Properties of Matter*, Plenum Press, New York.
- Touloukian, Y. S., DeWitt, D. P., and Hearn, R. S., eds. (1973). *Thermal Radiative Properties: Coatings*, Vol. 9 of *Thermophysical Properties of Matter*, Plenum Press, New York.
- Weast, R. C., ed. (1988). *CRC Handbook of Chemistry and Physics*, 68th ed., Chemical Rubber Company, Cleveland, OH.
- White, F. M. (1984). *Heat Transfer*, Addison-Wesley, Reading, MA.

Boiling

JOHN R. THOME

Laboratory of Heat and Mass Transfer
Faculty of Engineering Science
Swiss Federal Institute of Technology Lausanne
Lausanne, Switzerland

- 9.1 Introduction to boiling heat transfer
- 9.2 Boiling curve
- 9.3 Boiling nucleation
 - 9.3.1 Introduction
 - 9.3.2 Nucleation superheat
 - 9.3.3 Size range of active nucleation sites
 - 9.3.4 Nucleation site density
- 9.4 Bubble dynamics
 - 9.4.1 Bubble growth
 - 9.4.2 Bubble departure
 - 9.4.3 Bubble departure frequency
- 9.5 Pool boiling heat transfer
 - 9.5.1 Nucleate boiling heat transfer mechanisms
 - 9.5.2 Nucleate pool boiling correlations
 - Bubble agitation correlation of Rohsenow
 - Reduced pressure correlation of Mostinski
 - Physical property type of correlation of Stephan and Abdelsalam
 - Reduced pressure correlation of Cooper with surface roughness
 - Fluid-specific correlation of Gorenflo
 - 9.5.3 Departure from nucleate pool boiling (or critical heat flux)
 - 9.5.4 Film boiling and transition boiling
- 9.6 Introduction to flow boiling
- 9.7 Two-phase flow patterns
 - 9.7.1 Flow patterns in vertical and horizontal tubes
 - 9.7.2 Flow pattern maps for vertical flows
 - 9.7.3 Flow pattern maps for horizontal flows
- 9.8 Flow boiling in vertical tubes
 - 9.8.1 Chen correlation
 - 9.8.2 Shah correlation
 - 9.8.3 Gungor–Winterton correlation
 - 9.8.4 Steiner–Taborek method
- 9.9 Flow boiling in horizontal tubes
 - 9.9.1 Horizontal tube correlations based on vertical tube methods

- 9.9.2 Horizontal flow boiling model based on local flow regime
- 9.9.3 Subcooled boiling heat transfer
- 9.10 Boiling on tube bundles
 - 9.10.1 Heat transfer characteristics
 - 9.10.2 Bundle boiling factor
 - 9.10.3 Bundle design methods
- 9.11 Post-dryout heat transfer
 - 9.11.1 Introduction
 - 9.11.2 Thermal nonequilibrium
 - 9.11.3 Heat transfer mechanisms
 - 9.11.4 Inverted annular flow heat transfer
 - 9.11.5 Mist flow heat transfer
- 9.12 Boiling of mixtures
 - 9.12.1 Vapor–liquid equilibria and properties
 - 9.12.2 Nucleate boiling of mixtures
 - 9.12.3 Flow boiling of mixtures
 - 9.12.4 Evaporation of refrigerant–oil mixtures
- 9.13 Enhanced boiling
 - 9.13.1 Enhancement of nucleate pool boiling
 - 9.13.2 Enhancement of internal convective boiling

Nomenclature

References

9.1 INTRODUCTION TO BOILING HEAT TRANSFER

When heat is applied to a surface in contact with a liquid, if the wall temperature is sufficiently above the saturation temperature, boiling occurs on the wall. Boiling may occur under quiescent fluid conditions, which is referred to as *pool boiling*, or under forced-flow conditions, which is referred to as *forced convective boiling*. In this chapter a review of the fundamentals of boiling is presented together with numerous predictive methods. First the fundamentals of pool boiling are addressed and then those of flow boiling. To better understand the mechanics of flow boiling, a section is also presented on two-phase flow patterns and flow pattern maps. Then the effects of mixture boiling are described. Finally, the topic of enhanced heat transfer is introduced.

For more exhaustive treatments of boiling heat transfer, the following books are recommended for consultation: Tong (1965), Wallis (1969), Hsu and Graham (1976), Ginoux (1978), van Stralen and Cole (1979), Delhaye et al. (1981), Whalley (1987), Thome (1990), Carey (1992) and Collier and Thome (1994). In addition, Rohsenow (1973) provides a detailed historical presentation of boiling research.

9.2 BOILING CURVE

When heating a surface in a large pool of liquid, the heat flux q is usually plotted versus the wall superheat ΔT_{sat} , which is the temperature difference between the surface and the saturation temperature of the liquid. First constructed by Nukiyama (1934), the *boiling curve* depicted in Fig. 9.1 is also referred to as *Nukiyama's curve*, where four distinct heat transfer regimes can be identified:

1. *Natural convection*. This is characterized by single-phase natural convection from the hot surface to the saturation liquid without formation of bubbles on the surface.
2. *Nucleate boiling*. This is a two-phase natural convection process in which bubbles nucleate, grow, and depart from the heated surface.
3. *Transition boiling*. This is an intermediate regime between the nucleate boiling and film boiling regimes.

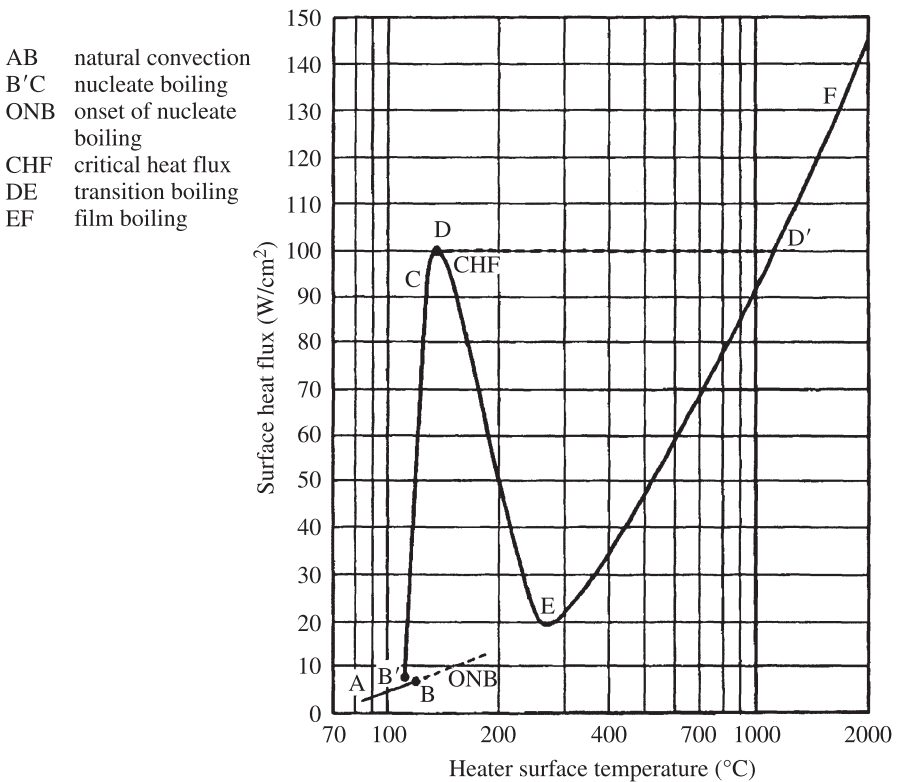


Figure 9.1 Nukiyama's boiling curve.

4. *Film boiling*. This mode is characterized by a stable layer of vapor that forms between the heated surface and the liquid, such that the bubbles form at the free interface and not at the wall.

Between these four regimes are three transition points. The first is called *incipience of boiling* (IB) or *onset of nucleate boiling* (ONB), at which the first bubbles appear on the heated surface. The second is the peak in the curve at the top of the nucleate boiling portion of the curve, referred to as *departure from nucleate boiling* (DNB), the *critical heat flux* (CHF), or *peak heat flux*. The last transition point is located at the lower end of the film boiling regime (at the letter *E*) and is called the *minimum film boiling* (MFB) point. These are all denoted in Fig. 9.1, while a representation of these regimes is shown in Fig. 9.2.

In the natural convection part of the curve, the wall temperature rises as the heat flux is increased until the first bubbles appear, signaling the incipience of boiling. These bubbles form (or nucleate) at small cavities in the heated surface, which are called *nucleation sites*. The active nucleation sites are located at pits and scratches in the surface. Increasing the heat flux, more and more nucleation sites become activated until the surface is covered with bubbles that grow and depart in rapid succession. The heat flux increases dramatically for relatively modest increases in ΔT_{sat} (defined as $T_w - T_{\text{sat}}$), noting that the scale is log-log. Increasing the heat flux even further, departing bubbles coalesce into vapor jets, changing the slope of the nucleate boiling curve. A further increase in q eventually prohibits the liquid from reaching the heated surface, which is referred to as the DNB or CHF, such that complete blanketing of the surface by vapor occurs, accompanied by a rapid rise in the surface temperature to dissipate the applied heat flux.

Following DNB, the process follows a path that depends on the manner in which the heat flux is applied to the surface. For heaters that impose a heat flux at the surface, such as electrical-resistance elements or nuclear fuel rods, the process progresses on a horizontal line of constant heat flux so that the wall superheat jumps to point D' , where film boiling prevails as shown in Fig. 9.1, and whose vapor bubbles grow and depart from the vapor-liquid interface of the vapor layer, not from the surface. A ulterior increase in q may bring the surface to the *burnout point* (letter *F*), where the surface temperature reaches the melting point of the heater. Reducing the heat flux, the film boiling curve passes below point D' until reaching point *E*, the MFB point. Here again, the process path depends on the mode of heating. For an imposed heat flux, the process path jumps horizontally at constant q to the nucleate boiling curve $B'C$. Consequently, a hysteresis loop is formed when heating a surface up past the DNB and then bringing it below MFB when q is the boundary condition imposed.

When the wall temperature is the externally controlled variable, such as by varying the saturation temperature of steam condensing inside a tube with boiling on the outside, the process path moves from the DNB to the MFB point, and vice versa, following the transition boiling path. In transition boiling, the process vacillates between nucleate boiling and film boiling, where each mode may coexist next to the

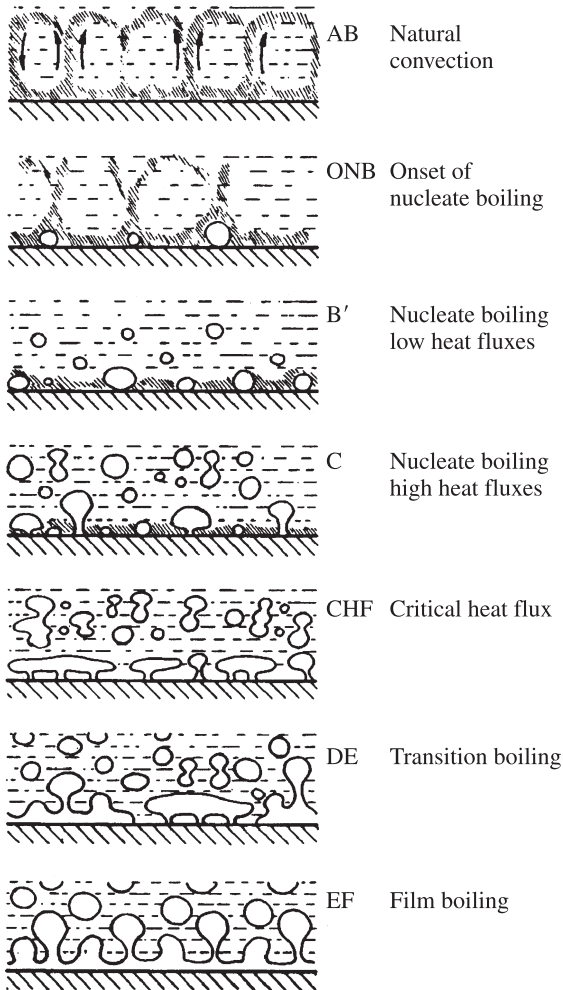


Figure 9.2 Pool boiling regimes.

another on the heated surface or may alternate at the same location on the surface. In film boiling, the wall is blanketed completely by a thin film of vapor, and therefore heat is conveyed by heat conduction across the vapor film and by radiation from the wall to the liquid or to the walls of the vessel. The vapor film is stable in that liquid does not normally wet the heater surface and relatively large bubbles are formed by evaporation at the free vapor–liquid interface, which then depart and rise up through the liquid pool. In the next sections, important aspects of the boiling curve, its phenomena, and predictive methods are described.

9.3 BOILING NUCLEATION

9.3.1 Introduction

In a pool of liquid, a vapor nucleus may form either at a heated surface or within the liquid itself if it is sufficiently superheated, a process called *nucleation*. If there is a preexistent vapor space above the liquid pool which is at its saturation temperature, then upon heating, vapor forms at the free interface without nucleation, which is referred to as *evaporation*. If nucleation is attained instead by reducing the pressure of the fluid rapidly or locally, this is called *cavitation* (e.g., that occurring on a rapidly rotating propeller of a ship).

Nucleation occurring in the bulk of a superheated, perfectly clean liquid is referred to as *homogeneous nucleation*, which may occur as a photon passes through a bubble chamber of superheated liquid hydrogen, leaving behind a photographic trace observed in early particle physics experiments. Homogeneous nucleation occurs when the free energy of formation of a cluster of molecules in the liquid phase is sufficient to form a vapor interface remote from the walls of the vessel. Instead, *heterogeneous nucleation* initiates at a solid surface when the free energy of formation there, or in a cavity in a surface, forms a vapor nucleus, or when a preexisting vapor nucleus in such a cavity reaches a superheat sufficient to initiate bubble growth. For homogeneous or heterogeneous nucleation to occur, the temperature must be elevated above the saturation temperature of the liquid to form or activate vapor nuclei. Hence, boiling does not begin when the saturation temperature is reached but instead, when a certain superheat is attained. Typically, nucleation occurs from a preexisting vapor nucleus residing within a cavity or from a vapor nucleus that protrudes into the thermal boundary layer formed at the wall.

9.3.2 Nucleation Superheat

The superheating of the liquid with respect to the saturation temperature that is required for nucleation to be achieved is referred to as the *nucleation superheat*. First, we consider the process of homogeneous nucleation. In Fig. 9.3 the mechanical equilibrium of forces at the interface of a spherical vapor nucleus (of radius r_{nuc}) in a liquid at uniform temperature T_G and pressure p_G is given by the Laplace equation,

$$p_G - p_L = \frac{2\sigma}{r_{\text{nuc}}} \quad (9.1)$$

where p_G is the vapor pressure inside the nucleus, p_L the local liquid pressure, and σ the surface tension. Since $p_G > p_L$, the surface tension balances the pressure difference across the interface and the pressure difference increases with decreasing nucleation radius, r_{nuc} . In addition, there is an effect of the curvature of the interface on the vapor pressure curve of the fluid, which lowers the pressure in the vapor nucleus relative to that above a planar interface p_∞ at the same fluid temperature, which has been shown by Lord Kelvin (1871) to be

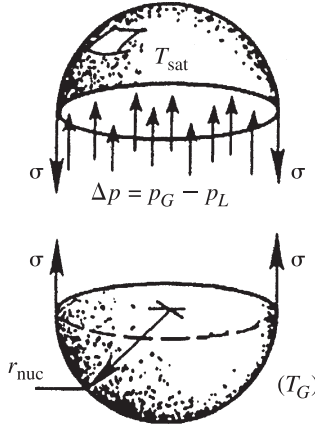


Figure 9.3 Vapor nucleus in a pool of liquid.

$$p_G = p_\infty \exp\left(\frac{-2\sigma v_L M}{r_{\text{nuc}} \bar{R} T}\right) \approx p_\infty \left(1 - \frac{2\sigma v_L}{p_\infty r_{\text{nuc}} v_G}\right) \quad (9.2)$$

where M is the molecular weight in kg/mol, \bar{R} is the ideal gas constant ($\bar{R} = 8.3144$ J/mol·K), and the specific volumes of the vapor and liquid are v_G and v_L , respectively. Introducing eq. (9.1) for $2\sigma/r_{\text{nuc}}$ into eq. (9.2) and rearranging yields

$$p_\infty - p_L = \frac{2\sigma}{r_{\text{nuc}}} \left(1 + \frac{v_L}{v_G}\right) \quad (9.3)$$

For a planar vapor–liquid interface, the slope of the vapor pressure curve is given by the Clausius–Clapeyron equation,

$$\left(\frac{dp}{dT}\right)_{\text{sat}} = \frac{h_{LG}}{T_{\text{sat}}(v_G - v_L)} \quad (9.4)$$

where T_{sat} is in K. Assuming that the vapor behaves as a perfect gas, then

$$Mp_G v_G = \bar{R} T \quad (9.5)$$

Thus, for $v_G \gg v_L$, eq. (9.4) becomes

$$\frac{1}{p} dp = \frac{h_{LG} M}{\bar{R} T^2} dT \quad (9.6)$$

Now integrating this expression from p_L to p_∞ and from T_{sat} to T_G , we have

$$\ln \frac{p_\infty}{p_L} = -\frac{h_{LG} M}{\bar{R}} \left(\frac{1}{T_G} - \frac{1}{T_{\text{sat}}}\right) = \frac{h_{LG} M}{\bar{R} T_G T_{\text{sat}}} (T_G - T_{\text{sat}}) \quad (9.7)$$

Substituting (9.3) and again rearranging gives us

$$T_G - T_{\text{sat}} = \frac{\bar{R}T_{\text{sat}}T_G}{h_{LG}M} \ln \left[1 + \frac{2\sigma}{p_L r_{\text{nuc}}} \left(1 + \frac{v_L}{v_G} \right) \right] \quad (9.8)$$

Since $v_G \gg v_L$ and $2\sigma/p_L r_{\text{nuc}} \ll 1$, this simplifies to

$$T_G - T_{\text{sat}} = \Delta T_{\text{nuc}} = \frac{\bar{R}T_{\text{sat}}^2}{h_{LG}M} \frac{2\sigma}{p_L r_{\text{nuc}}} \quad (9.9)$$

This expression gives the nucleation superheat ΔT_{nuc} , which is the difference between the saturation temperature of the vapor T_G at the pressure inside the nucleus p_G and the saturation temperature T_{sat} at the pressure in the surrounding liquid p_L . An equivalent and easier to use form is

$$\Delta T_{\text{nuc}} = \frac{2\sigma}{r_{\text{nuc}}(dp/dT)_{\text{sat}}} \quad (9.10)$$

where $(dp/dT)_{\text{sat}}$ is obtained with eq. (9.4) or, more accurately, from the equation of state of the fluid. Expression (9.10) is also obtainable by introducing $(dp/dT)_{\text{sat}}$ into eq. (9.1). The nucleation superheat ΔT_{nuc} represents the uniform superheating of the liquid required for a stable vapor bubble of radius r_{nuc} to exist. If the superheat is less than this, the nucleus will collapse, whereas if it is larger, it will grow as a bubble.

If air is trapped in the nucleus with the vapor, either while filling the vessel or by degassing of the liquid itself, the partial pressure of the gas, p_a , must be taken into consideration in eq. (9.1), so that

$$p_G + p_a - p_L = \frac{2\sigma}{r_{\text{nuc}}} \quad (9.11)$$

$$T_G - T_{\text{sat}} = \frac{\bar{R}T_{\text{sat}}T_G}{h_{LG}M} \ln \left(1 + \frac{2\sigma}{p_L r_{\text{nuc}}} - \frac{p_a}{p_L} \right) \quad (9.12)$$

Presence of a noncondensable gas thus reduces the nucleation superheat required to initiate boiling.

For heterogeneous nucleation at a flat surface, the free energy of formation required to create a vapor embryo is smaller than for homogeneous nucleation. Their respective nucleation superheats can be related by multiplying that for homogeneous nucleation by a factor ϕ . As illustrated in Fig. 9.4a ϕ depends on the contact angle β between the surface and the liquid:

$$\phi = \frac{2 + 2 \cos \beta \cos \beta \sin^2 \beta}{4} \quad (9.13)$$

$\beta = 0$ for a liquid that completely wets the surface, so in that case $\phi = 1$. If the surface is completely nonwetting, $\beta = \pi$, and thus in this case, $\phi = 0$ (i.e., no superheat is

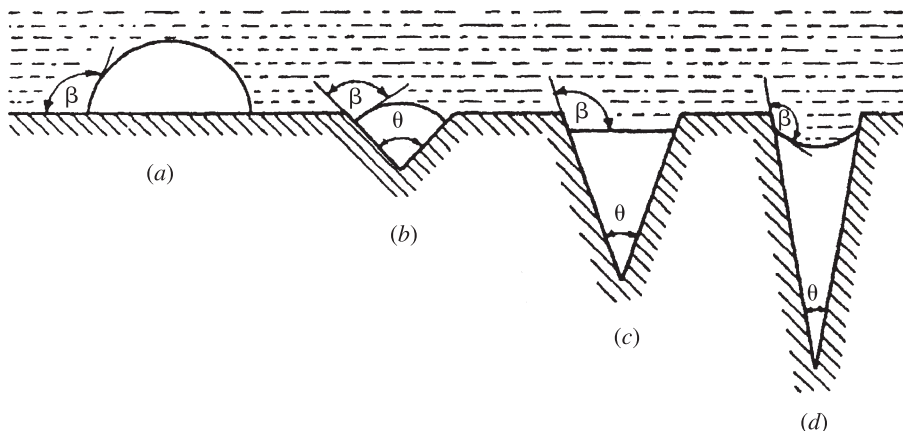


Figure 9.4 Nucleation: (a) plane surface; (b–d) triangular cavity.

required for nucleation). Typically, the contact angle ranges from $0 < \beta < \pi/2$, so possible values of ϕ are $\frac{1}{2} < \phi < 1$. However, bubbles are normally generated at microcavities in the solid surface, such as that illustrated in Fig. 9.4*b* with an included angle θ . The apparent contact angle β' for eq. (9.13) is then

$$\beta' = \beta + \frac{\pi - \theta}{2} \quad (9.14)$$

As a consequence, the energy required for formation of a bubble is less at these cavities than on a planar surface or in the bulk, and therefore bubble nucleation occurs preferentially at a cavity. Larger cavities with large θ give a value of β' closer to β than smaller cavities, implying that larger cavities will nucleate first.

The contact angle β between the wall and the liquid–vapor interface is generally unknown for most fluid–surface combinations, and no reliable prediction method is available, which also complicates the prediction of the nucleation superheat. Contact angle is a function of the surface finish, such as whether or not it is clean, oxidized, fouled, polished, or wettable at all, and also depends on whether the interface is advancing or receding. Table 9.1 lists contact angles of some common fluids on surfaces polished with emery paper. The mechanics of nucleation at a cavity are essentially as follows. As T_w of the cavity increases above T_{sat} , a vapor nucleus trapped in a cavity expands until it reaches the mouth of the cavity. If the liquid surrounding the protruding nucleus is superheated, the bubble will grow. As a bubble grows, less superheat is required to maintain its mechanical stability. Thus, it is this radius of the cavity mouth that determines the degree of superheat required to activate a boiling site.

TABLE 9.1 Advancing Contact Angles

Liquid	Surface	β (deg)
Water	Copper	86
	Brass	84
Benzene	Copper	25
	Brass	23
Ethanol	Copper	14–19
	Brass	14–18
Methanol	Copper	25
	Brass	22
<i>n</i> -Propanol	Copper	13
	Brass	8

Source: Shakir and Thome (1986).

9.3.3 Size Range of Active Nucleation Sites

Above, a single uniform temperature was assumed for the wall and liquid. A more practical case is when there is a temperature gradient in the form of a thermal boundary layer in the liquid adjacent to the wall, such as illustrated in Fig. 9.5 for a conical nucleation site, where a vapor nucleus of radius r_{nuc} sits at the cavity mouth. The bulk liquid temperature is T_∞ , the wall temperature is T_w (where $T_w \geq T_\infty$) and a linear temperature gradient is assumed in the thermal boundary layer of thickness δ . If α_{nc} is the natural convection heat transfer coefficient and λ_L is the thermal conductivity of the liquid, the boundary layer thickness is approximately

$$\delta = \frac{\lambda_L}{\alpha_{nc}} \tag{9.15}$$

Hsu (1962) postulated that a nucleus sitting in such a temperature gradient activates if the superheat at the top of the vapor nucleus is greater than that required for its equilibrium [i.e., eq. (9.10)], including the distortion of the temperature profile by the bubble nucleus itself. Nucleation occurs if the local liquid temperature profile intersects the equilibrium nucleation curve. The first site to activate is at the tangency between the nucleation superheat curve and the liquid temperature profile line. Hsu assumed that distortion put the location of this temperature at a distance $2r_{\text{nuc}}$ from the surface, while Han and Griffith (1965) put the distance at $1.5r_{\text{nuc}}$ based on potential flow theory. If the liquid pool is at the saturation temperature (i.e., if $T_\infty = T_{\text{sat}}$ and $1.5r_{\text{nuc}}$ is assumed for displacement of the isotherms), the cavity size satisfying the condition of tangency is $r_{\text{nuc}} = \delta/2$, which is approximately 50 μm for water at its normal boiling point.

Much larger superheats or heat fluxes are typically necessary, however, to initiate boiling on a heated surface. This discrepancy results from the fact that a range of cavity sizes exists on a real surface, and large cavities that respect the criterion above may

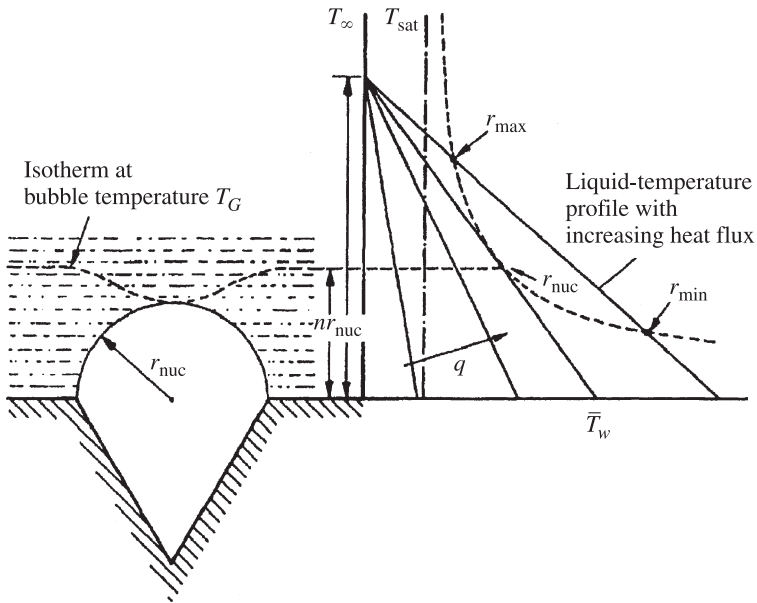


Figure 9.5 Nucleation in a temperature gradient.

not be available. In this case, T_w must be increased until the liquid temperature profile intersects the equilibrium bubble curve corresponding to a smaller cavity. Thus, there is a maximum nucleation radius r_{max} and a minimum nucleation radius r_{min} that will activate among those available, where r_{max} is the largest cavity size available that meets the nucleation criterion, and similarly, r_{min} is the smallest cavity size that meets the criterion nearer the surface. In reality, no such cavity may be available, or only one at the tangency point, or finally, numerous cavities in the size range from r_{min} to r_{max} , and hence this introduces the concept of a size range of active nucleation sites. Actual prediction of the nucleation superheat for a surface is complicated by our lack of knowledge of the size and shape of the cavities actually available. Consequently, it is more typical to observe the superheat at which nucleation occurs experimentally and then to back-calculate the effective nucleation radius using eq. (9.10).

9.3.4 Nucleation Site Density

As the heat flux at the surface is increased, more and more nucleation sites activate and the question arises as to *how many* sites are active per unit area. The nucleation site density can be determined using several approaches. First, active boiling sites can be counted with heat flux or wall superheat as the independent variable, typically using photographs or videos of the boiling process. Second, the nucleation site density can be inferred from the measured heat flux by postulating some heat transfer mechanisms. There is rarely agreement between these two approaches. Third, the

size and distribution of cavities on the surface can be determined using a scanning electron microscope. However, this is tedious and the resulting distribution of cavities only describes the actual surface investigated. As a consequence, prediction of the nucleation site density is only an approximate estimate.

9.4 BUBBLE DYNAMICS

The growth of vapor bubbles can be a particularly complex physical phenomenon. For example, bubble growth and departure are influenced by the orientation of the surface, the thickness and temperature profile in the thermal boundary layer, the proximity of neighboring bubbles, transient thermal diffusion within the wall to the adjacent liquid, wake effects of the previous bubble, bubble shape during growth, and so on. Bubble dynamics play a key role in the development of any analytical model purporting to predict nucleate pool boiling heat transfer coefficients. The simplest case to analyze is that of a single spherical bubble growing within an infinite, uniformly superheated liquid remote from a wall. This is presented below. A comprehensive treatment of bubble growth theory can be found in van Stralen and Cole (1979).

9.4.1 Bubble Growth

A spherical bubble growing in a uniformly superheated liquid is the simplest geometry to analyze. The pressure and temperature inside the bubble are p_G and T_G ; the bubble radius is R and is a function of time t from the initiation of growth (growth rate is dR/dt). The pressure and temperature in the liquid are p_∞ and T_∞ . Other effects influencing the bubble are ignored, such as the static head of the liquid, and the center point of the bubble is assumed to be immobile. At inception, the superheat is sufficient for nucleation. Then, as the bubble grows, the pressure inside the bubble decreases and with it, T_{sat} at the bubble interface. Enthalpy stored in the superheated liquid adjacent to the interface is converted into latent heat at the bubble interface and hence the interfacial temperature falls, creating a thermal diffusion shell around the bubble. Momentum is imparted to the surrounding liquid as the bubble grows and heat diffuses from the superheated bulk to the interface at a rate equal to the rate at which latent heat is liberated at the interface. In addition, the equilibrium vapor pressure curve is assumed to describe this dynamic process, and it is assumed that the vapor pressure in the bubble corresponds to the saturation pressure at the vapor temperature [i.e., that $p_G = p_{\text{sat}}(T_G)$]. Bubble growth under these conditions is controlled by two factors:

1. *Inertia.* The initial growth of a bubble is very fast, limited only by the momentum available to displace the surrounding liquid from its path. That is, inertia must be imparted to the liquid to accelerate it away in front of the growing bubble.
2. *Heat diffusion.* As the bubble grows in size, the effect of inertia becomes negligible, and growth continues by virtue of diffusion of heat from the superheated

liquid to the interface, although at a much slower growth rate than during the inertia-controlled stage of growth.

For inertia-controlled bubble growth during the initial stage of bubble growth, Rayleigh (1917) modeled incompressible radially symmetric flow of the liquid surrounding a bubble for a spherical bubble with a differential element of radius r and thickness dr for a bubble of radius R . The Rayleigh equation is

$$R \frac{d^2 R}{dt^2} + \frac{3}{2} \left(\frac{dR}{dt} \right)^2 = \frac{1}{\rho_L} \left(p_G - p_\infty - \frac{2\sigma}{R} \right) \quad (9.16)$$

where the vapor pressure in the bubble is p_G and that at the interface is p_L . Since $2\sigma/R \ll p_G - p_\infty$, the term $2\sigma/R$ can be ignored. Utilizing a linearized version of the Clapeyron equation for the small pressure differences involved, the Rayleigh equation reduces to

$$R \frac{d^2 R}{dt^2} + \frac{3}{2} \left(\frac{dR}{dt} \right)^2 = \frac{\rho_G}{\rho_L} \frac{T_\infty - T_{\text{sat}}(p_\infty)}{T_{\text{sat}}(p_\infty)} h_{LG} \quad (9.17)$$

Finally, integrating from the initial condition of $R = 0$ at $t = 0$, the Rayleigh bubble growth equation for inertia-controlled growth is obtained:

$$R(t) = \left\{ \frac{2}{3} \left[\frac{T_\infty - T_{\text{sat}}(p_\infty)}{T_{\text{sat}}(p_\infty)} \right] \frac{h_{LG} \rho_G}{\rho_L} \right\}^{1/2} t \quad (9.18)$$

For heat diffusion-controlled growth, Plesset and Zwick (1954) derived the following bubble growth equation for relatively large superheats:

$$R(t) = \text{Ja} \sqrt{\frac{12a_L t}{\pi}} \quad (9.19)$$

where a_L is the thermal diffusivity of the liquid:

$$a_L = \frac{\lambda_L}{\rho_L c_{pL}} \quad (9.20)$$

and the Jakob number is

$$\text{Ja} = \frac{\rho_L c_{pL} (T_\infty - T_{\text{sat}})}{\rho_G h_{LG}} \quad (9.21)$$

Thus, for heat diffusion-controlled bubble growth, the radius R increases with time as $t^{1/2}$, while it grows linearly with time during the initial inertia-controlled stage of growth. Mikic et al. (1970) combined the Rayleigh and Plesset–Zwick equations to arrive at an asymptotic bubble growth equation valid for the entire bubble growth period:

$$R^+ = \frac{2}{3} [(t^+ + 1)^{3/2} - (t^+)^{3/2} - 1] \quad (9.22)$$

where

$$R^+ = \frac{RA}{B^2} \quad (9.23)$$

$$t^+ = \frac{tA^2}{B^2} \quad (9.24)$$

$$A = \left\{ \frac{2[T_\infty - T_{\text{sat}}(p_\infty)] h_{LG} \rho_G}{3\rho_L T_{\text{sat}}(p_\infty)} \right\}^{1/2} \quad (9.25)$$

$$B = \left(\frac{12a_L}{\pi} \right)^{1/2} \text{Ja} \quad (9.26)$$

This expression reduces to eqs. (9.18) and (9.19) at the two extremes of t^+ , respectively.

Bubble growth at heated walls differs significantly from these ideal conditions since growth occurs in a thermal boundary layer that may be thicker or thinner than the bubble itself. The velocity field in the liquid created by the growing bubble is affected by the wall and with it the inertia force imposed on the liquid, which may change the bubble shape from spherical to hemispherical or to some other more complex shape. The hydrodynamic wake of a departing bubble may disturb the velocity field of the next bubble or that of adjacent bubbles. Furthermore, rapidly growing bubbles trap a thin evaporating liquid microlayer on the heated surface. For example, Fig. 9.6 illustrates microlayer evaporation underneath a growing bubble and macrolayer evaporation from the thermal boundary layer to the bubble as proposed in a model by van Stralen (1966).

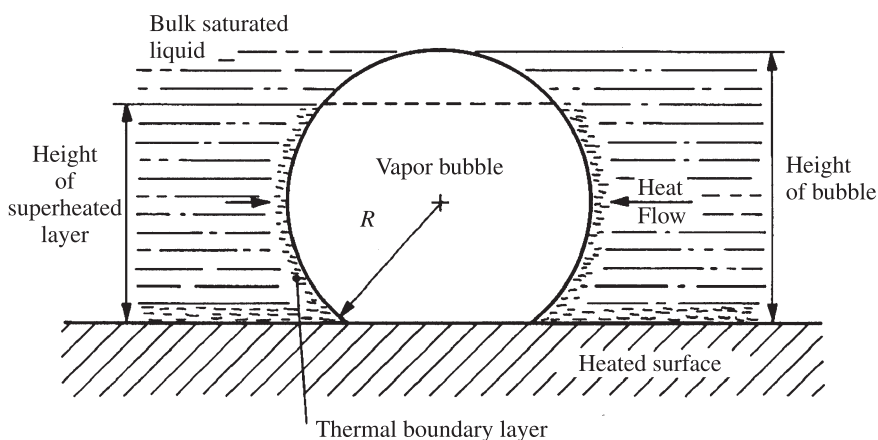


Figure 9.6 Bubble growth model of van Stralen (1966).

9.4.2 Bubble Departure

Bubble departure is another fundamental process of importance in nucleate boiling. The diameter at which a bubble departs from the surface during its growth is controlled by buoyancy and inertia forces (each attempting to detach the bubble from the surface) and surface tension and hydrodynamic drag forces (both resisting its departure). Furthermore, the shape of the bubble may deviate significantly from the idealized spherical shape. While slowly growing bubbles tend to remain spherical, rapidly growing bubbles tend to be hemispherical. Numerous other shapes are observed using high-speed movie cameras or videos.

The simplest case to analyze is that of a large, slowly growing bubble on a flat surface facing upward, for which the hydrodynamic and inertia forces are negligible. Departure occurs when the buoyancy force trying to lift the bubble off overcomes the surface tension force trying to hold it on. The surface tension force also depends on the contact angle β (i.e., a contact angle approaching 90° increases the surface tension force and hence the bubble departure diameter). Fritz (1935) proposed the first bubble departure equation that equated these two forces. The Fritz equation, utilizing the contact angle β (i.e., $\beta = \pi/2 = 90^\circ$ for a right angle) and surface tension σ , gives the bubble departure diameter as

$$d_{oF} = 0.0208\beta \left[\frac{\sigma}{g(\rho_L - \rho_G)} \right]^{1/2} \quad (9.27)$$

The contact angle relative to the surface (through the liquid) is input in degrees. The Fritz equation has been extended empirically to pressures ranging from 0.1 to 19.8 MPa with the following correction to d_{oF} :

$$d_o = 0.0012 \left(\frac{\rho_L - \rho_G}{\rho_G} \right)^{0.9} d_{oF} \quad (9.28)$$

More complex bubble departure models include the inertia, buoyancy, drag, and surface tension forces. The surface tension may also act to pinch off the bubble as it begins to depart from the surface. As an illustration of one of these theories, that of Keshock and Siegel (1964) is presented here. Assuming a spherical bubble, their force balance of the static and dynamic forces acting on a departing bubble is

$$F_b + F_p = F_i + F_\sigma + F_D \quad (9.29)$$

where F_b and F_p are the buoyancy and the excess pressure forces, respectively, acting to lift the bubble off the surface and F_i , F_σ , and F_D are the inertia, surface tension, and liquid drag forces resisting bubble departure. The buoyancy force is

$$F_b = \frac{\pi d_o^3}{6} (\rho_L - \rho_G) g \quad (9.30)$$

The excess pressure on the dry area where the bubble is attached to the wall is

$$\Delta p = \frac{2\sigma \sin \beta}{d_b} + \frac{\sigma}{r_b} \simeq \frac{2\sigma \sin \beta}{d_b} \quad (9.31)$$

The first term comes from the Laplace equation (9.1) applied to the bubble base diameter, including the contact angle β , while the second term accounts for the effect of curvature at the base of the bubble. Keshock and Siegel assumed that the second term is negligible compared to the first, such that the excess pressure force acting on the base area of diameter d_b is

$$F_p = \frac{\pi d_b}{2} \sigma \sin \beta \quad (9.32)$$

The inertia force imparted on the surrounding liquid by the growing bubble is

$$F_i = \frac{d}{dt} \mu \quad (9.33)$$

where m is the mass of the liquid displaced by the bubble and u is the interfacial velocity. Assuming that the liquid affected is 11/16 of the bubble volume, the inertia force is

$$F_i = \frac{d}{dt} \left[\left(\frac{11}{16} \rho_L \frac{4\pi [R(t)]^3}{3} \right) \left(\frac{dR(t)}{dt} \right) \right]_{d=d_o} \quad (9.34)$$

The interfacial velocity $dR(t)/dt$ may be determined with the Plesset and Zwick bubble growth model presented earlier. The surface tension force acting on the dry perimeter at the base of the bubble of diameter d_b is

$$F_\sigma = \pi d_b \sigma \sin \beta \quad (9.35)$$

Assuming a spherical bubble rising freely in a liquid at a velocity equal to that of bubble growth at the moment of departure, the hydrodynamic drag force resisting bubble departure is

$$F_D = \frac{1}{2} \rho_L C_D \pi [R(t)]^2 \left[\frac{dR(t)}{dt} \right]^2 \quad (9.36a)$$

or

$$F_D = \frac{\pi}{4} C_D \text{Re}_{\text{bub}} \mu_L [R(t)] \frac{dR(t)}{dt} \quad (9.36b)$$

where the drag coefficient is C_D and the bubble Reynolds number is

$$\text{Re}_{\text{bub}} = \frac{\rho_L [2R(t)] [dR(t)/dt]}{\mu_L} \quad (9.37)$$

The drag coefficient is related to the bubble Reynolds number as

$$C_D = \frac{a}{\text{Re}_{\text{bub}}} \quad (9.38)$$

(where Keshock and Siegel use $a = 45$), so the drag force is

$$F_D = \frac{\pi}{4} a \mu_L [R(t)] \frac{dR(t)}{dt} \quad (9.39)$$

In the model above, the drag force is typically negligible, while the inertia force becomes significant only at large ΔT . The excess pressure and surface tension forces are difficult to calculate for a real case since d_b is unknown (d_b would typically be larger than the cavity mouth since the liquid film trapped under a growing bubble partially dries out).

9.4.3 Bubble Departure Frequency

The bubble departure frequency is

$$f = \frac{1}{t_g + t_w} \quad (9.40)$$

where t_g is the bubble growth time and t_w is the waiting time between the departure of one bubble and the initiation of growth of the next. Bubble departure frequencies range from as low as 1 Hz at very small superheats to over 100 Hz at high superheats. The bubble growth time t_g can be obtained by calculating the bubble departure diameter [e.g., using eq. (9.28)] and solving for time t in the Plesset–Zwick bubble growth equation presented earlier. After a bubble departs, the length of pause before the next bubble begins to grow depends on the rate at which the surface and adjacent liquid are reheated by transient heat conduction from the wall.

Once the bubble departure diameter and frequency are known, the volumetric vapor flow rate from a single boiling site may be determined. Combining this with the bubble nucleation site density, the volumetric vapor flow rate per unit area from the heated surface can be estimated, and hence latent heat transport from the surface can also be calculated. Thus, the latent heat flux can be determined, and subtracting this from the total heat flux measured, the sensible heat flux leaving the surface in the form of superheated liquid is obtained. The effects of sequential bubbles and neighboring bubbles on one another and their competition for the heat stored within the thermal boundary layer, however, make an accurate prediction of the vapor flow rate from the surface very difficult to obtain.

9.5 POOL BOILING HEAT TRANSFER

Methods for predicting heat transfer coefficients in the various pool boiling regimes are described in this section. Most of the attention is placed on nucleate boiling, but

heat transfer in the film boiling and transition boiling regimes are also addressed. Methods are also provided to predict departure from nucleate boiling (referred to as DNB or critical heat flux) and the minimum heat flux of film boiling.

9.5.1 Nucleate Boiling Heat Transfer Mechanisms

Before presenting a selection of nucleate pool boiling correlations, the heat transfer mechanisms playing a role in nucleate pool boiling, illustrated in Fig. 9.7, are identified as follows:

1. *Bubble agitation.* The systematic pumping motion of the growing and departing bubbles agitates the liquid, pushing it back and forth across the heater surface, which in effect transforms the otherwise natural convection process into a localized forced convection process. Sensible heat is transported away in the form of superheated liquid and depends on the intensity of the boiling process.

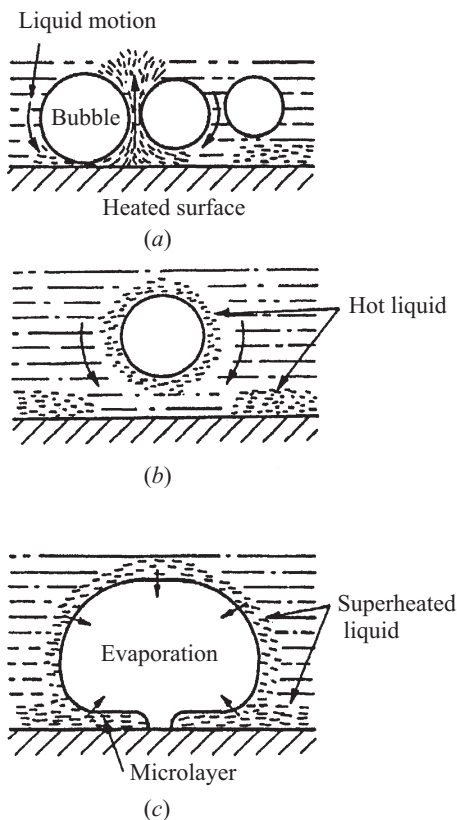


Figure 9.7 Heat transfer mechanisms in nucleate pool boiling: (a) bubble agitation; (b) vapor-liquid exchange; (c) evaporation.

2. *Vapor-liquid exchange.* The wakes of departing bubbles remove the thermal boundary layer from the heated surface, and this creates a cyclic thermal boundary layer stripping process. Sensible heat is transported away in the form of superheated liquid, whose rate of removal is proportional to the thickness of the layer, its mean temperature, the area of the boundary layer removed by a departing bubble, the bubble departure frequency, and the density of active boiling sites.

3. *Evaporation.* Heat is conducted into the thermal boundary layer and then to the bubble interface, where it is converted to latent heat. Macroevaporation occurs over the top of the bubble while microevaporation occurs underneath the bubble across the thin liquid layer trapped between the bubble and the surface, the latter often referred to as *microlayer evaporation*. The rate of latent heat transport depends on the volumetric flow of vapor away from the surface per unit area.

The mechanisms above compete for the same heat in the liquid and hence overlap with one another, thermally speaking. At low heat fluxes characteristic of the isolated bubble region, natural convection also occurs on inactive areas of the surface, where no bubbles are growing.

9.5.2 Nucleate Pool Boiling Correlations

The complexity of the nucleate pool boiling process is such that accurate, reliable analytically based design theories are yet to be available. Unresolved problems are related primarily to predicting such things as boiling nucleation superheats, boiling site densities for a given surface, and thermal interaction between neighboring boiling sites. As a consequence, completely empirical methods are used for predicting nucleate pool boiling heat transfer coefficients. In a pool boiling experiment, the wall superheat ΔT is measured versus the heat flux q , and the nucleate boiling heat transfer coefficient is obtained from its definition ($\alpha_{nb} \equiv q/\Delta T$). These data may be fit with expressions such as $q \propto \Delta T^n$, $\alpha_{nb} \propto \Delta T^n$, or $\alpha_{nb} \propto q^n$, where the exponent n is on the order of 3, 2, or 0.7, respectively. Pool boiling correlations are typically formulated in similar fashion where expressions in the form $\alpha_{nb} \propto q^n$ are the easiest to apply since heat flux is an imposed design variable while the wall temperature in ΔT is unknown and part of the solution. Literally hundreds of pool boiling correlations have been proposed; below a representative selection of recommended methods is presented plus the classic Rohsenow method.

Bubble Agitation Correlation of Rohsenow Rohsenow (1962) proposed the first widely quoted correlation. He assumed the boiling process is dominated by the bubble agitation mechanism depicted in Fig. 9.7, whose bubble-induced forced-convective heat transfer process could be correlated with the standard single-phase forced-convection correlation relation:

$$Nu = C_1 \cdot Re^x \cdot Pr^y \quad (9.41)$$

where the Nusselt number for boiling is defined as

$$\text{Nu} = \frac{\alpha_{nb}}{\lambda_L} \left[\frac{\sigma}{g(\rho_L - \rho_G)} \right]^{1/2} \tag{9.42}$$

using the bubble departure diameter [which is the bracketed term in eq. (9.42)] as the characteristic length, and α_{nb} is the nucleate pool boiling heat transfer coefficient. He defined the Reynolds number using the superficial velocity of the liquid as

$$\text{Re} = \frac{q}{h_{LG} \rho_L} \left[\frac{\sigma}{g(\rho_L - \rho_G)} \right]^{1/2} \frac{\rho_L}{\mu_L} \tag{9.43}$$

where Pr_L is the liquid Prandt number. For the lead constant C_1 , he introduced the empirical constant C_{sf} to account for the particular liquid–surface combination, so that

$$\text{Nu} = \frac{1}{C_{sf}} \text{Re}^{1-n} \cdot \text{Pr}^{-m} \tag{9.44}$$

which he presented in the form

$$\frac{c_{pL} \Delta T}{h_{LG}} = C_{sf} \left\{ \frac{q}{\mu_L h_{LG}} \left[\frac{\sigma}{g(\rho_L - \rho_G)} \right]^{1/2} \right\}^n [\text{Pr}]^{m+1} \tag{9.45}$$

Thus, this gives $\Delta T \propto q^n$ and α_{nb} is obtainable from its definition (i.e., $\alpha_{nb} = q/\Delta T$ where $\Delta T = T_w - T_{\text{sat}}$ and T_w is the wall temperature). The exponents are $m = 0.7$ and $n = 0.33$ (thus equivalent to $q \propto \Delta T^3$), except for water, where $m = 0$. Physical properties are evaluated at the saturation temperature of the fluid. Rohsenow provided a list of values of C_{sf} for various surface–fluid combinations that has been extended by Vachon et al. (1967) in Table 9.2. Because this method requires a surface–fluid factor, it is inconvenient to use for general thermal design.

TABLE 9.2 Values of C_{sf} for Rohsenow Correlation

Liquid–Surface Combination	C_{sf}
<i>n</i> -Pentane on polished copper	0.0154
<i>n</i> -Pentane on polished nickel	0.0127
Water on polished copper	0.0128
Carbon tetrachloride on polished copper	0.0070
Water on lapped copper	0.0147
<i>n</i> -Pentane on lapped copper	0.0049
<i>n</i> -Pentane on emery polished copper	0.0074
Water on scored copper	0.0068
Water on ground and polished stainless steel	0.0800
Water on PTFE pitted stainless steel	0.0058
Water on chemically etched stainless steel	0.0133
Water on mechanically polished stainless steel	0.0132

Reduced Pressure Correlation of Mostinski Mostinski (1963) applied the principle of corresponding states to the correlation of nucleate pool boiling data, arriving at a reduced pressure formulation without a surface–fluid parameter or fluid physical properties. His *dimensional* reduced pressure correlation is

$$\alpha_{nb} = 0.00417 q^{0.7} p_{\text{crit}}^{0.69} F_P \quad (9.46)$$

where α_{nb} is the nucleate pool boiling coefficient in $\text{W/m}^2 \cdot \text{K}$, q the heat flux in W/m^2 , and p_{crit} the critical pressure of the fluid in kN/m^2 (i.e., in kPa). Pressure effects on nucleate boiling are correlated using the factor F_P , determined from the expression

$$F_P = 1.8 p_r^{0.17} + 4 p_r^{1.2} + 10 p_r^{10} \quad (9.47)$$

where p_r is the reduced pressure, defined as $p_r = p/p_{\text{crit}}$. This correlation gives reasonable results for a wide range of fluids and reduced pressures.

Physical Property Type of Correlation of Stephan and Abdelsalam

Stephan and Abdelsalam (1980) developed individual correlations for four classes of fluids (water, organics, refrigerants, and cryogenics), utilizing a statistical multiple regression technique. These correlations used the physical properties of the fluid (evaluated at the saturation temperature) and are hence said to be physical property–based correlations. Their correlation applicable to organic fluids is

$$\frac{\alpha_{nb} d_o}{\lambda_L} = 0.0546 \left[\left(\frac{\rho_G}{\rho_L} \right)^{1/2} \frac{q d_o}{\lambda_L T_{\text{sat}}} \right]^{0.67} \left(\frac{h_{LG} d_o^2}{a_L^2} \right)^{0.248} \left(\frac{\rho_L - \rho_G}{\rho_L} \right)^{-4.33} \quad (9.48)$$

The term at the left is a Nusselt number and the bubble departure diameter d_o (meters) is calculated with a Fritz type of equation:

$$d_o = 0.0146 \beta \left[\frac{2\sigma}{g(\rho_L - \rho_G)} \right]^{1/2} \quad (9.49)$$

Note that the contact angle β is assigned a fixed value of 35° in this expression, irrespective of the fluid, such that the lead constant becomes 0.511. In the expressions above, T_{sat} is the saturation temperature of the fluid in Kelvin and a_L is the liquid thermal diffusivity in m^2/s .

Reduced Pressure Correlation of Cooper with Surface Roughness

Cooper (1984) proposed the following reduced pressure expression for the nucleate pool boiling heat transfer coefficient:

$$\alpha_{nb} = 55 p_r^{0.12 - 0.4343 \ln R_p} (-\log_{10} p_r)^{-0.55} M^{-0.5} q^{0.67} \quad (9.50)$$

Note that this is a *dimensional* correlation in which α_{nb} is in $\text{W/m}^2 \cdot \text{K}$, the heat flux q is in W/m^2 , and M is the molecular weight and R_p the mean surface roughness

in micrometers (R_p is set to $1.0 \mu\text{m}$ for undefined surfaces). Increasing the surface roughness has the effect of increasing the nucleate boiling heat transfer coefficient. Since R_p may be affected by fouling or oxidation of the surface, it is common to use his standard value of $1.0 \mu\text{m}$ for R_p . Although he recommends multiplying α_{nb} by a factor of 1.7 for horizontal copper cylinders, the equation more accurately predicts boiling of the new generation of refrigerants on copper tubes without applying this factor, and that is the approach recommended here. The correlation covers a database of reduced pressures from 0.001 to 0.9 and molecular weights from 2 to 200 and is highly recommended for general use.

Fluid-Specific Correlation of Gorenflo Gorenflo (1993) proposed a reduced pressure type of correlation that utilizes a fluid-specific heat transfer coefficient α_0 , defined for each fluid at the fixed reference conditions of $p_{r0} = 0.1$, $R_{p0} = 0.4 \mu\text{m}$, and $q_0 = 20,000 \text{ W/m}^2$. His values for α_0 are given in Table 9.3 for various fluids. The general expression for the nucleate boiling heat transfer coefficient α_{nb} at other conditions is

$$\alpha_{nb} = \alpha_0 F_{PF} (q/q_0)^n (R_p/R_{p0})^{0.133} \quad (9.51)$$

where the pressure correction factor F_{PF} is

$$F_{PF} = 1.2 p_r^{0.27} + 2.5 p_r + \frac{p_r}{1 - p_r} \quad (9.52)$$

and p_r is the reduced pressure. The exponent n on the heat flux ratio is also a function of reduced pressure:

$$n = 0.9 - 0.3 p_r^{0.3} \quad (9.53)$$

The value of n decreases with increasing reduced pressure, typical of experimental data. Surface roughness is included in the last term of eq. (9.51), where R_p is in micrometers (set to $0.4 \mu\text{m}$ when unknown). The method above is for all fluids listed except water and helium. For water, the corresponding equations are

$$F_{PF} = 1.73 p_r^{0.27} + \left(6.1 + \frac{0.68}{1 - p_r} \right) p_r^2 \quad (9.54)$$

$$n = 0.9 - 0.3 p_r^{0.15} \quad (9.55)$$

This method is applicable for $0.0005 \leq p_r \leq 0.95$ using the values of α_0 in the list. For other fluids, experimental values can be input at the standard reference conditions cited in the table, or another correlation can be used to estimate α_0 . This method is accurate over a very wide range of heat flux and pressure and is probably the most reliable of those presented. However, this approach is not extendable to boiling of mixtures, which is of interest in numerous industrial processes.

TABLE 9.3 Values of α_0 in $\text{W/m}^2 \cdot \text{K}$ at $p_{r0} = 0.1$, $q_0 = 20,000 \text{ W/m}^2$, and $R_{p0} = 0.4 \text{ } \mu\text{m}$, with p_{crit} in bar

Fluid	p_{crit}	M	α_0
Methane	46.0	16.04	7,000
Ethane	48.8	30.07	4,500
Propane	42.4	44.10	4,000
<i>n</i> -Butane	38.0	58.12	3,600
<i>n</i> -Pentane	33.7	72.15	3,400
<i>i</i> -Pentane	33.3	72.15	2,500
<i>n</i> -Hexane	29.7	86.18	3,300
<i>n</i> -Heptane	27.3	100.2	3,200
Benzene	48.9	78.11	2,750
Toluene	41.1	92.14	2,650
Diphenyl	38.5	154.2	2,100
Ethanol	63.8	46.07	4,400
<i>n</i> -Propanol	51.7	60.10	3,800
<i>i</i> -Propanol	47.6	60.10	3,000
<i>n</i> -Butanol	49.6	74.12	2,600
<i>i</i> -Butanol	43.0	74.12	4,500
Acetone	47.0	58.08	3,950
R-11	44.0	137.4	2,800
R-12	41.6	120.9	4,000
R-13	38.6	104.5	3,900
R-13B1	39.8	148.9	3,500
R-22	49.9	86.47	3,900
R-23	48.7	70.02	4,400
R-113	34.1	187.4	2,650
R-114	32.6	170.9	2,800
R-115	31.3	154.5	4,200
R-123	36.7	152.9	2,600
R-134a	40.6	102.0	4,500
R-152a	45.2	66.05	4,000
R-226	30.6	186.5	3,700
R-227	29.3	170.0	3,800
RC318	28.0	200.0	4,200
R-502	40.8	111.6	3,300
Chloromethane	66.8	50.49	4,400
Tetrafluoromethane	37.4	88.00	4,750
Hydrogen (on Cu)	12.97	2.02	24,000
Neon (on Cu)	26.5	20.18	20,000
Nitrogen (on Cu)	34.0	28.02	10,000
Nitrogen (on Pt)	34.0	28.02	7,000
Argon (on Cu)	49.0	39.95	8,200
Argon (on Pt)	49.0	39.95	6,700
Oxygen (on Cu)	50.5	32.00	9,500
Oxygen (on Pt)	50.5	32.00	7,200
Water	220.6	18.02	5,600
Ammonia	113.0	17.03	7,000
Carbon dioxide ^a	73.8	44.01	5,100
Sulfur hexafluoride	37.6	146.1	3,700

^aAt triple point.

9.5.3 Departure from Nucleate Pool Boiling (or Critical Heat Flux)

The maximum attainable heat flux in the nucleate boiling regime is the DNB or CHF point shown in Section 9.2. The maximum in the nucleate boiling curve heat flux is reached when a hydrodynamic instability destabilizes the vapor jets rising from the heater surface. Zuber (1959) was first to demonstrate that this process is governed by the Taylor and Helmholtz instabilities. His model was refined by Lienhard and Dhir (1973a) for an infinite flat heated surface facing upward and has been extended to other geometries.

Taylor instability governs the collapse of an infinite, horizontal planar interface of liquid above a vapor or gas, and the Taylor wavelength is that which predominates at the interface during the collapse. Applied to the DNB phenomenon, vapor jets are formed above a large, flat horizontal heater surface as illustrated in Fig. 9.8. For jets in a rotated square array as shown, their in-line spacing between jets is the two-dimensional Taylor wavelength λ_{d2} , but since $\lambda_{d2} = \sqrt{2}\lambda_{d1}$, the characteristic dimension can be considered to be λ_{d1} , which is equal to

$$\lambda_{d1} \left[\frac{(\rho_L - \rho_G)g}{\sigma} \right]^{1/2} = 2\pi\sqrt{3} \quad (9.56)$$

The *Helmholtz instability* is that which causes a planar liquid interface to go unstable when a vapor or gas flowing parallel to the interface reaches some critical velocity. Presently, it is the rising vapor jet that creates the instability. The critical velocity of the vapor u_G is

$$u_G = \sqrt{\frac{2\pi\sigma}{\rho_G\lambda_H}} \quad (9.57)$$

where λ_H is the Helmholtz wavelength of a disturbance in the jet wall. Setting $\lambda_{d1} = \lambda_H$ and performing an energy balance, the expression for q_{DNB} is obtained:

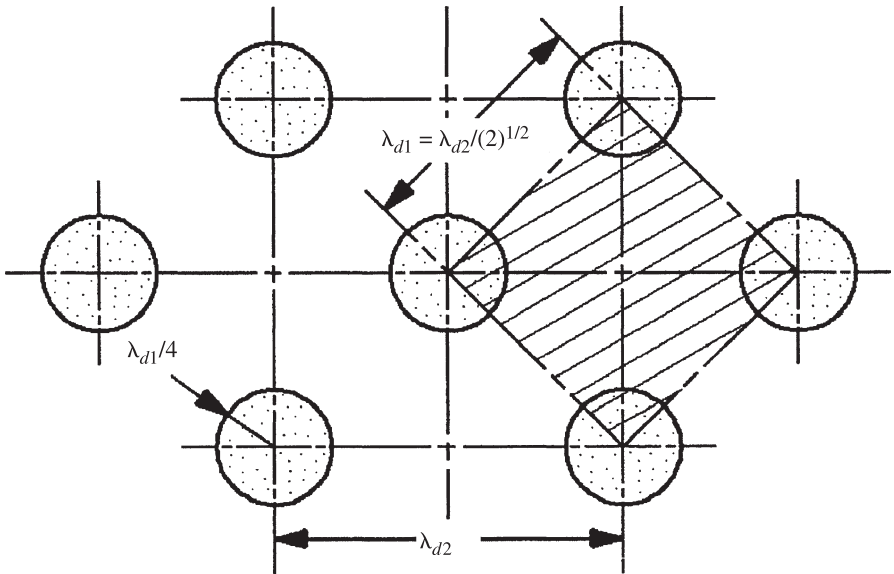
$$q_{\text{DNB}} = \rho_G h_{LG} \sqrt{\frac{2\pi\sigma}{\rho_G} \frac{1}{2\pi\sqrt{3}}} \sqrt{\frac{g(\rho_L - \rho_G)}{\sigma} \frac{\pi}{16}} \quad (9.58)$$

or

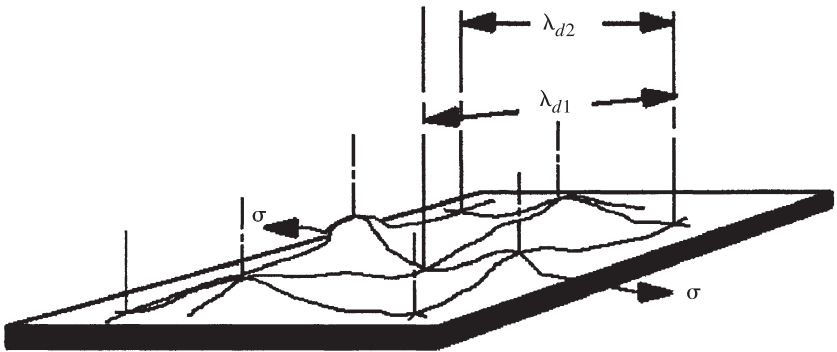
$$q_{\text{DNB}} = 0.149 \rho_G^{1/2} h_{LG} \sqrt[4]{g(\rho_L - \rho_G)\sigma} \quad (9.59)$$

This expression is valid for flat infinite heaters facing upward, providing good agreement with experimental results for large flat heaters with vertical sidewalls to prevent lateral liquid flow as long as the diameters or widths of the heaters are larger than $3\lambda_{d1}$. Using dimensional analysis, Kutateladze (1948) had already arrived at nearly the same result:

$$q_{\text{DNB}} = C \rho_G^{1/2} h_{LG} \sqrt[4]{g(\rho_L - \rho_G)\sigma} \quad (9.60)$$



(a) Plan view of vapor jets rising from the surface



(b) Wave-form underneath the vapor jets shown in (a)

Figure 9.8 Vapor jets on a horizontal heater at DNB showing the Taylor wavelengths.

where he found the empirical factor C to be 0.131 based on a comparison to experimental data. Zuber's original analysis yielded a nearly identical value of $C = \pi/24 = 0.1309$, while the Lienhard and Dhir solution gives $C = 0.149$, which is 15% higher.

Lienhard and Dhir (1973a,b) extended this theory to finite surfaces using the expression

$$\frac{q_{\text{DNB}}}{q_{\text{DNB},Z}} = \text{fn}(L') \quad (9.61)$$

TABLE 9.4 q_{DNB} Ratios for Finite Bodies

Geometry	$\frac{q_{\text{DNB}}}{q_{\text{DNB},Z}}$	Dimension	Range
Infinite flat plate	1.14	Width or diameter	$L' \geq 2.7$
Small flat heater	$1.14A_{\text{heater}}/\lambda_{d1}^2$	Width or diameter	$0.07 \leq L' \leq 0.2$
Horizontal cylinder	$0.89 + 2.27e^{-3.44\sqrt{R'}}$	Radius R	$R' \geq 0.15$
Large horizontal cylinder	0.90	Radius R	$R' \geq 1.2$
Small horizontal cylinder	$0.94/(R')^{1/4}$	Radius R	$0.15 \leq R' \leq 1.2$
Large sphere	0.84	Radius R	$4.26 \leq R'$
Small sphere	$1.734/(R')^{1/2}$	Radius R	$R' \leq 4.26$
Small horizontal ribbon oriented vertically ^a	$1.18/(H')^{1/4}$	Height of side H	$0.15 \leq H' \leq 2.96$
Small horizontal ribbon oriented vertically ^b	$1.4/(H')^{1/4}$	Height of side H	$0.15 \leq H' \leq 5.86$
Any large finite body	$\simeq 0.9$	Length L	About $L' \geq 4$
Small slender cylinder of any cross section	$1.4/(P')^{1/4}$	Transverse perimeter P	$0.15 \leq P' \leq 5.86$
Small bluff body	Constant/ $(L')^{1/2}$	Length L	About $L' \geq 4$

Source: Adapted from Lienhard (1981).

^aHeated on both sides.

^bOne side insulated.

where $q_{\text{DNB}}/q_{\text{DNB},Z}$ is a constant or a geometrical expression with a characteristic dimension of the particular surface, and eq. (9.60) with $C = \pi/24$ gives the value of $q_{\text{DNB},Z}$. The dimensionless length scale is

$$L' = 2\pi\sqrt{3}\frac{L}{\lambda_{d1}} \tag{9.62}$$

where λ_{d1} is given by eq. (9.56) and L may be a length L , a perimeter P , a height H , or a radius R , which give the values of L' , P' , H' , and R' , respectively, according to the type of geometry listed in Table 9.4. The methods are accurate to within about 20% for a wide range of fluids.

9.5.4 Film Boiling and Transition Boiling

Film boiling bears a strong similarity to falling film condensation, where the rising vapor film is analogous to the falling liquid film. Recognizing this fact, Bromley (1950) used the Nusselt equation for film condensation on horizontal cylinders to predict film boiling on the same geometry. He did this simply by changing the thermal conductivity and the kinematic viscosity from liquid to vapor properties and introducing an empirical lead constant of 0.62 rather than 0.728. Thus, for a cylinder of diameter D , the film boiling heat transfer coefficient α_{fb} is

$$\alpha_{fb} = 0.62 \left[\frac{\rho_G(\rho_L - \rho_G)gh'_{LG}\lambda_G^3}{D\mu_G(T_w - T_{\text{sat}})} \right]^{1/4} \quad (9.63)$$

The vapor properties are evaluated at the film temperature $(T_{\text{sat}} + \Delta T/2)$, the liquid properties at the saturation temperature T_{sat} , and the latent heat is corrected for sensible heating effects of the vapor as

$$h'_{LG} = h_{LG} \left[1 + 0.34 \left(\frac{c_{pG} \Delta T}{h_{LG}} \right) \right] \quad (9.64)$$

Berenson (1960) proposed a film boiling model for film boiling on cylinders, incorporating the Taylor hydrodynamic wave instability theory into the Bromley model, arriving at

$$\alpha_{fb} = 0.425 \left\{ \frac{\rho_G(\rho_L - \rho_G)gh'_{LG}\lambda_G^3}{\mu_G(T_w - T_{\text{sat}}) [\sigma/g(\rho_L - \rho_G)]^{1/2}} \right\}^{1/4} \quad (9.65)$$

where the physical properties are evaluated as above but 0.5 is used in eq. (9.64) rather than 0.34. For film boiling on spheres, Lienhard (1981) has similarly shown that

$$\alpha_{fb} = 0.67 \left[\frac{\rho_G(\rho_L - \rho_G)gh'_{LG}\lambda_G^3}{D\mu_G(T_w - T_{\text{sat}})} \right]^{1/4} \quad (9.66)$$

At large superheats, thermal radiation may be important, depending on the emissivity of the heated surface, ε_w . Bromley (1950) proposed combining the contributions of film boiling and thermal radiation on cylinders when $\alpha_{\text{rad}} < \alpha_{fb}$ as follows:

$$\alpha_{\text{total}} = \alpha_{fb} + \frac{3}{4}\alpha_{\text{rad}} \quad (9.67)$$

where the radiation heat transfer coefficient α_{rad} from the heater to the surrounding liquid or vessel is

$$\alpha_{\text{rad}} = \frac{q_{\text{rad}}}{T_w - T_{\text{sat}}} = \frac{\varepsilon_w \sigma_{\text{SB}}(T_w^4 - T_{\text{sat}}^4)}{T_w - T_{\text{sat}}} \quad (9.68)$$

and σ_{SB} is the Stephan–Boltzmann constant ($\sigma_{\text{SB}} = 5.67 \times 10^{-8} \text{ W/m}^2 \cdot \text{K}^4$). Applying this analogy to vertical plates is less tenable because in film boiling the liquid–vapor interface becomes Helmholtz unstable near the leading edge. Leonard et al. (1976) showed that replacing the diameter D in eq. (9.63) with the one-dimensional Taylor instability wavelength λ_{d1} given by eq. (9.56) gives satisfactory results for film boiling on relatively tall vertical plates.

The minimum heat flux at which film boiling can be maintained is again controlled by the Taylor instability of the interface (i.e., point MFB in Section 9.2). Zuber (1959) supposed that the minimum is reached when the vapor generation rate becomes too

small to sustain Taylor wave action on the free interface for stable generation of bubbles. For a horizontal cylinder, q_{MFB} is then

$$q_{\text{MFB}} = C \rho_G h_{LG} \sqrt[4]{\frac{\sigma g (\rho_L - \rho_G)}{(\rho_L + \rho_G)^2}} \quad (9.69)$$

where C is an arbitrary empirical constant, which Berenson (1960) identified experimentally to be equal to 0.09.

Transition boiling occurs between the heat fluxes at the DNB and MFB points on surfaces in which the surface temperature is the independent variable. For example, the transition boiling portion of the pool boiling curve may be obtained by quenching a hot sphere. If the Biot number of the sphere is small, an energy balance on the sensible heat removed from the body can be used to determine the transient surface heat flux during that portion of the cooling process. Thus, measuring the temperatures of the sphere and the liquid, the transition heat transfer coefficient can be obtained. However, tests show that the transition boiling curve obtained by cooling may differ significantly from that obtained by heating.

The heat transfer process in the transition regime can be thought of as a combination of nucleate and film boiling, occurring either side by side or one after another in rapid succession at the same location on the heater surface. The endpoints of this regime are given by the values of q_{DNB} and q_{MFB} . Very approximate values of the transition boiling heat transfer coefficient can be obtained by linear interpolation between their respective values at q_{DNB} and q_{MFB} . For more details on transition boiling, refer to Witte and Lienhard (1982) or Dhir and Liaw (1987).

9.6 INTRODUCTION TO FLOW BOILING

For evaporation under forced-flow conditions, heat transfer includes both a convective contribution and a nucleate boiling contribution, whose relative importance depends on the specific conditions. The process of flow boiling is most commonly used inside vertical tubes, in horizontal tubes, in annuli, and on the outside of horizontal tube bundles. The local flow boiling heat transfer coefficient is primarily a function of vapor quality, mass velocity, heat flux, flow channel geometry and orientation, two-phase flow pattern, and fluid properties. Because the flow boiling coefficient is a function of vapor quality, these calculations are typically done locally in thermal design methods. Flow boiling is the most typical of industrial applications; pool boiling is sometimes applied to cooling of electronic parts. In the next five sections we present a review of two-phase flow patterns (Section 9.7), flow boiling inside vertical tubes (Section 9.8), flow boiling in horizontal tubes (Section 9.9), boiling on tube bundles (Section 9.10) and post-dryout heat transfer inside tubes (Section 9.11).

9.7 TWO-PHASE FLOW PATTERNS

Flow boiling heat transfer is closely related to the two-phase flow structure of the evaporating fluid. Commonly observed flow structures are defined as two-phase flow

patterns that have particular identifying characteristics. Analogous to criteria for delineating laminar flow from turbulent flow in single-phase flow, two-phase flow pattern maps are used to predict the transition from one type of two-phase flow pattern to another and hence to identify which flow pattern is occurring at the particular local conditions under consideration. In this section, first the flow patterns themselves are described for internal tube flows, then a flow pattern map and its flow regime transition equations are presented for horizontal tubes. For a more comprehensive treatment of two-phase flow transitions, refer to Barnea and Taitel (1986).

9.7.1 Flow Patterns in Vertical and Horizontal Tubes

Flow patterns encountered in co-current upflow of gas and liquid in a vertical tube are shown in Fig. 9.9. The commonly identifiable flow patterns are:

- *Bubbly flow*. In this regime, the gas is dispersed in the form of discrete bubbles in the continuous liquid phase. The shapes and sizes of the bubbles may vary widely, but they are notably smaller than the pipe diameter.
- *Slug flow*. Increasing the gas fraction, bubbles collide and coalesce to form larger bubbles similar in size to the pipe diameter. These have a characteristic hemispherical nose with a blunt tail end, similar to a bullet, and are referred to as *Taylor bubbles*. Successive bubbles are separated by a liquid slug, which may include smaller entrained bubbles. These bullet-shaped bubbles have a thin film of liquid between them and the channel walls, which may flow downward due to the force of gravity, even though the net flow of liquid is upward.
- *Churn flow*. Further increasing the velocity, the flow becomes unstable and the liquid travels up and down in an oscillatory fashion, although the net flow is

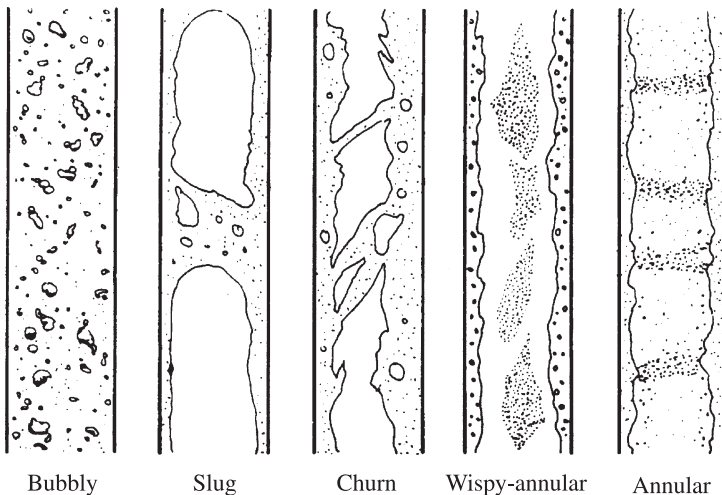


Figure 9.9 Flow patterns in vertical upflow.

upward. One explanation for the instability is that the gravity and shear forces acting on the thin film of liquid of Taylor bubbles become similar in magnitude, such that the flow direction of the film oscillates between upward and downward. This flow pattern is a transition regime between the slug flow and annular flow regimes. In small-diameter tubes, churn flow may not develop such that the flow passes directly from slug flow to annular flow.

- *Annular flow.* Here the bulk of the liquid flows as a thin film on the wall with the gas as the continuous phase flowing up the center of the tube, forming a liquid annulus with a gas core whose interface is disturbed by both large-magnitude waves and chaotic ripples. Liquid may be entrained in the high-velocity gas core as small droplets; the liquid fraction entrained may be similar to that in the film. This flow regime is quite stable and is often desirable for system operation and pipe flow.
- *Wispy annular flow.* When the flow rate is increased further, the entrained droplets congregate to form large lumps or wisps of liquid in the central vapor core with a very disturbed annular liquid film.
- *Mist flow.* When the flow rate is increased even further, the annular film becomes very thin, such that the shear of the gas core on the interface is able to entrain all the liquid as droplets in the continuous gas phase (i.e., the inverse of the bubbly flow regime). The wall is intermittently wetted locally by impinging droplets. The droplets in the mist may be too small to be seen without special lighting and/or magnification.

Flow patterns in horizontal two-phase flows are influenced by the effect of gravity, which acts to stratify the liquid to the bottom and the gas to the top of the channel. Flow patterns encountered in co-current flow of gas and liquid in a horizontal tube are shown in Fig. 9.10. The commonly identifiable flow patterns are:

- *Bubbly flow.* The bubbles are dispersed in the continuous liquid with a higher concentration in the upper half of the tube because of buoyancy effects. However, at high mass velocities, the bubbles tend to be dispersed uniformly in the tube as shear forces become dominant.
- *Stratified flow.* At low liquid and gas velocities, there is complete separation of the two phases, with the gas in the top and the liquid in the bottom, separated by an undisturbed horizontal interface.
- *Stratified–wavy flow.* With increasing gas velocity, waves form on the liquid–gas interface traveling in the direction of the flow. The amplitude of the waves depends on the relative velocity of the two phases, but their crests do not reach the top of the tube. The waves have a tendency to wrap up around the sides of the tube, leaving thin films of liquid on the wall after passage of the wave.
- *Intermittent flow.* Further increasing the gas velocity, the waves grow in magnitude until they reach the top of the tube. Thus, large amplitude waves wash the top of the tube intermittently, while slower-moving smaller-amplitude waves are often evident in between. The large-amplitude waves contain a large amount of

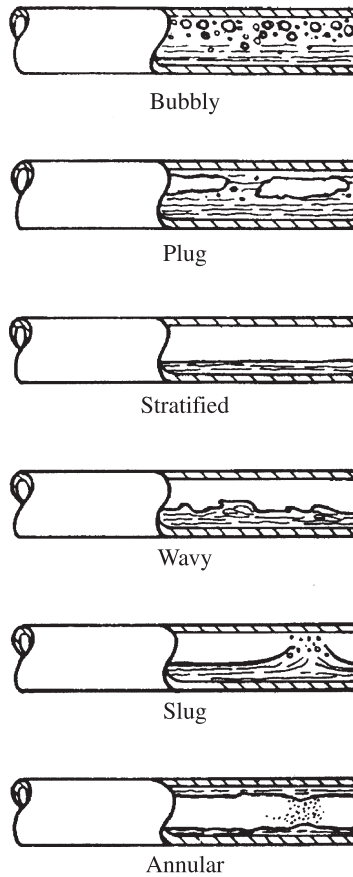


Figure 9.10 Flow patterns in horizontal flow.

liquid and often have entrained bubbles. The top wall is often wet continuously from the thin liquid film left behind by each large-amplitude wave.

- *Annular flow.* Similar to vertical upflow, at large gas flow rates the liquid forms a continuous annular film around the perimeter of the tube, which tends to be noticeably thicker at the bottom than the top. The interface of the film is typically disturbed by small-amplitude waves, and droplets may be dispersed in the gas core. At high gas fractions, the top of the tube eventually becomes dry first, with the flow reverting to the stratified–wavy flow regime.
- *Mist flow.* Similar to that occurring in vertical flow, all the liquid may become entrained as small droplets in the high-velocity continuous gas phase.

Intermittent flow is actually a composite of the plug and slug flow regimes. These subcategories may be described as follows:

- *Plug flow*. This pattern is characterized by liquid plugs that are separated by elongated gas bubbles. The diameters of the bubbles are smaller than the tube, such that the liquid phase is continuous along the bottom of the tube. Plug flow may also be referred to as *elongated bubble flow*.
- *Slug flow*. At higher gas velocities, bubbles are entrained in the liquid slugs, and the elongated bubbles become similar in size to the channel height. The liquid slugs can also be characterized as large-amplitude waves.

9.7.2 Flow Pattern Maps for Vertical Flows

For vertical upflow, Fig. 9.13 (shown later) shows the typical regimes that would be encountered from inlet to outlet of an evaporator tube. It is beyond our scope in this chapter to present flow pattern maps for vertical flows. A flow pattern map is a diagram utilized to delineate the transitions between the flow patterns, typically plotted on log-log axes using dimensionless parameters to represent the liquid and gas velocities. Hewitt and Roberts (1969) and Fair (1960) are widely quoted flow pattern maps for vertical upflows.

9.7.3 Flow Pattern Maps for Horizontal Flows

For evaporation, Fig. 9.14 (shown later) depicts the typical sectional views of the flow structure. For condensation, the flow regimes are similar with the exception that the top tube wall is not dry in stratified types of flow, but instead, is coated with a thin condensing film of condensate. The most widely quoted flow pattern maps for predicting the transition between two-phase flow regimes for adiabatic flow in horizontal tubes are those of Baker (1954) and Taitel and Dukler (1976), whose descriptions are available in numerous books and publications. Their transition curves should be considered as zones similar to that between laminar and turbulent flow.

For small-diameter tubes typical of heat exchangers, Kattan et al. (1998a) proposed a modification of the Steiner (1993) map, which itself is a modified Taitel–Dukler map, and included a method for predicting the onset of dryout at the top of the tube in evaporating annular flows. This flow pattern map is presented here as it is used in Section 9.9 for predicting local flow boiling coefficients based on the local flow pattern. The flow regime transition boundaries of the Kattan–Thome–Favrat flow pattern map are depicted in Fig. 9.11 (bubbly flow is at very high mass velocities and is not shown). This map provides the transition boundaries on a linear–linear graph with mass velocity plotted versus gas or vapor fraction for the particular fluid and flow channel, which is much easier to use than the log-log format of other maps.

The transition boundary curve between *annular and intermittent flows* to *stratified-wavy flow* is

$$\dot{m}_{\text{wavy}} = \left\{ \frac{16A_{Gd}^3 g d_i \rho_L \rho_G}{\chi^2 \pi^2 [1 - (2h_{Ld} - 1)^2]^{0.5}} \left[\frac{\pi^2}{25h_{Ld}^2} (1 - \chi)^{-F_1(q)} \left(\frac{\text{We}}{\text{Fr}} \right)_L^{-F_2(q)} + 1 \right] \right\}^{0.5} + 50 \quad (9.70)$$

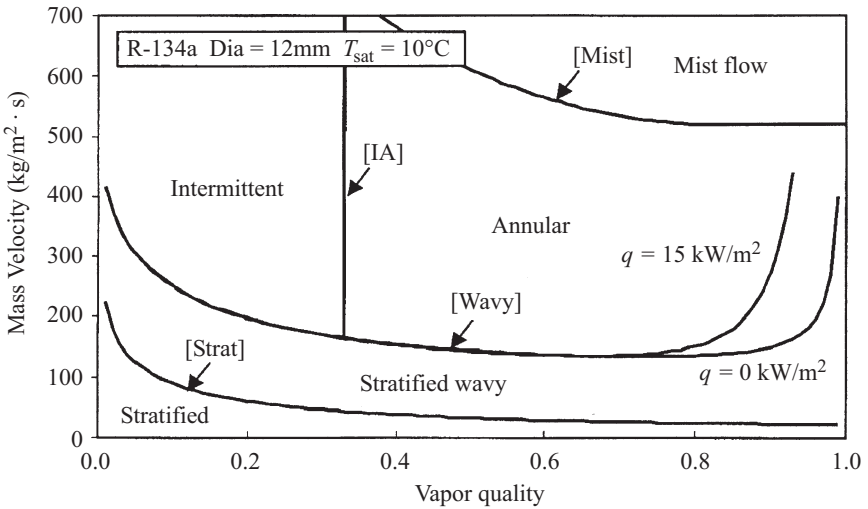


Figure 9.11 Kattan–Thome–Favrat flow pattern map illustrating flow regime transition boundaries.

The high-vapor-quality portion of this curve depends on the ratio of the Froude number (Fr_L) to the Weber number (We_L), where Fr_L is the ratio of the inertia to the surface tension forces and We_L is the ratio of inertia to gravity forces. The mass velocity threshold for the transition from *annular flow* to *mist flow* is

$$\dot{m}_{\text{mist}} = \left[\frac{7680 A_{Gd}^2 g d_i \rho_L \rho_G}{\chi^2 \pi^2 \xi_{ph}} \left(\frac{Fr}{We} \right)_L \right]^{0.5} \quad (9.71)$$

Evaluating the expression above for the minimum mass velocity of the mist flow transition gives the value of χ_{\min} , which for $\chi > \chi_{\min}$ is

$$\dot{m}_{\text{mist}} = \dot{m}_{\min} \quad (9.72)$$

The transition between *stratified–wavy flow* and *fully stratified flow* is given by the expression

$$\dot{m}_{\text{strat}} = \left\{ \frac{(226.3)^2 A_{Ld} A_{Gd}^2 \rho_G (\rho_L - \rho_G) \mu_L g}{\chi^2 (1 - \chi) \pi^3} \right\}^{1/3} \quad (9.73)$$

The transition threshold into *bubbly flow* is

$$\dot{m}_{\text{bubbly}} = \left[\frac{256 A_{Gd} A_{Ld}^2 d_i^{1.25} \rho_L (\rho_L - \rho_G) g}{0.3164 (1 - \chi)^{1.75} \pi^2 P_{id} \mu_L^{0.25}} \right]^{1/1.75} \quad (9.74)$$

In the equations above, the ratio of We to Fr is

$$\left(\frac{\text{We}}{\text{Fr}}\right)_L = \frac{g d_i^2 \rho_L}{\sigma} \quad (9.75)$$

and the friction factor is

$$\xi_{Ph} = \left(1.138 + 2 \log \frac{\pi}{1.5 A_{Ld}}\right)^{-2} \quad (9.76)$$

The nondimensional empirical exponents $F_1(q)$ and $F_2(q)$ in the \dot{m}_{wavy} boundary equation include the effect of heat flux on the onset of dryout of the annular film: the transition of annular flow into annular flow with partial dryout, the latter classified as stratified-wavy flow by the map. They are

$$F_1(q) = 646.0 \left(\frac{q}{q_{\text{DNB}}}\right)^2 + 64.8 \left(\frac{q}{q_{\text{DNB}}}\right) \quad (9.77a)$$

$$F_2(q) = 18.8 \left(\frac{q}{q_{\text{DNB}}}\right) + 1.023 \quad (9.77b)$$

The Kutateladze (1948) correlation for the heat flux of departure from nucleate boiling, q_{DNB} , is used to normalize the local heat flux:

$$q_{\text{DNB}} = 0.131 \rho_G^{1/2} h_{LG} [g(\rho_L - \rho_G)\sigma]^{1/4} \quad (9.78)$$

The vertical boundary between *intermittent flow* and *annular flow* is assumed to occur at a fixed value of the Martinelli parameter X_{tt} , equal to 0.34, where X_{tt} is defined as

$$X_{tt} = \left(\frac{1 - \chi}{\chi}\right)^{0.875} \left(\frac{\rho_G}{\rho_L}\right)^{0.5} \left(\frac{\mu_L}{\mu_G}\right)^{0.125} \quad (9.79)$$

Solving for χ , the threshold line of the intermittent-to-annular flow transition at χ_{IA} is

$$\chi_{IA} = \left\{ \left[0.2914 \left(\frac{\rho_G}{\rho_L}\right)^{-1/1.75} \left(\frac{\mu_L}{\mu_G}\right)^{-1/7} \right] + 1 \right\}^{-1} \quad (9.80)$$

Figure 9.12 defines the geometrical dimensions of the flow, where P_L is the wetted perimeter of the tube, P_G the dry perimeter in contact with only vapor, h the height of the completely stratified liquid layer, and P_i the length of the phase interface. Similarly, A_L and A_G are the corresponding cross-sectional areas. Normalizing with the tube internal diameter d_i , six dimensionless variables are obtained:

$$h_{Ld} = \frac{h}{d_i} \quad P_{Ld} = \frac{P_L}{d_i} \quad P_{Gd} = \frac{P_G}{d_i} \quad P_{id} = \frac{P_i}{d_i}$$

$$A_{Ld} = \frac{A_L}{d_i^2} \quad A_{Gd} = \frac{A_G}{d_i^2} \quad (9.81)$$

For $h_{Ld} \leq 0.5$:

$$P_{Ld} = \frac{8(h_{Ld})^{0.5} - 2[h_{Ld}(1 - h_{Ld})]^{0.5}}{3} \quad P_{Gd} = \pi - P_{Ld}$$

$$A_{Ld} = \frac{\{12[h_{Ld}(1 - h_{Ld})]^{0.5} + 8(h_{Ld})^{0.5}\} h_{Ld}}{15} \quad A_{Gd} = \frac{\pi}{4} - A_{Ld} \quad (9.82)$$

For $h_{Ld} > 0.5$:

$$P_{Gd} = \frac{8(1 - h_{Ld})^{0.5} - 2[h_{Ld}(1 - h_{Ld})]^{0.5}}{3} \quad P_{Ld} = \pi - P_{Gd}$$

$$A_{Gd} = \frac{\{12[h_{Ld}(1 - h_{Ld})]^{0.5} + 8(1 - h_{Ld})^{0.5}\} (1 - h_{Ld})}{15} \quad A_{Ld} = \frac{\pi}{4} - A_{Gd} \quad (9.83)$$

For $0 \leq h_{Ld} \leq 1$:

$$P_{id} = 2[h_{Ld}(1 - h_{Ld})]^{0.5} \quad (9.84)$$

Since h is unknown, an iterative method utilizing the following equation is necessary to calculate the reference liquid level h_{Ld} :

$$X_{tt}^2 = \left[\left(\frac{P_{Gd} + P_{id}}{\pi} \right)^{1/4} \frac{\pi^2}{64A_{Gd}^2} \left(\frac{P_{Gd} + P_{id}}{A_{Gd}} + \frac{P_{id}}{A_{Ld}} \right) \right] \left(\frac{\pi}{P_{Ld}} \right)^{1/4} \frac{64A_{Ld}^3}{\pi^2 P_{Ld}} \quad (9.85)$$

Once the reference liquid level h_{Ld} is known, the dimensionless variables are calculated from eqs. (9.82)–(9.84) and the transition curves for the new flow pattern map are determined with eqs. (9.70)–(9.80).

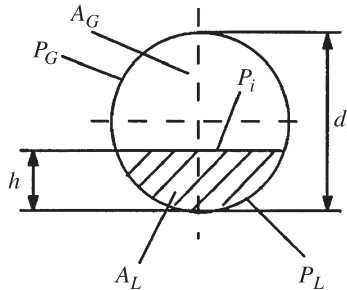


Figure 9.12 Cross-sectional and peripheral fractions in a circular tube.

This map was developed from a database for five refrigerants: two single-component fluids (R-134a and R-123), two near-azeotropic mixtures (R-402A and R-404A), and one azeotropic mixture (R-502). The test conditions covered the following range of variables: mass flow rates from 100 to 500 kg/m² · s, vapor qualities from 4 to 100%, heat fluxes from 440 to 36,500 W/m², saturation pressures from 0.112 to 0.888 MPa, Weber numbers from 1.1 to 234.5, and liquid Froude numbers from 0.037 to 1.36. The Kattan–Thome–Favrat flow pattern map correctly identified 96.2% of these flow pattern data.

Zürcher et al. (1997) obtained additional two-phase flow pattern observations for the zeotropic refrigerant mixture R-407C at an inlet saturation pressure of 0.645 MPa, and the map accurately identified these new flow pattern data. Zürcher et al. (1999) also obtained two-phase flow pattern data for ammonia with a 14-mm bore sight glass for mass velocities from 20 to 140 kg/m² · s, vapor qualities from 1 to 99% and heat fluxes from 5000 to 58,000 W/m², all taken at a saturation temperature of 4°C and saturation pressure of 0.497 MPa. Thus, the mass velocity range in the database was extended from 100 kg/m² · s down to 20 kg/m² · s. In particular, it was observed that the transition curve \dot{m}_{strat} was too low and eq. (9.73) was corrected empirically by adding +20 χ as follows:

$$\dot{m}_{\text{strat}} = \left[\frac{(226.3)^2 A_{Ld} A_{Gd}^2 \rho_G (\rho_L - \rho_G) \mu_{LG}}{\chi^2 (1 - \chi) \pi^3} \right]^{1/3} + 20\chi \quad (9.86)$$

where \dot{m}_{strat} is in kg/m² · s. The transition from stratified–wavy flow to annular flow at high vapor qualities was, instead, observed to be too high, and hence an additional empirical term with an exponential factor modifying the boundary at high vapor qualities was added to eq. (9.70) to take this into account as

$$\dot{m}_{\text{wavy}(\text{new})} = \dot{m}_{\text{wavy}} - 75e^{-(\chi^2 - 0.97)^2 / \chi(1 - \chi)} \quad (9.87)$$

where the mass velocity is in kg/m² · s. The movement of these boundaries has an effect on the dry angle calculation θ_{dry} in the Kattan et al. (1998c) flow boiling heat transfer model and shifts the onset of dryout to slightly higher vapor qualities, which is in agreement with the ammonia heat transfer test data.

To utilize this map, the following parameters are required: vapor quality (χ), mass velocity (\dot{m}), tube internal diameter (d_i), heat flux (q), liquid density (ρ_L), vapor density (ρ_G), liquid dynamic viscosity (μ_L), vapor dynamic viscosity (μ_G), surface tension (σ), and latent heat of vaporization (h_{LG}), all in SI units. The local flow pattern is identified by the following procedure:

1. Solve eq. (9.85) iteratively with eqs. (9.79), (9.82), (9.83), and (9.84).
2. Evaluate eq. (9.81).
3. Evaluate eqs. (9.75)–(9.78).
4. Evaluate eqs. (9.70), (9.71) or (9.72), (9.73), (9.74), and (9.80).
5. Compare these values to the given values of χ and \dot{m} to identify the flow pattern.

Note that eq. (9.87) should be used in place of eqs. (9.70) and (9.86) should be used in place of eq. (9.80) to utilize the most updated version. The map is thus specific to the fluid properties, flow conditions (heat flux), and tube internal diameter input into the equations. The map can be programmed into any computer language, evaluating the transition curves in incremental steps of 0.01 in vapor quality to obtain a tabular set of threshold boundary points, which can then displayed as a complete map with \dot{m} versus χ as coordinates.

9.8 FLOW BOILING IN VERTICAL TUBES

Convective evaporation in a vertical tube is depicted in Fig. 9.13. At the inlet, the liquid enters subcooled. As the liquid heats up, the wall temperature rises until it

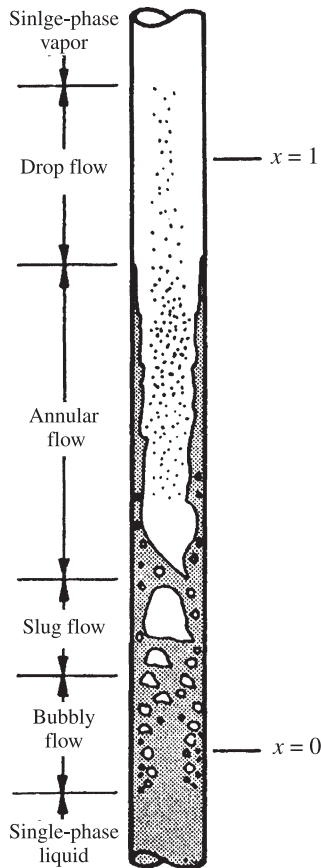


Figure 9.13 Flow patterns during evaporation in a vertical tube with a uniform heat flux. (From Collier and Thome, 1994.)

surpasses the saturation temperature of the liquid, at which point subcooled boiling begins, where bubbles nucleate and grow in the thermal boundary layer and condense in the subcooled core. Farther up the tube, the liquid bulk reaches its saturation temperature and the convective boiling process passes through the bubbly flow, churn flow, and finally, into the annular flow regime. At the dryout point, the annular liquid film is depleted completely, either by evaporation or by entrainment into the vapor core, and the wall temperature rises significantly in order to dissipate the applied heat flux. The process proceeds in the post-dryout (mist or drop flow) regime. First, saturated wet wall convective boiling is described, and post-dryout heat transfer is then described in Section 9.11.

In the forced-convective evaporation regime the heat transfer coefficient is less dependent on heat flux than in nucleate pool boiling, while its dependence on the local vapor quality appears as a new and important parameter. Both the nucleate and convective heat transfer mechanisms must be taken into account to predict heat transfer data in the convective boiling regime. Their relative importance varies from dominance of nucleate boiling at low vapor qualities and high heat fluxes to the dominance of convection at relatively high vapor qualities and low heat fluxes.

9.8.1 Chen Correlation

The Chen (1963) correlation was the first to attain widespread acclaim and has served as the starting point for the development of most other flow boiling correlations since. Superposition of the nucleate boiling and convective boiling mechanisms is assumed, such that the local two-phase flow boiling coefficient α_{tp} is obtained as

$$\alpha_{tp} = \alpha_{nb} + \alpha_{cb} \quad (9.88)$$

where α_{nb} is the nucleate boiling contribution and α_{cb} is the convective contribution, which Chen presented as

$$\alpha_{tp} = \alpha_{FZ} S + \alpha_L F \quad (9.89)$$

The Forster and Zuber (1955) correlation is used to calculate the pool boiling heat transfer coefficient α_{FZ} as

$$\alpha_{FZ} = 0.00122 \left(\frac{\lambda_L^{0.79} c_{pL}^{0.45} \rho_L^{0.49}}{\sigma^{0.5} \mu_L^{0.29} h_{LG}^{0.24} \rho_G^{0.24}} \right) \Delta T_{\text{sat}}^{0.24} \Delta p_{\text{sat}}^{0.75} \quad (9.90)$$

while for liquid-only heat transfer, coefficient α_L is obtained with the Dittus–Boelter correlation:

$$\alpha_L = 0.023 \text{Re}_L^{0.8} \cdot \text{Pr}_L^{0.4} \left(\frac{\lambda_L}{d_i} \right) \quad (9.91)$$

The liquid Reynolds number Re_L above is based on the fraction of liquid flowing alone in the channel [i.e., using $\dot{m}(1 - \chi)$ to calculate Re_L]. In the Forster–Zuber

equation, the wall superheat ΔT_{sat} and pressure difference Δp_{sat} are the active parameters: the pressure difference refers to that obtained with the fluid's vapor pressure curve evaluated at the wall and saturation temperatures, respectively, and Δp_{sat} is in N/m^2 . Thus, this approach leads to an iterative calculation when the heat flux is specified since the wall temperature is not known beforehand.

Forced flow creates a sharper temperature gradient at the wall relative to that in nucleate pool boiling, which has an adverse effect on bubble nucleation. Thus, nucleation is partially suppressed, which Chen accounted for by introducing a nucleation suppression factor S . The convective boiling contribution α_{cb} is a product of α_L times a two-phase multiplier F , which enhances this heat transfer mode. The suppression factor S , two-phase multiplier F , Martinelli parameter X_{tt} , and two-phase Reynolds number Re_{tp} used in his method are calculated as follows:

$$S = \frac{1}{1 + 0.00000253 \text{Re}_{tp}^{1.17}} \quad (9.92)$$

$$F = \left(\frac{1}{X_{tt}} + 0.213 \right)^{0.736} \quad (9.93)$$

$$X_{tt} = \left(\frac{1 - \chi}{\chi} \right)^{0.9} \left(\frac{\rho_G}{\rho_L} \right)^{0.5} \left(\frac{\mu_L}{\mu_G} \right)^{0.1} \quad (9.94)$$

$$\text{Re}_{tp} = \text{Re}_L \cdot F^{1.25} \quad (9.95)$$

Note, however, that when $1/X_{tt} \leq 0.1$, F is set equal to 1.0. The Chen correlation is applicable over the entire evaporation range in which the heated wall remains wet.

9.8.2 Shah Correlation

Shah (1982) proposed a method for implementing his chart method. Similar to Chen, he included two distinct mechanisms: nucleate boiling and convective boiling. However, instead of adding these two contributions, his method chooses the *larger* of the nucleate boiling coefficient α_{nb} and the convective boiling coefficient α_{cb} . In his method, the first step is to calculate the dimensionless parameter N , which for vertical tubes at all values of the liquid Froude number Fr_L is given as

$$N = C_0 \quad (9.96)$$

where C_0 is determined from

$$C_0 = \left(\frac{1 - \chi}{\chi} \right)^{0.8} \left(\frac{\rho_G}{\rho_L} \right)^{0.5} \quad (9.97)$$

For $N > 1.0$, the values of α_{nb} and α_{cb} are calculated from the following expressions and the larger value is chosen as the local heat transfer coefficient α_{tp} . The value of the liquid-only convective heat transfer coefficient α_L used in these expressions

is determined from the liquid fraction of the flow, $\dot{m}(1 - \chi)$, using eq. (9.91). The effect of heat flux on nucleate boiling is introduced using the *boiling number*, which is defined as

$$\text{Bo} = \frac{q}{\dot{m}h_{LG}} \quad (9.98)$$

This dimensionless group represents the ratio of the actual heat flux to the maximum heat flux achievable by complete evaporation of the liquid. For $\text{Bo} > 0.0003$,

$$\frac{\alpha_{nb}}{\alpha_L} = 230\text{Bo}^{0.5} \quad (9.99)$$

and for $\text{Bo} < 0.0003$,

$$\frac{\alpha_{nb}}{\alpha_L} = 1 + 46\text{Bo}^{0.5} \quad (9.100)$$

$$\frac{\alpha_{cb}}{\alpha_L} = \frac{1.8}{N^{0.8}} \quad (9.101)$$

For $1.0 > N > 0.1$, the value α_{cb} is determined from eq. (9.101) and the value of α_{nb} in the bubble suppression regime is calculated from

$$\frac{\alpha_{nb}}{\alpha_L} = F \cdot \text{Bo}^{0.5} \exp(2.74N - 0.1) \quad (9.102)$$

Then the larger value is chosen for α_{tp} . For $N < 0.1$, the value of α_{cb} is calculated with eq. (9.101) while α_{nb} in the bubble suppression regime is determined as

$$\frac{\alpha_{nb}}{\alpha_L} = F \cdot \text{Bo}^{0.5} \exp(2.74N - 0.15) \quad (9.103)$$

Again one chooses the larger value for α_{tp} . In the equations above, the constant F is 14.7 when $\text{Bo} > 0.0011$ and is 15.43 when $\text{Bo} < 0.0011$.

This method is also applicable to vertical annuli. For annular gaps between the inner and outer tubes greater than 4 mm, the equivalent diameter is the difference between the two diameters. For annuli less than 4 mm, the equivalent diameter is obtained by evaluating the hydraulic diameter using only the heated perimeter. Kandlikar (1990) has also proposed a fluid-specific correlation similar to that of Shah using an empirical constant specific to the particular fluid.

9.8.3 Gungor–Winterton Correlation

Gungor and Winterton (1986) proposed a Chen type of correlation based on a large database (3693 points) covering water, refrigerants (R-11, R-12, R-22, R-113, and R-114), and ethylene glycol for mostly vertical up flows and some vertical down flows as

$$\alpha_{tp} = E\alpha_L + S\alpha_{nb} \quad (9.104)$$

with α_L calculated from eq. (9.91) using the local liquid fraction of the flow, $\dot{m}(1 - \chi)$. Their convection enhancement factor E is

$$E = 1 + 24,000\text{Bo}^{1.16} + 1.37 \left(\frac{1}{X_{tt}} \right)^{0.86} \quad (9.105)$$

where X_{tt} is the Martinelli parameter defined in eq. (9.94). Their boiling suppression factor S is

$$S = (1 + 0.00000115E^2 \cdot \text{Re}_L^{1.17})^{-1} \quad (9.106)$$

with Re_L based on $\dot{m}(1 - \chi)$. The nucleate pool boiling coefficient is calculated with the Cooper (1984) reduced pressure correlation with R_p set to $1 \mu\text{m}$

$$\alpha_{nb} = 55p_r^{0.12} (-\log_{10} p_r)^{-0.55} M^{-0.5} q^{0.67} \quad (9.107)$$

This *dimensional* correlation gives the heat transfer coefficient in $\text{W/m}^2 \cdot \text{K}$ and the heat flux q must be input in W/m^2 . M is the molecular weight and p_r is the reduced pressure. Gungor and Winterton (1987) have also proposed a newer variation of this correlation.

9.8.4 Steiner–Taborek Method

Steiner and Taborek (1992) proposed a model for vertical tubes using a large database containing 10,262 data points for water plus 2345 data points for four refrigerants (R-11, R-12, R-22, and R-113), seven hydrocarbons (benzene, *n*-pentane, *n*-heptane, cyclohexane, methanol, ethanol, and *n*-butanol), three cryogenes (nitrogen, hydrogen, and helium), and ammonia. It is considered to be the most accurate vertical tube boiling correlation currently available. As opposed to the methods above, they assumed an asymptotic equation for the local two-phase flow boiling coefficient α_{tp} :

$$\alpha_{tp} = [(\alpha_{nb})^n + (\alpha_{cb})^n]^{1/n} \quad (9.108)$$

where $n = 3$ and the local flow boiling heat transfer coefficient is defined as

$$\alpha_{tp} = \frac{q}{T_{\text{wall}} - T_{\text{sat}}} \quad (9.109)$$

Here q , T_{wall} , and T_{sat} are local values along the evaporator tube and T_{sat} corresponds to the local saturation pressure. Expression (9.108) is rewritten introducing the parameters that affect heat transfer as

$$\alpha_{tp} = [(\alpha_{nb,0} F_{nb})^3 + (\alpha_L F_{tp})^3]^{1/3} \quad (9.110)$$

where:

- $\alpha_{nb,0}$ is the local nucleate pool boiling coefficient at a reference heat flux q_0 and reference reduced pressure of 0.1.
- F_{nb} is the nucleate boiling correction factor that accounts for the differences between pool and flow boiling, and the effects of pressure, heat flux, tube diameter, surface roughness, and so on, but not boiling suppression (which is not required in an asymptotic model).
- α_L is the local liquid-phase forced-convection coefficient based on the total flow as liquid obtained with the Gnielinski (1976) correlation.
- F_{tp} is the two-phase multiplier that accounts empirically for the enhancement of convection in a two-phase flow.

The term $\alpha_{nb,0}F_{nb}$ may be obtained from experimental data or from the nucleate pool boiling correlation of the user's choice (or from the method recommended below). The Gnielinski correlation is

$$\text{Nu}_L = \frac{\alpha_L d_i}{\lambda_L} = \frac{(f/8)(\text{Re}_L - 1000)\text{Pr}_L}{1 + 12.7(f/8)^{1/2}(\text{Pr}_L^{2/3} - 1)} \quad (9.111)$$

where the Fanning friction factor f is

$$f = [0.7904 \ln(\text{Re}_L) - 1.64]^{-2} \quad (9.112)$$

The total mass velocity of liquid plus vapor is used for evaluating Re_L in eqs. (9.111) and (9.112). Only liquid physical properties are used. The two-phase multiplier F_{tp} is for convective evaporation that will occur if $\chi < \chi_{\text{crit}}$ and $q > q_{\text{ONB}}$ or over the entire range of χ if $q < q_{\text{ONB}}$. For applications where $\chi < \chi_{\text{crit}}$ at the tube exit, the following equation is used:

$$F_{tp} = \left[(1 - \chi)^{1.5} + 1.9\chi^{0.6} \left(\frac{\rho_L}{\rho_G} \right)^{0.35} \right]^{1.1} \quad (9.113)$$

This expression is valid for values of ρ_L/ρ_G from 3.75 to 5000 and converges to unity as χ goes to zero. At low heat fluxes where only pure convective evaporation is present over the entire range from $\chi = 0.0$ to $\chi = 1.0$ (i.e., where the heat flux is too low for nucleation to occur), the following expression is used:

$$F_{tp} = \left(\left[(1 - \chi)^{1.5} + 1.9\chi^{0.6}(1 - \chi)^{0.01} \left(\frac{\rho_L}{\rho_G} \right)^{0.35} \right]^{-2.2} + \left\{ \frac{\alpha_G}{\alpha_L} \chi^{0.01} [1 + 8(1 - \chi)^{0.7}] \left(\frac{\rho_L}{\rho_G} \right)^{0.67} \right\}^{-2} \right)^{-0.5} \quad (9.114)$$

where $\chi^{0.01}$ and $(1 - \chi)^{0.01}$ take the expression to its proper limits at $\chi = 0$ and $\chi = 1$. This expression is valid for values of ρ_L/ρ_G from 3.75 to 1017. At $\chi = 1.0$, the value of α_{tp} corresponds to α_G , which is the forced-convection coefficient with the total flow as all vapor.

The nucleate boiling coefficient α_{nb} is determined similar to the Gorenflo (1993) nucleate pool boiling method. The *standard* nucleate flow boiling coefficients $\alpha_{nb,0}$ to use are listed in Table 9.5, where the standard conditions are a reduced pressure of 0.1, a mean surface roughness of 1 μm , and a heat flux q_0 equal to the value listed for each fluid. The nucleate boiling correction factor F_{nb} applied to the value of $\alpha_{nb,0}$ is

$$F_{nb} = F_{pf} \left(\frac{q}{q_0} \right)^{nf} \left(\frac{d_i}{d_{i,0}} \right)^{-0.4} \left(\frac{R_p}{R_{p,0}} \right)^{0.133} F(M) \quad (9.115)$$

where the pressure correction factor F_{pf} , valid for $p_r < 0.95$, is

$$F_{pf} = 2.816 p_r^{0.45} + \left(3.4 + \frac{1.7}{1 - p_r^7} \right) p_r^{3.7} \quad (9.116)$$

The nucleate boiling exponent nf for all fluids is

$$nf = 0.8 - 0.1 \exp(1.75 p_r) \quad (9.117)$$

except for cryogenics, where it is

$$nf = 0.7 - 0.13 \exp(1.105 p_r) \quad (9.118)$$

The standard tube reference diameter $d_{i,0}$ is equal to 0.01 m and the surface roughness term covers values of R_p from 0.1 to 18 μm . The standard value of $R_{p,0}$ is 1 μm and should be used if the surface roughness is not known. The Steiner–Taborek catch-all residual correction factor in terms of liquid molecular weight M is

$$F(M) = 0.377 + 0.199 \ln M + 0.000028427 M^2 \quad (9.119)$$

This expression is valid for $10 < M < 187$, with the maximum value of $F(M)$ of 2.5, even for cases when the expression gives a larger value. For cryogenic liquids H_2 and He , the designated values of $F(M)$ are 0.35 and 0.86, respectively.

The minimum heat flux q_{ONB} for determining the threshold for the onset of nucleate boiling is

$$q_{\text{ONB}} = \frac{2\sigma T_{\text{sat}} \alpha_L}{r_{\text{nuc}} \rho_G h_{LG}} \quad (9.120)$$

where $r_{\text{nuc}} = 0.3 \times 10^{-6}$ m is used for the critical nucleation radius. For $q > q_{\text{ONB}}$, nucleate boiling occurs, whereas below this value it does not. Notably, their method is applicable to pure fluids, but there is no simple way to determine the values of $\alpha_{nb,0}$ for mixtures.

TABLE 9.5 Standard Nucleate Flow Boiling Coefficients $\alpha_{nb,0}$ in $\text{W/m}^2 \cdot \text{K}$ at $p_r = 0.1$ for q_0 in W/m^2 and $R_{p,0} = 1 \mu\text{m}$ with p_{crit} in Bar

Fluid	p_{crit}	M	q_0	$\alpha_{nb,0}$
Methane	46.0	16.04	20,000	8,060
Ethane	48.8	30.07	20,000	5,210
Propane	42.4	44.10	20,000	4,000
<i>n</i> -Butane	38.0	58.12	20,000	3,300
<i>n</i> -Pentane	33.7	72.15	20,000	3,070
Isopentane	33.3	72.15	20,000	2,940
<i>n</i> -Hexane	29.7	86.18	20,000	2,840
<i>n</i> -Heptane	27.3	100.2	20,000	2,420
Cyclohexane	40.8	84.16	20,000	2,420
Benzene	48.9	78.11	20,000	2,730
Toluene	41.1	92.14	20,000	2,910
Diphenyl	38.5	154.2	20,000	2,030
Methanol	81.0	32.04	20,000	2,770
Ethanol	63.8	46.07	20,000	3,690
<i>n</i> -Propanol	51.7	60.10	20,000	3,170
Isopropanol	47.6	60.10	20,000	2,920
<i>n</i> -Butanol	49.6	74.12	20,000	2,750
Isobutanol	43.0	74.12	20,000	2,940
Acetone	47.0	58.08	20,000	3,270
R-11	44.0	137.4	20,000	2,690
R-12	41.6	120.9	20,000	3,290
R-13	38.6	104.5	20,000	3,910
R-13B1	39.8	148.9	20,000	3,380
R-22	49.9	86.47	20,000	3,930
R-23	48.7	70.02	20,000	4,870
R-113	34.1	187.4	20,000	2,180
R-114	32.6	170.9	20,000	2,460
R-115	31.3	154.5	20,000	2,890
R-123	36.7	152.9	20,000	2,600
R-134a	40.6	102.0	20,000	3,500
R-152a	45.2	66.05	20,000	4,000
R-226	30.6	186.5	20,000	3,700
R-227	29.3	170.0	20,000	3,800
RC318	28.0	200.0	20,000	2,710
R-502	40.8	111.6	20,000	2,900
Chloromethane	66.8	50.49	20,000	4,790
Tetrachloromethane	45.6	153.8	20,000	2,320
Tetrafluoromethane	37.4	88.00	20,000	4,500
Helium ^a	2.275	4.0	1,000	1,990
Hydrogen (para)	12.97	2.02	10,000	12,220
Neon	26.5	20.18	10,000	8,920
Nitrogen	34.0	28.02	10,000	4,380
Argon	49.0	39.95	10,000	3,870
Oxygen	50.8	32.00	10,000	4,120
Water	220.6	18.02	150,000	25,580
Ammonia	113.0	17.03	150,000	36,640
Carbon dioxide ^b	73.8	44.01	150,000	18,890
Sulfur hexafluoride	37.6	146.1	150,000	12,230

^aPhysical properties at $p_r = 0.3$ rather than 0.1.
^bCalculated with properties at T_{crit} .

9.9 FLOW BOILING IN HORIZONTAL TUBES

A composite schematic of convective evaporation in a horizontal tube is depicted in Fig. 9.14. At the inlet, the liquid enters subcooled. Farther along the tube, the liquid reaches its saturation temperature and the convective boiling process passes through various possible flow regimes, and flow can be either stratified or unstratified. In the latter case, dryout occurs at the top of the tube where the film thickness is thinnest, and dryout progresses around the perimeter from top to bottom along the tube.

9.9.1 Horizontal Tube Correlations Based on Vertical Tube Methods

Some of the better known methods proposed over the years for predicting local flow boiling heat transfer coefficients inside vertical plain tubes have been adapted to horizontal tubes: for example, those of Shah (1982), Gungor and Winterton (1986, 1987), Klimenko (1988), and Kandlikar (1990). The first two are described below.

The Shah (1982) vertical tube method described in Section 9.8 is applied to horizontal tubes by making an adjustment to N when the flow is stratified: that is, for $Fr_L < 0.04$,

$$N = 0.38Fr_L^{-0.3}C_0 \quad (9.121)$$

where the liquid Froude number Fr_L is defined as

$$Fr_L = \frac{\dot{m}^2}{\rho_L^2 g d_i} \quad (9.122)$$

Otherwise, for horizontal flow without stratification (i.e., $Fr_L \geq 0.04$), the Shah vertical tube method is used without change with $N = C_0$.

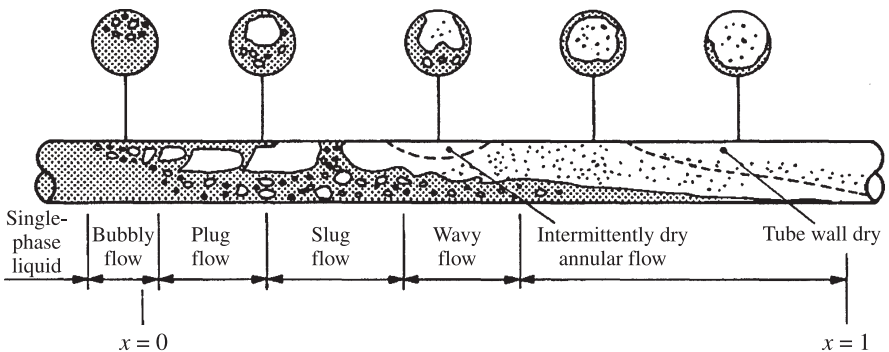


Figure 9.14 Flow patterns during evaporation in a horizontal tube with a uniform heat flux. (From Collier and Thome, 1994.)

Gungor and Winterton (1986) also used the liquid Froude number as the threshold criterion for flow stratification, but they set the threshold value a little higher: at $Fr_L < 0.05$. Their stratified flow correction factor E_2 is

$$E_2 = Fr_L^{0.1-2Fr_L} \quad (9.123)$$

and is applied to their convection enhancement factor E in eq. (9.104). In addition, when $Fr_L < 0.05$, their boiling suppression factor S must be multiplied by the correction factor

$$S_2 = (Fr_L)^{1/2} \quad (9.124)$$

Kattan et al. (1998a) have pointed out that the liquid Froude number is not reliable for predicting the stratification threshold, identifying it correctly only about 50% of the time. Therefore, the methods above can be used for annular and intermittent flows but do not predict heat transfer in stratified types of flow very accurately. Thome (1995a) summarized the pitfalls of applying vertical methods to horizontal flow boiling as follows:

- Vertical tube methods do not recognize the different flow patterns occurring in horizontal flow boiling, and their stratification criteria are not reliable.
- These methods are incapable of predicting the sharp peak in α_{tp} versus χ found in many experimental data sets, nor can they predict the subsequent sharp decline in α_{tp} after the onset of dryout at the top of the tube in annular flows at high vapor qualities.
- They do not attempt to model the two-phase flow structure itself and utilize a *tubular* flow correlation (Dittus–Boelter) as their starting point to predict annular *film* flow heat transfer.

Still, these methods are simple to implement and they predict flow boiling coefficients in the annular flow regime with reasonable accuracy as long as they are limited to vapor qualities below the peak in α_{tp} versus χ , which occurs at about 80 to 90% vapor quality.

9.9.2 Horizontal Flow Boiling Model Based on Local Flow Regime

Kattan et al. (1998a,b,c) proposed a flow boiling model that takes a more fundamental approach to predicting local flow boiling heat transfer coefficients by incorporating a simplified local two-phase flow structure into the prediction method as a function of the local flow pattern. So far, their model covers annular flows, annular flows with partial dryout, intermittent flows, stratified-wavy flows, and fully stratified flows, and methods for predicting heat transfer in bubbly flows and mist flows are under development. Their method identifies the local two-phase flow pattern using their flow pattern map described in Section 9.7.

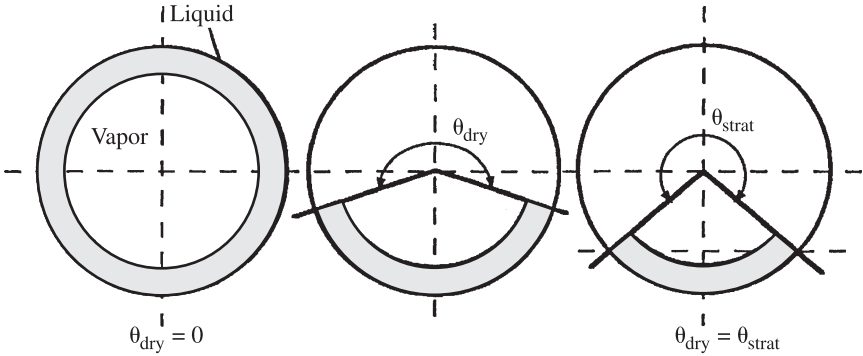


Figure 9.15 Geometric illustration of liquid and vapor areas, stratified and dry angles, and liquid film thickness used in the flow boiling model.

Their simplified two-phase flow structures assumed for the fully stratified, stratified-wavy, and annular flow regimes are depicted in Fig. 9.15. In annular flow, the liquid is assumed to form a uniform liquid ring on the tube wall, while for stratified-wavy flow a truncated annular ring is assumed to represent the flow structure. For fully stratified flow, the liquid is also assumed to form a truncated annular ring, with the same cross-sectional area of liquid as in its true stratified shape. Annular flow with partial dryout around the top of the tube is similar to stratified-wavy flow, and the heat transfer model treats it so. Currently, the complex intermittent flow structure is represented by the annular flow structure, an assumption that provides good representation of that heat transfer data.

Their general equation for the local flow boiling coefficient α_{tp} for evaporation in a horizontal, plain tube is

$$\alpha_{tp} = \frac{r_i \theta_{dry} \alpha_{vapor} + r_i (2\pi - \theta_{dry}) \alpha_{wet}}{2\pi r_i} \quad (9.125)$$

where the internal tube radius is r_i . The dry perimeter of the tube, if any, is given by $r_i \theta_{dry}$, where θ_{dry} is the dry angle around the top of the tube, and the wetted perimeter of the tube is $r_i (2\pi - \theta_{dry})$. The vapor-phase heat transfer coefficient α_{vapor} is applied to the dry perimeter, and the wet wall heat transfer coefficient α_{wet} is applied to the wet perimeter. The wet wall heat transfer coefficient is obtained from an asymptotic model that combines the nucleate boiling α_{nb} and convective boiling α_{cb} contributions to heat transfer by the third power as

$$\alpha_{wet} = (\alpha_{nb}^3 + \alpha_{cb}^3)^{1/3} \quad (9.126)$$

The nucleate boiling heat transfer coefficient α_{nb} is determined with the *dimensional* reduced pressure correlation of Cooper (1984):

$$\alpha_{nb} = 55 p_r^{0.12} (-\log_{10} p_r)^{-0.55} M^{-0.5} q^{0.67} \quad (9.127)$$

where a roughness equal to his standard surface roughness factor is assumed, α_{nb} is in $\text{W/m}^2 \cdot \text{K}$, p_r is the reduced pressure, M is the liquid molecular weight, and q is the heat flux at the tube wall in W/m^2 .

The convective boiling heat transfer coefficient α_{cb} for annular liquid film flow was formulated as a *film* flow, not as a *tubular* flow, as follows:

$$\alpha_{cb} = 0.0133 \left[\frac{4\dot{m}(1-\chi)\delta}{(1-\varepsilon)\mu_L} \right]^{0.69} \left(\frac{c_{pL}\mu_L}{\lambda_L} \right)^{0.4} \frac{\lambda_L}{\delta} \quad (9.128)$$

The term in brackets is the liquid film Reynolds number Re_L and the following term is the liquid Prandtl number Pr_L . The mean liquid velocity in the annular film is utilized in determining the liquid Reynolds number, which changes as a local function of the vapor quality χ , annular liquid film thickness δ , and vapor void fraction ε . Note that in this formulation, neither an empirical boiling suppression factor nor two-phase convection multiplier is required.

The vapor-phase heat transfer coefficient α_{vapor} is calculated with the Dittus-Boelter turbulent flow heat transfer correlation assuming *tubular* flow on the dry perimeter of the tube using the vapor properties and the mass velocity of the vapor:

$$\alpha_{\text{vapor}} = 0.023 \left(\frac{\dot{m}\chi d_i}{\varepsilon\mu_G} \right)^{0.8} \left(\frac{c_{pG}\mu_G}{\lambda_G} \right)^{0.4} \frac{\lambda_G}{d_i} \quad (9.129)$$

The vapor Reynolds number Re_G in the first term in parentheses above includes the vapor void fraction ε such that the mean vapor velocity in the cross section of the tube occupied by the vapor is used in its determination. The internal tube diameter is d_i , λ_L and λ_G are the liquid and vapor thermal conductivities, c_{pL} and c_{pG} are the liquid and vapor specific heats, and μ_L and μ_G are the liquid and vapor dynamic viscosities. The total mass velocity of the liquid plus vapor through the tube is \dot{m} , and χ is the local vapor quality.

The dry angle θ_{dry} in eq. (9.125) is the circumferential angle of the tube wall, which is assumed to be constantly dry for stratified types of flow and for annular flows with partial dryout. On the other hand, for annular and intermittent flows, the entire tube perimeter is always wetted and hence θ_{dry} is equal to zero, in which case α_{tp} is equal to α_{wet} . Methods for determining θ_{dry} , ε , and δ are described below.

The Rouhani-Axelsson (1970) drift flux type of void fraction model is used to calculate the vapor void fraction ε :

$$\varepsilon = \frac{\chi}{\rho_G} \left\{ [1 + 0.12(1-\chi)] \left(\frac{\chi}{\rho_G} + \frac{1-\chi}{\rho_L} \right) + \frac{1.18}{\dot{m}} \left[\frac{g\sigma(\rho_L - \rho_G)}{\rho_L^2} \right]^{1/4} (1-\chi) \right\}^{-1} \quad (9.130)$$

where ρ_L and ρ_G are the liquid and vapor densities and σ is the surface tension (all in SI units). The cross-sectional area of the tube occupied by the liquid-phase A_L is then obtainable as

$$A_L = A(1-\varepsilon) \quad (9.131)$$

and A is the total cross-sectional area of the tube. For the fully stratified flow regime illustrated on the right in Fig. 9.15, the stratified angle θ_{strat} of the liquid is defined geometrically as

$$A_L = 0.5r_i^2 [(2\pi - \theta_{\text{strat}}) - \sin(2\pi - \theta_{\text{strat}})] \quad (9.132)$$

where θ_{strat} is in radians. Equation (9.132) is an implicit expression and has to be solved iteratively using A_L to find the value of the stratified angle θ_{strat} . A simplified version of this expression that avoids an iterative solution is

$$\theta_{\text{strat}} \simeq 2 \left[\pi - \cos^{-1}(2\varepsilon - 1) \right] \quad (9.133)$$

The concept of a dry angle θ_{dry} is introduced for the dry perimeter of the stratified-wavy flow regime. The dry angle θ_{dry} at a particular vapor quality varies from its lower limit of $\theta_{\text{dry}} = 0$ for annular or intermittent flow on the \dot{m}_{wavy} transition curve with complete wall wetting to its maximum value of $\theta_{\text{dry}} = \theta_{\text{strat}}$ for fully stratified flow on the \dot{m}_{strat} transition curve. These mass velocities, called \dot{m}_{high} and \dot{m}_{low} , respectively, themselves are functions of vapor quality, and hence θ_{dry} changes as a function of vapor quality and mass velocity. The simple linear expression for θ_{dry} between \dot{m}_{high} and \dot{m}_{low} for any value of $\chi < \chi_{\text{max}}$ is

$$\theta_{\text{dry}} = \theta_{\text{strat}} \frac{\dot{m}_{\text{high}} - \dot{m}}{\dot{m}_{\text{high}} - \dot{m}_{\text{low}}} \quad (9.134)$$

At vapor qualities where $\chi > \chi_{\text{max}}$, an additional step is required to determine θ_{dry} since \dot{m}_{high} runs into the intersection of the \dot{m}_{wavy} and \dot{m}_{mist} curves, and for $\chi > \chi_{\text{max}}$ there is no \dot{m}_{wavy} curve for determining \dot{m}_{high} . Thus when $\chi > \chi_{\text{max}}$, the dry angle θ_{dry} is prorated *horizontally* as a linear function of vapor quality between θ_{max} and 2π , the latter being the upper limit since the tube wall is completely dry at $\chi = 1$, so that

$$\theta_{\text{dry}} = (2\pi - \theta_{\text{max}}) \frac{\chi - \chi_{\text{max}}}{1 - \chi_{\text{max}}} + \theta_{\text{max}} \quad (9.135)$$

Note that θ_{max} is determined from eq. (9.134) at $\chi = \chi_{\text{max}}$.

The annular liquid film thickness δ is determined by equating the cross-sectional area occupied by the liquid phase for this void fraction and dry angle to that of a truncated annular liquid ring, assuming that the thickness δ is small compared to the tube radius r_i , obtaining

$$\delta = \frac{A_L}{r_i(2\pi - \theta_{\text{dry}})} = \frac{A(1 - \varepsilon)}{r_i(2\pi - \theta_{\text{dry}})} = \frac{\pi d_i(1 - \varepsilon)}{2(2\pi - \theta_{\text{dry}})} \quad (9.136)$$

Figure 9.16 presents the heat transfer coefficients predicted by the Kattan–Thome–Favrat flow boiling model using their flow pattern map with the updated corrections to their wavy flow and stratified flow transitions made by Zürcher et al. (1999) to the flow pattern map. A 19.86-mm (0.01986-m)-internal-diameter tube is simulated for *n*-butane evaporating at saturation conditions of 60°C and 0.6394 MPa and a heat flux of 15,000 W/m². The heat transfer curves for α_{tp} cover:

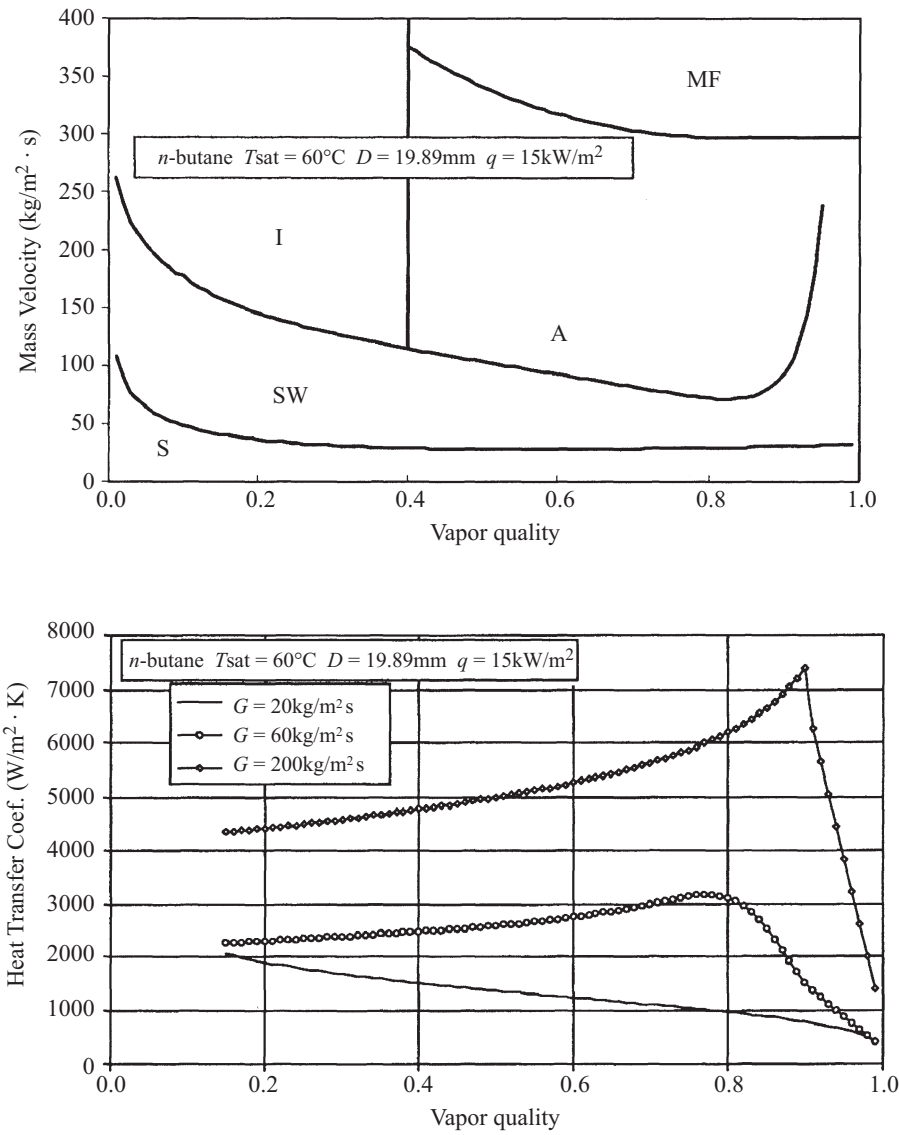


Figure 9.16 Simulation of Kattan–Thome–Favrat model for pure *n*-butane at 60°C, showing flow pattern map and heat transfer coefficients.

- Fully stratified flow for $\dot{m} = 20 \text{ kg/m}^2 \cdot \text{s}$ at all χ values, with a monotonic decrease in α_{tp} with increasing χ
- Stratified–wavy flow for $\dot{m} = 60 \text{ kg/m}^2 \cdot \text{s}$ at all χ values shown that give a moderate peak in α_{tp} versus χ
- Intermittent flow for $\dot{m} = 200 \text{ kg/m}^2 \cdot \text{s}$ with $\chi \leq 0.4$ that shows a moderate rise in α_{tp} versus χ

- *Annular flow* for $\dot{m} = 200 \text{ kg/m}^2 \cdot \text{s}$ with $0.4 < \chi < 0.93$ that results in an ever-steepier rise in α_{tp} versus χ as the annular film thins out before the onset of dryout occurs at $\chi = 0.93$
- *Annular flow with partial dryout* (modeled as stratified-wavy flow) for $\dot{m} = 200 \text{ kg/m}^2 \cdot \text{s}$ with $\chi \geq 0.93$, where a sharp decline in α_{tp} versus χ after the peak occurs

Although not illustrated, α_{tp} goes to its natural limit of α_{vapor} at $\chi = 0$. On the other hand, for all liquid flow, the convective boiling heat transfer coefficient α_{cb} for liquid film flow does *not* go to the tubular value. Hence, α_{cb} should be obtained with the Dittus–Boelter or Gnielinski correlation when $\chi = 0$. Including more recent data for evaporation of ammonia for mass velocities as low as $16.3 \text{ kg/m}^2 \cdot \text{s}$ and results for evaporation of refrigerant–oil mixtures, their flow boiling model is applicable over the following parameter ranges:

- $1.12 \leq p_{\text{sat}} \leq 8.9 \text{ bar}$
- $0.0085 \leq p_r \leq 0.225$
- $16.3 \leq \dot{m} \leq 500 \text{ kg/m}^2 \cdot \text{s}$
- $0.01 \leq \chi \leq 1.0$
- $440 \leq q \leq 71,600 \text{ W/m}^2$
- $17.03 \leq M \leq 152.9$ (but up to about 300 for refrigerant–oil mixtures)
- $74 \leq \text{Re}_L \leq 20,399$ and $1300 \leq \text{Re}_G \leq 376,804$
- $1.85 \leq \text{Pr}_L \leq 5.47$ (but up to 134 for refrigerant–oil mixtures)
- $0.00016 \leq \mu_L \leq 0.035 \text{ N} \cdot \text{s/m}^2$ (i.e., 0.16 to 35 cP)
- Tube metals (copper, carbon steel, and stainless steel)

For annular flows, the accuracy of this new method is similar to those of the Shah (1982), Jung et al. (1989), and Gungor–Winterton (1986, 1987) correlations; however, the latter methods do not provide a method to determine when annular flow conditions exist. For stratified–wavy flows, the Kattan–Thome–Favrat model has been shown to be twice as accurate as the best of these other methods, even though these other correlations have stratified flow threshold criteria and corresponding heat transfer correction factors. At $\chi > 0.85$, typical of direct-expansion evaporator applications, the Kattan–Thome–Favrat model is three times more accurate than the best of these other methods, which have standard deviations of over $\pm 80\%$.

The Kattan–Thome–Favrat model is implemented as follows for a given tube internal diameter, specific design conditions, and fluid physical properties:

1. Determine the local flow pattern corresponding to the local design condition using the Kattan–Thome–Favrat flow pattern map (Section 9.7) together with the local heat flux, vapor quality, and mass velocity.
2. Calculate the local vapor void fraction ϵ with eq. (9.130).
3. Calculate the local liquid cross-sectional area A_L with eq. (9.131).

4. If the flow is annular or intermittent (intermittent flow is thermally modeled as if it were annular), determine the annular liquid film thickness δ from eq. (9.136) with θ_{dry} set to 0.
5. If the flow is stratified–wavy (note that the flow pattern map classifies annular flow with partial dryout at the top of the tube as being stratified–wavy), eq. (9.132) is first utilized to calculate θ_{strat} , then the values of \dot{m}_{high} and \dot{m}_{low} are determined with the flow pattern map at vapor quality χ . Next, θ_{dry} is calculated with eq. (9.134) if $\chi \leq \chi_{\text{max}}$ or with eq. (9.135) if $\chi > \chi_{\text{max}}$, and then the annular liquid film thickness δ is determined from eq. (9.136) with this value of θ_{dry} .
6. If the flow is fully stratified, use eq. (9.132) to calculate θ_{strat} and then determine the annular liquid film thickness δ from eq. (9.136) using the value of θ_{strat} for θ_{dry} .
7. Determine the convective boiling heat transfer coefficient α_{cb} with eq. (9.128).
8. Calculate the vapor-phase heat transfer coefficient α_{vapor} with eq. (9.129) if part of the wall is dry.
9. For a pure, single-component liquid or an azeotropic mixture, the nucleate pool boiling heat transfer coefficient α_{nb} is determined with eq. (9.127) using the total local heat flux q .
10. Calculate the heat transfer coefficient on the wetted perimeter of the tube α_{wet} with eq. (9.126) using the values of α_{nb} and α_{cb} .
11. Determine the local flow boiling coefficient α_{tp} with eq. (9.125).

For evaporation of zeotropic mixtures and refrigerant–oil mixtures, refer to Section 9.12.

9.9.3 Subcooled Boiling Heat Transfer

Fully developed subcooled boiling is characterized by vapor formation at the heated wall in the form of single bubbles or as a bubbly layer parallel to the wall. These bubbles are swept into the subcooled area of the liquid flow by the variable shear stress on their boundary imposed by the turbulent flow velocity profile. The bubbles then condense in the subcooled core. To predict local heat transfer coefficients in the subcooled boiling regime, Gungor and Winterton (1986) have adapted their correlation by using separate temperature differences for driving the respective nucleate boiling and convective boiling processes so that the heat flux is calculated as a sum of their contributions as

$$q = \alpha_L [T_w - T_L(z)] + S\alpha_{nb}(T_{\text{wall}} - T_{\text{sat}}) \quad (9.137)$$

This formula predicted their database with a mean error of $\pm 25\%$. The methods presented earlier for saturated forced-convective evaporation may be adapted to subcooled flow boiling in an analogous manner.

9.10 BOILING ON TUBE BUNDLES

In the foregoing sections we addressed flow boiling when it occurs inside tubes. Boiling on the outside of horizontal tube bundles is another important process, typical of kettle and thermosyphon reboilers, waste heat boilers, fire tube steam generators, and flooded evaporators.

9.10.1 Heat Transfer Characteristics

Figure 9.17 depicts a simplified tube bundle layout. Subcooled liquid enters the bundle from below and flows upward past the tubes. Until the wall temperature surpasses the saturation temperature of the liquid, single-phase convective heat transfer occurs. Once the wall temperature is above T_{sat} , subcooled boiling may occur and the bubbly flow regime begins. Farther up the bundle, the bulk fluid temperature reaches the saturation temperature and saturated boiling begins. The rapid departure of sequential bubbles tends to form bubble jets from the top of tubes. With coalesce of these bubbles into a larger size, sliding bubbles are formed as they pass between adjacent tubes, characterized by a thin evaporating film of liquid between the bubble and the wall. The flow becomes ever more chaotic and locally unstable and the chugging flow regime is

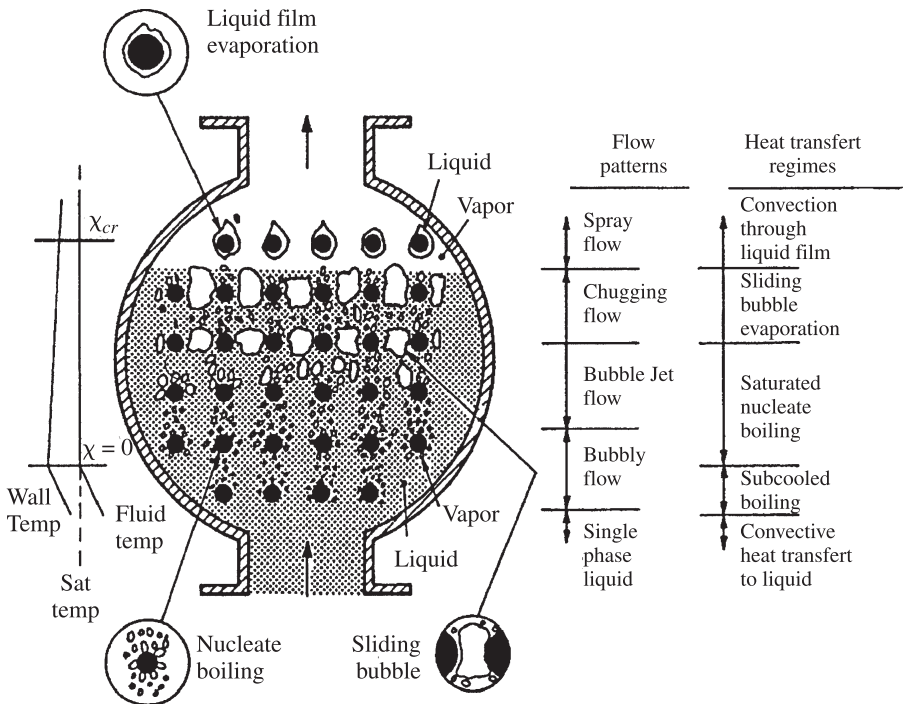


Figure 9.17 Boiling on a horizontal tube bundle. (From Collier and Thome, 1994.)

encountered. At higher vapor qualities with increasing vapor shear on the liquid films on the tubes, the liquid becomes entrained in the vapor, which becomes the continuous phase. This is the spray flow regime and the tubes are wetted by the impact of droplets that may maintain a continuous liquid film on the tubes. Thus, the active heat transfer modes in bundle boiling are nucleate boiling, convective boiling, and thin-film evaporation. At some critical condition x_{cr} illustrated in the diagram, dryout of the tubes may occur with a substantial decrease in the local heat transfer coefficient.

Typically, for saturated inlet conditions the local flow boiling coefficient at the bottom of the tube is similar in value to that for nucleate pool boiling on a single tube (methods described in Section 9.5). As the local vapor quality rises from bottom to top in the bundle, the influence of convection becomes more and more important. At the top of the bundle, the heat transfer coefficient may become as high as three to four times that at the bottom.

9.10.2 Bundle Boiling Factor

Bundle boiling coefficients can be analyzed by normalizing the bundle coefficient α_b with the single tube nucleate pool boiling coefficient α_{st} , where α_{st} is either measured or calculated using a nucleate pool boiling correlation and α_b may refer either to a local value within the bundle or to the mean value for the entire tube bundle. This ratio, known as the *bundle boiling factor* F_b , indicates the relative enhancing effect of two-phase convection in the bundle compared to the pool boiling coefficient, such that

$$F_b = \frac{\alpha_b}{\alpha_{st}} \quad (9.138)$$

The value of F_b tends toward 1.0 at high heat fluxes and high reduced pressures because the nucleate boiling coefficient becomes dominant. For plain tubes and low finned tubes, local values of F_b tend to range from about 1.0 at the bottom of the bundle, when the inlet flow is all liquid and thus the convective effect is minimal, up to as high as 3 or 4 near the top tube rows, where the convective contribution is very pronounced. Mean bundle values of F_b , on the other hand, are normally in the range 1.5 to 2.0.

9.10.3 Bundle Design Methods

The simplest thermal design method is to assume a value of the bundle boiling factor, such as $F_b = 1.5$ as a conservative value. Then, after calculating the single-tube boiling heat transfer coefficient using one of the methods in Section 9.5, the mean bundle boiling coefficient is obtainable from eq. (9.138). Another simple approach has been proposed by Palen (1983), where the mean bundle boiling heat transfer coefficient α_b is assumed to be a superposition of the contributions of boiling and natural convection as

$$\alpha_b = \alpha_{st} F_b F_c + \alpha_{nc} \quad (9.139)$$

Here α_{st} is the single-tube nucleate pool boiling coefficient, F_b the bundle boiling factor, F_c the mixture boiling correction factor (see Section 9.12), and α_{nc} the natural convection heat transfer coefficient for the tube bundle. Palen recommends using $\alpha_{nc} = 250 \text{ W/m}^2 \cdot \text{K}$ and $F_b = 1.5$. For pure fluids and azeotropic mixtures, F_c is equal to 1.0; for zeotropic mixtures, its value may vary from 0.1 to 1.0.

Various Chen-type *in-tube* boiling correlations have been proposed for evaporation on the *outside* of plain tube bundles. In this approach, the liquid-only heat transfer coefficient to the liquid phase in eq. (9.89) is calculated using a correlation for turbulent crossflow over a tube bundle rather than the Dittus–Boelter in-tube correlation, and the nucleate boiling coefficient is predicted with one of the methods in Section 9.5. New expressions for the boiling suppression factor S and two-phase multiplier F are then formulated, sometimes with the boiling suppression factor set to unity. So far, these methods have had only limited success in predicting local bundle boiling heat transfer coefficients since they are typically based on small databases composed of only one combination of tube diameter and tube pitch and one or two fluids, and hence are not applicable for general use.

9.11 POST-DRYOUT HEAT TRANSFER

9.11.1 Introduction

Post-dryout heat transfer occurs during forced-flow evaporation when the heated surface becomes dry before complete evaporation. It refers to the heat transfer process downstream from the point at which the surface became dry and may occur at any vapor quality or even during subcooled flow boiling. Post-dryout heat transfer is also referred to as the *liquid-deficient regime* or as *mist flow heat transfer*; however, these terms do not describe the process when it occurs at low vapor quality. In general, the post-dryout heat transfer regime is entered from the wet wall regime by passing through one of the following transitions in the evaporation process:

- *Dryout of the liquid film.* A liquid film (such as in an annular flow) may completely evaporate, leaving only the entrained liquid droplets in the vapor to be evaporated.
- *Entrainment of the liquid film.* For a high vapor shear stress on the liquid film, the liquid may be pulled from the surface and become entirely entrained in the vapor phase.
- *Critical heat flux.* Imposing a large heat flux or wall superheat at the wall may create a continuous layer of vapor on the wall, starting from dryout under a single small bubble, a large Taylor bubble, or a dense packing of bubbles.

For the transition from annular to mist flow, refer to Section 9.7 on two-phase flow maps. For further discussion on the mechanisms and prediction of the critical heat flux, refer to the reviews by Weisman (1992), Katto (1994, 1996), and Celata (1997).

The heated wall is not completely dry in the post-dryout heat transfer regime. Entrained droplets impinge on the surface and wet it locally before either evaporating or rebounding back into the vapor phase. Second, in horizontal channels, the upper portion of the heated periphery of the flow channel becomes dry while the bottom remains wetted by the flowing liquid, such that there is simultaneously flow boiling heat transfer on the bottom and post-dryout heat transfer around the top. This partial dryout of the perimeter of the heated channel may also occur when there is a significant variation in the peripheral heat flux, such as a boiler tube exposed to radiant heat from only one direction. The post-dryout regime may be reached during saturated boiling in a channel but may also be encountered during subcooled boiling at high heat fluxes. Only saturated boiling is discussed here.

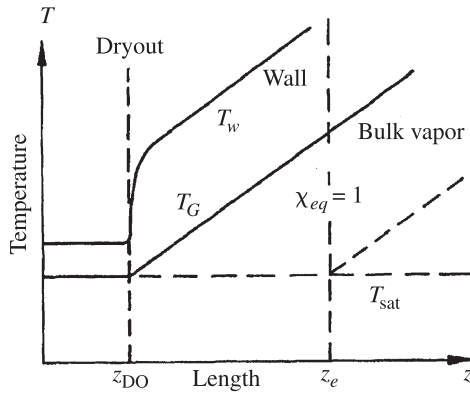
The post-dryout regime may be encountered in fossil-fuel boilers and fired heaters, on nuclear power plant fuel rod assemblies during a hypothetical loss-of-coolant accident, in direct-expansion evaporators and air-conditioning coils, and in cooling of various high-heat-flux devices. Heat transfer coefficients in the post-dryout regime are significantly lower than those for wet wall evaporation. In this chapter, first thermal nonequilibrium effects and heat transfer phenomena particular to post-dryout flow are described, and then methods for predicting heat transfer under post-dryout conditions inside channels with uniform boundary conditions are presented.

9.11.2 Thermal Nonequilibrium

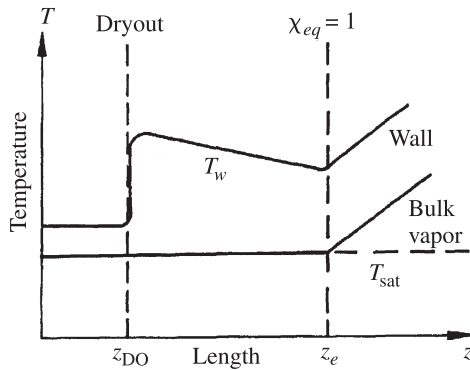
The wall superheat during wet wall evaporation remains relatively small, typically below 15 to 30 K. In the post-dryout regime, instead, the local wall temperature may become significantly higher than the saturation temperature, such that a departure from equilibrium occurs. The two limiting cases are illustrated in Fig. 9.18. For complete departure from equilibrium, heat is transferred only to the continuous vapor phase. If heat absorbed by the entrained droplets is insignificant, the vapor temperature $T_G(z)$ downstream from the point of dryout rises with the sensible heating of the vapor. Similarly, the wall temperature $T_w(z)$ rises like that of a single-phase convective flow, giving the temperature profile illustrated in Fig. 9.18a. Post-dryout evaporation tends toward the case of complete thermal nonequilibrium at low pressures and low mass flow rates at high vapor qualities.

For complete thermodynamic equilibrium, illustrated in Fig. 9.18b, the rate of heat transfer to the entrained droplets is assumed to be so effective that the vapor temperature $T_G(z)$ remains at the saturation temperature as the droplets evaporate. The wall temperature $T_w(z)$ varies depending on the intensity of the droplet evaporation process. Evaporation tends toward thermal equilibrium at high reduced pressures and very high mass flow rates.

A typical process path is illustrated in Fig. 9.19, where the local vapor temperature is lower than that occurring for complete nonequilibrium, but is still significantly above the local saturation temperature of the complete equilibrium case. Hence, for post-dryout heat transfer the temperature of the vapor is not known a priori but is part of the solution. Thermodynamic equilibrium means that all the heat absorbed by the fluid is utilized to evaporate the liquid, and hence the local equilibrium vapor quality



(a) Complete lack of thermodynamic equilibrium



(b) Complete thermodynamic equilibrium

Figure 9.18 Thermodynamic states in the post-dryout regime. (From Collier and Thome, 1994.)

is $\chi_e(z)$. If, instead, all the heat does into superheating the vapor after the onset of dryout, the vapor quality remains that at the dryout point $\chi_{DO}(z)$. In between, the actual local vapor quality $\chi_a(z)$ is somewhere between these two limits such that $\chi_{DO}(z) < \chi_a(z) < \chi_e(z)$.

Consider Fig. 9.19, which depicts post dryout in a vertical tube of internal diameter d_i heated uniformly with a heat flux of q . Dryout occurs at a length z_{DO} from the inlet, and it is assumed that thermodynamic equilibrium exists at the dryout point. If complete equilibrium is maintained after dryout, all the liquid will be evaporated when point z_e is reached. However, in the actual situation, only a fraction (κ) of the surface heat flux is used to evaporate the remaining liquid in the post-dryout region while the remainder is used to superheat the bulk vapor. The liquid is thus evaporated completely only when a downstream distance of z_a is reached. Assuming that the total heat flux $q(z)$ from the tube wall to the fluid is comprised of the heat flux associated

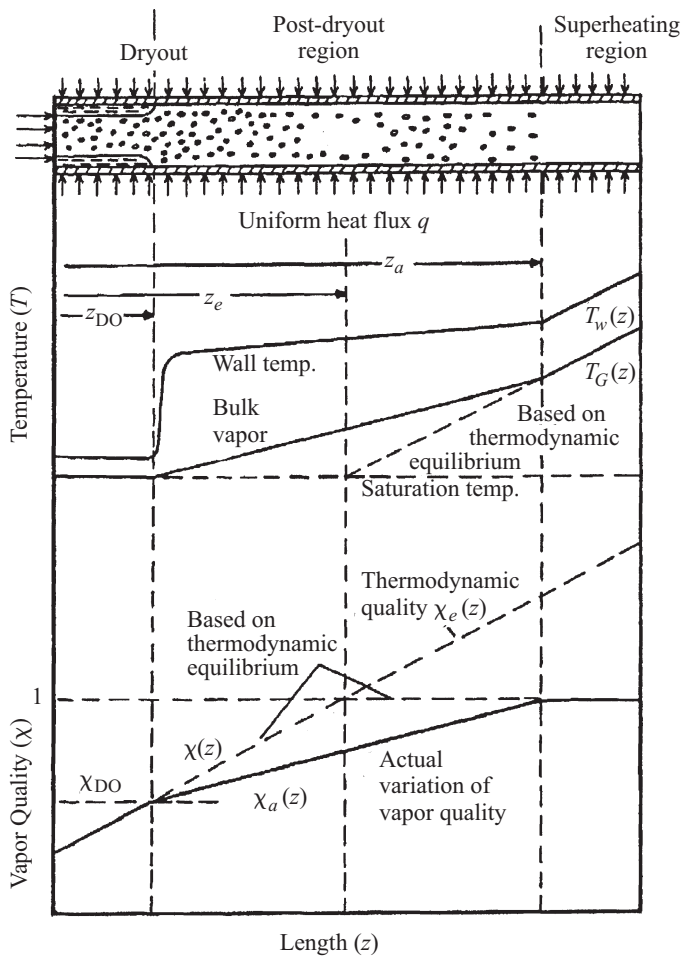


Figure 9.19 Departure from thermodynamic equilibrium in the post-dryout regime. (From Collier and Thome, 1994.)

with droplet evaporation $q_L(z)$ and the heat flux associated with vapor superheating $q_G(z)$, then

$$q(z) = q_L(z) + q_G(z) \tag{9.140}$$

Furthermore, let

$$\kappa = \frac{q_L(z)}{q(z)} \tag{9.141}$$

where κ is considered independent of tube length, so that the profiles of the actual bulk vapor temperature and actual vapor quality are linear. The vapor quality for $z < z_e$ is given by an energy balance

$$\chi(z) - \chi_{\text{DO}} = \frac{4}{d_i \dot{m} h_{LG}} (z - z_{\text{DO}}) \quad (9.142)$$

where h_{LG} is the latent heat of vaporization, \dot{m} is the total mass velocity, and point z_e is given by

$$z_e = \left[\frac{d_i \dot{m} h_{LG}}{4q} (1 - \chi_{\text{DO}}) \right] + z_{\text{DO}} \quad (9.143)$$

The variation in the actual vapor quality $\chi_a(z)$ with length for $z < z_a$ is

$$\chi_a(z) - \chi_{\text{DO}} = \frac{4\kappa q}{d_i \dot{m} h_{LG}} (z - z_{\text{DO}}) \quad (9.144)$$

where z_a is

$$z_a = \left[\frac{d_i \dot{m} h_{LG}}{4\kappa q} (1 - \chi_{\text{DO}}) \right] + z_{\text{DO}} \quad (9.145)$$

Combining eq. (9.142) with (9.145) yields

$$\kappa = \frac{\chi_a(z) - \chi_{\text{DO}}}{\chi(z) - \chi_{\text{DO}}} = \frac{z_a - z_{\text{DO}}}{z_e - z_{\text{DO}}} \quad (9.146)$$

The actual bulk vapor temperature $T_{G,a}(z)$ is thus

$$T_{G,a}(z) = T_{\text{sat}} + \frac{4(1 - \kappa)q(z - z_{\text{DO}})}{\dot{m} c_{pG} d_i} \quad (9.147)$$

for $z < z_a$, while for $z_a > z$ it is

$$T_{G,a}(z) = T_{\text{sat}} + \frac{4q(z - z_e)}{\dot{m} c_{pG} d_i} \quad (9.148)$$

The two limiting cases in Fig. 9.18 are obtained by setting $\kappa = 0$ and $\kappa = 1$, respectively, in the expressions above. In reality, κ is not independent of tube length and must be predicted from the actual process conditions. As illustrated in Fig. 9.19, small droplets may remain entrained in the vapor wall beyond the location of $\chi_e(z)$, where one is tempted to believe that all the flow is superheated vapor.

9.11.3 Heat Transfer Mechanisms

Post-dryout heat transfer may occur in the *dispersed flow regime*, in which the vapor phase becomes the continuous phase and all the liquid is entrained as dispersed droplets or as *inverted annular flow*, in which the vapor forms an annular film on the tube wall and the liquid is in the central core. The first typically occurs after dryout or entrainment of an annular film flow, while the second occurs when the critical heat flux is exceeded at low vapor quality or in a subcooled liquid. In inverted annular flow,

the wall is too hot to be rewetted by the liquid, and a continuous stable, if chaotic, vapor film is formed between the wall and the continuous liquid core. For horizontal and inclined tubes, dryout typically initiates on the upper perimeter of the tube while the lower perimeter remains wet, and may also occur only on one side of a vertical tube heated nonuniformly by, say, a radiant heat source. Post-dryout heat transfer is characterized by the following modes:

- *Wall-to-vapor heat transfer*: turbulent (or laminar) convection to the continuous vapor phase
- *Wall-to-droplet heat transfer*: evaporation of droplets that impinge on the hot wall
- *Vapor-to-droplet heat transfer*: convection from the bulk superheated vapor to the saturated liquid in the droplets, including any droplets passing through the thermal boundary layer on the wall that do not actually contact the wall
- *Radiation heat transfer from wall-to-droplets/vapor/upstream wall*: net radiation flux dependent on the view factor, emissive properties, transparency of the vapor, and respective temperatures.

9.11.4 Inverted Annular Flow Heat Transfer

This regime is also referred to as *forced-convective film boiling*. From observations of film boiling inside a vertical tube, Dougall and Rohsenow (1963) observed that the flow consisted of a central liquid core surrounded by a thin annular film of vapor on the heated wall when occurring at low vapor quality and low flow rates. The interface was not smooth but wavy. Because of the density difference between the two phases, the vapor was assumed to be traveling at a much higher velocity than the liquid core. Depending on the conditions imposed on vertical upward flow, the liquid core was observed to flow upward, remain more or less stationary, or even flow downward. Entrained vapor bubbles were also observed in the liquid core.

The simplest inverted annular flow to analyze is heat transfer through a laminar vapor film. For a vertical flat surface, this is similar to the Nusselt solution for falling film condensation on a vertical flat plate. The local heat transfer coefficient $\alpha(z)$ at a distance z from the point of onset of film boiling is

$$\alpha(z) = C \left[\frac{\lambda_G^3 \rho_G (\rho_L - \rho_G) g h_{LG}}{z \mu_G \Delta T} \right]^{1/4} \quad (9.149)$$

where the wall superheat is $\Delta T = T_w - T_{\text{sat}}$ and the value of C depends on the boundary conditions: $C = 0.707$ for zero interfacial stress and $C = 0.5$ for zero interfacial velocity, for example.

For turbulent flow in the vapor film, the heat transfer coefficient is inversely dependent on the distance z according to Wallis and Collier (1968):

$$\frac{\alpha(z)z}{\lambda_G} = 0.056 \text{Re}_G^{0.2} (\text{Pr}_G \cdot \text{Gr}_G)^{1/3} \quad (9.150)$$

where the vapor Reynolds number Re_G is that of the vapor fraction flowing alone in the tube, Pr_G is the vapor Prandtl number, and Gr_G is the vapor Grashof number:

$$Gr_G = \frac{z^3 g \rho_G (\rho_L - \rho_G)}{\mu_G^2} \quad (9.151)$$

Other important effects on inverted annular flow heat transfer are the flow structure at the interface (waves, periodic disturbances, instabilities), subcooling of the liquid core, thermal radiation, and so on.

9.11.5 Mist Flow Heat Transfer

A heat transfer model for the mist flow regime should ideally include the heat transfer mechanisms mentioned earlier and nonequilibrium effects on the local temperature and vapor quality. However, most methods include only one or several of these. For single-phase turbulent convection from the wall to the continuous vapor phase, Dougall and Rohsenow (1963) have used the Dittus–Boelter correlation:

$$Nu_G = \frac{\alpha d_i}{\lambda_G} = 0.023 Re_{GH}^{0.8} \cdot Pr_G^{0.4} \quad (9.152)$$

where the velocity was assumed to be the homogeneous velocity u_H :

$$u_H = \frac{\dot{m}}{\rho_H} = \dot{m} \left(\frac{\chi}{\rho_G} + \frac{1-\chi}{\rho_L} \right) \quad (9.153)$$

so that the Reynolds number of the homogeneous vapor is

$$Re_{GH} = \frac{\dot{m} d_i}{\mu_G} \left[\chi + \frac{\rho_G}{\rho_L} (1 - \chi) \right] \quad (9.154)$$

They used the equilibrium vapor quality χ_e in this expression with all properties evaluated at the saturation temperature. Hence, nonequilibrium effects and other heat transfer modes are neglected, so this method should only be used as a first approximation.

Groeneveld (1973) added another multiplying factor Y to this approach, where

$$Y = 1 - 0.1 \left[\left(\frac{\rho_L}{\rho_G} - 1 \right) (1 - \chi) \right]^{0.4} \quad (9.155)$$

$$Nu_G = 0.00327 \left\{ \frac{\dot{m} d_i}{\mu_G} \left[\chi + \frac{\rho_G}{\rho_L} (1 - \chi) \right] \right\}^{0.901} \cdot Pr_G^{1.32} \cdot Y^{-1.50} \quad (9.156)$$

The equilibrium vapor quality χ_e and saturation properties are used. His database covers flows in vertical and horizontal tubes and in vertical annuli for the following conditions:

- $2.5 \text{ mm} < d_i < 25 \text{ mm}$
- $34 \text{ bar} < p < 215 \text{ bar}$
- $700 \text{ kg/m}^2 \cdot \text{s} < \dot{m} < 5300 \text{ kg/m}^2 \cdot \text{s}$
- $0.1 < \chi < 0.9$
- $120 \text{ kW/m}^2 < q < 2100 \text{ kW/m}^2$

Use of his correlation beyond the range above is not recommended. Groeneveld and Delorme (1976) subsequently proposed a new correlation that accounts for non-equilibrium effects, whose simplified version is as follows. First the parameter ψ is obtained from

$$\psi = 0.13864 \text{Pr}_G^{0.203} \cdot \text{Re}_{GH,e}^{0.2} \left(\frac{q d_i c_{pG,e}}{\lambda_L h_{LG}} \right)^{-0.0923} (1.307 - 1.083 \chi_e + 0.846 \chi_e^2) \quad (9.157)$$

which is valid for $0 \leq \psi \leq \pi/2$. (Note: When $\psi < 0$, its value is set to 0.0; when $\psi > \pi/2$, it is set to $\pi/2$.) Their homogeneous Reynolds number $\text{Re}_{GH,e}$ based on the equilibrium vapor quality is

$$\text{Re}_{GH,e} = \frac{\dot{m} d_i}{\mu_G} \left[\chi_e + \frac{\rho_G}{\rho_L} (1 - \chi_e) \right] \quad (9.158)$$

For values of χ_e greater than unity (i.e., when the enthalpy added to the fluid places its equilibrium state in the superheated vapor region), χ_e is set equal to 1.0 in the expressions above. To determine the values of $T_{G,a}$ and χ_a , an energy balance is used where $h_{G,a}$ is the actual vapor enthalpy and $h_{L,\text{sat}}$ is the enthalpy of the saturated liquid, while χ_e is the equilibrium vapor quality and h_{LG} is the latent heat of evaporation. The actual vapor quality is obtained from

$$\chi_a = \frac{h_{LG} \chi_e}{h_{G,a} - h_{L,\text{sat}}} \quad (9.159)$$

and the change in enthalpy is

$$h_{G,a} - h_{L,\text{sat}} = h_{LG} + \int_{T_{\text{sat}}}^{T_{G,a}} c_{pG} dT_G \quad (9.160)$$

The difference between the actual vapor enthalpy $h_{G,a}$ and the equilibrium vapor enthalpy $h_{G,e}$ is

$$\frac{h_{G,a} - h_{G,e}}{h_{LG}} = \exp(-\tan \psi) \quad (9.161)$$

For $0 \leq \chi_e \leq 1$, the equilibrium vapor enthalpy $h_{G,e}$ is that of the saturated vapor, that is,

$$h_{G,e} = h_{G,\text{sat}} \quad (9.162)$$

For $\chi_e > 1$, the equilibrium vapor enthalpy $h_{G,e}$ is calculated as

$$h_{G,e} = h_{G,\text{sat}} + (\chi_e - 1)h_{LG} \quad (9.163)$$

Finally, the heat transfer coefficient, defined as $\alpha = q/(T_w - T_{G,a})$, is obtained from

$$\frac{\alpha d_i}{\lambda_{G,f}} = \frac{q d_i}{(T_w - T_{G,a})\lambda_{G,f}} = 0.008348 \left\{ \chi_a + \frac{\rho_G}{\rho_L}(1 - \chi_a) \right\}^{0.8774} \cdot \text{Pr}_{G,f}^{0.6112} \quad (9.164)$$

where the subscript “ G,f ” in these expressions indicates that the vapor properties should be evaluated at the film temperature

$$T_{G,f} = \frac{T_w + T_{G,a}}{2} \quad (9.165)$$

This iterative method predicts the values of α , $T_{G,a}$, and χ_a when given those of \dot{m} , χ_e , and q . The method includes the effect of departure from equilibrium but still ignores the contributions of wall-to-droplet, vapor-to-droplet, and radiation heat transfer. This method is more accurate than that of Groeneveld (1973) and has a similar application range.

A more complete model has been proposed by Ganic and Rohsenow (1977). In their model the total heat flux in mist flow was assumed to be the sum of wall-to-vapor convection q_G , wall-to-droplet evaporation q_L , and radiation q_{rad} , so that

$$q = q_G + q_L + q_r \quad (9.166)$$

The wall-to-vapor convection contribution was obtained by introducing the actual vapor velocity into the McAdams turbulent flow correlation as

$$q_G = 0.0023 \left(\frac{\lambda_L}{d_i} \right) \left(\frac{\dot{m} \chi d_i}{\varepsilon \mu_G} \right)^{0.8} \cdot \text{Pr}_G^{0.4} (T_w - T_{\text{sat}}) \quad (9.167)$$

using the void fraction ε (e.g., see Section 9.9 for an expression to calculate the void fraction), while the physical properties are evaluated at the saturation temperature. The total radiant heat flux from the wall to droplets and from the wall to vapor is

$$q_{\text{rad}} = F_{wL} \sigma_{\text{SB}} (T_w^4 - T_{\text{sat}}^4) + F_{wG} \sigma_{\text{SB}} (T_w^4 - T_{\text{sat}}^4) \quad (9.168)$$

where F_{wL} and F_{wG} are the respective view factors, σ_{SB} is the Stephan–Boltzmann constant ($\sigma_{\text{SB}} = 5.67 \times 10^{-8} \text{ W/m}^2 \cdot \text{K}^4$) and blackbody radiation is assumed. $F_{wG} = 0$ for a transparent vapor. The radiant heat flux is in fact negligible except at very large wall temperatures.

Although ignoring nonequilibrium effects, they predicted the heat flux due to impinging droplets on the wall as

$$q_L = u_d(1 - \varepsilon)\rho_L h_{LG} f_{cd} \exp \left[1 - \left(\frac{T_w}{T_{\text{sat}}} \right)^2 \right] \quad (9.169)$$

where the droplet deposition velocity u_d is

$$u_d = 0.15 \frac{\dot{m} \chi}{\rho_L \varepsilon} \sqrt{\frac{f_G}{2}} \quad (9.170)$$

f_{cd} is the cumulative deposition factor, and f_G is the single-phase friction factor calculated at the effective vapor Reynolds number (i.e., $\dot{m} \chi_e d_i / \varepsilon \mu_G$). The value of f_{cd} is a complicated function of droplet size. The importance of q_L relative to the total heat flux is significant at low to medium vapor qualities, where a large fraction of liquid is present in the flow.

For heat transfer from the superheated vapor to a single, isolated entrained liquid droplet, Ganic and Rohsenow (1977) predicted the convective heat transfer coefficient from the vapor to the droplet, α_D , in terms of a droplet Nusselt number as

$$\text{Nu}_D = 2 + 0.6 \text{Re}_D^{1/2} \cdot \text{Pr}_G^{1/3} \quad (9.171)$$

where

$$\text{Nu}_D = \frac{\alpha_D D}{\lambda_G} \quad (9.172)$$

$$\text{Re}_D = \frac{\rho_G D(u_G - u_D)}{\mu_G} \quad (9.173)$$

D is the droplet diameter, u_G the vapor velocity, u_D the droplet velocity, and the Prandtl number Pr_G is based on vapor properties:

$$\text{Pr}_G = \frac{\mu_G c_{pG}}{\lambda_G} \quad (9.174)$$

The factor of 2 on the right-hand side of eq. (9.171) is that resulting for pure conduction to the droplet, and the second term accounts for convection. The heat transfer rate to the droplet is

$$Q = \pi D^2 \alpha_D (T_{G,a} - T_D) \quad (9.175)$$

where $T_{G,a}$ is the superheated vapor temperature and T_D is the droplet temperature. T_D is assumed to be the saturation temperature, but a method for estimating the value of $T_{G,a}$ is required.

Methods to model mist flow heat transfer for internal flows numerically have progressed rapidly in recent years. For example, Andreani and Yadigaroglu (1997) have

developed a three-dimensional Eulerian–Lagrangian model of dispersed flow boiling that includes a mechanistic description of the formation of the droplet spectrum.

9.12 BOILING OF MIXTURES

Evaporation of pure fluids is typical of systems that operate on a closed cycle, such as water in a power plant or a refrigerant in an air-conditioning system. Instead, evaporation of mixtures is an important heat transfer process in the petrochemical processing industries, in the production of polymers, occurs in refrigeration systems when a miscible oil enters the refrigerant charge in the compressor, and so on. Thus, in this section, the basic principles of mixture boiling are presented. For a more complete discussion of this topic, refer to Thome and Shock (1984).

9.12.1 Vapor–Liquid Equilibria and Properties

Some knowledge of the principles of vapor–liquid equilibria is required to understand the basics of mixture boiling. Phase equilibrium of a binary mixture system is typically presented on a phase diagram such as the one depicted in Fig. 9.20 for a mixture that does not exhibit an azeotrope. This diagram shows the bubble point and dew point temperature curves at constant pressure, where the vertical axis is temperature and the horizontal axis gives the mole fraction of the two components in both the liquid and vapor phases. The component with the lower boiling point temperature at the particular pressure (i.e., in this case the one to the right at a mole fraction of 1.0) is referred to as the *more volatile* or *lighter component*; the other fluid is referred to as the *less volatile* or *heavier component*.

For a mixture with the mole fraction x in the liquid phase, its equilibrium mole fraction in the vapor phase is y . The bubble point temperatures T_{bub} are given by

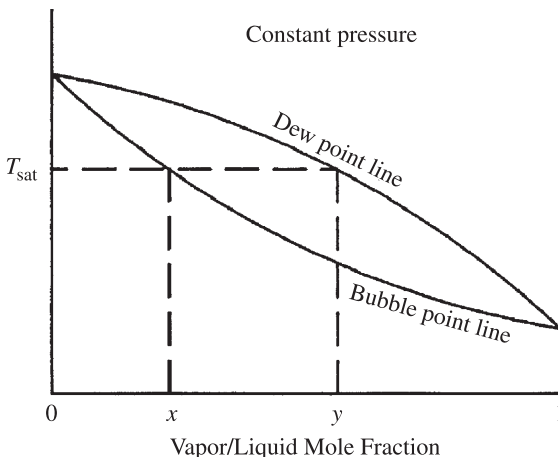


Figure 9.20 Phase equilibrium diagram of a binary mixture.

the bottom curve as a function of x , and the dew point temperatures T_{dew} are given by the upper curve as a function of y . The bubble point temperature represents the temperature at which a subcooled mixture of the liquid will first form vapor when heating the fluid. Similarly, the dew point temperature is the temperature at which a superheated vapor will first form liquid upon being cooled. The difference in the liquid and vapor mole fractions is caused by the different partial pressures exerted by each fluid, and $(y - x)$ is the driving force for mass transfer to the bubble during boiling. The temperature difference between the two curves at any vertical line at a liquid mole fraction x is referred to as the boiling range or temperature glide of the mixture, ΔT_{bp} .

The physical properties of mixtures often do not follow a linear interpolation between the pure component properties, whether using a mixing law based on mass fraction or on mole fraction. For instance, the liquid viscosity of a binary mixture may be higher or lower than that of its two components at the same temperature. Thus, it is important to use appropriate methods for the prediction of mixture properties for use in thermal design. A comprehensive treatment is available in Reid et al. (1987).

9.12.2 Nucleate Boiling of Mixtures

The basic relationship between the mixture boiling heat transfer coefficient α_{mixt} with respect to the ideal pure fluid boiling heat transfer coefficient α_{id} is

$$\frac{\alpha_{\text{mixt}}}{\alpha_{id}} = F_c = \frac{\Delta T_{id}}{\Delta T_{id} + dT_{bp}} \quad (9.176)$$

The ideal boiling coefficient is that which would be obtained by inserting the mixture physical properties into a nucleate pool boiling correlation in Section 9.5, so this can also be referred to as the *boiling coefficient of the equivalent pure fluid*. For a heat flux of q , the wall superheat for boiling of the equivalent pure fluid is ΔT_{id} . For a zeotropic mixture, mass transfer of the more volatile component to the bubble interface and evaporation into the bubble to provide its larger equilibrium mass fraction in the vapor phase has the effect of forming a mass diffusion layer around the bubble. Hence, the local mass fraction of the more volatile component is lower at the bubble interface, and thus the bubble point temperature of the mixture at the bubble interface is higher than in the bulk liquid. This rise in bubble point temperature dT_{bp} diminishes the superheat available for evaporation and hence slows down the bubble growth rate. The value of dT_{bp} ranges from a minimum value of zero for a pure fluid or an azeotrope up to the maximum possible value, which is the boiling range (or temperature glide) of a zeotropic mixture. The value of dT_{bp} is controlled by the combined heat and mass transfer diffusion process. A mixture in which the liquid and vapor mole fractions are the same is referred to as an *azeotrope*.

Schlünder (1983) proposed a simple solution predicting dT_{bp} for a bubble growing in a uniformly superheated fluid. That method was extended by Thome (1989) to multicomponent mixtures in terms of the boiling range ΔT_{bp} , and his analytically derived mass transfer factor F_c for nucleate pool boiling of mixtures is

$$F_c = \left\{ 1 + \frac{\alpha_{id}}{q} \Delta T_{bp} \left[1 - \exp \left(\frac{-q}{\rho_L h_{LG} \beta_L} \right) \right] \right\}^{-1} \quad (9.177)$$

For zeotropic mixtures, $F_c < 1.0$ since $\Delta T_{bp} > 0$, but F_c equals 1.0 for pure fluids and azeotropes since for these fluids $\Delta T_{bp} = 0$. The nucleate boiling heat transfer coefficient for zeotropic mixtures is thus obtained by including F_c in, for example, the Cooper correlation to give

$$\alpha_{nb} = 55 p_r^{0.12} (-\log_{10} p_r)^{-0.55} M^{-0.5} q^{0.67} F_c \quad (9.178)$$

where q is the heat flux and p_r and M are those of the liquid mixture. The ideal heat transfer coefficient α_{id} is first determined with eq. (9.178) by setting ΔT_{bp} to 0.0 such that $F_c = 1.0$. This method is valid for boiling ranges up to 30 K and hence covers many of the zeotropic refrigerant blends and hydrocarbon mixtures of industrial interest. In these expressions, the heat flux q is in W/m^2 , the liquid density ρ_L is in kg/m^3 , the latent heat h_{LG} is in J/kg , and the mass transfer coefficient β_L equals a fixed value of 0.0003 m/s.

9.12.3 Flow Boiling of Mixtures

Evaporation of mixtures inside vertical and horizontal tubes is typical of numerous industrial processes. More recently, with the retirement of the older refrigerants and their replacements in some cases by three-component zeotropic mixtures, for example R-407C, evaporation of mixtures has now become common to the design of air-conditioning systems. Mixtures have three important effects on thermal design. First, as a mixture evaporates along a tube, its local bubble point temperature rises as the more volatile component preferentially evaporates into the vapor phase. Hence the change in enthalpy also includes sensible heating of the liquid and vapor up this temperature gradient in addition to the latent heat of vaporization. The vapor produced has a mole fraction of y , while that of the liquid has a mole fraction of x . Hence, it is the enthalpy change between these two states that is used to calculate the latent heat change during flow boiling. Consequently, an enthalpy curve is required to do the energy balance between the evaporating fluid and the heating fluid in a heat exchanger.

The second effect is that of the mass transfer on nucleate pool boiling contribution to the flow boiling heat transfer coefficient. This can be introduced into heat transfer models that have explicit nucleate boiling and convective boiling contributions, such as most of those discussed in Sections 9.8 and 9.9. This can be accomplished by multiplying the nucleate boiling contribution in those methods by the mixture boiling correction factor F_c , discussed in Section 9.12.2.

The third effect is the gas-phase heat transfer resistance. The most widely used approach for predicting in-tube condensation of miscible mixtures where all components are condensable is commonly referred to as the *Silver-Bell-Ghaly* method. This method accounts for the need to cool the vapor phase when condensing a mixture along its dew point temperature curve in addition to removal of the latent heat.

Similarly, the vapor phase must be heated up when a mixture proceeds up the bubble point curve during evaporation. The effective flow boiling heat transfer coefficient α_{eff} for evaporation of a mixture is calculated by proration as

$$\frac{1}{\alpha_{\text{eff}}} = \frac{1}{\alpha_{tp}(\chi)} + \frac{Z_G}{\alpha_G} \quad (9.179)$$

The flow boiling heat transfer coefficient $\alpha_{tp}(\chi)$ is obtained with one of the in-tube correlations cited previously for pure fluids but using the local physical properties of the mixture and including the effect of F_c on the nucleate boiling coefficient. The other heat transfer coefficient is that of the vapor α_G , which is calculated with the Dittus–Boelter turbulent flow correlation using the vapor fraction of the flow in calculating the vapor Reynolds number. The parameter Z_G is the ratio of the sensible heating of the vapor to the total heating rate, which can be written as

$$Z_G = \chi c_{pG} \frac{dT_{bp}}{dh} \quad (9.180)$$

In this expression χ is the local vapor quality, c_{pG} is the specific heat of the vapor, and dT_{bp}/dh is the slope of the bubble point curve with respect to the enthalpy of the mixture as it evaporates (i.e., the slope of the enthalpy curve). This approach is based on two important assumptions in determining the value of α_G : (1) Mass transfer has no effect; and (2) the value of α_G is determined assuming that the vapor occupies the entire cross section of the tube.

Since the error in ignoring the first assumption becomes significant for mixtures with large boiling ranges, the method above is reliable only for mixtures with small to medium-sized boiling ranges (perhaps up to about 15 K). The second assumption, on the other hand, tends to be conservative since the interfacial waves in annular flows tend to enhance the vapor-phase heat transfer coefficient above that obtained with the Dittus–Boelter correlation.

9.12.4 Evaporation of Refrigerant–Oil Mixtures

Introduction of a miscible lubricating oil in a refrigerant often has a detrimental effect on nucleate pool boiling heat transfer, similar to that described for zeotropic mixtures discussed in Section 9.12.2. A refrigerant–oil mixture is, in fact, a very wide-boiling-range mixture with values of ΔT_{bp} of up to 300 K or more. Other effects are also important here, such as the three-order-of-magnitude difference between the oil's dynamic viscosity and that of the refrigerant liquid. For flow boiling of refrigerant–oil mixtures, similar to zeotropic mixtures, it is necessary to calculate the bubble point temperature of the mixture as a function of the local oil mass fraction and to apply the enthalpy profile approach to determine the change of enthalpy of the mixture. Simple algebraic methods were proposed by Thome (1995b) for both these purposes.

For flow boiling of refrigerant–oil mixtures, experimental data sometimes demonstrate an increase in the local heat transfer coefficient at low to medium vapor qualities, but typically, oil has only a detrimental effect, causing substantially reduced heat transfer coefficients at high vapor qualities, where the local oil mass fraction

risers rapidly. For plain tubes, Zürcher et al. (1998) conducted refrigerant–oil evaporation tests with local oil mass fractions up to 50 wt % oil and liquid viscosities up to $0.035 \text{ N} \cdot \text{s}/\text{m}^2$ (35 cP in common engineering units) with R-134a and R-407C. They showed that the Kattan–Thome–Favrat method described in Section 9.9 gave reasonable accuracy for these increasingly viscous mixtures using only the liquid viscosity of the mixture in the appropriate equations. They utilized the well-known Arrhenius logarithmic mixing law for viscosities of liquid mixtures, rearranged in the form

$$\frac{\mu_{\text{ref-oil}}}{\mu_{\text{ref}}} = \left(\frac{\mu_{\text{oil}}}{\mu_{\text{ref}}} \right)^w \quad (9.181)$$

The local viscosity of the refrigerant–oil mixture, $\mu_{\text{ref-oil}}$, thus calculated is used directly for the liquid viscosity μ_L in the boiling model and flow pattern map calculations described in Section 9.9, while refrigerant properties are used for all others. The refrigerant–oil viscosity, which changes by several orders of magnitude with respect to that of the pure refrigerant, completely dominates the much smaller changes experienced by other physical properties. The oil and refrigerant viscosities, μ_{ref} and μ_{oil} , are those at the respective local bubble point temperature of the mixture. The local oil mass fraction, w , in terms of the nominal inlet oil mass fraction w_{inlet} circulating in the system, is

$$w = \frac{w_{\text{inlet}}}{1 - \chi} \quad (9.182)$$

where χ is the local vapor quality, including the mass of the oil in the liquid phase. Note, however, that the expression above is undefined when $\chi = 1$ and that a local vapor quality greater than $(1 - w_{\text{inlet}})$ cannot be achieved since the oil is nonvolatile and remains totally in the liquid phase. Figure 9.21 illustrates the effect of oil on the

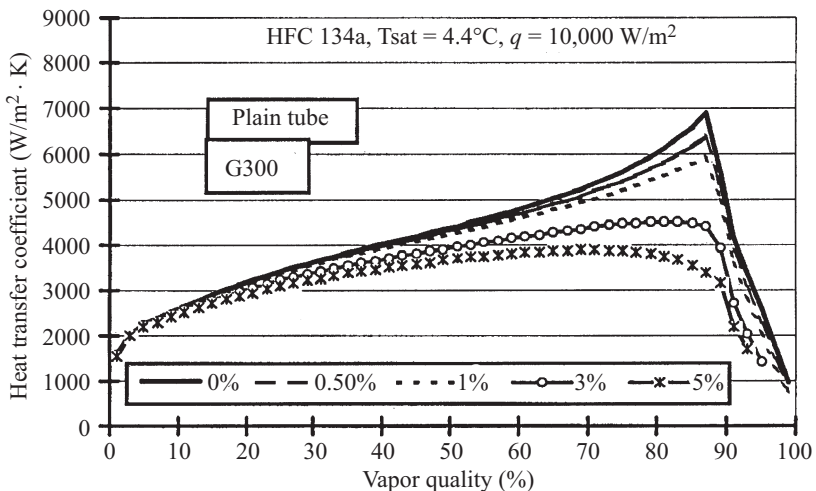


Figure 9.21 Simulation of Kattan–Thome–Favrat model for R-134a/oil mixtures.

local flow boiling heat transfer coefficient, which is most pronounced at high vapor qualities and at high local oil mass fractions.

9.13 ENHANCED BOILING

In the foregoing sections we have addressed boiling when it occurs on plain surfaces, either outside or inside tubes. Boiling on specially formed microsurfaces, to enhance nucleate boiling or convective boiling or both, is referred to as *enhanced boiling* and these surfaces as *enhanced boiling surfaces*. Typically, enhanced surfaces on the outside of tubes are for the purpose of enhancing nucleate boiling, whereas those on the inside are for enhancing forced-convective boiling. The exception is the porous layered surfaces that enhance nucleate boiling whether applied inside or outside a tube. In this section, first enhancement of nucleate boiling is discussed and then enhancement of forced-convective boiling. Both types of enhanced surfaces are used widely in industry, particularly in the refrigeration and air-conditioning industries. Refer to Bergles (1996), Thome (1990), and Webb (1994) for comprehensive treatments of this subject.

9.13.1 Enhancement of Nucleate Pool Boiling

Boiling on plain, smooth surfaces is a weak function of the roughness of the surface, which increases nucleate pool boiling heat transfer coefficient with increasing roughness. This is only marginal, on the order of up to 30%, and may also be temporary if the surface becomes fouled. For substantial and sustainable enhancement, numerous geometries have been proposed and patented over the years. The earliest commercially successful enhancement was the integral low finned tube (i.e., a continuous helical fin that is formed on the outside of an otherwise plain tube), which is still used for appropriate applications. Applying a porous metallic coating on the surface of a tube is another important historical development, giving up to *15 times* the heat transfer coefficient of a plain tube. In recent years, attention has focused on mechanically deformed low finned tubes, whose fins are notched, bent, and compressed to form reentrant channels, essentially mechanically emulating a porous coating.

Enhanced nucleate boiling surfaces provide significant performance advantages over those of a plain tube. For instance, the enhancement ratio of their coefficient relative to that of a comparable plain tube ranges from about 2 to 4 for low finned tubes and up to about 10 or more times for porous-coated tubes and mechanically deformed low finned tubes. Evaporation occurs both on the external surface of an enhanced boiling surface and inside its reentrant passageways. Hence, there are four possible paths by which heat can leave such a surface (Fig. 9.22):

1. As latent heat in the vapor formed within the reentrant passageways
2. As latent heat in bubbles growing on the exterior and on those emerging from the pores

3. As sensible heat to the liquid “pumped” through the reentrant passageways
4. As sensible heat to the liquid in the external thermal boundary layer

The factors contributing to the substantial increase in thermal performance of enhanced surfaces can be summarized as follows:

- *Nucleation superheat.* Enhanced surfaces have an abundant supply of reentrant nucleation (except for low finned tubes) and hence initiate boiling at very low wall superheats with respect to plain surfaces.
- *Wetted surface area.* Low finned tubes have from 2 to 3.5 times the surface area of a similar-sized plain tube, while complex enhancements have area ratios from 4 to 10 times that of a plain surface.
- *Thin-film evaporation.* Reentrant channels favor the formation of thin evaporating liquid films on the inner walls of the passageways.
- *Capillary evaporation.* In a porous coating, the myriad of liquid menisci can evaporate as heat is conducted into the liquid behind them.
- *Internal convection.* Liquid is pumped through the narrow channels by capillary forces and by growth and departure of bubbles. The small hydraulic diameters and entrance region effects yield very large laminar heat transfer coefficients for the liquid flow.
- *External convection.* The larger number of active boiling sites accentuates the external convection mechanisms (i.e., bubble agitation and thermal boundary layer stripping).

These mechanisms can be compared to those occurring on a plain surface in Section 9.5.1. The thermal effectiveness of these factors depends on the type of

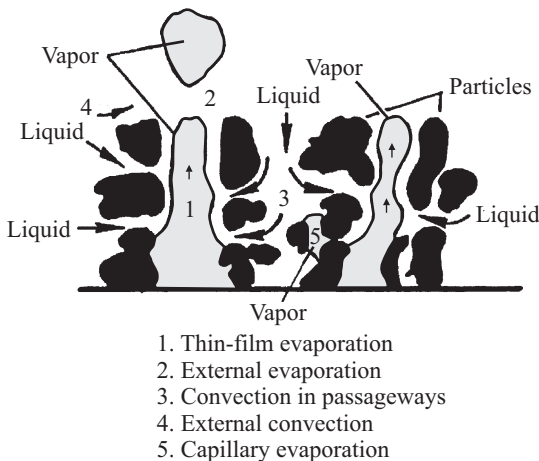


Figure 9.22 Heat transfer paths for boiling on a porous-coated surface.

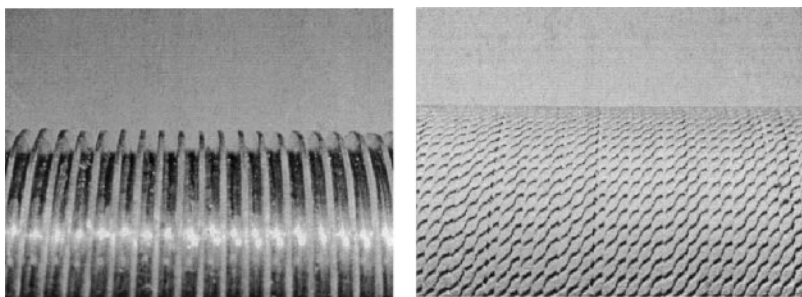


Figure 9.23 Low finned tube (left) and Turbo-Bii tube (right).

enhanced surface geometry and its characteristic dimensions. As an example, Fig. 9.23 depicts photographs of the surfaces of a low finned tube and a Turbo-Bii tube (trademark of Wolverine Tube Inc.).

9.13.2 Enhancement of Internal Convective Boiling

Numerous geometries exist for enhancing in-tube evaporation: porous coatings, corrugations, ribs, star inserts, twisted tapes, and microfins, to name just a few. The two most important geometries are the porous coating (commercially available as High Flux from UOP, Inc.) and the microfin (manufactured by numerous companies). The High Flux porous coating is used in large refrigeration systems working with propane or ethylene as the working fluids and also in vertical thermosyphon reboilers in the petrochemical industry for evaporation of nonfouling fluids, typically mixtures. Its nucleate boiling performance is so high that typically the convective contribution for forced-convective boiling becomes negligible in comparison. Hence, nucleate pool boiling data can be used for these design applications.

Microfin tubes are characterized by numerous small internal fins 0.1 to 0.4 mm in height that can be either longitudinal or helical and either two-dimensional (i.e., plain microfins) or three-dimensional (i.e., crosscut or notched microfins). Figure 9.24 depicts a typical geometry. The fins have a height-to-width at base ratio of about 1.0, and their fin profiles tend to be trapezoidal, triangular, or rectangular, depending on the particular tooling of the manufacturer. Most microfin tubes are seamless (manufactured by drawing a plain tube over an externally grooved mandrel), but manufacturers now also produce these tubes from strip by first rolling the enhancement geometry onto one side of the strip and then forming a longitudinally seamed tube from the strip. Microfin tubes are most commonly available in copper in diameters from about 5 to 16 mm outside diameter. Several versions are available in high alloys with 14 to 22-mm internal diameters (stainless steels and titanium) and also in carbon steel and aluminum (for ammonia systems). Nearly all microfin tubes tested in university labs have been used in their original production form; in some industrial applications of microfin tubes, such as air-conditioning coils with external aluminum fins, they are

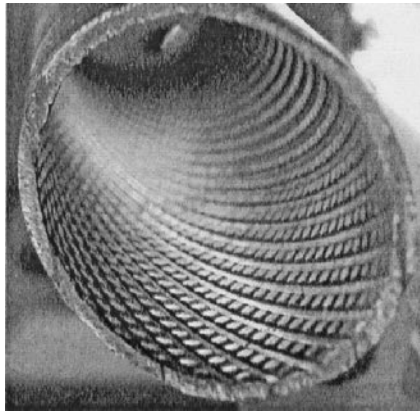


Figure 9.24 Microfin tube.

expanded mechanically into the coils, and hence their fin heights are reduced by a small margin and their internal diameters increased.

In-tube evaporation inside microfin tubes has become an important research topic because of their widespread application in direct-expansion evaporators in recent years. These are all horizontal units, and hence all the published test data for microfin tubes presented here will be for that orientation. Microfin tubes typically provide heat transfer augmentation on the order of 1.5 up to 4 times that of a plain tube operating at the same conditions. This significant enhancement relative to plain tubes, with only a small adverse augmentation of their two-phase pressure drops, has been attributed to the following heat transfer enhancement mechanisms:

- *Extended surface area effect.* Internal wetted surface area ratios for microfin tubes relative to their equivalent plain bore tubes range from about 1.3 to 1.9, depending on the number of fins and on their shape, height, and helix angle (typically, the area ratio represents the *lower* bound on the heat transfer enhancement level).
- *Enhanced convective heat transfer.* Microfins augment the convective heat transfer process across the annular liquid film, similar to internal ribs used for single-phase flow inside tubes, and this increases the two-phase convection contribution to annular flow boiling.
- *Flow pattern effect.* The helical microfins tend to convert what would otherwise be a stratified-wavy flow in plain tubes into the more thermally effective annular flow regime, meaning that all the internal tube wall perimeter is wetted and active rather than only the lower wetted fraction in plain tubes; this represents the principal reason for their very large augmentation ratios at low mass velocities.
- *Nucleate boiling heat transfer.* The microfins may favor the activation of nucleation sites by partially shielding the potential cavities from the flow; nucleate boiling will also occur on the total wetted extended surface area.

- *Swirl effects.* Swirl imparted to the annular liquid film by helical microfins may retard the onset of dryout to higher vapor qualities; swirl of the continuous vapor phase in mist flow and annular flow with partial dryout will augment vapor-phase heat transfer to the dry wall, similar to a single-phase turbulent flow inside an internally ribbed tube; swirl will also drive entrained droplets to the tube wall.
- *Grigorik film thinning effects.* The convex contours at the tips of microfins will tend to thin the evaporating liquid film on the fins, similar to that which occurs for film condensation on external low finned tubes, increasing the evaporating heat transfer coefficients on the microfins significantly.

In recent years, numerous methods have been proposed for predicting the flow boiling heat transfer coefficients in microfin tubes. Refer to Webb (1999) and Thome (1999) for a summary of these methods.

NOMENCLATURE

Roman Letter Symbols

a	drag constant, dimensionless
	empirical constant, dimensionless
a_L	liquid thermal diffusivity, m^2/s
A	cross-sectional area, m^2
	bubble growth parameter, m/s
A_G	cross-sectional area of vapor, m^2
A_{Gd}	dimensionless cross-sectional area of vapor, dimensionless
A_L	cross-sectional area of liquid, dimensionless
A_{Ld}	dimensionless cross-sectional area of liquid, m^2
b	empirical exponent, dimensionless
B	bubble growth parameter, $\text{m/s}^{1/2}$
c	empirical exponent, dimensionless
c_{pL}	liquid specific heat, $\text{J/kg} \cdot \text{K}$
C	empirical constant, dimensionless
	inverted annular flow constant, dimensionless
C_D	drag coefficient, dimensionless
C_0	boiling constant, dimensionless
C_{sf}	surface factor, dimensionless
C_1	lead constant, dimensionless
d_b	bubble base diameter, m
d_i	tube diameter, m
$d_{i,0}$	reference tube diameter, m
d_o	bubble departure diameter, m
d_{oF}	bubble departure diameter of Fritz, m
D	outside tube diameter, m
	droplet diameter, m
e	empirical constant, dimensionless

E	convection enhancement factor, dimensionless
E_2	stratified flow correction factor, dimensionless
f	bubble departure frequency, s^{-1} empirical constant, dimensionless Fanning friction factor, dimensionless friction factor, dimensionless
f_{cd}	cumulative deposition factor, dimensionless
f_G	vapor-phase friction factor, dimensionless
F	drag force, N two-phase multiplier, dimensionless constant of Shah, dimensionless
$F_1(q)$	nondimensional exponent, dimensionless
$F_1(q)$	nondimensional exponent, dimensionless
F_b	buoyancy force, N bundle boiling factor, dimensionless
F_c	mixture boiling correction factor, dimensionless
F_D	drag force, N
F_i	inertia force, N
$F(M)$	residual correction factor, dimensionless
F_{nb}	nucleate boiling correction factor, dimensionless
F_p	excess pressure force, N reduced pressure factor, dimensionless
F_{pf}	pressure correction factor, dimensionless
F_{PF}	pressure correction factor, dimensionless
F_{tp}	two-phase multiplier, dimensionless
F_{wG}	radiative view factor from wall to vapor, dimensionless
F_{wL}	radiative view factor from wall to liquid droplets, dimensionless
F_σ	surface tension force, N
g	acceleration of gravity, m/s^2 empirical exponent, dimensionless
h	liquid height, m
$h_{G,a}$	actual vapor enthalpy, J/kg
$h_{G,e}$	equilibrium vapor enthalpy, J/kg
$h_{G,sat}$	enthalpy of saturated vapor, J/kg
h_{Ld}	dimensionless liquid height, dimensionless
h_{LG}	latent heat of vaporization, J/kg
$h_{L,sat}$	enthalpy of saturated liquid, J/kg
H	characteristic height, m
H'	dimensionless height, dimensionless
L	characteristic length, m
L'	dimensionless length, dimensionless
m	mass, kg exponent, dimensionless
\dot{m}	total mass velocity of liquid and vapor, $kg/s \cdot m^2$

\dot{m}_{bubbly}	bubbly flow transition mass velocity, $\text{kg/s} \cdot \text{m}^2$
\dot{m}_{high}	value of wavy (new) flow mass velocity transition at χ , $\text{kg/s} \cdot \text{m}^2$
\dot{m}_{low}	value of stratified low mass velocity transition at χ , $\text{kg/s} \cdot \text{m}^2$
\dot{m}_{min}	minimum mist flow transition mass velocity, $\text{kg/s} \cdot \text{m}^2$
\dot{m}_{mist}	mist flow transition mass velocity, $\text{kg/s} \cdot \text{m}^2$
\dot{m}_{strat}	stratified flow transition mass velocity, $\text{kg/s} \cdot \text{m}^2$
\dot{m}_{wavy}	wavy flow transition mass velocity, $\text{kg/s} \cdot \text{m}^2$
$\dot{m}_{\text{wavy(new)}}$	new wavy flow transition mass velocity, $\text{kg/s} \cdot \text{m}^2$
M	molecular weight, kg/mol
n	exponent, dimensionless
nf	nucleate boiling exponent, dimensionless
N	dimensionless parameter, dimensionless
p	pressure, N/m^2
Δp	pressure difference, N/m^2
Δp_{sat}	saturation pressure difference, N/m^2
p_a	partial pressure of air, N/m^2
p_{crit}	critical pressure, N/m^2
p_G	vapor pressure, N/m^2
p_L	liquid pressure, N/m^2
p_r	reduced pressure, dimensionless
p_{sat}	saturation pressure, Pa
p_{∞}	vapor pressure at planar interface, N/m^2
P	characteristic perimeter, m
P'	characteristic perimeter, m
P_G	vapor perimeter, m
P_{Gd}	dimensionless vapor perimeter, dimensionless
P_i	length of liquid–vapor interface, m
P_{id}	interface length, dimensionless
P_L	wetted perimeter, m
P_{Ld}	liquid perimeter, dimensionless
P_v	dry perimeter, m
q	heat flux, W/m^2
q_{DNB}	heat flux at DNB, W/m^2
$q_{\text{DNB},z}$	heat flux at DNB according to Zuber, W/m^2
q_G	heat flux resulting from wall-to-droplet evaporation, W/m^2
q_L	heat flux resulting from droplet evaporation, W/m^2
q_{MFB}	heat flux at MFB, W/m^2
q_{ONB}	heat flux at onset of nucleate boiling, W/m^2
q_{rad}	radiation heat flux, W/m^2
q_0	reference heat flux, W/m^2
r_b	bubble base radius, m
r_i	internal radius of tube, m
r_{max}	maximum nucleation radius, m
r_{min}	minimum nucleation radius, m

r_{nuc}	nucleation radius, m
R	bubble radius, m
	characteristic radius, m
R'	radius, dimensionless
R^+	bubble radius, dimensionless
\bar{R}	ideal gas constant, J/mol · K
R_p	mean surface roughness, μm
R_{p0}	reference mean surface roughness, μm
$R_{p,0}$	reference mean surface roughness, μm
S	nucleation suppression factor, dimensionless
S_2	stratified flow correction factor, dimensionless
t	bubble growth time, s
t^+	bubble growth time, dimensionless
t_g	bubble growth time, s
t_w	bubble waiting time, s
T	absolute temperature, K
T_{bub}	bubble point temperature, K
T_{crit}	critical temperature, K
T_D	droplet temperature, K
T_{dew}	dew point temperature, K
T_G	vapor temperature, K
$T_{G,a}$	actual bulk vapor temperature, K
$T_{G,f}$	film temperature of vapor, K
T_L	subcooled liquid temperature, K
T_{sat}	saturation temperature, K or $^{\circ}\text{C}$
T_w	wall temperature, K or $^{\circ}\text{C}$
T_{∞}	bulk liquid temperature, K or $^{\circ}\text{C}$
ΔT	wall superheat, K
ΔT_{bp}	boiling range or temperature glide of mixture, K
ΔT_{id}	ideal wall superheat, K
ΔT_{nuc}	nucleation superheat, K
ΔT_{sat}	wall superheat, K
u	velocity, m/s
u_d	droplet deposition velocity, m/s
u_G	vapor velocity, m/s
u_H	velocity for homogeneous flow, m/s
v_G	vapor specific volume, m^3/kg
v_L	liquid specific volume, m^3/kg
w	local mass fraction of oil, kg/kg
w_{inlet}	inlet mass fraction of oil before expansion valve, kg/kg
x	mole fraction of liquid, dimensionless
X_{tt}	Martinelli parameter, dimensionless
y	mole fraction of vapor, dimensionless
Y	multiplying factor, dimensionless
z	axis along tube, m

z_a	length from inlet where liquid is actually completely evaporated, m
z_{DO}	length from inlet where dryout occurs, m
z_e	length from inlet under equilibrium conditions, m
Z_G	mixture boiling parameter, dimensionless

Greek Letter Symbols

α	mist flow heat transfer coefficient, $\text{W/m}^2 \cdot \text{K}$
α_b	bundle boiling heat transfer coefficient, $\text{W/m}^2 \cdot \text{K}$
α_{cb}	convective boiling heat transfer coefficient, $\text{W/m}^2 \cdot \text{K}$
α_D	convective boiling heat transfer coefficient from vapor to droplet, $\text{W/m}^2 \cdot \text{K}$
α_{eff}	effective mixture flow boiling heat transfer coefficient, $\text{W/m}^2 \cdot \text{K}$
α_{fb}	film boiling heat transfer coefficient, $\text{W/m}^2 \cdot \text{K}$
α_{FZ}	Forster–Zuber nucleate boiling heat transfer coefficient, $\text{W/m}^2 \cdot \text{K}$
α_G	vapor heat transfer coefficient, $\text{W/m}^2 \cdot \text{K}$
α_{id}	ideal pure fluid boiling heat transfer coefficient, $\text{W/m}^2 \cdot \text{K}$
α_L	liquid only heat transfer coefficient, $\text{W/m}^2 \cdot \text{K}$
α_{mixt}	mixture boiling heat transfer coefficient, $\text{W/m}^2 \cdot \text{K}$
α_{nb}	nucleate boiling heat transfer coefficient, $\text{W/m}^2 \cdot \text{K}$
$\alpha_{nb,0}$	reference nucleate boiling heat transfer coefficient for flow boiling, $\text{W/m}^2 \cdot \text{K}$
α_{nc}	natural convection heat transfer coefficient, $\text{W/m}^2 \cdot \text{K}$
α_{rad}	radiation heat transfer coefficient, $\text{W/m}^2 \cdot \text{K}$
α_{st}	single-tube nucleate boiling heat transfer coefficient, $\text{W/m}^2 \cdot \text{K}$
α_{total}	total heat transfer coefficient, $\text{W/m}^2 \cdot \text{K}$
α_{tp}	two-phase flow boiling heat transfer coefficient, $\text{W/m}^2 \cdot \text{K}$
α_{vapor}	vapor-phase heat transfer coefficient on dry wall, $\text{W/m}^2 \cdot \text{K}$
α_{wet}	wet wall heat transfer coefficient, $\text{W/m}^2 \cdot \text{K}$
α_0	reference nucleate boiling heat transfer coefficient, $\text{W/m}^2 \cdot \text{K}$
$\alpha(z)$	local heat transfer coefficient at position z , $\text{W/m}^2 \cdot \text{K}$
β	contact angle, rad
β'	apparent contact angle, rad
β_L	mass transfer coefficient, m/s
δ	thickness of annular liquid layer, m boundary layer thickness, m
ε	void fraction, dimensionless
θ_{dry}	dry angle around top perimeter of tube, rad
θ_{max}	dry angle at χ_{max} , rad
θ_{strat}	stratified angle around bottom perimeter of tube, rad
κ	ratio of droplet heat flux to total heat flux, dimensionless
λ	thermal conductivity, $\text{W/m}^2 \cdot \text{K}$

λ_{d1}	one-dimensional Taylor wavelength, m
λ_{d2}	two-dimensional Taylor wavelength, m
λ_H	Helmholtz wavelength, m
μ	dynamic viscosity, $\text{N} \cdot \text{s}/\text{m}^2$
μ_{oil}	dynamic viscosity of oil, $\text{N} \cdot \text{s}/\text{m}^2$
μ_{ref}	dynamic viscosity of refrigerant, $\text{N} \cdot \text{s}/\text{m}^2$
$\mu_{\text{ref-oil}}$	dynamic viscosity of refrigerant-oil mixture, $\text{N} \cdot \text{s}/\text{m}^2$
ξ_{Ph}	friction factor,
ξ_w	emissivity of the wall, dimensionless
ρ	density, kg/m^3
σ	surface tension, N/m
σ_{SB}	Stephan–Boltzmann constant, $\text{W}/\text{m}^2 \cdot \text{K}^4$
ϕ	heterogeneous nucleation factor, dimensionless
χ	vapor quality, kg/kg
χ_a	actual local vapor quality, dimensionless
χ_{DO}	vapor quality at dryout, dimensionless
χ_e	local equilibrium vapor quality, dimensionless
χ_{max}	vapor quality at intersection of mist and wavy flow transition curves, kg/kg
ψ	mist flow parameter, dimensionless

Dimensionless Numbers

Bo	boiling number
Fr_L	Froude number of liquid phase
Gr_G	Grashof number of vapor
Ja	Jakob number
Nu	Nusselt number
Pr	Prandtl number
Re	Reynolds number
Re_{bub}	bubble Reynolds number
Re_G	Reynolds number of vapor phase
Re_{GH}	Reynolds number for vapor in homogeneous flow
Re_L	Reynolds number of liquid phase
Re_{tp}	two-phase Reynolds number
We	Weber number

Subscripts

e	equilibrium
f	film
G	vapor
H	homogeneous
L	liquid

REFERENCES

- Andreani, M., and Yadigaroglu, G. (1997). A 3-D Eulerian-Lagrangian Model of Dispersed Flow Boiling Including a Mechanistic Description of the Droplet Spectrum Evolution, Parts 1 and 2, *Int. J. Heat Mass Transfer*, 40, 1753–1793.
- Baker, O. (1954). Design of Pipe Lines for Simultaneous Flow of Oil and Gas, *Oil Gas J.*, July, p. 26.
- Barnea, D., and Taitel, Y. (1986). Flow Pattern Transition in Two-Phase Gas-Liquid Flows, in *Encyclopedia of Fluid Mechanics*, Gulf Publishing, Houston, TX, Vol. 3, pp. 403–474.
- Berenson, P. J. (1960). Transition Boiling Heat Transfer from a Horizontal Surface, *MIT Heat Transfer Lab. Tech. Rep. 17*.
- Bergles, A. E. (1996). The Encouragement and Accommodation of High Heat Fluxes, *Proc. 2nd European Thermal Sciences and 14th UIT National Heat Transfer Conference 1996*, Edizioni ETS, Pisa, Vol. 1, pp. 3–11.
- Bromley, A. L. (1950). Heat Transfer in Stable Film Boiling, *Chem. Eng. Prog.*, 46, 221–227.
- Carey, V. P. (1992). *Liquid-Vapor Phase-Change Phenomena*, Hemisphere Publishing (Taylor & Francis), New York.
- Celata, G. P. (1997). Modeling of the Critical Heat Flux in Subcooled Flow Boiling, presented at the Convective Flow and Pool Boiling Conference, Kloster Irsee, Germany, May 18–23.
- Chen, J. C. (1963). A Correlation for Boiling Heat Transfer to Saturated Fluids in Convective Flow, *ASME-63-HT-34*, ASME, New York.
- Collier, J. G., and Thome, J. R. (1994). *Convective Boiling and Condensation*, 3rd ed., Oxford University Press, Oxford, U.K.
- Cooper, M. G. (1984). Heat Flow Rates in Saturated Nucleate Pool Boiling: A Wide Ranging Examination Using Reduced Properties, in *Advances in Heat Transfer*, Vol. 16, J. P. Hartnett and T. F. Irvine, eds., Academic Press, New York, pp. 157–239.
- Delhaye, J. M., Giot, M., and Riethmuller, M. L. (1981). *Thermohydraulics of Two-Phase Systems for Industrial Design and Nuclear Engineering*, Hemisphere Publishing, Washington, DC.
- Dhir, V. K., and Liaw, S. P. (1987). Framework for a Unified Model for Nucleate and Transition Pool Boiling, in *Radiation, Phase Change Heat Transfer and Thermal Systems*, *ASME-HTD-81*, ASME, New York, pp. 51–58.
- Dougall, R. S., and Rohsenow, W. M. (1963). Film Boiling on the Inside of Vertical Tubes with Upward Flow of the Fluid at Low Vapor Qualities, *Report 9079-26*, Mechanical Engineering Department, Engineering Project Laboratory, MIT, Cambridge, MA, Sept.
- Fair, J. R. (1960). What You Need to Design Thermosyphon Reboilers, *Pet. Refiner*, 39(2), 105.
- Forester, H. K., and Zuber, N. (1955). Dynamics of Vapor Bubbles and Boiling Heat Transfer, *AIChE J.*, 1(4), 531–535.
- Fritz, W. (1935). Berechnung des Maximal Volume von Dampfblasen, *Phys. Z.*, 36, 379–388.
- Ganic, E. N., and Rohsenow, W. M. (1977). Dispersed Flow Heat Transfer, *Int. J. Heat Mass Transfer*, 20, 855–866.
- Ginoux, J. J. (1978). *Two-Phase Flows and Heat Transfer with Application to Nuclear Reactor Design Problems*, Hemisphere Publishing, Washington, DC.
- Gnielinski, V. (1976). New Equations for Heat and Mass Transfer in Turbulent Pipe and Channel Flow, *Int. Chem. Eng.*, 16, 359–368.

- Gorenflo, D. (1993). Pool Boiling, in *VDI-Heat Atlas* (English version), VDI-Verlag, Düsseldorf, Germany.
- Groeneveld, D. C. (1973). Post-Dryout Heat Transfer at Reactor Operating Conditions, *Report AECL-4513*, ANS Topical Meeting on Water Reactor Safety, Salt Lake City, UT.
- Groeneveld, D. C., and Delorme, G. G. J. (1976). Prediction of the Thermal Non-Equilibrium in the Post-dryout Regime, *Nucl. Eng. Des.*, 36, 17–26.
- Gungor, K. E., and Winterton, R. H. S. (1986). A General Correlation for Flow Boiling in Tubes and Annuli, *Int. J. Heat Mass Transfer*, 29, 351–358.
- Gungor, K. E., and Winterton, R. H. S. (1987). Simplified General Correlation for Saturated Flow Boiling and Comparisons of Correlations with Data, *Chem. Eng. Res. Des.*, 65, 148–156.
- Han, C. Y., and Griffith, P. (1965). The Mechanism of Heat Transfer in Nucleate Pool Boiling, 1: Bubble Initiation, Growth and Departure, *Int. J. Heat Mass Transfer*, 8, 887.
- Hewitt, G. F., and Roberts, D. N. (1969). Studies of Two-Phase Flow Patterns by Simultaneous X-ray and Flash Photography, *AERE-M 2159*, Her Majesty's Stationery Office, London.
- Hsu, Y. Y. (1962). On the Size Range of Active Nucleation Cavities on a Heating Surface, *J. Heat Transfer*, 84, 207–213.
- Hsu, Y. Y., and Graham, R. W. (1976). *Transport Processes in Boiling and Two-Phase Systems*, Hemisphere Publishing, Washington, DC.
- Jung, D. S., McLinden, M., Radermacher, R., and Didion, D. (1989). A Study of Flow Boiling Heat Transfer with Refrigerant Mixtures, *Int. J. Heat Mass Transfer*, 32(9), 1751–1764.
- Kandlikar, S. G. (1990). A General Correlation of Saturated Two-Phase Flow Boiling Heat Transfer inside Horizontal and Vertical Tubes, *J. Heat Transfer*, 112, 219–228.
- Kattan, N., Thome, J. R., and Favrat, D. (1998a). Flow Boiling in Horizontal Tubes, 1: Development of a Diabatic Two-Phase Flow Pattern Map, *J. Heat Transfer*, 120, 140–147.
- Kattan, N., Thome, J. R., and Favrat, D. (1998b). Flow Boiling in Horizontal Tubes, 2: New Heat Transfer Data for Five Refrigerants, *J. Heat Transfer*, 120, 148–155.
- Kattan, N., Thome, J. R., and Favrat, D. (1998c). Flow Boiling in Horizontal Tubes, 3: Development of a New Heat Transfer Model Based on Flow Patterns, *J. Heat Transfer*, 120, 156–165.
- Katto, Y. (1994). Critical Heat Flux, *Int. J. Multiphase Flow*, 20, 53–90.
- Katto, Y. (1996). Critical Heat Flux Mechanisms, in *Convective Flow Boiling*, J. C. Chen, ed., Taylor & Francis, Washington, DC, pp. 29–44.
- Kelvin, Lord (1871). *Philos. Mag.*, 42(4), 448.
- Keshock, E. G., and Siegel, R. (1964). Forces Acting on Bubbles in Nucleate Boiling under Normal and Reduced Gravity Conditions, *NASA-TN-D-2299*.
- Klimenko, V. V. (1988). A Generalized Correlation for Two-Phase Forced Flow Heat Transfer, *Int. J. Heat Mass Transfer*, 31(3), 541–552.
- Kutateladze, S. S. (1948). On the Transition to Film Boiling under Natural Convection, *Kotlo-turbostroenie*, 3, 10.
- Lienhard, J. E., Sun, K. H., and Dix, G. E. (1976). Low Flow Film Boiling Heat Transfer on Vertical Surfaces, II: Empirical Formulations and Application to BWR-LOCA Analysis, presented at U.S. National Heat Transfer Conference, St. Louis, MO.
- Lienhard, J. H. (1981). *A Heat Transfer Textbook*, Prentice-Hall, Englewood Cliffs, NJ, p. 411.
- Lienhard, J. H., and Dhir, V. K. (1973a). Extended Hydrodynamic Theory of the Peak and Minimum Pool Boiling Heat Fluxes, *NASA-CR-2270*, July.

- Lienhard, J. H., and Dhir, V. K. (1973b). Hydrodynamic Prediction of Peak Pool Boiling Heat Fluxes from Finite Bodies, *J. Heat Transfer*, 95, 152–158.
- Mikic, B. B., Rohsenow, W. M., and Griffith, P. (1970). On Bubble Growth Rates, *Int. J. Heat Mass Transfer*, 13, 657–665.
- Mostinski, I. L. (1963). Application of the Rule of Corresponding States for Calculation of Heat Transfer and Critical Heat Flux, *Teploenergetika*, 4, 66.
- Nukiyama, S. (1934). The Maximum and Minimum Values of Heat Q Transmitted from Metal to Boiling Water under Atmospheric Pressure, *J. Jpn. Soc. Mech. Eng.*, 37, 367–374 (in Japanese). Trans. in *Int. J. Heat Mass Transfer*, 9, 1419–1433 (1966).
- Palen, J. W. (1983). Kettle and Internal Reboilers, in *Heat Exchanger Design Handbook*, Vol. 3, E. U. Schlünder, ed., Hemisphere Publishing, New York, pp. 3.6.1.1–3.6.5.6.
- Plesset, M. S., and Zwick, S. A. (1954). The Growth of Vapor Bubbles in Superheated Liquids, *J. Appl. Phys.*, 25, 493–500.
- Rayleigh, Lord (1917). On the Pressure Developed in a Liquid during the Collapse of a Spherical Cavity, *Philos. Mag.*, 34, 94–98; *Scientific Papers*, Vol. 6, Cambridge University Press, Cambridge, 1920, p. 504.
- Reid, R. C., Prausnitz, J. M., and Poling, B. E. (1987). *The Properties of Gases and Liquids*, 4th ed., McGraw-Hill, New York.
- Rohsenow, W. M. (1962). A Method of Correlating Heat Transfer Data for Surface Boiling of Liquids, *Trans. ASME*, 74, 969–975.
- Rohsenow, W. M. (1973). Boiling, in *Handbook of Heat Transfer*, W. M. Rohsenow and J. P. Hartnett, eds., McGraw-Hill, New York, Sec. 13.
- Rouhani, Z., and Axelsson, E. (1970). Calculation of Volume Void Fraction in the Subcooled and Quality Region, *Int. J. Heat Mass Transfer*, 13, 383–393.
- Schlünder, E. U. (1983). Heat Transfer in Nucleate Boiling of Mixtures, *Int. Chem. Eng.*, 23(4), 589–599.
- Shah, M. M. (1982). Chart Correlation for Saturated Boiling Heat Transfer Equations and Further Study, *ASHRAE Trans.*, 88, pt. 1, 185–196.
- Shakir, S., and Thome, J. R. (1986). Boiling Nucleation of Mixtures on Smooth and Enhanced Surfaces, *Proc. 8th International Heat Transfer Conference*, San Francisco, Vol. 4, pp. 2081–2086.
- Steiner, D. (1993). Heat Transfer to Boiling Saturated Liquids, in *VDI-Wärmeatlas (VDI Heat Atlas)*, for Verein Deutscher Ingenieure, VDI-Gesellschaft Verfahrenstechnik und Chemieingenieurwesen, Düsseldorf, Germany. Transl. J. W. Fullarton.
- Steiner, D., and Tabor, J. (1992). Flow Boiling Heat Transfer in Vertical Tubes Correlated by an Asymptotic Model, *Heat Transfer Eng.*, 13(2), 43–69.
- Stephan, K., and Abdelsalam, M. (1980). Heat Transfer Correlations for Natural Convection Boiling, *Int. J. Heat Mass Transfer*, 23, 73–87.
- Taitel, Y., and Dukler, A. E. (1976). A Model for Predicting Flow Regime Transitions in Horizontal and Near Horizontal Gas–Liquid Flow, *AIChE J.*, 22(2), 43–55.
- Thome, J. R. (1989). Prediction of the Mixture Effect on Boiling in Vertical Thermosyphon Reboilers, *Heat Transfer Eng.*, 12(2), 29–38.
- Thome, J. R. (1990). *Enhanced Boiling Heat Transfer*, Hemisphere Publishing (Taylor & Francis), Washington, DC.
- Thome, J. R. (1995a). Flow Boiling in Horizontal Tubes: A Critical Assessment of Current

- Methodologies, *Proc. International Symposium of Two-Phase Flow Modelling and Experimentation*, Rome, Vol. 1, pp. 41–52.
- Thome, J. R. (1995b). Comprehensive Thermodynamic Approach to Modelling Refrigerant–Lubricating Oil Mixtures, *Int. J. HVAC&R Res.*, 1(2), 110–126.
- Thome, J. R. (1999). Flow Boiling inside Microfin Tubes: Recent Results and Design Methods, in *Heat Transfer Enhancement of Heat Exchangers*, S. Kakaç et al., eds., Kluwer Academic Publishers, Dordrecht, The Netherlands, Series E: Applied Sciences, Vol. 355, pp. 467–486.
- Thome, J. R., and Shock, R. A. W. (1984). Boiling of Multicomponent Liquid Mixtures, in *Advances in Heat Transfer*, J. P. Harnett and T. F. Irvine, eds., Academic Press, New York, Vol. 16, pp. 59–156.
- Tong, L. S. (1965). *Boiling Heat Transfer and Two-Phase Flow*, Wiley, New York.
- Vachon, R. I., Nix, G. H., and Tanger, G. E. (1967). Evaluation of Constants for the Rohsenow Pool Boiling Correlation, 67-HT-33, U.S. National Heat Transfer Conference.
- van Stralen, S. J. D. (1966). The Mechanism of Nucleate Boiling in Pure Liquids and in a Binary Mixture, Parts I and II, *Int. J. Heat Mass Transfer*, 9, 995–1046.
- van Stralen, S. J. D., and Cole, R. (1979). *Boiling Phenomena*, Hemisphere Publishing, Washington, DC.
- Wallis, G. B. (1969). *One Dimensional Two-Phase Flow*, McGraw-Hill, New York.
- Wallis, G. B., and Collier, J. G. (1968). *Two-Phase Flow and Heat Transfer*, Vol. 3, pp. 33–46, Notes for a Summer Shortcourse, July 15–26, Dartmouth College, Hanover, NH.
- Webb, R. L. (1994). *Principles of Enhanced Heat Transfer*, Wiley, New York.
- Webb, R. L. (1999). Prediction of Condensation and Evaporation in Micro-fin and Micro-channel Tubes, in *Heat Transfer Enhancement of Heat Exchangers*, S. Kakaç et al., eds., Kluwer Academic Publishers, Dordrecht, The Netherlands, Series E: Applied Sciences, Vol. 355, pp. 529–550.
- Weisman, J. (1992). The Current Status of Theoretically Based Approaches to the Prediction of the Critical Heat Flux in Flow Boiling, *Nucl. Technol.*, 99, July, 1–21.
- Whalley, P. (1987). *Boiling, Condensation and Gas–Liquid Flow*, Oxford University Press, Oxford.
- Witte, L. C., and Lienhard, J. W. (1982). On the Existence of Two “Transition” Boiling Curves, *Int. J. Heat Mass Transfer*, 25, 771–779.
- Zuber, N. (1959). Hydrodynamic Aspects of Boiling Heat Transfer, *AEC Rep. AECU-4439*, Physics and Mathematics, Atomic Energy Commission, Washington, DC.
- Zürcher, O., Thome, J. R., and Favrat, D. (1997). Prediction of Two-Phase Flow Patterns for Evaporation of Refrigerant R-407C inside Horizontal Tubes, *Paper IX-1*, Convective Flow and Pool Boiling Conference, Engineering Foundation, Irsee, Germany.
- Zürcher, O., Thome, J. R., and Favrat, D. (1998). Intube Flow Boiling of R-407C and R-407C/Oil Mixtures, II: Plain Tube Results and Predictions, *Int. J. HVAC&R Res.*, 4(4), 373–399.
- Zürcher, O., Thome, J. R., and Favrat, D. (1999). Evaporation of Ammonia in a Smooth Horizontal Tube: Heat Transfer Measurements and Predictions, *J. Heat Transfer*, 121, 89–101.

Condensation

M. A. KEDZIERSKI

Building and Fire Research Laboratory
National Institute of Standards and Technology
Gaithersburg, Maryland

J. C. CHATO

Department of Mechanical and Industrial Engineering
University of Illinois–Urbana-Champaign
Urbana, Illinois

T. J. RABAS

Consultant
Downers Grove, Illinois

- 10.1 Introduction
- 10.2 Vapor space film condensation
 - 10.2.1 Nusselt's analysis of a vertical flat plate
- 10.3 Film condensation on low fins
 - 10.3.1 Introduction
 - 10.3.2 Surface tension pressure gradient
 - 10.3.3 Specified interfaces
 - 10.3.4 Bond number
- 10.4 Film condensation on single horizontal finned tubes
 - 10.4.1 Introduction
 - 10.4.2 Trapezoidal fin tubes
 - 10.4.3 Sawtooth fin condensing tubes
- 10.5 Electrohydrodynamic enhancement
 - 10.5.1 Introduction
 - 10.5.2 Vapor space EHD condensation
 - 10.5.3 In-tube EHD condensation
- 10.6 Condensation in smooth tubes
 - 10.6.1 Introduction
 - 10.6.2 Flow regimes in horizontal tubes
 - Flow regimes in horizontal two-phase flow
 - Effects of mass flux and quality
 - Effects of fluid properties and tube diameter
 - Potential role of surface tension
 - Flow regime mapping
 - Comparison of flow regime maps

- 10.6.3 Heat transfer in horizontal tubes
 - Effects of mass flux and quality
 - Effects of tube diameter
 - Effects of fluid properties
 - Effects of temperature difference
 - Gravity-driven condensation
 - Shear-driven annular flow condensation
 - Comparison of heat transfer correlations
- 10.6.4 Pressure drop
- 10.6.5 Effects of oil
- 10.6.6 Condensation of zeotropes
- 10.6.7 Inclined and vertical tubes
- 10.7 Enhanced in-tube condensation
 - 10.7.1 Microfin tubes
 - 10.7.2 Microfin tube pressure drop
 - 10.7.3 Twisted-tape inserts
- 10.8 Film condensation on tube bundles
 - 10.8.1 X-shell condensers (shell-side condensation)
 - Tube-side flow and temperature maldistribution
 - Condenser sizing methods
 - Noncondensable gas management and proper venting techniques
 - 10.8.2 In-tube condensers
 - Nonuniform outside inlet flow and temperature distributions
 - Noncondensable gas pockets
- 10.9 Condensation in plate heat exchangers
 - 10.9.1 Introduction
 - 10.9.2 Steam condensation heat transfer
 - 10.9.3 Effect of inclination on heat transfer performance
 - 10.9.4 Effect of inclination on pressure drop

Appendix A

Nomenclature

References

10.1 INTRODUCTION

Condensation is the process by which a vapor is converted to its liquid state. Because of the large internal energy difference between the liquid and vapor states, a significant amount of heat can be released during the condensation process. For this reason, the condensation process is used in many thermal systems.

In general, a vapor will condense to liquid when it is cooled sufficiently or comes in contact with something (e.g., a solid or another fluid) that is below its equilibrium temperature. This chapter is concerned primarily with convective condensation (condensation of a flowing vapor in a passage) and vapor space condensation (condensation of stagnate vapor onto a surface). Film condensation occurs when the condensate

completely wets the surface in a continuous liquid film and can be associated with either convective or vapor space condensation. Dropwise condensation, usually associated with vapor space condensation, occurs when the condensate “beads up” on the surface into drops of liquid as a consequence of the liquid’s lack of affinity for the surface. Heat transfer coefficients for dropwise condensation can be one to two orders of magnitude greater than those for film condensation. Unfortunately, dropwise condensation is not easily sustained in practice.

10.2 VAPOR SPACE FILM CONDENSATION

10.2.1 Nusselt’s Analysis of a Vertical Flat Plate

Nusselt (1916) published a solution for steady-state laminar film condensation on a vertical flat plate. This pioneering work laid the foundation on which those working in the field of condensation still build their research. The cross section of the liquid film as analyzed by Nusselt is shown in Fig. 10.1. The vapor condenses at its saturation temperature (T_{sat}) due to a cooler wall temperature (T_w) of the vertical plate. The thickness of the condensate film (δ) increases along the length (s) due to mass transfer to the liquid–vapor interface. The film is drained by the influence of gravity alone in the downward s direction. Consequently, the film velocities in the y and z directions can be neglected compared to the velocity in the s direction (u). Moreover, the

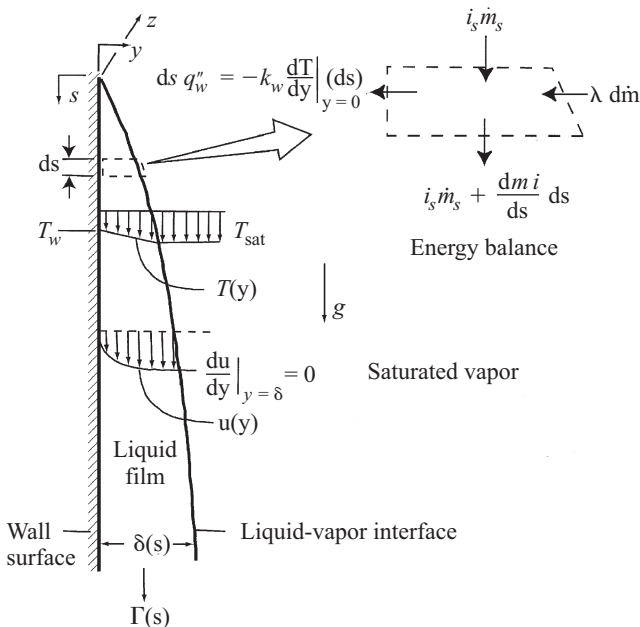


Figure 10.1 Nusselt condensation on vertical flat plate.

velocity and temperature changes in the y direction are much larger than those in the s and z directions. Accordingly, both momentum changes and convection in the s direction are negligible. As a result, if there is no shear stress at the liquid–vapor interface, the s -moment equation becomes

$$\mu_l \frac{d^2 u}{dy^2} = \frac{dP}{ds} - \rho_l g \quad (10.1)$$

Equation (10.1) shows that the viscous forces are balanced by the sum of the gravity force ($\rho_l g$) and pressure gradient in the s direction (dP/ds). The momentum equation can be integrated while using the no-slip condition at the wall and no shear at the liquid–vapor interface to yield the velocity profile of the film:

$$u = \frac{y}{\mu_l} \left(\frac{y}{2} - \delta \right) \left(\frac{dP}{ds} - \rho_l g \right) \quad (10.2)$$

The liquid mass flow rate of the film per unit width (Γ) is

$$\Gamma = \int_0^\delta \rho_l u_s dy = \frac{\delta^3}{3\nu_l} \left(\frac{dP}{ds} - \rho_l g \right) \quad (10.3)$$

Differentiating eq. (10.3) gives

$$\frac{d\Gamma}{ds} = \frac{1}{3\nu_l} \frac{d}{ds} \left[\delta^3 \left(\frac{dP}{ds} - \rho_l g \right) \right] \quad (10.4)$$

An energy balance on an incremental element of the film is shown in Fig. 10.1. If the convection of heat along the s direction is neglected, the heat balance becomes

$$\lambda d\Gamma = -k_l \frac{dT}{dy} ds \quad (10.5)$$

where λ , k_l , and T are the latent heat, thermal conductivity, and temperature of the film, respectively.

By applying the Nusselt assumptions to the energy equation, it reduces to

$$\frac{dT}{dy} = \frac{T_{\text{sat}} - T_w}{\delta} \quad (10.6)$$

where T_{sat} is the saturation temperature of the condensate and T_w is the local wall temperature.

Rearranging the incremental energy balance and substituting the temperature gradient gives the gradient of the mass flow rate:

$$\frac{d\Gamma}{ds} = \frac{-k_l (T_{\text{sat}} - T_w)}{\lambda \delta} \quad (10.7)$$

Equating the foregoing two expressions for the mass flow rate gradient yields the ordinary differential equation that models Nusselt condensation:

$$\frac{d}{ds} \left[\delta^3 \left(\frac{dP}{ds} - \rho_l g \right) \right] = \frac{-3\nu_l k_l (T_{\text{sat}} - T_w)}{\lambda \delta} \quad (10.8)$$

By applying the Nusselt assumption to the s -momentum equation for the vapor phase, one obtains $dP/ds = \rho_g g$; and using the expression $\delta(d\delta^3/ds) = \frac{3}{4}(d\delta^4/ds)$, the solution to eq. (10.8) becomes

$$\delta = \left[\frac{4k_l \mu_l (T_{\text{sat}} - T_w)s}{\rho_l g (\rho_l - \rho_g) \lambda} \right]^{1/4} \quad (10.9)$$

For film condensation, the convection of heat along length s can be neglected compared to conduction across the film. For these conditions, the temperature gradient of the film is approximately linear, and the heat transfer coefficient is k_l/δ . Consequently, the condensation heat transfer coefficient for a vertical flat plate for no interfacial shear is

$$h = \left[\frac{\rho_l g (\rho_l - \rho_g) k_l^3 \lambda}{4 \mu_l (T_{\text{sat}} - T_w)s} \right]^{1/4} \quad (10.10)$$

The average condensation heat transfer coefficient over $s = 0$ to $s = L$ is

$$h = 0.943 \left[\frac{\rho_l g (\rho_l - \rho_g) k_l^3 \lambda}{\mu_l (T_{\text{sat}} - T_w)L} \right]^{1/4} \quad (10.11)$$

Equation (10.11) gives the heat transfer coefficient for laminar film condensation on a vertical flat plate for low pressures ($\rho_v \ll \rho_g$) and $c_{p,1}(T_{\text{sat}} - T_w)/\lambda < 1$. The average condensation heat transfer coefficient for a horizontal tube of outer diameter D_o is obtained by replacing g with $g \sin \phi$ and integrating around the tube with respect to the cylindrical coordinate angle ϕ from 0 to 180°:

$$h = 0.729 \left[\frac{\rho_l g (\rho_l - \rho_g) k_l^3 \lambda}{\mu_l (T_{\text{sat}} - T_w) D_o} \right]^{1/4} \quad (10.12)$$

10.3 FILM CONDENSATION ON LOW FINS

10.3.1 Introduction

The first application of a finned surface to condense vapor was probably done with the intent to enhance the heat transfer via additional surface area for a given projected area. Today, low fins (<1.5 mm) are specially designed to enhance condensation significantly by inducing surface tension drainage forces that rid the fins of insulating condensate. Gravity forces are always present, but the influence of gravity on the

condensate drainage from a fin can be minimal for short or low fins. As described in the remainder of this section, the minimum fin height to encourage surface tension drainage depends on the surface tension of the fluid and shape of the fin.

10.3.2 Surface Tension Pressure Gradient

Laplace (1966) has shown that if a liquid–vapor interface is curved, a pressure difference across the interface must be present to establish mechanical equilibrium of the interface. The equilibrium condition is described by the difference between the pressure of the liquid (P_l) and the pressure of the vapor (P_g) by the two radii of curvature (r) of the interface and the surface tension of the fluid liquid–vapor interface (σ). This may be represented as

$$P_l - P_g = \sigma \left(\frac{1}{r_1} + \frac{1}{r_2} \right) \quad (10.13)$$

The radii of curvature are defined as positive from the liquid side of the interface. Figure 10.2 shows r_1 as the curvature in the Y – X plane; r_2 is the curvature in the X – Z plane.

Consider, for example, a still pond. Because the surface of a pond is flat or of infinite radius, eq. (10.13) predicts that the pressure of the water at the liquid side of the liquid–vapor interface is equal to the pressure of the surrounding air. Similarly, eq. (10.13) shows that the pressure of a curved liquid film for positive radii r_1 and r_2 must be greater than the vapor that surrounds it. A greater difference between the pressure of the liquid and vapor occurs for large surface tension and small radii of curvature (large curvature).

The liquid–vapor interface of a condensate film must have a curvature (κ_i) decrease along the fin length to exhibit surface tension drainage. The curvature decrease of

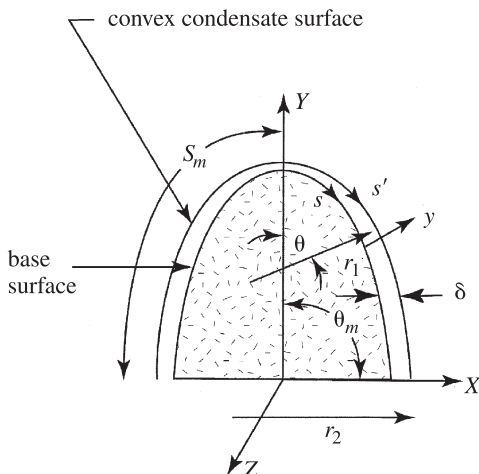


Figure 10.2 Convex fin and condensate film.

the interface induces a pressure decrease within the film. The expression for this pressure variation, known as the *surface tension pressure gradient*, is obtained by differentiating eq. (10.13) with respect to the fin arc length(s)

$$\frac{dP}{ds} = \sigma \frac{d(1/r_1)}{ds} = \sigma \frac{d\kappa_i}{ds} \quad (10.14)$$

where $1/r_2 = 0$ for a two-dimensional surface.

Figure 10.2 shows the coordinate system for a condensate film on a convex fin surface profile. The coordinate measured along the liquid–vapor interface is s' . The coordinate measured along the fin surface is s . The location $s = 0$ is the point of symmetry and is referred to the *fin tip*. The film has thickness δ . The condensate surface turns through a maximum angle of θ_m and a maximum arc length S_m . The coordinate measured perpendicular to the base-metal surface is y .

The curvature of the liquid–vapor interface, shown in Fig. 10.2, decreases for increasing values of the coordinate s' . In general, decreasing pressure gradients can be achieved with fin tips of small curvature. A general function for the liquid–vapor interface curvature (κ_i) can be represented as a function of s' :

$$\kappa_i = C_1 - C_2 s'^{\zeta} \quad (10.15)$$

where C_1 , C_2 , and ζ are arbitrary constants. As illustrated in the following section, specification of the interface curvature allows the fin designer to investigate the influence of the fin shape on the condensation performance.

10.3.3 Specified Interfaces

Gregorig (1954) proposed to increase Nusselt condensation by shaping a convex condensate surface such that surface tension forces alone would produce a film of constant thickness:

$$\delta = \left[\frac{k_l \mu_l (T_{\text{sat}} - T_w) S_m^3}{\sigma \lambda \rho_l \theta_m} \right]^{1/4} \quad (10.16)$$

By using $h = k_l/\delta$, the local heat transfer coefficient for Gregorig's surface becomes

$$h = \left[\frac{\sigma \lambda \theta_m k_l^3}{\nu_l (T_{\text{sat}} - T_w) S_m^3} \right]^{1/4} \quad (10.17)$$

Zener and Lavi (1974) proposed a convex shape that gives a constant-pressure gradient along the convex surface. The local heat transfer coefficient for the Zener and Lavi profile is

$$h = \left[\frac{\sigma \lambda \theta_m k_l^3}{2 \nu_l (T_{\text{sat}} - T_w) S_m^2 s'} \right]^{1/4} \quad (10.18)$$

The average heat transfer coefficient for the Zener and Lavi (1974) profile is 15% larger than that for the Gregorig (1954) surface.

Adamek (1981) showed that there is an entire family of convex shapes that utilize surface tension to drain the film. His curvature is defined as

$$\kappa_i = \frac{(\zeta + 1)\theta_m}{\zeta S_m} \left[1 - \left(\frac{s'}{S_m} \right)^\zeta \right] \tag{10.19}$$

Figure 10.3 shows five different Adamek profiles for ζ values within the range $-0.9 \leq \zeta \leq 2$. The profiles of the liquid–vapor interface, as shown in Fig. 10.3, start at $s' = 0$ at the fin tip and rotate through equal lengths of S_m . The local heat transfer coefficient for the Adamek profile is

$$h = \left[\frac{\sigma \lambda \theta_m k_l^3 (\zeta + 1)(\zeta + 2)}{12 \nu_l (T_{\text{sat}} - T_w) S_m^{\zeta+1} s'^{2-\zeta}} \right]^{1/4} \tag{10.20}$$

where $\zeta = -0.5$ gives the maximum heat transfer coefficient.

The region of surface tension influence is confined to a few molecular thicknesses at the liquid–vapor interface (Freundlich, 1922). The thinness of the film permits the base-metal shape to influence the shape of the liquid–vapor interface. Therefore, fins can be designed for large pressure gradients by carefully considering the fin size and the base-metal fin curvature (κ_b).

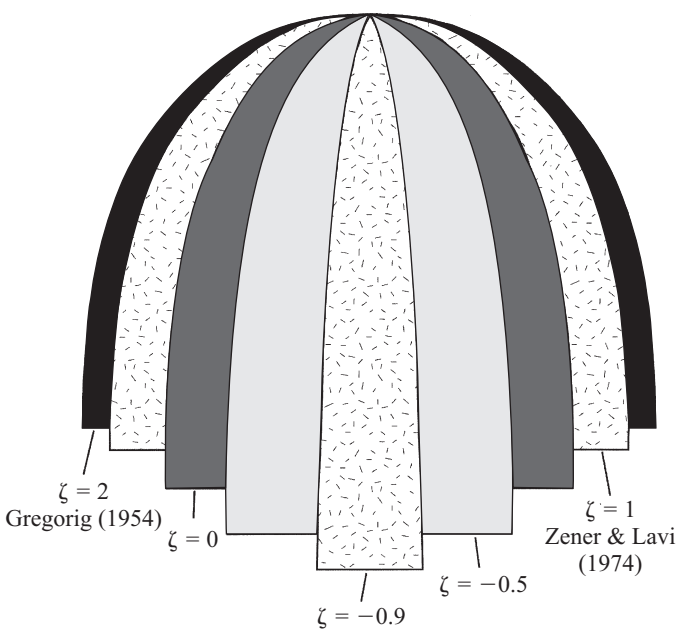


Figure 10.3 Family of Adamek (1981) liquid–vapor interface fin profiles.

It is not convenient to specify fins base on curvature. A designer would rather specify the geometry of the fin by controlled machining parameters. Kedzierski and Webb (1990) have defined an alternative set of condensate surface profiles (referred to here as the *K-W profiles*), where the fin tip radius (r_o), the fin thickness at the root (t_r), the fin height (e), the fin angle (θ_m), and the shape factor Z are independently specified. Smaller values of Z produce narrower fin tips. Appendix A presents the equations that describe the fin profiles. The thickness of the condensate film for the K-W profile is given by (Jaber and Webb, 1996)

$$\delta = \frac{k_l}{h} = 4Cp^{-1}r \left[3C_2(e^{Z\theta_m} - 1) \right] + 4Cp^{-1}r \left\{ \frac{C_3^{1/3}}{Z} \left[0.5 \ln \frac{N_m}{N_o} + \sqrt{3} (\tan^{-1} Y_m - \tan^{-1} Y_o) \right] \right\} \quad (10.21)$$

where $C = 3\mu_l k_l (T_{\text{sat}} - T_w) / \rho_l^2 g \lambda$, and C_2 , C_3 , p , N_m , N_o , Y_m , and Y_o are given in Appendix A.

10.3.4 Bond Number

Care must be taken to ensure that the fin height (e) is not so large that the surface tension pressure gradient has dissipated over a significant portion of the fin. The Bond number (Bd), which is the ratio of gravity forces to surface tension forces, can be used to test the strength of the surface tension pressure gradient. If the surface tension forces are dominant over gravity forces, the condensate drainage is determined by surface tension. The strength of the surface tension pressure gradient weakens as the film approaches the base of the fin. The Bond number at the base of the fin can be approximated by (Kedzierski and Webb, 1990)

$$\text{Bd} = \frac{(\rho_l - \rho_g)ge^2}{\sigma\theta_m} \quad (10.22)$$

Here, $\text{Bd} = 1$ implies that surface tension forces are equal to gravity forces at the end of the fin and that surface tension forces are greater than gravity forces for the remainder of the fin. Equation (10.22) should always be used to check first if surface tension forces are truly dominant ($\text{Bd} < 1$) over gravity forces before performing an analysis that assumes so. Equation (10.22) predicts that small fin heights and large θ_m give strong pressure gradients.

10.4 FILM CONDENSATION ON SINGLE HORIZONTAL FINNED TUBES

10.4.1 Introduction

Advances in metal-forming processes have enabled the use of surface tension drainage theory in the design of special finned surfaces for horizontal tubes. In this section

we review the condensing performance of the trapezoidal and sawtooth fin geometries for vapor space condensation. The trapezoidal fin is a relatively simple and inexpensive fin geometry. However, a greater heat transfer performance can be obtained with a more complicated and expensive sawtooth fin geometry.

10.4.2 Trapezoidal Fin Tubes

Figure 10.4 shows a sketch of the cross section of an integral finned tube with an envelope diameter of D_o and a root diameter of D_r . During manufacturing, the outer fin surface of the tube is lifted from the surface of a plane tube via a rolling process that leaves one side of the fin tip with a rounded corner. The sketch shows the key geometric parameters of the tube: the spacing between fins at the tip (b) and root (b_r) of the fin, fin pitch (p), fin height (e), fin tip thickness (t), and half-angle at the fin tip (β).

Compared to many passively enhanced condenser tubes, integral finned tubes are relatively inexpensive and can significantly improve the heat transfer performance over that of a plain tube. The heat transfer of a low fin (< 1.5 mm) tube is greater than that of a plain tube per unit length because the finned tube exhibits (1) additional surface area over a plain tube per unit tube length, (2) a short condensing length over the fin compared to the tube diameter, and (3) surface tension drainage forces along the fins.

Surface tension forces also cause a degradation in heat transfer through the retention of a relatively thick condensate film between the fins of the lower part of the tube. Honda et al. (1983) derived the following expression for the condensate retention angle (ϕ_f), defined as the angle between the top of the tube and the point where the tube begins to flood with condensate:

$$\phi_f = \cos^{-1} \left(\frac{4\sigma \cos \beta}{\rho_l g b D_o} - 1 \right) \quad \text{for } e > 2b(1 - \sin \beta) / \cos \beta \quad (10.23)$$

Equation (10.23) was also derived by Rudy and Webb (1981) for the case of $\beta = 0$.

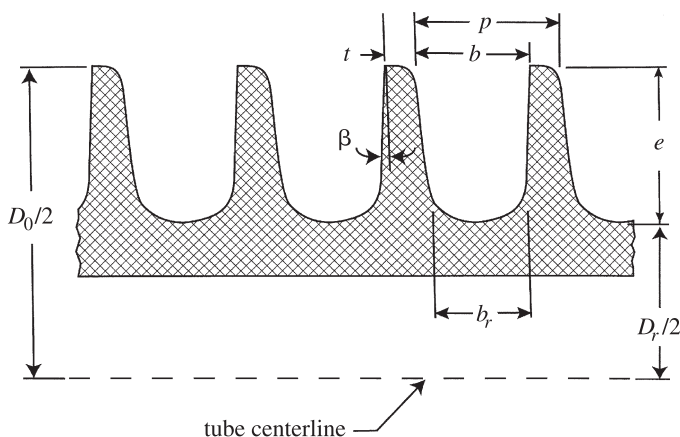


Figure 10.4 Cross section of integral-fin tube.

Typically, heat transfer in the flood zone is neglected. Analysis of the unflooded region focuses on calculating the condensate film thickness along the fin, that is, the solution to eq. (10.8). The key obstacle to solving eq. (10.8) is the determination of the appropriate expression for the surface tension pressure gradient (dP/ds) and the component of gravity ($\rho_l g$) that acts to drain the condensate from the fin. It is common to assume some relationship for dP/ds as a function of fin arch length. Researchers such as Webb et al. (1985), Adamek and Webb (1990), Rifert (1980), and Karkhu and Borovkov (1971) have assumed a linear pressure gradient along the fin length. Even with a linear assumption for the pressure gradient, an explicit solution that includes the effect of gravity has yet to be derived. Toward this end, Honda et al. (1987) have managed a numerical solution that couples the effects of surface tension and only the component of gravity along the fin arch. Consequently, this solution is strictly valid only at the top and bottom of a horizontal tube.

Considering that it is crucial to include the effects of gravity as the Bond number increases above 0.1, the explicit semiempirical calculation method of Rose (1994) is much welcomed. Rose (1994) couples the effects of surface tension and gravity through an expression for the average condensate thickness on the unflooded portion of the tube:

$$\delta = \left[\frac{\mu V}{A(\rho_l - \rho_g)g/l_g + B\sigma/l_\sigma^3} \right]^{1/3} \quad (10.24)$$

Here V is the mean volume of condensate flux per area of surface; A and B are constants representing the influence of gravity and surface tension, respectively; and l_g and l_σ are characteristic lengths for gravity- and surface tension-driven flows, respectively. The characteristic lengths and the constants are each assigned a value for the fin tip, fin root, and fin side regions for the unflooded portion of the tube. The gravity constant A is given as either 0.728 for tubelike surfaces or 0.943 for fin sides [see the leading coefficients in eqs. (10.11) and (10.12), respectively]. The B constants are obtained through regression against measured condensation heat transfer data on finned tubes.

By using $V = q''/h_{fg}\rho_l$, eq. (10.24), and $q'' = k_l(T_{\text{sat}} - T_w)/\delta$, the heat flux may be written for the fin tip, fin side, and tube surface between the fins. The flooded portion of the tube is assumed to be inactive for heat transfer. The heat fluxes for the three regions are summed and weighted by the appropriate surface areas and rearranged to give the heat transfer coefficient for the finned tube (h_f). Rose (1994) obtained the enhancement ratio by normalizing h_f by the heat transfer of the smooth tube (h_s) with an outside diameter equal to the root diameter of the finned tube:

$$\frac{\overline{h_f}}{\overline{h_s}} = \frac{\Psi_1 + \Psi_2 + \Psi_3}{0.728(b + t)}$$

$$\Psi_1 = \left(\frac{D_o}{D_r} \right)^{3/4} t \left[0.281 + \frac{B\sigma D_o}{t^3 g(\rho_l - \rho_g)} \right]^{1/4}$$

$$\Psi_2 = \frac{\phi_f}{\pi} \frac{1 - f_f}{\cos \beta} \frac{D_o^2 - D_r^2}{2e_v^{1/4} D_r^{3/4}} \left[0.791 + \frac{B\sigma e_v}{e^3 g(\rho_l - \rho_g)} \right]^{1/4}$$

$$\Psi_3 = \frac{\phi_f}{\pi} B_1 (1 - f_r) b_r \left\{ [\xi(\phi_f)]^3 + \frac{B\sigma D_r}{b_r^3 g(\rho_l - \rho_g)} \right\}^{1/4} \quad (10.25)$$

where

$$\xi(\phi_f) = 0.874 + 0.1991 \times 10^{-2} \phi_f - 0.2642 \times 10^{-1} \phi_f^2 + 0.5530 \times 10^{-2} \phi_f^3 - 0.1363 \times 10^{-2} \phi_f^4 \quad (10.26)$$

$$f_f = \frac{1 - \tan(\beta/2)}{1 + \tan(\beta/2)} \frac{2\sigma \cos \beta}{\rho_l g D_r e} \frac{\tan(\phi_f/2)}{\phi_f} \quad (10.27)$$

$$f_r = \frac{1 - \tan(\beta/2)}{1 + \tan(\beta/2)} \frac{4\sigma}{b_r \rho_l g D_r} \frac{\tan(\phi_f/2)}{\phi_f} \quad (10.28)$$

$$e_v = \frac{\phi_f}{\sin \phi_f} e \quad \phi_f \leq \frac{\pi}{2} \quad (10.29)$$

$$e_v = \frac{\phi_f}{2 - \sin \phi_f} e \quad \frac{\pi}{2} \leq \phi_f \leq \pi \quad (10.30)$$

Here f_f and f_r are the fraction of the fin side and root of the tube that are flooded with condensate, respectively, and e_v represents the mean vertical fin height of the tube.

The enhancement ratio is valid where h_f and h_s have the same driving temperature difference. The agreement that Rose (1994) obtained between the experimental data available and the fit of those data to eq. (10.25) was approximately $\pm 20\%$ for $B = 0.143$ and $B_l = 2.96$.

10.4.3 Sawtooth Fin Condensing Tubes

Figure 10.5 compares the cross sections of a sawtooth or notched tube (Turbo-CDI) to that of a tube with trapezoidal fins (Turbo-Chil). The Turbo-CDI has 1575 fins per meter, a 1-mm fin height before notching on the outside tube surface, with 35 ridges with a 0.5-mm ridge height on the inside tube surface. The fins on the outside of the Turbo-Chil (1024 ft/min) are 1.4 mm in fin height and the 10 ridges on the inside of the tube are 0.4 mm high. Both tubes have a wall thickness of 0.7 mm, the same envelope diameter (D_o), and internal fins. Coolant flows inside the tube while condensation takes place on the outside tube surface. The sharp tips of the sawtooth provide the large curvature and curvature gradients that are necessary to induce large surface tension pressure gradients, which act to thin the condensate and enhance condensation heat transfer.

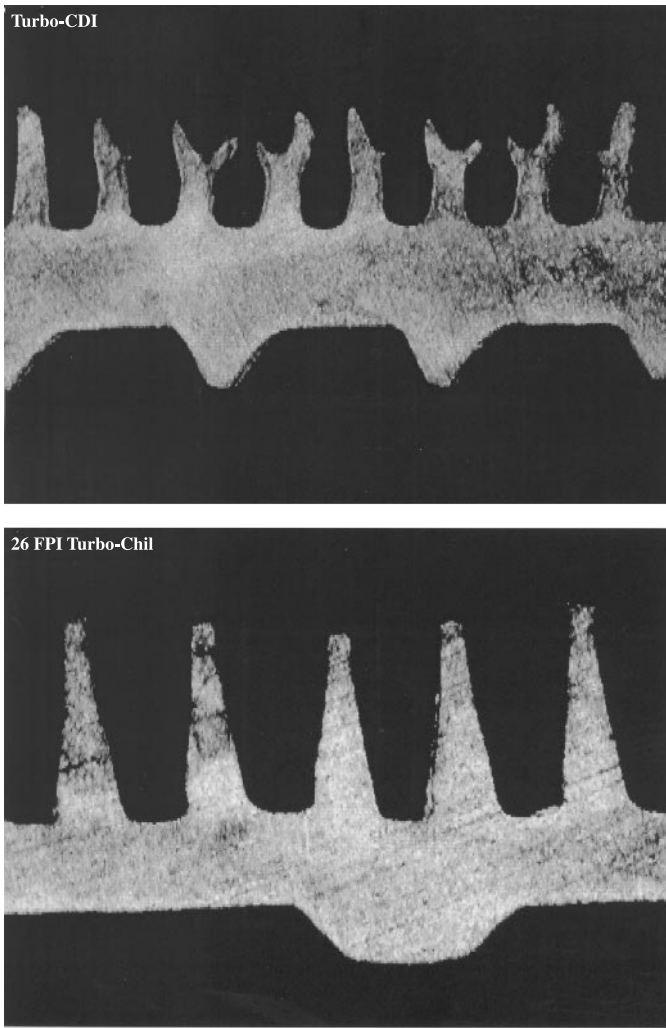


Figure 10.5 Cross sections of the Turbo-CDI and Turbo-Chil. (Courtesy of Wolverine Tube, Inc.)

According to Webb (1994), no model exists for condenser tubes with sawtooth fin shapes. Consequently, the heat transfer performance of select tubes is presented here graphically. Figure 10.6 provides the condensation heat transfer coefficient for a sawtooth and trapezoidal fin tube versus the heat flux, both based on the envelope area of the tube. Figure 10.6 illustrates that the heat transfer performance of the sawtooth tube is approximately twice that of a trapezoidal integral fin tube of the same envelope diameter. Both area increase and surface tension effects contribute to the performance increase.

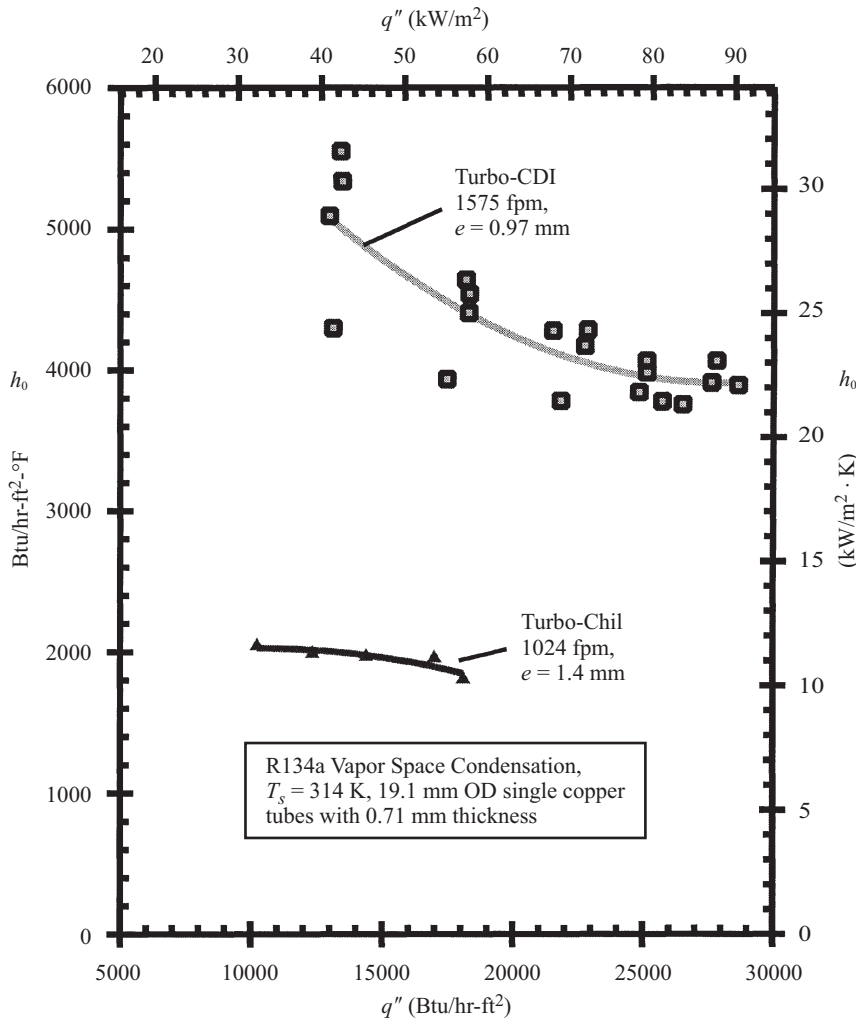


Figure 10.6 Condensation heat transfer performance of standard and sawtooth tubes. (Courtesy of Wolverine Tube, Inc.)

10.5 ELECTROHYDRODYNAMIC ENHANCEMENT

10.5.1 Introduction

The electrohydrodynamic (EHD) enhancement technique uses a high-voltage, low-current electric field to mix the condensate film or to remove it from the tube surface. EHD enhancement requires a fluid that has low electrical conductivity, such as refrigerants. Consequently, most of the EHD studies have been with refrigerants and refrigerant mixtures.

The magnitude and nature of the enhancement is a function of the (1) electric field, (2) flow parameter, and (3) heat transfer surface (Ohadi, 1991). The field potential, its polarity, and the electrode geometry and spacing determine the electric field. The Reynolds number and working fluid properties fix the flow parameters. The EHD technique is more effective for low Reynolds numbers. Bologna et al. (1987) reported enhancements as large as 2000% for film condensation on a plate.

10.5.2 Vapor Space EHD Condensation

Typically, the electrode is a screen wrapped around the tube and spaced a certain distance from the tube. The gap between the tube and the electrode and the dielectric strength influence the enhancement. Currently, there are no correlations that predict vapor space EHD condensation. However, it is possible to enhance plain tube and enhanced tube performance with EHD by ten- and threefold, respectively (Ohadi, 1991; Da Silva et al., 2000). Enhancements result from condensate removal from the tube. In fact, Yabe (1991) shows that the extraction of liquid from the tube surface can be effective enough to promote pseudo-dropwise condensation. In general, the heat transfer coefficient is directly proportional to the applied voltage.

10.5.3 In-Tube EHD Condensation

Typically, a helical or a straight-rod electrode is centered within the tube to enhance in-tube condensation. The tube is grounded to create an electric field between the electrode and the tube wall. EHD can be used to increase smooth tube condensation by a factor of nearly 6.5. Gidwani et al. (1998) developed R-404a and R-407c condensation heat transfer correlations for a 3.17-mm straight-rod electrode placed in a 11.1-mm-diameter smooth tube and a 10.60-mm-diameter corrugated tube with a 7.1-mm pitch and a 1-mm corrugation. The ratio of the in-tube condensation heat transfer coefficient with EHD (h_E) to that with no EHD (h) for R-404a is

$$\frac{h_E}{h} = 1 + cEs^{n_l} \left(\frac{G_T}{300} \right)^{n_2} \left(\frac{1-x_q}{x_q} \right)^{n_3} \text{Ja}^{n_4} \quad (10.31)$$

where the ranges for which the correlation holds are

$$70 \leq Es = \frac{\kappa\epsilon_o E^2 D_i}{\sigma} \leq 120$$

$$5 \text{ kg/m}^2 \cdot \text{s} \leq G_T \leq 300 \text{ kg/m}^2 \cdot \text{s}$$

$$0.06 \leq \text{Ja} \leq 2.8$$

$$950 \leq \text{Re}_{lo} \leq 13,000$$

$$0.1 \leq x_q \leq 0.9$$

where the constant c and the exponents are given in Table 10.1 and h is calculated from the smooth correlation given in Section 10.5. Hence ϵ_o is the dielectric

TABLE 10.1 Values of Coefficients for R-404a EHD In-Tube Condensation

Coefficient	Smooth Tube	Corrugated Tube
c	0.00174	0.00868
n_1	0.98833	0.70733
n_2	-0.54505	-0.33768
n_3	0.59805	0.37158
n_4	-0.27722	-0.15107

Source: Gidwani et al. (1998).

permittivity for a vacuum and $\kappa(= \varepsilon/\varepsilon_0)$ is the dielectric constant of the fluid. Most of the data were correlated to within $\pm 30\%$.

The electric field (E) for use in eq. (10.31) is estimated from the applied voltage (V) as

$$E = \frac{2V}{D_i \ln(D_i/D_{el})} \tag{10.32}$$

where D_i is the inner diameter of the tube and D_{el} is the outer diameter of the inner electrode. The ratio of the in-tube condensation heat transfer coefficient with EHD (h_E) to that with no EHD (h) for R-407c is

$$\frac{h_E}{h} = 1 + c(\log Es)^{n_1} \left(\frac{G_T}{300}\right)^{n_2} \left(\frac{1-x_q}{x_q}\right)^{n_3} \text{Ja}^{n_4} \tag{10.33}$$

TABLE 10.2 Values of Coefficients for R-407c EHD In-Tube Condensation

Coefficient	Smooth Tube	
	$\frac{x_q}{1-x_q} \frac{G_T P_r}{300} \leq 0.05$	$\frac{x_q}{1-x_q} \frac{G_T P_r}{300} > 0.05$
c	0.23173	0.0586
n_1	1.6711	0.46622
n_2	0.07777	-0.26072
n_3	0.22064	-0.09885
n_4	-0.16572	-1.77379
	Corrugated Tube	
c	0.06221	0.018457
n_1	2.53152	2.88447
n_2	0.10825	-0.06351
n_3	0.47615	0.25078
n_4	-0.00954	-0.70633

Source: Gidwani et al. (1998).

within the following ranges:

$$80 \leq Es = \frac{\kappa \epsilon_o E^2 D_i}{\sigma} \leq 102$$

$$5 \text{ kg/m}^2 \cdot \text{s} \leq G_T \leq 300 \text{ kg/m}^2 \cdot \text{s}$$

$$0.1 \leq Ja \leq 2.3$$

$$970 \leq Re_{lo} \leq 11,000$$

$$0.1 \leq x_q \leq 0.9$$

where the constant c and the exponents are given in Table 10.2 and h is calculated from the smooth correlation given in Section 10.6. Most of the data were correlated to within $\pm 15\%$.

10.6 CONDENSATION IN SMOOTH TUBES*

10.6.1 Introduction

Studies of condensation are numerous in the technical literature. These studies include analytical efforts to model the physics of condensation processes, experimental efforts to measure the heat transfer behavior of certain fluids, and various combinations of the two. Most investigators have collected data for a limited number of fluids under a range of operating conditions that was suitable for the applications of their interest. Efforts to match their data with existing correlations or to develop correlations to fit their own data have met with some success. Many correlations that are available come with no explicit range of parameters over which they can be expected to give accurate results. Although there are handbooks and design manuals supplying reasonable recommendations for a design engineer who is searching the technical literature, the overall literature provides seemingly diverse reports about which correlation is “best.” The differences between the lowest and highest predicted heat transfer coefficients, in certain cases, can be as high as a factor of 2 or 3 (Hinde et al., 1992).

There is agreement in the literature that the mechanisms of heat transfer and pressure drop are intimately linked with the prevailing two-phase flow regime. This has led to many studies aimed at predicting what dimensionless parameters govern specific flow regime transitions and at what values of these dimensionless parameters certain transitions are expected to occur. Although debates still exist in the literature concerning differences in the flow regime predictions of various researchers, a basic understanding has been established of what the various flow regimes are and, in most cases, what parameters are suitable for determining the transition from one flow regime to the next. Thus, the topics of heat transfer and flow regimes must be combined in the correlations that can be used in the design of condensers.

*This section is based on the work of Dobson and Chato (1998).

10.6.2 Flow Regimes in Horizontal Tubes

A detailed discussion of the background and the literature was given by Dobson (1994), Dobson et al. (1994a,b), and Dobson and Chato (1998). Other summaries were published by Breber (1988), Palen et al. (1993), and Wang and Chato (1995).

Flow Regimes in Horizontal Two-Phase Flow In small tubes, under 3 mm diameter, surface tension and vapor shear dominate the flow. At high void fractions annular or annular-mist flow occurs, whereas at medium and low void fractions, the flow is mostly of the slug-plug type, where traveling packets of liquid are separated by vapor. In larger tubes, the two factors controlling the flow are gravity and vapor shear. In this chapter only the larger tubes are considered. At low vapor velocities, gravity dominates and the condensate forms primarily on the top portion of the tube and flows downward into a liquid pool which is driven out axially, partly by the vapor flow and partly by a gravitational head. In terms of void fraction, the flow regimes can be divided into two groups: those that occur at high void fractions and those that occur only at low void fractions. The first category includes five flow regimes: stratified flow, wavy flow, wavy-annular flow, annular flow, and annular-mist flow. The second category includes slug, plug, and bubbly flow. The five flow regimes in the first category are arranged such that each successive flow regime corresponds to an increase in the vapor velocity. Thus, the first two are gravity dominated, the third is influenced about equally, and the last two are vapor shear dominated. The three flow regimes in the second category are arranged such that the transition from one flow regime to the next corresponds to an increase in the liquid inventory (a decrease in void fraction α).

At very low vapor velocities, the gravity-controlled stratified flow regime is observed. Because the vapor velocity is low, the liquid-vapor interface remains smooth (Chato, 1960, 1962). As the vapor velocity is increased, the liquid-vapor interface becomes Helmholtz unstable, giving rise to surface waves (Carey, 1992) and wavy flow. The condensation process on the top of the tube is similar to that in stratified flow. The condensation process on the portion of the tube wall near the interface between the liquid pool and the vapor is affected by the waves because it is alternately exposed to a thin condensate film flowing downward and the crest of a wave moving in the mean flow direction.

As the vapor velocity is increased further, the wavy flow becomes unstable and can result in two different transitions. At high liquid fractions, the slug flow case that is described subsequently occurs. At lower liquid fractions, the waves begin to wash up and around the tube wall, leading to annular flow. Before the annular flow pattern is reached, however, a transitional flow pattern called *wavy-annular flow* is observed in which some liquid from the waves begins to wash up and around the circumference of the tube, but not enough to create a symmetric annular film. This liquid moves primarily in the mean flow direction rather than downward, creating the primary difference from the wavy flow regime.

With still further increases in the vapor velocity, the liquid migration from the pool at the bottom of the tube to the top of the tube continues until the film thickness

becomes nearly uniform. The visual appearance of this type of flow is one of an annular film of liquid on the wall and a high-speed vapor core in the center, hence the name *annular flow*. The liquid–vapor interface in annular flow is nearly always characterized by surface waves due to the high-speed vapor flowing over it.

At yet higher vapor velocities, the crests of the waves on the liquid film are sheared off by the vapor flow and entrained in the core in the form of liquid droplets. This is referred to as the *annular–mist flow regime* because of the appearance of an annular film with a mixture of vapor and mist in the core flow.

At low void fractions *slug flow* is formed when interfacial waves grow sufficiently in amplitude to block the entire cross section at some axial locations, leading to the visual appearance of slugs of liquid flowing along the tube. These slugs have been shown by Hubbard and Dukler (1966) and Lin and Hanratty (1989) to create large pressure spikes, due to rapid deceleration of the vapor flow. In other cases, flow that would visually be identified as slug flow does not create these large pressure spikes. This regime has been designated by Lin and Hanratty as *pseudo-slug flow*. They proposed that unlike true slugs, pseudo-slugs either did not entirely block the tube or did so only momentarily. A regime with a qualitative description similar to pseudo-slug flow was designated as proto-slug flow by Nicholson et al. (1978) and as wavy–annular flow by Barnea et al. (1980). These references illustrate the considerable subjectivity in flow regime classifications.

As condensation continues, the slugs coalesce into a predominantly liquid flow with large bubbles within. This is referred to as the *plug flow regime*. Turbulent fluctuations within the liquid eventually break these plugs into smaller vapor bubbles that become dispersed throughout the liquid. This is called the *bubbly flow regime*. The slug, plug, and bubbly flow regimes occur at the end of the condensation process when the liquid inventory is large (the void fraction, α , is small). In combination, they occupy only 10 to 20% of the total quality range. The plug and bubbly flow regimes are confined to the bottom of the quality range and will not be discussed further because here the vapor mass fractions and, consequently, the energy transfer rates due to condensation are negligibly small. The heat transfer rates should be estimated on the basis of single-phase liquid flow.

Effects of Mass Flux and Quality At the lowest mass fluxes (e.g., $25 \text{ kg/s} \cdot \text{m}^2$), smooth-stratified flow can be expected to occur across the entire range of quality. As the mass flux is increased to, say, $75 \text{ kg/s} \cdot \text{m}^2$, interfacial waves develop and wavy flow occurs for the entire range of quality. For these two mass fluxes, the flow regime is not affected by changes in diameter or refrigerant.

At mass fluxes between 150 and $300 \text{ kg/s} \cdot \text{m}^2$, several different flow regimes occur as the quality changes. Slug flow is found at low qualities, followed sequentially by wavy, wavy–annular, and annular flow. At these mass fluxes, the tube diameter and fluid properties influence the range of quality over which each of the flow regimes occurred.

At even higher mass fluxes, the flow regimes include slug flow at low quality, followed by wavy–annular, annular, and annular–mist flow as the quality increases. Annular or annular–mist flow normally occurs for 70 to 80% of the condensation path.

At these high mass fluxes significant entrainment can occur, the magnitude of which tends to vary in time. Pure mist flow (without a stable wall film) was observed by Dobson (1994) only at qualities over 90% without condensation. Mist flows seem to develop a stable liquid film as soon as condensation begins. In the range of parameters tested by Dobson (1994), Dobson et al. (1994a,b), and Dobson and Chato (1998), Soliman's (1986) idea of pure mist flow as a distinct condensation regime was not verified.

Effects of Fluid Properties and Tube Diameter Although mass flux and quality are primary factors affecting the flow regimes, the thermophysical properties of the fluid and the tube diameter play a secondary role. Their influence is most evident at the intermediate mass fluxes of 150 to 300 kg/s · m², where the mass velocities are not so high nor low as to allow one flow regime to clearly dominate over the other. The primary fluid properties that affect the flow regimes are the vapor and liquid densities and viscosities and the surface tension. Much of the variation in the fluid properties can be related to the reduced pressure. At high values of reduced pressure, the liquid and vapor phases are more similar. Thus vapor density and viscosity are higher, and liquid density and viscosity are lower. The surface tension, which represents the work required to increase the interfacial area (Carey, 1992), also decreases as the reduced pressure increases and the phases become more similar.

The most noticeable effect of the property differences on the flow regimes is the extent to which annular flow prevails over wavy or wavy-annular flow. At a given mass flux where wavy, wavy-annular, and annular flows all occur, the size of the quality range occupied by annular flow is greater at lower reduced pressures.

Another item that is affected by the reduced pressure is the length of the slug flow region. Taitel and Dukler's (1976) criterion for slug flow is that $X_{tt} > 1.6$. Combining this value with the fact that

$$(\rho_g/\rho_l)^{0.5}(\mu_l/\mu_g)^{0.1} \simeq 0.551 P_r^{0.49} \quad (10.34)$$

Wattelet, 1994; Wattelet et al., 1994) yields an algebraic expression for the quality below which slug flow is expected to occur:

$$x_{\text{slug}} \leq \frac{1}{1 + 3.27 P_r^{-0.54}} \quad (10.35)$$

The tube diameter also affects the flow regime transitions. As the tube diameter is reduced at a fixed mass flux, the transition from wavy flow to wavy-annular flow and the transition from wavy-annular flow to annular flow shifts to lower qualities. At high mass fluxes most of the quality range is associated with annular flow and the diameter effects are less pronounced.

Pure stratified flow can be found only in tubes with relatively small length-to-diameter ratios. Entrainment can be expected only at high mass fluxes. Although estimating the amount of entrainment is difficult, it appears that entrainment is less pronounced in the smaller tubes.

Potential Role of Surface Tension In any situation where a free surface exists, the potential role of surface tension should not be overlooked. The analytical approach used in the original Taitel–Dukler maps clearly ignores surface tension forces. The consensus of subsequent investigators is that surface tension forces become increasingly important as the diameter is decreased and may dominate for sufficiently small tube sizes. Of primary interest is the effect on the wavy-to-annular transition. Galbiati and Andreini (1992) started with Taitel and Dukler's analysis of a Kelvin–Helmholtz instability for the wavy-to-annular flow transition. They included surface tension forces that supplement the stabilizing gravity forces. Their final result for the transition criterion can be obtained by plotting the following values of F_{td} on the Taitel–Dukler map:

$$\frac{F_{td}}{\sqrt{1 + 1.305\sigma/gD^2(\rho_l - \rho_g)}} = \frac{F_{td}}{\sqrt{1 + 1.305/Bd}} \quad (10.36)$$

F_{td} , called by Taitel and Dukler a modified Froude number, is defined by

$$F_{td} = \sqrt{\frac{\rho_g}{\rho_l - \rho_g}} \frac{Gx/\rho_g}{\sqrt{Dg \cos \alpha_T}} \quad (10.37)$$

The second term in eq. (10.37) is a superficial vapor Froude number (ratio of inertial to gravity forces in the vapor), while the first is a modifier depending on the density ratio.

For values of the Bond number Bd much greater than unity, surface tension plays no significant stabilizing role. Although eq. (10.36) shows the right trends, its magnitudes are questionable. The lowest value of the Bond number found by Dobson (1994), Dobson et al. (1994a,b), and Dobson and Chato (1998), that for R-134a at 35°C in a 3.14-mm-inside-diameter tube, was about 16. This Bond number results in a value of the denominator of eq. (10.36) of only 1.04, indicating gravity dominance. However, Galbiati and Andreini (1992) stated that the surface tension and gravity forces were of equal magnitude for $D = 3$ mm. The value of surface tension for their air–water system was significantly larger than that for high-temperature refrigerants. The value of the diameter at which surface tension forces become important is quite sensitive to what wavelength is considered most unstable ($1 = 5.5D$ was used by Galbiati and Andreini), so this issue warrants further attention if tubes in the range of 3 mm are used.

Flow Regime Mapping Because the flow patterns strongly influence the heat and momentum transfer processes, it is important for designers to predict what flow pattern is expected based on the flow rate, quality, fluid properties, and tube diameter. One of the earliest attempts at a flow regime map was by Baker (1954). The Baker map was based on observations of adiabatic gas–liquid flows in tubes ranging from 25.4 to 101.6 mm in diameter. The data used included both air–water and oil–water flows, providing a fairly wide range of fluid properties. The horizontal and vertical

coordinates on the Baker map are the superficial liquid and vapor mass fluxes times scaling factors that account for fluid property variations. Although subsequent flow regime maps have achieved improved accuracy, Baker's work is historically the first widely recognized flow regime map.

Mandhane et al. (1974) developed a flow regime map similar to Baker's using a larger database of 5935 observations. The abscissa and ordinate of the Mandhane map are the superficial gas velocity and superficial liquid velocity, which makes it rather simple to use. The Mandhane map correctly predicted the flow regime for 68% of the observations in their database, as opposed to 42% for the original Baker map. The boundaries of the Mandhane map were constructed primarily for air–water data in relatively large tubes. Comparisons with recent data for evaporating refrigerants revealed systematic problems with the Mandhane map (Wattelet, 1994; Wattelet et al., 1994). These problems were caused primarily by the much higher vapor densities of the refrigerants in Wattelet's study than the air densities in the Mandhane data. This problem would be worse for condensation because the vapor density is considerably higher at condensation temperatures than at evaporation temperatures.

Perhaps the most theoretically based flow regime map is that of Taitel and Dukler (1976). They reasoned that each flow regime transition was based on a different set of competing forces and that a single parameter or set of coordinates should not be expected to predict all flow regime transitions. The Taitel–Dukler map includes five flow regimes: stratified smooth, stratified–wavy, annular, intermittent (plug and slug), and dispersed bubble. The map was developed for adiabatic flows, but has been used with success by other investigators for diabatic flows (Barnhart, 1992; Wattelet, 1994; Wattelet et al., 1994). Taitel and Dukler developed various approaches for predicting the transitions between the various flow regimes based on the appropriate physical mechanisms. For the stratified-to-wavy flow transition, they hypothesized that waves would be formed when the pressure and shear forces acting on a wave were sufficient to overcome viscous dissipation in the wave. Their ideas were based on the work of Jeffreys (1925, 1926), and in dimensional form they deduced that waves would be expected to form when a critical vapor velocity was exceeded. In dimensionless form, the inequality can be expressed as

$$K_{td} = F_{td} \sqrt{\text{Re}_l} \geq \frac{20}{\tilde{u}_g \sqrt{\tilde{u}_l}} \quad (10.38)$$

The right-hand side of eq. (10.38) follows the nomenclature set forth by Taitel and Dukler, where quantities with tildes are dimensionless variables. In this scheme, actual phase velocities are scaled by superficial phase velocities and lengths are scaled by the tube diameter.

The transition from a stratified-wavy flow to an intermittent or annular flow was observed experimentally by Butterworth (1972) and Dukler and Hubbard (1975). They described wave growth on a stratified–wavy flow that led to one of two effects. At low liquid fractions, the wave washed liquid around the circumference of the tube, leading to an annular flow. At high liquid fractions, the wave bridged the tube cross section and led to an intermittent (slug or plug) flow. Taitel and Dukler predicted this

transition based on a modification of the Kelvin–Helmholtz stability analysis for an infinitesimal wave between two horizontal plates. Taitel and Dukler extended this theory to predict the stability of finite waves inside a tube. In dimensionless form, their correlation for the transition is

$$F_{td}^2 \left[\frac{1}{(1 - \tilde{h}_l)^2} \frac{\tilde{u}_g^2 \sqrt{1 - (2\tilde{h}_l - 1)^2}}{\tilde{A}_g} \right] \geq 1 \quad (10.39)$$

All terms in the bracketed portion of eq. (10.39) are exclusively functions of the Martinelli parameter, X_{tt} , so the boundary is a function of only F_{td} and X_{tt} . As discussed in what follows, the two transition criteria expressed by eqs. (10.38) and (10.39) are the only ones relevant to most practical cases.

Another approach to predicting flow regime transitions, specifically for condensation, has been developed by Soliman (1982, 1983). Soliman distinguished between three flow regimes that he deemed to be important for condensing flows: wavy flow, annular flow, and mist flow. He developed two flow regime transition criteria, one for the wavy-to-annular transition and one for the annular-to-mist transition. It is important to note that the wavy flow regime of Soliman includes the regimes commonly called stratified, slug, and wavy flow. Although these regimes have important differences from the standpoint of flow regime classification, particularly concerning the stability of the wavy interface, Soliman apparently concluded that these differences were less important than the significant stratification that they all had in common.

Soliman (1982) postulated that the wavy-to-annular transition was based on a balance between inertial and gravitational forces on the liquid film. The Froude number, $G^2/\rho_l^2 g L$, represents a balance between these forces. Soliman proposed that the appropriate velocity was the actual liquid velocity and the appropriate length scale was the film thickness δ . These parameters were not known based solely on G , x , and the fluid properties. Soliman obtained expressions for them based on relations for two-phase pressure drop in annular flow. Thus, his transition criterion is opposite to that of Taitel and Dukler in that it assumes that an annular flow exists and seeks to determine when gravitational forces will cause a transition to wavy flow. The resulting expression for the Froude number is given by

$$Fr_{so} = \begin{cases} 0.025 Re_l^{1.59} \left(\frac{1 + 1.09 X_{tt}^{0.039}}{X_{tt}} \right)^{1.5} \frac{1}{Ga^{0.5}} & \text{for } Re_l \leq 1250 \\ 1.26 Re_l^{1.04} \left(\frac{1 + 1.09 X_{tt}^{0.039}}{X_{tt}} \right)^{1.5} \frac{1}{Ga^{0.5}} & \text{for } Re_l > 1250 \end{cases} \quad (10.40a)$$

$$\quad (10.40b)$$

Based on comparisons with data in tubes 4.8 to 25 mm in diameter, and with fluids including water, refrigerants, and acetone, Soliman (1982) concluded that wavy flow was observed for $Fr_{so} < 7$, and annular flow was observed for $Fr_{so} > 7$. Dobson (1994) and Dobson et al. (1994a,b) reported that $Fr_{so} = 7$ served as a good indicator of the transition from wavy to wavy–annular flow, although a symmetric annular flow was not observed until around $Fr_{so} = 18$.

Solimon (1983, 1986) also developed a parameter for predicting the transition from annular to mist flow. He postulated that the primary forces tending to prevent entrainment were liquid viscous forces and surface tension forces, and that the primary force which promoted mist formation was vapor inertia. He formulated a modified Weber number that represented a balance between these forces:

$$We_{so} = \begin{cases} 2.45 \frac{Re_g^{0.64}}{Su_g^{0.3} (1 + 1.09 X_{tt}^{0.039})^{0.4}} & \text{for } Re_l \leq 1250 \end{cases} \quad (10.41a)$$

$$We_{so} = \begin{cases} 0.85 \left(\frac{\mu_g}{\mu_l} \right) \left(\frac{\rho_l}{\rho_g} \right)^{-0.084} \frac{Re_g^{0.79} X_{tt}^{0.157}}{Su_g^{0.3} (1 + 1.09 X_{tt}^{0.039})^{0.4}} & \text{for } Re_l > 1250 \end{cases} \quad (10.41b)$$

Based on visual observations from various studies, Soliman (1986) concluded that annular flow was always observed for $We_{so} < 20$, and pure mist flow with no stable liquid film on the wall was always observed for $We_{so} > 30$. The region of We_{so} between 20 and 30 was reported to be a mix of annular and mist flow called *annular-mist flow*.

Comparison of Flow Regime Maps Dobson (1994), Dobson et al. (1994a,b), and Dobson and Chato (1998) used their own data for refrigerants to compare various flow regime maps, and they proposed modifications. The validity of the maps for other diameters, fluids, and temperatures was addressed by examining how their predictions changed with diameter and reduced pressure.

Mandhane Map The predictions of the original Mandhane map were grossly different from the experimental observations, but this map was developed primarily from air–water data. At atmospheric pressure and temperature, the density of air is about 1.15 kg/m^3 . This is between 40 and 100 times lower than the vapor densities of refrigerants. Hanratty (1994) pointed out that the Mandhane map could be brought into better agreement with refrigerant data by accounting for the large differences in vapor density. To effect this change, the superficial vapor velocity of the refrigerant was multiplied by the square root of the ratio of the vapor density to the density of atmospheric air. The resulting quantity is referred to herein as a *modified superficial vapor velocity*:

$$j_v^{\text{corr}} = \sqrt{\frac{\rho_g}{\rho_a}} j_v \quad (10.42)$$

From a physical standpoint, this modified superficial velocity is proportional to the square root of the vapor kinetic energy. This simple change was made in both the vapor and liquid superficial velocities, and the results are plotted on the Mandhane coordinates in Fig. 10.7. The condensation paths are for mass fluxes ranging from 25 to $650 \text{ kg/s} \cdot \text{m}^2$ of R-134a. The points on the map cover a range of quality from 5 to 95% in 5% increments. Decreasing the quality corresponds to moving to the left on the map.

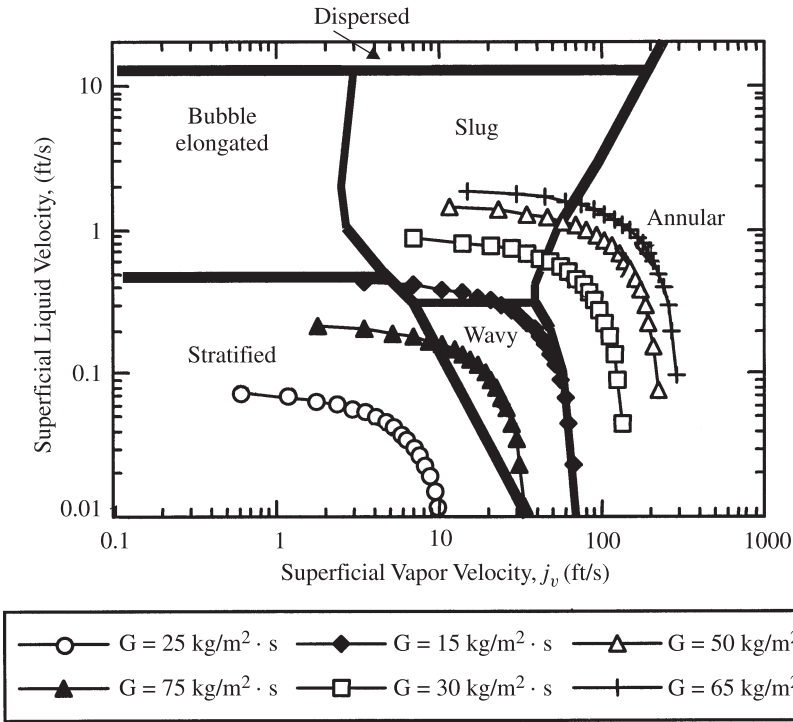


Figure 10.7 Predicted flow patterns for R-134a on the Mandhane et al. (1974) map using corrected superficial velocities. (From Dobson and Chato, 1998.)

Making this simple correction to the Mandhane map produced much better agreement with the experimental data. The only obvious deficiency was an overprediction in the length of the slug flow region, particularly at $300 \text{ kg/s} \cdot \text{m}^2$. Barnea et al. (1980), however, also noted that their wavy–annular flow data occupied the slug flow region on the Mandhane map. They suggested that this was due to different interpretations of what constituted slug flow and that data observed to be in the wavy–annular flow regime should be classified as slug flow for comparison with the Mandhane map (or, conversely, points lying near the right edge of Mandhane’s slug flow region might be expected to correspond to wavy–annular flow). Incorporating this suggestion results in excellent agreement with the Mandhane map.

Having established the basic validity of the corrected Mandhane map for the case of R-134a in the 7.04-mm-inside-diameter tube, questions remain about how it incorporates the effects of diameter and reduced pressure. Neither coordinate on the Mandhane map includes a diameter term, and investigators as early as Taitel and Dukler (1976) have noted systematic deviations in the Mandhane map because of this deficiency. Thus, the increased amount of annular flow in the 3.14-mm-inside-diameter and smaller tubes would not be predicted using the Mandhane map.

The effect of reduced pressure is correctly represented on the corrected Mandhane map. The trends predicted by the Mandhane map regarding the change in fluid properties are consistent with experimental observations, although a portion of the slug flow region was again found to be occupied by either wavy or wavy-annular flow.

Taitel–Dukler Map Figure 10.8 traces condensation paths for R-134a on the Taitel–Dukler map. The points range from 5 to 95% quality at 5% increments, with increasing quality corresponding to moving left on the map. Because the Taitel–Dukler map uses different coordinates for different transitions, in general three different lines would be needed for each mass flux. For the range of parameters examined by Dobson and Chato (1998), no dispersed bubble flow was observed or predicted. Thus, the only two parameters that were needed were K_{td} and F_{td} , used, respectively, for predicting the stratified to wavy and wavy to annular or intermittent transitions.

Plots of K_{td} versus X_{tt} are shown for the two lowest mass fluxes only, because these were the only mass fluxes at which any stratified flow was predicted. The map predicted stratified flow up to 80% for the 25-kg/s · m² flux case, where stratified flow was observed across the entire range of quality. It is interesting to note that the transition boundary is nearly parallel to the condensation path lines. This implies that a particular mass flux will be, to a close approximation, either wavy or annular across the entire range of quality. For mass fluxes slightly above the transition boundary (in the annular regime), the slug flow regime at low qualities was always followed by

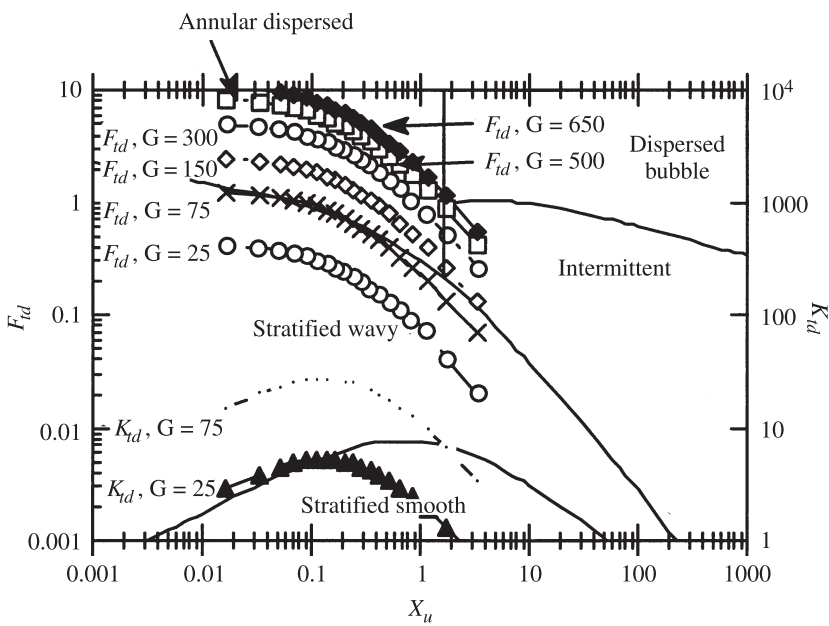


Figure 10.8 Flow regime predictions of the Taitel–Dukler (1976) map for R-134a at 35°C in the 7.04-mm-ID tube. (From Dobson and Chato, 1998.)

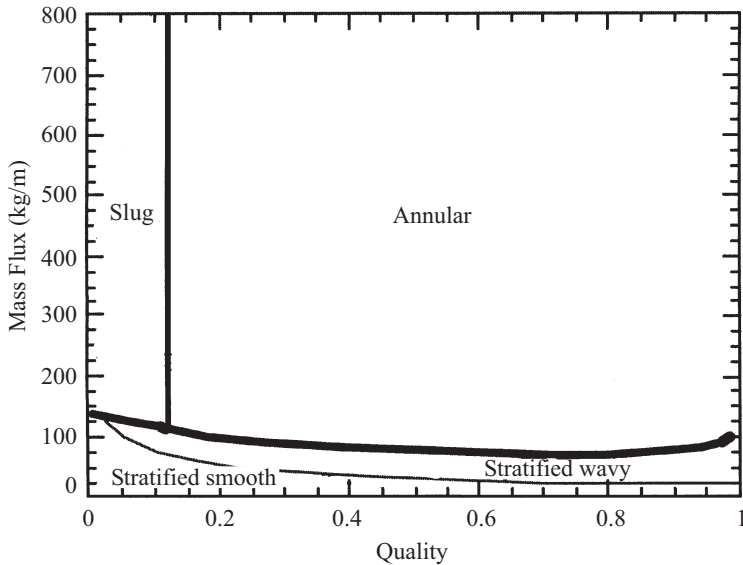


Figure 10.9 Taitel–Dukler (1976) predictions on G – x coordinates for R-134a at 35°C in a 7.04-mm-ID tube. (From Dobson and Chato, 1998.)

regions of wavy, wavy–annular, then annular flow. The quality range over which the wavy and wavy–annular flow regimes occurred decreased as mass flux was increased.

The predictions of the Taitel–Dukler map are translated onto mass flux–quality (G – x) coordinates in Fig. 10.9. At low mass fluxes, stratified flow is predicted across the entire range of quality. At slightly higher mass fluxes, wavy flow is predicted across most of the quality range with a small amount of stratified flow at low quality. At mass fluxes above $140 \text{ kg/s} \cdot \text{m}^2$, slug flow is predicted for qualities below 11.8% and annular flow is predicted for all higher qualities. It is close to this boundary that the observed flow regimes deviated most significantly from the Taitel–Dukler predictions. The length of the slug flow region was underpredicted, and this was consistently followed by some wavy or wavy–annular flow that was not predicted by the Taitel–Dukler map.

The apparent discrepancy between the observed and predicted flow regimes at mass fluxes slightly above the annular boundary of the Taitel–Dukler map is due largely to differences in terminology. In an early experimental verification of the Taitel–Dukler map, Barnea et al. (1980) used the term *wavy–annular flow* to refer to a hybrid pattern observed at the lowest gas rates where the slug-to-annular transition occurred. A similar regime has been termed *proto-slug flow* by Nicholson et al. (1978), and *pseudo-slug flow* by Lin and Hanratty (1989). Because this pattern occurs after the wavy flow has become unstable, it is properly labeled as *intermittent* or *annular flow* in Taitel–Dukler terminology. From a heat transfer standpoint, however, the instability of the wavy flow near this boundary is less important than the significant stratification due to gravity. At higher mass fluxes, the range of quality

occupied by this hybrid flow pattern becomes so small that proper classification is unimportant.

Of the boundaries from the Taitel–Dukler map that were used, only that between wavy and intermittent or annular flow depends on the diameter. The parameter that is used for predicting this transition, F_{td} , is proportional to $D^{-0.5}$ at a fixed mass flux and quality. Thus, decreasing the diameter increases the Froude number and decreases the mass flux at which the annular transition is expected to occur. This is consistent with the observed trend of more annular flow in the smaller tubes. Although the trend is physically correct, the predictions themselves were incorrect when applied to the data in the 3.14-mm-inside-diameter tube. The Taitel–Dukler method predicts annular flow across nearly the entire range of quality at a mass flux of $75 \text{ kg/s} \cdot \text{m}^2$, while wavy flow was observed exclusively at this mass flux. The predicted trend of the Taitel–Dukler map to an increase in the reduced pressure was consistent with the experimental observations. For example, the slug flow region was wider, as predicted by eq. (10.35).

At higher reduced pressures one would also expect the stratified-to-wavy and wavy-to-annular transitions to be shifted to higher mass fluxes, due to the lower vapor velocity at a given mass flux and quality. This small shift is due to two opposing trends brought about by the changes in fluid properties. At constant mass flux and quality, the value of F_{td} decreases with increasing pressures, moving the curve downward relative to the transition boundary on the Taitel–Dukler map. However, the value of X_{tt} at constant quality increases with pressure, moving the curve to the right on the Taitel–Dukler map and therefore closer to the boundary. From a practical standpoint, this predicted shift in the transition boundary is insignificant. The apparent discrepancy between the predictions and the observations at mass fluxes slightly above the annular flow boundary was also present with all the refrigerants used. For example, at a mass flux of $150 \text{ kg/s} \cdot \text{m}^2$, wavy flow persisted at qualities up to 50%, while the Taitel–Dukler map predicted annular flow above 20% quality.

Soliman Transitions Soliman (1982, 1986) developed criteria for two flow regime transitions for condensation: (1) wavy or slug flow to annular flow, and (2) annular flow to mist flow. His transition criteria are displayed on G – x coordinates in Fig. 10.10. Several interesting observations can be made from comparing the predictions of Soliman to those of Taitel and Dukler. First, at high qualities Soliman's prediction of the wavy-to-annular transition agrees fairly well with that of Taitel and Dukler. Unlike the Taitel–Dukler map, though, Soliman predicts a wavy region at low qualities over the entire mass flux range of this study. This occurs partially because Soliman lumps the wavy and slug flow regions together. At high mass fluxes, the region predicted to be wavy flow by Soliman corresponds almost exactly with the slug flow region on the Taitel–Dukler map. At lower mass fluxes, though, the region predicted to be occupied by wavy flow extends to higher qualities than the slug flow boundary on the Taitel–Dukler map. This is consistent with the experimental data in both magnitude and trend if the predicted transition line is considered to be that of wavy flow to wavy–annular flow. It was shown by Dobson (1994) and Dobson et al. (1994a,b) that the transition from wavy–annular flow to annular flow was well predicted by a value of $\text{Fr}_{so} = 18$, as opposed to $\text{Fr}_{so} = 7$ for the wavy-to-wavy–annular transition.

Unlike the maps of Mandhane and Taitel–Dukler, Soliman’s map also includes a distinct mist flow region. According to Soliman, mist or spray flow is a regime with all the liquid flowing as entrained droplets in the core flow and no stable film on the wall. Annular mist flow would refer to a regime with a stable liquid film on the wall and significant entrainment in the core flow. According to the observations made by Dobson (1994), most of the region labeled as mist flow by Soliman’s map would more properly be called annular–mist flow. Although the amount of entrainment was very significant, a stable liquid film was always observed on the wall at qualities below 90%. Even when the flow entered the sight glass at the inlet of the test section as mist flow, the outlet sight glass always had annular–mist flow. This observation suggests that the net mass flux toward the wall during condensation always results in a stable liquid film, no matter what the observations might indicate in an adiabatic section. This finding is important for interpreting the annular–mist flow heat transfer data. If Soliman’s mist flow region is interpreted as annular–mist flow, the predictions seem quite reasonable.

The diameter effects predicted by Soliman’s transition criteria are also shown in Fig. 10.10. The lower mass flux limit at which annular flow is predicted is relatively insensitive to the diameter change, much like the predictions of Taitel and Dukler. At mass fluxes slightly above this, however, the wavy-to-annular transition line was shifted to lower qualities with decreasing diameter. This was consistent with the

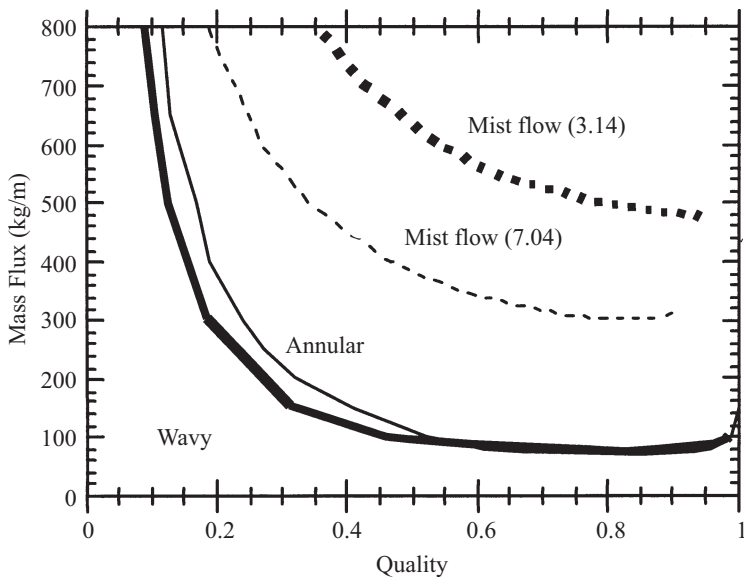


Figure 10.10 Soliman’s (1982, 1983) predicted flow regime on G – x coordinates for R-134a at 35°C. (From Dobson and Chato, 1998.)

experimental observations in both direction and magnitude. The predicted effect on the mist flow regime was much more dramatic, with a significant stabilizing effect on the liquid film being predicted as the tube diameter was decreased. This was consistent with the trend of the observations, although the transition was very difficult to detect visually.

The effect that increasing the reduced pressure has on the wavy-to-annular flow regime transition predicted by Soliman is shown in Fig. 10.11. This figure compares the predicted wavy-to-annular transition lines for R-134a at 35°C and R-32/R-125 at 45°C (low and high reduced pressures). The predicted trends are consistent with the experimental observations.

Because reliable surface tension data were not yet available for R-32/R-125 and drawing any conclusions concerning mist flow from the visualization was difficult, only the lines for the wavy-to-annular transition were included in Fig. 10.11. As another way of assessing the effect of increasing reduced pressure, the magnitude of the Weber number was examined as the temperature was increased for both R-134a and R-22. The Weber number increased as temperature increased due to the reduced liquid viscosity and surface tension, but only slightly (less than 10% as the temperature of both fluids was raised from 35°C to 55°C). This small change indicates that the decreased surface tension and liquid viscosity are nearly balanced by corresponding decreases in the density ratio. Based on these trends, one would

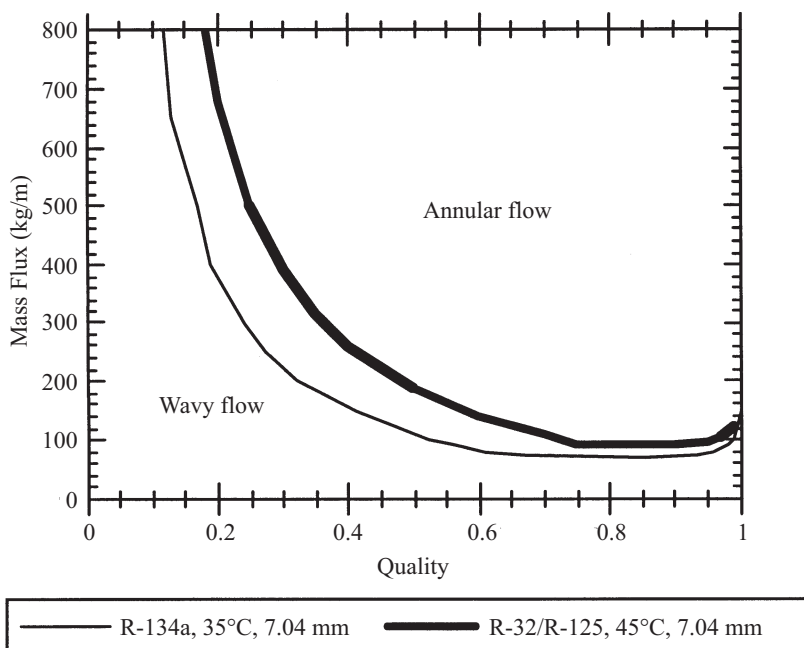


Figure 10.11 Effect of reduced pressure on Soliman's (1982) wavy-to-annular flow regime transition. (From Dobson and Chato, 1998.)

expect slightly more entrainment to occur at higher reduced pressures at identical mass flux and quality.

10.6.3 Heat Transfer in Horizontal Tubes

The following discussion is based on data of Dobson (1994) in the smooth-stratified, wavy-stratified, wavy-annular, annular, and annular-mist flow regimes.

Effects of Mass Flux and Quality Figure 10.12 presents typical heat transfer data for R-32/R-125 (60%/40%) in a 3.14-mm-inside-diameter tube at a saturation temperature of 35°C. At the lowest mass flux of 75 kg/s · m², the Nusselt number increases very modestly as the quality is increased. A similar quality dependence is exhibited as the mass flux is doubled to 150 kg/s · m². The Nusselt numbers remain nearly identical as the mass flux is doubled. At a mass flux of 300 kg/s · m², a different trend emerges. At low qualities, the heat transfer coefficients remain nearly identical to the lower mass flux cases. As the quality increases to around 30%, the Nusselt number displays a much more pronounced effect of quality. At mass fluxes above 300 kg/s · m², the dependence of the Nusselt number on quality remains similar. Even at low qualities, the Nusselt numbers are substantially higher than those for the low-mass-flux cases. If the same data were plotted as Nusselt number versus mass flux, the heat transfer coefficient would remain relatively constant at low mass fluxes. At a given mass flux, the slope of the heat transfer versus mass flux curve increases to a relatively constant value. The mass flux at which this change in slope occurs increases as the quality is decreased. For example, at 25% quality this shift occurs at a mass flux of 300 kg/s · m².

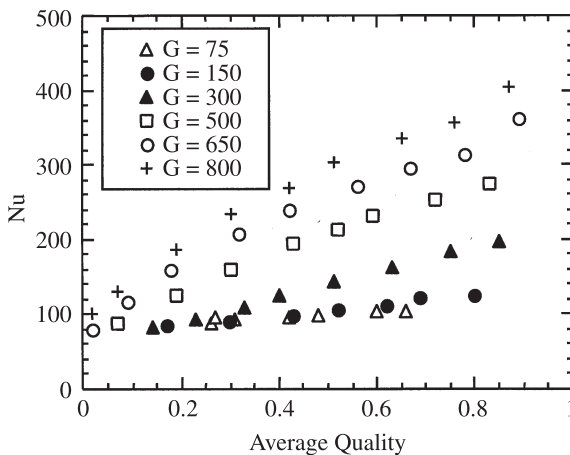


Figure 10.12 Variation of Nusselt number with quality for 60%/40% R-32/R-125 mixture at 35°C in 3.14-mm-ID test section. Mass flux G is in kg/s · m. (From Dobson and Chato, 1998.)

The change in heat transfer behavior exhibited in Fig. 10.12 is closely linked to changes in the two-phase flow regime. For the two lowest mass fluxes, 75 and 150 $\text{kg/s} \cdot \text{m}^2$, wavy or wavy-annular flow prevail over much of the quality range. The primary item affecting the heat transfer coefficient in this flow regime is the film thickness, which is insensitive to mass flux. Thus, wavy flow heat transfer coefficients are also relatively insensitive to mass flux.

At the highest mass fluxes, annular flow prevails over most of the quality range. In the annular flow regime, correlations such as those of Soliman et al. (1968) and Traviss et al. (1973) clearly illustrate the interdependence between pressure drop and heat transfer (h is proportional to $\sqrt{-\Delta P/\Delta Z}$). Because the pressure drop increases sharply as the quality is increased, the heat transfer coefficients in the annular flow regime show significant quality dependence.

At the intermediate mass flux of $300 \text{ kg/s} \cdot \text{m}^2$, the flat Nusselt number versus quality behavior that is characteristic of wavy flow occurs at low qualities whereas annular flow behavior appears at higher qualities. The change in slope in Fig. 10.12 occurs around 30% quality, corresponding closely to the observed change from the wavy-annular to the annular flow regime. At this mass flux, it would be inappropriate to use a single heat transfer model over the entire quality range.

Effects of Tube Diameter The relationships between h and D that were predicted by annular and wavy flow heat transfer coefficients agreed well with the experimental data. Although this was expected for the 7.04-mm-inside-diameter (ID) tube, a commonly used and tested size, some doubt existed about whether the heat transfer behavior in the 3.14-mm-ID tube would correspond with that predicted by "large tube" correlations. The most noticeable effect of the tube diameter has to do with the point at which the heat transfer mechanism changes from filmwise (wavy) to forced-convective (annular). The primary difference in the heat transfer behavior in the two tubes was observed at a mass flux of $300 \text{ kg/s} \cdot \text{m}^2$. In the 3.14-mm-ID tube, the heat transfer behavior showed a change in slope around 30% quality as the flow regime changed from wavy-annular to annular. In the larger 7.04-mm-ID tube, this transition was observed only at the highest quality point (89%), corresponding closely with observed transition to annular flow at around 80% quality. The heat transfer characteristics at the other mass fluxes were similar in both tubes.

Effects of Fluid Properties In the stratified and wavy flow regimes, the property index from the Chato (1960, 1962) correlation, $[\rho_l(\rho_l - \rho_g)k_l^3\lambda/\mu_l]^{0.25}$, can be used to compare the expected heat transfer behavior of different fluids. In the annular flow regime the single-phase liquid heat transfer index $k_l^{0.6}c_{pl}^{0.4}/\mu_l^{0.4}$ can be used at low qualities, but at higher qualities the two-phase multiplier, described below, becomes dominant.

Effects of Temperature Difference The refrigerant-to-wall temperature difference has an impact on the heat transfer coefficients in the wavy flow regime. This dependence occurs because for a falling film, a larger temperature difference results in a thicker film at a given location (hence, lower heat transfer coefficients). In the

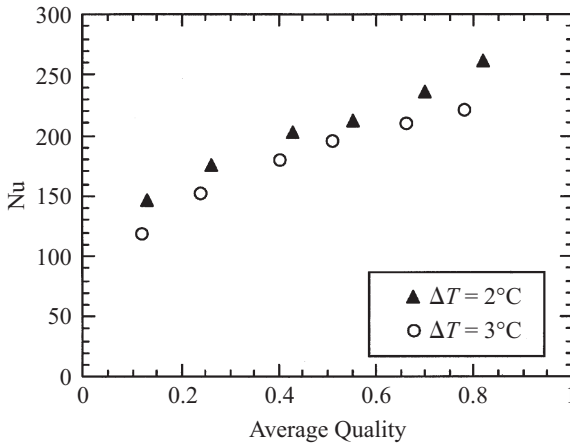


Figure 10.13 Effect of ΔT on Nu for R-32/R-125 in a 7.04-mm test section, $G = 75$ (kg/s · m), $T_{\text{sat}} = 35^\circ\text{C}$. (From Dobson and Chato, 1998.)

annular flow regime, a significant amount of experimental and analytical evidence suggests a negligible impact of temperature difference. Studying the effect of temperature difference on the heat transfer coefficients then provides a nonvisual method of assessing the extent of film wise and/or forced-convective condensation.

Precisely controlling the temperature difference during internal condensation experiments is very difficult. For this reason, few internal condensation data are available for which the temperature differences were controlled deliberately. Figure 10.13 shows the variation of Nusselt number with quality for R-32/R-125 at a saturation temperature of 35°C and a mass flux of $75 \text{ kg/s} \cdot \text{m}^2$. The two sets of points correspond to temperature differences of approximately 2°C (1.88 to 2.12°C) and 3°C (2.87 to 3.11°C). As predicted by the Nusselt theory, the Nusselt numbers are lower for the higher temperature difference data across the full range of quality. Using the quantity $Nu/(Ga \cdot Pr_l/Ja_l)^{0.25}$, based on liquid properties, on the vertical axis instead of Nu brings these data on a single line because at the very low mass flux almost all the heat transfer occurs by filmwise condensation on the top and very little occurs in the bottom of the tube. As the quality approaches unity and the liquid pool vanishes, the value of $Nu/(Ga \cdot Pr_l/Ja_l)^{0.25}$ properly approaches the value of 0.728 for condensation outside a horizontal cylinder.

Gravity-Driven Condensation The gravity-driven flow regimes include the stratified, wavy, and slug flow regions. These regimes are lumped together primarily because the dominant heat transfer mechanism in each regime is conduction across the film at the top of the tube. This type of condensation is commonly referred to as *film condensation*. Nusselt's (1916) heat transfer coefficient for gravity-driven condensation of a pure component on a vertical plate given by eq. (10.11) can be expressed as the mean Nusselt number at $z = L$:

$$\overline{\text{Nu}}_L = \frac{\bar{h}L}{k_l} = 0.943 \left[\frac{\rho_l g (\rho_l - \rho_g) L^3 \lambda}{k_l \mu_l (T_{\text{sat}} - T_w)} \right]^{1/4} \quad (10.43)$$

The bracketed term in eq. (10.43) can be expressed in dimensionless form as

$$\overline{\text{Nu}}_L = 0.943 \left(\frac{\text{Ga}_L \cdot \text{Pr}_l}{\text{Ja}_l} \right)^{1/4} \quad (10.44)$$

Dhir and Lienhard (1971) devised a simple way to extend the analysis for the vertical wall to arbitrary axisymmetric bodies. They showed that the local Nusselt number can be predicted by replacing g in eq. (10.43) with an effective acceleration of gravity:

$$g_{\text{eff}} = \frac{x(gr)^{4/3}}{\int_0^x g^{1/3} r^{4/3} dx} \quad (10.45)$$

In eq. (10.45), $r(x)$ is the local radius of curvature and $g(x)$ is the local gravity component in the x direction. For the horizontal cylinder, as was done for eq. (10.12), the effective gravity can be evaluated numerically and averaged over the circumference of the tube to obtain

$$\text{Nu} = 0.729 \left(\frac{\text{Ga} \cdot \text{Pr}_l}{\text{Ja}_l} \right)^{1/4} \quad (10.46)$$

The diameter is the length scale in Ga .

Based on integral analyses, Bromley (1952) and Rohsenow (1956) corrected for the assumption of a linear temperature profile by replacing the latent heat in these equations by a modified latent heat given by

$$\lambda' = \lambda(1 + 0.68\text{Ja}_l) \quad (10.47)$$

This correction shows that the assumption of a linear temperature profile in the original analysis is quite acceptable for Ja_l much less than unity.

During condensation inside horizontal, smooth tubes at low vapor velocities, gravitational forces, which tend to pull condensate down the tube wall, are much stronger than vapor shear forces, which tend to pull the condensate in the direction of the mean flow. Thus, a condensate film forms on the top of the tube and grows in thickness as it flows around the circumference. The bottom portion of the tube is filled with a liquid pool that transports the condensed liquid along the tube in the direction of the mean flow.

Chato (1960, 1962) concentrated on stratified flows with low vapor velocities, $\text{Re}_{\text{vo}} < 35,000$. He developed a similarity solution for the condensate film, which was patterned after Chen's (1961) analysis of falling-film condensation outside a horizontal cylinder. He applied this solution to the upper portion of the tube, where falling-film condensation existed (i.e., down to the liquid pool on the bottom). To

predict the depth of the liquid pool, he developed a separate model based on open channel hydraulics. Both his analytical model and experimental results for R-113 showed that the depth of the liquid level was relatively constant. This allowed his heat transfer data to be approximated quite well by the following correlation for the average Nusselt number:

$$\bar{Nu} = \frac{\bar{h}D}{k_l} = 0.555 \left[\frac{\rho_l g (\rho_l - \rho_g) D^3 \lambda}{k_l \mu_l (T_{\text{sat}} - T_w)} \right]^{1/4} \quad (10.48)$$

The constant 0.555 is 76% of the value of 0.728 for external condensation on a cylinder. This decrease in heat transfer is due to the thickness of the liquid pool on the bottom of the tube, which reduces the heat transfer to negligible amounts.

Jaster and Kosky (1976) proposed a correlation similar to Chato's for stratified flow condensation. To account for the variation of the liquid pool depth in a manner consistent with pressure-driven flow, they replaced the constant in the Chato correlation with a function of the void fraction α . This resulted in

$$\bar{Nu} = \frac{\bar{h}D}{k_l} = 0.728 \alpha^{3/4} \left[\frac{\rho_l g (\rho_l - \rho_g) D^3 \lambda}{k_l \mu_l (T_{\text{sat}} - T_w)} \right]^{1/4} \quad (10.49)$$

They recommend using Zivi's (1964) correlation for the void fraction:

$$\alpha = \left[1 + \frac{1-x}{x} \left(\frac{\rho_g}{\rho_l} \right)^{2/3} \right]^{-1} \quad (10.50)$$

Jaster and Kosky's correlation overpredicts the Chato correlation for all qualities to greater than about 0.2. It had a mean deviation of 37% with their own data, which it appeared to overpredict consistently.

The correlations of Chato and Jaster and Kosky both neglect the heat transfer that occurs in the liquid pool at the bottom of the tube. Chato showed that considering conduction only, this heat transfer was negligible compared to that through the upper part of the tube. This assumption is reasonable for low-speed stratified flows, but might not be so for higher-mass-flux low-quality situations where wavy or stratified flow could prevail, creating substantial convective heat transfer in the bottom of the tube. Rosson and Myers (1965) collected experimental data in what they called the *intermittent flow regime*, which included stratified, wavy, and slug flows. They measured the variation of heat transfer coefficient with angle around the tube and found, as expected, that the heat transfer coefficient decreased continuously from the top to the bottom of the tube. They proposed replacing the constant in the Nusselt's solution with an empirically determined function of the vapor Reynolds number:

$$Nu_{\text{top}} = 0.31 Re_g^{0.12} \left[\frac{\rho_l g (\rho_l - \rho_g) D^3 \lambda}{k_l \mu_l (T_{\text{sat}} - T_w)} \right]^{1/4} \quad (10.51)$$

In the bottom of the tube, they postulated forced-convective heat transfer. Using a heat and momentum transfer analogy, they recommended the following correlation:

$$\text{Nu}_{\text{bot}} = \frac{\phi_{l,lt} \sqrt{8\text{Re}_l}}{5 [1 + \ln(1 + 5 \text{Pr}_l)/\text{Pr}_l]} \quad (10.52)$$

where

$$\phi_{l,lt} = \sqrt{1 + \frac{1}{X_{lt}} + \frac{12}{X_{lt}^2}} \quad (10.53)$$

Rosson and Myers defined a parameter β that represented the fraction of the tube perimeter over which filmwise condensation occurred. They recommended predicting the value of β as follows:

$$\beta = \begin{cases} \text{Re}_g^{0.1} & \text{if } \frac{\text{Re}_g^{0.6} \cdot \text{Re}_l^{0.5}}{\text{Ga}} < 6.4 \times 10^{-5} \\ \frac{1.74 \times 10^{-5} \text{Ga}}{\sqrt{\text{Re}_g \cdot \text{Re}_l}} & \text{if } \frac{\text{Re}_g^{0.6} \cdot \text{Re}_l^{0.5}}{\text{Ga}} > 6.4 \times 10^{-5} \end{cases} \quad (10.54a)$$

$$(10.54b)$$

Then the circumferentially averaged Nusselt number was given by

$$\text{Nu} = \beta \cdot \text{Nu}_{\text{top}} + (1 - \beta) \text{Nu}_{\text{bot}} \quad (10.55)$$

Rosson and Myers compared their predicted values to their own experimental data for acetone and methanol, and the agreement was reasonable. A large number of scatter was inherent due to inaccuracies in their experimental techniques, so it is difficult to discern whether the deviations were due to theoretical deficiencies or experimental scatter.

Tien et al. (1988) presented an analysis for gravity-driven condensation that they proposed to be valid for stratified, wavy, and slug flow. Their analysis was similar to that of Rosson and Myers, although more deeply rooted in conservation equations than are empirically determined expressions. This analysis approaches the correct values in the asymptotic limits. That is, for a quality of zero it predicts a single-phase-liquid Nusselt number, and for situations where stratified flow exists rather than slug flow, it reduces to the form of Rosson and Myers. To use the Tien model, six simultaneous nonlinear equations must be solved. Although novel and well structured, the technique is probably too involved for a practical design correlation.

Dobson (1994), Dobson et al. (1994a,b), and Dobson and Chato (1998) developed correlations for wavy flows based primarily on their own data obtained with refrigerants. As the vapor velocities increase from very low values, the vapor shear causes an increase in the convective heat transfer in the pool at the bottom of the tube and it generates an axial velocity component in the condensate film at the top of the tube. The development of the correlation was guided by a combination of careful

data analysis and physical guidance from analytical solutions. The final correlation separates the heat transfer by film condensation in the upper part of the horizontal tube from the forced-convective heat transfer in the bottom pool:

$$\text{Nu} = \frac{0.23\text{Re}_{vo}^{0.12}}{1 + 1.11X_{tt}^{0.58}} \left(\frac{\text{Ga} \cdot \text{Pr}_l}{\text{Ja}_l} \right)^{0.25} + \left(1 - \frac{\theta_l}{\pi} \right) \text{Nu}_f \quad (10.56)$$

where θ_l is the angle subtended from the top of tube to the liquid level and

$$\text{Nu}_f = 0.0195\text{Re}_l^{0.8} \cdot \text{Pr}_l^{0.4} \sqrt{1.376 + \frac{C_1}{X_{tt}^{C_2}}} \quad (10.57)$$

For $0 < \text{Fr}_l < 0.7$,

$$C_1 = 4.172 + 5.48\text{Fr}_l - 1.564\text{Fr}_l^2 \quad (10.58a)$$

$$C_2 = 1.773 - 0.169\text{Fr}_l \quad (10.58b)$$

For $\text{Fr}_l > 0.7$,

$$C_1 = 7.242 \quad (10.59a)$$

$$C_2 = 1.655 \quad (10.59b)$$

where Fr_l is the liquid Froude number. Due to the 1.376 inside the radical of eq. (10.57), the correlation above matches the Dittus–Boelter single-phase correlation when $x = 0$.

If the area occupied by the thin condensate film is neglected, θ_l is geometrically related to the void fraction by

$$\alpha = \frac{\theta_l}{\pi} - \frac{\sin 2\theta_l}{2\pi} \quad (10.60)$$

If a void fraction model is assumed, this transcendental equation must be solved to obtain the desired quantity, θ_l . Jaster and Kosky (1976) deduced an approximate relationship which is much easier to use. In the context of the present topic, their simplification can be stated as

$$1 - \frac{\theta_l}{\pi} \simeq \frac{\arccos(2\alpha - 1)}{\pi} \quad (10.61)$$

The simplicity achieved by this assumption is well worth the modest errors associated with it. These errors are themselves mitigated by the fact that the forced-convective Nusselt number, by which the quantity in eq. (10.61) is multiplied, is normally considerably smaller than the filmwise Nusselt number. The void fraction correlation of Zivi (1964), eq. (10.50), was used with this correlation. Equation (10.56) is to be used when $G < 500 \text{ kg/s} \cdot \text{m}^2$ and $\text{Fr}_{so} < 20$. Even though the Dobson correlations yield reasonable results, available data suggest the need for further

development of heat transfer models in the wavy or wavy-annular regions at higher mass fluxes.

Shear-Driven Annular Flow Condensation The annular flow regime represents the situation where the interfacial shear stresses dominate and create a nearly symmetric annular film with a high-speed vapor core. A variety of approaches for predicting heat transfer during annular flow condensation have been developed. Although these approaches can be divided into many different categories, they can be reduced to three for the purposes of this review: two-phase multiplier approaches, shear-based approaches, and boundary layer approaches.

Two-Phase Multiplier Correlations The simplest method of heat transfer prediction in the annular flow regime is the two-phase multiplier approach. This approach was pioneered for predicting convective evaporation data by Denglor and Addoms (1956) and was adapted for condensation by Shah (1979). The theoretical hypothesis is that the heat transfer process in annular two-phase flow is similar to that in single-phase flow of the liquid (through which all the heat is transferred), and thus their ratio may be characterized by a two-phase multiplier. This reasoning is in fact very similar to that of Lockhart and Martinelli (1947), who pioneered the two-phase multiplier approach for predicting two-phase pressure drop. The single-phase heat transfer coefficients are typically predicted by modifications of the Dittus and Boelter (1930) correlation, which results in the form

$$\text{Nu} = 0.023\text{Re}_l^{0.8} \cdot \text{Pr}_l^m \cdot F \left(x, \frac{\rho_l}{\rho_g}, \frac{\mu_l}{\mu_g}, \text{Fr}_l \right) \quad (10.62)$$

where m is a constant between 0.3 and 0.4 and F is the two-phase multiplier. Although the two-phase multiplier can depend on more dimensionless groups than those indicated in eq. (10.62), the groups shown are the most relevant. The type of single-phase correlation shown is valid for turbulent flow and is based primarily on an analogy between heat and momentum transfer.

One of the most widely cited correlations of the two-phase multiplier type is that of Shah (1979). It was developed from his observation that the mechanisms of condensation and evaporation were very similar in the absence of nucleate boiling. With this idea, he set out to modify the convective component of his flow boiling correlation for use during condensation. The form of his correlation is

$$\text{Nu} = 0.023\text{Re}_l^{0.8} \cdot \text{Pr}_l^{0.4} \left[1 + \frac{3.8}{p_r^{0.38}} \left(\frac{x}{1-x} \right)^{0.76} \right] \quad (10.63)$$

The bracketed term is the two-phase multiplier. It properly approaches unity as x approaches 0, indicating that it predicts the single-phase liquid heat transfer coefficient when only liquid is present. As the reduced pressure is increased, the properties of the liquid and vapor become more alike and the two-phase multiplier decreases, as expected.

Cavallini and Zecchin (1974) used the results of a theoretical annular flow analysis to deduce the dimensionless groups that should be present in an annular flow correlation. They then used regression analysis to justify neglecting many of the groups that did not appear in their empirically developed correlation, which can be shown to be of the two-phase multiplier form by writing it in the following way:

$$\text{Nu} = 0.023\text{Re}_l^{0.8} \cdot \text{Pr}_l^{0.33} \left\{ 2.64 \left[1 + \left(\frac{\rho_l}{\rho_g} \right)^{0.5} \frac{x}{1-x} \right] \right\}^{0.8} \quad (10.64)$$

Here the bracketed term represents the two-phase multiplier.

The two-phase multiplier approach was selected for correlating the annular flow heat transfer data by Dobson (1994), Dobson et al. (1994a,b), and Dobson and Chato (1998). To make sure that the correlation was not biased by data outside the annular flow regime, only data with $\text{Fr}_{\text{so}} > 20$ were used to develop the correlation. This value was reported by Dobson (1994) to provide a good indicator of the transition from wavy-annular to annular flow and agreed well with the data from his study. The correlation developed was

$$\text{Nu} = 0.023\text{Re}_l^{0.8} \cdot \text{Pr}_l^{0.4} \left(1 + \frac{2.22}{X_{tt}^{0.89}} \right) \quad (10.65)$$

This form utilizes the single-phase heat transfer correlation of Dittus–Boelter (1930) with a Prandtl exponent of 0.4. At a quality of zero, the Lockhart–Martinelli parameter approaches infinity and eq. (10.65) becomes the single-phase liquid Nusselt number. This correlation is to be used for $G \geq 500 \text{ kg/s} \cdot \text{m}^2$ or for all mass fluxes if $\text{Fr}_{\text{so}} > 20$.

Shear-Based Correlations The use of shear-based correlations for annular flow condensation dates back to the early work of Carpenter and Colburn (1951). They argued that the resistance to heat transfer in the turbulent liquid flow was entirely inside the laminar sublayer and that the wall shear stress was composed of additive components due to friction, acceleration, and gravity. Although it was later pointed out by Soliman et al. (1968) that their equation for the accelerational shear component was incorrect, the framework that they established at a relatively early point in the history of forced-convective condensation remains useful.

Soliman et al. (1968) utilized the framework established by Carpenter and Colburn to develop their own semiempirical heat transfer correlation for annular flow. Neglecting the gravitational term (which is appropriate for horizontal flow), the Soliman correlation can be written as

$$\text{Nu} = 0.036\text{Re}_{lo} \cdot \text{Pr}_l^{0.65} \left(\frac{\rho_l}{\rho_g} \right)^{0.5} \sqrt{\frac{2(0.046)x^2}{\text{Re}_g^{0.2}} \phi_g^2 + \text{Bo} \sum_{n=1}^5 a_n \left(\frac{\rho_g}{\rho_l} \right)^{n/3}} \quad (10.66a)$$

where

$$a_1 = x(2 - \gamma) - 1 \quad (10.66b)$$

$$a_2 = 2(1 - x) \quad (10.66c)$$

$$a_3 = 2(\gamma - 1)(x - 1) \quad (10.66d)$$

$$a_4 = \frac{1}{x} - 3 + 2x \quad (10.66e)$$

$$a_5 = \gamma \left(2 - \frac{1}{x} - x \right) \quad (10.66f)$$

$$\gamma = \frac{\text{interface velocity}}{\text{mean film velocity}} = 1.25 \text{ for turbulent liquid} \quad (10.66g)$$

Soliman et al. (1968) compared the predictions of their correlation to data for steam, R-113, R-22, ethanol, methanol, toluene, and trichloroethylene. The agreement was correct in trend, although even on log-log axes the deviations appear quite large. No statistical information regarding deviations was given.

Chen et al. (1987) developed a generalized correlation for vertical flow condensation, which included several effects combined with an asymptotic model. They stated, as did Carey (1992), that their correlation for the shear-dominated regime was also appropriate for horizontal flow but made no comparison with horizontal flow data. Their correlation use the general form of Soliman et al. (1968), but the acceleration terms were neglected and the pressure drop model was replaced by one from Dukler (1960). The final result for the average modified Nusselt number is given in what follows in the discussion of flows in vertical channels, eq. (10.79).

Boundary Layer Correlation The most theoretical correlation, based on boundary layer considerations, is that of Traviss et al. (1973). Under its rather stringent assumptions, this method provides an analytical prediction of the Nusselt number. Before a pressure drop model is assumed, the correlation can be written as

$$\text{Nu} = \frac{D^+ \cdot \text{Pr}_l}{F_2(\text{Re}_l, \text{Pr}_l)} \quad (10.67)$$

The term D^+ is the tube diameter scaled by the turbulent length scale, $\mu_l / \sqrt{\tau_w \rho_l}$. A simple force balance indicates the proportionality between the wall shear and the pressure drop, establishing the fact that the annular flow Nusselt number is proportional to the square root of the pressure drop per unit length.

The denominator of eq. (10.67), F_2 , can be thought of as a dimensionless heat transfer resistance. Guidance as to its evaluation is given in eq. (10.69). Physically, this resistance increases as the dimensionless film thickness increases, as would be expected from conduction arguments. A plot of F_2 versus Re_l for various values of Pr_l shows that as Re_l increases from 0 to 1125 (the value where the fully turbulent region begins), F_2 increases very rapidly. As Re_l is increased further, F_2 increases much more slowly. Physically, this occurs because the primary resistance to heat transfer is contained in the laminar sublayer and buffer regions.

Although the Traviss et al. (1973) analysis was performed after the advent of the simple shear-based correlations, it provides a useful method for understanding them. For relatively small changes in Re_l when $Re_l > 1125$, one could reasonably assume a constant value of F_2 at a fixed Prandtl number. If the Prandtl number dependence could be expressed as a power law function, the Nusselt number could then be expressed as

$$Nu = a D^+ \cdot Pr_l^m \quad (10.68)$$

where a is a constant. This is exactly the form of the original shear-based correlation of Carpenter and Colburn (1951). Thus, these correlations are justified for a narrow range of conditions by the more theoretically sound analysis of Traviss et al. (1973).

Only a few manipulations are required to show the equivalence between the Traviss analysis and the two-phase-multiplier approach. The first important observation is that annular flow is seldom encountered for liquid Reynolds numbers less than 1125. Using the criterion for annular flow that $Fr_{so} = 18$ [eqs. (10.40a,b)], the corresponding equation was solved for the quality above which annular flow could exist with $Re_l = 1125$. The results indicated that the liquid film is seldom so thin that the fully turbulent region is not reached; thus the piecewise definition of F_2 is seldom necessary and its value can be well approximated by the function

$$F_2 \simeq 10.25 Re_l^{0.0605} \cdot Pr_l^{0.592} \quad (10.69)$$

If this approximation is used in eq. (10.68) and D^+ is evaluated with a pressure drop correlation using Lockhart and Martinelli's two-phase liquid multiplier approach, the following equation is obtained for the Nusselt number:

$$Nu = 0.0194 Re_l^{0.815} \cdot Pr_l^{0.408} \phi_l^2(X_{tt}) \quad (10.70)$$

This is identical in form, and close in value, to the commonly used two-phase multiplier correlations, such as eq. (10.63).

Comparison of Heat Transfer Correlations The following comparisons were developed by Dobson (1994), Dobson et al. (1994a,b), and Dobson and Chato (1998). Details may be obtained from these publications.

Gravity-Dominated Correlations Chato's correlation was developed for stratified flow and was recommended for use at vapor Reynolds numbers of less than 35,000, that is, at low mass fluxes in the stratified flow regime. It was compared with 210 experimental data points that met this criterion and had a mean deviation of 12.8%.

The range of applicability of the Jaster and Kosky (1976) correlation is specified by an upper limit of a dimensionless wall shear. The mean deviation between the 213 experimental points that met this criterion and the values predicted was 14.5%, slightly higher than for the simpler Chato (1962) correlation. Although the deviations between the Jaster and Kosky correlation and the present data were sometimes large,

the mean deviation of 14.5% was substantially better than the 37% standard deviation of their own data.

The correlations of Chato and Jaster and Kosky were both able to predict most of the experimental data for the wavy flow regime within a range of $\pm 25\%$. Chato's analysis implies an essentially constant void fraction which is independent of quality. Jaster and Kosky's correlation does not predict the variation with quality accurately. Neither accounted for heat transfer in the bottom of the liquid pool. For low mass fluxes, this approach is reasonable.

Because no guidelines were given for use of the Rosson and Myers (1965) correlation, it was compared against the full database of points that were later used to develop the wavy flow correlation. Although Rosson and Myers attempted to account for forced-convective condensation in the liquid pool at the bottom of the tube, their correlation was actually a poor predictor of the experimental data. The correlation had a mean deviation of 21.3% from the experimental data, almost 10% worse than the simpler Chato or Jaster and Kosky correlations. The most problematic part of the correlation seemed to be the prediction of the parameter β , which represents the fraction of the tube circumference occupied by filmwise condensation. At low mass fluxes, this parameter should clearly be related to the void fraction and approach unity as the quality approaches unity. However, the empirical expressions developed by Rosson and Myers do not behave in this manner. The trends were very erratic, particularly for mass fluxes over $25 \text{ kg/s} \cdot \text{m}^2$, where the relationship was not even monotonic.

Annular Flow Correlations The annular flow correlations that were selected for comparison with the experimental data encompass at least one member of each of the three broad classes: two-phase multiplier correlations (Shah, 1979; Cavallini and Zecchin, 1974; Dobson, 1994), shear-based correlations (Chen et al., 1987) and boundary layer analyses (Traviss et al., 1973).

Of the five correlations, Shah's and Dobson's came with specific guidelines for a lower limit of applicability. The Shah correlation should not be used at mass fluxes where the vapor velocity with $x = 1$ was less than 3 m/s. In all cases this represents a vapor velocity well above the wavy-to-annular transition line on the Taitel-Dukler map. This criterion was selected for each of the correlations, so that they would be compared on an equal basis.

The predictions of the Shah correlation agree fairly well with the data, with a mean deviation of 9.1%. Nearly all the data were predicted within $\pm 25\%$. The most significant deviations occurred for some low Nusselt number data that were in the wavy-annular flow regime, and for some very high-mass-flux, high-quality data. In general, the Shah correlation underpredicted the experimental data.

The mean deviation of the Cavallini and Zecchin correlation from the experimental data was 11.6%, slightly higher than that of the Shah correlation. Despite the slightly higher mean deviation, though, the predictions of the Cavallini and Zecchin correlation were more correct in trend than those of the Shah correlation. When the Cavallini and Zecchin correlation was in error, it tended to overpredict the experimental data. The largest errors occurred at low qualities because this correlation approaches a value of 2.18 times the single-phase Nusselt number at a quality of zero.

The mean deviation of the Traviss correlation was 11.8%, slightly higher than the Cavallini and Zecchin correlation. The Traviss correlation tended to overpredict the experimental data, particularly at high qualities, where their empirical correction was used. Without this correction, their correlation would have underpredicted the high-quality data.

The Chen correlation was the worst predictor of the annular flow data, with a mean deviation of 23.3%. This correlation significantly underpredicted nearly all the data. The correlation of Soliman (1968) generally predicts lower Nusselt numbers than the Chen correlation. Thus, it would have performed even worse against the data of Dobson.

The mean deviation of Dobson's wavy flow correlation, eq. (10.56), from his experimental data was 6.6%. The mean deviation of his annular flow correlation, eq. (10.65), was 4.5%. The maximum mean deviation of both of these correlations from other experimental data in the literature was 13.7%.

One problem with the annular flow correlations that is not apparent in a plot of experimental versus predicted Nusselt numbers concerns their range of applicability. The Nusselt numbers were well above the annular flow predictions at low qualities. As the quality reached about 70% and the flow pattern became fully annular, the predictions of the Cavallini and Zecchin correlation agreed very well with the experimental data. These data suggest the need for further development of heat transfer models in the wavy or wavy-annular regions at higher mass fluxes. Recently, Cavallini et al. (2002) suggested a set of correlations for annular, stratified, and slug flow which provide better results for high pressure refrigerants.

10.6.4 Pressure Drop

The discussion of pressure drop could take up a chapter of its own. Here only one representative method is given. The pressure drop ΔP in a tube is caused by friction and by the acceleration due to phase change. Souza et al. (1992, 1993) developed an expression for the total pressure drop in a short section Δz in which the quality can be considered constant at a mean value:

$$-\Delta P = \frac{2f_{lo}G^2}{\rho_l D} \phi_{lo}^2 \Delta z + G^2 \left\{ \left[\frac{x_o^2}{\rho_g \alpha_o} + \frac{(1-x_o)^2}{\rho_l(1-\alpha_o)} \right] - \left[\frac{x_i^2}{\rho_g \alpha_i} + \frac{(1-x_i)^2}{\rho_l(1-\alpha_i)} \right] \right\} \quad (10.71)$$

where

$$f_{lo} = 0.0791 \text{Re}_{lo}^{-0.25} \quad (10.72)$$

$$\phi_{lo}^2 = \left(1.376 + \frac{C_1}{X_{tt}^{C_2}} \right) (1-x)^{1.75} \quad (10.73a)$$

C_1 and C_2 are given in eqs. (10.58) and (10.59)

Souza and Pimenta (1995) developed another correlation:

$$\phi_{lo}^2 = 1 + (\Gamma - 1)x^{1.75} (1 + 0.952\Gamma X_{tt}^{0.4126}) \quad (10.73b)$$

$$\Gamma = \left(\frac{\rho_l}{\rho_g} \right)^{0.5} \left(\frac{\mu_g}{\mu_l} \right)^{0.125} \quad (10.73c)$$

Other pressure drop correlations were suggested by Friedel (1979) and Jung and Rademacher (1989), but neither one produced more accurate predictions than Souza's. Cavallini et al. (2002) proposed a correlation that better predicted the pressure drops for high pressure refrigerants.

10.6.5 Effects of Oil

Oil in the refrigerant decreases the heat transfer and increases the pressure drop. Gaibel et al. (1994) discussed these effects. He found that for oil mass fractions $\omega_o < 0.05$, the correction factor developed by Schlager et al. (1990) gave acceptable values for the Nusselt number with oil (Nu_o) when applied to the Dobson correlations (Nu) [eqs. (10.56) and (10.65)]:

$$Nu_o = Nu \cdot e^{-3.2\omega_o} \quad (10.74)$$

For the pressure drop with oil (ΔP_o), the Souza et al. (1992, 1993) correction factor applied to the pure refrigerant pressure drop (ΔP_p) was found acceptable in the same oil concentration range:

$$\Delta P_o = \Delta P_p (1 + 12.4\omega_o - 110.8\omega_o^2) \quad (10.75)$$

10.6.6 Condensation of Zeotropes

Sweeney (1996) and Sweeney and Chato (1996) correlated the data of Kenney et al. (1994) obtained with Refrigerant 407c, a zeotropic mixture of R-32, R-125, and R-134a (23, 25, and 52% by mass), in a smooth tube. They found that the Nusselt numbers for zeotropic mixtures (Nu_m) could be predicted by the following simple modification of the Dobson correlation (Nu) [eq. (10.65)] for the annular flow regime:

$$Nu_m = 0.7 \left(\frac{G}{300} \right)^{0.3} \cdot Nu \quad (10.76)$$

For the wavy regime, the mixture Nusselt number is obtained by a similar modification of the Dobson correlation (Nu) [eq. (10.56)]:

$$Nu_m = \left(\frac{G}{300} \right)^{0.3} \cdot Nu \quad (10.77)$$

where the mass flux G is in $\text{kg/s} \cdot \text{m}^2$. These correlations cannot be assumed to be generally applicable to zeotropes without additional data on other zeotropes, but they do indicate that the equations represent the underlying physical phenomena well.

10.6.7 Inclined and Vertical Tubes

Inclining the tube from the horizontal will affect only the gravity-dominated flows, (i.e., stratified and wavy patterns) significantly. For the shear-dominated annular flows, the correlations are essentially independent of tube orientation. Chato (1960) studied both analytically and experimentally the effects of a downward inclination of a condenser tube with stratified flows. He found improvement in the heat transfer up to about a 15° inclination, caused by the reduction in depth of the bottom condensate pool. However, this improvement decreases at increasing angles as the vertical orientation is approached because of the thickening of the condensate layer on the wall as it traverses longer distances before reaching the bottom pool. It can be shown from eqs. (10.43) and (10.48) that if the L/D ratio of the tube is greater than 8.3, the horizontal tube will have better heat transfer. It is obvious that an upward inclination of the tube is counterproductive because gravity will retard the liquid flow, reducing the heat transfer.

Chen et al. (1987) analyzed annular film condensation in a vertical tube and proposed the following approximate correlation for the average Nusselt number for complete condensation in the tube:

$$\overline{\text{Nu}}_d = \left(\text{Re}_T^{-0.44} + \frac{\text{Re}_T^{0.8} \cdot \text{Pr}_l^{1.3}}{1.718 \times 10^5} + \frac{C \cdot \text{Pr}_l^{1.3} \cdot \text{Re}_T^{1.8}}{2075.3} \right)^{0.5} \quad (10.78)$$

where

$$\overline{\text{Nu}}_d = \frac{\bar{h}_T}{k_l} \left(\frac{v_l^2}{g} \right)^{1/3} \quad \text{Re}_T = \frac{4m}{\mu_l \pi D}$$

$$C = \frac{0.252 \mu_l^{1.177} \mu_g^{0.156}}{D^2 g^{0.667} \rho_l^{0.553} \rho_g^{0.78}} \quad (\text{dimensionless})$$

Chen et al., contended that similar derivations can be applied to horizontal annular flows with the following result:

$$\overline{\text{Nu}}_d = 0.022 \sqrt{C} \cdot \text{Pr}_l^{0.65} \cdot \text{Re}_T^{0.9} \quad (10.79)$$

However, they did not verify this correlation with comparisons to experimental data. By the same argument, it can be suggested that the Dobson (1994) correlation of eq. (10.65) can be used for vertical, downward flow tubes at high mass fluxes. Although condensation in upward flow is worse than in horizontal or downward flow, it does occur in reflux condensers. Chen et al. (1987) treated this case in some detail.

10.7 ENHANCED IN-TUBE CONDENSATION

10.7.1 Microfin Tubes

Most evaporators and condensers of new unitary refrigeration and air-conditioning equipment are manufactured with microfin tubes. The microfin tube dominates unitary equipment design because it provides the highest heat transfer with the lowest pressure drop of the commercially available internal enhancements (Webb, 1994). Cavallini et al. (2000) quotes an 80 to 180% heat transfer enhancement over an equivalent smooth tube with a relatively modest 20 to 80% increase in pressure drop. Together, R-134a, R-22, and replacements for R-22 constitute by mass nearly all the refrigerants used in unitary products (Muir, 1989). As a result, much of the predictive development for convective condensation in microfin tubes has been focused on R-134a, R-22, and replacements for R-22.

Figure 10.14 shows the cross section and characteristic dimensions of a microfin tube. The outside diameter (D_o) of commercially available microfin tubes ranges from 4 to 15 mm. The root diameter (D_r) is depicted in Fig. 10.14. Microfin tubes

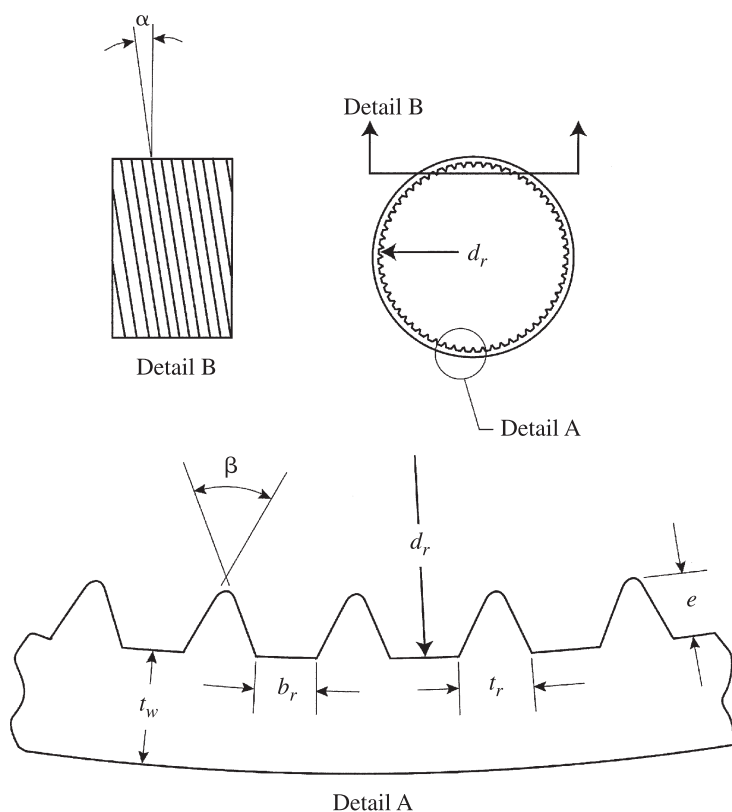


Figure 10.14 Cross section of microfin tube.

typically have 30 to 80 trapezoidal fins that spiral down the tube axis with a helix angle (α) between 6 and 30°. The fin height (e) ranges between 0.1 and 0.25 mm, which is approximately less than $0.04D_o$. The fin apex angle β varies from 20 to 60° for commercial microfin tubes, where most are close to the middle of this range.

Several factors are responsible for the passive enhancement of condensation in microfin tubes. First, the fins provide additional heat transfer area over that of a smooth tube of the same cross-sectional flow area. The fins add in the range of 50% more surface area per tube length. Surface tension is another mechanism that can act to thin the film on the fin tips for very high vapor qualities and low mass velocities. Yang and Webb (1997) have modeled surface tension effects on the fin and vapor shear effects for small-diameter extruded aluminum tubes with microgrooves. Swirl effects due to the riffling of the fins along the tube axis may improve heat transfer for certain operating conditions. Finally, the fins enhance heat transfer as a roughness would in the mixing of the flow at the wall.

Currently, the prediction of convective condensation heat transfer in microfin tubes is handicapped by the lack of flow pattern maps for microfin tubes. Consequently, correlations and models that presently exist for the prediction of the condensation heat transfer and pressure drop in microfin tubes do not use them. Cavallini et al. (2000) provides an excellent review of predictive correlations/models for flow condensation in microfin tubes. Cavallini et al. (2000) shows that the models of Cavallini et al. (1993, 1995), Yu and Koyama (1998), and Kedzierski and Goncalves (1999) produce similar results for various tube geometries and mass fluxes. The Kedzierski and Goncalves (1999) model is presented here because it has the simplest form and is based on the largest number of data points.

Although the Kedzierski and Goncalves (1999) model is based on 1489 data points, this data set was for the same tube geometry. The hydraulic diameter concept was used to generalize the correlation to other microfin true geometries. The hydraulic diameter of the microfin tube is defined as

$$D_h = \frac{4A_c \cos \alpha}{N_f S} \quad (10.80)$$

where S is the perimeter of one fin and channel taken perpendicular to the axis of the fin, N_f the number of fins, A_c the cross-sectional flow area, and α the helix angle of the fin. Equation (10.80) was used to derive an expression for the hydraulic diameter for the geometry given in Fig. 10.14:

$$D_h = \frac{(\pi D_r^2 - 2N_f t_b e) \cos \alpha}{N_f [b_r + 2e / \cos(\beta/2)]} \quad (10.81)$$

The local Nusselt number (Nu) was calculated based on the actual inner surface area of the tube as

$$Nu = \frac{h_{2\phi} D_h}{k_l} \quad (10.82)$$

The convective–condensation Nusselt numbers (Nu) were correlated following the law of corresponding states philosophy presented by Cooper (1984). Cooper suggested that the fluid properties that govern nucleate pool boiling can be well represented by a product of the reduced pressure (P_r/P_c), the modified acentric factor $[-\log_{10}(P_r/P_c)]$, and other dimensionless variables to various powers. The above reduced-pressure terms and several other locally evaluated terms were used to correlate locally measured convective condensation Nusselt number for the microfin tube:

$$\text{Nu} = \frac{h_{2\phi} D_h}{k_l} = 2.256 \text{Re}_{lo}^{\beta_1} \cdot \text{Ja}^{\beta_2} \cdot \text{Pr}_l^{\beta_3} \left(\frac{P_r}{P_c} \right)^{\beta_4} \left(-\log_{10} \frac{P_r}{P_c} \right)^{\beta_5} \cdot \text{Sv}^{\beta_6} \quad (10.83)$$

where

$$\begin{aligned} \beta_1 &= 0.303 & \beta_2 &= -0.232x_q & \beta_3 &= 0.393 \\ \beta_4 &= -0.578x_q^2 & \beta_5 &= -0.474x_q^2 & \beta_6 &= 2.531x_q \end{aligned}$$

and the ranges for which the correlation holds are

$$\begin{aligned} 3500 &\leq \text{Re}_{lo} = \frac{G_T D_h}{\mu_l} \leq 24,000 \\ 0.004 &\leq \text{Ja} = \frac{c_{pl}(T_{\text{sat}} - T_w)}{\lambda} \leq 0.16 \\ 1.7 &\leq \text{Pr}_l = \frac{c_{pl}\mu_l}{k_l} \leq 3.6 \\ 0.86 &\leq \text{Sv} = \frac{v_g - v_l}{v} \leq 10.3 \\ 0.22 &\leq \frac{P_r}{P_c} \leq 0.62 \\ 0.06 &\leq x_q \leq 1.0 \end{aligned}$$

where the liquid only Reynolds number (Re_{lo}), the Jakob number (Ja), the liquid Prandtl number (Pr_l), the reduced pressure (P_r/P_c), the dimensionless specific volume (Sv) and the quality (x_q) are all evaluated locally at the saturated condition. The Reynolds number is based on the total mass velocity (G_T).

10.7.2 Microfin Tube Pressure Drop

Kedzierski and Goncalves (1999) fitted Fanning friction factor (f_r) data for a 60-fin, 8.91-mm-root-diameter microfin tube to the equation

$$f = 0.00228 \text{Re}_{lo}^{-0.062} \Phi^{0.211} \left(3500 \leq \text{Re}_{lo} = \frac{G_T D_h}{\mu_l} \leq 24,000 \right) \quad (10.84)$$

The exponent on the two-phase number ($\Phi = \Delta x_q \lambda / \Delta L_g$) given in eq. (10.84), 0.211, is consistent with that given by Pierre (1964): 0.24. However, the exponent on the Reynolds number, -0.062 , is very different from that given by Pierre (1964): -0.24 . The exponent on the Reynolds number of eq. (10.84) is approximately equivalent to -0.06 which is the exponent that one would calculate from the transition zone of the Moody (1944) chart using the fin height (0.2 mm) for the roughness height.

The fact that the Reynolds number exponent is consistent with that obtained from the Moody (1944) chart suggests that the fins of a microfin tube act like a roughness to enhance the convective condensation heat transfer. If roughness mixing dominates the enhancement mechanism, neither swirl effects nor surface tension drainage have much influence on the heat transfer. The lack of importance of surface tension and swirl flow may be a consequence of the flow conditions and surface geometry.

The corroboration between the present Re exponent and Moody's (1944) also suggests that the frictional pressure drop of microfin tubes should depend on the fin height/root-tube diameter (e/D_i) ratio. If it is assumed that the fins act purely as a roughness, the Moody (1944) chart can be used to interpolate between the foregoing friction factor equation and Pierre's (1964) smooth tube friction factor for a given e/D_i ratio as follows:

$$f = \left[0.002275 + 0.00933 \exp \left(\frac{e/D_i}{-0.003} \right) \right] \text{Re}_{lo}^{-1/4.16+532(e/D_i)} \Phi^{0.211} \quad (10.85)$$

The pressure-drop equation for which eqs. (10.84) and (10.85) are valid is

$$\Delta P = \left[\frac{f(v_o + v_i) \Delta L}{D_h} + (v_o - v_i) \right] G_T^2 \quad (10.86)$$

where v_o and v_i are the specific volumes of the exiting and entering flows, respectively, while G_T is the total mass velocity of the flow.

10.7.3 Twisted-Tape Inserts

Twisted-tape inserts have been used to enhance heat transfer since the nineteenth century. Marine steam boilers were fitted with *retarders* (twisted tapes) to reduce coal consumption. Royal and Bergles (1978) surveyed horizontal convective condensation with twisted tapes and found improvements in heat transfer coefficients by as much as 30% over empty tube condensation. In addition, the most popular use of twisted tapes in flow boiling is to delay the occurrence of burnout.

Figure 10.15 shows a schematic of a twisted-tape insert in a tube. The flow enhancement of the twisted tape arises primarily from increased flow path length and swirl mixing. Swirl flow and increased path length are also expected to benefit two-phase heat transfer. Manglik and Bergles (1992) suggest that swirl flow effects may be correlated by the swirl parameter Sw:

$$\text{Sw} = \frac{\text{Re}_s}{\sqrt{y}} = \frac{\text{Re}_D}{\sqrt{y}} \frac{\sqrt{1 + (\pi/2y)^2}}{1 - 4\delta/\pi D_i} \quad (10.87)$$

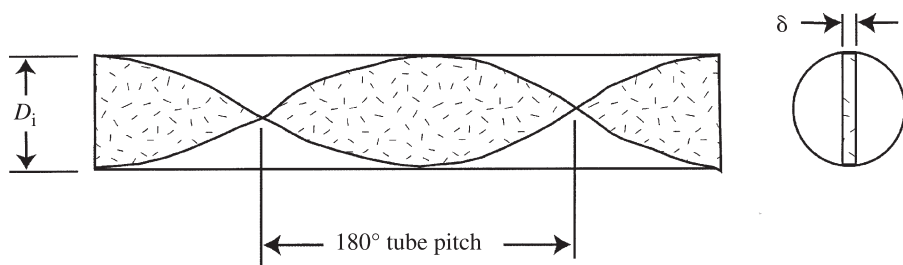


Figure 10.15 Cross section of twisted-tape insert in a tube.

where Re_D is the all-liquid empty-tube Reynolds number based on liquid properties $G_T D_i / \mu_l$, and y is the twist ratio of the tape. The twist ratio is defined as the ratio of the 180° twist pitch normalized by the internal diameter of the tube, D_i . The thickness of the tape is δ .

The $1/\sqrt{y}$ parameter accounts for convective inertia effects that are ignored by $1/y$, which has been used traditionally to correlate swirl flow data. Manglik and Bergles (1992) show that laminar flow heat transfer for three different twist ratios are correlated well with the swirl parameter. Agrawal et al. (1986) also correlated R-12 swirl flow boiling heat transfer coefficients to $y^{-0.5219}$ for Re_D approximately in the range 7000 to 14,000. Consequently, it is inferred that the $1/\sqrt{y}$ parameter is suitable for correlating flow boiling and convective condensation data for low and somewhat high Reynolds numbers.

Kedzierski and Kim (1998) correlated 2253 locally measured convective condensation Nusselt numbers for refrigerants R-12, R-22, R-152a, R-134a, R-290, R-290/R-134a, R-134a/R-600a, R-32/R-134a, and R-32/R-152a with a $y = 4.15$ twisted tape to the following equation:

$$Nu = 0.00136 Sw^{\alpha_1} \cdot Pr_l^{\alpha_2} \cdot P_r^{\alpha_3} (-\log_{10} P_r)^{\alpha_4} \cdot Ja^{\alpha_5} \quad (10.88)$$

where

$$\begin{aligned} \alpha_1 &= 0.613 + 0.647x_q & \alpha_2 &= 0.877 & \alpha_3 &= -1.735 + 2.362x_q \\ \alpha_4 &= -2.815 + 4.197x_q & \alpha_5 &= -0.528, \end{aligned}$$

and the ranges for which the correlation holds are

$$2200 \leq Sw \leq 18,000$$

$$0.14 \leq P_r = \frac{P}{P_c} \leq 3.6$$

$$2.4 \leq Pr_l = \frac{c_{p,l} \mu_l}{k_l} \leq 3.6$$

$$0.008 \leq \text{Ja} = \frac{c_{p,l}(T_{\text{sat}} - T_w)}{\lambda} \leq 0.1$$

$$0.023 \leq x_q \leq 0.9$$

Equation (10.88) correlated 95% of all the condensation Nusselt numbers to within approximately $\pm 20\%$ for R-12, R-22, R-152a, R-134a, R-290, R-290/R-134a, R-134a/R-600a, R-32/R-134a, and R-32/R-152a. The single equation was found to predict single-component and zeotropic Nusselt numbers equally well. This suggests that mass transfer has a negligible effect on condensation heat transfer with twisted-tape inserts for the low relatively temperature glide mixtures R-32/R-134a and R-32/R-152a. The intention of the swirl parameter is to generalize the correlation to other twist ratios, but this aspect of the correlation has not been validated.

10.8 FILM CONDENSATION ON TUBE BUNDLES

In this section we address how to size or rate multitube condensers using the prediction methods already discussed in this and earlier chapters. These prediction methods and most published data apply for a single tube. With large condensers, which sometimes contain many thousands of tubes, other factors must be considered because they can drastically reduce the performance compared to the single-tube results. The four major issues that adversely affect the condensor performance are (1) maldistribution of the shell-side and tube-side fluids, (2) shell-side condensate inundation (condensate from adjacent tubes), (3) saturation-temperature depression due to the vapor pressure drop, and (4) noncondensable gases.

Both shell-side and tube-side condensations are addressed. The common characteristics of most shell-side condensations are horizontal tubes, single-component shell-side condensation (limited inlet noncondensable gases), and either tube-side forced convection or in-tube evaporation. The vapor generally flows downward in crossflow to the tube bundle. This configuration, called an *X shell* (Fig. 10.16), is the most common, especially if the shell-side pressure drop can affect the thermal per-

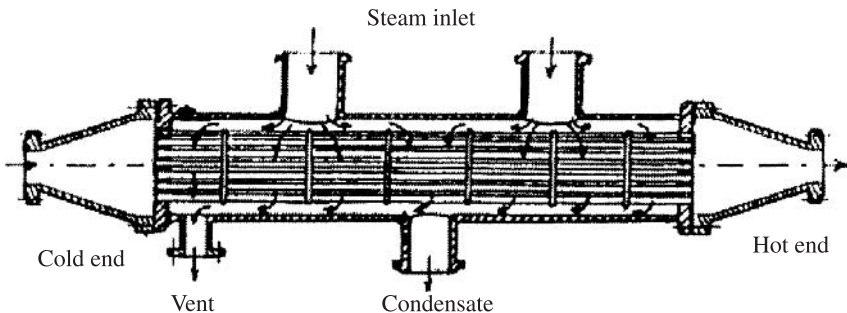


Figure 10.16 Longitudinal view of a typical X-shell condenser.

formance negatively because of the saturation temperature depression. For tube-side condensation, the discussion is restricted to the crossflow configuration. This design type is commonly used for all gas-cooled condensers.

10.8.1 X-Shell Condensers (Shell-Side Condensation)

Consider first the adverse effects of tube-side flow and temperature maldistributions on X-shell condensers. Next, a discussion of different condenser rating methods dealing with the other above-mentioned adverse bundle effects is presented. Some final comments are given regarding good noncondensable gas management and venting practices.

Tube-Side Flow and Temperature Maldistribution The major cause of tube-side flow maldistribution is a poor design of the inlet header. Flow variations (maximum/minimum flow rates per tubes) as much about 1.5 were measured by Gotoda and Izumi (1977). They also supplied an equation to estimate the velocity maldistribution:

$$\left(\frac{u_{g,\max}}{u_{g,\text{av}}}\right)^2 = 1 + \frac{1}{K_t} \left[\left(\frac{A_{\text{tube}}}{A_{\text{pipe}}}\right)^2 - \left(\frac{A_{\text{tube}}}{A_{\text{plate}}}\right)^2 \right] \quad (10.89)$$

where $u_{g,\max}$ is the maximum velocity; $u_{g,\text{av}}$ is the average or mean velocity; A_{tube} is the total inside cross-sectional area or $n_t(\pi/4)D_i^2$, n being the number of tubes and D_i the inside tube diameter; A_{pipe} is the nozzle or pipe cross-sectional area; A_{plate} is the inside area of the tube sheet; and K_t is the total loss coefficient. This coefficient is calculated with the equation

$$K_t = K_{\text{ent}} + K_{\text{ext}} + K_{\text{box}} + \frac{fL}{D_i} \quad (10.90)$$

where K_{ent} is the tube entrance loss, K_{ext} is the tube exit loss, K_{box} is the box loss, f is the friction factor, and L is the tube length. Note that the maldistribution, $u_{g,\max}/u_{g,\text{av}}$, decreases as the loss coefficient increases. Rabas (1985a) showed that only a 10% reduction of the outside condensing coefficient occurred with a $u_{g,\max}/u_{g,\text{av}}$ value of 1.66. With a $u_{g,\max}/u_{g,\text{av}}$ value of 1.22, only a 1% reduction occurred for different lengths, nozzle angles, and condensing vapors. The simple calculation of $u_{g,\max}/u_{g,\text{av}}$ will quickly determine if tube-side distribution is an important consideration.

A nonuniform inlet temperature distribution can exist for some X-shell condenser applications, such as the multistage flash evaporators used in the desalination industry and the multistage condensers sometime used in power plants. For both applications, the overall tube length is divided into stages with partitions perpendicular to the tube axis. Each stage operates at different pressure levels. The outlet temperature distribution of the lower-temperature stage is the inlet temperature of the higher-temperature stage; hence, a nonuniform inlet temperature distribution is obtained. Rabas (1987a) showed that these typical nonuniform temperature distributions have almost no effect on the thermal performance.

Condenser Sizing Methods We still need to consider the adverse effects of condensate inundation, noncondensable gas pockets, and the saturation temperature depression on the performance of X-shell condensers. There are three methods that are used to size and/or rate these condensers: (1) vertical row-number correction, (2) bundle-factor method, and (3) pointwise or numerical computer programs. Both the vertical row-number and bundle-factor methods use a single evaluation of the overall heat transfer coefficient using the standard summation of the separate heat transfer resistances. The major uncertainty in the calculation is the average, outside condensing heat transfer coefficient, $h_{o,av}$.

Vertical Row-Number Method The vertical row-number method is commonly used to size and rate small condensers (tube counts less than about 2000) with limited inlet concentrations of noncondensable gases. For small condensers, shell-side maldistribution and saturation temperature depression normally are not important considerations. A correction is made to the outside single-tube condensing coefficient to account only for the condensate loading or inundation for the additional tubes within the bundle:

$$h_{o,av} = f(n_t)h_{o,Nus} \quad (10.91)$$

where $h_{o,Nus}$, the outside condensing coefficient, is predicted with the single-tube Nusselt equation or eq. (10.12) and $f(n_t)$ is the bundle vertical row-number correction, an empirical function of the number of tubes in a vertical row. Some $f(n_t)$, expressions are

$$f(n_t) = \begin{cases} \left(\frac{1}{n_t}\right)^{0.25} & \text{Jakob (1949)} & (10.92a) \\ \left(\frac{1}{n_t}\right)^{0.1667} & \text{Kern (1958)} & (10.92b) \\ 0.6 + 0.4353 \left(\frac{1}{n_t}\right)^{0.2} & \text{Eissenberg (1974)} & (10.92c) \end{cases}$$

Marto (1984) compared these predictions with a broad range of these results and found that the data fell between the Eissenberg and Jakob (commonly referred to as Nusselt) predictions, the latter being the most conservative.

Before using the correction method, an estimate of the shell-side pressure drop is recommended to determine if the saturation temperature depression can be ignored. This estimate can be made based on the following assumptions:

1. The inlet velocity $u_{g,i}$ is uniform and can be calculated with the continuity equation ($m_{g,i} = \rho_g w L u_{g,i}$), where $m_{g,i}$ is the inlet vapor flow rate, L the tube length between the tube sheets, and w the minimum free-flow width for the top transverse row of the bundle.

2. The single-phase crossflow pressure-drop prediction methods and friction-factor correlations applies and the Reynolds number can be calculated based on $u_{g,i}/2$.
3. The distance of travel is the bundle depth, the distance between the top and bottom tube rows.
4. The velocity varies in a linear manner as the vapor flows through the bundle (a one-third reduction in the pressure drop or ΔP prediction evaluated using $u_{g,i}$ as the velocity value).

No concern is needed if the saturation depression, ΔT_{sat} , based on this ΔP value is small with respect to temperature difference between the inlet vapor and coolant temperatures. This simplistic approach was found to yield reasonable estimates for most feedwater heaters, some very small power plant condensers, and some condensers in smaller multistage flash evaporators.

The other restriction on the use of the row-correction method is that the noncondensable gases will not affect the performance significantly. Rabas and Mueller (1986) showed that noncondensable gases will not have a measurable impact if the mass ratio $m_{g,i}/m_{a,i}$ is greater than 1000, where $m_{g,i}$ is the vapor inlet flow rate and $m_{a,i}$ is the inlet noncondensable flow rate.

Bundle Factor Method The bundle factor method is very similar to the vertical row-number correction except that the correct factor now contains some corrections for noncondensable gas and the saturation temperature depression. It is expressed as follows:

$$h_{o,av} = F_{to} h_{o,Nus} \quad (10.93)$$

where $h_{o,Nus}$ is again the condensing coefficient obtained with the single-tube Nusselt equation (10.12). The bundle factor F_{to} is commonly obtained from field test results. Sklover and Grigor'ev (1975) and Sklover (1990) proposed a method to calculate F_{to} that contains corrections for condensation inundation, noncondensable gases, and vapor-velocity effects (the saturation temperature depression). This method has not received wide acceptance. However, many heat exchanger manufacturers have developed proprietary correlations for F_{to} based on field experimental data. These correlations are then applied for particular applications with similar design conditions—similar inlet flow rates (vapor, noncondensables, and coolant) and temperature levels. Rabas (1992) suggested that the same F_{to} obtained with a plain tube condenser could be used to evaluate the performance improvement obtained after retubing with enhanced tubes.

Pointwise or Numerical Computer Programs It is apparent that the two overall methods have difficulty capturing the impact of the bundle size and shape on the thermal performance. Pointwise or numerical methods were developed to account for these geometry effects and to incorporate the latest techniques to correct for condensate inundation, noncondensable gas accumulation or pockets, and saturation temperature depression.

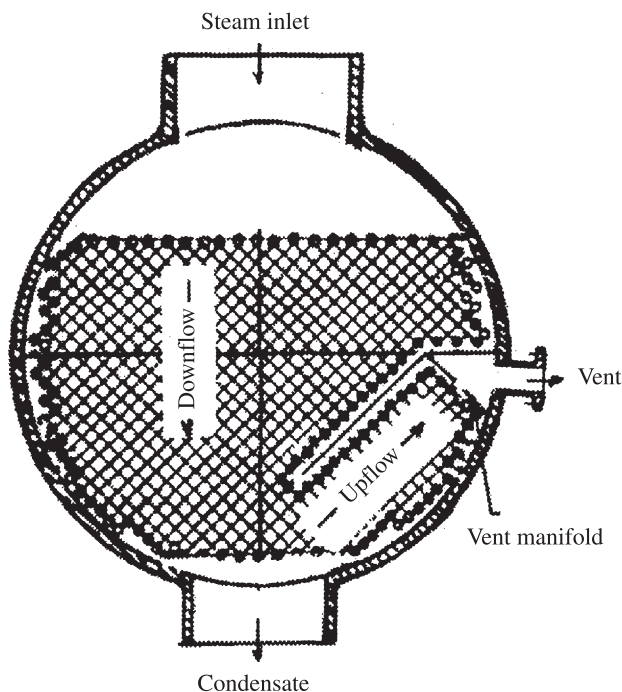


Figure 10.17 Tube bundle layout of a typical X-shell condenser.

An accurate computer model of an X-shell condenser need not be three-dimensional. Figure 10.17 shows that this single pass X-shell condenser is divided into a number of bays by the vertical tube supports. The three-dimensional nature of the condenser can therefore be modeled by repeated one- or two-dimensional predictions for each bay, with the inlet vapor flow being adjusted to satisfy the common overall pressure-drop constraint, the same pressure drop from the vapor inlet to the vent off-take.

A one-dimensional model is a realistic representation when the flow is essentially down or up through the bundle with limited bundle shell-side leakage. For example, a one-dimensional approach is reasonable for the condenser cross section shown in Figure 10.17 but not for many large surface condenser cross sections. There are some situations where a one-dimensional approach is acceptable, that is, when the transverse tube pitch is much less than the longitudinal pitch, as shown in Figure 10.18. The two-dimensional flow field within each bay can be considered as a series of one-dimensional parallel paths with dividing streamlines corresponding to these rays of tubes extending from the bundle exterior to the central core. Other power plant condenser manufacturers employ tube-layout patterns that can only be analyzed with a two-dimensional numerical model for each bay.

Computer codes were developed based on one-, two-, and three-dimensional models. Barsness (1963), Kistler and Kassem (1981), and Rabas and Kassem (1985) developed one-dimensional models. The model described by Kistler and Kassem was

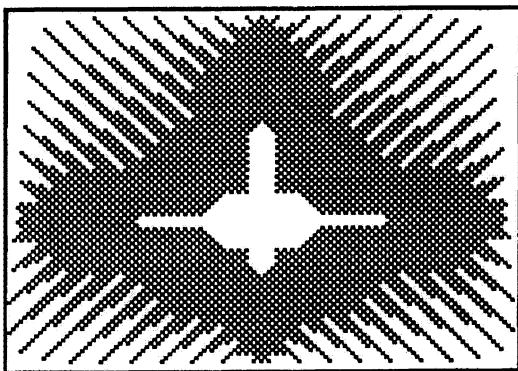


Figure 10.18 Tube pattern layout of a large power plant condenser.

the basis of an early Heat Transfer Research, Inc. (HTRI) code called CST that was commercially available and is also applicable for other shell types. Later developments are the two- and three-dimensional codes. Some recent publications that discuss these codes are Zhang (1994, 1996), Zhang et al. (1993), Zhang and Zhang (1994), Frisina et al. (1990), and Pouzenc (1990). These and some other codes are proprietary but can be purchased from organizations such as Heat Transfer Research, Inc., and Heat Transfer and Fluid Flow Services (HTFS). In addition to optimizing the tube bundle layout at the design stage, these codes have been very useful in correcting some performance problems on older units (Beckett et al., 1983). Because of the proprietary nature, no further discussion is presented.

Noncondensable Gas Management and Proper Venting Techniques The adverse effects of noncondensable gases and saturation temperature depression can be minimized with good condenser design practice, which includes proper management of the noncondensable gases and proper venting.

Management of the Noncondensable Gas There are three causes of noncondensable gas pockets in X-shell condensers: (1) radial flow maldistribution within a given bay, (2) longitudinal heat flux maldistribution for bay to bay, and (3) bottle-necking of the mixture in route from the bay exit to the vent. The pockets caused by the radial flow maldistribution can be located anywhere in the bundle cross section and in all the bays. The pockets caused by the longitudinal maldistribution are located around the air-cooling section in the cold-end bays of the condenser. Only the first two causes are discussed. The third is the result of poor design practice that can be corrected with straightforward fluid flow principles.

POCKETS FORMED BY RADIAL FLOW MALDISTRIBUTION Noncondensable gas pockets formed by a radial flow imbalance are most common with large power plant surface condensers with radial vapor flow into the bundle. A good tube bundle layout should

minimize or almost eliminate this type of noncondensable gas buildup or pockets. The important design concept is that the pressure drop from the top of the bundle to the air vent manifold is identical for all possible vapor paths. Figure 10.18 shows a good layout. Note that the vent manifold is not in the geometric center because of the difference between the two-phase pressure drop in countercurrent upflow and co-current downflow. A two-dimensional flow-field code is the most precise method to locate the true low-pressure point—the location of the vent manifold.

POCKETS CAUSED BY THE LONGITUDINAL HEAT FLUX MALDISTRIBUTION As shown in Fig. 10.16, the vapor is forced to flow nearly perpendicular to the tubes in each bay in a series of parallel flow paths. However, the vapor flow rate in each of the bays is different and is controlled by two common boundary conditions: (1) the outlet tube-side fluid temperature is the inlet temperature to the adjacent upstream bay, and (2) the shell-side pressure from the vapor inlet to the vent off-take is the same for all the bays. Because of the first, the condensing capability of each bay is different, due to the temperature rise along the length of the condenser. Because of the second, the pressure drops from the vapor inlet to the vent location for all the bays must be the same or balanced. The inlet vapor flow rates into each bay are controlled by these two boundary conditions and must decrease from the cold to the hot end of the condenser. This longitudinal heat flux maldistribution cannot be avoided because of the reduced temperature difference due to the rise in each successive bay.

Tinker (1933) presented the first and one of the best explanations for the longitudinal maldistribution problem. Figure 10.19 shows air pockets at the bottom of the three cold-end bays of a single-pass condenser with a single air removal vent. Because of the unequal heat flux and the uniform pressure-drop constraint, the cold-end bays “run out of steam” and air pockets will form on the remaining and inactive surface in each. These pockets can have a major impact on the performance because their size is somewhat controlled by the air in-leakage, vent location, and/or vent capacity.

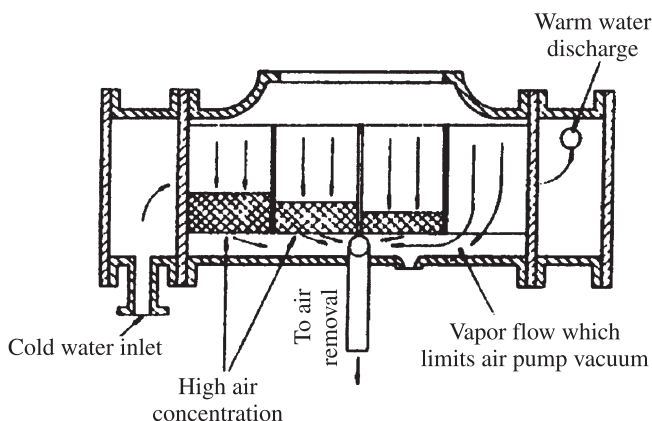


Figure 10.19 Air pockets due to longitudinal heat flux maldistribution. (From Tinker, 1933.)

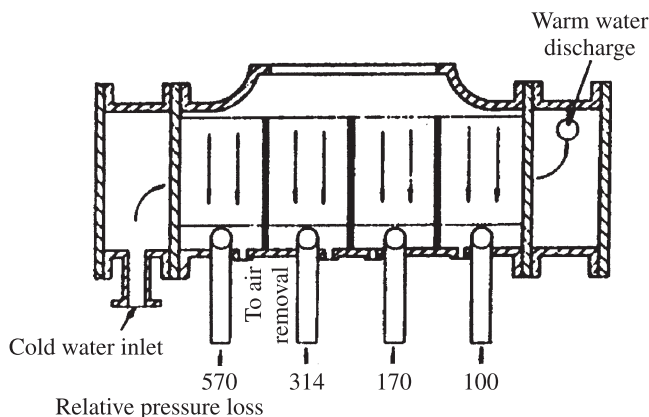


Figure 10.20 Relative pressure variations in each bay for air pocket removal with bay venting. (From Tinker, 1933.)

The longitudinal gas pockets can only be completely eliminated with unrealistic vent flow rates. Figure 10.20 shows that the pressure drop is increased by a factor of 5.7 in the cold-end bay if all the pockets are eliminated by venting each bay separately. It would not be practical and certainly not cost-effective to vent each bay separately because anywhere from about five to 15 separate, noncondensable gas-removal systems would be required for typical condenser applications. In addition, there would be a significant increase in the saturation temperature depression in the cold-end bays.

The negative impact of the gas pockets can be minimized or controlled by forcing more vapor into the cold-end bays by (1) orificing the vent manifold, (2) longitudinal vent flow cascading, (3) increasing the number of tube-side passes, and (4) increasing the vent flow rate. To force more vapor to the cold-end bay shown in Fig. 10.20, pressure drops must be introduced into the flow paths (blocking plates with different-sized openings or orifices) of the other three bays to obtain similar pressure-drop value for all four flow paths. Barsness (1963), Andrews (1974), Rabas (1985b), and Spencer and Hewitt (1990) discussed this concept in depth. Cascading, another concept used to minimize the size of cold-end pockets, was first proposed by Tinker (1933). The basis for this simple concept is to permit vapor to pass from a higher temperature bay to the lower temperature bay through the tube supports. This can be done for all the tube supports, a selected number, or just for the cold-end bay. Another approach is to increase the number of tube-side passes; however, this is not always feasible because of pumping limitations. Increasing the vent flow rate is discussed in the next section.

Noncondensable gas pockets will always exist even if the inlet gas concentration is small, or less than the 1000 rule mentioned above. With good design, the performance reduction due to the pockets can be limited to a couple of percent when based on the condition that all the heat transfer surface is active or not blanketed (Rabas and Kassem, 1985). It is interesting to note that these same two constraints are also

responsible for the formation of noncondensable pockets with in-tube condensers and will be discussed later.

Proper Venting Proper venting is necessary to minimize the adverse effect of noncondensable pockets. The first issue is the vent location. For single-pass X-shell condensers, this is at or near the center of the cold-end bay. A more general statement of Butterworth (1991) is that “the vent should be located as near as possible to the coldest part of the condenser, which, of course, is where the coolant enters.” Note that these statements are essentially the same. For a two-pass unit, the recommended approach is to vent each pass separately: If this is not feasible, care should be exercised to route the vapor-gas vent flow from the higher-temperature passes to the cold-end of the coldest pass.

The second issue is the vent flow rate. The condenser performance is always improved with an increasing rate, but the extent may or may not be significant. Figure 10.21 shows the predicted performance improvements (Rabas, 1985b) with increasing vent flow for two evaporator condensers used in multistage flash evaporators that are operating at different temperature levels. The important point is that the performance improvement of the low-temperature unit is limited by the saturation temperature depression. Another important consideration is the increased capital cost of the vacuum system and the increased quantity of vapor rejected to the environment. The desired goal is to vent the minimum amount of vapor, yet maintain reasonable condenser performance. Another issue that may override these considerations, the oxygen concentration in the condensate, is not addressed here.

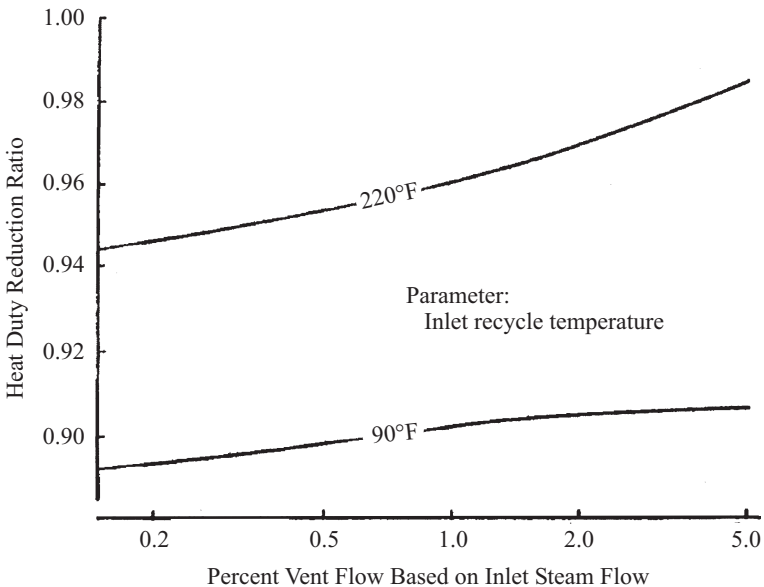


Figure 10.21 Effect of the vent flow rate on condenser performance.

Two methods are used by industry to select the vent flow rate. The first is simply to size the venting system for a percentage of the inlet vapor flow rate, the magnitude being based on experience. The second method is to select the vent flow rate based on estimates of the inlet gas flow rate and of the exit vapor/gas mass ratio. This ratio is calculated as follows:

$$\frac{m_{g,o}}{m_{a,i}} = \frac{M_g}{M_a} \frac{P_{g,o}}{P_{total,i} - P_{g,o}} \tag{10.94}$$

where $P_{g,o}$ is the saturation pressure at an assumed subcooled mixture outlet temperature and $T_{total,i}$ is the vapor pressure at the condenser inlet. The total vent flow is equal to the sum of $m_{a,i}$ and $m_{g,o}$. For example, the Heat Exchange Institute (1984) recommends 7.5°F subcooling and an air in-leakage rate based on the condenser volume.

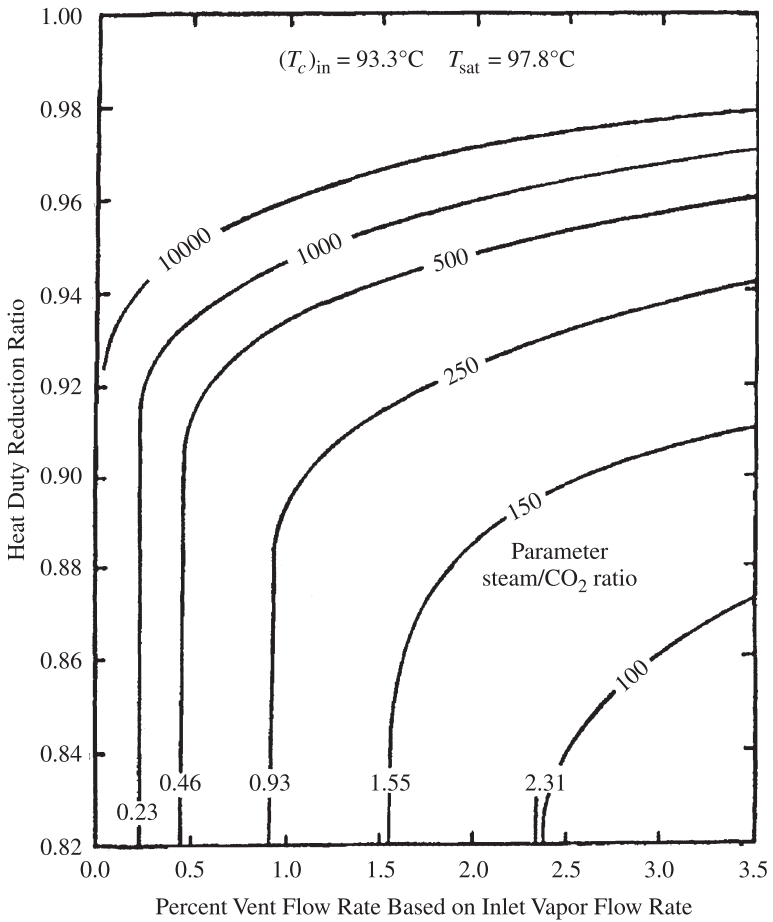


Figure 10.22 Effect of the vent flow rate on condenser performance.

Rabas and Mueller (1986) recommended an exit vapor/gas ratio that is about twice the minimum value calculated with eq. (10.94) with $P_{g,o}$ based on the inlet coolant temperature or the maximum subcooling. Figure 10.22 shows the effect of the vent flow rate on the heat duty reduction for a typical brine heater, the thermal performance now being evaluated with a pointwise method that contains a Colburn–Hougen analysis (Colburn and Hougen, 1933) to calculate the effect of the noncondensable gases (Rabas and Mueller, 1986). Note the very sharp drop in the performance when the vent flow rate approaches the minimum value for either air or carbon dioxide as the inlet noncondensable gas.

10.8.2 In-Tube Condensers

Most in-tube condensing applications use a crossflow arrangement with horizontal or slightly downward-sloping tubes. Similar bundle effects—maldistribution, noncondensable gas, and saturation temperature depression—also have a negative impact on the thermal performance. Only the effects of outside maldistribution and noncondensable gas pockets are discussed because the prediction of the in-tube condensing pressure drop has already been addressed.

Nonuniform Outside Inlet Flow and Temperature Distributions Standard design practice is to assume that the flow and temperature distributions are uniform at the exchanger face. However, these profiles can be very nonuniform and depend on the fan arrangement (induced or forced draft), the fan characteristics, the fan plenum design, and side obstructions. Of interest is to what extent these nonuniform flow distributions affect condenser thermal performance. The first investigations addressed only inlet flow variations and restricted the analysis to one dimension. Two later investigations removed these restrictions. Rabas (1987b) considered condensers with a constant saturation temperature, and later, Beiler and Kröger (1996) extended the analysis to condensers with a varying saturation temperature (the situation with a temperature drop due to the pressure drop, the presence of noncondensable gases, or multicomponent condensation). Both investigations showed that there is a heat load reduction with an increase departure from uniform distributions. However, the performance reduction was only about 7% with severe nonuniform distributions. The maldistribution occurring in well-designed cross-cooled heat exchangers reduces the thermal performance by only a few percent. In other words, be concerned about shell-side maldistributions only when very nonuniform flow distributions exist. Severe shell-side maldistributions are characterized with forced-draft fan arrangement, shallow tube banks, and a marginal fan plenum design.

Noncondensable Gas Pockets Berg and Berg (1980) stated that customary design practice is to assume that the inlet flow rates are the same for each tube and that all the vapor is condensed at the exit with condensate filling the tube. They and others—Breber et al. (1982) and Fabbri (1987)—clearly demonstrated that this is not the case. The same two reasons responsible for varying inlet flows into each bay and noncondensable pockets therein with shell-side condensation apply again: (1) The

approaching shell-side fluid temperature to each transverse tube row is increased because of the temperature rise(s) of the previous row(s), and (2) the tube-side pressure from the vapor inlet to the outlet headers is the same for all tubes. Fabbri (1987) evaluated the percentage of the total tube length that was blanketed with noncondensables or flooded with condensate with different transverse row numbers and row effectiveness values, the same value assumed for each row. With a row effective value of 0.5, the noncondensing percentages are about 15 and 30% for three and 10 rows, respectively. Manufacturers have developed many different techniques to minimize this ineffective portion of the tube bank. For more details, see Berg and Berg (1980), Henry et al. (1983), and Breber (1987).

10.9 CONDENSATION IN PLATE HEAT EXCHANGERS

10.9.1 Introduction

Figure 10.23 shows an isometric, cross-sectional view of a plate heat exchanger. Plate heat exchangers are made by stacking corrugated metal sheets to create channels that alternate between two fluid streams. Fluid paths are made by alternating the orientation of the chevron-shaped bumps as the plates are assembled. Areas where chevrons of adjacent plates touch create obstructions that mix the flow. The chevrons are approximately 62° with respect to the flow direction, as shown in Fig. 10.23. Some plate heat exchangers have chevrons that “point” perpendicularly to the flow direction. The 62° chevron angle (28° from the horizontal) arises from a compromise between increasing heat transfer and increased pressure drop.

Gasketed plate heat exchangers use O-rings to seal the edges of the plates, while the edges of compact brazed plate heat exchangers (CBEs) are brazed. The CBE has the advantage of relatively large operating pressures and the gasketed plate heat exchanger that of disassembling for cleaning. The same plate design can be used for the two heat exchanger types, which leads to similar condensation performance. Milk producers and other food and drink processors satisfied hygiene requirements by disassembling and cleaning the gasketed plate heat exchangers periodically (Saunders, 1988). Currently, the compactness of the CBE drives its use as refrigerant evaporators and condensers (Falls et al., 1992; Jonsson, 1985). For example, Saunders (1988) cites a case where one CBE replaced several shell-and-tube exchangers. Unfortunately, the available research on plate heat exchangers as condensers is not entirely comprehensive.

10.9.2 Steam Condensation Heat Transfer

Wang and Zhao (1993) have developed an expression for steam condensation in a plate heat exchanger where the chevrons point perpendicularly to the flow direction:

$$\text{Nu} = 0.00115 \left[\frac{\text{Re}_l \cdot \lambda (1 + 0.68\text{Ja})}{c_{p,l}(T_{\text{sat}} - T_w)} \right]^{0.983} \cdot \text{Pr}_l^{0.33} \left(\frac{\rho_l}{\rho_g} \right)^{0.248} \quad (10.95)$$

$$0.12 \text{ MPa} \leq P_s \leq 0.2 \text{ MPa}$$

$$10,000 \leq \text{Re}_l = \frac{G_T(1 - x_{qo})D_e}{\mu_l} \leq 45,000$$

where D_e is the equivalent round tube diameter based on the cross-sectional flow area between two plates. All steam transport properties are evaluated at

$$f = 0.00228 \text{Re}_{lo}^{-0.062} \Phi^{0.021} \quad \left(3500 \leq \text{Re}_{lo} = \frac{G_T D_h}{\mu_l} \leq 24,000 \right)$$

The latent heat and steam density are evaluated at the average steam temperature.

Equation (10.95) is valid for both complete and partial condensation. The x_{qo} is the mass quality of the steam exiting the plate heat exchanger. The quality term in the

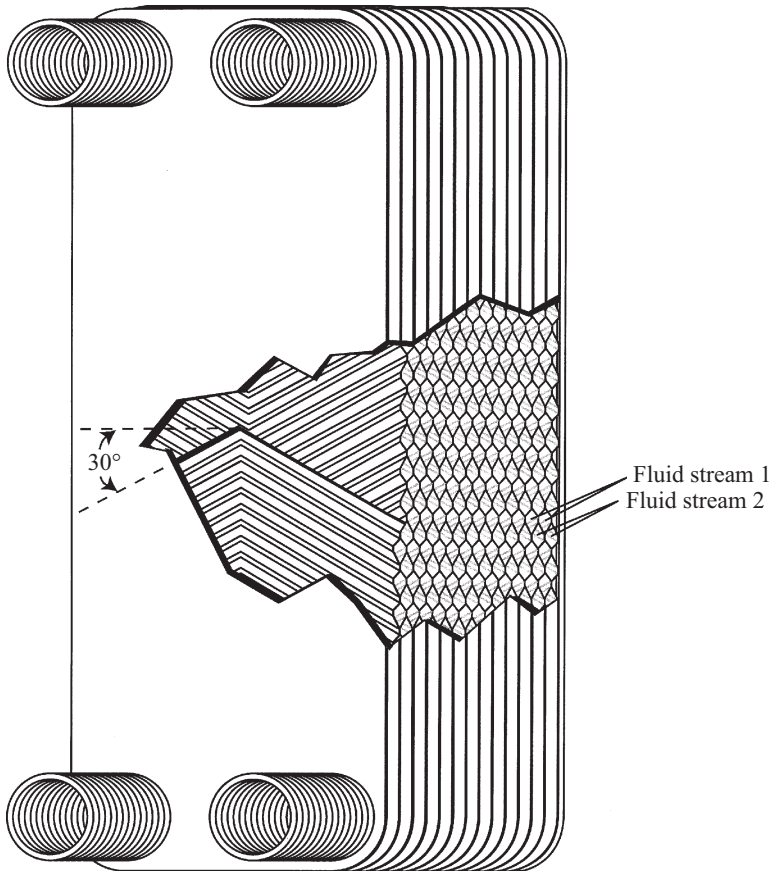


Figure 10.23 Cross-sectional view of a plate heat exchanger.

Reynolds number accounts for the partial condensation condition. Equation (10.95) predicted most of the Wang and Zhao (1993) data to within $\pm 15\%$.

10.9.3 Effect of Inclination on Heat Transfer Performance

It may be advantageous to install the CBE skewed in equipment to achieve a lower profile, and consequently, lower-cost unit enclosure. In the event of a redesign, equipment manufacturers require the effect of inclination on heat exchanger duty. Accordingly, Kedzierski (1997) quantified the change in performance associated with tilting a CBE from the designed vertical position. Detailed measurements of the effect of inclination on the performance of a CBE are required to weigh the performance change carefully against the production cost savings.

Figure 10.24 shows that the measured overall conductance of a CBE for R-22 condensation improved by approximately 17 to 30% by rotating it from the vertical to the horizontal position. Figure 10.24 shows the orientation of the rotation with respect to heat exchanger connections. The overall heat transfer coefficient of the condenser improved nearly linearly with rotation. The results suggest that a compact braze heat exchanger performs best as a condenser when the width is installed in the vertical direction to give the shortest condensing length.

The enhancement of the condenser performance in the horizontal orientation is due to shortening of the condensing length. The condensing length was 72 mm

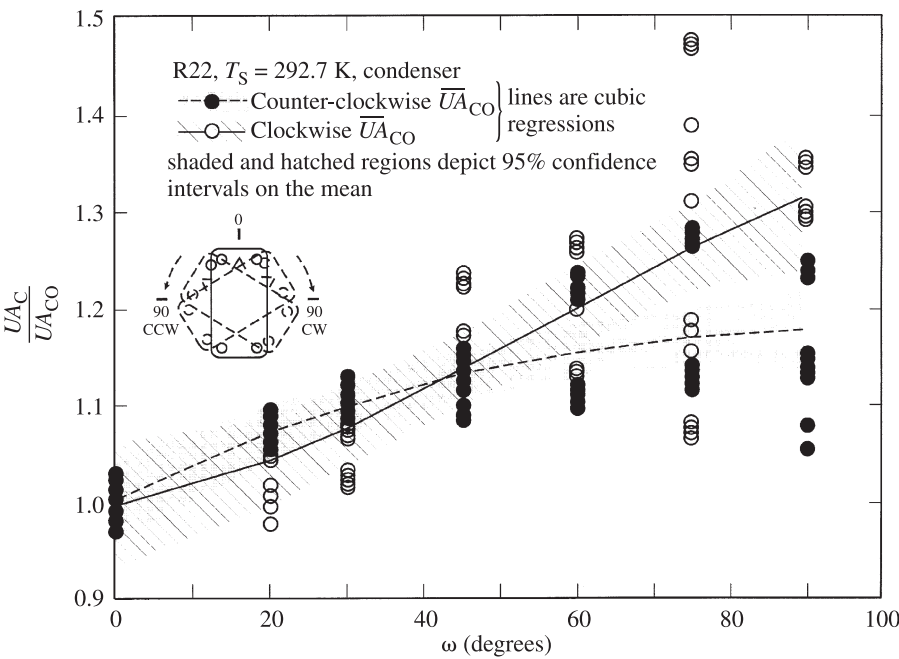


Figure 10.24 Normalized overall conductance of CBE as a function of inclination.

and 466 mm long when the condenser is in the horizontal and vertical positions, respectively. The longer condensing length permits the film thickness to increase through inundation. The thin-film region near the leading edge of the condensing length exhibits the most favorable heat transfer. The length of the leading edge for the condenser in the horizontal position is nearly 6.5 times that for the condenser in the vertical position. Consequently, the average condensate film thickness for the condenser in the horizontal position is thinner than that in the vertical position. Thin condensate films induce a greater overall heat transfer coefficient for the condenser in the horizontal position.

10.9.4 Effect of Inclination on Pressure Drop

Figure 10.25 shows the refrigerant-side condenser pressure drop (ΔP_c) as measured by Kedzierski (1997) for refrigerant downflow plotted against the rotation angle. The mean pressure drop remained within 2% of the vertical value (ΔP_{co}) for all angles of counterclockwise rotation. Gravitational effects were small because most of the volume (height) in the condenser was in the vapor phase. Conversely, gravity influences the pressure drop for the clockwise rotation past 45°. The refrigerant exit port is located near the top of the channel. Consequently, refrigerant must accumulate in the channel before exiting. The greater holdup of liquid in the condenser increased the pressure drop of the condenser for the clockwise rotation.

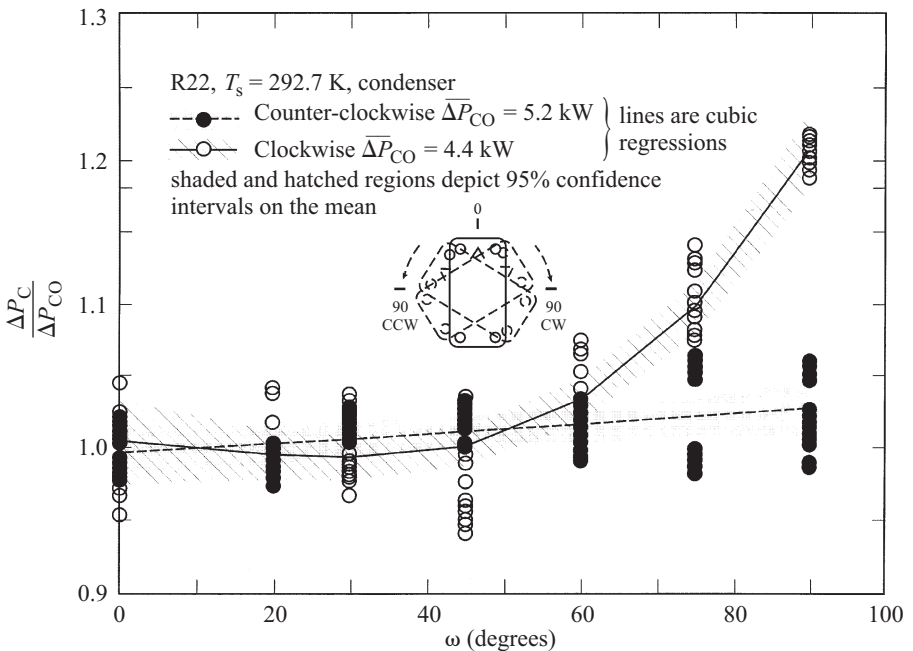


Figure 10.25 Condensation pressure drop of CBE as a function of inclination.

APPENDIX A

In this appendix we present the equations that describe the K-W fin profiles (Kedzier-ski and Webb (1990) and the constants used in eq. (10.21). The radius of curvature r of the new profile is defined by

$$r = C_1 + C_2 e^{Z\theta} + C_3 \theta \quad (10.A.1)$$

The constants C_1 , C_2 , C_3 , and C_4 are given by

$$C_1 = r_o - C_2 \quad (10.A.2)$$

$$C_2 = \frac{0.5t_r(\sin \theta_m - \theta_m \cos \theta_m) - e(\cos \theta_m + \theta_m \sin \theta_m - 1)}{C_4 - [2(1 - \cos \theta_m) - \theta_m \sin \theta_m]} + \frac{r_o - [\theta_m \sin \theta_m - 2(1 - \cos \theta_m)]}{C_4 - [2(1 - \cos \theta_m) - \theta_m \sin \theta_m]} \quad (10.A.3)$$

$$C_3 = \frac{0.5t_r - C_1 \sin \theta_m - C_2 Z e^{Z\theta_m} \cos \theta_m / (Z^2 + 1)}{\cos \theta_m + \theta_m \sin \theta_m - 1} - \frac{C_2(e^{Z\theta_m} \sin \theta_m - Z) / (Z^2 + 1)}{\cos \theta_m + \theta_m \sin \theta_m - 1} \quad (10.A.4)$$

$$C_4 = e^{Z\theta_m} [1 - \cos \theta_m + Z(\sin \theta_m - \theta_m)] + \frac{(Z\theta_m - 1) \cos \theta_m - (Z + \theta_m) \sin \theta_m + 1}{Z^2 + 1} \quad (10.A.5)$$

The constants defined by eqs. (10.A.2)–(10.A.5) are obtained by applying the following boundary conditions to eq. (10.A.1):

$$r = r_o \quad \text{at } \theta = 0 \quad (10.A.6)$$

$$t_r = 2 \int_0^{x/2} r \cos \theta d\theta \quad (10.A.7)$$

$$e = \int_0^{x/2} r \sin \theta d\theta \quad (10.A.8)$$

The procedure to solve for the radius of curvature r of the new profile is outlined in the following. First, select e , t_r , θ_m , r_o , and Z . Then evaluate C_4 given by eq. (10.A.5) and substitute C_4 into eq. (10.A.3) and solve for C_2 . Next, use C_2 to solve eq. (10.A.2) for C_1 . The constants C_1 and C_2 can now be used to solve for the remaining constant, C_3 .

$$N = \frac{(p - C_3^{1/3})^2}{p^2 - C_3^{1/3} p - C_3^{2/3}} \quad (10.A.9)$$

$$Y = \frac{2p + C_3^{1/3}}{\sqrt{3}C_3^{1/3}} \quad (10.A.10)$$

where p is defined as

$$p = \left(\frac{dr}{d\theta} \right)^{1/3} \quad (10.A.11)$$

The parameters N_m and Y_m are obtained by evaluating eqs. (10.A.9) and (10.A.10), respectively, at $\theta = \theta_m$. Similarly, the parameters N_o and Y_o are obtained by evaluating eqs. (10.A.9) and (10.A.10), respectively, at $\theta = 0$.

NOMENCLATURE

Roman Letter Symbols

A	constant in Rose (1994) model, dimensionless
A_{pipe}	pipe cross-sectional area, m^2 (ft^2)
A_{plate}	inside area of the tube sheet, m^2 (ft^2)
A_{tube}	total inside cross-sectional area of tube, m^2 (ft^2)
A_c	cross-sectional flow area, m^2 (ft^2)
A_g	cross-sectional area occupied by vapor, m^2 (ft^2)
\tilde{A}_g	cross-sectional area occupied by vapor, dimensionless [$= A_g/D^2$]
a_n	series described by eqs. (10.66b–f), dimensionless
b	spacing between fins at the tip, m (ft)
b_r	spacing between fins at the root, m (ft)
B	constant in Rose (1994) model, dimensionless
B_1	constant in Rose (1994) model, dimensionless
Bd	Bond number, dimensionless [$= g(\rho_l - \rho_g)D^2/\sigma$]
Bo	boiling number, dimensionless [$= q''/Gi_{lg}$]
c	constant in eq. (10.31), dimensionless
c_p	specific heat at constant pressure, $\text{W/m} \cdot \text{K}$ ($\text{Btu-hr-ft} \cdot ^\circ\text{R}$)
C	property constant in eq. (10.21), dimensionless
C_n	arbitrary constants in eq. (10.15), dimensionless
D	tube diameter, m (ft)
D^+	diameter, dimensionless [$= D\sqrt{\tau_w \rho_l / \mu_l}$]
D_e	equivalent round tube diameter based on the cross-sectional flow area, m (ft)
D_h	hydraulic diameter, m (ft)
E	electric field, V/m (V/ft)
e	fin height, m (ft)
e_v	average vertical fin height, m (ft)
f	friction factor, dimensionless

f_f	fraction of fin side that is flooded, dimensionless
f_{lo}	liquid-only friction factor defined by eq. (10.72), dimensionless
$f(n_t)$	row-number correction defined by eq. (10.91)
f_r	fraction of root of tube that is flooded, dimensionless
F	two-phase multiplier defined in eq. (10.62), dimensionless
F_2	denominator in eq. (10.67), dimensionless
F_{td}	defined by eq. (10.37), dimensionless
F_{to}	tube bundle correction factor defined by eq. (10.7.5), dimensionless
Fr_1	Froude number, dimensionless $[= G^2/\rho_l^2 g D]$
Fr_{so}	Soliman's modified Froude number, eqs. (10.40a and b), dimensionless
g	gravitational acceleration, m/s^2 (ft/s^2)
G	mass flux, $kg/m^2 \cdot s$ ($lb_m/ft^2 \cdot h$)
G_T	total liquid and vapor mass flux, $kg/m^2 \cdot s$ ($lb_m/ft^2 \cdot hr$)
Ga	Galileo number based on tube diameter, $[= g \rho_l (\rho_l - \rho_g) D^3 / \mu_l^2]$
Ga_L	Galileo number based on tube length, dimensionless $[= g \rho_l (\rho_l - \rho_g) L^3 / \mu_l^2]$
h	heat transfer coefficient, $W/m^2 \cdot K$, ($Btu/hr \cdot ft^2 \cdot ^\circ R$)
$h_{o,av}$	outside condensing heat transfer coefficient calculated with eqs. (10.91) and (10.93), dimensionless
$h_{o,Nus}$	outside condensing heat transfer coefficient calculated with eq. (10.12), dimensionless
h_l	liquid depth, m (ft)
\tilde{h}_l	liquid depth, dimensionless $[= h_l/D]$
i	specific enthalpy, J/kg (Btu/lbm)
j_v	superficial vapor velocity, dimensionless $[= Gx/\rho_g]$
j_v^{corr}	defined by eq. (10.42), dimensionless
Ja	liquid Jakob number, dimensionless, $[= C_{p,l}(T_{sat} - T_w)/\lambda]$
k	thermal conductivity, $W/m \cdot K$ ($Btu/hr \cdot ft \cdot ^\circ R$)
K_{box}	pipe entrance and exit loss in the tube box, dimensionless
K_{ent}	tube entrance loss coefficient, dimensionless
K_{ext}	tube exit loss coefficient, dimensionless
K_t	total loss coefficient defined by eq. (10.90), dimensionless
K_{td}	defined by eq. (10.38), dimensionless
l	characteristic length, m (ft)
L	tube or plate length, m (ft)
m	mass flow rate in tube, kg/s (lb_m/s)
$m_{a,i}$	mass flow rate of air in, kg/s (lb_m/s)
$m_{g,o}$	mass flow rate of vapor out, kg/s (lb_m/s)
M	molar mass, g/mol
N	constant in K-W profiles, dimensionless
N_f	total number of microfins in tube, dimensionless

Nu	Nusselt number (subscript indicates characteristic length, other than D), dimensionless $[= hD/k_l]$
Nu_d	in-tube Nusselt number, dimensionless
Nu_f	forced-convective Nusselt number as defined by eq. (10.57), dimensionless
n	exponents given in Table 10.3, dimensionless
n_t	number of tubes in the condenser, dimensionless
p	fin pitch, m^{-1} (ft^{-1})
P	pressure, N/m^2 (lb_f/ft^2)
P_c	critical pressure, N/m^2 (lb_f/ft^2)
$P_{g,o}$	partial pressure of vapor out, N/m^2 (lb_f/ft^2)
P_r	reduced pressure, dimensionless $[= P/P_c]$
$R_{total,i}$	inlet total pressure, N/m^2 (lb_f/ft^2)
Pr_l	liquid Prandtl number, dimensionless $[= \mu_l c_{p,l}/k_l]$
q''	heat flux, W/m^2 ($Btu/hr \cdot ft^2$)
Re_g	superficial vapor Reynolds number, dimensionless $[= GDx/\mu_g]$
Re_l	superficial liquid Reynolds number, dimensionless $[= GD(1-x)/\mu_l]$
Re_{lo}	liquid-only Reynolds number, dimensionless $[= GD/\mu_l]$
Re_{vo}	vapor-only Reynolds number, dimensionless $[= GD/\mu_g]$
r	local radius of curvature, m (ft)
s	coordinate direction along heat transfer surface, m (ft)
s'	coordinate direction along condensate surface, m (ft)
S	perimeter of one microfin, m (ft)
S_m	total or maximum arc length of fin, m (ft)
Su_g	Suratman number, dimensionless $[= \rho_g D \sigma / \mu_g^2]$
Sv	specific volume, dimensionless $[= (v_g - v_l)/v]$
Sw	swirl number defined by eq. (10.87), dimensionless
t	fin tip thickness, m (ft)
T	temperature, K ($^{\circ}R$)
u	velocity of condensate film in s direction, m/s (ft/h)
\tilde{u}_g	vapor velocity/superficial vapor velocity, dimensionless
\tilde{u}_l	liquid velocity/superficial liquid velocity, dimensionless
V	pseudo condensate velocity, m/s (ft/s)
We_{so}	Soliman's modified Weber number, eqs. (10.41 a and b), dimensionless
w	minimum free flow width, m (ft)
X_{lt}	laminar-turbulent Lockhart-Martinelli parameter, dimensionless
X_{tt}	turbulent-turbulent Lockhart-Martinelli parameter, dimensionless $\{(\rho_g/\rho_l)^{0.5}(\mu_l/\mu_g)^{0.1}[(1-x)/x]^{0.9}\}$
x	location from leading edge, circumferential direction, or vapor quality, dimensionless
x_q	thermodynamic quality, dimensionless

y	coordinate direction normal to condensing surface, m (ft) twist ratio, dimensionless
Y	constant for K–W profiles, dimensionless
z	axial location in tube, dimensionless
Z	shape parameter in K–W condensate profiles, dimensionless

Greek Letter Symbols

α	void fraction, dimensionless helix angle of microfin tube, rad exponents in eq. (10.88)
α_T	angle of inclination in Taitel–Dukler criterion, rad
β	fraction of the circumference where filmwise condensation prevails, eqs. (10.54a) and (10.54b), dimensionless half angle at the fin tip, rad microfin apex angle, rad exponents in eq. (10.83), dimensionless
Γ	mass flow rate of film per unit width, kg/m · s (lb _m /ft-hr)
γ	velocity ratio given in eq. (10.66g), dimensionless
δ	condensate film thickness, m (ft)
Δ	change in a parameter, dimensionless
ϵ_0	dielectric permittivity of a vacuum, dimensionless [$= 8.85 \times 10^{-12} \text{ N/V}^2 \text{ (lb}_f\text{/V}^2\text{)}]$]
ζ	constant in Adamek condensate profiles, dimensionless arbitrary constant given in eq. (10.15), dimensionless
θ	angle in cylindrical coordinate system, rad
θ_l	angle subtended from the top of tube to the bottom liquid level, rad
θ_m	total angle of rotation of fin through S_m , rad
κ	curvature, m ⁻¹ (ft ⁻¹) dielectric constant, dimensionless
λ	latent heat, J/kg (Btu/lbm)
λ'	Rohsenow's (1956) modified enthalpy of vaporization, eq. (10.47), dimensionless
μ	dynamic viscosity, N/m · s (lb _f /ft · h)
ν	kinematic viscosity, m ² /s (ft ² /h) [$= \mu/\rho$]
ξ	function given by eq. (10.26), dimensionless
ρ	density, kg/m ³ (lbm/ft ³)
σ	surface tension, kg/s ² (lb _f /ft)
τ_w	shear stress at the wall, N/m ² (lb _f /ft ²)
Φ	two-phase number in eq. (10.84), dimensionless
ϕ	cylindrical coordinate angle, rad
ϕ_f	condensate retention angle, rad
ϕ_g^2	two-phase pressure-drop multiplier, dimensionless [$= (dP/dz)/(dP/dz)_g$]
ϕ_l^2	two-phase pressure-drop multiplier, dimensionless [$= (dP/dz)/(dP/dz)_l$]

ϕ_{lc}^2	two-phase pressure-drop multiplier, dimensionless [= $(dP/dz)/(dP/dz)_{lo}$]
$\phi_{l,lt}$	defined by eq. (10.53), dimensionless
ω_o	mass fraction of oil in refrigerant, dimensionless

Roman Subscripts and Superscripts

-	average value
<i>a</i>	air
<i>av</i>	average
<i>b</i>	base metal
<i>bot</i>	bottom of tube
<i>box</i>	inlet or outlet header or water box
<i>E</i>	EHD enhanced
<i>eff</i>	fin effect
<i>el</i>	electrode
<i>ent</i>	entrance
<i>ext</i>	exit
<i>f</i>	fin
<i>g</i>	vapor, gravity effects
<i>i</i>	inlet, inner, liquid–vapor interface
<i>l</i>	liquid
<i>lt</i>	laminar–turbulent
<i>m</i>	maximum, fin root location
<i>max</i>	maximum
<i>o</i>	outlet, oil, fin tip location, outer or envelope diameter of tube
<i>q</i>	quality
<i>r</i>	root of fin
<i>s</i>	smooth tube
<i>sat</i>	saturated condition
<i>top</i>	top of tube
<i>w</i>	wall condition, vertical or tube

Greek Subscripts and Superscripts

σ	surface tension effects
2ϕ	two-phase vapor and liquid

REFERENCES

- Adamek, T. (1981). Bestimmung der Kondensationsgrößen auf feingewellten Oberflächen zur Auslegung optimaler Wandprofile, *Waerme- Stoffuebertrag.*, 15, 255–270.
- Adamek, T., and Webb, R. L. (1990). Prediction of Film Condensation on Horizontal Integral Fin Tubes, *Int. J. Heat Mass Transfer*, 33(8), 1721–1735.
- Agrawal, K. N., Varma, H. K., and Lal, S. (1986). Heat Transfer during Forced Convection Boiling of R12 under Swirl Flow, *J. Heat Transfer*, 108, 567–573.

- Andrews, E. F. C. (1974). A Review of the Thermal Performance Achievements of 500 MW Condenser Plant: Some Aspects of Steam-Side Venting, *NEL Report 619*, National Engineering Laboratory, E. Kilbridge, Glasgow, Scotland, pp. 114–129.
- Baker, O. (1954). Simultaneous Flow of Oil and Gas, *Oil Gas J.*, 53, 185–195.
- Barnea, D., Shoham, O., Taitel, Y., and Dukler, A. E. (1980). Flow Pattern Transition for Gas–Liquid Flow in Horizontal and Inclined Pipes: Comparisons of Experimental Data with Theory, *Int. J. Multiphase Flow*, 6, 217–225.
- Barnhart, J. (1992). An Experimental Investigation of Flow Patterns and Liquid Entrainment in a Horizontal-Tube Evaporator, Ph.D. dissertation, Department of Mechanical and Industrial Engineering, University of Illinois, Urbana-Champaign, IL.
- Barsness, E. J. (1963). Calculation of the Performance of Surface Condensers by Digital Computers, *ASME-63-PWR-2*, ASME, New York.
- Beckett, G., Davidson, B. J., and Ferrison, J. A. (1983). The Use of Computer Programs to Improve Condenser Performance, in *Condenser: Theory and Practice*, No. 77, Institute of Chemical Engineers, London, pp. 97–110.
- Beiler, M. G., and Kröger, D. G. (1996). Thermal Performance Reduction in Air-Cooled Heat Exchangers Due to Nonuniform Flow and Temperature Distributions, *Heat Transfer Eng.*, 17(1), 82–92.
- Berg, W. F., and Berg, J. L. (1980). Flow Patterns for Isothermal Condensation in One-Pass Air-Cooled Heat Exchangers, *Heat Transfer Eng.*, 1(4), 21–31.
- Bologa, M. K., Savin, I. K., and Didkovsky, A. B. (1987). Electric-Field-Induced Enhancement of Vapour Condensation Heat Transfer in the Presence of a Non-condensable Gas, *Int. J. Heat Mass Transfer*, 30(8), 1577–1585.
- Breber, G. (1987). Design Methods That Reduce Blackflow and Inert-Gas Blanketing in Cross-flow Condensers, in *Heat Transfer Equipment Design*, R. K. Shah, E. C. Subbarao, and R. A. Mashelkar, eds., Hemisphere Publishing, New York.
- Breber, G. (1988). Intube Condensation, in *Heat Transfer Equipment Design*, R. K. Shah, E. C. Subbarao, and R. A. Mashelkar, eds., Hemisphere Publishing, New York, pp. 1–23.
- Breber, G., Palen, J. W., and Taborek, J. (1982). Study on Noncondensable Vapor Accumulation in Air-Cooled Condensers, *Heat Exch.*, 18, 263–268.
- Bromley, L. A. (1952). Effect of Heat Capacity on Condensation, *Ind. Eng. Chem.*, 44, 2966–2969.
- Butterworth, D. (1972). A Visual Study of Mechanisms in Horizontal, Air–Water Flow, *Report M2556*, AERE, Harwell, England.
- Butterworth, D. (1991). Steam Power Plant and Process Condensers, in *Boilers, Evaporators, and Condensers*, S. Kakaç, ed., Wiley, New York, Chap. 11, p. 575.
- Carey, V. P. (1992). *Liquid–Vapor Phase Change Phenomena: An Introduction to the Thermophysics of Vaporization and Condensation Processes in Heat Transfer Equipment*, Hemisphere Publishing, New York.
- Carpenter, E. F., and Colburn, A. P. (1951). The Effect of Vapor Velocity on Condensation Inside Tubes, *Proc. General Discussion on Heat Transfer*, pp. 20–26.
- Cavallini, A., and Zecchin, R. (1974). A Dimensionless Correlation for Heat Transfer in Forced-Convective Condensation, *Proc. 5th International Heat Transfer Conference*, Japan Society of Mechanical Engineers, Vol. 3, pp. 309–313.
- Cavallini, A., Censi, G., Del Col, D., Doretti, L., Longo, G. A., and Rossetto, L. (2002). In-Tube Condensation of Halogenated Refrigerants, *ASHRAE Trans.*, 108(1), 146–161.

- Cavallini, A., Del Col, D., Doretti, L., Klammsteiner, N., Longo, G. A., and Rossetto, L. (1995). Condensation of New Refrigerants Inside Smooth and Enhanced Tubes, *Proc. 19th Int. Cong. of Refrig., The Hague*, 4, 105–114.
- Cavallini, A., Longo, G. A., and Rossetto, L. (1993). *Condensation Heat Transfer and Pressure Drop of Refrigerants in Tubes of Finned Tube Heat Exchangers: Theoretical and Practical Aspects*, DTI, Denmark, pp. 160–204.
- Cavallini, A., Del Col, D., Doretti, L., Longo, G. A., and Rossetto, L. (2000). Heat Transfer and Pressure Drop during Condensation of Refrigerants inside Horizontal Enhanced Tubes, *Int. J. Refrig.*, 23, 4–25.
- Chato, J. C. (1960). Laminar Condensation inside Horizontal and Inclined Tubes, Ph.D. dissertation, Department of Mechanical Engineering, MIT, Cambridge, MA.
- Chato, J. C. (1962). Laminar Condensation inside Horizontal and Inclined Tubes, *ASHRAE J.*, 4, 52–60.
- Chen, M. M. (1961). An Analytical Study of Laminar Film Condensation, II: Single and Multiple Horizontal Tubes, *J. Heat Transfer*, 83, 55–60.
- Chen, S. L., Gerner, F. M., and Tien, C. L. (1987). General Film Condensation Correlations, *Exp. Heat Transfer*, 1, 93–107.
- Colburn, A. P., and Hougen, O. A. (1933). Design of Cooler Condensers for Mixtures of Vapors and Noncondensable Gases, *Ind. Eng. Chem.*, 26, 1178–1182.
- Cooper, M. G. (1984). *Saturation Nucleate Pool Boiling: A Simple Correlation*, Department of Engineering Science, Oxford University, Oxford, pp. 86, 785–793.
- Da Silva, L. W., Molki, M., and Ohadi, M. M. (2000). Electrohydrodynamic Enhancement of R-134a Condensation on Enhanced Tubes, presented at the 35th IAS Annual Meeting and World Conference on Industrial Applications of Electrical Energy, in *Conference Record of the 2000 IEEE Industry Applications Conference*, Rome.
- Denglor, C. E., and Addoms, J. N. (1956). Heat Transfer Mechanism for Vaporization of Water in a Vertical Tube, *Chem. Eng. Prog. Symp. Ser.*, 52(18), 95–103.
- Dhir, V., and Lienhard, J. (1971). Laminar Film Condensation on Plane and Axisymmetric Bodies in Nonuniform Gravity, *J. Heat Transfer*, 93, 97–100.
- Dittus, F. W., and Boelter, L. M. K. (1930). Heat Transfer in Automobile Radiators of the Tubular Type, *Univ. Calif. (Berkeley) Publ. Eng.*, 2(13), 443.
- Dobson, M. K. (1994). Heat Transfer and Flow Regimes during Condensation in Horizontal Tubes, Ph.D. dissertation, Department of Mechanical and Industrial Engineering, University of Illinois, Urbana-Champaign, IL.
- Dobson, M. K., and Chato, J. C. (1998). Condensation in Smooth Horizontal Tubes, *J. Heat Transfer, Trans. ASME*, 120, 193–213.
- Dobson, M. K., Chato, J. C., Wattelet, J. P., Gaibel, J. A., Ponchner, M., Kenney, P. J., Shimon, R. L., Villanueva, T. C., Rhines, N. L., Sweeney, K. A., Allen, D. G., and Hershberger, T. T. (1994a). Heat Transfer and Flow Regimes during Condensation in Horizontal Tubes, *ACRC Tech. Rep. 57*, University of Illinois, Urbana-Champaign, IL.
- Dobson, M. K., Chato, J. C., Hinde, D. K., and Wang, S. P. (1994b). Experimental Evaluation of Internal Condensation of Refrigerants R-12 and R-134a, *ASHRAE Trans.*, 100(1), 744–754.
- Dukler, A. E. (1960). Fluid Mechanics and Heat Transfer in Vertical Falling-Film Systems, *Chem. Eng. Prog. Symp. Ser.*, 56(30), 1–10.

- Dukler, A. E., and Hubbard, M. G. (1975). A Model for Gas-Liquid Slug Flow in Horizontal and Near Horizontal Tubes, *Ind. Eng. Chem. Fundam.*, 14(4), 337-347.
- Eissenberg, D. M. (1974). An Investigation of the Variables Affecting Steam Condensation on the Outside of a Horizontal Tube Bundle, *Progress Report 74-943*, Office of Saline Water Research and Development, Oak Ridge National Laboratory, Knoxville, TN.
- Fabbri, G. (1987). Analysis of Noncondensable Contaminant Accumulation in Single-Pass Air-Cooled Condensers, *Heat Transfer Eng.*, 18(2), 50-60.
- Falls, R. S., Carter, J. R., and Kavanaugh, S. P. (1992). Test Results of a Water-to-Air Heat Pump with a Brazed Plate Heat Exchanger for Ground-Coupled Applications, *Proc. ASME-JSES-KSES International Solar Energy Conference*, Part 1, pp. 417-423.
- Freundlich, H. (1922). *Colloid and Capillary Chemistry*, E.P. Dutton, New York.
- Friedel, L. (1979). Improved Friction Pressure Drop Correlations for Horizontal and Vertical Two Phase Pipe Flow, *Paper E2*, European Two Phase Flow Group Meeting, Ispra, Italy.
- Frisina, V. C., Carlucci, L. N., and Campagna, A. O. (1990). SPOC: A Computer Program for Simulation of Power-Plant Condenser Performance, Electric Power Research Institute, presented at the Condenser Technology Conference, Boston.
- Gaibel, J. A., Chato, J. C., Dobson, M. K., Ponchner, M., Kenney, P. J., Shimon, R. L., Villanueva, T. C., Rhines, N. L., Sweeney, K. A., Allen, D. G., and Hershberger, T. T. (1994). Condensation of a 50/50 Blend of R-32/R-125 in Horizontal Tubes with and without Oil, *ACRC Technical Report 56*, University of Illinois, Urbana-Champaign, IL.
- Galbiati, L., and Andreini, P. (1992). The Transition between Stratified and Annular Regimes for Horizontal Two-Phase Flow in Small Diameter Tubes, *Int. Commun. Heat Mass Transfer*, 19(2), 185-190.
- Gidwani, A., Molki, M., Ohadi, M., Dessiatoun, S. V., and Da Silva, L. W. (1998). EHD-Enhanced Condensation Heat Transfer and Pressure Drop of Alternative Refrigerants/Refrigerant Mixtures for HVAC Applications, *ASHRAE Final Report Project 922-RP*.
- Gotoda, H., and Izumi, S. (1977). A Modern Condenser Design, *Proc. Inst. Mar. Eng.*, March, 253-273.
- Gregorig, R. (1954). Hautkondensation an feingewellten Oberflaechen bei Beruecksichtigung der Oberflaechenspannungen, *Z. Angew. Math. Phys.*, 5, 36-49.
- Hanratty, T. J. (1994). Private communication to M. K. Dobson, University of Illinois, Urbana-Champaign, IL.
- Heat Exchange Institute (1984). *Standards for Steam Surface Condensers*, 8th ed., HEI, Cleveland, OH.
- Henry, J. A. H., Grant, I. D. R., and Cotchin, C. D. (1983). A Method to Improve the Performance of an In-tube Condenser, in *Condenser: Theory and Practice*, Vol. 77, Institute of Chemical Engineers, London, pp. 459-468.
- Hinde, D. K., Dobson, M. K., Chato, J. C., Mainland, M. E., and Rhines, N. (1992). Condensation of R-134a with and without Oils, *ACRC Technical Report 26*, University of Illinois, Urbana-Champaign, IL.
- Honda, H., Nozu, S., and Mitsumori, K. (1983). Augmentation of Condensation on Finned Tubes by Attaching a Porous Drainage Plate, *Proc. ASME-JSME Thermal Engineering Joint Conference*, Vol. 3, pp. 289-295.
- Honda, H., Nozu, S., and Uchima, B. (1987). A Generalised Prediction Method for Heat Transfer during Film Condensation on a Horizontal Low-Finned Tube, *Proc. 2nd ASME-JSME Thermal Engineering Joint Conference*, Vol. 4, pp. 385-392.

- Hubbard, M. G., and Dukler, A. E. (1966). The Characterization of Flow Regimes for Horizontal Two-Phase Flow: Statistical Analysis of Wall Pressure Fluctuations, *Proc. 1966 Heat Transfer and Fluid Mechanics Institute*, pp. 100–121.
- Jaber, H. M., and Webb, R. L. (1996). Steam Condensation on Horizontal Integral-Fin Tubes of Low Thermal Conductivity, *J. Enhanced Heat Transfer*, 3(1), 55–71.
- Jakob, M. (1949). *Heat Transfer*, Vol. 1, Wiley, New York, pp. 667–675.
- Jaster, H., and Kosky, P. G. (1976). Condensation in a Mixed Flow Regime, *Int. J. Heat Mass Transfer*, 19, 95–99.
- Jeffreys, H. (1925). On the Formation of Water Waves by Wind, *Proc. R. Soc.*, A107, 189.
- Jeffreys, H. (1926). On the Formation of Water Waves by Wind, *Proc. R. Soc.*, A110, 241.
- Jonsson, I. (1985). Plate Heat Exchangers as Evaporators and Condensers for Refrigerants, *Aust. Refrig. Air Cond. Heat.*, 39(9), 30–31.
- Jung, D. S., and Rademacher, R. (1989). Prediction of Pressure Drop during Horizontal, Annular Flow Boiling of Pure and Mixed Refrigerants, *Int. J. Heat Mass Transfer*, 32, 2435–2446.
- Karkhu, V. A., and Borovkov, V. P. (1971). Film Condensation of Vapor at Finely-Finned Horizontal Tubes, *Heat Transfer Sov. Res.*, 3, 183–191.
- Kedzierski, M. A. (1997). Effect of Inclination on the Performance of a Compact Brazed Plate Condenser and Evaporator, *Heat Transfer Eng.*, 18(3), 25–38.
- Kedzierski, M. A., and Goncalves, J. M. (1999). Horizontal Convective Condensation of Alternative Refrigerants within a Micro-fin Tube, *J. Enhanced Heat Transfer*, 6(2/4), 161–178.
- Kedzierski, M. A., and Kim, M. S. (1998). Convective Boiling and Condensation Heat Transfer with a Twisted-Tape Insert for R12, R22, R152a, R134a, R290, R32/R134a, R32/R152a, R290/R134a, R134a/R600a, *Therm. Sci. Eng.*, 6(1), 113–122.
- Kedzierski, M. A., and Webb, R. L. (1990). Practical Fin Shapes for Surface Tension Drained Condensation, *J. Heat Transfer*, 112, 479–485.
- Kenney, P. J., Chato, J. C., Dobson, M. K., Wattlelet, J. P., Gaibel, J. A., Ponchner, M., Shimon, R. L., Villaneuva, T. C., Rhines, N. L., Sweeney, K. A., Allen, D. G., and Hershberger, T. T. (1994). Condensation of a Zeotropic Refrigerant R-32/R-125/R-134a (23%/25%/52%) in a Horizontal Tube, *ACRC Technical Report 62*, University of Illinois, Urbana-Champaign, IL.
- Kern, D. Q. (1958). Mathematical Development of Loading in Horizontal Condensers, *AIChE J.*, 4, 157–160.
- Kistler, R. S., and Kassem, A. E. (1981). Stepwise Rating of Condensers, *Chem. Eng. Prog.*, 77(7), 55–59.
- Laplace, P. S. (1966). *Celestial Mechanics*, translated to English by N. Bowditch, Chelsea Publishing, Bronx, NY.
- Lin, P. Y., and Hanratty, T. J. (1989). Detection of Slug Flow from Pressure Measurements, *Int. J. Multiphase Flow*, 15(2), 209–226.
- Lockhart, R. W., and Martinelli, R. C. (1947). Proposed Correlation of Data for Isothermal, Two-Phase, Two-Component Flow in Pipes, *Chem. Eng. Prog.*, 45(1), 39–48.
- Mandhane, J. M., Gregory, G. A., and Aziz, K. (1974). A Flow Pattern Map for Gas-Liquid Flow in Horizontal and Inclined Pipes, *Int. J. Multiphase Flow*, 1, 537–553.
- Manglik, R. A., and Bergles, A. E. (1992). Heat Transfer and Pressure Drop Correlations for Twisted-Tape Inserts in Isothermal Tubes, I: Laminar Flows, *Enhanced Heat Transfer, ASME-HTD-202*, ASME, New York, pp. 89–98.

- Marto, P. J. (1984). Heat Transfer and Two-Phase Flow during Steam-Side Condensation, *Heat Transfer Eng.*, 5(1/2), 31–61.
- Moody, L. F. (1944). Friction Factors for Pipe Flow, *Trans. ASME*, 66, 671–684.
- Muir, E. B. (1989). Commercial Refrigerants and CFCs, in CFCs: Today's Options—Tomorrow's Solutions, *Proc. ASHRAE's 1989 CFC Technology Conference*, pp. 81–86.
- Nicholson, M. K., Aziz, K., and Gregory, G. A. (1978). Intermittent Two Phase Flow: Predictive Models, presented at the 27th Canadian Chemical Engineering Conference, Calgary, Alberta, Canada.
- Nusselt, W. (1916). Die Oberflächenkondensation des Wasserdampfes, *Z. Ver. Dtsch. Ing.*, 60, 541–575.
- Ohadi, M. M. (1991). Heat Transfer Enhancement in Heat Exchangers, *ASHRAE J.*, 33(12), 42–50.
- Palen, J. W., Kistler, R. S., and Yang, Z. F. (1993). What We Still Don't Know about Condensation in Tubes, *Proc. ASME Symposium Condensation and Condenser Design*, pp. 19–53.
- Pierre, B. (1964). Flow Resistance with Boiling Refrigerants, 1, *ASHRAE J.*, 6(9), 58–65.
- Pouzenc, C. (1990). Use of Condenser Modeling Computer Programs, presented at the Electric Power Research Institute Condenser Technology Conference, Boston.
- Rabas, T. J. (1985a). The Effect of Tubeside Maldistribution on the Thermal Performance of Condensers Used in MSF Distillation Plants, *Desalination*, 55, 515–528.
- Rabas, T. J. (1985b). An Improved MSF Condenser Design, *Desalination*, 55, 169–184.
- Rabas, T. J. (1987a). The Effect of a Nonuniform Inlet Tubeside Temperature Distribution on the Thermal Performance of X-Shell Condensers Connected in Series, in *Maldistribution of Flow and Its Effect on Heat Exchanger Performance*, ASME-HTD-75, ASME, New York, pp. 97–104.
- Rabas, T. J. (1987b). The Effect of a Nonuniform Inlet Flow and Temperature Distribution on the Thermal Performance of Air-Cooled Condensers, in *Maldistribution of Flow and Its Effect on Heat Exchanger Performance*, ASME-HTD-75, ASME, New York, pp. 29–43.
- Rabas, T. J. (1992). Heat Exchanger Performance Calculations for Enhanced-Tube Condenser Applications, in *Enhanced Heat Transfer*, ASME-HTD-202, ASME, New York, pp. 139–147.
- Rabas, T. J., and Kassem, A. E. (1985). The Effect of Equal Shellside Pressure Drops on the Thermal Performance of Single-Pass, X-Shell, Steam Condensers, *ASME-HTD-44*, Two-Phase Heat Exchanger Symposium, Denver, CO, pp. 35–44.
- Rabas, T. J., and Mueller, A. C. (1986). The Effect of Noncondensable Gases and Vent Flow Rate on the Thermal Performance of Single-Pass, X-Shell Condensers, *Heat Transfer Eng.*, 7(3/4), 35–42.
- Rifert, V. G. (1980). A New Method for Calculating Rates of Condensation on Finned Tubes, *Heat Transfer Sov. Res.*, 12, 142–147.
- Rohsenow, W. M. (1956). Heat Transfer and Temperature Distribution in Laminar Film Condensation, *Trans. ASME*, 78, 1645–1648.
- Rose, J. W. (1994). An Approximate Equation for the Vapour-Side Heat-Transfer Coefficient for Condensation on Low-Finned Tubes, *Int. J. Heat Mass Transfer*, 37, 865–875.
- Rosson, H. F., and Myers, J. A. (1965). Point Values of Condensing Film Coefficients inside a Horizontal Tube, *Chem. Eng. Prog. Symp. Ser.*, 61(59), 190–199.

- Royal, J. H., and Bergles, A. E. (1978). Augmentation of Horizontal In-Tube Condensation by Means of Twisted-Tape Inserts and Internally Finned Tubes, *J. Heat Transfer*, 100, 17–24.
- Rudy, T. M., and Webb, R. L. (1981). Condensate Retention on Horizontal Integral-Fin Tubing, in *Advances in Enhanced Heat Transfer*, 20th National Heat Transfer Conference, ASME-HTD-18, ASME, New York, pp. 35–41.
- Saunders, E. A. D. (1988). *Heat Exchangers Selection, Design and Construction*, Wiley, New York.
- Schlager, L. M., Pate, M. B., and Bergles, A. E. (1990). Performance Predictions of Refrigerant–Oil Mixtures in Smooth and Internally Finned Tubes, *ASHRAE Trans.*, 96(1), 161–182.
- Shah, M. M. (1979). A General Correlation for Heat Transfer during Film Condensation inside Pipes, *Int. J. Heat Mass Transfer*, 22, 547–556.
- Sklover, G. G. (1990). Generalized Data of Steam Condensation Computation in Horizontal Tube Bundles, *Proc. 2nd International Symposium on Condensers and Condensation*, University of Bath, Bath, Somersetshire, England, pp. 203–212.
- Sklover, G. G., and Grigor'ev, V. G. (1975). Calculating the Heat Transfer Coefficient in Steam Turbine Condensers, *Teploenergetika*, 22(1), 86–91.
- Soliman, H. M. (1982). On the Annular-to-Wavy Flow Pattern Transition during Condensation inside Horizontal Tubes, *Can. J. Chem. Eng.*, 60, 475–481.
- Soliman, H. M. (1983). Correlation of Mist-to-Annular Transition during Condensation, *Can. J. Chem. Eng.*, 61, 178–182.
- Soliman, H. M. (1986). The Mist–Annular Transition during Condensation and Its Influence on the Heat Transfer Mechanism, *Int. J. Multiphase Flow*, 12(2), 277–288.
- Soliman, H. M., Schuster, J. R., and Berenson, P. J. (1968). A General Heat Transfer Correlation for Annular Flow Condensation, *J. Heat Transfer, Trans. ASME*, 90, 267–276.
- Souza, A. L., and Pimenta, M. M. (1995). Prediction of Pressure Drop during Horizontal Two-Phase Flow of Pure and Mixed Refrigerants, ASME Conference on Cavitation and Multiphase Flow, ASME-HTD-210, ASME, New York, pp. 161–171.
- Souza, A. L., Chato, J. C., Jabardo, J. M. S., Wattelet, J. P., Panek, J., Christoffersen, B., and Rhines, N. (1992). Pressure Drop during Two-Phase Flow of Refrigerants in Horizontal Smooth Tubes, *ACRC Technical Report 25*, University of Illinois, Urbana-Champaign, IL.
- Souza, A. L., Chato, J. C., Wattelet, J. P., and Christoffersen, B. R. (1993). Pressure Drop during Two-Phase Flow of Pure Refrigerants and Refrigerant–Oil Mixtures in Horizontal Smooth Tubes, *ASME-HTD-243*, ASME, New York, pp. 35–41.
- Spencer, E., and Hewitt, E. W. (1990). Analysis of an Earlier Geothermal Surface Condenser Design with Current Knowledge and Practice, *Proc. 2nd International Symposium on Condensers and Condensation*, University of Bath, Bath, Somerset, England, pp. 135–146.
- Sweeney, K. A. (1996). The Heat Transfer and Pressure Drop Behavior of a Zeotropic Refrigerant Mixture in a Microfinned Tube, M.S. thesis, Department of Mechanical and Industrial Engineering, University of Illinois, Urbana-Champaign, IL.
- Sweeney, K. A., and Chato, J. C. (1996). The Heat Transfer and Pressure Drop Behavior of a Zeotropic Refrigerant Mixture in a Microfinned Tube, *ACRC Technical Report 95*, University of Illinois, Urbana-Champaign, IL.
- Taitel, Y., and Dukler, A. E. (1976). A Model for Predicting Flow Regime Transitions in Horizontal and Near Horizontal Gas–Liquid Flow, *AIChE J.*, 22(1), 47–55.

- Tien, C. L., Chen, S. L., and Peterson, P. F. (1988). Condensation inside Tubes, *EPRI Project 1160-3 Final Report*.
- Tinker, T. (1933). Surface Condenser Design and Operating Characteristics, paper contributed by the Central Power Station Committee of the Power Division for the Semi-annual Meeting, Chicago, June 25 to July 1, of the American Society of Mechanical Engineers.
- Traviss, D. P., Rohsenow, W. M., and Baron, A. B. (1973). Forced-Convective Condensation in Tubes: A Heat Transfer Correlation for Condenser Design, *ASHRAE Trans.*, 79(1), 157–165.
- Wang, Z.-Z., and Zhao, Z.-N. (1993). Analysis of Performance of Steam Condensation Heat Transfer and Pressure Drop in Plate Condensers, *Heat Transfer Eng.*, 14(4), 32–41.
- Wang, S.-P., and Chato, J. C. (1995). Review of Recent Research on Heat Transfer with Mixtures, 1: Condensation, *ASHRAE Trans.*, 101(1), 1376–1386.
- Wattelet, J. P. (1994). Heat Transfer Flow Regimes of Refrigerants in a Horizontal-Tube Evaporator, Ph.D. dissertation, Department of Mechanical and Industrial Engineering, University of Illinois, Urbana-Champaign, IL.
- Wattelet, J. P., Chato, J. C., Christofferson, B. R., Gaibel, J. A., Ponchner, M., Shimon, R. L., Villaneuva, T. C., Rhines, N. L., Sweeney, K. A., Allen, D. G., and Hershberger, T. T. (1994). Heat Transfer Flow Regimes of Refrigerants in a Horizontal-Tube Evaporator, *ACRC Technical Report 55*, University of Illinois, Urbana-Champaign, IL.
- Webb, R. L. (1994). *Principles of Enhanced Heat Transfer*, Wiley-Interscience, New York.
- Webb, R. L., Rudy, T. M., and Kedzierski, M. A. (1985). Prediction of the Condensation Coefficient on Horizontal Integral-Fin Tubes, *ASME J. Heat Transfer*, 107, 369–376.
- Yabe, A. (1991). Active Heat Transfer Enhancement by Applying Electric Field, *Proc. 3rd ASME/JSME Thermal Engineering Conference*, Vol. 3, pp. xv–xxiii.
- Yang, C. Y., and Webb, R. L. (1997). A Predictive Model for Condensation in Small Hydraulic Diameter Tubes Having Axial Micro-fins, *J. Heat Transfer*, 119, 776–782.
- Yu, J., and Koyama, S. (1998). Condensation Heat Transfer of Pure Refrigerants in Microfin Tubes, *Proc. 1998 International Refrigeration Conference at Purdue*, pp. 325–330.
- Zener, C., and Lavi, A. (1974). Drainage Systems for Condensation, *J. Eng. Power*, 96, 209–215.
- Zhang, C. (1994). Numerical Modeling Using a Quasi-Three Dimensional Procedure for Large Power Plant Condensers, *J. Heat Transfer*, 116, 180–188.
- Zhang, C. (1996). Local and Overall Condensation Heat Transfer Behavior in Horizontal Tube Bundles, *Heat Transfer Eng.*, 17(1), 19–30.
- Zhang, C., and Zhang, Y. (1994). Sensitivity Analysis of Heat Transfer Coefficient Correlations on the Predictions of Steam Surface Condensers, *Heat Transfer Eng.*, 15(2), 54–63.
- Zhang, C., Sousa, A. C. M., and Venart, J. E. S. (1993). The Numerical and Experimental Study of a Power Plant Condenser, *J. Heat Transfer*, 115, 435–444.
- Zivi, S. M. (1964). Estimation of Steady-State Steam Void-Fraction by Means of the Principle of Minimum Entropy Production, *J. Heat Transfer, Trans. ASME*, 86, 247–252.

Heat Exchangers

ALLAN D. KRAUS

University of Akron
Akron, Ohio

- 11.1 Introduction
- 11.2 Governing relationships
 - 11.2.1 Introduction
 - 11.2.2 Exchanger surface area
 - 11.2.3 Overall heat transfer coefficient
 - 11.2.4 Logarithmic mean temperature difference
- 11.3 Heat exchanger analysis methods
 - 11.3.1 Logarithmic mean temperature difference correction factor method
 - 11.3.2 ϵ - N_{tu} method
 - Specific ϵ - N_{tu} relationships
 - 11.3.3 P - $N_{tu,c}$ method
 - 11.3.4 ψ - P method
 - 11.3.5 Heat transfer and pressure loss
 - 11.3.6 Summary of working relationships
- 11.4 Shell-and-tube heat exchanger
 - 11.4.1 Construction
 - 11.4.2 Physical data
 - Tube side
 - Shell side
 - 11.4.3 Heat transfer data
 - Tube side
 - Shell side
 - 11.4.4 Pressure loss data
 - Tube side
 - Shell side
- 11.5 Compact heat exchangers
 - 11.5.1 Introduction
 - 11.5.2 Classification of compact heat exchangers
 - 11.5.3 Geometrical factors and physical data
 - 11.5.4 Heat transfer and flow friction data
 - Heat transfer data
 - Flow friction data
- 11.6 Longitudinal finned double-pipe exchangers
 - 11.6.1 Introduction

- 11.6.2 Physical data for annuli
 - Extruded fins
 - Welded U-fins
- 11.6.3 Overall heat transfer coefficient revisited
- 11.6.4 Heat transfer coefficients in pipes and annuli
- 11.6.5 Pressure loss in pipes and annuli
- 11.6.6 Wall temperature and further remarks
- 11.6.7 Series-parallel arrangements
- 11.6.8 Multiple finned double-pipe exchangers
- 11.7 Transverse high-fin exchangers
 - 11.7.1 Introduction
 - 11.7.2 Bond or contact resistance of high-fin tubes
 - 11.7.3 Fin efficiency approximation
 - 11.7.4 Air-fin coolers
 - Physical data
 - Heat transfer correlations
 - 11.7.5 Pressure loss correlations for staggered tubes
 - 11.7.6 Overall heat transfer coefficient
- 11.8 Plate and frame heat exchanger
 - 11.8.1 Introduction
 - 11.8.2 Physical data
 - 11.8.3 Heat transfer and pressure loss
- 11.9 Regenerators
 - 11.9.1 Introduction
 - 11.9.2 Heat capacity and related parameters
 - Governing differential equations
 - 11.9.3 $\epsilon-N_{tu}$ method
 - 11.9.4 Heat transfer and pressure loss
 - Heat transfer coefficients
 - Pressure loss
- 11.10 Fouling
 - 11.10.1 Fouling mechanisms
 - 11.10.2 Fouling factors

Nomenclature

References

11.1 INTRODUCTION

A *heat exchanger* can be defined as any device that transfers heat from one fluid to another or from or to a fluid and the environment. Whereas in *direct contact* heat exchangers, there is no intervening surface between fluids, in *indirect contact* heat exchangers, the customary definition pertains to a device that is employed in the transfer of heat between two fluids or between a surface and a fluid. Heat exchangers may be classified (Shah, 1981, or Mayinger, 1988) according to (1) transfer processes,

(2) number of fluids, (3) construction, (4) heat transfer mechanisms, (5) surface compactness, (6) flow arrangement, (7) number of fluid passes, and (8) type of surface.

Recuperators are direct-transfer heat exchangers in which heat transfer occurs between two fluid streams at different temperature levels in a space that is separated by a thin solid wall (a parting sheet or tube wall). Heat is transferred by convection from the hot (hotter) fluid to the wall surface and by convection from the wall surface to the cold (cooler) fluid. The recuperator is a surface heat exchanger.

Regenerators are heat exchangers in which a hot fluid and a cold fluid flow alternately through the same surface at prescribed time intervals. The surface of the regenerator receives heat by convection from the hot fluid and then releases it by convection to the cold fluid. The process is transient; that is, the temperature of the surface (and of the fluids themselves) varies with time during the heating and cooling of the common surface. The regenerator is also a surface heat exchanger.

In *direct-contact* heat exchangers, heat is transferred by partial or complete mixing of the hot and cold fluid streams. Hot and cold fluids that enter this type of exchanger separately leave together as a single mixed stream. The temptation to refer to the direct-contact heat exchanger as a mixer should be resisted. Direct contact is discussed in Chapter 19. In the present chapter we discuss the shell-and-tube heat exchanger, the compact heat exchanger, the longitudinal high-fin exchanger, the transverse high-fin exchanger including the air-fin cooler, the plate-and-frame heat exchanger, the regenerator, and fouling.

11.2 GOVERNING RELATIONSHIPS

11.2.1 Introduction

Assume that there are two *process streams* in a heat exchanger, a hot stream flowing with a *capacity rate* $C_h = \dot{m}_h C_{ph}$ and a cooler (or cold stream) flowing with a capacity rate $C_c = \dot{m}_c C_{ph}$. Then, conservation of energy demands that the heat transferred between the streams be described by the enthalpy balance

$$q = C_h(T_1 - T_2) = C_c(t_2 - t_1) \quad (11.1)$$

where the subscripts 1 and 2 refer to the inlet and outlet of the exchanger and where the T 's and t 's are employed to indicate hot- and cold-fluid temperatures, respectively.

Equation (11.1) represents an ideal that must hold in the absence of losses, and while it describes the heat that will be transferred (the *duty* of the heat exchanger) for the case of prescribed flow and temperature conditions, it does not provide an indication of the size of the heat exchanger necessary to perform this duty. The size of the exchanger derives from a statement of the *rate equation*:

$$q = U \eta S \theta_m = U_h \eta_{ov,h} S_h \theta_m = U_c \eta_{ov,c} S_c \theta_m \quad (11.2)$$

where S_h and S_c are the surface areas on the hot and cold sides of the exchanger, U_h and U_c are the *overall heat transfer coefficients* referred to the hot and cold sides of

the exchanger and θ_m is some driving temperature difference. The quantities $\eta_{ov,h}$ and $\eta_{ov,c}$ are the respective overall fin efficiencies and in the case of an unfinned exchanger, $\eta_{ov,h} = \eta_{ov,c} = 1$.

The entire heat exchange process can be represented by

$$q = U_h \eta_{ov,h} S_h \theta_m = U_c \eta_{ov,c} S_c \theta_m = C_h (T_1 - T_2) = C_c (t_2 - t_1) \quad (11.3)$$

which is merely a combination of eqs. (11.1) and (11.2).

11.2.2 Exchanger Surface Area

Consider the unfinned tube of length L shown in Fig. 11.1a and observe that because of the tube wall thickness δ_w , the inner diameter will be smaller than the outer diameter and the surface areas will be different:

$$S_i = \pi d_i L \quad (11.4a)$$

$$S_o = \pi d_o L \quad (11.4b)$$

In the case of the finned tube, shown with one fin on the inside and outside of the tube wall in Fig. 11.1b, the fin surface areas will be

$$S_{fi} = 2n_i b_i L \quad (11.5a)$$

$$S_{fo} = 2n_o b_o L \quad (11.5b)$$

where n_i and n_o are the number of fins on the inside and outside of the tube wall, respectively, and it is presumed that no heat is transferred through the tip of either of the inner or outer fins. In this case, the *prime* or *base surface* areas

$$S_{bi} = (\pi d_i - n_i \delta_{fi}) L \quad (11.6a)$$

$$S_{bo} = (\pi d_o - n_o \delta_{fo}) L \quad (11.6b)$$

The total surface will then be

$$S_i = S_{bi} + S_{fi} = (\pi d_i - n_i \delta_{fi} + 2n_i b_i) L$$

or

$$S_i = [\pi d_i + n_i (2b_i - \delta_{fi})] L \quad (11.7a)$$

$$S_o = [\pi d_o + n_o (2b_o - \delta_{fo})] L \quad (11.7b)$$

The ratio of the finned surface to the total surface will be

$$\frac{S_{fi}}{S_i} = \frac{2n_i b_i L}{[\pi d_i + n_i (2b_i - \delta_{fi})] L} = \frac{2n_i b_i}{\pi d_i + n_i (2b_i - \delta_{fi})} \quad (11.8a)$$

$$\frac{S_{fo}}{S_o} = \frac{2n_o b_o L}{[\pi d_o + n_o(2b_o - \delta_{fi})]L} = \frac{2n_o b_o}{\pi d_o + n_o(2b_o - \delta_{fo})} \quad (11.8b)$$

The overall surface efficiencies $\eta_{ov,h}$ and $\eta_{ov,c}$ are based on the base surface operating at an efficiency of unity and the finned surface operating at fin efficiencies of η_{fi} and η_{fo} . Hence

$$\begin{aligned} \eta_{ov,i} S_i &= S_{bi} + \eta_{fi} S_{fi} \\ &= S_i - S_{fi} + \eta_{fi} S_{fi} \end{aligned}$$

or

$$\eta_{ov,i} = 1 - \frac{S_{fi}}{S_i} (1 - \eta_{fi}) \quad (11.9a)$$

and in a similar manner,

$$\eta_{ov,o} = 1 - \frac{S_{fo}}{S_o} (1 - \eta_{fo}) \quad (11.9b)$$

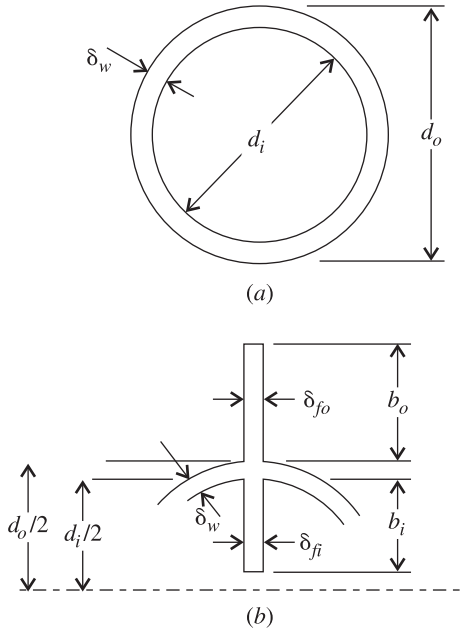


Figure 11.1 End view of (a) a bare tube and (b) a small central angle of a tube with both internal and external fins of length, L .

Notice that when there is no finned surface, $S_{fi} = S_{fo} = 0$ and eqs. (11.9) reduce to

$$\eta_{ov,i} = \eta_{ov,o} = 1$$

and that with little effort, the subscripts in eqs. (11.4) through (11.9) can be changed to reflect the hot and cold fluids.

11.2.3 Overall Heat Transfer Coefficient

In a heat exchanger containing hot and cold streams, the heat must flow, in turn, from the hot fluid to the cold fluid through as many as five thermal resistances:

1. Hot-side convective layer resistance:

$$R_h = \frac{1}{h_h \eta_{ov,h} S_h} \quad (\text{K/W}) \quad (11.10)$$

2. Hot-side *fouling* resistance due to an accumulation of foreign (and undesirable) material on the hot-fluid exchanger surface:

$$R_{dh} = \frac{1}{h_{dh} \eta_{ov,h} S_h} \quad (\text{K/W}) \quad (11.11)$$

Fouling is discussed in a subsequent section.

3. Resistance of the exchanger material, which has a finite thermal conductivity and which may take on a value that is a function of the type of exchanger:

$$R_m = \begin{cases} \frac{\delta_w}{k_m S_m} & (\text{K/W}) \quad \text{plane walls} \\ \frac{\ln(d_o/d_i)}{2\pi k_m L n_t} & (\text{K/W}) \quad \text{circular tubes} \end{cases} \quad (11.12)$$

where δ_m is the thickness of the metal, S_m the surface area of the metal, and n_t the number of tubes.

4. Cold-side fouling resistance:

$$R_{dc} = \frac{1}{h_{dc} \eta_{ov,c} S_c} \quad (\text{K/W}) \quad (11.13)$$

5. Cold-side convective layer resistance:

$$R_c = \frac{1}{h_c \eta_{ov,c} S_c} \quad (\text{K/W}) \quad (11.14)$$

The resistances listed in eqs. (11.10)–(11.14) are in *series* and the total resistance can be represented by

$$\frac{1}{US} = \frac{1}{h_h \eta_{ov,h} S_h} + \frac{1}{h_{dh} \eta_{ov,h} S_h} + R_m + \frac{1}{h_{dc} \eta_{ov,c} S_c} + \frac{1}{h_c \eta_{ov,c} S_c} \quad (11.15)$$

where, for the moment, U and S on the left side of eq. (11.16) are not assigned any subscript. Equation (11.16) is perfectly general and may be put into specific terms depending on the selection of the reference surface, whether or not fouling is present and whether or not the metal resistance needs to be considered. If eq. (11.16) is solved for U , the result is

$$U = \frac{1}{\frac{S}{h_h \eta_{ov,h} S_h} + \frac{S}{h_{dh} \eta_{ov,h} S_h} + SR_m + \frac{S}{h_{dc} \eta_{ov,c} S_c} + \frac{S}{h_c \eta_{ov,c} S_c}} \quad (11.16)$$

and if the thickness of the metal is small and thermal conductivity of the metal is high, the metal resistance becomes negligible and

$$U = \frac{1}{\frac{S}{h_h \eta_{ov,h} S_h} + \frac{S}{h_{dh} \eta_{ov,h} S_h} + \frac{S}{h_{dc} \eta_{ov,c} S_c} + \frac{S}{h_c \eta_{ov,c} S_c}} \quad (11.17)$$

Several forms of eq. (11.17) are:

- For a hot-side reference with fouling,

$$U_h = \frac{1}{\frac{1}{h_h \eta_{ov,h}} + \frac{1}{h_{dh} \eta_{ov,h}} + \frac{1}{h_{dc} \eta_{ov,c}} \frac{S_h}{S_c} + \frac{1}{h_c \eta_{ov,c}} \frac{S_h}{S_c}} \quad (11.18)$$

- For a cold-side reference with fouling,

$$U_c = \frac{1}{\frac{1}{h_h \eta_{ov,h}} \frac{S_c}{S_h} + \frac{1}{h_{dh} \eta_{ov,h}} \frac{S_c}{S_h} + \frac{1}{h_{dc} \eta_{ov,c}} + \frac{1}{h_c \eta_{ov,c}}} \quad (11.19)$$

- For a hot-side reference without fouling,

$$U_h = \frac{1}{\frac{1}{h_h \eta_{ov,h}} + \frac{1}{h_c \eta_{ov,c}} \frac{S_h}{S_c}} \quad (11.20)$$

- For a cold-side reference without fouling,

$$U_c = \frac{1}{\frac{1}{h_h \eta_{ov,h}} \frac{S_c}{S_h} + \frac{1}{h_c \eta_{ov,c}}} \quad (11.21)$$

- For an unfinned exchanger where $\eta_{ov,h} = \eta_{ov,c} = 1$ and a hot-side reference without fouling,

$$U_h = \frac{1}{\frac{1}{h_h} + \frac{1}{h_c} \frac{S_h}{S_c}} \tag{11.22}$$

- For an unfinned exchanger and a cold-side reference without fouling,

$$U_c = \frac{1}{\frac{1}{h_h} \frac{S_h}{S_c} + \frac{1}{h_c}} \tag{11.23}$$

11.2.4 Logarithmic Mean Temperature Difference

For the four basic simple arrangements indicated in Fig. 11.2, θ_m in eqs. (11.2) and (11.3) is the *logarithmic mean temperature difference*, which can be written as

$$\theta_m = \text{LMTD} = \frac{\Delta T_1 - \Delta T_2}{\ln(\Delta T_1/\Delta T_2)} = \frac{\Delta T_2 - \Delta T_1}{\ln(\Delta T_2/\Delta T_1)} \tag{11.24}$$

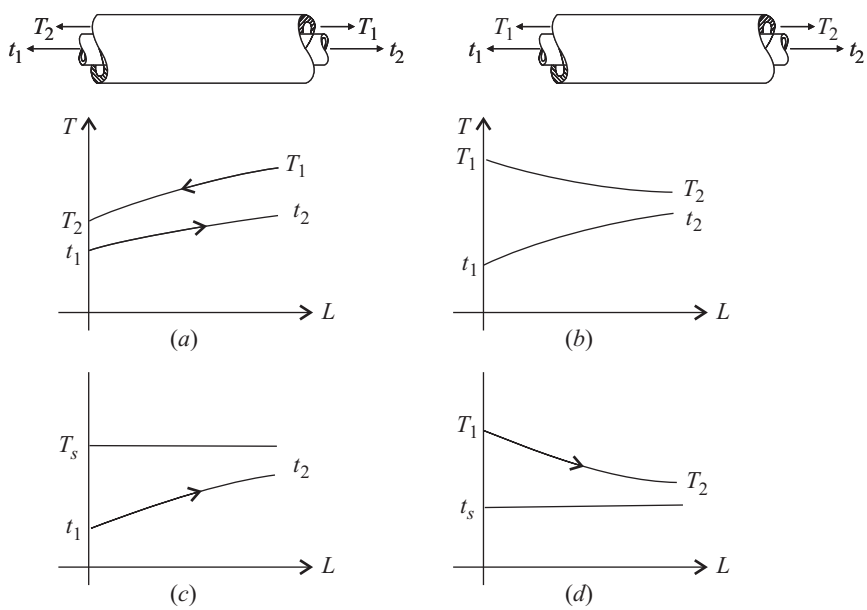


Figure 11.2 Four basic arrangements for which the logarithmic mean temperature difference may be determined from eq. (11.23): (a) counterflow; (b) co-current or parallel flow; (c) constant-temperature source and rising-temperature receiver; (d) constant-temperature receiver and falling-temperature source.

- For the *counterflow exchanger* where the fluids flow in opposite directions through the exchanger (Fig. 11.2a),

$$\text{LMTD} = \frac{(T_1 - t_2) - (T_2 - t_1)}{\ln [(T_1 - T_2)/(T_2 - t_1)]} \quad (11.25)$$

- For the *co-current or parallel flow exchanger* where the fluids flow in the same direction through the exchanger (Fig. 11.2b),

$$\text{LMTD} = \frac{(T_1 - t_1) - (T_2 - t_2)}{\ln [(T_1 - t_1)/(T_2 - t_2)]} \quad (11.26)$$

- For an exchanger that has a constant-temperature source, $T_s = T_1 = T_2$, and a rising-temperature receiver (Fig. 11.2c),

$$\text{LMTD} = \frac{t_2 - t_1}{\ln [(T_s - t_1)/(T_s - t_2)]} \quad (11.27)$$

- For an exchanger that has a constant-temperature receiver, $t_s = t_1 = t_2$, and a falling-temperature source (Fig. 11.2d),

$$\text{LMTD} = \frac{T_1 - T_2}{\ln [(T_1 - t_s)/(T_2 - t_s)]} \quad (11.28)$$

These simple expressions for the logarithmic mean temperature difference cannot be employed for arrangements other than those shown in Fig. 11.2. The procedure for the case of crossflow and multipass exchangers is given in the next section.

11.3 HEAT EXCHANGER ANALYSIS METHODS

11.3.1 Logarithmic Mean Temperature Difference Correction Factor Method

The logarithmic mean temperature difference developed in Section 11.2.4 is not applicable to multipass or crossflow heat exchangers. The temperature parameter θ_m in eqs. (11.2) and (11.3) is the true or effective mean temperature difference and is related to the logarithmic mean temperature difference:

$$\theta_m = \text{LMTD} = \frac{\Delta T_1 - \Delta T_2}{\ln(\Delta T_1/\Delta T_2)} = \frac{\Delta T_2 - \Delta T_1}{\ln(\Delta T_2/\Delta T_1)} \quad (11.24)$$

and the functions

$$P = \frac{t_2 - t_1}{T_1 - t_1} \quad (11.29a)$$

defined as the *cold-side effectiveness* and

$$R = \frac{T_1 - T_2}{t_2 - t_1} = \frac{C_c}{C_h} \tag{11.29b}$$

defined as a *capacity rate ratio*.

The true or effective mean temperature difference in multipass or crossflow exchangers, θ_m , will be related to the counterflow logarithmic mean temperature difference via

$$\theta_m = F(\text{LMTD}_c)$$

where the correction factor

$$F \equiv \frac{\theta_m}{\text{LMTD}_c} \tag{11.30}$$

is a function of P , R , and the flow arrangement.

The quest for the logarithmic mean temperature difference correction factor apparently began in the early 1930s (Nagle, 1933; Underwood, 1934; Fischer, 1938; Bowman et al., 1940). The correction factors are available in chart form, such as indicated in Figs. 11.3 and 11.4.

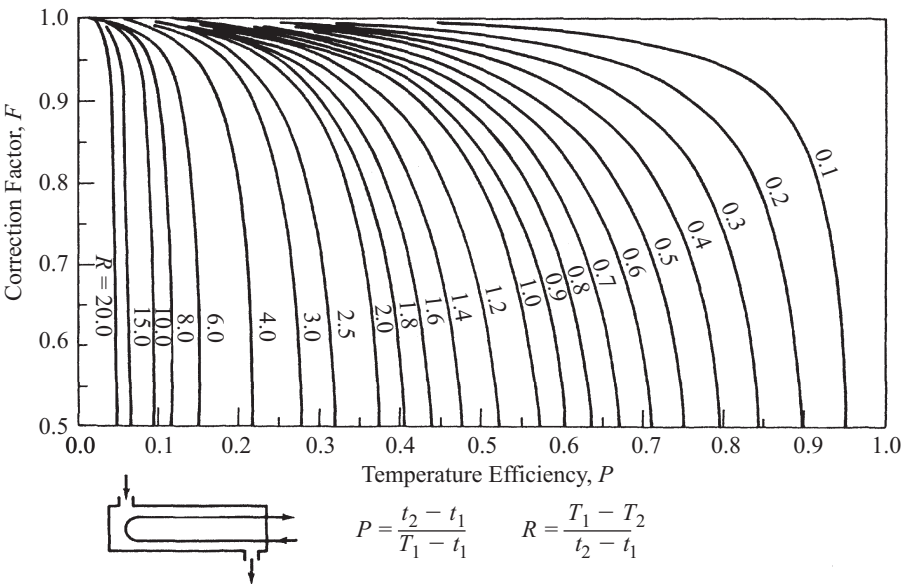


Figure 11.3 Logarithmic mean temperature difference correction factor for the shell-and-tube heat exchanger with one shell pass and two tube passes. (From Kakaç, 1991, with permission.)

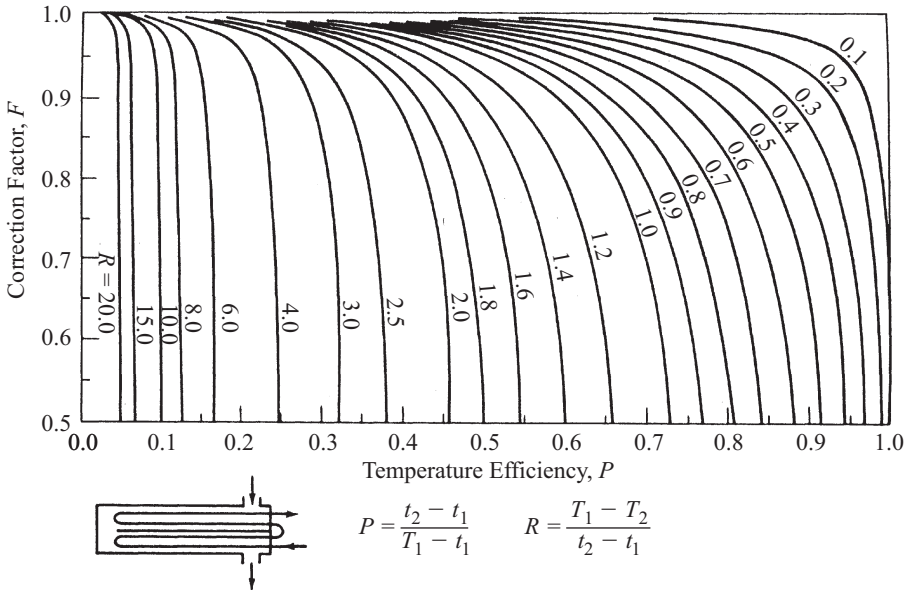


Figure 11.4 Logarithmic mean temperature difference correction factor for the shell-and-tube heat exchanger with two shell passes and four tube passes. (From Kakaç, 1991, with permission.)

11.3.2 ϵ - N_{tu} Method

The parameter P in the logarithmic mean temperature difference correction factor method requires three temperatures for its computation. The inlet temperature of both the hot and cold streams is usually a given, but when the cold-side outlet temperature is not known, a trial-and-error method is required to evaluate P . The trial-and-error procedure may be avoided in the ϵ - N_{tu} method, and because of its suitability for computer-aided design, the ϵ - N_{tu} method is gaining in popularity.

Kays and London (1984) have shown that the heat exchanger transfer equations may be written in dimensionless form, which results in three dimensionless groups:

1. Capacity rate ratio:

$$C^* = \frac{C_{\min}}{C_{\max}} \quad (0 \leq C^* \leq 1) \quad (11.31)$$

Notice that this differs from the capacity rate ratio R used in the determination of the logarithmic mean temperature difference correction factor. Here, the capacity ratio C^* is always less than unity.

2. Exchanger heat transfer effectiveness:

$$\epsilon = \frac{q}{q_{\max}} \quad (0 \leq \epsilon \leq 1) \quad (11.32)$$

This is the ratio of the actual heat transferred to the maximum heat that could be transferred if the exchanger were a counterflow exchanger.

3. *Number of transfer units:*

$$N_{tu} \equiv \frac{US}{C_{\min}} = \frac{1}{C_{\min}} \int_S U \, dS \quad (11.33)$$

The number of transfer units is a measure of the size of the exchanger.

The actual heat transfer is given by the enthalpy balance of eq. (11.1). Observe that if

$$C_h > C_c \quad \text{then } (T_1 - T_2) < (t_2 - t_1)$$

and if

$$C_c > C_h \quad \text{then } (t_2 - t_1) < (T_1 - T_2)$$

the fluid that “might” experience the maximum temperature change, $T_1 - t_1$, is the fluid that has the minimum capacity rate. Thus, the maximum possible heat transfer can be expressed as

$$q_{\max} = C_c(T_1 - t_1) \quad (C_c < C_h) \quad (11.34a)$$

or

$$q_{\max} = C_h(T_1 - t_1) \quad (C_h < C_c) \quad (11.34b)$$

and either of these can be obtained with the counterflow exchanger. Therefore, the exchanger effectiveness can be written as

$$\epsilon = \frac{q}{q_{\max}} = \frac{C_h(T_2 - T_1)}{C_{\min}(T_1 - t_1)} = \frac{C_c(t_2 - t_1)}{C_{\min}(T_1 - t_1)} \quad (11.35)$$

Observe that the value of ϵ will range between zero and unity and that for a given ϵ and q_{\max} , the actual heat transfer in the exchanger will be

$$q = \epsilon C_{\min}(T_1 - t_1) \quad (11.36)$$

Because

$$\epsilon = f(C^*, N_{tu}, \text{flow arrangement})$$

each exchanger arrangement has its own effectiveness relationship. The formal introduction of the ϵ - N_{tu} method of heat exchanger analysis was apparently by London and Seban (1942, 1980). However, Sekulic et al. (1999) point out that solutions for the single-pass crossflow exchanger were originally obtained by Nusselt (1911, 1930), Mason (1955), and Baclic and Heggs (1985). Additional solutions for single-pass

unmixed–unmixed crossflow can be attributed to Hausen (1943), Baclic (1978), and Li (1987). Stevens et al. (1957) provided data for one-, two-, and three-pass exchangers, and Baclic (1990) reported on an analysis of 36 different two-pass crossflow arrangements.

Solutions for shell-and-tube heat exchanger arrangements are also numerous. In addition to the Nagle (1933), Underwood (1934), Fischer (1938), and Bowman et al. (1940) studies already cited, Gardner (1941, 1942), Schindler and Bates (1960), Jaw (1964), and Crozier and Samuels (1977) all provided analyses of different arrangements. Kraus and Kern (1965) solved the problem of the $1 - n$ (n even) exchanger by direct integration, and this was later modified by Baclic (1989). Baclic (1997) also gave general explicit solutions for the $1 - n$ (n odd) exchanger. More complex situations with shell-and-tube heat exchangers with unbalanced passes and/or without axial flow nonuniformities have been the subject of papers by Roetzel and Spang (1987) and Spang (1991).

Specific ϵ – N_{tu} Relationships Specific ϵ – N_{tu} relationships along with their limiting values for 10 flow arrangements, summarized from the work of Kakaç et al. (1987), follow:

1. For counterflow,

$$\epsilon = \frac{1 - e^{-N_{tu}(1-C^*)}}{1 - C^*e^{-N_{tu}(1-C^*)}} \quad (11.37)$$

When $C^* = 1$,

$$\epsilon = \frac{N_{tu}}{1 + N_{tu}}$$

and when $N_{tu} \rightarrow \infty$,

$$\epsilon = 1 \quad \text{for all } C^*$$

2. For co-current (parallel) flow,

$$\epsilon = \frac{1 - e^{-N_{tu}(1+C^*)}}{1 + C^*} \quad (11.38)$$

When $C^* = 1$,

$$\epsilon = \frac{1}{2} (1 - e^{-2N_{tu}})$$

and when $N_{tu} \rightarrow \infty$,

$$\epsilon = \frac{1}{1 + C^*}$$

3. For crossflow with both fluids unmixed,

$$\epsilon = 1 - e^{-(1+C^*)N_{tu}} \left[I_0(2N_{tu}C^{*1/2}) + C^{*n/2} I_1(2N_{tu}C^{*1/2}) \right] - \frac{1-C^*}{C^*} \sum_{n=2}^{\infty} C^{*n/2} I_n(2N_{tu}C^{*1/2}) \quad (11.39)$$

When $C^* = 1$,

$$\epsilon = 1 - [I_0(2N_{tu}) + I_1(2N_{tu})] e^{-2N_{tu}}$$

and when $N_{tu} \rightarrow \infty$,

$$\epsilon = 1 \quad \text{for all } C^*$$

4. For crossflow with one fluid mixed and one fluid unmixed. With C_{\min} mixed and C_{\max} unmixed:

$$\epsilon = 1 - e^{\{-1-[1-e^{(-C^*N_{tu})}/C^*]\}} \quad (11.40a)$$

When $C^* = 1$,

$$\epsilon = 1 - e^{-(1-e^{-N_{tu}})}$$

and when $N_{tu} \rightarrow \infty$,

$$\epsilon = 1 - e^{-1/C^*}$$

With C_{\max} mixed and C_{\min} unmixed:

$$\epsilon = \frac{1}{C^*} \left\{ 1 - e^{-C^*(1-e^{-N_{tu}})} \right\} \quad (11.40b)$$

When $C^* = 1$,

$$\epsilon = 1 - e^{-(1-e^{-N_{tu}})}$$

and when $N_{tu} \rightarrow \infty$,

$$\epsilon = \frac{1 - e^{-C^*}}{C^*}$$

5. For crossflow with both fluids mixed,

$$\epsilon = \frac{1}{\frac{1}{1 - e^{-N_{tu}}} + \frac{C^*}{1 - e^{-C^*N_{tu}}} - \frac{1}{N_{tu}}} \quad (11.41)$$

When $C^* = 1$,

$$\epsilon = \frac{1}{\frac{2}{1 - e^{-N_{tu}}} + \frac{1}{N_{tu}}}$$

and when $N_{tu} \rightarrow \infty$,

$$\epsilon = \frac{1}{1 + C^*}$$

6. For the 1–2 shell-and-tube exchanger with the shell fluid mixed [Tubular Exchanger Manufacturers' Association (TEMA) E-shell],

$$\epsilon = \frac{2}{(1 + C^*) + (1 + C^{*2})^{1/2} \coth(\Gamma/2)} \quad (11.42)$$

where

$$\Gamma = N_{tu}(1 + C^{*2})^{1/2}$$

When $C^* = 1$,

$$\epsilon = \frac{2}{2 + 2^{1/2} \coth \Gamma/2}$$

where

$$\Gamma = 2^{1/2} N_{tu}$$

and when $N_{tu} \rightarrow \infty$,

$$\epsilon = \frac{2}{(1 + C^*) + (1 + C^{*2})^{1/2}}$$

7. For the 1–2 shell-and-tube exchanger with the shell fluid unmixed (TEMA E-shell). For $C_{\min} = C_{\text{tube}}$ and $C_{\max} = C_{\text{shell}}$:

$$\epsilon = 1 - \frac{2C^* - 1}{2C^* + 1} \left[\frac{2C^* + e^{-N_{tu}(C^*+1/2)}}{2C^* - e^{-N_{tu}(C^*-1/2)}} \right] \quad (11.43a)$$

When $C^* = \frac{1}{2}$,

$$\epsilon = 1 - \frac{1 + e^{-N_{tu}}}{2 + N_{tu}}$$

and when $N_{tu} \rightarrow \infty$,

$$\epsilon = \begin{cases} \frac{2}{1 + 2C^*} & \text{for } C^* \geq 0.5 \\ 1 & \text{for } C^* < 0.5 \end{cases}$$

For $C_{\min} = C_{\text{shell}}$ and $C_{\max} = C_{\text{tube}}$:

$$\epsilon = \frac{1}{C^*} - \frac{2 - C^*}{C^*(2 + C^*)} \left[\frac{2 + C^* e^{-N_{tu}(1+C^*/2)}}{2 - C^* e^{-N_{tu}(1+C^*/2)}} \right] \quad (11.43b)$$

When $C^* = 1$,

$$\epsilon = 1 - \frac{1}{3} \left[\frac{2 + e^{-3N_{tu}/2}}{2 - e^{-N_{tu}/2}} \right]$$

and when $N_{tu} \rightarrow \infty$,

$$\epsilon = \frac{2}{2 + C^*}$$

8. For the 1–4 shell-and-tube exchanger with the shell fluid mixed (TEMA E-shell). For $C_{\min} = C_{\text{tube}}$ and $C_{\max} = C_{\text{shell}}$:

$$\epsilon = \frac{4}{2(1 + C^*) + (1 + 4C^{*2})^{1/2} \coth(\Gamma/4) + \tanh(N_{tu}/4)} \quad (11.44a)$$

where

$$\Gamma = N_{tu} (1 + 4C^{*2})^{1/2}$$

When $C^* = 1$,

$$\epsilon = \frac{4}{4 + 5^{1/2} \coth(\Gamma/4) + \tanh(N_{tu}/4)}$$

where

$$\Gamma = 5^{1/2} N_{tu}$$

and when $N_{tu} \rightarrow \infty$ with $C_{\min} = C_{\text{tube}}$,

$$\epsilon = \frac{4}{2(1 + C^*) + (1 + 4C^{*2})^{1/2} + 1}$$

For $C_{\min} = C_{\text{shell}}$ and $C_{\max} = C_{\text{tube}}$:

$$\epsilon = \frac{4}{2(1 + C^*) + (4 + C^{*2})^{1/2} \coth(\Gamma/4) + C^* \tanh(C^* N_{tu}/4)} \quad (11.44b)$$

where

$$\Gamma = N_{tu} (4 + C^{*2})^{1/2}$$

When $C^* = 1$,

$$\epsilon = \frac{4}{4 + 5^{1/2} \coth(\Gamma/4) + \tanh(N_{tu}/4)}$$

where

$$\Gamma = 5^{1/2} N_{tu}$$

and when $N_{tu} \rightarrow \infty$,

$$\epsilon = \frac{4}{2(1 + C^*) + (4 + C^{*2})^{1/2} + C^*}$$

9. For the 1-2 split-flow shell-and-tube exchanger with the shell fluid mixed (TEMA G-shell). For $C_{\min} = C_{\text{tube}}$ and $C_{\max} = C_{\text{shell}}$:

$$\epsilon = \frac{(1 + G + 2C^*G) + (2C^* + 1)De^{-\alpha} - e^{-\alpha}}{(1 + G + 2C^*G) + 2C^*(1 - D) + 2C^*De^{-\alpha}} \quad (11.45a)$$

where

$$D = \frac{1 - e^{-\alpha}}{2C^* + 1} \quad G = \frac{1 - e^{-\beta}}{2C^* - 1}$$

$$\alpha = \frac{1}{4} N_{tu} (2C^* + 1) \quad \text{and} \quad \beta = \frac{1}{2} N_{tu} (2C^* - 1)$$

When $C^* = 1$,

$$\epsilon = \frac{4 - e^{-N_{tu}/2} - e^{-3N_{tu}/2}}{4 - 3e^{-N_{tu}/2} - \frac{2}{3}e^{-3N_{tu}/4} - e^{-3N_{tu}/2}} \quad (11.45b)$$

When $N_{tu} \rightarrow \infty$ and $C^* > \frac{1}{2}$,

$$\epsilon = \frac{2C^* + 1}{2C^{*2} + C^* + 1}$$

and when $C^* \leq \frac{1}{2}$,

$$\epsilon = 1$$

For $C_{\min} = C_{\text{shell}}$ and $C_{\max} = C_{\text{tube}}$: For the effectiveness, use eq. (11.45a) with C^* replaced by $1/C^*$, N_{tu} replaced by $C^* N_{\text{tu}}$, and ϵ replaced by $C^* \epsilon$. When $C^* = 1$, use eq. (11.45b). When $N_{\text{tu}} \rightarrow \infty$ with $C^* < 2$,

$$\epsilon = \frac{C^* + 2}{2C^{*2} + C^* + 2}$$

and with $C^* \geq 2$,

$$\epsilon = \frac{1}{C^*}$$

10. For the 1–2 divided-flow shell-and-tube exchanger with the shell fluid mixed (TEMA J-shell). For $C_{\min} = C_{\text{tube}}$ and $C_{\max} = C_{\text{shell}}$:

$$\epsilon = \frac{2}{1 + 2C^* \Phi'} \quad (11.46a)$$

where

$$\Phi' = 1 + \gamma \frac{1 + \Phi}{1 - \Phi} - 2\gamma \frac{\gamma\Phi + (1 - \Phi)e^{-C^* N_{\text{tu}}(\gamma-1)/2}}{(1 - \Phi)^2 + \gamma(1 - \Phi^2)}$$

$$\Phi = e^{-\gamma C^* N_{\text{tu}}}$$

$$\gamma = \frac{(1 + 4C^{*2})^{1/2}}{2C^*}$$

When $C^* = 1$,

$$\epsilon = \frac{2}{1 + 2\Phi'} \quad (11.46b)$$

where

$$\Phi' = 1 + \gamma \frac{1 + \Phi}{1 - \Phi} - 2\gamma \frac{\gamma\Phi + (1 - \Phi)e^{-N_{\text{tu}}(\gamma-1)/2}}{(1 - \Phi)^2 + \gamma(1 - \Phi^2)}$$

$$\Phi = e^{-\gamma N_{\text{tu}}}$$

$$\gamma = \frac{5^{1/2}}{2}$$

and when $N_{\text{tu}} \rightarrow \infty$,

$$\epsilon = \frac{2}{1 + 2C^{*2} + (1 + 4C^{*2})^{1/2}}$$

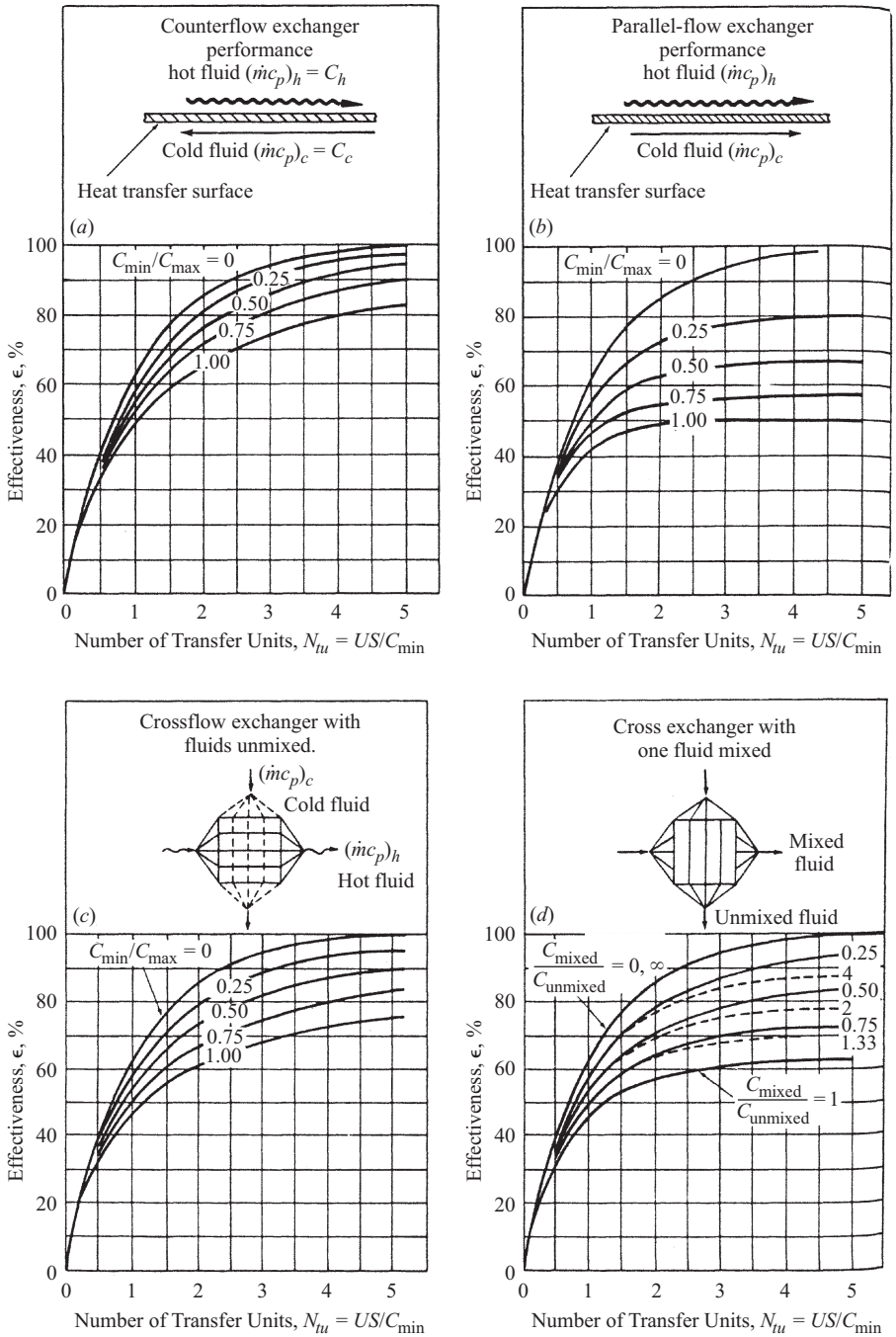


Figure 11.5 Heat exchanger effectiveness as a function of N_{tu} for 10 heat exchanger arrangements. (From Kakaç, 1991, with permission.)

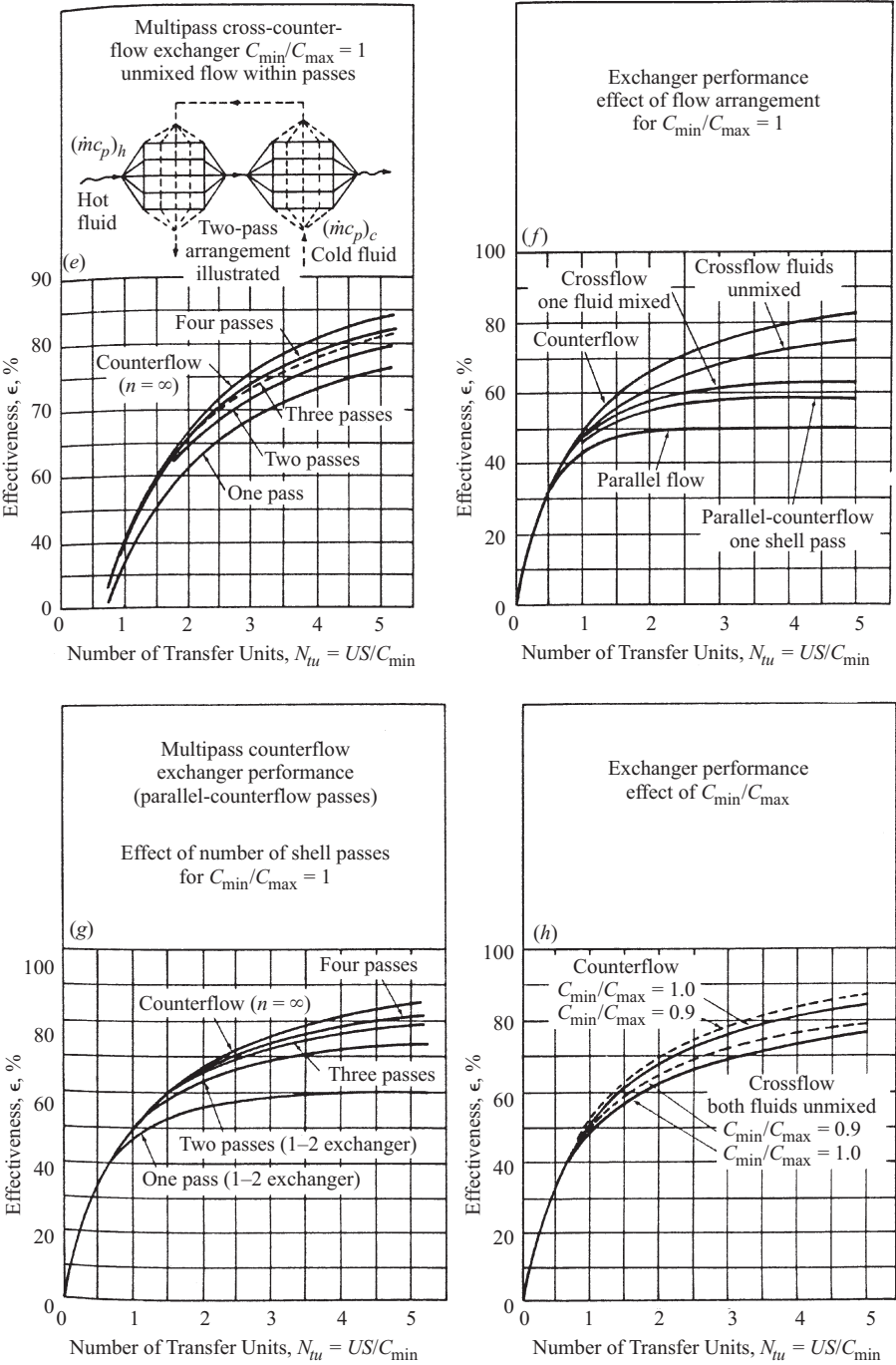


Figure 11.5 (Continued) Heat exchanger effectiveness as a function of N_{tu} for 10 heat exchanger arrangements. (From Kakaç, 1991, with permission.)

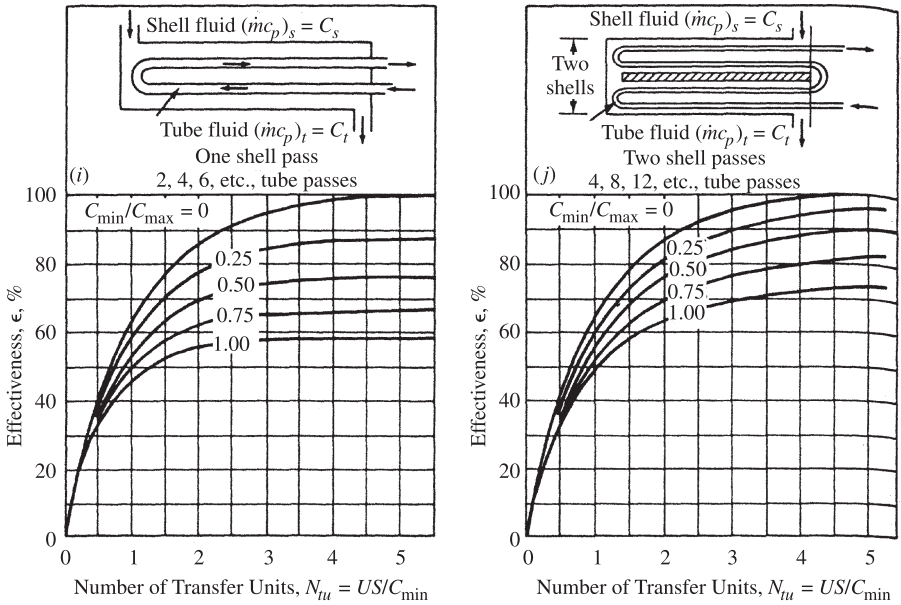


Figure 11.5 (Continued) Heat exchanger effectiveness as a function of N_{tu} for 10 heat exchanger arrangements. (From Kakaç, 1991, with permission.)

For $C_{min} = C_{shell}$ and $C_{max} = C_{tube}$: For the effectiveness, use eq. (11.46a) with C^* replaced by $1/C^*$, N_{tu} replaced by C^*N_{tu} , and ϵ replaced by $C^*\epsilon$. When $C^* = 1$, use eq. (11.46b), and when $N_{tu} \rightarrow \infty$ when $C_{min} = C_{shell}$,

$$\epsilon = \frac{2}{C^* + 2 + (C^*2 + 4)^{1/2}}$$

Graphs of the 10 arrangements just considered are shown in Fig. 11.5.

11.3.3 P - $N_{tu,c}$ Method

In shell-and-tube heat exchangers, any possible confusion deriving from selection of the C_{min} fluid is avoided through use of the P - $N_{tu,c}$ method. The method uses the cold-side capacity rate, so that

$$P = \frac{C_{min}}{C_c} \epsilon = \begin{cases} \epsilon & \text{for } C_c = C_{min} \\ \epsilon C^* & \text{for } C_c = C_{max} \end{cases} \quad (11.47)$$

$$N_{tu,c} = \frac{C_{min}}{C_c} N_{tu} = \begin{cases} N_{tu} & \text{for } C_c = C_{min} \\ N_{tu} C^* & \text{for } C_c = C_{max} \end{cases} \quad (11.48)$$

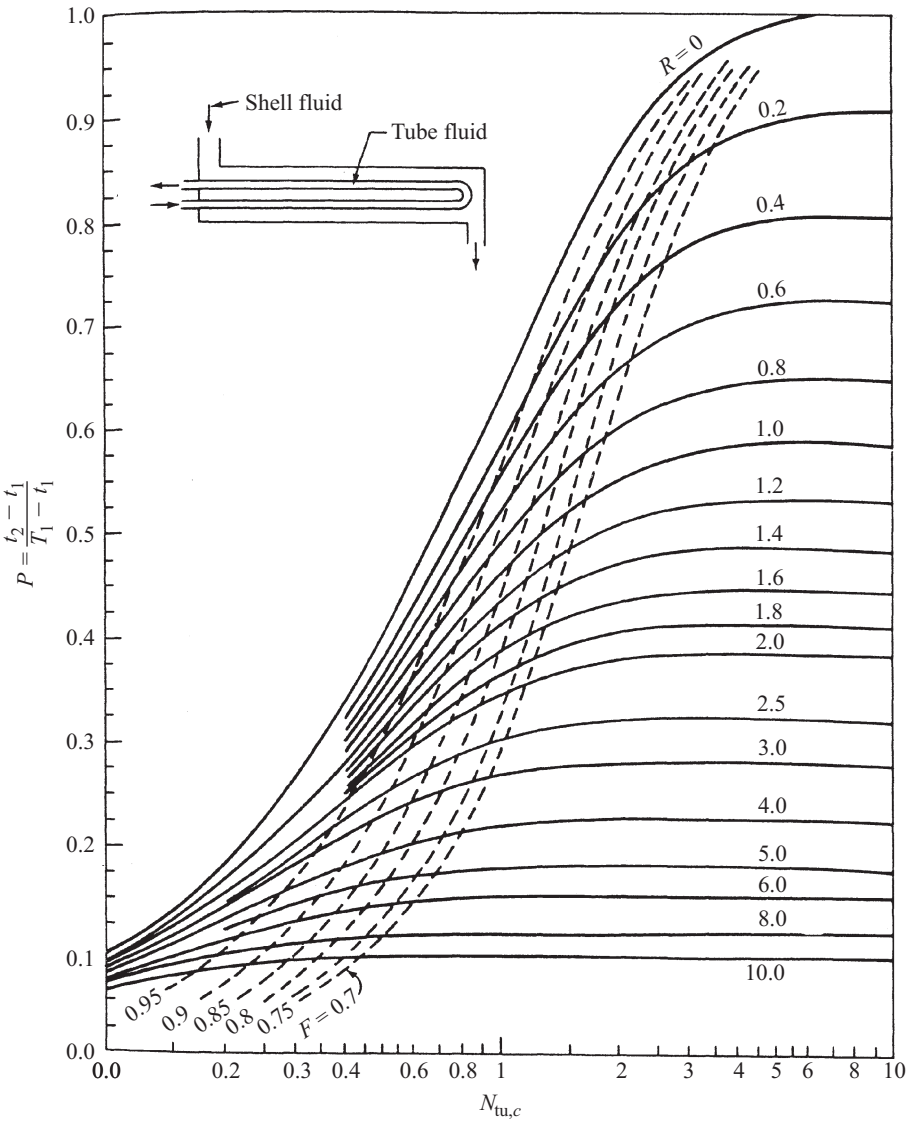


Figure 11.6 Temperature effectiveness P as a function of $N_{tu,c}$ and R for a 1-2 shell-and-tube heat exchanger with the shell fluid mixed. (From Kakaç, 1991, with permission.)

and it may be recalled that

$$R = \frac{C_c}{C_h} = \frac{T_1 - T_2}{t_2 - t_1} \tag{11.29b}$$

The parameter P is the temperature effectiveness and is similar to the exchanger effectiveness ϵ . It is a function of $N_{tu,c}$, R , and the flow arrangement

$$P = f(N_{tu,c}, R, \text{flow arrangement})$$

In the P – $N_{tu,c}$ method, the total heat flow from the hot fluid to the cold fluid will be

$$q = PC_c(T_1 - t_1) \quad (11.49)$$

and the P – $N_{tu,c}$ relationships can be derived from the ϵ – N_{tu} relationships by replacing C^* , ϵ and N_{tu} by R , P , and $N_{tu,c}$. For example, for the counterflow exchanger, which has an ϵ – N_{tu} representation of

$$\epsilon = \frac{1 - e^{-N_{tu}(1-C^*)}}{1 - C^*e^{-N_{tu}(1-C^*)}} \quad (11.37)$$

the P – $N_{tu,c}$ representation is

$$P = \frac{1 - e^{-N_{tu,c}(1-R)}}{1 - Re^{-N_{tu,c}(1-R)}}$$

Figure 11.6 is a chart of P plotted against $N_{tu,c}$ for the 1–2 shell-and-tube heat exchanger with the shell fluid mixed.

11.3.4 ψ – P Method

The ψ – P method proposed by Mueller (1967) combines the variables of the LMTD and ϵ – N_{tu} methods. Here ψ is introduced as the ratio of the true temperature difference to the *temperature head* (the inlet temperature difference of the two fluids, $T_1 - t_1$,

$$\psi = \frac{\theta_m}{T_1 - t_1} = \frac{\epsilon}{N_{tu}} = \frac{P}{N_{tu,c}} \quad (11.50)$$

The logarithmic mean temperature difference correction factor

$$F = \frac{\theta_m}{\text{LMTD}_c}$$

which can be written as

$$F = \frac{N_{cf}}{N_{tu,c}} \quad (11.51)$$

where N_{cf} is the number of transfer units for the counterflow exchanger obtained by solving eq. (11.37),

$$\epsilon = \frac{1 - e^{-N_{tu}(1-C^*)}}{1 - C^*e^{-N_{tu}(1-C^*)}} \quad (11.37)$$

for N_{tu} :

$$N_{cf} = \begin{cases} \frac{1}{1-R} \ln \frac{1-RP}{1-P} & \text{for } R \neq 1 \\ \frac{P}{1-P} & \text{for } R = 1 \end{cases} \quad (11.52)$$

Equations (11.30), (11.31), and (11.52) can be combined to yield

$$\psi = \frac{FP(1-R)}{\ln [(1-RP)/(1-P)]} \quad (11.53)$$

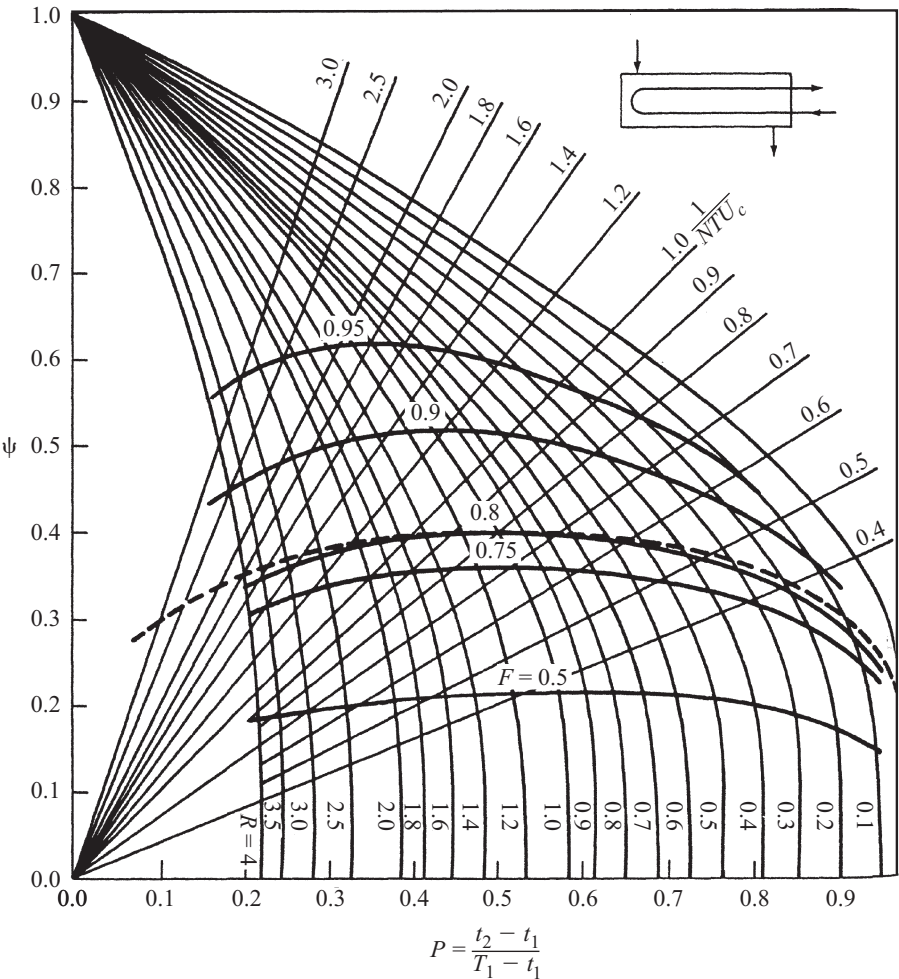


Figure 11.7 Mueller (1967) chart for Ψ as a function of P for a 1–2 shell-and-tube heat exchanger with the shell fluid mixed. (From Kakaç, 1991, with permission.)

so that

$$q = US\psi(T_1 - t_1) \quad (11.54)$$

which shows that

$$\psi = f(P, R, \text{flow arrangement})$$

The plot of ψ as a function of P is known as a *Mueller chart* (Mueller, 1967), and Fig. 11.7 shows such a chart for a 1–2 shell-and-tube heat exchanger with the shell fluid mixed.

11.3.5 Heat Transfer and Pressure Loss

The relationships presented thus far refer to the principles of heat transfer and the conservation of energy among the streams that make up the heat exchangers. The energy analysis is completed by taking into account the pumping power needed to force the streams through the heat exchanger structure. Relations for pumping power or pressure loss calculations are presented in Section 11.4.4.

Qualitatively speaking, in a heat exchanger with changing flow architecture, the heat exchanger performance and the pumping power performance compete with one another. For example, structural modifications such as the employment of extended surface (fins) that lead to heat transfer enhancement also cause an increase in pumping power. Trade-offs between these competing effects have been addressed extensively in thermal design (Bejan et al., 1996). For example, the confined thermodynamic irreversibility due to heat transfer and pumping power can be minimized by proper selection of the dimensions and aspect ratios of the flow passages (Bejan, 1997, 2000).

11.3.6 Summary of Working Relationships

A summary of the pertinent relationships employed in the analysis of heat exchangers follows.

- For the logarithmic mean temperature difference correction factor method (the LMTD method),

$$q = USF\theta_m$$

$$\theta_m = \text{LMTD} = \frac{\Delta T_1 - \Delta T_2}{\ln(\Delta T_1/\Delta T_2)} = \frac{\Delta T_2 - \Delta T_1}{\ln(\Delta T_2/\Delta T_1)} \quad (11.24)$$

where

$$\Delta T_1 = T_1 - t_2 \quad \Delta T_2 = T_2 - t_1$$

$$P = \frac{t_2 - t_1}{T_1 - t_1} \quad (11.29a)$$

$$R = \frac{T_1 - T_2}{t_2 - t_1} \quad (11.29b)$$

$$F = f(P, R, \text{flow arrangement})$$

- For the ϵ - N_{tu} method,

$$q = \epsilon C_{\min}(T_1 - t_1) \quad (11.37)$$

$$\epsilon = \frac{q}{q_{\max}} = \frac{C_h(T_2 - T_1)}{C_{\min}(T_1 - t_1)} = \frac{C_c(t_2 - t_1)}{C_{\min}(T_1 - t_1)} \quad (11.35)$$

$$C^* = \frac{C_{\min}}{C_{\max}} \quad (0 \leq C^* \leq 1) \quad (11.31)$$

$$N_{tu} \equiv \frac{US}{C_{\min}} = \frac{1}{C_{\min}} \int_S U dS \quad (11.33)$$

$$\epsilon = f(N_{tu}, C^*, \text{flow arrangement})$$

- For the P - $N_{tu,c}$ method,

$$q = PC_c(T_1 - t_1) \quad (11.49)$$

$$N_{tu,c} = \frac{US}{C_c} = \frac{C_{\min}}{C_c} N_{tu} \quad (11.48)$$

$$P = f(N_{tu,c}, R, \text{flow arrangement})$$

- For the ψ - P method,

$$q = US\psi(T_1 - t_2) \quad (11.54)$$

$$\psi = \frac{\theta_m}{T_1 - t_1} = \frac{\epsilon}{N_{tu}} = \frac{P}{N_{tu,c}} \quad (11.50)$$

$$\psi = f(P, R, \text{flow arrangement})$$

11.4 SHELL-AND-TUBE HEAT EXCHANGER

11.4.1 Construction

Shell-and-tube heat exchangers are fabricated with round tubes mounted in cylindrical shells with their axes coaxial with the shell axis. The differences between the many variations of this basic type of heat exchanger lie mainly in their construction features and the provisions made for handling differential thermal expansion between tubes and shell.

A widely accepted standard is published by the Tubular Exchanger Manufacturers' Association (TEMA). This standard is intended to supplement the ASME as well as other boiler and pressure vessel codes. The TEMA (1998) standard was prepared by a committee comprising representatives of 27 U.S. manufacturing companies, and their combined expertise and experience provide exchangers of high integrity at reasonable cost. TEMA provides a standard designation system that is summarized in Fig. 11.8. Six examples of the shell-and-tube heat exchanger arrangements are shown in Fig. 11.9.

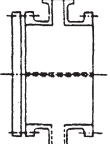
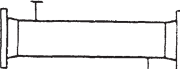
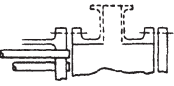
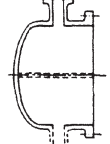
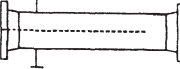

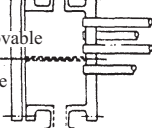
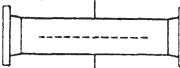
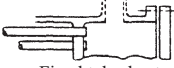
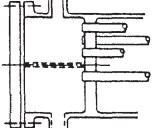
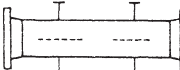
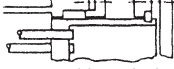
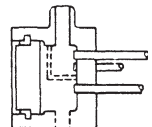
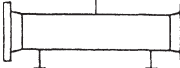

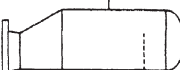
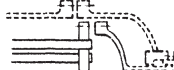
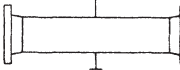

Front End Stationary Head Types		Shell Types		Rear End Head Types	
A		E		L	
	Channel and removable cover		One pass shell		Fixed tubesheet like "A" stationary head
B		F		M	
	Bonnet (integral cover)		Two pass shell with longitudinal baffle		Fixed tubesheet like "B" stationary head
C		G		N	
	Channel integral with tube-sheet and removable cover		Split flow		Fixed tubesheet like "N" stationary head
N		H		P	
	Channel integral with tube-sheet and removable cover		Double split flow		Outside packed floating head
D		J		S	
	Special high pressure closure		Divided flow		Floating head with backing device
X		K		T	
			Kettle type reboiler		Pull through floating head
U		X		W	
			Cross flow		Externally sealed floating tubesheet

Figure 11.8 TEMA standard designation system for shell-and-tube heat exchangers. (From Saunders, 1988, with permission.)

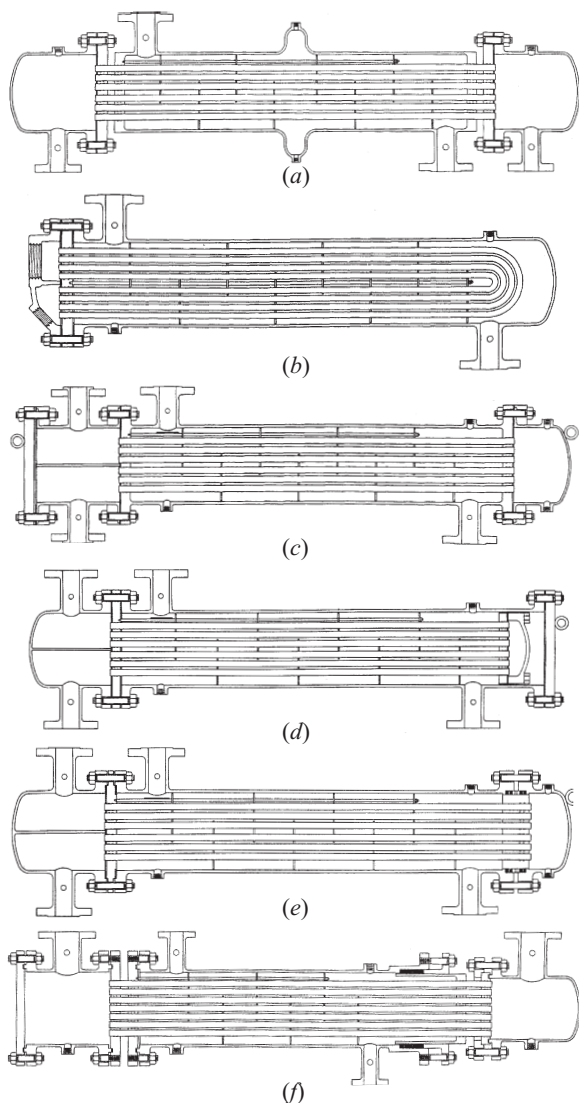


Figure 11.9 (a) Single-tube-pass baffled single-pass-shell shell-and-tube heat exchanger designed to give essentially counterflow conditions. The toroidal expansion joint in the center of the shell accommodates differential thermal expansion between the tubes and the shell. (b) U-tube single-pass-shell shell-and-tube heat exchanger. (c) Two-pass baffled single-pass-shell shell-and-tube heat exchanger. (d) Heat exchanger similar to that of (c) except for the floating head used to accommodate differential thermal expansion between the tubes and the shell. (e) Heat exchanger that is similar to the heat exchanger in (d) but with a different type of floating head. (f) Single-tube-pass baffled single-pass-shell shell-and-tube heat exchanger with a packed joint floating head and double header sheets to assure that no fluid leaks from one fluid circuit into the other. (Courtesy of the Patterson-Kelley Co. and reproduced from Fraas, 1989, with permission.)

Figure 11.9a shows a single-pass tube side and a baffled single-pass shell side. A toroidal expansion joint in the center of the shell accommodates the differential thermal expansion between the tubes and the shell. Figure 11.9b employs U-tubes within the baffled single-pass shell. In this case, account must be taken of the fact that approximately half of the tube-side surface is in counterflow and the other half of the tube-side surface is in co-current flow with the shell-side fluid. The unit shown in Fig. 11.9c has a flow pattern that is similar to the unit shown in Fig. 11.9b. However, the construction is more complex, to facilitate inspection of the inside of the tubes, the cleaning of the tubes mechanically, and the replacement of defective tubes. While the configuration of Fig. 11.9d does not provide for differential thermal expansion between the tubes and the shell, the *floating head* allows for thermal expansion between the tubes and the shell and for large temperature differences between the fluids. In Fig. 11.9e, leakage from one fluid stream into the other through the packed joints of the floating head goes directly to the exterior of the shell, where it can be detected readily and without contamination of the other stream. Figure 11.9f indicates a further variation of the type of exchanger shown in Fig. 11.9e.

11.4.2 Physical Data

Tube Side For a tube bundle containing n_t tubes of length L with outside and inside diameters of d_o and d_i , respectively, the flow area will be

$$A_f = \frac{\pi n_t d_i^2}{4n_p} \quad (11.55)$$

where n_p is the number of passes. The surface area for the n_t tubes is

$$S_o = \pi d_o L n_t \quad (11.56)$$

The equivalent diameter to be used in establishing the heat transfer coefficient is

$$d_e = d_i \quad (11.57)$$

and the length of the tube to be used in pressure loss computations is L_T :

$$L_T = L + 2\delta_{sh} \quad (11.58)$$

where δ_{sh} is the thickness of the tube sheet.

Because the tube side is concerned only with the number of tubes and tube passes and not with the tube layout, eqs. (11.55) through (11.58) pertain to tubes on square (\square), rotated square (\diamond), and equilateral triangular (\triangle) pitch. The number of tubes within a given shell can be obtained from a list of tube counts such as those provided by Kern (1950) and Saunders (1988).

Shell Side Saunders (1988) has provided the pertinent physical data for the shell side with segmented baffles. A concise pictorial summary of the various shell-side

parameters is shown in Fig. 11.10. With the nomenclature contained in Fig. 11.10, several flow areas can be identified.

The crossflow area is

$$A_c = C_1 + \frac{(D_s - C_1 - d_o)(p - d_o)}{yp} \quad (11.59)$$

where the tube pitch factor y varies with the tube arrangement:

$$y = \begin{cases} 1.000 & \text{for equilateral triangular } \triangleright, 30^\circ \text{ pitch} \\ 0.866 & \text{for equilateral triangular } \triangle, 60^\circ \text{ pitch} \\ 1.000 & \text{for square } \square \text{ pitch} \\ 0.707 & \text{for square rotated } \diamond 45^\circ \text{ pitch} \end{cases}$$

The tube bundle bypass area is

$$A_{bp} = C_1 L_{bc} \quad (11.60)$$

where L_{bc} is the central baffle spacing

The shell-to-baffle leakage area for one baffle is

$$A_{sb} = \frac{1}{2}(\pi + \theta_1) D_s \delta_{sb} \quad (11.61)$$

where δ_{sb} is the shell-to-baffle spacing:

$$\delta_{sb} = \frac{D_s - D_b}{2}$$

$$\theta_1 = \arcsin \left(1 - \frac{2l_c}{D_s} \right) \quad (\text{rad})$$

The fraction of the total number of tubes in one window is

$$F_w = \frac{\theta_3 - \sin \theta_3}{2\pi} \quad (11.62)$$

where

$$\theta_3 = 2 \arccos \frac{D_s - 2l_c}{D_s - C_1} \quad (\text{rad})$$

The tube-to-baffle leakage area for one baffle is

$$A_{tb} = \frac{\pi d_o (1 - F_w) n_t \delta_{tb}}{2} \quad (11.63)$$

where δ_{tb} is the tube to baffle spacing.

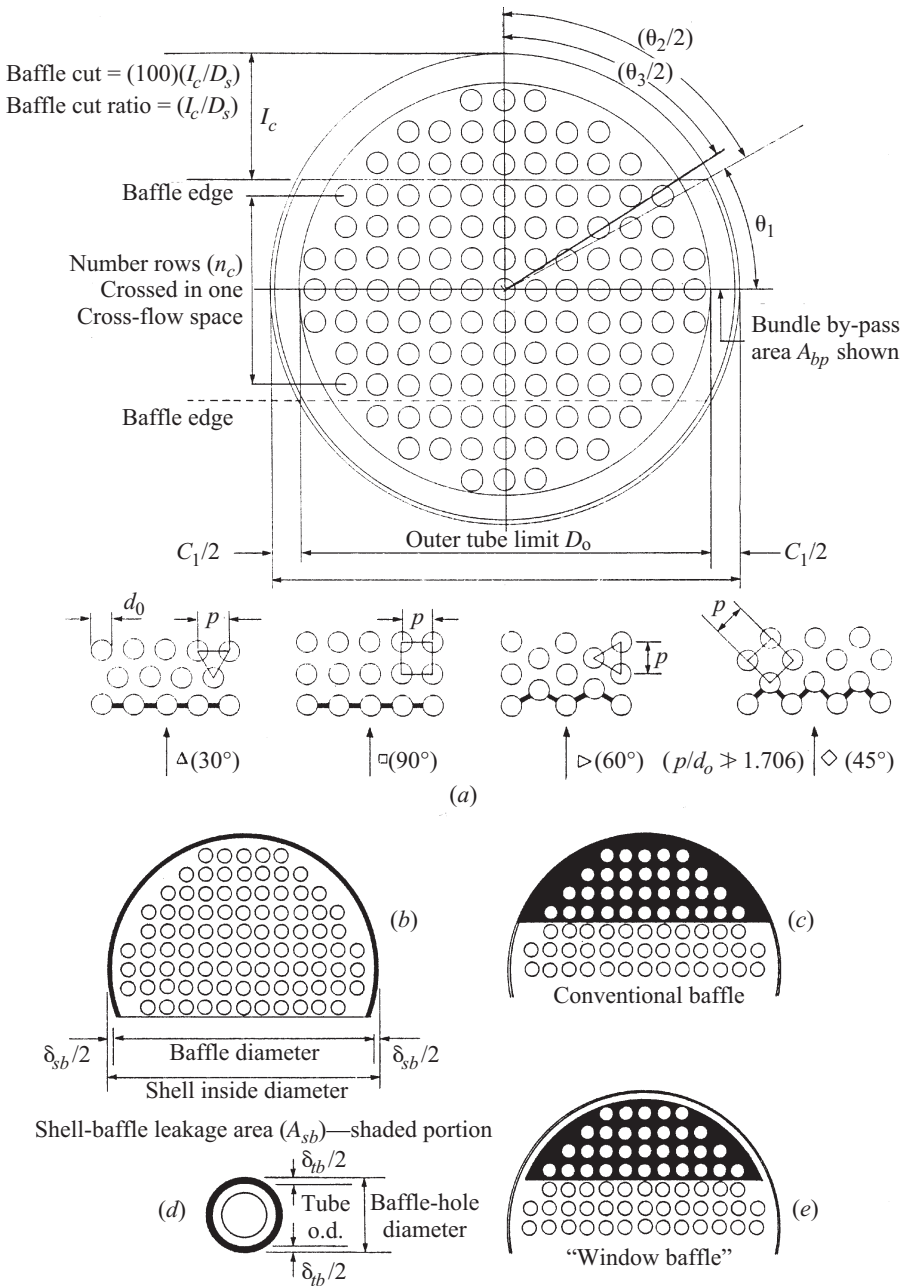


Figure 11.10 Shell-side terminology and areas for shells with segmental baffles: (a) end view showing tube layout and baffles; (b) shell-baffle leakage area; (c) conventional baffle arrangement; (d) tube-baffle leakage area; (e) window baffle. (From Saunders, 1988, with permission.)

The free area for fluid flow in one window section will be

$$A_w = A_{wg} - A_{wt}$$

where A_{wg} is the gross window area:

$$A_{wg} = \frac{D_s^2}{8} (\theta_2 - \sin \theta_2)$$

where

$$\theta_2 = \arccos \left(\frac{1 - 2l_c}{D_s} \right)$$

and the area occupied by the tubes in one window is

$$A_{wt} = \frac{\pi}{4} n_{tw} d_o^2$$

where the number of tubes in the window is

$$n_{tw} = F_w n_t$$

Hence

$$A_w = \frac{D_s^2}{8} (\theta_2 - \sin \theta_2) - \frac{\pi}{4} n_{tw} d_o^2 \quad (11.64)$$

The number of tubes crossed in one crossflow space is

$$n_c = \frac{D_s - 2l_c}{qp} \quad (11.65)$$

where the factor q varies with the tube pitch:

$$q = \begin{cases} 0.866 & \text{for equilateral triangle } \triangle, 30^\circ \text{ pitch} \\ 1.000 & \text{for equilateral triangle } \triangleright, 60^\circ \text{ pitch} \\ 1.000 & \text{for square } \square \text{ pitch} \\ 0.707 & \text{for square rotated } \diamond 45^\circ \text{ pitch} \end{cases}$$

The effective number of tubes crossed in one window is

$$n_{cw} = \frac{0.8l_c}{qp} \quad (11.66)$$

The equivalent diameter of one window to be used in establishing the heat transfer coefficient is

$$D_e = \frac{4A_w}{\pi d_o n_{tw} + D_s \theta_2 / 2} \quad (11.67)$$

11.4.3 Heat Transfer Data

The establishment of the heat transfer coefficient on the tube side and the shell side of a shell-and-tube exchanger is of fundamental importance to the design and analysis of the shell-and-tube heat exchanger.

Tube Side Investigations that pertain to heat transfer and friction data within tubes have been reported by Pohlhausen (1921), DeLorenzo and Anderson (1945), Deissler (1951), McAdams (1954), Hausen (1959, 1974), Stefan (1959), Barnes and Jackson (1961), Dalle Donne and Bowditch (1963), Yang (1962), Petukhov and Popov (1963), Perkins and Wörsæ-Schmidt (1965), Wörsæ-Schmidt (1966), Test (1968), Webb (1971), Oskay and Kakaç (1973), Shah and London (1978), Rogers (1980), Kays and Crawford (1993), Gnielinski (1976), Kakaç et al. (1985, 1987), Shah and Bhatti (1987), and Kakaç and Yener (1994). These are summarized by Kraus et al. (2001).

Some heat transfer correlations depend on a viscosity correction,

$$\phi^n = \left(\frac{\mu}{\mu_w} \right)^n \quad (11.68)$$

where μ and μ_w are the dynamic viscosities at the bulk and wall temperature, respectively, and where n is an exponent depending on whether the process is one of heating or one of cooling.

The heat transfer correlations that follow are subdivided into three listings: for laminar flow, for transition flow, and for turbulent flow. In all of these, unless otherwise indicated, all fluid properties are based on the bulk temperature:

$$T_b = \frac{T_1 + T_2}{2} \quad \text{and} \quad t_b = \frac{t_1 + t_2}{2}$$

Laminar Flow: $Re \leq 2300$ For situations in which the thermal and velocity profiles are fully developed, the Nusselt number depends only on the thermal boundary conditions. For circular tubes with $Pr \geq 0.60$ and $Re \cdot Pr \cdot L/d > 0.05$, the Nusselt numbers have been shown to be

$$Nu = 3.657 \quad (11.69)$$

for constant-temperature conditions and

$$Nu = 4.364 \quad (11.70)$$

for constant-heat-flux conditions. Here Re_d is the Reynolds number based on the tube diameter d , and L is the tube length.

In many cases, the Graetz number, which is the product of the Reynolds and Prandtl numbers and the diameter-to-length ratio:

$$Gz \equiv Re \cdot Pr \frac{d}{L}$$

is employed.

At the entrance of a tube, the Nusselt number is infinite and decreases asymptotically to the value for fully developed flow as the flow progresses along the length of the tube. The Sieder–Tate (1936) equation gives a good correlation for both liquids and gases in the region where the thermal and velocity profiles are both developing:

$$Nu = \frac{hd}{k} = 1.86 \left(Re \cdot Pr \frac{d}{L} \right)^{1/3} \phi^{0.14} \quad (11.71)$$

for T_w constant and within the following ranges:

$$0.48 \leq Pr \leq 16,700 \quad 0.0044 \leq \phi \leq 9.75 \quad \left(Re \cdot Pr \frac{d}{L} \right)^{1/3} \phi^{0.14} \geq 2$$

The limitations should be observed carefully as the Sieder–Tate equation yields a zero heat transfer coefficient for extremely long tubes.

The correlation of Hausen (1943) is good for both liquids and gases at constant wall temperature:

$$Nu = \frac{hd}{k} = 3.66 + \frac{0.668 Re \cdot Pr(d/L)}{1 + 0.40 [Re \cdot Pr(d/L)]^{2/3}} \quad (11.72)$$

The heat transfer coefficient obtained from this correlation is the average value for the entire length of the tube, and it may be observed that when the tube is sufficiently long, the Nusselt number approaches the constant value of 3.657.

Transition: $2300 \leq Re \leq 10,000$ For transition flow for both liquids and gases, the Hausen (1943) correlation for both liquids and gases may be employed:

$$Nu = \frac{hd}{k} = 0.116 (Re^{2/3} - 125) Pr^{1/3} \phi^{0.14} \left[1 + \left(\frac{d}{L} \right)^{2/3} \right] \quad (11.73)$$

Turbulent Flow: $Re \geq 10,000$ For both liquids and gases, Dittus and Boelter (1930) recommend

$$Nu = \frac{hd}{k} = 0.023 Re^{0.80} \cdot Pr^n \quad (11.74)$$

where $n = 0.30$ for cooling and $n = 0.40$ for heating.

Sieder and Tate (1936) removed the dependence on heating and cooling by setting the exponent on Pr to $1/3$ and adding a viscosity correction:

$$Nu = \frac{hd}{k} = 0.023 Re^{0.80} \cdot Pr^{1/3} \phi^{0.14} \quad (11.75)$$

This correlation is valid for liquids and gases for $L/d > 60$, $Pr > 0.60$, and moderate $T_w - T_b$.

The correlation of Petukhov (1970),

$$Nu = \frac{hd}{k} = \frac{(f/8)Re \cdot Pr}{1.07 + 12.7(f/8)^{1/2}(Pr^{2/3} - 1)} \quad (11.76)$$

where

$$f = \frac{1}{(1.82 \log_{10} Re - 1.64)^2} \quad (11.77)$$

is valid for $1 \leq Pr \leq 2000$ and $10^4 \leq Re \leq 5 \times 10^5$.

Bejan (1995) has suggested that the most accurate correlation is that of Gnielinski (1976), who provided a modification of the Petukhov (1970) correlation of eq. (11.76) with f given by eq. (11.64):

$$Nu = \frac{hd}{k} = \frac{(f/8)(Re - 1000)Pr}{1.00 + 12.7(f/8)^{1/2}(Pr^{2/3} - 1)} \quad (11.78)$$

in order to extend the range to $1.0 < Pr < 10^6$ and $2300 < Re < 5 \times 10^6$.

Two simpler alternatives to eq. (11.78) have been suggested by Gnielinski (1976):

$$Nu = \frac{hd}{k} = 0.0214(Re^{0.80} - 100)Pr^{0.40} \quad (11.79)$$

for $0.50 < Pr < 1.50$ and $10^4 < Re < 5 \times 10^6$, and

$$Nu = \frac{hd}{k} = 0.012(Re^{0.87} - 280)Pr^{0.40} \quad (11.80)$$

for $0.50 < Pr < 500$ and $3 \times 10^3 < Re < 10^6$.

Equation (11.76) can be modified to account for variable properties:

$$Nu = \frac{hd}{k} = \frac{(f/8)Re \cdot Pr}{1.07 + 12.7(f/8)^{1/2}(Pr^{2/3} - 1)} \phi^n \quad (11.81)$$

where $n = 0.11$ for heating and $n = 0.25$ for cooling and where f is given by eq. (11.64). In addition to the restrictions on L/d and Re cited with eq. (11.64), $1 \leq \phi \leq 40$ and $0.5 \leq Pr \leq 140$.

Sleicher and Rouse (1975) give

$$Nu = \frac{hd}{k} = 5 + 0.015Re^m \cdot Pr^n \quad (11.82)$$

where

$$m = 0.88 - \frac{0.24}{Pr + 4.00}$$

$$n = \frac{1}{3} + 0.5e^{-0.60\text{Pr}}$$

for $1 \leq \text{Pr} \leq 1000$ and $10^4 \leq \text{Re} \leq 10^6$.

Shell Side It is not practical to manufacture a shell-and-tube heat exchanger in which fluid flow between the baffles and the shell is prevented by welding each segmented baffle to the inside of the shell. It is also not practical to try and prevent fluid flow in the annular space between each tube and a baffle by fitting the annular space around each tube with a tightly fitting sleeve and or by trying to assure that the tubes completely fill the shell in a uniform manner such that there are no gaps between the tube bundle and the shell. Yet an exchanger with a shell side fabricated with these features would yield the idealized flow pattern shown in Fig. 11.11a. Notice that in this ideal flow pattern, there is no bypassing of the tube bundle within a baffle space and no leakage of the shell-side fluid between adjacent baffle spaces.

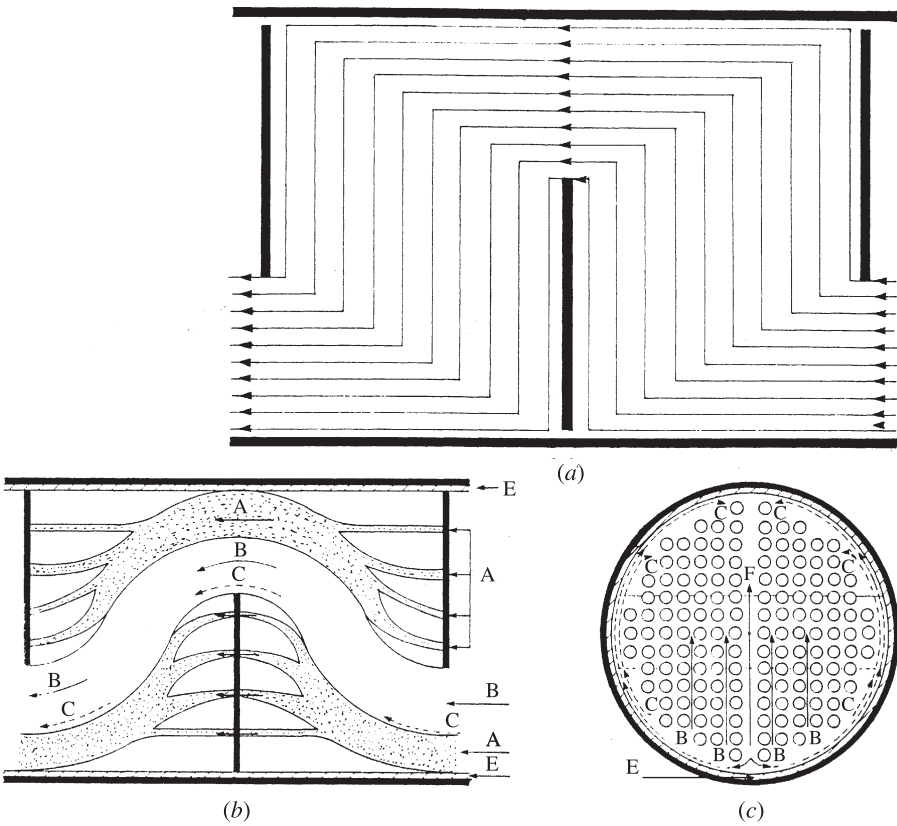


Figure 11.11 Tinker (1951) model for the shell-side flow streams: (a) idealized model; (b, c) model proposed by Tinker. (From Saunders, 1988, with permission.)

Because of the need to have certain tube bundles removable and because of the cost, shell-and-tube heat exchangers always possess gaps between the baffles and the shell and between the baffles and the tubes. Moreover, there may also be gaps between the tube bundle and the shell, and these gaps will be due to impingement baffles and/or pass partitions.

Tinker (1951) proposed the shell-side fluid flow model shown in Fig. 11.11*b* as the departure from the ideal. The stream designations *A*, *B*, *C*, and *E* were proposed by Tinker (1951), and later, stream *F*, shown in Fig. 11.8*c*, was added. Tinker also provided a method for determination of the individual flow stream components from which the overall heat transfer coefficient and pressure loss could be determined. While the Tinker (1951) approach was fundamentally sound, experimental data were sparse and unreliable, and, of course, there were no computers in the 1950s.

Although the Tinker (1951) method was later simplified by Tinker (1958) and simplified further by Devore (1962) and Fraas (1989), many heat exchanger designers continued to rely on the methods provided by Donohue (1949), Kern (1950), and Gilmour (1952–54), which assumed that *all* the shell-side fluid flowed across the tube bundle in crossflow without leakage, as shown in Fig. 11.11*a*. A correction factor was later applied to heat transfer coefficients obtained from these methods to account for all the leakage streams.

Bell (1963) published a method based on extensive research at the University of Delaware, and this produced the name *Bell–Delaware method*. This method accounts for the various leakage streams and involves relatively straightforward calculations. Details of the method, complete with supporting curves, have been presented by Bell (1988) and Taborek (1983).

In the Bell–Delaware method, an ideal heat transfer coefficient h_{id} is determined for pure crossflow using the entire shell-side fluid flow stream at (or near) the center of the shell. It is computed from the correlations of Zhukauskas (1987) outlined in Chapter 6 and repeated here as eqs. (11.83) and (11.84): For in-line tube bundles with the number of tube rows $n_r \geq 16$:

$$Nu_d = \begin{cases} 0.90Re_d^{0.4}Pr^{0.36}\Upsilon^{0.25} & \text{for } 1 \leq Re_d < 100 \\ 0.52Re_d^{0.5}Pr^{0.36}\Upsilon^{0.25} & \text{for } 100 \leq Re_d < 1000 \\ 0.27Re_d^{0.63}Pr^{0.36}\Upsilon^{0.25} & \text{for } 1000 \leq Re_d < 2 \times 10^5 \\ 0.033Re_d^{0.8}Pr^{0.36}\Upsilon^{0.25} & \text{for } 2 \times 10^5 \leq Re_d < 2 \times 10^6 \end{cases} \quad (11.83)$$

and for staggered tube bundles with the number of tube rows $n_r \geq 16$:

$$Nu_d = \begin{cases} 1.04Re_d^{0.4}Pr^{0.36}\Upsilon^{0.25} & \text{for } 1 \leq Re_d < 500 \\ 0.71Re_d^{0.5}Pr^{0.36}\Upsilon^{0.25} & \text{for } 500 \leq Re_d < 1000 \\ 0.35\phi^{0.2}Re_d^{0.63}Pr^{0.36}\Upsilon^{0.25} & \text{for } 1000 \leq Re_d < 2 \times 10^5 \\ 0.031\phi^{0.2}Re_d^{0.8}Pr^{0.36}\Upsilon^{0.25} & \text{for } 2 \times 10^5 \leq Re_d < 2 \times 10^6 \end{cases} \quad (11.84)$$

In eqs. (11.83) and (11.84),

$$\Upsilon = \frac{\text{Pr}}{\text{Pr}_w} \quad \text{and} \quad \varrho = \frac{X_T}{X_L}$$

The ideal heat transfer coefficient is then corrected using the product of five correction factors to provide the shell-side heat transfer coefficient h_s :

$$h_s = J_C J_L J_B J_S J_R h_{id} \quad (11.85)$$

The numerical values of the correction factors were determined by Bell (1963) and with a subsequent curve-fitting procedure due to Taborek (1998). They are now considered in detail.

J_C is the correction factor for the baffle cut and spacing and is the average for the entire exchanger. It is expressed as a fraction of the number of tubes in crossflow

$$J_C = 0.55 + 0.72 F_C \quad (11.86)$$

where with

$$\begin{aligned} \varphi &= \frac{D_s - 2l_c}{D_o} \\ F_C &= \frac{1}{\pi} [\pi + \varphi \sin(\arccos \varphi) - 2 \arccos \varphi] \end{aligned} \quad (11.87)$$

In eqs. (11.86) and (11.87), D_s is the shell inside diameter (m), D_o is the diameter at the outer tube limit (m), and l_c is the distance from the baffle tip to the shell inside diameter (m).

J_L is the correction factor for baffle leakage effects, including both the tube-to-baffle and the baffle-to-shell effects (the A and E streams in Fig. 11.11*b* and *c*):

$$J_L = 0.44(1 - r_a) + [1 - 0.044(1 - r_a)] e^{-2.2r_b} \quad (11.88)$$

where

$$r_a = \frac{A_{sb}}{A_{sb} + A_{tb}} \quad (11.89a)$$

$$r_b = \frac{A_{sb} + A_{tb}}{A_w} \quad (11.89b)$$

J_B is the correction factor for bundle and partition bypass effects (the C and F streams in Fig. 11.11*b* and *c*):

$$J_B = \begin{cases} 1 & \text{for } \zeta \geq \frac{1}{2} \\ e^{-C r_c [1 - 2\zeta^{1/3}]} & \text{for } \zeta < \frac{1}{2} \end{cases} \quad (11.90)$$

where

$$r_c = \frac{A_{bp}}{A_w} \quad (11.91a)$$

$$\zeta = \frac{N_{ss}}{N_{cc}} \quad (11.91b)$$

where with X_L as the longitudinal tube pitch and N_{ss} taken as the number of sealing strip pairs,

$$N_{cc} = \frac{D_s - 2l_c}{X_L}$$

$$C = \begin{cases} 1.35 & \text{for } \text{Re}_s \leq 100 \\ 1.25 & \text{for } \text{Re}_s > 100 \end{cases} \quad (11.91c)$$

Here

$$A_{bp} = L_{bc} (D_s - D_o + 0.5N_P w_P)$$

is the crossflow area for the bypass, where N_P is the number of bypass divider lanes that are parallel to the crossflow stream B , w_P is the width of the bypass divider lane (m), and L_{bc} is the central baffle spacing.

J_S is the correction factor that accounts for variations in baffle spacing at the inlet and outlet sections as compared to the central baffle spacing:

$$J_S = \frac{N_b - 1 + (L_i^*)^{(1-n)} - (L_o^*)^{(1-n)}}{N_b - 1 + (L_i^*)^{(1-n)} + (L_o^*)^{(1-n)}} \quad (11.92)$$

where N_b is the number of baffles and

$$L_i^* = \frac{L_{bi}}{L_{bc}} \quad (11.93a)$$

$$L_o^* = \frac{L_{bo}}{L_{bc}} \quad (11.93b)$$

$$n = \begin{cases} \frac{3}{5} & \text{for turbulent flow} \\ \frac{1}{3} & \text{for laminar flow} \end{cases} \quad (11.93c)$$

Here L_{bi} is the baffle spacing at the inlet (m), L_{bo} is the baffle spacing at the outlet (m), and L_{bc} is the central baffle spacing (m)

J_R is the correction factor that accounts for the temperature gradient when the shell-side fluid is in laminar flow:

$$J_R = \begin{cases} 1 & \text{for } \text{Re}_s \geq 100 \\ \left(\frac{10}{N_{r,c}} \right)^{0.18} & \text{for } \text{Re}_s \leq 20 \end{cases} \quad (11.94)$$

For $20 < \text{Re}_s < 100$, a linear interpolation should be performed between the two extreme values. In eq. (11.81), Re_s is the shell-side Reynolds number and $N_{r,c}$ is the number of effective tube rows crossed through one crossflow section.

11.4.4 Pressure Loss Data

Tube Side The pressure loss inside tubes of circular cross section in a shell-and-tube heat exchanger is the sum of the friction loss within the tubes and the turn losses between the passes of the exchanger. The friction loss inside the tubes is given by

$$\Delta P_f = \frac{4f\rho u^2}{2} \frac{L}{d_i} \quad (\text{Pa}) \quad (11.95a)$$

where u is the linear velocity of the fluid in the tubes, or

$$\Delta P_f = \frac{4fG^2}{2\rho} \frac{L}{d} \quad (\text{Pa}) \quad (11.95b)$$

where G is the mass velocity of the fluid in the tubes. In eqs. (11.95), f is the friction factor.

The fluid will undergo an additional pressure loss due to contractions and expansions that occur during fluid turnaround between tube passes. Kern (1950) and Kern and Kraus (1972) have proposed that this loss be given by one velocity head per turn:

$$\Delta P_t = \frac{4\rho u^2}{2} \quad (\text{Pa}) \quad (11.96)$$

In an exchanger with a single pass,

$$\Delta P_t = \frac{4\rho u^2}{2} = 2\rho u^2 \quad (\text{Pa}) \quad (11.97)$$

and in an exchanger with n_p passes, there will be $n_p - 1$ turns. Hence

$$\Delta P_t = 2(n_p - 1)\rho u^2 \quad (11.98)$$

Friction factors may be obtained from Fig. 11.12, which plots the friction factor as a function of the Reynolds number inside the tube and the relative roughness, ϵ/d_i . The figure is due to Moody (1944), and it may be noted that when the flow is laminar,

$$f = \frac{16}{\text{Re}} \quad (11.99)$$

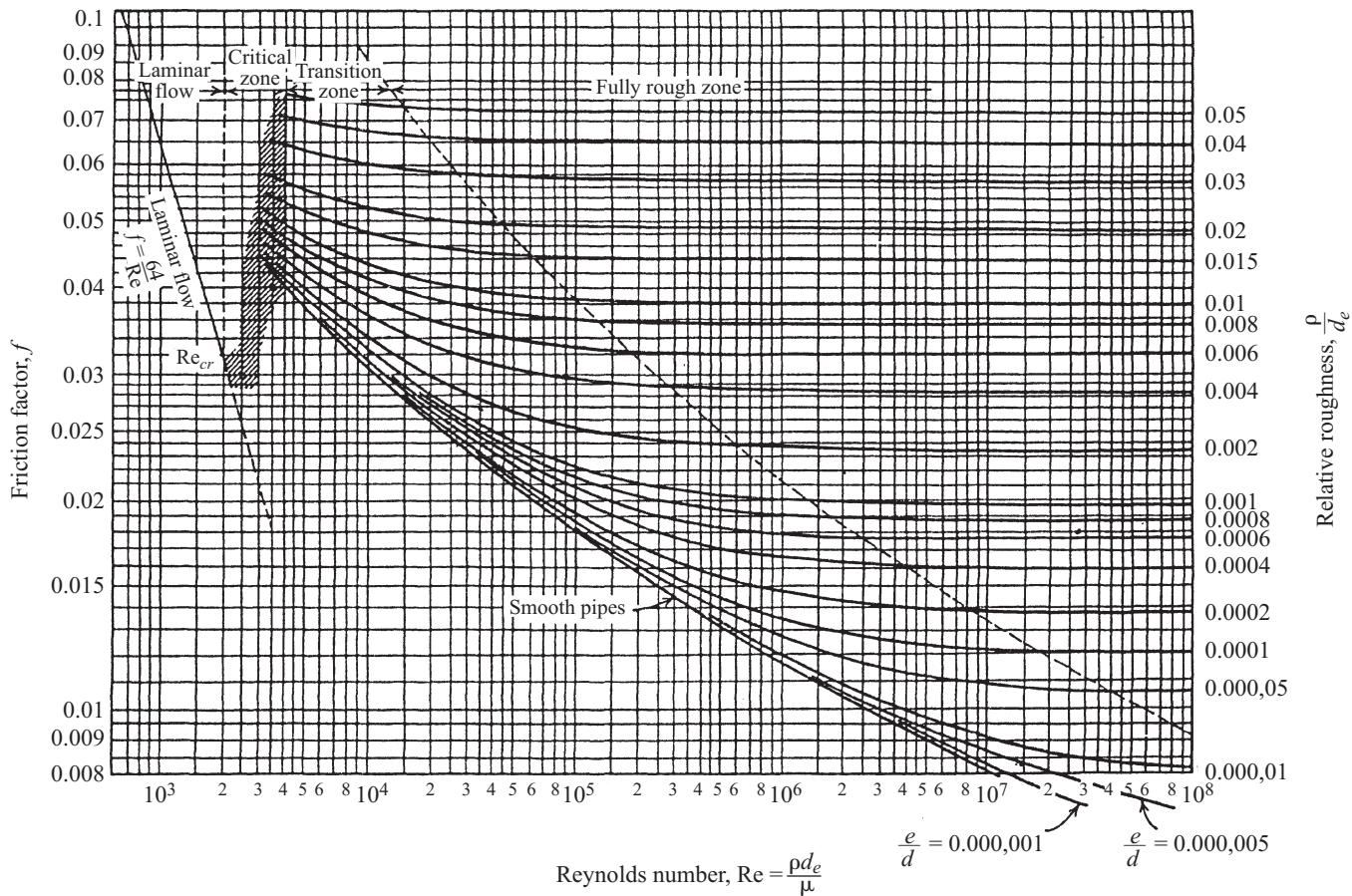


Figure 11.12 Moody chart for tube and annulus friction factors. (From Moody, 1944.)

Many investigators have developed friction factor relationships as a function of the Reynolds number. The use of the friction factor give by eq. (11.77) in the Petukhov and Gnielinski correlations of eqs. (11.76) and (11.78) has been noted. Other functions can be fitted to the curves in Fig. 11.10. Two of them for smooth tubes are

$$f = \begin{cases} \frac{0.046}{\text{Re}^{0.20}} & (3 \times 10^4 \leq \text{Re} \leq 10^6) \\ \frac{0.079}{\text{Re}^{0.25}} & (4 \times 10^3 \leq \text{Re} \leq 10^5) \end{cases} \quad (11.100)$$

$$(11.101)$$

Shell Side Tinker (1951) also suggested a flow stream model for the determination of shell-side pressure loss. However, the lack of adequate data caused him to make rather gross simplifications in arriving at the effects to be attributed to the various flow streams. Willis and Johnston (1984) developed a simpler method which extends Tinker's scheme to include end-space pressure losses and includes a simple method for nozzle pressure drop developed by Grant (1980).

The flow streams in the Willis and Johnston method are shown in Fig. 11.13. For each of the streams, a coefficient n is defined so that

$$n_i = \frac{\Delta p_i}{\dot{m}_i} \quad (i = b, c, s, t, w) \quad (11.102)$$

where the Δp_i 's and the \dot{m}_i 's are the pressure drops and mass flow rates for the i th stream, respectively.

The crossflow stream contains the actual crossflow path (path c) and the bypass path (path b). These paths merge into the window stream (path w), and continuity and compatability for these three paths give

$$\dot{m}_{cr} = \dot{m}_w \quad (11.103a)$$

where

$$\dot{m}_{cr} = \dot{m}_b + \dot{m}_c \quad (11.103b)$$

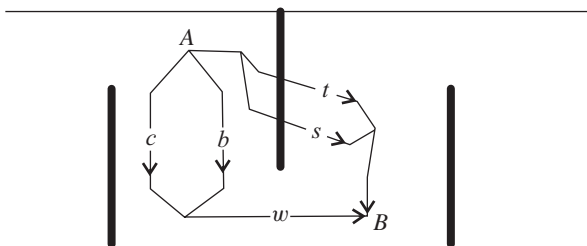


Figure 11.13 Shell-side flow streams for the Willis and Johnston (1984) pressure-drop method.

and the pressure loss between points A and B will be

$$\Delta p_{AB} = \Delta p_{cr} + \Delta p_w \quad (11.103c)$$

because $\Delta p_{cr} = \Delta p_b = \Delta p_c$. It can be shown that

$$\Delta p_{cr} = \left[\left(\frac{1}{n_b} \right)^{1/2} + \left(\frac{1}{n_c} \right)^{1/2} \right]^2 \dot{m}_w^2 \quad (11.104)$$

and in similar fashion, for the parallel combination of the shell-to-baffle leakage path (path s) and the tube-to-baffle leakage path (path t),

$$\Delta p_l = \left[\left(\frac{1}{n_s} \right)^{1/2} + \left(\frac{1}{n_t} \right)^{1/2} \right]^2 \dot{m}_l^2 \quad (11.105)$$

where the leakage flow rate is

$$\dot{m}_l = \dot{m}_s + \dot{m}_t \quad (11.106)$$

With the total flow rate given by

$$\dot{m}_T = \dot{m}_s + \dot{m}_t + \dot{m}_w \quad (11.107)$$

a combination of eqs. (11.102) and (11.104)–(11.107) gives

$$\dot{m}_w = \frac{\dot{m}_T}{1 + \left[\frac{(n_c^{-1/2} + n_b^{-1/2})^{-2} + n_w}{(n_s^{-1/2} + n_t^{-1/2})^{-2}} \right]^{1/2}} \quad (11.108)$$

and it is observed that the procedure depends on the values of the n_i 's.

For n_c , Butterworth (1979) has proposed that

$$n_c = C_c F_c^{-b} \quad (11.109a)$$

with

$$C_c = 4a \frac{d_o^2 d_V}{(p - d_o)^3} \left(\frac{\dot{m}_T d_o}{\mu A_c} \right)^{-b} \frac{\delta_{ov}}{2\rho d_o A_c^2} \quad (11.109b)$$

where for square or rotated square pitch, $a = 0.061$, $b = 0.088$, and $F_c = 1.00$; and for equilateral triangular pitch, $a = 0.45$, $b = 0.267$, and $F_c = 0.50$. In eq. (11.109b),

$$D_V = \frac{ap^2 - d_o^2}{d_o}$$

with $a = 1.273$ for square and rotated square pitch and $a = 1.103$ for equilateral triangular pitch. In addition,

$$\delta_{ov} = (1 - 0.02p_b)D_s$$

is the height of the baffle overlap region, p_b is the baffle cut, and

$$A_c = \frac{\pi D_o^2}{2} - 2 \frac{D_o^2}{2} \left(\frac{\theta_3}{2} - \sin \frac{\theta_3}{2} \cos \frac{\theta_3}{2} \right) \frac{L_{cb}}{\delta_{ov}} - N_p z L_{cb}$$

where n_p is the number of pass partitions and z is the path partition width in line with the flow.

For n_b ,

$$n_b = \frac{0.316(\delta_{ov}/X_L)(\dot{m}_T D'_e / \mu A_{bp})^{-0.25} + 2N_s}{2\rho A_{bp}^2} \quad (11.110)$$

where

$$A_{bp} = (2w + N_p z) L_{bc}$$

$$D'_e = \frac{2A_{bp}}{2(w + L_{bc}) + N_p(z + L_{bc})}$$

For n_s ,

$$n_s = \frac{4[0.0035 + 0.264(2\dot{m}_T \delta_{sb} / \mu A_{sb})]^{-0.42} + (\delta_b / 2\delta_{sb}) + 2.03(\delta_b / 2\delta_{sb})^{-0.177}}{2\rho A_{sb}^2} \quad (11.111)$$

where

$$A_{sb} = \pi(D_s - \delta_{sb})\delta_{sb}$$

For n_t ,

$$n_t = \frac{4[0.0035 + 0.264(2\dot{m}_T \delta_{tb} / \mu A_{tb})]^{-0.42} + (\delta_b / 2\delta_{tb}) + 2.03(\delta_b / 2\delta_{tb})^{-0.177}}{2\rho A_{tb}^2} \quad (11.112)$$

where

$$A_{tb} = n\pi(d_o - \delta_{tb})\delta_{tb}$$

For n_w ,

$$n_w = \frac{1.90e^{0.6856A_w/A_{CL}}}{2\rho A_w^2} \quad (11.113)$$

where A_w is the window flow area with n_{tw} taken as the number of tubes in the window:

$$A_w = A_{w1} - \frac{\pi d_o^2 n_{tw}}{4}$$

$$A_{w1} = \frac{d_s}{4} \left(\frac{\theta_1}{2} - \sin \frac{\theta_1}{2} \cos \frac{\theta_1}{2} \right)$$

and where for square and rotated square layouts,

$$A_{CL} = (D_s - N_{CL} d_o) L_{bc}$$

and for equilateral triangular layouts,

$$A_{CL} = 2(N_{CL} - 1)(p - D_o) + 2w$$

Here, to the nearest integer,

$$N_{CL} = \frac{D_o - d_o}{P_y}$$

with $P_y = p$ for square pitch, $P_y = 1.414p$ for rotated square pitch, and $P_y = 1.732p$ for equilateral triangular pitch.

Equation (11.108) establishes the window mass flow as a function of the total mass flow, and a simple computation then determines the total baffle-space pressure loss via

$$\Delta p_{AB} = \Delta P_{cr} + \Delta p_w \quad (11.103c)$$

where

$$\Delta p_{cr} = n_c \dot{m}_c \quad \text{or} \quad \Delta p_{cr} = n_b \dot{m}_b$$

$$\Delta p_w = n_w \dot{m}_w$$

The total pressure loss contains components due to the baffle-space pressure loss established by the foregoing procedure, the end-space pressure loss, and the nozzle pressure loss. The end-space pressure loss is taken as

$$\Delta p_e = N_e \dot{m}_e^2 + \frac{1}{2} n_w \dot{m}_w^2 \quad (11.114)$$

where

$$n_e = n_{cr} \frac{D_s + \delta_{ov}}{2\delta_{ov}} \left(\frac{L_{bc}}{L_{be}} \right)^2 \quad (11.115a)$$

with

$$n_{cr} = \left[\left(\frac{1}{n_c} \right)^{1/2} + \left(\frac{1}{n_c} \right)^{1/2} \right]^{-2} \quad (11.115b)$$

and where

$$n_{we} = \frac{1.9e^{0.6856(A_w L_{bc}/A_{CL} L)}}{2\rho A_w^2} \quad (11.115c)$$

The average end-space flow rate is

$$\dot{m}_e = \frac{\dot{m}_t + \dot{m}_w}{2}$$

Grant (1980) gives the pressure drop in the inlet nozzle as

$$\Delta p_{n1} = \frac{G_1^2 A_1}{\rho_1 A_2} \left(\frac{A_1}{A_2} - 1 \right) \quad (11.116)$$

where G_1 is the entry mass velocity, $G_1 = \rho_1 u_1$, A_1 is the inlet nozzle area, and A_2 is the bundle entry area. For the outlet-nozzle pressure loss,

$$\Delta p_{n2} = \frac{G_2^2}{2\rho_2} \left[1 - \left(\frac{A_3}{A_4} \right)^2 + \left(\frac{1}{c} - 1 \right)^2 \right] \quad (11.117)$$

where G_2 is the exit mass velocity, $G_2 = \rho_2 u_2$, A_3 is the outlet nozzle area, and A_4 is the bundle exit area. The recommended value of the contraction coefficient is $c = \frac{2}{3}$.

The total shell-side pressure loss will be

$$\Delta P_T = \Delta p_{n1} + (F_T + 1) \Delta p_e + (N_b - 1) \Delta p_{AB} \Delta p_{n2} \quad (11.118)$$

Equation (11.118) has assumed that the pressure losses in the end spaces at inlet and outlet are identical. The factor F_T is the transitional correction factor and is based on the crossflow Reynolds number

$$\text{Re}_c = \frac{\dot{m}_c d_o}{\mu A_c}$$

where for $\text{Re}_c < 300$, the entire method is not valid; $0 \leq \text{Re}_c < 1000$, $F_T = 3.646e^{-0.1934}$; and $\text{Re}_c \geq 1000$, $F_T = 1$.

11.5 COMPACT HEAT EXCHANGERS

11.5.1 Introduction

One variation of the fundamental compact exchanger element, the core, is shown in Fig. 11.14. The core consists of a pair of parallel plates with connecting metal

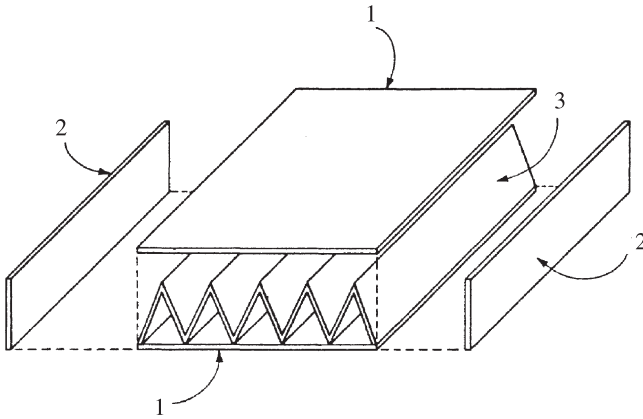


Figure 11.14 Exploded view of a compact heat exchanger core: 1, plates; 2, side bars; 3, corrugated fins stamped from a continuous strip of metal. By spraying braze powder on the plates, the entire assembly of plates, fins, and bars can be thermally bonded in a single furnace operation. (From Kraus et al., 2001, with permission.)

members that are bonded to the plates. The arrangement of plates and bonded members provides both a fluid-flow channel and prime and extended surface. It is observed that if a plane were drawn midway between the two plates, each half of the connecting metal members could be considered as longitudinal fins.

Two or more identical cores can be connected by *separation* or *splitter plates*, and this arrangement is called a *stack* or *sandwich*. Heat can enter a stack through either or both end plates. However, the heat is removed from the successive separating plates and fins by a fluid flowing in parallel through the entire network with a single average convection heat transfer coefficient. For this reason, the stack may be treated as a finned passage rather than a fluid–fluid heat exchanger, and, of course, due consideration must be given to the fact that as more and more fins are placed in a core, the equivalent or hydraulic diameter of the core is lowered while the pressure loss is increased significantly.

Next, consider a pair of cores arranged as components of a two-fluid exchanger in crossflow as shown in Fig. 11.15. Fluids enter alternate cores from separate headers at right angles to each other and leave through separate headers at opposite ends of the exchanger. The separation plate spacing need not be the same for both fluids, nor need the cores for both fluids contain the same numbers or kinds of fins. These are dictated by the allowable pressure drops for both fluids and the resulting heat transfer coefficients. When one coefficient is quite large compared with the other, it is entirely permissible to have no extended surface in the alternate cores through which the fluid with the higher coefficient travels. An exchanger built up with plates and fins as in Fig. 11.16 is a *plate fin* heat exchanger.

The discussion of plate fin exchangers has concentrated thus far on geometries involving two or more fluids that enter the body of the compact heat exchanger by

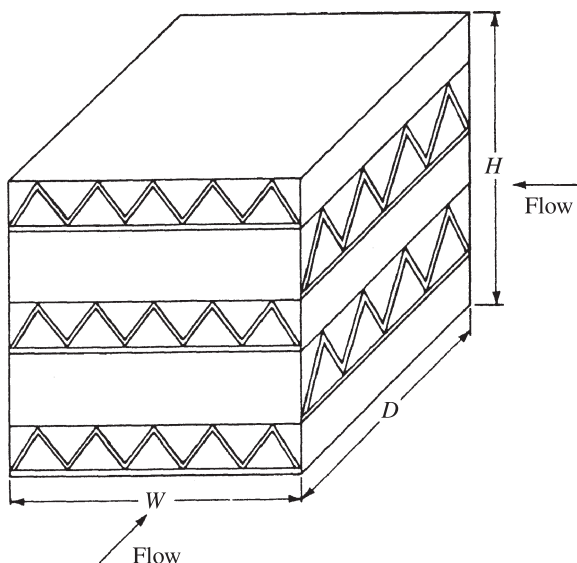


Figure 11.15 Two-fluid compact heat exchanger with headers removed. (From Kraus et al., 2001, with permission.)

means of headers. In many instances, one of the fluids may be merely air, which is used as a cooling medium on a once-through basis. Typical examples include the air-fin cooler and the *radiators* associated with various types of internal combustion engines. Similarly, there are examples in which the compact heat exchanger is a coil that is inserted into a duct, as in air-conditioning applications. A small selection of compact heat exchanger elements available is shown in Fig. 11.16.

11.5.2 Classification of Compact Heat Exchangers

Compact heat exchangers may be classified by the kinds of compact elements that they employ. The compact elements usually fall into five classes:

1. *Circular and flattened circular tubes.* These are the simplest form of compact heat exchanger surface. The designation ST indicates flow inside straight tubes (example: ST-1), FT indicates flow inside straight flattened tubes (example: FT-1) and FTD indicates flow inside straight flattened dimpled tubes. Dimpling interrupts the boundary layer, which tends to increase the heat transfer coefficient without increasing the flow velocity.

2. *Tubular surfaces.* These are arrays of tubes of small diameter, from 0.9535 cm down to 0.635 cm, used in service where the ruggedness and cleanability of the conventional shell-and-tube exchanger are not required. Usually, tubesheets are comparatively thin, and soldering or brazing a tube to a tubesheet provides an adequate seal against interleakage and differential thermal expansion.

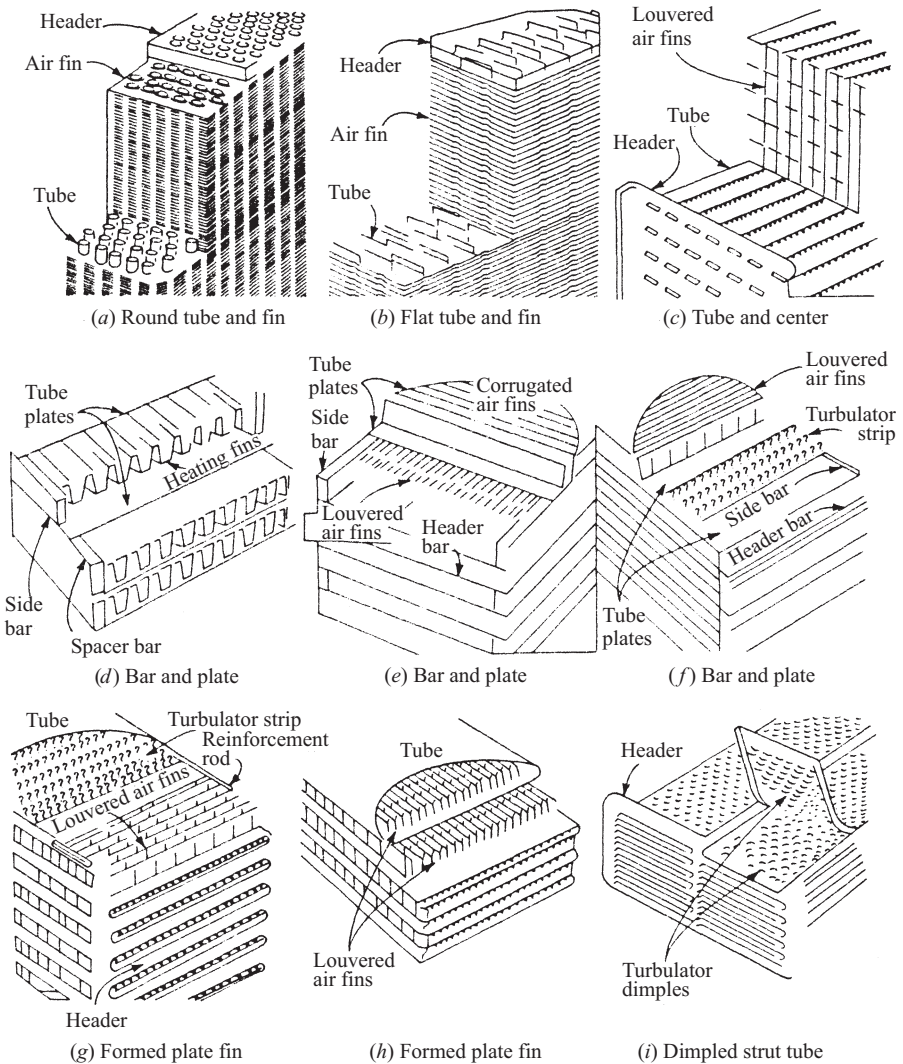


Figure 11.16 Some compact heat exchanger elements. (Courtesy of Harrison Radiator Division.)

3. *Surfaces with flow normal to banks of smooth tubes.* Unlike the radial low fin tubes, smooth round tubes are expanded into fins that can accept a number of tube rows, as shown in Fig. 11.16a. Holes may be stamped in the fin with a drawn hub or foot to improve contact resistance or as a spacer between successive fins, as shown, or brazed directly to the fin with or without a hub. Other types reduce the flow resistance outside the tubes by using flattened tubes and brazing, as indicated in Fig. 11.16b and c. Flat tubing is made from strips similar to the manufacture of welded circular tubing but is much thinner and is joined by soldering or brazing rather than welding.

The designation considers staggered (S) and in-line (I) arrangements of tubes and identifies transverse and longitudinal pitch ratios. The suffix (s) indicates data correlation from steady-state tests. All other data were correlated from a transient technique. Examples include the surface S1.50-1.25(s), which is a staggered arrangement with data obtained via steady-state tests with transverse pitch-to-diameter ratio of 1.50 and longitudinal pitch-to-diameter ratio of 1.25. The surface I1.25-1.25 has an in-line arrangement with data obtained from transient tests with both transverse and longitudinal pitch-to-diameter ratios of 1.25.

4. *Plate fin surfaces.* These are shown in Figs. 11.16*d* through *i*.

- (a) The *plain fin* is characterized by long uninterrupted flow passages and is designated by a numeral that indicates the number of fins per inch. The suffix T is appended when the passages are of definite triangular shape. Examples are the surfaces 19.86, 15.08, and 46.45T.
- (b) The *louvered fin* is characterized by fins that are cut and bent into the flow stream at frequent intervals and is designated by a fraction which indicates the length of the fin in the flow direction (inches) followed by a numeral that indicates the number of fins per inch. For example, the designation

$$\frac{1}{2} - 6.06$$

indicates 6.06 $\frac{1}{2}$ -in.-long fins per inch.

- (c) The *strip fin* is designated in the same manner as the louvered fin. The suffixes (D) and (T) indicate double and triple stacks. The strip fins are frequently referred to as *offset fins* because they are offset at frequent intervals and the exchanger is essentially a series of plate fins with alternate lengths offset.
- (d) The *wavy fin* is characterized by a continuous curvature. The change in flow direction introduced by the waves in the surface tends to interrupt the boundary layer, as in the case of louvered and strip fins. Wavy fin designations are always followed by the letter W. For example, the

$$11.44 - \frac{3}{8}W$$

is a wavy fin with 11.44 fins per inch and a $\frac{3}{8}$ -in. wave.

- (e) The *pin fin* surface is constructed from small-diameter wires. This surface yields very high heat transfer coefficients because the effective flow length is very small. The designation of the pin fin surfaces is nondescriptive.
- (f) The *perforated fin* surface has holes cut in the fins to provide boundary layer interruption. These fins are designated by the number of fins per inch followed by the letter P.

5. *Finned-tube surfaces.* Circular tubes with spiral radial fins are designated by the letters CF followed by one or two numerals. The first numeral designates the number of fins per inch, and the second (if one is used) refers to the nominal tube size. With circular tubes with continuous fins, no letter prefix is employed and the

two numerals have the same meaning as those used for circular tubes with spiral radial fins. For finned flat tubes, no letter prefix is used; the first numeral indicates the fins per inch and the second numeral indicates the largest tube dimension. When CF does not appear in the designation of the circular tube with spiral radial fins, the surface may be presumed to have continuous fins.

6. *Matrix surfaces.* These are surfaces that are used in rotating, regenerative equipment such as combustion flue gas–air preheaters for conventional fossil furnaces. In this application, metal is deployed for its ability to absorb heat with minimal fluid friction while exposed to hot flue gas and to give up this heat to incoming cold combustion air when it is rotated into the incoming cold airstream. No designation is employed.

11.5.3 Geometrical Factors and Physical Data

Compact heat exchanger surfaces are described in the literature by geometric factors that have been standardized largely through the extensive work of Kays and London (1984). These factors and the relationships between them are essential for application of the basic heat transfer and flow friction data to a particular design problem. They are listed and defined in Table 11.1. Physical data for a number of compact heat exchanger surfaces are given in Table 11.2. Relationships between the geometric factors in Table 11.1 will now be established.

Consider an exchanger composed of n_1 layers of one type of plate fin surface and n_2 layers of a second type, as shown in Fig. 11.13. The separation plate thickness is established by the pressure differential to which it is exposed or through designer discretion. Retaining the subscripts 1 and 2 for the respective types of surface, the overall exchanger height H is

$$H = n_1(b_1 + a) + n_2(b_2 + a) \quad (11.119)$$

where b_1 and b_2 are separation distances between the plates for the two kinds of surface. With the width W and depth D selected, the overall volume V is

$$V = WDH \quad (11.120)$$

In Fig. 11.15, the length L_1 is along the depth of the exchanger ($L_1 = D$) and the length L_2 is along the width ($L_2 = W$).

The frontal areas are also established. Again referring to Fig. 11.13, we have

$$A_{fr,1} = HW \quad (11.121a)$$

$$A_{fr,2} = HD \quad (11.121b)$$

If the entire exchanger consisted of a single exchanger surface, surface 1 or surface 2, the total surface area would be the product of the ratio of total surface to total

TABLE 11.1 Compact Heat Exchanger Geometric Factors

Factor and Symbol	Descriptive Comments
A	Free flow area on one side of the exchanger. To distinguish hot and cold sides, the free flow areas are frequently designated by A_h and A_c .
A_{fr}	Frontal area on one side of the exchanger. This is merely the product of the overall exchanger width and height or depth and height.
a	Separation plate thickness. This applies only to plate fin surfaces and its value is at the designer's discretion.
b	Separation plate spacing. This dimension is an approximation of the fin height. Applies to plate fin surfaces only.
d_e	Equivalent diameter used to correlate flow friction and heat transfer; four times the hydraulic radius, r_h .
L	Flow length on one side of the exchanger. Note that this factor <i>always</i> concerns the flow length of a <i>single</i> side of the exchanger, although two sides may be present, and that the ambiguity is avoided with the overall exchanger dimensions, which are designated <i>width</i> , <i>depth</i> , and <i>height</i> . It is therefore reasonable to have the overall exchanger depth be the length on one side of the exchanger and the overall width the length on the other side.
P	Perimeter of the passage.
p	Porosity, the ratio of the exchanger void volume to the total exchanger volume. Applies to matrix surfaces only.
r_h	Hydraulic radius; the ratio of the passage flow area to its wetted perimeter.
S	Heat transfer surface on one side of the exchanger. Subscripts are often appended to distinguish between hot- and cold-side surfaces.
S_f	Surface of the fins, only, on one side of the exchanger. Applies to finned surfaces only.
V	Total exchanger volume. This applies to both sides of the heat exchanger and is merely the product of the overall heat exchanger width, depth, and height.
α	Ratio of the total surface area on <i>one</i> side of the exchanger to the total volume on <i>both</i> sides of the exchanger. Applies to tubular, plate fin surfaces, and crossed-rod matrices only.
β	Ratio of the total surface area to the total volume on <i>one</i> side of the exchanger. The surface alone is S . The total volume includes the overall exchanger dimensions. Applies to plate fin surfaces only.
δ_f	Fin thickness.
η_f	Fin efficiency.
η_{ov}	Overall passage efficiency.
σ	Ratio of the free flow area to the frontal area on one side of the exchanger.

TABLE 11.2 Surface Geometry of Some Plate Fin Surfaces

Plain Plate Fins	11.1	15.08	19.86	46.45T
$b(\times 10^{-3} \text{ m})$	6.35	10.62	6.35	2.54
Fins per inch	11.1	15.08	19.86	46.45
$d_e(\times 10^{-3} \text{ m})$	3.08	2.67	1.875	0.805
$\delta_f(\times 10^{-3} \text{ m})$	0.152	0.152	0.152	0.051
$\beta(\text{m}^2/\text{m}^3)$	1204	1358.3	1840.6	4371.7
S_f/S	0.756	0.870	0.849	0.837
Louvered Fins	$\frac{3}{8}$ -6.06	$\frac{1}{2}$ -6.06	$\frac{3}{16}$ -11.1	$\frac{3}{4}$ -11.1
$b(\times 10^{-3} \text{ m})$	6.35	6.35	6.35	6.35
Fins per inch	6.06	6.06	11.1	11.1
$d_e(\times 10^{-3} \text{ m})$	4.453	4.453	3.084	3.084
$\delta_f(\times 10^{-3} \text{ m})$	0.152	0.152	0.152	0.152
$\beta(\text{m}^2/\text{m}^3)$	840	840	1204	1204
S_f/S	0.640	0.640	0.756	0.756
Strip Fins	$\frac{1}{8}$ -13.95	$\frac{1}{8}$ -16.00D	$\frac{1}{8}$ -19.82D	$\frac{1}{8}$ -20.06
$b(\times 10^{-3} \text{ m})$	9.54	6.48	5.21	5.11
Fins per inch	13.95	16.00	19.82	20.06
$d_e(\times 10^{-3} \text{ m})$	2.68	1.86	1.54	1.49
$\delta_f(\times 10^{-3} \text{ m})$	0.254	0.152	0.102	0.102
$\beta(\text{m}^2/\text{m}^3)$	1250	1804	2231	2290
S_f/S	0.840	0.845	0.841	0.843
Wavy and Pin Fins	11.5- $\frac{3}{8}$ W	17.8- $\frac{3}{8}$ W	AP-1	PF-3
$b(\times 10^{-3} \text{ m})$	9.53	10.49	6.10	19.1
Fins per inch or fin pattern	11.5	17.8	In-line	In-line
$d_e(\times 10^{-3} \text{ m})$	3.02	2.12	4.40	1.636
δ_f or pin diameter ($\times 10^{-3} \text{ m})$	0.254	0.152	1.02	0.79
$\beta(\text{m}^2/\text{m}^3)$	1138	1686	617	1112
S_f/S	0.822	0.892	0.512	0.834

volume $\beta(\text{m}^2/\text{m}^3)$ and the total volume V . However, where there are two surfaces, it is necessary to employ the factor α , which is the ratio of the total surface on *one* side to the total surface on *both* sides of the exchanger. By taking simple proportions,

$$\alpha_1 = \frac{b_1}{b_1 + b_2 + a} \beta_1 \quad (11.122a)$$

$$\alpha_2 = \frac{b_2}{b_1 + b_2 + a} \beta_2 \quad (11.122b)$$

and the total surfaces will be

$$S_1 = \alpha_1 V \quad (11.123a)$$

$$S_2 = \alpha_2 V \quad (11.123b)$$

The hydraulic radius is defined as the flow area divided by the wetted perimeter of the passage:

$$r_h = \frac{A}{P} = \frac{AL}{S} \quad (11.124)$$

and the ratio of the flow area to the frontal area is designated as σ :

$$\sigma = \frac{A}{A_{fr}} \quad (11.125)$$

For all but matrix surfaces, because eq. (11.124) leads to $A = Sr_h/L$,

$$\sigma = \frac{Sr_h}{A_{fr}L} = \frac{Sr_h}{V} = \alpha r_h \quad (11.126)$$

Thus, the flow areas are given by

$$A_1 = \sigma_1 A_{fr,1} \quad (11.127a)$$

$$A_2 = \sigma_2 A_{fr,2} \quad (11.127b)$$

11.5.4 Heat Transfer and Flow Friction Data

Heat Transfer Data Heat transfer data for compact heat exchangers are correlated on an individual surface basis using a Colburn type of representation. This representation plots the heat transfer factor j_h :

$$j_h = \text{St} \cdot \text{Pr}^{2/3} = \frac{h}{G c_p} \left(\frac{c_p \mu}{k} \right)^{2/3} \quad (11.128)$$

as a function of the Reynolds number, which is obtained by employing the equivalent diameter $d_e = 4r_h$:

$$\text{Re} = \frac{4r_h G}{\mu} = \frac{d_e G}{\mu} \quad (11.129)$$

The Stanton number St is the ratio of the Nusselt number Nu to the product of the Reynolds and Prandtl numbers, with the specific heat c taken as the value for constant pressure,

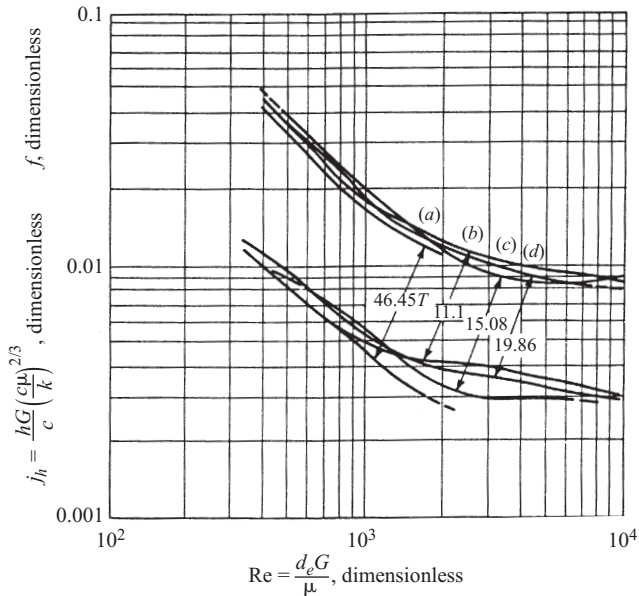
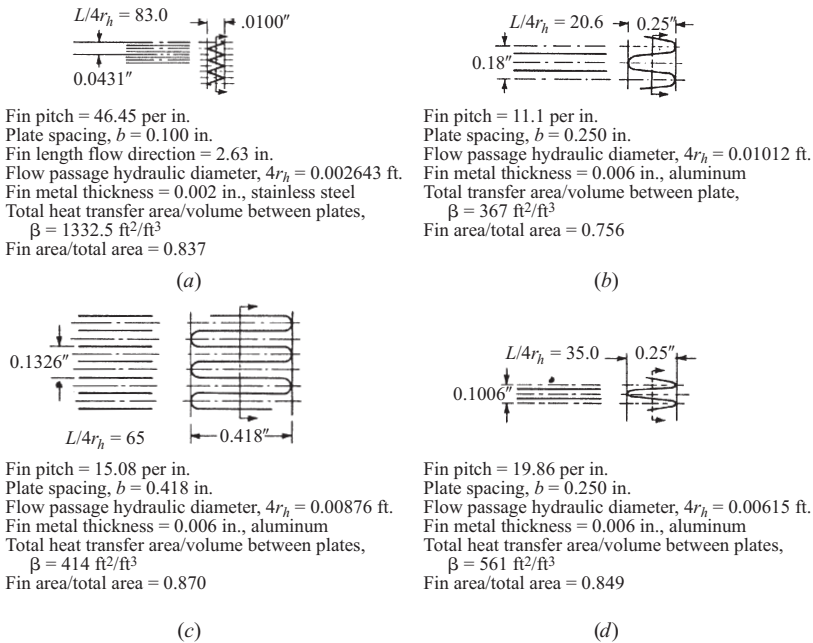


Figure 11.17 Heat transfer and flow friction characteristics of some plain plate fin compact heat exchanger surfaces. (From Kays and London, 1984.)

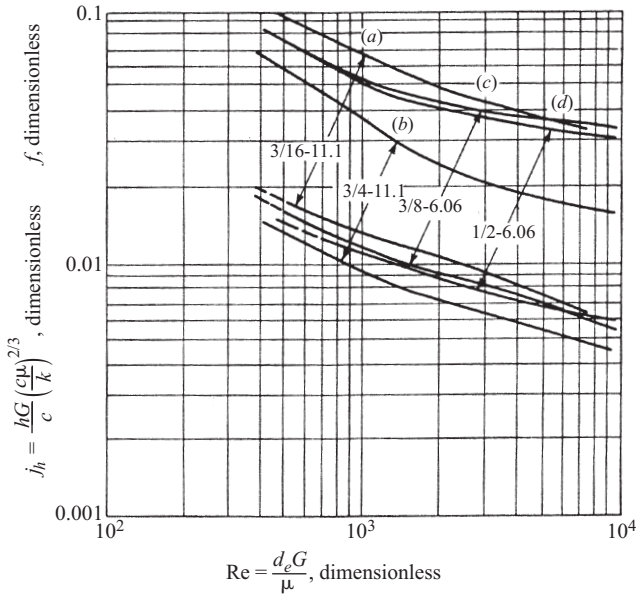
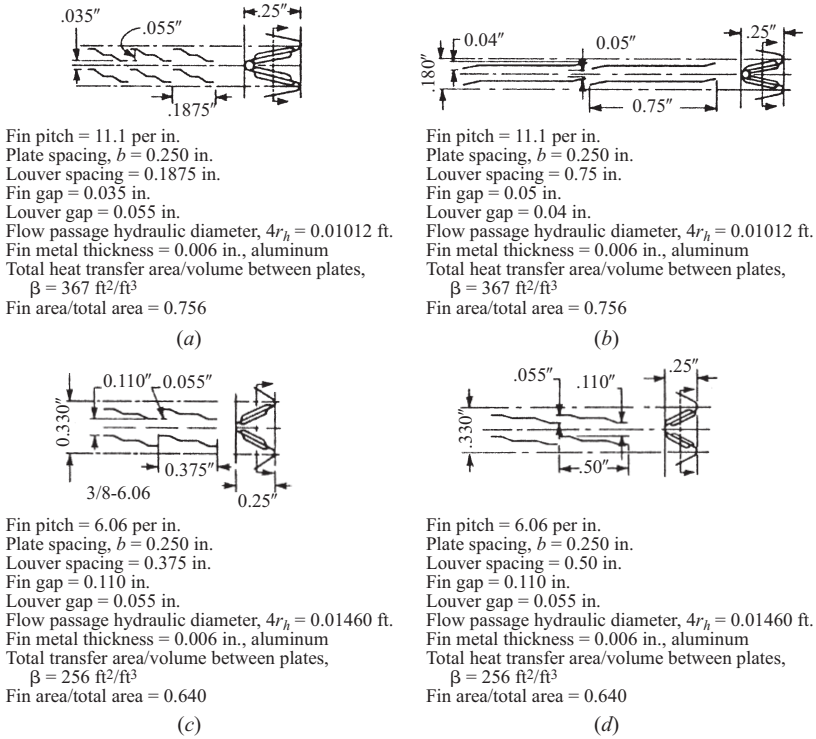
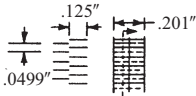
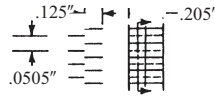


Figure 11.18 Heat transfer and flow friction characteristics of some louvered fin compact heat exchanger surfaces. (From Kays and London, 1984.)



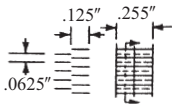
Fin pitch = 20.06 per in.
 Plate spacing, $b = 0.201$ in.
 Splitter symmetrically located
 Fin length flow direction = 0.125 in.
 Flow passage hydraulic diameter, $4r_h = 0.004892$ ft.
 Fin metal thickness = 0.004 in., aluminum
 Splitter metal thickness = 0.006 in.
 Total heat transfer area/volume between plates,
 $\beta = 698 \text{ ft}^2/\text{ft}^3$
 Fin area (including splitter)/total area = 0.843

(a)



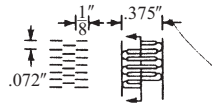
Fin pitch = 19.82 per in.
 Plate spacing, $b = 0.205$ in.
 Splitter symmetrically located
 Fin length flow direction = 0.125 in.
 Flow passage hydraulic diameter, $4r_h = 0.005049$ ft.
 Fin metal thickness = 0.004 in., nickel
 Splitter metal thickness = 0.006 in.
 Total heat transfer area/volume between plates,
 $\beta = 680 \text{ ft}^2/\text{ft}^3$
 Fin area (including splitter)/total area = 0.841

(b)



Fin pitch = 16.00 per in.
 Plate spacing, $b = 0.255$ in.
 Splitter symmetrically located
 Fin length flow direction = 0.125 in.
 Flow passage hydraulic diameter, $4r_h = 0.006112$ ft.
 Fin metal thickness = 0.006 in., aluminum
 Splitter metal thickness = 0.006 in.
 Total heat transfer area/volume between plates,
 $\beta = 550 \text{ ft}^2/\text{ft}^3$
 Fin area (including splitter)/total area = 0.845

(c)



Fin pitch = 13.95 per in.
 Plate spacing, $b = 0.375$ in.
 Fin length = 0.125 in.
 Flow passage hydraulic diameter, $4r_h = 0.00879$ ft
 Fin metal thickness = 0.010 in., aluminum
 Total heat transfer area/volume between plates,
 $\beta = 381 \text{ ft}^2/\text{ft}^3$
 Fin area/total area = 0.840
 Note: The fin surface area on the leading and trailing edges of the fins have not been included in area computations.

(d)

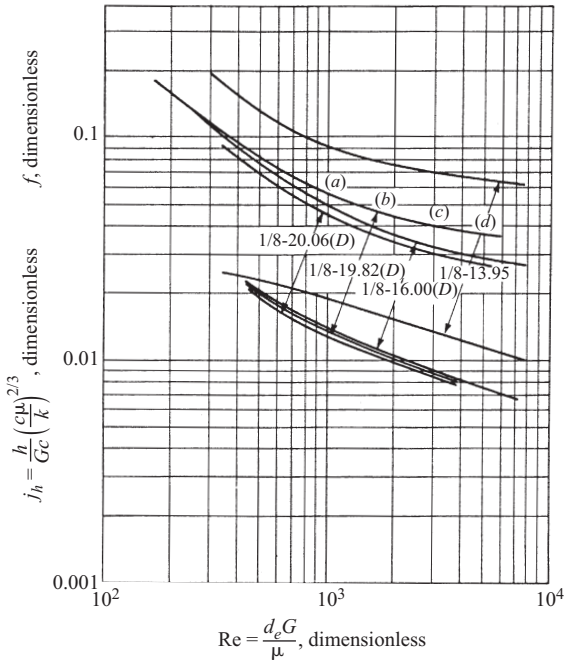


Figure 11.19 Heat transfer and flow friction characteristics of some strip fin compact heat exchanger surfaces. (From Kays and London, 1984.)

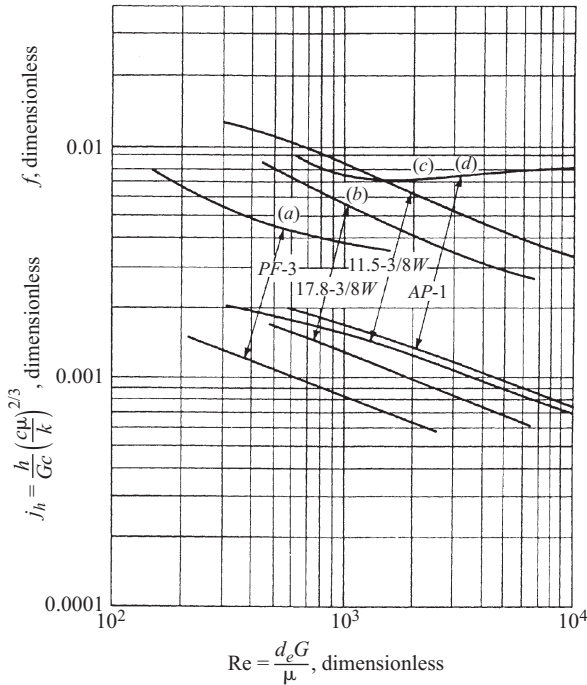
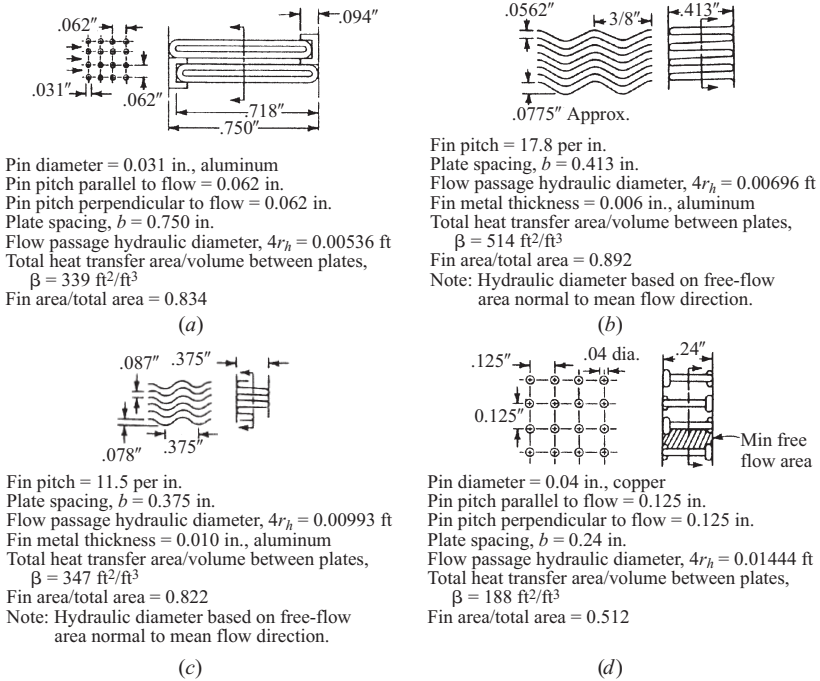


Figure 11.20 Heat transfer and flow friction characteristics of some wavy and pin fin compact heat exchanger surfaces. (From Kays and London, 1984.)

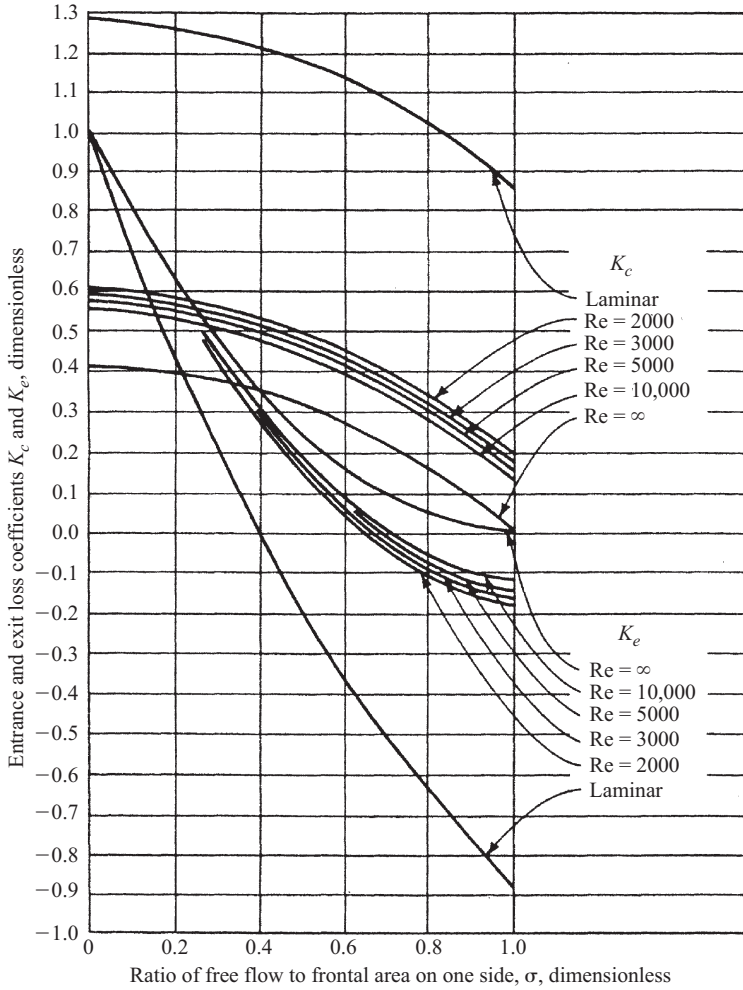


Figure 11.21 Entrance and exit loss coefficients for flow through plate fin exchanger cores. (From Kays and London, 1984).

$$St = \frac{Nu}{Re \cdot Pr} = \frac{hd_e/k}{(d_e G/\mu)(c\mu/k)} = \frac{h}{Gc} \quad (11.130)$$

The fluid properties in eqs. (11.129) and (11.130) are evaluated at the bulk temperature

$$T_b = \frac{1}{2}(T_1 + T_2) \quad (11.131a)$$

$$t_b = \frac{1}{2}(t_1 + t_2) \quad (11.131b)$$

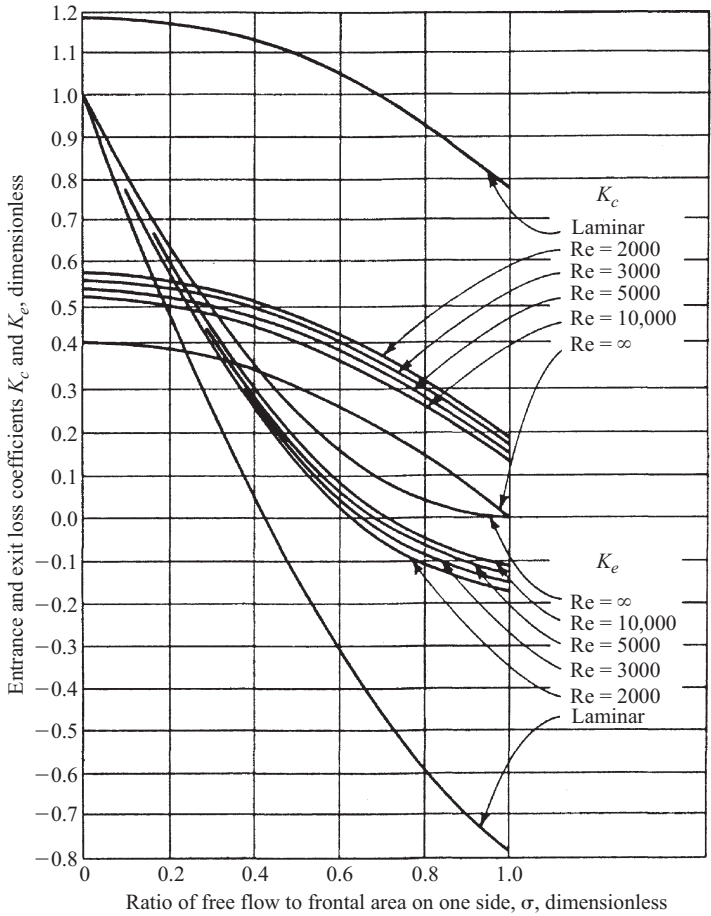


Figure 11.22 Entrance and exit loss coefficients for flow through rectangular passages. (From Kays and London, 1984.)

Flow Friction Data Kays and London (1984) suggest that the pressure drop ΔP in a compact heat exchanger be computed from the equation

$$\frac{\Delta P}{P_1} = \frac{G^2 v_1}{2g_c P_1} (\Phi_1 + \Phi_2 + \Phi_3 - \Phi_4) \quad (11.132)$$

where

$$\begin{aligned} \Phi_1 &= 1 + K_c - \sigma^2 \\ \Phi_2 &= 2 \left(\frac{v_2}{v_1} - 1 \right) \end{aligned}$$

$$\Phi_3 = f \frac{S}{A} \frac{v_m}{v_1}$$

$$\Phi_4 = (1 - \sigma^2 - K_e) \frac{v_2}{v_1}$$

Friction factors are correlated on an individual surface basis and are usually plotted as a function of the Reynolds number. The entrance and exit loss coefficients differ for the various types of passages and are plotted as functions of the parameter σ and the Reynolds number.

Four terms may be noted within the parentheses in eq. (11.132). These terms denote, respectively, the entrance or contraction loss as the fluid approaches the exchanger at line velocity and changes to the exchanger entrance velocity, acceleration loss, or acceleration gain as the fluid expands or contracts during its passage through the exchanger, flow friction loss, and exit loss.

Kays and London (1984) have presented heat transfer and flow friction data for approximately 120 surfaces described by the foregoing. Some typical examples are shown in Figs. 11.17 through 11.20. Entrance and exit loss coefficients for plate fin cores and rectangular passages are plotted in Figs. 11.21 and 11.22.

Because the pitch of the fins is small, the height of the fin is approximately equal to b , the distance between the separation plates. The fin efficiency for the parallel-plate heat exchanger may be taken as

$$\eta_f = \frac{\tanh mb/2}{mb/2} \quad (11.133)$$

where $b/2$ is half of the separation plate distance.

11.6 LONGITUDINAL FINNED DOUBLE-PIPE EXCHANGERS

11.6.1 Introduction

The double-pipe exchanger consists of a pair of concentric tubes or pipes. One process stream flows through the inner pipe, and the other flows, either in counter- or co-current (parallel) flow in the annular region between the two pipes. The inner pipe may be bare or it may contain as many as 48 longitudinal fins equally spaced around its periphery.

Consider the plain double-pipe exchanger shown in Fig. 11.23. It usually consists of *two pairs* of concentric pipes with a return bend and a return head made leaktight by packing glands. The packing glands and bends returning outside rather than inside the return head are used only where the annulus has low fluid pressure. If there is no problem with differential thermal expansion, the glands may be omitted and the outer and inner pipes may be welded together to provide a leaktight construction.

Two pairs of concentric pipes are used to form a *hairpin* because of the convenience the hairpin affords for manifolding streams and the natural loop it can provide

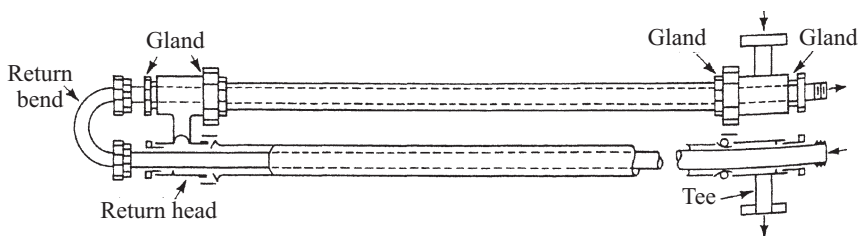


Figure 11.23 Plain double-pipe exchanger. (From Kraus et al., 2001, with permission.)

for differential thermal expansion between the inner and outer pipes. The hairpin brings all inlets and outlets close together at one end, which is particularly important when multiple hairpins are connected in batteries. Moreover, the hairpins need not have the same length. An additional merit of the double-pipe heat exchanger is the ease in which it usually can be disassembled for inspection and cleaning or reused in another service whenever a process becomes obsolete.

The longitudinal fin double-pipe exchanger is used advantageously where an appreciable inequity appears in the composite thermal resistance of a pair of fluids in a plain double-pipe exchanger. Because heat transfer equipment is usually purchased on the basis of its performance in the fouled condition, the composite thermal resistance is the sum of the convective film resistances and the fouling resistances. The advantage of the finned annulus lies in its ability to offset the effects of poorer heat transfer in one fluid by exposing more surface to it than the other. Indeed, even if the composite resistances of both fluids are low, as discussed subsequently, there may still be an advantage in the use of the finned inner pipe.

Fins are usually 0.089 cm thick (0.035 in. and 20 BWG). A steel fin with a thermal conductivity of $50 \text{ W/m} \cdot \text{K}$ and a height of 1.27 cm ($\frac{1}{2}$ in.) on exposure to a composite resistance of $0.004 \text{ m}^2 \cdot \text{K/W}$ (corresponding to a film coefficient of $250 \text{ W/m}^2 \cdot \text{K}$) has a fin efficiency of about 0.65. Exposed to a composite resistance of $0.002 \text{ m}^2 \cdot \text{K/W}$, the efficiency drops to about 0.5. Hence, the high fin has its limitations, although metals of higher thermal conductivity extend the range of application. Fin surface is inexpensive compared with prime surface, but its usefulness diminishes significantly below a composite resistance of $0.002 \text{ m}^2 \cdot \text{K/W}$. For the case where both composite resistances are very large, any improvement in the surface exposed to the higher resistance may save considerable linear meters of exchanger. Moreover, inner pipes are available with fins on the inside as well as the outside of the pipe, and the inner pipes are also available with continuous twisted longitudinal fins, which cause some mixing in the annulus. As a class, however, these show a small increase in heat transfer coefficient for a large expenditure of pressure loss, and for viscous fluids, the mixing and its effects decay rapidly.

The disposition of the fins about the pipe is shown clearly in Fig. 11.24. They form a radial array of channels, with each channel composed of two fins. Channels may be attached by continuously spot-welding them to the outside of the inner pipe or by other brazing or welding procedures. It should be noted that contact between the

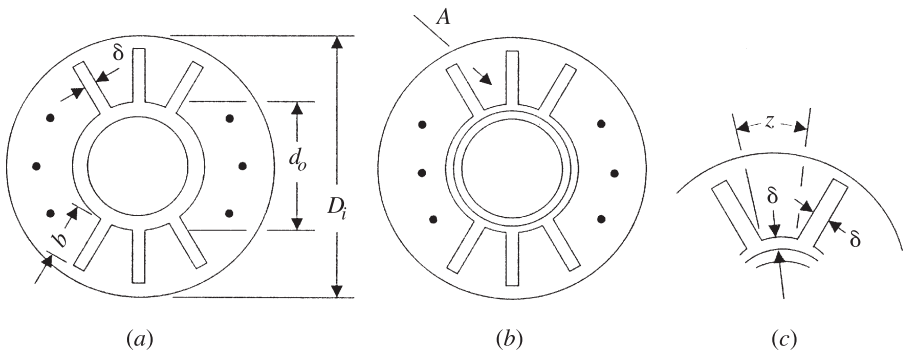


Figure 11.24 Configurations to be used for the determination of the flow area, wetted perimeter, and surfaces for the annular region in the double-pipe heat exchanger: (a) extruded fins; (b) welded U-fins; (c) detail of two welded U-fins. (From Kraus et al., 2001, with permission.)

channels and the other pipe should be continuous over the entire channel length but need not be very wide. In another method of attaching longitudinal fins, grooves are plowed in the outside diameter of the inner pipe. Metal ribbon is then inserted into the grooves as fins and the plowed-up metal is peened back to form a tight bond between fins and the inner pipe. In the laminar or transition flow regimes, fins are sometimes offset every 30 to 100 cm. The common double-pipe exchanger units available are summarized in Table 11.3.

TABLE 11.3 Dimensions of Double-Pipe Exchangers^a

Nominal Diameter (in.)	Outer Pipe Thickness (mm)	Outer Pipe OD (mm)	Max. No. of Fins	Inner Pipe OD (mm)	Inner Pipe Thickness (mm)	Fin Height (mm)
2	3.91	60.3	20	25.4	2.77	11.1
3	5.49	88.9	20	25.4	2.77	23.8
3	5.49	88.9	36	48.3	3.68	12.7
3½	5.74	101.6	36	48.3	3.68	19.05
3½	5.74	101.6	40	60.3	3.91	12.7
4	6.02	114.3	36	48.3	3.68	25.4
4	6.02	114.3	40	60.3	3.91	10.05
4	6.02	114.3	48	73.0	5.16	12.7

Source: After Saunders (1988).

^aOne outer tube—one inner tube: standard units. The fin thickness for extruded or soldered fins is 0.5 mm for fins up to 12.7 mm high and 0.8 mm high for greater heights. Fin thickness for welded fins is 0.89 mm for fin heights up to 25.4 mm. The dimensions shown here are for low-pressure units.

11.6.2 Physical Data for Annuli

Extruded Fins For the finned annular region between the inner and outer pipes shown in Fig. 11.24a, the cross-sectional area for n_t identically finned inner pipes each having n_f extruded fins will be

$$A = \frac{\pi}{4} D_i^2 - \left(\frac{\pi}{4} d_o^2 - n_f b_f \delta_f \right) n_t \quad (11.134)$$

There are two wetted perimeters. One of them is for heat transfer:

$$P_{Wh} = [\pi d_o + n_f (2b_f - \delta_f)] n_t \quad (11.135)$$

where the tips of the fins are presumed adiabatic. The other is for pressure loss:

$$P_{Wf} = \pi D_i + P_{Wh}$$

or

$$P_{Wf} = \pi D_i + [\pi d_o + n_f (2b_f - \delta_f)] n_t \quad (11.136)$$

The equivalent diameter for heat transfer will be

$$d_e = \frac{4A}{P_{Wh}} = \frac{(\pi/4) D_i^2 - [(\pi/4) d_o^2 - n_f b_f \delta_f] n_t}{(\pi d_o - n_f \delta_f + 2n_f b_f) n_t} \quad (11.137)$$

and the equivalent diameter for pressure drop will be

$$d_e = \frac{4A}{P_{Wf}} = \frac{(\pi/4) D_i^2 - [(\pi/4) d_o^2 - n_f b_f \delta_f] n_t}{\pi D_i + (\pi d_o - n_f \delta_f + 2n_f b_f) n_t} \quad (11.138)$$

The surface area per unit length per tube will be

$$S' = S = S_b + S_f$$

where S_b is the unfinned surface of the inner tube per unit length,

$$S_b = \pi d_o - n_f \delta_f \quad (11.139a)$$

Then, per unit length, with

$$S_f = 2b_f n_f \quad (11.139b)$$

the surface area on the annulus side of the inner pipe per unit length is

$$S' = S = \pi d_o + (2b_f - \delta_f) n_f \quad (11.139c)$$

Welded U-Fins The configuration for the annular region that accommodates welded U-fins is shown in Fig. 11.24*b*, and detail for a pair of the fins is shown in Fig. 11.24*c*. Observe that z is the fin root width *and* thickness, which is usually taken as $2\delta_f$. The free area for flow for n_f fins and n_t inner tubes with $\delta_f = z/2$ is

$$A = \frac{\pi}{4} D_i^2 - \left[\frac{\pi}{4} d_o^2 + n_f \delta_f \left(b_f + \frac{z}{2} \right) \right] n_t \quad (11.140)$$

If $d_o \gg z$, the wetted perimeter for heat flow will be the circumference of the inner tube less the thicknesses of the n_f fins plus twice the heights of the n_f fins.

$$P_{Wh} = [\pi d_o + n_f (2b_f - \delta_f)] n_t \quad (11.141)$$

Here, too, the tips are presumed to be adiabatic. The wetted perimeter for pressure loss is

$$P_{Wf} = \pi D_i + P_{Wh}$$

or

$$P_{Wf} = \pi D_i + [\pi d_o + n_f (2b_f - \delta_f)] n_t \quad (11.142)$$

Then the two equivalent diameters are, for heat transfer,

$$d_e = \frac{4A}{P_{Wh}} = \frac{(\pi/4) D_i^2 - [(\pi/4) d_o^2 + n_f \delta_f (b_f + z/2)] n_t}{[\pi d_o + n_f (2b_f - \delta_f)] n_t} \quad (11.143)$$

and for pressure drop,

$$d_e = \frac{(\pi/4) D_i^2 - [(\pi/4) d_o^2 + n_f \delta_f (b_f + z/2)] n_t}{\pi D_i + [\pi d_o + n_f (2b_f - \delta_f)] n_t} \quad (11.144)$$

The surface areas, S_b , S_f , S , and the surface area per unit length S' will be the same as those for the extruded fin configuration and are given by eqs. (11.139).

11.6.3 Overall Heat Transfer Coefficient Revisited

Kern (1950), Kern and Kraus (1972), and Kraus et al. (2001) all report on a method originally proposed by Kern for evaluation of the overall heat transfer coefficient when it has a component that involves fouling in the presence of fins. The equation for an overall heat transfer coefficient is a complicated expression because of the annulus fouling and the fin efficiency. It can be developed from a series summation of several thermal resistances that are identified in Fig. 11.25. These resistances are given in $\text{m}^2 \cdot \text{K}/\text{W}$.

After both inside and outside heat transfer coefficients, h_i and h_o , have been determined and after both fouling resistances, r_{di} and r_{do} , have been specified (either

However, when the diameter ratio $d_i/d_o \geq 0.75$, r_{mo} can be computed with an error of less than 1% from the arithmetic mean diameter:

$$r_{mo} = \frac{d_o - d_i}{2k_m} \frac{2\pi d_o}{\pi(d_o + d_i)} = \frac{d_o(d_o - d_i)}{k_m(d_o + d_i)} \quad (\text{m}^2 \cdot \text{K/W}) \quad (11.147)$$

4. At this point, the sum of the internal resistances referred to the outside of the inner pipe is

$$\sum R_{io} = r_{io} + r_{dio} + r_{mo} \quad (\text{m}^2 \cdot \text{K/W})$$

and this resistance must be referred to the gross outside surface of each inner pipe per meter:

$$S' = \pi d_o + (2b - \delta)n_f \quad (11.148)$$

Thus,

$$\sum R_{is} = \sum R_{io} \frac{S'}{\pi d_o} \quad (\text{m}^2 \cdot \text{K/W}) \quad (11.149)$$

5. The annulus heat transfer coefficient is h_o , so that

$$r_o = \frac{1}{h_o} \quad (\text{m}^2 \cdot \text{K/W}) \quad (11.150)$$

6. The annulus fouling resistance r_{do} must be combined with h_o to obtain the value of the annulus coefficient working on the fin and prime outer surface. Let this resistance be designated as r'_o , so that

$$r'_o = \frac{1}{h_o} + r_{do} = r_o + r_{do} \quad (\text{m}^2 \cdot \text{K/W})$$

$$h'_o = \frac{1}{r_o + r_{do}}$$

The fin efficiency will be given by

$$\eta_{fo} = \frac{\tanh mb}{mb} \quad (11.151)$$

where

$$m = \left(\frac{2h'_o}{k_m \delta_f} \right)^{1/2}$$

Then, with the weighted fin efficiency defined by eq. (11.9b),

$$\eta_{ov,o} = 1 - \frac{S_{fo}}{S_o}(1 - \eta_{fo}) \quad (11.9b)$$

or

$$\eta_{ov,o} = \frac{\eta_{fo}S_{fo} + S_{bo}}{S_{fo} + S_{bo}}$$

the value of the heat transfer coefficient to the finned and prime surface corrected for the weighted fin efficiency and based on the outside surface of the inner pipe will be

$$h'_{o\eta} = h'_o \eta_o$$

so that the resistance is

$$r'_{o\eta} = \frac{1}{h'_{o\eta}} \quad (\text{m}^2 \cdot \text{K/W}) \quad (11.152)$$

7. The overall resistance is the sum of eqs. (11.149) and (11.152). Thus,

$$\frac{1}{U_o} = \sum R_{is} + r'_{o\eta}$$

or

$$U_o = \frac{1}{\sum R_{is} + r'_{o\eta}} \quad (11.153)$$

The overall heat transfer coefficient given by eq. (11.153) is the coefficient to be used in the *rate equation*:

$$q = U_o S_o \theta_m \quad (11.154)$$

11.6.4 Heat Transfer Coefficients in Pipes and Annuli

Heat transfer coefficients for both the inside of the tubes and the annular region containing the fins have been presented in Section 11.4.3.

11.6.5 Pressure Loss in Pipes and Annuli

The friction relationships of eqs. (11.95) and the turn loss relationship of eq. (11.96) also pertain to the double-pipe heat exchanger. However, when hairpins are considered, the total friction loss in the inner pipe will be

$$\Delta P_f = \frac{8n_{hp} f \rho V^2 L}{2d} = 4n_{hp} f \rho V^2 \frac{L}{d_i} \quad (11.155)$$

For the annulus, the tube diameter is replaced with the equivalent diameter for pressure loss:

$$\Delta P_f = \frac{8n_{hp}f\rho V^2}{2} \frac{L}{d_e} = 4n_{hp}f\rho V^2 \frac{L}{d_e} \quad (11.156)$$

The turn loss for both inner pipe and annulus with N_{hp} hairpins is

$$\Delta P_t = 2(2n_{hp} - 1)\rho V^2 \quad (11.157)$$

11.6.6 Wall Temperature and Further Remarks

It may be noted that the wall resistance presents the lowest resistance to the flow of heat between the hot and cold fluids. Hence, an excellent approximation to the wall temperature may be obtained via the computation of the product of $\sum R_{is}$ and the heat flux. Then, if the hot fluid is carried within the inner tube, the wall temperature will be

$$T_w = T_b - \sum R_{is} \frac{q}{S} \quad (11.158)$$

where

$$\begin{aligned} \sum R_{is} &= \sum R_{io} \frac{S'}{\pi d_o} \\ \sum R_{io} &= r_{io} + r_{do} + r_{mo} \end{aligned} \quad (11.149)$$

In the event, that the cold fluid is carried in the inner tube, the wall temperature will be

$$T_w = t_b + \sum R_{is} \frac{q}{S} \quad (11.159)$$

11.6.7 Series-Parallel Arrangements

When two streams are arranged for counterflow, the LMTD represents the maximum thermal potential for heat transfer that can be obtained. Often, on the industrial scale, a single process service may entail the use of more than a single long hairpin. It then follows that it is desirable to connect the hairpins in series on both the annulus and inner pipe sides, as in Fig. 11.26. In this configuration, the temperature potential remains the LMTD for counterflow.

In some services, there may be a large quantity of one fluid undergoing a small temperature change and a small quantity of another fluid undergoing a large temperature change. It may not be possible to circulate the large volume of fluid through the required number of hairpins with the pressure drop available. Under these circumstances, the larger volume of fluid may be manifolded in the series-parallel arrangement shown in Fig. 11.27. The inner pipe fluid has been split between the exchangers

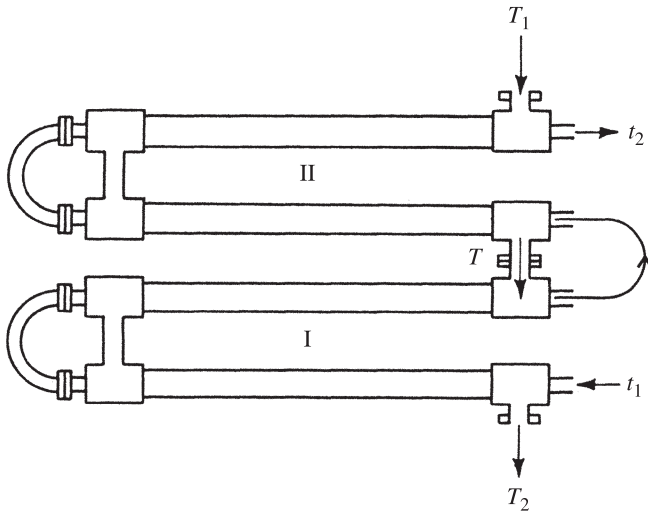


Figure 11.26 Double-pipe heat exchangers in series. (From Kraus et al., 2001, with permission.)

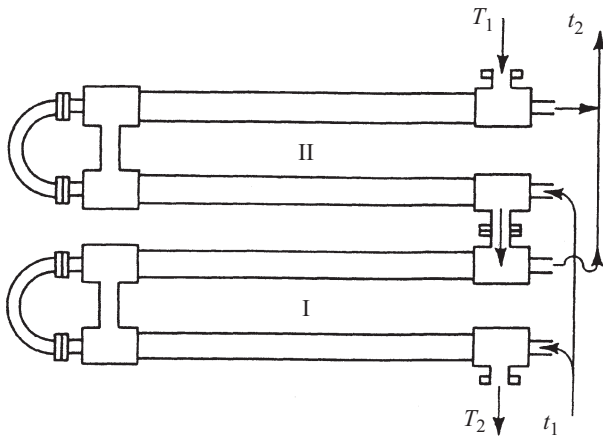


Figure 11.27 Double-pipe heat exchangers in series-parallel. (From Kraus et al., 2001, with permission.)

designated I and II. Both of these exchangers are in counterflow relative to each other but not in the same sense as in Fig. 11.26. In Fig. 11.27, the T 's refer to the *series* streams and the t 's refer to the *parallel* streams.

Departures from true counterflow and true co-current (parallel) flow can be handled by the logarithmic mean temperature difference correction factor F .

Kern (1950) presents a derivation for the factor γ to be used in a modification of the heat transfer rate equation

$$q = U_o S \gamma (T_1 - t_1) \quad (11.160)$$

where $T_1 - t_1$ represents the *total temperature potential*, the difference in the fluid stream inlet temperatures, in the exchanger configuration. After a laborious and detailed derivation, Kern (1950) gives, for one series hot fluid and n parallel cold fluid streams,

$$\gamma = \frac{\left(1 - \frac{T_2 - t_1}{T_1 - t_1}\right) \frac{Z - 1}{nZ}}{\ln \left[\frac{Z - 1}{Z} \left(\frac{T_1 - t_1}{T_2 - t_1} \right)^{1/n} + \frac{1}{Z} \right]} \quad (11.161)$$

where

$$Z = \frac{T_1 - T_2}{n(t_2 - t_1)}$$

For one series cold fluid and n parallel hot fluid streams, Kern (1950) gives

$$\gamma = \frac{\left(1 - \frac{T_1 - t_2}{T_1 - t_1}\right) \frac{1 - Z}{nz}}{\ln \left[(1 - Z) \left(\frac{T_1 - t_1}{T_1 - t_2} \right)^{1/n} + Z \right]} \quad (11.162)$$

TABLE 11.4 Dimensions of Multitube Double-Pipe Exchangers^a

Nom. Dia. (in.)	Pipe Thick. (mm)	Pipe OD (mm)	No. of Tubes	No. of Fins	Tube OD (mm)	Tube Thick. (mm)	Fin Height (mm)
4	6.02	114.3	7	16	19.02	2.11	5.33
	6.02	114.3	7	20	22.2	2.11	5.33
6	7.11	168.3	19	16	19.02	2.11	5.33
	7.11	168.3	14	16	19.02	2.11	5.33
	7.11	168.3	7	20	25.4	2.77	12.7
8	8.18	219.1	19	16	19.02	2.11	8.64
	8.18	219.1	19	20	22.2	2.11	7.11
	8.18	219.1	19	20	25.4	2.77	5.33
	8.18	219.1	19	16	19.02	2.11	7.11
	8.18	219.1	19	20	22.2	2.11	5.33

Source: After Saunders (1988).

^aFin thicknesses are identical to those listed in Table 11.3. The dimensions shown here are for low-pressure units.

where

$$Z = \frac{n(T_1 - T_2)}{t_2 - t_1}$$

11.6.8 Multiple Finned Double-Pipe Exchangers

There are numerous applications for longitudinal fin pipes and tubes. Closest to the double-pipe exchanger is the hairpin with multiple longitudinal-fin pipes. A variety of pipes and tubes are available with longitudinal fins whose numbers, heights, thicknesses, and materials differ. Data for some of these configurations are shown in Table 11.4.

The procedure for the design and analysis of the multiple-tube exchanger differs little for that used for the single-tube exchanger.

11.7 TRANSVERSE HIGH-FIN EXCHANGERS

11.7.1 Introduction

Pipes, tubes, and cast tubular sections with external transverse high fins have been used extensively for heating, cooling, and dehumidifying air and other gases. The fins are preferably called *transverse* rather than radial because they need not be circular, as the latter term implies, and are often helical. The air-fin cooler is a device in which hot-process fluids, usually liquids, flow inside extended surface tubes and atmospheric air is circulated outside the tubes by forced or induced draft over the extended surface.

Unlike liquids, gases are compressible, and it is usually necessary to allocate very small pressure drops for their circulation through industrial equipment or the cost of the compression work may entail a substantial operating charge. Except for hydrogen and helium, which have relatively high thermal conductivities, the low thermal conductivities of gases coupled with small allowable pressure drops tend toward low-external-convection heat transfer coefficients.

In the discussion of longitudinal high-fin tubes in Section 11.6.1, it was noted that a steel fin 1.27 cm high and 0.0889 cm thick could be used advantageously with a fluid producing a heat transfer coefficient as high as $250 \text{ W/m}^2 \cdot \text{K}$. Aluminum and copper have thermal conductivities much higher than steel, 200 and 380 versus $45 \text{ W/m} \cdot \text{K}$. It would appear that thin high fins made of aluminum or copper would have excellent fin efficiencies when exposed to various heating and cooling applications of air and other gases at or near atmospheric pressure.

In air-fin cooler services, the allowable pressure drop is measured in centimeters or inches of water and air can be circulated over a few rows of high-fin tubes with large transverse fin surfaces and, at the same time, require a very small pressure drop. Transverse high-fin tubular elements are found in such diverse places as economizers of steam power boilers, cooling towers, air-conditioning coils, indirect-fired heaters, waste-heat recovery systems for gas turbines and catalytic reactors, gas-cooled nuclear reactors, convectors for home heating, and air-fin coolers.

In the services cited involving high temperatures, hot gases flow over the fins and water or steam flows inside the tubes. The extended surface element usually consists of a chromium steel tube whose chromium content is increased with higher anticipated service temperatures. A ribbon, similar in composition to the tube, is helically wound and continuously welded to the tube. The higher and thicker the fins, the fewer the maximum number of fins per centimeter of tube which can be arc-welded because the fin spacing must also accommodate the welding electrode. High-temperature high-fin tubes on a closer spacing are fabricated by electrical resistance welding of the fins to the tube.

High-fin tubes can also be extruded directly from the tube-wall metal, as in the case of integral low-fin tubing. However, it becomes increasingly difficult to extrude a high fin from ferrous alloys as hard as those required for high-temperature services, which are often amenable to work hardening while the fin is being formed. Whether fins are attached by arc welding or resistance welding, the fin-to-tube attachment for all practical design considerations introduces a negligible bond or contact resistance.

High-fin tubes are used in increasing numbers in devices such as the air-fin cooler, in which a hot fluid flows within the tubes, and atmospheric air, serving as the cooling medium, is circulated over the fins by fans. Several high-fin tubes for air-fin cooler service are shown in Fig. 11.28. Type *a* can be made by inserting the tubes through sheet metal strips with stamped or drilled holes and then expanding the tubes slightly to cause pressure at the tube-to-strip contacts. The tubes and strips may then be brazed. If the tubes are only expanded into the plates to produce an "interference fit," some bond or contact resistance must be anticipated. For practical purposes, when the tubes and strips are brazed together, the joint may be considered a metallurgical bond and the bond resistance can be neglected.

In Fig. 11.28, tubes *b* through *e* are made by winding a metal ribbon in tension around the tube. These types are not metallurgically bonded and rely entirely upon the tension in the ribbon to provide good contact. Type *f* combines tension winding with brazing, and for the combination of a steel tube and an aluminum fin, the common tin-lead solder is not compatible and a zinc solder is used. Type *g* employs a tube as a liner, and high fins are extruded from aluminum, which, like copper, is a metal that can be manipulated to a considerable fin height. Types *d*, *e*, and *f* employ aluminum for the fins and are arranged to protect the tube from the weather because air-fin coolers are installed outdoors. Type *g*, sometimes called a *muff-type* high-fin tube, has its contact resistance between the inside of the integral finned tube and the liner or plain tube. Type *h* has a mechanical bond which can closely match a metallurgical bond for contact resistance. Type *i*, an elliptical tube with rectangular fins, may employ galvanized steel fins. When tube ends are circular, they are rolled into headers.

Consider a typical air-fin cooler application with a hot fluid inside the tubes. In many instances, carbon steel meets the corrosion-resistance requirements of the tube-side fluid. From the standpoint of high thermal conductivity and cost, aluminum ribbon is very suitable for tension-wound fins. However, aluminum has twice the thermal coefficient of expansion of steel, and the higher the operating temperature of the fluid inside the tubes, the greater the tendency of the fins to elongate away from their room-temperature tension-wound contact with the tube, and the greater is

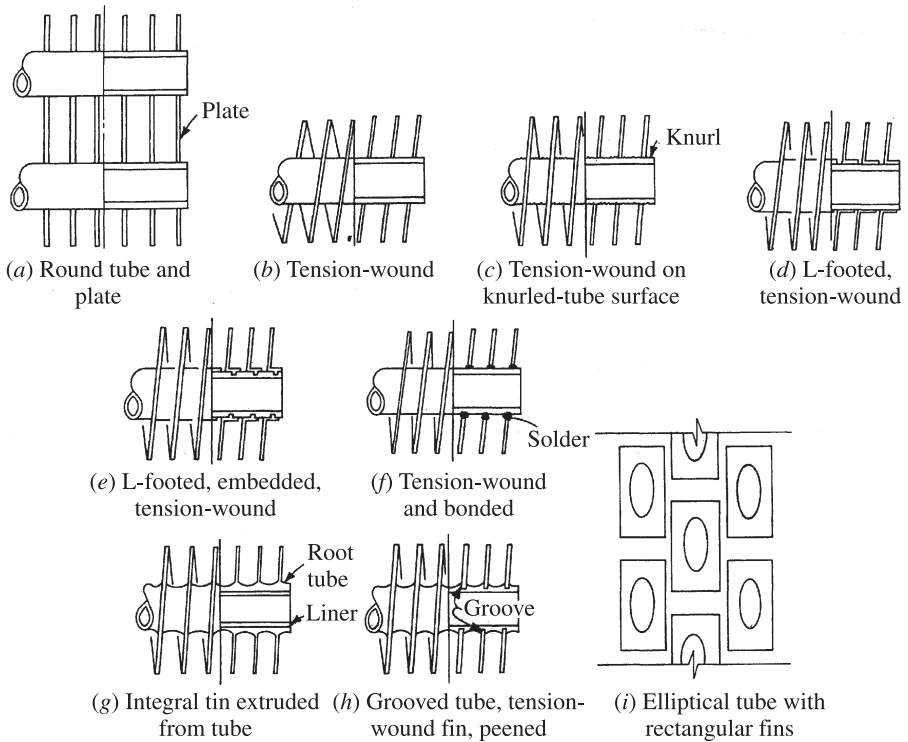


Figure 11.28 Various types of high-fin tubing. (From Kraus et al., 2001, with permission.)

the bond or contact resistance. In one variation of type *d* in Fig. 11.28, the ribbon is wound with *J* rather than *L* feet, with the *J*'s pressing against each other and the tube at room temperature. As the feet become heated during operation, they expand against each other.

11.7.2 Bond or Contact Resistance of High-Fin Tubes

The bond resistance of several types of interference-fit high-fin tubes shown in Fig. 11.28 has been studied by Gardner and Carnavos (1960), Shlykov and Ganin (1964), and Yovanovich (1981). Gardner and Carnavos pointed out that in its most general sense, the term *interference fit* implies the absence of a metallurgical bond, as opposed to the extrusion of a fin from a tube wall, and the welding, soldering, or brazing of a fin to the tube. The interference fit is produced by mechanically developing contact pressure through elastic deformation either by winding a ribbon under tension about a tube, as in types *b* through *e* in Fig. 11.28, or by expanding a tube against the fins as in type *a*, or a combination of pressing the root tube against the liner or the liner against the root tube, as in type *g*.

11.7.3 Fin Efficiency Approximation

The fin efficiency of the radial fin of rectangular profile was given in Chapter 3:

$$\eta = \frac{2r_b}{m(r_a^2 - r_b^2)} \frac{I_1(mr_a)K_1(mr_b) - K_1(mr_a)I_1(mr_b)}{I_0(mr_b)K_1(mr_a) + I_1(mr_a)I_0(mr_b)}$$

where

$$m = \left(\frac{2h}{k\delta}\right)^{1/2} \quad \rho = \frac{r_b}{r_a} \quad \phi = (r_a - r_b)^{3/2} \left(\frac{2h}{kA_p}\right)^{1/2}$$

$$R_a = \frac{1}{1 - \rho} \quad R_b = \frac{\rho}{1 - \rho}$$

The modified Bessel functions in the radial fin efficiency expressions are obtained from tables or from software, and their employment to obtain the efficiency involves a somewhat laborious procedure. An alternative has been provided by McQuiston and Tree (1972), who suggest the approximation

$$\eta = \frac{\tanh m\psi}{m\psi} \quad (11.163)$$

where

$$m = \left(\frac{2h}{k\delta}\right)^{1/2}$$

$$\psi = r_b \frac{1 - \rho}{\rho} \left(1 + 0.35 \ln \frac{1}{\rho}\right) \quad (11.164)$$

where ρ is the radius ratio,

$$\rho = \frac{r_b}{r_a}$$

11.7.4 Air-Fin Coolers

The air-fin cooler consists of one or more horizontal rows of tubes constituting a *section* through which air is circulated upward by mechanical draft. The fan that moves the air may be above the section providing an *induced draft* or it may be below the section, providing a *forced draft*.

In the induced-draft air-fin cooler, the heated air is thrown upward to a good height by its high exit velocity. A relatively small amount of the heated air is sucked back to reenter the air intake below the section and thereby cut down the temperature difference available between the ambient air and the process fluid. In a forced-draft unit, the air leaves at a low velocity at a point not far from the high entrance velocity

of the air to the fan below the section. Hot air is more apt to be sucked back into the fan intake, causing *recirculation*. Following a trend in cooling towers that started some years ago, induced-draft units now appear to be preferred. Usually, the section has cross bracing and baffles to increase rigidity and reduce vibration.

The design and analysis of air-fin coolers differs only in a few respects from the longitudinal fin exchangers in Section 11.6. The principal difference is in the air side, where air competes with other fluids as a coolant. Because air is incompressible and liquids are not, only a small pressure drop can be expended for air circulation across the finned tubes, lest the cost of air-compression work become prohibitive. In most applications, the allowable air-side pressure drop is only about 1.25 cm ($\frac{1}{2}$ in.) of water. The air passes over the finned tubing in crossflow, and this merely requires the use of the proper heat transfer and flow friction data. The temperature excursion of the air usually cannot be computed at the start of the calculations because the air volume, and hence the air temperature rise, are dependent on the air pressure drop and flow area of the cooler.

Most widely used are the integral-fin muff-type tube (Fig. 11.28g), the L-footed tension-wound tube (Fig. 11.28g), and the grooved and peened tension-wound tube (Fig. 11.28h). These tubes usually employ nine or eleven fins per inch. Numerous other tubes are manufactured in accordance with the types shown in Fig. 11.28b, c, and f. Other tubes have serrated or discontinuous fins. The latter tubes are fabricated to their own standards by manufacturers of air-fin coolers.

Physical Data As indicated in Fig. 11.29, tubes may be arranged in either triangular or in-line arrangements. Observe that the pitch in these arrangements is designated by P_t , P_l , or P_d , where P_t = transverse pitch (m), P_l = longitudinal pitch (m), and

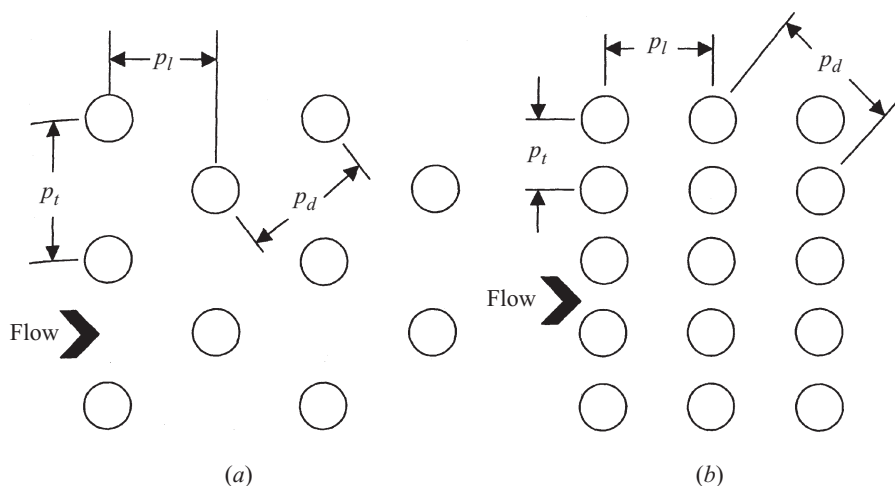


Figure 11.29 Tube arrangements: (a) triangular; (b) in-line. (From Kraus et al., 2001, with permission.)

P_d = diagonal pitch (m). The diagonal pitch is related to the transverse and longitudinal pitch by

$$P_d = \left[\left(\frac{P_t}{2} \right)^2 + P_l^2 \right]^{1/2} \quad (11.165)$$

and in the case of an equilateral triangular arrangement,

$$P_d = P_t$$

When there are n' tubes in a row and n_r rows, the total number of tubes will be

$$n_t = n' n_r \quad (11.166)$$

Let z be the clear space between the tubes, which are L meters long. The fins are b meters high:

$$b = \frac{d_a - d_b}{2}$$

where d_a and d_b are, respectively, the outer and inner diameters of the fin. The fins are δ_f thick and the minimum flow area $A = A_{\min}$ will depend on the transverse pitch P_t . For

$$P_t > 2P_d - d_b - \frac{2z\delta_f}{z + \delta_f}$$

$$A = A_{\min} = n' L \left(P_t - d_b - \frac{2z\delta_f}{z + \delta_f} \right) \quad (11.167)$$

and for

$$P_t < 2P_d - d_b - \frac{2z\delta_f}{z + \delta_f}$$

$$A = A_{\min} = 2n' L \left(P_d - d_b - \frac{2z\delta_f}{z + \delta_f} \right) \quad (11.168)$$

The surface area of the tube (between the fins) will be

$$S_b = \frac{\pi n_t L d_b z}{z + \delta_f} \quad (11.169)$$

and the surface of the fins, which accounts for the heat transfer from the tips of the fins, will be

$$S_f = \frac{\pi n_t L}{z + \delta_f} \left[\frac{1}{2} (d_a^2 - d_b^2) + d_a \delta_f \right] \quad (11.170)$$

This makes the total surface

$$S = S_b + S_f \quad (11.171a)$$

the finned surface per total surface,

$$\frac{S_f}{S} = \frac{S_f}{S_b + S_f} \quad (11.171b)$$

and the surface per unit length per tube,

$$S' = \frac{S}{NL} \quad (11.171c)$$

Heat Transfer Correlations Early investigations that pertain to heat transfer and friction data in tube bundles containing high-fin tubes have been reported by Jameson (1945), Kutateladze and Borishanskii (1966), and Schmidt (1963). The correlation of Briggs and Young (1963) is based on a wide range of data. Their general equation for tube banks containing six rows of tubes on equilateral triangular pitch is

$$\text{Nu} = \frac{hd_b}{k} = 0.134\text{Re}^{0.681} \cdot \text{Pr}^{1/3} \left[\frac{2(P_f - \delta_f)}{d_a - d_b} \right]^{0.20} \left(\frac{P_f - \delta_f}{\delta_f} \right)^{0.1134} \quad (11.172)$$

where

$$\text{Re} = \frac{d_b G}{\mu}$$

and where the range of parameters is

$$\begin{array}{ll} 1000 < \text{Re} < 18,000 & 0.33 \text{ mm} < \delta_f < 20.02 \text{ mm} \\ 11.13 \text{ mm} < d_b < 40.89 \text{ mm} & 1.30 \text{ mm} < P_f < 4.06 \text{ mm} \\ 11.42 \text{ mm} < b = d_a - \frac{d_b}{2} < 16.57 \text{ mm} & 24.99 \text{ mm} < P_t < 111 \text{ mm} \end{array}$$

Vampola (1966) proposed a correlation based on an extensive study of different finned tubes. For more than three tube rows,

$$\begin{aligned} \text{Nu} = \frac{hd_e}{k} &= 0.251\text{Re}^{0.67} \left(\frac{P_t - d_b}{d_b} \right)^{-0.20} \\ &\times \left(\frac{P_t - d_b}{P_f - \delta_f} + 1 \right)^{-0.20} \left(\frac{P_t - d_b}{P_d - d_b} \right)^{0.40} \end{aligned} \quad (11.173)$$

where

$$\text{Re} = \frac{d_e G}{\mu}$$

$$d_e = \frac{S_b d_a + S_f (S_f P_f / 2NL)^{1/2}}{S}$$

with the diagonal pitch given by eq. (11.165). In eq. (11.173), the range of parameters is

$$\begin{aligned} 1000 < \text{Re} < 10,000 & \quad 24.78 \text{ mm} < P_t < 49.55 \text{ mm} \\ 10.67 \text{ mm} < d_b < 26.01 \text{ mm} & \quad 16.20 \text{ mm} < d_e < 34.00 \text{ mm} \\ 5.20 \text{ mm} < b = \frac{d_a - d_b}{2} < 9.70 \text{ mm} & \quad 0.48 \text{ mm} < \frac{P_t - d_b}{d_b} < 1.64 \\ 0.25 \text{ mm} < \delta_f < 0.70 \text{ mm} & \quad 4.34 < \frac{P_t - d_b}{P_f - \delta_f} + 1 < 25.2 \\ 2.28 \text{ mm} < P_f < 5.92 \text{ mm} & \quad 0.45 < \frac{P_t - d_b}{P_d - d_r} < 2.50 \\ 20.32 \text{ mm} < P_l < 52.40 \text{ mm} & \end{aligned}$$

Ganguli et al. (1985) proposed the following correlation for three or more rows of finned tubes:

$$\text{Nu} = \frac{h d_b}{k} = 0.38 \text{Re}^{0.6} \cdot \text{Pr}^{1/3} \left(\frac{S_b}{S} \right)^{0.15} \quad (11.174)$$

where

$$\text{Re} = \frac{d_b G}{\mu}$$

The correlation of eq. (11.174) is valid for

$$\begin{aligned} 1800 < \text{Re} < 100,000 & \quad 2.30 \text{ mm} < P_f < 3.629 \text{ mm} \\ 11.176 \text{ mm} < d_b < 19.05 \text{ mm} & \quad 27.432 \text{ mm} < P_t < 98.552 \text{ mm} \\ 5.842 \text{ mm} < b = \frac{d_a - d_b}{2} < 19.05 \text{ mm} & \quad 1 < \frac{S}{S_b} < 50 \\ 0.254 \text{ mm} < \delta_f < 0.559 \text{ mm} & \end{aligned}$$

Other correlations include those of Brauer (1964), Schulenberg (1965), Kunttysh and Iokhvedor (1971), and Mirkovic (1974). More recent correlations include those of Zhukauskas (1974), Weierman (1976), Hofmann (1976), Ehlmdy and Biggs (1979), Biery (1981), Gianolio and Cuti (1981), Brandt and Wehle (1983), and Nir (1991). Many of them are cited by Kröger (1998).

11.7.5 Pressure Loss Correlations for Staggered Tubes

Some of the earlier correlations for the static pressure drop through bundles of circular finned tubes are those of Jameson (1945), Gunter and Shaw (1945), and Ward and

Young (1959). A frequently used correlation is that of Robinson and Briggs (1966) for staggered tubes:

$$\Delta P = 18.03 \frac{G^2}{\rho} n_r \cdot \text{Re}^{-0.316} \left(\frac{P_t}{d_b} \right)^{-0.927} \left(\frac{P_t}{P_d} \right)^{0.515} \quad (11.175)$$

for n_r rows and where

$$\text{Re} = \frac{d_b G}{\mu}$$

and where P_d is given by eq. (11.165). Equation (11.175) is valid for

$$\begin{array}{ll} 2000 < \text{Re} < 50,000 & 2.31 \text{ mm} < P_f < 2.82 \text{ mm} \\ 18.64 \text{ mm} < d_b < 40.89 \text{ mm} & 42.85 \text{ mm} < P_t < 114.3 \text{ mm} \\ 39.68 \text{ mm} < d_a < 69.85 \text{ mm} & 37.11 \text{ mm} < P_l < 98.89 \text{ mm} \\ 10.52 \text{ mm} < b = \frac{d_a - d_b}{2} < 14.48 \text{ mm} & 1.8 < \frac{P_t}{d_b} < 4.6 \end{array}$$

Vampola (1966) proposed the correlation

$$\begin{aligned} \Delta P = 0.7315 \frac{G^2}{\rho} n_r \cdot \text{Re}^{-0.245} & \left(\frac{P_t - d_b}{d_b} \right)^{-0.90} \\ & \times \left(\frac{P_t - d_b}{P_f - \delta} + 1 \right)^{0.70} \left(\frac{d_e}{d_b} \right)^{0.90} \end{aligned} \quad (11.176)$$

where the Reynolds number, equivalent diameter, and limits of applicability are identical to those following eq. (11.173).

11.7.6 Overall Heat Transfer Coefficient

Because the air- and tube-side heat transfer coefficients, the bond and tube metal resistances, and the tube-side fouling factor all apply at very dissimilar surfaces, it is important that all of these resistances be corrected and summed properly. No provision need be made for air-side fouling because the air-side heat transfer coefficient is low and becomes the controlling resistance. Usually, with the muff-type tube, the resistances are first referred to a hypothetical bare tube having outside diameter, d_b . With diameter designations in Fig. 11.30, there are five inside resistances:

1. The inside film resistance:

$$r_{io} = \frac{1}{h_i} \frac{d_b}{d_i} \quad (11.177)$$

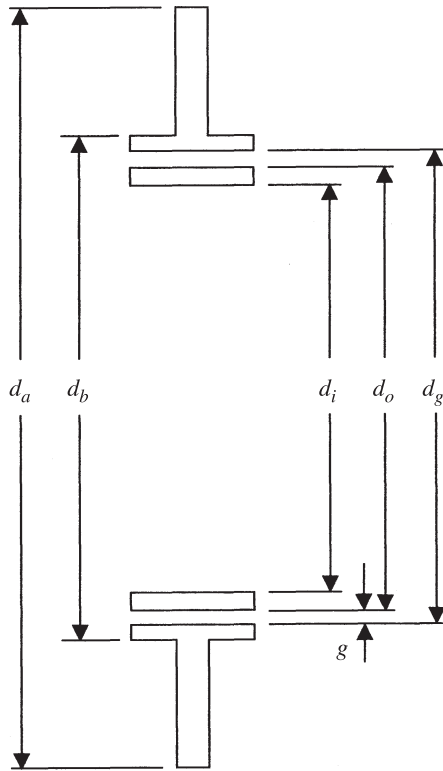


Figure 11.30 Single fin in muff-type tubing. Notice that the diameter at the tips and base of the fin are designated as d_a and d_b , respectively. (From Kraus et al., 2001, with permission.)

2. The inside fouling resistance:

$$r_{dio} = r_{di} \frac{d_b}{d_i} \quad (11.178)$$

3. The liner metal resistance is based on the mean liner diameter, and with the metal thickness

$$\delta_l = \frac{d_o - d_i}{2}$$

the liner metal resistance is

$$r_{mol} = \frac{\delta_l}{k_l} \frac{2d_b}{d_o + d_i} \quad (11.179)$$

4. The bond resistance given by the tube manufacturer or calculated from the procedure of Section 11.2.3 is transferred appropriately via

$$r_{Bo} = r_B \frac{d_b}{d_g} \quad (11.180)$$

5. The tube metal resistance is based on the mean tube diameter, and with the metal thickness

$$\delta_t = \frac{d_b - d_g}{2}$$

the tube metal resistance is

$$r_{mot} = \frac{\delta_t}{k_t} \frac{2d_b}{d_b + d_g} \quad (11.181)$$

The sum of these resistances is $\sum R_{io}$:

$$\sum R_{io} = r_{io} + r_{dio} + r_{mol} + r_{Bo} + r_{mot}$$

and it is noted that $\sum R_{io}$ is based on the equivalent bare outside tube surface. The gross outside surface to bare tube surface is $S'/\pi d_b$, so that the total resistance referred to the gross outside surface will be

$$\sum R_{is} = \sum R_{io} \frac{S'}{\pi d_b} \quad (11.182)$$

The air-side coefficient is h_o and the fin efficiency is computed from eq. (11.9b). Then, with no provision for fouling,

$$r_{o\eta} = \frac{1}{h_o \eta_{ov,o}} \quad (11.183)$$

where $\eta_{ov,o}$ is obtained from eq. (11.9b):

$$\eta_{ov,o} = 1 - \frac{S_f}{S} (1 - \eta_f)$$

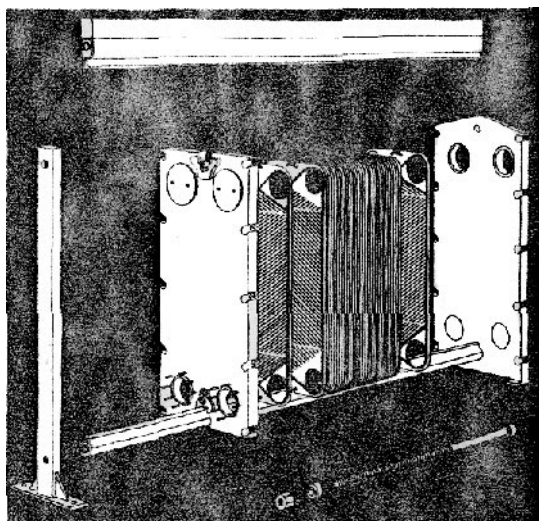
The overall heat transfer coefficient is then given by

$$U_o = \frac{1}{\sum R_{is} + r_{o\eta f}} \quad (11.184)$$

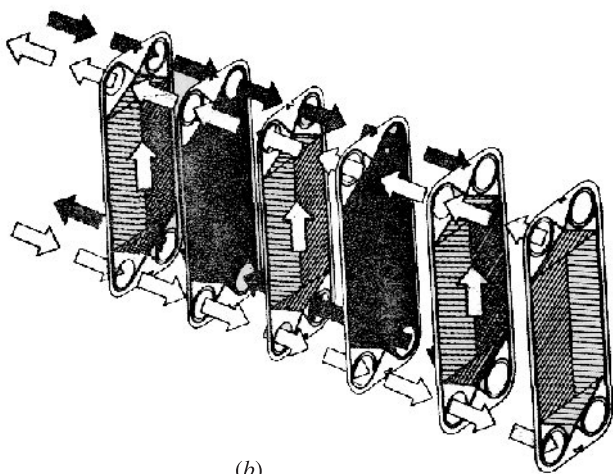
11.8 PLATE AND FRAME HEAT EXCHANGER

11.8.1 Introduction

An exploded view of the *plate and frame heat exchanger*, also referred to as a *gasketed plate heat exchanger*, is shown in Fig. 11.31a. The terminology *plate fin heat*



(a)



(b)

Figure 11.31 (a) Exploded view of a typical plate and frame (gasketed-plate) heat exchanger and (b) flow pattern in a plate and frame (gasketed-plate) heat exchanger. (From Saunders, 1988, with permission.)

exchanger is also in current use but is avoided here because of the possibility of confusion with the plate fin surfaces in compact heat exchangers. The exchanger is composed of a series of corrugated plates that are formed by precision pressing with subsequent assembly into a mounting frame using full peripheral gaskets. Figure 11.31*b* illustrates the general flow pattern and indicates that the spaces between the plates form alternate flow channels through which the hot and cold fluids may flow, in this case, in counterflow.

Plate and frame heat exchangers have several advantages. They are relatively inexpensive and they are easy to dismantle and clean. The surface area enhancement due to the many corrugations means that a great deal of surface can be packed into a rather small volume. Moreover, plate and frame heat exchangers can accommodate a wide range of fluids.

There are three main disadvantages to their employment. Because of the gasket, they are vulnerable to leakage and hence must be used at low pressures. The rather small equivalent diameter of the passages makes the pressure loss relatively high, and the plate and frame heat exchanger may require a substantial investment in the pumping system, which may make the exchanger costwise noncompetitive.

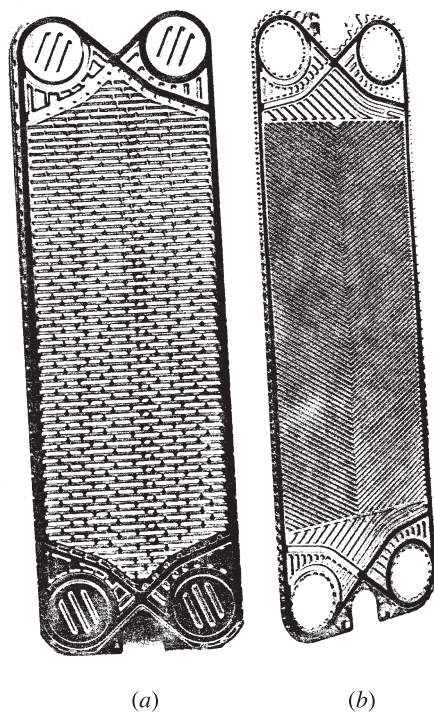


Figure 11.32 Typical plates in plate and frame (gasketed-plate) heat exchanger (a) Inter-mating or washboard type and (b) Chevron or herringbone type. (From Saunders, 1988, with permission.)

The two most widely employed corrugation types are the *intermating* or *washboard* type and the *chevron* or *herringbone* type. Both of these are shown in Fig. 11.32. The corrugations strengthen the individual plates, increase the heat transfer surface area, and actually enhance the heat transfer mechanism.

The outside plates of the assembly do not contribute the fluid-to-fluid heat transfer. Hence, the effective number of plates is the total number of plates minus two. This fact becomes less and less important as the number of plates becomes large. It may be noted that an odd number of plates must be used to assure an equal number of channels for the hot and cold fluids. Figure 11.31a indicates that the frame consists of a fixed head at one end and a movable head at the other. The fluids enter the device through *ports* located in one or both of the end plates. If both inlet and outlet ports for both fluids are located at the fixed-head end, the unit may be opened without disturbing the external piping.

A single traverse of either fluid from top to bottom (or indeed, bottom to top) is called a *pass* and single- or multipass flow is possible. Counterflow or co-current flow is achieved in what is called *looped flow* or *1/1 arrangement*, shown in Fig. 11.33a and b. In Fig. 11.33a, termed the *Z* or *zed arrangement*, two ports are present on both the fixed and movable heads. In the *U arrangement* of Fig. 11.33b, all four

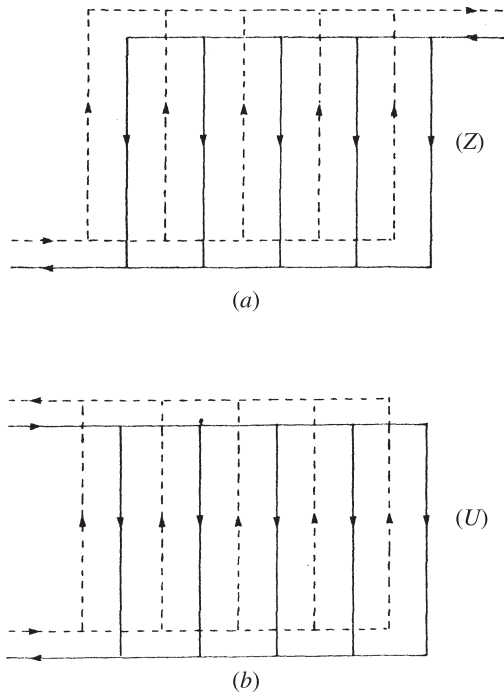


Figure 11.33 Countercurrent single-pass flow (a) *Z*-arrangement and (b) *U*-arrangement. (From Saunders, 1988, with permission.)

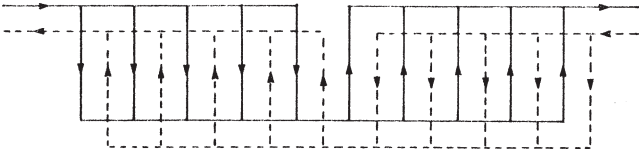


Figure 11.34 *Two-pass/two-pass flow.* (From Saunders, 1988, with permission.)

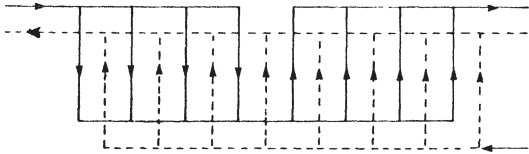


Figure 11.35 *Two-pass/one-pass flow.* (From Saunders, 1988, with permission.)

ports are at the fixed-head end. The *two pass/two pass flow* or *2/2 arrangement* is shown in Fig. 11.34, and the *two pass/one pass flow* or *2/1 arrangement* is shown in Fig. 11.35. Observe that in Fig. 11.34, the arrangement is in true counterflow except for the center plate, where co-current flow exists. In Fig. 11.35, one half of the unit is in counterflow and the other half is in co-current flow.

11.8.2 Physical Data

Figure 11.36*a* shows a sketch of a single plate for the chevron configuration. The *chevron angle* is designated by β , which can range from 25° to 65° . As shown in Fig. 11.36*b*, the mean flow channel gap is b , and it is seen that b is related to the plate pitch p_{pl} and plate thickness δ_{pl} :

$$b = p_{pl} - \delta_{pl} \tag{11.185}$$

Because the corrugations increase the flat plate area, an enlargement factor Λ is employed:

$$\Lambda = \frac{\text{developed length}}{\text{projected length}} \tag{11.186}$$

where typically, $1.10 < \Lambda < 1.25$.

The cross-sectional area of one channel, A_1 , is given by

$$A_1 = bw \tag{11.187}$$

where w is the effective plate width shown in Fig. 11.36*a*. With the wetted perimeter of one channel,

$$P_{W1} = 2(b + \Lambda w) \quad (11.188)$$

the channel equivalent diameter will be

$$d_e = \frac{4A_1}{P_{W1}} = \frac{4bw}{2(b + \Lambda w)}$$

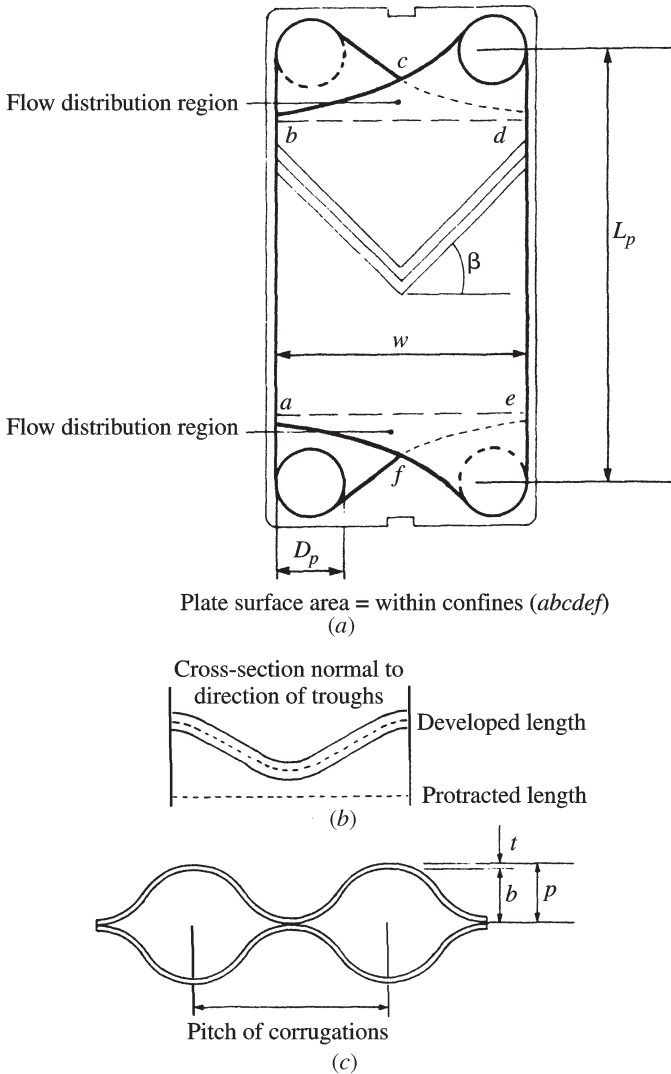


Figure 11.36 Plate geometry for Chevron plates in plate and frame (gasketed-plate heat exchanger). (From Saunders, 1988, with permission.)

and because $w \gg b$,

$$d_e = \frac{2b}{\Lambda} \quad (11.189)$$

If N_p is high, the total surface area for heat flow may be based on the projected area:

$$S = N_p L W \quad (11.190)$$

where L is the length of each plate in the flow direction and W is its width.

Because the hot- and cold-side surfaces are identical, the overall heat transfer coefficient will be given by

$$U = \frac{1}{1/h_c + 1/h_c + R_{dc} + R_{dh} + \delta_{pl}/k_{p1} S_m}$$

where R_{dc} and R_{dh} are the hot- and cold-side fouling resistances. For a thin plate of high thermal conductivity,

$$U = \frac{1}{1/h_c + 1/h_c + R_{dc} + R_{dh}} \quad (11.191)$$

If $R_{dc} = R_{dh} = 0$ (an unfouled or clean exchanger),

$$U = \frac{h_c h_h}{h_c + h_h} \quad (11.192)$$

In the case of plate and frame heat exchanger, the true temperature difference in

$$q = US\theta_m$$

depends on the flow arrangement. For true counterflow or co-current flow, eqs. (11.25) and (11.26) apply. For other arrangements, such as those shown in Figs. 11.34 through 11.36, the work of Shah and Focke (1988) should be consulted.

11.8.3 Heat Transfer and Pressure Loss

The heat transfer and pressure loss in a plate and frame heat exchanger are based on a channel Reynolds number evaluated at the bulk temperature of the fluid given by eqs. (11.131):

$$\text{Re}_{\text{ch}} = \frac{d_e G_{\text{ch}}}{\mu} \quad (11.131)$$

Then the channel Nusselt number will be

$$\text{Nu}_{\text{ch}} = \frac{h d_e}{k} = j_h k \text{Pr}^{1/3} \phi^{0.17}$$

where j_h is a heat transfer parameter and $\phi = \mu/\mu_w$:

$$j_h = C_h \text{Re}_{\text{ch}}^y \quad (11.193)$$

where C_h and y have been determined by Kumar (1984). Both of these values are listed in Table 11.5 as a function of the chevron angle β and the Reynolds number. Thus

$$h = \frac{j_h k \text{Pr}^{1/3} \phi^{0.17}}{d_e} \quad (11.194)$$

The channel pressure loss is the sum of the friction loss Δp_{ch} and the port pressure loss Δp_{port} , which accounts for the entrance and exit losses:

$$\Delta P = \Delta p_{\text{ch}} + \Delta p_{\text{port}} \quad (11.195)$$

In eq. (11.195),

$$\Delta p_{\text{ch}} = \frac{4 f_{\text{ch}} N_p L_p G^2}{2 \rho d_e \phi^{0.17}} \quad (11.196)$$

where N_p is the number of passes, L_p is indicated in Fig. 11.36a, and where

$$f_{\text{ch}} = \frac{K_p}{\text{Re}^z} \quad (11.197)$$

TABLE 11.5 Kumar's (1984) Constants for Single-Phase Heat Transfer and Pressure Loss in Plate and Frame Heat Exchangers

Chevron Angle (deg)	Reynolds Number	C_h	y	Reynolds Number	K_p	z
≤ 30	≤ 10	0.718	0.349	< 10	50.000	1.000
	> 10	0.348	0.663	10–100	19.400	0.589
				> 100	2.990	0.183
45	< 10	0.718	0.349	< 15	47.000	1.000
	10–100	0.400	0.598	15–300	18.290	0.652
	> 100	0.300	0.663	> 300	1.441	0.206
50	< 20	0.630	0.333	< 20	34.000	1.000
	20–300	0.291	0.591	20–300	11.250	0.631
	> 300	0.130	0.732	> 300	0.772	0.161
60	< 20	0.562	0.326	< 40	24.000	1.000
	20–400	0.306	0.529	40–400	3.240	0.457
	> 400	0.108	0.703	> 400	0.760	0.215
≥ 65	< 20	0.562	0.326	< 50	24.000	1.000
	20–500	0.331	0.503	50–500	2.800	0.451
	> 500	0.087	0.718	> 500	0.639	0.213

Source: After Saunders (1988).

According to Kumar (1984), the port pressure loss may be taken as

$$\Delta p_{\text{port}} = \frac{1.3N_p G^2}{2\rho} \quad (11.198)$$

so that the exchanger pressure loss, as required by eq. (11.195), will be

$$\Delta P = \frac{4f_{\text{ch}}N_p L_p G^2}{2\rho d_e \phi^{0.17}} + \frac{1.3N_p G^2}{2\rho}$$

The Kumar (1984) constants depend on the chevron angle and the channel Reynolds number. They are displayed in Table 11.5.

11.9 REGENERATORS

11.9.1 Introduction

The *regenerator* represents a class of heat exchangers in which heat is alternately stored and removed from a surface. This heat transfer surface is usually referred to as the *matrix* of the regenerator. For continuous operation, the matrix must be moved into and out of the fixed hot and cold fluid streams. In this case, the regenerator is called a *rotary regenerator*. If, on the other hand, the hot and cold fluid streams are switched into and out of the matrix, the regenerator is referred to as a *fixed matrix regenerator*. In both cases the regenerator suffers from leakage and fluid entrainment problems, which must be considered during the design process.

An example of a rotary regenerator is shown in Fig. 11.37. This is the *Lungstrom air preheater* used in power plants to warm the incoming combustion air using the exhaust or flue gases from the steam generator.

11.9.2 Heat Capacity and Related Parameters

A sketch of the end view of a rotary regenerator is shown in Fig. 11.38a. The shaded lines represent the radial shield between the hot sector represented by the angle ϕ_h and the cold sector represented by the angle ϕ_c . If the space occupied by the radial shield is represented by the angle ϕ_{sh} , the total periphery in terms of these angles will be

$$\phi_t = \phi_h + \phi_c + \phi_{sh} = 2\pi$$

and because the magnitude of ϕ_{sh} is much less than either ϕ_h or ϕ_c , ϕ_{sh} may be neglected, leaving

$$\phi_t = \phi_h + \phi_c = 2\pi \quad (11.199)$$

The entire assembly shown in Fig. 11.38a rotates in the counterclockwise direction at N_r (rev/s). The hot fluid with capacity rate $C_h = \dot{m}_h c_{ph}$ enters the hot sector (ϕ_h)

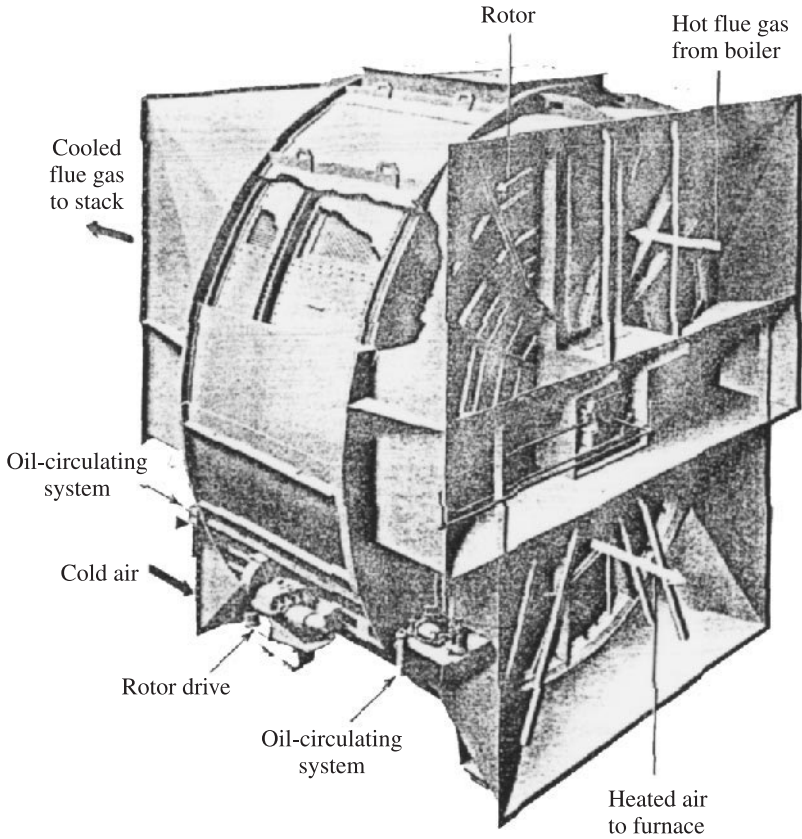


Figure 11.37 A Lungstrom air preheater. (From Fraas, 1989, with permission.)

at T_1 and flows *out of* the plane of the paper at T_2 . The cold fluid with capacity rate $C_c = \dot{m}_c c_{pc}$ enters the cold sector (ϕ_c) at t_1 and flows *into* the plane of the paper and leaves at t_2 .

Details of a single passage of the hot and cold sides of the matrix are indicated, respectively, in Fig. 11.38*b* and *c*. In Fig. 11.38*b*, which represents the hot side of the matrix, the fluid flows from left to right, so that

$$T(x=0) = T_2 \quad \text{and} \quad T(x=L) = T_1$$

The matrix surface S_h is presumed to be at T_{mh} . For the cold fluid shown in Fig. 11.38*c*, the fluid flows from right to left, making

$$t(x=0) = t_1 \quad \text{and} \quad t(x=L) = t_2$$

and the matrix surface S_c is presumed to be at T_{mc} .

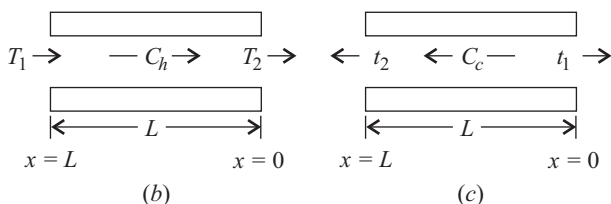
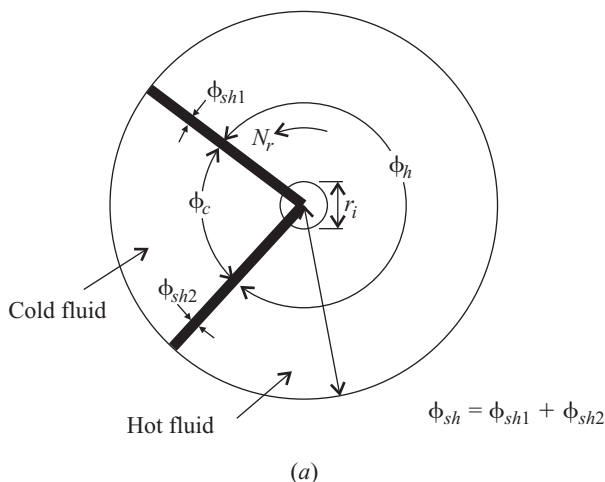


Figure 11.38 (a) End view of a rotary regenerator and (b) details of the hot and cold sides of the matrix.

If M_h and M_c are the masses of the hot and cold fluids contained in the regenerator matrix at any instant of time, u_h and u_c are the mean axial velocities, and τ_{dh} and τ_{dc} are the fluid *residence* or *dwel* times, the hot- and cold-side *heat capacitances* of the fluids within the regenerator are

$$\bar{C}_h = M_h c_{ph} = C_h \tau_{dh} = \frac{C_h L}{u_h} \quad (11.200a)$$

$$\bar{C}_c = M_c c_{pc} = C_c \tau_{dc} = \frac{C_c L}{u_c} \quad (11.200b)$$

In addition, the matrix material will possess a heat capacitance and heat capacity rate of

$$\bar{C}_m = M_m c_m \quad (11.201a)$$

$$C_m = M_m c_m N_r = \bar{C}_m N_r \quad (11.201b)$$

where M_m is the mass of the *entire* matrix and c_m is its specific heat.

With ϕ_{sh} neglected, it is observed that the matrix wall capacitances are related by

$$\bar{C}_{mh} = \bar{C}_m \frac{\phi_h}{\phi_t} \quad (11.202a)$$

$$\bar{C}_{mc} = \bar{C}_m \frac{\phi_c}{\phi_t} \quad (11.202b)$$

and the matrix wall heat capacity rates are related by

$$C_{mh} = \frac{\bar{C}_{mh}}{P_h} = C_m N_r \quad (11.203a)$$

$$\frac{\bar{C}_{mc}}{P_c} = C_m N_r \quad (11.203b)$$

where P_h and P_c are the hot- and cold-fluid time periods.

The heat transfer surface areas are related to the total heat transfer surface by

$$S_h = \frac{\alpha V \phi_h}{\phi_t} \quad (11.204a)$$

$$S_c = \frac{\alpha V \phi_c}{\phi_t} \quad (11.204b)$$

where α is the total surface per unit volume, (the packing density) and V is the total matrix volume.

Some of the matrix surfaces have been described in Section 11.5.2 and values of α and *porosity* p are given by Kays and London (1984). The minimum flow areas designated by A_h and A_c are related to the frontal areas:

$$A_{fr,h} = \pi(r_o^2 - r_i^2) \frac{\phi_h}{\phi_t} \quad (11.205a)$$

$$A_{fr,c} = \pi(r_o^2 - r_i^2) \frac{\phi_c}{\phi_t} \quad (11.205b)$$

The ratio of the free flow area to the frontal area is σ :

$$\sigma_h = \frac{A_h}{A_{fr,h}} \quad (11.206a)$$

$$\sigma_c = \frac{A_c}{A_{fr,c}} \quad (11.206b)$$

The value of σ for seven matrix surfaces is given by Kays and London (1984). For *porous flow passages*, σ is given by

$$\sigma_h = \frac{V_{\text{void}}}{A_{fr,h}L} \quad (11.207a)$$

$$\sigma_c = \frac{V_{\text{void}}}{A_{fr,c}L} \quad (11.207b)$$

The value of the hydraulic (equivalent) diameter will then be

$$D_h = \frac{4\sigma}{\alpha} \quad (11.208)$$

Governing Differential Equations The differential equation that governs the regenerator process is a partial differential equation because the temperatures are a function of the distance x into the regenerator matrix, $0 \leq x \leq L$, and the time τ . Figure 11.39a shows a control volume giving energy quantities during the flow of hot fluid through a passage of length dx during the period when the hot fluid rejects heat to the matrix surface. Figure 11.39b presents the control volume for the matrix surface and indicates that the heat transferred to the matrix surface is equal to the change the matrix internal energy. An energy balance using Fig. 11.39a shows that the difference between the enthalpy flow into and out of the control volume must equal the heat transferred to the matrix surface. This results in

$$\frac{\partial T_h}{\partial \tau_h} + \frac{L}{\tau_{dh}} \frac{dT}{dx} = \frac{h_h S_h}{C_h \tau_{dh}} (T_{mh} - T_h) \quad (11.209)$$

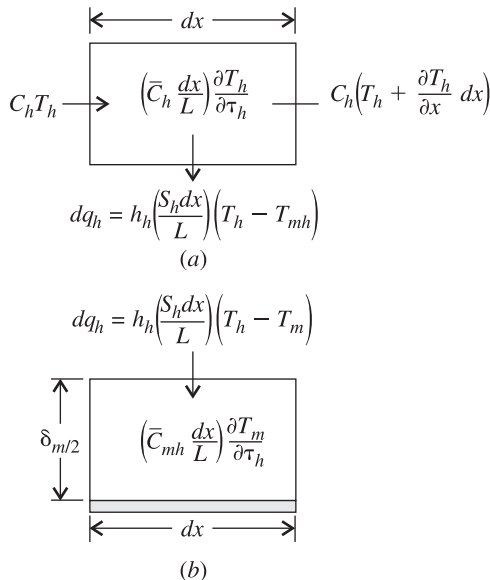


Figure 11.39 Control volume with energy quantities during the flow of hot fluid through (a) the regenerator matrix and (b) the control volume for the matrix surface.

With the value of \bar{C}_h given by eq. (11.200a) substituted into eq. (11.209), the result is

$$\frac{\partial T_h}{\partial \tau_h} + \frac{L}{\tau_{dh}} \frac{dT}{dx} = \frac{h_h S_h}{L} (T_{mh} - T_h) dx \quad (11.210)$$

With no lengthwise conduction, the energy balance for Fig. 11.39b provides

$$\bar{C}_{mh} \frac{\partial T_{mh}}{\partial \tau_h} dx = \frac{h_h S_h}{L} (T_h - T_{mh}) \quad (11.211)$$

Then eqs. (11.203b) and (11.211) can be combined to yield

$$\frac{\partial T_{mh}}{\partial \tau_h} = \frac{h_h S_h}{C_h P_h} (T_h - T_{mh}) \quad (11.212)$$

A similar set of equations can be developed for the cold-fluid flow period, with the result

$$-\frac{\partial T_{mc}}{\partial \tau_c} = \frac{h_c S_c}{C_c P_c} (T_{mc} - T_c) \quad (11.213)$$

In eqs. (11.212) and (11.213), the hot and cold periods are related to the hot- and cold-sector angles via

$$\frac{P_h}{P_t} = \frac{\phi_h}{\phi_t} \quad \text{and} \quad \frac{P_c}{P_t} = \frac{\phi_c}{\phi_t} \quad (11.214)$$

The boundary conditions for eqs. (11.212) and (11.213) are

$$T_h(0, \tau_h) = T_1 \quad (0 \leq \tau_h \leq P_h) \quad (11.215a)$$

$$T_c(L, \tau_c) = T_1 \quad (0 \leq \tau_c \leq P_c) \quad (11.215b)$$

Moreover, the periodic equilibrium conditions for wall at any time $\tau = n P_t$ are given by

$$T_m(x, \tau_h = P_h) = T_m(x, \tau_c = 0) \quad (0 \leq x \leq L) \quad (11.216a)$$

$$T_{mh}(x, \tau_h = 0) = T_{mc}(x, \tau_c = P_c) \quad (0 \leq x \leq L) \quad (11.216b)$$

11.9.3 ϵ - N_{tu} Method

The ϵ - N_{tu} method is employed to determine the performance of the rotary regenerator, while it is customary to use the Δ -II method for obtaining the performance of fixed-matrix regenerators. Because there is no complete analytical solution to eqs. (11.212) and (11.213) with the boundary conditions of eqs. (11.215), Coppage and London (1953) proposed a method where the regenerator effectiveness is a function of four dimensionless parameters:

$$\epsilon = f(N_{tu,o}, C^*, C_m^*, (hS)^*) \quad (11.217)$$

where

$$N_{tu,o} = \frac{1}{C_{\min}} \frac{1}{1/h_h S_h + 1/h_c S_c} \quad (11.218a)$$

$$C^* = \frac{C_{\min}}{C_{\max}} \quad (11.31)$$

$$C_m^* = \frac{C_m}{C_{\min}} \quad (11.218b)$$

$$h^* = \frac{(hS)_{\min}}{(hS)_{\max}} \quad (11.218c)$$

The effectiveness ϵ has been defined in eq. (11.35) as

$$\epsilon = \frac{q}{q_{\max}} = \frac{C_h(T_2 - T_1)}{C_{\min}(T_1 - t_1)} = \frac{C_c(t_2 - t_1)}{C_{\min}(T_1 - t_1)} \quad (11.35)$$

so that

$$q = \epsilon C_{\min}(T_1 - t_1) \quad (11.36)$$

Coppage and London (1953) have pointed out that for the special case of $C_h/C_c = \infty$, the behavior of the regenerator becomes identical to that of the counterflow recuperator given by eq. (11.37) and for the special case of $C^* = 1$,

$$\epsilon = \frac{N_{tu,o}}{N_{tu,o} + 1}$$

Based on the dimensionless groups of eqs. (11.31) and (11.218), the effectiveness of the rotary regenerator is given by Kays and London (1984) when $\epsilon \leq 0.90$ as

$$\epsilon = \epsilon_{cf} \left[1 - \frac{1}{9(C_m^*)^{1.93}} \right] \quad (11.219)$$

where ϵ_{cf} is the effectiveness of the counterflow recuperator given by eq. (11.37):

$$\epsilon = \frac{1 - e^{-N_{tu}(1-C^*)}}{1 - C^* e^{-N_{tu}(1-C^*)}} \quad (11.37)$$

When $\epsilon > 0.90$, Kays and London (1984) recommend the use of the *ineffectiveness*, $1 - \epsilon$, and they provide a plot of the ineffectiveness as a function of $N_{tu,c}$ and two cases of C^* , $C^* = 1.0$ and $C^* = 0.95$.

11.9.4 Heat Transfer and Pressure Loss

Heat Transfer Coefficients Many of the plate heat transfer surfaces described in Section 11.5.7 are used in rotary regenerators. Triangular passages and cross-rod matrices are also employed, and Kays and London (1984) provide a chart of $j_h = St \cdot Pr^{2/3}$ as a function of Re for six randomly stacked woven-wire screen matrix surfaces of several porosities in their Fig. 7.8. The chart is based on the work of Tong and London (1957).

Pressure Loss Friction factors are also given by Kays and London (1984) for the same woven-wire screen matrix surfaces in their Fig. 7.9. The friction factors are to be used in a modification of eq. (11.132) using the porosity ρ in place of σ :

$$\frac{\Delta P}{P_1} = \frac{G^2 v_1}{2g_c P_1} \left[(1 + p^2) \left(\frac{v_2}{v_1} - 1 \right) + f \frac{S}{A} \frac{v_m}{v_1} \right] \quad (11.220)$$

11.10 FOULING

11.10.1 Fouling Mechanisms

Somerscales and Knudsen (1981) have identified six categories of fouling:

1. *Particulate fouling.* The accumulation of solid particles is suspended in the process stream on the heat transfer surfaces. Typical examples include dust deposition, particles carried in condenser cooling water, and unburned fuel, or fly ash. If the solid deposition is due to gravity, the process is referred to as sedimentation fouling.

2. *Precipitation fouling.* Dissolved substances carried in the process stream are precipitated on the heat transfer surfaces. Examples include carbonates, sulfates, and carbonates. *Scaling* occurs when precipitation occurs on heated rather than cooled surfaces.

3. *Chemical reaction fouling.* In certain cases, deposits on the heat transfer surfaces which are not, in themselves, reactants are formed by chemical reactions. In this type of fouling, cracking and coking of hydrocarbons and polymerization are typical examples.

4. *Corrosion fouling.* In this type of fouling, the heat transfer surface reacts, at certain pH levels, to produce products that adhere to the heat transfer surfaces, and in turn, this may promote the attachment of additional fouling materials. Sulfur in fuel oil and sulfur products in the flue gas, such as sulfur dioxide, can lead to sulfuric acid. This has caused, for example, significant damage to heat exchange surfaces in air heaters in the power industry.

5. *Biological fouling.* Materials such as algae, bacteria, molds, seaweed, and barnacles carried in the process stream cause biological fouling of the heat transfer surfaces. A prime example of biological fouling is in marine power plant condensers.

6. *Freezing fouling.* In this type of fouling, a liquid, or some of its higher-melting-point components will deposit on a subcooled heat transfer surface.

11.10.2 Fouling Factors

When a heat exchanger is placed in service, the heat transfer surfaces are, presumably, clean. With time, in some services in the power and process industries, the apparatus may undergo a decline in its ability to transfer heat. This is due to the accumulation of heat insulating substances on either or both of the heat transfer surfaces. The Tubular Exchanger Manufacturers' Association (TEMA) undertook the establishment of standards defining design practices not covered by the ASME Code for Unfired Pressure Vessels. Because the ASME code is concerned primarily with safe pressure containment and the means for inspecting for it during construction, the contribution of TEMA to sound mechanical construction has been substantial.

In addition, TEMA published a table of *fouling factors* to assist the designer in preventing the fouling of a single item in a process, including several items of heat transfer equipment. Resistances were tabulated which were to be added to the film resistances ($1/S_i h_i$ and $1/h_o S_o$) of specific process streams so that the operating period of each would be similar and assure some desired period of continuous operation. The tables of fouling factors were intended as a crude guide toward the equalizations of cumulative fouling in all fouling streams in the assembly.

The fouling factors published by TEMA became entrenched in industrial heat exchanger design. Fouling factors, by the TEMA definition, are time dependent. They are not present when the apparatus is placed on stream; yet at some definite time in the future, when the apparatus has lost some of its heat transfer capabilities, the fouling factor is deemed to have arrived. TEMA does not delineate the in-between fouling process, and the fouling factor has shed little light on the nature of fouling. Significant is the fact that an item of equipment that failed to comply with the TEMA notion of a desired period of continuous operation became a *fouling problem*. Within the scope of the definition of a fouling factor, the only means for ameliorating fouling was to employ larger fouling factors for repetitive services.

The entire concept of the fouling factor is somewhat indefinite. It is an unsteady-state effect that is added indiscriminately to steady-state heat transfer resistances. The difference between a clean and a fouled exchanger is that an intolerable portion of the available temperature difference between fluids must be used to overcome fouling. Thus, if the outside surface S_o of a pipe or tube is the reference and r_{do} is the fouling or *dirt* factor, performance is defined by

$$q = \frac{1}{r_{do}} S \Delta T_{do}$$

where ΔT_{do} is the temperature drop across the fouling factor. After solving for the temperature drop,

$$\Delta T_{do} = r_{do} \frac{q}{S}$$

it is observed that the fouling factor only partially controls fouling. The heat flux q/S is of equal importance. If a fouling factor must be used, it would be more appropriate

TABLE 11.6 Fouling Resistances of Various Gas, Vapor, and Liquid Streams

Fluid	Fouling Resistance ($10^4 \text{ m}^2 \cdot \text{K/W}$)	Fluid	Fouling Resistance ($10^4 \text{ m}^2 \cdot \text{K/W}$)
Liquid water streams		Crude oil refinery streams	
Artificial spray pond water	1.75–3.5	Temperature $\approx 120^\circ\text{C}$	3.5–7
Boiler blowdown water	3.5–5.3	Temperature $\approx 120\text{--}180^\circ\text{C}$	5.25–7
Brackish water	3.5–5.3	Temperature $\approx 180\text{--}230^\circ\text{C}$	7–9
Closed-cycle condensate	0.9–1.75	Temperature $> 230^\circ\text{C}$	9–10.5
Closed-loop treated water	1.75	Petroleum streams	
Distilled water	0.9–1.75	Lean oil	3.5
Engine jacket water	1.75	Liquefied petroleum gases	1.75–3
River water	3.5–5.3	Natural gasolene	1.75–3.5
Seawater	1.75–3.5	Rich oil	1.75–3.5
Treated boiler feedwater	0.9	Process liquid streams	
Treated cooling tower water	1.75–3.5	Bottom products	1.75–3.5
Industrial liquid streams		Caustic solutions	3.5
Ammonia (oil bearing)	5.25	DEA solutions	3.5
Engine lube oil	1.75	DEG solutions	3.5
Ethanol	3.5	MEA solutions	3.5
Ethylene glycol	3.5	TEG solutions	3.5
Hydraulic fluid	1.75	Caustic solutions	3.5
Industrial organic fluids	1.75–3.5	Crude and vacuum liquids	
Methanol	3.5	Atmospheric tower bottoms	12.3
Refrigerants	1.75	Gasolene	3.5
Transformer oil	1.75	Heavy fuel oil	5.3–12.3
No. 2 fuel oil	3.5	Heavy gas oil	5.3–9
No. 6 fuel oil	0.9	Kerosene	3.5–5.3
Cracking and coking unit streams		Light distillates and gas oil	3.5–5.3
Bottom slurry oils	5.3	Naphtha	3.5–5.3
Heavy coker gas oil	7–9	Vacuum tower bottoms	17.6
Heavy cycle oil	5.3–7	Industrial gas or vapor streams	
Light coker gas oil	5.3–7	Ammonia	1.75
Light cycle oil	3.5–5.3	Carbon dioxide	3.5
Light liquid products	3.5	Coal flue gas	17.5
Overhead vapors	3.5	Compressed air	1.75
Light-end processing streams		Exhaust steam (oil bearing)	2.6–3.5
Absorption oils	3.5–5.3	Natural gas flue gas	9
Alkylation trace acid streams	3.5	Refrigerant (oil bearing)	3.5
Overhead gas	1.75	Steam (non-oil bearing)	9
Overhead liquid products	1.75		
Overhead vapors	1.75		
Reboiler streams	3–5.5		
Chemical process streams			
Acid gas	3.5–5.3		
Natural gas	1.75–3.5		
Solvent vapor	1.75		
Stable overhead products	1.75		

Source: Adapted from Chenoweth (1988).

to specify a fouling factor for a particular process stream along with some range of appropriate temperature differences. TEMA has made some attempt to anticipate temperature differences by classifying fouling factors according to various process services. The result is inexact, as there is much latitude in establishing a process service. In any event, fouling factors which are, in reality, *fouling resistances* are given by TEMA and may be specified by other standards.

Chenoweth (1990) provided a summary of the fouling resistances for various gas, vapor, and liquid streams. A partial list of his fouling factors is given in Table 11.6.

NOMENCLATURE

Roman Letter Symbols

A_{bp}	crossflow area for bypass, m^2
A_c	crossflow area, m^2
	cold-side flow area, m^2
A_{CL}	centerline flow area, m^2
A_f	flow area, m^2
A_{fr}	frontal area, m^2
$A_{fr,c}$	cold-side frontal area, m^2
$A_{fr,h}$	hot-side frontal area, m^2
$A_{fr,1}$	frontal area, side 1 of exchanger, m^2
$A_{fr,2}$	frontal area, side 2 of exchanger, m^2
A_w	window flow area, m^2
A_{wg}	gross window area, m^2
A_{wt}	crossflow area for bypass, m^2
A_1	inlet nozzle area, m^2
A_2	bundle entry area, m^2
A_3	outlet nozzle area, m^2
A_4	bundle exit area, m^2
a	coefficient, dimensionless
	separation or splitter plate thickness, m
b	coefficient, dimensionless
	distance between separation plates, m
	mean flow channel gap, m
b_f	fin height, m
b_i	inside fin height, m
b_o	outside fin height, m
C	constant, dimensionless
	capacity rate, W/K
C_c	cold-fluid capacity rate, W/K
C_h	hot-fluid capacity rate, W/K
	coefficient, dimensionless
C_m	matrix wall capacity rate, W/K

C_{\max}	maximum capacity rate, W/K
C_{\min}	minimum capacity rate, W/K
C_{mc}	cold-side matrix wall capacity rate, W/K
C_{mh}	hot-side matrix wall capacity rate, W/K
C_1	difference between shell inside diameter and outer tube limit, m
\bar{C}_c	cold-side heat capacitance, W/kg · K
\bar{C}_h	hot-side heat capacitance, W/kg · K
\bar{C}_m	matrix material heat capacitance, W/kg · K
\bar{C}_{mc}	cold-side matrix material heat capacitance, W/kg · K
\bar{C}_{mh}	hot-side matrix material heat capacitance, W/kg · K
C^*	capacity rate ratio, dimensionless
c_c	contraction coefficient, dimensionless
	counterflow coefficient, dimensionless
c_m	specific heat of rotor, J/kg · K
c_p	specific heat at constant pressure, J/kg · K
c_{pc}	cold-fluid specific heat at constant pressure, J/kg · K
c_{ph}	hot-fluid specific heat at constant pressure, J/kg · K
D	depth of exchanger, m
	parameter defined where used
D_b	baffle diameter, m
D_e	equivalent diameter, m
D'_e	equivalent diameter of bypass lane, m
D_o	outer tube limit diameter, m
D_s	shell inside diameter, m
d	diameter, m
d_e	equivalent diameter, m
d_h	hydraulic diameter, m
d_i	inner or inside diameter, m
d_o	tube diameter (outside diameter), m
F	logarithmic mean temperature difference correction factor, dimensionless
F_C	crossflow tube fraction, dimensionless
F_T	transitional correction factor, dimensionless
F_w	fraction of number of tubes in one window, dimensionless
f	friction factor, dimensionless
G	parameter, defined when used, dimensionless
	mass velocity, kg/m ² · s
G_{ch}	channel mass velocity, kg/m ² · s
Gr	Graetz number, dimensionless
g_c	proportionality factor in Newton's second law, dimensionless
H	height of exchanger, m
h	heat transfer coefficient, W/m ² · K
h_c	cold-side heat transfer coefficient, W/m ² · K
h_{dc}	cold-side fouling heat transfer coefficient, W/m ² · K

h_{dh}	hot-side fouling heat transfer coefficient, $\text{W/m}^2 \cdot \text{K}$
h_h	hot-side heat transfer coefficient, $\text{W/m}^2 \cdot \text{K}$
h_i	inside heat transfer coefficient, $\text{W/m}^2 \cdot \text{K}$
h_{io}	inside heat transfer coefficient referred to outside surface, $\text{W/m}^2 \cdot \text{K}$
$h'_{i\eta}$	annulus heat transfer coefficient corrected for the weighted fin efficiency, $\text{W/m}^2 \cdot \text{K}$
h'_o	annulus heat transfer coefficient including the effect of fouling, $\text{W/m}^2 \cdot \text{K}$
I	modified Bessel function of the first kind, dimensionless
J_B	correction factor for bundle bypass, dimensionless
J_C	correction factor for baffle cut, dimensionless
J_L	correction factor for baffle leakage, dimensionless
J_R	correction factor for temperature gradient, dimensionless
j_h	heat transfer parameter, dimensionless
k	thermal conductivity, $\text{W/m} \cdot \text{K}$
k_m	thermal conductivity of metal, $\text{W/m} \cdot \text{K}$
L	exchanger length, m
	tube length, m
	length of plate, m
L_{bc}	central baffle spacing, m
L_{bi}	baffle spacing at inlet, m
L_{bo}	baffle spacing at outlet, m
L_i^*	baffle spacing parameter, dimensionless
L_o^*	baffle spacing parameter, dimensionless
l_c	baffle cut, m
LMTD	logarithmic mean temperature difference, K
m	mass of matrix, kg
	fin performance factor, m^{-1}
\dot{m}	mass flow rate, kg/s
\dot{m}_b	bypass path mass flow rate, kg/s
\dot{m}_c	cold-fluid mass flow rate, kg/s
	crossflow path mass flow rate, kg/s
\dot{m}_{cr}	total crossflow mass flow rate, kg/s
\dot{m}_h	hot-fluid mass flow rate, kg/s
\dot{m}_l	leakage path mass flow rate, kg/s
\dot{m}_s	shell-to-baffle leakage path mass flow rate, kg/s
\dot{m}_T	total mass flow rate, kg/s
\dot{m}_t	tube-to-baffle leakage path mass flow rate, kg/s
\dot{m}_w	window mass flow rate, kg/s
N_{cc}	group of length terms, dimensionless
N_{cf}	number of transfer units for counter flow, dimensionless
N_{CL}	number of tubes on shell centerline, dimensionless
N_{cw}	number of tubes crossed in one window, dimensionless
N_p	number of plates, dimensionless

N_r	rotational speed, rev/s
N_{ss}	number of sealing strip pairs, dimensionless
N_{tu}	number of heat transfer units, dimensionless
$N_{tu,c}$	number of heat transfer units based on cold side, dimensionless
$N_{tu,o}$	overall number of heat transfer units, dimensionless
n	number of fins, dimensionless
n_b	flow resistance of bypass path, $N \cdot s/m^2 \cdot kg$
n_c	number of tubes crossed, dimensionless
	flow resistance of crossflow path, $N \cdot s/m^2 \cdot kg$
n_{cr}	flow resistance of total crossflow path, $N \cdot s/m^2 \cdot kg$
n_{cw}	number of tubes crossed in one window, dimensionless
n_{hp}	number of hairpins, dimensionless
n_i	number of fins on inside, dimensionless
n_o	number of fins on outside, dimensionless
n_p	number of passes, dimensionless
	number of in-line pass partitions, dimensionless
n_r	number of rows, dimensionless
n_s	flow resistance of shell-to-baffle leakage path, $N \cdot s/m^2 \cdot kg$
n_t	flow resistance of tube-to-baffle leakage path, $N \cdot s/m^2 \cdot kg$
	number of tubes, dimensionless
n_{tw}	number of tubes in one window, dimensionless
n_w	flow resistance of window path, $N \cdot s/m^2 \cdot kg$
n_{we}	exit space window flow resistance, $N \cdot s/m^2 \cdot kg$
n_1	number of stacks, side 1 of heat exchanger, dimensionless
n_2	number of stacks, side 2 of heat exchanger, dimensionless
n'	number of tubes in a row, dimensionless
Nu	Nusselt number, dimensionless
Nu_d	Nusselt number based on diameter, dimensionless
Nu_{ch}	channel Nusselt number, dimensionless
P	cold-side effectiveness, dimensionless
	perimeter of passage, m
	pressure, N/m^2 or Pa
P_c	cold-fluid time period, s
P_d	diagonal pitch, m
P_h	hot-fluid time period, s
P_l	longitudinal pitch, m
P_t	transverse pitch, m
P_{W1}	wetted perimeter for one channel, m
ΔP	pressure loss, N/m^2 or Pa
ΔP_{AB}	pressure loss from A to B, N/m^2 or Pa
ΔP_b	bypass path pressure loss, N/m^2 or Pa
ΔP_c	crossflow path pressure loss, N/m^2 or Pa
ΔP_{ch}	channel pressure loss, N/m^2 or Pa
ΔP_{cr}	total crossflow path pressure loss, N/m^2 or Pa

ΔP_e	end-space pressure loss, N/m ² or Pa
ΔP_f	friction pressure loss, N/m ² or Pa
ΔP_l	leakage path pressure loss, N/m ² or Pa
ΔP_{n1}	pressure loss at inlet nozzle, N/m ² or Pa
ΔP_{n2}	pressure loss at outlet nozzle, N/m ² or Pa
ΔP_{port}	port pressure loss, N/m ² or Pa
ΔP_s	shell-to-baffle path pressure loss, N/m ² or Pa
ΔP_t	turn pressure loss, N/m ² or Pa
	tube-to-baffle path pressure loss, N/m ² or Pa
ΔP_w	window pressure loss, N/m ² or Pa
p	porosity of matrix surface, dimensionless
p_b	baffle cut, m
p_{pl}	plate pitch, m
Pr	Prandtl number, dimensionless
Pr _w	Prandtl number based on wall thermal properties, dimensionless
q	heat flow, W
	tube pitch correction factor, dimensionless
R	capacity rate ratio, W/K
	thermal resistance, K/W
R_c	cold-side thermal resistance, K/W
R_{dc}	cold-side fouling thermal resistance, K/W
R_{dh}	hot-side fouling thermal resistance, K/W
R_h	hot-side thermal resistance, K/W
R_{io}	sum of internal resistances referred to the outside of the inner pipe, K/W
R_{is}	sum of internal resistances referred to gross outside surface, K/W
R_m	metal thermal resistance, K/W
r_a	area ratio, defined where used, dimensionless
r_b	area ratio, defined where used, dimensionless
r_c	area ratio, defined where used, dimensionless
r_{di}	inside fouling resistance, m ² · K/W
r_{dio}	inside fouling resistance referred to tube outside, m ² · K/W
r_{do}	outside fouling resistance, m ² · K/W
r_h	hydraulic radius, m
r_{io}	inside film resistance referred to tube outside, m ² · K/W
r_{mo}	pipe wall resistance referred to tube outside, m ² · K/W
r_o	annulus film resistance referred to tube outside, m ² · K/W
$r_{o\eta}$	annulus thermal resistance corrected for fouling, m ² · K/W
r'_o	refers to outside or annulus resistance with fouling, m ² · K/W
$r'_{o\eta}$	refers to outside or annulus resistance with fouling corrected for overall efficiency, m ² · K/W
Re	Reynolds number, dimensionless
Re _c	crossflow Reynolds number, dimensionless

Re_d	Reynolds number based on diameter, dimensionless
S	surface area, m^2
S'	annulus surface per unit length, m^2/m
S_b	base or prime surface area, m^2
S_{bi}	inside base surface area, m^2
S_{bo}	outside base surface area, m^2
S_c	cold side surface area, m^2
S_f	finned surface area, m^2
S_{fi}	inside finned surface area, m^2
S_{fo}	outside surface area, m^2
S_h	hot surface area, m^2
S_i	inside surface area, m^2
S_m	metal or matrix surface area, m^2
S_o	outside surface area, m^2
S'	surface area per unit length of tube, m^2/m
St	Stanton number, dimensionless
T	hot-fluid temperature, K
T_{mc}	cold-side matrix temperature, K
T_{mh}	hot-side matrix temperature, K
T_s	surface temperature, K
T_w	wall temperature, K
T_1	inlet hot-fluid temperature, K
T_2	outlet hot-fluid temperature, K
t	cold-fluid temperature, K
t_1	inlet cold-fluid temperature, K
t_2	outlet cold-fluid temperature, K
U	overall heat transfer coefficient, $W/m^2 \cdot K$
U_c	overall heat transfer coefficient referred to cold fluid, $W/m^2 \cdot K$
U_h	overall heat transfer coefficient referred to hot fluid, $W/m^2 \cdot K$
u	linear velocity, m/s
V	volume of exchanger, m^3
V_{void}	void volume, m^3
v	specific volume of fluid, m^3/kg
W	width of exchanger, m width of plate, m
w	effective plate width, m
w_p	width of bypass divider lane, m
X_L	longitudinal tube spacing, m
X_T	transverse tube spacing, m
Z	parameter used in multistream arrangements, dimensionless
z	clear space between tubes, m pass partition width, m fin root width, m

Greek Letter Symbols

α	parameter defined where used, dimensionless ratio of total area on one side of the exchanger to the total volume on both sides of an exchanger, m^2/m^3 packing density, m^2/m^3
β	parameter defined where used, dimensionless ratio of total area on to the total volume on one side of an exchanger, m^2/m^3 chevron angle, deg
Γ	parameter defined where used, dimensionless
γ	correction factor for multipass arrangements, dimensionless parameter defined where used, dimensionless
Δ	change in, dimensionless
δ_f	fin thickness, m
δ_{fi}	inside fin thickness, m
δ_{fo}	outside fin thickness, m
δ_m	metal thickness, m
δ_{ov}	height of baffle overlap region, m
δ_{pl}	plate thickness, m
δ_{sb}	shell-to-baffle spacing, m
δ_{sh}	tube sheet thickness, m
δ_{tb}	tube-to-baffle spacing, m
δ_{ts}	tube-to-shell gap thickness, m
ϵ	exchanger effectiveness, dimensionless
ζ	combination of terms, dimensionless
η	efficiency, dimensionless
η_c	cold-side fin efficiency, dimensionless
η_f	fin efficiency, dimensionless
η_{fi}	inside fin efficiency, dimensionless
η_{fo}	outside fin efficiency, dimensionless
η_h	hot-side fin efficiency, dimensionless
η_{ov}	overall efficiency, dimensionless
$\eta_{ov,c}$	cold-side overall efficiency, dimensionless
$\eta_{ov,h}$	hot-side overall efficiency, dimensionless
$\eta_{ov,i}$	inner or inside efficiency, dimensionless
$\eta_{ov,o}$	outer or outside efficiency, dimensionless
θ_m	true temperature difference, K
θ_1	angle between the horizontal and the point on the baffle edge on the baffle cut, rad
θ_2	angle, rad
θ_3	twice the angle between the vertical and the intersection of the baffle edge and the outer tube limit, rad
Λ	enlargement factor, dimensionless
μ	dynamic viscosity, $\text{N} \cdot \text{s}^2/\text{m}$
ρ	fluid density, dimensionless

ϱ	ratio of transverse to longitudinal tube spacing, dimensionless
σ	ratio of free flow area to frontal area, dimensionless
τ_{dc}	cold-side dwell time, s
τ_{dh}	hot-side dwell time, s
Υ	ratio of Prandtl numbers, dimensionless
Φ	parameter, defined where used, dimensionless
ϕ	viscosity correction factor, dimensionless
ϕ_c	cold-side face angle in a regenerator, rad
ϕ_h	hot-side face angle in a regenerator, rad
ϕ_{sh}	shield face angle in a regenerator, rad
ϕ_t	total face angle in a regenerator, rad
φ	group of length terms, dimensionless
ψ	ratio, dimensionless
	correction factor, dimensionless

Subscripts

a	particular area ratio
AB	distance between A and B
B	bundle bypass
b	bypass path
	particular area ratio
	base or prime surface
	baffle
	bulk temperature
bc	central baffle spacing
bi	inside base surface
bi	inlet baffle spacing
bo	outside base surface
bo	outlet baffle spacing
bp	bypass area
C	baffle cut
	crossflow tube fraction
CL	tubes on shell centerline
	centerline flow area
c	contraction coefficient
	baffle cut
	cold fluid
	crossflow
	number of tubes crossed
	particular area ratio
	crossflow path
cc	group of length terms
cf	counterflow
ch	channel
D	diameter

d	diameter
	diagonal
	dirt or fouling
dc	cold-side dwell time
dh	hot-side dwell time
di	inside fouling
dio	inside fouling condition referred to outside
do	outside fouling
e	end space
	equivalent
f	fin
	flow
fi	inside fin
fo	outside fin
fr	frontal area
h	heat transfer parameter
	hot fluid
	hydraulic
i	inner or inside
id	ideal condition
L	baffle leakage
l	longitudinal
m	matrix or metal
max	maximum
min	minimum
mo	metal condition referred to outside
n_1	nozzle 1 location
n_2	nozzle 2 location
o	outer or outside
	outer tube limit
p	number of bypass divider lanes
	width of bypass divider lane
	number of pass partitions
	number of bypass divider lanes
pl	plate
port	port
S	baffle spacing
s	shell
	surface
sb	shell-to-baffle leakage path
	shell-to-baffle spacing
sh	tube sheet
shell	shell
ss	sealing strips

T	temperature gradient total transitional correction factor
t	tube or number of tubes tube-to-baffle leakage path transverse
ts	tube sheet
tube	tube
tw	number of tubes in one window
V	volumetric volumetric equivalent diameter
void	void volume
Wf	wetted perimeter for friction
Wh	wetted perimeter for heat transfer
$W1$	wetted perimeter of one channel
w	window path wall window
we	end-space condition
wg	gross window area
wt	tubes in window
y	tube pitch factor
1	inlet
2	inlet or outlet
3	outlet
4	outlet

Superscripts

m	exponent, dimensionless
n	exponent, dimensionless
y	exponent, dimensionless

REFERENCES

- Baclic, B. S. (1978). A Simplified Formula for Cross-Flow Heat Exchanger Effectiveness, *J. Heat Transfer*, 100, 746–747.
- Baclic, B. S. (1989). 1–2N Shell-and-Tube Exchanger Effectiveness: A Simplified Kraus–Kern Equation, *J. Heat Transfer*, 111, 181–182.
- Baclic, B. S. (1990). ϵ – N_{tu} Analysis of Complicated Flow Arrangements, in *Compact Heat Exchangers*, R. K. Shah, A. D. Kraus, and D. Metzger, eds., Hemisphere Publishing, New York, pp. 31–90.
- Baclic, B. S. (1997). 1–(2N – 1) Shell-and-Tube Exchanger Effectiveness: Explicit Equations, *Heat Mass Transfer*, 33, 163–165.

- Baclic, B. S., and Heggs, P. J. (1985). On the Search for New Solutions of the Single-Pass Crossflow Heat Exchanger Problem, *Int. J. Heat Mass Transfer*, 28, 1965–1976.
- Barnes, J. F., and Jackson, J. D. (1961). Heat Transfer to Air, Carbon Monoxide and Helium Flowing through Smooth Circular Tubes under Conditions of Large Surface/Gas Temperature Ratio, *J. Mech. Eng. Sci.*, 3(4), 303–314.
- Bejan, A. (1995). *Convection Heat Transfer*, 2nd ed., Wiley, New York.
- Bejan, A. (1997). *Advanced Engineering Thermodynamics*, 2nd ed., Wiley, New York.
- Bejan, A. (2000). *Shape and Structure, from Engineering to Nature*, Cambridge University Press, Cambridge.
- Bejan, A., Tsatsaronis, G., and Moran, M. (1996). *Thermal Design and Optimization*, Wiley, New York.
- Bell, K. J. (1963). Final Report of the Cooperative Research Program on Shell-and-Tube Heat Exchangers, *Bulletin 5*, Engineering Experimental Station, University of Delaware, Newark, DE.
- Bell, K. J. (1988). Delaware Method for Shell Side Design, in *Heat Transfer Equipment Design*, R. K. Shah, E. C. Subbarao and R. A. Mashelkar, eds., Hemisphere Publishing, New York, pp. 145–166.
- Biery, J. C. (1981). Prediction of Heat Transfer Coefficients in Gas Flow Normal to Finned and Smooth Tube Banks, *J. Heat Transfer*, 103, 705–710.
- Bowman, R. A., Mueller, A. C., and Nagle, W. M. (1940). Mean Temperature Difference in Design, *Trans. ASME*, 62, 283–294.
- Brandt, F., and Wehle, W. (1983). Eine zusammenfassende Darstellung des Wärmeübergangs Rohrbündeln mit glatten Rohren und Rippenrohren, VGB-Konferenz.
- Brauer, H. (1964). Compact Heat Exchangers, *Chem. Proc. Eng.*, 451–458.
- Briggs, D. E., and Young, E. H. (1963). Convective Heat Transfer and Pressure Drop of Air Flowing across Triangular Pitch Banks of Finned Tubes, *Chem. Eng. Prog. Symp. Ser.*, 59(41), 1–8.
- Butterworth, D. (1979). The Correlation of Crossflow Pressure Drop Data by Means of the Permeability Concept, *Report AERE-R9435*, UKAEA, Harwell, Berkshire, England.
- Chenoweth, J. M. (1990). Final Report of the HTRI/TEMA Joint Committee to Review the Fouling Section of the TEMA Standards, *Heat Transfer Eng.*, 11(1), 73–107.
- Coppage, J. E., and London, A. L. (1953). The Period Flow Regenerator: A Summary of Design Theory, *Trans. ASME*, 75, 779–785.
- Crozier, R., Jr., and Samuels, M. (1977). Mean Temperature Difference in Old Tube Pass Heat Exchangers, *J. Heat Transfer*, 99, 487–489.
- Dalle Donne, M., and Bowditch, P. W. (1963). Experimental Local Heat Transfer and Friction Coefficients for Subsonic Laminar, Transitional and Turbulent Flow of Air or Helium in a Tube at High Temperatures, *Dragon Project Report 184*, Winfirth, Dorchester, Dorset, England.
- Deissler, R. G. (1951). Analytical Investigation of Fully Developed Laminar Flow in Tubes with Heat Transfer and Fluid Properties Variable along the Radius, *NACA-TN-2410*.
- DeLorenzo, B., and Anderson, R. B. (1945). Heat Transfer and Pressure Drop of Liquids in Double Pipe Exchangers, *Trans. ASME*, 67, 697–703.
- Devore, A. (1962). Use Nomograms to Speed Exchanger Calculations, *Hydrocarbon Process. Pet. Refiner*, 41(12), 101–106.

- Dittus, F. W., and Boelter, L. M. K. (1930). Heat Transfer in Automobile Radiators of the Tubular Type, *Univ. Calif. (Berkeley) Publ. Eng.*, 2 (13), 443–461; *Int. Comm. Heat Mass Transfer*, 12 (1985), 3–22.
- Donohue, D. A. (1949). Heat Transfer and Pressure Drop in Heat Exchangers, *Ind. Eng. Chem.*, 41(11), 2499–2511.
- Ehlmady, A. H., and Biggs, R. C. (1979). Finned Tube Heat Exchanger: Correlation of Dry Surface Heat Transfer Data, *Trans. ASHRAE*, 85, 117–123.
- Fischer, F. K. (1938). Mean Temperature Difference Correction in Multipass Exchangers, *Ind. Eng. Chem.*, 30(4), 377–383.
- Fraas, A. P. (1989). *Heat Exchanger Design*, Wiley, New York.
- Ganguli, A., Tung, S. S., and Taborek, J. (1985). Parametric Study of Air Cooled Heat Exchanger Finned Tube Geometry. *AIChE Symp. Ser.*, 81(245), 122–128.
- Gardner, K. A. (1941). Mean Temperature Difference in Multipass Exchangers: Correction Factors with Shell Fluid Unmixed, *Ind. Eng. Chem.*, 33, 1495–1500.
- Gardner, K. A. (1942). Mean Temperature Difference in an Array of Identical Exchangers, *Ind. Eng. Chem.*, 34, 1083–1087.
- Gardner, K. A., and Carnavos, T. C. (1960). Thermal Contact Resistance in Finned Tubing, *J. Heat Transfer*, 82, 279–287.
- Gianolio, E., and Cuti, F. (1981). Heat Transfer Coefficients and Pressure Drops for Air Coolers with Different Numbers of Rows under Induced and Forced Draft, *Heat Transfer Eng.*, 3(1), 38–46.
- Gilmour, C. (1952–54). Short Cut to Heat Exchanger Design, *Chem. Eng.*, Parts I–VII.
- Gnielinski, V. (1976). New Equations for Heat and Mass Transfer in Turbulent Pipe and Channel Flow, *Int. Chem. Eng.*, 16, 359–366.
- Grant, I. D. R. (1980). Shell-and-Tube Exchangers for Single-Phase Application, in *Developments in Heat Exchanger Technology*, Vol. 1, Applied Science Publishers, London.
- Gunter, A. Y., and Shaw, W. A. (1945). A General Correlation of Friction Factors for Various Types of Cross Flow, *Trans. ASME*, 67, 643.
- Hausen, H. (1943). Darstellung des Wärmeüberganges in Röhren durch verallgemeinerte Potenzbeziehungen, *Z. VDI*, 4, 91–95.
- Hausen, H. (1959). Neue Gleichungen für Wärmeübertragung bei Freier oder erzwungener Strömung, *Allg. Waermetechn.*, 9, 75–79.
- Hausen, H. (1974). Extended Equation for Heat Transfer in Tubes at Turbulent Flow, *Waermestoffuebertrag.*, 7, 222–225.
- Hofmann, H. (1976). Möglichkeiten zur Berechnung des Wärmeübergangs und des Druckverlustes von Rippenrohrbündeln, *Luft- Kältetechn.*, 12, 136–141.
- Jameson, S. L. (1945). Tube Spacing in Finned Tube Banks, *Trans. ASME*, 67, 633–640.
- Jaw, L. (1964). Temperature Relations in Shell-and-Tube Exchangers Having One-Pass-Split-Flow Shells, *J. Heat Transfer*, 86C, 408–416.
- Kakaç, S. (1991). *Boilers, Evaporators and Condensers*, Wiley, New York.
- Kakaç, S., and Yener, Y. (1994). *Convective Heat and Mass Transfer*, 2nd ed., CRC Press, Boca Raton, FL.
- Kakaç, S., Aung, W., and Viskanta, R. (1985). *Natural Convection: Fundamentals and Applications*, Hemisphere Publishing, New York.

- Kakaç, S., Shah, R. K., and Aung, W. (1987). *Handbook of Single-Phase Convective Heat Transfer*, Wiley, New York.
- Kays, W. M., and Crawford, M. E. (1993). *Convective Heat Transfer*, 3rd ed., McGraw-Hill, New York.
- Kays, W. M., and London, A. L. (1984). *Compact Heat Exchangers*, 3rd ed., McGraw-Hill, New York.
- Kern, D. Q. (1950). *Process Heat Transfer*, McGraw-Hill, New York.
- Kern, D. Q., and Kraus, A. D. (1972). *Extended Surface Heat Transfer*, McGraw-Hill, New York.
- Kraus, A. D., and Kern, D. Q. (1965). The Effectiveness of Heat Exchangers with One Shell Pass and Even Numbers of Tube Passes, *ASME-65-HT-18*, ASME, New York.
- Kraus, A. D., Aziz, A., and Welty, J. R. (2001). *Extended Surface Heat Transfer*, Wiley, New York.
- Kröger, D. (1998). *Air Cooled Heat Exchangers and Cooling Towers*, Tecpress, Uniedal, South Africa.
- Kumar, H. (1984). The Plate Heat Exchanger, Construction and Design, *Inst. Chem. Eng. Symp. Ser.*, 86, 1275–1282.
- Kunttyish, V. B., and Iokhvedor, F. M. (1971). Effect of Relative Interfin Distance on the Thermal Convective Heat Transfer in Finned Tube Bundles and on Augmenting Heat Transfer, *Heat Transfer Sov. Res.*, 3(2), 50–55.
- Kutateladze, S. S., and Borishanskii, V. M. (1958). *A Concise Encyclopedia of Heat Transfer*, Oxford; Pergamon Press, Oxford, UK.
- Li, C.-Ha. (1987). New Simplified Formula for Crossflow Heat Exchanger Effectiveness, *J. Heat Transfer*, 109, 521–522.
- London, A. L., and Seban, R. A. (1942). A Generalization of the Methods of Heat Exchanger Analysis, TR No $N_{tu} - 1$, Mechanical Engineering Department, Stanford University, Stanford, CA.
- London, A. L., and Seban, R. A. (1980). A Generalization of the Methods of Heat Exchanger Analysis, TR No $N_{tu} - 1$, *Int. J. Heat Mass Transfer*, 23, 5–16.
- Mason, J. (1955). Heat Transfer in Cross Flow, *Proc. 2nd U.S. National Congress on Applied Mechanics*, ASME, New York.
- Mayinger, F. (1988). Classification and Applications of Two-Phase Flow Heat Exchangers, in *Two-Phase Flow Heat Exchangers*, S. Kakaç, A. E. Bergles, and E. O. Fernandes, eds., Kluwer Academic, Dordrecht, The Netherlands.
- McAdams, W. H. (1954). *Heat Transmission*, 3rd ed., McGraw-Hill, New York.
- McQuiston, F. C., and Tree, D. R. (1972). Optimum Space Envelopes of the Finned Tube Heat Transfer Surface, *Trans. ASHRAE*, 78, 144–148.
- Mirkovic, Z. (1974). Heat Transfer and Flow Resistance Correlations for Helically Finned and Staggered Tube Banks in Cross Flow Heat Exchangers, in *Design and Theory Source Book*, N. H. Afgan and E. U. Schlünder, eds., McGraw-Hill, New York.
- Moody, L. F. (1944). Friction Factors for Pipe Flow, *Trans. ASME*, 66, 671–678.
- Mueller, A. C. (1967). New Charts for True Mean Temperature Difference in Heat Exchangers, AIChE Paper 10, 9th National Heat Transfer Conference.
- Nagle, W. M. (1933). Mean Temperature Difference in Multipass Heat Exchangers, *Ind. Eng. Chem.*, 25, 604–609.

- Nir, A. (1991). Heat Transfer and Friction Correlations for Crossflow over Staggered Finned Tube Banks, *Heat Transfer Eng.*, 12(1), 43–50.
- Nusselt, W. (1911). Der Wärmeübergang in Kreuzstrom, *Verh. Ver. Dtsch. Ing.*, 55, 2021–2024.
- Nusselt, W. (1930). The Condensation of Steam on Cooled Surfaces, *Verh. Ver. Dtsch. Ing.*, 60, 541–546. Translated into English by D. Fullerton, *Chem. Eng. Fundam.*, 1(2), 6–9.
- Oskay, R., and Kakaç, S. (1973). Effect of Viscosity Variations on Turbulent and Laminar Forced Convection in Pipes, *METU J. Pure Appl. Sci.*, 6, 211–230.
- Perkins, H. C., and Warsøe-Schmidt, P. (1965). Turbulent Heat and Momentum Transfer for Gases in a Circular Tube at Wall to Bulk Temperature Ratios of Seven, *Int. J. Heat Mass Transfer*, 8, 1011–1031.
- Petukhov, B. S. (1970). Heat Transfer and Friction in Turbulent Pipe Flow with Variable Physical Properties, in *Advances in Heat Transfer*, J. P. Hartnett and T. F. Irvine, eds., Academic Press, New York, pp. 504–514.
- Petukhov, B. S., and Popov, V. N. (1963). Theoretical Calculation of Heat Exchange and Frictional Resistance in Turbulent Flow in Tubes of Incompressible Fluid with Variable Physical Properties, *High Temp.*, 1(1), 69–73.
- Pohlhausen, E. (1921). Der Wärmeaustausch Zwischen Festen Körpern und Flüssigkeiten mit kleiner Reibung und kleiner Wärmeleitung, *Z. Angew. Math. Mech.*, 1, 115–121.
- Robinson, K. K., and Briggs, D. E. (1966). Pressure Drop of Air Flowing across Triangular Pitch Banks of Finned Tubes, *Chem. Eng. Prog. Symp. Ser.*, 62(64), 177–183.
- Roetzel, W., and Spang, B. (1987). Analytisches Verfahren zur thermischen Berechnungen mehrgängiger Rohrbündel-wärmeübertrager, *Fortschr. Ber. VDI*, 19(18).
- Rogers, D. G. (1980). Forced Convection Heat Transfer in a Single Phase Flow of Newtonian Fluid in a Circular Pipe, *CSIR Rep. CENG 322*, CSIR, Pretoria, South Africa.
- Saunders, E. A. D. (1988). *Heat Exchangers: Selection, Design and Construction*, Longman Scientific and Technical, Harlow, Essex, England.
- Schindler, D. L., and Bates, H. T. (1960). True Temperature Difference in a 1–2 Divided Flow Heat Exchanger, *Chem. Eng. Prog. Symp. Ser.*, 30, 56, 203–206.
- Schmidt, T. E. (1963). Wärmeübergang an Rippenrohe und Berechnung von Rohrbündelnevärmeanstauschern, *Kältetechnik*, 15(4), 370–376.
- Schulenberg, F. J. (1965). Wahl der Bezugslänge zur Darstellengun Wärmübergang und Druckverlust in Wärmetauschern, *Chem. Ing. Tech.*, 37, 431.
- Sekulic, D. P., Shah, R. K., and Pignotti, A. (1999). A Review of Solution Methods for Determining Effectiveness– N_{tu} Relationships of Heat Exchangers with Complex Flow Arrangements, *Appl. Mech. Rev.*, 52(3), 97–117.
- Shah, R. K. (1981). Classification of Heat Exchangers, in *Heat Exchangers: Thermal-Hydraulic Fundamentals and Design*, S. Kakaç, A. E. Bergles, and F. Mayinger, eds., Hemisphere Publishing, New York.
- Shah, R. K., and Bhatti, M. S. (1987). Laminar Convective Heat Transfer in Ducts, in *Handbook of Single Phase Convective Heat Transfer*, Wiley, New York, Chap. 3.
- Shah, R. K., and Focke, W. W. (1988). Plate Heat Exchangers and Their Design Theory, in *Heat Transfer Equipment Design*, R. K. Shah, E. C. Subbarao, and R. A. Mashelkar, eds., Hemisphere Publishing, New York, pp. 145–166.
- Shah, R. K., and London, A. L. (1978). *Laminar Flow Forced Connection in Ducts*, Academic Press, New York.

- Shlykov, Y. P., and Ganin, Y. E. (1964). Thermal Resistance of Metallic Contacts, *Int. J. Heat Mass Transfer*, 7, 921–926.
- Sieder, E. N., and Tate, G. E. (1936). Heat Transfer and Pressure Drop of Liquids in Tubes, *Ind. Eng. Chem.*, 28, 1429–1436.
- Sleicher, C. A., and Rouse, M. W. (1975). A Convenient Correlation for Heat Transfer to Constant and Variable Property Fluids in Turbulent Pipe Flow, *Int. J. Heat Mass Transfer*, 18, 677–684.
- Somerscales, E. F. C., and Knudsen, J. G. (1981). *Fouling of Heat Transfer Equipment*, Hemisphere Publishing, New York.
- Spang, B. (1991). Über das thermischen Verhalten von Rohrbündelwärmeübertragern mit Segmentumlenkblechen, *Fortschr. Ber. VDI*, 19(48).
- Stefan, K. (1959). Wärmeübertragung und Druckabfall Beinichtausgebildeter Laminarströmung in Röhren und in ebenen Spalten, *Chem. Ing. Tech.*, 31, 773–778.
- Stevens, R. A., Fernandez, J., and Woolf, J. R. (1957). Mean Temperature Difference in One-, Two- and Three-Pass Crossflow Heat Exchangers, *Trans. ASME*, 79, 287–297.
- Taborek, J. (1983). Shell-and-Tube Heat Exchangers, in *Heat Exchanger Design Handbook*, E. U. Schlünder, eds., Hemisphere Publishing, New York, Sect. 3.3.
- Taborek, J. (1998). Shell-and-Tube Heat Exchangers in Single Phase Flow, in *Handbook of Heat Exchanger Design*, G. F. Hewitt, ed., Begell House, New York, Secs. 3.3.3.1 to 3.3.11.5.
- TEMA (1998). *Standards of the Tubular Exchanger Manufacturers' Association*, 8th ed., TEMA, New York.
- Test, F. L. (1968). Laminar Flow Heat Transfer and Fluid Flow for Liquids with a Temperature Dependent Viscosity, *J. Heat Transfer*, 90, 385–393.
- Tinker, T. (1951). Shell Side, Characteristics of Shell-and-Tube Heat Exchangers, Parts I, II and III, *Proc. General Discussion on Heat Transfer*, IME, London, and ASME, New York, p. 89.
- Tinker, T. (1958). Shell Side, Characteristics of Shell-and-Tube Heat Exchangers: A Simplified Rating System for Commerical Heat Exchangers, *Trans. ASME*, 80, 231–237.
- Tong, L. S. and London, A. L. (1957). Heat Transfer and Flow Friction Characteristics of Woven Screen and Crossed-Rod Matrices, *Trans. ASME*, 79, 1558–1570.
- Underwood, A. J. V. (1934). The Calculation of Mean Temperature Difference in Multipass Heat Exchangers, *J. Inst. Pet. Technol.*, 20, 145–158.
- Vampola, J. (1966). Heat Transfer and Pressure Drop in Flow of Gases across Finned Tube Banks, *Strojirenstvi*, 7, 501–508.
- Ward, D. J., and Young, E. H. (1959). Heat Transfer and Pressure Drop of Air in Forced Convection across Triangular Pitch Banks of Finned Tubes, *Chem. Eng. Prog. Symp. Ser.*, 55(29), 37–46.
- Webb, R. L. (1971). A Critical Evaluation of Analytical Solutions and Reynolds Analogy Equations for Heat and Mass Transfer in Smooth Tubes, *Waerme- Stoffuebertrag.*, 4, 197–204.
- Weierman, C. (1976). Correlations Ease the Selection of Finned Tubes, *Oil Gas J.*, 74(36), 94–100.
- Willis, M. J. N., and Johnston, D. (1984). A New and Accurate Hand Calculation Method for Shell Side Pressure Drop and Flow Distribution, *ASME-HTD-36*, ASME, New York, pp. 67–79.

- Wörsæ-Schmidt, P. M. (1966). Heat Transfer and Friction for Laminar Flow of Helium and Carbon Dioxide in a Circular Tube at High Heating Rate, *Int. J. Heat Mass Transfer*, 9, 1291–1295.
- Yang, K. T. (1962). Laminar Forced Convection of Liquids in Tubes with Variable Viscosity, *J. Heat Transfer*, 8, 353–362.
- Yovanovich, M. M. (1981). New Contact and Gap Conductance Correlations for Conforming Rough Surfaces, *AIAA Paper 1164*, 16th AIAA Thermophysics Conference, Palo Alto, CA.
- Zhukauskas, A. A. (1974). Investigation of Heat Transfer in Different Arrangements of Heat Exchanger Surfaces, *Teploenergetika*, 21(5), 24.
- Zhukauskas, A. A. (1987). Convective Heat Transfer in Cross Flow, in *Handbook of Single-Phase Convective Heat Transfer*, S. Kakaç, R. K. Shah, and W. Aung, eds., Wiley, New York.

Experimental Methods

JOSÉ L. LAGE

Mechanical Engineering Department
Southern Methodist University
Dallas, Texas

- 12.1 Fundamentals
 - 12.1.1 Measurement
 - 12.1.2 Sensing
 - 12.1.3 Calibration
 - 12.1.4 Readability
- 12.2 Measurement error
 - 12.2.1 Uncertainty: bias and precision errors
 - 12.2.2 Mean and deviation
 - 12.2.3 Error distribution
 - 12.2.4 Chauvenet's criterion and the chi-square test
- 12.3 Calculation error
- 12.4 Curve fitting
- 12.5 Equipment
 - 12.5.1 Glass thermometers
 - 12.5.2 Thermocouples
 - 12.5.3 Resistance temperature detectors
 - 12.5.4 Liquid crystals
 - 12.5.5 Pyrometers
 - 12.5.6 Heat flow meters

Nomenclature

References

12.1 FUNDAMENTALS

12.1.1 Measurement

Measurement is one of the most important activities in science and engineering. Validation of new theories, determination of material property values, classification of new materials, performance evaluation of new and existing devices, and monitoring and control of existing and new processes are activities that depend on measurements.

Measurement, or *measuring*, is also the most important part of an experiment. Measuring is not *absolute*, as it does not define a quantity (standard) to be measured. Measuring is a *relative* effort and is made to compare and to evaluate. To be independent, a comparison requires a *measure*, a standard unit.

The art of measuring is at least as old as humanity itself. The human body performs measurements all the time. One of the most basic quantities continuously measured by the human body is the environment temperature. Feeling *hot* or *cold* is a consequence of this measuring. Although not descriptive (not quantified with a parameter such as temperature), the natural measuring of the environmental temperature by the human body is nevertheless a relative process. This process is based on a comparison of the environmental temperature with a certain standard, in this case the temperature at which the body feels neither hot nor cold—the *null point* of human thermal control.

In heat transfer, temperature and heat flow are unquestionably the most important quantities to be measured. Other quantities of interest to heat transfer include fluid speed, pressure (force), mechanical stress, electric current, voltage, length, surface area, volume, and displacement. In this chapter the focus is on temperature and heat flow measurements.

General measuring concepts such as *sensitivity*, *hysteresis*, *calibration*, *accuracy*, and *readability* are presented first. Then the discussion turns to statistical concepts such as *mean*, *deviation*, *standard deviation*, *normal distribution*, *Chauvenet's criterion*, and the *chi-square test*, related to the determination of precision, bias error, and measuring uncertainty. The final section of this chapter is devoted to a brief discussion of some common instruments for measuring temperature or heat flow.

12.1.2 Sensing

Among the two possible alternatives for sensing devices, the most common are the *contact* sensing devices such as thermocouples that measure by physical contact. In general, contact sensing devices are rugged, economical, relatively accurate, and easy to use. Disadvantages commonly associated with contact sensing devices include susceptibility to wear (e.g., breaking of thermocouple junction). They also require accessibility for physical contact. Because of the *contact* nature of these devices, they tend to interfere with the medium where measurement is to be taken, frequently affecting the state and the value of the quantity to be measured. The last disadvantage can be a serious problem. For instance, the conductive wires of a thermocouple will always provide a heat path when in contact with the medium where temperature is to be measured. This heat path can modify the state of the medium where temperature is to be measured by adding energy to, or extracting energy from, the medium.

Another alternative is a *non-contact* sensing device such as an infrared sensor or *pyrometer*. This type of sensing device is advantageous because it does not require physical contact; that is, the measurement can be made remotely. They are more convenient than the contact sensing devices for measuring quantities from surfaces in movement without contact with the surface. In addition, they do not interfere with the quantities being measured (no heat sink/source), are generally faster in

obtaining the measurement (because of the smaller thermal inertia), and are less prone to wear.

Some disadvantages include cost (generally more expensive than contact sensing devices), difficult calibration, and the effect of the environment on the measurement (e.g., dust and smoke in the field of view will affect the measurement of surface temperature using an infrared detector).

Most measuring devices do not measure the quantity of interest directly. In the case of thermocouples, for instance, what is measured is a voltage across the open-circuit terminals of the thermocouple wires. This voltage emanates from the electrical effect that temperature has on the electrical potential (EMF) along two distinct but connected conductive wires. By knowing how the voltage read by the electrical instrument relates to the temperature at the connection of the two thermocouple wires, the voltage can be *translated* into temperature. The same is true in relation to the more common mercury thermometers. The mercury thermometer does not measure the temperature directly but the variation caused by the temperature on the volume of mercury inside the thermometer. The scale printed on the thermometer glass, translating the mercury volume variation into temperature, allows the measurement of volume to be translated into temperature. These are types of *indirect* measurement.

The *sensitivity* of measuring devices is a very important characteristic for measuring. Sensitivity can be understood as the relation between cause and consequence. Thermocouples have sensitivities listed in $\text{mV}/^\circ\text{C}$ because the consequence of measuring an increase in temperature is a change in voltage across the thermocouple terminals.

Suppose that a thermocouple for measuring a temperature variation of 60°C is needed, and a multimeter having a scale from 0 to 100 mV is available. Unless the thermocouple has a sensitivity S smaller than 100 mV per 60°C , or equivalently, $S < 1.67 \text{ mV}/^\circ\text{C}$, measurement cannot be performed within the available voltage range. It should be kept in mind that small quantities are, in general, more difficult and expensive to be measured; that is, thermocouples with small sensitivities tend to be more costly.

The sensitivity of an instrument might not be uniform along the entire range available for measurement. In such cases, translation from the quantity actually measured to the quantity of interest is not linear. Moreover, the sensitivity of an instrument might depend on the direction of variation of the quantity being measured. For instance, when increasing the temperature, a certain thermocouple device might have a uniform sensitivity equal to $1.5 \text{ mV}/^\circ\text{C}$. But when the temperature to be measured decreases, the sensitivity might be nonuniform; for example $S(T) = 1.5\alpha(T) \text{ (mV}/^\circ\text{C})$, where $\alpha(T)$ is a certain function of temperature T . In this case, the temperature value corresponding to a certain voltage when the temperature increases will differ from the temperature value at the same measured voltage when the temperature decreases. The instrument is then said to exhibit *hysteresis*. Figure 12.1 demonstrates this phenomenon considering a thermocouple with uniform sensitivity equal to $1.5 \text{ mV}/^\circ\text{C}$ when measuring an increase in temperature (continuous line) from 0°C to 20°C , and nonuniform sensitivity equal to $1.5(2.33 - 0.133T + 0.0033T^2) \text{ mV}/^\circ\text{C}$ when measuring a decrease in temperature from 20°C to 0°C .

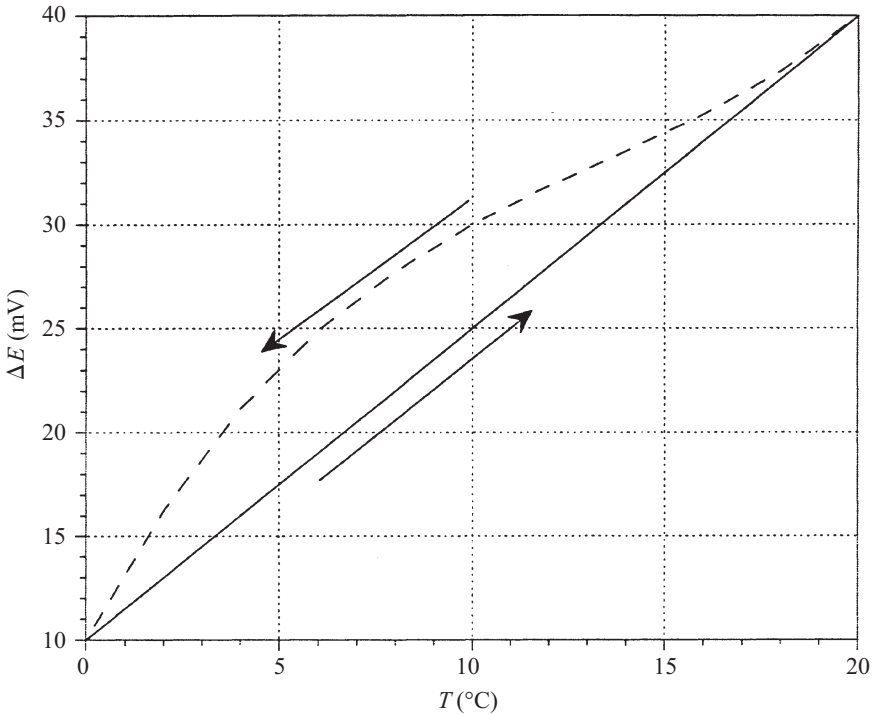


Figure 12.1 Voltage ΔE versus temperature T measurements from a thermocouple system exhibiting hysteresis. When measuring an increase in T (continuous line), the sensitivity of the instrument is uniform and equal to $1.5 \text{ mV}/^\circ\text{C}$. When measuring a decrease in T (dashed line), the sensitivity is nonuniform and equal to $1.5(2.33 - 0.133T + 0.033T^2) \text{ mV}/^\circ\text{C}$.

12.1.3 Calibration

All measuring instruments must be calibrated for determining their accuracy a . The *accuracy* quantifies an instrument's ability to measure a known value or standard. Standards define units of measurement and are essential in building measuring scales. Standards for measuring temperature and heat flow using different scales are maintained in the United States by the National Institute of Standards and Technology (NIST).

The International Temperature Scale of 1990 (ITS-90) is defined with several fixed temperature points, or standards, listed in Table 12.1. This scale evolved from the pioneering work of Lord Kelvin, who in 1884 proposed an absolute temperature scale, the Kelvin scale, for measuring temperatures. The Kelvin temperature scale (with only positive values) is an *absolute scale* because the scale covers the entire range of possible temperatures, as established by the second law of thermodynamics.

When calibrating a thermometer, for instance, the experimentalist compares the measured temperature value at a certain state to the standard temperature value set

TABLE 12.1 Some Fixed Temperature Points Used as Standards for Defining the ITS-90

State	$T(K)$
Triple equilibrium state of hydrogen	13.8033
Triple equilibrium state of neon	24.5561
Triple equilibrium state of oxygen	54.3584
Triple equilibrium state of argon	83.8058
Triple equilibrium state of water	273.16
Solid–liquid equilibrium of gallium at 1 atm	302.9146
Solid–liquid equilibrium of tin at 1 atm	505.078
Solid–liquid equilibrium of zinc at 1 atm	692.677
Solid–liquid equilibrium of silver at 1 atm	1234.93
Solid–liquid equilibrium of gold at 1 atm	1337.33
Solid–liquid equilibrium of copper at 1 atm	1357.77

Source: Holman (2001).

forth by the ITS-90 for that particular state. When the discrepancy (or *accuracy*) is uniform along the entire scale, the instrument can be *calibrated* simply by moving the origin of the scale so that the new values measured by the instrument agree with the standard values.

Often, standards provide a physical meaning to the values measured by the scale as is the case of the temperature measured with the Kelvin absolute temperature scale. Other temperature scales commonly used are the Celsius ($^{\circ}\text{C}$) and Fahrenheit ($^{\circ}\text{F}$). Neither is an absolute scale, as they both allow for negative temperature values. Although having different standards, a thermocouple system calibrated against the Celsius scale will have the same sensitivity as a thermocouple system calibrated against the Kelvin scale. That is, the thermocouple voltage variation per degree Celsius is the same as the voltage variation per degree Kelvin. Therefore, the Kelvin and Celsius scales are related for yielding the same sensitivity (the same variation per degree). The absolute Rankine scale ($^{\circ}\text{R}$) provides the same sensitivity as the Fahrenheit scale. The conversions from one temperature scale to another can be performed using

$$K = 273.15 + ^{\circ}\text{C} \quad (12.1)$$

$$^{\circ}\text{R} = 459.67 + ^{\circ}\text{F} \quad (12.2)$$

$$^{\circ}\text{F} = 32 + \frac{9}{5} ^{\circ}\text{C} \quad (12.3)$$

12.1.4 Readability

A measuring scale is based on standard values chosen to represent the measurement at certain states. It is possible to divide the space between standard values, marking equal increments along the instrument read out to obtain a better estimate of measurements for a state different from the standard state. The number of divisions in

the readout of an instrument determines the *readability* of the instrument. For example, if a thermometer using the Kelvin scale is built with 50 equal increments between the triple equilibrium state of oxygen (54.3584 K) and the triple equilibrium state of water (273.16 K), each increment of this thermometer (referred to as the *least count* L_c of the thermometer) would be $L_c = (273.16 \text{ K} - 54.3584 \text{ K})/50 = 4.3726 \text{ K}$. If instead of 50, 150 equal increments were employed, the least count of the thermometer would be $L_c = 1.4587 \text{ K}$.

The readability of an instrument, or the least count, determines how close the real value can actually be read from the instrument scale. For instance, in an attempt to measure the temperature T at the triple equilibrium state of argon (83.8058 K) using a thermometer calibrated for the triple equilibrium state of oxygen (54.3584 K) and with least count equal to 4.3726 K, the thermometer would indicate a value between the sixth (80.594 K) and seventh (84.967 K) marks on the scale. The measured value in this case could be any value between 80.594 and 84.976 K. The certainty of the measured value would be assured only to within the least count of the instrument, in this case 4.3726 K. One common representation for the measured value in this case is based on the arithmetic average of the two bounding values and half the least count, i.e., $T = \{[(80.594 \text{ K} + 84.976 \text{ K})/2] \pm (4.3726 \text{ K}/2)\}$. The resulting value, $T = 82.785 \pm 2.186 \text{ K}$, covers the entire range from 80.594 to 84.976 K. However, the use of the same thermometer, but now with least count equal to 1.4587 K, the same measurement would fall between the twentieth (83.532 K) and twenty-first (84.991 K) marks, and the certainty would be to within 1.4587 K. The measured value in this case could be $T = 84.261 \pm 0.73 \text{ K}$, which is closer to the precise value 83.8058 K than the value obtained by the thermometer with the least count 4.3726 K.

Even without knowing the precise value being measured, it can be stated that the certainty of the second reading ($\pm 0.73 \text{ K}$) is much better than the certainty of the first reading ($\pm 2.186 \text{ K}$). This conclusion is a direct consequence of the least count being smaller in the second thermometer than in the first thermometer.

When the state at which a value is being measured coincides with a standard state, the error of the instrument can always be checked by comparing the measurement with the standard value. However, the standards are values set at some prescribed (discrete) states. If the state at which a value is to be measured does not coincide with any of the standard states, the experimentalist cannot be certain of the accuracy of the measurement, even if the instrument has been calibrated.

12.2 MEASUREMENT ERROR

12.2.1 Uncertainty: Bias and Precision Errors

In the example described in Section 12.1, the error between the measured and real values could not be quantified precisely because the measured value was not a standard value. However, the error between measured and exact values could be estimated to be no more than one-half the least count of the instrument. Although *uncertain*, the measurement error in this case can be *estimated* or *determined* (*deterministic* as

opposed to *random*). Observe that this error is independent of the number of times the measurement is taken, or equivalently, independent of the sample size. This error (related to the least count) is then said to be a systematic error, contributing to the *bias error* B of the measurement.

The bias error remains constant if the measurement is performed under the same environmental conditions (under which condition, for instance, the least count of the measuring device would not change). All errors that are known to exist (deterministic) but that have not been eliminated (such as accuracy, hysteresis, and linearity) should be included in the bias error of the measurement.

The bias error is one of the components of the overall measurement error, called the *uncertainty* U of the measurement. The uncertainty of a measurement is affected not only by the bias error, but also by the *precision* σ_p of the instrument. In general, the uncertainty of a measurement can be obtained from the bias and precision errors (Wheeler and Ganji, 1996) as

$$U = (B^2 + \sigma_p^2)^{1/2} \quad (12.4)$$

The precision σ_p of an instrument is a measure of the repeatability of the measurement. Most instruments, especially when used in the field, are affected by uncontrollable effects such as ambient temperature, humidity, and pressure. Even when trying to calibrate an instrument by measuring a certain standard, the response of the instrument might not be the same when the measurement is repeated several times.

Assume, for example, that it is required to calibrate a mercury thermometer using the triple point of water. The thermometer is placed in contact with a mixture of solid (ice), liquid, and gas (vapor) water in thermal equilibrium. Once the thermometer reaches thermal equilibrium with the mixture, the location of the mercury meniscus in the thermometer is marked. In repeated performance of the same sequence of events with the same thermometer, the chances are that the location of mercury meniscus at equilibrium would not be the same as the location of the first measurement. The discrepancy gives a measure of the precision of the thermometer.

The precision of an instrument can be accessed by performing repeated measurements of the same state (not necessarily a standard state). Hence, to access the precision of an instrument, multiple measurements of the same state must be taken (one single measurement will never allow for the determination of the precision of the measuring instrument).

Keep in mind that *precision* and *accuracy* are very different concepts. The accuracy of a measurement is a deterministic error that can be eliminated by calibrating the instrument, hence it affects the bias error. The precision of the instrument, intrinsic to the instrument itself, is affected in most cases by the environment. This precision *error* cannot be eliminated unless the instrument is rebuilt. [Observe that even if the instrument is used in the same controlled environment (temperature, pressure, humidity, etc.), the deterioration of the instrument in time will affect the precision.]

Precision is a *random error* contributing to the uncertainty of the measurement. Although impossible to predict precisely, the precision of an instrument can often be estimated with reasonable confidence via statistical analysis.

Finally, it is important to point out that the readability error can influence not only the bias error (because of the least count) but also the precision error of the instrument (because it can change the resolution, or least count). For instance, when the environmental conditions change, the least count of the instrument might change as well due to the expansion–contraction of the scale. This contribution to the error is random, or nondeterministic. Therefore, this readability error adds to the precision error of the instrument.

12.2.2 Mean and Deviation

When n measurements T_i are taken of the same quantity, a single representative measured quantity can be found by calculating the arithmetic mean \bar{T} of all values,

$$\bar{T} = \frac{1}{n} \sum_{i=1}^n T_i \quad (12.5)$$

The deviation d_i from the mean \bar{T} of each measurement T_i is defined as

$$d_i = T_i - \bar{T} \quad (12.6)$$

The standard deviation σ can be used to quantify the spreading of the measured values with respect to the mean:

$$\sigma = \left[\frac{1}{n} \sum_{i=1}^n (T_i - \bar{T})^2 \right]^{1/2} \quad (12.7)$$

The standard deviation, eq. (12.7), is representative of the precision σ_p of the instrument when the number of measurements is large ($n > 20$). Otherwise, σ should be multiplied by $[n/(n-1)]^{1/2}$.

Notice that the standard deviation σ has the dimension(s) of the measured quantity T . Moreover, the standard deviation of the mean value \bar{T} , namely, $\sigma_{\bar{T}}$, can be estimated from

$$\sigma_{\bar{T}} = \frac{\sigma}{n^{1/2}} \quad (12.8)$$

where n is larger than 10.

The standard deviation of a set of measurements is an important parameter to represent the probability of a certain measurement to fall within a certain interval. Although similar, this concept differs from the readability concept discussed earlier. Recall that every measurement has a certain readability error associated with it and this error is proportional to the least count of the measuring device. The precision of the instrument (or measurement) is an additional uncertainty, as it relates to a series of measurements taken of the same state (or quantity).

12.2.3 Error Distribution

When several measurements of a quantity T are taken, and all of them are affected by small random errors equally likely to be positive or negative, the probability $\Gamma_G(T)$ of one of the measurements falling within T and $T + dT$ is given by the *Gaussian or normal error distribution* (also known as *random distribution*),

$$\Gamma_G(T) = \frac{1}{\sigma(2\pi)^{1/2}} e^{-(T-\bar{T})^2/2\sigma^2} \quad (12.9)$$

Figure 12.2 presents some normalized Gaussian distribution results $[\int_{-\infty}^{\infty} \Gamma_G(T) dT = 1.0]$ from simulated temperature measurements.

As expected, the most probable measurement is the one coinciding with the mean (average) value \bar{T} . Moreover, when the standard deviation σ is large, the spreading of the measurements is large as well. Hence, the probability of any measurement falling far from \bar{T} increases with σ , as predicted by $\Gamma_G(T)$.

Observe from eq. (12.9) that the probability of a measurement yielding the average value \bar{T} equals $1/[\sigma(2\pi)^{1/2}]$. In the cases presented in Fig. (12.2), the probabilities are $\Gamma_G(\bar{T}) = 0.997$ when $\sigma = 0.4$ and $\Gamma_G(\bar{T}) = 0.665$ when $\sigma = 0.6$.

Evidently, $\Gamma_G(\bar{T})$ will be greater than unity when σ is smaller than $(2\pi)^{-1/2}$, or equivalently, when $\sigma < 0.399$. Because of the relation with σ , the value of $\Gamma_G(\bar{T})$ is also a measure of the precision σ_p of the instrument.

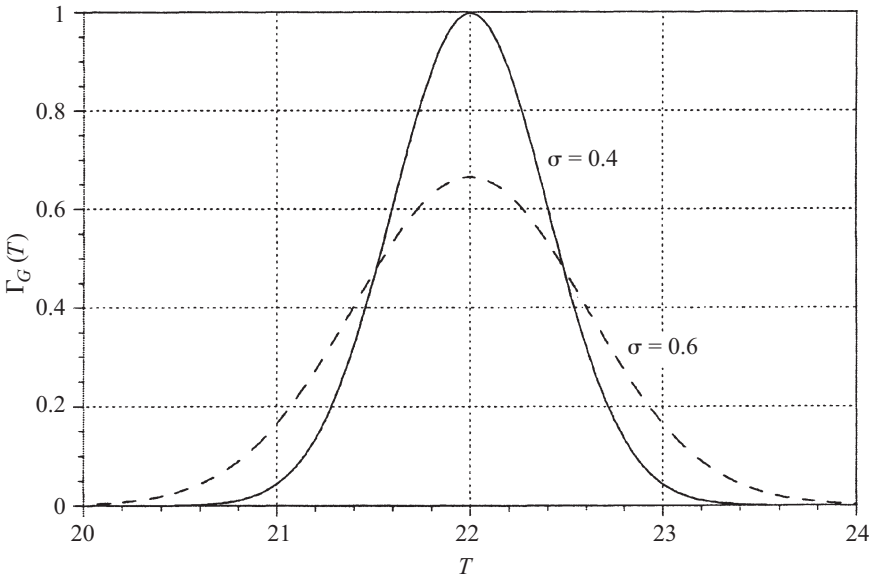


Figure 12.2 Simulated Gaussian distribution of temperature with standard deviation 0.4 and 0.6, and average temperature $\bar{T} = 22^\circ\text{C}$.

A more interesting and practical quantity is the probability that a certain measurement will fall within a certain distance (deviation) ΔT from the mean value \bar{T} . This deviation probability is given by $\Gamma_d(\Delta\zeta)$:

$$\Gamma_d(\Delta\zeta) = \left[\left(\frac{2}{\pi} \right)^{1/2} \right] \int_0^{\Delta\zeta} e^{-\zeta^2/2} d\zeta \quad (12.10)$$

where $\zeta = (T - \bar{T})/\sigma$ and $\Delta\zeta = \Delta T/\sigma$. It can be shown that the equation for $\Gamma_d(\Delta\zeta)$ can be written in terms of the error function:

$$\Gamma_d(\Delta\zeta) = \text{erf} \left(\frac{\Delta\zeta}{2^{1/2}} \right) \quad (12.11)$$

where

$$\text{erf}(x) = \frac{2}{\pi^{1/2}} \int_0^x e^{-m^2} dm \quad (12.12)$$

Results from eq. (12.11) are presented in Fig. 12.3. In practice, when trying to find the probability of a measurement falling within a distance ΔT from the mean value, it is only necessary to calculate $\Delta\zeta = \Delta T/\sigma$ and then find the corresponding $\Gamma_d(\Delta\zeta)$ value in Fig. 12.3.

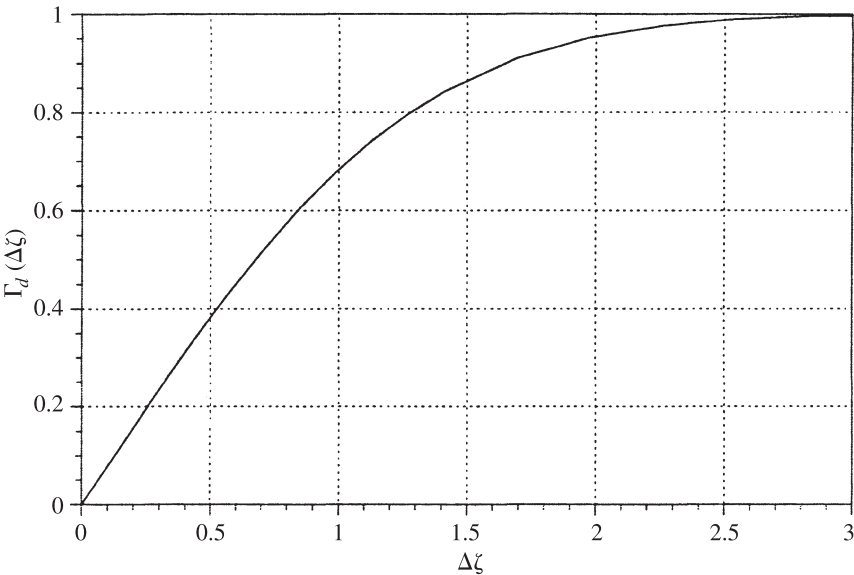


Figure 12.3 Graphical representation of eq. (12.11).

Consider, for instance, the case of a series of temperature measurements yielding a standard deviation $\sigma = 0.4$. The probability of a measurement falling within $\Delta T = 0.4$ unit from the mean value is approximately 0.68. This value is the $\Gamma_d(\Delta\zeta)$ value, obtained from Fig. 12.3, for $\Delta\zeta = \Delta T/\sigma = 1.0$. It is worth noting from Fig. 12.3 that the probability that a measurement is within 3σ units (or greater) of the mean value is precisely $\Gamma_d(3) = 0.997$, or approximately unity. Recall that these results are valid when the distribution of measurements follows a Gaussian distribution, which is generally valid when several measurements of the same quantity are taken.

Another interesting aspect related to $\Gamma_d(\Delta\zeta)$ is now considered. If it can be concluded from a series of measurements that the probability of any measurement falling within a ΔT interval from the mean is given by $\Gamma_d(\Delta T/\sigma)$, it can be stated that this same probability is the probability of the mean value falling within the same interval. When related to the mean, the probability $\Gamma_d(\Delta\zeta)$ is called the *confidence level*, and $\Delta\zeta$ is called the *confidence interval*. In the example described in the preceding paragraph, the measurements present a confidence level of 68% for a confidence interval of 1.0—that is, the probability that the mean value \bar{T} would fall within an interval of $\pm 1\sigma$ units is 68%!

Multiple measurements of the same quantity are very often written in terms of the mean value and the standard deviation representing the precision error, such as $\bar{T} \pm \sigma$. According to the previous assessment, this representation of the mean value (using a confidence interval equal to unity) has a confidence level of 68% if the probability of the measurements follows a Gaussian distribution.

The number of measurements necessary to achieve a certain confidence level can be determined from

$$n = \left(\frac{\sigma_p \Delta\zeta}{\sigma} \right)^2 \quad (12.13)$$

As an example, consider the measurement of temperature with a device having precision $\sigma_p = \pm 0.4^\circ\text{C}$. If the interest is in achieving a confidence interval $\Delta\zeta = \Delta T/\sigma = 2$ (equivalent to a confidence level of 95.4%; see Fig. 12.3) for a standard deviation of $\pm 0.2^\circ\text{C}$, at least 16 measurements would be required.

12.2.4 Chauvenet's Criterion and the Chi-Square Test

Frequently, repeated measurements of the same quantity might yield results that are far off the mean value. A criterion commonly used to identify unacceptable measurement values is *Chauvenet's criterion*. This criterion is based on the fact that the probability of obtaining a certain deviation from the mean by any measurement should not be smaller than $1/(2n)$, where n is the total number of measurements. This probability is equivalent to $[1 - \Gamma_d(\Delta T/\sigma)]$. Therefore, Fig. 12.3 can be employed to determine the maximum deviation $\Delta T = \sigma\Delta\zeta$ for any number of readings. Table 12.2 presents the corresponding maximum $\Delta\zeta$ acceptable for several numbers of measurements.

TABLE 12.2 Values of Maximum Deviation ΔT_{\max} from the Mean for Application of Chauvenet’s Criterion

n^a	$\Delta T_{\max}/\sigma$	n^a	$\Delta T_{\max}/\sigma$
2	1.28	9	1.91
3	1.38	10	1.96
4	1.54	20	2.24
5	1.65	40	2.52
6	1.73	60	2.64
7	1.80	80	2.73
8	1.85	100	2.82

^aNumber of measurements from which the standard deviation σ is calculated.

Notice that the criterion is applied only once to a set of measurements data, by comparing the deviation from the mean of each measurement with the maximum deviation ΔT obtained from Table 12.2 once the standard deviation σ of the data set is calculated.

The application of Chauvenet’s criterion on a data set allows not only consistent discard of questionable data, but also recalculation of the standard deviation from the remaining data. This new standard deviation is believed to be a more accurate representation of the average deviation of the experimental data from the mean value.

It is important to verify how close a certain data set follows a certain distribution before relying too heavily on statistical analysis. A common test for evaluating the closeness of the data to a certain distribution is the chi-square test. This test is based on χ^2 , defined as the relative deviation of the value observed from the value expected in a set of n measurements. If the value in question is the probability of a certain measurement,

$$\chi^2 = \sum_{i=1}^{n_v} \frac{(\Gamma_i - \Gamma_{Gi})^2}{\Gamma_{Gi}} \tag{12.14}$$

where n_v is the number of different values measured, Γ_i the observed probability of a certain measurement, and Γ_{Gi} the expected Gaussian distribution for the particular measurement.

To illustrate the use of the *chi-square test*, consider the temperature data set shown in Table 12.3, where $n_v = 11$. The mean temperature of the data set is $\overline{T} = 23^\circ\text{C}$ and the standard deviation is $\sigma = 0.724^\circ\text{C}$.

To verify if the observed probability distribution of the data follows a Gaussian distribution, an estimate Γ of each measurement is made by dividing the number of times the measurement is observed in the data set (number of *events*) by the total number of measurements (equal to 122). To normalize the results for comparison with the Gaussian distribution, the probability was divided by the increment in temperature, 0.2°C , and is presented in Table 12.3 as Γ . If this data set follows a Gaussian distribution, the probability of each measurement must be given by eq. (12.9), with

TABLE 12.3 Data Set of Measured Temperature T with Number of Events for Each Measurement, Observed Probability Γ , and Gaussian Probability Γ_G ^a

$T(^{\circ}\text{C})$	Events	$\Gamma (\times 10^{-1})$	$\Gamma_G (\times 10^{-1})$	$(\Gamma - \Gamma_G)^2$
				Γ_G
22.0	19	7.79	2.10	1.5500
22.2	12	4.92	2.96	0.1290
22.4	6	2.46	3.88	0.0520
22.6	8	3.28	4.71	0.0434
22.8	12	4.92	5.29	0.0026
23.0	13	5.33	5.51	0.0006
23.2	6	2.46	5.32	0.1540
23.4	9	3.69	4.75	0.0239
23.6	5	2.05	3.94	0.0906
23.8	6	2.46	3.02	0.0105
24.0	26	10.70	2.15	3.3700

^aThe final column shows values to be used in calculating χ^2 from eq. (12.14).

results shown in Table 12.3. Using both observed and predicted probability, the value of χ^2 using eq. (12.14), is obtained as $\chi^2 = 5.42$.

The chi-square probability Γ_{χ^2} , indicating how well the distribution observed follows the Gaussian distribution, is obtained from Table 12.4 once the number of degrees of freedom N is found. Observe that $N = n_v - p$, where p is the number of imposed conditions in the data set.

From Table 12.3 it is found that the number of conditions imposed equals unity (the only condition imposed is that the total number of measurements be equal to 122), hence $N = 10$. From Table 12.4, $\Gamma_{\chi^2} = 0.856$ is then obtained. As a rule of

TABLE 12.4 Measurement Data Obtained with Various Degrees of Freedom N ^a

N	Γ_{χ^2}				
	0.99	0.9	0.5	0.1	0.01
1	0.000157	0.0158	0.455	2.71	6.63
2	0.0201	0.211	1.39	4.61	9.21
3	0.115	0.584	2.37	6.25	11.3
4	0.297	1.06	3.36	7.78	13.3
5	0.554	1.61	4.35	9.24	15.1
6	0.872	2.20	5.35	10.6	16.8
7	1.24	2.83	6.35	12.0	18.5
8	1.65	3.49	7.34	13.4	20.1
9	2.09	4.17	8.34	14.7	21.7
10	2.56	4.87	9.34	16.0	23.2

Source: Holman (2001).

^aPresents the natural probability Γ_{χ^2} of chi-square being higher than the value calculated for χ^2 .

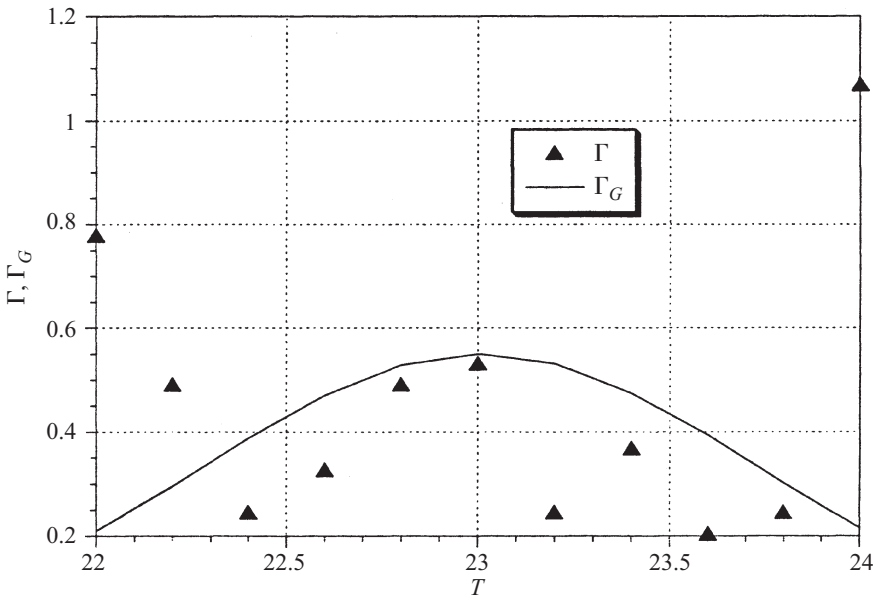


Figure 12.4 Graphical representation of the observed probability distribution Γ (shown as black triangles) and the Gaussian distribution Γ_G (straight line) from Table 12.3.

thumb, when $0.1 < \Gamma_{\chi^2} < 0.9$ it cannot be said with confidence whether or not the expected distribution is followed. However, if $\Gamma_{\chi^2} < 0.1$, the chi-square test shows that the distribution expected is not being followed. The other extreme range, when $\Gamma_{\chi^2} > 0.9$, is very unlikely to happen naturally; therefore, this range is regarded as *suspicious* (Dally et al., 1993). (*Note:* It is important that the number of events of each measurement be at least five for the result to be statistically meaningful.)

To bring into a better perspective the meaning of the chi-square test example considered in the preceding paragraph, the probability distribution Γ and Gaussian distribution Γ_G observed, presented in Table 12.3, are shown graphically in Fig. 12.4. It is clear from Fig. 12.4 that the distribution Γ diverges from the Gaussian distribution Γ_G at the extreme temperature values of $T = 22^\circ\text{C}$ and $T = 24^\circ\text{C}$.

12.3 CALCULATION ERROR

Once the uncertainty of a certain measured quantity is determined, the next complication arises when a quantity is calculated from this measurement. The question is how the uncertainty of a measured quantity will affect the uncertainty of the quantity calculated. This question becomes even more difficult to answer when more than one measuring quantity is used for the calculation. The most common procedure used to evaluate the uncertainty of the quantity calculated in this case is based on the Kline and McClintock (1953) method.

When a certain quantity Q is calculated from a number n of measured quantities T , and each measured quantity has uncertainty $\pm U$, the corresponding uncertainty of the calculated quantity U_Q can be estimated from

$$U_Q = \left[\left(U_1 \frac{\partial Q}{\partial T_1} \right)^2 + \left(U_2 \frac{\partial Q}{\partial T_2} \right)^2 + \cdots + \left(U_n \frac{\partial Q}{\partial T_n} \right)^2 \right]^{1/2} \quad (12.15)$$

The conceptual basis for eq. (12.15) is discussed by Coleman and Steel (1989). Equation (12.15) provides a good estimate of the uncertainty U_Q when the odds of each measured quantity T_i having uncertainty U_i is the same, and when the measured quantities T_1, T_2, \dots, T_n are independent of each other (i.e., the error of one quantity does not correlate with the errors of the remaining quantities). If the errors correlate, eq. (12.15) should be modified as suggested by Coleman and Steel (1989).

If the uncertainty of one measured quantity T_i is more probable than the uncertainty of another variable, say T_{i+1} , eq. (12.15) must be corrected. In general,

$$U_Q = \frac{1}{\Omega} \left[\left(\omega_1 U_1 \frac{\partial Q}{\partial T_1} \right)^2 + \left(\omega_2 U_2 \frac{\partial Q}{\partial T_2} \right)^2 + \cdots + \left(\omega_n U_n \frac{\partial Q}{\partial T_n} \right)^2 \right]^{1/2} \quad (12.16)$$

where ω_i represents the odds of variable T_i having uncertainty U_i , and Ω , a representative average of the odds, is defined as

$$\Omega = \frac{(\omega_1^2 + \omega_2^2 + \cdots + \omega_n^2)^{1/2}}{n^{1/2}} \quad (12.17)$$

Further relevant information on uncertainty analysis was provided by Moffat (1982, 1985).

12.4 CURVE FITTING

The most common curve-fitting technique is the least-squares technique. To apply this technique, the experimentalist must know (or guess) the form of the function for curve fitting a data set. Consider a certain data set of temperature values T_i obtained when varying the heating power \dot{q}_i . Considering the shape of the graph T versus \dot{q} , it could be assumed that $T = f(a_1, a_2, \dots, a_p, \dot{q})$, where a_1, a_2, \dots, a_p are all constants to be determined.

The least squares method entails minimization of the cumulative square of the deviations between the measured value T_i and the fitted value $f(a_1, a_2, \dots, a_p, \dot{q})$, namely, the minimization of D , where

$$D = \sum_{i=1}^n [T_i - f(a_1, a_2, \dots, a_p, \dot{q})]^2 \quad (12.18)$$

The minimization process then yields the best values for a_1, a_2, \dots , and a_p , by imposing

$$\frac{\partial D}{\partial a_1} = \frac{\partial D}{\partial a_2} = \dots = \frac{\partial D}{\partial a_p} = 0 \quad (12.19)$$

Each term of eq. (12.19) yields an algebraic equation involving a_1, a_2, \dots , and a_p , in the form

$$\frac{\partial D}{\partial a_j} = \sum_{i=1}^n \left\{ 2 [T_i - f(a_1, a_2, \dots, a_p, \dot{q})] \left(-\frac{\partial f}{\partial a_j} \right) \right\} = 0 \quad (12.20)$$

where j goes from 1 to p . There are p equation and p unknown. The solution of this system of algebraic equations leads to a_1, a_2, \dots , and a_p values that minimize the cumulative square of the deviations.

As an illustration of the applicability of the least squares fitting method, consider the temperature data set presented in Fig. 12.5. From the data distribution shown by the triangle symbols, the fitting polynomial function

$$f = T = a_1 \dot{q} + a_2 \dot{q}^2 \quad (12.21)$$

could be proposed. The minimization equations in this case are

$$\frac{\partial D}{\partial a_1} = \sum_{i=1}^n \{ 2 [T_i - (a_1 \dot{q}_i + a_2 \dot{q}_i^2)] (-\dot{q}_i) \} = 0 \quad (12.22)$$

$$\frac{\partial D}{\partial a_2} = \sum_{i=1}^n \{ 2 [T_i - (a_1 \dot{q}_i + a_2 \dot{q}_i^2)] (-\dot{q}_i^2) \} = 0 \quad (12.23)$$

When written in terms of coefficients a_1 and a_2 , these two equations read, respectively,

$$a_1 \sum_{i=1}^n \dot{q}_i^2 = \sum_{i=1}^n T_i \dot{q}_i - a_2 \sum_{i=1}^n \dot{q}_i^3 \quad (12.24)$$

$$a_2 \sum_{i=1}^n \dot{q}_i^4 = \sum_{i=1}^n T_i \dot{q}_i^2 - a_1 \sum_{i=1}^n \dot{q}_i^3 \quad (12.25)$$

Using eq. (12.25), eq. (12.24) can be rewritten in terms of a_1 only:

$$a_1 = \frac{\sum_{i=1}^n \dot{q}_i^4 \sum_{i=1}^n T_i \dot{q}_i - \sum_{i=1}^n T_i \dot{q}_i^2 \sum_{i=1}^n \dot{q}_i^3}{\sum_{i=1}^n \dot{q}_i^2 \sum_{i=1}^n \dot{q}_i^4 - \sum_{i=1}^n \dot{q}_i^3 \sum_{i=1}^n \dot{q}_i^3} \quad (12.26)$$

Now, using eq. (12.26), eq. (12.25) can be rewritten in terms of a_2 only:

$$a_2 = \frac{\sum_{i=1}^n \dot{q}_i^2 \sum_{i=1}^n T_i \dot{q}_i^2 - \sum_{i=1}^n T_i \dot{q}_i \sum_{i=1}^n \dot{q}_i^3}{\sum_{i=1}^n \dot{q}_i^2 \sum_{i=1}^n \dot{q}_i^4 - \sum_{i=1}^n \dot{q}_i^3 \sum_{i=1}^n \dot{q}_i^3} \quad (12.27)$$

Once a_1 and a_2 are determined, the standard error (representative deviation) of the curve fit from the measured quantities T_i can be estimated using (Figliola and Beasley, 1995)

$$\varepsilon = \left\{ \frac{\sum_{i=1}^n [T_i - f(a_1, a_2, \dots, a_p, \dot{q})]^2}{n - p} \right\}^{1/2} \quad (12.28)$$

The appearance of $n - p$ in the denominator of eq. (12.28) instead of n results from the use of the coefficients a_1, a_2, \dots , and a_p for determining f . Hence, p degrees of freedom have been removed from the system of data.

There are situations in which it is important to estimate the uncertainties of the coefficients a_1 and a_2 . One common example is determination of the permeability K

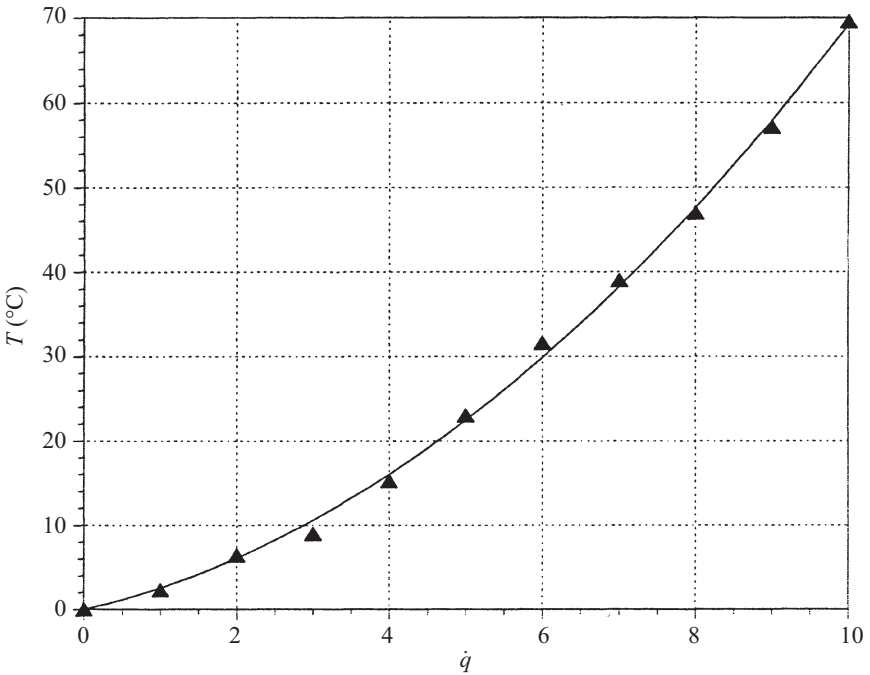


Figure 12.5 Graphical representation of experimental data (triangles) and curve-fit $T = a_1\dot{q} + a_2\dot{q}^2$. The least squares fit yields $a_1 = 2.0646$, $a_2 = 0.48645$, with $\chi^2 = 8.3096$ ($\Gamma_{\chi^2} = 0.5$) and fitting error $\varepsilon = 0.9608^\circ\text{C}$.

and the form coefficient C of porous materials from experimentally measured cross-section-averaged fluid speed v and pressure-drop ΔP data using the equation

$$\frac{\Delta P}{L} = \frac{\mu}{K} v + \rho C v^2 \quad (12.29)$$

Comparing eq. (12.29) and eq. (12.21) it is observed that $\Delta P/L$ plays the role of f , v of \dot{q} , μ/K of a_1 , and ρC of a_2 . The coefficients a_1 and a_2 (and consequently, K and C) can be determined from eqs. (12.26) and (12.27), respectively. The issue at hand is very simple: how to determine the uncertainties of the resulting coefficients a_1 and a_2 (or K and C)? This question was answered by Antohe et al. (1997). From the point of view of uncertainty analysis, the variables T_i and \dot{q}_i can be considered independent. Hence, using the Kline–McClintock method, eq. (12.15), the uncertainties can be estimated from

$$U_{a1} = \left\{ \sum_{i=1}^n \left[U_{\dot{q}_i} \left(\frac{\partial a_1}{\partial \dot{q}_i} \right) \right]^2 + \sum_{i=1}^n \left[U_{T_i} \left(\frac{\partial a_1}{\partial T_i} \right) \right]^2 \right\}^{1/2} \quad (12.30)$$

$$U_{a2} = \left\{ \sum_{i=1}^n \left[U_{\dot{q}_i} \left(\frac{\partial a_2}{\partial \dot{q}_i} \right) \right]^2 + \sum_{i=1}^n \left[U_{T_i} \left(\frac{\partial a_2}{\partial T_i} \right) \right]^2 \right\}^{1/2} \quad (12.31)$$

where $U_{\dot{q}}$ and U_T are, respectively, the uncertainties of each experimental data pair \dot{q}_i and T_i . This methodology for estimating the uncertainty of coefficients obtained from curve-fitting experimental data is general. The fundamental step is to utilize, in the Kline–McClintock model, the curve-fitting equations (e.g., least squares) to compute the local derivatives of the coefficients being considered.

In most cases, it is not known if a certain curve-fit equation is valid or not. Hence, it is very instructive to question the validation of the curve-fitting equation. A very useful procedure for validating (or not) a certain model (or curve-fit equation) was proposed by Davis et al. (1992). The first step in the validation procedure is to calculate the *residual* δ_i , defined as the deviation of the analytical value $f(\dot{q}_i)$ (or the curve-fit value) from the corresponding experimental value T_i ; that is,

$$\delta_i(\dot{q}_i) = T_i - f(\dot{q}_i) \quad (12.32)$$

A parameter called *semivariance*, defined as

$$\varphi(\Delta \dot{q}) = \frac{1}{2N(\Delta \dot{q})} \sum_{j=1}^{n(\Delta \dot{q})} [\delta_j(\dot{q}_j + \Delta \dot{q}) - \delta_j(\dot{q}_j)]^2 \quad (12.33)$$

can be used to estimate the appropriateness of the curve-fitting equation. The semivariance φ is a function of the lag distance $\Delta \dot{q}$ between two experimental points and of the number of experimental points (or pair of points) N that are $\Delta \dot{q}$ units apart. If the resulting semivariance tends to a finite value as the lag distance $\Delta \dot{q}$ increases,

the residuals do not correlate and the model (or curve fit) is valid. Otherwise, the residuals correlate and the theoretical model (or curve fit) is invalid. This procedure was tested successfully in a fluid mechanics application by Lage et al. (1997).

12.5 EQUIPMENT

12.5.1 Glass Thermometers

The oldest and most common human-made temperature-measuring device is the glass (fluid) thermometer. The basic principle of operation is the volumetric change of the working fluid (e.g., air, water, mercury) with temperature, commonly represented by the coefficient of volumetric thermal expansion β , defined as

$$\beta = \frac{1}{V} \frac{dV}{dT} \quad (12.34)$$

For compressible fluids, β must be measured at a constant pressure. The coefficient of volumetric thermal expansion varies with temperature, primarily for liquids and solids. Gases present similar volumetric coefficient of thermal expansion at atmospheric pressure. Some average values, from -20 to 100°C , are presented in Table 12.5.

Glass thermometers are commercially available for measuring temperatures from -80°C to approximately 600°C . They are designed with a bulb where most of the working fluid is stored, connected to a capillary to accommodate the increase in fluid volume.

Mercury-filled thermometers, also called *clinical thermometers*, are the most common glass thermometers, available in several sizes and designed for various ranges of operation. Mercury is advantageous as a glass thermometer working fluid, as it has a coefficient of volumetric thermal expansion almost independent of temperature. From -10 to 330°C , for instance, the coefficient of volumetric thermal expansion of mercury is almost constant and equal to $1.8 \times 10^{-4}\text{K}^{-1}$. Mercury thermometers are suitable for measuring temperatures from -40 to 550°C .

TABLE 12.5 Average Value of Coefficient of Volumetric Thermal Expansion β for Several Gases from -20 to 100°C

Gas	$\beta (\times 10^{-3}\text{K}^{-1})$
Air	3.6
NH_3	3.8
CO	3.7
CO_2	3.7
H_2	3.7
NO	3.7

Assuming β as a value independent of the temperature, eq. (12.34) can be integrated to yield

$$V_2 = V_1 e^{\beta(T_2 - T_1)} \tag{12.35}$$

with T_1 and T_2 being two distinct temperatures at which the fluid volume is V_1 and V_2 , respectively. Because β is generally a very small number, the exponential function of eq. (12.35) is very weak. In fact, the volume increment versus temperature variation for a mercury thermometer is almost linear, as can be seen in Fig. 12.6. This aspect facilitates calibration of the thermometer.

In the case of mercury, a variation of 1.0°C in temperature causes the volume to change by 0.018%. Hence, a volume of 8 mm^3 of mercury will expand to 8.00144 mm^3 . When this expansion is accommodated by a 0.1-mm-diameter capillary, the temperature change will cause the mercury column in the capillary to rise by 0.18 mm.

Observe that the sensitivity of this thermometer is $0.18\text{ mm}/^\circ\text{C}$. Increasing (or decreasing) the initial volume of mercury in the thermometer and decreasing (or increasing) the diameter of the capillary increases (or decreases) the sensitivity of the thermometer. For instance, using an initial volume equal to 10 mm^3 of mercury

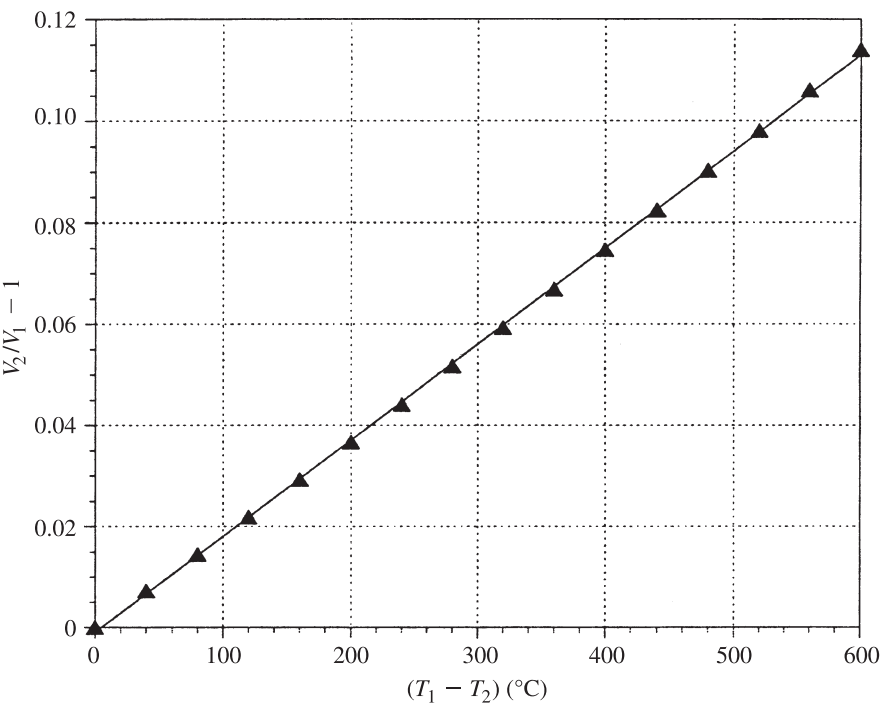


Figure 12.6 Volume variation versus temperature change for mercury. The straight line indicates the result of the least squares curve fitting the points of the graph with the linear function $(V_2/V_1) - 1 = -9.4885 \times 10^{-4} - 1.9005 \times 10^{-4}(T_2 - T_1)$.

and a capillary with diameter 0.05 mm leads to a thermometer with sensitivity equal to 0.92 mm/°C.

12.5.2 Thermocouples

Thermocouples are the most important components of thermoelectric systems functioning as electric thermometers. These thermometers operate based on the natural generation of electric potential through distinct but homogeneous electrical conductors with terminals exposed to different temperatures—a thermoelectric phenomenon.

The fundamental principle behind the operation of thermocouples is the cross-coupling between fluxes (heat and electricity) and driving forces (temperature and electric potential). A sound theoretical foundation for the study and design of thermoelectric systems, based on irreversible thermodynamics, is available in Bejan (1988). In this section, a brief review of the most important concepts is offered.

Two fundamental empirical effects are important for understanding thermal-electric interactions: the *Peltier effect* (named after the French physicist Jean Peltier, who discovered the phenomenon in 1834) and *Seebeck effect* (discovered by the German physicist Thomas Seebeck in 1826) which is the basis for the thermocouple operation.

The Peltier effect, observed experimentally, is the natural generation of a heat power flux of \dot{q}'' (in Watts per square meter) along a conductor by a finite electric potential gradient, even when the conductor is maintained at a uniform temperature (which brings to light one of the limitations of Fourier's law). A simple mathematical representation of this statement is

$$\dot{q}'' = -\alpha_1 \frac{1}{T} \frac{dE}{dx} \bigg|_{dT/dx=0} \quad (12.36)$$

where α_1 is a proportionality parameter, T the temperature of the conductor (in Kelvin), E the electrostatic potential (in volts), and x is the coordinate measured along the electric current direction (in meters).

It is known that a potential gradient along a conductor generates an electric current flux I'' (in amperes per meter-square) through the conductor. Therefore,

$$I'' = -\alpha_2 \frac{1}{T} \frac{dE}{dx} \bigg|_{dT/dx=0} \quad (12.37)$$

where α_2 is another proportionality parameter. By combining eqs. (12.36) and (12.37), the Peltier coefficient $\pi(T)$, measured in volts, can be defined as

$$\pi(T) = \frac{\dot{q}''}{I''} = \frac{\alpha_1}{\alpha_2} \quad (12.38)$$

Equation (12.38) can be rewritten by introducing $\epsilon_s(T)$, the absolute thermoelectric power of the conductor (in volts per Kelvin), also known as the *absolute Seebeck coefficient*, to obtain

$$\dot{q}'' = \pi(T)I'' = T\varepsilon_s(T)I'' \quad (12.39)$$

Equation (12.39) shows the existing relationship between electric current flux and generated heat power flux along an isothermal conductor more directly. This equation also presents the relationship between the Peltier $\pi(T)$ and Seebeck $\varepsilon_s(T)$ coefficients.

The phenomenon responsible for the Peltier effect can be understood more clearly when considering two dissimilar thermoelectric conductors connected and maintained at the same (uniform) temperature, as shown in Fig. 12.7. When a finite electric potential gradient is imposed along the conductors, a certain finite amount of electric current flux I'' can be transported through the conductors and across the junction. The discontinuity in the absolute thermoelectric power $\varepsilon_s(T)$ across the junction yields a net amount of heat released (or absorbed) at the junction, as shown in Fig. 12.7. This heat power flux, \dot{q}_c'' , generated (or depleted) by the electric current passing through the junction, is the difference between the power flux generated along conductor 1, \dot{q}_1'' , and the power flux generated along conductor 2, \dot{q}_2'' .

Expressions for \dot{q}_1'' and \dot{q}_2'' can be written using eq. (12.39):

$$\dot{q}_1'' = \pi_1(T_c)I'' = T_c\varepsilon_{s1}(T_c)I'' \quad (12.40)$$

$$\dot{q}_2'' = \pi_2(T_c)I'' = T_c\varepsilon_{s2}(T_c)I'' \quad (12.41)$$

where T_c is the junction temperature and $\varepsilon_{s1}(T)$ and $\varepsilon_{s2}(T)$ are the absolute thermoelectric power of each conductor.

Assuming \dot{q}_1'' greater than \dot{q}_2'' (which is equivalent to saying that conductor 1 is more sensitive than conductor 2 to the generation of heat power flux when transporting electric current, and subtracting eq. (12.41) from eq. (12.40) yields

$$\dot{q}_c'' = \dot{q}_1'' - \dot{q}_2'' = T_c [\varepsilon_{s1}(T_c) - \varepsilon_{s2}(T_c)] I'' \quad (12.42)$$

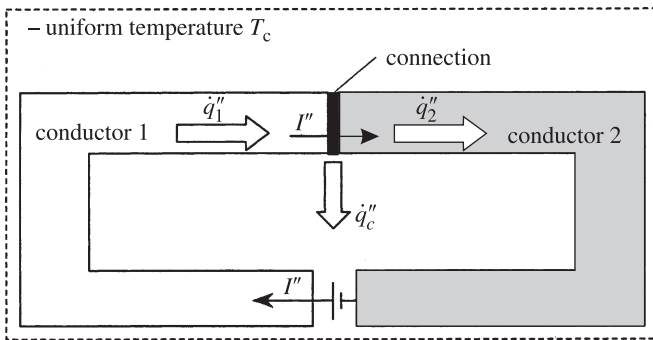


Figure 12.7 Peltier effect. It is necessary to remove (or add) a certain amount of heat at the junction to maintain two dissimilar thermoelectric conductors at the same uniform temperature when passing a current through them. The ratio of heat power flux \dot{q}'' to electric current flux I'' is dependent on the temperature T_c at which the conductors and the connection are maintained.

Observe that the configuration shown in Fig. 12.7 is suitable for evaluating the junction temperature T_c by measuring the heat power flux q_c'' and electric current flux I'' when the Seebeck coefficient of the two conductors $\varepsilon_{s1}(T)$ and $\varepsilon_{s2}(T)$ are known. Unfortunately, the measuring of the heat power flux q_c'' is very difficult in practice.

An alternative for measuring the junction temperature T_c is based on the Seebeck effect. This effect evolves from experimental observations that suggest the existence of a finite electromotive force when a temperature gradient is imposed along a conductor, even though no electric current passes through the conductor. The mathematical representation of the Seebeck effect is

$$\left. \frac{dE}{dx} \right|_{I=0} = \varepsilon_s(T) \left. \frac{dT}{dx} \right|_{I=0} \quad (12.43)$$

It can be shown from eq. (12.43) that the absolute Seebeck coefficient $\varepsilon_s(T)$ represents the variation of electrostatic potential E with temperature T when zero electric current passes through the conductor,

$$\varepsilon_s(T) = \left. \frac{dE}{dT} \right|_{I=0} \quad (12.44)$$

Observe how the Peltier and Seebeck effects are related. The Peltier effect, eq. (12.36), represents the production of heat power flux by an electric potential gradient along an isothermal conductor (zero temperature gradient). The Seebeck effect, eq. (12.43), represents the creation of an electric potential gradient by a temperature gradient when no current flows through the conductor. Moreover, the Peltier coefficient $\pi(T)$, eq. (12.38), is defined as the ratio of thermal flux to electric flux, while the Seebeck coefficient, eq. (12.43), is the ratio of electric potential gradient to thermal potential gradient.

Consider now the sketch shown in Fig. 12.8. Using eq. (12.40), the difference in electric potential along conductor 1 will be

$$E_c - E_1 = \int_{T_0}^{T_c} \varepsilon_{s1}(T) dT \quad (12.45)$$

and along conductor 2,

$$E_c - E_2 = \int_{T_0}^{T_c} \varepsilon_{s2}(T) dT \quad (12.46)$$

Subtraction of eq. (12.45) from eq. (12.46) provides the electric potential difference [electromotive force (EMF)] $\Delta E = E_2 - E_1$ generated across two homogeneous conductors connected at one extremity maintained at temperature T_c , with the other extremities maintained at temperature T_0 , as

$$\Delta E = E_2 - E_1 = \int_{T_0}^{T_c} [\varepsilon_{s1}(T) - \varepsilon_{s2}(T)] dT \quad (12.47)$$

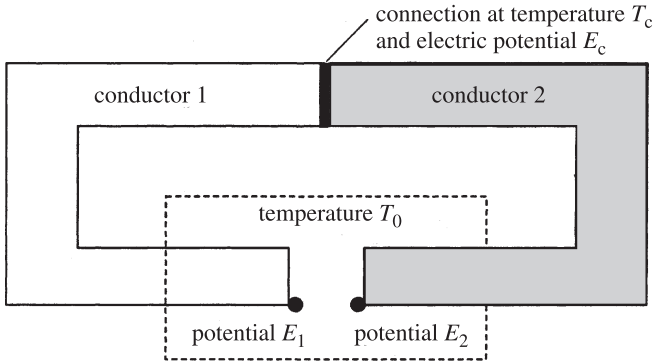


Figure 12.8 Seebeck effect (basic thermocouple). A difference in electrical potential across the thermal leads of two dissimilar but connected conductors is generated when a temperature gradient is imposed along each conductor. The ratio of electrical potential gradient to thermal potential gradient along each conductor is dependent on the local temperature of the conductor.

where ε_{s1} and ε_{s2} are the thermoelectrical characteristics of each conductor (total *thermoelectric power*, equal to the Seebeck coefficient). From eq. (12.47), ε_{s1} must differ from ε_{s2} for the potential generated by the two conductors to be nonzero. That is, the two conductors must be different. Observe also that the sensitivity of each conductor is proportional to ε_s . A very high ε_s value means that a small temperature variation will generate a large electric potential difference.

Figure 12.8 is the most fundamental representation of a thermocouple. By measuring the voltage ΔE across terminals 1 and 2 and the temperature T_0 , the junction temperature T_c can be found once the Seebeck coefficient of each conductor in the thermocouple is known. It is very important to recognize that the length of each conductor is irrelevant for determining the junction temperature T_c [see eq. (12.47)]. Moreover, the manner in which the temperature varies along the conductors is also irrelevant for determining the junction temperature T_c . With these two observations in mind, the effect of attaching a third conductor at the extremities of conductor 1 and 2 as shown in Fig. 12.9 can be predicted.

Using eq. (12.44) for conductor 1,

$$E_c - E_1 = \int_{T_0}^{T_c} \varepsilon_{s1}(T) dT \quad (12.48)$$

and for the leg of conductor 3 connected to conductor 1,

$$E_1 - E_3 = \int_{T_a}^{T_0} \varepsilon_{s3}(T) dT \quad (12.49)$$

Addition of eq. (12.48) to eq. (12.49) gives

$$E_c - E_3 = \int_{T_0}^{T_c} [\varepsilon_{s1}(T)] dT + \int_{T_a}^{T_0} [\varepsilon_{s3}(T)] dT \quad (12.50)$$

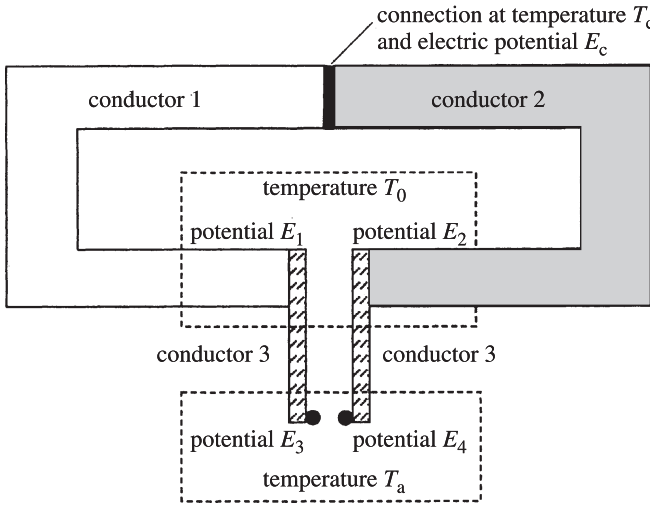


Figure 12.9 Third conductor attached to the leads of the two base thermocouple wires (conductors 1 and 2).

Doing the same for conductor 2,

$$E_c - E_2 = \int_{T_0}^{T_c} \varepsilon_{s2}(T) dT \quad (12.51)$$

and for the leg of conductor 3 connected to conductor 2, we have

$$E_2 - E_4 = \int_{T_a}^{T_0} \varepsilon_{s3}(T) dT \quad (12.52)$$

Addition of eq. (12.51) to eq. (12.52) yields

$$E_c - E_4 = \int_{T_0}^{T_c} [\varepsilon_{s2}(T)] dT + \int_{T_a}^{T_0} [\varepsilon_{s3}(T)] dT \quad (12.53)$$

Finally, subtraction of eq. (12.50) from eq. (12.53) provides

$$E_4 - E_3 = \int_{T_0}^{T_c} [\varepsilon_{s1}(T) - \varepsilon_{s2}(T)] dT \quad (12.54)$$

A comparison of eq. (12.54) with eq. (12.47) shows that the potential difference ($E_4 - E_3$) is identical to ($E_2 - E_1$). Therefore, the inclusion of a third homogeneous conductor is irrelevant to the determination of T_c using the thermocouple configuration shown in Fig. 12.9.

Existing standard pairs of conductors used as thermocouples have a wide range of temperature application, being commercially available for measuring temperatures

TABLE 12.6 Most Common Standard Thermocouples^a

Thermocouple Wires	Type	Range, T_{\min} to T_{\max} (°C)	S (mV/°C) T (°C)
Chromel (nickel–chromium) Constantan (copper–nickel)	E	−260 to 980	0.07313 300 to 1000
Iron Constantan (copper–nickel)	J	−180 to 870	0.05451 0 to 760
Chromel (nickel–chromium) Alumel (nickel–aluminum)	K	−260 to 1370	0.04079 0 to 1370
Tungsten Tungsten and 26% rhenium	G	15 to 2800	0.01474 800 to 2300

^aThermocouple *type* is a letter designation for certain thermocouples. *Range* refers to the applicability range and *sensitivity* S for specific temperature ranges with a reference junction temperature at 0°C included.

from approximately −270°C to approximately 2300°C. The most common are listed in Table 12.6, together with their temperature range of applicability and sensitivity.

Keep in mind when selecting a thermocouple that not only is the temperature range important but also the conditions under which the thermocouple will be operating. When two thermocouples cover approximately the same temperature range (such as thermocouples type E and J) the one that presents the largest sensitivity S tends, in general, to yield more accurate readings. However, they tend to be more expensive and require more expensive equipment for data acquisition.

Figure 12.10 is presented to assist in the verification of the linearity of the voltage as a function of temperature for each thermocouple. The straight lines are the best linear curve fit for each thermocouple within the temperature range shown.

Observe that the agreement between curve-fit and real values is quite good in most cases. If the measuring temperature range is small, the voltage versus temperature signal can be well approximated by a linear function. With this in mind, and eq. (12.47), Moffat (1990) devised a method for visualizing the temperature versus voltage relationship of any thermocouple arrangement.

For instance, consider the simple thermocouple configurations shown in Fig. 12.11. The first two thermocouples have wires A–B (left) and C–B (center), connected at the same temperature T_2 and with terminals at the same temperature T_1 . Each thermocouple will generate a certain electromotive force, which will be $\Delta E_{AB} = E_A - E_B$ and $\Delta E_{CB} = E_C - E_B$, respectively.

If the electric potential ΔE of each thermocouple is linear with the connection temperature T_2 , and the linearity function depends only on the thermocouple material, each thermocouple will follow a different voltage versus temperature line, as shown in Fig. 12.10. Hence, we can write $\Delta E_{AB} = \varepsilon_{sAB}(T_2 - T_1)$ and $\Delta E_{CB} = \varepsilon_{sCB}(T_2 - T_1)$.

A third thermocouple, made of wires A–C, also shown in Fig. 12.11 (right), can now be considered. This third thermocouple yields the resulting effect of combining

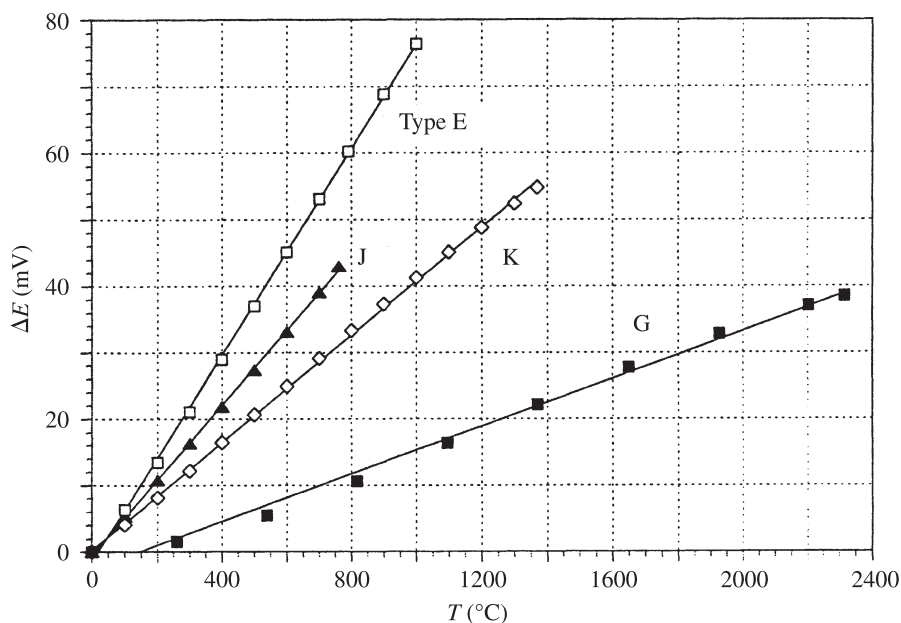


Figure 12.10 Electromotive force generated, ΔE , as a function of junction temperature T for thermocouple types E, J, K, and G. The reference temperature is equal to 0°C in all cases. The straight lines represent a linear curve fit of the results for each thermocouple. Values for subzero temperatures are not shown.

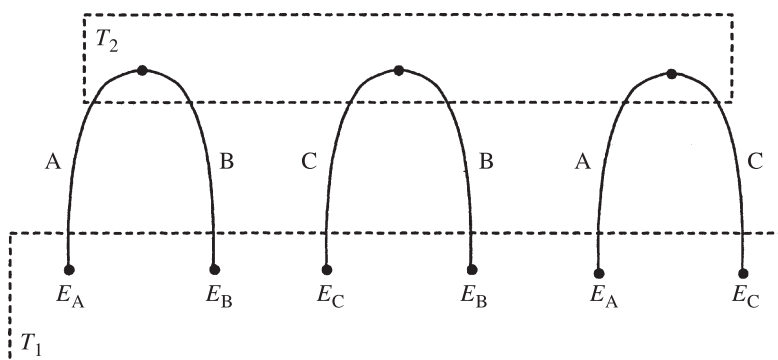


Figure 12.11 Two thermocouple arrangements, wires A–B (left), C–B (center), and A–C (right) connected at the same temperature T_2 and with terminals at the same temperature T_1 .

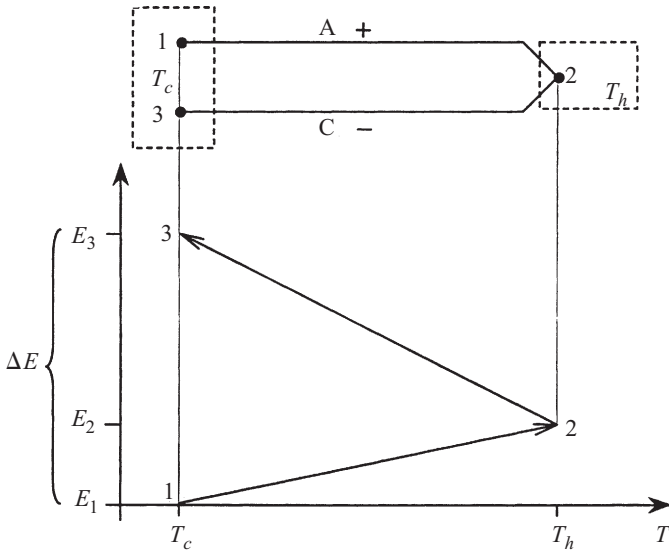


Figure 12.12 Thermocouple connection (top) and corresponding resulting electromotive force $\Delta E = E_3 - E_1$ as a function of temperature (bottom).

the first two because we can write $E_A - E_c = (E_A - E_B) - (E_C - E_B)$. In terms of the temperature variation, we can write

$$\Delta E_{AC} = \Delta E_{AB} - \Delta E_{CB} = \varepsilon_{sAB}(T_2 - T_1) - \varepsilon_{sCB}(T_2 - T_1)$$

This final result is shown in Fig. 12.12. The graph E versus T presents the curves for each original thermocouple (i.e., line 1–2 in Fig. 12.12 corresponds to curve ΔE_{AB} of thermocouple A – B , and line 2–3 corresponds to curve $-\Delta E_{CB}$ of thermocouple C – B), with arrows linking each connection.

Although the final result does not seem to depend on the thermocouple wire B , it is known that the inclination of each curve ΔE versus T (curves 1–2 and 2–3) depends on the material of wire B . If we obtain ΔE versus T curves, such as those of Fig. 12.10, for all thermocouple wires when connected to the same base wire B , the curves can be used to find the voltage of any thermocouple configuration.

This concept is utilized in analyzing the four-thermocouple *thermopile* shown in Fig. 12.13. The resulting ΔE versus T diagram indicates that the final voltage of the thermopile, $\Delta E_{1-9} = E_9 - E_1$, is four times the voltage of a single thermocouple, $\Delta E_{1-3} = E_3 - E_1$. Thermopiles are useful for amplifying the voltage signal.

12.5.3 Resistance Temperature Detectors

Resistance temperature detectors (RTDs) are devices designed for obtaining temperature values from measured changes in the resistance of an element. Many types of

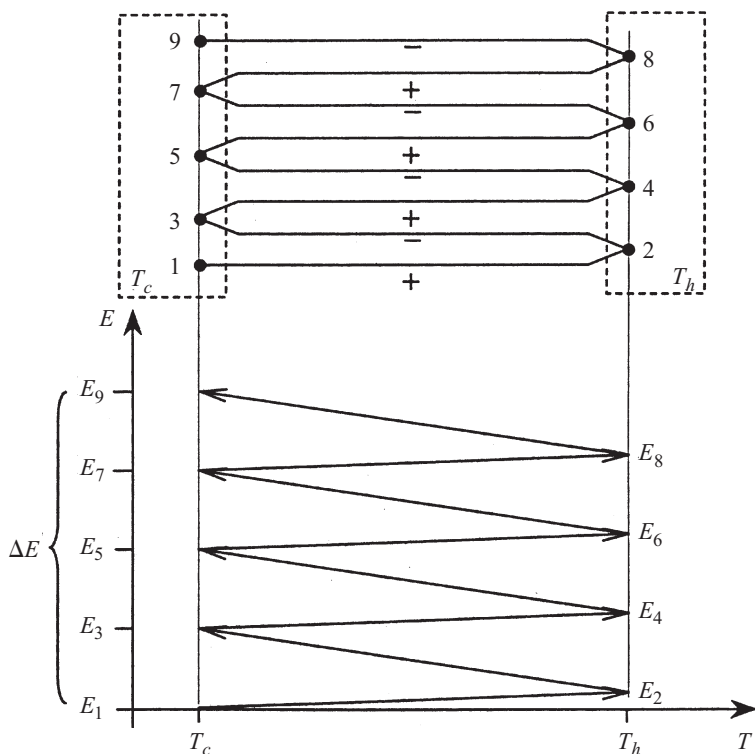


Figure 12.13 Four-thermocouple thermopile (top) and corresponding voltage versus temperature graph (bottom).

materials, such as gold, iron, mercury, nickel, and tungsten, can be used as resistive elements. As the temperature of the element changes, so does the resistance. Experimental correlations to obtain the temperature of the element by measuring the element resistance, are generally written as

$$R = R_0 [1 + c_1(T - T_0) + c_2(T - T_0)^2] \quad (12.55)$$

where R is the resistance of the element measured at temperature T , R_0 the resistance at $T = T_0$, and c_1 and c_2 are two experimentally determined correlation constants. For small temperature variation [i.e., small $(T - T_0)$], eq. (12.55) can be simplified to

$$R = R_0 [1 + c_1(T - T_0)] \quad (12.56)$$

where c_1 , the temperature coefficient of resistance, can vary from 0.001 to 0.007°C^{-1} , depending on the material used for the resistance element.

For most materials, the electrical resistance increases with the temperature of the element (i.e., c_1 is positive). However, there are semiconductors that present opposite

behavior. RTDs using semiconductors are called *thermistors*, and their resistance varies exponentially with temperature,

$$R = R_0 \exp \left[\alpha \left(\frac{1}{T} - \frac{1}{T_0} \right) \right] \quad (12.57)$$

where α is an experimentally determined constant.

The resistance of thermistors not only decreases with temperature, specific and their resistance is much higher than that of common metals. For instance, the specific resistance of copper is approximately $0.17 \mu\Omega \cdot \text{m}$, and for semiconductors used in thermistors is approximately $10^7 \mu\Omega \cdot \text{m}$. Some of the main advantages in using thermistors are related directly to their high resistivity: (1) small resistance effect of connecting leads (which is an important issue in most RTDs), and (2) reduced electric current for measuring resistance, and consequently, reduced self-heating. Other advantages are the very high sensitivity of the device [because of the exponential characteristics of eq. (12.57)] and very good accuracy. The accuracy of RTDs is about $\pm 0.0025^\circ\text{C}$, whereas the accuracy of thermistors can be as high as $\pm 0.005^\circ\text{C}$ which is much better than that of thermocouples. Moreover, the rapid time response to changes in temperature is also important. However, semiconductors tend to deteriorate rather rapidly, and thermistors are generally limited in application to benign environments at temperatures below 300°C .

12.5.4 Liquid Crystals

Liquid crystals, discovered in 1888 by Friedrich Reinitzer (an Austrian botanist), are now an integral part of the measuring arsenal available to the thermal engineer. They are suitable for temperature measurements because the molecular structure of the material changes with temperature, and by doing so, the optical characteristics (light diffraction) of the material changes as well.

Liquid crystals are ideal for surface temperature measurements and for volumetric clear liquid temperature measurement. Two particular types of liquid crystals, the cholesteric and the nematic, are used for thermal measurement. At present, liquid crystals are available in encapsulated form (microcapsules) that can be used as paint (thin film) for measuring surface temperature, or mixed with clear fluids (e.g., air, water) for volumetric temperature measurements. The microencapsulation of liquid crystal is extremely important for minimizing the effect of shear on the molecular structure of the material, which can induce changes in optical properties as the temperature does.

When temperature of an illuminated liquid crystal increases, the color of the crystal changes in bands. For instance, the crystal might seem yellow at temperatures from 31 to 34°C . The temperature range within which a single color is observed is called the *ambiguity band*. Liquid crystals are available in several different bands.

For quantitative measurement, liquid crystals must be calibrated against known temperatures, and this sometimes represents a nuisance. They can be calibrated in terms of color bands (ambiguity bands) or in terms of wavelength (chromaticity). The latter is more involved and more precise for providing continuous calibration

(calibration based on wavelength values instead of a single color). The time of response of liquid crystals is good, generally faster than 10^{-3} s. The microcapsules are also very close to being neutrally buoyant in water (specific gravity equal to 1.02), reducing the interference with the flow field.

12.5.5 Pyrometers

Pyrometers are devices based on radiation heat transfer commonly used for measuring the temperature of hot gases, above 500°C . However, their absolute accuracy is generally poor, about $\pm 10^{\circ}\text{C}$. They can be considered a subgroup of optical devices, as they require a line of sight for performing the measurement. The most common are specific to the radiation absorption technique, being particularly useful for steady or unsteady measurement of gas temperature.

Other existing devices are based on Rayleigh radiation scattering, spontaneous Raman scattering, laser-induced fluorescence, and spectral radiation emission. Some provide temporal resolution of more than 10^{-10} s. When using the laser as probe, the spatial resolution can be made extremely small, less than 10^{-9} m. These systems tend to be complex and very expensive, especially because of the base equipment. Some of these devices, such as laser-induced fluorescence, can be designed to provide concurrent multipoint measurement. Some require seeding the gas, which can be detrimental in certain circumstances for making the measuring process more intrusive.

12.5.6 Heat Flow Meters

Devices for measuring local heat flow based on measurements of the time evolution of local temperature are generally called the *bead calorimeter* or *slug calorimeter*. Here the preference is to call them *sensible capacitors*, which is more descriptive of the two main characteristics of the device: (1) it stores energy as a capacitor, and (2) energy is stored in the form of sensible heat.

When measuring temperature, the measuring device (e.g., a thermocouple) is to have very small thermal inertia (or heat capacity) to achieve thermal equilibrium (the same temperature) as fast as possible with the point where the temperature is being measured. In contrast, the measurement of heat flow by sensible capacitors requires large thermal inertia, so the time for thermal equilibrium is longer and measurable.

Thermal inertia can be adjusted by changing the mass m or the specific heat c of the material within the capacitor. The heat flow \dot{q} can be calculated using the first law of thermodynamics for a solid system,

$$\dot{q} = mc \frac{dT}{dt} \quad (12.58)$$

as long as the time evolution of the temperature dT/dt is measurable. It is important that the temperature within the device be as uniform as possible, to satisfy an implicit assumption of eq. (12.58). Consequently, materials with very high thermal conductivity (e.g., deoxidized copper) designed for a very small volume/surface area ratio are preferable (e.g., spherical shapes).

Some disadvantages of sensible capacitors include inaccuracy in obtaining dT/dt from the temperature–time evolution measurement, the need to cool the device to a temperature lower than the temperature where the heat flow is to be measured before measurements can be taken, and the intrusiveness of the device (for absorbing energy for measurement, the device disturbs the state or temperature of the region where a measurement is to be taken, which affects the existing heat flow).

A different family of heat flow gauges, called *diffusion meters*, operates based on Fourier’s law of conduction heat transfer for steady state,

$$\dot{q} = kA \frac{\Delta T}{\Delta x} \quad (12.59)$$

where k is the thermal conductivity of the material used for measurement, A the cross-sectional area of the material through which heat flows, and ΔT is the temperature difference measured across a distance Δx within the device.

The geometry of the meter is extremely important for the proper functioning of diffusion meters. It is necessary that the heat flow within the device be unidirectional for eq. (12.59) to be valid. Thin layers (films) of uniform and isotropic low-conductivity material help prevent multidimensional effects and provide a consistent frame for calculating the heat flow from eq. (12.5). More involve designs with different geometry are also common [e.g., the *Gardon gauge*, described by Moffat (1990)]. Heat fluxes as high as 0.6 MW/m^2 can be measured with this device.

Some disadvantages of diffusion meters include difficulty in obtaining unidirectional heat flow, the need for protective layers around the measuring elements (which increase the thermal inertia of the element, and as a consequence, is more disturbing to the state of the measuring region), and the need for steady-state measurement [eq. (12.59) is inappropriate if the heat flow varies in time].

NOMENCLATURE

Roman Letter Symbols

a	accuracy
A	area, m^2
B	bias error, dimensionless
c	specific heat, $\text{J/kg} \cdot \text{K}$
C	form coefficient, m^{-1}
d_i	deviation of measurement i , dimensionless
E	electrostatic potential, V
E_c	connection electrostatic potential, V
ΔE	EMF, voltage, V
f	function, dimensionless
I	electric current, A
I''	electric current flux, A/m^2
k	thermal conductivity, $\text{W/m} \cdot \text{K}$

K	permeability, m^2
L	length, m
L_c	least count, dimensionless
m	mass, kg
n	number of measurements, dimensionless
n_v	number of measures, dimensionless
N	number of degrees of freedom, dimensionless
p	number of imposed conditions, dimensionless
P	pressure, Pa
\dot{q}	heat power, W
\dot{q}''	heat power flux, W/m^2
Q	quantity calculated from T_i , dimensionless
R	electric resistance, Ω
R_0	reference resistance, Ω
S	sensitivity, dimensionless
t	time, s
T	temperature, K
T_c	connection temperature, K
T_i	measurement i, dimensionless
\bar{T}	mean value of measurements T_i , dimensionless
U	uncertainty, dimensionless
v	fluid speed, m/s
V	volume, m^3
x	coordinate, m

Greek Letter Symbols

α	proportionality/sensitivity parameter, dimensionless
β	volumetric coefficient of thermal expansion, K^{-1}
Γ	observed probability, dimensionless
Γ_d	deviation probability, confidence level, dimensionless
Γ_G	Gaussian probability, dimensionless
Γ_{χ^2}	χ^2 probability, dimensionless
δ_i	residual
ε	standard error of curve fitting, dimensionless
ε_s	Seebeck coefficient, dimensionless
μ	dynamic viscosity, dimensionless
π	Peltier coefficient, dimensionless
ρ	fluid density, kg/m^3
σ	standard deviation, dimensionless
σ_p	precision, dimensionless
φ	semivariance, dimensionless
χ^2	chi-square, dimensionless
ω	odds of variable T_i having uncertainty U_i , dimensionless
Ω	average of odds, dimensionless
$\Delta\zeta$	confidence interval, dimensionless

REFERENCES

- Antohe, B. V., Lage, J. L., Price, D. C., and Weber, R. M. (1997). Experimental Determination of Permeability and Inertia Coefficients of Mechanically Compressed Aluminum Porous Matrices, *J. Fluids Eng.*, 119, 404–412.
- Bejan, A. (1988). *Advanced Engineering Thermodynamics*, Wiley, New York.
- Coleman, H. W., and Steel, W. G. (1989). *Experimental Uncertainty Analysis for Engineers*, Wiley, New York.
- Dally, J. W., Riley, W. F., and McConnell, K. G. (1993). *Instrumentation for Engineering Measurements*, 2nd ed., Wiley, New York.
- Davis, P. A., Olague, N. E., and Goodrich, M. T. (1992). Application of a Validation Strategy to Darcy's Experiment, *Adv. Water Resources*, 15, 175–180.
- Figliola, R. S., and Beasley, D. E. (1995). *Theory and Design for Mechanical Measurements*, 2nd ed., Wiley, New York.
- Holman, J. P. (2001). *Experimental Methods for Engineers*, 7th ed., McGraw-Hill, New York.
- Kline, S. J., and McClintock, F. A. (1953). Uncertainty in Single Sample Experiments, *Mech. Eng.*, 75, 3–8.
- Lage, J. L., Antohe, B. V., and Nield, D. A. (1997). Two Types of Nonlinear Pressure-Drop versus Flow-Rate Relation Observed for Saturated Porous Media, *J. Fluids Eng.*, 119, 700–706.
- Moffat, R. J. (1982). Contributions to the Theory of Single-Sample Uncertainty Analysis, *J. Fluids Eng.*, 104, 250.
- Moffat, R. J. (1985). Uncertainty Analysis in the Planning of an Experiment, *J. Fluids Eng.*, 107, 173–181.
- Moffat, R. J. (1990). Some Experimental Methods for Heat Transfer Studies, *Exp. Therm. Fluid Sci.*, 3, 14–32.
- Wheeler, A. J., and Ganji, A. R. (1996). *Introduction to Engineering Experimentation*, Prentice Hall, Upper Saddle River, NJ.

Heat Transfer in Electronic Equipment

AVRAM BAR-COHEN

Department of Mechanical Engineering
University of Minnesota
Minneapolis, Minnesota

ABHAY A. WATWE and RAVI S. PRASHER

Intel Corporation
Chandler, Arizona

- 13.1 Introduction
 - 13.1.1 Cooling requirements
 - History
 - Present and future
 - 13.1.2 Thermal packaging goals
 - Preventing catastrophic failure
 - Achieving reliable operations
 - Life-cycle costs
 - 13.1.3 Packaging levels
- 13.2 Thermal resistances
 - 13.2.1 Introduction
 - 13.2.2 Basic heat transfer modes
 - Conduction
 - Convection
 - Radiation
 - 13.2.3 Chip package resistance
 - Internal resistance
 - External resistance
 - Flow resistance
 - Total resistance: single-chip packages
- 13.3 Length-scale effects on thermophysical properties
 - 13.3.1 Spreading resistance
 - 13.3.2 Heat flow across solid interfaces
 - Thermal contact resistance
 - Thermal boundary resistance
 - Interstitial materials
 - Thermal conductivity of particle-laden systems
 - Effect of filler concentration on mechanical strength
 - 13.3.3 First-order transient effects
 - Lumped heat capacity

- Thermal wave propagation
 - Chip package transients
 - 13.3.4 Heat flow in printed circuit boards
 - Anisotropic conductivity
 - Thermal vias
 - Effect of trace layers
 - 13.4 Convective phenomena in packaging
 - 13.4.1 Printed circuit boards in natural convection
 - 13.4.2 Optimum spacing
 - 13.4.3 Printed circuit boards in forced convection
 - 13.5 Jet impingement cooling
 - 13.5.1 Introduction
 - 13.5.2 Correlation
 - 13.5.3 First-order trends
 - 13.5.4 Figures of merit
 - 13.5.5 General considerations for thermal–fluid design
 - 13.5.6 Impingement on heat sinks
 - 13.6 Natural convection heat sinks
 - 13.6.1 Empirical results
 - 13.7 Phase-change phenomena
 - 13.7.1 Heat pipes and vapor chambers
 - Alternative designs
 - 13.7.2 Immersion cooling
 - 13.8 Thermoelectric coolers
 - 13.9 Chip temperature measurement
 - 13.10 Summary
- Nomenclature
- References

13.1 INTRODUCTION

13.1.1 Cooling Requirements

History Despite the precipitous drop in transistor switching energy that has characterized the solid-state semiconductor revolution, the cooling requirements of micro-electronic components have not diminished. As the twenty-first century begins, high-performance chip power dissipation exceeds 100 W, some three orders-of-magnitude above the SSI (small-scale integration) chips of the early 1960s, and informed opinion suggests that a 150-W chip will become reality within the first decade of the twenty-first century. Thermal management is thus one of the key challenges in advanced electronic packaging, and considerable improvement in thermal packaging will be needed to exploit successfully the Moore’s law acceleration in semiconductor technology.

In the early 1960s chip heat removal requirements for the 2- to 3-mm SSI silicon semiconductor devices were typically in the range 0.1 to 0.3 W. By the mid-1980s, increased chip transistor counts and functional densities pushed LSI (large-scale integration) ECL (emitter-coupled logic) power dissipation to 5 W for 5-mm chips (Bar-Cohen, 1987).

Although historical reliability data for silicon bipolar chips, based largely on military electronic systems, had established a “traditional” upper limit of 110 to 125°C on the junction temperature, in the 1980s reliability and performance considerations led to a lower standard, 65 to 85°C, in commercial applications, thus halving the allowable temperature rise of the chip above the ambient 45°C. The resulting LSI chip heat fluxes, approaching $25 \times 10^4 \text{ W/m}^2$ (25 W/cm²), combined with the lowered chip temperatures, necessitated the development of high-performance cooling systems and posed a formidable challenge to the electronic packaging community.

Mainframe computers of this era based on high-speed bipolar chips were characterized by water-cooled multichip modules, with an effective thermal resistance of 1 to 2 K/W · cm² (Bar-Cohen, 1987). However, although slower, the lower-power CMOS (complementary metal oxide on silicon) VLSI (very large scale integration) chips, with power dissipation often less than 1 W across a 10-mm chip, were becoming the technology of choice for workstations and desktop computers. These chips, requiring effective thermal resistances some 25 times lower than the mainframe bipolar chips, could often be cooled passively (conduction spreading and air natural convection) and rarely required more than modest forced-convection and simple air-cooled extended surface heat sinks.

In the mid-1990s, the thirst of the marketplace for greater integrated-circuit speed and functionality, along with growing on-chip heating which accompanied lower operating voltages and higher currents, pushed CMOS microprocessor chip power dissipation to the range 15 to 30 W and forced the use of ever more aggressive air-cooling technology. As the end of the decade approached, chips in high-performance workstations were routinely dissipating in excess of 75 W, with heat fluxes that were once again approaching $25 \times 10^4 \text{ W/m}^2$. To facilitate continued air cooling of these higher-power chips and in recognition of the vast reliability improvements in silicon devices, the allowable junction temperatures in the final years of the 1990s rose to values close to 100°C in desktop computers and workstations.

Present and Future To understand the future trends in the cooling requirements for microelectronic components, it is helpful to examine the consensus emerging from industrywide “road-mapping” efforts, including the Semiconductor Industry Association’s (SIA’s) *National Technology Roadmap for Semiconductors: Technology Needs* (1997) and National Electronics Manufacturing Institute’s (NEMI’s) *Technology Roadmap* (1996). These trends are summarized in Table 13.1, where the salient thermal and related parameters, starting with the 1999 state of the art and extending to 2012, are classified by application categories. In the low-cost or commodity product category, including disk drives, displays, microcontrollers, boom-boxes, and video cassette recorders, power dissipation is very modest, and only incidental cooling expenditures can be tolerated. In this category, today and for the foreseeable

future, thermal management rarely involves more than reliance on buoyancy-induced natural circulation of air, augmented perhaps by passive heat spreading. Operation at an elevated chip temperature of typically 125°C in an anticipated internal ambient temperature of 55°C , resulting in a driving force of 70°C , provides some compensation for the relatively high chip-to-air thermal resistance associated with this approach.

Similar constraints severely limit the options for today's battery-operated hand-held products, including PDAs (personal digital assistants) and cellular phones, where clever use of heat spreaders generally makes it possible to maintain the 1 to 2 W integrated circuits (ICs) at temperatures at or below 115°C . Significantly, in this category, thermal management capability is today in rough equilibrium with the battery power available for extended operation, but an anticipated doubling of the available battery power by the late years of the current decade may well necessitate more aggressive approaches.

Natural convection cooling is also generally the rule for memory devices. But when many such DRAMs and/or SRAMs, each typically dissipating 1 W, are stacked together or densely packed on a printed circuit board, forced convection is used to keep these devices from exceeding their allowable temperature of approximately 100°C . Such techniques can be expected to be more broadly applied for thermal management of future memory devices, dissipating, perhaps, so much as 2.5 W, by the end of the decade.

During the 1990s, the automotive category claimed the "harsh environment" mantle previously worn by "mil-spec" components. The elevated ambient temperatures under the hood and elsewhere in a vehicle, reaching as high as 165°C , make it necessary for automotive ICs, dissipating 10 to 15 W, to operate reliably at temperatures as high as 175°C . This category also includes equipment used in mining and resource exploration and in the upper spectrum of military applications. The relatively small chip size of 53 mm^2 in 1999, projected to grow to just 77 mm^2 by 2012, and an anticipated constant power dissipation of 14 W, result in chip heat fluxes that are comparable to those encountered in the most demanding, high-performance category.

However, due to the small allowable temperature difference for these components, the automotive category poses the most demanding of electronic cooling requirements. While a wide variety of heat-spreading and air-cooling strategies, for elevated chip temperature operation, have been implemented successfully in this product category, development efforts are also addressing conventional temperature operation based on the use of refrigerated cold plates. Throughout the 1990s, heat-sink-assisted air cooling was the primary thermal packaging approach for the cost/performance category, which included both desktop and notebook computers. Thermal management of the microprocessors used in desktop computers often relied on clip-attached or adhesively bonded extruded aluminum heat sinks, cooled by remotely located fans. But as the chip power reached 50 W by the end of the decade, thermal packaging for this product category required progressively more refined designs as well as lower-thermal-resistance interface materials. Returning to Table 13.1, it may be seen that cost/performance chip heat fluxes are forecasted to peak by 2006, at approximately 40% higher values than in 1999.

Table 13.1 Thermal Characteristics of Current and Future Semiconductor Packages

	Year of Commercialization				
	1999	2001	2003	2006	2012
Commodity					
Power dissipation (W)	n/a	n/a	n/a	n/a	n/a
Chip size (mm ²)	53	56	59	65	77
On-chip frequency (MHz)	300	415	530	633	1044
Junction temperature (°C)	125	125	125	125	125
Ambient temperature	55	55	55	55	55
Pin count	40–236	40–277	40–325	40–413	40–666
Handheld					
Power dissipation (W)	1.4	1.7	2	2.4	3.2
Chip size (mm ²)	53	56	59	65	77
Heat flux (W/cm ²)	2.6	3.0	3.4	3.7	4.2
On-chip frequency (MHz)	300	415	530	633	1044
Junction temperature (°C)	115	115	115	115	115
Ambient temperature (°C)	55	55	55	55	55
Pin count	117–400	137–469	161–413	205–524	330–846
Memory (DRAM)					
Power dissipation (W)	0.8	1.1	1.5	2	3
Chip size (mm ²)	400	445	560	790	1580
Heat flux (W/cm ²)	0.20	0.25	0.27	0.25	0.19
On-chip frequency (MHz)	100	100	125	125	150
Bits/chip (mega)	1,000		4,000	16,000	256,000
Junction temperature (°C)	100	100	100	100	100
Ambient temperature	45	45	45	45	45
Pin count	30–82	34–96	36–113	40–143	48–231
Cost performance					
Power dissipation (W)	48	61	75	96	109
Chip size (mm ²)	340	285	430	520	750
Heat flux (W/cm ²)	13.5	15.8	17.4	18.5	14.5
On-chip frequency (MHz)	526	727	928	1108	1827
Junction temperature (°C)	100	100	100	100	100
Ambient temperature	45	45	45	45	45
Pin count	300–976	352–895	413–1093	524–1476	846–2690
High performance					
Power dissipation (W)	88	108	129	160	174
Chip size (mm ²)	340	385	430	520	750
Heat flux (W/cm ²)	25.9	28.1	30.0	30.7	23.2
On-chip frequency (MHz)	958	1570	1768	2075	3081
Transistor (MHz/cm ²)	6	10	18	39	180
Junction temperature (°C)	100	100	100	100	100
Ambient temperature	45	45	45	45	45
Pin count	1991	1824	2228	3008	5480
Automotive					
Power dissipation (W)	14	14	14	14	14
Chip size (mm ²)	53	56	59	65	77
Heat flux (W/cm ²)	26.4	25.0	23.7	21.5	18.2
On-chip frequency (MHz)	150	150	200	200	250
Junction temperature (°C)	175	175	180	180	180
Ambient temperature	165	165	170	170	170
Pin Count	40–236	40–277	40–325	40–413	40–666

Source: Data from NEMI (1996) and SIA (1997).

In an attempt to minimize the performance gap between notebook and desktop computers, fan-cooled heat sinks did begin to appear in notebook computers toward the end of the 1990s. However, throughout much of this decade, battery power limitations made it necessary to harness naturally convecting air, circulating past low-fin heat sinks and heat pipes, as well as metal cases heated by spreading, to provide the requisite cooling for the 3- to 5-W chips. In the coming years, advanced notebook computers using modified cost/performance chips will pose extreme challenges to the thermal management community.

In the late 1990s, under the influence of market forces, thermal management of nearly all the products in the high-performance category devolved to the aggressive use of air cooling, exploiting technology that was a natural outgrowth of the air-cooled multichip modules of the 1980s. By the end of the decade, a renaissance in thermal packaging produced heat sinks for high-end commercial workstations and servers that were routinely dissipating 60 to 70 W with chip heat fluxes of some 26 W/cm². As may be seen in Table 13.1, the packaging community consensus suggests that early in the second decade of the twenty-first century, power dissipation will rise to 175 W for chips operating at some 3 GHz. However, it is anticipated that chip area, growing from 3.8 cm² to some 7.5 cm², will keep pace with chip power dissipation in the coming years, yielding chip heat fluxes that increase only marginally above the present values to approximately 30 W/cm² by 2006, before beginning a slow decline in later years.

13.1.2 Thermal Packaging Goals

Preventing Catastrophic Failure In today's high-performance microelectronic systems, catastrophic failure may be associated with an immediate and total loss of electronic function and package integrity, or drastic, though reversible, deterioration in performance. The prevention of permanent as well as intermittent catastrophic failure is the primary and foremost goal of electronics thermal management and often requires the elimination of large temperature excursions. Excessive temperatures, inducing large thermomechanical stresses, may lead to excessive strain and/or stress levels in the silicon, delamination of the die attach and heat sink or spreader bond layer, as well as broken wire, solder, or gold bonds. Furthermore, elevated temperatures, which exceed the design specification of the package, may result in melting, vaporization, or even combustion of low-temperature packaging materials. Alternatively, unanticipated chip and package temperature variations beyond the specified tolerance may lead to shifts in semiconductor behavior (e.g., CMOS switching frequency) or that of adjacent photonic (e.g., emitted wavelength, conversion efficiency) or microwave components (e.g., phase shift), as well as to structural misalignment and signal delays that undermine the ability of the package to deliver the requisite performance. A detailed understanding of the catastrophic vulnerability of the specified component(s) provides the basis for establishing the thermal management strategy for a particular package or product, including selection of the appropriate fluid, heat transfer mode, and inlet coolant temperature required to meet design specifications.

Achieving Reliable Operations Following selection of the thermal packaging strategy, attention can be turned to meeting the desired level of reliability and the associated target failure rates of each component and subassembly. Individual solid-state electronic devices are inherently reliable. However, because a single microelectronic chip may include as many as 15 million transistors and 600 leads, and because many tens of such components may be used in a single system, achieving failure-free operation over the useful life of a product is a formidable challenge. The suppression of thermally induced failures often requires adherence to strict limits on the temperature rise or fall relative to the ambient temperature and the minimization of spatial and temporal temperature variations in a package.

The reliability of a system is the probability that the system will meet the required specifications for a given period of time. As an individual electronic component contains no moving parts, it can often perform reliably for many years, especially when operating at or near room temperature. In practice, integrated circuits operate at temperatures substantially above ambient, and unfortunately, most electronic components are prone to failure from prolonged exposure to these elevated temperatures. This accelerated failure rate results from the interplay of numerous factors, including the consequences of thermal strain and stress in the bonding and encapsulation materials, parasitic chemical reactions, dopant diffusion, and dielectric breakdown (Pecht et al., 1992). Although accurate failure rate predictions defy simple correlations, under some conditions a modest 10 to 20°C increase in chip temperature can double the component failure rate. Consequently, for many package categories, temperature is the strongest contributor to the loss of reliability. In such systems, thermal management is critical to success of the electronic system.

Life-Cycle Costs In the final stages of thermal design of an electronic system, the reliability, availability, and maintainability of the proposed thermal control alternatives must be evaluated and used to guide the final technology and equipment choice. It is the role of the packaging engineer to assure that the enhanced reliability of the components, resulting from lower operating temperature as well as the minimization of spatial and temporal temperature variations, is sufficient to compensate for the additional life-cycle cost and inherent failure rate of fans, pumps, heat pipes, interface materials, and other elements of the cooling system. Successful thermal packaging requires a judicious and insightful combination of materials and heat transfer mechanisms to stabilize the component temperatures at an acceptable level.

13.1.3 Packaging Levels

To initiate the development of a thermal design for a specified electronic product, it is first necessary to define the relevant packaging level (see Fig. 13.1). The commonly accepted categorization places the chip package, which houses and protects the chip, at the bottom of the packaging hierarchy (*level 1*). The printed circuit board (PCB), which provides the means for chip-to-chip communication, constitutes *level 2*, while the backplane or *motherboard*, which interconnects the printed circuit boards, is termed *level 3* packaging. The box, rack, or cabinet, that houses the entire system

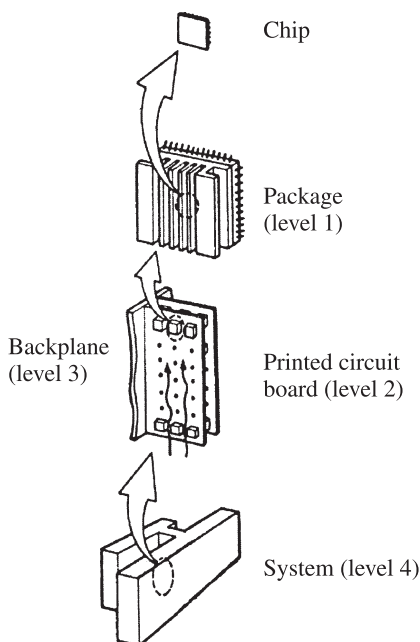


Figure 13.1 Electronic packaging levels.

is generally referred to as *level 4*. The primary thermal transport mechanisms and commonly used heat removal techniques vary substantially from one packaging level to the next as the scale of the thermal transport phenomena shifts from the microscale (or even nanoscale in future years) at level 1, to the mesoscale at level 2, and on to the macroscale in packaging levels 3 and 4.

Level 1 thermal packaging is concerned primarily with conducting heat from the chip to the package surface and then into the printed circuit board. At this packaging level, reduction in thermal resistance between the silicon die and the outer surface of the package is the most effective way to lower the chip temperature. As shown in Table 13.2, a variety of passive cooling techniques are available to reduce the thermal resistance. For example, improved thermal performance can be obtained by using die-attach adhesives, with diamond, silver, or other high-conductivity filler material, thermal greases, and phase-change materials, which soften at the operating temperature to conform better to the surface of the chip. Alternatively, attaching metal-plate heat spreaders to the chip, and using thermally enhanced molding compounds and embedded heat slugs [for plastic ball grid array (PBGA) and lead frame packages], can also lead to beneficial results. It is also quite common to attach heat sinks to the surface of a package to create additional surface area for heat removal by natural and/or forced convection. In very high power applications, it may be necessary to cool the chip directly by attachment to a heat pipe, by direct attachment of a

TABLE 13.2 Thermal Management Techniques for Distinct Packaging Levels

Packaging Level	Passive Cooling Techniques	Active Cooling Techniques
Level 1: chip package	High-conductivity adhesive Greases Phase-change materials High-conductivity molding compound Heat spreader Heat slug Heat sinks Dielectric liquid immersion Heat pipes	Fans Air jet impingement Dielectric liquid Thermoelectric cooler
Level 2: PCB	Thick power and ground planes Insulated metal substrates Heat pipes Natural convection	Fans Ducted air Dielectric liquids Cold plates
Levels 3 + 4: module and rack	Natural convection Heat pipes	Ducted air Air-handling system Cold plates Refrigeration systems

heat sink, by impingement of high-velocity air jets, or by immersion in a dielectric liquid.

Heat removal at level 2 typically occurs both by conduction in the printed circuit board and by convection to the ambient air. Use of printed circuit boards with thick, high-conductivity power and ground planes and/or embedded heat pipes provides improved thermal spreading at this level of packaging. Use of electrically insulated metal substrates can also be considered. Often, heat sinks are attached to the back surface of the printed circuit board. In many airborne systems or in systems designed for very harsh environments, convective cooling of the component is not possible; instead, heat must be conducted to the edge of the printed circuit board. Attachment of a heat sink or a heat exchanger at this edge then serves to remove the heat dissipated by the components populating the printed circuit board or substrate.

As might be surmised from the frequent use of the term *computer on a chip* or *computer in a package*, many of today's electronic systems can be packaged adequately at level 1 or 2. Heat sinks or finned surfaces protruding into the airstream are often used at levels 1 and 2 to aid in the transfer of heat to the ambient air. When levels 3 and 4 are present, thermal packaging generally involves the use of active thermal control measures such as air-handling systems, refrigeration systems, or water pipes, heat exchangers, and pumps. Often, however, it is possible to cool the module and/or rack by relying on natural circulation of the heated air.

13.2 THERMAL RESISTANCES

13.2.1 Introduction

To determine the component temperatures and temperature gradients encountered in the flow of heat within electronic systems, it is necessary to define the relevant heat transfer mechanisms and establish their governing relations. In a typical system, heat removal from active regions of the microcircuit(s) or chip(s) may require the use of several mechanisms, some operating in series and others in parallel, to transport to the coolant or ultimate heat sink the heat generated. Practitioners of the thermal arts and sciences generally deal with four basic thermal transport modes: conduction, including contact resistance; convection; phase change; and radiation.

The expression of the governing heat transfer relations in the form of thermal resistances (Kraus, 1958) greatly simplifies the first-order thermal analysis of electronic systems. Recognizing that heat flow q is analogous to electrical current and that the temperature drop ΔT is analogous to a voltage drop, it is possible to define a general thermal resistance R as

$$R = \frac{\Delta T}{q} \quad (13.1)$$

Although, strictly speaking, this analogy applies only to conduction heat transfer, it is possible to generalize this definition to all the modes of thermal transport. Thus, following the established rules for resistance networks, thermal resistances that occur sequentially can be summed to yield the overall thermal resistance along that heat flow path. Conversely, the reciprocal of the overall thermal resistance of several parallel heat transfer paths or mechanisms can be found by summing the reciprocals of the individual resistances.

In refining the thermal design of an electronic system, primary attention should be devoted to reducing the largest thermal resistances along a specified thermal path and/or providing parallel paths for heat removal from a critical area or component. While thermal resistances associated with various paths and thermal transport mechanisms constitute the building blocks for the development of a thermal packaging solution, they have also found widespread application as figures of merit in evaluating and comparing the thermal efficacy of various packaging techniques and strategies.

13.2.2 Basic Heat Transfer Modes

Conduction Based on Fourier's equation for one-dimensional thermal diffusion (Incropera and DeWitt, 1996), the thermal resistance for conduction heat transfer is given by

$$R = \frac{L}{kA} \quad (13.2)$$

where L is the length of the heat flow path, k the thermal conductivity of the medium, and A the cross-sectional area for heat flow. Table 13.3 lists the values of the thermal

Table 13.3 Room-Temperature Thermal Properties of Commonly Used Electronic Packaging Materials

Material	Density (kg/m ³)	Specific Heat (J/kg · K)	Thermal Conductivity (W/m · K)
Air	1.16	1,005	0.024
Epoxy (dielectric)	1,500	1,000	0.23
Epoxy (conductive)	10,500	1,195	0.35
Polyimide	1,413	1,100	0.33
FR4	1,500	1,000	0.30
Water	1,000	4,200	0.59
Thermal grease	—	—	1.10
Alumina	3,864	834	22.0
Aluminum	2,700	900	150
Silicon	2,330	770	120
Copper	8,800	380	390
Gold	19,300	129	300
Diamond	3,500	51	2,000

Source: Incropera and DeWitt (1996).

conductivity, density, and specific heat of some of the commonly used electronic packaging materials. Conduction resistance values for typical packaging materials are displayed in Fig. 13.2 as a function of the thermal conductivity and the ratio of thickness to cross-sectional area of a single layer. This figure reveals the conduction resistance to range from 2 K/W for a 1-mm-thick 1000-mm² layer of a typical epoxy encapsulant to 6×10^{-4} W/K for a 25- μ m-thick layer of copper 100 mm² in area. Similarly, typical soft bonding materials are found to pose resistances of 0.1 K/W for solders and 1 to 3 K/W for epoxies and thermal greases for typical L/A ratios ranging from 0.25 to 1.0 m⁻¹.

Equation (13.2) is strictly valid only for one-dimensional heat conduction. However, for geometrically complex electronic packages, in which heat flow is two- or three-dimensional, the shape factor approach can be used to define the internal resistance of the package via

$$R = \frac{L}{kA} = \frac{1}{k(A/L)} = \frac{1}{kS} \quad (13.3)$$

The shape factor S in eq. (13.3) is solely geometry dependent and can be found tabulated in many of the popular heat transfer textbooks (McAdams, 1954; Incropera and DeWitt, 1996; Swartz and Pohl, 1989).

Convection Following the form of the conventional relations for convective heat transfer, often referred to as *Newton's law of cooling* (Incropera and DeWitt, 1996), the thermal resistance in convective thermal transport can be written in the form of eq. (13.3):

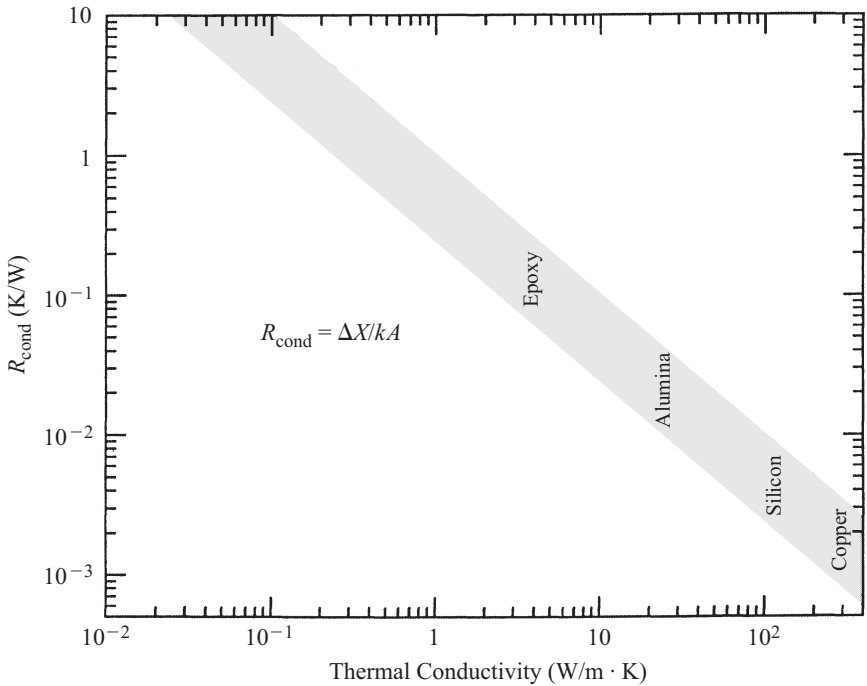


Figure 13.2 Conduction thermal resistances for packaging materials.

$$R = \frac{1}{hA} \tag{13.4}$$

where h is the coefficient of heat transfer. The heat transfer coefficients for typical fluids and specified domains relevant to electronic packaging vary by nearly three orders of magnitude, from approximately $5 \text{ W/m}^2 \cdot \text{K}$ for air in natural convection and $25 \text{ W/m}^2 \cdot \text{K}$ for air in forced convection, to some $150 \text{ W/m}^2 \cdot \text{K}$ for high-velocity air jets, perhaps $1000 \text{ W/m}^2 \cdot \text{K}$ for forced convection of water in cold plates, and values approaching $5,000 \text{ W/m}^2 \cdot \text{K}$ for the pool boiling of fluorocarbon liquids.

The heat transfer literature contains many theoretical equations and empirical correlations that can be used to determine the heat transfer coefficient for specified fluids flowing within channels or along surfaces of various geometries. Many of these relations are expressed in nondimensional form as

$$\text{Nu} = C \cdot \text{Re}^n \cdot \text{Pr}^m \tag{13.5}$$

where Nu is the Nusselt number, C a geometric constant, Re the Reynolds number, and Pr the Prandtl number. Many of the commonly used empirical correlations for convective heat transfer in geometries encountered in electronic packaging configurations are summarized in Table 13.4. Alternatively, simplified heat transfer coefficient

TABLE 13.4 Correlation for Convective Heat Transfer Coefficients

Mode of Convection	Correlation
Natural convection from an isothermal vertical surface	$h = C(\text{Ra})^n = C \frac{k_f}{L} \left(\frac{\rho_f^2 \beta g C_p \Delta T L^3}{\mu_f k_f} \right)^n$ $C = 0.59, n = \frac{1}{4} \text{ for } 1 < \text{Ra} < 10^9$ $C = 0.10, n = \frac{1}{3} \text{ for } 10^9 < \text{Ra} < 10^{14}$
Natural convection from a vertical isoflux surface	$h = 0.631 \left(\frac{k_f}{L} \right) \left[\frac{C_p \rho_f^2 g \beta q'' H^5}{\mu_f k_f^2 L} \right]^{1/5}$
Natural convection on an isothermal horizontal surface	$h = C(\text{Ra})^n = C \frac{k_f}{L} \left(\frac{\rho_f^2 \beta g C_p \Delta T L^3}{\mu_f k_f} \right)^n$ $C = 0.54, n = \frac{1}{4} \text{ for } 10 \leq \text{Ra} \leq 10^7$ $C = 0.15, n = \frac{1}{3} \text{ for } 10^7 \leq \text{Ra} \leq 10^{11}$
Forced convection on an isothermal flat plate	$h = C(\text{Re})^n (\text{Pr})^{1/3} = C \frac{k_f}{L} \left(\frac{\rho_f V L}{\mu_f} \right)^n \left(\frac{\mu_f C_p}{k_f} \right)^{1/3}$ $\text{Laminar: } C = 0.664, n = \frac{1}{2}$ $\text{Turbulent: } C = 0.0296, n = \frac{4}{5}$
Forced convection on an isoflux flat plate	$h = C(\text{Re})^n (\text{Pr})^{1/3} = C \frac{k_f}{L} \left(\frac{\rho_f V L}{\mu_f} \right)^n \left(\frac{\mu_f C_p}{k_f} \right)^{1/3}$ $\text{Laminar: } C = 0.453, n = \frac{1}{2}$ $\text{Turbulent: } C = 0.0308, n = \frac{4}{5}$
Laminar forced convection in a circular tube	$h = \frac{k_f}{D} \left\{ 3.66 + \frac{0.0668(D/L) \cdot \text{Re} \cdot \text{Pr}}{1 + 0.04[(D/L) \cdot \text{Re} \cdot \text{Pr}]^{2/3}} \right\}$ $\text{Re} = \frac{\rho_f V D}{\mu_f}, \quad \text{Pr} = \frac{\mu_f C_p}{k_f} \quad \text{for } \text{Re} < 2000$
Turbulent forced convection in a circular tube	$h = \frac{k_f}{D} (0.023 \text{Re}^{0.8} \cdot \text{Pr}^n) (\text{Re} > 2000)$ $n = 0.4 \text{ for heating, } n = 0.3 \text{ for cooling}$

Source: Incropera and DeWitt (1996).

TABLE 13.5 Simplified Equations for Convective Heat Transfer Coefficients for Air at 50°C

Mode of Convection	Correlation
Natural convection from an isothermal vertical surface	$h = \frac{1.51}{L} (\Delta T L^3)^{1/4}$
Natural convection from a vertical isoflux surface	$h = \frac{1.338}{L} \left(\frac{q'' H^5}{L} \right)^{1/5}$
Natural convection on an isothermal horizontal surface	$h = \frac{1.381}{L} (\Delta T L^3)^{1/4}$
Forced convection on an isothermal flat plate	$h = \begin{cases} 3.886 \left(\frac{V}{L} \right)^{0.5} & \text{for laminar flow} \\ 0.099 \left(\frac{V^4}{L} \right)^{0.2} & \text{for turbulent flow} \end{cases}$
Forced convection on an isoflux flat plate	$h = \begin{cases} 2.651 \left(\frac{V}{L} \right)^{0.5} & \text{for laminar flow} \\ 0.103 \left(\frac{V^4}{L} \right)^{0.2} & \text{for turbulent flow} \end{cases}$
Laminar forced convection in a circular tube	$h = \frac{1}{D} \left[0.131 + \frac{1563 (VD^2/L)}{1 + 32.50 (VD^2/L)^{2/3}} \right]$
Turbulent forced convection in a circular tube	$h = \begin{cases} 0.00071 \left(\frac{V^4}{D} \right)^{0.2} & \text{for heating} \\ 0.000736 \left(\frac{V^4}{D} \right)^{0.2} & \text{for cooling} \end{cases}$

equations and/or tabulated values for specific fluids and geometries of interest can be used to streamline the determination of this most important parameter. Table 13.5 lists such simplified equations for calculation of heat transfer coefficients for air at an average temperature of 50°C.

Values of convection resistance for a variety of coolants and heat transfer mechanisms are shown in Fig. 13.3 for a typical heat source area of 10 cm² and the velocity range 2 to 8 m/s. These resistances are seen to vary from 100 K/W for natural convection in air, to 33 K/W for forced convection in air, to 0.5 K/W for boiling in fluorocarbon liquids.

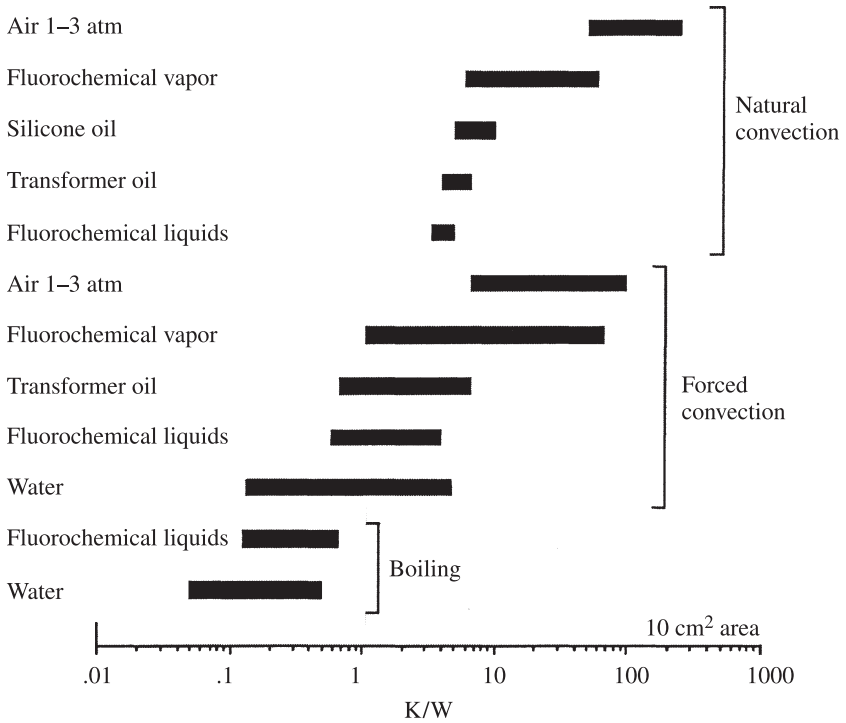


Figure 13.3 Convective thermal resistances for typical coolants.

Radiation Thermal radiation is governed by the difference between the source and sink temperatures, each raised to the fourth power:

$$q = \varepsilon \sigma A F_{12} (T_1^4 - T_2^4) \quad (13.6)$$

where ε is the emissivity; σ the Stefan–Boltzmann constant, equal to $5.67 \times 10^{-8} \text{ W/m}^2 \cdot \text{K}^4$; and F_{12} the radiation *view factor* between surfaces 1 and 2. For highly absorbing and emitting surfaces placed in close proximity to each other, F_{12} is close to unity. The value of F_{12} also approaches unity when determining the flow of radiant heat from a small, highly emitting surface to a large, highly absorbing surface which surrounds it on all sides. Relations for estimating the view factor for simple geometries and a variety of surface conditions can be found in textbooks by Incropera and DeWitt (1996) and Swartz and Pohl (1989). View factors for a variety of complex geometries have also been tabulated by Howell (1982).

For modest temperature differences, eq. (13.6) can be linearized to the form

$$q = h_r A (T_1 - T_2) \quad (13.7)$$

where h_r is the effective radiation heat transfer coefficient and is approximately equal to

$$h_r = 4\epsilon\sigma F_{12}(T_1T_2)^{3/2} \tag{13.8}$$

Noting the form of eq. (13.7), the radiation thermal resistance—analogueous to the convective resistance—is seen to be expressible as

$$R = \frac{1}{h_r A} \tag{13.9}$$

13.2.3 Chip Package Resistance

The thermal performance of alternative chip and packaging is commonly compared on the basis of the overall (junction-to-coolant) thermal resistance R_T . This packaging figure of merit is generally defined in a purely empirical fashion:

$$R_T = \frac{T_j - T_f}{q} \tag{13.10}$$

where T_j and T_f are the junction and coolant (fluid) temperatures, respectively, and q is the chip heat dissipation. To lower chip temperatures at a specified power, it is clearly necessary to select and/or design a chip package with the lowest thermal resistance. Examination of various packaging techniques reveals that the junction-to-coolant thermal resistance is, in fact, composed of an internal, largely conductive resistance and an external, primarily convective resistance. As shown in Fig. 13.4, the internal resistance R_j is encountered in the flow of dissipated heat from the active chip

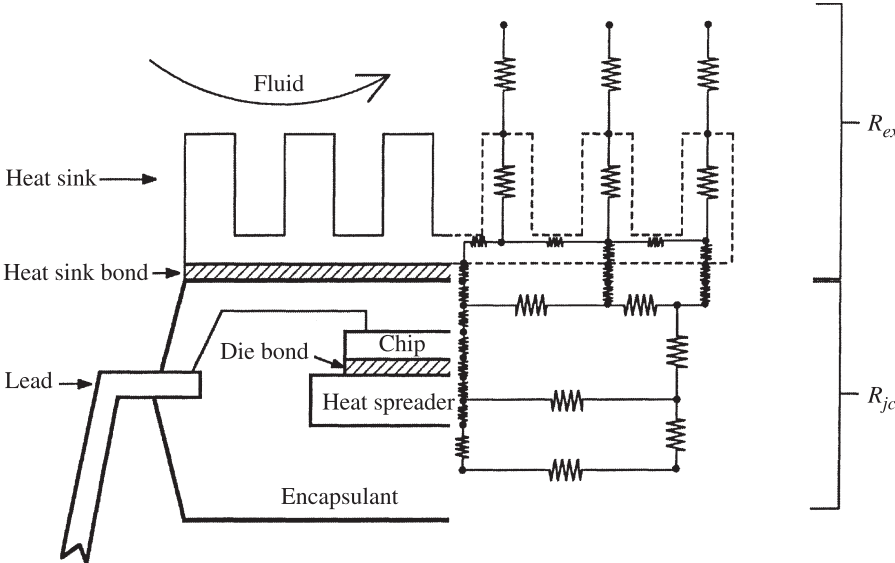


Figure 13.4 Primary thermal resistances in a single-chip package.

surface through the materials used to support and bond the chip and on to the case of the integrated-circuit package. The flow of the heat from the case directly to the coolant, or indirectly through a fin structure and then to the coolant, must overcome the external resistance R_{ex} .

Internal Resistance In flowing from the chip to the package surface or case, the heat encounters a series of resistances associated with individual material layers such as silicon, copper, alumina, and epoxy, as well as the contact resistances that occur at the interfaces between layers of materials. Although the actual heat flow paths within the chip package are rather complex and may shift to accommodate varying external cooling situations, it is possible to obtain a first-order estimate of the internal resistance by assuming that power is dissipated uniformly across the chip surface and that the heat flow is largely one-dimensional.

Equation (13.11) can be used to determine the internal chip module resistance, where the summed terms represent the conduction thermal resistances posed by the individual layers, each with thickness Δx .

$$R_T \equiv \frac{T_j - T_c}{q} = \sum \frac{\Delta x}{kA} \quad (13.11)$$

External Resistance To determine the resistance to thermal transport from the surface of a component to a fluid in motion (i.e., the convective resistance), it is necessary to quantify the heat transfer coefficient h . The heat transfer coefficient can be calculated by using the various correlations listed in Tables 13.4 and 13.5 for both natural and forced convection. The external resistance R_{ex} for convective cooling can be expressed as shown in eq. (13.4). When a heat sink or compact heat exchanger is attached to the package, the external resistance accounting for the bond-layer conduction and the total resistance of the heat sink R_{sk} can be expressed as

$$R_{\text{ex}} = \frac{T_c - T_f}{q} = \sum \frac{\Delta x}{kA} + R_{\text{sk}} \quad (13.12)$$

where

$$R_{\text{sk}} = \left(\frac{1}{nhA_{\text{fin}}\eta} + \frac{1}{h_bA_b} \right)^{-1} \quad (13.13)$$

is the parallel combination of the resistance R_{fin} of the n fins:

$$R_{\text{fin}} = \frac{1}{nhA_{\text{fin}}\eta} \quad (13.14)$$

where η is the fin efficiency, and the exposed or base surface resistance R_b not occupied by the fins,

$$R_b = \frac{1}{h_bA_b} \quad (13.15)$$

Here the base surface area ($A_b = A_T - nA_f$), and the heat transfer coefficient h_b are used because the heat transfer coefficient that is applied to the base surfaces is not necessarily equal to that on the fins. In an optimally designed fin structure, the fin efficiency η can be expected to fall in the range 0.5 to 0.7 (Kraus and Bar-Cohen, 1983).

Flow Resistance The transfer of heat to a flowing gas or liquid that is not undergoing phase change results in an increase in the coolant temperature from the inlet temperature T_{in} to an outlet temperature T_{out} , which results in a flow resistance R_{fl} given by (Kraus and Bar-Cohen, 1983)

$$R_{fl} = \frac{Q}{q} \frac{1}{2\dot{m}} \quad (13.16)$$

where Q is the heat absorbed by the fluid from all the components in its flow path, q the heat dissipation of a single component, and \dot{m} the mass flow rate.

Total Resistance: Single-Chip Packages The overall single-chip package resistance relating the chip temperature to the inlet temperature of the coolant can be found by summing the internal, external, flow resistance, and various spreading resistances to yield

$$R_T = R_{jc} + R_{sp} + R_{ex} + R_{fl} \quad (13.17)$$

where R_{sp} is the spreading resistance arising from the three-dimensional nature of heat flow in the heat spreader and heat sink base. R_{sp} is discussed in greater detail in Section 13.3.1.

13.3 LENGTH-SCALE EFFECTS ON THERMOPHYSICAL PROPERTIES

Thermal analysis and control of electronic equipment occurs across the wide range of length scales encountered in packaged microelectronic components: from the nanoscale features characteristic of advanced semiconductor devices, to the micro-scale functional cells on the silicon, to the mesoscale dimensions of individual chips and the macroscale of packages and printed circuit boards. In the preceding discussion, it was assumed that thermophysical properties are independent of the size of the specimen or the length scale involved in a particular thermal transport process. However, extensive research on heat transport in miniaturized systems, such as occurs in microelectronic devices, and thermal processes occurring at a very fast rate, such as encountered in pulsed laser heating, has shown that at very small length scales, thermophysical properties such as the thermal conductivity and the specific heat can deviate significantly from the commonly accepted macroscale values.

Two distinct length scales govern the diffusion of heat through solids: the mean free path of electrons or phonons, and the characteristic wavelength of the energy

carrier. Variations in the mean free path produce the *classical size effect* on the thermal conductivity of any material (Tien and Chen, 1994). The *quantum size effect*, reflecting the impact of the characteristic wavelength of the energy carrier (Tien and Chen, 1994), has been shown to affect both the thermal transport properties and the thermodynamic properties.

The Asheghi et al. (1996) results for the effect of film thickness on the thermal conductivity of silicon at various temperatures are shown in Fig. 13.5. This figure reveals that thermal conductivity is more sensitive to film thickness at cryogenic temperatures, at which the mean free path of the energy carriers grows to become comparable to the size of the specimen. In this domain, thermal transport is limited by boundary scattering of phonons or electrons. Majumdar (1993) has derived an expression for calculation of the effective thermal conductivity of thin, dielectric films where phonons are the dominant thermal carriers:

$$\frac{k_{\text{film}}}{k_{\text{bulk}}} = \frac{1}{1 + \frac{4}{3}(l/\delta)} \quad (13.18)$$

where l is the mean free path and δ is the thickness of the film. Equation (13.18) is valid only at temperatures below the Debye temperature.

Prasher and Phelan (1998) calculated the size effect on the bulk phonon heat capacity of thin films and various other microstructures showing that if the characteristic length of the microstructure approaches the dominant phonon wavelength, the specific heat per unit volume becomes dependent on the dimension of the thin films. They

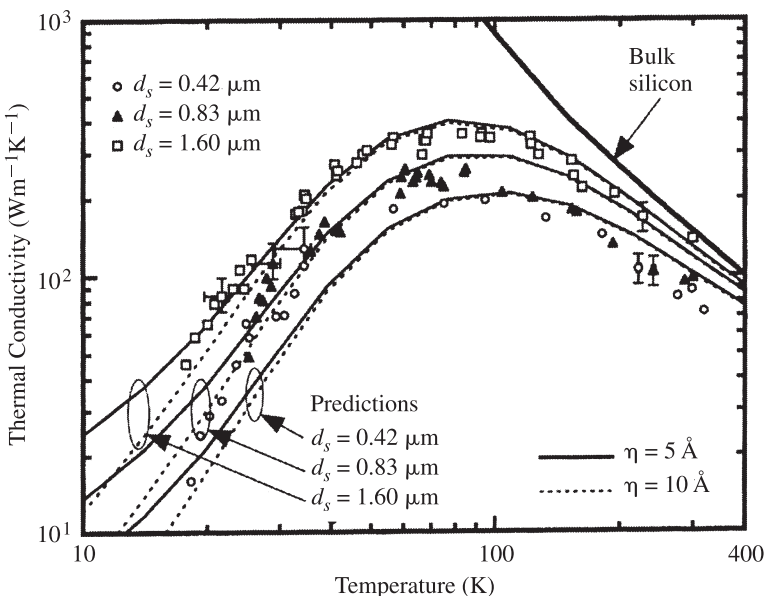


Figure 13.5 Thin-film thermal conductivity of silicon. (From Tien and Chen, 1994.)

suggested that when the grouping, NT/ϕ , where N is the number of atomic layers in the thin film, T the temperature, and ϕ the Debye temperature, is less than unity, the heat capacity can be expected to display sensitivity to the characteristic dimension. Their results show that such size effects on the thermodynamic properties are more important at cryogenic temperatures.

13.3.1 Spreading Resistance

In chip packages that provide for lateral spreading of the heat generated in the chip, the increasing cross-sectional area for heat flow in the “layers” adjacent to the chip reduces the heat flux in successive layers and hence the internal thermal resistance. Unfortunately, however, there is an additional resistance associated with this lateral flow of heat, which must be taken into account in determination of the overall chip package temperature difference. The temperature difference across each layer of such a structure can be expressed as

$$\Delta T = q R_T \quad (13.19)$$

where

$$R_T = R_{1D} + R_{sp} \quad (13.20)$$

or

$$R_T = \frac{\Delta x}{kA} + R_{sp} \quad (13.21)$$

For the circular and square geometries common in microelectronic applications, Negus et al. (1989) provide an engineering approximation for the spreading resistance R_{sp} of a small heat source on a thick substrate or heat spreader, insulated on the sides and held at a fixed temperature along the base as

$$R_{sp} = \frac{(0.475 - 0.626\zeta + 0.13\zeta^3)}{k\sqrt{a}} \quad (13.22)$$

where ζ is the square root of the heat source area divided by the substrate area, k the thermal conductivity of the substrate, and a the area of the heat source.

The spreading resistance R_{sp} from eq. (13.22) can now be added to the one-dimensional conduction resistance to yield the overall thermal resistance of that layer. It is to be noted that the use of eq. (13.22) requires that the substrate be three to five times thicker than the square root of the heat source area. Consequently, for relatively thin layers on thicker substrates, such as thin lead frames or heat spreaders interposed between the chip and the substrate, eq. (13.22) cannot be expected to provide an acceptable prediction of R_{sp} . Instead, use can be made of the numerical results plotted in Fig. 13.6 to obtain the appropriate value of the spreading resistance.

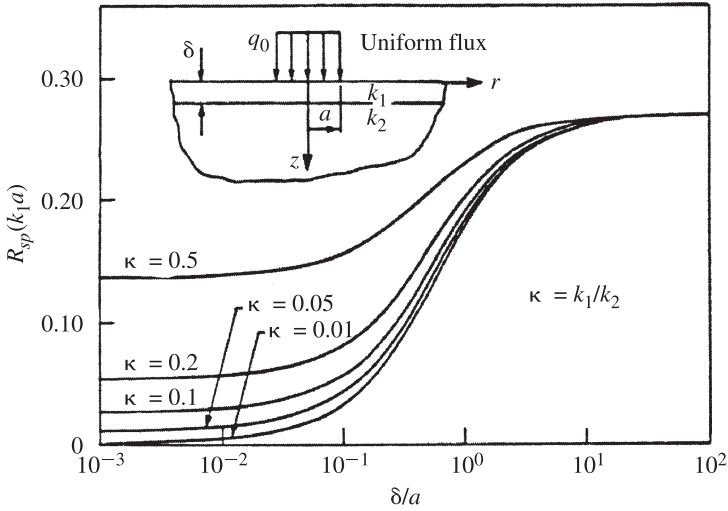


Figure 13.6 Spreading resistance on thin layers.

Kennedy (1959) analyzed heat spreading from a circular uniform heat flux source to a cylindrical substrate with isothermal temperature boundaries at the edges, the bottom, or both, and presented the results in graphic form. Spreading resistance charts prepared originally by Kennedy (1959) were reproduced by Sergent and Krum (1994). Although the boundary conditions and geometry assumed by Kennedy (1959) do not match the mixed boundary conditions and rectangular shapes found in most electronic packages, the spreading resistance results can be used with acceptable accuracy in many design situations (Simons et al., 1997). Using the spreading resistance factor H from the appropriate Kennedy graph, the spreading resistance is calculated using

$$R_{sp} = \frac{H}{k\pi\sqrt{a}} \quad (13.23)$$

where k is the thermal conductivity and a is the heat source area (Figs. 13.7 to 13.9).

Song et al. (1994) developed an analytical model to estimate the constriction–spreading thermal resistance R_{sp} from a circular or rectangular heat source to a similarly shaped convectively cooled substrate. Lee et al. (1995) extended the solutions provided by Song et al. (1994) to present closed-form expressions for dimensionless constriction–spreading thermal resistance based on average and maximum temperature rise through the substrate. Their set of equations is

$$R_{sp,avg} = \frac{0.5(1 - \zeta)^{3/2}\phi_c}{k\sqrt{A_{source}}} \quad (13.24)$$

$$R_{sp,max} = \frac{(1/\sqrt{\pi})(1 - \zeta)^{3/2}\phi_c}{k\sqrt{A_{source}}} \tag{13.25}$$

$$\phi_c = \frac{\tanh\lambda_c\tau + (\lambda_c \cdot Bi)}{1 + (\lambda_c \cdot Bi) \tanh\lambda_c\tau} \tag{13.26}$$

$$\lambda_c = \pi + \frac{1}{e\sqrt{\pi}} \tag{13.27}$$

$$\tau = \frac{\delta}{b} \tag{13.28}$$

$$Bi = \frac{hr}{k} \tag{13.29}$$

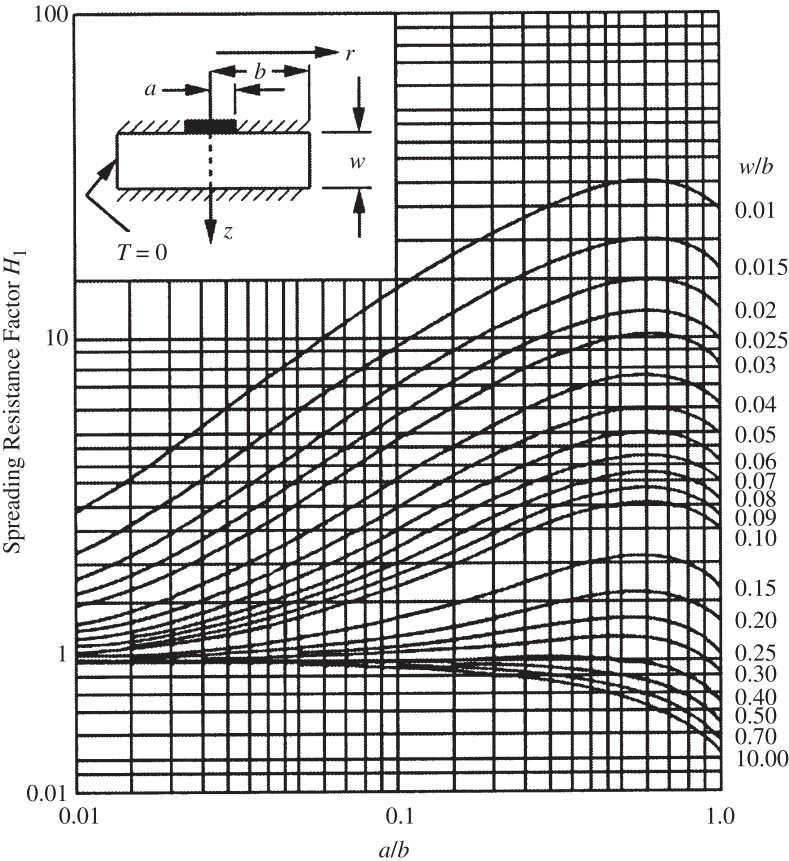


Figure 13.7 Spreading resistance factor H_1 for surface $z = w$ at zero temperature. (From Simons et al., 1997.)

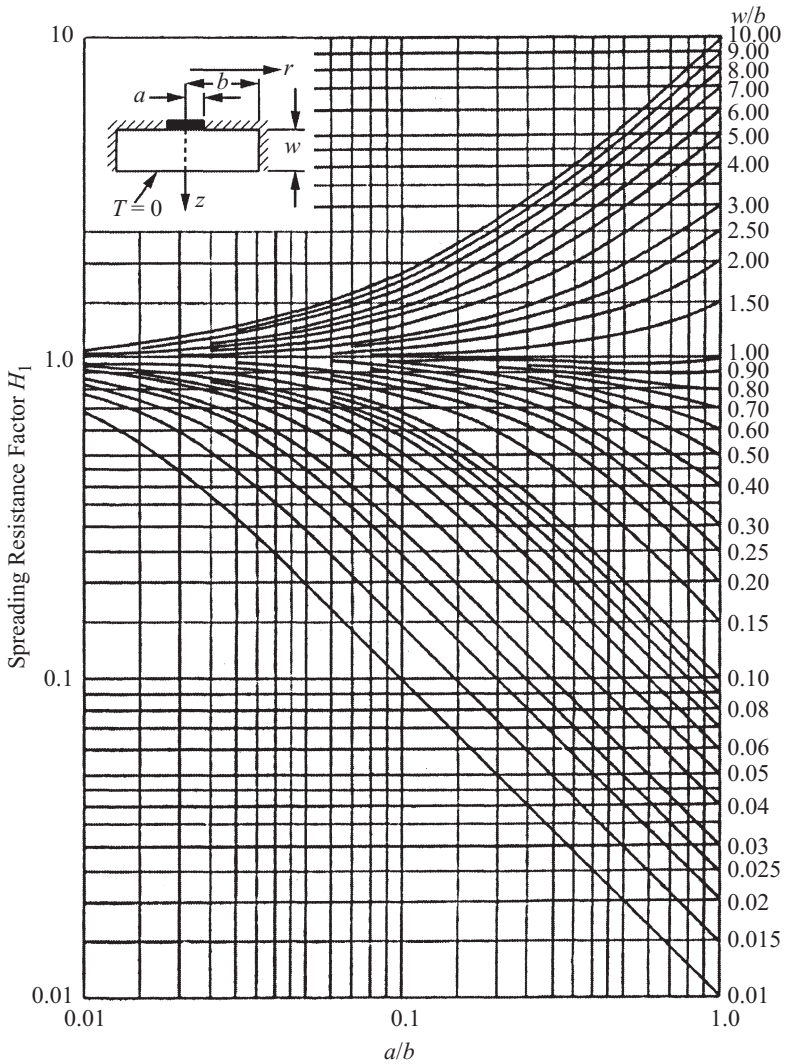


Figure 13.8 Spreading resistance factor H_2 for surface $z = w$ at zero temperature. (From Simons et al., 1997.)

In eqs. (13.24)–(13.29), $R_{sp,ave}$ is the constriction resistance based on the average source temperature, $R_{sp,max}$ the constriction resistance based on the maximum source temperature, δ the fin thickness, r the outer radius of the substrate, h the convective heat transfer coefficient, and k the thermal conductivity. The authors claim the expressions to be accurate to within 10% for a range of source and substrate shapes and for source and substrate rectangularity aspect ratios less than 2.5. Use of the convective boundary condition on the substrate base makes these relations especially

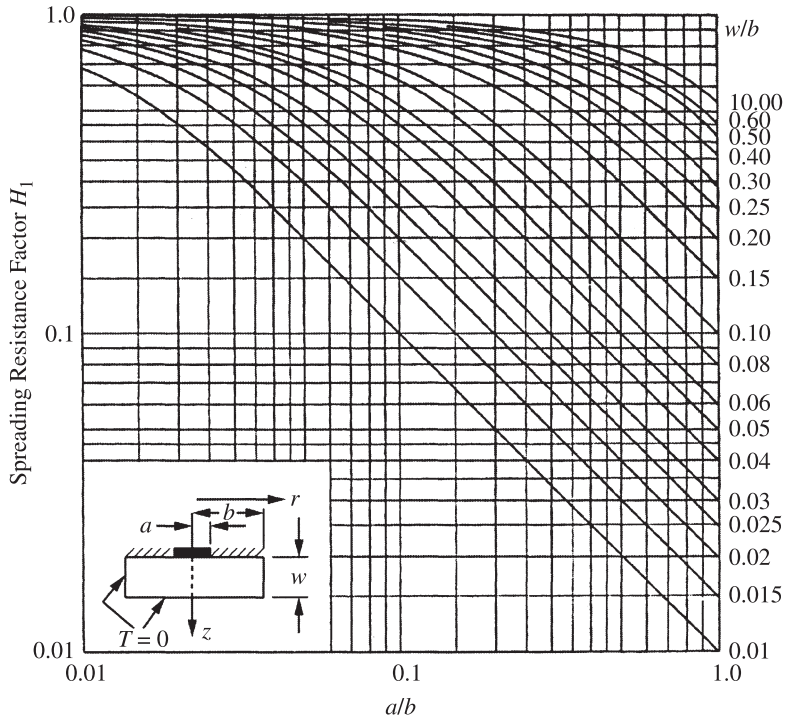


Figure 13.9 Spreading resistance factor H_3 for surface $z = w$ at zero temperature. (From Simons et al., 1997.)

well suited to the analytical determination of the spreading resistance of a chip-to-heat sink assembly as well as a chip encapsulated in a convectively cooled plastic package.

13.3.2 Heat Flow across Solid Interfaces

Heat transfer across an interface formed by the joining of two solids is accompanied by a temperature difference caused by imperfect contact between the two solids. Even when perfect adhesion is achieved between the solids, the transfer of heat is impeded by the acoustic mismatch in the properties of the phonons on either side of the interface. Traditionally, the thermal resistance arising due to imperfect contact has been called the *thermal contact resistance*. The resistance due to the mismatch in the acoustic properties is usually termed the *thermal boundary resistance*. The thermal contact resistance is a macroscopic phenomenon, whereas thermal boundary resistance is a microscopic phenomenon.

Thermal Contact Resistance When two surfaces are joined, as shown in Fig. 13.10, asperities on each of the surfaces limit the actual contact between the two

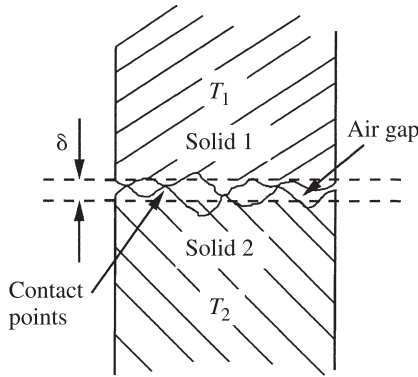


Figure 13.10 Contact and heat flow at a solid–solid interface.

solids to a very small fraction, perhaps just 1 to 2% for lightly loaded interfaces, of the apparent area. As a consequence, the flow of heat across such an interface involves solid-to-solid conduction in the area of actual contact, A_{co} , and conduction through the fluid occupying the noncontact area, A_{nc} , of the interface. At elevated temperatures or in vacuum, radiation heat transfer across the open spaces may also play an important role. The pressure imposed across the interface, along with microhardness of the softer surface and the surface roughness characteristics of both solids, determine the interfacial gap δ and the contact area A_{co} . Assuming plastic deformation of the asperities and a Gaussian distribution of the asperities over the apparent area, for the contact resistance R_{co} , Cooper et al. (1969) proposed

$$R_{co} = \left[1.45 \frac{k_s (P/H)^{0.985}}{\sigma} |\overline{\tan \theta}| \right]^{-1} \quad (13.30)$$

where k_s is the harmonic mean thermal conductivity, defined as $k_s = 2k_1k_2/(k_1+k_2)$; P the apparent contact pressure; H the hardness of the softer material; and σ the root-mean-square (rms) roughness, given by

$$\sigma_1 = \sqrt{\sigma_1^2 + \sigma_2^2} \quad (13.31)$$

where σ_1 and σ_2 are the roughness of surface 1 and 2, respectively. The term $|\overline{\tan \theta}|$ in eq. (13.30) is the average asperity angle:

$$|\overline{\tan \theta}|^2 = |\tan \theta_1|^2 + |\tan \theta_2|^2 \quad (13.32)$$

This relation neglects the heat transfer contribution of any trapped fluid in the interfacial gap.

In the pursuit of a more rigorous determination of the contact resistance, Yovanovich and Antonetti (1988) found it possible to predict the area-weighted interfacial gap, Y , in the form

$$Y = 1.185\sigma \left(-\ln \frac{3.132P}{H} \right)^{0.547} \quad (13.33)$$

where σ is the effective rms as given by eq. (13.31), P the contact pressure (Pa), and H the surface microhardness (Pa) of the softer material, to a depth of the order of the penetration of the harder material. Using Y as the characteristic gap dimension and incorporating the solid–solid and fluid gap parallel heat flow paths, Yovanovich (1990) derived for the total interfacial thermal resistance,

$$R_{co} = \left[1.25k_s \frac{|\overline{\tan \theta}|}{\sigma} \left(\frac{P}{H} \right)^{0.95} + \frac{k_g}{Y} \right]^{-1} \quad (13.34)$$

where k_g is the interstitial fluid thermal conductivity. In the absence of detailed information, $\sigma/|\overline{\tan \theta}|$ can be expected to range from 5 to 9 μm for relatively smooth surfaces.

Thermal Boundary Resistance When dealing with heat removal from a chip and thermal transport in various packaging structures at room temperature and above, the thermal boundary resistance R_b is generally negligible compared to the contact resistance. However, at the transistor level, where interfaces—often formed by epitaxial thin film deposition, through atomistic processes such as physical vapor deposition—may be nearly perfect, the thermal boundary resistance should be included. Two theoretical models are widely used to predict the thermal boundary resistance R_b : the *acoustic mismatch model* (AMM) and the *diffuse mismatch model* (DMM). The former is based on the specular reflection of sound waves at the interface and the latter is based on the diffuse scattering of phonons at the interface. Swartz and Pohl (1989) provide a comprehensive discussion of both AMM and DMM models for the thermal boundary resistance and have shown that the microscopic thermal boundary resistance resulting from the mismatch in the acoustic properties in the low-temperature limit can be obtained by the following DMM equation:

$$R_b = \frac{\pi^2 k_b^4}{30 \hbar^3} \frac{\sum_{jj} c_{1,jj}^{-2} \times \sum_j c_{2,jj}^{-2}}{\sum_{jj} c_{1,jj}^{-2} + \sum_{jj} c_{2,jj}^{-2}} T^{-3} \quad (13.35)$$

where k_b is the Boltzmann constant, \hbar the Planck constant divided by 2π , c the speed of sound, jj the mode of sound ($jj = 1$ for the longitudinal mode, and $jj = 2$ for the transverse mode), and the subscripts 1 and 2 refer to the two solids in contact. Note that this relation is strictly valid only at very low temperatures. Similar equations to estimate R_b using DMM at high temperatures or AMM can be obtained from Swartz and Pohl (1989). Although AMM and DMM are based on very different physical arguments, they appear to yield identical results for most material pairs (Swartz and Pohl, 1989). Both these models are very good in predicting R_b at very low temperatures but fail miserably at high temperatures for various reasons, such

as increased scattering of phonons and deviation from the Debye density of states (Swartz and Pohl, 1989).

Interstitial Materials In describing heat flow across an interface, eq. (13.34) assumed the existence of a fluid gap, which provides a parallel heat flow path to that of the solid–solid contact. Because the noncontact area may occupy in excess of 90% of the projected area, heat flow through the interstitial spaces can be of great importance. Consequently, the use of high-thermal-conductivity interstitial materials, such as soft metallic foils and fiber disks, conductive epoxies, thermal greases, and polymeric phase-change materials, can substantially reduce the contact resistance. The enhanced thermal capability of many of high-performance epoxies, thermal greases, and phase-change materials commonly in use in the electronic industry is achieved through the use of large concentrations of thermally conductive particles. Successful design and development of thermal packaging strategies thus requires the determination of the effective thermal conductivity of such particle-laden interstitial materials and their effect on the overall interfacial thermal resistance.

Comprehensive reviews of the general role of interstitial materials in controlling contact resistance have been published by several authors, including Sauer (1992). When interstitial materials are used for control of the contact resistance, it is desirable to have some means of comparing their effectiveness. Fletcher (1972) proposed two parameters for this purpose. The first of these parameters is simply the ratio of the logarithms of the conductances, which is the inverse of the contact resistance, with and without the filler:

$$\chi = \frac{\ln \kappa_{cm}}{\ln \kappa_{bj}} \quad (13.36)$$

in which κ is the contact conductance, and cm and bj refer to control material and bare junctions respectively. The second parameter takes the thickness of the filler material into account and is defined as

$$\eta = \frac{(\kappa \delta_{\text{filler}})_{cm}}{(\kappa \delta_{\text{gap}})_{bj}} \quad (13.37)$$

in which δ is the equivalent thickness.

The performance of an interstitial interface material as decided by the parameter defined by Fletcher (1972), in eqs. (13.36) and (13.37) includes the bulk as well as the contact resistance contribution. It is for this reason that in certain cases the thermal resistance of these thermal interface materials is higher than that for a bare metallic contact because the bulk resistance is the dominant factor in the thermal resistance (Madhusudan, 1995). To make a clear comparison of only the contact resistance arising from the interface of the substrate and various thermal interface materials, it is important to measure it exclusively. Separation of the contact resistance and bulk resistance will also help researchers to model the contact resistance and the bulk resistance separately.

Equations (13.36) and (13.37) by Fletcher (1972), show that the thermal resistance of any interface material depends on both the bond line thickness and thermal conductivity of the material. As a consequence, for materials with relatively low bulk conductivity, the resistance of the added interstitial layer may dominate the thermal behavior of the interface and may result in an overall interfacial thermal resistance that is higher than that of the bare solid–solid contact (Madhusudan, 1995). Thus, both the conductivity and the achievable thickness of the interstitial layer must be considered in the selection of an interfacial material. Indeed, while the popular phase-change materials have a lower bulk thermal conductivity (at a typical value of $0.7 \text{ W/m} \cdot \text{K}$) than that of the silicone-based greases (with a typical value of $3.1 \text{ W/m} \cdot \text{K}$), due to thinner phase-change interstitial layers, the thermal resistance of these two categories of interface materials is comparable.

To aid in understanding the thermal behavior of such interface materials, it is useful to separate the contribution of the bulk conductivity from the interfacial resistance, which occurs where the interstitial material contacts one of the mating solids. Following Prasher (2001), who studied the contact resistance of phase-change materials (PCMs) and silicone-based thermal greases, the thermal resistance associated with the addition of an interfacial material, R_{TIM} can be expressed as

$$R_{\text{TIM}} = R_{\text{bulk}} + R_{co1} + R_{co2} \quad (13.38)$$

where R_{bulk} is the bulk resistance of the thermal interface material, and R_{co} the contact resistance with the substrate, and subscripts 1 and 2 refer to substrates 1 and 2. Prasher (2001) rewrote eq. (13.38) as

$$R_{\text{TIM}} = \frac{\delta}{\kappa_{\text{TIM}}} + \frac{\sigma_1}{2\kappa_{\text{TIM}}} \frac{A_{\text{nom}}}{A_{\text{real}}} + \frac{\sigma_2}{2\kappa_{\text{TIM}}} \frac{A_{\text{nom}}}{A_{\text{real}}} \quad (13.39)$$

where R_{TIM} is the total thermal resistance of the thermal interface material, δ the bond-line thickness, κ_{TIM} the thermal conductivity of the interface material, σ_1 and σ_2 the roughness of surfaces 1 and 2, respectively, A_{nom} the nominal area, and A_{real} the real area of contact of the interface material with the two surfaces. Equation (13.39) assumes that the thermal conductivity of the substrate is much higher than that of the thermal interface material. The first term on the right-hand side of eq. (13.39) is the bulk resistance, and other terms are the contact resistances. Figure 13.11 shows the temperature variation at the interface between two solids in the presence of a thermal interface material associated with eq. (13.39). Unlike the situation with the more conventional interface materials, the actual contact area between a polymeric material and a solid is determined by capillary forces rather than surface hardness, and an alternative approach is required to determine A_{real} in eq. (13.39). Modeling each of the relevant surfaces as a series of notches, and including the effects of surface roughness, the slope of the asperities, the contact angle of the polymer with each the substrates, the surface energy of the polymer, and the externally applied pressure, a surface chemistry model was found to match very well with the experimental data for PCM and greases at low pressures (Prasher, 2001), as shown in Fig. 13.12 for

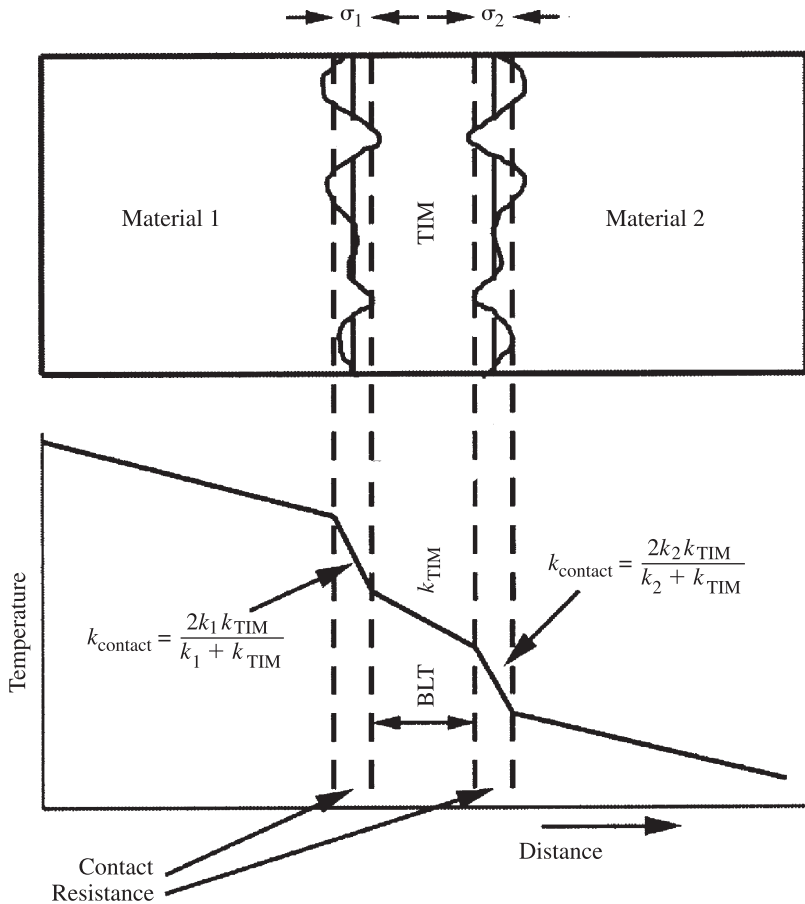


Figure 13.11 Temperature drops across an interface.

PCM. Unfortunately, it has not yet been found possible to determine the contact area with a closed-form expression. It is also to be noted that eq. (13.39) underpredicts the interface thermal resistance data at high pressures.

Thermal Conductivity of Particle-Laden Systems Equation (13.39) shows that the bulk and contact resistance of the thermal interface material are dependent on the thermal conductivity of the interface material. The thermal conductivity of a particle-laden polymer increases nonlinearly with increasing volume fraction of the conducting particle, as suggested in Fig. 13.13. One of the most commonly used models for predicting the thermal conductivity of a particle-laden, two-phase system is the Lewis and Nielsen (1970) model. This model calculates the thermal conductivity of two-phase system using

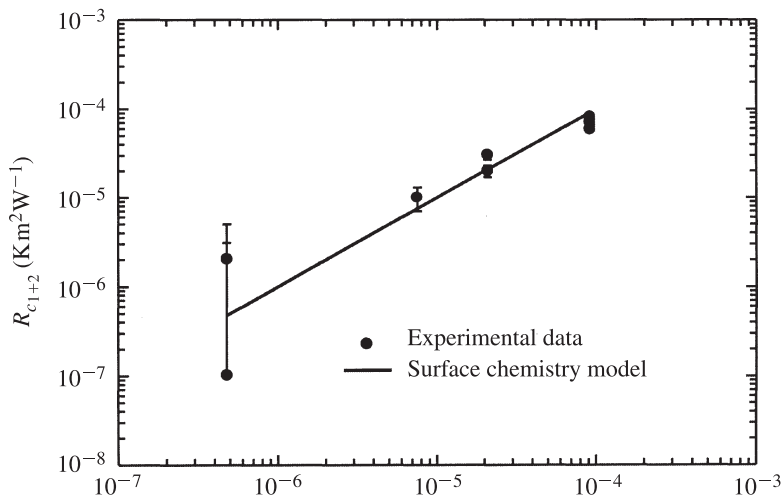


Figure 13.12 Surface chemistry model of contact resistance.

$$k = k_m \frac{1 + SB\varphi}{1 - B\psi\varphi} \tag{13.40}$$

where k_m is the thermal conductivity of the continuous phase or base polymer, φ the particle volume fraction, and S a shape parameter that increases with aspect ratio. Table 13.6 provides the value of A for dispersed polymers. The constant B in eq. (13.40) can be estimated using the expression

$$B = \frac{k_p/k_m - 1}{k_p/k_m + S} \tag{13.41}$$

where k_p is the thermal conductivity of the filler and

TABLE 13.6 Values of A for Several Dispersed Types

	Aspect Ratio of Dispersed Phase (Length/Diameter)	A
Spheres	1	1.5
Randomly oriented rods	2	1.58
	4	2.08
	6	2.8
	10	4.93
	15	8.38

Source: Cross (1996).

$$\psi = 1 + \frac{1 - \phi_m}{\phi_m^2} \phi \quad (13.42)$$

where ϕ_m is the maximum packing fraction. Table 13.7 lists values of ϕ_m for spheres and rods in different packing configurations.

Another commonly used model for predicting thermal conductivity of two-phase systems is *effective medium transport* (EMT), discussed by Devpura et al. (2000). Both the EMT and Lewis–Nielsen models were developed for moderate filler density (up to around 40% by volume) and often fail to predict the thermal conductivity at higher percentages of the filler. The Nielsen model becomes unstable above a 40% volume fraction, as shown by Devpura et al. (2000), whereas the EMT model underpredicts the thermal conductivity above 40%.

Devpura et al. (2000) have proposed a new model, based on the formation of a percolation network of the filler, for calculating the thermal conductivity of high-volume-fraction particle-laden systems. The change in the conductivity of the matrix from its value at the percolation threshold (percentage of filler particles at which percolation starts) is given by

$$\Delta k = [k_f(p - p_c)]^{0.95 \pm 0.5} \quad (13.43)$$

where p_c is the volume fraction at the percolation threshold and p is the volume fraction. The thermal conductivities calculated using the percolation, EMT, and Lewis–Nielsen models are shown in Fig. 13.13, where the percolation model appears to provide a useful upper bound on the thermal conductivity. Unfortunately, however, the threshold value p_c needed in eq. (13.43) can only be determined from a full numerical simulation. Devpura et al. (2000) have provided an algorithm for the percolation modeling of particle-laden systems.

The effective thermal conductivity of a particle-laden polymeric system is also dependent on the interfacial resistance between the particle and the matrix. Devpura

TABLE 13.7 Maximum Packing Fraction ϕ_m

Shape of Particles	Type of Packing	ϕ_m
Spheres	Face-centered cubic	0.7405
	Hexagonal close	0.7405
	Body-centered cubic	0.6
	Simple cubic	0.524
	Random close	0.637
	Random loose	0.601
Rods or fibers	Uniaxial hexagonal close	0.907
	Uniaxial simple cubic	0.785
	Uniaxial random	0.82
	Three-dimensional random	0.52

Source: Cross (1996).

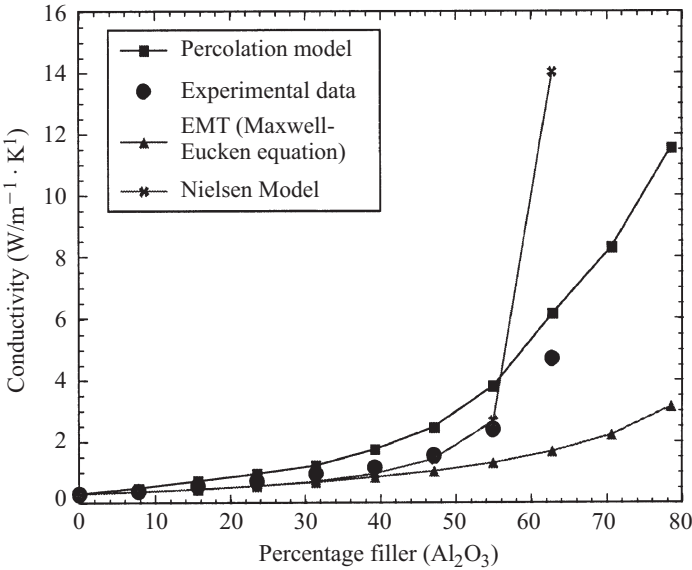


Figure 13.13 Comparing the percolation model with experimental data and other existing models for a bimodal distribution of Al₂O₃ filler (65 μm : 9μm = 4 : 1) in polyethylene matrix ($k_f = 42.34/\text{W/m} \cdot \text{K}$, $k_m = 0.36 \text{ W/m} \cdot \text{K}$, $y = 25$, $z = 40$). (From Devpura et al., 2000.)

et al. (2000) and Davis and Artz (1995) have shown that below a critical dimension of the particles, the thermal conductivity of a two-phase polymeric system may decrease relative to the thermal conductivity of the matrix, despite the use of highly conducting fillers, owing to high interfacial resistance at the particle–matrix interface. For spherical particles in low volume fractions, Davis and Artz (1995) have used the *effective medium theory* to provide an expression for the thermal conductivity for a particle-laden system:

$$\frac{k}{k_m} = \frac{[k_p(1 + 2\alpha) + 2k_m] + 2\varphi[k_p(1 - \alpha) - k_m]}{[k_p(1 + 2\alpha) + 2k_m] - \varphi[k_p(1 - \alpha) - k_m]} \quad (13.44)$$

where φ is the volume fraction of the particles and α is given by

$$\alpha = \frac{R_{mc}k_m}{r} \quad (13.45)$$

where r is the radius of the particle and R_{mc} is the interface resistance between the particle and the matrix. Higher values of α , which can be due to either higher values of R_{mc} , higher values of k_m , or smaller radius of the particles, will lead to a decrease in the thermal conductivity of the particle-laden systems. Nan et al. (1997) provide a comprehensive comparison of EMT with the interfacial term in it with experimental

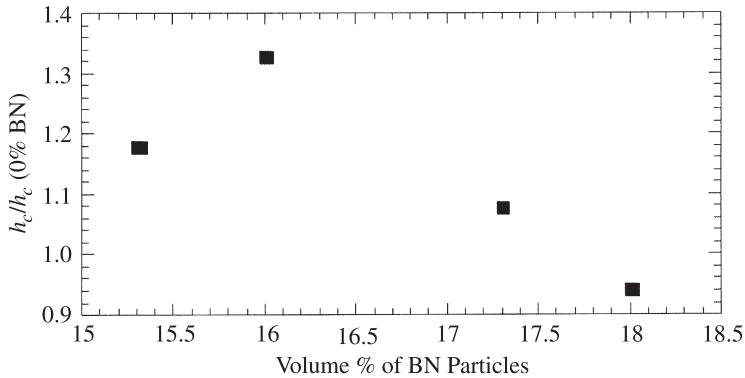


Figure 13.14 Measured thermal contact conductance of a sodium silicate-based thermal interface material, as a function of volume percentage of boron nitride (BN) particles, normalized with respect to h_c for no BN particles. (From Xu et al., 2000.)

data available in the literature. It is to be noted that eq. (13.44) can be used for a low-volume fraction, probably up to 40%. For a higher-volume fraction, numerical techniques such as the percolation model of Devpura et al. (2000) must be used. Devpura et al. (2000) have shown that increasing values of α increases the percolation threshold. The thermal characteristics of other types of high-performance thermally enhanced interface materials are described in Madhusudan (1995).

Effect of Filler Concentration on Mechanical Strength Along with the beneficial effect on thermal conductivity, increasing the particle volume fraction results in an increase in the mechanical rigidity of the material, as reflected in the variation in the shear modulus of particle-laden systems shown by Lewis and Nielsen (1970). Consequently, at a given pressure, a higher particle volume fraction in the interface material may result in a higher bond-line thickness and smaller A_{real} than those for a material with a low particle volume fraction. As a result of this trade-off between thermal conductivity and mechanical rigidity, the minimum thermal resistance may not occur at the maximum particle loading condition. No analytical study concerning this phenomenon has been reported in the literature; however, Xu et al. (2000) did confirm that the minimum thermal resistance occurs at less than the maximum particle loading. Their results, presented in terms of contact conductance, which is the inverse of resistance, are shown in Fig. 13.14.

13.3.3 First-Order Transient Effects

Variations in component power dissipation, including power-up and power-down protocols, power-line surges, and lightning strikes, as well as performance-driven fluctuations, can result in significant thermal transients at all the relevant packaging levels. Common commercial practice in the early years of the twenty-first century

generally involves design and analysis for the worst-case steady-state conditions. However, detailed design and development of avionics for terrestrial and space applications, as well as equipment design for other harsh environments, often includes detailed numerical modeling of the complete performance- and environmentally driven temporal temperature variations in critical devices. Moreover, predictions of die attach, wire bond, solder bump, and encapsulant failure rates—even under more benign circumstances—often require knowledge of the history of the die-bond temperature gradient and the temperature difference between the chip and the encapsulant. A detailed treatment of thermal transients in electronic equipment, on multiple length and time scales, is beyond the scope of the present discussion. Nevertheless, some insight into these effects can be gained from the use of judiciously selected first-order equations.

Lumped Heat Capacity For an internally heated solid of relatively high thermal conductivity which is experiencing no external cooling, solution of the energy equation reveals that the temperature will undergo a constant rise rate, according to

$$\frac{dT}{dt} = \frac{q}{mC_p} \quad (13.46)$$

where q is the rate of internal heating (W), m the mass of the solid (kg), and C_p the specific heat of the solid (J/kg · K). Values of C_p are given in Table 13.3 for a wide variety of packaging materials. Equation (13.46) assumes that internal temperature variations are small enough to allow the entire solid to be represented by a single temperature. This relation, frequently called the *lumped-capacity solution*, can be used with confidence when the thermal conductivity of the solid is high. If the solid of interest is subjected to convective heating or cooling by an adjacent fluid, the temperature can be expected to rise to an asymptotic, steady-state limit. If the convective heat exchange is represented by a heat transfer coefficient boundary condition, the temperature of the solid is found to vary as

$$T(t) = T(0) + \Delta T_{ss} (1 - e^{-hAt/mC_p}) \quad (13.47)$$

where ΔT_{ss} is the steady-state temperature determined by the convection relation of eq. (13.5) and mC_p/hA is the thermal time constant of this solid.

Heat flow from such a convectively cooled solid to the surrounding fluid encounters two resistances, a conduction resistance within the solid and a convection resistance at the external surface. When the internal resistance is far smaller than the external resistance, the temperature variations within the solid may be neglected and use made of the lumped capacity solution. The Biot number Bi , representing the ratio of the internal conduction resistance to the external convective resistance, can be used to determine the suitability of this assumption:

$$Bi = \frac{\text{internal conduction resistance}}{\text{external surface convection resistance}} = \frac{L/kA}{1/hA} = \frac{hL}{k} \quad (13.48)$$

where h is the heat transfer coefficient at the external surface, k the thermal conductivity of the solid, and L the characteristic dimension, best defined by the quotient of the volume divided by the external surface area. For $Bi < 0.1$ it is generally acceptable to determine the solid temperature with the lumped capacity approximation.

Thermal Wave Propagation Thermal diffusion into a previously unheated solid can be viewed as an ever-expanding wave whose propagation rate is determined by the thermal diffusivity of the material. For one-dimensional heat flow into a solid with invariant properties, which experiences a step change in surface temperature, the penetration depth δ can be expressed approximately as (Eckert and Drake, 1987)

$$\delta = \sqrt{12\alpha t} \quad (13.49)$$

where α is the thermal diffusivity, equal to $k/\rho C_p$. Strictly speaking, this relation can only be used to determine the location of the thermal front in a homogeneous solid. However, with a stepwise change in properties and/or a judicious choice of the effective thermal diffusivity, it can often provide insight into the thermal behavior of the chip, substrate, package, or module affected by the thermal transient of interest.

Chip Package Transients In a typical IC package (see Fig. 13.15), the flow of heat from the active layer of the silicon chip through the die bond and encapsulant to the external package surfaces provides inherent time intervals for the thermal modeling and analysis of IC packages. Following Mix and Bar-Cohen (1992), the temporal behavior of chip packages can be classified into four time intervals: an *early* or *chip period*, when effects are confined to the chip; an *intermediate period*, when the die bond and local encapsulant (or package case) are involved; the *quasi-steady period*, when the entire package is responding to the dissipation and transfer of heat; and finally, the *steady-state period*, when the temperatures everywhere have stabilized. In Fig. 13.16 a semilog plot is used to display the temporal temperature variation of the active surface of the silicon for a convectively cooled package subjected to a constant power dissipation and a 1-ms duration pulse of energy followed by a constant power dissipation. A comparison of these temperature variations reveals the pulse-constant

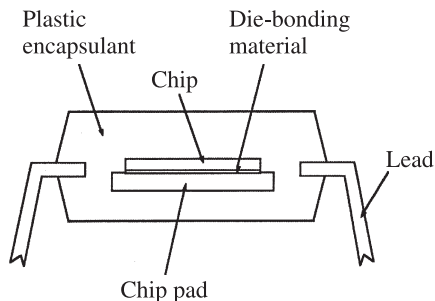


Figure 13.15 Typical plastic chip package.

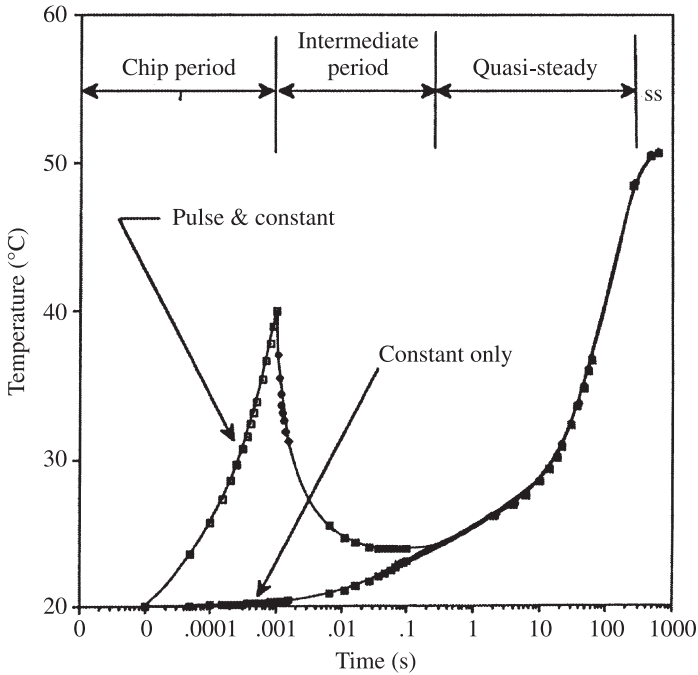


Figure 13.16 Thermal response of a typical plastic package.

condition to generate a far more complex response than the constant power condition. It is therefore this condition that will serve as the vehicle for this brief exploration of the transient thermal behavior of a plastic IC package.

During the initial period, heat dissipated by the circuitry just below the surface of the chip propagates into the silicon and across the nearby interface into the encapsulant. During this chip period, of order $0.0 < t < 1$ ms, the chip temperature can be expected to follow eq. (13.50), commonly used to determine the temperature of a semi-infinite body that is subjected to a uniform heat flux (Eckert and Drake, 1987):

$$T(x, t) = \frac{q''}{k} \sqrt{\frac{4\alpha t}{\pi}} \left[e^{-x^2/4\alpha t} - x \sqrt{\frac{\pi}{4\alpha t}} \operatorname{erfc} \left(\frac{x}{\sqrt{4\alpha t}} \right) \right] \tag{13.50}$$

It must be noted, however, that the presence of encapsulant above the chip reduces the heat flowing through the chip, in proportion to the ratio of the thermal effusivities, defined as the $\rho C_p k$ product, of the joined materials. Assuming perfect contact between the silicon and the encapsulant and uniform power dissipation at the interface, the effusivities can be used to define a partitioning coefficient for the silicon that can be used to obtain the net heat flow into the silicon or encapsulant:

$$\frac{q_s}{q_s + q_e} = \frac{(\sqrt{\rho C_p k})_s}{(\sqrt{\rho C_p k})_s + (\sqrt{\rho C_p k})_e} \tag{13.51}$$

For typical encapsulants (e.g., polysulfides, polyurethane, epoxides), the effusivity of silicon is found to dominate this relation, and as a result, 90% or more of the heat generated diffuses into the silicon. In recognition of the contact resistance between the encapsulant and the chip and/or in the interest of an upper-bound estimate, the chip temperature in eq. (13.50) can be evaluated at the full surface heat flux (i.e., q_e is negligible).

Although the internal thermal response of a multilayered structure can be related to the thermal time constants for diffusion across individual layers, it is often the convective time constant for the entire package that determines the gross thermal behavior. A composite convective thermal time constant for a plastic IC package can be expressed as

$$\tau = \sum_n \frac{(\rho C_p V)_n}{hA} \quad (13.52)$$

where $\sum(\rho C_p V)_n$ is the summed lumped heat capacity of all the materials constituting the package and A is the surface area available for external heat transfer. For a typical plastic package in which the mass of the chip and metallization is nearly negligible, $\sum(\rho C_p V)_n$ is approximately equal to the heat capacity of the plastic encapsulant. The IC package time constant τ_{ICP} can be expected to apply when the thermal front has reached the external surfaces (or case) of the package and is found to be valid for the time interval $\tau < t < t_{ss}$.

Using the package time constant, the temperature during this time period can be expressed to a first approximation by a relation of the form

$$\Delta T_{r,z} = (1 - e^{-t/\tau})(\Delta T_{r,z})_{ss} \quad (13.53)$$

where $(\Delta T_{r,z})_{ss}$ represents the steady-state temperature at the location of interest. Figures 13.17 through 13.20 display the results of finite-element simulations for a typical plastic package (Mix and Bar-Cohen, 1992) and lend credence to the existence of distinct time domains in the thermal transient behavior of an IC package. Comparison of these values with the temperatures obtained from the analytical relations, eqs. (13.50) through (13.53), suggest that judiciously selected analytical relations can yield results that are within some 5% of the more detailed computational results.

13.3.4 Heat Flow in Printed Circuit Boards

Anisotropic Conductivity Prediction of the temperature distribution in a conductively cooled printed circuit board (PCB) necessitates modeling of heat flow in a multilayer composite structure with two materials (electrical conductor and dielectric) of vastly different thermal properties. The complex heat flow patterns that develop in the PCB as a result of heat diffusing from high-power components into the surrounding board and/or as heat flows toward the cooled edges of the board may be analyzed with the aid of a resistive network. The multidimensional nature of the heat flow requires that effective thermal resistances be determined for each of the primary directions, although often a bi-directional description distinguishing between

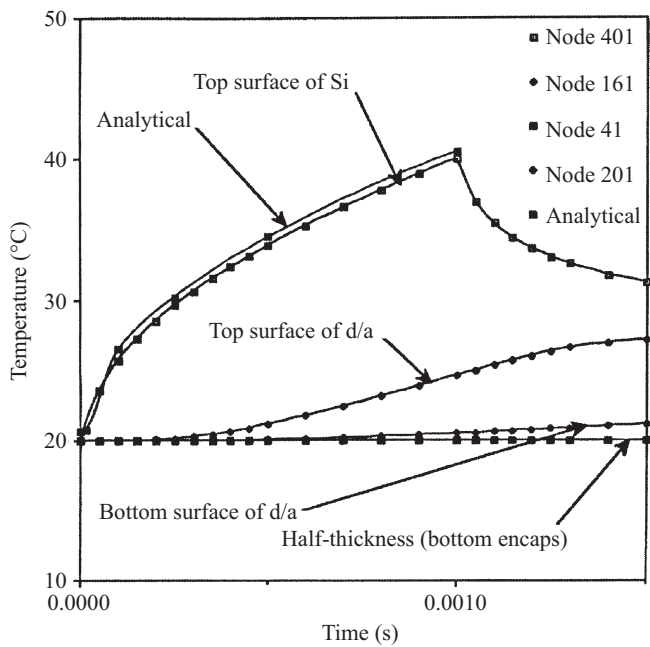


Figure 13.17 Temperature as a function of time (early time).

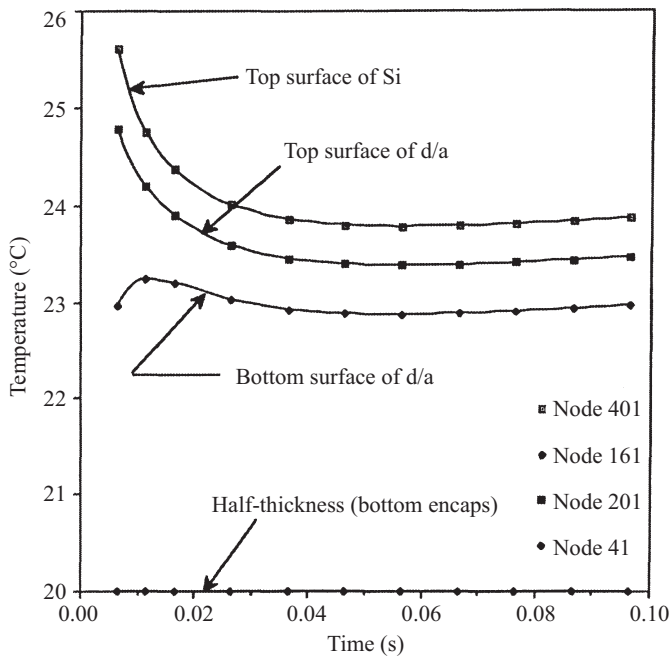


Figure 13.18 Temperature as a function of time (intermediate time).

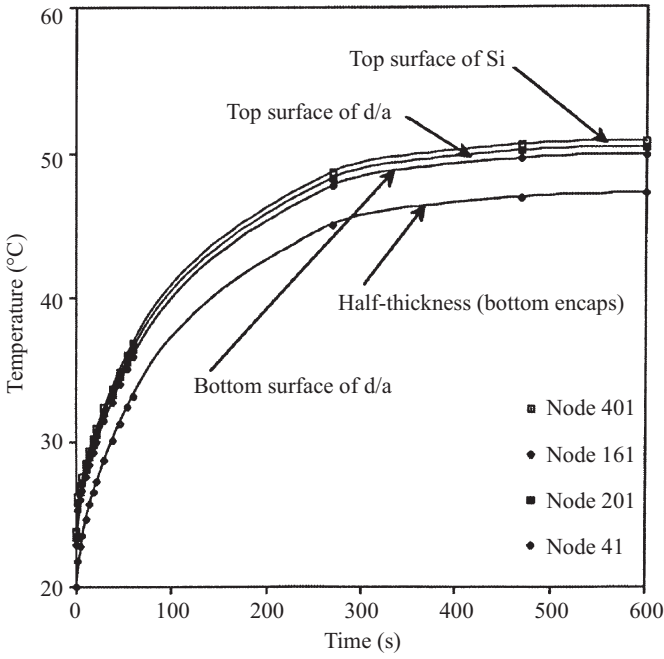


Figure 13.19 Temperature as a function of time (quasi-steady).

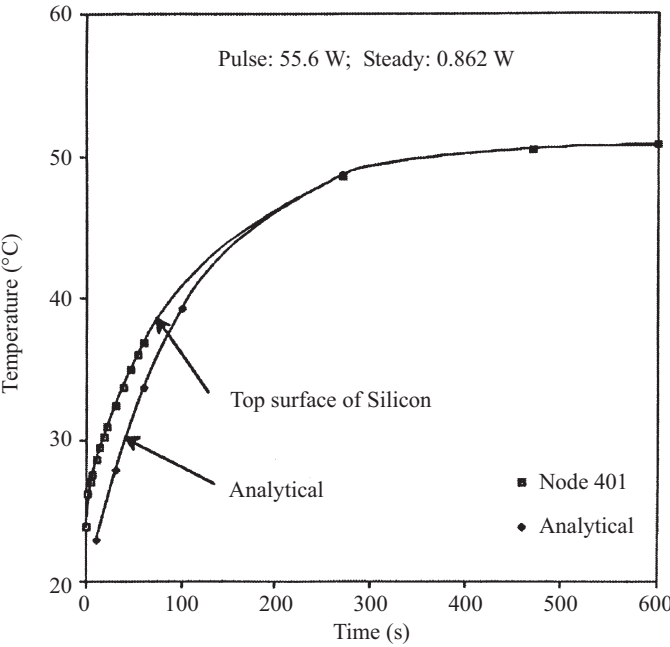


Figure 13.20 Comparison of model as a function of analytical predictions (quasi-steady).

the lateral conductivity and the transverse (through the thickness) conductivity is sufficient to achieve the desired accuracy. As in all discretized thermal models, the error inherent in this technique is inversely proportional to the volume represented by each resistor.

Because the copper and dielectric layers in the board may not be continuous, due to the presence of traces and vias, it is very difficult to model the conduction in this layer in full detail. If n_c is the number of cutouts (holes for interconnection and etched copper) in the copper layers and d_c is the diameter of each cutout, a conduction factor for conduction normal to the copper layers may be defined as

$$\kappa_n = \frac{WL - n_c(\pi d_c^2/4)}{WL} \quad (13.54)$$

where W and L are the width and length of the printed circuit board, respectively. The factor κ_n simply represents the fraction of the conduction area missing due to the cutouts.

Similarly, a conduction factor for the in-plane direction may be defined as

$$\kappa_p = \frac{W - n_c d_c}{W} \quad (13.55)$$

The thermal resistance of each of the layers making up the printed circuit board in the normal direction can be written as

$$R_x^n = \frac{\delta_x}{\kappa_p k_x L W} \quad (13.56)$$

where δ_x and k_x are the thickness and thermal conductivity of layer x . Similarly, the thermal resistance of each of the layers in the in-plane direction can be written as

$$R_x^p = \frac{L}{\kappa_p k_x \delta_x W} \quad (13.57)$$

The thermal resistances of the various layers are in series in the normal direction and in parallel in the in-plane direction. Using the law of electrical resistances, the total resistance R_t^n in the normal direction can be written as

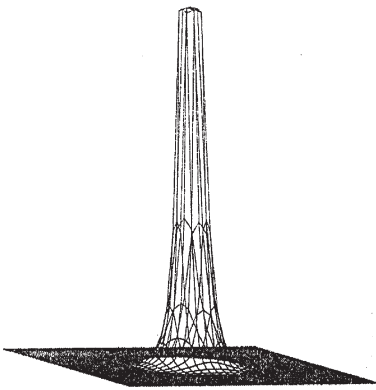
$$R_t^n = \frac{\delta_t}{k_{en} L W} = \sum \frac{\delta_x}{k_x L W} \quad (13.58)$$

where δ_t is the total thickness of the interposer or motherboard and k_{en} is the equivalent normal thermal conductivity. Similarly, the total resistance R_t^p in the in-plane direction can be written as

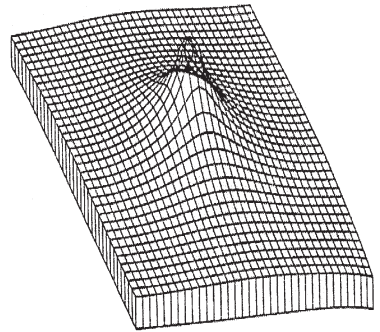
$$\frac{1}{R_t^p} = \frac{k_{ep} \delta_t W}{L} = \sum \frac{k_x \delta_x W}{L} \quad (13.59)$$

Equations (13.56) and (13.57) can be used to estimate the equivalent in-plane and normal thermal conductivities for the motherboard and interposer layers.

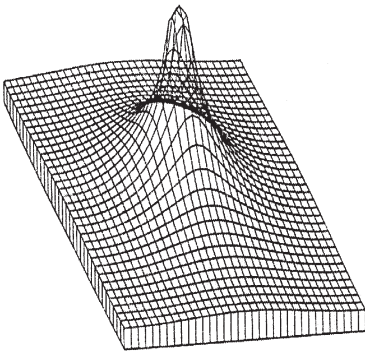
Thermal Vias Existing electrical *vias*, or *plated through holes*, as well as “thermal vias” embedded in the board, enhance the transverse thermal conductivity of a PCB and help to reduce the resistance to heat flow in the direction perpendicular to the plane of the PCB. Thermal vias are also used in chip scale packages (CSPs) and ball grid array (BGA) packages to provide thermal paths of reduced resistance from the chip directly to the PCB. Due to the geometric complexity of most PCBs, a combination of analytical and experimental approaches is usually needed to estimate



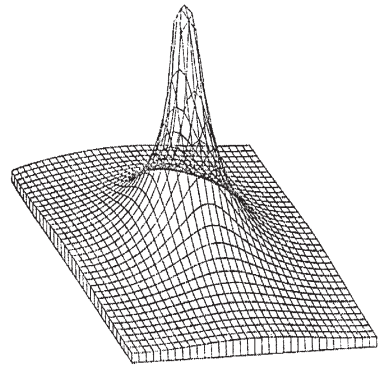
(a) Epoxy-glass substrate without copper plane, $\Delta T_{\max} = 160^{\circ}\text{C}$



(b) Epoxy-glass substrate, 1-oz copper plane, $\Delta T_{\max} = 21.8^{\circ}\text{C}$



(c) Epoxy-glass substrate, 2-oz copper plane, $\Delta T_{\max} = 13.9^{\circ}\text{C}$



(d) Epoxy-glass substrate, 4-oz copper plane, $\Delta T_{\max} = 8.9^{\circ}\text{C}$

Figure 13.21 Temperature distribution in an epoxy-glass substrate with and without copper planes. (From Howard et al., 1984.)

the thermal conductivity of a particular board, but much can be learned from the analysis of a PCB with a relatively simple wiring pattern.

When a large number of vias are present, it is possible to determine the thermal conductivity in the normal direction by assuming that the higher-conductivity vias provide the dominant thermal conduction path for heat. The thermal conductivity of the dielectric can therefore be neglected and the thermal conductivity of the dielectric layer in the normal direction can be computed using

$$k_n = (1 - \kappa_n)k_{cu} \quad (13.60)$$

where the factor k_n is computed using the via diameter and eq. (13.54). The conductivity in the in-plane direction for the dielectric layers can still be assumed to be that of the dielectric alone.

Effect of Trace Layers Use of additional in-plane (or artificially thickened) copper layers can serve to substantially increase the effective lateral thermal conductivity of a PCB, as achieved by Hewlett-Packard in the “finstrate” technology of the mid-1980s. The reduced in-plane thermal resistance can help transport heat to the edges of the board and/or dramatically reduce the local temperature rise of a high-power component mounted to the PCB. The beneficial effect of such trace layers can best be illustrated with a specific example using a finite-element model and numerical simulation to generate the temperature distributions (Lewis et al., 1996).

The following results were obtained with a 7.47-mm-square chip size, dissipating 1 W, mounted on various PCBs (Howard et al., 1984). The results for case 1, using an epoxy–glass substrate without any copper, are shown in Fig. 13.21*a* in the form of a three-dimensional plot of the temperature distribution in the substrate. The poor thermal conductivity of the epoxy glass is seen to yield a 160°C maximum temperature rise under the center of the chip. With a 1-oz copper trace, maximum temperature rise under the center of the chip is reduced to 21.8°C, whereas with 2-oz copper it is 13.9°C and with 4-oz copper it is 8.9°C, as shown in Fig. 13.21*b*, *c*, and *d*, respectively.

13.4 CONVECTIVE PHENOMENA IN PACKAGING

13.4.1 Printed Circuit Boards in Natural Convection

Despite increasing performance demands and advances in thermal management technology, natural convection air cooling of electronic equipment continues to command substantial attention. The simplicity, reliability, and low cost of air natural convection make this cooling mode a popular choice for individual IC packages, populated printed circuit boards, and the heat sinks attached to modules, power supplies, and chip packages. The heat transfer coefficient for natural convection can be related to the temperature difference between the surface and the ambient fluid, along with the fluid’s thermal and fluid properties, as seen in the correlations listed in Tables 13.4 and 13.5, respectively.

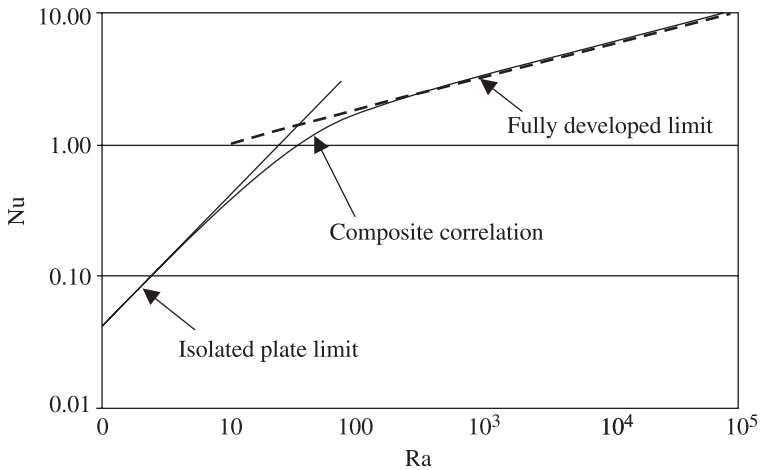


Figure 13.22 Composite correlation for parallel isothermal plates.

Vertical heated channels formed by parallel PCBs are a frequently encountered configuration in natural convection cooling of electronic equipment. The historical work of Elenbaas (1942) provides the foundation for much of the effort dealing with natural convection in such smooth, isothermal, parallel-plate channels. His experimental results for isothermal plates were confirmed via numerical simulation by Bodoia and Osterle (1964), who showed that the results could also be used for the constant heat flux condition. Other researchers have extended this pioneering work to include asymmetrically heated channels, including the case of the single insulated wall (Aung, 1972; Aung et al., 1972; Miyatake et al., 1973; Miyatake and Fujii, 1972). These many studies revealed that the value of the convective heat transfer coefficient lies between two extremes associated with the separation distance between the plates or the channel width.

For wide spacing, the plates appear to have little influence upon one another, and the heat transfer coefficient in this case achieves its isolated plate limit. On the other hand, for closely spaced plates or for relatively long channels, the fluid attains the fully developed velocity profile and the heat transfer rate reaches its fully developed value. Intermediate values of the heat transfer coefficient can be obtained from a judicious superposition of these two limiting phenomena, as presented in the composite expressions proposed by Bar-Cohen and Rohsenow (1984). Figure 13.22 shows one such correlation for natural convection heat transfer from isothermal parallel plates. Composite correlation for other situations such as symmetrically heated isothermal or isoflux surfaces are available in the literature (Kraus and Bar-Cohen, 1983).

A compilation of these natural convection heat transfer correlations for an array of vertically heated channels is listed in Table 13.8. The heat transfer from isothermal plates is expressed in terms of the Elenbaas number, defined as

TABLE 13.8 Natural Convection Heat Transfer Correlations for an Array of Heated Vertical Channels

Condition	Fully Developed Limit	Composite Correlation
Symmetric isothermal plates	$Nu_0 = \frac{El}{24}$	$Nu_0 = \left(\frac{576}{El^2} + \frac{2.873}{\sqrt{El}} \right)^{-1/2}$
Asymmetric isothermal plates	$Nu_0 = \frac{El}{12}$	$Nu_0 = \left(\frac{144}{El^2} + \frac{2.873}{\sqrt{El}} \right)^{-1/2}$
Symmetric isoflux plates	$Nu_0 = \sqrt{\frac{El}{48}}$	
Asymmetric isoflux plates	$Nu_0 = \sqrt{\frac{El}{24}}$	
Symmetric isoflux plates based on midheight temperature	$Nu_0 = \sqrt{\frac{El}{12}}$	$Nu_0 = \left[\frac{12}{El} + \frac{1.88}{(El)^{2/5}} \right]^{-1/2}$
Asymmetric isoflux plates based on midheight temperature	$Nu_0 = \sqrt{\frac{El}{6}}$	$Nu_0 = \left[\frac{6}{El} + \frac{1.88}{(El)^{2/5}} \right]^{-1/2}$

$$El = \frac{C_p \rho^2 g \beta (T_w - T_{amb}) b^4}{\mu k_f L} \tag{13.61}$$

In eq. (13.61), b is the channel spacing, L the channel length, and $(T_w - T_{amb})$ the temperature difference between the channel wall and the ambient or channel inlet. The equations for the uniform heat flux boundary condition are defined in terms of the modified Elenbaas number, which is defined as

$$El' = \frac{C_p \rho^2 g \beta q'' b^5}{\mu k_f^2 L} \tag{13.62}$$

In eq. (13.62), q'' is the heat flux leaving the channel wall(s).

A different type of asymmetry can occur if adjacent channel walls are isothermal but at different temperatures or isoflux but dissipating different heat fluxes. For the case where the walls are isothermal but at different wall temperatures T_{w1} and T_{w2} , Aung (1972) defined an asymmetry parameter as

$$r_T = \frac{T_{w1} - T_0}{T_{w2} - T_0} \tag{13.63}$$

in which T_0 is the air temperature at the channel inlet. Then the heat transfer could be calculated using the parameters listed in Table 13.9. In the case of symmetric isoflux plates, if the heat flux on the adjacent walls is not identical, the equations in Table 13.8 can be used with an average value of the heat flux on the two walls.

TABLE 13.9 Nusselt Number for Symmetric Isothermal Walls at Different Temperatures

r_T	\overline{Nu}_0/El
1.0	1/24
0.5	17/405
0.1	79/1815
0.0	2/45

Source: Aung (1972).

13.4.2 Optimum Spacing

The composite relations presented in Section 13.4.1 may be used in optimizing the spacing between PCBs. For isothermal arrays, the optimum spacing maximizes the total heat transfer from a given base area or the volume assigned to an array of PCBs. Figure 13.23 shows the maximum power dissipation from a PCB card cage as a function of the PCB spacing. It is clear from the figure that there is an optimum PCB spacing at which maximum power can be dissipated in the PCBs for the same PCB-to-ambient temperature difference.

In the case of isoflux parallel-plate arrays, the power dissipation may be maximized by increasing the number of plates indefinitely. Thus, it is more practical to define the optimum channel spacing for an array of isoflux plates as the spacing that will yield the maximum volumetric heat dissipation rate per unit temperature difference. Despite this distinction, the optimum spacing is found in the same manner.

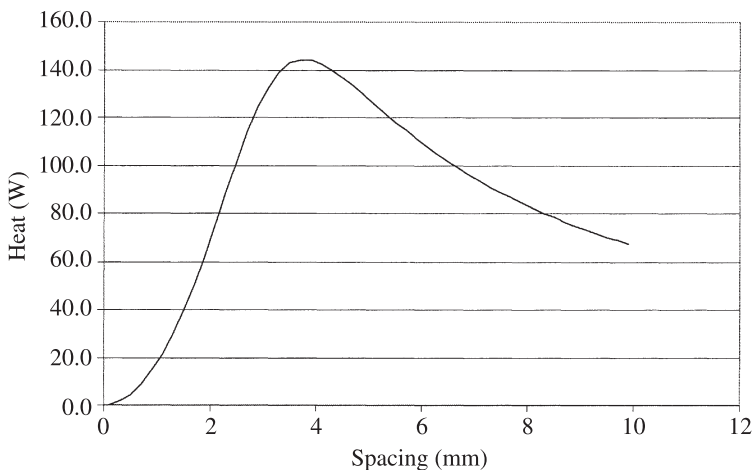


Figure 13.23 Variation of total power dissipation from a PCB array with PCB spacing.

TABLE 13.10 Optimum Spacing for Natural Convection Cooled Arrays of Vertical Plates or Printed Circuit Boards

Condition	Optimum Spacing
Symmetric isothermal plates	$b_{\text{opt}} = \frac{2.714}{P^{1/4}}$
Asymmetric isothermal plates	$b_{\text{opt}} = \frac{2.154}{P^{1/4}}$
Symmetric isoflux plates	$b_{\text{opt}} = 1.472R^{-0.2}$
Asymmetric isoflux plates	$b_{\text{opt}} = 1.169R^{-0.2}$

Source: Kraus and Bar-Cohen (1983).

The optimal spacings for different conditions are tabulated in Table 13.10. The parameter b_{opt} in Table 13.10 represents the optimal spacing, and the plate to air parameter P is given as

$$P = \frac{C_p(\rho_f)^2 g \beta \Delta T_0}{\mu_f k_f L} \tag{13.64}$$

where ΔT_0 is the temperature difference between the PCB and the ambient. The parameter R in Table 13.10 is given by

$$R = \frac{C_p(\rho_f)^2 g \beta q''}{\mu_f k^2 L} \tag{13.65}$$

These smooth-plate relations have proved useful in a wide variety of applications and have been shown to yield very good agreement with measured empirical results for heat transfer from arrays of PCBs. However, when applied to closely spaced PCBs, these equations tend to underpredict heat transfer in the channel due to the presence of between-package wall flow and the nonsmooth nature of the channel surfaces.

13.4.3 Printed Circuit Boards in Forced Convection

The thermal analysis for PCB arrays exposed to forced airflow can be performed in a manner similar to that described for natural convection. If the PCB spacing is large enough that the boundary layers developing on adjacent boards are not expected to interfere with each other, the heat transfer correlations developed for the isolated flat plate in Table 13.4 can be used. Note that in doing so, it is implicitly assumed that the PCBs are densely populated and that the gap between adjacent components on the PCB is small enough such that the developing boundary layers are not interrupted. Additionally, for such cases, even though heat is generated within discrete components on the board, it is possible to assume that there is a uniform heat flux condition on the surface of the components because the component spacing is very small. When

TABLE 13.11 Nusselt Number for Developing Laminar Flow in Isoflux Channels

$x^+ = 2 \left(\frac{x/D_h}{\text{Re} \cdot \text{Pr}} \right)$	Nu
0.002	18.50
0.010	9.62
0.020	7.68
0.10	5.55
0.20	5.40
∞	5.39

Source: Heaton et al. (1964).

the spacing between the PCBs is small, the boundary layers from the adjacent boards are expected to merge. In such cases the heat transfer coefficient can be estimated using the channel flow correlations discussed later in this section.

The channels formed by PCBs are generally relatively short and the ratio of channel length to the spacing between the boards is rarely larger than 100. In such cases, distinct velocity and temperature boundary layers are expected to develop over much of the length of the PCB. Consequently, correlations or tables for developing flow solutions must be used to correctly estimate the heat transfer from the PCBs. Heaton et al. (1964) determined the local Nusselt numbers expected during developing laminar flow between isoflux walls. These are listed in Table 13.11. It is clear from the tabulated values that the heat transfer coefficient in the developing region can be two to three times higher than that obtained using the fully developed flow correlations. Similar data for a variety of flow geometries have been summarized by Kays and Crawford (1993).

It is often necessary in the thermal analysis of electronics equipment to evaluate the heat transfer coefficient for a discrete component located on a poorly conducting PCB, positioned at a downstream location in a channel. Thermal performance of such a discrete component can be assessed by assuming a uniform heat flux condition on the component surface and assuming that the boundary layer development begins at the leading edge of the component. The Nusselt number values tabulated in Table 13.11 can now be used to evaluate the heat transfer coefficient.

For forced laminar flow in long or very narrow parallel-plate channels, the heat transfer coefficient attains an asymptotic value under fully developed conditions (the fully developed limit), which for symmetrically heated channel surfaces is approximately equal to

$$h = \frac{4k_f}{D_h} \quad (13.66)$$

where D_h is the hydraulic diameter defined in terms of the flow area A and the wetted perimeter of the channel P_w :

TABLE 13.12 Nusselt Numbers for Fully Developed Laminar Flow in Channels

Cross Section	Aspect Ratio	Nu for T Constant	q'' Constant
Rectangular	1	2.98	3.61
	2	3.39	4.12
	4	4.44	5.33
	Infinite	7.54	8.23
	Infinite with only one wall heated	4.86	5.38
Circular	—	3.66	4.36
Triangular	—	2.35	3.00

Source: Kays and Crawford (1993).

$$D_h = \frac{4A}{P_w} \tag{13.67}$$

Table 13.12 provides the values of the fully developed Nusselt numbers Nu and heat transfer coefficient h for several channel geometries and for both isoflux (q'' const) and isothermal (T const) conditions.

For the case where adjacent channel walls each have a different uniform value of heat flux, Kays and Crawford (1993) also provide

$$Nu_1 = \frac{5.385}{1 - 0.346(q''_2/q''_1)} \tag{13.68}$$

In the inlet zones of such parallel-plate channels and along isolated plates, the heat transfer coefficient varies with the distance from the leading edge and can be computed using the flat plate correlations provided in Tables 13.4 and 13.5.

For calculation of the junction temperatures of components mounted on PCBs and cooled by forced convection, Witzman (1998) proposed

$$T_j - T_a = \Delta T_a + \Delta T_{jc} + \Delta T_{ca} \tag{13.69}$$

where ΔT_a is the rise in the temperature of air as it flows over the PCB, ΔT_{jc} is the temperature drop between the silicon junction and the outer surface of the PCB-mounted component, and ΔT_{ca} is the temperature drop between the component surface and the local ambient temperature. With increasing component power dissipation and more densely populated PCBs, it is important to determine the heat transfer coefficient on the component surface accurately in order to compute ΔT_{ca} . Witzman (1998) and Graham and Witzman (1988) obtained the local heat transfer coefficients through careful empirical measurements. They found that in most cases the temperature varied axially, as well as laterally, along the surface of the PCB, creating a high-temperature area in the center of the PCB rack. Based on their measurements for 20-mm board spacing and uniform component power dissipation ranging from 10 to 30 W, Witzman (1998) proposed

$$T_j - T_a = 76.1q^{0.8} [1 + 0.23(n - 2)^{0.62}] \quad (13.70)$$

where n is the position of the component ($n = 1$ is the bottom row), $T_j - T_a$ the average temperature rise of the n th component above the ambient temperature, and q the component power dissipation.

Moffat and Ortega (1988) recommended that a heat transfer coefficient h_{ad} based on the adiabatic temperature of the heated element be used when utilizing correlations for heat transfer determined from actual measurements of simulated electronic cooling systems. This recommendation is based on the fact that h_{ad} is independent of the geometry and flow and does not depend on the upstream flow pattern. Additionally, h_{ad} can be measured by heating up only one element on the PCB and allows for superposition of solutions. The superposition formulation for computing the junction temperature of the i th component on a PCB can be written as

$$T_j - T_{in} = \frac{q_i}{h_i A_i} + \sum_{j=1}^j \theta_{ij} \frac{q_j}{h_j} \quad (13.71)$$

where T_{in} is the inlet coolant temperature and θ_{ij} is the thermal wake function, defined as

$$\theta_{ij} = \frac{T_i - T_{in}}{T_j - T_{in}} \quad (13.72)$$

In eq. (13.71), j represents the components upstream from component i . The first term in eq. (13.71) calculates the temperature rise of the component above its own adiabatic temperature and the second term adds the difference between the adiabatic temperature of the component and the inlet temperature of the coolant. Moffat and Ortega (1988) have also summarized an extensive set of experimental data for several geometric arrangements in a channel.

The convective resistance in the fluid region adjacent to the wall in turbulent flow is nearly independent of the exact thermal boundary condition on the channel wall or on any discrete component. Consequently, the correlations listed in Table 13.4 can be used to obtain a fairly accurate estimate of the heat transfer coefficient in turbulent flow for both isothermal and isoflux wall boundary conditions. The constants and eigenvalues required to estimate a heat transfer coefficient in developing turbulent flow have been summarized by Kays and Crawford (1993).

13.5 JET IMPINGEMENT COOLING

13.5.1 Introduction

In recent years the use of impinging fluid jets for thermal management of electronic components has received extensive attention. The high heat transfer coefficients that can be attained in this cooling mode, the ability to vary and control the heat transfer

rates across a large substrate or PCB with an appropriately configured distribution plate or nozzle array, and the freedom to tailor the jet flow to the local cooling requirements, have made impingement cooling one of the most promising alternatives for the cooling of high-heat-flux components.

Impingement cooling may involve a single jet or multiple jets directed at a single component or an array of electronic components. Circular orifices, slot-shaped orifices, or nozzles of various cross sections may form the jets. The axis of the impinging jet may be perpendicular or inclined to the surface of the component. Moreover, in the application of liquid jets, a distinction can be made between free jets, which are surrounded by ambient air and submerged jets, for which the volume surrounding the jet is filled with the working liquid. Whereas heat transfer associated with gas jets has been the subject of active research since the mid-1950s, jet impingement cooling with dielectric liquids is a far more recent development. Many of the pioneering studies in this field were reviewed by Bergles and Bar-Cohen (1990). More recent studies of heat transfer to free jets of dielectric liquids have been performed by Stevens and Webb (1989), Nonn et al. (1988), and Wang et al. (1990). Womac et al. (1990) examined free as well as submerged liquid jets, while submerged jet impingement heat transfer was the subject of the investigations by Wadsworth and Mudawar (1990) and Mudawar and Wadsworth (1990).

As a final distinction, jet impingement cooling of electronic components may involve forced convection alone or localized flow boiling, with or without net vapor generation. The discussion in this section is limited to single-phase forced convection.

13.5.2 Correlation

Despite the complex behavior of the local heat transfer coefficient resulting from parametric variations in the impinging jet flow, it has been found possible to correlate the average heat transfer coefficient with a single expression, for both individual jets and arrays of jets impinging on isothermal surfaces. Based on earlier results by Schlünder et al. (1970) and Krotzsch (1968), Martin (1977) proposed a relation to capture the effects of jet Reynolds number, nondimensional distance of separation (H/D), impinging area ratio (f), Prandtl number (Pr), and fluid thermal conductivity on the jet Nusselt number:

$$Nu_D = \left[1 + \left(\frac{H/D}{0.6/\sqrt{f}} \right)^3 \right]^{-0.05} \left\{ \sqrt{f} \frac{1 - 2.2\sqrt{f}}{1 + 0.2 [(H/D) - 6] \sqrt{f}} \right\} Re_D^{0.667} \cdot Pr^{0.42} \quad (13.73)$$

The range of validity for this correlation developed from extensive gas jet data, as well as some data for water and other, higher Prandtl number liquids, including some high-Schmidt-number mass transfer data, was given by Martin (1977) as $2 \times 10^3 \leq Re_D \leq 10^5$, $0.6 < Pr(Sc) < 7(900)$, $0.004 \leq f \leq 0.04$, and $2 \leq H/D \leq 12$. Martin found this correlation to provide a predictive accuracy of 10 to 20% over the stated parametric range. The average Nu was also found to be nearly unaffected by the

angle of inclination of the jet (Martin, 1977). It is to be noted that for jets produced by sharp-edged orifices, jet contraction immediately after the orifice exit must be taken into consideration in calculating the average velocity, jet diameter, and nozzle area ratio f .

In applying the Martin correlation to the cooling of electronic components, constituting discrete heat sources on a large surface, it is necessary to alter the definition of the jet area ratio f . Recognizing that in this application, the impingement area is usually equal to the component area, f can be expressed as

$$f = \frac{nA_{\text{jet}}}{A} = \frac{0.785 D^2 n}{A} \quad (13.74)$$

Womac (1989) found the Martin correlation to give reasonable agreement with his submerged jet data for small-diameter jets (< 3 mm) of water and FC-77. Two other studies of submerged jet impingement were conducted by Brdlik and Savin (1965) for air and by Sitharamayya and Raju (1969) for water. The correlations from these studies are plotted in Fig. 13.24 along with the Martin correlation for a specific condition of $f = 0.008$, $H/D = 3$, and $\text{Pr} = 13.1$, which falls well within the ranges of all three correlations. The maximum deviation of these correlations from the Martin correlation in this plot was 32%. The Martin correlation was chosen over these alternatives primarily because of the broad range of parameters in the database from which it was developed. Also, the Martin correlation generally falls below the other correlations, making it the most conservative choice.

Although the Martin (1977) correlation does not explicitly address the effect of escaping crossflow at the perimeter of a chip or board, this behavior was investigated by Kraitshev and Schlünder (1973) in mass transfer experiments using several configurations of circular jets with varying liquid escape paths. Kraitshev and Schlünder

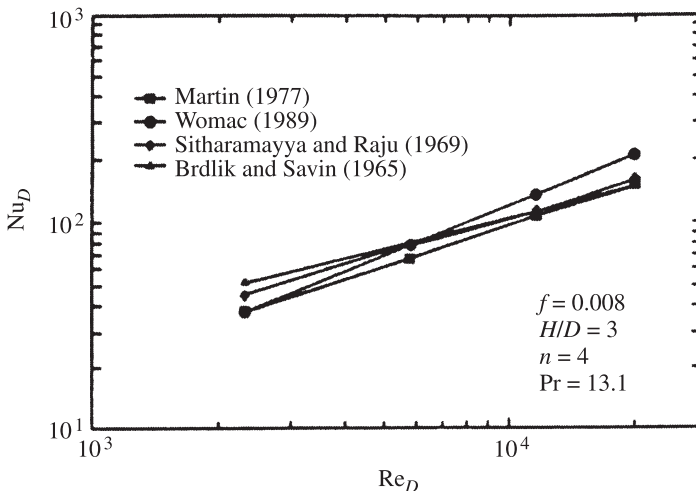


Figure 13.24 Comparison of various submerged jet correlations.

(1973) found that for $H/D < 3$, the effects of acceleration of the crossflow offset losses due to interference with the jets and that at high values of H/D the heat transfer was unaffected. Only in an intermediate range of H/D , which varied with the configuration, was the heat transfer found to degrade in the outer regions of the array.

13.5.3 First-Order Trends

The variation of the Nusselt number with each of the three primary factors influencing jet impingement in the range of the Martin correlation, eq. (13.73), is shown in Figs. 13.25 through 13.27, respectively. Examining these figures it may be seen that the Nusselt number increases steadily with the Reynolds number (Fig. 13.25) and decreases with the ratio of jet distance to jet diameter (Fig. 13.26). More surprisingly, the curves shown in Fig. 13.27 indicate that the Nusselt number reaches an asymptote in its dependence on the ratio of jet area to component area. Interestingly, Martin (1977) found that a nozzle/heater area ratio f of 0.0152 and a jet aspect ratio H/D of 5.43 yielded the highest average transfer coefficient for a specified pumping power per unit area.

Returning to eq. (13.73), it may be observed that in the range of interest, the first term on the right side can be approximated as

$$\left[1 + \left(\frac{H/D}{0.6/f^{0.5}} \right)^6 \right]^{-0.05} \simeq \left(\frac{H/D}{0.6/f^{0.5}} \right)^{-0.3}$$

(13.75)

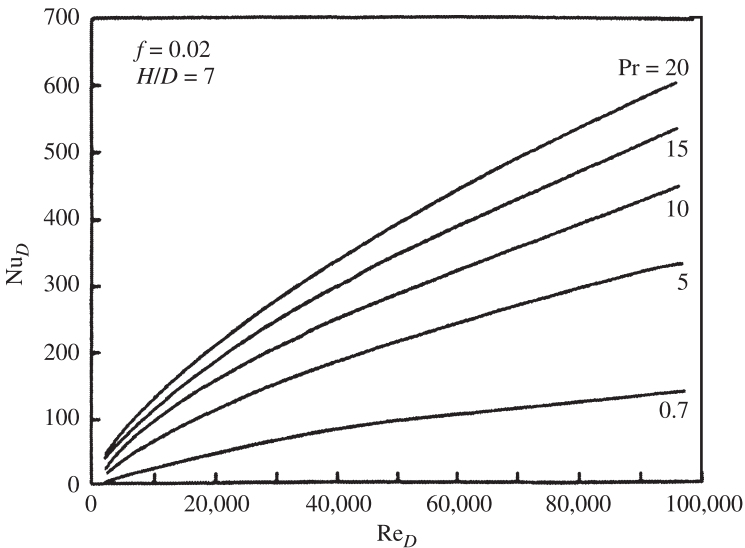


Figure 13.25 Effect of Reynolds and Prantl numbers on heat transfer.

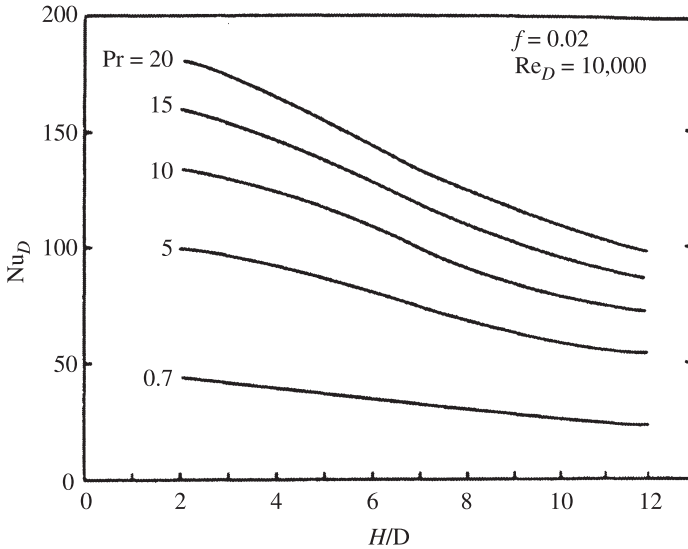


Figure 13.26 Effect of jet aspect ratio on heat transfer.

and that the second term is not far different from $0.6f^{0.5}$. Reexpressing eq. (13.73) with these simplifications, the average heat transfer coefficient h is found to approximately equal

$$\text{Nu} \simeq 0.5 \left(\frac{H}{D} \right)^{-0.3} f^{0.35} \cdot \text{Re}_D^{0.667} \cdot \text{Pr}^{0.42} \quad (13.76)$$

This approximation falls within 30% of eq. (13.73) throughout the parametric range indicated but is within 10% $H/D < 3$.

13.5.4 Figures of Merit

Recalling the definition of the jet Nusselt number, $\text{Nu} = hD/k$, and substituting for the area ratio f from eq. (13.74), the heat transfer coefficient produced by impinging liquid jet(s) is found to be proportional to

$$h \propto kH^{-0.3} \left(\frac{n}{A} \right)^{0.35} \cdot \text{Re}_D^{0.67} \cdot \text{Pr}^{0.42} \quad (13.77)$$

Or, expanding the Reynolds and Prandtl numbers yields

$$h \propto (k^{0.58} \rho^{0.67} \mu^{-0.25}) \left[\left(\frac{n}{A} \right)^{0.35} D^{0.67} \right] \frac{V^{0.67}}{H^{0.3}} \quad (13.78)$$

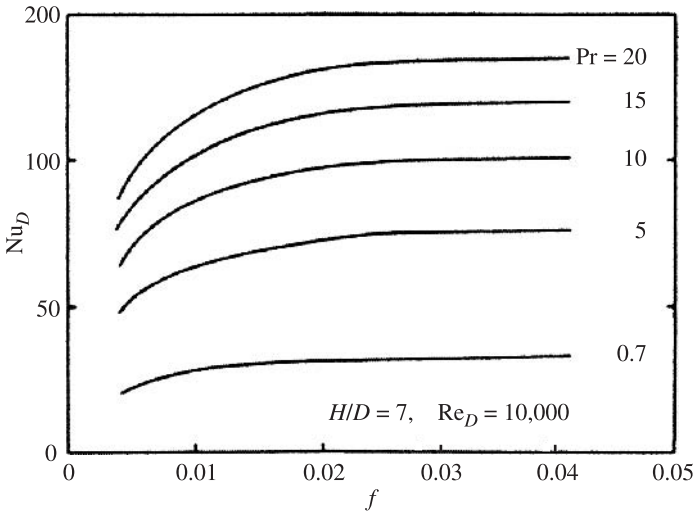


Figure 13.27 Effect of jet area/heater area ratio on heat transfer.

The first term on the right-hand side in eq. (13.78) represents a fluid figure of merit for submerged-jet heat transfer, the second term constitutes a thermal figure of merit for the jet plate, and the third the operating conditions of an impingement cooling system. Clearly, to maximize the jet heat transfer rate, it is desirable to choose a fluid with high thermal conductivity and density but relatively low viscosity. To the accuracy of the approximations used to derive eq. (13.78) (and especially in the low- f range), the thermally preferred jet plate would contain many large-diameter nozzles per component. Due to the strong dependence of the heat transfer rate on the jet Reynolds number, maximization of the heat transfer coefficient also requires increasing the fluid velocity at the nozzle and decreasing the distance of separation between the nozzle and the component. Alternatively, if a fluid has been selected and if the jet Reynolds number is to remain constant, a higher heat transfer coefficient can be obtained only by increasing n/A or decreasing H .

13.5.5 General Considerations for Thermal–Fluid Design

Although the thermal relations discussed in Section 13.5.4 can be used to establish the gross feasibility of submerged jet impingement cooling for high-power chips, successful implementation of this thermal management technique requires consideration of system-level issues and design trade-offs (Maddox and Bar-Cohen, 1991). The minimization of life-cycle costs is a crucial element in electronic systems, and consequently, attention must be devoted to the “consumed” fluid flow rate, pressure drop, and pumping power as well as to the limitations imposed by manufacturing tolerances and costs. The gross impact of these considerations on the design of impinging jet cooling systems can be seen with the aid of eq. (13.78).

The nozzle pressure drop and hence plenum pressure required to achieve a specified jet velocity has direct bearing on the choice and cost of the coolant circulation system and the structural design, as well as cost, of the jet plate. Since eqs. (13.73) and (13.78) show the jet heat transfer coefficient to increase with velocity to the 0.67 power while nozzle pressure losses generally depend on the square of the velocity, concern about the plenum operating pressure would lead the designer to choose the lowest possible jet velocity.

Examination of the approximate relation for the jet heat transfer coefficient, eq. (13.78), suggests that to maintain high heat transfer rates at low jet velocities would necessitate increasing the number of nozzles (n/A), increasing the diameter of each nozzle (D), or decreasing the spacing between the nozzle exit and the component (H). The minimum value of H is likely to be determined by the precision of assembly and deflection under pressure of the jet plate and thus it will benefit from reduced operating pressure. Because the maximum heat transfer rates are approached asymptotically as the total jet area increases to approximately 4% of the component area (see Fig. 13.27), there is coupling between the number of jets and the jet diameter. The heat transfer rate can thus be improved by increasing both jet diameter and the number of jets up to this value, but if operating near the maximum rate, the jet diameter is inversely related to the square root of n/A .

In the use of liquid jets, the operating costs are often dominated by the pumping power, or product of total volumetric flow rate and pressure drop, needed to provide a specified heat removal rate. The pumping power can easily be shown to vary with $D^2 V^3 n/A$. Examining this dependence in light of the approximate heat transfer coefficient relation, eq. (13.78), it is again clear that reduced costs are associated with low liquid velocity and a relatively large total nozzle area.

These results suggest that optimum performance, based on system level as well as thermal considerations, and as represented by the average heat transfer coefficient, would be achieved by designing jet impingement systems to provide approximately 4% jet-to-component area ratios and operate at relatively low jet velocities. Improved surface coverage, more uniform heat removal capability, and decreased vulnerability to blockage of a single (or a few) nozzles would appear to be favored by the use of a relatively large number of jets per component, allowing reduction in the diameter of individual jets. Alternatively, the cost of manufacturing and the probability of nozzle blockage can be expected to increase for small-diameter nozzles and thus place a lower practical limit on this parameter. Given the approximate nature of eq. (13.78), these relationships must be viewed as indicative rather than definitive, and the complete Martin correlation [eq. (13.73)] should be used for any detailed exploration of these trends.

13.5.6 Impingement on Heat Sinks

El Sheikh and Garimella (2000) carried out extensive research on jet impingement cooling of electronic components and derived heat transfer correlations for impingement-cooled pin-fin heat sinks. Results were presented in terms of Nu_{base} , based on the heat sink footprint area, and on Nu_{HS} , based on the total heat sink surface area:

$$\text{Nu}_{\text{base}} = 3.361 \text{Re}^{0.724} \cdot \text{Pr}^{0.4} \left(\frac{D}{d} \right)^{-0.689} \left(\frac{S}{d} \right)^{-0.210} \quad (13.79)$$

$$\text{Nu}_{\text{HS}} = 1.92 \text{Re}^{0.716} \cdot \text{Pr}^{0.4} \left(\frac{A_{\text{HS}}}{A_d} \right)^{-0.689} \left(\frac{D}{d} \right)^{0.678} \left(\frac{S}{d} \right)^{-0.181} \quad (13.80)$$

These equations are valid for $2000 \leq \text{Re} \leq 23000$, $S/d = 2$ and 3 . The term D refers to the jet diameter and d refers to the pin diameter.

13.6 NATURAL CONVECTION HEAT SINKS

Despite the decades-long rise in component heat dissipation, the inherent simplicity and reliability of buoyantly driven flow continues to make the use of natural convection heat sinks the cooling technology of choice for a large number of electronic applications. An understanding of natural convection heat transfer from isothermal, parallel-plate channels provides the theoretical underpinning for the conceptual design of natural convection cooled plate-fin heat sinks. However, detailed design and optimization of such fin structures requires an appreciation for the distinct characteristics of such phenomena as buoyancy-induced fluid flow in the interfin channels and conductive heat flow in the plate fins.

The presence of the heat sink *base*, or prime surface area, along one edge of the parallel-plate channel, contrasting with the open edge at the tip of the fins, introduces an inherent asymmetry in the flow field. The resulting three-dimensional flow pattern generally involves some inflow from (and possibly outflow through) the open edge. For relatively small fin spacings with long and low fins, this edge flow may result in a significant decrease in the air temperature between the fins and alter the performance of such heat sinks dramatically. For larger fin spacings, especially with wide, thick fins, the edge flow may well be negligible. Thus, Sparrow and Bahrami (1980), who studied 7.6-cm-wide vertically oriented isothermal plates, found the edge flow to have a negligible effect on the heat transfer coefficient for values of the Elenbaas number greater than 10, but to produce deviations of up to 30% in the equivalent Nusselt number when the Elenbaas number was less than 4.

Heat flow in extended surfaces must result in a temperature gradient at the fin base. When heat flow is from the base to the ambient, the temperature decreases along the fin, and the average fin surface temperature excess is typically between 50 and 90% of the base temperature excess. As a consequence of the anisothermality of the fin surface, exact analytic determination of the heat sink capability requires a combined (or conjugate) solution of the fluid flow in the channel and heat flow in the fin. Due to the complexity of such a conjugate analysis, especially in the presence of three-dimensional flow effects, the thermal performance of heat sinks is frequently based on empirical results. In recent years, extensive use has also been made of detailed numerical solutions to quantify heat sink performance. Alternatively, a satisfactory estimate of heat sink capability can generally be obtained by decoupling the flow and temperature fields and using an average heat transfer coefficient, along with an

average fin surface temperature, to calculate the thermal transport from the fins to the ambient air.

13.6.1 Empirical Results

Starner and McManus (1963) were perhaps the first to investigate in detail the thermal performance of natural convection heat sinks as a function of the geometry (spacing and height) and angle of base plate orientation (vertical, horizontal, and 45°). Their configuration, with the present terminology, is shown in Fig. 13.28. For a base surface area of $254 \text{ mm} \times 127 \text{ mm}$, supporting 14 and 17 1.02-mm fins (with the cases summarized in Table 13.13), Starner and McManus found that the measured heat transfer coefficients for the vertical orientation were generally lower than the values expected for parallel-plate channels. The inclined orientation (45°) resulted in an additional 5 to 20% reduction in the heat transfer coefficient. Results for the horizontal orientation showed a strong contribution from three-dimensional flow.

Welling and Wooldridge (1965) performed an extensive study of heat transfer from vertical arrays of 2- to 3-mm-thick fins attached to an identical $203 \text{ mm} \times 66.3 \text{ mm}$ base (the individual cases are summarized in Table 13.14). Their results revealed that in the range $0.6 < \text{El} < 100$, associated with 4.8- to 19-mm spacings and fin heights from 6.3 to 19 mm, the heat transfer coefficients along the total wetted surface were lower than attained by an isolated flat plate but generally above those associated with parallel-plate flow. This behavior was explained in terms of the competing effects of channel flow, serving to preheat the air, and inflow from the open edge, serving to mix the heated air with the cooler ambient fluid. In this study it was observed for the first time that for any given interfin spacing there is an optimum fin height b beyond which thermal performance per unit surface area deteriorates. A similar study of upward- and downward-facing fin arrays on a horizontal base was reported by Jones and Smith

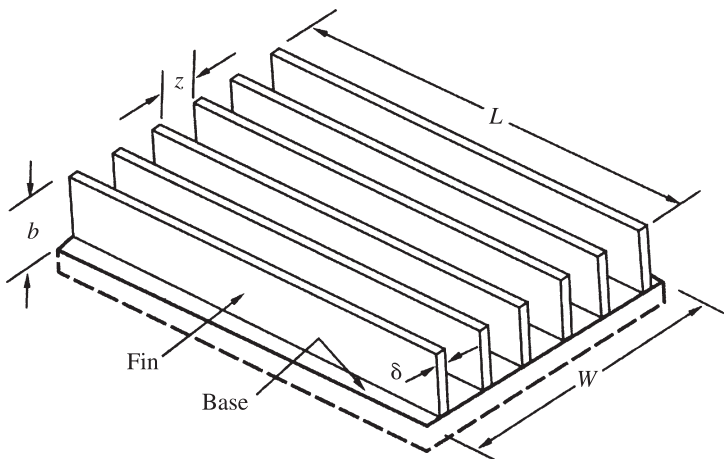


Figure 13.28 Geometric parameters for Starner and McManus (1963) fin arrays.

TABLE 13.13 Geometric Parameters for Starner and McManus (1963) Fin Arrays

Array	<i>N</i>	<i>L</i>		<i>W</i>		<i>b</i>		<i>Z</i>		δ	
		in.	mm	in.	mm	in.	mm	in.	mm	in.	mm
1	17	10.0	254	5.0	127	0.5	12.7	0.25	6.35	0.04	1.016
2	17	10.0	254	5.0	127	1.5	38.1	0.25	6.35	0.04	1.016
3	17	10.0	254	5.0	127	0.25	6.35	0.25	6.35	0.04	1.016
4	14	10.0	254	5.0	127	1.0	25.4	0.313	7.95	0.04	1.016

(1970). The Welling and Woldridge (1965) data formed the basis for the Van de Pol and Tierney (1973) correlation discussed later in this chapter.

In 1986, Bilitzky completed a comprehensive investigation of natural convection heat transfer from multiple heat sink geometries that differed primarily in fin height and spacing. The heat sinks were operated at different heat dissipations as well as different angles of inclination and orientation. Twelve distinct heat sinks and a flat plate were tested in a room within which extraneous convection had been suppressed. The range of angles is indicated in Fig. 13.29. The base was first kept vertical, while the fins were rotated through four different positions (90°, 60°, 30°, and 0°). Then the base was tilted backward toward the horizontal orientation through four different positions (90°, 60°, 30°, and 0°). Six of the heat sinks used bases 144 mm long \times 115 mm wide to support plate fins, nominally 2 mm in thickness and 6 to 13.8 mm apart, ranging in height from 8.6 to 25.5 mm. Six additional heat sinks, with identical fin geometries, were supported on bases 280 mm long and 115 mm wide. The geometric parameters of the 12 heat sinks were selected to span the base and fin dimensions encountered in electronics cooling applications and are summarized in Table 13.15.

TABLE 13.14 Geometric Parameters for Welling and Wooldridge (1965) Fin Arrays

Array	<i>N</i>	<i>L</i>		<i>W</i>		<i>b</i>		<i>Z</i>		δ	
		in.	mm	in.	mm	in.	mm	in.	mm	in.	mm
1	4	8.0	203.2	2.61	66.3	0.75	19.05	0.75	19.05	0.09	2.29
2	6	8.0	203.2	2.61	66.3	0.75	19.05	0.414	10.52	0.09	2.29
3	8	8.0	203.2	2.61	66.3	0.75	19.05	0.27	6.86	0.09	2.29
4	10	8.0	203.2	2.61	66.3	0.75	19.05	0.19	4.83	0.09	2.29
5	4	8.0	203.2	2.61	66.3	0.5	12.7	0.75	19.05	0.09	2.29
6	6	8.0	203.2	2.61	66.3	0.5	12.7	0.414	10.52	0.09	2.29
7	8	8.0	203.2	2.61	66.3	0.5	12.7	0.27	6.86	0.09	2.29
8	10	8.0	203.2	2.61	66.3	0.5	12.7	0.19	4.83	0.09	2.29
9	4	8.0	203.2	2.61	66.3	0.25	6.35	0.75	19.05	0.09	2.29
10	6	8.0	203.2	2.61	66.3	0.25	6.35	0.414	10.52	0.09	2.29
11	8	8.0	203.2	2.61	66.3	0.25	6.35	0.27	6.86	0.09	2.29
12	10	8.0	203.2	2.61	66.3	0.25	6.35	0.19	4.83	0.09	2.29
13	0	8.0	203.2	2.61	66.3	0.00	0.00	2.61	66.3	0.00	0.00

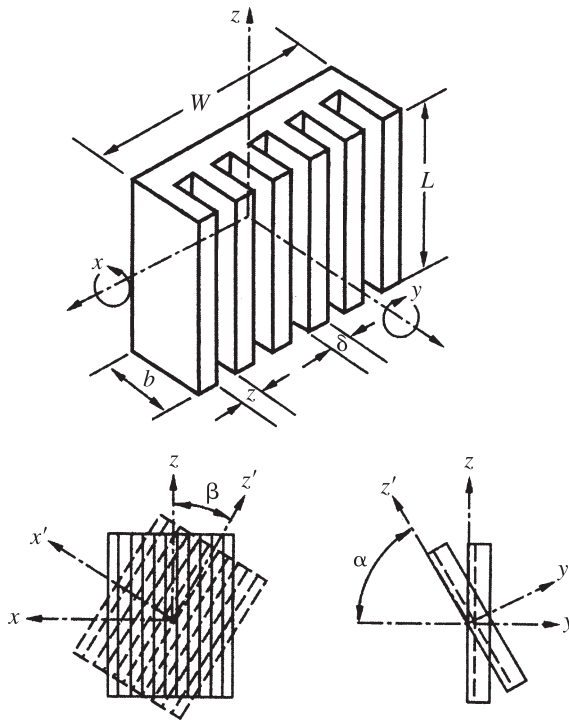


Figure 13.29 Geometry and orientation of Bilitzky (1986) fin arrays.

TABLE 13.15 Geometric Parameters for Bilitzky (1986) Fin Arrays

Array	L		W		b		Z		δ	
	in.	mm	in.	mm	in.	mm	in.	mm	in.	mm
1	5.67	144	4.53	115	1.004	25.5	0.236	6.0	0.075	1.9
2	5.67	144	4.53	115	0.677	17.2	0.232	5.9	0.079	2.0
3	5.67	144	4.53	115	0.339	8.6	0.228	5.8	0.083	2.1
4	5.67	144	4.53	115	1.004	25.5	0.547	13.9	0.075	1.9
5	5.67	144	4.53	115	0.677	17.2	0.543	13.8	0.079	2.0
6	5.67	144	4.53	115	0.339	8.6	0.539	13.7	0.083	2.1
7	11.02	280	4.53	115	1.004	25.5	0.236	6.0	0.075	1.9
8	11.02	280	4.53	115	0.669	17.0	0.232	5.9	0.079	2.0
9	11.02	280	4.53	115	0.335	8.5	0.228	5.8	0.083	2.1
10	11.02	280	4.53	115	1.004	25.5	0.547	13.9	0.075	1.9
11	11.02	280	4.53	115	0.669	17.0	0.543	13.8	0.079	2.0
12	11.02	280	4.53	115	0.335	8.5	0.539	13.7	0.083	2.1

In all 12 heat sinks studied, the vertical-vertical orientation, that is, a vertically oriented base with vertical fins and channels, yielded the highest heat transfer coefficients most often. However, in a relatively large number of situations, the thermal performance of the vertical-vertical arrays was indistinguishable from that attained by a vertical base plate with fins rotated 30° from the axis, a horizontal base plate, and a base plate inclined 60° from the horizontal with unrotated fins. On the other hand, vertical-horizontal orientation, that is, the base plate vertical and the fins rotated 90° from the axis, led to the lowest heat dissipation rates. For the unrotated fins, the lowest heat transfer coefficients were almost always found to occur at a base plate angle of 30° from the horizontal. The use of smoke revealed a relatively complex three-dimensional flow pattern around the heat sinks, with very substantial inflow from the direction of the fin tips when the base plate was strongly inclined and when the heat sinks were in the vertical base-horizontal fins orientation.

The influence of the spacing z between the fins for short and long base plates was examined by comparing pairs of heat sinks that differed only in geometric parameters, z (fin arrays 1 and 4, 2 and 5, 3 and 6, 7 and 10, 8 and 11, and 9 and 12 in Table 13.15). Bilitzky (1986) observed that in nearly all the configurations and operating conditions examined, the highest heat transfer coefficients were attained with the larger fin spacing. However, the improvement in the heat transfer coefficient was not always sufficient to compensate for the loss of wetted fin surface area. Moreover, for the horizontal base plate configurations as well as for the vertical base with horizontal fins, the total array dissipation appeared not to depend on this parameter.

13.7 PHASE-CHANGE PHENOMENA

13.7.1 Heat Pipes and Vapor Chambers

Among the various available cooling techniques, the use of heat pipe technology is increasing rapidly, especially in portable computers. Heat pipes can provide a low-thermal-resistance path for heat transfer within electronic equipment, linking a high-power component with a remotely placed heat sink or cold plate, without adding substantial weight to the system. A heat pipe is a thermal transport device that uses phase-change processes and vapor diffusion to transfer large quantities of heat over substantial distances, with no moving parts and at nearly a constant temperature. A heat pipe is composed of a sealed slender tube containing a wick structure, which lines the inner surface, saturated by a small amount of fluid (such as water), as shown in Fig. 13.30. It is composed of three sections: the evaporator section at one end, where heat is absorbed and the fluid is vaporized; a condenser section at the other end, where the vapor is condensed and heat is rejected; and the adiabatic section, in between, where the vapor and the liquid phases of the fluid flow in opposite directions through the core and the wick, respectively, and in which no significant heat transfer occurs between the fluid and the surrounding medium.

The evaporation and condensation processes yield extremely high heat transfer coefficients, and only a modest pressure difference is required to transport the vapor

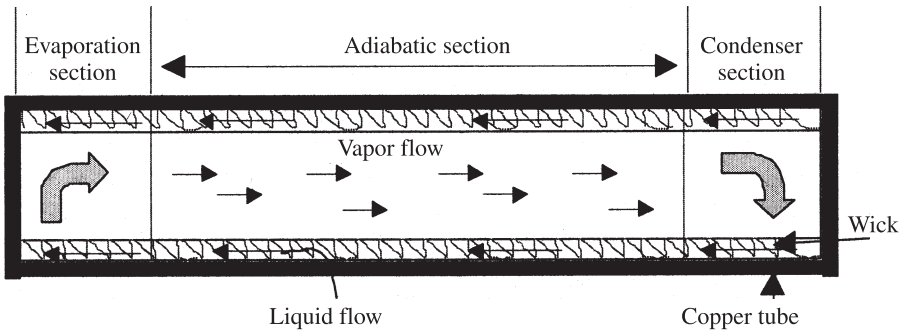


Figure 13.30 Longitudinal cross section of a heat pipe.

from the evaporator to the condenser end of the heat pipe. However, very careful wick design and assembly is required to ensure that capillary forces, in the wick structure, will be successful in pumping the liquid back to the evaporator. Unfortunately, even modest accumulations of noncondensable gas in the vapor space, especially in the region adjacent to the condenser, can lead to severe deterioration in heat pipe performance, often in just a few weeks or months of operation. Contamination and trapping of air and/or other noncondensable gases, during the fabrication process, as well as gas leakage and/or generation due to material incompatibilities, can all contribute to such a loss of heat pipe performance.

Due to the small axial gradient in vapor pressure, required to propel the vapor from the evaporator to the condenser, and the strong dependence of vapor pressure on temperature embodied in the Clausius–Clapeyron equation (Dunn and Reay, 1994), even a modest internal temperature difference is sufficient to effect considerable thermal transport. Moreover, since much of the working volume of a heat pipe is occupied by vapor, such heat pipes may weigh just a few grams. Indeed, a simple heat pipe with water as the working fluid may have an effective axial thermal conductivity on the order of $100,000 \text{ W/m} \cdot \text{K}$, compared with about $400 \text{ W/m} \cdot \text{K}$ for copper. For example, a 0.6-cm-diameter 15-cm-long horizontal cylindrical heat pipe, with water as the working fluid can transfer 300 W at just a 2- to 3-K temperature difference between the evaporator end and the condenser end of the pipe.

However, the resistance to heat flow in the radial direction, or perpendicular to the heat pipe surface, is often far higher than in the axial direction. The relatively low thermal conductivity of the commonly used wick materials, the high porosity of the wick, and the use of low-thermal-conductivity working fluids all combine to impede the flow of heat from the heat pipe wall to the liquid–vapor interface. Moreover, the interface thermal resistance between the heat pipe and the microelectronic device, heat sink, cold plate, and/or other elements in the thermal path frequently poses a substantial thermal resistance that may well govern the cooling capability of the heat pipe.

Although most heat pipes are cylindrical in shape, they can be manufactured in a variety of shapes, involving right-angle bends, S-turns, or spirals. Heat pipes can also

be made in a flat configuration, with a minimum thickness that currently is close to 0.3 cm (Zorbil et al., 1988). Flat heat pipes, attached directly to the back surface of a PCB, have been used successfully for cooling high-power boards in avionic applications, in which heat must be conducted to the edges of the board, which are attached to an air- or water-cooled, cold plate. When the ultimate heat sink is the ambient air, cooling fins are usually attached to the condenser end of the heat pipe, to increase the heat transfer area and reduce the convective resistance.

Recent years have seen growing interest in a special category of flat heat pipes, popularly known as *vapor chambers*. Vapor chambers differ from traditional cylindrical heat pipes in relying on two-dimensional rather than one-dimensional flow of vapor and liquid in the chamber core and in the wick, respectively. Vapor chambers are used in the base of a heat sink for enhanced lateral spreading of heat from a high-heat-flux component. Although the high lateral thermal conductivity of the vapor chambers is most advantageous in this regard, the relatively low axial conductivity of the vapor chamber, often due to the low thermal conductivity of the wick, high wick porosity, and low fluid conductivity, can compromise the effectiveness of a poorly designed vapor chamber. Recently, Chesser et al. (2000) provided a simplified scheme to predict the capillary limits of a vapor chamber and suggested ways in which this same analysis could also be used to predict the temperature variations in the flowing vapor.

Alternative Designs Murthy et al. (2000) presented a micromachined thermosyphon design to be used as heat spreader. The thermosyphon included a central evaporator section, with integrated fins for cooling along the edges and a microfabricated three-dimensional copper structure for enhancing boiling heat transfer. Zeng et al. (2000) have proposed a two-phase cooling design based on the use of an electrokinetic (EK) pump delivering 0.05 to 10 mL/min of electroosmotic flow for the cooling of microelectronic devices in the range 1 to 200 W. Such pumps have no moving parts and are expected to develop pressure heads in excess of 1 atm, substantially above values reported for other micropumps.

13.7.2 Immersion Cooling

Thermal control of operational electronic components by direct immersion in low-boiling-point dielectric liquids dates back to the late 1940s. In the mid-1980s use of immersion cooling for the Cray 2 and ETA-10 supercomputers, as well as substantial research on jet impingement and spray cooling, led to renewed interest in this technology. Due to elimination of the solid-to-solid interface resistance, immersion cooling is well suited to the cooling of advanced, high-heat-flux electronic components now under development.

Table 13.16 lists the thermophysical properties for some of the most commonly used dielectric liquids. It is clear from the data in this table that these fluids have higher thermal conductivities, densities, and specific heats than air and that, consequently, use of these fluids can be expected to offer substantial improvements relative to conventional air cooling. However, the table also indicates that due to the inferiority of the thermophysical properties to those of water, the thermal performance afforded

TABLE 13.16 Thermophysical Properties of Typical Dielectric Coolants

Property	FC-87	L-1402	FC-72	FC-84	R-113
Boiling point (°C)	30	51	52	83	48
Liquid density (kg/m ³)	1633	1635	1592	1575	1511
Vapor density (kg/m ³)	11.58	11.25	12.68	13.28	7.40
Dynamic viscosity (N · m/s ²)	4.2×10^{-4}	5.2×10^{-4}	4.5×10^{-4}	4.2×10^{-4}	5.0×10^{-4}
Specific heat (J/kg · K)	1088	1059	1088	1130	979
Thermal conductivity (W/m · K)	0.0551	0.0596	0.0545	0.0535	0.0702
Prandtl number	8.3	9.2	9.0	8.9	7.0
Heat of vaporization (J/kg)	87,927	104,675	87,927	79,553	146,824
Surface tension (N/m)	8.9×10^{-3}	1.1×10^{-2}	8.5×10^{-3}	7.7×10^{-3}	1.5×10^{-3}

Source: Danielson et al. (1987).

by these fluids is significantly lower than that expected from the use of water as a coolant.

Immersion cooling systems can be classified as passive or active. Passive systems are those in which no pumping devices are used to circulate the coolant. In such systems, heat transfer from the hot component to the coolant may occur due to natural convection or pool boiling. In an active system, on the other hand, the heat transfer from the immersed component is governed by forced convection and/or by flow boiling to the fluid actively circulated by a pump.

As seen from Table 13.16, the Prandtl number for most commonly used dielectric fluids is very high. In addition, the length scales of electronic components are usually smaller than those used to establish the free- and forced-convection correlations listed in Table 13.4. The effect of length scale is much more pronounced on the natural convection heat transfer coefficient. Park and Bergles (1988) provided a correlation accounting for the effect of heater length on the natural convection heat transfer coefficient from vertically oriented heaters immersed in dielectric fluids:

$$\text{Nu} = a \cdot \text{Ra}_*^b \quad (13.81)$$

where

$$a = 0.906 \left[1.0 + \frac{0.0111}{(W/W_\infty)^{3.965}} \right]^{0.2745} \quad (13.82)$$

$$b = 0.184 \left[1.0 + \frac{2.64 \times 10^{-5}}{(W/W_\infty)^{9.248}} \right]^{-0.0362} \quad (13.83)$$

Although eq. (13.81) was developed from measurements taken on vertically oriented heaters, it predicts natural convection on horizontal silicon chips quite well.

The importance of substrate conduction on natural convection heat transfer from a package to a dielectric coolant has been addressed by Sathe and Joshi (1992) and by

Wroblewski and Joshi (1992). Both numerical studies found that a significant portion of the heat was conducted from the power-dissipating component into the substrate and then convected to the surrounding coolant. Sathe and Joshi (1992) also found that natural convection liquid cooling was preferable to natural convection air cooling only if the ratio of the package thermal conductivity to the fluid thermal conductivity was less than 1.

Due to the large liquid densities and the flow rates commonly encountered in active immersion cooling methods, the liquid flow regime is usually transitional or turbulent. The equations listed in Table 13.4 can be used to obtain fairly accurate estimates of forced-convection heat transfer coefficients on electronic components being cooled by flowing dielectric coolants. Although single-phase natural or forced convection of the dielectric coolants can be used for cooling of electronics, the high heat transfer efficiency of nucleate boiling makes this phase-change process a highly attractive mode of heat transfer. Once boiling is initiated on the component very large changes in component heat dissipation can be accommodated with a very small change in component temperature. This is clear from the steep slope of the pool boiling curve for FC-72 shown in Fig. 13.31.

Most commonly used electronic cooling fluids have rather large air solubilities and very low surface tension. Consequently, prolonged exposure of any surface to these fluids allows the fluid to dissolve air out of the microscopic surface cavities. In the

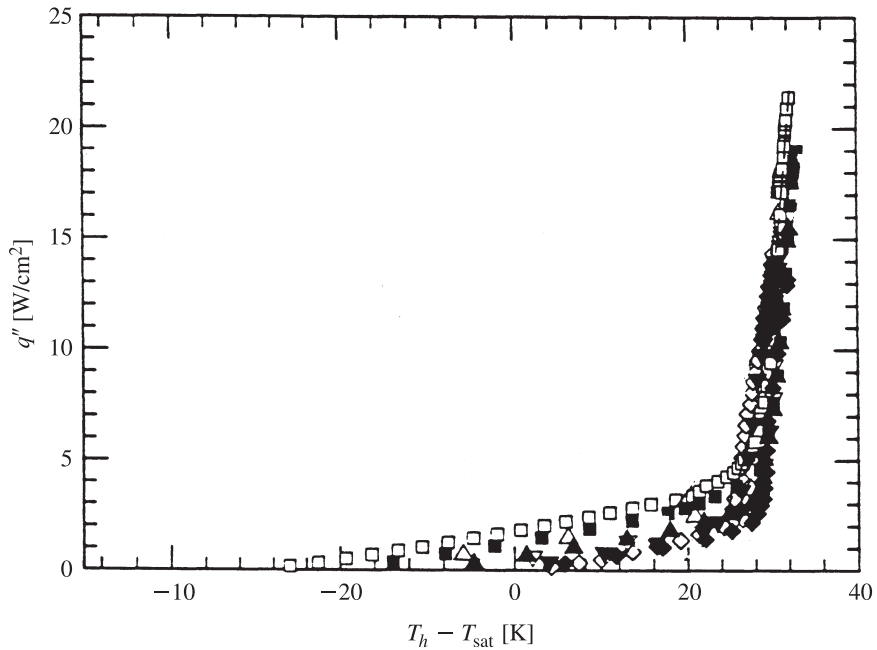


Figure 13.31 Nucleate pool boiling curve for FC-72 on a horizontal silicon chip. (From Watwe et al., 1997.)

absence of these air-filled surface cavities, boiling cannot be initiated on the surface of the silicon. Thus with increasing component heat flux the die temperature increases rapidly, while heat transfer from the component occurs primarily via natural convection, as shown in Fig. 13.31. When the temperature difference between the component surface and the bulk coolant is sufficiently large, boiling may be initiated, causing a rapid decrease in the component temperature. The initial increase in component temperature followed by the temperature drop subsequent to the onset of boiling is termed *incipience overshoot*. Such a thermal shock is rather undesirable in the design of an immersion cooled system due to component reliability considerations.

Although it is very difficult to predict incipience overshoot, You et al. (1990) have presented a comprehensive investigation of the parameters that affect nucleate boiling incipience for the highly wetting dielectric coolants. Bar-Cohen and Simon (1986) have proposed the following equation to obtain an engineering estimate of the incipience temperature excursion ΔT_{ex} :

$$\Delta T_{\text{ex}} \leq \frac{2T_s \sigma_l}{h_{fv}} \left[4 \times 10^6 \left(\frac{1}{\rho_f} - \frac{1}{\rho_l} \right) \frac{\rho_f}{\rho_f - \rho_v} \right] - 0.003 \left[\frac{q'' h_{fv}^2}{C_p^3 \mu_f} \sqrt{\frac{\sigma_f}{g(\rho_f - \rho_v)}} \right]^{1/3} \cdot \text{Pr}^{1.7} \quad (13.84)$$

Once nucleate boiling initiates on the component, the relationship between the component heat flux and its temperature rise above that of the coolant saturation temperature is given by the Rohsenow (1951) correlation:

$$q'' = \mu_f h_{fg} \sqrt{\frac{g(\rho_f - \rho_g)}{\sigma}} \left(\frac{C_{sf}}{a \cdot \text{Pr}_f^{1.7} \cdot h_{fg}} \right) (T_w - T_{\text{sat}})^n \quad (13.85)$$

Watwe et al. (1997) determined that values of a and n in eq. (1.52) were 0.0075 and 7.5, respectively, for fluorocarbon FC-72 boiling on a 1-cm² silicon chip. Danielson et al. (1987) have reported values of a ranging from 0.003 to 0.0093 and values of n ranging from 4 to 8 for nucleate boiling of FC-72. Watwe et al. (1997) have also shown that eq. (13.85) can be used to predict the boiling heat transfer characteristics accurately at elevated ambient pressure or under subcooled liquid conditions.

Flow boiling in channels occurs due to bubble generation at the channel walls. Depending on the fluid velocity, channel orientation with respect to gravity and hydrodynamic effects due to vapor and liquid density differences, several different flow regimes can be identified. Following initiation of boiling, the heat transfer coefficient at the wall increases significantly while the vapor bubbles are carried away by the flowing liquid. This is the bubbly flow regime. With increasing vapor volume fraction, individual bubbles coalesce to form large vapor slugs. This constitutes the slug flow regime.

At very high heat flux levels, the rate of vapor generation is so high that the individual bubbles coalesce into large vapor mushrooms. These large vapor mushrooms depart from the heated surface periodically due to hydrodynamic instabilities caused

by density differences between the vapor and liquid flow. If the surface of the heater cannot be rewetted following the cyclic departure of these vapor mushrooms, the surface temperature is expected to rise rapidly and cause the heater to melt or burnout. The heat flux at which such a dryout/burnout phenomenon occurs is called *critical heat flux* (CHF). It is extremely essential to ensure that the critical heat flux condition does not occur on an immersion-cooled electronic component to ensure its functionality and reliability. Watwe et al. (1997) extended the classical Kutateladze (1951)–Zuber (1959) Haramura-Katto (1983) model of the pool boiling critical heat flux to propose the equation

$$\text{CHF} = \left\{ \frac{\pi}{24} h_{fg} \sqrt{\rho_g} [\sigma_f g (\rho_f - \rho_g)]^{1/4} \right\} \frac{\delta \sqrt{\rho_s C_s k_s}}{\delta \sqrt{\rho_s C_s k_s} + 0.1} \\ \times [1.3014 - 0.01507 L'] \left\{ 1 + 0.03 \left[\left(\frac{\rho_f}{\rho_g} \right)^{0.75} \frac{C_{pf}}{h_{fg}} \right] (T_{\text{sat}} - T_{\text{bulk}}) \right\} \quad (13.86)$$

where

$$L' = L \sqrt{\frac{g(\rho_f - \rho_g)}{\sigma_f}} \quad (13.87)$$

and δ is the heater thickness. Equation (13.86) is a composite equation that includes effects such as heater size, heater thermophysical properties, system pressure, and bulk liquid subcooling (temperature difference between the saturation temperature and bulk liquid temperature can be used to estimate critical heat flux during pool boiling of dielectric coolants).

Lee and Simon (1989) proposed the following equation to compute the critical heat flux on heater lengths ranging from 0.25 to 3 mm for flow velocities from 1 to 17 m/s and subcooling ranging from 13 to 68°C:

$$\text{CHF} = \rho_v h_{fv} U \left[0.04 \left(\frac{\rho_f}{\rho_v} \right)^{0.99} \left(\frac{\sigma_f}{\rho_f U^2 L} \right)^{0.33} \right] \\ \left[1 + 3.03 \left(\frac{\rho_f}{\rho_v} \right)^{0.78} \left(\frac{C_p \Delta T_{\text{sub}}}{h_{fv}} \right)^{0.42} \right] \quad (13.88)$$

Most practical immersion cooling systems operate in a closed loop, where the vapor of the dielectric liquid is condensed and returned to the electronic enclosure. Two such systems are shown in Fig. 13.32*a* and *b*. In Fig. 13.32*a* a “remote” condenser, external to the electronic enclosure and cooled by water, air, or other fluid, condenses the vapor leaving the enclosure and directs the condensate back to the enclosure for reuse. In the configuration represented by Fig. 13.32*b*, the condenser is located in the vapor

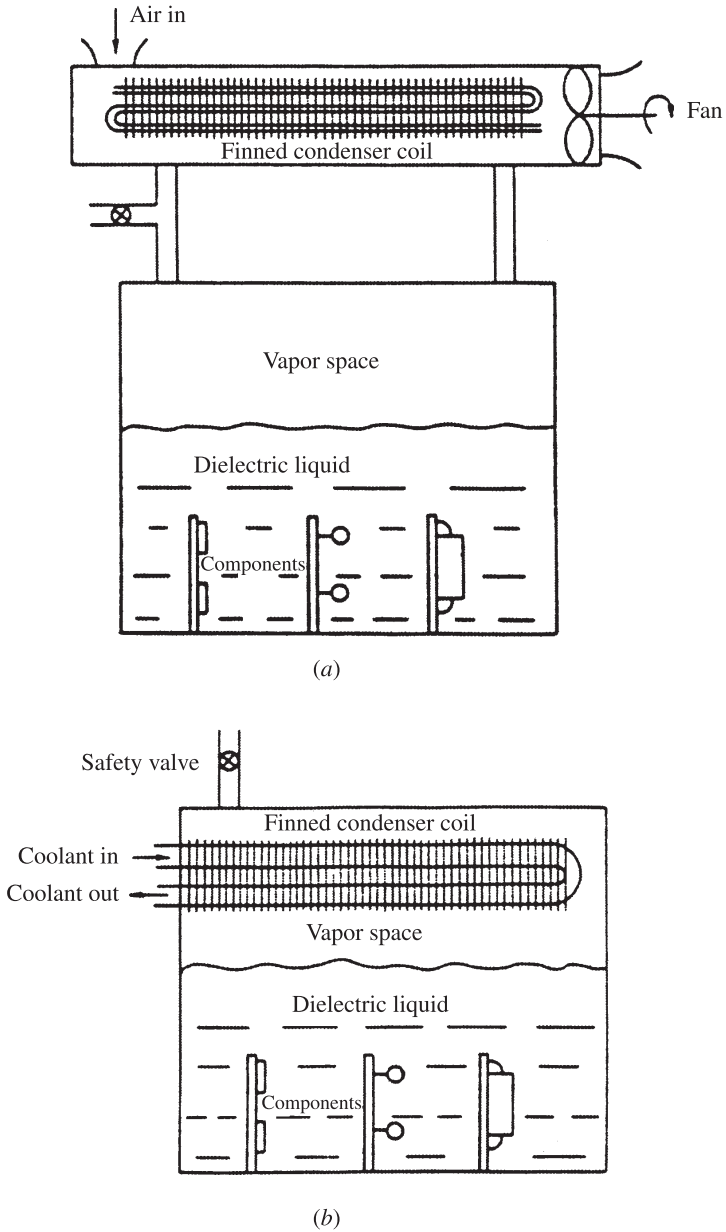


Figure 13.32 Two closed-loop immersion cooling systems.

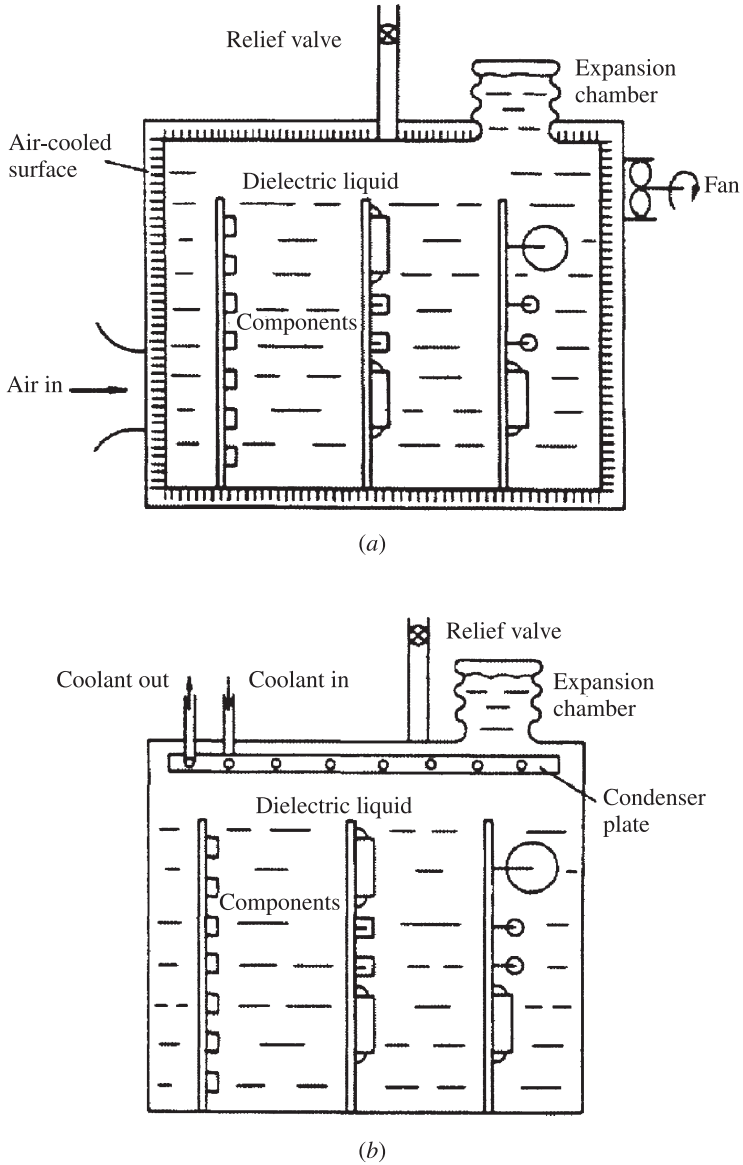


Figure 13.33 Submerged condenser immersion cooling systems.

space above the liquid—producing a more compact immersion module design—and the condensate drips back into the liquid.

As discussed previously, due to the high solubility of air in the perfluorinated fluorocarbons, often used as immersion cooling liquids, it is not uncommon for vapor space condensers to be affected adversely by a buildup of noncondensable gas.

Such difficulties can be avoided by submerging the condenser (i.e., heat exchanger tubes) in the liquid, as shown in Fig. 13.33*a*. The circulating water through the tubes absorbs the heat from the dielectric liquid, thus subcooling the liquid. Any vapor bubbles generated by boiling on the component surfaces collapse and condense in the subcooled liquid.

As a further modification of this approach, it is possible to use the side and top walls of the liquid-filled enclosure to serve as the submerged condenser, which can then be externally air- or liquid-cooled, as shown in Fig. 13.33*b*. Nelson et al. (1994), Kitching et al. (1995), and Geisler et al. (1996) have performed empirical studies on the cooling capabilities of “passive immersion cooled multichip modules” based on the concepts discussed above. Nelson et al. (1994) showed that the overall thermal performance of these modules was not affected by the presence of uneven chip power densities. The maximum power that can be dissipated from such modules depends on the nucleate pool boiling critical heat flux on the power-dissipating component as well as the condensation limit of the condenser. The thermal behavior of the module can be plotted on performance maps where the lower bound marked is determined by natural convection heat transfer on both heater and condenser sections. The natural convection correlation by Park and Bergles (1988) and those listed in Table 13.4 can be used to estimate the lower bound.

Once pool boiling is initiated on the heaters, one of the following two scenarios determines the cooling limit:

1. The maximum power dissipation from the module can be limited by the occurrence of the critical heat flux condition on the heater. Geisler et al. (1996) have shown that it may be possible to raise the critical heat flux limit by reducing the module-to-ambient thermal resistance, thereby increasing the subcooling of the coolant inside the module. The Watwe et al. (1997) correlation [see eq. (13.86)] can be used to compute the critical heat flux limit.

2. The maximum power dissipation from the module can also be limited if the condenser is unable to condense the volume of vapor generated at the heater. The uncondensed vapor will occupy the near wall regions of the condenser, thereby dramatically reducing the condenser efficiency.

The condensation limit on an unfinned flat plate condenser can be computed using the following correlation proposed by Gerstmann and Griffith (1966):

$$\text{Nu} = \begin{cases} 0.81\text{Ra}^{0.193} & \text{for } 10^{10} > \text{Ra} > 10^8 \\ 0.69\text{Ra}^{0.20} & \text{for } 10^8 > \text{Ra} > 10^6 \end{cases} \quad (13.89)$$

$$(13.90)$$

where the Nusselt number Nu and the Rayleigh number Ra are defined as follows:

$$\text{Nu} = \frac{h}{k_f} \left[\frac{\sigma_f}{g(\rho_f - \rho_v) \cos \theta} \right]^{1/2} \quad (13.91)$$

$$\text{Ra} = \frac{g \cos \theta \rho_f (\rho_f - \rho_v) h_{fv}}{k \mu \Delta T} \left[\frac{\sigma_f}{g(\rho_f - \rho_v) \cos \theta} \right]^{3/2} \quad (13.92)$$

where θ is a configuration factor which must be determined empirically. However, to obtain engineering estimates of the thermal performance, Bar-Cohen et al. (1987) have proposed a value of 31.5 for θ . The upper bound on the performance maps is therefore marked with both the CHF limit and the condensation limit.

13.8 THERMOELECTRIC COOLERS

The Peltier effect is the basis for the thermal electric cooler (TEC), which is a solid-state heat pump. If a potential is placed across two junctions, heat will be absorbed into one junction and expelled from the other in proportion to the current. Most material combinations exhibit the Peltier effect to some degree. However, it is most obvious across a p - n junction as shown in Fig. 13.34. As electrons are transported from the p -side of a junction to the n -side, they are elevated to a higher-energy state and thus absorb heat, resulting in cooling the surrounding area. When they are transported from the p -side to the n -side, they release heat.

The materials that have been used to make TEC include bismuth telluride (Bi_2Te_3), lead telluride (PbTe), and silicon germanium (SiGe). To obtain optimum parameters, these semiconductors are doped during fabrication. Bi_2Te_3 has the best performance at temperatures of interest for electronic components and is most commonly used. A TEC device is constructed by placing from one to several hundred thermocouples electrically in series and thermally in parallel between two pieces of metallized, thermally conductive ceramic acting as an electrical insulator. For continuous cooling at the low-temperature side of the TEC, the heat absorbed at the cold side, as well as the heat generated by the flow of electricity, must be removed from the hot side by one of the thermal transport mechanisms described previously. Solution of the governing equations for a thermoelectric couple yields a relation for the maximum temperature differential obtainable with such a device, as

$$\Delta T_{\max} = \frac{\alpha^2 T_c^2}{2KR} \quad (13.93)$$

$$K = \frac{k_a A_a}{L_a} + \frac{k_b A_b}{L_b} \quad (13.94)$$

$$R = \frac{\rho_a L_a}{A_a} + \frac{\rho_b L_b}{A_b} \quad (13.95)$$

It may thus be observed that the maximum temperature differential can be enhanced by minimizing the product of the thermal conductance K and electrical resistance R .

A TEC device is frequently rated by a figure of merit, as given by

$$\text{FOM} = \frac{\alpha_s^2}{\rho_{\text{TE}} k_{\text{TE}}} \quad (13.96)$$

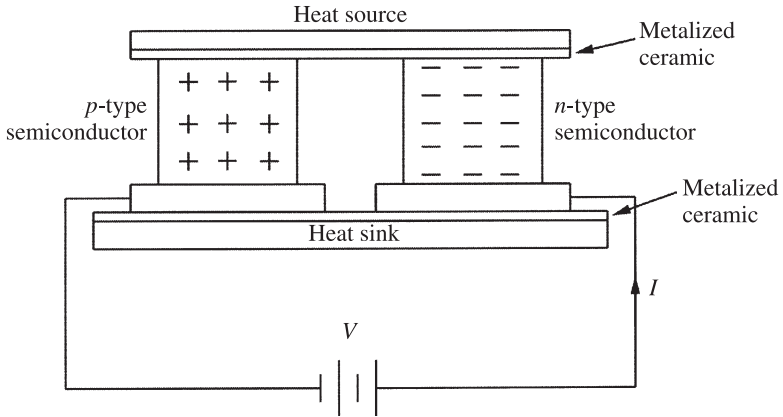


Figure 13.34 Thermoelectric cooler.

where α_s^2 is the Seebeck coefficient and ρ_{TE} is the resistivity of the TEC element. Values of this figure of merit are typically in the range 0.002 to 0.005 K^{-1} , but extensive research is under way to improve this FOM by as much as an order of magnitude in the next few years. The coefficient of performance of a TEC is defined as the ratio of heat pumped to the input power:

$$\text{COP} = \frac{\text{heat pumped}}{\text{input power}} = \frac{q_c}{P_{\text{in}}} \quad (13.97)$$

The optimum COP is given by

$$\text{COP}_{\text{opt}} = \frac{T_{\text{avg}}}{\Delta T} \frac{B - 1}{B + 1} - 0.5 \quad (13.98)$$

where

$$B = \sqrt{1 + (\text{FOM} \cdot T_{\text{avg}})} \quad (13.99)$$

A TEC may be selected from the performance and COP curves for a given set of design criteria. It is essential that the TEC and heat sink, as well as the power supply used to operate the TEC, be selected together. For increased cooling capacity, TECs may be operated in parallel. However, for lower chip temperatures it may be necessary to cascade several TEC devices or to operate them in series.

The biggest limitation in the use of a TEC for commercial electronics is the very low FOM. Recent years have witnessed extensive research in the area of TECs from a material point of view to increase the FOM. Thin-film superlattice and quantum-well structures have shown evidence of providing high FOM compared to the state-of-the-art TEC.

13.9 CHIP TEMPERATURE MEASUREMENT

As mentioned previously, the total thermal resistance of a package is usually the sum of θ_{jc} (junction to case) and θ_{ca} (case to ambient). The object of most experimental programs is to determine these resistances. This knowledge then allows the junction temperature to be predicted as a function of power and cooling medium temperature and flow rate. θ_{jc} and θ_{ca} are typically measured in a lab environment with the help of test chips popularly known as test vehicles. There are basically two measurement methods commonly used to determine the temperature of a test vehicle die. The first makes use of a temperature-sensitive parameter on the test vehicle to determine the die temperature, such as one or more dedicated diodes or resistors. Calibration of these temperature sensors can be very time consuming. Furthermore, as a test vehicle can have more than one temperature sensor and there could also be part-to-part variability in the test vehicle coming out of the factory, time to calibrate each temperature sensor could be enormous. Solbrekken and Chiu (1998) introduced a simplified calibration procedure that utilizes single-resistance measurements either at room temperature or at the anticipated test temperature. In their proposed method 30 temperature sensors are selected randomly and are calibrated at three set-point temperatures. Then the average intercept of resistance versus temperature for the 30 temperature sensors is calculated. Later, for the calibration of other test vehicles for the same generation of products, the die is calibrated at a single temperature and the average intercept calculated for the 30 samples is used in conjunction with the single-point calibration for determining the temperature of the test vehicle. A second category of chip temperature measurement techniques includes liquid crystals, thermographic phosphors, laser scanners, infrared camera, and so on. Each of these methods presents a unique set of concerns, ranging from temperature resolution to cost of implementation.

13.10 SUMMARY

The fundamental principles and concepts for thermal management of electronics were presented in this chapter. Simplified equations for first-order analysis of the temperature on electronic components were also introduced. A variety of cooling techniques, including heat sinks, jet impingement cooling, liquid immersion cooling, and thermoelectric cooling, were also discussed.

NOMENCLATURE

Roman Letter Symbols

<i>A</i>	area, m ²
<i>a</i>	heat source area, m ²
<i>B</i>	constant, dimensionless
<i>b</i>	heat source size, m
	PCB spacing, m

Bi	Biot number, dimensionless [= hL/k]
C	constant in heat transfer coefficient correlations, dimensionless
C_p	specific heat, J/kg · K
CHF	critical heat flux, dimensionless
COP	coefficient of performance, dimensionless
c	speed of sound, m/s
D	diameter, m
d	diameter, m
El	Elenbaas number, dimensionless
El'	modified Elenbaas number, dimensionless
F_{ij}	radiation view factor from i to j , dimensionless
FOM	figure of merit, dimensionless
f	impingement area ratio, dimensionless
g	gravitational acceleration, m/s ²
H	height, m
	Kennedy (1959) spreading resistance factor, dimensionless
	hardness, N/m ²
h	heat transfer coefficient, W/m ² · K
h_{fv}	latent heat of vaporization, J/kg · K
\hbar	Planck's constant, dimensionless
K	conductance, W/K
k	thermal conductivity, W/m · K
k_b	Boltzmann constant, dimensionless
L	length, width, or thickness, m
l	mean free path, m
m	mass, kg
\dot{m}	mass flow rate, kg/s
N	number of atomic layers, dimensionless
n	number, dimensionless
Nu	Nusselt number, dimensionless [= hL/k]
P	pressure, N/m ²
	plate to air parameter, dimensionless
	perimeter, m
p	volume fraction, dimensionless
p_c	threshold volume fraction, dimensionless
Pr	Prandtl number, dimensionless [= $\mu C_p/k$]
Q	total heat flow, W
q	heat flow, W
q''	heat flux, W/m ²
R	thermal resistance, °C/W or K/W
r	radius, m
	asymmetry parameter, dimensionless
r_T	asymmetry parameter, dimensionless
Ra	Rayleigh number, dimensionless [= $(g\beta\Delta TL^3/\nu^2)\text{Pr}$]
Re	Reynolds number, dimensionless [= $\rho VL/\mu$]

S	shape factor, m^2
	shape parameter, dimensionless
T	temperature, $^{\circ}C$ or K
t	time, s
V	velocity, m/s
	volume, m^3
W	characteristic length (length or width), m
x	length or distance, m
Y	area-weighted interfacial gap, m
z	clear space between fins, m
Δk	change in thermal conductivity, $W/m \cdot K$
ΔT	temperature difference, $^{\circ}C$ or K
Δx	distance between two points, m

Greek Letter Symbols

α	thermal diffusivity, m^2/s
	Seebeck coefficient, dimensionless
β	volumetric expansion coefficient, K^{-1}
δ	thickness or gap width, m
	penetration depth, m
	heater thickness, m
ε	emissivity, dimensionless
ζ	ratio of heat source area to substrate area, dimensionless
η	fin efficiency, dimensionless
θ	thermal resistance, $^{\circ}C/W$
	asperity angle, deg
κ	conductance, W/K
	conduction factor, dimensionless
μ	dynamic viscosity, $N \cdot s/m^2$
ν	kinematic viscosity, m^2/s
π	pi, dimensionless
ρ	density, kg/m^3
σ	Stefan–Boltzmann constant, $W/m^2 \cdot K^4$
	surface tension, N/m
	surface roughness, m
τ	time constant, s
ϕ	Debye temperature, K
φ	particle volume fraction, dimensionless
	maximum packing fraction, dimensionless
φ_m	maximum packing fraction, dimensionless
χ	ratio of logarithmic conductances, dimensionless

Subscripts

0	initial (at time = 0) or based on channel inlet
1	item or entity 1

1D	one-dimensional
2	item or entity 2
<i>a</i>	ambient or entity <i>a</i>
<i>ad</i>	adiabatic
amb	ambient
avg	average
<i>b</i>	boundary or base or entity <i>b</i>
bj	bare junction
base	heat sink base area
bulk	bulk
<i>c</i>	case or cutout
<i>ca</i>	case to ambient
cm	control material
<i>co</i>	contact
<i>D</i>	diameter
<i>e</i>	encapsulant
<i>en</i>	equivalent normal
eq	equivalent in-plane
ex	external or excursion
<i>f</i>	fluid
<i>f_g</i>	between saturated liquid and saturated vapor
filler	filler
film	film
fin	fin
<i>fl</i>	flow
<i>g</i>	interstitial fluid or gas (vapor)
gap	gap
<i>h</i>	hydraulic
HS	heat sink
<i>i</i>	counter
ICP	integrated circuit package
in	inlet
<i>j</i>	junction a counter
<i>jc</i>	junction to case
jet	jet
<i>jj</i>	mode of sound
<i>m</i>	continuous phase or matrix and maximum packing fraction
max	maximum
<i>mc</i>	between interface and matrix
<i>nc</i>	noncontacting
nom	nominal
opt	optimum
out	outlet
<i>p</i>	particle
	plane

	filler at constant pressure
r	radiation or radial direction
real	real
s	silicon
	mean condition
sat	saturation
sk	heat sink
source	source
sp	spreading
ss	steady state
sub	subcooled
T	total or overall
TE	thermoelectric device
TIM	thermal interface material
v	vapor
w	wall or wetted
x	layer designation
z	position along the z -coordinate direction

Superscripts

n	normal direction
p	in-plane direction

REFERENCES

- Asheghi, M., Touzelbaev, M. N., Goodson, K. E., Leung, Y. K., and Wong, S. S. (1996). Temperature Dependent Thermal Conductivity of Single Crystal Silicon Layers in SOI Substrates, *Proc. International Mechanical Engineering Congress and Exposition*, Atlanta, GA, Nov. 17–22, DSC-Vol. 59.
- Aung, W. (1972). Fully Developed Laminar Free Convection between Vertical Plates Heated Asymmetrically, *Int. J. Heat Mass Transfer*, 15, 1577–1580.
- Aung, W., Fletcher, L. S., and Sernas, V. (1972). Developing Laminar Free Convection between Vertical Flat Plates with Asymmetric Heating, *Int. J. Heat Mass Transfer*, 15, 2293–2308.
- Bar-Cohen, A. (1987). Thermal Management of Air and Liquid-Cooled Multi-chip Modules, *IEEE Trans. Components Hybrids Manuf. Technol.*, 10(2), 159–175.
- Bar-Cohen, A., and Rohsenow, W. M. (1984). Thermally Optimum Spacing of Vertical Natural Convection Cooled, Parallel Plates, *J. Heat Transfer*, 106, 116–123.
- Bar-Cohen, A., and Simon, T. W. (1986). Wall Superheat Excursions in the Boiling Incipience of Dielectric Fluids, *Heat Transfer Eng.*, 9(3), 19–30.
- Bar-Cohen, A., Perelman, A., and Sabag, A. (1987). Bubble Pumped Convective Augmentation on Vertical Submerged Condenser Surfaces, *Proc. ASME/JSME Thermal Engineering Joint Conference*, Vol. 3, pp. 431–440.
- Bergles, A. E., and Bar-Cohen, A. (1990). Direct Liquid Cooling of Microelectronic Components, in *Advances in Thermal Modeling of Electronic Components and Systems*, Vol. II, A. Bar-Cohen and A. D. Kraus, eds., ASME, New York, pp. 233–342.

- Bilitzky, A. (1986). The Effect of Geometry on Heat Transfer by Free Convection from a Fin Array, M.S. thesis, Department of Mechanical Engineering, Ben-Gurion University of the Negev, Beer Sheva, Israel.
- Bodoia, J. R., and Osterle, J. F. (1964). The Development of Free Convection between Heated Vertical Plates, *J. Heat Transfer*, 84, 40–44.
- Brdlik, P. M., and Savin, V. K. (1965). Heat Transfer between an Axisymmetric Jet and a Plate Normal to the Flow, *J. Eng. Phys.*, 8, 91–98.
- Chesser, J. B., Peterson, G. P., and Lee, S. (2000). A Simplified Method for Determining the Capillary Limitation of Flat Plate Heat Pipes in Electronic Cooling Applications, in *Proc. 34th National Heat Transfer Conference*, Pittsburgh, PA.
- Cooper, M. G., Mikic, B. B., and Yovanovich, M. M. (1969). Thermal Contact Resistance, *Int. J. Heat Mass Transfer*, 12, 279–300.
- Cross, R. (1996). Synergistic Combinations of Thermally Conductive Fillers in Polymer Matrices, *Microelectron. Int.*, 41, 27–29.
- Danielson, R. D., Tousignant, L., and Bar-Cohen, A. (1987). Saturated Pool Boiling Characteristics of Commercially Available Per-fluorinated Inert Liquids, *Proc. 1987 ASME/JSME Thermal Engineering Joint Conference*, Honolulu, HI, Vol. 3, pp. 419–430.
- Davis, L. C., and Artz, B. E. (1995). Thermal Conductivity of Metal Matrix Composites, *J. Appl. Phys.*, 77, 4954–4960.
- Devpura, A., Phelan, P. E., and Prasher, R. S. (2000). Percolation Theory Applied to the Analysis of Thermal Interface Materials in Flip-Chip Technology, *Proc. Itherm*, May 23–26, Vol. 1, pp. 21–29.
- Dunn, P. D., and Reay, D. A. (1994). *Heat Pipes*, 4th ed., Elsevier Science, Oxford.
- Eckert, E. R. G., and Drake, R. M., Jr. (1987). *Analysis of Heat and Mass Transfer*, Hemisphere Publishing, New York.
- El Sheikh, H. A., and Garimella, S. V. (2000). Heat Transfer from Pin-Fin Heat Sinks under Multiple Impinging Jets, *IEEE Trans. Adv. Packag.*, Vol. 23(1), 113–120.
- Elenbaas, W. (1942). Heat Dissipation of Parallel Plates by Free Convection, *Physica*, 9(1), 665–671.
- Fletcher, L. S. (1972). A Review of Thermal Control Materials for Metallic Junctions, *J. Spacecr. Rockets*, 9(12), 849–850.
- Geisler, K. J., Kitching, D., and Bar-Cohen, A. (1996). A Passive Immersion Cooling Module with a Finned Submerged Condenser, presented at Arthur E. Bergles Symposium on Process, Enhanced and Multi-phase Heat Transfer.
- Gerstmann, J., and Griffith, P. (1967). Laminar Film Condensation on the Underside of Horizontal and Inclined Surfaces, *Int. J. Heat and Mass Transfer*, 10, 551–580.
- Graham, K., and Witzman, S. (1988). Analytical Correlation of Thermal Design of Electronic Packages, in *Cooling Technology for Electronic Equipment*, Hemisphere Publishing, New York.
- Haramura, Y., and Katto, Y. (1983). A New Hydrodynamic Model of Critical Heat Flux Applicable Widely to Both Pool and Forced Convection Boiling on Submerged Bodies in Saturated Liquids, *Int. J. Heat Mass Transfer*, 26, 389–399.
- Heaton, H. S., Reynolds, W. C., and Kays, W. M. (1964). Heat Transfer in Annular Passages: Simultaneous Development of Velocity and Temperature Fields in Laminar Flow, *Int. J. Heat Mass Transfer*, 7, 763–781.

- Howard, R. T., Furkay, S. S., Kilburn, R. F., and Monti, G., Jr. (1984). *Thermal Management Concepts in Micro Electronic Packaging: From Component to System*, International Society for Hybrid Microelectronics, Silver Spring, MD.
- Howell, J. R. (1982). *A Catalog of Radiative Transfer Factors*, McGraw-Hill, New York.
- Incropera, F. P., and DeWitt, D. P. (1996). *Fundamentals of Heat and Mass Transfer*, 4th ed., Wiley, New York.
- Jones, C. D., and Smith, L. F. (1970). Optimum Arrangement of Rectangular Fins on Horizontal Surfaces for Free Convection Heat Transfer, *J. Heat Transfer*, 92, 6.
- Kays, W. M., and Crawford, M. E. (1993). *Convective Heat and Mass Transfer*, McGraw-Hill, New York.
- Kennedy, D. P. (1959). Heat Conduction in a Homogeneous Solid Circular Cylinder of Isotropic Media, *IBM Report TR 00.15072.699*.
- Kitching, D., Ogata, T., and Bar-Cohen, A. (1995). Thermal Performance of a Passive Immersion-Cooling Multi-chip Module, *J. Enhanced Heat Transfer*, 2(1/2), 95–103.
- Kraitshev, S. G., and Schlünder, E. U. (1973). Paper presented at the Fachausschuss Trocknungstechnik der Verfahrenstechnischen Gesellschaft im Verein Deutscher Ingenieure (VDI), Colmar, France; synopsis in 1973, *Chem. Ing. Tech.*, 42, 1324.
- Kraus, A. D. (1958). The Use of Steady State Electrical Network Analysis in Solving Heat Flow Problems, *Proc. 2nd National ASME/AICHE Heat Transfer Conference*, Chicago, Aug.
- Kraus, A. D., and Bar-Cohen, A. (1983). *Thermal Analysis and Control of Electronic Equipment*, McGraw-Hill/Hemisphere Publishing, New York.
- Krotzsch, P. (1968). Wärme und Stoffübertragung bei Pallströmung aus Düsen und Blendentel dem *Chem. Ing. Tech.*, 40(7), 339–344.
- Kutateladze, S. S. (1951). A Hydrodynamic Theory of Changes in the Boiling Process under Free Convection Conditions, *Izv. Akad. Nauk SSSR, Otd. Tekhn. Nauk*, 4, 529 (translation in *AEC-TR-1441*).
- Lee, T. Y., and Simon, T. W. (1989). High-Heat-Flux Forced Convection Boiling from Small Regions, *Heat Transfer in Electronics, 1989, ASME-HTD-111*, ASME, New York, p. 7.
- Lee, S., Song, S., Au, V., and Moran, K. P. (1995). Constriction/Spreading Resistance Model for Electronic Packaging, *Proc. 4th ASME/JSME Thermal Engineering Joint Conference*, Vol. 4, pp. 199–206.
- Lewis, T. B., and Nielsen, L. E. (1970). Dynamic Mechanical Properties of Particulate Filled Composites, *J. Appl. Polym. Sci.*, 14, 1449–1471.
- Lewis, R. W., Morgan, K., Thomas, H. R., and Seetharamu, K. N. (1996). *The Finite Element Method in Heat Transfer Analysis*, Wiley, New York.
- Maddox, D. E., and Bar-Cohen, A. (1991). Thermofluid Design of Submerged-Jet Impingement Cooling for Electronic Components, *Proc. ASME/AICHE National Heat Transfer Conference*, Minneapolis, MN.
- Madhusudan, C. V. (1995). *Thermal Contact Conductance*, Springer-Verlag, New York.
- Majumdar, A. (1993). Microscale Heat Conduction in Dielectric Thin Films, *J. Heat Transfer*, 115, 7–16.
- Martin, H. (1977). Heat and Mass Transfer between Impinging Gas Jets and Solid Surfaces, in *Advances in Heat Transfer*, Vol. 13, J. P. Hartnett and T. F. Irvine, Jr., eds., Academic Press, New York, pp. 1–60.
- McAdams, W. H. (1954). *Heat Transmission*, McGraw-Hill, New York.

- Mix, D., and Bar-Cohen, A. (1992). Transient and Steady-State Thermo-structural Modeling of a PDIP Package, *ASME Publication 92-WA/EEP-10*, ASME 1992 Winter Annual Meeting, Anaheim, CA, Nov.
- Miyatake, O., and Fujii, T. (1972). Free Convective Heat Transfer between Vertical Parallel Plates: One Plate Isothermally Heated and the Other Thermally Insulated, *Heat Transfer Jpn. Res.*, 3, 30–38.
- Miyatake, O., Fujii, T., Fujii, M., and Tanaka, H. (1973). Natural Convective Heat Transfer between Vertical Parallel Plates: One Plate with a Uniform Heat Flux and the Other Thermally Insulated, *Heat Transfer Jpn. Res.*, 4, 25–33.
- Moffat, R. J., and Ortega, A. (1988). Direct Air-Cooling of Electronic Components, in *Advances in Thermal Modeling of Electronic Components and Systems*, Vol. 1, A. Bar-Cohen and A. D. Kraus, eds., ASME, New York, pp. 129–265.
- Mudawar, I., and Wadsworth, D. C. (1990). Critical Heat Flux from a Simulated Electronic Chip to a Confined Rectangular Impinging Jet of Dielectric Liquid, *Int. J. Heat Mass Transfer*, 34, 1465–1480.
- Murthy, S. S., Joshi, Y. K., and Nakayama, W. (2000). Single Chamber Compact Thermosyphons with Micro-fabricated Components, *Proc. Itherm*, May 23–26, pp. 321–327.
- Nan, C. W., Birringer, R., Clarke, D. R., and Gleiter, H. (1997). Effective Thermal Conductivity of Particulate Composites with Interfacial Thermal Resistance, *J. Appl. Phys.*, 81, 6692–6699.
- National Electronics Manufacturing Institute (1996). *Technology Roadmap*, NEMI, Herndon, VA.
- Negus, K. J., Yovanovich, M. M., and Beck, J. V. (1989). On the Non-dimensionalization of Constriction Resistance for Semi-infinite Heat Flux Tubes, *J. Heat Transfer*, 111, 804–807.
- Nelson, R. D., Sommerfeldt, S., and Bar-Cohen, A. (1994). Thermal Performance of an Integral Immersion Cooled Multi-chip Module Package, *IEEE Trans. Components Packag. Manuf. Technol.*, A17(3), 405–412.
- Nonn, T., Dagan, Z., and Jiji, L. M. (1988). Boiling Jet Impingement Cooling of Simulated Microelectronic Heat Sources, *ASME-88-WA/EEP-3*, ASME, New York.
- Park, K. A., and Bergles, A. E. (1988). Effects of Size of Simulated Microelectronic Chips on Boiling and Critical Heat Flux, *J. Heat Transfer*, 110, 728–734.
- Pecht, M., Lall, P., and Hakim, E. (1992). The Influence of Temperature on Integrated Circuit Failure Mechanisms, in *Advances in Thermal Modeling of Electronic Components and Systems*, Vol. 3, A. Bar-Cohen and A. D. Kraus, eds., ASME, New York, pp. 61–152.
- Prasher, R. S. (2001). Surface Chemistry and Characteristics Based Model for the Contact Resistance of Polymeric Interstitial Thermal Interface Materials, *J. Heat Transfer*, 123, 969–975.
- Prasher, R. S., and Phelan, P. E. (1998). Size Effects on the Thermodynamic Properties of Thin Solid Films, *J. Heat Transfer*, 120(4), 1078–1081.
- Rohsenow, W. M. (1951). A Method of Correlating Heat Transfer Data for Surface Boiling of Liquids, *Trans. ASME*, 74, 969–976 (reprinted in *Proc. 3rd ASME/JSME Thermal Engineering Joint Conference*, Vol. 1, pp. 503–512).
- Sathe, S. B., and Joshi, Y. (1992). Natural Convection Liquid Cooling of a Substrate-Mounted Protrusion in a Square Enclosure: A Parametric Study, *J. Heat Transfer*, 114, 401–409.
- Sauer, H. J., Jr. (1992). Comparative Enhancement of Thermal Contact Conductance of Various

- Classes of Interstitial Materials, *Proc. NSF/DITAC Workshop*, Monash University, Melbourne, Victoria, Australia, pp. 103–115.
- Schlünder, E. U., Krotzsch, P., and Hennecke, F. W. (1970). Gesetzmäßigkeiten der Wärme- und Stoffübertragung bei der Prallströmung aus Ring- und Schlitzdüsen, *Chem. Ing. Tech.*, 42, 333–338.
- Sergeant, J., and Krum, A. (1994). *Thermal Management Handbook for Electronic Assemblies*, McGraw-Hill, New York.
- Semiconductor Industry Association (1997). *National Technology Roadmap for Semiconductors: Technology Needs*, Semiconductor Industry Association, Washington, DC.
- Simons, R. E., Antonetti, V. W., Nakayama, W., and Oktay, S. (1997). Heat Transfer in Electronic Packages, in *Microelectronics Packaging Handbook*, 2nd ed. Part I, Tummala, R. R., Rymaszewski, E. J., and Klopfenstein, A. G., eds., pp. 1-315 to 1-403, Chapman and Hall, New York, N.Y.
- Sitharamayya, S., and Raju, K. S. (1969). Heat Transfer between an Axisymmetric Jet and a Plate Held Normal to the Flow, *Can. J. Chem. Eng.*, 47, 365–368.
- Solbrekken, G. L., and Chiu, C.-P. (1998). Single Temperature Calibration Method for Die Level Temperature Sensors. Using a Single Temperature Technique, *IEEE Trans. Components and Packaging Tech.*, 23(1), 40–46.
- Song, S., Lee, S., and Au, V. (1994). Closed Form Equation for Thermal Constriction/Spreading Resistances with Variable Resistance Boundary Condition, *Proc. 1994 IEPS Conference*, pp. 111–121.
- Sparrow, E. M., and Bahrami, P. A. (1980). Experiments on Natural Convection from Vertical Parallel Plates with Either Open or Closed Edges, *J. Heat Transfer*, 102, 221–227.
- Starner, K. E., and McManus, H. N. (1963). An Experimental Investigation of Free Convection Heat Transfer from Rectangular Fin Arrays, *J. Heat Mass Transfer*, 85, 273–278.
- Stevens, J., and Webb, B. W. (1989). Local Heat Transfer Coefficients under an Axisymmetric, Single-Phase Liquid Jet, *Proc. National Heat Transfer Conference*, Philadelphia, pp. 113–119.
- Swartz, E. T., and Pohl, R. O. (1989). Thermal Boundary Resistance, *Rev. Modern Phys.*, 61(3).
- Tien, C. L., and Chen, G. (1994). Challenges in Microscale Conductive and Radiative Heat Transfer, *J. Heat Transfer*, 116, 799–807.
- Van de Pol, D. W., and Tierney, J. K. (1973). Free Convection Nusselt Number for Vertical U-Shaped Channels, *J. Heat Transfer*, 95, 542–543.
- Wadsworth, D. C., and Mudawar, I. (1990). Cooling of a Multichip Electronic Module by Means of Confined Two Dimensional Jets of Dielectric Liquid, *J. Heat Transfer*, 112, 891–898.
- Wang, X. S., Dagan, Z., and Jiji, L. M. (1990). Heat Transfer between a Laminar Free-Surface Impinging Jet and a Composite Disk, *Proc. 9th International Heat Transfer Conference*, Vol. 4, Hemisphere Publishing, New York, p. 137.
- Watwe, A. A., Bar-Cohen, A., and McNeil, A. (1997). Combined Pressure and Subcooling Effects on Pool Boiling from a PPGA Chip Package, *J. Electron. Packag.*, 119(2), 95–105.
- Welling, J. R., and Wooldridge, C. B. (1965). Free Convection Heat Transfer Coefficients from Rectangular Vertical Fins, *J. Heat Transfer*, 87, 439–444.
- Witzman, S. (1998). Thermal Modeling of Air Cooled Components Mounted on Printed Circuit Boards, in *Advances in Thermal Modeling of Electronic Components and Systems*, Vol. 4, A. Bar-Cohen and A. D. Kraus, eds., ASME, New York, pp. 179–250.

- Womac, D. H. (1989). Single-Phase Axisymmetric Liquid Jet Impingement Cooling of Discrete Heat Sources, M.S. thesis, Department of Mechanical Engineering, Purdue University, West Lafayette, IN.
- Womac, D. J., Aharoni, G., Ramadhyani, S., and Incropera, F. P. (1990). Single Phase Liquid Jet Impingement Cooling of Small Heat Sources, in *Heat Transfer 1990 (Proc. 9th International Heat Transfer Conference)*, Vol. 4, Hemisphere Publishing, New York, pp. 149–154.
- Wroblewski, D., and Joshi, Y. (1992). Transient Natural Convection from a Leadless Chip Carrier in a Liquid Filled Enclosure: A Numerical Study, *J. Electron. Packag.*, 114, 271–279.
- Xu, Y., Luo, X., and Chung, D. D. L. (2000). Sodium Silicate Based Thermal Interface Material for High Thermal Contact Conductance, *J. Electron. Packag.*, 122, 128–131.
- You, S. M., Simon, T. W., and Bar-Cohen, A. (1990). Experiments on Boiling Incipience with a Highly-Wetting Dielectric Fluid: Effects of Pressure, Subcooling and Dissolved Gas Content, *Proc. 9th International Heat Transfer Conference*, Jerusalem, Israel, Vol. 3, pp. 337–342.
- Yovanovich, M. M. (1990). Personal communication.
- Yovanovich, M. M., and Antonetti, V. W. (1988). Application of Thermal Contact Resistance Theory to Electronic Packages, in *Advances in Thermal Modeling of Electronic Components and Systems*, Vol. 1, A. D. Kraus, and A. Bar-Cohen, eds., Hemisphere Publishing, New York.
- Zeng, S., Chen, C.-H., Mikkelsen, J. C., and Santiago, J. G. (2000). Fabrication and Characterization of Electrokinetic Micro Pumps, *Proc. Itherm*, May 23–26, pp. 31–36.
- Zorbil, V., Stulc, P., and Polase, F. (1988). Enhancement Cooling of Boards with Integrated Circuits by Heat Pipes, *Proc. 3rd International Heat Pipe Symposium*, Tsukuba, Japan, pp. 273–279.
- Zuber, N. (1959). Atomic Energy Commission Technical Information Service, *Report AECU-4439*, Atomic Energy Commission, Washington, DC.

Heat Transfer Enhancement

R. M. MANGLIK

Thermal-Fluids and Thermal Processing Laboratory
Department of Mechanical, Industrial and Nuclear Engineering
University of Cincinnati, Cincinnati, Ohio

- 14.1 Introduction
 - 14.1.1 Classification of enhancement techniques
 - 14.1.2 Performance evaluation criteria
- 14.2 Treated surfaces
 - 14.2.1 Boiling
 - 14.2.2 Condensing
- 14.3 Rough surfaces
 - 14.3.1 Single-phase flow
 - 14.3.2 Boiling
 - 14.3.3 Condensing
- 14.4 Extended surfaces
 - 14.4.1 Single-phase flow
 - 14.4.2 Boiling
 - 14.4.3 Condensing
- 14.5 Displaced enhancement devices
 - 14.5.1 Single-phase flow
 - 14.5.2 Boiling
 - 14.5.3 Condensing
- 14.6 Swirl flow devices
 - 14.6.1 Single-phase flow
 - 14.6.2 Boiling
 - 14.6.3 Condensing
- 14.7 Coiled tubes
 - 14.7.1 Single-phase flow
 - 14.7.2 Boiling
 - 14.7.3 Condensing
- 14.8 Additives for liquids
 - 14.8.1 Single-phase flow
 - 14.8.2 Boiling
- 14.9 Active techniques
- 14.10 Compound enhancement

Nomenclature

References

14.1 INTRODUCTION

The conversion, utilization, and recovery of energy in every industrial, commercial, and domestic application involve a heat exchange process. Some common examples are steam generation and condensation in power and cogeneration plants; sensible heating and cooling of viscous media in thermal processing of chemical, pharmaceutical, and agricultural products; refrigerant evaporation and condensation in air conditioning and refrigeration; gas flow heating in manufacturing and waste-heat recovery; air and liquid cooling of engine and turbomachinery systems; and cooling of electrical machines and electronic devices. Improved heat exchange, over and above that in the usual or standard practice, can significantly improve the thermal efficiency in such applications as well as the economics of their design and operation.

The engineering cognizance of the need to increase the thermal performance of heat exchangers, thereby effecting energy, material, and cost savings as well as a consequential mitigation of environmental degradation had led to the development and use of many heat transfer *enhancement* techniques. These methods have in the past been referred to variously as *augmentation* and *intensification*, among other terms. There is an enormous database of technical literature on the subject, now estimated at over 8000 technical papers and reports, which has been disseminated periodically in numerous bibliographic reports (Bergles et al., 1983, 1991, 1995; Jensen and Shome, 1994), reviews (Webb and Bergles, 1983a; Webb, 1987; Shatto and Peterson, 1996; Bergles, 1998, 1999; Manglik and Bergles, 2002a), and monographs and edited texts (Thome, 1990; Webb, 1994; Manglik and Kraus, 1996; Kakaç et al., 1999). This information growth, represented by the typical yearly distribution of technical publications depicted in Fig. 14.1, urgently warrants that a digital library of enhanced heat and mass transfer be established (Bhatnagar and Manglik, 2002). This literature documents the extensive research effort devoted to establishing the conditions under which enhancement techniques will improve the heat or mass transfer in various applications. An effort that began more than 140 years ago, when the first attempt to enhance heat transfer coefficients in condensing steam was reported in the classical study by J. P. Joule (1861), continues to be a major research and development activity (Manglik et al., 2000; Bergles, 2000).

Enhancement techniques essentially reduce the thermal resistance in a conventional heat exchanger by promoting higher convective heat transfer coefficient with or without surface area increases (as represented by fins or extended surfaces). As a result, the size of a heat exchanger can be reduced, or the heat duty of an existing exchanger can be increased, or the pumping power requirements can be reduced, or the exchanger's operating approach temperature difference can be decreased. The latter is particularly useful in thermal processing of biochemical, food, plastic, and pharmaceutical media, to avoid thermal degradation of the end product. On the other hand, heat exchange systems in spacecraft, electronic devices, and medical applications, for example, may rely primarily on enhanced thermal performance for their successful operation. The commercialization of enhancement techniques, where the technology has been transferred from the research laboratory to full-scale industrial use of those that are more effective and workable (Bergles et al., 1991; Fletcher and

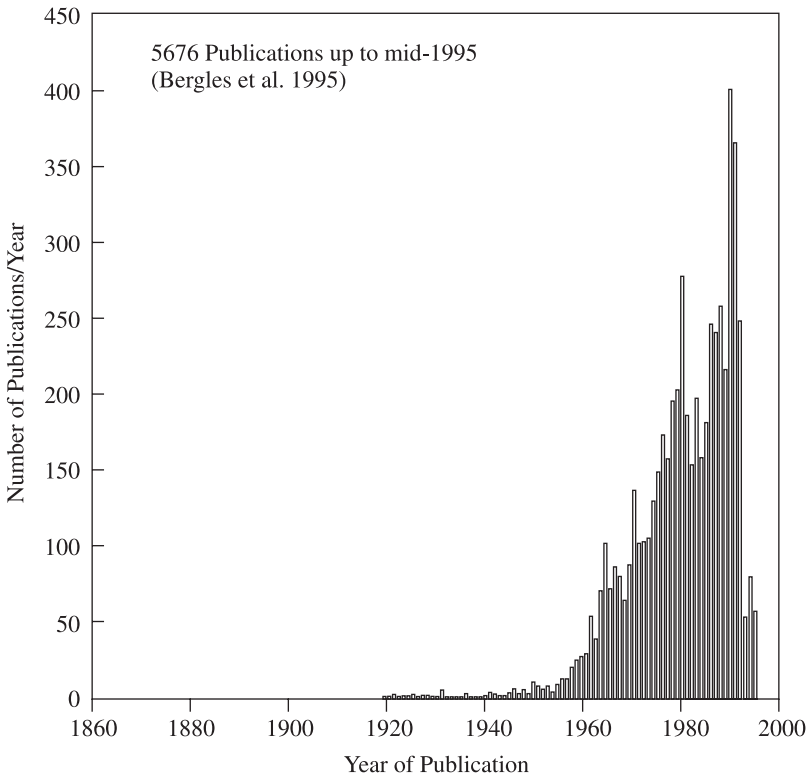


Figure 14.1 Yearly growth of the published technical literature on heat transfer enhancement (citations up to mid-1995). (From Bergles et al., 1995.)

Andrews, 1994), has also led to a larger number of patents (Webb et al., 1983; Bergles et al., 1991; Webb et al., 1993, 1994).

In this chapter we give an overview of the state of the art in heat transfer enhancement in various applications and provide a review of the pertinent literature. The use of many different techniques, their thermal–hydraulic performance (with lists of predictive correlations for the heat transfer and pressure drop, or reference to design databases, wherever available), and some methodologies for design optimization and overall performance evaluation of heat exchangers are outlined.

14.1.1 Classification of Enhancement Techniques

Sixteen different enhancement techniques have been identified by Bergles et al. (1983, 1991, 1995), which can be classified broadly as *passive* and *active* techniques. A list of the various methods or devices under each of these two categories is given in Table 14.1. The primary distinguishing feature is that unlike active methods, passive techniques do not require direct input of external power. They generally use surface

TABLE 14.1 Classification of Various Heat Transfer Enhancement Techniques

Passive Techniques	Active Techniques
Treated surfaces	Mechanical aids
Rough surfaces	Surface vibration
Extended surfaces	Fluid vibration
Displaced enhancement devices	Electrostatic fields
Swirl flow devices	Injection
Coiled tubes	Suction
Surface tension devices	Jet impingement
Additives for liquids	
Additives for gases	
Compound Enhancement	
Two or more passive and/or active techniques that are employed together	

or geometrical modifications to the flow channel, or incorporate an insert, material, or additional device. Except for extended surfaces, which increase the effective heat transfer surface area, these passive schemes promote higher heat transfer coefficients by disturbing or altering the existing flow behavior. This, however, is accompanied by an increase in the pressure drop. In the case of active techniques, the addition of external power essentially facilitates the desired flow modification and the concomitant improvement in the rate of heat transfer. The use of two or more techniques (passive and/or active) in conjunction constitutes *compound enhancement*.

The effectiveness of any of these methods is strongly dependent on the mode of heat transfer (single-phase free or forced convection, pool boiling, forced convection boiling or condensation, and convective mass transfer), and type and process application of the heat exchanger. In considering their specific applications, a descriptive characterization of each of the 16 techniques is useful in assessing their potential. The descriptions of *passive techniques*, as given by Bergles (1998), are as follows:

1. *Treated surfaces* are heat transfer surfaces that have a fine-scale alteration to their finish or coating. The alteration could be continuous or discontinuous, where the roughness is much smaller than what affects single-phase heat transfer, and they are used primarily for boiling and condensing duties.
2. *Rough surfaces* are generally surface modifications that promote turbulence in the flow field, primarily in single-phase flows, and do not increase the heat transfer surface area. Their geometric features range from random sand-grain roughness to discrete three-dimensional surface protuberances.
3. *Extended surfaces*, more commonly referred to as *finned surfaces*, provide an effective heat transfer surface area enlargement. Plain fins have been used routinely

in many heat exchangers. The newer developments, however, have led to modified finned surfaces that also tend to improve the heat transfer coefficients by disturbing the flow field in addition to increasing the surface area.

4. *Displaced enhancement devices* are inserts that are used primarily in confined forced convection, and they improve energy transport indirectly at the heat exchange surface by “displacing” the fluid from the heated or cooled surface of the duct with bulk fluid from the core flow.

5. *Swirl flow devices* produce and superimpose swirl or secondary recirculation on the axial flow in a channel. They include helical strip or cored screw-type tube inserts, twisted ducts, and various forms of altered (tangential to axial direction) flow arrangements, and they can be used for single-phase as well as two-phase flows.

6. *Coiled tubes* are what the name suggests, and they lead to relatively more compact heat exchangers. The tube curvature due to coiling produces secondary flows or Dean vortices, which promote higher heat transfer coefficients in single-phase flows as well as in most regions of boiling.

7. *Surface tension devices* consist of wicking or grooved surfaces, which direct and improve the flow of liquid to boiling surfaces and from condensing surfaces.

8. *Additives for liquids* include the addition of solid particles, soluble trace additives, and gas bubbles in single-phase flows, and trace additives, which usually depress the surface tension of the liquid, for boiling systems.

9. *Additives for gases* include liquid droplets or solid particles, which are introduced in single-phase gas flows in either a dilute phase (gas–solid suspensions) or dense phase (fluidized beds).

Descriptions for the various *active techniques* have been given as follows:

1. *Mechanical aids* are those that stir the fluid by mechanical means or by rotating the surface. The more prominent examples include rotating tube heat exchangers and scraped-surface heat and mass exchangers.

2. *Surface vibration* has been applied primarily, at either low or high frequency, in single-phase flows to obtain higher convective heat transfer coefficients.

3. *Fluid vibration* or fluid pulsation, with vibrations ranging from 1.0 Hz to ultrasound (~ 1.0 MHz), used primarily in single-phase flows, is considered to be perhaps the most practical type of vibration enhancement technique.

4. *Electrostatic fields*, which could be in the form of electric or magnetic fields, or a combination of the two, from dc or ac sources, can be applied in heat exchange systems involving dielectric fluids. Depending on the application, they can promote greater bulk fluid mixing and induce forced convection (corona “wind”) or electro-magnetic pumping to enhance heat transfer.

5. *Injection*, used only in single-phase flow, pertains to the method of injecting the same or a different fluid into the main bulk fluid either through a porous heat transfer interface or upstream of the heat transfer section.

6. *Suction* involves either vapor removal through a porous heated surface in nucleate or film boiling, or fluid withdrawal through a porous heated surface in single-phase flow.

7. *Jet impingement* involves the direction of heating or cooling fluid perpendicularly or obliquely to the heat transfer surface. Single or multiple jets (in clusters or staged axially along the flow channel) may be used in both single-phase and boiling applications.

As acknowledged by Bergles et al. (1983, 1996), there are some difficulties in classifying a few techniques, and the somewhat arbitrarily fuzzy distinctions between them should be recognized. A good example to illustrate this is the classification of some of the newer structured surfaces used in boiling (Bergles, 2000; Webb, 1994; Thome, 1990) as treated, rough, or extended surfaces. Perhaps a future subcategorization and/or recategorization of the enhancement techniques might be needed to sort out such issues in the ever-expanding database.

Furthermore, as mentioned earlier, any two or more of these techniques (passive and/or active) may be employed simultaneously to obtain enhancement in heat transfer that is greater than that produced by only one technique itself. This simultaneous utilization is termed *compound enhancement*. Some promising applications, for example, are in heat or mass exchangers where one technique may preexist; this is particularly so when the existing enhancement is from an active method.

14.1.2 Performance Evaluation Criteria

The issue of quantifying and evaluating the performance of enhancement devices, with a very broad and universal set of criteria, is complex and difficult. As Bergles (1998) has pointed out in his survey of the subject: "It seems impossible to establish a generally applicable selection criterion. . . ." Besides the relative thermal-hydraulic performance improvements brought about by the enhancement devices, there are many factors that may have to be considered. They include economic (engineering development, capital, installation, operating, maintenance, and other such costs), manufacturability (machining, forming, bonding, and other production processes), reliability (material compatibility, integrity, and long-term performance), and safety, among others. The assessment of these factors, as well as the enhanced convection performance, is usually application driven. The discussion in this chapter, however, will be restricted only to the convective thermal-hydraulic behavior, for which several criteria have been developed to quantify the relative enhancement in different applications (Bergles, 1998; Webb, 1994; Kays and London, 1984; Bergles et al., 1974a,b).

The enhanced heat transfer obtained in forced convection is always accompanied by an increase in the pressure drop. This is illustrated in Fig. 14.2 for typical cases of single-phase flows in (a) enhanced plate fin cores, and (b) tubes with structured surface roughness. As recommended by Marner et al. (1983), the results for the enhanced geometries are based on an equivalent parallel-plate duct (same plate separation) in the first case, and the "envelope" or "empty" tube diameter in the second case. This allows direct comparison of enhancement data with the "normal" or "smooth tube"

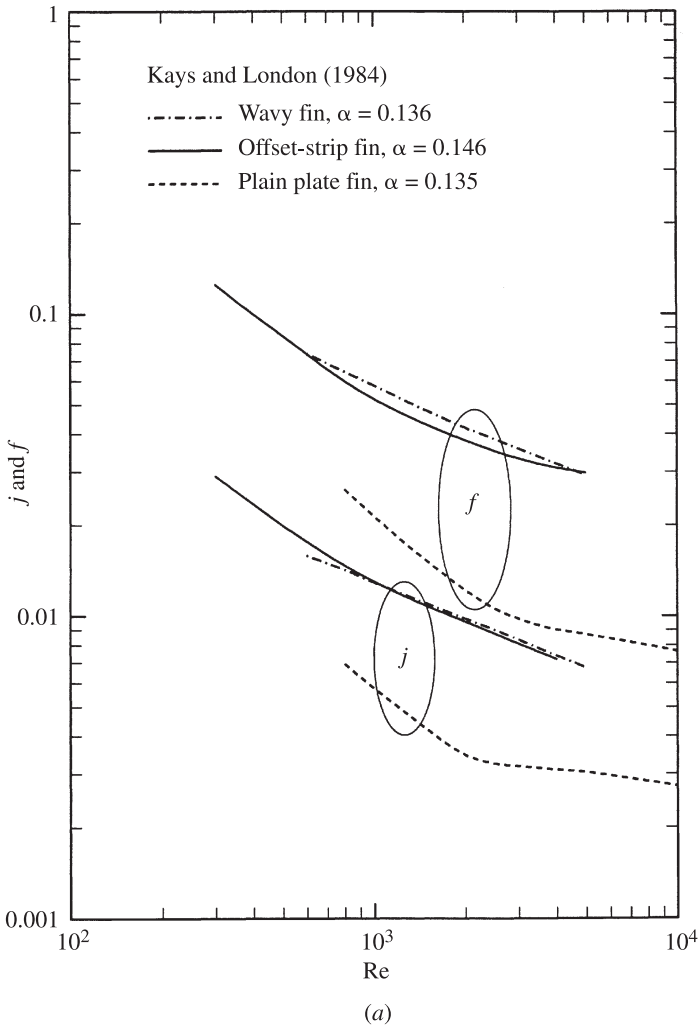


Figure 14.2 Typical thermal-hydraulic performance of enhanced surfaces: (a) enhanced plate fin geometries; (*continued*)

performance. It may be noted that in many enhanced duct geometries, particularly with inserts and extended surfaces, the hydraulic diameter is different from their “parent” flow channel. The improved heat transfer coefficients due to enhancement are evident from Fig. 14.2, as are the concomitant friction factors. Thus, the problem is essentially one of finding the optimum or net gain after considering the overall energy use of the heat exchanger.

In most practical applications of enhancement techniques, the following *performance objectives*, along with a set of *operating constraints* and *conditions*, are usually considered for optimizing the use of a heat exchanger:

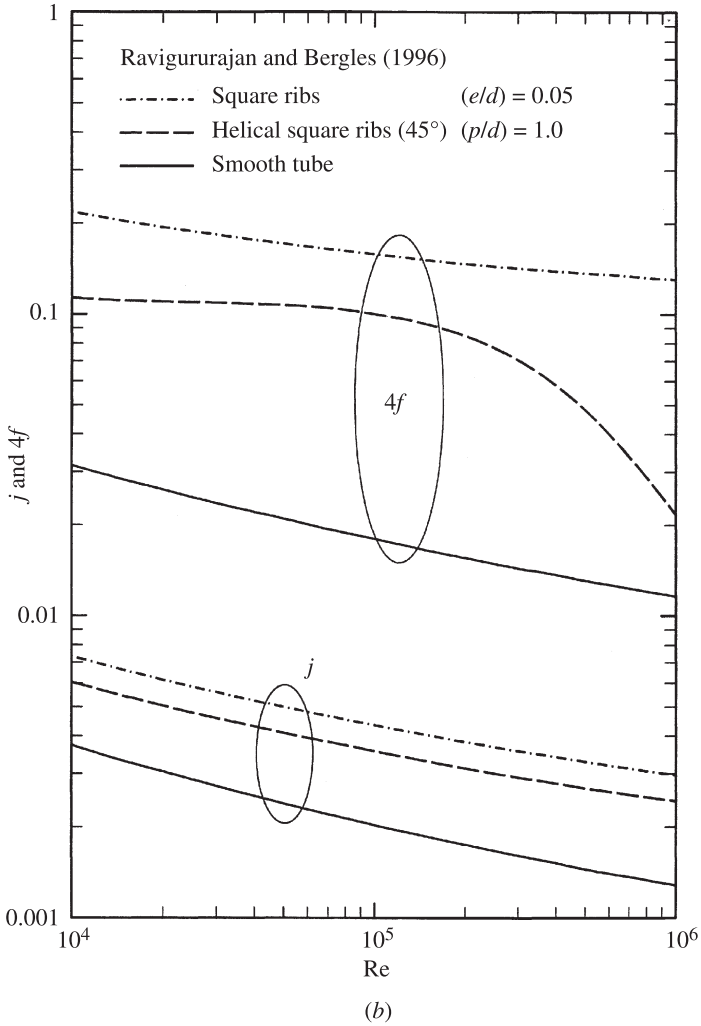


Figure 14.2 (Continued) (b) tubes with different internal roughness.

1. Increase the heat duty of an existing heat exchanger without altering the pumping power (or pressure drop) or flow rate requirements.
2. Reduce the approach temperature difference between the two heat-exchanging fluid streams for a specified heat load and size of exchanger.
3. Reduce the size or heat transfer surface area requirements for a specified heat duty and pressure drop.
4. Reduce the process stream's pumping power requirements for a given heat load and exchanger surface area.

It may be noted that objectives 1, 2, and 4 yield savings in operating (or energy) costs, and objective 3 lends to material savings and reduced capital costs. These objective functions and constraints have been described by many different performance evaluation criteria (PEC) in the literature (Bergles et al., 1974a,b; Webb, 1981, 1994; Bergles, 1998; for example). It is instructive to consider some of these PEC for the more common case of applying enhancement techniques to the conventional shell-and-tube heat exchanger.

The heat exchanger performance is represented by two dependent variables: heat transfer rate Q and pressure drop Δp or pumping power P , which can be expressed as

$$Q = (UA) \Delta T_m \quad (14.1)$$

$$\Delta p = 2f \frac{L}{d_i} \frac{G^2}{\rho} \quad \text{and} \quad P = \Delta p \frac{GA_c}{\rho} \quad (14.2)$$

Here the primary independent operating variables are the approach temperature difference ΔT_i [$\Delta T_m = \phi(\Delta T_i)$] and the mass flow rate \dot{m} , and in the case of the tubular geometry, the design variables (heat transfer surface area A or exchanger size) are the diameter d_i and length L of tubes and number of tubes N per pass. PEC are established for the process stream of interest by selecting one of the operational variables for the performance objective and applying the design constraints on the remaining variables.

For *single-phase flow heat transfer* inside enhanced and smooth tubes of the same envelope diameter, PEC for 12 different cases outlined by Bergles (1998) and Webb (1994) are listed in Table 14.2. They represent criteria for comparing the

TABLE 14.2 Performance Evaluation Criteria for Single-Phase Forced Convection in Enhanced Tubes of Same Envelope Diameter (d_i) as the Smooth Tube

Case	Geometry	Fixed				Objective
		\dot{m}	P	Q	ΔT_i	
FG-1a	N, L	\times			\times	$Q \uparrow$
FG-1b	N, L	\times		\times		$\Delta T_i \downarrow$
FG-2a	N, L		\times		\times	$Q \uparrow$
FG-2b	N, L		\times	\times		$\Delta T_i \downarrow$
FG-3	N, L			\times	\times	$P \downarrow$
FN-1	N		\times	\times	\times	$L \downarrow$
FN-2	N	\times		\times	\times	$L \downarrow$
FN-3	N	\times		\times	\times	$P \downarrow$
VG-1	—	\times	\times	\times	\times	$(NL)^a \downarrow$
VG-2a	$(NL)^a$	\times	\times		\times	$Q \uparrow$
VG-2b	$(NL)^a$	\times	\times	\times		$\Delta T_i \downarrow$
VG-3	$(NL)^a$	\times		\times	\times	$P \downarrow$

^aThe product of N and L .

enhanced performance on the basis of the following three broad exchanger geometry constraints:

1. *FG criteria.* The area of flow cross section (N and d_i) and tube length L are kept constant. This would typically be applicable for retrofitting the smooth tubes of an existing exchanger with enhanced tubes, thereby maintaining the same basic geometry and size (N , d_i , L). The objectives then could be to increase the heat load capacity Q for the same approach temperature ΔT_i and mass flow rate \dot{m} or pumping power P ; or decrease ΔT_i or P for fixed Q and \dot{m} or P ; or reduce P for fixed Q .

2. *FN criteria.* The flow frontal area or cross section (N and d_i) is kept constant, and the heat exchanger length is allowed to vary. Here the objectives are to seek a reduction in either the heat transfer surface area ($A \rightarrow L$) or the pumping power P for a fixed heat load.

3. *VG criteria.* The number of tubes and their length (N and L) are kept constant, but their diameter can change. A heat exchanger is often sized to meet a specified heat duty Q for a fixed process fluid flow rate \dot{m} . Because the tube-side velocity reduces in such cases so as to accommodate the higher friction losses in the enhanced surface tubes, it becomes necessary to increase the flow area to maintain constant \dot{m} . This is usually accomplished by using a greater number of parallel flow circuits. It may also be noted that with a constant exchanger \dot{m} , the penalty of operating a higher thermal effectiveness inherent in the *FG* and *FN* cases is avoided.

For the quantitative evaluation of these PEC, algebraic expression can be obtained that relate the enhanced surface performance (Nu or j and $f \cdot Re$) with that of an equivalent smooth duct. For a specified tube bundle geometry (N , L , d_i) in a shell-and-tube heat exchanger, the heat transfer coefficient h and pumping power P can be expressed as

$$h = \frac{c_p j G}{Pr^{2/3}} \quad (14.3)$$

$$P = \frac{f AG^3}{2\rho^2} \quad (14.4)$$

Thus, the performance of enhanced tubes can be related to that of equivalent smooth tubes (N , L , d_i same) as

$$\frac{hA/h_oA_o}{(P/P_o)^{1/3}(A/A_o)^{2/3}} = \frac{j/j_o}{(f/f_o)^{1/3}} \quad (14.5)$$

Given either j (or Nu) and f data or correlations for both the enhanced and smooth duct, evaluation of the objectives for the PEC in Table 14.2 is rather straightforward. One of the groupings hA/h_oA_o , P/P_o , and A/A_o becomes the objective function, with the other two set as 1.0 for the corresponding operating constraints, which also provide the mass flux ratio G/G_o required to satisfy eq. (14.5). Extended details for obtaining the requisite relationships are given by Webb (1994), Webb and Bergles

(1983b), and Nelson and Bergles (1986), and two illustrative examples are outlined briefly below.

A common enhancement objective for many batch-processing applications in the chemical and process industry is to increase the thermal performance of a given heat exchanger (fixed geometry) by using enhancement techniques, but without changing the pumping power and approach temperature difference requirements. This corresponds to the FG-2a criterion of Table 14.2, which can be implemented by expressing the ratio of heat transfer rate for the enhanced and smooth duct, respectively, as

$$\frac{Q}{Q_o} = \left(\frac{\text{Nu}}{\text{Nu}_o} \right)_{N, L, d_i, \Delta T_i, P} \quad (14.6)$$

The constraint of fixed pumping power can be expressed as

$$(f \cdot \text{Re}^3) = (f_o \cdot \text{Re}_o^3) \quad (14.7)$$

to establish the relationship between the Reynolds numbers (or mass fluxes G and G_o) for the enhanced and smooth flow passages. Because the enhanced duct geometry has higher friction factors than those of the equivalent smooth passage, this constraint requires that for a given flow rate (Re or G) in the former case, Re_o (or G_o) must be higher. Typical results for the single-phase flow-enhanced performance of tubes with twisted-tape inserts, evaluated according to the FG-2a criterion expressed in eq. (14.6), are presented in Fig. 14.3. As can be seen from this graph, using twisted tapes promotes considerable enhancement; details of their specific thermal-hydraulic performance characteristics are discussed later in the chapter.

In designing new enhanced-surface heat exchangers for a specified heat duty, approach temperature difference, and pressure drop, a reduction of the required heat transfer surface area is often the primary objective. The consequent FN-1 criterion of Table 14.2 can be stated as

$$\frac{A}{A_o} = \left(\frac{\text{Nu}_o}{\text{Nu}} \right)_{N, d_i, Q, \Delta T_i, \Delta p} \quad (14.8)$$

In this case, the Reynolds numbers or mass fluxes in the enhanced and smooth duct geometries are related by the fixed Δp requirements as follows:

$$(f \cdot \text{Re}^2) = (f_o \cdot \text{Re}_o^2) \quad (14.9)$$

Typical surface area savings (FN-1 criterion) due to the enhanced heat transfer in wavy-plate (flow-cross-section aspect ratio $\alpha = 0$, or parallel wavy plates, with a plate separation to waviness depth ratio $\beta = 1.0$) cores of a compact heat exchanger, for laminar liquid flow convection, are depicted in Fig. 14.4. As high as 95% reduction in thermal size is obtainable, depending on the operating conditions and wavy-surface geometry. In this case, the reference smooth channel is that of a flat parallel-plate core of the same β , and, once again, Re_o or G_o would be larger than that in the wavy or enhanced channel in order to meet the constraints of eq. (14.9).

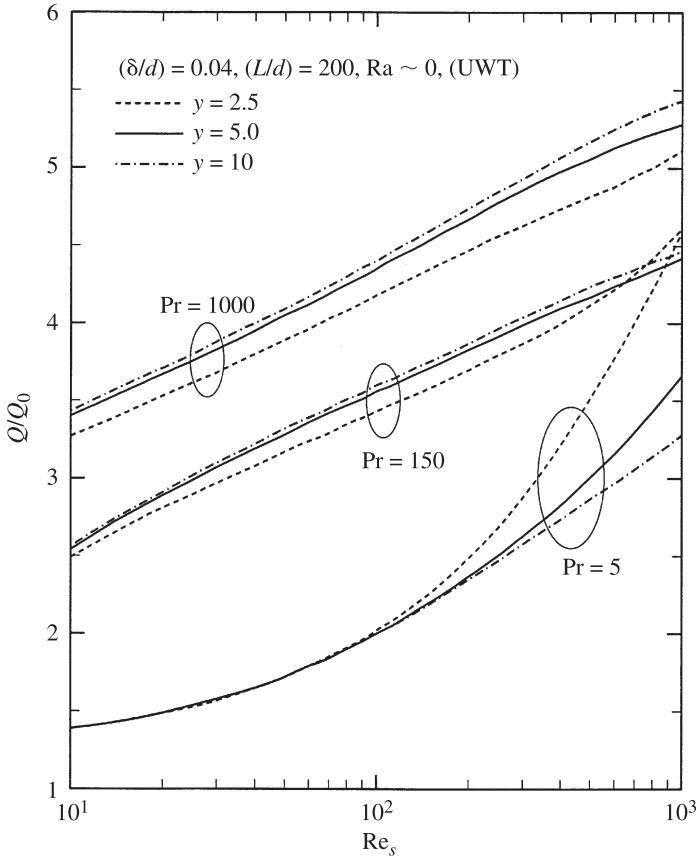


Figure 14.3 Typical enhanced heat transfer performance (FG-2a criterion) of circular tubes fitted with twisted-tape inserts and uniform wall temperature conditions. (From Manglik and Yerra, 2002.)

Some additional considerations and variations of these PEC (Table 14.2) for *single-phase convection*, which are based on a systems or complete heat exchanger unit approach, have also been considered. Bergles et al. (1974b), Nelson and Bergles (1986), and Webb (1994) provide the necessary guidance and details of their algebraic development. Furthermore, in a very recent study, Zimparov (2001) has outlined the application of PEC to *compound enhancement* that involves use of twisted-tape inserts in spirally corrugated (rough) tubes.

The formulation of appropriate PEC for *two-phase flow heat transfer* (boiling and condensation) is a rather complex task. The difficulty stems from the dependence of the local heat transfer coefficient on the local temperature difference and/or quality, and that the pressure gradient is also involved (although a simplification is often made by considering a constant pressure level). A variety of different strategies, which

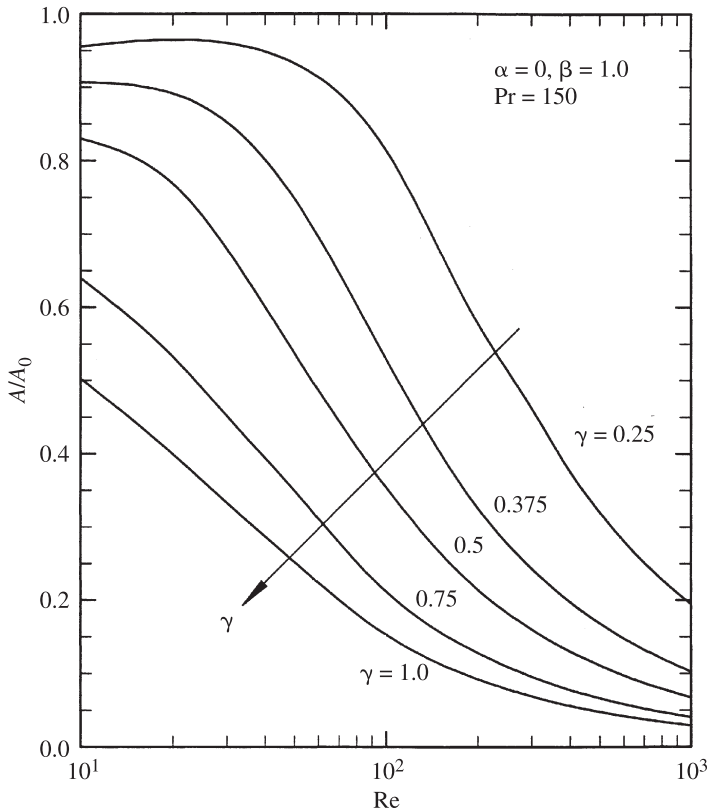


Figure 14.4 Typical surface area reductions (FN-1 criterion) in compact heat exchangers with parallel wavy-plate cores maintained at uniform wall temperature conditions.

include relating heat transfer, pressure drop or pumping power, and vapor–liquid quality in some fashion, have been used in the literature to evaluate the enhanced performance.

In forced-convective boiling, the enhanced critical heat flux (CHF) in tubes with twisted-tape inserts has been related to the pumping power by Gambill et al. (1961), and for tubes with brush and mesh inserts by Megerlin et al. (1974); in the latter case, a ratio of the dissipated power at CHF and pumping power was presented. Matzner et al. (1965) developed an efficiency index based on the increased exit quality, or critical power, that could be achieved with tube inserts, which in turn can be compared with the pumping power. Royal and Bergles (1978a) have devised two PEC for enhanced condensation in finned tubes and tubes with twisted-tape inserts: (1) size reduction made possible by replacing plain tubes with enhanced tubes of similar nominal diameter, assuming constant pressure level, and (2) a measure of the pressure drop consequences of an enhanced surface or insert. Kubanek and Milette

(1979) have considered heat transfer and pressure drop in the evaluation of refrigerant evaporators with internally finned tubes. Luu and Bergles (1981) have similarly examined refrigerant condensers with internally finned tubes, helically ribbed tubes, and spirally fluted tubes.

An extended discussion of enhanced performance evaluation of two-phase systems is given by Webb (1988, 1994). In fact, Webb (1988) has developed the only known analysis of PEC for two-phase flows that considers the effect of Δp on the ΔT_{lm} in two-fluid heat exchangers. Both *work-producing* (e.g., Rankine power cycle) and *work-absorbing* (e.g., vapor-compression refrigeration cycle) systems have been considered. In work-producing systems, enhancement techniques may influence their performance by way of (1) reduced boiler and/or condenser surface area (reduced heat exchanger size) for fixed turbine power output or (2) increased turbine power output with fixed boiler heat input and/or condenser heat rejection. Similarly, the following performance objectives and operating constraints may be considered for work-absorbing systems: (1) reduced heat transfer surface area of evaporator and/or condenser (reduced heat exchanger size) for fixed compressor power; (2) increased evaporator heat load for pressure difference between condenser and evaporator (compressor lift); (3) reduced power input to the compressor for fixed evaporator heat load; as a consequence, the ΔT_{lm} value of the evaporator and/or condenser would decrease. Based on this assessment of two-phase flow systems, Webb (1988) modified the PEC of Table 14.2 for evaporators/boilers and condensers, and these are listed in Table 14.3. Procedures for computing these PEC, which may be applied to both flows inside tubes and outside tube bundles, are also given by Webb (1988, 1994).

TABLE 14.3 Modified Performance Evaluation Criteria for Two-Phase Flow Heat Exchange Systems with Enhanced Tubes of Same Envelope Diameter (d_i) as the Smooth Tube

Case	Geometry	Fixed				Objective
		\dot{m}	P	Q	ΔT_i	
FG-1a	N, L				\times	$Q \uparrow$
FG-1b	N, L	\times	\times	\times		$\Delta T_i^a \downarrow$
FG-3	N, L	\times		\times	\times	$P^b \downarrow$
FN-1	N	\times		\times	\times	$L \downarrow$
FN-2	N	\times		\times	\times	$L \downarrow$
FN-3	N	\times		\times		$P^b \downarrow$
VG-1	—	\times	\times	\times		$(NL)^c \downarrow$
VG-2a	$(NL)^c$		\times		\times	$Q \uparrow$
VG-2b	$(NL)^c$	\times		\times		$\Delta T_i^a \downarrow$
VG-3	$(NL)^c$	\times		\times		$P^b \downarrow$

^aDefined as the temperature difference between the exit boiling fluid and inlet process fluid for vaporizers, and the approach temperature difference between the vapor and coolant streams for condensers.

^bPower output (turbine power) for work-producing systems and power input (compressor power) for work-consuming systems.

^cThe product of N and L .

14.2 TREATED SURFACES

As indicated earlier, treated surfaces are applicable primarily in two-phase heat transfer, and they consist of a variety of structured surfaces (continuous or discontinuous integral surface roughness or alterations) and coatings. In the event that this treatment provides a “roughness” to the surface, its size (normal protrusion to the surface) is not large enough to influence single-phase forced convection.

14.2.1 Boiling

The influence of surface finish on nucleate and transition pool boiling has been studied for more than four decades now (Bergles, 1998; Webb, 1994; Rohsenow, 1985; Berenson, 1962; Kurihari and Myers, 1960). A variety of methods have been employed to alter the surface finish by producing different types of *structured surfaces* (Bergles, 1998; Webb, 1994). These include the following types of surfaces, along with a few representative citations of patents and experimental studies that have considered them:

- *Machined or grooved surfaces* (Bonilla et al., 1965; Kun and Czikk, 1969; Chu and Moran, 1977; Fujikake, 1980; Hwang and Moran, 1981; Zhong et al., 1992)
- *Formed or modified low-fin surfaces* (Webb, 1972; Zateell, 1973; Nakayama et al., 1975; Arai et al., 1977; Pais and Webb, 1991)
- *Multilayered surfaces* made up of stamped or perforated cover foils and fine-wire or wire-screen wraps (Ragi, 1972; Hasegawa et al., 1975; Schmittle and Starner, 1978; Asakavičius et al., 1979)
- *Coated surfaces*, which include nonwetting coatings and particle deposits or material coatings that form artificial surface porosity (Griffith and Wallis, 1960; Young and Hummel, 1965; Marto and Rohsenow, 1966; Milton, 1971; Oktay and Schmeckenbecher, 1974; Dahl and Erb, 1976; Warner et al., 1978; Fujii et al., 1979; Nishikawa et al., 1983; Cieslinski, 2002).

An illustrative sampling of machined, formed, and coated surfaces that have been used in practice or tested in the laboratory is given in Fig. 14.5. Also, some types of fouling on and oxidation of the boiling surface, which perhaps improves the wettability, have been found to increase pool-boiling CHF.

Much of the work on developing structured surfaces for enhanced boiling is fundamentally driven by the principle of producing a large number of stable vapor traps, or nucleation sites, on the surface that lend to early or reduced ΔT incipience. This is particularly relevant to boiling applications for highly wetting fluids (e.g., refrigerants, organic liquids, cryogenes, and alkali liquid metals), where the normal cavities present on the heated surface tend to experience subcooled liquid flooding. By selective surface treatment (machining, forming, and coating or sintering), doubly reentrant cavities may be produced that would ensure vapor trapping in low-surface-tension fluids. The phase-change mechanism on such structured surfaces, however, is different from “normal” cavity boiling, and extended discussions of different models

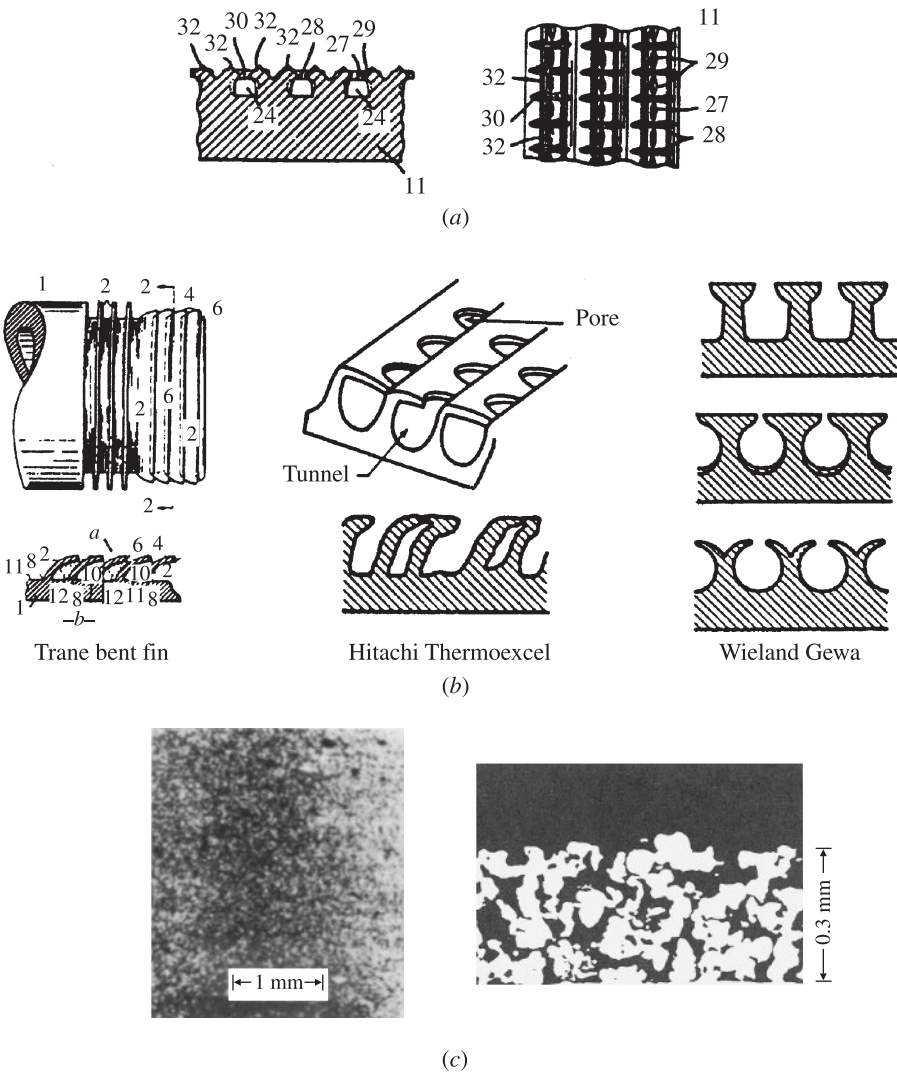


Figure 14.5 Examples of structured boiling surfaces produced by machining, forming, or coating: (a) deeply knurled surface; (b) different commercial formed-low-fin surfaces; (c) sintered particle-coated surface.

are given by Czikk and O'Neill (1979), Nakayama et al. (1980a,b), Kovalev et al. (1990), Webb and Haider (1992), and Webb (1994), among others. A study (Kulenovic et al., 2002) using high-speed image-processing techniques provides new information on bubble departure diameters, bubble generation frequency, and their up-flow velocities in pool boiling of propane over a structured surface with reentrant cavities.

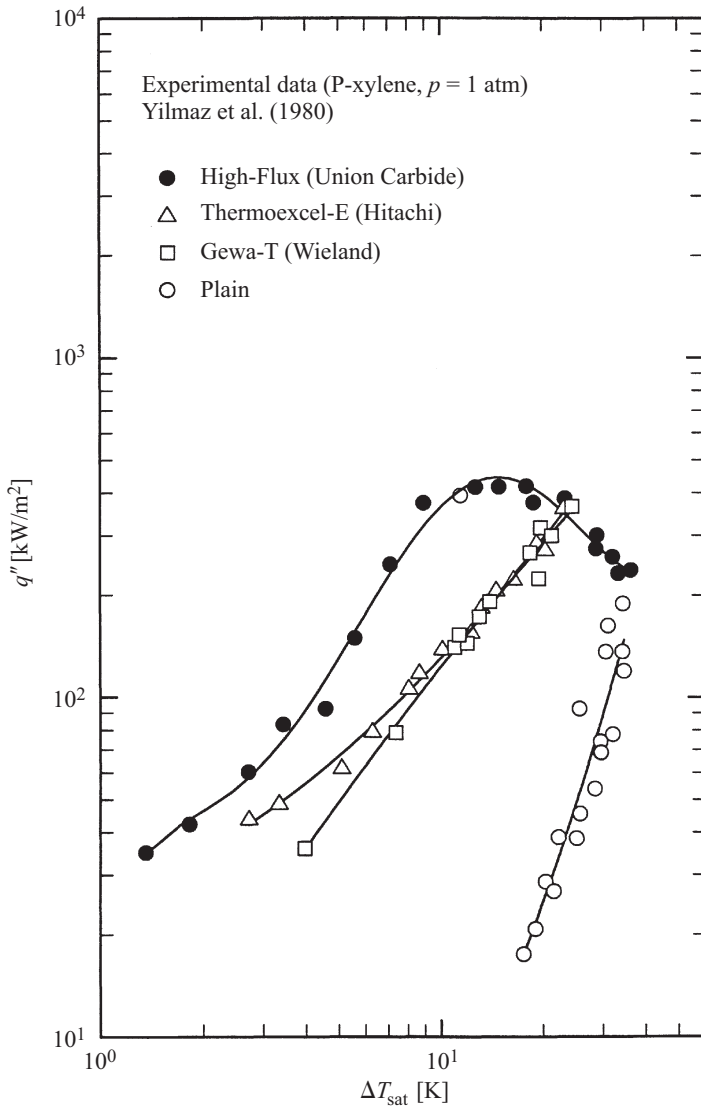


Figure 14.6 Experimental data reported by Yilmaz et al. (1980) for pool boiling of *p*-xylene at 1 atm from smooth and structured (Gewa-T, Thermoexcel-E, and High-Flux) surfaces.

Considerable enhancement with an order-of-magnitude reduction in wall superheat has been reported (Thome, 1990; Webb, 1994; Bergles, 1998) for boiling with some of these structured surfaces. Yilmaz et al. (1980) and Yilmaz and Westwater (1981) have reported a rather comprehensive comparison of the nucleate boiling performances of several commercially available structured surfaces. These involved the Wieland Gewa-T, Hitachi Thermoexcel-E, and Union Carbide High-Flux tubular

surfaces, among others. Their P-xylene boiling performance data for these three enhanced tubes as well as that for a reference smooth tube are give in Fig. 14.6. A shift in their boiling curves well to the left of that for the smooth tube, with a significant reduction in ΔT_{sat} , is shown clearly. Moreover, most of these surfaces have been found to increase the CHF as well. In saturated pool boiling of isopropyl alcohol, Yilmaz and Westwater (1981) have reported up to 40% higher CHF with some configurations of structured surfaces. It may be noted that the heat flux in all these cases is based on the area of the equivalent smooth tube of the same outside diameter.

The phenomenon of temperature overshoot or incipience hysteresis, which is commonly seen in boiling of highly wetting fluids over smooth surfaces and where the boiling curve exhibits different characteristics with increasing and decreasing heat flux, has also been reported with sintered-particle coated surfaces (Bergles and Chyu, 1982; Kim and Bergles, 1985) and multilayered (sintered screens) surfaces (Liu et al., 1987). This starting temperature overshoot and hysteresis are shown in Fig. 14.7, where the Bergles and Chyu (1982) data for pool boiling of R-113 on a horizontal, electrically heated, sintered surface (High-Flux) tube are presented. The boiling data of Ma et al. (1986) for methanol with similarly coated surfaces, however, show substantially less hysteresis. In any event, this suggests that some commercial equipment for boiling applications that use enhanced or structured surfaces may encounter

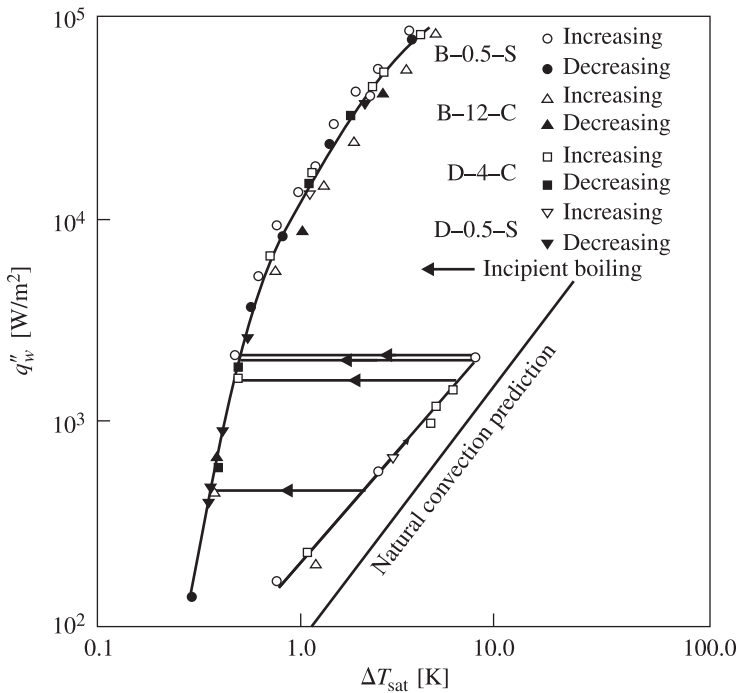


Figure 14.7 Temperature excursion or startup hysteresis in pool boiling of R-113 on a horizontal tube with a sintered (High-Flux) surface. (From Bergles and Chyu, 1982.)

potential startup problems (Thome, 1990; Webb, 1994; Bergles, 1998). Furthermore, there are limited data which indicate that the tube bundle performance in a thermosyphon reboiler may be different from that of a single tube (Yilmaz et al., 1981). A later study (Jensen et al., 1992), however, suggests that single-tube results may be used to predict tube bundle behavior.

Several attempts have been made to model the nucleate boiling mechanisms on structured surfaces and to develop predictive correlations. These analyses have tried to scale and correlate the effects of geometrical properties of the structured surface, or

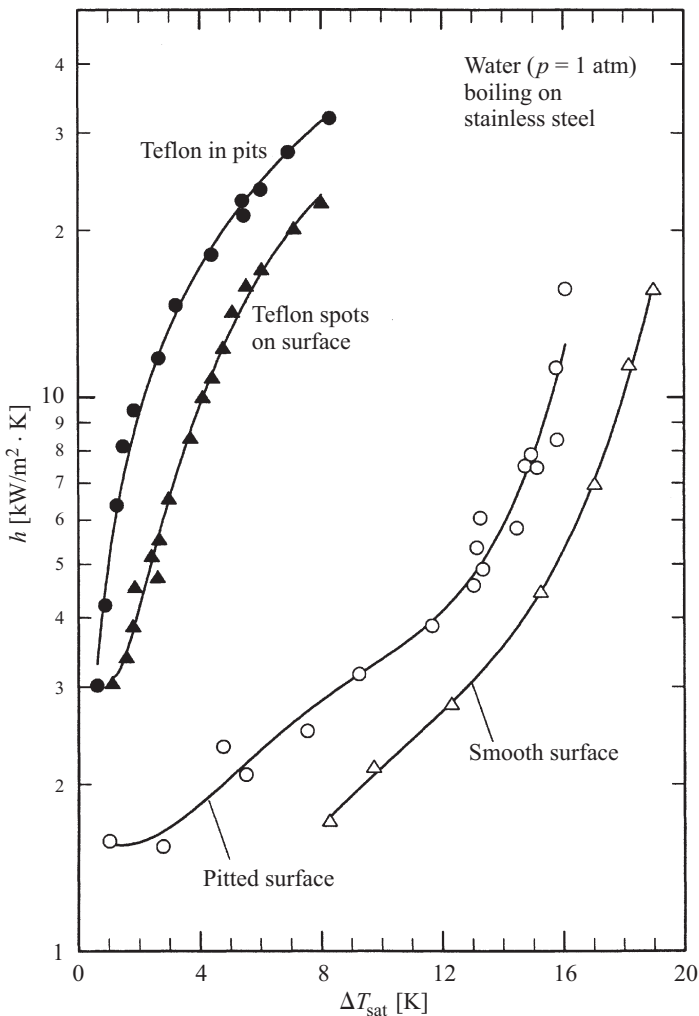


Figure 14.8 Enhanced boiling heat transfer characteristics of water at 1 atm from a stainless steel surface coated with Teflon spots. (From Young and Hummel, 1965.)

the characteristics of nucleating cavities and liquid-replenishing intercavity channels, on the heat transfer. Extended discussions of several different models can be found in Nakayama et al. (1980a,b), Webb (1994), Chien and Webb (1998), Yabe et al. (1999), and Kim and Choi (2001), among others.

For less wetting or relatively higher-surface-tension fluids, coatings of nonwetting material (e.g., Teflon) on either the heated surface or its pits and cavities have been found to improve stable nucleation and reduce the required wall superheat (Griffith and Wallis, 1960; Young and Hummel, 1965; Gaertner, 1967; Vachon et al., 1969). Young and Hummel (1965) sprayed a smooth as well as a “pitted” stainless steel surface with Teflon to create spots of the no-wetting material on the heated surface and in the pits. This was found to promote nucleate boiling in water, with relatively low wall superheat and three- to four-times-higher heat transfer coefficients, as shown in Fig. 14.8. In a more recent study of boiling of alcohols (methanol, ethanol, and isopropanol) at atmospheric and subatmospheric pressures on a horizontal brass tube coated with polytetrafluoroethylene, Vijaya Vittala et al. (2001) have reported a significant enhancement in the heat transfer. A typical set of their data for ethanol is presented in Fig. 14.9. Surfaces coated with thin films of low-thermal-conductivity materials have also been shown to enhance pool boiling heat transfer under heater surface temperature-controlled experimental conditions (Zhukov et al., 1975). This

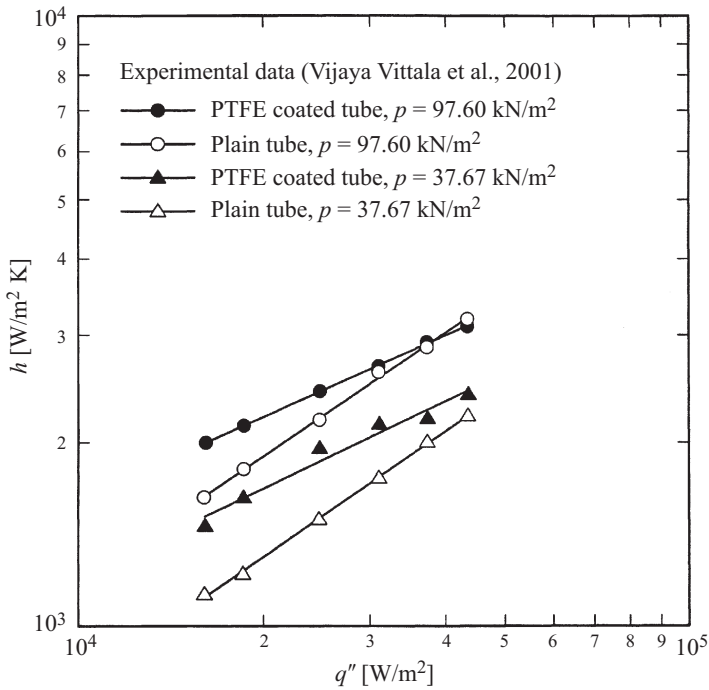


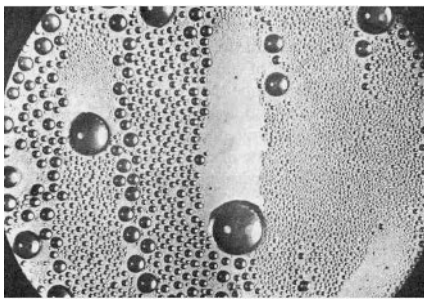
Figure 14.9 Enhancement in the boiling heat transfer coefficient for ethanol at different subatmospheric pressures and heat fluxes from PTFE-coated tubes.

essentially breaks up film boiling by reducing the fluid-surface interface temperature to promote a more effective transition or nucleate boiling. This has also been found to be the case with scale or oxide coatings, which destabilize film boiling and significantly reduce the quench times of a heated surface (Bergles and Thompson, 1970).

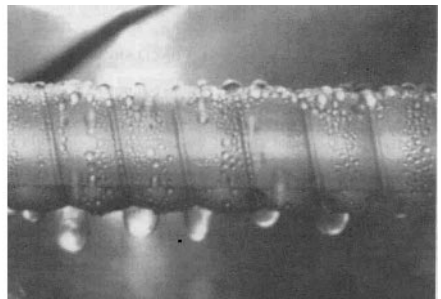
14.2.2 Condensing

Vapor space condensation heat transfer can be enhanced primarily by treated surfaces that promote dropwise condensation. The intent here is to prevent surface wetting and break up the condensate film into droplets, as depicted in Fig. 14.10, which lends to better drainage and more effective vapor renewal at the cold heat transfer interface. This technique had been found to enhance the heat transfer by factors of 10 to 100 in comparison with that in filmwise condensation (Bergles, 1998). Nonwetting coatings of several different materials have been used effectively in different investigations (Hannemann, 1977; Tanasawa, 1978; Griffith, 1985). This includes coating the condensing surface with a thin film of an inorganic compound, a thin-film plating of a noble metal, or a film of an organic polymer (Rose et al., 1999; Das et al., 2000). Of these, organic coatings have been used considerably in steam systems, and Marto et al. (1986) and Holden et al. (1987) have given a comprehensive evaluation of their performance in promoting dropwise condensation. However, this technique is useful in promoting dropwise condensation in steam (or other relatively high-surface-tension fluid) condensers, as there seem to be no nonwetting (or “Freonophobic”) substances that would induce dropwise condensation in refrigerants and other low-surface-tension fluids (Iltisheff, 1971).

Glicksman et al. (1973) have shown that by strategically placing strips of Teflon or other nonwetting material in a helical or axial arrangement around the circumference of horizontal tubes, the average condensation heat transfer coefficients of steam on horizontal tubes can be improved by 20 to 50%. In such an arrangement, the condensate flow is interrupted near the leading edge of the nonwetting strip, and



(a)



(b)

Figure 14.10 Examples of dropwise condensation of steam: (a) on a plain surface (from Hampson and Ozisik, 1952); (b) on a SAM-coated corrugated tube (from Das et al., 2000).

the condensate film that reforms at its downstream edge is much thinner. Cary and Mikic (1973) suggest further that Marangoni convection (surface tension–gradient or interfacial temperature–gradient, driven flow) at the liquid–vapor–strip interface may also be a contributing factor in enhancing the heat transfer. There are, however, several practical issues relating to the application and surface integrity of nonwetting material coating, as discussed by Tanasawa (1978), Marto et al. (1986), and Das et al. (2000).

There have been a few attempts to develop theoretical models for dropwise condensation as well. In this, the studies reported by Le Fevre and Rose (1966), Rose (1988), and Tanaka (1975a,b) are particularly noteworthy, and their brief assessment is provided by Rose et al. (1999). The application of a hydrophobic coating of self-assembled monolayers, formed by a chemisorption of alkylthiols on metallic surfaces, to promote dropwise condensation has been investigated by Das et al. (2000). Experiments on steam condensation on coated corrugated tubes with gold and copper–nickel alloy surfaces under atmospheric (101 kPa) and subatmospheric (10 kPa) pressure conditions with wall subcooling of about 16°C and 6°C, respectively, showed that condensation heat transfer coefficients increased by factors of 2.3 to 3.6 compared to those for uncoated tubes. The characteristic condensation behavior is illustrated photographically in Fig. 14.10*b*. Although technically, this study would fall under the compound enhancement category, the noteworthy and novel technique to effect dropwise condensation is particularly relevant here.

In a different scheme to enhance film condensation, Notaro (1979) has described a patent for a tube surface that is intermittently coated with small-diameter metal particles. The objective of this scheme is that condensation would occur over the strategically coated surface, and liquid film would then drain along the uncoated, bare tube surface. With a typical configuration (a 6-m vertical tube with 0.5-mm-diameter particle coatings interspaced over 50% of the tube surface), up to 17 times higher steam condensation coefficients than that in normal film condensation have been reported (Notaro, 1979; Webb, 1984).

14.3 ROUGH SURFACES

14.3.1 Single-Phase Flow

One of the earliest and perhaps simplest and yet highly effective techniques is the use of surface roughness in turbulent single-phase flows (Nikuradse, 1933; Dippert and Sabersky, 1963; Webb et al., 1971); in laminar flows, small-scale surface roughness tends to have little effect. It essentially disturbs the viscous sublayer in the near-wall turbulent flow structure to promote higher momentum and heat transport (Nikuradse, 1933). Much of the early work focused on “naturally” occurring roughness in commercial tubes. However, as pointed out by Bergles (1998), because such natural roughness is not well defined, artificial or structured roughness is now commonly employed in most applications. Structured roughness can be integral to the surface, or the protuberances can be introduced in the form of wire-coil-type inserts. The former can be produced by machining (e.g., knurling, threading, grooving), forming,

casting, or welding, and the resulting surface protuberances or grooves can be two-dimensional or discrete three-dimensional in their geometrical arrangement (Webb, 1994; Bergles, 1998). As a result, almost an infinite number of geometric variations are possible for structured roughness, and this is also reflected in the more than 700 studies, and still counting (Bergles et al., 1995; Bhatnagar and Manglik, 2002) that have been reported in the literature.

Rough surfaces have been employed to enhance heat transfer in single-phase flows both inside tubes and outside tubes, rods, and tube bundles. A collection of studies and patents that deal with their thermal-hydraulic performance as well as fabrication and manufacturing methods is given by Webb et al. (1983), Ravigururajan and Bergles (1986), Webb (1994), Bergles et al. (1995), and Bergles (1998). Some of the two-dimensional structured roughness used inside tubes includes repeated or transverse ribs, helical ribs, and wire coil inserts, in a variety of profiles, as illustrated in Fig. 14.11. Of these, tubes with grooves are often referred to as corrugated, roped, indented, fluted, or convoluted tubes, among other names, and are illustrated in Fig. 14.12*a*. They provide an external rough surface as well and have been used in double-pipe and shell-and-tube bundles to enhance annulus- or shell-side heat transfer. Two representative tubes with three-dimensional roughness, composed of serrated ribs, dimples, and cross-ribbed surfaces, are also depicted in Fig. 14.12*b* and *c*. Besides these, knurling (to form diamond knurls), discrete slotting, rolling, and particle deposition have been investigated as possible candidates for three-dimensional roughness (Durant et al., 1965; Groehn and Scholz, 1976; Achenbach, 1977; Fenner and Ragi, 1979; Menze et al., 1994; Webb, 1994).

Over the last five decades, a fairly extensive set of experimental data for heat transfer coefficients and friction factors in rough tubes has been obtained (Ravigururajan and Bergles, 1986; Esen et al., 1994; Bergles, 1998). Several attempts have also been made to develop predictive equations for the turbulent flow regime. One of the first such efforts was the momentum heat transfer analogy solution proposed by Dipperry and Sabersky (1963) for sand-grain roughness. Subsequently, Webb et al. (1971, 1972) devised another analogy-based correlation for heat transfer coefficients for different fluids ($0.7 \leq \text{Pr} \leq 38$) and tubes with transverse repeated-rib roughness ($\alpha = 90^\circ$, $0.01 \leq e/d \leq 0.04$, $10 \leq p/e \leq 15$; Fig. 14.11). Withers (1980*a,b*), similarly, extended this correlating technique to commercial single- and multiple-helix internally ridged tubes. A detailed discussion of these solutions and their prediction efficacy is given by Webb (1994). In a more recent experimental study on turbulent flows of water and oil in spirally corrugated tubes, Dong et al. (2001) have developed a new set of analogy-based friction factor and Nusselt number correlations. Adopting an empirical approach, combined with a statistical analysis of a fairly large database for heat transfer coefficients and friction factors for the various types of roughness shown in Fig. 14.11, Ravigururajan and Bergles (1996) have proposed the following Nusselt number and Fanning friction factor correlations:

$$\text{Nu} = \text{Nu}_o \left\{ 1 + \left[2.64 \text{Re}^{0.036} \left(\frac{e}{d} \right)^{0.212} \left(\frac{p}{d} \right)^{-0.21} \left(\frac{\alpha}{90} \right)^{0.29} \cdot \text{Pr}^{-0.024} \right]^7 \right\}^{1/7} \quad (14.10)$$

$$f = f_o \left\{ 1 + \left[29.1 \text{Re}^{a1} \left(\frac{e}{d} \right)^{a2} \left(\frac{p}{d} \right)^{a3} \left(\frac{\alpha}{90} \right)^{a4} \left(1 + 2.94 \sin \frac{\beta}{n} \right) \right]^{15/16} \right\}^{16/15} \quad (14.11a)$$

where

$$\begin{aligned} a1 &= 0.67 - 0.06 \left(\frac{p}{d} \right) - 0.49 \left(\frac{\alpha}{90} \right) & a2 &= 1.37 - 0.157 \left(\frac{p}{d} \right) \\ a3 &= -1.66 \times 10^{-6} \text{Re} - 0.33 \left(\frac{\alpha}{90} \right) & a4 &= 4.59 + 4.11 \times 10^{-6} \text{Re} - 0.15 \left(\frac{p}{d} \right) \end{aligned} \quad (14.11b)$$

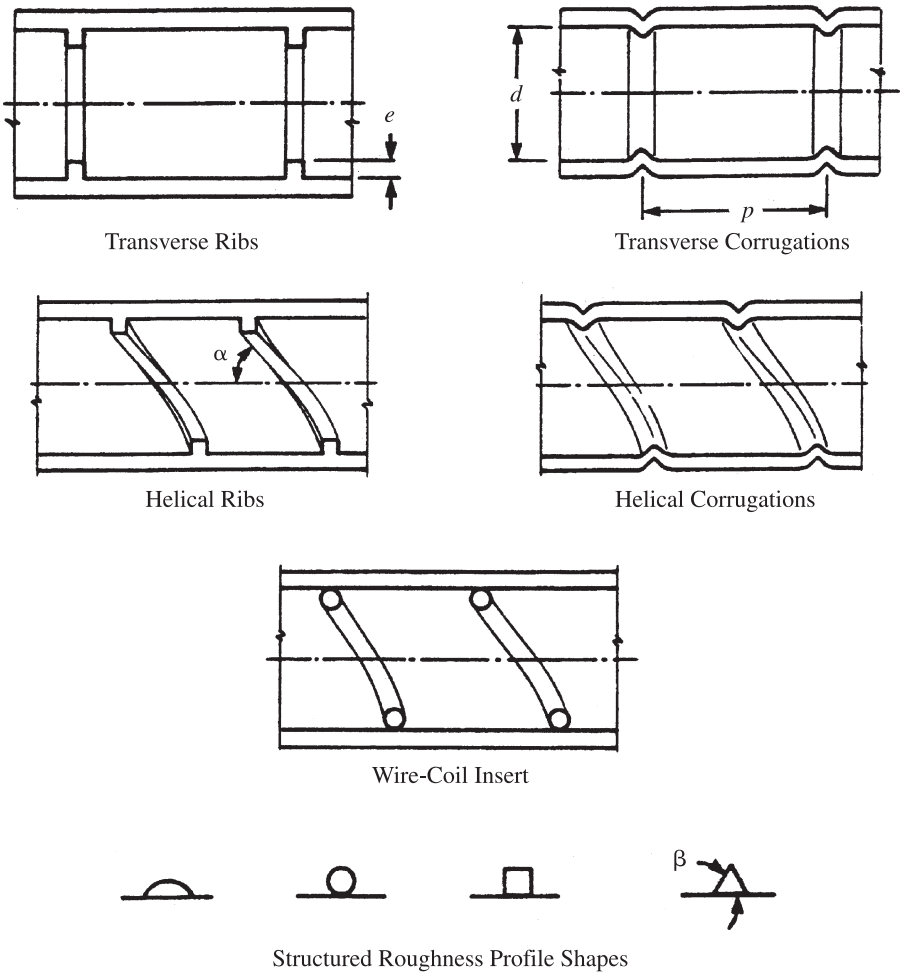


Figure 14.11 Different type of structured roughness and their profile shapes considered by Ravigururajan and Bergles (1986, 1996).

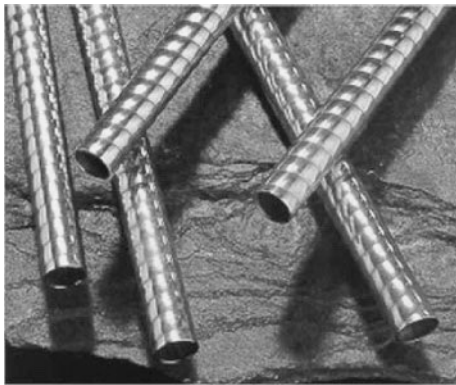
and the respective smooth tube Nu_o and f_o performances are given by

$$Nu_o = \frac{Re \cdot Pr(f_o/2)}{1 + 12.7\sqrt{f_o/2}(Pr^{2/3} - 1)} \quad (14.12)$$

$$f_o = (1.58 \ln Re - 3.28)^{-2} \quad (14.13)$$

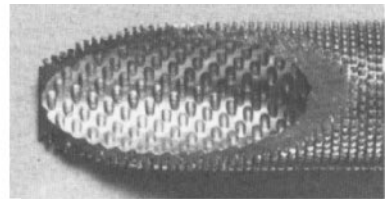
The prediction reliability and accuracy of eqs. (14.10) and (14.11) have been shown to be very good compared with more than 1800 experimental data points, representing the full range of roughness types and profiles depicted in Fig. 14.11 (Ravigururajan and Bergles, 1986; Bergles, 1998), and some typical predictions are graphed in Fig. 14.2b.

A novel technique to provide variable-roughness “on demand” inside tubes has recently been proposed and tested by Champagne and Bergles (2001). The concept involves using a wire-coil insert made of a shape-memory alloy (SMA) that alters its geometry in response to changes in temperature (Bergles and Champagne, 1999). With a fixed roughness height (e/d), the wire-coil insert changes from a compressed shape, which occupies a small fraction of the tube length, to an expanded shape that has the desired or “trained” roughness pitch (p/d) and helix pitch ($\alpha/90^\circ$) upon being heated. In essence, the SMA insert can be designed to provide the required roughness to meet “active” changes in process conditions, which are usually reflected by the variations in the tube wall temperature and enhancement objectives. A schematic rendering of this concept is given in Fig. 14.13. In a proof-of-concept experimental

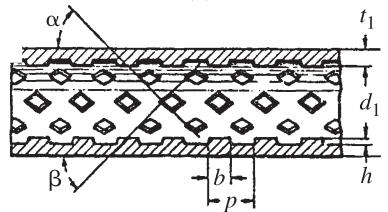


(a)

Two-Dimensional Roughness



(b)



(c)

Three-Dimensional Roughness

Figure 14.12 Tubes with two- and three-dimensional structured roughness: (a) corrugated tubes (courtesy of Wolverine Tube, Inc.); (b) serrated ribs on outer surface and staggered dimples on inner surface (courtesy of Sumitomo Light Metal Industries); and (c) Cross-ripled inner surface (from Nakamura and Tanaka, 1973).

test, Champagne and Bergles (2001) have further shown that depending on the flow rate, a typical SMA (NiTi) wire coil insert can produce 30 to 64% increases in the heat transfer coefficients in single-phase turbulent flows.

Flows in annuli with an inner rough surface, commonly encountered in a double-pipe heat exchanger with an inner tube that is convoluted or corrugated, or has some other structured roughness on its outer surface, have also been investigated in the literature (Kemeny and Cyphers, 1961; Brauer, 1961; Dalle Donne and Meyer, 1977; Hudina, 1979; Garimella and Christensen, 1995a,b; Salim et al., 1999; Kang and Christensen, 2000). In an early study with helical grooves and helical protuberances, the experimental data of Kemeny and Cyphers (1961) suggest enhancement factors of 1.25 to 2.0 for different flow rates and roughness (Bergles, 1998). Surface protrusions had a relatively higher performance than grooves. Some of the more recent work with water and propylene glycol flows in annuli with fluted or corrugated tubes (Garimella and Christensen, 1995a,b; Salim et al., 1999; Kang and Christensen, 2000) indicate up to four times higher Nusselt numbers, with up to 10 times higher friction factors in the turbulent flow regime. Two different sets of correlations have also been devised by Garimella and Christensen (1995a,b), and Salim et al. (1999) that are based on their own respective data. No attempt appears to have been made to consolidate and compare the various data sets available in the literature. For high-viscosity fluids (e.g., propylene glycol) and/or large temperature-dependent viscosity variations in the flow field, Kang and Christensen (2000) suggest incorporating a Sieder and Tate (1936) type of viscosity-ratio correction factor in the predictive equation.

The heat transfer enhancement in annuli with three-dimensional diamond-knurls type of roughness on the inner heated tube's outer surface has been investigated by Durant et al. (1965). At fixed pumping power conditions, the heat transfer coefficients for the knurled annuli were found to be up to 75% higher than those for the equivalent smooth annuli. Dalle Donne (1978) provides turbulent flow data for three-dimensional roughness made up of rows of staggered studs. The Stanton numbers were found to increase by factors of 3 and 4; the associated friction factors were 8 to 12 times higher. For their application in gas-cooled reactors, the grouping $\sqrt{St^3/f}$ is often used as a figure of merit to interpret the performance data. This translates into enhancement ratios of up to 2.3 for the three-dimensional roughness. Similarly, annuli data have been "transformed" for application to the rod-bundle geometry (Hall, 1962; Lewis, 1974; Hudina, 1979; Webb, 1994). Some work has also been reported

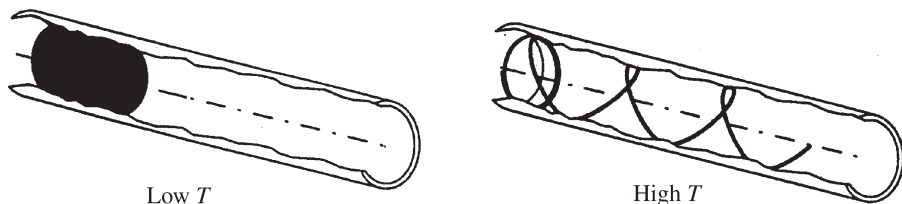


Figure 14.13 Conceptual representation of "roughness on demand" provided by a shape-memory alloy wire coil insert. (From Champagne and Bergles, 2001.)

on crossflow over tube bundles that have roughness on the outer surface, particularly for gas-cooled reactors and shell-and-tube heat exchangers (Bergles, 1998). Much of this work is based on the extended experimental investigations with cross flows over a single rough cylinder. The case of pyramid-shaped roughness elements has been considered by Achenbach (1977) and Zhukauskas et al. (1978), with air and water flows, respectively, and up to 150% increase in the Nusselt number has been reported.

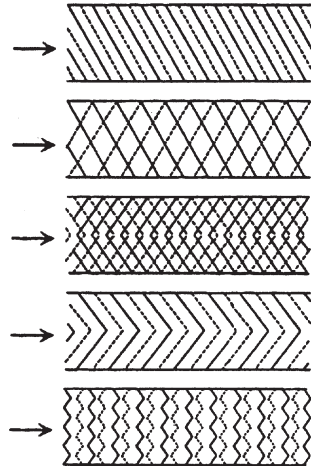
Structured roughness, usually in the form of ribs, in both two-dimensional and discrete three-dimensional arrangements, has also been applied to plate-type and rectangular channels (Han, 1988; Han et al., 1991; Liou and Hwang, 1992; Prakash and Zerkle, 1995; Ekkad and Han, 1997; Olsson and Sundén, 1998; Sundén, 1999; Gao and Sundén, 2001). Much of this work is directed toward compact heat exchangers and gas turbine cooling and regeneration systems. A variety of arrangements for rectangular ribs attached to two opposite heated walls of rectangular (or plate) channels have been considered (Han et al., 1991; Zhang et al., 1994; Olsson and Sundén, 1998). With ribs angled at 60° , some examples of the geometrical schemes investigated experimentally by Olsson and Sundén (1998) and Sundén (1999) are depicted in Fig. 14.14. Their relative enhanced performance, as represented by the *volume goodness factor* or heat transfer coefficient versus pumping power expended per unit heat transfer area [the development of this figure of merit is given in Kays and London (1984) and Shah and London (1978)], is also presented in this figure. Of the five configurations shown here, the last one, with short rib segments, essentially constitutes three-dimensional structured roughness. An interesting variation in the form of wedge- and delta-shaped ribs, which tend to produce longitudinal vortices in the near-wall region of the flow field, have been suggested by Han et al. (1993).

Finally, as noted by Bergles (1998), surface roughness is usually not considered in applications with free or natural convection. In this thermal-fluid-transport regime, the buoyancy-induced fluid flow velocities are generally very low and are not easily disrupted by small-scale surface roughness so as to produce flow separation and recirculation (the primary mechanisms for roughness-induced enhancement). Bergles et al. (1979) reviewed the limited data available in the literature up to that time, which are for air, water, and oil with machined or formed roughness on the surface exposed to free convection. Where up to 100% increases in heat transfer have been reported in an air system, it is questionable if radiation effects have been accounted for adequately; in liquids, on the other hand, the enhancement has been found to be considerably small.

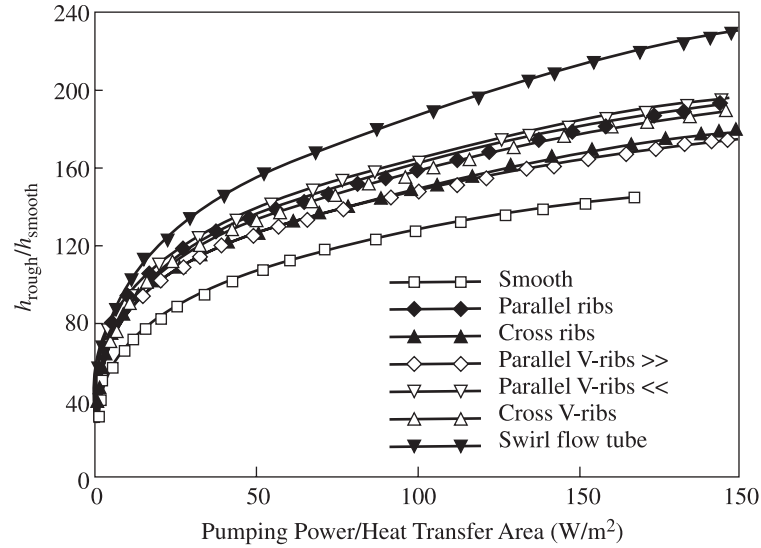
14.3.2 Boiling

The application of rough-structured surfaces in pool boiling situations has been classified under *treated surfaces* (Bergles, 1998), and their performance was discussed earlier. Their use in forced convection or flow boiling is primarily addressed here.

The earliest works on the effects of surface roughness in forced-convection boiling were the investigation of improvements in subcooled CHF by knurling or threading the heated surface (Durant and Mishak, 1959; Durant et al., 1965). When compared



(a)



(b)

Figure 14.14 Enhanced performance of rectangular channels with structured roughness reported by Sundén (1999): (a) different rib orientations; (b) variation of heat transfer coefficient with specific pumping power (volume goodness factor performance).

on the basis of equal pumping power, it was shown that CHF for the rough tubes were up to 80% higher than those for smooth tubes. Murphy and Truesdale (1972) have shown further that subcooled CHF tends to decrease by as much as 15 to 30% with increasing roughness height. In another study (Gomelaury and Magrakvelidze, 1978) with two-dimensional structured roughness, CHF is found to be dependent on the degree of subcooling. Swenson et al. (1962) and Watson et al. (1974) employed integral multistart helical ribs and found that at subcritical pressures, film boiling was inhibited and much higher heat fluxes could be sustained with lower mass fluxes in comparison with a smooth tube. Kitto and Wiener (1982) have reported as much as a threefold increase in CHF under nonuniform circumferential heating ribbed tubes. Three more recent studies (Celata et al., 1994; Kabata et al., 1996; Lan et al., 1997) have experimented with wire-coil inserts and found considerable enhancement in CHF. Celata et al. (1994) have reported up to 50% higher subcooled boiling CHF in comparison with that in a smooth tube for the same conditions. The subcooled water boiling data of Kabata et al. (1996) show as much as 90% CHF enhancement. Similarly, Lan et al. (1997) found two- to threefold increases in CHF in a R-113 system; they have also proposed a tentative correlation for predicting CHF under subcooled conditions.

The use of helical ribbed tubes in high-pressure power boilers have long been considered in the literature (Bergles, 1998), and they have been shown to increase the heat transfer coefficient and CHF in once-through boiling of water (Swenson et al., 1962). Ribbed tubes also tend to suppress pseudo-film boiling (Ackerman, 1970) and increase the heat transfer coefficient in the post-CHF, dispersed-flow film boiling regime (Bergles, 1998). Commercial structured rough surfaces in the form of corrugated (or fluted, or convoluted) tubing have come to be employed extensively in refrigerant evaporators. Withers and Habdas (1974) have reported up to 100% increase in the heat transfer coefficient and up to 200% enhancement in CHF in bulk boiling of R-12 in helically corrugated tubes. In a more recent study on flow boiling of R-134a in a horizontal spirally fluted tube (MacBain et al., 1997), considerable enhancement in the heat transfer coefficient, which tends to increase with quality (a condition contrary to that in a smooth tube), has been reported.

Artificial roughness in the form of longitudinal ribs or grooves has also been applied in gravity-driven, horizontal-tube, spray-film evaporators. However, although this type of surface might promote turbulence, it tends to impede film drainage (Bergles, 1998). Three-dimensional roughness, as obtained in knurled surfaces, for example, tends to promote turbulence as well as the liquid spreading over the surface. In this case, heat transfer coefficients have been found to increase as much as 100% (Cox et al., 1969). The contrasting recommendation of Newson (1978), based on the results for single-phase film or trickle coolers, is to employ longitudinal-rib-type roughness for horizontal-tube multiple-effect evaporators.

14.3.3 Condensing

Film condensation of steam on vertical tubes with external pyramid-shaped, closely knurled artificial surface roughness was perhaps first investigated by Medwell and

Nicol (1965), and Nicol and Medwell (1966). With gravity-driven condensate drainage, the mean heat transfer coefficient was found to increase significantly, with the roughest tube providing a twofold higher h than that in the reference smooth tube. Similarly, four- to fivefold higher condensing coefficients for R-11 have been reported by Carnavos (1980) or knurled tubes, although part of this enhancement may be due to an area increase. Thomas (1967) attached axial wires around the periphery of vertical smooth tubes, which facilitated better surface tension-driven condensate film drainage, to produce three- to fourfold enhancement in heat transfer. It was shown further that square-profiled wires were more effective than circular ones of the same roughness height (Thomas, 1968). These findings have been further corroborated by the analysis presented by Rifert and Leont'yev (1976), and the patent obtained by Kun and Ragi (1981) also describes closely spaced, attached-wire surface roughness on vertical tubes.

Commercial corrugated or fluted tubes have been considered extensively for enhancement of vapor space condensation, and their application was perhaps first advocated and shown to be beneficial by Withers and Young (1971). Subsequently, one of the most comprehensive investigations of steam condensation on vertical fluted tubes was performed by Newson and Hodgson (1973). Experimental data for 32 tubes with flute (or different helical corrugation) geometries were obtained, and the condensation heat transfer coefficient was found to be enhanced by factors of 1.45 to 6.75 over that for smooth tubes. In steam condensation on horizontal helically corrugated tubes, Mehta and Raja Rao (1979) and Zimparov et al. (1991), among some others (Webb, 1994; Das et al., 2000), have reported about 1.1 to 1.4 enhancement factors (ratio of rough to smooth tube h 's). Typical enhancement in the Mehta and Raja Rao (1979) data is shown in Fig. 14.15. Similarly, Dreitser et al. (1988) have reported 1.8 to 2.65 times higher steam condensation heat transfer coefficients on horizontal tubes with transverse grooves or corrugations.

Rough surfaces have been found to enhance in-tube forced-convective condensation as well. In an early study on the performance of horizontal-tube, multiple-effect desalination plants, Cox et al. (1970) could improve the overall heat transfer coefficients, with forced convection condensation inside and spray film evaporation outside, by using spirally indented and V-grooved tubes; although, it may be noted, a knurled surface tube was ineffective. Luu and Bergles (1979, 1981) have reported experimental data for condensation of R-113 in tubes with helical repeated rib internal roughness and deep spirally fluted tubes. The average coefficients were found to increase by as much as 80% above smooth-tube values in the former case, and by 50%, on an envelope diameter basis, in the latter. Similarly, for R-22, Shinohara and Tobe (1985) observed a 59% increase in the condensation coefficients with a corrugated tube, and Chiang (1993) has reported a 10 to 20% increase with a helically grooved tube. Wang (1987) has considered wire-coil inserts for stratified flow, in-tube condensation of R-12, to obtain 35 to 40% average enhancement. Wire-coil inserts ($0.051 \leq e/d \leq 0.118$, $0.512 \leq p/d \leq 1.024$) have also been used in a more recent study (Akhavan-Behabadi et al., 2000) on condensation of R-22, and up to 100% enhancement in heat transfer coefficients is reported; a Nusselt number correlation, based on their own data set, has also been proposed. A method to produce

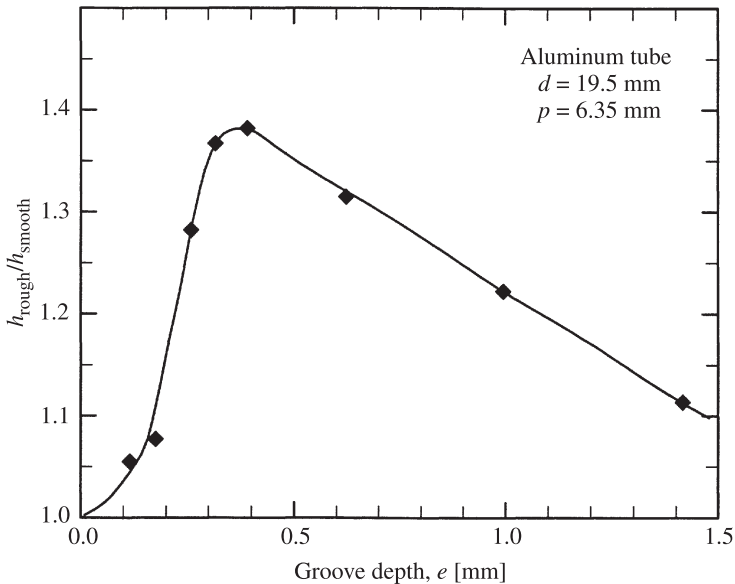


Figure 14.15 Data for enhanced steam condensation heat transfer on a horizontal corrugated tube reported by Mehta and Raja Rao (1979).

sand-grain-type random roughness by attaching metallic particles, which cover 50% of the surface area with an average roughness of $e/d = 0.031$, is described in a U.S. patent by Fenner and Ragi (1979). They have also shown that condensation increased by 300% for $x > 0.6$ and by 140% for lower qualities in a refrigerant R-12 system.

14.4 EXTENDED SURFACES

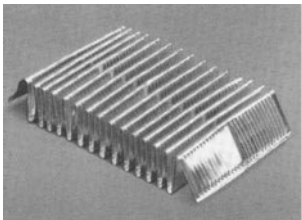
Extended or finned surfaces are perhaps the most widely used and researched of all enhancement techniques. Their applications cover a broad spectrum of heat exchange devices, which include finned tubes for shell-and-tube exchanges (Fig. 14.16), plate fins for compact heat exchanger (Fig. 14.17), and finned heat sinks for electronic cooling (Fig. 14.18), among others. Several monographs, reviews, and edited texts (e.g., Kern and Kraus, 1972; Zhukauskas, 1989; Shah et al., 1990; Bergles, 1990; Manglik and Kraus, 1996; Kakaç et al., 1999; Kraus et al., 2001) provide extended discussions on various aspects of fins, their design optimization, and applications.

14.4.1 Single-Phase Flow

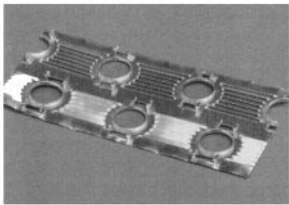
Enhanced heat transfer from finned surfaces by buoyancy-driven natural or free convection has been considered primarily for cooling of electrical and electronic devices and for hot-water baseboard room heaters. Of these, with new advancements in



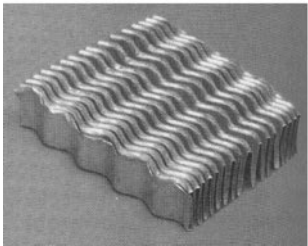
Figure 14.16 Tubes with circumferential and strip fins on their outer surface for shell-and-tube heat exchangers. (Courtesy of Wieland-Werke AG.)



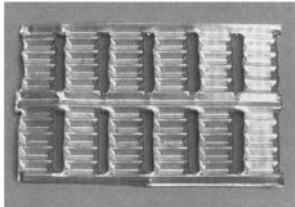
Louvered plate fins



Circular-tube louvered fin



Wavy plate fins
(a)



Oval-tube louvered fin
(b)

Figure 14.17 Some enhanced fin geometries used in (a) plate fin and (b) tube plate fin compact heat exchangers.

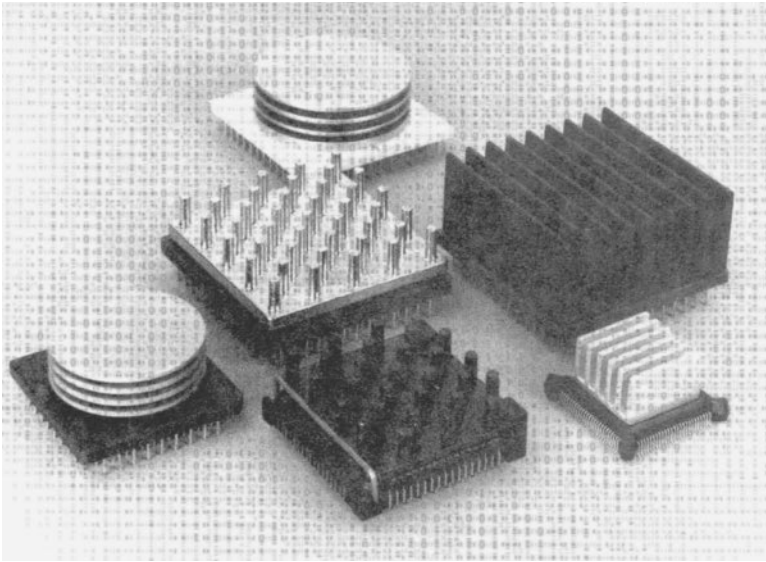


Figure 14.18 Typical finned heat sinks used for electronic cooling. (Courtesy of EG&G Wakefield Engineering.)

building/room heating equipment, the use of baseboard heaters has declined considerably; in fact, this practice is close to being discontinued. For thermal management of microelectronic devices, on the other hand, much recent effort has been directed toward the development of high-performance extended-surface heat sinks, and it continues to attract attention in the worldwide literature. A variety of fins are used, and some typical geometries are shown in Fig. 14.18. The design of these heat sinks entails optimization of the shape, size, and spacing of fin arrays, and their heat transfer characteristics have been covered in great detail in several reviews and monographs (Kraus, 1982; Nakayama and Bergles, 1990; Kraus and Bar-Cohen, 1995). In this context, one of the earliest studies on free convection from a pair of isothermal plates or fins was reported by Elenbaas (1942). It may also be noted that the use of extended surfaces for cooling electronic devices is not restricted to the natural convection heat transfer regime, but, in fact, the ever-increasing developments in high-performance microelectronics demand forced-convective heat transfer as well as other enhancement strategies (Bergles, 1986, 1990).

In single-phase forced-convective applications, tubes with fins on the inner, outer, or both surfaces have long been used in double-pipe and shell-and-tube heat exchangers (Kern and Kraus, 1972; Fraas, 1989; Hewitt, 1992; Hewitt et al., 1993; Kraus et al., 2001, Kakaç and Liu, 2002). Some examples of finned tubes that are typically employed are shown in Figs. 14.16 and 14.19. Although experimental data for several different geometries and flow arrangements are reported in the literature (Webb, 1994; Bergles, 1998), few predictive correlations for the Nusselt number and friction factor have been devised. In recent times, theoretical studies based on computational

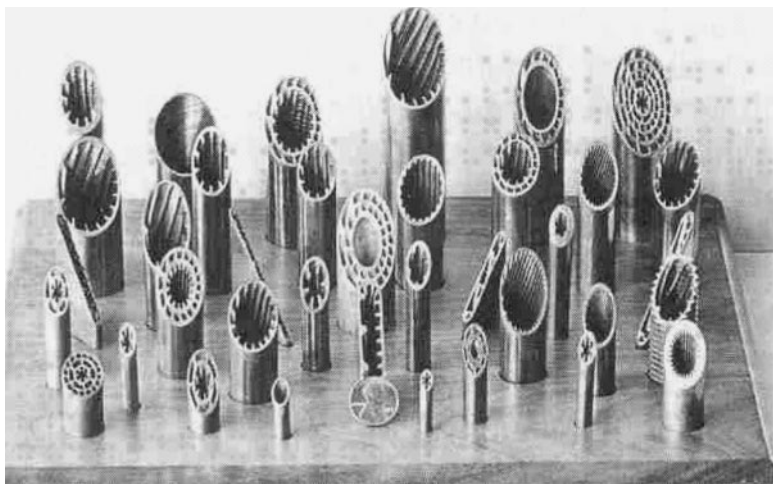


Figure 14.19 Examples of the variety in inner-finned tubes used in heat exchangers. (Courtesy of Noranda Metal Industries, Inc.)

simulations of forced convection in finned tubes and annuli have also been reported in the literature. These analyses have addressed both laminar (Masliyah and Nandakumar, 1976; Prakash and Liu, 1985; Rustom and Soliman, 1988; Kettner et al., 1991; Shome and Jensen, 1996; and several others) and turbulent (Patankar et al., 1979; Said and Trupp, 1984; Edwards and Jensen, 1994; Liu and Jensen, 1999, 2001; and others) flows, where, in some cases, the modeling includes fins of finite thickness, helical or spiral fins, and a conjugate analysis-based fin effectiveness. Extended discussions of some of the computational modeling issues and their implications for the numerical results are given by Webb (1994), Edwards and Jensen (1994), Shome and Jensen (1996), and Liu and Jensen (2001).

For internally finned tubes with straight or spiral fins and laminar flows, Watkinson et al. (1975) give the following hydraulic-diameter-based common expression for the isothermal Fanning friction factor and two different equations for the respective Nusselt numbers:

$$f_h = \frac{16.4}{\text{Re}_h} \left(\frac{d_h}{d} \right)^{1.4} \quad (14.14)$$

For straight fin tubes,

$$\text{Nu}_h = \frac{1.08 \times \log \text{Re}_h}{n^{0.5} (1 + 0.01 \text{Gr}_h^{1/3})} \text{Re}_h^{0.46} \cdot \text{Pr}^{1/3} \left(\frac{L}{d_h} \right)^{1/3} \left(\frac{\mu_w}{\mu_b} \right)^{0.14} \quad (14.15)$$

For spiral fin tubes,

$$\text{Nu}_h = \frac{8.533 \times \log \text{Re}_h}{1 + 0.01 \text{Gr}_h^{1/3}} \text{Re}_h^{0.26} \cdot \text{Pr}^{1/3} \left(\frac{t}{p} \right)^{0.5} \left(\frac{L}{d_h} \right)^{1/3} \left(\frac{\mu_w}{\mu_b} \right)^{0.14} \quad (14.16)$$

For f_h and Nu_h in turbulent flows in tubes with straight and spiral fins, Carnavos (1979a) has recommended the following:

$$f_h = 0.046 Re_h^{-0.2} \left(\frac{A_f}{A_{fi}} \right)^{0.5} (\sec \alpha)^{0.75} \quad (14.17)$$

$$Nu_h = 0.023 Re_h^{0.8} \cdot Pr^{0.4} \left(\frac{A_f}{A_{fi}} \right)^{0.1} \left(\frac{A_i}{A} \right)^{0.5} (\sec \alpha)^3 \quad (14.18)$$

These correlations have been shown to describe the data for air, water, oil, and ethylene glycol (Watkinson et al., 1975; Carnavos, 1979a; Marner and Bergles, 1989).

An attractive variation is to use segmented or interrupted longitudinal fins inside circular tubes, which are considered to promote enhanced heat transfer by periodically disrupting and restarting the boundary layer on the fin surface and perturbing the bulk flow field in general. The experimental data for airflows in such tubes reported by Hilding and Coogan (1964) indicate thermal-hydraulic performance improvements in the laminar and transition flow regimes; very few benefits were seen in turbulent flows. Kelkar and Patankar (1990) have also considered segmented fins inside circular tubes and have computationally simulated laminar forced convection in tubes with zero-thickness fin segments arrayed along the length of the tube in both an in-line and staggered arrangement. The in-line segmented fins, which had half the fin surface area of staggered or continuous fins, were found to perform better with 6% higher Nu and 22% lower f . Longitudinal fins and their modified varieties of the interrupted cut-and-twisted (Gunter and Shaw, 1942), perforated, and serrated types, as well as offset strip or lanced-type fins (see Fig. 14.16), are also commonly used in the annuli of double-pipe heat exchangers (Kern and Kraus, 1972; Webb, 1994; Bergles, 1998). Some design guidelines, data, and limited sets of predictive correlations are given by Kern and Kraus (1972), Guy (1983), Taborek (1997), and Kakaç and Liu (2002). Also, internally finned tubes can be “stacked” to provide multiple internal passages of the type shown in Fig. 14.19 with rather small hydraulic diameters (Soliman and Feingold, 1977; Carnavos, 1979b; Soliman, 1989).

For crossflow over finned tube banks, a fairly large set of experimental data can be found in the Russian literature (Zhukauskas, 1989), and the recommended correlations for tubes with circular or helical fins are given below. It should be noted here that the Reynolds number is based on the maximum flow velocity in the tube bank given by

$$U_{\max} = U_{\infty} \times \max \left[\frac{S_T}{S_T - D}, \frac{S_T/2}{[S_L^2 + (S_T/2)^2]^{1/2} - D} \right] \quad \text{and} \quad Re = \frac{\rho U_{\max} D}{\mu} \quad (14.19)$$

where S_T and S_L are the transverse and longitudinal pitch, respectively, of the tube array. Also, based on the work of Lokshin and Fomina (1978) and Yudin (1982), the friction loss is given in terms of the Euler number and the pressure drop is obtained from

$$\Delta p = \text{Eu}(\rho V_\infty^2 N_L) C_z \quad (14.20)$$

where C_z is a correction factor for tube bundles with $N_L < 5$ rows of tubes in the flow direction, and is as follows:

N_L	Aligned	Staggered
1	2.25	1.45
2	1.6	1.25
3	1.2	1.1
4	1.05	1.05
≥ 5	1.0	1.0

For in-line tubes with circular or helical fins,

$$\text{Eu} = 0.068 \varepsilon^{0.5} \left(\frac{S_T - 1}{S_L - 1} \right)^{-0.4} \quad (14.21)$$

for $10^3 \leq \text{Re} \leq 10^5$, $1.9 \leq \varepsilon \leq 16.3$, $2.38 \leq S_T/D \leq 3.13$, and $1.2 \leq S_L/D \leq 2.35$.

$$\text{Nu} = 0.303 \varepsilon^{-0.375} \cdot \text{Re}^{0.625} \cdot \text{Pr}^{0.36} \left(\frac{\text{Pr}}{\text{Pr}_w} \right)^{0.25} \quad (14.22)$$

for $5 \times 10^3 \leq \text{Re} \leq 10^5$, $5 \leq \varepsilon \leq 12$, $1.72 \leq S_T/D \leq 3.0$, $1.8 \leq S_L/D \leq 4.0$.

For staggered tubes with circular or helical fins,

$$\text{Eu} = C_1 \cdot \text{Re}^a \cdot \varepsilon^{0.5} \left(\frac{S_T}{D} \right)^{-0.55} \left(\frac{S_L}{D} \right)^{-0.5} \quad (14.23)$$

where

$$C_1 = \begin{cases} 67.6, & a = -0.7 & \text{for } 10^2 \leq \text{Re} < 10^3, 1.5 \leq \varepsilon \leq 16, \\ & & 1.13 \leq S_T/D \leq 2.0, 1.06 \leq S_L/D \leq 2.0 \\ 3.2, & a = -0.25 & \text{for } 10^3 \leq \text{Re} < 10^5, 1.9 \leq \varepsilon \leq 16, \\ & & 1.6 \leq S_T/D \leq 4.13, 1.2 \leq S_L/D \leq 2.35 \\ 0.18, & a = 0 & \text{for } 10^5 \leq \text{Re} < 1.4 \times 10^6, 1.9 \leq \varepsilon \leq 16, \\ & & 1.6 \leq S_T/D \leq 4.13, 1.2 \leq S_L/D \leq 2.35 \end{cases}$$

$$\text{Nu} = C_2 \cdot \text{Re}^a \cdot \text{Pr}^b \left(\frac{S_T}{S_L} \right)^{0.2} \left(\frac{p_f}{D} \right)^{0.18} \left(\frac{h_f}{D} \right)^{-0.14} \left(\frac{\text{Pr}}{\text{Pr}_w} \right)^{0.25} \quad (14.24)$$

where

$$C_2 = \begin{cases} 0.192, & a = 0.65, \quad b = 0.36 & \text{for } 10^2 \leq \text{Re} \leq 2 \times 10^4 \\ 0.0507, & a = 0.8, \quad b = 0.4 & \text{for } 2 \times 10^4 \leq \text{Re} \leq 2 \times 10^5 \\ 0.0081, & a = 0.95, \quad b = 0.4 & \text{for } 2 \times 10^5 \leq \text{Re} \leq 1.4 \times 10^6 \end{cases}$$

and the general range of the following fin and tube pitch parameters:

$$0.06 \leq \frac{pf}{D} \leq 0.36, 0.07 \leq \frac{h_f}{D} \leq 0.715, 1.1 \leq \frac{S_T}{D} \leq 4.2, 1.03 \leq \frac{S_L}{D} \leq 2.5$$

In eqs. (14.22)–(14.24), the variables that describe the fin dimensions are $\varepsilon \equiv$ finned surface extension ratio (i.e., ratio of total surface area and the bare tube surface area), $p_f \equiv$ fin pitch, and $h_f \equiv$ fin height.

Plate-fin or tube-and-plate fin type of compact heat exchangers, where the finned surfaces provide a very large surface area density, are being used increasingly in many automotive, waste-heat recovery, refrigeration and air-conditioning, cryogenic, propulsion system, and other heat recuperation applications. A variety of finned surfaces are used, typical among which include offset strip fins, louvered fins, perforated fins, and wavy fins, as illustrated in Fig. 14.17, which not only provide a surface-area enlargement but also increase the heat transfer coefficient by altering the flow field. Their development, thermal–hydraulic performance, and design methodologies, primarily for gas or air flows, have been the subject of several reviews and monographs (Manglik and Bergles, 1990; Kays and London, 1984; Shah et al., 1997; Webb, 1994; Smith, 1997; Shah et al., 1999; Hesselgreaves, 2001). The forced-convective gas flow in the interfin channels is rather complex, where the enhancement is generally due to flow separation, secondary flow, or periodic starting of the boundary layer, and relatively few generalized correlations or predictive methods are available.

Of the many different compact heat exchanger enhanced plate-fin geometries, a more popular surface that finds wide use is the offset strip fin whose geometrical features are described in Fig. 14.20. Based on the experimental data for 18 different rectangular offset-strip-fin cores listed in Kays and London (1984) the following power law correlations for the Fanning friction factor f and Colburn factor j have been proposed (Manglik and Bergles, 1995):

$$f_h = 9.6243 \text{Re}_h^{-0.7422} \alpha^{-0.1856} \delta^{0.3053} \gamma^{-0.2659} (1 + 7.669 \times 10^{-8} \text{Re}_h^{4.429} \alpha^{0.920} \delta^{3.767} \gamma^{0.236})^{0.1} \quad (14.25)$$

$$j_h = 0.6522 \text{Re}_h^{-0.5403} \alpha^{-0.1541} \delta^{0.1499} \gamma^{-0.0678} (1 + 5.269 \times 10^{-5} \text{Re}_h^{1.340} \alpha^{0.504} \delta^{0.456} \gamma^{-1.055})^{0.1} \quad (14.26)$$

It should be noted that f_h , j_h , and Re_h in these equations are based on the hydraulic diameter that is defined as

$$d_h = \frac{4shl}{2(sl + hl + th) + ts} \quad (14.27)$$

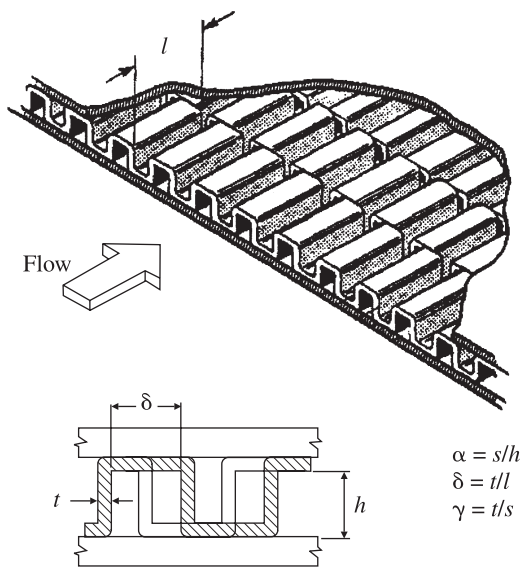


Figure 14.20 Geometrical features of rectangular offset strip plate fins. (From Manglik and Bergles, 1995.)

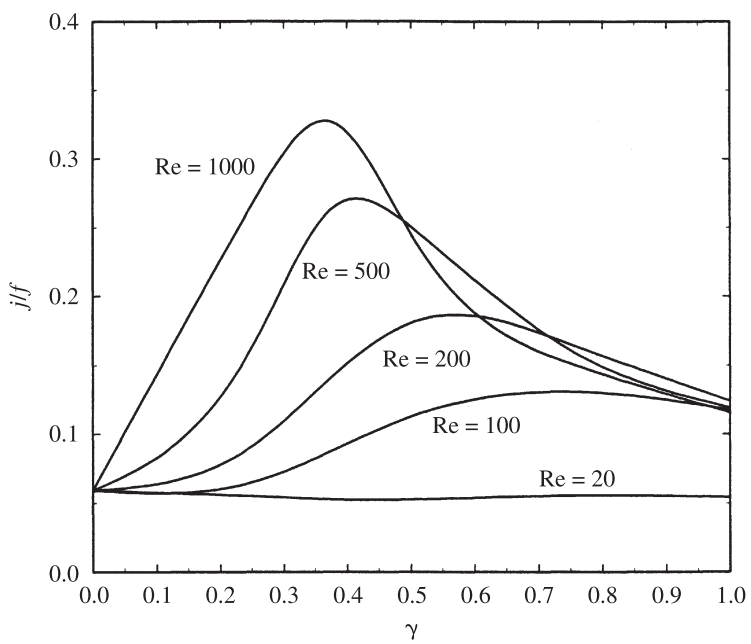


Figure 14.21 Enhanced performance of sinusoidal wavy plate fin channels in periodically developed laminar flows as measured by the area goodness factor. (From Metwally and Manglik, 2000.)

where each geometric variable is identified in Fig. 14.20. These equations quite accurately represent the experimental data continuously in the laminar, transition, and turbulent flow regimes (Manglik and Bergles, 1995).

For tube fin heat exchangers, Wang (2000) has given a comprehensive review of 51 patents issued in the period 1981–1991 for a variety of louvered-, wavy-, and slit fin and punched tab (protruded-tab vortex generators) fin surfaces. Wang et al. (2001) have also provided an extended review and compilation of correlations for plain, wavy, louvered, and slit fins. The applicability of these predictive equations to both dry and wet (dehumidifying) conditions has been discussed, along with the issue of hydrophilic coatings. For the wavy fin tube fin coil, a numerical simulation for the air-side performance has been reported by Min and Webb (2001). Metwally and Manglik (2000) have analyzed periodically developed laminar forced convection in wavy plate fin cores. Their numerical model considers two-dimensional sinusoidal-wavy plate fins, which is applicable when the fin height \gg fin spacing, and the results depicted in Fig. 14.21 show a strong influence of the wall waviness on the enhanced performance represented by the area goodness factor (j/f); the development and applicability of this figure of merit for compact heat exchangers are outlined in Shah and London (1978). Subsequent work on three-dimensional wavy plate fin channels (finite fin height) shows trends that are similar, albeit different in magnitude (Muley et al., 2002; Zhang et al., 2002).

14.4.2 Boiling

Internally finned tubes are commonly in refrigerant evaporators as well as some other applications for flow boiling. A variety of different geometries are used, and some typical cases made up of large, medium, or low and microfin heights are shown in Fig. 14.22. As pointed out by Bergles (2000), increases in the average heat transfer coefficient of up to 200%, based on the smooth or “empty” tube of the same diameter, have been reported. Their boiling performance, particularly with refrigerants, has been investigated for almost five decades now, with some of the earliest studies reported by Boling et al. (1953), Katz et al. (1955), and Lavin and Young (1965).

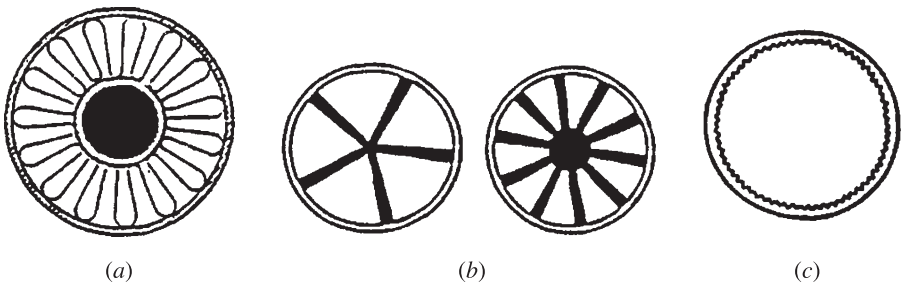


Figure 14.22 Some types of internally finned tubes used for refrigerant evaporators: (a) strip fin inserts; (b) star-shaped shrunk-fit fin inserts; (c) microfinned tubes. (From Bergles, 2000.)

Extended reviews of this literature are given by Thome (1990), Webb (1994), Bergles (1998), and Kandlikar et al. (1999).

In pool boiling of R-114, Hesse (1973) has shown that finned tubes have higher heat transfer coefficients compared with the performance of equivalent smooth tubes. There was, however, no change in the CHF (with q''_{cr} referenced to the smooth tube area), which may perhaps be due to the bubble interference in the interfin spaces. Based on an extended survey of finned tubes for pool boiling, Westwater (1973) has suggested that this situation may be remedied by keeping the fin spacing close to the departure diameter of the nucleate boiling bubble for the evaporating fluid; the issues of fin shape and boiling regimes that provide high enhancement levels have also been addressed. Several other studies have shown enhanced boiling of refrigerants and organics from finned surfaces (Bergles et al., 1981; Kakaç et al., 1988; Thome, 1990; Webb, 1994; Bergles, 1998).

Of the three different types of internally finned tubes shown in Fig. 14.22, Schlünder and Chawla (1969) and Pearson and Young (1970) have reported boiling data for R-11 and R-22, respectively, with different star-shaped shrunk-fit fin inserts (Fig. 14.22*b*). Additional data for R-122 and R-22 are given by Lavin and Young (1965), and for R-22 by Kubanek and Milette (1979). In the former study, the effects of subcooling as well as boiling in different flow regimes are also discussed.

However, in most heat exchangers for refrigeration and air-conditioning systems that are manufactured today, microfinned tubes (Fig. 14.22*c*) are invariably used

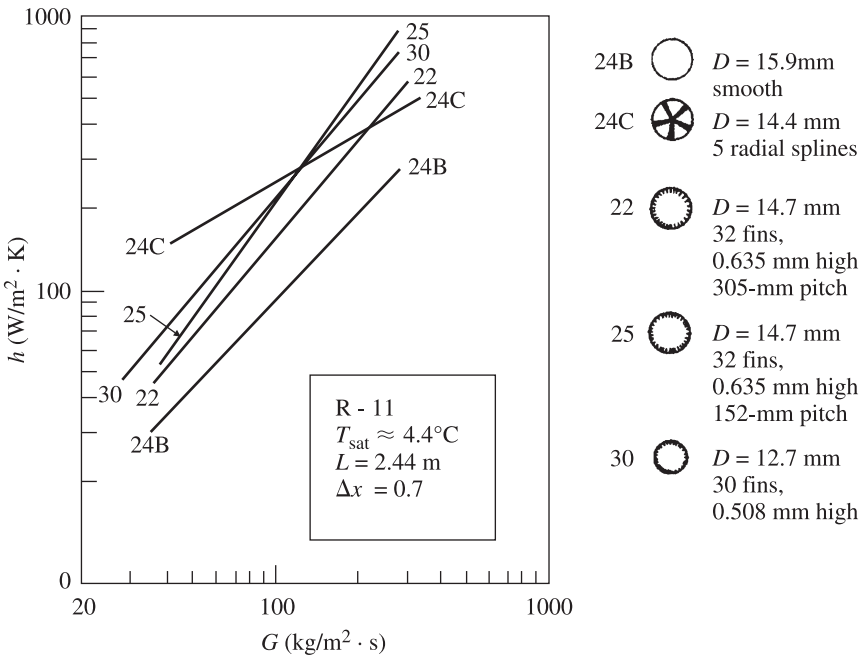


Figure 14.23 Enhanced boiling heat transfer coefficients for R-11 flows in internally finned tubes reported by Kubanek and Milette (1979).

(Webb, 1994). Some of the earliest experimental studies with such tubes were reported by Fujie et al. (1977), Itoh and Kimura (1979), Kubanek and Milette (1979), and Shinohara et al. (1987). The R-11 boiling data of Kubanek and Milette (1979) for finned tubes, which includes a tube with a star-shaped fin insert and a smooth tube, are shown in Fig. 14.23. Here the heat transfer coefficients are based on the same-diameter smooth tube surface area, and the enhanced performance is self-evident. Much of the current focus of work on microfin tubes is their performance with boiling of alternative (or chlorine-free substitutes) refrigerants. New data have been reported, for example, by Kedzierski (1993) for R-123 and by Eckels et al. (1994a) for R-134a. In a very recent new development, microfins machined in a herringbone fashion, instead of the conventional spiral or helical pattern, on the inner tube surface have been produced and tested with R-22 and R-407c (Ebisu and Torikoshi, 1998; Torikoshi and Ebisu, 1999). The data suggest a 80 to 100% increase in the average boiling heat transfer coefficients compared to that for conventional microfin tubes for the same conditions. As shown schematically in Fig. 14.24, Ebisu and Torikoshi (1998) attribute this improved performance to a better distribution of the liquid layer at the wall and its more circumferentially uniform thinning.

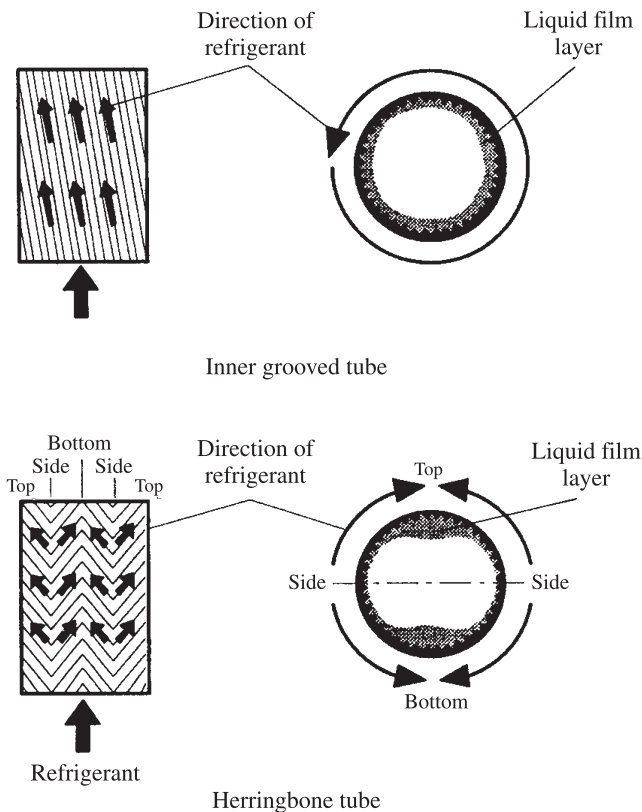


Figure 14.24 Liquid film distribution and enhancement mechanisms in conventional spiral and herringbone microfin tubes. (From Ebisu and Torikoshi, 1998.)

14.4.3 Condensing

Extended surfaces that include a variety of large-, medium-, and micro-sized fins are used extensively for condensation heat transfer enhancement in power, process, air-conditioning, and refrigeration applications. The heat exchangers in these duties involve both horizontal and vertical tube condensers, with fins on the inside or outside surfaces (or both) of tubes. In some applications, compact plate fin heat exchangers with offset strip fin cores have also been considered, and Fujii (1995) and Torikoshi and Ebisu (1999) have presented good review summaries of some of the newer developments.

For integral fin tubes, besides the increased surface area, higher heat transfer coefficients are obtained because a relatively thin condensate film tends to be formed near the fin tips, and surface tension forces pull the condensate into the interfin grooved spaces, thereby promoting better drainage and reduction of liquid film resistance. The fin profile or shape plays an important role in promoting this surface tension-induced condensate film drainage, as was established almost a half-century ago by Gregorig (1954) in perhaps the first analytical study to address this issue. Since then, several surface tension-drained models have been proposed to predict the enhanced heat transfer coefficients and design fin profile shapes (Adamek, 1981; Honda and Nozu, 1987; Honda et al., 1988; Webb et al., 1985; Adamek and Webb, 1990; Honda and Kim, 1995; Honda and Rose, 1999).

A fairly large body of data for condensation on horizontal tubes with external integral fins is available in the literature, which has been reviewed insightfully by Marto (1988). This data set includes measurements for steam, refrigerants (R-11, R-22, and R-113), and several organic fluids. One of the first attempts to devise a correlation was made by Beatty and Katz (1948), who proposed the following equation for the average heat transfer coefficient based on the total area of the finned tube:

$$h_m = 0.689 \left(\frac{k_l^3 \rho_l^2 i_{lg}}{\mu_l \Delta T} \right)^{1/4} \left\{ 1.3 \eta_f \frac{A_f}{A_e [\pi(D_o^2 - D_r^2)/4D_o]^{0.25}} + \frac{A_r}{A_e D_r^{0.25}} \right\} \quad (14.28)$$

Here the total outside surface area of a finned tube is taken to be the effective surface area A_e . This semiempirical correlation is based on their data for methyl chloride, sulfur chloride, *n*-pentane, propane, and R-22 and the assumption that the condensate is readily drained by gravity. However, as pointed out by Webb (1994), this is perhaps not a generally valid assumption, as the surface tension force and not gravity primarily controls condensate film drainage from the fin surface. Webb (1994), and Shah et al. (1999) have compiled and comparatively reviewed the available correlations and models that account for surface tension-induced drainage. The role of fin geometry (profile and height) has been discussed by Honda et al. (1994) and Das et al. (1999). Comparing the performance of four different fin shapes, a profile “with a monotonically increasing radius of curvature near the fin tip and a constant thickness near the fin root” (Honda et al., 1994), tube C of the four fin tubes in Fig. 14.25 has been shown to provide the highest condensation enhancement with CFC-11 and HCFC-123. Furthermore, for a fixed fin profile and spacing, the effect of fin height

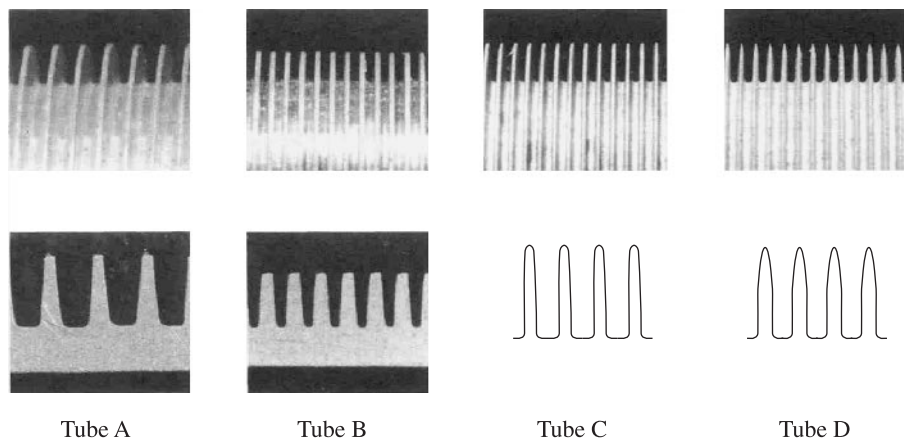


Figure 14.25 Cross-sectional fin profiles of various finned tubes tested by Honda et al. (1994) for condensation of CFC-11 and HCFC-123.

is depicted by the data of Das et al. (1999) in Fig. 14.26. Based on these assessments it appears that the Honda et al. (1988) and Rose (1994a,b)–Briggs and Rose (1994) correlations are preferred.

Heat transfer enhancement in vertical condensers has been considered for several large-scale power and process industry applications. Several different types of finned tubes and other enhanced surfaces have been tested (Thomas, 1967, 1968; Alexander and Hoffman, 1971; Bergles, 1998). An excellent analysis for designing a fin profile

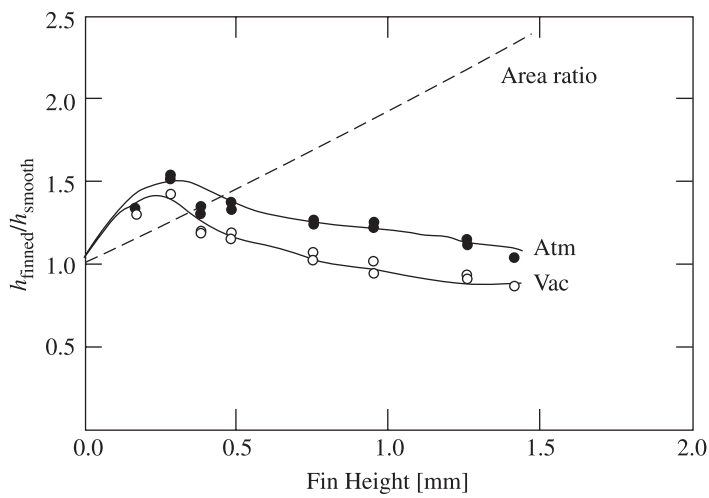


Figure 14.26 Effect of fin height on enhanced steam condensation heat transfer. (From Das et al., 1999.)

to optimize the surface-tension-induced film condensation drainage is described by Mori et al. (1981). The preferred geometry according to this analysis is characterized by four factors: a sharp leading edge, gradually changing curvature of the fin surface from its tip to root, wide grooves or spaces between fins to collect condensate, and horizontal disks attached to the tube at periodic intervals to strip off the accumulated condensate. Their experimental data for R-113 showed further that such an arrangement indeed enhances the condensation performance.

Refrigerant and steam condensation inside horizontal low-fin and microfin tubes have been studied extensively for air-conditioning and refrigeration and process applications (Vrable et al., 1974; Royal and Bergles, 1978a,b; Luu and Bergles, 1979; Khanpara et al., 1986; Schlager et al., 1988, 1990; Shizuya et al., 1995; Kwon et al., 2000). Enhancements ranging from 100% up to 300% over the equivalent smooth tube performance are reported for steam, R-12, R-113, R-22, and R-410A, among others. For predicting the average steam condensation heat transfer coefficient, based on the inside or envelope diameter of the tube, Royal and Bergles (1978b) have proposed the following correlation:

$$h_{m,i} = 0.0265 \left(\frac{k_l}{d_h} \right) \left(\frac{G_e d_h}{\mu_l} \right)^{0.8} \cdot \text{Pr}_l^{1/3} \left[1 + 160 \left(\frac{h_f^2}{s d} \right)^{1.91} \right] \quad (14.29a)$$

where

$$G_e = G \left[(1 - x_m) + x_m \sqrt{\frac{\rho_l}{\rho_g}} \right] \quad (14.29b)$$

Similarly, for refrigerants, Luu and Bergles (1979) give the following predictive equation:

$$h_{m,i} = 0.024 \left(\frac{k_l}{d_h} \right) \left(\frac{G d_h}{\mu_l} \right)^{0.8} \cdot \text{Pr}_l^{0.43} \left(\frac{h_f^2}{s d} \right)^{-0.22} \frac{1}{2} \left[\left(\frac{\rho}{\rho_m} \right)_{\text{in}}^{0.5} + \left(\frac{\rho}{\rho_m} \right)^{0.5} \right] \quad (14.30a)$$

where

$$\frac{\rho}{\rho_m} = 1 + x_m \left(\frac{\rho_l - \rho_g}{\rho_g} \right) \quad (14.30b)$$

Much of the current work is now focused on the use of microfin tubes (Khanpara et al., 1986; Schlager et al., 1990; Shizuya et al., 1995; Chamra et al., 1996; Shikazono et al., 1998; Kwon et al., 2000). Also, the effort is now directed toward ascertaining their performance with a variety of alternative refrigerants or replacements for CFCs (Eckels et al., 1994b; Kedzierski and Goncalves, 1997; Tang et al., 2000).

Three-dimensional finned surfaces have been shown to enhance condensation heat transfer from horizontal tubes over and above that normally obtained from

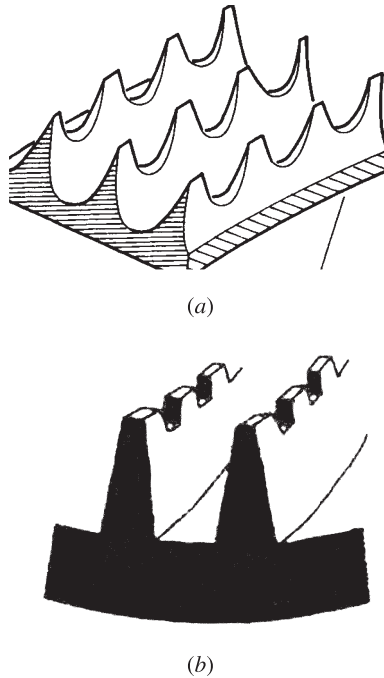


Figure 14.27 Three-dimensional finned surfaces for enhanced condensation: (a) notched fins (from Nakayama et al., 1975); (b) serrated-tip microfins (from Itoh et al., 1997).

conventional low-fin tubes. The improvements in the envelope area-based heat transfer coefficients can be as much as seven times smooth tube values. A typical three-dimensional finned surface developed in Japan (Nakayama et al., 1975; Arai et al., 1977) is shown in Fig. 14.27a, and the notched fin profiles apparently provide better multidirectional condensate drainage from the fin tips. In an experimental study with circular pin fins, Chandran and Watson (1976) found the average heat transfer coefficients, based on the total surface area, to be as much as 20% higher than those for a smooth tube. Webb and Gee (1979) have proposed square-profiled spine fins on the basis of a theoretical value using the gravity drainage model.

Similarly, for in-tube condensation, Itoh et al. (1997) have shown that microfins with serrated tips (uniformly spaced secondary discrete grooves on fin tips as shown in Fig. 14.27b) provide 30 to 60% improvements in the average heat transfer coefficients over same-sized conventional microfin tubes. The herringbone arrangement for microfins inside a tube proposed by Ebisu and Torikoshi (1998) and Torikoshi and Ebisu (1999), which essentially provide a cross-corrugated three-dimensional finned surface, has also been found to enhance R-22 and R-407C condensation heat transfer (see also the discussion in Section 14.4.2 on refrigerant boiling inside this herringbone microfin tube).

14.5 DISPLACED ENHANCEMENT DEVICES

14.5.1 Single-Phase Flow

The use of several different types of inserts, which are categorized as displaced enhancement devices, is documented in the literature (Bergles et al., 1995; and Bergles 1998). They include static mixer elements (e.g., Kenics, Sulzer), metallic mesh, disks, rings, or balls, which tend to “displace” the fluid from the core of the channel to its heated or cooled wall, and vice versa; the heat transfer surface itself remains unaltered. The earliest set of data on displaced enhancement devices was perhaps reported by Koch (1958), who tested two such devices: suspended rings and disks as inserts, and tubes packed with Raschig rings and round balls. The disks were found to promote higher heat transfer with rather moderate increases in the friction factor penalty. In the case of rings and round balls, although the heat transfer improvements were comparable to that with disks, the friction factors were exorbitantly high (more than 1600%). Several studies (Van Der Meer and Hoogenedoorn, 1978; Marnier and Bergles, 1978; Lin et al., 1978; Pahl and Muschelknautz, 1979) have reported the performance of different types of static mixers, and a comprehensive review of their characteristic features is given by Pahl and Muschelknautz (1979). Most of these devices are, however, effective only in laminar flows, as in turbulent flows, the pressure-drop penalties are extremely high (Bergles, 1998). The application of static mixers is generally restricted to chemical processing with heat transfer, where fluid mixing is the primary need.

One of the newer displaced enhancement devices commercially available at the present time is the wire matrix insert shown in Fig. 14.28. A coiled-wire matrix, shaped in assorted size cloverleaf patterns, is metallurgically attached to a core rod, and this assembly, with different coil-matrix densities, is used as a tube insert. The wires tend to disrupt the core as well as boundary layer flows, thereby promoting better mixing and enhanced heat transfer. Oliver and Aldington (1986) have reported limited data for laminar flows of viscous liquids.

For high-temperature gas applications, classical examples that continue to be employed are bent tab, bent strip, punched-tab strip, and other types of inserts placed in

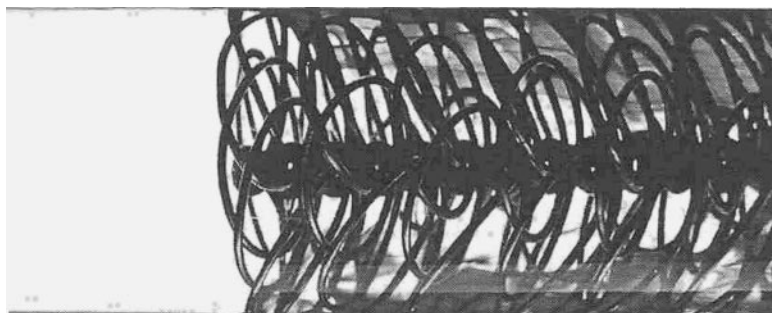


Figure 14.28 Heatex wire matrix tube inserts. (Courtesy of Cal Gavin Ltd.)

the flue tubes of fire-tube boilers and hot-water heaters. Although often referred to as baffles or retarders or turbulators, these inserts are basically mixing devices that increase the convective heat transfer coefficient in turbulent flows (Koch, 1958; Evans and Churchill, 1963; Nirmalan et al., 1986; Junkhan et al., 1988). Similarly, spiral brush inserts in short channels with turbulent flows and high wall heat flux have been tested by Megerlin et al. (1974). Although the heat transfer coefficients improved by as much as 8.5 times that in a smooth tube, the pressure drop was exorbitantly high. The latter aspect of displaced enhancement devices in general has restricted their use in practical applications.

14.5.2 Boiling

A limited number of studies have reported the use of displaced enhancement devices in boiling applications to increase CHF (Bergles, 1998). These have included rings, spacers, inserts (mesh or brush type), and so on, for both bulk and subcooled boiling conditions (Megerlin et al., 1974; Ryabov et al., 1977; Bergles, 1998). Much of this work was carried out in the late 1960s and early 1970s, driven primarily by the needs to address ways to increase CHF in nuclear power plants, and such devices have not received attention recently.

14.5.3 Condensing

As in the case of boiling, displaced enhancement devices have not found much use in condensation applications. Only two rather dated studies (Azer et al., 1976; Fan et al., 1978) appear to have considered the use of Kenics static mixer inserts experimentally. The improvements in heat transfer coefficients, however, were once again accompanied by a very high pressure-drop penalty.

14.6 SWIRL FLOW DEVICES

Swirl flow devices generally consist of a variety of tube inserts, geometrically varied flow arrangements, and duct geometry modifications that produce secondary flows. Typical examples of each of these techniques include twisted-tape inserts, periodic tangential fluid injection, and helically twisted tubes, shown schematically in Fig. 14.29. Of these, twisted-tape inserts have received considerable attention in the literature, and their thermal-hydraulic performance in single-phase, boiling, and condensation forced convection, as well as design and application issues, have been discussed in great detail (Manglik and Bergles, 2002a).

14.6.1 Single-Phase Flow

Perhaps the most effective and widely used swirl flow device for single-phase flows is the twisted-tape insert, which has design and application literature dating back more than a century (Whitham, 1986). It has been shown to increase significantly

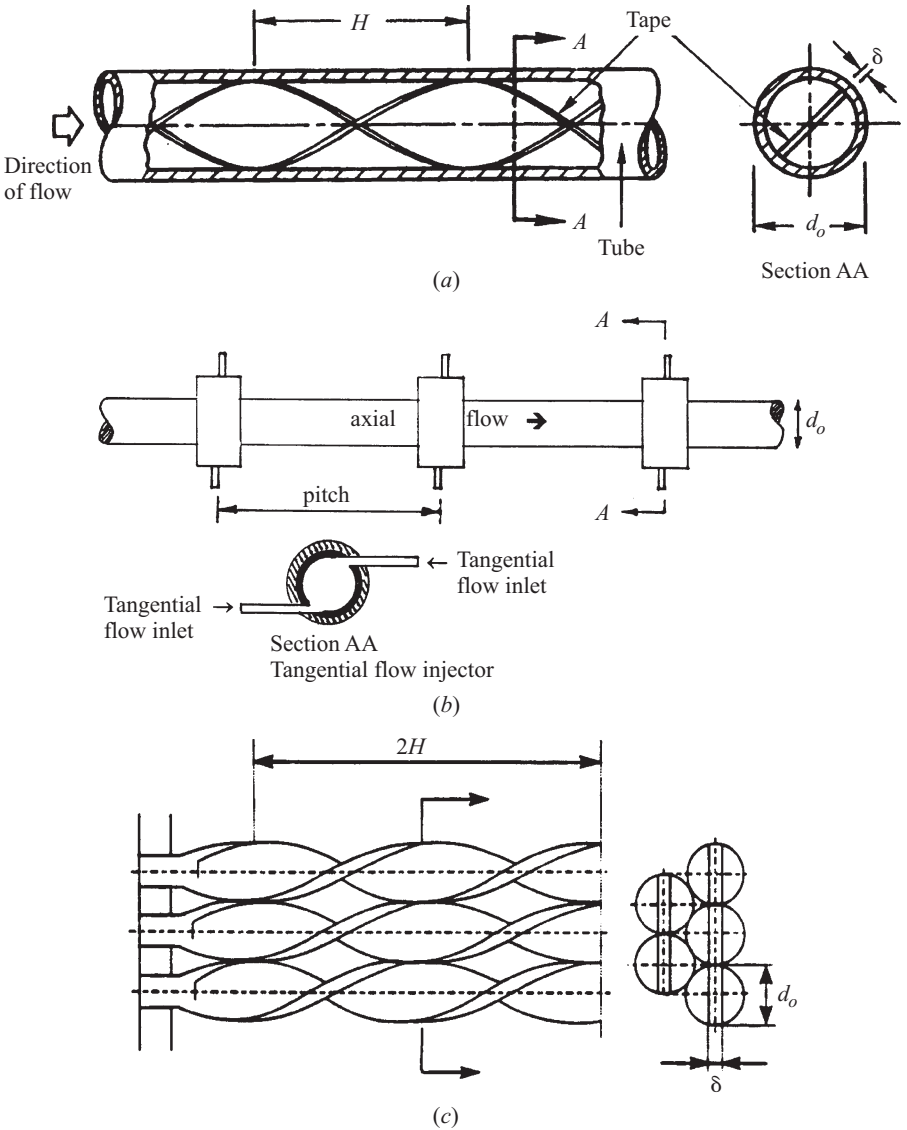


Figure 14.29 Typical examples of swirl flow devices: (a) twisted-tape insert; (b) altered tube flow arrangement; (c) twisted duct. (From Manglik and Bergles, 2002a.)

the heat transfer coefficient with a relatively small pressure-drop penalty (Smithberg and Landis, 1964; Lopina and Bergles, 1969; Date and Singham, 1972; Hong and Bergles, 1976; Marner and Bergles, 1989; Manglik and Bergles, 1991; 1992; Manglik and Yera, 2002). Frequent use of twisted tapes is in retrofit of existing shell-and-tube heat exchangers to upgrade their heat duties. Also, when employed in a new

exchanger for a specified heat duty, significant reduction in size can be achieved. The ease of fitting multitube bundles with tape inserts and their removal, as depicted in Fig. 14.30*a*, makes them particularly useful in fouling situations, where frequent tube-side cleaning may be required.

The characteristic geometrical features of a twisted tape, as shown in Fig. 14.30*b*, include the 180° twist pitch H , tape thickness δ , and tape width w (which is usually about the same as the tube inside diameter d in snug- to tight-fitting tapes). The severity of tape twist is described by the dimensionless twist ratio $y(= H/d)$, and depending on the tube diameter and tape material, inserts with a very small twist ratio can be employed. When placed inside a circular tube, the flow field gets altered in several different ways: increased axial velocity and wetted perimeter due to the blockage and partitioning of the flow cross section, longer effective flow length in the helically twisting partitioned duct, and tape's helical curvature-induced secondary fluid circulation or swirl. Of these, the most dominant mechanism is swirl generation, which effects transverse fluid transport across the tape-partitioned duct, thereby promoting greater fluid mixing and higher heat transfer coefficients. The growth and structure of this tape-induced swirl in the laminar flow regime, as characterized by experimental flow visualization (Manglik and Ranganathan, 1997) and computational simulations

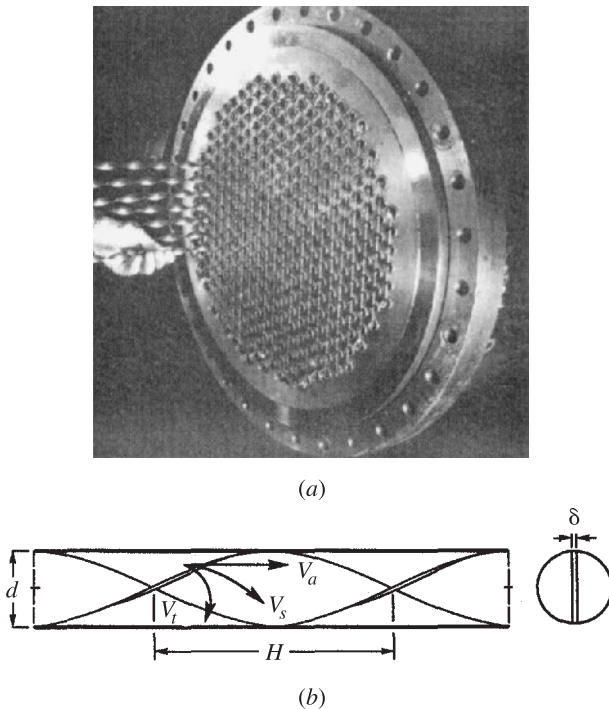


Figure 14.30 Twisted-tape inserts: (a) typical application in a shell-and-tube heat exchanger (courtesy of Brown Fintube Company); (b) characteristic geometrical features.

(Manglik and You, 2002), are depicted in Fig. 14.31. The fully developed laminar swirl flows, which consist of two asymmetrical counter-rotating helical vortices, have been shown (Manglik and Bergles, 1993a; Manglik et al., 2001a) to scale by a dimensionless swirl parameter defined on the basis of a primary force balance as

$$Sw = \frac{Re_s}{\sqrt{y}} \tag{14.31a}$$

where

$$Re_s = \frac{\rho V_s d}{\mu} \qquad V_s = \frac{G}{\rho} \left[1 + \left(\frac{\pi}{2y} \right)^2 \right]^{1/2} \tag{14.31b}$$

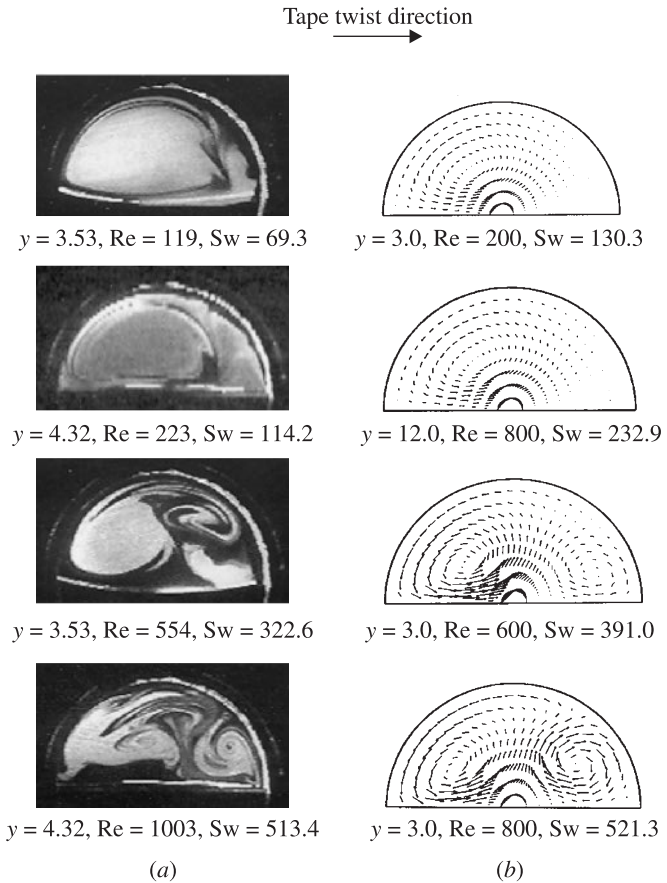


Figure 14.31 Structure of swirl produced by twisted-tape inserts in laminar flows in circular tubes: (a) experimental visualization of secondary flow patterns (from Manglik and Ranganathan, 1997); (b) results of numerical simulations (From Manglik and You, 2002).

Based on this scaling of the swirl behavior in the *laminar flow* regime, the following correlation for predicting the isothermal Fanning friction factor has been proposed (Manglik and Bergles, 1993a):

$$f_s = \frac{15.767}{\text{Re}_s} \left[\frac{\pi + 2 - 2(\delta/d)}{\pi - 4(\delta/d)} \right]^2 (1 + 10^{-6} \text{Sw}^{2.55})^{1/6} \quad (14.32)$$

where f_s is based on the effective swirl velocity and swirl flow length, or

$$f_s = \frac{\Delta p d}{2\rho V_s^2 L_s} \quad L_s = L \left[1 + \left(\frac{\pi}{2y} \right)^2 \right]^{1/2} \quad (14.33)$$

Equation (14.32) has been shown to predict within $\pm 10\%$ a fairly large set of experimental data for a very wide range of flow conditions and tape geometry: $0 \leq \text{Sw} \leq 2000$, $1.5 \leq y \leq \infty$, $0.02 \leq (\delta/d) \leq 0.12$ (Manglik and Bergles, 1993a; Manglik et al., 2001a). For laminar flow heat transfer in tubes maintained at a uniform wall temperature (UWT), the following correlation developed by Manglik and Bergles (1993a) is recommended:

$$\text{Nu}_m = \underbrace{4.612(\mu_b/\mu_w)^{0.14}}_{\text{fully developed flow}} \left\{ \underbrace{\left[(1 + 0.0951 \text{Gz}^{0.894})^{2.5} \right]}_{\text{thermal entrance}} \right. \\ \left. + \underbrace{6.413 \times 10^{-9} (\text{Sw} \cdot \text{Pr}^{0.391})^{3.835}}_{\text{swirl flows}} \right]^2 + \underbrace{2.132 \times 10^{-14} (\text{Re}_a \cdot \text{Ra})^{2.23}}_{\text{free convection}} \left. \right\}^{0.1} \quad (14.34)$$

Here each of the terms that account for various convection effects is highlighted, and the interplay between thermal entrance effects and fully developed tape-induced swirl flows is depicted in Fig. 14.32. With $\text{Ra} \sim 0$, their respective asymptotes are represented by $\text{Sw} \rightarrow 0$, $\text{Gz} \rightarrow \infty$ (entrance effects), and $\text{Sw} \rightarrow \infty$, $\text{Gz} \rightarrow 0$ (swirl-dominated flows). Similarly, in flows where $\text{Gr} > \text{Sw}^2$, free convection effects dominate and they are scaled by the grouping $(\text{Re}_a \cdot \text{Ra})$, as shown in Fig. 14.33. For tubes with the uniform heat flux (UHF) condition, the correlation devised by Hong and Bergles (1976) for fully developed swirl flows may be considered after incorporating the classical viscosity-ratio correction factor to account for viscous property variations as follows:

$$\text{Nu}_z = 5.172 \left[1 + 5.484 \times 10^{-3} \text{Pr}^{0.7} \left(\frac{\text{Re}_a}{y} \right)^{1.25} \right]^{0.5} \left(\frac{\mu_b}{\mu_w} \right)^{0.14} \quad (14.35)$$

Furthermore, to account for the influence of free convection on swirl flows in UHF tubes, Bandyopadhyay et al. (1991) have extended the Hong and Bergles correlations to include mixed convection as

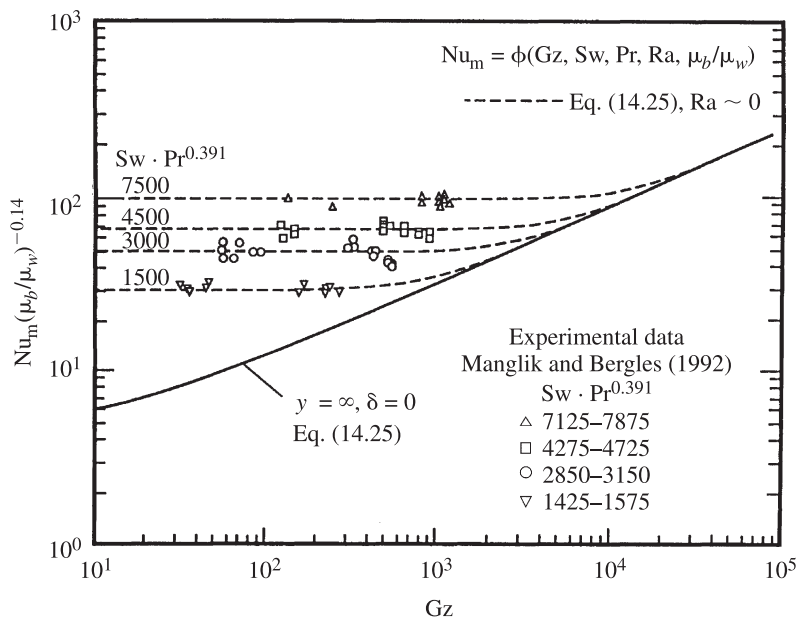


Figure 14.32 Influence of twisted-tape-generated swirl and tube partitioning on the average Nusselt number in thermal developing and fully developed laminar flows in circular tubes with uniform wall temperature. (From Manglik and Bergles, 1993a.)

$$Nu_z = \left[Nu_{z,HB}^9 + 1.17 (Ra^{*0.181})^9 \right]^{1/9} \tag{14.36}$$

For predicting friction factors under the more practical diabatic (heating or cooling) conditions, based on the theoretical results of Harms et al. (1998) for the limiting case of a straight-tape insert ($y = \infty, \delta = 0$) for liquids and the experimental results of Watanabe et al. (1983), a first-order correction to the isothermal results of eq. (14.32) can be made as

$$\frac{f}{f_{iso}} = \begin{cases} \left(\frac{\mu_b}{\mu_w} \right)^m & \text{for liquids} \\ \left(\frac{T_b}{T_w} \right)^{0.1} & \text{for gases} \end{cases} \tag{14.37a}$$

where

$$m(UWT) = \begin{cases} 0.65 & \text{heating} \\ 0.58 & \text{cooling} \end{cases} \quad \text{or} \quad m(UHF) = \begin{cases} 0.61 & \text{heating} \\ 0.54 & \text{cooling} \end{cases} \tag{14.37b}$$

In the *turbulent flow regime*, which is characterized inherently by fluctuating velocities, a well-mixed cross-stream eddy structure, and flow instabilities in the transition process, the scaling of swirl flows due to twisted-tape inserts with Sw is

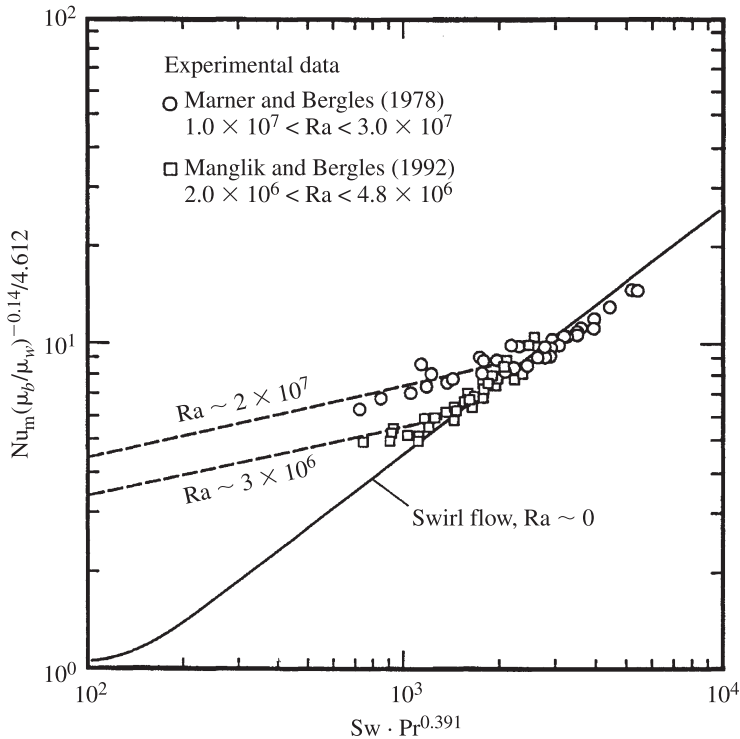


Figure 14.33 Mixed convection effects in laminar fully developed twisted-tape-induced swirl-flow heat transfer in circular tubes with uniform wall temperature. (From Manglik and Bergles, 1993a.)

found to be inapplicable (Manglik and Bergles, 1993b). Instead, the friction factor correlates with a power law reciprocal of the twist ratio as

$$f = \frac{0.0791}{\text{Re}^{0.25}} \left(1 + \frac{2.752}{y^{1.29}} \right) \left[\frac{\pi}{\pi - (4\delta/d)} \right]^{1.75} \left[\frac{\pi + 2 - (2\delta/d)}{\pi - (4\delta/d)} \right]^{1.25} \quad (14.38)$$

and it describes the available experimental data within $\pm 5\%$ (Manglik and Bergles, 1993b; Tong et al., 1996; Manglik and Bergles, 2002a). Again, to correct for heating and cooling conditions in predicting the friction factors, the following recommendations given by Lopina and Bergles (1969) for liquids, and by Watanabe et al. (1983) for gases, may be adopted:

$$\frac{f}{f_{\text{iso}}} = \begin{cases} \left(\frac{\mu_b}{\mu_w} \right)^{0.35(d_h/d)} & \text{for liquids} \\ \left(\frac{T_b}{T_w} \right)^{0.1} & \text{for gases} \end{cases} \quad (14.39)$$

For turbulent flow heat transfer with $Re \geq 10^4$, Manglik and Bergles (1993b) have proposed a Nusselt number correlation that is expressed as

$$Nu = 0.023Re^{0.8} \cdot Pr^{0.4} \left(1 + \frac{0.769}{y}\right) \left[\frac{\pi + 2 - (2\delta/d)}{\pi - (4\delta/d)}\right]^{0.2} \left[\frac{\pi}{\pi - (4\delta/d)}\right]^{0.8} \phi \quad (14.40a)$$

where the property correction factor ϕ is given by

$$\phi = \left(\frac{\mu_b}{\mu_w}\right)^n \quad \text{or} \quad \left(\frac{T_b}{T_w}\right)^m \quad (14.40b)$$

where

$$n = \begin{cases} 0.18 & \text{liquid heating} \\ 0.30 & \text{liquid cooling} \end{cases} \quad \text{and} \quad m = \begin{cases} 0.45 & \text{gas heating} \\ 0.15 & \text{gas cooling} \end{cases} \quad (14.40c)$$

The predictions of eq. (14.40) have been found (Manglik and Bergles, 1993b; 2002a) to describe within $\pm 10\%$ the majority of experimental data for a very wide range of tape-twist ratios ($2 \leq y \leq \infty$) reported in the literature for both gas and liquid turbulent flows in circular tubes with twisted-tape inserts.

14.6.2 Boiling

Of all the swirl flow devices, twisted tapes have also found extensive use in boiling applications. Two recent reviews (Shatto and Peterson, 1996; Manglik and Bergles, 2002a) have covered most aspects of their thermal-hydraulic performance, which includes bulk boiling with net vapor generation, subcooled boiling, and critical heat flux. A schematic synopsis of the effects of twisted-tape inserts on the heat transfer in a uniformly heated tube with once-through boiling (typically encountered in power boilers and refrigerant evaporators) is given in the bulk fluid and tube wall temperature map of Fig. 14.34. Variations in the wall temperature of an empty smooth tube and one fitted with a twisted tape and in the bulk fluid temperature are depicted for a typical case of fixed mass flux, inlet temperature, and pressure level in a uniformly heated tube. The heat transfer enhancement due to the tape insert is reflected in the reduced wall temperature along the tube length in the single-phase liquid, subcooled boiling, bulk boiling, dispersed-flow film boiling, and post-dryout single-phase vapor regimes. Also, dryout is delayed to significantly higher quality. The primary enhancement mechanism is perhaps tape-induced swirl, which tends to improve vapor removal and wetting of the heated surface.

Enhancement of subcooled boiling is of particular interest for cooling and thermal management of high-heat-flux devices (e.g., electrical machines, electronic and microelectronic devices, and nuclear reactors cores). Gambill et al. (1961), Feinstein and Lundberg (1963), and Lopina and Bergles (1973) have reported a limited set of experimental data, and the typical boiling curves for the influence of a tape-twist

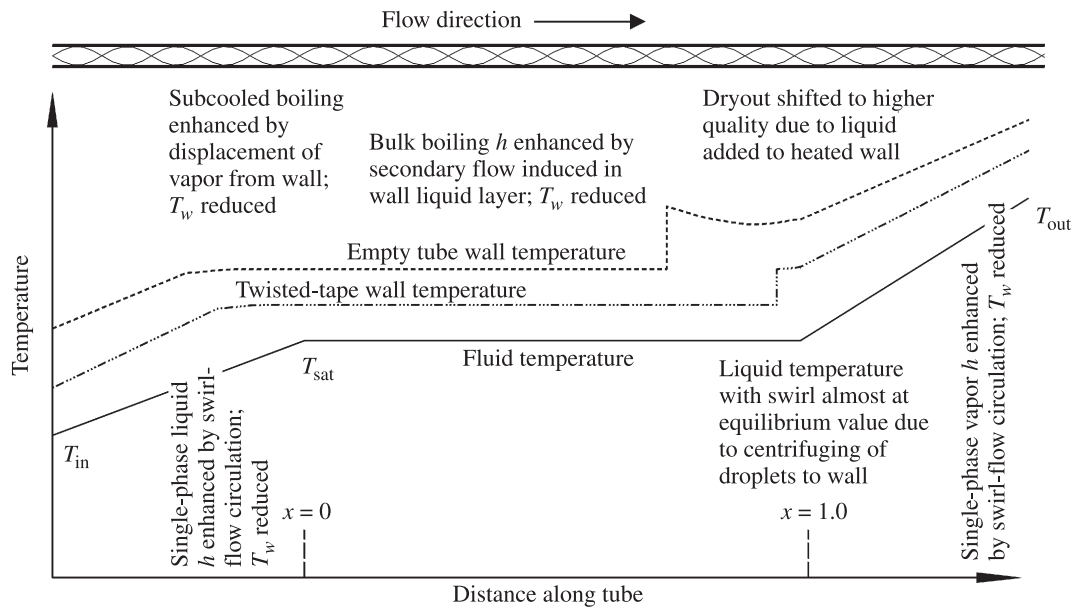


Figure 14.34 Characteristic axial evolution of tube wall and bulk fluid temperatures in forced convection boiling in a uniformly heated circular tube with and without a twisted-tape insert. (From Manglik and Bergles, 2002a.)

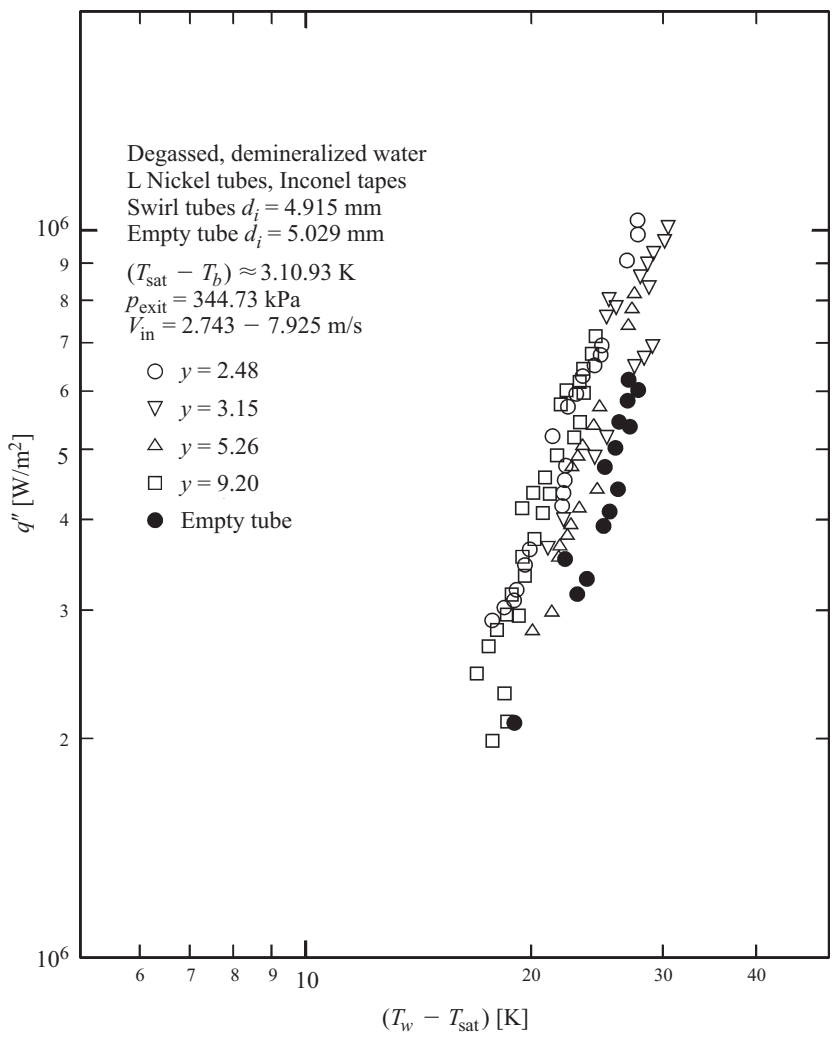


Figure 14.35 Boiling curves for fully developed subcooled flow boiling heat transfer in a tube with twisted-tape inserts of different twist severity. (From Lopina and Bergles, 1973.)

ratio, as characterized by the results of Lopina and Bergles (1973), are depicted in Fig. 14.35. The slight leftward shift of the swirl flow boiling curves relative to that for an empty tube suggests some heat transfer enhancement, although the change in the y values seems to have no significant effect.

A more effective use of twisted tapes in subcooled boiling has been shown for increasing the critical heat flux (Bergles, 1998; Manglik and Bergles, 2002a). Higher wall heat fluxes are essentially sustained because swirl-induced radial pressure gradients promote greater vapor removal from and transport of liquid droplets to the heated

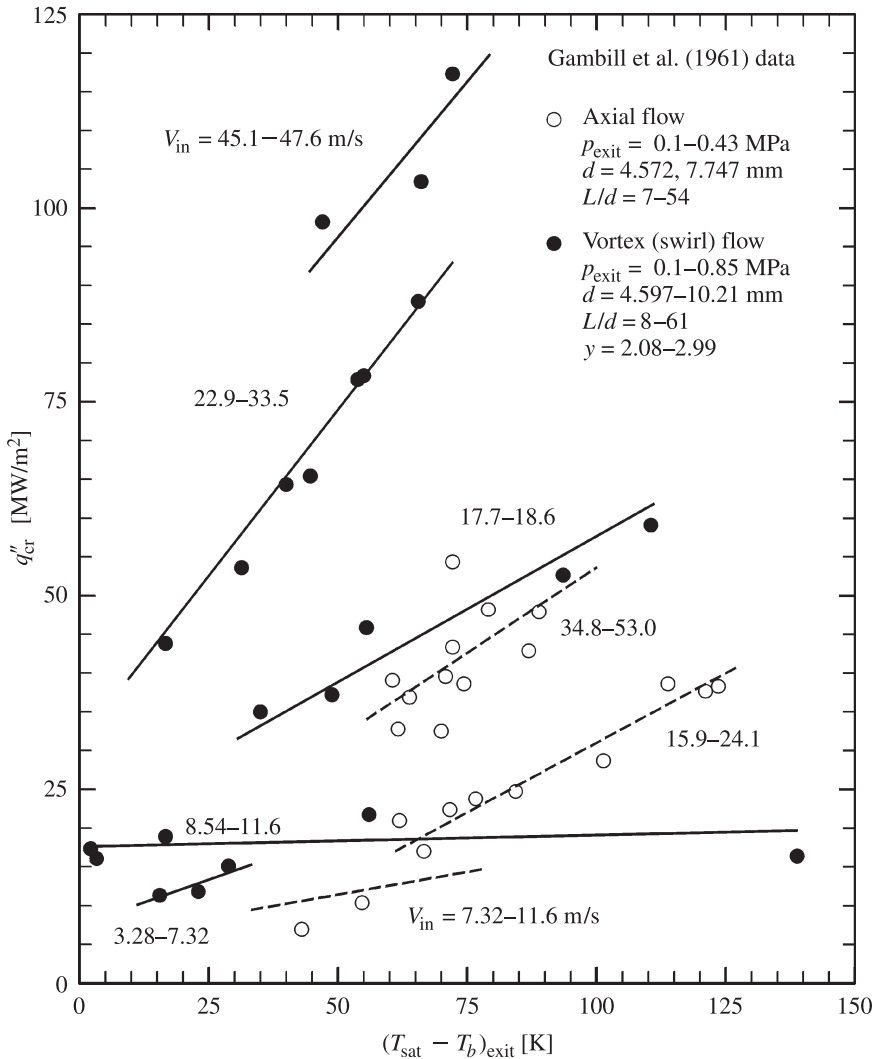


Figure 14.36 Enhanced CHF in subcooled boiling due to twisted-tape-induced swirl flows. (From Gambill et al., 1961.)

surface. This enhancement is seen in the experimental data of Gambill et al. (1961) in Fig. 14.36, where increase in CHF of up to 100% is seen. In fact, Gambill et al. (1961) have shown that the CHF is higher by a factor of 2 in tubes with twisted-tape inserts compared to that in smooth empty tubes for the same pumping power. Drižius et al. (1978) measured CHF in a 1.6-mm-diameter tube fitted with $2 \leq y \leq 10$ tapes, and found the data to be independent of subcooling but dependent on mass flux y and heated length. In a more recent study, Gaspari and Cattadori (1994) reconfirmed the

enhanced performance of twisted tapes with their CHF data, which is 1.4 to 2.1 times higher with twist ratios of $y = 2.0$ and 1.0 , respectively. Similarly, in their experiments with small-diameter ($2.44 \leq d \leq 6.54$ mm) stainless steel tubes and different twist ratio ($1.9 \leq y \leq \infty$) tapes, Tong et al. (1996) found the CHF enhanced by a factor of 1.5 with the tightest twisted tape and a mass flux of $15,000 \text{ kg/m}^2 \cdot \text{s}$. They also deduced that CHF was inversely proportional to y , d , T_i , and l/d , but directly proportional to G and p_e . Based on this parametric analysis, the following empirical correlation has been proposed:

$$q''_{\text{cr}} = 31.554 \frac{(G/G_o)^{0.6657} (p_e/p_{e,o})^{0.2787}}{(y/y_o)^{0.2412} (d/d_o)^{0.0735}} \left[\frac{(L_h/d)_o}{(L_h/d)} \right]^{0.2191} \left(\frac{T_{\text{sub},e} - T_i}{T_{\text{sat},e} - T_{i,o}} \right)^{1.041} \quad (14.41)$$

Here the variables with the subscript o pertain to a reference condition (see Tong et al. for details), and the predictions of eq. (14.41) have been shown to describe within $\pm 25\%$ most of their own experimental data as well as those of Gambill et al. (1961), Drižius et al. (1978), Inasaka et al. (1991), and Gaspari and Cattadori (1994).

For the pressure drop in subcooled flow boiling, needed to size the pumping system, determine the exit pressure, and assess the thermal-hydraulic stability of the system (Manglik and Bergles, 2002a), Pabisz and Bergles (1997) have devised an empirical correlation. Their equation is based on the Tong et al. (1996) data, where any gravitational component has been subtracted from the measured pressure drop and is expressed as

$$\Delta p = (\Delta p''_{\text{fluid only}} + \Delta p''_{\text{subcooled boiling}})^{1/n} \quad (14.42)$$

The details of procedures for calculating the single-phase fluid only and subcooled boiling contributions can be found in Pabisz and Bergles (1997), and the predictions of this correlation have been shown to describe most of the experimental data within $\pm 15\%$.

In bulk or saturated boiling conditions, twisted-tape inserts have been shown to enhance the heat transfer coefficient throughout the entire quality region ($0 \leq x \leq 1$), as well as to increase the CHF (or dryout quality) and the heat transfer coefficients in the post-dryout dispersed-flow film boiling region (Shatto and Peterson, 1996; Manglik and Bergles, 2002a). Enhanced performance data have been reported for a variety of fluids, including water, refrigerants, cryogenic fluids, and liquid metals (Bergles et al., 1995; Manglik and Bergles, 2002a). As reviewed by Shatto and Peterson (1996), several different correlations have been proposed by different investigators (Gambill et al., 1961; Blatt and Adt, 1963; Jensen and Bensler, 1986; Agarwal et al., 1986; Kedzierski and Kim, 1997). For predicting the CHF, Jensen (1984) provides an empirical correlation based on data for water and R-22 that describes the experimental results within an average deviation of $\pm 10\%$. Bergles et al. (1971) have considered the dispersed flow (post-dryout) regime and have devised a rather elaborate correlation. Their equation is based on several variables that affect and describe swirl flow behavior and on the assumption that the vapor remains at saturated conditions. Blatt and Adt (1963), and Agarwal et al. (1982) have also given correlations for the two-phase flow pressure drop in bulk boiling that are based on their respective data for R-11 and R-12.

14.6.3 Condensing

In-tube condensation of both steam and refrigerant vapor in the presence of twisted-tape inserts have been considered in the literature (Manglik and Bergles, 2002a). For describing condensing heat transfer with and without twisted-tape inserts, Fig. 14.34 for a once-through flow system is once again relevant, but with the sequence of event reversed. That is, entering from the right of the performance map in this figure, the flow is initially desuperheated, followed by condensation (with a change in quality from $x = 1$ to $x = 0$) and subsequent liquid subcooling. As in the case of boiling, phase-changer coefficients for condensation are inherently large, and twisted-tape inserts may enhance them further. Thus, for their practical use, due attention must be given to the controlling thermal resistance in a two-fluid heat exchanger, as well as an assessment of the relative thermal benefits by considering the increased pressure drop. The latter generally entails a reduced saturation temperature and the driving temperature difference in the heat exchanger.

Royal and Bergles (1978a,b) appear to have reported the only study on steam condensation in tubes fitted with twisted-tape inserts. They found that the average heat transfer coefficient was increased by 30% over the empty-tube values with snug-fitting tapes of $y = 3.3$ and 7.0, where the higher enhancement was for the tighter tape twist. Based on these data, the following correlation has been given:

$$\text{Nu}_{h,m} = 0.0265 \left[\frac{Gd_h}{\mu_l} \left(1 - x_m + \frac{x_m \rho_l}{\rho_g} \right) \right]^{0.8} \text{Pr}_l^{0.33} \left[1 + 160 \left(\frac{H^2}{Ld} \right)^{1.91} \right] \quad (14.43)$$

It may be noted, however, that the associated pressure drop also tends to be large (two to four times the empty tube value at constant mass flux and inlet pressure), and the relative performance enhancement should be ascertained by the appropriate evaluation criteria (Royal and Bergles, 1978a; see also Section 14.1.2). In a somewhat related process, the impact of a twisted tape on dehumidification of moist air has been investigated by Helmer and Iqbal (1980).

Refrigeration condensation in tubes with twisted-tape inserts has received considerably more attention in the literature (Luu and Bergles, 1979, 1980; Azer and Said, 1981; Said and Azer, 1983; Kedzierski and Kim, 1997). Luu and Bergles (1979, 1980) found up to a 30% increase in the nominal area-basis average heat transfer coefficients for R-113 with $y = 2.8$ and 4.6 tapes. The concomitant pressure drop, however, was also 3.5 times higher than in a smooth tube. Similar results for heat transfer and pressure drop with R-113 have been reported by Azer and Said (1981) and Said and Azer (1983). Based on curved fits through their heat transfer data, Luu and Bergles give the following correlation:

$$h_m = 0.024 F \frac{k_e}{d_h} \left(\frac{Gd_h}{\mu_l} \frac{8y^2}{3\pi^2} \left\{ \left[\left(\frac{\pi}{2y} \right)^2 + 1 \right]^{1.5} - 1 \right\} \right)^{0.8} \cdot \text{Pr}_l^{0.43} \\ \times \frac{(\rho/\rho_m)_m^{0.5} + (\rho/\rho_m)_e^{0.5}}{2} \quad (14.44)$$

where $F = 1$ for snug- and loose-fitting tapes, and ρ/ρ_m is given by eq. (14.30b). In the more recent study by Kedzierski and Kim (1997) twisted-tape condensation of a wide range of refrigerants has been investigated. They have also proposed an equation for the heat transfer coefficient that uses the Manglik and Bergles (1993a) swirl parameter Sw to correlate the twisted-tape effects, and it describes 95% of their sectional-average heat transfer coefficients within $\pm 20\%$.

14.7 COILED TUBES

A coiled or curved tube has long been recognized as a swirl-producing flow geometry (Eustice, 1911; Dean, 1927, 1928; Taylor, 1929). The secondary fluid motion is generated essentially by the continuous change in direction of the tangential vector to the bounding curved surface of the duct, which results in the local deflection of the bulk flow velocity vector. Rather complex flow patterns are obtained that are characterized by multiple helical vortices superimposed over the main axial flow, and the consequent fluid mixing lends to enhance heat or mass transfer. Coiled tubes are now used in a wide variety of applications, including domestic hot water heaters, chemical process reactors, industrial and marine boilers, kidney dialysis devices, and blood oxygenators, among many others (Bergles et al., 1991; Nandakumar and Masliyah, 1986).

14.7.1 Single-Phase Flow

The single-phase flow behavior, thermal-hydraulic performance, and applications of curved and coiled tubes of circular as well as noncircular cross section have been presented in several literature reviews (Nandakumar and Masliyah, 1986; Shah and Joshi, 1987; Bergles et al., 1991; Ebdian and Dong, 1998). The curvature-induced swirl flow characteristics of curved or helically coiled tubes are strongly dependent on their geometrical attributes, and a typical representation for circular cross-section tubes is given in Fig. 14.37. The consequent nondimensional parameters (Dean number, radius of curvature, and helical number) that describe the flow behavior and duct geometry scaling are usually defined as follows:

$$De = Re \sqrt{\frac{d}{2R}} \quad (14.45a)$$

$$R_c = R \left[1 + \left(\frac{H}{2\pi R} \right)^2 \right] \quad (14.45b)$$

$$He = Re \sqrt{\frac{d}{2R_c}} = De \left[1 + \left(\frac{H}{2\pi R} \right)^2 \right]^{1/2} \quad (14.45c)$$

It may be noted that the helical number reduces to the Dean number when $H = 0$ (i.e., the helicoidal pitch is zero and a simple curved duct is considered). The tube curvature

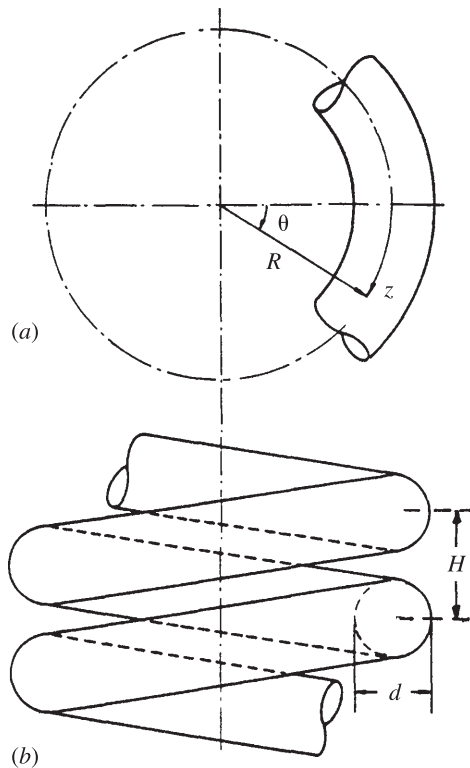


Figure 14.37 Geometrical representation of (a) a curved tube, and (b) a helical coiled tube of circular cross sections.

acts to impose a centrifugal force on the fluid motion, thereby generating a secondary circulation that in laminar flows has been shown to consist of two symmetrical counterrotating helical vortices (Mori and Nakayama, 1965; Collins and Dennis, 1975; Nandakumar and Masliyah, 1982; Prusa and Yao, 1982; Cheng and Yuen, 1987). This helically swirling flow is often referred to as *Dean flow* in the literature, and its strength and cross-stream fluid-mixing intensity, which produces enhanced heat transfer, increases with De .

Several investigators have reported experimental data and theoretical (analytical or computational) results for laminar flow and heat transfer in curved and coiled circular tubes, and numerous correlations have been presented (White, 1929; Kubair and Kuloor, 1963, 1966a,b; Mori and Nakayama, 1965, 1967a,b; Manlapaz and Churchill, 1980, 1981; Nandakumar and Masliyah, 1986; Austen and Soliman, 1988). For isothermal friction factors in fully developed swirl flows, the following Manlapaz and Churchill (1980) correlation perhaps provides the most generalized predictions for a wide range of coiled tube geometry and operating conditions (Nandakumar and Masliyah, 1986; Gnielinski, 1986; Shah and Joshi, 1987):

$$f = f_{st} \left[\left\{ 1 - \frac{0.18}{[1 + (35/\text{He})^2]^{0.5}} \right\}^m + \left(1 + \frac{d}{6R} \right)^2 \frac{\text{He}}{88.33} \right]^{0.5}$$

$$m = \begin{cases} 2 & \text{De} < 20 \\ 1 & 20 < \text{De} < 40 \\ 0 & \text{De} > 40 \end{cases} \quad (14.46)$$

Manlapaz and Churchill (1980) have also given two separate but similar expressions for predicting average Nusselt numbers in fully developed flows with uniform wall temperature (UWT) and uniform heat flux (UHF) conditions, respectively:

$$\text{Nu}_{m,T} = \left[\left\{ 3.657 + \frac{4.343}{[1 + (957/\text{Pr} \cdot \text{He}^2)]^2} \right\}^3 + 1.158 \left\{ \frac{\text{He}}{[1 + (0.477/\text{Pr})]} \right\}^{3/2} \right]^{1.3} \quad (14.47)$$

$$\text{Nu}_{m,H} = \left[\left\{ 4.364 + \frac{4.636}{[1 + (1342/\text{Pr} \cdot \text{He}^2)]^2} \right\}^3 + 1.816 \left\{ \frac{\text{He}}{[1 + (1.15/\text{Pr})]} \right\}^{3/2} \right]^{1/3} \quad (14.48)$$

Their predictive results have been shown to agree with a fairly large data set from different experimental investigations (Manlapaz and Churchill, 1980; Nandakumar and Masliyah, 1986; Shah and Joshi, 1987; Austen and Soliman, 1988). For estimating the thermal entry region, Janssen and Hoogenedoorn (1978) give the following equation:

$$\frac{L_{\text{th}}}{d} \leq 20\text{Pr}^{0.2} \sqrt{\frac{d}{2R_c}} \quad (14.49)$$

The more recent theoretical analysis of Acharya et al. (1994) provides a different expression:

$$\frac{L_{\text{th}}}{d} = 1.66 + 0.102 \left(\frac{\text{Re}^{0.25}}{\text{Pr}^{0.5}} \right) \sqrt{\frac{2R}{d}} \quad (14.50)$$

In general, the thermal entrance region for curved tubes is significantly smaller than that for straight tubes for the same flow conditions.

As in the case of swirl flows generated by twisted-tape inserts, it has been widely observed that the flow inside coiled tubes remains in the viscous regime up to a much higher Reynolds number than that for straight tubes (White, 1929; Taylor, 1929; Ito, 1959; Srinivasan et al., 1968). The curvature-induced helical vortices tend to suppress the onset of turbulence and delay transition. Several different expressions have been developed to determine the critical Reynolds number for transition (Nandakumar and

Masliyah, 1986), and the following correlation given by Srinivasan et al. (1968) is more widely cited:

$$\text{Re}_{tr} = 2100 \left(1 + 12 \sqrt{\frac{d}{2R}} \right) \quad 10 < \frac{2R}{d} < \infty \quad (14.51)$$

Mishra and Gupta (1979) have suggested that the finite-pitch effects of coiled tubes can be incorporated by employing R_c instead of R . For fully developed turbulent flows in curved or coiled circular tubes, Mishra and Gupta (1979) have devised a friction factor correlation by superposition of swirl flow effects on straight flows that is expressed as

$$f = \frac{0.079}{\text{Re}^{0.25}} + \left(0.0075 \sqrt{\frac{d}{2R_c}} \right) \quad (14.52)$$

This equation is valid for $\text{Re}_{tr} < \text{Re} < 10^5$, $6.7 < 2R/d < 346$, and $0 < H/2R < 25.4$, and has been shown to describe the literature database rather well (Gnielinski, 1986). For turbulent fully developed flow heat transfer, Mori and Nakayama (1967b) suggest the following correlations:

$$\text{Nu} = \begin{cases} \frac{\text{Pr}}{26.2(\text{Pr}^{2/3} - 0.074)} \text{Re}^{4/5} \left(\frac{d}{2R} \right)^{1/10} \left[1 + 0.098 \left\{ \text{Re} \left(\frac{d}{2R} \right)^2 \right\}^{1/5} \right] & \text{for } \text{Pr} \approx 1 \end{cases} \quad (14.53a)$$

$$\text{Nu} = \begin{cases} \frac{\text{Pr}^{0.4}}{41.0} \text{Re}^{5/6} \left(\frac{d}{2R} \right)^{1/12} \left[1 + 0.061 \left\{ \text{Re} \left(\frac{d}{2R} \right)^{2.5} \right\}^{1/6} \right] & \text{for } \text{Pr} > 1 \end{cases} \quad (14.53b)$$

Furthermore, more recently, single-phase flow-enhanced heat transfer in curved or coiled ducts of a variety of noncircular cross sections (square, rectangular, elliptical, semicircular, and annular) have been considered in the literature. Brief reviews of some of these studies are given by Nandakumar and Masliyah (1986) and Ebadian and Dong (1998).

14.7.2 Boiling

Coiled tubes are commonly employed in commercial vapor generators, as they provide a substantial improvement in the evaporation heat transfer coefficient with a significantly smaller surface area-to-volume footprint (Bergles et al., 1991; Jensen and Shome, 1994). Jensen (1980), Jensen and Bergles (1981), Jensen and Shome (1994), and Bergles (1998) have reviewed the rather sparse literature on flow boiling heat transfer and two-phase pressure drop in curved or helically coiled tubes.

In forced-convective evaporation of refrigerants, Barskii and Chukhman (1971) have reported up to 60% enhancement in the heat transfer coefficients with R-12

flows in tightly coiled tubes at high heat fluxes. The pressure-drop penalty, however, is also of about the same relative magnitude as the heat transfer increase. A similar performance was obtained with R-22 boiling in coiled tubes in a follow-up study by Chukhman (1972).

Significant enhancement in the CHF for refrigerant boiling has also been found in several studies. Hughes and Olson (1975) report a 60% increase for R-113 relative to a straight circular tube. By evaluating the coiled-to-straight tube burnout power ratio for R-12 flows, Cumo et al. (1972) indicate as high as 600% enhancement. In a more detailed study of R-113 boiling, Jensen and Bergles (1981) found the subcooled region q''_{cr} to be lower than the comparable straight tube value. However, the CHF was substantially enhanced when the outlet quality was greater than 0.1. With $x = 0.1$, $2R/d = 54$, and $G = 2800 \text{ kg/m}^2 \cdot \text{s}$, for example, the CHF for the coiled tube is 150% higher than that in a straight tube. In a subsequent study, Jensen and Bergles (1982) have explored the effect of nonuniform heat flux on CHF, which is observed to have a rather complex dependence on mass flux, tube curvature, and heat flux variation or tilt.

14.7.3 Condensing

Condensation applications for curved or coiled tubes appear to have received negligible attention in the literature. This is not entirely surprising, as it may be speculated that the centrifugal action of curvature-induced swirl flows would tend to maintain the wall liquid film, thereby impairing condensate drainage and core flow vapor contact with the cold wall. Notwithstanding this contention, modest improvements in condensation rates have been reported in curved tubes (return bends) by Traviss and Rohsenow (1973) and in coiled tubes by Shklover and Gerasimov (1963) and Miropolskii and Kurbanmukhamedov (1975).

14.8 ADDITIVES FOR LIQUIDS

14.8.1 Single-Phase Flow

Much of the work on this technique for single-phase liquid flows has focused primarily on the drag-reducing consequences of the additives. See, for example, studies by Toms (1948), Virk et al. (1970), Gupta et al. (1967), Cho and Hartnett (1980), Fossa and Tagliafico (1995), Gasljevic and Matthys (1997), Sato et al. (1999), Aguilar et al. (2001), and Li et al. (2001), among many others. The lowering of frictional losses has the indirect effect of providing heat transfer enhancement when evaluated on a fixed pressure drop or pumping power basis. In the case of soluble polymeric additives in water, where the solution has a shear-thinning rheology, the non-Newtonian effects lead to a significant reduction in friction loss as well as a modest increase in the heat transfer coefficient (Joshi and Bergles, 1981; Prusa and Manglik, 1994; Manglik and Prusa, 1995; Hartnett and Cho, 1998; Chhabra and Richardson, 1999; Manglik and Fang, 2002). With polymeric additives that impart a viscoelastic character to the

solution, the heat transfer has been found to be further enhanced in rectangular ducts due to a viscoelasticity-driven secondary circulation that is imposed over the bulk flow (Hartnett and Kostic, 1985; Hartnett, 1992; Hartnett and Cho, 1998).

Some other considerations in the literature have included polystyrene sphere suspensions in oil, and injection of gas bubbles (Bergles, 1998). In the former case, Watkins et al. (1976) have reported up to 40% improvements in the laminar flow heat transfer coefficients. By injecting air bubbles at the base of a heated vertical wall, Tamari and Nishikawa (1976) found up to 400% higher free-convection heat transfer coefficients in both water and ethylene glycol. In a turbulent flow of water, Kenning and Kao (1972) obtained up to 50% increases in heat transfer by injecting nitrogen bubbles.

14.8.2 Boiling

The use of various additives (surfactants, polymers, etc.) that lower the surface tension of the solution and binary mixtures of liquids (wetting agents, alcohols, etc.) have long been recognized to enhance pool boiling heat transfer substantially (Thome, 1990; Bergles, 1997; Wasekar and Manglik, 1999). Depending on their concentration, increases in the nucleate boiling heat transfer coefficients of 20 to 160% in surfactant solutions (Tzan and Yang, 1990; Ammerman and You, 1996; Wu et al., 1998; Manglik, 1998; Hetsroni et al., 2000; Wasekar and Manglik, 2000, 2002), and 20 to 40% in binary liquid mixtures with wetting agents or alcohols (Morgan et al., 1949; van Wijk et al., 1956; Lowery and Westwater, 1957; van Stralen, 1959; Shakir et al., 1985) have been reported.

Enhanced nucleate boiling heat transfer in surfactant solutions has attracted considerable recent attention in the literature (Wasekar and Manglik, 1999; Zhang and Manglik, 2003). The improved thermal performance is strongly dependent on the type and concentration of the surfactant additive, its chemistry (ionic nature, molecular and chemical composition, and structure) and the diffusion kinetics at the dynamic vapor–liquid interface. A typical set of pool boiling data for aqueous SDS (sodium dodecyl sulfate) solutions of various concentrations is presented in Fig. 14.38. The boiling curve is seen to shift to the left to indicate enhanced heat transfer, which is also characterized by early onset of nucleate boiling (ONB) or incipience, except in solutions with surfactant concentrations $C > \text{c.m.c.}^*$ The ebullient behavior is also found to be more vigorous with clusters of smaller, more regularly shaped bubbles and minimal coalescence between neighboring bubbles. The lowering of the solution's surface tension promotes nucleation of smaller bubbles, with a clustered activation of nucleation sites which depart at much higher frequencies than seen in pure water (Wasekar and Manglik, 2000, 2002). Comparative and qualitative snapshots of the boiling behavior of aqueous surfactant solutions at different wall heat flux levels are depicted in Fig. 14.39.

*The c.m.c. of a surfactant is its *critical micelle concentration* when colloid-sized clusters or aggregates are formed in the bulk phase (Edwards et al., 1991).

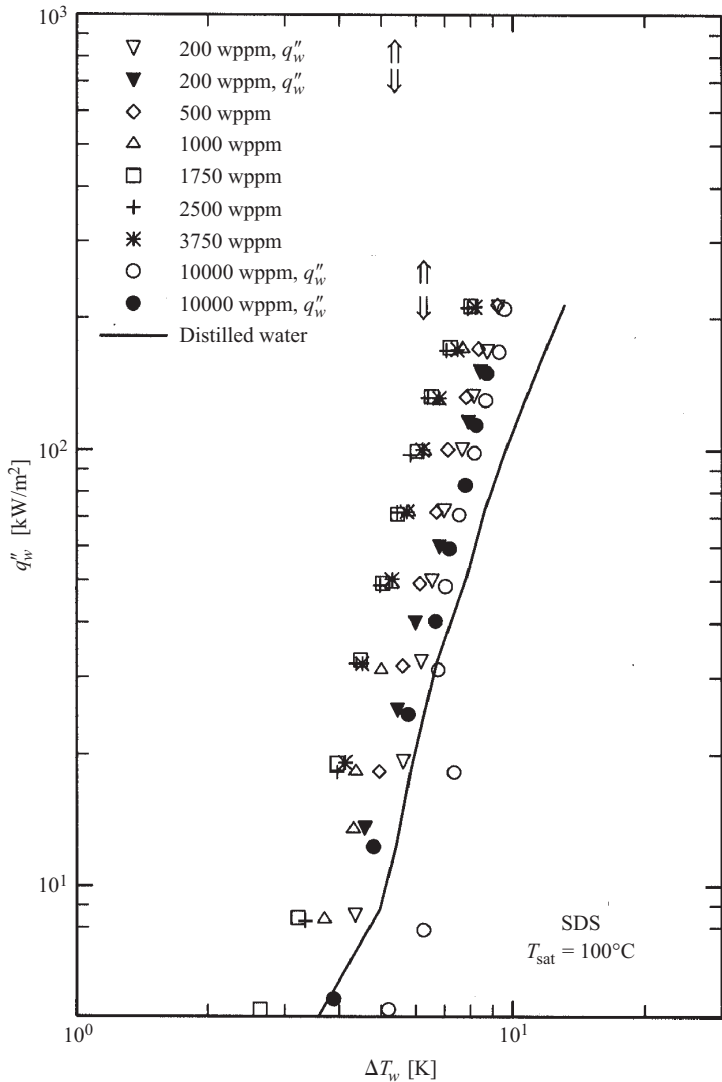


Figure 14.38 Pool boiling data for aqueous sodium dodecyl sulfate (SDS) solutions. (From Wasekar and Manglik, 2000.)

The influence of additive concentration on the extent of nucleate boiling enhancement, relative to that in pure water at atmospheric saturation conditions, is shown in Fig. 14.40. Up to 65% enhancement in 2500 wppm aqueous SDS solution is seen, with the optimum performance dependent on the surfactant concentration and wall heat flux. Similar results have been reported by Tzan and Yang (1990), Manglik (1998), Hetsroni et al. (2000), and Wasekar and Manglik (2002). Figure 14.40 also shows that there is a decrease in the boiling heat transfer enhancement in very high

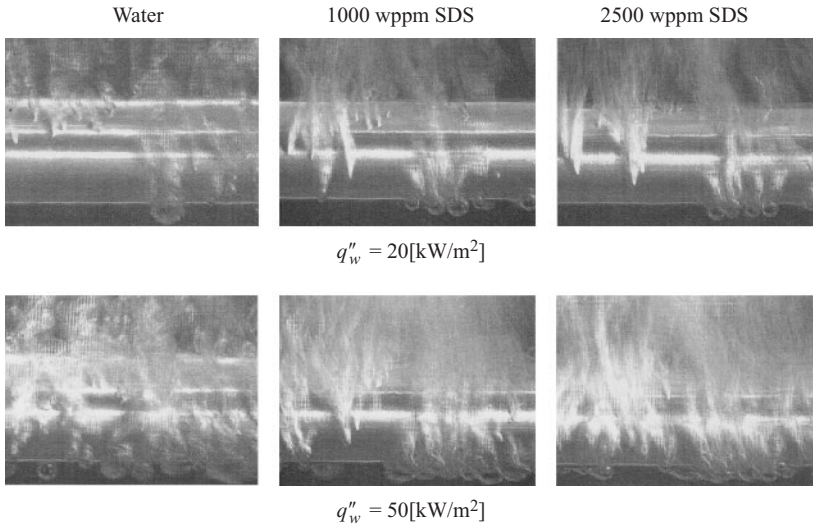


Figure 14.39 Photographic record of pool boiling behavior of distilled water and aqueous SDS solution at different heat flux levels. (From Wasekar and Manglik, 2000.)

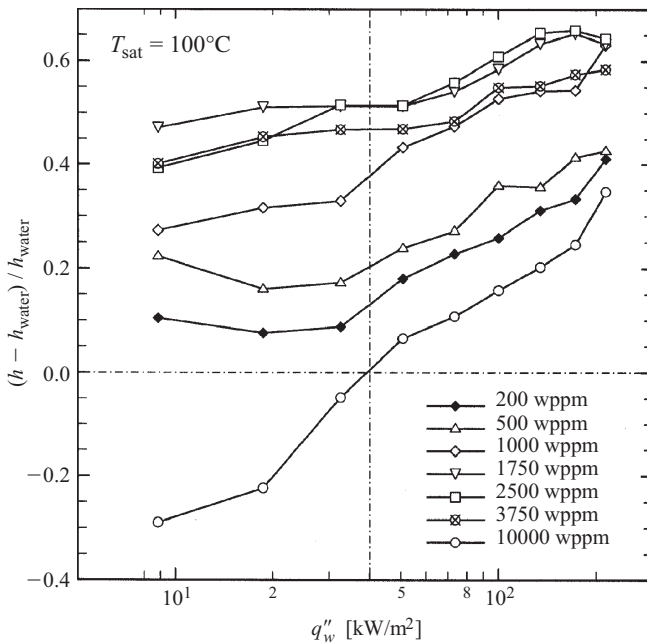


Figure 14.40 Enhanced nucleate boiling heat transfer performance of aqueous SDS solutions and its variation with heat flux and surfactant concentration. (From Wasekar and Manglik, 2000.)

concentration solutions ($C > 2500$ wppm), and, in fact, there is even a deterioration in h at low heat fluxes ($q''_w \leq 40$ kW/m²) and $C = 10,000$ wppm. This has been observed to be the general trend in most surfactant solutions, where the optimum enhancement appears to be obtained in aqueous solutions with $C \approx$ c.m.c. (Wasekar and Manglik, 2002); the c.m.c. for SDS is about 2500 wppm at 23°C (Manglik et al., 2001b). The optimum enhancement in the boiling heat transfer coefficient for four different surfactants in partially and fully developed nucleate boiling regimes are presented in Fig. 14.41. The improved performance is further seen to be a function of the ionic nature of surfactant, its molecular weight, and dynamic surface tension characteristics (evaluated at near-boiling bubble frequencies and bulk temperature at atmospheric pressure). Other factors of influence include diffusion kinetics of additive and Marangoni (both thermocapillary and diffusocapillary) convection (Wasekar and Manglik, 2001, 2002).

The addition of volatile additives to liquids to increase the CHF has also been considered in the literature (van Wijk et al., 1956; van Stralen, 1959; 1970; Bergles, 1998). Depending on the system pressure, van Wijk et al. (1956) and van Stralen (1959) have reported 2.5 to 3.5 times higher CHF values with low concentrations (2

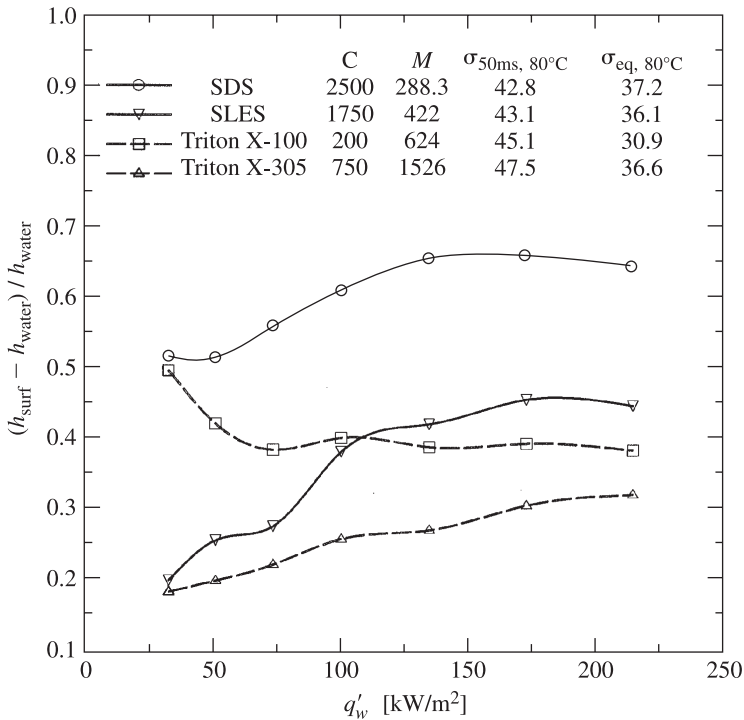


Figure 14.41 Optimum enhancement of nucleate boiling heat transfer in aqueous solutions of different surfactants: the effects of additive ionic nature, molecular weight, and dynamic surface tension. (From Wasekar and Manglik, 2002.)

to 3% by weight) of 1-pentanol in saturated pool boiling of water. In another study, van Stralen (1970) reports up to 80% improvement in the film boiling coefficient in a 4:1 weight percent mixture of 2-butanone and water. Bergles and Scarola (1966) and Pabisz and Bergles (1997) have considered subcooled flow boiling of water [a 1-pentanol (2.2% by weight) mixture] and found a distinct reduction in CHF at low subcooling. Contrarily, with the addition of a surfactant to seawater, the overall heat transfer coefficient was found to be doubled in vertical upflow boiling in a desalination application.

14.9 ACTIVE TECHNIQUES

A variety of active techniques, including mechanical aids (stirring, surface scraping, and rotating surfaces), surface vibration, fluid vibration, electrostatic (electric and magnetic) fields, injection, suction, and jet impingement, have been investigated in the literature (Bergles, 1998). As indicated earlier, all of these methods and devices require the input of external power to promote the desired enhancement, which should be accounted for appropriately when evaluating the improved thermal-hydraulic performance.

For *stirring* and *surface scraping* devices, Uhl (1970) and Hagge and Junkhan (1974) provide early reviews and the applications include both single-phase and boiling heat transfer. *Rotating surfaces* commonly preexist in cooling of rotating electrical machinery and gas turbine rotor blades, and substantial enhancement (of up to 350%) in heat transfer coefficients for laminar flows in straight tubes rotating around their own axis or a parallel axis have been reported (Mori and Nakayama, 1967c; McElhiney and Preckshot, 1977; Vidyanidhi et al., 1977). Tang and McDonald (1971) have reported that with high-speed rotation of heated cylinders in saturated pools, the convective coefficients are so high that boiling can be suppressed. Enhanced steam condensation on a rotating vertical cylinder has been documented by Nicol and Gacesa (1970). In most recent studies, however, compound use of surface rotation has generally been considered, with some other technique for enhanced cooling of gas turbine blades (Eliades et al., 2001; Hwang et al., 2001).

For almost three decades, starting in the late 1930s, much work was done on inducing enhanced heat or mass transfer by effecting sufficiently intense *surface vibrations* or oscillations, particularly in the free convection mode (Martinelli and Boelter, 1939; McAdams, 1954; Fand and Peebles, 1962; Lemlich and Rao, 1965; Bergles, 1969). Depending on oscillation amplitude-to-tube diameter ratios and vibration Reynolds numbers, up to 20-fold increases in heat transfer coefficients compared with those for stationary tubes have been reported (Bergles, 1998). Substantial improvements in heat transfer induced by heated surface vibrations in forced-convection applications have also been recorded. A caveat on using this technique is that cavitation becomes a problem when the vibration intensity becomes too large, which causes a sharp degradation of heat transfer. Hsieh and Marsters (1973) have further extended this method to an array of five horizontal cylinders and reported up to a 54% increase in the average heat transfer coefficients at the highest surface vibration intensity. Based on experiments

with saturated as well as subcooled boiling, Bergles (1969) has shown that heater-surface vibrations have little effect on the heat transfer. However, the CHF increased by a maximum of about 10% at an average velocity of 0.25 m/s. Other experiments have confirmed that fully developed boiling is essentially unaffected by vibration (McQuiston and Parker, 1967; Price and Parker, 1967; Fuls and Geiger, 1970). In a few studies (e.g., Brodov et al., 1977), up to 10 to 15% enhancement in the condensation heat transfer coefficients have been obtained in a vibrating horizontal tube.

There has been considerable research on the use of *fluid vibrations* (or pulsations) to enhance heat transfer, particularly the application of acoustic fields (Bergles, 1998). Improvements of 100 to 200% over natural convection heat transfer coefficients in air were obtained by Sprott et al. (1960), Fand and Kaye (1961), and Lee and Richardson (1965) by generating intense sound fields and directing them transversely to a horizontal heated cylinder, although there could be large circumferential variations in the local heat transfer coefficients at these acoustic vibration intensities (Fand et al., 1962). In liquids, ultrasonic frequencies may be used to the desired acoustic streaming (about 1 MHz produces a type of streaming called *crystal wind*), although these intensities may still be high enough to cause cavitation. Robinson et al. (1958), Zhukauskas et al. (1961), Larson and London (1962), Fand (1965), and Li and Parker (1967), among others, report 30 to 45% increases in free convection heat transfer by means of sonic and ultrasonic vibrations. In his experiments with high surface temperatures, where it was possible to achieve cavitation, Bergles (1964) found that lower-frequency vibrations (80 Hz) provided up to 50% enhancement in the heat transfer. Furthermore, while ultrasonic vibrations appear to promote no improvements in nucleate pool boiling (Wong and Chon, 1969), they enhance vapor removal and lend to an increase in CHF by almost 50% (Ornatskii and Shcherbakov, 1959). Internal duct flow boiling is also reported to be unaffected irrespective of the ultrasonic vibration intensity (Bergles and Newell, 1965). Mathewson and Smith (1963) investigated the effects of up to a 176-dB acoustic field with frequencies in the range 50 to 330 Hz and found laminar film condensation coefficients for isopropanol to be enhanced by about 60% at low vapor flow rates.

The use of *electric and magnetic fields* to enhance heat transfer, or electrohydrodynamic (EHD) enhancement, has received considerable attention in the literature for more than four decades. Several recent reviews of its applications and extended discussion of the fundamental electromagnetic field effects on heat transport have been published (Jones, 1978; Viskanta, 1985; Poulter and Allen, 1986; Yabe, 1991). Much of this work has focused on improvement of single-phase heat transfer, where the technique has been shown to be particularly effective (Webb, 1994; Bergles, 1998; Nelson et al., 2000). In laminar forced convection in transformer oil, several early studies have shown at least 100% enhancement in the heat transfer (Savkar, 1971; Newton and Allen, 1977); it may be pointed out here that electric transformers provide a preexisting electromagnetic field. More recent work has addressed the application of electric fields with its attendant corona discharge (or corona wind) for enhancing air- and gas-flow heat transfer in tubular exchangers (Davidson et al., 1987; Ohadi et al., 1994; Nelson et al., 2000). EHD use has been also extended to phase-changer systems, where enhancement of nucleate boiling and CHF as well as film condensation

have been investigated (Choi, 1961; Velkoff and Miller, 1965; Cooper, 1990; Ogata and Yabe, 1993; Xu et al., 1995; Chen and Liu, 1999; Chu et al., 2000). Attempts to model the electric field effects on boiling heat transfer analytically and/or computationally have also been reported in the literature (Karayiannis and Xu, 1998a,b). For some other novel applications, a U.S. patent (Blomgren and Blomgren, 1972) describes the cooling of cutting tools by point electrodes, and a few proposals have considered compound use of electric fields with finned surfaces to improve the single-phase heat dissipation (Reynolds and Holmes, 1976), and condensation heat transfer (Chu et al., 2001).

Jet impingement techniques have gained considerable recent interest, particularly for their significant potential in microelectronic cooling, MEMS, and other microscale devices (Chu and Chrysler, 1998; Behnia et al., 2001; Honma et al., 2001; Amon et al., 2001), gas-turbine blade cooling (Ekkad et al., 2000; Hwang and Chang, 2000; Cornaro et al., 2001), and manufacturing, drying, heat treating, and quenching applications (Viskanta, 1998; Hall et al., 2001a,b). These applications involve both single-phase and boiling heat transfer, and jet impingement techniques have been found to enhance the heat transfer considerably. Strategies to develop optimum arrays of jets for specific duties (San and Lai, 2001) and computational modeling (Kumagai et al., 2002) have also been proposed in the literature.

14.10 COMPOUND ENHANCEMENT

As Bergles (2000) has pointed out, “*compound techniques* offer a way to further elevate heat transfer coefficients,” and this area of enhancement technology holds much promise for future development. Indications of their emerging development and growth are evident in a recent survey of the 2001 literature (Manglik and Bergles, 2002b). Conceptually, with compound techniques, heat transfer coefficients can be increased above each of the techniques acting alone. A variety of combinations for two or more enhancement methods or devices have been considered, and some representative examples are discussed in this section.

Perhaps the most attractive potential for compound technique use are offered by systems where one form of enhancement preexists “naturally.” Good examples are rotating systems, which include rotor windings of large turbogenerators or electric motors, and gas-turbine blades, among others. A few different passive techniques have been applied in rotating tubes and ducts in the literature. Muralidhar Rao and Sastri (1995) have used twisted-tape inserts in a tube that rotates around a parallel axis (to simulate the coolant channel of an electric machine), and their results for laminar flow of air are presented in Fig. 14.42. The Nusselt number is seen to increase with rotational speed (J_a) and is greater than that predicted for a stationary tube with a twisted-tape insert of $y = 5$; the latter, in turn, has been found to be higher than empty rotating tube performance. Similarly, in rotating U-bend flat or rectangular ducts that simulate internal flow passages of a gas-turbine airfoil, structured roughness or ribs have been considered to enhance integral blade cooling (Hwang et al., 2001; Iacovides et al., 2001; Lin et al., 2001; Murata and Mochizuki, 2001). In another example, both

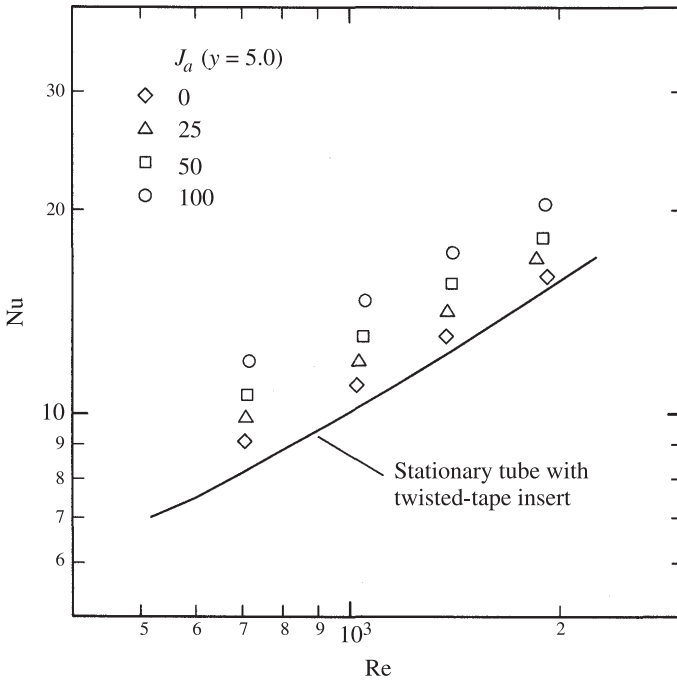


Figure 14.42 Effect of tube rotational speed (J_a) on Nusselt number enhancement in laminar flow heat transfer in a circular tube with a twisted-tape insert. (From Muralidhar Rao and Sastri, 1995.)

ribbed roughness and vortex generators have been used in a two-pass rotating duct (Acharya et al., 2000; Eliades et al., 2001).

Many different compound schemes involving twisted-tape inserts have been considered for single-phase forced-convective and boiling applications (Manglik and Bergles, 2002a). For single-phase flows, besides the rotating tube example discussed previously (Rao, 1983; Muralidhar Rao and Sastri, 1995), experimental data for rough tubes or ribbed ducts with twisted-tape inserts (Bergles et al., 1969; Shivkumar and Raja Rao, 1988; Zhang et al., 2000; Zimparov, 2001), and internally finned tubes with twisted-tape inserts (Van Rooyen and Kröger, 1978; Usui et al, 1984; Zhou et al., 1990) are available. Additionally, Wu et al. (2000) have tested the performance of decaying swirl flows (produced by inlet axial vanes) in spirally corrugated tubes. The heat transfer coefficients are generally enhanced to a greater extent than that with each individual technique in these cases. However, an interesting forced convection boiling study by Pabisz and Bergles (1996) reports a rather surprising consequence of using twisted-tape inserts along with 1-pentanol additive to water in a 3 to 4% mixture by weight. Here the CHF was found to be *reduced* below that with the twisted tape and pure water.

Some other representative examples of promising compound enhancement techniques for varied practical applications that have been proposed in the literature are as follows:

- Corrugated (rough) tube with a hydrophobic coating (treated surface) to promote dropwise condensation of steam (Das et al., 2000)
- Application of EHD fields in pool boiling of refrigerant R-134a from microfinned and treated tubes (Darabi et al, 2000)
- Single-phase mass transfer enhancement in grooved (finned) channel with flow pulsations (Nishimura et al., 1998), and heat transfer in an acoustically excited flow field over a rough cylinder (Kryukov and Boykov, 1973)
- Gas–solid suspension flows in an electric field (Min and Chao, 1966; Elsdon and Shearer, 1977; Bologna et al., 1985)
- Fluidized-bed (air-particle suspension) heat transfer with airflow pulsations (Bhattacharya and Harrison, 1976) and across finned tubes (Bartel and Genetti, 1973)
- Surfactant additive for seawater evaporation in spirally corrugated or doubly fluted (rough surface) tubes (Sephton, 1971, 1975)

Again, as in the CHF reduction case with twisted-tape inserts as a volatile liquid additive to water (Pabisz and Bergles, 1996), another surprise in compound enhancement is reported by Masliyah and Nandakumar (1977). Their computational results revealed that average Nu for internally finned coiled tubes was lower than that in plain coiled tubes for the same flow conditions. Bergles (2000) refers to another example where there was reduction in average single-phase heat transfer coefficients in a coiled tube with pulsating flow (fluid vibration) compared with coiled tube performance in steady flow.

Finally, issues relating to the performance of enhancement techniques under fouling conditions remain relatively unresolved (Bergles, 2000; Somerscales and Bergles, 1997). Several instances of enhancement techniques acting to mitigate fouling are cited. Many patents for different devices also claim that their use not only enhances heat (and/or mass) transfer, but also reduces fouling (Bergles et al., 1991; Somerscales and Bergles, 1997).

NOMENCLATURE

Roman Letter Symbols

A	heat transfer surface area, m^2
A_c	area of flow cross section, m^2
A_e	effective heat transfer surface area, m^2
A_f	heat transfer surface area of fins, m^2
A_r	area of unfinned (or root) portion of tube, m^2
C	concentration, wppm

c_p	specific heat of fluid, J/kg · K
c_s	correction factor, dimensionless
c.m.c.	critical micelle concentration of a surfactant at equilibrium conditions, wppm
D	outside diameter of tube, m
D_o	outside diameter of circular finned tube, m
D_r	root diameter of externally finned tube, m
De	Dean number, dimensionless
d	inside or envelope tube diameter, m
d_h	hydraulic diameter, m [= $4A_c/P_w$]
d_i	tube inside or envelope diameter, m
Eu	Euler number, dimensionless pressure drop
e	roughness or rib height, m
f	Fanning friction factor, dimensionless
G	mass flux kg/m ² · s [= \dot{m}/A_c]
Gr	Grashof number, dimensionless [= $g\rho^2 d^3 \beta \Delta T_w / \mu^2$]
Gz	Graetz number, dimensionless [= $\dot{m}c_p/kL$]
H	180° tape-twist pitch, m
	pitch of a helical coil, m
He	helical number, dimensionless
h	heat transfer coefficient, W/m ² · K
	offset strip fin height, m
h_f	fin height, m
i_{lg}	specific enthalpy of vaporization, J/kg
J_a	tube rotation speed, dimensionless
j	Colburn factor, dimensionless [= $St \cdot Pr^{2/3} = Nu/Re \cdot Pr^{1/3}$]
k	thermal conductivity, W/m · K
L	tube length, m
L_h	heated length of tube, m
L_s	effective swirl flow length, m
L_{th}	thermal entrance length of duct, m
l	offset length in offset strip fin cores, m
\dot{m}	mass flow rate, kg/s
N	number of tubes, dimensionless
N_L	number of tube rows in flow direction in a tube bundle, dimensionless
n	number of fins, dimensionless
Nu	Nusselt number, dimensionless
Nu_z	axially local Nusselt number, dimensionless
P	pumping power, N · m/s
P_w	wetted perimeter, m
p	pressure, N/m ²
	pitch, m
p_f	fin pitch, dimensionless

Δp	pressure drop, N/m^2
Pr	Prandtl number, dimensionless $[= \mu c_p / k]$
Q	heat transfer rate, W
q''	heat flux, $\text{W/m}^2 [= q / A]$
R	curvature radius of a curved tube or zero-pitch coil, m
R_c	radius of curvature of a helical coil, m
Ra	Rayleigh number, dimensionless $[= \text{Gr} \cdot \text{Pr}]$
Ra^*	modified Rayleigh number based on the wall heat flux, dimensionless
Re	Reynolds number, dimensionless
	empty tube Reynolds number, $[= 4\dot{m} / \pi d \rho \mu]$
Re_a	tape-partitioned tube Reynolds number, dimensionless $[= Gd / \mu]$
S_L	longitudinal pitch of tube centers in a tube bundle, m
S_T	transverse pitch of tube centers in a tube bundle, m
St	Stanton number, dimensionless $[\text{Nu} / \text{Re} \cdot \text{Pr}]$
Sw	swirl parameter, dimensionless
s	interfin separation in offset strip fins, m
	average spacing between adjacent fins, m
T	temperature, K
ΔT_i	approach temperature difference, K
ΔT_{lm}	log-mean temperature difference, K
t	fin thickness, m
U	mean axial velocity, m/s
	overall heat transfer coefficient, $\text{W/m}^2 \cdot \text{K}$
UHF	uniform wall heat flux boundary condition
UWT	uniform wall temperature boundary condition
V_a	mean axial velocity in a tape-partitioned tube, $[= G / \rho]$, m/s
V_s	swirl velocity, m/s
w	width of twisted-tape insert, m
x	average mass quality of vapor–liquid flow, dimensionless
y	twist ratio of a twisted-tape insert, dimensionless $[= H / d]$

Greek Letter Symbols

α	spiral fin helix angle, deg
	aspect ratio of the flow cross section of noncircular duct (height/width), dimensionless
	aspect ratio for offset strip fin channel, dimensionless $[= s / h]$
β	wavy plate fin density factor, dimensionless $[= \text{fin separation} / \text{waviness depth}]$
γ	aspect ratio of corrugated plate or fin waviness, dimensionless $[= \text{waviness depth} / \text{pitch}]$
	ratio of fin thickness to fin separation of offset strip fins, dimensionless $[= t / s]$

δ	ratio of fin thickness and fin offset length, dimensionless [$= t/l$]
	thickness of a twisted tape, m
ε	fin surface extension ratio, dimensionless [$=$ total surface area/bare tube surface area]
η_f	fin efficiency, dimensionless
μ	dynamic viscosity, $\text{N/m}^2 \cdot \text{s}$
ρ	fluid density, kg/m^3

Subscripts

b	bulk or mean temperature conditions
cr	critical heat flux
e	exit conditions
g	gas or vapor state
H	UHF thermal boundary condition
h	hydraulic diameter
i	inlet condition
	inner surface
	inside (envelope) diameter
iso	adiabatic isothermal conditions
l	liquid state
m	bulk mean or average quantity
	length-averaged quantity
max	maximum value
o	smooth tube, channel, or surface
s	twisted-tape-induced swirl flows
sat	saturation condition or the wall superheat
st	a straight tube
sub	subcooled condition
	subcooling
T	UWT thermal boundary condition
tr	laminar-turbulent transition flow regime
w	wall condition
	heat transfer surface
∞	free stream conditions

REFERENCES

- Acharya, N., Sen, M., and Chang, H.-C. (1994). Thermal Entrance Length and Nusselt Numbers in Coiled Tubes, *Int. J. Heat Mass Transfer*, 37(2), 336–340.
- Acharya, S., Hibbs, R. G., Chen, Y., and Nikitopoulos, D. E. (2000). Mass/Heat Transfer in a Ribbed Passage with Cylindrical Vortex Generators: The Effect of Generator-Rib Spacing, *J. Heat Transfer*, 122(4), 641–652.
- Achenbach, E. (1977). The Effect of Surface Roughness on the Heat Transfer from a Circular Cylinder to the Cross Flow of Air, *Int. J. Heat Mass Transfer*, 20, 359–369.

- Ackerman, J. W. (1970). Pseudoboiling Heat Transfer to Supercritical Pressure Water in Smooth and Ribbed Tubes, *J. Heat Transfer*, 92, 490–498.
- Adamek, T. A. (1981). Bestimmung der Kondensationsgrossen auf feingewellten Oberflächen zur Auslegen optimaler Wandprofile, *Waerme Stoffuebertrag.*, 15, 255–270.
- Adamek, T. A., and Webb, R. L. (1990). Prediction of Film Condensation on Horizontal Integral-Fin Tubes, *Int. J. Heat Mass Transfer*, 33(8), 1721–1735.
- Agarwal, K. N., Varma, H. K., and Lal, S. (1982). Pressure Drop during Forced Convection Boiling of R-12 under Swirl Flow, *J. Heat Transfer*, 104, 758–762.
- Agarwal, K. N., Varma, H. K., and Lal, S. (1986). Heat Transfer during Forced Convection Boiling of R-12 under Swirl Flow, *J. Heat Transfer*, 108, 567–573.
- Aguilar, G., Gasljevic, K., and Matthys, E. F. (2001). Asymptotes of Maximum Friction and Heat Transfer Reductions for Drag-Reducing Surfactant Solutions, *Int. J. Heat Mass Transfer*, 44, 2835–2843.
- Akhavan-Behabadi, M. A., Varma, H. K., and Agarwal, K. N. (2000). Enhancement of Heat Transfer Rates by Coiled Wires during Forced Convective Condensation of R-22 inside Horizontal Tubes, *J. Enhanced Heat Transfer*, 7(2), 69–80.
- Alexander, L. G., and Hoffman, H. W. (1971). Performance Characteristics of Corrugated Tubes for Vertical Tube Evaporators, *ASME-71-HT-30*, ASME, New York.
- Ammerman, C. N., and You, S. M. (1996). Determination of Boiling Enhancement Mechanism Caused by Surfactant Addition to Water, *J. Heat Transfer*, 118, 429–435.
- Amon, C. H., Murthy, J., Yao, S. C., Narumanchi, S., Wu, C.-F., and Hsieh, C.-C. (2001). MEMS-Enabled Thermal Management of High-Heat-Flux Devices, EDIFICE: Embedded Droplet Impingement for Integrated Cooling of Electronics, *Exp. Therm. Fluid Sci.*, 25(5), 231–242.
- Arai, N., Fukushima, T., Arai, A., Nakajima, T., Fujie, K., and Nakayama, Y. (1977). Heat Transfer Tubes Enhancing Boiling and Condensation in Heat Exchangers of a Refrigerant Machine, *ASHRAE Trans.*, 83(2), 58–70.
- Asakavičius, J. P., Žukauskas, A. A., Gaigalis, V. A., and Eva, V. K. (1979). Heat Transfer from Freon-113, Ethyl Alcohol and Water with Screen Wicks, *Heat Transfer Sov. Res.*, 11(1), 92–100.
- Austen, D. S., and Soliman, H. M. (1988). Laminar Flow and Heat Transfer in Helically Coiled Tubes with Substantial Pitch, *Exp. Therm. Fluid Sci.*, 1, 183–194.
- Azer, N. Z., and Said, S. A. (1981). Augmentation of Condensation Heat Transfer by Internally Finned Tubes and Twisted Tapes, *Final Technical Report*, Department of Mechanical Engineering, Kansas State University, Manhattan, KS.
- Azer, N. Z., Fan, L. T., and Lin, S. T. (1976). Augmentation of Condensation Heat Transfer with In-Line Static Mixers, *Proc. 1976 Heat Transfer and Fluid Mechanics Institute*, Stanford University Press, Stanford, CA, pp. 512–526.
- Bandyopadhyay, P. S., Gaitonde, U. N., and Sukhatme, S. P. (1991). Influence of Free Convection on Heat Transfer during Laminar Flow in Tubes with Twisted Tapes, *Exp. Therm. Fluid Sci.*, 4, 577–586.
- Barskii, M. A., and Chukhman, G. I. (1971). Study of Heat Transfer in Boiling of Freons in Spiral Tubes, *Kholod. Tekh.*, 48(2), 18–21.
- Bartel, W. J., and Genetti, W. E. (1973). Heat Transfer from a Horizontal Bundle of Bare and Finned Tubes in an Air Fluidized Bed, *AIChE Symp. Ser.*, 69(128), 85–93.

- Beatty, K. O., Jr., and Katz, D. L. (1948). Condensation of Vapors on Outside of Finned Tubes, *Chem. Eng. Prog.*, 44(1), 55–70.
- Behnia, M., Pralits, J., and Nakayama, W. (2001). Numerical Simulation of Jet Impingement/Channel Flow Cooling of an Array of Heated Strips by a Fluor Inert Liquid, *Int. J. Transp. Phenomena*, 3(4), 437–448.
- Berenson, P. J. (1962). Experiments on Pool Boiling Heat Transfer, *Int. J. Heat Mass Transfer*, 5, 985–999.
- Bergles, A. E. (1964). The Influence of Flow Vibrations on Forced-Convection Heat Transfer, *J. Heat Transfer*, 86, 559–560.
- Bergles, A. E. (1969). The Influence of Heated-Surface Vibration on Pool Boiling, *J. Heat Transfer*, 91, 152–154.
- Bergles, A. E. (1986). Evolution of Cooling Technology for Electrical, Electronic, and Micro-electronic Equipment, *Heat Transfer Eng.*, 7(3–4), 97–106.
- Bergles, A. E. (1990). *Electronic and Microelectronic Equipment*, Hemisphere Publishing, New York.
- Bergles, A. E. (1997). Enhancement of Pool Boiling, *Int. J. Refrig.*, 20(8), 545–551.
- Bergles, A. E. (1998). Techniques to Enhance Heat Transfer, in *Handbook of Heat Transfer*, 3rd ed., (Rohsenow W. M., Hartnett, J. P., and Cho, Y. I., eds.), McGraw-Hill, New York, Chap. 11.
- Bergles, A. E. (1999). The Imperative to Enhance Heat Transfer, *Heat Transfer Enhancement of Heat Exchangers* (Kakaç, S., Bergles, A. E., Mayinger, F., and Yüncii, H., eds.) Kluwer, Dordrecht, The Netherlands, 13–29.
- Bergles, A. E. (2000). New Frontiers in Enhanced Heat Transfer, in *Advances in Enhanced Heat Transfer*, 2000, (Manglik, R. M., Ravigururijan, T. S., Muley, A., Papar, A. R., and Kim, J., eds.), ASME, New York, pp. 1–8.
- Bergles, A. E., and Champagne, P. (1999). Novel Variable Roughness Technique to Enhance, on Demand, Heat Transfer in a Single-Phase Heat Exchanger, provisional U.S. patent application 60/144,563, July 16.
- Bergles, A. E., and Chyu, M. C. (1982). Characteristics of Nucleate Pool Boiling from Porous Metallic Coatings, *J. Heat Transfer*, 104, 279–285.
- Bergles, A. E., and Newell, P. H., Jr. (1965). The Influence of Ultrasonic Vibrations on Heat Transfer to Water Flowing in Annuli, *Int. J. Heat Mass Transfer*, 8, 1273–1280.
- Bergles, A. E., and Scarola, L. S. (1966). Effect of a Volatile Additive on the Critical Heat Flux for Surface Boiling of Water in Tubes, *Chem. Eng. Sci.*, 21, 721–723.
- Bergles, A. E., and Thompson, W. G., Jr. (1970). The Relationship of Quench Data to Steady-State Pool Boiling Data, *Int. J. Heat Mass Transfer*, 13, 55–68.
- Bergles, A. E., Lee, R. A., and Mikic, B. B. (1969). Heat Transfer in Rough Tubes with Tape-Generated Swirl Flow, *J. Heat Transfer*, 91, 443–445.
- Bergles, A. E., Fuller, W. D., and Hynek, S. J. (1971). Dispersed Flow Film Boiling of Nitrogen with Swirl Flow, *Int. J. Heat Mass Transfer*, 14(9), 1343–1354.
- Bergles, A. E., Blumenkrantz, A. R., and Taborek, J. (1974a). Performance Evaluation Criteria for Enhanced Heat Transfer Surfaces, in *Heat Transfer 1974 (Proc. 5th International Heat Transfer Conference)*, Vol. 2, JSME, Tokyo, pp. 234–238.
- Bergles, A. E., Bunn, R. L., and Junkhan, G. H. (1974b). Extended Performance Evaluation Criteria for Enhanced Heat Transfer Surfaces, *Lett. Heat Mass Transfer*, 1, 113–120.

- Bergles, A. E., Junkhan, G. H., and Webb, R. L. (1979). Energy Conservation via Heat Transfer Enhancement, *Report COO-4649-5*, Heat Transfer Laboratory, Iowa State University, Ames, IA.
- Bergles, A. E., Collier, J. G., Delhay, J. M., Hewitt, G. F., and Mayinger, F. (1981). *Two-Phase Flow and Heat Transfer in the Power and Process Industries*, Hemisphere Publishing, Washington, DC.
- Bergles, A. E., Nirmalan, V., Junkhan, G. H., and Webb, R. L. (1983). Bibliography of Augmentation of Convective Heat and Mass Transfer, II, *Report HTL-31, ISU-ERI-Ames-84221*, Heat Transfer Laboratory, Iowa State University, Ames, IA.
- Bergles, A. E., Jensen, M. K., Somerscales, E. F. C., and Manglik, R. M. (1991). Literature Review of Heat Transfer Enhancement Technology for Heat Exchanges in Gas-Fired Applications, *Report GRI 91-0146*, Gas Research Institute, Chicago.
- Bergles, A. E., Jensen, M. K., and Shome, B. (1995). Bibliography on Enhancement of Convective Heat and Mass Transfer, *Report HTL-23*, Heat Transfer Laboratory, Rensselaer Polytechnic Institute, Troy, NY.
- Bergles, A. E., Jensen, M. K., and Shome, B. (1996). The Literature on Enhancement of Convective Heat and Mass Transfer, *J. Enhanced Heat Transfer*, 4(1), 1–6.
- Bhatnagar, R. K., and Manglik, R. M. (2002). Enhanced Heat and Mass Transfer Literature: Case for a Digital Library with Intelligent Information Retrieval, Thermal Fluids and Thermal Processing Laboratory, *Report TFTPL-CSI*, University of Cincinnati, Cincinnati, OH.
- Bhattacharya, S. C., and Harrison, D. (1976). Heat Transfer in a Pulsed Fluidized Bed, *Trans. Inst. Chem. Eng.*, 54, 281–286.
- Blatt, T. A., and Adt, R. R. (1963). The Effects of Twisted Tape Swirl Generators on the Heat Transfer Rate and Pressure Drop of Boiling Freon 11 and Water, *ASME-63-WA-42*, ASME, New York.
- Blomgren, O. C., Sr., and Blomgren, O. C., Jr. (1972). Method and Apparatus for Cooling the Workpiece and/or the Cutting Tools of a Machining Apparatus, U.S. patent 3,670,606.
- Boling, C., Donovan, W. J., and Decker, A. S. (1953). Heat Transfer of Evaporating Freon with Inner-Fin Tubing, *Refrig. Eng.*, 61, 1338–1340, 1384.
- Bologa, M. K., Pushkov, V. V., and Berkov, A. B. (1985). Electric Field Induced Heat Transfer Enhancement in a Gas–Solid Suspension Heat Exchanger, *Int. J. Heat Mass Transfer*, 20, 1245–1255.
- Bonilla, C. F., Grady, J. J., and Avery, G. A. (1965). Pool Boiling Heat Transfer from Scored Surfaces, *Chem. Eng. Prog. Symp. Ser.*, 61(57), 281–288.
- Brauer, H. (1961). Strömungswiderstand und Wärmeübergang bei Ringspalten mit rauhen Rohren, *Atomkernenergie*, 4, 152–159.
- Briggs, A., and Rose, J. W. (1994). Effect of Fin Efficiency on a Model for Condensation Heat Transfer on a Horizontal Integral-Fin Tube, *Int. J. Heat Mass Transfer*, 37, 457–463.
- Brodov, Y. M., Salev'yev, R. Z., Permayakov, V. A., Kuptsov, V. K., and Gal'perin, A. G. (1977). The Effect of Vibration on Heat Transfer and Flow of Condensing Steam on a Single Tube, *Heat Transfer Sov. Res.*, 9(1), 153–155.
- Carnavos, T. C. (1979a). Heat Transfer Performance of Internally Finned Tubes in Turbulent Flow, in *Advances in Heat Transfer*, ASME, New York, pp. 61–67.

- Carnavos, T. C. (1979b). Cooling Air in Turbulent Flow with Internally Finned Tubes, *Heat Transfer Eng.*, 1(2), 41–46.
- Carnavos, T. C. (1980). An Experimental Study: Condensing R-11 on Augmented Tubes, *ASME-80-HT-54*, ASME, New York.
- Cary, J. D., and Mikic, B. B. (1973). The Influence of Thermocapillary Flow on Heat Transfer in Film Condensation, *J. Heat Transfer*, 95, 20–24.
- Celata, G. P., Cumo, M., and Mariani, A. (1994). Enhancement of Water Subcooled Flow Boiling CHF in Tubes with Helically Coiled Wires, *Int. J. Heat Mass Transfer*, 37(1), 53–67.
- Champagne, P. R., and Bergles, A. E. (2001). Development and Testing of a Novel, Variable-Roughness Technique to Enhance, on Demand, Heat Transfer in a Single-Phase Heat Exchanger, *J. Enhanced Heat Transfer*, 8(5), 341–352.
- Chamra, L. M., Webb, R. L., and Randlett, M. R. (1996). Advanced Micro-fin Tubes for Condensation, *Int. J. Heat Mass Transfer*, 39(9), 1839–1846.
- Chandran, R., and Watson, F. A. (1976). Condensation on Static and Rotating Pinned Tubes, *Trans. Inst. Chem. Eng.*, 54, 65–72.
- Chen, Y., and Liu, Z. (1999). Study on Enhancement of Nucleate Boiling Heat Transfer by EHD Effect, *J. Enhanced Heat Transfer*, 6(6), 457–466.
- Cheng, K. C., and Yuen, F. P. (1987). Flow Visualization Studies on Secondary Flow Patterns in Straight Tubes Downstream of a 180 deg Bend and in Isothermally Heated Horizontal Tubes, *J. Heat Transfer*, 109(1), 49–54.
- Chhabra, R. P., and Richardson, J. F. (1999). *Non-Newtonian Flow in the Process Industries*, Butterworth-Heinemann, Oxford.
- Chiang, R. (1993). Heat Transfer and Pressure Drop during Evaporation and Condensation of R-22 in 7.5 mm and 10 mm Diameter Axial and Helical Grooved Tubes, *AIChE Symp. Ser.*, 89(295), 205–210.
- Chien, L.-H., and Webb, R. L. (1998). A Nucleate Boiling Model for Structured Enhanced Surfaces, *Int. J. Heat Mass Transfer*, 41(14), 2183–2195.
- Cho, Y. I., and Hartnett, J. P. (1980). Heat Transfer Performance of Concentrated Polyethylene Oxide and Polyacrylamide Solutions, *AIChE J.*, 26, 250–256.
- Choi, H. Y. (1961). Electrohydrodynamic Boiling Heat Transfer, *Report 63-12-1*, Department of Mechanical Engineering, Tufts University, Medford, MA.
- Chu, R. C., and Chrysler, G. M. (1998). Recent Developments of Cooling Technology and Thermal Design for Leading-Edge Electronic Products, *Int. J. Transp. Phenomema*, 1(1), 31–40.
- Chu, R. C., and Moran, K. P. (1977). Method for Customizing Nucleate Boiling Heat Transfer from Electronic Units Immersed in Dielectric Coolant, U.S. patent 4,050,507.
- Chu, R. C., Takano, K., Nishio, S., and Tanasawa, I. (2000). Study on Enhancement of Condensation Heat Transfer Using Electric Field, *Heat Transfer Asian Res.*, 29(4), 269–279.
- Chu, R. C., Nishio, S., and Tanasawa, I. (2001). Enhancement of Condensation Heat Transfer on a Finned Tube Using an Electric Field, *J. Enhanced Heat Transfer*, 8(4), 215–229.
- Chukhman, G. I. (1972). The Internal Heat Transfer in Evaporative Air Coolers with Flow Turbulization, *Heat Transfer Sov. Res.*, 4(4), 67–70.
- Cieśliński, J. T. (2002). Nucleate Pool Boiling on Porous Metallic Coatings, *Exp. Therm. Fluid Sci.*, 25(7), 557–564.

- Collins, W. M., and Dennis, S. C. R. (1975). The Steady Motion of a Viscous Fluid in a Curved Tube, *Q. J. Mech. Appl. Math.*, 28, 133–156.
- Cooper, P. (1990). EHD Enhancement of Nucleate Boiling, *J. Heat Transfer*, 112, 458–464.
- Cornaro, C., Fleischer, S. A., Rounds, M., and Goldstein, J. R. (2001). Jet Impingement Cooling of a Convex Semi-cylindrical Surface, *Int. J. Thermal Sci.*, 40(10), 890–898.
- Cox, R. B., Pascale, A. S., Matta, G. A., and Stromberg, K. S. (1969). Pilot Plant Tests and Design Study of a 2.5 MGD Horizontal-Tube Multiple-Effect Plant, *Report 492*, Office of Saline Water Research and Development, Washington, DC.
- Cox, R. B., Matta, G. A., Pascale, A. S., and Stomberg, K. G. (1970). Second Report on Horizontal Tubes Multiple-Effect Process Pilot Plant Tests and Design, *Reprot 592*, Office of Saline Water Research and Development, Washington, DC.
- Cumo, M., Farello, G. E., and Ferrari, G. (1972). The Influence of Curvature in Post Dry-Out Heat Transfer, *Int. J. Heat Mass Transfer*, 15, 2045–2062.
- Czikk, A. M., and O'Neill, P. S. (1979). Correlation of Nucleate Boiling from Porous Metal Films, in *Advances in Enhanced Heat Transfer*, (Chenoweth, J. M., Kaellis, J., Michel, J. W., and Shenkman, S., eds.), ASME, New York, pp. 53–60.
- Dahl, M. M., and Erb, L. D. (1976). Liquid Heat Exchanger Interface and Method, U.S. patent 3,990,862.
- Dalle Donne, M. (1978). Heat Transfer in Gas Cooled Fast Reactor Cores, *Ann. Nucl. Energy*, 5, 439–453.
- Dalle Donne, M., and Meyer, L. (1977). Turbulent Convective Heat Transfer from Rough Surfaces with Two-Dimensional Rectangular Ribs, *Int. J. Heat Mass Transfer*, 20, 583–620.
- Darabi, J., Ohadi, M. M., and Dessiatoun, S. V. (2000). Compound Augmentation of Pool Boiling on Three Selected Commercial Tubes, *J. Enhanced Heat Transfer*, 7(5), 347–360.
- Das, A. K., Incheck, G. A., and Marto, P. J. (1999). The Effect of Fin Height during Steam Condensation on a Horizontal Stainless Steel Integral-Fin Tube, *J. Enhanced Heat Transfer*, 6(2–4), 237–250.
- Das, A. K., Kilty, H. P., Marto, P. J., Kumar, A., and Andeen, G. B. (2000). Dropwise Condensation of Steam on Horizontal Corrugated Tubes Using an Organic Self-Assembled Monolayer Coating, *J. Enhanced Heat Transfer*, 7(2), 109–123.
- Date, A. W., and Singham, J. R. (1972). Numerical Prediction of Friction and Heat Transfer Characteristics of Fully Developed Laminar Flow in Tubes Containing Twisted Tapes, *ASME-72-HT-17*, ASME, New York.
- Davidson, J. H., Kulacki, F. A., and Dunn, P. F. (1987). Convective Heat Transfer with Electric and Magnetic Fields, in *Handbook of Single-Phase Convective Heat Transfer*, (Kakaç, S., Shah, R. K., and Aung, W., eds.), Wiley, New York, Chap. 9.
- Dean, W. R. (1927). Note on the Motion of Fluid in a Curved Pipe, *Philos. Mag.*, Ser. 7, 4, 208–233.
- Dean, W. R. (1928). The Stream Line Motion of Fluid in a Curved Pipe, *Philos. Mag.*, Ser. 7, 5(30), 673–695.
- Dippery, D. F., and Sabersky, R. H. (1963). Heat and Momentum Transfer in Smooth and Rough Tubes at Various Prandtl Numbers, *Int. J. Heat Mass Transfer*, 6, 329–353.
- Dong, Y., Huixiong, L., and Tingkuan, C. (2001). Pressure Drop, Heat Transfer and Performance of Single-Phase Turbulent Flow in Spirally Corrugated Tubes, *Exp. Therm. Fluid Sci.*, 24, 131–138.

- Dreitser, G. A., Levin, E. S., and Mikhailov, A. V. (1988). Intensification of Heat Transfer in the Condensation of Water Vapor on Horizontal Tube with Annular Grooves, *J. Eng. Phys.*, 55(5), 789–793.
- Drižius, M.-R., Shkema, R. K., and Shlančiauskas, A. A. (1978). Boiling Crisis in Swirled Flow of Water in Pipes, *Heat Transfer Sov. Res.*, 10(4), 1–7.
- Durant, W. S., and Mirshak, S. (1959). *Roughening of Heat Transfer Surfaces as a Method of Increasing Heat Flux at Burnout*, E.I. Dupont de Nemours and Co., Savannah, GA.
- Durant, W. S., Towell, R. H., and Mirshak, S. (1965). Improvement of Heat Transfer to Water Flowing in an Annulus by Roughening the Heated Wall, *Chem. Eng. Prog. Symp. Ser.*, 60(61), 106–113.
- Ebadian, M. A., and Dong, Z. F. (1998). Forced Convection, Internal Flow in Ducts, in *Handbook of Heat Transfer*, 3rd ed., (Rohsenow, W. M., Hartnett, J. P., and Cho, Y. I., eds.), McGraw-Hill, New York, Chap. 5.
- Ebisu, T., and Torikoshi, K. (1998). Experimental Study on Evaporation and Condensation Heat Transfer Enhancement for R407C Using Herringbone Heat Transfer Tube, *ASHRAE Trans.*, 104, Pt. 2, 1044–1052.
- Eckels, S. J., Doerr, T. M., and Pate, M. B. (1994a). Heat Transfer and Pressure Drop of R-134a and Ester Lubricant Mixtures in a Smooth and a Micro-fin Tube, I: Evaporation, *ASHRAE Trans.*, 100(2), 265–281.
- Eckels, S. J., Doerr, T. M., and Pate, M. B. (1994b). Heat Transfer and Pressure Drop of R-134a and Ester Lubricant Mixtures in a Smooth and a Micro-fin tube, II: Condensation, *ASHRAE Trans.*, 100(2), 283–294.
- Edwards, D. P., and Jensen, M. K. (1994). An Investigation of Turbulent Flow and Heat Transfer in Longitudinally Finned Tubes, *Report HTL-18*, Heat Transfer Laboratory, Rensselaer Polytechnic Institute, Troy, NY.
- Edwards, D. A., Brenner, H., and Wassan, D. T. (1991). *Interfacial Transport Processes and Rheology*, Butterworth-Heinemann, Boston, MA.
- Ekkad, S. V., and Han, J. C. (1997). Detailed Heat Transfer Distributions in Two-Pass Square Channels with Rib Turbulators, *Int. J. Heat Mass Transfer*, 40, 2525–2537.
- Ekkad, S. V., Pamula, G., and Acharya, S. (2000). Influence of Crossflow-Induced Swirl and Impingement on Heat Transfer in an Internal Coolant Passage of a Turbine Airfoil, *J. Heat Transfer*, 122(3), 587–597.
- Elenbaas, W. (1942). Heat Dissipation of Parallel Plates by Free Convection, *Physica*, 9(1), 1–28.
- Eliades, V., Nikitopoulos, E. D., and Acharya, S. (2001). Mass-Transfer Distribution in Rotating, Two-Pass, Ribbed Channels with Vortex Generators, *J. Thermophys. Heat Transfer*, 15(3), 266–274.
- Elsdon, R., and Shearer, C. J. (1977). Heat Transfer in Gas Fluidized Bed Assisted by an Alternating Electric Field, *Chem. Eng. Sci.*, 32, 1147–1153.
- Esen, E. B., Obot, N. T., and Rabas, T. J. (1994). Enhancement, I: Heat Transfer and Pressure Drop Results for Air Flow through Passages with Spirally Shaped Roughness, *J. Enhanced Heat Transfer*, 1(2), 145–156.
- Eustice, J. (1911). Experiments on Stream-Line Motion in Curved Pipes, *Proc. R. Soc.*, A85, 119–131.
- Evans, L. B., and Churchill, S. W. (1963). The Effect of Axial Promoters on Heat Transfer and Pressure Drop inside a Tube, *Chem. Eng. Prog. Symp. Ser.*, 41(59), 36–46.

- Fan, L. T., Lin, S. T., and Azer, N. Z. (1978). Surface Renewal Model of Condensation Heat Transfer in Tubes with In-Line Static Mixers, *Int. J. Heat Mass Transfer*, 21, 849–854.
- Fand, R. M. (1965). The Influence of Acoustic Vibrations on Heat Transfer by Natural Convection from a Horizontal Cylinder to Water, *J. Heat Transfer*, 87, 309–310.
- Fand, R. M., and Kaye, J. (1961). The Influence of Sound on Free Convection from a Horizontal Cylinder, *J. Heat Transfer*, 83, 133.
- Fand, R. M., and Peebles, E. M. (1962). A Comparison of the Influence of Mechanical and Acoustical Vibrations on Free Convection from a Horizontal Cylinder, *J. Heat Transfer*, 84, 268–270.
- Fand, R. M., Roos, J., Cheng, P., and Kaye, J. (1962). The Local Heat-Transfer Coefficient around a Heated Horizontal Cylinder in an Intense Sound Field, *J. Heat Transfer*, 84, 245–250.
- Feinstein, L., and Lundberg, R. E. (1963). Study of Advanced Techniques for Cooling Very High Power Microwave Tubes, *Report RADC-TDR-63-242*, Rome Air Development Center, Rome, NY.
- Fenner, G. W., and Ragi, E. (1979). Enhanced Tube Inner Surface Heat Transfer Device and Method, U.S. patent 4,154,291.
- Fletcher, L. S., and Andrews, M. J. (1994). Technical/Market Assessment of Heat Exchanger Technology for Users of Natural Gas, *Report GRI-94/0248*, Gas Research Institute, Chicago.
- Fossa, M., and Tagliafico, L. A. (1995). Experimental Heat Transfer of Drag-Reducing Polymer Solutions in Enhanced Surface Heat Exchangers, *Exp. Therm. Fluid Sci.*, 10, 221–228.
- Fraas, A. P. (1989). *Heat Exchanger Design*, 2nd ed., Wiley, New York.
- Fujie, K., Itoh, N., Innami, T., Kimura, H., Nakayama, N., and Yanugidi, T. (1977). Heat Transfer Pipe, U.S. patent 4,044,797.
- Fujii, T. (1995). Enhancement to Condensing Heat Transfer: New Developments, *J. Enhanced Heat Transfer*, 2(1/2), 127–137.
- Fujii, M., Nishiyama, E., and Yamanaka, G. (1979). Nucleate Pool Boiling Heat Transfer from Microporous Heating Surface, in *Advances in Enhanced Heat Transfer*, J. M. Chenoweth et al., eds., ASME, New York, pp. 45–51.
- Fujikake, J. (1980). Heat Transfer Tube for Use in Boiling Type Heat Exchangers and Method of Producing the Same, U.S. patent 4,216,826.
- Fuls, G. M., and Geiger, G. E. (1970). Effect of Bubble Stabilization on Pool Boiling Heat Transfer, *J. Heat Transfer*, 97, 635–640.
- Gaertner, R. F. (1967). Methods and Means for Increasing the Heat Transfer Coefficient between a Wall and Boiling Liquid, U.S. patent 3,301,314.
- Gambill, W. R., Bundy, R. D., and Wansbrough, R. W. (1961). Heat Transfer, Burnout, and Pressure Drop for Water in Swirl Flow Tubes with Internal Twisted Tapes, *Chem. Eng. Prog. Symp. Ser.*, 57(32), 127–137.
- Gao, X., and Sundén, B. (2001). Heat Transfer and Pressure Drop Measurements in Rib-Roughened Rectangular Ducts, *Exp. Therm. Fluid Sci.*, 24, 25–34.
- Garimella, S., and Christensen, R. N. (1995a). Heat Transfer and Pressure Drop Characteristics of Spirally Fluted Annuli, I: Hydrodynamics, *J. Heat Transfer*, 117, 54–60.
- Garimella, S., and Christensen, R. N. (1995b). Heat Transfer and Pressure Drop Characteristics of Spirally Fluted Annuli, II: Heat Transfer, *J. Heat Transfer*, 117, 61–68.

- Gasljevic, K., and Matthys, E. F. (1997). Experimental Investigation of Thermal and Hydrodynamic Development Regions for Drag-Reducing Surfactant Solutions, *J. Heat Transfer*, 119, 80–88.
- Gaspari, G. P., and Cattadori, G. (1994). Subcooled Flow Boiling in Tubes with and without Turbulence Promoters, *Exp. Therm. Fluid Sci.*, 8, 28–34.
- Glicksman, L. R., Mikic, B. B., and Snow, D. F. (1973). Augmentation of Film Condensation on the Outside of Horizontal Tubes, *AIChE J.*, 19, 636–637.
- Gnielinski, V. (1986). Correlations for the Pressure Drop in Helically Coiled Tubes, *Int. Chem. Eng.*, 26(1), 36–44.
- Gomelaury, V. I., and Magrakvelidze, T. S. (1978). Mechanism of Influence of Two Dimensional Artificial Roughness on Critical Heat Flux in Subcooled Water Flows, *Therm. Eng.*, 25(2), 1–3.
- Gregorig, R. (1954). Hautkondensation an Feingewellten Oberflächen bei Berücksichtigung der Oberflächenspannungen, *Z. Angew. Math. Phys.*, 5, 36–49.
- Griffith, P. (1985). Dropwise Condensation, in *Handbook of Heat Transfer Fundamentals*, W. M. Rohsenow, J. P. Hartnett, and E. N. Ganic, eds., McGraw-Hill, New York, Chap. 11, Pt. 2.
- Griffith, P., and Wallis, J. D. (1960). The Role of Surface Conditions in Nucleate Boiling, *Chem. Eng. Prog. Symp. Ser.*, 56(49), 49–63.
- Groehn, H. G., and Scholz, F. (1976). Heat Transfer and Pressure Drop of In-Line Tube Banks with Artificial Roughness, in *Heat and Mass Transfer Sourcebook*, Scripta Publishing, Washington, DC, pp. 21–24.
- Gunter, A. Y., and Shaw, W. A. (1942). Heat Transfer, Pressure Drop and Fouling Rates of Liquids for Continuous and Noncontinuous Longitudinal Fins, *Trans. ASME*, 64, 795–802.
- Gupta, M. K., Herzener, A. L., and Hartnett, J. P. (1967). Turbulent Heat Transfer Characteristic of Viscoelastic Fluids, *Int. J. Heat Mass Transfer*, 10, 1211–1224.
- Guy, A. R. (1983). Double-Pipe Heat Exchangers, in *Heat Exchanger Design Handbook*, E. U. Schlünder, ed., Vol. 3, Hemisphere Publishing, Washington, DC, Sec. 3.2.
- Hagge, J. K., and Junkhan, G. H. (1974). Experimental Study of a Method of Mechanical Augmentation of Convective Heat Transfer Coefficients in Air, *Report HTL-3, ISU-ERI-Ames-74158*, Iowa State University, Ames, IA.
- Hall, W. B. (1962). Heat Transfer in Channels Having Rough and Smooth Surfaces, *J. Mech. Eng. Sci.*, 4, 287–291.
- Hall, D. E., Incropera, F. P., and Viskanta, R. (2001a). Jet Impingement Boiling from a Circular Free-Surface Jet during Quenching, 1: Single Phase Jet, *J. Heat Transfer*, 123(5), 901–910.
- Hall, D. E., Incropera, F. P., and Viskanta, R. (2001b). Jet Impingement Boiling from a Circular Free-Surface Jet during Quenching, 2: Two Phase Jet, *J. Heat Transfer*, 123(5), 911–917.
- Hampson, H., and Ozisik, N. (1952). An Investigation into the Condensation of Steam, *Proc. Inst. Mech. Eng.*, 1B, 282.
- Han, J.-C. (1988). Heat Transfer and Friction Characteristics in Rectangular Channels with Rib Turbulators, *J. Heat Transfer*, 110, 321–328.
- Han, J.-C., Zhang, Y. M., and Lee, C. P. (1991). Augmented Heat Transfer in Square Channels with Parallel, Crossed and V-Shaped Angled Ribs, *J. Heat Transfer*, 113, 590–596.
- Han, J.-C., Huang, J. J., and Lee, C. P. (1993). Augmented Heat Transfer in Square Channels with Wedge-Shaped and Delta-Shaped Turbulence Promoters, *J. Enhanced Heat Transfer*, 1(1), 37–52.

- Hannemann, R. J. (1977). Recent Advances in Dropwise Condensation Theory, *ASME-77-WA/HT-21*, ASME, New York.
- Harms, T. M., Jog, M. A., and Manglik, R. M. (1998). Effects of Temperature-Dependent Viscosity Variations and Boundary Conditions on Fully Developed Laminar Forced Convection in a Semicircular Duct, *J. Heat Transfer*, 120, 600–605.
- Hartnett, J. P. (1992). Viscoelastic Fluids: A New Challenge in Heat Transfer, *J. Heat Transfer*, 114, 296–303.
- Hartnett, J. P., and Cho, Y. I. (1998). Non-Newtonian Fluids, in *Handbook of Heat Transfer*, 3rd ed., W. M. Rohsenow, J. P., Hartnett, and Y. I. Cho, eds., McGraw-Hill, New York, Chap. 10.
- Hartnett, J. P., and Kostic, M. (1985). Heat Transfer to a Viscoelastic Fluid in Laminar Flow through a Rectangular Channel, *Int. J. Heat Mass Transfer*, 28, 1147.
- Hasegawa, S., Echigo, R., and Irie, S. (1975). Boiling Characteristics and Burnout Phenomena on a Heating Surface Covered with Woven Screens, *J. Nuc. Sci. Technol.*, 12(II), 722–724.
- Helmer, W. A., and Iqbal, I. (1980). Laminar Heat Transfer in a Circular Tube with Twisted Tapes during Condensation, *ASHRAE Trans.*, 86, Pt. 2, 662–674.
- Hesse, G. (1973). Heat Transfer in Nucleate Boiling, Maximum Heat Flux and Transition Boiling, *Int. J. Heat Mass Transfer*, 16, 1611–1627.
- Hesseltgreaves, J. E. (2001). *Compact Heat Exchangers: Selection, Design and Operation*, Pergamon Press, Amsterdam, The Netherlands.
- Hetsroni, G., Zakin, J. L., Lin, Z., Mosyak, A., Pancallo, E. A., and Rozenblit, R. (2000). The Effect of Surfactants on Bubble Growth, Wall Thermal Patterns and Heat Transfer in Pool Boiling, *Int. J. Heat Mass Transfer*, 44, 485–497.
- Hewitt, G. F. (1992). *Handbook of Heat Exchanger Design*, Begell House, New York.
- Hewitt, G. F., Shires, G. L., and Bott, T. R. (1993). *Process Heat Transfer*, CRC Press, Boca Raton, FL.
- Hilding, W. E., and Coogan, C. H., Jr. (1964). Heat Transfer and Pressure Loss Measurements in Internally Finned Tubes, *Proc. Symposium on Air-Cooled Heat Exchangers*, ASME, New York, pp. 57–85.
- Holden, K. M., Wanniarachchi, A., Marto, P. J., Boone, D. H., and Rose, J. W. (1987). The Use of Organic Coatings to Promote Dropwise Condensation of Steam, *J. Heat Transfer*, 109(3), 768–774.
- Honda, H., and Kim, K. (1995). Effect of Fin Geometry on the Condensation Heat Transfer Performance of a Bundle of Horizontal Low-Finned Tubes, *J. Enhanced Heat Transfer*, 2(1/2), 139–147.
- Honda, H., and Nozu, S. (1987). A Prediction Method for Heat Transfer during Film Condensation on Horizontal Low Integral-Fin Tubes, *J. Heat Transfer*, 109(1), 218–225.
- Honda, H., and Rose, J. (1999). Augmentation Techniques in External Condensation, in *Handbook of Phase Change: Boiling and Condensation*, (Kandlikar, S. G., Shoji, M., and Dhir, V. K., eds.), Taylor & Francis, Philadelphia, Chap. 22.
- Honda, H., Nozu, S., and Uchima, B. (1988). A Generalized Prediction Method for Heat Transfer during Film Condensation on a Horizontal Low Finned Tube, *JSME Int. J.*, Ser. 2, 31(4), 709–717.
- Honda, H., Takamatsu, H., and Kim, K. (1994). Condensation of CFC-11 and HCFC-123 in In-Line Bundles of Horizontal Finned Tubes: Effect of Fin Geometry, *J. Enhanced Heat Transfer*, 1(2), 197–209.

- Hong, S. W., and Bergles, A. E. (1976). Augmentation of Laminar Flow Heat Transfer in Tubes by Means of Twisted-Tape Inserts, *J. Heat Transfer*, 98, 251–256.
- Honma, M., Nishihara, A., and Atarashi, T. (2001). Numerical Analysis of Impinging Air Flow and Heat Transfer in Plate-Fin Type Heat Sinks, *J. Electron. Packag.*, 123(3), 315–318.
- Hsieh, R., and Marsters, G. F. (1973). Heat Transfer from a Vibrating Vertical Array of Horizontal Cylinders, *Can. J. Chem. Eng.*, 51, 302–306.
- Hudina, M. (1979). Evaluation of Heat Transfer Performances of Rough Surfaces from Experimental Investigation in Annular Channels, *Int. J. Heat Mass Transfer*, 22, 1381–1392.
- Hughes, T. G., and Olson, D. R. (1975). Critical Heat Fluxes for Curved Surfaces during Subcooled Flow Boiling, *Trans. Can. Soc. Mech. Eng.*, 3(3), 122–130.
- Hwang, J.-J., and Chang, B.-Y. (2000). Effect of Outflow Orientation on Heat Transfer and Pressure Drop in a Triangular Duct with an Array of Tangential Jets, *J. Heat Transfer*, 122(4), 669–678.
- Hwang, U. P., and Moran, K. P. (1981). Boiling Heat Transfer of Silicon Integrated Circuits Chip Mounted on a Substrate, in *Heat Transfer in Electronic Equipment*, M. D. Kelleher and M. M. Yovanovich, eds., ASME-HTD-20, ASME, New York, pp. 53–59.
- Hwang, G. J., and Tzeng, S. C., Mao, C. P., and Soong, C. Y. (2001). Heat Transfer in a Radially Rotating Four-Pass Serpentine Channel with Staggered Half-V Rib Turbulators, *J. Heat Transfer*, 123(1), 39–50.
- Iacovides, H., Jackson, D. C., Kelemenis, G., Launder, B. E., and Yuan, Y. M. (2001). Flow and Heat Transfer in a Rotating U-Bend with 45° Ribs, *Int. J. Heat Fluid Flow*, 22(3), 308–314.
- Iltscheff, S. (1971). Über einige Versuche zur Erzielung von Tropfkondensation mit Fluorierten Kältemitteln, *Kultetech. Klim.*, 23, 237–241.
- Inasaka, F., Nariai, H., Fujisaki, W., and Ishiguro, H. (1991). Critical Heat Flux of Subcooled Flow Boiling in Tubes with Internal Twisted Tape, *Proc. ASME/JSME Thermal Engineering Joint Conference*, Vol. 2, ASME, New York, pp. 65–70.
- Ito, H. (1959). Friction Factors for Turbulent Flow in Curved Pipes, *Trans. ASME, J. Basic Eng.*, 81, 123–134.
- Itoh, M., and Kimura, H. (1979). Boiling Heat Transfer and Pressure Drop in Internal Spiral-Grooved Tubes, *Bull. Jpn. Soc. Mech. Eng.*, 22(171), 1251–1257.
- Itoh, M., Shikazono, N., and Uchida, M. (1997). Enhancement of Condensation Heat Transfer in a Horizontal Micro-fin Tube for Zeotropic Refrigerant Mixtures, *Proc. Oji International Seminar*, Japan, pp. 233–238.
- Janssen, L. A. M., and Hoogenedoorn, C. J. (1978). Laminar Convective Heat Transfer in Helical Coiled Tubes, *Int. J. Heat Mass Transfer*, 21, 1179–1206.
- Jensen, M. K. (1980). Boiling Heat Transfer and Critical Heat Flux in Helical Coils, Ph.D. dissertation, Iowa State University, Ames, IA.
- Jensen, M. K. (1984). A Correlation for Predicting Critical Heat Flux Condition with Twisted Tape Swirl Generators, *Int. J. Heat Mass Transfer*, 27(11), 2171–2173.
- Jensen, M. K., and Bensler, H. P. (1986). Saturated Forced Convective Boiling Heat Transfer with Twisted Tape Inserts, *J. Heat Transfer*, 108, 93–99.
- Jensen, M. K., and Bergles, A. E. (1981). Critical Heat Flux in Helically Coiled Tubes, *J. Heat Transfer*, 103, 660–666.
- Jensen, M. K., and Bergles, A. E. (1982). Critical Heat Flux in Helical Coils with a Circumferential Heat Flux Tilt toward the Outside Surface, *Int. J. Heat Mass Transfer*, 25, 1383–1395.

- Jensen, M. K., and Shome, B. (1994). Literature Survey on Heat Transfer Enhancement Techniques in Refrigeration Applications, *Report ORNL/Sub/91-SL794*, Oak Ridge National Laboratory, Oak Ridge, TN.
- Jensen, M. K., Trewin, R. R., and Bergles, A. E. (1992). Crossflow Boiling in Enhanced Tube Bundles, in *Two-Phase Flow in Energy Systems*, ASME-HTD-220, ASME, New York, pp. 11–17.
- Jones, T. B. (1978). Electrohydrodynamically Enhanced Heat Transfer in Liquids: A Review, *Adv. Heat Transfer*, 14, 107–148.
- Joshi, S. D., and Bergles, A. E. (1981). Analytical Study of Laminar Flow Heat Transfer to Pseudoplastic Fluids with Uniform Wall Temperature, *AIChE Symp. Ser.*, 77(208), 114–122.
- Joule, J. P. (1861). On the Surface Condensation of Steam, *Philos. Trans. R. Soc. London*, 151, 133–160.
- Junkhan, G. H., Bergles, A. E., Nirmalan, V., and Hanno, W. (1988). Performance Evaluation of the Effects of a Group of Turbulator Inserts on Heat Transfer from Gases in Tubes, *ASHRAE Trans.*, 94(2), 1195–1201.
- Kabata, Y., Nakajima, R., and Shioda, K. (1996). Enhancement of Critical Heat Flux for Flow Boiling of Water in Tubes with a Twisted Tape and Helically Coiled Wire, *Proc. ASME-JSME 4th International Conference on Nuclear Engineering*, Vol. 1, Pt. B, 639–646.
- Kakaç, S., and Liu, H. (2002). *Heat Exchangers: Selection, Rating, and Thermal Design*, 2nd ed., CRC Press, Boca Raton, FL.
- Kakaç, S., Bergles, A. E., and Oliveira Fernandes, E. (1988). *Two-Phase Flow Heat Exchangers: Thermal-Hydraulic Fundamentals and Design*, Kluwer Academic, Dordrecht, The Netherlands.
- Kakaç, S., Bergles, A. E., Mayinger, F., and Yüncü, H. (1999). *Heat Transfer Enhancement of Heat Exchangers*, Kluwer Academic, Dordrecht, The Netherlands.
- Kandlikar, S. G., Shoji, M., and Dhiri, V. K. (1999). *Handbook of Phase Change: Boiling and Condensation*, Taylor & Francis, Philadelphia.
- Kang, Y. T., and Christensen, R. N. (2000). The Effect of Fluid Property Variations on Heat Transfer in Annulus Side of a Spirally Fluted Tube, *J. Enhanced Heat Transfer*, 7(1), 1–9.
- Karayiannis, T. G., and Xu, Y. (1998a). Electric Field Effect in Boiling Heat Transfer, A: Simulation of the Electric Field and Electric Forces, *J. Enhanced Heat Transfer*, 5(4), 217–229.
- Karayiannis, T. G., and Xu, Y. (1998b). Electric Field Effect in Boiling Heat Transfer, B: Electrode Geometry, *J. Enhanced Heat Transfer*, 5(4), 213–247.
- Katz, D. L., Meyers, J. E., Young, E. H., and Balekjian, G. (1955). Boiling outside Finned Tubes, *Pet. Refiner*, 34, 113–116.
- Kays, W. M., and London, A. L. (1984). *Compact Heat Exchangers*, 3rd ed., McGraw-Hill, New York.
- Kedzierski, M. A. (1993). Simultaneous Visual and Calorimetric Measurements of R-11, R-123, and R-123 Alkylbenzene Nucleate Flow Boiling, in *Heat Transfer with Alternative Refrigerants*, ASME-HTD-423, ASME, New York, pp. 27–33.
- Kedzierski, M. A., and Goncalves, J. M. (1997). Horizontal Convective Condensation of Alternative Refrigerants within a Micro-fin Tube, *NISTIR 6095*, National Institute of Standards and Technology, Gaithersburg, MD.

- Kedzierski, M. A., and Kim, M. S. (1997). Convective Boiling and Condensation Heat Transfer with a Twisted-Tape Insert for R12, R22, R152a, R134a, R290, R32/R134a, R32/R152a, R290/R134a, R134a/R600a, *Report NISTIR 5905*, National Institute of Standards and Technology, Gaithersburg, MD.
- Kelkar, K. M., and Patankar, S. V. (1990). Numerical Prediction of Fluid Flow and Heat Transfer in a Circular Tube with Longitudinal Fins Interrupted in the Streamwise Direction, *J. Heat Transfer*, 112, 342–348.
- Kemeny, G. A., and Cyphers, J. A. (1961). Heat Transfer and Pressure Drop in an Annulus Gap with Surface Spoilers, *J. Heat Transfer*, 83, 189–198.
- Kenning, D. B. R., and Kao, Y. S. (1972). Convective Heat Transfer to Water Containing Bubbles: Enhancement Not Dependent on Thermocapillarity, *Int. J. Heat Mass Transfer*, 15, 1709–1718.
- Kern, D. Q., and Kraus, A. D. (1972). *Extended Surface Heat Transfer*, McGraw-Hill, New York.
- Kettner, I. J., Degani, D., and Guffinger, G. (1991). Numerical Study of Heat Transfer in Internally Finned Tubes, *Numer. Heat Transfer*, A20, 159–180.
- Khanpara, J. C., Bergles, A. E., and Pate, M. D. (1986). Augmentation of R-113 In-Tube Condensation with Micro-fin Tubes, in *Heat Transfer in Air Conditioning and Refrigeration Equipment*, ASME-HTD-65, ASME, New York, pp. 21–32.
- Kim, C.-J., and Bergles, A. E. (1985). Structured Surfaces for Enhanced Nucleate Boiling, *Report HTL-36, ISU-ERI-Ames-86220*, Iowa State University, Ames, IA.
- Kim, N.-H., and Choi, K.-K. (2001). Nucleate Pool Boiling on Structured Enhanced Tubes Having Pores with Connecting Gaps, *Int. J. Heat Mass Transfer*, 44(1), 17–28.
- Kitto, J. B., and Wiener, M. (1982). Effects of Nonuniform Circumferential Heating and Inclination on Critical Heat Flux in Smooth and Ribbed Bore Tubes, in *Heat Transfer*, 1982, Vol. 4, Hemisphere Publishing, New York, pp. 297–302.
- Koch, R. (1958). Druckverlust und Wärmeübergang bei verwirbelter Strömung, *VDI Forschungsh.*, B24(469), 1–44.
- Kovalev, S. A., Solov'yev, S. L., and Ovodkov, O. A. (1990). Theory of Boiling Heat Transfer on a Capillary Porous Surface, *Proc. 9th International Heat Transfer Conference*, Vol. 2, pp. 105–110.
- Kraus, A. D. (1982). *Analysis and Evaluation of Extended Surface Thermal Systems*, Hemisphere Publishing, New York.
- Kraus, A. D., and Bar-Cohen, A. (1995). *Design and Analysis of Heat Sinks*, Wiley, New York.
- Kraus, A. D., Aziz, A., and Welty, J. (2001). *Extended Surface Heat Transfer*, Wiley, New York.
- Kryukov, Y. V., and Boykov, G. P. (1973). Augmentation of Heat Transfer in an Acoustic Field, *Heat Transfer Sov. Res.*, 5(1), 26–28.
- Kubair, V., and Kuloor, N. R. (1963). Pressure Drop and Heat Transfer in Spiral Tube Coils, *Indian J. Technol.*, 1, 336–338.
- Kubair, V., and Kuloor, N. R. (1966a). Comparison of Performance of Helical and Spiral Coil Heat Exchangers, *Indian J. Technol.*, 4, 1–8.
- Kubair, V., and Kuloor, N. R. (1966b). Heat Transfer to Newtonian Fluids in Coiled Pipes in Laminar Flow, *Int. J. Heat Mass Transfer*, 9, 63–75.
- Kubaneck, G. R., and Milette, D. L. (1979). Evaporative Heat Transfer and Pressure Drop Performance of Internally-Finned Tubes with Refrigerant 22, *J. Heat Transfer*, 101, 447–452.

- Kulenovic, R., Mertz, R., and Groll, M. (2002). High Speed Flow Visualization of Pool Boiling from Structured Tubular Heat Transfer Surfaces, *Exp. Therm. Fluid Sci.*, 25(7), 547–555.
- Kumagai, M., Amano, R. S., and Jensen, M. K. (2002). Heat Transfer Enhancement by Turbulent Impinging Jets Using a Universal Function Method, *J. Enhanced Heat Transfer*, 9(1), 47–55.
- Kun, L. C., and Czikk, A. M. (1969). Surface for Boiling Liquids, U.S. patent 3,454,081 (reissued Aug. 21, 1979, Re. 30,077).
- Kun, L. C., and Ragi, E. G. (1981). Enhancement for Film Condensation Apparatus, U.S. patent 4,253,519.
- Kurihari, H. M., and Meyers, J. E. (1960). Effects of Superheat and Roughness on the Boiling Coefficients, *AIChE J.*, 6(1), 83–91.
- Kwon, J. T., Park, S. K., and Kim, M. H. (2000). Enhanced Effect of a Horizontal Micro-fin Tube for Condensation Heat Transfer with R-22 and R-410A, *J. Enhanced Heat Transfer*, 7(2), 97–107.
- Lan, J., Disimile, P., and Weisman, J. (1997). Two Phase Flow Patterns and Boiling Heat Transfer in Tubes Containing Helical Wire Insets, II: Critical Heat Flux Studies, *J. Enhanced Heat Transfer*, 4(2), 283–296.
- Larson, M. B., and London, A. L. (1962). A Study of the Effects of Ultrasonic Vibrations on Convection Heat Transfer to Liquids, *ASME-62-HT-44*, ASME, New York.
- Lavin, J. G., and Young, E. H. (1965). Heat Transfer to Evaporating Refrigerants in Two-Phase Flow, *AIChE J.*, 11, 1124–1132.
- Lee, B. H., and Richardson, P. D. (1965). Effect of Sound on Heat Transfer from a Horizontal Circular Cylinder at Large Wavelength, *J. Mech. Eng. Sci.*, 7, 127–130.
- Le Fevre, E. J., and Rose, J. W. (1966). A Theory of Heat-Transfer by Dropwise Condensation, *Proc. 3rd International Heat Transfer Conference*, Vol. 2, pp. 362–375.
- Lemlich, R., and Rao, M. A. (1965). The Effect of Transverse Vibration on Free Convection from a Horizontal Cylinder, *Int. J. Heat Mass Transfer*, 8, 27–33.
- Lewis, M. J. (1974). Roughness Functions, the Thermohydraulic Performance of Rough Surfaces and the Hall Transformation: An Overview, *Int. J. Heat Mass Transfer*, 17, 809–814.
- Li, K. W., and Parker, J. D. (1967). Acoustical Effects on Free Convective Heat Transfer from a Horizontal Wire, *J. Heat Transfer*, 89, 277–278.
- Li, P.-W., Kawaguchi, Y., and Yabe, A. (2001). Transitional Heat Transfer and Turbulent Characteristics of Drag-Reducing Flow through a Contracted Channel, *J. Enhanced Heat Transfer*, 8, 23–40.
- Lin, S. T., Fan, L. T., and Azer, N. Z. (1978). Augmentation of Single Phase Convective Heat Transfer with In-Line Static Mixers, *Proc. 1978 Heat Transfer and Fluid Mechanics Institute*, Stanford University Press, Stanford, CA, pp. 117–130.
- Lin, Y.-L., Shih, T. I.-P., Stephens, M. A., and Chyu, M. K. (2001). A Numerical Study of Flow and Heat Transfer in a Smooth and Ribbed U-Duct with and without Rotation, *J. Heat Transfer*, 123(2), 219–232.
- Liou, T.-M., and Hwang, J.-J. (1992). Developing Heat Transfer and Friction in a Ribbed Rectangular Duct with Flow Separation at Inlet, *J. Heat Transfer*, 114(3), 565–573.
- Liu, X., and Jensen, M. K. (1999). Numerical Investigation of Turbulent Flow and Heat Transfer in Internally Finned Tubes, *J. Enhanced Heat Transfer*, 6(2/4), 105–119.
- Liu, X., and Jensen, M. K. (2001). Geometry Effects on Turbulent Flow and Heat Transfer in Internally Finned Tubes, *J. Heat Transfer*, 123(6), 1035–1044.

- Liu, X., Ma, T., and Wu, J. (1987). Effects of Porous Layer Thickness of Sintered Screen Surfaces on Nucleate Boiling Characteristics, in *Heat Transfer Science and Technology*, B-X. Wang, ed., Hemisphere Publishing, New York, pp. 577–583.
- Lokshin, V. A., and Fomina, V. N. (1978). Correlation of Experimental Data on Finned Tube Bundles, *Teploenergetika*, 6, 36–39.
- Lopina, R. F., and Bergles, A. E. (1969). Heat Transfer and Pressure Drop in Tape Generated Swirl Flow of Single-Phase Water, *J. Heat Transfer*, 91, 434–442.
- Lopina, R. F., and Bergles, A. E. (1973). Subcooled Boiling of Water in Tape Generated Swirl Flow, *J. Heat Transfer*, 95, 281–283.
- Lowery, A. J., Jr., and Westwater, J. W. (1957). Heat Transfer to Boiling Methanol: Effect of Added Agents, *Ind. Eng. Chem.*, 19, 1445–1448.
- Luu, M., and Bergles, A. E. (1979). Experimental Study of the Augmentation of the In-Tube Condensation of R-113, *ASHRAE Trans.*, 85(2), 132–146.
- Luu, M., and Bergles, A. E. (1980). Enhancement of Horizontal In-Tube Condensation of R-113, *ASHRAE Trans.*, 86(1), 293–312.
- Luu, M., and Bergles, A. E. (1981). Augmentation of In-Tube Condensation of R-113 by Means of Surface Roughness, *ASHRAE Trans.*, 87(2), 33–50.
- Ma, T., Liu, X., and Li, H. (1986). Effects of Geometrical Shapes and Parameters of Reentrant Grooves on Nucleate Pool Boiling Heat Transfer from Porous Surfaces, in *Heat Transfer 1986*, Vol. 4, pp. 2013–2018.
- MacBain, S. M., Bergles, A. E., and Raina, S. (1997). Heat Transfer and Pressure Drop Characteristics of Flow Boiling in a Horizontal Deep Spirally Fluted Tube, *HVAC&R Res.*, 3(1), 65–80.
- Manglik, R. M. (1998). Pool Boiling Characteristics of High Concentration Aqueous Surfactant Emulsions, in *Heat Transfer 1998*, Vol. 2, KSME, Seoul, Korea, pp. 449–453.
- Manglik, R. M., and Bergles, A. E. (1990). The Thermal-Hydraulic Design of the Rectangular Offset-Strip-Fin Compact Heat Exchanger, in *Compact Heat Exchangers*, (Shah, R. K., Kraus, A. D., and Metzger, D., eds.), Hemisphere Publishing, New York, pp. 123–149.
- Manglik, R. M., and Bergles, A. E. (1991). Heat Transfer Enhancement of Intube Flows in Process Heat Exchangers by Means of Twisted-Tape Inserts, *Report HTL-8*, Heat Transfer Laboratory, Rensselaer Polytechnic Institute, Troy, NY.
- Manglik, R. M., and Bergles, A. E. (1992). Heat Transfer Enhancement and Pressure Drop in Viscous Liquid Flows in Isothermal Tubes with Twisted-Tape Inserts, *Waerme Stoffuebertrag.*, 27, 249–257.
- Manglik, R. M., and Bergles, A. E. (1993a). Heat Transfer and Pressure Drop Correlations for Twisted-Tape Inserts in Isothermal Tubes, I: Laminar Flows, *J. Heat Transfer*, 115(4), 881–889.
- Manglik, R. M., and Bergles, A. E. (1993b). Heat Transfer and Pressure Drop Correlations for Twisted-Tape Inserts in Isothermal Tubes, II: Transition and Turbulent Flows, *J. Heat Transfer*, 115(4), 890–896.
- Manglik, R. M., and Bergles, A. E. (1995). Heat Transfer and Pressure Drop Correlations for the Rectangular Offset-Strip-Fin Compact Heat Exchanger, *Exp. Therm. Fluid Sci.*, 10(2), 171–180.
- Manglik, R. M., and Bergles, A. E. (2002a). Swirl Flow Heat Transfer and Pressure Drop with Twisted-Tape Inserts, in *Advances in Heat Transfer*, Vol. 36, Academic Press, New York, pp. 183–266.

- Manglik, R. M., and Bergles, A. E. (2002b). Enhanced Heat Transfer in the New Millenium: A Review of the 2001 Literature, Thermal-Fluids and Thermal Processing Laboratory Report No. TFTPL-EB01, University of Cincinnati, Cincinnati, OH.
- Manglik, R. M., and Fang, P. (2002). Thermal Processing of Viscous Non-Newtonian Fluids in Annular Ducts: Effects of Power-Law Rheology, Duct Eccentricity, and Thermal Boundary Conditions, *Int. J. Heat Mass Transfer*, 45(4), 803–814.
- Manglik, R. M., and Kraus, A. D. (1996). *Process, Enhanced, and Multiphase Heat Transfer*, Begell House, New York.
- Manglik, R. M., and Prusa, J. (1995). Viscous Dissipation in Non-Newtonian Flows: Implications for the Nusselt Number, *J. Thermophys. Heat Transfer*, 9(4), 733–742.
- Manglik, R. M., and Ranganathan, C. (1997). Visualization of Swirl Flows Generated by Twisted-Tape Inserts in Circular Tubes, in *Experimental Heat Transfer, Fluid Mechanics and Thermodynamics, 1997*, (Giot, M., Mayinger, F., and Celata, G. P., eds.), Edizioni ETFS, Pisa, Italy, pp. 1631–1636.
- Manglik, R. M., and You, L. (2002). Computational Modeling of Laminar Swirl Flows and Heat Transfer in Circular Tubes with Twisted-Tape Inserts, *Report TFTPL-7*, Thermal-Fluids and Thermal Processing Laboratory, University of Cincinnati, Cincinnati, OH.
- Manglik, R. M., and Yerra, K. (2002). Application of Twisted-Tape Inserts in Shell-and-Tube Exchangers: Optimization of Enhanced Thermal-Hydraulic Performance, Thermal-Fluids and Thermal Processing Laboratory Report No. TFTPL-8, University of Cincinnati, Cincinnati, OH.
- Manglik, R. M., Ravigururajan, T. S., Muley, A., Papar, R. A., and Kim, J. (2000). *Advances in Enhanced Heat Transfer, 2000*, ASME, New York.
- Manglik, R. M., Maramaju, S., and Bergles, A. E. (2001a). The Scaling and Correlation of Low Reynolds Number Swirl Flows and Friction Factors in Circular Tubes with Twisted-Tape Inserts, *J. Enhanced Heat Transfer*, 8(6) (in press).
- Manglik, R. M., Wasekar, V. M., and Zhang, J. (2001b). Dynamic and Equilibrium Surface Tension of Aqueous Surfactant and Polymeric Solutions, *Exp. Therm. Fluid Sci.*, 25(1/2), 55–64.
- Manlapaz, R. L., and Churchill, S. W. (1980). Fully Developed Laminar Flow in a Helically Coiled Tube of Finite Pitch, *Chem. Eng. Commun.*, 7, 57–78.
- Manlapaz, R. L., and Churchill, S. W. (1981). Fully Developed Laminar Convection from a Helical Coil, *Chem. Eng. Commun.*, 9, 185–200.
- Marner, W. J., and Bergles, A. E. (1978). Augmentation of Tubeside Laminar Flow Heat Transfer by Means of Twisted-Tape Inserts, Static-Mixer Inserts and Internally Finned Tubes, *Heat Transfer 1978*, Vol. 2, Hemisphere Publishing, Washington, DC, pp. 583–588.
- Marner, W. J., and Bergles, A. E. (1989). Augmentation of Highly Viscous Laminar Heat Transfer inside Tubes with Constant Wall Temperature, *Exp. Therm. Fluid Sci.*, 2, 252–257.
- Marner, W. J., Bergles, A. E., and Chenoweth, J. M. (1983). On the Presentation of Performance Data for Enhanced Tubes Used in Shell-and-Tube Heat Exchangers, *J. Heat Transfer*, 105, 358–365.
- Martinelli, R. C., and Boelter, L. M. K. (1939). The Effect of Vibration on Heat Transfer by Free Convection from a Horizontal Cylinder, *Heat. Piping Air Cond.*, 11, 525–527.
- Marto, P. J. (1988). An Evaluation of Film Condensation on Horizontal Integral-Fin Tubes, *J. Heat Transfer*, 110, 1287–1305.

- Marto, P. J., and Rohsenow, W. M. (1966). Effects of Surface Conditions on Nucleate Pool Boiling of Sodium, *J. Heat Transfer*, 88, 196–204.
- Marto, P. J., Looney, D. J., Rose, J. W., and Wanniarachchi, A. (1986). Evaluation of Organic Coatings for the Promotion of Dropwise Condensation of Steam, *Int. J. Heat Mass Transfer*, 29(8), 1109–1117.
- Masliyah, J. H., and Nandakumar, K. (1976). Heat Transfer in Internally Finned Tubes, *J. Heat Transfer*, 98, 257–261.
- Masliyah, J. H., and Nandakumar, K. (1977). Fluid Flow and Heat Transfer in Internally Finned Helical Coils, *Can. J. Chem. Eng.*, 55, 27–36.
- Mathewson, W. F., and Smith, J. C. (1963). Effect of Sonic Pulsation on Forced Convective Heat Transfer to Air and on Film Condensation of Isopropanol, *Chem. Eng. Prog. Symp. Ser.*, 41(59), 173–179.
- Matzner, B., Casterline, J. E., Moek, E. O., and Wikhammer, G. A. (1965). Critical Heat Flux in Long Tubes at 1000 psi, *ASME-65-WA/HT-30*, ASME, New York.
- McAdams, W. H. (1954). *Heat Transmission*, 3rd ed., McGraw-Hill, New York, p. 267.
- McElhiney, J. E., and Preckshot, G. W. (1977). Heat Transfer in the Entrance Length of a Horizontal Rotating Tube, *Int. J. Heat Mass Transfer*, 20, 847–854.
- McQuiston, F. C., and Parker, J. D. (1967). Effect of Vibration on Pool Boiling, *ASME-67-HT-49*, ASME, New York.
- Medwell, J. O., and Nicol, A. A. (1965). Surface Roughness Effects on Condensate Films, *ASME-65-HT-43*, ASME, New York.
- Megerlin, F. E., Murphy, R. W., and Bergles, A. E. (1974). Augmentation of Heat Transfer in Tubes by Means of Mesh and Brush Inserts, *J. Heat Transfer*, 96, 145–151.
- Mehta, M. H., and Raja Rao, M. (1979). Heat Transfer and Frictional Characteristics of Spirally Enhanced Tubes for Horizontal Condensers, in *Advances in Enhanced Heat Transfer*, J. M. Chenoweth et al., eds., ASME, New York, pp. 11–22.
- Menze, K., Fujii, M., and Webb, R. L. (1994). Review of Patents in Europe, Japan, and the U.S. for 1992, *J. Enhanced Heat Transfer*, 1(2), 135–143.
- Metwally, H. M., and Manglik, R. M. (2000). Numerical Solutions for Periodically-Developed Laminar Flow and Heat Transfer in Sinusoidal Corrugated Plate Channels with Constant Wall Temperature, *Proc. 34th National Heat Transfer Conference*, ASME, New York, Paper NHTC 2000-12216.
- Milton, R. M. (1971). Heat Exchange System with Porous Boiling Layer, U.S. patent 3,587,730.
- Min, K., and Chao, B. T. (1966). Particle Transport and Heat Transfer in Gas–Solid Suspension Flow under the Influence of an Electric Field, *Nucl. Sci. Eng.*, 26, 534–546.
- Min, J., and Webb, R. L. (2001). Numerical Predictions of Wavy Fin Coil Performance, *J. Enhanced Heat Transfer*, 8(3), 2001.
- Miropolskii, Z. L., and Kurbanmukhamedov, A. (1975). Heat Transfer with Condensation of Steam within Coils, *Therm. Eng.*, 5, 111–114.
- Mishra, P., and Gupta, S. N. (1979). Momentum Transfer in Curved Pipes, 1: Newtonian Fluids; 2: Non-Newtonian Fluids, *Ind. Eng. Chem. Process Des. Dev.*, 18, 130–142.
- Morgan, A. I., Bromley, L. A., and Wilke, C. R. (1949). Effect of Surface Tension on Heat Transfer in Boiling, *Ind. Eng. Chem.*, 41, 2767–2769.
- Mori, Y., and Nakayama, W. (1965). Study on Forced Convective Heat Transfer in Curved Pipes (1st Report, Laminar Region), *Int. J. Heat and Mass Transfer*, 8, 67–82.

- Mori, Y., and Nakayama, W. (1967a). Study on Forced Convective Heat Transfer in Curved Pipes (2nd Report, Turbulent Region), *Int. J. Heat Mass Transfer*, 10, 37–59.
- Mori, Y., and Nakayama, W. (1967b). Study on Forced Convective Heat Transfer in Curved Pipes (3rd Report, Theoretical Analysis under the Condition of Uniform Wall Temperature and Practical Formulae), *Int. J. Heat Mass Transfer*, 10, 681–695.
- Mori, Y., and Nakayama, W. (1967c). Forced Convection Heat Transfer in a Straight Pipe Rotating around a Parallel Axis, *Int. J. Heat Mass Transfer*, 10, 1179–1194.
- Mori, Y., Hijikata, K., Hirasawa, S., and Nakayama, W. (1981). Optimized Performance of Condensers with Outside Condensing Surfaces, *J. Heat Transfer*, 103, 96–102.
- Muley, A., Borghese, J. B., Manglik, R. M., and Kundu, J. (2002). Experimental and Numerical Investigation of Thermal–Hydraulic Characteristics of a Wavy-Channel Compact Heat Exchanger Heat Transfer 2002, *Proc. 12th International Heat Transfer Conference*, (4), 417–422.
- Muralidhar, Rao, M., and Sastri, V. M. K. (1995). Experimental Investigation of Fluid Flow and Heat Transfer in a Rotating Tube with Twisted-Tape Inserts, *Heat Transfer Eng.*, 16(2), 19–28.
- Murata, A., and Mochizuki, S. (2001). Large Eddy Simulation of Heat Transfer in an Orthogonally Rotating Square Duct with Angled Rib Turbulators, *J. Heat Transfer*, 123(5), 858–867.
- Murphy, R. W., and Truesdale, K. L. (1972). The Mechanism and the Magnitude of Flow Boiling Augmentation in Tubes with Discrete Surface Roughness Elements (III), *Report B12-7294*, Raytheon Co., Bedford, MA.
- Nakamura, H., and Tanaka, M. (1973). Cross-Rifled Vapor Generating Tube, U.S. patent 3,734,140.
- Nakayama, W., and Bergles, A. E. (1990). Cooling Electronic Equipment: Past, Present and Future, in *Electronic and Microelectronic Equipment*, A. E. Bergles, ed., Hemisphere Publishing, New York, pp. 3–39.
- Nakayama, W., Daikoku, T., Kuwahara, H., and Kakizaki, K. (1975). High-Flux Heat Transfer Surface Thermoexcel, *Hitachi Rev.*, 24, 329–333.
- Nakayama, W., Daikoku, T., Kuwahara, H., and Nakajima, T. (1980a). Dynamic Model of Enhanced Boiling Heat Transfer on Porous Surfaces, I: Experimental Investigation, *J. Heat Transfer*, 102, 445–450.
- Nakayama, W., Daikoku, T., Kuwahara, H., and Nakajima, T. (1980b). Dynamic Model of Enhanced Boiling Heat Transfer on Porous Surfaces, II: Analytical Modeling, *J. Heat Transfer*, 102, 451–456.
- Nandakumar, K., and Masliyah, J. H. (1982). Bifurcation in Steady Laminar Flow through Curved Tubes, *J. Fluid Mech.*, 119, 475–490.
- Nandakumar, K., and Masliyah, J. H. (1986). Swirling Flow and Heat Transfer in Coiled and Twisted Pipes, in *Advances in Transport Processes*, A. S. Mujumdar and R. A. Mashelkar, eds., Vol. IV, Wiley Eastern, New Delhi, India, pp. 49–112.
- Nelson, R. M., and Bergles, A. E. (1986). Performance Evaluation for Tubeside Heat Transfer Enhancement of a Flooded Evaporator Water Chiller, *ASHRAE Trans.*, 92(1B), 739–755.
- Nelson, D. A., Zia, S., Whipple, R. L., and Ohadi, M. M. (2000). Corona Discharge Effects on Heat Transfer and Pressure Drop in Tube Flows, *J. Enhanced Heat Transfer*, 7(2), 81–95.
- Newson, I. H. (1978). Heat Transfer Characteristics of Horizontal Tube Multiple Effects (HTME) Evaporators: Possible Enhanced Tube Profiles, *Proc. 6th International Symposium on Fresh Water from the Sea*, Vol. 2, pp. 113–124.

- Newson, I. H., and Hodgson, T. D. (1973). The Development of Enhanced Heat Transfer Condenser Tubing, *Desalination*, 14, 291–323.
- Newton, D. C., and Allen, P. H. G. (1977). Senftleben Effect in Insulating Oil under Uniform Electric Stress, *Lett. Heat Mass Transfer*, 4(1), 9–16.
- Nicol, A. A., and Gacesa, M. (1970). Condensation of Steam on a Rotating Vertical Cylinder, *J. Heat Transfer*, 97, 144–152.
- Nicol, A. A., and Medwell, J. O. (1966). The Effect of Surface Roughness on Condensing Steam, *Can. J. Chem. Eng.*, 44(6), 170–173.
- Nikuradse, J. (1933). Strömungsgesetze in rauhen Rohren, *Forsch. Arb. Ing. Wes.*, 361; English translation as *NACA-TM-1292* (1965).
- Nirmalan, V., Junkhan, G. H., and Bergles, A. E. (1986). Investigation of the Effects of Turbulence-Producing Inserts on Heat Transfer in Tubes with Application to Fire-Tube Boilers, *ASHRAE Trans.*, 92(1B), 791–809.
- Nishikawa, K., Ito, T., and Tanaka, K. (1983). Augmented Heat Transfer by Nucleate Boiling at Prepared Surfaces, *Proc. 1983 ASME-JSME Thermal Engineering Conference*, Vol. 1, ASME, New York, pp. 387–393.
- Nishimura, T., Kunitsugu, K., and Morega, A. M. (1998). Fluid Mixing and Mass Transfer Enhancement in Grooved Channels for Pulsatile Flow, *J. Enhanced Heat Transfer*, 5(1), 23–37.
- Notaro, P. (1979). Enhanced Condensation Heat Transfer Device and Method, U.S. patent 4,154,294.
- OGata, J., and Yabe, A. (1993). Basic Study on the Enhancement of Nucleate Boiling Heat Transfer by Applying Electric Fields, *Int. J. Heat Mass Transfer*, 36(3), 775–782.
- Ohadi, M. M., Li, S. S., and Dessiatoun, S. (1994). Electrostatic Heat Transfer Enhancement in a Tube Bundle Gas-to-Gas Heat Exchanger, *J. Enhanced Heat Transfer*, 1, 327–335.
- Oktay, S., and Schmeckenbecher, A. F. (1974). Preparation and Performance of Dendritic Heat Sinks, *J. Electrochem. Soc.*, 21, 912–918.
- Oliver, D. R., and Aldington, R. W. J. (1986). Enhancement of Laminar Flow Heat Transfer Using Wire Matrix Turbulators, in *Heat Transfer 1986*, Vol. 6, Hemisphere Publishing, Washington, DC, pp. 2897–2902.
- Olsson, C.-O., and Sundén, B. (1998). Experimental Study of Flow and Heat Transfer in Rib-Roughened Rectangular Channels, *Exp. Therm. Fluid Sci.*, 16, 349–365.
- Ornatskii, A. P., and Shcherbakov, V. K. (1959). Intensification of Heat Transfer in the Critical Region with the Aid of Ultrasonics, *Teploenergetika*, 6(1), 84–85.
- Pabisz, R. A., Jr., and Bergles, A. E. (1996). Enhancement of Critical Heat Flux in Subcooled Flow Boiling Using Alcohol Additives and Twisted-Tape Inserts, *Report HTL-25*, Heat Transfer Laboratory, Rensselaer Polytechnic Institute, Troy, NY.
- Pabisz, R. A., Jr., and Bergles, A. E. (1997). Using Pressure Drop to Predict the Critical Heat Flux in Multiple Tube, Subcooled Boiling Systems, in *Experimental Heat Transfer, Fluid Mechanics and Thermodynamics*, 1997, (Giot, M., Mayinger, F., and Celata, C. P., eds.), Edizioni ETS, Pisa, Italy, pp. 851–858.
- Pahl, M. H., and Muschelknaute, E. (1979). Einsatz und Auslegung statischer Mischers, *Chem. Ing. Tech.*, 51, 347–364.
- Pais, C., and Webb, R. L. (1991). Literature Survey of Pool Boiling on Enhanced Surfaces, *ASHRAE Trans.*, 97, Pt. 1, 79–89.

- Patankar, S. V., Ivanovic, M., and Sparrow, E. M. (1979). Analysis of Turbulent Flow and Heat Transfer in Internally Finned Tubes and Annuli, *J. Heat Transfer*, 101, 29–37.
- Pearson, J. F., and Young, E. H. (1970). Simulated Performance of Refrigerant-22 Boiling inside of Tubes in a Four Pass Shell and Tube Heat Exchanger, *AIChE Symp. Ser.*, 66(102), 164–173.
- Poulter, R., and Allen, P. H. G. (1986). Electrohydrodynamically Augmented Heat and Mass Transfer in the Shell/Tube Heat Exchanger, in *Heat Transfer 1986*, Vol. 6, Hemisphere Publishing, Washington, DC, pp. 2963–2968.
- Prakash, C., and Liu, Y.-D. (1985). Analysis of Laminar Flow and Heat Transfer in the Entrance Region of an Internally Finned Circular Duct, *J. Heat Transfer*, 107, 84–91.
- Prakash, C., and Zerkle, R. (1995). Prediction of Turbulent Flow and Heat Transfer in Ribbed Rectangular Duct with and without Rotation, *J. Turbomachinery*, 117, 255–264.
- Price, D. C., and Parker, J. D. (1967). Nucleate Boiling on a Vibrating Surface, *ASME-67-HT-58*, ASME, New York.
- Prusa, J., and Manglik, R. M. (1994). Asymptotic and Numerical Solutions for Thermally Developing Flows of Newtonian and Non-Newtonian Fluids in Circular Tubes, *Num. Heat Transfer*, A26(2), 199–217.
- Prusa, J., and Yao, L. S. (1982). Numerical Solution for Fully Developed Flow in Heated Curved Tubes, *J. Fluid Mech.*, 123, 503–522.
- Ragi, E. G. (1972). Composite Structure for Boiling Liquids and Its Formation, U.S. patent 3,684,007.
- Rao, K. S. (1983). Augmentation of Heat Transfer in the Axial Ducts of Electrical Machines with Tape Generated Swirl Flow, *IEEE Trans. Power Apparatus Syst.*, 102(8), 2750–2756.
- Ravigururajan, T. S., and Bergles, A. E. (1986). Study of Water-Side Enhancement for Ocean Thermal Energy Conversion Heat Exchangers, *Report HTL-44, ISU-ERI-Ames-87197*, Heat Transfer Laboratory, Iowa State University, Ames, IA.
- Ravigururajan, T. S., and Bergles, A. E. (1996). Development and Verification of General Correlations for Pressure Drop and Heat Transfer in Single-Phase Turbulent Flow in Enhanced Tubes, *Exp. Therm. Fluid Sci.*, 13, 55–70.
- Reynolds, B. L., and Holmes, R. E. (1976). Heat Transfer in a Corona Discharge, *Mech. Eng.*, Oct., pp. 44–49.
- Rifert, V. G., and Leont'yev, G. G. (1976). An Analysis of Heat Transfer with Steam Condensing on a Vertical Surface with Wires to Promote Heat Transfer, *Teploenergetika*, 23(4), 74–80.
- Robinson, G. C., McClude, C. M., III, and Hendricks, R., Jr. (1958). The Effects of Ultrasonics on Heat Transfer by Convection, *Am. Ceram. Soc. Bull.*, 37, 399–404.
- Rohsenow, W. M. (1985). Boiling, in *Handbook of Heat Transfer Fundamentals*, W. M. Rohsenow, J. P. Hartnett, and E. M. Ganic, eds., McGraw-Hill, New York, Chap. 12.
- Rose, J. W. (1988). Some Aspects of Dropwise Condensation Theory, *Int. Commun. Heat Mass Transfer*, 15, 449–473.
- Rose, J. W. (1994a). Condensation on Low-Finned Tubes: An Equation for Vapor-Side Enhancement, in *Condensation and Condenser Design*, ASME, New York, pp. 317–333.
- Rose, J. W. (1994b). An Approximate Equation for the Vapor-Side Heat Transfer Coefficient for Condensation on Low-Finned Tubes, *Int. J. Heat Mass Transfer*, 37, 865–875.
- Rose, J., Utaka, Y., and Tanasawa, I. (1999). Dropwise Condensation, in *Handbook of Phase*

- Change: Boiling and Condensation*, S. G. Kandlikar, M. Shoji, and V. K. Dhir, eds., Taylor & Francis, Philadelphia, Chap. 20.
- Royal, J. H., and Bergles, A. E. (1978a). Pressure Drop and Performance Evaluation of Augmented In-Tube Condensation, in *Heat Transfer 1978*, Vol. 2, Hemisphere Publishing, Washington, DC, pp. 459–464.
- Royal, J. H., and Bergles, A. E. (1978b). Augmentation of Horizontal In-Tube Condensation by Means of Twisted-Tape Inserts and Internally-Finned Tubes, *J. Heat Transfer*, 100, 17–24.
- Rustum, I. M., and Soliman, H. M. (1988). Numerical Analysis of Laminar Forced Convection in the Entrance Region of Tubes with Longitudinal Internal Fins, *J. Heat Transfer*, 110, 310–313.
- Ryabov, A. N., Kamen'shchikov, F. T., Filipov, V. N., Chalykh, A. F., Yugay, T., Stolyarov, Y. V., Blagovestova, T. I., Mandrazhitskiy, V. M., and Yemelyanov, A. I. (1977). Boiling Crisis and Pressure Drop in Rod Bundles with Heat Transfer Enhancement Devices, *Heat Transfer Sov. Res.*, 9(1), 112–122.
- Said, S. A., and Azer, N. Z. (1983). Heat Transfer and Pressure Drop during Condensation inside Horizontal Tubes with Twisted-Tape Inserts, *ASHRAE Trans.*, 89, Pt. 1, 96–113.
- Said, M. N. A., and Trupp, A. C. (1984). Predictions of Turbulent Flow and Heat Transfer in Internally Finned Tubes, *Chem. Eng. Commun.*, 31, 65–99.
- Salim, M. M., France, D. M., and Panchal, C. B. (1999). Heat Transfer Enhancement on the Outer Surface of Spirally Indented Tubes, *J. Enhanced Heat Transfer*, 6(5), 327–341.
- San, J.-Y., and Lai, M.-D. (2001). Optimum Jet-to-Jet Spacing of Heat Transfer for Staggered Arrays of Impinging Air Jets, *Int. J. Heat Mass Transfer*, 44(21), 397–407.
- Sato, K., Mimatsu, J., and Kumada, M. (1999). Turbulent Characteristics and Heat Transfer Augmentation of Drag Reducing Surfactant Solution Flow, *Therm. Sci. Eng.*, 7(1), 41–51.
- Savkar, S. D. (1971). Dielectrophoretic Effects in Laminar Forced Convection between Two Parallel Plates, *Phys. Fluids*, 14, 2670–2679.
- Schlager, L. M., Pate, M. B., and Bergles, A. E. (1988). Evaporation and Condensation of Refrigerant–Oil Mixture in a Smooth Tube and a Micro-fin Tube, *ASHRAE Trans.*, 94(1), 149–166.
- Schlager, L. M., Pate, M. B., and Bergles, A. E. (1990). Evaporation and Condensation Heat Transfer and Pressure Drop in Horizontal, 12-7-mm Micro-fin Tubes with Refrigerant 22, *J. Heat Transfer*, 112, 1041–1047.
- Schlünder, E. U., and Chawla, M. (1969). Ortlicher Wärmeübergang und Druckabfall bei der Strömung verdampfender Kältemittel in innenberippten, waggerechten Rohren, *Kaeltetechn. Klim.*, 21(5), 136–139.
- Schmittle, K. V., and Starnner, T. E. (1978). Heat Transfer in Pool Boiling, U.S. patent 4,074,753.
- Sephton, H. H. (1971). Interface Enhancement for Vertical Tube Evaporator: A Novel Way of Substantially Augmenting Heat and Mass Transfer, *ASME-71-HT-38*, ASME, New York.
- Sephton, H. H. (1975). Upflow Vertical Tube Evaporation of Sea Water with Interface Enhancement: Process Development by Pilot Plant Testing, *Desalination*, 16, 1–13.
- Shah, R. K., and Joshi, S. D. (1987). Convective Heat Transfer in Curved Ducts, in *Handbook of Single-Phase Convective Heat Transfer*, (Kakaç, S., Shah, R. K., and Aung, W., eds.), Wiley, New York, Chap. 5.
- Shah, R. K., and London, A. L. (1978). *Laminar Flow Convection in Ducts*, Supplement 1 to *Advances in Heat Transfer*, T. F. Irvine, Jr., and J. P. Hartnett, eds., Academic Press, New York.

- Shah, R. K., Kraus, A. D., and Metzger, D. (1990). *Compact Heat Exchangers: A Festschrift for A.L. London*, Hemisphere Publishing, New York.
- Shah, R. K., Bell, K. J., Mochizuki, S., and Wadekar, V. V. (1997). *Compact Heat Exchangers for the Process Industries*, Begell House, New York.
- Shah, R. K., Zhou, S. Q., and Tagavi, K. A. (1999). The Role of Surface Tension in Film Condensation in Extended Surface Passages, *J. Enhanced Heat Transfer*, 6(2/4), 179–216.
- Shakir, S., Thome, J. R., and Lloyd, J. R. (1985). Boiling of Methanol–Water Mixtures on Smooth and Enhanced Surfaces, in *Multiphase Flow and Heat Transfer*, ASME-HTD-47, ASME, New York, pp. 1–6.
- Shatto, D. P., and Peterson, G. P. (1996). A Review of Flow Boiling Heat Transfer with Twisted Tape Inserts, *J. Enhanced Heat Transfer*, 3(4), 233–257.
- Shikazono, N., Itoh, M., Uchida, M., Fukushima, T., and Hatada, T. (1998). An Analytical Model to Predict the Condensation Heat Transfer Coefficient in Horizontal Micro-fin Tube, *ASHRAE Trans.*, 104(2), 143–152.
- Shinohara, Y., and Tobe, M. (1985). Development of an Improved Thermofin Tube, *Hitachi Cable Rev.*, 4, 47–50.
- Shinohara, Y., Oizumi, K., Itoh, Y., and Hori, M. (1987). Heat Transfer Tubes with Grooved Inner Surface, U.S. patent 4,658,892.
- Shivkumar, C., and Raja Rao, M. (1988). Studies on Compound Augmentation of Laminar Flow Heat Transfer to Generalized Power Law Fluids in Spirally Corrugated Tubes by Means of Twisted Tape Inserts, *Proc. 1988 National Heat Transfer Conference*, ASME-HTD-96, Vol. 1, ASME, New York, pp. 685–691.
- Shizuya, M., Itoh, M., and Hijikata, K. (1995). Condensation of Nonazeotropic Binary Refrigerant Mixtures including R22 as a More Volatile Component inside a Horizontal Tube, *J. Heat Transfer*, 117(2), 538–543.
- Shklover, G. G., and Gerasimov, A. V. (1963). Heat Transfer of Moving Steam in Coil-Type Heat Exchangers, *Teploenergetika*, 10(5), 62–65.
- Shome, B., and Jensen, M. K. (1996). Numerical Investigation of Laminar Flow and Heat Transfer in Internally Finned Tubes, *J. Enhanced Heat Transfer*, 4(1), 35–51.
- Sieder, E. N., and Tate, G. E. (1936). Heat Transfer and Pressure Drop of Liquids in Tubes, *Ind. Eng. Chem.*, 28, 1429–1435.
- Smith, E. M. (1997). *Thermal Design of Heat Exchangers*, Wiley, Chichester, West Sussex, England.
- Smithberg, E., and Landis, F. (1964). Friction and Forced Convection Heat Transfer Characteristics in Tubes with Twisted Tape Swirl Generators, *J. Heat Transfer*, 86, 39–49.
- Soliman, H. M. (1989). Performance Evaluation of Multipassage Tubes for Laminar Flow Applications, *J. Thermophys. Heat Transfer*, 3(4), 461–469.
- Soliman, H. M., and Feingold, A. (1977). Heat Transfer, Pressure Drop, and Performance Evaluation of Quintuplex Internally Finned Tube, *ASME-77-HT-46*, ASME, New York.
- Somerscales, E. F. C., and Bergles, A. E. (1997). Enhancement of Heat Transfer and Fouling Mitigation, *Adv. Heat Transfer*, 30, 197–253.
- Sprott, A. L., Holman, J. P., and Durand, F. L. (1960). An Experimental Study of the Effects of Strong, Progressive Sound Fields on Free-Convection Heat Transfer from a Horizontal Cylinder, *ASME-60-HT-19*, ASME, New York.

- Srinivasan, P. S., Nandapurkar, S. S., and Holland, F. A. (1968). Pressure Drop and Heat Transfer in Coils, *Chem. Eng.*, 218, 113–119.
- Sundén, B. (1999). Enhancement of Convective Heat Transfer in Rib-Roughened Rectangular Ducts, *J. Enhanced Heat Transfer*, 6(2/4), 89–103.
- Swenson, H. S., Carver, J. R., and Szoeko, G. (1962). The Effects of Nucleate Boiling versus Film Boiling on Heat Transfer in Power Boiler Tubes, *J. Eng. Power*, 84, 365–371.
- Taborek, J. (1997). Double-Pipe and Multitube Heat Exchangers with Plain and Longitudinal Finned Tubes, *Heat Transfer Eng.*, 18(2), 34–45.
- Tamari, M., and Nishikawa, K. (1976). The Stirring Effect of Bubbles upon the Heat Transfer to Liquids, *Heat Transfer Jpn. Res.*, 5(2), 31–44.
- Tanaka, H. (1975a). A Theoretical Study on Dropwise Condensation, *J. Heat Transfer*, 97, 72–78.
- Tanaka, H. (1975b). Measurement of Drop-Size Distribution during Transient Dropwise Condensation, *J. Heat Transfer*, 97, 341–346.
- Tanasawa, I. (1978). Dropwise Condensation: The Way to Practical Applications, in *Heat Transfer 1978*, Vol. 6, Hemisphere Publishing, Washington, DC, pp. 393–405.
- Tang, S. I., and McDonald, T. W. (1971). A Study of Heat Transfer from a Rotating Horizontal Cylinder, *Int. J. Heat Mass Transfer*, 14, 1643–1658.
- Tang, L., Ohadi, M. M., and Johnson, A. T. (2000). Flow Condensation in Smooth and Microfin Tubes with HCFC-22, HFC-134a and HFC-410A Refrigerants, I: Experimental Results, *J. Enhanced Heat Transfer*, 7(5), 289–310.
- Taylor, G. I. (1929). The Criterion for Turbulence in Curved Pipes, *Proc. R. Soc.*, A124, 243–249.
- Thomas, D. G. (1967). Enhancement of Film Condensation Rates on Vertical Tubes by Vertical Wires, *Ind. Eng. Chem. Fundam.*, 6(1), 97–102.
- Thomas, D. G. (1968). Enhancement of Film Condensation Rate on Vertical Tubes by Longitudinal Fins, *AIChE J.*, 6(1), 644–649.
- Thome, J. R. (1990). *Enhanced Boiling Heat Transfer*, Hemisphere Publishing, New York.
- Toms, B. A. (1948). Some Observations on the Flow of Linear Polymer Solutions through Straight Tubes at Large Reynolds Numbers, *Proc. International Congress on Rheology*, Vol. II, p. 135.
- Tong, W., Bergles, A. E., and Jensen, M. K. (1996). Critical Heat Flux and Pressure Drop of Subcooled Flow Boiling in Small-Diameter Tubes with Twisted-Tape Inserts, *J. Enhanced Heat Transfer*, 3(2), 95–108.
- Torikoshi, K., and Ebisu, T. (1999). Japanese Advanced Technologies of Heat Exchanger in Air-Conditioning and Refrigeration Applications, in *Compact Heat Exchangers and Enhancement Technology for the Process Industry*, (Shah, R. K., Bell, K. J., Honda, H., and Thonon, B., eds.), Begell House, New York, pp. 17–24.
- Traviss, D. P., and Rohsenow, W. M. (1973). The Influence of Return Bends on the Downstream Pressure Drop and Condensation Heat Transfer in Tubes, *ASHRAE Trans.*, 79(1), 129–137.
- Tzan, Y. L., and Yang, Y. M. (1990). Experimental Study of Surfactant Effects on Pool Boiling Heat Transfer, *J. Heat Transfer*, 112, 207–212.
- Uhl, V. W. (1970). Mechanically Aided Heat Transfer to Viscous Materials, in *Augmentation of Convective Heat and Mass Transfer*, A. E. Bergles and R. L. Webb, eds., ASME, New York, pp. 109–117.
- Usui, H., Sano, Y., and Iwashita, K. (1984). Heat Transfer Enhancement Effects by Combined

- Use of Internally Grooved Rough Surfaces and Twisted Tapes, *Heat Transfer Jpn. Res.*, 13(4), 19–32.
- Vachon, R. I., Nix, G. H., Tanger, G. E., and Cobb, R. O. (1969). Pool Boiling Heat Transfer from Teflon-Coated Stainless Steel, *J. Heat Transfer*, 91, 364–370.
- Van Der Meer, T. H., and Hoogenedoorn, C. J. (1978). Heat Transfer Coefficients for Viscous Fluids in a Static Mixer, *Chem. Eng. Sci.*, 33, 1277–1282.
- Van Rooyen, R. S., and Kröger, D. G. (1978). Laminar Flow Heat Transfer in Internally Finned Tubes with Twisted-Tape Inserts, in *Heat Transfer 1978*, Vol. 2, Hemisphere Publishing, Washington, DC, pp. 577–581.
- van Stralen, S. J. D. (1959). Heat Transfer to Boiling Binary Liquid Mixtures, *Br. Chem. Eng.*, I(4), 8–17; II(4), 78–82.
- van Stralen, S. J. D. (1970). Nucleate Boiling in Binary Systems, in *Augmentation of Convective Heat and Mass Transfer*, A. E. Bergles, and R. L. Webb, eds., ASME, New York, pp. 133–147.
- van Wijk, W. R., Vos, A. S., and van Stralen, S. J. D. (1956). Heat Transfer to Boiling Binary Liquid Mixtures, *Chem. Eng. Sci.*, 5, 68–80.
- Velkoff, H. R., and Miller, J. H. (1965). Condensation of Vapor on a Vertical Plate with a Transverse Electrostatic Field, *J. Heat Transfer*, 87, 197–201.
- Vidyanidhi, V., Suryanarayana, V. V. S., and Chenchu Raju, V. C. (1977). An Analysis of Steady Freely Developed Heat Transfer in a Rotating Straight Pipe, *J. Heat Transfer*, 99, 148–150.
- Vijaya Vittala, C. B., Gupta, S. C., and Agarwal, V. K. (2001). Boiling Heat Transfer from a PTFE Coated Heating Tube to Alcohols, *Exp. Therm. Fluid Sci.*, 25, 125–130.
- Virk, P. S., Mickley, H. S., and Smith, K. A. (1970). The Ultimate Asymptote and Mean Flow Structure in Toms' Phenomenon, *J. Appl. Mech.*, 37, 448–493.
- Viskanta, R. (1985). Electric and Magnetic Fields, in *Handbook of Heat Transfer Fundamentals*, W. M. Rohsenow et al., eds., McGraw-Hill, New York, Chap. 10.
- Viskanta, R. (1998). Convective and Radiative Flame Jet Impingement Heat Transfer, *Int. J. Transp. Phenomena*, 1(1), 1–15.
- Vrable, D. L., Yang, W. J., and Clark, J. A. (1974). Condensation of Refrigerant-12 inside Horizontal Tubes with Internal Axial Fins, in *Heat Transfer 1974*, Vol. III, JSME, Tokyo, pp. 250–254.
- Wang, W. (1987). The Enhancement of Condensation Heat Transfer for Stratified Flow in a Horizontal Tube with Inserted Coil, in *Heat Transfer Science and Technology*, B.-X. Wang, ed., Hemisphere Publishing, Washington, DC, pp. 805–811.
- Wang, C.-C. (2000). Technology Review: A Survey of Recent Patents of Fin-and-Tube Heat Exchangers, *J. Enhanced Heat Transfer*, 7(5), 333–345.
- Wang, C.-C., Lee, W.-S., Sheu, W.-J., and Liaw, J.-S. (2001). Empirical Airside Correlations of Fin-and-Tube Heat Exchangers under Dehumidifying Conditions, *Int. J. Heat Exchangers*, II(2), 151–178.
- Warner, D. F., Mayhan, K. G., and Park, E. L., Jr. (1978). Nucleate Boiling Heat Transfer of Liquid Nitrogen from Plasma Coated Surfaces, *Int. J. Heat Mass Transfer*, 21, 137–144.
- Wasekar, V. M., and Manglik, R. M. (1999). A Review of Enhanced Heat Transfer in Nucleate Pool Boiling of Aqueous Surfactant and Polymeric Solutions, *J. Enhanced Heat Transfer*, 6(2/4), 135–150.

- Wasekar, V. M., and Manglik, R. M. (2000). Pool Boiling Heat Transfer in Aqueous Solutions of an Anionic Surfactant, *J. Heat Transfer*, 122(4), 708–715.
- Wasekar, V. M., and Manglik, R. M. (2001). Computation of Marangoni Convection at the Vapor–Liquid Interface in Aqueous Surfactant Solutions, in *Computational Fluid and Solid Mechanics*, Vol. 2, Elsevier, Amsterdam, pp. 1412–1416.
- Wasekar, V. M., and Manglik, R. M. (2002). The Influence of Additive Molecular Weight and Ionic Nature on the Pool Boiling Performance of Aqueous Surfactant Solutions, *Int. J. Heat Mass Transfer*, 45(3), 483–493.
- Watanabe, K., Taira, T., and Mori, Y. (1983). Heat Transfer Augmentation in Tubular Flow by Twisted Tapes at High Temperatures and Optimum Performance, *Heat Transfer Jpn. Res.*, 12(3), 1–31.
- Watkins, R. W., Robertson, C. R., and Acrivos, A. (1976). Entrance Region Heat Transfer in Flowing Suspensions, *Int. J. Heat Mass Transfer*, 19, 693–695.
- Watkinson, A. P., Miletto, D. C., and Kubanek, G. R. (1975). Heat Transfer and Pressure Drop of Internally Finned Tubes in Laminar Oil Flows, *ASME-75-HT-41*, ASME, New York.
- Watson, G. B., Lee, R. A., and Wiener, M. (1974). Critical Heat Flux in Inclined and Vertical Smooth and Ribbed Tubes, in *Heat Transfer 1974*, Vol. IV, JSME, Tokyo, pp. 275–279.
- Webb, R. L. (1972). Heat Transfer Having a High Boiling Heat Transfer Coefficient, U.S. patent 3,696,861.
- Webb, R. L. (1981). Performance Evaluation Criteria for Use of Enhanced Heat Transfer Surfaces in Heat Exchanger Design, *Int. J. Heat Mass Transfer*, 24, 715–726.
- Webb, R. L. (1987). Enhancement of Single-Phase Heat Transfer, in *Handbook of Single-Phase Convective Heat Transfer*, S. Kakaç, R. K. Shah, and W. Aung, eds., Wiley, New York, Chap. 17.
- Webb, R. L. (1988). Performance Evaluation Criteria for Enhanced Tube Geometries Used in Two-Phase Heat Exchangers, in *Heat Transfer Equipment Design*, R. K. Shah, E. C. Subbarao, and R. A. Mashelkar, eds., Hemisphere Publishing, New York, pp. 697–704.
- Webb, R. L. (1994). *Principles of Enhanced Heat Transfer*, Wiley, New York.
- Webb, R. L., and Bergles, A. E. (1983a). Heat Transfer Enhancement: Second Generation Technology, *Mech. Eng.*, 105(6), 60–67.
- Webb, R. L., and Bergles, A. E. (1983b). Performance Evaluation Criteria for Selection of Heat Transfer Surface Geometries Used in Low Reynolds Number Heat Exchangers, in *Low Reynolds Number Flow Heat Exchangers*, S. Kakaç, R. K. Shah, and A. E. Bergles, eds., Hemisphere Publishing, Washington, DC, pp. 735–752.
- Webb, R. L., and Gee, D. L. (1979). Analytical Predictions for a New Concept Spine-Fin Surface Geometry, *ASHRAE Trans.*, 85(2), 274–283.
- Webb, R. L., and Haider, S. I. (1992). An Analytical Model for Nucleate Boiling on Enhanced Surfaces, in *Pool and External Flow Boiling*, V. K. Dhir and A. E. Bergles, eds., ASME, New York, pp. 345–360.
- Webb, R. L., Eckert, E. R. G., and Goldstein, R. J. (1971). Heat Transfer and Friction in Tubes with Repeated-Rib Roughness, *Int. J. Heat Mass Transfer*, 14, 601–618.
- Webb, R. L., Eckert, E. R. G., and Goldstein, R. J. (1972). Generalized Heat Transfer and Friction Correlations for Tubes with Repeated-Rib Roughness, *Int. J. Heat Mass Transfer*, 15, 180–184.
- Webb, R. L., Bergles, A. E., and Junkhan, G. H. (1983). Bibliography of U.S. Patents on

- Augmentation of Convective Heat and Mass Transfer, *Report HTL-32, ISU-ERI-Ames-84257*, Iowa State University, Ames, IA.
- Webb, R. L., Rudy, T. M., and Kedzierski, M. A. (1985). Prediction of the Condensation Coefficient on Horizontal Integral-Fin Tubes, *J. Heat Transfer*, 107, 369–376.
- Webb, R. L., Fujii, M., Menze, K., Rudy, T., and Ayub, Z. (1993). Technology Review, *J. Enhanced Heat Transfer*, 1(1), 1–4.
- Webb, R. L., Menze, K., Rudy, T., Ayub, Z., and Fujii, M. (1994). Technology Review, *J. Enhanced Heat Transfer*, 1(2), 127–130.
- Westwater, J. W. (1973). Development of Extended Surfaces for Use in Boiling Liquids, *AIChE Symp. Ser.*, 69(131), 1–9.
- White, C. M. (1929). Streamline Flow through Curved Pipes, *Proc. R. Soc.*, A123, 645–663.
- Whitham, J. M. (1986). The Effect of Retarders in Fire Tube Boilers, *Street Railw. J.*, 12(6), 374.
- Withers, J. G. (1980a). Tube-Side Heat Transfer and Pressure Drop for Tubes Having Helical Internal Ridging with Turbulent/Transitional Flow of Single-Phase Fluid, 1: Single-Helix Ridging, *Heat Transfer Eng.*, 2(1), 48–58.
- Withers, J. G. (1980b). Tube-Side Heat Transfer and Pressure Drop for Tubes Having Helical Internal Ridging with Turbulent/Transitional Flow of Single-Phase Fluid, 2: Multiple-Helix Ridging, *Heat Transfer Eng.*, 2(2), 43–50.
- Withers, J. G., and Haddas, E. P. (1974). Heat Transfer Characteristics of Helical Corrugated Tubes for Intube Boiling of Refrigerant R-12, *AIChE Symp. Ser.*, 70(138), 98–106.
- Withers, J. G., and Young, E. H. (1971). Steam Condensation on Vertical Rows of Horizontal Corrugated and Plain Tubes, *Ind. Eng. Chem. Process Des. Dev.*, 10(1), 19–30.
- Wong, S. W., and Chon, W. Y. (1969). Effects of Ultrasonic Vibrations on Heat Transfer to Liquids by Natural Convection and by Boiling, *AIChE J.*, 15, 281–288.
- Wu, W. T., Yang, Y. M., Maa, J. R. (1998). Nucleate Pool Boiling Enhancement by Means of Surfactant Additives, *Exp. Therm. Fluid Sci.*, 18, 195–209.
- Wu, H., Cheng, H., and Zhou, Q. (2000). Compound Enhanced Heat Transfer inside Tubes by Combined Use of Spirally Corrugated Tubes and Inlet Axial Vane Swirlers, *J. Enhanced Heat Transfer*, 7(4), 247–257.
- Xu, Y., Al-Dadah, R. K., Karayiannis, T. G., and Allen, P. H. G. (1995). Incorporation of EHD Enhancement in Heat Exchangers, *J. Enhanced Heat Transfer*, 2(1/2), 87–93.
- Yabe, A. (1991). Active Heat Transfer Enhancement by Applying Electric Fields, *Proc. 3rd ASME-JSME Thermal Engineering Joint Conference*, Vol. 3, JSME, Tokyo, and ASME, New York, pp. xv–xxiii.
- Yabe, A., Nakayama, W., and Di Marco, P. (1999). Enhancement Techniques in Pool Boiling, in *Handbook of Phase Change: Boiling and Condensation*, S. G. Kandlikar, M. Shoji, and V. K. Dhir, eds., Taylor & Francis, Philadelphia, Chap. 5.
- Yilmaz, S., and Westwater, J. W. (1981). Effect of Commercial Enhanced Surfaces on the Boiling Heat Transfer Curve, in *Advances in Enhanced Heat Transfer 1981*, (Webb, R. L., Carnavos, T. C., Park Jr., E. F., and Hustetler, K. M., eds.), *ASME-HTD-18*, ASME, New York, pp. 73–92.
- Yilmaz, S., Hwalck, J. J., and Westwater, J. W. (1980). Pool Boiling Heat Transfer Performance for Commercial Enhanced Tube Surfaces, *ASME-80-HT-41*, ASME, New York.

- Yilmaz, S., Palen, J. W., and Taborek, J. (1981). Enhanced Surfaces as Single Tubes and Tube Bundles, in *Advances in Heat Transfer 1981*, R. L. Webb, et al., eds., ASME-HTD-18, ASME, New York, pp. 123–129.
- Young, R. X., and Hummel, R. L. (1995). Improved Nucleate Boiling Heat Transfer, *Chem. Eng. Prog. Symp. Ser.*, 61(59), 264–470.
- Yudin, V. F. (1982). *Teploobmen Poperechnoobrennykh Trub* (Heat Transfer of Crossfinned Tubes), Mashinostroyeniye Publishing House, Leningrad, Russia.
- Zatell, V. A. (1973). Method of Modifying a Finned Tube for Boiling Enhancement, U.S. patent 3,768,290.
- Zhang, J., and Manglik, R. M. (2003). Pool Boiling Heat Transfer in Aqueous Solutions of a Cationic Surfactant, Proc. of the 6th ASME-JSME Thermal Engineering Joint Conference, Paper No. TED-AJ03-248, Tokyo, Japan.
- Zhang, J., Manglik, R. M., Muley, A., and Borghese, J. B. (2002). Three-Dimensional Numerical Simulation of Laminar Air Flows in Wavy Plate-Fin Channels, *Proc. 13th International Symposium on Transport Phenomena (ISTP-13)*, Victoria, British Columbia, Canada.
- Zhang, Y. M., Azad, G. M., Han, J.-C., and Lee, C. P. (2000). Turbulent Heat Transfer Enhancement and Surface Heating Effect in Square Channels with Wavy, and Twisted Tape Inserts with Interrupted Ribs, *J. Enhanced Heat Transfer*, 7(1), 35–49.
- Zhang, Y. M., Gu, W. Z., and Han, J.-C. (1994). Heat Transfer and Friction in Rectangular Channels with Ribbed or Ribbed-Grooved Walls, *J. Heat Transfer*, 116, 58–65.
- Zhong, L., Tan, Y., and Wang, S. (1992). Investigation of the Heat Transfer Performance of Mechanically Made Porous Surface Tubes with Ribbed Channels, *Proc. 2nd International Symposium on Multiphase Flow and Heat Transfer*, X.-J. Chen, T. N. Veziroğlu, and C. L. Tien, eds., Vol. 1, Hemisphere Publishing, New York, pp. 700–707.
- Zhou, Q. T., Ye, S. Y., Ou-Yang, Y. H., and Gu, N. Z. (1990). Combined Enhancement of Tube-Side Heat Transfer in Cast-Iron Air Preheater, in *Heat Transfer 1990*, Vol. 4, Hemisphere Publishing, New York, pp. 39–44.
- Zhukauskas, A. (1989). *High-Performance Single-Phase Heat Exchangers*, Hemisphere Publishing, New York, Chap. 14.
- Zhukauskas, A. A., Shlanchyauskas, A. A., and Yaronees, Z. P. (1961). Investigation of the Influence of Ultrasonics on Heat Exchange between Bodies in Liquids, *J. Eng. Phys.*, 4, 58–61.
- Zhukauskas, A., Ziugzda, J., and Daujotas, P. (1978). Effects of Turbulence on the Heat Transfer of a Rough Surface Cylinder in Cross-Flow in the Critical Range of Re, in *Heat Transfer 1978*, Vol. 4, Hemisphere Publishing, Washington, DC, pp. 231–236.
- Zhukov, V. M., Kazakov, G. M., Kovalev, S. A., and Kuzmakichta, Y. A. (1975). Heat Transfer in Boiling of Liquids on Surfaces Coated with Low Thermal Conductivity Films, *Heat Transfer-Soviet Research*, 7(3), 16–26.
- Zimparov, V. (2001). Enhancement of Heat Transfer by a Combination of Three-Start Spirally Corrugated Tubes with a Twisted Tape, *Int. J. Heat Mass Transfer*, 44(3), 551–574.
- Zimparov, V. D., Vulchanov, N. L., and Delov, L. B. (1991). Heat Transfer and Frictional Characteristics of Spirally Enhanced Tubes for Power Plant Condensers, *Int. J. Heat Mass Transfer*, 34(9), 2187–2197.

Porous Media

ADRIAN BEJAN

Department of Mechanical Engineering and Materials Science
Duke University
Durham, North Carolina

- 15.1 Introduction
- 15.2 Basic principles
 - 15.2.1 Mass conservation
 - 15.2.2 Flow models
 - 15.2.3 Energy conservation
- 15.3 Conduction
- 15.4 Forced convection
 - 15.4.1 Plane wall with constant temperature
 - 15.4.2 Sphere and cylinder
 - 15.4.3 Concentrated heat sources
 - 15.4.4 Channels filled with porous media
 - 15.4.5 Compact heat exchangers as porous media
- 15.5 External natural convection
 - 15.5.1 Vertical walls
 - 15.5.2 Horizontal walls
 - 15.5.3 Sphere and horizontal cylinder
 - 15.5.4 Concentrated heat sources
- 15.6 Internal natural convection
 - 15.6.1 Enclosures heated from the side
 - 15.6.2 Cylindrical and spherical enclosures
 - 15.6.3 Enclosures heated from below
 - 15.6.4 Penetrative convection
- 15.7 Other configurations

Nomenclature

References

15.1 INTRODUCTION

Heat and mass transfer through saturated porous media is an important development and an area of very rapid growth in contemporary heat transfer research. Although the mechanics of fluid flow through porous media has preoccupied engineers and physicists for more than a century, the study of heat transfer has reached the status

of a separate field of research during the last three decades (Nield and Bejan, 1999). It has also become an established topic in heat transfer education, where it became a part of the convection course in 1984 (Bejan, 1984, 1995). The reader is directed to a growing number of monographs that outline the fundamentals (Scheidtger, 1957; Bear, 1972; Bejan, 1987; Kaviany, 1995; Ingham and Pop, 1998, 2002; Vafai, 2000; Pop and Ingham, 2001; Bejan et al., 2004).

Porous media and transport are becoming increasingly important in heat exchanger analysis and design. It was pointed out in Bejan (1995) that the gradual miniaturization of heat transfer devices leads the flow toward lower Reynolds numbers and brings the designer into a domain where dimensions are considerably smaller and structures considerably more complex than those covered by the single-configuration correlations developed historically for large-scale heat exchangers. The race toward small scales and large heat fluxes in the cooling of electronic devices is the strongest manifestation of this trend. It is fair to say that the reformulation of heat exchanger analysis and design as the basis of porous medium flow principles is the next area of growth in heat exchanger theory for small-scale applications.

The objective of this chapter is to provide a concise and effective review of some of the most basic results on heat transfer through porous media. This coverage is an updated and condensed version of a review presented first in Bejan (1987). More detailed and tutorial alternatives were developed subsequently in Bejan (1995, 1999) and Nield and Bejan (1999), to which the interested reader is directed.

15.2 BASIC PRINCIPLES

The description of heat and fluid flow through a porous medium saturated with fluid (liquid or gas) is based on a series of special concepts that are not found in the pure-fluid heat transfer. Examples are the porosity and the permeability of the porous medium, and the volume-averaged properties of the fluid flowing through the porous medium. The porosity of the porous medium is defined as

$$\phi = \frac{\text{void volume contained in porous medium sample}}{\text{total volume of porous medium sample}} \quad (15.1)$$

The engineering heat transfer results assembled in this chapter refer primarily to fluid-saturated porous media that can be modeled as nondeformable, homogeneous, and isotropic. In such media, the volumetric porosity ϕ is the same as the area ratio (void area contained in the sample cross section)/(total area of the sample cross section). Representative values are shown in Table 15.1.

The phenomenon of convection through the porous medium is described in terms of volume-averaged quantities such as temperature, pressure, concentration, and velocity components. Each volume-averaged quantity (ψ) is defined through the operation

$$\langle \psi \rangle = \frac{1}{V} \iiint_V \psi \, dV \quad (15.2)$$

TABLE 15.1 Properties of Common Porous Materials

Material	Porosity, ϕ	Permeability, K (cm ²)	Surface per unit Volume (cm ⁻¹)
Agar-agar	—	2×10^{-10} – 4.4×10^{-9}	
Black slate powder	0.57–0.66	4.9×10^{-10} – 1.2×10^{-9}	7×10^3 – 8.9×10^3
Brick	0.12–0.34	4.8×10^{-11} – 2.2×10^{-9}	
Catalyst (Fischer–Tropsch, granules only)	0.45	—	5.6×10^5
Cigarette	—	1.1×10^{-5}	
Cigarette filters	0.17–0.49		
Coal	0.02–0.12		
Concrete (bituminous)	—	1×10^{-9} – 2.3×10^{-7}	
Concrete (ordinary mixes)	0.02–0.07		
Copper powder (hot-compacted)	0.09–0.34	3.3×10^{-6} – 1.5×10^{-5}	
Corkboard	—	2.4×10^{-7} – 5.1×10^{-7}	
Fiberglass	0.88–0.93	—	560–770
Granular crushed rock	0.45		
Hair (on mammals)	0.95–0.99		
Hair felt	—	8.3×10^{-6} – 1.2×10^{-5}	
Leather	0.56–0.59	9.5×10^{-10} – 1.2×10^{-9}	1.2×10^4 – 1.6×10^4
Limestone (dolomite)	0.04–0.10	2×10^{-11} – 4.5×10^{-10}	
Sand	0.37–0.50	2×10^{-7} – 1.8×10^{-6}	150–220
Sandstone (“oil sand”)	0.08–0.38	5×10^{-12} – 3×10^{-8}	
Silica grains	0.65		
Silica powder	0.37–0.49	1.3×10^{-10} – 5.1×10^{-10}	6.8×10^3 – 8.9×10^3
Soil	0.43–0.54	2.9×10^{-9} – 1.4×10^{-7}	
Spherical packings (well shaken)	0.36–0.43		
Wire crimps	0.68–0.76	3.8×10^{-5} – 1×10^{-4}	29–40

Source: Data from Nield and Bejan (1999), Scheidegger (1957), and Bejan and Lage (1991).

where ψ is the actual value of the quantity at a point inside the sample volume V . Alternatively, the volume-averaged quantity equals the value of that quantity averaged over the total volume occupied by the porous medium. The volume sample is called *representative elementary volume* (REV). The length scale of the REV is much larger than the pore scale but considerably smaller than the length scale of the macroscopic flow domain.

15.2.1 Mass Conservation

The principle of mass conservation or mass continuity applied locally in a small region of the fluid-saturated porous medium is

$$\frac{D\rho}{Dt} + \rho \nabla \cdot \mathbf{v} = 0 \quad (15.3)$$

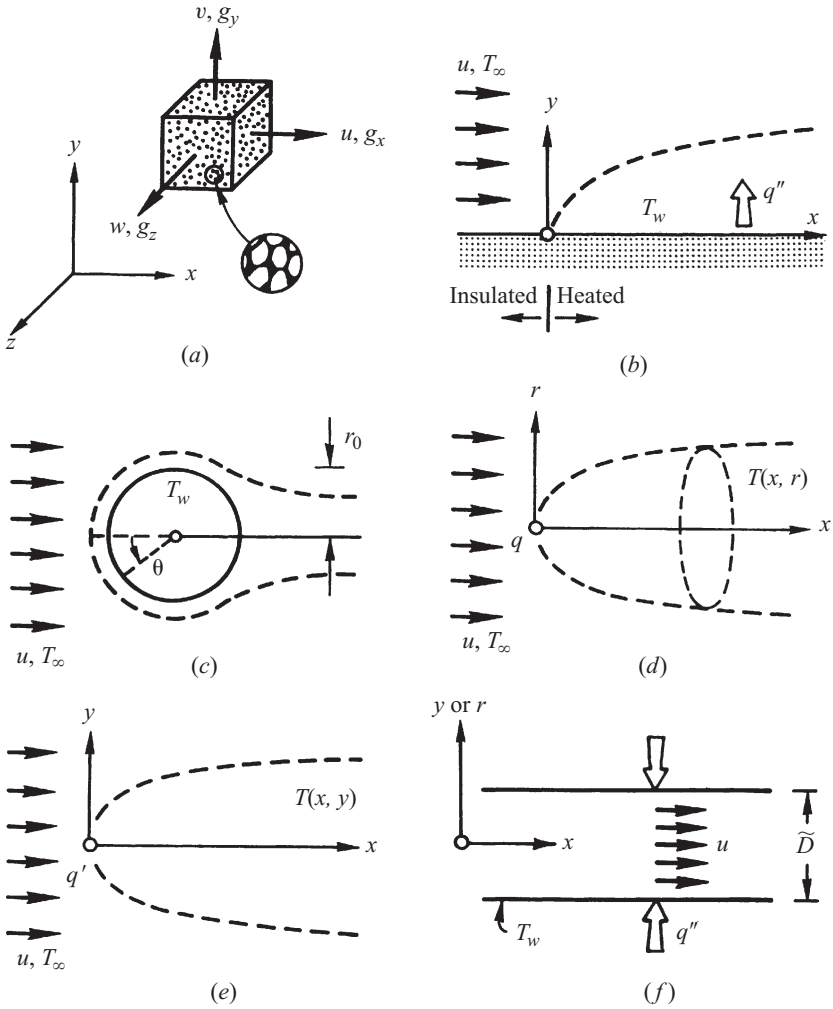


Figure 15.1 Configurations for forced-convection heat transfer: (a) Cartesian coordinate system; (b) boundary layer development over a flat surface in a porous medium; (c) boundary layer development around a cylinder or sphere embedded in a porous medium; (d) point heat source in a porous medium; (e) horizontal line source in a porous medium; (f) duct filled with porous medium.

where D/Dt is the material derivative operator:

$$\frac{D}{Dt} = \frac{\partial}{\partial t} + u \frac{\partial}{\partial x} + v \frac{\partial}{\partial y} + w \frac{\partial}{\partial z} \quad (15.4)$$

and where \mathbf{v} (u, v, w) is the volume-averaged velocity vector (Fig. 15.1a). For example, the volume-averaged velocity component u in the x direction is equal to

ϕu_p , where u_p is the average velocity through the pores. In many single-phase flows through porous media, the density variations are small enough so that the $D\rho/Dt$ term may be neglected in eq. (15.3). The incompressible flow model has been invoked in the development of the majority of the analytical and numerical results reviewed in this section. The incompressible flow model should not be confused with the incompressible-substance model encountered in thermodynamics (Bejan, 1997).

15.2.2 Flow Models

The most frequently used model for volume-averaged flow through a porous medium is the Darcy flow model (Nield and Bejan, 1999; Bejan, 1995). According to this model, the volume-averaged velocity in a certain direction is directly proportional to the net pressure gradient in that direction,

$$u = \frac{K}{\mu} \left(-\frac{\partial P}{\partial x} \right) \quad (15.5)$$

In three dimensions and in the presence of a body acceleration vector $\mathbf{g} = (g_x, g_y, g_z)$ (Fig. 15.1a), the Darcy flow model is

$$\mathbf{v} = \frac{K}{\mu} (-\nabla P + \rho \mathbf{g}) \quad (15.6)$$

The proportionality factor K in Darcy's model is the permeability of the porous medium. The units of K are m^2 . In general, the permeability is an empirical constant that can be determined by measuring the pressure drop and the flow rate through a column-shaped sample of porous material, as suggested by eq. (15.5). The permeability can also be estimated from simplified models of the labyrinth formed by the interconnected pores. Modeling the pores as a bundle of parallel capillary tubes of radius r_0 yields (Bejan, 1995)

$$K = \frac{\pi r_0^4}{8} \frac{N}{A} \quad (15.7)$$

where N is the number of tubes counted on a cross section of area A . Modeling the pores as a stack of parallel capillary fissures of width B and fissure-to-fissure spacing $a + b$ yields the permeability formula (Bejan, 1995)

$$K = \frac{b^3}{12(a + b)} \quad (15.8)$$

Modeling the porous medium as a collection of solid spheres of diameter d , Kozeny obtained the relationship (Nield and Bejan, 1999)

$$K \sim \frac{d^2 \phi^3}{(1 - \phi)^2} \quad (15.9)$$

A more applicable version of eq. (15.9) was obtained by considering a bed of particles or fibers with an effective average particle or fiber diameter D_p . The hydraulic radius theory of Carman-Kozeny leads to the relationship (Nield and Bejan, 1999)

$$K = \frac{D_p^2 \phi^3}{180(1 - \phi)^2} \quad (15.10)$$

where

$$D_p^2 = \frac{\int_0^\infty D_p^3 h(D_p) dD_p}{\int_0^\infty D_p^2 h(D_p) dD_p} \quad (15.11)$$

and $h(D_p)$ is the density function for the distribution of diameters D_p . The constant 180 in eq. (15.10) was obtained by seeking a best fit with experimental results. Equation (15.10) gives satisfactory results for media that consist of particles of approximately spherical shape and whose diameters fall within a narrow range. The equation is often not valid in the cases of particles that deviate strongly from the spherical shapes, broad particle-size distributions and consolidated media. Nevertheless, it is widely used because it seems to be the best simple expression available. Additional limitations to the use of eq. (15.10) and alternate statistical models leading to Darcy's law are reviewed in Nield and Bejan (1999).

The Darcy flow model is valid in circumstances where the order of magnitude of the *local pore Reynolds number*, based on the local volume-averaged speed $(u^2 + v^2 + w^2)^{1/2}$ and $K^{1/2}$, is smaller than 1 (Ward, 1964). At pore Reynolds numbers of order 1 and greater, the measured relationship between pressure gradient and volume-averaged velocity is correlated by Forchheimer's modification of Darcy's model of eq. (15.5) (Nield and Bejan, 1999):

$$-\frac{\partial P}{\partial x} = \frac{\mu}{K}u + b\rho u^2 \quad (15.12)$$

The term $b\rho u^2$ accounts for the increasingly important role played by fluid inertia. In three dimensions and in the presence of body acceleration, the Forchheimer modification of the Darcy flow model is

$$\mathbf{v} + \frac{b\rho K}{\mu}|\mathbf{v}|\mathbf{v} = \frac{K}{\mu}(-\nabla P + \rho\mathbf{g}) \quad (15.13)$$

Experimental measurements (Ward, 1964) suggest that as the local pore Reynolds number exceeds the order of 10, Forchheimer's constant b approaches asymptotically the value

$$b = 0.55K^{-1/2} \quad (15.14)$$

Extensive measurements involving gas flow through columns of packed spheres, sand, and pulverized coal (Ergun, 1952) led to the following correlations for K and b :

$$K = \frac{d^2 \phi^3}{150(1 - \phi)^2} \quad (15.15)$$

$$b = \frac{1.75(1 - \phi)}{\phi^3 d} \quad (15.16)$$

Brinkman's (1947) modification of the Darcy flow model accounts for the transition from Darcy flow to highly viscous flow (without porous matrix), in the limit of extremely high permeability:

$$\mathbf{v} = \frac{K}{\mu} (-\nabla \rho + \rho \mathbf{g}) + K \nabla^2 \mathbf{v} \quad (15.17)$$

The more appropriate way to write Brinkman's equation is (Nield and Bejan, 1999)

$$\nabla P = -\frac{\mu}{K} \mathbf{v} + \tilde{\mu} \nabla^2 \mathbf{v} \quad (15.18)$$

which is similar to eq. (15.17) without the body force term and multiplied by K/μ . In eqs. (15.17) and (15.18), two viscous terms are evident. The first is the usual Darcy term, and the second is analogous to the Laplacian term that appears in the Navier–Stokes equation. The coefficient $\tilde{\mu}$ is an effective viscosity. Brinkman set μ and $\tilde{\mu}$ equal to each other, but in general that is not true. The reader is referred to Nield and Bejan (1999) for a critical discussion of the applicability of eq. (15.18).

There are situations in which it is convenient to use the Brinkman equation. One such situation is when flows in porous media are compared with those in clear fluids. The Brinkman equation has a parameter K (the permeability) such that the equation reduces to a form of the Navier–Stokes equation as $K/L^2 \rightarrow \infty$ and to the Darcy equation as $K/L^2 \rightarrow 0$. Another situation is when it is desired to match solutions in a porous medium and in an adjacent viscous fluid.

The two modifications of the Darcy flow model discussed above, the Forchheimer model of eq. (15.13) and the Brinkman model of eq. (15.17), were used simultaneously by Vafai and Tien (1981) in a study of forced-convection boundary layer heat transfer. In the presence of gravitational acceleration, Vafai and Tien's momentum equations would read

$$\mathbf{v} + \frac{b\rho K}{\mu} |\mathbf{v}| \mathbf{v} = \frac{K}{\mu} (-\nabla P + \rho \mathbf{g}) + K \nabla^2 \mathbf{v} \quad (15.19)$$

None of the foregoing models account adequately for the transition from porous medium flow to pure fluid flow as the permeability K increases. Note that in the high- K limit, the terms that survive in eq. (15.17) or (15.19) account for momentum conservation only in highly viscous flows in which the effect of fluid inertia is negligible relative to pressure and friction forces. A model that bridges the entire gap between the Darcy–Forchheimer model and the Navier–Stokes equations was proposed by Vafai and Tien (1981):

$$\frac{\nu}{K} \mathbf{v} + b|\mathbf{v}|\mathbf{v} = -\frac{D\mathbf{v}}{Dt} - \frac{1}{\rho} \nabla P + \nu \nabla^2 \mathbf{v} + \mathbf{g} \quad (15.20)$$

As the permeability K increases, the left-hand side vanishes and gives way to the complete vectorial Navier–Stokes equation for Newtonian constant-property flow. The state of the art in the development of flow models and new questions about the older models are discussed in Nield and Bejan (1999).

15.2.3 Energy Conservation

Consider now the first law of thermodynamics for flow through a porous medium. For simplicity, assume that the medium is isotropic and that radiative effects, viscous dissipation, and the work done by pressure changes are negligible. For most cases, it is acceptable to assume that there is local thermal equilibrium so that $T_s = T_f = T$, where T_s and T_f are the temperatures of the solid and fluid phases, respectively. Also assume that heat conduction in the solid and fluid phases takes place in parallel so that there is no net heat transfer from one phase to the other. Taking averages over an elemental volume of the medium give, for the solid phase (Nield and Bejan, 1999),

$$(1 - \phi)(\rho c)_s \frac{\partial T_s}{\partial t} = (1 - \phi) \nabla \cdot (k_s \nabla T_s) + (1 - \phi) q_s''' \quad (15.21)$$

and for the fluid phase,

$$\phi(\rho c_p)_f \frac{\partial T_f}{\partial t} + (\rho c_p)_f \mathbf{v} \cdot \nabla T_f = \phi \nabla \cdot (k_f \nabla T_f) + \phi q_f''' \quad (15.22)$$

Here the subscripts s and f refer to the solid and fluid phases, respectively, c is the specific heat of the solid, c_p is the specific heat at constant pressure of the fluid, k is the thermal conductivity, and q''' (W/m³) is the heat generation rate per unit volume.

In writing eqs. (15.21) and (15.22) it has been assumed that the surface porosity is equal to the porosity. For example, $-k_s \nabla T_s$ is the conductive heat flux through the solid, and thus $\nabla \cdot (k_s \nabla T_s)$ is the net rate of heat conduction into a unit volume of the solid. In eq. (15.21), this appears multiplied by the factor $(1 - \phi)$, which is the ratio of the cross-sectional area occupied by solid to the total cross-sectional area of the medium. The other two terms in eq. (15.21) also contain the factor $(1 - \phi)$, because this is the ratio of volume occupied by solid to the total volume of the element. In eq. (15.22) there also appears a convective term, due to the seepage velocity. We recognize that $\mathbf{v} \cdot \nabla T_f$ is the rate of change of temperature in the elemental volume due to the convection of fluid into it, so this, multiplied by $(\rho c_p)_f$, must be the rate of change of thermal energy, per unit volume of fluid, due to the convection. Note further that in writing eq. (15.22), use has been made of the Dupuit–Forchheimer relationship (Nield and Bejan, 1999), $\mathbf{v} = \phi \mathbf{V}$.

Setting $T_s = T_f = T$ and adding eqs. (15.21) and (15.22) yields

$$(\rho c)_m \frac{\partial T}{\partial t} + (\rho c)_f \mathbf{v} \cdot \nabla T = \nabla \cdot (k_m \nabla T) + q_m''' \quad (15.23)$$

where

$$(\rho c)_m = (1 - \phi)(\rho c)_s + \phi(\rho c_p)_f \quad (15.24)$$

$$k_m = (1 - \phi)k_s + \phi k_f \quad (15.25)$$

$$q_m''' = (1 - \phi)q_s''' + \phi q_f''' \quad (15.26)$$

are, respectively, the overall heat capacity per unit volume, overall thermal conductivity, and overall heat production per unit volume of the medium. Equation (15.24) may also be written as

$$(\rho c)_m = (\rho c_p)_f \sigma \quad (15.27)$$

where σ is the heat capacity ratio,

$$\sigma = \phi + (1 + \phi) \frac{(\rho c)_s}{(\rho c_p)_f} \quad (15.28)$$

The energy balance of eq. (15.24) becomes

$$\sigma \frac{\partial T}{\partial t} + \mathbf{v} \cdot \nabla T = \nabla \cdot (\alpha_m \nabla T) + \frac{q_m'''}{(\rho c_p)_f} \quad (15.29)$$

where α_m is the thermal diffusivity of the fluid saturated porous medium,

$$\alpha_m = \frac{k_m}{(\rho c_p)_f} \quad (15.30)$$

If the assumption of local thermal equilibrium is abandoned, account must be taken for the local heat transfer between solid and fluid. Equations (15.21) and (15.22) are replaced by

$$(1 - \phi)(\rho c)_s \frac{\partial T}{\partial t} = (1 - \phi) \nabla \cdot (k_s \nabla T_s) + (1 - \phi) q_s''' + h(T_f - T_s) \quad (15.31)$$

$$\phi(\rho c_p)_f \frac{\partial T_f}{\partial t} + (\rho c_p)_f \mathbf{v} \cdot \nabla T = \phi \nabla \cdot (k_f \nabla T) + \phi q_f''' + h(T_s - T_f) \quad (15.32)$$

where h is the heat transfer coefficient. A critical aspect of using this approach lies in the determination of the appropriate value of h . Experimental values of h are found in an indirect manner and methods are reviewed by Nield and Bejan (1999).

In situations where the fluid that saturates the porous structure is a mixture of two or more chemical species, the equation that expresses the conservation of species is (Bejan, 1995)

$$\phi \frac{\partial C}{\partial t} + \mathbf{v} \cdot \nabla C = D \nabla^2 C + \dot{m}_i''' \quad (15.33)$$

In this equation C is the concentration of i , expressed in kilograms of i per unit volume of porous medium; D is the mass diffusivity of i through the porous medium with the fluid mixture in it; and \dot{m}_i''' is the number of kilograms of i produced by a chemical reaction per unit time and per unit volume of porous medium.

15.3 CONDUCTION

Pure thermal diffusion is the mechanism for heat transfer when there is no motion through the pores of the solid structure. The conservation of energy is described by eq. (15.29), in which the convection term is absent:

$$\sigma \frac{\partial T}{\partial t} = \nabla \cdot (\alpha_m \nabla T) + \frac{q'''}{(\rho c_p)_f} \quad (15.34)$$

Except for the heat capacity ratio σ that appears on the left side, eq. (15.34) is the same as the equation for time-dependent conduction through a solid (Bejan, 1993). This means that the mathematical methods developed for conduction in solids (Bejan, 1993; Carslaw and Jaeger, 1959) apply to porous media saturated with stagnant fluid. For example, the thermal penetration depth due to time-dependent conduction into a semiinfinite porous medium without fluid motion is of order $(\alpha_m t / \sigma)^{1/2}$. The reader is directed to Chapter 3 in this book for additional mathematical solutions for key configurations.

The overall thermal conductivity of a porous medium depends in a complex fashion on the geometry of the medium (Nield and Bejan, 1999; Nield, 1991). If the heat conduction in the solid and fluid phases occurs in parallel, the overall conductivity k_A is the weighted arithmetic mean of the conductivities k_s and k_f :

$$k_A = (1 - \phi)k_s + \phi k_f \quad (15.35)$$

On the other hand, if the structure and orientation of the porous medium is such that the heat conduction takes place in series, with all the heat flux passing through both solid and fluid, the overall conductivity k_H is the weighted harmonic mean of k_s and k_f :

$$\frac{1}{k_H} = \frac{1 - \phi}{k_s} + \frac{\phi}{k_f} \quad (15.36)$$

In general, k_A and k_H will provide upper and lower bounds, respectively, on the actual overall conductivity k_m . It is always true that $k_H \leq k_A$, with equality if and only if $k_s = k_f$. For practical purposes, a rough-and-steady estimate for k_m is provided by k_G , the weighted geometric mean of k_s and k_f , defined by

$$k_G = k_s^{1-\phi} k_f^\phi \quad (15.37)$$

This provides a good estimate as long as k_s and k_f are not too different from each other (Nield, 1991). More complicated correlation formulas for the conductivity of packed beds have been proposed. Experiments by Prasad et al. (1989) showed that eqs.

(15.35)–(15.37) gave reasonably good results provided that k_f was not significantly greater than k_s . Additional thermal conductivity models are discussed in Nield and Bejan (1999).

15.4 FORCED CONVECTION

15.4.1 Plane Wall with Constant Temperature

The newer results developed for heat transfer through porous media refer to forced and natural convection. The heat transfer results listed next refer to a uniform unidirectional seepage flow through a homogeneous and isotropic porous medium. They are based on the idealization that the solid and fluid phases are locally in thermal equilibrium.

Consider the uniform flow (u, T_∞) parallel to a solid wall heated to a constant temperature T_w , as shown in Fig. 15.1*b*. The boundary layer solution for the local Nusselt number is available analytically (Bejan, 1995):

$$\text{Nu}_x = \frac{q''}{T_w - T_\infty} \frac{x}{k_m} = 0.564 \text{Pe}_x^{1/2} \quad (15.38)$$

where Pe_x is the Péclet number based on the local longitudinal position, $\text{Pe}_x = ux/\alpha_m$. The heat flux q'' and the heat transfer coefficient $q''/(T_w - T_\infty)$ decrease as $x^{-1/2}$. The overall Nusselt number based on the heat flux, $\overline{q''}$ averaged from $x = 0$ to a given wall length $x = L$ is

$$\overline{\text{Nu}}_L = \frac{\overline{q''}}{T_w - T_\infty} \frac{L}{k_m} = 1.128 \text{Pe}_L^{1/2} \quad (15.39)$$

where the overall Péclet number is $\text{Pe}_L = uL/\alpha_m$. The total heat transfer rate through the wall is $q' = \overline{q''}L$. Related boundary layer solutions are reviewed in Nield and Bejan (1999).

The local Nusselt number for boundary layer heat transfer near a wall with constant heat flux is also available in closed form (Bejan, 1995):

$$\text{Nu}_x = \frac{q''}{T_w(x) - T_\infty} \frac{x}{k_m} = 0.886 \text{Pe}_x^{1/2} \quad (15.40)$$

where $\text{Pe}_x = ux/\alpha_m$. The temperature difference $T_w(x) - T_\infty$ increases as $x^{1/2}$. The overall Nusselt number that is based on the average wall temperature $\overline{T_w}$ (specifically, the temperature averaged from $x = 0$ to $x = L$ is

$$\overline{\text{Nu}}_L = \frac{\overline{q''}}{\overline{T_w} - T_\infty} \frac{L}{k_m} = 1.329 \text{Pe}_L^{1/2} \quad (15.41)$$

where $\text{Pe}_L = uL/\alpha_m$. Equations (15.38)–(15.41) are valid when the respective Péclet numbers are greater than 1 in an order-of-magnitude sense. Mass transfer counterparts to these heat transfer formulas are obtained through the notation transformation

$Nu \rightarrow Sh, q'' \rightarrow j'', T \rightarrow C, k_m \rightarrow D$, and $\alpha_m \rightarrow D$, where Sh , j'' , C , and D are the Sherwood number, mass flux, species concentration, and mass diffusivity constant.

From a fluid mechanics standpoint, these results are valid if the flow is parallel, that is, in the Darcy regime or Darcy–Forchheimer regime through a homogeneous and isotropic porous medium. The special effect of the flow resistance exerted by the solid wall was documented numerically in Vafai and Tien (1981).

15.4.2 Sphere and Cylinder

Consider the thermal boundary layer region around a sphere or around a circular cylinder that is perpendicular to the uniform flow with volume-averaged velocity u . As indicated in Fig. 15.1c, the sphere or cylinder radius is r_0 and the surface temperature is T_w . The distributions of heat flux around the sphere and cylinder in Darcy flow were determined in Cheng (1982). With reference to the angular coordinate θ defined in Fig. 15.1c, the local peripheral Nusselt numbers are, for the sphere,

$$Nu_\theta = 0.564 \left(\frac{ur_0\theta}{\alpha_m} \right)^{1/2} \left(\frac{3}{2}\theta \right)^{1/2} \sin^2 \theta \left(\frac{1}{3} \cos^3 \theta - \cos \theta + \frac{2}{3} \right)^{-1/2} \quad (15.42)$$

and for the cylinder,

$$Nu_\theta = 0.564 \left(\frac{ur_0\theta}{\alpha_m} \right)^{1/2} (2\theta)^{1/2} \sin \theta (1 - \cos \theta)^{-1/2} \quad (15.43)$$

The Péclet number is based on the swept arc $r_0\theta$: namely, $Pe_\theta = ur_0\theta/\alpha_m$. The local Nusselt number is defined as

$$Nu_\theta = \frac{q''}{T_w - T_\infty} \frac{r_0\theta}{k_m} \quad (15.44)$$

Equations (15.42) and (15.43) are valid when the boundary layers are distinct (thin), that is, when the boundary layer thickness $r_0 \cdot Pe_\theta^{-1/2}$ is smaller than the radius r_0 . This requirement can also be written as $Pe_\theta^{1/2} \gg 1$ or $Nu_\theta \gg 1$.

The conceptual similarity between the thermal boundary layers of the cylinder and the sphere (Fig. 15.1c) and that of the flat wall (Fig. 15.1b) is illustrated further by Nield and Bejan's (1999) correlation of the heat transfer results for these three configurations. The heat flux averaged over the area of the cylinder and sphere, $\overline{q''}$, can be calculated by averaging the local heat flux q'' expressed by eqs. (15.42)–(15.44). The results are for the sphere,

$$\overline{Nu}_D = 1.128 Pe_D^{1/2} \quad (15.45)$$

and for the cylinder,

$$\overline{Nu}_D = 1.015 Pe_D^{1/2} \quad (15.46)$$

In these expressions, the Nusselt and Péclet numbers are based on the diameter $D = 2r_0$:

$$\overline{\text{Nu}}_D = \frac{\overline{q''}}{T_w - T_\infty} \frac{D}{k_m} \quad \text{Pe}_D = \frac{uD}{\alpha_m} \quad (15.47)$$

15.4.3 Concentrated Heat Sources

In the region downstream from the hot sphere or cylinder of Fig. 15.1c, the heated fluid forms a thermal wake whose thickness increases as $x^{1/2}$. This behavior is illustrated in Fig. 15.1d and e, in which x measures the distance downstream from the heat source. Seen from the distant wake region, the embedded sphere appears as a point source (Fig. 15.1d), while the cylinder perpendicular to the uniform flow (u, T_∞) looks like a line source (Fig. 15.1e).

Consider the two-dimensional frame attached to the line source q' in Fig. 15.1e. The temperature distribution in the wake region, $T(x, y)$, is

$$T(x, y) - T_\infty = 0.282 \frac{q'}{k_m} \left(\frac{\alpha_m}{ux} \right)^{1/2} e^{-uy^2/4\alpha_m x} \quad (15.48)$$

This shows that the width of the wake increases as $x^{1/2}$, while the temperature excess on the centerline $[T(x, 0) - T_\infty]$ decreases as $x^{-1/2}$. The corresponding solution for the temperature distribution $T(x, r)$ in the round wake behind the point source q of Fig. 15.1d is

$$T(x, r) - T_\infty = \frac{q}{4\pi k_m x} e^{-ur^2/4\alpha_m x} \quad (15.49)$$

In this case, the excess temperature on the wake centerline decreases as x^{-1} , that is, more rapidly than on the centerline of the two-dimensional wake. Equations (15.48) and (15.49) are valid when the wake region is slender, in other words, when $\text{Pe}_x \gg 1$. When this Péclet number condition is not satisfied, the temperature field around the source is dominated by the effect of thermal diffusion, not convection. In such cases, the effect of the heat source is felt in all directions, not only downstream.

In the limit where the flow (u, T_∞) is so slow that the convection effect can be neglected, the temperature distribution can be derived by the classical methods of pure conduction. A steady-state temperature field can exist only around the point source (Bejan, 1993),

$$T(r) - T_\infty = \frac{q}{4\pi k_m r} \quad (15.50)$$

The pure-conduction temperature distribution around the line source remains time-dependent. When the time t is sufficiently long so that $(x^2 + y^2)/(4\alpha_m t) \ll 1$, the excess temperature around the line source is approximated by

$$T(x, y, t) - T_\infty \simeq \frac{q'}{4\pi k_m} \left[\ln \frac{4\alpha_m t}{\sigma(x^2 + y^2)} - 0.5772 \right] \quad (15.51)$$

15.4.4 Channels Filled with Porous Media

Consider now the forced-convection heat transfer in a channel or duct packed with a porous material as in Fig. 15.1f. In the Darcy flow regime the longitudinal volume-averaged velocity u is uniform over the channel cross section. When the temperature field is fully developed, the relationship between the wall heat flux q'' and the local temperature difference ($T_w - T_b$) is analogous to the relationship for fully developed heat transfer to slug flow through a channel without a porous matrix (Bejan, 1995). The temperature T_b is the mean or bulk temperature of the stream that flows through the channel,

$$T_b = \frac{1}{A} \int_A T \, dA \quad (15.52)$$

in which A is the area of the channel cross section. In cases where the confining wall is a tube with the internal diameter D , the relation for fully developed heat transfer can be expressed as a constant Nusselt number (Rohsenow and Choi, 1961):

$$\text{Nu}_D = \begin{cases} \frac{q''(x)}{T_w - T_b(x)} \frac{D}{k} = 5.78 & (\text{tube}, T_w = \text{constant}) \\ \frac{q''}{T_w(x) - T_b(x)} \frac{D}{k_m} = 8 & (\text{parallel plates}, q'' = \text{constant}) \end{cases} \quad (15.53)$$

$$\quad (15.54)$$

When the porous matrix is sandwiched between two parallel plates with the spacing D , the corresponding Nusselt numbers are (Rohsenow and Hartnett, 1973)

$$\text{Nu}_D = \begin{cases} \frac{q''(x)}{T_w - T_b(x)} \frac{D}{k_m} = 4.93 & (\text{parallel plates}, T_w = \text{constant}) \\ \frac{q''}{T_w(x) - T_b(x)} \frac{D}{k_m} = 6 & (\text{parallel plates}, q'' = \text{constant}) \end{cases} \quad (15.55)$$

$$\quad (15.56)$$

The forced-convection results of eqs. (15.53)–(15.56) are valid when the temperature profile across the channel is fully developed (sufficiently far from the entrance $x = 0$). The entrance length, or length needed for the temperature profile to become fully developed, can be estimated by noting that the thermal boundary layer thickness scales as $(\alpha_m x / u)^{1/2}$. Setting $(\alpha_m x / u)^{1/2} \sim D$, the thermal entrance length $x_T \sim D^2 u / \alpha_m$ is obtained. Inside the entrance region $0 < x < x_T$, the heat transfer is impeded by the forced-convection thermal boundary layers that line the channel walls, and can be calculated approximately using eqs. (15.38)–(15.41).

One important application of the results for a channel packed with a porous material is in the area of heat transfer augmentation. The Nusselt numbers for fully developed heat transfer in a channel without a porous matrix are given by expressions similar to eqs. (15.53)–(15.56) except that the saturated porous medium conductivity k_m is replaced by the thermal conductivity of the fluid alone, k_f . The relative heat transfer augmentation effect is indicated approximately by the ratio

$$\frac{h_x \text{ (with porous matrix)}}{h_x \text{ (without porous matrix)}} \sim \frac{k_m}{k_f} \quad (15.57)$$

in which h_x is the local heat transfer coefficient $q''/(T_w - T_b)$. In conclusion, a significant heat transfer augmentation effect can be achieved by using a high-conductivity matrix material, so that k_m is considerably greater than k_f .

Key results for forced convection in porous media have also been developed for tree networks of cracks (constructal theory) (Bejan, 2000), time-dependent heating, annular channels, stepwise changes in wall temperature, local thermal nonequilibrium, and other external flows (such as over a cone or wedge). These are also reviewed in Nield and Bejan (1999), which also describes improvement in porous-medium modeling that account for fluid inertia, thermal dispersion, boundary friction, non-Newtonian fluids, and porosity variation.

The concepts of heatfunctions and heatlines were introduced for the purpose of visualizing the true path of the flow of energy through a convective medium (Bejan, 1995). The heatfunction accounts simultaneously for the transfer of heat by conduction and convection at every point in the medium. The heatlines are a generalization of the flux lines used routinely in the field of conduction. The concept of heatfunction is a spatial generalization of the concept of the Nusselt number, that is, a way of indicating the magnitude of the heat transfer rate through any unit surface drawn through any point on the convective medium. The heatline method was extended recently to several configurations of convection through fluid-saturated porous media (Morega and Bejan, 1994).

15.4.5 Compact Heat Exchangers as Porous Media

An important application of the formalism of forced convection in porous media is in the field of heat exchanger simulation and design. Heat exchangers are a century-old technology based on information and concepts stimulated by the development of large-scale devices. The modern emphasis on heat transfer augmentation, and the more recent push toward miniaturization in the cooling of electronics, have led to the development of compact devices with much smaller features than in the past. These devices operate at lower Reynolds numbers, where their compactness and small dimensions ("pores") make them candidates for modeling as saturated porous media. Such modeling promises to revolutionize the nomenclature and numerical simulation of the flow and heat transfer through heat exchangers (Bejan et al., 2004).

To illustrate this change, consider Zhukauskas's (1987) classical chart for the pressure drop in crossflow through arrays of staggered cylinders (e.g., Fig. 9.38 in Bejan, 1993). The four curves drawn on this chart for the transverse pitch/cylinder diameter ratios 1.25, 1.5, 2, and 2.5 can be made to collapse into a single curve (Bejan and Morega, 1993), as shown in Fig. 15.2. The technique consists of treating the bundle as a fluid-saturated porous medium and using the volume-averaged velocity U , the pore Reynolds number $UK^{1/2}/\nu$ on the abscissa, and the dimensionless pressure gradient group $(\Delta P/L)K^{1/2}/\rho U^2$ on the ordinate.

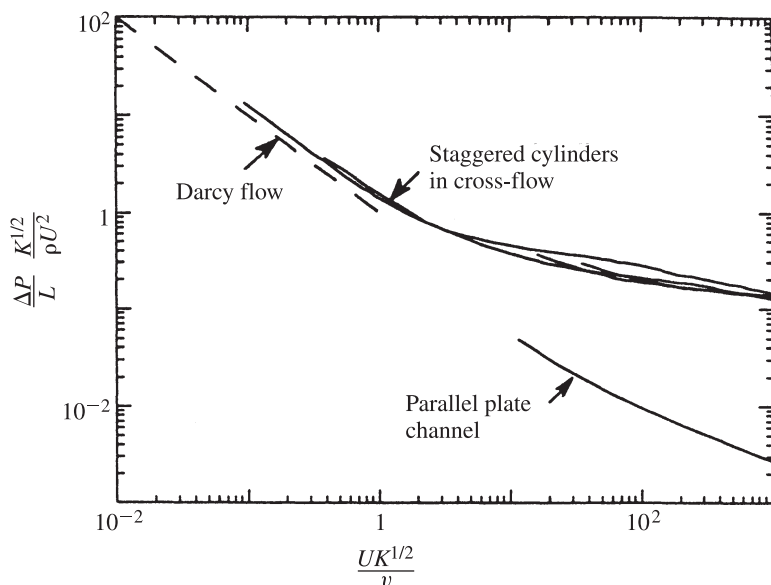


Figure 15.2 Porous medium representation of the classical pressure-drop data for flow through staggered cylinders and stacks of parallel plates. (From Bejan and Morega, 1993).

The method of presentation of Fig. 15.2 deserves to be extended to other heat exchanger geometries. Another reason for pursuing this direction is that the heat and fluid flow process can be simulated numerically much more easily if the heat exchanger is replaced at every point by a porous medium with volume-averaged properties.

Another important application of porous media concepts in engineering is in the optimization of the internal spacings of heat exchangers subjected to overall volume constraints. Packages of electronics cooled by forced convection are examples of heat exchangers that must function in fixed volumes. The design objective is to install as many components (i.e., heat generation rate) as possible, while the maximum temperature that occurs at a point (hot spot) inside the given volume does not exceed a specified limit. A very basic trade-off exists with respect to the number of components installed (Bejan and Sciubba, 1992) regarding the size of the pores through which the coolant flows. This trade-off is evident when the two extremes are imagined, these extremes being numerous components (small pores) and few components (large spacings).

When the components and pores are numerous and small, the package functions as a heat-generating porous medium. When the installed heat generation rate is fixed, the hot-spot temperature increases as the spacings become smaller, because in this limit the coolant flow is being shut off gradually. In the opposite limit, the hot-spot temperature increases again because the heat transfer contact area decreases as the component size and spacing become larger. At the intersection of these two

asymptotes, an optimal spacing (pore size) where the hot-spot temperature is minimal when the heat generation rate and volume are fixed is found.

The same spacing represents the design with maximal heat generation rate and fixed hot-spot temperature and volume. Analytical and numerical results have been developed for optimal spacings in applications with solid components shaped as parallel plates (Bejan, 1995). Optimal spacings for cylinders in crossflow were determined analytically and experimentally in Stanescu et al. (1996). The spacings of heat sinks with square pin fins and impinging flow were optimized numerically and experimentally in Ledezma et al. (1996). All the dimensionless results developed for optimal spacings (S_{opt}) have the form

$$\frac{S_{\text{opt}}}{L} \sim \text{Be}_L^{-n} \quad (15.58)$$

where L is the dimension of the given volume in the flow direction, and Be_L is a new dimensionless group (the Bejan number) that serves as the forced-convection analog of the Rayleigh number of natural convection (Bhattacharjee and Grosshandler, 1988; Petrescu, 1994),

$$\text{Be}_L = \frac{\Delta P \cdot L^2}{\mu_f \alpha_f} \quad (15.59)$$

In this definition ΔP is the pressure difference maintained across the fixed volume. For example, the exponent n in eq. (15.58) is equal to $\frac{1}{4}$ in the case of laminar flow through stacks of parallel-plate channels, and is comparable to $\frac{1}{4}$ in other configurations.

The frequency of pulsating flows through microchannels in parallel can be optimized for global system performance subject to total volume and void space constraints. The fundamentals of this optimization opportunity are outlined in Bejan (2000) and Bejan et al. (2004).

15.5 EXTERNAL NATURAL CONVECTION

15.5.1 Vertical Walls

In natural convection the body force is due to internal density differences that are induced by heating or cooling effects. The equations of motion reviewed in Section 15.2.2 are complemented by the assumption that density and temperature changes are sufficiently small so that the linear approximation is valid. This is known as the Oberbeck–Boussinesq approximation

$$\rho \approx \rho_0 [1 - \beta(T - T_0)] \quad (15.60)$$

where β is the thermal expansion coefficient

$$\beta = -\frac{1}{\rho} \left(\frac{\partial P}{\partial T} \right)_p \quad (15.61)$$

Note that the gravitational acceleration points in the negative y direction, in other words, the body acceleration vector \mathbf{g} appearing in eq. (15.6) and Fig. 15.1a, has $(0, -g, 0)$ as components.

Consider the heat and fluid flow in a porous medium adjacent to a heated vertical flat plate on which a thin thermal boundary layer is formed when the Rayleigh number Ra takes large values. Using the method of scale analysis (Bejan, 1984, 1995), the two-dimensional boundary layer equations take the form (Nield and Bejan, 1999)

$$\frac{\partial u}{\partial x} + \frac{\partial v}{\partial y} = 0 \quad (15.62)$$

$$v = -\frac{K}{\mu} \left[\frac{\partial P'}{\partial y} - \rho g \beta (T - T_\infty) \right] \quad (15.63)$$

$$\frac{\partial P'}{\partial x} = 0 \quad (15.64)$$

$$\sigma \frac{\partial T}{\partial t} + u \frac{\partial T}{\partial x} + v \frac{\partial T}{\partial y} = \alpha_m \frac{\partial^2 T}{\partial x^2} \quad (15.65)$$

Here the subscript ∞ denotes the reference value at a large distance from the heated boundary, and P' denotes the difference between the actual static pressure and the local hydrostatic pressure. It has been assumed that the Oberbeck–Boussinesq approximation and Darcy's law are valid. These equations were solved subject to a variety of boundary conditions, and the existing solutions are cataloged in Nield and Bejan (1999). The most important are the solutions for walls with constant temperature and constant heat flux.

The local Nusselt number for a vertical isothermal wall (Fig. 15.3a) is (Cheng and Minkowycz, 1977)

$$Nu_y = 0.444 Ra_y^{1/2} \quad (15.66)$$

where $Nu_y = q'' y / (T_w - T_\infty) k_m$ and the local Rayleigh number is defined as $Ra_y = K g \beta y (T_w - T_\infty) / \alpha_m \nu$. Equation (15.66) is valid in the boundary layer regime, $Ra_y^{1/2} \gg 1$. The overall Nusselt number is

$$\overline{Nu}_H = 0.888 Ra_H^{1/2} \quad (15.67)$$

where $\overline{Nu}_H = \overline{q''} H / [k_m (T_w - T_\infty)]$ and $Ra_H = K g \beta H (T_w - T_\infty) / \alpha_m \nu$ and where H is the height of the wall.

For convection near walls with uniform heat flux, the local Nusselt number (Cheng and Minkowycz, 1977) can be rearranged (Bejan, 1984):

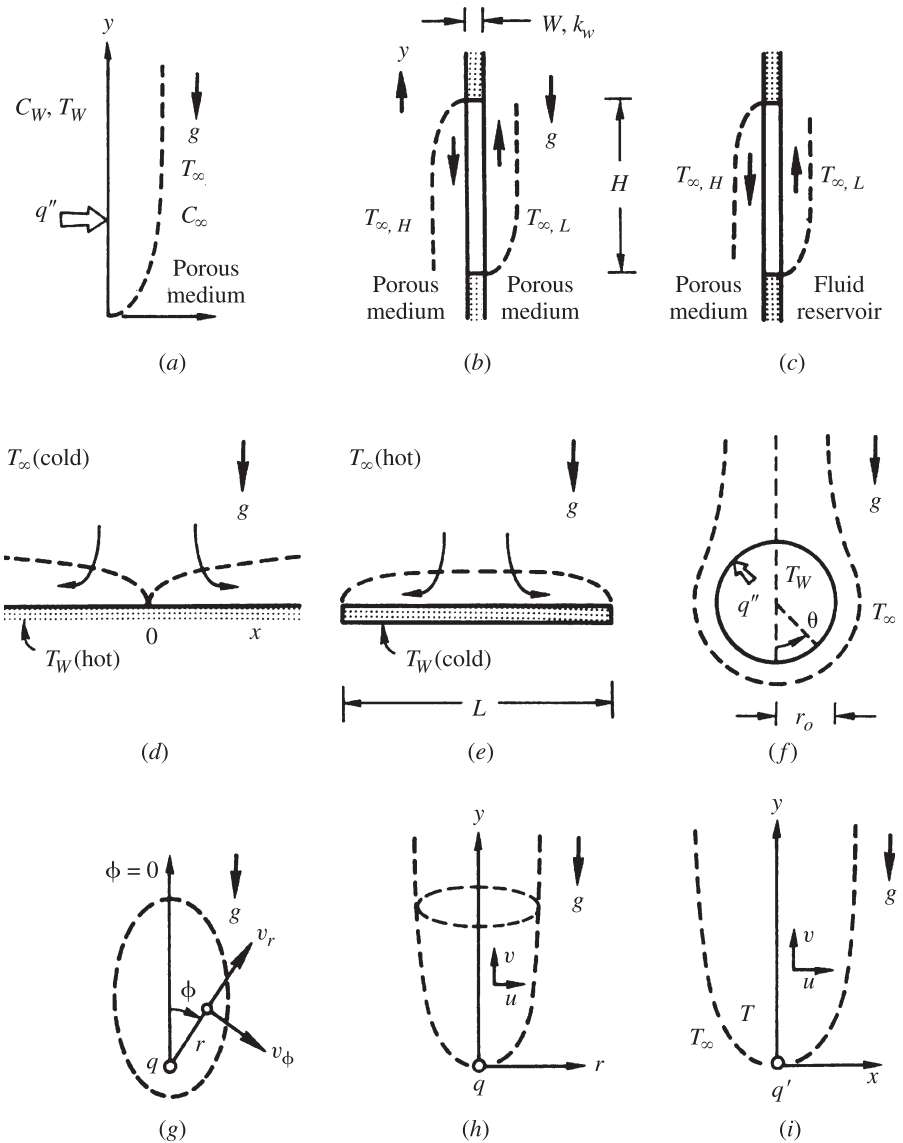


Figure 15.3 Natural convection in external flow: (a) impermeable vertical wall; (b) vertical partition embedded in a porous medium; (c) vertical wall separating a porous medium and a fluid reservoir; (d) hot surface facing upward in a porous medium; (e) cold surface facing upward in a porous medium; (f) impermeable sphere or cylinder embedded in a porous medium; (g) point heat source, low-Rayleigh-number regime; (h) point heat source, high-Rayleigh-number regime; (i) horizontal line source.

$$\text{Nu}_y = 0.772 \text{Ra}_y^{*1/3} \quad (15.68)$$

where $\text{Nu}_y = q'' y / k_m [T_w(y) - T_\infty]$ and $\text{Ra}_y^* = K g \beta y^2 q'' / \alpha_m \nu k_m$. Equation (15.68) holds in the boundary layer regime, $\text{Ra}_y^{*1/3} \gg 1$. The corresponding formula for the overall Nusselt number is

$$\overline{\text{Nu}}_H = 1.044 \text{Ra}_H^{*1/3} \quad (15.69)$$

where $\overline{\text{Nu}}_H = q'' H / k_m (\overline{T}_w - T_\infty)$ and $\text{Ra}_H^* = K g \beta H^2 q'' / \alpha_m \nu k_m$. Other formulations of the boundary layer problem, such as the time-dependent development of the flow near a vertical wall, and the flow near a permeable wall with blowing or suction, are reviewed in Nield and Bejan (1999).

When the porous medium of Fig. 15.3a is finite in both directions, the discharge of the heated vertical stream into the rest of the medium leads in time to thermal stratification. This problem was considered in Bejan (1984). As shown in the upper part of Fig. 15.4, the original wall excess temperature is $T_0 - T_{\infty,0}$, and the porous medium is stratified according to the positive vertical gradient $\gamma = dT_\infty/dy$. The local temperature difference $T_0 - T_\infty(y)$ decreases as y increases, which is why a monotonic decrease in the total heat transfer rate as γ increases should be expected. This trend is confirmed by the lower part of the figure, which shows the integral solution developed for this configuration. The overall Nusselt number, Rayleigh number, and stratification parameter are defined as

$$\overline{\text{Nu}}_H = \frac{\overline{q''} H}{k_m (T_0 - T_{\infty,0})} \quad (15.70)$$

$$\text{Ra}_H = \frac{K g \beta H}{\alpha_m \nu} (T_0 - T_{\infty,0}) \quad (15.71)$$

$$b = \frac{\gamma H}{T_0 - T_{\infty,0}} \quad (15.72)$$

The accuracy of this integral solution can be assessed by comparing its $b = 0$ limit,

$$\frac{\overline{\text{Nu}}_H}{\text{Ra}_H^{1/2}} = 1 \quad (b = 0) \quad (15.73)$$

with the similarity solution for an isothermal wall adjacent to an isothermal porous medium, eq. (15.67). The integral solution overestimates the global heat transfer rate by only 12.6%.

Referring again to the single-wall geometry of Fig. 15.3a, the corresponding problem in a porous medium saturated with water near the temperature of maximum density was solved by Ramilison and Gebhart (1980). In place of the Oberbeck–Boussinesq model, this solution was based on $\rho = \rho_m (1 - \alpha_m |T - T_m|^q)$, where ρ_m and T_m are the maximum density and the temperature of the state of maximum

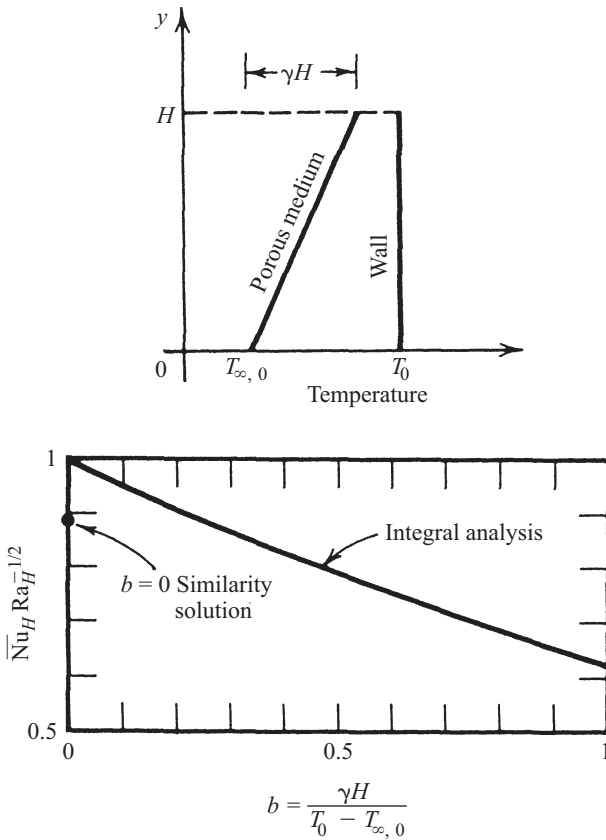


Figure 15.4 Heat transfer solution for a vertical isothermal wall bordering a linearly stratified porous medium saturated with fluid. (From Bejan, 1984.)

density. The parameters ρ_m , T_m , q , and $\overline{\alpha_m}$ (not to be confused with the thermal diffusivity α_m) depend on the pressure and salinity, and are reported in Gebhart and Mollendorf (1977). Data on the local Nusselt number are reported in graphical form (Ramilison and Gebhart, 1980); a closed-form analytical substitute for this graphical information for pure water at atmospheric pressure was found by the present author,

$$\overline{Nu}_y = 0.42 \times 0.35 - \left| \frac{T_m - T_\infty}{T_w - T_\infty} \right|^{0.46} \left[\frac{2\overline{\alpha_m} K g y (T_w - T_\infty)}{\alpha_m \nu} \right]^{1/2} \quad (15.74)$$

Equation (15.74) is accurate within 1% in the range $-16 < (T_m - T_\infty)/(T_w - T_\infty) < 5$.

The breakdown of the Darcy flow model in vertical boundary layer natural convection was the subject of several studies (Plumb and Huenefeld, 1981; Bejan and Poulikakos, 1984; Nield and Joseph, 1985). Assuming the Forchheimer modification of the Darcy flow model, at local pore Reynolds numbers greater than 10, the local

Nusselt number for the vertical wall configuration of Fig. 15.3a approaches the following limits (Bejan and Poulidakos, 1984):

$$\text{Nu}_y = \begin{cases} 0.494\text{Ra}_{\infty,y}^{1/4} & \text{for the isothermal wall} \\ 0.804\text{Ra}_{\infty,y}^{*1/5} & \text{for the constant heat flux wall} \end{cases} \quad (15.75)$$

where $\text{Ra}_{\infty,y} = g\beta y^2(T_w - T_\infty)/(b\alpha_m^2)$ and $\text{Ra}_{\infty,y}^* = g\beta y^3 q''/(k_m b\alpha_m^2)$. Equations (15.75) and (15.76) are valid provided that $G \ll 1$, where $G = (v/K)[bg\beta(T_w - T_\infty)]^{-1/2}$. In the intermediate range between the Darcy limit and the inertia-dominated limit, that is, in the range where G is of order 1, numerical results (Bejan and Poulidakos, 1984) for a vertical isothermal wall are correlated within 2% by the closed-form expression

$$\text{Nu}_y = \left[(0.494)^n + (0.444G^{-1/2})^n \right]^{1/n} \cdot \text{Ra}_{\infty,y}^{1/4} \quad (15.77)$$

The heat transfer results summarized in this section also apply to configurations where the vertical wall is inclined (slightly) to the vertical. In such cases, the gravitational acceleration that appears in the definition of Rayleigh-type numbers in this section must be replaced by the gravitational acceleration component that acts along the early vertical wall.

When a vertical wall divides two porous media and a temperature difference exists between the two systems, there is a pair of conjugate boundary layers, one on each side of the wall, with neither the temperature nor the heat flux specified on the wall but rather, to be found as part of the solution of the problem (Fig. 15.3b) (Bejan and Anderson, 1981). The overall Nusselt number results for this configuration are correlated within 1% by the expression

$$\overline{\text{Nu}}_H = 0.382(1 + 0.615\omega)^{-0.875} \cdot \text{Ra}_H^{1/2} \quad (15.78)$$

where $\overline{\text{Nu}}_H = \overline{q''}H/(T_{\infty,H} - T_{\infty,L})k_m$ and where $\overline{q''}$ is the heat flux averaged over the entire height H . In addition, $\text{Ra}_H = Kg\beta H(T_{\infty,H} - T_{\infty,L})/(\alpha_m v)$; the wall thickness parameter ω is defined as

$$\omega = \frac{W}{H} \frac{k_m}{k_w} \text{Ra}_H^{1/2} \quad (15.79)$$

In this dimensionless group, W and H are the width and height of the wall cross section, k_m and k_w are the conductivities of the porous medium and wall material, respectively, and Ra_H is the Rayleigh number based on H and the temperature difference between the two systems.

In thermal insulation and architectural applications, the porous media on both sides of the vertical partition of Fig. 15.3b may be thermally stratified. If the stratification on both sides is the same and linear (e.g., Fig. 15.4), so that the vertical temperature gradient far enough from the wall is $dT/dy = b_1(T_{\infty,H} - T_{\infty,L})/H$, where b_1 is a constant, and if the partition is thin enough so that $\omega = 0$, it is found that the overall

Nusselt number increases substantially with the degree of stratification (Bejan and Anderson, 1983). In the range $0 < b_1 < 1.5$, these findings are summarized by the correlation

$$\overline{\text{Nu}}_H = 0.382 (1 + 0.662b_1 - 0.073b_1^2) \cdot \text{Ra}_H^{1/2} \quad (15.80)$$

Another configuration of engineering interest is sketched in Fig. 15.3c: a vertical impermeable surface separates a porous medium of temperature $T_{\infty,H}$ from a fluid reservoir of temperature $T_{\infty,L}$ (Bejan and Anderson, 1983). When both sides of the interface are lined by boundary layers, the overall Nusselt number is

$$\overline{\text{Nu}}_H = [(0.638)^{-1} + (0.888B)^{-1}]^{-1} \cdot \text{Ra}_{H,f}^{1/4} \quad (15.81)$$

where $\overline{\text{Nu}}_H = \overline{q''}H/(T_{\infty,H} - T_{\infty,L})k_m$ and $B = k_m \cdot \text{Ra}_H^{1/2}/(k_f \cdot \text{Ra}_{H,f}^{1/4})$. The parameter k_f is the fluid-side thermal conductivity, and the fluid-side Rayleigh number $\text{Ra}_{H,f} = g(\beta/\alpha\nu)_f H^3(T_{\infty,H} - T_{\infty,L})$. Equation (15.81) is valid in the regime where both boundary layers are distinct, $\text{Ra}_H^{1/2} \gg 1$ and $\text{Ra}_{H,f}^{1/4} \gg 1$; it is also assumed that the fluid on the right side of the partition in Fig. 15.3c has a Prandtl number of order 1 or greater. Additional solutions for boundary layer convection in the vicinity of vertical partitions in porous media are reviewed in Nield and Bejan (1999).

15.5.2 Horizontal Walls

With reference to Fig. 15.3d, boundary layers form in the vicinity of a heated horizontal surface that faces upward (Cheng and Chang, 1976). Measuring x horizontally away from the vertical plane of symmetry of the flow, the local Nusselt number for an isothermal wall is

$$\text{Nu}_x = 0.42\text{Ra}_x^{1/3} \quad (15.82)$$

where $\text{Nu}_x = q''x/k_m(T_w - T_\infty)$ and $\text{Ra}_x = Kg\beta x(T_w - T_\infty)/\alpha_m\nu$. The local Nusselt number for a horizontal wall heated with uniform flux is

$$\text{Nu}_x = 0.859\text{Ra}_x^{*1/4} \quad (15.83)$$

where $\text{Ra}_x^* = Kg\beta x^2 q''/k_m\alpha_m\nu$. Equations (15.82) and (15.83) are valid in the boundary layer regime, $\text{Ra}_x^{1/3} \gg 1$ and $\text{Ra}_x^{*1/4} \gg 1$, respectively. They also apply to porous media bounded from above by a cold surface; this new configuration is obtained by rotating Fig. 15.3d by 180° . The transient heat transfer associated with suddenly changing the temperature of the horizontal wall is documented in Pop and Cheng (1983).

The other horizontal wall configuration, the upward-facing cold plate of Fig. 15.3e, was studied in Kimura et al. (1985). The overall Nusselt number in this configuration is

$$\text{Nu} = 1.47\text{Ra}_L^{1/3} \quad (15.84)$$

where $Nu = q' / [k_m(T_\infty - T_w)]$ and $Ra_L = Kg\beta L(T_\infty - T_w) / \alpha_m \nu$ and where q' is the overall heat transfer rate through the upward-facing cold plate of length L . Equation (15.84) holds if $Ra_L \gg 1$ and applies equally to hot horizontal plates facing downward in an isothermal porous medium. Note the exponent $\frac{1}{3}$, which is in contrast to the exponent $\frac{1}{2}$ for the vertical wall in eq. (15.67). Other solutions and flow instabilities in natural convection above or under horizontal walls are reviewed in Nield and Bejan (1999).

15.5.3 Sphere and Horizontal Cylinder

With reference to the coordinate system shown in the circular cross section sketched in Fig. 15.3f, the local Nusselt numbers for boundary layer convection around an impermeable sphere or a horizontal cylinder embedded in an infinite porous medium are, in order,

$$Nu_\theta = \begin{cases} 0.444 Ra_\theta^{1/2} \left(\frac{3}{2}\theta\right)^{1/2} \sin^2 \theta \left(\frac{1}{3} \cos^3 \theta - \cos \theta + \frac{2}{3}\right)^{-1/2} & (15.85) \\ 0.444 Ra_\theta^{1/2} (2\theta)^{1/2} \sin \theta (1 - \cos \theta)^{-1/2} & (15.86) \end{cases}$$

where $Nu_\theta = q'' r_0 \theta / [k_m(T_w - T_\infty)]$ and $Ra_\theta = Kg\beta r_0(T_w - T_\infty) / \alpha_m \nu$. These steady-state results have been reported in Cheng (1982); they are valid provided that the boundary layer region is slender enough, that is, if $Nu_\theta \gg 1$. The overall Nusselt numbers for the sphere and horizontal cylinder are, respectively (Nield and Bejan, 1999),

$$\overline{Nu}_D = \begin{cases} 0.362 Ra_D^{1/2} & (15.87) \\ 0.565 Ra_D^{1/2} & (15.88) \end{cases}$$

where $\overline{Nu}_D = \overline{q''} D / [k_m(T_w - T_\infty)]$ and $Ra_D = Kg\beta D(T_w - T_\infty) / \alpha_m \nu$. The transient flow of and heat transfer near a horizontal cylinder are described in Ingham et al. (1983). Solutions for convection at low and intermediate Rayleigh numbers are summarized in Nield and Bejan (1999).

15.5.4 Concentrated Heat Sources

The convection generated in a porous medium by a concentrated heat source has been studied in two limits: first, the *low-Rayleigh-number regime*, where the temperature distribution is primarily due to thermal diffusion, and second, the *high-Rayleigh-number regime*, where the flow driven by the source is a slender vertical plane (this second regime may be called the *boundary layer regime*).

In the low-Rayleigh-number regime, the transient flow and temperature fields around a constant-strength heat source q that starts to generate heat at $t = 0$ is (Bejan, 1978)

$$\psi = \alpha_m K^{1/2} \cdot \text{Ra}_q \frac{\tau^{1/2}}{8\pi} \sin^2 \phi \left[2\eta \operatorname{erfc} \eta + \frac{1}{\eta} \operatorname{erf} \eta - \frac{2}{\pi^{1/2}} \exp(-\eta^2) \right] \quad (15.89)$$

$$\begin{aligned} T - T_\infty = \frac{q}{k_m K^{1/2}} & \left[\frac{1}{4\pi R} \operatorname{erfc} \left(\frac{R}{2\tau^{1/2}} \right) + \text{Ra}_q \frac{\cos \phi}{64\pi^2 \tau^{1/2}} \right. \\ & \times \left(\frac{1}{\eta} - \frac{4}{3\pi^{1/2}} + \frac{6}{5\pi^{1/2}} \eta^2 - \frac{16}{45\pi} \eta^3 - \frac{152}{315\pi^{1/2}} \eta^4 \right. \\ & + \frac{64}{315\pi} \eta^5 + \frac{517}{3780\pi^{1/2}} \eta^6 - \frac{992}{14,175\pi} \eta^7 \\ & \left. \left. - \frac{2039}{69,300\pi^{1/2}} \eta^8 + \frac{2591}{155,929\pi} \eta^9 + \dots \right) \right] \quad (15.90) \end{aligned}$$

where

$$\eta = \frac{R}{2\tau^{1/2}} \quad R = \frac{r}{K^{1/2}} \quad \tau = \frac{\alpha_m t}{\sigma K} \quad (15.91)$$

and

$$\text{Ra}_q = \frac{Kg\beta q}{\alpha_m \nu k_m} \quad (15.92)$$

is the Rayleigh number based on point-source strength. The stream function ψ is defined in the axisymmetric spherical coordinates of Fig. 15.3g via

$$v_r = \frac{1}{r^2 \sin \phi} \frac{\partial \psi}{\partial \phi} \quad v_\phi = -\frac{1}{r \sin \phi} \frac{\partial \psi}{\partial r} \quad (15.93)$$

The time-dependent solution of eqs. (15.89)–(15.93) is valid in the range $0 < \eta < 1$. The steady-state flow and temperature fields around a constant point source q in the low-Rayleigh-number regime is (Bejan, 1978)

$$\begin{aligned} \psi = \frac{\alpha r}{8\pi} & \left[\text{Ra}_q \sin^2 \phi + \frac{\text{Ra}_q^2}{24\pi} \sin \phi \sin 2\phi \right. \\ & \left. - \frac{5\text{Ra}_q^3}{18,432\pi^2} (8 \cos^4 \phi - 3) + \dots \right] \quad (15.94) \end{aligned}$$

$$\begin{aligned} T - T_\infty = \frac{q}{4\pi k r} & \left[1 + \frac{\text{Ra}_q}{8\pi} \cos \phi + \frac{5\text{Ra}_q^2}{768\pi^2} \cos 2\phi \right. \\ & \left. + \frac{\text{Ra}_q^3}{55,296\pi^3} \cos \phi (47 \cos^2 \phi - 30) - \dots \right] \quad (15.95) \end{aligned}$$

The series solution of eqs. (15.94) and (15.95) is sufficiently accurate if Ra_q is on the order of 20 or less. Numerical solutions for the point-source steady-state problem at Rayleigh numbers in the range 10^{-1} to 10^2 are reported in Hickox and Watts (1980). The same authors reported analytical results for the limit $Ra_q \rightarrow 0$ and numerical results in the Ra_q range 10^{-1} to 10^2 for steady-state flow near a point source located at the base of a semi-infinite porous medium bounded from below by an impermeable and insulated surface. A subsequent paper (Hickox, 1981) shows that the transient and steady-state solutions for the point source in the strict $Ra \rightarrow 0$ limit can be superimposed to predict the flow and temperature fields around buried objects of more complicated geometries.

In the high-Rayleigh-number regime, the point source generates a vertical plume flow the thickness of which scales as $y \cdot Ra_q^{-1/2}$, where y is the vertical position along the plume axis (Fig. 15.3*h*). The analytical solution for the flow and temperature field was constructed in Bejan (1984),

$$\frac{T - T_\infty}{q/(k_m y)} = \frac{v}{(\alpha_m/y)Ra_q} = \frac{2C_1^2}{1 + (C_1\eta/2)^2} \quad (15.96)$$

where $\eta = (r/y)Ra_q^{1/2}$ and $C_1 = 0.141$. The solution holds provided the plume region is slender (i.e., when $Ra_q^{1/2} \gg 1$).

The two-dimensional frame of Fig. 15.3*i* shows a plume above a horizontal line heat source. The temperature and flow fields generated in a porous medium at high Rayleigh numbers by a horizontal line source of strength q' (W/m) are

$$\frac{T - T_\infty}{(q'/k_m)Ra_{q'}^{-1/3}} = \frac{v}{(\alpha_m/y)Ra_{q'}^{2/3}} = \frac{C_2^2/6}{\cosh^2(C_2\eta/6)} \quad (15.97)$$

where $C_2 = 1.651$, $\eta = (x/y)Ra_{q'}^{1/3}$, and $Ra_{q'} = Kg\beta y q'/\alpha_m \nu k_m$ is the Rayleigh number based on line source strength. The derivation of this solution can be found in Wooding (1963) and is a special case of vertical boundary layer convection (Cheng and Minkowycz, 1977). The boundary layer solution in eq. (15.97) is valid at sufficiently high Rayleigh numbers $Ra_{q'}^{1/3} \gg 1$. The low-Rayleigh-number regime for convection near a horizontal line source (in an infinite medium or near a vertical insulated and impermeable surface) is described in Nield and Bejan (1999).

15.6 INTERNAL NATURAL CONVECTION

15.6.1 Enclosures Heated from the Side

The most basic configuration of a porous layer heated in the horizontal direction is sketched in Fig. 15.5*a*. In Darcy flow, the heat and fluid flow driven by buoyancy depends on two parameters: the geometric aspect ratio H/L , and the Rayleigh number based on height, $Ra_H = Kg\beta H(T_h - T_c)/\alpha_m \nu$. There exist four heat transfer regimes

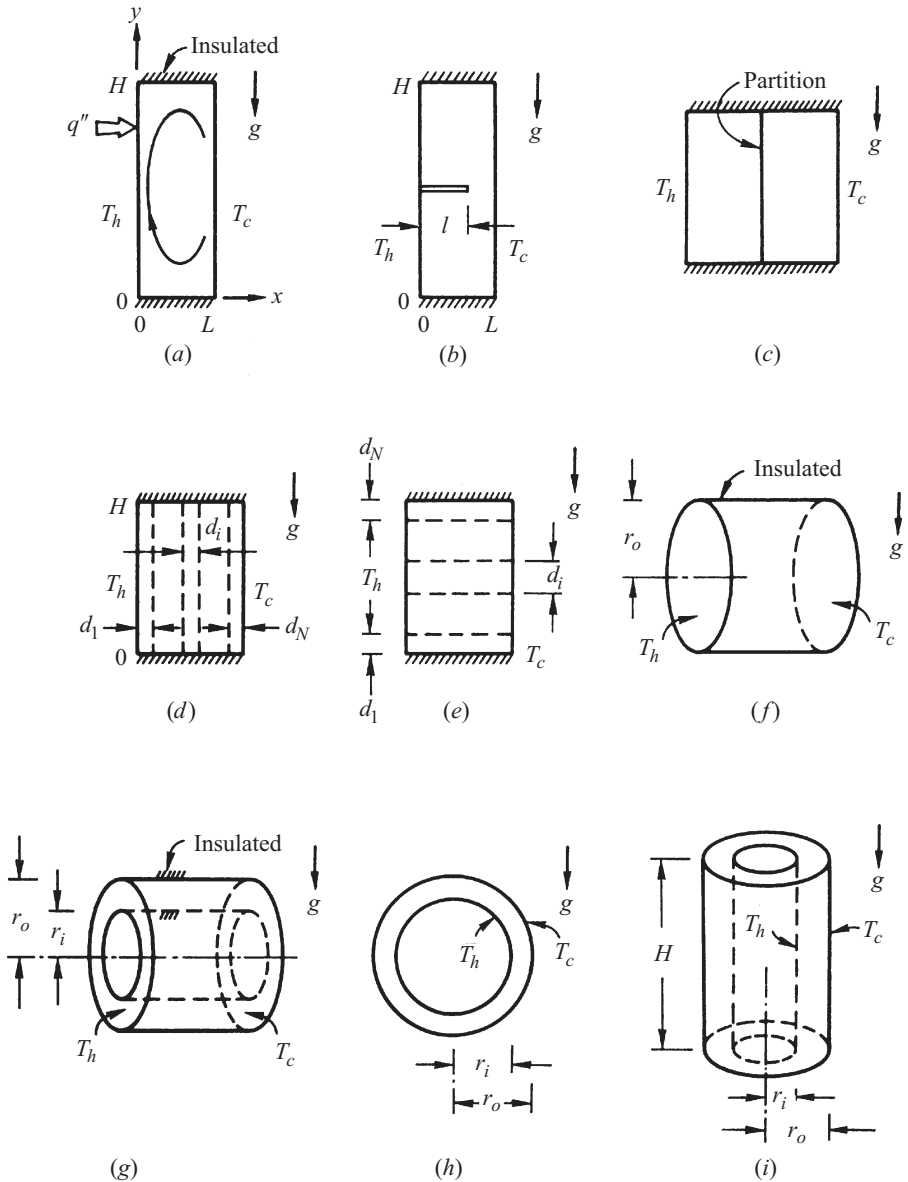


Figure 15.5 Natural convection heat transfer in confined porous media heated from the side: (a) rectangular enclosure; (b) rectangular enclosure with a horizontal partial partition; (c) rectangular enclosure with a vertical full partition midway; (d) rectangular enclosure made up of N vertical sublayers of different K and α ; (e) rectangular enclosure made up of N horizontal sublayers of different K and α ; (f) horizontal cylindrical enclosure; (g) horizontal cylindrical annulus with axial heat flow; (h) horizontal cylindrical or spherical annulus with radial heat flow; (i) vertical cylindrical annulus with radial heat flow.

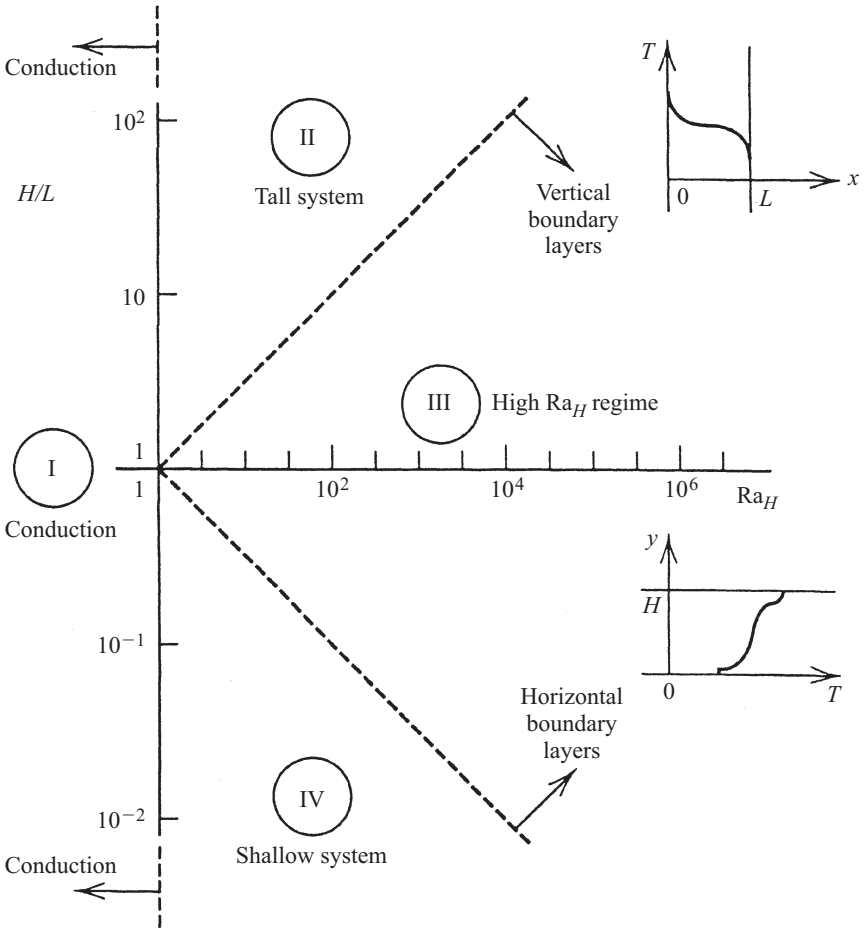


Figure 15.6 Four heat transfer regimes for natural convection in an enclosed porous layer heated from the side. (From Bejan, 1984.)

(Bejan, 1984), that is, four ways to calculate the overall heat transfer rate $q' = \int_0^H q'' dy$. These are summarized in Fig. 15.6.

- *Regime I:* the pure conduction regime, defined by $Ra_H \ll 1$. In this regime, q' is approximately equal to the pure conduction estimate $k_m H (T_h - T_c) / L$.
- *Regime II:* the conduction dominated regime in tall layers, defined by $H/L \gg 1$ and $(L/H) Ra_H^{1/2} \ll 1$. In this regime, the heat transfer rate scales as $q' \geq k_m H (T_h - T_c) / L$.
- *Regime III:* the convection-dominated regime (or high-Rayleigh-number regime), defined by $Ra_H^{-1/2} < H/L < Ra_H^{1/2}$. In this regime, q' scales as $k_m (T_h - T_c) Ra_H^{1/2}$.

- *Regime IV*: the convection-dominated regime in shallow layers, defined by $H/L \ll 1$ and $(H/L)\text{Ra}_H^{1/2} \ll 1$. Here the heat transfer rate scales as $q \leq k_m(T_h - T_c)\text{Ra}_H^{1/2}$.

Considerable analytical, numerical, and experimental work has been done to estimate more accurately the overall heat transfer rate q' or the overall Nusselt number:

$$\text{Nu} = \frac{q'}{kH(T_h - T_c)/L} \quad (15.98)$$

Note that unlike the single-wall configurations of Section 15.5.1, in confined layers of thickness L the Nusselt number is defined as the ratio of the actual heat transfer rate to the pure conduction heat transfer rate. An analytical solution that covers the four heat transfer regimes smoothly is (Bejan and Tien, 1978)

$$\text{Nu} = K_1 + \frac{1}{120} K_1^3 \left(\text{Ra}_H \frac{H}{L} \right)^2 \quad (15.99)$$

where $K_1(H/L, \text{Ra}_H)$ is obtained by solving the system

$$\frac{1}{120} \delta_e \cdot \text{Ra}_H^2 \cdot K_1^3 \left(\frac{H}{L} \right)^3 = 1 - K_1 = \frac{1}{2} K_1 \frac{H}{L} \left(\frac{1}{\delta_e} - \delta_e \right) \quad (15.100)$$

This result is displayed in chart form in Fig. 15.7, along with numerical results from Hickox and Gartling (1981). The asymptotic values of this solution are

$$\text{Nu} \sim \begin{cases} 0.508 \frac{L}{H} \text{Ra}_H^{1/2} & \text{as } \text{Ra}_H \rightarrow \infty \\ 1 + \frac{1}{120} \left(\text{Ra}_H \frac{H}{L} \right)^2 & \text{as } \frac{H}{L} \rightarrow 0 \end{cases} \quad (15.101)$$

$$(15.102)$$

The heat transfer in the convection-dominated regime III is represented well by eq. (15.101) or by alternative solutions developed solely for regime III: for example (Weber, 1975),

$$\text{Nu} = 0.577 \frac{L}{H} \text{Ra}_H^{1/2} \quad (15.103)$$

Equation (15.103) overestimates experimental and numerical data from three independent sources (Bejan, 1979) by only 14%. More refined estimates for regime III were developed in Bejan (1979) and Simpkins and Blythe (1980), where the proportionality factor between Nu and $(L/H)\text{Ra}_H^{1/2}$ is replaced by a function of both H/L and Ra_H . This alternative is illustrated in Fig. 15.8. For expedient engineering calculations of heat transfer dominated by convection, Fig. 15.7 is recommended for shallow layers ($H/L < 1$), and Fig. 15.8 for square and tall layers ($H/L \gtrsim 1$) in the boundary layer regime, $\text{Ra}_H^{-1/2} < H/L < \text{Ra}_H^{1/2}$.

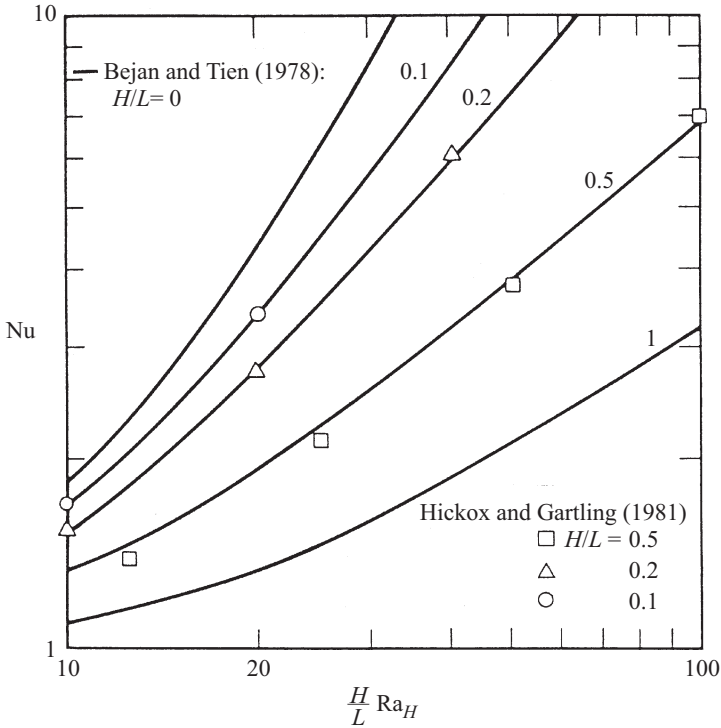


Figure 15.7 Total heat transfer rate through an enclosed porous layer heated from the side. (From Bejan and Tien, 1978.)

In the field of thermal insulation engineering, a more appropriate model for heat transfer in the configuration of Fig. 15.5a is the case where the heat flux q'' is distributed uniformly along the two vertical sides of the porous layer. In the high-Rayleigh-number regime (regime III), the overall heat transfer rate is given by (Bejan, 1983a)

$$Nu = \frac{1}{2} \left(\frac{L}{H} \right)^{4/5} \cdot Ra_H^{*2/5} \tag{15.104}$$

where $Ra_H^* = Kg\beta H^2 q'' / \alpha_m \nu k_m$. The overall Nusselt number is defined as in eq. (15.98), where $T_h - T_c$ is the height-averaged temperature difference between the two sides of the rectangular cross section. Equation (15.104) holds in the high-Rayleigh-number regime $Ra_H^{*-1/3} < H/L < Ra_H^{*1/3}$.

Impermeable partitions (flow obstructions) inserted in the confined porous medium can have a dramatic effect on the overall heat transfer rate across the enclosure (Bejan, 1983b). With reference to the two-dimensional geometry of Fig. 15.5b, in the convection-dominated regimes III and IV the overall heat transfer rate decreases

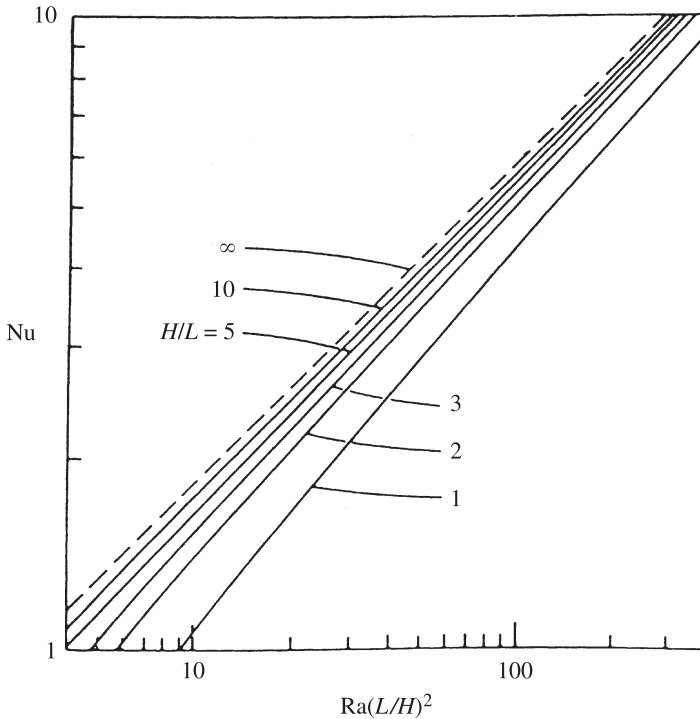


Figure 15.8 Heat transfer rate in regime III through a porous layer heated from the side. (From Bejan, 1979.)

steadily as the length l of the horizontal partition approaches L , that is, as the partition divides the porous layer into two shorter layers. The horizontal partition has practically no effect in regimes I and II, where the overall heat transfer rate is dominated by conduction. If the partition is oriented vertically (Fig. 15.5c), in the convection-dominated regime the overall heat transfer rate is approximately 40% of what it would have been in the same porous medium without the internal partition.

The nonuniformity of permeability and thermal diffusivity can have a dominating effect on the overall heat transfer rate (Poulikakos and Bejan, 1983b). In cases where the properties vary so that the porous layer can be modeled as a sandwich of vertical sublayers of different permeability and diffusivity (Fig. 15.5d), an important parameter is the ratio of the peripheral sublayer thickness (d_1) to the thermal boundary layer thickness ($\delta_{T,1}$) based on the properties of the d_1 sublayer (note that $\delta_{T,1}$ scales as $H \cdot \text{Ra}_{H,1}^{-1/2}$, where the Rayleigh number $\text{Ra}_{H,1} = K_1 g \beta H (T_h - T_c) / \alpha_1 \nu$ and where the subscript 1 represents the properties of the d_1 sublayer). If $d_1 > \delta_{T,1}$, the heat transfer through the left side of the porous system of Fig. 15.5d is impeded by a thermal resistance of order $\delta_{T,1} / k_1 H$. If the sublayer situated next to the right wall (d_N) has exactly the same properties as the d_1 sublayer, and if $\delta_{T,1} < (d_1, d_N)$, the overall heat transfer rate in the convection-dominated regime can be estimated using

eq. (15.101), in which both Nu and Ra_H are based on the properties of the peripheral layers.

When the porous-medium inhomogeneity may be modeled as a sandwich of N horizontal sublayers (Fig. 15.5e), the scale of the overall Nusselt number in the convection-dominated regime can be evaluated as (Poulikakos and Bejan, 1983a)

$$Nu \sim 2^{-3/2} Ra_{H,1}^{1/2} \frac{L}{H} \sum_{i=1}^N \frac{k_i}{k_1} \left(\frac{K_i d_i \alpha_i}{K_1 d_1 \alpha_i} \right)^{1/2} \quad (15.105)$$

where both Nu and $Ra_{H,1}$ are based on the properties of the d_1 sublayer (Fig. 15.5e). The correlation of eq. (15.105) was tested via numerical experiments in two-layer systems.

The heat transfer results reviewed in this section are based on the idealization that the surface that surrounds the porous medium is impermeable. With reference to the two-dimensional geometry of Fig. 15.5a, the heat transfer through a shallow porous layer with one or both end surfaces permeable is anticipated analytically in Bejan and Tien (1978). Subsequent laboratory measurements and numerical solutions for Ra_H values up to 120 validate the theory (Haajizadeh and Tien, 1983).

Natural convection in cold water saturating the porous-medium configuration of Fig. 15.5a was considered in Poulikakos (1984). Instead of the linear approximation of eq. (15.60), this study used the parabolic model

$$\rho_m - \rho = \gamma \rho_m (T - T_m)^2 \quad (15.106)$$

where $\gamma \approx 8.0 \times 10^{-6} K^{-2}$ and $T_m = 3.98^\circ C$ for pure water at atmospheric pressure. The parabolic density model is valid in the temperature range 0 to $10^\circ C$. In the convection-dominated regime $Nu \gg 1$, the scale analysis (Bejan, 1995) leads to the Nusselt number correlation (Bejan, 1987)

$$Nu = c_3 \frac{L/H}{Ra_{\gamma h}^{-1/2} + c_4 Ra_{\gamma c}^{-1/2}} \quad (15.107)$$

where $Ra_{\gamma h} = Kg\gamma H(T_h - T_m)^2/\alpha_m \nu$, $Ra_{\gamma c} = Kg\gamma H(T_m - T_c)^2/\alpha_m \nu$, and where the Nusselt number is defined in eq. (15.98). For the convection-dominated regime, the numerical study (Poulikakos, 1984) tabulated results primarily for the case $T_c = 0^\circ C$, $T_h = 7.96^\circ C$; using these data for cases in which T_c and T_h are symmetrically positioned around T_m (i.e., when $Ra_{\gamma h} = Ra_{\gamma c}$), the scaling-correct correlation in eq. (15.107) takes the form (Bejan, 1987)

$$Nu \approx 0.26 \frac{L}{H} Ra_{\gamma h}^{1/2} \quad (15.108)$$

In other words, the two constants that appear in eq. (15.107) satisfy the relationship $c_3 \approx 0.26(1 + c_4)$. More experimental data for the high-Rayleigh-number regime in vertical layers with $Ra_{\gamma h} \neq Ra_{\gamma c}$ are needed to determine c_3 and c_4 uniquely.

15.6.2 Cylindrical and Spherical Enclosures

The convection occurring in a porous medium confined in a horizontal cylinder with disk-shaped ends at different temperatures (Fig. 15.5f) has features similar to the problem of Fig. 15.5a. A parametric solution for the horizontal cylinder problem is reported in Bejan and Tien (1978). The corresponding phenomenon in a porous medium in the shape of a horizontal cylinder with annular cross section (Fig. 15.5g) is documented in Bejan and Tien (1979).

A pivotal important geometric configuration in thermal insulation engineering is a horizontal annular space filled with fibrous or granular insulation (Fig. 15.5h). In this configuration the heat transfer is radial between the concentric cylindrical surfaces of radii r_i and r_o , unlike in the earlier sketch (Fig. 15.5g), where the cylindrical surfaces were insulated and the heat transfer was axial. Experimental measurements and numerical solutions for the overall heat transfer in the configuration of Fig. 15.5h have been reported in Caltagirone (1976) and Burns and Tien (1979). These results were correlated based on scale analysis (Bejan, 1987) in the range $1.19 \leq r_o/r_i \leq 4$ and the results are correlated by

$$\text{Nu} = \frac{q'_{\text{actual}}}{q'_{\text{conduction}}} \approx 0.44 \text{Ra}_{r_i}^{1/2} \frac{\ln(r_o/r_i)}{1 + 0.916(r_i/r_o)^{1/2}} \quad (15.109)$$

where $\text{Ra}_{r_i} = K\beta r_i(T_h - T_c)/\alpha_m \nu$ and $q'_{\text{conduction}} = 2\pi k_m(T_h - T_c)/\ln(r_o/r_i)$. This correlation is valid in the convection-dominated limit, $\text{Nu} \gg 1$.

Porous media confined to the space formed between two concentric spheres are also an important component in thermal insulation engineering. Figure 15.5h can be interpreted as a vertical cross section through the concentric-sphere arrangement. Numerical heat transfer solutions for discrete values of Rayleigh number and radius ratio are reported graphically in Burns and Tien (1979). Using the scale analysis method (Bejan, 1984, 1995) the data that correspond to the convection-dominated regime ($\text{Nu} \gtrsim 1.5$) are correlated within 2% by the scaling-correct expression (Bejan, 1987)

$$\text{Nu} = \frac{q_{\text{actual}}}{q_{\text{conduction}}} = 0.756 \text{Ra}_{r_i}^{1/2} \frac{1 - r_i/r_o}{1 + 1.422(r_i/r_o)^{3/2}} \quad (15.110)$$

where $\text{Ra}_{r_i} = K\beta r_i(T_h - T_c)/\alpha_m \nu$ and $q_{\text{conduction}} = 4\pi k_m(T_h - T_c)/(r_i^{-1} - r_o^{-1})$. In terms of the Rayleigh number based on the insulation thickness $\text{Ra}_{r_o-r_i} = K\beta(r_o - r_i)(T_h - T_c)/\alpha_m \nu$, the correlation (15.110) becomes

$$\text{Nu} = 0.756 \text{Ra}_{r_o-r_i}^{1/2} \frac{[r_i/r_o - (r_i/r_o)^2]^{1/2}}{1 + 1.422(r_i/r_o)^{3/2}} \quad (15.111)$$

In this form, the Nusselt number expression has a maximum in r_i/r_o (at $r_i/r_o = 0.3$).

Heat transfer by natural convection through an annular porous insulation oriented vertically (Fig. 15.5i) was investigated numerically (Havstad and Burns, 1982) and experimentally (Prasad et al., 1985). For systems where both vertical cylindrical

surfaces may be modeled as isothermal (T_h and T_c), results were correlated with the five-constant empirical formula (Havstad and Burns, 1982)

$$\text{Nu} = 1 + a_1 \left[\frac{r_i}{r_o} \left(1 - \frac{r_i}{r_o} \right) \right]^{a_2} \cdot \text{Ra}_{r_o}^{a_4} \left(\frac{H}{r_o} \right)^{a_5} \exp \left(-a_3 \frac{r_i}{r_o} \right) \quad (15.112)$$

where $a_1 = 0.2196$, $a_2 = 1.334$, $a_3 = 3.702$, $a_4 = 0.9296$, and $a_5 = 1.168$ and where $\text{Ra}_{r_o} = K g \beta r_o (T_h - T_c) / \alpha_m \nu$. The Nusselt number is defined as $\text{Nu} = q_{\text{actual}} / q_{\text{conduction}}$, where $q_{\text{conduction}} = 2 \pi k_m H (T_h - T_c) / \ln(r_o / r_i)$. The correlation of eq. (15.112) fits the numerical data in the range $1 \leq H / r_o \leq 20$, $0 < \text{Ra}_{r_o} < 150$, $0 < r_i / r_o \leq 1$, and $1 < \text{Nu} < 3$. In the boundary layer convection regime (at high Rayleigh and Nusselt numbers), the scale analysis of this two-boundary-layer problem suggests the following scaling law (Bejan, 1987):

$$\text{Nu} = c_1 \frac{\ln(r_o / r_i)}{c_2 + r_o / r_i} \frac{r_o}{H} \text{Ra}_H^{1/2} \quad (15.113)$$

where $\text{Ra}_H = K g \beta H (T_h - T_c) / \alpha_m \nu$. Experimental data in the convection-dominated regime $\text{Nu} \gg 1$ are needed to determine the constants c_1 and c_2 (note that Havstad and Burns's data are for moderate Nusselt numbers $1 < \text{Nu} < 3$, i.e., for cases where pure conduction plays an important role). There is a large and still-growing volume of additional results for enclosed porous media heated from the side, for example, with application to cavernous bricks and walls for buildings (Lorente et al., 1996, 1998; Lorente 2002; Lorente and Bejan, 2002; Vasile et al., 1998).

15.6.3 Enclosures Heated from Below

The most basic configuration of a confined porous layer heated in the vertical direction is shown in Fig. 15.9a. An important difference between heat transfer in this configuration and heat transfer in confined layers heated from the side is that in Fig. 15.9a convection occurs only when the imposed temperature difference or heating rate exceeds a certain, finite value. Recall that in configurations such as Fig. 15.5a, convection is present even in the limit of vanishingly small temperature differences (Fig. 15.6).

Assume that the fluid saturating the porous medium of Fig. 15.9a expands upon heating ($\beta > 0$). By analogy with the phenomenon of Bénard convection in a pure fluid, in the convection regime the flow consists of finite-sized cells that become more slender and multiply discretely as the destabilizing temperature difference $T_h - T_c$ increases. If $T_h - T_c$ does not exceed the critical value necessary for the onset of convection, the heat transfer mechanism through the layer of thickness H is that of pure thermal conduction. If $\beta > 0$ and the porous layer is heated from above (i.e., if T_h and T_c change places in Fig. 15.9a), the fluid remains stably stratified and the heat transfer is again due to pure thermal conduction: $q' = k_m L (T_h - T_c) / H$.

The onset of convection in an infinitely long porous layer heated from below as examined on the basis of linearized hydrodynamic stability analysis (Nield and Bejan, 1999; Horton and Rogers, 1945; Lapwood, 1948). For fluid layers confined between

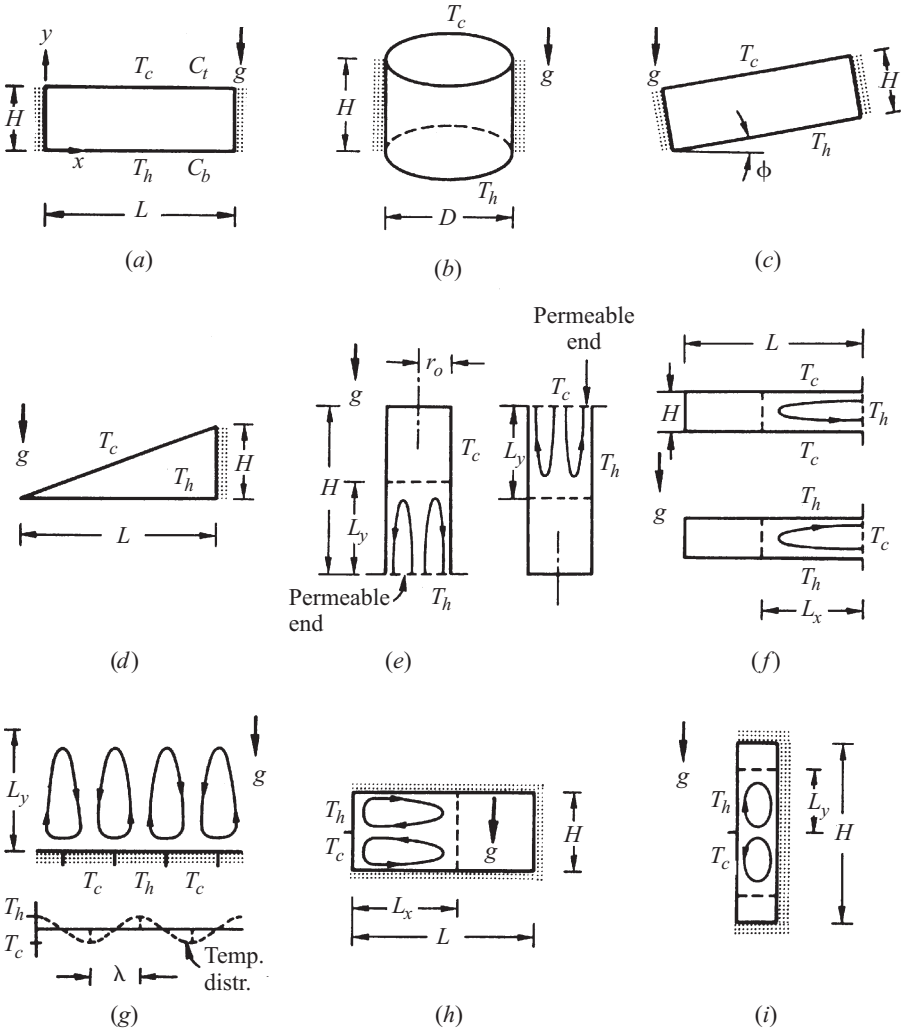


Figure 15.9 Natural convection heat transfer in confined porous layers heated from below (a–d), and due to penetrative flows (e–i): (a) rectangular enclosure; (b) vertical cylindrical enclosure; (c) inclined rectangular enclosure; (d) wedge-shaped enclosure; (e) vertical cylindrical enclosure; (f) horizontal rectangular enclosure; (g) semi-infinite porous medium bounded by a horizontal surface with alternate zones of heating and cooling; (h) shallow rectangular enclosure heated and cooled from one vertical wall; (i) slender rectangular enclosure heated and cooled from one vertical wall.

impermeable and isothermal horizontal walls, it was found that convection is possible if the Rayleigh number based on height exceeds the critical value

$$\text{Ra}_H = \frac{Kg\beta H(T_h - T_c)}{\alpha_m \nu} = 4\pi^2 = 39.48 \quad (15.114)$$

A much simpler closed-form analysis based on constructal theory (Nelson and Bejan, 1998; Bejan, 2000) predicted the critical Rayleigh number $12\pi = 37.70$, which approaches within 5% the hydrodynamic stability result. For a history of the early theoretical and experimental work on the onset of Bénard convection in porous media, and for a rigorous generalization of the stability analysis to convection driven by combined buoyancy effects, the reader is directed to Nield (1968), where it is shown that the critical Rayleigh number for the onset of convection in infinitely shallow layers depends to a certain extent on the heat and fluid flow conditions imposed along the two horizontal boundaries.

Of practical interest in heat transfer engineering is the heat transfer rate at Rayleigh numbers that are higher than critical. There has been a considerable amount of analytical, numerical, and experimental work devoted to this issue. Reviews of these advances may be found in Nield and Bejan (1999) and Cheng (1978). Constructal theory anticipates the entire curve relating heat transfer to Rayleigh number (Nelson and Bejan, 1998; Bejan, 2000).

The scale analysis of the convection regime with Darcy flow (Bejan, 1984) concludes that the Nusselt number should increase linearly with the Rayleigh number, whence the relationship

$$\text{Nu} \approx \frac{1}{40} \text{Ra}_H \quad \text{for} \quad \text{Ra}_H > 40 \quad (15.115)$$

This linear relationship is confirmed by numerical heat transfer calculations at large Rayleigh numbers in Darcy flow (Kimura et al., 1986). The experimental data compiled in Cheng (1978) show that the scaling law of eq. (15.115) serves as an upper bound for some of the high- Ra_H experimental data available in the literature.

Most of the data show that in the convection regime Nu increases as Ra_H^n , where n becomes progressively smaller than 1 as Ra_H increases. This behavior is anticipated by the constructal-theory solution (Nelson and Bejan, 1998; Bejan, 2000). The exponent $n \sim \frac{1}{2}$ revealed by data at high Rayleigh numbers was anticipated based on a scale analysis of convection rolls in the Forchheimer regime (Bejan, 1995):

$$\frac{\text{Nu}}{\text{Pr}_p} \sim \left(\frac{\text{Ra}_H}{\text{Pr}_p} \right)^{1/2} \quad (\text{Ra}_H > \text{Pr}_p) \quad (15.116)$$

where Pr_p is the *porous-medium Prandtl number* for the Forchheimer regime (Bejan, 1995),

$$\text{Pr}_p = \frac{H\nu}{bK\alpha_m} \quad (15.117)$$

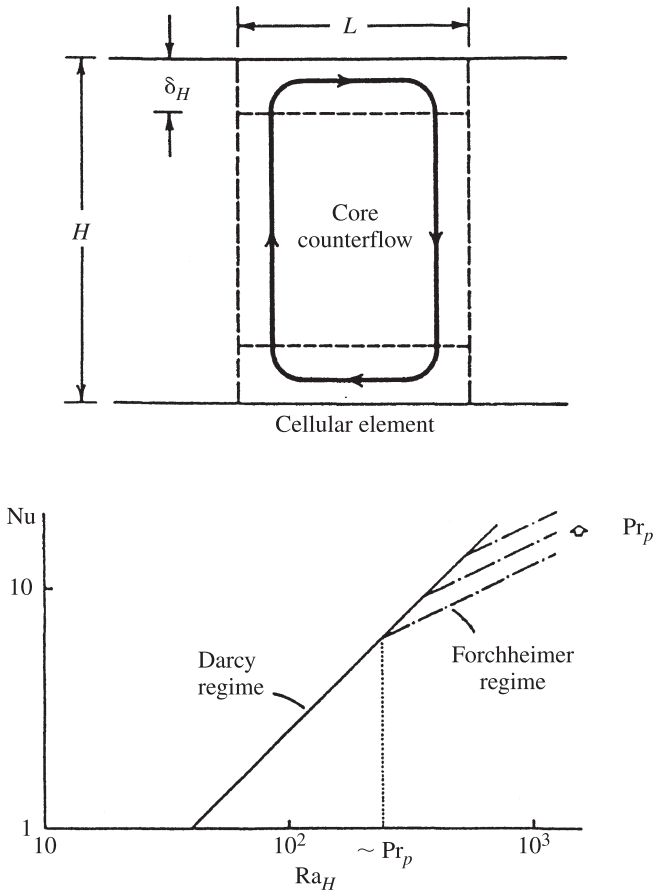


Figure 15.10 Asymptotes of the function $Nu(Ra_H, Pr_p)$ for convection in a porous layer heated from below. (From Bejan, 1995.)

In this formulation Nu is a function of two groups, Ra_H and Pr_p , in which Pr_p accounts for the transition from Darcy to Forchheimer flow (Fig. 15.10). In this formulation the Darcy flow result of eq. (15.115) becomes

$$\frac{Nu}{Pr_p} \sim \frac{1}{40} \frac{Ra_H}{Pr_p} \quad (40 < Ra_H < Pr_p) \quad (15.118)$$

The experimental data for convection in the entire regime spanned by the asymptotes given by eqs. (15.116) and (15.118) are correlated by

$$Nu = \left\{ \left(\frac{Ra_H}{40} \right)^n + \left[c (Ra_H \cdot Pr_p)^{1/2} \right]^n \right\}^{1/n} \quad (15.119)$$

where $n = -1.65$ and $c = 1896$ are determined empirically based on measurements reported by many independent sources. The effects of fluid inertia and other departures from Darcy flow are discussed in detail in Nield and Bejan (1999).

The correlations of eqs. (15.115)–(15.119) refer to layers with length/height ratios considerably greater than 1. They apply when the length (lateral dimension L perpendicular to gravity) of the confined system is greater than the horizontal length scale of a single convective cell (i.e., greater than $H \cdot \text{Ra}_H^{-1/2}$) according to the scale analysis of Bejan (1984).

Natural convection studies have also been reported for porous layers confined in rectangular parallelepipeds heated from below, horizontal circular cylinders, and horizontal annular cylinders. The general conclusion is that the lateral walls have a convection-suppression effect. For example, in a circular cylinder of diameter D and height H (Fig. 15.9b), in the limit $D \ll H$ the critical condition for the onset of convection is (Bau and Torrance, 1982)

$$\text{Ra}_H = 13.56 \left(\frac{H}{D} \right)^2 \quad (15.120)$$

In inclined porous layers that deviate from the horizontal position through an angle ϕ (Fig. 15.9c), convection sets in at Rayleigh numbers that satisfy the criterion (Combarous and Bories, 1975)

$$\text{Ra}_H > \frac{39.48}{\cos \phi} \quad (15.121)$$

where it is assumed that the boundaries are isothermal and impermeable. The average heat transfer rate at high Rayleigh numbers can be estimated by

$$\text{Nu} = 1 + \sum_{s=1}^{\infty} k_s \left(1 - \frac{4\pi^2 s^2}{\text{Ra}_H \cos \phi} \right) \quad (15.122)$$

where $k_s = 0$ if $\text{Ra}_H \cos \phi < 4\pi^2 s^2$ and $k_s = 2$ if $\text{Ra}_H \cos \phi \geq 4\pi^2 s^2$.

In a porous medium confined in a wedge-shaped (or attic-shaped) space cooled from above (Fig. 15.9d), convection consisting of a single counterclockwise cell exists even in the limit $\text{Ra}_H \rightarrow 0$, because in this direction the imposed heating is not purely vertical. The same observation holds for Fig. 15.9c. Numerical solutions of transient high-Rayleigh-number convection in wedge-shaped layers show the presence of a Bénard-type instability at high enough Rayleigh numbers (Poulikakos and Bejan, 1983b). When $H/L = 0.2$, the instability occurs above $\text{Ra}_H \simeq 620$. It was found that this critical Rayleigh number increases as H/L increases.

The onset of convection in the layer of Fig. 15.9a saturated with water near the state of maximum density has been studied using linear stability analysis (Sun et al., 1970) and time-dependent numerical solutions of the complete governing equations (Blake et al., 1984). In both studies, the condition for the onset of convection is reported graphically or numerically for a discrete series of cases. The numerical results (Blake

et al., 1984) for layers with $T_c = 0^\circ\text{C}$ and $5^\circ\text{C} \leq T_h \leq 8^\circ\text{C}$ suggested the following criterion for the onset of convection:

$$\frac{KgH}{\alpha_m \nu} > 1.25 \times 10^5 \exp[\exp(3.8 - 0.446T_h)] \quad (15.123)$$

In this expression T_h must be expressed in $^\circ\text{C}$. Finite-amplitude heat and fluid flow results for Rayleigh numbers $Kg\gamma(T_h - T_c)^2 H / \alpha_m \nu$ of up to 10^4 (i.e., about 50 times greater than critical) are also reported in Blake et al. (1984).

Nuclear safety considerations have led to the study of natural convection in horizontal saturated porous layers (Fig. 15.9a) heated volumetrically at a rate q''' . Boundary conditions and observations regarding the onset of convection and overall Nusselt numbers are presented in Nield and Bejan (1999). It is found that convection sets in at internal Rayleigh numbers (Kulacki and Freeman, 1979)

$$\text{Ra}_I = \left(\frac{k_m \beta}{\alpha_m \nu} \right)_f \frac{KgH^3 q'''}{2k_m} \quad (15.124)$$

in the range 33 to 46, where the subscript f indicates properties of the fluid alone. Top and bottom surface temperature measurements in the convection-dominated regime are adequately represented by (Buretta and Berman, 1976)

$$\frac{q''' H^2}{2k_m (T_h - T_c)} \approx 0.116 \text{Ra}_I^{0.573} \quad (15.125)$$

where T_h and T_c are the resulting bottom and top temperatures if q''' is distributed throughout the layer of Fig. 15.9a. The empirical correlation (11.25) is based on experiments that reach into the high Ra_I range of 10^3 to 10^4 .

15.6.4 Penetrative Convection

In this section attention is focused on buoyancy-driven flows that penetrate the enclosed porous medium only partially. This class of convection phenomena have been categorized as *penetrative flows* (Bejan, 1984). With reference to the two vertical cylindrical configurations sketched in Fig. 15.9e, if the cylindrical space is slender enough, the flow penetrates vertically to the distance

$$L_y = 0.085 r_o \cdot \text{Ra}_{r_o} \quad (15.126)$$

where $\text{Ra}_{r_o} = Kg\beta r_o (T_h - T_c) / \alpha_m \nu$ and $L_y < H$. The overall convection heat transfer rate through the permeable horizontal end is

$$q = 0.255 r_o k_m (T_h - T_c) \text{Ra}_{r_o} \quad (15.127)$$

A similar partial penetration mechanism is encountered in the two horizontal geometries of Fig. 15.9f. The length of lateral penetration, L_x , and the convection heat transfer rate in the two-dimensional geometry, q' (W/m), are (Bejan, 1984, 1995)

$$L_x = 0.16H \cdot \text{Ra}_H^{1/2} \quad (15.128)$$

$$q' = 0.32k_m(T_h - T_c)\text{Ra}_H^{1/2} \quad (15.129)$$

where $\text{Ra}_h = Kg\beta(T_h - T_c)H/\alpha_m\nu$ and $L_x < L$.

In a semi-infinite porous medium bounded from below or from above by a horizontal surface with alternating zones of heating and cooling (Fig. 15.9g), the buoyancy-driven flow penetrates vertically to a height or depth approximately equal to $\lambda \cdot \text{Ra}_\lambda^{1/2}$, where $\text{Ra}_\lambda = Kg\beta\lambda(T_h - T_c)/\alpha_m\nu$ and λ is the distance between a heated zone and an adjacent cooled zone. Numerical and graphic results are reported in Poulikakos and Bejan (1984a) for the Ra_λ range 1 to 100.

There are many other circumstances in which penetrative flows can occur, steady and transient (Nield and Bejan, 1999). For example, in a porous medium heated and cooled along the same vertical wall of height H , the incomplete penetration can be either horizontal (Fig. 15.9h) or vertical (Fig. 15.9i) (Poulikakos and Bejan, 1984b). In the case of incomplete horizontal penetration, the penetration length and convective heat transfer rate scale as

$$L_x \sim H \cdot \text{Ra}_H^{1/2} \quad (15.130)$$

$$q' \sim k_m(T_h - T_c)\text{Ra}_H^{1/2} \quad (15.131)$$

The derivation of these order-of-magnitude results can also be found in Bejan (1995). They are valid if $\text{Ra}_H^{1/2} < L/H$ and $\text{Ra}_H \gtrsim 1$. The corresponding scales of incomplete vertical penetration (Fig. 15.9i) are

$$L_y \sim H \left(\frac{L}{H} \right)^{2/3} \cdot \text{Ra}_H^{-1/3} \quad (15.132)$$

$$q' \sim k_m(T_h - T_c) \left(\frac{L}{H} \cdot \text{Ra}_H \right)^{1/3} \quad (15.133)$$

and are valid if $\text{Ra}_H^{1/2} > L/H$ and $\text{Ra}_H^{1/2} > H/L$. The penetrative flows of Fig. 15.9h and i occur when the heated section T_h is situated above the cooled section T_c . When the positions of T_h and T_c are reversed, the buoyancy-driven flow fills the entire space $H \times L$.

15.7 OTHER CONFIGURATIONS

Research on heat and mass transfer in porous media has grown impressively during the past two decades, beyond the fundamental results highlighted in Sections 15.1 and 15.6. The most up-to-date review of the current state of the literature on heat transfer in porous media is provided in the latest edition of Nield and Bejan's (1999)

book, which contains over 1600 references and in a new book (Bejan et al., 2004). This closing section is a brief review of some of the subfields that have emerged.

When the flow is due to a combination of driving forces, buoyancy and imposed pressure differences, the heat transfer characteristics depend greatly on which force dominates. Two papers (Lai et al., 1991; Vargas et al., 1995) review most of what is known on mixed convection in two-dimensional external flow, along walls (vertical, inclined, horizontal) and in wedge-shaped domains. The free and forced-convection effects are governed by the Rayleigh and Péclet numbers, respectively,

$$\text{Ra}_x = \frac{g_x \beta K x (T_w - T_\infty)}{\alpha_m \nu} \quad (15.134)$$

$$\text{Pe}_x = \frac{U_\infty x}{\nu} \quad (15.135)$$

where x is the position from the leading edge measured along the wall and g_x is the acceleration component aligned with x . The graphic presentation of the heat transfer results suggests that, in broad terms, free convection is the dominating effect when $\text{Ra}_x/\text{Pe}_x > O(1)$.

The corresponding class of mixed convection problems concerning the embedded sphere and horizontal cylinder in a uniform vertical flow was treated in Cheng (1982). Inertial effects were introduced in the modeling of these problems by several authors. The most comprehensive treatment is the unifying analysis (Nakayama and Pop, 1991) for mixed convection based on the Darcy–Forchheimer model, which is valid for plane walls and axisymmetric bodies of arbitrary shape. This unifying treatment and other configurations (internal flow) can also be found in Nield and Bejan (1999).

Another combination or competition of driving forces occurs when the local density variations that cause buoyancy are due not only to temperature gradients but also to concentration gradients. This class of phenomena is also known as *double-diffusive* or *thermohaline convection*. As an example, consider the onset of convection in a horizontal porous layer subjected to heat and mass transfer between the confining bottom and top walls (Fig. 15.9a). An additional buoyancy effect is due to the concentration of constituent i maintained along the bottom wall (C_b) and the top wall (C_t). The linearized density–temperature relation is

$$\rho \approx \rho_b [1 - \beta(T - T_h) - \beta_C(C - C_b)] \quad (15.136)$$

where β_C is the concentration expansion coefficient,

$$\beta_C = -\frac{1}{\rho} \left(\frac{\partial \rho}{\partial C} \right)_p \quad (15.137)$$

For saturated porous layers confined between impermeable walls with uniform T and C distributions, convection is possible if (Nield, 1968)

$$\text{Ra}_H + \text{Ra}_{D,H} > 39.48 \quad (15.138)$$

where

$$Ra_H = \frac{Kg\beta H(T_h - T_c)}{\alpha_m \nu} \quad (15.139)$$

$$Ra_{D,H} = \frac{Kg\beta_C H(C_b - C_t)}{\nu D} \quad (15.140)$$

with D as the mass diffusivity of constituent i through the solution-saturated porous medium. Therefore, because β_C can be positive or negative, the effect of mass transfer from below can be, respectively, either to decrease or increase the critical Ra_H for the onset of convection. Alternatives to eq. (15.138) for horizontal porous layers subjected to other boundary conditions are presented in Nield and Bejan (1999) and Nield (1968).

In the single-wall vertical flow configuration of Fig. 15.3a, the additional buoyancy effect caused by the imposed concentration difference $C_w - C_\infty$ can either aid or oppose the familiar flow due to $T_w - T_\infty$ (Bejan, 1984, 1995). An important role is played by the buoyancy ratio

$$N = \frac{\beta_C(C_w - C_\infty)}{\beta(T_w - T_\infty)} \quad (15.141)$$

In heat-transfer-driven flows ($|N| \ll 1$), the heat transfer rate is given by eq. (15.66). The overall mass transfer rate can be estimated based on the scaling laws

$$\frac{j'}{D(C_w - C_\infty)} \sim \begin{cases} Ra_H^{1/2} \cdot Le^{1/2} & \text{for } Le \gg 1 \\ Ra_H^{1/2} \cdot Le & \text{for } Le \ll 1 \end{cases} \quad (15.142)$$

where $j'/(kg/s \cdot m)$ is the overall mass transfer rate per unit length and Le is the Lewis number of the solution-saturated porous medium, α_m/D . In mass transfer-driven situations ($|N| \gg 1$), the overall mass transfer rate is

$$\frac{j'}{D(C_w - C_\infty)} = 0.888(Ra_H \cdot Le|N|)^{1/2} \quad (15.143)$$

for all Lewis numbers. The corresponding overall Nusselt number obeys the scaling laws

$$\frac{q'}{k(T_w - T_\infty)} \sim \begin{cases} (Ra_H|N|)^{1/2} & \text{for } Le \ll 1 \\ Le^{-1/2}(Ra_H|N|)^{1/2} & \text{for } Le \gg 1 \end{cases} \quad (15.144)$$

The order-of-magnitude results of eqs. (15.142) and (15.144) agree within 15% with overall heat and mass transfer calculations based on similarity solutions to the same problem (Bejan and Khair, 1985). The corresponding enclosure problem, where the vertical walls are maintained at different temperatures and concentrations, the

heat and mass transfer due to convection driven by combined buoyancy effects was documented in terms of numerical experiments in Trevisan and Bejan (1985, 1986).

Another expanding area is the study of conduction and convection in the presence of phase change: melting, solidification, boiling, and condensation. These problems are recommended by specialized applications in diverse fields such as geophysics, manufacturing, small-scale heat exchangers, and spaces filled with fibers coated with energy storage (phase-change) material. These and other applications are treated in detail in the most recent edition of Nield and Bejan (1999).

NOMENCLATURE

Roman Letter Symbols

A	cross-sectional area, m^2
a	fissure spacing, m
B	width of stack, m
	combination of terms, dimensionless
Be	Bejan number, dimensionless
b	fissure spacing, m
	coefficient in Forchheimer's modification of Darcy's law, m^{-1}
	stratification parameter, dimensionless
C	constituent concentration, kg/m^3
c	specific heat, $\text{J}/\text{kg} \cdot \text{K}$
c_p	specific heat at constant pressure, $\text{J}/\text{kg} \cdot \text{K}$
D	mass diffusivity, m^2/s
	diameter of round tube, m
	distance between parallel plates, m
D_p	fiber diameter, m
D/Dt	material derivative operator, s^{-1}
d	diameter, m
	peripheral sublayer thickness, m
g	gravitational acceleration, m/s^2
H	height, m
h	heat transfer coefficient, $\text{W}/\text{m}^2 \cdot \text{K}$
h_m	local mass transfer coefficient, m/s
j'	constituent mass flow per unit length, $\text{kg}/\text{m} \cdot \text{s}$
j''	constituent mass flow per unit area, $\text{kg}/\text{m}^2 \cdot \text{s}$
K	permeability, m^2
k	thermal conductivity, $\text{W}/\text{m} \cdot \text{K}$
k_A	overall average thermal conductivity, $\text{W}/\text{m} \cdot \text{K}$
k_G	weighted geometric mean thermal conductivity, $\text{W}/\text{m} \cdot \text{K}$
k_H	weighted harmonic mean thermal conductivity, $\text{W}/\text{m} \cdot \text{K}$
k_m	porous medium thermal conductivity, $\text{W}/\text{m} \cdot \text{K}$

L	length, m
L_x	penetration length, m
L_y	penetration height, m
Le	Lewis number, dimensionless
m'''	mass produced in chemical reaction, kg/m^3
N	buoyancy ratio, dimensionless
	number of horizontal sublayers, dimensionless
Nu	Nusselt number, dimensionless
Nu_H	Nusselt number based on height, dimensionless
Nu_L	Nusselt number based on wall length, dimensionless
Nu_θ	peripheral Nusselt number, dimensionless
Nu_x	Nusselt number based on local longitudinal position, dimensionless
Nu_y	Nusselt number based on heat flux, dimensionless
P	pressure, Pa
Pe	Péclet number, dimensionless
Pe_L	overall Péclet number, dimensionless
Pe_x	Péclet number based on local longitudinal position, dimensionless
Pr_p	porous medium Prandtl number, dimensionless
q	heat transfer rate, W
q'	heat transfer rate per unit length, W/m
q''	heat transfer rate per unit area, W/m^2
q'''	volumetric heat generation rate, W/m^3
R	parameter defined in eq. (15.91), dimensionless
r	radial coordinate, m
	spherical coordinate, m
r_i	inner radius, m
r_o	outer radius, m
Ra_H	Rayleigh number based on height and temperature difference, dimensionless
Ra_H^*	Rayleigh number based on heat flux, dimensionless
Ra_I	internal Rayleigh number based on volumetric heat generation rate, dimensionless
Ra_y	Darcy-modified Rayleigh number, dimensionless
	Rayleigh number based on heat flux, dimensionless
$Ra_{\infty,y}^*$	Rayleigh number for inertial flow based on heat flux, dimensionless
Ra_{yc}	Rayleigh number for the cold side of a porous medium saturated with fluid near the density maximum, dimensionless
Ra_{yh}	Rayleigh number for the hot side of a porous medium saturated with fluid near the density maximum, dimensionless
S	spacing, m

Sh	Sherwood number, dimensionless
t	time, s
T	temperature, K
u	velocity component in the x direction, m/s
V	volume, m^3
\mathbf{V}	volume averaged velocity vector, m/s
W	width, m
w	velocity component in the z direction, m/s
x	Cartesian coordinate, m
y	Cartesian coordinate, m
z	Cartesian coordinate, m

Greek Letter Symbols

α_m	porous medium thermal diffusivity, m^2/s
$\bar{\alpha}_m$	empirical factor in the density–temperature relation for water, dimensionless
β	coefficient of thermal expansion, K^{-1}
β_C	coefficient of concentration expansion, m^3/kg
γ	vertical temperature gradient, K/m
δ_T	thermal boundary layer thickness, m
η	similarity variable, dimensionless
λ	distance, m
μ	dynamic viscosity, $Pa \cdot s$
ν	kinematic viscosity, m^2/s
ρ	density, kg/m^3
σ	capacity ratio, dimensionless
τ	time, dimensionless
ϕ	porosity, dimensionless
	spherical coordinate, rad
	angle, rad
ψ	stream function, m^2/s
	spherical coordinate, dimensionless
ω	wall thickness parameter, dimensionless

Subscripts

A	overall
b	bottom or bulk
c	cold
f	fluid (liquid or gas) phase
G	geometric mean
H	harmonic mean
h	hot
i	inner
L	property based on plate length
m	bulk property

	property of the state of maximum density
	porous medium
<i>o</i>	outer
<i>opt</i>	optimum
<i>p</i>	constant pressure condition
<i>s</i>	solid phase
<i>w</i>	wall
<i>x</i>	local property
∞	free stream condition

REFERENCES

- Bau, H. H., and Torrance, K. E. (1982). Low Rayleigh Number Thermal Convection in a Vertical Cylinder Filled with Porous Materials and Heated from Below, *J. Heat Transfer*, 104, 166–172.
- Bear, J. (1972). *Dynamics of Fluids in Porous Media*, American Elsevier, New York.
- Bejan, A. (1978). Natural Convection in an Infinite Porous Medium with a Concentrated Heat Source, *J. Fluid Mech.*, 89, 97–107.
- Bejan, A. (1979). On the Boundary Layer Regime in a Vertical Enclosure Filled with a Porous Medium, *Lett. Heat Mass Transfer*, 6, 93–102.
- Bejan, A. (1983a). The Boundary Layer Regime in a Porous Layer with Uniform Heat Flux from the Side, *Int. J. Heat Mass Transfer*, 26, 1339–1346.
- Bejan, A. (1983b). Natural Convection Heat Transfer in a Porous Layer with Internal Flow Obstructions, *Int. J. Heat Mass Transfer*, 26, 815–822.
- Bejan, A. (1984). *Convection Heat Transfer*, Wiley, New York.
- Bejan, A. (1987). Convective Heat Transfer in Porous Media, in *Handbook of Single-Phase Convective Heat Transfer*, S. Kakaç, R. K. Shah, and W. Aung, eds., Wiley, New York.
- Bejan, A. (1993). *Heat Transfer*, Wiley, New York.
- Bejan, A. (1995). *Convection Heat Transfer*, 2nd ed., Wiley, New York.
- Bejan, A. (1997). *Advanced Engineering Thermodynamics*, 2nd ed., Wiley, New York.
- Bejan, A. (1999). Heat Transfer in Porous Media, in *Heat Exchanger Design Update*, G. F. Hewitt, ed., Begell House, New York, Vol. 6, Sec. 2.11.
- Bejan, A. (2000). *Shape and Structure, from Engineering to Nature*, Cambridge University Press, Cambridge, UK.
- Bejan, A., and Anderson, R. (1981). Heat Transfer across a Vertical Impermeable Partition Imbedded in a Porous Medium, *Int. J. Heat Mass Transfer*, 24, 1237–1245.
- Bejan, A., and Anderson, R. (1983). Natural Convection at the Interface between a Vertical Porous Layer and an Open Space, *J. Heat Transfer*, 105, 124–129.
- Bejan, A., and Khair, K. R. (1985). Heat and Mass Transfer by Natural Convection in a Porous Medium, *Int. J. Heat Mass Transfer*, 28, 909–918.
- Bejan, A., and Lage, J. L. (1991). Heat Transfer from a Surface Covered with Hair, in *Convective Heat and Mass Transfer in Porous Media*, S. Kakaç, B. Kilis, F. A. Kulacki, and F. Arinc, eds., Kluwer Academic, Dordrecht, The Netherlands, pp. 823–845.

- Bejan, A., and Morega, A. M. (1993). Optimal Arrays of Pin Fins and Plate Fins in Laminar and Forced Convection, *J. Heat Transfer*, 115, 75–81.
- Bejan, A., and Poulikakos, D. (1984). The Non-Darcy Regime for Vertical Boundary Layer Natural Convection in a Porous Medium, *Int. J. Heat Mass Transfer*, 27, 717–722.
- Bejan, A., and Sciubba, E. (1992). The Optimal Spacing of Parallel Plates Cooled by Forced Convection, *Int. J. Heat Mass Transfer*, 35, 3259–3264.
- Bejan, A., and Tien, C. L. (1978). Natural Convection in a Horizontal Porous Medium Subjected to End-to-End Temperature Difference, *J. Heat Transfer*, 100, 191–198; errata (1983), 105, 683–684.
- Bejan, A., and Tien, C. L. (1979). Natural Convection in Horizontal Space Bounded by Two Concentric Cylinders with Different End Temperatures, *Int. J. Heat Mass Transfer*, 22, 919–927.
- Bejan, A., Dincer, I., Lorent, S., Miguel, A. F., and Reis, A. H. (2004). *Porous and Complex Flow Structures, in Modern Technologies*, Springer, New York.
- Bhattacharjee, S., and Grosshandler, W. L. (1988). The Formation of a Wall Jet near a High Temperature Wall under Microgravity Environment, *ASME-HTD-96*, ASME, New York, pp. 711–716.
- Blake, K. R., Bejan, A., and Poulikakos, D. (1984). Natural Convection near 4°C in a Water Saturated Porous Layer Heated from Below, *Int. J. Heat Mass Transfer*, 27, 2355–2364.
- Brinkman, H. C. (1947). A Calculation of the Viscous Force Extended by a Flowing Fluid on a Dense Swarm of Particles, *Appl. Sci. Res.*, A1, 26–34.
- Buretta, R. J., and Berman, A. S. (1976). Convective Heat Transfer in a Liquid Saturated Porous Layer, *J. Appl. Mech.*, 43, 249–253.
- Burns, P. J., and Tien, C. L. (1979). Natural Convection in Porous Media Bounded by Concentric Spheres and Horizontal Cylinders, *Int. J. Heat Mass Transfer*, 22, 929–939.
- Caltagirone, J. P. (1976). Thermoconvective Instabilities in a Porous Medium Bounded by Two Concentric Horizontal Cylinders, *J. Fluid Mech.*, 76, 337–362.
- Carslaw, J. S., and Jaeger, J. C. (1959). *Conduction of Heat in Solids*, 2nd ed., Oxford University Press, Oxford.
- Cheng, P. (1978). Heat Transfer in Geothermal Systems, *Adv. Heat Transfer*, 14, 1–105.
- Cheng, P. (1982). Mixed Convection about a Horizontal Cylinder and a Sphere in a Fluid Saturated Porous Medium, *Int. J. Heat Mass Transfer*, 25, 1245–1247.
- Cheng, P., and Chang, I. D. (1976). Buoyancy Induced Flows in a Saturated Porous Medium Adjacent to Impermeable Horizontal Surfaces, *Int. J. Heat Mass Transfer*, 19, 1267–1272.
- Cheng, P., and Minkowycz, W. J. (1977). Free Convection about a Vertical Plate Embedded in a Saturated Porous Medium with Application to Heat Transfer from a Dike, *J. Geophys. Res.*, 82, 2040–2044.
- Combarnous, M. A., and Bories, S. A. (1975). Hydrothermal Convection in Saturated Porous Media, *Adv. Hydrosol.*, 10, 231–307.
- Ergun, S. (1952). Fluid Flow through Packed Columns, *Chem. Eng. Prog.*, 48(2), 89–94.
- Gebhart, B., and Mollendorf, J. C. (1977). A New Density Relation for Pure and Saline Water, *Deep Sea Res.*, 24, 831–841.
- Haajizadeh, M., and Tien, C. L. (1983). Natural Convection in a Rectangular Porous Cavity with One Permeable End wall, *J. Heat Transfer*, 105, 803–808.

- Havstad, M. A., and Burns, P. J. (1982). Convective Heat Transfer in Vertical Cylindrical Annuli Filled with a Porous Medium, *Int. J. Heat Mass Transfer*, 25, 1755–1766.
- Hickox, C. E. (1981). Thermal Convection at Low Rayleigh Number from Concentrated Sources in Porous Media, *J. Heat Transfer*, 103, 232–236.
- Hickox, C. E., and Gartling, D. K. (1981). A Numerical Study of Natural Convection in a Horizontal Porous Layer Subjected to an End-to-End Temperature Difference, *J. Heat Transfer*, 103, 797–802.
- Hickox, C. E., and Watts, H. A. (1980). Steady Thermal Convection from a Concentrated Source in a Porous Medium, *J. Heat Transfer*, 102, 248–253.
- Horton, C. W., and Rogers, F. T. (1945). Convection Currents in a Porous Medium, *J. Appl. Phys.*, 16, 367–370.
- Ingham, D. B., and Pop, I., eds. (1998). *Transport Phenomena in Porous Media*, Pergamon Press, Oxford.
- Ingham, D. B., and Pop, I., eds. (2002). *Transport Phenomena, in Porous Media II*, Pergamon Press, Amsterdam.
- Ingham, D. B., Merkin, H., and Pop, I. (1983). The Collision of Free-Convective Boundary Layers on a Horizontal Cylinder Embedded in a Porous Medium, *Q. J. Mech. Appl. Math.*, 36, 313–335.
- Kaviany, M. (1995). *Principles of Heat Transfer in Porous Media*, 2nd ed., Springer-Verlag, New York.
- Kimura, S., Bejan, A., and Pop, I. (1985). Natural Convection near a Cold Plate Facing Upward in a Porous Medium, *J. Heat Transfer*, 107, 819–825.
- Kimura, S., Schubert, G., and Straus, J. M. (1986). Route to Chaos in Porous-Medium Thermal Convection, *J. Fluid Mech.*, 166, 305–324.
- Kulacki, F. A., and Freeman, R. G. (1979). A Note on Thermal Convection in a Saturated Heat-Generating Porous Layer, *J. Heat Transfer*, 101, 169–171.
- Lai, F. C., Kulacki, F. A., and Prasad, V. (1991). Mixed Convection in Saturated Porous Media, in *Convective Heat and Mass Transfer in Porous Media*, S. Kakaç, B. Kilis, F. A. Kulacki, and F. Arinc, eds., Kluwer Academic, Dordrecht, The Netherlands, pp. 225–287.
- Lapwood, E. R. (1948). Convection of a Fluid in a Porous Medium, *Proc. Cambridge Philos. Soc.*, 44, 508–521.
- Ledezma, G. A., Morega, A. M., and Bejan, A. (1996). Optimal Spacing between Fins with Impinging Flow, *J. Heat Transfer*, 118, 570–577.
- Lorente, S. (2002). Heat Losses through Building Walls with Closed, Open and Deformable Cavities, *Int. J. Energy Res.*, 26, 611–632.
- Lorente, S., and Bejan, A. (2002). Combined ‘Flow and Strength’ Geometric Optimization: Internal Structure in a Vertical Insulating Wall with Air Cavities and Prescribed Strength, *Int. J. Heat Mass Transfer*, 45, 3313–3320.
- Lorente, S., Petit, M., and Javelas, R. (1996). Simplified Analytical Model for Thermal Transfer in a Vertical Hollow Brick, *Energy and Buildings*, 24, 95–103.
- Lorente, S., Petit, M., and Javelas, R. (1998). The Effects of Temperature Conditions on the Thermal Resistance of Walls Made with Different Shapes Vertical Hollow Brick, *Energy and Buildings*, 28, 237–240.
- Morega, A. M., and Bejan, A. (1994). Heatline Visualization of Convection in Porous Media, *Int. J. Heat Fluid Flow*, 15, 42–47.

- Nakayama, A., and Pop, I. (1991). A Unified Similarity Transformation for Free, Forced and Mixed Convection in Darcy and Non-Darcy Porous Media, *Int. J. Heat Mass Transfer*, 34, 357–367.
- Nelson, R. A., Jr., and Bejan, A. (1998). Constructal Optimization of Internal Flow Geometry in Convection, *J. Heat Transfer*, 120, 357–364.
- Nield, D. A. (1968). Onset of Thermohaline Convection in a Porous Medium, *Water Resour. Res.*, 4, 553–560.
- Nield, D. A. (1991). Estimation of the Stagnant Thermal Conductivity of Saturated Porous Media, *Int. J. Heat Mass Transfer*, 34, 1575–1576.
- Nield, D. A., and Bejan, A. (1999). *Convection in Porous Media*, 2nd ed., Springer-Verlag, New York.
- Nield, D. A., and Joseph, D. D. (1985). Effects of Quadratic Drag on Convection in a Saturated Porous Medium, *Phys. Fluids*, 28, 995–997.
- Petrescu, S. (1994). Comments on the Optimal Spacing of Parallel Plates Cooled by Forced Convection, *Int. J. Heat Mass Transfer*, 37, 1283.
- Plumb, O. A., and Huenefeld, J. S. (1981). Non-Darcy Natural Convection from Heated Surfaces in Saturated Porous Media, *Int. J. Heat Mass Transfer*, 24, 765–768.
- Pop, I., and Ingham, D. B. (2001). *Convective Heat Transfer: Mathematical and Computational Modelling of Viscous Fluids and Porous Media*, Pergamon Press, Oxford.
- Pop, I., and Cheng, P. (1983). The Growth of a Thermal Layer in a Porous Medium Adjacent to a Suddenly Heated Semi-infinite Horizontal Surface, *Int. J. Heat Mass Transfer*, 26, 1574–1576.
- Poulikakos, D. (1984). Maximum Density Effects on Natural Convection in a Porous Layer Differentially Heated in the Horizontal Direction, *Int. J. Heat Mass Transfer*, 27, 2067–2075.
- Poulikakos, D., and Bejan, A. (1983a). Natural Convection in Vertically and Horizontally Layered Porous Media Heated from the Side, *Int. J. Heat Mass Transfer*, 26, 1805–1814.
- Poulikakos, D., and Bejan, A. (1983b). Numerical Study of Transient High Rayleigh Number Convection in an Attic-Shaped Porous Layer, *J. Heat Transfer*, 105, 476–484.
- Poulikakos, D., and Bejan, A. (1984a). Penetrative Convection in Porous Medium Bounded by a Horizontal Wall with Hot and Cold Spots, *Int. J. Heat Mass Transfer*, 27, 1749–1758.
- Poulikakos, D., and Bejan, A. (1984b). Convection in a Porous Layer Heated and Cooled along One Vertical Side, *Int. J. Heat Mass Transfer*, 27, 1879–1891.
- Prasad, V., Kulacki, F. A., and Keyhani, M. (1985). Natural Convection in Porous Media, *J. Fluid Mech.*, 150, 89–119.
- Prasad, V., Kladas, N., Bandyopadhyaya, A., and Tian, Q. (1989). Evaluation of Correlations for Stagnant Thermal Conductivity of Liquid-Saturated Porous Beds of Spheres, *Int. J. Heat Mass Transfer*, 32, 1793–1796.
- Ramilison, J. M., and Gebhart, B. (1980). Buoyancy Induced Transport in Porous Media Saturated with Pure or Saline Water at Low Temperatures, *Int. J. Heat Mass Transfer*, 23, 1521–1530.
- Rohsenow, W. M., and Choi, H. Y. (1961). *Heat, Mass and Momentum Transfer*, Prentice-Hall, Englewood Cliffs, NJ.
- Rohsenow, W. M., and Hartnett, J. P. (1973). *Handbook of Heat Transfer*, McGraw-Hill, New York.

- Scheidtdeger, A. E. (1957). *The Physics of Flow through Porous Media*, Macmillan, New York.
- Simpkins, P. G., and Blythe, P. A. (1980). Convection in a Porous Layer, *Int. J. Heat Mass Transfer*, 23, 881–887.
- Stanescu, G., Fowler, A. J., and Bejan, A. (1996). The Optimal Spacing of Cylinders in Free-Stream Cross-Flow Forced Convection, *Int. J. Heat Mass Transfer*, 39, 311–317.
- Sun, Z. S., Tien, C., and Yen, Y. C. (1970). Onset of Convection in a Porous Medium Containing Liquid with a Density Maximum, *Heat Transfer 1970*, Vol. IV, Paper NC 2.11.
- Trevisan, O. V., and Bejan, A. (1985). Natural Convection with Combined Heat and Mass Transfer Buoyancy Effects in a Porous Medium, *Int. J. Heat Mass Transfer*, 28, 1597–1611.
- Trevisan, O. V., and Bejan, A. (1986). Mass and Heat Transfer by Natural Convection in a Vertical Slot Filled with Porous Medium, *Int. J. Mass Transfer*, 29, 403–415.
- Vafai, K., ed. (2000). *Handbook of Porous Media*, Marcel Dekker, New York.
- Vafai, K., and Tien, C.-L. (1981). Boundary and Inertia Effects on Flow and Heat Transfer in Porous Media, *Int. J. Heat Mass Transfer*, 24, 195–203.
- Vargas, J. V. C., Laursen, T. A., and Bejan, A. (1995). Nonsimilar Solutions for Mixed Convection on a Wedge Embedded in a Porous Medium, *Int. J. Heat Fluid Flow*, 16, 211–216.
- Vasile, C., Lorente, S., and Perrin, B. (1998). Study of Convective Phenomena inside Cavities Coupled with Heat and Mass Transfers through Porous Media—Application to Vertical Hollow Bricks—A First Approach, *Energy and Buildings*, 28, 229–235.
- Ward, J. C. (1964). Turbulent Flow in Porous Media, *J. Hydraul. Div. ASCE*, 90(HY5), 1–12.
- Weber, J. E. (1975). The Boundary Layer Regime for Convection in a Vertical Porous Layer, *Int. J. Heat Mass Transfer*, 18, 569–573.
- Wooding, R. A. (1963). Convection in a Saturated Porous Medium at Large Rayleigh or Péclet Number, *J. Fluid Mech.*, 15, 527–544.
- Zhukauskas, A. (1987). Convective Heat Transfer in Cross Flow, in *Handbook of Single-Phase Convective Heat Transfer*, S. Kakaç, R. K. Shah, and W. Aung, eds., Wiley, New York.

Heat Pipes

JAY M. OCHTERBECK

Department of Mechanical Engineering
Clemson University
Clemson, South Carolina

- 16.1 Introduction
 - 16.1.1 Heat pipe basics
 - 16.1.2 Wick structures
 - 16.1.3 Classification by type of control
 - 16.1.4 Capillary action
- 16.2 Transport limitations
 - 16.2.1 Introduction
 - 16.2.2 Capillary limit
 - 16.2.3 Boiling limit
 - 16.2.4 Entrainment limit
 - 16.2.5 Viscous limit
 - 16.2.6 Sonic limit
 - 16.2.7 Condenser limit
- 16.3 Heat pipe thermal resistance
- 16.4 Figures of merit
- 16.5 Transient operation
 - 16.5.1 Continuum vapor and liquid-saturated wick
 - 16.5.2 Wick depriming and rewetting
 - 16.5.3 Freeze–thaw issues
 - 16.5.4 Supercritical startup
- 16.6 Special types of heat pipes
 - 16.6.1 Variable conductance heat pipes
 - 16.6.2 Micro and miniature heat pipes
 - 16.6.3 Pulsating heat pipes
 - 16.6.4 Loop heat pipes and capillary pumped loops

Nomenclature

References

16.1 INTRODUCTION

16.1.1 Heat Pipe Basics

Capillary-driven two-phase systems offer significant advantages over traditional single-phase systems. With the typically increased thermal capacity associated with the phase change of a working fluid, considerably smaller mass flow rates are required to transport equivalent amounts than in single-phase liquid or gas systems for a given temperature range. Moreover, heat transfer coefficients of two-phase systems are much greater than in single-phase flows and result in enhanced heat transfer. Lower mass flow rates and enhanced thermal characteristics provide the benefits of smaller system size (and weight) while providing increased performance. The thermal capacity of a single-phase system depends on the temperature change of the working fluid; thus, a large temperature gradient or a high mass flow rate is required to transfer a large amount of heat. However, a two-phase system can provide essentially isothermal operation regardless of variations in the heat load. Additionally, single-phase systems require the use of mechanical pumps and fans to circulate the working fluid, while capillary-driven two-phase systems have no external power requirements, which make such systems more reliable and free of vibration.

The best known capillary-driven two-phase system is the heat pipe, where a schematic of a conventional heat pipe is shown in Fig. 16.1. The concept of the heat pipe was first presented by Gaugler (1944) and Trefethen (1962), but was not widely publicized until an independent development by Grover et al. (1964) at the Los Alamos Scientific Laboratories. Heat pipes are passive devices that transport heat from a heat source (evaporator) to a heat sink (condenser) over relatively long distances via the latent heat of vaporization of a working fluid. As shown, a heat pipe generally has three sections: an evaporator section, an adiabatic (or transport) section, and a condenser section. The major components of a heat pipe are a sealed container, a wick structure, and a working fluid. The wick structure is placed on the inner surface of the heat pipe wall and is saturated with the liquid working fluid and provides the structure to develop the capillary action for liquid returning from the condenser to the evaporator section.

With evaporator heat addition, the working fluid is evaporated as it absorbs an amount of heat equivalent to the latent heat of vaporization, while in the condenser section, the working fluid vapor is condensed. The mass addition in the vapor core of the evaporator section and mass rejection in the condenser end results in a pressure gradient along the vapor channel which drives the corresponding vapor flow. Return of the liquid to the evaporator from the condenser is provided by the wick structure. As vaporization occurs in the evaporator, the liquid meniscus recedes correspondingly into the wick structure, as shown in Fig. 16.1. Similarly, as vapor condenses in the condenser region, the mass addition results in an advanced meniscus. The difference between the capillary radii in the evaporator and condenser ends of the wick structure results in a net pressure difference in the liquid-saturated wick. This pressure difference drives the liquid from the condenser through the wick structure to the evaporator region, thus allowing the overall process to be continuous.

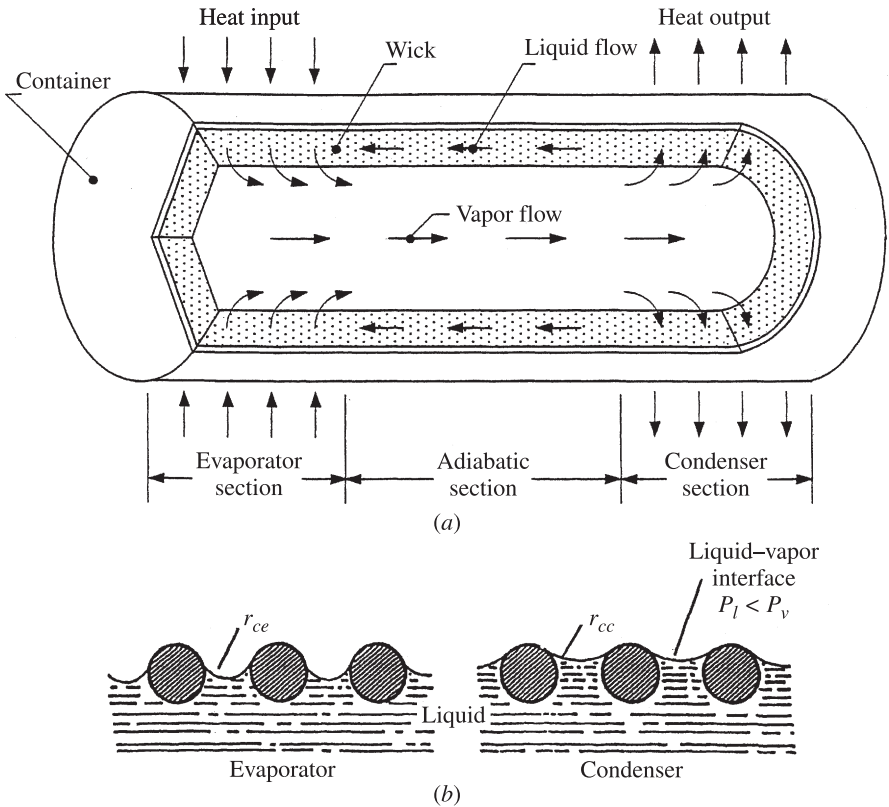


Figure 16.1 (a) Typical heat pipe construction and operation; (b) radii of curvature of the liquid-vapor interface in the evaporator and condenser.

Due to the two-phase characteristics, the heat pipe is ideal for transferring heat over long distances with a very small temperature drop and for creating a nearly isothermal surface for temperature stabilization. As the working fluid operates in a thermodynamic saturated state, heat is transported using the latent heat of vaporization instead of sensible heat or conduction where the heat pipe then operates in a nearly isothermal condition. This nearly isothermal condition offers benefits of transporting large amounts of heat efficiently, decreasing the overall heat transfer area and saving system weight. The amount of heat that can be transported through the use of latent heat is typically several orders of magnitude greater than transported by sensible heat for a geometrically equivalent system. Additionally, no mechanical pumping systems are required due to the capillary-driven working fluid. Given the wide range of operating temperatures for working fluids, the high efficiencies, the low relative weights, and the absence of external pumps in heat pipes, these systems are seen as attractive options in a wide range of heat transfer applications.

TABLE 16.1 Typical Heat Pipe Working Fluids

Working Fluid	Triple Point (K)	Critical Point (K)	Useful Range (K)
Oxygen	54.3	154.8	55–154
Nitrogen	63.1	126.2	65–125
Ethane	89.9	305.5	100–305
Butane	134.8	425.0	260–350
Methanol	175.2	513.2	273–503
Toluene	178.1	593.9	275–473
Acetone	180.0	508.2	250–475
Ammonia	195.5	405.6	200–405
Mercury	234.3	1763	280–1070
Water	273.2	647.3	273–643
Potassium	336.4	2250	400–1800
Sodium	371.0	2500	400–1500
Lithium	453.7	3800	500–2100
Silver	1234	7500	1600–2400

Theoretically, heat pipe operation is possible at any temperature between the triple state and the critical point of the working fluid utilized, albeit at significantly reduced transport capabilities near the two extremes due to the fluid property characteristics of surface tension and viscosity. Several typical heat pipe working fluids are given in Table 16.1, along with the corresponding triple point, critical point, and most widely utilized temperature range for each individual fluid. Classification of heat pipes may be in terms of geometry, intended applications, or the type of working fluid utilized.

Each heat pipe application has a temperature range in which the heat pipe is intended to operate. Therefore, the working fluid must be chosen to take into account this operating temperature (along with the pressure condition), but also its chemical compatibility with the container and wick materials. Depending on operating temperature, four different types of heat pipes are usually described with regard to commonly used working fluids:

1. *Cryogenic heat pipes* designed to operate from 1 to 200 K, with working fluids such as helium, argon, neon, nitrogen, and oxygen. These typically have relatively low heat transfer capabilities, due to very low values of the latent heat of vaporization, h_{fg} , and low surface tensions of the working fluids. In addition, startup of the heat pipe involves transitioning from a supercritical state to an operating liquid–vapor condition.
2. *Room (low)-temperature heat pipes* with operating temperatures ranging between 200 and 550 K. Working fluids typically used in this range include methanol, ethanol, ammonia, acetone, and water.
3. *Medium-temperature heat pipes* with operating temperatures ranging from 550 to 700 K. Mercury and sulfur are typical fluids in this range, along with some organic fluids (e.g., naphthalene and biphenyl).

4. *High (liquid-metal)-temperature heat pipes* operating above 700 K. Very high heat fluxes can be obtained using liquid metals due to the characteristics of the fluid: namely, very large surface tensions and high latent heats of vaporization. Examples of liquid metals commonly used include potassium, sodium, and silver. In the case of liquid metal heat pipes, startup typically involves starting from an initially frozen working fluid.

Because the amount of heat transferred by a heat pipe depends on the latent heat of vaporization, the transfer of appreciable quantities of heat is possible, even for long distances. Axial heat flows of 10^8 W/m^2 are easily reachable with sodium heat pipes. By calculating an effective thermal conductivity k_{eff} , values may reach $10^8 \text{ W/m} \cdot \text{K}$ (sodium heat pipe) (Ivanovskii et al., 1982), which is several orders of magnitude greater than the conductivity of the best conductors.

One of the most common applications of a heat pipe is that of a heat flux transformer. Using a heat pipe, high heat fluxes from a heat source can be injected over a small surface area, which is then rejected over a larger condenser surface area. Thermal flux transformation ratios greater than 10:1 can allow systems to employ final heat rejection with low cooling capability methods, such as natural convection or single-phase cooling.

16.1.2 Wick Structures

The wick provides a means for the flow of liquid from the condenser to the evaporator section of the heat pipe. It also provides surface pores that are required at the liquid–vapor interface for development of the required capillary pressure. The wick structure also has an impact on the radial temperature drop at the evaporator end between the inner heat pipe surface and the liquid–vapor surface. Thus, an effective wick requires large internal pores in a direction normal to the heat flow path. This will minimize liquid flow resistance. In addition, small surface pores are required for the development of high capillary pressure and a highly conductive heat flow path for minimization of the radial surface to liquid–vapor surface temperature drop. To satisfy these requirements, two types of wick structure have been developed. These are the homogeneous wicks made of a single material, examples of which are shown in Fig. 16.2, and the composite wicks containing two or more materials, with some typical examples displayed in Fig. 16.3.

One common wick structure is the wrapped screen wick shown in Fig. 16.2a. This type of wick structure is designated by its mesh number, which is an indication of the number of pores per unit length or unit surface area. The surface pore size is inversely proportional to the mesh number and the liquid flow resistance can be controlled by the tightness of the wrapping. This is attractive, but because of the interruptions in the wick metal by a liquid of low thermal conductivity in the moderate-range heat pipe, the radial temperature drop from the inner pipe surface to the liquid–vapor surface at the evaporator end can be quite high. This problem can be alleviated through use of the sintered metal wick structure shown in Fig. 16.2b. Notice here that the pore size is small but the small pores will make it more difficult for the liquid to flow from the condenser to the evaporator.

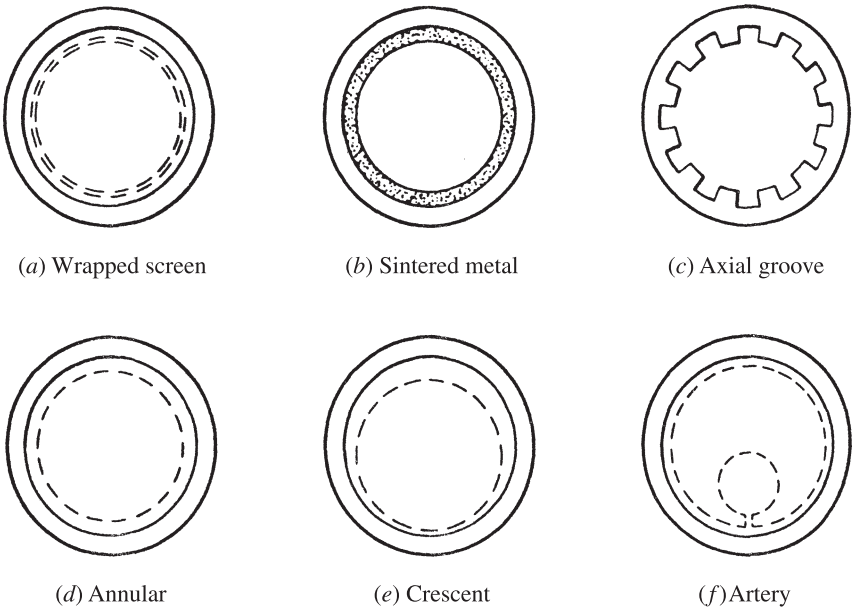


Figure 16.2 Cross sections of homogeneous wick structures. (From Chi, 1976, with permission.)

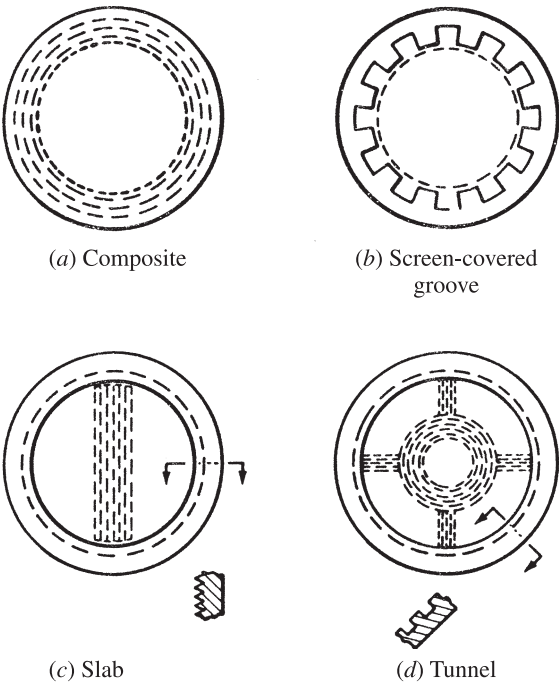


Figure 16.3 Cross sections of composite wick structures. (From Chi, 1976, with permission.)

The axially grooved wick shown in Fig. 16.2*c* possesses highly conductive metal paths for the minimization of radial temperature drop. Axially grooved heat pipes are most commonly found in space applications. The annular and crescent wicks, shown respectively in Fig. 16.2*d* and *e*, have small resistance to liquid flow but are vulnerable to liquids of low thermal conductivity. The artery wick, shown in Fig. 16.2*f* was developed to reduce the thickness of the radial heat flow path through the structure and to provide a low-resistance path for the liquid flow from the condenser to the evaporator. However, these wicks often lead to operating problems if they are not self-priming, because the arteries must fill automatically at startup or after a dryout.

All the composite wicks shown in Fig. 16.3 have a separate structure for development of the capillary pressure and liquid flow. Notice that in some of the structures in Fig. 16.3, a separation of the heat flow path from the liquid flow path can be provided. For example, the screen-covered groove wick shown in Fig. 16.3*b* has a fine mesh screen for high capillary pressure, axial grooves to reduce flow resistance, and a metal structure to reduce the radial temperature drop. The slab wick displayed in Fig. 16.3*c* is inserted into an internally threaded container. High capillary pressure is derived from a layer of fine mesh screen at the surface, and liquid flow is assured by the coarse screen inside the slab. The threaded grooves tend to provide uniform circumferential distribution of liquid and enhance radial heat transfer.

16.1.3 Classification by Type of Control

In addition to classification by the temperature range of the working fluid, heat pipes may be classified by the type of control employed. Control is often necessary because a heat pipe without control will self-adjust its operating temperature in accordance with the heat source at the evaporator end and the heat sink at the condenser end. For example, it may be desirable to control the temperature in the range prescribed in the presence of a wide range of variations in heat source and heat sink temperatures. On the other hand, it may be required to permit the passage of heat under one set of conditions and block the heat flow completely under another set of conditions. This leads to a consideration of the performance of heat pipes known as *thermal switches* and *thermal diodes*.

There are four major control approaches that are illustrated in Fig. 16.4 and described in what follows.

1. *Gas-loaded heat pipe.* The presence of a noncondensable gas has a marked effect on the performance of a condenser. This effect can be exploited for heat pipe control. Any noncondensable gas present in the vapor space is swept to the condenser section during operation, and gas will block a portion of the condenser surface. The heat flow at the condenser can be controlled by controlling the volume of the noncondensable gas. Examples of self-controlled devices, those that can be controlled by the vapor pressure of the working fluid, are shown in Fig. 16.4*a*, *b*, and *c*. Examples of feedback-controlled devices are shown Fig. 16.4*d* and *e*.

2. *Excess-liquid heat pipe.* Control can also be attained by condenser flooding with excess working fluid. In the excess-liquid heat pipe, excess working fluid in

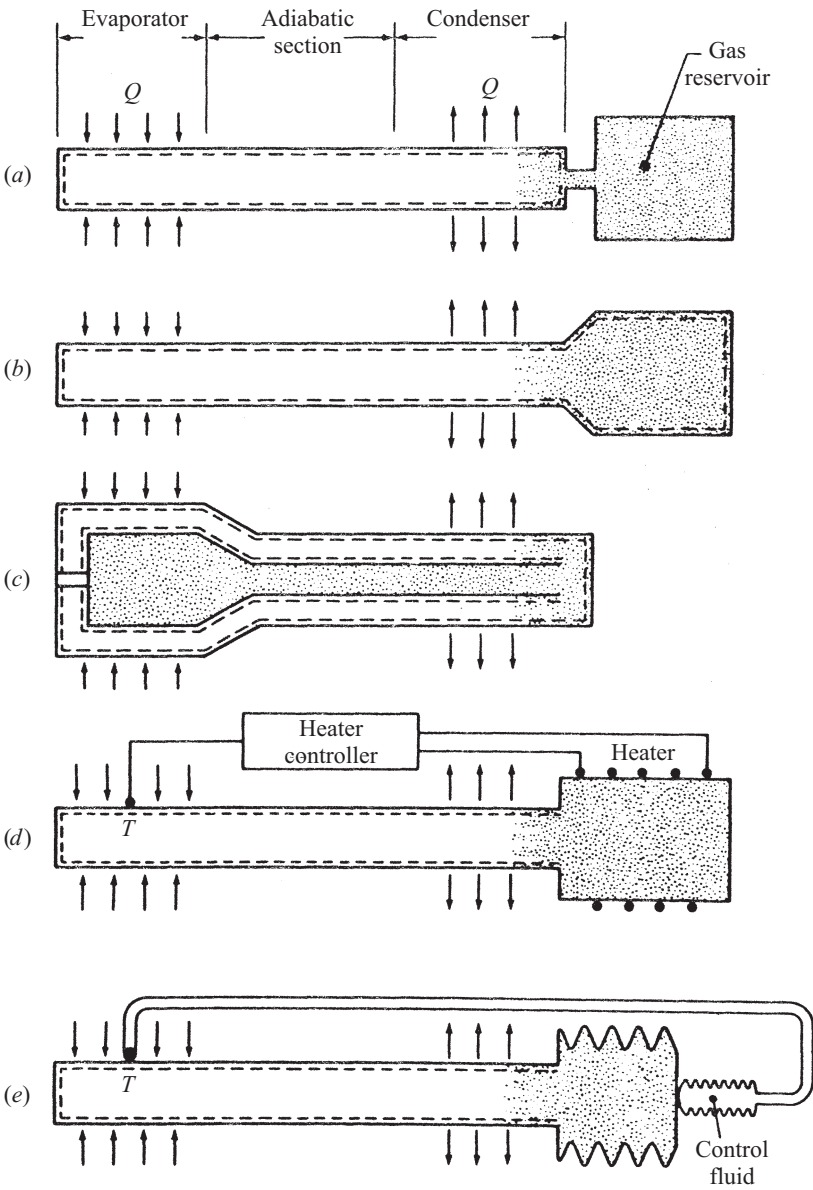


Figure 16.4 Representative gas-loaded heat pipes. (From Chi, 1976, with permission.)

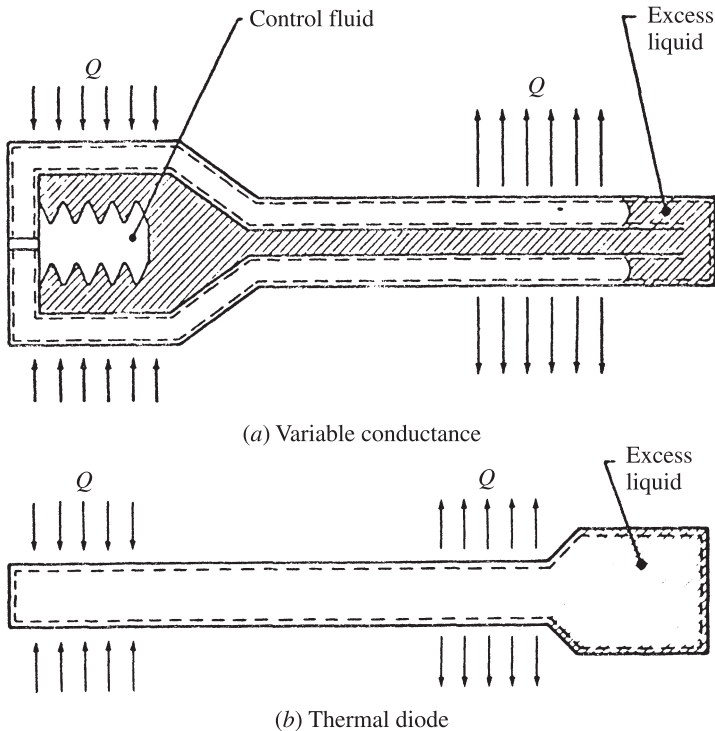


Figure 16.5 Representative excess liquid heat pipes. (From Chi, 1976, with permission.)

the liquid phase is swept into the condenser and blocks a portion of the condenser. Observe in Fig. 16.5a that a decrease in vapor temperature will expand the control fluid in the bellows, which forces excess liquid to block a portion of the condenser. An example of a thermal diode is displayed in Fig. 16.5b.

3. *Vapor flow-modulated heat pipe.* The performance of the heat pipe can be controlled by the vapor flow through the adiabatic section as shown in Fig. 16.6a, an increase in heat input or an increase in heat source temperature felt at the surface of the evaporator causes a rise in the temperature and pressure of the vapor in the evaporator section. The flow of this vapor through the throttling valve creates a temperature and pressure drop that results in a reduction in the magnitudes of these quantities in the condenser section. Thus, the condensing temperature and pressure can be held at values that yield the required condenser performance even though the temperature at the heat source has increased. In the event that the heat input increases, the condenser can keep pace with this increase and adjust its performance by means of the throttling valve. Figure 16.6b shows a thermal switch where the flow of vapor through the throttling valve can be cut off entirely.

4. *Liquid flow-modulated heat pipe.* Liquid flow control is also an effective way of maintaining control over heat pipe performance. One way of controlling liquid flow is through the use of a liquid trap, as shown in Fig. 16.7a. This trap is a wick-lined

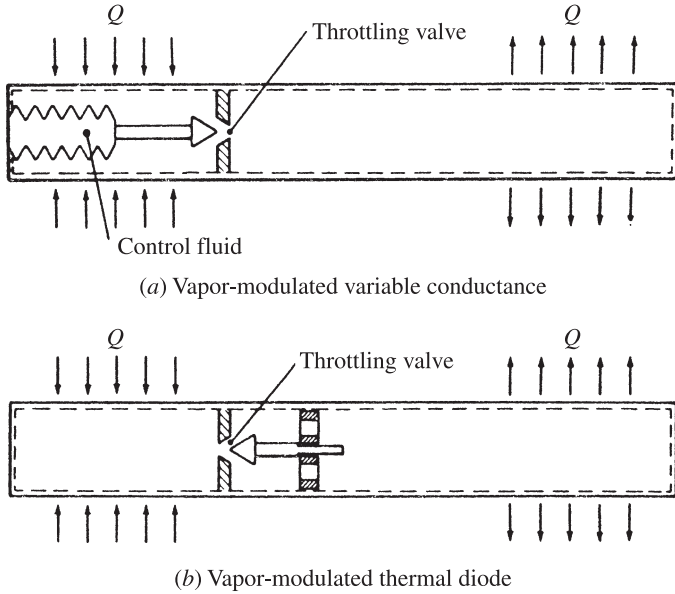


Figure 16.6 Representative vapor flow-modulated heat pipes. (From Chi, 1976, with permission.)

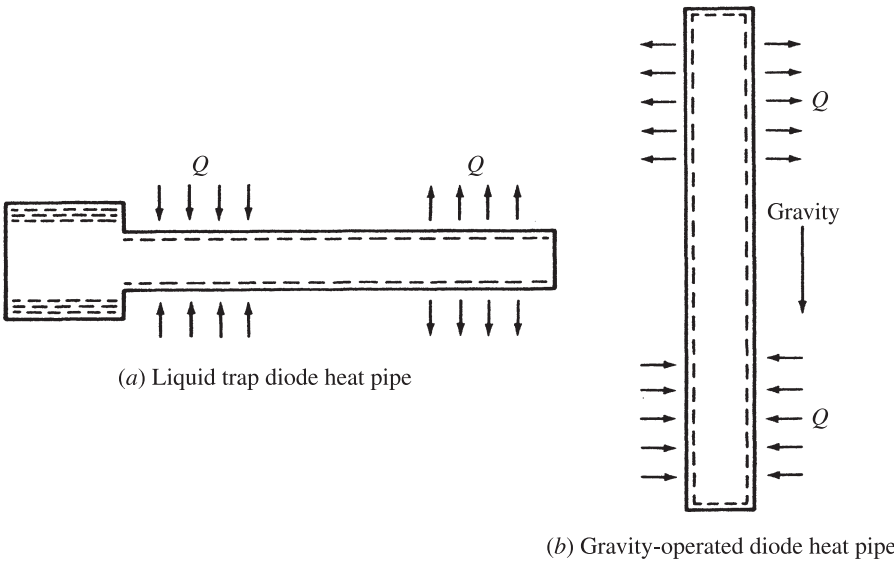


Figure 16.7 Representative liquid flow-modulated heat pipes. (From Chi, 1976, with permission.)

reservoir located in the evaporator end. The wick in the trap, referred to as the *trap wick*, is not connected to the operating wick in the rest of the heat pipe. In the normal mode of operation with the heat pipe operating in the standard fashion, the trap wick is dry. If the heat input increases or the attitude of the heat pipe changes, condensation may occur in the trap and the liquid trap may become an alternate condensing end of the pipe. As liquid accumulates in the trap, the main wick begins dryout which results in operational failure. An example of a heat pipe with the evaporator section below the condenser section is shown in Fig. 16.7*b*. This, in itself, is a type of control because the heat pipe can function as a thermal diode providing that the wick is designed appropriately. Notice that the condensed liquid is returned to the evaporator section with the assistance of the gravitational force. This type of heat pipe is commonly referred to as a *thermosyphon*.

16.1.4 Capillary Action

In capillary-driven systems, the driving potential for the working fluid circulation is provided by the difference in the curvature of the evaporating and condensing liquid–vapor interfaces. Consequently, determining the maximum pumping capacity, and the corresponding heat transfer performance, of these systems depends strongly on the accuracy of the prediction of the shapes of the evaporating and condensing interfaces. On a microscopic scale, a liquid–vapor interface is a volumetric transition zone across which the molecule number density varies continuously. However, on a macroscopic scale, an interface between a liquid and its vapor is modeled as a surface of discontinuity and characterized by the property of surface tension. The surface tension is defined thermodynamically to be the change in surface excess free energy (or work required) per unit increase in interfacial area

$$\sigma = \left(\frac{\partial E}{\partial A_s} \right)_{T,n} \quad (16.1)$$

As the capillary pressure at the liquid–vapor interface is due to the curvature of the menisci and the surface tension of the working fluid and is given by the Young–Laplace equation (see Carey, 1992 for a detailed derivation)

$$\Delta P_c = \sigma \left(\frac{1}{R_1} + \frac{1}{R_2} \right) \quad (16.2)$$

where σ is the surface tension and R_1 and R_2 are the principal radii of the meniscus, as shown in Fig. 16.8. Limitations to use of the Young–Laplace equation are typically that the liquid–vapor interface is static, interfacial mass fluxes (evaporation) are low, and disjoining pressure effects are negligible. For cases of very thin films where disjoining pressure effects must be included to provide a physically correct and accurate prediction of the capillary pressure across an interface, a review of techniques has been provided by Wayner (1999).

In predicting the maximum capillary pressure available for a given heat pipe wick structure, the two principal radii of curvature are typically combined into an effective

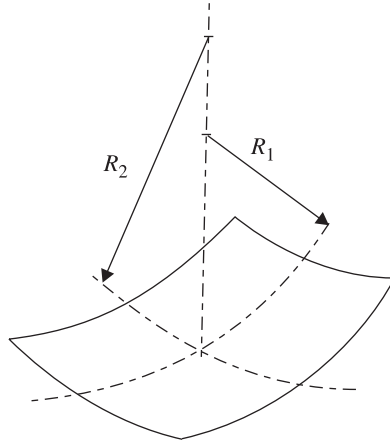


Figure 16.8 The radii of the meniscus.

radius of curvature for the wick structure. This method produces an effective capillary radius equivalent to the inner radius of a circular tube ($R_1 = R_2 = r_{\text{eff}} / \cos \theta$) and allows for easy comparison between capillary structures with different structures. In this case, the capillary pressure is expressed as

$$\Delta P_c = \frac{2\sigma}{r_{\text{eff}}} \cos \theta \quad (16.3)$$

where θ , the apparent contact angle (Fig. 16.9), is dependent on the fluid–wick pair used. The contact angle is a measure of the degree of wettability of the liquid on the wick structure, where $\theta = 0^\circ$ relates to a perfectly wetting system. Carey (1992) provides a detailed discussion on parameters affecting wettability. For this expression to be maximized, the wetting angle must be zero (i.e., the liquid wets the wick perfectly). Thus, the maximum capillary pressure with a perfectly wetting fluid will be

$$(\Delta P_c)_{\text{max}} = \frac{2\sigma}{r_{\text{eff}}} \quad (16.4)$$

where r_{eff} is the effective pores radius of the wick and can be determined for various wick structures.

The difference in the curvature of the menisci between the evaporator and the condenser section implies a difference in the capillary pressure at the interface along the length of the heat pipe. The capillary pressure developed by the wick between points 1 and 2 can be expressed as

$$(\Delta P_c)_{1 \rightarrow 2} = \Delta P_{c,1} - \Delta P_{c,2} \quad (16.5)$$

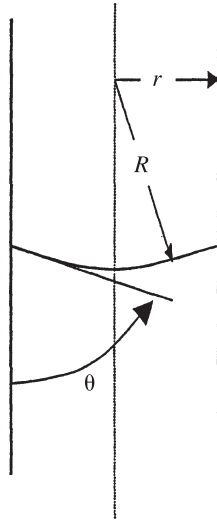


Figure 16.9 Meniscus in a cylindrical pore.

The maximum capillary pressure developed by the wick between the *wet point* (defined as the point where the meniscus is flat) and the *dry point* (defined as the point where the curvature of the menisci is maximum) is then

$$(\Delta P_c)_{\max} = \frac{2\sigma}{r_{\text{eff}}} \quad (16.6)$$

This capillary pressure differential circulates the fluid against the liquid and vapor pressure losses and any adverse body forces such as gravity.

16.2 TRANSPORT LIMITATIONS

16.2.1 Introduction

Limitations of the maximum heat input that may be transported by a heat pipe can be divided into two primary categories: limits that result in heat pipe failure and limits that do not. For the limitations resulting in heat pipe failure, all are characterized by insufficient liquid flow to the evaporator for a given heat input, thus resulting in *dryout* of the evaporator wick structure. The heat input to the heat pipe, Q , is related directly to the mass flow rate of the working fluid being circulated and the latent heat, h_{fg} , of the fluid as the heat input is the driving mechanism, or

$$Q = \dot{m}h_{fg} \quad (16.7)$$

However, limitations not resulting in heat pipe failure do require that the heat pipe operate at an increased temperature for an increase in heat input. The two categories and basic phenomena for each limit may be summarized as follows:

Limitations (Failure)

1. *Capillary limit.* The capillary limit relates to the fundamental phenomenon governing heat pipe operation which is development of capillary pressure differences across the liquid–vapor interfaces in the evaporator and condenser. When the driving capillary pressure is insufficient to provide adequate liquid flow from the condenser to the evaporator, dryout of the evaporator wick will occur. Generally, the capillary limit is the primary maximum heat transport limitation of a heat pipe.

2. *Boiling limit.* The boiling limit occurs when the applied evaporator heat flux is sufficient to cause nucleate boiling in the evaporator wick. This creates vapor bubbles that partially block the liquid return and can lead to evaporator wick dryout. The boiling limit is sometimes referred to as the *heat flux limit*.

3. *Entrainment limit.* The entrainment limit refers to the case of high shear forces developed as the vapor passes in the counterflow direction over the liquid saturated wick, where the liquid may be entrained by the vapor and returned to the condenser. This results in insufficient liquid flow to the wick structure.

Limitations (Nonfailure):

1. *Viscous limit.* The viscous limit occurs at low operating temperatures, where the saturation vapor pressure may be of the same order of magnitude as the pressure drop required to drive the vapor flow in the heat pipe. This results in an insufficient pressure available to drive the vapor. The viscous limit is sometimes called the *vapor pressure limit*.

2. *Sonic limit.* The sonic limit is due to the fact that at low vapor densities, the corresponding mass flow rate in the heat pipe may result in very high vapor velocities, and the occurrence of choked flow in the vapor passage may be possible.

3. *Condenser limit.* The condenser limit is based on cooling limitations such as radiation or natural convection at the condenser. For example, in the case of radiative cooling, the heat pipe transport may be governed by the condenser surface area, emissivity, and operating temperature.

Additionally, the capillary, viscous, entrainment, and sonic limits are axial heat flux limits, that is, functions of the axial heat transport capacity along the heat pipe. However, the boiling limit is a radial heat flux limit occurring in the evaporator.

Using the analysis techniques for each limitation independently, the heat transport capacity as a function of the mean operating temperature (the adiabatic vapor temperature) can be determined. This procedure yields a heat pipe performance region similar to that shown in Fig. 16.10. As shown, the separate performance limits define an operational range represented by the region bounded by the combination of the individual limits. In effect, this operational range defines the region or combination of temperatures and maximum transport capacities at which the heat pipe will function. Thus, it is possible to ensure that the heat pipe can transport the required thermal

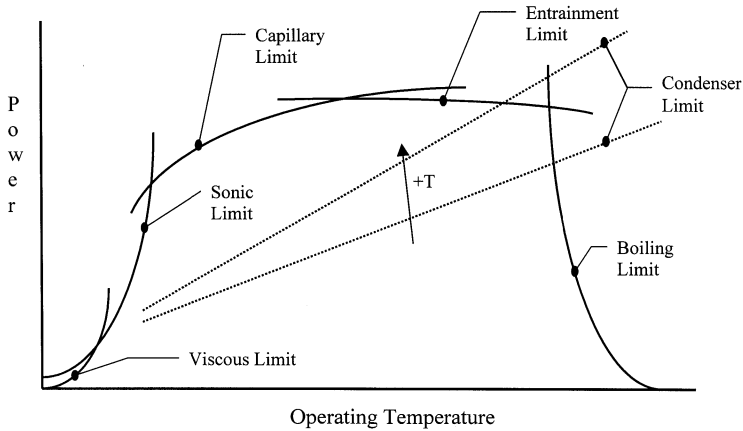


Figure 16.10 Typical heat pipe performance map.

load or to improve the design. It is important to note that in the determination of the heat transport capacity, the mean operating temperature must be identified. However, the operating temperature of a standard heat pipe is a function of the heat input, thus resulting in a mutually dependent case between the heat transport and the operating temperature. In Section 16.3 a method is described by which the operating temperature can be estimated based on the heat pipe characteristics, the heat input, and the condenser cooling conditions.

16.2.2 Capillary Limit

Because the driving potential for the circulation of the working fluid is the capillary pressure difference, the maximum capillary pressure must be greater than the sum of all pressure losses inside the heat pipe:

$$(\Delta P_c)_{\max} \geq \Delta P_{\text{tot}} \quad (16.8)$$

The pressure losses in heat pipes can be separated into the frictional pressure drops along the vapor and liquid paths, the pressure drop in liquid as a result of body forces (e.g., gravity, centrifugal, electromagnetic), and the pressure drop due to phase transition

$$\Delta P_{\text{tot}} = \Delta P_V + \Delta P_l + \Delta P_b + \Delta P_{\text{ph}} \quad (16.9)$$

During heat pipe operation, the menisci naturally adjust the radii of curvature for the capillary pressure differential to balance the pressure losses ΔP_{tot} . However, the maximum radius of curvature is limited to the capillary dimension of the wick structure such that the maximum transport occurs when $(\Delta P_c)_{\max} = \Delta P_{\text{tot}}$. It is

important to note that the pressure drop associated with phase transition, ΔP_{ph} , is significant only under very high condensation or evaporation rates and represents the jump condition associated with the kinetic energy change in the liquid–vapor process. Except for very specific conditions (e.g., liquid metal heat pipes with extremely high evaporation rates), the phase transition pressure drop is typically negligible and will not be considered further in following discussions. However, for further information, Ivanovskii et al. (1982) and Delhay (1981) provide more details related to the phase transition condition.

Figure 16.11 shows a pressure-drop diagram along the length of a heat pipe working under low heat flux. If the total pressure drop exceeds the maximum capillary pressure, the return rate of liquid to the evaporator will be insufficient and the heat pipe will experience dryout of the wick. The maximum capillary pressure ΔP_c developed within the heat pipe wick structure is given by the Laplace–Young equation of eq. (16.2). Values of the effective capillary radius r_{eff} for different wick structures are provided in Table 16.2.

The body forces result from any gravitational field against which the liquid must be pumped. This includes any inclination of the heat pipe

$$\Delta P_{\parallel} = \rho_l g L \sin \phi \tag{16.10}$$

as well as any hydrostatic pressure drop related to the drawing of the fluid to the top portion of the heat pipe cross section

$$\Delta P_{\perp} = \rho_l g d_v \cos \phi \tag{16.11}$$

It is important to note that the inclination of the heat pipe can either be an *adverse tilt* (evaporator above condenser) or a *favorable tilt* (condenser above evaporator) such that the hydrostatic pressure either subtracts from, or adds to, the capillary pumping pressure. In cases where the liquid flow to the evaporator becomes dominated by gravitational forces, the system is operating as a *thermosyphon* as opposed to a traditional heat pipe. For basics of a thermosyphon, Faghri (1995) may be consulted.

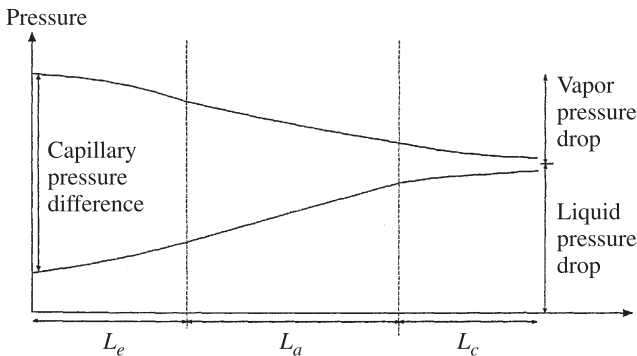


Figure 16.11 Pressure variation along the length of a heat pipe working under low heat flux.

TABLE 16.2 Expressions for the Effective Capillary Radius r_c for Several Wick Structures

Structure	r_c	Data
Circular cylinder (artery or tunnel wicks)	$r_{\text{eff}} = r$	r = radius of liquid flow passage
Rectangular groove	$r_{\text{eff}} = \frac{w}{2}$	w = groove width
Triangular groove	$r_{\text{eff}} = \frac{w}{\cos \beta}$	w = groove width β = half-included angle
Parallel wires	$r_{\text{eff}} = \frac{w}{2}$	w = wire spacing
Wire screens	$r_{\text{eff}} = \frac{w + d_w}{2} = \frac{1}{2N}$	N = screen mesh number w = wire spacing d_w = wire diameter
Packed spheres	$r_c = 0.41r_s$	r_s = sphere radius

Source: Chi (1976), with permission.

The differential liquid pressure drop in the wick structure assuming one-dimensional laminar flow can be expressed as

$$\frac{dP_l}{dx} = -\frac{\mu_l \dot{m}_l(x)}{KA_w \rho_l} \quad (16.12)$$

where K represents the wick permeability. The wick permeability is related directly to the porosity of the wick structure, which is defined as the ratio of pore volume to total volume, or $\varepsilon = V_{\text{pore}}/V_{\text{tot}}$, and is given by

$$K = \frac{2\varepsilon(r_h)^2}{f_l \cdot \text{Re}_l} \quad (16.13)$$

As the hydraulic radius of the porous structure is typically small and the liquid flow velocity is low, the liquid flow can be assumed laminar. Thus, the values of $(f_l \cdot \text{Re}_l)$ can be assumed constant and depend only on the flow passage shape, where typical values of the permeability for different wick structures are given in Table 16.3.

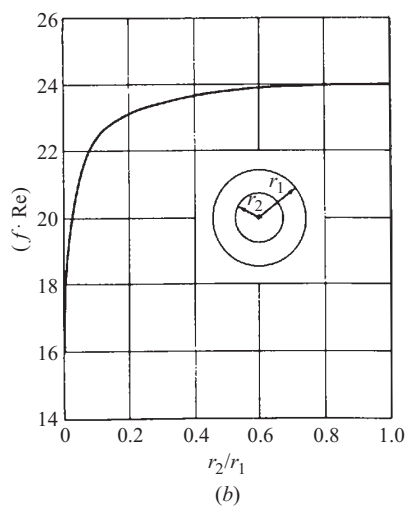
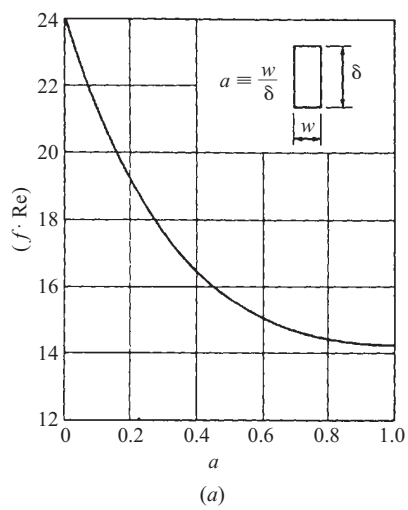
Assuming one-dimensional vapor flow, the differential vapor pressure drop can be expressed in terms of the pressure drops due to frictional forces and dynamic pressure, or

$$\frac{dP_v}{dx} = \frac{(f \cdot \text{Re}_v \mu_v \dot{m}_v(x))}{2A_v r_{h,v}^2 \rho_v} - \frac{2\dot{m}_v}{A_v^2 \rho_v} \frac{d\dot{m}_v(x)}{dx} \quad (16.14)$$

Recognizing that the total vapor mass flow rate and liquid mass flow rate are equal at steady-state conditions, the mass flow rate through the system can be expressed in terms of the heat transport rate and the latent heat of vaporization of the fluid, or

TABLE 16.3 Expressions of Wick Permeability K for Several Wick Structures

Wick Structure	K Expression	
Circular artery	$K = \frac{r^2}{8}$	
Open rectangular grooves	$K = \frac{2\epsilon r_{h,l}^2}{f_l \cdot Re_l}$	$\epsilon = \text{porosity} = \frac{w}{s}$ $s = \text{groove pitch}$ $r_{h,l} = \frac{2w\delta}{w + 2\delta}$ $w = \text{groove width}$ $\delta = \text{groove depth}$ $(f_l \cdot Re_l) \text{ from (a) below}$
Circular annular wick	$K = \frac{2r_{h,l}^2}{f_l \cdot Re_l}$	$r_{h,l} = r_1 - r_2$ $(f_l \cdot Re_l) \text{ from (b) below}$
Wrapped screen wick	$K = \frac{d^2 \epsilon^3}{122(1 - \epsilon)^2}$	$d = \text{wire diameter}$ $\epsilon = 1 - \frac{1.05\pi Nd}{4}$ $N = \text{mesh number}$
Packed sphere	$K = \frac{r_s^2 \epsilon^3}{37.5(1 - \epsilon)^2}$	$r_s = \text{sphere radius}$ $\epsilon = \text{porosity (value depends on packing mode)}$



Source: Chi (1976), with permission.

$$\dot{m}_l = \dot{m}_v = \frac{Q}{h_{fg}} \quad (16.15)$$

The effective length of the heat pipe, L_{eff} , is used to represent the average distance that the liquid and vapor must travel along the heat pipe

$$L_{\text{eff}} = \frac{1}{\dot{m}} \int_0^L \dot{m}(x) dx = \frac{1}{Q} \int_0^L Q(x) dx \quad (16.16)$$

Assuming uniform evaporation and condensation in the evaporator and condenser regions, the mass flow rates in the evaporator and condenser vary linearly and the effective length of a heat pipe becomes

$$L_{\text{eff}} = \frac{L_e}{2} + L_a + \frac{L_c}{2} \quad (16.17)$$

and the total liquid pressure drop can then be expressed as

$$\Delta P_l = \int_0^L \frac{dP_l}{dx} dx = \frac{\mu_l Q L_{\text{eff}}}{K A_w \rho_l h_{fg}} \quad (16.18)$$

Assuming that the dynamic pressure drop is fully recovered in the condenser region, the vapor pressure drop will be

$$\Delta P_v = \int_0^L \frac{dP_v}{dx} dx = \frac{(f \cdot \text{Re})_v \mu_v Q L_{\text{eff}}}{2 A_v r_{h,v}^2 \rho_v h_{fg}} \quad (16.19)$$

For cases where compressibility effects must be included and the dynamic pressure is not fully recovered, see Busse (1973) or Ivanovskii et al. (1982). Due to low liquid velocities and the small characteristic dimensions of the wick structure, the liquid flow is always generally assumed to be laminar. However, the vapor flow velocities may be sufficient to correspond to turbulent flow. In this case, the heat transfer rate Q and the Reynolds number Re are related, and the term $(f \cdot \text{Re})_v$ must be evaluated from a friction factor correlation for turbulent flow.

To determine the friction factor f_v , the vapor flow regime must be evaluated. Expressing the Reynolds number in terms of the heat input Q , the flow regime is determined from

$$\text{Re}_v = \frac{2r_v Q}{A_v \mu_v h_{fg}} \quad (16.20)$$

For laminar flow ($\text{Re} < 2300$) in a circular cross section, the term $(f \cdot \text{Re})_v$ is a constant

$$f_v \cdot \text{Re}_v = 16 \quad (16.21)$$

while for turbulent flow ($\text{Re} > 2300$) in a circular cross section the Blasius correlation can be used

$$f_v = \frac{0.038}{\text{Re}_v^{0.25}} \quad (16.22)$$

Values for $f \cdot \text{Re}$ for noncircular cross sections can be obtained from most convective heat transfer textbooks as a function of the cross-sectional geometry.

In the case of laminar vapor flow, the substitution of the individual pressure-drop terms into the capillary limit, eq. (16.9), results in an algebraic expression that can be solved directly for Q . For turbulent vapor flow, different methods exist for solving for Q . The first method for determining the capillary limit when the vapor flow is turbulent is that of an iterative solution. This procedure begins with an initial estimation of the capillary limit where the solution first assumes laminar, incompressible vapor flow. Using these assumptions, the maximum heat transport capacity Q can be determined by substituting the values for individual pressure drops and solving for the axial heat transfer. Once this value has been obtained, the axial heat transfer can be substituted into expressions for the vapor Reynolds number to determine the accuracy of the original assumptions. Using this iterative approach, accurate values for the capillary limitation as a function of the operating temperature can be determined where the operating temperature effects the capillary limit due to the temperature dependence of the fluid properties.

For a more direct solution of the capillary limit when turbulent flow is present in the vapor channel, it is possible to substitute the Blasius correlation into the vapor pressure-drop term. Then, separating all terms other than heat input $Q(x)$ and length x into friction coefficients F_v and F_l , the capillary limit can be expressed as

$$(\Delta P_c)_{\max} - \Delta P_{\perp} - \Delta P_{\parallel} = \int_0^L (F_l + F_v) Q dx \quad (16.23)$$

where the liquid frictional coefficient F_l is given by

$$F_l = \frac{\mu_l}{KA_w \rho_l h_{fg}} \quad (16.24)$$

and the vapor frictional coefficient F_v is evaluated from the expression

$$F_v = \frac{(f_v \cdot \text{Re}_v) \mu_v}{2r_v^2 A_v \rho_v h_{fg}} \quad (16.25)$$

For the case of turbulent vapor flow, the vapor friction coefficient was modified by substituting eq. (16.22) for $(f \cdot \text{Re})_v$ which results in an expression for the vapor friction coefficient of

$$F_v = \frac{0.038}{2} \frac{\mu_v}{r_v^2 A_v \rho_v h_{fg}} \text{Re}_v^{0.75} = 0.019 \frac{\mu_v}{r_v^2 A_v \rho_v h_{fg}} \left(\frac{2r_v Q}{A_v \mu_v h_{fg}} \right)^{0.75} \quad (16.26)$$

Substitution of this expression and combining with those discussed previously results in a general pressure balance relationship for turbulent vapor flow which takes the form

$$(\Delta P_c)_{\max} - \Delta P_{\perp} - \Delta P_{\parallel} = \frac{0.019 \mu_v}{r_v^2 A_v \rho_v h_{fg}} \left(\frac{2r_v}{A_v \mu_v h_{fg}} \right)^{0.75} \int_0^L Q^{7/4} dx + F_l \int_0^L Q dx \quad (16.27)$$

This expression and a Newton–Raphson method to determine the roots from the resulting polynomial equation, the maximum heat transport capacity (i.e., the capillary limit) for a given heat pipe can be determined as a function of the evaporator and condenser lengths and the operating temperature.

To solve for the capillary limit without iteration or numerical integration, an estimation of the capillary limit may be obtained where the friction factor is estimated and assumed constant for the entire operating range. Inspection of a traditional Moody (1944) friction factor diagram reveals that beyond a Reynolds number of 10^5 the friction factor becomes constant as the flow enters the fully turbulent region. By assuming a friction factor for $Re > 10^5$, the capillary limit results in a quadratic equation for Q and a much easier solution. This method typically produces reasonable results that tend more on the conservative side.

16.2.3 Boiling Limit

At higher heat fluxes, nucleate boiling may occur in the wick structure, which may allow vapor to become trapped in the wick, thus blocking liquid return and resulting in evaporator dryout. This phenomenon, referred to as the *boiling limit*, differs from the other limitations discussed previously, as it depends on the radial or circumferential heat flux applied to the evaporator, as opposed to the axial heat flux or total thermal power transported by the heat pipe.

Determination of the heat flux or boiling limit is based on nucleate boiling theory and is comprised of two separate phenomena: (1) bubble formation and (2) subsequent growth or collapse of the bubbles. Bubble formation is governed by the size (and number) of nucleation sites on a solid surface and the temperature difference between the heat pipe wall and the working fluid. The temperature difference, or superheat, governs the formation of bubbles and can typically be defined in terms of the maximum heat flux as

$$Q = \frac{k_{\text{eff}}}{T_w} \Delta T_c \quad (16.28)$$

where k_{eff} is the effective thermal conductivity of the liquid–wick combination. The critical superheat ΔT_c is defined by Marcus (1965) as

$$\Delta T_c = \frac{T_{\text{sat}}}{h_{fg} \rho_v} \left[\frac{2\sigma}{r_n} - (\Delta P_c)_{\max} \right] \quad (16.29)$$

where T_{sat} is the saturation temperature of the fluid and r_n is the critical nucleation site radius, which according to Dunn and Reay (1982) ranges from 0.1 to 25.0 μm for conventional metallic heat pipe case materials. As discussed by Brennan and Kroliczek (1979), this model yields a very conservative estimate of the amount of

TABLE 16.4 Effective Thermal Conductivity k_e for Liquid-Saturated Wick Structures

Wick Structure	k_e Expression	
Wick and liquid in series	$k_e = \frac{k_l k_w}{e k_w + k_l (1 - \epsilon)}$	k_e = effective thermal conductivity
Wick and liquid in parallel	$k_e = e k_l + k_w (1 - \epsilon)$	k_l = liquid thermal conductivity
Wrapped screen	$k_e = \frac{k_l [(k_l + k_w) - (1 - \epsilon)(k_l - k_w)]}{(k_l + k_w) + (1 - \epsilon)(k_l - k_w)}$	k_w = wick material thermal conductivity
Packed spheres	$k_e = \frac{k_l [(2k_l + k_w) - 2(1 - \epsilon)(k_l - k_w)]}{(2k_l + k_w) + (1 - \epsilon)(k_l - k_w)}$	ϵ = wick porosity
Rectangular grooves	$k_e = \frac{(w_f k_l k_w \delta) + w k_l (0.185 w_f k_w + \delta k_l)}{(w + w_f)(0.185 w_f k_f + \delta k_l)}$	w_f = groove fin thickness w = wick thickness δ = groove depth

Source: Chi (1976), with permission.

superheat required for bubble formation and is true even when using the lower bound for the critical nucleation site radius. This is attributed to the absence of adsorbed gases on the surface of the nucleation sites caused by the degassing and cleaning procedures used in the preparation and charging of heat pipes.

The growth or collapse of a given bubble once established on a flat or planar surface is dependent on the liquid temperature and corresponding pressure difference across the liquid–vapor interface caused by the vapor pressure and surface tension of the liquid. By performing a pressure balance on any given bubble and using the Clausius–Clapeyron equation to relate the temperature and pressure, an expression for the heat flux beyond which bubble growth will occur may be developed (Chi, 1976) and expressed as

$$Q_b = \frac{2\pi L_{\text{eff}} k_{\text{eff}} T_v}{A_v h_{fg} \rho_v \ln(r_i/r_v)} \left[\frac{2\sigma}{r_n} - (\Delta P_c)_{\text{max}} \right] \quad (16.30)$$

where r_i is the inner pipe wall radius and r_v is the vapor core radius. Relationships to determine the effective conductivity, k_{eff} , of the liquid saturated wick are given in Table 16.4.

16.2.4 Entrainment Limit

Examination of the basic flow conditions in a heat pipe shows that the liquid and vapor flow in opposite directions. The interaction between the countercurrent liquid and vapor flow results in viscous shear forces occurring at the liquid–vapor interface,

which may inhibit liquid return to the evaporator. In the most severe cases, waves may form and the interfacial shear forces may become greater than the liquid surface-tension forces, resulting in liquid droplets being picked up or entrained in the vapor flow and carried to the condenser.

The majority of previous work has been for thermosyphons or for gravity-assisted heat pipes. Of all the limits for heat pipes, the entrainment limit has produced one of the largest amounts of work, even though much is debated about when, and if, this limit occurs. Busse and Kemme (1980) expressed doubt as to whether entrainment actually occurs in a capillary-driven heat pipe because the capillary structure would probably retard the growth of any surface waves. In a majority of cases studied, the wick structure of the heat pipe was flooded (i.e., excess liquid), which allowed entrainment to occur. Additionally, much of the work has been an adaptation to work conducted in the study of annular two-phase flow, where the onset of droplet formation, the rates of entrainment, and the contribution to momentum transfer by the entrained droplets have been investigated in much detail (Langer and Mayinger, 1979; Hewitt, 1979; Nguyen-Chi and Groll, 1981). It is important to note that for thermosyphons, the entrainment and flooding limitation is typically the most important factor limiting heat transport (Faghri, 1995).

The most common approach to estimating the entrainment limit in heat pipes is to use a Weber number criterion. Cotter (1967) presented one of the first methods to determine the entrainment limit. This method utilized the *Weber number*, defined as the ratio of the viscous shear force to the forces resulting from the surface tension, or

$$\text{We} = \frac{2r_{h,w}\rho_v V_h^2}{\sigma} \quad (16.31)$$

By relating the vapor velocity and the heat transport capacity to the axial heat flux as

$$v_v = \frac{Q}{A_v \rho_v h_{fg}} \quad (16.32)$$

and assuming that to prevent entrainment of liquid droplets in the vapor flow, the Weber number must be less than unity, the maximum transport capacity based on entrainment can be written as

$$Q_e = A_v \lambda \left(\frac{\sigma \rho_v}{2r_c} \right)^{0.5} \quad (16.33)$$

where r_c is the capillary radius of the wick structure. However, this assumption typically results in an overestimation of the entrainment limit since the axial critical wavelength may be much greater than the width of the capillary structure.

In addition to the Weber number criterion, several different onset velocity criteria have been proposed for use with this expression. These include one by Busse (1973)

$$U_c = \left(\frac{2\pi\sigma}{\rho_v d} \right)^{1/2} \quad (16.34)$$

and another by Rice and Fulford (1987)

$$U_c = \left(\frac{8\sigma}{P_v d} \right)^{1/2} \quad (16.35)$$

These relations can be converted into the heat transport limitation due to entrainment by combining with the continuity equation, which yields

$$Q_e = A_v \rho_v \lambda \left(\frac{2\pi\sigma}{\rho_v d} \right)^{1/2} \quad (16.36)$$

or

$$Q_e = A_v \rho_v \lambda \left(\frac{8\sigma}{\rho_v d} \right)^{1/2} \quad (16.37)$$

respectively, where d is the wire spacing for screen wicks or the groove width for grooved wicks. However, as mentioned earlier, these criteria may overestimate the entrainment limit, due to problems associated with the characteristic dimensions.

Tien and Chung (1979) presented correlations for vertical (gravity-assisted) heat pipes. This correlation was applied to data reported by Kemme (1976), who expanded the Weber number criterion suggested by Cotter (1967), to include the balancing force term of buoyancy, or

$$Q_e = A_v \lambda \left[\frac{\rho_v}{A^*} \left(\frac{2\pi\sigma}{\iota} + \rho_l g D \right) \right]^{0.5} \quad (16.38)$$

Prenger (1984) developed a correlation for textured wall, gravity-assisted heat pipes. A model was presented which included both liquid and vapor inertia terms. It was found that for textured wall heat pipes, the liquid inertia term was dominant because the liquid was partially shielded from the vapor flow. This fact allowed the vapor inertia term to be neglected and the model to be reduced to

$$Q_e = 2A_v \lambda \frac{D_{\text{wire}}}{D_{\text{pipe}}} \left(\frac{\rho_l \sigma}{\pi D_{\text{pipe}}} \right)^{0.5} \quad (16.39)$$

which correlated well with previous data taken by Prenger and Kemme (1981). While the model presented by Tien and Chung (1979) found that heat flux limited by entrainment or flooding (as a function of the capillary structure), Prenger (1984) found the entrainment limit to be a function of the depth of the liquid layer or flow channel.

A review paper by Peterson and Bage (1991) provides a full description of work in the entrainment area as well as comparisons of available models. An interesting item in this comparison is that the models resulted in values for the heat pipe entrainment limit which varied by as much as a factor of 27 and demonstrate the level of unresolved issues in predicting the entrainment limit.

16.2.5 Viscous Limit

When operating at low temperatures, the available vapor (saturation) pressure in the evaporator region may be very small and be of the same magnitude as the required pressure gradient to drive the vapor from the evaporator to the condenser. In this case, the total vapor pressure will be balanced by opposing viscous forces in the vapor channel. Thus, the total vapor pressure within the vapor region may be insufficient to sustain an increased flow. This low-flow condition in the vapor region is referred to as the *viscous limit*. As the viscous limit occurs at very low vapor pressures, the viscous limit is most often observed in longer heat pipes when the working fluid used is near the melting temperature (or during frozen startup conditions) as the saturation pressure of the fluid is low.

Busse (1973) provided an analytical investigation of the viscous limit. The model first assumed an isothermal ideal gas for the vapor and that the vapor pressure at the condenser end was equal to zero, which provides the absolute limit for the condenser pressure. Using these assumptions, a one-dimensional model of the vapor flow assuming laminar flow conditions was developed and expressed as

$$Q_v = \frac{A_v r_v^2 h_{fg} \rho_v P_v}{16 \mu_v L_{\text{eff}}} \quad (16.40)$$

where P_v and ρ_v are the vapor pressure and density at the evaporator end of the heat pipe. The values predicted by this expression were compared with the results of previous experimental investigations and were shown to agree well (Busse, 1973). For cases where the condenser pressure is not selected to be zero, as could be the case when the viscous limit is reached for many conditions, the following expression is used

$$Q_v = \frac{A_v r_v^2 h_{fg} \rho_v P_v}{16 \mu_v L_{\text{eff}}} \left(1 - \frac{P_{v,c}^2}{P_v^2} \right) \quad (16.41)$$

where $P_{v,c}$ is the vapor pressure in the condenser. Busse (1973) noted that the viscous limit could be reached in many cases when $P_{v,c}/P_v \sim 0.3$.

To determine whether the viscous limit should be considered as a possible limiting condition, the vapor pressure gradient relative to the vapor pressure in the evaporator may be evaluated. In this case, when the pressure gradient is less than one-tenth of the vapor pressure, or $\Delta P_v/P_v < 0.1$, the viscous limit can be assumed not to be a factor. Although this condition can be used to determine the viscous limit during normal operating conditions, during startup conditions from a cold state, the viscous limit given by Busse (1973) will probably remain the limiting condition. As noted earlier, the viscous limit does not represent a failure condition. In the case where the heat input exceeds the heat input determined from the viscous limit, this results in the heat pipe operating at a higher temperature with a corresponding increase in the saturation vapor pressure. However, this condition typically is associated with the heat pipe transitioning to being sonic limited, as discussed in the following section.

16.2.6 Sonic Limit

The sonic limit is typically experienced in liquid metal heat pipes during startup or low-temperature operation due to the associated very low vapor densities in this condition. This may result in choked, or sonic, vapor flow. For most heat pipes operating at room temperature or cryogenic temperatures, the sonic limit is typically not a factor, except in the case of very small vapor channel diameters. With the increased vapor velocities, inertial, or dynamic, pressure effects must be included. It is important to note that in cases where inertial effect of the vapor flow are significant, the heat pipe may no longer operate in a nearly isothermal case, resulting in a significantly increased temperature gradient along the heat pipe. In cases of heat pipe operation where the inertial effects of the vapor flow must be included, an analogy between heat pipe operation and compressible flow in a converging–diverging nozzle can be made. In a converging–diverging nozzle, the mass flow rate is constant and the vapor velocity varies due to the varying cross-sectional area. However, in heat pipes, the area is typically constant and the vapor velocity varies due to mass addition (evaporation) and mass rejection (condensation) along the heat pipe.

As in nozzle flow, decreased outlet (back) pressure, or in the case of heat pipes, condenser temperatures, results in a decrease in the evaporator temperature until the sonic limit is reached. Any further increase in the heat rejection rate does not reduce the evaporator temperature or the maximum heat transfer capability but only reduces the condenser temperature due to the existence of choked flow. Figure 16.12 illustrates the relationship between the vapor temperature along a heat pipe with

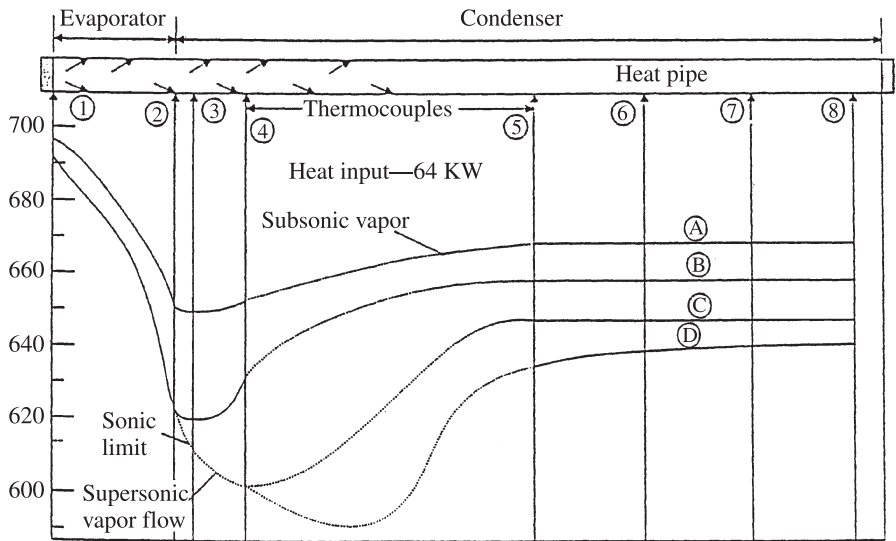


Figure 16.12 Temperature as a function of axial position. (From Dunn and Reay, 1982, with permission.)

inertial vapor effects. Curve A represents the temperature distribution typical of a heat pipe with subsonic flow conditions and partial pressure recovery (some inertial effects are present in the vapor flow). Increasing the heat rejection rate and lowering the condenser temperature will decrease the evaporator temperature as shown in curve B. Continued increases in the heat flux and reductions in the condenser temperature will result in a decrease in the overall average vapor temperature. However, eventually the vapor velocity at the condenser inlet approaches the sonic velocity and a critical or choked flow condition exists. For this situation, continued reductions in the condenser temperature only serve to decrease the temperature in the condenser region and have no effect on the vapor temperature in the evaporator.

Unlike the heat transport limits discussed previously, the sonic limitation actually serves as an upper bound to the axial heat transport capacity and does not necessarily result in dryout of the evaporator wick or total heat pipe failure. Attempts to exceed the sonic limit result in increasing both the evaporator temperature and the axial temperature gradient along the heat pipe, thus reducing further the isothermal characteristics typically found in the vapor flow region.

Levy (1968) developed a closed-form expression for the sonic limit derived from one-dimensional vapor flow theory. This analysis assumed that the frictional effects may be neglected; thus inertial effects dominate, and the vapor behaves as a perfect gas. Combining these assumptions with the energy and momentum equations results in expressions for the temperature and pressure ratios. Substituting the local Mach number and relating the axial heat flux to the density and velocity, the relationship between the static and stagnation temperatures and pressure can be rewritten as

$$\frac{T_o}{T_v} = 1 + \frac{\gamma_v - 1}{2} Ma_v^2 \quad (16.42)$$

$$\frac{P_o}{P_v} = 1 + \gamma_v Ma_v^2 \quad (16.43)$$

where the subscripts o and v indicate the stagnation and static states of the vapor, respectively. Combining the temperature and pressure ratios with the ideal gas law yields an expression for the density ratio, which when combined with the two relationships, yields an equation for the axial heat flux in terms of the physical properties, geometrical dimensions, and Mach number. For choked flow, the Mach number will equal unity, which yields an expression for the maximum axial heat transport:

$$Q_s = A_v \rho_o \lambda \left[\frac{\gamma_v R_v T_o}{2(\gamma_v + 1)} \right]^{1/2} \quad (16.44)$$

Busse (1973) presented an alternative approach by assuming that only inertial effects are present in one-dimensional flow. In this case the momentum equation yields

$$\frac{dP}{dx} = -\frac{d}{dx} \overline{\rho v^2} \quad (16.45)$$

Integration of this expression, combining it with the continuity equation, and assuming that the vapor behaves as an ideal gas yields an expression for the maximum heat transport capacity as a function of the thermophysical and geometric properties

$$Q = \lambda \left(\frac{\rho_v P_v}{A} \right)^{1/2} \left[\frac{P}{P_v} \left(1 - \frac{P}{P_v} \right) \right]^{1/2} \quad (16.46)$$

A determination of the point where the first derivative, dQ/dP , vanishes yields a relationship for the sonic limit

$$Q_s = 0.474 \lambda A_v (\rho_v P_v)^{1/2} \quad (16.47)$$

where ρ_v and P_v are the vapor density and pressure at the evaporator exit. The greatest difficulty in determining the sonic limit is determining these two quantities along with the inlet pressure to the condenser. In addition, fractional effects have been included by Levy and Chou (1973) to improve correlation with experimental data. Other experimental and theoretical investigations of the sonic limitation have been performed by Kemme (1969) and Deverall et al. (1970).

Several attempts to describe the sonic limit from solutions to the two-dimensional Navier–Stokes equations have been developed. Bankston and Smith (1971) and Rohani and Tien (1974) all used numerical methods. The former study indicated that axial flow reversal occurred for high condensation rates at the end of the condenser. Comparison with the predicted results of a one-dimensional model developed by Busse (1973) indicated good agreement for high condensation rates in the condenser region despite this flow reversal (Rohani and Tien, 1974).

It is interesting to compare the results for the viscous limit and sonic limit where a relationship between the two exist with respect to the quantity $P_v \rho_v$. Inertial effects are found to vary with the product $(P_v \rho_v)^{1/2}$, while the viscous effects vary linearly with respect to $P_v \rho_v$. As a result, when this product is small, the transport capacity is typically limited by viscous effects but with increasing $P_v \rho_v$, inertial effects begin to dominate and a transition occurs from the viscous to the sonic limit. The boundary between these two limits can be determined by setting these two equations equal to each other and solving for the combined terms as a function of temperature (Ivanovskii et al., 1982; Busse, 1973). The results indicate that the transition temperature is dependent on the thermophysical properties of the working fluid, the geometry of the heat pipe, and the length of the evaporator and condenser regions. Experimental work by Vinz and Busse (1973) verified that this transition compared quite well with predicted values.

16.2.7 Condenser Limit

The heat transfer rate in the condenser section is governed by the coupling of the condenser with the system heat sink. At steady state, the heat rejection rate in the condenser must equal the heat addition rate in the evaporator. Typically, the condenser

coupling is either by convection and/or radiation. In this case the heat transfer from the condenser, assuming a constant condenser temperature, is determined from

$$Q_c = Q_{\text{conv}} + Q_{\text{rad}} = hA(T_c - T_\infty) + \epsilon A\sigma (T_c^4 - T_{\text{surr}}^4) \quad (16.48)$$

where h is the convective heat transfer coefficient, A the condenser surface area, and ϵ the emissivity of the surface. If either convective or radiation effects are negligible, the first or second term, respectively, in eq. (2.6.1) is neglected. Examples of reaching the condenser limit can be low convective heat transfer coefficients (e.g., natural convection), low surface emissivity, or limited surface area. In these cases, increased heat addition to the heat pipe results in an increased temperature of the heat pipe because an increased temperature difference between the heat pipe condenser and heat sink is required. Methods to improve the condenser limit may include augmentation of the heat transfer coefficient (e.g., forced convection), increasing the surface emissivity (e.g., surface coatings), and increasing the condenser surface area (e.g., fins). For cases where the condenser surface temperature is not uniform, integration of the differential heat transfer along the condenser surface is required. Moreover, if the heat pipe condenser is in an enclosure, radiation view factors between the heat pipe and surroundings need to be determined. For both of the latter two cases, information can be used from any standard heat transfer textbook (e.g., Incropera and DeWitt, 2002).

16.3 HEAT PIPE THERMAL RESISTANCE

The overall temperature difference between the heat sink and the heat source is an important characteristic for thermal control systems utilizing heat pipes. As the heat pipe is typically referred to as an overall structure of very high effective thermal conductivity, an electrical resistance analogy similar to that found in conduction heat transfer analysis is used. As the heat transfer occurs from the heat source to the heat sink, each part of the heat pipe can be separated into an individual thermal resistance. The combined resistances provide a mechanism to model the overall thermal resistance and the temperature drop from heat sink to heat source associated with the given heat input. In addition, the resistance analogy provides a means to estimate the mean operating temperature (adiabatic vapor temperature) that is typically needed in determining the transport limit at a given operating condition. The temperature gradient is found utilizing a thermal resistance network, where Fig. 16.13 illustrates the analogy for a simple cylindrical heat pipe. The overall thermal resistance of the heat pipe only is comprised typically of nine resistances arranged in a series-parallel combination. The resistances can be summarized along with estimates of typical magnitudes as follows:

1. $R_{p,e}$: pipe wall radial resistance, evaporator ($\sim 10^{-1} \text{ }^\circ\text{C/W}$)
2. $R_{w,e}$: saturated liquid/wick radial resistance, evaporator ($\sim 10^{+1} \text{ }^\circ\text{C/W}$)

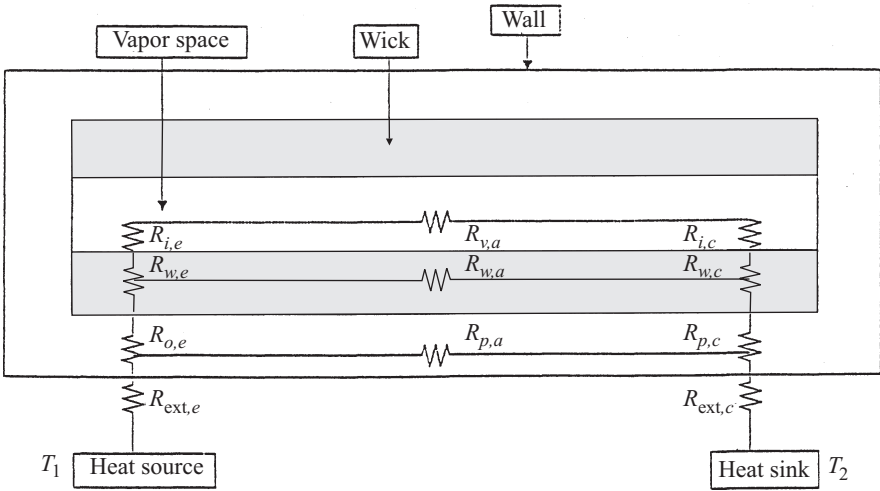


Figure 16.13 Equivalent thermal resistance of a heat pipe. (From Peterson, 1994, with permission.)

3. $R_{i,e}$: liquid–vapor interface resistance, evaporator ($\sim 10^{-5} \text{ }^{\circ}\text{C/W}$)
4. $R_{v,a}$: adiabatic vapor section resistance ($\sim 10^{-8} \text{ }^{\circ}\text{C/W}$)
5. $R_{p,a}$: pipe wall axial resistance ($\sim 10^{+2} \text{ }^{\circ}\text{C/W}$)
6. $R_{w,a}$: saturated liquid–wick axial resistance ($\sim 10^{+4} \text{ }^{\circ}\text{C/W}$)
7. $R_{i,c}$: liquid–vapor interface resistance, condenser ($\sim 10^{-5} \text{ }^{\circ}\text{C/W}$)
8. $R_{w,c}$: saturated liquid–wick radial resistance, condenser ($\sim 10^{+1} \text{ }^{\circ}\text{C/W}$)
9. $R_{p,c}$: pipe wall radial resistance, condenser ($\sim 10^{-1} \text{ }^{\circ}\text{C/W}$)

By examination of the typical range of resistance values, several simplifications are possible. First, due to comparative magnitudes of the resistance of the vapor space and the axial resistances of the pipe wall and liquid–wick combinations, the axial resistance of the pipe wall, $R_{p,a}$, and the liquid–wick combination, $R_{w,a}$, may be treated as open circuits and neglected. Second, the liquid–vapor interface resistances and the axial vapor resistance (in most situations) can be assumed negligible. Thus, the primary resistances of the heat pipe are the pipe wall radial resistances and the liquid–wick resistances in the evaporator and condenser.

The pipe wall resistances are found using for flat plates

$$R_{p,e} = \frac{\delta}{k_p A_e} \quad (16.49)$$

where δ is the plate thickness and A_e is the evaporator surface area, and for cylindrical pipes as

$$R_{p,e} = \frac{\ln(d_o/d_i)}{2\pi L_e k_p} \quad (16.50)$$

where L_e is the evaporator length (or is replaced by the condenser length when evaluating $R_{p,c}$). The resistance of the liquid–wick combination is also found from eq. (16.50), where the effective conductivity k_{eff} is used instead of the pipe wall value k_p . Relationships for calculating k_{eff} are given in Table 16.3.

Two other resistances shown in Fig. 16.13 have a significant role in the design of heat pipe thermal control systems. These are the external resistances occurring between the heat source and heat pipe evaporator and the heat pipe sink and heat pipe condenser, $R_{\text{ext},e}$ and $R_{\text{ext},c}$, respectively. The external resistances are found by using information related to contact resistances and convective resistance where information on these can be found in most heat transfer textbooks. In many applications, these two resistances combined are greater than the overall heat pipe resistance, thus, these are typically the controlling resistances in applications.

One additional important observation from the resistance analogy can be made. This is the case where the heat pipe reaches a dryout condition, such as exceeding the capillary limit. In the case of dryout, the vapor flow from the evaporator to the condenser will be discontinued and the resistance $R_{v,a}$ will increase significantly, such that this circuit now may be considered as an open circuit. Thus, any heat input to the system must be transported along the heat pipe wall, $R_{p,a}$, and the wick structure combination, $R_{w,a}$. As the difference between the axial resistances is several orders of magnitude, the temperature drop along the heat pipe will correspond to an increase of several orders of magnitude. This is as expected since the heat must now be transferred by conduction instead of using the latent heat of vaporization of the working fluid.

16.4 FIGURES OF MERIT

As a first step in the steady-state modeling of the transport capacity of a heat pipe, it can be useful initially to select a working fluid and/or to compare one fluid with another regardless of the heat pipe geometry. To maximize heat transport, the ideal fluid has a high surface tension to increase capillary pumping, high fluid density, and latent heat of vaporization to reduce mass flow rates (and thus frictional losses) and low viscosity. These properties are combined to form a figure of merit (FM) for a given fluid in terms of fluid properties. In conventional heat pipes, the greatest pressure loss is typically associated with the liquid flow in the wick structure. Equating the Young–Laplace equation for capillary pressure to the wick pressure drop predicted by Darcy’s law, Chi (1976) was able to separate the fluid terms from the geometric and produce a figure of merit (liquid based)

$$\text{FM} = \frac{\rho_l \sigma h_{fg}}{\mu_l} \quad (16.51)$$

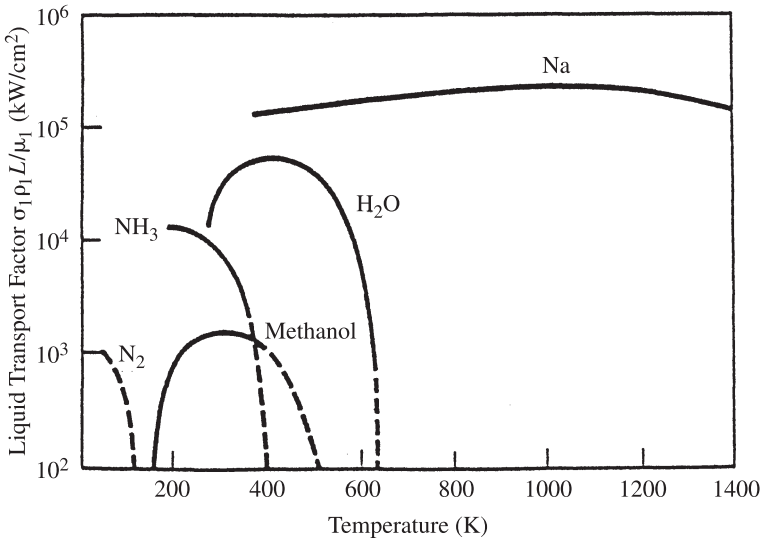


Figure 16.14 Heat pipe liquid-based figure of merit as a function of operating temperature for several working fluids.

which has units of heat flux (W/m^2). Working fluid candidates with high figures of merit are considered to have better performance characteristics. The figure of merit (liquid based) as a function of operating temperature for several working fluids is shown in Fig. 16.14. For a given heat pipe geometry, this provides a good estimation of the working fluid potentially providing the greatest transport capacity at a specific temperature.

In cases where the pressure drop due to flow through the wick structure is not the dominant pressure drop (e.g., the loop heat pipe, discussed later), Dunbar and Cadell (1998) developed a figure of merit under the assumption that the pressure drop in the vapor flow is the dominate pressure loss term. The analysis equated the frictional pressure drop due to turbulent flow in the vapor channel to the Young–Laplace equation for capillary pressure and separated the fluid terms from geometric terms to yield the figure of merit (vapor based)

$$\text{FM} = \frac{\rho_v \sigma h_{fg}^{1.75}}{\mu_v^{0.25}} \tag{16.52}$$

16.5 TRANSIENT OPERATION

16.5.1 Continuum Vapor and Liquid-Saturated Wick

The most common transient occurring for a heat pipe is when the vapor is in a continuum flow condition and the wick is saturated with liquid. As the effective

thermal conductivity of the heat pipe is very high and the overall mass is relatively low, a heat pipe typically has a low thermal capacitance and a low overall thermal resistance compared to the overall thermal control systems. In these situations, the heat pipe can be modeled using a lumped capacitance method assuming uniform heat pipe temperature at any given time. This approach may also be applicable in numerous situations, such as when free convection is used as the heat addition or heat rejection mechanism due to large convective resistances between the heat pipe and the airstreams. Applying an energy balance to the entire heat pipe, the general energy equation for using a lumped capacitance approach is given by

$$Q_e(t) - Q_c(t) = (\rho c_p)_{\text{eff}} V \frac{dT}{dt} \quad (16.53)$$

where $Q_e(t)$ is the evaporator heat input, $Q_c(t)$ the condenser heat rejection, and $(\rho c_p)_{\text{eff}} V$ the effective thermal mass of the heat pipe and must include the specific heats of the case, wick, and fluid. Solutions to eq. (16.53) depend directly on the boundary conditions (convection, radiation, conduction) corresponding to the heat input and heat rejection for the given system. In some cases it will be required to know more accurate axial temperatures and pressures occurring in the heat pipe; thus a more detailed spatial-temporal model may be required. For these situations, numerical techniques commonly are utilized, even for cases of one-dimensional approximations. Information regarding numerical analyses of heat pipe transients can be found in Colwell and Modlin (1992), Bowman (1991), and Faghri (1995).

16.5.2 Wick Depriming and Rewetting

Heat pipes utilized in spacecraft thermal management systems may be subjected to orbital attitude adjustments, reboots, and docking maneuvers, which may result in accelerations sufficient to cause redistribution of the liquid within the heat pipes. When the magnitude, direction, and/or duration of the acceleration is sufficient, liquid will flow out of the wick and accumulate in the ends of the liquid and vapor channels opposite to the direction of acceleration. For accelerations in the direction of an evaporator, dryout may easily occur. To predict the performance of a thermal management system following an evaporator dryout, the process of repriming/rewetting the heat pipe evaporator must be evaluated to determine the time required and conditions for the heat pipe to become operational once again. Additionally, evaporator dryout will occur if the thermal loading on a heat pipe exceeds the heat pipe transport capability. Typical scenarios where this condition may occur are excess power input in electronic chip cooling, cold plate/heat sink cooling in electronics or spacecraft, initial clamping of a heat pipe to a heat source, and heat pipe heat exchangers. In the event of evaporator dryout, the power or thermal loading to the heat pipe must be decreased. Investigations examining the time required to rewet/reprime the wick structure have been conducted by Ambrose et al. (1987), Ivanovskii et al. (1982), and Ochterbeck et al. (1995).

16.5.3 Freeze–Thaw Issues

Heat pipe startup from the frozen state involves the preliminary phase-change process of melting the working fluid before the heat pipe becomes fully functional. The heat input must effectively melt the working fluid in the wick structure and allow for liquid return to the evaporator prior to evaporator dryout. The presence of all three phases of the working fluid during the melting process significantly affects the startup characteristics and complicates the investigation of frozen startup.

Heat pipes experiencing frozen startup can be divided distinctly into two regimes (liquid metal and room temperature). The primary difference between startup of liquid metal heat pipes and room-temperature heat pipes is the absence of the conduction-dominated regime, which exists in early periods with free molecular vapor flow conditions, common to liquid metals. In room-temperature heat pipe frozen startup, a saturated solid–vapor phase and continuum flow conditions exist; thus sublimation of the working fluid is possible, which results in heat and mass transport by the working fluid vapor in addition to heat diffusion in the solid regions. The sublimation and corresponding loss of mass in the evaporator is a direct disadvantage to the restart process for room-temperature heat pipes, since there is no mass return to the evaporator.

Previous investigations of liquid metal and room-temperature heat pipes have demonstrated that prior to continuum vapor flow conditions, heat and mass transfer in the vapor channel are essentially negligible under free molecular flow regimes. Negligible evaporation results from an insufficient vapor pressure P_v to sustain vaporization or from the collision of vapor molecules with the physical boundaries instead of other vapor molecules. Transition criteria, usually based on a transition temperature T^* , is evaluated where the mean free molecular path of the vapor molecules becomes much less than the minimum vapor space dimension. This criterion is represented mathematically by the Knudsen number

$$\text{Kn} \equiv \frac{\lambda}{D_v} \quad (16.54)$$

where λ is the mean free molecular path. Specific ranges regarded to exist for the various flow regimes have been given as (Zucrow and Hoffman, 1976)

- *Continuum vapor flow:* $\text{Kn} < 0.01$
- *Free molecular flow:* $\text{Kn} > 3.0$
- *Transition region:* $0.01 < \text{Kn} < 3.0$

In terms of the vapor temperature and pressure, an expression for the transition temperature T^* is given by

$$T^* = \frac{2}{\pi} \frac{\text{Kn}^2}{R} \left(\frac{P_v D_v}{\mu_v} \right)^2 \quad (16.55)$$

where R is the working fluid gas constant. The transition corresponds to the specified Knudsen number, generally 0.01, at which continuum flow conditions will exist for

temperatures greater than T^* and for a specific vapor channel diameter D_v . Equation (16.55) provides a relationship for the transition temperature expressed in terms of the fluid properties and the vapor channel diameter. However, there is a difficulty in evaluating eq. (16.55) because of the temperature dependence of the vapor viscosity; thus an iterative solution using individual fluid properties is required. Results of the transition temperature versus vapor channel diameter are shown in Fig. 16.15.

For room-temperature working fluids (water and ammonia), continuum flow conditions exist for temperatures below the melting point, T_{mp} , where the fluid exists in a saturated solid-vapor phase, while continuum flow conditions do not exist until approximately $2T_{mp}$ for liquid metal working fluids. In this case, due to a saturated solid-vapor phase in the frozen state, and due to the existence of continuum flow conditions, sublimation of the working fluid is therefore possible. This results in heat and mass transport by the working fluid vapor in addition to heat diffusion in the solid regions. Because the free molecular regime is no longer present, the condition of melting a significant portion of the working fluid by conduction prior to large-scale vaporization is not found in room-temperature heat pipes. The sublimation and corresponding loss of mass in the evaporator is a direct disadvantage to the restart process for room-temperature heat pipes. Thus, the entire thermal history of room-temperature heat pipes that may undergo freeze-thaw cycles is important.

Although frozen startup is always required at least once for liquid metal heat pipes, conditions occur for other working fluids where the heat pipe or heat sink is at sub-freezing temperatures. In liquid metal heat pipe startup, it is often possible to melt a significant amount of the working fluid before evaporation begins. This is not the

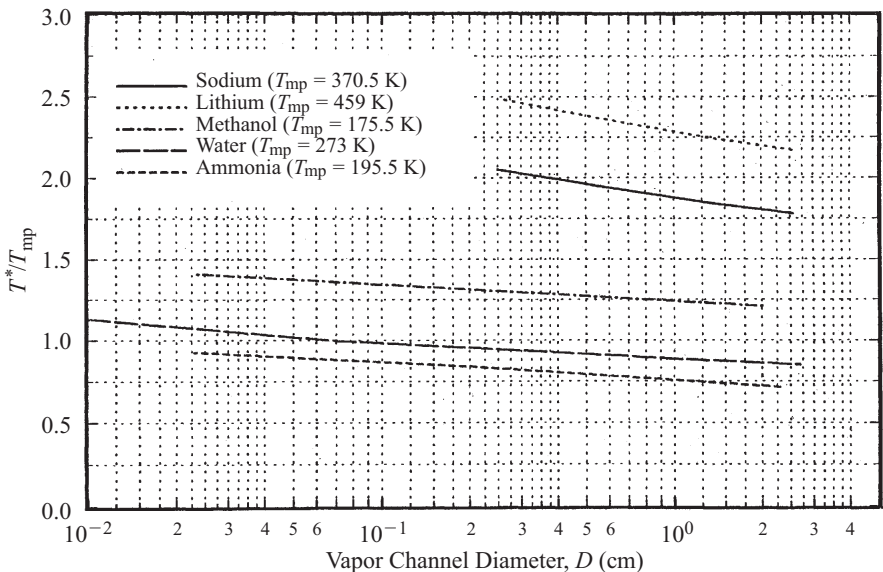


Figure 16.15 Transition temperature as a function of vapor channel diameter for several fluids.

case with room-temperature heat pipes, especially those without a noncondensable gas charge. For room-temperature heat pipes, the frozen-state temperature is generally not far below that of the triple point. For heat pipe fluids such as water, the vapor pressure may be great enough to allow migration of the working fluid toward the colder regions of the heat pipe (condenser). Also, relatively higher vapor pressures at the melting point can lead to significant evaporation immediately after the working fluid has melted, for which the condenser may remain in a frozen state, thus hindering the return of sufficient liquid.

In the analysis of frozen startup for room-temperature heat pipes (122 to 630 K) (Ochterbeck, 1997), all reported experiments, not including noncondensable gas charging, have resulted in evaporator dryout. Although several tested frozen heat pipes have been restarted successfully, these instances of startup have involved evaporator dryout followed by evaporator rewetting. Increases in the noncondensable gas level resulted in aiding restart by effectively blocking the sublimation–migration process of working fluid, and the heat pipe restarted in a gas-controlled mode.

During startup of a gas-loaded liquid metal heat pipe, the noncondensable gas initially occupies the entire vapor space under frozen conditions, with this condition prevailing until the vapor pressure $P(T_e)$ is equivalent in magnitude to the initial gas pressure, P_i . Also, this condition of $P_v(T_e) = P_i$ typically occurs at temperatures well above the working fluid melting point. The movement of the vapor–gas front and melt front essentially propagate at the same rate; thus freezeout of the working fluid is hindered by the noncondensable gas. However, in a room-temperature heat pipe, the vapor–gas front and melt front do not necessarily coincide. Increases in the evaporator temperature correspond to an increased evaporator vapor pressure, which drives the movement of the vapor–gas front, even with a frozen working fluid. The initiation of a melt front within the wicking structure does not occur until the evaporator temperature is greater than the working fluid triple state (Faghri, 1995; Ivanovskii et al., 1982).

16.5.4 Supercritical Startup

In heat pipes for cryogenic applications, a gaseous or supercritical state prevails for the working fluids (e.g., hydrogen, nitrogen, oxygen) at room-temperature conditions. During startup, the heat pipe must be cooled until the fluid temperature is below the critical point, requiring condensation of the working fluid and wetting of the wicking structure before the heat pipe becomes operational (Chang and Colwell, 1985). The investigation by Chang and Colwell (1985) of supercritical startup in cryogenic heat pipes utilized a finite-difference numerical analysis and gave good insight into the problem. However, as finite-difference techniques may be difficult to utilize, an analytical model was presented by Yan and Ochterbeck (1999). The basics of this model utilized two underlying assumptions in the analysis: that the condenser temperature is uniform and that condensation within the heat pipe begins at $T = T_c$. For the system, the analysis is separated into two regions. First, the condenser temperature remains above the critical point temperature, $T_{\text{cond}} > T_{\text{cr}}$, such that condensation within the heat pipe, and phase-change heat transfer, do not yet

occur. Thus, this stage is entirely conduction controlled and solution of the problem is found using any of various solution techniques (e.g., the integral method) to transient heat conduction equation. Once the heat pipe condenser temperature and pressure decrease below the critical state and the working fluid corresponds to saturation conditions, the heat pipe is modeled using a coupled hydrodynamic rewetting model for an advancing liquid in the wick structure along with the heat conductance equation for the remaining dry region.

16.6 SPECIAL TYPES OF HEAT PIPES

16.6.1 Variable Conductance Heat Pipes

Heat pipes operate at the saturation temperature of the working fluids given by the pressure inside the pipe. If the heat input and/or condenser coolant conditions change, the operating conditions of the heat pipe also change along the temperature–pressure saturation curve; that is, a new coupled set of temperature and pressure values are set by the new steady-state operating condition. This mode of heat pipe operation is referred to as a *fixed-conductance mode*.

The interest of variable conductance heat pipes (VCHPs) is that a VCHP maintains the same operating temperature under varying heat input or condenser cooling conditions. For gas-loaded heat pipes, the most common type of variable conductance heat pipe, this is achieved by connecting the heat pipe with a reservoir containing a noncondensable gas, as shown in Fig. 16.16. The pressure is set by the reservoir pressure using either active control by pressure regulation or passive control where the volume of the reservoir is large compared with the volume of the heat pipe (practically, at least four to five times larger).

During operation, the noncondensable gas is swept down the length of the heat pipe by the working fluid vapor to the condenser section. Because condensation of the working fluid does not take place where noncondensable gas is present, a portion of the condenser is blocked from transferring heat to the heat sink. If the heat input to the

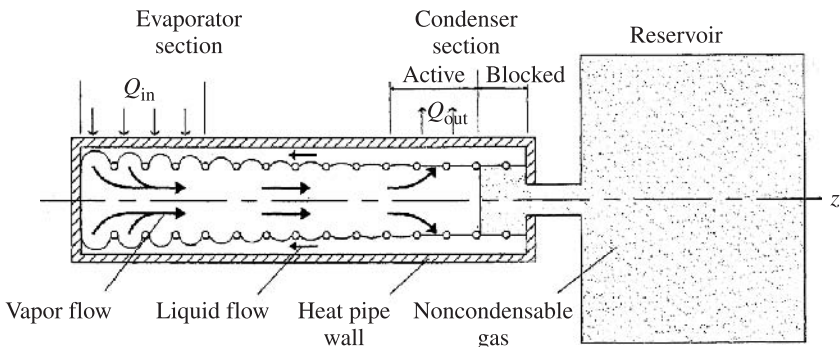


Figure 16.16 Variable-conductance heat pipe.

evaporator section is increased, the vapor pressure increases, which leads to compression of the inert gas until the vapor pressure reaches the pressure set by the reservoir. This, in turn, increases the amount of condenser surface available to transfer heat, increasing the quantity of heat removed, and maintaining the temperature constant. On the other hand, if the heat input decreases, the pressure will also decrease, leading to an expansion of the gas and a reduction in the active surface of the condenser. The quantity of heat removed by the condenser will then decrease, and the temperature will remain constant. Thus, the operating temperature of the variable-conductance heat pipe remains nearly constant for variations of heat input–output. Regulating the pressure in the reservoir permits setting the operating temperature of the heat pipe.

16.6.2 Micro and Miniature Heat Pipes

The concept of the micro heat pipe was first proposed as a method to provide more uniform temperature distributions in semiconductor devices and thus to eliminate local hot spots generated by these devices. These micro heat pipes are formed by wickless, noncircular geometries in generally sharp-cornered geometries (e.g., triangular) with internal channel diameters on the order of 30 to 1000 μm . The sharp-angled corners serve as the liquid arteries and provide the capillary structure necessary for supporting the liquid–vapor interface, as in Fig. 16.17.

Since initially proposed, several investigations have been directed toward the micro heat pipe concept (Peterson, 1994). The first investigations essentially concentrated on miniature heat pipes with characteristic dimensions on the order of 1.0 mm and provided good insight into the fundamental differences that would be expected to occur between conventional and micro heat pipes (Wu et al., 1991). Recently, micro heat pipe arrays with characteristic dimensions on the order of 30 to 100 μm have been constructed in silicon wafers using both chemical etching and vapor deposition techniques. These micro heat pipe arrays have been tested in both steady-state and transient operations and demonstrated significant improvement over plain silicon wafers by reducing the maximum surface temperatures or hot spots, thus providing more uniform temperature distributions in the wafers. These tests proved the concept of micro heat pipes to be feasible.

Prior to utilization of micro heat pipes in electronic applications, several issues must be addressed. Included herein is the determination of the effects on the operational performance by the amount of working fluid present and determination of the distribution of the working fluid within the micro heat pipe during operation. In a conventional heat pipe, the amount of working fluid necessary is governed by the requirement that the wicking structure be effectively saturated over the operating temperature range of the heat pipe. As the sharp corner regions in the micro heat pipe serve as the wick structure, the amount of working fluid required for optimal performance is not easily determined. Both undercharging and overcharging the micro heat pipes will result in severe degradation of heat pipe performance.

The location of the working fluid is very complex in nature and is determined by the geometry of the micro heat pipe, amount of working fluid, and the corresponding heat input. As the heat input is increased, the liquid meniscus in the evaporator region

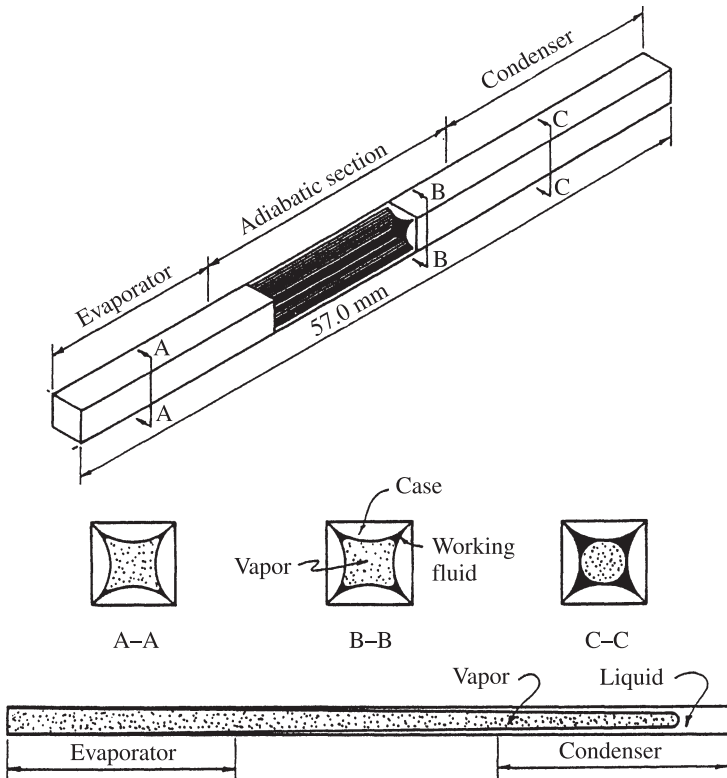


Figure 16.17 Tapezoidal micro heat pipe modeled by Babin et al. (1990).

recedes into the sharp corners due to a required larger capillary-pumping requirement to transport the liquid from the condenser to the evaporator. Because the micro heat pipe contains a fixed amount of working fluid, the decreased mass in the evaporator must correspond to an increased mass inventory in the condenser. However, as the meniscus recedes, the area by which liquid may flow decreases, resulting in increased frictional forces acting against the return of the liquid. The liquid flow area may vary additionally along the length of the micro heat pipe, further complicating the performance evaluation.

The amount of working fluid not only affects the working fluid distribution in the heat pipe but also significantly affects the maximum performance of the heat pipe. If the heat pipe is overcharged, the resistances to heat transfer are increased, as the heat must travel through the additional fluid and may in fact result in a system with inferior heat transfer characteristics than would exist without the heat pipe. Similarly, if the heat pipe is undercharged, the liquid flow passage size may be reduced and result in increased frictional losses in the liquid. An optimal charge must exist which allows the maximum performance of a micro heat pipe to be achieved.

16.6.3 Pulsating Heat Pipes

The pulsating heat pipe (PHP) (Akachi and Polasek, 1995) is one of the latest developments in the area of heat pipe technology. In contrast to a conventional heat pipe, where the working fluid inside the heat pipe circulates continuously by capillary forces between the heat source and the heat sink in the form of countercurrent flow, the working fluid in a PHP oscillates in its axial direction. The basic heat transfer mechanism in a pulsating heat pipe is the oscillating movement of the fluid associated with phase change (evaporation and condensation) phenomena. To operate, a PHP must take advantage of capillary forces to form liquid and vapor slugs, as shown in Fig. 16.18. A PHP is composed of a bundle of turns of one continuous capillary tube.

The diameter of the capillary tube must be small enough to allow liquid and vapor plugs to coexist. For this condition, the maximum diameter was determined by Akachi and Polasek (1995) to be

$$d \leq 2 \left(\frac{\sigma}{\rho_L g} \right)^{1/2} \quad (16.56)$$

where some results for common fluids at ambient temperature are:

- *Water*: $d < 5.34$ mm
- *Acetone*: $d < 3.36$ mm
- *Ethanol*: $d < 3.25$ mm
- *R-142b*: $d < 2.04$ mm

Akachi and Polasek (1995) described the basic principle of a PHP: “When one end of the bundle of turns of the undulating capillary tube is subjected to high temperature, the working fluid inside evaporates and increases the vapor pressure, which causes the bubbles in the evaporator zone to grow. This pushes the liquid

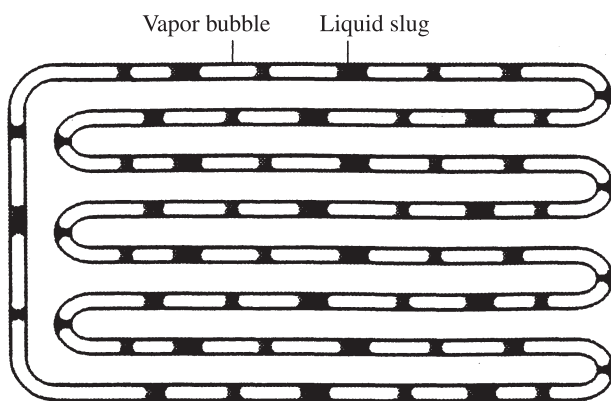


Figure 16.18 Pulsating heat pipe.

column toward the low temperature end (condenser). The condensation at the low temperature end will further increase the pressure difference between the two ends. Because of the interconnection of the tubes, the motion of liquid slugs and vapor bubbles at one section of the tube toward the condenser also leads to the motion of slugs and bubbles in the next section toward the high temperature end (evaporator). This works as the restoring force. The inter-play between the driving force and the restoring force leads to oscillation of the vapor bubbles and liquid slugs in the axial direction. The frequency and the amplitude of the oscillation are expected to be dependent on the heat flow and mass fraction of the liquid in the tube.”

Thus, heat can be transferred from the heated section to the cooled section. The PHP has the advantage of not needing a wick structure to transport the liquid. There is also no pump, so the PHP is passive and to operate needs no power other than the heat that is being rejected. Although the overall resistance of a pulsating heat pipe is typically greater than that of a traditional heat pipe, the pulsating heat pipe can operate at higher heat fluxes, as the system utilizes boiling and is not limited by a boiling limit other than the critical heat flux.

16.6.4 Loop Heat Pipes and Capillary Pumped Loops

A main drawback of the conventional heat pipe is the presence of the wick along the entire internal surface, which causes increased pressure losses in the liquid flow. The losses increase rapidly with increasing transfer length. This is also one reason why conventional heat pipes are sensitive to the orientation in the gravitational field. Therefore, separation of the vapor passage from the liquid passage and reducing the presence of the wick in the heat pipes resulted in the loop heat pipe (LHP), developed primarily in the former Soviet Union, and capillary pumped loops (CPL), developed primarily in the United States. Figure 16.19 shows the evolution from conventional heat pipes to the LHP and CPL (Maidanik and Fershtater, 1997). In an LHP/CPL, the wick is located only in the evaporator sections; the remainder of the systems are replaced by smooth-walled tubing, which makes it possible for an LHP/CPL system to transport the working fluid through a long distance with a small hydraulic pressure loss. LHP/CPL systems are therefore considered as prime candidates for thermal management systems for large modern space systems. The essence of an LHP and a CPL are actually the same, the major difference being that the LHP usually operates in a constant-conductance mode, while a CPL usually operates in a variable-conductance mode by keeping the operation temperature unchanged.

As mentioned, the adiabatic and condenser sections in a capillary pumped loop are replaced by smooth-walled tubing, so that the frictional pressure drops in these sections are reduced significantly. In general, the thermal capability of a capillary pumped loop can be one to two orders of magnitude greater than that of a conventional heat pipe with the same wick material.

A schematic of a typical CPL is shown in Fig. 16.20. It consists of an evaporator pump, a vapor transport line, a condenser, a subcooler, a liquid return line, and a two-phase reservoir. Heat is applied to the evaporator and vaporizes the liquid, while at the condenser the heat is rejected to a heat sink and the vapor is condensed. The vapor

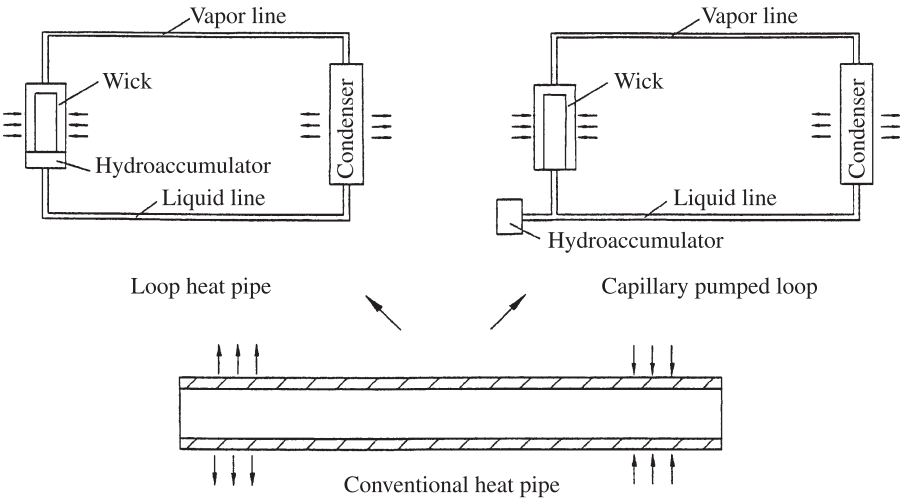


Figure 16.19 Evolution from conventional to LHP/CPL heat pipes.

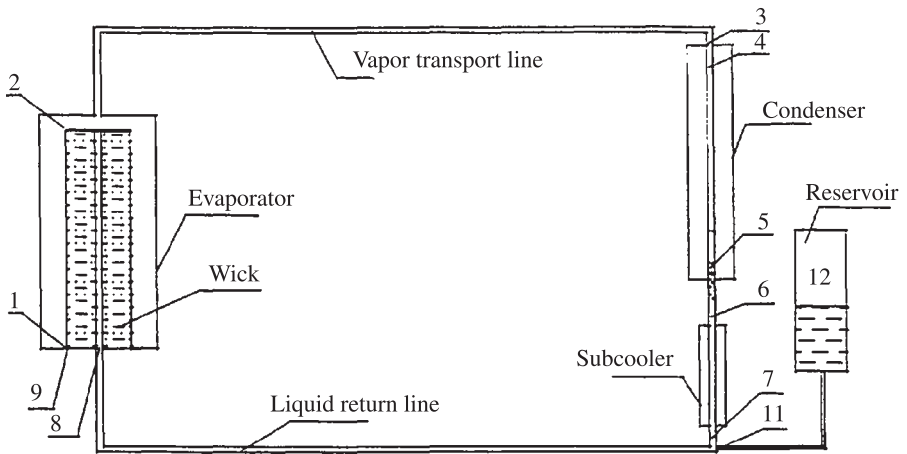


Figure 16.20 Capillary pumped loop (CPL) heat pipes.

transport and liquid return lines provide flow paths for the working fluid between the evaporator and the condenser. The two-phase reservoir is used to set the operation temperature of the loop and serves as an accumulator to store any excess liquid not required in the loop during operation.

Prior to applying power to the CPL evaporator, referred to as *startup*, the reservoir is typically heated to a set-point temperature higher than the temperature of the rest of the loop. The temperature difference gives rise to a pressure difference, and the higher pressure, corresponding to the higher temperature in the reservoir, will drive

the liquid to fill the entire loop with liquid. This process, called *pressure priming*, is critical for proper operation of a CPL. After filling the entire loop with liquid, heat is applied to the evaporator. As the evaporator is heated to the reservoir set-point temperature, liquid begins to evaporate (with boiling during the initial stage) and menisci are formed at the liquid–vapor interface. The capillary pressure is then developed in the evaporator wick and forces the vapor to flow to the condenser section via the vapor transport line. Liquid originally in the vapor line is displaced to the reservoir during startup. In the condenser, heat is removed and the vapor condenses. Before returning to the evaporator, the condensed liquid can be passed through a subcooler, where any remaining vapor bubbles are collapsed. After initial transient conditions in the startup process, the CPL reaches a constant operation state such that vapor condenses at a temperature very close to the set temperature in the reservoir.

The mechanism of using the reservoir to control the operating temperature of a CPL can be explained by examining the pressure balance for the loop. Since the reservoir contains a two-phase fluid, its pressure is governed by the set temperature (saturation temperature) and will be maintained constant as long as the set-point temperature is constant. Any changes in the heat load on the evaporator or temperature of the condenser heat sink will cause the local pressure to increase or decrease and give rise to a pressure imbalance. The pressure imbalance will then drive liquid into or out of the condenser and reservoir to balance the local pressure change. The net result is that except for a slight difference, the operating pressure in the loop will be kept at the same value as that of the reservoir and the system operating temperature is kept at the temperature set by the reservoir.

Figure 16.21 is the ideal P – T diagram for the typical CPL system shown in Fig. 16.20. It can be seen that the liquid vaporizes at a temperature range of $(T_2 - T_1)$ in the evaporator due to frictional loss, and is superheated at the exit. From point 2 to point 3, the superheated vapor undergoes an adiabatic extension process. At point 4, the vapor begins to condense after the superheat is absorbed. The temperature T_4 is very close to the reservoir temperature, T_{12} , the slight difference being caused by the fluid flow between the two points. At point 5, all the vapor is condensed and the liquid is further subcooled to T_7 at the exit of the subcooler. From point 7 to point 8 the pressure is reduced further. In the wick, the liquid is superheated until T_1 and vaporized. The difference between P_1 and P_9 is the capillary pressure.

The concept of the CPL was initially proposed by Stenger (1966) at the NASA Lewis Research Center in the mid-1960s. However, serious development efforts on the CPL did not begin until the late 1970s, when larger space systems demanded more powerful thermal control systems. In the United States, numerous ground and flight CPL experiments were carried out by NASA and its contractors. Most of the experiments demonstrated the CPL to be a powerful thermal management system. Some unique CPL characteristics, such as passive operation, pressure priming under heat loads, and low sensitivity to noncondensable gases, were noted. Similar experiments were also carried out in Europe and Japan. The potential of a CPL as a heat transport system for larger applications was confirmed (Wulz and Embacher, 1990; Dunbar and Supper, 1997; Ku, 1997). Several advantages exist for a CPL:

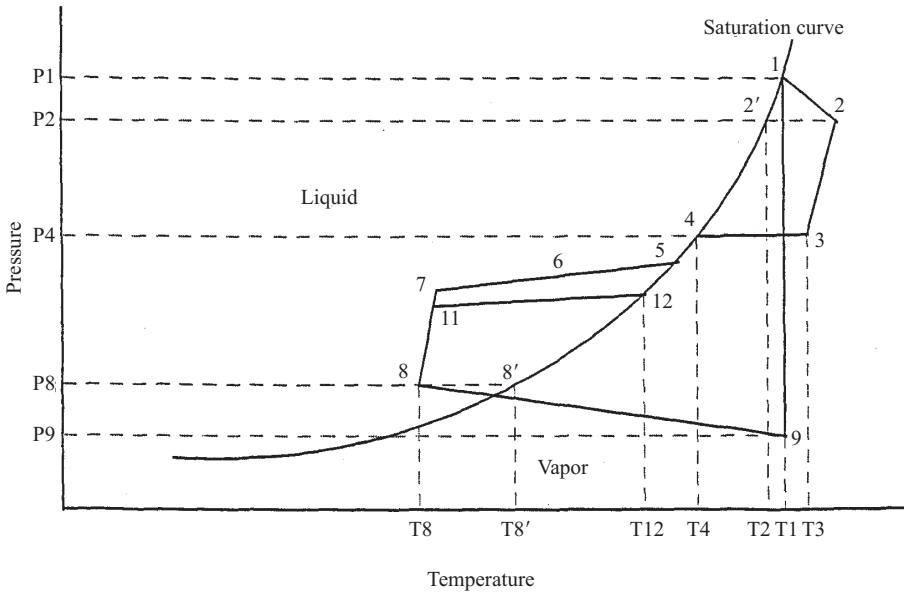


Figure 16.21 Ideal P - T diagram for a typical CPL system. (From Ku, 1997.)

1. Because the fluid is transferred in smooth-walled tubing, the fluid can be transferred through a long distance with a small pressure drop. This characteristic makes CPL especially suitable for systems with increased power.
2. More than one evaporator/condenser is possible in a single CPL system. The multiple evaporators/condensers can work in parallel mode to enhance the thermal capacity. Furthermore, the evaporator could work as a condenser when it is exposed to a heat sink. In practical applications, this can save substantial power when some instruments are not operating.
3. The use of a reservoir makes it possible to control the operating temperature. While in a conventional heat pipe, the operation temperature depends on the heat load.
4. In the CPL, the fluid cannot be pumped continuously back to the evaporator section from the condenser section even if the condenser temperature rises above the saturation temperature, because there is no wick in the condenser. In some systems using heat pipes as the heat transport device, a special design is required to prevent heat from being transferred from the condenser to the evaporator. Therefore, a CPL is essentially a thermal diode.

Multiple parallel evaporators and condensers may be used within a single CPL to maximize the heat transport capabilities and to accommodate multiple heat sources and multiples heat sinks. With multiple evaporators, isolators are added in application CPLs to each of the evaporators, to keep the failure of one evaporator from affecting the others. An isolator consists of an inner layer of porous media on the inside walls

of the liquid inlet, at the entrance of each evaporator. If one evaporator deprimes and dries out, the capillary pressure developed by the wick of its isolator will prevent the vapor from entering the main liquid line and affecting the other evaporators.

Heat-load sharing is an intrinsic but most valuable characteristic of CPLs. The multiple parallel evaporators serve a dual function: heat can be added to, as well as removed from, the evaporators. This feature permits heat sharing among individual evaporators. Because the pressure head in the loop is established by capillary forces, one or more of the evaporators can work in a reverse mode, that is, as condensers.

When an evaporator works in a reverse mode, it can be considered as another condenser. The pressure drop in the evaporator working in reverse mode is due mainly to flow resistance through the evaporator and the isolator wicks. When this evaporator reaches its heat-dissipating limit, menisci are formed at the surface of the wick, and capillary forces are developed to resist any further increase in the flow rate; that is, the wick acts as a flow regulator.

NOMENCLATURE

Roman Letter Symbols

A	area, m^2
b	thickness, m
c	speed of sound, m/s
c_p	specific heat, $\text{J/kg} \cdot \text{K}$
c'	experimental constant, dimensionless
C	constant, dimensionless
d	diameter, m
f	friction factor, dimensionless
F	force, N
g	gravitational acceleration, m/s^2
h	heat transfer coefficient, $\text{W/m}^2 \cdot \text{K}$
	liquid column length, m
j	molecular flux, $\text{kg/m}^2 \cdot \text{s}$
k	thermal conductivity, $\text{W/m} \cdot \text{K}$
K	wick permeability, m^2
L	length, m
m	mass, kg
\underline{m}	mass flow rate, kg/s
Ma	Mach number, dimensionless
N	screen mesh number, m^{-1}
P	pressure, N/m^2
Pr	Prandtl number, dimensionless
q	heat transfer, W
Q	heat transfer, J
r	capillary radius, m
	radius of curvature, m

R	thermal resistance, K/W
	gas constant, J/kg · K
Re	Reynolds number, dimensionless
Re_r	Radial Reynolds number, dimensionless
s	penetration depth, m
S	crimping factor, dimensionless
t	time, s
T	temperature, K
U	velocity, m/s
u	x component of velocity, m/s
V	volume, m ³
v	velocity, m/s
	axial component of velocity, m/s
w	groove width, m
	wire spacing, m
We	Weber number, dimensionless
x	axial position, m
	coordinate, m
z	axial position, m

Greek Letter Symbols

α	thermal diffusivity, m ² /s
β	angle of inclination, deg or radians
	contact angle, deg or radians
γ	groove cone angle, deg or radians
	specific heat ratio, dimensionless
ΔT	wall superheat at rewet point, K
δ	thickness, m
ε	wick porosity, dimensionless
ξ	rewetting front position, m
η	liquid transport factor, dimensionless
θ	angle, deg or radians
ι	characteristic length of the wick, m
λ	latent heat of vaporization, J/kg
μ	absolute viscosity, N · s/m ²
ρ	density, kg/m ³
σ	surface tension, N/m
Ψ	angle with respect to horizontal, deg or radians

Subscripts

a	adiabatic section
	air
b	boiling
c	capillary, condenser

cr	critical
<i>d</i>	droplet
	dry
	dryout
<i>e</i>	entrainment
	evaporator section
eff	effective
ext	external
<i>f</i>	frictional
	fin
<i>g</i>	gravitational
<i>h</i>	hydraulic
<i>I</i>	inner
	inertial
	interface
<i>l</i>	liquid
<i>m</i>	maximum
<i>n</i>	nucleation
<i>o</i>	outer
<i>p</i>	pipe
<i>s</i>	sonic
	surface
<i>t</i>	total
<i>v</i>	vapor
<i>w</i>	wire spacing
	wick
	wetting
	axial hydrostatic pressure
+	normal hydrostatic pressure

REFERENCES

- Akachi, H., and Polasek, F. (1995). Pulsating Heat Pipe Review of the Present State of the Art, *Technical Report ITRI-ERL*, Chutung, Taiwan, May.
- Ambrose, J. H., Chow, L. C., and Beam, J. E. (1987). Transient Heat Pipe Response and Rewetting Behavior, *J. Thermophys. Heat Transfer*, 1(3), 222–227.
- Babin, B. R., Peterson, G. P., and Wu, D. (1990). Experimental Investigation of a Flexible Bellows Heat Pipe for Cooling Discrete Heat Sources, *J. Heat Transfer*, 112(3), 602–607.
- Bankston, C. A., and Smith, J. H. (1971). Incompressible Laminar Vapor Flow in Cylindrical Heat Pipes, *ASME-71-WA/HT-15*, ASME, New York.
- Bowman, W. J. (1991). Numerical Modeling of Heat-Pipe Transients, *J. Thermophys. Heat Transfer*, 5(3), 374–379.

- Brennan, P. J., and Kroliczek, E. J. (1979). *Heat Pipe Design Handbook*, NASA Contract Report NAS5-23406.
- Busse, C. A. (1973). Theory of the Ultimate Heat Transfer of Cylindrical Heat Pipes, *Int. J. Heat Mass Transfer*, 16, 169–186.
- Busse, C. A., and Kemme, J. E. (1980). Dry-out Phenomena in Gravity-Assist Heat Pipes with Capillary Flow, *Int. J. Heat Mass Transfer*, 23, 643–654.
- Carey, V. P. (1992). *Liquid–Vapor Phase-Change Phenomena*, Taylor & Francis, Washington, DC.
- Chang, W. S., and Colwell, G. T. (1985). Mathematical Modeling of the Transient Operating Characteristics of a Low-Temperature Heat Pipe, *Numer. Heat Transfer*, 8, 169–186.
- Chi, S. W. (1976). *Heat Pipe Theory and Practice*, Hemisphere Publishing, Washington, DC.
- Colwell, G. T., and Modlin, J. M. (1992). Mathematical Heat Pipe Models, *Proc. 8th International Heat Pipe Conference*, Vol. 1, pp. 162–166.
- Cotter, T. P. (1967). Heat Pipe Startup Dynamics, *Proc. SAE Thermionic Conversion Specialist Conference*, Palo Alto, CA.
- Delhaye, J. M. (1981). Basic Equations for Two-Phase Flow Modeling, in *Two-Phase Flow and Heat Transfer in the Power and Process Industries*, A. E. Bergles, J. G. Collier, and J. M. Delhaye, eds., Hemisphere Publishing, Washington, DC.
- Deverall, J. E., Kemme, J. E., and Florschuetz, L. W. (1970). Sonic Limitations and Startup Problems of Heat Pipes, *Report LA-4578*, Los Alamos Scientific Laboratory, Los Alamos, NM.
- Dunbar, N., and Cadell, P. (1998). Working Fluids and Figures of Merit for CPL/LHP Applications, *CPL-98 Workshop Proc.*, Aerospace Corporation, El Segundo, CA, Mar. 2–3.
- Dunbar, N., and Supper, W. (1997). Spacecraft Capillary Pumped Loop Technology towards a Qualified Thermal Control Tool, *Proc. 10th International Heat Pipe Conference*, Stuttgart, Germany.
- Dunn, P. D., and Reay, D. A. (1982). *Heat Pipes*, 3rd ed., Pergamon Press, New York.
- Faghri, A. (1995). *Heat Pipe Science and Technology*, Taylor & Francis, Washington, DC.
- Gaugler, R. S. (1944). Heat Transfer Devices, U.S. patent 2,350,348.
- Grover, G. M., Cotter, T. P., and Erikson, G. F. (1964). Structures of Very High Thermal Conductivity, *J. Appl. Phys.*, 218, 1190–1191.
- Hewitt, G. F. (1979). Liquid Mass Transport in Annular Two-Phase Flow, *Two-Phase Momentum, Heat and Mass Transfer in Chemical, Process, and Energy Engineering Systems*, Vol. 1, Hemisphere Publishing, New York, pp. 273–302.
- Incropera, F. P., and DeWitt, D. P. (1996). *Fundamentals of Heat and Mass Transfer*, 4th ed., Wiley, New York.
- Ivanovskii, M. N., Sorokin, V. P., and Yagodkin, I. V. (1982). *The Physical Properties of Heat Pipes*, Clarendon Press, Oxford.
- Kemme, J. E. (1969). Ultimate Heat Pipe Performance, *IEEE Trans. Electron Devices*, 16, 717–723.
- Kemme, J. E. (1976). Vapor Flow Consideration in Conventional and Gravity-Assist Heat Pipes, *Proc. 2nd International Heat Pipe Conference*, pp. 11–21.
- Ku, J. (1997). Recent Advances in Capillary Pumped Loop Technology, *AIAA-97-3870*, AIAA, New York.

- Langer, H., and Mayinger, F. (1979). Entrainment in Annular Two-Phase Flow under Steady and Transient Flow Conditions, *Two-Phase Momentum, Heat and Mass Transfer in Chemical, Process, and Energy Engineering Systems*, Vol. 2, Hemisphere Publishing, New York, pp. 695–706.
- Levy, E. K. (1968). Theoretical Investigation of Heat Pipes Operating at Low Vapor Pressure, *J. Eng. Ind.*, 90, 547–552.
- Levy, E. K., and Chou, S. F. (1973). The Sonic Limit in Sodium Heat Pipes, *J. Heat Transfer*, 95, 218–223.
- Maidanik, Y. F., and Fershtater, Y. G. (1997). Theoretical Basis and Classification of Loop Heat Pipes and Capillary Pumped Loops, *Proc. 10th International Heat Pipe Conference*, Stuttgart, Germany, Sept.
- Marcus, B. D. (1965). On the Operation of Heat Pipes, *Report 9895-6001-TU-000*, TRW, Redondo Beach, CA.
- Moody, L. F. (1944). Friction Factors for Pipe Flow, *Trans. ASME*, 66, 671–684.
- Nguyen-Chi, H., and Groll, M. (1981). Entrainment or Flooding Limit in a Closed Two-Phase Thermosyphon, *Proc. 4th International Heat Pipe Conference*, pp. 147–162.
- Ochterbeck, J. M. (1997). Modeling of Room-Temperature Heat Pipe Startup from the Frozen State, *J. Thermophys. Heat Transfer*, 11(2), 165–172.
- Ochterbeck, J. M., Peterson, G. P., and Ungar, E. (1995). Depriming/Rewetting of External Artery Heat Pipes: Comparison with SHARE-II Flight Experiment, *J. Thermophys. Heat Transfer*, 9(1), 101–108.
- Peterson, G. P. (1994). *An Introduction to Heat Pipe*, Wiley, New York.
- Peterson, G. P., and Bage, B. (1991). Entrainment Limitations in Thermosyphons and Heat Pipes, *J. Energy Resour. Technol.*, 113(3), 147–154.
- Prenger, F. C. (1984). Performance Limits of Gravity-Assist Heat Pipes, *Proc. 5th International Heat Pipe Conference*, pp. 1–5.
- Prenger, F. C., and Kemme, J. E. (1981). Performance Limits of Gravity-Assist Heat Pipes with Simple Wick Structures, *Proc. 4th International Heat Pipe Conference*, pp. 137–146.
- Rice, G., and Fulford, D. (1987). Influence of a Fine Mesh Screen on Entrainment in Heat Pipes, *Proc. 6th International Heat Pipe Conference*, pp. 168–172.
- Rohani, A. R., and Tien, C. L. (1974). Analysis of the Effects of Vapor Pressure Drop on Heat Pipe Performance, *Int. J. Heat Mass Transfer*, 17, 61–67.
- Stenger, F. J. (1966). Experimental Feasibility Study of Water-Filled Capillary Pumped Heat Transfer Loops, *NASA X-1310, NASA LeRC Report*.
- Tien, C. L., and Chung, K. S. (1979). Entrainment Limits in Heat Pipes, *AIAA J.*, 17(6), 643–646.
- Trefethen, L. (1962). On the Surface Tension Pumping of Liquids or a Possible Role of the Candlewick in Space Exploration, GE Tech. Int. Ser. No. G15-D114, General Electric Co., Schenectady, NY.
- Vinz, P., and Busse, C. A. (1973). Axial Heat Transfer Limits of Cylindrical Sodium Heat Pipes between 25 W-cm^{-2} and 15.5 kW-cm^{-2} , *Proc. 1st International Heat Pipe Conference*, Stuttgart, Germany, Paper 2-1.
- Wayner, P. C., Jr. (1999). Long Range Intermolecular Forces in Change-of-Phase Heat Transfer, *Proc. 33rd National Heat Transfer Conference*, Albuquerque, NM, Aug. 15–17.

- Wu, D., Peterson, G. P., and Chang, W. S. (1991). Transient Experimental Investigation of Micro Heat Pipes, *J. Thermophys. Heat Transfer*, 5(4), 539–545.
- Wulz, H., and Embacher, E. (1990). Capillary Pumped Loops for Space Applications: Experimental and Theoretical Studies on the Performance of Capillary Evaporator Designs, *AIAA-90-1739*, AIAA, New York.
- Yan, Y., and Ochterbeck, J. M. (1999). Analysis of the Supercritical Startup Behavior for Cryogenic Heat Pipes, *J. Thermophys. Heat Transfer*, 13(1), 140–145.
- Zucrow, M. J., and Hoffman, J. D. (1976). *Gas Dynamics*, Wiley, New York.

Heat Transfer in Manufacturing and Materials Processing

RICHARD N. SMITH

Department of Mechanical Engineering, Aeronautical Engineering and Mechanics
Rensselaer Polytechnic Institute
Troy, New York

C. HARIS DOUMANIDIS

Department of Mechanical Engineering
Tufts University
Medford, Massachusetts

RANGA PITCHUMANI

Department of Mechanical Engineering
University of Connecticut
Storrs, Connecticut

- 17.1 Introduction
- 17.2 Heat transfer to moving materials undergoing thermal processing
 - 17.2.1 Uniform thermal environment
 - Thin solid model
 - Two-dimensional workpieces
 - 17.2.2 Interaction between a discrete heat source and a continuously moving work-piece
 - Thin plate or rod with a moving planar heat source
 - Thin plate with a moving line heat source
 - Semi-infinite solid with a moving point source
 - Semi-infinite plane with finite size moving heat source
- 17.3 Thermal issues in heat treatment of solids
- 17.4 Machining processes: metal cutting
 - 17.4.1 Background
 - 17.4.2 Thermal analysis
 - Tool–chip interface temperature rise
 - Energy generation at the shear plane
 - Assessment of steady-state metal cutting temperature models
- 17.5 Machining processes: grinding
 - 17.5.1 Background
 - 17.5.2 Workpiece temperatures during grinding
- 17.6 Thermal–fluid effects in continuous metal forming processes
 - 17.6.1 Background

- 17.6.2 Considerations for thermal–fluid modeling in extrusion and drawing
 - Deformation heating considerations
 - Frictional heating considerations
- 17.7 Processing of polymer-matrix composite materials
 - 17.7.1 Introduction
 - 17.7.2 Processing of thermosetting-matrix composites
 - Thermal model
 - Kinetics model
 - Laminate consolidation model
 - 17.7.3 Processing of thermoplastic-matrix composites
 - Heat transfer
 - Void dynamics
 - Interlaminar bonding
 - Polymer degradation
 - Solidification (crystallization)
- 17.8 Thermal process control for manufacturing
 - 17.8.1 Control of SISO thermal systems
 - Thermostatic (on–off) control
 - Proportional–integral–derivative (PID) control
 - Software implementation of SISO controllers
 - 17.8.2 Control of MIMO thermal systems
 - State controllers by pole placement
 - State observers by pole placement
 - 17.8.3 Optimal formulation: linear quadratic Gaussian
 - Optimal control: linear quadratic regulator (LQR)
 - Optimal observation: Kalman–Bucy filter
 - 17.8.4 Smith prediction
 - 17.8.5 Sliding mode control
 - 17.8.6 Adaptive control
 - Model reference adaptive control (MRAC)
 - Self-tuning regulation
 - 17.8.7 Parameter identification
 - Orthogonal projection
 - Least squares

Nomenclature

References

17.1 INTRODUCTION

The last two decades of the twentieth century have witnessed a significant move in the thermal-fluid sciences toward studying fundamental problems motivated by applications in manufacturing and materials processing. Establishment of a number of industrially supported research centers within universities had the express purpose of developing advances that could directly affect U.S. industrial competitiveness in manufacturing and that could train a new generation of technical specialists.

Recognition that many processes, such as casting, welding, spray deposition, quenching, crystal growth, extrusion and drawing, rolling, and metal cutting, are enabled and/or controlled by heat transfer and fluid mechanics phenomena has led heat transfer researchers to turn their attention to these types of problems. The report of the National Science Foundation (NSF)-sponsored workshop on critical technologies in the thermal systems (Jacobs and Hartnett, 1992) emphasized the importance of work in this area. The proceedings of several recent international symposia (Shah et al., 1992; Tanasawa and Lior, 1992; Guceri, 1993) have provided significant collections of review articles and of recent research results which can be of great utility to engineers and researchers. In 1988, the Heat Transfer Division of the American Society of Mechanical Engineers (ASME) initiated a new technical committee (K-15, Heat and Mass Transfer in Manufacturing and Materials Processing, referred to subsequently as MMP) to coordinate the orderly presentation of research results at division-sponsored meetings. These activities were recently celebrated with a more focused NSF-sponsored workshop (Prasad et al., 1998). Kitto et al. (1995) highlighted critical technologies associated with thermal phenomena, with particular emphasis on MMP. A new journal devoted to this subject was also initiated (Guceri, 1992), and two other handbook chapters have appeared (Radford and Tong, 2000; Viskanta and Bergman, 2000).

Necessarily, the scope of this presentation must be limited. First, MMP is an extremely broad subject, and it is difficult to identify common technological foundations among such disparate topics as, for example, machining and injection molding and chemical vapor deposition, even with a focus strictly on thermal-fluid aspects. Furthermore, the thermal-fluid elements of even a single process cannot be separated fully from other fundamental engineering elements, such as material behavior, mechanics, and control. Indeed, entire books have been devoted even to a single type of manufacturing process (e.g., DeVries, 1992; Steen, 1991). Nonetheless, the goal of the present chapter is to characterize the important transport phenomena, particularly heat transfer, that are associated with a number of manufacturing and materials processing operations. The general approach will be to introduce and review the essential features of a particular manufacturing process, to identify appropriate physical models of the process that are useful for describing the thermal and transport fields, to show how the physical model leads to a mathematical model of the process, and to interpret these models in light of experimental results and in terms of the expected performance and operation of the actual process.

The particular subjects have been chosen largely from segments of three graduate courses taught by the authors, developed independently between 1995 and 2000. The focus is more on manufacturing operations than on materials processes (as much as those two can be distinguished), and there is limited overlap with similar monographs (Radford and Tong, 2000; Viskanta and Bergman, 2000), so that no specific reference will be made to them. Examples of topics that have reluctantly been omitted are most phases of solidification processing, chemical and vapor deposition processes, polymer processes (except for composites processing), and others that the reader will note. Some texts that may serve as appropriate background in some of these areas are Poirier and Poirier (1992), Guthrie (1989), Gaskell (1992), Flemings (1974), Poirier

and Geiger (1994), Yang et al. (1994), and Kou (1996). For background on general manufacturing and materials processes, the reader is referred to classical texts (Schey, 2000; Kalpakjian, 1996; DeGarmo et al., 1997). The authors have chosen not to attempt a complete literature review of the particular subjects. Rather, important references that comprise the essential focus will be cited, in addition to broad background references.

Most of the necessary background in conduction, convection, and radiation phenomena has been discussed in earlier chapters of this book. Unique features of MMP that must be considered carefully in developing appropriate physical models are unusual boundary conditions, conjugate heat transfer problems, in which two adjoining media are thermally coupled; moving heat sources or sinks; multimode heat transfer (convection and radiation); and phase change. Some background material on conduction heat transfer to objects in motion and on the thermal response of a solid to a moving, local, or distributed heat source is offered first. These elements are common to several of the process descriptions that follow. Section 17.3 contains a very brief review of some of the issues in heat treatment. In Sections 17.4 to 17.6 some material removal and metal forming processes are discussed. In Section 17.7 some thermal characteristics of composite materials manufacturing are introduced. Finally, in Section 17.8 we present an introduction to analysis for thermal control, which has common application in almost any manufacturing operation involving an applied heat source. In all cases, the heat transfer elements are emphasized over considerations of mechanical behavior and material property response.

17.2 HEAT TRANSFER TO MOVING MATERIALS UNDERGOING THERMAL PROCESSING

A large variety of processes involve the continuous movement of a workpiece or manufactured part through a thermal environment. These can include rolling, extrusion and drawing, continuous casting, crystal growth, welding, and heat treatment. The thermal environment can be localized, such as the forming zone of a rolling process, or continuous, such as quenching of a wire following a drawing process. When a heat source is localized, it may be that the source itself is moving and the workpiece stationary, although it is often convenient to consider the thermal field from the point of view of a stationary source. Processing speeds can vary from a few centimeters per hour (Czochralski crystal growth) to several meters per second (wire drawing).

17.2.1 Uniform Thermal Environment

Consider first the case of a continuously moving workpiece exposed to a uniform thermal environment. Jaluria (1993) has discussed three basic approaches in the mathematical modeling of such processes. In the first approach, only conduction heat transfer in the solid material (workpiece), including the advection associated with the workpiece motion, is considered. The external heating or cooling is accommodated by a known surface heat transfer coefficient and/or radiative environment or

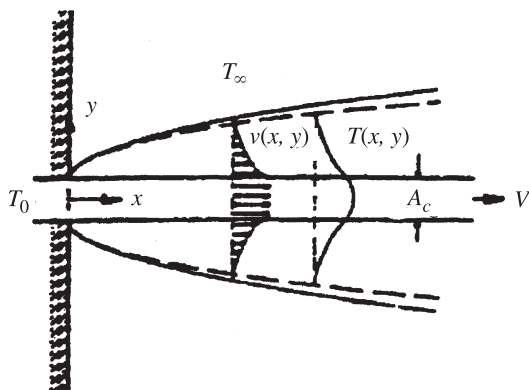


Figure 17.1 Conjugate temperature and velocity fields in a moving material undergoing convective cooling.

by a specified distribution of surface heat flux. The second approach focuses on the convective flow field in the surroundings, which is induced, at least partially, by the workpiece movement. One attempts to obtain a distribution of the local surface heat transfer coefficient from the thermal field *calculated* in the fluid. The thermal conditions in the solid workpiece are prescribed as boundary conditions. (This would be considered a classical convection problem.) The third approach is a combination of the first two, called a *conjugate problem* of heat transfer, as illustrated schematically in Fig. 17.1. The thermal fields in the workpiece and in the surroundings are both determined, with a coupling of the thermal and fluid conditions at the solid–fluid interface. The concentration here is only on the first approach, because attention is necessarily focused on the workpiece thermal response. However, it should be recognized that a determination of surface heat transfer coefficients, presumed as being known and uniform in most of what follows, is seldom a straightforward task.

Thin Solid Model Consider the case in which the temperature variation through the cross section of the workpiece is negligible compared to that along its length. For a workpiece moving at a uniform velocity (implying that the cross section of the workpiece is uniform in the direction of motion), an energy balance on a differential control volume of size $dA_c \times dx$ yields the following equation for the temperature distribution as a function of time and distance x along the workpiece (Fig. 17.2):

$$\frac{1}{\alpha} \frac{\partial T}{\partial t} = \frac{\partial^2 T}{\partial x^2} - \frac{V}{\alpha} \frac{\partial T}{\partial x} - \frac{hP}{kA_c} (T - T_\infty) \quad (17.1a)$$

with some very simple boundary conditions:

$$\begin{aligned} T &= T_o & \text{at } x &= 0 \\ \frac{\partial T}{\partial x} &= 0 & \text{at } x &= L \end{aligned} \quad (17.1b)$$

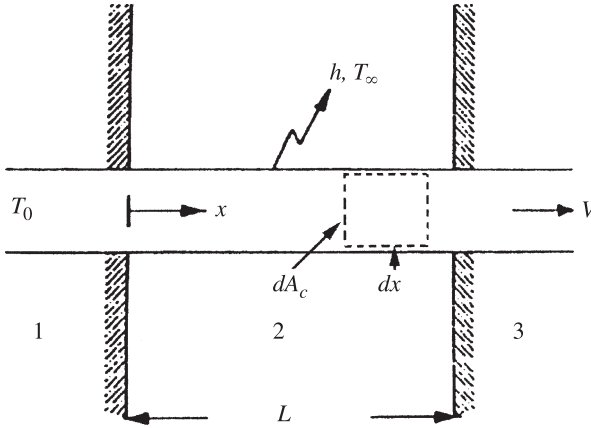


Figure 17.2 Continuously moving material whose surface is exposed to a convective heat transfer environment.

Under steady-state conditions, the following dimensionless parameters may conveniently be introduced:

$$\begin{aligned} x^* &= \frac{x}{L} & \theta &= \frac{T - T_\infty}{T_o - T_\infty} & \text{Pe} &= \frac{V\gamma}{\alpha} \\ L^* &= \frac{L}{\gamma} & \text{Bi} &= \frac{h\gamma}{k} \end{aligned} \quad (17.2)$$

where $\gamma \equiv A_c/P$ (P is the perimeter). The dimensionless form of eq. (17.1a) is

$$\frac{d^2\theta}{dx^{*2}} - \text{Pe} \frac{d\theta}{dx^*} - \text{Bi} \cdot \theta = 0 \quad (17.3a)$$

subject to

$$\begin{aligned} \theta &= \theta_o & \text{at } x^* &= 0 \\ \frac{\partial\theta}{\partial x^*} &= 0 & \text{at } x^* &= L^* \end{aligned} \quad (17.3b)$$

The solution to eq. (17.3) is straightforward:

$$\frac{\theta(x)}{\theta_o} = \frac{m_1 e^{m_1 L^*} e^{m_2 x^*} - m_2 e^{m_2 L^*} e^{m_1 x^*}}{m_1 e^{m_1 L^*} - m_2 e^{m_2 L^*}} \quad (17.4)$$

where

$$m_1 \text{ and } m_2 = \frac{\text{Pe} \pm \sqrt{\text{Pe}^2 + 4 \text{Bi}}}{2} \quad (17.5)$$

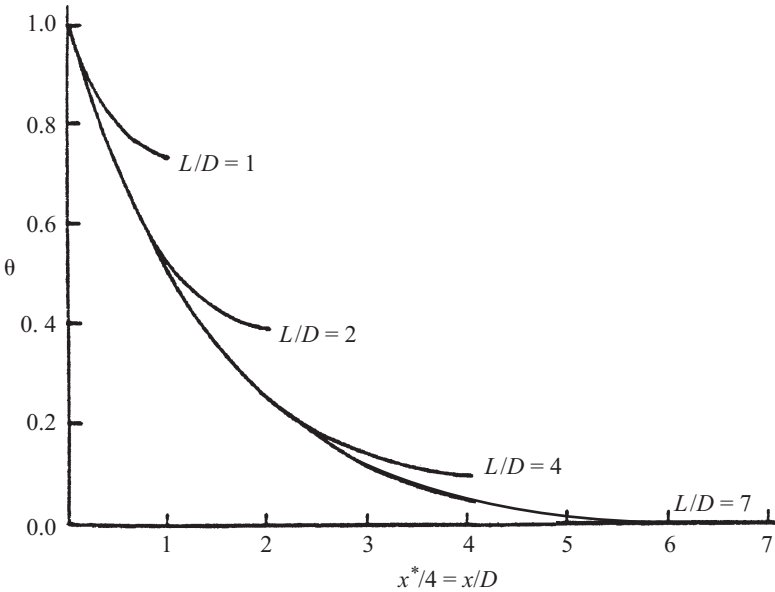


Figure 17.3 Steady-state temperature distributions in a continuously moving cylindrical rod for different values of L/D ($4\text{ Pe} = VD/\alpha = 0.4$; $4\text{ Bi} = hD/k = 0.2$).

Figure 17.3 shows the results for the temperature distribution in a circular rod ($\gamma = D/4$) for one particular case. Note that when $L/D > 7$ (for this case), the condition of an infinitely long rod is attained and the temperature at the end of the rod approaches asymptotically that of the environment. Under those conditions, it is easily shown that eq. (17.4) reduces to

$$\frac{\theta(x^*)}{\theta_o} = \exp\left(\frac{\text{Pe} - \sqrt{\text{Pe}^2 + 4\text{ Bi}}}{2}x^*\right) \quad (17.6)$$

Necessarily, eqs. (17.4) and (17.6) are valid only when the value of Bi is sufficiently small, to ensure that the temperature variation across the rod is negligible compared to that along its length. Furthermore, when $\text{Pe} \rightarrow 0$, the problem reduces to that of a stationary extended surface.

The problem depicted in Fig. 17.2 may be extended to include a more realistic boundary condition at $x^* = 0$ and L^* , taking into account the upstream and downstream thermal conditions. If $\theta(x^* \rightarrow -\infty) = \theta_o$ and θ must remain finite as $x^* \rightarrow +\infty$, the temperature distribution in the region exposed to the thermal environment is governed by the following three equations:

$$\frac{d^2\theta_1}{dx^{*2}} - \text{Pe}\frac{d\theta_1}{dx^*} = 0 \quad \text{for } x^* < 0$$

$$\begin{aligned} \frac{d^2\theta_2}{dx^{*2}} - \text{Pe} \frac{d\theta_2}{dx^*} - \text{Bi}\theta &= 0 & \text{for } 0 < x^* < L^* \\ \frac{d^2\theta_3}{dx^{*2}} - \text{Pe} \frac{d\theta_3}{dx^*} &= 0 & \text{for } x^* > L^* \end{aligned} \quad (17.7)$$

for which Jaluria has provided the solutions as

$$\begin{aligned} \theta_1 &= \left[1 + \frac{\text{Pe} (m_2 e^{m_2 L^*} - m_1 e^{m_1 L^*})}{m_1^2 e^{m_1 L^*} - m_2^2 e^{m_2 L^*}} \right] e^{Pe x^*} \\ \theta_2 &= 1 + \frac{\text{Pe} (m_2 e^{m_2 L^*} e^{m_1 x^*} - m_1 e^{m_1 L^*} e^{m_2 x^*})}{m_1^2 e^{m_1 L^*} - m_2^2 e^{m_2 L^*}} \\ \theta_3 &= 1 + \frac{\text{Pe} (m_2 - m_1) e^{Pe L^*}}{m_1^2 e^{m_1 L^*} - m_2^2 e^{m_2 L^*}} \end{aligned} \quad (17.8)$$

As in the more limited case, three physical parameters emerge from the analysis. The Péclet number Pe represents a dimensionless speed of the workpiece and serves to compare the ability of the workpiece to advect energy through its motion to its ability to transfer energy along its length due to thermal conduction. The Biot number Bi may be thought of as a ratio of internal thermal resistance to external thermal resistance. These analytical results are limited to small values of Bi , because temperature gradients in the direction transverse to the workpiece motion have been neglected. Finally, L^* is the dimensionless length of the workpiece. When L^* is large enough (the value depends on Bi and Pe), the workpiece will approach thermal equilibrium with the thermal environment at T_∞ .

Figure 17.4 shows some typical results. For increasing speed (Pe) there is a shorter time for heat loss up to given distance, so that the temperature decay is more gradual. Similarly, the thermal penetration of the temperature field upstream due to conduction is lower for increased Pe , because advection effects begin to dominate over thermal conduction. A large value of Bi implies more effective cooling by the external thermal environment, and the increased thermal gradient in the active heat transfer region leads to increased thermal penetration upstream. (It should be noted that the results in Fig. 17.4b are obtained for values of the Biot number for which the assumption of a one-dimensional temperature distribution is not fully justified. However, the analysis does illustrate effectively the physical significance of the dimensionless parameters, and this significance is repeated for many other MMPs.) Finally, when L^* is large enough (about 5 in Fig. 17.4b), the temperature at the end of region 2 (at $x^* = L^*$) is very close to the ambient temperature, and any increase in L^* will not affect the heat transfer.

Two-Dimensional Workpieces When temperature variations over the cross section of the workpiece are important relative to those in the direction of motion, a differential control volume of size $dA_c \times dx$ must be used to establish an energy balance

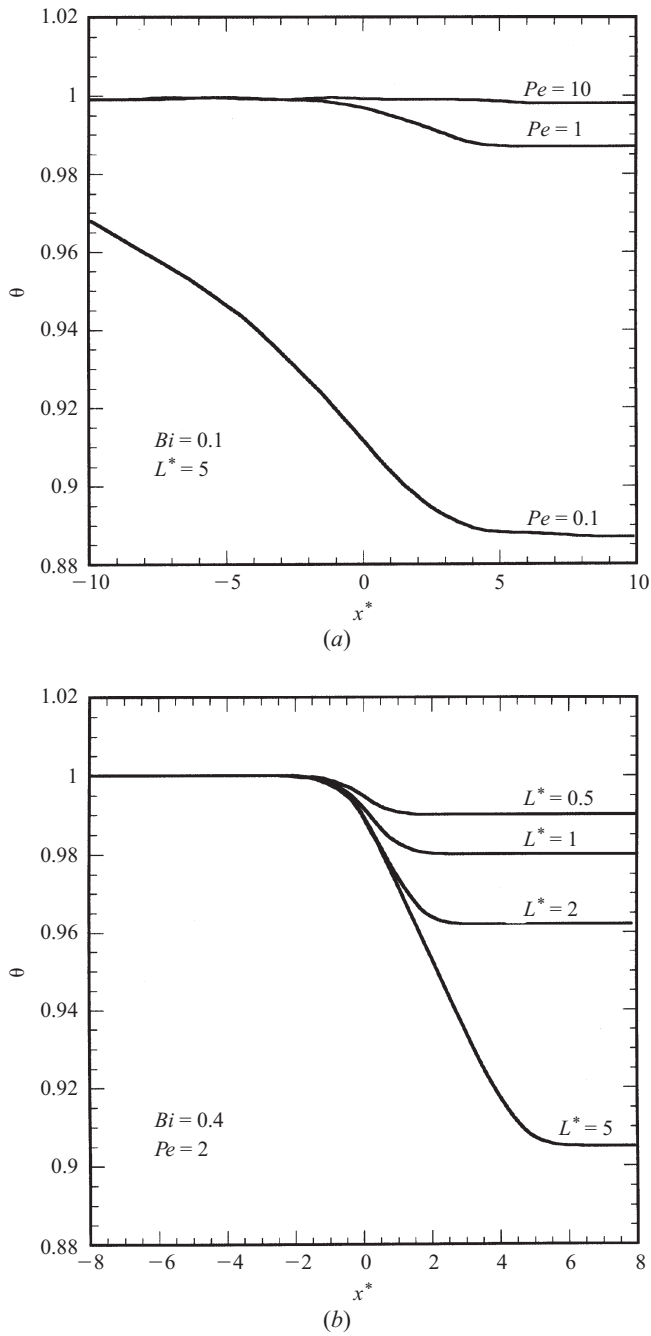
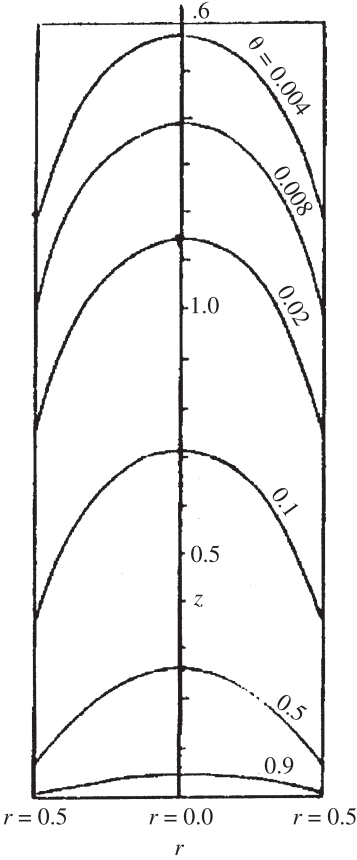
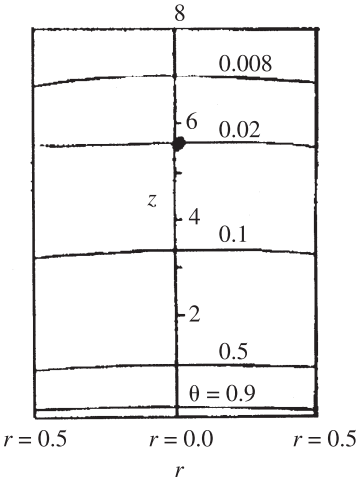


Figure 17.4 (a) Effect of varying Pe on the temperature distribution in a continuously moving solid ($Bi = 0.1$; $L^* = L/D = 0.2$); (b) Effect of varying exposed rod length ($L^* = L/D$) on the temperature distribution ($Bi = 0.4$; $Pe = 2.0$). (From Jaluria, 1993.)



(a)



(b)

Figure 17.5 Isotherms for a long moving cylindrical rod: (a) $Bi_D = 10, Pe_D = 0.4$; (b) $Bi_D = 0.2, Pe_D = 0.4$.

that will yield the temperature distribution. Now the coordinate system chosen must be more specific. For example, for a circular rod of diameter D , the steady-state conduction equation becomes

$$\frac{\partial \theta}{\partial \tau} + Pe \frac{\partial \theta}{\partial X} = \frac{1}{R} \frac{\partial}{\partial R} \left(R \frac{\partial \theta}{\partial R} \right) + \frac{\partial^2 \theta}{\partial X^2} \tag{17.9}$$

where $\tau = \alpha t / D^2$, $X = x / D$, and $R = r / D$. Initial and boundary conditions are as follows:

$$\begin{aligned}
 \tau > 0: \quad & \text{at } X = 0, \quad \theta = 1.0 \quad \text{for } 0 \leq R \leq 0.5 \\
 & \text{at } X = L(\tau), \quad \frac{\partial \theta}{\partial X} = -\text{Bi} \cdot \theta \quad \text{for } 0 \leq R \leq 0.5 \\
 & \text{at } R = 0, \quad \frac{\partial \theta}{\partial R} = 0 \quad \text{for } 0 \leq X \leq L(\tau) \\
 & \text{at } R = 0.5, \quad \frac{\partial \theta}{\partial R} = -\text{Bi} \cdot \theta \quad \text{for } 0 \leq X \leq L(\tau)
 \end{aligned} \tag{17.10}$$

In this case, the length of the rod is a function of time, $L = V_t$, and convective heat loss is presumed to occur from the end of the rod. As L^* increases, a steady-state temperature distribution is attained and $\theta \rightarrow 0$ as $L^* \rightarrow \infty$. Jaluria (1993) presented some typical results of a computational solution for a planar strip [for which eq. (17.9) must be modified slightly— D refers to the strip thickness in Bi_D and Pe_D] and for a cylindrical rod. Figure 17.5 shows some typical isotherms for the latter case. Note that when $\text{Bi}_D = 0.2$, the temperature variation through the rod is negligible.

17.2.2 Interaction between a Discrete Heat Source and a Continuously Moving Workpiece

The situation in which a source of heat is confined to a small region on the surface of the workpiece is considered next. The one-dimensional case is discussed first, for a discrete and a distributed heat source. Then the two- and three-dimensional response of a solid to a moving heat source is also presented. These form the basis for understanding the behavior of a wide variety of manufacturing systems.

Thin Plate or Rod with a Moving Planar Heat Source The situation is depicted in Fig. 17.6. The magnitude of the heat source is Q (in watts), and the surface is considered to transfer heat by convection to an environment at T_∞ with a heat transfer coefficient h . For a coordinate system fixed to the heat source moving

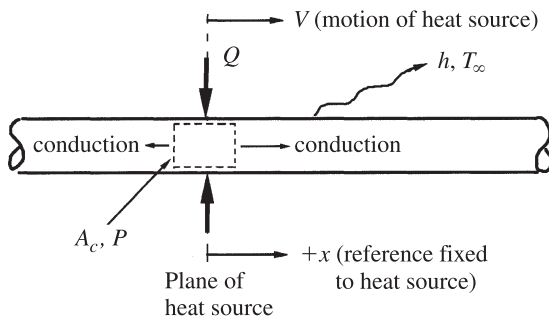


Figure 17.6 Thin plate or rod with a moving planar heat source.

in the direction $+x$ with velocity V (the workpiece is moving toward the source $-x$ direction at a velocity of $-V$), the quasi-steady temperature distribution in the workpiece is given by

$$T(x^*) - T_\infty = \begin{cases} (T_{\max} - T_\infty) \exp \left[+ \left(\sqrt{\text{Pe}^2 + 4 \text{Bi}} - \text{Pe} \right) \frac{x^*}{2} \right] & \text{for } x^* \leq 0 \\ (T_{\max} - T_\infty) \exp \left[- \left(\sqrt{\text{Pe}^2 + 4 \text{Bi}} + \text{Pe} \right) \frac{x^*}{2} \right] & \text{for } x^* \geq 0 \end{cases} \quad (17.11)$$

where the maximum temperature occurring in the workpiece is

$$T_{\max} - T_\infty = \frac{Q\gamma}{k} \frac{1}{\sqrt{\text{Pe}^2 + 4 \text{Bi}}} \quad (17.12)$$

The maximum temperature is proportional to the magnitude of the heat source, decreases with increasing workpiece speed, and is also lower for plates that are good conductors. The temperature drops quickly in the $+x$ direction, and more slowly in the $-x$ direction. Two limiting cases provide additional physical insight: When the workpiece speed is very large ($\text{Pe}^2 \gg 4 \text{Bi}$),

$$T(x^*) - T_\infty = \begin{cases} (T_{\max} - T_\infty) & \text{for } x^* \leq 0 \\ (T_{\max} - T_\infty) \exp(-\text{Pe} \cdot x^*) & \text{for } x^* \geq 0 \end{cases} \quad (17.13)$$

$$T_{\max} - T_\infty = \frac{Q}{\rho c A_c V}$$

All the mass that passes by the source is heated to T_{\max} , which depends on the heat capacity of the material, ρc . For very low speeds ($\text{Pe}^2 \ll 4 \text{Bi}$), the workpiece functions essentially as an infinitely long extended surface with a perfectly symmetric temperature profile:

$$T - T_\infty = (T_{\max} - T_\infty) \exp(-\sqrt{\text{Bi}} \cdot x^*)$$

$$T_{\max} - T_\infty = \frac{Q\gamma/k}{2\sqrt{\text{Bi}}} \quad (17.14)$$

Thin Plate with a Moving Line Heat Source Applications involving welding or heat treating with a localized source of energy (electron beam, laser beam, welding torch) provide an additional set of heat transfer problems. If the workpiece is very thin, temperature gradients through the thickness may be neglected compared to those in the direction of motion or transverse to it. When the surface loses heat to the surroundings at T_∞ with a heat transfer coefficient h , the temperature distribution is given by

$$T - T_\infty = \frac{Q/H}{2\pi k} \exp\left(\frac{\text{Pe}_H x^*}{2}\right) K_o \left[\sqrt{\left(\frac{\text{Pe}_H}{2}\right)^2 + (\text{Bi}_H)^2} r^* \right] \quad (17.15)$$

where H is the plate thickness, $x^* = x/H$ is the dimensionless distance upstream of source, $r^* = \sqrt{x^* + y^*}$, $y^* = y/H$ is the dimensionless distance transverse to the heat source, $Pe_H = VH/\alpha$, $Bi_H = hH/k$, and K_o is the modified Bessel function. When surface heat losses can be neglected, Bi_H is set to zero in eq. (17.15).

Semi-infinite Solid with a Moving Point Source The three-dimensional temperature distribution for the case of negligible surface heat losses is given by

$$T - T_\infty = \frac{Q}{2\pi kr} \exp \left[-\frac{V(x+r)}{2\alpha} \right] \quad (17.16)$$

The symbols in eq. (17.16) are the same as used previously, with $r = \sqrt{x^2 + y^2 + z^2}$. There is not a convenient length scale because the plate is infinite in the x and y directions and semi-infinite in the z direction. If a finite plate thickness is introduced, eq. (17.16) may be rewritten in a dimensionless form as

$$T - T_\infty = \frac{Q/H}{2\pi kr^*} \exp \left[-\frac{Pe_H(x^* + r^*)}{2} \right] \quad (17.17)$$

However, it must be remembered that H must be significantly larger than the thermal penetration in the z direction.

Semi-infinite Plane with a Finite Size Moving Heat Source The quasi-steady state thermal response of a workpiece to frictional heating (e.g., in machining, extrusion, or drawing) or to heating from a moving finite source may be obtained from the solution for transient stationary heating of a semi-infinite solid (Incropera and DeWitt, 1996) with a constant surface heat flux. These results are applied to the case of a moving solid under a uniform heat flux q_s'' , which acts over a distance $x = 0$ to $x = l$, with the remaining surface being insulated, to yield the following result for the dimensionless surface temperature rise:

$$\frac{(T_s - T_\infty)\pi k V}{2\alpha q_s''} = \begin{cases} \sqrt{\pi \cdot Pe_l} \left[\sqrt{x^*} - \sqrt{x^* - 1} \right] & \text{for } x^* \geq 1 \\ \sqrt{\pi \cdot Pe_l} \cdot x^* & \text{for } x^* \leq 1 \end{cases} \quad (17.18)$$

The peak temperature occurs at $x = l$, with a drop in temperature downstream of the heat source. Equations (17.18) neglect any effects of heat conduction in the direction of motion. The more general results, cited by Carslaw and Jaeger (1959), may be expressed by

$$\frac{(T_s - T_\infty)\pi k V}{2\alpha q_s''} = \int_{(x^*-1)(Pe_l/2)}^{x^*(Pe_l/2)} e^u K_o(|u|) du \quad (17.19)$$

The integral in eq. (17.19) has an analytical form with distinct results expressible for the three regions of interest, $x^* \leq 0$, $0 \leq x^* \leq 1$, and $1 \leq x^*$, and is shown

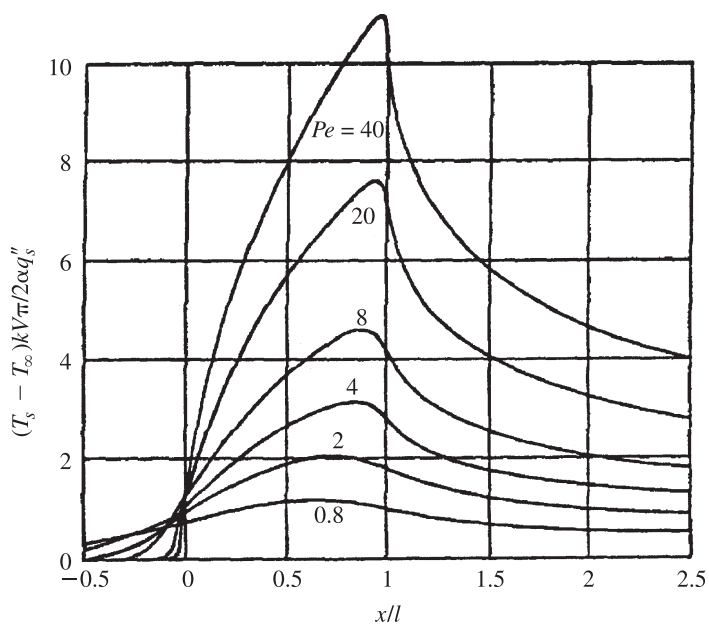


Figure 17.7 Surface temperature distribution due to a moving heat source of length l ($Pe = Vl/\alpha$).

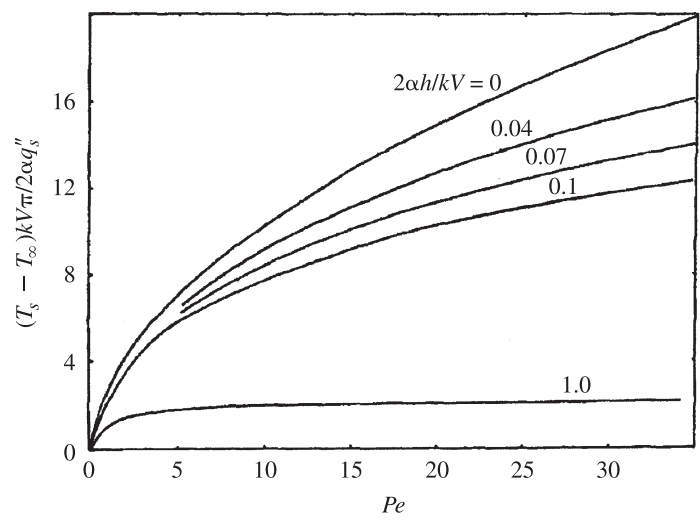


Figure 17.8 Peak surface temperature due to a moving heat source of length l , including effects of convective cooling. (From DesRuisseaux and Zerkle, 1970.)

graphically in Fig. 17.7. When $Pe_l \geq 20$, the simpler result, eq. (17.18), is quite adequate and is usually the one cited when analyzing temperature rises in machining and grinding processes, which usually occur at speeds sufficiently high to yield large values of the Péclet number.

DesRuisseaux and Zerkle (1970) extended these results to account for convective heat losses from the surface. The dimensionless temperature at the trailing edge of the heating zone ($x = l$) is shown in Fig. 17.8 in terms of the heat transfer coefficient h , expressed dimensionlessly as $2 Bi_l / Pe_l = 2\alpha h / kV$. When the region between $0 \leq x \leq l$ is not convectively cooled, they suggest an approximation to the temperature in the heated zone obtained by increasing the heat source strength by an amount equal to the average convective flux that would have occurred in the heated zone.

17.3 THERMAL ISSUES IN HEAT TREATMENT OF SOLIDS

Heat treatment is generally regarded as the controlled heating and cooling of metals for the purpose of altering their mechanical and physical properties. The material remains in a solid phase (usually below the eutectoid or the bulk melting temperature), and neither material removal nor significant alteration of shape occurs. Analysis of the heat transfer processes involved is straightforward, in principle, to obtain the appropriate temporal and spatial temperature response of the solid. However, achieving a desired result requires that the thermal behavior of a solid be carefully integrated with an understanding of the equilibrium properties, the kinetics of phase transformations and diffusion at various temperatures, and the relationship of the mechanical properties of a solid to its material structure. Consequently, study of this subject is usually confined to the expertise of metallurgists and materials specialists rather than heat transfer specialists. The interested reader is referred to Chapter 5 of DeGarmo et al. (1997) or Chapter 6 of Schey (2000) for an introductory discussion of the metallurgical issues, and to a large number of publications of the American Society of Metals (e.g., ASM, 1991) for more detailed information.

A useful but oversimplified categorization of heat treatment processes divides them into bulk and surface heat treating. In the former the entire solid is maintained at an elevated temperature to obtain a metallurgical state indicated by the equilibrium phase diagram. The key processing step is then the cooling process, in which the material goes through a nonequilibrium transformation. Under some conditions, a final stage of the process may occur at room temperature (e.g., natural aging), where diffusion occurs to convert an unstable supersaturated solution into a stable two-phase structure. An important tool in adapting such cooling processes is the *time-temperature transformation (TTT) diagram*, which characterizes the kinetics of solid-solid transformations at various temperatures. For example, thin specimens of a metal are heated to obtain an equilibrium condition, followed by rapid quenching to a specified temperature. The transformation to a new stable metallurgical state is then observed as a function of time, and the points where a transformation begins and ends are noted. The locus of these points usually takes the shape of a pair of "C"

curves. The nose of the “C” is at an intermediate temperature, which is where the transformation occurs most rapidly, a compromise between the equilibrium driving force for the transformation and the species diffusion rates. Real quenching processes occur under a continuous cooling condition, and a modification of the TTT diagram known as the *continuous cooling transformation (CCT) curve* is often overlaid on the TTT diagram. Then an actual temperature vs. time plot provides the metallurgist with information on the materials characteristics that will result from a particular cooling path. Achieving a uniform cooling rate and a resulting uniform structure is rarely possible for large workpieces, because quenching or cooling is naturally a nonhomogeneous process. Viskanta and Bergman (2000) have discussed in more detail some of the heat transfer issues related to quenching of metals.

An example of *surface heat treatment* is a local annealing and quenching process to achieve a hard, wear-resistant surface coupled to a tough, fracture resistance core. Common heating techniques include flame heating, induction heating, laser beam heating, and electron beam heating. An important issue is that of control of the motion of the heat source and of the workpiece, because only a portion of the surface may be exposed at a time (see Section 17.8).

17.4 MACHINING PROCESSES: METAL CUTTING

The goals of this section are to review the mechanisms of heat generation in metal cutting, discuss the relevant modeling assumptions used in thermal analysis, and describe the limitations of these models.

17.4.1 Background

The process of chip formation during machining consumes a great deal of power. The overall cutting power is given by

$$P = VF_p \quad (17.20)$$

where F_p is the power component of the cutting force, which is parallel with the workpiece velocity, and V is the velocity of the workpiece material. Most of this power is converted into heat and then partitioned to the workpiece chip and cutting tool. Some of the detrimental effects of high temperatures include (1) increased tool wear, and hence shortened tool life (high temperature at the cutting edge is the primary factor associated with accelerated wear); (2) decreased process efficiency (escalation of temperature limits the rate of material removal, specifically the cutting speed); and (3) decreased surface quality as a result of residual stresses and thermal distortion.

The simplest case of metal cutting, which has been the focus of most modeling effort regarding thermal behavior, is *orthogonal cutting*. A single cutting edge is oriented normal to the direction of motion, and the chip flows up the surface of the wedge-shaped cutting edge, with a velocity V_c , in the same plane as the velocity of the workpiece. Figure 17.9a illustrates the chip, tool, and workpiece geometry. The chip

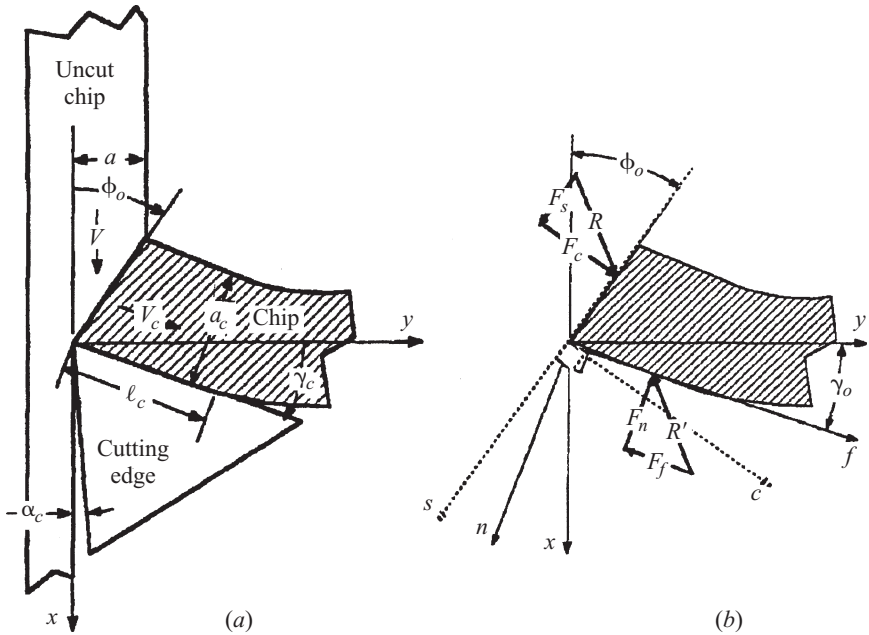


Figure 17.9 Chip formation during orthogonal metal cutting. (From DeVries, 1992.)

is assumed to be continuous, at least in the vicinity of the cutting tool, characteristic of a ductile workpiece such as brass, low-carbon steel, or an aluminum alloy.

Plastic shear is the principal mechanism of chip formation. There is a finite volume to the shear zone; however, at common cutting speeds, the angle between the planes, which defines the deformation zone, collapses, so that the deformation appears to occur in a single plane. For this reason, an infinitely thin zone of deformation is assumed in most models. Figure 17.9b shows the force components between the cutting tool and the workpiece that are needed to characterize the cutting process, including the heat generation and temperature distributions.

DeVries (1992) has described the relationships among these forces and the geometrical features of chip formation, all based on the classical literature. Several theories are available to determine the shear plane angle ϕ_o . One that minimizes the cutting power is

$$\phi_o = \frac{\pi}{4} - 0.5 (\beta - \gamma_o) \quad (17.21)$$

where β is the friction angle, defined by $\tan^{-1} \mu$, and μ is the coefficient of friction between the chip and the tool, F_f/F_n . The resultant force at the shear plane must equal the resultant force at the tool–chip interface.

$$\mathbf{R} = \mathbf{F}_c + \mathbf{F}_s \quad - \mathbf{R} = \mathbf{F}_f + \mathbf{F}_n \quad (17.22)$$

The shear force is then given by

$$F_s = (l_s b) \tau_s = \tau_s \frac{ba}{\sin \phi_0} \quad (17.23)$$

where τ_s is the plastic flow stress of the material, l_s the length of the shear zone, a the depth of cut, and b the width of cut. Combining this information, one may obtain results for the force components F_c and F_n as

$$F_c = F_s \frac{\mu \cos(\phi_0 - \gamma_0) + \sin(\phi_0 - \gamma_0)}{\cos(\phi_0 - \gamma_0) - \mu \sin(\phi_0 - \gamma_0)} \quad (17.24a)$$

$$F_n = F_s \frac{1}{\cos(\phi_0 - \gamma_0) - \mu \sin(\phi_0 - \gamma_0)} \quad (17.24b)$$

The x component of the resultant force, F_p , is also easily obtained.

17.4.2 Thermal Analysis

Typically, the heat sources in orthogonal cutting can be regarded as being localized in three places in the cutting zone. Mechanical energy dissipated in the *shear zone* consists of that needed to cause plastic flow (a relatively small amount) and that converted into internal energy (heat). Usually, this is modeled as a planar heat source. The second significant source of heating is the *rake face* between the moving chip and the cutting tool face. The heat generated there by sliding friction is usually modeled as a uniformly distributed planar heat source. A tertiary source is frictional heating between the *flank face* of the cutting tool and the moving workpiece. For sharp tools, the contact area is very small, resulting in the neglect of this source in most models. The engineering information sought at the simplest analytical level is the temperature rise at the tool–chip interface, which is due to a combination of the *shear plane* heating of the chip and the frictional heating between the chip and the tool face. The focus in the remainder of this section is on these two processes and is based on the classical work of Trigger and Chao (1951) as described in DeVries (1992).

Tool–Chip Interface Temperature Rise The (assumed) uniform heating of the chip as it passes through the shear zone is dealt with in the next section. Its temperature is assumed to be T_c and it moves with a velocity V_c as it passes over the tool surface through a frictional contact length l_c . The total rake face heat flux is given by

$$q_r'' = \frac{F_f V_c}{b l_c} \quad (17.25)$$

Adapting the solution for the surface temperature rise due to a constant heat flux, eq. (17.16), we may determine the *average* temperature rise at the chip/tool interface to be

$$(T_r - T_0)_{avg} = (T_c - T_0) + \frac{4}{3\sqrt{\pi}} \frac{B_3 q_r''}{\rho_c c_c V_c} \sqrt{\text{Pe}_{l_c}} \quad (17.26)$$

where B_3 is the fraction of the frictional heat flux that is conducted into the chip, which is regarded as being infinitely thick for the short times associated with this process. Trigger and Chao (1951) provided an ad hoc theory for the value of B_3 ; however, a conservative estimate of the rake face temperature rise is obtained if B_3 is set equal to 1.

Energy Generation at the Shear Plane The heat flux through the uncut chip cross section, bl_s , the area of the shear plane, results in a temperature rise in the chip as it passes through the shear plane:

$$q_c'' = (T_c - T_0) c_c \rho_c V \quad (17.27)$$

In turn, q_c'' is given by the following expression:

$$q_c'' = \frac{B_1 (F_s V_{c/s} - F_p V B_2)}{bl_s} = \frac{B_1 [F_p V (1 - B_2) - F_f V_c]}{bl_s} \quad (17.28)$$

where B_1 is the fraction of the energy at the shear zone that goes into raising the temperature of the chip as opposed to plastic deformation energy (typical values: $0.85 < B_1 < 0.95$). The quantity B_2 is the fraction of the power dissipated in chip formation that is conducted into the workpiece (typical values: $0.05 < B_2 < 0.15$).

In a more complete numerical study of the thermal field in the vicinity of the shear plane, Dawson and Malkin (1984) found that the average temperature rise of the chip as it crosses the shear plane may be expressed approximately as

$$\frac{\pi k V (T_{c,avg} - T_o)}{2\alpha q_c''} = 3.11 (1 - 0.22e^{-2.9\phi_o}) e^{-0.7\phi_o} \cdot \text{Pe}_{l_s}^{0.5e^{-3\phi_o}} \quad (17.29)$$

and the fraction of the shear plane energy removed by the chip in cutting is given by

$$R = 1 - B_2 = \frac{V (2 \sin \phi_o) (\rho c) (T_{c,avg} - T_o)}{2q_c''} \quad (17.30)$$

A plot of this result is given as Fig. 17.10.

Assessment of Steady-State Metal Cutting Temperature Models This section concludes with a brief summary of a study by Stephenson (1991) which compared calculations from four steady-state metal cutting temperature models [Loewen-Shaw (Shaw, 1984); Boothroyd, 1975 (as modified by Tay et al., 1976); Wright et al., 1980; Venuvinod and Lau, 1986] with experimental results. Both tool-chip interface temperatures and deformation zone temperatures were considered.

All the models assume that there are two heat sources, as discussed previously. Differences arise in the method in which heat generation is partitioned among the tool, chip, and workpiece, whether variations of thermal properties are considered,

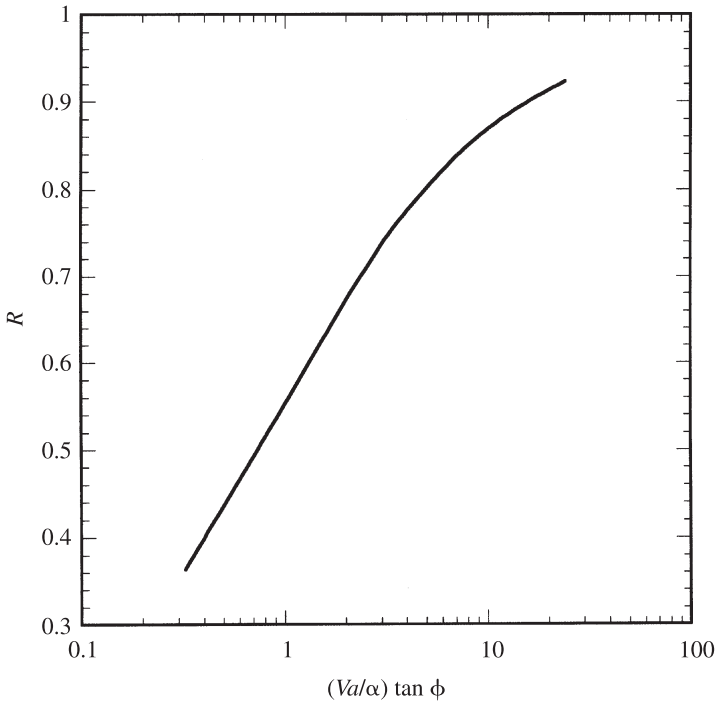


Figure 17.10 Fraction of shear plane energy that enters the chip during metal cutting.

and how the rake face heat source is modeled. The Boothroyd and Wright models use an energy partition analysis due to Weiner (1955) and thus assume less heat flow into the workpiece than do the other two models, which use analysis based on Trigger and Chao (1951). The Loewen–Shaw and Venuvinod–Lau models take into consideration the variation of thermal properties, whereas the Boothroyd and Wright models do not. Finally, the Boothroyd and Loewen–Shaw models assume that the rake face source is a uniform heat source, while the Wright and Venuvinod–Lau models can be applied with more general source strength distributions. Stephenson (1991) found that the best results were obtained with the Loewen–Shaw and Venuvinod–Lau models, while the Boothroyd and Wright models overestimated both rake face and shear zone temperature rises by approximately a factor of 2 for a variety of materials and cutting conditions. All models failed when chips produced were discontinuous so that tool–chip contact length was not constant. Finally, all the models predicted shear plane temperatures that were too high, probably due to their common assumption of planar heat generation in the shear zone.

17.5 MACHINING PROCESSES: GRINDING

The goals of this section are to review the mechanisms of heat generation in metal grinding and to provide an overview of some of the relevant modeling assumptions

used in thermal analysis. A detailed exposition of mathematical modeling for grinding is beyond the scope of this chapter; however, some key references to the literature are cited.

17.5.1 Background

Grinding is a precision machining process capable of delivering surface roughness 10 times lower than that achieved by metal cutting and with dimensional accuracy that is 10 times better. Grinding accounts for approximately 20% of all machining in the United States.

One of the major differences between cutting and grinding relates to the number and geometry of the cutting edges. Grinding uses an abrasive wheel with many randomly oriented cutting edges, while metal cutting uses a known number of cutting edges with a controlled geometry. Orthogonal metal cutting involves the use of positive or “moderately” negative rake angles. In grinding, the small abrasive grits with random orientation give rise to large negative rake angles. The chips or *swarf* produced in grinding are typically an order of magnitude smaller than that produced in metal cutting. These differences are illustrated in Fig. 17.11. Although surface grinding is not the most common type of production grinding, it is the simplest to model, and like orthogonal cutting, has been the focus of most modeling effort, much of which has occurred since 1990. Conventional grinding is characterized by small depths of cut (0.005 to 0.05 mm) and fast workpiece velocities (100 to 500 mm/s), whereas creep-feed grinding yields cut depths of 1 to 20 mm with very slow workpiece velocities (1 to 50 mm/s). In both cases the wheel velocity (typically, 20 to

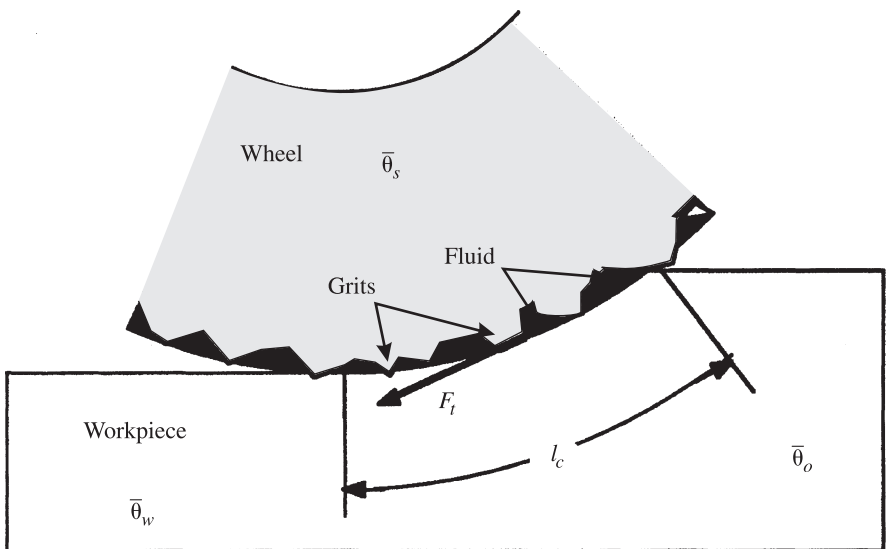


Figure 17.11 Schematic of the wheel–workpiece interface for a grinding process. (From DeVries, 1992.)

80 m/s) is much larger than the workpiece velocity. Other types of grinding are external and internal cylindrical grinding, in which both the workpiece and the grinding wheel are cylindrical; face grinding, which uses the flat edges of a cylindrical wheel against a workpiece that moves perpendicular to the wheel motion; and abrasive cut-off, in which a thin cutting wheel slices through a workpiece. In every case, however, the basic process involves the cutting action of individual abrasive grains acting against the workpiece.

In grinding, more of the energy provided at the spindle is converted into heat, making the potential for thermal damage to the workpiece significant. In orthogonal metal cutting, the tool cutting edge experiences elevated temperatures. In the case of grinding, more of the heat generated goes into the workpiece, which can lead to elevated workpiece temperatures and metallurgical changes and subsurface damage called *burning*, as discussed by Malkin (1984) and Guo and Malkin (1992). Additional review and recent advances in thermal modeling of grinding processes is contained in Jen and Lavine (1995), Guo and Malkin (1996), Zhang and Faghri (1996), and Ju et al. (1998).

17.5.2 Workpiece Temperatures during Grinding

At the level of an individual grain, heat generation occurs in the shear plane, at the chip–grain interface due to friction there, and at the grain–workpiece interface. At this scale, the methods described in Section 17.4 may be used to estimate local temperatures, which may locally attain over 1000°C. Although these temperatures may be important with respect to wear of the abrasive, they are not usually indicative of the effects on workpiece quality, because they are so very localized (temporally and spatially) and since material experiencing such temperatures will quickly be removed by another grain. More relevant to workpiece damage is the average interference zone temperature that results from the overall effect of all the grains in the contact region and from the grinding fluid that is almost always present.

In this way, Malkin (1984) determined an expression for the maximum grinding zone temperature rise to be

$$T_m - T_o = \frac{\beta \alpha_w^{1/2} \varepsilon P}{k_w b d_s^{1/4} a^{1/4} V_w^{1/2}} \quad (17.31)$$

where P is the grinding power, ε the fraction of the grinding power entering the workpiece as heat, a and b the depth and width of cut, V_w the workpiece velocity, d_s the wheel diameter, k_w the thermal conductivity of the workpiece, α_w the thermal diffusivity of the workpiece, and β a constant that depends on the heat source shape (1.13 for rectangular and 1.06 for triangular). Malkin used a semiempirical analysis to determine

$$\varepsilon = \frac{u - 0.45u_{ch}}{u} \quad (17.32)$$

where the specific grinding energy u is equal to the grinding power divided by the volumetric removal rate, and u_{ch} is the chip formation component of this energy, which

may be regarded as a material property (about 13.8 J/mm^3 for ferrous materials). Typical values of ε determined in this way are 0.7 to 0.9. Equation (17.31) neglects heat transfer to the wheel (through the grains) and the grinding fluid, which may restrict its validity to dry grinding or to the occurrence of film boiling in the grinding fluid. However, it does permit determination of the onset of workpiece burn (critical grinding zone temperature) in terms of a measured level of the grinding power.

If a grinding fluid is present, a very approximate analysis yields the following for the fraction ε :

$$\varepsilon = \frac{1}{1 + (V_s/V_w)^{1/2} [(k\rho c)_c / (k\rho c)_w]^{1/2}} \quad (17.33)$$

where k_c and $(\rho c)_c$ in the product $(k\rho c)_c$ are weighted volumetric averages of the thermal properties of the grain, grinding fluid, and air (porosity), and V_s is the wheel velocity. When applied to creep-feed grinding conditions, the energy partition to the workpiece is determined to be a small fraction of that in conventional grinding.

Equation (17.33) may be modified for cubic boron nitride (CBN) grinding wheels to account for the much higher thermal conductivity of the CBN abrasive grains than that for aluminum oxide, by neglecting the effects of the grinding fluid (valid for conventional grinding), to yield

$$(k\rho c)_c = (1 - \phi)^2 (k\rho c)_g \quad (17.34)$$

for insertion into eq. (17.33). The average wheel surface porosity ϕ is difficult to estimate reliably; however, ad hoc estimates based on experimental measurements imply that $\varepsilon \approx 0.2$ and $\phi \approx 0.9$ for typical conditions with ferrous workpieces.

More recent attempts to predict temperature rise during grinding have sought to eliminate the need to estimate a partition of the grinding energy or to determine effective fluid/grinding wheel thermal properties. The analytical details are too involved to present here. However, the general approach, indicated schematically in Fig. 17.12, is as follows. Separate analytical solutions are determined analytically for the conduction heat transfer to an individual abrasive grain, in terms of a heat flux q_g'' ; for conduction into the grinding fluid from the workpiece, in terms of a heat flux q_f'' ;

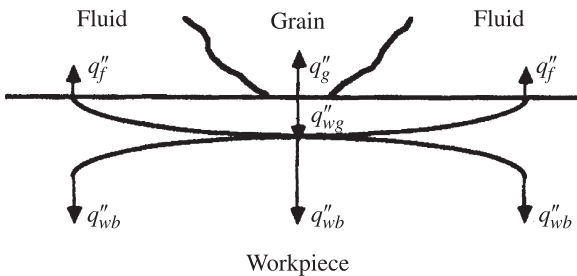


Figure 17.12 Heat flow paths in the vicinity of an abrasive grain–workpiece interface. (After Lavine and Jen, 1991.)

for the background heat transfer into the workpiece from the entire grinding zone, in terms of a heat flux q''_{wb} ; and for the heat transfer into the workpiece from an individual grain, in terms of a heat flux q''_{wg} . Then an appropriate coupling of these solutions is established using continuity of temperature and conservation of energy applied in a mathematically consistent way to each interface. The reader is referred to Jen and Lavine (1995), Lavine and Jen (1991), and Ju et al. (1998) for additional details.

17.6 THERMAL-FLUID EFFECTS IN CONTINUOUS METAL FORMING PROCESSES

In this section we review briefly some of the important thermal and fluid considerations in continuous deformation processes such as drawing, rolling, and extrusion. Metal forming processes exploit the property of metals that allows them to flow plastically in the solid state. By simply moving the material to the shape desired, as opposed to removing unwanted regions, there is little or no waste. In general, a temperature increase in the workpiece brings about a decrease in material strength, an increase in ductility, and a decrease in the rate of strain hardening (all of these effects tend to promote the ease of deformation).

17.6.1 Background

Deformation processes tend to be classified as *hot working* (recrystallization occurs simultaneously; $T_{\text{initial}} \geq 0.6T_{\text{melt}}$), *cold working* ($T_{\text{initial}} = 0.3T_{\text{melt}}$), or *warm working*. However, because the general principles governing deformation at different temperatures are basically the same, classification according to specific input and output geometries and material and production rate conditions is often more useful. Therefore, one may broadly characterize forming operations under the headings of forging, sheet metal forming, drawing, extrusion, and rolling, the latter three being examples of continuous processing. An understanding of thermal effects in such systems is integrally coupled to a characterization of the metal flow, stresses, lubrication, and material handling and design of the forming equipment, so that a simple thermal analysis even for generic types of systems may not characterize a process completely. Among classical references, Altan et al. (1983) and Schey (1983) are detailed and complete, albeit with limited consideration of thermal and heat transfer effects. Yang (1992) and Tseng et al. (1990) also provide useful discussions of thermal effects in extrusion and drawing and in rolling, respectively. The focus of the present section is on factors associated with the temperature rise of the workpiece and the die (or roll).

17.6.2 Considerations for Thermal–Fluid Modeling in Extrusion and Drawing

Figure 17.13 includes schematic illustrations of generic continuous deformation processes. (Although extrusion is a batch process, it is often studied as a quasi-steady-state process.) The principal distinctions among these are the delivery of the force to

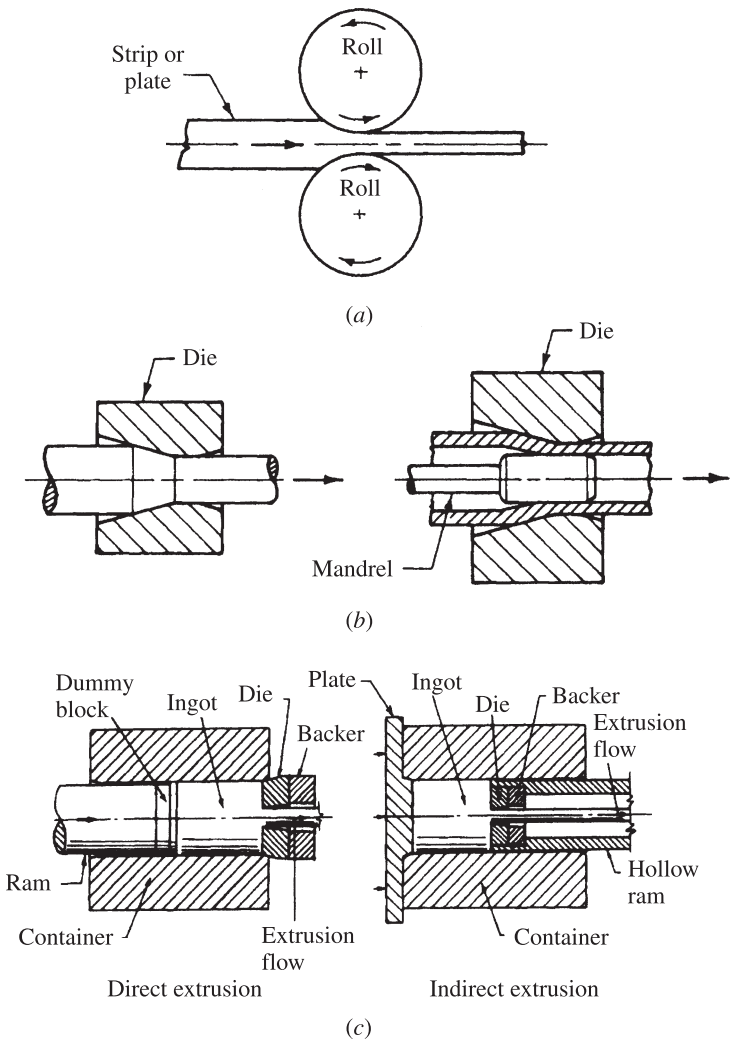


Figure 17.13 Schematic diagrams of rolling, drawing, and extrusion processes. (After Altan et al., 1983.)

the workpiece, the reduction in the cross section of the workpiece, and the speed. Heat generation arises from two sources: plastic deformation heating of the workpiece and frictional heating between the workpiece and the die (Fig. 17.14).

Deformation Heating Considerations In wire drawing and often in rolling, the deformation and hence the heating of the workpiece due to the plastic flow of the material may be considered to be nearly uniform (Wright, 1976). Under these conditions, the uniform temperature increase of the wire is given by

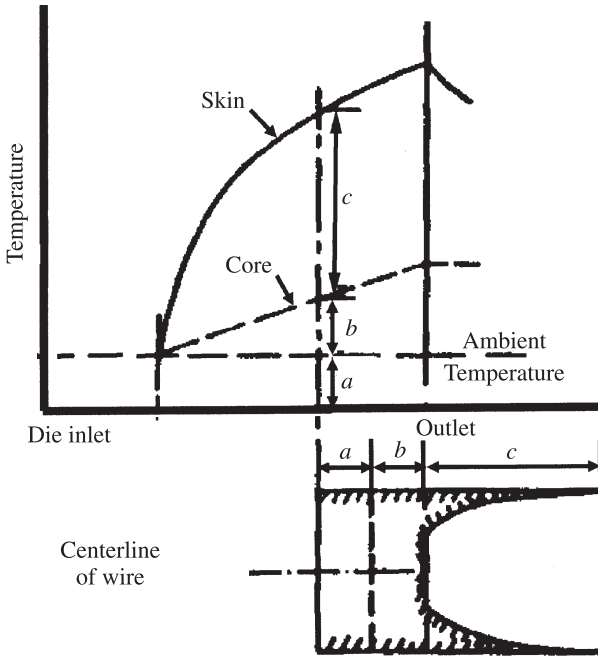


Figure 17.14 Surface and core temperature distributions during a drawing process.

$$\Delta T_{DH} = \frac{W_D}{\rho_w c_w} \simeq \frac{\tau_s \ln(A_o/A_1)}{\rho_w c_w} \quad (17.35)$$

where W_D is the deformation work per unit volume, τ_s the flow stress of the workpiece, A_o and A_1 the initial and final cross-sectional areas, and $\rho_w c_w$ the volumetric specific heat of the workpiece.

Frictional Heating Considerations Frictional heating is concentrated near the wire–die interface, resulting in severe temperature gradients. In the simplest physical model, the latter is regarded as arising from a friction coefficient (assumed known and constant) and the normal stress on the workpiece, which is usually assumed to be the yield stress of the workpiece. Apparent friction coefficients can vary from 0.01 (hydrodynamic lubrication) up to 0.5 (boundary lubrication). Then if a suitable partition coefficient for the transfer of heat between the workpiece and die can be discerned, an estimate of temperature levels may be obtained. Even though uniform friction and heat partition coefficients may not be realistic, many modeling efforts are based on their use (Snidle, 1977; El-Domiaty and Kassab, 1998). Figure 17.15 shows results for a calculation of two-dimensional temperature distributions in a drawn steel wire using a similar model for the die–workpiece interface; Fig. 17.16 shows a similar result for a hot aluminum extrusion process.

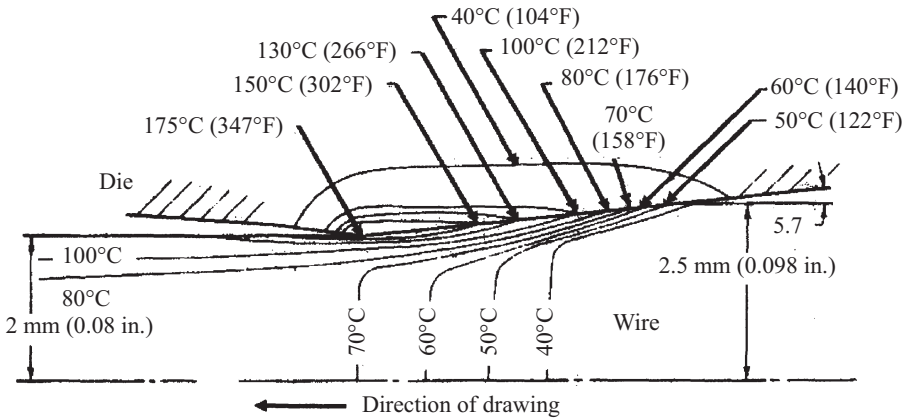


Figure 17.15 Coupled die and workpiece temperature distributions in wire drawing. (From Altan et al., 1983.)

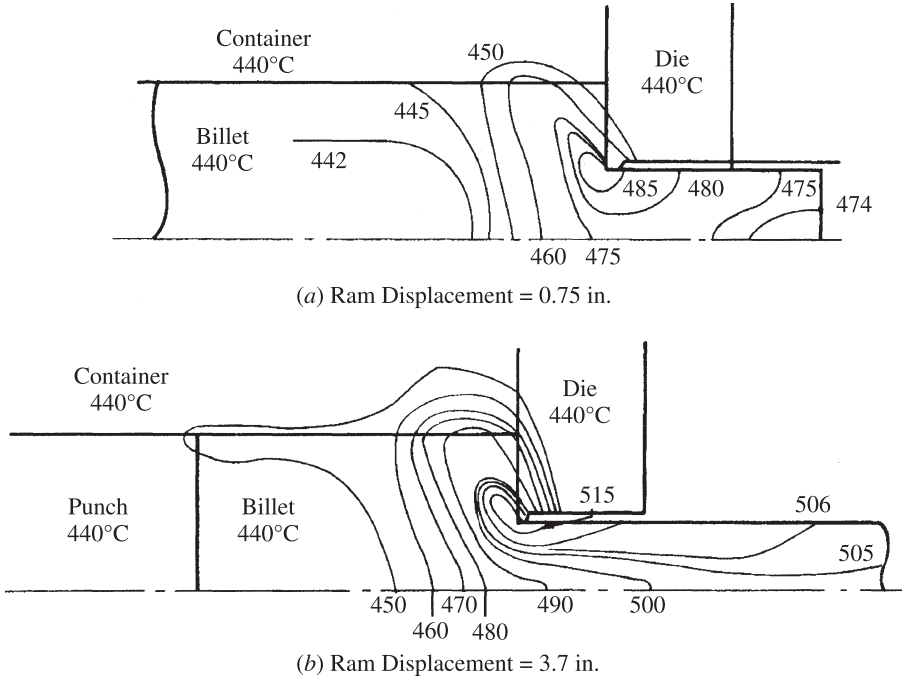


Figure 17.16 Coupled die and workpiece temperature distributions in metal extrusion. (From Altan et al., 1983.)

A more realistic model of these processes would include several important elements that are ignored in the discrete heat source approach (Yang, 1992). These include a Reynolds equation for the pressure distribution in a lubricating film for a given film thickness variation along the die–workpiece interface. However, the film thickness must be determined by the thermoelasto–viscoplastic deformation behavior of the die and the workpiece. An energy equation for the lubricating film introduces heat generation by viscous dissipation and pressure work. (Local boundary lubrication and the associated metal-to-metal shearing of contacting asperities still may be present.) Temperature and pressure dependence of the density and the viscosity of the lubricant must be known, as pressures can be exceedingly high in such films. Heat conduction in the deforming solids, including heat generation due to plastic deformation in the workpiece, must be accounted for. Suitable compatibility conditions at the solid–liquid interfaces must be established. Heat losses from the extruded or drawn workpiece after it exits the die must also be accommodated.

Figure 17.17 shows a physical model of the elastohydrodynamic lubrication phenomenon in wire or strip drawing that is often the basis for a more complete analysis. The contact area is divided into four regions: (1) an elastohydrodynamic inlet region; (2) a plastohydrodynamic region of strip deformation; (3) a plastohydrodynamic outlet region and (4) an elastohydrodynamic outlet region. In an early study, Dowson et al. (1972) found that almost 90% of the pressure rise in the film occurs in the last 0.25% of the inlet length. There is a gradual decrease of pressure through regions 2 and 3, followed by a recovery to ambient pressure at the region 4 exit. There is a large decrease in the film thickness at the plastic–elastic boundary, followed by a gradual decrease in region 2. It is nearly a constant over region 3, decreasing to a minimum at the parallel–divergent interface of region 4. To date, only portions of

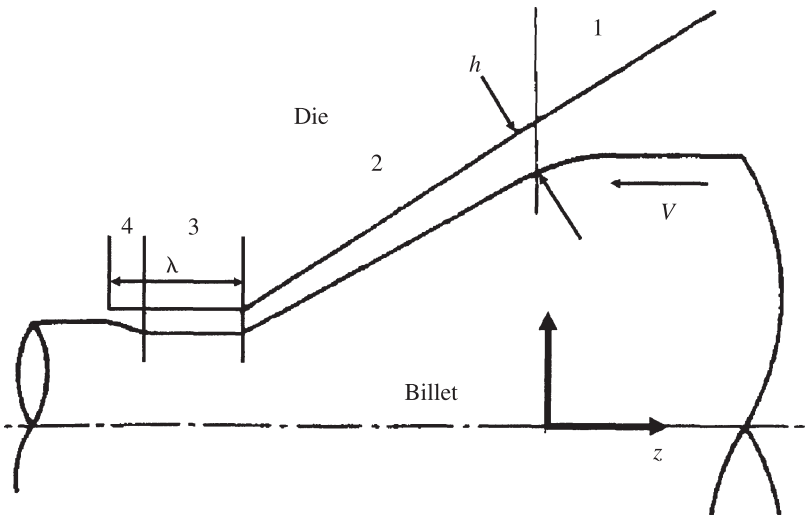


Figure 17.17 Film regions during elastic–plastic hydrodynamic lubrication. (From Dowson et al., 1972.)

all these elements have been treated, and usually for specific operating conditions, so that general results are still largely unavailable (Snidle et al., 1976; Wilson and Mahdavian, 1974; Lucca and Wright, 1996).

17.7 PROCESSING OF POLYMER-MATRIX COMPOSITE MATERIALS

17.7.1 Introduction

Composite materials—consisting of a dispersed *reinforcement phase* embedded in a bulk *matrix phase*—provide designers with increased opportunities for tailoring structures to meet a variety of property and performance requirements. Although the matrix phase gives to a composite its net shape, surface appearance, environmental resistance, and overall durability, it is the reinforcements that carry most of the structural loads and thus dictate the overall stiffness and strength. The matrix constituent may be metallic, ceramic, or polymeric in origin, while the reinforcement morphology could be fibrous or particulate. Polymer matrix composites reinforced with fibers are by far the most widely used and form the focus of this section.

Polymers used in composites may be either thermosetting or thermoplastic. A vast majority of the current composite applications utilize thermosetting polymers, which solidify through an irreversible crosslinking chemical reaction called *cure*. Thermoplastics, on the other hand, exhibit a reversible phase change with respect to heating and cooling, without any accompanying chemical reaction. The processing of these two classes of polymer matrix composites therefore involves fundamentally different mechanisms, discussed in this section. The objective of the section is not that of providing a comprehensive review of the literature in the field; instead, we highlight the transport phenomena aspects involved in the processing and the modeling of the governing phenomena.

17.7.2 Processing of Thermosetting-Matrix Composites

Manufacture of thermosetting-matrix composites, in principle, consists of exposing a multilayered fiber–resin–catalyst mixture to elevated temperature and pressure variation with time, called *cure temperature and pressure cycles*. The high temperatures initiate and sustain a crosslinking, exothermic chemical reaction, called the *cure reaction*, while the applied pressure serves to consolidate and expel voids in the composite and the volatile compounds that may form during the reaction. The cure process transforms the initially soft fiber–resin mixture to a structurally hard composite product, and due to the irreversible nature of the cure reaction, the structural integrity is retained upon withdrawal of the external temperature and pressure variations.

Thermosetting-matrix composite fabrication is well served by many continuous and batch processes, such as pultrusion, tape laying/filament winding, autoclave curing, and liquid composite molding, among others. Three representative processes are shown schematically in Fig. 17.18. In the pultrusion process (Fig. 17.18a), fibers are drawn from supply reels through a resin bath and fed into a heated die shaped to produce the desired cross section. A prescribed temperature cycle maintained along

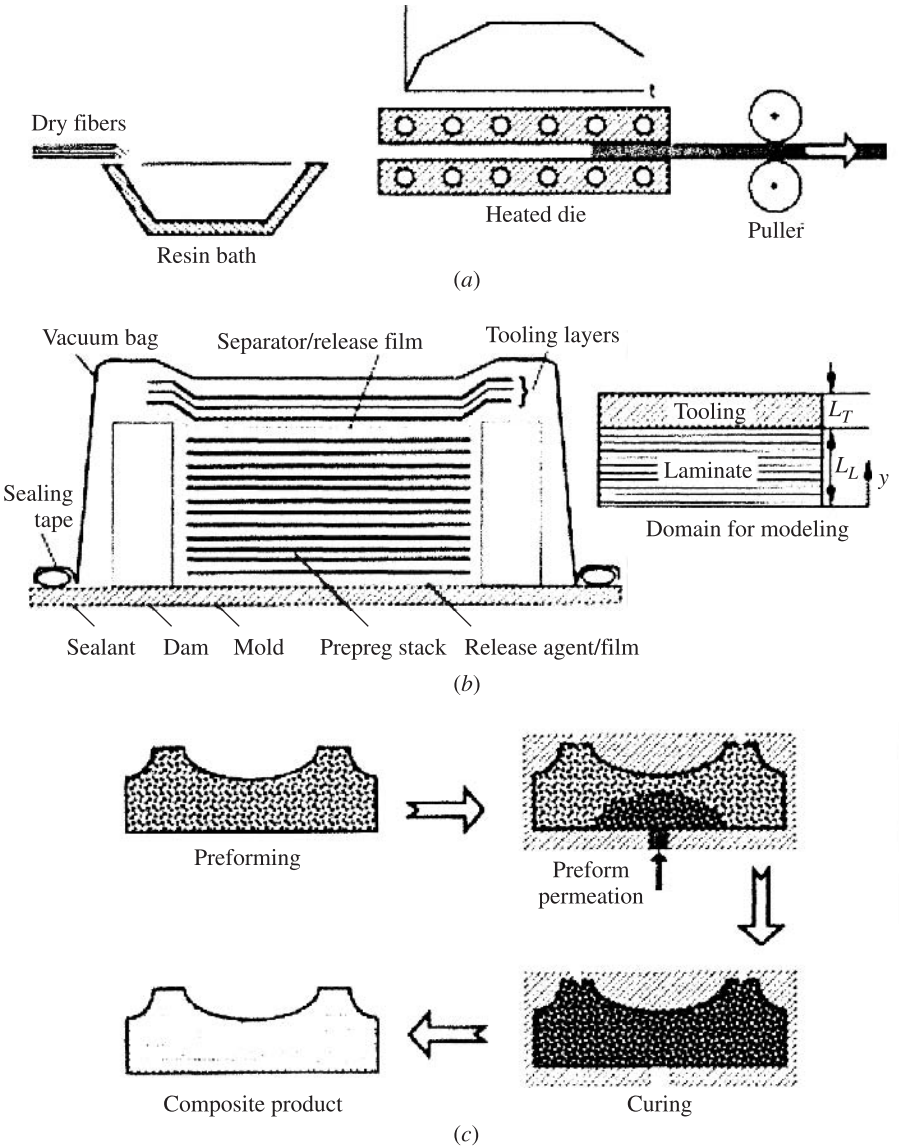


Figure 17.18 (a) Pultrusion, (b) autoclave, and (c) liquid composite molding processes for fabrication of thermosetting matrix composites.

the die length cures the fiber–resin mixture. The cured material emerging from the die is cut to the desired length to form the product. The process has been used for fabrication of composite parts with fixed cross-sectional geometry, such as tubes, rods, and I-beam sections. In autoclave curing, a batch process, a composite layup consisting of stacks of either partially cured resin-preimpregnated fiber layers (called

prepregs) or resin-coated fiber layers is prepared by hand or by automated means. The layup is sandwiched between tooling materials and enclosed in a vacuum bag, as shown schematically in Fig. 17.18*b*. The assembly is subjected to a temperature and vacuum cycle in an autoclave oven to consolidate the layers and produce a cured composite product. The process is capable of fabricating quality laminates and has been used extensively in the aerospace industry. The basic steps in a liquid composite molding process, exemplified by resin transfer molding, are shown schematically in Fig. 17.18*c*. The process begins with the stacking of fibrous reinforcement units to obtain a porous net-shaped structure termed a *preform*. The preform is placed into a closed mold cavity and subsequently infiltrated by injecting a reactive polymeric resin into the mold. The resin-saturated preform is then exposed to a prescribed cure temperature schedule which transforms the materials in the mold cavity to a structurally hard composite product. The process offers potential for fabricating high-performance composite parts of various size and shape complexities cost-effectively and at high throughputs.

As seen from the foregoing description, all the fabrication methods share the common step of *cure*. The cure process is discussed here by considering the autoclave process (Fig. 17.18*b*). The dominant physical phenomena involved in the process are the heat transfer associated with the heating of the laminate and the tooling, the chemical reaction effecting the cure process, and the consolidation of the laminates and reduction of voids. Mathematical models for the foregoing physical phenomena are widely reported in the literature (Broyer and Macosko, 1976; Loos and Springer, 1983; Han et al., 1986; Gutowski et al., 1987; Walsh and Charmchi, 1988; Bogetti and Gillespie, 1991; Davè et al., 1990; Martinez, 1991; Pitchumani and Yao, 1993). Although the details of the modeling may be found there, the principal steps in the model formulation are presented below.

Thermal Model The thermal model consists of solving the energy equation (in Cartesian coordinates, for the configuration shown in Fig. 17.18*b*) for the temperature distribution in the layup cross section. If the heating in the autoclave is assumed to be uniform across the width and length of the layup (x and z directions in the figure), and if the layup thickness is small compared to those in the other dimensions, the energy transfer is predominantly one-dimensional through the layup thickness (y direction). It is further assumed here that symmetric heating conditions prevail on the top and bottom surfaces of the layup, which together with the fact that the layup geometry is symmetric about the laminate midthickness, reduces the problem domain to one-half of the layup thickness.

The governing equation for the one-dimensional heat transfer in the two-material domain formed by the laminate and the tooling, accounting for the internal heat generation due to the exothermic cure reaction in the composite, may be written as

$$\frac{\partial [(\rho c T)_L]}{\partial t} = \frac{\partial}{\partial y} \left(k_L \frac{\partial T_L}{\partial y} \right) + C_{A0} \Delta H_R (1 - v_f) \cdot \frac{d\varepsilon}{dt}$$

$$0 \leq y \leq L_L \quad (\text{laminate})$$

$$\frac{\partial [(\rho c T)_T]}{\partial t} = \frac{\partial}{\partial y} \left(k_T \frac{\partial T_T}{\partial y} \right)$$

$$L_L \leq y \leq L_L + L_T \quad (\text{tooling}) \quad (17.36)$$

where ρc is the volumetric specific heat, T the temperature, t and y the time and location in the layup thickness, respectively, k the thermal conductivity of the composite, C_{A0} the initial resin concentration in the resin-catalyst mixture, ΔH_R the heat of the cure reaction, and v_f the fiber volume fraction in the composite. The subscripts L and T refer to the laminate and tooling, respectively. Further, $d\varepsilon/dt$ denotes the rate of the cure reaction, which together with the heat of reaction determines the heat release rate during the cure process. The expression for the reaction rate is given by the kinetics model, discussed below.

The governing equation set, eq. (17.36), is subject to an initial temperature field in the laminate and tooling, given by

$$T_L(y, 0) = T_T(y, 0) = T_o(y) \quad (17.37)$$

The boundary conditions associated with eq. (17.36) are convective heating of the top surface of the tooling in the autoclave ($y = L_L + L_T$ in Fig. 17.18b) and an insulated condition at the laminate midthickness ($y = 0$) if symmetric heating conditions are assumed. Further, temperature and heat flux must be continuous at the laminate-tooling interface ($y = L_L$). These conditions may be written as follows:

$$\begin{aligned} -k_T \frac{\partial T_T}{\partial y} &= h [T_T - T_{\text{cure}}(t)] & \text{at } y = L_L + L_T \\ \frac{\partial T_T}{\partial y} &= 0 & \text{at } y = 0 \\ T_T = T_L \quad k_T \frac{\partial T_T}{\partial y} &= k_L \frac{\partial T_L}{\partial y} & \text{at } y = L_L \end{aligned} \quad (17.38)$$

where h is the heat transfer coefficient, and $T_{\text{cure}}(t)$ denotes the cure temperature cycle.

Kinetics Model The heat release due to the cure reaction, appearing as a source term in the laminate energy equation [eq. (17.36)] is a function of the reaction kinetics. Empirical as well as mechanistic models for the cure kinetics are available (Loos and Springer, 1983; Han et al., 1986; Chiao and Lyon, 1990; Ramakrishnan et al., 2000). While mechanistic models account explicitly for the different reaction steps and track the processes of monomers diffusing into growing molecules or molecular chains, empirical models have been employed successfully in describing the dominant effects of the cure reaction in a simple-to-use manner. The kinetics of the cure reaction is described empirically in terms of an Arrhenius-type rate equation, which is expressed functionally as

$$\frac{d\varepsilon}{dt} = f(\varepsilon, T) \quad (17.39)$$

where ε is the degree of cure, defined as the fraction of the initial resin concentration C_{A0} , that has reacted; that is, $\varepsilon = (C_{A0} - C_A)/C_{A0}$, in which C_A is the resin concentration at any time during the reaction. Note that the degree of cure is zero initially (when $C_A = C_{A0}$) and reaches unity at the completion of the reaction.

The kinetics models for several resin-catalyst systems are summarized in Table 17.1. The approach to obtaining the heat of the reaction and the kinetic parameters follows a standard procedure as given in Han et al. (1986), Han and Lem (1983), and Sourour and Kamal (1976). The principal steps in the procedure are outlined in what follows and the reader is referred to the foregoing publications for further details. The characterization is based on analysis of carefully measured resin-catalyst samples in a differential scanning calorimeter (DSC). First, the heat generated during the cure reaction is measured by completing the reaction nonisothermally, in which the sample is heated in a DSC from room temperature at a prescribed rate until there is no more heat being generated by reaction. Figure 17.19 shows the rate of heat generated, dQ/dt , as a function of time t , referred to as a *thermogram*, for the nonisothermal DSC run on an EPON 815 epoxy resin catalyzed with an Epicure 3274 curing agent. The total heat generated due to the reaction, ΔH_R , is obtained as the area under the thermogram by integrating the measured heat flow with respect to time. Note that a secondary heating may be necessary to cure the sample completely, in which case the residual heat generated during the second run is added to obtain the heat of the reaction.

The kinetic parameters (e.g., K_{10} , K_{20} , E_1 , E_2 , m , and n in Table 17.1) are obtained from isothermal scans of the resin system in the differential scanning calorimeter to obtain dQ/dt versus time t for various temperatures. Since the total amount of heat generated by the cure reaction at any time $Q(t)$ is directly proportional to the degree of cure ε of the sample at that particular instant, the rate of cure $d\varepsilon/dt$ can be defined as

$$\frac{d\varepsilon}{dt} = \frac{1}{\Delta H_R} \frac{dQ(t)}{dt} \quad (17.40)$$

Using eq. (17.40), the isothermal thermograms are cast as plots of $d\varepsilon/dt$ versus time t and the degree of cure ε is obtained by integrating these plots with respect to time. Figure 17.20 shows the cure rate $d\varepsilon/dt$ as a function of the degree of cure ε at various isothermal conditions. The empirical parameters in the kinetics equation are then obtained as follows. First, the $d\varepsilon/dt$ versus ε data for each temperature is fitted to the right-hand side of the kinetics model to determine K_1 , K_2 , m , and n , where $K_i = K_{i0}e^{-E_i/RT}$, $i = 1, 2$. The natural logarithm of K_1 and K_2 when plotted against $1/T(K^{-1})$ yields the K_{10} , K_{20} , E_1 , and E_2 values reported in Table 17.1.

The coupled energy and kinetics equations are solved simultaneously to obtain the temperature and degree of cure variations with time in the composite section. An example temperature and degree of cure profile during a cure process is illustrated in Fig. 17.21 for the case of fabricating a Cycom-4102 laminate. Note that due to the

TABLE 17.1 Kinetics Models and Model Parameters for Various Resin Systems

Material	Kinetics Model	Kinetic Parameters
AS4/3501-6	For $\varepsilon \leq 0.3$	$K_{10} = 2.101 \times 10^9 \text{ s}^{-1}$
Lee et al. (1982)	$\frac{d\varepsilon}{dt} = (K_{10}e^{-E_1/RT} + K_{20}e^{-E_1/RT}\varepsilon^m)(B - \varepsilon)^b$ $(1 - \varepsilon^d)^c$	$K_{20} = -2.014 \times 10^9 \text{ s}^{-1}$ $A_1 = 1.960 \times 10^5 \text{ kJ/kmol}$ $E_1 = 8.07 \times 10^4 \text{ kJ/kmol}$ $E_2 = 7.78 \times 10^4 \text{ kJ/kmol}$ $\Delta H_R = 474 \text{ kJ/kg}$ $B = 0.47$ $m = b = c = d = 1.0$
	For $\varepsilon > 0.3$	
	$\frac{d\varepsilon}{dt} = A_1e^{-E_1/RT}(1 - \varepsilon^d)^c$	
Cycom-4102	$\frac{d\varepsilon}{dt} = (K_{10}e^{-E_1/RT} + K_{20}e^{-E_1/RT}\varepsilon^m)(1 - \varepsilon)^n$	$K_{10} = 0 \text{ min}^{-1}$ $K_{20} = 3.7 \times 10^{22} \text{ min}^{-1}$ $E_1 = 0 \text{ kJ/kmol}$ $E_2 = 1.66 \times 10^5 \text{ kJ/kmol}$ $\Delta H_R = 74.1 \text{ kJ/kg}$ $m = 0.524; n = 1.476$
Pillai et al. (1994)	(This equation applies to all the remaining kinetics models.)	
OC-E701/P16N/BPO		$K_{10} = 5.69 \times 10^{12} \text{ s}^{-1}$ $K_{20} = 8.61 \times 10^8 \text{ s}^{-1}$ $E_1 = 1.07 \times 10^5 \text{ kJ/kmol}$ $E_2 = 7.51 \times 10^4 \text{ kJ/kmol}$ $\Delta H_R = 200 \text{ kJ/kg}$ $m = 0.58; n = 1.42$
Han et al. (1986)		
OC-E701/P16N/TBPP		$K_{10} = 5.28 \times 10^{17} \text{ s}^{-1}$ $K_{20} = 2.96 \times 10^{10} \text{ s}^{-1}$ $E_1 = 1.7 \times 10^5 \text{ kJ/kmol}$ $E_2 = 8.41 \times 10^4 \text{ kJ/kmol}$ $\Delta H_R = 1000 \text{ kJ/kg}$ $m = 0.56; n = 1.44$
Han et al. (1986)		
Epon-815/Epicure-3274		$K_{10} = 0 \text{ s}^{-1}$ $K_{20} = 4.18 \times 10^5 \text{ s}^{-1}$ $E_1 = 0 \text{ kJ/kmol}$ $E_2 = 55.92 \text{ kJ/kmol}$ $\Delta H_R = 384 \text{ kJ/kg}$ $m = 0.25; n = 1.75$
Ramakrishnan et al. (2000)		
Phthalic Anhydride/maleic Anhydride/propylene Glycol (2:1:3) Crosslinking agent: styrene monomer (28%) Initiator: 60% MEK in dimethyl phthalate		$K_{10} = 0 \text{ s}^{-1}$ $K_{20} = 2.60 \times 10^9 \text{ min}^{-1}$ $E_1 = 0 \text{ kJ/kmol}$ $E_2 = 71.34 \times 10^3 \text{ kJ/kmol}$ $\Delta H_R = 309.4 \text{ kJ/kg}$ $m = 0.445; n = 1.500$
Pusatcioglu et al. (1979)		

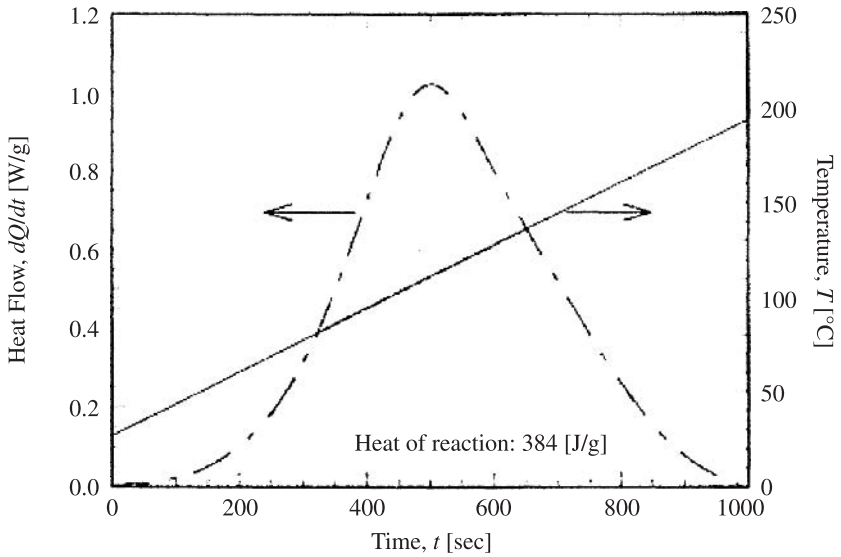


Figure 17.19 Example nonisothermal DSC scan for Epon 815/Epicure 3274 resin-catalyst system, showing the heat flow as a function of time. The area under the curve is the heat of reaction. (After Ramakrishnan et al., 2000.)

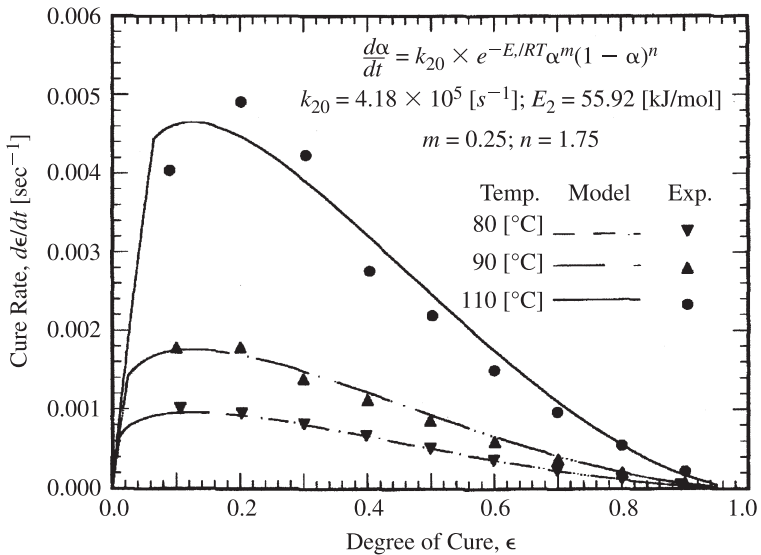


Figure 17.20 Model parameters for the kinetics of the Epon 815/Epicure 3274 resin-catalyst system obtained from isothermal DSC scans. (After Ramakrishnan et al., 2000.)

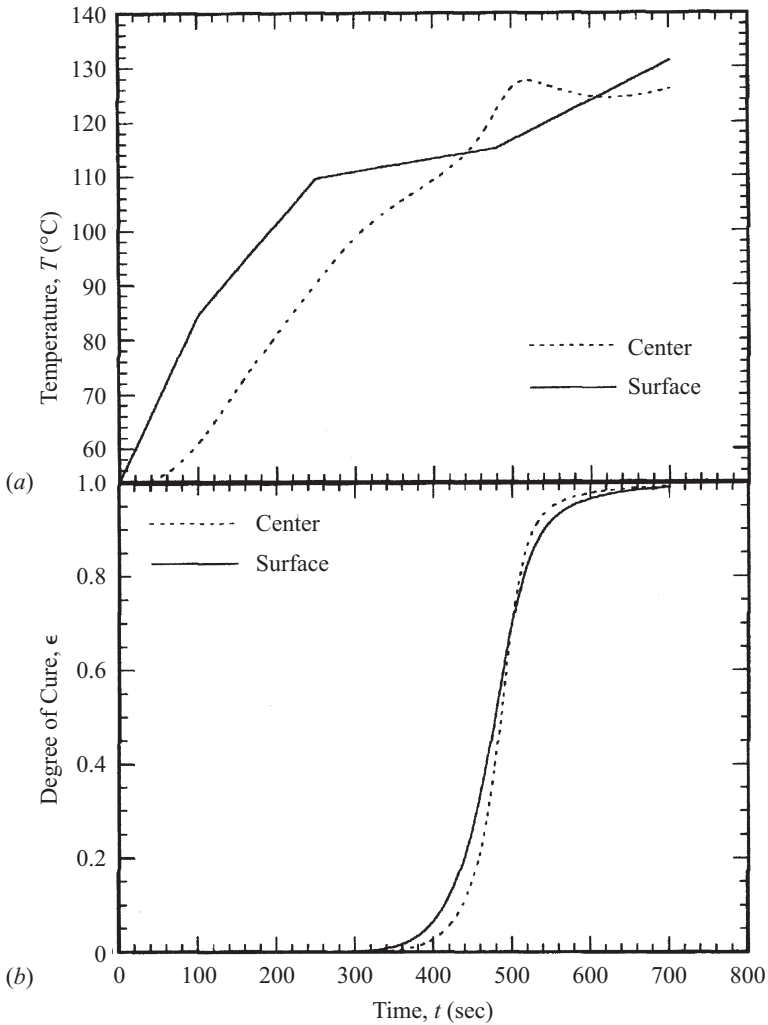


Figure 17.21 (a) Temperature variation and (b) degree of cure evolution with time during a typical cure process. The results correspond to the cure of a Cycom-4102 laminate.

exothermic reaction, the temperature inside the laminate exceeds that of the surface during later stages of the cure (Fig. 17.21a). The cure rate is also observed to be very rapid in Fig. 17.21b in the time interval corresponding to the peak exotherm. Controlling the exotherm and preventing/minimizing processing-induced stresses is an important consideration in the design of cure cycles.

Laminate Consolidation Model The goal of consolidation is to produce a monolithic structure with simultaneous void reduction, which is accomplished

through application of an external pressure (or vacuum) cycle on the laminate. The process is influenced by the resin viscosity, which is a function of the temperature and degree of cure in the laminate, and the applied pressure. The resin viscosity decreases initially with temperature; however, as the cross-linking reactions proceed, the viscosity sharply increases near the gel point, at which the viscosity is theoretically infinite. Thus, the cure pressure cycle is designed to take advantage of the window during processing when the viscosity is low.

Mathematically, the consolidation process is described as that of resin flow through a porous bed formed by the reinforcing fibers. Models for the consolidation process have been presented by Springer (1982), Davè et al. (1987), and Gutowski et al. (1987), among others. The models by Davè et al. (1987) and Gutowski et al. (1987) consider the composite to contain a deformable fiber network in which resin flow in all directions is governed by Darcy's law. The fiber network also takes part in carrying the load due to the applied pressure (or vacuum) during processing. The total force σ acting on the porous fiber bed is balanced by the sum of the force due to the springlike behavior of the fiber network p and the hydrostatic force due to the pressure of the resin in the layup, P .

The hydrostatic pressure is obtained as the solution of the governing equation for consolidation of a porous bed within a given time interval with three-dimensional flow and a one-dimensional confined compression condition (no boundary motion in the x and y directions), given by (Davè et al., 1987)

$$\frac{1}{\mu m_v} \left[\frac{\partial}{\partial x} \left(\kappa_x \frac{\partial P}{\partial x} \right) + \frac{\partial}{\partial y} \left(\kappa_y \frac{\partial P}{\partial y} \right) + \frac{\partial}{\partial z} \left(\kappa_z \frac{\partial P}{\partial z} \right) \right] = \frac{\partial P}{\partial t} \quad (17.41)$$

where μ is the viscosity of the resin in the porous fiber bed; κ_x , κ_y , and κ_z are the specific permeabilities in the x , y , and z directions, which depend on the stress level; t is time; and m_v is the coefficient of volume change, which describes the stress-strain behavior of a body in confined compression. For a porous medium, it is the ratio of change in porosity to axial (normal) stress for confined compression of the porous body with its vertical side faces constrained from any motion (Kardos, 1997).

Solution of the foregoing equation requires information on the anisotropic permeability tensor and its variation as the fiber bed consolidates during processing. Several theoretical and experimental studies have been conducted to determine this information (Gutowski et al., 1986; Lam and Kardos, 1991; Adams and Rebenfeld, 1991a,b; Skartsis et al., 1992; Skartsis and Kardos, 1990), which is provided predominantly in terms of the Carman-Kozeny relationship

$$\kappa = \frac{\varphi^3}{(1 - \varphi)^2} \frac{1}{s k_o} \quad (17.42)$$

where φ is the resin volume fraction; k_o is the Kozeny constant, determined empirically; and s is the specific surface of the fibers and is related to the fiber radius r_f as $4/r_f^2$. The Kozeny constant is reported to remain relatively constant over a wide range of resin volume fractions, except near the extreme limits of φ . For flow parallel to the

fibers, values of k_o in the range 0.5 to 0.7 have been reported, while for transverse flow the values range from 11 to 18 (Gutowski et al., 1987; Lam and Kardos, 1988). Viscoelastic characteristics of the resin, such as near the gel point, are accounted for through the use of a pseudo-Kozeny constant, k_o^* , which is a function of both fluid and fiber bed properties (Skartsis et al., 1992).

Resin viscosity is another important parameter that affects resin flow and transport of voids during the consolidation process. The viscosity is a function of the temperature and the degree of cure and is often given by an empirical correlation of the form

$$\mu = \mu_{\infty} \exp \left(\frac{E}{RT} + \lambda \varepsilon \right) \quad (17.43)$$

where μ_{∞} is a constant, E the activation energy for viscosity, and λ a constant that is independent of temperature, all of which are determined empirically. For the Hercules 3501-6 resin, Lee et al. (1982) reported the values of the model parameters as: $\mu_{\infty} = 7.93 \times 10^{-14}$ Pa · s, $E = 9.08 \times 10^4$ J/mol, and $\lambda = 14.1 \pm 1.2$.

Gutowski and co-workers (Gutowski, 1985; Gutowski et al., 1987) modeled fiber deformation by assuming that a composite is a porous, nonlinear elastic medium that is filled with a viscous resin. They modeled the deformation of bundles of fibers as beams bending between multiple contact points, and derived an expression for the stiffness p as

$$p = 3\pi \frac{E}{\beta^4} \frac{\sqrt{v_f/v_i} - 1}{(\sqrt{v_a/v_f} - 1)^4} \quad (17.44)$$

where E is the bending stiffness of the fiber and v_a , v_f , and v_i are the maximum fiber volume fraction, the instantaneous fiber volume fraction, and the initial fiber volume fraction, respectively. The term β is a geometric parameter that is related to the fiber architecture and fiber diameter. For well-aligned fiber bundles, the parameters, β , v_i , and v_a , determined by fitting experimental measurements to the model, were given by Gutowski and co-workers as $\beta = 225$, $v_i = 0.50$, and $v_a = 0.829$. The values increase with increasing fiber alignment.

A model for diffusion-controlled void growth and dissolution in an epoxy resin system during consolidation was developed by Kardos et al. (1986). The model provides the size of a void located in an infinite isotropic medium as a function of the processing parameters and identifies conditions under which void growth can be prevented or voids can be made to collapse during the cure process. Based on their model, they proposed that the resin pressure (atm) at any point within the laminate being cured must be greater than a minimum value as given below:

$$P \geq P_{\min} \quad P_{\min} = 4.962 \times 10^3 \exp \left(-\frac{4892}{T} \right) \omega_o \quad (17.45)$$

where P is the pressure (atm) in the resin, obtained as solution of eq. (17.41), P_{\min} the minimum resin pressure required to prevent void growth by moisture diffusion at

any time during cure, w_o the relative humidity (%) to which the resin in the prepreg is equilibrated prior to processing, and T the temperature (K).

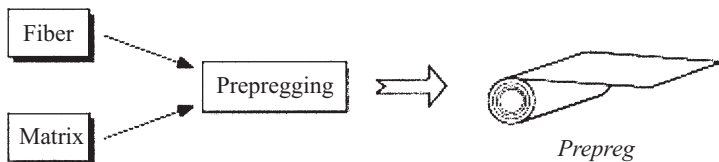
Design of the cure process calls for selecting the optimum temperature and pressure cycles so as to minimize the fabrication time and simultaneously minimize the void content and processing-induced stresses. Optimization of cure cycles utilizing the physical models has been reported by Pillai et al. (1994), Rai and Pitchumani (1997a,b), Diwekar and Pitchumani (1993), and Pitchumani and Diwekar (1994).

17.7.3 Processing of Thermoplastic-Matrix Composites

Unlike thermosetting resins, thermoplastic melts have significantly higher viscosity, which renders fabrication of quality composites via impregnation of a net-shaped fiber structure as a single step impractical. Continuous fiber-reinforced thermoplastic composites are commonly fabricated in two stages, as shown schematically in Fig. 17.22. In the first stage, called *prepregging*, thin reinforcement layers are impregnated with the thermoplastic to form *prepregs* (short for *preimpregnated reinforcements*). Because the reinforcement layers in prepregs are usually about 150 to 200 μm in thickness, a high degree of impregnation can be achieved under controlled conditions. Thermoplastic prepregs are commercially available in a variety of widths, ranging from small-width ribbons or tows to wider tapes and sheets, and have a low void content with a fairly uniform fiber distribution. Processes for the fabrication of prepregs are outside the scope of this chapter (discussed in detail in Pitchumani, 2002).

The focus of this section is on the second stage, referred to as *consolidation*, in which the prepregs are stacked to the desired shape and thickness and fusion-bonded and solidified to obtain the final composite product. Consolidation of prepreg layers is achieved by a number of processes, including prepreg layup with autoclave

Stage 1: Prepregging



Stage 2: Consolidation

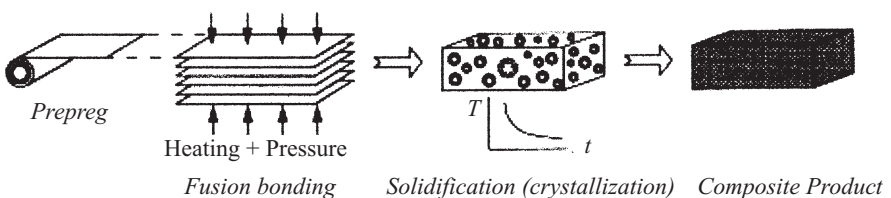


Figure 17.22 Two main steps in thermoplastic composite processing.

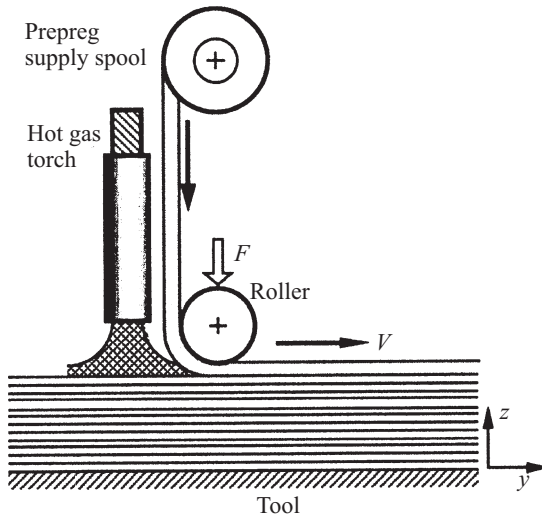


Figure 17.23 Tow placement/tape laying process with in situ consolidation.

consolidation, and pultrusion, which are similar to processes described in the context of thermosetting matrix composites processing, with the notable difference that there is usually a cooling step to solidify the consolidated composite. Thermoplastic tape laying and automated tow placement, illustrated in Fig. 17.23, are processes based on incrementally laying down and continuously consolidating prepreg layers to build the composite product. The nip point formed by the incoming tow and the substrate layer at the entry to the roller region is heated by an appropriate means (such as the hot-gas torch shown in Fig. 17.23). The mechanisms leading to consolidation and bonding take place under the roller, and the fully consolidated structure emerges ready to form the substrate for new tows added during subsequent passes of the process. The rollers and torches, along with the supply spool, are mounted on a common frame, called the *tow-placement head*, which is translated with a line speed V during the process. Unlike the autoclave process, which involves batch consolidation of tow layers, tow placement and tape-laying processes involve consolidation in situ and offer the potential for rapid fabrication. These processes can be used to produce part geometries with intricate features and are particularly suited for fabrication of large structures such as aircraft wing skins and the fuselage (Lamontia et al., 1992, 1995). Tape laying and tow placement differ principally in the size of the prepreps used; while wider tapes are used in tape laying, the prepreg tows used in tow placement are smaller (on the order of about 0.25 in. wide). In this process, a thermoplastic impregnated tow is passed under a lay-down roller onto a substrate formed of previously deposited and consolidated tows on a cylindrical or flat tool.

Fabrication of composites from prepreps using the aforementioned processes is based on the principle of *fusion bonding*, which fundamentally consists of application of heat and pressure at the interface of two layers of thermoplastic prepreps in contact,

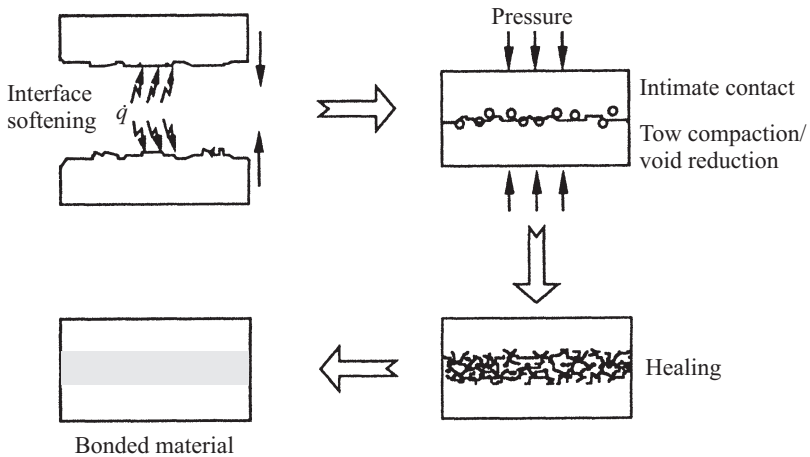


Figure 17.24 Mechanisms involved in the fusion bonding process.

and subsequently, cooling down of the interface to obtain a bonded product. The mechanisms involved in fusion bonding of two thermoplastic surfaces are illustrated schematically in Fig. 17.24. The applied high temperatures cause the interface to soften, and the simultaneous application of pressure serves to flatten the surface asperities and establish an area contact at the interface, referred to as the *intimate contact* process. Further, the elevated temperatures cause an interdiffusion of polymer molecules, termed *autohesion* or *healing*, across the interfacial areas in intimate contact, resulting in the development of bond strength in the laminate. Polymer *degradation* refers to the cumulative effect of exposure of the polymer matrix to high temperatures during the process. The cooling down of the bonded layers causes *solidification* of the molten thermoplastic matrix, which in the case of semicrystalline thermoplastics, influences the crystalline morphology of the polymer matrix in the composite product.

The dominant transport mechanisms involved in the process and their relationship to the pressure and temperature cycles applied are shown in Fig. 17.25. As the material is heated, when its temperature reaches a certain value known as the *glass transition temperature* T_g , the crystal structure of semicrystalline thermoplastics begins to break, and material softening takes place. At temperatures exceeding T_g , the crystalline structure disintegrates progressively until the material melting point T_{mp} is reached, whereupon all crystallinity is lost and the polymer is fully molten. For amorphous thermoplastics, owing to the absence of any significant crystalline structure, the glass transition temperature and the melting point are nearly identical. As seen in Fig. 17.25, the material temperature exceeding the glass transition temperature is a prerequisite for most of the mechanisms of fusion bonding, while *heat transfer* and *polymer degradation* occur throughout the process. *Healing* takes place as long as the temperature is above the melting point, and *polymer crystallization* accompanying solidification occurs when the material is cooled down from the melting point

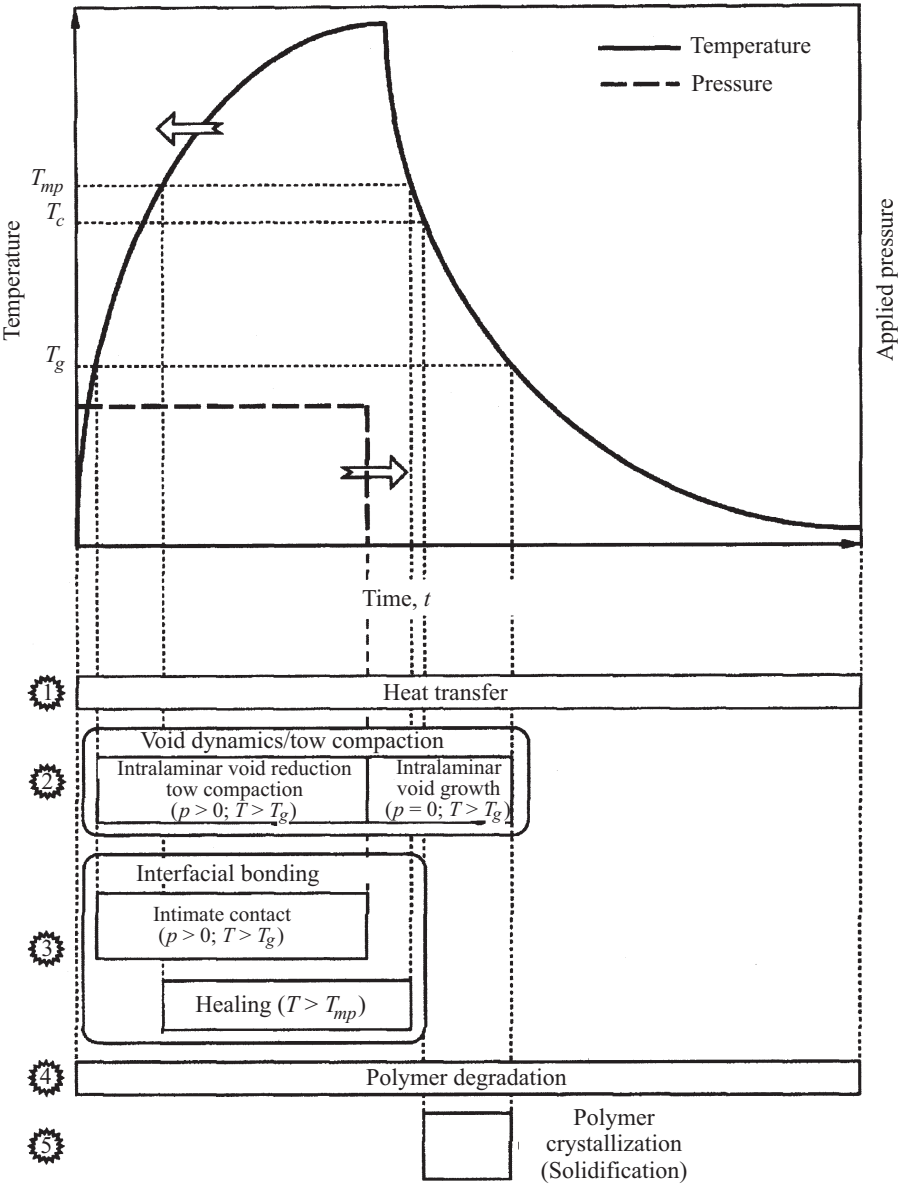


Figure 17.25 Dominant mechanisms during thermoplastic composites processing and their relationship to the temperature and pressure cycles.

past the crystallization temperature (T_c) to the glass transition point. *Intimate contact*, *intralaminar void reduction* (i.e., reduction of voids present within prepregs), and *tow compaction* processes prevail during the application of pressure, whereas *intralaminar void growth* occurs in the absence of applied pressure and while the temperature is greater than the glass transition point. The mechanisms are discussed in detail next by considering the tape-laying and tow-placement processes.

Heat Transfer Heat transfer during thermoplastic composites processing has been studied extensively by many investigators [see Pitchumani (2002) for a detailed list] in the context of autoclave, filament winding, tape/tow placement, and pultrusion processes. The goal of heat transfer analysis is to predict the transient temperature field within the tow layers, which is utilized in the analysis of the other mechanisms involved in the process. The thermal model formulation consists of the energy equation in an appropriate coordinate system with a source term corresponding to the heat of crystallization. The material domain modeled is usually two-dimensional along the fiber length (the y direction) and through the thickness of the tow layers (the z direction). Considering a tape laying or tow-placement process for rectangular product geometries, the governing equations for the transient temperature field in the composite may be written as follows:

$$\begin{aligned} \frac{\partial}{\partial t}(\rho c T) + \frac{\partial}{\partial y}(\rho c V T) &= \frac{\partial}{\partial y} \left(k_y \frac{\partial T}{\partial y} \right) + \frac{\partial}{\partial z} \left(k_z \frac{\partial T}{\partial z} \right) \\ &+ \rho_m (1 - v_f) \Delta H_c \frac{d\hat{c}}{dt} \end{aligned} \quad (17.46)$$

where ρ and c are the density and specific heat of the composite medium, T the temperature, t the time, V refers to the tow velocity in the direction of travel, and v_f refers to the fiber volume fraction in the composite. The anisotropic conductivities of the composite medium, k_y and k_z , are evaluated as the conductivities of an equivalent homogeneous medium. The longitudinal conductivity in the fiber direction (k_y) is determined using the *rule of mixtures*, which is simply a volume average of the fiber and the matrix conductivities, while the transverse conductivity (k_z) is obtained by any of a number of analytical models available [see Hashin (1983), Han and Cosner (1981), and Pitchumani (1999) and references therein].

The last term in eq. (17.46) denotes the source/sink effects due to the crystallization, in which ΔH_c is the heat of crystallization, ρ_m the matrix density, and $d\hat{c}/dt$ the crystallization rate. Generally, the magnitude of the crystallization source term is very small in comparison to the other terms in the energy equation, during the heating process, and it has been customary to neglect the source term in the heat transfer analysis of the process during the heating stage. Crystallization, however, plays a significant role in the cooling-down step, which is discussed later in the section on solidification. The governing equations are subject to initial conditions on the temperature and appropriate boundary conditions, specific to the process and the product geometry under consideration. For example, in the tape-laying or tow-placement processes (Pitchumani et al., 1996), the bottom surface of the prepreg layers in contact

with a tool surface is subject to a prescribed temperature either with perfect contact or with a finite contact resistance. The top surface condition is, in general, a combination of convection to the ambient, exposure to the heat source, and contact with the roller or tool/die surfaces. The heat transfer coefficients and contact resistance values used in the problem formulation are generally determined from experiments, or assumed empirically. The equations are solved numerically using a finite difference or finite element method.

Void Dynamics The application of a pressure cycle to a prepreg tow heated to above its glass transition temperature causes deformation, referred to as *tow compaction*, due to flow of the softened material, whereby the tow thickness decreases accompanied by a corresponding increase in the width. During the process, owing to the high viscosity of thermoplastics, the fibers in the prepregs move along with the thermoplastic resin rather than relative to the resin (Pitchumani et al., 1996; Ranganathan et al., 1995). Therefore, the process may best be described as a squeeze flow instead of a Darcy flow. The fiber–resin–voids mixture is modeled as an equivalent homogeneous fluid with the rheological properties of the continuum dependent on the temperature, the fiber volume fraction, and the void content.

The compaction process is accompanied by void reduction, and the regions outside the compaction zone subject to high temperature are areas of void growth. The void reduction and void growth mechanisms are collectively referred to in this discussion as *void dynamics*. Several mechanisms contribute to void dynamics, including void migration, void compression and expansion, void coalescence, gas diffusion from the void to the melt, and void bubbling (Ranganathan et al., 1995). The dominant consolidation-related void dynamics mechanisms in thermoplastics processing are those of void migration along with resin and void compression due to the effects of cooling, and compaction under the applied pressure. The diffusion of gases across the void–tow melt interface may be assumed to be negligible in the analysis (Pitchumani et al., 1996; Ranganathan et al., 1995), owing to the poor solubility of the gases in the thermoplastic melt. The effect of void migration is accounted for in a *macroscopic* flow model, while the void compression effects are considered in a *microscopic* void dynamics model. These two models are coupled and necessitate a simultaneous solution for the void fraction in the composite. The *macroscopic* flow model further yields the pressure field in the consolidation region, which governs the intimate contact process discussed in a later subsection.

Pressure Field in the Consolidation Region (Macroscopic Model) Pitchumani et al. (1996) and Ranganathan et al. (1995) presented models for tow compaction for consolidation under a roller as encountered in tow/tape placement, and filament winding processes. Figure 17.26 shows an enlarged view of the modeling domain, which is the region under the compaction roller. A tow of a given height h_i and width w_i enters the region under the roller with a specified line speed V , and in the compaction process, its height reduces to h_f while its width increases to w_f . Since the tow dimension in the y direction is much larger than the x and z dimensions, flow in the y direction may be neglected. Further, owing to the high viscosity of the

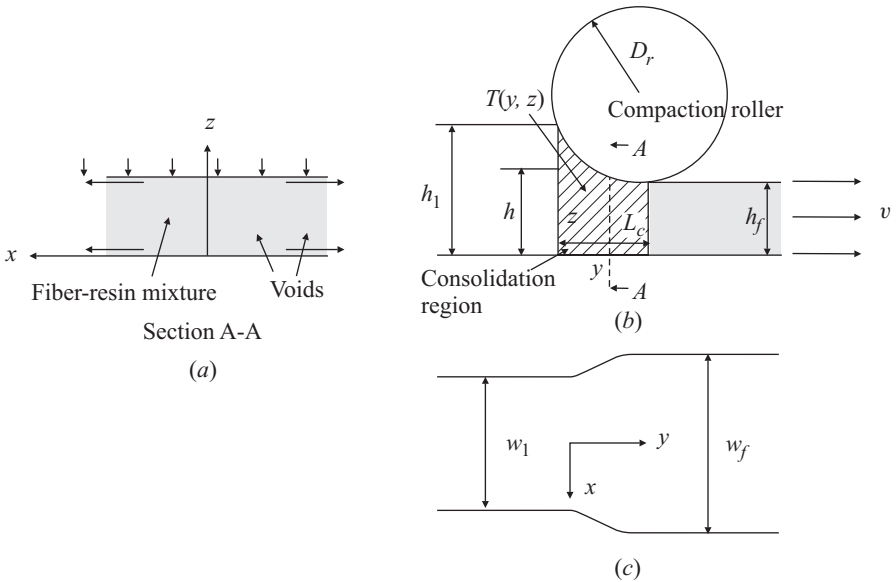


Figure 17.26 Region under the consolidation roller illustrating the tow compaction process.

matrix resin, the inertial effects may be neglected and the consolidation process may be treated as a creeping flow problem.

The fluid motion under the compaction roller is governed by the continuity and momentum equations in Cartesian coordinates, which may be simplified by utilizing the fact that the tow thicknesses (typically about 0.006 in.) are small relative to the width and length. Further, because the quantity of interest in the consolidation region is the pressure field under the rollers and not the actual velocity profiles, the governing equations may be cast in an integral form, as described in Pitchumani et al. (1996). The resulting integral equation is given by eq. (17.47), which constitutes the *macroscopic* governing equation for determining the pressure distribution under the rollers.

$$\begin{aligned}
 h \frac{\partial \rho^*}{\partial \tau} + \rho^* \frac{dh}{d\tau} + \frac{\partial}{\partial x} \left\{ \rho^* \int_0^h \left[v_x(0) + \frac{dp}{dx} \int_0^z \frac{\xi}{\mu} d\xi \right. \right. \\
 \left. \left. + C_1(x) \int_0^z \frac{1}{\mu} d\xi \right] dz \right\} = 0
 \end{aligned}
 \quad (17.47)$$

where the process is assumed to be at steady state, ξ is a dummy variable of integration, $C_1(x)$ is a constant of integration, ρ^* is the density of the fiber-resin-voids mixture scaled with respect to the density of the mixture in the absence of voids, and τ is the Lagrangian time, which is related to the line speed V and the location under the roller (measured from the entrance to the roller region) y , as $\tau = y/V$. The term h

is the instantaneous thickness of the tow under the compaction roller, which is related to the under-roller distance y , based on geometric considerations (Pitchumani et al., 1996), and $v_x(0)$ is the width-wise velocity component at the tow–substrate interface ($z = 0$ in Fig. 17.26).

The boundary conditions on the pressure p correspond to the tow being unconstrained along its width, which implies that $p(x = \pm w/2) = p_{\text{atm}}$, the atmospheric pressure. Furthermore, the unknowns $C_1(x)$ and $v_x(0)$, which result from integration of the continuity equation across the instantaneous tow thickness, are determined using the no-slip condition at the tow–substrate interface and a partial slip condition at the tow–roller interface (Pitchumani et al., 1996).

Void Compression (Microscopic Model) The time derivative of the dimensionless density, $\partial \rho^* / \partial \tau$, appearing in eq. (17.47) is evaluated from a *microscopic* model which accounts for void compression (one of the void reduction mechanisms) during the consolidation process. A typical void at any location may be approximated by a sphere of radius R and is assumed to be surrounded by a concentric spherical resin shell of outer radius S . The ratio of R and S is determined by the void fraction at the location under consideration. Void growth or collapse is governed by a balance between the pressure inside and outside the void and the surface tension σ and resin viscosity μ . Using conservation of the incompressible resin mass, and the ideal gas law for the gas within the void, the *microscopic* void dynamics equation may be written as (Pitchumani et al., 1996)

$$4\mu \left(\frac{R^{*3}}{S_o^{*3} + R^{*3} - 1} - 1 \right) \frac{dR^*}{d\tau} + \left(\frac{p_{go}}{R^{*3}} \frac{T}{T_o} - p_f \right) \frac{R^*}{\mu} - \frac{2\sigma}{\mu R_o} = 0 \quad (17.48)$$

where the bubble and outer shell radii are scaled with respect to the initial radius of the void, R_o , which is determined based on the void fraction in the tow at the entrance to the consolidation roller. In eq. (17.48) p_g and p_{go} are the instantaneous and initial pressures inside the voids, respectively, and the fluid pressure surrounding the void is labeled p_f .

Further, for the concentric spherical shell description, the rate of change of ρ^* with respect to time can be expressed in terms of the rate of change of the nondimensional radius of void as (Ranganathan et al., 1995)

$$\frac{\partial \rho^*}{\partial \tau} = \frac{-3R^{*2} (S_o^{*3} - 1)}{(S_o^{*3} - 1 + R^{*3})^2} \frac{dR^*}{d\tau} \quad (17.49)$$

For a set of given initial conditions on the void radii, density, pressure, and temperature, the rate of change of the nondimensional density with respect to time may be obtained using eqs. (17.48) and (17.49). This expression may be used in eq. (17.47) to compute the pressure distribution in the consolidation region. Equation (7.14) can then be used to compute the change in radius of the voids and update the void radius at various locations in the domain. Similarly, eq. (17.49) may be integrated numerically to obtain the local densities in the tow as a function of x and τ .

Void Growth (Microscopic Model) In the regions outside the consolidation rollers, the tow matrix melt is exposed to the ambient atmospheric pressure (i.e., $p_f = p_{\text{atm}}$). The reduced fluid pressure outside the voids, combined with the high void pressures (resulting from the high temperatures under the torches) causes the voids to grow in size. Furthermore, because the tow surfaces are unconstrained and the matrix melt is assumed incompressible, the increase in void size leads to an increase in tow dimensions. The goal of the void growth analysis is therefore that of determining the void fraction and tow thickness as a function of the axial location along the process (y direction in Fig. 17.26). Because the fluid pressure is known (ambient), the *macroscopic* model equations need not be solved in the void growth analysis. The change in the void dimensions is given by the *microscopic* model, eq. (17.48), with p_f replaced by p_{atm} , and the corresponding density change is obtained from eq. (17.49). The volume change in the tow due to void growth will, in general, manifest itself in a dimensional change in the tow width and thickness. However, owing to bonding of the contacted areas at the tow–substrate interface, the tow is assumed to be constrained along its width. The void growth therefore directly translates to a thickness change in the tow.

The relationship between tow thickness and the void fraction is obtained by noting that the volume of the incompressible matrix melt is constant in the tow during the process. The instantaneous tow thickness h is therefore related to the instantaneous width-averaged void fraction v as follows:

$$h(1 - v) = \text{constant} \quad (17.50a)$$

where

$$v = \frac{R^{*3}}{S_o^{*3} + R^{*3} - 1} \quad (17.50b)$$

Interlaminar Bonding Interfacial bonding and development of bond strength during the process are attributed to the mechanisms of intimate contact and healing at the tow–substrate interface. Theoretical models for the two mechanisms are now reviewed briefly and are followed by a discussion on the coupling of the two mechanisms toward evaluation of the bond strength in the composite.

Intimate Contact An intimate contact process refers to the flattening of the softened surface asperities as two thermoplastic prepreg plies are brought in contact. The mechanism of intimate contact is strongly influenced by the pressure in the consolidation region, the temperature field at the tow–substrate interface, the time for which the pressure is nonzero and the temperature is greater than the glass transition point, material viscosity, and the geometric parameters of the relative surface asperity profiles.

The modeling of the intimate contact process focuses on predicting the evolution of the extent of interfacial area contact with time. The interfacial area contact is usually expressed in terms of a nondimensional *degree of intimate contact*, D_{ic} , which is

defined as the ratio of the area in contact to the planar area of the thermoplastic tape. Thus, a value of $D_{ic} = 1$ denotes complete intimate contact. A model for intimate contact development was first proposed by Dara and Loos (1985), who considered the thermoplastic surfaces to be made of a statistical distribution of rectangular elements of varying widths and heights. Lee and Springer (1987) followed the model of Dara and Loos with a simplification of the geometry, taking the rectangular elements to be of the *same size* and distributed periodically. During the intimate contact process, the rectangular elements flatten under the applied pressure, resulting in a decrease in the element height (a) and a simultaneous increase in its width (b). The flattening of the rectangular elements was described as a squeeze flow into the troughs of the periodic distribution. Mantell and Springer (1992) generalized the model for time-varying pressure and viscosity during the process and obtained an expression for the degree of intimate contact:

$$D_{ic}(\tau_{ic}) = \frac{1}{w^*} \left[1 + a^* \int_0^{\tau_{ic}} \frac{p_{app}}{\mu} d\tau \right]^{1/5} \quad (17.51)$$

$$w^* = 1 + \frac{w_o}{b_o} \quad a^* = 5w^* \left(\frac{a_o}{b_o} \right)^2$$

Equation (17.51) assumes that the fiber-matrix material behaves as a Newtonian fluid in laminar flow under an applied pressure, p_{app} . The other terms appearing in eq. (17.51) are as follows: μ is the temperature-dependent fiber-matrix viscosity, τ_{ic} the time available for intimate contact, w the instantaneous width of the trough in the periodic asperity distribution, and the subscripts 0 refer to the initial dimensions of the asperity elements (prior to the beginning of the intimate contact process).

Lee and Springer (1987) and Mantell and Springer (1992) suggested that the second term in the brackets in eq. (17.51) is often large compared to unity; equivalently, the initial fraction of the area in contact (at the start of the process) is negligible. Retaining only the dominant term, the degree of intimate contact may be approximated as

$$D_{ic}(\tau_{ic}) = R_c \left(\int_0^{\tau_{ic}} \frac{p_{app}}{\mu} d\tau \right)^{1/5} \quad R_c = \frac{a^{*1/5}}{w^*} \quad (17.52)$$

The factor R_c incorporates the geometric parameters of the asperity representation and is determined by fitting the model to experimental data. For AS4 carbon fibers reinforcing poly-ether-ether-ketone (PEEK) thermoplastic prepregs, the value of R_c was reported to be 0.40 by Lee and Springer (1987) and 0.29 by Mantell and Springer (1992). As an approximation, the applied pressure may be taken to be the average pressure estimated by distributing the applied consolidation force uniformly over the planar area of the tow. However, the consolidation pressure field obtained from the void dynamics model serves as a more accurate representation of the driving force for intimate contact and has been used in the process simulations (Pitchumani et al., 1994, 1996, 1997). The intimate contact model of eqs. (17.51) and (17.52) suggests

that the degree of intimate contact increases as the one-fifth power of time, increases with the applied pressure, and decreases with increasing material viscosity (which, for a given material, corresponds to lower processing temperatures).

Improved models that eliminate the ambiguity associated with the model parameter values have been developed by Yang (2002) and Yang and Pitchumani (1998, 2001a,b, 2002). Their model utilizes a fractal geometry-based description of the intrinsic multiscale features of tow surfaces, in which the parameters can be determined uniquely from profilometric measurements on a tow surface rather than an *a posteriori* fitting of the model to experimental data. The interested reader is referred for details to the publications cited.

Polymer Healing Healing is a temperature-dependent phenomenon that is governed by the interdiffusion of polymer chains across the interfacial areas in intimate contact. Polymer interdiffusion under isothermal conditions is described by the reptation theory of de Gennes (1971). According to this theory, the strength buildup at the interface with time t is governed by

$$D_h = \frac{\sigma}{\sigma_\infty} = \left(\frac{t}{t_r} \right)^{1/4} \quad (17.53)$$

where D_h is a degree of healing defined as the ratio of the instantaneous interfacial strength σ to the ultimate strength σ_∞ such that a value of $D_h = 1$ corresponds to complete healing. Further, t_r is a temperature-dependent characteristic time which denotes the time at which full interfacial strength is realized.

The reptation theory, originally developed for isothermal healing, was extended by Bastien and Gillespie (1991) and Agarwal (1991) to incorporate nonisothermal effects encountered in composites processing techniques. The approach was that of dividing an arbitrary nonisothermal history into discrete time intervals, $\Delta\tau (= \tau_j - \tau_{j-1})$. Within each time interval, the temperature T_j is assumed constant and equal to the average of the temperatures at times τ_j and τ_{j-1} . In each of these isothermal steps, the reptation theory of de Gennes, eq. (17.53), was applied. The degree of healing, based on strength considerations, for a nonisothermal process was obtained as a summation of the incremental strength buildup in each of the discrete time intervals as

$$D_h(\tau_h) = \sum_{j=1}^{\tau_h/\Delta\tau} \frac{\tau_j^{1/4} - \tau_{j-1}^{1/4}}{[t_r^* a_T(T_j)]^{1/4}} \quad a_T(T) = \exp \left[\frac{E_a}{R} \left(\frac{1}{T} - \frac{1}{T_{\text{ref}}} \right) \right] \quad (17.54)$$

where a shift factor a_T is applied to the reptation time t_r^* at a reference temperature T_{ref} . In eq. (17.54), E_a is the activation energy of diffusion of the polymer, R the universal gas constant, and τ_h the time for the healing process. For PEEK, the following values of the constants were given by Agarwal (1991): $E_a = 57.3$ kJ/mol, $t_r^* = 0.11$ s, at T_{ref} of 400°C.

It must be noted that in the foregoing model, the expression for the incremental strength buildup in any isothermal time interval τ_j to τ_{j-1} —the terms immediately following the summation sign in eq. (17.54)—is strictly appropriate if the process

had been isothermal at temperature T_j from the beginning (i.e., over $0 \leq \tau \leq \tau_j$). However, the fact that this is not generally valid for a nonisothermal history constitutes the principal limitation of the model. A more rigorous description of the total degree of healing under nonisothermal conditions is provided by Yang (2002) and Yang and Pitchumani (2002)

$$D_h(J_h) = \left[\int_0^{\tau_h} \frac{dt}{t_r(T)} \right]^{1/4} \quad (17.55)$$

where the repetition time t_r and its time derivative are temperature-dependent functions.

Coupling between Healing and Intimate Contact The net bond strength developed at the interface after a time τ_h is a result of the coupled effects of the mechanisms of healing and intimate contact. It is given by an area average of the bond strengths (healing) of each of the incremental areas that come into intimate contact throughout the duration τ_{ic} of the applied pressure. In a dimensionless form, the net degree of bonding D_b may be written as (Butler et al., 1998, Yang and Pitchumani, 2003)

$$D_b(\tau_h) = D_{ic}(0)D_h(\tau_h) + \int_0^{\tau_{ic}} D_h(\tau_h - \tau) \frac{dD_{ic}(\tau)}{d\tau} d\tau \quad (17.56)$$

where D_b is the interfacial bond strength scaled with respect to the maximum realizable bond strength in the composite, and D_{ic} and D_h are the intimate contact and healing functions given in eqs. (17.51) [or (17.52)] and (17.54) (or 17.55), respectively. The first term on the right-hand side of eq. (17.56) corresponds to the strength buildup at the areas initially in intimate contact.

During processing, if the time available for intimate contact to develop τ_{ic} is small in comparison to the time available for healing to occur τ_h , $D_h(\tau_h - \tau)$ with $0 \leq \tau \leq \tau_{ic}$ may be approximated as $D_h(\tau_h)$. By virtue of this simplification, eq. (17.56) may be simplified as

$$D_b(\tau_h) \approx D_h(\tau_h)D_{ic}(\tau_{ic}) \quad (17.57)$$

Equation (17.57) allows for a simplified, yet reasonably accurate evaluation of the degree of interfacial bonding without resorting to a rigorous numerical computation (Pitchumani et al., 1996, 1997, Steiner et al., 1995, Yang and Pitchumani, 2003).

Polymer Degradation Polymer thermal degradation refers to the property and performance deterioration in the composite due to prolonged exposure of the polymer to high temperatures (Schnabel, 1981). While other chemical mechanisms may additionally contribute to the overall property and performance degradation of the composite, the material weight loss has been the principal measure of degradation modeled in the literature. The goal of degradation modeling is that of developing an appropriate expression for the kinetics relating a degree of degradation to temperature and time. Day et al. (1989) investigated the degradation of PEEK in a nitrogen

atmosphere and explored different models for the degradation rate kinetics. They reported kinetic parameters based on different isothermal analysis methods. Nam and Seferis (1992) developed an empirical model for describing polymer weight loss due to thermal degradation under nonisothermal conditions. The degradation process was treated to comprise two reaction mechanisms, and the kinetics was expressed as an Arrhenius-type rate equation of the form

$$\frac{d\alpha}{d\tau} = A \exp\left(\frac{-E_a}{RT}\right) [y(1 - \alpha) + (1 - y)\alpha(1 - \alpha)] \quad (17.58)$$

where α is the degree of degradation defined based on weight loss, such that it lies in the range $0 \leq \alpha \leq 1$, with $\alpha = 1$ corresponding to approximately 36% weight loss; τ is the time defined previously; E_a is an activation energy for degradation; and A is a preexponential factor. The values of the constants for PEEK were given as $A = 4.959 \times 10^{14} \text{ min}^{-1}$, $E_a = 240.2 \text{ kJ/mol}$, and $y = 0.0215$.

Solidification (Crystallization) The final step in thermoplastic composites fabrication is the cooling down of the fusion bonded structure to obtain the solidified product. As discussed above, the processing inherently involves exposing the materials to high temperatures. Consequently, the material undergoes complex cooling histories and severe temperature gradients during the solidification step. During solidification, semicrystalline polymers develop a partially ordered structure from the disordered melt phase, a process referred to as *crystallization* (Young and Lovell, 1991). Accompanying crystallization is a volumetric shrinkage, which together with the difference in the properties of the fibers and the matrix is a source of processing-induced stress that may lead to defects and dimensional instabilities in finished parts.

The extent of the crystallization process is quantified in terms of a degree of crystallinity, defined as the ratio of the volume of the crystalline phase at any instant during the solidification process to that of the total thermoplastic material. The analysis of the solidification step during thermoplastic composites processing is based on the heat transfer model presented earlier in this section. The last term in eq. (17.46) represents the source term due to crystallization and is a function of the crystallization kinetics. The kinetics of the crystallization process is governed by the cooling rate dT/dt , the instantaneous degree of crystallization \hat{c} , and the instantaneous temperature T , and may be expressed functionally as

$$\frac{dc}{d\tau} = f\left(\frac{dT}{dt}, \hat{c}, T\right) \quad (17.59)$$

Studies on crystallization kinetics are aimed at developing specific expressions for the function f . Two models that have been used in the context of thermoplastic composites processing are presented below.

Lee and Springer (1987) adopted the expression proposed by Ozawa (1971) to analyze the processing of PEEK-based composites. Ozawa's model, as applied by Lee and Springer for the case of PEEK 150P thermoplastic, may be expressed as

$$\frac{d\hat{c}_r}{d\tau} = -(1 - \hat{c}_r) \frac{d\varphi/dt}{(dT/dt)^{n-1}}$$

$$\begin{aligned} \text{For PEEK 150P: } \hat{c}_r &= \frac{H_T}{H_u} \hat{c} = 0.42 - 0.03 \ln \frac{dT}{dt} \quad \varphi = \exp(-0.037T + 11.3) \\ n &= 0.8 \quad H_u = 130 \text{ J/g} \end{aligned} \quad (17.60)$$

where \hat{c}_r is the relative crystallinity and related to the degree of crystallization \hat{c} , in which H_u is the theoretical ultimate heat of crystallization of the polymer and H_T is the total heat of crystallization at the given cooling rate.

Velisaris and Seferis (1986) proposed an Avrami model based on dual crystal nucleation and growth processes occurring in parallel and reported that the model was able to predict isothermal and nonisothermal crystallization processes in the case of neat and carbon fiber-reinforced PEEK samples in a unified manner. The first mechanism, F_{vc1} , is based on preexisting nuclei for crystallization and is dominated by crystal growth kinetics. The second nucleation mechanism, F_{vc2} , reflects additional nucleation followed by crystal growth. The complete expression for the kinetic model is given by eq. (17.61), expressed in an integral form of the functional representation given by eq. (17.59).

$$\frac{\hat{c}}{\hat{c}_\infty} = w F_{vc1} + (1 - w) F_{vc2} \quad (17.61a)$$

where

$$F_{vc1} = 1 - \exp \left\{ -C1_1 \int_0^\tau T \exp \left[\frac{C2_1}{T - T_g + 51.6} - \frac{C3_1}{T(T_{m1} - T)^2} \right] n_1 \tau^{n_1-1} dt \right\} \quad (17.61b)$$

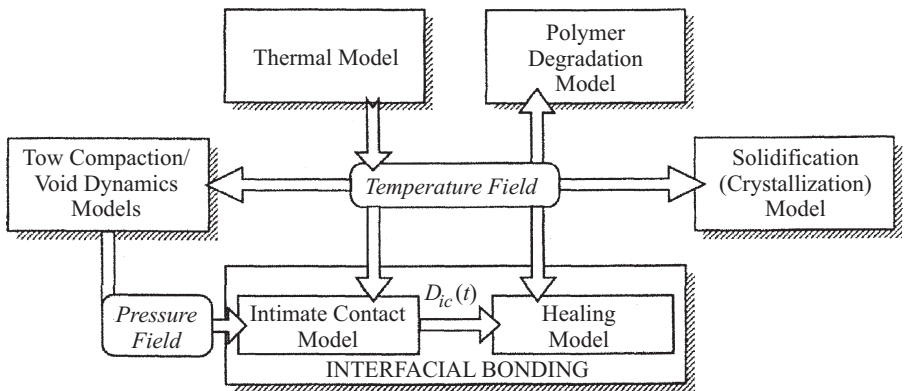
$$F_{vc2} = 1 - \exp \left\{ -C1_2 \int_0^\tau T \exp \left[\frac{C2_2}{T - T_g + 51.6} - \frac{C3_2}{T(T_{m2} - T)^2} \right] n_2 \tau^{n_2-1} dt \right\} \quad (17.61c)$$

The model constants Ci_j in the foregoing equations are determined from crystallization experiments, \hat{c}_∞ is the equilibrium volume fraction crystallinity, and \hat{c} is the crystallinity based on volume fraction. The glass transition temperature is denoted by T_g , T_{m1} and T_{m2} represent the crystallization onset temperatures for the two crystallization mechanisms, and w is a weighting factor ($0 \leq w \leq 1$) for the dual mechanisms and depends on the cooling rate and fiber volume fraction. The model constants are tabulated in Table 17.2. Under normal processing conditions, the first mechanism is reported to dominate over the second (Velisaris and Seferis, 1986; Chapman et al., 1990).

TABLE 17.2 Constants in the Crystallization Kinetics Model of Velisaris and Seferis (1986), Eqs. (17.61)

	Process 1 (Growth)	Process 2 (Nucleation)	Cooling Rate (°C/s)	<i>w</i>	
				Neat PEEK	AS4/PEEK
<i>n</i>	2.50	1.50	0 (isothermal)	0.085	0.05
<i>T_m</i> (K)	593	615	0.032	0.100	
<i>C</i> _{1<i>i</i>} (s ^{-<i>n</i>} K ⁻¹)	2.08 × 10 ¹⁰	2.08 × 10 ¹⁰	0.160	0.700	0.61
<i>C</i> _{2<i>i</i>} (K)	4050	7600	0.320	0.710	0.61
<i>C</i> _{3<i>i</i>} (K ³)	1.80 × 10 ⁷	3.20 × 10 ⁶	0.620	0.720	0.61
<i>C</i> _∞	0.37	0.37	0.930	0.720	0.61
			7.600	0.720	
			45.00	0.740	
			114.0	0.750	

Simulation of a thermoplastic composite processing technique calls for simultaneous solution of the equations governing the various phenomena. In an integrated simulation, the thermal model provides the temperature field in the composite, which is utilized in the tow compaction model to obtain the pressure field in the consolidation region. The pressure and temperature profiles govern void reduction and growth and intimate contact development at the interface between the prepregs being fusion bonded. The temperature field and intimate contact evolution in turn drive the healing process and the bond strength development at the interface. Polymer degradation and crystallization mechanisms are a function of the temperature field in the composite. The interactions among the various physical models in an integrated simulator are shown in Fig. 17.27. Process optimization using the integrated model base is discussed in Pitchumani et al. (1997).

**Figure 17.27** Interactions among the models of physical phenomena governing thermoplastic composite processing.

17.8 THERMAL PROCESS CONTROL FOR MANUFACTURING

In this section we review briefly several thermal control tools for thermal processing of materials, with particular attention to serial, localized heating processes such as welding and cutting. The control objective is to achieve a desirable dynamic temperature distribution by modulation of the supplied heat input. We also briefly review several open- and closed-loop regulation methods for single-input single-output (SISO) and multiple-input multiple-output (MIMO) thermal systems, including linear and nonlinear controllers.

For thermal processes with certain invariant model descriptions of temperature $T = f(Q, T_o, T_s)$, that is, as a function of the heat input Q and the initial T_o and boundary conditions T_s , open-loop control can be based on model inversion. Given a desired temperature specification T_d (usually dictated by the material structure and properties to be obtained), the required heat (see Fig. 17.28) can be determined as $Q = f^{-1}(T_d, T_o, T_s)$. Since open-loop control does not employ sensing and feedback of the output, it cannot reject process disturbances or alterations of the system parameters. However, when disturbances in the initial DT_o or boundary conditions DT_s can be assessed, they can be compensated through feedforward by proper correction DQ of the heat input to restore the desired temperature on the basis of the thermal model (i.e., $Df = 0$).

Closed-loop control uses real-time output sensing h and feedback of the temperature output, which is compared to the desired specification (Fig. 17.29). The resulting error $e = T_d - T$ defines the supplied heat input through the thermal controller g . For such a linear error-based controller with a heat input disturbance Q_d ,

$$\left. \begin{array}{l} T = f(ge + Q_d) \\ e = T_d - hT \end{array} \right\} \Rightarrow T = \frac{fg}{1 + fgh} T_d + \frac{f}{1 + fgh} Q_d \quad (17.62)$$

The sensor calibration and high speed usually dictate that $h = 1$. Therefore, by properly increasing the controller gain g , it is clear that the effect of Q_d on T is diminished (disturbance rejection), while the output T follows the specification T_d ($T \rightarrow T_d$,

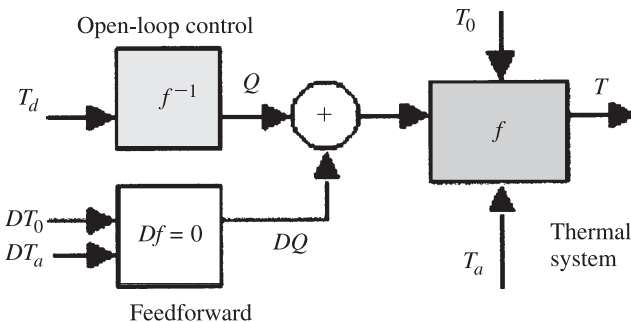


Figure 17.28 Open-loop control with feedforward.

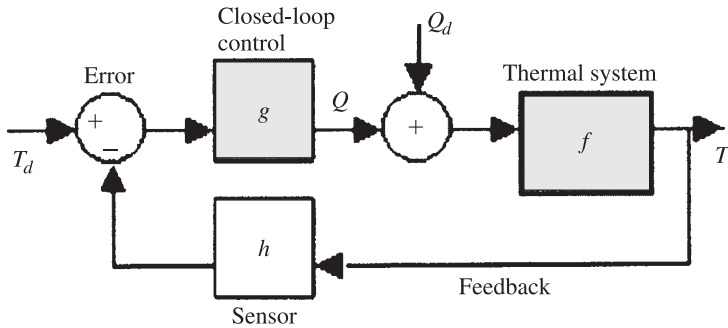


Figure 17.29 Closed-loop thermal control.

command tracking). Stability of the closed loop must be ensured by designing the system poles (denominator roots) with negative real parts. Feedback can also be supplemented by feedforward to further reduce the disturbance effects if necessary.

17.8.1 Control of SISO Thermal Systems

Thermostatic (On-Off) Control This popular type of thermal controller is based on simple one- or two-sided nonlinear elements such as on-off, differential gap, and saturation:

• *On-Off*:

$$N_c(\hat{e}) = \frac{4c}{\pi \hat{e}} \quad (17.63)$$

• *Differential gap*:

$$N_c(\hat{e}) = \frac{4c}{\pi \hat{e}} \sin^{-1} \frac{b}{\hat{e}} \quad (17.64)$$

• *Saturation*:

$$N_c(\hat{e}) = \frac{2c}{\pi b} \left[\sin^{-1} \frac{b}{\hat{e}} + \frac{b}{\hat{e}} \sqrt{1 - \left(\frac{b}{\hat{e}} \right)^2} \right] \quad (17.65)$$

The describing functions N_c of the error amplitude \hat{e} are equivalent to the transfer functions for linear systems but correspond to only the first harmonic for a sinusoidal excitation. In closed-loop operation, thermostatic controllers usually result in a limit cycle (or self-excited oscillation) of the regulated temperature at steady state, which can be determined by setting the closed-loop denominator to zero (Fig. 17.30a):

$$1 + N_c G_p = 0 \quad \Rightarrow \quad |G_p(j\omega)| = |N_c^{-1}(\hat{e})| \quad (17.66)$$

In a polar (Nyquist) plot on the complex plane, the amplitude \hat{e} and frequency ω of the steady-state limit cycle correspond to the stable (outward) intersection of the

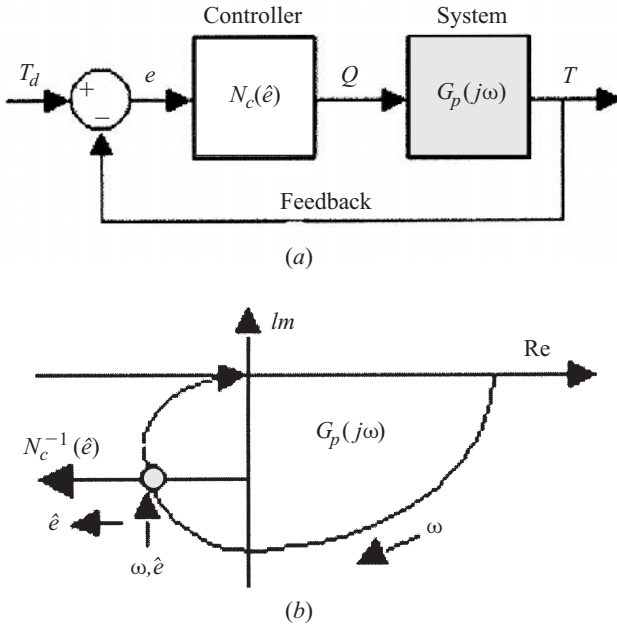


Figure 17.30 (a) Thermostatic control system and (b) determination of the thermostatic control system limit cycle from its Nyquist plot.

process transfer function G_p and the controller inverse describing function N_c^{-1} (Fig. 17.30b).

Proportional–Integral–Derivative (PID) Control This general linear controller can be expressed in the time and Laplace domain as

$$Q = K_p e + K_i \int_0^t e \, dt + K_d \frac{de}{dt} \Rightarrow G_c(s) = \frac{Q(s)}{e(s)} = K_p + \frac{K_i}{s} + K_d s \quad (17.67)$$

where K_p , K_i , and K_d are the proportional, integral, and derivative gains, respectively. Therefore, for a first-order thermal system G_p , the transfer function G_{cl} of the closed-loop system (Fig. 17.29) can be derived as

$$G_p(s) = \frac{T(s)}{Q(s)} = \frac{K}{\tau s + 1} \Rightarrow \quad (17.68)$$

$$G_{cl}(s) = \frac{T(s)}{T_d(s)} = \frac{G_c(s)G_p(s)}{1 + G_c(s)G_p(s)} = \frac{KK_d s^2 + KK_p s + KK_i}{(KK_d + \tau)s^2 + (KK_p + 1)s + KK_i}$$

The PID gains are generally selected to ensure the closed-loop system stability and performance characteristics. Generally, the proportional gain K_p increases speed

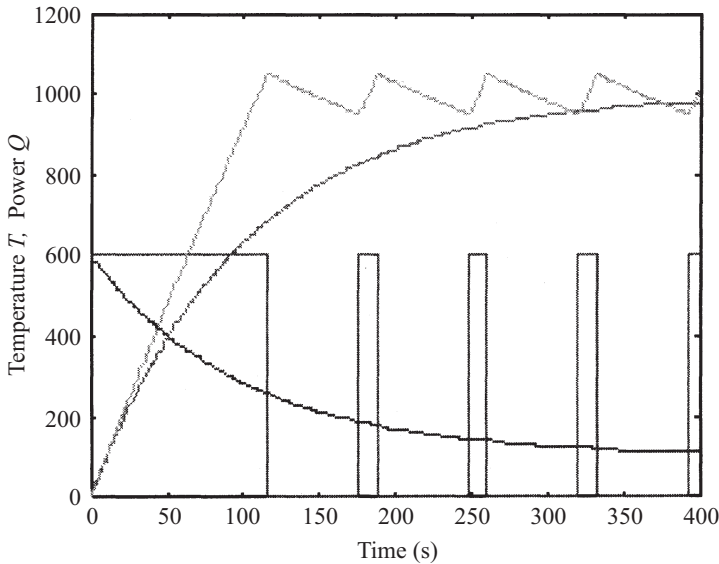


Figure 17.31 Comparison of closed-loop step responses of a first-order thermal system with PI and thermostatic control.

but decreases damping. The integral gain K_i improves the tracking accuracy but decreases damping and system stability. The derivative gain K_d improves the speed and damping, but increases the sensitivity to measurement noise.

For a linear first-order thermal system with gain $K = 10$ K/W and time constant $\tau = 600$ s, Fig. 17.31 compares the closed-loop performance of a PID and a thermostatic controller with the differential gap during a step command to a desired temperature increase $T_d = 1000$ K. The PI controller has the gains $K_p = 0.6$ W/K and $K_i = 0.001$ W/K. The thermostatic controller switches on to $c = 600$ W when $e > b = 50$ K and switches off to zero when $e \leq b = -50$ K. For the same power saturation level, the PID controller gives smoother but slower asymptotic tracking; the thermostatic controller may be tuned to the optimal actuator power level, but its relay operation may accelerate wear.

Software Implementation of SISO Controllers The controllers designed must be converted from the continuous to the discrete time domain to be programmed in software for sampled (computer) control. First, the sampling period \mathcal{T} can be selected by rules of thumb based on the step response of the open-loop thermal system:

$$\frac{d}{3} < \mathcal{T} < \frac{t_s}{3} \quad \text{with} \quad t_s \approx 3\tau \quad \text{and} \quad \tau \approx \frac{L^2}{4\alpha} \quad (17.69)$$

where t_s is the settling time, d the delay, and τ the time constant of the thermal system, which for conduction depends on the characteristic length L and diffusivity α . Next,

the controller Laplace variable s is approximated by the discrete z variable, through a differential approximation such as

$$s \approx \frac{2}{T} \frac{z-1}{z+1} \Rightarrow \frac{Q(s)}{E(s)} = G_c(s) \rightarrow G_c(z) = \frac{Q(z)}{E(z)} \quad (17.70)$$

Finally, the discretized control relation of power $Q(k)$ to the error $e(k)$ for the k th sampling period is converted to the time domain via the delay operator z^{-1} . For example, the PID controller of Fig. 17.31 with a sampling period $T = 100$ s can be programmed as

$$\begin{aligned} G_c(s) &= 0.6 + \frac{0.001}{s} \\ \Rightarrow G_c(z) &= 0.6 + 0.001 \frac{100}{2} \frac{z+1}{z-1} = \frac{0.65 - 0.55z^{-1}}{1 - z^{-1}} = \frac{Q(z)}{E(z)} \quad (17.71) \\ \Rightarrow Q(k) &= Q(k-1) + 0.65e(k) - 0.55e(k-1) \end{aligned}$$

17.8.2 Control of MIMO Thermal Systems

Controller design methods in the Laplace domain similar to those for SISO systems, that is, based on the transfer matrix description, are usually impractical for MIMO thermal processes. Rather, state-space techniques in the time domain are employed, on the basis of linearized thermal models derived from finite-difference or finite-element analyses:

$$\dot{T} = AT + BQ \quad (17.72)$$

where the vector T contains the n temperature states and the vector Q contains the l power inputs. The elements of both T and Q represent deviations from the nominal process conditions T_o, Q_o , respectively, at which the thermal system model is linearized. A is the $n \times n$ state matrix and B the $n \times l$ input matrix.

State Controllers by Pole Placement If real-time measurement and feedback of the full temperature state T is possible, the control scheme of Fig. 17.32 uses the

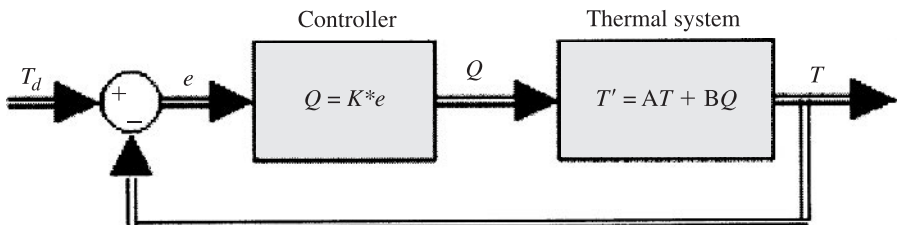


Figure 17.32 Full state feedback control.

error vector $\mathbf{e} = \mathbf{T}_d - \mathbf{T}$ to regulate the state to the desired specification \mathbf{T}_d . The power vector \mathbf{Q} is modulated by the error \mathbf{e} through the $l \times n$ controller matrix \mathbf{K} .

$$\left. \begin{array}{l} \text{System: } \dot{\mathbf{T}} = \mathbf{A}\mathbf{T} + \mathbf{B}\mathbf{Q} \\ \text{Controller: } \mathbf{Q} = \mathbf{K}(\mathbf{T}_d - \mathbf{T}) \end{array} \right\} \Rightarrow \dot{\mathbf{T}} = (\mathbf{A} - \mathbf{B}\mathbf{K})\mathbf{T} + \mathbf{B}\mathbf{K}\mathbf{T}_d \equiv \hat{\mathbf{A}}\mathbf{T} + \hat{\mathbf{B}}\mathbf{T}_d \quad (17.73)$$

where $\hat{\mathbf{A}} = \mathbf{A} - \mathbf{B}\mathbf{K}$ and $\hat{\mathbf{B}} = \mathbf{B}\mathbf{K}$ are the $n \times n$ closed-loop state and input matrices, respectively. If the system controllability matrix \mathbf{P}_c has full rank, that is,

$$\mathbf{P}_c = [\mathbf{B} : \mathbf{A}\mathbf{B} : \mathbf{A}^2\mathbf{B} : \cdots : \mathbf{A}^{n-1}\mathbf{B}] \quad \text{has} \quad \text{rank}(\mathbf{P}_c) = n \quad (17.74)$$

the $l \times n$ gains of the controller matrix \mathbf{K} can be chosen so that the eigenvalues (poles) of the resulting closed-loop state matrix $\hat{\mathbf{A}}$ can be placed at the desired values $\mu_i, i = 1 \cdots n$, as dictated by the stability and performance requirements for the feedback system. For example, Ackermann's formula for the controller design \mathbf{K} yields

$$\mathbf{K} = [0 \ 0 \ 0 \cdots 1] \mathbf{P}_c^{-1} \phi(\mathbf{A}) \quad \text{where} \quad \phi(s) = (s - \mu_1)(s - \mu_2) \cdots (s - \mu_n) \quad (17.75)$$

with $\phi(s)$ the characteristic polynomial of the desired closed-loop system matrix $\phi(s) = |s\mathbf{I} - \hat{\mathbf{A}}|$.

State Observers by Pole Placement If the full state vector \mathbf{T} is not measurable, but only m thermal outputs in vector \mathbf{Y} can be sensed directly in real time, the previous control scheme can employ feedback of the state estimates $\hat{\mathbf{T}}$ from a full-state observer. The state and output equations of the system are

$$\dot{\mathbf{T}} = \mathbf{A}\mathbf{T} + \mathbf{B}\mathbf{Q} \quad \mathbf{Y} = \mathbf{C}\mathbf{T} + \mathbf{D}\mathbf{Q} \quad (17.76)$$

where \mathbf{C} is the $m \times n$ output matrix and \mathbf{D} the $m \times l$ direct matrix. The observer is a system model implemented computationally in parallel to the actual thermal process, that is, receiving the same input values \mathbf{Q} , and compensating for uncertainties in the system matrices ($\mathbf{A}, \mathbf{B}, \mathbf{C}, \mathbf{D}$) by comparison of its outputs $\hat{\mathbf{Y}}$ to the actual system outputs \mathbf{Y} , as in Fig. 17.33.

$$\dot{\hat{\mathbf{T}}} = \hat{\mathbf{A}}\hat{\mathbf{T}} + \mathbf{B}\mathbf{Q} + \mathbf{L}\mathbf{C}(\mathbf{T} - \hat{\mathbf{T}}) \quad \hat{\mathbf{Y}} = \mathbf{C}\hat{\mathbf{T}} + \mathbf{D}\mathbf{Q} \quad (17.77)$$

where \mathbf{L} is the $n \times m$ observer matrix. The state equation of the observer contains a correction term of the state deviation $\boldsymbol{\varepsilon} = \mathbf{T} - \hat{\mathbf{T}}$.

$$\mathbf{L}(\mathbf{Y} - \hat{\mathbf{Y}}) = \mathbf{L}\mathbf{C}(\mathbf{T} - \hat{\mathbf{T}}) = \mathbf{L}\mathbf{C}\boldsymbol{\varepsilon} \quad (17.78)$$

By combining the previous state equations for the system and the observer,

$$\dot{\boldsymbol{\varepsilon}} = (\mathbf{A} - \mathbf{L}\mathbf{C})\boldsymbol{\varepsilon} \quad (17.79)$$

and the state deviation can vanish if the matrix $\mathbf{A} - \mathbf{L}\mathbf{C}$ has eigenvalues with negative real parts. If the system observability matrix \mathbf{P}_o has full rank, that is,

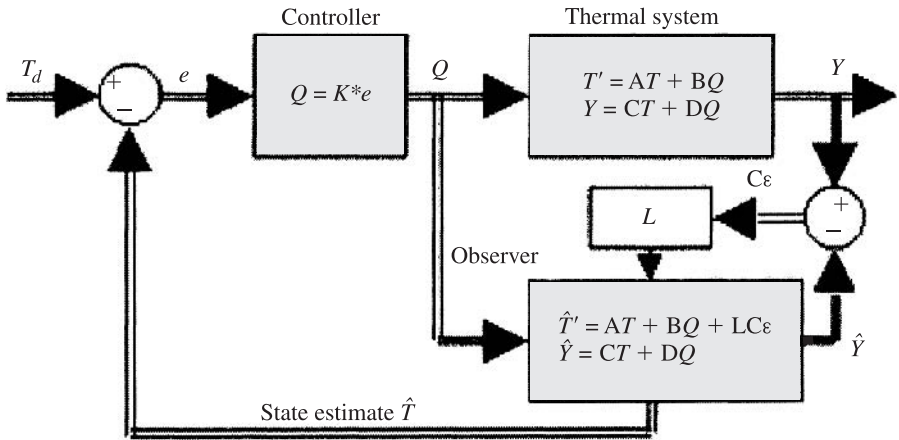


Figure 17.33 MIMO feedback control with state observer via pole placement.

$$\mathbf{P}_o = [\mathbf{C} : \mathbf{CA} : \mathbf{CA}^2 : \dots : \mathbf{CA}^{n-1}]^T \quad \text{has} \quad \text{rank}(\mathbf{P}_o) = n \quad (17.80)$$

then the $n \times m$ gains of the observer matrix \mathbf{L} can be chosen so that the eigenvalues (poles) of the resulting matrix $\mathbf{A} - \mathbf{LC}$ can be placed at the desired values λ_i , $i = 1 \dots n$. These eigenvalues λ_i are usually selected with a real part 5 to 10 times larger (more negative) than the specified poles μ_i of the closed-loop system, to ensure faster convergence of the estimates $\hat{\mathbf{T}}$ to the actual states \mathbf{T} . For example, Ackermann's formula for the observer design \mathbf{L} yields

$$\mathbf{L} = \boldsymbol{\varphi}(\mathbf{A})\mathbf{P}_o^{-1}[0 \ 0 \ 0 \ \dots \ 1]^T \quad \text{where} \quad \boldsymbol{\varphi}(s) = (s - \lambda_1)(s - \lambda_2) \dots (s - \lambda_n) \quad (17.81)$$

with $\phi(s)$ the characteristic polynomial of the desired matrix $\phi(s) = |s\mathbf{I} - (\mathbf{A} - \mathbf{LC})|$. The combined full state feedback and observation arrangement of Fig. 17.32 can be described by the state equations

$$\begin{bmatrix} \dot{\hat{\mathbf{T}}} \\ \dot{\boldsymbol{\varepsilon}} \end{bmatrix} = \begin{bmatrix} \mathbf{A} - \mathbf{BK} & \mathbf{BK} \\ \mathbf{0} & \mathbf{A} - \mathbf{LC} \end{bmatrix} \begin{bmatrix} \mathbf{T} \\ \boldsymbol{\varepsilon} \end{bmatrix} + \begin{bmatrix} \mathbf{BK} \\ \mathbf{0} \end{bmatrix} \mathbf{T}_d \quad (17.82)$$

where the eigenvalues of this augmented system are those of $\mathbf{A} - \mathbf{BK}(\mu_i)$ and $\mathbf{A} - \mathbf{LC}(\lambda_i)$. Thus, according to the separation principle, the controller \mathbf{K} and observer \mathbf{L} can be designed independently of each other. Alternatively, when partial measurements of the state \mathbf{T} can be made, a minimal (Luenberger) observer can be designed to estimate the unmeasurable states only.

17.8.3 Optimal Formulation: Linear Quadratic Gaussian

Instead of the pole placement in Section 17.8.2, an alternative design methodology for both the linear controller \mathbf{K} and observer \mathbf{L} for a thermal system in Fig. 17.33

can be based on optimization of a quadratic performance index during closed-loop system operation.

Optimal Control: Linear Quadratic Regulator (LQR) The design of an optimal controller (LQR) for the feedback system in Fig. 17.32 is based on minimization of a performance index J , penalizing the state errors $\mathbf{e} = \mathbf{T}_d - \mathbf{T}$ and the input values \mathbf{Q} over the full time horizon of operation:

$$J = \int_0^\infty (\mathbf{e}^T \mathbf{Q} \mathbf{e} + \mathbf{Q}^T \mathbf{R} \mathbf{Q}) dt \quad (17.83)$$

where \mathbf{Q} is a $x \times n$ positive-definite real square matrix ($\mathbf{Q} = \mathbf{S}^T \mathbf{S}$) containing cost factors for the state error squares and/or products, and \mathbf{R} is a $l \times l$ positive-definite real square matrix with similar penalties for the heat input squares and products. The closed-loop system, referenced by the matrix $\mathbf{A} - \mathbf{BK}$, is stabilizable if the matrix

$$\mathbf{P}_s = \left[\mathbf{S} : \mathbf{SA} : \mathbf{SA}^2 : \dots : \mathbf{SA}^{n-1} \right] \quad \text{has} \quad \text{rank}(\mathbf{P}_s) = n \quad (17.84)$$

Then a $n \times n$ matrix \mathbf{P} can be determined by solving the algebraic Riccati equation:

$$\mathbf{A}^T \mathbf{P} + \mathbf{PA} - \mathbf{PBR}^{-1} \mathbf{B}^T \mathbf{P} + \mathbf{Q} = 0 \quad (17.85)$$

If the performance index J is defined over a finite time horizon ($t = 0 \dots D$), the differential Riccati equation must be integrated backward in time, starting at $\mathbf{P}(D) = \mathbf{0}$:

$$-\dot{\mathbf{P}}(t) = \mathbf{A}^T \mathbf{P}(t) + \mathbf{P}(t) \mathbf{A} - \mathbf{P}(t) \mathbf{BR}^{-1} \mathbf{B}^T \mathbf{P}(t) + \mathbf{Q} \quad (17.86)$$

In either case the optimal controller \mathbf{K} can be determined as

$$\mathbf{K} = \mathbf{R}^{-1} \mathbf{B}^T \mathbf{P} \quad \text{and} \quad \mathbf{Q} = \mathbf{K}(\mathbf{T}_d - \mathbf{T}) \quad (17.87)$$

yielding a resulting value of the performance index for the closed-loop thermal system:

$$J = \mathbf{e}^T(0) \mathbf{P} \mathbf{e}(0) \quad (17.88)$$

Optimal Observation: Kalman–Bucy Filter If thermal noise is present in the system input and/or the sensor measurements, optimal observation attempts to minimize its effects in estimating the temperature states $\hat{\mathbf{T}}$. The optimal observer \mathbf{L} in Fig. 17.33 must minimize the variance J of the state deviations $\mathbf{\varepsilon} = \mathbf{T} - \hat{\mathbf{T}}$:

$$J = E(\mathbf{\varepsilon}^T \mathbf{\varepsilon}) = \int_0^\infty \mathbf{\varepsilon}(t)^T \mathbf{\varepsilon}(t) dt \quad (17.89)$$

The noise components \mathbf{w} and \mathbf{v} are included in the state and output equation of the system as

$$\dot{\mathbf{T}} = \mathbf{A}\mathbf{T} + \mathbf{B}\mathbf{Q} + \mathbf{w} \quad \mathbf{Y} = \mathbf{C}\mathbf{T} + \mathbf{v} \quad (17.90)$$

It is assumed that noise is Gaussian with zero mean [$E(\mathbf{w}) = \mathbf{0}$, $E(\mathbf{v}) = \mathbf{0}$] and covariance matrices $\mathbf{Q} = E(\mathbf{w} \mathbf{w}^T)$ and $\mathbf{R} = E(\mathbf{v} \mathbf{v}^T)$, respectively. The $n \times n$ matrix \mathbf{Q} and the $m \times m$ matrix \mathbf{R} are thus both positive definite real symmetric ($\mathbf{Q} = \mathbf{H}^T \mathbf{H}$). The system is observable if the matrix

$$\mathbf{P}_0 = [\mathbf{H} : \mathbf{H}\mathbf{A} : \mathbf{H}\mathbf{A}^2 : \dots : \mathbf{H}\mathbf{A}^{n-1}] \quad \text{has} \quad \text{rank}(\mathbf{P}_0) = n \quad (17.91)$$

Then an $n \times n$ matrix \mathbf{S} can be determined by solving the Riccati equation:

$$\mathbf{A}\mathbf{S} + \mathbf{S}\mathbf{A}^T - \mathbf{S}\mathbf{C}^T \mathbf{R}^{-1} \mathbf{C}\mathbf{S} + \mathbf{Q} = \mathbf{0} \quad (17.92)$$

and the optimal observer \mathbf{L} (Kalman–Bucy filter) can be designed as

$$\mathbf{L} = \mathbf{S}\mathbf{C}^T \mathbf{R}^{-1} \quad \text{with state correction} \quad \mathbf{L}(\mathbf{Y} - \hat{\mathbf{Y}}) = \mathbf{L}\mathbf{C}\boldsymbol{\varepsilon} \quad (17.93)$$

with resulting state deviation variance

$$J = \text{trace}(\mathbf{S}) \quad (17.94)$$

Again the separation principle allows for independent design of the optimal controller \mathbf{K} and observer \mathbf{L} . There is a clear duality between the controller/observer design methodology, as in the pole placement case.

17.8.4 Smith Prediction

Thermal systems often involve considerable measurement delays (transport lags, such as $G_p(s)e^{-sd}$), compromising the stability and performance of closed-loop control systems. An observation technique can be used to overcome such delays d , in which a process model $G_m(s)$ (the Smith predictor) is computationally implemented in parallel to the actual thermal process (Fig. 17.34). Its real-time estimates provide undelayed substitute feedback, while the deviations of its predictions (delayed by $D = d/\mathcal{T}$ sampling periods) from the actual measurements are also fed back for correction:

$$\boldsymbol{\varepsilon}(t) = \mathbf{T}(t) - \hat{\mathbf{T}}(t - d) \quad (17.95)$$

It is clear that for a perfect model of the process [i.e., $G_m(s) = G_p(s)$] the closed-loop transfer function is identical for that for an undelayed system, except of course for the delay term e^{-sd} :

$$G_{cl}(s) = \frac{G_c(s)G_p(s)}{1 + G_c(s)G_p(s)} e^{-sd} \quad (17.96)$$

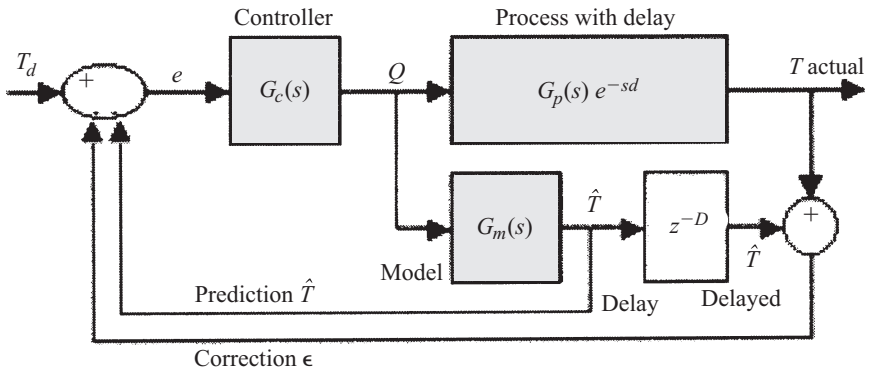


Figure 17.34 Smith predictor for delay compensation in closed-loop control.

17.8.5 Sliding Mode Control

Besides linear error-based controllers (PID, pole placement, LQR), nonlinear techniques such as switching methods similar to the thermostatic control for SISO systems are also applicable to MIMO thermal processes. Figure 17.34 illustrates such a sliding mode control algorithm. Setting the previous linear control laws to zero (with the controller \mathbf{K} designed by pole placement or optimal methods),

$$Q = \mathbf{K}(T_d - T) = 0 \quad (17.97)$$

defines a plane in the n -dimensional state space \mathbf{T} (the phase plane of Fig. 17.35) with no control action ($Q = 0$). This plane separates the state space in two half-spaces, for which a two-position switching controller can be defined as

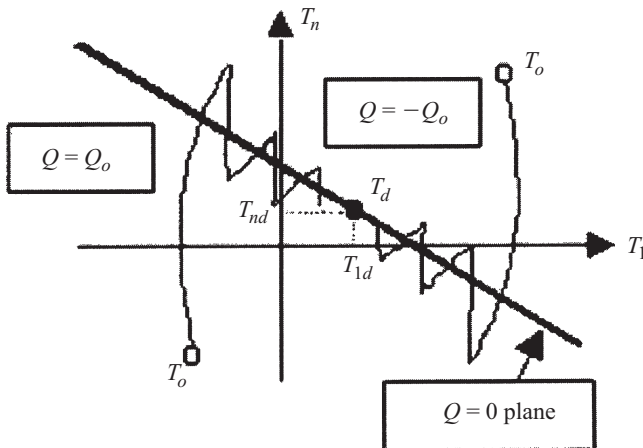


Figure 17.35 Sliding mode control on phase plane.

$$\begin{aligned} \text{if } \mathbf{K}(\mathbf{T}_d - \mathbf{T}) > 0 \quad \text{then} \quad Q &= Q_o \\ \text{if } \mathbf{K}(\mathbf{T}_d - \mathbf{T}) < 0 \quad \text{then} \quad Q &= -Q_o \end{aligned} \quad (17.98a)$$

which can be represented as

$$Q(t) = Q_o \operatorname{sgn}[\mathbf{K}(\mathbf{T}_d - \mathbf{T})] \quad (17.98b)$$

Similar nonlinear switching controllers can be based on on-off, differential algorithms. These result in a chattering state response around the switching plane above, sliding toward the desired specification \mathbf{T}_d (Fig. 17.35).

17.8.6 Adaptive Control

For thermal systems with nonlinear time-varying or uncertain dynamics, adaptive controllers adjust their parameters in real time accordingly to ensure the desired closed-loop performance. For a priori known alterations of the thermal process characteristics, simple gain scheduling of the controller off-line is effective. In this section we describe briefly two particular representative nonlinear algorithms of model reference adaptive systems and self-tuning regulators.

Model Reference Adaptive Control (MRAC) This control scheme is illustrated in Fig. 17.36. The desired behavior of the feedback system, which consists of the time-variable/uncertain process and the adaptive controller, is specified via an ideal open-loop reference model, implemented computationally in parallel to the closed-loop actual system. The reference model usually is defined by simple linear dynamics:

$$\dot{\mathbf{T}}_d = \mathbf{A}\mathbf{T}_d + \mathbf{B}\mathbf{v} \quad (17.99)$$

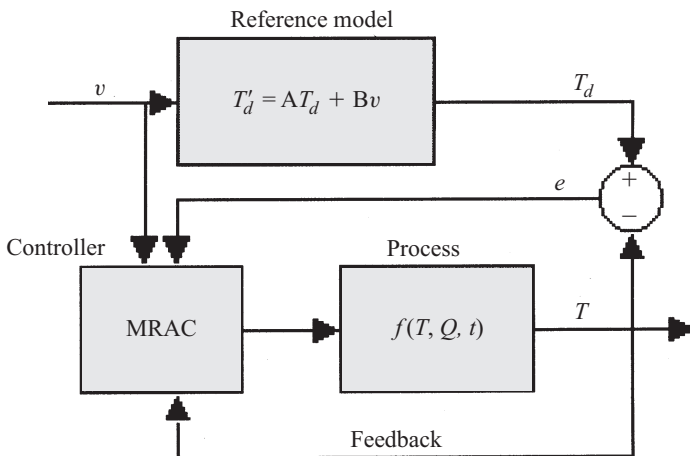


Figure 17.36 Model reference adaptive system.

describing the desired reference state T_d in response to an excitation signal v . Thus, the MRAC algorithm is designed so that the control signal Q forces the thermal process $f(T, Q, t)$ to closed-loop behavior following the reference model responses.

To ensure the stability of the feedback system, a candidate Lyapunov function is proposed as

$$V(e) = e^T P e \quad (17.100)$$

with $e = T_d - T$ the state error and P a $n \times n$ positive-definite real symmetric matrix. To qualify for a Lyapunov function and ensure the system stability, the scalar function V must satisfy

$$\dot{V}(e) = e^T (A^T P + P A) e + 2e^T P [A T + B v - f(T, Q, t)] \leq 0 \quad (17.101)$$

by proper choice of the control Q . To this purpose, the matrix P is first chosen to satisfy the Lyapunov equation:

$$A^T P + P A = -Q \quad (17.102)$$

where Q is a positive-definite real symmetric matrix (usually selected as the identity $I_{n \times n}$ matrix). Second, the control input Q is selected so that the second term is a nonpositive scalar M :

$$e^T P [A T + B v - f(T, Q, t)] = M \leq 0 \quad (17.103)$$

This feedback linearization method of the process f by the control Q ensures stable convergence of the state error e to zero, that is, the tracking of the desired T_d by the actual temperature state T .

Self-Tuning Regulation The basic controller structure (such as PID) of the self-tuning regulator is designed on the basis of a linearized nominal process model at the operating process conditions. However, the controller parameters are adjusted in real time via identification of the process parameters through input/output measurements (Fig. 17.37). For example, a discrete-time model of a linear time invariant (LTI) thermal process,

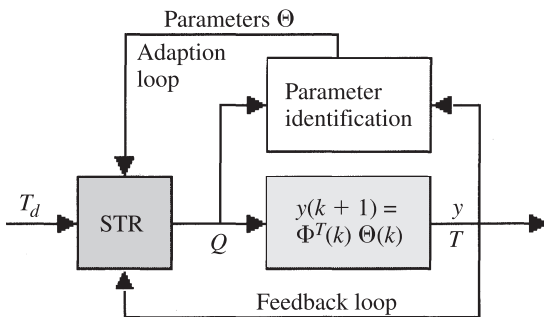


Figure 17.37 Self-tuning regulator.

$$\mathbf{T}(k+1) = \mathbf{GT}(k) + \mathbf{HQ}(k) \quad \mathbf{Y}(k) = \mathbf{CT}(k) + \mathbf{DQ}(k) \quad (17.104)$$

can be written as a system of m MISO output difference equations in an autoregressive moving average (ARMA) form as ($h = 1 \cdots m$)

$$y_h(k+1) = \sum_{i=0}^{n-1} a_i y(k-i) + \sum_{j=1}^l \sum_{i=0}^{n-1} b_{ij} Q_j(k-i) \Rightarrow y(k+1) = \Phi^T(k) \Theta(k) \quad (17.105)$$

where $\Phi = [y(k)'s \quad Q(k)'s]$ is the augmented vector containing the n last values of the outputs and inputs [all known except for the present inputs $Q_j(k)$], and $\Theta = [a'_i s b'_{ij} s]$ is the respective process parameter vector. The latter can be identified in real time by one of the identification techniques of the next section. Using this process parametrization, a deadbeat (one-step-ahead) control law can be established to set the future output $y(k+1)$ to the desired one y_d , by solving for the necessary current inputs $Q_j(k)$:

$$y_d = \Phi^T(k) \Theta(k) \leftarrow \text{solve for } Q_j(k) \text{ in } \Phi(k) \quad (17.106)$$

The adaptation loop in Fig. 17.37 is typically executed at a lower frequency (larger period, 5 to 10 times \mathcal{T}) than the feedback loop.

17.8.7 Parameter Identification

Beyond its off-line use in thermal process analysis and control system design, identification of thermal parameters is applied in real time for controller adaptation. This is based on in-process data of the applied heat inputs $\mathbf{Q}(k)$ and the measured thermal outputs $\mathbf{y}(k)$. In this section we review two popular methodologies based on orthogonal projection and least squares.

Orthogonal Projection The process parameters in vector Θ are updated at a rate proportional to their corresponding factors in the augmented vector Φ , to eliminate the resulting output deviation $\varepsilon = y - y_d$:

$$\dot{\Theta} = -\gamma \varepsilon \frac{\partial \varepsilon}{\partial \Theta} \quad (17.107)$$

where γ is an adaptation gain. This intuitive algorithm (also known as the MIT rule) corresponds to an orthogonal projection of the parameter vector on the hypersurface of the output deviations, according to the respective direction cosines. In discrete time, this can be expressed in difference form as

$$\Theta(k) = \Theta(k-1) + \gamma [\Phi^T(k-1) \Phi(k-1)]^{-1} [y(k) - \Phi^T(k-1) \Theta(k-1)] \Phi(k-1) \quad (17.108)$$

Least Squares If N consecutive measurements of the output $y(i)$, $1 = 1 \cdots N$, are made at successive sampling periods, these can be concatenated in a measured output vector \mathbf{Y} as

$$\mathbf{Y} = [y(n+1)y(n+2) \cdots y(n+N)]^T \quad (17.109)$$

These will be compared with their respective predictions $\hat{\mathbf{Y}}$ by the ARMA process model, in which the corresponding augmented vectors Φ can be assembled in matrix Φ :

$$\Phi = [\Phi^T(n) \Phi^T(n+1) \cdots \Phi^T(n+N-1)]^T \quad (17.110)$$

where the elementary vectors Φ also contain the previously measured outputs $y(i)$, $i = 1 \cdots n$ and inputs $Q(i)$, $i = 1 \cdots n$. Thus the ARMA model of the thermal system can be written as $\mathbf{Y} = \Phi\Theta$. The least squares method minimizes the quadratic index of the output deviations $\epsilon = \mathbf{Y} - \hat{\mathbf{Y}}$ (i.e., $J = \epsilon^T \epsilon$) setting the parameters Θ to

$$\Theta = (\Phi^T \Phi)^{-1} \Phi^T \mathbf{Y} \quad (17.111)$$

where Φ^\dagger is the pseudoinverse of Φ .

NOMENCLATURE

Roman Letter Symbols

a	grinding cut depth, m
A	ARMA output coefficient, dimensionless
A_1	state matrix, dimensionless
A_c, A_o, A_1	preexponential frequency factor in cure kinetics model, s^{-1}
b	cross-sectional area, m^2
	chip width, m
	grinding width, m
B	saturation point, dimensionless
B_1, B_2, B_3	ARMA input coefficient, dimensionless
	input matrix, dimensionless
Bi	parameters defined in eqs. (17.26)–(17.28), dimensionless
\hat{c}	Biot number, dimensionless
c	degree of crystallization, dimensionless
	specific heat capacity, $kJ/kg \cdot K$
C	saturation level, dimensionless
C_A	output matrix, dimensionless
	instantaneous resin concentration in the resin–catalyst mixture at any time, t , kg/m^3
C_{A0}	initial resin concentration in the resin–catalyst mixture, kg/m^3
d	delay, dimensionless

d_s	grinding wheel diameter, m
D	diameter, m
	differential, dimensionless
	period, dimensionless
D	direct matrix, dimensionless
D_b	degree of bonding, dimensionless
D_h	degree of healing, dimensionless
D_{ic}	degree of intimate contact, dimensionless
e	error, dimensionless
E	activation energy for viscosity in the chemorheological model, kJ/kmol
	error (Laplace transform), dimensionless
	expectation, dimensionless
E_1, E_2	activation energies in the cure kinetics models, kJ/kmol
f	transfer function, dimensionless
F, \mathbf{F}	forces associated with cutting, N
g	controller transfer function, dimensionless
G	transfer function, dimensionless
G	discrete state matrix, dimensionless
h	heat transfer coefficient, $\text{W/m}^2 \cdot \text{K}$
	depth of cut, m
	thermoplastic tow thickness, m
	sensor transfer function, dimensionless
	discrete-time index, dimensionless
H	plate thickness, m
H	detectability matrix, dimensionless
	discrete input matrix, dimensionless
H_T	total heat of crystallization, kJ/kg
H_u	theoretical ultimate heat of crystallization, kJ/kg
ΔH_c	heat of crystallization, kJ/kg
ΔH_R	heat of the cure reaction, kJ/kg
i	discrete time index, dimensionless
I	identity matrix, dimensionless
J	quadratic performance index, dimensionless
k	thermal conductivity, $\text{W/m} \cdot \text{K}$
	discrete time index, dimensionless
k_o	Kozeny constant, dimensionless
K	gain, dimensionless
K	controller matrix, dimensionless
K_o	modified Bessel function of the first kind, of order zero, dimensionless
K_{10}, K_{20}	preexponential frequency factors in the cure kinetics models, s^{-1}
l	input number, dimensionless
	length of heated region, m

l_c	frictional contact length, m
l_s	shear length, m
L	length, m
	thickness, m
	characteristic length, m
L	observer matrix, dimensionless
m, n	exponents in the cure kinetics models, dimensionless
	output number and state number, dimensionless
m_1, m_2	$(Pe \pm \sqrt{Pe^2 + 4 Bi})/2$, dimensionless
N	describing function, dimensionless
	sample number, dimensionless
p	stiffness of a fiber network, Pa
P	perimeter, m
	grinding power, W
	pressure, Pa
P	pdrs matrix, dimensionless
Pe	Péclet number, dimensionless
q''	heat flux, W/m ²
Q	heat source strength, W
$Q(t)$	heat release during cure per unit mass of resin-catalyst sample, kJ/kg
Q	state penalty matrix, dimensionless
r, x, y, z	spatial coordinates, m
r_f	fiber radius, m
R	fraction of shear energy removed by the chip, dimensionless
	void radius, m
	universal gas constant, kJ/kmol · K
R, X, Y	coordinates, dimensionless
R	resultant force, N
	input penalty matrix, dimensionless
s	Laplace variable, dimensionless
S	radius of a resin shell surrounding a void, m
S	stabilizability matrix, dimensionless
t	time, s
T	temperature, K
	sampling period, s
u	grinding energy, J/m ³
	integration variable, dimensionless
v	velocity, m/s
	void fraction, dimensionless
	output noise, dimensionless
	excitation, dimensionless
v_a	maximum fiber volume fraction, dimensionless
v_f	fiber volume fraction in the composite, dimensionless

v_I	initial fiber volume fraction, dimensionless
V	velocity, m/s
	Lyapunov function, dimensionless
w	state noise, dimensionless
W_D	deformation work per unit volume, J/m ³
y	parameter in the degradation kinetics model, dimensionless
	output, dimensionless
y	output measurement, dimensionless
Y	measured output, dimensionless
z	Z-transform variable, dimensionless

Greek Letter Symbols

α	thermal diffusivity, m ² /s
	degree of degradation, dimensionless
β	friction angle
	shape constant, dimensionless
γ	characteristic thickness, m [= A_c/P]
	adaptation gain, dimensionless
γ_o	rake angle, deg
ε	fraction of grinding power entering the workpiece as heat, dimensionless
	degree of cure, dimensionless [= $(C_{A0} - C_A)/C_{A0}$]
	state deviation, dimensionless
θ	temperature, dimensionless
Θ	parameters, dimensionless
κ	permeability, m ²
λ	constant in the chemorheological model, dimensionless
	eigenvalue (observer), dimensionless
μ	coefficient of friction, dimensionless
	dynamic viscosity, Pa · s
	eigenvalue (controller), dimensionless
ρ	density, kg/m ³
σ	interfacial bond strength, Pa
τ	time, dimensionless
	time (Lagrangian), s
τ_s	flow stress, N/m ²
ϕ	porosity, dimensionless
	characteristic polynomial, dimensionless
ϕ_o	shear plane angle, deg
φ	resin volume fraction in the fiber–resin mixture, dimensionless [= $1 - v_f$]
Φ	augmented state, dimensionless
ω	angular frequency, s ⁻¹

Subscripts and Superscripts

*	dimensionless
\wedge	closed-loop
	estimated
.	time derivative
-1	inverse
\dagger	pseudoinverse
app	applied
atm	atmospheric
c	chip
	controller
	controllability
cl	closed loop
d	desired reference
	derivative
f	fluid, fiber
g	grain
	gas
i	integral
L	laminate
m	model
max	maximum
min	minimum
o	initial
	ambient
	reference
p	process
	proportional
r	rake
ref	reference value
s	surface
	setting
T	tooling
T	transpose
W	workpiece
x, y, z	along the respective coordinate directions
∞	ultimate (maximum realizable) value

REFERENCES

- Adams, K. L., and Rebenfeld, L. (1991a). Permeability Characteristics of Multilayer Fiber Reinforcements, I: Experimental Observations, *Polym. Compos.*, 12, 179–185.
- Adams, K. L., and Rebenfeld, L. (1991b). Permeability Characteristics of Multilayer Fiber Reinforcements, II: Theoretical Model, *Polym. Compos.*, 12, 186.

- Agarwal, V. (1991). The Role of Molecular Mobility in the Consolidation and Bonding of Thermoplastic Composite Materials, *Technical Report 91-39*, Center for Composite Materials, University of Delaware, Newark, DE.
- Altan, T., Oh, S., and Gegel, H. (1983). *Metal Forming: Fundamentals and Applications*, American Society for Metals, Metals Park, OH.
- ASM (1991). ASM Handbook Volume 4: Heat Treating, American Society for Metals, Metals Park, OH.
- Bastien, L. J., and Gillespie, J. W., Jr. (1991). A Non-isothermal Healing Model for Amorphous Thermoplastics, *Polym. Eng. Sci.*, 31(24), 1720–1730.
- Bogetti, T. A., and Gillespie, J. W., Jr. (1991). Two-Dimensional Cure Simulation of Thick Thermosetting Composites, *J. Compos. Mater.*, 25(3), 239–273.
- Boothroyd, G. (1975). *Fundamentals of Metal Cutting and Machine Tools*, Hemisphere Publishing, Washington, DC, Chap. 3.
- Broyer, E., and Macosko, C. W. (1976). Heat Transfer and Reaction in Polymer Reaction Injection Molding, *AIChE J.*, 22(2), 268–276.
- Butler, C. A., McCullough, R. L., Pitchumani, R., and Gillespie, J. W., Jr. (1998). An Analysis of Mechanisms Governing Fusion Bonding of Thermoplastic Composites, *J. Thermoplastic Compos. Mater.*, 11(4), 338–363.
- Carslaw, H. S., and Jaeger, J. C. (1959). *Conduction of Heat in Solids*, 2nd ed., Oxford University Press, London.
- Chapman, T. J., Gillespie, J. W., Jr., Pipes, R. B., Manson, J.-A. E., and Seferis, J. C. (1990). Prediction of Process-Induced Residual Stresses in Thermoplastic Composites, *J. Compos. Mater.*, 24, 616–643.
- Chiao, L., and Lyon, R. E. (1990). A Fundamental Approach to Resin Cure Kinetics, *J. Compos. Mater.*, 24, 739–752.
- Dara, P. H., and Loos, A. C. (1985). Thermoplastic Matrix Composite Processing Model, *Report CCMS-85-10*, Center for Composite Materials and Structures, Virginia Polytechnic Institute and State University, Blacksburg, VA.
- Davè, R. S., Kardos, J. L., and Dudukovic, M. P. (1987). A Model for Resin Flow during Composite Processing, I: General Mathematical Development, *Polym. Compos.*, 8, 29.
- Davè, R. S., Mallow, A., Kardos, J. L., and Dudukovic, M. P. (1990). Science-Based Guidelines for the Autoclave Process for Composites Manufacturing, *SAMPE J.*, 26(3), 31.
- Dawson, P. R., and Malkin, S. (1984). Inclined Moving Heat Source Model for Calculating Metal Cutting Temperatures, *ASME J. Eng. Ind.*, 106, 179–186.
- Day, M., Cooney, J. D., and Wiles, D. M. (1989). A Kinetic Study of the Thermal Decomposition of Poly(Aryl-Ether-Ether-Ketone) (PEEK) in Nitrogen, *Polym. Eng. Sci.*, 29(1), 19–22.
- DeGarmo, E. P., Black, J. T., and Kohser, R. A. (1997). *Materials and Processing in Manufacturing*, 8th ed., Prentice Hall, Upper Saddle River, NJ.
- de Gennes, P. G. (1971). Reptation of a Polymer Chain in the Presence of Fixed Obstacles, *J. Chem. Phys.*, 55(2), 572–579.
- DesRuisseaux, N. R., and Zerkle, R. D. (1970). Temperature in Semi-infinite and Cylindrical Bodies Subjected to Moving Heat Sources and Surface Cooling, *J. Heat Transfer*, 92, 456–464.
- DeVries, W. R. (1992). *Analysis of Material Removal Processes*, Springer-Verlag, New York.
- Diwekar, U. M. and Pitchumani, R. (1993). Optimal Cure Cycles for Thermoset Composites

- Manufacture, in *Advanced Computations in Materials Processing*, V. Prasad and R. V. Arimilli, eds., ASME-HTD-241, ASME, New York, pp. 23–31.
- Dowson, D., Parsons, B., and Lidgitt, P. J. (1972). An Elasto-plasto-hydrodynamic Lubrication Analysis of the Wire Drawing Process, *Proc. Symposium on Elasto-hydrodynamic Lubrication*, Institute of Mechanical Engineers, London, pp. 94–106.
- El-Domiaty, A., and Kassab, S. Z. (1998). Temperature Rise in Wire Drawing, *J. Mater. Process. Technol.*, 83, 72–83.
- Flemings, M. C. (1974). *Solidification Processing*, McGraw-Hill, New York.
- Gaskell, D. R. (1992). *An Introduction to Transport Phenomena in Materials Engineering*, Macmillan, New York.
- Guceri, S. I., ed. (1992). *Journal of Materials Processing and Manufacturing Science*, Technomic Publishing, Lancaster, PA (Vol. 1, No. 1).
- Guceri, S. I., ed. (1993). *Transport Phenomena in Processing*, Technomic Publishing, Lancaster, PA.
- Guo, C., and Malkin, S. (1992). Heat Transfer in Grinding, *J. Mater. Process. Manuf. Sci.*, 1, 16–27.
- Guo, C., and Malkin, S. (1996). Inverse Heat Transfer Analysis of Grinding, 1 and 2, *J. Eng. Ind.*, 118, 137–149.
- Guthrie, R. I. L. (1989). *Engineering in Process Metallurgy*, Oxford Science Publishers, Clarendon Press, Oxford.
- Gutowski, T. G. (1985). A Resin Flow/Fiber Deformation Model for Composites, *SAMPE Q.*, 16(4), 58–65.
- Gutowski, T. G., Cai, Z., Kingery, J., and Wineman, S. J. (1986). Resin Flow/Fiber Deformation Experiments, *SAMPE Q.*, 17, 54–58.
- Gutowski, T. G., Morigaki, T., and Cai, Z. (1987). The Consolidation of Laminate Composites, *J. Compos. Mater.*, 21, 172–188.
- Han, L. S., and Cosner, A. A. (1981). Effective Thermal Conductivities of Fibrous Composites, *J. Heat Transfer*, 103, 387–392.
- Han, C. D., and Lem, K. W. (1983). Chemorheology of Thermosetting Resins, I: The Chemorheology and Curing Kinetics of Unsaturated Polyester Resin, *J. Appl. Polym. Sci.*, 28, 3155–3182.
- Han, C. D., Lee, D. S., and Chin, H. B. (1986). Development of a Mathematical Model for the Pultrusion Process, *Polym. Eng. Sci.*, 26(6), 393–404.
- Hashin, Z. (1983). Analysis of Composite Materials: A Survey, *J. Appl. Mech.*, 50, 481–505.
- Incropera, F. P., and DeWitt, D. P. (1996). *Fundamentals of Heat Transfer*, 3rd ed., Wiley, New York.
- Jacobs, H. R., and Hartnett, J. P., eds. (1992). *Thermal Engineering: Emerging Technologies and Critical Phenomena*, NSF Workshop Report, Grant CTS-91-04006, National Science Foundation, Washington, DC.
- Jaluria, Y. (1993). Transport from Continuously Moving Materials Undergoing Thermal Processing, *Annu. Rev. Heat Transfer*, 4, 187–245.
- Jen, T. C., and Lavine, A. S. (1995). A Variable Heat Flux Model of Heat Transfer in Grinding: Model Development, *J. Heat Transfer*, 117, 473–478.
- Ju, Y., Farris, T. N., and Chandrasekar, S. (1998). Theoretical Analysis of Heat Partition and Temperatures in Grinding, *J. Tribol.*, 120, 789–794.

- Kalpajian, S. (1996). *Manufacturing Engineering and Technology*, 3rd ed., Addison-Wesley, Reading, MA.
- Kardos, J. L. (1997). The Processing Science of Reactive Polymer Composites, in *Advanced Composites Manufacturing*, T. G. Gutowski, ed., Wiley, New York, pp. 43–80.
- Kardos, J. L., Dudukovic, M. P., McKague, E. L., and Lehman, M. W. (1986). Void Formation and Transport during Processing of Thermosetting Matrix Composites, in *Advances in Polymer Science*, Vol. 80, K. Dusek, ed., Springer-Verlag, Berlin.
- Kitto, J. B., Fiveland, W. A., Latham, C. E., and Peterson, G. P. (1995). Advances in Thermal Engineering, *Mech. Eng.*, 117(3), 88–92.
- Kou, S. (1996). *Transport Phenomena in Materials Processing*, Wiley, New York.
- Lam, R. C., and Kardos, J. L. (1988). The Permeability of Aligned and Cross-Plied Fiber Beds during Processing of Continuous Fiber Composites, in *Proc. American Society for Composites, 3rd Conference*, Seattle, WA, pp. 3–11.
- Lam, R. C., and Kardos, J. L. (1991). The Permeability and Compressibility of Aligned and Cross-Plied Carbon Fiber Beds during Processing of Composites, *Polym. Eng. Sci.*, 31, 1064.
- Lamontia, M. A., Gruber, M. B., and Gillespie Jr., J. W. (1992). Design, Manufacture and Testing of AS-4 Graphite/PEEK Thermoplastic Composite 24-inch Ring-Stiffened Cylinder Model, in *Proc. Submarine Technology Symposium*, Applied Physics Laboratory, Johns Hopkins University, Baltimore.
- Lamontia, M. A., Gruber, M. B., Smoot, M. A., Sloan, J., and Gillespie Jr., J. W. (1995). Performance of a Filament Wound Graphite/Thermoplastic Composite Ring-Stiffened Pressure Hull Model, *J. Thermoplastic Compos. Mater.*, 8(1), 15–36.
- Lavine, A. S., and Jen, T. C. (1991). Thermal Aspects of Grinding: Heat Transfer to Workpiece, Wheel and Fluid, *J. Heat Transfer*, 113, 296–303.
- Lee, W. I., and Springer, G. S. (1987). A Model of the Manufacturing Process of Thermoplastic Matrix Composites, *J. Compos. Mater.*, 21, 1017–1055.
- Lee, W. I., Loos, A. C., and Springer, G. S. (1982). Heat of Reaction, Degree of Cure, and Viscosity of Hercules 3501–6 Resin, *J. Compos. Mater.*, 16, 510.
- Loos, A. C., and Springer, G. S. (1983). Curing of Epoxy Matrix Composites, *J. Compos. Mater.*, 17, 135–169.
- Lucca, D. A., and Wright, R. N. (1996). Heating Effects in the Drawing of Wire and Strip under Hydrodynamic Lubrication Conditions, *J. Manuf. Sci. Eng.*, 118, 628–638.
- Malkin, S. (1984). Grinding of Metals: Theory and Application, *J. Appl. Metalwork.*, 3, 95–109.
- Mantell, S. C., and Springer, G. S. (1992). Manufacturing Process Models for Thermoplastic Composites, *J. Compos. Mater.*, 26(16), 2348–2377.
- Martinez, G. M. (1991). Fast Cures for Thick Laminated Organic Matrix Composites, *Chem. Eng. Sci.*, 46(2), 439–450.
- Nam, J. D., and Seferis, J. C. (1992). Generalized Composite Degradation Kinetics for Polymeric Systems under Isothermal and Nonisothermal Conditions, *J. Polym. Sci. B Polym. Phys.*, 30, 455–463.
- Ozawa, T. (1971). Kinetics of Non-isothermal Crystallization, *Polymer*, 12, 150–158.
- Pillai, V., Beris, A., and Dhurjati, P. (1994). Implementation of Model-Based Optimal Temperature Profiles for Autoclave Curing of Composites Using a Knowledge-Based System, *Ind. Eng. Chem. Res.*, 33, 2443–2452.

- Pitchumani, R. (1999). Evaluation of Thermal Conductivities of Disordered Composite Media Using a Fractal Model, *J. Heat Transfer*, 121(1), 163–166.
- Pitchumani, R. (2002). Processing of Thermoplastic-Matrix Composites, in *Annual Reviews of Heat Transfer*, Vol. XIII, Begell House, New York.
- Pitchumani, R., and Diwekar, U. M. (1994). Process Optimization for the Fabrication of Partially-Cured Composites, in *Transport Phenomena in Manufacturing and Materials Processing*, ASME-HTD-280, ASME, New York, pp. 1–11.
- Pitchumani, R., and Yao, S. C. (1993). Nondimensional Analysis of a Thermoset Composites Manufacture, *J. Compos. Mater.*, 27(6), 613–636.
- Pitchumani, R., Ranganathan, S., Don, R. C., and Gillespie, J. W., Jr. (1994). Analysis of On-Line Consolidation during the Thermoplastic Tow-Placement Process, in *Thermal Processing of Materials: Thermo-mechanics, Controls, and Composites*, V. Prasad et al., eds., ASME-HTD-289, ASME, New York, pp. 223–234.
- Pitchumani, R., Ranganathan, S., Don, R. C., Gillespie, J. W., Jr., and Lamontia, M. A. (1996). Analysis of Transport Phenomena Governing Interfacial Bonding and Void Dynamics during Thermoplastic Tow-Placement, *Int. J. Heat Mass Transfer*, 39(9), 1883–1897.
- Pitchumani, R., Gillespie, J. W., Jr., and Lamontia, M. A. (1997). Design and Optimization of a Thermoplastic Tow-Placement Process with In-situ Consolidation, *J. Compos. Mater.*, 31(3), 244–275.
- Poirier, D. R., and Geiger, G. H. (1994). *Transport Phenomena in Materials Processing*, TMS, Warrendale, PA.
- Poirier, D. R., and Poirier, E. J. (1992). *Heat Transfer Fundamentals for Metal Casting*, TMS, Warrendale, PA.
- Prasad, V., Lavine, A., Zumbrennen, D., and Longtin, J., eds. (1998). Thermal Aspects of Manufacturing and Materials Processing: Emerging Technologies and Research Issues, Report of an NSF/ASME Workshop, Anaheim, CA, Nov. 18–19.
- Pusatcioglu, S. Y., Fricke, A. L., and Hassler, J. C. (1979). Heats of Reaction and Kinetics of a Thermoset Polyester, *J. Appl. Polym. Sci.*, 24, 937–946.
- Radford, D. W., and Tong, T. W. (2000). Heat Transfer in Manufacturing, in *CRC Handbook of Thermal Engineering*, F. Kreith, ed., CRC Press, Boca Raton, FL, pp. 4.264–4.286.
- Rai, N., and Pitchumani, R. (1997a). Optimal Cure Cycles for the Fabrication of Thermosetting-Matrix Composites, *Polym. Compos.*, 18(1), 566–581.
- Rai, N., and Pitchumani, R. (1997b). Neural Network-Based Optimal Curing of Composite Materials, *J. Mater. Process. Manuf. Sci.*, 6(1), 39–62.
- Ramakrishnan, B. T., Zhu, L., and Pitchumani, R. (2000). Curing of Composites Using Internal Resistive Heating, *J. Manuf. Sci. Eng.*, 122(1), 124–131.
- Ranganathan, S., Advani, S. G., and Lamontia, M. A. (1995). A Non-isothermal Process Model for Consolidation and Void Reduction during In-situ Tow-Placement of Thermoplastic Composites, *J. Compos. Mater.*, 29(8), 1040–1062.
- Schey, J. A. (1983). *Tribology in Metalworking: Friction, Lubrication and Wear*, American Society for Metals, Metals Park, OH.
- Schey, J. A. (2000). *Introduction to Manufacturing Processes*, 3rd ed., McGraw-Hill, New York.
- Schnabel, W. (1981). *Polymer Degradation: Principles and Practical Applications*, Macmillan, New York.

- Shah, R. K., Roshan, H. Md., Sastri, V. M. K., and Padmanabhan, K. A., eds. (1992). *Thermo-mechanical Aspects of Manufacturing and Materials Processing*, Hemisphere Publishing, New York.
- Shaw, M. C. (1984). *Metal Cutting Principles*, Oxford University Press, Oxford, Chap. 12.
- Skartsis, L., and Kardos, J. L. (1990). The Newtonian Permeability and Consolidation of Oriented Carbon Fiber Beds, *Proc. American Society for Composites, 5th Technical Conference*, p. 548.
- Skartsis, L., Khomami, B., and Kardos, J. L. (1992). Resin Flow through Fiber Beds during Composite Manufacturing Processes, II: Numerical and Experimental Studies of Newtonian Flow through Ideal and Actual Fiber Beds, *Polym. Eng. Sci.*, 32, 231.
- Snidle, R. W. (1977). Contribution to the Theory of Frictional Heating and the Distribution of Temperature in Wires and Strips during Drawing, *Wear*, 44, 270–294.
- Snidle, R. W., Parsons, B., and Dowson, D. (1976). A Thermal Hydrodynamic Lubrication Theory for Hydrostatic Extrusion of Low Strength Materials, *J. Lubr. Technol.*, 98, 335–343.
- Sourour, S., and Kamal, M. R. (1976). Differential Scanning Calorimetry of Epoxy Cure: Isothermal Cure Kinetics, *Thermochim. Acta*, 41, 14.
- Springer, G. S. (1982). Resin Flow during the Cure of Fiber Reinforced Composites, *J. Compos. Mater.*, 16, 400.
- Steen, W. M. (1991). *Laser Material Processing*, Springer-Verlag, London.
- Steiner, K. V., Bauer, B. M., Pitchumani, R., and Gillespie, J. W., Jr. (1995). An Experimental Verification of Modeling and Control for Thermoplastic Tape Placement, *Proc. SAMPE International Conference*, Anaheim, CA, Apr., pp. 1550–1559.
- Stephenson, D. P. (1991). Assessment of Steady-State Metal Cutting Temperature Models Based on Simultaneous Infrared and Thermocouple Data, *J. Eng. Ind.*, 113, 121–128.
- Tanasawa, I., and Lior, N., eds. (1992). *Heat and Mass Transfer in Materials Processing*, Hemisphere Publishing, New York.
- Tay, A. O., Stevenson, M. G., de Vahl Davis, G., and Oxley, P. L. B. (1976). A Numerical Method for Calculating Temperature Distributions in Machining, *Int. J. Mach. Tool Des. Res.*, 16, 335–349.
- Trigger, K. J., and Chao, B. T. (1951). An Analytical Evaluation of Metal Cutting Temperatures, *Trans. ASME*, 73, 57–68.
- Tseng, A. A., Tong, S. X., Maslen, S. H., and Mills, J. J. (1990). Thermal Behavior of Aluminum Rolling, *J. Heat Transfer*, 112, 301–308.
- Velisaris, C. N., and Seferis, J. C. (1986). Crystallization Kinetics of Polyetheretherketone (PEEK) Matrices, *Polym. Eng. Sci.*, 26(22), 1574–1581.
- Venuvinod, P. K., and Lau, W. S. (1986). Estimation of Rake Temperatures for Oblique Cutting, *Int. J. Mach. Tool Des. Res.*, 26, 1–14.
- Viskanta, R., and Bergman, T. (2000). Heat Transfer in Materials Processing, in *Handbook of Heat Transfer Applications*, 3rd ed., W. M. Rohsenow, J. P. Hartnett, and E. N. Ganic, eds., McGraw-Hill, New York, pp. 18.1–18.74.
- Walsh, S. M., and Charmchi, M. (1988). Heat Transfer Characteristics in a Pultrusion Process, *Proc. National Heat Transfer Conference*, Houston, TX, Vol. 23.
- Weiner, J. H. (1955). Shear Plane Temperature Distribution in Orthogonal Cutting, *ASME Trans.*, 77, 1331–1341.

- Wilson, W. R. D., and Mahdavian, S. M. (1974). A Thermal Reynolds Equation and Its Application in the Analysis of Plasto-hydrodynamic Inlet Zones, *J. Lubr. Technol.*, 96, 572–578.
- Wright, R. N. (1976). Practical Use of Mechanical Analysis in Wire Drawing, *Wire Technol.*, 9, 57–61.
- Wright, P. K., McCormick, S. P., and Miller, T. R. (1980). Effect of Rake Face Design on Cutting Tool Temperature Distributiouns, *J. Eng. Ind.*, 102, 123–128.
- Yang, K. T. (1992). Thermal and Friction Effects in Metal Extrusion and Wire Drawing, in *Thermomechanical Aspects of Manufacturing and Materials Processing*, R. K. Shah et al., eds., Hemisphere Publishing, New York, pp. 245–262.
- Yang, F. (2002). Studies on Interface and Interphase Phenomena in Polymer Composites Processing, Ph.D. dissertation, Composites Processing Laboratory, Department of Mechanical Engineering, University of Connecticut, Storrs, CT.
- Yang, F., and Pitchumani, R. (1998). A Fractal Model for Intimate Contact Development during Thermoplastic Fusion Bonding, *Proc. 13th Technical Conference of the American Society for Composites*, A. J. Vizzini, ed., pp. 1134–1146.
- Yang, F., and Pitchumani, R. (2001a). Fractal Description of Interlaminar Contact Development during Thermoplastic Composites Processing, *J. Reinf. Plastics Compos.*, 20(7), 536–546.
- Yang, F., and Pitchumani, R. (2001b). A Fractal Cantor Set-based Description of Intimate Contact Evolution during Thermoplastic Composites Processing, *J. Mater. Sci.*, 36(19), 4661–4671.
- Yang, F., and Pitchumani, R. (2002). Interlaminar Contact Development in Thermoplastic Fusion Bonding, *Polym. Eng. Sci.*, 42(2), 424–438.
- Yang, F., and Pitchumani, R. (2003). Nonisothermal Heating and Interlaminar Bond Strength Evolution During Thermoplastic Matrix Composites Processing, *Polymer Composites*, 24(2), in press.
- Yang, W.-J., Mochizuki, S., and Nishiwaki, N. (1994). *Transport Phenomena in Manufacturing and Materials Processing*, Elsevier, Amsterdam.
- Young, R. J., and Lovell, P. A. (1991). *Introduction to Polymers*, Chapman & Hall, London.
- Zhang, Z., and Faghri, A. (1996). An Integral Approximate Solution of Heat Transfer in the Grinding Process, *Int. J. Heat Mass Transfer*, 39, 2653–2662.

Microscale Heat Transfer

ANDREW N. SMITH

Department of Mechanical Engineering
United States Naval Academy
Annapolis, Maryland

PAMELA M. NORRIS

Department of Mechanical and Aerospace Engineering
University of Virginia
Charlottesville, Virginia

- 18.1 Introduction
- 18.2 Microscopic description of solids
 - 18.2.1 Crystalline structure
 - 18.2.2 Energy carriers
 - 18.2.3 Free electron gas
 - 18.2.4 Vibrational modes of a crystal
 - 18.2.5 Heat capacity
 - Electron heat capacity
 - Phonon heat capacity
 - 18.2.6 Thermal conductivity
 - Electron thermal conductivity in metals
 - Lattice thermal conductivity
- 18.3 Modeling
 - 18.3.1 Continuum models
 - 18.3.2 Boltzmann transport equation
 - Phonons
 - Electrons
 - 18.3.3 Molecular approach
- 18.4 Observation
 - 18.4.1 Scanning thermal microscopy
 - 18.4.2 3ω technique
 - 18.4.3 Transient thermoreflectance technique
- 18.5 Applications
 - 18.5.1 Microelectronics applications
 - 18.5.2 Multilayer thin-film structures
- 18.6 Conclusions
- Nomenclature
- References

18.1 INTRODUCTION

The microelectronics industry has been driving home the idea of miniaturization for the past several decades. Smaller devices equate to faster operational speeds and more transportable and compact systems. This trend toward miniaturization has an infectious quality, and advances in nanotechnology and thin-film processing have spread to a wide range of technological areas. A few examples of areas that have been affected significantly by these technological advances include diode lasers, photovoltaic cells, thermoelectric materials, and microelectromechanical systems (MEMSs). Improvements in the design of these devices have come mainly through experimentation and macroscale measurements of quantities such as overall device performance. Most studies of the microscale properties of these devices and materials have focused on either electrical and/or microstructural properties. Numerous thermal issues, which have been largely overlooked, currently limit the performance of modern devices. Hence the thermal properties of these materials and devices are of critical importance for the continued development of high-tech systems.

The need for increased understanding of the energy transport mechanisms of thin films has given rise to a new field of study called *microscale heat transfer*. Microscale heat transfer is simply the study of thermal energy transfer when the individual carriers must be considered or when the continuum model breaks down. The continuum model for heat transfer has classically been the conservation of energy equation coupled with Fourier's law for thermal conduction. In an analogous manner, the study of "gas dynamics" arose when the continuum fluid mechanics models were insufficient to explain certain phenomena. The field of microscale heat transfer bears some striking similarities. One area of similarity is in the methodology. Usually, the first attempt at modeling is to modify the continuum model in such a way that the microscale considerations are taken into account. The more common and slightly more difficult method is application of the Boltzmann transport equation. Finally, when both of these methods fail, the computationally exhaustive molecular dynamics approach is typically adopted. These three methods and specific applications will be discussed in more detail.

Figure 18.1 demonstrates four different mechanisms by which electrons, the primary heat carriers in metallic films, can be scattered. All of these scattering mechanisms are important in the study of microscale heat transfer. The mean free path of an electron in a bulk metal is typically on the order of 10 to 30 nm, where electron lattice scattering is dominant. However, when the film thickness is on the order of the mean free path, boundary scattering comes important. This is referred to as a *size effect* because the physical size of the film influences the transport properties. Thin films are manufactured using a number of methods and under a wide variety of conditions. This can have a serious influence on the microstructure of the film, which influences defect and grain boundary scattering. Finally, when heated by ultrashort pulses, the electron system becomes so hot that electron-electron scattering can become significant. Thus, microscale heat transfer requires consideration of the microscopic energy carriers and the full range of possible scattering mechanisms.

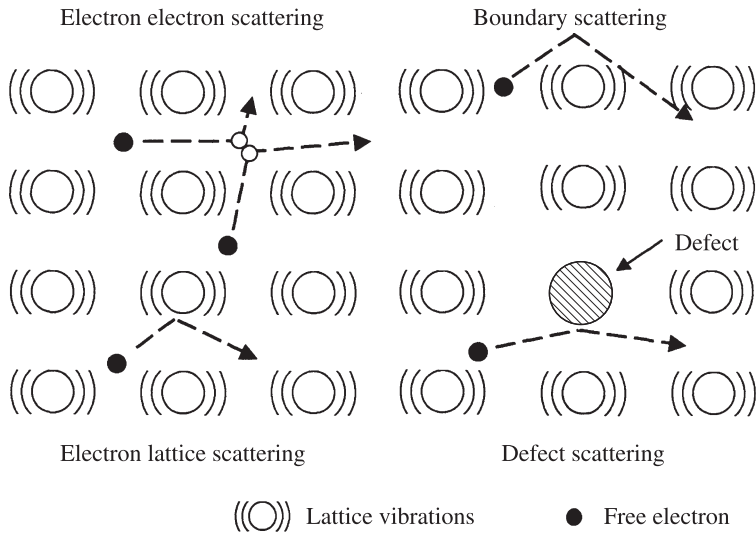


Figure 18.1 Primary scattering mechanisms of free electrons within a metal.

In the first section of this chapter we focus on defining and describing the microscopic heat carriers. The free electrons are typically responsible for thermal transport in metals. The governing statistical distribution is presented and discussed, along with equations for thermal conduction and the electron heat capacity. In an insulating material, thermal transport is accomplished through the motion of lattice vibrations called *phonons*. These lattice vibrations or phonons are discussed in detail. The primary heat carriers in semiconductor materials are also phonons, and therefore the thermal transport properties of semiconductors are determined in the same manner as for insulating materials. The formulations for these energy carriers are then used to explain and calculate the phonon thermal conductivity and lattice heat capacity of crystalline materials.

Experimental observation and measurement of microscale thermophysical properties is the subject of the next section. These techniques can be either steady-state, modulated, or pulsed transient techniques. Steady-state techniques typically focus on measuring the surface temperature with high spatial resolution, while the transient techniques are better suited for measuring transport properties on microscopic length scales. The majority of these techniques utilize either one or more of the following methods for determining thermal effects; nanoscale thermocouples, the temperature dependence of the electrical resistance of a microbridge, or thermal effects on the refractive index monitored using optical techniques. Three common methods for measuring microscale thermal phenomena are discussed in more detail.

In the final section we focus on specific applications where consideration of microscale heat transfer is important. For example, the microelectronics industry is perpetually looking for materials with lower dielectric constants to keep pace with the

miniaturization trend. Unfortunately, materials that are good electrical insulators are typically also good thermal insulators. As another example, high-power diode lasers and, particularly, vertical cavity surface-emitting laser diodes are often limited by the dissipation of thermal energy. These devices are an example of the increased trend toward multilayer thin-film structures. Recently, developers of thermoelectric materials have been using multilayer superlattice structures to reduce thermal transport normal to the material. This could significantly increase the efficiency of thermoelectric coolers. These examples represent just a few areas in which advancements in nanotechnology will have a dramatic impact on our lives.

18.2 MICROSCOPIC DESCRIPTION OF SOLIDS

To proceed with a discussion of microscale heat transfer, it is necessary first to examine the microscopic energy carriers and the basic heat transfer mechanisms. In metals, thermal transport occurs primarily from the motion of free electrons, while in semiconductors and insulators, thermal transport occurs due to lattice vibrations that travel about the material much like acoustic waves. In this chapter a conscious decision was made to minimize the presentation of quantum mechanical derivations and focus on a more physical presentation. More detailed descriptions of the material presented in this section can be found in most basic solid-state physics textbooks such as those of Ashcroft and Mermin (1976) and Kittel (1996). The theoretical descriptions of electrons and phonons usually include an assumption that the material has a crystalline structure. Therefore, this section begins with the basic relevant concepts of crystalline structures.

18.2.1 Crystalline Structure

The atoms within a solid structure arrange themselves in an organized manner such that the potential energy stored within the lattice is minimized. If the structure has long-range order, the material is referred to as *crystalline*. Once this structure is formed, smaller individual pieces of the crystalline can usually be identified that, when repeated in each direction, comprise the entire solid material. This type of material is then referred to as *single crystalline*. Most real materials contain grains, which are single crystalline; however, when the grains meet, a grain boundary is formed and the material is described as *polycrystalline*. In this section the assumption is made that the materials are single crystalline. However, the issues of grain size and boundaries, which arise in polycrystalline materials, are very important to the study of microscale heat transfer since the grain boundaries can scatter energy carriers and impede thermal transport.

The smallest of the individual structures that make up the entire crystal are called *unit cells*. Once the crystal has been broken down into unit cells, it must be determined whether the unit cells make up a *Bravais lattice*. Several criteria must be satisfied before a Bravais lattice can be identified. First, it must be possible to define a set of vectors, \mathbf{R} , which can describe the location of all points within the lattice,

$$\mathbf{R} = n_1 \mathbf{a}_1 = n_1 \mathbf{a}_1 + n_2 \mathbf{a}_2 + n_3 \mathbf{a}_3 \quad (18.1)$$

where n_1 , n_2 , and n_3 are integers. The set of primitive vectors \mathbf{a}_i are defined in the same manner. The three independent vectors \mathbf{a}_i can be used to translate between any of the lattice points using a linear combination of these vectors. Second, the structure of the lattice must appear exactly the same regardless of the point from which the array is viewed. Described in another way, if the lattice is observed from the perspective of an individual atom, all the surrounding atoms should appear to be identical, independent of which atom is chosen as the observation point.

There are 14 three-dimensional lattice types (Kittel, 1996). However, the most important are the *simple cubic* (SC), *face-centered cubic* (FCC), and *body-centered cubic* (BCC). These structures are Bravais lattices only when all the atoms are identical, as is the case with any element. When the atoms are different, these structures are not Bravais lattices. The NaCl structure is an example of a simple cubic structure, as shown in Fig. 18.2a, where the sodium and chloride atoms occupy alternating positions. For this structure to meet the criteria of a Bravais lattice, to be seen as identical regardless of the viewing point, the Na and Cl atoms must be grouped. Whenever two atoms are grouped, the lattice is said to have a *two-point basis*. In a Bravais lattice each unit cell contains only one atom, while each unit cell of a lattice with a two-point basis will contain the two grouped atoms. When each sodium atom is grouped with a chlorine atom, the result is a Bravais lattice with a two-point basis, shown in Fig. 18.2b by dark solid lines.

It is also possible to have a lattice with a basis even if all the atoms are identical; the most important crystal structure that falls into this category is the diamond structure. The group IV elements C, Si, Ge, and Sn can all have this structure. In addition, many III–V semiconductors, such as GaAs, also have the diamond structure. The diamond structure is a FCC Bravais lattice with a two-point basis, or equivalently, the diamond structure is composed of two offset FCC lattices.

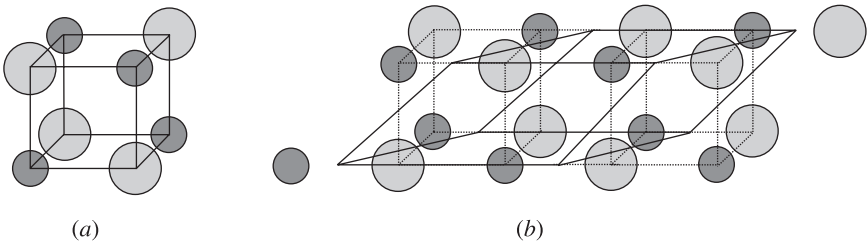


Figure 18.2 (a) NaCl structure shown as a simple cubic unit cell where the Na atom is the solid circle and the Cl atom is the shaded circle. (b) Each Na atom has been grouped with the Cl atom on its left, this pair of atoms form the two-point basis. The NaCl structure can then be arranged as a Bravais lattice using the two-point basis, where the unit cell is shown by the dark solid lines.

For the purposes of understanding microscale heat transfer, there are two important concepts regarding crystalline structures that must be understood. The first is the concept of a Bravais lattice, which has just been presented. It is important in the study of energy transport on a microscale basis to know the Bravais lattice structure of the material of interest and whether or not the crystal is a lattice with a basis. The second important concept is the idea of the reciprocal lattice.

The structure of a crystal has an intrinsic periodicity that begins with the Bravais lattice unit cell. Certain properties, such as the electron density of the material, will vary between lattice sites but will vary periodically with the lattice. It is also common to be dealing with waves or particles with wavelike properties traveling within the crystal. In both cases, it is advantageous to define a *reciprocal lattice*. The set of all wave vectors \mathbf{k} , which represent plane waves with the periodicity of a given Bravais lattice, is described by the reciprocal lattice vectors. Given the Bravais lattice vector \mathbf{R} , the reciprocal lattice vectors can be defined as the set of vectors that satisfy the equation

$$e^{i\mathbf{k}\cdot(\mathbf{r}+\mathbf{R})} = e^{i\mathbf{k}\cdot\mathbf{r}} \quad (18.2)$$

where \mathbf{r} is any vector within the lattice. It can be shown that the reciprocal lattice of a Bravais lattice is also a Bravais lattice, which also has a set of primitive vectors \mathbf{b} . It turns out that the reciprocal lattice of a FCC lattice is a BCC lattice, the reciprocal lattice of a BCC lattice is FCC, and the reciprocal lattice of a SC lattice is still simple cubic.

Once the reciprocal lattice vectors have been defined, the *Brillouin zone* can be found. The Brillouin zone is a unit cell of the reciprocal lattice centered on a particular lattice site and containing all points that are closer to that lattice site than to any other lattice site. According to the definition of a Bravais lattice, if the Brillouin zone is drawn around each lattice point, the entire volume will be filled and each Brillouin zone will be identical. The manner in which the Brillouin zone is constructed geometrically is: (1) draw lines from one reciprocal lattice site to all neighboring sites, (2) draw planes normal to each line that bisect the line, and (3) end each plane once it has intersected with another plane. The result is a choppy sphere that contains all the points closer to the central reciprocal lattice point than any other reciprocal lattice point. Three-dimensional representation of the Brillouin zone can be found in most solid-state physics texts (Kittel, 1996).

18.2.2 Energy Carriers

Thermal conduction through solid materials takes place both by the transport of vibrational energy within the lattice and by the motion of free electrons in a metal. In the next two sections a basic theoretical description of these energy carriers is presented. There are several significant differences in the behavior of these carriers that must be understood when dealing with microscale problems. There are also many similarities in the manner in which the problems are approached, despite the differences in the energy carriers.

18.2.3 Free Electron Gas

Many of the properties of metals can be explained adequately with the free electron Fermi gas theory (Ashcroft and Mermin, 1976). Although free electron gas theory does not adequately explain some properties, such as bandgaps in semiconductors, transport properties such as the electrical resistivity and thermal conductivity are well described by this theory. The assumption is made that each ion contributes a certain number of valence electrons to the Fermi gas and that these electrons are then free to move about the entire volume of the metal. The electron cloud is described appropriately as a gas, because any interactions other than collisions between electrons are neglected. Electron–electron collisions are usually negligible at or below room temperature, and electron collisions occur most frequently with the lattice, although scattering with defects, grain boundaries, and surfaces can also be significant.

Because the electrons have been assumed to be free and noninteracting, the allowable energy levels can be calculated using the free-particle Schrödinger equation. The allowable wavevectors in Cartesian coordinates that satisfy periodic boundary conditions in a three-dimensional cubic crystal, where the length of each side of the crystal is L , are found to be of the form

$$\mathbf{k}_x = \frac{2\pi n_x}{L} \quad \mathbf{k}_y = \frac{2\pi n_y}{L} \quad \mathbf{k}_z = \frac{2\pi n_z}{L} \quad (18.3)$$

where n_x , n_y , and n_z are integer quantities. The allowable energy levels can be expressed in terms of the electron wavevectors \mathbf{k} :

$$\varepsilon_{\mathbf{k}} = \frac{\hbar^2 \mathbf{k}^2}{2m} \quad (18.4)$$

where m is the effective mass of an electron and \hbar is Planck's constant. Each atom contributes a certain number of electrons to give a total number N_e of free electrons. According to the *Pauli exclusion principle*, no two electrons can occupy the same energy state. The electrons start filling energy levels beginning with the lowest energy level and the energy of the highest level that is occupied at zero temperature is called the *Fermi energy*.

The Fermi energy ε_F is often visualized as a sphere plotted as a function of wavevector \mathbf{k} , where the radius is given by the Fermi wavevector k_F , which is the wavevector of the highest occupied energy level. In theory, the surface of this sphere is not continuous, but rather, a collection of discrete wavevectors. However, because the value of N_e is usually very large, the assumption of a smooth sphere is typically reasonable. According to the Pauli exclusion principle, each electron must have a particular wavevector. However, since there are two spin states, there are two allowable energy levels for each wavevector. Thus, there must be $N_e/2$ wavevectors contained within the sphere. As shown in eq. (18.3), the linear distance between allowable wavevectors is $2\pi/L$. Therefore, the volume of each wavevector element in reciprocal space is $(2\pi/L)^3$ or $8\pi^3/V$. The number of wavevectors contained in the

sphere times the volume taken up by each wavevector must equal the volume of the sphere of radius k_F . Therefore, the Fermi wavevector can be calculated as

$$\frac{8\pi^3}{V} \frac{N_e}{2} = \frac{4}{3} \pi k_F^3 \rightarrow k_F = \left(\frac{3\pi^2 N_e}{V} \right)^{1/3} \quad (18.5)$$

which when substituted into eq. (18.4) yields an expression for the Fermi energy:

$$\varepsilon_F = \frac{\hbar^2 k_F^2}{2m} = \frac{\hbar^2}{2m} \left(\frac{3\pi^2 N_e}{V} \right)^{2/3} \quad (18.6)$$

where m is the effective mass of an electron and \hbar is Planck's constant.

Up to this point, the temperature of the electron gas has been assumed to be zero; therefore, all the energy levels up to the Fermi energy are occupied, whereas all energy levels above the Fermi energy are vacant. The occupational probability of a free electron gas as a function of temperature is given by the Fermi–Dirac distribution,

$$f(\varepsilon) = \frac{1}{e^{(\varepsilon - \mu)/k_B T} + 1} \quad (18.7)$$

where μ is the thermodynamic potential, k_B the Boltzmann constant, and T the temperature of the electron gas. The chemical potential μ is a function of temperature but can be approximated by the Fermi energy for temperatures at or below room temperature (Kittel, 1996).

Now that the allowable energy levels and the governing statistics have been defined for the free electron systems, it is possible to calculate the transport properties of the free electron systems. This was first done by Sommerfeld in 1928 using the Fermi–Dirac statistics (Wilson, 1954). However, in many instances it will be more convenient to integrate over energy states of the electron system rather than wavevectors. Therefore, the density of states $D(\varepsilon)$ is defined such that a single integration can be performed over the energy. The density of states can be determined by the following expression for the electron number density n_e :

$$n_e = \int \frac{1}{4\pi^3} f(\mathbf{k}) d\mathbf{k} = \int_0^\infty D(\varepsilon) f(\varepsilon) d\varepsilon \quad (18.8)$$

Using eq. (18.8), the electron density of states, which represents the number of available states of energy ε , can be calculated as

$$D(\varepsilon) = \frac{m}{\hbar^2 \pi^2} \sqrt{\frac{2m\varepsilon}{\hbar^2}} \quad (18.9)$$

where m is the effective mass of an electron. Once the density of states has been determined, the specific internal energy stored within the electron system can be found by the integration

$$u_e = \int_0^\infty \varepsilon D(\varepsilon) f(\varepsilon) d\varepsilon \quad (18.10)$$

18.2.4 Vibrational Modes of a Crystal

In this section, the manner in which vibrational energy is transported through a crystalline lattice is discussed. For this discussion, the primary emphasis is on the positions of the ions within the lattice and the interatomic forces. Several assumptions are made at this point to simplify the analysis. The first is that the mean equilibrium position of each ion is about its assigned lattice site within the Bravais lattice given by the vector \mathbf{R} . The second is that the distance between the ion and the lattice site is much smaller than the interatomic spacing. Therefore, the position of each ion can be expressed in terms of the stationary Bravais lattice site and some displacement:

$$\mathbf{r}(\mathbf{R}) = \mathbf{R} + u(\mathbf{R}) \quad (18.11)$$

Calculation of the vibrational modes in three dimensions is involved; therefore, the discussion will begin with the one-dimensional case. The observations that are made based on the one-dimensional model will generally hold true in a three-dimensional crystal. The analysis begins with a simple linear chain of atoms, shown in Fig. 18.3, where solid vertical lines give the positions of the equilibrium lattice sites. Their positions are given by an integer times a , the distance between lattice sites. The atoms are connected by springs, with spring constant K , that represent a linearization of the restoring forces that act between ions. The displacement u_n of each ion from the lattice is measured relative to the n th lattice site.

The equations of motion for the atoms within the system are given by the expression

$$M \frac{d^2 u_n}{dt^2} = K(u_{n+1} - 2u_n + u_{n-1}) \quad (18.12)$$

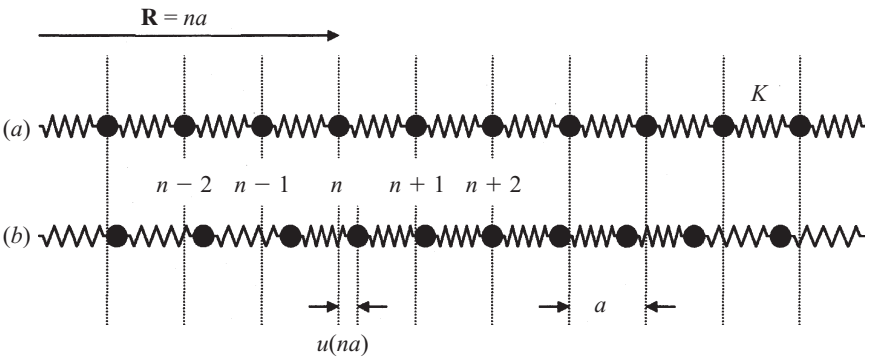


Figure 18.3 (a) Linear chain of atoms at their equilibrium lattice sites, $\mathbf{R} = na$; (b) linear chain of atoms where the individual atoms are displaced from their equilibrium positions by $u(na)$.

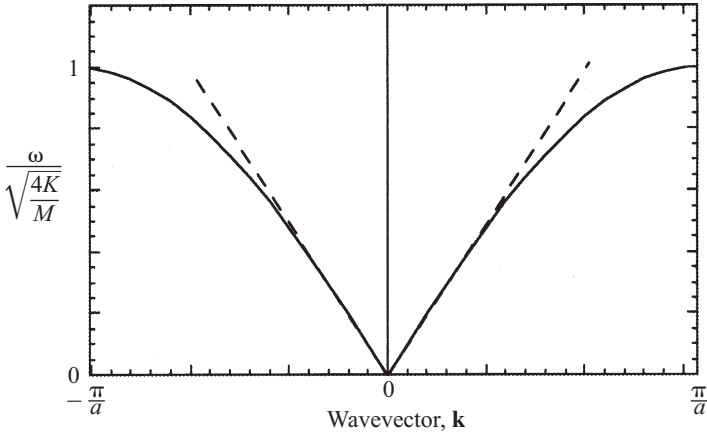


Figure 18.4 Plot of the frequency of a plane wave propagating in the crystal as a function of wavevector. Note that the relationship is linear until $\mathbf{k} \simeq 1/a$.

where M is the mass of an individual atom. By taking the time dependence of the solution to be of the form $\exp(-i\omega t)$, the frequency of the solution as a function of the wavevector can be determined as given by eq. (18.13). Figure 18.4 shows the results of this equation plotted over all the values that produce independent results. Values of \mathbf{k} larger than π/a correspond to plane waves with wavelengths less than the interatomic spacing. Because the atoms are located at discrete points, solutions to the equations above yielding wavelengths less than the interatomic spacing are not unique solutions, and these solutions can be equally well represented by long-wavelength solutions.

$$\omega(\mathbf{k}) = \sqrt{\frac{4K}{M}} \left| \sin \frac{1}{2} \mathbf{k} \mathbf{a} \right| \quad (18.13)$$

The results shown in Fig. 18.4 apply for a Bravais lattice in one dimension, which can be represented by a linear chain of identical atoms connected by springs with the same spring constant, K . A Bravais lattice with a two-point basis can be represented in one dimension by either a linear chain of alternating masses M_1 and M_2 , separated by a constant spring constant K , or by a linear chain of constant masses M , with the spring constant of every other spring alternating between K_1 and K_2 . The theoretical results are similar in both cases, but only the case of a linear chain with atoms connected by two different springs, K_1 and K_2 , where the springs alternate between the atoms, is discussed. The results are shown in Fig. 18.5. The displacement of each atom from each equilibrium point is given by either $u(na)$ for atoms with the K_1 spring on their right and $v(na)$ for atoms with the K_1 spring on their left.

The reason for selecting this case is its similarity to the diamond structure. Recall that the diamond structure is a FCC Bravais lattice with a two-point basis; all the atoms are identical, but the spacing between atoms varies. As the distance varies

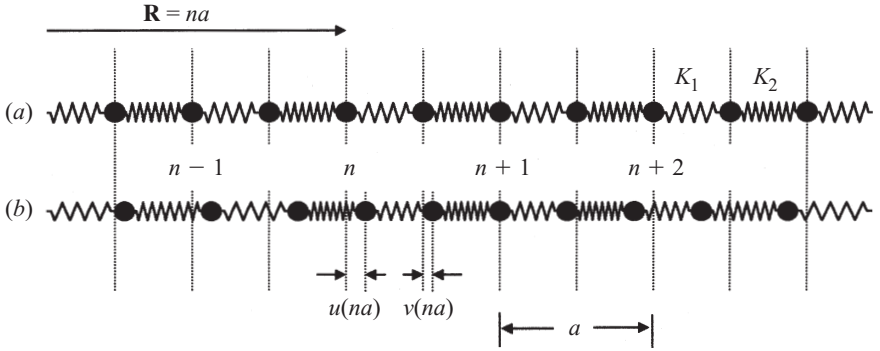


Figure 18.5 (a) One-dimensional Bravais lattice with two atoms per primitive cell shown in their equilibrium positions. The atoms are identical in mass; however, the atoms are connected by springs with alternating strengths K_1 and K_2 . (b) One-dimensional Bravais lattice with two atoms per primitive cell where the atoms are displaced by $u(na)$ and $v(na)$.

between atoms, so do the intermolecular forces, which are represented here by two different spring constants. The equations of motion for this system are given by

$$M \frac{d^2 u_n}{dt^2} = -K_1(u_n - v_n) - K_2(u_n - v_{n-1}) \quad (18.14a)$$

$$M \frac{d^2 v_n}{dt^2} = -K_1(v_n - u_n) - K_2(v_n - u_{n+1}) \quad (18.14b)$$

where u_n and v_n represent the displacement of the first and second atoms within the primitive cell, and K_1 and K_2 are the spring constants of the alternating springs. Again taking the time dependence of the solution to be of the form $e^{-i\omega t}$, the frequency of the solutions as a function of the wavevector can be determined as given by eq. (18.15) and shown in Fig. 18.6, assuming that $K_2 > K_1$:

$$\omega^2 = \frac{K_1 + K_2}{M} \pm \frac{1}{M} \sqrt{K_1^2 + K_2^2 + 2K_1 K_2 \cos \mathbf{k}a} \quad (18.15)$$

The expression relating the lattice vibrational frequency ω and wavevector \mathbf{k} is typically called the *dispersion relation*. There are several significant differences between the dispersion relation for a Bravais lattice without a basis [eq. (18.13)] versus a lattice with a basis [eq. (18.15)]. One of the most valuable pieces of information that can be gathered from the dispersion relation is the group velocity. The group velocity v_g governs the rate of energy transport within a material and is given by the expression

$$v_g = \frac{\partial \omega}{\partial \mathbf{k}} \quad (18.16)$$

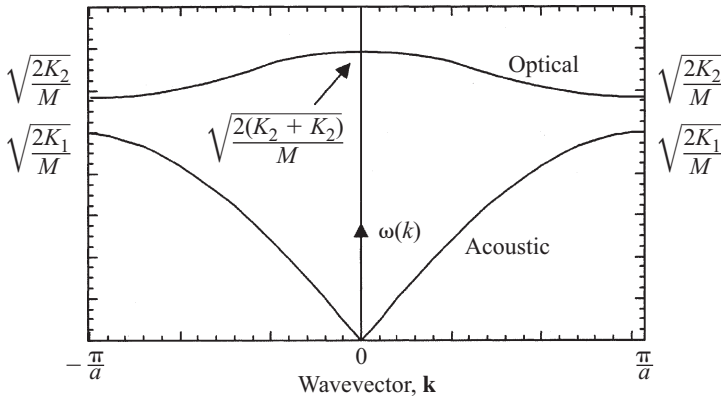


Figure 18.6 Dispersion relation for a one-dimensional Bravais lattice with a two-point basis.

The dispersion relations shown in Fig. 18.4 and in the lower curve in Fig. 18.6 are both roughly linear until $\mathbf{k} \simeq 1/a$, at which point the slope decreases and vanishes at the edge of the Brillouin zone, where $\mathbf{k} = \pi/a$. From these dispersion relations it can be observed that the group velocity stays constant for small values of \mathbf{k} and goes to zero at the edge of the Brillouin zone. It follows directly that waves with small values of \mathbf{k} , corresponding to longer wavelengths, contribute significantly to the transport of energy within the material. These curves represent the acoustic branch of the dispersion relation because plane waves with small \mathbf{k} , or long wavelength, obey a linear dispersion relation $\omega = c\mathbf{k}$, where c is the speed of sound or acoustic velocity.

The upper curve shown in Fig. 18.6 is commonly referred to as the *optical branch* of the dispersion relation. The name comes from the fact that the higher frequencies associated with these vibrational modes enable some interesting interactions with light at or near the visible spectrum. The group velocity of these waves is typically much less than for the acoustic branch. Therefore, contributions from the optical branch are usually considered negligible when evaluating the transport properties. Contributions from the optical branch must be considered when evaluating the specific heat.

Dispersion relations for a three-dimensional crystal in a particular direction will look very similar to one-dimensional relations except that there are transverse modes. The transverse modes arise due to the shear waves that can propagate in a three-dimensional crystal. The two transverse modes travel at velocities slower than the longitudinal mode; however, they still contribute to the transport properties. The optical branch can also have transverse modes. Again, optical branches occur only in three-dimensional Bravais lattices with a basis and do not contribute to the transport properties, due to their low group velocities.

Figure 18.7 shows the dispersion relations for lead at 100 K (Brockhouse et al., 1962). This is an example of a monoatomic Bravais lattice, since lead has a face-centered cubic (FCC) crystalline structure. Therefore, there are only acoustic branches, one longitudinal branch and two transverse. In the $[110]$ direction it is

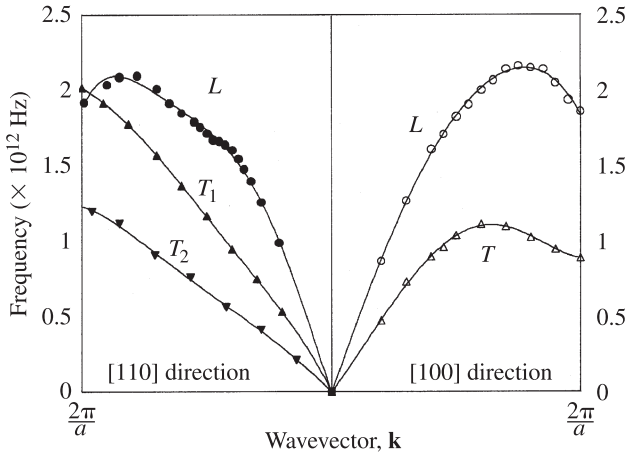


Figure 18.7 Dispersion relation for lead at 100 K plotted in the [110] and [100] directions. (From Brockhouse et al., 1962.)

possible to distinguish between the two transverse modes; however, due to the symmetry of the crystal, the two transverse modes happen to be identical in the [100] direction (Ashcroft and Mermin, 1976).

Finally, the concept of phonons must be introduced. The term *phonon* is commonly used in the study of the transport properties of the crystalline lattice. The definition of a phonon comes directly from the equation for the total internal energy U_l of a vibrating crystal:

$$U_l = \sum_{\mathbf{k}, s} \left[n_s(\mathbf{k}) + \frac{1}{2} \right] \hbar \omega(\mathbf{k}, s) \quad (18.17)$$

The simple explanation of eq. (18.17) is that the crystal can be seen as a collection of $3N$ simple harmonic oscillators, where N is the total number of atoms within the system and there are three modes of oscillation, one longitudinal and two transverse. Using quantum mechanics, one can derive the allowable energy levels for a simple harmonic oscillator, which is exactly the expression within the summation of eq. (18.17). The summation is taken over the allowable phonon wavevectors \mathbf{k} and the three modes of oscillation s . The definition of a phonon comes from the following statement: The integer quantity $n_s(\mathbf{k})$ is the mean number of phonons with energy $\hbar \omega(\mathbf{k}, s)$. Therefore, the number of phonons at a particular frequency simply represents the amplitude to which that vibrational mode is excited. Phonons obey the Bose–Einstein statistical distribution; therefore, the number of phonons with a particular frequency ω at an equilibrium temperature T is given by the equation

$$n_s(\mathbf{k}) = \frac{1}{e^{\hbar \omega(\mathbf{k}, s)/k_B T} - 1} \quad (18.18)$$

where k_B is the Boltzmann constant. Most thermal engineers are familiar with the concept of photons. Photons also obey the Bose–Einstein distribution; therefore, there are many conceptual similarities between phonons and photons.

The ability to calculate the energy stored within the lattice is important in any analysis of microscale heat transfer. Often, the calculations, which can be quite cumbersome, can be simplified by integrating over the allowable energy states. These integrations are actually performed over frequency, which is linearly related to energy through Planck’s constant. The specific internal energy of the lattice, u_l , is then given by the equation

$$u_l = \sum_s \int D_s(\omega) n_s(\omega) \hbar \omega_s \, d\omega_s \quad (18.19)$$

where $D_s(\omega)$ is the phonon density of states, which is the number of phonon states with frequency between ω and $(\omega + d\omega)$ for each phonon branch designated by s . The actual density of states of a phonon system can be calculated from the measured dispersion relation; although often, simplifying assumptions are made for the density of states that produce reasonable results.

18.2.5 Heat Capacity

The rate of thermal transport within a material is governed by the thermal diffusivity, which is the ratio of the thermal conductivity to the heat capacity. The heat capacity of a material is thus of critical importance to thermal performance. In this section the heat capacity of crystalline materials is examined. An understanding of the heat capacity of the different energy carriers, electrons and phonons, is important in the following section, where thermal conductivity is discussed. The heat capacity is defined as the change in internal energy of a material resulting from a change in temperature. The energy within a crystalline material, which is a function of temperature, is stored in the free electrons of a metal and within the lattice in the form of vibrational energy.

Electron Heat Capacity To solve for the electron heat capacity of a free electron metal, C_e , the derivative of the internal energy, stored within the electron system, is taken with respect to temperature:

$$C_e = \frac{\partial u_e}{\partial T} = \frac{\partial}{\partial T} \int_0^\infty \varepsilon D(\varepsilon) f(\varepsilon) \, d\varepsilon \quad (18.20)$$

The only temperature-dependent term within this integral is the Fermi–Dirac distribution. Therefore, the integral can be simplified, yielding an expression for the electron heat capacity:

$$C_e = \frac{\pi^2 k_B^2 n_e}{2\varepsilon_F} T \quad (18.21)$$

where C_e is a linear function of temperature and n_e is the electron number density. The approximations made in the simplification of foregoing integral hold for electron temperatures above the melting point of the metal.

Phonon Heat Capacity Deriving an expression for the heat capacity of a crystal is slightly more complicated. Again, the derivative of the internal energy, stored within the vibrating lattice, is taken with respect to temperature:

$$C_l = \frac{\partial u_l}{\partial T} = \frac{\partial}{\partial T} \left[\sum_s \int D_s(\omega) n_s(\omega) \hbar \omega_s \partial \omega \right] \quad (18.22)$$

To calculate the lattice heat capacity, an expression for the phonon density of states is required. There are two common models for the density of states of the phonon system, the Debye model and the Einstein model. The *Debye model* assumes that all the phonons of a particular mode, longitudinal or transverse, have a linear dispersion relation. Because longer-wavelength phonons actually obey a linear dispersion relation, the Debye model predominantly captures the effects of the longer-wavelength phonons. In the *Einstein model*, all the phonons are assumed to have the same frequency and hence the dispersion relation is flat; this assumption is thus more representative of optical phonons. Because both optical and acoustic phonons contribute to the heat capacity, both models play a role in explaining the heat capacity. However, the acoustic phonons alone contribute to the transport properties; therefore, the Debye model will typically be used for calculating the transport properties.

Debye Model The basic assumption of the Debye model is that the dispersion relation is linear and all three acoustic branches have the speed of sound c :

$$\omega(\mathbf{k}) = c\mathbf{k} \quad (18.23)$$

However, unlike photons, this dispersion relation does not extend to infinity. Since there are only N primitive cells within the lattice, there are only N independent wavevectors for each acoustic mode. Using spherical coordinates again, conceive of a sphere of radius k_D in wavevector space, where the total number of allowable wavevectors within the sphere must be N and each individual wavevector occupies a volume of $(2\pi/L)^3$:

$$\frac{4}{3}\pi k_D^3 = N \left(\frac{2\pi}{L} \right)^3 \rightarrow k_D = \left(\frac{6\pi^2 N}{V} \right)^{1/3} \quad (18.24)$$

Using eq. (18.24), the maximum frequency allowed by the Debye model, known as the *Debye cutoff frequency* ω_D , is

$$\omega_D = c \left(\frac{6\pi^2 N}{V} \right)^{1/3} \quad (18.25)$$

Now that the maximum frequency allowed by the Debye model is known and it is assumed that the dispersion relation is linear, an expression for the phonon density of states is required. Again, the concept of a sphere in wavevector space can be used to find the number of allowable phonon modes N with wavevector less than k . Each allowable wavevector occupies a volume in reciprocal space equal to $(2\pi/L)^3$.

Therefore, the total volume of the sphere of radius k must be equal to the number of phonon modes with wavevector less than k multiplied times $(2\pi/L)^3$:

$$\frac{4}{3}\pi k^3 = N \left(\frac{2\pi}{L} \right)^3 \rightarrow N = \frac{V}{6\pi^2} k^3 \quad (18.26)$$

The phonon density of states $D(\omega)$ is the number of allowable states at a particular frequency and can be determined by the expression

$$D(\omega) = \frac{\partial N}{\partial \omega} = \frac{V}{2\pi^2 c^3} \omega^2 \quad (18.27)$$

Returning to eq. (18.22), all the information needed to calculate the lattice heat capacity is known. Again simplifying the problem by assuming that all three acoustic modes obey the same dispersion relation, $\omega(\mathbf{k}) = c\mathbf{k}$, the lattice heat capacity can be calculated using

$$C_l(T) = \frac{3V\hbar^2}{2\pi^2 c^3 k_B T^2} \int_0^{\omega_D} \omega^4 \frac{e^{\hbar\omega/k_B T}}{(e^{\hbar\omega/k_B T} - 1)^2} d\omega \quad (18.28)$$

which can be simplified further by introducing a term called the *Debye temperature*, θ_D . The Debye temperature is calculated directly from the Debye cutoff frequency,

$$k_B \theta_D = \hbar \omega_D \rightarrow \theta_D = \frac{\hbar \omega_D}{k_B} \quad (18.29)$$

With this new quantity, the lattice specific heat calculated under the assumptions of the Debye model can be expressed as

$$C_l(T) = 9Nk_B \left(\frac{T}{\theta_D} \right)^3 \int_0^{\theta_D/T} \frac{x^4 e^x}{(e^x - 1)^2} dx \quad (18.30)$$

Figure 18.8 shows the molar values of the specific heat of Au compared to the results of eq. (18.30) using a Debye temperature of 170 K. Although a theoretical value of the Debye temperature can be calculated using eq. (18.29), the published values are typically determined by comparing the theoretical predictions of the specific heat to measured values.

The low-temperature specific heat is important in the analysis of the lattice thermal conductivity. If the temperature is much less than the Debye temperature, the lattice heat capacity is proportional to T^3 . This proportionality is easily seen in Fig. 18.9, where the information contained in Fig. 18.8 is plotted on a logarithmic plot to highlight the exponential dependence on temperature. The Debye model accurately predicts this T^3 dependence.

Einstein Model The Einstein model for the phonon density of states is based on the assumption that the dispersion relation is flat. In other words, the assumption is

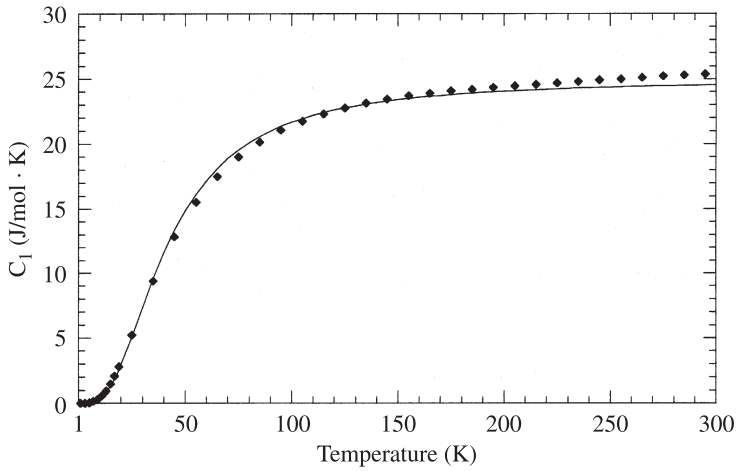


Figure 18.8 Molar specific heat of Au compared to the Debye model (eq. 18.30) using 170 K for the Debye temperature. (From Weast et al., 1985.)

made that all N simple harmonic oscillators are vibrating at the same frequency, ω_0 ; therefore, the density of states can be written as

$$D(\omega) = N\delta(\omega - \omega_0) \quad (18.31)$$

The method for calculating the heat capacity is exactly the same as that followed with the Debye model, although the integrals are simpler, due to the delta function.

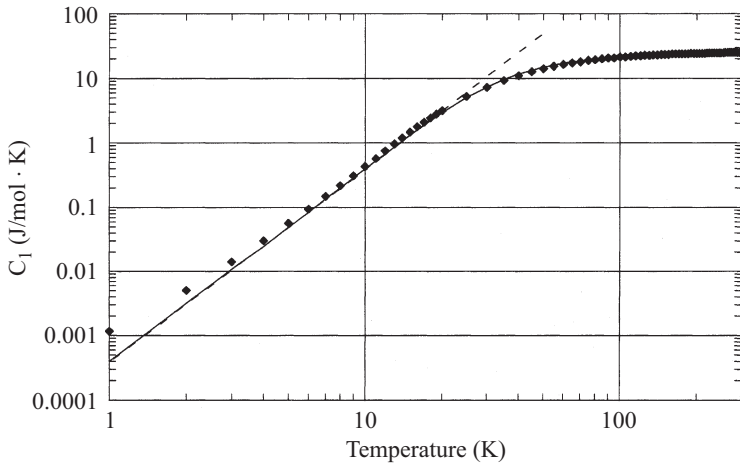


Figure 18.9 The T^3 dependence of the lattice specific heat is very apparent on a logarithmic plot of the molar specific heat of Au (Weast et al., 1985), compared to the Debye model (eq. 18.30) using 170 K for the Debye temperature.

This model provides better results than the Debye model for elements with the diamond structure. One reason for the improvement is the optical phonons in these materials. Optical phonons have a roughly flat dispersion relation, which is better represented by the Einstein model.

18.2.6 Thermal Conductivity

The specific energy carriers have been discussed in previous sections. The manner in which these carriers store energy, and the appropriate statistics that describe the energy levels that they occupy, have been presented. In the next section we focus on how these carriers transport energy and the mechanisms that inhibit the flow of thermal energy. Using very simple arguments from the kinetic theory of gases, an expression for the thermal conductivity K can be obtained:

$$K = \frac{1}{3} C v l \quad (18.32)$$

where C is the heat capacity of the particle, v the average velocity of the particles, and l the mean free path or average distance between collisions.

Electron Thermal Conductivity in Metals Thermal conduction within metals occurs due to the motion of free electrons within the metal. According to eq. (18.32), there are three factors that govern thermal conduction: the heat capacity of the energy carrier, the average velocity, and the mean free path. As shown in eq. (18.21), the electron heat capacity is linearly related to temperature. As for the velocity of the electrons, the Fermi–Dirac distribution, eq. (18.7), dictates that the only electrons within a metal that are able to undergo transitions, and thereby transport energy, are those located at energy levels near the Fermi energy. The energy contained within the electron system is purely kinetic and can therefore be converted into velocity. Because all electrons involved in transport of energy have an amount of kinetic energy close to the Fermi energy, they are all traveling at velocities near the Fermi velocity. Therefore, the assumption is made that all the electrons within the metal are traveling at the Fermi velocity, which is given by

$$v_F = \sqrt{\frac{2}{m} \varepsilon_F} \quad (18.33)$$

The third important contributor to the thermal conductivity is the electron mean free path, obviously a direct function of the electron collisional frequency. Electron collisions can occur with other electrons, the lattice, defects, grain boundaries, and surfaces. Assuming that each scattering mechanism is independent, *Matthiessen's rule* states that the total collisional rate is simply the sum of the individual scattering mechanisms (Ziman, 1960):

$$\nu_{\text{tot}} = \nu_{ee} + \nu_{ep} + \nu_d + \nu_b \quad (18.34)$$

where ν_{ee} is the electron–electron collisional frequency, ν_{ep} the electron–lattice collisional frequency, ν_d the electron–defect collisional frequency, and ν_b the electron–boundary collisional frequency. Consideration of each of these scattering mechanisms is important in the area of microscale heat transfer.

The temperature dependence of the collisional frequency can also be very important. Electron–defect and electron–boundary scattering are both typically independent of temperature, whereas for temperatures above the Debye temperature, the electron–lattice collisional frequency is proportional to the lattice temperature. Electron–electron scattering is proportional to the square of the electron temperature:

$$\nu_{ee} \simeq AT_e^2 \quad \nu_{ep} = BT_l \quad (18.35)$$

where A and B are constant coefficients and T_e and T_l are the electron and lattice temperatures. In clean samples at low temperatures, electron–lattice scattering dominates. However, electron–lattice scattering occurs much less frequently than simple kinetic theory would predict. In very pure samples and at very low temperatures, the mean free path of an electron can be as long as several centimeters, which is more than 10^8 times the distance between lattice sites. This is because the electrons do not scatter directly off the ions, due to the wavelike nature that allows the electrons to travel freely within the periodic structure of the lattice. Scattering occurs only when there are disturbances in the periodic structure of the lattice.

The temperature dependence of the thermal conductivity often allows us to isolate effects from several different mechanisms that affect the thermal conductivity. Figure 18.10 shows the thermal conductivity of three metals commonly used in the microelectronics industry: Cu, Al, and W. The general temperature dependence of all three metals is very similar. At very low temperatures, below 10 K, the primary

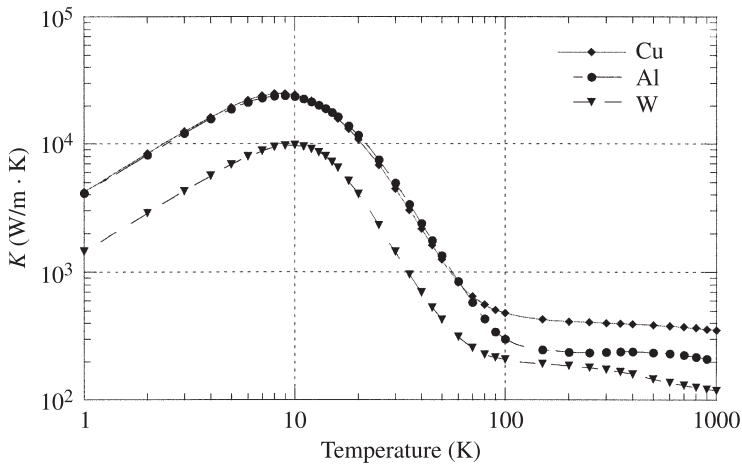


Figure 18.10 Thermal conductivity of Cu, Al, and W plotted as a function of temperature. (From Powell et al., 1966.)

scattering mechanism is due to either defect or boundary scattering, both of which are independent of temperature. The linear relation between the thermal conductivity and temperature in this regime arises from the linear temperature dependence of the electron heat capacity. At temperatures above the Debye temperature, the thermal conductivity is roughly independent of temperature as a result of competing temperature effects. The electron heat capacity is still linearly increasing with temperature [eq. (18.21)], but the mean free path is inversely proportional to temperature, due to increased electron–lattice collisions, as indicated by eq. (18.35).

Lattice Thermal Conductivity Thermal conduction within the crystalline lattice is due primarily to acoustic phonons. The original definition of phonons was based on the amplitude of a particular vibrational mode and that the energy contained within a phonon was finite. In this section, phonons are treated as particles, which is analogous to assuming that the phonon is a localized wave packet. Acoustic phonons generally follow a linear dispersion relation; therefore, the Debye model will generally be adopted when modeling the thermal transport properties, and the group velocity is assumed constant and equal to the speed of sound within the material. Thus, all the phonons are assumed to be traveling at a velocity equal to the speed of sound, which is independent of temperature. At very low temperatures the phonon heat capacity is proportional to T^3 , while at temperatures above the Debye temperature, the heat capacity is nearly constant.

The kinetic theory equation for the thermal conductivity of a diffusive system, eq. (18.32), is also very useful for understanding conduction in a phonon system. However, for this equation to be applicable, the phonons must scatter with each other, defects, and boundaries. If these interactions did not occur, the transport would be more radiative in nature. In some problems of interest in microscale heat transfer, the dimensions of the system are small enough that this is actually the case, and for these problems a model was developed called the *equations of phonon radiative transport* (Majumdar, 1993). However, in bulk materials, the phonons do scatter and the transport is diffusive. The phonons travel through the system much like waves, so it is easy to envision reflection and scattering occurring when waves encounter a change in the elastic properties of the material. Boundaries and defects obviously represent changes in the elastic properties. The manner in which scattering occurs between phonons is not as straightforward.

Two types of phonon–phonon collisions occur within crystals, described by either the *normal* or *N process* or the *Umklapp* or *U process*. In the simplest case, two phonons with wavevectors \mathbf{k}_1 and \mathbf{k}_2 collide and combine to form a third phonon with wavevector \mathbf{k}_3 . This collision must conserve energy:

$$\hbar\omega(\mathbf{k}_1) + \hbar\omega(\mathbf{k}_2) = \hbar\omega(\mathbf{k}_3) \quad (18.36)$$

Previously, the reciprocal lattice vector was defined as a vector through which any periodic property can be translated and still result in the same value. Since the dispersion relation is periodic throughout the reciprocal lattice,

$$\hbar\omega(\mathbf{k}) = \hbar\omega(\mathbf{k} + \mathbf{b}) \quad (18.37)$$

can be written. Here, \mathbf{b} is the reciprocal lattice vector. If eq. (18.37) is substituted into eq. (18.36) and a linear dispersion relation is assumed, $\omega(\mathbf{k}) = c\mathbf{k}$, then

$$\mathbf{k}_1 + \mathbf{k}_2 = \mathbf{k}_3 + \mathbf{b} \quad (18.38)$$

This equation is often referred to as the *conservation of quasi-momentum*, where $\hbar\mathbf{k}$ represents the phonon momentum. If $\mathbf{b} = 0$, the collision is called a normal or N process, and if $\mathbf{b} \neq 0$, the process is referred to as an Umklapp or U process. Examples of normal and Umklapp processes in one dimension are shown in Fig. 18.11.

The importance of distinguishing between N processes and U processes becomes apparent at low temperatures. At low temperatures, only long-wavelength phonons are excited, and these phonons have small wavevectors. Therefore, only normal scattering processes occur at low temperatures. Normal processes do not contribute to thermal resistance; therefore, phonon-phonon collisions do not contribute to low-temperature thermal conductivity. For higher temperatures, above the Debye temperature, however, all allowable modes of vibration are excited and the overall phonon population increases with temperature. Therefore, the frequency of U processes increases with increasing temperatures. This is the case for high temperatures, $T > \theta_D$, where the mean free path l_{pp} is inversely proportional to temperature:

$$l_{pp} \propto \frac{1}{T} \quad (18.39)$$

Figure 18.12 shows the thermal conductivity of three elements, all of which have the diamond structure and all of which exhibit the same general trend of thermal conductivity. At low temperatures, the normal processes do not affect the thermal conductivity. Defect and boundary scattering are independent of temperature; therefore, the temperature dependence arises from the heat capacity and follows the expected T^3 behavior. As the temperature increases, the heat capacity becomes constant, while the mean free path decreases, resulting in the approximately T^{-1} behavior at higher temperatures.

The thermal conductivity of crystalline SiO_2 , quartz, is shown in Fig. 18.13. The thermal conductivity has the same T^3 behavior at low temperature and T^{-1} behavior

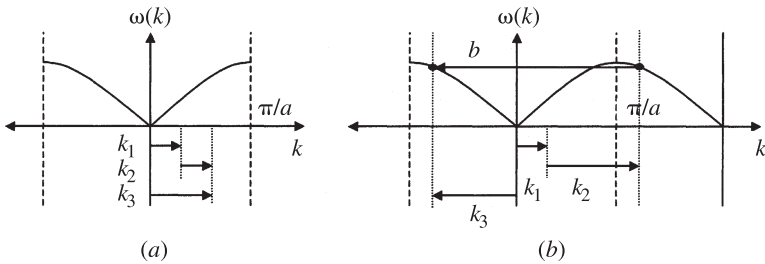


Figure 18.11 (a) Normal process where two phonons collide and the resulting phonon still resides within the Brillouin zone. (b) Umklapp process where two phonons collide and the resulting wavevector must be translated by the reciprocal lattice vector \mathbf{b} to remain within the original Brillouin zone.

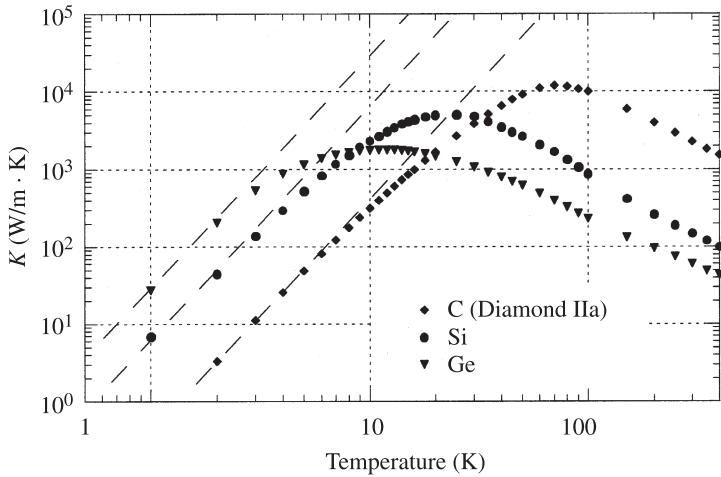


Figure 18.12 Thermal conductivity of the diamond structure shown as a function of temperature. (From Powell et al., 1974.)

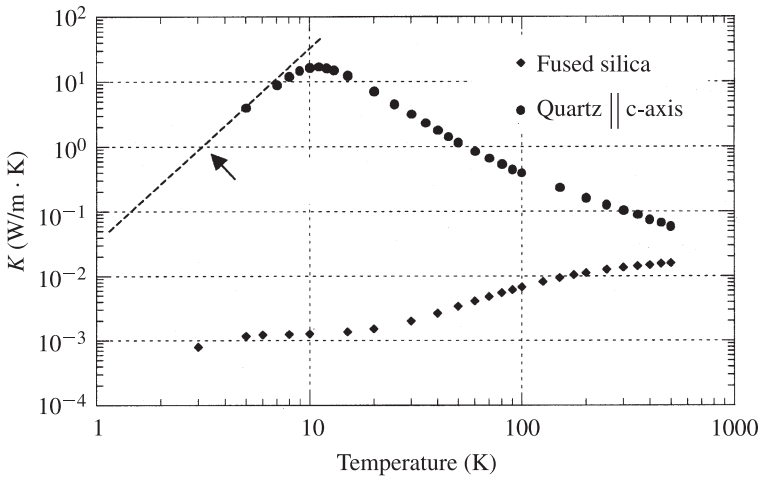


Figure 18.13 Thermal conductivity of crystalline and amorphous forms of SiO_2 . (From Powell et al., 1966.)

at high temperature. The thermal conductivity is plotted for the direction parallel to the c -axis because quartz has a hexagonal crystalline structure. The thermal conductivity of fused silica, also shown in Fig. 18.13, does not follow this behavior since it is an amorphous material and does not have a crystalline structure. The thermal conductivity of amorphous materials is an entirely different subject, and the reader is referred to several good references on the subject, such as Cahill and Pohl (1988) and Mott (1993).

18.3 MODELING

Now that an understanding of the basic energy carriers and the statistical procedures for dealing with these carriers has been developed, in this section we focus on a discussion of the methods for modeling heat transfer on the microscale. The first and simplest approach is to modify the continuum models to incorporate microscale heat transfer effects. Typically, continuum models can be used as long as meaningful local temperatures can be established. The next approach is to make use of the Boltzmann transport equation (Majumdar, 1998). With this approach, the transport equations developed are no longer dependent on temperature but on the statistical distributions of the energy carriers. The collisional term in the Boltzmann transport equation, however, is very difficult to model, and the assumptions made when modeling this term eventually limit the accuracy of this approach. Finally, the transport of thermal energy can be modeled using more molecular approaches, such as lattice dynamics, molecular dynamics, and Monte Carlo simulations (Klistner et al., 1988; Chou et al., 1999; Tamura et al., 1999). These approaches are the most fundamental in concept; however, they are computationally difficult and are ultimately limited by knowledge of the intermolecular forces between the atoms.

18.3.1 Continuum Models

Microscale heat transfer continuum models can be separated in several categories, depending on the basic transport mechanisms and the type of energy carriers involved. The first distinction is based on the manner in which heat transport occurs. If the energy carrier undergoes frequent collisions, transport is diffusive and the heat flux q is given by Fourier's law:

$$q = -K \nabla T \quad (18.40)$$

where K is the thermal conductivity. When eq. (18.40) is combined with the conservation of energy equation, the result is a parabolic differential equation. One theoretical problem with Fourier's law is that it yields an infinite speed of propagation of thermal energy. In other words, if the surface of a material is instantaneously heated, Fourier's law dictates that the thermal effect is felt immediately throughout the entire system. Typically, this effect is extremely small, and the speed with which the average of the thermal energy density travels is actually quite slow. Consider the one-dimensional heat equation for an instantaneous pulse that arrives at the surface at time zero:

$$C \frac{\partial T}{\partial t}(x, t) = \frac{\partial}{\partial x}(q) + S_o \delta(x) \delta(t) \quad (18.41)$$

where C is the heat capacity of the material, x the direction of heat flow, S_o the amount of energy deposited, and δ is a delta function. The solution to this problem is given by (Kittel and Kroemer, 1980)

$$T(x, t) = \frac{2S_o}{C} \sqrt{4\pi\alpha t} \exp\left(\frac{-x^2}{4\alpha t}\right) \quad (18.42)$$

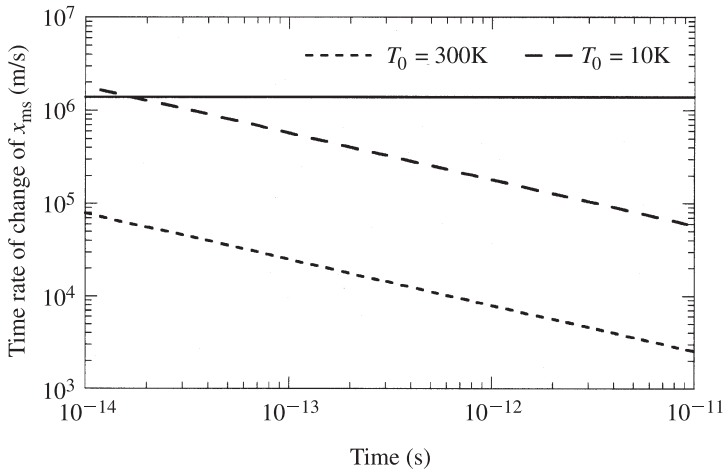


Figure 18.14 Time rate of change of the root mean square of the distance to which the effects of the instantaneous pulse have propagated plotted as a function of time.

where α is the thermal diffusivity of the material. The root mean square of the distance to which the effects of the instantaneous pulse have propagated is given by

$$x_{\text{rms}}(t) = \sqrt{2\alpha t} \quad (18.43)$$

Taking the derivative of this expression yields the average velocity with which the thermal energy propagates. Figure 18.14 shows the time rate of change of x_{rms} plotted versus time for Au at two different temperatures. In the low-temperature case, the time rate of change of x_{rms} , which represents the velocity of the energy carriers, exceeds the Fermi velocity for the first several hundred picoseconds. It is not possible for the thermal energy to propagate at this rate because the Fermi velocity represents the speed of the electrons. This illustrates that a time scale exists where a finite speed of propagation must be considered.

Cattaneo's equation was introduced to account for the finite speed of thermal energy propagation (Joseph and Preziosi, 1989). Essentially, Cattaneo's equation accounts for the time required for the heat flux to develop after a temperature gradient has been applied and is given by

$$\tau \frac{\partial q}{\partial t} + q = -K \nabla T \quad (18.44)$$

where τ is the relaxation time of the heat carrier. When this heat flux equation is combined with the conservation of energy equation, the result is a hyperbolic differential equation. This equation reduces to Fourier's law when the relaxation time is much less than the time scale of interest.

Another manner in which continuum thermal models have been modified to account for microscale heat transfer phenomena deals with equilibrium versus nonequilibrium systems. There are instances when multiple energy carriers may be involved

in a problem, and the representative temperature of each energy carrier system is different. Ultrashort pulsed laser heating and nonequilibrium Joule heating in field-effect transistors are two examples where nonequilibrium thermal systems occur. During ultrashort pulsed laser heating of metals, the electron and phonon systems can be treated separately. The conservation of energy equations for both systems are given by

$$C_e(T_e) \frac{\partial T_e}{\partial t} = \nabla(q_e) + G(T_e - T_l) + S_e \quad (18.45a)$$

$$C_l(T_l) \frac{\partial T_l}{\partial t} = \nabla(q_l) - G(T_e - T_l) + S_l \quad (18.45b)$$

where $G(T_e - T_l)$ is the rate of energy exchange between the two systems, G the electron–phonon coupling factor, and S_e and S_l are the source terms for the electron and lattice systems, respectively. The resulting system of equations can again be parabolic or hyperbolic, depending on the appropriate equation for the heat flux, eq. (18.40) or (18.44).

Even when continuum heat transfer equations are appropriate, the thermophysical properties can be influenced by microscale phenomena. The thermal conductivity can be reduced significantly due to increased defect and/or grain boundary scattering (Mayadas et al., 1969). When the length scale of the film is on the order of the heat carrier mean free path, there can be changes in the transport properties due to increased boundary scattering (Fuchs, 1938).

18.3.2 Boltzmann Transport Equation

The Boltzmann transport equation (BTE) is a conservation equation, where the conserved quantity is the number of particles. The general form of the BTE is given by the following equation for classical particles (Ziman, 1960):

$$\underbrace{\frac{\partial}{\partial t} [f(\mathbf{x}, \mathbf{P}, t) dV_x dV_P]}_{\text{total time rate of change of number of particles}} + \underbrace{\mathbf{v} \cdot \nabla_x [f(\mathbf{x}, \mathbf{P}, t) dV_x dV_P]}_{\text{convection of particles in physical space}} + \underbrace{\mathbf{F} \cdot \nabla_P [f(\mathbf{x}, \mathbf{P}, t) dV_x dV_P]}_{\text{convection of particles in momentum space}} = \underbrace{\left\{ \frac{\partial}{\partial t} [f(\mathbf{x}, \mathbf{P}, t) dV_x dV_P] \right\}_{\text{coll}}}_{\text{time rate of change of number of particles due to collisions}} \quad (18.46)$$

total time rate of change of number of particles	convection of particles in physical space	convection of particles in momentum space	time rate of change of number of particles due to collisions
--	--	--	--

where f is the distribution of particles, dV_x a differential control volume located at position x , and dV_P a differential control volume located at momentum P . The first term represents the quantity of interest, the time rate of change of the number of particles at position x that have velocity v . The second term represents particles

that physically cross the boundaries of the differential control volume in physical space. The third term accounts for particles that are acted on by an external force F and are therefore accelerated into or out of the differential control volume in velocity space. Finally, the right-hand side of the equation accounts for changes in position and velocity which can occur whenever two particles collide. This equation is directly applicable to electrons and classical particles where the momentum is represented by $\mathbf{P} = m\mathbf{v}$. In the case of electrons, the momentum can be expressed in terms of the wavevector using the expression $\mathbf{P} = \hbar\mathbf{k}$. This equation for the momentum is also used with phonons and photons; however, momentum is not strictly conserved, eq. (18.38).

When applying eq. (18.46) in the solution of microscale heat transfer problems, the greatest difficulty comes from the collisional term on the right-hand side. General expressions for the collisional frequencies of electron–electron, electron–phonon, and phonon–phonon scattering have already been presented as eqs. (18.35) and (18.39). However, the detailed nature of these collisions has not been examined fully. Typically, the relaxation time approximation is utilized. Under this approximation, the following expression is used:

$$\left(\frac{\partial f}{\partial t}\right)_{\text{collisions}} = -\frac{f - f_o}{\tau} \quad (18.47)$$

where f_o is the equilibrium distribution and τ is the relaxation time. The relaxation time approximation is based on the assumption of a distribution that is slightly perturbed from its equilibrium distribution f such that the distribution function can be written as $f = f_o + f'$. Collisions within the system will then act to bring about an equilibrium distribution. Substituting this expression into eq. (18.47) and solving for the deviation from equilibrium as a function of time due solely to collisional effects yields

$$\frac{\partial f'}{\partial t} = -\frac{f'}{\tau} \rightarrow f'(t) = e^{-t/\tau} \quad (18.48)$$

Therefore, by using eq. (18.47) for the collisional term, the assumption has been made that the collisions within the system will bring any deviation back to equilibrium according to an exponential decay. The relaxation time τ is simply the time required for the collisional effects to decrease the deviation by a factor of $1/e$. Although the relaxation time is not exactly the mean free time between collisions, the two are often assumed to be of the same order of magnitude and will sometimes be used interchangeably. When multiple relaxation times are applicable, such as electron–lattice and electron–defect scattering, they may be combined by again using Matthiessen's rule, eq. (18.34), assuming that the collisional mechanisms are independent. Note that the relaxation time is inversely proportional to the collisional frequency.

Phonons A general form of the Boltzmann transport equation for a phonon system is given by

$$\begin{aligned} \frac{\partial}{\partial t} [N(\mathbf{x}, \mathbf{k}, t) dV_x dV_k] + \mathbf{v} \cdot \nabla_x [N(\mathbf{x}, \mathbf{k}, t) dV_x dV_k] \\ = - \left(\frac{N(\mathbf{x}, \mathbf{k}, t) - N_o(\mathbf{x}, \mathbf{k}, t)}{\tau} \right) \end{aligned} \quad (18.49)$$

where $N(\mathbf{x}, \mathbf{k}, t)$ is the Bose-Einstein distribution as a function of position, wavevector, and time, and $\hbar \mathbf{k}$ is used to express the quasi-momentum of the phonon. The assumption is made that no external forces act on the phonons within the crystal. Using this form, the rate of heat transfer due to phonons can be determined within a crystal under a steady-state temperature gradient applied in the x direction. The one-dimensional Boltzmann transport equation can be written as

$$v_x \frac{\partial N}{\partial x} = - \frac{N - N_o}{\tau} \quad (18.50)$$

Thermal transport within the crystal occurs due to slight deviations from an equilibrium distribution, $N = N_o + N'$. The assumption that $\partial N_o / \partial x \gg \partial N / \partial x$ yields

$$N' = -v_x \tau \frac{\partial N_o}{\partial x} \quad (18.51)$$

Because the equilibrium distribution does not contribute to heat flux, N' yields the only contribution. The heat flux of a phonon system can be written in terms of the number of electrons traveling in the x direction carrying energy $\hbar \omega$:

$$q_x = \int v_x N'(\omega) \hbar \omega D(\omega) d\omega \quad (18.52)$$

where $D(\omega)$ is the phonon density of states. Substituting the expression for N' given in eq. (18.51) into eq. (18.52) yields

$$q_x = \begin{cases} \int v_x \left(-v_x \tau \frac{\partial N_o}{\partial x} \right) \hbar \omega D(\omega) d\omega & (18.53a) \\ \int v_x \left(-v_x \tau \frac{\partial N_o}{\partial T} \frac{\partial T}{\partial x} \right) \hbar \omega D(\omega) d\omega & (18.53b) \\ -v_x^2 \tau \left[\int \frac{\partial N_o}{\partial T} \hbar \omega D(\omega) d\omega \right] \frac{dT}{dx} & (18.53c) \end{cases}$$

The expression inside the brackets in eq. (18.53c) is, by definition, the lattice heat capacity, eq. (18.22). The mean free path of a phonon is equal to the product of the mean free time between collisions and the speed of the particle, $l = v \tau_p$. The speed of sound in the solid is equal to the square root of the sum of the three velocity components squared. If all the velocity components are equal, $v_x = \frac{1}{3} v^2$. Substituting all these expressions into eq. (18.53c) gives the same expression for the thermal conductivity that was presented as eq. (18.32):

$$q_x = -\frac{1}{3} C v \Lambda \frac{dT}{dx} \quad (18.54)$$

If the problem is transient rather than steady state, the time derivative term must be retained in the Boltzmann transport equation. Making the same assumptions as were made for the steady-state case, the BTE can be reduced to the form

$$\tau \frac{\partial f'}{\partial t} + f' = -v_x \tau \frac{\partial f_o}{\partial x} \quad (18.55)$$

This solution can then be used to derive an equation for the heat flux, which is identical to Catteneo's equation for hyperbolic heat conduction:

$$\tau \frac{\partial q}{\partial t} + q = -\frac{1}{3} C v \Lambda \frac{\partial T}{\partial x} \quad (18.56)$$

Despite this result, experience indicates that Fourier's law is applicable for most transient problems. This is because in most heat transfer problems the time scale of interest is much larger than the relaxation time of the energy carrier, in which case the first term can be neglected.

Electrons When dealing with the transport properties of metals, such as current density and thermal conduction due to the electrons, it is useful to begin with the general form of the Boltzmann transport equation for an electron system as given by the expression

$$\begin{aligned} \frac{\partial}{\partial t} [f(\mathbf{x}, \mathbf{k}, t) dV_x dV_k] + \mathbf{v} \cdot \nabla_x [f(\mathbf{x}, \mathbf{k}, t) dV_x dV_k] - \frac{e\mathbf{E}}{m} \cdot \nabla_k [f(\mathbf{x}, \mathbf{k}, t) dV_x dV_k] \\ = \left\{ \frac{\partial}{\partial t} [f(\mathbf{x}, \mathbf{k}, t) dV_x dV_k] \right\}_{\text{coll}} \end{aligned} \quad (18.57)$$

where $\hbar \mathbf{k}$ is used to express the momentum of the electron, m is the effective mass of an electron, and the force on an electron in the presence of an electric field \mathbf{E} is given by $\mathbf{F} = -e\mathbf{E}$. Again assuming that there is a temperature gradient in the x direction and that the distribution is only slightly perturbed from an equilibrium distribution, the Boltzmann transport equation reduces to

$$f' = - \left(\mathbf{v}_x \tau \frac{\partial f_o}{\partial T} \right) \frac{dT}{dx} - \left(\frac{e\tau}{m} \frac{\partial f_o}{\partial v_x} \right) \mathbf{E} \quad (18.58)$$

The following equations can be used to calculate the current density j and heat flux q of a metal based on the number of electrons traveling in a certain direction:

$$j = \int e \cdot v f(\epsilon) D(\epsilon) d\epsilon \quad (18.59)$$

$$q = \int \epsilon \cdot v f(\epsilon) D(\epsilon) d\epsilon \quad (18.60)$$

Again, only the deviation from the equilibrium distribution contributes to the transport properties. Therefore, the current density and heat flux can be written in terms of the thermal gradient and electrical field with four linear coefficients (Ziman, 1960):

$$j = L_{EE}\mathbf{E} + L_{ET} \nabla T \quad (18.61)$$

$$q = L_{TE}\mathbf{E} + L_{TT} \nabla T \quad (18.62)$$

If the thermal gradient is zero, eq. (18.61) reduces to Ohm's law, where $j = \sigma\mathbf{E}$ and $L_{EE} = \sigma$. Using eqs. (18.58) and (18.59), it is possible to solve for the electrical conductivity using the fact that $\partial f / \partial \varepsilon \approx \delta(\varepsilon - \varepsilon_F)$ and $\varepsilon = \frac{1}{2}mv^2$:

$$\sigma = \frac{ne^2\tau}{m} \quad (18.63)$$

If the material is electrically insulated such that $j = 0$ and a thermal gradient is placed across the material, an electric field will be created within the material such that

$$\mathbf{E} = Q \nabla T \rightarrow Q = -\frac{L_{ET}}{L_{EE}} \quad (18.64)$$

where Q is the thermopower of the material. Returning briefly to the case where the thermal gradient is zero, $\nabla T = 0$, there is still a heat flux occurring across the material, as seen from

$$q = L_{TE}E = \Pi j \rightarrow \Pi = \frac{L_{TE}}{L_{EE}} \quad (18.65)$$

where Π is the *Peltier coefficient*. This ability to create a heat flux simply by passing a current through a material is the basis for thermoelectric coolers. The effect of microscale heat transfer in these devices is a topic of current interest and is discussed in Section 18.5.

Whenever a thermal gradient is applied to a material with free electrons, an electric field is established within the material. This electric field actually creates a heat flux that opposes the thermal gradient. Taking this effect into account yields the following expression for the thermal conductivity:

$$K = -\left(L_{TT} - \frac{L_{TE}L_{ET}}{L_{EE}}\right) \quad (18.66)$$

For most metals the electrical conductivity, L_{EE} , is large enough that the thermoelectric effect on the thermal conductivity can be neglected. The less electrically conducting the material, however, the more important it becomes to account for this reduction in the thermal conductivity. If the thermoelectric effects are neglected, the thermal conductivity takes the same form as was found for the case of phonons:

$$K = \frac{1}{3}C_e v l = \frac{1}{3}C_e v_F^2 \tau \quad (18.67)$$

Using the relaxation time approximation and Boltzmann transport equation expressions for the electrical and thermal conductivity have been derived in terms of a relaxation time, eqs. (18.63) and (18.67). Because both quantities are related linearly to the relaxation time, their ratio is independent of the relaxation time:

$$\frac{K}{\sigma} = \frac{\frac{1}{3}(\pi^2 k_B^2 n / 2eF) v_F^2 \tau}{ne^2 \tau / m} = \frac{\pi^2}{3} \left(\frac{k_B}{e} \right)^2 T \quad (18.68)$$

where eq. (18.21) is used for the electron heat capacity. This result, known as the *Wiedemann-Franz law*, relates the electrical conductivity to the thermal conductivity for metals at all but very low temperature. The proportionality constant is known as the *Lorentz number*:

$$L = \frac{K}{\sigma T} = \frac{\pi^2}{3} \left(\frac{k_B}{e} \right)^2 = 2.45 \times 10^{-8} \text{ W} \cdot \Omega / \text{K}^2 \quad (18.69)$$

18.3.3 Molecular Approach

Recent advances in computational capabilities have increased interest in molecular approaches to solving microscale heat transfer problems. These approaches include lattice dynamic approaches (Tamura et al., 1999), molecular dynamic approaches (Voltz and Chen, 1999; Lukes et al., 2000), and Monte Carlo simulations (Klistner et al., 1988; Woolard et al., 1993). In lattice dynamical calculations the ions are assumed to be at their equilibrium positions, and the intermolecular forces are modeled using appropriate expressions for the types of bonds present. This technique can be very effective in calculating phonon dispersion relations (Tamura et al., 1999) and has also been applied to calculating interfacial properties (Young and Maris, 1989). It is difficult, however, to take into account defects and grain boundaries.

The molecular dynamics approach is very similar; however, more emphasis placed on modeling the interatomic potential and the assumption of a rigid crystalline structure is no longer imposed (Chou et al., 1999). Most molecular dynamics approaches have utilized the Lennard-Jones potential:

$$\phi(r) = 4\xi \left[\left(\frac{r_c}{r} \right)^{12} - \left(\frac{r_c}{r} \right)^6 \right] \quad (18.70)$$

where ξ is a measure of the strength of the attractive forces and r_c is a measure of the radius of the repulsive core. Basically, the ions attract each other with a potential that varies with $1/r^6$ at large separation; however, they become strongly repulsive at short distance due to the Pauli exclusion principle. The noble gases in solid form have been shown to be well characterized by the Lennard-Jones potential; however, some modification is typically required for use of this potential with other crystalline materials. Chou et al. (1999) provide a comprehensive review of the molecular dynamics approaches that have been taken in microscale thermophysical problems.

Monte Carlo simulation is very similar to the Boltzmann transfer equation approach, in that the energy carriers are dealt with as particles. In Monte Carlo simulation, the particle's trajectory begins from a particular point traveling in a random

direction and the path is calculated based on parameters that govern the collisional behavior of the particles. The accuracy of this approach is limited by knowledge of the particular collisional events. This technique has been applied to both electron (Woolard et al., 1993) and phonon systems (Klistner et al., 1988).

18.4 OBSERVATION

Numerous experimental methods have been employed to monitor microscale heat transfer phenomena. In an attempt to discuss most of these techniques in a broader context, the methods are grouped into two categories. The techniques are either steady state or transient. The steady-state techniques usually involve thermography or surface temperature measurements. The transient techniques use either a modulated or pulsed heating source and monitor the temperature response as a function of time in order to measure the thermophysical properties. The next distinguishing feature is the manner in which the thermal response is observed. The three most common methods of observing microscale thermal phenomena include thin-film thermocouples, thin-film microbridges, and optical techniques.

Nanometer-scale thermocouples are typically used in conjunction with an atomic force microscope (AFM) (Majumdar, 1999; Shi et al., 2000). This technique is nondestructive because the AFM brings the probe into contact with the sample very carefully. Another series of investigators have used thin-film microbridges, which are usually thinner than 100 nm with a width that depends on the application (Cahill et al., 1994; Lee and Cahill, 1997; Borca-Tasciuc et al., 2000). This technique relies on the fact that the electrical resistance of the microbridge is a strong function of temperature. Because the microbridge must be deposited onto the material of interest, this technique is neither noncontact nor nondestructive. Finally, optical techniques have been employed where a laser is used as either the heating source and/or the thermal probe. The thermal effects can be monitored optically in a number of different ways. One set of techniques relies on the temperature dependence of reflectance and these techniques are referred to as thermoreflectance techniques (Paddock and Eesley, 1986; Hostetler et al., 1997). The thermal expansion that results at the surface can also be used to deflect the probe beam, and the deflection can be related to temperature. These techniques are referred to as *photothermal techniques* (Welsh and Ristau, 1995). Finally, “mirage” techniques use the fact that the air just above the surface is also heated, which causes changes in the index of refraction that bend the probe beam by varying amounts, depending on the change in temperature (Gonzales et al., 2000).

Three different techniques are described in the next few sections. The first technique is scanning thermal microscopy (SThM) (Majumdar, 1999). This is an example of the steady-state approach using a nanometer-scale thermocouple. The thermocouple is fabricated onto the tip of an AFM probe. The next technique presented is the 3ω technique, which uses a thin-film microbridge as both the heating source and as a thermal probe (Cahill et al., 1994). This is an example of a modulated transient technique. The last example is the transient thermoreflectance (TTR) technique (Paddock and Eesley, 1986), an optical technique in which a pulsed laser is used to heat and probe the sample. This is an excellent example of a pulsed transient technique.

These examples demonstrate steady-state, modulated, and pulsed transient techniques and the use of thin-film thermocouples, microbridges, and optical methods, respectively, although numerous other combinations or variations of these techniques have been used. Steady-state microbridge techniques have been used to measure thermal boundary resistance (Swartz and Pohl, 1987). For example, an AFM has been used to monitor the expansion and contraction of thin-film materials, which results from a modulated heating source (Varesi and Majumdar, 1998). Lasers have been used as modulated heating sources (Yao, 1987), and to monitor the effects of the pulse heating source on the surface temperature (Kading et al., 1994). A technique called *near-field optical thermometry* was recently developed based on near-field scanning microscopy technology, which uses an optical heating source and can beat the diffraction limit associated with far-field optical thermometry (Goodson and Asheghi, 1997).

18.4.1 Scanning Thermal Microscopy

In this section a brief introduction to scanning thermal microscopy (SThM) is presented. Majumdar (1999) published a comprehensive review article that provides more detail and historical development of SThM. Majumdar categorized the majority of techniques into (1) thermovoltage techniques (Shi et al., 2000), (2) electrical resistive techniques (Fiege et al., 1999), and (3) thermal expansion techniques (Varesi and Majumdar, 1998). A single reference has been provided here for each technique, but by no means do these represent the complete literature on the subject.

The majority of SThM experiments fall into the first category of thermovoltage techniques. These techniques require a nanometer-scale thermocouple, which is made

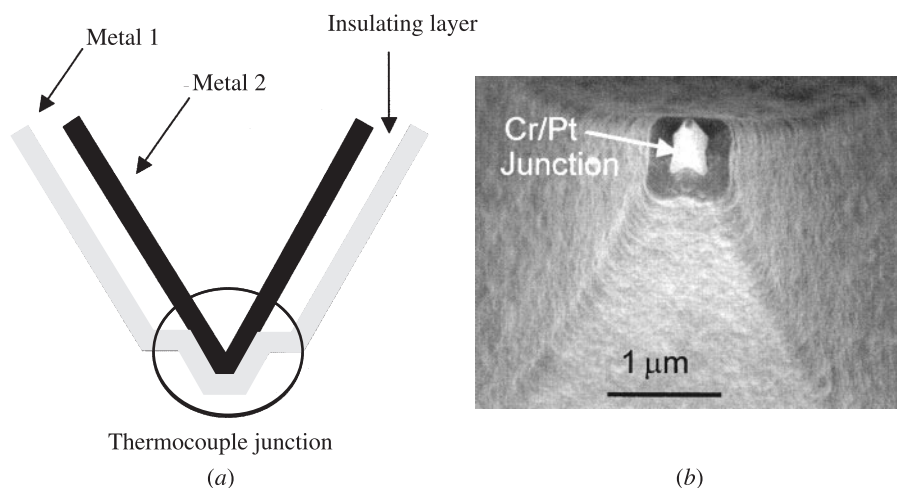


Figure 18.15 (a) Nanometer-scale thermocouple manufactured on the tip of a commercially available AFM cantilever; (b) micrograph of a Cr/Pt thermocouple deposited on a SiN_x cantilever. (Reproduced with permission of L. Shi and A. Majumdar, from Shi et al., 2000.)

by depositing thin metallic films onto commercially available AFM probes. Figure 18.15*a* is a schematic of the final thermocouple junction. Majumdar (1999) describes several methods for manufacturing these nanometer thermocouples. Figure 18.15*b* is a micrograph of a Cr/Pt thermocouple junction (Shi et al., 2000). The size of the tip of the thermocouple obviously affects the spatial resolution of the technique. Thermocouples have been fabricated with tip radii between 20 and 50 nm. However, several other factors also affect the spatial resolution. These include the mean free path of the energy carrier of the material to be characterized and the mechanism of heat transfer between the sample and the thermocouple.

Operation of the AFM cantilever is identical to that for a standard AFM probe (Fig. 18.16). The sample is mounted on a x-y-z stage that raises the sample vertically until the sample comes into contact with the cantilever, at which point the cantilever is deflected. The deflection of the cantilever is detected by a reflection of a laser beam off the cantilever. A slight deflection in the cantilever results in a measurable deflection of the laser beam. This information is used in a feedback control loop to maintain contact between the probe and the sample while the sample is being scanned.

Ideally, the thermocouple tip would come into contact with the sample and the thermocouple would quickly reach thermal equilibrium with the sample without affecting the temperature of the surface. Unfortunately, the situation is far from ideal. Thermal energy is transferred to the thermocouple through several mechanisms. There is solid-solid thermal conduction from the sample to the thermocouple where the two are brought into contact. There is also thermal conduction through the gas surrounding the thermocouple tip, and conduction through a liquid layer that condenses in

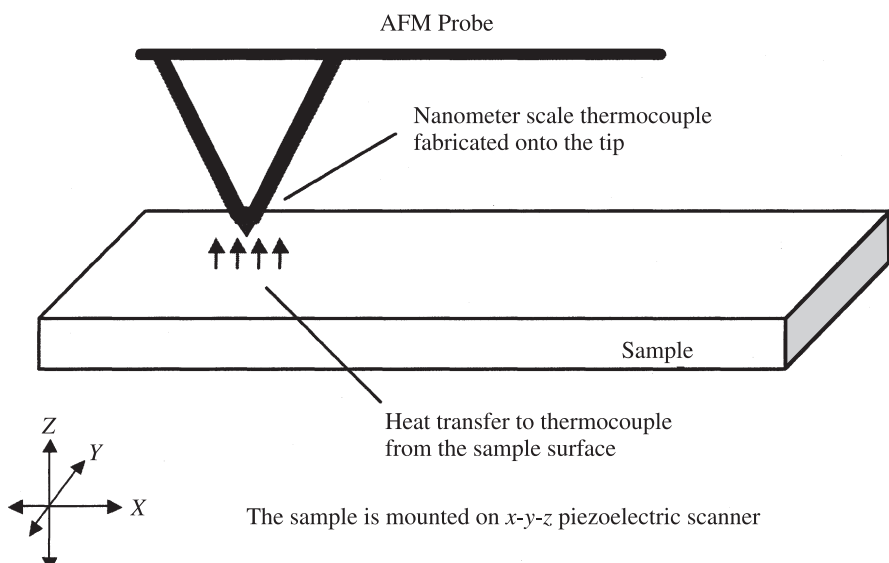


Figure 18.16 Use of a scanning thermal microscope probe to measure the thermal profile of a field-effect transistor.

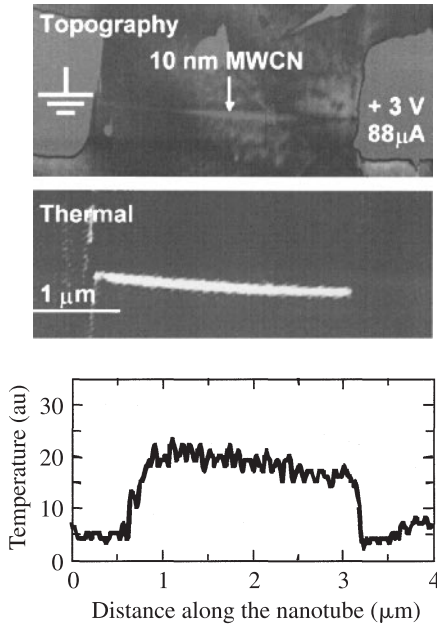


Figure 18.17 Topographical and thermal profile of a multiwalled carbon nanotube that has been heated with a dc electrical current. (Courtesy of L. Shi and A. Majumdar at the University of California–Berkeley.)

the small gap between the tip and the sample. Shi et al. (2000) demonstrated that conduction through this liquid layer dominates the heat transfer under normal atmospheric conditions. Figure 18.17 shows a topographical and thermal image of a 10-nm multiwalled carbon nanotube.

18.4.2 3ω Technique

The 3ω technique has been one of the most widely used and perhaps the most effective technique for measuring the thermophysical properties of dielectric thin films (Cahill, 1990; Lee and Cahill, 1997). Figure 18.18*a* shows a top view of a microbridge used for the 3ω technique. Figure 18.18*b* shows a side view of a microbridge that has been deposited onto the thin film to be measured. There are four electrical pads shown in Figure 18.18*a*; the outer two pads are used to send current through the microbridge, which provides the modulated heating, while the inner two pads are used for measuring the voltage drop across the microbridge.

The current sent through the microbridge is modulated at a certain frequency where $I = I_0 \cos \omega t$. The technique is called the 3ω technique because the temperature oscillations of the sample surface from the modulated current are evident in the microbridge voltage signal at the third harmonic of the current modulation frequency. The microbridge has a resistance R , and the power loss or Joule heating that occurs within the system is proportional to the square of the current:

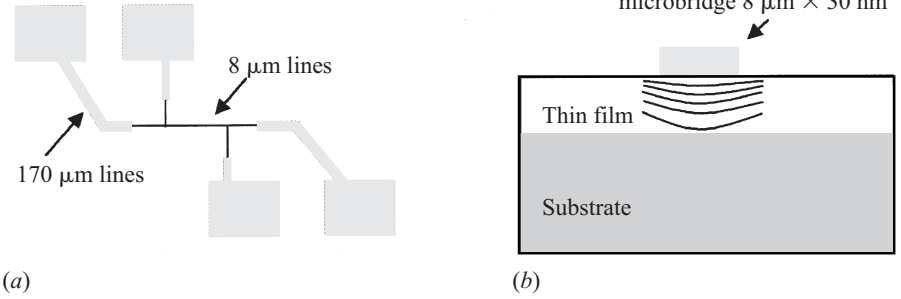


Figure 18.18 (a) Top view of the thin-film microbridge setup used by Lee and Cahill (1997) to measure heat transport in thin dielectric films (from Lee and Cahill, 1997); (b) microbridge deposited onto a dielectric thin-film material. The film thickness and width are much less than the length of the microbridge, making the problem essentially two-dimensional.

$$P = I^2 R = \frac{I_0^2 R}{2} (1 + \cos 2\omega) \quad (18.71)$$

The power loss term has a steady-state component and a sinusoidal term. The modulated component of the heat generation occurs at a frequency of 2ω , which will result in a temperature fluctuation within the system at a frequency of 2ω :

$$T(x, t) = T_s(x) + T_m(x) \cos \omega t \quad (18.72)$$

where T_s is the steady-state temperature distribution and T_m is the amplitude of the temperature oscillations at a frequency of 2ω . Electrical resistance in metals arises due to several electron scattering mechanisms, which include defect scattering, grain boundary scattering, and electron–phonon scattering. As discussed in Section 18.2, the electron–phonon collisional frequency is proportional to the lattice temperature. Therefore, the electrical resistance of metals increases linearly with temperature, $R = R_0 + R_1 T$. This change in the electrical resistance of the film is the basic thermal mechanism that allows for detection of the temperature changes using microbridge techniques:

$$V_{mb} = IR_{mb} = I_0 \cos \omega t [R_0 + R_1 (T_s + T_m \cos 2\omega t)] \quad (18.73)$$

Oscillations occur within the microbridge voltage signal at frequencies of ω and 3ω , where the 3ω signal contains information about the amplitude of the temperature fluctuations of the microbridge. The amplitude of the temperature oscillation is then compared to a thermal model as a function of the heating frequency to determine the effective thermal diffusivity of the underlying material.

One interesting aspect of modulated techniques is that the modulation frequency can be varied, which affects the amount of material that influences the measurement. Essentially, higher oscillation frequencies will only probe the thermal properties near

the surface, while lower frequencies allow more time for diffusion and can be used to probe thicker films. This effect can easily be understood by examining the one-dimensional solution to the heat equation for a semi-infinite material where according to Majumdar (1999), the surface temperature is being modulated at frequency ω_s :

$$T(x, t) \propto \exp\left(-x\sqrt{\frac{\omega_s}{2\alpha_{\text{eff}}}}\right) \exp\left[i\left(\omega_s t - x\sqrt{\frac{\omega_s}{2\alpha_{\text{eff}}}}\right)\right] \quad (18.74)$$

where α_{eff} is the effective thermal diffusivity of the material. These temperature oscillations occurring throughout the film at the modulation frequency are sometimes referred to as *thermal waves* (Rosencwaig et al., 1985). Notice that the amplitude of the temperature oscillation decays exponentially. The penetration depth is inversely proportional to the square root of the modulation frequency:

$$\delta_{rw} = \sqrt{\frac{2\alpha}{\omega}} \quad (18.75)$$

where δ_{rw} is the penetration depth of the thermal wave. Equation (18.74) also demonstrates that the modulation undergoes a phase shift as the thermal wave propagates through the material. This phase shift is a result of the time required for thermal diffusion, which is a relatively slow process. Experimental techniques have been employed that monitor this phase shift and use this information to calculate the thermal diffusivity (Yu et al., 1996).

18.4.3 Transient Thermoreflectance Technique

Ultrashort pulsed lasers with pulse durations of a few picoseconds to subpicoseconds are rapidly becoming viable as an industrial tool. These lasers, used in combination with the transient thermoreflectance (TTR) technique, are capable of measuring the thermal diffusivity of thin films normal to the surface (Paddock and Eesley, 1986; Hostetler et al., 1997). This is an example of a pulsed transient technique where the ultrashort pulsed laser provides the transient phenomena. A pump-probe experimental setup is used to monitor the change in reflectance of the sample surface as a function of time. Once the change in reflectance of the sample surface is known as a function of time, reflectance must be related to temperature. The reflectance of most metals is a function of temperature due to the thermal effects on the absorption from interband transitions. In general, the change in reflectance is linearly related to temperature for small changes in temperature.

The experimental setup is called *pump-probe* because each pulse is split into an intense heating or pump pulse and a weaker probe pulse. The heating pulse is used to generate or initiate the transient phenomena to be observed. The optical path length of the probe pulse is controlled such that the probe can arrive at the sample surface just before, during, or after the heating event. The probe then takes a snapshot of the reflectance at a specific time delay relative to the pump, where the temporal resolution of the snapshot is on the order of the probe pulse duration.

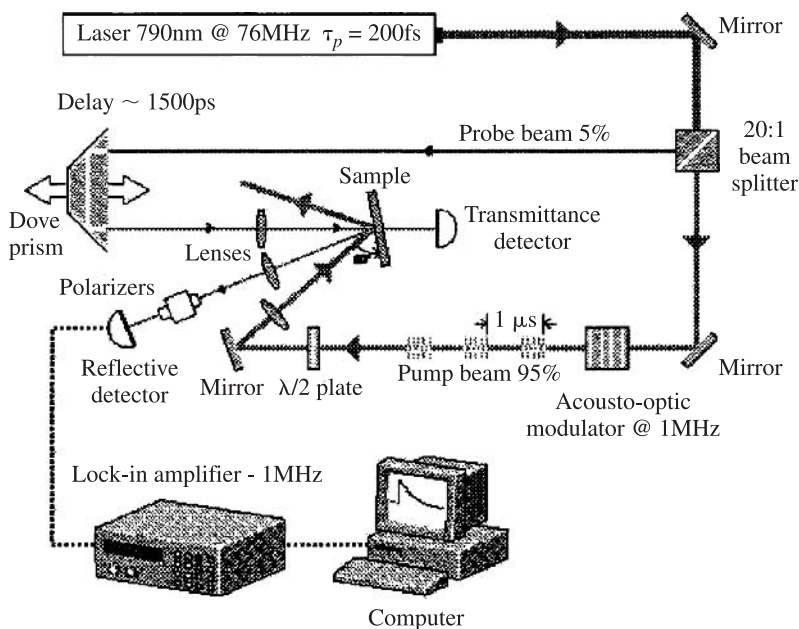


Figure 18.19 Experimental setup for the transient thermoreflectance (TTR) technique.

A schematic of the transient thermoreflectance (TTR) technique is shown in Fig. 18.19. The pump beam is modulated at a frequency on the order of 1 MHz with an acousto-optic modulator. A half-wave plate is then used to rotate the heating beam's polarization parallel to the plane of incidence. The pump beam is focused on the sample surface, which results in an estimated fluence of between 1 and 10 J/m², depending on the spot size and laser power. The probe beam is focused on the center of the region heated by the pump pulse. The probe beam is then sent through a polarizer to filter the scattered pump light and then onto a photodiode.

Because the pump beam is modulated at 1 MHz while the probe beam is not modulated, there is a period of time where the probe is affected by the pump beam, followed by a period where it is not affected. The reflectance of the probe beam, which is always present, will then have a slight modulation occurring at a frequency of 1 MHz. The amplitude of this modulation is proportional to the change in reflectance of the sample surface due to the pump pulse. This amplitude modulation of the probe beam is detected using a lock-in amplifier, which monitors the photodiode response at a frequency of 1 MHz. By slowly changing the optical path length of the probe using a variable delay stage, the change in reflectance of the sample due to the pump pulse (i.e., the thermal relaxation) can be reconstructed on a picosecond time scale.

The advantage of using an ultrashort pulsed laser for this experiment is that the heating caused by the laser pulse is highly localized near the surface. This is not true with longer pulses because thermal energy will diffuse across a 100-nm metal film within several hundred picoseconds. However, ultrashort pulsed lasers deposit their

energy so rapidly that the electrons and phonons within the metal are not always in thermal equilibrium. This phenomena is referred to as *nonequilibrium heating*.

It has been theorized that for subpicosecond laser pulses, the radiant energy is first absorbed by the electrons and then transferred to the lattice (Anisimov et al., 1974). This exchange of energy occurs within a few picoseconds. In 1974, Anisimov presented a two-temperature model, later called the *parabolic two-step (PTS) model*, which assumes that the lattice (or phonons) and electrons can be described by separate temperatures T_l and T_e :

$$C_e(T_e) \frac{\partial T_e}{\partial t} = \frac{\partial}{\partial x} \left[K_e(T_e, T_l) \frac{\partial T_e}{\partial x} \right] - G [T_e - T_l] + S(x, t) \quad (18.76a)$$

$$C_l \frac{\partial T_l}{\partial t} = G [T_e - T_l] \quad (18.76b)$$

The electron–phonon coupling factor G is a material property that represents the rate of energy transfer between the electrons and the lattice. The heat capacity of the electrons and the lattice, C_e and C_l , and the thermal conductivity of the electrons K_e are also material properties. The appropriate expressions for the electron heat capacity was given as eq. (18.21). The electron thermal conductivity can be determined to be $K_e = K_{eq}(T_e/T_l)$ using eqs. (18.32)–(18.35).

Thermal diffusivity of the thin film can be obtained by comparing the transient reflectance response to the thermal model presented as eqs. (18.76a) and (18.76b). This model requires that the electron–phonon coupling factor be known. While values

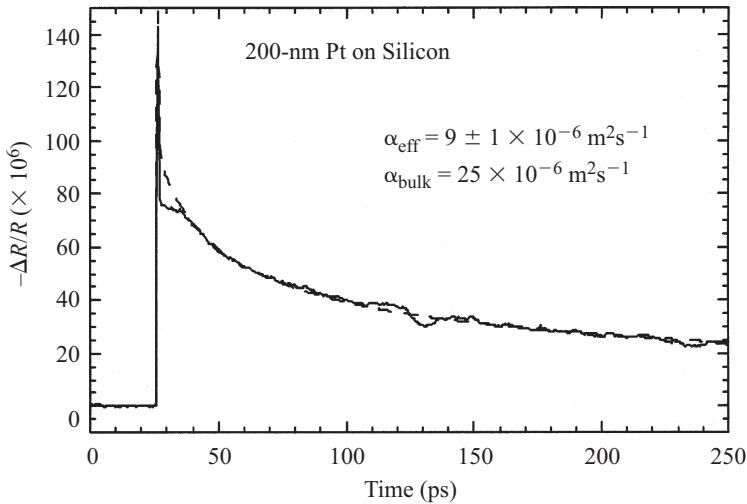


Figure 18.20 Change in reflectance of a 200-nm Pt thin film on silicon where the phase and magnitude of the signal have been taken into account. The experimental results are compared to the PTS model to determine the thermal diffusivity.

are available in the literature for most metals, the electron–phonon coupling factor can be affected by the microstructure of the film (Elsayed-Ali et al., 1991). The electron–phonon coupling factor can be measured with the TTR technique using an optically thin film to minimize the effects of diffusion. The electron–phonon coupling can then be directly observed in the first few picoseconds of the transient response (Hostetler et al., 1999). Figure 18.20 shows a TTR scan taken on a 200-nm Pt film evaporated onto a silicon substrate. The value of the thermal diffusivity was determined to be $9 \pm 1 \times 10^6 \text{ m}^2/2$ using a least squares fitting routine. This value is significantly less than the bulk value for platinum.

18.5 APPLICATIONS

Microscale heat transfer was defined in Section 18.1 as the study of heat transfer when the individual carriers must be considered or when the continuum model breaks down. Several examples are presented next that illustrate how microscale heat transfer is of critical importance to the microelectronics industry. Thermal transport in multilayer and superlattice structures is covered, where increased scattering of energy carriers leads to increased thermal resistance within these materials.

18.5.1 Microelectronics Applications

To keep pace with the demand for faster, smaller devices, there is a continual need for materials with lower dielectric constants. Unfortunately, materials that are good electrical insulators are also typically good thermal insulators. Increased operating temperatures in these new devices would lead to increases in electrical crosstalk and electromigration, which would defeat the purpose of employing a better electrical insulator. These thermal considerations can directly affect the ultimate packing density of new devices (Goodson and Flik, 1992). Currently, continuum models are sufficient to model the thermal performance of these devices, and microscale thermal effects are usually taken into account by employing measured material properties for the thin-film materials. These properties are measured using the methods described in Section 18.4. The effective use of these material properties is typically the subject of electronic cooling, which represents another large area of research. Novel phase-change materials (Pal and Joshi, 1997), and micro heat pipes (Peterson et al., 1998) are just a few examples of cutting-edge research activities aimed at improvements in device thermal management.

Traditional metal-oxide semiconductor field-effect transistors (MOSFETs) are manufactured directly on the bulk silicon substrate. Because crystalline silicon is a very good thermal conductor, the removal of thermal energy is usually not a primary concern. However, because these transistors are made directly on the silicon substrate, there can be, at most, one layer of transistors. Silicon-on-insulator (SOI) transistors, which are not limited to a single layer, are extremely desirable for use in manufacturing a three-dimensional chip. The presence of an insulating layer between the device and the silicon substrate also reduces the leakage current, the threshold

voltage, and the junction capacitance of the device. While these reductions all represent improvements, the insulating layer also decreases the ability of the device to dissipate heat. SOI transistors are an excellent example of a modern microelectronics device in which microscale heat transfer plays an important role in the overall device performance. Ju and Goodson (1999) cover the subject of microscale heat conduction in integrated circuits in great detail.

Figure 18.21 is a basic schematic of a SOI transistor where the individual components have been labeled. This device is a field-effect transistor, which means that when a voltage is applied to the gate, a small conductive channel is created in the doped silicon device layer just underneath the gate. This conductive channel allows current to flow from the source to the drain. However, the majority of the resistive heating of the device occurs within this channel. This results in highly localized heating in the silicon layer underneath the gate. The presence of the insulating oxide layer forces the thermal energy to propagate through the silicon device layer and then through the metal leads of the source and drain. The thickness of the silicon device layer can be less than 100 nm, which is on the order of the mean free path of a phonon in silicon. Several experimental studies have been performed to quantify size effects in thin silicon films. The source and drain lines are made of metallic materials which act like fins, moving the thermal energy away from the device (Goodson and Flik, 1992). The thickness of these metal leads is currently on the order of several hundred nanometers, which is greater than the mean free path of an electron. However, as these dimensions continue to diminish, continuum models will no longer be applicable.

Another interesting thermal effect that occurs in field-effect transistors which falls into the area of microscale heat transfer is nonequilibrium Joule heating. Nonequilibrium Joule heating can occur in the area of the drain due to the very high electric field that is established in the region just underneath the gate. The strength of this electric field is inversely proportional to the channel length. The channel length directly

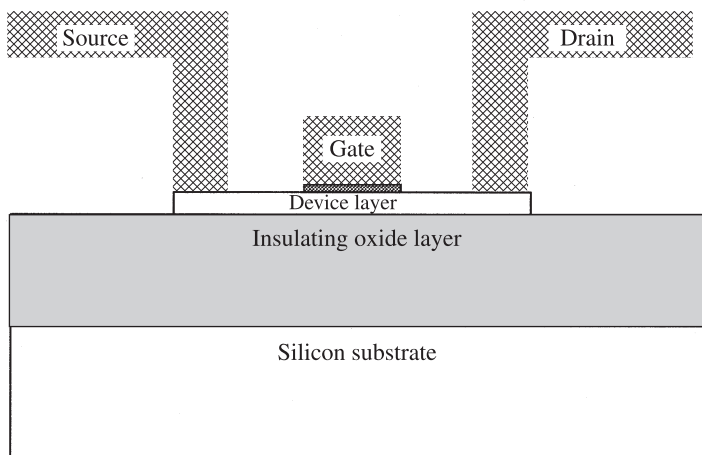


Figure 18.21 Individual components of a silicon-on-insulator (SOI) field-effect transistor.

affects the time required for the transistor to switch; therefore, efforts are constantly under way to reduce the channel length. Operation of a field-effect transistor with a channel length of 61 nm was recently demonstrated (Timp, 1997), and manufacturing of channel lengths with sub-100-nm dimensions is expected within the first decade of the twenty-first century. The high electric field present between the source and the drain creates highly energetic electrons, which are not in thermal equilibrium with the lattice when they arrive at the drain. Lai and Majumdar (1996) present a simple thermal and electrical model for submicron silicon semiconductor devices using hydrodynamic equations for the electron system and conservation equations for the optical and acoustic phonons. Another thermal analysis of nonequilibrium Joule heating was performed on GaAs metal semiconductor field-effect transistors (Fushinobu et al., 1995). In both cases, the nonequilibrium electron temperatures were predicted to be on the order of 1000 K, while changes in the lattice temperature were on the order of tens of Kelvin. This behavior is very similar to the nonequilibrium heating that occurs in metals and semiconductors when heated with ultrashort pulsed lasers, as discussed in Section 18.4.

18.5.2 Multilayer Thin-Film Structures

Multilayer thin films and superlattice structures are currently being utilized in numerous modern devices due to their unique material properties. One example is giant magnetoresistance (GMR) technology, which holds great promise for increasing memory density, access speed, and power requirements for memory maintenance. GMR devices are created using multilayer metallic superlattices where the individual layers are on the order of a few nanometers (Baibich et al., 1988). Quantum well lasers are another example of multilayer thin-film structures, where the layer thickness is on the order of the mean free path of the heat carrier. A certain amount of thermal resistance is associated with each interface within the multilayer structure, due to phonon scattering that occurs at each interface. Yu et al. (1995) showed that the thermal conductivity of a 700 Å/700 Å GaAs/AlAs superlattice is significantly less than that of the corresponding bulk materials but larger than that of the corresponding alloy. Reduced values for the thermophysical properties of superlattice materials have been incorporated into continuum models to predict the increases in operating temperatures. One example is a thermal analysis performed on vertical cavity surface-emitting laser diodes (VCSELs), which showed a significant increase in the operating temperature (Norris et al., 1994).

Recently, the increased thermal resistance associated with superlattice structures has been under investigation as a means of improving the performance of thermoelectric materials (Hicks and Dresselhaus, 1993). Reduced thermal transport properties typically represent a nuisance effect, causing devices to operate at higher, less desirable temperatures. In the case of thermoelectric materials, however, the reduction in thermal transport is being used to engineer better materials. Heat transfer through the thermoelectric device significantly reduces the overall efficiency, and new materials are being fabricated using multilayer superlattice structures to reduce thermal transport by phonons. Figure 18.22 shows a schematic of a basic thermoelectric cooler.

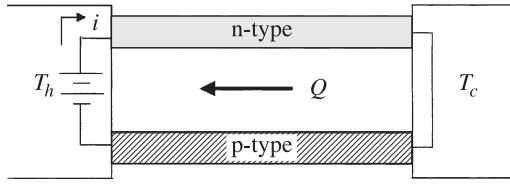


Figure 18.22 Thermoelectric device fabricated using *n*- and *p*-type doped semiconductor materials.

Because electrons carry both thermal energy and charge, the thermal and electrical properties of metals are interrelated. As was shown in Section 18.3, the current density and heat flux can be written in terms of the thermal gradient and electrical field with four linear coefficients (Ziman, 1960):

$$j = L_{EE} E + L_{ET} \nabla T \quad (18.61)$$

$$q = L_{TE} E + L_{TT} \nabla T \quad (18.62)$$

From these equations we can see that in the case of zero current, an electric field will be present whenever a thermal gradient exists. This phenomenon is referred to as the *Seebeck effect*. The thermoelectric power, or *Seebeck coefficient*, can be expressed as

$$S = \frac{L_{ET}}{L_{EE}} \quad (18.77)$$

The higher the thermoelectric power, the more energy the device can move from the cold side of the device to the hot side. However, the higher the thermopower, the more electrically resistive the device becomes, which creates more thermal energy due to Joule heating, some of which is conducted to the cold side of the device. In addition, thermal conduction through the device from the hot side to the cold side reduces the efficiency. The thermoelectric figure of merit, Z , accounts for these conflicting effects and is given by

$$Z = \frac{S^2 \sigma}{K} \quad (18.78)$$

where σ is the electrical conductivity and K is the thermal conductivity. As mentioned previously, increasing the thermoelectric power leads to a decrease in the electrical conductivity. The thermal conductivity has two components, one from phonons and another from electrons in the semiconductor:

$$K = K_e + K_p \quad (18.79)$$

The electronic thermal conductivity is related to the electrical conductivity through the Wiedemann–Franz law discussed in Section 18.3. However, any reduction in

thermal conduction from phonons through the device can increase the figure of merit. Some examples of materials that have high values of Z include Bi_2Te_3 and SiGe alloys.

It has been shown that depending on the layer thickness, it is possible for superlattice materials to have a thermal conductivity that is less than that of the corresponding alloy (Borca-Tasçiuç et al., 2000). While alloying materials typically reduces the thermal properties due to increased scattering sites, the interface between two materials can also be a strong source of thermal resistance. This resistance, called *thermal boundary resistance*, is caused by either the reflection of heat carriers at the interface or by differences in the phonon density of states between the materials (Swartz and Pohl, 1989). Figure 18.23 shows the cross-plane thermal conductivity of several SiGe superlattice materials with different periods. The thermal conductivity was measured using a differential 3ω method (Borca-Tasçiuç et al., 2000). The thermal conductivity was approximately 50% less than the alloy for the samples with 9- and 14.4-nm periods. The sample with the smallest period, 4 nm, had a thermal conductivity closer to that of the alloy.

It has recently been proposed that two-dimensional structures may be able to achieve higher thermoelectric figures of merit. Hicks et al. (1996) propose that these two-dimensional structures can be prepared in the form of quantum well structures. In our earlier discussion, the multilayer thermoelectric devices were oriented in the cross-plane direction to reduce thermal conduction. The devices proposed would be oriented in the in-plane direction to capitalize on increased thermoelectric effects.

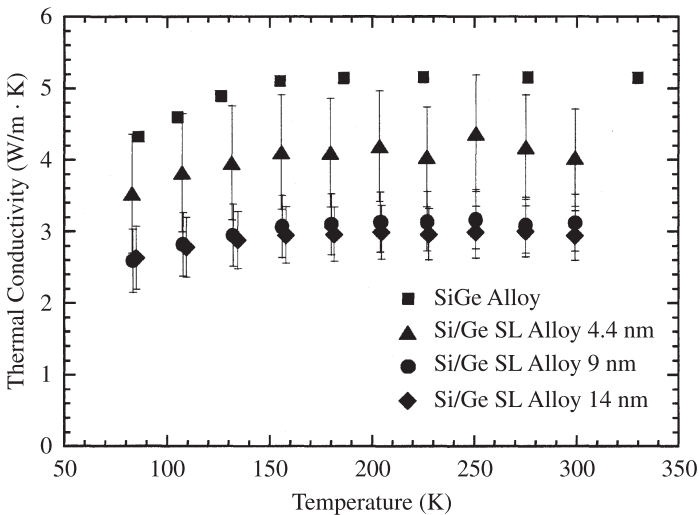


Figure 18.23 Temperature dependence of the thermal conductivity of Si/Ge superlattices of varying period as compared to a SiGe alloy material. (Reproduced with permission of Theodorian Borca-Tasçiuç.)

18.6 CONCLUSIONS

Microscale heat transfer is a new subject in concept but not in practice. The microscopic study of the thermal properties of solids has been a topic within condensed matter physics for at least five decades. As discussed in Section 18.1, many of the thermal properties of bulk materials can be adequately explained with rather simple models of the electron and lattice systems. These concepts provide the foundation necessary to tackle many of the problems facing microscale heat transfer.

This chapter has provided an overview of the primary theoretical methods used for approaching microscale heat transfer problems. The first and simplest approach is a continuum model, where microscale effects are taken into account by employing accurate values for the thermophysical properties of the thin-film materials employed in the device. When the length scales of the thermal problem are on the order of the mean free path of the energy carrier, however, continuum models are no longer applicable. The Boltzmann transport equation was discussed and can be used to solve a number of problems; however, to model the collisional term, certain assumptions must be made. Finally, molecular dynamics and Monte Carlo simulations were discussed briefly, but again, these techniques typically require a large number of assumptions which limit the accuracy.

Several methods for observing the effects of microscale heat transfer were discussed. To see the effects of microscale heat transfer, the observer must look on very short time or length scales. This often requires the development of new experimental techniques. Scanning thermal microscopy (SThM) was given as an example of a technique capable of resolving surface temperature on nanometer length scales, and the transient thermorefectance technique was given as an example of a technique used to monitor transport phenomena on a picosecond timescale. Development of a technique capable of both ultrashort length scale and ultrashort time scale measurements remains a challenge.

Finally, a few applications were presented that demonstrate the importance of considering microscale heat transfer. As the nanotechnology revolution continues, the need for accurate modeling of thermal transport on ultrashort time and length scales will be vital to the success of many new devices. The distinction between thermal engineers and physicists will begin to blur, as engineers continue to draw on the concepts of condensed matter physics to explain and predict the transport properties of microscopic energy carriers. These advances require the education of a new breed of thermal engineers; those trained in modern physics as well as in mechanics. This is an exciting period in the field of heat transfer and many challenges remain.

NOMENCLATURE

Roman Letter Symbols

A	electron-electron scattering coefficient ($\text{K}^{-2}\text{s}^{-1}$)
a	interatomic spacing (m)
\mathbf{a}_i	primitive lattice vectors (m)

B	electron-phonon scattering coefficient ($\text{K}^{-1}\text{s}^{-1}$)
\mathbf{b}_i	reciprocal primitive lattice vectors (m^{-1})
C	heat capacity ($\text{Jm}^{-3}\text{K}^{-1}$)
c	speed of sound (ms^{-1})
D	density of states
E	electric field (Vm^{-1})
e	electrical charge (C)
F	force (N)
f	Fermi-Dirac distribution
f'	change in Fermi-Dirac distribution
G	electron-phonon coupling factor ($\text{Wm}^{-3}\text{K}^{-1}$)
\hbar	Planck's constant (eVs)
I	current (A)
j	current density (Am^{-2})
K	thermal conductivity ($\text{Wm}^{-1}\text{K}^{-1}$)
K	spring constant (NM^{-1})
\mathbf{k}	wavevector (m^{-1})
k_B	Boltzmann constant (eVK^{-1})
L	length (m)
\mathcal{L}	Lorentz number (WOhmK^{-2})
L_{ET}	thermoelectric coefficient ($\text{Am}^{-1}\text{K}^{-1}$)
L_{EE}	thermoelectric coefficient ($\text{Am}^{-1}\text{V}^{-1}$)
L_{TE}	thermoelectric coefficient ($\text{Wm}^{-1}\text{V}^{-1}$)
L_{TT}	thermoelectric coefficient ($\text{Wm}^{-1}\text{K}^{-1}$)
l	mean free path (m)
M	mass of an ion (kg)
m	effective mass of an electron (kg)
N	Bose-Einstein distribution
N_l	number of lattice sites
N_e	number of free electrons
n	integer
n_e	electron number density (m^{-3})
P	momentum (kgms^{-1})
\mathcal{P}	power (W)
Q	thermopower (VK^{-1})
q	heat flux (Wm^{-2})
\mathbf{R}	position of lattice site (m)
\mathcal{R}	resistance (Ohms)
\mathbf{r}	position of ions (m)
r_c	radius of repulsive core (m)
S	heating source (Wm^{-3})
S_b	Seebeck coefficient (VK^{-1})
T	temperature (K)
t	time (s)
U	internal energy (J)

u	specific internal energy (Jkg^{-1})
u	displacement (m)
V	volume (m^3)
\mathcal{V}	potential difference (V)
v	velocity (ms^{-1})
v	displacement (m)
x	direction normal to surface (m)
Z	thermoelectric figure of merit

Greek Symbols

α	thermal diffusivity (m^2s^{-1})
δ_{tw}	thermal wave penetration depth (m)
ε	electron energy (eV)
ϕ	interatomic potential (N)
μ	chemical potential (eV)
Π	Peltier coefficient (WA^{-1})
θ_D	Debye temperature (K)
σ	electrical conductivity ($\text{Am}^{-1}\text{V}^{-1}$)
τ	relaxation time (s)
ω	frequency (rad)
ν	collisional frequency (s^{-1})
ξ	strength of interatomic forces (N)

Subscripts

b	boundary
e	electron
ee	electron-electron
eff	effective
ep	electron-phonon
D	Debye
d	defect
F	Fermi
g	group
k	wavevector
l	lattice
m	modulated
n	n^{th} lattice site
o	equilibrium
P	momentum
pp	phonon-phonon
rms	root mean square
s	phonon branches
ss	steady state
tot	total

REFERENCES

- Anisimov, S. I., Kapeliovich, B. L., and Perelman, T. L. (1974). Electron Emission from Metal Surfaces Exposed to Ultrashort Laser Pulses, *Sov. Phys. JETP*, 39, 375–377.
- Ashcroft, N. W., and Mermin, N. D. (1976). *Solid State Physics*, Saunders College Publishing, Fort Worth, TX.
- Baibich, M. N., Broto, J. M., Fert, A., Dau, F. N. V., and Petroff, F. (1988). Giant Magnetoresistance of (001)Fe/(001)Cr Magnetic Superlattices, *Phys. Rev. Lett.*, 61, 2472–2475.
- Borca-Tasçiuc, T., Liu, W., Zeng, T., Song, D. W., Moore, C. D., Chen, G., Wang, K. L., Goorsky, M. S., Radetic, T., and Gronsky, T. (2000). Thermal Conductivity of Symetrically Strained Si/Ge Superlattices, *Superlattices Microstruct.*, 28, 199–206.
- Brockhouse, B. N., Arase, T., Caglioti, G., Rao, K. R., and Wods, A. D. B. (1962). Crystal Dynamics of Lead, I: Dispersion Curves at 100 K, *Phys. Rev.*, 128, 1099–1111.
- Cahill, D. G. (1990). Thermal Conductivity Measurements from 30–750 K: The 3ω Method, *Rev. Sci. Instrum.*, 61, 802–808.
- Cahill, D. G., and Pohl, R. O. (1988). Lattice Vibrations and Heat Transport in Crystals and Glasses, *Annu. Rev. Phys. Chem.*, 39, 93–121.
- Cahill, D. G., Katiyar, M., and Abelson, J. R. (1994). Thermal Conductivity of a-Si:H Thin Films, *Phys. Rev. B*, 50, 6077–6081.
- Chou, F. C., Lukes, J. R., Liang, X. G., Takahashi, K., and Tien, C. L. (1999). Molecular Dynamics in Microscale Thermophysical Engineering, in *Annual Review of Heat Transfer*, C. L. Tien, ed., Begell House, New York, pp. 141–176.
- Elsayed-Ali, H. E., Juhasz, T., Smith, G. O., and Bron, W. E. (1991). Femtosecond Thermoreflectivity and Thermotransmissivity of Polycrystalline and Single-Crystalline Gold Films, *Phys. Rev. B*, 43, 4488–4491.
- Fiege, G. B. M., Altes, A., Heiderhoff, R., and Balk, L. J. (1999). Quantitative Thermal Conductivity Measurements with Nanometre Resolution, *J. Phys. D Appl. Phys.*, 32, L13–L17.
- Fuchs, K. (1938). The Conductivity of Thin Metallic Films According to the Electron Theory of Metals, *Proc. Cambridge Philos. Soc.*, 34, 100–108.
- Fushinobu, K., Majumdar, A., and Hijikata, K. (1995). Heat Generation and Transport in Submicron Semiconductor Devices, *J. Heat Transfer*, 117, 25–31.
- Gonzales, E. J., Bonevich, J. E., Stafford, G. R., White, G., and Josell, D. (2000). Thermal Transport through Thin Films: Mirage Technique Measurements on Aluminum/Titanium Multilayers, *J. Mater. Res.*, 15, 764–771.
- Goodson, K. E., and Asheghi, M. (1997). Near-Field Optical Thermometry, *Microscale Thermophys. Eng.*, 1, 225–235.
- Goodson, K. E., and Flik, M. I. (1992). Effect of Microscale Thermal Conduction on the Packing Limit of Silicon-on-Insulator Electronic Devices, *IEEE Trans. Components Hybrids Manuf. Technol.*, 15, 715–722.
- Hicks, L. D., and Dresselhaus, M. S. (1993). Effect of Quantum-Well Structures on the Thermoelectric Figure of Merit, *Phys. Rev. B*, 47, 12727–12731.
- Hicks, L. D., Harmon, T. C., Sun, X., and Dresselhaus, M. S. (1996). Experimental Study of the Effect of Quantum-Well Structures on the Thermoelectric Figure of Merit, *Phys. Rev. B*, 53, R10493–R10496.

- Hostetler, J. L., Smith, A. N., and Norris, P. M. (1997). Thin Film Thermal Conductivity and Thickness Measurements Using Picosecond Ultrasonics, *Microscale Thermophys. Eng.*, 1, 237–244.
- Hostetler, J. L., Smith, A. N., and Norris, P. M. (1999). Measurement of the Electron–Phonon Coupling Factor Dependence on Film Thickness and Grain Size in Au, Cr and Al, *Appl. Opt.*, 38, 3614–3620.
- Joseph, D. D., and Preziosi, L. (1989). Heat Waves, *Rev. Mod. Phys.*, 61, 41–73.
- Ju, Y. S., and Goodson, K. E. (1999). *Microscale Heat Conduction in Integrated Circuits and Their Constituent Films*, Kluwer Academic, Boston.
- Kading, O. W., Shurk, H., and Goodson, K. E. (1994). Thermal Conduction in Metallized Silicon-Dioxide Layers on Silicon, *Appl. Phys. Lett.*, 65, 1629–1631.
- Kittel, C. (1996). *Introduction to Solid State Physics*, Wiley, New York.
- Kittel, C., and Kroemer, H. (1980). *Thermal Physics*, W.H. Freeman, San Francisco.
- Klistner, T., Vanleve, J. E., Fischer, H. E., and Pohl, R. O. (1988). Phonon Radiative Heat Transfer and Surface Scattering, *Phys. Rev. B*, 38, 7576–7594.
- Lai, J., and Majumdar, A. (1996). Concurrent Thermal and Electrical Modeling of Sub-micrometer Silicon Devices, *J. Appl. Phys.*, 79, 7353–7361.
- Lee, S. M., and Cahill, D. G. (1997). Heat Transport in Thin Dielectric Films, *J. Appl. Phys.*, 81, 2590–2595.
- Lukes, J. R., Li, D. Y., Liang, X. G., and Tien, C. L. (2000). Molecular Dynamics Study of Solid Thin-Film Thermal Conductivity, *J. Heat Transfer*, 122, 536–543.
- Majumdar, A. (1993). Microscale Heat Conduction in Dielectric Thin Films, *J. Heat Transfer*, 115, 7–16.
- Majumdar, A. (1998). Microscale Energy Transport in Solids, in *Microscale Energy Transport*, C. L. Tien, A. Majumdar, and F. M. Gerner, eds., Taylor & Francis, Washington, DC, pp. 3–94.
- Majumdar, A. (1999). Scanning Thermal Microscopy, *Annu. Rev. Mater. Sci.*, 29, 505–585.
- Mayadas, A. F., Shatzkes, M., and Janak, J. F. (1969). Electrical Resistivity Model for Polycrystalline Films: The Case of Specular Reflection at External Surfaces, *Appl. Phys. Lett.*, 14, 345–347.
- Mott, N. F. (1993). *Conduction in Non-crystalline materials*, Oxford University Press, Oxford.
- Norris, P. M., Chen, G., and Tien, C. L. (1994). Size-Effects on the Temperature Rise in Vertical Cavity Surface-Emitting Laser Diodes, *Int. J. Heat Mass Transfer*, 37, 9–14.
- Paddock, C. A., and Eesley, G. L. (1986). Transient Thermorefectance from Thin Metal Films, *J. Appl. Phys.*, 60, 285–290.
- Pal, D., and Joshi, Y. K. (1997). Application of Phase Change Materials to Thermal Control of Electronic Modules: A Computational Study, *J. Electron. Packag.*, 119, 40–50.
- Peterson, G. P., Swanson, L. W., and Gerner, F. M. (1998). Micro Heat Pipes, in *Microscale Energy Transport*, C. L. Tien, A. Majumdar, and F. M. Gerner, eds., Taylor & Francis, Washington, DC, pp. 295–337.
- Powell, R. W., Ho, C. Y., and Liley, P. E. (1966). *Thermal Conductivity of Selected Elements*, U.S. Government Printing Office, Washington, DC.
- Powell, R. W., Ho, C. Y., and Liley, P. E. (1974). *Thermal Conductivity of the Elements: A Comprehensive Review*, American Chemical Society, Washington, DC.

- Rosencwaig, A., Opsal, J., Smith, W. L., and Willenborg, D. L. (1985). Detection of Thermal Waves through Optical Reflectance, *Appl. Phys. Lett.*, 46, 1013–1015.
- Shi, L., Plyasunov, S., Bachtold, A., McEuen, P. L., and Majumdar, A. (2000). Scanning Thermal Microscopy of Carbon Nanotubes Using Batch-Fabricated Probes, *Appl. Phys. Lett.*, 77, 4295–4297.
- Swartz, E. T., and Pohl, R. O. (1987). Thermal Resistance at Interfaces, *Appl. Phys. Lett.*, 51, 2200–2202.
- Swartz, E. T., and Pohl, R. O. (1989). Thermal Boundary Resistance, *Rev. Mod. Phys.*, 61, 605–668.
- Tamura, S., Tanaka, Y., and Maris, H. J. (1999). Phonon Group-Velocity and Thermal Conduction in Superlattices, *Phys. Rev. B*, 60, 2627–2630.
- Timp, G. (1997). Low Leakage, Ultra-thin Gate Oxides for Extremely High Performance Sub-100 nm nMOSFETs, *IEDM Tech. Dig.*, Cat. No. 97CH36103, 930–932.
- Varesi, J., and Majumdar, A. (1998). Scanning Joule Expansion Microscopy at Nanometer Scales, *Appl. Phys. Lett.*, 72, 37–39.
- Voltz, S., and Chen, G. (1999). Molecular Dynamics Simulation of Thermal Conductivity of Silicon Nanowires, *Appl. Phys. Lett.*, 75, 2056–2058.
- Weast, R. C., Astle, M. J., and Beyer, W. H., eds. (1985). *CRC Handbook of Chemistry and Physics*, CRC Press, Boca Raton, FL.
- Welsh, E., and Ristau, D. (1995). Photothermal Measurements on Optical Thin Films, *Appl. Opt.*, 34, 7239–7253.
- Wilson, A. H. (1954). *The Theory of Metals*, Cambridge University Press, Cambridge.
- Woolard, D. L., Tian, H., Littlejohn, M. A., Kim, K. W., Trew, R. J., Leong, M. K., and Tang, T. W. (1993). Construction of Higher-Moment Terms in the Hydrodynamic Electron-Transport Model, *J. Appl. Phys.*, 74, 6197–6207.
- Yao, T. (1987). Thermal Properties of AlAs/GaAs Superlattices, *Appl. Phys. Lett.*, 51, 1798–1800.
- Young, D. A., and Maris, H. J. (1989). Lattice-Dynamical Calculation of the Kapitza Resistance between FCC Lattices, *Phys. Rev. B*, 40, 3685–3693.
- Yu, X. Y., Chen, G., Verma, A., and Smith, J. S. (1995). Temperature Dependence of Thermophysical Properties of GaAs/AlAs Periodic Structure, *Appl. Phys. Lett.*, 67, 3554–3556.
- Yu, X. Y., Zhang, L., and Chen, G. (1996). Thermal-Wave Measurements of Thin-Film Thermal Diffusivity with Different Laser Beam Configurations, *Rev. Sci. Instrum.*, 67, 2312–2316.
- Ziman, J. M. (1960). *Electrons and Phonons*, Oxford University Press, London.

Direct Contact Heat Transfer

ROBERT F. BOEHM

University of Nevada–Las Vegas
Las Vegas, Nevada

- 19.1 Introduction
- 19.2 Sensible heat exchange
 - 19.2.1 General comments
 - 19.2.2 External convection to spheres
 - 19.2.3 Heat transfer inside spheres
- 19.3 Evaporation and condensation
 - 19.3.1 General considerations
 - 19.3.2 Condensation of a vapor on or in a liquid
 - Film condenser
 - Condensation on liquid droplets
 - Condensation on liquid jets
 - Condensation in a liquid
 - 19.3.3 Evaporation of a liquid by a surrounding vapor, gas or liquid
 - Droplet evaporation in a vapor or gas
 - Droplet evaporation in a liquid
- 19.4 Columns and other contactors
 - 19.4.1 Spray columns
 - Global treatments
 - Differential treatment
 - Melting and solidification applications
 - 19.4.2 Baffled columns
 - 19.4.3 Packed columns
- 19.5 Concluding comments
- Nomenclature
- References

19.1 INTRODUCTION

Direct contact heat transfer can occur whenever two substances at different temperatures touch each other physically. The implication is that there is not an intervening wall between the two substances. Heat transfer where there is a surface between the two streams is sometimes called *indirect*, or the heat transfer device is one of

the *closed* types. The physical interaction of the two streams can accomplish heat transfer very efficiently. Without an intervening wall, the energy transport between the two streams can take place across small thermal resistances. In addition, the fact that a wall is not present can allow a mass transfer process to take place. In some cases, this is a desirable phenomenon (open cooling towers), but in other cases it may not be.

Costs are often more favorable for direct contact heat transfer devices than for their closed counterparts. The thermal resistances present in closed heat exchangers result in less heat transfer than might be accomplished in direct contact, and this often translates to lower operating costs for the latter. In addition, the equipment to accomplish the direct contact processes is generally less expensive than the counterpart closed heat exchangers. Both aspects can result in considerable life-cycle cost savings for the direct contact approach over that of the closed type of heat exchanger.

Some potential limitations are inherent in direct contact processes. There is a requirement that the two streams be at the same pressure. Although this requirement does not often cause significant problems, it could be very important. Also, as noted above, the mass transfer possibility in direct contact may not be desirable.

Direct contact heat transfer is a field with a wide range of potential applications. The actual situation is that with some notable exceptions, such as open feedwater heaters and wet cooling towers, few of these applications have been used to any great extent. Reasons for this are numerous, but one of the main reasons is that engineers are not as knowledgeable as they might be about the design of these types of systems. This chapter is an attempt to expose some of these possibilities so that the design of more efficient industrial processes might result.

To present a description of direct contact processes within the limited space of this chapter, some restriction in scope is necessary. Because the direct contact of any number of generic streams is possible (and most have in fact been proposed to transfer heat), only some of the more important applications will be noted here. Solid-solid transfer processes are not covered, nor are high-temperature situations included where radiative heat transfer is important. Open cooling towers are not discussed here to any great extent, even though they are the single most widely-applied type of direct contact heat exchangers. Although some information related to cooling towers is provided in the Section 19.4, this will by no means cover a very significant fraction of the total literature on the subject. The previous work on cooling towers is voluminous and tends to use quite specialized design approaches. Interested readers can find current overviews by ASHRAE (2000) and Mills (1999). An earlier review of the literature on the numerical modeling developed to predict cooling tower performance was given by Johnson et al. (1987).

The literature contains reports of studies of interaction between different substances as well as the same substances. For example, a great deal of interest has been directed to the use of water in phase-change situations, particularly the condensation of steam on liquid water. On the other hand, interest has also been directed to the use of fluids of different types. For example, a great deal of literature on heat transfer in immiscible liquids was cited years ago by Sideman (1966), and many studies on this topic have appeared since then.

Generally, the prediction of mass transfer has been given more attention over the years than has the field of direct contact heat transfer. Because of mass transfer and heat transfer analogies, some information from the mass transfer literature can be used in direct contact heat transfer design. This analog is exposed minimally here, however. Emphasis here is on surveying predictions and applications, the main thrusts of benefit to designers.

19.2 SENSIBLE HEAT EXCHANGE

19.2.1 General Comments

Heat transfer from a continuous fluid to droplets or bubbles of another fluid is a complicated situation involving not only the typical convection-related variables (e.g., geometry, velocity, and thermophysical properties) but also the proximity of the objects to one another where more than one is present. The latter characteristic can be handled in an overall way through the definition of the *void fraction* or *holdup*, the latter denoted here by the symbol ϕ . Either of these relates to the volumetric ratio of the amount of the dispersed phase (droplet or bubble) to the total volume. Holdup has a profound effect on direct contact heat transfer, as noted several times in this chapter.

Another aspect that influences the heat transfer to droplets or bubbles is the shape of these objects. It has been well documented that droplets and bubbles can experience a wide variety of shapes, depending on the object size and the flow situation (Grace, 1983). Despite this, much work has been done on a variety of systems assuming that the droplet is spherically-shaped. A great deal of the early work was reviewed by Sideman (1966).

19.2.2 External Convection to Spheres

Convection to spheres has been the focus of many studies. Some benchmark work on this was that of Vliet and Leppert (1961) for a single sphere in forced convection with water. The examination of their data for convection from water to solid spheres, as well as existing data from others, led them to propose the following correlation:

$$\frac{hd}{k} = (1.2 + 0.53\text{Re}^{0.54}) \text{Pr}^{0.3} \left(\frac{\mu_c}{\mu_w} \right)^{0.25} \quad (19.1)$$

which is stated to hold for $1 < \text{Re} < 300,000$ and $2 < \text{Pr} < 380$.

More recently, Ahmad and Yovanovich (1994) have revisited this problem. They recommend the following correlation for swarms of spherical and rigid droplets for situations when the holdup is less than 5%:

$$\frac{hd}{k} = 2 + \frac{0.775\text{Pr}^{1/3}[\text{Re}/(2\chi + 1)]^{1/2}}{1 + [1/(2\chi + 1)^3 \text{Pr}]^{1/6}} \quad (19.2)$$

where $\chi = 1.0/\text{Re}^{1/4}$ for $\chi < 1$ and $\chi = 1.0$ for $\chi > 1$.

For holdups greater than 5%, the problem becomes much more complicated. Here interactions with the other droplets in the swarm change the continuous fluid flow pattern over each individual droplet. Wilson and Jacobs (1993) used a numerical approach to show that the heat transfer on individual particles in this more populous situation is given by the following:

$$\frac{hd}{k} = [1 - 0.186(\phi - 0.42)] (0.877\text{Re}^{1/2} + 0.152\text{Re}^{2/3}) \text{Pr}^{1/3} \quad (19.3)$$

In this correlation, the velocity used in the Reynolds number is the superficial value.

19.2.3 Heat Transfer inside Spheres

Interior to droplets and bubbles, the heat transfer is affected by the amount of circulation and whether or not impurities are present. Although the latter is more generally viewed as a problem of correctly identifying the appropriate properties to use, the former can be very difficult to predict. If there is no circulation at all, a conduction solution will apply. For a spherically shaped bubble or droplet without circulation, the solution to the transient conduction problem using a convective boundary condition to a constant environmental temperature (this may not always be an appropriate assumption) gives the following:

$$\frac{T - T_\infty}{T_o - T_\infty} = 2 \sum_{n=1}^{\infty} \frac{\sin \lambda_n R - \lambda_n R \cos \lambda_n R}{\lambda_n R - \sin \lambda_n R \cos \lambda_n R} \frac{\sin \lambda_n r}{\lambda_n r} \exp(-\lambda_n^2 R^2 \cdot \text{Fo}) \quad (19.4)$$

Here the λ_n are the infinite number of roots to the transcendental equation:

$$\lambda_n R \cos \lambda_n R = (1 - \text{Bi}) \sin \lambda_n R$$

For the other extreme, which finds a great deal of internal circulation within the droplet, Sideman (1966) recommends the following correlation after examining the results that were known at the time of his review:

$$\frac{hd}{k} = 2 + 1.13(\text{Re} \cdot \text{Pr} \cdot K)^{0.5} \quad (19.5)$$

and where

$$K \equiv 1 - \frac{2.9 + 4.35(\mu_d/\mu_c)}{1 + (\rho_d\mu_d/\rho_c\mu_c)^{1/2}} \text{Re}^{-1/2}$$

This equation holds for $\text{Re} \cdot \text{Pr} \gg 1$.

Intermediate between the conduction limit and the well-mixed limit is an area investigated numerically and experimentally by Hutchins and Marschall (1989). They found that natural convection is a major mode of transfer in addition to conduction. The internal heat transfer coefficient was seen to decrease with time until a “nearly

constant" value was reached, and this value was set by natural convection as represented by

$$\frac{\bar{h}_d d}{k_d} = 0.806(\text{Ra})^{0.2321} = 0.806 \left[\frac{g\beta d^3 (T_w - T_0)}{\nu\alpha} \right]^{0.2321} \quad (19.6)$$

A problem that involves primarily sensible heat exchange, but where some evaporation also plays a part, is the bubbling of air into a stagnant column of water. Ghazi (1991) reported such a study. The results were given in a different form from some other relations presented here. Data correlated with the following relationship:

$$\frac{UL}{k_{\text{air}}} = 0.027\text{Re}^{1.36} \cdot \text{Pr}^{0.33} \quad (19.7)$$

L is the depth of the water pool, and the overall heat transfer coefficient U was determined from the equation

$$UA = \frac{\dot{m}_{\text{air}} C_{p,\text{air}} (T_{\text{air,out}} - T_{\text{air,in}})}{\text{LMTD}} \quad (19.8)$$

with A as a reference area, taken as that for the orifice in this correlation.

19.3 EVAPORATION AND CONDENSATION

19.3.1 General Considerations

Lock (1994) has summarized the various modes in which condensation and evaporation can take place in simple direct contact systems. These include the evaporation–condensation interactions with droplets and jets in the presence of an incondensable gas. Consider a representation of the regimes shown in Fig. 19.1. In this figure the italic notations relate to the state of the vapor, with four regions defined by the intersection of the interface isobar and the interface isotherm. The nonshaded areas, hot evaporation on the upper right and cold condensation on the lower left, are the normally anticipated regions where those phenomena occur. Above the isotherm T_I the region of vapor heat gain is demarcated from the region of vapor heat loss.

In the hot evaporation region, the vapor–gas mixture is at a higher temperature than the liquid. This superheated mixture drives the process by the transfer of heat to the cooler liquid. Below the isotherm, but still on the same side of the isobar, the process can take place only if the liquid is superheated and thus furnishes the heat necessary for the evaporation process. Cool evaporation is limited by the liquid superheat, as would be represented by the liquid Jakob number.

Condensation processes take place in the region shown to the left of the interface isobar in Fig. 19.1. These are normally considered to occur when the vapor is cooler than the liquid, and this region is denoted as cold condensation (lower left).

Clearly, the liquid source or sink available for evaporation or condensation is limited in real situations. Hence the finite heat capacity of the liquid is a critical

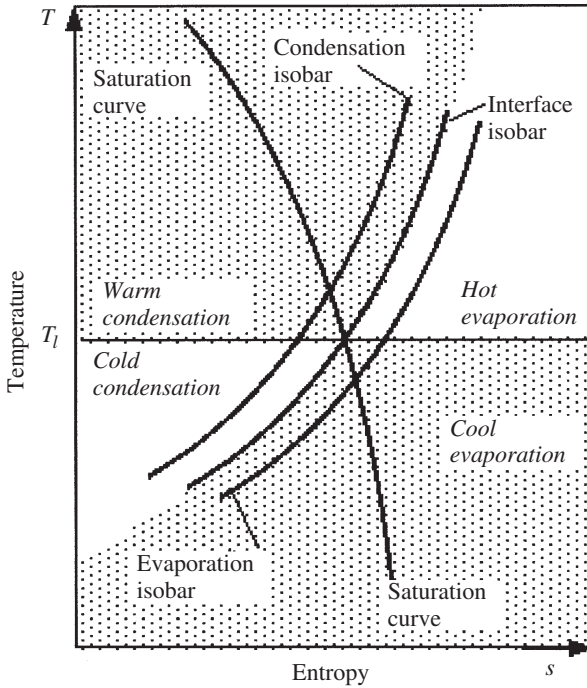


Figure 19.1 Four regimes of a vapor–gas mixture. (Adapted from Lock, 1994.)

element in the determination of the amount of heat and mass transfer that can occur. For the cool evaporation and warm condensation regions, this can be assessed by examining the Jakob number for the liquid. By examining a simple energy balance, it can be shown that the mass of vapor that can be added to or removed from the liquid by a change of phase is given by

$$m_v \leq m_L \frac{Ja_L}{1 + Ja_v} \quad (19.9)$$

where $Ja_L = C_{P,L}|T_l - T_0|/h_{fg}$ and $Ja_v = C_{P,V}|T_\infty - T_l|/h_{fg}$ represent, respectively, the liquid and vapor Jakob numbers. The Jakob number plays an important descriptive role in virtually all direct contact processes that involve a change of phase.

For direct contact situations where cool evaporation or warm condensation occurs, the interface temperature is very close to the saturation temperature. This results in a vapor Jakob number that is quite small. In this case the equation shown above for the amount of mass of vapor formed or removed reduces to the following.

$$m_v \leq m_L \cdot Ja_L \quad (19.10)$$

Often in these situations, the liquid Jakob number is very small, and very large amounts of liquid will be required to condense or evaporate small amounts of vapor.

A practical issue that can arise is the presence of a noncondensable gas, often air, in a condensing or evaporating system. In evaporating systems, small amounts of a component of this type do not cause much effect, and the phase-change processes are relatively unimpeded. In condensing systems, the situation is quite different. Here the phase-change process can be grossly hindered. Thus it is very important in condensing systems to know the extent of the presence of noncondensables and account for them appropriately.

19.3.2 Condensation of a Vapor on or in a Liquid

Condensation of a vapor on or in a liquid, whether or not that liquid is the same substance as the vapor, is commonly encountered in engineering systems. Direct contact processes differ from their indirect counterparts in many respects already noted. In indirect transfer, the extent of the process is limited by the area of the surface and the heat transfer rate possible through the surface. In direct contact processes, the situation is limited by the interplay between the latent heat of condensation and the amount of sensible heat the liquid can absorb. The amount of the liquid used for condensing purposes and its subcooling determines the extent of condensation that can be accomplished.

The presence of noncondensables during the condensation process affects performance in negative ways. Details of the many studies of this will not, in general, be summarized here because of the effects of the multitude of variables that influence individual situations. Condensation of a vapor that contains noncondensable elements on a surface finds that a noncondensable layer builds up near the surface. This causes both a heat transfer and a mass transfer resistance that impedes the basic condensation process. In many respects this is similar to what is found in surface condensers when noncondensable gases are present. In vapor droplet direct contact condensation in a liquid, this same phenomenon is present at the inner interface of the bubble. Additionally, though, the presence of noncondensables results in a decreased vapor pressure inside the bubble compared to that of a pure substance in the same situation. This then lowers the condensation temperature, decreasing the driving potential for heat transfer.

Many studies of direct contact condensation are reported in the literature. An extensive review of this literature was given by Sideman and Moalem-Marón (1982).

Film Condenser We start with a description of a situation that will be of value primarily for visualization purposes. This is the direct contact film condenser shown in Fig. 19.2. In this situation, a bulk vapor is condensed on another liquid, the latter serving as the sink. Patterned after the model used for Nusselt's solution for laminar film condensation, and described in most elementary heat transfer texts, the concepts form a basis for other systems that follow below.

Consider the heat transfer processes that occur in the direct contact film condenser. The pure saturated vapor condenses on the liquid of the same substance. Heat then flows by conduction through the condensed liquid to the sink liquid. Since it is assumed here that there is no other place for the heat to be absorbed ultimately than

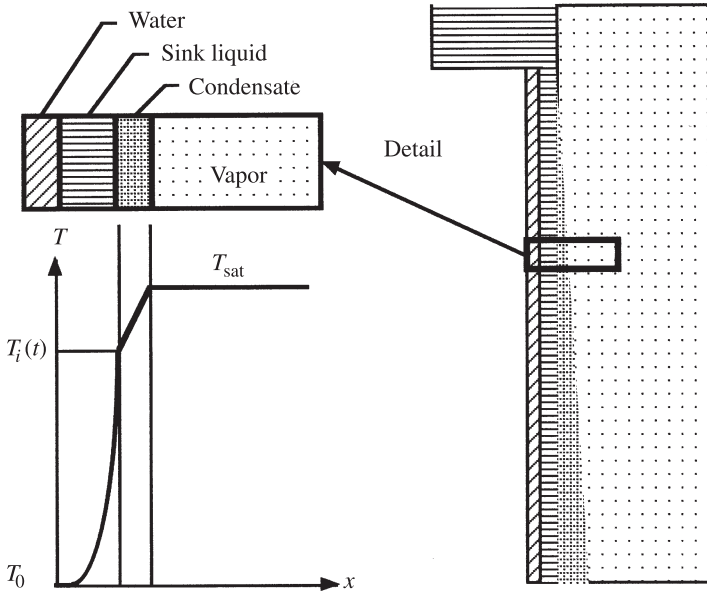


Figure 19.2 Some details of a direct-contact film condenser where a vapor condenses on the liquid.

the sink liquid, the heat capacity of that liquid is the determining factor for the duty possible from devices of this type.

The heat transfer processes that must be analyzed for this type of system are the diffusion phenomena through the two liquid films. For short times, the sink liquid is considered as being semi-infinite at the interface between it and the condensed liquid.

Condensation on Liquid Droplets A more practical geometry is that of droplets. Here spheres of the cooler sink fluid are sprayed at a velocity v into the saturated vapor of the fluid of interest. Due to heat exchange between the warmer vapor and cooler sink fluid, the vapor condenses and builds up a film on the droplets. This process then slows with time because the fluid film that builds up on the droplet causes increasing thermal resistance to heat flow (although this effect can often be neglected in analyses because the film thickness is small). Also, the temperature of the sink fluid increases, causing a diminishing temperature driving force, a true limit to the process. Consider the situation when the equality sign holds in eq. (19.10). For a film thickness of δ , this equation can be written as

$$4\pi \left(\frac{d}{2}\right)^2 \delta \cdot \rho_c = \frac{4\pi}{3} \left(\frac{d}{2}\right)^3 \rho_s \cdot \text{Ja}_s \quad (19.11)$$

yielding

$$\delta = \frac{d}{6} \frac{\rho_S}{\rho_c} \text{Ja}_S \quad (19.12)$$

Generally, the densities of the two liquids are of the same order of magnitude. If the Jakob number of the sink is very much less than unity, the condensate thickness δ will be small relative to the sink droplet diameter. In this situation, the heat transfer across the condensed film can be assumed to be by conduction.

Heat transfer in the droplet can also be assumed to be by conduction. The governing descriptive equation for temperature is then one-dimensional conduction in spherical coordinates. With this model, the heat transfer into the composite film/droplet is given by (Lock, 1994)

$$\frac{\bar{h}_x x}{k_S} = \frac{2}{\pi^{1/2}} \left(\frac{vX}{\alpha_S} \right)^{1/2} \quad (19.13)$$

where X is defined here as the droplet travel distance in the vapor: $X \equiv vt$. These results hold for the times and situations when the film thickness is small. The term in parentheses is sometimes called the *travel Péclet number*.

Condensation on Liquid Jets Although less important from an applications' viewpoint than the situation of condensation on droplets, condensation on jets yields to direct analysis. Again assume that the thermal transport in the jet is due primarily to heat conduction and neglect the thermal resistance of the condensate film. As is often the case, the Jakob number in the vapor is assumed to be small. An alternative phrasing of this assumption is that the vapor superheat is assumed not to be large. For this situation, the average heat transfer is given as (Lock, 1994)

$$\frac{\bar{h}_S d_{\text{jet}}}{k_S} = \frac{2}{\pi^{1/2}} \left(\frac{v_0 d_{\text{jet}}^2}{\alpha_S X} \right)^{1/2} \quad (19.14)$$

The combination of variables in the parentheses is the Graetz number, based on the assumed constant diameter of the jet, and v_0 is the jet velocity.

Several researchers have reported experimental studies, including Celata et al. (1989). An empirical relationship that does not require all of the idealizations inherent in the equations given above was published by Kim and Mills (1989):

$$\frac{h d_{\text{jet}}}{k} = 3.2 \left(\frac{v_0 d_{\text{jet}}}{v} \right)^{0.8} \left(\frac{v}{\alpha} \right)^{0.3} \left(\frac{f_{\text{rough}}}{f_{\text{smooth}}} \right)^{0.18} \left(\frac{\rho v^2}{\sigma d_{\text{jet}}} \right)^{0.19} \left(\frac{d_{\text{jet}}}{L} \right)^{0.57} \quad (19.15)$$

Here the symbol f denotes the friction factor of the nozzle and σ represents the surface tension.

Condensation in a Liquid

Single-Bubble Studies The condensation of a single bubble in a liquid of the same component or a liquid of a different component has been of great interest to researchers over the years. Included have been studies of a stationary bubble in a

liquid of the same or a different liquid, as well as a moving bubble in the same or a different liquid. A primary motivation for this has been to develop an understanding that might be applicable to more realistic systems that consist of many bubbles. When fluids of different types are involved (called *three-phase exchanges* because the liquid and vapor of the condensing component as well as the liquid of the sink are present), the number of variables that influence performance goes up significantly over that for two-phase-exchange systems. As shown in a review of this work by Sideman and Moalem-Marón (1982), most studies tend to focus on the time required to condense the bubble in a given situation. Hence the bubble radius variation with time is an oft-cited result.

Some measured results for the condensation heat transfer coefficient were given recently by Terasaka et al. (1999). They also compared the measurements to some theoretical predictions and found the results to compare quite well. In the experiments reported, they condensed single bubbles of hexane and, separately, vinyl acetate in water. The experimental results fit the following equations. For hexane,

$$h_d = \frac{7.89 \times 10^4}{\sqrt{T_V - T_L}} \quad (19.16)$$

while for vinyl acetate, the following was found:

$$h_d = \frac{8.77 \times 10^4}{\sqrt{T_V - T_L}} \quad (19.17)$$

These relationships can be compared to the theoretical result:

$$h_d = \frac{h_{fg}}{M_W} \sqrt{\frac{2\rho_V}{T_V \Delta T (1/\rho_V - 1/\rho_C)}} \quad (19.18)$$

In this result, M_W denotes the molecular weight of water.

Bubble Trains A train of single bubbles is a more-complicated idealization of more realistic systems consisting of swarms of condensing bubbles. In this model, some degree of interaction of individual bubbles, including the effects of local heating of the bulk liquid, can be analyzed. Another important aspect that can be examined in the train studies is the effect on rise velocity of preceding bubbles. This has a significant impact on the liquid height necessary to accomplish a desired amount of condensation.

The transport properties of fluids involved in the condensing systems have a profound impact on the magnitude of the heat transfer coefficients. This is like the situation in surface condensers. In direct contact, the properties of the fluid where the condensation is taking place add an additional effect. An example quoted in Sideman and Moalem-Marón (1982) serves to illustrate this effect. The relative ratios of heat transfer coefficients for pentane condensing in pentane to those for pentane condensing in water to those for a water–water system are 1 : 1.5 : 3.9. The superior heat transfer performance of water over organic fluids can be seen in these ratios.

Phenomena Related to LOCA Interest in the condensation of a vapor in a liquid has been motivated by concern about loss-of-coolant accidents (LOCA) in light-water nuclear reactors. In this situation, unwanted steam generated in the core is forced through a pool of water. These phenomena can be quite complicated because of the various forms of unsteady steam flow that can exist. The heat transfer coefficients and the liquid temperatures can experience wide-ranging time fluctuations here.

Aya and Nariai (1991) have summarized the various modes of condensation that can occur in this situation. They have indicated the importance of pool water subcooling. Note that these types of phenomena occur normally near standard atmospheric pressure. They gave an approximate map that shows the differentiation between the various types of behavior. This is shown in Fig. 19.3 and is discussed below.

If a steam jet is directed into a liquid water pool at lower mass flux rates (i.e., the lower-left-hand region of Fig. 19.3), a phenomenon denoted as *chugging* can occur. For this situation, the results of Young et al. (1974) can be used:

$$h = 6.5\rho_L C_{P,L} v_S^{0.6} \left(\frac{v_L}{d} \right)^{0.4} \quad (19.19)$$

Aya and Nariai (1991) noted that this result did not include the effect of subcooling, which they felt was very important.

At higher mass flux rates (say, greater than about $25 \text{ kg/s} \cdot \text{m}^2$) than those associated with eq. (19.19), another type of oscillation can occur. The frequency of this

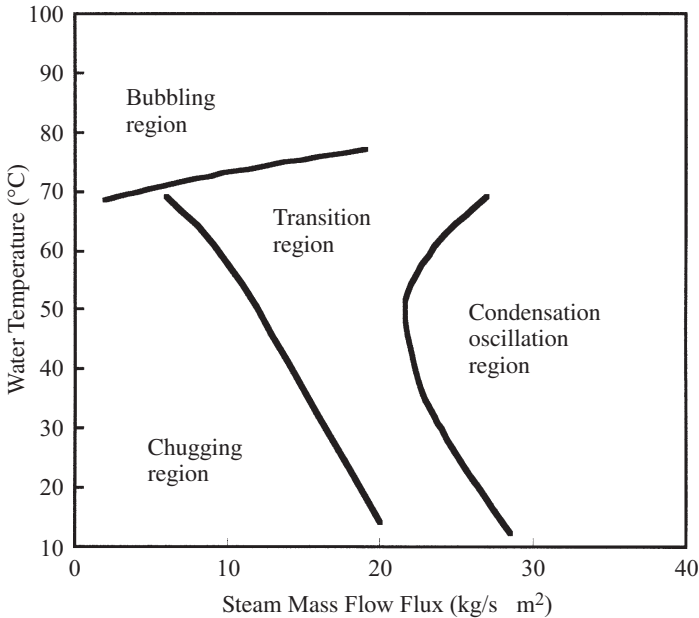


Figure 19.3 Map of condensation phenomena that can develop in loss of coolant accidents. (After Aya and Nariai, 1991.)

one is closely related to that of the periodic growth and reduction of a steam bubble attached to the jet exit. This phenomenon is referred to in the literature simply as *condensation oscillation*. The region where this phenomenon takes place is shown on the right-hand side of Fig. 19.3. A correlation that represents the data quite well has been given by Fukuda (1982):

$$\bar{h} = 43.78 \frac{k_L}{d} \left(\frac{dG_S}{\rho_L v_L} \right)^{0.9} \frac{C_{P,L} \Delta T}{h_{fg}} \tag{19.20}$$

Aya and Nariai (1991) also outlined the magnitudes of the various types of condensation phenomena when steam is condensed in pool water. These are shown in Fig. 19.4. Although the values are affected by numerous variables, including time, and are difficult to illustrate exactly, general trends can be shown.

The highest of these modes is the film coefficient on the vapor side (not the overall value). This is denoted as “steam-side interfacial” in the figure. Moving down in Fig. 19.4, the next variation is shown for the “chugging” region. Along the line indicated,

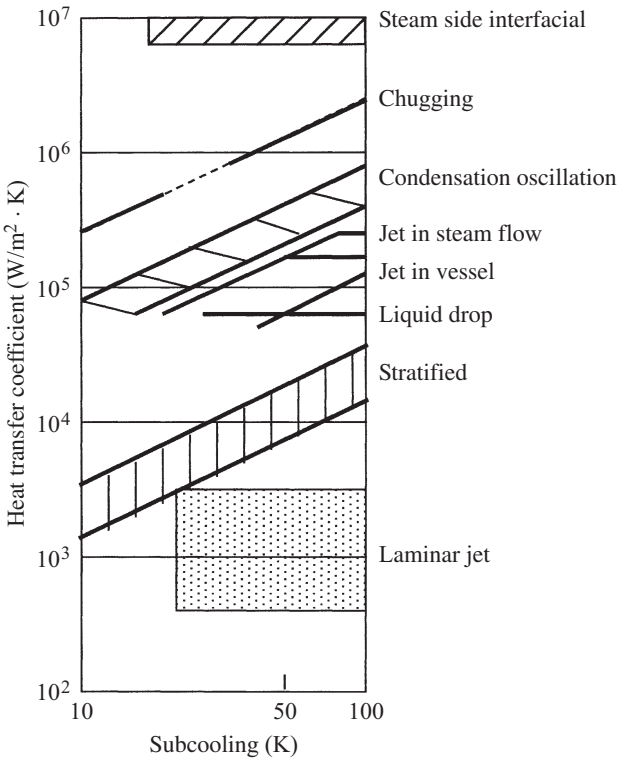


Figure 19.4 Various regimes of condensation of steam in water according to Aya and Nariai (1991).

the higher values are for the individual transient processes, while the lower values denote the average values. “Condensation oscillation” is affected by both the pool subcooling as well as the steam mass flow flux. Higher values of the latter are found in the upper portion of the shaded region. Heat transfer coefficients for this regime can be predicted using eq. (19.20). Near the middle levels, the “jet in steam flow” and the “jet in vessel” typical ranges are shown. Values in the former category are affected by the steam mass flux at higher levels of subcooling. The water pool water can be stratified in certain situations. When this is the case, the heat transfer coefficients are then decreased. This variation is shown by the range denoted as “stratified” in Fig. 19.4. Here the heat transfer is influenced by many variables, including the mass flux and the degree of stratification.

Ranges of the heat transfer coefficients for laminar jets and droplets (Sideman and Moalem-Marón, 1982) are also shown for comparison purposes. The jet values are influenced by the diameter of the jet as well as mass flux rate. The droplet variations shown assume a small contact time. Longer contact times would greatly reduce the magnitudes of h .

More recently, Ju et al. (2000) reported a study on details of the condensation process. They used holographic interferometry to determine the heat transfer to condensing bubbles associated with the application of core makeup tanks.

19.3.3 Evaporation of a Liquid by a Surrounding Vapor, Gas or Liquid

Droplet Evaporation in a Vapor or Gas A problem of great importance in applications is the spray cooling of a hot gas. In this situation, liquid droplets are evaporated by the warmer gas, cooling the latter. Unlike condensing systems, the presence of the gas does not impede the process. Several workers have focused on this problem, motivated by a variety of applications. Using a stochastic modeling approach, Carey and Hawks (1995) analyzed small droplets evaporating in their own superheated vapor. For larger microdroplets, they found the following relationship:

$$\frac{hd}{k} = 2 \frac{\ln(\text{Ja}_v - 1)}{\text{Ja}_v} \quad (19.21)$$

where the Jakob number is given by $\text{Ja} = C_{pv}(T_\infty - T_R)/h_{fg}$. A more complicated result is given for microdroplets.

Tong and Sirignano (1984) analyzed the evaporation of multicomponent droplets in a hot gas. They used a simplified model for this problem that has application to evaporation of fuel in combustion systems. No correlation was presented in this work, but time-varying results were shown for some specific cases.

Droplet Evaporation in a Liquid Çoban and Boehm (1989) modified the results given by several others for the evaporation of immiscible droplets in a continuous liquid. Their particular application was for organic liquids evaporating in water. In the model, the extremely high heat transfer coefficients associated with the evaporating

portion of the droplet were combined in appropriate ways with the poorer heat transfer through the vaporized portion of the droplet. This result is

$$\frac{hd}{k_L} = (\text{Re}_c \cdot \text{Pr}_c)^{1/3} \mathfrak{S} + \frac{5k_c}{k_L}(1 - \mathfrak{S}) \quad (19.22)$$

where

$$\mathfrak{S} \equiv [0.466(\pi - \beta + 0.5 \sin 2\beta)^{2/3}]$$

and β is vapor half-opening angle of the droplet, assuming that the vapor portion of the evaporating droplet accumulates in the top part of the droplet. When the flow of the two fluids is in the same direction, operational aspects change considerably. This is discussed further in Section 19.4.1.

Work has also been performed for a three-phase exchanger where the dispersed phase is injected into a stagnant continuous phase (Smith et al., 1982). Specific results were found for cyclopentane injected into a vessel of water, and these results were compared to a numerical approach that used the drift flux model. Only short transient runs were possible for this situation. Both a preagglomeration state and a postagglomeration stage were considered. In both cases, the thermal resistance of the dispersed phase was assumed to be negligible, and single-droplet velocity was assumed to be of the form

$$v = v_0 r^{c_1} \quad (19.23)$$

In this equation and the two below, the 0 subscript denotes the initial value of the droplet. Further, the single droplet heat transfer was calculated as

$$\frac{hd}{k_c} = c_2 \cdot \text{Re}_c^{c_3} \cdot \text{Pr}_c^{1/3} \quad (19.24)$$

The value of c_3 is known to be in the range 0.7 to 1.0. For the preagglomeration stages, the heat transfer of the bubble as a function of the travel distance in the stagnant water was expressed by

$$h(z) = 2\psi\phi_0 \frac{h_{d0}}{d_0} \frac{(1 + \psi z)^{3/\psi} - 1}{\psi B z} \quad (19.25)$$

where

$$B \equiv \frac{2h_0 \Delta T}{v_0 d_0 h_{fg}} \frac{\rho_{d,L} - \rho_{d,V}}{\rho_{d,L} \rho_{d,V}} \quad \text{and} \quad \psi \equiv (1 - c_1)(1 + c_3) + 1$$

and with c_1 , c_2 , and c_3 as defined by comparison to eqs. (19.23) and (19.24). For the postagglomeration correlation, Smith et al. (1982) found the following result:

$$\frac{h(z)d_0Bz}{2h_{d0}} = \phi_0[(1 + \psi_0Bz_a)^{3/\psi_0} - 1] + \frac{\phi_{\max}}{1 - \phi_{\max}} \times \left\{ \left[1 + \psi_aBz_a + 6(1 - \phi_{\max})^{1-c_3}\psi_aB(z - z_a) \right]^{1/2\psi_a} - (1 + \psi_aBz_a)^{1/2\psi_a} \right\} \quad (19.26)$$

In this equation the subscript a is used to denote the onset of agglomeration. The same order of magnitude of predicted heat transfer coefficients for evaporation were noted as those for results reported in the literature.

Studies of direct-contact evaporation of R114 injected into stagnant water near saturation were reported by Celata et al. (1995). Photographic means were used to quantify the rate at which the refrigerant evaporated and the amount of the liquid remaining at after the droplet. More recently they investigated a related problem, but with set amounts of subcooling (Celata et al., 1999).

19.4 COLUMNS AND OTHER CONTACTORS

19.4.1 Spray Columns

Columns, including spray columns and columns with internals, can be used for a variety of direct contact heat transfer processes. Columns with internals can include tray columns and columns with packing. Packings can range from spheres to more complicated geometries called *structured packings*. The latter are preferred from the perspective of minimizing cost and maximizing performance. Columns allow intimate contact between a dispersed phase and a continuous phase. In condensation situations, the liquid (sink) phase is usually continuous. A review of a variety of process heating devices has been given by Jacobs (1988b).

Three analysis approaches have been used. One draws on previous design practice for conventional, indirect heat exchangers, another uses concepts from mass transfer device analysis, and the third uses more detailed analyses of the behavior of a typical droplet in the device and accumulates the effects for all, to find overall performance. Both the first and third approaches are discussed here in some detail.

First consider the design approach analogous to that used for closed heat exchangers. No matter which of the many types of heat transfer phenomena are present (e.g., desuperheating, condensation, and subcooling could all be taking place in a given device), the overall heat transfer is calculated using the LMTD approach. If the area between the two separate fluids is known, the calculation can be made:

$$Q = U_A A_i \cdot \text{LMTD} = U_A A_i \frac{\Delta T_1 - \Delta T_2}{\ln(\Delta T_1 / \Delta T_2)} \quad (19.27)$$

In this equation, U_A denotes the overall heat transfer coefficient based upon the fluid interface area A_i . The subscripts 1 and 2 denote the temperature differences between the two fluids at each of the ends of the contacting device. Several problems exist with this approach. For one, the area-based heat transfer coefficient on the fundamental droplet level may be difficult to estimate. Second, the area of that interface can also be difficult to determine. Third, even if the area is known, it is not unusual for it to vary considerably throughout the contactor. A more easily evaluated approach to this that has been used in many studies reported in the literature is to replace the area-based heat transfer characteristics with volume-based values. This is given as

$$Q = U_V V \cdot \text{LMTD} = U_V V \frac{\Delta T_1 - \Delta T_2}{\ln (\Delta T_1 / \Delta T_2)} \quad (19.28)$$

In this equation, V denotes the total contactor internal volume and U_V is the volumetric heat transfer coefficient based on that volume. Although the latter can suffer from imprecision about details of the heat transfer variations as indicated in the area-based approach, the assumption made here is that the result is a composite for the overall situation.

Another way of dealing with the elusive concept of the basis for the overall heat transfer coefficient is to use a term for the surface area of the droplets per unit volume of the column. In this manner, the heat transfer coefficient can be written as $U_A a$. Here the U_A is the traditional surface heat transfer coefficient, but it is now based on the area of the droplets, while a is the area of the droplets per unit volume of the heat exchanger. Hence

$$U_A a = U_V \quad (19.29)$$

This does not simplify the problems of determining the area-to-volume information explained above; it is simply another notation used in the literature.

Reminiscent of mass transfer operations, where columns have traditionally been used most frequently, the *transfer unit* technique is often applied. In this approach, a volumetric heat transfer coefficient, usually determined from empirical data, is used. The concept of a *stage* comes into play. This is illustrated in Fig. 19.5.

One situation that occurs frequently is that of partial condensation of a superheated vapor by a cool liquid. In this case, the volumetric heat transfer coefficient can be written as (Fair, 1972; Sideman and Moalem-Maron, 1982)

$$U_V = \frac{1}{1/h_{V,L} + (1/\beta h_{V,G})(Q_G/Q_T)} \quad (19.30)$$

In this equation, $h_{V,L}$ and $h_{V,G}$ represent the heat transfer coefficients on the liquid side and the gas (vapor) side in direct contact, respectively; and Q_T and Q_G , respectively, are the total heat transfer and the amount of heat transfer involved in removing the superheat. The subscript G is used to differentiate it from locations where actual condensation is occurring. Finally, the term β is used for the following:

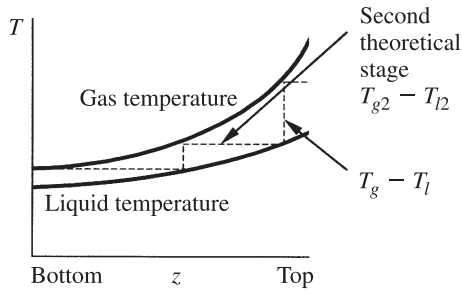


Figure 19.5 Temperature versus distance plot of heat exchanger with stages outlined. The first stage is at the left, the second is indicated explicitly, and a portion of a third exists at the right.

$$\beta \equiv \frac{\hat{N}C_{P,G}/h_{V,G}V}{1 - e^{-\hat{N}C_{P,G}/h_{V,G}V}} \quad (19.31)$$

Here the term \hat{N} is used to denote the mass transfer rate. Note that when the contactor only includes condensation (no desuperheating) and the liquid (sink) is the same compound as the vapor, the vapor–liquid portion is not present, and the vapor-side heat transfer coefficient in the overall computation can be neglected. For this case, the following results:

$$U_V = h_{L,V} \quad (19.32)$$

The overall height of a heat transfer unit ($Z_{i,T}$) can be written as

$$Z_{i,T} = Z_{i,G} + Z_{i,L} \frac{G_G C_{P,G}}{G_L C_{P,L}} \frac{Q_L}{Q_G} \quad (19.33)$$

This is a characteristic of the specific heat transfer equipment and process. Finally, the number of transfer units (NTUs) can be found:

$$\text{NTU}_g = \int_{T_{g1}}^{T_{g2}} \frac{dT_g}{T_g - T} \approx \ln \frac{T - T_{g1}}{T - T_{g2}} \quad (19.34)$$

From this the total column height can be found:

$$Z_T = \frac{V_T}{A} = \text{NTU}_g \cdot Z_{i,T} \quad (19.35)$$

In this equation, A denotes the cross-sectional area of the empty column.

Global Treatments Spray columns offer the simplest contactor configuration. In this arrangement, a column is outfitted with inlets for each of the continuous

and dispersed fluids and their corresponding outlets. The lighter fluid is admitted at the bottom of the column and flows upward in a down-coming heavier fluid, due to the influence of gravity. The lighter fluid can serve as either the *dispersed* or the *continuous* component, although most applications find it as the former. Special arrangements (often called *disengagement zones*) are incorporated in both the top and bottom of the column to allow the two fluids to be separated. A simple schematic of one of these types of columns is shown in Fig. 19.6. Although the details of the actual introduction of the two fluids is not shown in this figure, the general arrangement is quite simple.

One of the more important variables that affect heat transfer in a spray column is the *holdup* (denoted here by the symbol ϕ). This is defined as the amount of the

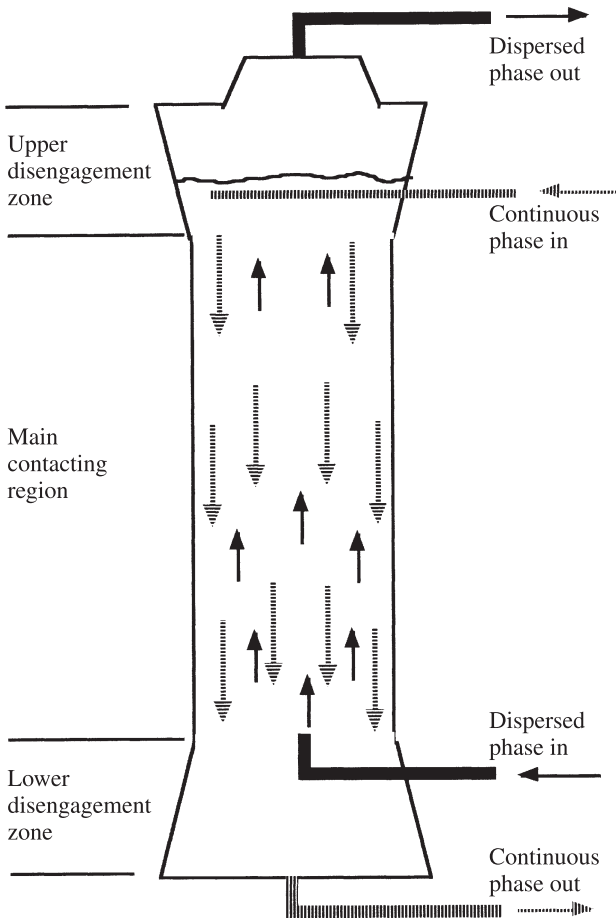


Figure 19.6 Spray column when the dispersed phase enters from the bottom. Other than as a means of introducing the two fluids, the column does not contain any internals.

dispersed fluid in the continuous fluid at any time. In a general heat transfer device, the holdup can vary with distance up the column. The holdup is often used to correlate both heat transfer and mass transfer.

Other variables of interest in discussions of spray columns are the *superficial* velocities (\tilde{V}) of each of the phases and the slip velocity. The superficial velocity is the actual velocity that the dispersed or continuous phase is moving, and this depends on the holdup. For the dispersed phase, this is

$$\tilde{V}_d = \frac{v_d}{\phi} \quad (19.36)$$

while the continuous phase velocity is given as

$$\tilde{V}_c = \frac{v_c}{1 - \phi} \quad (19.37)$$

Finally, the *slip velocity* \tilde{V}_{slip} is given as the difference of the two component velocities shown above. As shown by Letan (1988), the operational relation of the system, in terms of the terminal velocity v_T , is

$$v_T(1 - \phi)^{\gamma-1} = \frac{\tilde{V}_d}{\phi} + \frac{\tilde{V}_c}{1 - \phi} \quad (19.38)$$

The flooding holdup can then be found. The flooding situation is found at the following condition (Letan, 1988):

$$\left. \frac{\partial \tilde{V}_c}{\partial \phi} \right|_{\tilde{V}_d} = 0 \quad (19.39)$$

With this condition, the flooding limit on holdup can be found:

$$\phi_f = \frac{[(\gamma + 1)^2 + 4\gamma(1/R - 1)]^{1/2} - (\gamma + 1)}{2\gamma(1/R - 1)} \quad (19.40)$$

where $R \equiv \tilde{V}_d/\tilde{V}_c$ and γ is as defined in eq. (19.38). At the limit where the continuous phase velocity is zero (R becomes unlimited), the maximum holdup can be determined:

$$\phi_{f,\text{max}} = \frac{1}{\gamma} \quad (19.41)$$

Finally, the pressure drop in the continuous phase in a vertical column is found as follows:

$$\frac{\Delta P}{\Delta Z} = (\rho_c - \rho_d)g\phi \quad (19.42)$$

As will be noted again in the discussion of columns that incorporate internals (baffles, packings, etc.), the spray column offers some benefits and shortcomings. Of the benefits, by far the most important is the relative simplicity and resulting low cost of these devices. Also, the heat transfer performance can be very high. One of the shortcomings is that there could be a fair amount of backmixing, which would hinder overall performance. Examples of possible temperature versus distance traces that might be encountered are given in Fig. 19.7.

Means of estimating the heat transfer in these devices have been addressed in the literature. For example, for gas-liquid systems, Fair (1988) has given the following correlation:

$$U_{V,G}(\text{W/m}^3 \cdot \text{K}) = 867 G_G^{0.82} G_L^{0.47} Z_T^{-0.38} \quad (19.43)$$

In this equation, Z_T denotes the height of a single spray zone. Fair indicates that this equation is only for the gas side of the heat transfer process, but because of circulation inside the droplets, there is relatively little resistance to heat transfer in the liquid phase.

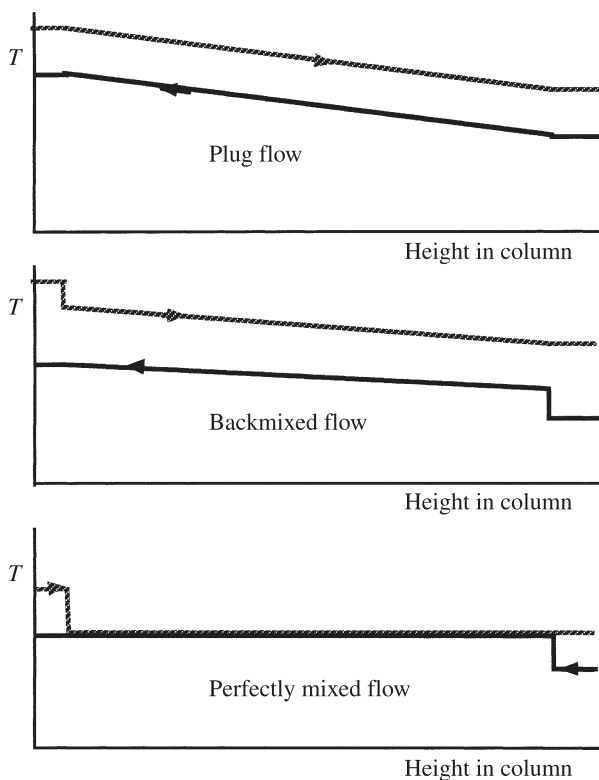


Figure 19.7 Various types of performance of a spray column that can result from mixing phenomena. (After Letan, 1988.)

Heat transfer results for liquid–liquid spray columns were correlated by Plass et al. (1979). For holdups greater than 5% ($\phi > 0.05$),

$$U_V (\text{Btu/hr-ft}^2 \cdot ^\circ\text{F}) = 4.5 \times 10^4 (\phi - 0.05) e^{-0.75(\dot{m}_d/\dot{m}_c)} + 600 \quad (19.44)$$

For columns where vaporization is taking place, the heat transfer can be calculated as follows (Jacobs and Boehm, 1980):

$$\text{St} = \frac{U_v V}{\dot{m}_L C_{P,L}} = \frac{Q}{\text{LMTD} \cdot \dot{m}_L C_{P,L}} = 2(\text{Ja}_V \cdot \text{Pr}_V)^{0.6} R_m^{-0.15} \quad (19.45)$$

To determine this result, data from a variety of systems were analyzed, including some where boiling took place on a liquid surface.

An even simpler result was given by Walter (1981). For all configurations with light hydrocarbons or refrigerants vaporizing in water, the following was recommended:

$$U_V = 894\phi \quad (19.46)$$

The only complication in applying this relationship is that the ϕ is the value coming into the boiling section. Hence, if preheating and boiling are taking place in the same column, this would be the holdup leaving the preheater portion.

More recently, Siqueros and Bonilla (1999) have evaluated the correlation above against experimental results they determined from vaporizing normal pentane in water. Although they found that the qualitative aspects of the performance matched well with that equation, their results were approximately 30% higher for the overall heat transfer coefficient.

Direct contact boiling phenomena have been proposed for a variety of applications, including nuclear reactors. A proposal has been presented (Kinoshita and Nishi, 1994; Kinoshita et al., 1995) for an innovative steam generator system for fast breeder reactors that utilizes water and a molten metal. In experiments using Wood's alloy (Bi–Pb–Sn–Cd) as the continuous phase fluid and water, volumetric heat transfer coefficients in the range 4 to 34 kW/m³ · K were demonstrated.

Spray columns have been applied for waste heat recovery, and several of the papers cited in this chapter address this application. One clever approach is to use a falling cloud of solid particles in a stream of exhaust gas (Sagoo, 1981, 1982). No specific performance correlations were given, but the approach was deemed to be quite successful.

The simplicity of the spray columns can lead to some undesirable aspects in overall performance. In many situations, the spray pattern may deteriorate at some distance from the nozzle. Spray columns are also prone to backmixing. Even in relatively organized flows, the wake following a droplet can impede heat transfer (Letan, 1988).

A method was reported by Letan (1988) for designing liquid–liquid spray columns. Crucial aspects of this are the column diameter and the column length. Of course, the appropriate diameter of the column is that required to pass the necessary flows. As

the relative flow rate increases, the drag on the droplets increases. At some point, too much holdup of the dispersed fluid could occur. *Flooding* is the point where the flow rate of the dispersed fluid and its imposed drag on the droplets do not allow the dispersed fluid to flow completely through the column. Considering these types of interactions, Letan presented a result to determine the proper diameter of the column:

$$D_{\text{column}} = 2 \left\{ \frac{\dot{V}_C [(V_d/V_c)(1 - \bar{\phi}) + \bar{\phi}]}{\pi V_T \bar{\phi} (1 - \bar{\phi})^\zeta} \right\}^{1/2} \quad (19.47)$$

In this equation, the exponent ζ is given by the following empirical relationships:

$$\begin{aligned} \text{Re} &\leq 0.2 & \zeta &= 4.65 \\ 0.2 < \text{Re} < 1 & & \zeta &= 4.35 \text{Re}^{-0.03} \\ 1 \leq \text{Re} \leq 500 & & \zeta &= 4.45 \text{Re}^{-0.01} \\ 500 < \text{Re} & & \zeta &= 2.4 \end{aligned}$$

Here the Reynolds number is based on the terminal velocity of the droplets. The length of the column is determined to accomplish the necessary heat transfer. Letan (1988) has given a method that includes the effect of the wake of the droplets. This results in a fairly lengthy computational method, and the reference noted should be consulted to use this approach.

An approximate approach has been recommended by Jacobs (1988a). This uses a formulation based on concepts used in closed heat exchangers to determine their length:

$$Z = \frac{\dot{m}_d \Delta h_d}{U_V [(\pi/4) D^2] \cdot \text{LMTD}} \quad (19.48)$$

When the flow of the two fluids is in the same direction, several column operational characteristics are quite different. No longer is flooding a limitation to operation, as both fluids are being forced through the column co-currently. On the other hand, the residence time is generally less than in a counterflow tower, and the temperature differentials are less favorable. A recent comprehensive study of such a system was reported by Shiina (1997). In this work, R-113 was used for the dispersed phase injected through a jet, and water was used for the continuous phase. Work was performed in a 50-mm-inner-diameter column with a maximum length of 1.5 m. The injector level could be varied to show the effects of contact height on the results. A complicated set of correlations was presented that fit the general form

$$\text{St} = \frac{U_V V}{\dot{m}_d C_{P,d}} = c_1 + c_2 (R_m)^{c_3} (\text{Ja} \cdot \text{Pr}_{d,v})^{c_4} \left(\frac{Z}{D_{\text{column}}} \right)^{c_5} \left(\frac{D_{\text{nozzle}}}{D_{\text{column}}} \right)^{c_6} \quad (19.49)$$

The constants for this equation are shown in Table 19.1.

TABLE 19.1 Empirical Correlation Constants for Eq. (19.49)

Conditions ^a	c_1	c_2	c_3	c_4	c_5	c_6
$R_m > 50, Ja < 11$	0.37	-1.45	0.12	0.08	1.97	57.93
$R_m > 50, Ja > 11$	0.37	0.12	0.12	0.08	4.73	2.27
$R_m < 50, Ja > 11$	-0.29	0.11	0.39	0.08	1.30	13.95
$R_m < 50, Ja < 11$	-0.29	-1.22	0.39	0.08	14.52	114.82

Source: Shiina (1997).

^aRange of applicability for table is $6.3 < R_m < 380, 4.8 < Ja < 37$.

Differential Treatment If predictive information on the detailed behavior of discrete zones inside a spray column is desired, a differential approach can be used. In this formulation, the behavior of a typical bubble is predicted when it is interacting with various elevations of the continuous phase. Models of this type have been cast in terms of a one-dimensional equation set, with the height in the column being the independent parameter. There is no reason why two- and three-dimensional formulations cannot be used, but one-dimensional models generally yield good predictions for the overall performance of a spray column. The added complexity of higher-order models is normally not considered to be worthwhile.

Several formulations have appeared. Among those found in the literature are formulations for liquid-liquid spray columns given by Jacobs and Golafshani (1989), Hutchins and Marschall (1989), and Summers and Crowe (1991), and three-phase exchanges in spray columns by Çoban and Boehm (1988), Tadrist et al. (1987, 1991), Ay et al. (1994), and Song et al. (1998). Brickman and Boehm (1994a,b) used a formulation similar to that of Çoban and Boehm (1988) to study design optimization of various configurations.

A basic approach to the analysis of a three-phase spray column will now be outlined. This draws on the work of Çoban and Boehm (1988) and Brickman and Boehm (1994a). First, consider the one-dimensional equations representing continuity, momentum, and energy. These are written for the region influenced by each stream of bubbles as follows:

$$\frac{dP}{dz} = -\frac{\dot{m}_d}{A} \frac{dv_d}{dz} - \frac{\dot{m}_c}{A} \frac{dv_c}{dz} - [\rho_c(1 - \phi) + \rho_d\phi]g \quad (19.50)$$

$$\frac{d\bar{h}_d}{dz} = \frac{A}{\dot{m}_d} \frac{Q_d}{V} \quad (19.51)$$

$$\frac{d\bar{h}_c}{dz} = \frac{A}{\dot{m}_c} \frac{\eta Q_c}{V} \quad (19.52)$$

Here the term η is used to denote the amount of heat that leaves (enters) the dispersed phase and is transferred to (from) the continuous phase. Heat loss to the surroundings from the column will render this parameter less than unity.

A relationship for the droplet velocity can be written in terms the drag coefficient and the other parameters is modified slightly from the result given by Raina et al. (1984).

$$v = \frac{1.1547\{[1 - (\rho_d/\rho_c)(R_0/R)^3](2Rg/C_D)\}^{1/2}\bar{R}^{[(5/6) - (\bar{R}/T_c)]}}{[(T_c^2 + T_d^2)/2T_dT_c]\bar{R}(C_P\mu_c/k_c)^{R_0/1.6R}} \quad (19.53)$$

In this equation, the subscript 0 denotes beginning values, C_D is the drag coefficient on a single droplet defined below, R is the droplet radius, and \bar{R} is the average droplet radius from insertion to the point of interest in the column. This average droplet radius is given by the relationship

$$\bar{R} \equiv \frac{R_0^2 + R^2}{2R_0R} \quad (19.54)$$

The drag coefficient on a single droplet can now be found (White, 1974):

$$C_D = \left(\frac{24}{\text{Re}} + \frac{6}{1 + \text{Re}^{1/2}} + 0.4 \right) \frac{1 + (2\mu_c/3\mu_d)}{1 + (\mu_c/\mu_d)} \quad (19.55)$$

In general, heat transfer coefficient calculations must be made for both the interior and the exterior surfaces of the droplet. A variety of correlations can be used for this, as discussed earlier in the chapter. One distinction is if the droplet is all liquid, all vapor, or if there is evaporation or condensation taking place inside. For purposes of discussion here, it is assumed that the droplet is initially all liquid, and then at some point in the column vaporization begins.

On the outside of the droplet, a variety of correlations are available, as noted previously. For example, eqs. (19.1), (19.2), or (19.3) could be applied, but a variety of other correlations appear in the literature [see, e.g., Sideman and Shabtai (1964)]. Any of these can be used to find the external heat transfer coefficient h_e .

Then a correlation for the interior-to-the-bubble heat transfer is determined. Again, a wide variety of correlations are available, depending on the presumed flow (or stationary) situation inside the bubble. Remember that the shape and size of the bubble have an influence on these aspects, as discussed by Grace (1983). One possible approach to this if the droplets are small is to assume that the internal heat transfer is solely by conduction when the droplet is all liquid. If and when evaporation begins, eq. (19.22) can be applied to find the h_i . With both the external and internal heat transfer coefficients found, the overall heat transfer coefficient can be calculated:

$$U = \frac{h_e h_i}{h_e + h_i} \quad (19.56)$$

With this heat transfer coefficient determined, the heat transfer can be calculated. This is given by

$$Q_d = U(4\pi R^2)N(T_c - T_d) \quad (19.57)$$

Here the term N denotes the number of bubble trains in a given spray column. Note that all of these factors just discussed are found at a given elevation z , and then the effect of height in the column is found from the mass, momentum, and energy balances shown in eqs. (19.50)–(19.52).

If the droplet number density does not change throughout the column, the droplet radius follows the dispersed phase density in the following manner.

$$R = R_0 \left(\frac{\rho_{d0}}{\rho_d} \right)^{1/3} \quad (19.58)$$

This may not always be a good assumption, depending on possible breakup of droplets, agglomeration, and other factors.

Droplet agglomeration or breakup could be included in the model. This could also include a variety of droplet sizes as may be the actual situation in a column. Both of these general aspects have been discussed by Song et al. (1998). They used probability functions to describe each of these aspects.

A general design problem is one where the two fluids are flowing countercurrently and their corresponding mass flow rates and incoming temperatures are known. From a design standpoint, it is desired to estimate the outgoing temperatures of the two fluids as they might be influenced by various physical parameters of the column (e.g., column diameter, column length, droplet diameter, operational pressure).

Analysis next considers the differential zone. An example of this is shown in Fig. 19.8. Here N injection areas are considered for the dispersed fluid. It is assumed that these injectors are essentially equidistant from one another so that the volume of the active zone is made up of N more or less equal subvolumes that run the full length of the active portion of the column.

Note that a particular arrangement (dispersed fluid in at the bottom that is vaporized by the continuous fluid as it travels up the column) has been assumed. This is done here only to give specific discussion points. The method can be applied to any general spray column combination of fluids, or particles flowing through a fluid.

To proceed, thermodynamic and thermal–physical properties are needed. Many such routines have been developed over the years and are now found almost routinely using thermodynamics and heat transfer texts or commercially available mathematical solver software. A variety of numerical approaches can be used to solve this system of equations. Brickman and Boehm (1994a) used a fourth-order Runge–Kutta solution algorithm. At the bottom of the column, the dispersed phase temperature is known. This is the location where the solution begins. Unknown from the standpoint of the solution method are the velocity gradients and the temperature of continuous fluid. What is known is the incoming temperature of the continuous fluid at the top of the column. To handle this problem, a shooting type of method is used. The unknown temperature at the bottom is estimated, the solution carried out, and the continuous phase temperature calculated at the top is compared to the one given. If these temperatures do not correspond to within a predetermined limit, a new value for the exiting continuous-fluid temperature is estimated and the calculation repeated.

Using an approach similar to the one just described, Çoban and Boehm (1988) made comparisons to experimental results determined in large-scale direct contact

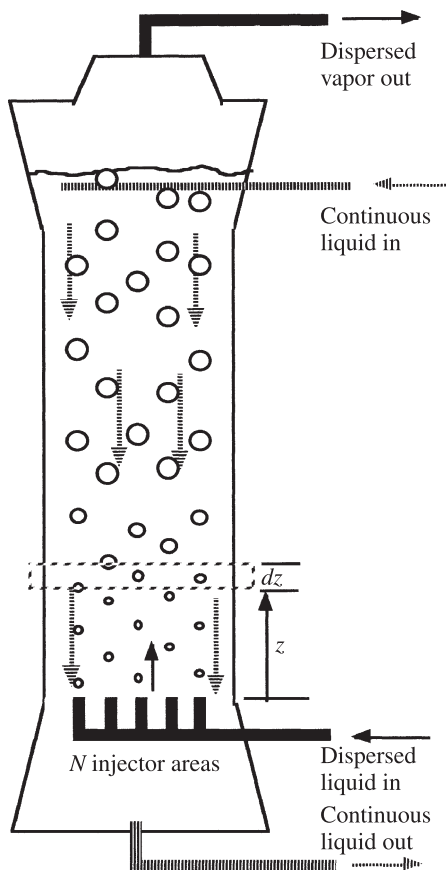


Figure 19.8 One-dimensional differential analysis volume that can be used to study performance of spray columns.

spray towers used in energy conversion systems. Very good comparisons were found. Later Brickman and Boehm (1994a,b, 1995) applied this type of solution technique to optimize designs of direct contact heat exchangers of the spray column type. They showed the influence of a variety of parameters on the overall performance of the direct contact heat exchanger. It was noted that a wide range in overall performance could be effected by simple adjustments to the operational parameters.

Melting and Solidification Applications One application of spray columns that has drawn interest over the years is that of solidification of a medium, typically for thermal storage or chemical separation. This can be accomplished in a batch mode, where the solidifying medium does not circulate outside the column. Alternatively, a means of moving a slurry can be used to circulate the partially solidified medium for

steady operation. The number of studies is sufficiently limited, and the working substances and physical systems sufficiently numerous, that no broadly encompassing predictive technique has been developed. However, individual summaries of some the specific work are given here.

Kim and Mersmann (1998) studied melt crystallization of *n*-dodecanol from a *n*-decanol/*n*-dodecanol mixture for separation purposes. In this set of experiments they used various coolants, including a gas, a liquid, and a vapor. Several semiempirical relationships were given to describe the data they found. Agitated columns were used for some of these studies, and the impeller diameter was used as a correlation variable in those cases. For a *gas-liquid* system, the following relationship fit the data very well:

$$\frac{U_V D^2}{k_{\text{melt}}} = 1.79\phi \text{We}^{-1.2} \quad (19.59)$$

Here the Weber number (We) is based on the droplet superficial velocity and the column diameter. For the situation when a *liquid-liquid* system is used, the authors separated the correlation into three ranges of holdup ratio:

$$0 < \phi < 0.2: \quad \frac{U_V D_{im}^2}{k_m} = 1.06\phi \text{We}_{im}^{-1.2} \quad (19.60a)$$

$$0.2 < \phi < 0.8: \quad \frac{U_V D_{im}^2}{k_m} = 0.18\text{We}_{im}^{-1.2} \quad (19.60b)$$

$$0.8 < \phi < 1: \quad \frac{U_V D_{im}^2}{k_m} = 0.34\phi \text{We}_{im}^{-1.2} \quad (19.60c)$$

In these correlations, the impeller characteristics are used.

Moderately high temperature thermal storage (around 48°C) using direct contact processes was examined by Kiatsiriroat et al. (2000). In these studies, sodium thiosulfate pentahydrate exchanged heat with a heat transfer oil. A direct contact storage unit made of acrylic and having a diameter of 0.12 m and a length of 0.7 m was used. The phase-change material remained in the unit. They found an empirical equation that fit the solidification data very well:

$$\text{St} = 67.48 \text{Ste}^{-1.4033} \cdot \text{Pr}^{-0.3508} \quad (19.61)$$

This also fit data they found for water-oil and water/R-12 systems.

A direct contact technique applicable to cold storage investigated by Utaka et al. (1998) was related to earlier work they performed (Utaka et al., 1987). Their approach used a closed vessel partially filled with water where the hydration of HCFC142b took place. For this system, the critical decomposition temperature of the gas hydrate is 13.1°C, and the formation temperature of the gas hydrate depends on the system pressure. For their system, the pressure was controlled. Although no heat transfer correlation was recommended in this study of transient phenomena, they did show

how the overall heat transfer coefficient varied with time (from about $4 \text{ kW/m}^3 \cdot \text{K}$ down to an order of magnitude smaller) and showed how this was dominated by the heat transfer coefficient on the liquid side.

A study of direct-contact freezing of tetradecane by a water–ethylene glycol solution in a spray column was reported by Inaba and Sato (1996). Both solidification rate versus temperature and some visual results were given. No correlation of heat transfer rate was noted.

In a study related to the one just noted, latent heat transfer for cold storage using direct contact means has also been investigated by Inaba and Sato (1997). In this work, tetradecane (paraffin) oil was used as the phase-change material, and cold water was used to accomplish the solidification. This phase change takes place at 5.8°C and liberates 229 kJ/kg of heat. Heat transfer characteristics were not given explicitly, but they did correlate volume fraction solidified as a function of the Stefan number based on the solid phase, the Reynolds number, and a dimensionless temperature ratio.

A combined direct contact freezer and ice slurry district cooling system has been reported (Knodel, 1989). In this approach, the evaporator section of the refrigeration system was a direct contact heat transfer device. The ice slurry that resulted was then moved through a distribution system. No specific heat transfer performance was given.

Thermal storage for solar heating was investigated by Fouda et al. (1980, 1984). A mixture of 68.2% Na_2SO_4 and 31.8% water was used throughout the work as the latent heat storage material and the paraffinic solvent Varsol was used as the immiscible heat transfer fluid. For most runs a spray column was used, but a limited number were performed using a screen packing (see the discussion on packed columns below). Volumetric heat transfer data, based on the salt volume, were correlated with the relationship

$$U_V = c_1 \tilde{V}^{c_2} \tag{19.62}$$

In this equation, \tilde{V} is the superficial velocity of the heat transfer fluid based on the total column cross-sectional area. The correlation constants varied with the size of the column, the fluid combination used, and whether or not the column had packing in it. These are listed in Table 19.2.

TABLE 19.2 Correlation Constants of Volumetric Heat Transfer Coefficients in Eq. (19.62)

System	<i>D</i> (cm)	Packing	\tilde{V} Range (cm/s)	<i>c</i> ₁	<i>c</i> ₂
Sodium sulfate	27.8	No	0.13–0.73	31.4	1.28
	27.8	Yes	0.10–0.39	18.6	0.78
	12.7	No	0.61–1.48	25.2	1.16
Water–Varsol	27.8	No	0.07–0.20	34.6	1.26
	12.7	No	0.61–0.91	29.8	0.43

Adapted from data presented by Fouda et al. (1984).

Farid and Yacoub (1989) and Farid and Khalaf (1994) have reported studies on latent heat storage at temperatures in the approximate range 20 to 50°C. In the first of these studies a single column was used, and three hydrated salts were the focus of the work: $\text{Na}_2\text{CO}_3 \cdot 10\text{H}_2\text{O}$, $\text{Na}_2\text{SO}_4 \cdot 10\text{H}_2\text{O}$, and $\text{Na}_2\text{HPO}_4 \cdot 12\text{H}_2\text{O}$. Volumetric heat transfer coefficients in the range 2 to 12 $\text{kW/m}^3 \cdot \text{K}$ were demonstrated. The authors fit these data with a correlation like that shown eq. (19.62) for a variety of cases with values for the first constant in the range $23.1 \leq c_1 \leq 46.5$ and the second constant in the range $0.70 \leq c_2 \leq 1.28$. In the second study, two columns were used with $\text{Na}_2\text{CO}_3 \cdot 10\text{H}_2\text{O}$ and $\text{Na}_2\text{S}_2\text{O}_3 \cdot 5\text{H}_2\text{O}$. The volumetric heat transfer coefficients were not correlated, but they were in the same general range as noted in the earlier paper. In this second work, a thermal efficiency was defined as the ratio of the actual energy removed (or stored) from both columns to the energy theoretically available in both columns. Values for this parameter of 45.3 to 91% were demonstrated.

19.4.2 Baffled Columns

Baffled columns are used as means of improving on the performance of spray columns. These devices rearrange flow that can be more favorable to heat transfer in both the dispersed and continuous phases. However, as internals are added to the column, the capital cost increases: hence the improvements in performance need to outweigh the additional expense of installation.

The flow and heat transfer situation in baffled-tray columns is more complicated to describe than that in spray columns. Figure 19.9 is a schematic showing some elements of this type of column. Important variables are the diameter of the column, the curtain area (shown in the figure), and the window area (column area minus the tray area). For this situation, Fair (1972, 1988) has given a heat transfer correlation for typical designs of baffles spaced about 0.6 m apart and window areas of 40 to 50% of the column area:

$$U_v (\text{W/m}^3 \cdot \text{K}) = 585 G_G^{0.7} G_L^{0.4} \quad (19.63)$$

This correlation fits data approximately for a range of systems, including air–water as well as hydrogen–light hydrocarbon/oil units.

Baffled columns have also been the basis of increasing heat transfer to immersed tubes. The use of a slurry in a bubble column has been reported by Saxena and Chen (1994). They gave the following correlation for the heat transfer in this situation:

$$\text{St} = 0.0389 (\text{Re} \cdot \text{Fr} \cdot \text{Pr}^2)^{-0.25} [\mu_L (\text{Pa} \cdot \text{s})]^{-0.15} \quad (19.64)$$

In this equation, the liquid viscosity has the units shown.

Sieve tray or perforated tray columns are a form of the baffled type. These can be used for applications of liquid–liquid and three-phase systems. In this arrangement, each of the baffles serves to catch the dispersed fluid and re-form the droplets. A typical tray interaction is shown in Fig. 19.10. At least two positive characteristics can result from this. One is that the droplet can be resized, which could be very

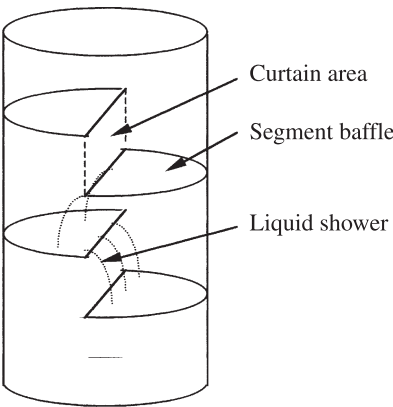


Figure 19.9 Conceptual schematic of a baffled tray column with the liquid indicated.

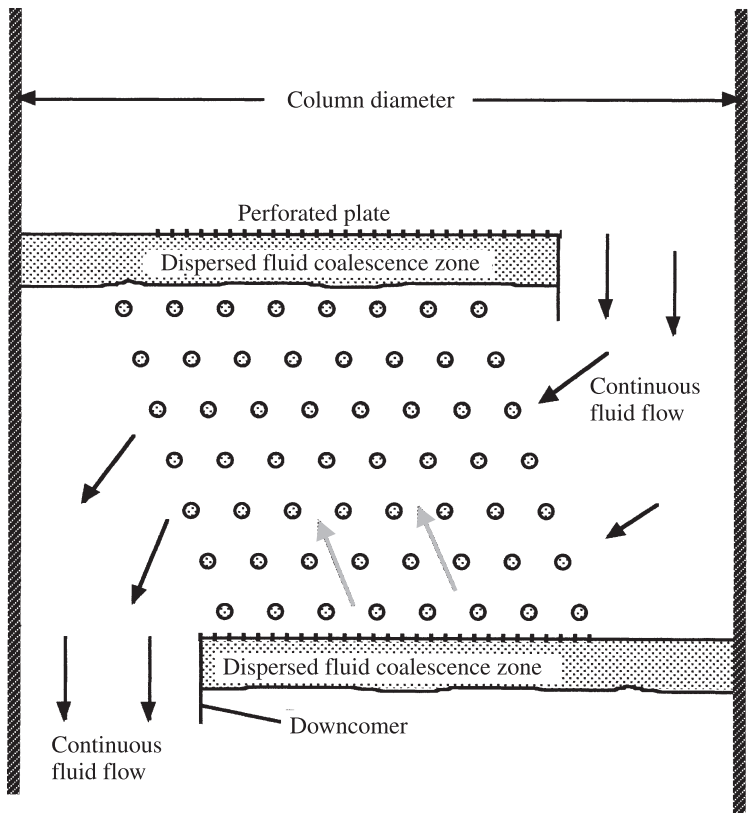


Figure 19.10 Fluid interactions at one unit in a perforated tray, baffled column direct-contact heat exchanger.

important in vaporizing systems, where the droplets can grow in size quite substantially throughout the column. Generally, heat transfer per unit of droplet surface area decreases as the droplet grows. Another positive factor is that the wake behind the droplet can be stripped away at each tray. The net result of both of these aspects is that the heat transfer can be increased substantially compared to a corresponding spray column.

19.4.3 Packed Columns

Another approach to improving on spray column performance is to use packed-bed arrangements. In this configuration, the main contacting zone (as shown in the spray column diagram) would be filled with objects of potentially any shape. Both packed beds and baffled towers can be contrasted to spray columns in several ways. Certainly, the cost is higher than the latter for either of these options. The spray column can yield higher performance than that for columns with internals [see, e.g., the report by Kunesh (1993)]. However, there are situations when backmixing can seriously degrade performance of spray columns. Also, if a vapor is introduced into a thick layer of liquid such as might be the case for a spray column, a significant pressure drop through the liquid might be encountered. This would increase the power required for moving the vapor. In both of these cases, packed columns or other devices with internals might offer beneficial performance improvements.

Usually, packings are used when a liquid is in contact with a gas or vapor. It is desired to have as much liquid surface in contact with the vapor or gas as possible. As the liquid flows over the packings, essentially wetting the latter, the area in contact between the two fluids is related to the area of the packing. Packings can also be used in liquid-liquid systems to assist in removing the wake from the dispersed liquid and increasing the heat transfer.

Although a simple configuration can be imagined where packed spheres are used, in fact, this is not a normally favored approach because of trade-offs between cost and performance. Instead, more complicated shapes such as structured packings are used. Some examples of these are shown in Fig. 19.11. Objects like those have a very high surface-area-to-volume ratio. These products can achieve ratios up to about $1000 \text{ m}^2/\text{m}^3$. In contrast, this ratio might be a couple of orders of magnitude smaller for spheres. Another factor of concern is the pressure drop for any flows through the bed. Generally, this is related to the solid volume fraction of packing. For solid spheres this is on the order of 40 to 50%, but for some modern packing shapes, this fraction might be less than a few percent. This is accomplished with a low total weight in modern packings, simplifying the design and construction of the column. Another appealing factor about some modern packing materials is that they fill the bed quite uniformly without special attention being required to remove large void spaces. The latter can affect bed performance negatively.

Packings of these types can be made of one of a variety of materials, depending on the application requirements. Plastic can be used for low-cost applications where the working temperatures are not too high. On the other hand, metals or ceramics can be used for higher-temperature applications.

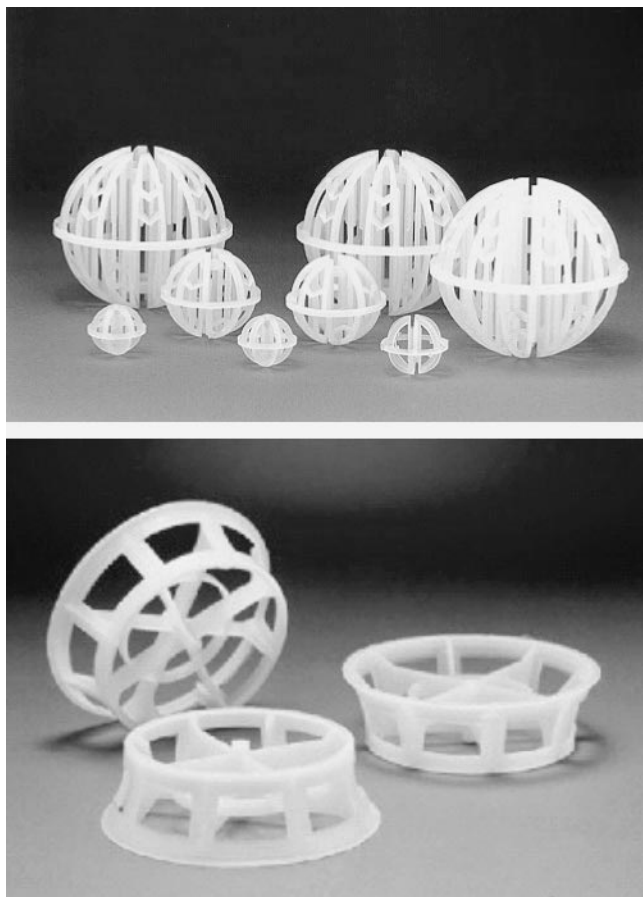


Figure 19.11 Types of bed packings: (above) Jaeger Tripaks (in North America) or Hacketten (in Europe) (printed with permission of Jaeger Products, Inc.); (below) Cascade MiniRings (printed with permission from Century Plastics, Inc. and Jaeger Products, Inc., the exclusive licensee for the product in North America).

Heat transfer data in the literature for systems with packings are limited. Part of this paucity of data is due to the fact that there are so many forms and sizes of packings. When this is coupled with the range of heat transfer stream compositions, the range of possibilities is virtually unlimited. Despite this, some data are given in the literature.

Thomas et al. (1979) reported a study of condensation of R-113 on water using ceramic spheres or Berl saddles. They also considered Cheng's (1963) results for Aroclor-steam in a bed of Raschig rings and the methylene chloride-water data of Harriott and Weigandt (1964). A relationship that provides a reasonable fit for all these data is as follows:

$$\text{St} \equiv \frac{U_V}{\dot{m}_V C_{P,V} a(a_w/a_t)} = 0.4 \text{Ja} \cdot C^{-0.21} H^{-0.67} \quad (19.65)$$

where

$$\text{Ja} \equiv \frac{h_{fg}}{C_{P,V}(T_s - T_a)}$$

$$C \equiv \frac{\dot{m}_L C_{P,L}}{\dot{m}_V C_{P,V}}$$

and H represents the packing height Z ratioed to the characteristic packing diameter. A factor is included to account for the packing wetted area and the total packing area.

Others have focused on the details of particular bed configurations and the heat transfer that results. For example, Fair and his co-workers were quite active in this area. Results for a variety of packings, including Raschig rings, Intalox saddles, Pall rings, and HyPak rings, were reported for an air–water or oil system (Huang and Fair, 1989; Fair, 1990). Key aspects of these data are presented in Table 19.3. All are for some combination of liquid and gas. The correlation equations are of the form

$$U_v = c_1 G_G^{c_2} G_L^{c_3} \quad (19.66)$$

In some cases the data are presented for the volumetric heat transfer coefficient on either the gas or liquid side separately. These data were reported as being for $h_G a$ or $h_L a$ and are so denoted in the table, but all are correlated with the same form as shown above. When the component values are given, the overall value can be found from the following equation

$$U_V = \frac{1}{(1/h_G a) + (1/h_L a)} \quad (19.67)$$

TABLE 19.3 Summary of Heat Transfer Correlations Appearing in the Literature

System	Coefficient	Packing ^a	c_1	c_2	c_3
Air/oil	U_V	RR-1	1.15	0.54	0.067
	U_V	RR-0.5	0.0032	1.57	0.14
	U_V	RR-1	0.083	0.94	0.25
Air/water	$h_G a$	RR	0.0201	0.7	0.7
	$h_G a$	RR-1, RR-1.5	0.117	1.0	0.2
	$h_L a$	RR-1, RR-1.5	8.0	0.0	0.80
	$h_G a$	RR-1	$1.78e^{0.0023Tf}$	0.7	0.07
	$h_L a$	RR-1	0.82	0.7	0.5
	U_V	PR-2	0.0279	0.57	0.806

Source: Adapted from data presented by Huang and Fair (1989).

^aRR-0.5, RR-1, and RR-1.5 denote Raschig rings of 0.5-, 1.0-, 1.5-in. size, while PR-2 denotes Pall rings of 2.0-in. size.

TABLE 19.4 Heat Transfer Correlation Constants for Air–Water Packed-Bed Systems

Packing	Size (cm)	Coefficient	c_1	c_2	c_3
Raschig rings	2.5	h_{La}	26,680	0.51	0.63
		h_{Ga}	6,947	1.10	0.02
	3.8	h_{La}	46,060	0.48	0.75
		h_{Ga}	6,130	1.45	0.16
Intalox saddles	2.5	h_{La}	36,900	0.20	0.84
		h_{Ga}	7,228	1.01	0.25
	3.8	h_{La}	42,570	0.20	0.69
		h_{Ga}	6,174	1.38	0.10
Pall rings	2.5	h_{La}	33,460	0.45	0.87
		h_{Ga}	5,065	1.12	0.33
	3.8	h_{La}	32,910	0.31	0.80
		h_{Ga}	5,310	1.28	0.26
HyPak rings	3.0	h_{La}	43,670	0.15	0.76
		h_{Ga}	8,150	0.99	0.18

Source: Adapted from data presented by Huang and Fair (1989).

The results shown in Table 19.3 were determined using columns ranging from 0.1016 to 0.76 m in diameter. It is interesting to note the wide variation in the results for these types of systems, even for the same-size columns.

Huang and Fair (1989) also reported some heat transfer measurements of their own on air–water systems. For these studies they used a variety of packing materials. Work was performed in a square column, modified to eliminate corner effects. The net cross-sectional area of the column was 0.079 m². A summary of these experiments is shown in Table 19.4. Again it is assumed that a form like eq. (19.66) represents the performance.

There is interest in the operation of packed-bed condensers when noncondensables are present, as noncondensables are frequently found in these types of systems. One such reported study uses water to condense steam in a steam–carbon dioxide mixture (Bontozolou and Karabelas, 1995). It was found that the region along the column where the bulk of the condensation takes place can be controlled by a suitable choice of the steam–water ratio. The amount of CO₂ dissolution in the water was found to be unexpectedly high and a strong function of liquid temperature.

19.5 CONCLUDING COMMENTS

It is hoped that the information included in this chapter will help engineers become more familiar with the various options available through the use of direct contact heat transfer. The methods of analysis outlined here, and the correlations included,

should facilitate this. Although designs can be performed for many types of systems with the computer approach outlined, still missing from this field is something akin to the effectiveness–NTU approach to closed exchangers. Hopefully, designers will recognize the significant performance improvements possible for many applications with the use of direct contact processes.

NOMENCLATURE

Roman Letter Symbols

a	area of bubbles/droplets per unit volume of column, m^{-1}
A	flow area, m^2
B	combination of variables defined below eq. (19.25)
Bi	Biot number, dimensionless
c_1, c_2, \dots	constants, dimensionless
C	ratio of mass-flow-rate specific heat products, dimensionless
C_D	drag coefficient on a single droplet, dimensionless
C_P	specific heat at constant pressure, $\text{kJ/kg} \cdot \text{K}$
d	droplet diameter, m
D	column diameter or impeller diameter, m
f	friction factor of the nozzle, dimensionless
Fo	Fourier number, dimensionless
Fr	Froude number, dimensionless
g	acceleration of gravity, 9.8 m/s^2
G	mass flow flux, $\text{kg/m}^2 \cdot \text{s}$
h	heat transfer coefficient, $\text{W/m}^2 \cdot \text{K}$
\bar{h}	average heat transfer coefficient, $\text{W/m}^2 \cdot \text{K}$
\underline{h}	enthalpy, kJ/kg
h_{fg}	latent heat of vaporization, kJ/kg
H	ratio: packing height to packing diameter, dimensionless
Ja	Jakob number, dimensionless
k	thermal conductivity, $\text{W/m} \cdot \text{K}$
K	factor used in eq. (19.5), dimensionless
LMTD	log mean temperature difference, K
m	mass, kg
	empirical exponent, dimensionless
\dot{m}	mass flow rate, kg/s
M	molecular weight, dimensionless
n	empirical exponent, dimensionless
N	number of bubble trains in a column, dimensionless
\hat{N}	mass transfer rate, kg/s
NTU	number of transfer units, dimensionless
P	pressure, kPa
Pr	Prandtl number, dimensionless
Q	heat transfer, W

r	radius of sphere, m
R	droplet radius, dimensionless
	volumetric flow ratio, dispersed to continuous, dimensionless
R_m	mass flow ratio, dispersed to continuous, dimensionless
\bar{R}	average dimension radius, $[\equiv (R_0^2 + R^2)/2R_0R]$, dimensionless
Ra	Rayleigh number, dimensionless
Re	Reynolds number, dimensionless
St	Stanton number, dimensionless
Ste	Stefan number, dimensionless
T	temperature, K
\mathfrak{Z}	quantity defined below eq. (19.22), dimensionless
U	overall heat transfer coefficient, $\text{W/m}^2 \cdot \text{K}$
U_V	volumetric heat transfer coefficient, $\text{W/m}^3 \cdot \text{K}$ [= Ua for a direct contact device]
v	velocity, m/s^2
V	volume, m^3
\bar{V}	volume of influence of a single column of bubbles, m^3
\tilde{V}	volumetric flow rate, m^3/s
\tilde{V}	denotes superficial or slip velocity, m^3/s
We	Weber number in a bubble column, $\sigma/\rho\tilde{V}^2D$
We_{im}	Weber number in an agitation system, $[= \sigma/\rho N^2 D_{im}^2]$, dimensionless
X	jet length or travel distance, m
z	local height, m (ft)
Z	total height of column or active zone, m

Greek Letter Symbols

α	thermal diffusivity, m^2/s
β	term defined in eqs. (19.22 and 19.31)
	vapor half opening angle, deg
	coefficient of thermal expansion, dimensionless
γ	function defined in eq. (19.38), dimensionless
δ	film thickness, m
ζ	exponent defined below eq. (19.47), dimensionless
η	fraction of heat transfer from dispersed to continuous phase, dimensionless
λ	eigenvalue, m^{-1}
μ	dynamic viscosity, $\text{N/m} \cdot \text{s}$
ν	kinematic viscosity, m^2/s
ρ	density, kg/m^3
σ	surface tension, N/m
ϕ	local holdup (fraction of volume occupied by droplets), dimensionless
$\bar{\phi}$	averaged holdup over whole column, dimensionless

χ	function defined under eq. (19.2), dimensionless
ψ	function defined below eq. (19.25), dimensionless

Subscripts

a	onset of agglomeration
a_w	air
c	continuous condensate
column	column
d	dispersed droplet
e	external value
f	flooding value
fg	heat of vaporization
g, G	gas or vapor
i	considered element of a series or internal value
im	impeller
jet	jet
L	liquid
max	maximum value
nozzle	nozzle
rough	rough nozzle surface value
S	thermal sink
slip	slip component of velocity
smooth	smooth nozzle surface value
T	height of single tray zone or total or terminal
V	volume vapor
w	wall interface water
0	initial value
1, 2	ends of heat exchanger constant indices
∞	ambient condition

REFERENCES

- Ahmad, G. R., and Yovanovich, M. M. (1994). Approximate Analytical Solution of Forced Convection Heat Transfer from Isothermal Spheres for All Prandtl Numbers, *J. Heat Transfer*, 116, 838–843.
- ASHRAE (2000). Cooling Towers, in *ASHRAE Systems and Equipment Handbook*, ASHRAE, Atlanta, GA, 36.1–36.19.
- Ay, H., Johnson, R., and Yang, W.-J. (1994). Direct-Contact Heat Transfer between a Rising Dispersed Phase in a Counterflow Stream, *Numer. Heat Transfer*, A26, 667–682.

- Aya, I., and Nariai, H. (1991). Evaluation of Heat-Transfer Coefficient at Direct-Contact Condensation of Cold Water and Steam, *Nucl. Eng. Des.*, 131, 17–24.
- Bontozoglou, V., and Karabelas, A. (1995). Direct-Contact Steam Condensation with Simultaneous Noncondensable Gas Absorption, *AIChE J.*, 41(2), 241–250.
- Brickman, R. A., and Boehm, R. F. (1994a). Maximizing Three-Phase Direct-Contact Heat Exchanger Output, *Numer. Heat Transfer*, A26 (3), 287–299.
- Brickman, R. A., and Boehm, R. F. (1994b). Optimization Considerations of Balanced, Liquid–Liquid Direct Contact Heat Exchangers, *ASME- 94-WA/HT-29*, ASME, New York.
- Brickman, R. A., and Boehm, R. F. (1995). Optimization Analyses of Balanced Liquid–Liquid Direct Contact Heat Exchangers, *Proc. ASME/JSME Thermal Engineering Conference*, Vol. 4, ASME, New York, pp. 373–379.
- Carey, V., and Hawks, N. (1995). Stochastic Modeling of Molecular Transport to an Evaporating Microdroplet in a Superheated Gas, *J. Heat Transfer*, 117, 432–439.
- Celata, G. P., Cumo, M., Farello, G. E., and Focardi, G. (1989). A Comprehensive Analysis of Direct Contact Condensation of Saturated Steam on Subcooled Liquid Jets, *Int. J. Heat Mass Transfer*, 32, 639–654.
- Celata, G., Cumo, M., D’Annibale, F., Gugliermetti, F., and Ingui, G. (1995). Direct Contact Evaporation of Nearly Saturated R 114 in Water, *Int. J. Heat Mass Transfer*, 38, 1495–1504.
- Celata, G., Cumo, M., D’Annibale, F., Gugliermetti, F., and Ingui, G. (1999). Direct Contact Boiling of Initially Subcooled R 114 into Water, *Heat Technol.*, 17, 75–84.
- Cheng, C. T. (1963). Direct Contact Condensation in a Packed Tower, M.S. thesis, University of California, Berkeley, CA.
- Çoban, T., and Boehm, R. (1989). Performance of a Three-Phase, Spray-Column, Direct-Contact Heat Exchanger, *J. Heat Transfer*, 111, 166–172.
- Fair, J. R. (1972). Designing Direct-Contact Coolers/Condensers, *Chem. Eng.*, June 12, pp. 91–100.
- Fair, J. R. (1988). Industrial Practice and Needs, in *Direct Contact Heat Transfer*, F. Kreith and R. Boehm, eds., Hemisphere Publishing, New York, pp. 25–39.
- Fair, J. R. (1990). Direct Contact Gas–Liquid Heat Exchange for Energy Recovery, *J. Sol. Energy Eng.*, 112, 216–222.
- Farid, M., and Khalaf, A. N. (1994). Performance of Direct Contact Latent Heat Storage Units with Two Hydrated Salts, *Sol. Energy*, 52, 179–189.
- Farid, M., and Yacoub, K. (1989). Performance of Direct Contact Latent Heat Storage Unit, *Sol. Energy*, 43, 237–251.
- Fouda, A., Despault, G., Taylor, J., and Capes, C. (1980). Solar Storage Systems Using Salt Hydrate Latent Heat Transfer and Direct Contact Heat Exchange, I: Preliminary Design Considerations, *Sol. Energy*, 25, 437–443.
- Fouda, A., Despault, G., Taylor, J., and Capes, C. (1984). Solar Storage Systems Using Salt Hydrate Latent Heat Transfer and Direct Contact Heat Exchange, II: Characteristics of Pilot System Operating with Sodium Sulfate Solution, *Sol. Energy*, 32, 57–65.
- Fukuda, S. (1982). Pressure Variations Due to Vapor Condensation in Liquid (II) Phenomena at Large Vapor Mass Flow Flux, *J. Atom. Energy Soc. Jpn.*, 24(6), 466–474.
- Ghazi, H. (1991). Direct-Contact Heat Transfer for Air Bubbling through Water, *J. Heat Transfer*, 113, 71–74.

- Grace, J. R. (1983). Hydrodynamics of Liquid Drops in Immiscible Liquids, in *Handbook of Fluids in Motion*, N. Cheremisinoff and R. Gupta, eds., Ann Arbor Science, Ann Arbor, MI, pp. 1003–1025.
- Harriott, P., and Wiegandt, H. F. (1964). Countercurrent Heat Exchange Using Vaporizing Immiscible Transfer Agents, *AIChE J.*, 10, 755–758.
- Huang, C.-C., and Fair, J. R. (1989). Direct-Contact Gas–Liquid Heat Transfer in a Packed Column, *Heat Transfer Eng.*, 10(2), 19–28.
- Hutchins, J., and Marschall, E. (1989). Studies in Liquid–Liquid Direct-Contact Heat Transfer, *Chem. Eng. Technol.*, 12, 388–394.
- Inaba, H., and Sato, K. (1996). Fundamental Study on Latent Cold Heat Storage by Means of Direct-Contact-Freezing between Oil Droplets and Cold Water Solution, *J. Heat Transfer*, 118, 799–802.
- Inaba, H., and Sato, K. (1997). Latent Cold Heat Energy Storage Characteristics by Means of Direct-Contact-Freezing between Oil Droplets and Cold Water Solution, *Int. J. Heat Mass Transfer*, 40, 3189–3200.
- Jacobs, H. R. (1988a). Thermal and Hydraulic Design of Direct-Contact Spray Columns for Use in Extracting Heat from Geothermal Brines, in *Direct Contact Heat Transfer*, F. Kreith and R. Boehm, eds., Hemisphere Publishing, New York, pp. 343–369.
- Jacobs, H. R. (1988b). Direct Contact Heat Transfer for Process Technologies, *J. Heat Transfer*, 110, 1259–1274.
- Jacobs, H. R., and Boehm, R. F. (1980). Direct Contact Binary Cycles, in *Sourcebook on the Production of Electricity from Geothermal Energy*, J. Kestin et al., eds., DOE/RA/4051-1, pp. 413–471.
- Jacobs, H. R., and Golafshani, M. (1989). A Heuristic Evaluation of the Governing Mode of Heat Transfer in a Liquid–Liquid Spray Column, *J. Heat Transfer*, 111, 773–779.
- Johnson, B. M., Nomura, K. K., and Bartz, J. A. (1987). Review of Numerical Models to Predict Cooling Tower Performance, *ASME-87-WA/CRTD-1*, ASME, New York.
- Ju, S. H., No, H. C., and Mayinger, F. (2000). Measurement of Heat Transfer Coefficients for Direct Contact Condensation in Core Makeup Tanks Using Holographic Interferometer, *Nucl. Eng. Des.*, 199, 75–83.
- Kiatsiriroat, T., Tainsuwan, J., Suparos, T., and Na Thalang, K. (2000). Performance Analysis of a Direct-Contact Thermal Energy Storage-Solidification, *Renewable Energy*, 20, 195–206.
- Kim, K.-J., and Mersmann, A. (1998). Direct Contact Heat Transfer in Melt Crystallization, *J. Chem. Eng. Jpn.*, 31, 527–535.
- Kim, S., and Mills, A. F. (1989). Condensation on Coherent Turbulent Liquid Jets, I: Experimental Study, *J. Heat Transfer*, 111, 1068–1074.
- Kinoshita, I., and Nishi, Y. (1994). Heat Transfer Characteristics of a Direct Contact Steam Generator with Low Melting Point Alloy and Water, *Proc. 10th International Heat Transfer Conference*, G. Hewitt, ed., Vol. 3, pp. 209–214.
- Kinoshita, I., Nishi, Y., and Furuya, M. (1995). Direct-Contact Heat-Transfer Characteristics between a Melted Alloy and Water, *Heat Transfer Jpn. Res.*, 24(4), 397–407.
- Knodel, B. (1989). Phase II: Direct Freeze Ice Slurry District Cooling, *Proc. 80th Annual Conference of the International District Heating and Cooling Association*, pp. 240–244.
- Kunesh, J. G. (1993). Direct-Contact Heat Transfer from a Liquid Spray into a Condensing Vapor, *Ind. Eng. Chem.*, 32, 2387–2389.

- Letan, R. (1988). Liquid-Liquid Processes, in *Direct Contact Heat Transfer*, F. Kreith and R. Boehm, eds., Hemisphere Publishing, New York, pp. 83-118.
- Lock, G. S. H. (1994). *Latent Heat Transfer: An Introduction to Fundamentals*, Oxford University Press, Oxford, Chap. 7.
- Mills, A. F. (1999). Cooling Towers, in *CRC Handbook of Thermal Engineering*, F. Kreith, ed., CRC Press, Boca Raton, FL, Sec. 4, pp. 253-263.
- Plass, S. B., Jacobs, H. R., and Boehm, R. F. (1979). Operational Characteristics of a Spray Column Type Direct Contact Preheater, *AIChE Symp. Ser.*, 74(179), 227-234.
- Raina, G., Wanchoo, R., and Grover, P. (1984). Direct Contact Heat Transfer with Phase Change: Motion of Evaporating Droplets, *AIChE J.*, 30(5), 835-837.
- Sagoo, M. S. (1981). Development of a Falling Cloud Heat Exchanger: Air and Particle Flow and Heat Transfer, *Heat Recov. Syst.*, 1(2), 133-138.
- Sagoo, M. S. (1982). The Falling Cloud Heat Exchanger Commercial Pilot Plant Operation, *Heat Recov. Syst.*, 2(1), 23-30.
- Saxena, S. C., and Chen, Z. D. (1994). Heat Transfer in Baffled Slurry Bubble Columns, *Proc. 10th International Heat Transfer Conference*, G. Hewitt, ed., Vol. 6, pp. 253-258.
- Shiina, K. (1997). Boiling Heat Transfer Characteristics in Liquid-Liquid Direct Contact Parallel Flow of Immiscible Liquids, *Heat Transfer Jpn. Res.*, 26, 493-514.
- Sideman, S. (1966). Direct Contact Heat Transfer between Immiscible Liquids, in *Advances in Chemical Engineering*, Vol. 6, T. Drew et al., eds., Academic Press, New York, pp. 207-286.
- Sideman, S., and Moalem-Maroon, D. (1982). Direct Contact Condensation, in *Advances in Heat Transfer*, Vol. 15, J. Hartnett and T. Irvine, eds., Academic Press, New York, pp. 227-281.
- Sideman, S., and Shabtai, S. (1964). Direct Contact Heat Transfer between a Single Drop and an Immiscible Medium, *Can. J. Chem. Eng.*, 42, 107-117.
- Siqueiros, J., and Bonilla, O. (1999). An Experimental Study of a Three-Phase, Direct-Contact Heat Exchanger, *Appl. Therm. Eng.*, 19, 477-493.
- Smith, R., Rohsenow, W., and Kazimi, M. (1982). Volumetric Heat-Transfer Coefficients for Direct-Contact Evaporation, *J. Heat Transfer*, 104, 264-270.
- Song, M., Steiff, A., and Weinspach, P.-M. (1998). Parametric Analysis of Direct Contact Evaporation Process in a Bubble Column, *Int. J. Heat Mass Transfer*, 41, 1749-1758.
- Summers, S. M., and Crowe, C. T. (1991). One-Dimensional Numerical Model for a Spray Column Exchanger, *AIChE J.*, 37(11), 1673-1679.
- Tadrist, L., Shehu Diso, I., Santini, R., and Pantaloni, J. (1987). Vaporization of a Liquid by Direct Contact in Another Immiscible Liquid, I: Vaporization of a Single Droplet; II: Vaporization of Rising Multidroplets, *Int. J. Heat Mass Transfer*, 30, 1773-1785.
- Tadrist, L., Sun, J., Santini, R., Pantaloni, J. (1991). Heat Transfer with Vaporization of a Liquid by Direct Contact in Another Immiscible Liquid: Experimental and Numerical Study, *J. Heat Transfer*, 113, 705-713.
- Terasaka, K., Sun, W., Prakoso, T., and Tsuge, H. (1999). Measurement of Heat Transfer Coefficient for Direct-Contact Condensation during Bubble Growth in Liquid, *J. Chem. Eng. Jpn.*, 32(5), 594-599.
- Thomas, K. D., Jacobs, H. R., and Boehm, R. F. (1979). Direct Contact Condensation of Immiscible Fluids in Packed Beds, in *Condensation Heat Transfer*, ASME, New York, pp. 103-110.

- Tong, A. Y., and Sirignano, W. A. (1984). Multicomponent Droplet Vaporization in a High Temperature Gas, *ASME-84-WA/HT-17*, ASME, New York.
- Utaka, Y., Saito, A., Niimi, M., and Nakata, N. (1987). Ice Cold Energy Storage Using Direct-Contact Phase Change Heat Transfer between Refrigerant and PCM in an Enclosure, *Trans. Jpn. Soc. Mech. Eng.*, 62(12), 3757–3762.
- Utaka, Y., Saito, A., and Seki, T. (1998). Gas Hydrate Cold Storage Using Direct-Contact Heat Transfer of Liquid–Vapor Phase Change and Natural Circulation of Refrigerant in Closed Vessel, *JSME Int. J. Ser. B*, 36, 150–155.
- Vliet, G., and Leppert, G. (1961). Forced Convection Heat Transfer from an Isothermal Sphere to Water, *J. Heat Transfer*, May, pp. 163–175.
- Walter, D. (1981). An Experimental Investigation of Direct Contact Three-Phase Boiling Heat Transfer, Ph.D. dissertation, University of Tennessee, Knoxville, TN.
- White, F. (1974). *Viscous Fluid Flow*, McGraw-Hill, New York.
- Wilson, M., and Jacobs, H. (1993). A Numerical Solution of the Heat Transfer from a Dense Array of Spherical Particles, *ANS Proc. National Heat Transfer Conference*, Vol. 7, pp. 225–233.
- Young, R. J., Yang, K. T., and Novotny, J. L. (1974). Vapor Liquid Interaction in a High Velocity Vapor Jet Condensing in a Coaxial Water Flow, *Proc. 5th International Heat Transfer Conference*, Vol. 3, pp. 226–230.

- Abbott, G L, 140, 146, 588, 589, 632
 Abib, A, 555, 556, 560, 563, 565, 568
 Abdelsalam, M, 655, 716
 Abelson, J R, 1339, 1355
 Abramowitz, M, 174, 257, 275, 276, 278,
 282, 283, 285, 286, 290, 297, 300,
 309, 320, 322, 326, 385
 Acharya, N, 1090, 1104
 Acharya, S, 1097, 1099, 1100, 1104, 1110
 Achenbach, E, 1051, 1055, 1105
 Ackerman, J W, 1057, 1105
 Acrivos, A, 1093, 1128
 Adamek, T, 726, 729, 789, 1070, 1105
 Adams, K L, 1267, 1301
 Addoms, J N, 756, 791
 Adebisi, G A, 235, 257
 Adt, R R, 1086, 1107
 Advani, S G, 1274, 1276, 1305
 Agarwal, K N, 768, 769, 1058, 1086, 1105
 Agarwal, V, 1279, 1302
 Agarwal, V K, 1048, 1127
 Aharoni, G, 996, 1027
 Akavan-Behabadim M A, 1058, 1105
 Ahmad, G R, 1361, 1395
 Akachi H, 1220, 1229
 Aguilar, G, 1092, 1105
 Al-Dadah, R K, 1099, 1129
 Aldington, R W J, 1074, 1122
 Alexaidas, V, 243, 247, 253, 254, 257, 260
 Alexander, L G, 1071, 1105
 Allam, T A, 629, 632
 Allen, D G, 736, 738–42, 754, 757, 760, 762,
 791–93, 796
 Allen, P H G, 1098, 1099, 1122, 1123
 Altan, T, 1254, 1255, 1257, 1302
 Altes, A, 1340, 1355
 Amano, R S, 1099, 1117
 Amato, W S, 545, 568
 Ambrose, J W, 1213, 1227
 Ammerman, C N, 1093, 1105
 Amon, C, 1099, 1105
 Andeen, G B, 1049, 1050, 1058,
 1109
 Anderson, A M, 497, 522
 Anderson, R, 1152, 1153, 1176
 Anderson, R B, 829, 906
 Andreani, M, 698, 714
 Andreini, P, 739, 792
 Andrews, E F C, 776, 790
 Andrews, L C, 168, 169, 173, 257
 Andrews, M J, 1030, 1031, 1111
 Angus, S, 50, 142
 Anisimov, S I, 1346, 1355
 Anno, J N, 319, 336, 337, 392
 Antohe, B V, 930, 931, 946
 Antonetti, V W, 4, 5, 42, 264, 271–73, 284,
 302, 303, 342, 346, 347, 351, 357,
 363–71, 375, 385, 393, 967–71, 1026,
 1027
 Arai, A, 1043, 1063, 1105
 Arai, N, 1043, 1073, 1105
 Arase, T, 1320, 1355
 Archard, J F, 340, 390, 392
 Armstrong, B, 50, 141
 Arp, V D, 49, 142, 144, 146
 Arpaci, V S, 239, 243, 257, 561, 571
 Artz, B E, 978, 1023
 Arvizu, D E, 192, 522
 Asako, Y, 404, 436
 Asakavičius, J P, 1043, 1105
 Ashcroft, N W, 1312, 1315, 1321, 1355
 Ashegi, M, 965, 1022, 1340, 1355
 Ashiwake, N, 497, 522
 Ashley, E J, 594, 595, 631
 ASHRAE, 1360, 1395
 ASM, 1245, 1302
 Astle, M J, 1325, 1357
 ASTM Standards, 122, 140, 142
 Atarashi, T, 1099, 1114
 Austen, D S, 1089, 1090, 1105
 Au, V, 294, 295, 388, 391, 967, 1024
 Augi, R, 360, 391

- Aung, W, 526, 569–71, 097, 911, 989, 990,
 1022, 1109, 1124
 Avery, G A, 1043, 1107
 Axelsson, E, 682, 716
 Ay, H, 1381, 1395
 Aya, I, 1369, 1370, 1396
 Ayub, Z, 1031, 1129
 Azad, G M, 1100, 1130
 Azer, N Z, 1074, 1075, 1087, 1105, 1111,
 1117, 1124
 Aziz, A, 174, 188, 201, 208, 212, 215, 218,
 228, 239, 250, 251, 255, 258, 259,
 829, 843, 844, 857, 858, 861, 870,
 872, 877, 908, 1059, 1061, 1116
 Aziz, K, 737, 740, 745, 794
 Aziz, R A, 116, 146
- Babin, B, R 1219, 1227
 Bachtold, A, 1339–42, 1357
 Baclic, B S, 808, 809, 906
 Baehr, H D, 49, 51, 121, 142, 143, 148
 Bahrami, P A, 1002, 1026
 Baibich, M N, 1349, 1355
 Baker, O, 666, 714, 739, 790
 Balachandar, A M, 487, 488, 523
 Balekjian, G, 1067, 1115
 Balk, L J, 1340, 1355
 Bandyopadhyay, P S, 1079, 1105
 Bandyopadhyaya, A, 1140, 1179
 Bankston, C A, 1208, 1227
 Bar-Cohen, A, 264, 287, 414, 436, 949,
 964, 981, 983, 989, 992, 996, 1000,
 1010–12, 1022–27, 1061, 1116
 Barnea, D, 663, 714, 737, 743, 745, 790
 Barnes, J F, 829, 906
 Barnhart, J, 740, 790
 Baron, A B, 750, 758–60, 796
 Barskii, M A, 1091, 1106
 Barsness, E J, 773, 776, 790
 Bartel, W J, 1101, 1106
 Bartz, J A, 1360, 1397
 Bastien, L J, 1279, 1302
 Batchelor, G K, 552, 568
 Bates, H T, 809, 909
 Bau, H H, 1168, 1176
 Bauer, B M, 1280, 1306
 Bayazitoglu, Y, 492, 522
 Beam, J E, 1213, 1227
 Bear, J, 1132, 1176
- Beasley, D E, 929, 946
 Beatty Jr, K O, 1070, 1106
 Beck, J V, 121, 140, 143, 254, 258, 285, 299,
 309, 385, 389, 966, 1025
 Beckett, G, 774, 790
 Begej, S, 356, 357, 387
 Beiler, M G, 779, 790
 Bejan, A, 27, 28, 30, 41, 121, 142, 216,
 217, 231, 236, 254, 258, 396–99,
 402–09, 414–18, 422, 423, 427,
 436–38, 483, 486, 497, 522, 523, 535,
 568, 821, 831, 906, 933, 946, 1132,
 1133, 1135–48, 1150–56, 1158–64,
 1166–73, 1176–80
 Behnia, M, 1099, 1106
 Bell, K J, 833, 834, 906, 1065, 1125, 1126
 Beltzer, A I, 255, 258
 Bennett, H E, 594, 595, 631
 Bensler, H P, 1086, 1114
 Berenson, P J, 61, 662, 714, 750, 757, 758,
 774, 795, 1–43, 1106
 Berg, J L, 779, 780, 790
 Berg, W F, 779, 780, 790
 Bergles, A E, 704, 714, 762, 768, 769, 793,
 794, 795, 908, 909, 996, 1015, 1022,
 1025, 1030–32, 1034, 1036–43,
 1045–47, 1049–55, 1057–59, 1061,
 1063, 1065–68, 1071–76, 1078–84,
 1086–88, 1091–93, 1096–99, 1100,
 1101, 1106–08, 1114–16, 1118–27,
 1128
 Bergman, T, 1233, 1246, 1306
 Beris, A, 1264, 1269, 1304
 Berkov, A B, 1101, 1107
 Berman, A S, 1169, 1177
 Bernstein, M, 483, 522
 Beyer, W H, 1320, 1357
 Beyerlein, S W, 51, 145
 Bhattacharjee, S, 415, 436, 1147, 1177
 Bhattacharya, S C, 1101, 1107
 Bhatnagar, R K, 1230, 1251, 1107
 Bhatti, M S, 396, 412, 436, 829, 909
 Bich, E, 49, 148
 Biery, J C, 875, 906
 Bigg, D M, 121, 143
 Biggs, R C, 175, 907
 Bilitsky, A, 1004–06, 1025
 Bird, R V, 115, 144
 Birringer, R, 978, 1025

- Black, J T, 1234, 1245, 1302
Blackwell, B F, 121, 140, 143, 234, 254, 258,
285, 285, 390
Blackwell, J H, 305
Blagovestova, T I, 1075, 1124
Blake, K R, 1168, 1169, 1177
Blatt, T I, 1086, 1107
Blasius, H, 455, 522
Blomgren Jr, O C, 1099, 1107
Blomgren Sr, O C, 1099, 1107
Blumenkrantz, A R, 1034, 1037
Blythe, P A, 1159, 1179
Bodoia, J R, 9, 42, 989, 1023
Boehm, R F, 1371, 1379, 1381, 1383, 1384,
1390, 1396–98
Boelter, L M K, 424, 437, 756, 757, 791,
830, 907, 1097, 1119
Bogetti, T A, 1261, 1302
Bohren, C F, 629, 631
Boling, C, 1067, 1107
Bologa, M K, 733, 790
Bonevich, J E, 1339, 1355
Bonilla, C F, 1043, 1107
Bonilla, O, 1379, 1398
Bontozoglu, V, 1392, 1396
Boone, D H, 1049, 1113
Boothroyd, G, 1249, 1302
Borca-Tasciuc, T, 1339, 1351, 1355
Borghese, J B, 1067, 1121, 1130
Bories, S A, 1168, 1177
Borishanskii, V M, 874, 908
Borisov, S E, 325, 358, 390
Borovkov, V P, 729, 793
Bose, T K, 253, 260
Bott, T R, 1061, 1013
Bowditch, P W, 829, 906
Bowman, R A, 806, 809, 906
Bowman, W J, 1213, 1227
Boykov, G P, 1101, 1116
Bradshaw, P, 466, 468–70, 522
Brandenberg, W M, 587, 593, 632
Brandt, F, 875, 906
Brauer, H, 875, 906
Braun, D, 354, 355, 385
Brdlik, P M, 997, 1023
Breber, G, 736, 779, 780, 790
Brennen, P J, 1201, 1228
Brenner, H, 1093, 1110
Brickman, R A, 1381, 1383, 1384, 1396
Briggs, A, 1071, 1107
Briggs, D E, 874, 876, 906, 909
Brinkman, H C, 1137, 1177
Brockhouse, B N, 1320, 1355
Brodov, Y M, 1098, 1107
Broerman, A W, 120, 140, 143
Bromley, L A, 660, 661, 714, 752, 790, 1093,
1120
Bron, W E, 147, 1355
Broto, J M, 1349, 1355
Broyer, E, 1261, 1302
Brown, F C, 119, 120, 121, 143
Brown, L R, 616, 632
Buck, E, 122, 145
Buckingham, E, 30, 42
Buckius, R O, 620, 632
Budhia, H, 254, 258
Bundy, R D, 1041, 1082, 1085, 1086, 1111
Bunn, R L, 1034, 1037, 1040, 1106
Burde, S S, 272, 279, 282, 283, 294, 339,
340, 385, 393
Buretta, R J, 1169, 1177
Burkhard, D G, 312, 390
Burns, P J, 1163, 1164
Bush, A W, 351, 385, 386
Busse, C A, 1199, 1203, 1205, 1207, 1209,
1228, 1229
Butler, C A, 1280, 1302
Butler, C P, 140, 146
Butterworth, D, 740, 777, 790, 939, 906
Byrd, P F, 276, 278, 283, 320, 326, 386

Cadell, P, 1212, 1228
Caglioti, G, 1330, 1339, 1342, 1343, 1355,
1356
Cahill, D G, 140, 143
Cai, Z, 1261, 1267, 1269, 1303
Caltagirone, J S, 1163, 1167
Cambernous, M A, 1168, 1177
Campagna, A O, 774, 792
Campo, A, 416, 436
Camy-Peyret, C, 616, 629, 632, 633
Capes, C, 1386, 1396
Carey, V P, 636, 714, 736, 738, 758, 790,
1191, 1192, 1228, 1371, 1396
Carlucci, L N, 774, 792
Carlson, W, 553, 568
Carnavos, T C, 870, 907, 158, 1062, 1107,
1108, 1120

- Carpenter, E F, 757, 759, 790
 Carslaw, H S, 122, 143, 164, 247, 248, 271,
 272, 275–77, 280, 309, 386, 1140,
 1177, 1243, 1302
 Carter, J R, 780, 792
 Carver, J R, 1057, 1126
 Cary, J D, 1050, 1108
 Casterline, J E, 1041, 1120
 Cattadori, G, 1085, 1086, 1112
 Catton, I, 565, 568
 Cavallini, A, 757, 760–62, 764, 765, 790,
 791
 Cebeci, T, 466, 468–70, 522, 545, 568
 Celata, G P, 689, 714, 1057, 1108, 1119,
 1122, 1367, 1373, 1396
 Censi, G, 761, 762, 790
 Cetinkale, T N, 356, 386
 Cezailliyan, A, 122, 140, 145, 147
 Chai, J C, 627, 632
 Chalyk, A F, 1025, 1124
 Champagne, P R, 1053, 1054, 1106, 1108
 Chamra, L M, 1072, 1108
 Chance, K V, 616, 632
 Chandra, S, 312, 392
 Chandran, R, 1073, 1108
 Chandrasekhar, S M, 557, 568, 1252, 1254,
 1304
 Chang, B Y, 1099, 1114
 Chang, H C, 1090, 1104
 Chang, I D, 1153, 1177
 Chang, W S, 1216, 1218, 1228, 1229
 Chao, B T, 339, 386, 1248–1250, 1101, 1120,
 1306
 Chapman, T J, 1182, 1302
 Chapplelear, P S, 116, 145
 Charmchi, M, 1261, 1306
 Chato, J C, 121, 143, 735, 736, 738, 739,
 741–52, 754, 757, 759, 760–62,
 791–93, 795, 796
 Chawla, M, 1068, 1124
 Cheesewright, R, 560, 568
 Chen, C-H, 1008, 1027
 Chen, F C, 120, 122, 143
 Chen, G, 164, 260, 965, 1026, 1338, 1344
 1349, 1351, 1355–57
 Chen, J C, 672, 714
 Chen, M M, 752, 791
 Chen, S L, 754, 758, 760, 762, 791, 795
 Chen, W T, 330–32, 386
 Chen, Y, 1099, 1100, 1104, 1108
 Chen, Z D, 1387, 1398
 Chenchu Raju, V C, 1097, 1127
 Cheng, C T, 1390, 1396
 Cheng, H C, 1100, 1129
 Cheng K C, 243, 258, 1089, 1108
 Cheng, P, 1142, 1148, 1153, 1154, 1156,
 1166, 1171, 1177, 1179, 1098, 1111
 Chenoweth, J M, 895, 896, 906, 1034, 1109,
 1119
 Chesser, M G, 1008, 1023
 Chhabra, R P, 1092, 1108
 Chi, S W, 1186, 188–90, 1197, 1198, 1202,
 1211, 1228
 Chiang, R, 1058, 1108
 Chiang, T, 545, 568
 Chiao, L, 1262, 1302
 Chien, L H, 1048, 1108
 Chin, H B, 1261–64, 1302
 Chiu, C-P, 1018, 1026
 Chiu, E H, 627, 632
 Cho, Y I, 1093, 1106, 1108, 1110, 1113
 Cho, S H, 247, 258
 Choi, C L, 120, 122, 143
 Choi, H Y, 26, 42, 1099, 1108, 1144, 1179
 Choi, K K, 1048, 1116
 Chon, W Y, 198, 1129
 Chou, F C, 1331, 1338, 1355
 Chou, S F, 1208, 1229
 Chow, L C, 1213, 1227
 Chow, Y L, 294, 386, 388
 Christensen, R N, 1054, 1111, 1115
 Christoffersen, B, 738, 740, 761, 762, 795,
 796
 Chrysler, G M, 1099, 1108
 Chu, H H S, 561, 563, 564, 568
 Chu, R C, 1043, 1099, 1108
 Chukman, G I, 1091, 1092, 1105, 1108
 Chung, D D L, 979, 1027
 Chung, K S, 1204, 1229
 Churchill, S W, 9, 42, 246, 258, 334, 386,
 413, 437, 483, 522, 547, 548, 561,
 563–65, 568, 569, 1075, 1089, 1090,
 1110, 1119
 Chyu, M C, 1046, 1099, 1108, 1117
 Cieslinski, J T, 1043, 1108
 Claasen, L, 541, 563, 570
 Clark, J A, 1072, 1127
 Clarke, D R, 978, 1025

- Clausen, D W, 587, 632
Clausing, A M, 339, 386
Çoban, T, 1371, 1381, 1396
Cobb, R, 1048, 1127
Colburn, A P, 423, 437, 757, 759, 779, 790, 791
Cole, K D, 254, 258
Cole, W A, 50, 143
Cole, R, 636, 646, 717
Coleman, H W, 927, 946
Collier, J G, 636, 671, 679, 688, 691, 692, 694, 714, 717, 1068, 1107
Collins, W M, 1089, 1108
Colwell, G T, 1213, 1216, 1228
Comini, G, 216, 254, 258, 259
Coogan Jr, C H, 1063, 1113
Cooney, J D, 1280, 1302
Cooper, M G, 340–42, 345, 351, 352, 386, 655, 675, 681, 714, 766, 791, 971, 1023
Cooper, P, 1099, 1109
Cooper, T E, 121, 143
Coppage, J E, 891, 892, 906
Cornero, C, 1099, 1109
Cosner, H M, 1273, 1303
Cotchin, C D, 780, 792
Cotta, R M, 254, 255, 259
Cotter, T P, 1182, 1203, 1208
Cox, G, 555, 570
Cox, R B, 1057, 1058, 1109
Craven, R J B, 50, 143
Crawford, M G, 474, 480, 523, 829, 909, 993–95, 1024
Cremers, C J, 140, 145
Crocker, D S, 253, 259
Cross, R, 976, 977, 1023
Crowe, C T, 1381, 1398
Crozier Jr, J R, 809, 906
Culham, J R, 292–94, 296, 299, 305, 307–10, 312, 314, 316, 317, 330–33, 362, 372, 374, 390, 391, 393
Cummo, M, 1057, 1092, 1108, 1109, 1367, 1373, 1396
Curtiss, C F, 115, 144
Cusco, L, 49, 51, 147
Cuti, F, 875, 9107
Cyphers, J A, 1054, 1116
Czikk, A M, 1043, 1044, 1109, 1117
Dagan, Z, 996, 1025, 1026
Dahl, M M, 1043, 1109
Daikoku, T, 497, 522, 1043, 1044, 1048, 1073, 1121
Dalle Donne, M, 829, 906, 1054, 1109
Dally, J, 926, 946
Dana, V, 616, 632
Danielson, R D, 1009, 1023
D'Annibale, F, 1373, 1376
Dara, P H, 1280, 1302
Darabi, J, 1101, 1109
Das, A K, 1049, 1050, 1058, 1070, 1101, 1109
Dashora, P, 121, 143
Da Silva, L W, 733, 734, 791, 792
Date, A W, 1076, 1109
Dau, F N V, 1339, 1349, 1355
Daubert, T E, 122, 145
Daujotas, P, 1055, 1130
Davalath, J, 492, 522
Dave, R S, 1261, 1267, 1302
Davidson, B J, 774, 790
Davidson, J H, 1098, 1109
Davis, P A, 930, 946
Davis, L C, 978, 1023
Dawson, P R, 1249, 1302
Day, M, 1280, 1302
Day, W A, 120, 143
Deakin, A S, 285, 386
Dean, W R, 1098, 1109
Decker, A S, 1057, 1107
Degani, D, 1062, 1116
De Garmo, E P, 1234, 1245, 1302
De Gennes, P G, 1279, 1302
Degiovanni, A, 140, 145
Deissler, R G, 829, 906
DeJong, N C, 487, 488, 523
Del Col, D, 761, 762, 764, 765, 790, 791
Del Guidice, S, 216, 254, 258, 259
DeLorenzo, B, 829, 906
Delhaye, J M, 636, 714, 1068, 1107, 1196, 1228
Delorme, G G J, 696, 715
Delov, L B, 1058, 1130
Dengler, C E, 756, 791
Dennis, S C R, 1089, 1108
de Reuck, K M, 49, 50, 142, 143
Desai, P D, 121, 148
Despault, G, 1386, 1396

- DesRuisseaux, N R, 1244, 1245, 1302
 Dessiatoun, S V, 733, 734, 792, 1098, 1101, 1109, 1122
 De Vaal, J W, 340–41, 344, 352, 357, 386, 393
 De Vahl Davis, G, 555, 570, 1249, 1306
 Deverall, J E, 1208, 1228
 Devore, A, 833, 906
 Devpura, A, 977–79, 1023
 DeVries, B, 51, 143
 Devries, W R, 1233, 1247, 1248, 1251, 1304
 DeWitt, D P, 119, 144, 194, 259, 503–05, 523 596, 633, 956, 957, 959, 961, 1024, 1209, 1228, 1243, 1303
 Dhir, V K, 658, 659, 662, 714, 716, 752, 791, 1068, 1113, 1115
 Dhurjati, P, 1263, 1304
 Didion, D, 685, 715
 Didkovsky, A B, 733, 790
 DiMarco, P 1048, 1129
 Dincer, I, 1132, 1171, 1177
 Dippery, D F, 1050, 1051, 1109
 Disimile, P, 1057, 1117
 Dittus, F W, 424, 437, 756, 757, 791, 830, 907
 Diweker, V M, 1269, 1302, 1305
 Dix, G E, 661, 715
 Dobson, M K, 735, 736, 738, 739, 741–44, 751, 757, 759, 760, 762, 763, 791–93
 Doerr, T M, 1069, 1072, 1110
 Domato, G A, 194, 259
 Don, R C, 1273–76, 1278, 1280, 1305
 Donaldson, A B, 140, 143
 Dong, Y, 1051, 1109
 Dong, Z F, 1088, 1091, 1110
 Donohue, D A, 833, 907
 Donovan, W J, 1067, 1107
 Doretti, L, 761, 762, 764, 765, 790, 791
 Doss, D J, 120, 122, 140, 143, 146
 Dougall, R S, 694, 695, 714
 Dowding, L J, 121, 140, 143
 Dowson, D, 1258, 1259, 1303
 Drake, R M, 981, 982, 1023
 Drazin, P G, 557, 568
 Dreitser, G A, 1058, 1109
 Dresselhaus, M S, 1349, 1350, 1355
 Drew, T B, 409, 437
 Drizzius, M R, 1085, 1086, 1110
 Dropkin, D, 565, 569
 Dryden, J R, 285, 295, 296, 386
 Duck, D P, 254, 260
 Dudukovic, M P, 1261, 1267, 1268, 1302
 Dukler, A E, 666, 716, 737, 738, 740, 743–45, 758, 790, 791, 793, 795
 Dunbar, N, 1212, 1224, 1228
 Duncan, A B, 164, 259
 Dunkle, R V, 588, 594, 595, 632
 Dunn, P D, 1007, 1023, 1206, 1228
 Dunn, P F, 1098, 1109
 Durand, F L, 1098, 1125
 Durant, W S, 1051, 1054, 1055, 1110
 Dykshoorn, P, 497, 524
 Easley, G L, 1339, 1344, 1356
 Eaton, B E, 49, 144
 Ebadian, M A, 1088, 1091, 1110
 Eberhart, R C, 121, 143
 Ebisu, T, 1069, 1070, 1073, 1110, 1126
 Echigo, R, 1043, 1113
 Eckels, S, 1069, 1072, 1110
 Eckert, E R G, 553, 568, 584, 633, 981, 982, 1023, 1050, 1051, 1128
 Ede, A J, 545, 570
 Edison, T A, 51, 145
 Edwards, D A, 1093, 1110
 Edwards, D P, 616, 632, 1062, 1110
 Ehlmdady, A H, 875, 570
 Eiermann, K, 121, 143
 Eissenberg, D M, 771, 792
 Ekkad, S V, 1055, 1099, 1110
 Elder, J W, 552, 554, 568, 569
 El-Domiatty, A, 1256, 1303
 Elenbaas, W, 9, 42, 989, 1023, 1061, 1110
 Eliades, V, 1097, 1100, 1110
 Elsayed-Ali, H E, 1347, 1355
 Elsdon, R, 1001, 1110
 El Sheikh, H A, 1001, 1023
 Ely, J F, 49, 51, 115, 116, 143, 144, 145, 149
 Embacher, L E, 1224, 1230
 Emmons, H W, 551, 569
 Engel, P A, 330–32, 386
 Erb, L D, 1043, 1109
 Ergun, 1136, 1177
 Erikson, G F, 1182, 1228
 Esen, E B, 1051, 1110
 Eto, T K, 243, 260
 Eustice, J, 1088, 1110

- Eva, V K, 1043, 1105
Evans, L B, 246, 258
- Fabbri, G, 779, 780, 792
Faghri, A, 1196, 1203, 1213, 1216, 1228, 1252, 1307
Faghri, M, 404, 436
Fair, J R, 666, 714, 1374, 1387, 1391, 1392, 1396, 1397
Falls, R S, 780, 792
Fan, L T, 1074, 1075, 1105, 1111, 1117
Fand, R M, 1097, 1098, 1111
Fang, P, 1092, 1119
Farag, I H, 628, 632
Farello, G E, 1367, 1396, 1092, 1109
Farid, M, 1387, 1396
Farris, T N, 1252, 1254, 1303
Favrat, D, 666, 670 680, 683, 702, 715, 717
Feingold, A, 1063, 1125
Feinstein, L, 1081, 1111
Felske, J D, 620, 632
Fenghour, A, 49, 143
Fenner, G W, 1051, 1059, 1111
Fernandes, E O, 908
Fernandez, J, 809, 910
Ferrari, G, 1092, 1109
Ferrison, J A, 774, 790
Fershtater, Y G, 1221, 1229
Fert, A, 1349, 1355
Fiege, G B M, 1340, 1355
Figliola, R S, 929, 946
Filipov, V N, 1075, 1124
Fine, H A, 140, 145
Fischer, F K, 896, 809, 907
Fischer, H E, 1331, 1356
Fishenden, M, 356, 386
Fisher, N J, 330, 386
Fiveland, W A, 627, 632, 1233, 1304
Flaud, J M, 616, 629, 632, 633
Fleischer, S A, 1099, 1109
Flemings, M C, 1233, 1303
Fletcher, L S, 187, 259, 264, 339, 340, 362, 378, 386, 388, 973, 974, 989, 1022, 1023, 1030, 1111
Flik, M I, 1347, 1348, 1355
Florschuetz, L W, 1208, 1228
Focardi, G, 1367, 1396
Focke, W W, 884, 909
Fomina, G M, 1063, 1118
Forester, H K, 672, 714
Fossa, M, 1092, 1111
Fouda, A, 1386, 1396
Fowler, A J, 416, 417, 437, 438
Fraas, A P, 833, 887, 907, 1061, 1111
France, D M, 1054, 1124
Freeman, R G, 1169, 1178
Freundlich, H, 726, 792
Fricke, A L, 1262, 1306
Friedel, L, 762, 792
Friedman, J N, 628, 633
Friedman, M D, 276, 278, 283, 320, 326, 386
Friend, D G, 49, 113, 115, 116, 142, 144, 145
Frisina, V C, 774, 792
Fritz, W, 649, 714
Frohn, A, 354, 355, 385
Fuchs, K, 1333, 1355
Fugii, K, 1043, 1069, 1073, 1111, 1120
Fujii, M, 140, 144, 989, 1029, 1031, 1051 1111, 1120
Fujii, T, 541, 543, 562, 563, 569, 989, 1029, 1070, 1111
Fujikake, J, 1043, 1111
Fujisaki, W M, 1086, 1114
Fukuda, S, 1370, 1396
Fukushima, T, 1043, 1072, 1073, 1105, 1125
Fulford, D, 1204, 1229
Fuller, J J, 1086, 1106
Fullerton, D, 909
Fuls, G M, 1098, 1111
Furkay, S S, 987, 988, 1024
Furuya, M, 1379, 1397
Fushinobu, K, 1349, 1355
- Gacesa, M, 1097, 122
Gaertner, R F, 1048, 1111
Gaibel, J A, 736, 738, 739–42, 746, 754, 757, 760, 762, 791–93, 796
Gaigalis, V A, 1043, 1045
Gaitonde, U N, 1079, 1105
Galbiati, L, 739, 792 629, 632, 633
Gal'perin, A G, 1098, 1107
Gamache, R R, 616, 629, 632, 633
Gambill, W R, 1082, 1085, 1086, 1111
Gangi, A R, 919, 946
Ganguli, A, 875, 907
Ganic, E N, 697, 698, 714
Ganin, Y E, 870, 910
Gao, V, 1055, 1111

- Gardner, K A, 809, 870, 907
 Garnier, J E, 356, 357, 387
 Garrabos, Y, 49, 148
 Garimella, S V, 1001, 1023, 1054, 1111
 Gartling, D K, 1159, 1178
 Gaskell, D R, 1233, 1103
 Gasljevic, K, 1092, 1105, 1112
 Gaspari, G P, 1085, 1086, 1112
 Gaugler, R S, 1182, 1228
 Gebhart, B, 164, 198, 259, 453, 462, 523, 526, 531, 532, 538, 539, 541–43, 545–50, 552, 555, 557, 558, 560, 569, 570, 1150, 1151, 1177, 1179
 Gee, D L, 1073, 1128
 Gegel, H, 1254, 1255, 1257, 1302
 Geiger, G E, 1098, 1111
 Geiger, G H, 1234, 1205
 Geisler, K J, 1015, 1023
 Genetti, W E, 1101, 1106
 Gerasimov, A V, 1092, 1125
 Gerner, F M, 164, 260, 758, 760, 762, 791, 1347, 1356
 Gerstmann, J, 1015, 1023
 Ghazi, H, 2363, 1396
 Gianolio, E, 875, 907
 Gibson, R D, 299, 300, 351, 385–87
 Gidwani, A, 733, 734, 792
 Gier, J T, 594, 595, 632
 Gillespie Jr, J W, 1261, 1270, 1273–76, 1278–80, 1282, 1283, 1303, 1304–06
 Gilmour, C, 833, 907
 Ginoux, J J, 636, 714
 Giot, M, 636, 714, 1119, 1122
 Gleiter, H, 978, 1025
 Glicksman, L R, 1049, 1112
 Globe, S, 565, 569
 Gnielinski, V, 676, 714, 829, 831, 907, 1089, 1091, 1112
 Godovsky, Y K, 121, 143
 Goel, P, 486, 523
 Golafshani, M, 1381, 1397
 Goldman, A, 616, 619, 632, 633
 Goldstein, J R, 1099, 1109
 Goldstein, R J, 555, 570, 1050, 1051, 1128
 Gomelaui, V I, 1057, 1112
 Goncalves, J M, 765, 766, 793, 1072, 1115
 Gonzales, E J, 1339, 1355
 Goodier, J N, 318–22, 327, 336, 337, 391
 Goodman, F O, 325, 357, 391
 Goodman, T R, 259, 260
 Goodrich, M T, 930, 946
 Goodson, K E, 140, 144, 965, 1022, 1340, 1347, 1348, 1355, 1356
 Goodwin, A R H, 49, 147
 Goody, R M, 629, 632
 Goorsky, M S, 1339, 1351, 1355
 Goorvitch, D, 629, 633
 Gorenflo, D, 655, 677, 715
 Gorski, M A, 491, 523
 Gotoda, H, 770, 792
 Grace, J R, 1361, 1382, 1397
 Gradshteyn, J S, 278, 387
 Grady, J J, 1043, 1107
 Graetz, L, 408, 437
 Graham, A D, 555, 570
 Graham, R W, 636, 715
 Grant, I D R, 838, 842, 780, 792, 907
 Green, D W, 122, 144, 145
 Greene, P R, 288, 387
 Greenwood, J A, 339, 340, 350, 351, 387
 Gregg, J L, 538–40, 545, 570
 Gregorig, R, 725, 726, 740, 792, 1070, 1112
 Gregory, G A, 737, 745, 794
 Grieg, D, 122, 144
 Griffith, P, 644, 647, 715, 1015, 1023, 1043, 1048, 1049, 1112
 Grigor'ev, V G, 772, 795
 Groen, H G, 1051, 1112
 Groeneveld, D C, 695–97, 715, 716
 Groll, M, 1203, 1229, 1044, 1117
 Gronsky, R, 1339, 1351, 1355
 Grosshandler, W L, 415, 436, 1147, 1177
 Grover, G M, 1182, 1228
 Grover, P, 1382, 1398
 Gruber, M B, 1270, 1304
 Gu, N Z, 1055, 1110, 1130
 Guceri, S I, 1233, 1303
 Guffinger, G, 1062, 1116
 Gugliermetti, F, 1373, 1396
 Gungor, K E, 674, 675, 677, 679, 680, 685, 686, 715
 Gunter, A Y, 1063, 1112
 Guo, C, 1252, 1303
 Gupta, M K, 1112, 1120
 Gupta, S C, 1048, 1127
 Gupta, S N, 1091, 1120
 Gurova, A N, 49, 51, 147
 Guthrie, R I L, 1233, 1303

- Gutowski, T G, 1261, 1267, 1268, 1303
Guy, A R, 1063, 1112
- Haajizadeh, M, 1162, 1177
Habdas, A P, 1057, 1129
Hagen, G, 401, 437
Hagge, J K, 1097, 1112
Haider, S I, 1044, 1128
Haji Sheikh, A, 254, 258
Hakim, E, 953, 1025
Hall, D E, 1099, 1112
Hall, W B, 1054, 1112
Hamad, G, 230, 258
Hampson, H, 1049, 1112
Han, C Y, 644, 715
Han, C D, 1261–64, 1303
Han, J C, 1055, 1110, 1112
Han, L S, 1273, 1303
Hands, B A, 49, 144
Hanley, H J M, 115, 116, 143, 144
Hannemann, R J, 1049, 1113
Hanno, W, 1075, 1115
Hanratty, T J, 737, 742, 745, 792, 793
Haramura, Y, 1012, 1023
Harmon, T C, 1350, 1355
Harms, T J, 1080, 1113
Harms-Watsenberg, F, 49, 148
Harriott, P 1390, 1397
Harrison, D, 1101, 1107
Hartnett, J P, 325, 358, 387, 570, 1092, 1093
1106, 1108, 1110, 1112, 1113, 1144,
1179, 1233, 1303
Hasegawa, S, 1043, 1113
Hashim, Z, 1273, 1303
Hassler, J C, 1262, 1305
Hatada, T, 1072, 1125
Hausen, H, 10, 42, 809, 829, 830, 907
Havstad, M A, 1163, 1164, 1177
Hawkins, R L, 629, 633
Hawks, N, 1371, 1396
Haynes, B D, 253, 259
Heat Exchanger Institute, 778, 792
Heaton, H S, 993, 1023
Heiderhoff, R, 1340, 1355
Hegazy, A A, 341, 343, 344, 346, 347, 351,
352, 356, 357, 363, 376, 387, 393
Heggs, P J, 808, 906
Hellums, J D, 547, 569
Helmer, W A, 1087, 1113
Hendricks Jr, R, 1098, 1123
Hennecke, F W, 996, 1026
Henry, J A H, 780, 792
Hernicz, R S, 596, 633
Hertz, H R, 319, 387
Herzener, A L, 1092, 1112
Hesse, G, 1068, 1113
Hesselgreaves, J E, 1065, 1113
Hetsroni, G, 1093, 1113
Hewitt, E W, 775, 792
Hewitt, G F, 666, 715, 910, 1061, 1068,
1107, 1113, 1203, 1228
Hibbs, R G, 1100, 1104
Hicks, L D, 1349, 1350, 1355
Hickox, C E, 1156, 1159, 1178
Hijikata, K, 1072, 1121, 1125, 1349, 1355
Hilder, D S, 548, 569
Hilding, W E, 1063, 1113
Hill, P G, 49, 144
Hill, P R, 356, 358
Hinde, D K, 735, 736, 738, 739, 741, 742,
746, 754, 757, 759, 791, 792
Hinze, J O, 558, 569
Hirasawa, S, 1072, 1121
Hirschfelder, J O, 115, 144
Ho, C Y, 122, 144, 1327, 1330, 1356
Hodgson, T D, 1058, 1121
Hoffmann, E, 423, 437
Hoffman, H, 875, 907
Hoffman, H W, 1070, 1105
Hoffmann, J D, 1214, 1230
Holden, K M, 1049, 1113
Holland, F A, 1090, 1091, 1125
Holland P M, 49, 144
Hollands, K G T, 555, 565, 566, 569, 570
Holm, R, 297, 339, 340, 387
Holman, J P, 917, 925, 946, 1098, 1125
Holmes, R E, 1091, 1113
Honda, H, 728, 729, 792, 1070, 1071, 1113,
1126
Hong, S W, 1076, 1079, 1114
Honma, M, 1099, 1114
Hoogenedoorn, C J, 10744, 1090, 1114, 1127
Hori, M, 1069, 1125
Hornbeck, R W, 408, 410, 437
Horton, C W, 1164, 1178
Hostetler, J L, 1339, 1344, 1347, 1356
Hostetler, K M, 1129
Hottel, H C, 627, 628, 632

- Hougen, O A, 779, 791
Howard, R T, 987, 988, 1024
Howell, J R, 606, 633, 961, 1024
Howley, J B, 49, 51, 145, 147
Hsieh, R, 1097, 1099, 1114
Hsu, Y Y, 636, 644, 715
Huang, C C, 1391, 1392, 1397
Huang, C L, 251, 259
Huang, J J, 1055, 1112
Huang, P N S, 253, 260
Hubbard, M G, 737, 740, 791, 792
Huber, M L, 115, 116, 144
Hudina, M, 1054, 1114
Huenefeld, J S, 1151, 1179
Huffman, D R, 629, 631
Hughes, T G, 1092, 1114
Hui, P, 296, 387
Huixiong, L, 1051, 1109
Hummel, R L, 1043, 1047, 1048, 1129
Humphrey, J D, 120, 146
Hunley, H J M, 49, 144
Hutchins, J, 1362, 1381, 1397
Hwalck, J J, 1045, 1129
Hwang, D C, 620, 632
Hwang, G-J, 1097, 1099, 1114
Hwang, J J, 1099, 1114, 1117
Hwang, U P, 1043, 1114
Hynek, S J, 1086, 1106
- Iacovidas, H, 1099, 1114
IAPWS, 49, 50, 144
Iltscheff, S, 1049, 1114
Imura, H, 541, 543, 562, 563, 569
Inaba, H, 1386, 1397
Inasaka, F, 1086, 1114
Incheck, G A, 1070, 1071, 1101, 1109
Incropera, F P, 119, 144, 194, 259, 503–07,
523, 524, 551, 569, 956, 957, 959,
961 996, 1024, 1027, 1099, 1132,
1209, 1228, 1293, 1303
Ingham, D B, 1132, 1154, 1178, 1179
Ingham, H, 49, 144
Ingui, G, 1372, 1396
Innami, T, 1069, 1111
Iokhvedor, F M, 875, 908
Iqbal, I, 1087, 1113
Irie, S, 1043, 1113
Ishiguro, H, 1086, 1114
Ito, H, 1090, 1114
Ito, T, 1043, 1069, 1122
Itoh, M, 1072, 1073, 1114, 1115
Itoh, N, 1069, 1111
Itoh, Y, 1069, 1125
Ivanov, D Y, 49, 148
Ivanovic, M, 1062, 1222
Ivanovskii, M N, 1185, 1196, 1199, 1208,
1213, 1216, 1228
Iwashita, K, 1110, 1126
Izumi, S, 770, 792
- Jabardo, J M S, 761, 762, 795
Jaber, H M, 727, 793
Jackson, D C, 1099, 1114
Jackson, J D, 829, 906
Jacobs, H R, 1233, 1303, 1362, 1373,
1379–81, 1390, 1397–99
Jacobi, A M, 487, 488, 523
Jacobsen, R T, 49–51, 113, 144, 145, 147
Jaeger, J C, 122, 143, 164, 247, 258, 271 272,
275–77, 280, 386, 1140, 1177, 1243,
1302
Jahangiri, M, 50, 145
Jakob, M, 119, 122, 144, 771, 793
Jaluria, Y, 216, 259, 526, 529, 531, 532, 539,
545, 546, 549–52, 555–58, 560 568,
569, 1234, 1239, 1303
Jameson, S L, 874–76, 907
Janak, J F, 1333, 1356
Janssen, L A M, 1090, 1114
Janzen, A R, 116, 146
Japiske, D, 555, 570
Jaster, H, 753, 755, 759, 793
Jaw, L, 809, 907
Jeans, J, 277, 387
Jeffreys, H, 740, 793
Jen, T C, 1252–54, 1303, 1304
Jenkins, R J, 140, 146
Jensen, M K, 1030, 1031, 1034, 1047, 1051,
1062, 1074, 1081, 1086, 1088, 1091,
1092, 1099, 1101, 1107, 1110, 1114,
1115, 1117, 1125, 1126
Jessie, J P, 627, 632
Jiji, L M, 164, 259, 996, 1025, 1026
Jog, M A, 1080, 1113
Johnson, A T, 1072, 1176
Johnson, B M, 1360, 1397
Johnson, K L, 319, 322, 335, 340, 346, 352,
378, 387

- Johnson, R, 1381, 1395
 Johnston, D, 838, 911
 Jones, C D, 1003, 1024
 Jones, T B, 1098, 1115
 Jones, T M, 356, 390
 Jonsson, I, 780, 793
 Josell, D, 1339, 1355
 Joseph, D D, 120, 144, 1151, 1179, 1332, 1356
 Joule, J P, 1030, 1115
 Joshi, H M, 488, 489, 523
 Joshi, Y K, 1008–10, 1025, 1027, 1347, 1356
 Joshi, S D, 1088, 1089, 1090, 1092, 1115, 1124
 Ju, Y, 1252, 1254, 1303
 Ju, Y S, 140, 144, 1348, 1356
 Jucks, K W, 616, 632
 Juhasz, T, 1347, 1355
 Jung, D S, 685, 715, 762, 793
 Junkan, G H, 1030, 1031, 1034, 1037, 1040, 1051, 1055, 1075, 1097, 1106, 1107, 1112 115, 1122, 1128

 Kabata, Y, 1057, 1115
 Kading, O W, 1340, 1356
 Kaellis, J, 1109
 Kakac, S, 526, 569–71, 806, 807, 815–18, 820, 829, 907–09, 911, 1030, 1059, 1061 1063, 1068, 1106, 1109, 1115, 1124
 Kakizaki, K, 1043, 1073, 1121
 Kalman, H, 207, 208, 209, 260
 Kalpakjian, S, 1234, 1304
 Kamal, M R, 1263, 1306
 Kamei, A 51, 145
 Kamen'Shchikov, F T, 1075, 1124
 Kandlikar, S G, 674, 679, 715, 1068, 1113, 1115
 Kang, Y T, 1054, 1115
 Kapeliovich, B L, 1346, 1355
 Karabelas, A, 1392, 1396
 Karayannis, T G, 1099, 1115
 Kardos, J L, 1261, 1267, 1268, 1302, 1304, 1306
 Karkhu, V A, 729, 783
 Kassab, S Z, 1255, 1303
 Kassem, A E, 773, 776, 794
 Katiyar, M, 1339, 1355
 Kattan, N, 666, 670, 680, 715

 Katti, R S, 50, 145
 Katto, Y, 689, 715, 1012, 1023
 Katz, D L, 1067, 1070, 1106, 1115
 Kavanaugh, S P, 780, 792
 Kaviany, M, 535, 570, 1132, 1178
 Kaye, J, 1098, 1111
 Kays, W M, 421, 437, 474, 480, 523, 807, 829, 845, 851–57, 889, 892, 893, 908 993–95, 1023, 1024, 1024, 1035, 1055 1065, 1115
 Kawaguchi, Y, 1092, 1117
 Kazakov, G M, 1048, 1130
 Kazimi, M, 1372, 1398
 Kedzierski, M, 727, 729, 765, 766, 768, 782–84, 793, 796, 1069, 1070, 1072, 1086–88, 1115, 1116, 1128
 Kelemenis, G, 1099, 1114
 Kelkar, K M, 1063, 1116
 Kelleher, M, 548, 569
 Kelvin, Lord, 640, 1115
 Keltner, N R, 285, 387
 Kemeny, G A, 1059, 1116
 Kemme, J E, 1203, 1204, 1208, 1228, 1229
 Kennedy, D P, 294, 300, 387, 967, 1024
 Kenney, P J, 736, 738–42, 754, 757, 760 762, 791–93, 796
 Kenning, D B R, 1093, 1116
 Keshok, E G, 649–51, 715
 Kern, D Q, 174, 259, 771, 793, 809, 825, 833, 836, 861, 866, 867, 908, 1059, 1063, 1081, 1116
 Kettner, I J, 1062, 1116
 Keyhani, M, 1163, 1179
 Khair, K R, 1171, 1176
 Khalaf, A N, 1387, 1396
 Khanpura, J C, 1072, 1116
 Khomami, B, 1267, 1306
 Kiatsiriroat, T, 1385, 1397
 Kilburn, L F, 987, 988, 1024
 Kilty, H P, 1049, 1050, 1058, 1109
 Kim, C J, 1046, 1116
 Kim, J, 1067, 1106, 1109
 Kim, K, 1070, 1113
 Kim, K J, 1367, 1385, 1397
 Kim, K W, 1338, 1357
 Kim, M S, 768, 793, 1086–88, 1116
 Kim, N H, 1048, 1116, 1117
 Kim, S J, 415, 416, 437, 490, 523
 Kimura, H, 1089, 1111, 1114

- Kimura, S, 1089, 1166, 1178
 Kingery, J, 1267, 2303
 Kinihara, H M, 1043, 1143
 Kinoshita, I, 1379, 1397
 Kirby, R K, 121, 148
 Kirilov, V V, 425, 438
 Kistler, R S, 736, 773, 794
 Kitching, D E, 1015, 1023, 1024
 Kitscha, W W, 319, 324–28, 339, 387, 393
 Kittel, C, 119, 121, 145, 1312–14, 1331, 1356
 Kitto, J B, 1057, 1116, 1233, 1304
 Kladius, N, 1140, 1179
 Klammsteiner, N, 765, 791
 Klein, S A, 115, 117, 145, 146
 Klemens, P G, 119, 145
 Klimenko, V V, 679, 715
 Kline, S J, 926, 946
 Klistner, T, 1331, 1338, 1339, 1356
 Kloptenstein, A G, 1026
 Knodel, B, 1386, 1397
 Knudsen, J G, 893, 910
 Koch, R, 1074, 1075, 1116
 Khoser, R A, 1234, 1245, 1116
 Konicek, L, 555, 565, 566, 569
 Kosky, P G, 753, 755, 759, 793
 Koslov, A D, 50, 145
 Kostic, M, 1093, 1213
 Kou, S, 1234, 1304
 Kovalev, S A, 1044, 1048, 1116, 1130
 Koyama, S, 765, 796
 Kraitsev, S G, 997, 1065
 Kraus, A D, 174, 201, 208, 212, 215, 258, 259, 284, 387, 809, 829, 836, 843, 844, 858, 859, 861, 870, 872, 877, 908, 956, 964, 989, 992, 1022, 1024–27
 Krauss, R, 51, 145
 Kreith, F, 254, 258, 1305
 Kroemer, H, 1331, 1356
 Kröger, D G, 779, 780, 875, 908, 1100, 1127
 Krolczek, E J, 1201, 1228
 Krotzch, P, 996, 1024, 1026
 Krum, A, 967, 1026
 Kryukov, Y V, 1101, 1116
 Ku, J, 1224, 1228
 Kubair, V, 1089, 1116
 Kubanik, G R, 1041, 1063, 1068, 1069, 1116, 1128
 Kuechenmeister, C, 49, 149
 Kuehn, T, 555, 570
 Kulacki, F A, 1099, 1109, 1163, 1169, 1171, 1178, 1179
 Kulanovic, R, 1044, 1117
 Kuloor, N, 1089, 1116
 Kumada, M, 1092, 1124
 Kumagai, M, 1099, 1115
 Kumar, A, 885, 886, 908, 1049, 1050, 1058, 1109
 Kumar, H, 885, 886, 908
 Kun, L C, 1043, 1058, 1116
 Kundu, J, 1067, 1121
 Kunesht, J G, 1389, 1397
 Kunitsugu, K, 1101, 1122
 Kuntysht, V B, 875, 908
 Kuptsov, V K, 1098, 1107
 Kurabayashi, K, 140, 144
 Kurbanmukhamedov, A, 1092, 1120
 Kurihari, H, 1043, 1044, 1048, 1073, 1117
 Kutateladze, S S, 658, 668, 714, 874, 908, 1012, 1024
 Kuzmakichta, Y A, 1048, 1130
 Kwon, J T, 1072, 1117
 Lachi, M, 140, 145
 Laesecke, A, 49, 51, 115, 117, 145, 148
 Lage, J L, 930, 931, 946, 133, 1176
 Lai, F C, 1171, 1178
 Lai, J, 1349, 1356
 Lai, M D, 1099, 1124
 Lal, S, 768, 789, 1086, 1304
 Lall, P, 9953, 1025
 Lam, R C, 1233, 1267, 1268, 1304
 Lambert, M A, 264, 339, 340, 387, 388
 Lamontia, M A, 1270, 1273–76, 1278, 1280, 1304, 1305
 Lan, J, 1057, 1117
 Landis, F, 1076, 1125
 Langer, H, 1203, 1229
 Langhaar, H L, 399, 437
 Laplace, P S, 724, 793
 Lapwood, E R, 1164, 1178
 Larson, M B, 1098, 1117
 Lau, W S, 1249, 1306
 Laursen, T A, 418, 437, 1171, 1180
 Lavi, A, 725, 726, 796
 Lavin, J G, 1067, 1069, 1117
 Lavine, A, 1233, 1252–54, 1303–05

- Launder, B E, 560, 570
Leckner, B, 617, 618, 632
Ledezma, G A, 416, 418, 437, 497, 523, 1147, 1178
Lee, B H, 1098, 1117
Lee, C P, 1955, 1100, 1112, 1130
Lee, D S, 1261–64, 1303
Lee, H S, 627, 632
Lee, R A, 1057, 1100, 1106, 1128
Lee, S, 294, 295, 357, 338, 360, 378 388, 391, 967, 1008, 1023, 1024, 1026
Lee, S M, 1339, 1342, 1343, 1356
Lee, S W, 415, 416, 437, 485, 486, 523
Lee, T Y, 1011, 1024
Lee, T Y R, 121, 148
Lee, V, 49, 144
Lee, W I, 1264, 1268, 1278, 1281, 1304
Lee, W S, 1067, 1127
LeFevre, E J, 545, 570, 1050, 1117
LeGal, E, 120, 146
Lehman, G L492, 523
Lehman, M W, 1268, 1304
Leland, T W, 116, 145
Lem, K W, 1263, 1303
Lemlich, R, 1097, 1117
Lemmon, E W, 49, 50, 113, 144, 145, 147
LeNeindre, B, 49, 148
Leong, M K, 1338, 1357
Leont'yev, G G, 1058, 1123
Leppert, G, 1361, 1399
Letan, R, 1377–80, 1398
Lewis, M J, 1054, 1117
Lewis, R W, 254, 258, 988, 1024
Lewis, T B, 975, 979, 1024
Levin, E S, 1058, 1109
Levy, E K, 1207, 1208, 1229
Li, C H, 809, 908
Li, D Y, 1338, 1356
Li, G, 416, 437
Li, H, 1046, 1118
Li, K W, 1098, 1117
Li, P W, 1092, 1117
Li, S S, 1098, 1122
Liang, X G, 1331, 1338, 1355, 1356
Liaw, J S, 1067, 1127
Liaw, S P, 662, 714
Lidgitt, P J, 1258, 1303
Lienhard, J H, 658–62, 715–17, 751, 791
Liley, P E, 122, 144, 145, 1327, 1330, 1356
Lin, P Y, 737, 745, 793
Lin, S T, 1074, 1075, 1105, 1111, 1117
Lin, Y-L, 1099, 1117
Lin, Z, 1093, 1094, 1108, 1113
Lior, N, 1233, 1306
Liou, T M, 1055, 1117
Litkouhi, B, 254, 258
Littlejohn, M A, 1338, 1357
Liu, C K, 560, 561, 571
Liu, H, 1061, 1063, 1115
Liu, W, 1339, 1351, 1355
Liu, X, 1046, 1062, 1117, 1118
Liu, Y D, 1062, 1123
Liu, Z, 1099, 1108
Lloyd, J R, 556, 571, 1093, 1125
Lloyd, W R, 356, 388
Lock, G H S, 253, 259, 1363, 1364, 1367, 1398
Lockhart, R W, 756, 793
Lokshin, V A, 1063, 1118
London, A L, 396, 403, 408–12, 438, 807, 808, 829, 845, 851–57, 889, 891–93, 906, 908–10, 1034, 1035, 1055, 1065, 1067, 1081, 1089, 1090, 1115, 1117, 1124
Longo, G A, 761, 762, 764, 765, 790, 791
Longtin, J, 1233, 1305
Looney, D J, 1049, 1118
Loos, A C, 1261, 1262, 1264, 1268, 1278, 1302, 1304
Lopina, R F, 1076, 1081, 1082, 1084, 1118
Lorente, S, 1132, 1145, 1164, 1171, 1177, 1178, 1180
Lovell, P A, 1281, 1287
Lowery Jr, A J, 1092, 1118
Loyalka, S K, 356, 358, 388
Lucca, D A, 1259, 1304
Luk, W A, 120, 122, 143
Lukes, J R, 1331, 1338, 1355, 1356
Lumley, J L, 558, 571
Lunardini, V J, 218, 239, 243, 247, 258, 259
Lundberg, R E, 1081, 1111
Luo, X, 919, 927
Luu, M, 1042, 1058, 1072, 1087, 1118
Lynch, J R, 204, 209
Lyon, R E, 1262, 1302
Ma, T, 1046, 1118
Maa, J R, 1093

- Macosko, C W, 1261, 1302
 MacBain, S M, 1057, 1118
 Macmillan, R D C, 49, 144
 Maddox, D E, 1000, 1024
 Madhusudana, C V, 187, 259, 264, 271, 325,
 362, 378, 388, 973, 974, 979, 1024
 Magee, J W, 51, 145
 Maglic, K D, 122, 140, 145, 147
 Magnus, W, 278, 388
 Magrakavelidze, V M, 1057, 1112
 Mahdavian, S M, 1259, 1306
 Mahajan, R, 526, 529, 532, 534, 546, 552,
 555, 569
 Maidanik, Y F, 1221, 1229
 Mainland, M E, 735, 792
 Majumdar, A, 164, 260, 965, 973, 974, 1024,
 1328, 1331, 1339–42, 1349, 1355–57
 Malin, M R, 555, 570
 Malkin, S, 1249, 1252, 1302–94
 Mallet, D, 140, 145
 Mallinson, G D, 555, 570
 Mallow, A, 1261, 1302
 Maloney, J O, 122, 144, 145
 Mandhane, J M, 740, 793
 Mandin, J Y, 616, 632
 Mandrazhitskiy, V M, 1075, 1124
 Manglik, R M, 1030, 1040, 1051, 1059,
 1065–67, 1075–84, 1086–89, 1091–
 96, 1099, 1106, 1107, 1113, 1118–20,
 1123, 1127, 1128, 1130
 Manlapaz, R L, 1089, 1090, 1119
 Manson, J E, 1282, 1302
 Mantell, S C, 1278, 1304
 Mantelli, M B H, 378, 388
 Mao, C P, 1097, 1099, 1114
 Maranraju, S, 1078, 1079, 1119
 Marcus, B D, 1201, 1229
 Mariani, A, 1057, 1108
 Maris, H J, 1331, 1338, 1357
 Marotta, E E, 340, 363, 372–74, 387, 388,
 390
 Marner, W J, 1034, 1063, 1074, 1076, 1081,
 1119
 Marschall, E, 350, 351, 389, 1362, 1381,
 1397
 Marsh, K, 49, 146
 Marsters, G F, 1097, 1114
 Martin, H, 503, 504, 523
 Martin, K A, 284, 368
 Martinelli, R C, 756, 793, 1097, 1119
 Martinez, G M, 1261, 1304
 Marto, P J, 771, 793, 1043, 1049, 1050,
 1058, 1070, 1071, 1101, 1109, 1113,
 1119, 1120
 Marx, V, 50, 146
 Maslen, S H, 1254, 1306
 Masliyah, J H, 1062, 1088–91, 1101, 1120,
 1121
 Mason, J, 808, 908
 Massie, S T, 616, 632
 Mathewson, W F, 1098, 1120
 Matta, G A, 1057, 1058, 1109
 Matthys, E F, 1092, 1105, 1112
 Matos, R S, 418, 437
 Matsushima, H, 486, 498, 523
 Matzner, B, 1047, 1120
 Maurer, G, 49, 50, 147
 Mayadas, A F, 1333, 1356
 Mayhan, K G, 1043, 1127
 Mayinger, F, 798, 908, 909, 1030, 1059,
 1068, 1106, 1107, 1115, 1119, 1122,
 1203, 1229, 1371, 1397
 McAdams, W H, 561, 563, 564, 570, 829,
 908, 957, 1024, 1097, 1120
 McCann, A, 616, 632
 McCarty, R D, 49, 50, 142, 146
 McClintock, F A, 926, 946
 McConnell, K G, 926, 946
 McClude, C M, 1098, 1123
 McCormick, S P, 1249, 1307
 McCullough, R L, 1280, 1302
 McDonald, T W, 1097, 1126
 McElhiney, J E, 1097, 1120
 McEuen, P L, 1339–42, 1357
 McGee, G R, 326, 337–39, 388
 McIntosh, J E, 356, 390
 McKague, E L, 1268, 1304
 McLinden, M, 51, 115, 1171, 145, 146, 148,
 149, 685, 715
 McManus, H N, 1003, 1004, 1026
 McNeill, A, 1010–12, 1015, 1026
 McCuiston, F C, 871, 908, 1098, 1120
 McWaid, T H, 350, 351, 389
 Medwell, J O, 1057, 1058, 1120, 1122
 Megerlin, F E, 1041, 1075, 1120
 Mehta, M H, 1058, 1059, 1120
 Menze, K, 1031, 1051, 1120
 Mereu, S, 415, 437

- Merk, H J, 543–45, 570
Merkin, H, 1154, 1178
Mermin, N D, 1312, 1321, 1351, 1355
Mersmann, A, 1385, 1397
Mertz, R, 1044, 1117
Metwally, H M, 1066, 1067, 1120
Metzger, D E, 905
Meyer, L, 1054, 1109
Meyers, J E, 1043, 1067, 1115, 1117
Michel, J W, 1109
Mickley, H S, 1092, 1127
Mikhailov, A V, 1058, 1109
Mikhailov, M D, 254, 255, 259
Mikic, B B, 173, 294, 298, 299, 300, 309,
340, 341, 345, 349, 351, 352, 372,
373, 386, 389, 647, 716, 971, 1023,
1049, 1050
Mikkelsen, J C, 1008, 1017
Millat, J, 49, 143, 148
Miletti, D L, 1041, 1063, 1068, 1069, 1116,
1128
Miller, J H, 1099, 1127
Miller, T R, 1249, 1307
Mills, A F, 1360, 1367, 1397, 1398
Mills, J J, 1254, 1306
Milton, R M, 1043, 1120
Mimaten, J, 1092, 1124
Min, J, 1067, 1120
Min, K, 1101, 1120
Minkowycz, W J, 239, 260, 545, 570, 1148,
1156, 1177
Mirkovic, Z, 875, 908
Miropolskii, Z L, 1092, 1120
Mirshak, S, 1051, 1054, 1055, 1110
Mishra, S, 1091, 1120
Mitsumori, K, 778, 792
Mix, D, 981, 983, 1025
Miyamoto, H, 49, 51, 146
Miyatake, O, 989, 1025
Moalem-Marón, D, 1365, 1368, 1371, 1374,
1398
Mochizuki, S, 1065, 1099, 1121, 1125, 1234,
1307
Modest, M F, 586, 599, 600, 606, 627–29,
632
Modlin, J M, 1213, 1228
Moek, E O, 1041, 1120
Moffat, R J, 492, 497, 522, 523, 927, 938,
944, 946, 995, 1025
Mohr, P J, 111, 146
Molki, M, 733, 734, 791, 792
Mollendorf, J C, 1151, 1177
Monti, Jr, G, 987, 988
Moody, L F, 33, 42, 421, 422, 437, 767, 794,
836, 837, 908, 1201, 1229
Moore, C D, 1339, 1351, 1355
Moran, K P, 294, 295, 357, 358, 360, 378,
388, 390, 967, 1024, 1043, 1108,
1114
Moran, M, 821, 908
Morega, A M, 418, 427, 436, 437, 485,
486, 497, 523, 1101, 1122, 1145–47,
1176, 1178
Morgan, A I, 1093, 1120
Morgan, V T, 563, 570, 988, 1024
Mori, Y, 1072, 1080, 1081, 1089, 1091,
1097, 1120, 1121, 1128
Morigaki, T, 1261, 1267, 1268, 1303
Mostinski, I L, 655, 716
Mosyak, A, 1093, 1094, 1113
Mott, N F, 1330, 1356
Mudawar, I, 996, 1025, 1026
Mueller, A C, 772, 779, 794, 806, 809,
819–21, 908
Muir, E B, 764, 794
Muley, A, 1067, 1106, 1121, 1130
Muralidhar R, M, 1099, 1100, 1121
Murata, A, 1099, 1121
Murphy, R W, 1041, 1057, 1075, 1120, 1121
Murthy, J, 1099, 1105
Murthy, S S, 1008, 1025
Muschelknautz, E, 1074, 1122
Muzychka, Y S, 302, 303, 305, 307–10, 312,
314, 316, 317, 389, 393
Myers, G E, 239, 243, 259
Myers, J E, 753, 760, 794
Na, T Y, 250, 251
Nagashima, A, 45, 148
Nagle, W M, 806, 809, 906, 908
Nakajima, R, 1057, 1115
Nakajima, T, 1043, 1044, 1048, 1053, 1105,
1121
Nakamura, H, 404, 436, 1053, 1121
Nakayama, A, 1171, 1178
Nakayama, N, 1069, 1101
Nakayama, W, 486, 495, 497, 522, 523,
967–70, 1008, 1025, 1026, 1043,

- Nakayama, W, (*continued*)
 1044, 1048, 1061, 1072, 1073, 1089,
 1091, 1097, 1099, 1106, 1120, 1121
 Nakayama, Y, 1043, 1073, 1105
 Nan, C W, 978, 1025
 Nandakumar, K, 1062, 1088–91, 1101,
 1119–21, 1125
 Nandapurkar, S S, 1090, 1091
 Nariai, H, 1086, 1114, 1369, 1370, 1396
 Na Thalong, K, 1385, 1397
 Naylor, A, 479, 523, 535, 538, 570
 Negus, K J, 284, 285, 297–300, 302, 389,
 393, 966, 1025
 Nelson, D A, 1098, 1121
 Nelson Jr, R A, 1166, 1178, 1179
 Nelson, R D, 1015, 1025
 Nelson, R M, 1039, 1040, 1121
 Nemchinov, V, 618, 632
 NEMI, 949, 951, 1025
 Neufeld, P D, 116, 146
 Newell Jr, P H, 1098, 1106
 Newson, I H, 1057, 1058, 1121
 Newton, D C, 1098, 1122
 Nguyen, H, 212, 259
 Nguyen-Chi, H, 1203, 1229
 Nho, K J, 325, 351, 355, 358, 389, 391
 Nicol, A A, 1057, 1058, 1097, 1122
 Nicholson, M K, 737, 745, 794
 Nield, D A, 931, 946, 1132, 1133, 1135–42,
 1145–48, 1150, 1151, 1153, 1154,
 1156, 1164, 1168–73, 1179
 Nielson, L E, 975, 979, 1024
 Nieto de Castro, C A, 49, 147
 Niimi, M, 1385, 1399
 Nikatopoulos, E D, 1097, 1100, 1104, 1110
 Nikuradse, J, 422, 437
 Nir, A, 875, 908
 Nirmilan, V, 1030, 1031, 1034, 1075, 1107,
 1122
 Nishi, Y, 1379, 1397
 Nishihara, A, 1099, 1114
 Nishikawa, K, 1043, 1122, 1126
 Nishio, S, 1099, 1108
 Nishimura, T, 1101, 1122
 Nishiwaka, K, 1093, 1122
 Nishiwaki, N, 1234, 1307
 Nishiyama, E, 1043, 1111
 NIST, 49, 50
 Nix, G H, 654, 717, 1048, 1107
 No, H C, 1371, 1397
 Nomura, K K, 1360, 1397
 Nonino, C, 216, 259
 Nonn, J, 996, 1025
 Normington, E J, 285, 390
 Norris, P M, 1339, 1344, 1347, 1349, 1356
 Notaro, P, 1050, 1122
 Notter, R H, 425, 437
 Novotny, J L, 1369, 1399
 Nozu, S, 7128, 729, 792, 1070, 1113
 Nukiyama, S, 637, 716
 Nusselt, W, 721, 753, 794, 808, 809
 Oberhettinger, F, 278, 388
 Obot, N T, 1051, 1110
 Ochterbeck, J M, 1213, 1216, 1229, 1230
 Ogata, J, 1099, 1122
 Ogata, T, 1015, 1024
 Oh, S, 1254, 1255, 1257, 1302
 Ohadi, M M, 733, 734, 791, 792, 1072, 1098,
 1101, 1109, 1121, 1126
 Oizumi, K, 1069, 1125
 Oktay, S, 967–70, 1026, 1043, 1122
 Olague, N E, 930, 946
 Olchoway, G A, 49, 148
 Oliver, D R, 1074, 1122
 Oliviero Fernandes, E, 1068, 1115
 Olson, D R, 1092, 1114
 Olsson, C O, 1055, 1122
 O'Neill, K, 254, 259
 O'Neill, P S, 1044, 1109
 Onions, R A, 340, 390,
 Oosthuizen, P H, 479, 523, 535, 538, 570
 Oppenheim, A K, 612, 632
 Opsal, J, 1344, 1357
 Orlande, H R B, 254, 259
 Ornatkii, A P, 1098, 1122
 Ortega, A, 490, 492, 497, 523, 524, 995,
 1025
 Ortt, E, 120, 146
 Oskay, R, 829, 909
 Ossin, A, 545, 568
 Osterle, J F, 9, 42, 989, 1023
 Ostrach, S, 535–37, 551, 555, 570
 Ou-Yang, Y H, 1100, 1130
 Ovodkov, O A, 1044, 1116
 Outcalt, S L, 51, 145, 146
 Oxley, P L B, 1249, 1306
 Ozawa, T, 1281, 1304

- Ozisik, M N, 120, 146, 164, 165, 216, 217, 219, 224, 229, 249, 254, 259, 546, 547, 570, 1049, 1112
- Ozoe, H, 413, 437
- Pabisz Jr, R A, 1086, 1097, 1101, 1122
- Paddock, C A, 1339, 1344, 1356
- Padmanabhan, C A, 1233, 1304
- Pahl, M H, 1074, 1122
- Pais, C B, 1043, 1122
- Pal, D, 1347, 1356
- Palen, J W, 688, 716, 736, 779, 790, 794, 1047, 1129
- Pamula, G, 1099, 1110
- Pancallo, E A, 1093, 1094, 1113
- Panchal, C B, 1054, 1124
- Panek, J, 761, 762, 795
- Pantaloni, J, 1381, 1392
- Papar, R A, 1067, 1106, 1119
- Parang, M, 253, 259
- Park, C, 257, 358, 391
- Park Jr, E L, 1043, 1127, 1129
- Park, K A, 1015, 1025
- Park, S C, 140, 144
- Park, S H, 495, 523
- Parker, J D, 1098, 1117, 1120, 1123
- Parker, W J, 140, 146, 558, 589, 632
- Parrott, J E, 119, 120, 122, 147
- Parsons, B, 1258, 1259, 1303
- Pascale, A S, 1057, 1058, 1109
- Patankar, S V, 627, 632, 1057, 1058, 109
- Pate, M B, 762, 632, 1057, 1058, 1109
- Pearson, J F, 1068, 1123
- Pecht, M, 953, 1025
- Pedroso, R I, 253, 259
- Peebles, E M, 1097, 1111
- Peletsky, V E, 122, 140, 145, 147
- Penoncello, S G, 49–51, 113, 144, 145, 147
- Pera, L, 541–43, 549, 550, 569, 570
- Perelman, A, 1016, 1022
- Perelman, T L, 1346, 1355
- Perkins, H C, 421, 437, 829, 909
- Perkins, R A, 49, 115, 117, 145–47
- Permayakov, V A, 1098, 1107
- Perrin, A, 616, 632
- Perrin, B, 1164, 1179
- Peterson, G P, 164, 259, 378, 388, 1008, 1023, 1030, 1082, 1086, 1125, 1203, 1210, 1213, 1218, 1219, 1227, 1229, 1233, 1304, 1347, 1356
- Peterson, P F, 754, 795
- Petit, M, 1164, 1178
- Petrescu, S, 415, 416, 438
- Petroff, F, 1349, 1355
- Petukkov, B S, 424, 438, 829, 831, 909
- Phelan, P E, 965, 977–79, 1023, 1025
- Pierre, B, 767, 794
- Pignotti, A, 808, 909
- Pillai, V, 1284, 1269, 1304
- Pimenta, M M, 762, 795
- Pipes, R E, 1282, 1302
- Pitchumani, R, 1262, 1264, 1265, 1269, 1273–76, 1278–80, 1283, 1302, 1304–07
- Plass, S B, 1379, 1398
- Platzer, B, 49, 50, 147
- Plesset, M S, 647, 716
- Pletcher, R H, 239, 260
- Plumb, O A, 491, 523, 1151, 1179
- Plyasunov, S, 1339–42, 1359
- Pohl, R O, 957, 961, 972, 973, 1026, 1330, 1331, 1338–40, 1350, 1355–57
- Pohlhausen, E, 463, 524, 829, 909
- Poirier, D R, 1233, 1234, 1305
- Poirier, E J, 1233, 1305
- Poiseuille, J, 401, 438
- Polase, F, 1008, 1027
- Polasek, F, 1220, 1227
- Poling, B E, 700, 716
- Polt, A, 49, 50, 147
- Poncher, M, 736, 738–42, 754, 757, 760, 762, 791–93, 796
- Pop, I, 1132, 1153, 1154, 1171, 1178, 1179
- Popov, V N, 424, 438
- Poulikakos, D, 164, 217, 219, 239, 240, 243, 260, 1151, 1152, 1161, 1162, 1168–70, 1177, 1179
- Poulter, R, 1098, 1123
- Pouzenc, C, 774, 794
- Powell, R W, 122, 144, 1327, 1330, 1356
- Prakash, C, 1055, 1062, 1123
- Prakoso, T, 1368, 1398
- Pralits, J, 1099, 1106
- Prasad, V, 1140, 1171, 1178, 1179, 1233, 1305
- Prasher, R S, 362, 374, 376, 377, 390, 997, 1026

- Prausnitz, J M, 700, 716
 Preckshot, G W, 1097, 1120
 Prenger, F C, 1204, 1229
 Preziosi, L, 120, 144, 1332, 1356
 Price, D C, 930, 946, 1098, 1123
 Price, D J, 587, 632
 Prins, J A, 543–45, 570
 Prusa, J, 50, 146, 148
 Pruss, A
 Pusatcioglu, S Y, 1262, 1305
 Pushkov, J, 1101, 1229
- Rabas, T J, 770, 772, 773, 776, 777, 779,
 794, 1051, 1110
 Radetic, T, 1339, 1351, 1355
 Radford, D W, 1233, 1305
 Rademacher, R, 685, 715, 762, 793
 Rai, N, 1269, 1305
 Raina, G, 1382, 1398
 Raina, S, 1057, 1118
 Raithby, G D, 555, 565, 566, 569, 570, 627,
 632
 Raja Rao, M, 1958, 1059, 1100, 1120
 Raji, E G, 1043, 1051, 1058, 1059, 1111
 1123
 Raju, K S, 997, 1026
 Ramadhyani, S, 504, 506, 524, 996, 1027
 Ramakrishnan, B T, 1282, 1264, 1265, 1305
 Ramilson, J M, 1150, 1151, 1179
 Ramires, M L V, 49, 51, 146, 147
 Randlett, M R, 1072, 1108
 Ranganathan, C, 1077, 1078
 Ranganathan, S, 1273–76, 1278, 1280, 1305
 Rao, K R, 1320, 1355
 Rao, K S, 1100, 1123
 Rao, M A, 1097, 1117
 Rapier, A C, 356, 390
 Ravigururjan, T S, 1036, 1051–53, 1119,
 1123
 Rayleigh, Lord, 647, 716
 Reay, D A, 1007, 1023, 1206, 1228
 Rebenfeld, L, 1267, 1301
 Reichard, H, 421, 438
 Reid, R C, 700, 716
 Reid, W H, 567, 568
 Reif, F, 119, 120, 121, 147
 Reis, A H, 1132, 1145, 1171, 1173
 Reithmuller, M L, 636, 653, 714
 Reynolds, B L, 1099, 1123
- Reynolds, W C, 993, 1023
 Rhines, N, 735, 736, 738–42, 754, 757, 760,
 762, 791–93, 795, 796
 Rich, B R, 541, 570
 Richardson, J F, 1092, 1108
 Richardson, M J, 140, 147
 Richardson, P D, 1098, 1117
 Rifert, V G, 729, 794, 1058, 1123
 Riley, D S, 254, 260
 Riley, W F, 254, 260, 926, 946
 Rinsland, C P, 616, 632
 Ristau, D, 1339, 1357
 Roberts, D N, 666, 715
 Robertson, C R, 1093, 1128
 Robinson, G C, 1098, 1123
 Robinson, K K, 876, 909
 Rocha, L A O, 416, 438
 Roeller, P T, 493, 524
 Roess, L C, 298, 300, 341, 351, 389, 390
 Roetzel, W, 809, 909
 Rogers, D G, 829, 909
 Rogers, F T, 1164, 1177
 Rohani, A R, 1208, 1229
 Rohsenow, W M, 11, 26, 42, 294, 298–300,
 309, 341, 351, 389, 414, 436, 570,
 636, 647, 694, 695, 697, 698, 714,
 716, 750, 752, 758–60, 794, 1011,
 1022, 1025, 1043 1092, 1106, 1110,
 1119, 1123, 1126, 1144 1179, 1372,
 1398
 Roos, J, 1098, 1111
 Rose, J W, 729, 730, 794, 1049, 1050, 1070,
 1071, 1107, 1113, 1120, 1123
 Rosencwaig, A, 1344, 1359
 Rosenblit, R, 1093, 1094, 1113
 Roshan, H Md, 1233, 1305
 Ross, D C 560, 562, 571
 Rosseto, L, 761, 762, 764, 765, 790, 791
 Rosson, H F, 753, 760, 794
 Rotem, Z, 541, 563, 570
 Rothman, L S, 616, 629, 632, 633
 Rouhani, Z, 682, 716
 Rounds, M, 1099, 1109
 Rouse, M W, 831, 910
 Royal, J H, 769, 794, 1041, 1072, 1087, 1124
 Rubinsky, B, 243, 260
 Rudy, T M, 728, 729, 795, 796, 1031, 1070,
 1128
 Rustum, T M, 1062, 1124

- Ryalov, A N, 1075, 1124
 Rymaszewski, E J, 1026
 Ryzhik, I M, 278, 387

 Sabag, A, 1016, 1022
 Sabersky, R H, 1050, 1051, 1109
 Saboya, F E M, 418, 437
 Sagoo, M S, 1379, 1398
 Sahin, A Z, 234, 260
 Said, M N A, 1062, 1124
 Said, S A, 1062, 1087, 1105, 1124
 Saito, A, 1385, 1399
 Sahota, M, 122, 144
 Salev'yev, R Z, 1098, 1107
 Salim, M M, 1054, 1124
 Sammakia, B, 526, 529, 532, 534, 552, 556, 558, 569
 Samuels, M, 809, 906
 San, J Y, 1099, 1124
 Sano, Y, 1100, 1126
 Santiago, J G, 1008, 1027
 Santini, R, 1381, 1398
 Sarofim, A F, 627, 628, 631
 Sastri, V M K, 1099, 1100, 1121, 1123, 1305
 Sathe, S B, 1009, 1010, 1025
 Sato, H, 50, 148
 Sato, K, 1092, 1124, 1386, 1397
 Sauer, Jr, H J, 973, 1025
 Saunders, E A D, 780, 795, 823, 825, 827, 832, 859, 867, 879–83, 885, 909
 Savija, I, 362, 290
 Savin, I K, 733, 790
 Savin, V K, 997, 1023
 Savkar, S D, 1098, 1124
 Saxena, S C, 1387, 1398
 Sayers, W A, 294, 195, 389
 Sayles, R S, 340, 390
 Scarola, L S, 1097, 1106
 Schankula, M H, 326, 337–39, 388
 Schatzes, M, 1333, 1356
 Scheiber, J D, 120, 140, 143
 Scheidigger, A E, 1132, 1133, 1179
 Schey, J A, 1234, 1245, 1254, 1305
 Schindler, D L, 809, 900
 Schlager, L M, 762, 795, 1072, 1124
 Schlichting, H, 397, 423, 438
 Schlünder, E U, 234, 260, 569, 700, 716, 908, 996, 997, 1025, 1026, 1068, 1114
 Schmeckenbecher, A F, 1043, 1122
 Schmidt, E, 584, 633
 Schmidt, R, 50, 147
 Schmidt, T E, 874, 909
 Schmittle, K V, 1043, 1124
 Schnabel, W, 1280, 1385
 Schneider, G E, 239, 260, 272, 281, 283, 285, 288, 289, 294, 301, 390, 391, 393
 Schneider, P J, 164, 260
 Scholz, F, 1051, 1112
 Schorr, A W, 549, 550, 569
 Schroeder, J, 616, 629, 632, 633
 Schubert, G, 1166, 1178
 Schuh, H, 535, 570
 Schulenberg, F J, 875, 909
 Schuster, J R, 750, 757, 758, 795
 Sciubba, E, 414, 415, 417, 436, 437, 497, 522, 1146, 1179
 Seban, R L, 808, 908
 Seetharamu, K N, 988, 1024
 Seferis, J C, 1281, 1282, 1302, 1304, 1306
 Seki, N, 243, 258
 Seki, T, 1385, 1389
 Sekulic, D P, 808, 909
 Selby, J E A, 629, 633
 Semyonov, G L, 325, 358, 390
 Sen, A K, 212, 260
 Sen, M, 1090, 1104
 Seniraj, R V, 253, 260
 Sengers, J V, 45, 49, 51, 145, 148
 Sephton, H H, 1101, 1124
 Sergeant, J, 967, 1026
 Sernas, V, 989, 1022
 Setzmann, U, 49, 112, 147
 Sexl, R U, 312, 390
 Shabtai, S, 1382, 1398
 Shah, M M, 673, 679, 685, 716, 756, 760, 795
 Shah, R K, 396, 403, 408–12, 438, 571, 798, 808, 809, 829, 874, 905–07, 908, 911, 1055, 1059, 1065, 1067, 1088–90, 1109, 1118, 1124–26, 1233, 1305
 Shakir, S, 644, 716, 1093, 1125
 Shamsundar, N, 254, 260
 Shan, Z, 51, 147
 Shatto, D P, 1030, 1082, 1086, 1125
 Shaw, M C, 1249, 1306
 Shaw, W A, 875, 907, 1063, 1112
 Shcherbakov, V K, 1098, 1122
 Shearer, C J, 1101, 1110

- Shehu Diso, I, 1382, 1398
 Shen, Z F, 628, 633
 Shenkman, S, 1107
 Sheu, W J, 1067, 1127
 Shi, L, 1339, 1340, 1357
 Shih, T I-P, 1099, 1117
 Shih, Y P, 251, 259
 Shiina, K, 1380, 1381, 1398
 Shikazono, N, 1072, 1073, 1114, 1115
 Shimon, R L, 736, 738–42, 754, 757, 760, 762, 791–93, 796
 Shinohara, Y, 1058, 1069, 1125
 Shioda, K, 1057, 1115
 Shires, G L, 1061, 1113
 Shirliffe, C J, 122, 147
 Shitzer, A, 121, 143
 Shivkumar, Y, 1072, 1125
 Shizuya, M, 1072, 1125
 Shkema, R K, 1085, 1086, 1110
 Shklover, G G, 772, 795
 Shlancýauskas, A A, 1085, 1086, 1110
 Shlykov, Y P, 356, 390, 870, 910
 Shock, R A W, 699, 717
 Shoham, O, 737, 743, 745, 790
 Shoji, M, 1068, 1072, 1113, 1115
 Shome, B, 1030, 1031, 1034, 1051, 1062, 1074, 1086, 1091, 1107, 1115, 1125
 Shurk, H, 1340, 1360
 SIA, 949, 951, 1026
 Sideman, S, 1360–62, 1365, 1368, 1371, 1374, 1382, 1398
 Sieder, E N, 10, 42, 424, 438, 830, 910, 1054, 1125
 Siegel, R, 606, 633, 649–51, 715
 Silver, M, 594, 595, 631
 Simon, T E, 1011, 1022, 1024, 1027
 Simons, R E, 342, 385, 967–70, 1026
 Simpkins, P G, 1159, 1179
 Singham, J R, 1076, 1109
 Siqueiros, W A, 1279, 1398
 Sirignano, W A, 1371, 1399
 Sitharamayya, S, 997, 1026
 Skartis, L, 1269, 1306
 Sleicher, C A, 425, 437, 831, 910
 Sloan, J, 1270, 1304
 Smith, A G, 466, 469, 524
 Smith, A N, 1339, 1334, 1347, 1356
 Smith, E M, 1065, 1125
 Smith, G O, 1347, 1355
 Smith, K A, 1092, 1127
 Smith, J C, 1098, 1120
 Smith, J H, 1208, 1227
 Smith, J S, 1349, 1357
 Smith, L F, 1003, 1024
 Smith, R, 1372, 1398
 Smith, T F, 628, 633
 Smith, W L, 1344, 1357
 Smithberg, E, 1076, 1125
 Smoot, J S, 1270, 1304
 Smukala, J, 49, 147
 Smythe, W R, 277, 283, 313, 390
 Sneddon, I N, 274, 283, 390
 Snidle, R W, 1255, 1259, 1306
 Snow, D F, 1049, 1112
 Sohal, R, 499, 524
 Solbrekken, G L, 1018, 1026
 Soliman, H M, 738, 741, 642, 746–48, 750, 757, 758, 795, 1062, 1063, 1089, 1090, 1105, 1124, 1125
 Solomon, A D, 243, 247, 253, 254, 257, 260
 Solov'yev S L, 1044, 1116
 Somerscales, E F C, 10893, 910, 1030, 1088, 1091, 1101, 107, 1125
 Sommerfeldt, S, 1015, 1025
 Song, D W, 1339, 1351, 1355
 Song, M, 1381–83, 1398
 Song, S, 294, 295, 325, 344, 345, 352, 354–62, 378, 388–91, 967, 1024, 1026
 Soni, R P, 278, 388
 Soong, C Y, 1097, 1099, 1114
 Sorokin, V P, 1185, 1196, 1199, 1208, 1213, 1216, 1228
 Sotani, T, 51, 148
 Soufiani, A, 629, 633
 Sourour, S, 1263, 1306
 Souza, A c m, 774, 796
 Souza, A L, 761, 751, 795
 Spalding, D B, 466, 469, 524, 560, 570
 Span, R, 48–50, 145, 147, 148
 Spang, B, 809, 909, 910
 Sparrow, E M, 239, 260, 398, 438, 538–40, 545, 570, 1002, 1026, 1062, 1122
 Springer, G S, 354, 355, 391, 1261, 1262, 1264, 1267, 1268, 1278, 1281, 1304, 1306
 Sprott, A L, 1098, 1125

- Sridhar, M R, 302, 303, 334, 335, 346, 349, 352, 391
Srinivasan, P S1090, 1125
Stafford, G R, 1339, 1355
Stanescu, G, 417, 438
Steiff, A, 1381–83, 1398
Starner, K E, 1003, 1004, 1026, 1147, 1179
Starner, T E, 1043, 1124
St. Clair Jr, C A, 254, 258
Stefan, K, 51, 121, 142, 143, 145, 412, 438, 655, 716, 821, 910
Stegun, I A 174, 257, 275, 276, 278, 282, 283, 285, 286, 290, 297, 300, 309, 320, 322, 326, 385
Steiner, D, 666, 675, 716
Steiner, K V, 1280, 1306
Stenger, F J, 1224, 1229
Steel, W G, 917, 946
Steen, W M, 1233, 1306
Stephens, M A, 1099, 1117
Stephenson, D P, 1249, 1250, 1306
Stevens, J, 996, 1026
Stevens, R A, 809, 910
Stevenson, M G, 1249, 1306
Stevanovic, M, 330–33, 391
Stevens, J, 493, 524
Stewart, R B, 50, 145
Stolyarov, Y, 1075, 1124
Stratton, J A, 177, 391
Straus, J M, 1166, 1178
Stromberg, K S, 1057, 1058, 1109
Strong, A B, 285, 301, 390, 391
Stuckes, A D, 119, 120, 122, 147
Stulc, P, 1008, 1027
Subbarao, E C, 906, 909
Suetin, P E, 325, 358, 390
Sukatme, S P, 1079, 1105
Summers, S M, 1281, 1398
Sun, J, 1381, 1398
Sun, K H, 661, 715
Sun, X, 1350, 1355
Sun, W, 1368, 1398
Sun, Z S, 1180
Sunaga, H, 51, 149
Sunden, B, 1055, 1056, 1111, 1122, 1126
Sunderland, J E, 247, 258
Suparos, T, 1385, 1397
Supper, W, 1224, 1228
Suryanarayana, V V S, 1097, 1127
Swanson, L W, 1347, 1356
Swartz Jr, E T, 957, 961, 972, 973, 1026, 1340, 1350, 1357
Sweeney, K A, 736, 738–42, 754, 757, 760, 762, 791–93, 795, 796
Swenson, H S, 1057, 1126
Szoeké, G, 1057, 1126
Tabor, D, 346, 391
Taborek, J, 675, 716, 779, 790, 833, 834, 875, 907, 910, 1034, 1037, 1047, 1063 1106, 1126
Tadrist, L, 1381, 1398
Tafti, D K, 487, 488, 523
Tagavi, K A, 1065, 1070, 1125
Tagliafico, L A, 1092, 1111
Taine, J, 629, 633
Tainsuwan, J, 1385, 1397
Taira, T, 1080, 1081, 1128
Taitel, Y, 616, 663, 714, 716, 737, 738, 740, 743–45, 790, 795
Takahashi, K, 1331, 1338, 1355
Takamatsu, H, 1070, 1113
Takano, K, 1043, 1099, 1108
Tamari, Y, 1093, 1126
Tamura, S, 1331, 1338, 1357
Tan, H S, 296, 387
Tan, Y, 1043, 1130
Tanaka, H, 989, 1025, 1050, 1126
Tanaka, K, 1043, 1122
Tanaka, M, 1053, 1121
Tanaka, Y, 51, 148, 1331, 1338, 1357
Tanasawa, I, 1049, 1050, 1099, 1108, 1123, 1126
Tanasawa, L, 1233, 1306
Tang, L, 1072, 1097, 1126
Tang, S I, 1097, 1126
Tang, T W, 1338, 1357
Tanger, G E, 654, 717, 1048, 1127
Tao, L N, 247, 260
Tate, G E, 10, 42, 424, 438, 830, 910, 1054, 1125
Tay, A O, 1249, 1306
Taylor, B N, 111, 146
Taylor, G I, 1088, 1090, 1126
Taylor, J, 1386, 1396
Taylor, R E, 140, 143, 148
Teerstra, P, 292–94, 296, 299, 372, 393
TEMA, 823, 910

- Tegeler, Ch, 558, 571
 Tenneckes, H, 558, 571
 Terasaka, K, 1368, 1398
 Test, F L, 829, 910
 Thomas, D G, 1071, 1126
 Thomas, G E, 1058, 1071, 1126
 Thomas, H R, 988, 1024
 Thomas, K D, 1390, 1398
 Thomas, L B, 325, 358, 391
 Thomas, T R, 349, 351, 196, 390
 Thome, J R, 636, 644, 666, 670, 671 679,
 680, 683, 686, 691, 692, 699, 700,
 702, 704, 708, 714–16
 Thompson, J C, 272, 279, 284, 297, 298,
 389, 393
 Thompson Jr, W G, 1049, 1106
 Thomson, G H, 122, 145
 Thonon, B A, 1092, 1126
 Tian, H, 1338, 1357
 Tian, Q, 1140, 1179
 Tien, C, 545, 563, 565, 568, 1168, 1180
 Tien, C H, 288, 289, 393
 Tien, C L, 164, 260, 545, 568, 620, 632, 754,
 758, 760, 762, 791, 795, 965, 1026
 1137, 1142, 1159, 1160, 1162, 1163,
 1177, 1180, 1204, 1208, 1229, 1331,
 1338, 1349, 1355, 1356
 Tierney, J K, 1004, 1026
 Tillner-Roth, 49, 51, 143, 148
 Timoshenko, S P, 318–22, 327, 336, 337, 391
 Timp, G, 1347, 1357
 Tingkuen, C, 1051, 1109
 Tinker, T, 775, 776, 795, 832, 833, 838, 910
 Tobe, M, 1058, 1125
 Tomimura, T, 140, 144
 Toms, B A, 1092, 1126
 Tong, A Y, 1371, 1399
 Tong, L S, 636, 717, 893, 910
 Tong, S X, 1254, 1306
 Yong, T W, 1233, 1305
 Tong, W, 1081, 1086, 1126
 Torrance, K E, 216, 259, 551, 571, 1168,
 1176
 Torikoshi, K, 1069, 1070, 1073, 1110, 1126
 Touloukian, Y S, 121, 148, 596, 633
 Toussignant, L, 1009, 1023
 Touzelbaev, M N, 965, 1022
 Towell, R H, 1051, 1055, 1059, 1110
 Traviss, D P, 750, 758–60, 796, 1092, 1126
 Tree, D R, 871, 908
 Trefethen, L, 1182, 1229
 Trevisan, O V, 1172, 1180
 Trew, R J, 1338, 1357
 Trewin, R R, 1047, 1115
 Trezek, G J, 121, 143
 Trigger, K J, 1248–505, 1306
 Trinh, S, 212, 260
 Truesdale, K L, 1057, 1121
 Trumpler, P R, 325, 358, 392
 Trupp, A C, 339, 340, 350, 351, 387, 1062,
 1124
 Tsatsaronis, G, 821, 908
 Tseng, A A, 1254, 1306
 Tsuge, H, 1368, 1398
 Tufeu, R, 49, 148
 Tung, S S, 875, 907
 Turner, G S, 526, 551, 571
 Turyk, P J, 285, 313, 392
 Tye, R P, 122, 147
 Tzan, Y L, 1093, 1094, 1126
 Tzeng, S P, 1097, 1099, 1114
 Tzou, D Y, 164, 260
 Uchida, M, 1072, 1073, 1114, 1125
 Uchima, B, 729, 792, 1070, 1071, 1113,
 1114
 Uhl, V W, 1079, 1126
 Ullman, A, 207–09, 260
 Underwood, A J V, 806, 809, 910
 Ungar, E, 1213, 1229
 Unny, T E, 555, 565, 566, 569
 Usagi, H H H, 9, 42
 Usagi, R, 9, 42, 334, 386, 548, 568
 Usui, H, 1100, 1126
 Utaka, Y, 1049, 1050, 1123, 1395, 1399
 Uzzell Jr, J C, 49, 259
 Vachon, R I, 654, 717, 1048, 1127
 Vafai, K, 1132, 1137, 1142, 1179, 1180
 Vampola, J, 874, 876, 910
 Van de Pohl, D W, 1004, 1026
 VanDerMeer, T H, 1074, 1127
 Vanleve, J E, 1331, 1338, 1339, 1356
 van Wijk, W R, 1093, 1096, 1127
 Van Rooyen, R S, 1100, 1127
 van Stralen, S J D, 636, 646, 648, 717, 1093,
 1096, 1097, 1127
 Varanasi, P, 616, 632

- Varesi, G, 1340, 1357
 Vargas, J V C, 418, 437, 1171, 1179
 Varma, H K, 768, 789, 1058, 1086, 1105
 Vasile, 1164, 1180
 Velisaris, C N, 1282, 1306
 Velkoff, H R, 1099, 1127
 Venart, J E S, 774, 796
 Venerus, D C, 120, 140, 143
 Venuvinod, P K, 1249, 1306
 Verma, A, 1349, 1357
 Vesovic, V, 49, 143, 148
 Veziroglu, T N, 312, 356, 392
 Vidyaniidhi, V, 1097, 1126
 Vijaya, Vittala, C B, 1048, 1126
 Villanueva, T C, 736, 738–42, 754, 757, 760, 762, 791–93, 796
 Vinz, P, 1208, 1229
 Virk, P S, 1092, 1126
 Viskanta, R, 243, 245, 260, 526, 569–71, 809, 829, 909, 911, 1098, 1099, 1112, 1126, 1233, 1246, 1306, 1361, 1399
 Vliet, G C, 541, 560–62, 571
 Vogel, E, 49, 143, 148
 Voltz, S, 1338, 1357
 Vos, A S, 1093, 1096, 1127
 Vrable, D L, 1072, 1126
 Vulchanov, N L, 1058, 1130

 Wachman, H Y, 352, 358, 392
 Wadekar, V V, 1065, 1125
 Wadsworth, D C, 996, 1025, 1026
 Wagner, W, 48–50, 112, 146–48
 Wakeham, W A, 45, 49, 143, 148
 Wallis, G B, 1043, 1048, 1112
 Wallis, J D, 636, 694, 717
 Walowit, J A, 319, 336, 337, 392
 Walsh, S M, 1261, 1306
 Walter, D, 1379, 1399
 Wanchoo, R, 1382, 1398
 Wang, C C, 1067, 1126
 Wang, H, 499, 500, 524
 Wang, K L, 1339, 1351, 1355
 Wang, S, 1043, 1098, 1130
 Wang, S P, 736, 738, 739, 741, 742, 746, 754, 757, 759, 791, 796
 Wang, W, 1058, 1127
 Wang, W-J, 1381, 1395
 Wang, X S, 996, 1026
 Wang, Z Z, 790, 992, 796

 Wanniararchchi, A, 1049, 1050, 1113, 1120
 Wansbrough, R W, 1041, 1082, 1085, 1086, 1111
 Ward, J C, 1136, 1179,
 Warner, C Y, 561, 571
 Warner, D F, 1043, 1126
 Wasekar, V M, 1093, 1095, 1096, 1119, 1127, 1128
 Wassan, D T, 1093, 1110
 Watanabe, K, 49, 51, 146, 148, 1080, 1081, 1121
 Watkins, R W, 1093, 1128
 Watkinson, A P, 1063, 1128
 Watson, F A, 1073, 1108
 Watson, G B, 1057, 1128
 Watson, J T R, 49, 143, 148
 Watts, H A, 1156, 1178
 Wattson, R B, 616, 629, 632, 633
 Wattelet, J P, 736, 738–42, 746, 754, 757, 760–62, 791, 793, 795, 796
 Watwe, A A, 1010–12, 1026
 Wayner, Jr, P C, 1191, 1229
 Weast, R C, 596, 633, 1325, 1357
 Webb, B W, 493, 524, 996, 1026
 Webb, R L, 488, 489, 523, 704, 708, 717, 727–29, 713, 764, 765, 784, 789, 793, 795, 796, 829, 910, 1020, 1031, 1034, 1037, 1038, 1040, 1042–45, 1047, 1048, 1050, 1051, 1057, 1058, 1061–63, 1067–70, 1072, 1073, 1098, 1105, 1108, 1117, 1120, 1122, 1128, 1129
 Weber, L A, 49, 50, 146
 Weber, J E, 1159, 1179
 Weber, W M, 930, 946
 Wehle, W, 875, 906
 Weierman, C, 875, 910
 Weinspach, P M, 1381–8333, 1398
 Weisman, J, 689, 717
 Weiss, V C, 51, 145
 Weissman, J, 689, 717
 Welling, J R, 1003, 1004, 1026
 Welsh, E, 1339, 1357
 Welty, J R, 174, 201, 208, 212, 215, 259, 829, 843, 844, 858, 859, 861, 870, 872, 877, 908, 1059, 1061, 1116
 Werner, K, 234, 260
 Wesley, D A, 325, 358, 392

- Westwater, J W, 1045, 1046, 1068, 1093,
1118, 1129
- Whalley, P, 636, 617
- Wheeler, A J, 919, 946
- Whipple, R L, 1098, 1121
- Whitaker, S, 483, 504
- White, C M, 1089, 1090, 1129
- White, F M, 584, 585, 633, 1382, 1399
- White, G, 1339, 1355
- Whitehouse, D J, 340, 392
- Whitham, J M, 1075, 1129
- Whittle, T D, 342, 385
- Wiedmann, M L, 325, 358, 392
- Wiegandt, H F, 1390, 1397
- Wiener, J H, 1250, 1306
- Wiener, M, 1057, 1116, 1128
- Wikhammer, G A, 1041, 1120
- Wiles, D M, 1280, 1302
- Wilhamson, J B P, 340, 350, 351, 387
- Willenborg, D L, 1344, 1357
- Wilke, C R, 1093, 1120
- Wilkins, D R, 256, 388
- Willis, M J N, 838, 911
- Wilson, A H, 1316, 1357
- Wilson, D G, 247, 260
- Wilson, M, 247, 260
- Wilson, W R D, 1259, 1306
- Wineman, S J, 1267, 1303
- Winterton, R H S, 674–77, 679, 680, 685,
686, 715
- Wirth, U, 490, 524
- Wirtz, R A, 492, 497, 499, 500, 523, 524
- Withers, J G, 1051, 1057, 1058, 1129
- Witte, L C, 662, 717
- Witzman, S, 994, 1023, 1026
- Wods, A D B, 1320, 1355
- Womac, D H, 504, 506, 524
- Womac, D J, 996, 997, 1027
- Wooding, R A, 1156, 1179
- Woolard, D L, 1338, 1357
- Wörsoe-Schmidt, P, 829, 909, 911
- Wong, S S, 965, 1022
- Wong, S W, 1098, 1129
- Wooldridge, C B, 1003, 1004, 1026
- Woolf, J R, 809, 910
- Wright, N T, 102, 122, 140, 143, 146
- Wright, R N, 1254, 1259, 1304, 1306
- Wright, P K, 1249, 1307
- Wroblewski, D, 1010, 1027
- Wu, C F, 1105
- Wu, D, 1218, 1219, 1227, 1229
- Wu, H, 1100, 1129
- Wu, J, 1046, 1118
- Wu, W T, 1093, 1100, 1119
- Wulz, H, 1224, 1230
- Xu, Y, 979, 1027, 1099, 1115, 1129
- Yabe, A, 733, 796, 1048, 1092, 1098, 1117,
1122, 1129
- Yacoub, K, 1387, 1396
- Yadigaroglu, G, 698, 714
- Yagodkin, Y V, 1185, 1196, 1198, 1208,
1213, 1216, 1228
- Yan, M M, 253, 260
- Yan, Y, 1216, 1230
- Yanagida, T, 498, 523, 1069, 1123
- Yang, C Y, 765, 796
- Yang, F, 1279, 1280, 1307
- Yang, K T, 551, 560, 571, 829, 911, 1254,
1258, 1307, 1369, 1399
- Yang, Y M, 1072, 1127
- Yang, W J, 1234, 1307, 1072, 1127
- Yang, Z F, 736, 794
- Yamanaka, G, 1043, 1111
- Yao, L S, 1089, 1099, 1123
- Yao, S C, 1261, 1305
- Yao, T, 1340, 1357
- Ye, S Y, 1099, 1105, 1100, 1130
- Yemelyanov, A I, 1075, 1124
- Yen, Y C, 1168, 1180
- Yener, Y, 829, 907
- Yerra, K, 1040, 1076, 1119
- Yilmaz, S, 1045–47, 1129
- Yokozeki, A, 51, 148
- Yoshino, K, 616, 632
- You, L, 1078, 1119
- You, S M, 1011, 1027, 1093, 1105
- Young, D A, 1338, 1357
- Young, E H, 874–76, 906, 910, 1067–69,
1115, 1117, 1123
- Young, R J, 1281, 1307
- Young, R X, 1043, 1047, 1049, 1058, 1129
- Younglove, B A, 49–51, 148, 149
- Yovanovich, M M, 4, 5, 42, 264, 271–73,
276–80, 282–89, 292–94, 296–303,
305, 307–10, 312–14, 316–19,
321–28, 330–42, 344–46, 349–42,

- 355–58, 362–72, 374, 378, 385, 386,
388–93, 1013, 1025, 1027, 1361,
1395
- Yu, J, 765, 796
- Yu, X Y, 1344, 1349, 1357
- Yuan, Y M, 1099, 1114
- Yudin, V F, 1063, 1129
- Yuen, F P, 1089, 1108
- Yüncü, H, 1030, 1059, 1106, 1115
- Yugay, T, 1075, 1124
- Yuge, T, 563, 564, 571
- Yung, Y L, 629, 632
- Zakim, J L, 1093, 1084, 1123
- Zatell, V A, 1043, 1130
- Zecchin, R, 757, 760, 790
- Zeng, S, 1008, 1027
- Zeng, T, 1339, 1351, 1355
- Zerkle, R D, 1244, 1245, 1302, 1055, 1123
- Zener, C, 725, 726, 796
- Zhang, C, 774, 796
- Zhang, J, 1067, 1093, 1096, 1119, 1130
- Zhang, L, 1344, 1357
- Zhang, L W, 487, 488, 523
- Zhang, X, 140, 144
- Zhang, Y, 774, 796
- Zhang, Y M, 1055, 1100, 1112, 1130
- Zhang, Z, 1252, 1307
- Zhao, Z N, 780, 792, 796
- Zhong, L, 1043, 1130
- Zhou, Q T, 1100, 1130
- Zhou, S Q, 1065, 1070, 1125
- Zhu, L, 1262, 1264, 1265, 1305
- Zhuang, J R, 234, 260
- Zhukauskas, A, 457, 483–85, 524, 833, 875,
911, 1055, 1098, 1130, 1145, 1179
- Zhukov, V M, 1048, 1130
- Zia, S, 1098, 1121
- Zienkiewicz, O G, 254, 258
- Ziman, J M, 1326, 1332, 1337, 1350, 1357
- Zimparov, V, 1040, 1058, 1150
- Zugzda, J, 1005, 1130
- Zivi, S M, 753, 755, 796
- Zorbil, V, 1009, 1027
- Zuber, N, 658, 661, 672, 714, 717, 1012,
1027
- Zucrow, J D, 1214, 1230
- Zukauskov, J, 1043, 1059, 1083, 1105
- Zumbrunnen, D, 1233, 1305
- Zürcher, O, 670, 683, 702, 717
- Zwick, S A, 647, 716

- Absolute mean asperity slope, 341, 342
- Absolute Seebeck coefficient, 933–934
- Absorptance, 583
- Absorption coefficient, 596, 615–616, 621, 625
- Absorptivity, 583
- Acceleration (due to gravity), 36
- Accuracy, 914, 916, 919
- Acentric factor, 52–54
- Acoustic mismatch model (AMM), 972
- Active enhancement techniques, 1031, 1033–1034, 1097–1099
- Active nucleation sites, size range of, 644–645
- Adamek profile, 726
- Adaptive control (for manufacturing), 1294–1296
- Additives:
 - for gases, 1033
 - for liquids, 1033, 1092–1097
- Adiabatic heat transfer coefficient, 496
- Adiabatic temperature, 496
- Adverse pressure gradient, 482
- Adverse tilt, 1196
- AFM, *see* Atomic force microscope
- Air-fin coolers, 844, 869, 871–875
- Algebraic turbulence models, 472
- Alloys, 1351
- Altered tube flow arrangement, 1076
- Alternating direction explicit methods, 238–239
- Aluminum, 123
 - joint conductance enhancement, 370, 372, 373
 - spectral, normal emittance of, 594–595
 - transverse high-fin exchangers, 868, 869
- Ambiguity bands, 942
- American Society of Mechanical Engineers (ASME), 894, 1233
- AMM (acoustic mismatch model), 972
- Ammonia (R-717), 70
- Amplitude decay function, 242
- Analogy solutions:
 - for boundary layer flow, 475–481
 - for turbulent boundary layer, 471–472
- Analysis methods (heat exchangers), *see* Heat exchangers
- Andreani—Yadigaroglu model, 698–699
- Angle factor, 600
- Anisotropic conductivity:
 - and conservation of energy, 120
 - in printed circuit boards, 983, 986–987
- Anisotropic materials, 164
- Annular fins, 206
- Annular flow, 663–668, 745
 - condensation in smooth tubes, 737
 - with partial dryout, 685
 - smooth horizontal tubes, 760–761
- Annular-mist flow, 737, 742
- Annular wicks, 1186, 1187, 1198
- Annuli:
 - fouling resistance, 863–864
 - physical data for, 860–861
 - pressure loss, 864–865
- Annulus heat transfer coefficient, 863
- Antimony, 123
- Antonetti—Yovanovich thermomechanical model, 366
- Area goodness factor, 1066, 1067
- Argon, 70–71, 359–360, 362
- Arrays of submerged jets, 514, 515
- Arrhenius logarithmic mixing law for
 - viscosities of liquid mixtures, 702–704
- Artery wicks, 1186, 1187, 1198
- Ash dispersions, fly, 620–621
- ASME, *see* American Society of Mechanical Engineers
- Asperities, 187
- Asymmetric isoflux plates, 990
- Asymmetric isothermal plates, 990

- Asymptotic values for dimensionless spreading resistances, 300, 301
- Atomic force microscope (AFM), 1339–1341
- Augmentation, 1030
- Autoclave, 1260–1261
- Autohesion, 1271
- Automotive industry, 950
- Axial heat flow method, 122
- Axially grooved wicks, 1186, 1187
- Axisymmetric flows, 469–471
- Axisymmetric objects, 510
- Azeotropes, 700, 701

- Backmixing, 1378, 1379
- Baffled columns, 1387–1389
- Ball-bearing resistance, 336
- Band approximation method, 614–615
- Base surface, 204
- BCC lattice, *see* Body-centered cubic lattice
- Bead calorimeters, 943
- Bed packings, 1390
- Bei (x), 176–177
- Bejan number, 415, 1147
- Bell—Delaware method, 833
- Benchmarking, 445
- Benzene, 71
- Ber (x), 176–177
- Beryllium, 123
- Bessel functions, 172–177
- Beta functions, 169–170, 172
- Bias error, 919, 920
- Bilitzky fin arrays, 1004, 1005
- Biological fouling, 893
- Biothermal engineering, 254
- Biot number (Bi), 218, 1238–1241
- Bipolar chips, 949
- Bismuth, 123–124
- Blackbodies, 575
- Blackbody emissive power, 575–580
- Blackbody radiation, 348, 349
- Black surfaces, 575
 - radiative intensity of, 581
 - thermal radiation between, 609–610
- Block arrays, 492–493, 495–497, 513
- Body-centered cubic (BCC) lattice, 1313, 1314
- Body of revolution, 470
- Boiling, 635–713
 - bubble dynamics, 646–651
 - bubble departure, 649–651
 - bubble departure frequency, 651
 - bubble growth, 646–648
 - curve, boiling, 637–639
 - direct contact boiling, 1379
 - enhancement of, 704–708
 - additives for liquids, 1093–1097
 - coiled tubes, 1091–1092
 - displaced enhancement devices, 1075
 - extended surfaces, 1067–1069
 - internal convective boiling, 706–708
 - nucleate pool boiling, 704–706
 - rough surfaces, 1055, 1057
 - swirl flow devices, 1082–1086
 - treated surfaces, 1043–1049
 - flow boiling, 662–699
 - flow pattern maps for horizontal flows, 666–671
 - flow pattern maps for vertical flows, 666
 - in horizontal tubes, 679–686
 - of mixtures, 701–702
 - post-dryout heat transfer, 689–699
 - on tube bundles, 687–689
 - two-phase flow patterns, 662–671
 - in vertical and horizontal tubes, 663–666
 - in vertical tubes, 671–679
 - forced convective boiling, 636
 - of mixtures, 699–704
 - evaporation of refrigerant—oil mixtures, 702–704
 - flow boiling, 701–702
 - nucleate boiling, 700–701
 - vapor-liquid equilibria and properties, 699–700
 - nomenclature for, 708–713
 - nucleation of, 640–646
 - nucleation superheat, 640–644
 - site density, 645–646
 - size range of active nucleation sites, 644–645
 - pool boiling, 636, 651–662
 - departure from nucleate pool boiling, 658–660
 - film boiling, 660–662
 - nucleate boiling heat transfer mechanisms, 652–653
 - nucleate pool boiling correlations, 653–657
 - transition boiling, 662

- Boiling coefficient of the equivalent pure fluid, 700
- Boiling curve, 637–639
- Boiling limit, 1194, 1201–1202
- Boiling nucleation, 640–646
 - nucleation superheat, 640–644
 - site density, 645–646
 - size range of active nucleation sites, 644–645
- Boiling number, 674
- Boiling point temperature, 48, 52–54
- Bolted joints, 378
- Boltzmann transport equation (BTE), 1333–1338
- Bonding, interlaminar, 1277–1280
- Bond number, 727
- Bond resistance, 870, 878
- Boron, 124
- Boundary conditions, 165–167
- Boundary layer, 397
 - in flow entrance region, 396–398
 - forced convection, 463–466
 - in fully developed flow region, 400–401
 - turbulent forced convection, 469–472
 - turbulent transition, 510
- Boundary layer assumption, 531–532
- Boundary layer correlation, 758–759
- Boundary layer flow:
 - analogy solutions for, 475–481
 - similarity transformation technique for laminar, 452–455
- Boundary layer regime, 1154
- Boundary scattering, 1310, 1311
- Boussinesq approximations, 531, 532
- Bravais lattice, 1312–1314, 1318–1320
- Brdlik and Savin correlation, 997
- Brillouin zone, 1314, 1320
- Brinell hardness, 334, 343–344, 346
- Brinkman flow model, 1137
- Bromley—Rohsenow correlation, 752
- BTE, *see* Boltzmann transport equation
- Bubble, studies of single, 1367–1368
- Bubble agitation, 652
 - nucleate boiling heat transfer by, 652
 - Rohsenow correlation of, 653–654
- Bubble departure, 649–651
- Bubble departure frequency, 651
- Bubble dynamics, 646–651
 - bubble departure, 649–651
 - bubble departure frequency, 651
 - bubble growth, 646–648
- Bubble growth, 646–648
- Bubble trains, 1368
- Bubbly flow, 663–665, 667
- Bubbly flow regime, 737
- Buckingham- π theorem, 30–31
- Buffer region, 474
- Bundle boiling factor, 688
- Bundle design methods, 688–689
- Bundle factor method, 772
- Burning, 1252
- Burnout point, 638
- Butane (R-600), 64
- Cadmium, 124
- Calcium, 124
- Calculation error, 926–927
- Calibration, 914, 916–917
- Calorimeters, 943
- Capacitance, thermal, 7
- Capacity rate ratio, 806, 807
- Capillary-driven systems, 1191–1193
- Capillary-driven two-phase system, 1182, 1183
- Capillary evaporation, 705
- Capillary limit, 1194–1201
- Capillary pumped loops (CPLs), 1221–1225
- Carbon, 125
- Carbon dioxide, 72, 616, 617
- Carbon monoxide, 72–73
- Carman—Kozeny flow model, 1136
- Carman—Kozeny relationship, 1267
- Cartesian coordinate system, 13, 14
 - heat conduction equations in, 165, 166
 - two-dimensional steady conduction, 223, 225, 226
- Catteneo's equation, 1332
- Cavallini—Zecchin correlation, 760–761
- Cavitation, 640
- CBEs, *see* Compact brazed plate heat exchangers
- CBN (cubic boron nitride) grinding wheels, 1253
- CCT (continuous cooling transformation) curve, 1246
- Cellular phones, 950
- Celsius temperature scale, 917

- Center for Information and Numerical Data Synthesis and Analysis (CINDAS), 121, 122
- Centerline-average (CLA) roughness, 340–341
- Central differences, 238
- Cerium, 125
- Cesium, 125
- CFD (computational fluid dynamics) codes, 445
- CF tubes, *see* Circular fin tubes
- Channels:
- optimal sizes for, 413–419
 - porous media as fill in, 1144–1145
 - thermal spreading and contact resistances in, 272–274
- Channel Elenbaas number (El), 9
- Chapman—Enskog dilute gas contribution, 115
- Chapman—Enskog dilute gas viscosity, 115
- Char, 619
- Chato's correlation, 752–753, 759–760
- Chauvenet's criterion, 923–924
- Chemical reaction fouling, 893
- Chen correlation, 672–673, 761, 763
- Chen—Engel model, 331, 332
- Chevron angle, 882, 883
- Chevron corrugation, 880, 881
- CHF, *see* Critical heat flux
- Chip formation, 1246–1250
- Chip packages, 952–955
- Chip package resistance, 962–964
- Chip package transients, 981–985
- Chip period (chip package temporal behavior), 981–984
- Chip temperature measurement, 1018
- Chi-square test, 924–926
- Chromium, 125, 869
- Churchill—Usagi method, 334
- Churn flow, 663, 664
- CINDAS, *see* Center for Information and Numerical Data Synthesis and Analysis
- Circle correlation coefficients, 285
- Circular annular area, 283–284
- Circular area:
- on a half-space, 274–277
 - isoflux, 285–286
 - on single layer (coating) on half-space, 295–296
- Circular fin (CF) tubes, 846–847
- Circular flux tubes:
- with multiple layers, 302–304
 - semi-infinite isotropic, 298–302
- Circular tubes:
- compact heat exchangers, 844
 - laminar force convection in, 959, 960
 - thermal spreading and contact resistances, 298–304
 - turbulent force convection in, 959, 960
- Circular-tube louvered fins, 1060
- Circumferential fins, 206
- CLA, *see* Centerline-average roughness
- Classical size effect, 965
- Clinical thermometers, 931
- Closed-loop immersion cooling systems, 1012–1014
- CMOS (complementary metal oxide on silicon), 949
- Coal dispersions, pulverized, 620–621
- Coatings:
- assumed nominal property values of, 370
 - circular area on a half-space, 295–296
 - effectiveness of, 371–372
 - metallic, 363–372
- Cobalt, 126
- Co-current flow, $\varepsilon - N_{tu}$ method for, 809
- Co-current flow exchangers, 805
- Coefficient of performance (COP), 1017
- Coiled tubes, 1033, 1088–1092
- boiling, 1091–1092
 - condensing, 1092
 - single-phase flow, 1088–1091
- Cold-side convective layer resistance, 802–804
- Cold-side effectiveness, 806
- Cold-side fouling resistance, 802, 803
- Cold working, 1254
- Columns, 1373–1392
- baffled, 1387–1389
 - packed, 1389–1392
 - spray, 1373–1387
- Compact brazed plate heat exchangers (CBEs), 780, 782, 783
- Compact heat exchangers, 842–857
- classification of, 844–847
 - circular and flattened circular tubes, 844

- finned-tube surfaces, 846–847
- matrix surfaces, 847
- plate fin surfaces, 846
- surfaces with flow normal to banks of
 - smooth tubes, 845–846
 - tubular surfaces, 844
- examples of, 845
- flow friction data, 851–857
- geometrical factors/physical data, 847–850
- heat transfer data, 850–857
 - as porous media, 1145–1147
- Complementary error function, 167, 168
- Complementary metal oxide on silicon (CMOS), 949
- Composites, fabrication of, 1270–1271
- Composite hollow cylinders, 185–186
- Composite hollow spheres, 186–187
- Composite materials, *see* Polymer-matrix composite materials
- Composite plane walls, 183–184
- Composite wicks, 1186, 1187
- Compound disks, 288–294
- Compound enhancement techniques, 1032, 1034, 1040, 1099–1101
- Compound rectangular channels, 304–309
- Compressibility factor, 112
- Computational fluid dynamics (CFD) codes, 445
- Computer programs, 45
- Concave parabolic fins:
 - longitudinal convecting, 203, 205–206
 - optimal dimensions of convecting, 212–214
- Concave parabolic spines:
 - convecting, 209–211
 - optimal dimensions of convecting, 214–215
- Concentrated heat sources:
 - external natural convection, 1154–1156
 - forced convection, 1143
- Condensation, 719–789
 - definition of, 720
 - direct contact heat transfer, 1363–1371
 - electrohydrodynamic enhancement technique, 732–735
 - in-tube, 733–735
 - vapor space, 733
 - enhanced in-tube, 764–769
 - microfin tubes, 764–767
 - twisted-tape inserts, 767–769
 - enhancement techniques
 - coiled tubes, 1092
 - displaced enhancement devices, 1075
 - extended surfaces, 1070–1073
 - rough surfaces, 1057–1059
 - swirl flow devices, 1087–1088
 - treated surfaces, 1049–1050
 - film, *see* Film condensation
 - in heat pipes, 1182, 1183
 - nomenclature for, 785–789
 - Nusselt's analysis of vertical flat plate, 721–723
 - in plate heat exchangers, 780–783
 - inclination and heat transfer performance, 782–783
 - inclination and pressure drop, 783
 - steam condensation heat transfer, 780–782
 - in smooth tubes, 735–763
 - condensation of zeotropes, 762–763
 - flow regimes in, 736–749
 - heat transfer in horizontal tubes, 749–761
 - inclined and vertical tubes, 763
 - oil's effects, 762
 - pressure drop, 761–762
 - of vapor on or in a liquid, 1365–1371
 - of zeotropes, 762–763
- Condensation limit, 1015–1016
- Condensation oscillation, 1370–1371
- Condenser limit, 1194, 1208–1209
- Condenser sizing methods, 771–774
 - bundle factor method, 772
 - pointwise or numerical computer programs, 772–774
 - vertical row-number method, 771–772
- Conduction:
 - in electronic equipment, 956–957
 - porous media basic principles, 1140–1141
- Conduction-controlled freezing and melting, 243–254
 - approximate analytical solutions, 250–253
 - exact solutions for planar freezing, 247
 - exact solutions in cylindrical freezing, 247–249
 - multidimensional freezing (melting), 254
 - one-region Neumann problem, 243–245
 - two-region Neumann problem, 245–247

- Conduction heat transfer, 2–4, 161–257
 - basic equations for, 164–167
 - boundary and initial conditions, 165–167
 - Fourier's Law, 164–165
 - general, 165
 - Bessel functions, 172–177
 - beta functions, 169–170, 172
 - conduction-controlled freezing and melting, 243–254
 - approximate analytical solutions, 250–253
 - exact solutions for planar freezing, 247
 - exact solutions in cylindrical freezing, 247–249
 - multidimensional freezing (melting), 254
 - one-region Neumann problem, 243–245
 - two-region Neumann problem, 245–247
 - contemporary topics in, 254–255
 - convecting spines, 208–211
 - error functions, 167–170
 - exponential integral function, 172, 173
 - extended surfaces, 201–215
 - convecting spines, 208–211
 - longitudinal convecting fins, 202–207
 - longitudinal convecting—radiating fins, 212
 - longitudinal radiating fins, 211–212
 - optimum dimensions of convecting fins and spines, 212–215
 - radial convecting fins, 206–209
 - gamma function, 168–169, 171
 - Legendre functions, 177–179
 - nomenclature for, 255–257
 - one-dimensional, 2, 3
 - one-dimensional conduction with internal heat generation, 2–4
 - optimum dimensions of convecting fins and spines, 212–215
 - periodic, 239–243
 - cooling of a lumped system in an oscillating temperature environment, 239
 - finite plane wall with periodic surface temperature, 241–242
 - infinitely long semi-infinite hollow cylinder with periodic surface temperature, 242–243
 - semi-infinite solid with periodic ambient temperature, 240–241
 - semi-infinite solid with periodic surface heat flux, 240
 - semi-infinite solid with periodic surface temperature, 239–240
- porous media, 1140–1141
- steady one-dimensional, 178, 180–201
 - composite hollow cylinder, 185–186
 - composite hollow sphere, 186–187
 - composite plane wall, 183–184
 - contact conductance, 187–188
 - critical thickness of insulation, 188
 - hollow cylinder, 180–181, 190–191
 - hollow sphere, 181–182, 192–193
 - location-dependent energy generation, 198–199
 - location-dependent thermal conductivity, 194–195
 - plane wall, 178, 180, 189–190
 - radiative—convective cooling of solids
 - with uniform energy generation, 201
 - solid cylinder, 191–192
 - solid sphere, 193–194
 - temperature-dependent energy generation, 199–200
 - temperature-dependent thermal conductivity, 196–198
 - thermal resistance, 182–183
 - uniform internal energy generation effect, 188–194
- transient, 229–239
 - finite-difference method, 236–239
 - finite-sized solid model, 235–236
 - lumped thermal capacity model, 229–231
 - multidimensional transient conduction, 236
 - semi-infinite solid model, 232–234
- two-dimensional steady conduction, 215–229
 - conduction shape factor method, 222–225
- finite-difference method, 223, 225–229
 - method of superposition, 221–222
 - rectangular plate with specified boundary temperatures, 216–217
 - solid cylinder with surface convection, 217–220

- solid hemisphere with specified base and surface temperatures, 219–221
- Conduction shape factor method, 222–225
- Conductive, thermally, 289
- Conductivity:
 - anisotropic, 983, 986–987
 - dilute gas thermal, 58–59
- Confidence interval, 923
- Confidence level, 923
- Configuration factor, 600
- Conforming joints, 265–266
- Conforming rough solids, 266–269
- Conforming rough surfaces, 340–362
 - elastic contact model, 349–351
 - elastic—plastic contact conductance model, 351–353
 - gap conductance for joints between, 355–359
 - gap conductance for large parallel isothermal plates, 353–355
 - joint conductance for joints between, 359–361
 - models for, 340–342
 - plastic contact model, 342–347
 - radiation resistance/conductance for, 347–349
- Conical spines, convecting, 209–211, 214
- Conjugate heat transfer, 443
- Conservation:
 - of energy, 23–30, 119–120
 - of momentum, 20, 21
 - of quasi-momentum, 1329
- Consolidation (of prepreg layers), 1269–1270
- Constriction resistance, 271
- Constructal theory, 254
- Contact conductance:
 - dimensionless, 346–347, 350, 352, 367
 - spreading resistance affected by, 284–285
 - and steady one-dimensional conduction, 187–188
- Contact pressure:
 - and dimensionless contact conductance, 367
 - dimensionless joint conductance vs. dimensionless, 374
 - and joint conductance, 368
 - relative, 345–346
- Contact resistance, 970–972
 - channels, 272–274
 - circular flux tube, 298–304
 - high-fin tubes, 870
 - of isothermal elliptical contact areas, 323–324
 - at line contact, 337–338
 - solid interfaces, 970–972
- Contact sensing devices, 914–916
- Contact strip, 336–337
- Continuity equation, 16–19
- Continuous component, 1376, 1377
- Continuous cooling transformation (CCT) curve, 1246
- Continuous metal forming processes, 1254–1259
- Continuum models, microscale heat transfer, 1331–1333
- Continuum vapor, 1212–1213
- Contour area, 264, 266
- Controls:
 - heat pipe, 1187–1191
 - excess-liquid, 1187, 1189
 - gas-loaded, 1187, 1188
 - liquid-flow-modulated, 1189–1191
 - vapor flow-modulated, 1189, 1190
 - manufacturing thermal process, *see* Thermal process control for manufacturing
- Convecting fins:
 - longitudinal, 202–207, 212
 - optimum dimensions, 212–215
- Convecting spines:
 - longitudinal, 208–211
 - optimum dimensions for, 212–215
- Convection, 7–10
 - coefficient for, 7–8
 - convective phenomena in packaging, 988–995
 - dimensionless parameters in, 8
 - double-diffusive, 1169
 - in electronic equipment, 957–961
 - external, 705, 1361–1362
 - forced, *see* Forced convection
 - natural, *see* Natural convection
 - surface, 232, 233, 250
- Convection transport, 446
- Convective—radiative cooling, simultaneous, 231
- Conversion factors (for English to SI units), 37–38

- Convex parabolic fins, 203, 206
- Convex parabolic spines, 210, 211, 215
- Convex surface exposed to large isothermal enclosure, 612
- Coolant pool, heat capacity of, 231
- Cooling:
 - electronic equipment requirements for, 948–952
 - immersion, 1008–1016
 - jet impingement, 995–1002
 - Newton's law of, 183, 957
 - radiation, 230–231
 - radiative—convective, 201
- Cooling limit, 1015
- Cooper's correlation, 655–656, 766
- Coordinate systems, 12–16
 - cylindrical, 13–15
 - general curvilinear, 16
 - rectangular (Cartesian), 13, 14
 - spherical, 13, 15
- COP (coefficient of performance), 1017
- Copper, 126, 868
- Correction factor method, 805–807
- Correlation equations, 294–295, 301–302
- Corresponding states:
 - extended, 114–115
 - model of, 116–117
- Corrosion fouling, 893
- Corrugation, 880–884
- Cosines, direction, 606
- Costs, life-cycle, 953
- Counterflow, $\varepsilon - N_{tu}$ method for, 809
- Counterflow exchangers, 805
- Coupling, 1280
- CPLs, *see* Capillary pumped loops
- Crank—Nicholson method, 238
- Crescent wicks, 1186, 1187
- Critical density (for fluids), 48, 52–54
- Critical enhancement (superscript “crit”), 115
- Critical heat flux (CHF), 638, 639, 689, 1012, 1041
- Critical pressure (for fluids), 48, 52–54
- Critical superheat, 1201
- Critical temperature (for fluids), 48, 52–54
- Crossed-strings method, 608–609
- Crossflow:
 - across bank of cylinders, 511
 - $\varepsilon - N_{tu}$ method for, 810–811
 - external flow forced convection, 482–485
 - laminar, 509
- Crossover wavelengths, 589
- Cross sections:
 - finned tubes profiles, 1071
 - fully developed flow affected by shape of, 403–404
 - hydraulic diameter, 402
 - spreading resistance for an abrupt change in, 312–313
- Cryogen graphs, 149–151
- Cryogenic heat pipes, 1184
- Crystals:
 - conservation of energy and crystalline elements, 120
 - structure of, 1312–1314
 - vibrational modes of, 1317–1322
- Crystallization, 1271, 1281–1283
- Crystal wind, 1098
- CST code, 774
- Cubic boron nitride (CBN) grinding wheels, 1253
- Cure process, 1259–1261
- Cure reaction, 1259
- Cure temperature and pressure cycles, 1259
- Curve fitting methods, 927–931
- Cyclohexane, 73
- Cyclopropane, 74
- Cycom-4102 laminate, 1263, 1266
- Cylinder(s):
 - conduction heat transfer with, 217–220
 - in crossflow, 482–483
 - crossflow across bank of, 511
 - external flow forced convection, 482–483
 - external laminar natural convection flow, 543–546
 - forced convection, 482–483, 1142–1143
 - hollow, 180–181, 185–186, 190–191, 242–243
 - horizontal, 543–545
 - natural convection in, 563–565
 - porous media, 1142–1143
 - solid, 217–220
 - surface convection, 217–220
 - at uniform surface temperature in laminar cross flow, 509
 - vertical, 545–546
- Cylinder bundles, 431

- Cylindrical coordinate systems, 13–15
 - heat conduction equations in, 165, 166
 - two-dimensional steady conduction, 225, 227–229
- Cylindrical enclosures, 1163–1164
- Cylindrical freezing, 247–252
- Cylindrical spines, 209, 210, 214
- Darcy—Fanning head-loss relationship, 33
- Darcy flow model, 1135–1137
- Databases, 45
- Dean number, 1088
- Debye cutoff frequency, 1323
- Debye model, 1323–1325
- Debye temperature, 1324
- Defect scattering, 1310, 1311
- Deformation heating considerations, 1255–1256
- Deformation processes, 1254–1259
- Degradation, 1271, 1280–1281
- Degree of intimate contact, 1277–1279
- Degrees of freedom, 925
- Delrin, 373–374
- Density:
 - critical, 48, 52–54
 - measurement of, 122
 - mixture, 114
 - of states, 1316
- Density-dependent contributions, 116–117
- Departure from nucleate boiling (DNB), 638
- Depriming, wick, 1213
- Deuterium, 74–75
- Developing flow, 407–413
 - Hagen—Poiseuille flow, 408–412
 - thermal entrance region, 407–408
 - thermally and hydraulically developing flow, 412–413
- Deviation (measurement error), 920
- Dhir—Lienhard correlation, 752
- Diamond, 121
- Diamond structure, 1313
- Dielectric coolants, 1008, 1009
- Differential approximation, 625
- Differential equations (for regenerators), 890–891
- Differential methods, 466
- Differential scanning calorimetry (DSC), 140, 1263
- Diffuse emitters, 583, 584, 587
- Diffuse mismatch model (DMM), 972
- Diffuse surfaces, 600
 - gray, 610–612
 - nongray, 614–615
- Diffusion approximation, thermal radiation, 623, 624
- Diffusion meters, 944
- Diffusivity, thermal:
 - and conservation of energy, 120
 - measurement of, 122, 140
- Dilute-gas contributions, 115–116
- Dilute gas thermal conductivity, 58–59
- Dilute gas viscosity, 60–61
- Dimensional analysis, 30–34
- Dimensionless contact conductance, 346–347, 350, 352, 367
- Dimensionless groups, 33–34
- Dimensionless joint conductance, 374
- Dimensionless length scale, 658
- Dimensionless numbers (for boiling), 713
- Dimensionless parameters (in natural convection), 532–533
- Dimensionless source temperature (table), 276
- Dimensionless spreading—constriction resistance parameter, 366
- Dimensionless spreading resistance, 272
 - asymptotic values for, 300, 301
 - coefficients for correlations of, 302
 - effect of n on, 282
 - in flux channels, 312
 - of isoflux rectangular area, 280
 - of isothermal ellipse, 279–280
 - of isothermal rectangular area, 281
 - of rectangular source area, 307
- Dipole moment, 52–54
- Direct-contact heat exchangers, 798, 799
- Direct contact heat transfer, 1359–1395
 - columns for, 1373–1392
 - condensation, 1363–1371
 - evaporation, 1363–1365, 1371–1373
 - external convection to spheres, 1361–1362
 - indirect contact vs., 1359–1360
 - inside spheres, 1362–1363
 - nomenclature for, 1393–1395
- Direct electrical heating method, 122
- Direct extrusion diagram, 1255
- Direct integration, view factors of, 600, 606

- Directional dependence:
 metal radiative properties, 586–587
 nonconductor radiative properties, 591, 593
- Directional emittance, 585
- Direction cosines, 606
- Direct-transfer heat exchangers, 799
- Dirt factor, 894
- Discrete heat sources:
 between continuously moving workpiece and, 1241–1245
 semi-infinite plane with finite size moving heat source, 1243–1245
 semi-infinite solid with moving point heat source, 1243
 thin plate/rod with moving planar heat source, 1241–1242
 thin plate with moving line heat source, 1242–1243
- Discrete ordinate method, 627
- Disengagement zones, 1376
- Disks, compound, 288–294
- Dispersed component, 1376, 1377
- Dispersed flow regime, 693
- Dispersion relation, 1319–1320
- Displaced enhancement devices, 1033, 1074–1075
 boiling, 1075
 condensing, 1075
 single-phase flow, 1074–1075
- Dittus—Boelter correlation, 695, 702, 755
- Divided-flow shell-and-tube exchangers, 814, 817
- DMM (diffuse mismatch model), 972
- DNB (departure from nucleate boiling), 638
- Dobson correlation, 760–763
- Double-diffusive convection, 1169
- Double-pipe exchangers, 857–859
 dimensions of multiple, 867
 multiple finned, 868
 in series—parallel arrangements, 865–868
- Doubly connected regular polygons, 284–285
- Drag coefficient, 650–651, 1382
- Drawing:
 deformation heating considerations for, 1255–1256
 frictional heating considerations for, 1256–1259
 thermal—fluid modeling in, 1254–1259
- Drift flux type of void fraction model, Rouhani—Axelsson, 682
- Droplet evaporation:
 in a liquid, 1371–1373
 in a vapor or gas, 1371
- Droplets:
 condensation on liquid, 1366–1367
 hemispherical, 219–221
- Drude theory, 586
- Dryout:
 of evaporator wick structure, 1193
 of the liquid film, 689
- Dry point, 1193
- DSC, *see* Differential scanning calorimetry
- Dupuit—Forchheimer flow model, 1138
- Dwell times, 888
- Early period (chip package temporal behavior), 981–984
- Eccentric rectangular area on rectangular plate with cooling, 314–318
- ECL (emitter-coupled logic), 949
- ECS, *see* Extended corresponding states
- Effective medium transport (EMT), 977, 978
- Effective microhardness, 347
- Effective solar temperature, 576
- EHD enhancement technique, *see* Electrohydrodynamic enhancement technique
- Einstein model (for phonon density of states), 1324–1326
- Elastic contact model, 349–351
- Elastic—plastic contact conductance model, 351–353
- Elastic—plastic contacts of hemispheres and flat surfaces in vacuum, 333–335
- Elastic—plastic contact region, 333, 335
- Elastoconstriction parameter, 321
- Elastogap resistance model, 324–326
- Elastomeric inserts, 372–374
- Electrical resistance, 182
- Electric fields, 1098–1099
- Electrohydrodynamic (EHD) enhancement technique, 732–735
- Electromagnetic wave theory, 583
- Electrons:
 Boltzmann transport equation for, 1336–1338
 transport of, 121

- Electron-electron scattering, 1310, 1311
- Electron heat capacity, 1322
- Electronic equipment, 947–1022
 - chip temperature measurement, 1018
 - convective phenomena in packaging, 988–995
 - optimum spacing, 991–992
 - printed circuit boards in forced convection, 992–995
 - printed circuit boards in natural convection, 988–991
- cooling requirements, 948–952
- finned heat sink examples of, 1061
- jet impingement cooling, 995–1002
 - correlation, 996–998
 - figures of merit, 999, 1000
 - first-order trends, 998–1000
 - impingement on heat sinks, 1001–1002
 - thermal—fluid design general considerations, 1000–1001
- length-scale effects on thermophysical properties, 964–988
 - first-order transient effects, 979–985
- heat flow across solid interfaces, 970–979
- heat flow in printed circuit boards, 983, 986–988
 - spreading resistance, 966–970
- natural convection heat sinks, 1002–1006
- nomenclature for, 1018–1022
- packaging levels, 953–955
- phase-change phenomena, 1006–1016
 - heat pipes and vapor chambers, 1006–1008
- immersion cooling, 1008–1016
- thermal packaging goals, 952–953
- thermal resistances, 956–964
 - basic heat transfer modes, 956–962
 - chip package resistance, 962–964
- thermoelectric coolers, 1016–1017
- Electron lattice scattering, 1310, 1311
- Electron scattering mechanisms, 1310–1311
- Electron thermal conductivity in metals, 1326–1328
- Electrostatic fields, 1033
- Elenbaas number (El), 9
- Ellipses, isoflux hyper-, 286–287
- Elliptical contact area, 319–322
- Elliptical source area, 277–280
- Elongated bubble flow, 666
- Emissive power, 575–580
- Emittance, 583
 - directional, 585
 - hemispherical, 584
 - spectral aluminum normal, 594–595
 - total hemispherical, 585, 588, 589
 - total normal, 597–598
- Emitter-coupled logic (ECL), 949
- EMT, *see* Effective medium transport
- Enclosures:
 - idealized, 599
 - internal natural convection
 - non-rectangular, 554–556
 - rectangular, 551–554
 - natural convection in, 565–566
 - porous media
 - cylindrical and spherical, 1163–1164
 - heated from below, 1164–1169
 - heated from the side, 1156–1162
 - radiative properties of, 582–586
- Energy carriers, 1314
- Energy conservation:
 - law of, 23–30
 - porous media basic principles, 1138–1140
- Energy exchange, imperfect, 353
- Energy generation:
 - constant surface heat flux and exponentially decaying, 234
 - location-dependent, 198–199
 - nuclear, *see* Nuclear energy generation
 - semi-infinite solid model, 234
 - at the shear plane, 1249
 - steady one-dimensional conduction, 188–194
 - temperature-dependent, 199–200
 - uniform internal, 188–194
- English engineering system (of units), 35–38
- Enhanced boiling, 704
- Enhanced convective heat transfer, 707
- Enhanced in-tube condensation, 764–769
- Enhance joint conductance, 361–377
- Enhancement, critical, 115
- Enhancement techniques, 1029–1104
 - active, 1031, 1033–1034, 1097–1099
 - active techniques, 1097–1099
 - additives for liquids, 1092–1097
 - boiling, 1093–1097
 - single-phase flow, 1092–1093

Enhancement techniques (*continued*)

- for boiling, 704–708
 - internal convective boiling, 706–708
 - nucleate pool boiling, 704–706
 - classification of, 1031–1034
 - coiled tubes, 1088–1092
 - boiling, 1091–1092
 - condensing, 1092
 - single-phase flow, 1088–1091
 - compound, 1099–1101
 - displaced enhancement devices, 1074–1075
 - boiling, 1075
 - condensing, 1075
 - single-phase flow, 1074–1075
 - electrohydrodynamic, 732–735
 - in-tube EHD condensation, 733–735
 - vapor space EHD condensation, 733
 - extended surfaces, 1059–1073
 - boiling, 1067–1069
 - condensing, 1070–1073
 - single-phase flow, 1059–1067
 - nomenclature for, 1101–1104
 - performance evaluation criteria for, 1034–1043
 - for rough surfaces, 1050–1059
 - boiling, 1055, 1057
 - condensing, 1057–1059
 - single-phase flow, 1050–1056
 - for single-phase flow heat transfer, 1037–1040
 - swirl flow devices, 1075–1088
 - boiling, 1082–1086
 - condensing, 1087–1088
 - single-phase flow, 1075–1082
 - for treated surfaces, 1043–1050
 - boiling, 1043–1049
 - condensing, 1049–1050
 - for two-phase flow heat transfer, 1040–1042
- Enthalpy, 46, 111, 112
- Entrainment limit, 1194, 1202–1204
- Entrainment of the liquid film, 689
- Entrance length, 396–397
- Entrance length region, 396–398
- Entropy, 111, 112
- $\epsilon - N_{tu}$ analysis method:
 - for heat exchangers, 807–817, 822
 - for 1–2 divided-flow shell-and-tube exchanger with the shell fluid mixed, 814, 817
 - for 1–2 shell-and-tube exchanger with the shell fluid mixed, 811
 - for 1–2 shell-and-tube exchanger with the shell fluid unmixed, 811–812
 - for 1–2 split-flow shell-and-tube exchanger with the shell fluid mixed, 813–814
 - for 1–4 shell-and-tube exchanger with the shell fluid mixed, 812–813
 - for co-current flow, 809
 - for counterflow, 809
 - for crossflow with both fluids mixed, 810–811
 - for crossflow with both fluids unmixed, 810
 - for crossflow with one fluid mixed and one fluid unmixed, 810
 - for heat exchangers, 807–817
 - for regenerators, 891–892
- Epon 815/Epicure 3274 resin—catalyst system, 1263, 1265
- Equations:
 - of phonon radiative transport, 1328
 - of state, 46–51, 111–112
- Equipment:
 - electronic, *see* Electronic equipment
 - experimental methods, 931–944
 - glass thermometers, 931–933
 - heat flow meters, 943–944
 - liquid crystals, 942–943
 - pyrometers, 943
 - resistance temperature detectors, 940–942
 - thermocouples, 933–941
- Equivalent isothermal circular contact, 295–296
- Equivalent isothermal circular source, 300
- Equivalent isothermal contact area, 297–298
- Equivalent isothermal distribution, 289
- Equivalent substance reducing ratios, 117
- Error distribution, 921–923
- Error functions, 167–170
- E-shells, TEMA, 811–813
- Estimated experimental uncertainty, 47
- Ethane, 62–63
- Ethane-based refrigerant graphs, 158–159
- Ethene, 75

- Ethylene, 75
- Eulerian—Lagrangian model of dispersed flow boiling, 699
- Euler integral, 168
- Evaporation, 640
 - direct contact heat transfer, 1363–1365, 1371–1373
 - in heat pipes, 1182, 1183
 - of liquid by a surrounding vapor or gas, 1371–1373
 - nucleate boiling heat transfer by, 653
 - of refrigerant—oil mixtures, 702–704
- Excess-liquid heat pipes, 1187, 1189
- Exchangers, heat, *see* Heat exchangers
- Exchanger heat transfer effectiveness, 807–808
- Exchanger surface area, 800–802
- Expansion, thermal, 140
- Experimental methods, 913–945
 - calculation error, 926–927
 - calibration, 916–917
 - curve fitting, 927–931
 - equipment, 931–944
 - glass thermometers, 931–933
 - heat flow meters, 943–944
 - liquid crystals, 942–943
 - pyrometers, 943
 - resistance temperature detectors, 940–942
 - thermocouples, 933–941
 - measurement, 913–914
 - measurement error, 918–926
 - bias error, 919, 920
 - Chauvenet's criterion, 923–924
 - chi-square test, 924–926
 - error distribution, 921–923
 - mean and deviation, 920
 - precision error, 919–920
 - uncertainty, 918–920
 - nomenclature for, 944–945
 - readability, 917–918
 - sensing, 914–916
- Explicit method, 236–238
- Exponential integral function (of conduction heat transfer), 172, 173
- Extended corresponding states (ECS), 114–115
- Extended surfaces:
 - conduction heat transfer with, 201–215
 - convecting spines, 208–211
 - longitudinal convecting fins, 202–207
 - longitudinal convecting—radiating fins, 212
 - longitudinal radiating fins, 211–212
 - optimum dimensions of convecting fins and spines, 212–215
 - radial convecting fins, 206–209
- enhancement techniques, 1032–1033, 1059–1073
 - boiling, 1067–1069
 - condensing, 1070–1073
 - single-phase flow, 1059–1067
- examples of, 1060–1062
- Extended surface area effect, 707
- External convection:
 - nucleate pool boiling enhancement, 705
 - to spheres, 1361–1362
- External flow (definition), 396
- External flow heat transfer, *see* Forced convection (external flows)
- External natural convection, 529
 - concentrated heat sources, 1154–1156
 - horizontal walls, 1153–1154
 - laminar flow, 543–551
 - over horizontal cylinder and sphere, 543–545
 - over vertical cylinder, 545–546
 - in plumes/wakes/other free boundary flows, 548–551
 - transient, 546–548
- porous media, 1147–1156
 - concentrated heat sources, 1154–1156
 - horizontal walls, 1153–1154
 - sphere and horizontal cylinder, 1154
 - vertical walls, 1147–1153
 - sphere and horizontal cylinder, 1154
 - vertical walls, 1147–1153
- External resistance, 963–964
- Extinction coefficient, 620, 621
- Extruded fins, 860
- Extrusion:
 - diagram of, 1255
 - frictional heating considerations for, 1256–1259
 - thermal—fluid modeling in, 1254–1259

- Fabrication of composites, 1270–1271
- Face-centered cubic (FCC) lattice, 1313, 1314, 1320–1321
- Fahrenheit temperature scale, 917
- Falkner—Skan flow, 454–455
- Fan-cooled heat sinks, 952
- Favorable tilt, 1196
- FCC lattice, *see* Face-centered cubic lattice
- Fermi—Dirac distribution, 1316
- Fermi energy, 1315–1316
- Ferrous alloys, 869
- FG criteria, 1038
- Fiber deformation, 1268
- Fiber network, 1267
- Figures of merit (FOM), 1016, 1017
 - heat pipes, 1211–1212
 - jet impingement cooling, 999, 1000
- Filler concentration, 979
- Films:
 - liquid, 689
 - lubricating, 1258–1259
 - oxide, 594–595
- Film boiling, 638, 660–662
- Film condensation, 723–732, 751
 - bond number, 727
 - on low-fins, 723–727
 - sawtooth fin condensing tubes, 730–732
 - on single horizontal finned tubes, 727–732
 - specified interfaces, 725–727
 - surface tension pressure gradient, 724–725
 - trapezoidal fin tubes, 728–730
 - on tube bundles, 769–780
 - in-tube condensers, 779–780
 - X-shell condensers, 770–779
 - vapor space, 721–723
- Film condensers, 1365–1366
- Film resistance:
 - high-fin exchangers, 876–877
 - longitudinal finned double-pipe heat exchangers, 862
- Filters, Kalman—Bucy, 1291–1292
- Fins:
 - annular, 206
 - circular-tube louvered, 1060
 - circumferential, 206
 - concave parabolic, 203, 205–206, 212–214
 - longitudinal convecting, 203, 205–206
 - optimal dimensions of convecting, 212–214
 - conduction heat transfer with, 201
 - longitudinal convecting fins, 202–207
 - longitudinal convecting—radiating fins, 212
 - longitudinal radiating fins, 211–212
 - optimum dimensions of convecting fins and spines, 212–215
 - radial convecting fins, 206–209
 - convecting, 202–207, 212–215
 - longitudinal, 202–207
 - longitudinal convecting—radiating, 212
 - optimal dimensions of, 212–214
 - radial, 206–209
 - convex parabolic, 203, 206
 - extruded, 860
 - film condensation on low-fins, 723–727
 - hyperbolic, 208, 209
 - longitudinal convecting, 202–207
 - longitudinal convecting—radiating, 212
 - longitudinal radiating, 211–212
 - louvered, 846, 1060
 - low-fins, 723–727
 - notched, 1073
 - offset, 846
 - oval-tube louvered, 1060
 - perforated, 846
 - pin, 846
 - plain, 846, 849, 851
 - radial convecting, 206–209
 - radiating, 211–212
 - rectangular, 202–205, 207, 213
 - longitudinal convecting, 202–205
 - optimal dimensions of convecting, 212, 213
 - radial convecting, 206–208
 - rectangular offset strip plate, 1066
 - serrated-tip micro-, 1073
 - strip, 846, 849, 853, 1060
 - trapezoidal, 203, 205
 - triangular
 - longitudinal convecting, 203, 205
 - optimal dimensions of convecting, 212, 213
 - radial convecting, 208
 - wavy, 846, 849, 854
 - wavy plate, 1060
 - welded U-, 861
- Fin arrays, 1003–1006
- Fin effectiveness, 204–212

- Fin efficiency approximation, 871
- Fin heat sinks:
 - pin, 498–500, 513
 - plate, 497–498
- Finite-difference method:
 - of transient conduction, 236–239
 - of two-dimensional steady conduction, 223, 225–229
- Finite-sized solid model, 235–236
- Finite size moving heat source, 1243–1245
- Finned surfaces:
 - conduction heat transfer of
 - longitudinal convecting, 202–207
 - longitudinal convecting—radiating, 212
 - longitudinal radiating, 211–212
 - optimum dimensions, 212–215
 - radial convecting, 206–209
 - cross-sectional profiles of finned tubes, 1071
 - enhancement techniques, 1032–1033
 - exchanger surface area, 800–801
 - heat transfer, 11
 - heat transfer with, 11
 - K-W profiles of, *see* Kedzierski—Webb profiles
- Finned-tube surfaces, 846–847
- First law of thermodynamics, 23–24
- First-order closure model, 471
- First-order transient effects:
 - chip package transients, 981–983
 - electronic equipment, 979–985
 - lumped heat capacity, 980–981
 - thermal wave propagation, 981
- Fixed matrix regenerators, 886
- Fixed points (for fluids), 52–54
- Flank face, 1248
- Flat plate(s):
 - forced convection external flows from, 456, 461–463, 485–490
 - forced convection on an isoflux, 959, 960
 - forced convection on an isothermal, 959, 960
 - incompressible flow past, with viscous dissipation, 461–463
 - isoflux, 959, 960
 - isothermal, 508–510, 959, 960
 - isothermal rough, 510–511
 - offset strips, 487–490
 - similarity solutions for, at uniform temperature, 456
 - stack of parallel plates, 485–486
 - with turbulent boundary layer, 510–511
 - with unheated starting length in turbulent flow, 479–480
 - in uniform laminar flow, 508–509
- Flat plate boundary layers, 463–466
- Flat surfaces:
 - inclined and horizontal, 562–563
 - laminar flow, 533–543
 - vertical, 561–562
- Flattened circular tubes, 844
- Floating head, 825
- Flooding, 1380
- Flooding holdup, 1377
- Flow(s):
 - axisymmetric, 470–471
 - configurations of, 443
 - developing, 407–413
 - fully developed, 404–407
 - over isothermal sphere, 483
 - in smooth tube condensation, 736–749
 - tube-side flow, 770
 - turbulent, 528
 - turbulent duct, 419–425
 - unconfined/partially confined, 502
- Flow boiling, 662–699, 701–702
 - flow pattern maps for horizontal flows, 666–671
 - flow pattern maps for vertical flows, 666
 - in horizontal tubes, 679–686
 - correlations based on vertical tube methods, 679–680
 - model based on local flow regime, 680–686
 - subcooled boiling heat transfer, 686
 - of mixtures, 701–702
 - post-dryout heat transfer, 689–699
 - heat transfer mechanisms, 693–694
 - inverted annular flow heat transfer, 694–695
 - mist flow heat transfer, 695–699
 - thermal nonequilibrium, 690–693
 - on tube bundles, 687–689
 - two-phase flow patterns, 662–671
 - in vertical and horizontal tubes, 663–666
 - in vertical tubes, 671–679
 - Chen correlation, 672–673

- Flow boiling (*continued*)
 Gungor—Winterton correlation, 674–675
 Shah correlation, 673–674
 Steiner—Taborek method, 675–678
- Flow entrance region, 396–399
- Flow friction data, 851–857
- Flow (hydrodynamic) entrance length, 396
- Flow models, 1135–1138
- Flow pattern effect, 707
- Flow pattern maps:
 for horizontal flows, 665–671
 for vertical flows, 663, 666
- Flow regions, 396–401
- Flow resistance, 11–12, 964
- Fluids:
 graphs of selected, 152–153
 properties of, 45, 738, 750
 thermodynamic properties of, 46–114
 calculation of, 112–113
 dilute gas thermal conductivity, 58–59
 dilute gas viscosity, 60–61
 equation of state, 46–51, 111–112
 estimated experimental uncertainty, 47
 ideal gas isobaric heat capacity, 55–57
 for mixtures, 113–114
 physical constants and fixed points, 52–54
 along the saturation line, 62–110
 transport properties of, 114–118
 density-dependent contributions, 116–117
 dilute-gas contributions, 115–116
 extended corresponding states, 114–115
 for mixtures, 117–118
- Fluid friction:
 in flow entrance region, 396, 397
 in fully developed flow region, 401, 403–404
- Fluid-specific correlation of Gorenflo, 656–657
- Fluid vibrations, 1033, 1098
- Fluorine, 75–76
- Flush-mounted heat sources, 491–492, 512
- Flux distribution:
 of the form $(1 - u^2)^\mu$, 300
 over isothermal elliptical area, 280
- Flux tubes, 272–274, 291–293, 298–302
- Fly ash dispersions, 620–621
- FM, *see* Figures of merit
- FN criteria, 1038
- Foils, metallic, 363–372
- FOM, *see* Figures of merit
- Forced convection, 9–10
 on an isoflux flat plate, 959, 960
 on an isothermal flat plate, 959, 960
 external flows, *see* Forced convection (external flows)
 internal flows, *see* Forced convection (internal flows)
 natural convection vs., 526
 porous media, 1141–1147
 channels filled with porous media, 1144–1145
 compact heat exchangers as porous media, 1145–1147
 concentrated heat sources, 1143
 configurations, 1134
 plane wall with constant temperature, 1141–1142
 sphere and cylinder, 1142–1143
 printed circuit boards in, 992–995
 summary of relationships, 427–434
- Forced convection (external flows), 439–522
 analysis of, 445–446
 from arrays of objects, 483–490
 crossflow across tube banks, 483–485
 flat plates, 485–490
 heat transfer correlations, 508–515
 morphology of, 440–445
 nomenclature for, 515–522
 from objects on substrate, 490–500
 block arrays, 495–497
 flush-mounted heat sources, 491–492
 isolated blocks, 493–495
 pin fin heat sinks, 498–500
 plate fin heat sinks, 497–498
 two-dimensional block array, 492–493
 from single objects in uniform flow, 446–483
 algebraic turbulence models, 472
 analogy solutions for boundary layer flow, 475–481
 axisymmetric nonsimilar flows, 469
 cylinder in crossflow, 482–483
 flow over isothermal sphere, 483
 high Reynolds number flow over a wedge, 446–452

- incompressible flow past flat plate with viscous dissipation, 461–463
- integral solutions for flat plate boundary layer with unheated starting length, 463–466
- near-wall region in turbulent flow, 472–475
- Prandtl number effect, 459–460
- similarity solutions for flat plate at uniform temperature, 456
- similarity solutions for wedge, 456–459
- similarity transformation technique for laminar boundary layer flow, 452–455
- Smith—Spalding integral method, 466–468
- surface roughness effect, 481–482
- turbulent boundary layer, 469–472
- two-dimensional nonsimilar flows, 466
- turbulent jets, 500–508
 - submerged jets, 502–508
 - thermal transport in jet impingement, 500–502
- Forced convection (internal flows), 395–436
 - heat transfer in developing flow, 407–413
 - Hagen—Poiseuille flow, 408–412
 - thermal entrance region, 407–408
 - thermally and hydraulically developing flow, 412–413
 - heat transfer in fully developed flow, 404–407
 - mean temperature, 404–405
 - thermally fully developed flow, 405–407
 - laminar flow, 396–404
 - flow entrance region, 396–399
 - fully developed flow region, 399–401
 - hydraulic diameter and pressure drop, 401–404
 - optimal channel sizes for, 413–419
 - and pressure drop, 396–404
 - nomenclature for, 434–436
 - summary of relationships, 427–434
 - total heat transfer rate, 425–427
 - isothermal wall, 426
 - uniformly heated wall, 427
 - turbulent duct flow, 419–425
 - fully developed flow, 420–423
 - heat transfer in fully developed flow, 423–425
 - optimum channel size for, 427
 - time-averaged equations, 419–420
- Forced convective boiling, 636
- Forced-convective film boiling, 694
- Forced draft, 871
- Forchheimer flow model, 1137
- Forward differences, 237
- Fouling, heat exchanger, 802, 893–896
- Fouling factors, 894–896
- Fouling problem, 894
- Fouling resistance, 877
- Fourier's equation, 119
- Fourier's Law, 2, 164–165
- Frame heat exchangers, plate and, *see* Plate and frame heat exchangers
- Free boundary flows, 548–551
- Freedom, degrees of, 925
- Free electron Fermi gas theory, 1315
- Free electron gas, 1314–1317
- Free surface jets, 506–508, 515
- Freeze—thaw issues, 1214–1216
- Freezing:
 - conduction-controlled, *see* Conduction-controlled freezing and melting
 - multidimensional, 254
- Freezing fouling, 893
- Fresnel's relations, 586
- Friction, fluid, 396, 397
- Frictional heating considerations, 1256–1259
- Friction factor, 421–422, 428
 - in compact heat exchangers, 857
 - in heat pipes, 1200
 - turbulent flow, 432
- Friction loss:
 - longitudinal finned double-pipe heat exchangers, 864–865
 - in pipe flow, 31–33
- Friction velocity, 421
- Froude number, 679, 680, 741
- Full-spectrum correlated k distribution method (FSCK), 628
- Fully developed flow, 404–407, 442
 - laminar flow, 399–401
 - mean temperature, 404–405
 - thermally, 405–407
 - turbulent duct flow, 420–425
- Fully developed limit, 9
- Fully developed value, 9
- Fully rough limit, 422–423

- Fully stratified flow, 667, 684
 Fundamental equation, 46
 Fusion bonding, 1270–1271
- Gamma function, 168–169, 171
 Ganic—Rohsenow model, 697, 698
 Gap conductance:
 for joints between conforming rough surfaces, 355–359
 for large parallel isothermal plates, 353–355
 Gap resistance, 338–339
 Gardon gauge, 944
 Gas(es):
 additives for, 1033
 dilute, 58–61, 115–116
 evaporation of a liquid by a surrounding gas, 1371–1373
 gray, 627–628
 isobaric heat capacity for ideal, 55–57
 Gasketed plate heat exchanger, 878, 879
 Gas—liquid systems, 1385
 Gas-loaded heat pipes, 1187, 1188
 Gas management, noncondensable, 774–777
 Gas pressure, 328, 329
 Gas rarefaction parameter, 357
 Gas theory, standard kinetic, 115–116
 Gaussian error distribution, 921
 General curvilinear coordinate systems, 16
 General elastogap resistance model, 338
 Giant magnetoresistance (GMR), 1349
 Gibbs energy, 46, 112
 Glass thermometers, 931–933
 Global thermal resistance, 418
 GMR (giant magnetoresistance), 1349
 Gnielinski correlation, 676
 Gold, 126
 Gorenflo's correlation of fluid-specific correlation, 656–657
 Graetz number, 413
 Grashof number (Gr), 8, 694
 Gravity, standard acceleration of, 36
 Gravity-dominated correlations, 759–760
 Gravity-driven condensation, 751–756
 Gray, diffuse surfaces, 585
 Gray gases, 627–628
 Gray surfaces, 585–586, 610–612
 Greases, thermal, 374–376
 Greek letter subscripts, 41
 for condensation, 789
 for external flow forced convection, 522
 for thermal radiation, 631
 Greek letter symbols, 40
 for boiling, 712–713
 for condensation, 788–789
 for conduction heat transfer, 256–257
 for direct contact heat transfer, 1394–1395
 for electronic equipment, 1020
 for enhancement techniques, 1103–1104
 for experimental methods, 945
 for external flow forced convection, 520–521
 for forced convection internal flows, 435–436
 for heat exchangers, 902–903
 for heat pipes, 1226
 for manufacturing and materials processing, 1300
 for microscale heat transfer, 1354
 for natural convection, 567–568
 for porous media, 1175
 for thermal radiation, 630
 for thermal spreading and contact resistances, 382–383
 thermophysical properties, 142
 Gr (Grashof number), 8
 Grigorik film thinning effects, 708
 Grinding, 1250–1254
 Groeneveld—Delorme correlation, 696
 G-shell, TEMA, 813–814
 Guarded hot plate method, 122
 Gungor—Winterton correlation, 674–675, 680, 685
- Hagen—Poiseuille flow, 401, 403, 408–412, 428, 429
 Hagen—Rubens relation, 586, 588–589
 Hairpin loops, 857–858, 864–865
 Half-space, 270–272
 circular area on a, 274–277
 circular area on single layer (coating) on, 295–296
 isothermal elliptical source area on a, 277–280
 isotropic, 270–272
 circular source areas, 274–277
 dimensionless spreading resistance, 279–280

- flux distribution over isothermal elliptical area, 280
- isoflux circular source, 275–277
- isothermal circular source, 274–275
- isothermal elliptical source area, 277–280
- rectangle on, 309
- thermal spreading and contact resistances in, 274–280
- transient spreading resistance, 285–288
- rectangle on layer on, 309
- rectangular source on a, 308
- spreading resistance in, 291–293
- Hankel transform method, 297
- Healing, 1271, 1272, 1279–1280
- Heat capacity:
 - of coolant pool, 231
 - ideal gas isobaric, 55–57
 - microscale heat transfer, 1322–1326
 - regenerator heat exchangers, 886–891
 - transient conduction, 231
- Heat conduction, 2, 165
- Heat convection, 2
- Heat diffusion, bubble growth, 646–647
- Heat exchangers, 797–905
 - analysis methods, 805–822
 - $\varepsilon - N^{tu}$, 807–817
 - heat transfer and pressure loss, 821
 - logarithmic mean temperature difference correction factor method, 805–807
 - $P - N_{tu,c}$, 817–819
 - $\phi - P$, 819–822
 - compact, *see* Compact heat exchangers
 - definition of, 798
 - fouling, 893–896
 - governing relationships for, 799–805
 - exchanger surface area, 800–802
 - logarithmic mean temperature difference, 804–805
 - overall heat transfer coefficient, 802–804
 - longitudinal finned double-pipe, *see* Longitudinal finned double-pipe heat exchangers
 - nomenclature for, 896–905
 - plate and frame, *see* Plate and frame heat exchangers
 - plate fin, 843, 845
 - regenerators, *see* Regenerators
 - shell-and-tube, *see* Shell-and-tube heat exchangers
 - transverse high-fin, *see* Transverse high-fin heat exchangers
- Heatex wire matrix tube inserts, 1074
- Heat flow:
 - across solid interfaces, 970–979
 - effect of filler concentration on mechanical strength, 979
 - interstitial materials, 973–975
 - in printed circuit boards, 983, 986–988
 - thermal boundary resistance, 972–973
 - thermal conductivity of particle-laden systems, 975–979
 - thermal contact resistance, 970–972
- Heat flow meters, 943–944
- Heat flux, 164
 - arbitrarily varying, 480
 - critical, *see* Critical heat flux
 - longitudinal maldistribution of, 775–777
 - maximum, 1201
 - radiative, 581–582
 - semi-infinite solid model, 232–234
 - semi-infinite solid with periodic surface, 240
- Heat flux limit, 1194
- Heat flux transformer, 1185
- Heat pipes, 1181–1227
 - capillary action, 1191–1193
 - as capillary-driven two-phase system, 1182
 - capillary pumped loops, 1221–1225
 - classification of, 1184–1185, 1187–1191
 - cryogenic, 1184
 - effective length of, 1199
 - excess-liquid, 1187, 1189
 - figures of merit, 1211–1212
 - gas-loaded, 1187, 1188
 - high (liquid-metal)-temperature, 1185
 - liquid-modulated, 1189–1191
 - loop, 1221–1222
 - major components of, 1182
 - medium-temperature, 1184
 - micro/miniature, 1218–1219
 - nomenclature for, 1225–1227
 - operation of, 1182–1183
 - performance map for, 1194–1195
 - phase-change phenomena, 1006–1008

- Heat pipes (*continued*)
 pulsating, 1220–1221
 room (low)-temperature, 1184
 thermal resistance, 1209–1211
 transient operation of, *see* Transient operation, heat pipe
 transport limitations of, *see* Transport limitations, heat pipe
 vapor flow-modulated, 1189, 1190
 variable conductance, 1217–1218
 wick structures, 1185–1187
 working fluids, 1184
- Heat radiation, *see* Thermal radiation
- Heat-sink assisted cooling, 950
- Heat sinks:
 finned examples of, 1061
 jet impingement on, 1001–1002
 natural convection, 1002–1006
 pin fin, 498–500, 513
 plate fin, 496–497
- Heat sources:
 concentrated, 1143, 1154–1156
 discrete, *see* Discrete heat sources
 flush-mounted, 491–492, 512
 moving, *see* Moving heat sources
 rectangular, 308, 317–318
- Heat transfer, 2
 conduction, *see* Conduction heat transfer
 convective, *see* Convection
 in developing flow, 407–413
 dimensionless groups used in, 34
 direct contact, *see* Direct contact heat transfer
 enhancement techniques for, *see* Enhancement techniques
 finned surfaces, *see* Finned surfaces
 flow boiling, 693–694
 flow resistance, 11–12
 in fully developed flow, 404–407
 heat exchanger analysis methods, 821
 heat exchangers, *see* Heat exchangers
 in horizontal tubes, 749–761
 inclination effect on performance of, 782–783
 interface—contact resistance, 4–7
 internal flow forced convection, 404–413
 jet area/heater area ratio effect on, 998, 1000
 jet aspect ratio effect on, 998, 999
 lumped-capacity heating and cooling, 7
 microscale, *see* Microscale heat transfer
 phase-change, 11
 plate and frame heat exchangers, *see* Plate and frame heat exchangers
 post-dryout, 693–694
 radiative, *see* Thermal radiation
 smooth tube condensation, 749–761
 spreading resistance, 4, 5
 thermoplastic-matrix composites
 processing, 1273–1274
- Heat Transfer and Fluid Flow Services (HTFS), 774
- Heat transfer coefficient(s):
 adiabatic, 496
 annulus, 863
 overall, *see* Overall heat transfer coefficient
 regenerators, 893
 temperature-dependent, 231
- Heat transfer correlations, 874–875
- Heat transfer data:
 compact heat exchangers, 850–857
 shell-and-tube heat exchangers, 829–836
- Heat Transfer Research, Inc. (HTRI) code, 774
- Heat transfer to moving materials undergoing thermal processing, 1234–1245
- Heat treatment (of solids), 1245–1246
- Heavier component, 699
- Heavy water (deuterium oxide), 76–77
- Heisler charts, 236
- Helium, 77, 359–360, 362
- Helmholtz energy, 46, 48, 111–113
- Helmholtz instability, 658
- Hemispherical droplets, 219–221
- Hemispherical emittances, 584
- Hemispherical properties, 587–588
- Heptane, 68–69
- Herringbone corrugation, 880, 881
- Herringbone microfin tubes, 1069
- Hertz contract parameters, 321
- Hertz distributed-load model, 318, 319
- Hertz elastic parameters, 320
- Heterogeneous nucleation, 640
- Hexane, 67–68
- High-fin tubes, 868–869
- High (liquid-metal)-temperature heat pipes, 1185

- High-Rayleigh-number regime, 1154, 1156
High Reynolds number flow over a wedge, 446–452
HITEMP database, 616, 629
HITRAN database, 616
Holdup, 1361, 1376, 1377, 1379
Hollow cylinders:
 composite, 185–186
 infinitely long semi-infinite, 242–243
 radial and axial conduction in, 217–218
 steady one-dimensional conduction in, 180–181, 190–191, 195, 197
Hollow spheres:
 composite, 186–187
 steady one-dimensional conduction in, 181–182, 186–187, 192–193, 197–198
 temperature-dependent thermal conductivity, 197–198
Homogeneous nucleation, 640
Horizontal cylinders, 543–545, 1154
Horizontal finned tubes, 727–732
Horizontal flat surfaces:
 natural convection in, 562–563
 natural convection in laminar flow over, 539–543
Horizontal surfaces, 959, 960
Horizontal tubes:
 flow boiling in, 664–666, 679–686
 correlations based on vertical tube methods, 679–680
 model based on local flow regime, 680–686
 subcooled boiling heat transfer, 686
 flow regimes in smooth, 736–749
 comparison of maps, 742–749
 effects of fluid properties and tube diameter, 738
 effects of mass flux and quality, 737–738
 mapping, 739–742
 potential role of surface tension, 739
 two-phase flow, 736–737
 heat transfer in smooth, 749–761
 annular flow correlations, 760–761
 correlation comparisons, 759–761
 effects of fluid properties, 750
 effects of mass flux and quality, 749–750
 effects of temperature difference, 750–751
 effects of tube diameter, 750
 gravity-dominated correlations, 759–760
 gravity-driven condensation, 751–756
 shear-driven annular flow condensation, 756–759
Horizontal walls, 1153–1154
Hot plate method, guarded, 122
Hot-side convective layer resistance, 802–804
Hot-side fouling resistance, 802, 803
Hot wire method, 122
Hot working, 1254
HTFS (Heat Transfer and Fluid Flow Services), 774
HTRI (Heat Transfer Research, Inc.) code, 774
Hybrid analytic—numeric methodology, 254
Hydraulically developing flow, 412–413
Hydraulic diameter, 9–10, 401–404
Hydraulic radius and diameter, 428
Hydrocarbon graphs, 154–155
Hydrodynamic entrance length, 396
Hydrodynamic stability, 557
Hydrogen, 78
Hydrogen sulfide, 78–79
Hydrostatic pressure, 1267
Hyperbolic fins, 208, 209
Hyperellipse, isoflux, 286–287
Hysteresis, 914, 915

IB (incipience of boiling), 638
ICs (integrated circuits), 950
Ideal gas isobaric heat capacity, 55–57
Idealized enclosures, 599
I (in-line) arrangements, 846
Immersion cooling, 1008–1016
Impingement on heat sinks, 1001–1002
Impingement zone, 503
Impurities, 122
Incident radiation, 626
Incipience of boiling (IB), 638
Incipient overshoot, 1011
Inclination:
 of flat surfaces
 natural convection in, 562–563
 natural convection in laminar flow over, 539–543

- heat transfer performance affected by, 782–783
- Inclination (*continued*)
 - pressure drop affected by, 783
 - of tubes, 763
- Incomplete beta function, 172
- Incomplete gamma function, 169, 171
- Incompressible flow past flat plate, 461–463
- Indentation diagonal, 343
- Indirect contact heat exchangers, 798
- Indirect contact heat transfer, 1359–1360
- Indirect extrusion diagram, 1255
- Induced draft, 871
- Ineffectiveness (term), 892
- Inertia, bubble growth, 646, 650
- Infinitely long semi-infinite hollow cylinder, 242–243
- Initial conditions (for conduction heat transfer), 165–167
- Injection, 1033
- In-line (I) arrangements, 846
- Inner-finned tubes, 1062
- Insulation, critical thickness of, 188
- Integral solutions for flat plate boundary layer, 463–466
- Integrated circuits (ICs), 950
- Intensification, 1030
- Interface—contact resistance, 4–7
- Interface location parameter, 245, 249
- Interfaces, *see* Joints
- Interference fit, 870
- Interlaminar bonding, 1277–1280
- Interlaminar corrugation, 880, 881
- Intermediate period (chip package temporal behavior), 981, 984
- Intermittent flow, 664–668, 684, 745
- Intermittent flow regime, 753
- Internal convection, 705
- Internal convective boiling, 706–708, 1361–1362
- Internal energy, 46, 112
- Internal energy generation, 230
- Internal flow convection, *see* Forced convection (internal flows)
- Internal flow (definition), 395
- Internal motions (superscript “int”), 115
- Internal natural convection, 529, 551–556
 - in non-rectangular enclosure configurations, 554–556
 - porous media, *see* Porous media
 - in rectangular enclosures, 551–554

- Internal resistance, 963
- International Temperature Scale of 1990 (ITS-90), 916, 917
- Interstitial materials, 973–975
- Intimate contact process, 1271–1273, 1277–1280
- Intralaminar void reduction, 1273
- Intralamination void growth, 1273
- In-tube condensers, 779–780
- In-tube EHD condensation, 733–735
- Inverse heat conduction, 254
- Inverted annular flow heat transfer, 693–695
- Inward cylindrical freezing, 251–252
- Iron, 126
- Irradiation, 600
- Isobaric heat capacity, 112
- Isobutane (2-methylpropane, R-600a), 65
- Isochoric heat capacity, 112
- Isoflux area, 308
- Isoflux circular annulus, 283
- Isoflux circular area, 285–286
- Isoflux circular contact, 296–297
- Isoflux circular source, 275–277, 300
- Isoflux contact area, 297
- Isoflux flat plates, 959, 960
- Isoflux hyperellipse, 286–287
- Isoflux plates, 990
- Isoflux rectangular area, 280
- Isoflux regular polygonal area, 281–282
- Isoflux regular polygons, 287–288
- Isoflux surfaces, 959, 960
- Isolated blocks, 493–495, 512–513
- Isolated plate limit, 9
- Isopentane (2-methylbutane), 66–67
- Isothermal circular annulus, 283–284
- Isothermal circular contact, 295–296
- Isothermal circular source, 274–275
- Isothermal contact area, 297–298
- Isothermal elliptical source area, 277–280
- Isothermal flat plate:
 - forced convection on an, 959, 960
 - with turbulent boundary layer, 510
 - with turbulent boundary layer transition from laminar to turbulent, 510
 - in uniform laminar flow, 508–509
- Isothermal horizontal surfaces, 959, 960
- Isothermal plates, 990
- Isothermal rectangular area, 281
- Isothermal rough flat plates, 510–511
- Isothermal sphere, 483
- Isothermal target surfaces:
 - array of round submerged jets impinging on, 514
 - array of submerged slot jets impinging on, 515
 - single round free surface jet impinging on square, 515
 - single round submerged jet impinging on, 513–514
 - single submerged slot jet impinging on, 514
- Isothermal vertical surfaces, 959, 960
- Isothermal walls, 426, 433
- Isotropic circular flux tubes, 298–302
- Isotropic finite disks with conductance:
 - circular area on single layer (coating) on half-space, 295–296
 - correlation equations, 294–295
 - equivalent isothermal contact area, 297–298
 - isoflux circular contact, 296–297
 - isoflux contact area, 297
 - isothermal contact area, 298
 - spreading resistance in, 291–294
 - thermal spreading and contact resistances, 294–298
- Isotropic flux tubes, 313
- Isotropic half-space, 270–272
 - circular source areas, 274–277
 - isoflux circular source, 275–277
 - isothermal circular source, 274–275
 - isothermal elliptical area, 279–280
 - isothermal elliptical source, 277–280
 - thermal spreading and contact resistances in, 274–280
 - transient spreading resistance, 285–288
- Isotropic materials, 164
- Isotropic semi-infinite two-dimensional channel, 313–314
- ITS-90, *see* International Temperature Scale of 1990
- Jakob numbers, 647, 1363–1364
- Jaster—Kosky correlation, 759–760
- Jets:
 - average Nusselt number for array of, 504–506

- average Nusselt number for single, 503–504
- condensation on liquid, 1367
- free surface, 506–508
- submerged, 502–508
- turbulent, 500–508
- Jet area/heater area ratio, 998, 1000
- Jet impingement, 1099
 - enhancement techniques, 1034
 - thermal transport in, 500–502
- Jet impingement cooling:
 - correlation, 996–998
 - in electronic equipment, 995–1002
 - figures of merit, 999, 1000
 - first-order trends, 998–1000
 - impingement on heat sinks, 1001–1002
 - thermal—fluid design general considerations, 1000–1001
- Jet in steam flow, 1371
- Jet in vessel, 1371
- Joints, 264
 - bolted, 378
 - characteristics of real, 269
 - parameters influencing resistance of, 269–270
 - types of, 264–266
- Joint conductance:
 - dimensionless contact pressure vs. dimensionless, 374
 - effect of layer thickness and contact pressure on, 368–371
 - enhancement methods for, 361–377
 - elastomeric inserts, 372–374
 - metallic coatings and foils, 363–372
 - phase-change materials, 377
 - thermal greases and pastes, 374–376
 - for joints between conforming rough surfaces, 359–361
- Joint resistances. *See also* Thermal spreading and contact resistances
 - at line contact, 339
 - of nonconforming rough surfaces, 339–340
- Joule (J), 36
- J-shell, TEMA, 814, 817
- Kalman—Bucy filter, 1291–1292
- Kármán—Nikuradse relation, 421
- Kattan—Thome—Favrat flow pattern map, 666, 667, 670
- Kattan—Thome—Favrat model, 683–686, 703
- Kedzierski—Goncalves model, 765, 766–767
- Kedzierski—Kim correlation, 768–769
- Kedzierski—Webb (K-W) profiles, 727, 784–785
- Kei (x), 176–177
- Kelvin temperature scale, 916, 917
- Ker (x), 176–177
- Kinetic gas theory, 115–116
- Kinetics model, 1262–1266
- Kirchhoff's law, 575
- Kirchhoff transformation, 196, 197
- Kline-McClintock model, 930
- Kozeny flow model, 1135
- Krypton, 79–80
- Kumar's constants, 885
- Kutateladze correlation, 668
- K-W profiles, *see* Kedzierski—Webb profiles
- Lambert surfaces, 583
- Laminar boundary layer flow, 452–455
- Laminar cross flow, 509
- Laminar flow:
 - forced convection (internal flows), 396–404
 - flow entrance region, 396–399
 - fully developed flow region, 399–401
 - hydraulic diameter and pressure drop, 401–404
 - optimal channel sizes for, 413–419 and pressure drop, 396–404
 - isothermal flat plate in uniform, 508–509
 - natural convection
 - external, 543–551
 - over flat surfaces, 533–543
 - over horizontal cylinder and sphere, 543–545
 - over inclined and horizontal surfaces, 539–543
 - over vertical cylinder, 545–546
 - over vertical surfaces, 533–540
 - in plumes/wakes/other free boundary flows, 548–551
 - transient, 546–548
 - optimal channel sizes, 430

- with parallel plates, 430
- in shell-and-tube heat exchangers, 832–830
- swirl flow devices, 1079
- transition from, to turbulent flow, 557
- uniform, 510
- Laminar flow entrance length, 427
- Laminar force convection, 959, 960
- Laminar fully developed flow, 428
- Laminar thermal entrance length, 429
- Laminate consolidation model, 1266–1269
- Large-scale integration (LSI) chips, 949
- Lasers, 1340, 1344–1345
- Lattice(s):
 - Bravais, 1312–1314, 1318–1320
 - reciprocal, 1314
- Lattice thermal conductivity, 1328–1330
- Layers, surface, 594–595
- Layer thickness, 368, 370
- Lead, 127, 370, 371, 1320–1321
- Leading edge, 449
- Least squares, 1297
- Legendre functions, 177–179
- Length-scale effects on thermophysical properties, 964–988
 - first-order transient effects, 979–985
 - heat flow across solid interfaces, 970–979
 - heat flow in printed circuit boards, 983, 986–988
 - spreading resistance, 966–970
- Lennard-Jones fluid, 116
- Less volatile component, 699
- Levels, packaging, 953–955
- Lewis—Nielsen model, 975, 977, 978
- Lewis numbers, 1172
- LHPs, *see* Loop heat pipes
- Life-cycle costs, 953
- Light, speed of, 574–575
- Lighter component, 699
- Linear quadratic Gaussian formulation, 1290–1292
- Linear quadratic regulators (LQRs), 1291
- Linear time invariant (LTI) thermal process, 1295
- Line contact models, 336–340
- Liner metal resistance, 877
- Liquids:
 - additives for, 1033, 1092–1097
 - condensation in, 1367–1371
 - evaporation of a, by a surrounding vapor or gas, 1371–1373
 - radiative properties of, 582–598
- Liquid composite molding process, 1260, 1261
- Liquid crystals, 942–943
- Liquid-deficient regime, 689
- Liquid droplets, 1366–1367
- Liquid film, 689
- Liquid Froude number, 679, 680
- Liquid jets, 1367
- Liquid—liquid systems, 1385
- Liquid-metal heat pipes, 1185
- Liquid-modulated heat pipes, 1189–1191
- Liquid-saturated wicks:
 - effective thermal conductivity for, 1202
 - transient operation of heat pipes, 1212–1213
- Lithium, 127
- LMTD method, *see* Logarithmic mean temperature difference correction factor method
- LOCA, *see* Loss-of-coolant accidents
- Local flow regime model, 680–686
- Local gap thickness, 322–323, 336, 337
- Local pore Reynolds number, 1136
- Local skin-friction coefficient, 397–399
- Location-dependent energy generation, 198–199
- Location-dependent thermal conductivity, 194–195
- Logarithmic mean temperature difference, 804–805
- Logarithmic mean temperature difference (LMTD) correction factor method, 805–807, 819, 821–822
- Longitudinal convecting fans, 202–207
- Longitudinal convecting—radiating fins, 212
- Longitudinal finned double-pipe heat exchangers, 857–868
 - components of, 857–859
 - multiple finned double-pipe, 868
 - and overall heat transfer coefficient, 861–864
 - physical data for annuli, 860–861
 - plain double-pipe exchangers vs., 857–859
 - pressure loss in pipes and annuli, 864–865
 - series—parallel arrangements, 865–868
 - uses of, 858

- wall temperature, 865
- Longitudinal heat flux maldistribution, 775–777
- Longitudinal radiating fins, 211–212
- Looped flow arrangement, 881
- Loop heat pipes (LHPs), 1221–1222
- Loss-of-coolant accidents (LOCA), 1369–1371
- Louvered fins, 846, 849, 852, 1060
- Low-finned tube, 706
- Low-fins, 723–727
- Low-Rayleigh-number regime, 1154–1156
- Low-temperature heat pipes, 1184
- LQRs (linear quadratic regulators), 1291
- LSI (large-scale integration) chips, 949
- LTI (linear time invariant) thermal process, 1295
- Lubricating film, 1258–1259
- Luminous, 619
- Lumped-capacity heating and cooling, 7, 239
- Lumped-capacity model for transient heating, 7, 229–231
- Lumped-capacity solution, 980
- Lumped heat capacity, 980–981
- Lungstrom air preheaters, 886, 887
- McAdams turbulent flow correlation, 697
- Machining processes:
 - grinding, 1250–1254
 - metal cutting, 1246–1250
- Mach number, 1207
- Macrocontacts, 264
- Macrocontacts, 265
- Macrohardness, 343–344
- Macroscopic flow model, 1274–1276
- Magnesium, 127
- Magnetic fields, 1098–1099
- Mainframe computers, 949
- Mandhane Map, 740, 742–744
- Manganese, 127
- Mangler transformation, 469
- Manglik—Bergles correlation, 767–768
- Manufacturing and materials processing (MMP), 1231–1301
 - heat transfer to moving materials undergoing thermal processing, 1234–1245
 - interaction between discrete heat source and continuously moving workpiece, 1241–1245
 - in uniform thermal environment, 1234–1241

Manufacturing and materials processing
(continued)

- heat treatment of solids, 1245–1246
- machining processes
 - grinding, 1250–1254
 - metal cutting, 1246–1250
- nomenclature for, 1297–1301
- polymer-matrix composite materials, 1259–1283
 - thermoplastic-matrix composites, 1269–1283
 - thermosetting-matrix composites, 1259–1269
- thermal-fluid effects in continuous metal forming processes, 1254–1259
- thermal process control for manufacturing, 1284–1297
 - adaptive control, 1294–1296
 - MIMO thermal systems, 1288–1290
 - optimal formulation: linear quadratic Gaussian, 1290–1292
 - parameter identification, 1296–1297
 - SISO thermal systems, 1285–1288
 - sliding mode control, 1293–1294
 - Smith prediction, 1292–1293
- thermoplastic-matrix composites
 - processing, 1269–1283
 - fabrication of composites, 1270–1271
 - heat transfer, 1273–1274
 - interlaminar bonding, 1277–1280
 - polymer degradation, 1280–1281
 - solidification (crystallization), 1281–1283
 - stages of, 1269–1270
 - transport mechanisms involved in, 1271–1273
 - void dynamics, 1274–1277
- thermosetting-matrix composites
 - processing
 - kinetics model, 1262–1266
 - laminate consolidation model, 1266–1269
 - thermal model, 1261–1262
 - unique features of, 1234
- Maple V*, 254
- Mapping (of smooth horizontal tube flow regimes), 739–742
 - Mandhane Map, 740, 742–744
 - Soliman Transitions, 741–742, 746–749
 - Taitel—Dukler Map, 740–741, 744–746
- Martin correlation, 996–997
- Mass conservation, 1133–1135
- Mass flux and quality, 737–738, 749–750
- Mass transfer, 34
- Mathematica*, 255
- Matrix phase, 1259
- Matrix surfaces, 847
- Matthiessen's rule, 1326
- Maximum heat flux, 1201
- Maximum packing fraction, 977
- Maxwell—Cattaneo equation, 120
- Maxwell criterion, 47
- Mean, 920
- Mean beam length method, 623, 624
- Mean free path, 325, 964–965
- Mean temperature, 404–405
- Mean temperature difference, logarithmic, 804–805
- Measurement:
 - of chip temperature, 1018
 - experimental methods for, 913–914
 - of thermophysical properties of solids, 122, 140
- Measurement error, experimental methods for, 918–926
 - bias error, 919, 920
 - Chauvenet's criterion, 923–924
 - chi-square test, 924–926
 - error distribution, 921–923
 - mean and deviation, 920
 - precision error, 919–920
 - uncertainty, 918–920
- Mechanical aids, 1033
- Mechanical contact model, 344, 363–365
- Mechanical strength, 979
- Medium-temperature heat pipes, 1184
- Melting:
 - conduction-controlled, *see* Conduction-controlled freezing and melting
 - multidimensional, 254
 - spray column applications, 1384–1387
- Memory devices, 950
- MEMS (microelectromechanical systems), 1310
- Mercury-filled thermometers, 931–933
- Metals:
 - electron thermal conductivity in, 1326–1328

- radiative properties of, 586–589
 - directional dependence, 586–587
 - hemispherical properties, 587–588
 - surface temperature effects, 588–589
 - total properties, 588
 - wavelength dependence, 586
- thermal conductivity for metallic elements, 121
- thermal radiation, 586–589
- Metal cutting, 1246–1250
- Metal forming processes, 1254–1259
- Metallic alloys, 132–133
- Metallic coatings and foils, 363–372
- Metal-oxide semiconductor field-effect transistors (MOSFETs), 1347
- Methane, 62
- Methane-based refrigerant graphs, 156–157
- Methanol, 80
- MFB (minimum film boiling) point, 638
- Microcontacts, 266
- Microelectromechanical systems (MEMs), 1310
- Microelectronics applications (of microscale heat transfer), 1347–1349
- Microfin tubes, 706–708, 764–767
- Microgaps, 266
- Microhardness layer, 343–346
- Micro heat pipes, 1218–1219
- Microlayer evaporation, 653
- Microscale heat conduction, 254
- Microscale heat transfer, 1309–1354
 - applications, 1347–1351
 - microelectronics, 1347–1349
 - multilayer thin-film structures, 1349–1351
 - definition of, 1310
 - electron scattering mechanisms, 1310–1311
 - methodology of, 1310
 - microscopic description of solids, 1312–1330
 - crystalline structure, 1312–1314
 - energy carriers, 1314
 - free electron gas, 1314–1317
 - heat capacity, 1322–1326
 - thermal conductivity, 1326–1330
 - vibrational modes of a crystal, 1317–1322
 - modeling methods, 1331–1339
 - Boltzmann transport equation, 1333–1338
 - continuum models, 1331–1333
 - molecular approach, 1338–1339
 - monitoring techniques, 1339–1347
 - scanning thermal microscopy, 1340–1342
 - 3w technique, 1342–1344
 - transient thermorefectance, 1344–1347
 - nomenclature for, 1352–1354
- Microscopic flow model, 1274, 1276–1277
- MIMO thermal systems, *see* Multiple-input multiple-output thermal systems
- Miniature heat pipes, 1218–1219
- Minimum film boiling (MFB) point, 638
- Mirage techniques, 1339
- Mist flow, 663–665, 667
- Mist flow heat transfer, 689, 695–699
- Mixed boundary conditions, 476
- Mixtures:
 - boiling of, 699–704
 - evaporation of refrigerant—oil mixtures, 702–704
 - flow boiling, 701–702
 - nucleate boiling, 700–701
 - vapor-liquid equilibria and properties, 699–700
 - flow boiling of, 701–702
 - rule of, 1273
 - thermodynamic properties of, 113–114
 - transport properties of, 117–118
- MMP, *see* Manufacturing and materials processing
- Model(s):
 - acoustic mismatch, 972
 - algebraic turbulence, 472
 - Andreani—Yadigaroglu, 698–699
 - Antonetti—Yovanovich thermomechanical, 366
 - Brinkman flow, 1137
 - Carman—Kozeny flow, 1136
 - Chen—Engel, 331, 332
 - for conforming rough surfaces, 340–342
 - of corresponding states, 116–117
 - Darcy flow, 1135–1137
 - Debye, 1323–1325
 - diffuse mismatch, 972
 - Dupuit—Forchheimer flow, 1138
 - Einstein, 1324–1326

- Model(s) (*continued*)
 elastic contact, 349–351
 elastic—plastic contact conductance, 351–353
 elastogap resistance, 324–326
 Eulerian—Lagrangian, 699
 finite-sized solid, 235–236
 first-order closure, 471
 flow, 1135–1138
 Forchheimer flow, 1137
 Ganic—Rohsenow, 697, 698
 general elastogap resistance, 338
 Hertz distributed-load, 318, 319
 Kattan—Thome—Favrat, 683–686, 703
 Kedzierski—Goncalves, 765–767
 kinetics, 1262–1266
 Kline-McClintock, 930
 Kozeny flow, 1135
 laminate consolidation, 1266–1269
 Lewis—Nielsen, 975, 977, 978
 line contact, 336–340
 local flow regime, 680–686
 lumped-capacity, 7, 229–231
 macroscopic flow, 1274–1276
 mechanical contact, 344, 363–365
 microscopic flow, 1274, 1276–1277
 Nielsen, 977, 978
 for nonconforming smooth solids, 318–319
 parabolic two-step, 1346
 percolation, 977, 978
 plastic contact, 342–347
 Plesset—Zwick bubble growth, 647–648, 650, 651
 point contact, 319–322
 Rosson—Myers, 754, 760
 Rouhani—Axelsson drift flux type of void fraction, 682
 semi-infinite solid, 232–234
 spreading—constriction resistance, 323–324
 steady-state metal cutting temperature, 1249–1250
 thermal, 264, 366–371, 1261–1262
 thermally decoupled, 325
 thermomechanical, 366
 thin solid, 1235–1239
 three-layer, 476–479
 Tien, 754
 Vafai and Tien flow, 1137–1138
 Van Stralen bubble growth, 648
 Zero-equation, 471
Modeling methods, microscale heat transfer, 1331–1339
 Boltzmann transport equation, 1333–1338
 continuum models, 1331–1333
 molecular approach, 1338–1339
Model reference adaptive control (MRAC), 1294–1295
Modified Bessel functions, 174, 175
Modified Gaussian bell-shaped terms, 112
Molecular approach (to microscale heat transfer), 1338–1339
Molecular gases:
 particulates and mixtures of, 621
 radiative properties of, 615–619
 thermal radiation, 615–619
Molecular weight, 48, 52–54
Momentum, 19–23
Momentum theorem, 19, 21–23
Monitoring techniques, microscale heat transfer, 1339–1347
 scanning thermal microscopy, 1340–1342
 3ω technique, 1342–1344
 transient thermorefectance, 1344–1347
Monte Carlo methods:
 for microscale heat transfer, 1338–1339
 thermal radiation, 627
 for view factors, 600
Moody charts, 421, 422, 836, 837
Moore's law, 948
More volatile component, 699
MOSFETs (metal-oxide semiconductor field-effect transistors), 1347
Mostinski correlation of reduced pressure, 655
Moving heat sources:
 finite size, 1243–1245
 line, 1242–1243
 planar, 1241–1242
 point, 1243
Moving workpieces:
 heat transfer to, undergoing thermal processing, 1234–1245
 interaction between discrete heat source and continuously, 1241–1245
 in uniform thermal environment, 1234–1241

- MRAC, *see* Model reference adaptive control
- Mueller charts, 820–821
- Muff-type high-fin tubes, 869, 876–878
- Multidimensional freezing (melting), 254
- Multidimensional transient conduction, 236
- Multilayer thin-film structures, 1349–1351
- Multiple finned longitudinal double-pipe heat exchangers, 868
- Multiple-input multiple-output (MIMO) thermal systems, 1284, 1288–1290
- Multiple rectangular heat sources on isotropic plate, 317–318
- Nanometer-scale thermocouples, 1339–1341
- NASA Lewis Research Center, 1224
- National Electronics Manufacturing Institute (NEMI), 949
- National Institute of Standards and Technology (NIST), 45, 113, 122, 916
- National Science Foundation (NSF), 1233
- Natural convection, 8–9, 525–568
 - on an isothermal horizontal surface, 959, 960
 - from an isothermal vertical surface, 959, 960
 - boiling curve, 637
 - common approximations, 531–532
 - dimensionless parameters, 532–533
 - empirical correlations, 560–566
 - cylinders and spheres, 563–565
 - enclosures, 565–566
 - inclined and horizontal flat surfaces, 562–563
 - vertical flat surfaces, 561–562
 - external, *see* External natural convection
 - external laminar flow, 543–551
 - over horizontal cylinder and sphere, 543–545
 - over vertical cylinder, 545–546
 - in plumes/wakes/other free boundary flows, 548–551
 - transient, 546–548
 - forced convection vs., 526
 - governing equations, 529–530
 - internal, 551–556
 - cylindrical and spherical enclosures, 1162–1164
 - enclosures heated from below, 1164–1169
 - enclosures heated from the side, 1156–1162
 - in non-rectangular enclosure configurations, 554–556
 - penetrative convection, 1169–1170
 - porous media, 1156–1170
 - rectangular enclosures, 551–554
 - laminar flow over flat surfaces, 533–543
 - inclined and horizontal surfaces, 539–543
 - vertical surfaces, 533–540
 - nomenclature for, 566–568
 - physical nature of, 526–529
 - printed circuit boards in, 988–991
 - turbulent flow, 557–560
 - from a vertical isoflux surface, 959, 960
- Natural convection cooling, 950
- Natural convection heat sinks, 1002–1006
- Navier—Stokes equations, 21–23
- Near-field optical thermometry, 1340
- Near-wall region in turbulent flow, 472–475
- NEMI (National Electronics Manufacturing Institute), 949
- Neon (R-720), 80–81
- Network analogy, 612
- Neumann problem:
 - one-region, 243–245, 250
 - two-region, 245–247
- Newton (N), 35
- Newton—Raphson method, 331, 332
- Newton's law of cooling, 183, 957
- Nickel, 128, 361, 362, 365, 367, 369
- Nielsen model, 977, 978
- NIST, *see* National Institute of Standards and Technology
- Nitrogen, 81–82, 359–360, 362
- Nitrogen trifluoride, 82
- Nodes, 223, 226
- Nomenclature, 38–41
 - for boiling, 708–713
 - for condensation, 785–789
 - for conduction heat transfer, 255–257
 - for direct contact heat transfer, 1393–1395
 - for electronic equipment, 1018–1022
 - for enhancement techniques, 1101–1104
 - for experimental methods, 944–945

for external flow forced convection,
515–522
Greek letter subscripts, 41

Nomenclature (*continued*)

Greek letter symbols, 40
for heat exchangers, 896–905
for heat pipes, 1225–1227
for internal flow forced convection,
434–436
for manufacturing and materials
processing, 1297–1301
for microscale heat transfer, 1352–1354
for natural convection, 566–568
for porous media, 1173–1176
Roman letter subscripts, 40–41
Roman letter symbols, 38–40
superscripts, 41
for thermal radiation, 629–631
for thermal spreading and contact
resistances, 378–385
for thermophysical properties, 141–142
Noncondensable gas management, 774–777
Nonconductors:
radiative properties of, 589–593
directional dependence, 591, 593
temperature dependence, 592, 593
wavelength dependence, 589–592
semitransparent sheets, 596
surface conditions' effects on, 593–595
surface layers and oxide films, 594–595
surface roughness, 593–594
thermal radiation, 589–593
Nonconforming joints, 264–265
Nonconforming smooth solids, 267–268
ball-bearing resistance, 336
contact resistance of isothermal elliptical
contact areas, 323–324
elastic—plastic contacts of hemispheres
and flat surfaces in vacuum, 333–335
elastogap resistance model, 324–326
line contact models, 336–340
local gap thickness, 322–323
models for, 318–319
point contact model, 319–322
radiative resistance, 326–327
sphere and layered substrate, 329–333
sphere—flat contact, 327–329
thermal spreading and contact resistances,
318–340
Non-contact sensing devices, 914–916
Nonequilibrium heating, 1346
Nongray surfaces, 614–615

- Nonmetallic solids, 134–139
- Nonparticipating media, 598–599
- Non-rectangular enclosure configurations, 554–556
- Nonsimilar flows:
 - axisymmetric, 469
 - two-dimensional, 466
- Normal error distribution, 921
- Normal process (of phonon—phonon collisions), 1328, 1329
- Notched fins, 1073
- Notebook computers, 952
- NSF (National Science Foundation), 1233
- NTUs (number of transfer units), 1375
- Nuclear energy generation, 188, 358, 1169
 - direct contact boiling phenomena for, 1379
 - loss-of-coolant accidents, 1369–1371
- Nucleate boiling, 639, 700–701
- Nucleate boiling curve, 6371010
- Nucleate boiling heat transfer, 707
 - bubble agitation, 653
 - evaporation, 653
 - pool boiling, 652–653
 - vapor—liquid exchange, 653
- Nucleate flow boiling coefficients, standard, 677, 678
- Nucleate pool boiling, 704–706
 - correlations, 653–657
 - bubble agitation correlation of Rohsenow, 653–654
 - fluid-specific correlation of Gorenflo, 656–657
 - physical property type of correlation of Stephan and Abdelsalam, 655
 - reduced pressure correlation of Cooper with surface roughness, 655–656
 - reduced pressure correlation of Mostinski, 655
 - departure from, 658–660
 - enhancement of, 704–706
- Nucleation, boiling, 640–646
 - nucleation superheat, 640–644
 - site density, 645–646
 - size range of active nucleation sites, 644–645
- Nucleation sites, 638, 644–645
- Nucleation superheat:
 - boiling, 640–644
 - nucleate pool boiling enhancement, 705
- Null point, 914
- Number of transfer units (NTUs), 1375
- Numerical computer programs, 772–774
- Nusselt number (Nu), 8–10, 429, 528
 - average, for array of jets, 504–506
 - average, for single jets, 503–504
 - for developing laminar flow in isoflux channels, 993
 - for fully developed laminar flow in channels, 994
 - gravity-driven condensation, 751–755
 - in Hagen-Poiseuille flow, 408–412
 - for heat transfer to laminar flow through ducts, 404
 - high-fin tubes, 874–875
 - horizontal tube heat transfer, 749
 - inclined and vertical tubes, 763
 - for internally finned tubes, 1062–1063
 - microfin enhanced in-tube condensation, 765–766
 - mist flow heat transfer, 698
 - plate and frame heat exchangers, 884–885
 - porous materials, 1141–1144, 1148, 1150–1154, 1159–1164, 1166–1168
 - for swirl flows, 1079, 1081
 - twisted-tape inserts, 768–769
- Nusselt's analysis of vertical flat plate condensation, 721–723
- Oberbeck—Boussinesq approximation, 1147–1148
- Objectives, enhancement performance, 1035
- Octane, 69
- Offset fins, 846
- Offset strips, 487–490, 511–512
- Ohm's law, 182
- Oil, 762
- Oil—refrigerant mixtures, 702–704
- ONB, *see* Onset of nucleate boiling
- 1–4 shell-and-tube exchanger, 812–813
- One-region Neumann problem, 243–245, 250–253
- 1/1 arrangement, 881
- 1–2 divided-flow shell-and-tube exchanger, 814, 817
- 1–2 shell-and-tube exchanger, 811–812, 820, 821
- 1–2 split-flow shell-and-tube exchanger, 813–814

- On—off control, 1285–1286
- Onset of nucleate boiling (ONB), 638, 639, 1093
- Opaque surfaces, 575, 577, 579–586
- Open rectangular grooves wicks, 1198
- Operating constraints and conditions, 1035–1037
- Optical branch (of the dispersion relation), 1320
- Optically smooth surfaces, 593
- Optically thick medium, 623, 625
- Optimum spacing (packaging), 991–992
- Orthogonal cutting, 1246–1248
- Orthogonal projection, 1296
- Outer region, 474
- Outward cylindrical freezing, 250–251
- Outward spherical freezing, 252–253
- Oval-tube louvered fins, 1060
- Overall heat transfer coefficient, 799–800
 - heat exchangers, 802–804
 - and longitudinal finned double-pipe heat exchangers, 861–864
 - transverse high-fin heat exchangers, 876–878
- Oxide films, 594–595
- Oxygen (R-732), 83
- Packaging:
 - convective phenomena in, 988–995
 - optimum spacing, 991–992
 - printed circuit boards in forced convection, 992–995
 - printed circuit boards in natural convection, 988–991
 - resistance and, 962–964
- Packaging levels (for electronic equipment), 953–955
- Packed columns, 1389–1392
- Packed sphere wicks, 1198
- Packings, 1373, 1389–1392
- Parabolic flux distribution, 300
- Parabolic two-step (PTS) model, 1346
- Paraffin, 378
- Parahydrogen, 83–84
- Parallel arrangements (double-pipe exchangers), 865–868
- Parallel flow exchangers, 805
- Parallel plates:
 - heat transfer from, 485–486
- Parallel plates (*continued*)
 - with isothermal surfaces, 429
 - with uniform heat flux, 430
- Parameter identification, manufacturing
 - thermal process control, 1296–1297
- Partially confined flow, 502
- Particle clouds:
 - radiative properties of, 619–621
 - thermal radiation, 619–621
- Particle-laden systems, 975–979
- Particulates, 621
- Particulate fouling, 893
- Pascal (Pa), 35
- Passive enhancement techniques, 1031–1033
- Pastes, thermal, 374–376
- Pauli exclusion principle, 1315
- PCBs, *see* Printed circuit boards
- PCM (phase-change materials), 377
- PDAs (personal digital assistants), 950
- Peak heat flux, 638
- Peaks, 187
- PEC, *see* Performance evaluation criteria
- Péclet number, 1141
 - moving materials in uniform thermal environment, 1238–1241
 - porous materials, 1171
 - travel, 1367
- PEEK thermoplastic prepregs, *see* Poly-ether-ether-ketone thermoplastic prepregs
- Peltier effect, 933–935, 1337
- Penetrative convection, 1169–1170
- Penetrative flows, 1169
- Pentane, 65–66
- Percolation model, 977, 978
- Perfect absorbers, 575
- Perfluorobutane (decafluorobutane), 84–85
- Perfluoropentane (dodecafluoropentane), 85
- Perfluoropropane (octafluoropropane, R-218), 85–86
- Perforated fins, 846
- Performance evaluation criteria (PEC), 1034–1043
- Performance objectives, enhancement, 1035
- Periodic conduction, 239–243
 - cooling of a lumped system in an oscillating temperature environment, 239

- finite plane wall with periodic surface temperature, 241–242
- infinitely long semi-infinite hollow cylinder with periodic surface temperature, 242–243
- semi-infinite solid with periodic ambient temperature, 240–241
- semi-infinite solid with periodic surface heat flux, 240
- semi-infinite solid with periodic surface temperature, 239–240
- Personal digital assistants (PDAs), 950
- Phase-change heat transfer, 2, 11
- Phase-change materials (PCM), 377
- Phase-change phenomena:
 - electronic equipment, 1006–1016
 - heat pipes and vapor chambers, 1006–1008
 - immersion cooling, 1008–1016
- Phonon heat capacity, 1323–1326
- Phonons, 120–121, 1311, 1321–1322, 1334–1336
- Photons, 1322
- Photothermal techniques, 1339
- PHPs, *see* Pulsating heat pipes
- Physical constants (for fluids), 52–54
- Physical property type of correlation of Stephan and Abdelsalam, 655
- PID control, *see* Proportional—integral—derivative control
- Pierre's smooth tube friction factor, 767
- Pin arrays, 431
- Pin fins, 846, 849, 854
- Pin fin heat sinks, 498–500, 513
- Pipes:
 - heat, *see* Heat pipes
 - longitudinal finned double-pipe heat exchangers, *see* Longitudinal finned double-pipe heat exchangers
- Pipe flow, 31–33
- Pipe fouling resistance, 862
- p terms, 31
- Plain double-pipe exchangers, 857–858
- Plain fins, 846, 849, 851
- Planar freezing, 247
- Planck function, 581
- Planck's constant, 575
- Plane surface, 643
- Plane wall(s):
 - composite, 183–184
 - with constant temperature, 1141–1142
 - finite, with periodic surface temperature, 241–242
 - steady one-dimensional conduction
 - in, 178, 180, 183–184, 189–190, 194–201
 - location-dependent energy generation, 198–199
 - location-dependent thermal conductivity, 194–195
 - temperature-dependent energy generation, 200
 - temperature-dependent thermal conductivity, 196–197
- Plastic contact geometric parameters, 345
- Plastic contact model, 342–347
- Plastic deformation, 346–347
- Plastic shear, 1247
- Plate and frame heat exchangers, 878–886
 - advantages/disadvantages of, 880
 - condensation in, 780–783
 - exploded view of, 879
 - heat transfer and pressure loss, 884–886
 - physical data, 882–884
- Plate fin heat exchangers, 843, 845, 878, 880
 - entrance and exit loss coefficients for flow through, 855
 - surface geometry of, 849
- Plate fin heat sinks, 497–498
- Plate fin surfaces, 846
- Plate heat exchangers:
 - condensation in, 780–783
 - inclination and heat transfer performance, 782–783
 - inclination and pressure drop, 783
 - steam condensation heat transfer, 780–782
- Plate stack, 511
- Plate through holes, 987
- Platinum, 128
- Plesset—Zwick bubble growth model, 647–648, 650, 651
- Plug flow, 665, 666, 737
- Plumes, 548–551
- $P - N_{tu,c}$ analysis method, 817–819, 822
- Point contact model, 319–322
- Pointwise computer programs, 772–774
- Poiseuill flow, *see* Hagen—Poiseuille flow
- Pole placement, 1288–1290
- Polycarbonate, 373–374

- Polycrystalline, 1312
- Poly-ether-ether-ketone (PEEK) thermoplastic prepregs, 1278, 1281–1282
- Polygons, isoflux regular, 287–288
- Polymers, 120
- Polymer crystallization, 1271–1273
- Polymer healing, *see* Healing
- Polymer-matrix composite materials, 1259–1283
 - thermoplastic-matrix composites, 1269–1283
 - thermosetting-matrix composites, 1259–1269
- Polymer thermal degradation, 1271, 1280–1281
- P-1 approximation (thermal radiation), 625–626
- Pool boiling, 636, 639
 - departure from nucleate pool boiling, 658–660
 - film boiling, 660–662
 - heat transfer, 651–662
 - nucleate boiling heat transfer mechanisms, 652–653
 - nucleate pool boiling correlations, 653–657
 - transition boiling, 662
- Pores, 1145
- Porosity, 1132
- Porous flow passages, 889–890
- Porous media, 1131–1176
 - basic principles, 1132–1140
 - conduction, 1140–1141
 - energy conservation, 1138–1140
 - flow models, 1135–1138
 - mass conservation, 1133–1135
 - external natural convection, 1147–1156
 - concentrated heat sources, 1154–1156
 - horizontal walls, 1153–1154
 - sphere and horizontal cylinder, 1154
 - vertical walls, 1147–1153
 - forced convection, 1141–1147
 - channels filled with porous media, 1144–1145
 - compact heat exchangers as porous media, 1145–1147
 - concentrated heat sources, 1143
 - plane wall with constant temperature, 1141–1142
- sphere and cylinder, 1142–1143

Porous media (*continued*)

- internal natural convection, 1156–1170
 - cylindrical and spherical enclosures, 1162–1164
 - enclosures heated from below, 1164–1169
 - enclosures heated from the side, 1156–1162
 - penetrative convection, 1169–1170
 - nomenclature for, 1173–1176
 - properties of common, 1133
 - subfields of, 1171–1173
- Porous-medium Prandtl number, 1166
- Post-dryout heat transfer, 689–699
 - heat transfer mechanisms, 693–694
 - inverted annular flow heat transfer, 694–695
 - mist flow heat transfer, 695–699
 - thermal nonequilibrium, 690–693
- Potassium, 128
- Prandtl number effect, 459–460
- Prandtl number (Pr), 8, 44
 - graphs of, 151, 153, 155, 157, 159
 - heat transfer affected by, 998
 - porous-medium, 1166
 - turbulent, 480–481
- Precipitation fouling, 893
- Precision error, 919–920
- Preforms, 1261
- Preimpregnated reinforcements (prepregs), 1261, 1269, 1278
- Prepregging, 1269
- Pressure, 112
 - critical, 48, 52–54
 - in fully developed flow region, 400–401
 - and solids, 122
- Pressure correlations, 655–656
- Pressure drop, 429
 - in compact heat exchangers, 856–857
 - in continuous phase in vertical column, 1377
 - in fully developed flow region, 401–404
 - heat pipe, 1196–1197, 1199–1201
 - heat pipe diagram of, 1196
 - and inclination, 783
 - in internal forced convection, 415
 - laminar flow, 401–404
 - and laminar flow, 396–404

- microfin tube, 766–767
- smooth tube condensation, 761–762
- Pressure field in the consolidation region, 1274–1276
- Pressure loss:
 - heat exchanger analysis methods, 821
 - heat exchangers
 - regenerators, 893
 - shell-and-tube, 836–842
 - longitudinal finned double-pipe heat exchangers
 - in pipes and annuli, 864–865
 - plate and frame heat exchangers, 884–886
 - regenerators, 893
 - shell-and-tube heat exchangers, 836–842
- Pressure loss correlations, 875–876
- Pressure prime, 1223
- Printed circuit boards (PCBs):
 - convective phenomena in packaging
 - in forced convection, 992–995
 - in natural convection, 988–991
 - heat flow in, 983, 986–988
 - anisotropic conductivity, 983, 986–987
 - effect of trace layers, 988
 - thermal vias, 987–988
- Propagation speed, 120
- Propane, 63–64
- Property formulation, 46
- Proportional—integral—derivative (PID) control, 1286–1287
- Propylene (propene, R-1270), 86
- Propyne (methyl acetylene), 87
- Proto-slug flow, 745
- Pseudo-slug flow, 745
- PTS (parabolic two-step) model, 1346
- Pulsating heat pipes (PHPs), 1220–1221
- Pultrusion, 1259, 1260
- Pulverized coal dispersions, 620–621
- Pump-probe, 1344
- Pure fluids, 49–51
- Pure radiation cooling, 230–231
- Purity of samples, 122
- PVC, 373–374
- Pyrometers, 914, 943
- Quantum size effect, 965
- Quartz, 1329, 1330
- Quasi-momentum, conservation of, 1329

- Quasi-steady period (chip package temporal behavior), 981, 985
- R-11 (trichlorofluoromethane, CFC-11), 91
- R-12 (dichlorodifluoromethane, CFC-12), 94–95
- R-13 (chlorotrifluoromethane, CFC-13), 97–98
- R-14 (tetrafluoromethane, FC-14), 99
- R-22 (chlorodifluoromethane, HCFC-22), 103
- R-23 (trifluoromethane, HCFC-23), 104–105
- R-32 (difluoromethane, HFC-32), 108
- R-41 (fluoromethane, HFC-41), 109
- R-113 (1,1,2-trichloro-1,2,2-trifluoroethane, CFC-113), 91–92
- R-114 (1,2-dichloro-1,1,2,2-tetrafluoroethane, CFC-114), 92–93
- R-115 (chloropentafluoroethane, CFC-115), 93
- R-116 (hexafluoroethane, FC-116), 94
- R-123 (2,2-dichloro-1,1,1-trifluoroethane, HCFC-123), 95–96
- R-124 (1-chloro-1,2,2,2-tetrafluoroethane, HCFC-124), 96
- R-125 (pentafluoroethane, HFC-125), 97
- R-134a (1,1,1,2-tetrafluoroethane, HFC-134a), 98–99
- R-141b (1,1-dichloro-1-fluoroethane, HCFC-141b), 100
- R-142b (1-chloro-1,1-difluoroethane, HCFC-142b), 100–101
- R-143a (1,1,1-trifluoroethane, HFC-143a), 101–102
- R-152a (1,1-difluoroethane, HFC-152a), 102
- R-227ea (1,1,1,2,3,3,3-heptafluoropropane, HFC-227ea), 103–104
- R-236ea (1,1,1,2,3,3,3-hexafluoropropane, HFC-236ea), 105
- R-236fa (1,1,1,3,3,3-hexafluoropropane, HFC-236fa), 106
- R-245ca (1,1,2,2,3-pentafluoropropane, HFC-245ca), 106–107
- R-245fa (1,1,1,3,3-pentafluoropropane, HFC-245fa), 107–108
- Radial convecting fins, 206–209
- Radial flow imbalance, 774–775
- Radial heat flow method, 122
- Radiating fins, 211–212
- Radiation cooling:
in electronic equipment, 961–962
transient conduction, 230–231
- Radiation heat transfer, 694. *See also*
Thermal radiation
- Radiation resistance/conductance, 347–349
- Radiation shields, 612–613
- Radiative—convective cooling of solids with uniform energy generation, 201
- Radiative exchange:
within participating media, 621–629
diffusion approximation, 623, 624
discrete ordinate method, 627
mean beam length method, 623, 624
Monte Carlo or statistical methods, 627
P-1 approximation, 625–626
weighted sum of gray gases, 627–628
zonal method, 627
between surfaces, 598–615
black surfaces, 609–610
diffuse gray surfaces, 610–612
diffuse nongray surfaces, 614–615
radiation shields, 612–613
view factors, 600–609
- Radiative heat flux, 581–582
- Radiative heat transfer, *see* Thermal radiation
- Radiative intensity, 581
- Radiative properties:
of participating media, 615–621
molecular gases, 615–619
particle clouds, 619–621
of solids and liquids, 582–598
metals, 586–589
nonconductors, 589–593
semitransparent sheets, 596
surface conditions' effects on, 593–595
- Radiative resistance, 326–327, 612
- Radiative transfer equation (RTE), 621–622
- Radiators, 844
- Rake face, 1248
- Random distribution, 921
- Random error, 919
- Rankine scale, 917
- Rate equation, heat exchange, 799
- Rayleigh bubble growth equation, 647
- Rayleigh number (Ra), 8, 415–416
low vs. high, 1154–1156
porous materials
external natural convection, 1150, 1155

- Rayleigh number (*continued*)
 internal natural convection, 1156,
 1160–1162, 1164, 1166, 1168, 1169
 mixed convection, 1171–1172
 penetrative convection, 1169–1170
 RC318 (octafluorocyclobutane, FC-C318),
 109–110
 Readability, experimental methods for, 914,
 917–918
 Real area of contact, 266
 Reciprocal lattice, 1314
 Reciprocity rule, view factors, 607
 Recirculation, 872
 Rectangles, 309
 Rectangular (Cartesian) coordinate system,
 13, 14
 Rectangular channels, 304–310
 Rectangular enclosures, 551–554
 Rectangular fins:
 longitudinal convecting, 202–205
 optimal dimensions of convecting, 212,
 213
 radial convecting, 206–208
 Rectangular heat sources, 308, 317–318
 Rectangular offset strip plate fins, 1066
 Rectangular passages, 856
 Rectangular plates:
 single eccentric area on compound,
 316–317
 with specified boundary temperatures,
 216–217
 with two nonhomogeneous boundary
 conditions, 221, 222
 Rectangular source area, 280–285
 arbitrary singly connected area, 282–283
 circular annular area, 283–284
 doubly connected regular polygons,
 284–285
 isoflux rectangular area, 280
 isoflux regular polygonal area, 281–282
 isothermal rectangular area, 281
 Rectangular sources, 308
 Recuperators, 799
 Reduced pressure correlations, 655–656
 Reducing ratios, 117
 Reflectance, 583
 Reflectivity, 583
 REFPROP program, 113
 Refractive index, 575
 Refrigerant—oil mixtures, 702–704
 Regenerators, 799, 886–893
 $\varepsilon - N_{tu}$ method, 891–892
 heat capacity and related parameters,
 886–891
 heat exchangers, 886–893
 $\varepsilon - N_{tu}$ method, 891–892
 heat capacity and related parameters,
 886–891
 heat transfer and pressure loss, 893
 heat transfer and pressure loss, 893
 Reinforcement phase, 1259
 Relative contact pressure, 345–346, 369
 Relative roughness, 33
 Reliability, 953
 Representative elementary volume (REV),
 1133
 Residence times, 888
 Residual, 930–931
 Resin systems, 1263, 1264
 Resistance:
 ball-bearing, 336
 at bolted joints, 378
 bond, 870, 878
 boundary, 972–973
 chip package, 962–964
 cold-side convective layer, 802–804
 cold-side fouling, 802, 803
 conforming rough surface models, 340–
 362
 constriction, 271
 contact, *see* Contact resistance
 convective layer, 802–804
 elastogap resistance model, 324–326
 electrical, 182
 electronic equipment thermal, 956–962
 of the exchanger material, 802
 external, 963–964
 film, 862, 876–877
 flow, 11–12, 964
 fouling, 802–803, 863–864, 877
 gap, 338–339
 high-fin exchangers, 876–878
 hot-side convective layer, 802–804
 hot-side fouling, 802, 803
 interface—contact, 4–7
 internal, 963
 joint, 328, 329

- longitudinal finned double-pipe heat exchangers, 862–864
- and overall heat transfer coefficient, 802–804
- spreading, *see* Spreading resistance
- temperature detectors, 940–942
- thermal, 182–183, 956–964, 1209–1211
- Resistance temperature detectors (RTDs), 940–942
- Resistive, thermally, 289
- Reststrahlen bands, 589–591
- Retarders, 767
- Revolution, body of, 470–471
- REV (representative elementary volume), 1133
- Rewetting, wick, 1213
- Reynolds number (Re), 8, 10, 408, 416
 - bubble, 650–651
 - compact heat exchangers, 850
 - heat pipes, 1199–1200
 - heat transfer affected by, 998
 - high, 446–452
 - local pore, 1136
 - mist flow heat transfer, 695, 696
 - plate and frame heat exchangers, 884
 - porous materials, 1145
- Rigidity, 330–331
- Rms, *see* Root-mean-square roughness
- Rockwell macrohardness values, 343–344, 346
- Rohsenow correlation of bubble agitation, 653–654
- Rolling (process), 1275
 - deformation heating considerations for, 1255–1256
 - diagram of, 1255
- Roman letter subscripts, 40–41
 - for condensation, 789
 - for conduction heat transfer, 257
 - for external flow forced convection, 521–522
 - for thermal radiation, 631
- Roman letter symbols, 38–40
 - for boiling, 708–712
 - for condensation, 785–788
 - for conduction heat transfer, 255–256
 - for direct contact heat transfer, 1393–1394
 - for electronic equipment, 1018–1020
 - for enhancement techniques, 1101–1103
 - for experimental methods, 944–945
 - for external flow forced convection, 515–520
 - for forced convection (internal flows), 434–435
 - for heat exchangers, 896–901
 - for heat pipes, 1225–1226
 - for manufacturing and materials processing, 1297–1300
 - for microscale heat transfer, 1352–1354
 - for natural convection, 566–567
 - for porous media, 1173–1175
 - for thermal radiation, 629–630
 - for thermal spreading and contact resistances, 378–382
 - thermophysical properties, 141
- Room (low)-temperature heat pipes, 1184
- Root-mean-square (rms) roughness, 340–342
- Rosseland mean absorption coefficient, 625
- Rosson—Myers model, 754, 760
- Rotary regenerators, 886, 888
- Rotating surfaces, 1097
- Rough flat plate, 510–511
- Roughness:
 - and duct flow, 422–423
 - relative, 33
 - surface, 376, 593–594
- Roughness effect, surface, 481–482
- Roughness Reynolds number, 481
- Rough surfaces:
 - enhancement techniques, 1032, 1050–1059
 - boiling, 1055, 1057
 - condensing, 1057–1059
 - single-phase flow, 1050–1056
 - profiles of, 1052
- Rouhani—Axelsson drift flux type of void fraction model, 682
- Round free surface jet, 515
- Round submerged jet(s), 513–514
- Round tubes, 429, 430
- RTDs, *see* Resistance temperature detectors
- RTE, *see* Radiative transfer equation
- Rule of mixtures, 1273
- Sandwich arrangement, 843
- Saturation line, 62–110
- Sawtooth fin condensing tubes, 730–732
- Scale analysis, 30

- Scanning thermal microscopy (SThM),
1340–1342
- Scattering, electron, 1310–1311
- Scattering coefficient, 620, 621
- Scattering phase function, 621
- SC lattice, *see* Simple cubic lattice
- Screen-covered groove wicks, 1186, 1187
- SDS solutions, *see* Sodium dodecyl sulfate solutions
- Sealed container, heat pipe, 1182
- Second law of thermodynamics, 35–37
- Seebeck coefficient, 1350
- Seebeck effect, 933–936, 1350
- Self-tuning regulation, 1295–1296
- Semiaxes of elliptical contact area, 319–322
- Semiconductors, 948, 951, 1311
- Semiconductor Industry Association (SIA),
949
- Semigray approximation method, 614
- Semi-infinite flux tubes, 291–293, 313–314
- Semi-infinite hollow cylinders, 242–243
- Semi-infinite isotropic circular flux tubes,
298–302
- Semi-infinite planes, 1243–1245
- Semi-infinite solid model, 232–234
- Semi-infinite solids:
with moving point heat source, 1243
with periodic ambient temperature,
240–241
with periodic surface heat flux, 240
periodic surface temperature, 239–240
- Semitransparent sheets, 596
- Semivariance, 930
- Sensible heat exchange, 1361–1363
- Sensing devices, 914–916
- Sensitivity, 914, 915
- Separation plates, 843
- Series arrangements, double-pipe exchanger,
865–868
- Series composite plane walls, 183, 184
- Series—parallel arrangements, double-pipe
exchanger, 865–868
- Series—parallel composite walls, 183, 184
- Serrated-tip microfins, 1073
- Shah correlation, 673–674, 679, 685, 760
- Shape factor, 600
- Shear-based correlations, 757–758
- Shear-driven annular flow condensation:
horizontal tubes affected by, 756–759
boundary layer correlation, 758–759
heat transfer, 756–759
shear-based correlations, 757–758
two-phase multiplier correlations,
756–757
- Shear planes, 1248, 1249
- Shear stress, 401
- Shear zone, 1247–1248
- Sheets, semitransparent, 596
- Shells (in shell-and-tube heat exchangers):
heat transfer data, 832–836
physical data, 825–828
pressure loss data, 838–842
- Shell-and-tube heat exchangers, 822–842
construction, 822–825
 $\epsilon - N_{tu}$ analysis method for, 811–814, 817
examples of, 823–824
fin examples for, 1060
heat transfer data, 829–836
shell side, 832–836
tube side, 829–832
physical data, 825–828
shell side, 825–828
tube side, 825
pressure loss data, 836–842
shell side, 838–842
tube side, 836–838
with the shell fluid mixed, 811–813
divided-flow, 814, 817
split-flow, 813–814
with the shell fluid unmixed, 811–812
 $\phi - P$ analysis method for, 820, 821
- Shell-side condensation, *see* X-shell
condensers
- SIA (Semiconductor Industry Association),
949
- Silicon, 128
spectral, normal reflectance of, 590, 591
thin-film thermal conductivity of, 965
- Silicon bipolar chips, 949
- Silicon-on-insulator (SOI) transistors,
1347–1348
- Silver, 129, 365, 369–371
- Silver—Bell—Ghaly method, 701
- Similarity solutions, external flow forced
convection:
for flat plate at uniform temperature,
456
for wedge, 456–459

- Similarity transformation technique for laminar boundary layer flow, 452–455
- Simple correlation equations, 301
- Simple cubic (SC) lattice, 1313, 1314
- Simultaneous convective—radiative cooling, 231
- Single-bubble studies, 1367–1368
- Single crystalline, 1312
- Single eccentric area on compound rectangular plate, 316–317
- Single horizontal finned tubes:
 - film condensation on, 727–732
 - sawtooth fin condensing tubes, 730–732
 - trapezoidal fin tubes, 728–730
- Single-input single-output (SISO) thermal systems, 1284–1288
- Single-phase flow heat transfer:
 - additives for liquids, 1092–1093
 - coiled tubes, 1088–1091
 - displaced enhancement devices, 1074–1075
 - enhancement of, 1037–1040
 - extended surfaces, 1059–1067
 - rough surfaces, 1050–1056
 - swirl flow devices, 1075–1082
- Single round free surface jets, 515
- Single round submerged jets, 513–514
- Single submerged slot jets, 514
- Singly connected source areas, 282–283
- Sintered metal wicks, 1185, 1186
- SISO thermal systems, *see* Single-input single-output thermal systems
- SI System (of units), *see* Système International d'Unités
- Site density, 645–646
- Sitharamayya and Raju correlation, 997
- Size effect (term), 1310
- Skin-friction, 397–399
- Skin friction coefficient, 428
- Slab wicks, 1186, 1187
- Sliding mode control, 1293–1294
- Slip regions, 353
- Slip velocity, 1377
- Slot jets, 514, 515
- Slug calorimeters, 943
- Slug flow, 663, 665, 666, 737
- Small-scale integration (SSI) chips, 948, 949
- Smith prediction, 1292–1293
- Smith—Spalding integral method, 466–468
- Smooth tubes, 735–763
 - compact heat exchangers, 845–846
 - condensation in, 735–763
 - condensation of zeotropes, 762–763
 - flow regimes in, 736–749
 - heat transfer in horizontal tubes, 749–761
 - inclined and vertical tubes, 763
 - oil's effects, 762
 - pressure drop, 761–762
 - surfaces with flow normal to banks of, 845–846
- Sodium, 129
- Sodium dodecyl sulfate (SDS) solutions, 1094–1096
- Software implementation of SISO controllers, 1287–1288
- SOI transistors, *see* Silicon-on-insulator transistors
- Solar absorptance, 597–598
- Solar temperature, effective, 576
- Solids:
 - heat treatment of, 1245–1246
 - metals, 586–589
 - microscale heat transfer, 1312–1330
 - crystalline structure, 1312–1314
 - energy carriers, 1314
 - free electron gas, 1314–1317
 - heat capacity, 1322–1326
 - thermal conductivity, 1326–1330
 - vibrational modes of a crystal, 1317–1322
 - properties of, 45–46
 - radiative—convective cooling of, 201
 - radiative properties of, 582–598
 - thermal spreading and contact resistances
 - conforming rough, 266–267
 - conforming rough, single layer between, 268–269
 - nonconforming rough, 268
 - nonconforming smooth, 267–268
- thermophysical properties of, 118–140
 - behavior of, 120–121
 - conservation of energy, 119–120
 - measuring, 122, 140
 - property values of, 121–139
 - table, 123–139
- with uniform energy generation, 201

Solid angles, 577, 579–581

Solid cylinders:

conduction heat transfer with, 217–220

radial and axial conduction in, 225,
227–229

steady one-dimensional conduction in
location-dependent energy generation,
199

temperature-dependent energy
generation, 199

surface convection, 217–220

Solid hemispheres, 219–221

Solidification, 1271

spray column applications, 1384–1387

thermoplastic-matrix composites
processing, 1281–1283

Solid interfaces, 970–979

Solid model, semi-infinite, 232–234

Solid spheres, 193–194, 199

Soliman correlation, 761

Sonic limit, 1194, 1206–1208

Soot, 619–620

Souza correlation, 761

Souza—Pimenta correlation, 762

Specific heat:

at constant pressures, 28

measurement of, 122, 140

temperature-dependent, 230

Specified interfaces, film condensation on,
725–727

Spectral:

directional emittance, 585

hemispherical emittance, 584

Spectral absorptivity, 623

Spectral blackbody intensity, 581

Spectral emissive power, 575

Spectral emissivity, 623

Speed:

of propagation, 120

of sound, 112, 113

Sphere(s):

direct contact heat transfer inside, 1362–
1363

external convection to, 1361–1362

external natural convection, 543–545,
1154

flow over isothermal, 483

forced convection, 1142–1143

forced convection external flows from, 483

hollow, 181–182, 186–187, 192–193

horizontal, 543–545

laminar flow, 543–545

and layered substrate, 329–333

natural convection, 563–565

porous media, 1142–1143, 1154

solid, 193–194

steady one-dimensional conduction in,
181–182, 186–187, 192–194

Sphere—flat contact, 327–329

Spherical coordinate systems, 13, 15, 165,
166

Spherical enclosures, 1163–1164

Spherical freezing, 252–253

Spherical harmonics method, 625

Spined surfaces:

convecting, 208–211

optimum dimensions, 212–215

Spiral fin tubes, 1062

Spiral microfin tubes, 1069

Split-flow shell-and-tube exchangers, 813–
814

Splitter plates, 843

Spray columns, 1373–1387

differential treatments, 1381–1384

global treatments, 1375–1381

melting and solidification applications,
1384–1387

Spreading—constriction parameter, 334

Spreading—constriction resistance model,
323–324

Spreading resistance, 4, 5. *See also* Thermal
spreading and contact resistances

for an abrupt change in cross sections,
312–313

contact conductance effects on, 284–285

correlation equations for, 301–302

definition of, 271

dimensionless, *see* Dimensionless
spreading resistance

and electronic equipment, 966–970

in electronic equipment, 966–970

in flux tubes, 291–293

in half-space, 291–293

in isotropic finite disks with conductance,
291–294

transient, 285–288

Spreading resistance parameter, 272

Squares, correlation coefficients for, 285

- Square area, 309
Square isothermal target surface, 515
Square plates, 225, 226
SRMs (standard reference materials), 122
SSI, *see* Small-scale integration chips
S (staggered) arrangements, 846
Stack arrangement, 843
Stages (of column direct contact heat transfer), 1374–1375
Staggered plates, optimal channel sizes for, 431
Staggered (S) arrangements, 846
Staggered tubes, pressure loss correlations for, 875–876
Stagnation point, 442
Stagnation zone, 503
Stainless steel, 360
Standard acceleration of gravity, 36
Standard kinetic gas theory, 115–116
Standard Reference Data Program (NIST), 113
Standard reference materials (SRMs), 122
Standard reference quality sources, 45
Stanton number, 850, 855
Starner and McManus fin arrays, 1003–1004
State controllers by pole placement, 1288–1289
State observers by pole placement, 1289–1290
Statistical methods, 627
Steady one-dimensional conduction, 178, 180–201
 composite hollow cylinder, 185–186
 composite hollow sphere, 186–187
 composite plane wall, 183–184
 contact conductance, 187–188
 critical thickness of insulation, 188
 hollow cylinder, 180–181, 190–191
 hollow sphere, 181–182, 192–193
 location-dependent energy generation, 198–199
 location-dependent thermal conductivity, 194–195
 plane wall, 178, 180, 189–190
 radiative—convective cooling of solids with uniform energy generation, 201
 solid cylinder, 191–192
 solid sphere, 193–194
 temperature-dependent energy generation, 199–200
 temperature-dependent thermal conductivity, 196–198
 thermal resistance, 182–183
 uniform internal energy generation effect, 188–194
Steady-state metal cutting temperature models, 1249–1250
Steady-state methods, 122
Steady-state period (chip package temporal behavior), 981, 985
Steam condensation heat transfer, 780–782
Stefan-Boltzmann constant (s), 12, 577
Stefan number (St), 33, 34, 244–249
Steiner—Taborek method, 675–678
Stephan and Abdelsalam correlation of physical property type, 655
SThm, *see* Scanning thermal microscopy
Stirring devices, 1097
Straight fin tubes, 1062
Straight tubes (ST), 844
Stratified flow, 664–667
Stratified—wavy flow, 664, 665, 667, 684
Strength, mechanical, 979
Stress power, 119
Strip(s):
 on finite channel with cooling, 310–311
 on infinite flux channel, 312
 offset, 487–490
Strip fins, 846, 849, 853, 1060
Strip heat source, 308
Structured packings, 1373
Structured roughness, 1050–1056
ST (straight tubes), 844
Subcooled boiling heat transfer, 686
Submerged condenser cooling systems, 1013, 1014
Submerged jet(s), 502–508
 array of round, impinging on isothermal target surface, 514
 array of slot, impinging on isothermal target surface, 515
 single round, impinging on isothermal target surface, 513–514
 single slot, impinging on isothermal target surface, 514
Subscripts:

- for boiling, 713
- for conduction heat transfer, 257
- for direct contact heat transfer, 1395
- for electronic equipment, 1020–1022
- for enhancement techniques, 1104
- for forced convection (internal flows), 436
- Greek letter, 41
- for heat exchangers, 903–905
- for heat pipes, 1226–1227
- for manufacturing and materials processing, 1301
- for microscale heat transfer, 1354
- for porous media, 1175–1176
- Roman letter, 40–41
- for thermal spreading and contact resistances, 384–385
- thermophysical properties, 142
- Substantial derivative, 18
- Substrates, 288
 - block arrays, 495–497
 - flush-mounted heat sources, 491–492
 - forced convection external flows from, 490–500
 - isolated blocks, 493–495
 - objects on, 444, 490–500
 - pin fin heat sinks, 498–500
 - plate fin heat sinks, 497–498
 - two-dimensional block array, 492–493
- Suction, 1034
- Sulfur dioxide, 87–88
- Sulfur hexafluoride, 88
- Summation rule, 606–607
- Supercritical startup, 1216–1217
- Superficial vapor velocity, 742, 743
- Superficial velocities, 1377
- Superheat:
 - critical, 1201
 - nucleation, 640–644
- Superposition, 221–222, 496
- Superscripts, 41
 - for condensation, 789
 - for conduction heat transfer, 257
 - “crit” (critical enhancement), 115
 - for electronic equipment, 1022
 - for external flow forced convection, 522
 - for forced convection (internal flows), 436
 - for heat exchangers, 905
 - “int” (internal motions), 115
 - for manufacturing and materials processing, 1301
 - for thermal radiation, 631
 - for thermal spreading and contact resistances, 385
 - thermophysical properties, 142
 - “trans” (translational term), 115
- Surfaces:
 - diffuse, 600
 - enhanced boiling, 704
 - extended, *see* Extended surfaces
 - with flow normal to banks of smooth tubes
 - compact heat exchangers, 845–846
 - rough, *see* Rough surfaces
 - thermal radiation between, 598–615
 - black surfaces, 609–610
 - diffuse gray surfaces, 610–612
 - diffuse nongray surfaces, 614–615
 - radiation shields, 612–613
 - view factors, 600–609
 - total emittance/solar absorptance of
 - selected, 597–598
 - treated, *see* Treated surfaces
- Surface conditions:
 - effects of, on nonconductors, 593–594
 - nonconductors affected by, 593–595
 - thermal radiation affected by, 593–595
- Surface convection:
 - one-region Neumann problem with, 250
 - semi-infinite solid model and, 232–233
- Surface heat flux:
 - semi-infinite solid model, 232–234
 - semi-infinite solid with periodic, 240
- Surface heat treatment, 1246
- Surface layers, 594–595
- Surface properties, 599
- Surface radiosity, 611
- Surface roughness:
 - and grease thermal conductivity, 376
 - and grinding, 1251
 - nucleate pool boiling, 655–656
 - reduced pressure correlation of Cooper, 655–656
- Surface roughness effect, 481–482
- Surface scraping devices, 1097
- Surface temperature:
 - arbitrarily varying, 465–466
 - finite plane wall with periodic, 241–242
 - radiative properties of metals, 588–589

- semi-infinite solid model, 232–233
- specified, 232–233
- uniform
 - axisymmetric object at, in uniform laminar flow, 510
 - crossflow across bank of cylinders at, 511
 - cylinder at, in laminar cross flow, 509
- Surface temperature effects, 588–589
- Surface tension, 739, 1191
- Surface tension devices, 1033
- Surface tension pressure gradient, 724–725
- Surface vibration, 1033, 1097
- Swirl effects, 708, 767–769
- Swirl flow devices, 1033
 - boiling, 1082–1086
 - condensing, 1087–1088
 - heat transfer enhancement, 1075–1088
 - single-phase flow, 1075–1082
- Symbols:
 - Greek letter, *see* Greek letter symbols
 - Roman letter, *see* Roman letter symbols
- Symmetric isoflux plates, 990
- Symmetric isothermal plates, 990
- Système International d'Unités (SI System), 35–38
- Taitel—Dukler map, 739–741, 744–746, 760
- Tantalum, 129
- Taylor bubbles, 663
- Taylor instability, 658
- TECs, *see* Thermal electric coolers
- Teflon, 373
- TEMA, *see* Tubular Exchanger Manufacturers' Association
- TEMA E-shell, 811–813
- TEMA G-shell, 813–814
- TEMA J-shell, 814, 817
- Temperature:
 - adiabatic, 496
 - boiling point for fluids, 48, 52–54
 - calibrating for, 916–917
 - critical, 48, 52–54
 - effective solar, 576
 - and electronic equipment, 948–953
 - finite plane wall with periodic, 241–242
 - and grinding, 1252–1254
 - horizontal tubes affected by, 750–751
 - longitudinal finned double-pipe heat exchangers, 865
 - maldistribution of, 770
 - and metal cutting, 1248–1250
 - mixture, 114
 - periodic conduction
 - oscillating, 239
 - semi-infinite solid with periodic ambient, 240–241
 - semi-infinite solid with periodic surface, 239–240
 - plane wall with constant, 1141–1142
 - porous media, 1141–1142
 - semi-infinite solid model
 - constant surface heat flux and nonuniform initial, 234
 - specified surface, 232–233
 - surface, 241–242
 - triple-point, 48, 52–54
 - uniform surface
 - axisymmetric object at, in uniform laminar flow, 510
 - crossflow across bank of cylinders at, 511
 - cylinder at, in laminar cross flow, 509
 - wall, 865
 - wedge at uniform, 509
 - X-shell condensers, 770
- Temperature change (in solids), 120
- Temperature dependence, 592, 593
- Temperature-dependent energy generation, 199–200
- Temperature-dependent heat transfer coefficient, 231
- Temperature-dependent specific heat, 230
- Temperature-dependent thermal conductivity, 196–198
- Temperature difference, logarithmic mean, 804–805
- Temperature gradient, 164
- Temperature head, 819
- Thermal boundary resistance, 970, 972–973, 1351
- Thermal capacitance, 7
- Thermal conductivity, 115, 164–165
 - dilute gas, 58–59
 - in ECS model, 117
 - graphs of, 149–150, 152, 154, 156, 158
 - location-dependent, 194–195

- Thermal conductivity (*continued*)
 measurement of, 122, 140
 microscale heat transfer, 1326–1330
 in mixtures, 117–118
 of particle-laden systems, 975–979
 of solids, 119–120
 temperature-dependent, 196–198
- Thermal contact resistance, *see* Contact resistance
- Thermal diffusivity:
 and conservation of energy, 120
 graphs of, 151, 153, 155, 157, 159
 measurement of, 140
- Thermal diodes, 1187
- Thermal elastoconstriction parameter, 324
- Thermal electric coolers (TECs), 1016–1017
- Thermal entrance length, 396
- Thermal entrance region, 407–408
- Thermal expansion:
 measurement of, 140
 volumetric coefficient of, 28
- Thermal—fluid design general considerations, 1000–1001
- Thermal-fluid effects in continuous metal forming processes, 1254–1259
- Thermal greases and pastes, 374–376
- Thermal heat radiation, *see* Thermal radiation
- Thermally and hydraulically developing flow, 430
- Thermally conductive, 289
- Thermally decoupled model, 325
- Thermally developing flow, 412–413, 429
- Thermally developing Hagen—Poiseuille flow, 429–430
- Thermally fully developed flow, 405–407
- Thermally resistive, 289
- Thermal management, 948–952
- Thermal model:
 metallic coatings and foils, 264, 366–371
 thermosetting-matrix composites processing, 1261–1262
- Thermal nonequilibrium, 690–693
- Thermal packaging goals, 952–953
- Thermal process control for manufacturing, 1284–1297
 adaptive control, 1294–1296
 MIMO thermal systems, 1288–1290
 optimal formulation: linear quadratic Gaussian, 1290–1292
 parameter identification, 1296–1297
 SISO thermal systems, 1285–1288
 sliding mode control, 1293–1294
 Smith prediction, 1292–1293
- Thermal radiation, 2, 573–631
 definition of, 574
 emissive power, 575–579
 nomenclature for, 629–631
 radiative exchange within participating media, 621–629
 diffusion approximation, 623, 624
 discrete ordinate method, 627
 mean beam length method, 623, 624
 Monte Carlo or statistical methods, 627
 P-1 approximation, 625–626
 weighted sum of gray gases, 627–628
 zonal method, 627
 radiative heat flux, 581–582
 radiative heat transfer, 12
 radiative intensity, 581
 radiative properties of participating media, 615–621
 molecular gases, 615–619
 particle clouds, 619–621
 radiative properties of solids and liquids, 582–598
 metals, 586–589
 nonconductors, 589–593
 semitransparent sheets, 596
 surface conditions' effects on, 593–595
 solid angles, 577, 579–581
 between surfaces, 598–615
 black surfaces, 609–610
 diffuse gray surfaces, 610–612
 diffuse nongray surfaces, 614–615
 radiation shields, 612–613
 view factors, 600–609
- Thermal resistance, 2
 in electronic equipment, 956–964
 basic heat transfer modes, 956–962
 chip package resistance, 962–964
 in heat pipes, 1209–1211
 and steady one-dimensional conduction, 182–183
- Thermal spreading and contact resistances, 261–385
 assumptions for resistance/conductance model development, 270
 at bolted joints, 378

- circular flux tube with multiple layers, 302–304
- within compound disk with conductance, 288–294
- in compound rectangular channels, 304–309
 - rectangle on isotropic half-space, 309
 - rectangle on layer on half-space, 309
 - square area on semi-infinite square flux tube, 309
- conforming rough solids, 266–267
- conforming rough surface, 340–362
 - elastic contact model, 349–351
 - elastic—plastic contact conductance model, 351–353
 - gap conductance for joints between, 355–359
 - gap conductance for large parallel isothermal plates, 353–355
 - joint conductance for joints between, 359–361
 - models for, 340–342
 - plastic contact model, 342–347
 - radiation resistance/conductance for, 347–349
- definitions
 - in flux tubes/channels, 272–274
 - in isotropic half-space, 270–272
- eccentric rectangular area on rectangular plate with cooling, 314–318
- multiple rectangular heat sources on isotropic plate, 317–318
- ingle eccentric area on compound rectangular plate, 316–317
- of isotropic finite disks with conductance, 294–298
 - circular area on single layer (coating) on half-space, 295–296
 - correlation equations, 294–295
 - equivalent isothermal contact area, 297–298
 - isoflux circular contact, 296–297
 - isoflux contact area, 297
 - isothermal contact area, 298
- in isotropic half-space, 274–280
 - circular source areas, 274–277
 - dimensionless spreading resistance, 279–280
 - flux distribution over isothermal elliptical area, 280
 - isoflux circular source, 275–277
 - isothermal circular source, 274–275
 - isothermal elliptical source area, 277–280
 - transient spreading resistance, 285–288
- joint conductance enhancement methods, 361–377
 - elastomeric inserts, 372–374
 - metallic coatings and foils, 363–372
 - phase-change materials, 377
 - thermal greases and pastes, 374–376
- nomenclature for, 378–385
- nonconforming rough solids, 268
- nonconforming smooth solids, 267–268, 318–340
 - ball-bearing resistance, 336
 - contact resistance of isothermal elliptical contact areas, 323–324
 - elastic—plastic contacts of hemispheres and flat surfaces in vacuum, 333–335
 - elastogap resistance model, 324–326
 - line contact models, 336–340
 - local gap thickness, 322–323
 - models for, 318–319
 - point contact model, 319–322
 - radiative resistance, 326–327
 - sphere and layered substrate, 329–333
 - sphere—flat contact, 327–329
- parameters influencing resistance/conductance, 269–270
- of rectangular source area, 280–285
 - arbitrary singly connected area, 282–283
 - circular annular area, 283–284
 - doubly connected regular polygons, 284–285
 - isoflux rectangular area, 280
 - isoflux regular polygonal area, 281–282
 - isothermal rectangular area, 281
- semi-infinite circular flux tubes and two-dimensional channels, 313–314
- semi-infinite isotropic circular flux tube, 298–302
 - accurate correlation equations, 302
 - general expression, 299–302

single layer between two conforming
rough solids, 268–269

Thermal spreading and contact resistances
(*continued*)

solids

conforming rough, 266–267

conforming rough, single layer between,
268–269

nonconforming rough, 268

nonconforming smooth, 267–268

from strip on finite channel with cooling,
310–311

from strip on infinite flux channel,
312–313

types of joints, 264–266

Thermal switches, 1187

Thermal time constant, 7

Thermal transport, 500–502

Thermal vias, 987–988

Thermal waves, 1343

Thermal wave propagation, 981

Thermistors, 942

Thermocouples, 140, 915, 933–941, 1339–
1341

arrangements of, 938–940

common standard, 938

nanometer-scale, 1339, 1340

Thermodynamics:

first law of, 23–24

second law of, 35–37

Thermodynamic properties:

of fluids, 46–114

of mixtures, 113–114

Thermoelectric power, 936, 1350

Thermogram, 1263

Thermohaline convection, 1169

Thermomechanical model, 366

Thermometers, 916–918, 931–933

Thermophysical properties, 43–142, 149–
159

of fluids, 46–118

along the saturation line, 62–110

calculation of, 112–113

dilute gas thermal conductivity, 58–59

dilute gas viscosity, 60–61

equation of state, 46–51, 111–112

estimated experimental uncertainty, 47

ideal gas isobaric heat capacity, 55–57

for mixtures, 113–114

physical constants and fixed points,
52–54

- thermodynamic properties, 46–114
- transport properties, 114–118
- graphs of, 149–159
- nomenclature for, 141–142
- saturation line, 62–110
- of solids, 118–140
 - behavior of, 120–121
 - conservation of energy, 119–120
 - measuring, 122, 140
 - property values of, 121–139
- as term, 44
- transport properties, 62–110
- Thermophysical Properties Research Center (TPRC), 121
- Thermoplastic-matrix composites, 1269–1283
 - fabrication of composites, 1270–1271
 - heat transfer, 1273–1274
 - interlaminar bonding, 1277–1280
 - polymer degradation, 1280–1281
 - solidification (crystallization), 1281–1283
 - stages of, 1269–1270
 - transport mechanisms involved in, 1271–1273
 - void dynamics, 1274–1277
- Thermorefectance techniques, 1339
- Thermosetting-matrix composites, 1259–1269
 - kinetics model, 1262–1266
 - laminar consolidation model, 1266–1269
 - thermal model, 1261–1262
- Thermostatic (on—off) control, 1285–1286
- Thermosyphon, 1196
- Thin-film evaporation, 705
- Thin-film microbridge, 1342, 1343
- Thin plate with moving heat source, 1241–1243
- Thin rod with moving planar heat source, 1241–1242
- Thin solid model, 1235–1239
- Thome method, 700–701
- Thomson functions, 176–177
- 3ω technique, 1342–1344
- Three-layer model for a “physical situation,” 476–479
- Three-phase exchanges, 1368
- Three-phase spray column, 1381–1384
- Three-time-level scheme, 238
- Tien model, 754
- Time-averaged equations, 419–420
- Time—temperature transformation (TTT) diagram, 1245–1246
- Tin, 129, 370, 371
- Titanium, 130
- Toluene (methylbenzene), 88–89
- Tool—chip interface temperature rise, 1248–1249
- Total, normal emittance, 597–598
- Total emissive power, 575
- Total heat transfer rate, 425–427, 433
- Total hemispherical emittance, 585, 588, 589
- Total properties, 588
- Total resistance, 964
- Total temperature potential, 867
- Tow compaction, 1273, 1274
- Tow-placement head, 1270
- TPRC (Thermophysical Properties Research Center), 121
- Trace layers, 988
- Transfer unit technique, 1374–1375
- Transient conduction, 229–239
 - finite-difference method, 236–239
 - finite-sized solid model, 235–236
 - lumped thermal capacity model, 229–231
 - multidimensional, 236
 - semi-infinite solid model, 232–234
- Transient effects, first-order, 979–985
- Transient natural convection in external laminar flow, 546–548
- Transient operation, heat pipe, 1212–1217
 - continuum vapor and liquid-saturated wick, 1212–1213
 - freeze—thaw issues, 1214–1216
 - supercritical startup, 1216–1217
 - wick depriming and rewetting, 1213
- Transient spreading resistance, 285–288, 313–314
- Transient thermorefectance (TTR), 1344–1347
- Transistors, 1347–1349
- Transition boiling, 639
 - boiling curve, 637
 - pool boiling, 662
- Transition flow, 830
- Transition region, 10, 528
- Transition temperature, 1271
- Translational term (superscript “trans”), 115
- Transmissivity, 583

- Transmittance, 583
- Transport, convection, 446
- Transport correlations, 482–483
- Transport equations, 49–51
- Transport limitations, heat pipe, 1193–1209
 - boiling limit, 1201–1202
 - capillary limit, 1195–1201
 - condenser limit, 1208–1209
 - entrainment limit, 1202–1204
 - leading to failure, 1194
 - nonfailure, 1194
 - sonic limit, 1206–1208
 - viscous limit, 1205
- Transport mechanisms, 1271–1273
- Transport properties, 44–45
 - density-dependent contributions, 116–117
 - dilute-gas contributions, 115–116
 - extended corresponding states, 114–115
 - of fluids, 114–118
 - for mixtures, 117–118
- Transverse high-fin heat exchangers, 868–878
 - air-fin coolers, 871–875
 - bond/contact resistance of high-fin tubes, 870
 - fin efficiency approximation, 871
 - overall heat transfer coefficient, 876–878
 - pressure loss correlations for staggered tubes, 875–876
- Trapezoidal fins, 203, 205
- Trapezoidal fin tubes, 728–730
- Trap wicks, 1191
- Travel Péclet number, 1367
- Treated surfaces, 1032, 1043–1050
 - boiling, 1043–1049
 - condensing, 1049–1050
- Triangular cavity, nucleation on, 643
- Triangular fins:
 - longitudinal convecting, 203, 205
 - optimal dimensions of convecting, 212, 213
 - radial convecting, 208
- Triple-point temperature, 48, 52–54
- True isothermal strip on infinite flux channel, 312
- TTR, *see* Transient thermorefectance
- TTT diagram, *see* Time—temperature transformation diagram
- Tubes:
 - air-fin cooler arrangements of, 872–874

- Tubes (*continued*)
- coiled, 1033, 1088–1092
 - boiling, 1091–1092
 - condensing, 1092
 - single-phase flow, 1088–1091
 - condensation in smooth, 735–763
 - enhanced in-tube condensation, 764–767
 - exchanger surface area, 800–802
 - film condensation on, 727–732
 - horizontal, 749–761
 - horizontal finned, 727–732
 - laminar force convection in circular, 959, 960
 - low-finned, 706
 - microfin, 706–708, 764–767
 - in shell-and-tube heat exchangers
 - heat transfer data, 829–832
 - physical data, 825
 - pressure loss data, 836–838
 - smooth, *see* Smooth tubes
 - Turbo-Bii, 706
 - turbulent force convection in circular, 959, 960
- Tube banks, 442, 483–485
- Tube bundles:
- film condensation on, 769–780
 - in-tube condensers, 779–780
 - X-shell condensers, 769–779
 - flow boiling on, 687–689
 - bundle boiling factor, 688
 - bundle design methods, 688–689
 - heat transfer characteristics, 687–688
- Tube diameter:
- flow regimes, 738
 - heat transfer, 750
- Tube metal resistance, 878
- Tube-side flow, 770
- Tubular Exchanger Manufacturers' Association (TEMA), 811, 823, 894, 896
- Tubular surfaces, 844
- Tungsten, 130, 590
- Turbo-Bii tube, 706
- Turbo-Cdi, 731
- Turbo-Chil, 731
- Turbulence, 557–560
- Turbulent boundary layer:
- flat plate with, 510
 - forced convection external flows from, 469–472
 - isothermal rough flat plate with, 510–511
 - uniform flux plate with, 510
- Turbulent boundary layer transition, 510
- Turbulent duct flow, 419–425
- fully developed flow, 420–423
 - heat transfer in fully developed flow, 423–425
 - optimal channel sizes for, 431–432
 - optimum channel sizes for, 427
 - time-averaged equations, 419–420
- Turbulent flow, 528
- and entrance lengths, 432
 - external flow forced convection, 472–475
 - flat plate with unheated starting length in, 479–480
 - natural convection in, 557–560
 - near-wall region in, 472–475
 - optimal channel sizes, 432
 - in shell-and-tube heat exchangers, 830–831
 - swirl flow devices, 1080–1082
- Turbulent flow friction factor, 432
- Turbulent flow heat transfer, 432–433
- Turbulent force convection, 959, 960
- Turbulent jets:
- external flow forced convection, 500–508
 - submerged jets, 502–508
 - thermal transport in jet impingement, 500–502
- Twisted duct, 1076
- Twisted-tape inserts:
- boiling, 1082–1086
 - condensation enhanced in-tube, 767–769
 - condensing, 1087–1088
 - enhanced in-tube condensation, 767–769
 - single-phase flow, 1076–1082
- Two-dimensional block array, 492–493
- Two-dimensional nonsimilar flows, 466
- Two-dimensional steady conduction, 215–229
- conduction shape factor method, 222–225
 - finite-difference method, 223, 225–229
 - method of superposition, 221–222
 - rectangular plate with specified boundary temperatures, 216–217
 - solid cylinder with surface convection, 217–220

- solid hemisphere with specified base and surface temperatures, 219–221
- Two-dimensional workpieces, 1238, 1240–1241
- Two pass/one pass flow arrangement, 882
- Two pass/two-pass flow arrangement, 882
- Two-phase flow heat transfer:
 - condensation in smooth tubes, 736–737
 - enhancement of, 1040–1042
- Two-phase flow patterns, 662–671
- Two-phase multiplier correlations, 756–757
- Two-phase system, capillary-driven, 1182, 1183
- Two-point basis, 1313
- Two-region Neumann problem, 245–247
- 2/1 arrangement, 882
- 2/2 arrangement, 882
- U arrangement, 881, 882
- Umklapp process (of phonon—phonon collisions), 1328, 1329
- Uncertainty:
 - estimated experimental, 47
 - measurement error, 918–920
- Unconfined flow, 502
- Unheated starting length:
 - external flow forced convection, 463–466
 - flat plate boundary layer with, 463–466
 - flat plate with, 479–480, 509
 - in turbulent flow, 479–480
 - uniform laminar flow with, 509
- Uniform energy generation, 201
- Uniform flow, forced convection external
 - flows from single objects in, 446–483
 - algebraic turbulence models, 472
 - analogy solutions for boundary layer flow, 475–481
 - axisymmetric nonsimilar flows, 469
 - cylinder in crossflow, 482–483
 - flow over isothermal sphere, 483
 - high Reynolds number flow over a wedge, 446–452
 - incompressible flow past flat plate with viscous dissipation, 461–463
 - integral solutions for flat plate boundary layer with unheated starting length, 463–466
 - near-wall region in turbulent flow, 472–475
 - Prandtl number effect, 459–460
 - similarity solutions for flat plate at uniform temperature, 456
 - similarity solutions for wedge, 456–459
 - similarity transformation technique for laminar boundary layer flow, 452–455
 - Smith—Spalding integral method, 466–468
 - surface roughness effect, 481–482
 - turbulent boundary layer, 469–472
 - two-dimensional nonsimilar flows, 466
- Uniform flux plate, 510
- Uniform heat flux, 433
- Uniform internal energy generation effect, 188–194
- Uniform laminar flow:
 - axisymmetric object at uniform surface temperature in, 510
 - flat plate in, with unheated starting length, 509
 - isothermal flat plate in, 508–509
- Uniformly heated wall, 427
- Uniform surface temperature:
 - axisymmetric object at, in uniform laminar flow, 510
 - crossflow across bank of cylinders at, 511
 - cylinder at, in laminar cross flow, 509
- Uniform thermal environment:
 - moving materials in, 1234–1241
 - thin solid model, 1235–1239
 - two-dimensional workpieces, 1238, 1240–1241
 - wedge at, 509
- Units, 34–38
 - conversion factors, 37–38
 - English engineering system, 36–37
 - SI System, 35–36
- Unit cells, 1312
- Unit vectors, 606
- Uranium, 130
- Vacuum:
 - coated joint operating in, 363
 - joint resistance in a, 328, 330, 333–335, 339
- Vafai and Tien flow model, 1137–1138
- Vanadium, 130
- Van Stralen bubble growth model, 648
- Vapor, evaporation of a liquid by a surrounding gas, 1371–1373

- Vapor chambers, 1008
Vapor flow-modulated heat pipes, 1189, 1190
Vapor inertia, 1204
Vapor-liquid equilibria and properties, 699–700
Vapor—liquid exchange, 653
Vapor space, 721–723
Vapor space EHD condensation, 733
Vapor-to-droplet heat transfer, 694
Vapor velocity, modified superficial, 742, 743
Variable conductance heat pipes (VCHPs), 1217–1218
Varisol, 1386
VCHPs, *see* Variable conductance heat pipes
VCSELs (vertical cavity surface-emitting laser diodes), 1349
Velocity:
 friction, 421
 in fully developed flow region, 399–400
 slip, 1377
 superficial, 1377
Vent flow rate, 777–779
Venting, noncondensable gas, 777–779
Vertical cavity surface-emitting laser diodes (VCSELs), 1349
Vertical cylinder, 545–546
Vertical flat plate, 721–723
Vertical flat surfaces:
 laminar flow, 533–540
 turbulent flow, 561–562
Vertical isoflux surface, 959, 960
Vertical row-number method, 771–772
Vertical surfaces, 959, 960
Vertical tubes:
 flow boiling in, 663–664, 666, 671–679
 Chen correlation, 672–673
 Gungor—Winterton correlation, 674–675
 horizontal tube correlations based on, 679–680
 Shah correlation, 673–674
 Steiner—Taborek method, 675–678
 smooth tube condensation, 763
Vertical walls, 1147–1153
Very large scale integration (VLSI) chips, 949
VG criteria, 1038
Vias, thermal, 987–988
Vibration(s), 1097–1098
 enhancement techniques, 1033
 fluid, 1033, 1098
Vibrational modes of a crystal, 1317–1322
Vickers microhardness, 343–346
View factors:
 in electronic equipment, 961
 evaluation of, between two surfaces, 605
 graphs of, 604–605
 radiative exchange between surfaces, 600–609
 crossed-strings method, 608–609
 direct integration, 600, 606
 reciprocity rule, 607
 summation rule, 606–607
 view factor algebra, 607–608
 thermal radiation, 600–609
 types of, 601–603
View factor algebra, 607–608
Viscosity, 115
 Chapman—Enskog dilute gas, 115
 dilute gas, 60–61
 in ECS model, 117
 graphs of, 150, 152, 154, 156, 158
 of mixtures, 118
 resin, 1268
Viscous dissipation:
 incompressible flow past flat plate with, 461–463
 isothermal flat plate in uniform laminar flow with appreciable, 508–509
Viscous dissipation function, 27–30
Viscous limit, 1194, 1205
Viscous sublayer, 473
VLSI (very large scale integration) chips, 949
Void compression, 1276
Void dynamics, 1274–1277
Void fraction, 1361
Void fraction model, Rouhani—Axelsson drift flux type of, 682
Void growth, 1277
Volatile component, 699
Volume-averaged quantity, 1132
Volumetric coefficient of thermal expansion, 28
Von Kármán constant, 474
Wakes, 548–551

Walls:

- horizontal, 1153–1154
- isothermal, 426, 433
- law of the, 474
- near-wall region in turbulent flow, 472–475
- opaque, 582–586
- plane, *see* Plane wall(s)
- series—parallel composite, 183, 184
- total heat transfer rate, 426, 427
- uniformly heated, 427
- vertical, 1147–1153

Wall jet region, 503

Wall resistance, 862–863

Wall temperature, 865

Wall-to-droplet heat transfer, 694

Wall-to-vapor heat transfer, 694

Warm working, 1254

Washboard corrugation, 880, 881

Waste heat recovery, 1379

Water, 89–90

Water vapor, 616, 617

Wavelength, characteristic, 964–966

Wavelength dependence:

- metal radiative properties, 586
- nonconductor radiative properties, 589–592

Wavy—annular flow, 745

Wavy fins, 846, 849, 854

Wavy plate fins, 1060

Weber number, 742, 1203–1204

Wedge:

- high Reynolds number flow over a, 446–452
- similarity solutions for, 456–459
- at uniform temperature, 509

Wedge flow limits, 458–459

Weighted sum of gray gases (WSGG), 627–628

Welded U-fins, 861

Welling and Wooldridge fin arrays, 1004

Wet point, 1193

Wettability, degree of, 1192

Wetted surface area, 705

Wicks:

- depriming and rewetting of, 1213

effective capillary radius for various, 1196, 1197

liquid-saturated, 1212–1213

Wick permeability, 1197, 1198

Wick structures, 1182, 1185–1187

Wiedemann—Franz law, 1338

Wien's displacement law, 577

Wien's distribution, 577

Willis and Johnston method, 838

Wispy annular flow, 663, 664

Womac correlation, 997

Work-absorbing systems, 1042

Work hardened contacts, 333

Working fluids, 1182–1184

Work-producing systems, 1042

Wrapped screen wicks, 1185, 1186, 1198

WSGG, *see* Weighted sum of gray gases

Xenon, 90

X-shell condensers (shell-side condensation), 769–779

condenser sizing methods, 771–774

bundle factor method, 772

pointwise or numerical computer programs, 772–774

vertical row-number method, 771–772

noncondensable gas management, 774–777

tube-side flow and temperature maldistribution, 770

venting, 777–779

 $\Psi - P$ analysis method:

heat exchanger, 819–821

heat exchangers, 819–822

Zener—Lavi profile, 725–726

Zeotropes, condensation of, 762–763

Zeotropic mixtures, 700–701

Zero-equation model, 471

Zinc, 131, 869

Zivi's correlation, 753

Zonal method (thermal radiation), 627

Z (zed) arrangement, 881